List of Acronyms

AE3	Third generation modal CMAQ aerosol model
AORGA	Anthropogenic secondary organic aerosol
AORGB	Biogenic secondary organic aerosol
AORGPA	Primary organic matter
APLT	Appalachian Lee Trough
AU	Analytical Uncertainty
BC	Black Carbon (aerosol)
BEIS	Biogenic Emissions Inventory System
BOTW	Beyond On the Way (emission scenario)
C	Carbon
CAIR	Clean Air Interstate Rule
CALPUFF	California Puff Model
CASTNet	Clean Air Status and Trends Network
CBM-IV or CB-IV	Carbon Bond Mechanism, Version 4, gas phase chemistry module
CEM	Continuous Emission Monitoring
CENRAP	Central Regional Air Planning Association
CH_2	Methylene
CMAQ	Community Multiscale Air Quality modeling system
CMAS	Community Modeling and Analysis System (modeling center)
CO	Carbon Monoxide
D.C. or DC	District of Columbia
DDM	Direct Decoupled Method
DRI_F	Desert Research Institute Sequential Filter Sampler
EC	Elemental Carbon
EDT	Eastern Daylight Time
EMS	Emissions Modeling System
EPA	U.S. Environmental Protection Agency
EPS	Emissions Preprocessor System
EST	Eastern Standard Time
FIPS	Federal Information Processing Standards
FRM	Federal Reference Method for PM2.5 Sampling
FT	Free Troposphere

List of Acronyms

GEOS-CHEM	Goddard Earth Observing System with Chemistry (Global Chemical Transport Model)
GOCART	Goddard Chemistry Aerosol Radiation and Transport (GOCART) model
Hr	Hour
HY-SPLIT	HYbrid Single-Particle Lagrangian Integrated Trajectory Model
I/O API	Input/Output Applications Programming Interface
ID	(site) Identifier
IMPROVE	Interagency Monitoring of Protected Visual Environments (air quality monitoring network)
ISORROPIA	Aerosol Thermodynamic Equilibrium Model (Note: ISORROPIA, “equilibrium” in Greek)
LFT	Lower Free Troposphere
LLJ	Nocturnal Low level Jet
MACT	Maximum Available Control Technology
MANE-VU	Mid-Atlantic Northeast Visibility Union
MAQSIP	Multiscale Air Quality Simulation Platform
MARAMA	Mid-Atlantic Regional Air Management Association
MCIP	Meteorology-Chemistry Interface Processor—processes MM5 output for CMAQ
MD	Maryland
MDE	Maryland Department of the Environment
MM5	Penn State-NCAR Mesoscale Model 5
MODIS	MODerate Imaging Spectrometer
MRPO	Midwest Regional Planning Organization
MSA	Metropolitan Statistical Area
MSL	Mean Sea Level
NAA	Non-Attainment Area
NAAQS	National Ambient Air Quality Standard
NADP	National Atmospheric Deposition Program
NEI	National Emissions Inventory
NESCAUM	Northeast States for Coordinated Air Use Management
NH	New Hampshire
NH_3	Ammonia

List of Acronyms

NH_4	Ammonium
NJ	New Jersey
NJDEP	New Jersey Department of Environmental Protection
NO	Nitric Oxide
NO_2	Nitrogen Dioxide
NO_3^-	Nitrate
NO_x	Reactive oxides of nitrogen, the sum of NO and NO_2
NO_y	Total reactive nitrogen oxides
NYSDEC	New York State Department of Environmental Conservation
OC	Organic Carbon
OM	Organic Matter
OPP	Other inorganic Primary PM2.5, also Soil/Crustal Material
OTB	On the Books
OTC	Ozone Transport Commission
OTR	Ozone Transport Region
PA	Pennsylvania
PAMS	Photochemical Assessment Monitoring Stations
PAVE	Package for Analysis and Visualization of Environmental data
PBL	Planetary Boundary Layer
PBW	Particle Bound Water
PM	Particulate Matter
PM2.5	Particulate Mass of aerosols less than 2.5 microns in diameter
PMF2	Positive Matrix Factorization model version 2
RACT	Reasonably Available Control Technology
RAMMPP	Regional Atmospheric Measurement, Modeling and Prediction Program
REMSAD	Regional Modeling System for Aerosols and Deposition
RH	Relative Humidity
RMSc	Root Mean Square error after Correcting for the bias
RPO	Regional Planning Organization
RRF	Relative Response Factor
SCC	Standard Classification Code
SIC	Standard Industrial Classification code

List of Acronyms

SIP	State Implementation Plan
SMOKE	Sparse Matrix Operator Kernel Emissions modeling system, the emissions preprocessor for CMAQ
SO_2	Sulfur Dioxide
SO_4	Sulfate
SOA	Secondary Organic Aerosols
SOIL	Crustal Material
SORGAM	Secondary Organic Aerosol Model
STN	Speciated Trends Network
STN_R	Speciation Trends Network—Thermo Scientific Reference Ambient Air Sampler
STN_S	Speciation Trends Network—Met One Instruments Speciation Air Sampling System
SW	Southwest
TEOM	Tapered Element Oscillating Microbalance instrument
UAM	Urban Airshed Model
$\mu g\ m^{-3}\ yr^{-1}$	Micrograms per cubic meter per year
UMBC	University of Maryland Baltimore County
UMD	University of Maryland College Park
UNMIX	Multivariate receptor model to deduce aerosol sources
URM-1ATM	Urban-to-Regional Multiscale – One Atmosphere Model
US	United States
UTM	Universal Transverse Mercator projection
UV	Ultraviolet
VA	Virginia
VADEQ	Virginia Department of Environmental Quality
VISTAS	Visibility Improvement State and Tribal Association of the Southeast
VOC	Volatile Organic Compounds
WNW	West Northwest
WV	West Virginia

Speciated PM2.5 in Maryland: Analysis of Extended Data Set from Essex

William F. Ryan
Debra Y. Harrington
Department of Meteorology
The Pennsylvania State University
University Park, PA

July, 2005

Executive Summary

1. This report contains an analysis of Speciated Trends Network (STN) data collected at Essex, Maryland for the period January, 2001-October, 2003. Data is also available from the monitor located at Fort Meade, Maryland. However, concentrations were measured only every 6 days at Fort Meade and, with a relatively large number of missing data days, the data set was not sufficiently robust to provide the statistical depth of analysis necessary for this study.

2. The STN monitor at Essex is located at 39.31ºN, 76.47ºW or approximately 10 miles E of Baltimore Inner Harbor. The local area is primarily residential and light industrial but there are a number of significant interstate highways and large arterial roads quite close to the monitor.

3. In addition to analyzing the entire data set at Essex, this analysis also investigated several subsets of data. These subsets included monthly and seasonal averages, the extremes of the distribution (10^{th} and 90^{th} percentile), and a set of high $PM_{2.5}$ episodes. The episode analysis includes a study of the unique data set of daily (rather than every third day) observations taken during July, 2002.

4. As is typical of observations from the eastern US, the major constituents of $PM_{2.5}$ at Essex are ammonium (NH_4), sulfate (SO_4), organic carbon (OC), elemental carbon (EC), and nitrate (NO_3). The relative fraction of OC, whose primary source is motor vehicle emissions, is uncertain. As measured by the STN monitors, it accounts for 23% of total $PM_{2.5}$ but its actual contribution is certainly higher as carbon particles also contain additional elements not directly measured. A correction factor (*k*) is typically applied to account for this additional amount of material and varies with type of particle and age. The range of *k* ranges from 1.4 to as much as 2.4 depending on the type and age of air mass measured.

5. Essex, due to its near urban location, is expected to sample air masses with high concentrations of OC. However, $PM_{2.5}$ is most closely correlated with SO_4 (r = 0.78) and NH_4 (r = 0.83). OC has a lower correlation (0.60) and its concentrations in high $PM_{2.5}$ cases ($PM_{2.5} > 30$ μgm^{-3}) are highly variable.

6. In terms of the seasonal cycle, SO_4 concentrations are highest in the summer (JJA) and account for nearly 50% of the $PM_{2.5}$ mass. Correlations for SO_4 (0.95) and NH_4 (0.92) are extremely strong in the summer months. OC has a bimodal seasonal signal with highest concentrations in both winter and summer seasons. EC, mainly from primary emissions, shows little seasonal differences. NO_3 is highest in the winter months but accounts for a small total fraction - ~ 12%.

7. Winter season $PM_{2.5}$ is dominated by OC and NH_4 and appears to be driven by local emissions. In winter, the correlation between OC and EC (0.77) is much higher than in the summer months (0.26) suggesting that local, primary emissions are important.

8. The 90th percentile of $PM_{2.5}$ cases (> 30 μgm^{-3}) is strongly weighted (65%) to the summer season and SO_4 is the most strongly correlated constituent in these cases (0.78).

9. Toxic compounds measured at Essex are difficult to assess because a large fraction of observations are below the method detection limit (MDL). There are no clear correlations between toxic compounds and $PM_{2.5}$ overall or in high $PM_{2.5}$ cases.

10. Weather patterns associated with summer season high $PM_{2.5}$ cases are, in many respects, quite similar to high O_3 cases. A strong upper level ridge of high pressure is typically located over or west of the mid-Atlantic in both $PM_{2.5}$ and O_3 cases. This alignment leads to consistent westerly transport of pollutants into the region. On a daily basis, O_3 and $PM_{2.5}$ peaks often, but not always, coincide. The main factor that limits peak O_3 in summer – cloud cover and convection – has a lesser impact on 24-hour average $PM_{2.5}$ concentrations.

11. In the winter season high $PM_{2.5}$ cases, a strong upper level ridge is also present along with westerly transport aloft. However, winter season $PM_{2.5}$ cases are more likely to be characterized by significant stagnation near the surface and by a very stable boundary layer – often enhanced by snow cover.

12. Low $PM_{2.5}$ cases are characterized by a weather pattern of an opposite phase as high $PM_{2.5}$ cases. Aloft, a trough of low pressure replaces the ridge, wind speed are much higher, and the source of the air mass entering Maryland is from the north and northwest - rural Canadian in origin.

13. A closer analysis of specific multi-day $PM_{2.5}$ cases in summer shows that large increases in $PM_{2.5}$ are driven primarily by increases in SO_4 concentrations. Although some episode days do include periods of stagnation, the longer range sources of the stagnant air masses are to the west of the region.

14. Winter season multi-day episodes are characterized by stagnation and a very stable boundary layer. This traps pollutants by limiting both vertical and horizontal mixing. OC is the most dominant constituent in these cases.

Section 1. Introduction

Fine particulate matter with aerodynamic diameter of ≤ 2.5 μm ($PM_{2.5}$) has been measured on a routine basis across the United States beginning in 1999 – although scattered locations, primarily through the EPA IMPROVE program, have measured $PM_{2.5}$ for more than a decade.

Total mass measurements are useful for determining the relative magnitude of the public health problem posed by $PM_{2.5}$ and the local and regional scale of the phenomena. A previous study prepared for the Maryland Department of the Environment looked at the overall concentrations of $PM_{2.5}$.[1]

Total mass measurements cannot determine the relative importance of different type and sources of pollution and so provides little guidance on optimal control strategies. Data on specific constituents of $PM_{2.5}$ are provided by Speciated Trends Network (STN) monitors. This study looks at $PM_{2.5}$ data from the STN monitors in Maryland and focuses on the site operated by the Maryland Department of the Environment at Essex, Maryland. The goal of this study is to determine the relative importance of various constituents of $PM_{2.5}$ to total mass. While an analysis of this dataset cannot identify specific sources of pollution, it can provide detailed information on categories of sources and therefore provide insight into preferred control strategies.

[1]Ryan, W.F., and P. Mangione, *$PM_{2.5}$ in Maryland: Visualization, Statistics and Preliminary Conceptual Model*, report prepared for the Maryland Department of the Environment, December, 2003.

Section 2. The STN Monitor at Essex, Maryland

a. Location of Monitor and Characteristics

Our analysis focuses on data collected at the STN monitor at Essex, Maryland. Data is also available from the monitor located at Fort Meade, Maryland. However, concentrations were measured only every 6 days at Fort Meade and, with a relatively large number of missing data days, the data set was not sufficiently robust to provide the statistical depth of analysis necessary for this study.

The STN monitor at Essex is located at 39.31ºN, 76.47ºW or approximately 10 miles E of Baltimore Inner Harbor (*Figure 2.1*). The neighborhood surrounding the monitor site is primarily residential and light industrial (*Figure 2.2*). The monitor is on a quiet side street although it is close to a busy arterial street (Eastern Avenue) with traffic flow of ~ 30,000 vehicles per day (*Figure 2.3*). In addition to Eastern Avenue, a number of large interstate routes encircle the area (within a radius of 1-2 miles) including the Baltimore Beltway (I-695) (*Figure 2.4*). Large point sources associated with power plants or heavy industrial sites are located at a greater distance (7-10 miles) but may also impact the monitor. These include Bethlehem Steel at Sparrows Point and power plants at Brandon Shores (*Figure 2.5 and Figure 2.6*).

The location of the Essex monitor suggests that it will be impacted primarily by motor vehicle emissions with intermittent impacts of large point sources. The unknown component is the impact of longer range, or regional, sources.

b. STN Sampler

The STN monitor located at Essex is one of a handful of STN monitors in the region. The purpose of the monitor is to determine the relative contributions of various constituents of $PM_{2.5}$ to the total mass measured. The main constituents of $PM_{2.5}$ include, but are not limited to, sulfate (SO_4), nitrate (NO_3), ammonium (NH_4), elemental carbon (EC), and organic carbon (OC). EC is often referred to as “black” carbon.

The Essex monitor is a RAAS-401 sampler set up as a 4-stage filter system. The sampler is more fully described in **Appendix A**. A short description is included here to assist in understanding the later data analysis sections. The RAAS-401 operates by directing a stream of ambient air into 4 distinct channels (**Appendix A**, *Figure A1*). These channels, or stages, measure various groups of $PM_{2.5}$ constituents.

Stage 1: EC and OC

The first stage captures sampled air particles on a quartz filter that is analyzed for concentrations of EC and OC. Because carbon compounds are ubiquitous, the quartz filters may already contain measurable concentrations of carbon compounds prior to deployment at the field site. To account for this, measured values of carbon are adjusted by subtracting an approximate value for the concentration of carbon found on clean

filters. To meet sampling protocol, the concentration of carbon was measured on approximately 100 clean filters. An average concentration of pre-existing carbon was calculated and then subtracted from each measured sample concentration. The resulting values for OC and EC, as reported in this study, are considered to be "blank corrected". The adjustment for pre-existing carbon represents one of many uncertainties involved in the measurement of carbon compounds (*Turpin and Lim, 2001; Subramanian et al., 2004*). A brief discussion of other uncertainties is included in **Appendix B**.

Stage 2: Total $PM_{2.5}$ Mass and Trace Elements

The second stage captures total particulate mass of particles less than 2.5 μm in diameter on a Teflon filter. The filter is weighed in the lab before deployment in the field and again after collecting a 24-hour sample. The resulting difference in the weights of the filter, combined with the 24-hour flow rate, yields the total concentration of particulate mass. After weighing, the filter is subjected to x-ray analyses to generate the concentrations of 48 trace elements[2]. A subset of elements, highlighted in bold in Footnote 1, are considered toxic elements. The measured mass concentration of toxic elements tends to be small; typically less than 0.01 $\mu g\ m^{-3}$.

Every measured element has a specified method detection limit (MDL) that is calculated at the laboratory and is based on uncertainties and measurement limits in all aspects of the measurement process, from the sample flow rate to the analysis conducted in the lab. The MDL is unique to each element. For the toxic elements analyzed in this report, 5 have well known MDL values. In a not insignificant number of cases, the measured concentration of a specific toxic element is below its known MDL; therefore, the measured value cannot be considered reliable. Table 2.1 lists the MDL of these 5 toxic elements and the percentage of cases which yielded concentrations below the MDL. Clearly, there are a significant number of cases in which the measured concentration is less than the MDL for a given toxic element. For lead (Pb), the measured value is below the MDL in almost a quarter of the total cases. This leads to a lack of confidence in the concentrations of the toxic compounds, and by extension, the trace elements as a whole.

Stage 3: Anion and cations

A Teflon filter on the third stage of the sampler is analyzed for specific anions (negatively charged ions) and cations (positively charged ions) using ion chromatography. The measured ions include sodium (Na), potassium (K), NH_4 and SO_4. The confidence level in these measurements is high, in part because the measured

[1] Antimony, **Arsenic**, Aluminum, Barium, Bromine, **Cadmium**, Calcium, **Chromium**, **Cobalt,** Copper, **Chlorine**, Cerium, Cesium, Europium, Gallium, Gold, Iron, Hafnium, **Lead**, Indium, Iridium, Lanthanum, **Manganese**, Magnesium, **Mercury**, **Nickel**, Niobium, **Phosphorous**, Potassium, Rubidium, Selenium, Samarium, Scandium, **Selenium**, Silicon, Silver, Sodium, Strontium, Sulfur, Tantalum, Terbium, Tin, Titanium, Tungsten, Vanadium, Yttrium, Zinc, and Zirconium.

[2] An ion in this application refers to a molecule that has acquired an electric charge by the loss or gain of one or more electron. An example of an anion is SO_4^{2-}, which has gained two electrons, and an example of a cation is NH_4^+, which has lost one electron.

concentrations are well above the MDL for each element. For example, the MDL for sulfate measured with the RAAS-401 is 0.011 μg m^{-3} while the lowest measured concentration found during this study period is 1 μgm^{-3}.

Stage 4: Nitrate

The fourth filter stage is set up to capture particulate NO_3 on a nylon filter. Nylon is used because it has a special affinity for nitrate. NO_3 occurs in particulate form as ammonium nitrate (NH_4NO_3), which readily dissociates into nitric acid (HNO_3) and ammonia (NH_3) vapors. To avoid measuring gas-phase nitrate, the sampled air is passed though a magnesium oxide (MgO) denuder to remove nitric acid.

Element	**MDL (μg m^{-3})**	**Percent of cases < MDL**
Arsenic	0.001	47.5
Chromium	0.0006	59.1
Lead	0.0022	20.2
Manganese	0.0009	20.2
Selenium	0.0009	31.0

Table 2.1 Method detection limits for toxic elements.

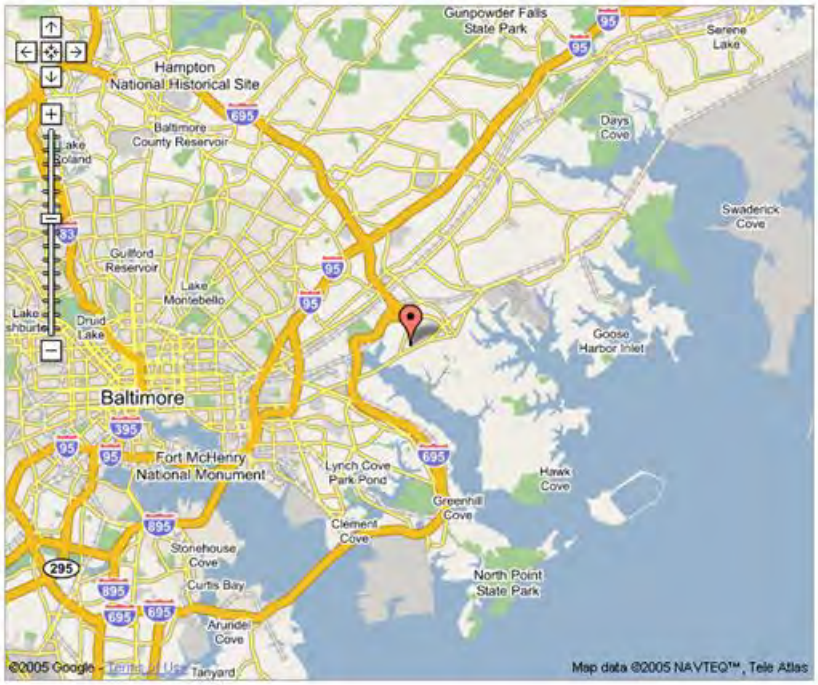

Figure 2.1. Location of Essex monitor relative to the City of Baltimore and surrounding highways (Figure courtesy Google Earth).

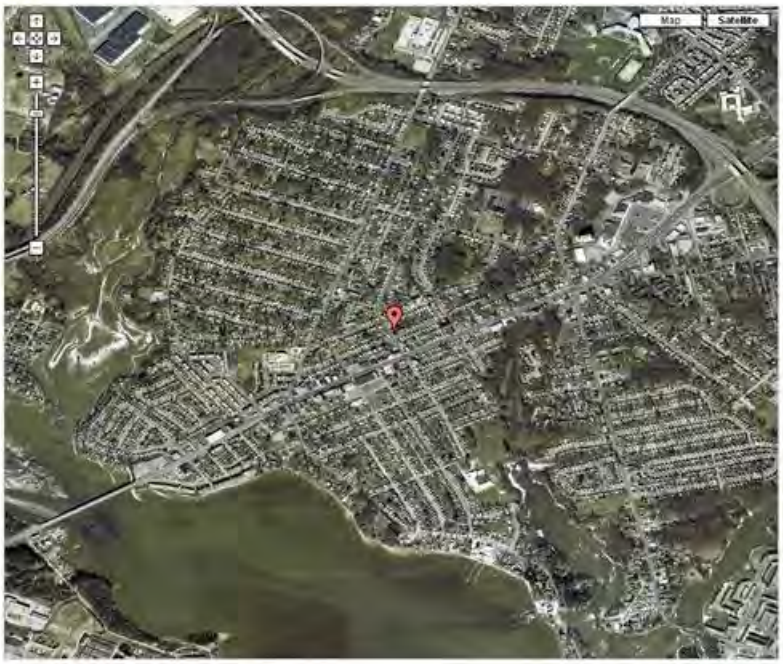

Figure 2.2. Satellite image of location of Essex monitor (Google Earth).

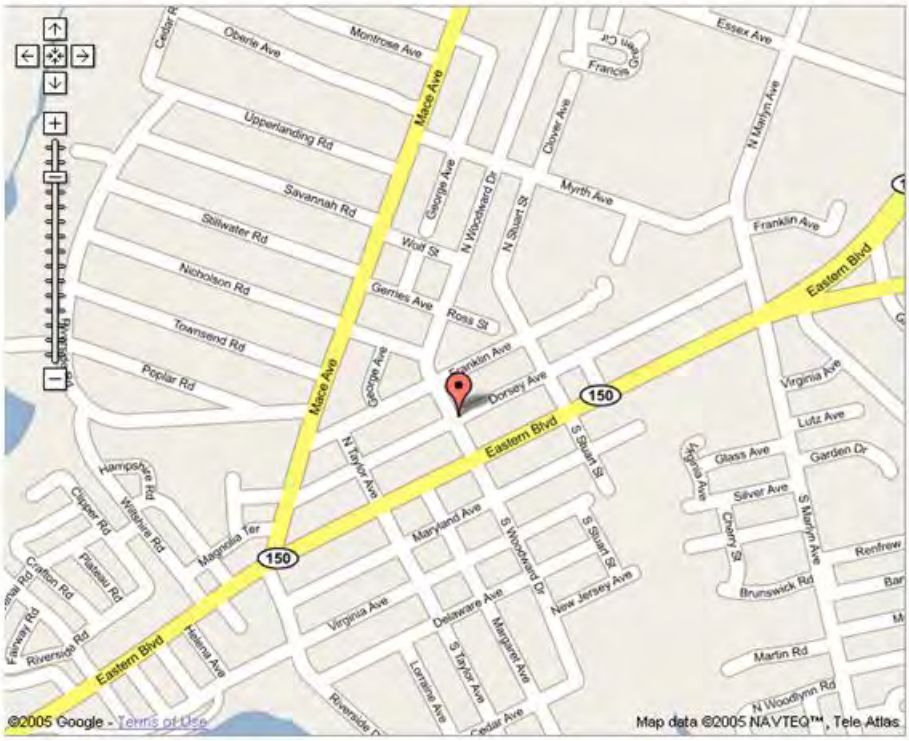

Figure 2.3. Street scale location of the Essex monitor

Figure 2.4. Larger scale satellite image of Essex monitor showing local highway system (Google Earth).

Figure 2.5. Satellite image of Essex monitor location relative to the metropolitan Baltimore region (Google Earth)

Figure 2.6. Location of large point sources near the Essex monitor, and insert shows the Brandon Shores power plant at bottom left of main image (Google Earth).

Section 3. Data Set Description

The data from the Essex monitor analyzed for this report is available from the EPA through the MARAMA website (http://www.marama.org/Projects). Measurements have been taken at this site since October, 2000 and continue today. The dates used for the analyses in this report are 1/31/2001 through 10/12/2003. As noted above, the dataset from Fort Meade was significantly less comprehensive and not sufficient for the analysis undertaken here. For details on previous measurements at Fort Meade, see *Chen et al., 2002*.

While the standard STN dataset consists of data samples collected every three days, samples were taken daily at Essex during July of 2002. For consistency, and so that the daily sampling in 2002 did not unfairly bias the statistical calculations, we reduced the July 2002 data so that every 3rd day sampling was represented. We retained the data which would have been captured using the standard, every 3-day sampling protocol, and set the remaining July 2002 data aside. The daily observations in July 2002 are a unique dataset and are separately analyzed as a case study in **Appendix C**. Additionally, we discarded the data for July 7, 2002, because the organic carbon component was overwhelmingly enhanced (ten times "normal" concentrations) by smoke advected into the region from forest fires in Quebec (*Debell et al., 2004*). For consistency, we eliminated the data for all species and $PM_{2.5}$ for this date. There were a total of 89 cases with no data reported, which represents approximately 27% of the total possible number of cases for data capture.

In addition to analyzing the dataset in its entirety (i.e. 1/31/2001 – 10/12/2003), we subdivided the data for three separate analyses. First, the data were aggregated into seasons using standard meteorological conventions as shown in *Table 3.1*. Second, a subset of very high and very low concentration cases were selected. Based on the distribution of all $PM_{2.5}$ values, the 90th percentile at Essex was chosen to define the high $PM_{2.5}$ cases, as shown in *Figure 3.1*. Because the dataset is skewed to the right (higher $PM_{2.5}$), the selection of low $PM_{2.5}$ cases is made more arbitrarily and were chosen so that the total number of high and low $PM_{2.5}$ cases are approximately the same. This subdivision generated 17 low $PM_{2.5}$ cases ($PM_{2.5} < 6.5$ μgm^{-3}) and 21 high $PM_{2.5}$ cases ($PM_{2.5} > 30$ μgm^{-3}). The third, and final, disaggregation of the dataset coincided with a selection of MARAMA-defined "clean" and "dirty" regional scale episodes. (see **Appendix D** for this list). For the time period of our study, MARAMA defined 6 "dirty" episodes, where the average high $PM_{2.5}$ concentration was 57 $\mu g\ m^{-3}$, and 5 "clean" episodes where the average high $PM_{2.5}$ concentration was 17 $\mu g\ m^{-3}$. These episodes ranged in duration between 7 and 16 days. With our 3-day sampling protocol, we generally have only a couple of data points in each episode. In one case we only had 1 data point to represent this episode and in another we had zero points. To amass a reasonable dataset to describe the clean and dirty MARAMA episodes, one date on either side of the beginning and end of the episodes was added, resulting in 24 dirty dates and 22 clean dates. For the episodes in which we had sufficient data capture to look at Essex results versus the other MARAMA sites, we were able to conclude that the episodes had a regional nature to them, as Essex values largely matched values found at other MARAMA sites.

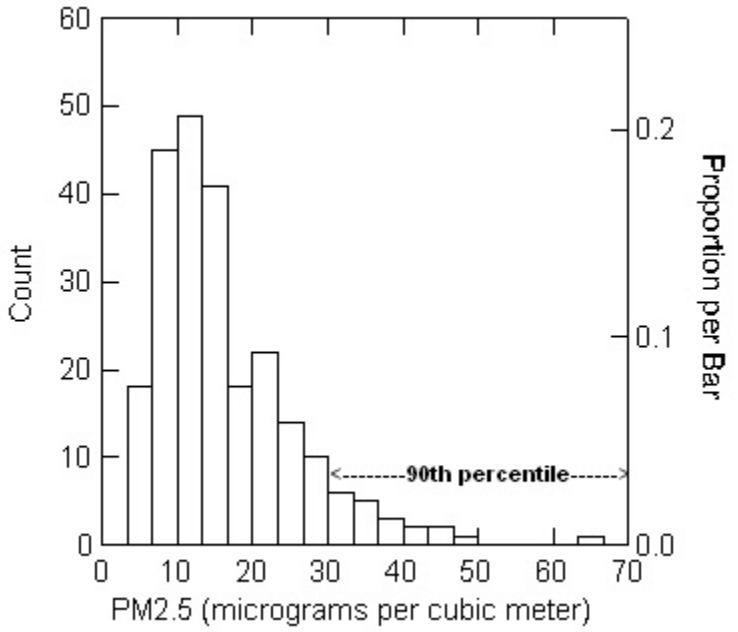

Figure 3.1 Frequency distribution of $PM_{2.5}$ concentrations at Essex

Winter (48 cases)	**Spring (65 cases)**	**Summer (72 cases)**	**Fall (58 cases)**
December	March	June	September
January	April	July	October
February	May	August	November

Table 3.1 Division of months and total number of cases for each season

Section 4. Statistical Summary

There are five constituents (or species) that account for more than 80% of the total $PM_{2.5}$ mass. These elements, their annual averages, and the annual averages of $PM_{2.5}$ are shown in *Table 4.1*. *Figure 4.1* shows the breakdown, in percentages, of the annual averages of the main constituents of $PM_{2.5}$. The biggest fraction of $PM_{2.5}$ is SO_4, followed by OC. No correction factor for OC, discussed more fully below, is applied at this stage of the analysis. The concentrations observed at Essex are nearly identical to those measured during a study at Fort Meade in 1999-2000 (*Chen et al., 2002*). The only significant difference is a higher percentage of NO_3 (12% compared to 8%) measured at Essex than Fort Meade. This difference may be due, in part, to a smaller frequency of winter season measurements made in the Fort Meade study or to local emissions differences between the two sites. The relative contribution of each main constituent measured at Essex is also consistent with observations at urban and near urban locations in New York State (*Schwab et al., 2004*).

(i) Organic carbon and reconstructed mass

The calculation of the concentration of $PM_{2.5}$ is done gravimetrically, while the concentrations of the key constituents are determined chemically. The gravimetric calculation is simply the difference between the mass on the dirty filter versus the mass on the clean filter. Summation of the chemically measured components should yield a value comparable to the gravimetrically measured $PM_{2.5}$. However, this is often not the case. Typically, the sum of the chemically measured constituents is less than the gravimetric mass. As noted in *Figure 4.1*, this fraction (noted "Other") is not insignificant. One reason for the sum of the chemically measured components being less than the total $PM_{2.5}$ is the calculation of total organic aerosol (OA), which is a function of the concentration of organic carbon,

$$[OA] = k * [OC],$$

where k represents the average molecular weight per carbon weight of a variety of carbon compounds.

In other words, carbon compounds emitted from primary sources (e.g., motor vehicle exhaust) contain atomic carbon chemically bound to other elements. Benzene (C_6H_6), for example, contains carbon and hydrogen atoms. Atomic oxygen and nitrogen are also commonly found, along with carbon, in emissions of this type. As the primary emissions linger in the atmosphere, they undergo further reactions, most often oxidation by the ubiquitous hydroxyl radical (OH), to form additional compounds. In the final step, particles are formed from these compounds that can contain a very heterogeneous mix of elements. As a result, the particles measured at the STN monitor, while containing carbon, will also contain a highly variable mix of other elements. The exact nature of the mixture, and hence the "correct" value for k, varies with a large number of factors, including season, time of day, and location. The value of k can also be a representation of the age of the air mass. Aged air masses are more likely to be subject to oxygenation and thus become "heavier" – i.e., a larger k value is appropriate. In general, higher values of k indicate a more aged air mass. Values for k used in previous studies (*Tanner*

et al., 2004; Turpin and Lim, 2001) have ranged between 1.4 and 2.4. The Essex site, in close proximity to a number of highways, is likely subject to "fresh" carbon emissions from auto exhaust. This suggests a low *k* value should be used. However, Essex may also be impacted by regional scale (aged) air masses. The large fraction of SO_4 noted in *Table 4.1* and *Figure 4.1* suggests a substantial, although likely highly varying, regional impact. In fact, the mix of local motor vehicle exhaust and regional scale transport may result in a value of *k* that changes significantly on a day-to-day basis and may even change within a given day. For example, early morning measurements may include a larger fraction of automobile exhaust, trapped in the nocturnal boundary layer, while afternoon observations, sampling a well-mixed layer including transported air parcel in the residual layer, and may be more regional in nature. In this work, a value in the middle of the typical range of *k* (1.9) is applied when calculating the reconstructed mass (RM),

$$RM = k * [OC] + [EC] + [NO_3] + [SO_4] + [NH_4] + Trace + f_1(Crust) + f_2(Salt).$$

A thorough discussion of the *k* factor, its history, what is represents, and typical values measured in laboratory work can be found in *Turpin and Lim., 2001*.

The ratio of the gravimetric mass to the reconstructed mass is given in *Figure 4.2*. For the majority of cases in this study (76.44%), the reconstructed mass was larger than the gravimetrically measured mass. There may be many possible reasons for the difference in total mass measured and reconstructed. Two likely reasons are:

1. The gravimetric measurement of $PM_{2.5}$ suffers from a loss of semi-volatile material.
2. The factor used to convert organic carbon concentration to organic aerosol concentration is too high.

The difference in the ratio of gravimetric mass to the reconstructed mass using different *k* values is shown in *Table 4.2*. As expected, the percentage of cases with an RM value greater than the $PM_{2.5}$ value increases along with *k*. An interesting feature of *Figure 4.2* is the seasonal cycle in the $PM_{2.5}$:RM ratio. In winter, the ratio is consistently < 1 ($RM > PM_{2.5}$). The seasonal difference may reflect greater loss of semi-volatile matter in the cooler winter season, perhaps due to volatilization of NO_3 which forms a higher fraction of $PM_{2.5}$ or differences in the structure of carbon compounds by season.

(ii) Annual Average Concentrations

Using all of the data for the available time period (1/31/2001 – 10/12/2003), correlations were calculated using simple linear regressions for each key constituent and total $PM_{2.5}$. The complete sets of resulting correlation coefficients are listed in **Appendix E**. As can be seen in *Figure 4.3*, NH_4 and SO_4 are highly correlated with $PM_{2.5}$, which is expected because a large fraction of the aerosol is composed of ammonium sulfate (see, *Figure 4.1*). *Figure 4.3* also illuminates the bimodal nature of the relationship between sulfate and $PM_{2.5}$. While, in the majority of cases, SO_4 rises linearly with $PM_{2.5}$ mass there is also a subset of cases, also linearly organized, with a distinctly flatter slope. In these cases $PM_{2.5}$ can rise to near the Code Orange range (40.5 μg m^{-3}) with SO_4 concentrations remaining below 10 μg m^{-3}. The flat sloped line of observations (i.e.,

$PM_{2.5}$ > 25 µg m^{-3} and SO_4 <10 µg m^{-3}) consists entirely of winter or late fall cases and illustrates the seasonal variations in $PM_{2.5}$ constituents that will be discussed in more detail below.

Overall, OC is also a large fraction of the total aerosol, and is relatively well correlated with $PM_{2.5}$, while EC is not well correlated with $PM_{2.5}$. This is shown in *Figure 4.4*. Concentrations of OC in *Figure 4.4* are shown without application of the *k* (correction) factor (see discussion of *k* above). The insertion of a *k*-factor will increase the total concentrations of OC and vary the slope line but will not affect the correlation coefficient or overall pattern of the plot. The lack of correlation between EC and $PM_{2.5}$ reflects, in part, the location of the Essex monitor. With major roadways situated nearby on all sides, the influx of primary emissions from car exhausts – the main source of EC – is expected to be nearly constant at Essex regardless of weather conditions and this appears to be the case. Concentrations of OC are more variable, particularly in the higher end of the $PM_{2.5}$ distribution. In fact, 9 of the highest 10 OC cases occur in the winter season (if November is included) as well as 70% of the top 20 cases.

Nitrate, on the other hand, is not well correlated with any other key constituent or with $PM_{2.5}$. The absence of a correlation between $PM_{2.5}$ and nitrate (or EC) most likely reflects nearby emission sources from motor vehicles. Linear regression analysis applied to the toxic components generated no relationships among the constituents or between the toxic and the key constituents.

(iii) Monthly Averages

Figure 4.5 shows the monthly average concentrations for the 5 key constituents. SO_4 exhibits a strong seasonal cycle with peak concentrations occurring during the summer months. Elemental carbon does not have a strong seasonal cycle. EC is a primary pollutant and strong nearby motor vehicle sources have little seasonal variation in emissions rates.

OC shows both winter and summer season peaks with a minimum in spring and fall. OC comes from a variety of sources. A large fraction is due to motor vehicle emissions but there are also contributions from the combustion of oil products for residential heating and industrial processes as well as natural sources. OC can be primary (e.g., by-products of combustion) but a large, and highly variable fraction, is secondary in nature. Secondary organic aerosols (SOA) form efficiently in a strongly oxidizing atmosphere. This accounts for the summer season maximum. In the winter season, the maximum in OC is likely dominated by primary emissions and the effects of strong low level inversions trapping local emissions. Examples of these effects will be seen in the case studies that follow.

Nitrate has a seasonal cycle with the highest values in the winter months and lowest in the summer months. The cool and moist conditions in the winter months are favorable for nitrate formation. There is also more ammonium available to form ammonium nitrate in the winter when sulfate values are relatively low. NH_4 bonds preferentially with SO_4 so that high sulfate concentrations found during the summer months favor ammonium sulfate formation rather than ammonium nitrate formation.

(iv) Seasonal Variations

The data was divided into 4 seasons defined as defined in *Table 3.1*. Using this seasonal breakdown of data, linear regressions were applied and correlation coefficients were calculated. The full set of correlation coefficients is in **Appendix F**. The best correlations are found between total $PM_{2.5}$, sulfate, and ammonium, and the highest correlation coefficients between these constituents are found in the summer months. *Figure 4.6* and *Figure 4.7* illustrate this. The good correlations between $PM_{2.5}$, SO_4, and $NH4^+$ in the summer months echoes the correlations found using the entire dataset.

Correlations between organic and elemental carbon are shown in *Figure 4.8*. They are not well correlated in the summer season when conditions are favorable for secondary organic aerosol formation. In the winter, the formation mechanism for SOA is essentially shut off so the main source of carbon is primary vehicle exhaust; thus a much tighter correlation exists between the carbon components.

(v) Low and High $PM_{2.5}$ Cases

The full dataset was subdivided in order to look at the days with the highest $PM_{2.5}$ concentration values. The 90^{th} percentile was determined using the histogram shown in *Figure 3.1*. The resulting datasets were analyzed using linear regression to see what correlations may or may not exist between the species and $PM_{2.5}$. The resulting correlation coefficients are shown in **Appendix G.**

The majority (13 out of 20) of the high $PM_{2.5}$ cases occurred in the summer months when meteorological conditions are ripe for secondary aerosol formation. The resulting correlation coefficients from the high $PM_{2.5}$ dataset show a strong relationship between $PM_{2.5}$, $NH4^+$, and SO_4, but, there is very little correlation between OC and $PM_{2.5}$. This follows the pattern shown in *Figure 4.4* where OC concentrations vary considerably in high $PM_{2.5}$ cases. This reflects the summer season bias of high $PM_{2.5}$ in Maryland. The relationship of winter and summer season cases and SO_4 is shown in *Figure 4.9*. For this plot, five winter cases of high $PM_{2.5}$ mass are indicated by a circle. In these cases, $PM_{2.5}$ is quite high but SO_4 remains at low concentrations. When these 5 cases, along with the highest $PM_{2.5}$ value (which may be an outlier), are removed, the correlation coefficient between sulfate and $PM_{2.5}$ is considerably improved, to 0.78.

The majority (12 out of 17) of the low $PM_{2.5}$ cases occurred during the transitional seasons of spring and fall. The resulting correlation coefficients from the low $PM_{2.5}$ dataset show a relationship between ammonium and nitrate, and ammonium and sulfate, shown in *Figure 4.10*, while a weaker relationship exists between organic carbon and sulfate ($r^2 = 0.517$).

d. Toxic Compounds

The lists of toxic compounds that are measured from the Teflon filter were given in Section 2. The sources of these toxic elements are both natural and anthropogenic.

Many of them are natural elements of the Earth's crust (i.e. Arsenic, Cadmium, Mercury, Chromium, Cobalt, Manganese, Nickel, Phosphorus, Selenium). Many of them are found in auto exhaust (i.e. Lead, Nickel, Manganese). Most of them are the products of industrial processes.

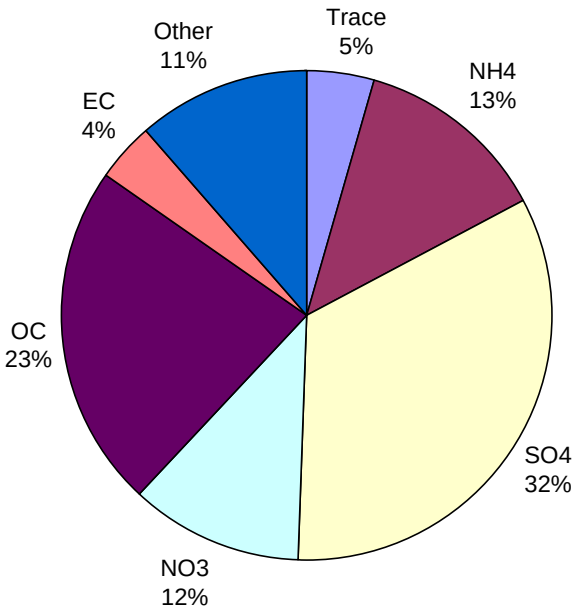

Figure 4.1 Pie chart of speciated pm concentrations at Essex for the entire study period. No correction factor (k) is applied to OC as discussed in text.

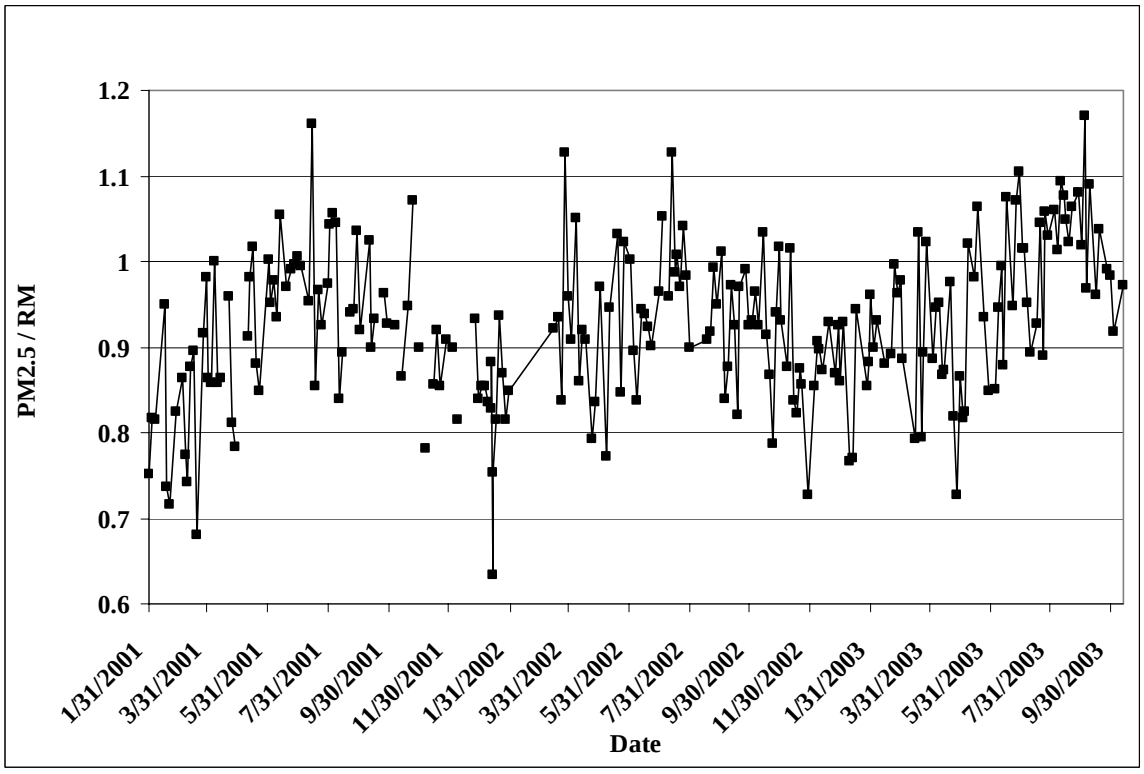

Figure 4.2. Ratio of $PM_{2.5}$ to reconstructed mass (RM) calculated using k=1.9.

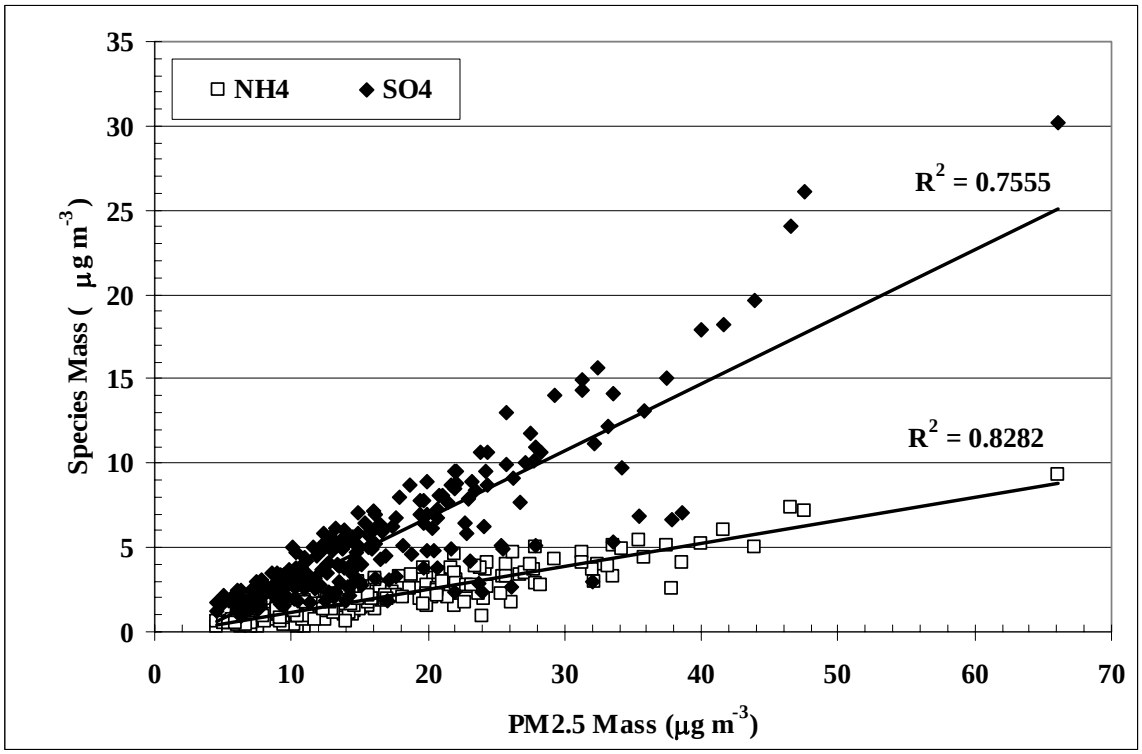

Figure 4.3. Relationship between ammonium and sulfate ions and $PM_{2.5}$ mass

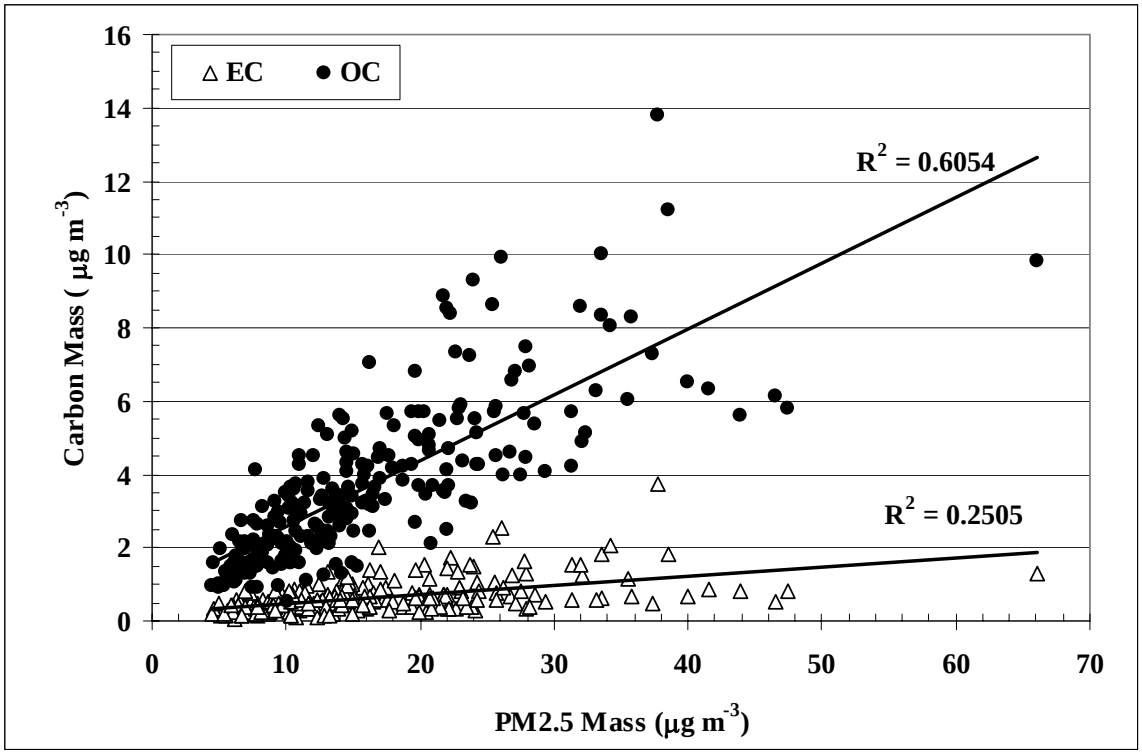

Figure 4.4 Relationship between elemental and organic carbon and $PM_{2.5}$ mass.

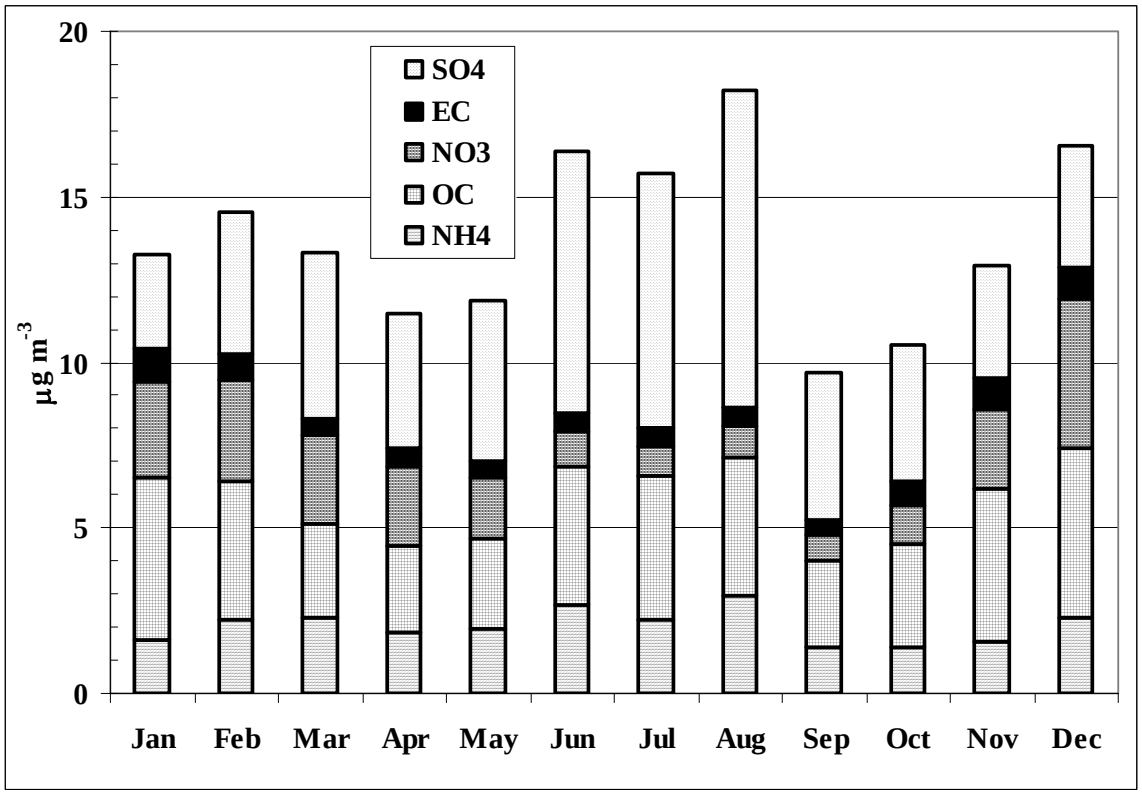

Figure 4.5. Monthly averages of $PM_{2.5}$ constituents

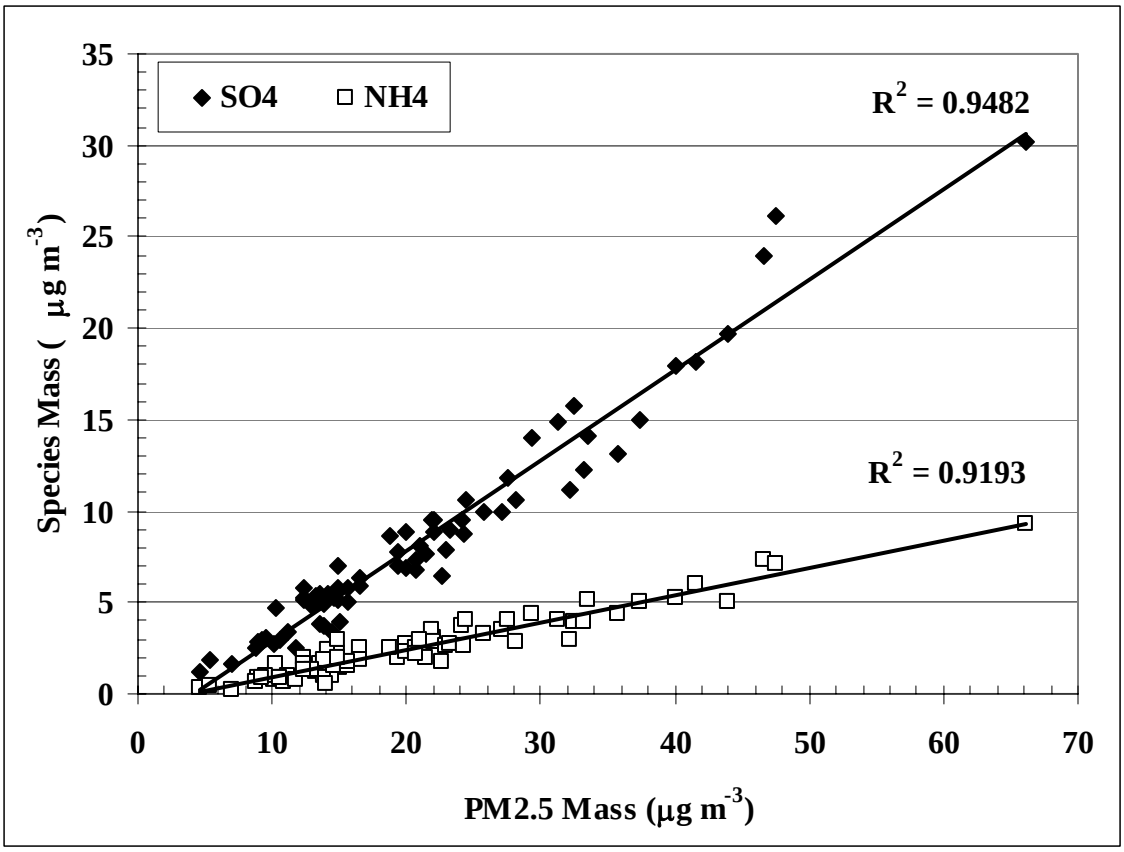

Figure 4.6 Relationship between sulfate and ammonium ions and $PM_{2.5}$ mass during the summer months of June, July, and August.

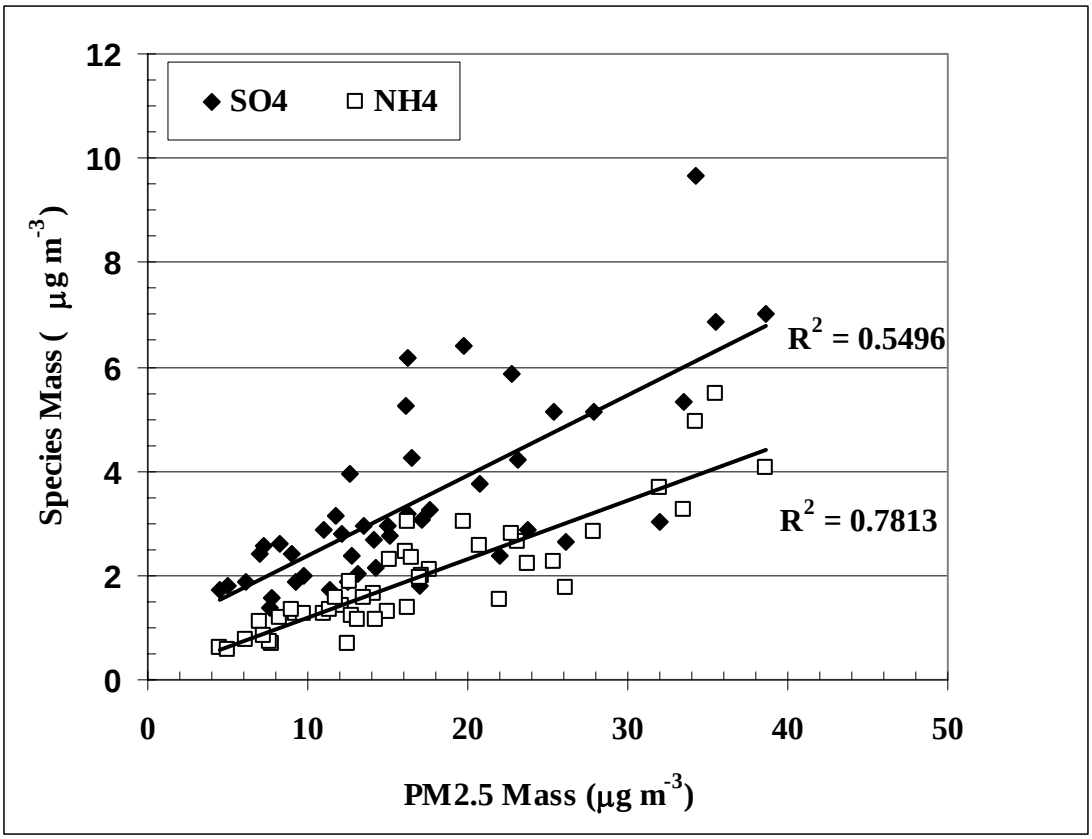

Figure 4.7 Relationship between sulfate and ammonium anions and $PM_{2.5}$ mass during the winter months of December, January, and February.

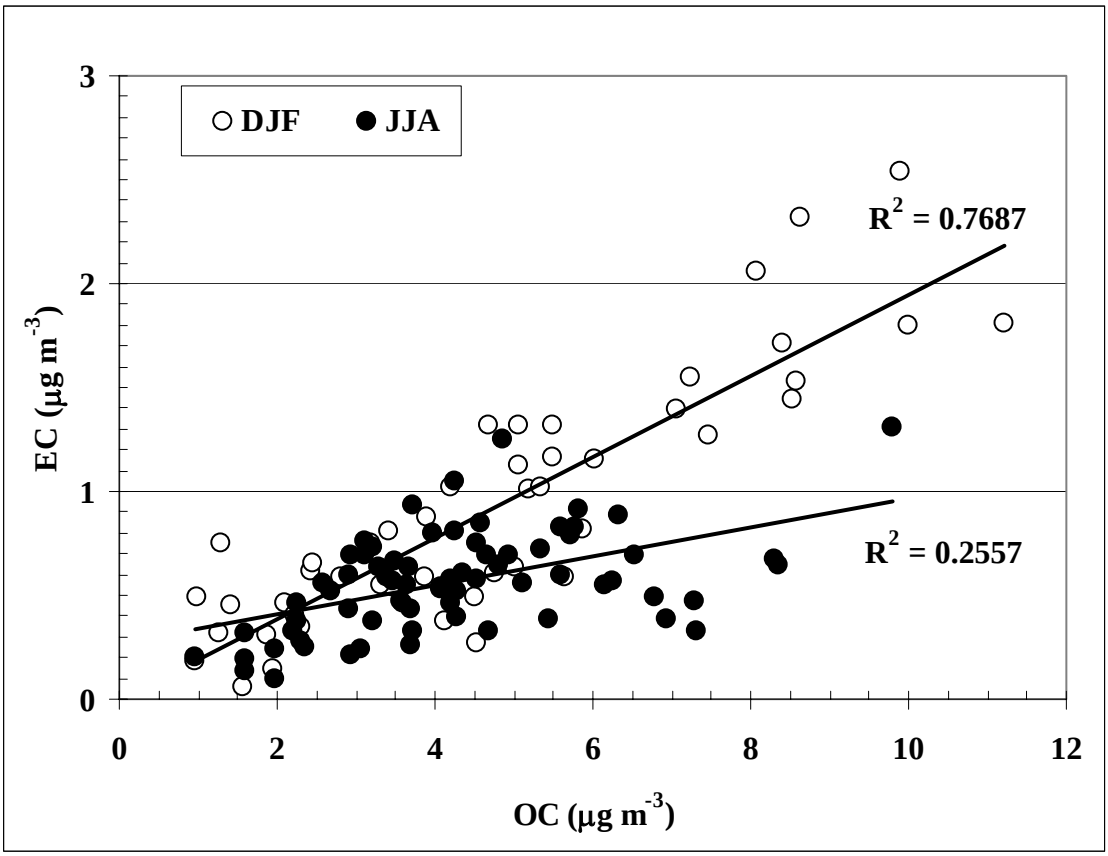

Figure 4.8 Seasonal correlation coefficients for organic and elemental carbon.

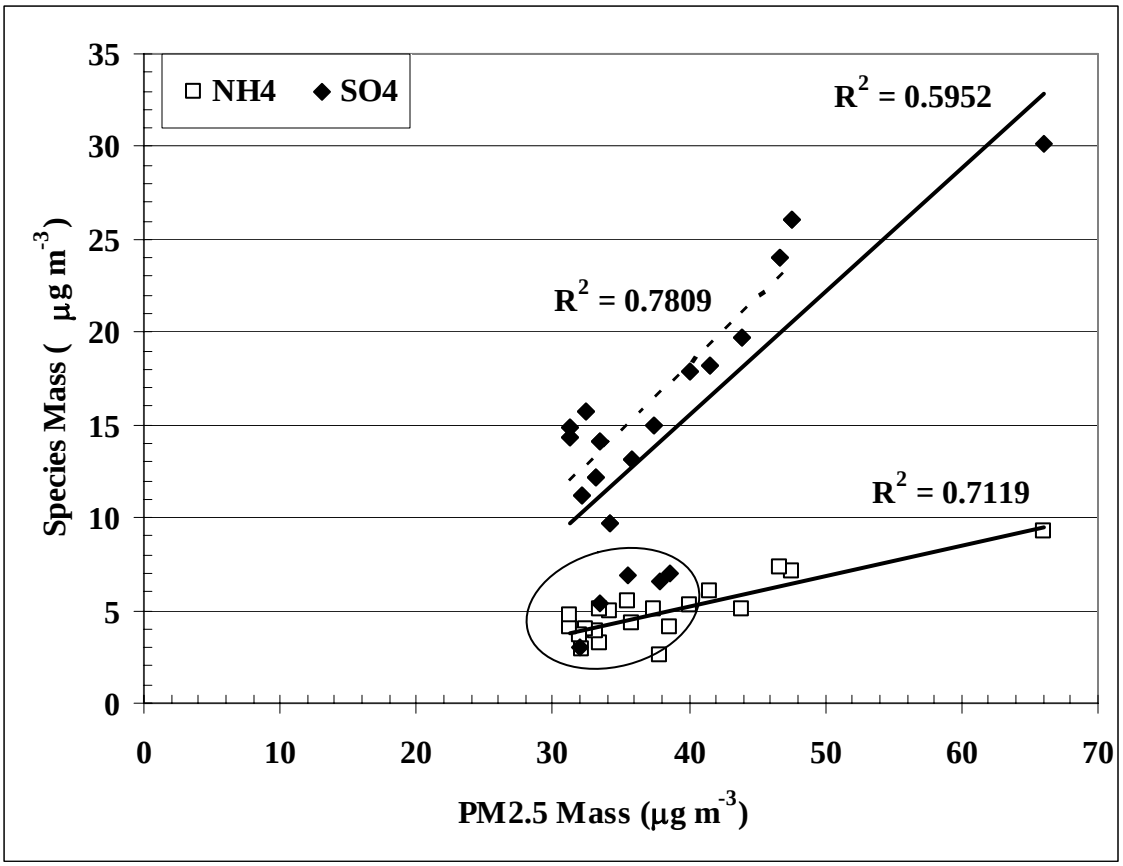

Figure 4.9 Relationship between sulfate and ammonium ions and $PM_{2.5}$ mass for high $PM_{2.5}$ cases.

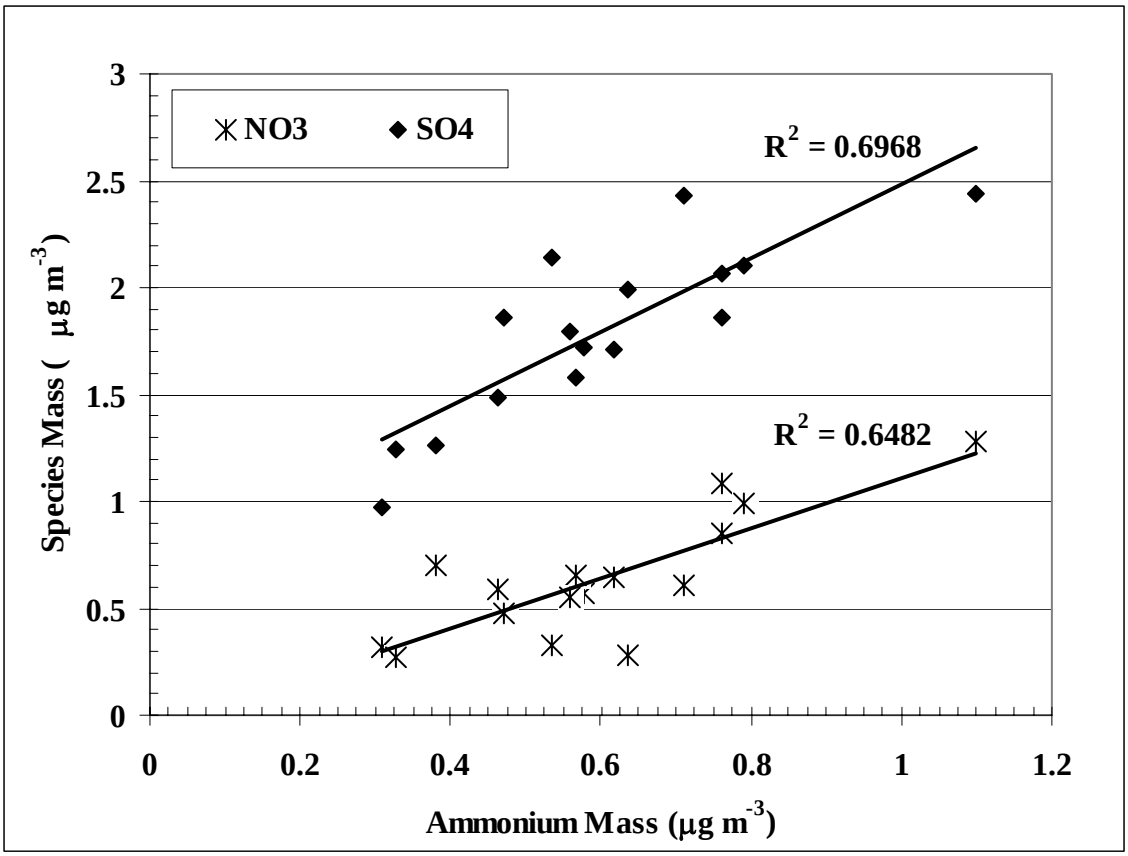

Figure 4.10 Relationship between sulfate and nitrate ions and ammonium ion for low $PM_{2.5}$ cases

Element	2001	2002	2003*
$PM_{2.5}$	16.47	16.08	16.18
SO4	5.52	5.06	5.64
OC	4.04	3.91	3.10
NH4	2.09	1.91	2.15
NO3	1.99	1.77	1.87
EC	0.61	0.74	0.58
Trace	0.24	0.27	0.25

*2003 data is not a complete year (ends 10/12/2003)

Table 4.1 Annual averages (µg m^{-3}) of $PM_{2.5}$ and its constituents. Note: No correction factor (k) applied to OC at this stage.

k value	Number cases < 1	Percent cases < 1
1.4	94	39 %
1.9	185	76 %
2.4	229	95 %

Table 4.2 Relationship between k-value and the number of cases where the reconstructed mass is greater than the gravimetric PM2.5 mass

Section 5. Meteorology of High and Low $PM_{2.5}$ Cases

Because the relative importance of the constituents of $PM_{2.5}$ change season by season (see, **Appendix E**), it is possible that the weather patterns conducive to high $PM_{2.5}$ also have seasonal differences. As a result, this section, presenting the meteorology of high $PM_{2.5}$ cases, will be separated by season with composite weather patterns for both winter and summer high $PM_{2.5}$ cases presented.

(i) Summer Season

The larger (synoptic scale) weather pattern for summer season high $PM_{2.5}$ cases are similar, in many respects to high O_3 cases (see, *Ryan et al., 1998* and *Chen et al., 2003*). In the upper troposphere, a strong ridge of high pressure is present. This ridge is significantly stronger than average conditions (*Figure 5.1*). The presence of an amplified upper level ridge means that vertical motion will be limited. In particular, locations at or east of the ridge's major axis will be characterized by subsidence, or downward, motion.

The presence of an upper air ridge, and its attendant subsidence field, suppresses cloud formation. Plots of average outgoing long wave radiation (OLR) measurements during these cases (not shown) are near maximum values. High values of OLR mean that there are few, or no, clouds to block the radiation emitted by the earth's surface. The lack of clouds is one of the reasons why this large scale pattern is conducive to high O_3 concentrations. $PM_{2.5}$ concentrations can also be enhanced under sunny skies, for example, formation of secondary organic aerosols is enhanced in a highly oxidizing (sunny) environment. Although the large scale weather pattern discussed here is conducive to multi-pollutant episodes, high O_3 and $PM_{2.5}$ do not always occur simultaneously. For the thirteen highest summer season PM cases at Essex, only 4 were also Code Red O_3 cases in the Baltimore metropolitan area. A number of factors can affect O_3 but not $PM_{2.5}$. For example, afternoon cloud cover, and convection, can reduce 8-hour O_3 concentrations markedly but have only a limited impact on $PM_{2.5}$.

In addition to clear skies and a strong upper level ridge, high $PM_{2.5}$ cases are also characterized by moist conditions in the boundary layer. In *Figure 5.2*, relative humidity at 850 mb (~ 1500 m) is shown. While relative humidity in these cases is only slightly higher than normal for summer for this region, it is moist in an absolute sense. Temperatures at this level are much higher than average, as is also consistent with high O_3 cases (*Figure 5.3*).

The near surface wind and pressure fields are also quite similar to high O_3 cases. With a strong upper level ridge just west of the region, surface high pressure tends to form over the mid-Atlantic or just slightly west. Often a high pressure area of continental origin will move west into the mid-Atlantic and then stall and become absorbed into the large semi-permanent Bermuda high centered offshore. In *Figure 5.4*, mean sea level pressure fields associated with high $PM_{2.5}$ episodes are shown. The extension of the Bermuda high is slightly further south than is found in high O_3 cases.

Back trajectories for the set of summer high $PM_{2.5}$ cases are given in *Figure 5.5*. These back trajectories show a generally westerly mean transport that is consistent with previous field studies carried out in the region (*Figure 5.6*). In addition to the westerly transport cases, there is a subset of cases of re-circulation along the Baltimore-Washington Corridor. The transport pattern in the high $PM_{2.5}$ is quite similar to that seen in high O_3 cases (*Figure 5.7* and *Figure 5.8*). While O_3 concentrations, on the regional scale, are sensitive to NO_x concentrations, $PM_{2.5}$ is impacted both by NO_x and SO_2 emissions. These compounds are typically emitted together by large point sources burning coal. The coincidence of enhanced NO_x and sulfur compounds has previously been seen in this region (*Figure 5.9*).

(ii) Winter Season

Winter season cases are a smaller subset than summer season high $PM_{2.5}$ cases but share some factors in common. The upper air pattern has a strong ridge north and west of Maryland (*Figure 5.10*, compare with *Figure 5.1*). Winds aloft are westerly (*Figure 5.11*) and, while stronger than the summer season cases, are only slightly weaker than the average winds for this time of year (Figure *5.12*). The back trajectories aloft are very similar to summer cases (*Figure 5.13*).

There are some subtle differences as well. Surface high pressure is nearly overhead during the winter cases (*Figure 5.14*) and suggests a strong stagnation pattern than in summer season cases (*Figure 5.4*). The extent of stagnation is seen in the near surface average winds (*Figure 5.15*). The light near surface winds, coupled with westerly winds aloft, suggest a complex interaction of both regional and local emissions in creating high $PM_{2.5}$ in these winter cases.

(iii) Clean Cases

At the other end of the distribution are cases with very low $PM_{2.5}$ concentrations. These cases occur in all seasons but are concentrated in the fall, winter and spring seasons. In general, they represent the opposite phase of the weather pattern associated with high $PM_{2.5}$. In the upper atmosphere, the "clean" cases are characterized by a trough, or region of lower than normal pressure (*Figure 5.16*). Large scale troughs are typically associated with stronger than normal winds and this is certainly true for this subset of cases (*Figure 5.17*). The air mass associated with the low $PM_{2.5}$ cases is typically Canadian in origin. As example of a surface pressure pattern typical of an outbreak of Canadian air is shown in *Figure 5.18*. These air masses are typically quite dry which also tends to reduce particle formation.

(iv) Analysis of High $PM_{2.5}$ Multi-Day Episodes

The full analysis of a set of high $PM_{2.5}$ episodes is contained in **Appendix C**. A few general comments are included here.

In the summer season, $PM_{2.5}$ concentrations are generally in the upper moderate range (20-30 μgm^{-3}) for much of these episodes but increase rapidly to concentrations above 30 μgm^{-3} (90^{th} percentile) only as the boundary layer transport pattern shifts westerly. The bulk of the increase in these cases is due to rapid increases in SO_4

concentrations (*Figure 5.19*). These increases are often coincident with increases in low level humidity as moist conditions enhance conversion from gaseous SO_2 to particulate sulfate. For episodes in June of 2003 and July of 2002, the increase of SO_4 from the onset (relatively clean day) to the mature phase (high $PM_{2.5}$) is on the order of 22-28 μgm^{-3}. The increase of SO_4 relative to other constituents has previously been seen in other mid-Atlantic cases. *Chen et al., 2003* reported a change in OC: SO_4 ratio from 3:1 prior to the onset of a high $PM_{2.5}$ episode to 1:3 at its peak. A similar ratio was observed in the June 2003 episode. Short bursts of high $PM_{2.5}$ (e.g., June 29, 2003) can occur in stagnant summer weather but an analysis of back trajectories of longer duration show preceding westerly transport. That is, the air mass is "primed" for high $PM_{2.5}$ before stagnation enhances the effect. This pattern has been seen in winter season $PM_{2.5}$ cases from 2001.

In the winter season, strong stability in the boundary layer is a critical issue. During the episode of February, 2003, this stability was driven by a combination of warm air arriving aloft over a snow covered surface. The cold surface, coupled with warm air (arriving from the west), leads to a strong inversion trapping emissions. In previous studies for cases prior to this dataset (see, **Appendix C**), the warmer air aloft can be advected from the east, in association with a developing offshore low pressure system, with re-circulation present over the mid-Atlantic as winds shift from west to east. The onshore wind also adds considerably to the moisture content of the atmosphere allowing for more efficient gas to particle conversion.

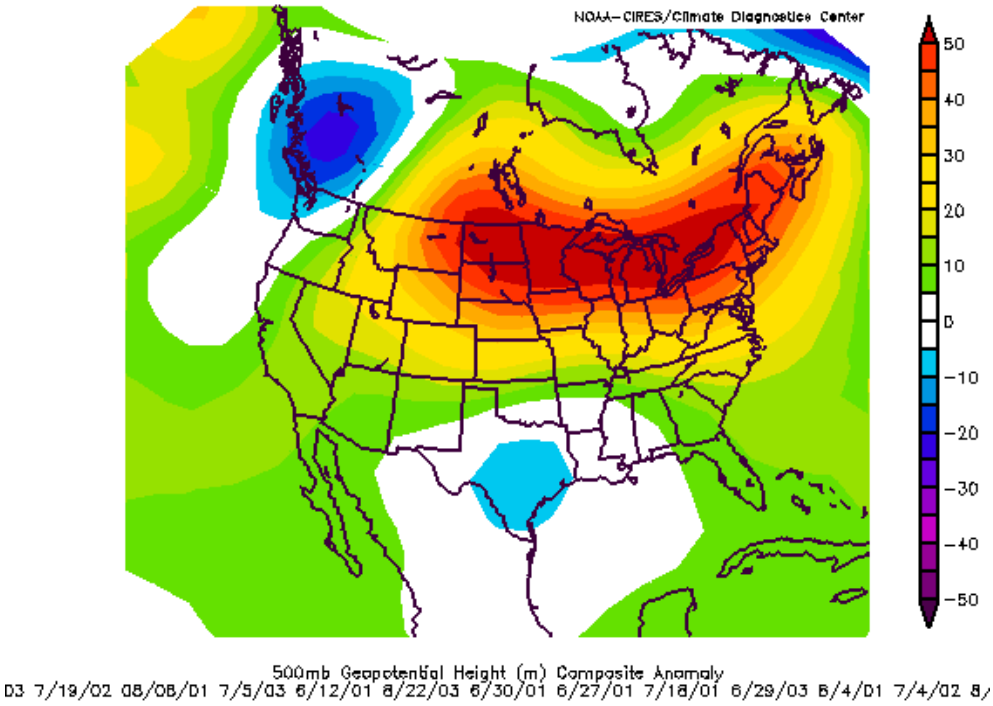

Figure 5.1. 500 mb geopotential height differences from normal for high summer season $PM_{2.5}$ cases. Figure courtesy of NOAA-Climate Diagnostics Center (CDC).

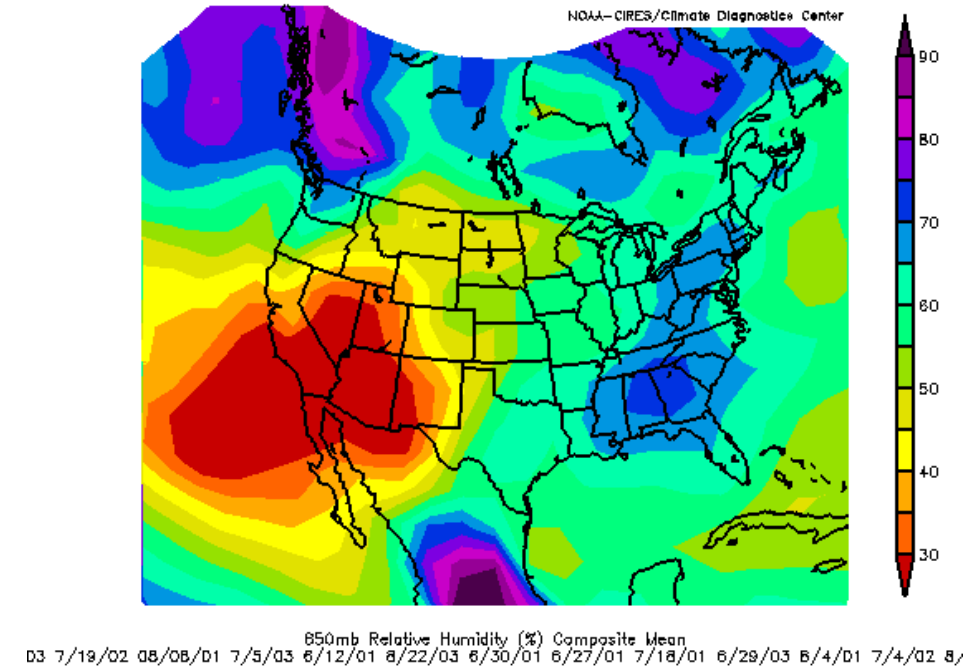

Figure 5.2. 850 mb mean relative humidity (%) for high summer season $PM_{2.5}$ cases. Figure courtesy of NOAA-Climate Diagnostics Center (CDC).

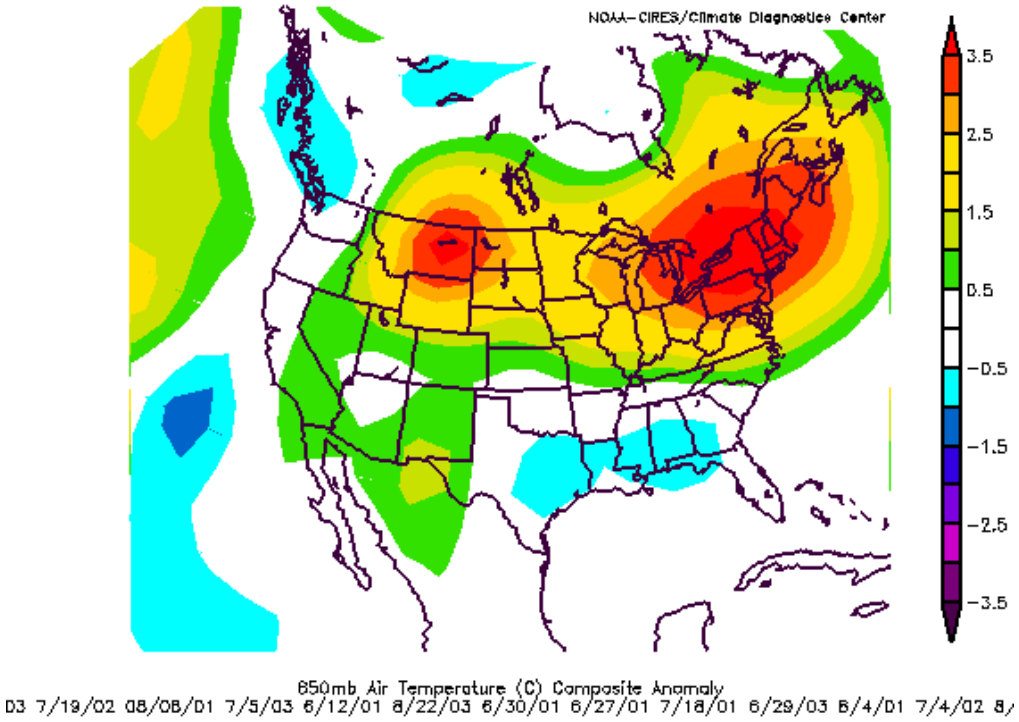

Figure 5.3. 850 mb temperature differences (ºC) from normal for high summer season $PM_{2.5}$ cases. Figure courtesy of NOAA-Climate Diagnostics Center (CDC).

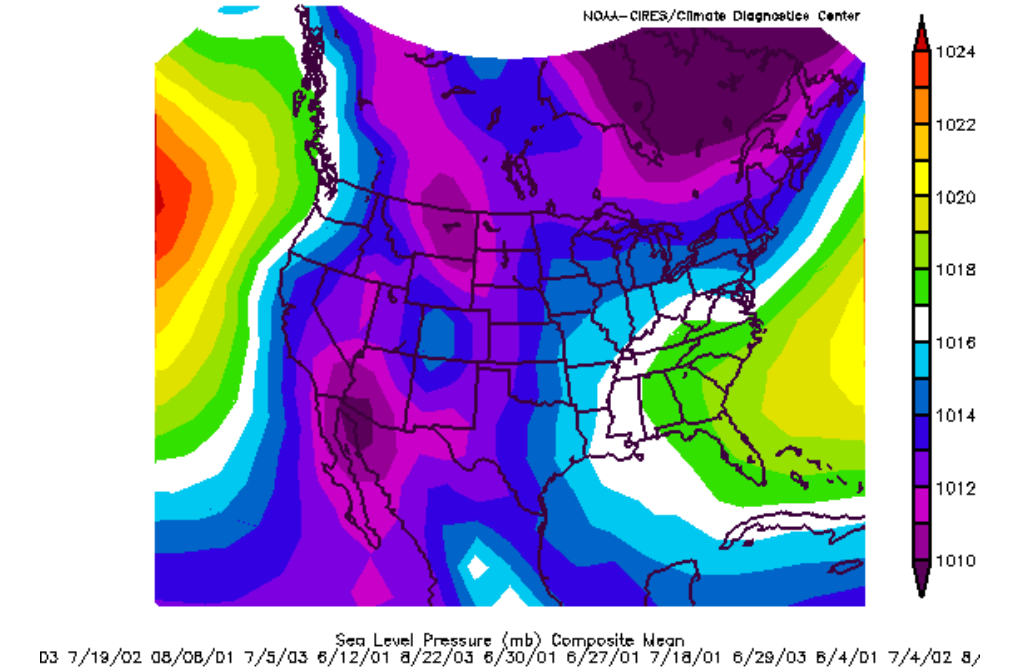

Figure 5.4. Mean sea level pressure field for high summer season $PM_{2.5}$ cases. Figure courtesy of NOAA-CDC.

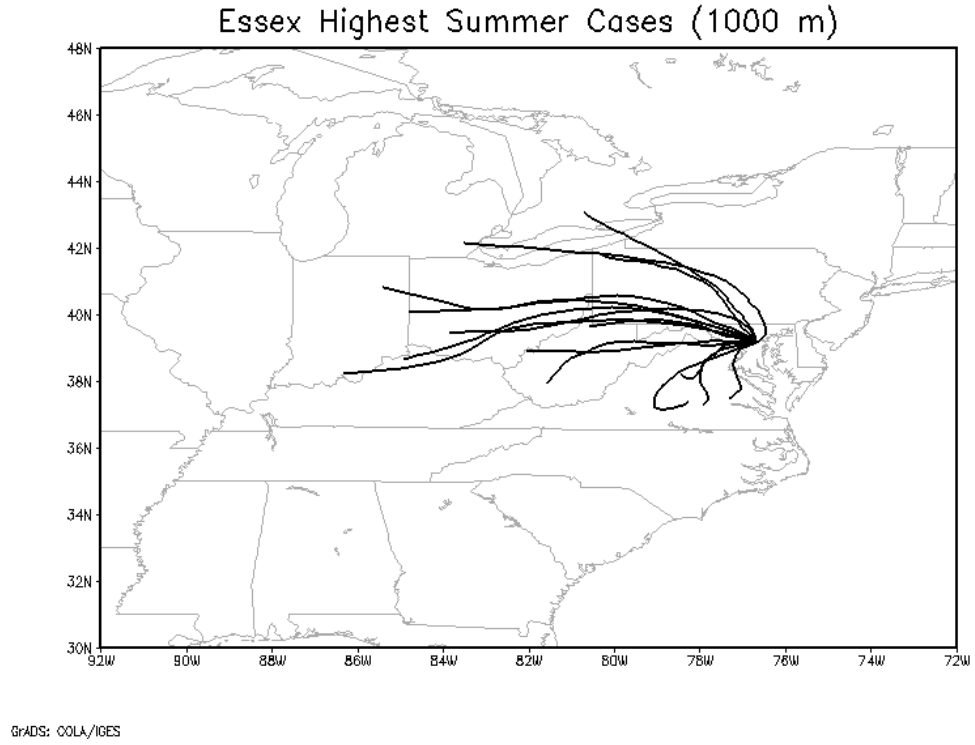

Figure 5.5. 24-hour back trajectories at 1000 m above ground level (agl) for summer season high $PM_{2.5}$ cases. Back trajectories courtesy of the NOAA-ARL HYSPLIT model

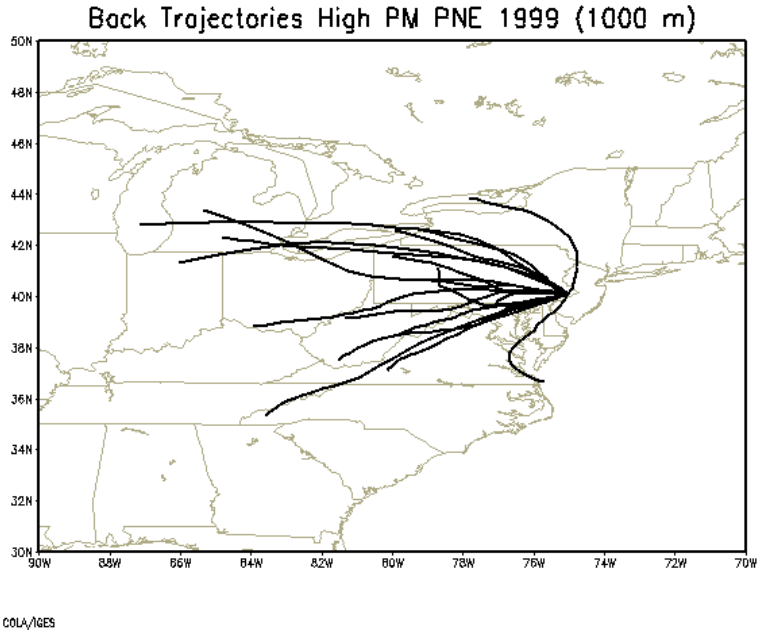

Figure 5.6. As in Figure 5.5 but for Philadelphia during the summer of 1999

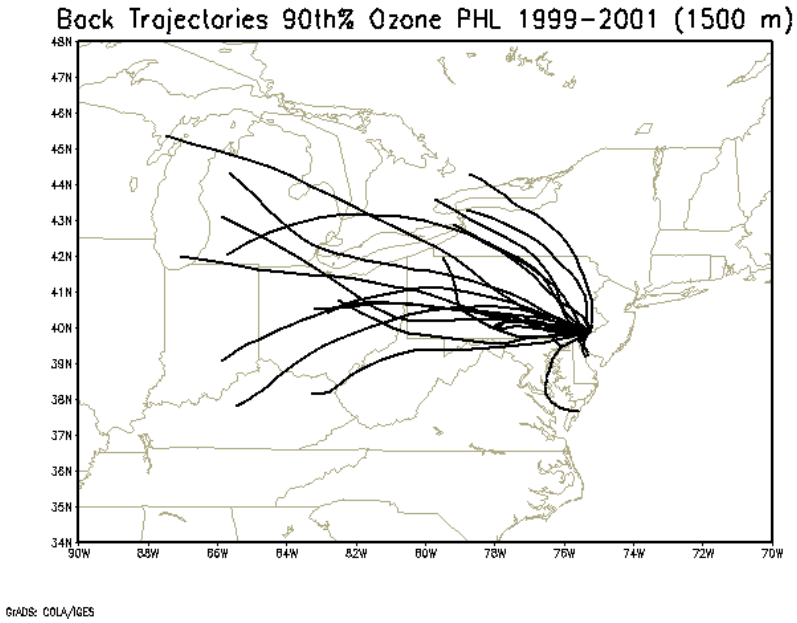

Figure 5.7. As in Figure 5.5 but for the 90th percentile of high O_3 cases in Philadelphia for the period 1999-2001. Back trajectories in this case at 1500 m agl

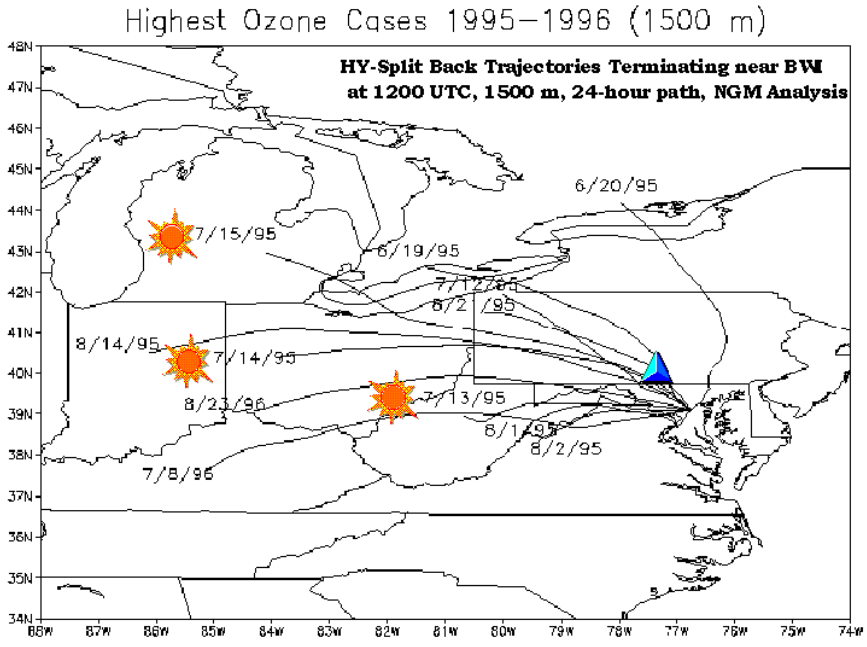

Figure 5.8. As in Figure 5.7 but for the highest O_3 cases in Baltimore during the summers of 1995-1996.

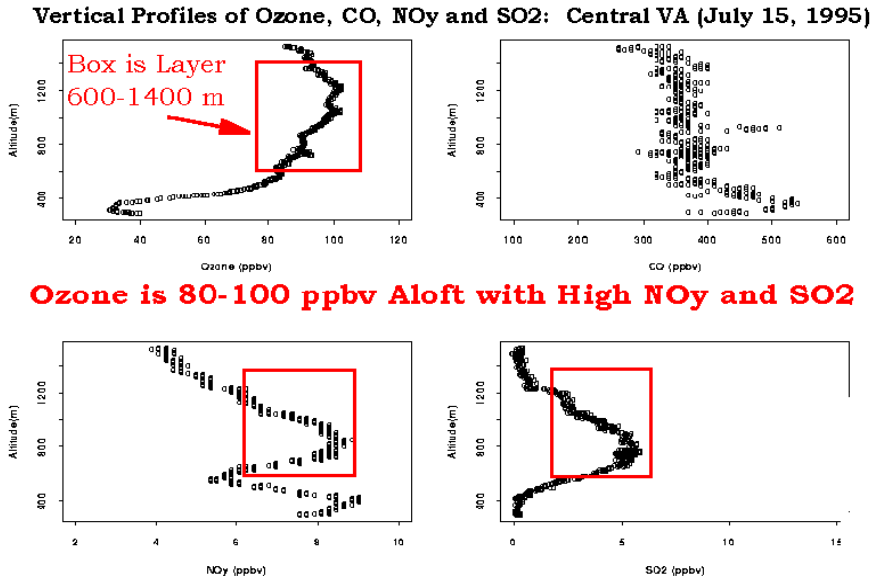

Figure 5.9. Aircraft observations of O_3 (top left), CO (top right), total reactive nitrogen (NO_y) (bottom left) and SO2 (bottom right) for high O_3 case of July 15, 1995. Data courtesy of NARSTO-NE (see, *Ryan et al., 1998*).

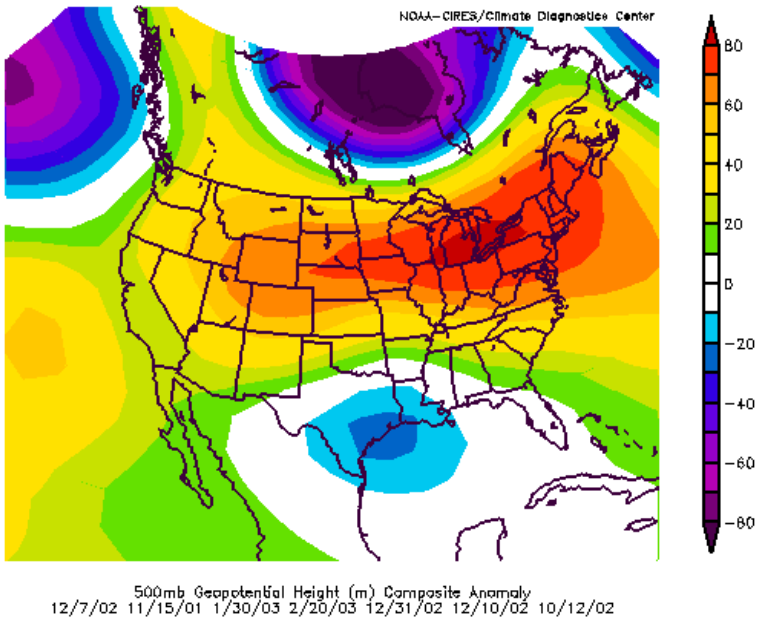

Figure 5.10. As in Figure 5.1 but for winter season high $PM_{2.5}$ cases (Figure courtesy of NOAA-CDC).

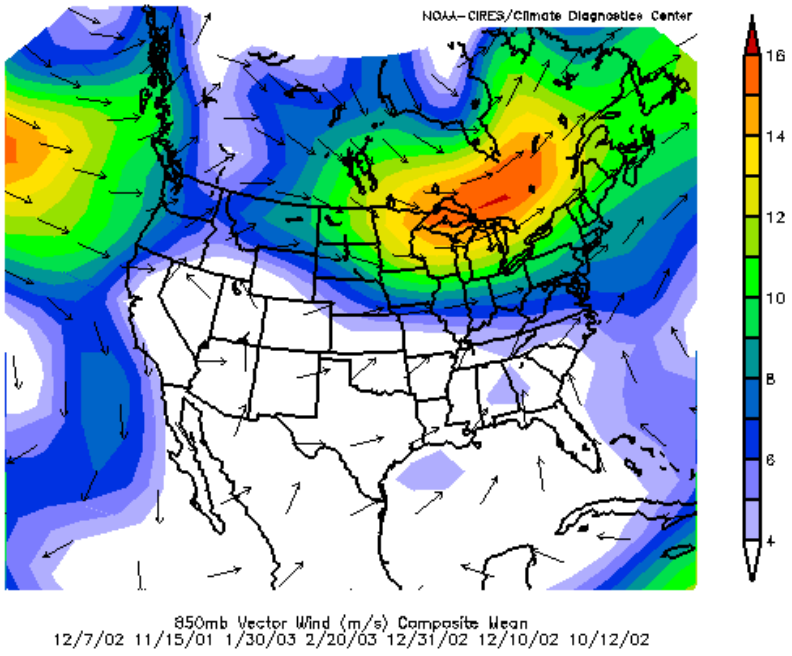

Figure 5.11. Mean 850 mb winds (in m s^{-1}) for winter season high $PM_{2.5}$ cases (Figure courtesy of NOAA-CDC).

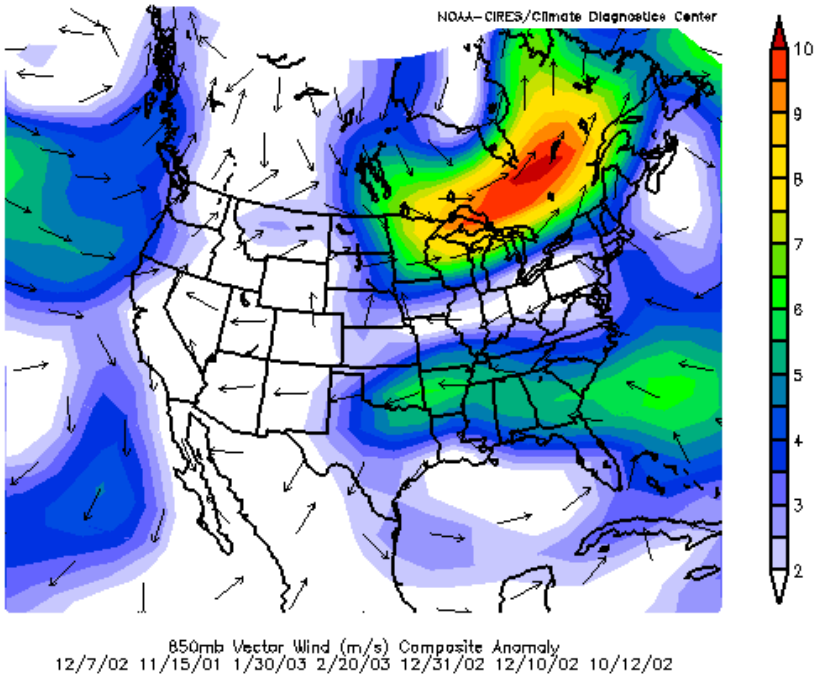

Figure 5.12. Difference from average of 850 mb winds (in m s^{-1}) for winter season high $PM_{2.5}$ cases (Figure courtesy of NOAA-CDC)

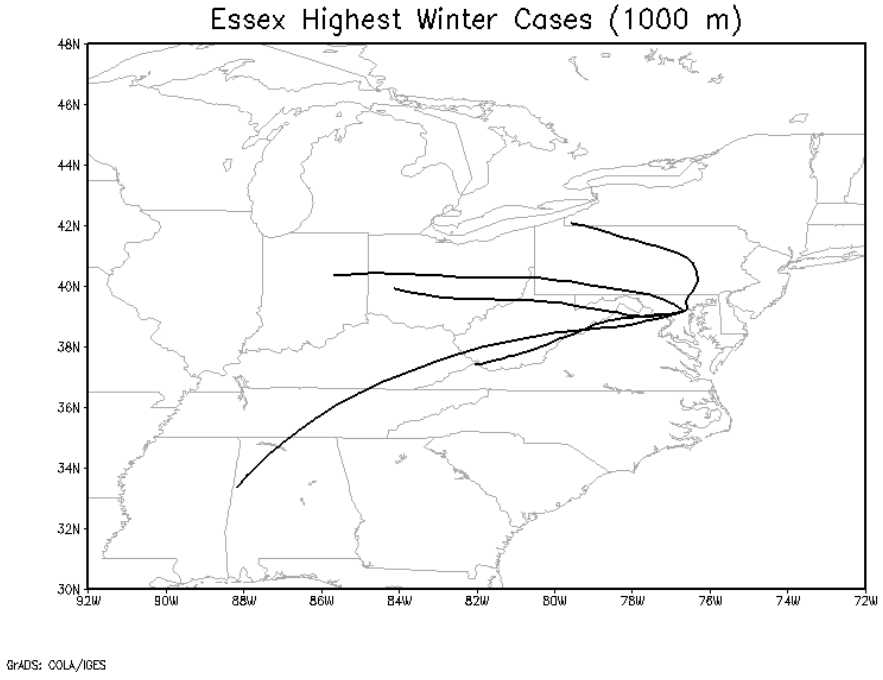

Figure 5.13. As in Figure 5.5 but for winter season high $PM_{2.5}$ cases

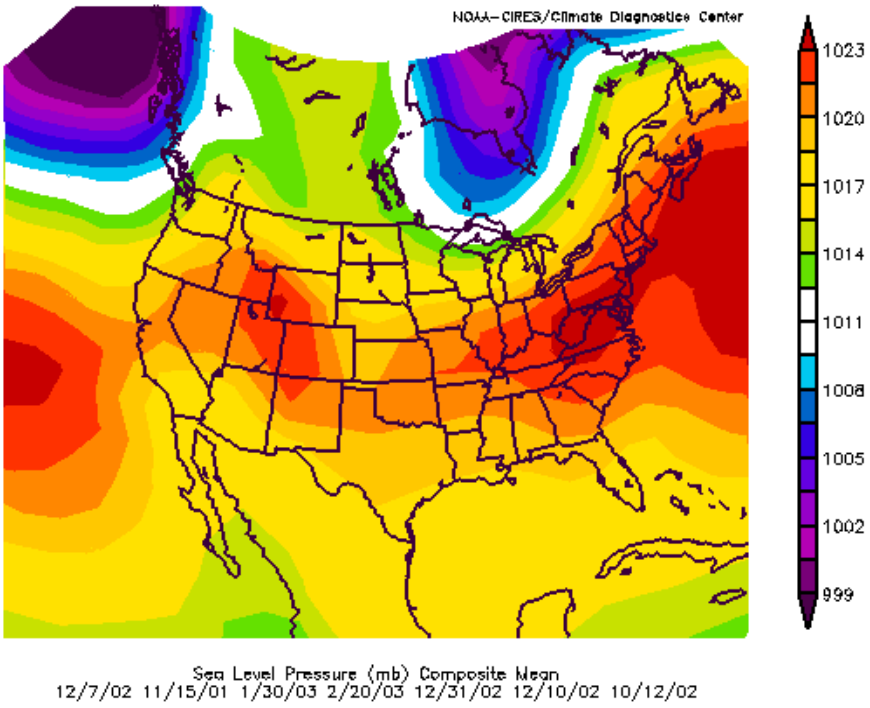

Figure 5.14. Mean sea level pressure field for summer season $PM_{2.5}$ cases. Figure courtesy of NOAA-CDC.

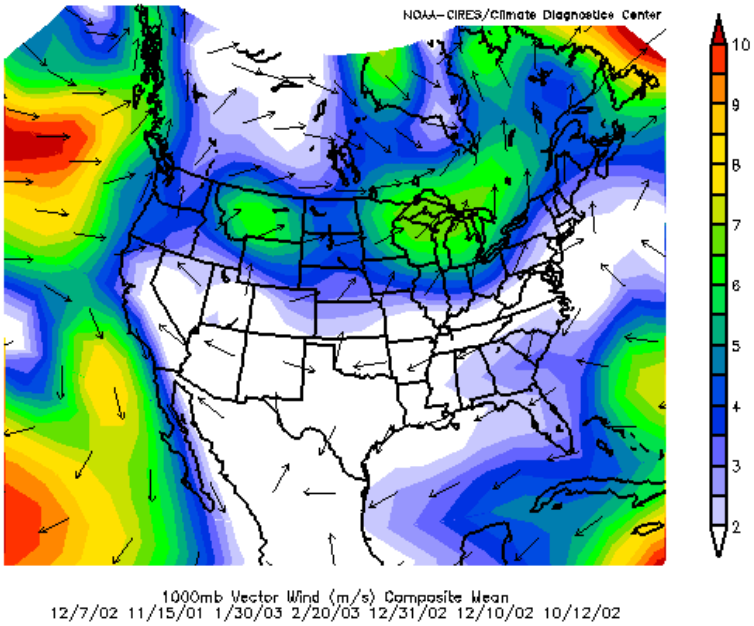

Figure 5.15. Mean 1000 mb (near surface) winds for high Mean sea level pressure field for high summer season $PM_{2.5}$ cases. (Figure courtesy of NOAA-CDC)

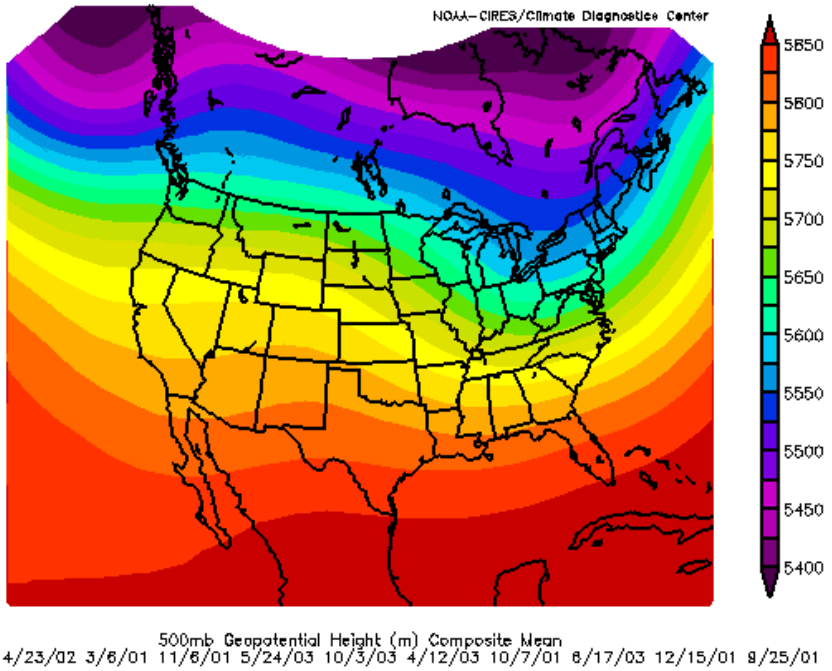

Figure 5.16. Mean 500 mb geopotential low $PM_{2.5}$ cases. (Figure courtesy of NOAA-Climate Diagnostics Center (CDC))

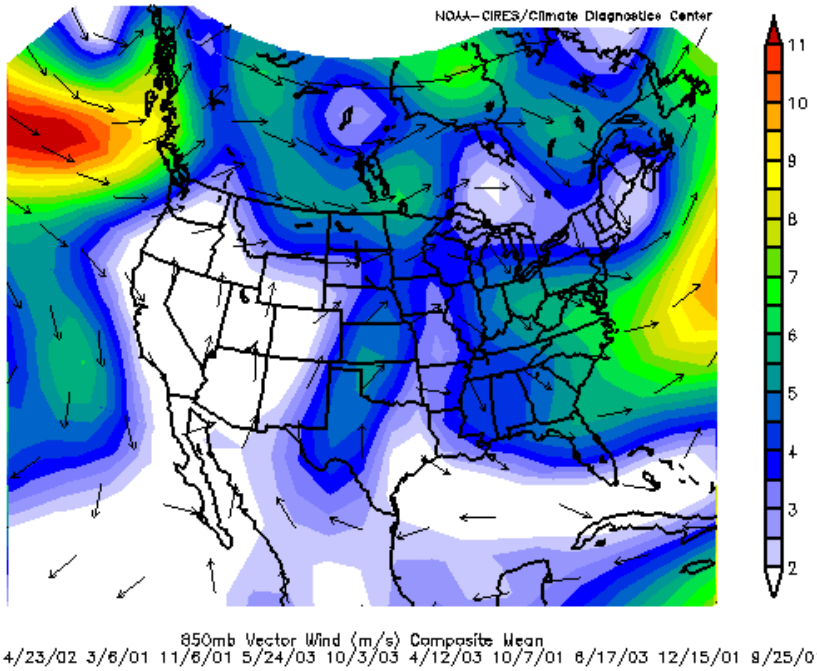

Figure 5.17. Mean 850 mb winds (in ms^{-1}) for low $PM_{2.5}$ cases (Figure courtesy of NOAA-CDC).

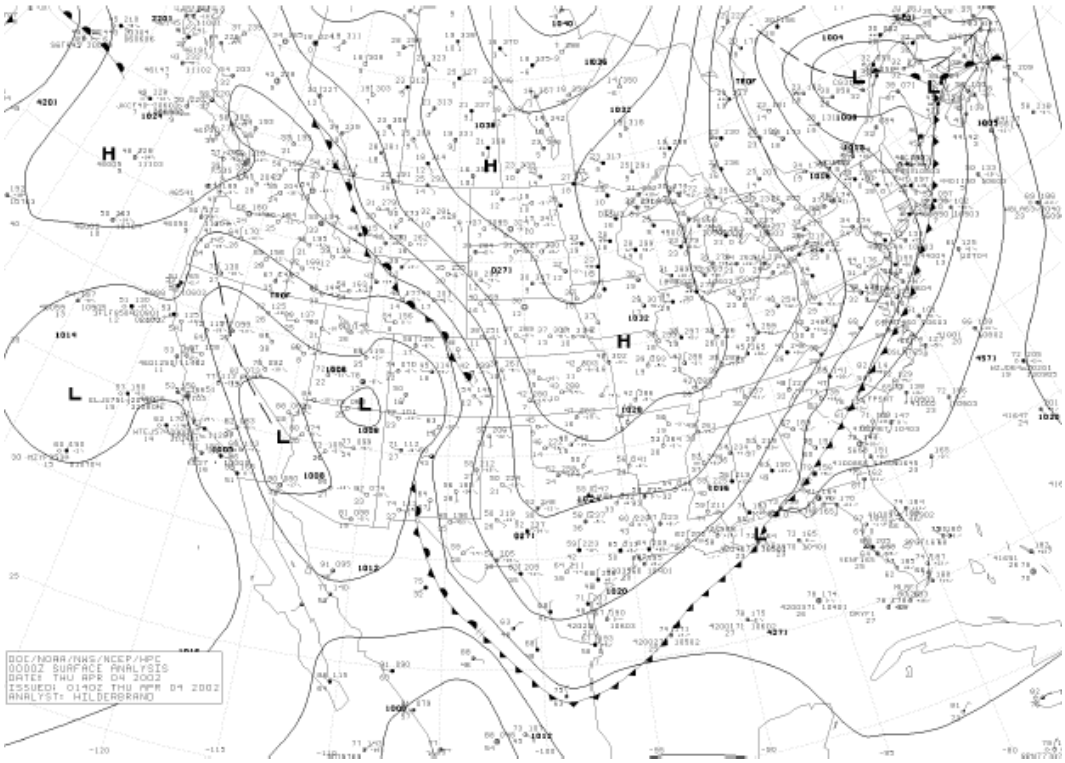
H
H
H
L
L
L
L
L
L
L
1014
1032
1028
1020
1012
1008
1004
1000
1016
1024
1036
1040
1044
1048
1052
1056
1060
1064
1068
1072
1076
1080
1084
1088
1092
1096
1100
1104
1108
1112
1116
1120
1124
1128
1132
1136
1140
1144
1148
1152
1156
1160
1164
1168
1172
1176
1180
1184
1188
1192

Section 6. Conclusion

This report contains an analysis of Speciated Trends Network (STN) data collected at Essex, Maryland for the period January, 2001-October, 2003. The STN monitor at Essex is located at 39.31ºN, 76.47ºW or approximately 10 miles E of Baltimore Inner Harbor. The local area is primarily residential and light industrial but there are a number of significant interstate highways and large arterial roads quite close to the monitor.

As is typical of observations from the eastern US, the major constituents of $PM_{2.5}$ at Essex are ammonium (NH_4), sulfate (SO_4), organic carbon (OC), elemental carbon (EC), and nitrate (NO_3). The relative fraction of OC, whose primary source is motor vehicle emissions, is uncertain. As measured by the STN monitors, it accounts for 23% of total $PM_{2.5}$ but its actual contribution is certainly higher as carbon particles also contain additional elements not directly measured. A correction factor (*k*) is typically applied to account for this additional amount of material and varies with type of particle and age. The range of *k* ranges from 1.4 to as much as 2.4 depending on the type and age of air mass measured.

The overall contributions of the various constituents to total $PM_{2.5}$ are consistent with recent observations at Fort Meade, Maryland and in urban and near urban sites in New York.

An analysis of the correlations between total $PM_{2.5}$ and its main constituents shows that $PM_{2.5}$ is most closely correlated with SO_4 ($r = 0.78$) and NH_4 ($r = 0.83$). OC has a lower correlation (0.60) and its concentrations in high $PM_{2.5}$ cases ($PM_{2.5} > 30$ μgm^{-3}) are highly variable. In terms of the seasonal cycle, SO_4 concentrations are highest in the summer (JJA) and account for nearly 50% of the $PM_{2.5}$ mass. Correlations for SO_4 (0.95) and NH_4 (0.92) are extremely strong in the summer months. OC has a bimodal seasonal signal with highest concentrations in both winter and summer seasons. EC, mainly from primary emissions, shows little seasonal differences. NO_3 is highest in the winter months but accounts for a small total fraction - ~ 12%. Winter season $PM_{2.5}$ is dominated by OC and NH_4 and appears to be driven by local emissions. In winter, the correlation between OC and EC (0.77) is much higher than in the summer months (0.26) suggesting that local, primary emissions are important.

The 90^{th} percentile of $PM_{2.5}$ cases (> 30 μgm^{-3}) is strongly weighted (65%) to the summer season and SO_4 is the most strongly correlated constituent in these cases (0.78). Toxic compounds measured at Essex are difficult to assess because a large fraction of observations are below the method detection limit (MDL). There are no clear correlations between toxic compounds and $PM_{2.5}$ overall or in high $PM_{2.5}$ cases.

Weather patterns associated with summer season high $PM_{2.5}$ cases are, in many respects, quite similar to high O_3 cases. A strong upper level ridge of high pressure is typically located over or west of the mid-Atlantic in both $PM_{2.5}$ and O_3 cases. This alignment leads to consistent westerly transport of pollutants into the region. On a daily basis, O_3 and $PM_{2.5}$ peaks often, but not always, coincide. The main factor that limits

peak O_3 in summer – cloud cover and convection – has a lesser impact on 24-hour average $PM_{2.5}$ concentrations.

In the winter season high $PM_{2.5}$ cases, a strong upper level ridge is also present along with westerly transport aloft. However, winter season $PM_{2.5}$ cases are more likely to be characterized by significant stagnation near the surface and by a very stable boundary layer – often enhanced by snow cover.

Low $PM_{2.5}$ cases are characterized by a weather pattern of an opposite phase as high $PM_{2.5}$ cases. Aloft, a trough of low pressure replaces the ridge, wind speed are much higher, and the source of the air mass entering Maryland is from the north and northwest - rural Canadian in origin.

A closer analysis of specific multi-day $PM_{2.5}$ cases in summer shows that large increases in $PM_{2.5}$ are driven primarily by increases in SO_4 concentrations. Although some episode days do include periods of stagnation, the longer range sources of the stagnant air masses are to the west of the region. Winter season multi-day episodes are characterized by stagnation and a very stable boundary layer. This traps pollutants by limiting both vertical and horizontal mixing. OC is the most dominant constituent in these cases.

Appendix A: Measurement and Analysis at the Essex, Maryland STN site

I. *Measurement*

The data analyzed in this report were gathered with a chemical speciation sampler (RAAS-401; Reference Ambient Air Sampler) manufactured by the Thermo-Electron Corporation. A schematic of the airflow through the mechanism is shown in Figure 1. Ambient air is collected by the inlet port which is insensitive to wind speed and direction. Particles larger than 10 μm in diameter do not pass through this main inlet. The airflow is then divided into two separate airflows, each with a precise flow rate of 24 Liters per minute (Lpm). This is the flow rate required by the sampler so that 50% of the sampled particles with diameters of 2.5 μm penetrate the inlet. Each of these airflows enters a cyclone fractionator which imparts a circular motion to the air and the particles are thus directed to the walls of the collection tube via the centripetal force generated by the circular motion. The airflow is then split again, resulting in a 7.3 Lpm flow rate and a 16.7 Lpm flow rate. Thus, there are four filters on which particles are gathered for analysis. The first is a quartz-fiber filter which is analyzed for carbon constituents. The second is a polytetrafluoroethylene (otherwise known as teflon) filter which is analyzed for total particulate mass concentration and for the mass concentration of individual trace elements. The third is also a teflon filter which is analyzed for anions (NH_4, K, Na.) and cations (SO_4, Cl). Two separate teflon filters are used because the analysis process for particulate elemental mass leads to a loss of volatile species. The fourth filter is a nylon filter which is analyzed for particulate nitrate. The air impacting this filter is first passed through an MgO denuder which removes nitric acid vapor (HNO_3) so that only particulate nitrate ends up on the nylon filter. The air flow rate through the sampler is critically important and is monitored at numerous points along the air flow path.

II.Analysis

The analysis of the particulate matter collected on the four filters is done at Research Triangle Institute (RTI). The quartz-fiber filter is analyzed for elemental and organic carbon using the Thermal Optical Reflectance Method (TOR). Using this method, carbon compounds are liberated from the filter sample under various temperature and oxidation environments. The details of the methods employed using TOR can be found in the EPA document, 'Guideline on Speciated Particle Monitoring' (1998). There are three different carbon compounds that are typically quantified from samples collected on quartz-fiber filters. The three types are organic, elemental (or black), and carbonate carbon. In this study, carbonate carbon was not separately analyzed for but is assumed to be included in either the elemental or organic carbon component. (Acidification of a section of the filter is required to analyze for carbonate carbon). The meaning of the elemental and organic carbon concentrations is dependent upon the operation used to analyze the filter. The TOR method can differentiate between four type of organic carbon and 3 types of elemental carbon. Carbon concentrations as reported here do not

have the same operational meaning as those analyzed with an alternate operational technique.

The first Teflon filter is analyzed using Photon-Induced X-ray Fluorescence (XRF). Using this method, volatile compounds are evaporated when the filter is place in a vacuum, thereby necessitating the second Teflon filter for which Ion Chromatography is used to analyze for cations and anions. IC is also used to analyze the nylon filter for particulate nitrate.

III. *Method Detection Limit*

Each element which is analyzed for has a unique Method Detection Limit (MDL). This limit is the minimum concentration that can be determined with 99% confidence that the concentration is greater than zero. The MDL is a statistical calculation and is based on everything involved in the sampling and analysis processes so it is unique to the mechanism used to sample the air and the type of filter used to collect the particles. Calculation of the MDL follows these steps:

1 Spike a solution with 1-5x the suspected DL for a given analyte
2 Measure the amount of analyte 7 times
3 Calculate the standard deviation and look up the t-value
4 Spike a new solution with a slightly different amount of analyte
5 Repeat steps 2 and 3
6 Determine that the 2 sample variances are statistically insignificant
7 Combine the two sample variances to get a std dev and tval
8 MDL = std dev * tval

Some MDL values for the species in this report are shown in *Table 1*.

Species	**MDL (ng m^{-3})**
PM2.5	300
OC	130
EC	130
SO_4	11
NO_3	8
NH_4	15
S	3
Si	3

Species	**MDL (ng m^{-3})**
Ca	1
Fe	0.8
Cr	0.6
Se	0.9
As	1
Cu	0.5
Pb	2.2
Mn	0.9
Zn	0.6

Appendix A. Table 1. Method Detection Limits using the RAAS-401

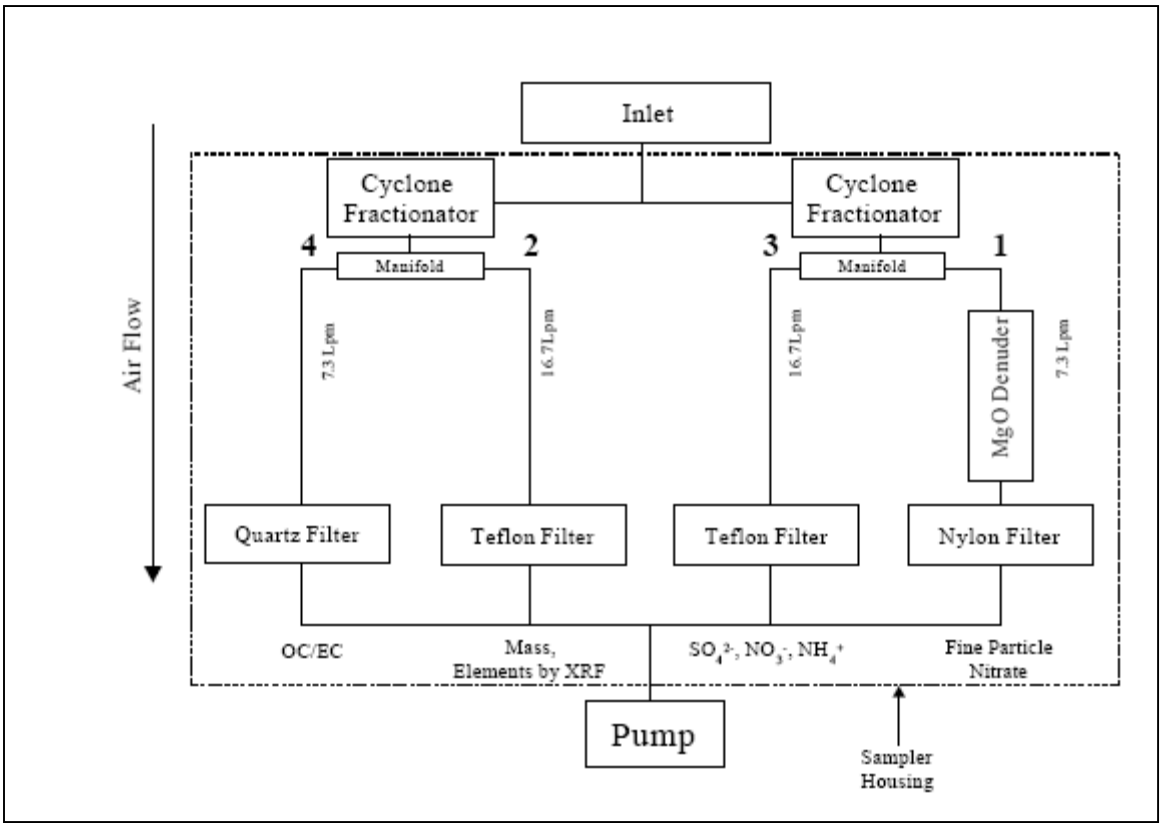

Appendix A. Figure 1. Schematic of the Anderson RAAS-401

Appendix B. Semi-Volatile Carbon Compounds

Semi-volatile (SVOL) material is composed of a variety of organic aerosol compounds (primarily carbon and hydrogen atoms) that have boiling points greater than 200° C. Measurement and analysis of the organic carbon component of $PM_{2.5}$ is subject to many uncertainties due to the SVOL portion of the aerosol.

The $PM_{2.5}$ carbon measurement is taken on a quartz filter using the Andersen RAAS-401. The quartz filter is subject to adsorption of gaseous OC which leads to overestimation of the OC particulate concentration. The quartz filter is also subject to volatilization of the collected particulate matter (due to extreme temperatures which the filter is exposed to during analysis) which leads to an underestimation of the OC particulate concentration.

The positive artifact can be almost eliminated by using a denuder ahead of the quartz filter. The denuder removes gas-phase material from the air stream before it reaches the filter. In another method, the amount of gas-phase material that is collected on the filter can be estimated by placing a second quartz filter behind the main quartz filter. This second filter will measure only the gas-phase OC material whose concentration can be subtracted from the concentration measured on the main quartz filter, yielding the resulting particulate OC concentration.

The negative artifact caused by volatilization of particulate material can be handled by using an adsorbent filter downstream of the main quartz filter. The adsorbent filter will capture the volatilized material. However, because the SVOL organic material has various absorptive properties, one type of adsorbent filter may not work for all compounds.

It should be noted that the methods described here to correct for positive and negative artifacts encountered during measurement and analysis of the SVOL portion of OC are capable of producing their own positive and negative artifacts.

Subramanian, et al.,(2004) (AS & T v. 38 supp1, 2004) found that, using a single quartz filter to measure $PM_{2.5}$ OC, the concentration of overestimated material was almost constant in Pittsburgh at 0.5 μgm^{-3}. This value was found to not vary seasonally. Simultaneous samples taken on a quartz filter with a denuder upstream (to remove the gaseous phase carbon) produced only a small loss of volatilized carbon particulate matter (as measured using a carbon-impregnated glass filter). Therefore, it was estimated that the single quartz filter measurement suffered from only a small negative artifact.

Appendix C: Case Studies of High $PM_{2.5}$ Cases

The case studies are available only on disc due to the size of the supporting images.

Episodes Discussed in Detail:

July 11-26, 2002 (Daily STN data available)
February 16-23, 2003
June 21-28, 2003

Other Episode Discussions Prior to STN Data base:

January 7-8, 2001
January 12-15, 2001
February 3-5, 2000
February 9-11, 2000
February 22-25, 2000
June 27-30, 2001
August 5-10, 2001

Appendix D: MARAMA Defined Episode List

Episode Number	Dates	Duration (Days)	Year	Season	Approximate Low (ug/m3)	Approximate High (ug/m3)	Type of Episode
1	2/8-12/00	5	2000	Winter	8	67	Dirty
2	5/29-6/6/00	9	2000	Summer	4	45	Dirty
3	10/9-19/00	11	2000	Fall	2	46	Dirty
4	1/9-16/01	8	2001	Winter	7	71	Dirty
5	1/21-25/01	5	2001	Winter	7	74	Dirty
6	6/24-7/2/01	9	2001	Summer	3	62	Dirty
7	7/12-7/20/01	9	2001	Summer	3	49	Dirty
8	3/30-4/11/02	13	2002	Spring	3	23	Clean
9	7/11-26/02	16	2002	Summer	2	57	Dirty
10	8/7-15/02	11	2002	Summer	3	54	Dirty
11	10/11-18/02	8	2002	Fall	2	13	Clean
12	12/20-26/02	7	2002	Fall	2	14	Clean
13	2/16-23/03	8	2003	Winter	5	49	Dirty
14	4/18-26/03	10	2003	Spring	3	21	Clean
15	6/21-28/03	8	2003	Summer	4	71	Dirty
16	8/31-9/7/03	8	2003	Fall	2	14	Clean

Appendix E: Correlation Coefficients Calculated Using Linear Regression Analysis on the Entire Dataset

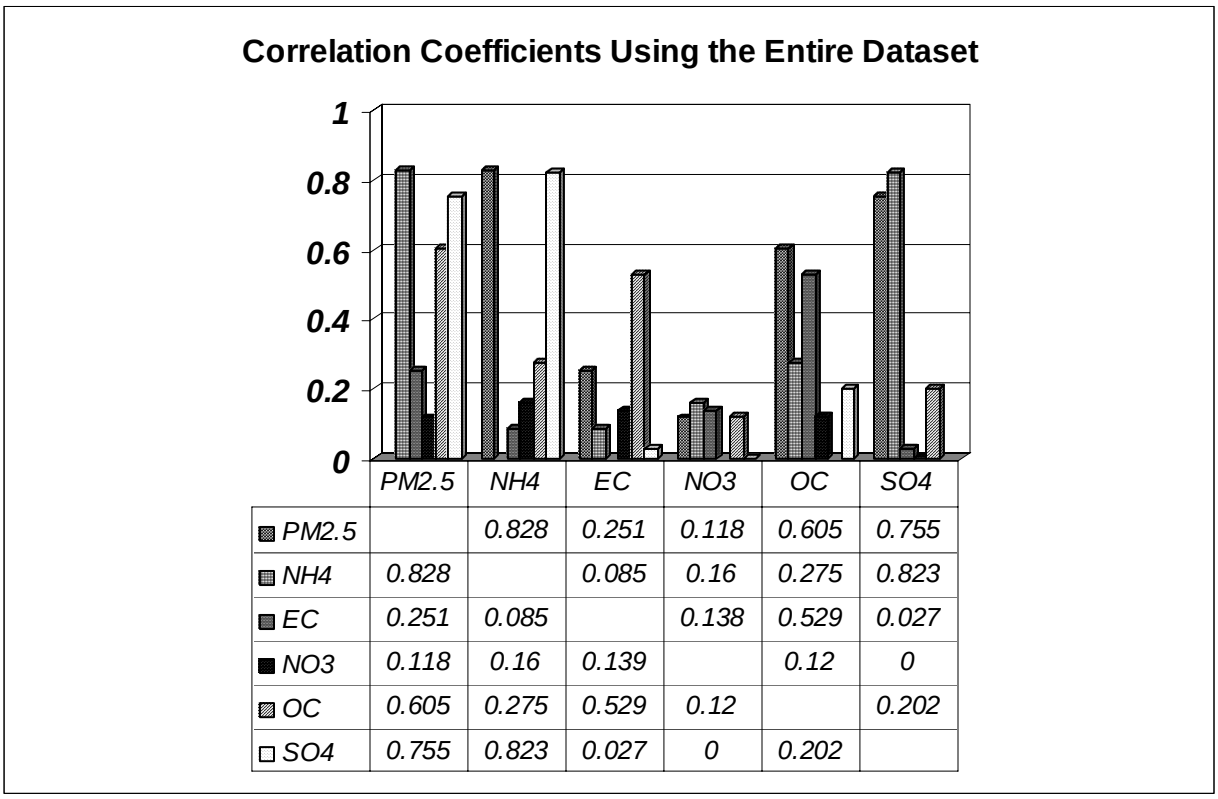

	PM2.5	NH4	EC	NO3	OC	SO4
PM2.5		0.828	0.251	0.118	0.605	0.755
NH4	0.828		0.085	0.16	0.275	0.823
EC	0.251	0.085		0.138	0.529	0.027
NO3	0.118	0.16	0.139		0.12	0
OC	0.605	0.275	0.529	0.12		0.202
SO4	0.755	0.823	0.027	0	0.202	

Appendix E, Table 1. Correlation coefficients for $PM_{2.5}$ and key constituents using the entire dataset

	Arsenic	Cadmium	Chromium	Cobalt	Chlorine	Lead	Manganese	Mercury
PM2.5	0.037	0.001	0.006	0	0.062	0.21	0.085	0.041
Arsenic	1	0.001	0.031	0	0.009	0.005	0.017	0.009
Cadmium	0.001	1	0.002	0.002	0.009	0.011	0.003	0
Chromium	0.031	0.002	1	0.016	0.004	0.011	0.003	0
Cobalt	0	0.002	0.016	1	0.002	0	0.006	0.001
Chlorine	0.009	0.009	0.004	0.002	1	0.131	0.008	0.016
Lead	0.005	0.011	0.001	0	0.131	1	0.078	0.007
Manganese	0.017	0.003	0.003	0.006	0.008	0.078	1	0
Mercury	0.009	0	0	0.001	0.016	0.007	0	1
Nickel	0.005	0	0	0.015	0.063	0.066	0.084	0.007
Phosphorus	0.002	0.003	0.003	0.102	0.004	0.003	0.028	0.001
Selenium	0.005	0.003	0.003	0.008	0.019	0.061	0.049	0.011

	Nickel	Phosphorus	Selenium
PM2.5	0.144	0.001	0.311
Arsenic	0.005	0.002	0.005
Cadmium	0	0.003	0.003
Chromium	0.006	0.031	0.006
Cobalt	0.015	0.102	0.008
Chlorine	0.063	0.004	0.019
Lead	0.066	0.003	0.061
Manganese	0.084	0.028	0.049
Mercury	0.007	0.001	0.011
Nickel	1	0.011	0.14
Phosphorus	0.011	1	0.002
Selenium	0.14	0.002	1

Appendix E, Table 2. As in Table 1 but for $PM_{2.5}$ and toxic constituents

	NH4	EC	NO3	OC	SO4
Arsenic	0.02	0.093	0.014	0.067	0.016
Cadmium	0	0.001	0.003	0	0
Chromium	0.002	0.058	0.005	0.023	0
Cobalt	0.002	0.008	0.007	0.004	0.004
Chlorine	0.019	0.166	0.23	0.144	0.004
Lead	0.107	0.161	0.122	0.232	0.06
Manganese	0.029	0.15	0.004	0.133	0.027
Mercury	0.024	0.004	0	0.03	0.027
Nickel	0.091	0.095	0.14	0.151	0.03
Phosphorus	0.004	0.015	0	0.003	0.007
Selenium	0.242	0.099	0.036	0.186	0.219

Appendix E, Table 3. As in Table 1 but for key and toxic constituents

Appendix F: Seasonal Correlations

Species	PM2.5	NH4	OCB	NO3	ECB	SO4
PM2.5	1.000	0.781	0.764	0.672	0.636	0.550
NH4	0.781	1.000	0.332	0.722	0.263	0.766
OCB	0.764	0.332	1.000	0.298	0.769	0.240
NO3	0.672	0.722	0.298	1.000	0.173	0.270
ECB	0.636	0.263	0.769	0.173	1.000	0.208
SO4	0.550	0.766	0.240	0.270	0.208	1.000

Appendix F, Table 1. Winter season correlation coefficients

Species	PM2.5	NH4	OCB	NO3	ECB	SO4
PM2.5	1.000	0.824	0.536	0.477	0.177	0.833
NH4	0.824	1.000	0.216	0.627	0.053	0.867
OCB	0.536	0.216	1.000	0.149	0.256	0.237
NO3	0.477	0.627	0.149	1.000	0.002	0.306
ECB	0.177	0.053	0.256	0.002	1.000	0.101
SO4	0.833	0.867	0.237	0.306	0.101	1.000

Appendix F, Table 2. Spring season correlation coefficients

Species	PM2.5	NH4	OCB	NO3	ECB	SO4
PM2.5	1.000	0.919	0.668	0.048	0.313	0.948
NH4	0.919	1.000	0.487	0.109	0.249	0.956
OCB	0.668	0.487	1.000	0.015	0.256	0.489
NO3	0.048	0.109	0.015	1.000	0.077	0.042
ECB	0.313	0.249	0.256	0.077	1.000	0.227

SO4	0.948	0.956	0.489	0.042	0.227	1.000

Appendix F, Table 3. Summer season correlation coefficients

Species	PM2.5	NH4	OCB	NO3	ECB	SO4
PM2.5	1.000	0.649	0.771	0.319	0.574	0.547
NH4	0.649	1.000	0.248	0.272	0.200	0.861
OCB	0.771	0.248	1.000	0.244	0.701	0.188
NO3	0.319	0.272	0.244	1.000	0.264	0.051
ECB	0.574	0.200	0.701	0.264	1.000	0.108
SO4	0.547	0.861	0.188	0.051	0.108	1.000

Appendix F, Table 4. Fall season correlation coefficients

Appendix G: Correlations for Low and High $PM_{2.5}$ Cases

Species	PM2.5	NH4	OCB	NO3	ECB	SO4
PM2.5	1.000	0.061	0.080	0.157	0.126	0.004
NH4	0.061	1.000	0.237	0.648	0.092	0.697
OCB	0.080	0.237	1.000	0.008	0.010	0.517
NO3	0.157	0.648	0.008	1.000	0.054	0.216
ECB	0.126	0.092	0.010	0.054	1.000	0.037
SO4	0.004	0.697	0.517	0.216	0.037	1.000

Appendix G, Table 1. Correlation coefficients for low $PM_{2.5}$ cases

Species	PM2.5	NH4	OCB	NO3	ECB	SO4
PM2.5	1.000	0.71	0.033	0.076	0.007	0.595
NH4	0.712	1.000	0.026	0.064	0.164	0.700
OCB	0.033	0.026	1.000	0.103	0.559	0.122
NO3	0.076	0.064	0.103	1.000	0.113	0.486
ECB	0.007	0.164	0.559	0.113	1.000	0.231
SO4	0.595	0.700	0.122	0.486	0.231	1.000

Appendix G, Table 2. Correlation coefficients for high $PM_{2.5}$ cases

Mid-Atlantic Regional Air Management Association

An Analysis of Speciated $PM_{2.5}$ Data in the MARAMA Region

May 31, 2006

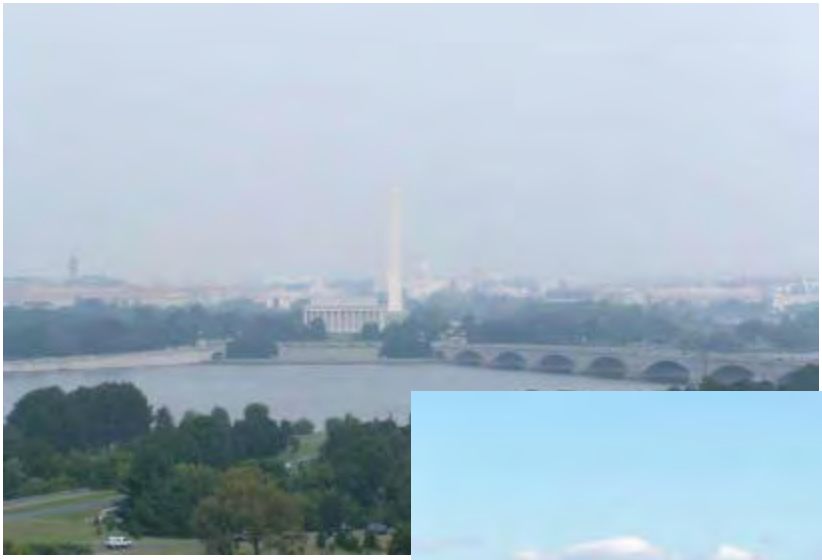

Prepared by

William G. Gillespie and Patrick Davis

Mid-Atlantic Regional Air Management Association

About MARAMA

The Mid-Atlantic Regional Air Management Association is a voluntary, non-profit association of ten state and local air pollution control agencies. MARAMA's mission is to strengthen the skills and capabilities of member agencies and to help them work together to prevent and reduce air pollution impacts in the Mid-Atlantic Region.

MARAMA provides cost-effective approaches to regional collaboration by pooling resources to develop and analyze data, share ideas, and train staff to implement common requirements.

The following State and Local governments are MARAMA members: Delaware, the District of Columbia, Maryland, New Jersey, North Carolina, Pennsylvania, Virginia, West Virginia, Philadelphia, and Allegheny County, Pennsylvania.

On the Cover: Images from the National Park Service WebCam looking east from the Netherlands Carillon in Washington, DC. The upper left photograph was taken at 2 p.m. August 22, 2003, 24-hour $PM_{2.5}$ concentration approximately 40 $\mu g/m^3$. The lower right photograph was taken at 2 p.m. October 3, 2003, 24-hour $PM_{2.5}$ concentration approximately 5 $\mu g/m^3$.

For copies of this report contact:

MARAMA
Mid-Atlantic Regional Air Management Association
711 West 40th Street
Suite 312
Baltimore, MD 21211

Telephone 410.467.0170
Fax 410.467.1737
http://www.marama.org/

An Analysis of Speciated $PM_{2.5}$ Data in the MARAMA Region

May 31, 2006

Prepared by

William G. Gillespie and Patrick Davis

Mid-Atlantic Regional Air Management Association

Preface

State and local air quality agencies in the MARAMA Region operate a variety of monitors that measure particulate matter (PM) less than or equal to 2.5 micrometers in aerodynamic diameter. These very small particles are referred to as $PM_{2.5}$. The measurement of $PM_{2.5}$ is important because scientific studies link $PM_{2.5}$ pollution to numerous health problems.

Some of the monitors that measure $PM_{2.5}$ pollution in the MARAMA Region are speciation monitors, monitors that measure the chemical composition of fine particles. This report provides information about $PM_{2.5}$ speciation monitors and the network of speciation monitors that has been deployed in the MARAMA Region. The major focus of the report is an analysis of the speciation data collected at eleven monitors from September 10, 2001 through October 12, 2003. Comparisons are made between the eleven monitors. The comparisons provide insights as to how the major components of $PM_{2.5}$ mass vary across the region by location and season. The report includes detailed site-by-site analyses of speciation data showing how the major species of $PM_{2.5}$ mass varied over time. The site-by-site analyses also provide back trajectories for periods of high and low $PM_{2.5}$ concentration.

Acknowledgements

MARAMA would like to acknowledge the state and local agency staff who operate and maintain the network of $PM_{2.5}$ speciation monitors in the MARAMA region. Without the hard work and dedication of state and local monitoring staff, speciation data would not be available to understand the complexities of fine particle pollution. MARAMA would also like to acknowledge the work of Research Triangle Institute International, Inc., the laboratory EPA has hired to analyze filters collected in the $PM_{2.5}$ speciation program. RTI analyzes a steady stream of filters from over 200 speciation monitors in the United States. Chemical analyses are performed for over 50 analytes. RTI staff provided important quality assurance and other information regarding the speciation data used in this report. Jim Flanagan and Dr. Max Peterson from RTI deserve special mention for their assistance in helping MARAMA staff understand the quality assurance and measurement uncertainty of speciation data.

This analysis would not have been possible without the funding and assistance of the U.S. Environmental Protection Agency (EPA). Funding support was provided by the EPA Region III, EPA grant number PM-983988-01-0. Numerous EPA staff assisted MARAMA in accessing and compiling speciation data. Other EPA staff provided information on the speciation program or provided suggestions as to how to best analyze speciation data. The following EPA staff provided important support or assistance for this project.

Ted Erdman, EPA Region III
Jim Homolya, EPA, Office of Air Quality Planning and Standards
Joann Rice, EPA, Office of Air Quality Planning and Standards
Paul Solomon, EPA, Office of Research and Development

Special thanks to Ted Erdman at EPA Region III for supporting this analytical effort and for promoting the idea of preparing a "Guide to Speciation Data." It is the hope of the authors that this document provides analysts with the basic information they need to access and use speciation data in air quality analyses.

MARAMA would like to thank Rich Poirot from the Vermont Department of Environmental Conservation for guidance and assistance in running the Combined Aerosol Tracking Tool (CATT), Dr. Richard Tropp from Desert Research Institute for his assistance in understanding the intricacies of mass reconstruction equations, and Dr. Barbara Turpin with Rutgers University for her insights regarding organic mass/organic carbon ratios.

To prepare this report, MARAMA received support and assistance from many MARAMA members, MARAMA staff, and other interested parties. We would like to acknowledge and thank the following individuals who provided us with data, analytical assistance and/or comments and suggestions on the report.

Pat Adkins - West Virginia Department of Environmental Protection
Tim Carroll - West Virginia Department of Environmental Protection
Katie Cooney - MARAMA, Air Quality Specialist
Wayne Cornelius - North Carolina Department and Natural Resources
Robert Day - District of Colombia Department of Health
Larry English - West Virginia Department of Environmental Protection
Betsy Frey - Delaware Department of Natural Resources and Environmental Control
Edwin Gluth - Maryland Department of the Environment

Jayme Graham - Allegheny County Health Department
John Graham - Northeast States for Coordinated Air Use Management
John Haus - Maryland Department of the Environment
Jessica Hermes - MARAMA, Administrative Assistant
Loretta Hayden - Philadelphia Department of Public Health
Tom Jennings - Virginia Department of Environmental Quality
Henry Kim - Philadelphia Department of Public Health
Hoke Kimball - North Carolina Department and Natural Resources
David Krask - Maryland Department of the Environment
Alan Leston - Northeast States for Coordinated Air Use Management (NESCAUM)
Jason Maranche - Allegheny County Health Department
Tom McKenna - New Jersey Department of Environmental Protection
George Mentzer - Pennsylvania Department of Environmental Protection
Charlie Pietarinen - New Jersey Department of Environmental Protection
Ron Savukas - Allegheny County Health Department
Matthew Seybold - Maryland Department of the Environment
Joette Steger - North Carolina Department and Natural Resources
Darrell Stern - Allegheny County Health Department
Carolyn Stevens - Virginia Department of Environmental Quality
Jeanne Wagner - West Virginia Department of Environmental Protection
Tom Weir - Philadelphia Department of Public Health
Susan Wierman- MARAMA Executive Director

Table of Contents

List of Figures

List of Tables

List of Abbreviations and Symbols

ATAD – Atmospheric Transport and Dispersion Model

AIRNow – EPA's air quality forecasting web site, available online at http://www.epa.gov/airnow/

AQI – Air Quality Index

AQS – Air Quality System

ASCII – American Standard Code for Information Interchange

BAM – Beta Attenuation Monitor

C – Centigrade

CAIR – Clean Air Interstate Rule

CAFO – Concentrated Animal Feeding Operation(s)

CFR – Code of Federal Regulations

EPA – U.S. Environmental Protection Agency

EDXRF – Energy Dispersive X-Ray Fluorescence

FDMS^{TM} – Filter Dynamics Measurement System; a trademark of Rupprecht & Patashnick, Co., Inc.

FRM – Federal Reference Method

IC – Ion chromatography

IMPROVE – Interagency Monitoring of Protected Visual Environments

km – Kilometer(s)

NAAQS – National Ambient Air Quality Standards

NESCAUM – Northeast States for Coordinated Air Use Management

NIOSH – National Institute for Occupational Safety and Health

NOAA – National Oceanic and Atmospheric Administration.

µm – Micrometer(s)

µg/m3 – Micrograms per cubic meter

OM/OC ratio – Organic Mass/Organic Carbon ratio

PAMS – Photochemical Assessment Monitoring Stations

PM – Particulate matter

$PM_{2.5}$ – Air borne particles with a mean aerometric diameter equal to or smaller than 2.5 μm.

POC – Parameter Occurrence Code

R^2 – the coefficient of determination

Rawinsonde – an instrument package, including a radio transmitter and sensors, carried aloft by an unmanned balloon to measure, temperature, pressure, wind speed, and other meteorological parameters

SLAMS – State and Local Air Monitoring Stations

SOP – Standard Operating Procedure

STAPPA/ALAPCO – the State and Territorial Air Pollution Program Administrators (STAPPA) and the Association of Local Air Pollution Control Officials (ALAPCO)

STN – Speciation Trends Network

TEOM – Tapered Element Oscillating Microbalance

TOR – Thermal Optical Reflectance

TOT – Thermal Optical Transmittance, NIOSH Method 5040

TTN – Technology Transfer Network

URL – Uniform Resource Locators

VIEWS – Visibility Information Exchange Web System

VOC – Volatile organic compound(s)

1 Executive Summary

1.1 Background and Approach

The data collected in the $PM_{2.5}$ speciation monitoring program is important to EPA, State and local air quality agencies, and others who are trying to understand the nature and extent of fine particle pollution at a specific site or in an entire region. Speciation data is the "grist" used in source apportionment analyses and it will play an increasingly important role in the development of strategies to control of fine particle pollution.

Given the importance of speciation data, MARAMA's Executive Board asked MARAMA staff to analyze speciation data in the MARAMA Region and show member agencies how to effectively use these data. In this report, MARAMA provides background information on the speciation monitoring program and analyzes speciation data for twelve sites across the MARAMA Region. The report also provides information about how to access and process speciation data. The data Methodology and Data Handling Techniques for Speciation Data section of the report serves as a practical guide to analysts who wish to obtain and process $PM_{2.5}$ speciation data.

This report makes regional comparisons between eleven monitoring sites from North Carolina to New Jersey using 25 months of data from September 10, 2001 through October 12, 2003. The regional comparisons show how the five major species that make up $PM_{2.5}$ mass – ammonium, elemental carbon, organic carbon mass, nitrate, and sulfate – vary across the region and season to season.

In addition to the regional comparisons, the report provides detailed "site-specific" analyses for the eleven sites analyzed regionally plus a site located in South Charleston, WV. Site-specific analyses provide detailed information about the composition of $PM_{2.5}$ mass over 2001-2003 and the seasonal variation of $PM_{2.5}$ constituents. Site-specific analyses also include back trajectories for the five percent "cleanest" and "dirtiest" days observed over the study period.

This analysis found that three of the five major contributors to $PM_{2.5}$ mass – ammonium, nitrate, and sulfate – are routinely measured with reasonable certainty. The average percent error for ammonium, nitrate, and sulfate measurements were 7.1, 11.8, and 8.6 respectively. Organic carbon mass and elemental carbon measurements were much less certain, however. An important source of error associated with the estimation of organic carbon mass was the assignment of the organic carbon mass to organic carbon OM/OC ratio, a factor used to estimate the mass of organic carbon aerosol collected in a speciation sample. Since OM/OC ratios have not been empirically determined at monitoring sites in the region, estimates of organic carbon mass are much less certain than other measurements.

To better understand how different OM/OC ratios affect organic carbon mass estimation, MARAMA performed a sensitivity analysis using OM/OC ratios of 1.6 and 1.9. Better mass closure, the comparison of reconstructed mass with gravimetric mass, was achieved using an OM/OC ratio of 1.6 at most urban sites. An OM/OC ratio of 1.9 produced better mass closure at rural sites, although even higher OM/OC ratios are probably appropriate for the most rural sites.

1.2 Findings

The following paragraphs summarize the major findings of this analytical effort.

- Speciation data is very valuable in understanding the nature and composition of fine particle pollution. The analysis of these data will help air quality planners develop appropriate and effective air quality control programs for fine particle pollution.
- The speciation monitoring network is producing data that will help assess the impacts of programs such as CAIR that are expected to reduce the concentration of $PM_{2.5}$ precursors between now, 2009, and thereafter.
- The analysis of speciation data is complex and requires increased knowledge of the nature and limitations of the data. State, local and regional air quality agencies will need training and practice to reap the full benefits of these data.
- Currently, a data analyst must gather information on how to process and analyze speciation data from a wide range of sources including EPA, regional associations, university researchers, contractors, etc.
- The OM/OC ratios used to convert organic carbon measurements from the speciation network into estimates of organic carbon mass have risen in recent years as research scientists improve the measurement of organic carbon species in the atmosphere. Higher OM/OC ratios increase the amount of mass attributed to organic carbon species.
- Organic carbon mass and sulfate were the largest contributors to $PM_{2.5}$ mass at all sites for the period from September 10, 2001 through October 12, 2003.
    - Using an OM/OC ratio of 1.6, organic carbon mass was the largest contributor to $PM_{2.5}$ mass at seven of the eleven sites analyzed. Sulfate was the largest average contributor to $PM_{2.5}$ mass at the other four sites.
    - The average organic carbon mass concentration, averaged regionally over 2001-2003 was 5.41 $\mu g/m^3$. Average organic carbon mass levels ranged from a high of 6.93 $\mu g/m^3$ in Elizabeth, NJ to a low of 3.63 $\mu g/m^3$ in Dover, DE. At most sites, organic carbon mass concentrations were highest in summer and lowest in the spring.
    - Empirically determined site-specific and/or site-specific and season-specific OM/OC values would greatly improve estimates of organic carbon mass at monitoring sites in the MARAMA Region.
    - More needs to be known about organic carbon mass, since it constitutes a large part of total $PM_{2.5}$ mass in the MARAMA Region. More work is needed to determine or better understand: which organic carbon species are present and in what concentration, how do organic carbon mass species vary over time and place, are the organic carbon mass species the result of anthropogenic or biogenic emissions, and what constituents and processes are important to secondary organic aerosol formation, etc.
- Sulfate was a strong contributor to $PM_{2.5}$ mass at all sites and was the largest contributor to $PM_{2.5}$ mass at four of the eleven sites analyzed.

- Sulfate concentrations were highest in summer, were often episodic in nature, and were correlated well with ammonium concentrations.
- If the average concentrations of sulfate and ammonium are added together, the combined concentration was the largest contributor to $PM_{2.5}$ mass at all sites averaged over 2001-2003.
- The average sulfate concentration, averaged regionally over 2001-2003 was 5.11 $\mu g/m^3$. Average sulfate levels ranged from a high of 6.12 $\mu g/m^3$ in Arendtsville, PA to a low of 4.11 $\mu g/m^3$ in Kinston, NC.

· Nitrate species made a much smaller contribution to $PM_{2.5}$ mass than organic carbon mass and sulfate species. The average nitrate concentration, averaged regionally over 2001-2003 was 1.76 $\mu g/m^3$. Average nitrate levels ranged from a high of 2.48 $\mu g/m^3$ in Wilmington, DE to a low of 0.94 $\mu g/m^3$ in Charlotte, NC. Nitrate concentrations peaked in the winter and were low in the summer. Nitrate concentrations appear linked to winter/cold weather conditions that produce solid phase nitrate species (Wittig et al., 2004). Lower average nitrate concentrations occurred in the southern part of the MARAMA Region and higher average nitrate concentrations occurred in northern areas.

· Ammonium species also made a much smaller contribution to $PM_{2.5}$ mass than organic carbon mass and sulfate species. The average ammonium concentration, averaged regionally over 2001-2003 was 2.01 $\mu g/m^3$. Average ammonium levels ranged from a high of 2.36 $\mu g/m^3$ in Arendtsville, PA to a low of 1.51 $\mu g/m^3$ in Kinston, NC. Ammonium concentrations were fairly uniform across the MARAMA Region. In many cases, urban sites produced higher ammonium concentrations than rural sites.

· Elemental carbon concentrations were generally small relative to other $PM_{2.5}$ mass constituents. Despite this, elemental carbon particles are important from a human health perspective, since they are considered air toxins and are associated with increased risk of cancer and other disease.

- The average elemental carbon concentration, averaged regionally over 2001-2003 was 0.75 $\mu g/m^3$. Average elemental carbon levels ranged from a high of 1.82 $\mu g/m^3$ in Elizabeth, NJ to a low of 0.36 $\mu g/m^3$ in Kinston, NC.
- Elemental carbon concentration was strongly correlated with population; higher concentrations occurred in urban sites and lower concentrations in rural areas.

· Over the period studied, $PM_{2.5}$ concentrations often rose and fell sympathetically over wide areas of the MARAMA Region.

· Many back trajectories for days when $PM_{2.5}$ concentrations were low originated in relatively "clean" areas in western or central Canada or northern states and moved quickly over great distances to receptor sites in the MARAMA Region. In contrast to back trajectories associated with high $PM_{2.5}$ concentrations, these "clean day" trajectories did not remain or re-circulate over air pollution source regions.

· Many back trajectories for days when $PM_{2.5}$ concentrations were high were tracks of air masses that spent the last five days over the continental U.S. In many cases, the air circulated or re-circulated through air pollution source regions in the Midwest, Mid-Atlantic, Northeast and South. Many "dirty day" trajectories passed through the Ohio River Valley.

- Speciation data can be used to characterize air quality at a particular site as well as to provide information about regional conditions.
- Speciation data can be used to analyze and confirm exceptional events like forest fires and other phenomena.
- The error/uncertainty of many trace element measurements in the speciation program is poorly known.
- Many trace element measurements in the speciation program are below the Method Detection Limit (MDL) of the analytical equipment used to make these measurements.

The Future Directions section of this report provides a list of follow-up activities and analyses that will improve the speciation monitoring program and the analysis of these data.

2 Introduction

2.1 The $PM_{2.5}$ National Ambient Air Quality Standards

On July 17, 1997, the U.S. Environmental Protection Agency (EPA) revised the National Ambient Air Quality Standards (NAAQS) for particulate matter (PM). After reviewing peer-reviewed scientific studies, EPA determined that modifications to the existing PM standards were necessary to protect public health and the environment. The new standards applied to air borne particles with a mean aerometric diameter equal to or smaller than 2.5 µm. These small particles, referred to as $PM_{2.5}$, were deemed to be the particles in the air that were of greatest concern in terms of public health. EPA revised the primary, health-based standard by creating a new annual $PM_{2.5}$ standard set at 15 $\mu g/m^3$ and a new 24-hour $PM_{2.5}$ standard set at 65 $\mu g/m^3$.

2.2 $PM_{2.5}$ Nonattainment Areas in the MARAMA Region

At the same time that EPA promulgated the new $PM_{2.5}$ standards, EPA announced new monitoring requirements to support the new standards. EPA established new Federal Reference Methods (FRM) for measuring $PM_{2.5}$ and put in place new criteria for sitting monitors and new procedures for operating monitoring networks and quality assuring the network's data. Soon after, states and local agencies began to establish $PM_{2.5}$ monitoring networks in conformance with EPA requirements. The first $PM_{2.5}$ FRM monitors were in place in 1998. Today, state and local air quality agencies and other organizations operate large networks to monitor $PM_{2.5}$ concentrations in the atmosphere.

Using the data collected in the $PM_{2.5}$ monitoring network, EPA designated areas in the United States that do not meet the NAAQS for $PM_{2.5}$ on December 17, 2004. The designations were based on 2001-2003 data. Because EPA's designations occurred close to the end of 2004, EPA provided states an opportunity to have 2002-2004 data considered in the final designation process. After reviewing certified, quality-assured data for 2002-2004, EPA found that eight areas previously identified as not attaining the $PM_{2.5}$ standards were attaining the standards. Figure 2-1 depicts final designations for $PM_{2.5}$ in the MARAMA Region including the changes that resulted from using 2002-2004 data.

2.3 EPA Region III Support for the Analysis of Speciated $PM_{2.5}$ Data

Given that large areas of the MARAMA Region do not meet national standards fine particles, the air quality agencies in the MARAMA Region were eager to analyze data that would shed light on the problem and provide information to help guide air pollution control strategy development. Analyzing $PM_{2.5}$ speciation data offered an excellent opportunity to study the constituents of fine particles and how particle composition varies season-to-season and place-to-place. It was hoped that understanding the components of $PM_{2.5}$ mass would provide important information about the air pollution sources that contribute to the $PM_{2.5}$ problem. Analysis of speciated $PM_{2.5}$ data could serve as an important part of a state's "weight of evidence" analyses supporting their State Implementation Plan (SIP). With all this in mind, states asked EPA to provide funds to MARAMA to facilitate regional data analysis.

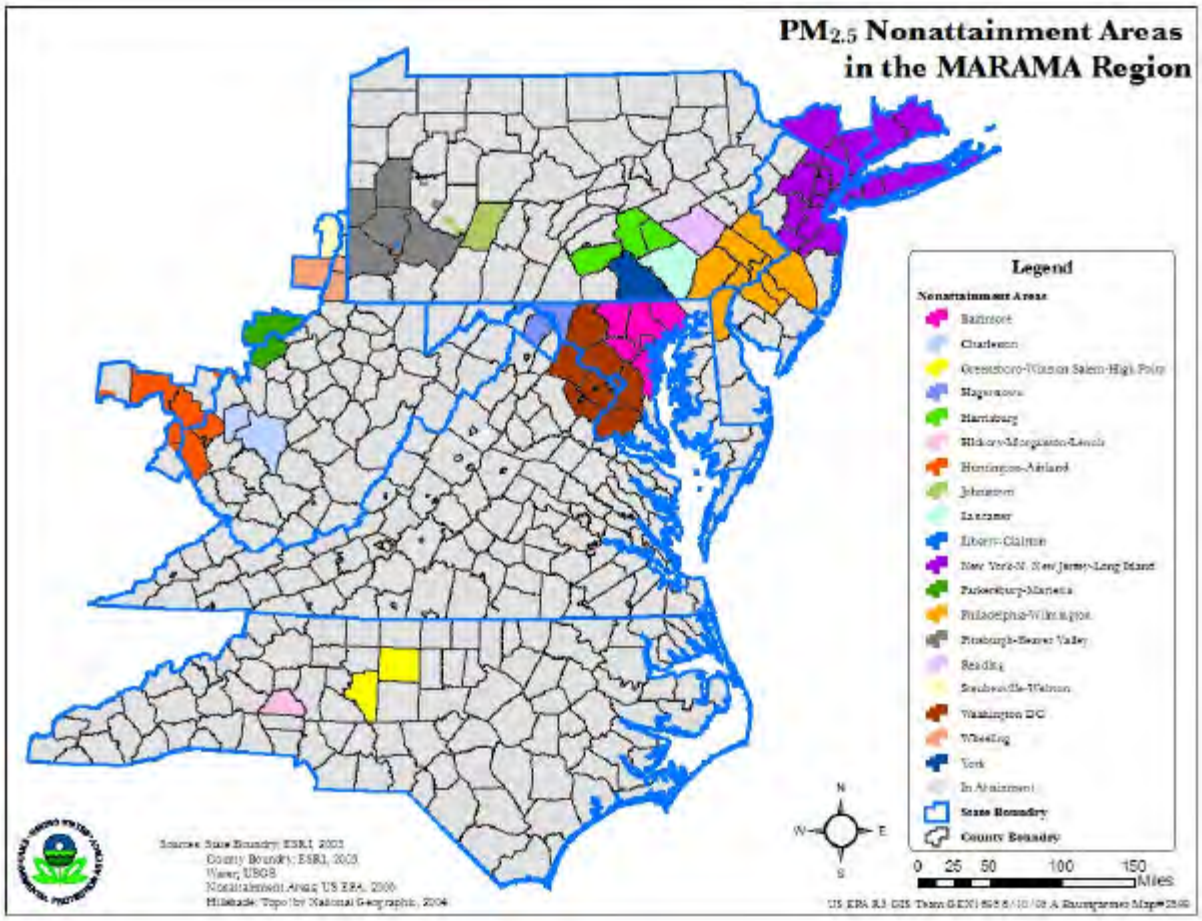

Figure 2-1 $PM_{2.5}$ Nonattainment Areas in the MARAMA Region

On January 19, 2004, EPA Region III awarded MARAMA a grant to complete the development of $PM_{2.5}$ forecasting tools, a task that was already well underway, and to analyze speciated data to support regional efforts to control $PM_{2.5}$ pollution. As grant deliverables, MARAMA committed to:

- Foster and develop analytical capabilities in MARAMA member agencies in order to help agencies make use of their $PM_{2.5}$ data, and
- Analyze $PM_{2.5}$ data to provide monitoring staff, air quality managers, decision makers, and the public with a deeper understanding of $PM_{2.5}$ pollution.

This report provides information to assist MARAMA agencies in analyzing $PM_{2.5}$ data and represents MARAMA's analysis of speciated $PM_{2.5}$ data in the Mid-Atlantic Region, a deliverable of EPA Region III grant number PM-983988-01-0.

2.4 The $PM_{2.5}$ Air Quality Monitoring Network

2.4.1 The State and Local Monitoring Network for Fine Particles in the MARAMA Region

The largest monitoring network for fine particles in the MARAMA Region is operated by state and local air quality agencies. These agencies run an extensive network of FRM monitors, continuous monitors, and speciation monitors. FRM monitors are used to determine an area's compliance with the NAAQS. They collect a sample over 24-hours. They either take a sample

every day or operate on an intermittent schedule of one-in-three days or one-in-six days. As the name implies, continuous monitors continuously measure $PM_{2.5}$ concentration. Typically, they report data on an hourly basis and are used for air quality mapping, reporting air quality levels, air quality forecasting, and other "real-time" applications. Speciation monitors are used by air quality agencies to determine the composition of fine particulate matter. Like FRM monitors, speciation monitors collect a sample over 24-hours. Because of the expense and effort involved in analyzing speciation samples, speciation monitors usually operate on a one-in-three or one-in-six day schedule. Figure 2-2 shows the location of $PM_{2.5}$ FRM and continuous monitors in the MARAMA Region.

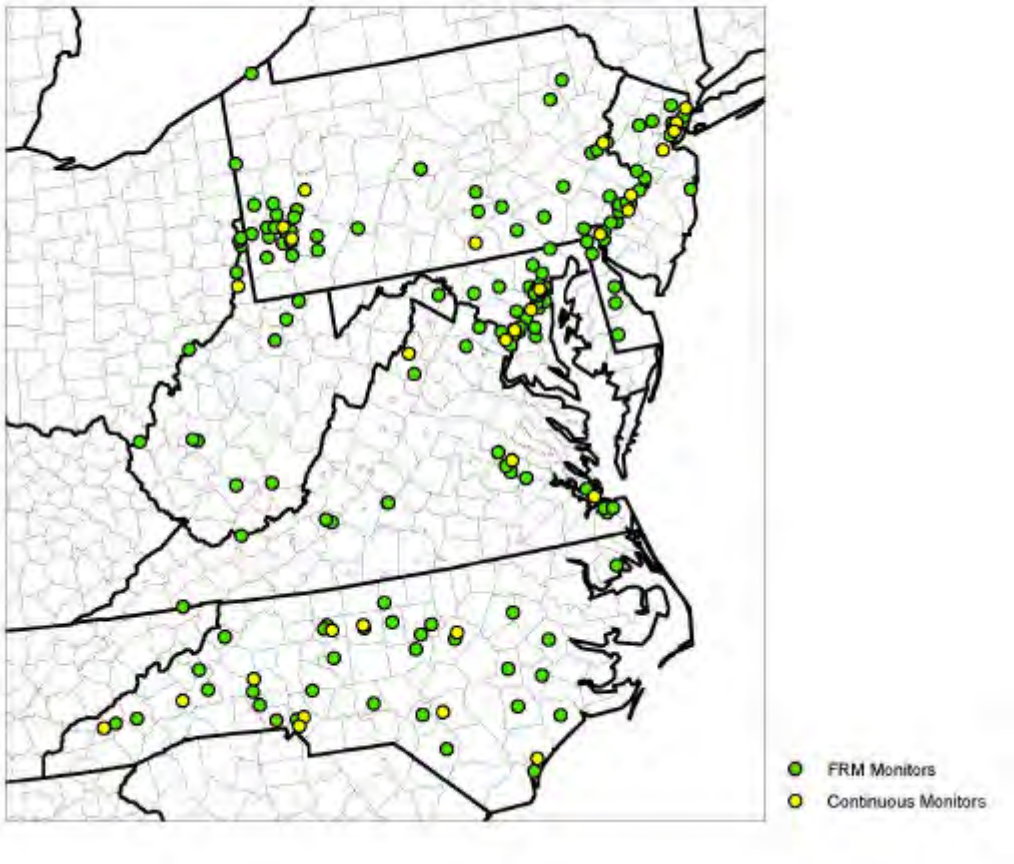

Figure 2-2 FRM and Continuous $PM_{2.5}$ Monitors in the MARAMA Region

2.4.2 Other Fine Particle Monitoring Networks in the MARAMA Region

There are several other monitoring networks in the MARAMA Region that measure fine particles and fine particle species. The Interagency Monitoring of Protected Visual Environments (IMPROVE) program operates monitors that measure visibility in federal Class I areas, which include national parks greater than 6,000 acres, wilderness areas and national memorial parks greater than 5,000 acres, and international parks that existed as of August 1977. IMPROVE monitors identify the chemical species of particles that are responsible for visibility impairment. Through photography, the measurement of optical extinction, and the measurement of particle species, the IMPROVE network tracks regional haze. The IMPROVE program has grown in recent years. Many "IMPROVE Protocol sites" have been established that use

IMPROVE measurement techniques but are not located in Class I areas. Figure 2-3 shows the location of IMPROVE and IMPROVE Protocol sites in the MARAMA Region.

EPA's Clean Air Status and Trends Network (CASTNET) also measures particle species in the MARAMA Region**.** The CASTNET program is designed to monitor trends in regional air quality and atmospheric deposition, provide data and information on how atmospheric pollution is affecting ecosystems, and provide measurements for validating and improving atmospheric models.

In the past, the program was primarily focused on measuring dry acidic deposition and rural ozone. The program is now moving into the continuous measurement of $PM_{2.5}$ species. In Beltsville, MD, CASTNET is testing a prototype instrument that will produce hourly measurements of particle and gaseous species. The CASTNET network is shown in Figure 2-3. While the National Atmospheric Deposition Program (NADP) does not directly measure fine particles in the MARAMA Region, NADP does measure many of the major constituents of particles that are "rained out" in precipitation. The monitoring sites in the NADP program are mapped in Figure 2-3.

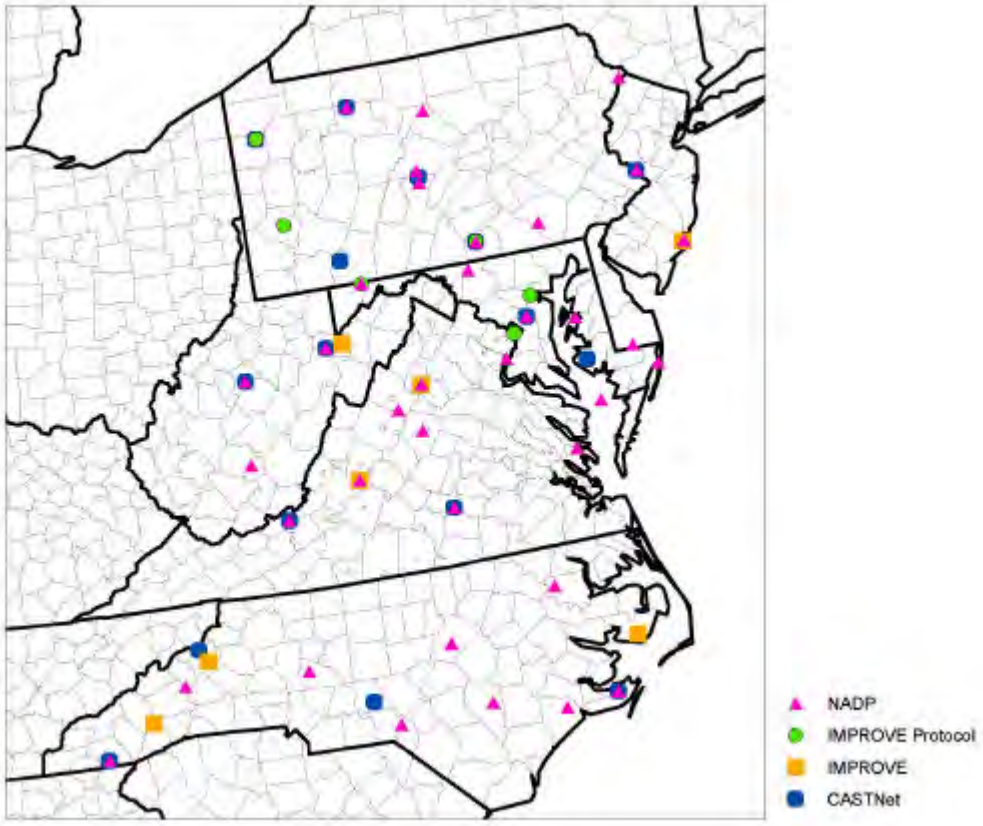

Figure 2-3 IMPROVE, IMPROVE Protocol, CASTNET, and NADP Monitoring Sites in the MARAMA Region

2.5 The $PM_{2.5}$ Speciation Monitoring Program

2.5.1 Objectives and Extent of the Speciation Monitoring Program

EPA established the speciation program after the new $PM_{2.5}$ NAAQS was promulgated to help understand the chemical composition of fine particle pollution. The objectives of the program are to:

- Assess the effectiveness of emission reduction strategies through the characterization of air quality trends,
- Support the development of predictive modeling tools and the application of source apportionment modeling for control strategy development,
- Support programs to improve environmental welfare such as the Regional Haze program, and
- Support health effects and exposure research studies.

The original program called for the establishment of 50 speciation sites that would analyze for various elements and ions. The program has grown and today there are 54 Speciation Trends Network (STN) sites and about 185 supplemental State and Local Air Monitoring Sites (SLAMS) sites. STN and SLAMS sites are very similar operating similar samplers on similar schedules. All STN samplers collect samples every third day. SLAMS samplers operate on either a one-in-three day or one-in-six day schedule. They are synchronized to collect samples on the same days as STN samplers.

2.5.2 Speciation Samplers Operated in the MARAMA Region

Forty-four speciation samplers are operated in the MARAMA Region. Met One SASS™ samplers are operated at 40 sites. Anderson RAAS samplers are operated at four sites in Maryland and Washington, DC. Figure 2-4 shows the location of speciation monitors in MARAMA Region.

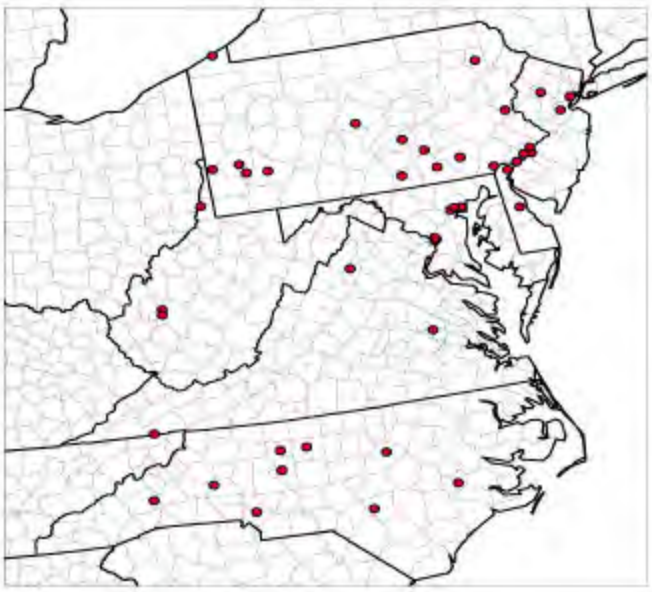

Figure 2-4 Speciation $PM_{2.5}$ Monitors in the MARAMA Region

A Met One SASS™ sampler is shown in Figure 2-5. The unit includes a solar radiation shield and canister collection assembly (shown at top), a control box (shown at center), a tripod, and vacuum pump box (shown at bottom). A disassembled sampling canister for the monitor is shown in Figure 2-6. Figure 2-6 shows the sharp cut cyclone (the device shown at upper right); a magnesium oxide denuder (the sleeve shown at center); three canister screws; two filter cassettes and filter spacer (ring-shaped parts at lower right); and the protective canister (the two parts on far left).

Figure 2-5 Met One SASS™ Monitor. Courtesy of Met One Instruments, Inc.

Figure 2-6 Disassembled Met One SASS canister. Courtesy of Met One Instruments, Inc.

On a sample day, a speciation sampler runs from midnight to midnight local time. In the MARAMA Region, a "sample" consists of three filters. A nylon filter collects particulate matter for the analysis of ammonium, nitrate, sulfate, potassium, and sodium ions. A quartz filter collects material for elemental and organic carbon analysis. A Teflon filter is used to measure total mass and to collect material for the analysis of elements collected over the 24-hour sampling period. Table 2-1 summarizes information about the three filters used in speciation samplers and the analyses performed on these filters.

Table 2-1 Speciation Filters, Analytes, Analytical Method and Number of Species

Filter	Analyte	Analytical Method	Number of Species
Nylon	Ammonium, Potassium, Sodium, Nitrate, Sulfate	Ion Chromatography	5
Quartz	Elemental and Organic Carbon	Thermal Optical Transmittance	7[1]
Teflon	Elements and Total Mass	Energy Dispersive X-Ray Fluorescence and Gravimetric Mass	49

[1] Includes elemental carbon, organic carbon, four organic carbon fractions, and pyrolyzed carbon. See Appendix A.

As one can see from Table 2-1, a single sampling day can produce data for about 61 different analytes. These data, amassed over years, serve as the input data for source apportionment studies and other analyses of fine particulate matter. Appendix A provides a complete annotated list of all of the analytes in EPA's chemical speciation program.

2.6 Selection of Monitors for the Analysis

The speciation program generates large and complex data. A single speciation monitor can generate 7,442 observations per year for 61 species or analytes (see Appendix A for a complete list of speciation analytes). The raw data needs to be quality assured and in some cases adjusted before it can be used in comparative analyses. Given the large and complex nature of the data and the limited resources available for analyzing these data, MARAMA and MARAMA members chose to analyze the data from eleven monitors in the speciation network. The monitors chosen for this analysis are listed in Table 2-2.

Table 2-2 Monitors Selected for the MARAMA $PM_{2.5}$ Speciation Data Analysis Project

AIRS Site ID	Site Name (City)	County Name	Date Monitoring Started	Date Monitoring Ended	Collection Frequency	Make	Model
Allegheny Co.							
420030008	Lawrenceville (Pittsburgh)	Allegheny	06/30/01		3	Met One	SASS
Delaware							
100010003	Dover	Kent	02/11/99		6	Met-One	SASS
100032004	MLK Jr. Avenue (Wilmington)	New Castle	02/14/99		6	Met-One	SASS
Washington, DC							
110010043	McMillan Reservoir	Washington, DC	03/26/01		3	Andersen	RAAS-401
Maryland							
240053001	Essex (Baltimore)	Baltimore	10/01/00		3	Andersen	RAAS-401
New Jersey							
340390004	Elizabeth Laboratory (Elizabeth)	Union	05/13/01		3	Met-One	SASS
North Carolina							
371190041	Garinger H.S. (Charlotte)	Mecklenburg	10/01/00		3	Met-One	SASS
371070004	Kinston	Lenoir	01/01/02		6	Met-One	SASS
Pennsylvania							
420010001	Arendtsville	Adams	07/01/01		6	Met-One	SASS
Philadelphia							
421010004	Air Mgt. Services (AMS) Laboratory	Philadelphia	02/04/99		3	Met-One	SASS
Virginia							
517600020	DEQ Monitoring Office	Richmond	03/02/01	12/26/03	3	Met-One	SASS

The following general criteria were used to select monitors for inclusion in this analysis:

- Select at least one monitor in each of MARAMA's ten member jurisdictions
- Provide good geographical coverage (good spatial distribution of monitors) across the MARAMA Region,
- Analyze monitoring data in nonattainment areas,
- Include at least some "rural" monitors and
- Ensure monitors analyzed have adequate data records.

In some cases, all of these criteria could not be completely met. For example, a West Virginia speciation monitor could not be included in the regional analysis found in this report because speciation monitoring only began in West Virginia in late 2003. The short data record for West Virginia monitors precluded them from being used in regional comparisons that were based on 2001 to 2003 data.

Since the speciation program is primarily an urban air monitoring network, there are very few rural monitors in the MARAMA Region. Some speciation monitors have been put in place in rural areas, however. The monitors at Luray Caverns, VA and State College, PA are good examples. In most cases, however, the data record for rural speciation monitors in the Region was too short for use in this analysis. There are rural IMPROVE and rural IMPROVE Protocol monitors in the Region. If care is exercised, speciation data from IMPROVE monitors can be compared with speciation data collected by state and local agencies. While these comparisons are possible, they were not made in this analysis.

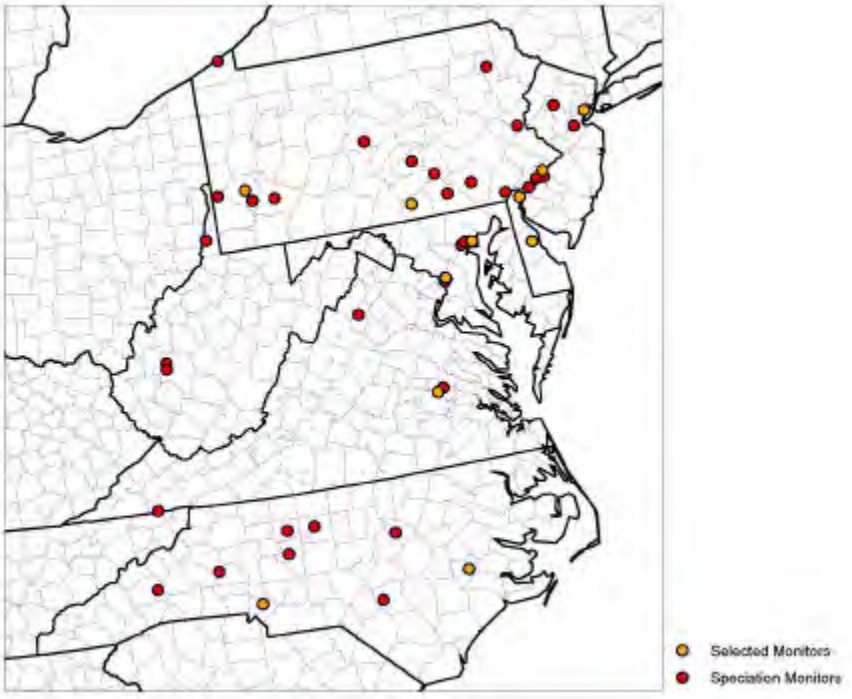

Figure 2-7 Selected and Non-Selected Speciation $PM_{2.5}$ Monitors in the MARAMA Region

In spite of the limitations mentioned above, MARAMA and MARAMA members were able to identify a collection of urban and rural monitors that were well distributed geographically across

the Region and provided data for many nonattainment areas. The monitors selected are mapped in Figure 2-7.

2.7 The Episodic Nature of $PM_{2.5}$ Pollution

From prior work in developing air quality forecasting tools that predicted $PM_{2.5}$ concentrations, MARAMA was aware that $PM_{2.5}$ concentrations often rise and fall sympathetically across much of the MARAMA Region. An example of this behavior is shown in Figure 2-8, a time series plot of twenty-two FRM monitors that measured $PM_{2.5}$ mass every day from April through June 2003. As one would expect over such a wide area, monitors in different locations did not always measure the same or similar mass concentration on a given day. What is surprising, however, is how often monitors in different locations did in fact measure the same or similar mass concentration on a given day. The episode in late June 2003 shown in Figure 2-8 is a case in point when all 22 monitors in the region rose to concentrations above 38 $\mu g/m^3$ during a large scale ammonium sulfate event. Appendix B provides a time series covering the period from January 1, 2001 through December 31, 2003. As the extended time series in the Appendix shows, there were many periods when monitors across the region rose and fell together.

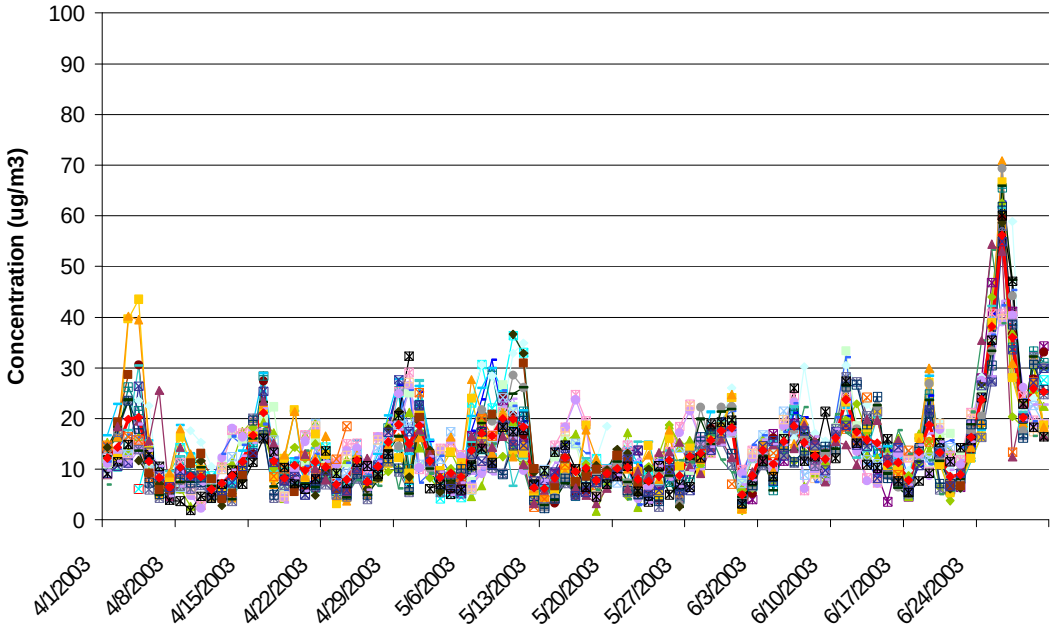

Figure 2-8 April – June 2003 Time Series, 22 FRM Monitors in the MARAMA Region

Initially, MARAMA planned to analyze a few "clean" episodes when $PM_{2.5}$ mass concentrations were low and a few "dirty" episodes when $PM_{2.5}$ mass concentrations were high in the region. As MARAMA began addressing the complexities of processing and adjusting the speciation data from eleven monitoring sites, it became clear that an analysis of episodes would be outside the scope of the current project. Episode analysis work could and should be done, however. For example, it would be interesting to know what meteorological regimes and air pollution source regions are involved when $PM_{2.5}$ mass concentrations are high and low. The back trajectory

analyses included in each site-analysis in this report provide some initial insights as to which source regions are involved on high and low $PM_{2.5}$ days at a particular monitoring site.

3 Methodology and Data Handling Techniques for Speciation Data

Today, EPA Region III spends about $1 million per year funding state and local speciation monitoring programs. Nationally, EPA has spent about $50 million on the speciation program since its inception. State and local agencies have also spent large amounts of time and money on the program. In short, large amounts of resources have been spent implementing and operating the speciation program.

The complex nature of the speciation data has been an impediment to wide scale use of speciation data. Recognizing that EPA and state agencies spend large amounts of money collecting speciation data, and that scientists, health researchers, and the air quality community need speciated data for their work and analyses, MARAMA developed a step-by-step guide that helps analysts access and use speciation data. By summarizing the data handling techniques needed to access and process speciation data, MARAMA hoped to make the data more accessible and foster the data's use in air quality analyses. The following paragraphs provide a straightforward, step-by-step guide to speciation data. The paragraphs describe in detail how to access, process, and use speciation data.

3.1 Where Speciation Data can be Obtained

$PM_{2.5}$ speciation data is available from three main sources: EPA's AQS database, files posted on an EPA web site, and through state and local agencies. Speciation data can be obtained directly from EPA's Air Quality System (AQS) if one has access to this enormous database. Access to AQS is provided through the Information Management Group of EPA's Office of Air Quality Planning and Standards (OAQPS) or through EPA regional offices. In general, access to AQS is restricted to registered users who upload and process raw AQS data. The general public, scientists, and researcher are usually not granted access to AQS because of the load this large number of users would place on the system. In July 2006 however, EPA plans to open an AQS "Data Mart" which will make large amounts of AQS data available to the general public. For more information on the AQS Data Mart see: http://www.epa.gov/ttn/airs/aqsdatamart/. Before the Data Mart opens, speciation data and other AQS data can be requested directly from EPA without becoming a registered user of AQS. Data requests can be submitted on-line at: http://www.epa.gov/ttn/airs/airsaqs/detaildata/datarequest.html.

Files posted on the Internet offer a second way to access speciation data. EPA has compiled raw speciation data from AQS in large data files that can be downloaded from EPA's Technology Transfer Network (TTN). Speciation and a wealth of other data can be downloaded from: http://www.epa.gov/ttn/airs/airsaqs/detaildata/downloadaqsdata.htm. On this web site, speciation data is found in the row of data marked, "PM Fine Speciation[2, 3] RD_501_SPEC_yyyy.ZIP." In the row, EPA has posted files for 2000 through 2005. Current year data files are incomplete because there is a time lag between the date a field measurement is made and the date the data is uploaded to AQS or posted on EPA's website. Speciation data files from the EPA web site can be quite large, sometimes as large as 100 MB. Section 3.2 below describes how to open and process these large files.

MARAMA has also posted speciation data on its web site. On MARAMA's website, data is available for eleven monitoring sites in the MARAMA Region. Reformatted, "user-friendly" speciation datasets are available under the heading, "MARAMA's Particulate Matter ($PM_{2.5}$) Data Analysis Project" on MARAMA's "Projects" web page at: http://www.marama.org/Projects/.

A third way to obtain speciated data is through state and local air quality agencies. Contact information for your state or local air quality agency is available from the State and Territorial Air Pollution Program Administrators (STAPPA) and the Association of Local Air Pollution Control Officials (ALAPCO) at: http://www.4cleanair.org/.

3.2 Processing Speciation Data

3.2.1 Obtaining Speciation Data Directly from the AQS Database

If you have access to EPA's AQS database, you will find it provides easy access to speciation data. AQS allows a user to download data by monitor, which makes for smaller more manageable data files than those posted on EPA's TTN web site. AQS will also allow a user to download data for a date range, not just a single year, which is a timesaver for many users. The file format for an AQS query will be exactly the same as the files downloaded from EPA's website. To obtain speciation data from AQS, run a query to "Extract Raw Data", report code "AMP 501." In the monitor selection window, input the AIRS number for the monitor, the date range, the POC code. Under the "Pollutant Type" select "Speciation". If you select output in a text file, the file generated by AQS can be imported directly into Microsoft Excel as a pipe delimited (|) data file.

3.2.2 Downloading "Zipped" Data Files from EPA's TTN Web Site

If you do not have access to EPA AQS database, you can obtain speciation data from EPA's TTN website. Go to: http://www.epa.gov/ttn/airs/airsaqs/detaildata/downloadaqsdata.htm. On this page you will find a table of files organized by year and type data. Each file in the table is a detailed raw data file extracted from the AQS database. For speciation data, locate the row marked, "PM Fine Speciation[2, 3] RD_501_SPEC_yyyy.ZIP." In this row you will find speciation data files for 2000 through 2005, one data file per column. The most recent year is marked "SPEC 2005." The files contain data for every speciation monitor in the United States and every analyte measured at those monitors for every sample day in that year. Select the years you wish to analyze and download these files to your computer.

3.2.3 "Unzipping" Downloaded Files and Importing Data into Microsoft Access

The file you download from the TTN will be a text file in "zipped" (compressed) format. Use WinZip or another zip program to unzip (decompress) it. See www.winzip.com. If you are operating in a Microsoft Office environment and have the full suite of Microsoft programs, you can import the downloaded, unzipped text file into Microsoft Access. Importing the file directly into Microsoft Excel would save a step, but Excel has an internal limit of 65,536 rows of data and a full year of speciation data from the TTN website will exceed that number of rows. In Access, import the "pipe delimited" ("|") text file using Access's "Import" feature. The file is now ready to be filtered for your specific needs.

The first row of the imported Access file is a "column header row" that contains field names/descriptions for each of the records in the file. Each row under the header row is a data record. Specific monitoring sites can be identified by their AIRS code. The AIRS code is a nine-digit numeric code that combines the two-digit state code, the three-digit county code, and the four-digit site ID for the monitoring site. A full list of state and county codes is available from: http://www.epa.gov/ttn/airs/airsaqs/manuals/StateandCountyCodes.htm to help you identify states and counties of interest.

In Access, filters for the state or specific monitoring site you wish to analyze. After the filtering process, copy all rows and columns from the filtered database and paste them into a Microsoft Excel workbook. If you selected all the data for a particular state in Access, you can filter again in Microsoft Excel for a specific monitor by filtering on the fields: State Code, County Code, and Site ID.

3.2.4 Filtering for the Correct POC Code and Parameter Codes

Each data file from the TTN contains not only speciation data but also $PM_{2.5}$ Federal Reference Method (FRM) data and continuous $PM_{2.5}$ data, if data for those monitors was collected at the site. To select only speciated data, filter the Excel data for Parameter Occurrence Code ("POC code") five. This should result in daily measurement data with a variety of parameter codes including the codes between 88101 and 88403, the speciation data. Parameter codes are numeric codes that indicate the specie being measured. For example, the parameter code for sulfate is 88403. For a complete list of parameter codes, see: http://www.epa.gov/ttn/airs/airsaqs/manuals/parmcodesbyclasscode.htm#SPECIATION.

Caution must be exercised when filtering the data by POC code. In some cases, speciation data has been assigned POC code three or six or some other number. Data assigned POC code one or two are usually $PM_{2.5}$ FRM data. POC code three data is usually continuous $PM_{2.5}$ data. In any case, speciation data can be identified as data:

- Obtained over a 24-hour period,
- On either a 1-in-3 or 1-in-6 day sampling schedule, and
- With parameter codes from 88101 (total $PM_{2.5}$ mass) through 88403 (sulfate).

Once the correct POC code has been identified and the Excel spreadsheet has been filtered for this POC code, the data can be filtered for the correct Parameter Codes. Filter the Parameter Codes for values greater than or equal to 88101 to select all the analytes in the speciation program. This will remove meteorological data, Parameter Codes 68103 to 68108, associated with the POC code you selected. At this point, the dataset is filtered by: State Code, County Code, Site ID, POC Code and Parameter Code.

3.2.5 Handling Null and Flagged Data

The data obtained from the EPA web site or AQS will contain null and flagged records. Null data are records with no sample value recorded. Flagged data are data that are special in some way and are assigned a qualifier code to denote what is special about this observation. Null Data Codes and Qualifiers (flags) are fields in the dataset that appear as columns to the right of the dataset's sample values. An explanation of Null Value Codes is provided in Table B.10.9 on page 81 of *Volume I, Quality Assurance Project Plan, Chemical Speciation of $PM_{2.5}$ Filter Samples*. This important document, the QAPP for the speciation program, is available at: http://www.epa.gov/ttn/amtic/specguid.html. Null Data Codes explain why data values are missing for a record. Research Triangle Institute, Inc. (RTI), the laboratory analyzing speciation samples, assigns Null Data Codes based on information received from the monitoring agency that provided the sample.

Qualifiers (flags) are explained in Table B.10.8 on page 80 of the QAPP. Flags provide additional information about a measurement. Many flags describe special circumstances associated with a measurement (high winds, volcanic eruptions, sandblasting, forest fire, etc.) Other flags give some indication why a sample should be considered invalid for example, "flow range average out of specification." Some flags are vague, for example "outlier – cause

unknown" and provide little guidance as to whether to include or exclude a data point in an analysis.

Flags are assigned to the data by RTI and the state and local agencies. Flags may be generated at any stage in the process of taking, analyzing, and quality-assuring a sample. A flag can be generated by sampler equipment, the field technician servicing the sampler, lab staff inspecting incoming samples, lab staff performing chemical analyses, and lab staff performing "Level 0" and "Level 1" data validation checks. The data validation process and the assignment of flags are described in detail in the RTI publication, *"Data Validation Process for the $PM_{2.5}$ Chemical Speciation Network"* which is available at: http://www.epa.gov/ttn/amtic/specdat.html. Many flags found in speciated data are generated during Level 1 data validation checks when mass balance and ion ratio checks are performed. For a look at the flag structure of the data used in this report, see Appendix C.

In the datasets posted on MARAMA's web site and in the data used in preparing this report, null values (missing data) and flagged data have been removed. While some valid data may have been excluded by removing flagged data, removing flagged data from consideration seemed the prudent thing to do given that the amount of data removed from consideration was small and that there was no straightforward method to determine which flagged data should be retained or excluded.

If you determine you would like to remove null and flagged data in the dataset you are preparing, filter the Null Data Code field for and the Qualifier (flag) fields for non-blanks and delete these data.

3.2.6 Pivoting the Data

While analyses can be performed on the filtered dataset described above, many analysts like to take the dataset one step further that makes the data even more user friendly. In this step, the filtered data is rearranged or "pivoted" into a new collection of columns ordered by date. Excel's pivot table feature easily accomplishes this task. In Excel's "Data" menu, select "PivotTable and PivotChart Report." When pivoting the filtered data, click, drag, and drop:

- The "Dates" field where Excel says "Drop Row Fields Here"
- The "POC" and "Parameter Code" fields where Excel says "Drop Column Fields Here", and
- The "Sample Value" field in the "Drop Data Items Here" area.

The resulting table, organized by date and parameter, makes a good "working dataset" that can be used to easily draw time series and reconstruct total PM mass from mass constituents.

3.2.7 Blank Correcting Organic Carbon Measurements

Measuring organic carbon aerosol is technically challenging. It is challenging because of the large number of compounds being measured, the changing physical conditions that occur during typical sampling periods (changing temperature and relative humidity, for example), gas phase/solid phase dynamics, and many other factors.

When organic carbon aerosol is measured in the sampling equipment deployed in the speciation network, there can be both positive and negative sampling biases. These biases are frequently referred to as "sampling artifacts." Sampling artifacts are a function of:

- Volatile organic compound or semi-volatile organic compound concentration or specie,
- Temperature,
- Relative humidity,
- Filter lot, filter preparation, filter storage, or filter handling,
- Sampler flow rate, and
- Other variables.

Positive artifacts occur when sample filters adsorb organic carbon gases and these gases add mass to the organic carbon particulate matter mass measurement. Negative artifacts occur when particulate matter on a sample filter volatilizes and is lost before weighing (Solomon, 2004).

Sophisticated techniques can be used to evaluate organic carbon artifacts, but these techniques are usually employed in research settings. These techniques utilize back up filters, parallel sampling ports and additional filters, and denuders. These techniques are not employed in the speciation network.

To help correct for positive artifacts in the STN/SLAM speciation network, organic carbon measurements made by the network should be "blank corrected." While blank correcting does not resolve all the issues associated with organic carbon artifacts, it does compensate for the organic carbon found on field and trip blanks.

Field blanks are filters that are taken to a monitoring site by a field technician. They are placed in the sampler briefly and then removed and sent to the analytical lab for analysis. Field blanks attempt to measure contamination and measurement artifacts associated with shipping and field handling. Trip blanks are handled in similar fashion except they are not placed in the sampler. They are simply taken into the field to a monitoring site and then sent on to a lab for analyses. Trip blanks attempt to measure contamination and measurement artifacts associated with shipping. The field and trip blanks for organic carbon used in the STN/SLAM speciation network are usually positive. That is, un-sampled field and trip filters contain measurable amounts of organic carbon. This un-sampled amount of organic carbon mass must be subtracted from measurements to improve the accuracy of these measurements. Organic carbon blank values vary across the various samplers in the speciation program (Anderson, Met One, Rupprecht & Patashnick, and URG). They also vary over time.

There are several methods for blank correcting organic carbon measurements. Two approaches are frequently commonly applied. Tolocka et al. and more recently Kim et al. (Tolocka et al., 2001; Kim et al., 2005) have demonstrated the regression technique where linear regression is applied to total $PM_{2.5}$ mass data and speciated organic carbon data. Total mass measurements are plotted on the x-axis and speciated organic carbon measurements are plotted on the y-axis. The y-intercept, the value of organic carbon when total mass is zero, is an estimate of the organic carbon blank. A typical regression plot for Charlotte, NC is shown in Figure 3-1. After the estimated carbon blank is determined by regression, this value is subtracted from actual measurements to blank correct the data. The regression approach generally produces good results and is the only method available if organic carbon blank data are not available. Since the approach relies on linear regression for its result, the usual cautions associated with linear regression apply (Neter, et al., 1996).

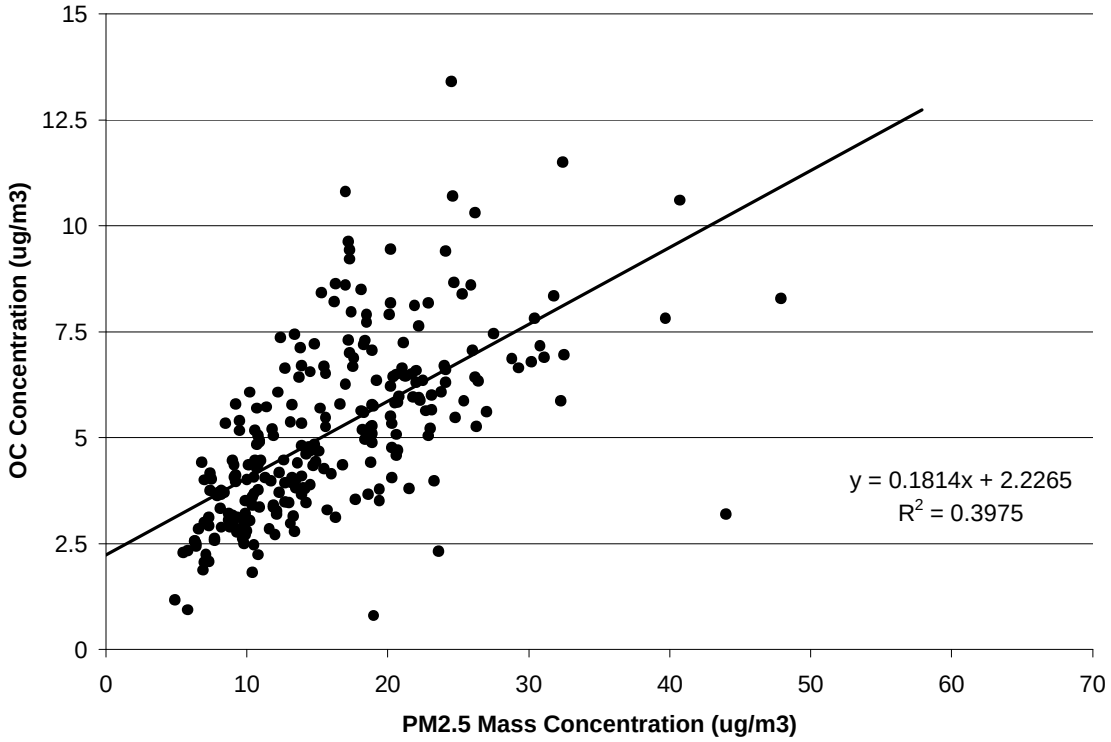

Figure 3-1 Example of an Organic Carbon vs. $PM_{2.5}$ Mass Concentration Plot (Charlotte, NC)

Another method of blank correcting organic carbon data involves averaging organic carbon blanks over time. This straightforward technique has the advantage of being based on actual blank measurements. When applying this technique, it is a good idea to plot organic blank values over time. Time series plots provide important "history" on blank levels, reveal trends if present, give a sense of the variability of the blank data, and provide an opportunity to identify extreme or possibly extraneous values. A typical time series plot is shown in Figure 3-2.

MARAMA plotted organic carbon blank values over time for each site, analyzed these plots, and calculated the average organic carbon blank for the site. The average blank value was subtracted from the organic carbon data for the site. To provide some sense of the variability of organic carbon blanks, time series plots of blank values for each sampling site are presented in Appendix D.

In the early years of the speciation program, blank data were not posted in EPA's AQS database. Starting in July of 2004, Research Triangle Institute, Inc., EPA's speciation contractor, began posting blank data for all analytes in the speciation program in the AQS database. Blank data for measurements made before July 2004 will be "backfilled" in AQS at some future date. The blank data MARAMA used in this analysis was obtained directly from RTI.

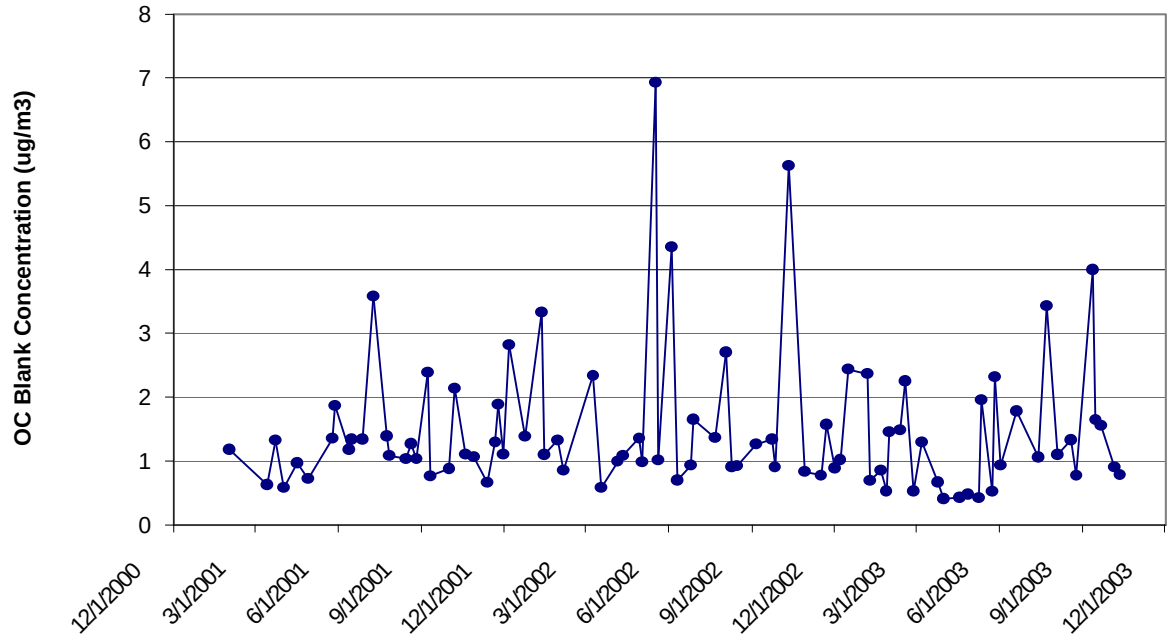

Figure 3-2 An Example of a Time Series plot for Organic Carbon Blanks (Charlotte, NC)

Since the regression technique and the blank averaging technique are viable methods of estimating organic blank concentrations, MARAMA compared the two methods at five sites. Table 3-1 compares the organic carbon blank values obtained from the two approaches.

Table 3-1 Comparison of Organic Carbon Blank Values from the Regression and Average Blank Approaches

			Regression Approach		Averaging Approach
AIRS Site Number	**Site**	**County, State**	**Y-Intercept/ OC Blank (µg/m^3)**	**R^2**	**OC Blank (µg/m^3)**
420030008	Lawrenceville	Allegheny, PA	1.97	0.50	1.22
371190041	Charlotte	Mecklenburg, NC	2.23	0.40	1.47
371070004	Kinston	Lenoir, NC	0.25	0.73	1.49
340390004	Elizabeth	Union, NJ	2.45	0.59	1.41
420010001	Arendtsville	Adams, PA	1.56	0.67	1.24
Average			1.64		1.33
Std. Dev.			0.79		0.14

The average organic carbon blank value, averaged across all sites and seasons, was 1.27 µg/m^3. The average seasonal organic carbon blank, averaged across all sites, was highest in the summer at about 1.36 µg/m^3 and lowest in the spring at 1.19 µg/m^3. Many sites did not behave like the regional average, however. Six sites, for example, had their highest blank levels in the winter and fall. The highest average blank value, averaged over the study period, was measured at Charlotte, NC at 1.56 µg/m^3; the lowest blank value was measured at Baltimore, MD at 0.94

µg/m^3. MARAMA applied average, site-specific organic carbon blank corrections in its calculations. Applying season-specific blank corrections would have improved the accuracy of organic carbon mass estimates, but this refinement was not pursued given the large uncertainties associated with assigning an OM/OC ratio to the organic carbon data.

After consultation with RTI, MARAMA decided it was not appropriate to blank correct elemental carbon measurements. RTI believed there was little chance blanks would be contaminated with elemental carbon. Perhaps more importantly, prior to a software upgrade to lab equipment in the fall of 2003, some organic carbon in the TOT analysis of field and trip blanks was being mistakenly assigned to elemental carbon. As a result, elemental carbon blanks during the period of this study may actually represent small amounts (about 0.1 µg/m^3) of organic carbon, not elemental carbon. Fortunately, the incorrect assignment of organic carbon as elemental carbon occurred only in the analysis of blanks.

3.2.8 Converting Blank Values from Units of µg/filter to Units of µg/m^3

Blank data obtained from the AQS database or RTI are in units of µg/filter. Before these data can be averaged and applied to actual measurements, they need to be converted from units of µg/filter to units of concentration (µg/m^3). Conversions are a function of flow rate and vary between samplers. The conversion equation below is for a Met One SASS Speciation sampler with a flow rate of 6.7 liters per minute. The Met One SASS sampler is by far the most frequently used sampler in the MARAMA Region. Conversions from units of µg/filter to units of concentration (µg/m^3) can be made for other samplers, if the sampler's flow rate is known.

$$\frac{\mu g}{meters^3} = \frac{\mu g}{filter} \times \frac{1}{6.7\ liters/minute} \times \frac{1}{1{,}440\ minutes} \times \frac{1{,}000\ liters}{meters^3}$$

3.2.9 Reconstructing $PM_{2.5}$ Mass

3.2.9.1 The Equations for Reconstructing Mass

Reconstructing $PM_{2.5}$ mass from its component parts is an important part of the analysis of speciated data. Comparing reconstructed mass (RCM) values to measured total mass, either measured by the speciation monitor or a collocated FRM monitor, provides a good quality-assurance check of the mass data from the site. Calculating reconstructed mass through mass balance techniques provides important information about the types of species measured at the site and their relative importance in terms of their contribution to total mass.

To calculate reconstructed mass, MARAMA used a modified version of the "traditional" reconstructed mass equation developed by the Desert Research Institutes (Tropp, 2004). DRI's traditional equation is shown below.

DRI Traditional Reconstructed Mass Equation

1. Unidentified Material	= Measured Mass - Reconstructed Mass
2. Geological	= 1.89*Al + 2.4*Si + 1.4*Ca + 1.43*Fe
3. Organics	= 1.2*Organic Carbon
4. Soot	= Elemental Carbon
5. Nitrate	= Nitrate
6. Sulfate	= Sulfate
7. Ammonium	= Ammonium
8. Salt	= 1.65*Cl
9. Trace Elements	= S(XRF Measured Species) - (Al+Si+Ca+Fe+S+Cl)
10. Reconstructed Mass	= S(Items 2-9)

In the equation, "Measured Mass" is the total mass as measured gravimetrically by the speciation monitor. Reconstructed Mass is the sum of items 2 through 9. The chemical symbols in the equations represent the measured concentrations of these chemical species from the lab analysis of the sample filters. The constants in the geological equation estimate the mass associated with soil or windblown dust. The constants estimate the mass of "typical" U.S. soil: average AlO/AlO_2, SiO_2, CaO, and FeO/FeO_2 concentration. The factor 1.2 for organic carbon is the Organic Mass to Organic Carbon OM/OC ratio. This ratio coverts the organic carbon value from the speciation dataset into an estimate of organic carbon mass concentration. The factor 1.65 for salt estimates the presence of sodium chloride from the XRF chlorine measurement. Finally, the "Trace Elements" is a summation of all the elemental substances measured by XRF less the trace elements already accounted for in other constituent calculations.

3.2.9.2 A Modified Equation for the Geological Component of $PM_{2.5}$ Mass

Because aluminum measurements are often less than the minimum detection limit (MDL) of the x-ray fluorescence equipment used in the chemical speciation program, analysts have suggested an alternative equation for estimating the geological component of reconstructed $PM_{2.5}$ mass (Frank, 2005 and Poirot, 2001). The alternative equation does not rely on aluminum measurements. Instead, it uses factors for silicon, calcium, iron and titanium to estimate the geological component of $PM_{2.5}$ mass. Using the alternative equation for geological material proved to be a good solution since MARAMA found, like others, that aluminum measurements were often zero or beneath the XRF's MDL. In the datasets MARAMA examined, about 80 percent of aluminum measurements were beneath the MDL. Using the alternative equation for the geological component of $PM_{2.5}$ mass did increase the amount of mass allocated to this mass fraction by about 40 percent. While this is a large increase, the increase was small in relative terms when considering total mass. Since the geological component of $PM_{2.5}$ mass is quite small in the MARAMA Region, increasing the size of the geological component by about 40 percent made little difference in the contribution the major species make to total mass. It should be noted that the equation for the geological component of $PM_{2.5}$ mass is an estimate of the soil component that assumes that all of the silicon, calcium, iron and titanium found in the sample are associated with soil or crustal material. While this assumption may be reasonable for rural sites, it may not be a reasonable assumption for urban sites where iron or other "soil" elements may be emitted from non-soil sources. As a result, estimates of the geological component of $PM_{2.5}$ mass, especially in urban areas, should be viewed as just that, estimates.

3.2.9.3 Increasing the OM/OC Ratio from 1.2 to 1.6

In addition to the refinement for the geological component, MARAMA also applied a larger OM/OC ratio in calculations that estimate organic carbon mass than the one used in early reconstruction equations. Work by Dr. Barbara Turpin (Turpin, 2001) and recent research suggested that the OM/OC ratio used in early mass reconstruction equations, 1.2, was too low for correctly estimating organic carbon mass (El-Zanan et al., 2005; Polidori, 2005; Zhang, 2005). A literature search revealed that much higher values were being measured or estimated for the OM/OC ratio. Dr. Andrea Polidori, when he was a doctoral student at Rutgers University, determined the OM/OC ratio for a site in downtown Pittsburgh to be 1.91 +/- 0.24 (1s), if only extractable organic carbon was considered in calculating the OM/OC ratio. If both extractable and non-extractable organic carbon were used to calculate the OM/OC ratio, the 13-month average OM/OC ratio was 2.05 +/- 0.18. Dr. Polidori's OM/OC ratio determinations were based on July 2001 to July 2002 sample data. Q. Zhang et al. independently calculated an OM/OC ratio of 1.8 for submicron organic aerosol in Pittsburgh using data from September 2002.

In estimating organic carbon mass for the sites in this analysis, MARAMA was faced with the dilemma of selecting the best possible OM/OC ratio for these sites knowing that these ratios vary site-by-site, season-to-season, even measurement-to-measurement. Site-specific OM/OC ratios had not been determined for sites examined in this analysis, although Dr. Polidori had determined an OM/OC ratio for a site in Pittsburgh not far from the Lawrenceville monitoring site.

After reviewing technical papers on the measurement of organic carbon aerosol, consulting researchers, and conducting a sensitivity analysis, MARAMA chose to use an OM/OC ratio of 1.6 for all sites because:

- 1.6 is viewed as a good estimate of the OM/OC ratio at urban sites (Turpin, 2001) and most sites analyzed in this report are urban sites,
- 1.6 yielded better mass closure than higher ratios at urban sites, and many urban sites are of special interest to MARAMA members since some of these sites violate the $PM_{2.5}$ annual NAAQS, and
- Using the same OM/OC ratio at all sites provided insight as to what the actual OM/OC ratio might be if it were experimentally determined.

While applying an OM/OC ratio of 1.6 to organic carbon data allows qualitative comparisons between monitoring sites, it is important to remember that organic carbon mass concentrations presented in this report are estimates of actual concentrations. To more accurately estimate organic carbon measurements at any particular site, site-specific OM/OC ratios would have to be determined for that site. Site-specific OM/OC ratios are determined experimentally by extracting and measuring the organic compounds deposited on sample filters. This has not been done for the sites analyzed in this report.

In a sensitivity analysis, MARAMA explored the application of OM/OC ratios of 1.6 and 1.9 at the sites studied. An OM/OC ratio of 1.6 was thought to be a good estimate of urban organic aerosol (Turpin, 2001). An OM/OC ratio of 1.9 was measured at one site within the region (Polidori, 2005) and was a potential estimate of "reasonably aged" organic aerosol that might approximate the OM/OC ratio at many monitoring sites in the MARAMA Region.

Tables 3-2 and 3-3 show that the mass closure achieved by applying different OM/OC ratios to a site's data was site dependent. A ratio of 1.6 produced better mass closure than 1.9 at urban sites like Baltimore, MD, Elizabeth, NJ, Philadelphia, PA, Pittsburgh, PA, Richmond, VA, Washington, DC, and Wilmington, DE. A ratio of 1.9 resulted in better mass closure than 1.6 at rural sites like Arendtville, PA, Dover, DE, Kinston, NC. As research has shown, larger OM/OC ratios need to be applied at rural sites where "aged organic aerosol" (higher molecular weight aerosol) is present. (Turpin, 2001; Kiss et al., 2002; Russell, 2003; El-Zanan et al., 2005; Reff, 2005; Takegawa et al., 2005). Surprisingly, a ratio of 1.9 also produced good mass closure in urban Charlotte, NC.

Tables 3-4 and 3-5 show results of the sensitivity analysis applied to just the urban sites analyzed. Considering just the urban sites, an OM/OC ratio of 1.6 underestimates gravimetric mass by only about 1.4 percent across all sites while an OM/OC ratio of 1.9 overstates gravimetric mass by about 8.2 percent. Thus, 1.6 appears to be a better OM/OC ratio for making comparisons between sites, especially urban sites, for the purpose of this study. Hopefully, future work will establish site-specific OM/OC ratios. Known OM/OC ratios will allow accurate site-to-site comparisons of organic carbon mass concentration.

Table 3-2 Sensitivity Analysis of OM/OC Ratios, OM/OC = 1.6

Site	Gravimetric Mass (µg/m3)	Reconstructed Mass (OM/OC = 1.6) (µg/m3)	Difference (µg/m3)	Percent Difference	Absolute Value of % Difference
Arendtsville, PA	16.46	15.15	-1.31	-7.95	7.95
Baltimore, MD	15.93	16.32	0.39	2.47	2.47
Charlotte, NC	15.68	14.68	-1.00	-6.36	6.36
Dover, DE	14.56	13.35	-1.21	-8.32	8.32
Elizabeth, NJ	17.96	19.07	1.11	6.20	6.20
Kinston, NC	13.74	12.56	-1.18	-8.61	8.61
Philadelphia, PA	16.66	17.21	0.55	3.30	3.30
Pittsburgh, PA	17.49	17.37	-0.12	-0.66	0.66
Richmond, VA	15.44	16.16	0.72	4.69	4.69
Washington, DC	15.98	16.43	0.45	2.82	2.82
Wilmington, DE	16.93	16.75	-0.18	-1.07	1.07
Average	**16.08**	**15.91**	**-0.16**	**-1.23**	**4.77**

Table 3-3 Sensitivity Analysis of OM/OC Ratios, OM/OC = 1.9

Site	Gravimetric Mass (µg/m3)	Reconstructed Mass (OM/OC = 1.9) (µg/m3)	Difference (µg/m3)	Percent Difference	Absolute Value of % Difference
Arendtsville, PA	16.46	15.86	-0.60	-3.63	3.63
Baltimore, MD	15.93	17.40	1.47	9.26	9.26
Charlotte, NC	15.68	15.77	0.09	0.58	0.58
Dover, DE	14.56	14.03	-0.52	-3.60	3.60
Elizabeth, NJ	17.96	20.36	2.40	13.36	13.36
Kinston, NC	13.74	13.42	-0.32	-2.36	2.36
Philadelphia, PA	16.66	18.37	1.71	10.23	10.23
Pittsburgh, PA	17.49	18.39	0.90	5.17	5.17
Richmond, VA	15.44	17.45	2.01	13.05	13.05
Washington, DC	15.98	17.49	1.51	9.46	9.46
Wilmington, DE	16.93	17.70	0.76	4.51	4.51
Average	**16.08**	**16.93**	**0.86**	**5.09**	**6.84**

Table 3-4 Sensitivity Analysis of OM/OC Ratios, OM/OC = 1.6 with Rural Sites Removed

Site	Gravimetric Mass (µg/m3)	Reconstructed Mass (OM/OC = 1.6) (µg/m3)	Difference (µg/m3)	Percent Difference	Absolute Value of % Difference
Baltimore, MD	15.93	16.32	0.39	2.47	2.47
Charlotte, NC	15.68	14.68	-1.00	-6.36	6.36
Elizabeth, NJ	17.96	19.07	1.11	6.20	6.20
Philadelphia, PA	16.66	17.21	0.55	3.30	3.30
Pittsburgh, PA	17.49	17.37	-0.12	-0.66	0.66
Richmond, VA	15.44	16.16	0.72	4.69	4.69
Washington, DC	15.98	16.43	0.45	2.82	2.82
Wilmington, DE	16.93	16.75	-0.18	-1.07	1.07
Average	**16.51**	**16.75**	**0.24**	**1.42**	**3.44**

Table 3-5 Sensitivity Analysis of OM/OC Ratios, OM/OC = 1.9 with Rural Sites Removed

Site	Gravimetric Mass (µg/m3)	Reconstructed Mass (OM/OC = 1.9) (µg/m3)	Difference (µg/m3)	Percent Difference	Absolute Value of % Difference
Baltimore, MD	15.93	17.40	1.47	9.26	9.26
Charlotte, NC	15.68	15.77	0.09	0.58	0.58
Elizabeth, NJ	17.96	20.36	2.40	13.36	13.36
Philadelphia, PA	16.66	18.37	1.71	10.23	10.23
Pittsburgh, PA	17.49	18.39	0.90	5.17	5.17
Richmond, VA	15.44	17.45	2.01	13.05	13.05
Washington, DC	15.98	17.49	1.51	9.46	9.46
Wilmington, DE	16.93	17.70	0.76	4.51	4.51
Average	**16.51**	**17.87**	**1.36**	**8.20**	**8.20**

3.2.9.4 The Modified DRI Reconstructed Mass Equation

The modified mass reconstruction equations, incorporating the new geological equation and the revised OM/OC ratio, are shown below. These equations were used in this analysis to reconstruct $PM_{2.5}$ mass and calculate the component parts of total mass. These equations were also coded into Excel spreadsheets to reconstruct $PM_{2.5}$ mass in the "user friendly" speciation datasets MARAMA developed for its members and posted on its web site.

1. Unidentified Material = Measured Mass - Reconstructed Mass
2. Geological = 3.73*Si + 1.63*Ca + 2.42*Fe+1.94*Ti
3. Organics = 1.6*Organic Carbon
4. Soot = Elemental Carbon
5. Nitrate = Nitrate
6. Sulfate = Sulfate
7. Ammonium = Ammonium
8. Salt = 1.65*Cl
9. Trace Elements = S(XRF Measured Species) - (Si+Ca+Fe+Ti+S+Cl)
10. Reconstructed Mass = S(Items 2-9)

3.2.9.5 Comparing Reconstructed Mass against Gravimetric Mass

After calculating reconstructed mass, it is important to compare the result with the gravimetric mass as determined by the speciation sampler and/or the co-located FRM monitor. The reconstructed mass and the gravimetric mass will probably not agree exactly, but they should be close in value. Large differences in the two values should be investigated. Large differences might indicate an error in the gravimetric mass measurement, error in one or more of the speciated mass measurements, selection of an inappropriate OM/OC ratio, or other problems.

3.3 Data Beneath the Method Detection Limit

This report focuses on compiling, processing, and analyzing data for the five major components of $PM_{2.5}$ mass – ammonium, elemental carbon, nitrate, organic carbon, and sulfate. The focus is on these components because they often make up 90 percent or more of the measured mass. In addition to the data for the five major species, however, a large amount of data on the elements

in a sample is reported in the speciation program. The program analyzes for 48 elements using energy dispersive x-ray fluorescence as the analytical method.

To gain some insight into whether the major species were being measured above the Method Detection Limit (MDL) of the analytical laboratory processing filters, MARAMA evaluated the speciation data from the Wilmington, DE. MARAMA calculated the MDL for all analytes in the speciation program and determined the percentage of measurements for each analyte that fell below the MDL. Appendix E lists these results. Table 3-6 is a subset of the information presented in Appendix E. As the Table shows, all measurements of the five major species at Wilmington from June 12, 2001 to December 29, 2003 are not zero and all measurements, except a few for elemental carbon, are above the MDL. As Table 3-7 shows, however, many measurements for trace elements are zero or below the MDL. The large number of measurements at zero or beneath the MDL raises many questions such as:

- How accurate and precise are the measurements below the MDL?
- Is it cost effective to continue to make these measurements?
- If trace element measurements are important for source identification or source apportionment modeling, how can these measurements be improved?

In the limited scope of MARAMA's project, MARAMA did not address these important questions. MARAMA did briefly examine data from two identical speciation samplers located in New Brunswick, NJ that sampled from February 6, 2001 to November 12, 2005. MARAMA found poor correlation between some of the trace element measurements made by these co-located samplers. For example, correlation between selenium measurements made beneath the MDL was very poor ($R^2 = 0.09$). This may be important because selenium is a marker specie for coal combustion sources and some source apportionment modelers may be using these "less than the MDL data" in their modeling.

Further work should be done to explore the quality of trace element measurements, made both above and below the MDL, since these data are frequently used to identify sources of $PM_{2.5}$ pollution. Analysts should use caution in using trace element data especially data that is near or below the MDL.

Table 3-6 Percentage of Measurements Made Beneath the MDL at Wilmington, DE, Five Major Species

Analyte	Ammonium	Elemental Carbon	Organic Carbon	Nitrate	Sulfate
Analyte Number	88301	88307	88305	88306	88403
High MDL (µg/filter)	0.16	2.352	2.352	0.084	0.12
Low MDL (µg/filter)	0.16	2.352	2.352	0.084	0.12
High MDL (µg/m^3)	0.0166	0.2438	0.2438	0.0087	0.0124
Low MDL (µg/m^3)	0.0166	0.2438	0.2438	0.0087	0.0124
Number of Measurements	136	138	138	136	136
Percent of Measurements Equal to Zero	0.0%	0.0%	0.0%	0.0%	0.0%
Percent of Measurements <=HMDL but not Zero	0.0%	0.7%	0.0%	0.0%	0.0%
Percent of Measurements <=HMDL or Zero	0.0%	0.7%	0.0%	0.0%	0.0%

Table 3-7 Percentage of Measurements Made Beneath the MDL at Wilmington, DE, Selected Analytes

Analyte	Arsenic	Aluminum	Lead	Manganese	Selenium
Analyte Number	88103	88104	88128	88132	88154
High MDL (ug/filter)	0.037	0.219	0.085	0.033	0.033
Low MDL (ug/filter)	0.014	0.157	0.027	0.015	0.025
High MDL (ug/m3)	0.0038	0.0227	0.0088	0.0034	0.0034
Low MDL (ug/m3)	0.0015	0.0163	0.0028	0.0016	0.0026
Number of Measurements	138	138	138	138	138
Percent of Measurements Equal to Zero	31.2%	44.9%	18.8%	18.1%	13.8%
Percent of Measurements <=HMDL but not Zero	62.3%	37.7%	71.0%	49.3%	71.7%
Percent of Measurements <=HMDL or Zero	93.5%	82.6%	89.9%	67.4%	85.5%

4 Regional Comparisons of $PM_{2.5}$ Species

4.1 The Data Used to Make Regional Comparisons

This report compares speciation data from eleven sites in the MARAMA Region. The eleven sites represent a quarter of the speciation monitors in the Region. The data used to make regional comparisons were obtained from EPA's TTN web site. When the data was downloaded and quality-assured, only 2001-2003 data were available. Since that time, 2004 and partial 2005 data have become available. While complete 2001-2003 data were downloaded for analysis, in many cases only partial data were available for 2001 since many monitors began operation is the summer of that year. As described in the previous section of this report, MARAMA performed a number of steps to process the speciation data.

MARAMA initially explored making regional comparisons using a subset of all possible measurements, measurements that had been collected on the same days. Ensuring all samples being compared were taken on the same days seemed to be a good way to avoid the problem of two monitors not agreeing simply because they sampled on different days. This "matching the sample day" approach was not viable however, because it severely reduced the size of the dataset. Seven of the monitoring sites evaluated sampled every third day (1-in-3 day monitors). The remaining four monitoring sites sampled only every sixth day (1-in-6 day monitors). Imposing "same sample day criteria" on the entire dataset removed one half of the data from the 1-in-3 day monitors, those days when 1-in-6 day monitors did not sample. Even more data were removed from consideration when days were removed because one of the eleven monitors did not sample for operational reasons. The resultant dataset was so small that regional comparisons could not be made with confidence, especially on a seasonal basis.

Since matching measurements by sample day was not a viable approach, MARAMA reports regional comparisons between monitors using all available data for the 2001-2003 but with null and flagged data removed. Fortunately, all the monitors on a 1-in-3 day schedule sample on the same day so direct comparisons between these monitors can be made. Similarly, all 1-in-6 day monitors sample on the same day so comparisons between these monitors are also quite robust. Comparison between 1-in-3 and 1-in-6 day monitors should be made with caution however, because of the possible bias introduced by different sampling days. In a report titled, "2002: A Year in Review," NESCAUM explored some of the issues associated with analyzing data collected from monitors that operate on different sampling schedules (NESCAUM, 2004). For analysts interested in this issue, the NESCAUM report provides interesting insights.

Since most of the $PM_{2.5}$ mass measured at a site can be attributed to five species – ammonium, elemental carbon, nitrate, organic carbon, and sulfate – these species were used in regional comparisons. Regional comparisons of the other analytes measured in the speciation program were not made. The data used to make regional comparisons included data from September 10, 2001 through October 12, 2003 (25 months). If a monitoring agency ran "intensives" and collected samples every day instead of every third or sixth day, the additional measurements were removed from consideration in regional comparisons. This avoided biases that could be introduced because an agency collected large amounts of data during a particular period when concentrations were unusually high or low, for example during a summer sulfate event. Data for July 7, 2002 was excluded from consideration in regional comparisons since many sites recorded extraordinary organic carbon measurements on this day when Canadian forest fire smoke moved

into the region. Some monitors recorded very high values due to the smoke while others did not. Some agencies flagged data for this day as an exceptional event while others did not. To ensure fair and consistent regional comparisons, data for July 7, 2002 was removed from consideration. By July 10, 2002, the next sample day in the 1-in-3 day sampling schedule, the Canadian forest fire smoke had moved out of the Mid-Atlantic Region.

Several sites analyzed did not operate continuously over the study period from September 10, 2001 through October 12, 2003 making these sites less comparable with others in the region. The rural sampler at Arendtsville, PA that operated on a 1-in-6 sampling schedule was not in operation from September 10, 2001 to April 2, 2002. Similarly, the rural sampler at Kinston, NC was not in operation from September 10, 2001 to January 14, 2002. As a result of these data gaps, the 2001-2003 averages and the seasonal averages for these monitors should be compared to other monitors in the region with caution. Fortunately, since the two monitors had gaps in their data records over much the same period, they compare quite well between themselves.

Several gaps in the data records of urban 1-in-3 day monitors were also observed. The Baltimore monitor did not operate from January 31, 2002 to March 14, 2002. The missing six weeks of winter data represents fourteen measurements or seven percent of the total data for the study period. The affect the missing data has on 2001-2003 averages and winter averages for Baltimore may be slight but it should be borne in mind when making inter-site comparisons. The Pittsburgh site also had a gap in its data record from November 22, 2001 to February 27, 2002. These missing data in fall and winter represented thirty records or about nineteen percent of the total data for the study period. As with Baltimore, the missing data for Pittsburgh has an affect on the calculation of 2001-2003 averages and winter averages. The affect may not be large, but it should be borne in mind when making inter-site comparisons. Finally, a substantial gap was found in the sulfate data record in Richmond, VA. Only two sulfate records were found in the Richmond data set from May 16, 2003 through October 2, 2003. The missing data represent twenty percent of the sulfate records at this site. The missing sulfate data during the prime sulfate season (late spring, summer, and early fall) mean Richmond's 2001-2003 averages and the seasonal sulfate averages (especially the summer average) are likely lower than they should be. This should be considered when comparing Richmond's average sulfate concentrations with other sites.

4.2 Regional Comparisons, 2001 to 2003

As one would expect, $PM_{2.5}$ mass constituents vary in concentration from place to place and season-to-season. Table 4.1 summarizes how average concentrations vary from site-to-site for the five major contributors to $PM_{2.5}$ mass. In the following paragraphs, we briefly describe how average concentrations for the five major species varied across the Region using data from September 10, 2001 through October 12, 2003. With the exception of the chart for organic carbon mass, the error bars shown in the bar charts are the average uncertainties associated with measuring ammonium, elemental carbon, nitrate and sulfate. The error bars for organic carbon mass include the uncertainty associated with applying an OM/OC ratio between 1.4 and 2.2.

Table 4-1 Regional Comparison of Major $PM_{2.5}$ Species, 2001 to 2003

Site and State	Organic Carbon Mass (µg/m^3)[1] (OM/OC =1.6)	Sulfate (µg/m^3)	Ammonium (µg/m^3)	Nitrate (µg/m^3)	Elemental Carbon (µg/m^3)
Arendtsville, PA	3.90	6.12	2.36	1.95	0.39
Baltimore, MD	5.82	5.13	1.94	1.84	0.77
Charlotte, NC	5.86	4.96	1.60	0.94	0.62
Dover, DE	3.62	4.65	1.89	1.87	0.47
Elizabeth, NJ	6.93	4.81	2.19	2.27	1.82
Kinston, NC	4.47	4.11	1.51	1.10	0.36
Philadelphia, PA	5.96	4.74	2.08	2.25	0.85
Pittsburgh, PA	5.47	6.00	2.28	1.77	0.85
Richmond, VA	6.81	4.97	1.89	1.20	0.56
Washington DC	5.70	5.44	2.02	1.68	0.73
Wilmington, DE	5.02	5.24	2.33	2.48	0.78
Average	**5.41**	**5.11**	**2.01**	**1.76**	**0.75**
Maximum	6.93	6.12	2.36	2.48	1.82
Minimum	3.62	4.11	1.51	0.94	0.36
Uncertainty Reported in AQS[2]	13%	9%	7%	12%	51%

[1] Organic carbon mass concentrations were calculated from blank-corrected organic carbon data. Organic carbon mass estimates are based on an OM/OC ratio of 1.6.

[2] Uncertainty is the average 1sigma error currently being reported in the EPA AQS database for that specie. The 13% 1sigma uncertainty reported for organic carbon mass does not include the error associated with application of an OM/OC ratio. The OM/OC ratio for the sites studied is expected to range between about 1.4 and 2.2.

EPA's contractor for the speciation program, Research Triangle Institute International, Inc. (RTI), did not post uncertainty data in the AIRS database during 2001-2003 so uncertainty information for the data used in this report was not available in AQS or in EPA web site data files. Since operating procedures and analytical equipment have not changed appreciably since the 2001-2003 data were collected, RTI believes current estimates of measurement error are good estimates of 2001-2003 measurement error. RTI is currently "backfilling" uncertainty data in AQS for previously collected speciation data including the 2001-2003 data used in this report.

4.2.1 Organic Carbon Mass

As explained in the Methodology and Data Handling Techniques section of this report, estimating the organic carbon mass concentration at a site is a complex process that requires the quality assurance of the organic carbon data, an examination of the organic carbon artifact, and the application of an OM/OC ratio to the measurement data. As noted previously, MARAMA applied an OM/OC ratio of 1.6 to the organic carbon data used in regional comparisons. This was done because experimentally derived OM/OC ratios had not been determined for monitoring sites in the MARAMA Region, yet some ratio had to be applied to estimate organic carbon mass. An OM/OC ratio of 1.6 was viewed as a good estimate of the OM/OC ratio at urban sites (Turpin, 2001) and most sites analyzed in this report are urban sites. It is clear from researcher work that OM/OC ratios vary from site-to-site, season-to-season, even measurement-to-

measurement. Given this variability, organic carbon mass estimates presented in this report should be viewed as estimates of actual values. As MARAMA's sensitivity analysis shows, an OM/OC ratio of 1.6 may overestimate organic carbon mass at some highly urban monitors, like the monitor located in Elizabeth, NJ and it likely underestimates the organic carbon mass concentration at rural sites such as Arendtsville, PA, Dover, DE, and Kinston, NC.

Given the application of an OM/OC ratio of 1.6, over 2001-2003, organic carbon mass was often the largest contributor to $PM_{2.5}$ mass. Organic carbon mass concentrations averaged 5.4 micrograms per cubic meter ($\mu g/m^3$) over the eleven sites studied. The highest average concentration, 6.9 $\mu g/m^3$, occurred at the Elizabeth, NJ monitoring site. The Elizabeth speciation monitor is located in an industrial area very close to toll booths on the New Jersey Turnpike. The site is likely dominated by mobile source emissions from both the New Jersey Turnpike and the Staten Island Expressway and nearby industrial emissions. While the Elizabeth site produced the highest average organic carbon mass concentration over the 2001-2003 period, Richmond was not far behind at 6.8 $\mu g/m^3$. Virginia monitoring personnel believe the Richmond site, like the Elizabeth, NJ site, is strongly influenced by mobile source emissions. Many large urban areas, namely Baltimore, Charlotte, Philadelphia, and Washington, had organic carbon mass concentrations between 5.7 and 5.9 $\mu g/m^3$.

The lowest organic carbon mass concentrations for 2001-2003 were observed at the rural monitoring sites at Arendtsville, PA, Dover, DE, and Kinston, NC. Average concentrations over the period were 3.9, 3.6, and 4.5, respectively. These low values probably result from applying too low an OM/OC ratio. Applying a higher OM/OC ratio, that represents more "aged" (higher molecular weight) organic carbon species, would increase organic carbon mass at these sites (El-Zanan et al., 2005; Polidori, 2005; Zhang, 2005). If the convention holds true that rural sites exhibit higher OM/OC ratios than urban sites, applying site-specific OM/OC ratios would likely have the effect of increasing estimated rural concentrations and reducing estimated urban concentrations of organic carbon mass. This would decrease the disparity between urban and rural concentrations of organic carbon mass.

Figure 4-1 depicts average organic carbon mass concentrations in the Region assuming an OM/OC ratio of 1.6 at all sites. Figure 4-2 maps these values. All regional comparisons of organic carbon mass concentration were made after removing data for the exceptional event that occurred on July 7, 2002 when Canadian forest fire smoke was present in the Mid-Atlantic Region.

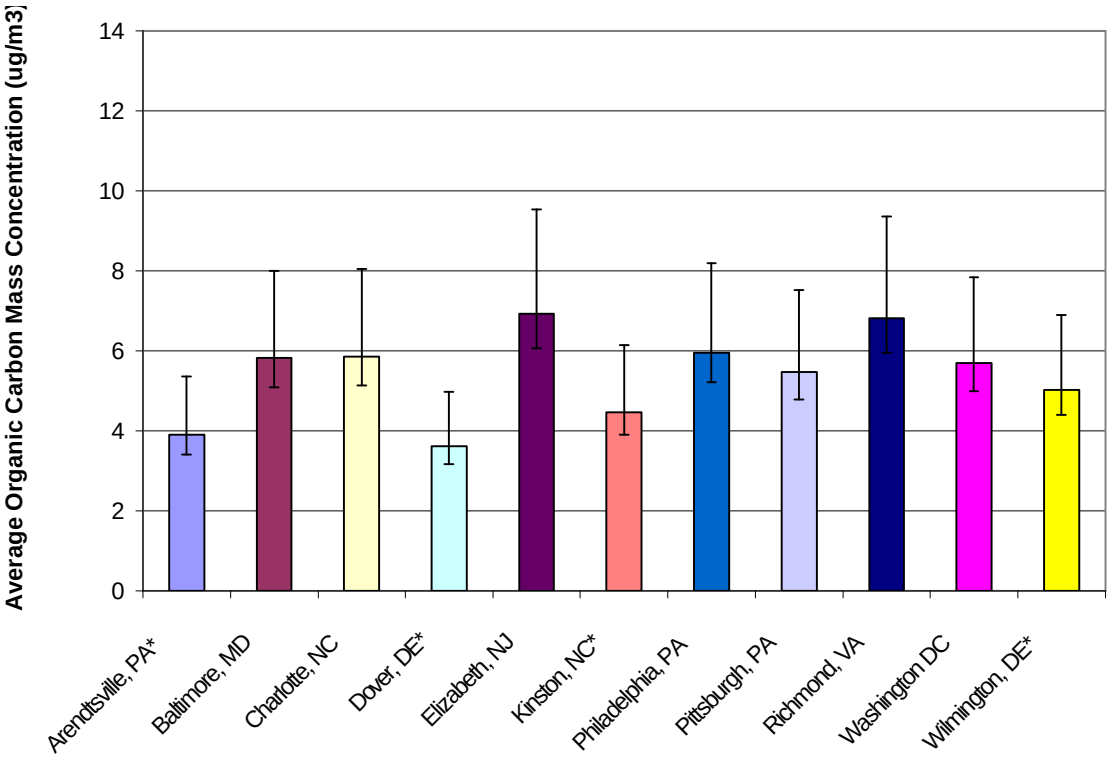

Figure 4-1 Average Organic Carbon Mass Concentrations in the MARAMA Region

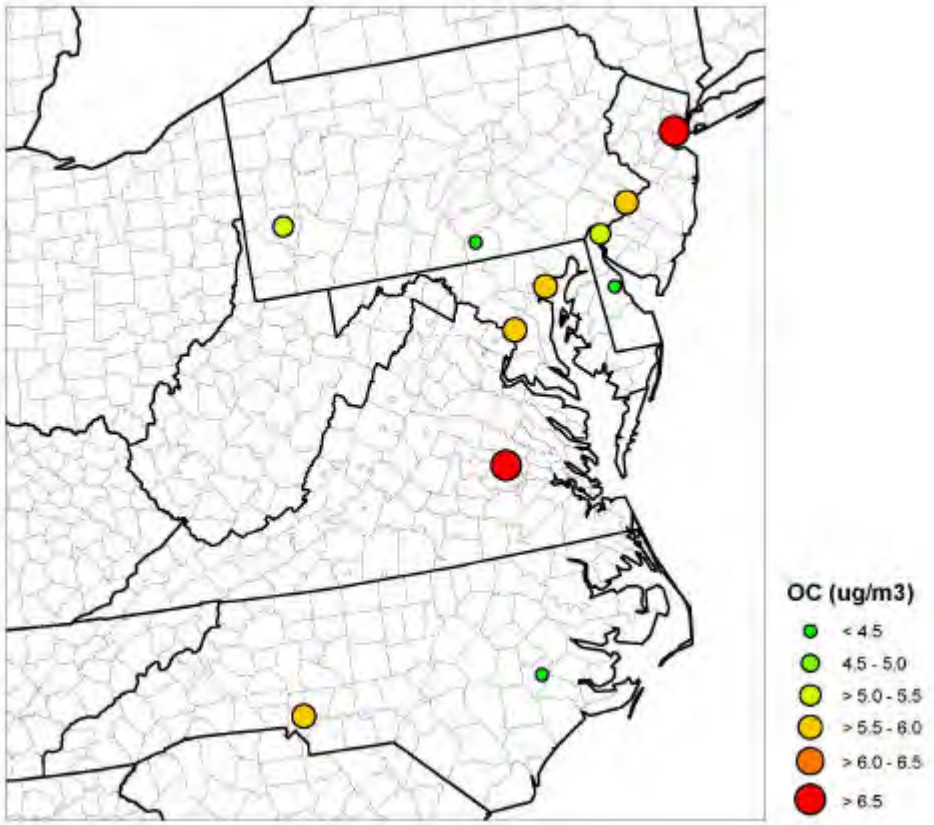

Figure 4-2 Average Organic Carbon Mass Concentration Map

4.2.2 Sulfate

Over the period, sulfate was also a large contributor to $PM_{2.5}$ mass. Sulfate concentrations averaged 5.1 µg/m^3 over the eleven sites studied. The highest average concentrations, 6.1 and 6.0 µg/m^3 occurred at Arendtsville and Pittsburgh, PA. Most sites had average concentrations between 4.7 and 5.4 µg/m^3. The lowest concentration, 4.1 µg/m^3 was observed at the Kinston monitoring site in rural southeastern North Carolina. Figure 4-3 depicts average sulfate concentrations in the Region. Figure 4-4 maps these values.

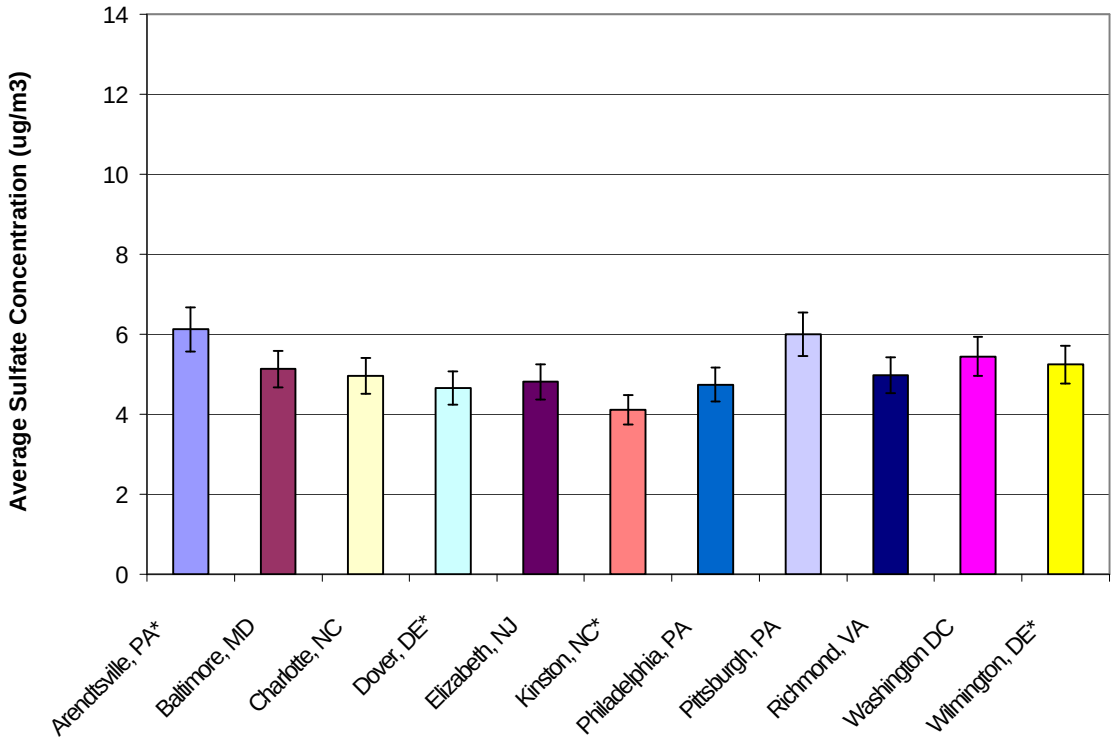

Figure 4-3 Average Sulfate Concentrations in the MARAMA Region

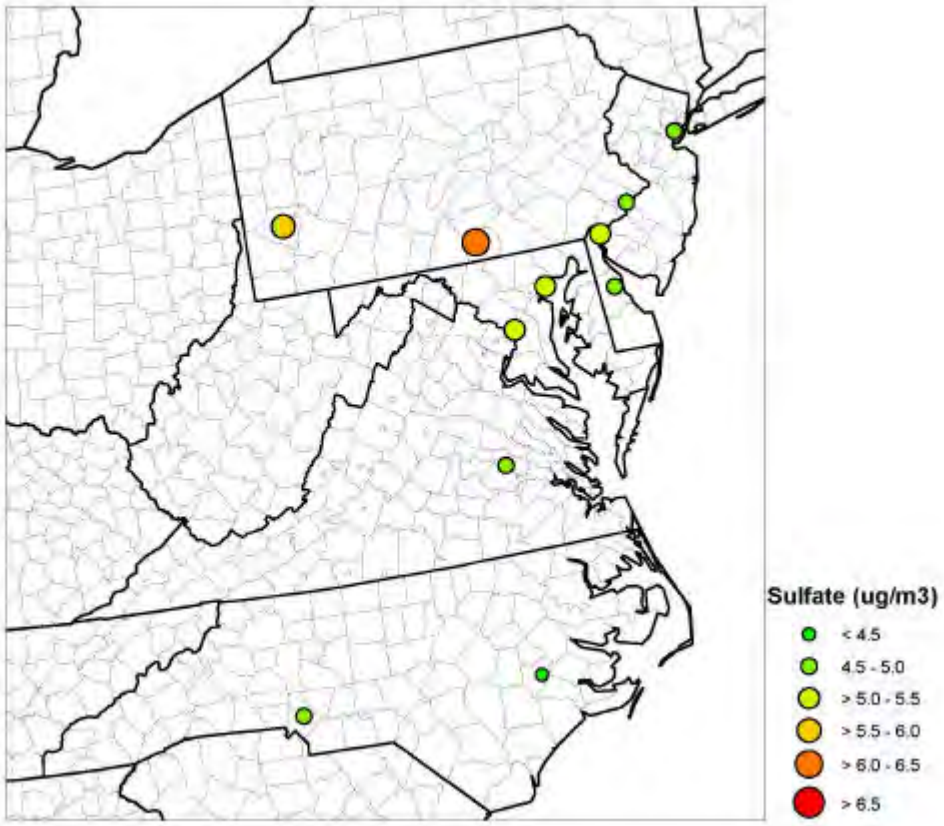

Figure 4-4 Average Sulfate Concentration Map

4.2.3 Ammonium

Over 2001-2003, ammonium concentration averaged 2.0 µg/m^3 across the Region. The highest average concentration, 2.4 µg/m^3 occurred in Arendtsville, PA followed closely by Wilmington, DE (2.3 µg/m^3) and Pittsburgh, PA (2.3 µg/m^3). The lowest concentration, 1.4 µg/m^3 was observed at the Kinston monitoring site in rural southeastern North Carolina. The low average concentration of ammonium at Kinston was surprising given that the monitor is located in an area of North Carolina known for Concentrated Animal Feeding Operations (CAFOs). In general, ammonium concentrations were highest in locations with high sulfate and/or nitrate concentrations. This may help explain the low average ammonium concentration in Kinston, NC where both sulfate and nitrate concentrations were low compared to other sites. Figure 4-5 depicts average ammonium concentrations in the Region. Figure 4-6 maps these values.

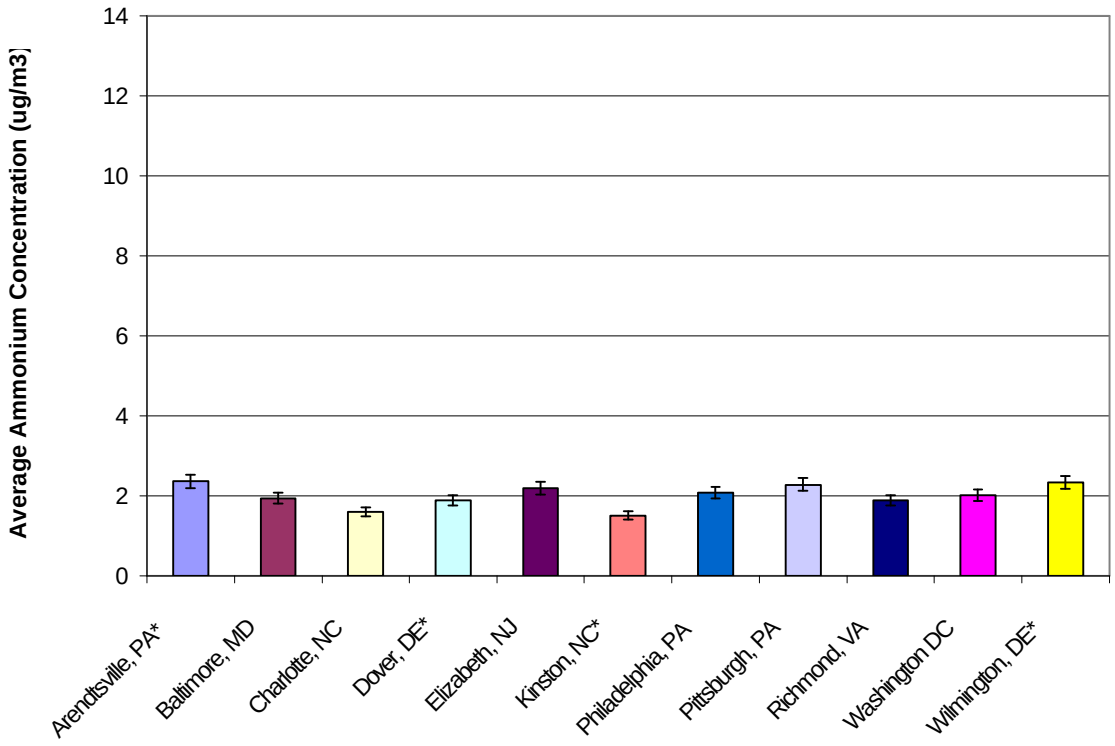

Figure 4-5 Average Ammonium Concentrations in the MARAMA Region

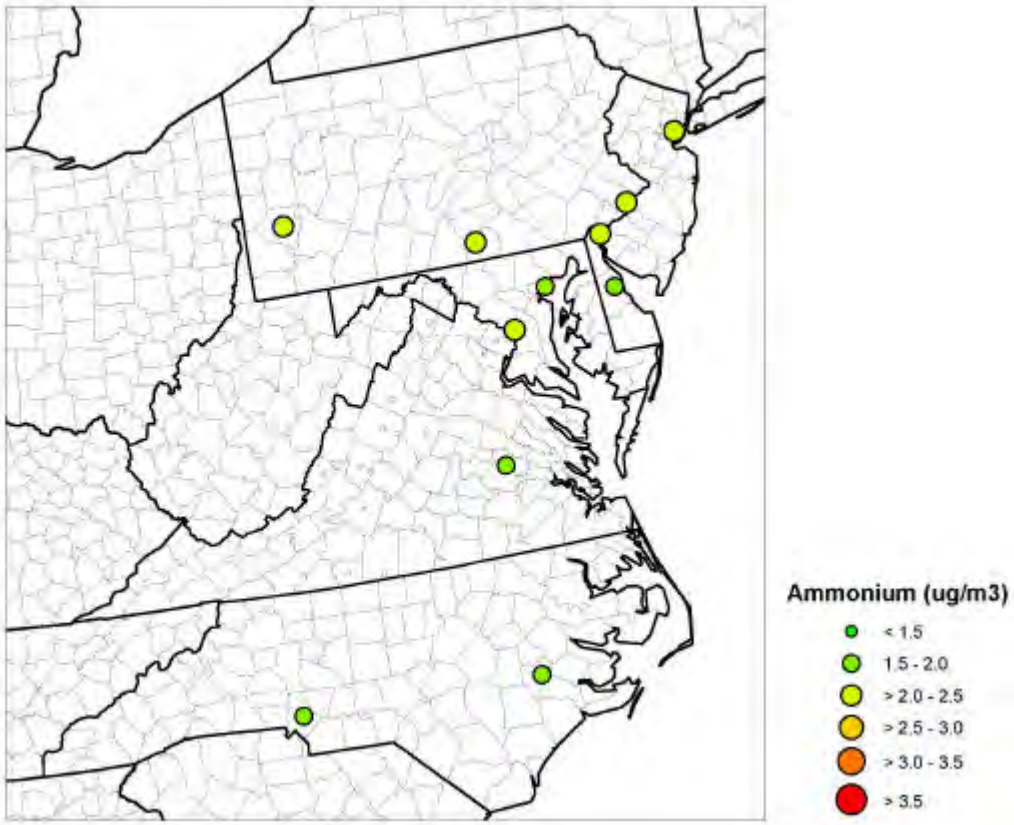

Figure 4-6 Average Ammonium Concentration Map

4.2.4 Nitrate

Nitrate concentrations averaged 1.8 µg/m^3 for the eleven monitors studied. The highest average concentration, 2.5 µg/m^3, occurred in Wilmington, DE. The lowest concentration, 0.9 µg/m^3, was observed in Charlotte, NC. Relatively low values were also measured in Kinston, NC (1.1 µg/m^3) and Richmond, VA (1.2 µg/m^3). Average nitrate concentrations appear correlated with the wintertime conditions that favor the formation of solid phase nitrate species. Figure 4-7 depicts average nitrate concentrations in the Region and Figure 4-8 maps these values.

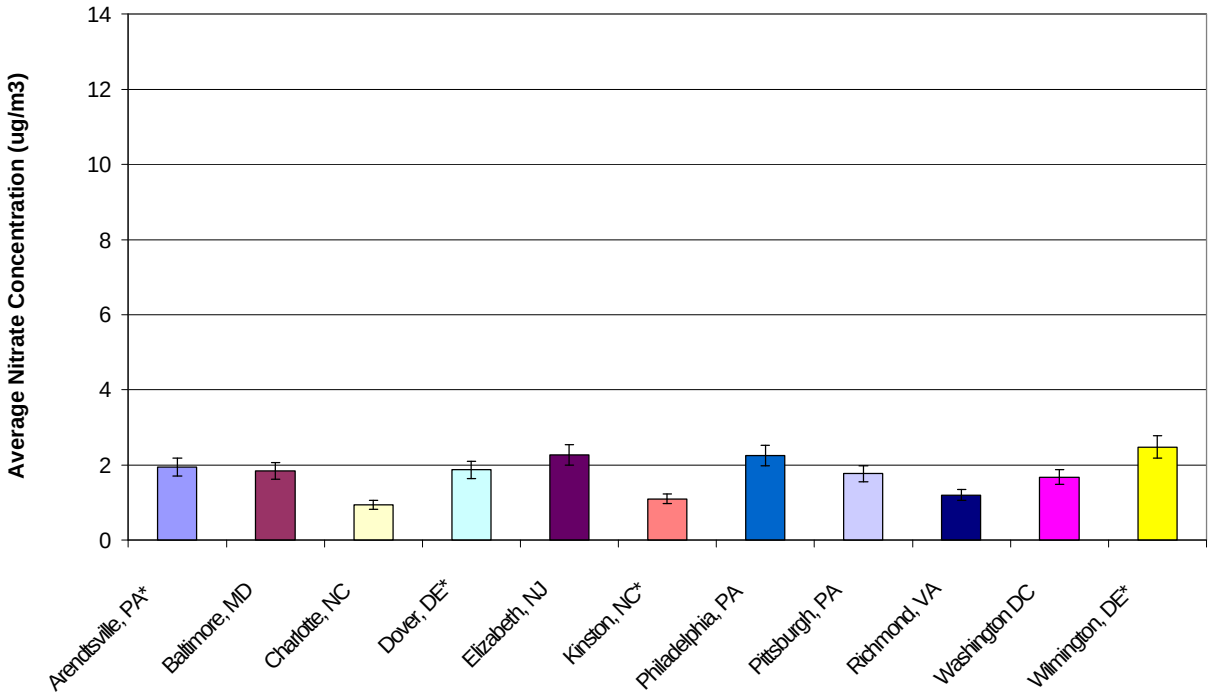

Figure 4-7 Average Nitrate Concentration in the MARAMA Region

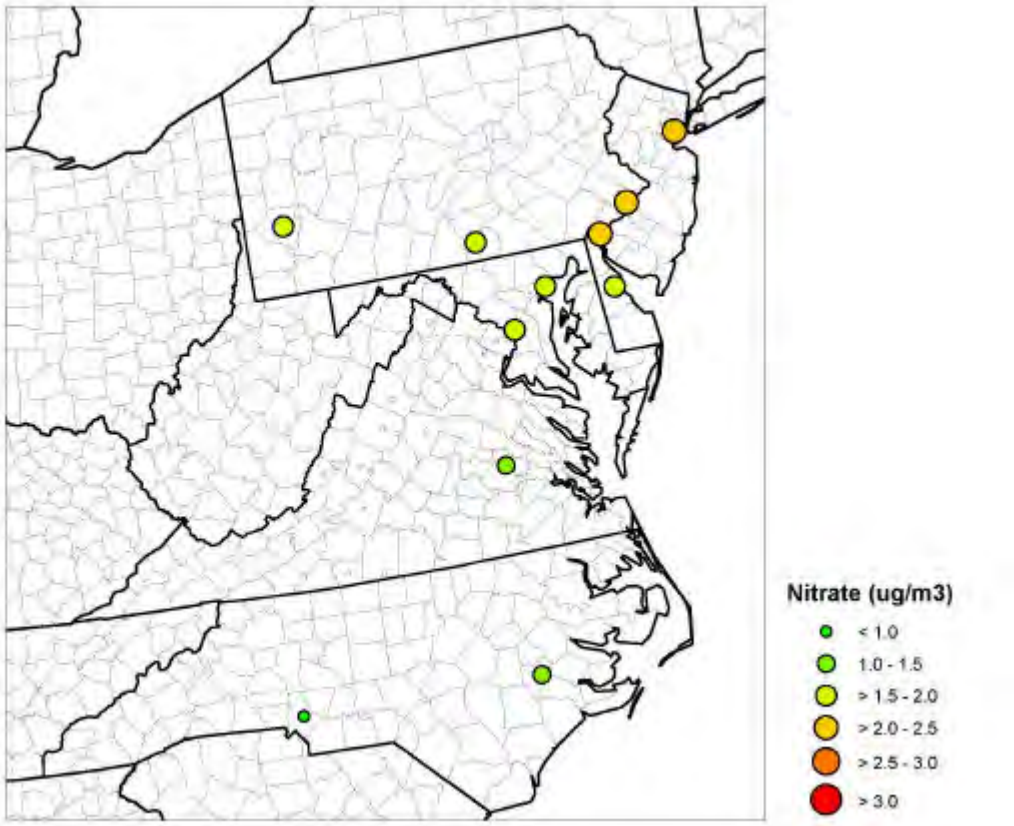

Figure 4-8 Average Nitrate Concentration Map

4.2.5 Elemental Carbon

Elemental carbon concentrations averaged 0.75 µg/m^3 over the eleven monitors over the study period. Average concentrations ranged from a high of 1.8 µg/m^3 at the highly urban site in Elizabeth, NJ to lows of 0.36 µg/m^3 in rural Kinston, NC and 0.39 µg/m^3 in rural Arendtsville, PA. The Dover, DE monitor, another fairly rural site, also recorded a relatively low average elemental carbon concentration of 0.47 µg/m^3 over the 2001-2003 period. The high elemental carbon concentration at the Elizabeth, NJ monitoring site was likely due to the monitor's proximity to a toll plaza on the New Jersey Turnpike and a nearby industrial area. In the case of elemental carbon concentrations, the Elizabeth site is about five times the average concentration of a rural site and more than twice the average concentration of other urban sites.

Large urban areas such as Baltimore, MD, Philadelphia, PA, Pittsburgh, PA, Washington, DC and Wilmington, DE exhibited average concentrations between about 0.7 and 0.9 µg/m^3, about twice the concentration of rural sites. Elemental carbon appeared strongly correlated with population. Population was defined as the population of the counties within 24.1 km (15 miles) of the monitoring site. Figure 4-9 shows a correlation between average elemental carbon concentration and population for the eleven monitoring sites studied. Figure 4-10 compares average elemental carbon concentrations across the Region. Figure 4-11 plots average elemental carbon concentrations on a map of urban areas.

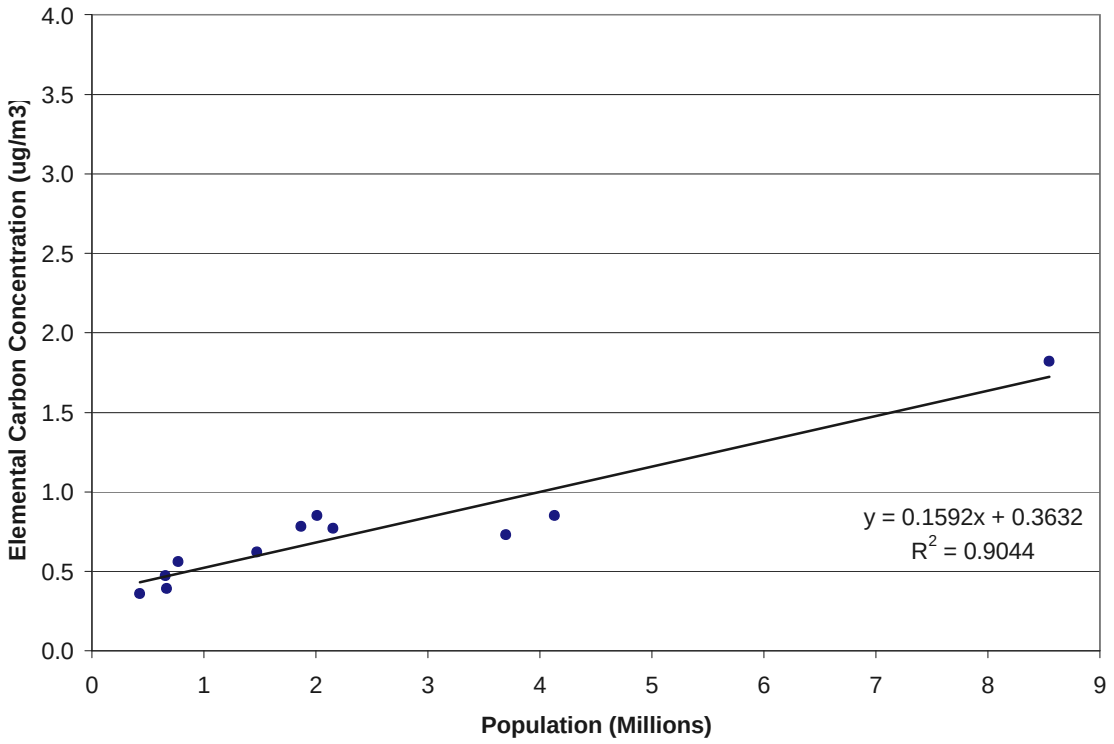

Figure 4-9 Correlation of Average Elemental Carbon Concentration and Population

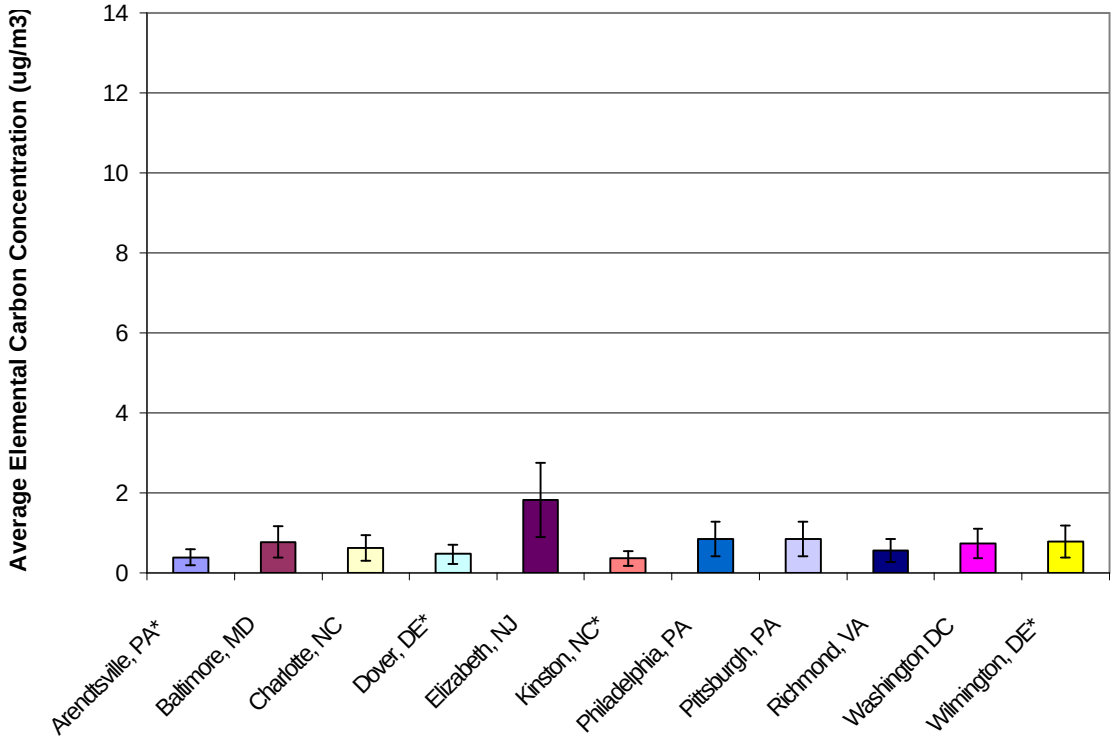

Figure 4-10 Average Elemental Carbon Concentrations in the MARAMA Region

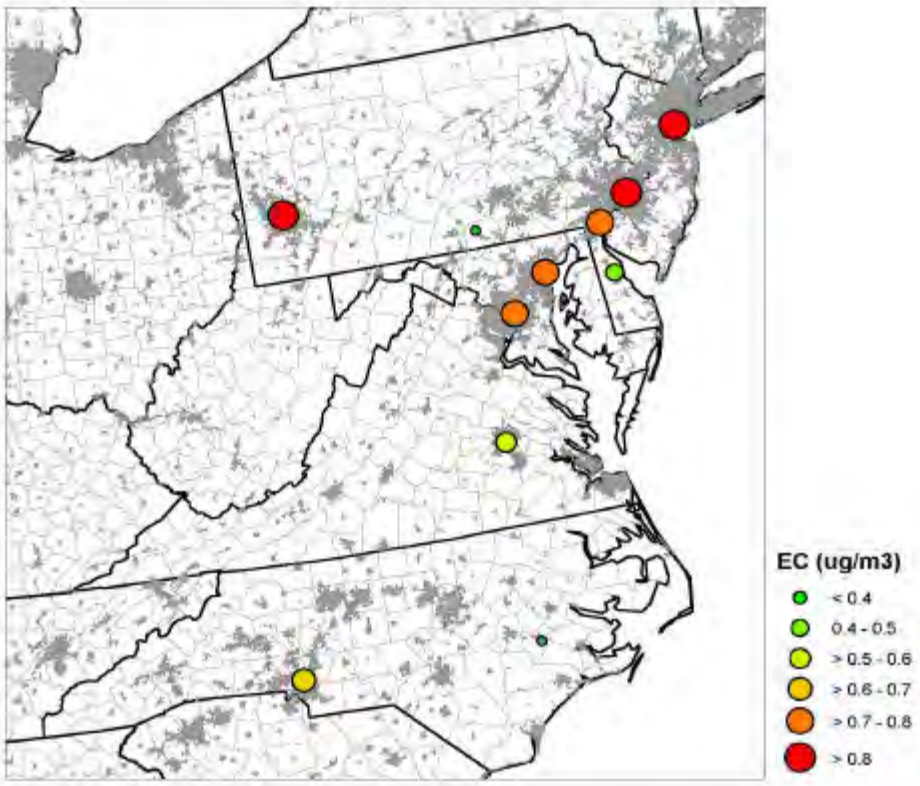

Figure 4-11 Map of Elemental Carbon Concentrations and Urban Areas

It is interesting to note that all of the more rural sites show similar average concentrations for elemental carbon even though they are located in different parts of the MARAMA Region. Further analytical work may determine if the elemental carbon concentrations observed at these rural sites represent "regional background concentrations" of this important specie.

4.3 Seasonal Comparisons, 2001 to 2003

Since several of the major constituents of $PM_{2.5}$ mass vary in concentration from season to season, MARAMA analyzed speciation data over 2001-2003 from a seasonal perspective. In this analysis, MARAMA followed the convention of placing June, July and August in the summer season. The other seasons and the months associated with them are listed in Table 4-2.

Table 4-2 Months Included in Each Season

Season	Months	Number of Days
Winter	December, January, February	90/91
Spring	March, April, May	92
Summer	June, July, August	92
Fall	September, October, November	91

At most of the eleven monitoring sites studied, the mass of the five largest contributors to $PM_{2.5}$ mass was highest in summer and lowest in spring and fall. The largest contributors to $PM_{2.5}$

mass, in order of importance, were organic carbon, sulfate, ammonium, nitrate, and elemental carbon. Averaged across the entire region, the average concentration of the five major constituents of $PM_{2.5}$ mass was highest in the summer at about 18.5 µg/m^3. A secondary peak in average concentration occurred in winter at about 15.4 µg/m^3. Spring and fall were characterized by lower concentrations. Averaged across the region, the average concentration of the five major constituents of $PM_{2.5}$ mass were 12.9 µg/m^3 in spring and 13.2 µg/m^3 in fall. Figure 4-12 shows how the mass of the five major constituents to $PM_{2.5}$ mass varied season to season when averaged over 2001-2003 and across all eleven monitors studied.

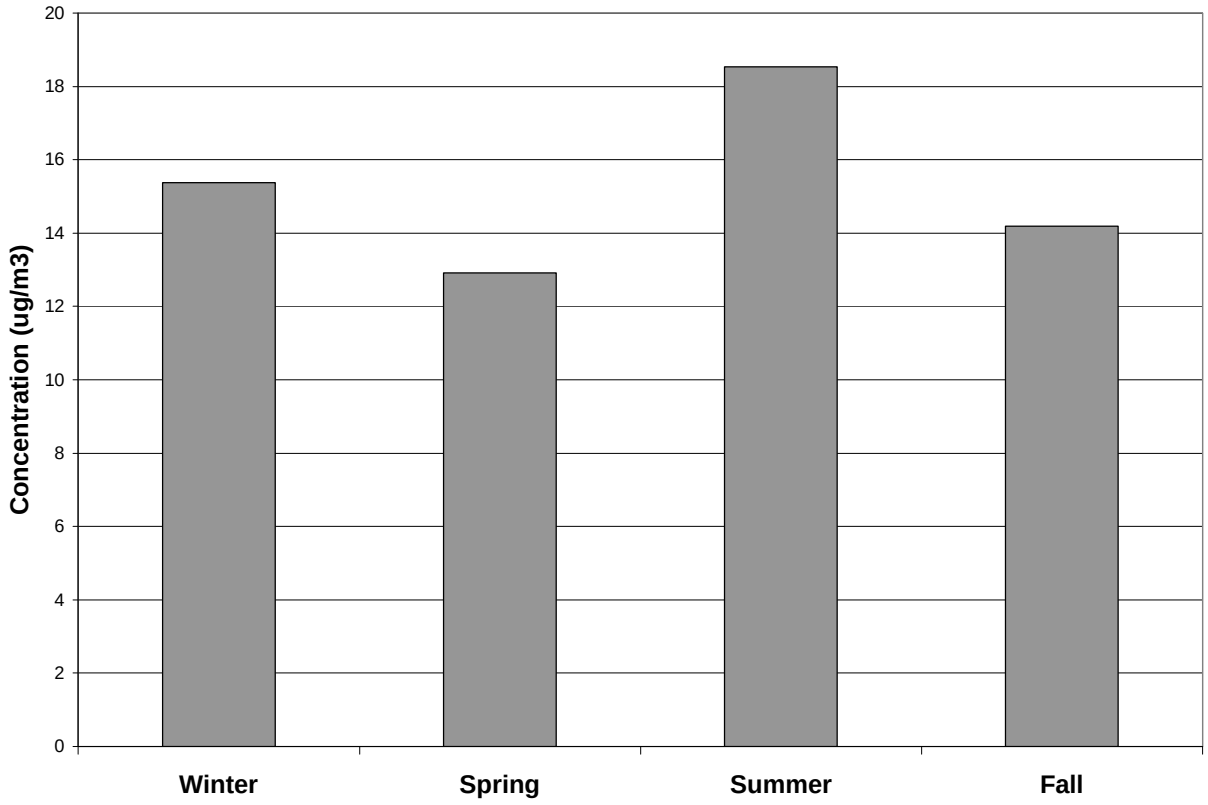

Figure 4-12 Seasonal Variation of the Five Major Contributors to $PM_{2.5}$ Mass

At an OM/OC ratio of 1.6, organic carbon mass and sulfate were the two largest contributors to $PM_{2.5}$ mass in the MARAMA Region. In winter, organic carbon mass was the dominate specie at all sites except Arendtsville, PA where sulfate contributed the most to $PM_{2.5}$ mass. In the fall, organic carbon mass was the largest contributor to $PM_{2.5}$ mass at six sites and sulfate was the largest contributor at the other five. In spring and summer, sulfate was the dominate specie at most sites. Even in the summer, however, organic carbon mass was the largest contributor to $PM_{2.5}$ mass at Elizabeth, NJ and Richmond, VA (although the OM/OC ratio of 1.6 may be too high for these sites). Organic carbon mass was also the largest contributor to $PM_{2.5}$ mass in the summer at rural Kinston, NC where sulfate concentrations are low.

As will be discussed in the site-specific analyses that follow in section 5 below, organic carbon mass concentrations were variable throughout the study period. On average however, regionally averaged organic carbon mass concentration peaked during the summer at 6.7 µg/m^3. Average organic carbon mass concentration declined in the fall to 5.2 µg/m^3 then increased somewhat in winter to 5.9 µg/m^3. Average organic carbon mass concentration was at its lowest level in the

spring at 4.0 µg/m^3. Figures 4-13 through 4-16 plot the behavior of organic carbon mass and the other major species through the seasons. The plots utilize data from September 10, 2001 through October 12, 2003. Data for the Canadian forest fire event that occurred July 7, 2002 was removed from the data used to develop these seasonal bar charts.

The development of seasonal, site-specific OM/OC ratios would very likely modify the seasonal behavior of organic carbon mass concentrations. Since researchers (Polidori, 2005) have shown at one site in the MARAMA Region that OM/OC ratios are slightly higher in the summer and winter than in the spring and fall, swings in organic carbon mass concentration are likely to be even greater if seasonal, site-specific OM/OC ratios are developed for speciation monitors in the Mid-Atlantic Region.

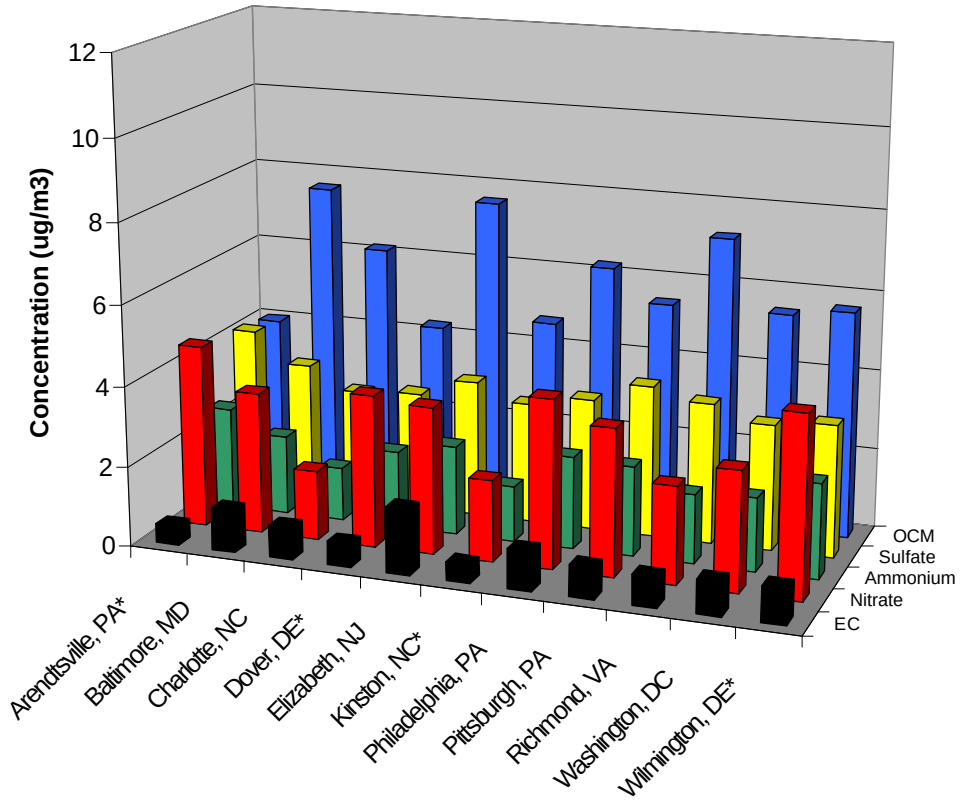

Figure 4-13 Seasonal Comparison of the Five Major $PM_{2.5}$ Species, Winter

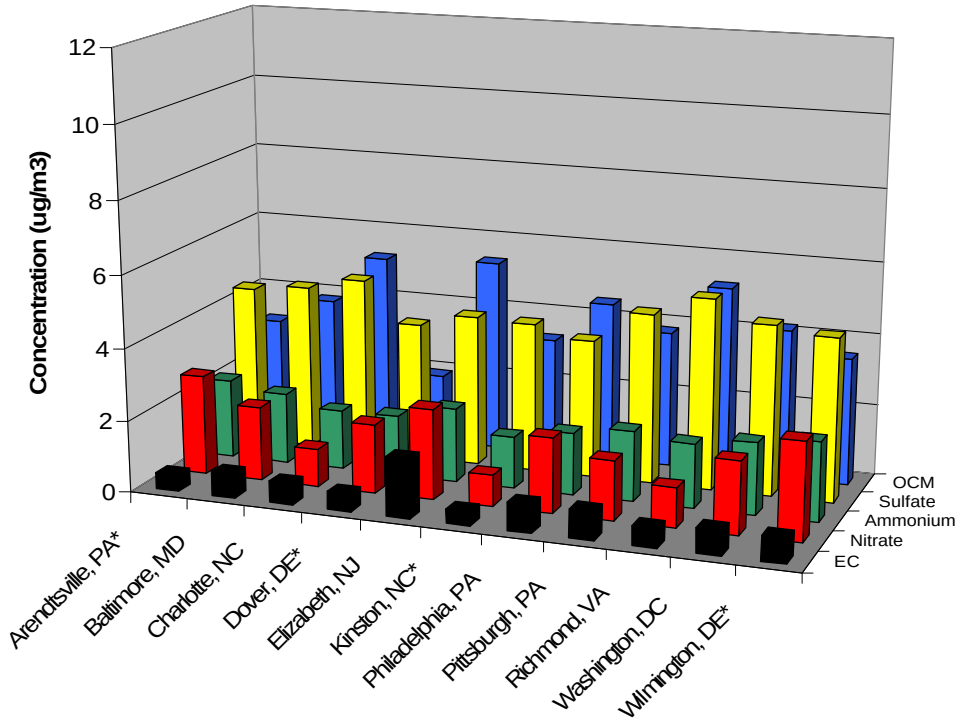

Figure 4-14 Seasonal Comparison of the Five Major $PM_{2.5}$ Species, Spring

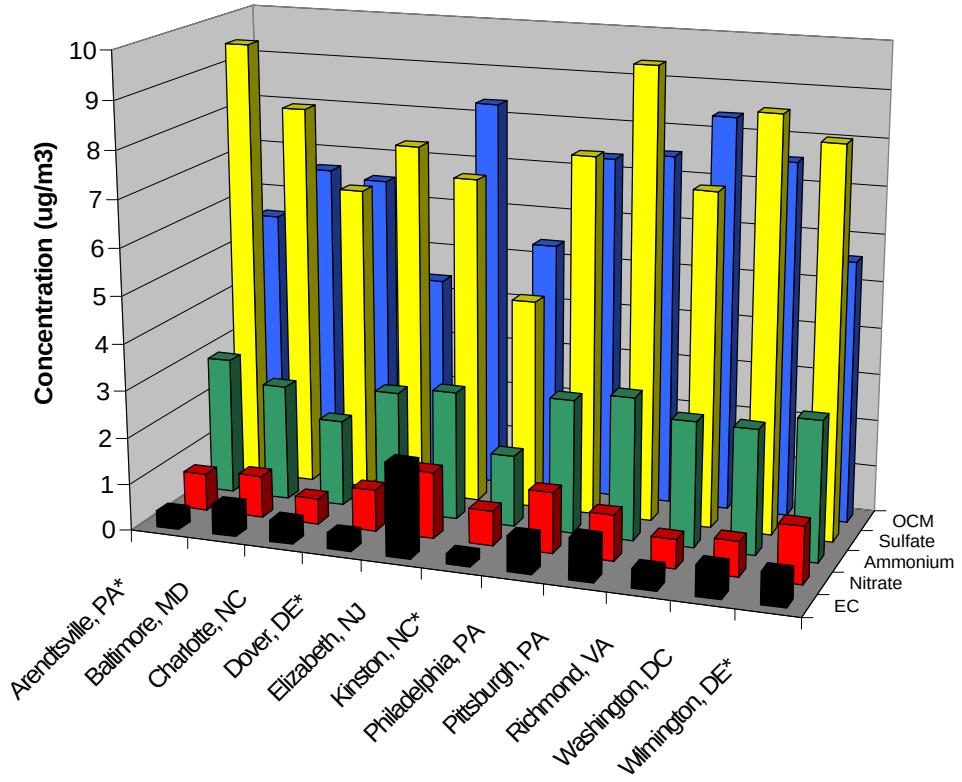

Figure 4-15 Seasonal Comparison of the Five Major $PM_{2.5}$ Species, Summer

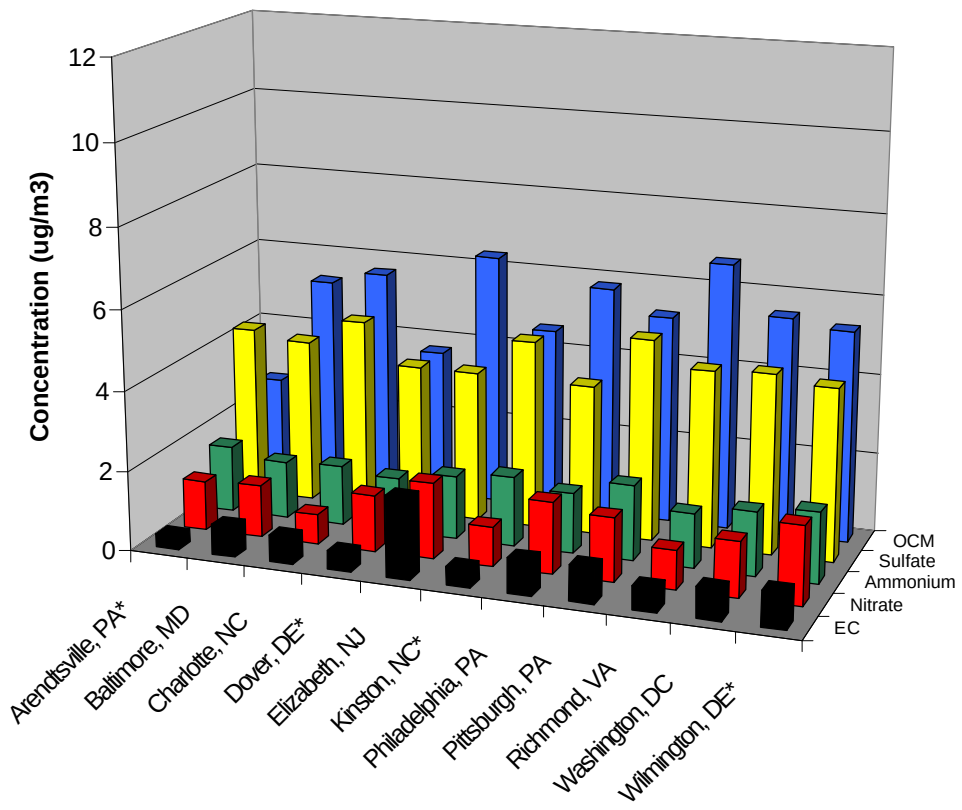

Figure 4-16 Seasonal Comparison of the Five Major $PM_{2.5}$ Species, Fall

Sulfate was an extremely important contributor to $PM_{2.5}$ mass at all sites in the Region, particularly in spring and summer when it was the largest contributor to total $PM_{2.5}$ mass at most sites studied. Sulfate concentrations peaked in summer. The regionally averaged sulfate concentration in summer was 7.7 $\mu g/m^3$. The regionally averaged concentration fell to 4.3 $\mu g/m^3$ in the fall and reached its lowest level in the winter at 3.3 $\mu g/m^3$. Spring levels, averaged across the region, were about 4.5 $\mu g/m^3$.

Unlike organic carbon mass and sulfate species, nitrate species peaked in winter, not summer. While an important contributor to winter $PM_{2.5}$ concentrations, nitrate concentrations were relatively modest when compared to the summertime contributions made by organic carbon and sulfate species. Regionally averaged nitrate concentration peaked in winter at 3.4 $\mu g/m^3$. Regionally averaged nitrate concentration was at its lowest level in the summer at 0.9 $\mu g/m^3$. Spring and fall concentrations were 1.9 $\mu g/m^3$ and 1.4 $\mu g/m^3$ respectively.

Ammonium ion is a modest but important contributor to $PM_{2.5}$ mass in all seasons. Across the seasons, the regional ammonium load was about 2 $\mu g/m^3$. Over the 2001-2003 period, the regionally averaged ammonium concentration was 2.6 $\mu g/m^3$ in the summer, 1.6 $\mu g/m^3$ in the fall, 2.0 $\mu g/m^3$ in the winter, and 1.9 $\mu g/m^3$ in the spring.

Elemental carbon did not exhibit the seasonal variability seen in organic carbon, sulfate, and nitrate concentrations. In general, this contributor to $PM_{2.5}$ mass appeared to consistently present in relatively low concentration season-to-season.

Tables 4-3 through 4-6 provide seasonal averages by site and specie for the eleven monitors studied. For more information about specific sites and the data from those sites, see Section 5.

Table 4-3 Winter Averages by Site and Specie

Site	Organic Carbon Mass (µg/m³) (OM/OC=1.6)	Sulfate (µg/m³)	Ammonium (µg/m³)	Nitrate (µg/m³)	Elemental Carbon (µg/m³)	Total (µg/m³) (OM/OC=1.6)
Arendtsville, PA[1]	4.02	4.14	2.52	4.55	0.47	15.70
Baltimore, MD	7.62	3.38	1.97	3.52	1.05	17.55
Charlotte, NC	6.15	2.85	1.33	1.73	0.80	12.86
Dover, DE[1]	4.27	2.96	1.92	3.80	0.59	13.53
Elizabeth, NJ	7.60	3.42	2.23	3.66	1.64	18.54
Kinston, NC[1]	4.67	3.01	1.38	2.03	0.46	11.56
Philadelphia, PA	6.22	3.29	2.31	4.19	0.99	17.00
Pittsburgh, PA	5.43	3.78	2.24	3.65	0.79	15.89
Richmond, VA	7.21	3.50	1.73	2.43	0.75	15.61
Washington, DC	5.45	3.14	1.82	2.99	0.84	14.24
Wilmington, DE[1]	5.65	3.30	2.36	4.50	0.89	16.71
Average	**5.85**	**3.34**	**1.98**	**3.37**	**0.84**	**15.38**
Maximum Value	7.62	4.14	2.52	4.55	1.64	18.54
Minimum Value	4.02	2.85	1.33	1.73	0.46	11.56

[1] Samplers at these sites sampled every sixth day.

Table 4-4 Spring Averages by Site and Specie

Site	Organic Carbon Mass (µg/m³) (OM/OC=1.6)	Sulfate (µg/m³)	Ammonium (µg/m³)	Nitrate (µg/m³)	Elemental Carbon (µg/m³)	Total (µg/m³) (OM/OC=1.6)
Arendtsville, PA[1]	3.08	4.43	2.19	2.76	0.45	12.92
Baltimore, MD	3.82	4.60	1.97	2.05	0.68	13.11
Charlotte, NC	5.20	4.94	1.65	1.05	0.59	13.43
Dover, DE[1]	1.91	3.82	1.67	1.91	0.49	9.81
Elizabeth, NJ	5.34	4.20	2.05	2.51	1.63	15.73
Kinston, NC[1]	3.27	4.15	1.43	0.87	0.39	10.11
Philadelphia, PA	4.46	3.83	1.72	2.08	0.78	12.87
Pittsburgh, PA	3.79	4.73	1.95	1.64	0.79	12.89
Richmond, VA	5.19	5.30	1.78	1.10	0.54	13.91
Washington, DC	4.17	4.74	1.99	2.01	0.69	13.59
Wilmington, DE[1]	3.53	4.55	2.19	2.71	0.68	13.66
Average	**3.98**	**4.48**	**1.87**	**1.88**	**0.70**	**12.91**
Maximum Value	5.34	5.30	2.19	2.76	1.63	15.73
Minimum Value	1.91	3.82	1.43	0.87	0.39	9.81

[1] Samplers at these sites sampled every sixth day.

Table 4-5 Summer Averages by Site and Specie

Site	Organic Carbon Mass (µg/m^3) (OM/OC=1.6)	Sulfate (µg/m^3)	Ammonium (µg/m^3)	Nitrate (µg/m^3)	Elemental Carbon (µg/m^3)	Total (µg/m^3) (OM/OC=1.6)
Arendtsville, PA[1]	5.51	9.51	2.94	0.79	0.35	19.10
Baltimore, MD	6.64	8.21	2.48	0.89	0.64	18.87
Charlotte, NC	6.49	6.55	1.84	0.55	0.45	15.88
Dover, DE[1]	4.40	7.59	2.61	0.89	0.34	15.82
Elizabeth, NJ	8.34	6.98	2.75	1.42	1.99	21.47
Kinston, NC[1]	5.38	4.48	1.52	0.75	0.22	12.35
Philadelphia, PA	7.36	7.65	2.85	1.29	0.76	19.92
Pittsburgh, PA	7.50	9.60	3.05	0.98	0.89	22.02
Richmond, VA	8.40	7.13	2.68	0.62	0.41	19.23
Washington, DC	7.56	8.79	2.66	0.75	0.66	20.42
Wilmington, DE[1]	5.59	8.28	2.98	1.22	0.68	18.75
Average	**6.65**	**7.71**	**2.58**	**0.92**	**0.67**	**18.53**
Maximum Value	8.40	9.60	3.05	1.42	1.99	22.02
Minimum Value	4.40	4.48	1.52	0.55	0.22	12.35

[1] Samplers at these sites sampled every sixth day.

Table 4-6 Fall Averages by Site and Specie

Site	Organic Carbon Mass (µg/m^3) (OM/OC=1.6)	Sulfate (µg/m^3)	Ammonium (µg/m^3)	Nitrate (µg/m^3)	Elemental Carbon (µg/m^3)	Total (µg/m^3) (OM/OC=1.6)
Arendtsville, PA[1]	2.55	4.31	1.65	1.23	0.33	9.98
Baltimore, MD	5.31	4.12	1.43	1.31	0.75	14.11
Charlotte, NC	5.64	4.78	1.50	0.75	0.68	14.42
Dover, DE[1]	3.73	3.77	1.36	1.41	0.47	12.10
Elizabeth, NJ	6.34	3.77	1.58	1.90	2.01	16.58
Kinston, NC[1]	4.59	4.72	1.75	0.98	0.47	12.49
Philadelphia, PA	5.80	3.74	1.51	1.79	0.88	15.19
Pittsburgh, PA	5.22	5.07	1.89	1.59	0.90	15.29
Richmond, VA	6.68	4.44	1.37	0.98	0.59	15.96
Washington, DC	5.49	4.51	1.60	1.39	0.76	14.77
Wilmington, DE[1]	5.30	4.34	1.77	1.96	0.89	15.24
Average	**5.15**	**4.32**	**1.58**	**1.39**	**0.79**	**14.19**
Maximum Value	6.68	5.07	1.89	1.96	2.01	16.58
Minimum Value	2.55	3.74	1.36	0.75	0.33	9.98

[1] Samplers at these sites sampled every sixth day.

5 Site Information and Analyses

The following sections provide detailed information about each monitoring site included in this study and a brief analysis of the speciation data collected at that site. Each site analysis includes:

- a site description,
- maps locating the site,
- a brief summary of the major constituents of $PM_{2.5}$ mass,
- a comparison of reconstructed mass and gravimetric mass,
- a time series showing how the five major constituents of $PM_{2.5}$ mass vary over time, and
- trajectory plots for some of the "cleanest" and "dirtiest" days during the 2001-2003 period.

The Combined Aerosol Trajectory Tool (CATT) was used to plot back trajectories for each site. CATT is an on-line, browser-based analytical tool that links air quality monitoring and other data with back trajectory information. Using CATT, one can select a pollutant of interest, a period of interest, a single site or multiple sites and then plot back trajectories for the site or sites selected. The trajectory features of CATT are useful in exploring and describing the air movements associated with observed air pollution phenomena.

The back trajectories in CATT are calculated by the Atmospheric Transport and Dispersion (ATAD) model. The version of ATAD used in CATT was developed in 1980 by the Air Resources Laboratory (ARL) of the National Oceanic and Atmospheric Administration (NOAA). ATAD is a Lagrangian model that calculates five-day trajectories over North America using rawinsonde data. The rawinsonde data includes data from balloon launches at 00Z, 06Z, 12Z, and 18Z each day. The model calculates four back trajectories per day using one vertical layer. In most cases, the vertical layer starts at 300 meters above ground level. The model calculates the transport layer depth and upper bound for the vertical layer. When no "critical inversion layer" exists, the top of the transport layer is assumed to be 3,000 meters above ground level.

CATT was developed by the Center for Air Pollution Impact and Trend Analysis (CAPITA) at Washington University in St. Louis, Missouri. CAPITA worked closely with the Cooperative Institute for Research in the Atmosphere (CIRA) to create CATT. For more information on CATT contact, Rudi Husar at Washington University in St. Louis at rhusar@me.wustl.edu or visit the CATT web site at: http://datafed.net/projects/catt/CATT_Links.htm. For more information on ATAD contact, Kristi Gephart at CIRA at gebhart@cira.colostate.edu. ATAD is no longer supported by ARL.

5.1 Arendtsville, PA

Site Name: Arendtsville
AIRS Number: 42-001-0001
Latitude: 39.9233 North
Longitude: -77.3081 West
Elevation: 240 meters (787 feet)
Agency Operating the Monitor: Pennsylvania Department of Environmental Protection
Speciation Sampling Frequency: 1-in-6 days

5.1.1 Site Description

The Arendtsville monitoring site is located in south central Pennsylvania. It is approximately 16 kilometers (10 miles) northwest of Gettysburg, PA and about 59 km (37 miles) southwest from Harrisburg, PA. Figure 5-1 shows the monitoring site's location relative to the interstate highway system and large eastern population centers.

Arendtsville is a rural monitoring site. The population of the borough of Arendtsville is only 848. Harrisburg, PA is the closest moderately sized city. Baltimore, MD is the closest metropolitan area about 113 km (70 miles) to the southeast. Figure 5-2 is a detailed map showing the topographic features around the monitoring site and the small town of Arendtsville, PA. Figure 5-3 is a photograph of the site looking east.

Figure 5-1 Location of the Arendtsville, PA Monitoring Site

Source: TopoZone

Figure 5-2 Topographic Map of the Arendtsville, PA Monitoring Site

Figure 5-3 Photograph of the Arendtsville, PA Monitoring Site

The monitoring site occupies a 50 by 50 meter clearing on a knoll west of the town of Arendtsville. The area around the monitoring site is agricultural characterized by rolling hills of pastureland and forested areas. Cows are raised on nearby farms. The site is immediately adjacent to an experimental peach farm. Peach orchard operations including oil spraying and smudge pot burning could have some impact on monitored values at the site.

The Pennsylvania Department of Environmental Protection has no record of any major SO_2 or NO_x sources within 25 miles of the monitoring site. The site is 200 meters from the nearest secondary road.

5.1.2 Major Constituents of $PM_{2.5}$ Mass

The major constituents of $PM_{2.5}$ mass at Arendtsville were sulfate and organic carbon species followed by ammonium and nitrate species. Over 2001-2003, average sulfate concentration was about 6.1 µg/m^3. Using an OM/OC ratio of 1.6, the average organic carbon mass concentration over the three-year period was about 3.9 µg/m^3. At an OM/OC ratio of 1.9, the average organic carbon mass concentration over the period would have been 4.6 µg/m^3. Figure 5-4 shows the relative contribution each major species makes to the total mass measured at the site.

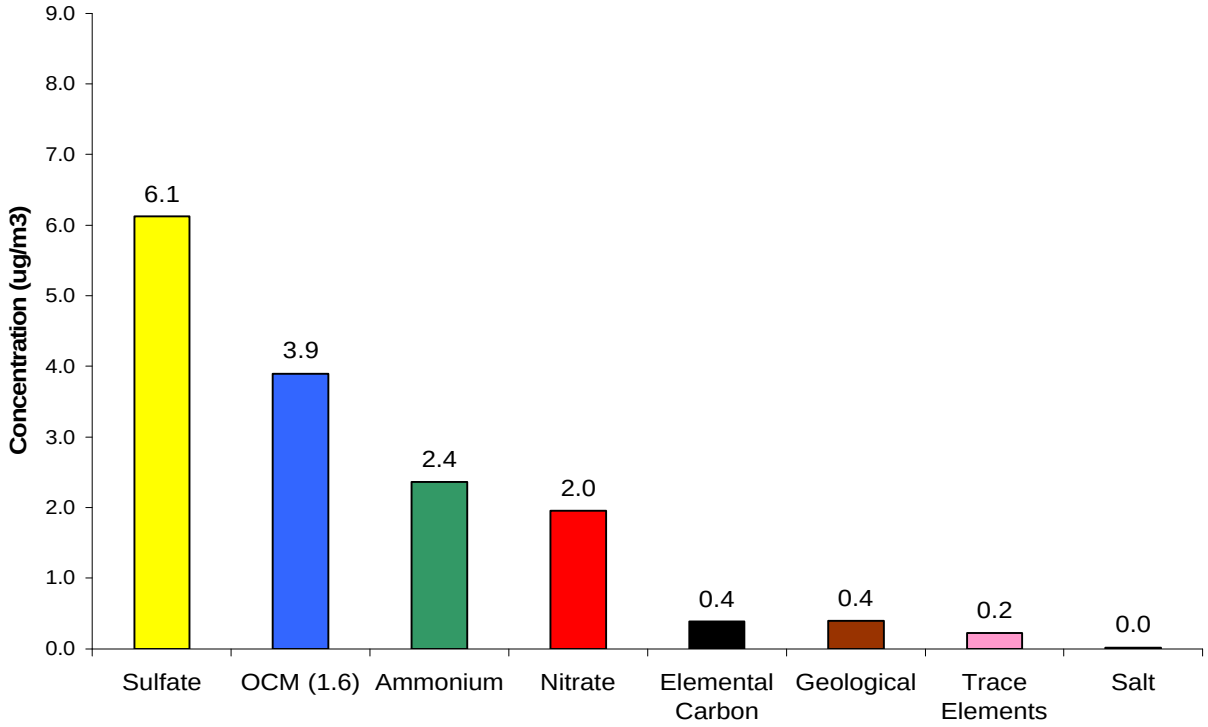

Figure 5-4 Major Constituents of $PM_{2.5}$ Mass, Arendtsville, PA

The average reconstructed mass calculated for this site was about 8 percent lower than the average gravimetric mass measured by the speciation sampler. Average reconstructed mass was 15.2 µg/m^3 whereas the average gravimetric mass was 16.5 µg/m^3. Figure 5-5 visually compares the average reconstructed mass with the average gravimetric mass.

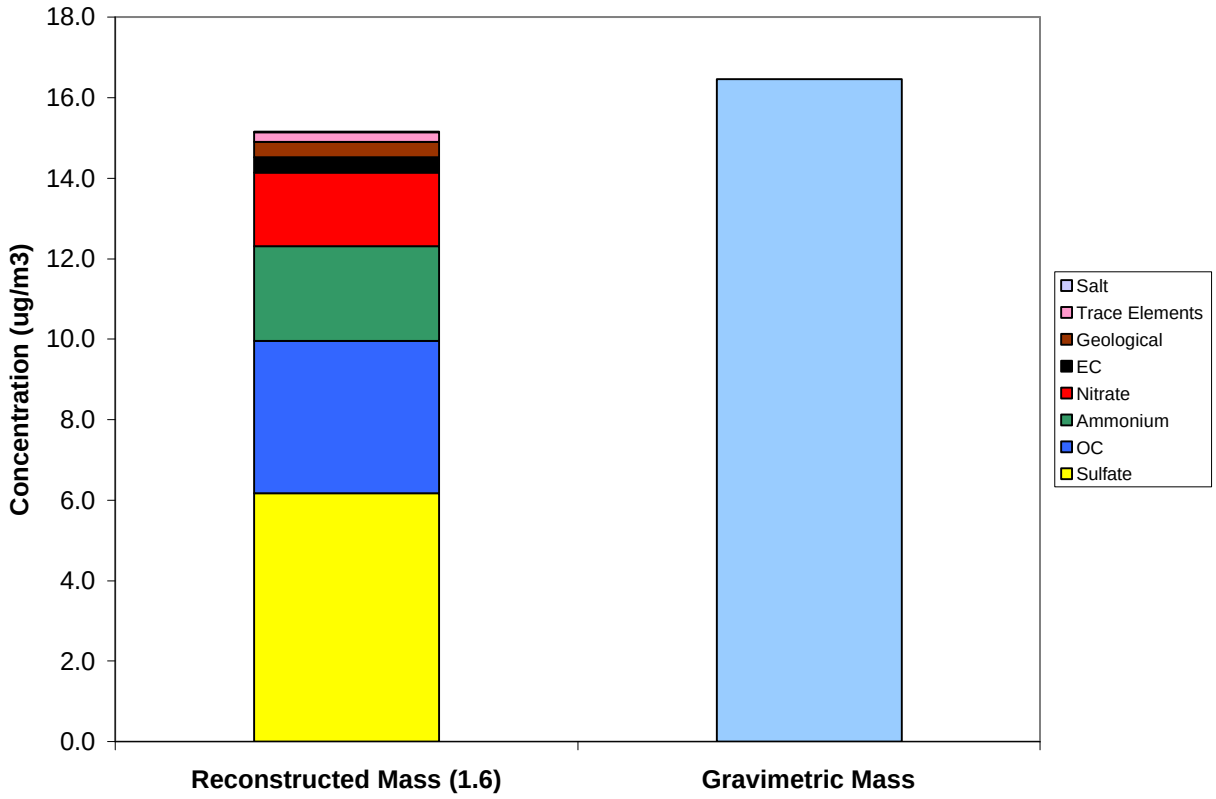

Figure 5-5 Comparison of Average Reconstructed Mass and Average Gravimetric Mass, Arendtsville, PA

5.1.3 Time Series Analysis of $PM_{2.5}$ Species

A speciation sampler was installed at the Arendtsville monitoring site in June 2001. The monitor ran on a 1-in-3 sampling schedule from June 30, 2001 to August 3, 2001. When the monitor returned to service on April 2, 2002, it began sampling on a 1-in-6 day schedule. Figure 5-6 shows a time series for the five major species measured at Arendtsville. Figures 5-7 through 5-11 show how each of the five major constituents of $PM_{2.5}$ mass varied over time. The black line in Figures 5-7 through 5-11 is the 30-day rolling average concentration for the specie. The early 1-in-3 measurement period includes 27 measurements. The later period, April 2, 2003 to December 31, 2003, includes 97 measurements. As noted previously, organic carbon mass concentrations were estimated using an OM/OC ratio of 1.6.

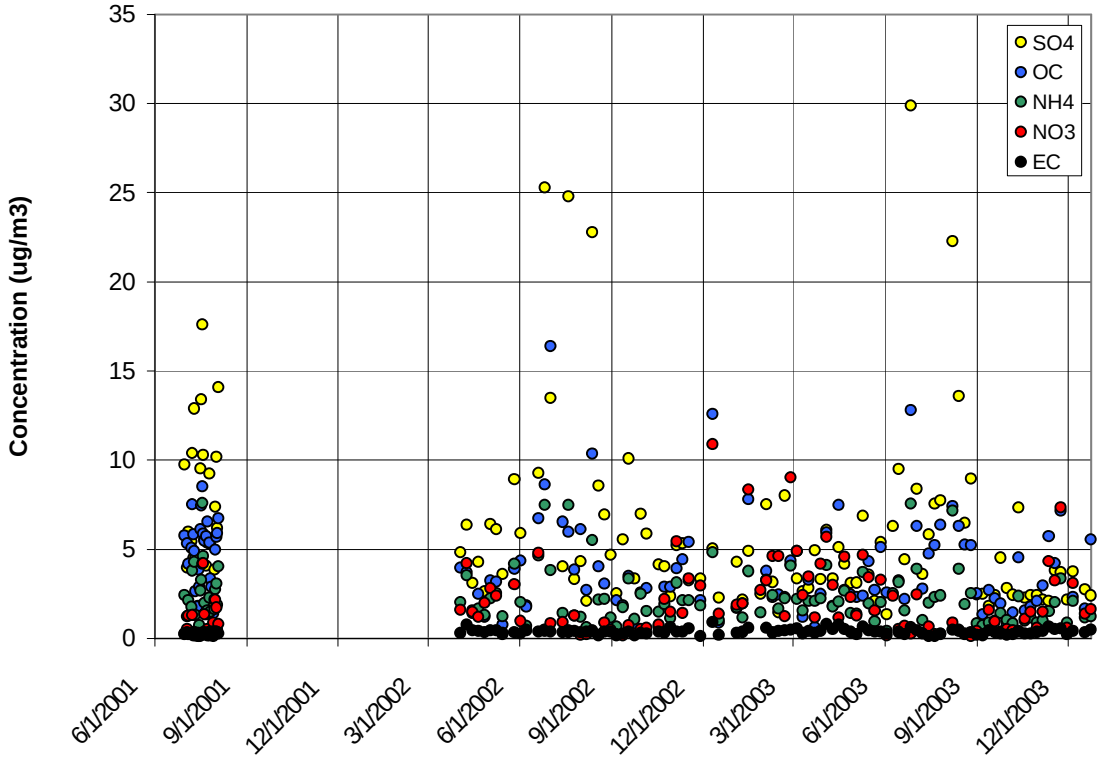

Figure 5-6 Time Series for the Arendtsville, PA Monitor

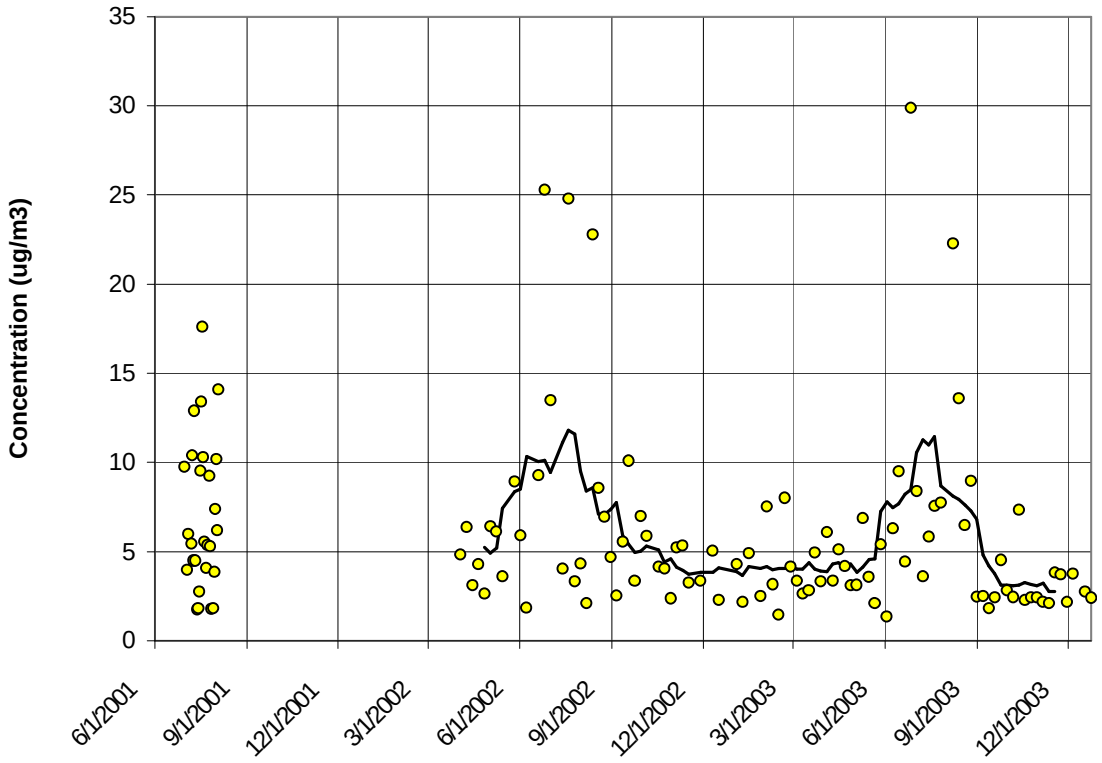

Figure 5-7 Sulfate Time Series for the Arendtsville, PA Speciation Monitor

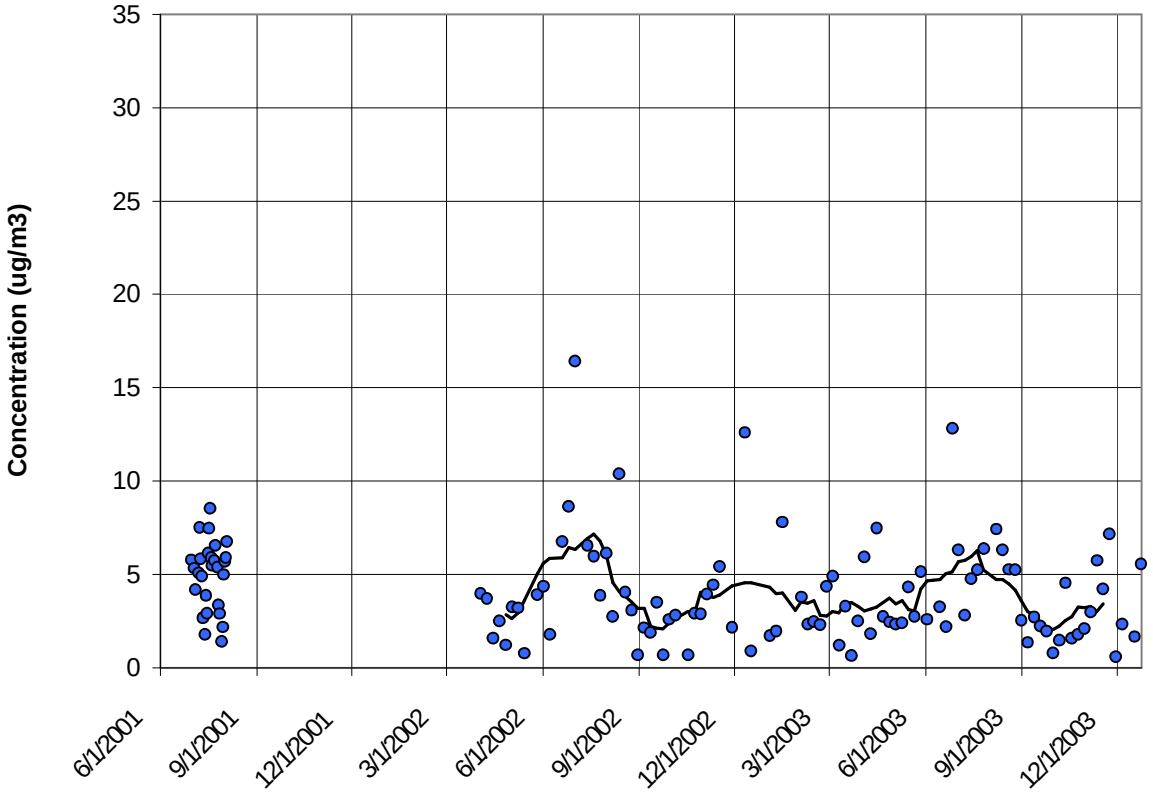

Figure 5-8 Organic Carbon Mass Time Series for the Arendtsville, PA Speciation Monitor

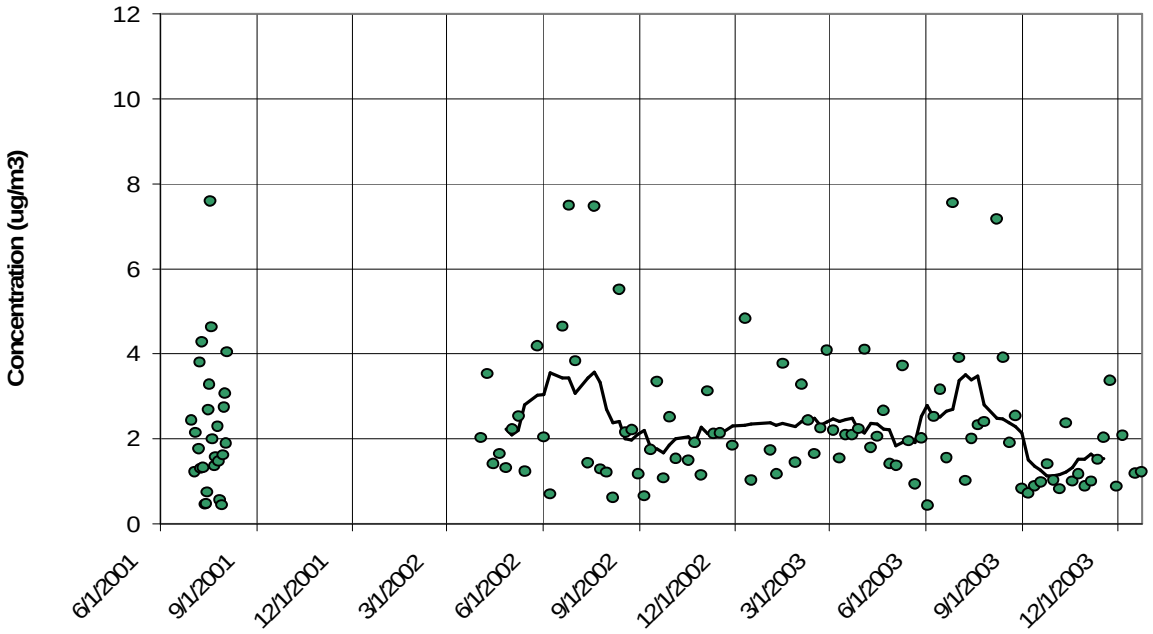

Figure 5-9 Ammonium Time Series for the Arendtsville, PA Speciation Monitor

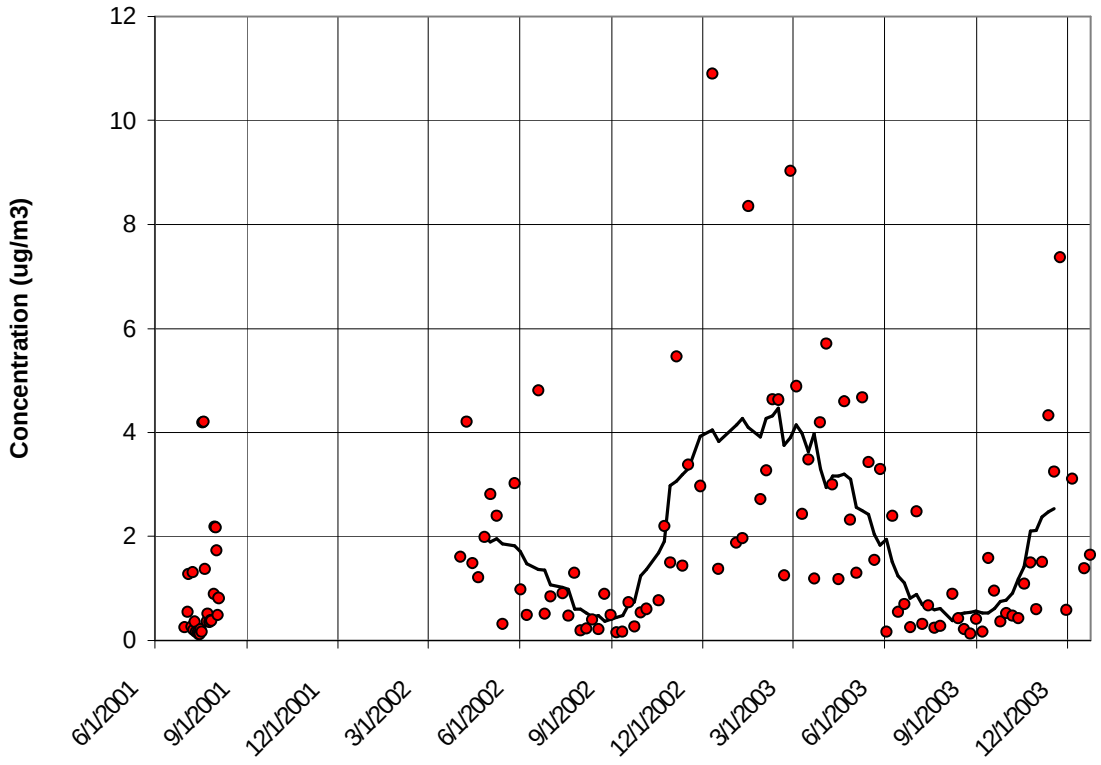

Figure 5-10 Nitrate Time Series for the Arendtsville, PA Speciation Monitor

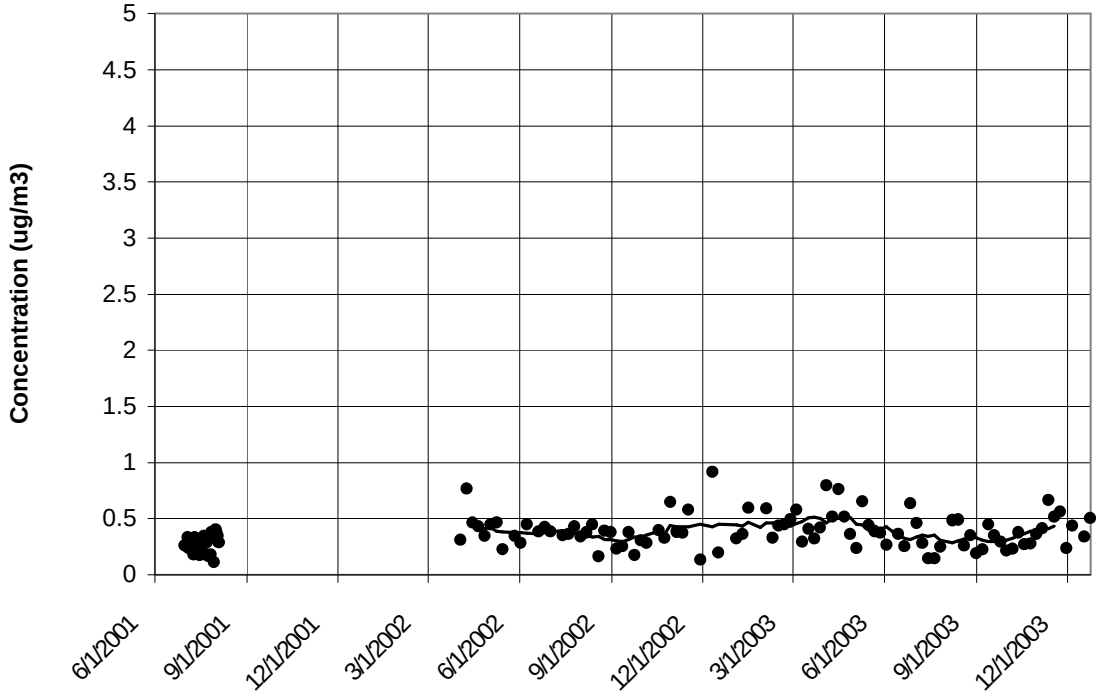

Figure 5-11 Elemental Carbon Time Series for the Arendtsville, PA Speciation Monitor

As Figure 5-7 shows, sulfate peaked during the summer but was an important contributor to $PM_{2.5}$ mass in other seasons as well. Average sulfate concentrations, averaged over all seasons over the 2001-2003 period, was 6.12 µg/m^3. This was the highest average concentration of any of the eleven monitors studied. The average summer sulfate concentration over the study period was 9.51 µg/m^3. As the time series shows, sulfate levels declined in the fall and rose again in late spring. Average fall, winter, and spring concentrations were similar at 4.31 µg/m^3, 4.14 µg/m^3, and 4.43 µg/m^3, respectively. The summer season was noteworthy for the very high concentrations that were occasionally measured. During this study, peak values of 20 to 30 µg/m^3 were recorded.

Over 2001-2003, the average concentration for organic carbon mass was 3.90 µg/m^3. Summer produced the highest seasonal average of 5.51 µg/m^3. Average spring and fall concentrations were lower at 3.08 and 2.55 µg/m^3 respectively. The average winter concentration of 4.02 µg/m^3 fell between summer and spring/fall levels. Organic carbon concentration appears to vary season to season as seen at other sites with summer peaks and weaker winter peaks. This pattern was not as clearly evident at Arendtsville as at other sites. Additional data will likely help resolve how organic carbon concentrations rise and fall seasonally at this site.

Over 2001-2003, the average ammonium concentration at Arendtsville, was 2.36 µg/m^3, the highest average of the eleven monitors studied. During the summer, the average ammonium concentration was 2.94 µg/m^3. On particular days, 24-hour concentrations were as high as 7 µg/m^3. Average ammonium concentration was lowest in the fall. Over 2001-2003, which included only two fall seasons, average ammonium concentration was 1.65 µg/m^3. While ammonium concentration rose in the summer and declined in the fall, what is most obvious from the time series is the relatively constant presence of ammonium species, season-to-season.

Ammonium and sulfate concentrations were well correlated ($R^2 = 0.78$). In the summer, when sulfate concentrations were high, ammonium levels were also high. Table 5-1 lists ammonium and sulfate concentrations on days when sulfate concentration exceeded 15 µg/m^3.

Table 5-1 High Ammonium and Sulfate Days for the Arendtsville, PA Monitor

Date	Ammonium Concentration (µg/m^3)	Sulfate Concentration (µg/m^3)
7/18/01	7.6	17.6
6/25/02	7.5	25.3
7/19/02	7.5	24.8
8/12/02	5.5	22.8
6/26/03	7.6	29.9
8/7/03	7.2	22.3

Nitrate concentration, shown in Figure 5-10, showed strong seasonal behavior. Nitrate concentration was lowest in the late summer/early fall when 24-hour concentrations were sometimes less than 0.5 µg/m^3. Average summer concentration was 0.79 µg/m^3. In the late fall, nitrate concentrations climbed and showed more day-to-day variability. Peak winter concentrations were as high as 8 to 11 µg/m^3. Average winter concentration was 4.55 µg/m^3. Spring was characterized by declining nitrate concentrations.

The average elemental carbon concentration over 2001-2003, was 0.39 µg/m^3, a relatively low concentration compared to other major constituents. Nonetheless, elemental carbon was almost always present in low concentration. Average elemental carbon concentration at Arendtsville

was very similar to the average elemental carbon concentration observed at Kinston, NC another rural site in the region. While additional rural sites in the region should be analyzed, 0.36 to 0.39 µg/m^3 may approximate average rural elemental carbon concentration in the region. This value is about half the average concentration observed at many urban sites.

As the time series in Figure 5-11 shows, elemental carbon exhibits little seasonal variation although concentrations are slightly higher in winter and spring. As the data record is extended, a seasonal pattern may become more evident. On several days over the 2001-2003 period, elemental carbon concentrations reached 0.7 to 0.9 µg/m^3. Since these values represent a doubling of the average concentration, it would be interesting to see if some cause can be found to explain these relatively large increases in concentration.

Seasonal averages for the major constituents of $PM_{2.5}$ mass are summarized in Table 5-2.

Table 5-2 Seasonal Averages for the Major Constituents of $PM_{2.5}$ Mass (µg/m^3) for Arendtsville, PA

	Organic Carbon	Sulfate	Ammonium	Nitrate	Elemental Carbon
Winter	4.02	4.14	2.52	4.55	0.47
Spring	3.08	4.43	2.19	2.76	0.45
Summer	5.51	9.51	2.94	0.79	0.35
Fall	2.55	4.31	1.65	1.23	0.33

5.1.4 Trajectory Analysis

Figure 5-12 shows CATT back trajectories for the cleanest days in the speciation record over the period studied from June 2001 through December 2003. While even lower concentration days can be found in the data record for Federal Reference Method monitors at the site, the trajectories plotted in Figure 5-12 are the lowest concentration days in the speciation record over the period studied. These "clean" days represent the five percent days with the lowest total $PM_{2.5}$ mass.

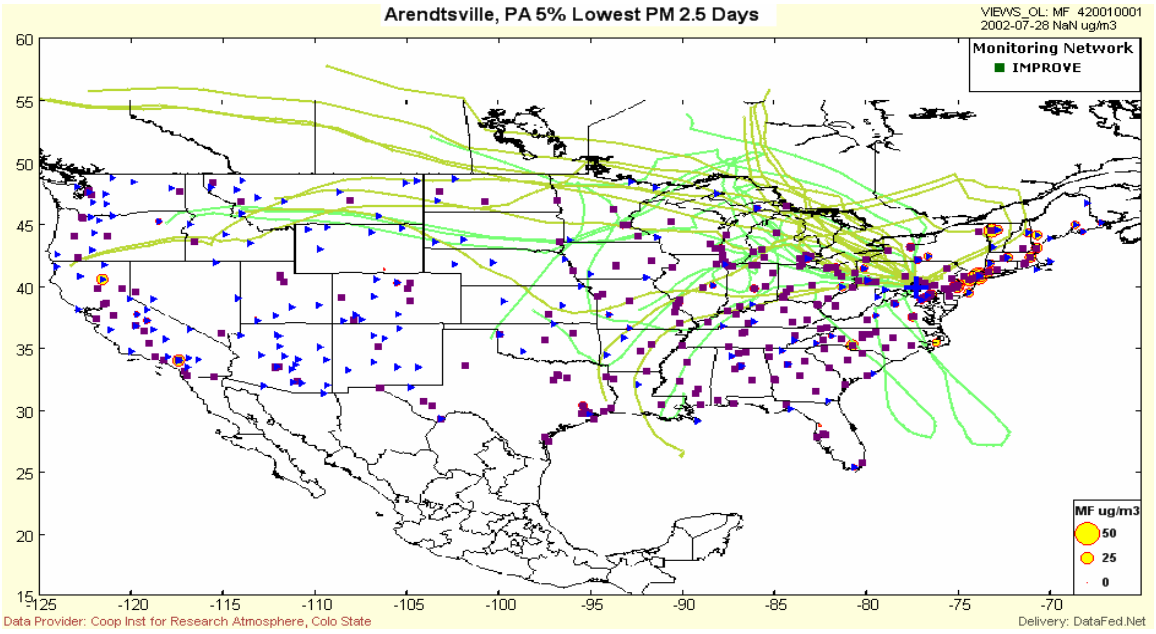

Figure 5-12 Back Trajectories for the Five Percent Cleanest Days, Arendtsville, PA

Clean day trajectories often originated in the Hudson Bay area of Canada and stream in from the northwest. These trajectories do not originate from or move through areas where air pollution emissions are high. Other clean day trajectories come from distant points in Canada or western states or track over the Atlantic Ocean. Generally, "cleaner" trajectories are those that: do not originate from high source regions, do not pass through source regions, or pass quickly through high source regions. Most of the trajectories plotted in Figure 5-12 exhibited these features. Table 5-3 lists the five percent cleanest days and the total mass concentration measured by the speciation monitor on that day.

Table 5-3 Five Percent Lowest Days for Arendtsville, PA

Date	$PM_{2.5}$ Mass ($\mu g/m^3$)
11/29/2003	4.7
8/06/2002	5.2
12/11/2002	5.4
7/14/2001	6.4
9/05/2002	6.8
6/07/2002	6.9
12/16/2002	6.9
Average	6.0

Figure 5-13 shows back trajectories for the dirtiest days, the five percent days with the highest total $PM_{2.5}$ mass. These trajectories show re-circulation over the Ohio River valley and other source regions. The trajectory plot also shows westerly transport to the Arendtsville monitoring site.

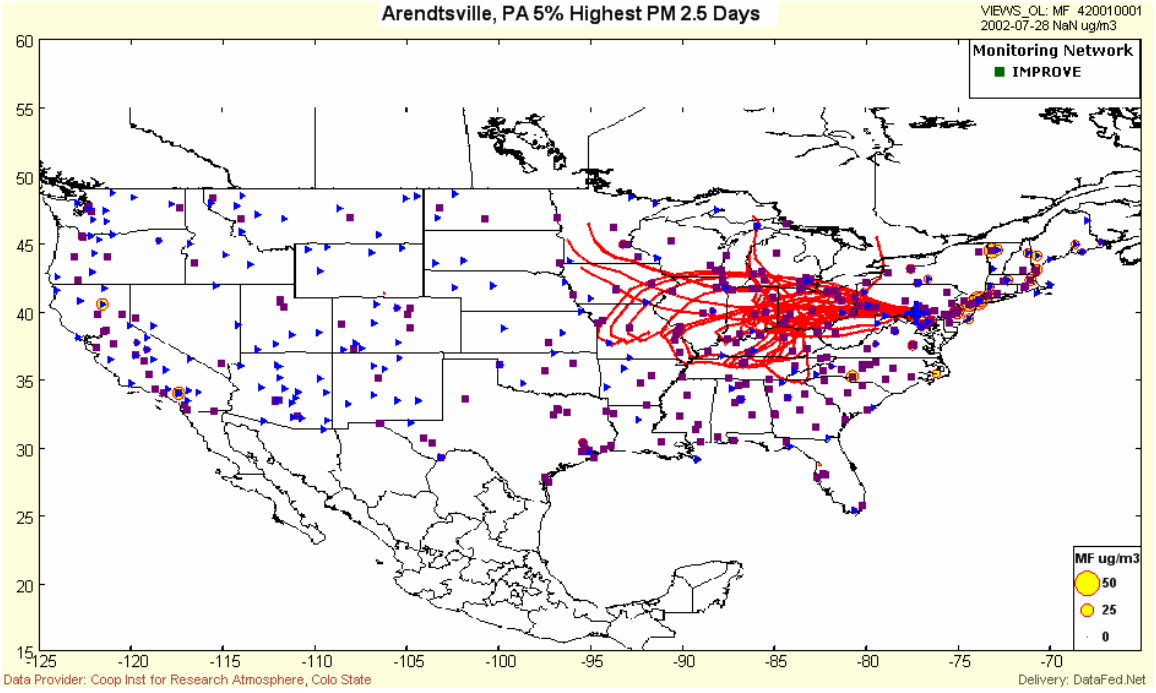

Figure 5-13 Back Trajectories for the Five Percent Dirtiest Days, Arendtsville, PA

Table 5-4 lists the five percent dirtiest days and the total mass concentration measured by the speciation monitor on that day.

Table 5-4 Five Percent Highest Days for Arendtsville, PA

Date	$PM_{2.5}$ Mass ($\mu g/m^3$)
7/01/2002	38.0
8/07/2003	40.8
7/19/2002	42.0
8/12/2002	45.6
7/18/2001	46.4
6/25/2002	51.1
6/26/2003	61.7
Average	46.5

5.2 Baltimore, MD

Site Name: Essex
AIRS Number: 24-005-3001
Latitude: 39.3108 North
Longitude: -76.4744 West
Elevation: 5.5 meters (18 feet)
Agency Operating the Monitor: Maryland Department of the Environment
Speciation Sampling Frequency: 1-in-3 days

5.2.1 Site Description

The Essex monitoring site is located in Essex, MD, a suburban community about 14.5 km (nine miles) east of downtown Baltimore. Figure 5-14 shows the monitoring site's location relative to the interstate highway system and large population centers. As the figure shows, the Essex site is located directly in the Interstate 95 corridor. Washington, DC is about 76 km (47 miles) to the southwest and Philadelphia, PA is about 152 km (94 miles) to the northeast.

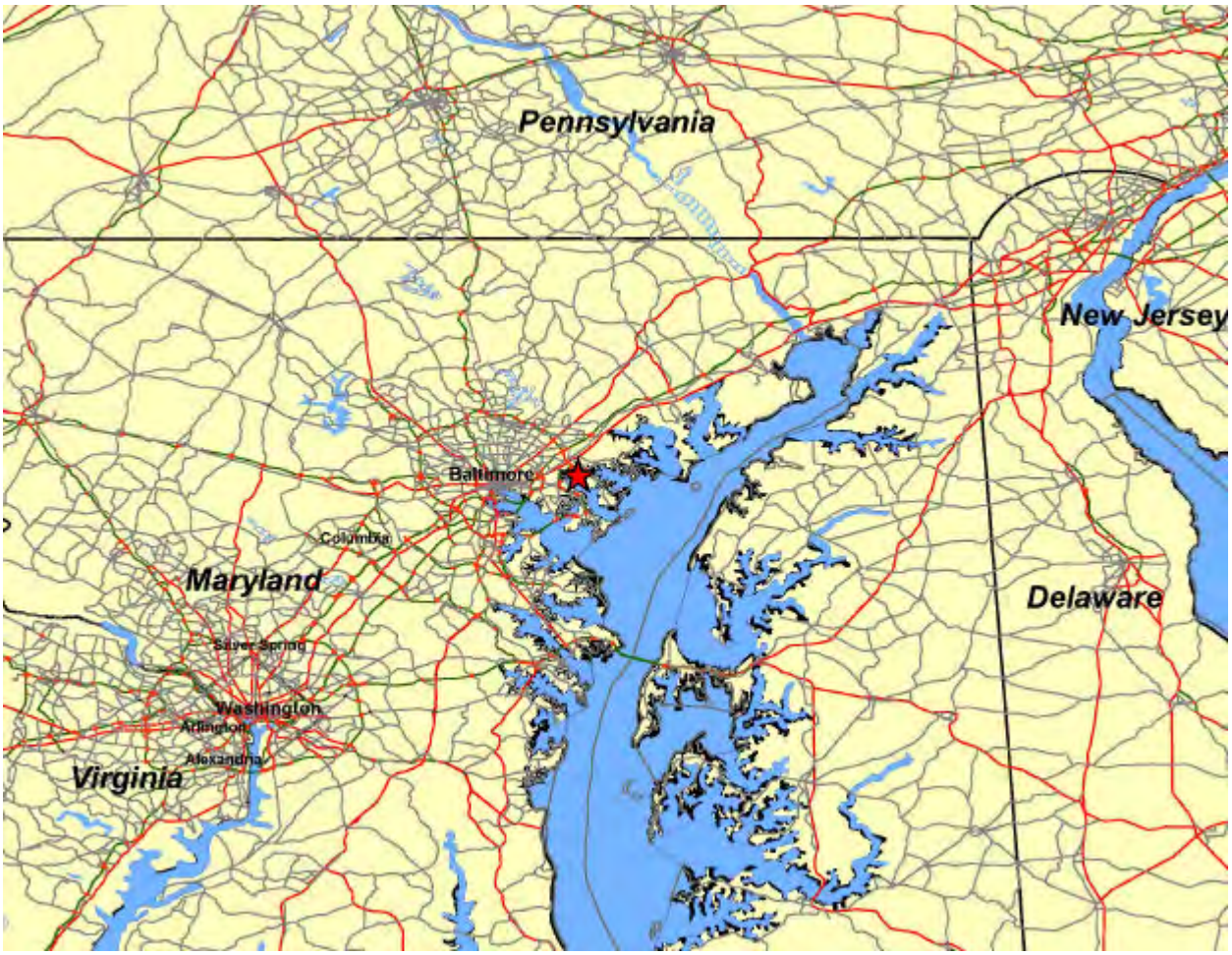

Figure 5-14 Location of the Essex, MD (Baltimore) Monitoring Site

The Essex monitor is a neighborhood scale monitor. The immediate area surrounding the site is residential in all directions. Several malls and shopping centers are within 4 km (2.5 miles) of

the site and four large industrial parks are within 5.6 km (3.5 miles) of the site. A large sewage treatment plant, the Back River Sewage Treatment plant, is about 2.4 km (1.5 miles) southwest from the site. The Baltimore Beltway is about 2.4 km (1.5 miles) west of the site and Interstate 95, the major north/south Interstate highway on the east coast, is about 4.8 km (3 miles) west of the monitor. The urban core of Baltimore to the west of the monitoring site has a population of 636,251 (2000 U.S. Bureau of the Census data). The entire Baltimore area has a population of 2,552,994 (2000 U.S. Bureau of the Census data). Essex lies at the beginning of the peninsula formed by the Back River and Middle Rivers, two estuaries of the Chesapeake Bay. Figure 5-15 is a detailed map showing the topographic features around the monitoring site. Figure 5-16 is a photograph of the site looking southwest.

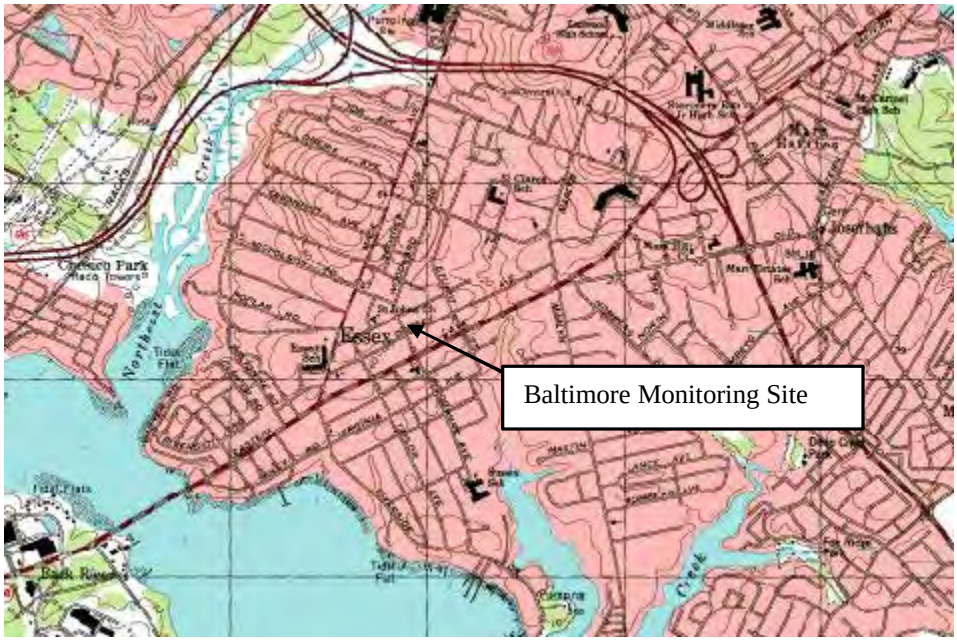

Source: TopoZone

Figure 5-15 Topographic Map of the Baltimore, MD Monitoring Site

Figure 5-16 Photograph of the Baltimore, MD Monitoring Site

The Maryland Department of the Environment reports there are a variety of air pollution sources in the vicinity of the monitoring site. There are 12 facilities within a 14 km (nine miles) of the Essex monitor. Many of the emission sources are south or southwest of the monitoring location. The facilities listed in Table 5-5 are located within about 11 km (seven miles) of the site.

Table 5-5 Emission Sources within 11 km of the Baltimore, MD Monitoring Site

Distance & Direction from Monitoring Site	Facility Type	Emissions
2.4 km, north	Fabricated Metal	VOC
6.4 km, west southwest	Brick & Stone Plant	NO_x
8.1 km, southwest	Auto Assembly Plant	NO_x, VOC
8.9 km, east northeast	Power Plant	CO, NH_3, NO_x, $PM_{2.5-10}$, SO_2, VOC
9.7 km, south	Cement Plant	$PM_{2.5}$, PM_{10}
9.7 km, south	Steel Mill; Blast Furnaces	CO, NH_3, NO_x, $PM_{2.5-10}$, SO_2, VOC
10.1 km, south southwest	Gypsum Plant	NO_x
10.9 km, south southwest	Chemical Plant	CO, NO_x, SO_2, NH_3
11.3 km miles, southwest	Petro Terminal	VOC
11.3 km, southwest	Power Plant	CO, NO_x, VOC, SO_2, $PM_{2.5-10}$, NH_3
12.1 km, southwest	Chemical Plant	NO_x, VOC, SO_2, NH_3
13.7 km, southwest	Chemical Plant	NO_x, VOC, $PM_{2.5-10}$, NH_3

Source: Maryland Department of the Environment

5.2.2 Major Constituents of $PM_{2.5}$ Mass

The major constituents of $PM_{2.5}$ mass at Baltimore were organic carbon and sulfate species followed by ammonium and nitrate species. Using an OM/OC ratio of 1.6, average organic carbon mass concentration over the study period was about 5.82 µg/m^3. Average sulfate concentrations were about 5.13 µg/m^3. Ammonium added about 1.94 µg/m^3 and nitrate added 1.84 µg/m^3 to the average concentration observed. Elemental carbon, geological components, and trace elements contributed about 1.7 µg/m^3 to the average mass measured. Figure 5-17 shows the contribution each species makes to the total mass measured at the site.

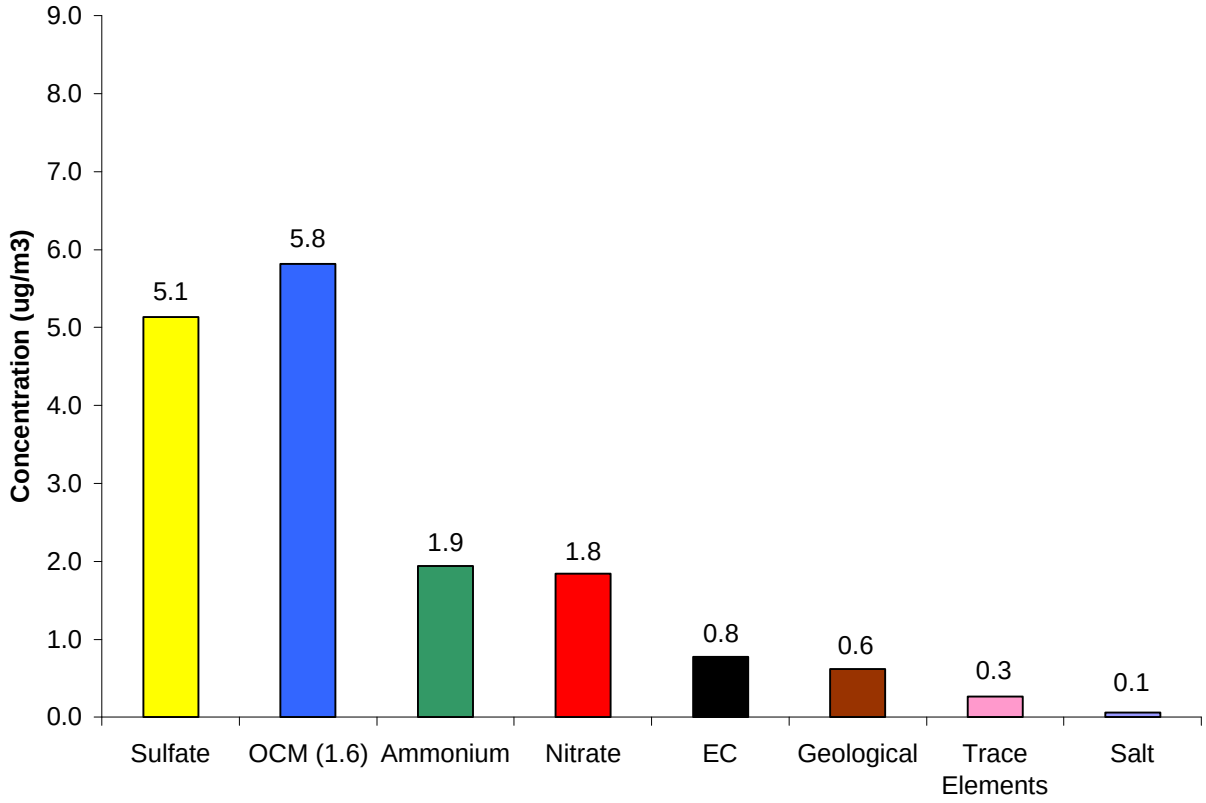

Figure 5-17 Major Constituents of $PM_{2.5}$ Mass, Baltimore, MD

The average reconstructed mass calculated for this site was 2.5 percent higher than the average gravimetric mass measured by the speciation sampler. Average reconstructed mass was 16.3 µg/m^3 whereas the average gravimetric mass was 15.9 µg/m^3. Figure 5-18 visually compares the average reconstructed mass with the average gravimetric mass.

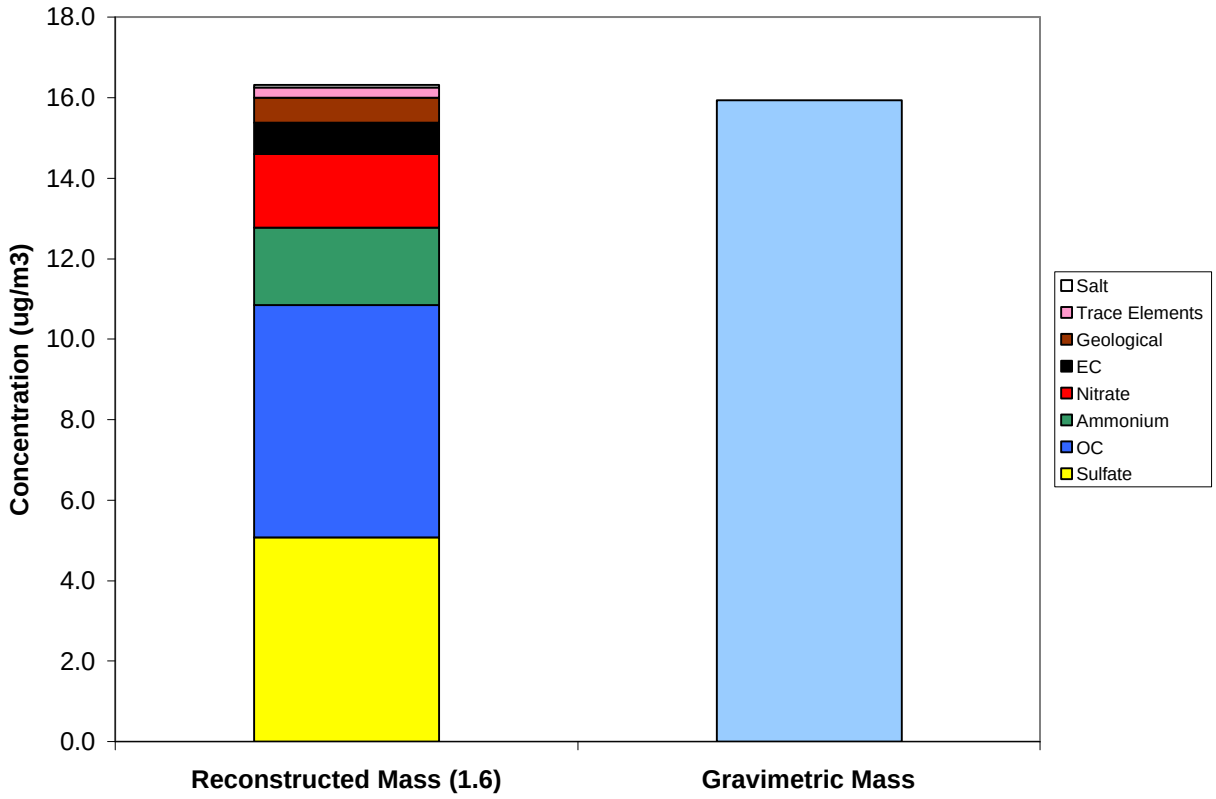

Figure 5-18 Comparison of Average Reconstructed Mass and Average Gravimetric Mass, Baltimore, MD

5.2.3 Time Series Analysis of $PM_{2.5}$ Species

An Anderson RAAS-401 speciation sampler was installed at the Baltimore monitoring site on October 1, 2000. It has operated on a 1-in-3 sampling schedule from its installation to the present time. Data was not collected from February through the March 2002 and from October 15 through December 31, 2003. From July 1-31, 2002, the Maryland Department of the Environment conducted a summer intensive at the Essex monitoring site and collected daily speciation samples. Figure 5-19 shows a composite time series for the five major species measured at the Essex monitoring site. Figures 5-20 through 5-24 show time series for each of the five major species. In the time series plots for the five major species, the black line is the 30-day rolling average concentration for the specie. The 30-day rolling average is not shown during the 30-day intensive in July 2002 when daily samples were taken.

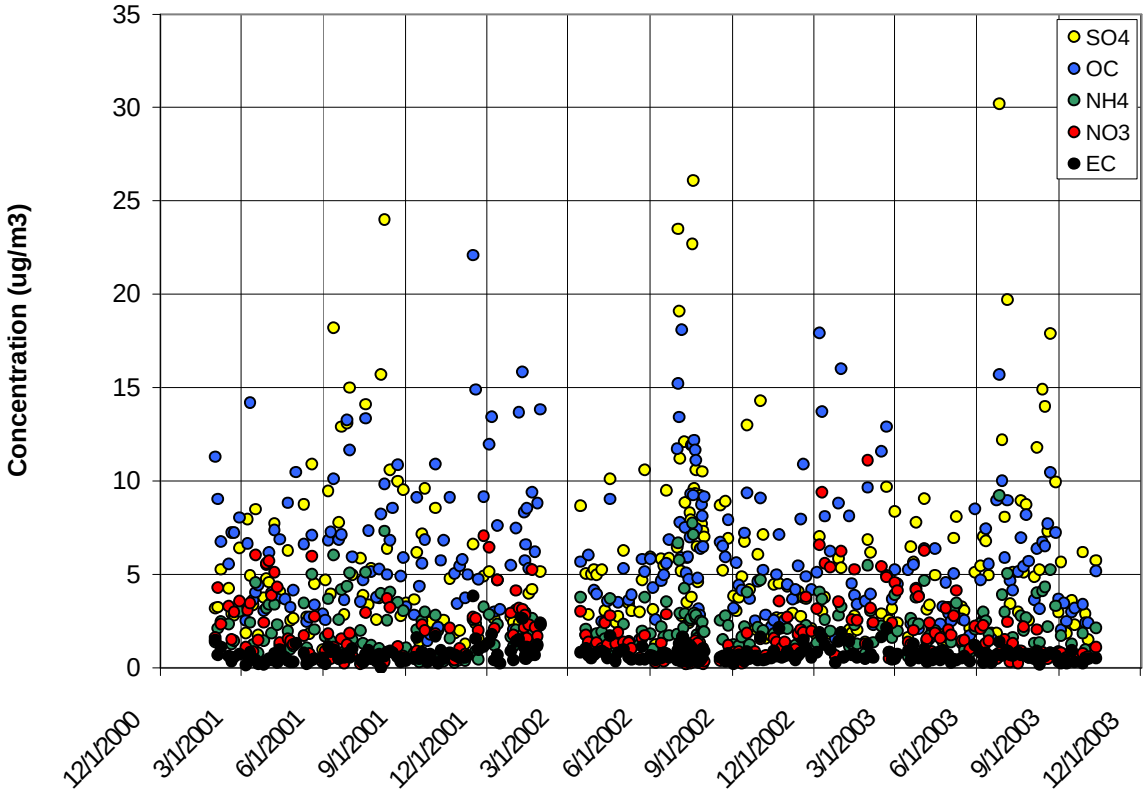

Figure 5-19 Time Series for the Baltimore, MD Monitor

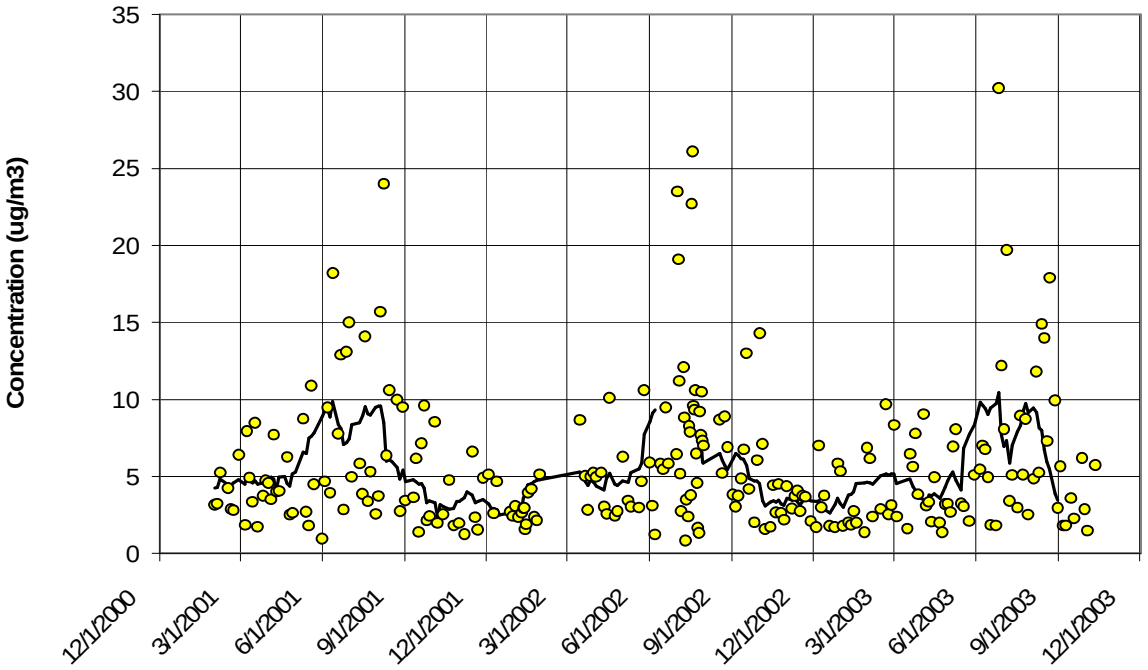

Figure 5-20 Sulfate Time Series for the Baltimore, MD Monitor

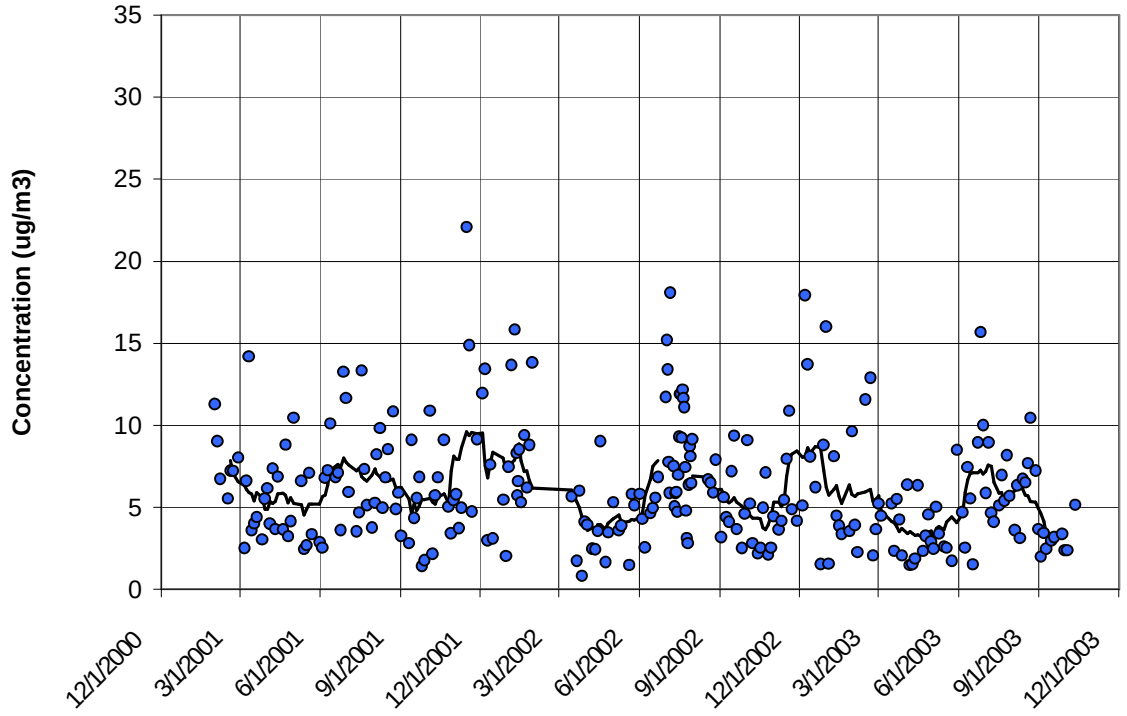

Figure 5-21 Organic Carbon Mass Time Series for the Baltimore, MD Monitor

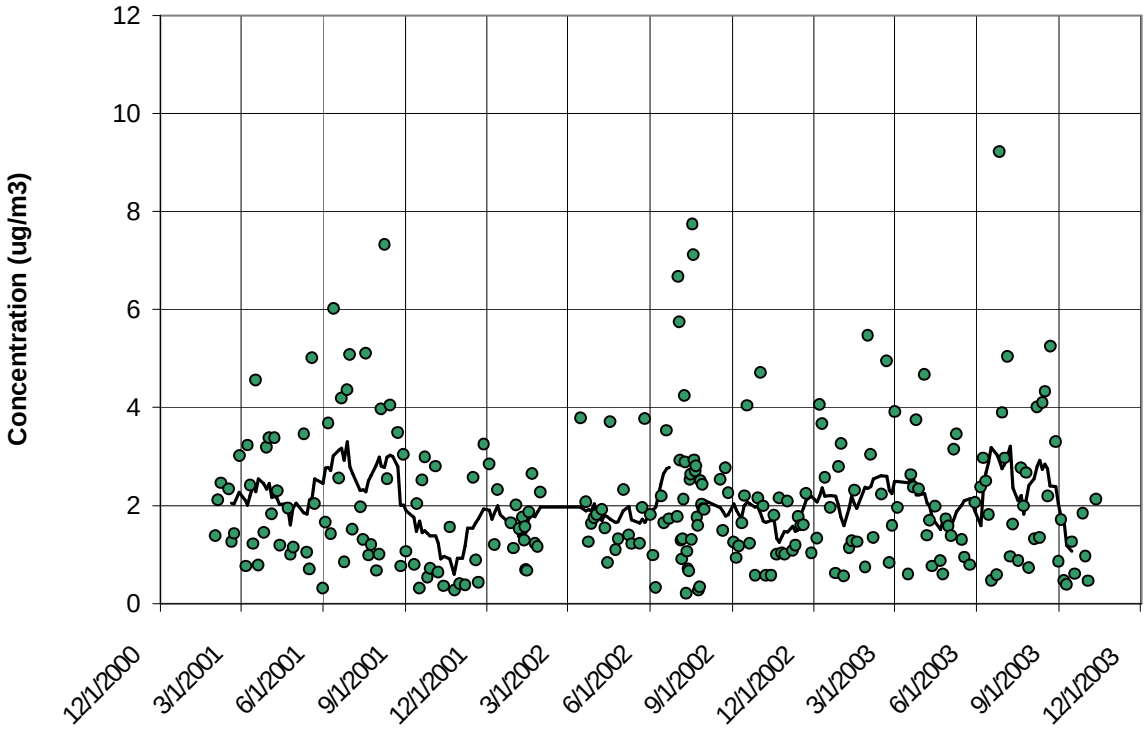

Figure 5-22 Ammonium Time Series for the Baltimore, MD Monitor

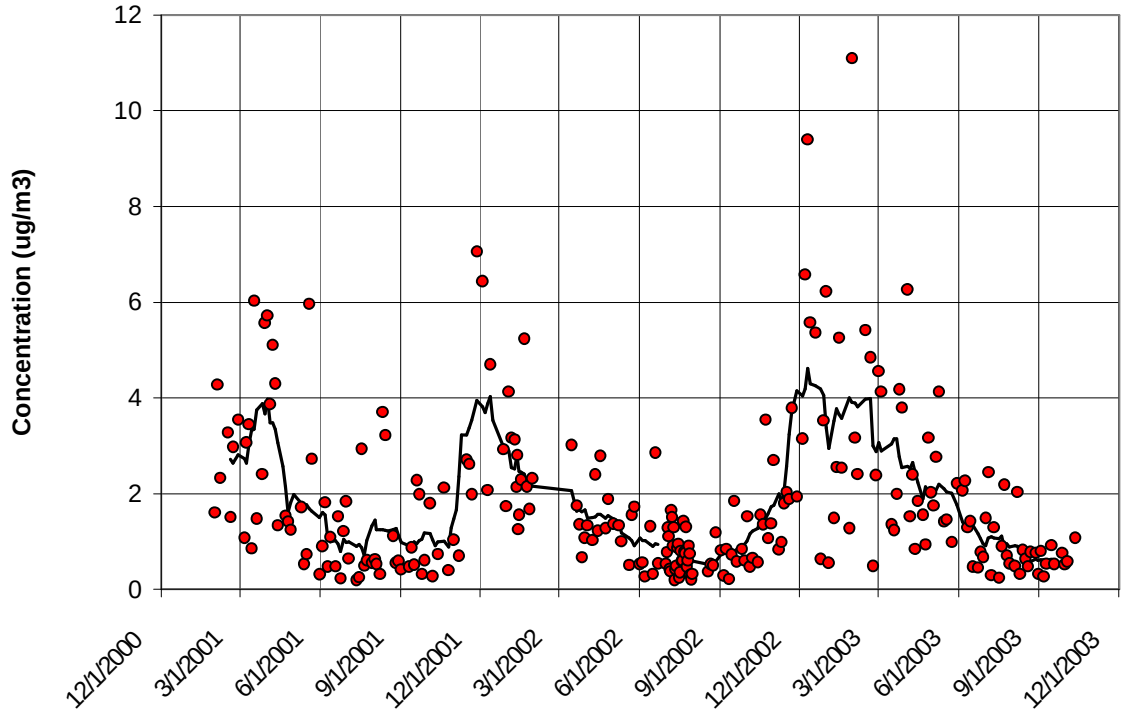

Figure 5-23 Nitrate Time Series for the Baltimore, MD Monitor

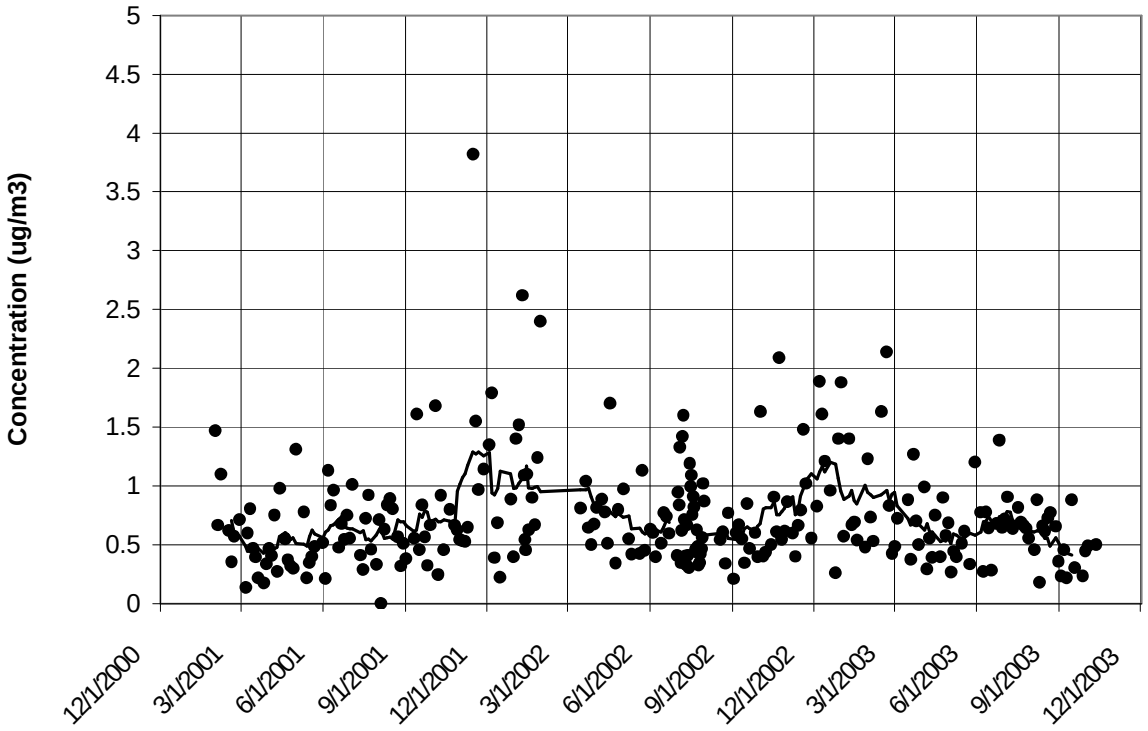

Figure 5-24 Elemental Carbon Time Series for the Baltimore, MD Monitor

The 30-day rolling average sulfate concentration in Figure 5-20 shows how sulfate varied seasonally over the 2001-2003 period. Sulfate concentration was lowest in winter at an average value of about 3.38 µg/m^3. In late January or February, sulfate concentration began to rise and continued rising until peak values were reached in summer. Average summer sulfate concentration was 8.21 µg/m^3. Peak summer values were as high as 20-30 µg/m^3. In late August, sulfate concentrations began to decline and continued declining through the fall until winter levels were reached. As the sulfate time series shows, sulfate concentrations were much more variable in summer than in winter.

At an OM/OC ratio of 1.6, organic carbon was the largest contributor to $PM_{2.5}$ mass in Baltimore. While organic carbon did not exhibit the dramatic seasonal behavior seen in the sulfate time series, seasonal patterns can be discerned. In Figure 5-21, the 30-day rolling average shows modest increases in organic carbon concentration during summer months and in late fall/ early winter. High organic carbon mass concentrations were recorded on July 7-9, 2002 when smoke from Canadian forest fires moved into the Baltimore area. These high values, 65.0, 41.0, and 19.7 µg/m^3 respectively, were considered exceptional events and were removed from the dataset.

Over 2001-2003, using an OM/OC ratio of 1.6, organic carbon mass concentration averaged 5.82 µg/m^3 and ranged from about 1.0 to 22.1 µg/m^3. The average summer concentration was 6.64 µg/m^3 and the average winter concentration was 7.62 µg/m^3. Baltimore had the highest winter organic carbon mass concentration in the region. Baltimore's average winter organic carbon concentration was greater than nearby Washington, DC (5.45 µg/m^3) and Wilmington, DE (5.65 µg/m^3). Average spring and fall concentrations were 3.82 µg/m^3 and 5.31 µg/m^3.

Over 2001-2003, average ammonium concentration was 1.94 µg/m^3. This average concentration was similar to concentrations observed in other nearby urban areas. For example, the 2001-2003 average ammonium concentration was 2.02 µg/m^3 in Washington, DC and 2.08 µg/m^3 in Philadelphia, PA. Figure 5-22 shows how ammonium concentration rose and fell over the period. Summer had the highest average concentration at 2.48 µg/m^3 followed by winter and spring with an average concentration of about 1.97 µg/m^3 each. Average ammonium concentration was lowest in the fall at about 1.43 µg/m^3. Ammonium concentrations were more variable in the summer than during other times of the year. Occasionally, summer concentrations rose above 6 µg/m^3.

Ammonium and sulfate concentrations were well correlated (R^2 = 0.84); when ammonium concentrations were high, sulfate concentrations were usually high. Table 5-6 lists ammonium and sulfate concentrations on days when sulfate concentration exceeded 15 µg/m^3.

The average nitrate concentration for Baltimore over the 2001-2003 period was 1.84 µg/m^3. Out of the eleven sites analyzed in the regional analysis, Baltimore fell somewhere in the middle between the average high at Wilmington, DE (2.48 µg/m^3) and the average low at Charlotte, NC (0.94 µg/m^3) and close to the regional average of 1.76 µg/m^3. As Figure 5-23 shows, nitrate measurements exhibited the seasonal variation seen at other sites. Nitrate concentrations were lowest and least variable during the summer and noticeably higher and more variable in the winter. Over 2001-2003, the average summer concentration was 0.89 µg/m^3 whereas the average winter concentration was 3.52 µg/m^3. In spring and fall, the average nitrate concentrations were 2.05 µg/m^3 and 1.31 µg/m^3 respectively.

Table 5-6 High Ammonium and Sulfate Days for the Baltimore, MD Monitor

Date	Ammonium Concentration (µg/m^3)	Sulfate Concentration (µg/m^3)
6/12/01	6.0	18.2
8/4/01	4.0	15.7
8/8/01	7.3	24.0
7/2/02	6.7	23.5
7/3/02	5.8	19.1
7/18/02	7.7	22.7
7/19/02	7.1	26.1
6/26/03	9.2	30.2
7/5/03	5.0	19.7
8/22/03	5.3	17.9

Figure 5-24 displays the time series for elemental carbon. Average elemental carbon concentration was lowest during the summer at about 0.64 µg/m^3 and highest during the winter at about 1.05 µg/m^3. Average spring concentration was 0.68 µg/m^3 and average fall concentration was 0.75 µg/m^3. Peak levels were observed in the late fall and winter months. Many values between 1.5 and 3.8 µg/m^3 were recorded.

Seasonal averages for the major constituents of $PM_{2.5}$ mass are summarized in Table 5-7.

Table 5-7 Seasonal Averages for the Major Constituents of $PM_{2.5}$ Mass (µg/m^3) for Baltimore, MD

Season	Organic Carbon	Sulfate	Ammonium	Nitrate	Elemental Carbon
Winter	7.62	3.38	1.97	3.52	1.05
Spring	3.82	4.60	1.97	2.05	0.68
Summer	6.64	8.21	2.48	0.89	0.64
Fall	5.31	4.12	1.43	1.31	0.75

5.2.4 Trajectory Analysis

Figure 5-25 shows CATT back trajectories for the cleanest days in the speciation record over the period studied from January 2001 through the end of August 2003. While even lower concentration days can be found in the data record of Federal Reference Method monitors at the Essex site, the trajectories plotted in Figure 5-25 are the lowest concentration days in the speciation record over the period studied. These “clean” days represent the five percent days with the lowest total $PM_{2.5}$ mass.

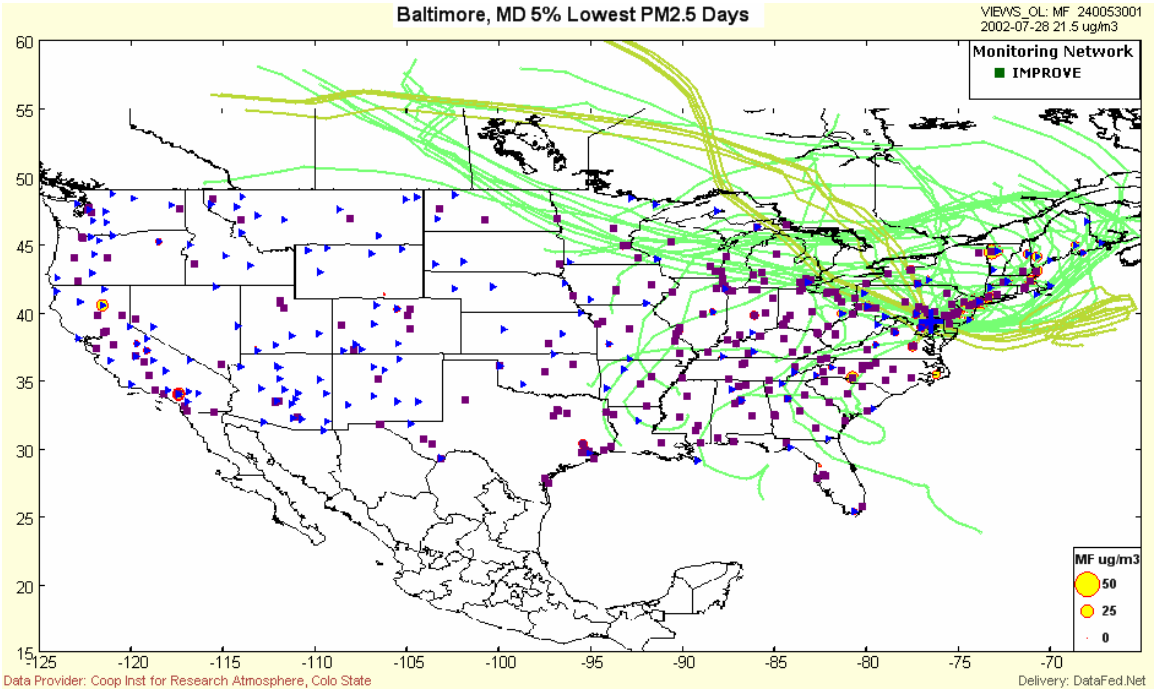

Figure 5-25 Back Trajectories for the Five Percent Cleanest Days, Baltimore, MD

Many "clean day" trajectories travel great distances from the northern or western Canadian provinces to Baltimore. These tracks indicate fast moving air masses probably associated with large-scale weather systems. In contrast to trajectories associated with high concentrations, these trajectories do not remain or re-circulate over source regions. Most other clean day trajectories are maritime trajectories tracking in from the Atlantic Ocean. Table 5-8 lists the five percent cleanest days at Baltimore, MD and the total mass concentration measured by the speciation monitor on that day.

Table 5-8 Five Percent Lowest Days for Baltimore, MD

Date	$PM_{2.5}$ Mass ($\mu g/m^3$)
9/25/2001	5.0
10/7/2001	5.5
11/6/2001	6.0
12/15/2001	5.1
6/7/2002	4.6
7/11/2002	4.5
7/26/2002	5.7
12/25/2002	4.5
1/3/2003	5.0
4/12/2003	5.7
5/24/2003	6.0
6/17/2003	5.4
10/3/2003	5.9

Figure 5-26 shows back trajectories for the dirtiest days, the five percent days with the highest total $PM_{2.5}$ mass. With the exception of the trajectories associated with the July 2002 Canadian forest fires that move through southeastern Canada, "dirty day" trajectories are tracks of air masses that have spent the past five days over the continental U.S and arrive in Baltimore from the west. In many cases, the air circulates or re-circulates through air pollution source regions in the Midwest.

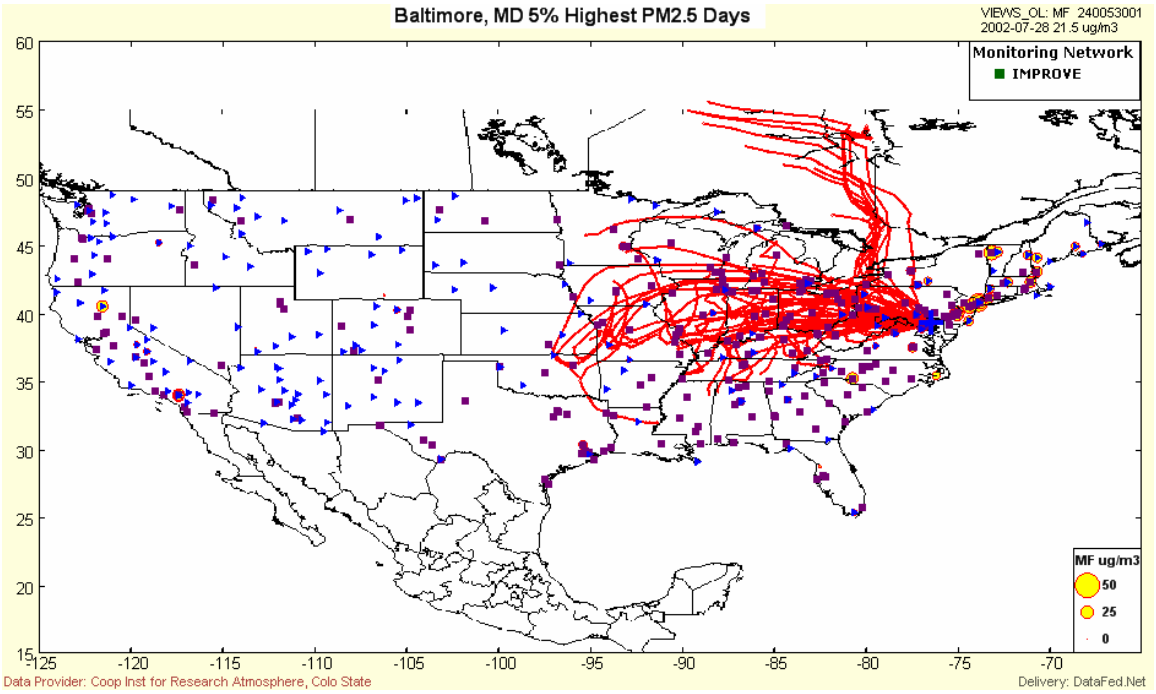

Figure 5-26 Back Trajectories for the Five Percent Dirtiest Days, Baltimore, MD

Table 5-9 lists the five percent dirtiest days and the total mass concentration measured by the speciation monitor on that day. All of the five percent dirtiest days occurred during the months of June, July and August.

Table 5-9 Baltimore, MD, Five Percent Highest Days

Date	$PM_{2.5}$ Mass ($\mu g/m^3$)
6/12/2001	41.6
8/8/2001	46.6
7/2/2002	51.8
7/3/2002	48.8
7/7/2002	78.5
7/8/2002	58.8
7/9/2002	43.0
7/18/2002	49.3
7/19/2002	47.5
6/26/2003	66.1
7/5/2003	43.9
8/22/2003	40.0

5.3 South Charleston, WV

Site Name: South Charleston Public Library
AIRS Number: 54-039-1005
Latitude: 38.3681 North
Longitude: -81.6936 West
Elevation: 183 meters (600 feet)
Agency Operating the Monitor: West Virginia Department of Environmental Protection, Division of Air Quality
Speciation Sampling Frequency: 1-in-6 days

5.3.1 Site Description

The South Charleston monitoring site is located about 5.6 km (3.5 miles) northwest of Charleston, WV. Figure 5-27 shows the monitoring site's general location relative to the interstate highway system and large population centers. The closest major cities to South Charleston are Columbus, OH about 209 km (130 miles) to the north northwest, Cincinnati, OH about 257 km (160 miles) to the northwest, and Pittsburgh, PA about 270 km (168 miles) to the northeast.

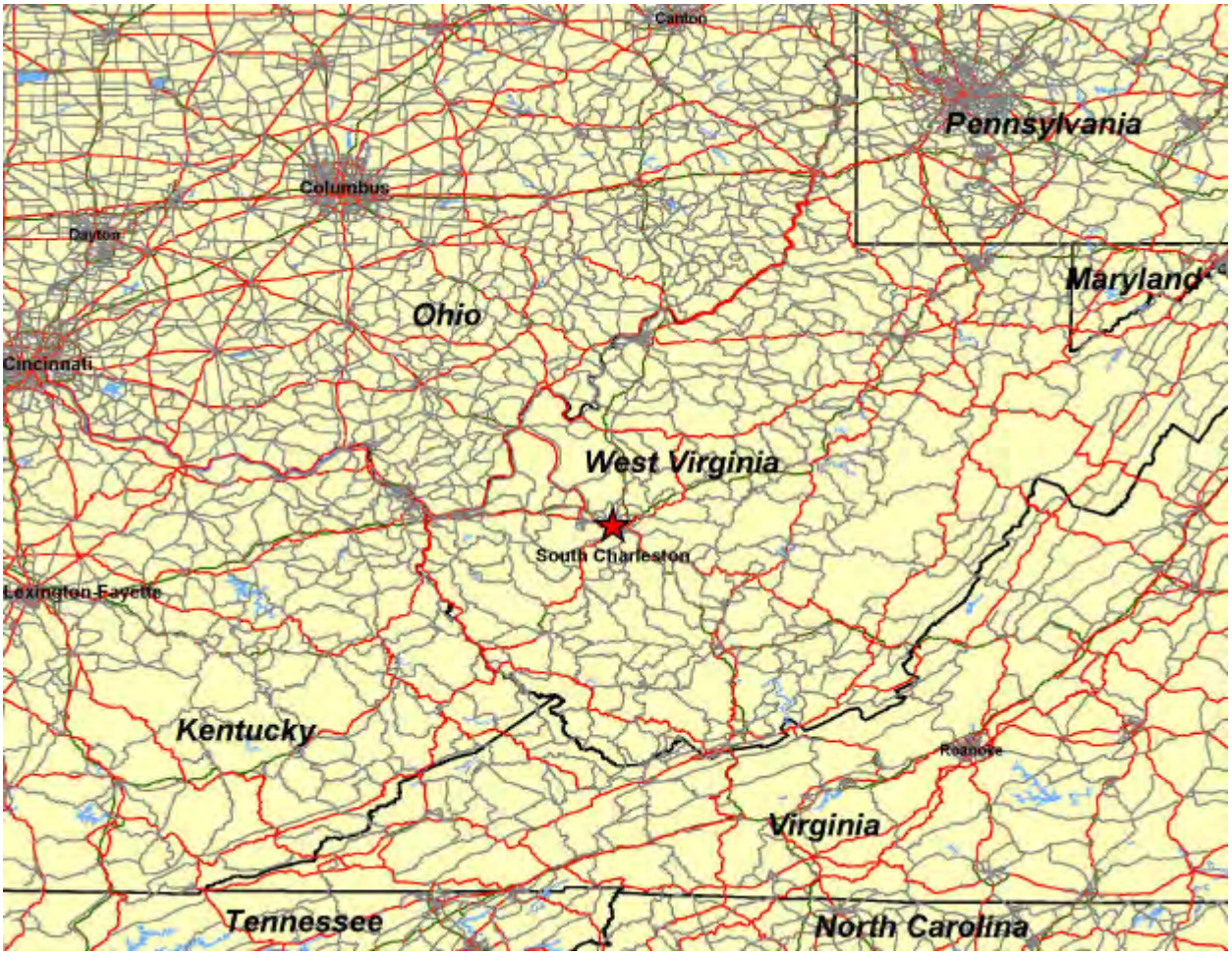

Figure 5-27 Location of the Charleston, WV Monitoring Site

The monitoring site is located on the roof of the South Charleston Public Library, a one-story building at the corner of 4th and D Streets in downtown South Charleston. The area immediately around the monitoring site is a mix of residential, commercial, and industrial properties. While the city of South Charleston has a population of 13,390, the city of Charleston, only a short distance to the southeast, has a population of 53, 421.

South Charleston lies in the Kanawha River valley. At the monitoring site's location the river valley is only about 1.3 km (0.8 mile) wide. Steep hills rise sharply on both sides of the valley, climbing to elevations 200 to 300 feet above the river. While the monitor is sited in a location with urban characteristics, the surrounding terrain outside of the valley is mountainous, forested land. General land use quickly changes from urban to rural as one climbs out of the Kanawha River valley. Figure 5-28 is a detailed map showing the topographic features around the monitoring site. Figure 5-29 is a photograph of the monitoring site.

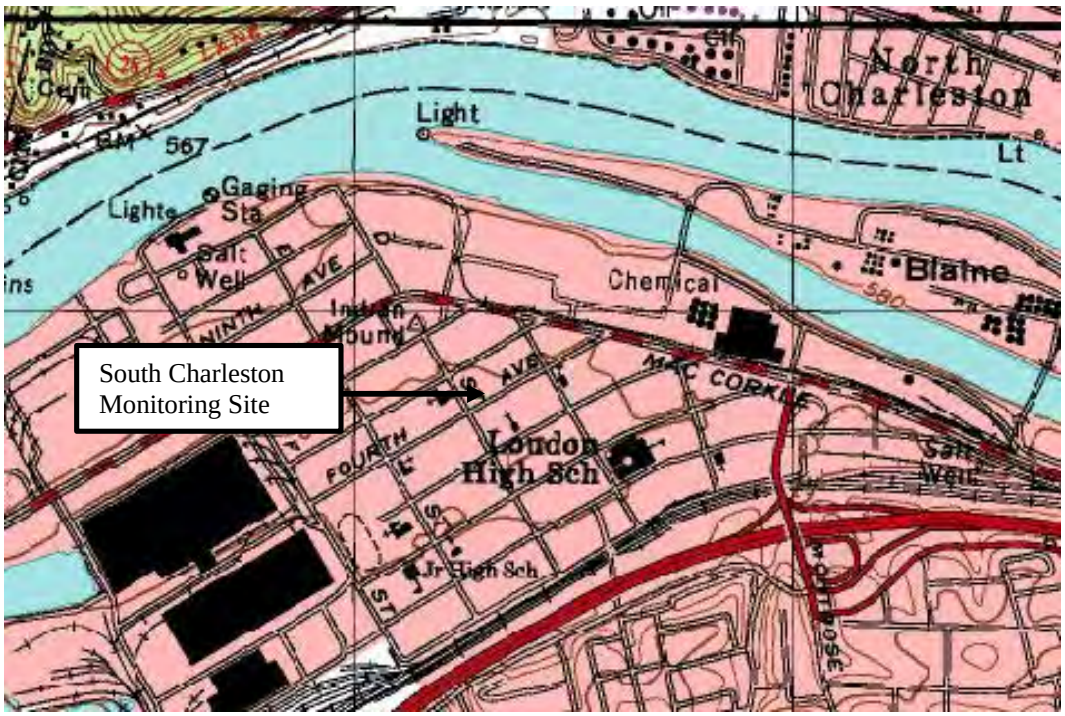

Source: TopoZone

Figure 5-28 Topographic Map of the Charleston, WV Monitoring Site

Figure 5-29 Photograph of the South Charleston, WV Monitoring Site

The West Virginia Division of Air Quality is engaged in an investigation of differences in $PM_{2.5}$ speciation between "in valley" sites like the South Charleston monitoring site and "out of valley" sites. The out of valley companion site for the South Charleston monitor is the Guthrie monitoring station about 7-8 miles to the north of the South Charleston location.

Mobile source and industrial emissions likely contribute to $PM_{2.5}$ speciation measurements made at the South Charleston monitor. U.S Route 60 (McCorkle Avenue) is about 274 meters (900 feet) north of the monitor. Route 60 is a four-lane street with many traffic lights and turning lanes. Interstate 64, a major east-west artery in West Virginia, is 0.5 km (0.3 miles) south of the monitor. In South Charleston, I-64 is a four-lane highway that carries both commuter and interstate traffic. Interstate 77/79 is approximately 4.8 km (3.0 miles) east of the monitor.

The Division of Air Quality of the West Virginia Department of Environmental Protection reports there were a variety of point sources of air pollution in the vicinity of the monitoring site. Table 5-10 lists some of the largest sources. Dow Chemical and Clearon Corporation also emit NO_x, SO_2, and VOCs.

Table 5-10 Emission Sources in the Vicinity of the South Charleston, WV Monitoring Site

Facility Name	Site Description	Distance (km)	Direction	$PM_{2.5}$ (tons/yr)
Dow Chemical	Chemical manufacturing	1.6	NE	40
Clearon Corporation	Chemical manufacturing	0.8	W	46.9
Mayflower Vehicle Systems	Steel automotive parts stamping	0.5	W	NA[1]

[1] Not Applicable

5.3.2 Major Constituents of $PM_{2.5}$ Mass

The West Virginia Department of Environmental Protection requested that MARAMA summarize the 2004-2005 $PM_{2.5}$ speciation data for their South Charleston monitoring site even though these data cannot be directly compared with other sites presented in this report. The South Charleston site cannot be directly compared with other sites because other sites utilize 2001-2003 data. The following analysis of speciation data is based on data from January 1, 2004 through November 12, 2005. Data for November 13 through December 31, 2005 was not available at the time this analysis was prepared.

From January 2004 to November 2005, the major constituents of $PM_{2.5}$ mass at the South Charleston monitor were organic carbon mass and sulfate species followed by ammonium and nitrate species. Using an OM/OC ratio of 1.6, organic carbon species contributed about 5.92 $\mu g/m^3$ to the average $PM_{2.5}$ concentration measured. Average sulfate concentration was about 5.67 $\mu g/m^3$. Average ammonium and nitrate concentrations were 1.90 $\mu g/m^3$ and 1.10 $\mu g/m^3$ respectively. Average elemental carbon concentration was about 0.94 $\mu g/m^3$. Figure 5-30 shows the contribution the major five species made to the average $PM_{2.5}$ concentration measured at the site. The average concentration of geological material, trace elements, and salt were not calculated for the South Charleston monitor.

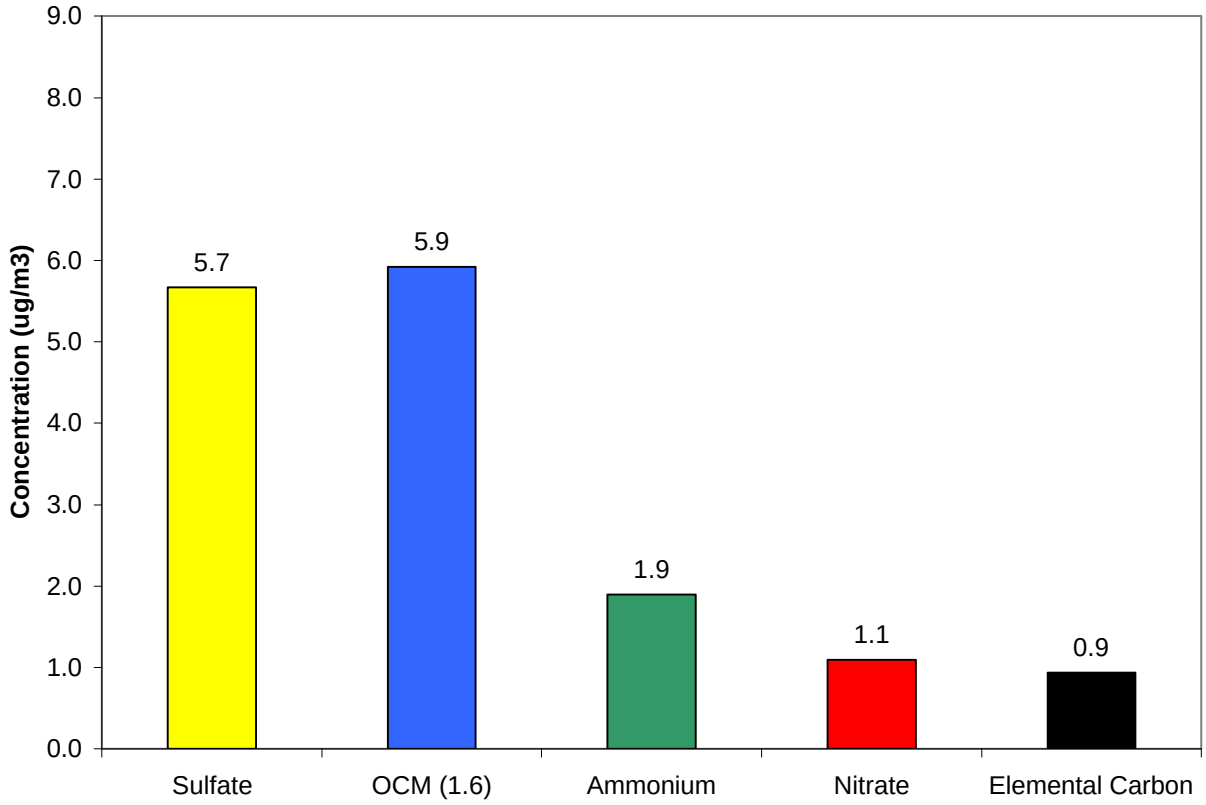

Figure 5-30 Major Constituents of $PM_{2.5}$ Mass, South Charleston, WV

5.3.3 Time Series Analysis of $PM_{2.5}$ Species

A Met One SASS speciation sampler was installed at the South Charleston monitoring site on November 23, 2003. It has operated on a 1-in-6 sampling schedule from its installation to the present time. Figure 5-31 shows a composite time series for the five major species measured at

South Charleston and Figures 5-32 through 5-36 show time series for each of the five major species. The black line in Figures 5-32 through 5-36 is the 30-day rolling average concentration for the specie.

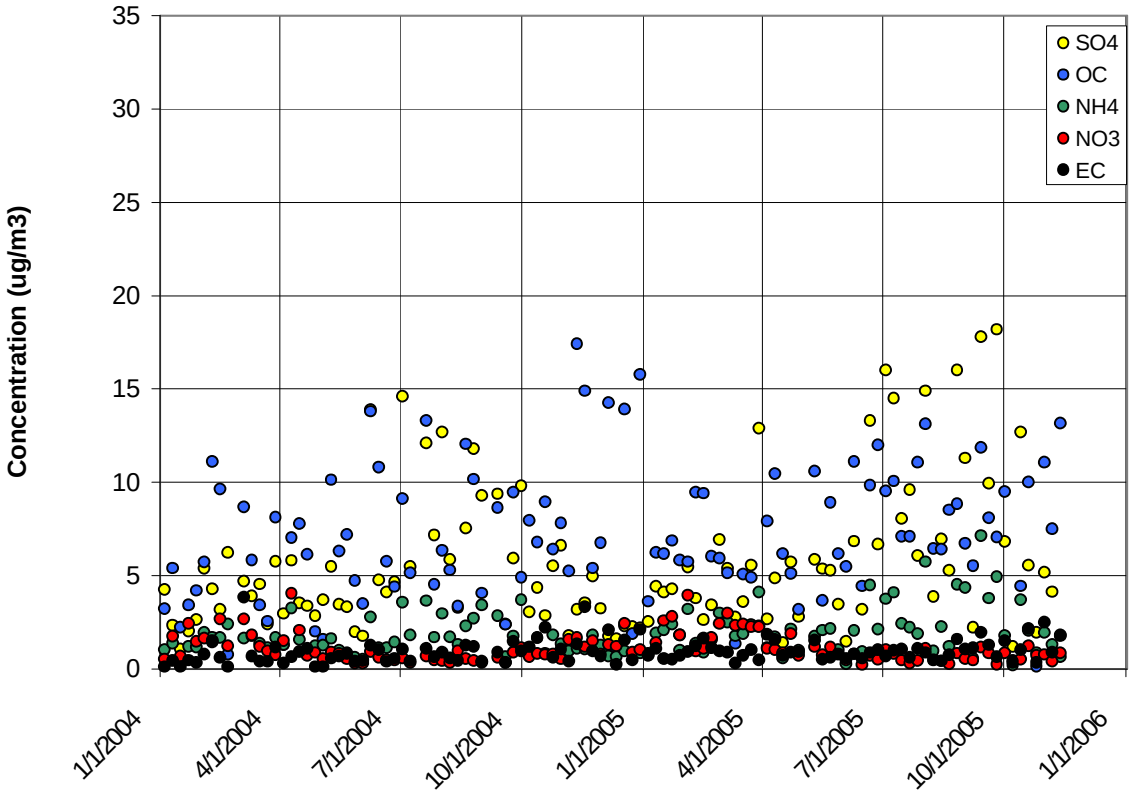

Figure 5-31 Time Series for the South Charleston, WV Monitor

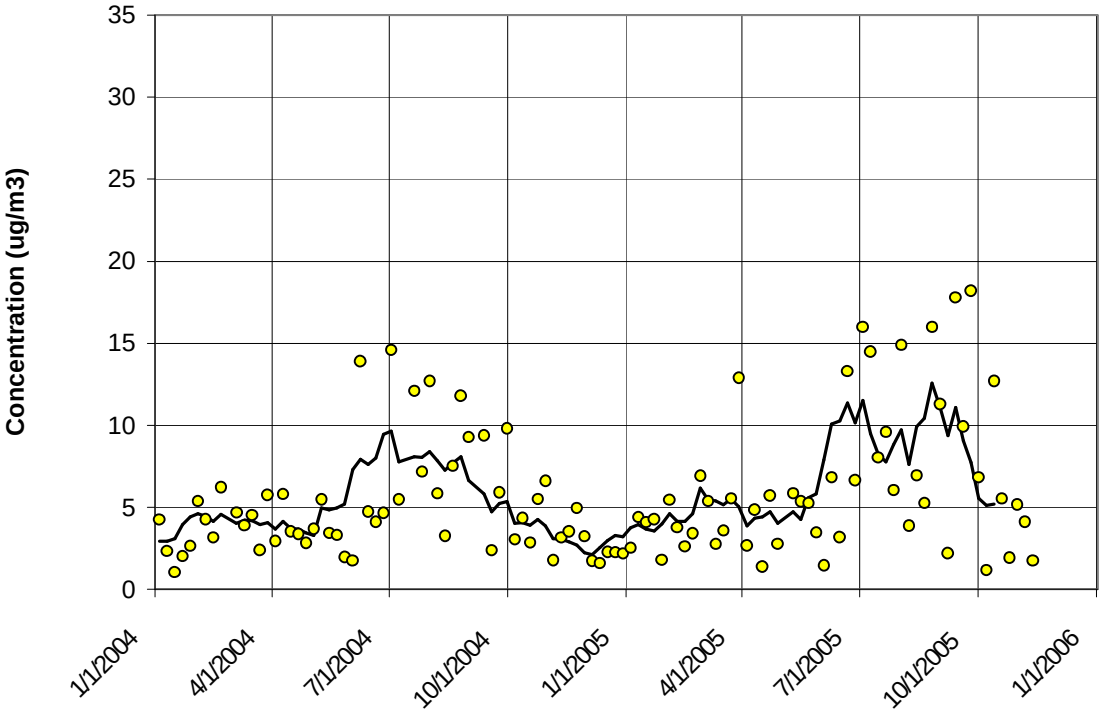

Figure 5-32 Sulfate Time Series for the South Charleston, WV Monitor

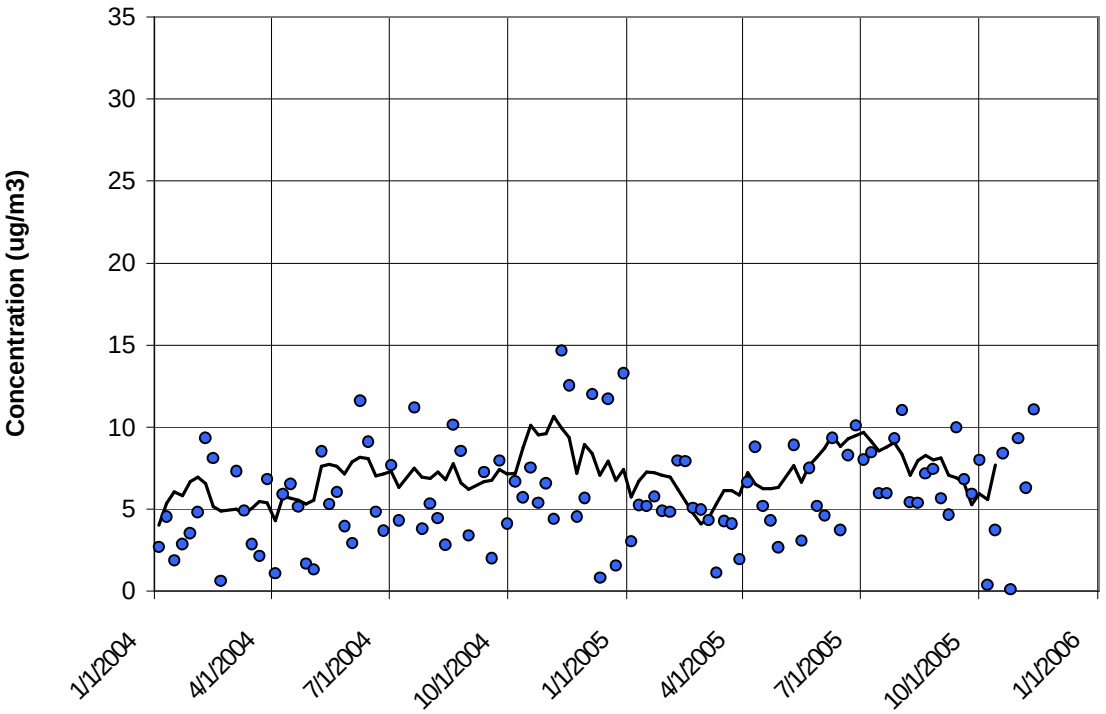

Figure 5-33 Organic Carbon Mass Time Series for the South Charleston, WV Monitor

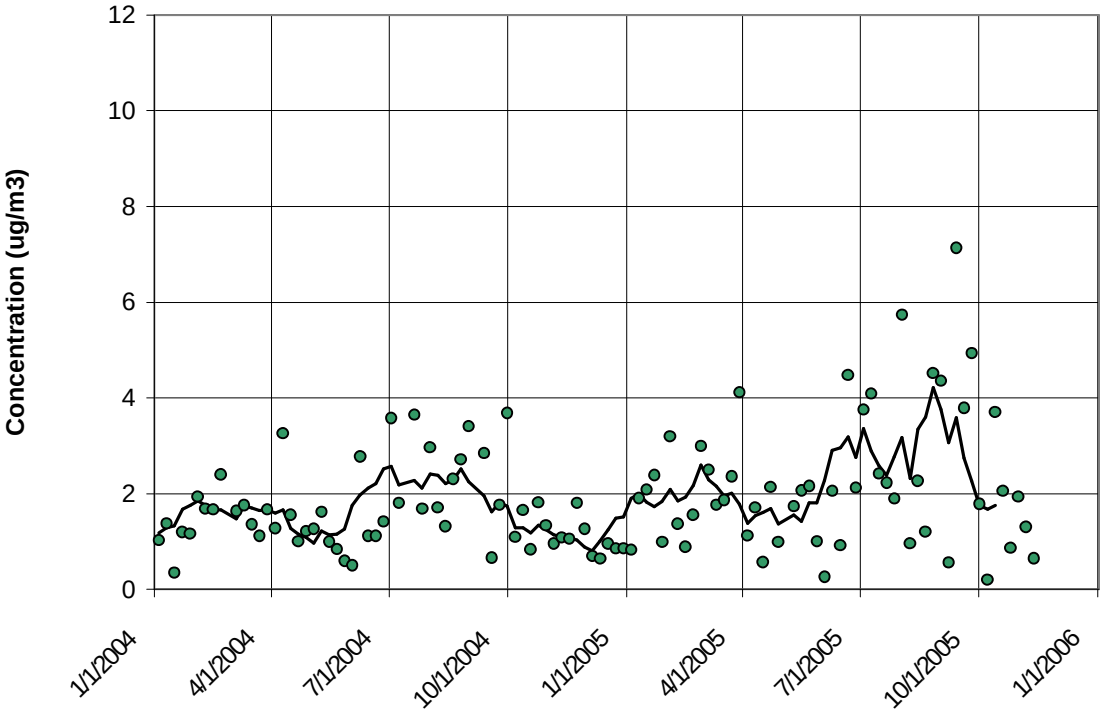

Figure 5-34 Ammonium Time Series for the South Charleston, WV Monitor

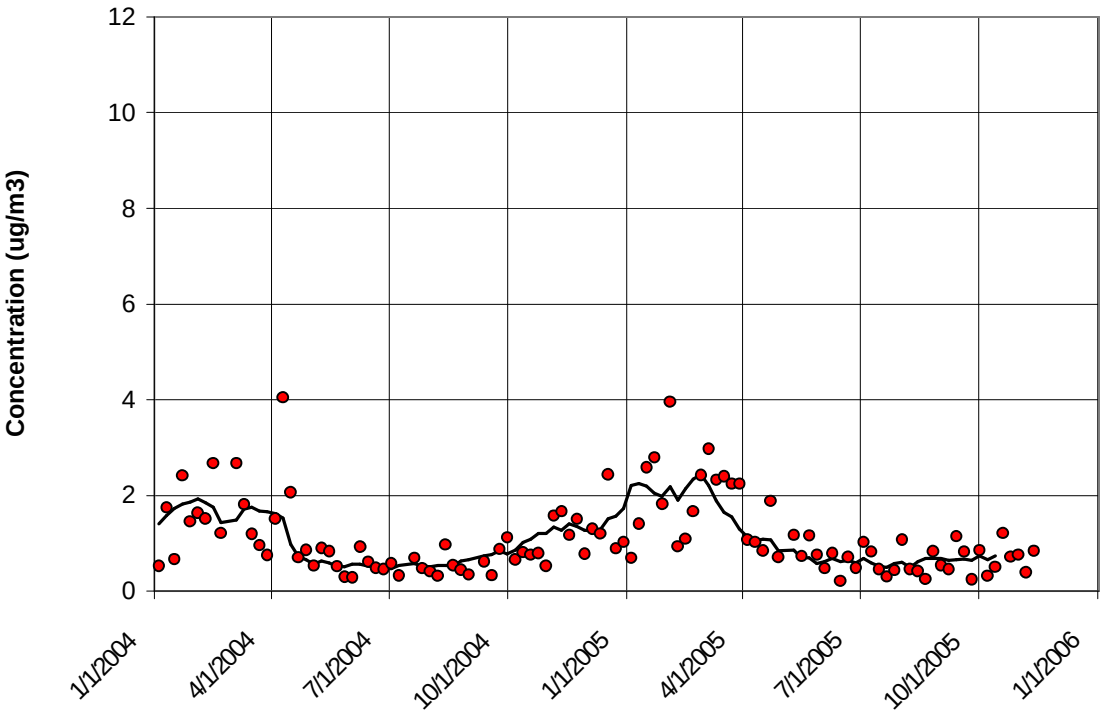

Figure 5-35 Nitrate Time Series for the South Charleston, WV Monitor

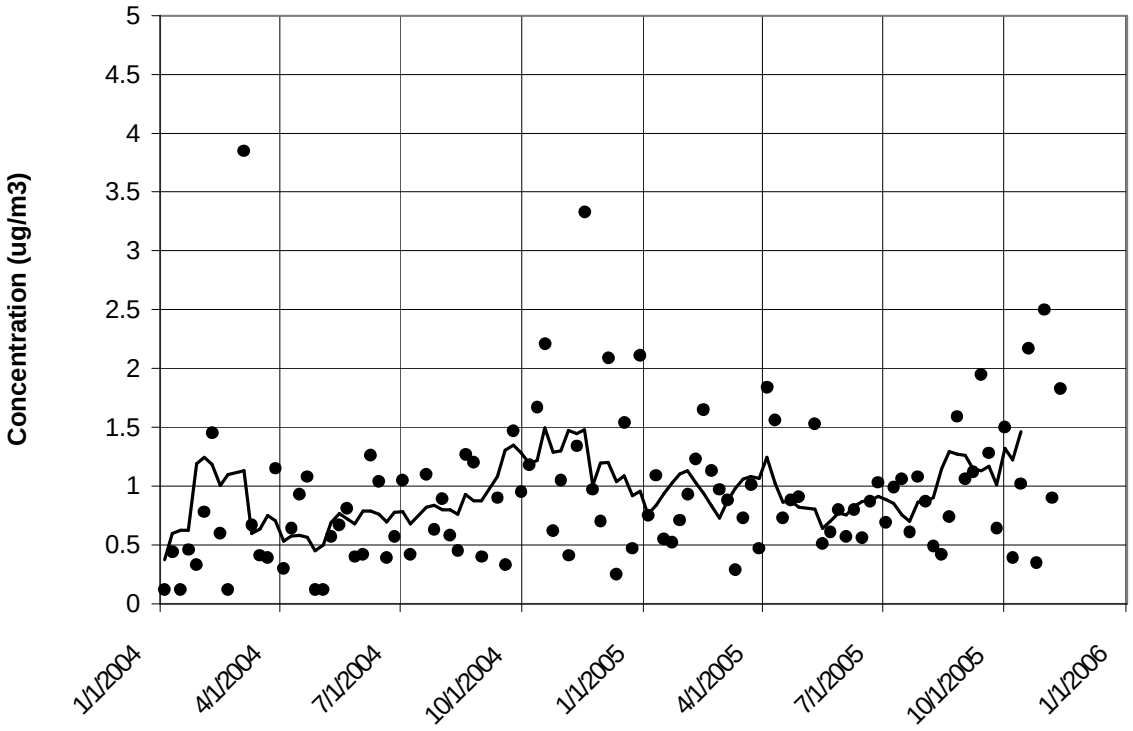

Figure 5-36 Elemental Carbon Time Series for the South Charleston, WV Monitor

The 30-day rolling average sulfate concentration in Figure 5-32 shows how sulfate varied from January 2004 through November 2005. Sulfate concentrations were lowest in winter at an average concentration of about 3.37 µg/m^3. The average summer sulfate concentration was much higher at 8.39 µg/m^3, more than twice the winter concentration. Average spring and fall concentrations were 4.32 and 6.12 µg/m^3 respectively. As the time series shows, sulfate concentration was much more variable in summer than in winter.

Average organic carbon mass concentration was highest in summer at 6.81 µg/m^3 followed by fall at 6.51 µg/m^3. Average winter concentration was about 5.54 µg/m^3. The lowest seasonal organic carbon mass concentration occurred in spring at 4.76 µg/m^3. As Figure 5-33 shows, organic carbon mass concentration was quite variable any time of year. Concentrations ranged between a low near zero and a high near 14.7 µg/m^3.

Average ammonium concentration was highest in the summer at about 2.37 µg/m^3. Winter and spring average concentrations were lower at 1.46 µg/m^3 and 1.63 µg/m^3. The average concentration in the fall was 2.05 µg/m^3. Figure 5-34 shows how ammonium concentration varied over time. Ammonium concentration was most variable in summer when fairly high concentrations occurred.

Ammonium and sulfate concentrations were well correlated (R^2 = 0.84); when sulfate concentrations were high, ammonium concentrations were usually high. Table 5-11 lists ammonium and sulfate concentrations on days when sulfate concentration exceeded 15 µg/m^3.

Table 5-11 High Ammonium and Sulfate Days for the South Charleston, WV Monitor

Date	Ammonium Concentration (µg/m^3)	Sulfate Concentration (µg/m^3)
7/3/05	3.8	16.0
8/26/05	4.5	16.0
9/13/05	7.1	17.8
9/25/05	4.9	18.2

As Figure 5-35 shows, nitrate measurements at South Charleston exhibited strong seasonal variation. Nitrate concentrations were lowest in the summer and noticeably higher in winter and early spring. The average summer concentration was 0.56 µg/m^3 whereas the average winter and spring concentrations were 1.68 µg/m^3 and 1.43 µg/m^3 respectively. Average fall concentration was 0.82 µg/m^3. As Figure 5-35 shows, nitrate values were much more variable in winter and early spring than in late spring and summer when they were consistently low.

Figure 5-36 displays the time series for elemental carbon. The highest seasonal average concentration occurred in the fall at 1.25 µg/m^3. Winter, spring, and summer had similar average concentrations of 0.85, 0.86, and 0.8 µg/m^3 respectively. Occasionally, relatively high elemental carbon concentrations were observed. Two especially high concentrations occurred on March 4, 2004 (3.9 µg/m^3) and on November 17, 2004 (3.3 µg/m^3).

Seasonal averages for the major constituents of $PM_{2.5}$ mass at South Charleston are summarized in Table 5-12.

Table 5-12 Seasonal Averages for the Major Constituents of $PM_{2.5}$ Mass (µg/m^3) for South Charleston, WV

	Organic Carbon Mass	Sulfate	Ammonium	Nitrate	Elemental Carbon
Winter	5.54	3.37	1.46	1.68	0.85
Spring	4.76	4.32	1.63	1.43	0.86
Summer	6.81	8.39	2.37	0.56	0.80
Fall	6.51	6.12	2.05	0.82	1.25

5.3.4 Trajectory Analysis

Trajectory analysis was not performed for the South Charleston monitor.

5.4 Charlotte, NC

Site Name: Garinger High School
AIRS Number: 37-119-0041
Latitude: 35.24028 North
Longitude: -80.78556 West
Elevation: 232 meters (761 feet)
Agency Operating the Monitor: Mecklenburg County Land Use and Environmental Services Agency
Speciation Sampling Frequency: 1-in-3 days

5.4.1 Site Description

The Garinger monitoring site is located on the grounds of Garinger High School in Charlotte, NC. The site is about 5.6 km (3.5 miles) northeast of the central business district in Charlotte. Figure 5-37 shows the monitoring site's location relative to the interstate highway system and large population centers. As the figure shows, the closest cities to Charlotte are Winston-Salem, NC about 134 km (83 miles) to the northeast, Greensboro, NC about 148 km (92 miles) to the northeast, and Columbia, SC about 150 km (93 miles) to the southeast. Atlanta, GA is 393 km (244 miles) to the southwest.

Figure 5-37 Location of the Charlotte, NC Monitoring Site

The Garinger monitor is a neighborhood scale monitor in a suburban location. The area immediately adjacent to the high school is residential in nature with many single-family homes. Most of the metropolitan area of Charlotte, population 582,502, lies to the west and south of the monitoring site. Charlotte is located in the piedmont region of North Carolina, a transitional area of rolling country between the Appalachian Mountains to the west and the coastal plain to the east. The mountains are about 80 miles northwest of Charlotte. The Atlantic Ocean is about 160 miles southeast. Figure 5-38 is a detailed map showing the topographic features around the monitoring site. Figure 5-39 is a photograph of the site.

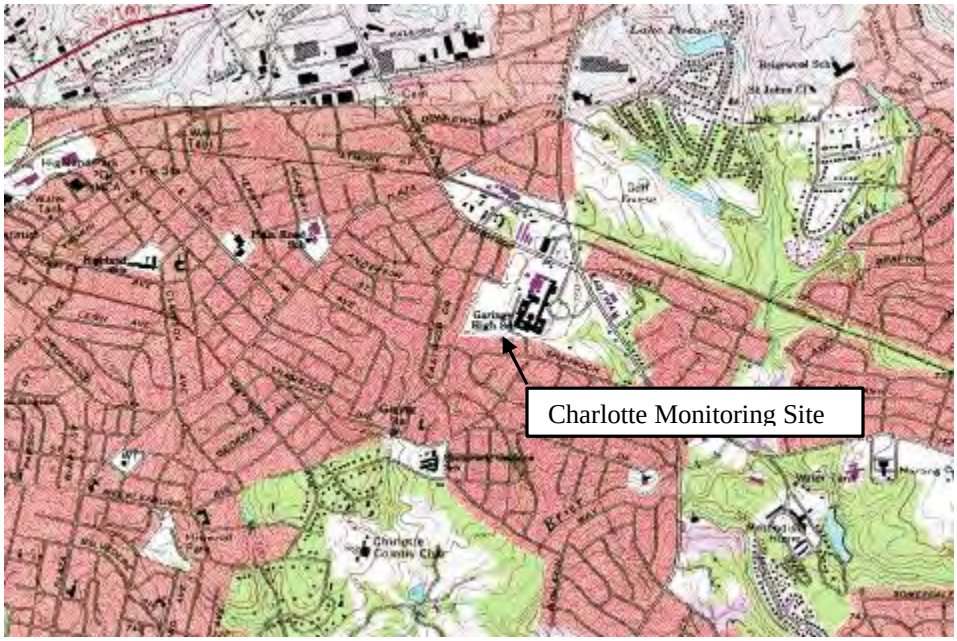

Source: TopoZone

Figure 5-38 Topographic Map of Charlotte, NC Monitoring Site

Figure 5-39 Photograph of the Charlotte, NC Monitoring Site

The North Carolina Division of Air Quality reports there are a variety of air pollution sources in the vicinity of the monitoring site. Table 5-13 lists the industries located within 24 km (fifteen miles) of the site.

Table 5-13 Emission Sources within 24km of the Charlotte, NC Monitoring Site

Facility	Actual Direct $PM_{2.5}$ Emissions (Tons/Year)
Charlotte Pipe & Foundry Co. Inc.	106[1]
Caraustar Mill Group, Inc.	9
Industrial Container Services- NC, LLC	4
Interstate Brands Corporation	1[1]
Gerdau Ameristeel US Inc., Charlotte Steel Mill Division	32[1]
Cargill, Inc.	13
InteliCoat Technologies, LLC	0
BMWNC, Inc.	0[1]
Continental Tire North America, Inc.	45
Frito-Lay, Inc.	1
Duke Energy Corporation - Allen Steam Station	2,012

[1] PM_{10} emissions. $PM_{2.5}$ emissions have not been estimated for this source.

The largest source of direct $PM_{2.5}$ emissions within a 24 km (15 mile) radius of the monitor is Duke Energy Corporation's Allen Steam Station, a 1,140 megawatt coal-fired power plant located in Belmont, NC. Belmont is about 14 miles west of the monitoring site. Many of the facilities listed in Table 5-13 also emit CO, NO_x, PM_{10}, SO_2, and VOCs.

5.4.2 Major Constituents of $PM_{2.5}$ Mass

The major constituents of $PM_{2.5}$ mass at Charlotte were organic carbon and sulfate species followed by ammonium and nitrate species. Using an OM/OC ratio of 1.6, the average organic carbon mass concentration over 2001-2003 was 5.86 µg/m^3. Average sulfate concentration was 4.96 µg/m^3. Average ammonium and nitrate concentrations were 1.60 µg/m^3 and 0.94 µg/m^3 respectively. Elemental carbon, geological components, and trace elements contributed about 1.5 µg/m^3 to the average mass concentration measured over 2001-2003. Figure 5-40 shows the contribution each major specie made to the total mass measured at the site.

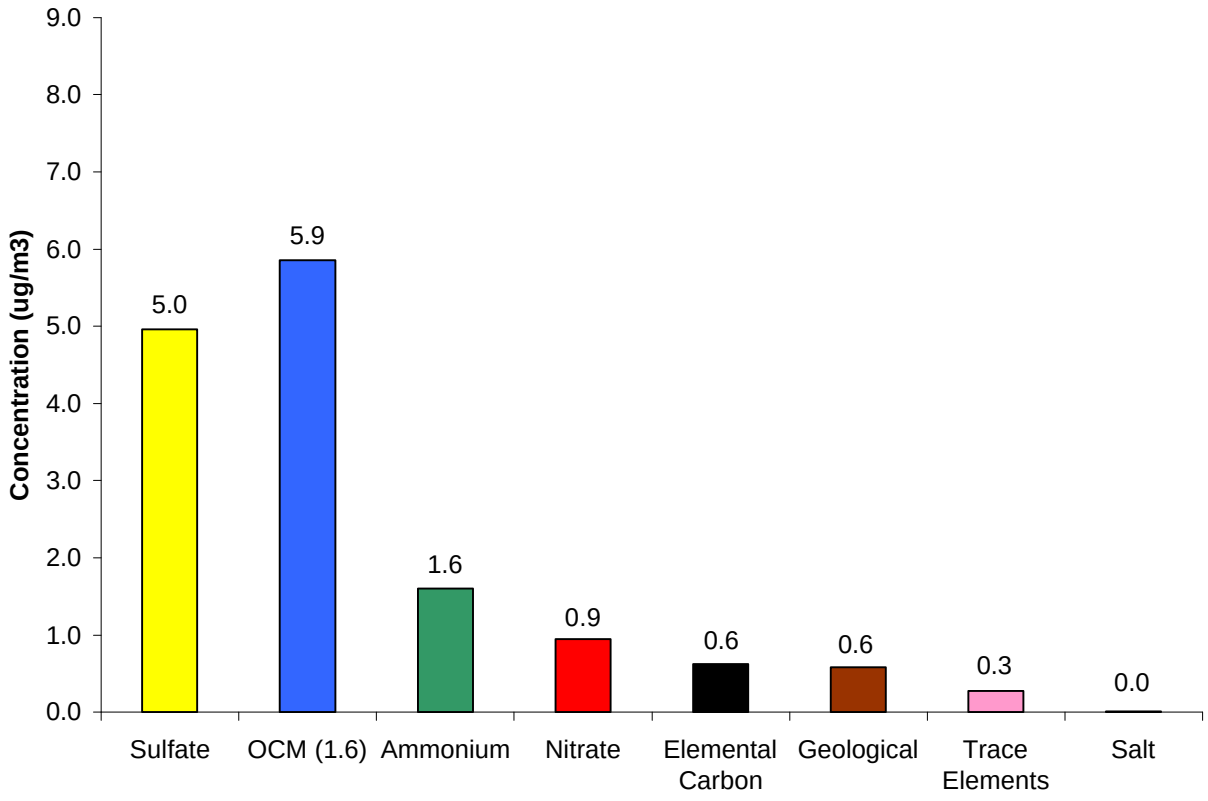

Figure 5-40 Major Constituents of $PM_{2.5}$ Mass, Charlotte, NC

The average reconstructed mass calculated for this site was 6.4 percent lower than the average gravimetric mass measured by the speciation sampler. Average reconstructed mass was 14.7 µg/m^3 whereas the average gravimetric mass was 15.7 µg/m^3. Figure 5-41 visually compares the average reconstructed mass with the average gravimetric mass. It should be noted that the Division of Air Quality of North Carolina's Department of Environment and Natural Resources has found that the MetOne SASS speciation sampler produces gravimetric measurements of $PM_{2.5}$ mass that are about ten percent higher than co-located FRM monitors.

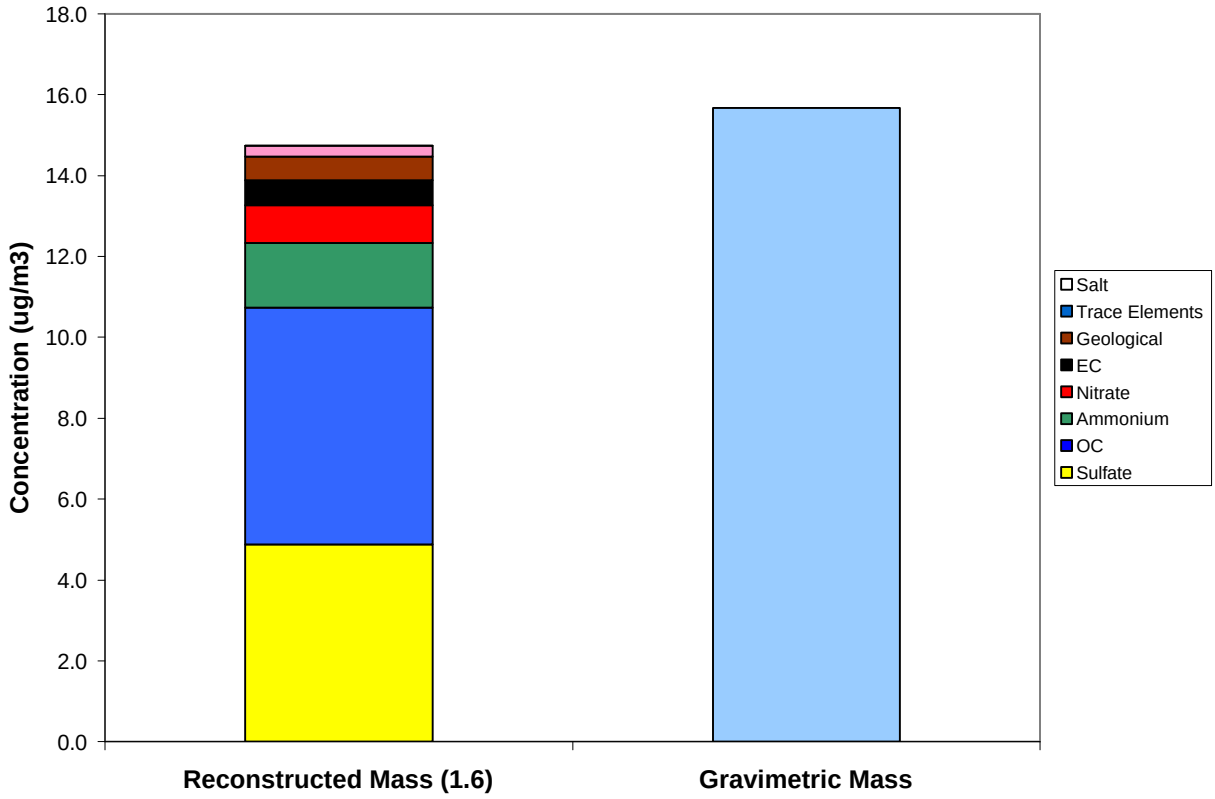

Figure 5-41 Comparison of Average Reconstructed Mass and Average Gravimetric Mass, Charlotte, NC

5.4.3 Time Series Analysis of $PM_{2.5}$ Species

A Met One SASS speciation sampler was installed at the Charlotte monitoring site on January 13, 2001. It has operated on a 1-in-3 sampling schedule from its installation to the present time. Figure 5-42 shows a composite time series for the five major species measured at Charlotte and Figures 5-43 through 5-47 show time series for each of the five major species. The black line in Figures 5-43 through 5-47 is the 30-day rolling average concentration for the species. In May 2001, the monitoring site was moved 230 meters to the southwest to allow room for the construction of a new school parking lot. This move accounts for the break in the data in May 2001.

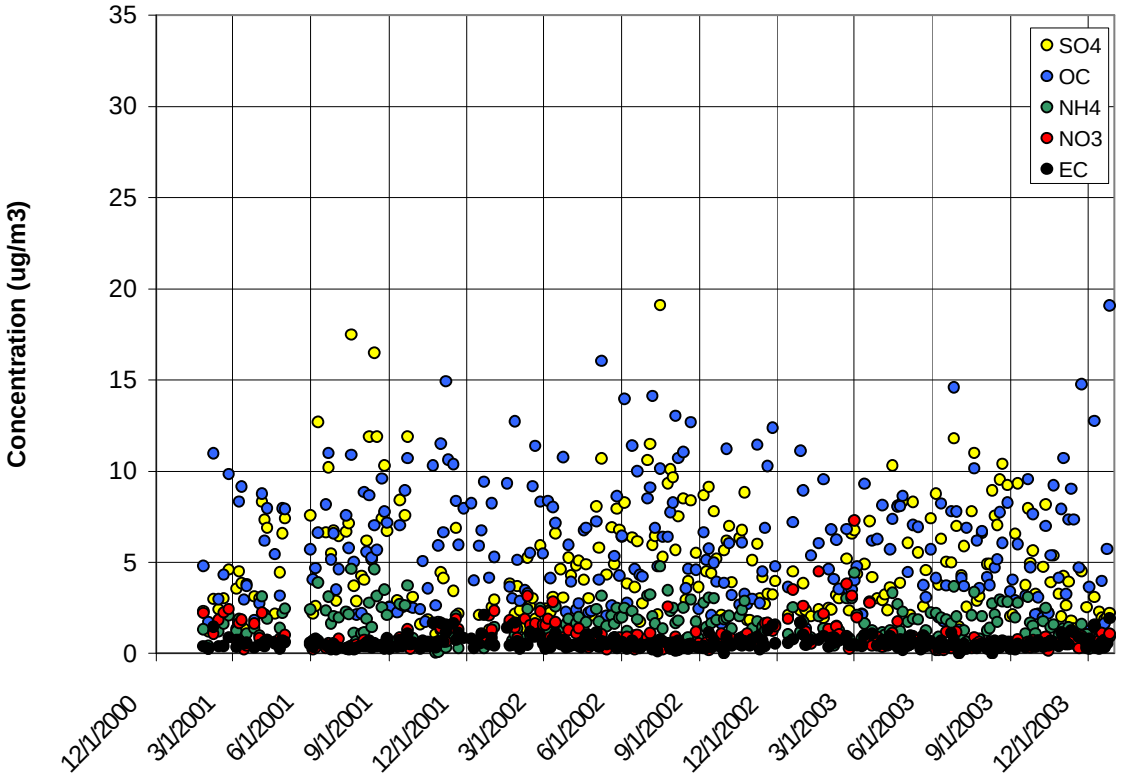

Figure 5-42 Time Series for the Charlotte, NC Monitor

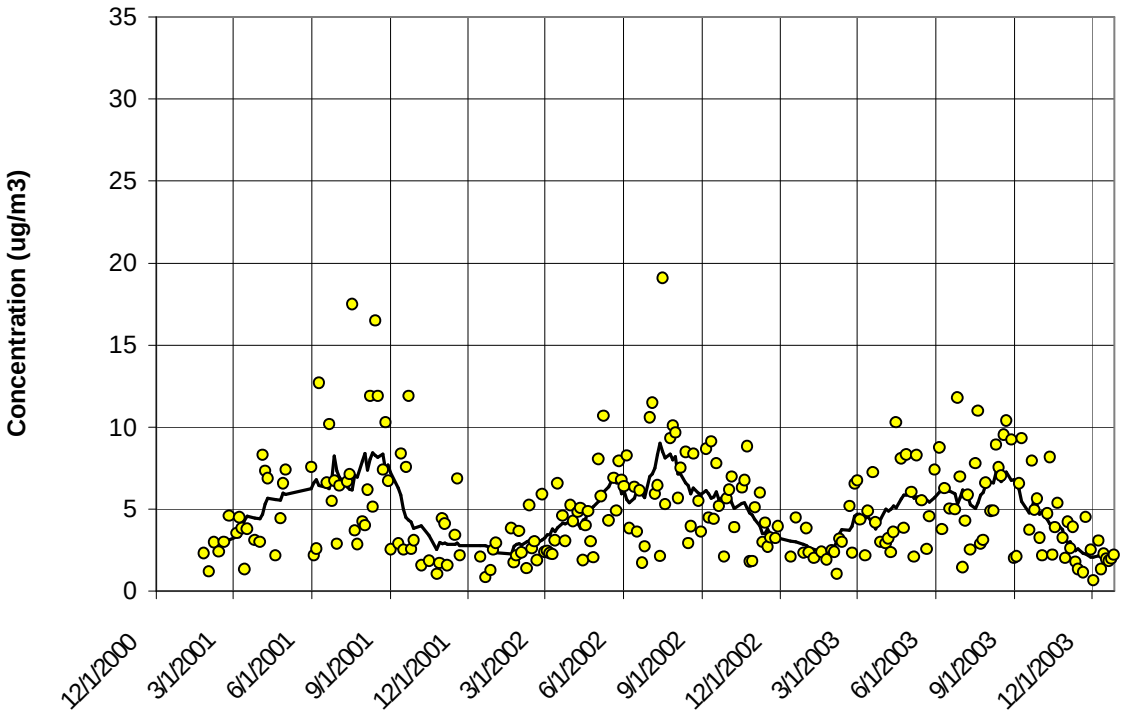

Figure 5-43 Sulfate Time Series for the Charlotte, NC Monitor

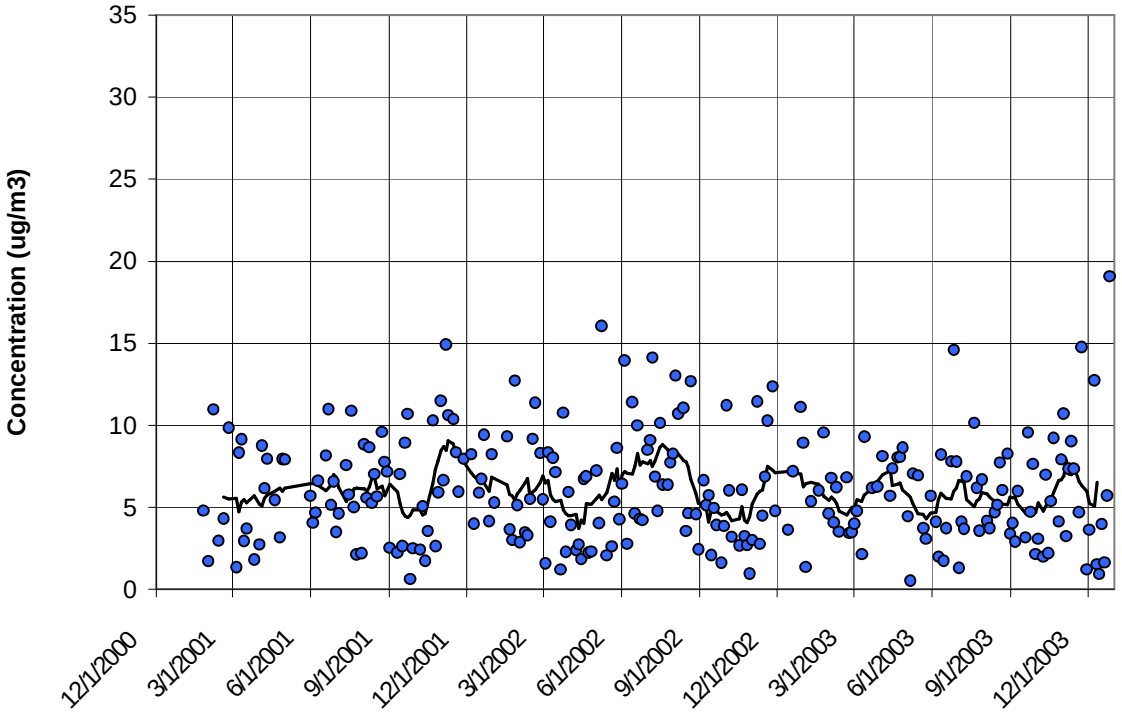

Figure 5-44 Organic Carbon Mass Time Series for the Charlotte, NC Monitor

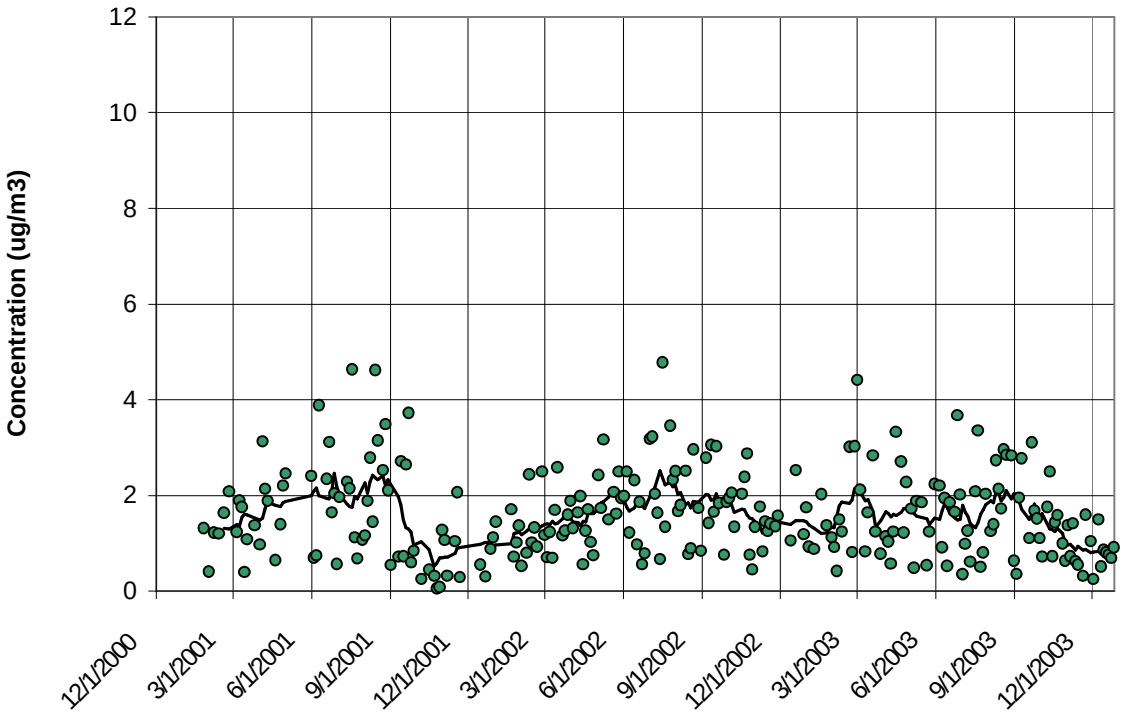

Figure 5-45 Ammonium Time Series for the Charlotte, NC Monitor

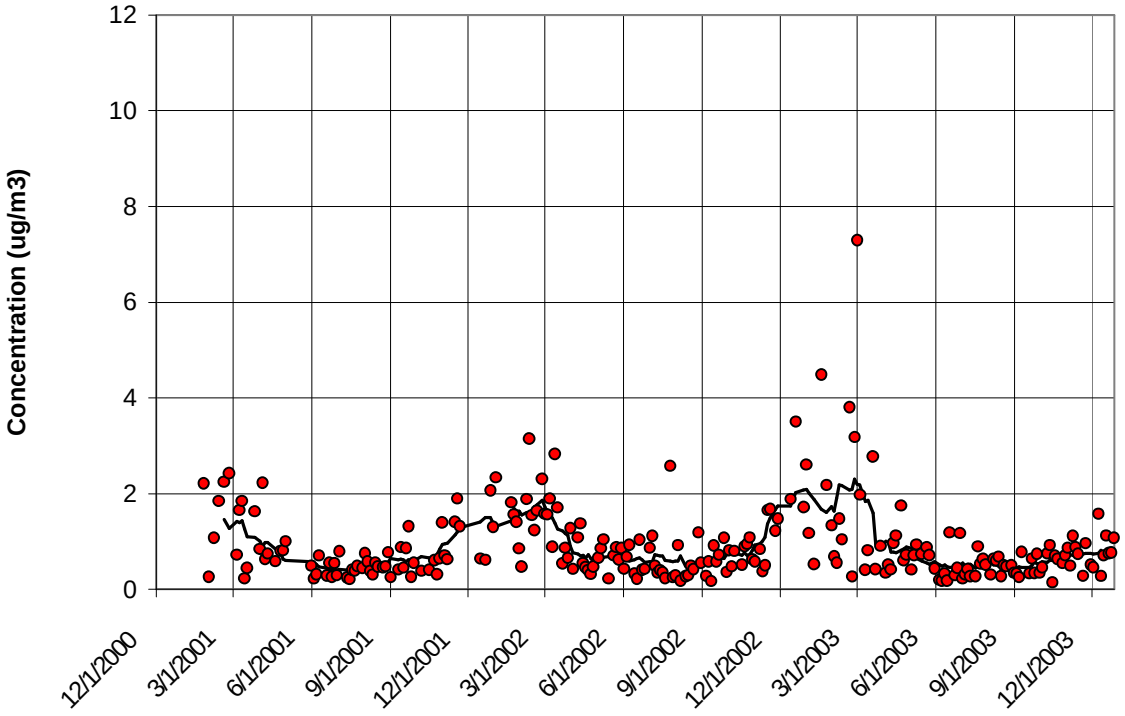

Figure 5-46 Nitrate Time Series for the Charlotte, NC Monitor

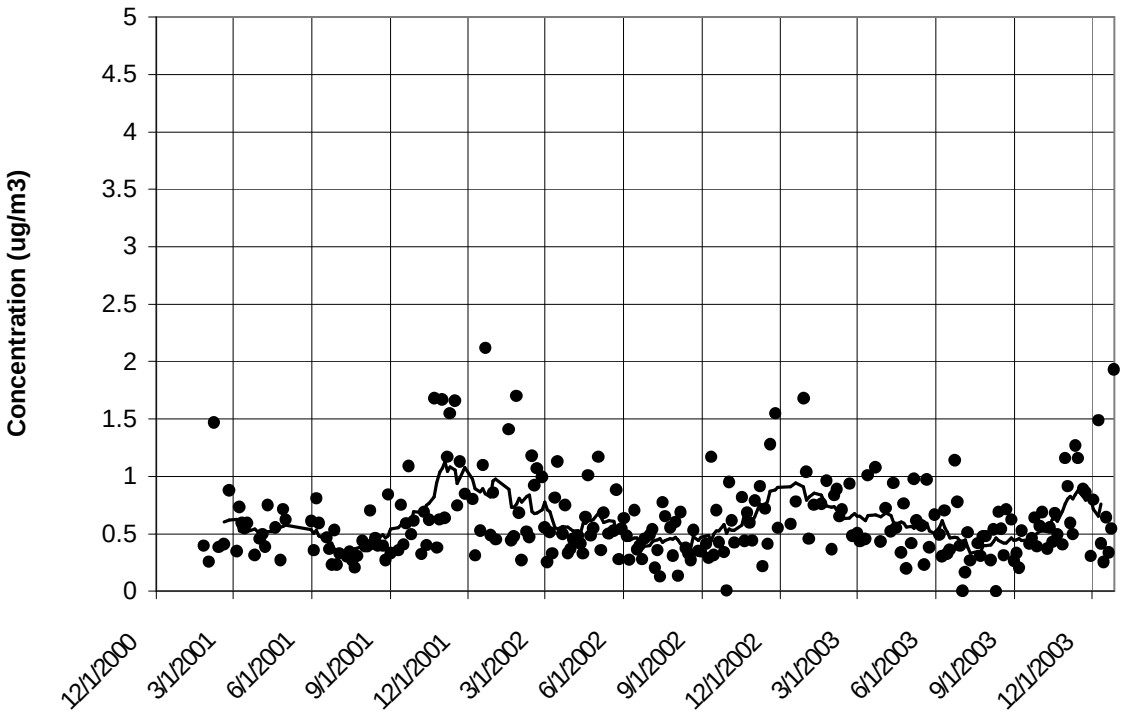

Figure 5-47 Elemental Carbon Time Series for the Charlotte, NC Monitor

The 30-day rolling average sulfate concentration in Figure 5-43 shows how sulfate varied seasonally over the 2001-2003 period in Charlotte, NC. Sulfate concentrations were lowest in winter at an average value of about 2.85 µg/m^3. In late January or February, concentrations began to rise and continued rising until peak values were reached in summer. The average summer sulfate concentration was 6.55 µg/m^3. Peak 24-hour summer concentrations were as high as 15-20 µg/m^3. In late August, or in the case of 2002 in mid-July, sulfate concentrations began to decline and continued declining through the fall until winter levels were reached in about February. As the sulfate time series shows, sulfate concentrations were much more variable in summer than in winter.

Organic carbon mass, the largest contributor to $PM_{2.5}$ mass in Charlotte, did not exhibit the clear seasonal behavior seen in the sulfate time series. As Figure 5-44 shows, organic carbon mass concentrations were quite variable over the data record studied making it difficult to discern seasonal patterns. Using an OM/OC ratio of 1.6, over the course of 2001-2003, organic carbon mass concentration averaged 5.86 µg/m^3 and ranged from about 0.6 to 19.1 µg/m^3. The 30-day rolling average concentration reveals a number of peaks and valleys. Over the 2001-2003 period, the average summer concentration was 6.49 µg/m^3 and the average winter concentration was 6.15 µg/m^3. Average spring and fall concentrations were 5.20 µg/m^3 and 5.64 µg/m^3 respectively. The analysis of additional data collected over future years may help explain what appears to be summer and winter peaks at this monitoring site.

Over 2001-2003, the average ammonium concentration was 1.60 µg/m^3. Only Kinston, NC had a lower average ammonium concentration (1.51 µg/m^3). Figure 5-45 shows how ammonium concentrations varied over time. The highest ammonium values usually occurred in summer and ranged from about 3 to 5 µg/m^3. Some high concentrations were also observed in the spring and fall. Summer had the highest average concentration at 1.84 µg/m^3 followed by spring with an average concentration of about 1.65 µg/m^3. Average winter concentration was about 1.33 µg/m^3. Over the 2001-2003 period, average ammonium levels in Charlotte were less than the average concentration observed in many other sites in the MARAMA Region.

Ammonium and sulfate concentrations were well correlated (R^2 = 0.85); when sulfate concentrations were high, ammonium concentrations were usually high. Table 5-14 lists ammonium and sulfate concentrations on days when sulfate concentration exceeded 15 µg/m^3.

Table 5-14 High Ammonium and Sulfate Days for the Charlotte, NC Monitor

Date	Ammonium Concentration (µg/m^3)	Sulfate Concentration (µg/m^3)
7/18/01	4.64	17.5
8/14/01	4.62	16.5
7/16/02	4.78	19.1

Of the eleven sites analyzed, the Charlotte site had the lowest average nitrate concentration (0.94 µg/m^3) over 2001-2003. As recent research has shown (Wittig, 2004), solid phase nitrate species are a function of temperature, relative humidity and ultraviolet radiation with higher concentrations occurring during cold weather/winter conditions. It is not surprising therefore that Charlotte, the most southern site studied, produced the lowest nitrate concentration. In this study, lower average nitrate concentrations were found in the southern part of the MARAMA Region and higher average concentrations in northern areas.

As Figure 5-46 shows, nitrate measurements at Charlotte exhibited some of the seasonal variation seen at other sites. Nitrate concentrations were lowest during the summer and noticeably higher in winter. Over 2001-2003, the average summer concentration was 0.55 µg/m^3 whereas the average winter concentration was 1.73 µg/m^3. In spring and fall, the average nitrate concentrations were 1.05 µg/m^3 and 0.75 µg/m^3, respectively. As Figure 5-46 shows, nitrate values were much more variable in winter than in summer.

Figure 5-47 displays the time series for elemental carbon. Average elemental carbon concentration was at its lowest during the summer at about 0.45 µg/m^3. Concentrations began to gently rise in late summer or early fall. Peak levels were observed in the fall and winter months. Average elemental carbon concentrations in the fall and winter were 0.68 µg/m^3 and 0.80 µg/m^3 respectively.

Seasonal averages for the major constituents of $PM_{2.5}$ mass measured in Charlotte, NC are summarized in Table 5-15.

Table 5-15 Charlotte, NC Seasonal Averages for the Major Constituents of $PM_{2.5}$ Mass (µg/m^3)

	Organic Carbon Mass	Sulfate	Ammonium	Nitrate	Elemental Carbon
Winter	6.15	2.85	1.33	1.73	0.80
Spring	5.20	4.94	1.65	1.05	0.59
Summer	6.49	6.55	1.84	0.55	0.45
Fall	5.64	4.78	1.50	0.75	0.68

5.4.4 Trajectory Analysis

Figure 5-48 shows CATT back trajectories for the cleanest days in the speciation record over the period studied from June 2001 through December 2003. While even lower concentration days

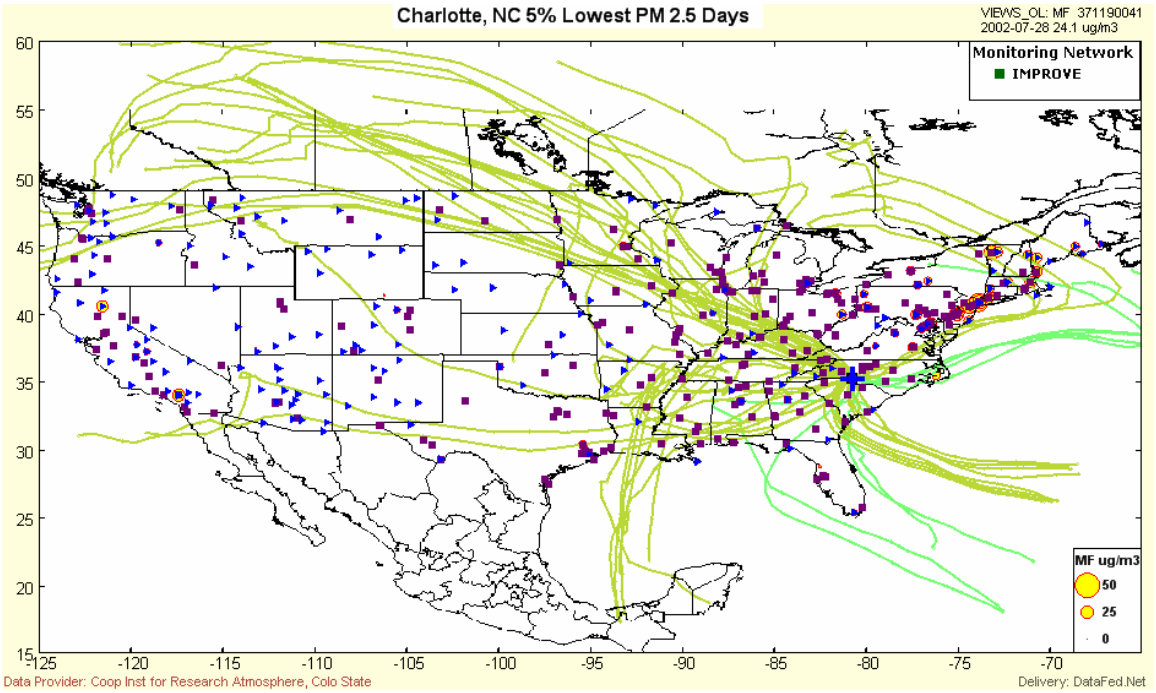

Figure 5-48 Charlotte, NC Back Trajectories for the Five Percent Cleanest Days

can be found in the data record for Federal Reference Method monitors at the site, the trajectories plotted in Figure 5-48 are the lowest concentration days in the speciation record over the period studied. These "clean" days represent the five percent days with the lowest total $PM_{2.5}$ mass.

Many "clean day" trajectories move quickly over great distances from the Pacific Northwest or the northern or western Canadian provinces to Charlotte. These tracks indicate fast moving air masses probably associated with large-scale weather systems. In contrast to trajectories associated with high concentrations, these trajectories do not remain or re-circulate over source regions. Other clean day trajectories are maritime in nature, tracking in from the Gulf of Mexico, the Caribbean Sea, or the Atlantic Ocean. Table 5-16 lists the five percent cleanest days at Charlotte, NC and the total mass concentration measured by the speciation monitor on that day.

Table 5-16 Charlotte, NC Five Percent Lowest Days

Date	$PM_{2.5}$ Mass ($\mu g/m^3$)
1/31/2001	6.3
9/25/2001	6.9
10/07/2001	7.0
10/13/2001	6.3
1/03/2003	5.8
4/09/2003	5.8
5/18/2003	4.9
7/02/2003	5.5
9/03/2003	7.0
10/15/2003	6.6
11/20/2003	6.8
12/11/2003	6.4
12/20/2003	6.4
Average	6.3

Figure 5-49 shows back trajectories for the dirtiest days, the five percent days with the highest total $PM_{2.5}$ mass. With the exception of one trajectory that appears to originate in the Gulf of Mexico, most "dirty day" trajectories are tracks of air masses that have spent the past five days over the continental U.S. In many cases, the air circulates or re-circulates through air pollution source regions in the South, Midwest, or Northeast and Mid-Atlantic states.

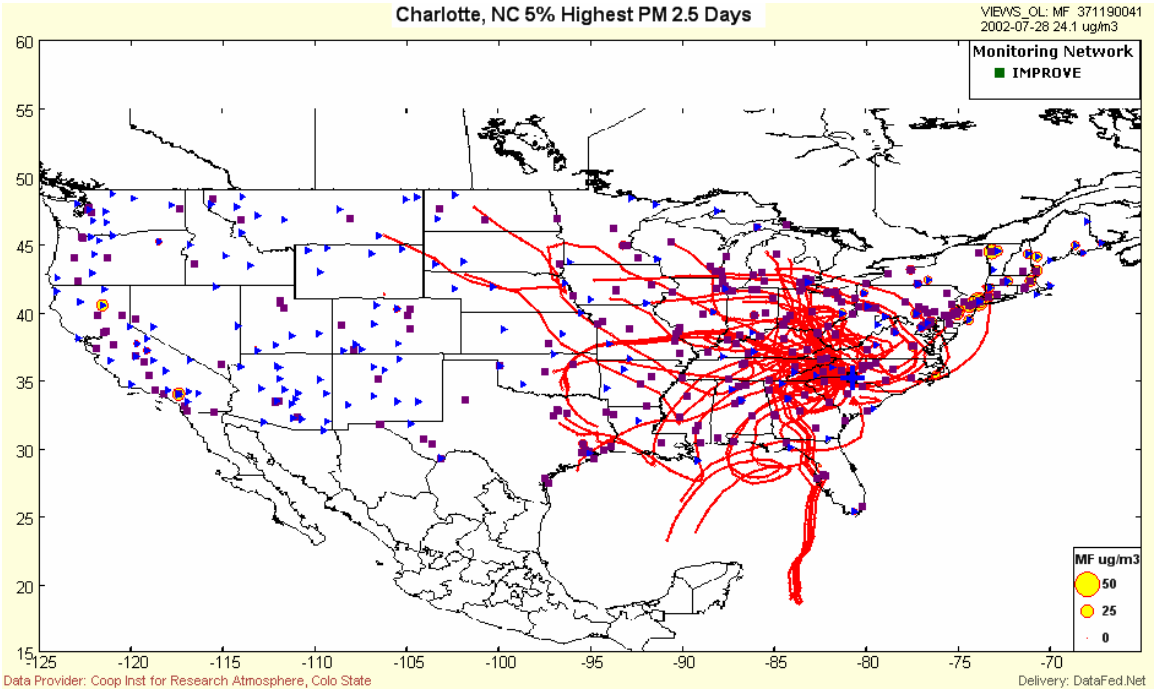

Figure 5-49 Charlotte, NC Back Trajectories for the Five Percent Dirtiest Days

Table 5-17 lists the five percent dirtiest days and the total mass concentration measured by the speciation monitor on that day.

Table 5-17 Charlotte, NC, Five Percent Highest Days

Date	$PM_{2.5}$ Mass ($\mu g/m^3$)
4/01/2001	44.0
4/04/2001	32.5
6/21/2001	31.8
7/18/2001	47.9
8/08/2001	31.1
8/14/2001	32.3
5/08/2002	32.4
7/01/2002	30.2
7/04/2002	30.8
7/16/2002	39.7
6/26/2003	40.7
7/20/2003	30.4
Average	35.3

5.5 Dover, DE

Site Name: Dover
AIRS Number: 10-001-0003
Latitude: 39.15500 North
Longitude: -75.51805 West
Elevation: 10 meters (33 feet)
Agency Operating the Monitor: Delaware Department of Natural Resources and Environmental Control (DNREC), Division of Air and Waste Management (DAWM), Air Quality Management Section (AQM), Air Surveillance
Speciation Sampling Frequency: 1-in-6 days

5.5.1 Site Description

The Dover monitoring site is located in Dover, DE, population 32,135. Dover is about 64 km (40 miles) south of Wilmington, DE and the I-95 corridor. Baltimore, MD is about 96 km (60 miles) west of Dover across the Chesapeake Bay. Washington, DC is about 130 km (81 miles) to the southwest also across the Chesapeake Bay. While the Dover monitor is located in a small city, the area immediately outside the city is rural in nature and dedicated for the most part to farming and other agricultural activities. Figure 5-50 shows the monitoring site's location relative to the interstate highway system and large eastern population centers.

Figure 5-50 Location of the Dover, DE Monitoring Site

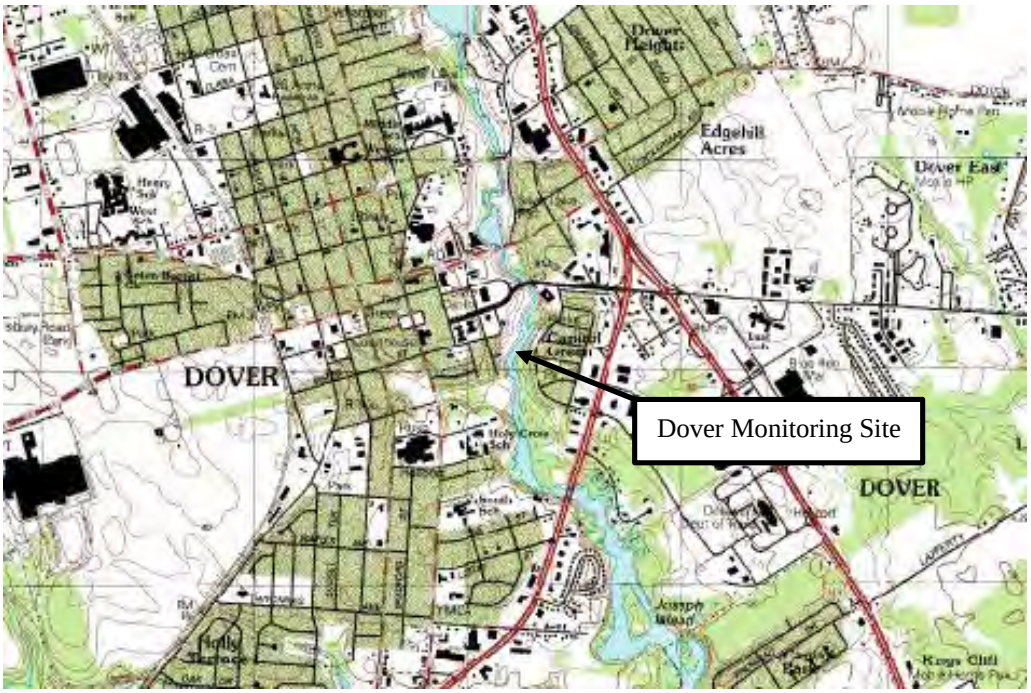

Source: TopoZone

Figure 5-51 Topographic Map of the Dover, DE Monitoring Site

Figure 5-52 Photograph of the Dover, DE Monitoring Site

The monitor is sited on a grassy strip of undeveloped land 100 meters (328 feet) west of the St. Jones River. The St. Jones River and the undeveloped land along its banks forms a green "buffer zone" in the heart of Dover. The monitoring site is only 210 meters (689 feet) from the state capital. Administrative offices are a short distance north and west of the monitor. Residential areas along the St. Jones lie east of the monitor. The St. Jones River and park-like lowlands are south of the monitor. Figure 5-51 is a detailed map showing the topographic features around the monitoring site. Figure 5-52 is a photograph of the site looking south.

Table 5-18 Emission Sources within 16 km of the Dover, DE Monitoring Site

Facility Name	Site Description	Distance (km)	Direction (degrees)	PM25[1] (tons/yr)
Bayhealth Medical Center, Kent General Hospital	Health services	0.7	222	0.1
Camdel Metals Corporation	Stainless steel tubing manufacturing	6.2	211	ND[2]
City of Dover, McKee Run Generating Station	Electric power generation	3.1	313	36.7
City of Dover, Van Sant Generating Station	Electric power generation	2.9	246	0.0
Delaware State University	College/university campus	4.0	328	0.3
Dover Air Force Base	Air Force base	3.5	132	2.5
Dow Reichhold Specialty Latex, LLC	Chemicals and allied products	6.8	319	0.9
Harris Manufacturing Co. Inc.	Fabricated rubber products	15.9	335	ND[2]
Hirsh Industries	Metal file cabinet manufacturer	5.1	313	0.0
Kraft Foods North America	Food preparation and processing	2.3	252	0.2
NRG Energy Center Dover, LLC	Coal-fired power plant	2.6	254	104.9
Proctor and Gamble, Dover Wipes Company	Hygiene products production	2.9	256	6.3
Quality Kitchen Corp.	Food service	6.0	221	ND[2]
Tilcon Delaware, Bay Road Facility	Asphalt concrete plant	7.0	144	3.7
Tilcon Delaware, Horsepond Road Facility	Asphalt concrete plant	3.3	110	3.8

[1] Primary (directly emitted) $PM_{2.5}$ emissions.
[2] No data.

The monitoring site is located near three major roadways. East Water Street, a local two-lane road is about 50 m (164 feet) to the east and west of the site. U.S. Route 13/113, a major highway that carries north and south bound traffic, is approximately 0.5 km (0.3 mile) to the east of the monitoring site. Delaware Route 1, another major north/south highway is 2 km (1.2 miles) to the east. While the Dover monitor is not located in the heart of a large urban complex like the Wilmington, DE monitor, there are some air pollution sources nearby. Table 5-18, provided by the Delaware Department of Natural Resources and Environmental Control, lists the 15 facilities within a 16 km (10 mile) radius of the monitor.

The largest source of direct $PM_{2.5}$ emissions within a 16 km (10 mile) radius of the monitor is NRG Energy Center Dover, LLC, a coal-fired power plant located 2.6 km to the west of the monitoring site. Many of the facilities listed in Table 5-18 also emit CO, NO_x, PM_{10}, SO_2, and VOCs.

5.5.2 Major Constituents of $PM_{2.5}$ Mass

The major constituents of $PM_{2.5}$ mass at Dover were organic carbon mass and sulfate species followed by ammonium and nitrate species. Using an OM/OC ratio of 1.6, average organic carbon mass averaged 3.62 µg/m^3 over 2001-2003. Sulfate species averaged 4.65 µg/m^3. Average ammonium and nitrate concentrations were 1.89 and 1.87 µg/m^3. Elemental carbon, geological components, and trace elements averaged about 1.3 µg/m^3 over 2001-2003. Figure 5-53 compares the average concentrations of the major species measured at the site.

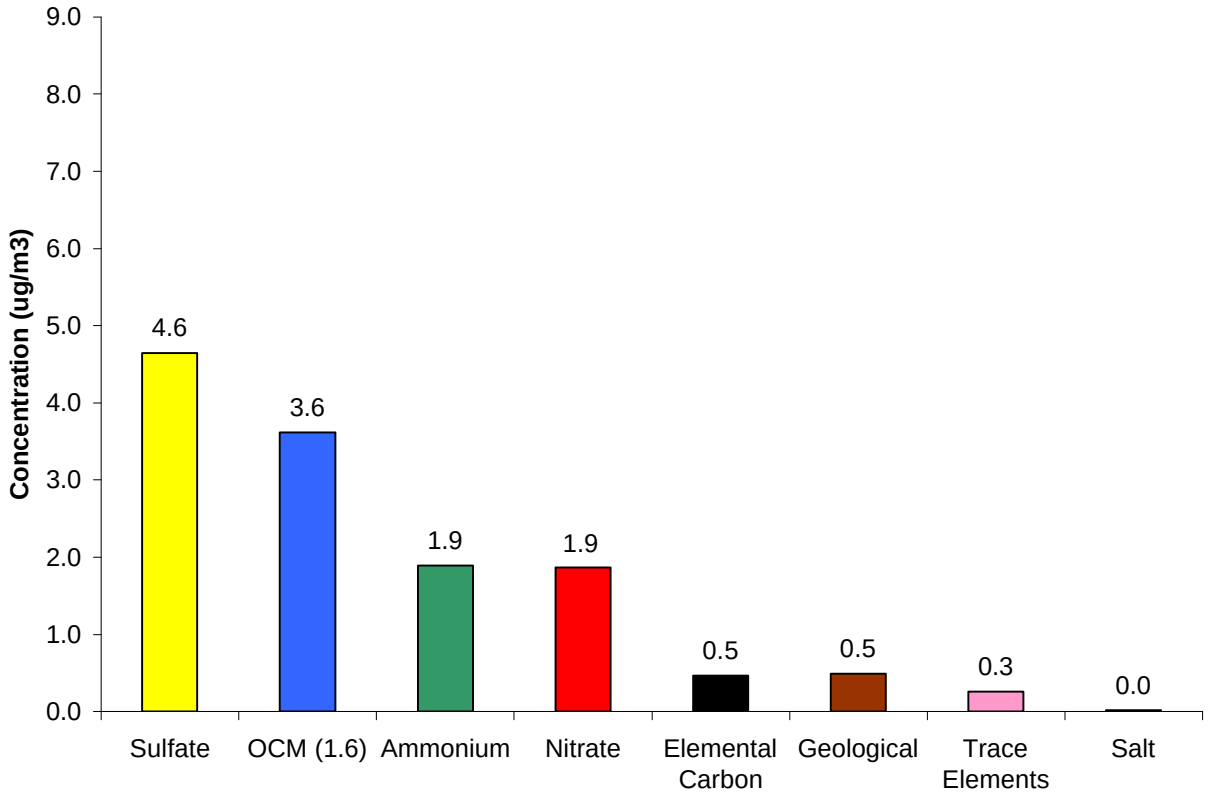

Figure 5-53 Major Constituents of $PM_{2.5}$ Mass, Dover, DE

The average reconstructed mass calculated for this site was about 8.3 percent lower than the average gravimetric mass measured by the speciation sampler. Average reconstructed mass was 13.4 µg/m^3 whereas the average gravimetric mass was 14.6 µg/m^3. Figure 5-54 visually compares the average reconstructed mass with the average gravimetric mass.

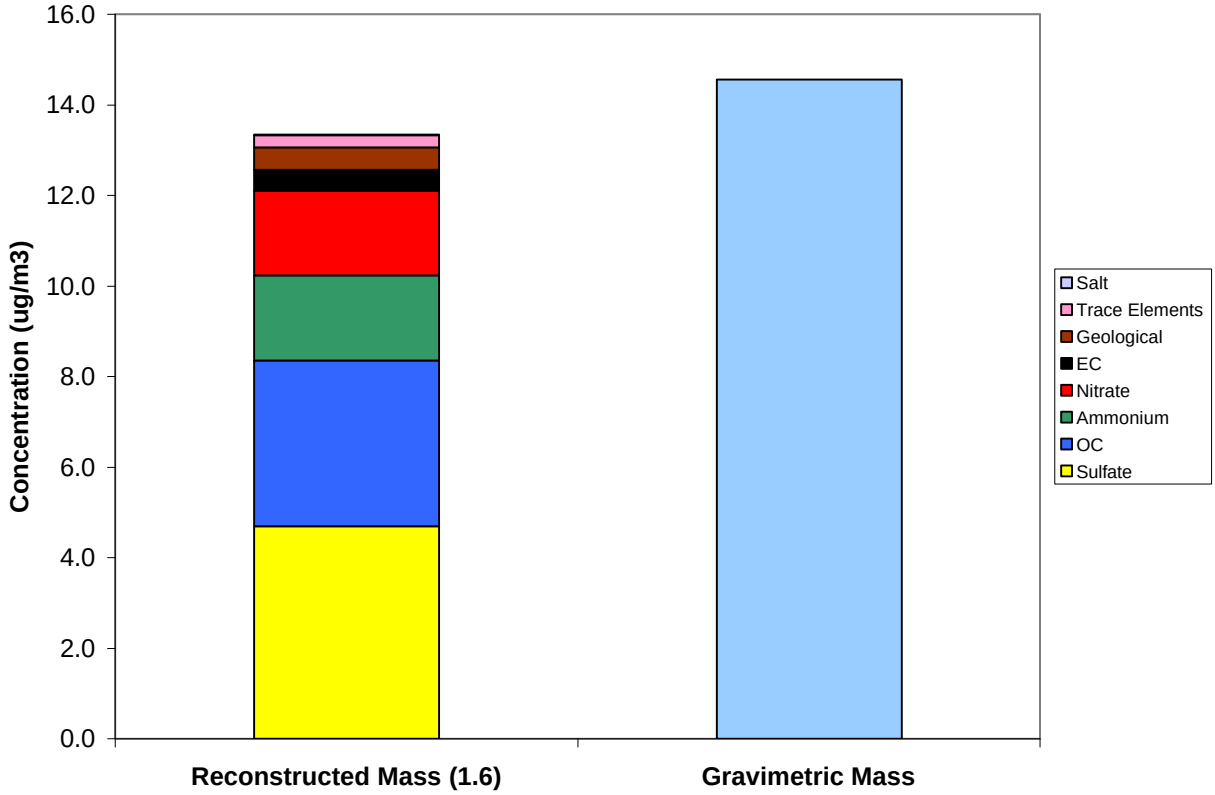

Figure 5-54 Comparison of Average Reconstructed Mass and Average Gravimetric Mass, Dover, DE

5.5.3 Time Series Analysis of $PM_{2.5}$ Species

The $PM_{2.5}$ speciation monitor at Dover, DE was installed and put in service in June 2001. It has operated on a 1-in-6 sampling schedule from its installation to the present time. Figure 5-55 shows a composite time series for the five major species measured at Dover. Figures 5-56 through 5-60 show time series for each of the five major species. The black line in Figures 5-56 through 5-60 is the 30-day rolling average concentration for the specie.

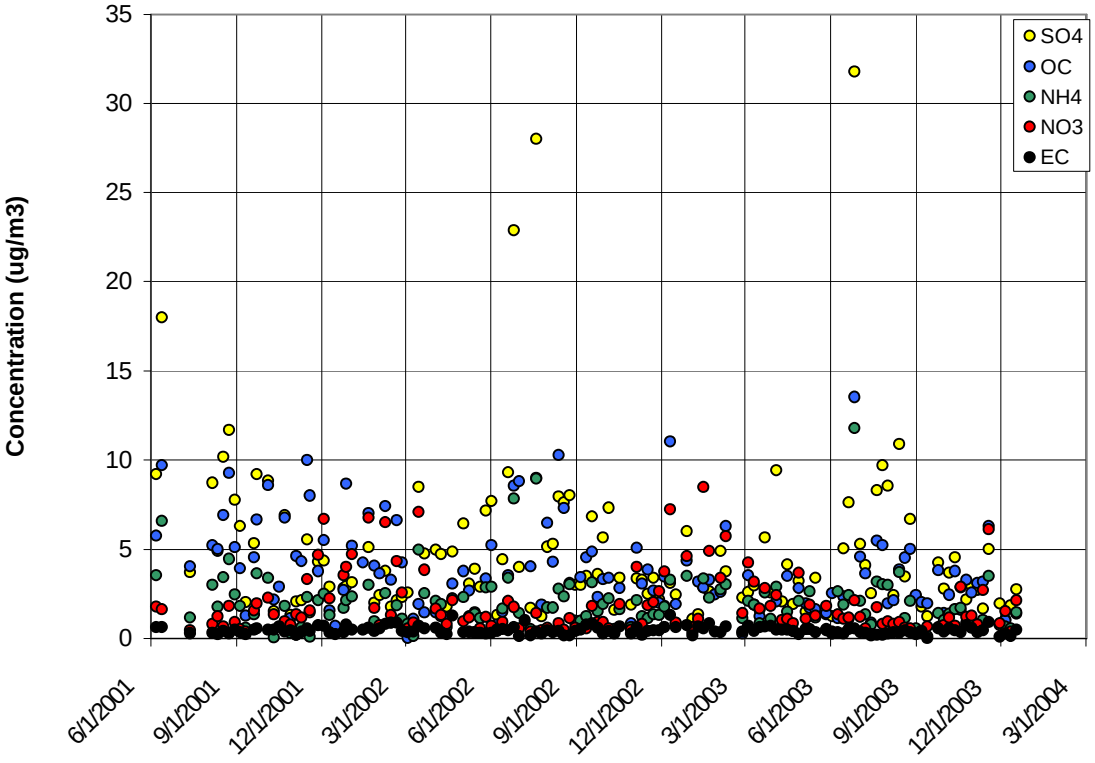

Figure 5-55 Time Series for the Dover, DE Monitor

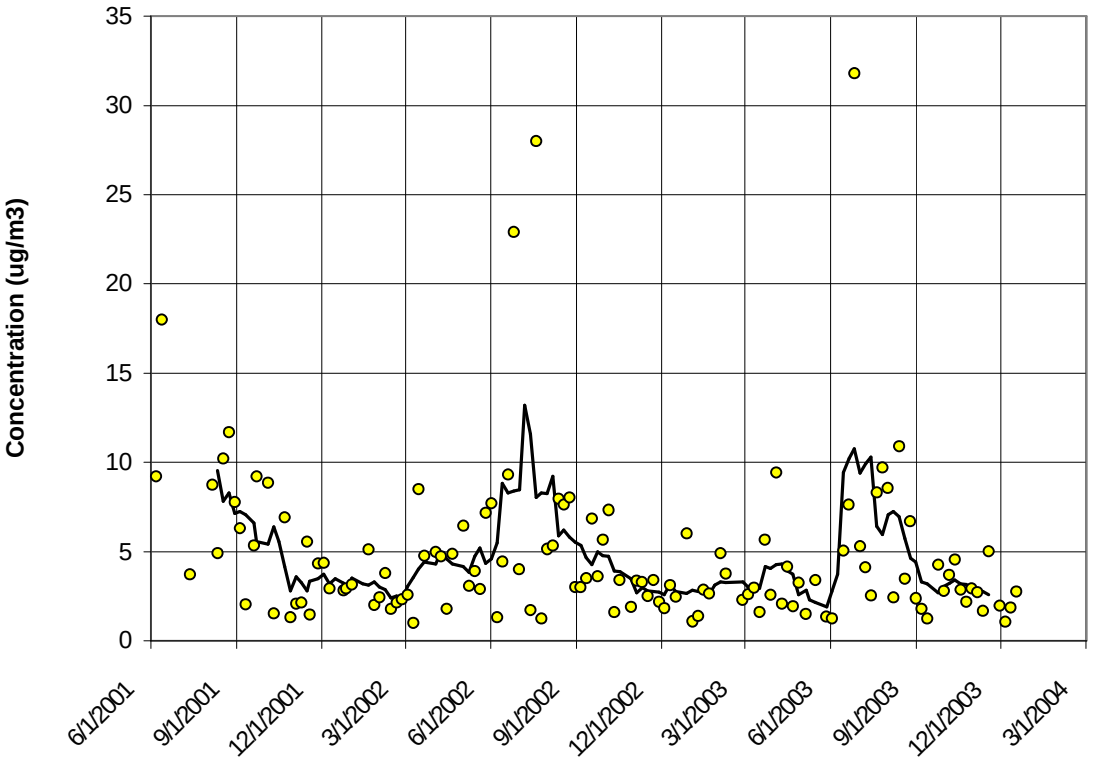

Figure 5-56 Sulfate Time Series for the Dover, DE Monitor

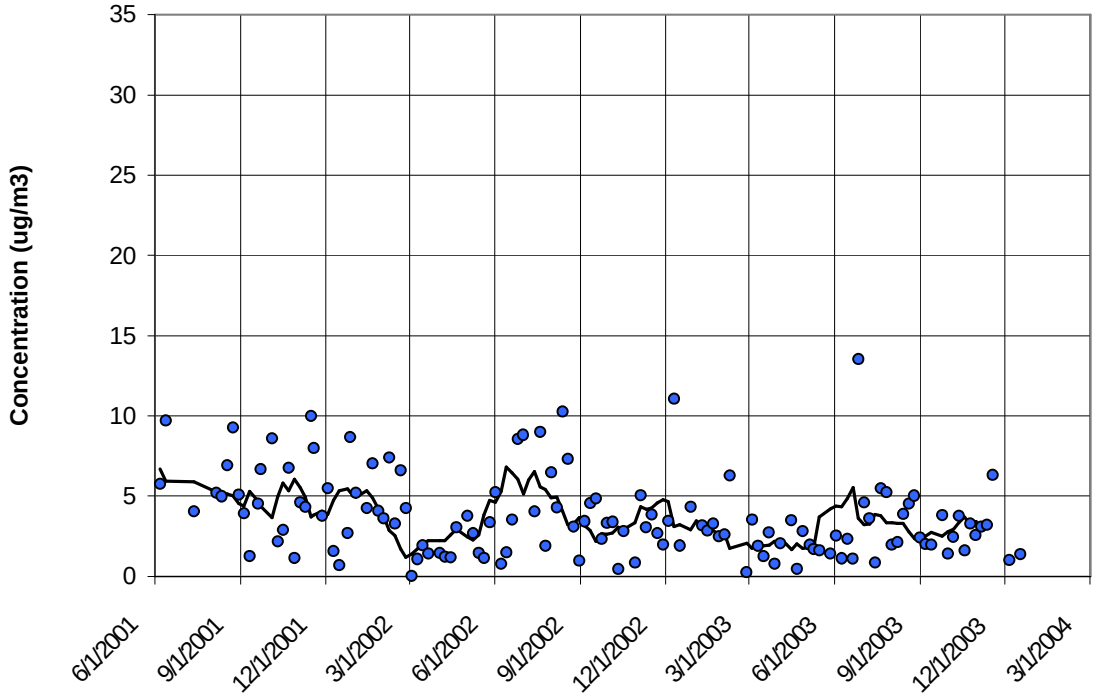

Figure 5-57 Organic Carbon Mass Time Series for the Dover, DE Monitor

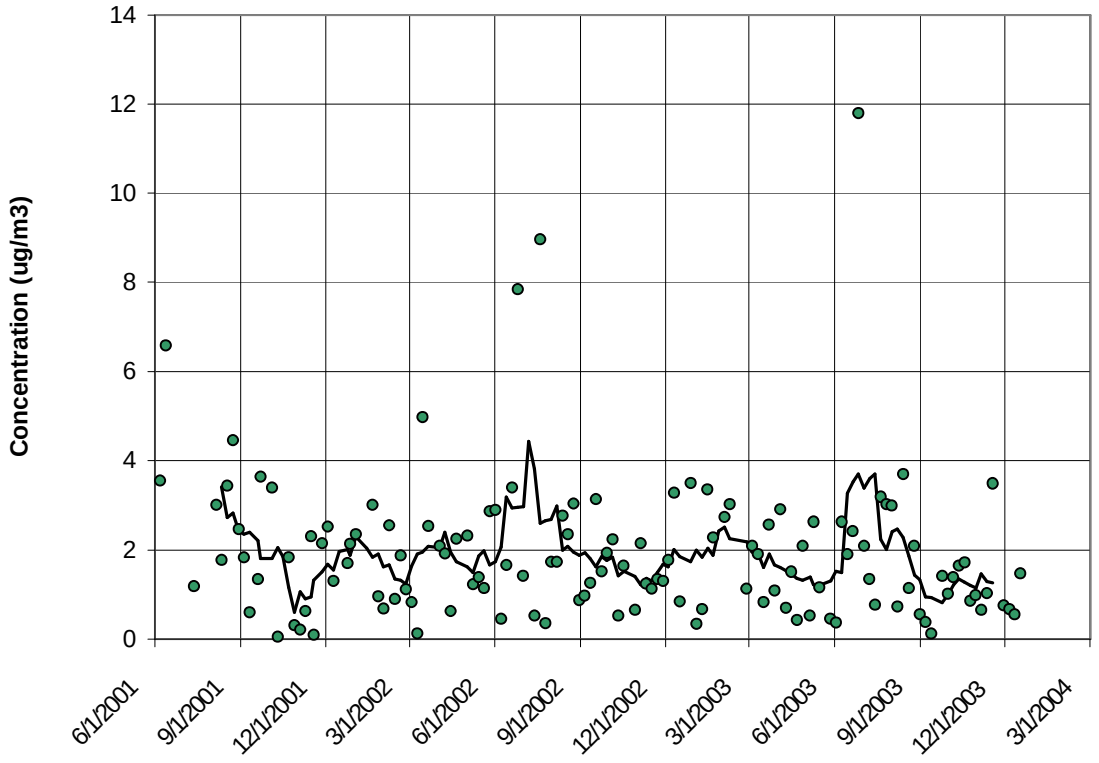

Figure 5-58 Ammonium Time Series for the Dover, DE Monitor

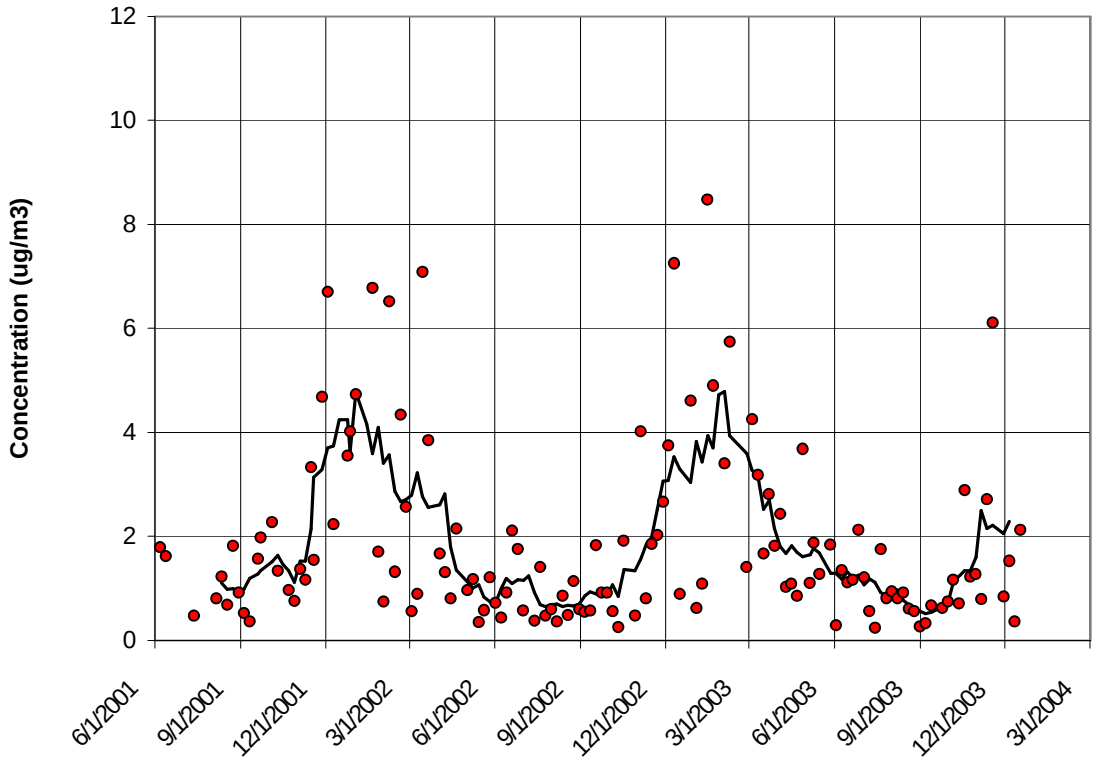

Figure 5-59 Nitrate Time Series for the Dover, DE Monitor

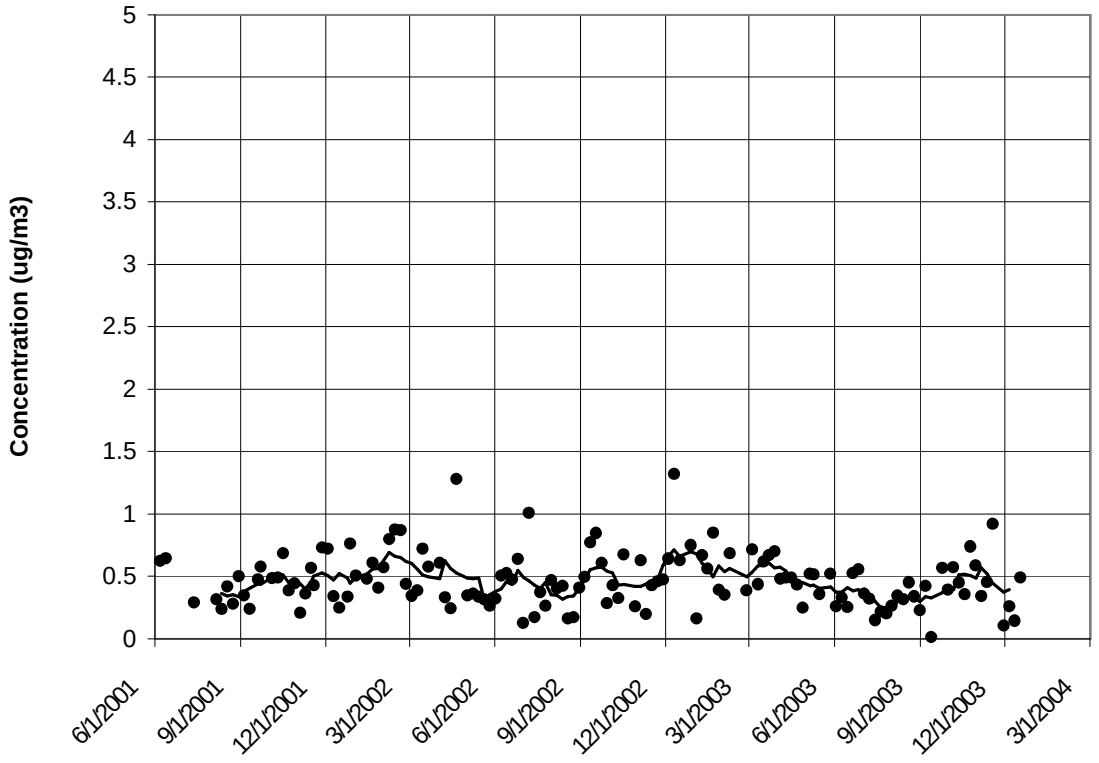

Figure 5-60 Elemental Carbon Time Series for the Dover, DE Monitor

Sulfate was the largest contributor to $PM_{2.5}$ mass concentration in Dover over 2001-2003. Average sulfate concentration was lowest in winter at 2.96 µg/m^3. Average summer concentration was much higher at 7.59 µg/m^3. Average spring and fall concentrations lay between the winter and summer concentrations at 3.82 and 3.77 µg/m^3. Figure 5-56 shows the 30-day rolling average sulfate concentration over 2001-2003. Most sulfate measurements were between 1 and 5 µg/m^3. During the summer and occasionally at other times of year, sulfate measurements were higher between about 5 and 10 µg/m^3. Some very high concentrations occurred in summer. Over 2001-2003, the peak summer sulfate concentration was 31.8 µg/m^3 on June 26, 2003.

Using an OM/OC ratio of 1.6, organic carbon mass was the second largest contributor to $PM_{2.5}$ mass in Dover, DE. Average organic carbon mass concentration was highest during the summer at 4.4 µg/m^3. Average organic carbon mass concentration was 4.27 and 3.73 µg/m^3 in winter and fall and lowest at 1.91 µg/m^3 in the spring. The time series in Figure 5-57 reveals a number of peaks and valleys. Elevated concentrations often occurred in summer and in late fall and winter. Lower, less variable concentrations occurred in spring. The variable nature of organic carbon mass and the relatively short data record over 2001-2003 makes it difficult to clearly identify seasonal patterns. The analysis of additional data collected over future years may help explain the season behavior of organic carbon mass. The organic carbon mass measurement for the exceptional event that occurred July 7, 2002 was removed from the organic carbon mass time series shown in this report and from seasonal average calculations. On July 7, 2002, smoke from Canadian forest fires moved into the Mid-Atlantic Region.

Over 2001-2003, the average ammonium concentration was 1.89 µg/m^3. This was close to the region wide average of 2.01 µg/m^3, the same as the concentration observed in Richmond (1.89 µg/m^3), and similar to the average concentration found in Baltimore (1.94 µg/m^3). The average ammonium concentration in Dover over 2001-2003 was less the average concentration observed in Wilmington, DE (2.33 µg/m^3) 64 km (40 miles) away.

As shown in Figure 5-58, average ammonium concentration was highest in the summer at 2.61 µg/m^3 followed by winter with an average concentration of about 1.92 µg/m^3. Average spring concentration was 1.67 µg/m^3 and fall had the lowest average concentration at 1.36 µg/m^3. Figure 5-58 shows how ammonium concentration varied over time. While the 30-day rolling average shows peaks and valleys, ammonium concentration is variable between about zero and 4 µg/m^3 most times of the year. Occasional “spikes” of high concentration occurred in summer. The highest ammonium concentration occurred on June 26, 2003 at 11.8 µg/m^3.

Ammonium and sulfate concentrations were well correlated (R^2 = 0.88); when sulfate concentrations were high, ammonium concentrations were usually high. Table 5-19 lists ammonium and sulfate concentrations on days when sulfate concentration exceeded 15 µg/m^3.

Table 5-19 High Ammonium and Sulfate Days for the Dover, DE Monitor

Date	Ammonium Concentration (µg/m^3)	Sulfate Concentration (µg/m^3)
6/12/01	6.6	18.0
6/25/02	7.8	22.9
7/19/02	9.0	28.0
6/26/03	11.8	31.8

As the time series in Figure 5-59 shows, nitrate concentrations at Dover exhibited the strong seasonal behavior seen at other sites. Nitrate concentrations were lowest during the summer and noticeably higher in the winter. Over 2001-2003, the average summer concentration was 0.89 $\mu g/m^3$ whereas the average winter concentration was 3.80 $\mu g/m^3$. In spring and fall, average nitrate concentrations were 1.91 $\mu g/m^3$ and 1.41 $\mu g/m^3$ respectively. As Figure 5-59 shows, nitrate values are much more variable in winter than in summer. Wintertime ammonium and nitrate measurements were strongly correlated ($R^2 = 0.84$).

Figure 5-60 displays the time series for elemental carbon. As the Figure shows, average concentration remained fairly constant over 2001-2003. Average elemental carbon concentration over the entire period was 0.47 $\mu g/m^3$. Elemental carbon concentration was slightly lower during the summer at 0.34 $\mu g/m^3$ and slightly higher during the winter at 0.59 $\mu g/m^3$. The unusually high values on April 20, 2002 (1.3 $\mu g/m^3$) and December 10, 2002 (1.3 $\mu g/m^3$) may have been due to special circumstances.

Table 5-20 shows the seasonal averages for the major constituents of $PM_{2.5}$ mass.

Table 5-20 Seasonal Averages for the Major Constituents of $PM_{2.5}$ Mass ($\mu g/m^3$) for Dover, DE

	Organic Carbon Mass	Sulfate	Ammonium	Nitrate	Elemental Carbon
Winter	4.27	2.96	1.92	3.80	0.59
Spring	1.91	3.82	1.67	1.91	0.49
Summer	4.40	7.59	2.61	0.89	0.34
Fall	3.73	3.77	1.36	1.41	0.47

[1] Does not include the exceptional event that occurred July 7, 2002, the smoke event associated with Canadian forest fires.

5.5.4 Trajectory Analysis

Figure 5-61 shows CATT back trajectories for the "cleanest" days in the speciation record over the period studied from January 2001 through December 2003. While even lower concentration days can be found in the data record for Federal Reference Method monitors at the site, the trajectories plotted in Figure 5-62 are the lowest concentration days in the speciation record over the period studied. These "clean" days represent the five percent days with the lowest total $PM_{2.5}$ mass.

"Clean day" trajectories arriving at the Dover monitor include sets of four trajectories that:

- Originate in North and South Dakota, Manitoba and Saskatchewan Canada and travel over the Great Lakes,
- Start in British Columbia Canada and travel over central Canada and the Great Lakes,
- Originate in Ontario Canada and move down to Dover over western New York and east central Pennsylvania,
- Begin in the Louisiana and Arkansas and loops northeast into Quebec and Maine and arrived in Dover from the northeast,
- Arrive from the northeast off the Atlantic Ocean, and
- Originate in the Atlantic off Florida and travels to Dover over the Appalachian Mountains and the southeastern states.

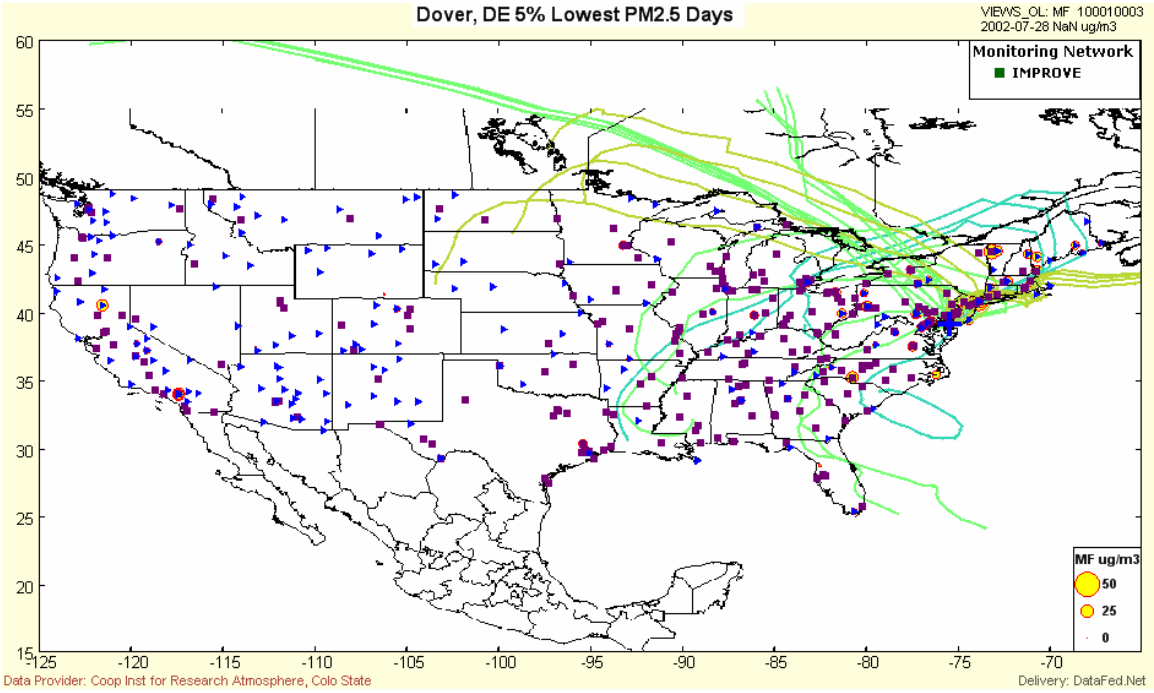

Figure 5-61 Back Trajectories for the Five Percent Cleanest Days, Dover, DE

In general, these trajectories do not originate or travel through high air pollution source regions. Table 5-21 lists the five percent cleanest days at Dover, DE and the total mass concentration measured by the speciation monitor on that day.

Table 5-21 Dover, DE Five Percent Lowest Days

Date	$PM_{2.5}$ Mass ($\mu g/m^3$)
10/28/2001	4.9
12/15/2001	5.5
6/7/2002	4.2
10/29/2002	6.3
5/27/2003	6.0
12/5/2003	5.0
Average	5.3

Figure 5-62 shows back trajectories for the "dirtiest" days, the five percent days with the highest total $PM_{2.5}$ mass. With the exception of a set of four trajectories that originate in Ontario and Manitoba Canada, most "dirty day" trajectories begin and re-circulate over source rich regions. Four of the six dirtiest days are high ammonium/high sulfate days that occurred during summer months. Many dirty day trajectories arrive in Dover from the west after traveling through the Ohio River Valley and states along the Ohio River. The set of trajectories that originate in Ontario and Quebec Canada are associated with the Canadian forest fire event of July 7-9, 2002.

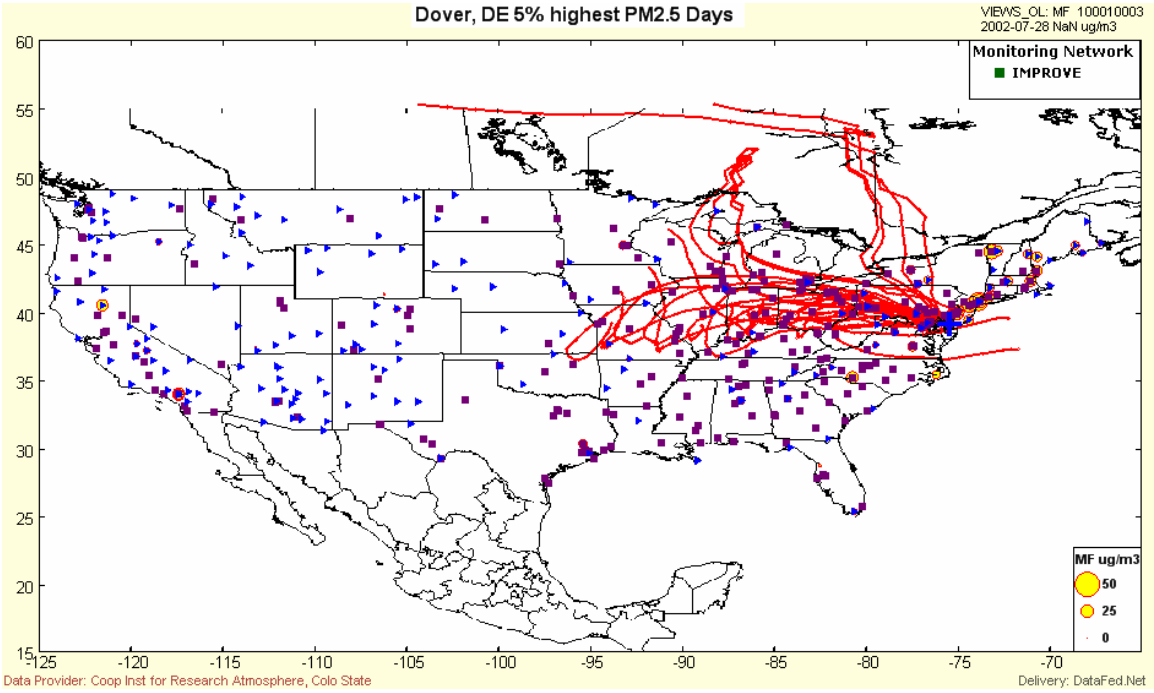

Figure 5-62 Back Trajectories for the Five Percent Dirtiest Days

Table 5-22 lists the five percent dirtiest days and the total mass concentration measured by the speciation monitor on that day.

Table 5-22 Dover, DE, Five Percent Highest Days

Date	$PM_{2.5}$ Mass ($\mu g/m^3$)
6/6/2001	32.8
6/12/2001	51.4
6/25/2002	46.5
7/7/2002	114
7/19/2002	56.5
6/26/2003	64.3
Average	60.9

5.6 Elizabeth, NJ

Site Name: Elizabeth Lab
AIRS Number: 34-039-0004
Latitude: 40.6411 North
Longitude: -74.2078 West
Elevation: 4.9 meters (16 feet)
Agency Operating the Monitor: New Jersey Department of Environmental Protection
Speciation Sampling Frequency: 1-in-3 days

5.6.1 Site Description

The Elizabeth monitoring site is located about 2.9 km (1.8 miles) south of downtown Elizabeth, NJ. It is located about 10.5 km (6.5 miles) south of Newark NJ and about 12 miles southwest of New York City. Figure 63 shows the monitoring site's location relative to the interstate highway system and large population centers.

Figure 5-63 Location of the Elizabeth, NJ Monitoring Site

The Elizabeth monitor is located in a highly urban and industrial area close to many emission sources. The most important feature of the site is its proximity to major mobile source emissions. The site is located adjacent to a toll plaza on the New Jersey Turnpike. Both the

New Jersey Turnpike and the Staten Island Expressway (I-278) are less than 200 meters (656 feet) from the monitoring shelter. The area immediately north of the highway interchange is residential in character. The area south of the interchange is industrial and includes extensive tank farms and other industrial facilities. The Newark International Airport is approximately 6 km (3.8 miles) to the north of the Elizabeth monitor. The nearby Port Newark/Elizabeth marine terminal is the world's largest containership port.

The site is relatively low lying. It is less than a 1.6 km (1 mile) west from the Arthur Kill, the body of water separating New Jersey from Staten Island, NY. The Atlantic Ocean is 27.4 km (17 miles) east of the monitoring site. Figure 5-64 shows the topographic features.

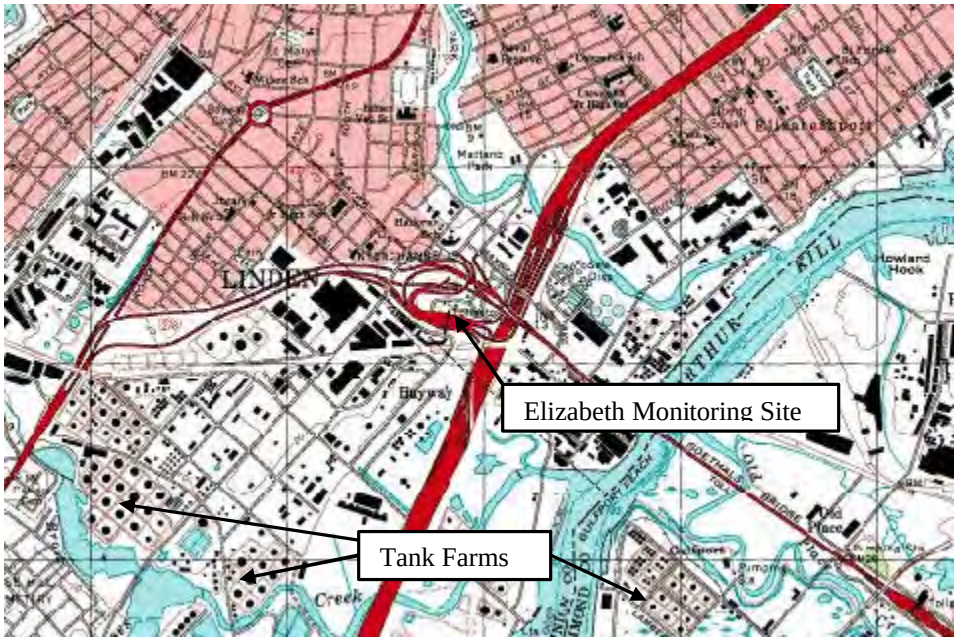

Source: TopoZone

Figure 5-64 Topographic Map of the Elizabeth, NJ Monitoring Site

The population of Elizabeth, NJ is 124,724. This population figure however does not properly characterize the urban nature of this monitoring site, especially given that New York City is only 12 miles to the northeast. The population of the New York City metropolitan area was estimated to be 21,199,865 in 2000 (2000 U.S. Census Bureau data).

5.6.2 Major Constituents of $PM_{2.5}$ Mass

For 2001-2003, the major constituents of $PM_{2.5}$ mass at Elizabeth were organic carbon and sulfate species followed by ammonium and nitrate species. Using an OM/OC ratio of 1.6, over 2001-2003, average organic carbon mass was 6.93 µg/m^3 whereas average sulfate concentration was 4.81 µg/m^3. Average ammonium and nitrate concentration were 2.19 and 2.27 µg/m^3. Elemental carbon contributed about 1.82 µg/m^3 of the total mass. Geological components, trace elements and salt added about 1.2 µg/m^3 to the mass. Figure 5-65 shows the contribution each species makes to the total mass measured at the site.

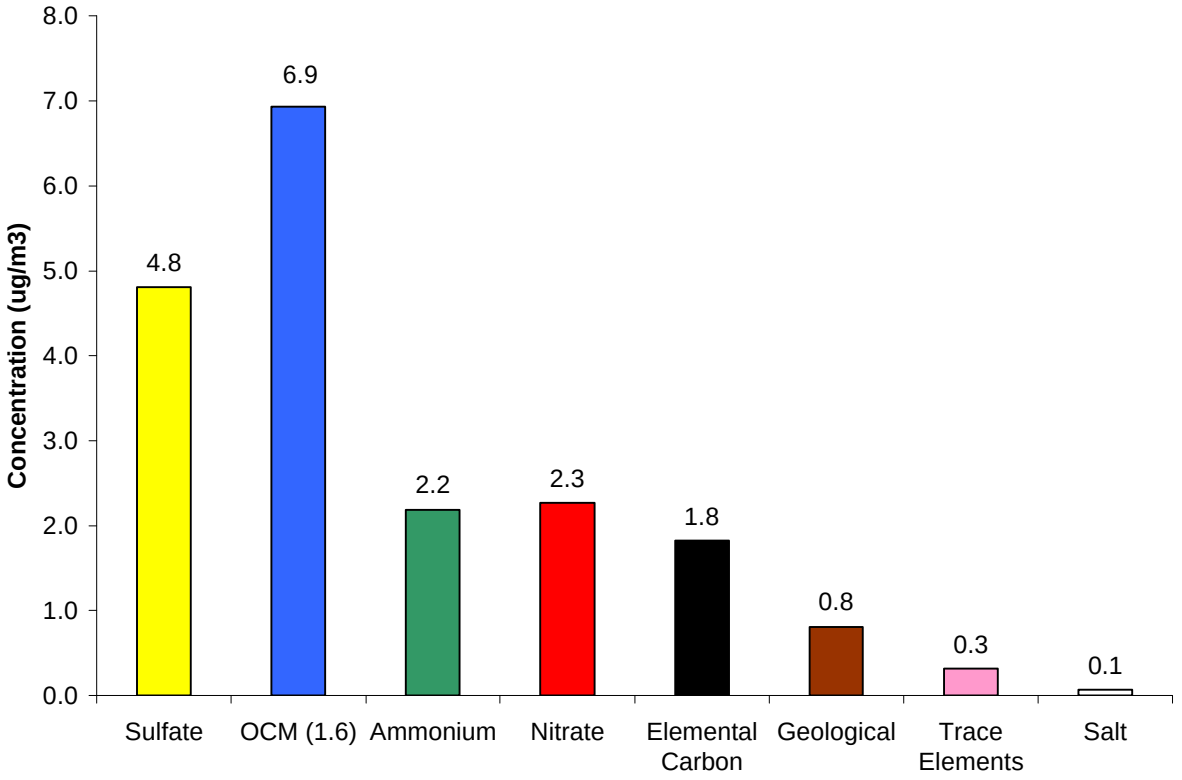

Figure 5-65 Major Constituents of $PM_{2.5}$ Mass, Elizabeth, NJ

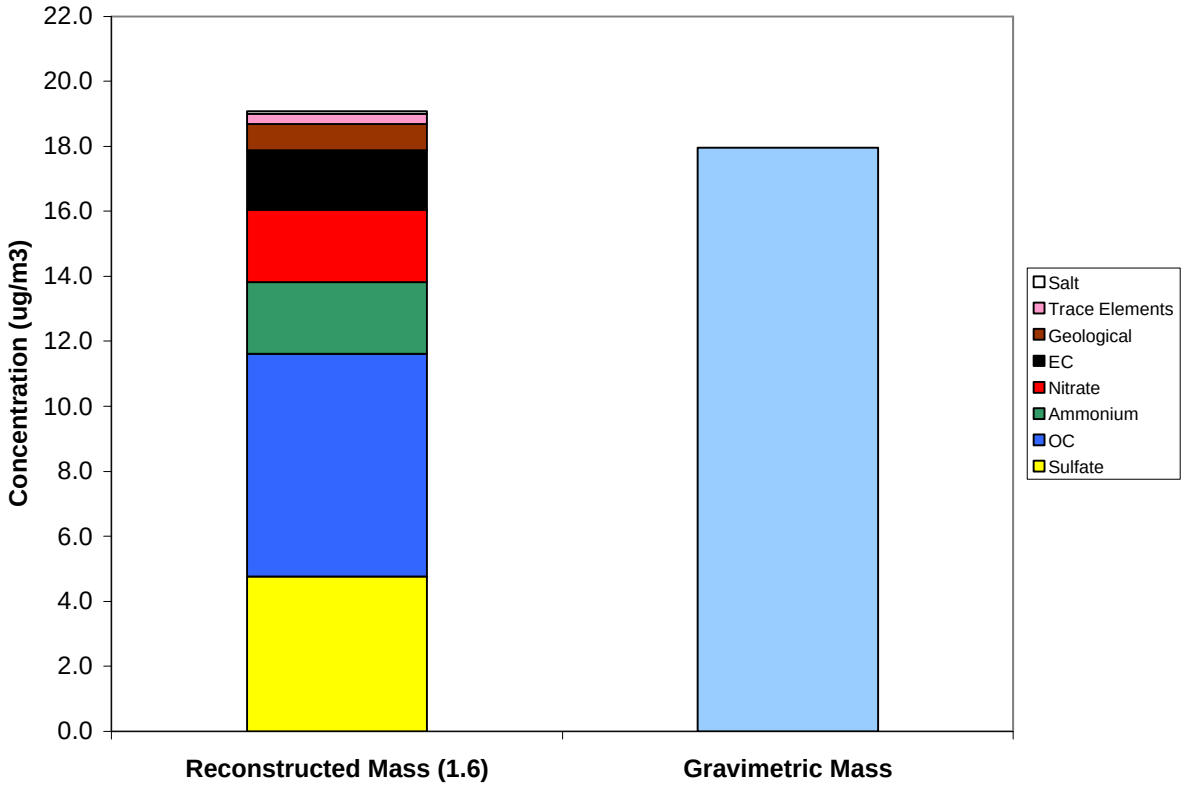

Figure 5-66 Comparison of Average Reconstructed Mass and Average Gravimetric Mass, Elizabeth, NJ

The average reconstructed mass calculated for this site was 6.2 percent higher than the average gravimetric mass measured by the speciation sampler. Average reconstructed mass was 19.1 $\mu g/m^3$ whereas the average gravimetric mass was 18.0 $\mu g/m^3$. Figure 5-66 visually compares the average reconstructed mass with the average gravimetric mass. The OM/OC ratio of 1.6 applied at this site may be too high, given the relatively "fresh" mobile source emissions that are thought to present near the Elizabeth monitor.

5.6.3 Time Series Analysis of $PM_{2.5}$ Species

The data record for the Met One SASS speciation sampler installed at the Elizabeth, NJ begins on June 6, 2001. The sampler has operated on a 1-in-3 sampling schedule from its installation to the present time. Figure 5-67 shows a composite time series for the five major species measured at Elizabeth and Figures 5-68 through 5-72 show time series for each of the five major species. In the time series plots for the five major species, the black line is the 30-day rolling average concentration for the specie.

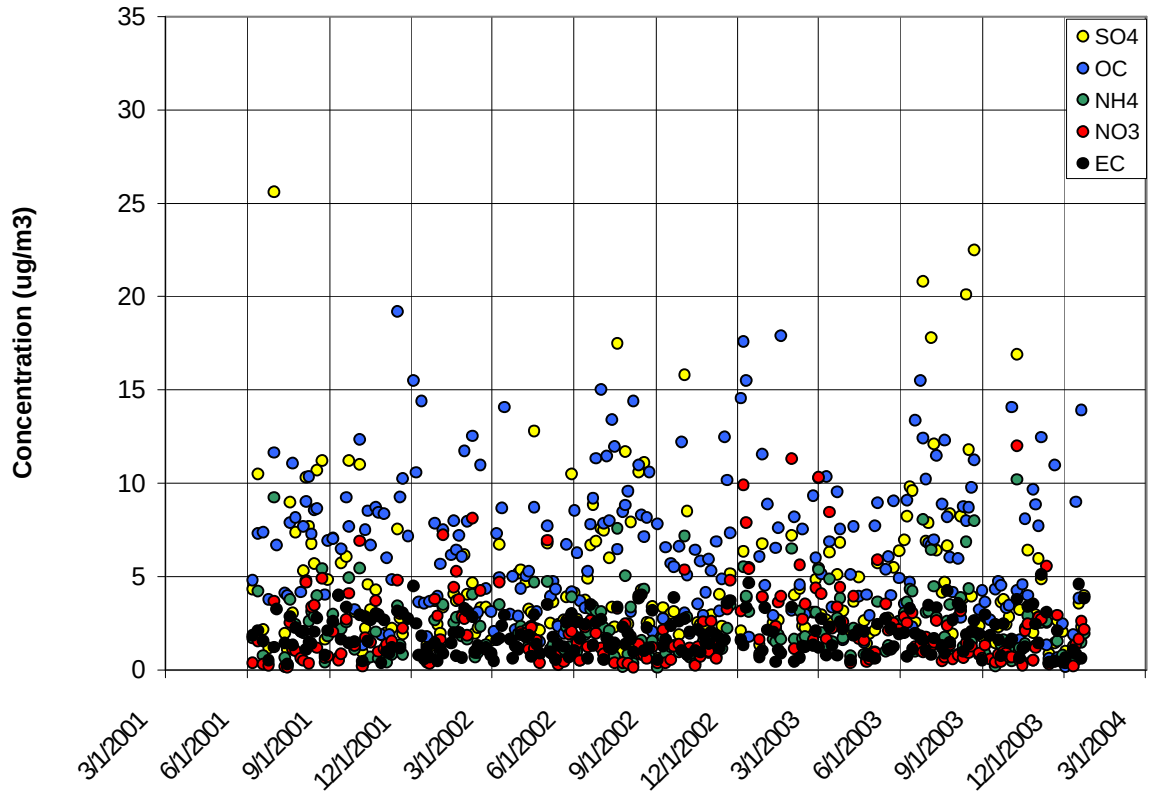

Figure 5-67 Time Series for the Elizabeth, NJ Monitor

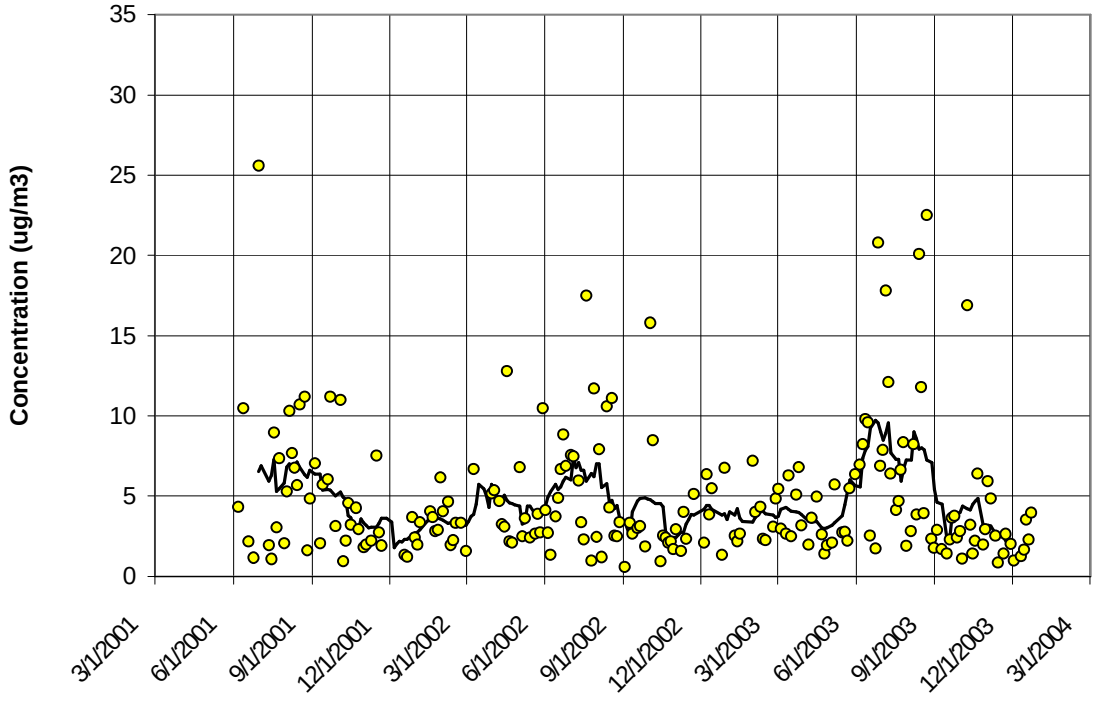

Figure 5-68 Sulfate Time Series for the Elizabeth, NJ Monitor

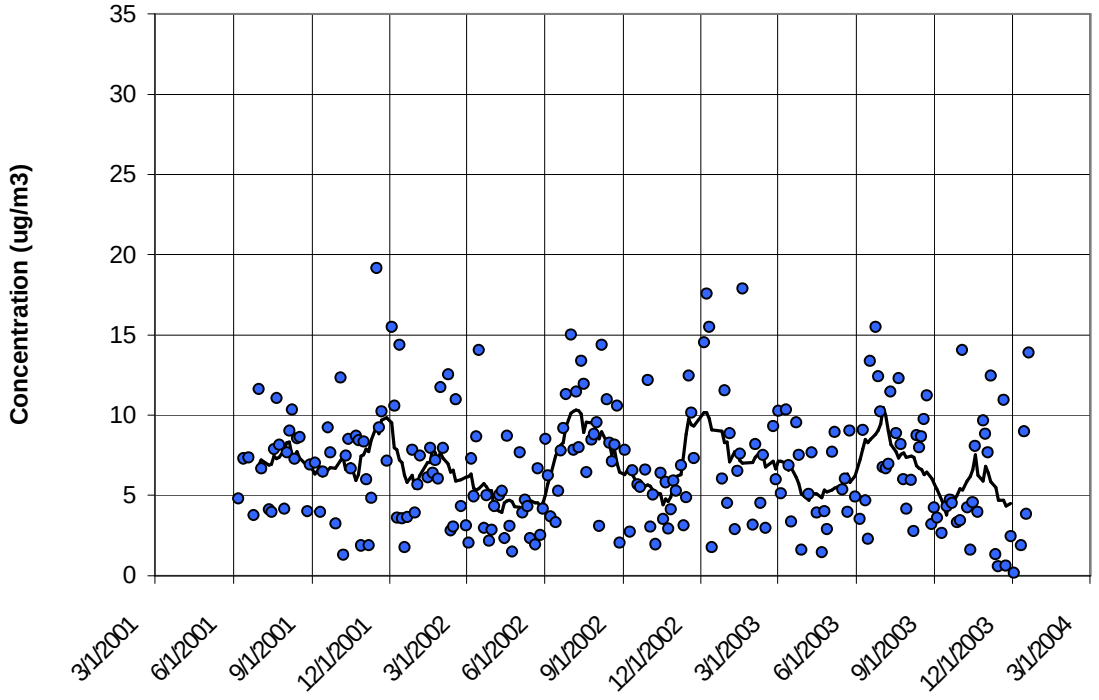

Figure 5-69 Organic Carbon Mass Time Series for the Elizabeth, NJ Monitor

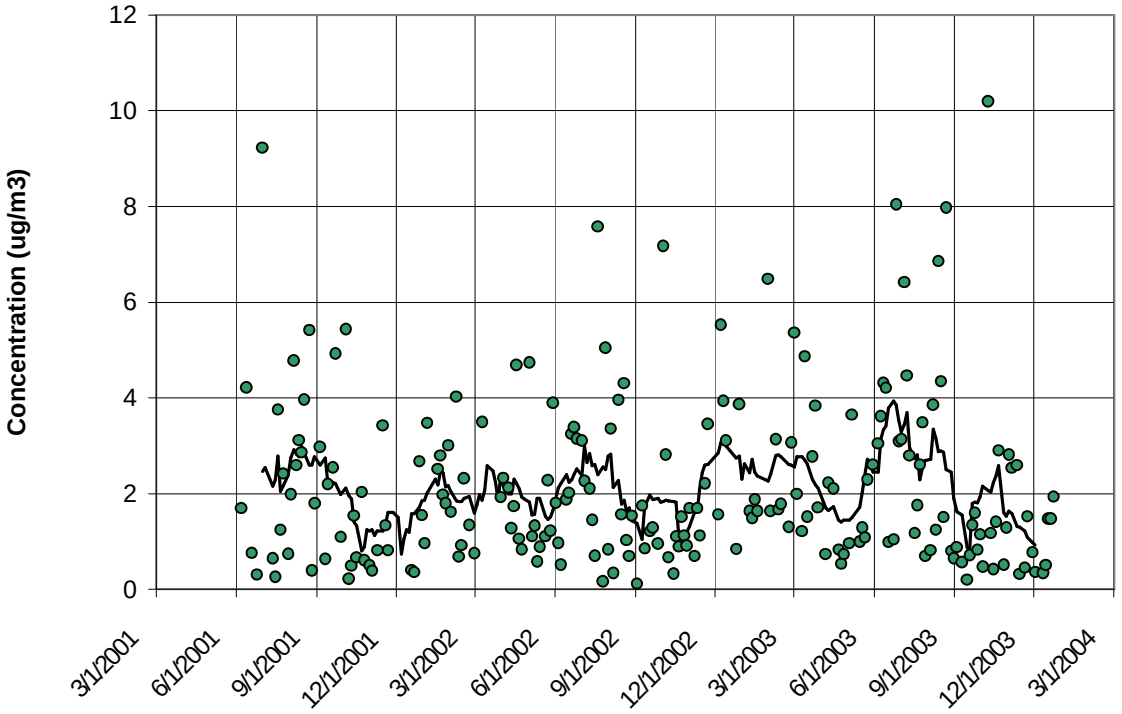

Figure 5-70 Ammonium Time Series for the Elizabeth, NJ Monitor

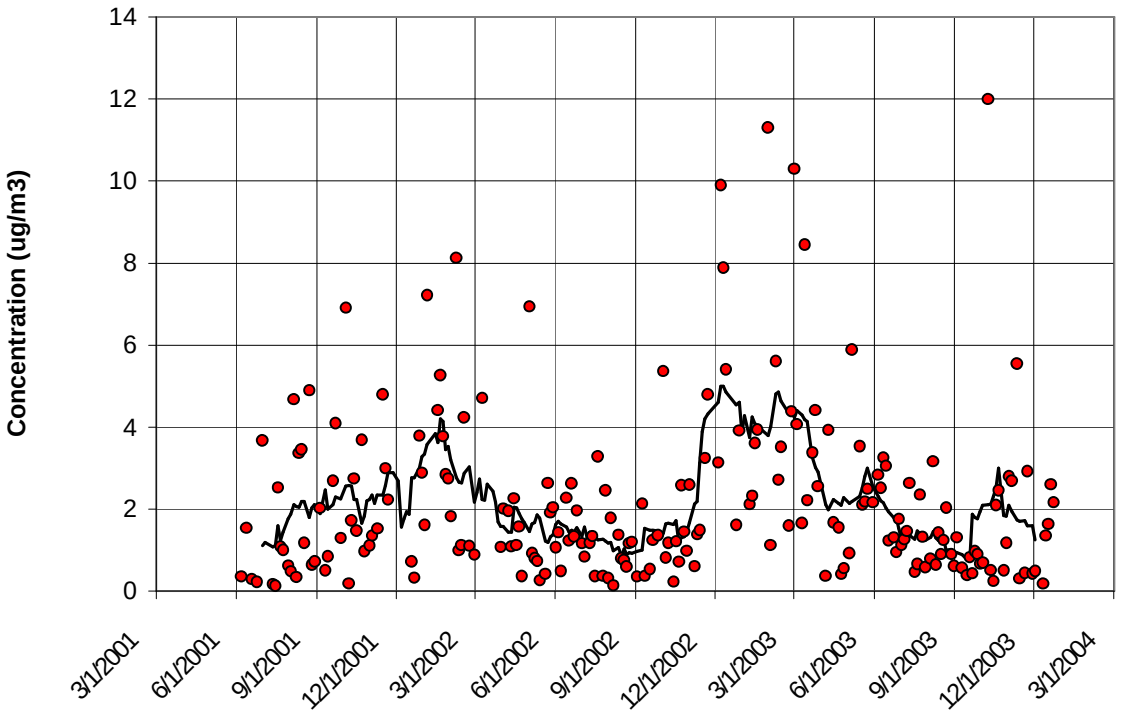

Figure 5-71 Nitrate Time Series for the Elizabeth, NJ Monitor

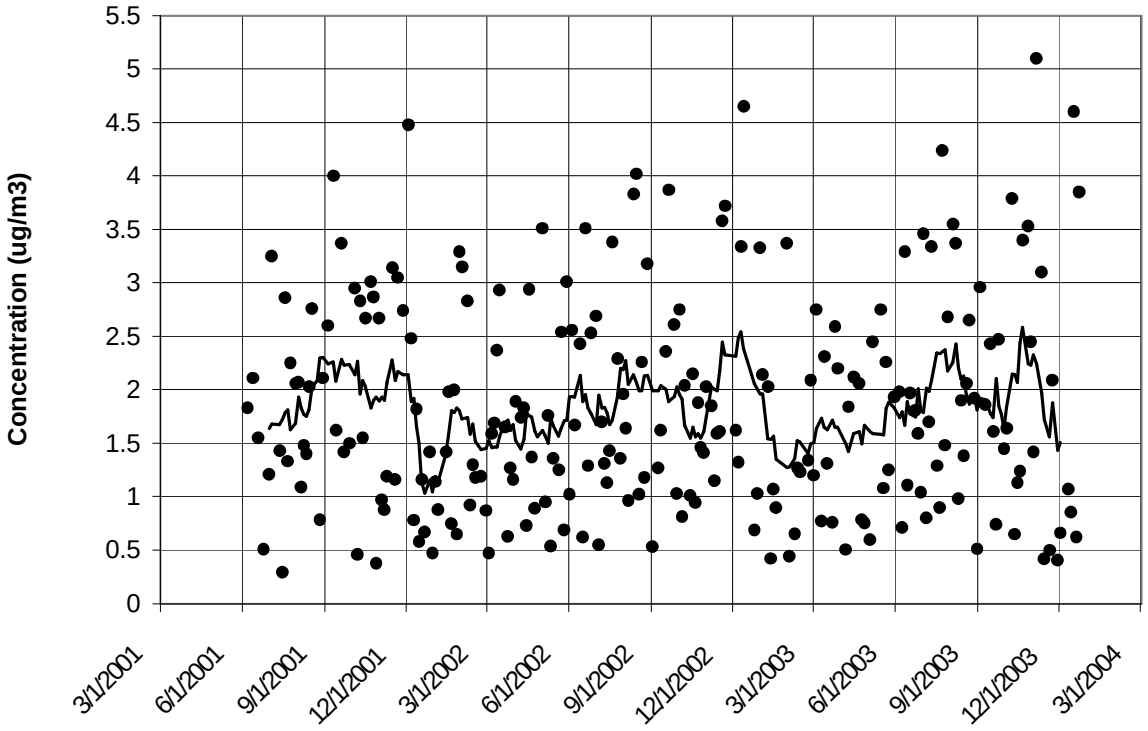

Figure 5-72 Elemental Carbon Time Series for the Elizabeth, NJ Monitor

The 30-day rolling average sulfate concentration in Figure 5-68 shows how sulfate varied seasonally over the 2001-2003 period in Elizabeth, NJ. The average sulfate concentration over all seasons at Elizabeth, 4.81 µg/m^3 was somewhat lower than the regional average regional sulfate concentration of 5.11 µg/m^3. Sulfate concentrations were highest in the summer and lowest in the winter. Average summer concentration over 2001-2003 was 6.98 µg/m^3; average winter concentration was 3.42 µg/m^3. As observed at other sites, sulfate concentration was much more variable during the summer than during other times of the year. Peak summer concentrations were in the 20-25 µg/m^3 range.

Organic carbon was the largest contributor to $PM_{2.5}$ mass at Elizabeth, NJ. The average organic carbon concentration over 2001-2003 was about 6.93 µg/m^3. This average concentration was similar to the average observed in Richmond, VA (6.81 µg/m^3) but higher than the average of 5.96 µg/m^3 observed at Philadelphia, PA, geographically the closest other monitor studied. Elizabeth's average organic carbon mass concentration was almost twice the average concentration estimated for Dover, DE, (3.62 µg/m^3), the lowest average concentration observed in the study. The high organic carbon concentrations at Elizabeth were likely due to the monitor's location in an area rich in mobile source emissions and perhaps industrial or other organic carbon emissions. High organic carbon mass concentrations estimated for Elizabeth, NJ may also be partially due to the OM/OC ratio applied to this site. If the Elizabeth monitoring site is in fact a site that receives large amounts of freshly emitted organic carbon species, the OM/OC ratio applied here of 1.6 may be too high for this monitoring station. Applying a lower OM/OC ratio would reduce estimates of organic carbon mass at this monitoring site.

As the 30-day rolling average in Figure 5-69 shows, organic carbon measurements appeared to exhibit some seasonal variation. Concentrations were often higher in summer and late fall/winter months than at other times of the year. While summer concentrations did not rise appreciably in 2001, increased concentrations were observed during the summers of 2002 and 2003. Over 2001-2003 period, the average summer concentration was 8.34 µg/m^3 followed by the average winter concentration of 7.60 µg/m^3. The average spring and fall concentrations were 5.34 µg/m^3 and 6.34 µg/m^3, respectively. The extraordinarily high organic carbon mass concentration of 72.0 µg/m^3 observed on July 7, 2002, was removed from the dataset. On this day, smoke from Canadian forest fires was in the Mid-Atlantic Region. Data associated with the Canadian forest fires was treated as an exceptional event.

Over 2001-2003, the average ammonium concentration was 2.19 µg/m^3. This average concentration was close to the regional average concentration of 2.01 µg/m^3 calculated for all monitors studied. Figure 5-70 shows how ammonium concentrations varied over time. Summer had the highest average concentration at 2.75 µg/m^3. Winter averaged 2.23 µg/m^3 and spring averaged 2.05 µg/m^3. Fall had the lowest concentration at 1.58 µg/m^3.

Ammonium and sulfate concentrations were well correlated (R^2 = 0.85); when ammonium concentrations were high, sulfate concentrations were usually high. Table 5-23 lists ammonium and sulfate concentrations on days when sulfate concentration exceeded 15 µg/m^3.

Table 5-23 High Ammonium and Sulfate Days for the Elizabeth, NJ Monitor

Date	Ammonium Concentration (µg/m^3)	Sulfate Concentration (µg/m^3)
6/30/01	9.2	25.6
7/19/02	7.6	17.5
10/2/02	7.2	15.8
6/26/03	8.1	20.8
7/5/03	3.5	17.8
8/13/03	6.9	20.1
8/22/03	8.0	22.5
10/9/03	10.2	16.9

Over 2001-2003, the Elizabeth monitor had an average nitrate concentration of 2.27 µg/m^3, an average somewhat higher than the average concentration of 1.76 µg/m^3 calculated for all monitors studied. Recent research has shown (Wittig, 2004) that the formation of solid phase nitrate species is a function of temperature, relative humidity, and ultraviolet radiation with higher concentrations occurring during cold weather/winter conditions. It is not surprising therefore that Elizabeth, NJ produced nitrate concentrations somewhat higher than monitors to the south.

As Figure 5-71 shows, nitrate measurements at Elizabeth exhibited the seasonal variation seen at other sites. Nitrate concentrations were lowest during the summer and noticeably higher in winter. Over 2001-2003, the average summer concentration was 1.42 µg/m^3 whereas the average winter concentration was 3.66 µg/m^3. In the spring and fall, average nitrate concentrations were 2.51 µg/m^3 and 1.90 µg/m^3, respectively. As Figure 5-71 shows, nitrate values are much more variable in winter than in summer.

Figure 5-72 displays the time series for elemental carbon. Over 2001-2003, the Elizabeth monitor had the highest average elemental carbon concentration (1.82 µg/m^3) of the eleven monitors studied. This average concentration was more than double the average concentration observed at other urban sites like Philadelphia, Pittsburgh, Baltimore, Washington, DC, and Wilmington, DE. The average elemental carbon concentration was about four to five times the average concentration observed at rural sites like Kinston, NC (0.36 µg/m^3) or Arendtsville, PA (0.39 µg/m^3). Average elemental carbon concentration was highest during the summer at 1.99 µg/m^3 and lowest during the winter and spring, 1.63 µg/m^3 and 1.64 µg/m^3 respectively.

The seasonal averages of the major species analyzed at Elizabeth, NJ are shown in Table 5-24.

Table 5-24 Seasonal Averages for the Major Constituents of $PM_{2.5}$ Mass (µg/m^3) for Elizabeth, NJ

	Organic Carbon	Sulfate	Ammonium	Nitrate	Elemental Carbon
Winter	7.60	3.42	2.23	3.66	1.64
Spring	5.34	4.20	2.05	2.51	1.63
Summer	8.34	6.98	2.75	1.42	1.99
Fall	6.34	3.77	1.58	1.90	2.01

5.6.4 Trajectory Analysis

Figure 5-73 shows CATT back trajectories for the cleanest days in the speciation record over the period studied from May 2001 through December 2003. While even lower concentration days can be found in the data record for Federal Reference Method monitors at the site, the trajectories plotted in Figure 5-73 are the lowest concentration days in the speciation record over the period studied. These "clean" days represent the five percent days with the lowest total $PM_{2.5}$ mass.

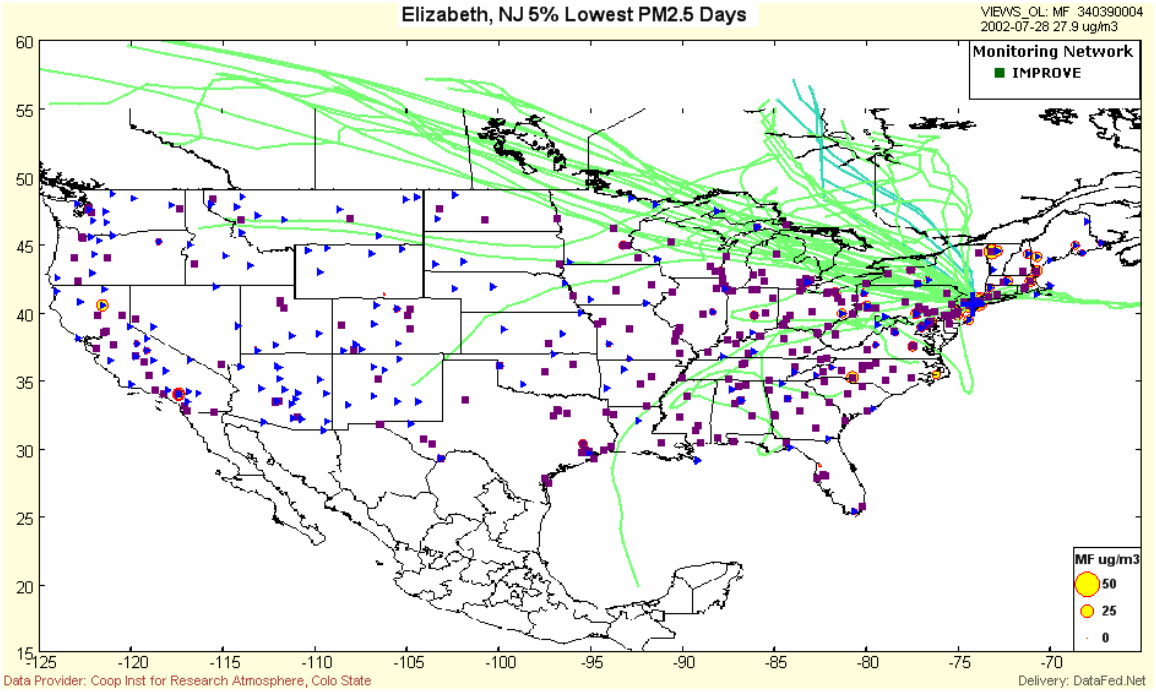

Figure 5-73 Elizabeth, NJ Back Trajectories for the Five Percent Cleanest Days

Most "clean day" trajectories show air parcels moving quickly from western Canadian directly to Elizabeth, NJ. These tracks originate in areas where there are relatively few source emissions. Most of these trajectories also do not pass through areas associated with high source emissions. In contrast to trajectories associated with high $PM_{2.5}$ concentrations, these trajectories do not remain or re-circulate over source regions. Other clean day trajectories come from Ontario, Canada and a few are maritime in nature.

Table 5-25 lists the five percent cleanest days at Elizabeth, NJ and the total mass concentration measured by the speciation monitor on that day.

Table 5-25 Elizabeth, NJ Five Percent Lowest Days

Date	$PM_{2.5}$ Mass ($\mu g/m^3$)
7/15/2001	5.4
10/7/2001	5.0
10/28/2001	3.7
11/6/2001	4.6
12/21/2001	5.1
9/2/2002	4.7
10/14/2002	5.0
4/6/2003	5.6
10/15/2003	5.2
11/14/2003	4.8
11/29/2003	5.5
Average	5.0

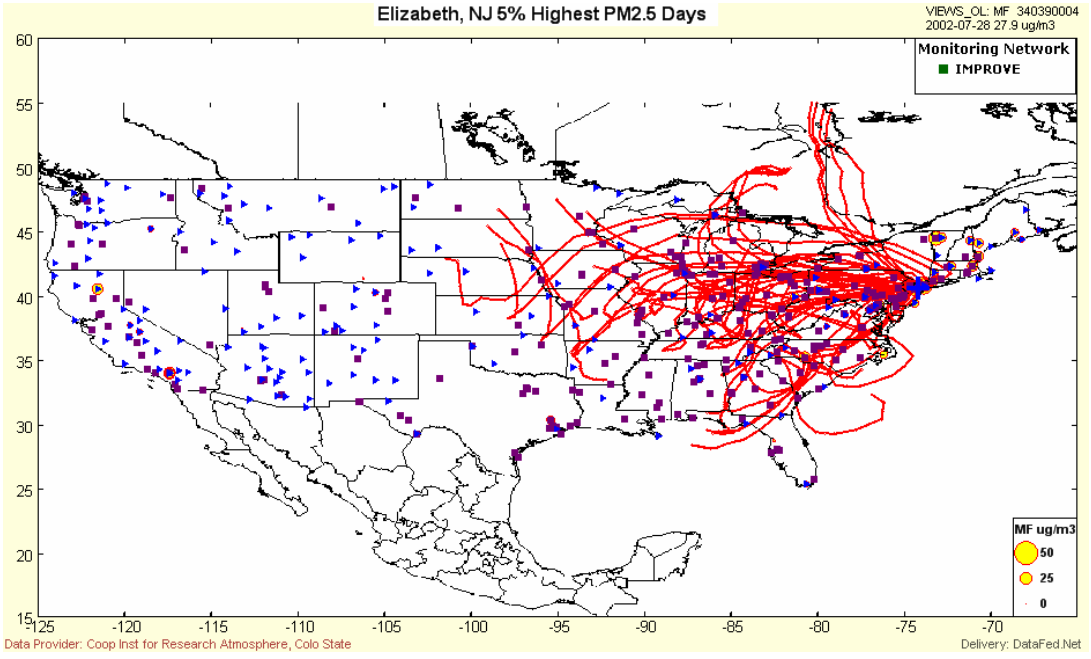

Figure 5-74 Elizabeth, NJ Back Trajectories for the Five Percent Dirtiest Days

Figure 5-74 shows back trajectories for the dirtiest days, the five percent days with the highest total $PM_{2.5}$ mass. With the exception of a few trajectories that appear to originate in the Gulf of Mexico, Atlantic Ocean and Ontario, Canada, most "dirty day" trajectories are tracks of air masses that have spent the past five days over the continental U.S. In many cases, the air circulates or re-circulates through air pollution source regions in the South, Midwest, or Northeast and Mid-Atlantic states.

Table 5-26 lists the five percent dirtiest days and the total mass concentration measured by the speciation monitor on that day.

Table 5-26 Elizabeth, NJ Five Percent Highest Days

Date	$PM_{2.5}$ Mass ($\mu g/m^3$)
6/30/2001	49.7
8/23/2001	38.3
3/15/2002	43.3
7/7/2002	85.7
7/19/2002	44.3
1/30/2003	44.0
6/26/2003	56.2
8/13/2003	41.0
8/22/2003	49.6
10/9/2003	51.0
Average	50.3

5.7 Kinston, NC

Site Name: Kinston
AIRS Number: 37-107-0004
Latitude: 35.2314 North
Longitude: -77.5686 West
Elevation: approximately 13.4 meters (44 feet)
Agency Operating the Monitor: North Carolina Division of Air Quality
Speciation Sampling Frequency: 1-in-6 days

5.7.1 Site Description

The Kinston monitoring site is located near the town of Kinston, NC, which is located in east central North Carolina. Kinston is in the coastal plane region of North Carolina, an area characterized by flat land or areas of gently rolling hills and valleys. The monitor is approximately 126 km (78 miles) southeast of Raleigh, NC and about 144 km (89 miles) north and slightly east of Wilmington, NC. Figure 5-75 shows the monitoring site's location relative to the interstate highway system and large population centers.

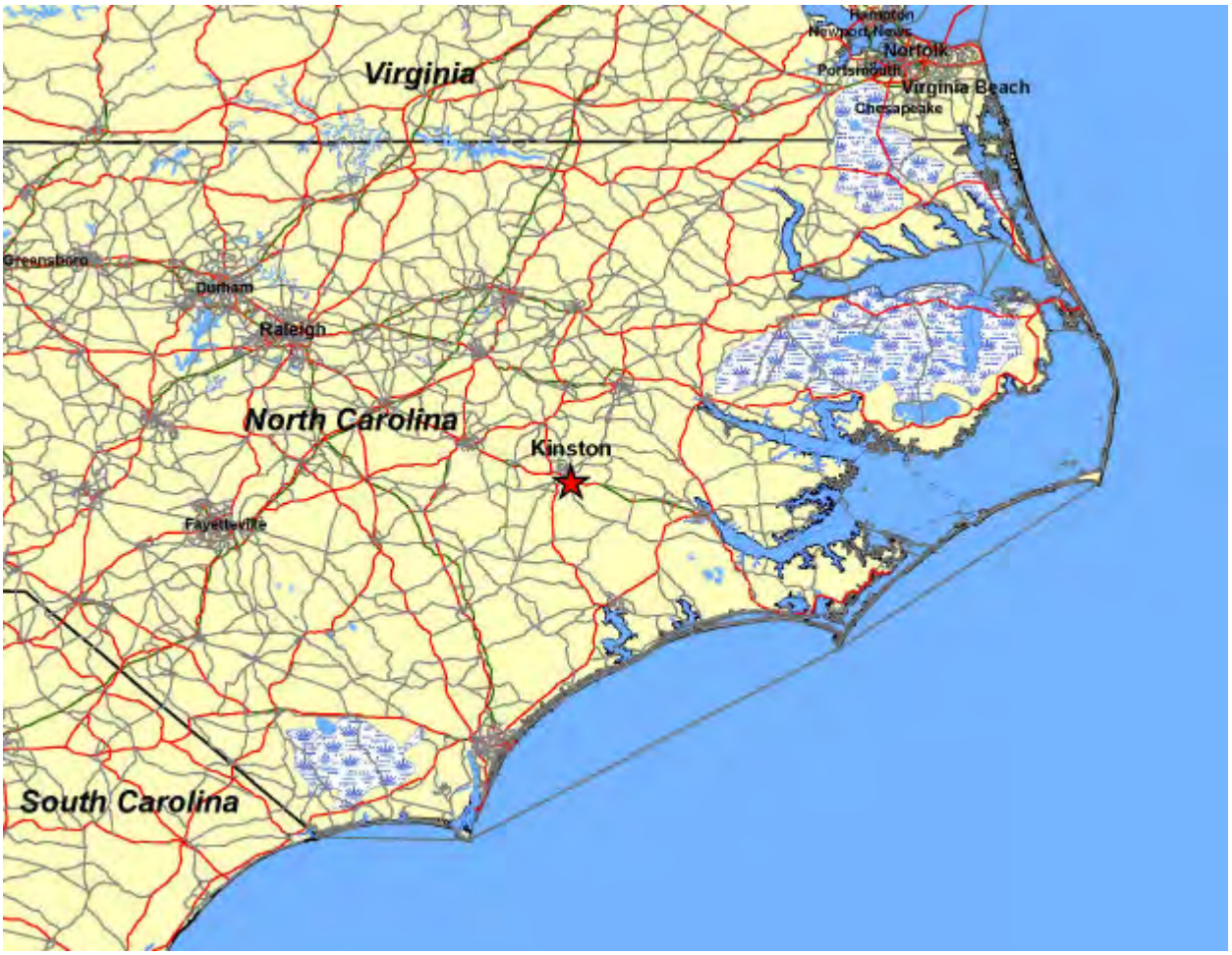

Figure 5-75 Location of the Kinston, NC Monitoring Site

While the Kinston monitoring site is located just south of the town of Kinston, it is considered a rural monitoring site. The population of Kinston is only 23,688 and the site is relatively far from large metropolitan areas. The site is located on the south end of the athletic fields of Lenoir Community College. With the exception of the town of Kinston to the north and the residential areas north and west of the town, the land around the monitoring site is either in agricultural production or marshland associated with the Neuse River. Figure 5-76 is a detailed map showing the topographic features around the monitoring site. Figure 5-77, a photograph looking south from the monitor, captures the rural nature of the landscape south of the monitor.

Source: TopoZone

Figure 5-76 Topographic Map of Kinston, NC Monitoring Site

The North Carolina Division of Air Quality reports there are a variety of air pollution sources in the vicinity of the monitoring site. Within 1.6 km (one mile) of the site there are woodworking and wood finishing operations that emit VOCs and particulate matter. Within about 16 km (ten miles) of the site, there are a range of air pollution sources including a plant that makes plastic products, three boilers, curing ovens, heating facilities, and other sources. The boilers, curing ovens, heating facilities and other sources in the area are general emitters of CO, NO_x, PM, SO_2, and VOCs. The area around Kinston, NC is noted for large hog farms and concentrated animal feeding operations (CAFOs).

Figure 5-77 View from the Kinston, NC Monitoring Site Looking South

5.7.2 Major Constituents of $PM_{2.5}$ Mass

The major constituents of $PM_{2.5}$ mass at Kinston were organic carbon and sulfate species followed by ammonium and nitrate species. Using an OM/OC ratio of 1.6, over 2001-2003, average organic carbon mass concentration was 4.47 $\mu g/m^3$. Average sulfate concentration was 4.11 $\mu g/m^3$. Average ammonium and nitrate concentrations were 1.51 and 1.10 $\mu g/m^3$, respectively. Elemental carbon, geological components, and trace elements added about 1.2 $\mu g/m^3$ to the average concentration measured at Kinston. OM/OC ratios larger than 1.6 are often applied at rural sites similar to Kinston, NC so the OM/OC ratio applied here may understate organic carbon mass measured at this site. If a larger OM/OC ratio was applied to the data, organic carbon mass would represent an even larger percent of total mass. Figure 5-78 shows the relative contribution each species made to the average concentration measured at Kinston, NC.

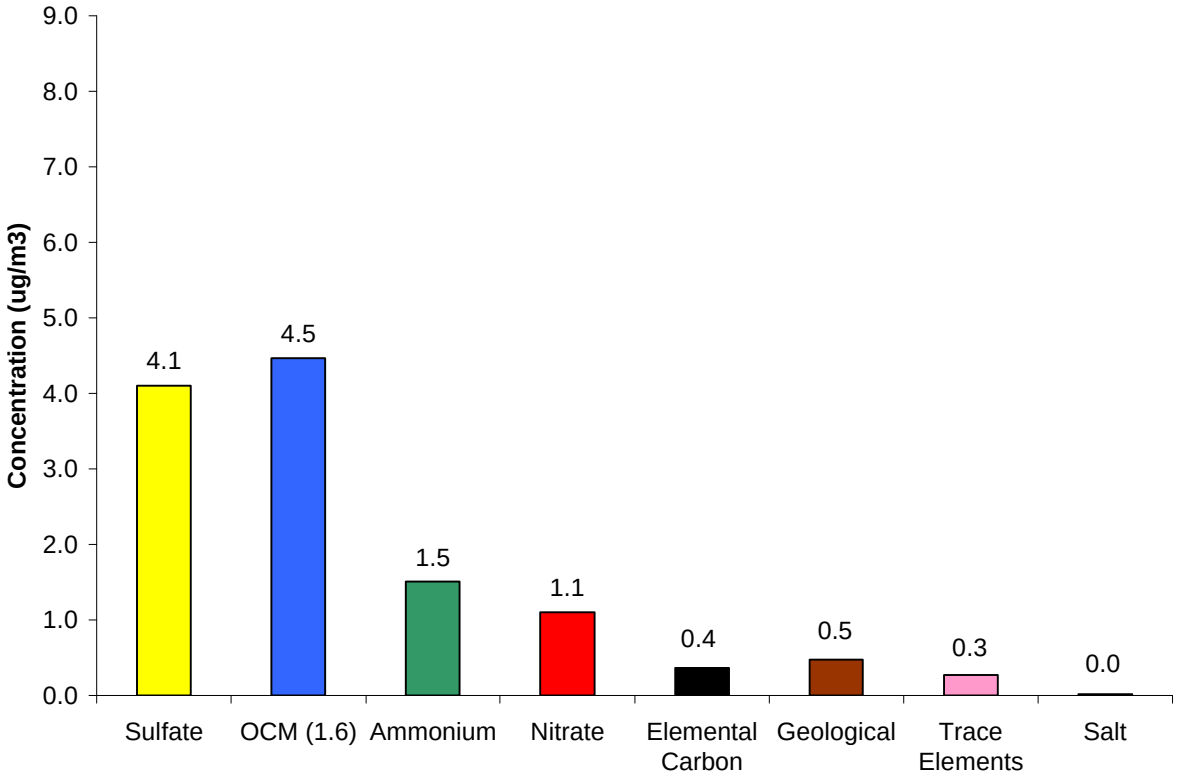

Figure 5-78 Major Constituents of $PM_{2.5}$ Mass, Kinston, NC

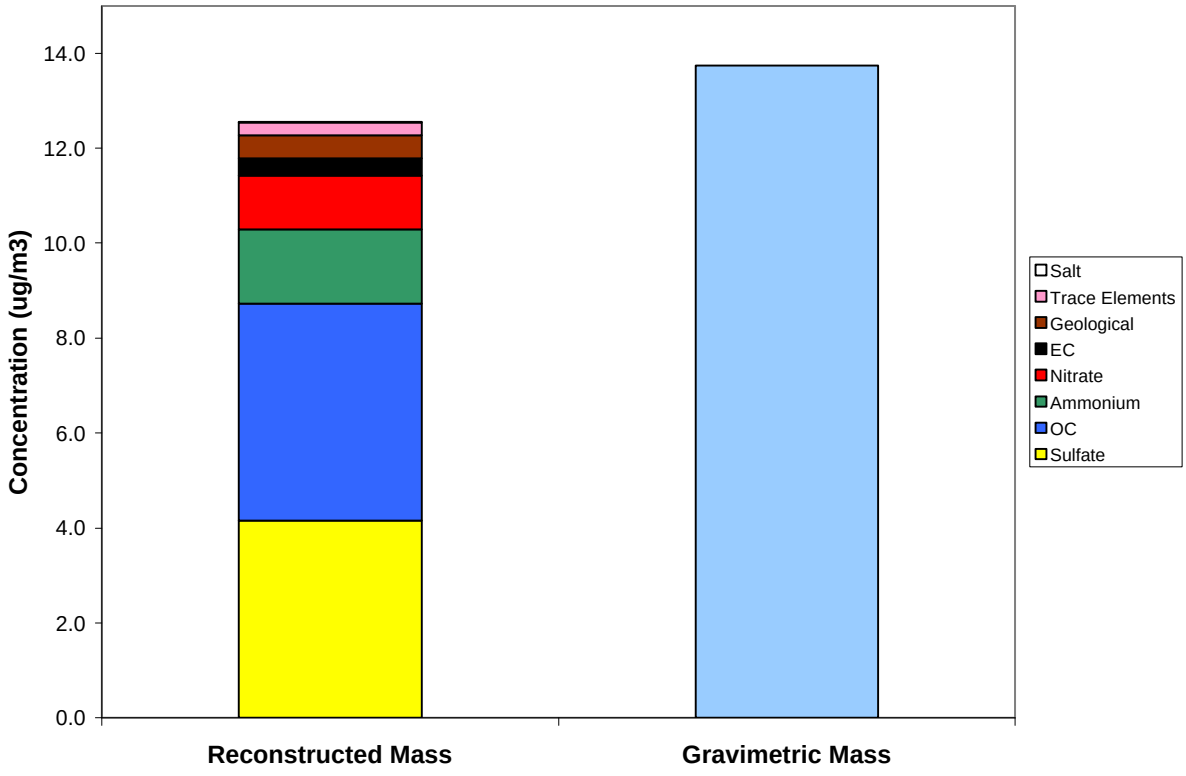

Figure 5-79 Comparison of Average Reconstructed Mass and Average Gravimetric Mass, Kinston, NC

The average reconstructed mass calculated for this site was 8.6 percent lower than the average gravimetric mass measured by the speciation sampler. Average reconstructed mass was 12.6 $\mu g/m^3$ whereas the average gravimetric mass was 13.7 $\mu g/m^3$. Figure 5-79 visually compares the average reconstructed mass with the average gravimetric mass.

5.7.3 Time Series Analysis of $PM_{2.5}$ Species

A speciation sampler was installed at the Kinston monitoring site in January 2002. It has operated on a 1-in-6 sampling schedule from its installation to the present time. Figure 5-80 shows a composite time series for the five major species measured at Kinston and Figures 5-81 through Figure 5-85 show time series for individual species. In the time series plots for the five major species, the black line is the 30-day rolling average concentration for the specie.

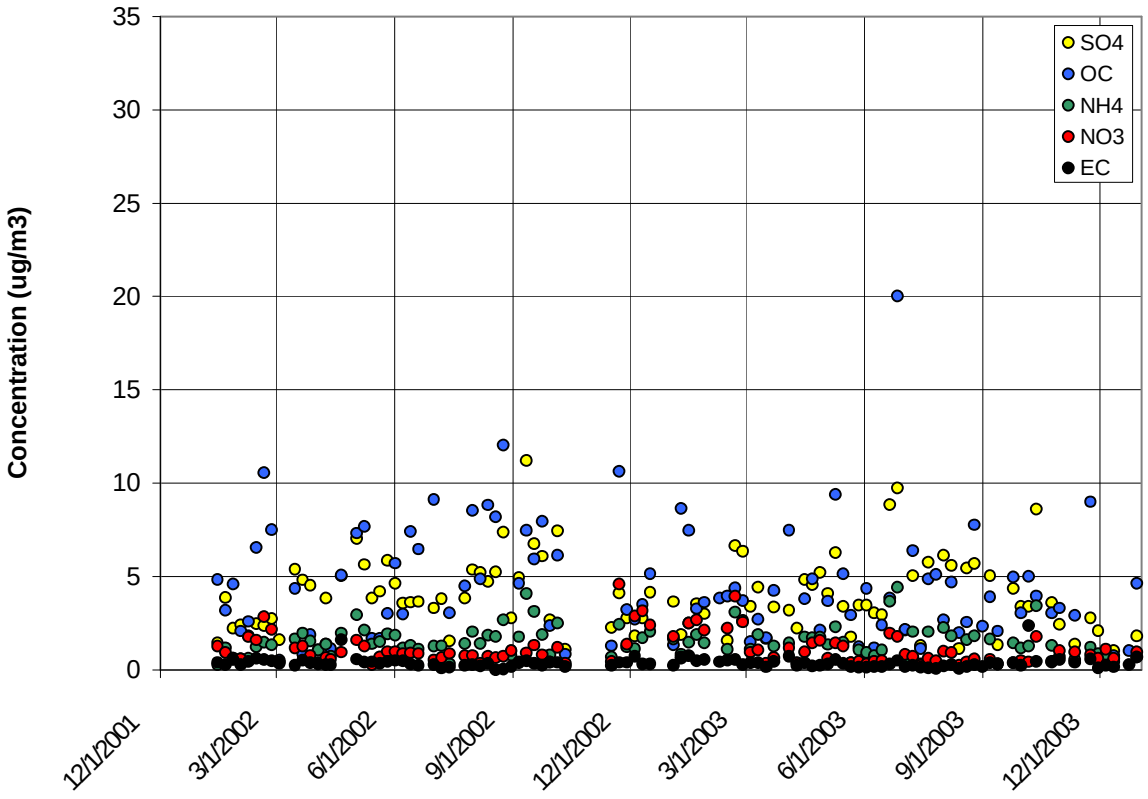

Figure 5-80 Time Series for the Kinston, NC Monitor

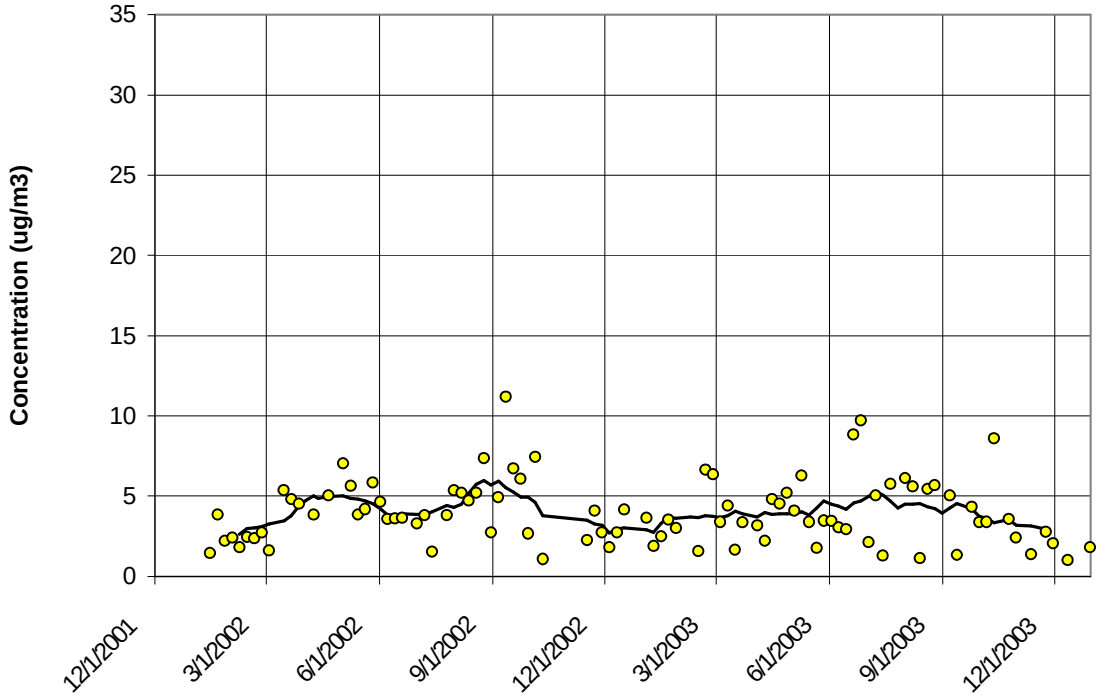

Figure 5-81 Sulfate Time Series for the Kinston, NC Monitor

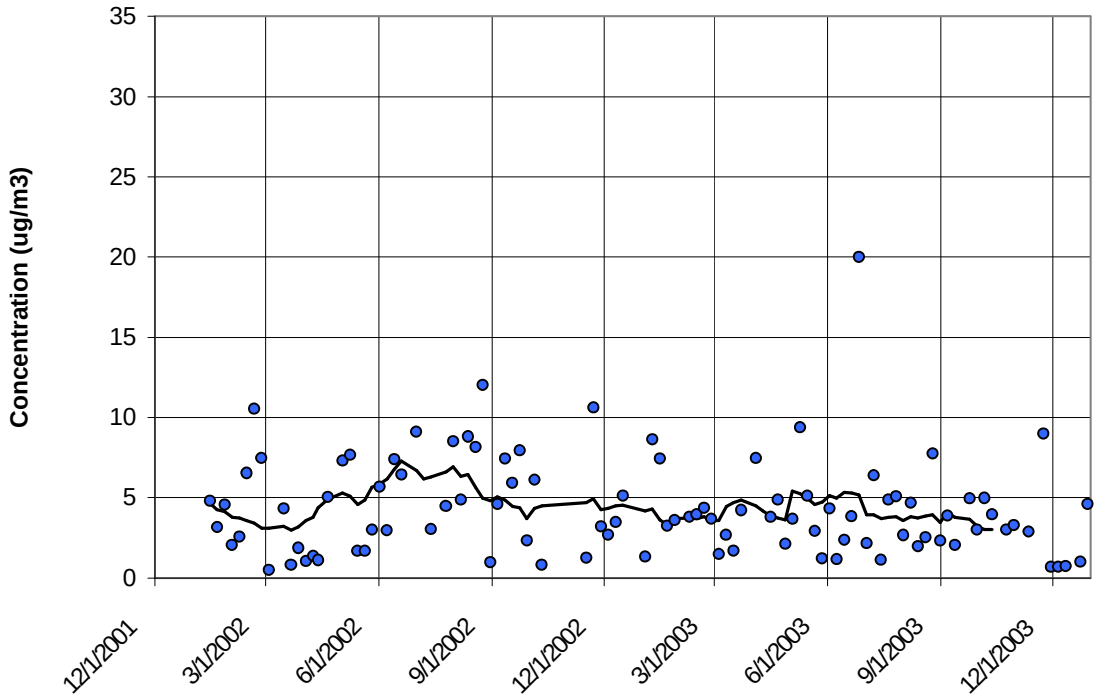

Figure 5-82 Organic Carbon Mass Time Series for the Kinston, NC Monitor

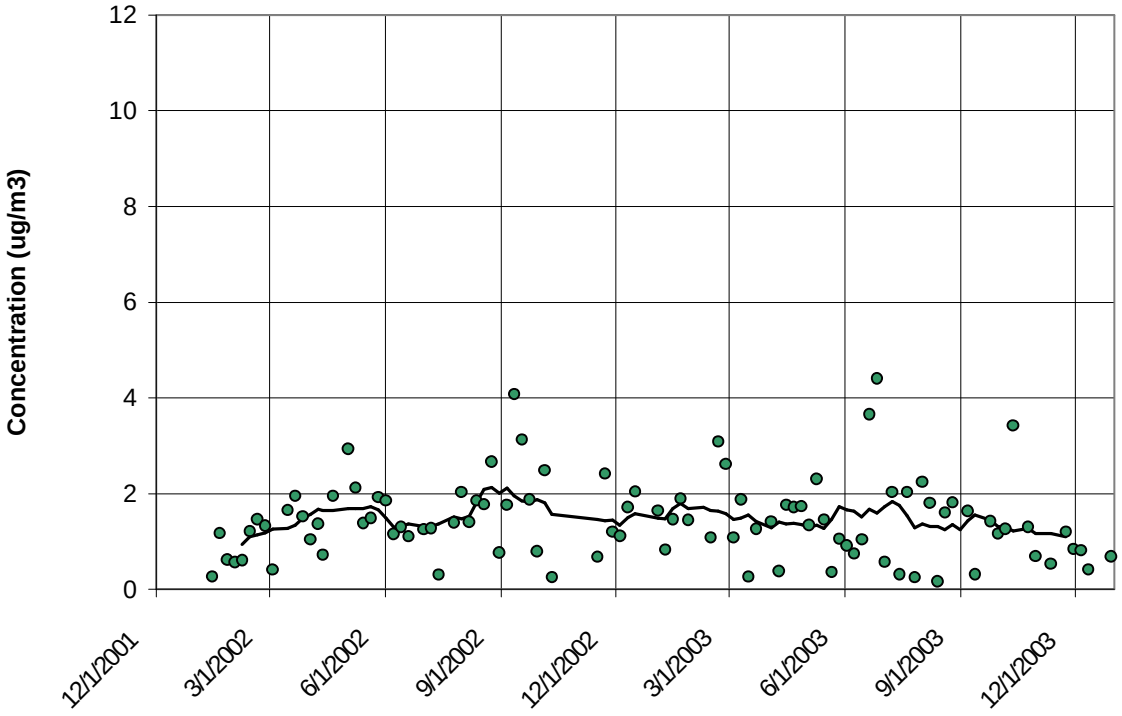

Figure 5-83 Ammonium Time Series for the Kinston, NC Monitor

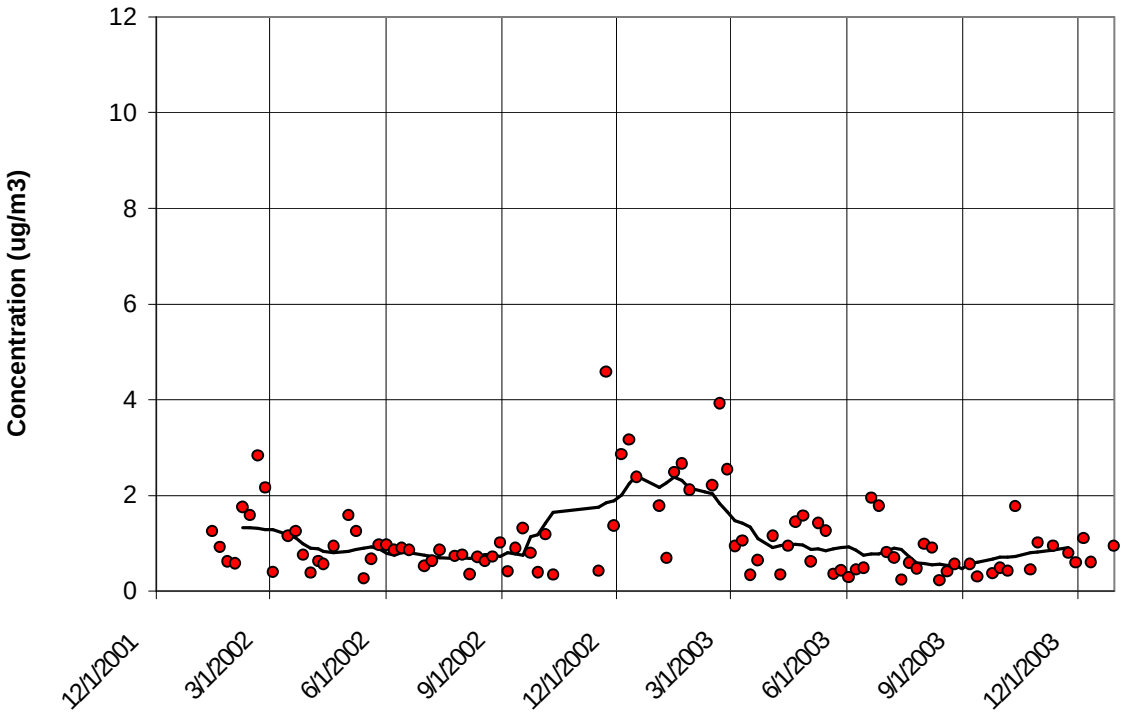

Figure 5-84 Nitrate Time Series for the Kinston, NC Monitor

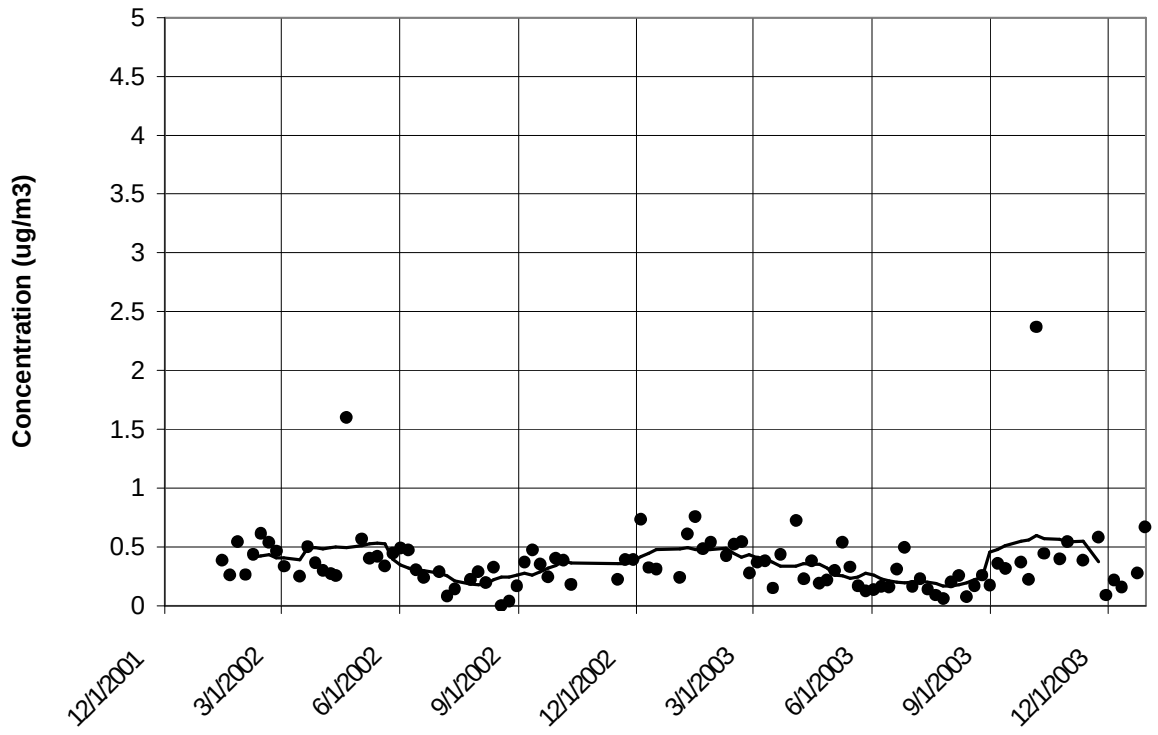

Figure 5-85 Elemental Carbon Time Series for the Kinston, NC Monitor

While sulfate species were an important contributor to total mass at Kinston, NC, sulfate concentrations, shown in Figure 5-81, did not rise sharply in summer as observed at other sites in the Region. Some higher sulfate concentrations occurred in summer and early fall, but they were modest increases compared to the behavior seen at other sites in the Region. The lack of a strong "sulfate signal" in summer may partially account for organic carbon mass supplanting sulfate as the largest contributor to total mass at this monitoring site. Over the two-year period, the average sulfate concentration was 4.11 $\mu g/m^3$ with most values falling between about 1.0 $\mu g/m^3$ and 7.0 $\mu g/m^3$.

Figure 5-82 gives a sense for how organic carbon mass, the largest contributor to total mass, varies over time. The average organic carbon mass concentration over the period was 4.47 $\mu g/m^3$. The average summer concentration was 5.38 $\mu g/m^3$ followed by average winter and fall concentrations of 4.67 and 4.59 $\mu g/m^3$. The average spring concentration was lowest at 3.27 $\mu g/m^3$. It would be interesting to know if the high value observed on June 26, 2003 can be explained by special circumstances.

Over 2001-2003, ammonium concentration averaged 1.51 $\mu g/m^3$, the lowest average concentration of any of the eleven sites analyzed. Initially, it was thought the Kinston site might exhibit high ammonium concentrations because of the site's general proximity to concentrated animal feeding operations (CAFOs). High average concentrations were not observed however.

Figure 5-83 shows how ammonium concentrations track over time. Average winter concentration (1.38 $\mu g/m^3$) was somewhat lower than average concentrations calculated for other times of year, but a strong seasonal pattern was not obvious over the 2001-2003 time period. A

table of high ammonium and sulfate days was not prepared for this site, because the sulfate concentration did not exceed 15.0 µg/m^3 over the course of the study period.

Of the eleven sites analyzed, the Kinston site had the second lowest average nitrate concentration (1.10 µg/m^3) over the 2001-2003 period. Only Charlotte, NC had a lower average nitrate concentration at 0.94 µg/m^3. Recent research has shown (Wittig, 2004) that solid phase nitrate species are a function of temperature, relative humidity and ultraviolet radiation with higher concentrations occurring during cold weather/winter conditions. It is not surprising therefore that Kinston and Charlotte, NC, the two most southern sites studied, produced the lowest nitrate concentrations.

As Figure 5-84 shows, nitrate measurements at Kinston exhibited some of the seasonal variation seen at other sites. Nitrate concentrations were lowest during the summer and noticeably higher in winter. Over 2001-2003, the average summer concentration was 0.75 µg/m^3 whereas the average winter concentration was 2.03 µg/m^3. In spring and fall, the average nitrate concentration was 0.87 and 0.98 µg/m^3 respectively. As Figure 5-84, shows, nitrate values were much more variable in the late fall and winter than in summer months.

Figure 5-85 displays the time series for elemental carbon. The plot shows fairly constant concentrations ranging between close to zero to about 0.80 µg/m^3. The average concentration over 2001-2003 was 0.36 µg/m^3, the lowest average concentration of any of the eleven monitors studied. Over 2001-2003, the average summer concentration was 0.22 µg/m^3 whereas the average fall and winter concentrations were more than twice as much at 0.47 and 0.46 µg/m^3, respectively. In the spring, the average elemental carbon concentration was 0.39 µg/m^3. It would be interesting to know if the high values observed on April 20, 2002 (1.6 µg/m^3) and on October 6, 2003 (2.4µg/m^3) can be attributed to special circumstances since these days appear exceptional given the other measurements.

The rural speciation monitors examined at Arendtsville, PA and Kinston, NC had very similar average elemental carbon concentrations over 2001-2003. The average concentrations at Arendtsville, PA (0.39 µg/m^3) and Kinston, NC (0.36 µg/m^3), may approximate the "regional background concentration" of elemental carbon, since these rural sites have relatively few sources of elemental carbon. The analysis of data from additional monitors around the Region would help confirm what regional background concentrations of elemental carbon actually are.

Seasonal averages for the major constituents of $PM_{2.5}$ mass measured in Kinston, NC are summarized in Table 5-27.

Table 5-27 Seasonal Averages for the Major Constituents of $PM_{2.5}$ Mass (µg/m^3) for Kinston, NC

	Organic Carbon	Sulfate	Ammonium	Nitrate	Elemental Carbon
Winter	4.67	3.01	1.38	2.03	0.46
Spring	3.27	4.15	1.43	0.87	0.39
Summer	5.38	4.48	1.52	0.75	0.22
Fall	4.59	4.72	1.75	0.98	0.47

5.7.4 Trajectory Analysis

Figure 5-86 shows CATT back trajectories for the cleanest days in the speciation record over the period studied from June 2001 through December 2003. While even lower concentration days can be found in the data record for Federal Reference Method monitors at the site, the

trajectories plotted in Figure 5-86 are the lowest concentration days in the speciation record over the period studied. These "clean" days represent the five percent days with the lowest total $PM_{2.5}$ mass.

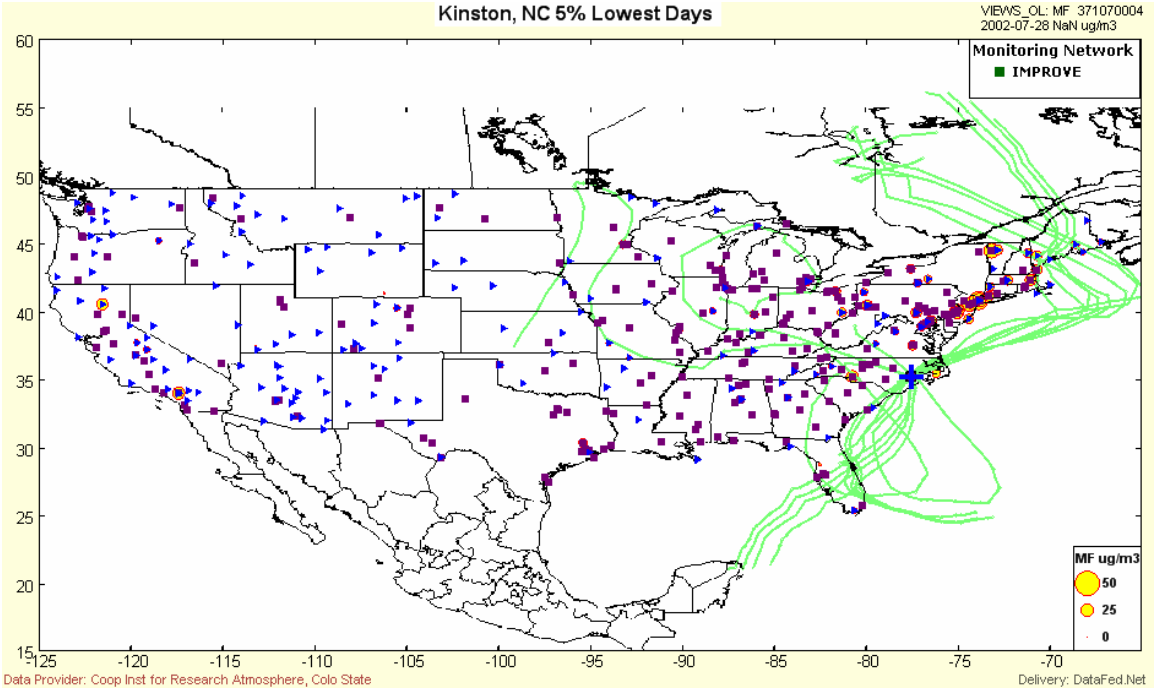

Figure 5-86 Kinston, NC Back Trajectories for the Five Percent Cleanest Days

Two clean day trajectories (two sets of four lines) originate in the Hudson Bay area of Canada or eastern provinces of Canada and arrive at Kinston after fairly long distances over the Atlantic Ocean. Another clean day trajectory originates in the Gulf of Mexico off the Yucatan peninsula and takes a mostly maritime track over the Gulf of Mexico and the Atlantic Ocean. The two other trajectories either re-circulate south of Kinston over the Atlantic or come in from the west without tracking over major source regions. Table 5-28 lists the five percent cleanest days at Kinston, NC and the total mass concentration measured by the speciation monitor on that day.

Table 5-28 Kinston, NC Five Percent Lowest Days

Date	$PM_{2.5}$ Mass ($\mu g/m^3$)
4/9/2003	4.8
7/14/2003	5.1
8/13/2003	4.5
9/12/2003	5.2
12/11/2003	4.7
Average	4.9

Figure 5-87 shows back trajectories for the dirtiest days, the five percent days with the highest total $PM_{2.5}$ mass. These trajectories generally show air arriving at Kinston after tracking through source regions to the southeast, west and north.

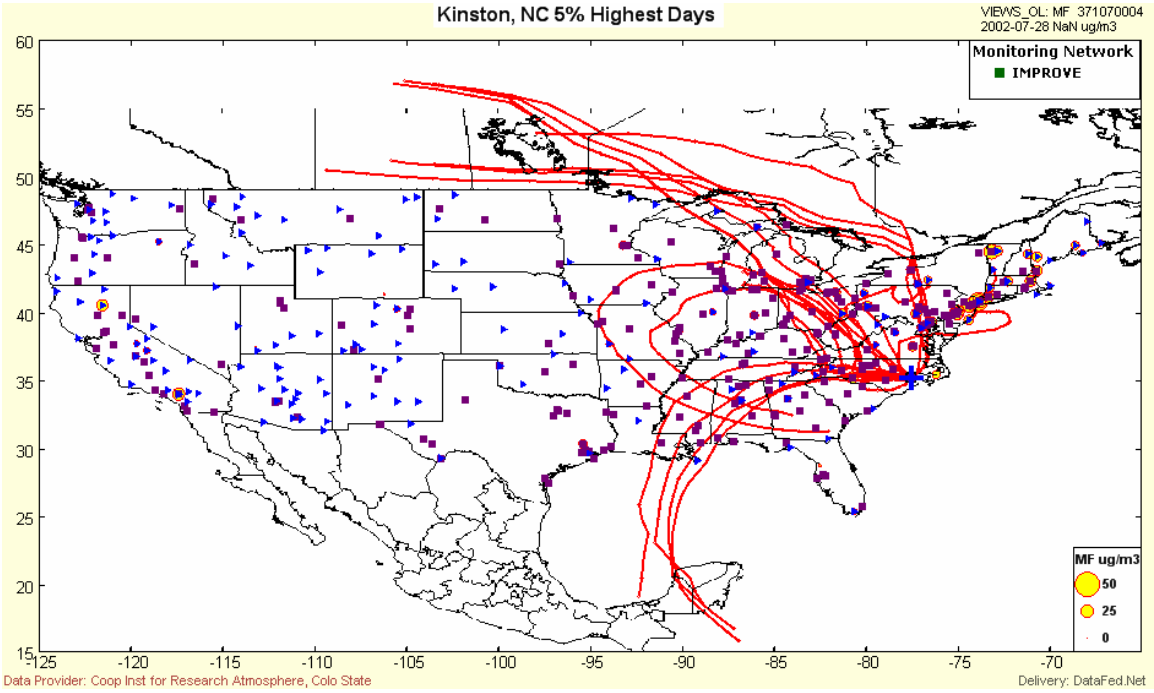

Figure 5-87 Kinston, NC Back Trajectories for the Five Percent Dirtiest Days

Table 5-29 lists the five percent dirtiest days and the total mass concentration measured by the speciation monitor on that day.

Table 5-29 Kinston, NC Five Percent Highest Days

Date	$PM_{2.5}$ Mass ($\mu g/m^3$)
2/19/2002	26.2
7/7/2002	29.5
9/11/2002	25.7
5/9/2003	23.7
6/26/2003	41.3
Average	29.3

5.8 Philadelphia, PA

Site Name: Air Management Services (AMS) Laboratory
AIRS Number: 42-101-0004
Latitude: 40.0089 North
Longitude: -75.0978 West
Elevation: 22 meters (72 feet)
Agency Operating the Monitor: Philadelphia Department of Public Health, Air Management Services
Speciation Sampling Frequency: 1-in-3 days

5.8.1 Site Description

The Air Management Services (AMS) Laboratory monitoring site is located in northeast Philadelphia, PA about 8.5 km (5.3 miles) northeast of the central business district of the city. Figure 5-88 shows the monitoring site's location relative to the interstate highway system and large population centers. Camden, NJ is approximately 7.2 km (4.5 miles) south of the monitoring site. The closest cities outside of the Philadelphia metropolitan area are Wilmington, DE about 48 km (30 miles) to the southwest, New York, NY about 121 km (75 miles) to the northeast, and Harrisburg, PA about 154 km (96 miles) to the west.

Figure 5-88 Location of the Philadelphia, PA Monitoring Site

The Philadelphia monitor is an urban scale monitor. It is located on the roof of a building 30.5 meters (100 feet) from the corner of Castor Avenue and East Lycoming Street. The area immediately adjacent to the monitoring site is a high-density residential neighborhood of row houses. Most of the metropolitan area of Philadelphia, population 1,470,151, lies to the southwest of the monitoring site. Like many urban monitors, there are a variety of roadways near the monitoring site, ranging from two-lane local streets to a four-lane artery 168 meters (550 feet) north of the site. Interstate 95 runs through Philadelphia and this major interstate highway is only 1.9 km (1.2 miles) east of the monitor. The Delaware River and the industry along it are 4 km (2.5 miles) south and east of the monitoring site. Figure 5-89 is a detailed map showing the topographic and other major features around the monitoring site.

Source: TopoZone

Figure 5-89 Topographic Map of the Philadelphia, PA Monitoring Site

The Philadelphia Department of Public Health reports there are a variety of air pollution sources in the vicinity of the monitoring site. Table 5-30 lists total PM and PM_{10} emission data for sources within 18 km (11.2 miles) of the monitor. $PM_{2.5}$ emissions have not been estimated for these sources.

Table 5-30 Emission Sources within 18 km of the Philadelphia, PA Monitoring Site

Name	Site Description	Distance (km)	Direction	SO2	Total PM	PM10	NO2	CO	VOC
Sun Refining and Marketing	Petroleum refinery	13.0	SSW	3,828.6	0.0	276.2	3,177.2	1,990.4	726.2
Sunoco Logistics, Belmont Terminal	Petroleum liquid terminal	12.6	SSW	0.0	0.0	0.0	0.0	0.0	94.5
Sunoco Belmont, Remediation System	Remediation system	12.6	SSW						

Name	Site Description	Distance (km)	Direction	SO2	Total PM	PM10	NO2	CO	VOC
Sun Company, Schuylkill Tank Farm	Tank farm	13.0	SSW	0.0	0.0	0.0	1.6	8.7	288.1
Rohm & Haas Company	Miscellaneous chemical mfg.	3.0	ESE	3.8	0.5	0.5	9.0	1.9	10.4
Calpine Philadelphia, NE	Cogeneration plant	2.2	SSE	2.8	0.0	0.0	2.1	4.3	0.7
Calpine Philadelphia, SW	Cogeneration plant	17.0	SSW	0.0	0.0	0.2	0.2	0.5	0.0
Sunoco Chemical, Frankford Plant	Chemical plant	1.8	ESE	502.3	157.6	35.1	393.7	39.1	94.5
Jefferson Smurfit Corporation (U.S.)	Box board mill division	12.0	WNW	131.1	21.3	19.2	109.9	19.1	13.2
Kvaerner Philadelphia Shipyard, Inc.	Ship building yard	14.0	ESE	0.0	19.7	19.7	3.0	2.1	49.5
Sun Chemical Corporation, GPI Division	Printing ink manufacturer	7.3	WSW	0.0	0.1	0.0	0.3	0.1	30.5
Inolex Chemical Company	Specialty organic chemicals	10.6	SSW	90.4	7.0	6.3	54.5	6.5	6.7
Lawrence McFadden Company	Paint manufacturer	6.3	ENE	0.3	0.0	0.0	0.2	0.0	26.0
Smith, Edwards, Dunlap Company	Commercial printing	2.9	SSW	0.4	0.0	0.0	0.4	0.1	4.2
Graphic Arts, Inc.	Printing facility	10.8	WSW	0.0	0.0	0.0	0.1	0.1	6.8
Kraft Foods N.A., Inc. (Nabisco)	Cookie and cracker baking	13.4	NNE	6.7	1.4	0.8	10.4	5.3	6.5
Catalyst International/Gasket Materials	Gasket manufacturing	3.8	ENE	0.0	0.0	0.0	0.1	0.0	4.9
Allied Tube & Conduit Corporation	Tube and conduit mfg.	11.8	ENE	0.0	0.0	0.0	0.0	0.0	71.2
Newman & Company	Paper recycler	3.8	ENE	142.0	14.2	9.9	106.4	9.2	0.5
Arbill Industries, Inc.	Industrial dry cleaner	6.4	WSW	0.2	0.0	0.0	0.2	0.1	22.7
Cardone Industries, Inc.	Auto parts re-mfg.	3.4	NNW	0.0	4.7	0.1	5.1	1.0	154.6
SEPTA Berridge/Courtland Maintenance Shop	Bus maintenance shop	3.0	WNW	0.0	0.1	0.0	4.0	1.3	5.8
Exelon Generation Company, Delaware Station	Electric utility	5.3	SSW	72.1	5.9	5.4	59.1	5.8	0.5
Trigen, Edison Station	District steam heating	8.2	SSW	251.2	7.6	6.8	137.2	17.6	1.0
Exelon Generating Company,	Electric utility	3.1	SSE	2.8	1.2	1.2	11.0	0.1	0.0

Name	Site Description	Distance (km)	Direction	SO2	Total PM	PM10	NO2	CO	VOC
Richmond Plant									
Exelon Generation Company, Schuylkill Station	Electric utility	13.3	WSW	200.0	16.0	14.6	80.6	14.4	1.2
Exelon Generation Company, Southwark Plant	Electric utility	10.9	SSW	0.1	0.0	0.1	0.8	0.0	0.0
Philadelphia Gas Works, Richmond Plant	Natural gas utility	2.9	SSE	0.1	1.0	1.0	90.2	36.2	10.4
Trigen, Schuylkill Station	Steam generating	10.5	WSW	483.0	30.4	30.4	300.0	31.8	1.2
Grays Ferry Cogeneration Partnership	Cogeneration plant	10.5	WSW	3.9	2.1	2.1	172.9	9.8	0.0
Kinder Morgan Liquids Terminals, LLC	Bulk terminal	3.3	SSE	5.6	0.2	0.2	3.9	1.0	29.8
ConocoPhillips Company, Philadelphia Terminal	Petroleum transfer/tank facility	1.2	WNW	0.0	0.0	0.0	0.0	0.0	19.0
ExxonMobil Oil Corporation	Gasoline terminal	15.5	SSW	0.0	0.0	0.0	0.0	0.0	68.0
Pacific Atlantic Terminals, LLC	Petroleum storage & distribution	14.8	SSW	1.2	0.0	0.0	0.6	0.1	11.0
Interstate Brands Corporation	Bread baking facility	10.4	NNE	6.8	0.9	0.6	22.5	6.1	40.0
Philadelphian Condominiums	Apartment building	8.3	WSW	9.3	1.2	1.0	46.0	39.4	7.2
Bellevue	Cogeneration plant	8.7	SSW	2.7	0.2	0.1	2.3	0.6	0.0
Park Towne Place Apartments	Apartment building	8.4	WSW	3.2	0.6	0.4	3.2	1.9	0.1
Temple University Hospital, Episcopal Cam	Hospital	3.4	WSW	5.9	0.6	0.4	5.9	2.0	0.2
The Children's Hospital of Philadelphia	Hospital	10.5	WSW	7.2	1.6	1.0	19.1	11.7	1.4
Temple University, Main Campus	University	5.5	WSW	129.4	10.0	6.4	88.7	11.9	2.2
Temple University Health Sciences Campus	Hospital steam plant	4.4	WSW	142.2	10.8	7.0	84.5	9.2	2.0
University of Pennsylvania	Education and research	10.2	WSW	0.5	0.5	0.5	7.5	2.2	0.5
Northeast WPCP	Water pollution control plant	2.2	SSE	4.1	1.2	1.2	4.5	17.9	14.6
Philadelphia Water Department (SW/BRC)	Sewage treatment plant	17.0	SSW	3.2	1.6	1.6	5.0	14.2	43.3

Name	Site Description	Distance (km)	Direction	SO2	Total PM	PM10	NO2	CO	VOC
Philadelphia Prison System	Correctional facility	7.0	ENE	0.6	1.1	0.5	13.7	7.9	0.6
Naval Foundry and Propeller Center	Naval base	15.0	SSW	0.0	5.7	4.4	0.6	0.1	1.6
U.S. Mint	U.S. coin production	7.4	SSW	0.0	0.0	0.1	1.8	2.2	2.7
Paid Steam Boiler Plant	Philadelphia naval business center	15.1	SSW	70.4	5.4	4.8	39.5	4.8	0.3
Naval Surface Warfare Center, Carderock Div.	Naval base	14.7	SSW	3.7	0.9	0.8	25.8	5.0	1.0

5.8.2 Major Constituents of $PM_{2.5}$ Mass

The major constituents of $PM_{2.5}$ mass at Philadelphia were organic carbon and sulfate species followed by nitrate and ammonium species. Using an OM/OC ratio of 1.6, organic carbon mass contributed about 6.0 µg/m^3 to the average concentration measured over 2001-2003. Average sulfate concentration over the period was about 4.7 µg/m^3 while average nitrate and ammonium concentrations were 2.2 and 2.1 µg/m^3 respectively. Elemental carbon, geological components, and trace elements added about 1.7 µg/m^3 to the average $PM_{2.5}$ concentration measured. Figure 5-90 compares the contributions each major specie made to the average concentration measured at the site.

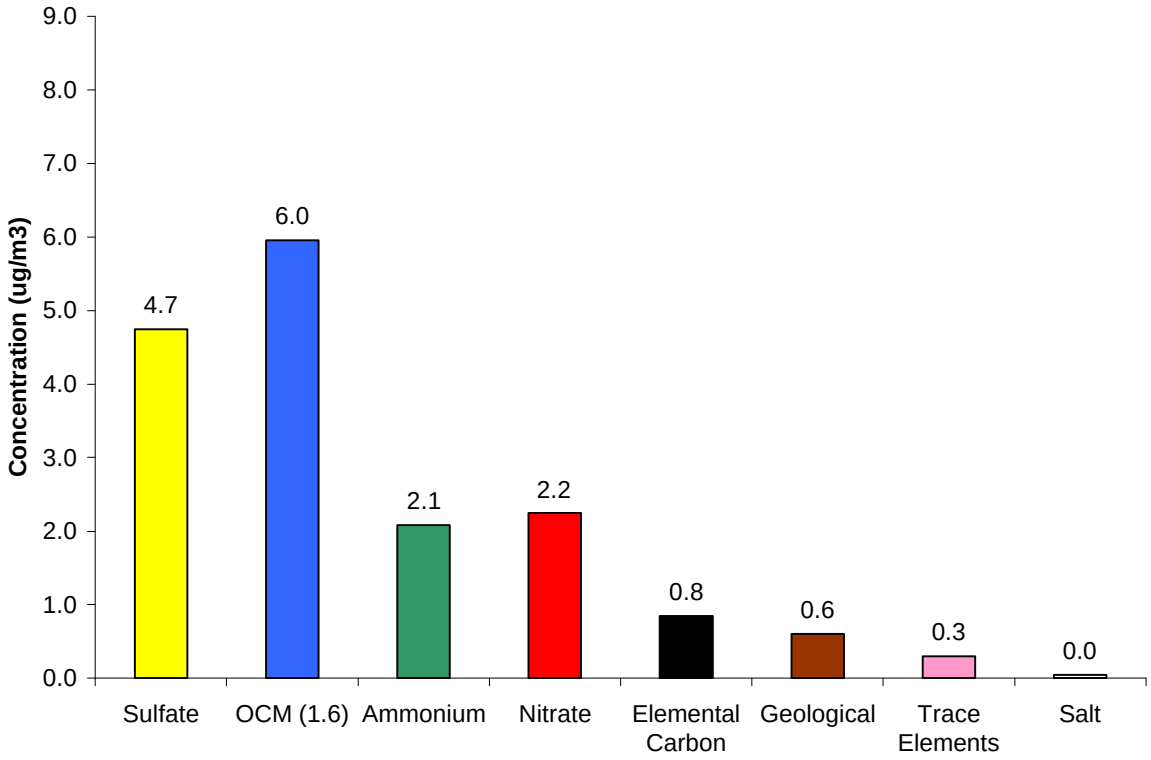

Figure 5-90 Major Constituents of PM2.5 Mass, Philadelphia, PA

The average reconstructed mass calculated for this site was about 0.6 percent greater than the average gravimetric mass measured by the speciation sampler. Average reconstructed mass was 17.2 µg/m^3 whereas the average gravimetric mass was 16.7 µg/m^3. Figure 5-91 visually compares the average reconstructed mass with the average gravimetric mass.

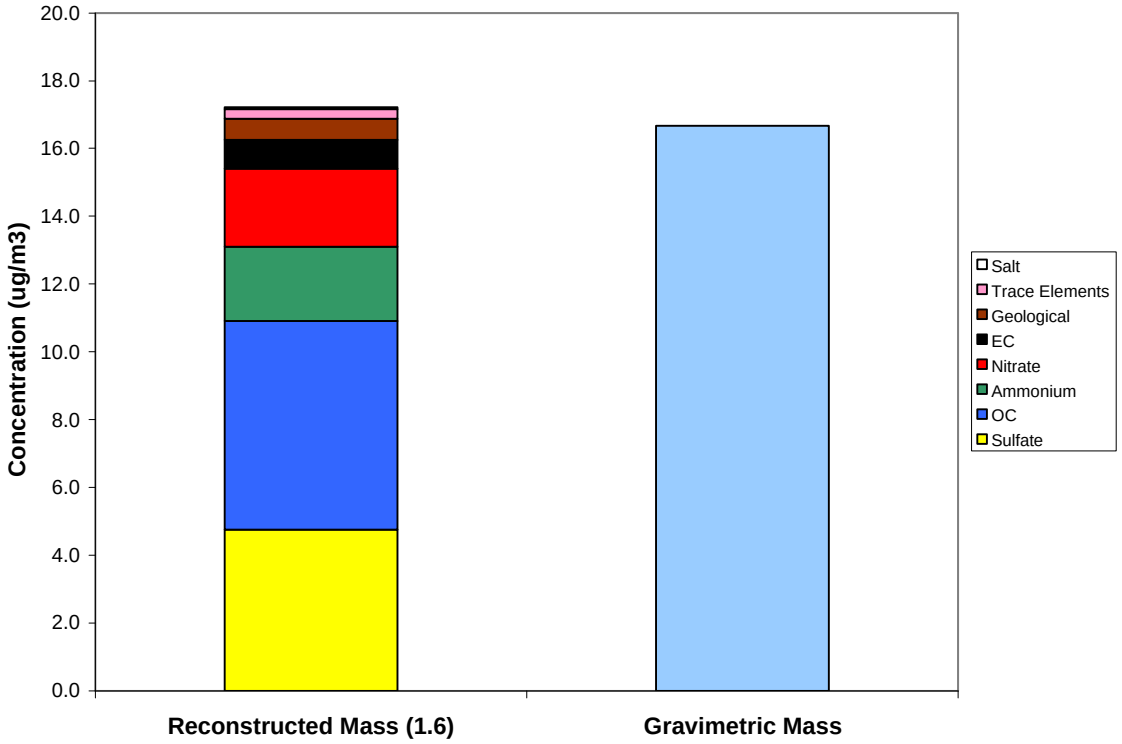

Figure 5-91 Comparison of Average Reconstructed Mass and Average Gravimetric Mass, Philadelphia, PA

5.8.3 Time Series Analysis of $PM_{2.5}$ Species

A Met One SASS speciation sampler was installed at the Philadelphia monitoring site in February 2000 with a break in service as noted below. It has operated on a 1-in-3 sampling schedule from its installation to the present time. Figure 5-92 shows a composite time series for the five major species measured at Philadelphia. Figures 5-93 through 5-97 show time series for each of the five major species. The black line in Figures 5-93 through 5-97 is the 30-day rolling average concentration for the specie. The 30-day rolling average is not shown during periods when the monitor was down or did not report data for more than two consecutive sample days. As the figures show, the Philadelphia speciation monitor was not in service from mid-June through early September 2001.

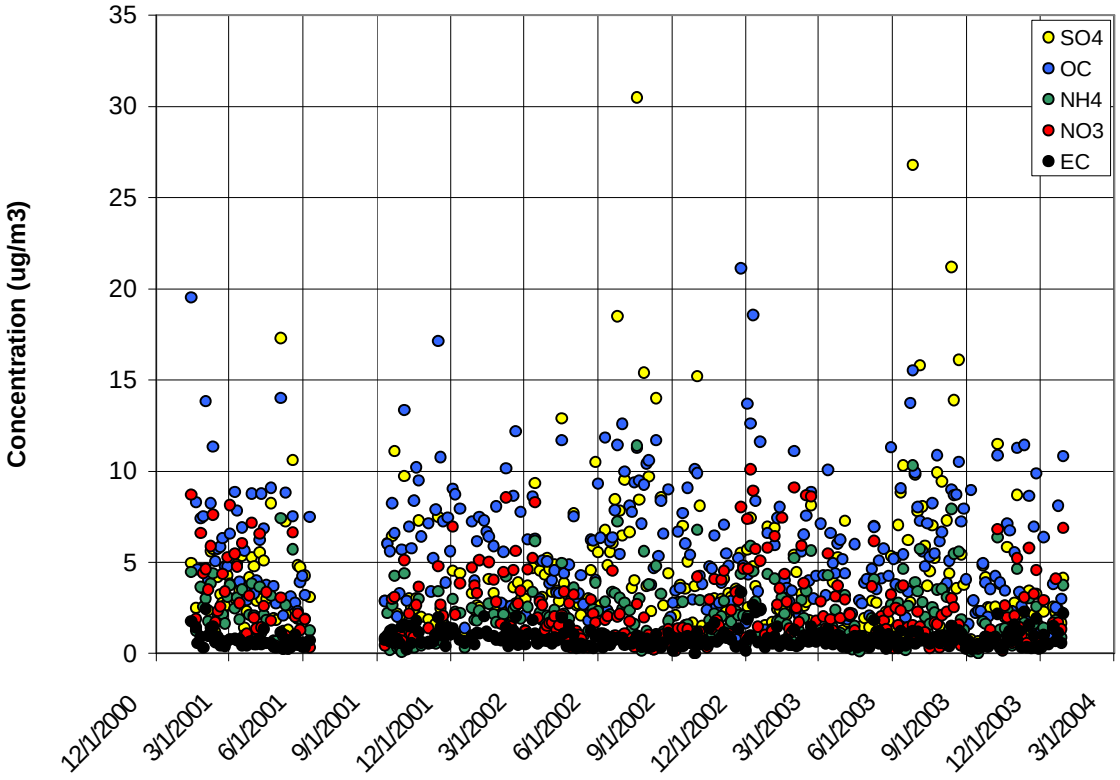

Figure 5-92 Time Series for the Philadelphia, PA Monitor

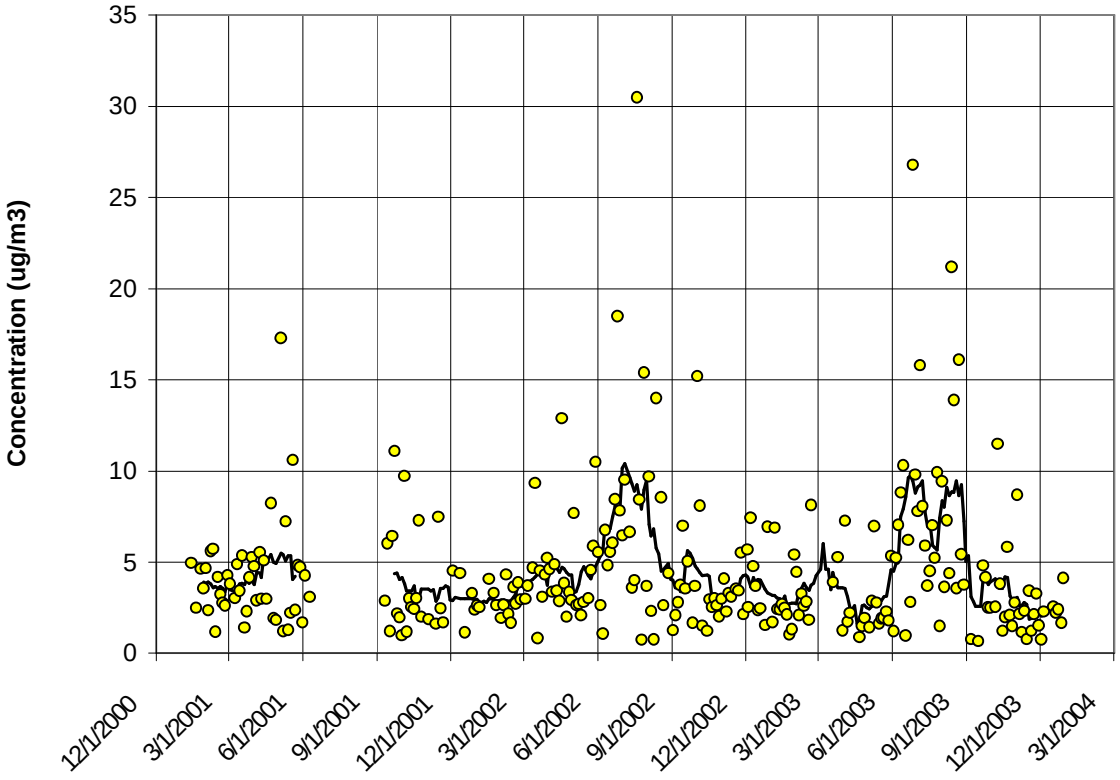

Figure 5-93 Sulfate Time Series for the Philadelphia, PA Monitor

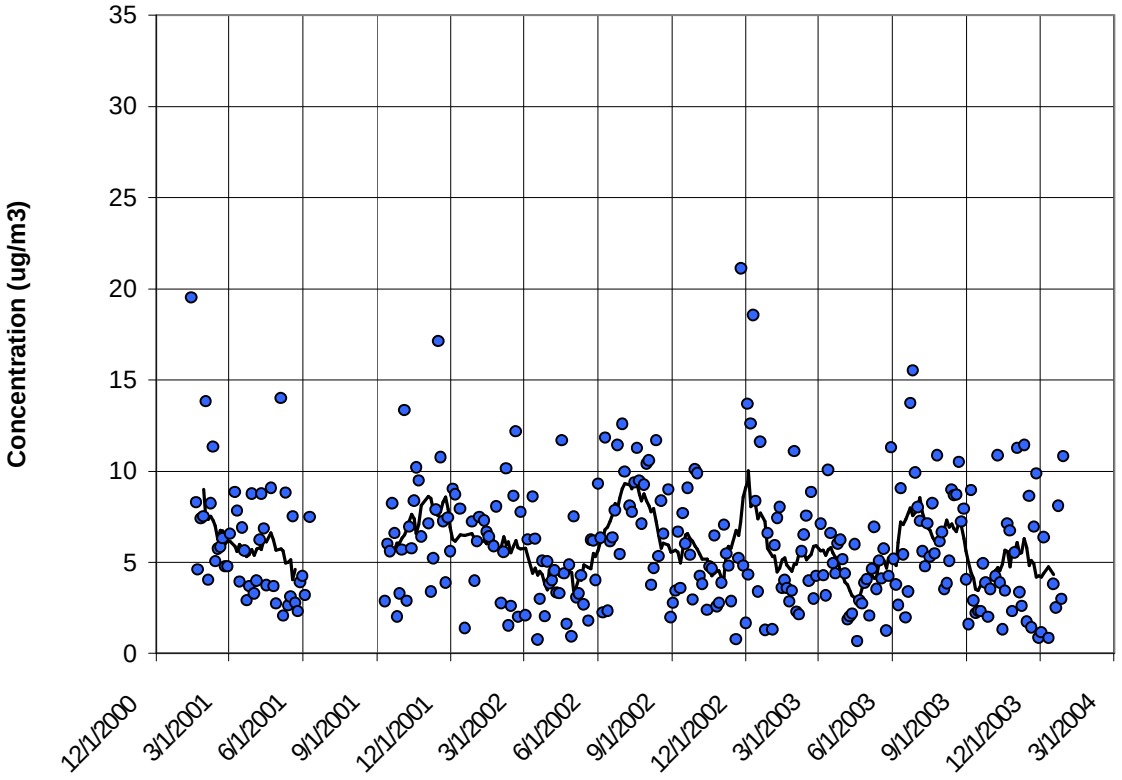

Figure 5-94 Organic Carbon Mass Time Series for the Philadelphia, PA Monitor

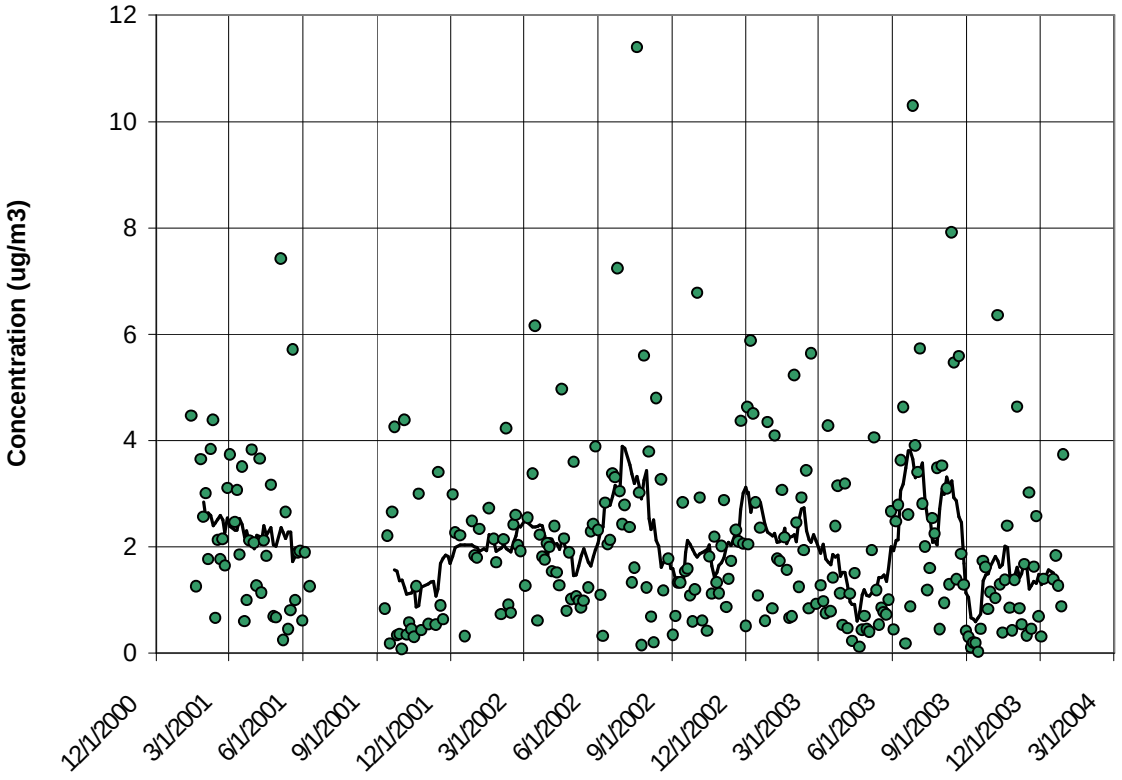

Figure 5-95 Ammonium Time Series for the Philadelphia, PA Monitor

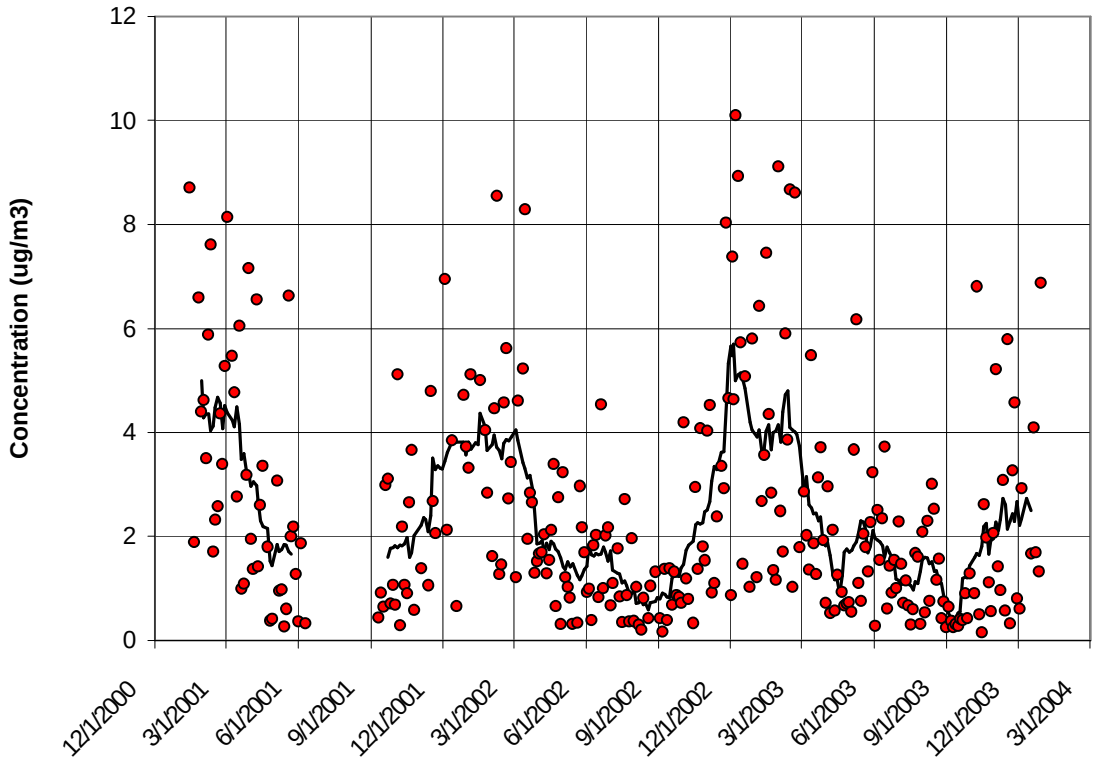

Figure 5-96 Nitrate Time Series for the Philadelphia, PA Monitor

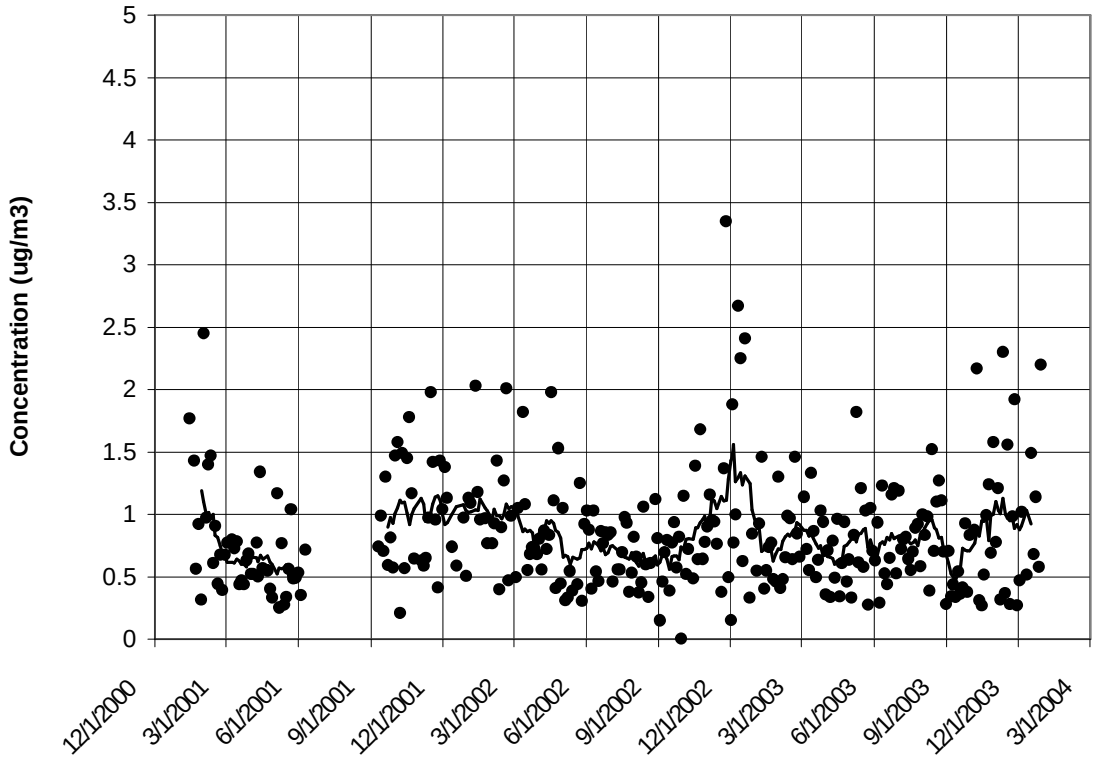

Figure 5-97 Elemental Carbon Time Series for the Philadelphia, PA Monitor

Average sulfate concentration over 2001-2003 was 4.74 µg/m^3 somewhat less than the average concentration of 5.11 µg/m^3 calculated for the MARAMA Region. The average concentration in Philadelphia was lower than the average concentration observed at most sites studied including Elizabeth, NJ (4.81 µg/m^3) to the northeast and the nearby cities of Wilmington, DE (5.24 µg/m^3) and Washington, DC (5.44 µg/m^3) to the southwest. The only monitors with lower average sulfate concentrations were the monitors in Dover DE, (4.65 µg/m^3) and Kinston, NC (4.11 µg/m^3). The break in service from June 9 through September 10, 2001 occurred during the peak sulfate season, which may explain the somewhat lower 2001-2003 average sulfate concentration and lower average summer sulfate concentration at this site.

The 30-day rolling average sulfate concentration in Figure 5-93 shows how sulfate varied seasonally over the 2001-2003 period. Average sulfate concentration was lowest in winter at a concentration of about 3.29 µg/m^3. As seen elsewhere, the average summer sulfate concentration was much higher. In Philadelphia, the average summertime sulfate concentration was 7.65 µg/m^3, more than twice the winter concentration. Average spring and fall concentrations were 3.83 and 3.74 µg/m^3 respectively. As the time series shows, sulfate concentration is much more variable in summer than in winter. Over 2001-2003, summer concentrations ranged from a low of 0.8 µg/m^3 to a high of 30.5 µg/m^3. The break in the 30-day rolling average in Figure 5-93, during the summer of 2001, corresponds to a period when the Philadelphia speciation monitor was not in service.

Applying an OM/OC ratio of 1.6, the average organic carbon mass over 2001-2003 was 5.96 µg/m^3. This average concentration was somewhat higher than the average concentration of 5.4 µg/m^3 calculated for the MARAMA Region. The average concentration for Philadelphia was somewhat higher than the average concentration measured in Washington DC (5.70 µg/m^3), Wilmington, DE (5.02 µg/m^3), Baltimore, MD (5.82 µg/m^3). The average concentration of organic carbon mass was much higher than average concentrations measured at rural sites such as Dover, DE (3.62 µg/m^3), Arendtsville, PA (3.90 µg/m^3), and Kinston, NC (4.47 µg/m^3).

As Figure 5-94 shows, organic carbon mass concentration was quite variable across the years. Individual measurements ranged from a low near 1.0 µg/m^3 to a high of 25.1 µg/m^3. Average organic carbon mass concentration was highest in summer at 7.36 µg/m^3 and lowest in the spring at 4.46 µg/m^3. Average fall and winter concentrations were 5.80 µg/m^3 and 6.22 µg/m^3 respectively. The 30-day rolling average in Figure 5-94 reveals elevated concentrations in summer and late fall/winter and lower concentrations in spring. Additional data from future years will help analyst explore what appears to be seasonal behavior. The data point for July 7, 2002, one of the days smoke from Canadian forest fires affected the region, was removed from the data for Philadelphia. This data point had been flagged as a forest fire in the raw data set and was subsequently removed. The organic carbon mass value on July 7, 2002 was 81.4 µg/m^3.

The average ammonium concentration was 2.08 µg/m^3 over 2001-2003. This concentration was close to the average concentration of 2.01 µg/m^3 observed across the MARAMA Region. Summer had the highest average concentration at 2.85 µg/m^3. Winter had the second highest seasonal average at 2.31 µg/m^3. Spring and fall had average concentrations of 1.72 and 1.51 µg/m^3 respectively. Figure 5-95 shows how ammonium concentrations varied over time. While the 30-day rolling average shows elevated concentrations during the two summers in the data record, there were high values and wide variability during most seasons. Additional data is needed to explore the seasonal behavior of ammonium at this monitoring site.

Ammonium and sulfate concentrations were well correlated ($R^2 = 0.81$); when sulfate concentrations were high, ammonium concentrations were usually high. Table 5-31 lists ammonium and sulfate concentrations on days when sulfate concentration exceeded 15 µg/m^3.

Table 5-31 High Ammonium and Sulfate Days for the Philadelphia, PA Monitor

Date	Ammonium Concentration (µg/m^3)	Sulfate Concentration (µg/m^3)
5/4/01	7.4	17.3
6/25/02	7.2	18.5
7/19/02	11.4	30.5
7/28/02	5.6	15.4
10/2/02	6.8	15.2
6/26/03	10.3	26.8
7/5/03	5.7	15.8
8/13/03	7.9	21.2
8/22/03	5.6	16.1

The average nitrate concentration over 2001-2003 was 2.25 µg/m^3 higher than the average concentration of 1.76 µg/m^3 calculated for the MARAMA Region. The average concentration for Philadelphia was somewhat lower than the average concentration measured in Wilmington DE (2.48 µg/m^3), where the highest average concentration in the region was measured. As Figure 5-96 shows, nitrate measurements in Philadelphia exhibited the seasonal variation seen at other sites. Nitrate concentrations were lowest in the summer/early fall and noticeably higher in winter. Over 2001-2003, the average summer concentration was 1.29 µg/m^3 whereas the average winter concentration was 4.19 µg/m^3. In spring and fall, average nitrate concentrations were 2.08 µg/m^3 and 1.79 µg/m^3 respectively. As Figure 5-96 shows, nitrate values were much more variable in winter than in summer.

The average elemental carbon concentration over 2001-2003 was 0.85 µg/m^3 somewhat more than the average concentration of 0.75 µg/m^3 calculated for the MARAMA Region. The average concentration for Philadelphia was similar to the average concentration measured Pittsburgh, PA (0.85 µg/m^3) and somewhat higher than the average concentration measured in Baltimore, MD (0.77 µg/m^3), Washington, DC (0.73 µg/m^3), and Wilmington, DE (0.78 µg/m^3).

Figure 5-97 displays the time series for elemental carbon. As the 30-day rolling average shows, higher concentrations occurred in the late fall and winter and occasionally at other times of year. The elevated concentrations observed in late fall and winter were reflected in average seasonal concentrations. The highest seasonal average concentration was winter at 0.99 µg/m^3 followed by fall at 0.88 µg/m^3. Spring and summer had the lowest average concentrations at 0.78 and 0.76 µg/m^3 respectively.

Seasonal averages for the major constituents of $PM_{2.5}$ mass measured in Philadelphia, PA are summarized in Table 5-32.

Table 5-32 Seasonal Averages for the Major Constituents of $PM_{2.5}$ Mass (µg/m^3) for Philadelphia, PA

	Organic Carbon Mass	Sulfate	Ammonium	Nitrate	Elemental Carbon
Winter	6.22	3.29	2.31	4.19	0.99
Spring	4.46	3.83	1.72	2.08	0.78
Summer	7.36	7.65	2.85	1.29	0.76
Fall	5.80	3.74	1.51	1.79	0.88

5.8.4 Trajectory Analysis

Figure 5-98 shows CATT back trajectories for the cleanest days in the speciation record over the period studied from January 2001 through December 2003. While even lower concentration days can be found in the data record for Federal Reference Method monitors at the site, the trajectories plotted in Figure 5-98 are the lowest concentration days in the speciation record over the period studied. These "clean" days represent the five percent days with the lowest total $PM_{2.5}$ mass.

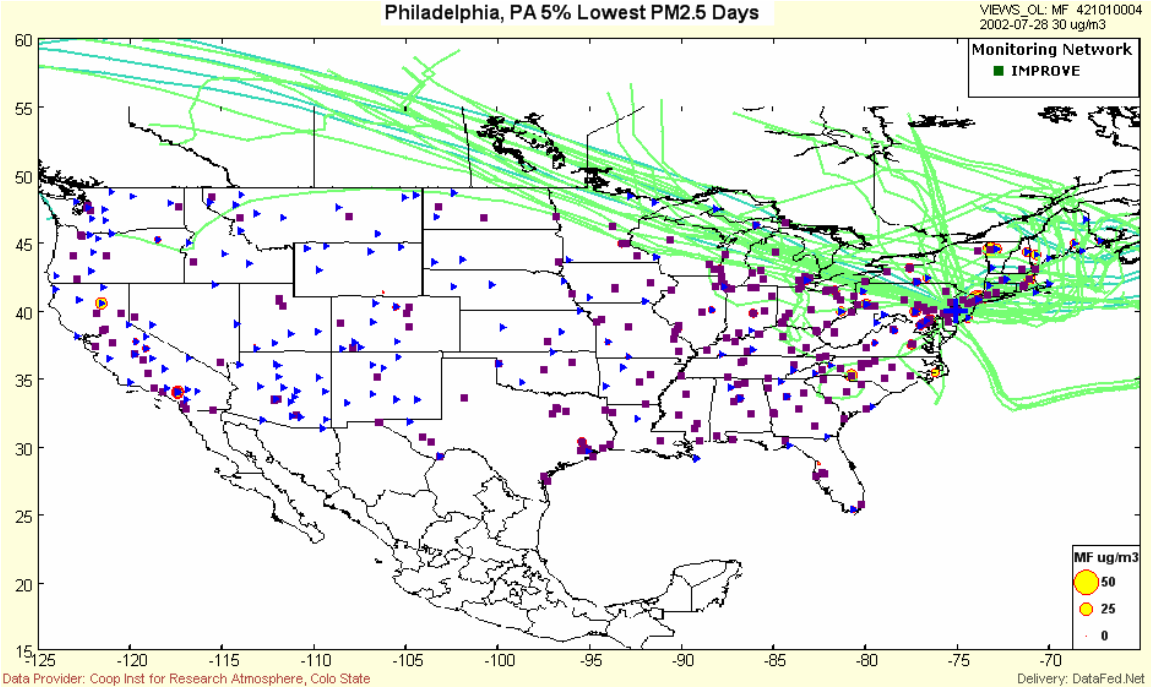

Figure 5-98 Philadelphia, PA Back Trajectories for the Five Percent Cleanest Days

As Figure 5-98 shows, many "clean day" trajectories originate in the western provinces of Canada and take very direct paths over southern Canada and the Great Lakes. They arrive in Philadelphia after passing over northern Pennsylvania and southern New York State. Other clean day trajectories take a direct path south from east central Canada or loop clockwise out of Canada over the Atlantic Ocean, arriving in Philadelphia from the southeast. In contrast to trajectories associated with high concentrations, these trajectories do not originate in high air pollution source regions and do not remain long in or re-circulate over these regions.

Table 5-33 lists the five percent cleanest days at Philadelphia, PA and the total mass concentration measured by the speciation monitor on that day.

Table 5-33 Philadelphia, PA Five Percent Lowest Days

Date	$PM_{2.5}$ Mass ($\mu g/m^3$)
10/7/2001	5.3
11/6/2001	5.0
3/18/2002	5.2
6/7/2002	5.5
8/9/2002	5.4
8/30/2002	4.1
9/2/2002	5.1
12/1/2002	5.5
12/25/2002	4.4
4/12/2003	4.8
6/17/2003	5.2
9/15/2003	4.8
10/15/2003	4.9
11/14/2003	4.4
12/2/2003	3.3
Average	4.9

Figure 5-99 shows back trajectories for the dirtiest days, the five percent days with the highest total $PM_{2.5}$ mass. With the exception of a set of trajectories that may be associated with fires in Mexico, most "dirty day" trajectories are trajectories that have spent the past five days over the continental U.S. In most cases, they are slower moving air masses than the clean day air masses. Many dirty day trajectories move through air pollution source regions in the South, Midwest and Ohio River Valley.

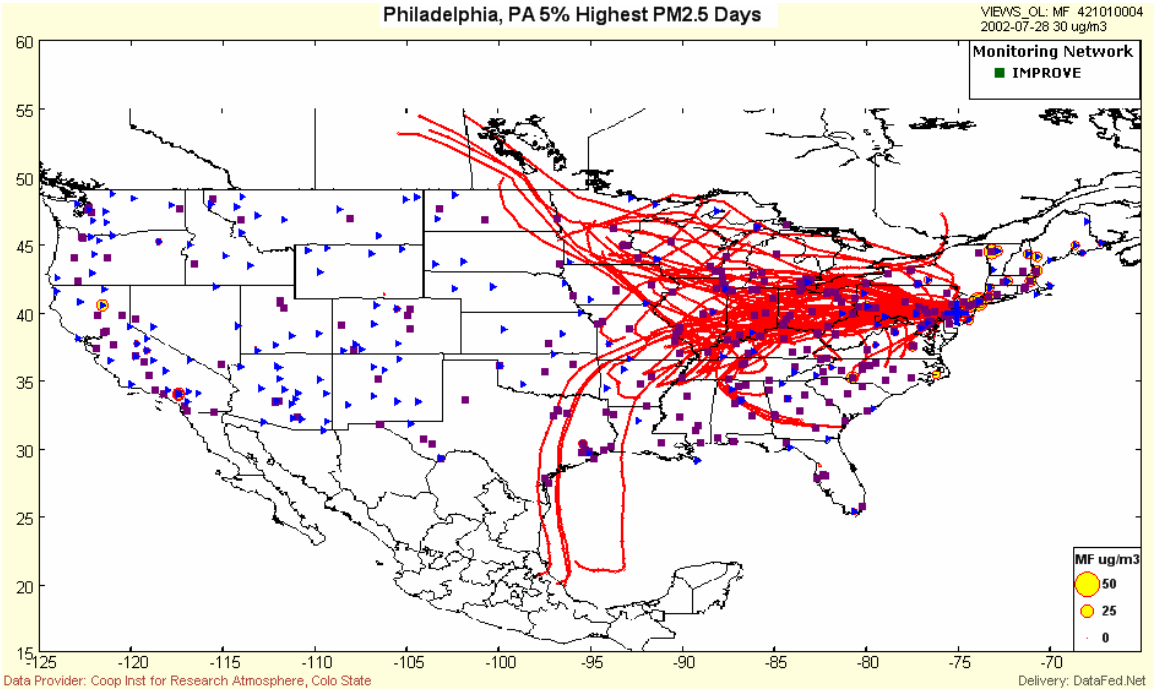

Figure 5-99 Philadelphia, PA Back Trajectories for the Five Percent Dirtiest Days

Table 5-34 lists the five percent dirtiest days and the total mass concentration measured by the speciation monitor on that day.

Table 5-34 Philadelphia, PA, Five Percent Highest Days

Date	$PM_{2.5}$ Mass ($\mu g/m^3$)
3/17/2001	239
5/4/2001	42.8
6/25/2002	41.4
7/19/2002	61.9
12/7/2002	35.3
3/13/2003	41.3
6/26/2003	65.4
7/5/2003	35.4
8/16/2003	38.5
8/22/2003	43.6
10/9/2003	40.1
11/12/2003	37.7
12/29/2003	37.1
Average	58.4

5.9 Pittsburgh, PA

Site Name: Lawrenceville
AIRS Number: 42-003-0008
Latitude: 40.4655 North
Longitude: -79.9611 West
Elevation: 267 meters (875 feet)
Agency Operating the Monitor: Allegheny County Health Department
Speciation Sampling Frequency: 1-in-3 days

5.9.1 Site Description

The Lawrenceville monitoring site is located in a residential neighborhood of Pittsburgh, PA about 4.0 km (2.5 miles) northeast of the city's central business district. The site is approximately 81 meters (264 feet) northwest of the intersection of 39th Street and Penn Avenue. Figure 5-100 shows the monitoring site's location relative to the interstate highway system and large population centers. As the figure shows, the closest cities to Pittsburgh are Youngstown, OH about 106 km (66 miles) to the northwest, Akron, OH about 68 km (110 miles) to the northwest, and Cleveland, OH about 214 km (133 miles) to the northwest.

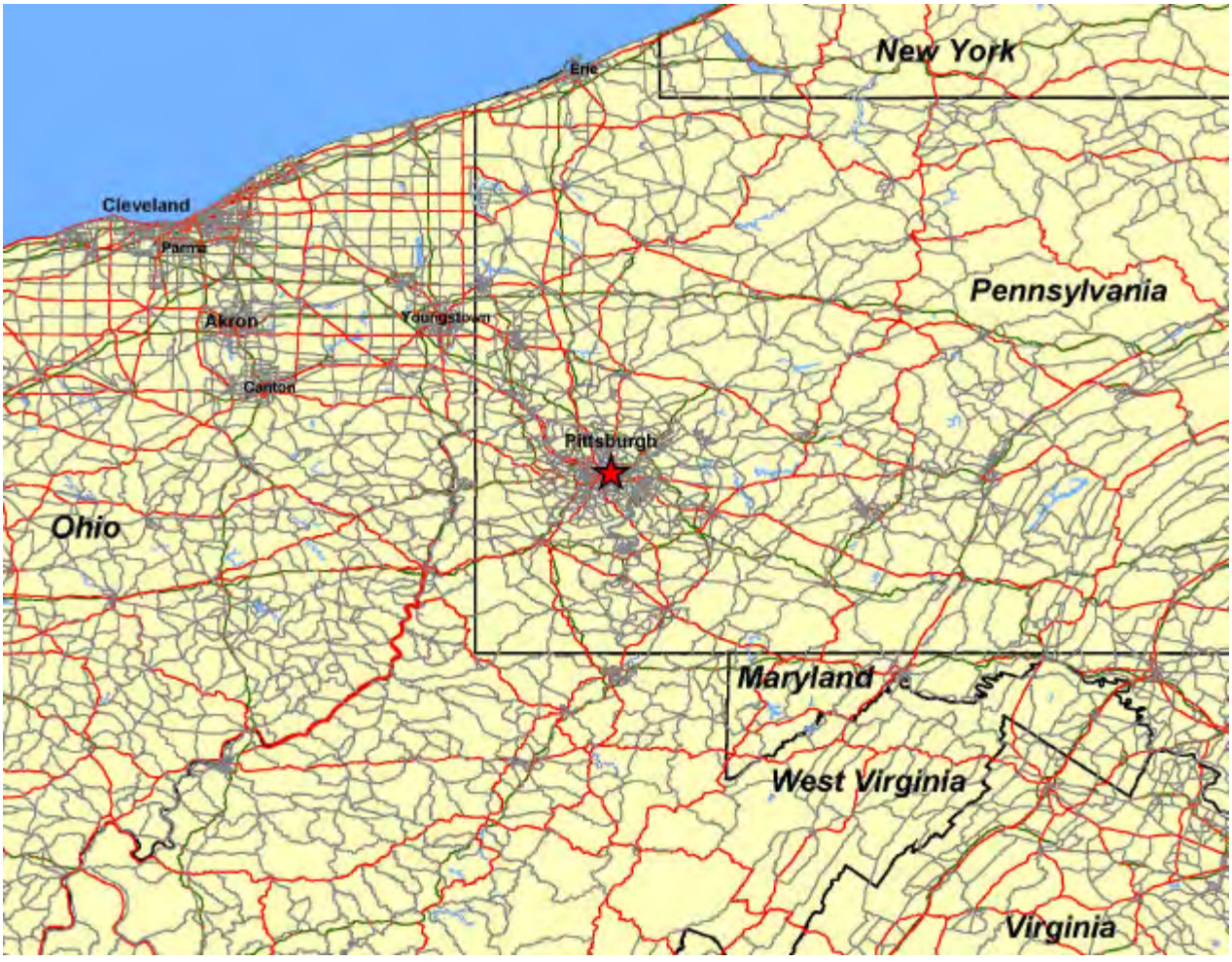

Figure 5-100 Location of the Pittsburgh, PA Monitoring Site

The Lawrenceville monitor is an urban scale monitor. The area immediately adjacent to the monitor is residential, a neighborhood of single-family homes. Large-scale commercial facilities along the Allegheny River are just 0.8 km (0.5 mile) away however. Heavy industry is located in the Monongahela River Valley south and southeast of the monitor. Large power generation and other industrial facilities also exist along the Ohio River northwest, west, and southwest of the monitor. Most of the metropolitan area of Pittsburgh, population 322,450, lies to the southwest of the monitoring site. The 40th Street Bridge, a major crossing over the Allegheny River, is only 0.8 km (0.5 mile) north and west of the monitor. Interstate 279 is about 3.2 km (two miles) to the west and Interstate 376 is about 3.2 km (two miles) to the south of the monitoring site.

Figure 5-101 shows the topographic features in the vicinity of the monitoring site. The Allegheny County Health Department believes some high $PM_{2.5}$ concentrations observed at the Lawrenceville monitor are partially the result of the monitor's location in the Allegheny River Valley. During temperature inversions, emissions can become trapped in the river valley. Figure 5-102 is a photograph of the roof-top site looking southwest toward downtown Pittsburgh.

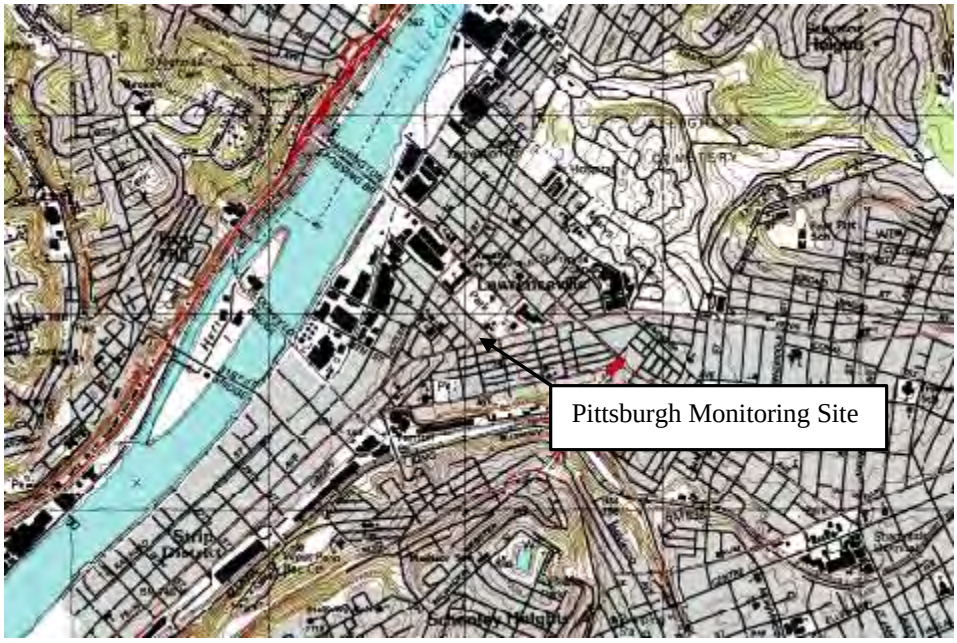

Source: TopoZone

Figure 5-101 Topographic Map of the Pittsburgh, PA Monitoring Site

Figure 5-102 Photograph of the Pittsburgh, PA Monitoring Site

The Allegheny County Health Department reports that a variety of air pollution sources are located in the vicinity of the monitoring site. Table 5-35 lists the industries within 11 km (seven miles) of the site.

Table 5-35 Emission Sources within 11 km of the Pittsburgh, PA Monitoring Site

Facility/Source	Direction	Distance	Emissions
Pittsburgh Brewing, coal-fired boiler	SSE	0.65 km	SO_2, HCl, HF, NH_3, Pb, $PM_{2.5}$[1]
Del Monte, coal-fired boiler	WSW	2.9 km	SO_2, HCl, HF, NH_3, Pb, $PM_{2.5}$[1]
Gulf Oil Storage	WSW	0.65 km	HAPs[2]
Shenango Coke Works	WNW	10.5 km	HAPs[2], metals, $PM_{2.5}$[1]
Neville Chemical	WNW	11 km	HAPs[2], metals
Pressure Chemical	WNW	10.9 km	SO_2, HCl, HF, Pb, Hexane
Bellefield Boiler, coal/oil-fired boilers	SW	2.5 km	HAPs[2], metals, $PM_{2.5}$[1]

[1] $PM_{2.5}$ emissions not known.
[2] HAP is an abbreviation for Hazardous Air Pollutant.

There are seven large point sources within an 11 km (seven mile) radius of the monitoring site. The Gulf Oil Storage and Pittsburgh Brewing facilities are the closest facilities. Both facilities are only 0.65 km (0.41 miles) away. With the exception of the Pittsburgh Brewing facility, all of the facilities listed above are west of the Lawrenceville monitor.

5.9.2 Major Constituents of $PM_{2.5}$ Mass

The major constituents of $PM_{2.5}$ mass at Pittsburgh were sulfate and organic carbon species followed by ammonium and nitrate species. Over 2001-2003, the average sulfate concentration was about 6.0 µg/m^3. Using an OM/OC ratio of 1.6, average organic carbon mass concentration was about 5.5 µg/m^3. While important constituents in $PM_{2.5}$, ammonium and nitrate made up a much smaller percentage of the total measured mass concentration from 2001 to 2003. Average ammonium concentration was 2.3 µg/m^3 while average nitrate concentration was 1.8 µg/m^3. Elemental carbon, geological components, and trace elements contributed about 1.9 µg/m^3 to the average concentration observed over the 2001-2003 period. Figure 5-103 shows the relative contributions the major species made to the total mass concentration measured at the site.

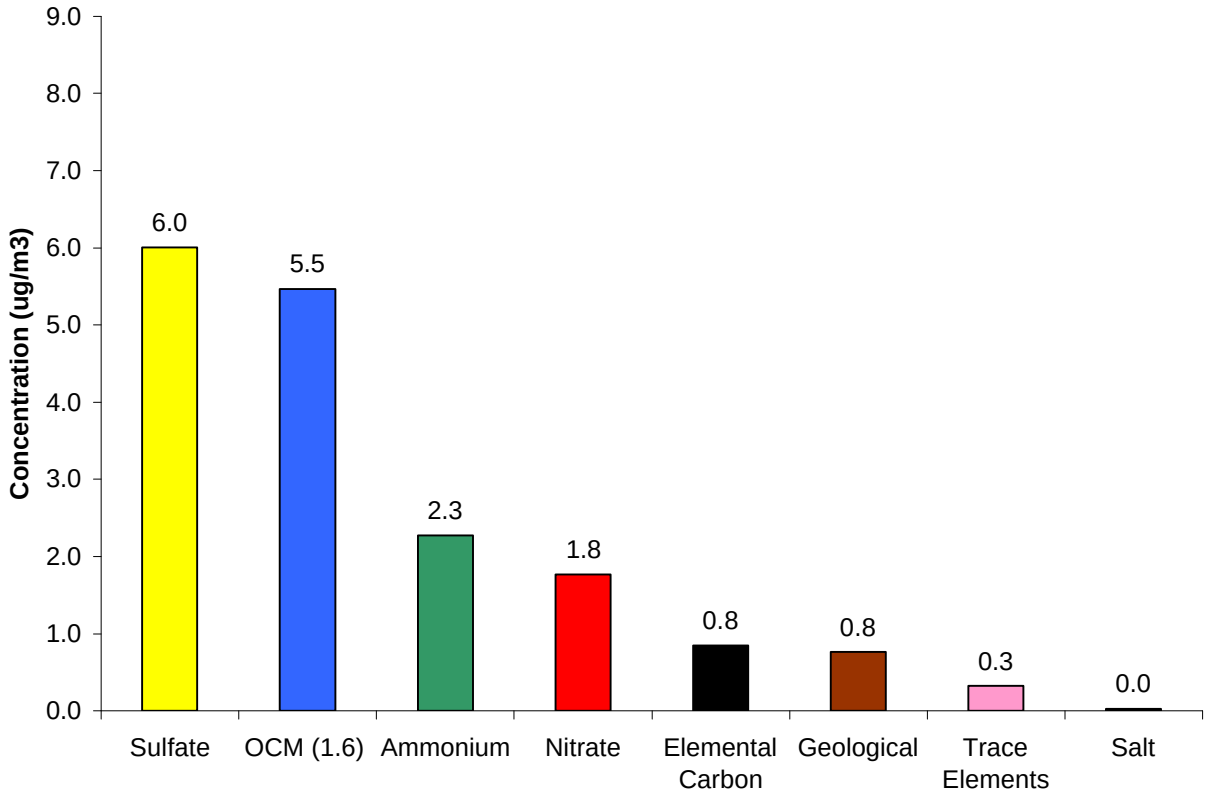

Figure 5-103 Major Constituents of $PM_{2.5}$ Mass, Pittsburgh, PA

The average reconstructed mass calculated for this site was very close to the average gravimetric mass measured by the speciation sampler. The average reconstructed mass over the study period was 17.4 µg/m^3. The average gravimetric mass was 17.5 µg/m^3. Figure 5-104 visually compares the average reconstructed mass with the average gravimetric mass.

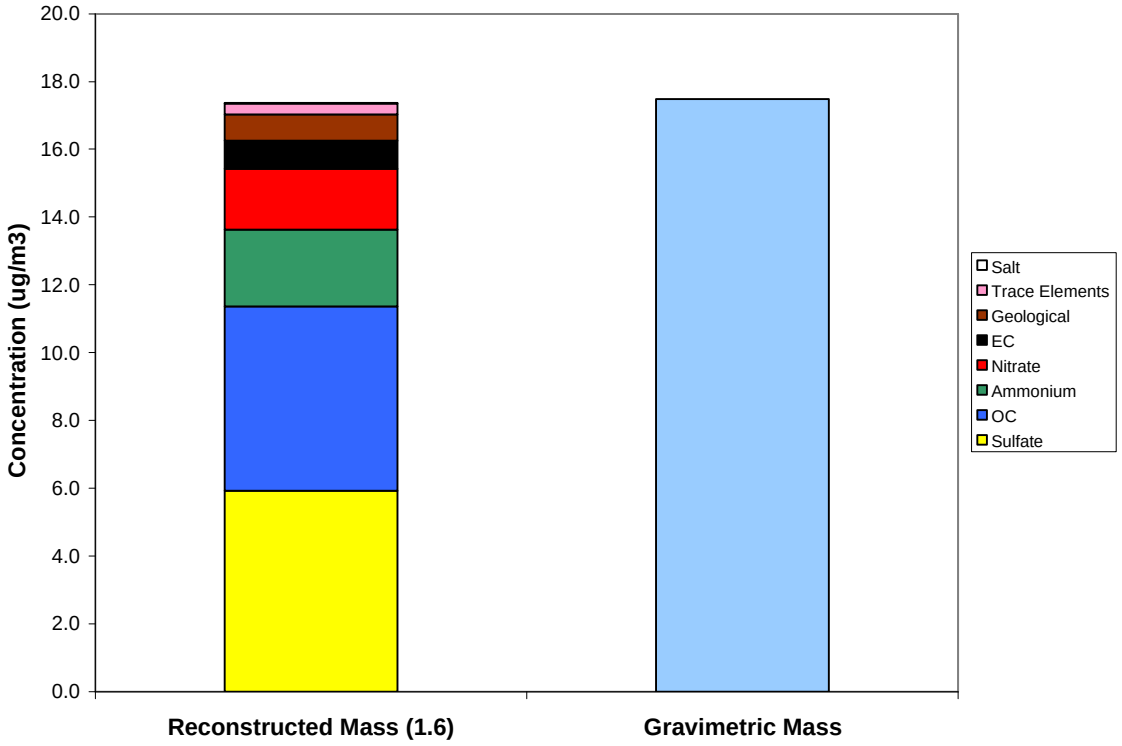

Figure 5-104 Comparison of Average Reconstructed Mass and Average Gravimetric Mass, Pittsburgh, PA

5.9.3 Time Series Analysis of $PM_{2.5}$ Species

A Met One SASS speciation sampler was installed at the Pittsburgh monitoring site on June 30, 2001. With the exception of monitor downtime and three "intensives" when the monitor collected a sample every day, the Met One SASS has operated on a 1-in-3 sampling schedule from its installation to the present time. Figure 5-105 shows a composite time series for the five major species measured at Pittsburgh and Figures 5-106 through 5-10 show time series for each of the five major species. In the time series plots for the five major species, the black line is the 30-day rolling average concentration for the specie. The 30-day rolling average is not shown during periods when the monitor was down or during periods when the monitor sampled everyday.

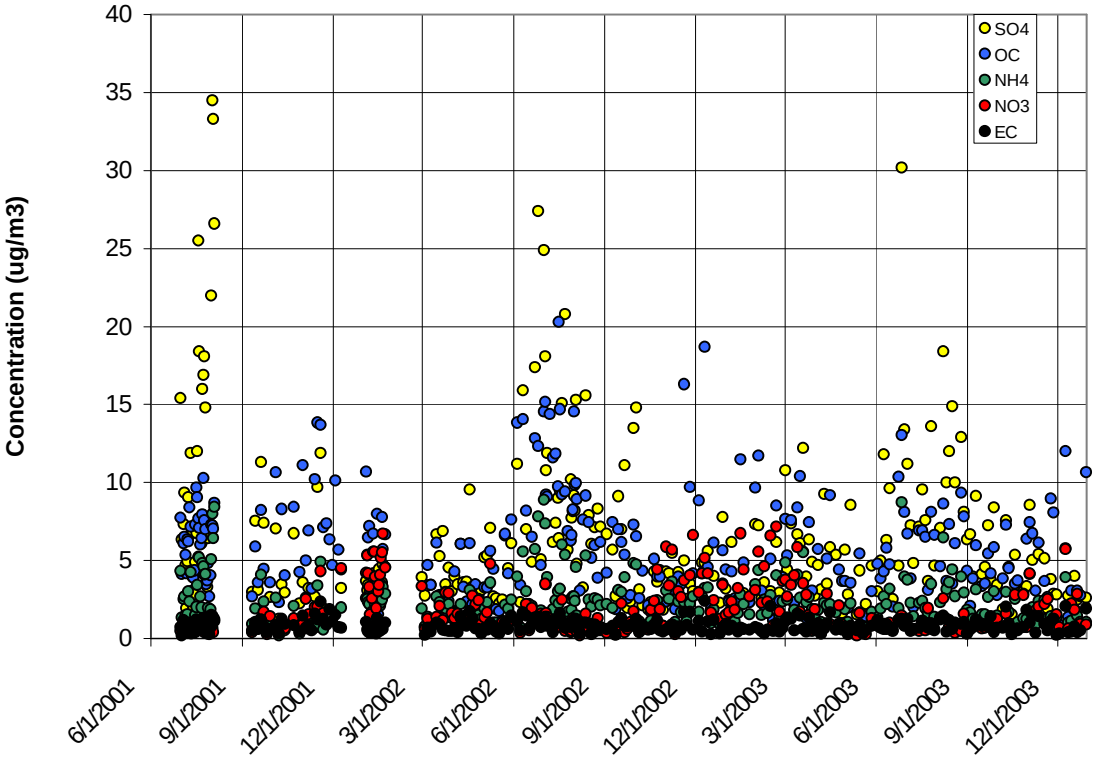

Figure 5-105 Time Series for the Pittsburgh, PA Monitor

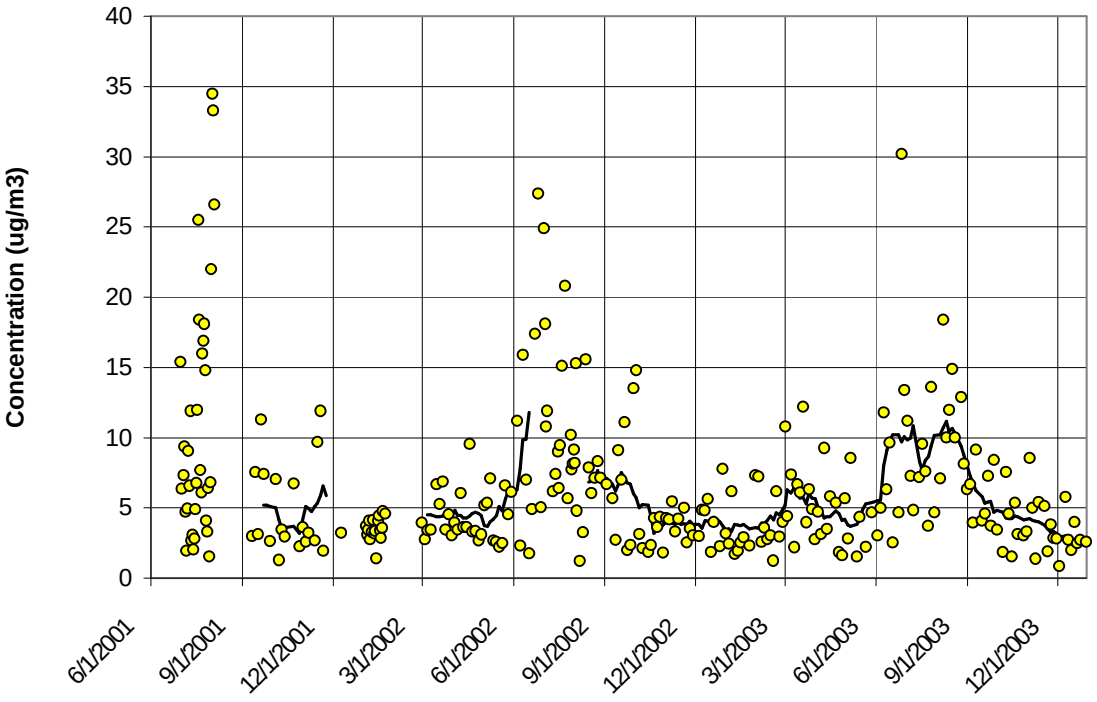

Figure 5-106 Sulfate Time Series for the Pittsburgh, PA Monitor

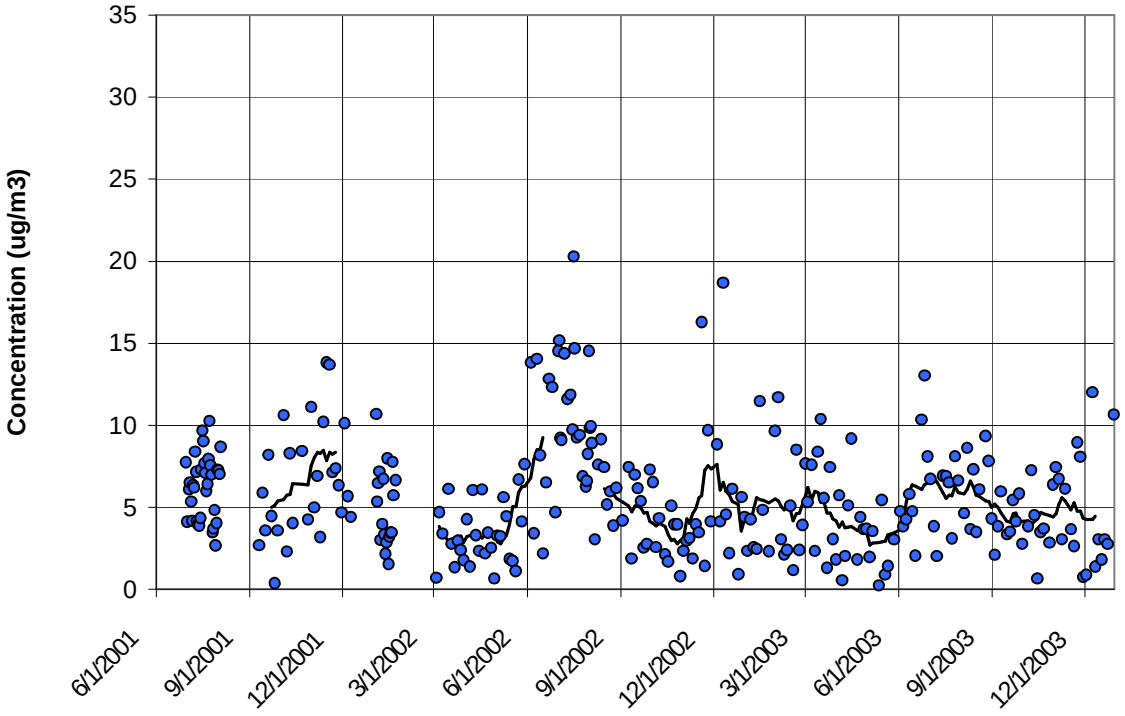

Figure 5-107 Organic Carbon Mass Time Series for the Pittsburgh, PA Monitor

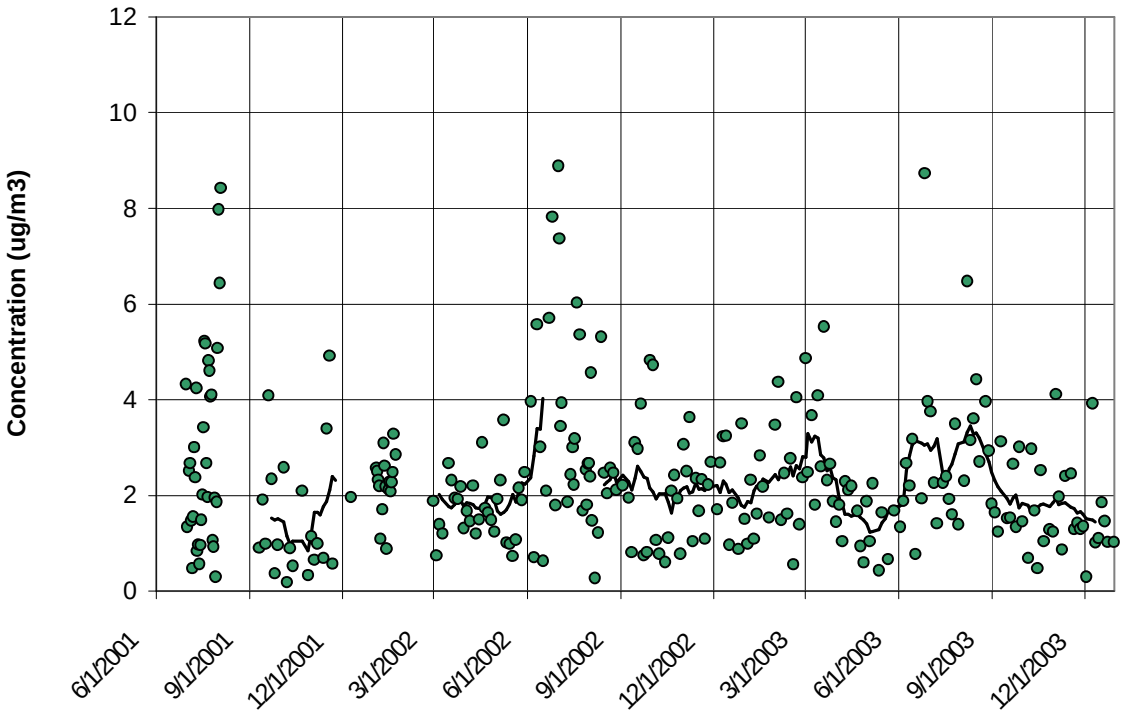

Figure 5-108 Ammonium Time Series for the Pittsburgh, PA Monitor

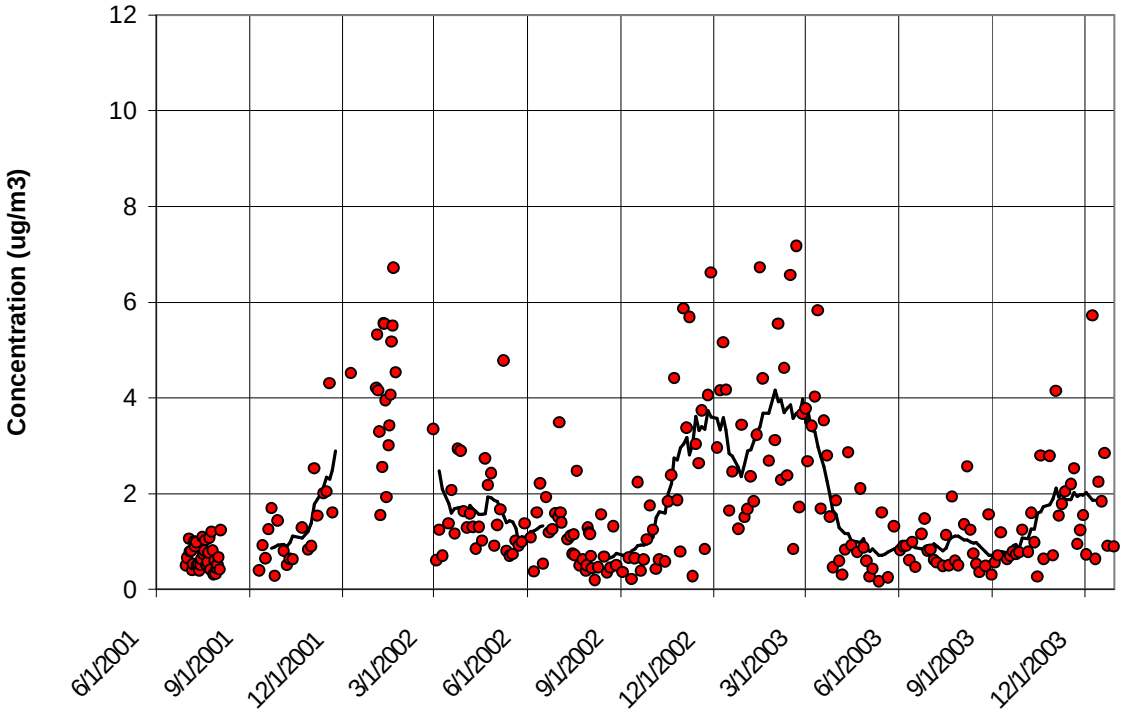

Figure 5-109 Nitrate Time Series for the Pittsburgh, PA Monitor

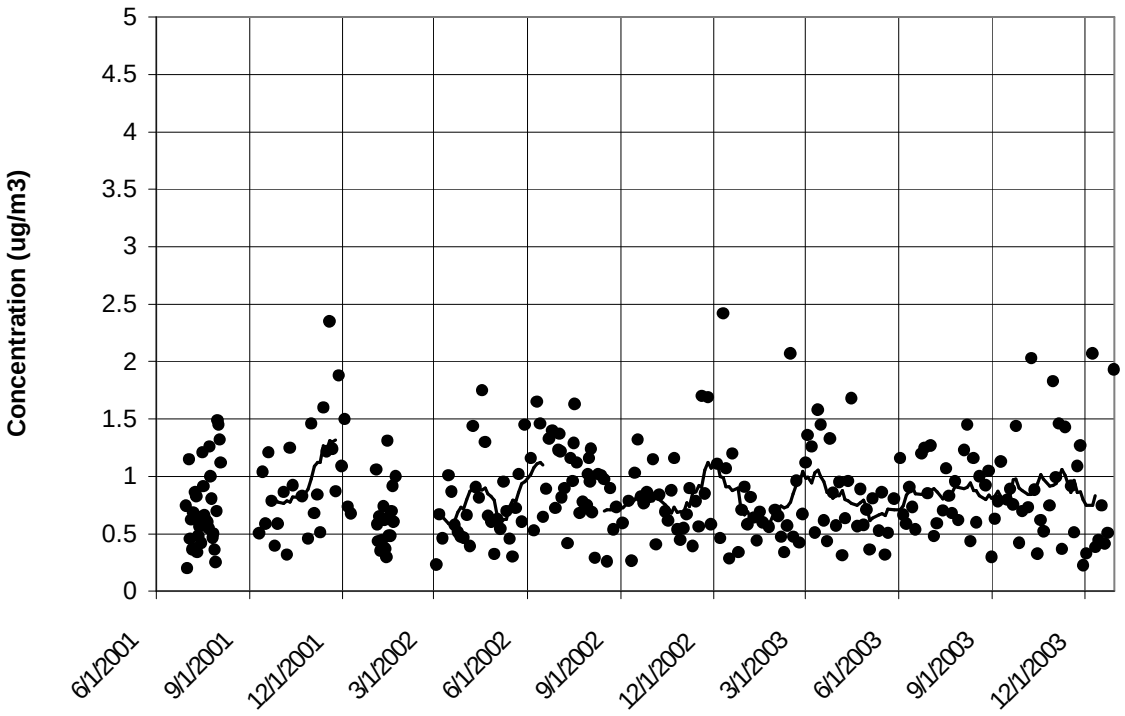

Figure 5-110 Elemental Carbon Time Series for the Pittsburgh, PA Monitor

The 30-day rolling average sulfate concentration in Figure 5-106 shows how sulfate varied seasonally over 2001-2003 in Pittsburgh, PA. Average sulfate concentration was lowest in winter at about 3.78 µg/m^3. Average concentrations were somewhat higher during the spring and fall at 4.73 and 5.07 µg/m^3, respectively. As seen at other sites, large concentrations of sulfate were observed during the summer months. In Pittsburgh, the average summer sulfate concentration was about 9.60 µg/m^3, the highest seasonal average concentration observed in the region. On peak days, summer concentrations ranged as high as 25-35 µg/m^3. Of the eleven sites analyzed, Pittsburgh had the second highest sulfate concentration averaged over all seasons (6.00 µg/m^3), only slightly less than the highest site, Arendtsville, PA which recorded a average concentration for all seasons of 6.12 µg/m^3. As the sulfate time series shows, sulfate concentrations were much more variable in summer than in winter.

Organic carbon mass was the second largest contributor to total $PM_{2.5}$ mass at the Pittsburgh monitoring site. Using an OM/OC ratio of 1.6, over the course of 2001-2003, organic carbon mass concentration averaged 5.47 µg/m^3. The average summer concentration was 7.50 µg/m^3 and the average winter concentration was 5.43 µg/m^3. Average spring and fall concentrations were 3.79 and 5.22 µg/m^3, respectively. Organic carbon mass concentrations were quite variable. They ranged from a low of about 0.2 to a high of 20.3 µg/m^3.

The 30-day rolling average concentration shown in Figure 5-107 reveals a number of peaks and valleys over 2001-2003. For example, a strong peak occurred during the summer of 2002 followed by a trough in mid-fall followed by a peak in late fall/early winter. A strong peak was not observed during the summer of 2003 nor did a trough or peak occur in the fall of 2003. Given the relatively short data record at this site, it is difficult to discern clear seasonal variability in the organic carbon mass at the Lawrenceville monitoring site. Data for additional years will likely help identify seasonal patterns if they are present.

Over 2001-2003, the average ammonium concentration was 2.28 µg/m^3. Only Wilmington, DE (2.33 µg/m^3) and Arendtsville, PA (2.36 µg/m^3) had higher average ammonium concentrations in the MARAMA Region. Figure 5-108 shows how ammonium concentrations varied over time. Summer had the highest average concentration at 3.05 µg/m^3 followed by winter with an average concentration of about 2.24 µg/m^3 each. Average spring and fall concentrations were about 1.95 and 1.89 µg/m^3. The highest 24-hour ammonium concentrations occurred in the summer between 8 and 9 µg/m^3. Some high values also occasionally occurred in the spring and fall.

Ammonium and sulfate concentrations were well correlated (R^2 = 0.81); when sulfate concentrations are high, ammonium concentrations are usually high. Table 5-36 lists ammonium and sulfate concentrations on days when sulfate concentration exceeded 15 µg/m^3. The Pittsburgh monitor recorded more high ammonium/sulfate days than other sites because the Allegheny County Health Department ran several summer intensives when the monitor sampled every day. The summer intensives captured more high ammonium/sulfate concentrations than regular 1-in-3 day sampling would have recorded.

Table 5-36 High Ammonium and Sulfate Days for the Pittsburgh, PA Monitor

Date	Ammonium Concentration (µg/m^3)	Sulfate Concentration (µg/m^3)
6/30/01	4.3	15.4
7/18/01	5.2	25.5
7/19/01	5.2	18.4
7/22/01	4.8	16.0
7/23/01	4.6	16.9
7/24/01	4.1	18.1
7/31/01	5.1	22.0
8/1/01	8.0	34.5
8/2/01	6.4	33.3
8/3/01	8.4	26.6
6/10/02	5.6	15.9
6/22/02	5.7	17.4
6/25/02	7.8	27.4
7/1/02	8.9	24.9
7/2/02	7.4	18.1
7/19/02	6.0	15.1
7/22/02	5.4	20.8
8/2/02	4.6	15.3
8/12/02	5.3	15.6
6/26/03	8.7	30.2
8/7/03	6.5	18.4

Over 2001-2003, the Pittsburgh site had approximately the same average nitrate concentration, 1.77 µg/m^3 as the average nitrate concentration for the entire Mid-Atlantic Region (1.76 µg/m^3). As noted in the regional analysis, nitrate concentration appears to be a function of temperature, relative humidity, and other factors (Wittig, 2004) with lower average concentrations occurring in the southern part of the MARAMA Region and higher average concentrations occurring in northern areas.

As Figure 5-109 shows, nitrate measurements at Pittsburgh exhibited the strong seasonal variation seen at other sites. Nitrate concentrations were lowest during the summer and noticeably higher in winter. Over 2001-2003, the average summer concentration was 0.98 µg/m^3 whereas the average winter concentration was 3.65 µg/m^3. In spring and fall, the average nitrate concentration was 1.64 and 1.59 µg/m^3 respectively. As Figure 5-109 shows, nitrate values were much more variable in winter than in summer.

Figure 5-110 displays the time series for elemental carbon. As the plot shows, while high concentrations were occasionally measured, overall, the elemental carbon concentration did not vary much season-to-season. Over 2001-2003, the average elemental carbon concentration was 0.85 µg/m^3. Average concentrations were highest in the summer and fall at 0.89 and 0.90 µg/m^3, respectively and 0.79 µg/m^3 in the winter and spring.

Seasonal averages for the major constituents of $PM_{2.5}$ mass measured in Pittsburgh, PA are summarized in Table 5-37.

Table 5-37 Seasonal Averages for the Major Constituents of $PM_{2.5}$ Mass (µg/m^3) for Pittsburgh, PA

	Organic Carbon Mass	Sulfate	Ammonium	Nitrate	Elemental Carbon
Winter	5.43	3.78	2.24	3.65	0.79
Spring	3.79	4.73	1.95	1.64	0.79
Summer	7.50	9.60	3.05	0.98	0.89
Fall	5.22	5.07	1.89	1.59	0.90

5.9.4 Trajectory Analysis

Figure 5-111 shows CATT back trajectories for the cleanest days in the speciation record over the period studied from June 2001 through December 2003. While even lower concentration days can be found in the data record for Federal Reference Method monitors at the site, the trajectories plotted in Figure 5-111 are the lowest concentration days in the speciation record over the period studied. These "clean" days represent the five percent days with the lowest total $PM_{2.5}$ mass.

Many "clean day" trajectories move quickly over great distances from western or central Canada or the northern states to Pittsburgh. These tracks indicate fast moving air masses probably associated with large-scale weather systems. In contrast to trajectories associated with high concentrations, these trajectories do not remain or re-circulate over source regions. Several clean day trajectories pass through eastern Canada and New England or originate over the Atlantic Ocean.

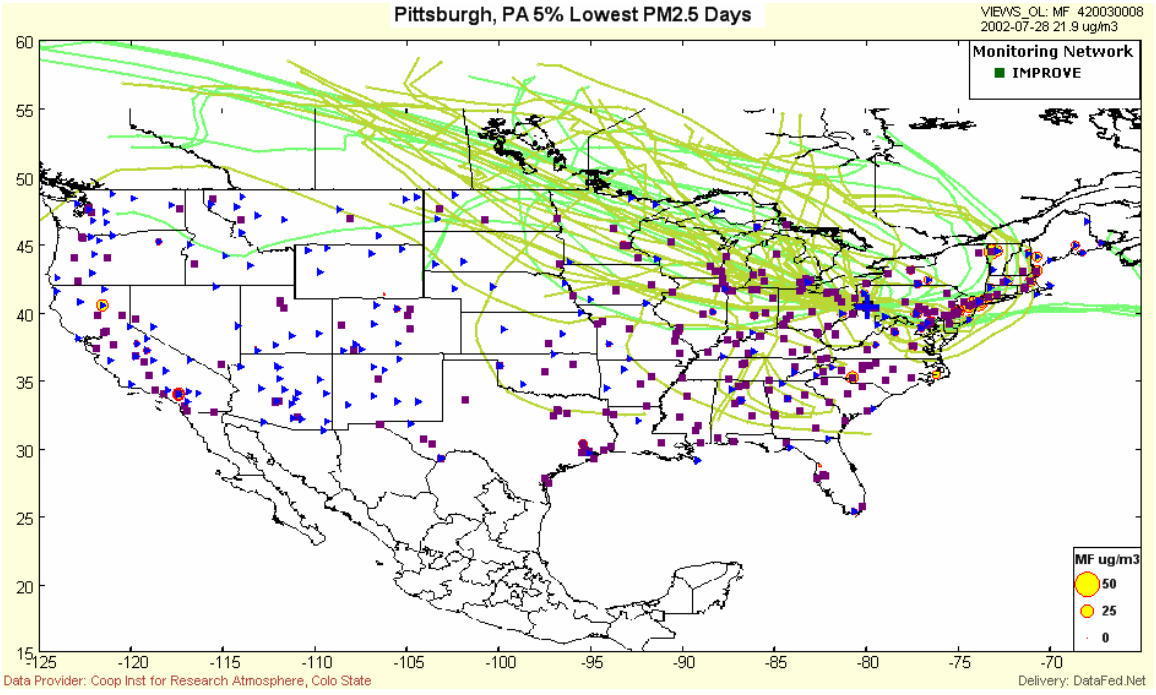

Figure 5-111 Pittsburgh, PA, Back Trajectories for the Five Percent Cleanest Days

Table 5-38 lists the five percent cleanest days at Pittsburgh, PA and the total mass concentration measured by the speciation monitor on that day.

Table 5-38 Pittsburgh, PA Five Percent Lowest Days

Date	$PM_{2.5}$ Mass ($\mu g/m^3$)
7/29/2001	6.1
9/25/2001	5.9
10/7/2001	6.1
1/13/2002	6.4
4/29/2002	6.5
6/16/2002	7.0
8/6/2002	5.9
9/11/2002	7.0
10/29/2002	5.7
12/25/2002	6.5
2/17/2003	4.6
5/12/2003	4.8
5/18/2003	4.3
10/15/2003	5.3
12/2/2003	5.2
Average	5.8

Figure 5-112 shows back trajectories for the dirtiest days, the five percent days with the highest total $PM_{2.5}$ mass. With the exception of a few trajectories that move south from Massachusetts along the Atlantic coast, most "dirty day" trajectories are tracks of air masses that have spent the past five days over the continental U.S. In many cases, the air circulates or re-circulates through air pollution source regions in the Ohio River Valley.

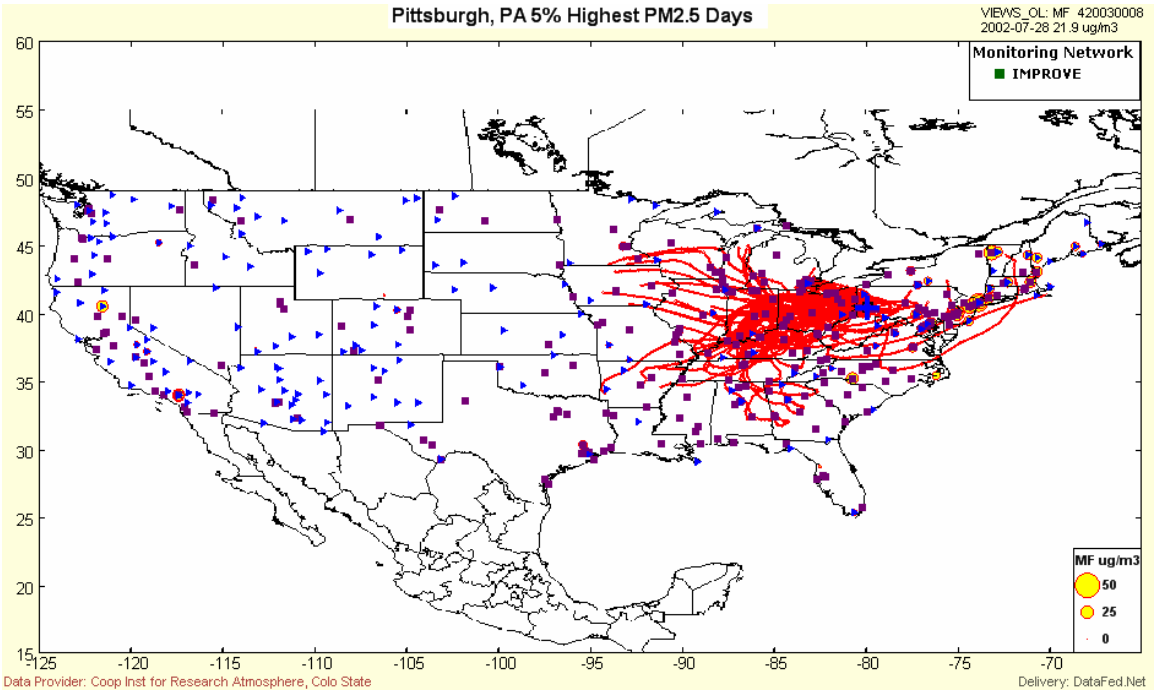

Figure 5-112 Pittsburgh, PA, Back Trajectories for the Five Percent Dirtiest Days

Table 5-39 lists the five percent dirtiest days and the total mass concentration measured by the speciation monitor on that day. As Table 5-39 shows, all of the five percent dirtiest $PM_{2.5}$ mass days occurred in the summer months, June through August.

Table 5-39 Pittsburgh, PA Five Percent Highest Days

Date	$PM_{2.5}$ Mass ($\mu g/m^3$)
7/18/2001	47.6
7/19/2001	39.5
7/24/2001	39.8
7/31/2001	41.2
8/1/2001	57.2
8/2/2001	60.2
8/3/2001	51.5
6/10/2002	39.6
6/22/2002	40.6
6/25/2002	54.7
7/1/2002	57.9
7/2/2002	48.5
7/22/2002	39.8
6/26/2003	62.1
Average	48.6

5.10 Richmond, VA

Site Name: VA DEQ Air Monitoring Office
AIRS Number: 51-760-0020
Latitude: 37.5106 North
Longitude: -77.4983 West
Elevation: 61 meters (200 feet)
Agency Operating the Monitor: Virginia Department of Environmental Quality (DEQ), Office of Air Quality Monitoring
Speciation Sampling Frequency: 1-in-3 days

5.10.1 Site Description

The Department of Environmental Quality's Richmond monitor was put in service in March 2001 in southwest Richmond, VA. The monitor was taken out of service September 1, 2004 when the DEQ moved its offices to a new location in northwest Richmond. The analysis that follows uses data from the monitor that was located at the southwest Richmond site. Figure 5-113 shows the monitor's location relative to the interstate highway system and large population centers. As the figure shows, Norfolk, VA was about 130 km (81 miles) to the southeast, Washington, DC about 162 km (100 miles) to the north, and the Raleigh Durham area about 225 km (140 miles) to the southwest.

Figure 5-113 Location of the Richmond, VA Monitoring Site

The DEQ's monitoring station in southwest Richmond was established in July 1981 as a total suspended particulate matter (TSP) monitoring site. The original objective of the site was to monitor air quality in the Midlothian Turnpike corridor. The monitoring site was located on the roof of the Office of Air Monitoring on Distributor Drive, one block north of Midlothian Turnpike, Virginia Route 60. In the area near the monitor site, Midlothian Turnpike was a six lane divided highway with a twenty-foot grass median.

The area immediately south of the monitor was very commercial in nature and was dominated by the east-west Midlothian Turnpike corridor. Commercial establishments along the highway included car dealerships, trucking firms, gas stations and garages, fast food restaurants, banks, etc. South of the Midlothian Turnpike corridor, land use was residential in character. The area northwest, north, and northeast of the monitoring site was mostly residential. Some light commercial use properties such as gas stations, grocery stores, a hospital, etc. were also located north of the monitor. Figure 5-114 is a detailed map showing the topographic features around the monitoring site. Figure 5-115 is a photograph of the site.

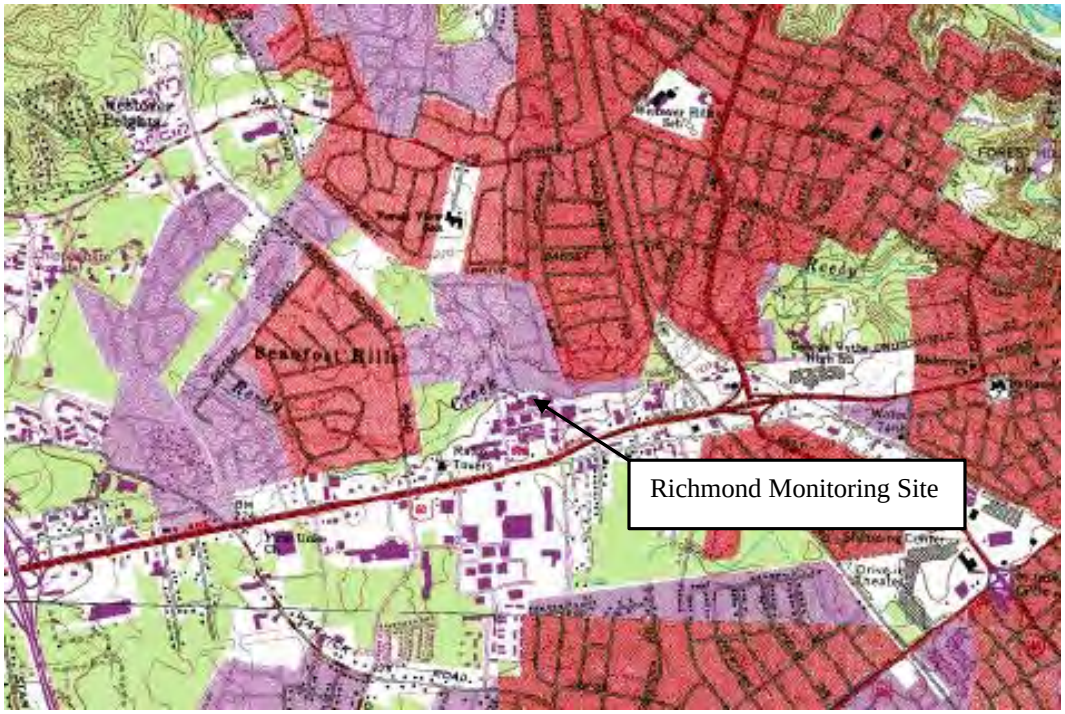

Source: TopoZone

Figure 5-114 Topographic Map of the Richmond, VA Monitoring Site

The Virginia DEQ Office of Air Quality Monitoring believes the speciation measurements made at the southwest Richmond monitor were heavily influenced by vehicular emissions. Midlothian Turnpike was only a block away and two trucking companies were located near the monitor. The DEQ reports there were a variety of air pollution sources in the vicinity of the monitoring site. Table 5-40 lists the sources that were located within 18 km (11 miles) of the site.

Figure 5-115 Photograph of the Richmond, VA Monitoring Site

Table 5-40 Emission Sources within 18 km of the Richmond, VA Monitoring Site

Facility/Source	Distance (km)	Direction	Emissions
Venetian Marble	0.158	West	Styrene, VOCs
Trucking Firm	0.183	West	CO, NO_x, PM
Midlothian Turnpike	0.198	South	CO, NO_x, PM
Trucking Firm	0.259	South-Southeast	CO, NO_x, PM
Residential Space heating	0.274	NW, N, NE	PM
Virginia Dominion Power	17.4	Southeast	NO_x, PM, SO_2

5.10.2 Major Constituents of $PM_{2.5}$ Mass

The major constituents of $PM_{2.5}$ mass at Richmond were organic carbon mass and sulfate species followed by ammonium and nitrate species. Using an OM/OC ratio of 1.6, organic carbon mass was the largest contributor to total $PM_{2.5}$ mass in Richmond. The average organic carbon mass concentration was 6.8 $\mu g/m^3$ over 2001-2003. Average sulfate concentration was about 5.0 $\mu g/m^3$. Average ammonium and nitrate concentration were about 1.9 and 1.2 $\mu g/m^3$ respectively. Elemental carbon, geological components, and trace elements added about 1.4 $\mu g/m^3$ to the average concentration measured over the period. Figure 5-116 compares the contributions each specie made to the average concentration measured at the site.

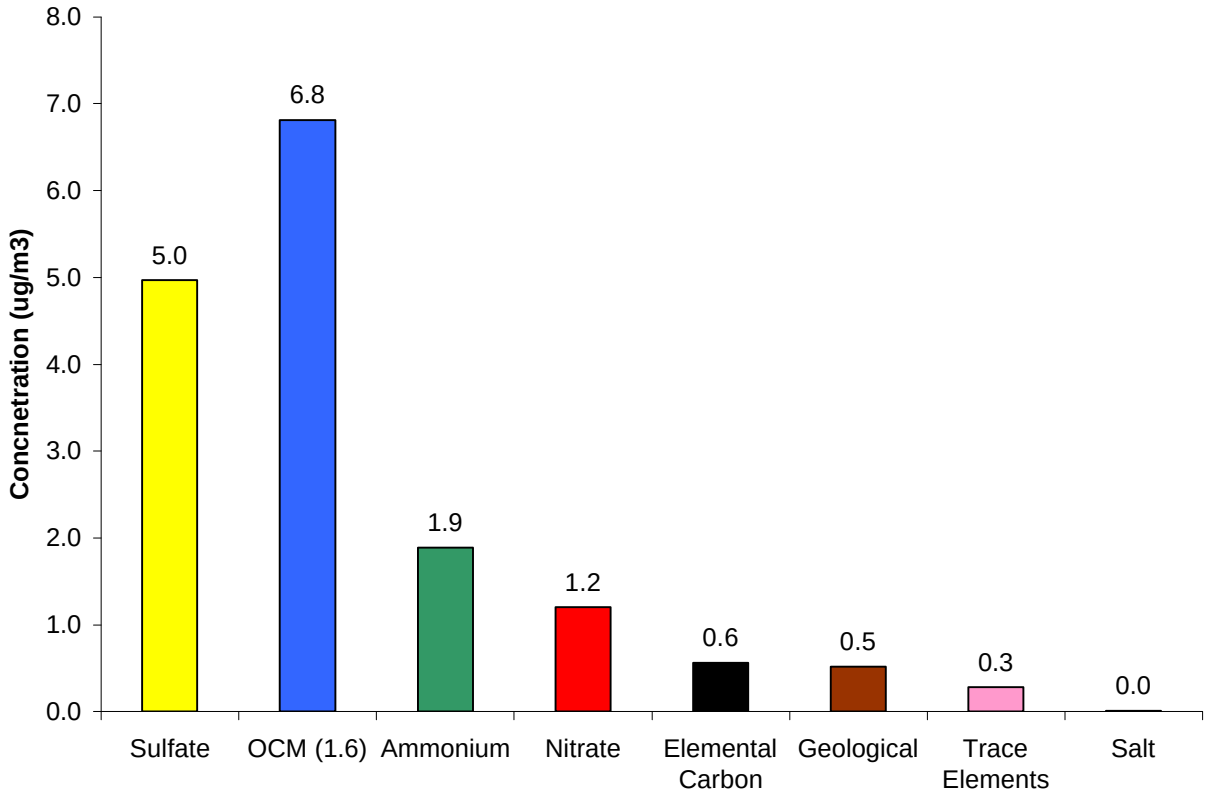

Figure 5-116 Major Constituents of $PM_{2.5}$ Mass, Richmond, VA

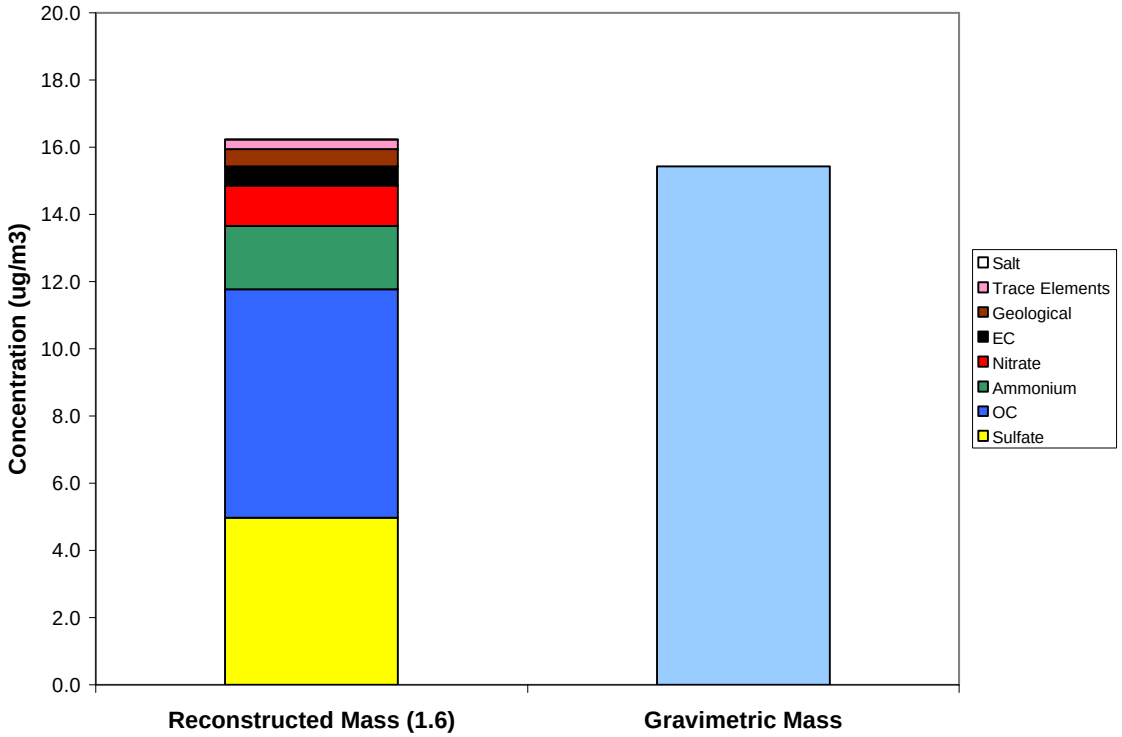

Figure 5-117 Comparison of Average Reconstructed Mass and Average Gravimetric Mass, Richmond, VA

The average reconstructed mass calculated for this site was about 4.7 percent higher than the average gravimetric mass measured by the speciation sampler. Average reconstructed mass was 16.2 µg/m^3 whereas the average gravimetric mass was 15.4 µg/m^3. Figure 5-117 visually compares the average reconstructed mass with the average gravimetric mass.

5.10.3 Time Series Analysis of $PM_{2.5}$ Species

A Met One SASS speciation sampler was installed at the Richmond monitoring site on March 2, 2001. It operated on a 1-in-3 sampling schedule from its installation until September 1, 2004. Figure 5-118 shows a composite time series for the five major species measured at Richmond. Figures 5-119 through 5-123 show time series for each of the five major species. The black line in Figures 5-119 through 5-123 is the 30-day rolling average concentration for the specie. The 30-day rolling average is not shown during periods when the monitor was down or did not report data for more than two consecutive sample days.

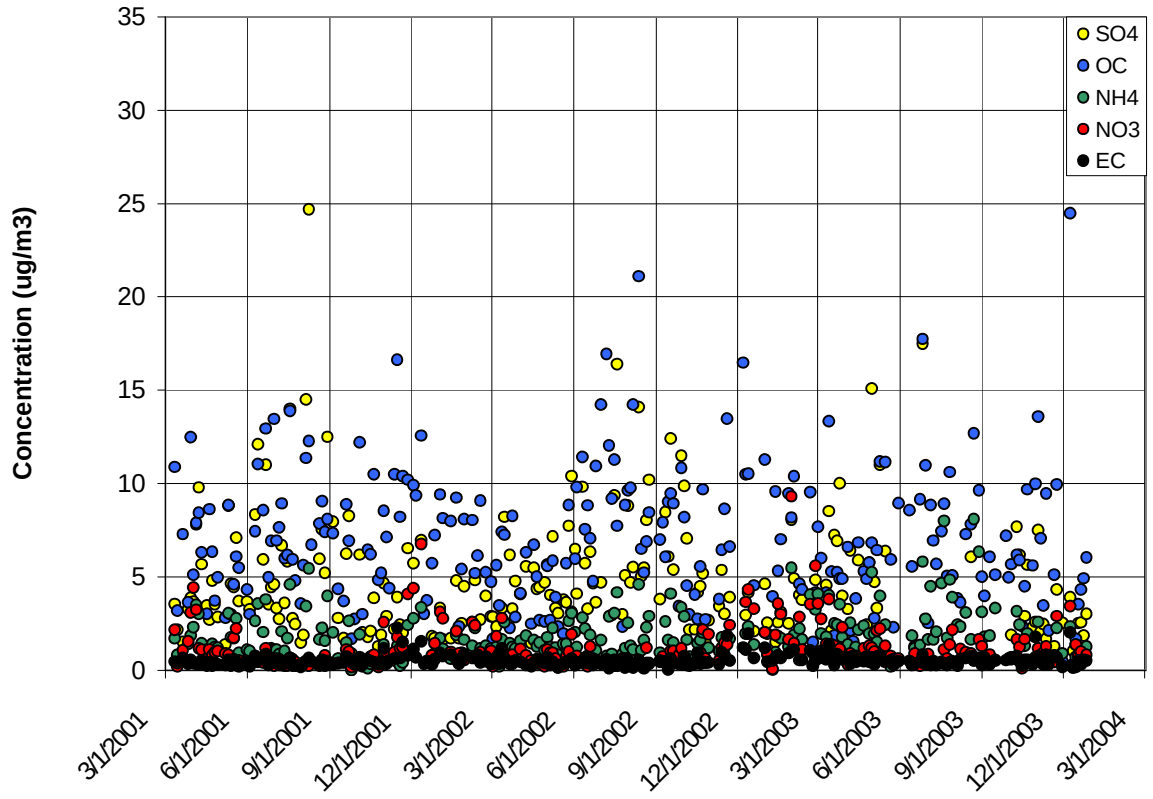

Figure 5-118 Time Series for the Richmond, VA Monitor

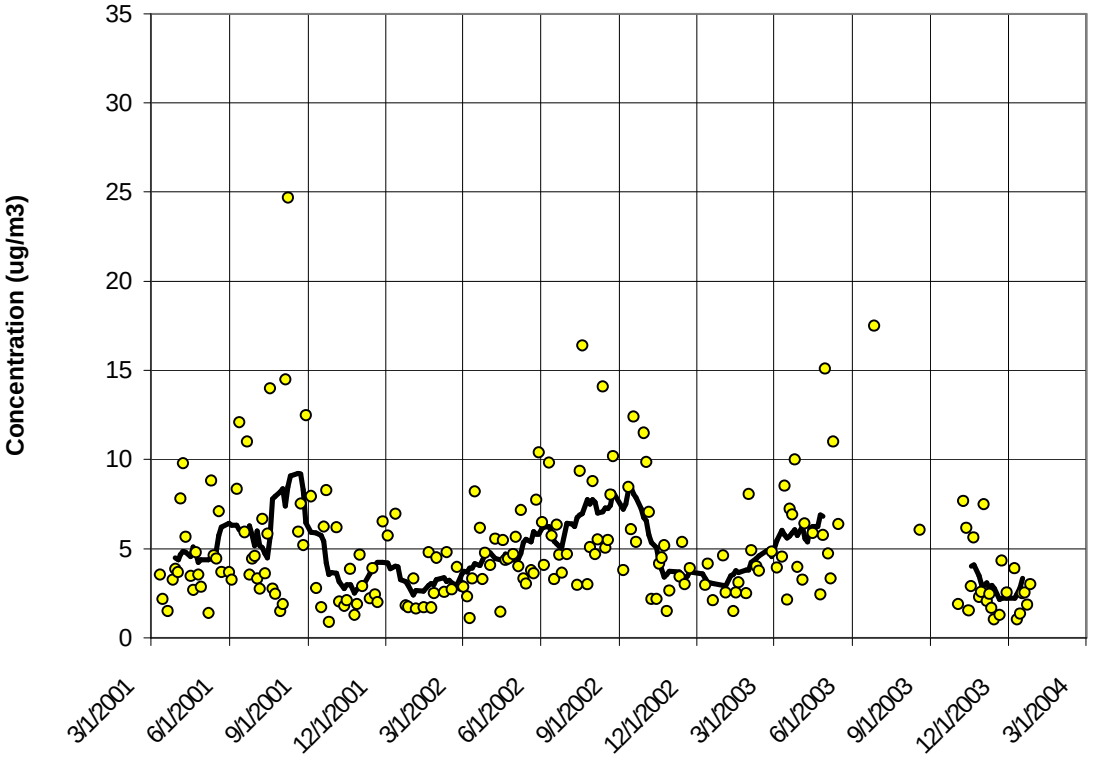

Figure 5-119 Sulfate Time Series for the Richmond, VA Monitor

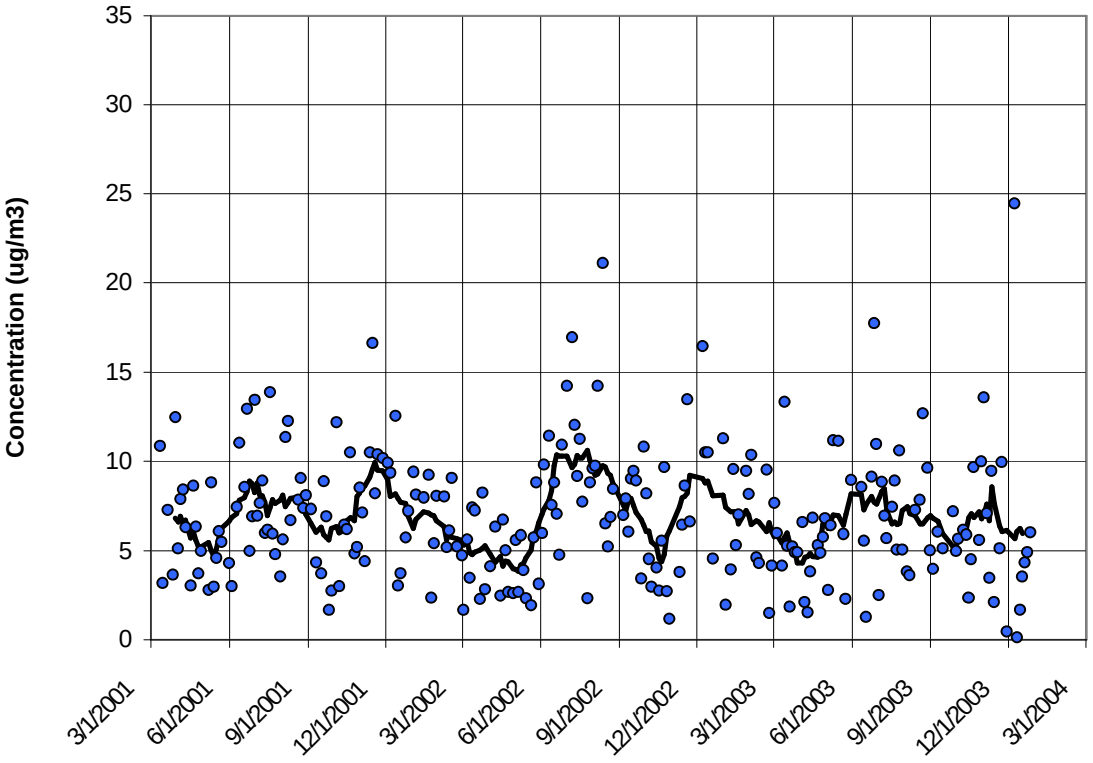

Figure 5-120 Organic Carbon Mass Time Series for the Richmond, VA Monitor

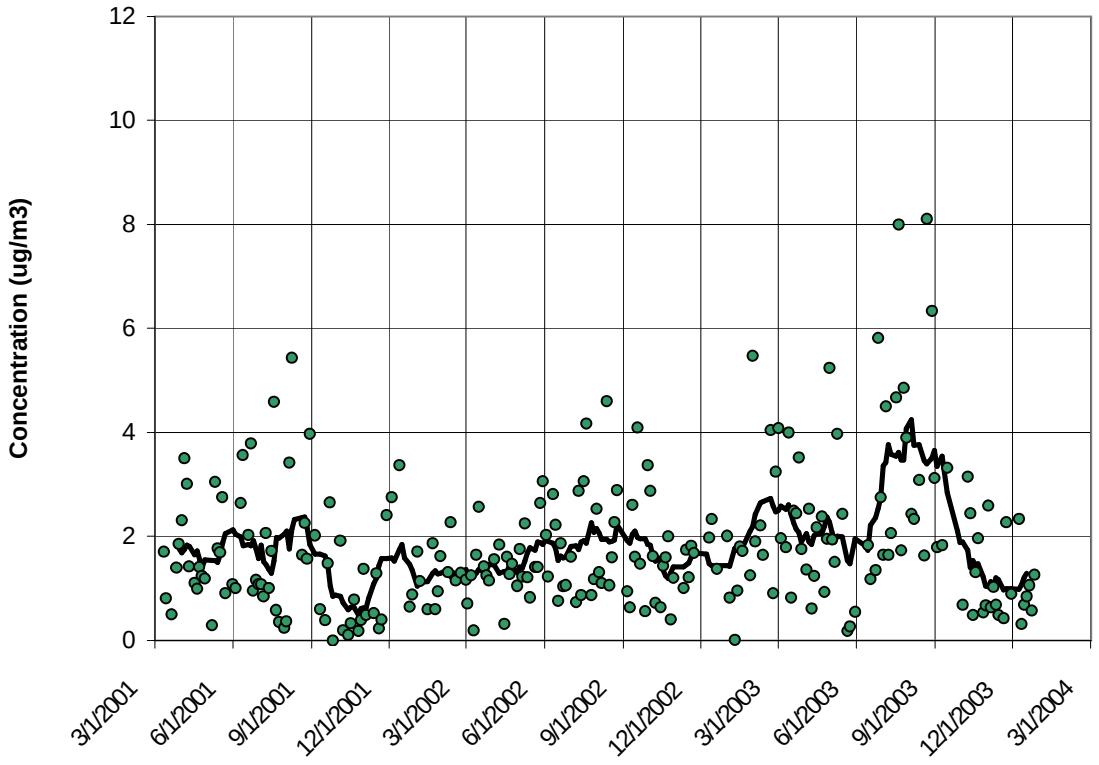

Figure 5-121 Ammonium Time Series for the Richmond, VA Monitor

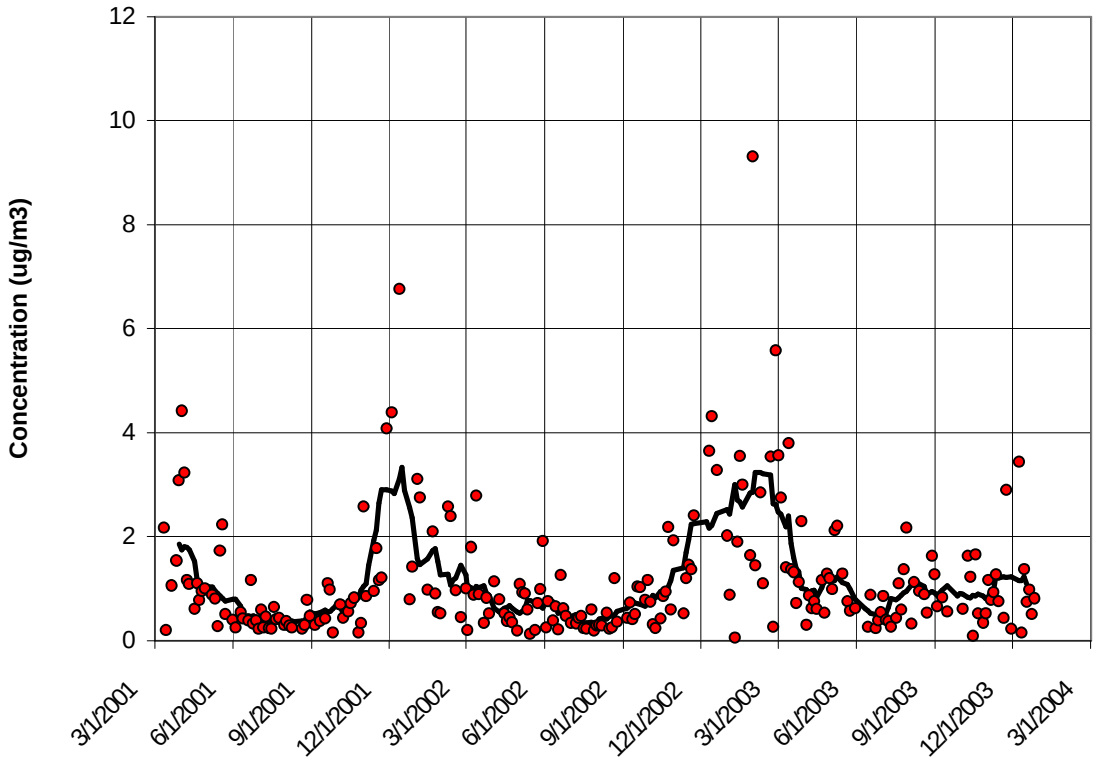

Figure 5-122 Nitrate Time Series for the Richmond, VA Monitor

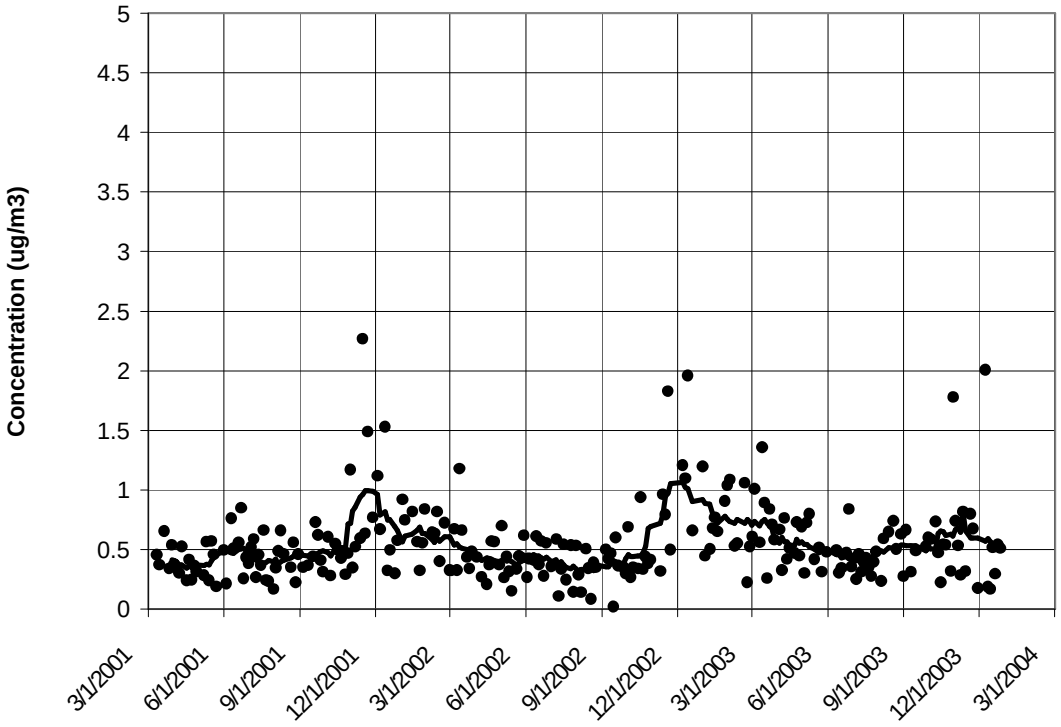

Figure 5-123 Elemental Carbon Time Series for the Richmond, VA Monitor

Average sulfate concentration over 2001-2003 was 4.97 µg/m^3 somewhat less than the regional average concentration of 5.11 µg/m^3 calculated for the MARAMA Region. The average concentration for Richmond was about the same as the average concentration measured in Charlotte, NC (4.96 µg/m^3). The average concentration for Richmond was somewhat lower than the average concentration for Washington, DC (5.44 µg/m^3), the closest other site studied. It is likely that missing sulfate data during the summer of 2003 lowered the 2001-2003 average sulfate concentration and the spring, summer and fall seasonal average concentrations for Richmond from what they would have been if sulfate data had been collected. Because of the missing sulfate data, direct comparisons between average sulfate concentrations and average sulfate concentrations at other sites should be made with caution.

The 30-day rolling average sulfate concentration in Figure 5-119 shows how sulfate varied seasonally over 2001-2003 in Richmond. Sulfate concentrations were the lowest in winter at an average concentration of about 3.50 µg/m^3. As seen elsewhere, the average summer sulfate concentration was much higher. In Richmond, the average summertime sulfate concentration was 7.13 µg/m^3, slightly more than twice the winter concentration. Average spring and fall concentrations were 5.30 and 4.44 µg/m^3 respectively. As the time series shows, sulfate concentration is much more variable in summer than in winter. Over 2001-2003, summer concentrations ranged from a low of 1.5 µg/m^3 to a high of 24.7 µg/m^3. The break in the 30-day rolling average in Figure 5-119, from early May through mid-October 2003, corresponds to a period when only two sulfate measurements were made. The rolling average was not calculated during this period.

Average organic carbon mass concentration over 2001-2003 was 6.81 µg/m^3. This average concentration was much higher than the average concentration of 5.41 µg/m^3 calculated for the

MARAMA Region. The average concentration for Richmond was similar to the average concentration measured in Elizabeth, NJ, another site that is believed to be strongly influenced by mobile source emissions. The average concentration of organic carbon mass in Richmond was higher than average concentrations measured in Washington, DC (5.70 µg/m^3) and Charlotte, NC (5.86 µg/m^3) and much higher than the average concentrations measured at rural sites such as Arendtsville, PA (3.90 µg/m^3) and Kinston, NC (4.47 µg/m^3).

The average organic carbon mass concentration in summer was about 8.40 µg/m^3 and the average concentration in winter was 7.21 µg/m^3. Average spring and fall concentrations were lower at 5.19 µg/m^3 and 6.68 µg/m^3 respectively. As Figure 5-120 shows, organic carbon mass concentration was quite variable any time of year. Concentrations ranged between a low near zero and high near 29.1 µg/m^3. The 30-day rolling average line in Figure 5-120 reveals peaks in summer and late fall/winter and troughs in the spring. Additional data would help confirm what appears to be seasonal behavior. The data for July 7, 2002, the day smoke from Canadian forest fires swept into the Mid-Atlantic Region, was removed from the data for Richmond. The organic carbon mass value on July 7, 2002 was high (20.1 µg/m^3), but less than other organic carbon mass concentrations measured over 2001-2003.

Over 2001-2003, the average ammonium concentration was 1.89 µg/m^3. This concentration was close to the average concentration of 2.01 µg/m^3 calculated for the MARAMA Region. Summer had the highest average concentration at 2.68 µg/m^3. Winter and spring had similar average concentrations at 1.73 and 1.78 µg/m^3 respectively. Average ammonium concentration was lowest in the fall at 1.37 µg/m^3. Figure 5-121 shows how ammonium concentrations varied over time. Ammonium concentration was most variable in summer when fairly high concentrations can occur. In the summer of 2003, several peak ammonium concentrations were measured at about 8 µg/m^3.

Ammonium and sulfate concentrations were well correlated ($R^2 = 0.80$); when sulfate concentrations were high, ammonium concentrations were usually high. Table 5-41 lists ammonium and sulfate concentrations on days when sulfate concentration exceeded 15 µg/m^3.

Table 5-41 High Ammonium and Sulfate Days for the Richmond, VA Monitor

Date	Ammonium Concentration (µg/m^3)	Sulfate Concentration (µg/m^3)
8/8/01	5.4	24.7
7/19/02	4.2	16.4
4/30/03	5.2	15.1
6/26/03	5.8	17.5
7/20/03	8.0	ND[1]
8/22/03	8.1	ND[1]

[1] No data

The average nitrate concentration over 2001-2003 was 1.20 µg/m^3 somewhat less than the average concentration of 1.76 µg/m^3 calculated for the MARAMA Region. The average concentration for Richmond was higher than the average concentration measured in Charlotte, NC (0.94 µg/m^3), and similar to the average concentration measured in Kinston, NC (1.10 µg/m^3). As noted in the regional analysis section, the formation of solid phase (particle) nitrate appears to be a function of temperature, relative humidity, and UV radiation (Wittig, 2004). Low temperatures and winter condition favor the formation of solid phase nitrate. Given this behavior, it is not surprising that average nitrate concentrations observed in Richmond and other

southern sites were lower than concentrations observed at more northern, colder monitoring locations.

As Figure 5-122 shows, nitrate measurements at Richmond exhibited the seasonal variation seen at other sites. Nitrate concentrations were low in the summer and noticeably higher in winter. Over 2001-2003, the average summer concentration was 0.62 µg/m^3 whereas the average winter concentration was 2.43 µg/m^3. In spring and fall, average nitrate concentrations were 1.10 µg/m^3 and 0.98 µg/m^3 respectively. As Figure 5-122 shows, nitrate values were much more variable in winter than in summer when they were consistently low.

The average elemental carbon concentration over 2001-2003 was 0.56 µg/m^3 somewhat less than the regional average concentration of 0.75 µg/m^3 calculated for the MARAMA Region. The average concentration for Richmond was lower, but similar to, the average concentration measured in Charlotte, NC (0.62 µg/m^3).

Figure 5-123 displays the time series for elemental carbon. Over 2001-2003, elemental carbon concentration varied in a fairly narrow band centered on 0.4 to 0.5 µg/m^3. As the 30-day rolling average shows, however, higher concentrations occurred in the late fall and winter. The late fall/winter peak was reflected in the season average concentrations. The highest seasonal average concentration was winter at 0.75 µg/m^3 followed by fall at 0.59 µg/m^3. Spring and summer had the lowest average concentrations at 0.54 and 0.41 µg/m^3 respectively.

Table 5-42 shows the seasonal averages for the major constituents of $PM_{2.5}$ mass at the Richmond, VA monitoring site.

Table 5-42 Seasonal Averages for the Major Constituents of $PM_{2.5}$ Mass (µg/m^3) for Richmond, VA

	Organic Carbon Mass	Sulfate	Ammonium	Nitrate	Elemental Carbon
Winter	7.21	3.50	1.73	2.43	0.75
Spring	5.19	5.30	1.78	1.10	0.54
Summer	8.40	7.13	2.68	0.62	0.41
Fall	6.68	4.44	1.37	0.98	0.59

5.10.4 Trajectory Analysis

Figure 5-124 shows CATT back trajectories for the cleanest days in the speciation record over the period studied from March 2001 through December 2003. While even lower concentration days can be found in the data record for Federal Reference Method monitors at the site, the trajectories plotted in Figure 5-124 are the lowest concentration days in the speciation record over the period studied. These “clean” days represent the five percent days with the lowest total $PM_{2.5}$ mass.

Many “clean day” trajectories move quickly over great distances from Canada’s western provinces, take a circular path from Canada’s eastern provinces out over the Atlantic Ocean, or loop in off the Atlantic. In contrast to trajectories associated with high $PM_{2.5}$ days, these trajectories do not remain for long periods over source regions or re-circulate through high source regions. Table 5-43 lists the five percent cleanest days at Richmond and the total mass concentration measured by the speciation monitor on that day.

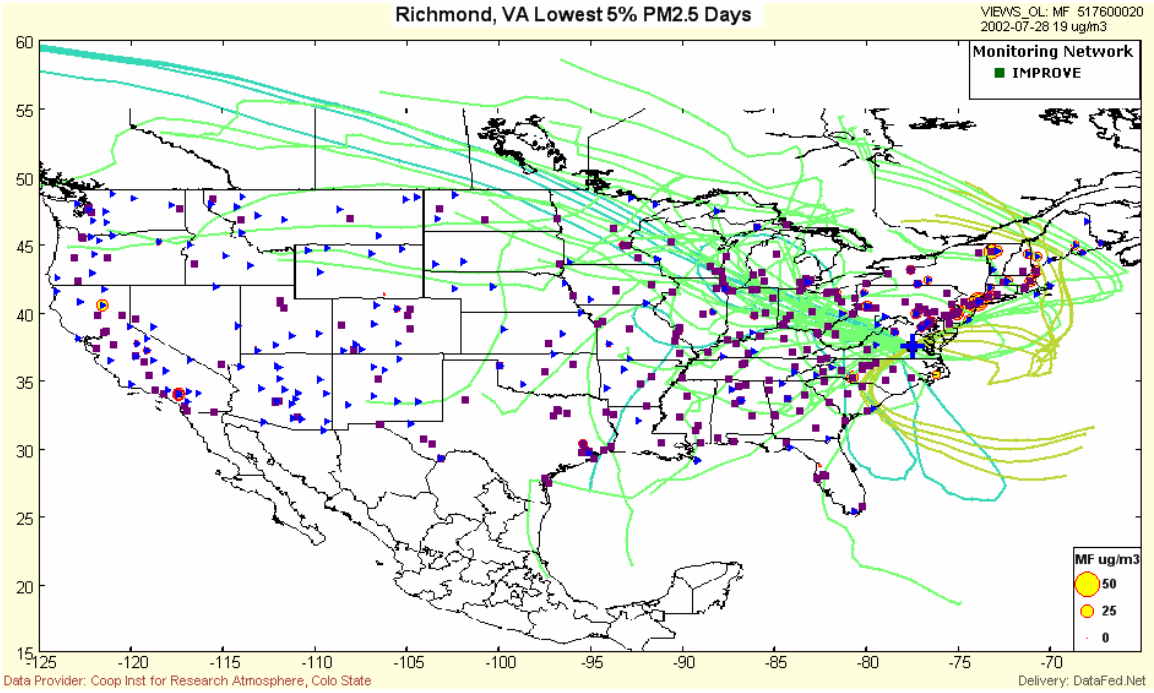

Figure 5-124 Richmond, VA Back Trajectories for the Five Percent Cleanest Days

Table 5-43 Richmond, VA Five Percent Lowest Days

Date	$PM_{2.5}$ Mass (µg/m^3)
7/30/2001	5.8
9/25/2001	4.3
12/18/2001	5.6
4/14/2002	5.9
5/14/2002	5.6
10/26/2002	5.2
2/23/2003	5.6
4/9/2003	5.7
10/15/2003	4.6
11/14/2003	4.1
11/29/2003	5.4
12/11/2003	3.2
Average	5.1

Figure 5-125 shows back trajectories for the dirtiest days, the five percent days with the highest total $PM_{2.5}$ mass. Most "dirty day" trajectories are tracks of air masses that have spent the past five days over the continental U.S. In many cases, the air circulates or re-circulates through air pollution source regions in the South, Midwest, and Mid-Atlantic states.

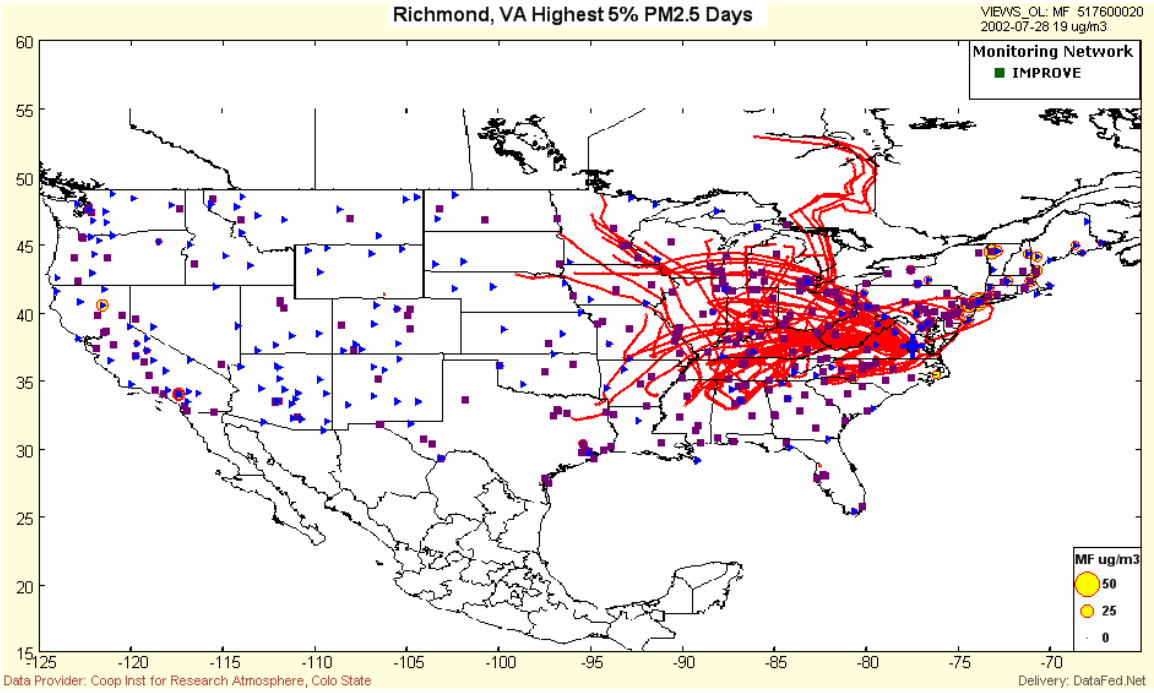

Figure 5-125 Richmond, VA, Back Trajectories for the Five Percent Dirtiest Days

Table 5-44 lists the five percent dirtiest days and the total mass concentration measured by the speciation monitor on that day.

Table 5-44 Richmond, VA, Five Percent Highest Days

Date	$PM_{2.5}$ Mass ($\mu g/m^3$)
6/12/2001	36.1
6/21/2001	35.4
7/18/2001	43.5
8/5/2001	42.3
8/8/2001	50.9
7/19/2002	31.6
8/12/2002	44.6
1/30/2003	30.4
6/26/2003	44.6
7/20/2003	41.2
8/22/2003	38.8
12/8/2003	31.9
Average	39.3

5.11 Washington, DC

Site Name: McMillan Reservoir
AIRS Number: 11-001-0043
Latitude: 38.9189 North
Longitude: -77.0125 West
Elevation: 51 meters (167 feet)
Agency Operating the Monitor: District of Columbia Department of Health
Speciation Sampling Frequency: 1-in-3 days

5.11.1 Site Description

The McMillan monitoring site is located near the southeast corner of the McMillan Reservoir in Washington, DC. The site is within the Washington Beltway about 3.2 km (2.0 miles) northeast of the central business district in Washington. Figure 5-126 shows the monitoring site's location relative to the interstate highway system and large population centers. The closest cities to Washington are Baltimore, MD about 53 km (33 miles) to the northeast and Richmond, VA about 158 km (98 miles) to the south.

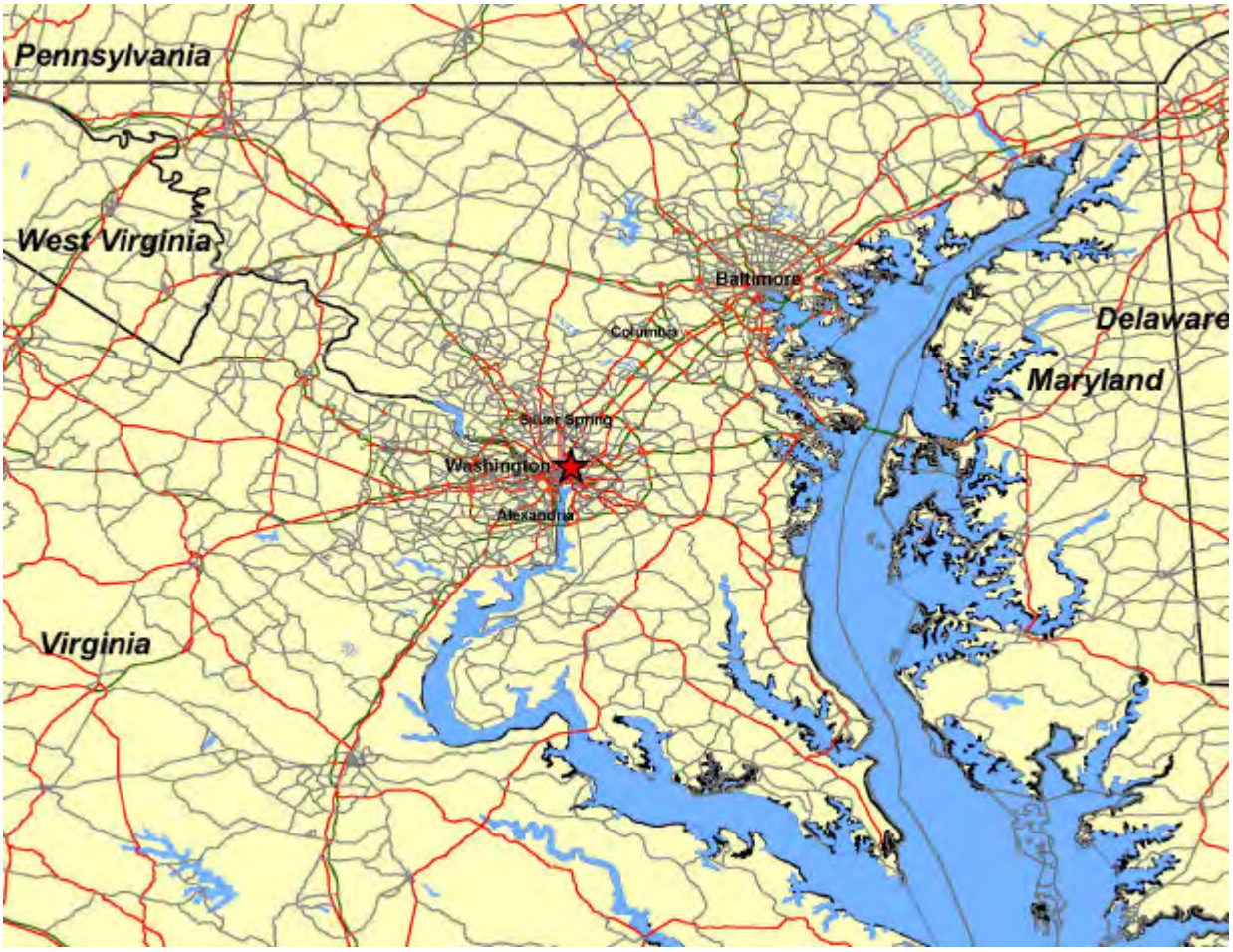

Figure 5-126 Location of the Washington, DC Monitoring Site

A residential neighborhood of row houses lies immediately south of the McMillan monitor. The compact campus of Howard University is 0.5 km (0.3 mile) to the west. A large complex made

up of the Washington Hospital Center and the Children's National Medical Center is about 0.8 km (0.5 miles) north of the monitor. The Glenwood and Prospect Hill cemeteries are about two city blocks east of the monitor.

In its urban environment, the Washington monitoring site is close to many streets that produce mobile source emissions. Bryant Street and First Street, NW, both two-lane streets, is about 80 meters (265 feet) south and east of the monitoring trailer. The monitor is about 0.3 km (0.2 mile) west of North Capital Street, a busy four-lane, north-south artery in the city. Rhode Island Avenue, U.S. Routes 1 and 29 in Washington, is about 0.6 km (0.4 miles) south and east of the monitoring site. The heavily traveled New York Avenue corridor and the rail yards associated with Union Station are south and east of the monitoring site. Figure 5-127 is a detailed map showing the urban features around the monitoring site.

Source: TopoZone

Figure 5-127 Topographic Map of the Washington, DC Monitoring Site

5.11.2 Major Constituents of $PM_{2.5}$ Mass

The major constituents of $PM_{2.5}$ mass at Washington were organic carbon and sulfate species followed by ammonium and nitrate species. Using an OM/OC ratio of 1.6, the average organic carbon mass concentration over 2001-2003 was 5.70 $\mu g/m^3$. Average sulfate concentration was slightly less at about 5.44 $\mu g/m^3$. While important constituents of $PM_{2.5}$ mass at the site, ammonium and nitrate contributed less to total mass measured than organic carbon and sulfate species. Average ammonium and nitrate concentrations were 2.02 $\mu g/m^3$ and 1.68 $\mu g/m^3$ respectively. Elemental carbon, geological components, and trace elements contributed about 1.6 $\mu g/m^3$ to the average concentration observed at the monitoring site. Figure 5-128 shows the contribution each specie made to the average concentration measured at McMillan Reservoir over the study period.

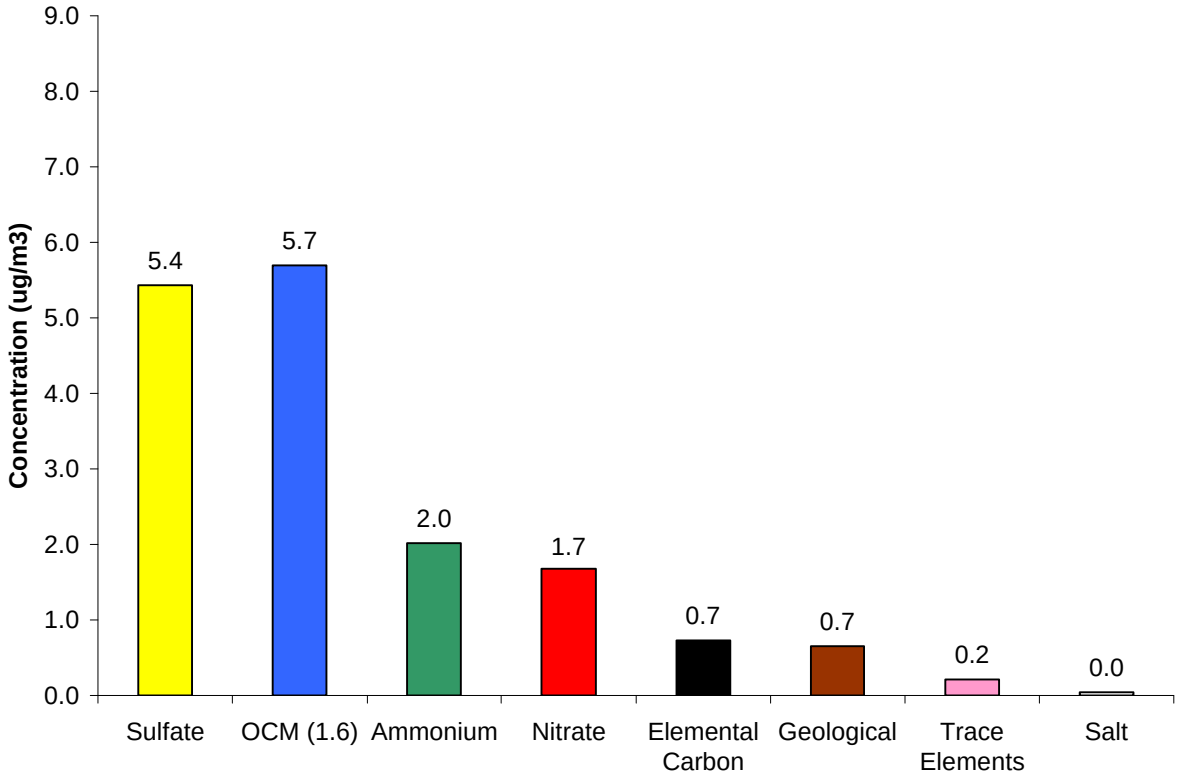

Figure 5-128 Major Constituents of $PM_{2.5}$ Mass, Washington, DC

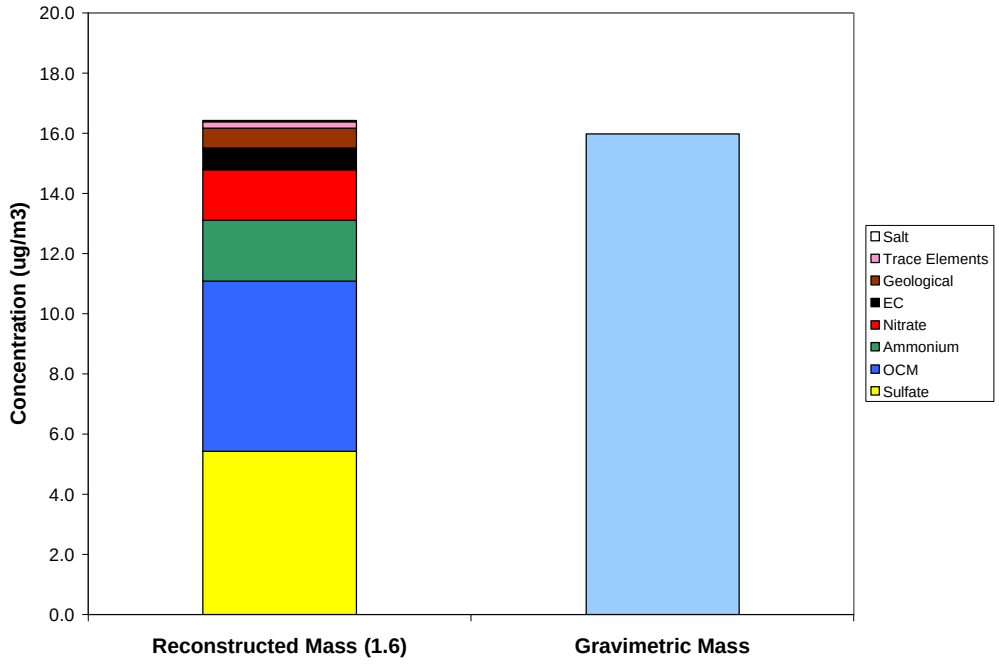

Figure 5-129 Comparison of Average Reconstructed Mass and Average Gravimetric Mass, Washington, DC

The average reconstructed mass calculated for this site was about 2.8 percent higher than the average gravimetric mass measured by the speciation sampler. Average reconstructed mass was

16.4 µg/m^3 whereas the average gravimetric mass was 16.0 µg/m^3. Figure 5-129 visually compares the average reconstructed mass with the average gravimetric mass.

5.11.3 Time Series Analysis of $PM_{2.5}$ Species

An Anderson RAAS-401 speciation sampler was installed at the Washington monitoring site on March 26, 2001. It has operated on a 1-in-3 sampling schedule from its installation to the present time. Figure 5-130 shows a composite time series for the five major species measured at Washington. Figures 5-131 through 5-135 show time series for each of the five major species. The black line in Figures 5-131 through 5-135 is the 30-day rolling average concentration for the specie. The 30-day rolling average is not shown during periods when the monitor was down or did not report data for more than two consecutive sample days.

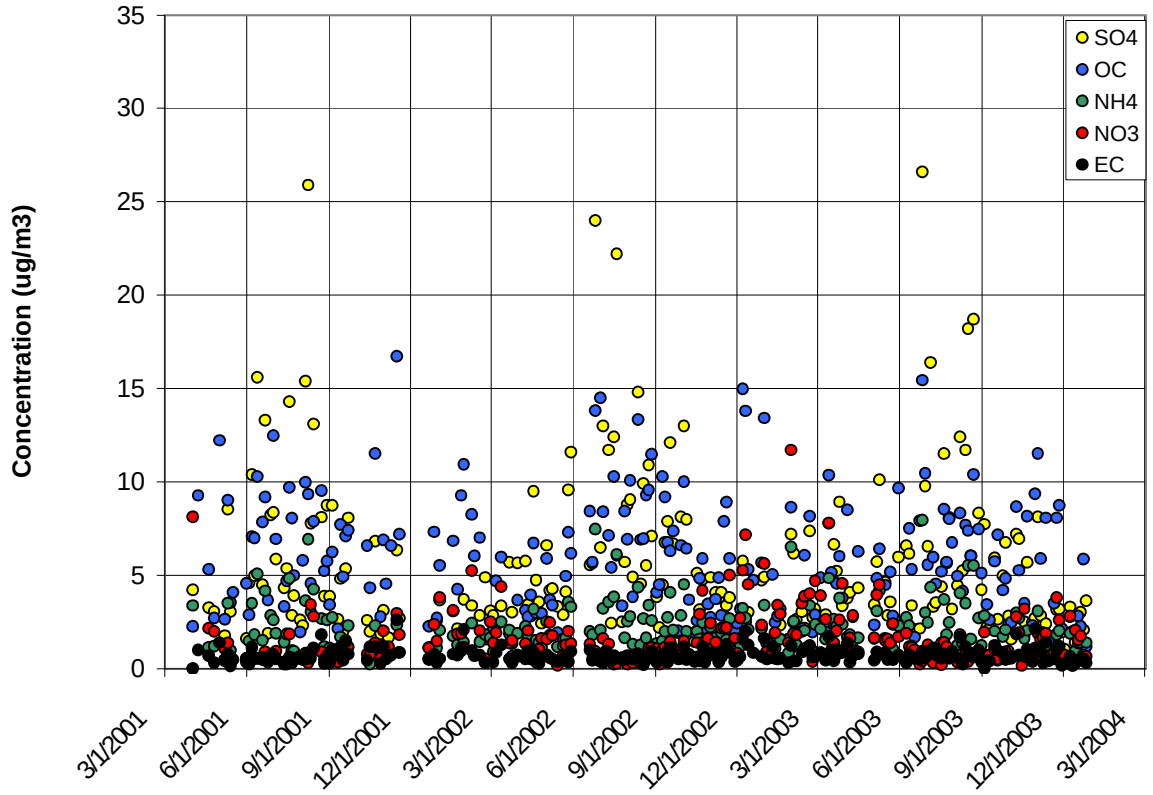

Figure 5-130 Time Series for the Washington, DC Monitor

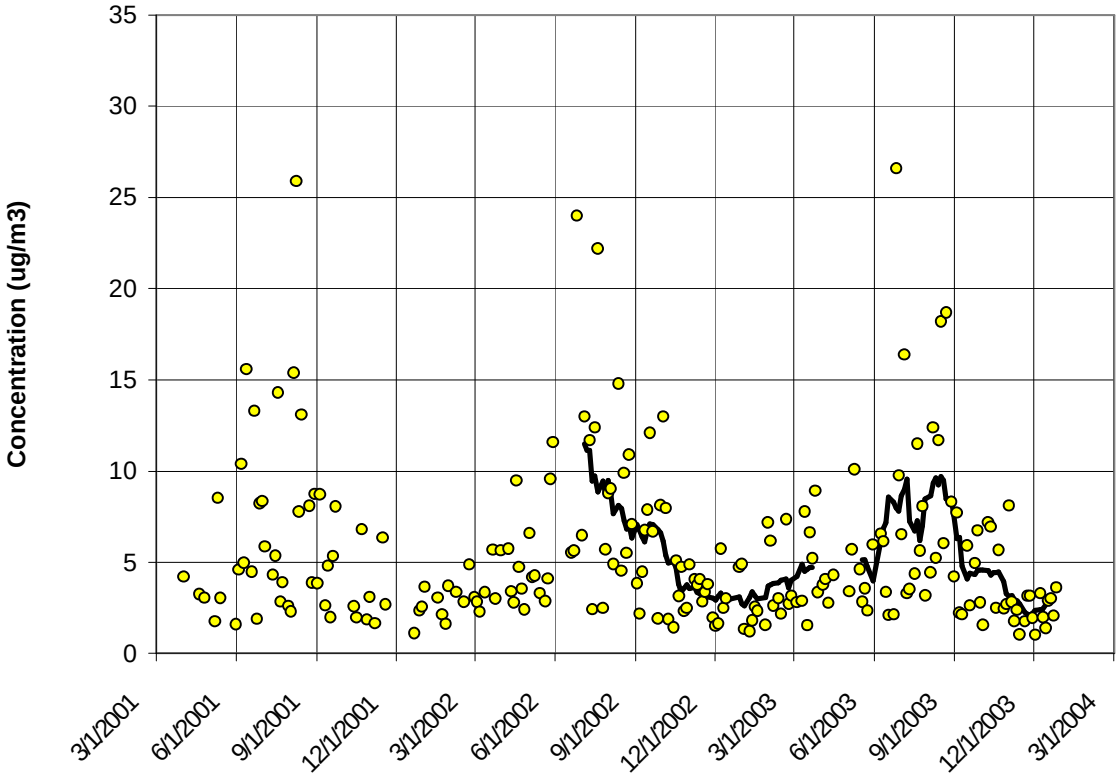

Figure 5-131 Sulfate Time Series for the Washington, DC Monitor

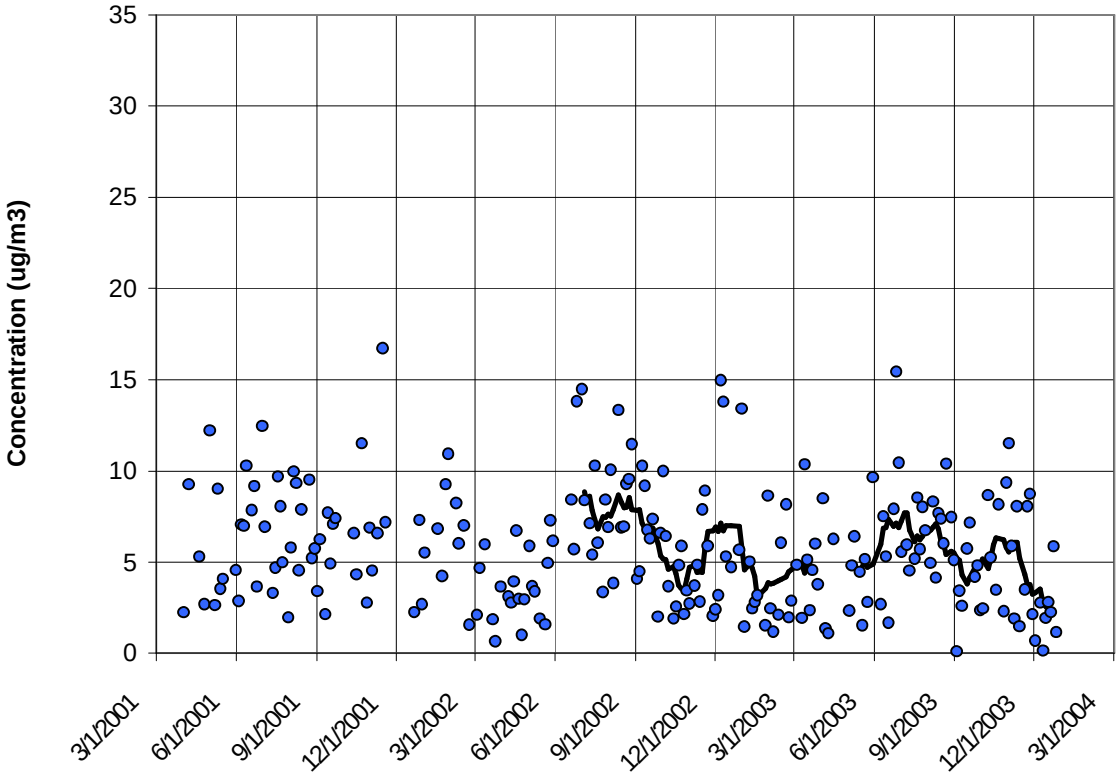

Figure 5-132 Organic Carbon Mass Time Series for the Washington, DC Monitor

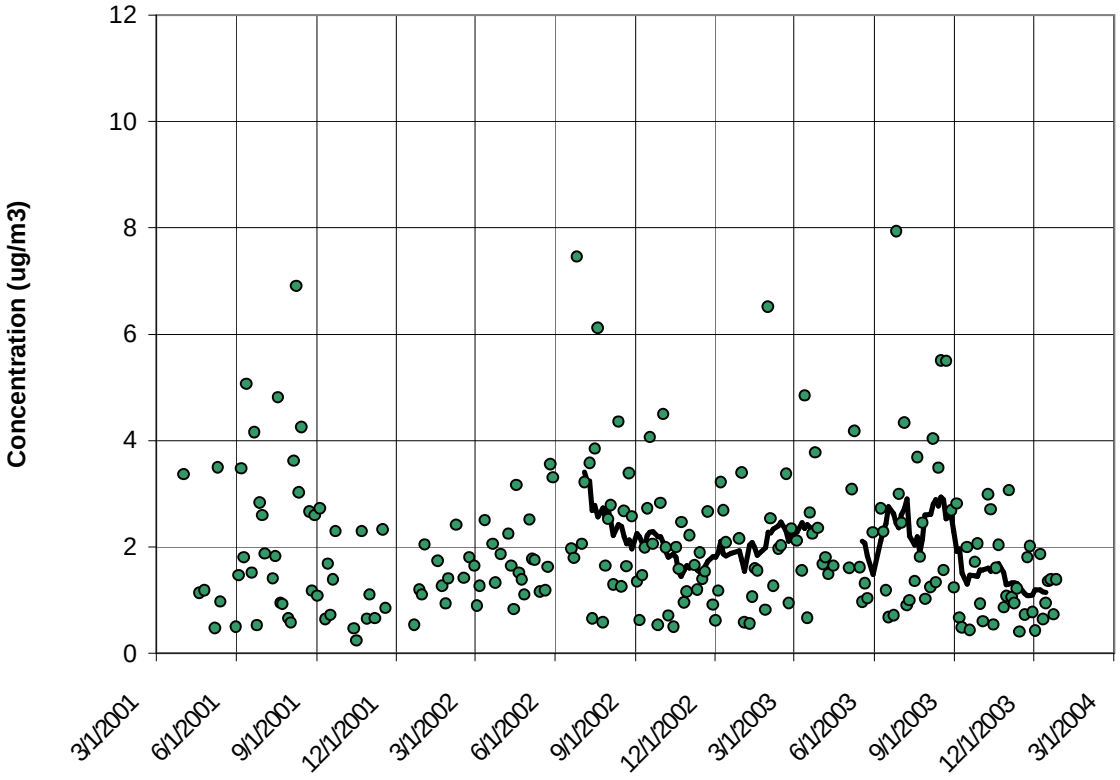

Figure 5-133 Ammonium Time Series for the Washington, DC Monitor

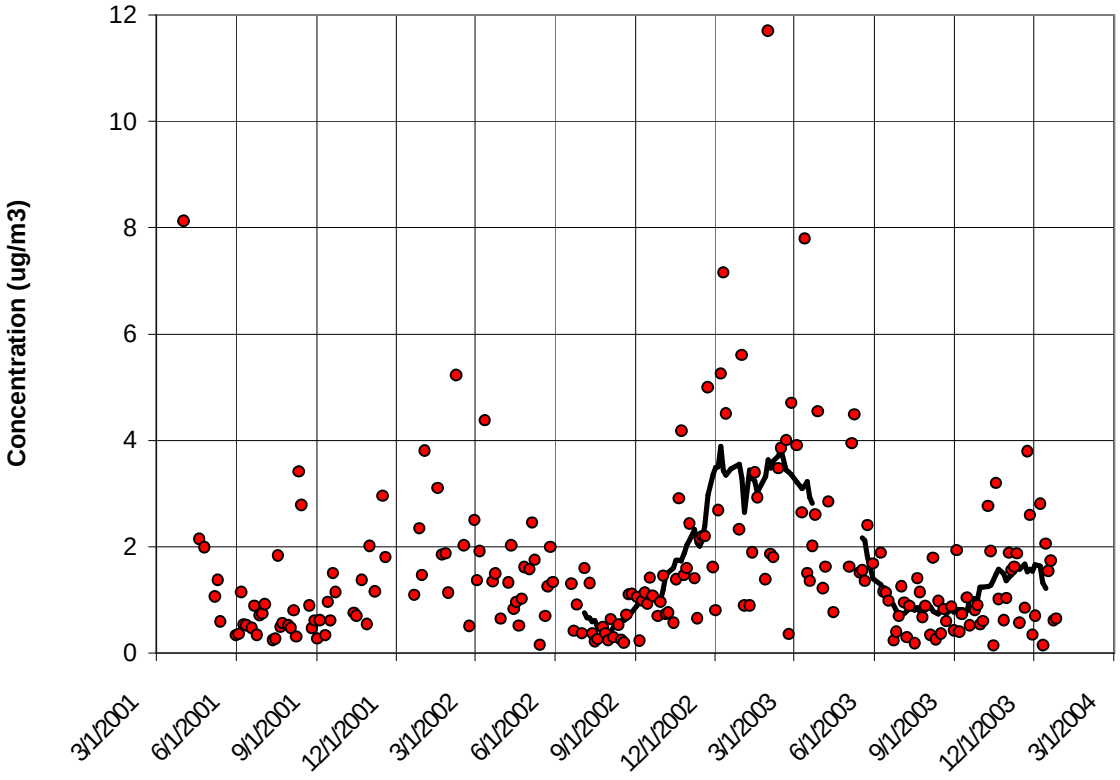

Figure 5-134 Nitrate Time Series for the Washington, DC Monitor

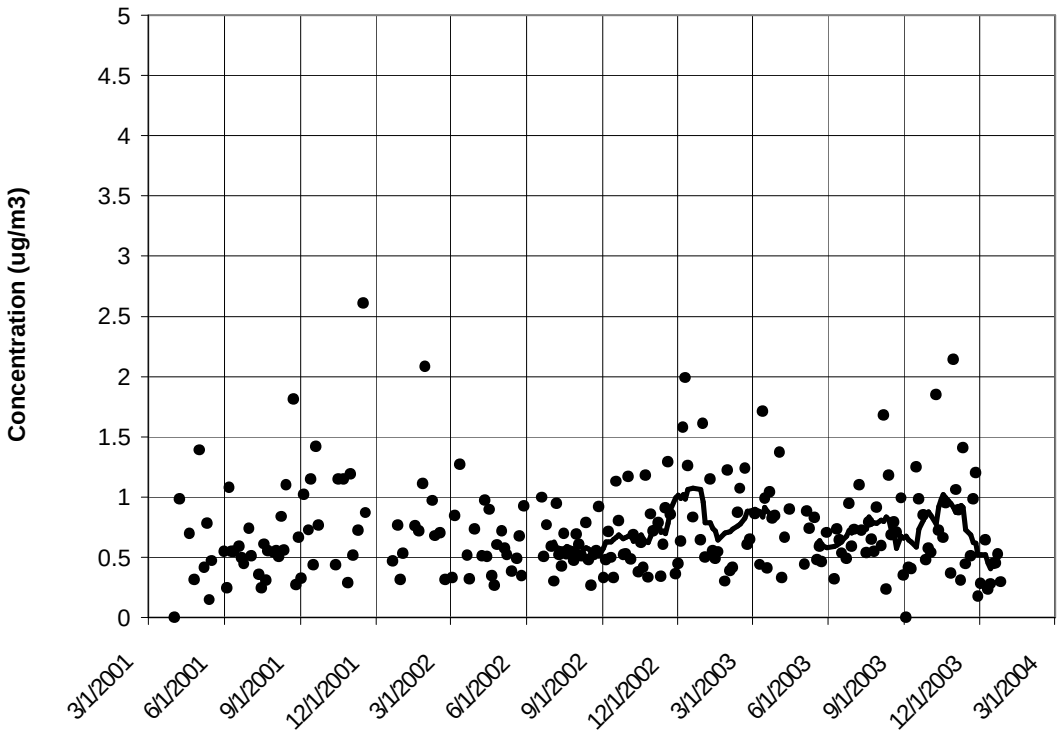

Figure 5-135 Elemental Carbon Time Series for the Washington, DC Monitor

Average sulfate concentration over 2001-2003 was 5.44 µg/m^3 somewhat more than the average concentration of 5.11 µg/m^3 calculated for the MARAMA Region. The average concentration for Washington was slightly higher than the average concentration measured in Richmond, VA (4.97 µg/m^3) and Baltimore (5.13 µg/m^3) the nearest other large cities.

Figure 5-131 shows how sulfate concentration varied seasonally over the 2001-2003. Sulfate concentrations were the lowest in winter at an average concentration of about 3.14 µg/m^3. As seen elsewhere, the average summer sulfate concentration was much higher. In Washington, the average summer sulfate concentration was 8.79 µg/m^3, almost three times the winter concentration. Average spring and fall concentrations were 4.74 and 4.51 µg/m^3 respectively. As the time series shows, sulfate concentration was much more variable in summer than in winter. Over 2001-2003, summer concentrations ranged from a low of 1.9 µg/m^3 to a high of 26.6 µg/m^3.

Over 2001-2003, average organic carbon mass concentration was 5.70 µg/m^3. This concentration was slightly higher than the average concentration of 5.41 µg/m^3 calculated for the MARAMA Region. Average organic carbon mass concentration was much less than the average concentrations measured at Elizabeth, NJ (6.93 µg/m^3) and Richmond, VA (6.81 µg/m^3), two sites believed to be strongly influenced by mobile source emissions. Washington's average concentration of organic carbon mass was much higher than the average concentrations measured at rural sites such as Arendtsville, PA (3.90 µg/m^3), Dover, DE (3.62 µg/m^3), and Kinston, NC (4.47 µg/m^3).

Average organic carbon mass concentration was highest in summer at about 7.56 µg/m^3. Lowest average concentration was observed in the spring at about 4.17 µg/m^3. Average fall and winter concentrations were lower at 5.49 and 5.45 µg/m^3 respectively. As Figure 5-132 shows, organic

carbon mass concentration was quite variable almost any time of year. Concentrations ranged between a low of 0.10 µg/m^3 and high near 16.7 µg/m^3. A 30-day rolling average line was not calculated and plotted for the first part of the 2001-2003 period because of the large amount of missing data during this period. Additional data for future years would allow the investigation of seasonal behavior at this site. The data for July 7, 2002, the day smoke from Canadian forest fires was present in the Mid-Atlantic Region, was removed from the dataset for Washington. The organic carbon mass value on this day was 29.7 µg/m^3.

The average ammonium concentration was 2.02 µg/m^3 over 2001-2003. This concentration was very close to the average concentration calculated for the entire MARAMA Region. Summer had the highest average concentration at 2.66 µg/m^3 followed by spring (1.99 µg/m^3) winter (1.82 µg/m^3), and fall (1.60 µg/m^3). Figure 5-133 shows how ammonium concentrations varied over time. Ammonium concentration was most variable in summer when fairly high concentrations occurred.

Ammonium and sulfate concentrations were well correlated (R^2 = 0.83); when sulfate concentrations were high, ammonium concentrations were usually high. Table 5-45 lists ammonium and sulfate concentrations on days when sulfate concentration exceeded 15 µg/m^3.

Table 5-45 High Ammonium and Sulfate Days for the Washington, DC Monitor

Date	Ammonium Concentration (µg/m^3)	Sulfate Concentration (µg/m^3)
6/12/01	5.1	15.6
8/5/01	3.6	15.4
8/8/01	6.9	25.9
6/25/02	7.5	24.0
7/19/02	6.1	22.2
6/26/03	7.9	26.6
7/5/03	4.3	16.4
8/16/03	5.5	18.2
8/22/03	5.5	18.7

The average nitrate concentration over 2001-2003 was 1.68 µg/m^3 slightly less than the average concentration of 1.76 µg/m^3 calculated for the MARAMA Region. The average concentration for Washington was higher than the average concentration measured in Richmond, VA (1.20 µg/m^3) and Charlotte, NC (0.94 µg/m^3) and higher average concentrations measured in Philadelphia, PA (2.25 µg/m^3), Elizabeth, NJ (2.27 µg/m^3), and Wilmington, DE (2.48 µg/m^3). As noted in the regional analysis section, nitrate concentration appears to be a function of cold temperature/wintertime conditions so it is not surprising that lower average concentrations were observed at sites south of Washington and higher average concentrations were observed at sites north of Washington.

As Figure 5-134 shows, nitrate measurements at Washington exhibited the strong seasonal variation seen at other sites. Nitrate concentrations were low and not very variable during the summer and noticeably higher and more variable in winter. Over the 2001-2003 period, the average summer concentration was 0.75 µg/m^3 whereas the average winter concentration was 2.99 µg/m^3. In spring and fall, average nitrate concentrations were 2.01 µg/m^3 and 1.39 µg/m^3 respectively.

The average elemental carbon concentration over 2001-2003 was 0.73 µg/m^3, very close to the average concentration calculated for the entire MARAMA Region. The average concentration for Washington was higher than the average concentration measured in Richmond, VA (0.56 µg/m^3) and slightly below the average concentration measured in Baltimore, MD (0.77 µg/m^3).

Figure 5-135 displays the time series for elemental carbon. The highest seasonal average concentration was winter and fall at 0.84 µg/m^3. Spring and summer each had the lowest average concentrations at 0.69 and 0.66 µg/m^3.

Table 5-46 shows the seasonal averages for the major constituents of $PM_{2.5}$ mass for the Washington D.C. monitoring site.

Table 5-46 Seasonal Averages for the Major Constituents of $PM_{2.5}$ Mass (µg/m^3) for Washington, D.C.

	Organic Carbon Mass	Sulfate	Ammonium	Nitrate	Elemental Carbon
Winter	5.45	3.14	1.82	2.99	0.84
Spring	4.17	4.74	1.99	2.01	0.69
Summer	7.56	8.79	2.66	0.75	0.66
Fall	5.49	4.51	1.60	1.39	0.76

5.11.4 Trajectory Analysis

Figure 5-136 shows CATT back trajectories for the cleanest days in the speciation record over the period studied from April 2001 through December 2003. While even lower concentration days can be found in the data record for Federal Reference Method monitor at the site, the trajectories plotted in Figure 5-136 were the lowest concentration days in the speciation record over the period studied. These "clean" days represent the five percent days with the lowest total $PM_{2.5}$ mass.

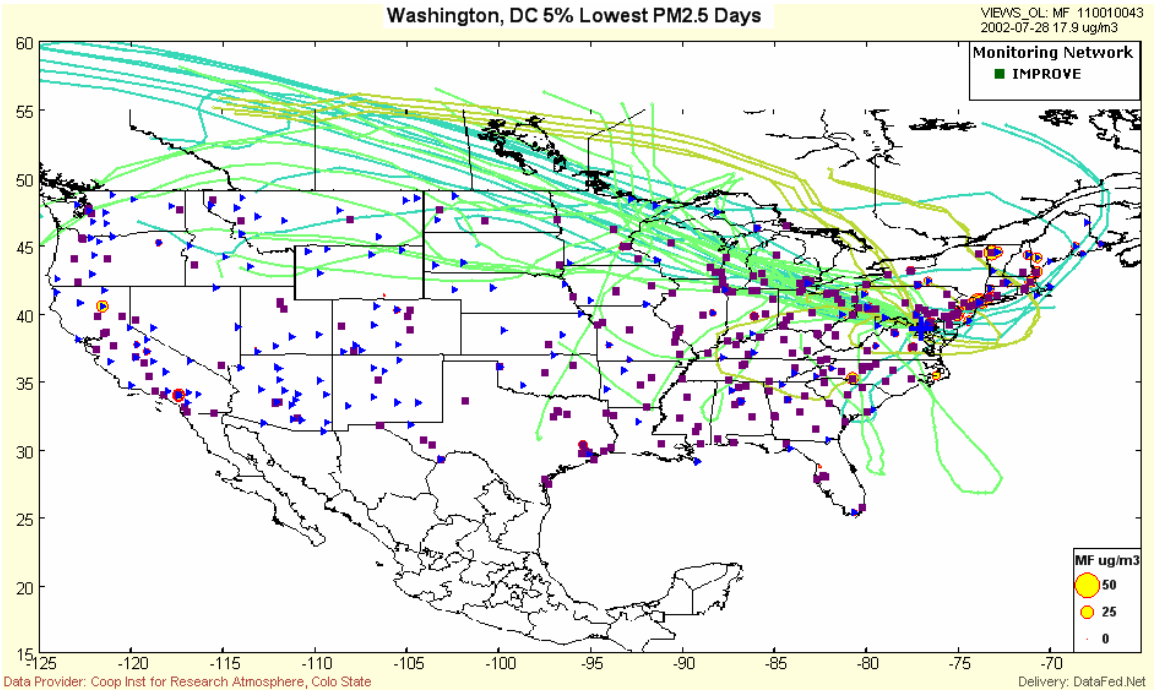

Figure 5-136 Washington, DC, Back Trajectories for the Five Percent Cleanest Days

Most “clean day” trajectories take paths from distant points in western Canada or northwestern states to Washington. One set of clean day trajectories originates in the eastern provinces of Canada and loops clockwise into Washington from the Atlantic Ocean. Most clean day trajectories originate over relatively clean areas and spend only minimal time over emission rich areas.

Table 5-47 lists the five percent cleanest days in Washington, DC and the total mass concentration measured by the speciation monitor on that day.

Table 5-47 Washington, DC Five Percent Lowest Days

Date	$PM_{2.5}$ Mass (µg/m^3)
11/6/2001	5.8
12/21/2001	4.7
10/14/2002	5.2
10/26/2002	5.8
12/1/2002	5.2
1/3/2003	4.1
10/15/2003	4.2
11/14/2003	4.0
11/29/2003	5.2
12/2/2003	3.3
12/11/2003	4.5
Average	4.7

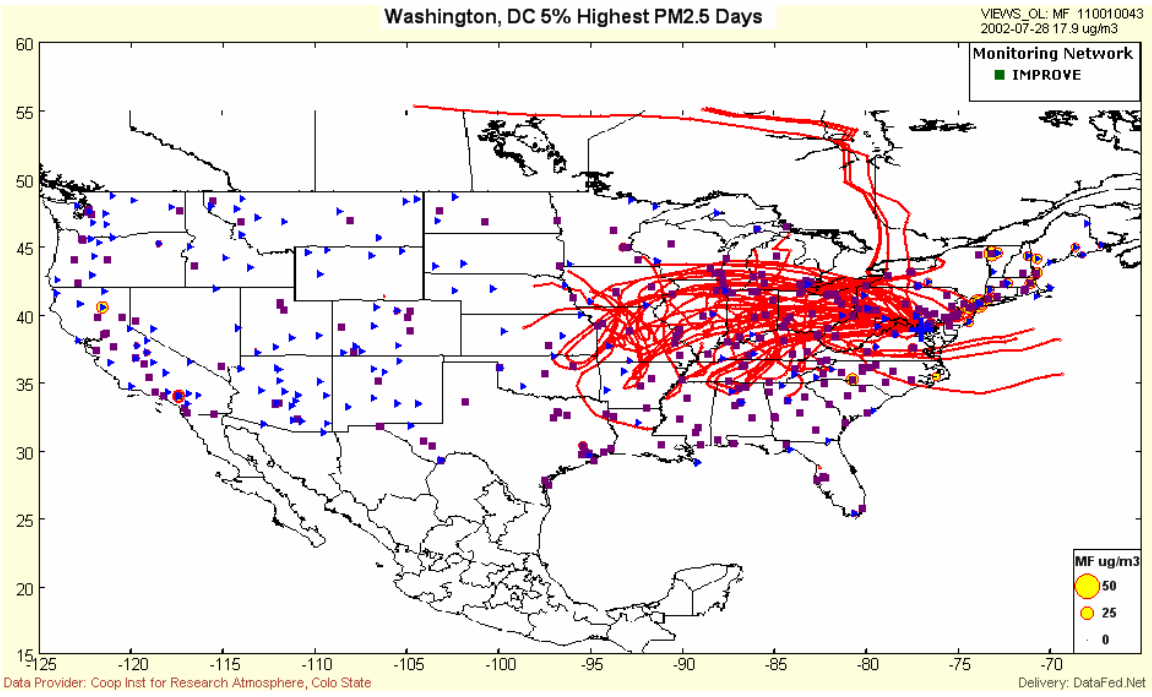

Figure 5-137 Washington, DC, Back Trajectories for the Five Percent Dirtiest Days

Figure 5-137 shows back trajectories for the dirtiest days, the five percent days with the highest total $PM_{2.5}$ mass. With the exception of a few trajectories that originate in the Atlantic Ocean and Canada, most "dirty day" trajectories are tracks that have spent the last five days over the continental U.S. In most cases, the trajectories circulate or re-circulate through air pollution source regions in the Midwest and Ohio River Valley. The four trajectories that originate in the Ontario and Quebec provinces of Canada are the trajectories for July 7, 2002. These trajectories capture the movement of smoke from Canadian forest fires into Washington, DC.

Table 5-48 lists the five percent dirtiest days and the total mass concentration measured by the speciation monitor on that day.

Table 5-48 Washington, DC, Five Percent Highest Days

Date	$PM_{2.5}$ Mass ($\mu g/m^3$)
6/12/2001	38.8
7/18/2001	35.7
8/8/2001	48.8
6/25/2002	53.3
7/4/2002	37.4
7/7/2002	40.3
7/19/2002	39.4
1/30/2003	37.2
6/26/2003	60.0
8/16/2003	35.8
8/22/2003	41.3
Average	42.5

5.12 Wilmington, DE

Site Name: Martin Luther King Jr. Avenue (MLK)
AIRS Number: 10-003-2004
Latitude: 39.7394 North
Longitude: -75.5581 West
Elevation: 30.5 meters (100 feet)
Agency Operating the Monitor: Delaware Department of Natural Resources and Environmental Control (DNREC), Division of Air and Waste Management (DAWM), Air Quality Management Section (AQM), Air Surveillance
Speciation Sampling Frequency: 1-in-6 days

5.12.1 Site Description

The MLK monitoring site is located in the urban core of Wilmington, DE. It is one of many monitoring sites located along I-95 corridor on the east coast. Figure 5-138 shows the monitoring site's location relative to the interstate highway system and large population centers. Philadelphia, PA is about 47 km (29 miles) to the northeast, Baltimore, MD is about 119 km (74 miles) to the southwest, and Harrisburg, PA is about 159 km (99 miles) to the west-northwest.

Figure 5-138 Location of the Wilmington, DE Monitoring Site

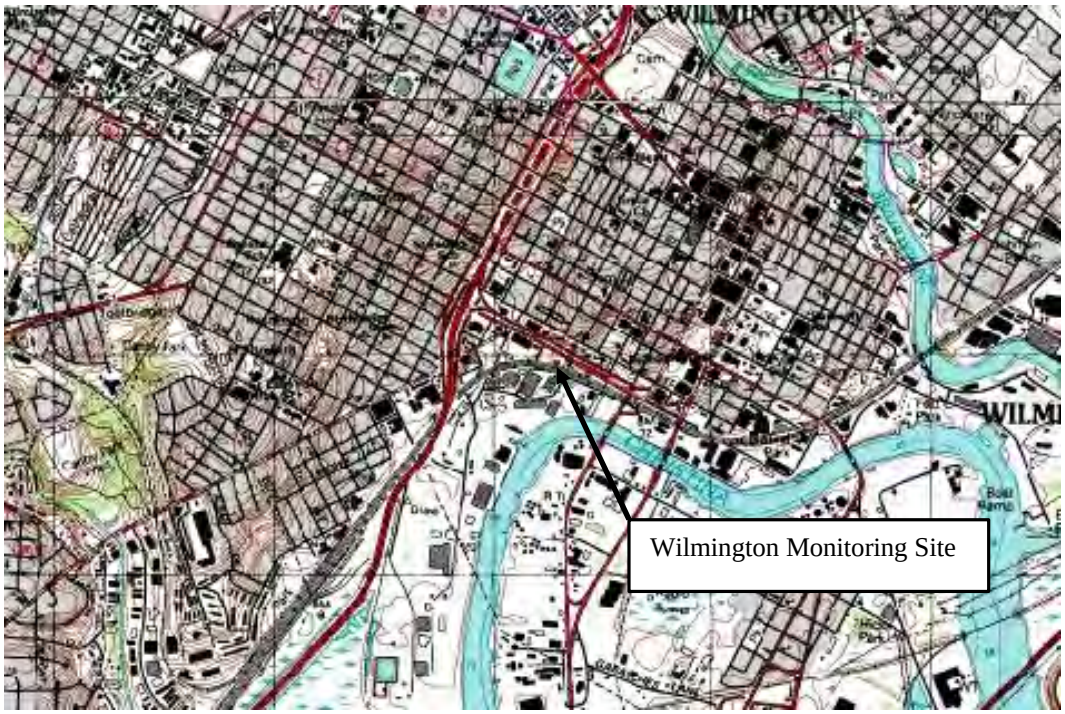

Source: TopoZone

Figure 5-139 Topographic Map of the Wilmington, DE Monitoring Site

Figure 5-140 Photograph of the Wilmington, DE Monitoring Site

The monitoring site is located 350 meters (1,148 feet) north of the Christiana River and 5.6 km (3.5 miles) west of the Delaware River. Figure 5-139 is a detailed map showing the topographic features and urban character of the monitoring site. Figure 5-140 is a photograph of the site.

The Wilmington monitor is an urban monitor and many emission sources are nearby. The major rail line carrying AMTRAK trains along the east coast is 35 meters (115 feet) south of the monitoring site. I-95, the major north-south interstate highway in the region, is about 410 meters (1,345 feet) west of the monitoring site. Route 13, a north-south urban arterial highway is about 410 meters (1,345 feet) east. There are many urban streets nearby including heavily traveled Martin Luther King Jr. Avenue 38 meters (125 feet) north of the monitoring station. A bus depot is about 285 meters west-northwest of the monitoring site.

The Delaware Department of Natural Resources and Environmental Control reports there are a variety of point sources in the vicinity of the monitoring site. Table 5-49 lists the emission sources located within 4.8 km (3 miles) of the site. The largest source of primary (directly emitted) $PM_{2.5}$ emissions within a 4.8 km radius of the monitor is Connectiv/Delmarva Power's fossil fuel fired power plant 4.6 km (2.9 miles) to the west of the monitor. Many of the emission sources listed in Table 5-49 also emit CO, NO_x, PM_{10}, SO_2, and VOCs.

Table 5-49 Emission Sources within 4.8 km of the Wilmington, DE Monitoring Site

Facility/Source	Site Description	Distance (km)	Direction (degrees)	$PM_{2.5}$[1] (tons/yr)
Alfred I. Dupont Hospital for Children	Medical/surgical hospital	4.4	2	2.6
American Minerals Inc.	Mineral processing/sizing	3.7	147	0.7
AMTRAK, Wilmington Maintenance Facility	Locomotive/rail car repairs	3.2	75	0.2
Christiana Materials	Hot mix asphalt plant	1.5	26	1.8
Clean Earth of New Castle	Soil remediation facility	3.2	152	6.3
Connectiv/Delmarva Power, Christiana Station	Electric power generation, peaking station	2.0	120	ND[2]
Connectiv/Delmarva Power, Edge Moor Station	Electric power generation	4.6	91	521.5
Connectiv/Delmarva Power, Hay Road Station	Electric power generation	4.5	83	48.4
Connectiv/Delmarva Power, Madison Street Station	Electric power generation, peaking station	0.8	220	ND[2]
Contractors Materials, LLC	Hot mix asphalt plant	1.8	161	2.3
Delaware Solid Waste Authority, Cherry Island	Municipal solid waste landfill	3.9	111	0.0
Delaware Recyclable Products, Inc.	Dry waste landfill	4.0	199	0.3
Delaware Refrigerated Srvs.	Refrigerated warehouse	3.4	154	ND[2]
Delaware Terminal Co.	Petroleum storage	4.0	144	0.3

Facility/Source	Site Description	Distance (km)	Direction (degrees)	$PM_{2.5}$[1] (tons/yr)
Diamond Materials, LLC	Hot mix asphalt plant	2.1	156	3.4
Dupont, Chestnut Run	R&D lab	4.2	287	8.7
Dupont, Experimental Station	R&D labs/incinerator	3.9	341	36.7
Dupont, Wilmington Office Building	Office building	1.1	48	2.9
Edgemoor Materials, Inc.	Hot mix asphalt plant	3.0	89	1.5
Industraplate Corporation	Electroplating	1.5	173	0.0
International Petroleum Corporation of Delaware	Oil recycling facility	0.9	181	0.4
Lafarge of North America, Inc.	Gypsum wallboard production	3.8	133	11.3
Laidlaw Corporation	Metal hanger coating	3.8	152	
Noramco Inc.	Pharmaceutical manufacturing	1.6	99	0.4
Pepsi Cola	Beverage bottling	3.5	62	ND[2]
Pure Green Industries, Inc.	Hot mix asphalt batch plant	2.6	80	0.8
St. Francis Hospital	Hospital	1.4	327	0.3
Tilcon Delaware, Terminal Avenue Plant	Hot mix asphalt plant	3.0	143	5.2
Veterans Administration Hospital	Medical & surgical hospital	4.0	273	0.3
Wilmington Piece Dye Company	Textile finisher	3.2	352	0.2
Wilmington Wastewater Treatment Plant	Wastewater treatment plant	3.5	100	0.3

[1] Primary (directly emitted) $PM_{2.5}$ emissions
[2] No data

5.12.2 Major Constituents of $PM_{2.5}$ Mass

The major constituents of $PM_{2.5}$ mass at Wilmington were organic carbon mass and sulfate species followed by ammonium and nitrate species. Using an OM/OC ratio of 1.6, organic carbon species contributed about 5.02 $\mu g/m^3$ to the average $PM_{2.5}$ mass concentration measured over 2001-2003. Sulfate species contributed about 5.24 $\mu g/m^3$ to the average concentration measured. Average ammonium concentration was about 2.33 $\mu g/m^3$ and average nitrate concentration was 2.48 $\mu g/m^3$. Elemental carbon, geological components, and trace elements contributed about 1.7 $\mu g/m^3$ to the average concentration observed over 2001-2003. Figure 5-141 compares the average concentrations of the major species measured at the site.

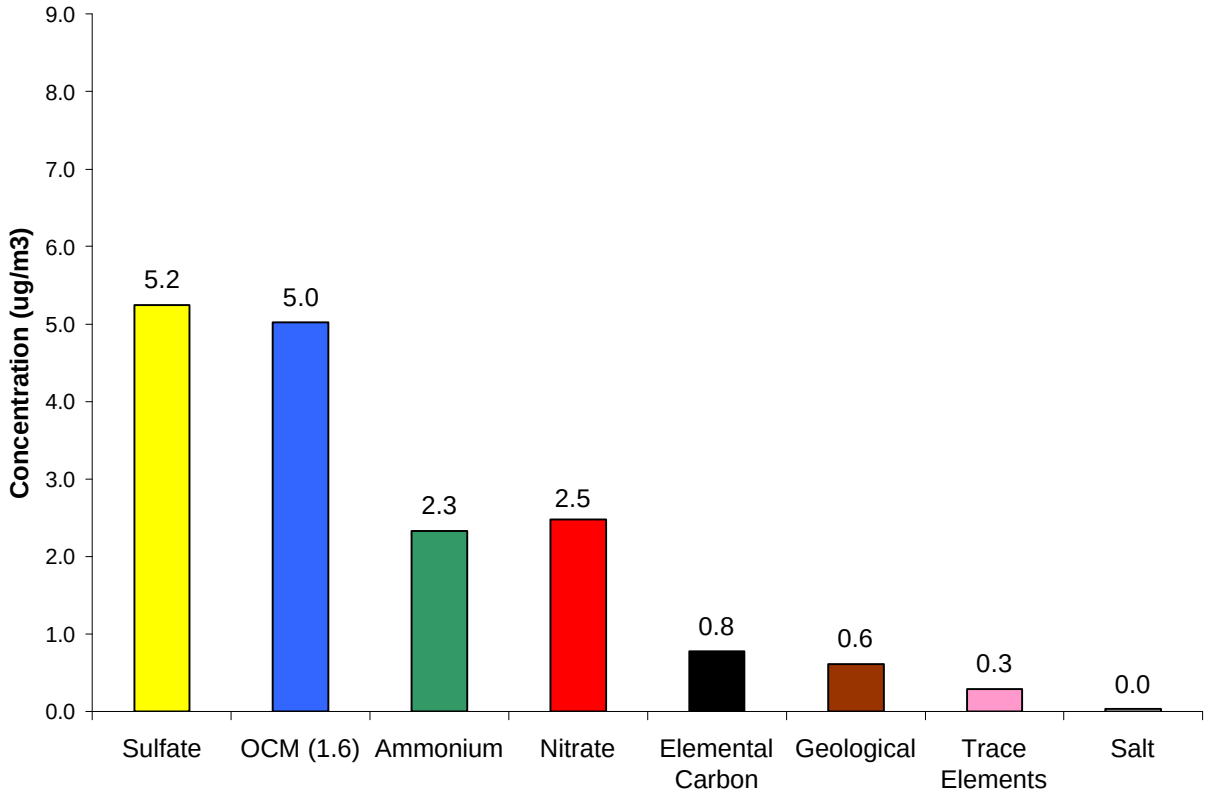

Figure 5-141 Major Constituents of $PM_{2.5}$ Mass, Wilmington, DE

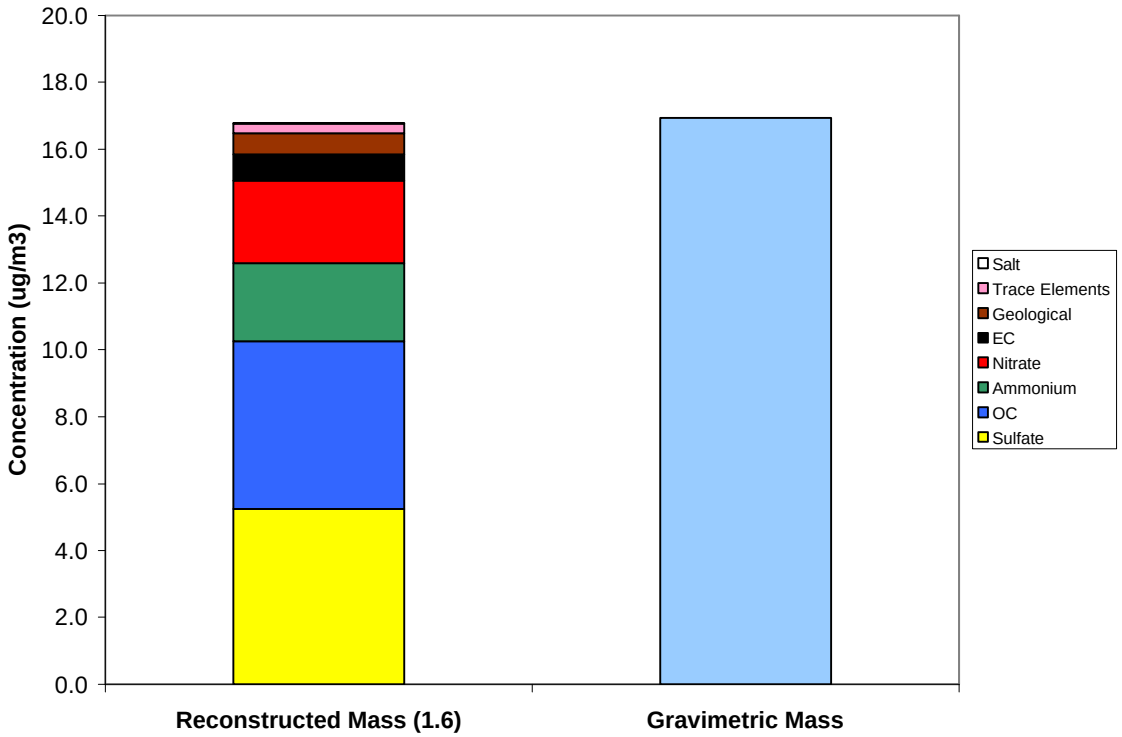

Figure 5-142 Comparison of Average Reconstructed Mass and Average Gravimetric Mass, Wilmington, DE

The average reconstructed mass calculated for this site was 0.6 percent lower than the average gravimetric mass measured by the speciation sampler. Average reconstructed mass was 16.8 $\mu g/m^3$ whereas the average gravimetric mass was 16.9 $\mu g/m^3$. Figure 5-142 visually compares the average reconstructed mass with the average gravimetric mass.

5.12.3 Time Series Analysis of $PM_{2.5}$ Species

A Met One SASS speciation sampler was installed at the Wilmington monitoring site on February 14, 1999. It has operated on a 1-in-6 sampling schedule from its installation to the present time. Figure 5-143 shows a composite time series for the five major species measured at Wilmington. Figures 5-144 through 5-148 show time series for each of the five major species. The black line in Figures 5-144 through 5-148 is the 30-day rolling average concentration for the specie.

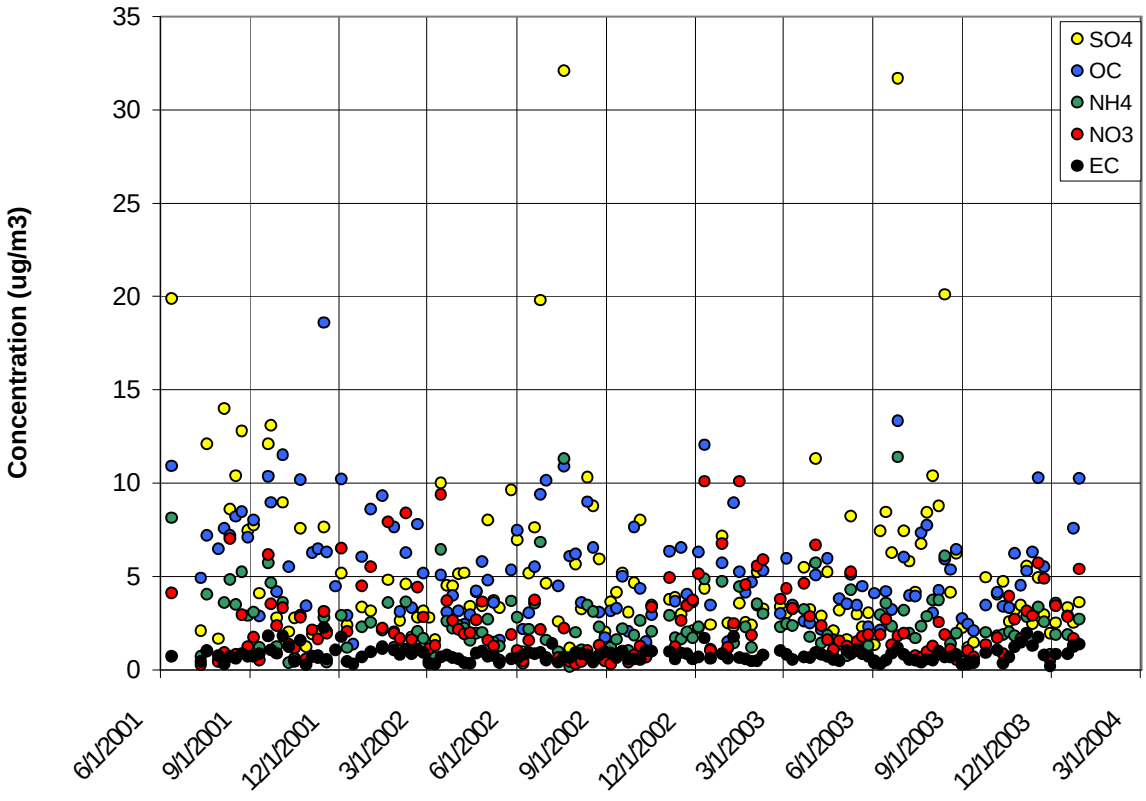

Figure 5-143 Time Series for the Wilmington, DE Monitor

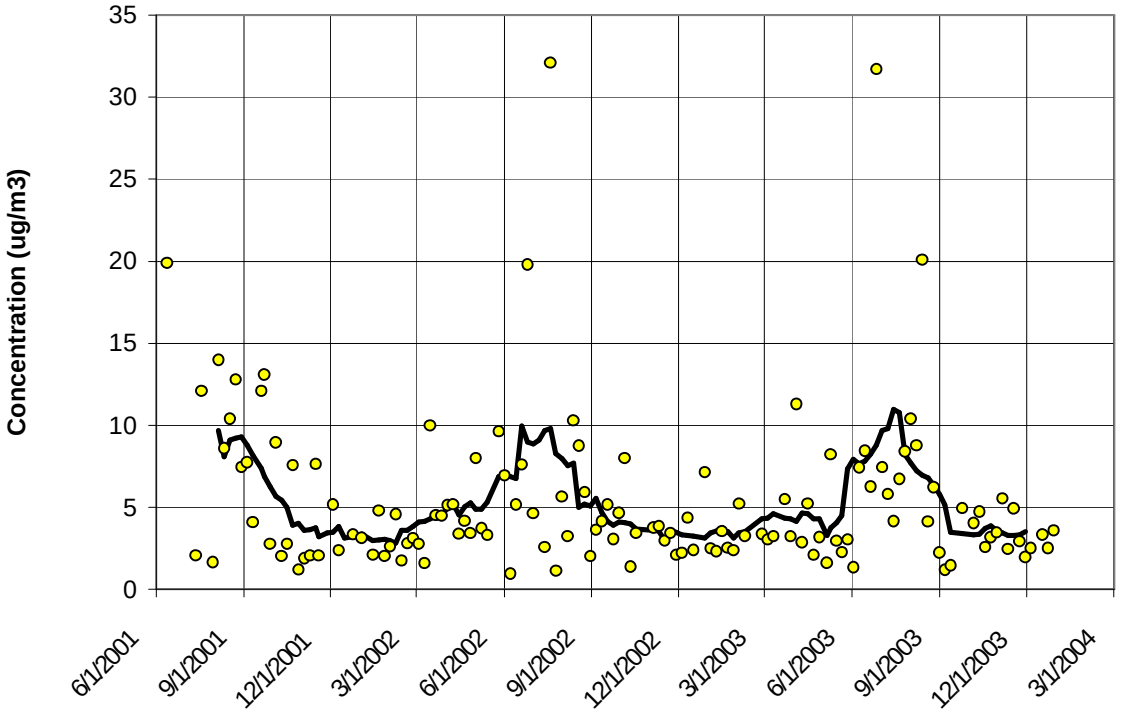

Figure 5-144 Sulfate Time Series for the Wilmington, DE Monitor

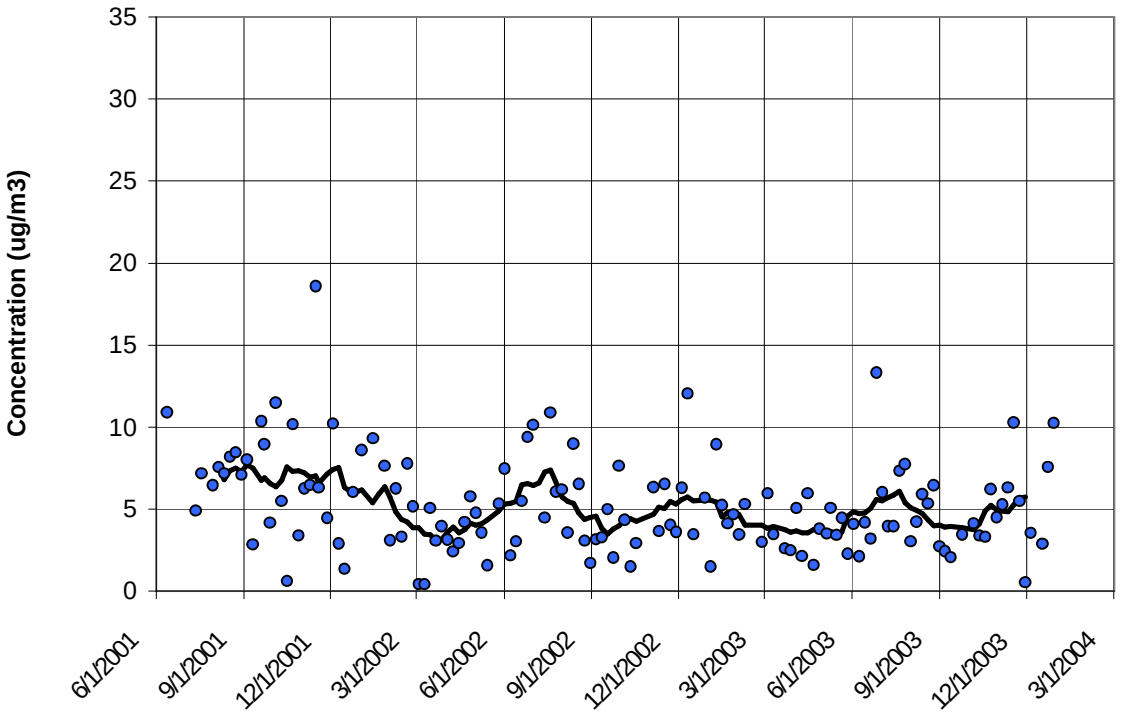

Figure 5-145 Organic Carbon Mass Time Series for the Wilmington, DE Monitor

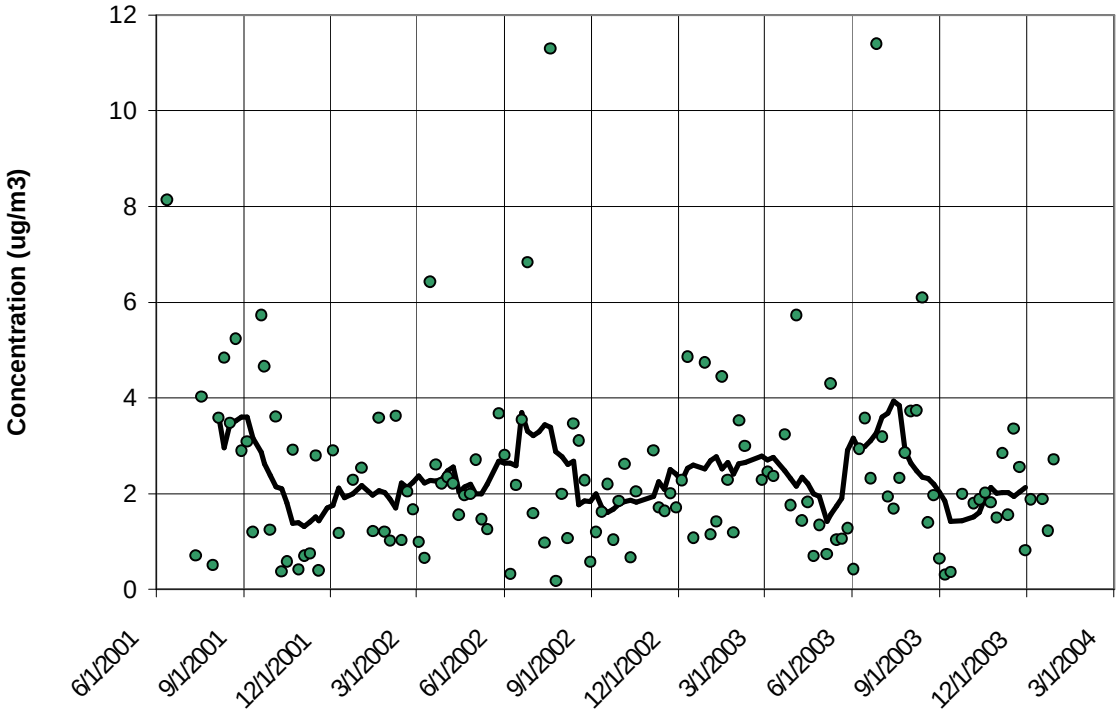

Figure 5-146 Ammonium Time Series for the Wilmington, DE Monitor

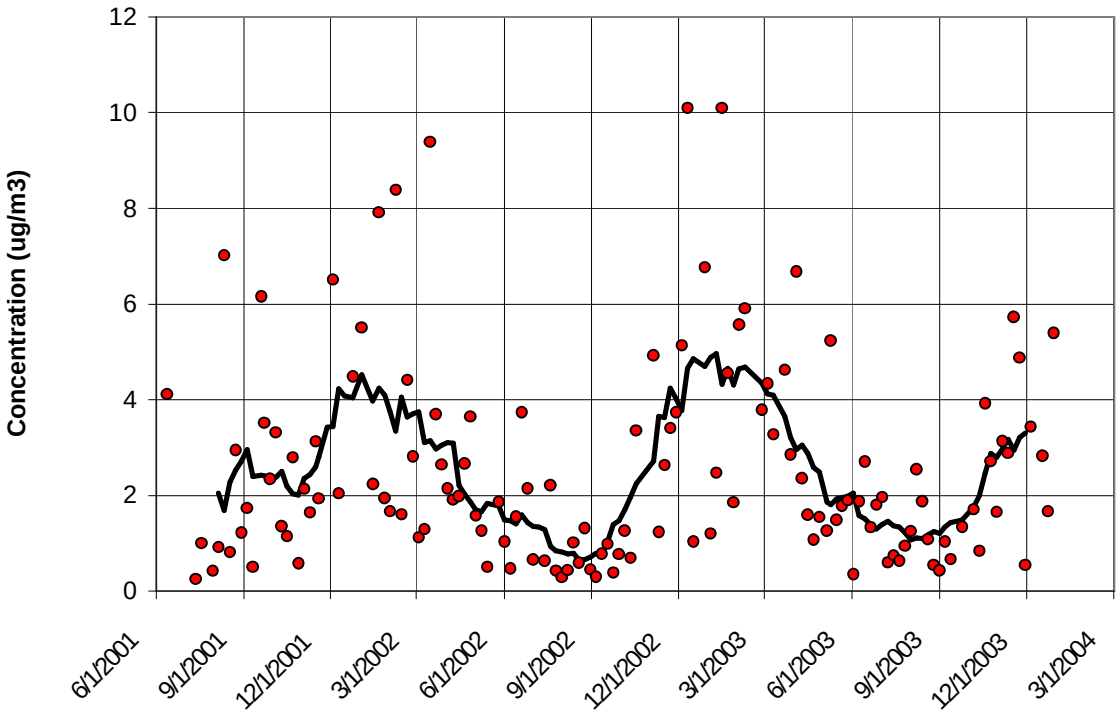

Figure 5-147 Nitrate Time Series for the Wilmington, DE Monitor

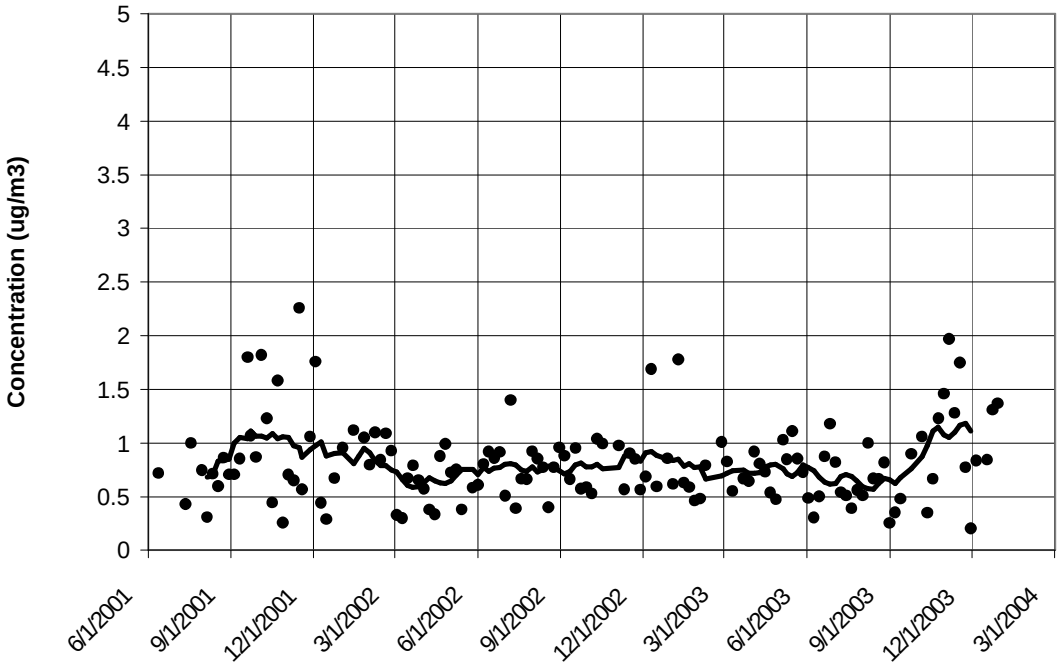

Figure 5-148 Elemental Carbon Time Series for the Wilmington, DE Monitor

The 30-day rolling average sulfate concentration in Figure 5-144 shows how sulfate concentration varied seasonally over 2001-2003 in Wilmington, DE. As seen elsewhere, sulfate showed strong season variation. Sulfate concentration was lowest in winter at an average value of about 3.30 µg/m^3. Sulfate concentrations were much higher in summer. The average summertime sulfate concentration was about 8.28 µg/m^3. Peak summer sulfate concentrations, averaged over 24-hours, were as high as 32 µg/m^3, however. As the sulfate time series shows, sulfate concentrations were much more variable in summer than in winter.

Using an OM/OC ratio of 1.6, organic carbon mass was the second largest contributor to $PM_{2.5}$ mass in Wilmington. Organic carbon mass averaged 5.02 µg/m^3 over all seasons. Over 2001-2003, average organic carbon concentration was highest during the winter months at 5.65 µg/m^3. Average summer concentration was similar at 5.59 µg/m^3. The average fall concentration was lower at 5.30 µg/m^3 and the lowest average concentration occurred in spring at 3.53 µg/m^3. The analysis of additional data collected over future years will help analysts better understand the season behavior of organic carbon mass at this site. The exceptionally high organic carbon concentration that occurred on July 7, 2002 during the Quebec fire event was removed from the data set used to calculate the seasonal averages presented here.

Over 2001-2003, the average ammonium concentration in Wilmington was 2.33 µg/m^3. This was the second highest average concentration observed among the eleven monitors analyzed behind Arendtsville, PA. Baltimore, MD and Philadelphia, PA, cities not far from Wilmington, had average ammonium concentrations of 1.94 and 2.08 µg/m^3 respectively.

Figure 5-146 shows how ammonium concentrations varied over time. Summer had the highest average concentration at 2.98 µg/m^3 followed by winter with an average concentration of about 2.36 µg/m^3. Average spring and fall concentrations were about 2.19 and 1.77 µg/m^3

respectively. The highest ammonium values occurred in summer. Some 24-hour measurements were as high as 11.4 µg/m^3. Some high values also occasionally occurred in other seasons.

Ammonium and sulfate concentrations were well correlated (R^2 = 0.84); when sulfate concentrations were high, ammonium concentrations were usually high. Table 5-50 lists ammonium and sulfate concentrations on days when sulfate concentration exceeded 15 µg/m^3.

Table 5-50 High Ammonium and Sulfate Days for the Wilmington, DE Monitor

Date	Ammonium Concentration (µg/m^3)	Sulfate Concentration (µg/m^3)
6/12/01	8.1	19.9
6/25/02	6.8	19.8
7/19/02	11.3	32.1
6/2603	11.4	31.7
8/13/03	6.1	20.1

Of the eleven sites analyzed, the Wilmington site had the highest average nitrate concentration (2.48 µg/m^3) over the 2001-2003 period. As noted in the regional analysis, for the sites and time period studied here, the formation of nitrate appeared to be associated with cold temperatures and winter weather conditions. In general, lower average concentrations occurred in the southern part of the MARAMA Region and higher average concentrations occurred in northern areas. As Figure 5-147 shows, nitrate concentrations were lowest during the summer and noticeably higher in winter. Over 2001-2003, the average winter concentration was 4.50 µg/m^3 whereas the average summer concentration was 1.22 µg/m^3. In spring and fall, the average nitrate concentrations were 2.71 µg/m^3 and 1.96 µg/m^3 respectively. As Figure 5-147 shows, nitrate values were much more variable in winter than in summer.

Figure 5-148 displays the time series for elemental carbon. The plot shows that elemental carbon concentration remained fairly constant season-to-season, at least over 2001-2003. Some high 24-hour values occurred in the fall of 2001 and 2003 but similarly high values did not occur in the fall of 2002. The average elemental carbon concentration over all seasons was 0.78 µg/m^3, which was similar to the average concentrations observed in other major cities in the region. Baltimore to the southwest had an average concentration of 0.77 µg/m^3. Philadelphia to the northeast had an average elemental carbon concentration somewhat higher than Wilmington at 0.85 µg/m^3. Wilmington's average elemental carbon concentration was about twice the average concentration observed at rural sites. Arendtsville, PA and Kinston, NC had average elemental carbon concentrations of 0.39 µg/m^{3}and 0.36 µg/m^3 respectively.

Table 5-51 provides the seasonal averages for the major constituents of $PM_{2.5}$ mass for the Wilmington, DE monitoring site.

Table 5-51 Seasonal Averages for the Major Constituents of $PM_{2.5}$ Mass (µg/m^3)

	Organic Carbon Mass	Sulfate	Ammonium	Nitrate	Elemental Carbon
Winter	5.65	3.30	2.36	4.50	0.89
Spring	3.53	4.55	2.19	2.71	0.68
Summer	5.59	8.28	2.98	1.22	0.68
Fall	5.30	4.34	1.77	1.96	0.89

5.12.4 Trajectory Analysis

Figure 5-149 shows CATT back trajectories for the cleanest days in the speciation record over the period studied from January 2001 through December 2003. While even lower concentration days may be found in the data record for Federal Reference Method monitors at the site, the trajectories plotted in Figure 5-149 are the lowest concentration days in the speciation record over the period studied. These "clean" days represent the five percent days with the lowest total $PM_{2.5}$ mass.

Many "clean day" trajectories in the MARAMA Region travel to the receptor site from areas in the northern and western states or from the western provinces of Canada. In the case of the Wilmington monitor, only one set of trajectories fits this description. Other clean day trajectories arrive in Wilmington from the central or eastern Canadian provinces or the Atlantic Ocean. Most clean day trajectories do not originate from or send long periods over major air pollution source regions

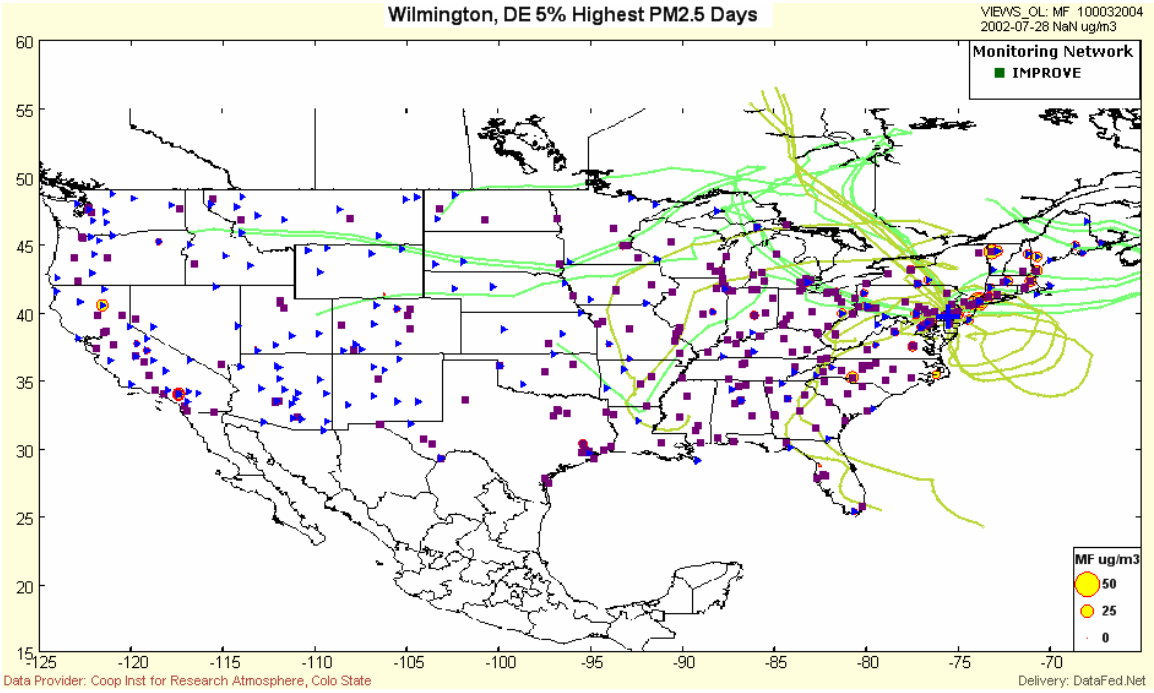

Figure 5-149 Wilmington, DE, Back Trajectories for the five Percent Cleanest Days

Table 5-52 lists the five percent cleanest days at Wilmington, DE and the total mass concentration measured by the speciation monitor on that day.

Table 5-52 Wilmington, DE Five Percent Lowest Days

Date	$PM_{2.5}$ Mass ($\mu g/m^3$)
10/28/2001	6.2
12/15/2001	6.6
8/30/2002	5.5
10/11/2002	6.4
9/6/2003	5.5
11/29/2003	5.6

Figure 5-150 shows back trajectories for the dirtiest days, the five percent days with the highest total $PM_{2.5}$ mass. Most "dirty day" trajectories have spent the last five days over the continental U.S. and show westerly transport from the Midwest. The trajectories from Canada are associated with the July7-9, 2002 forest fire event.

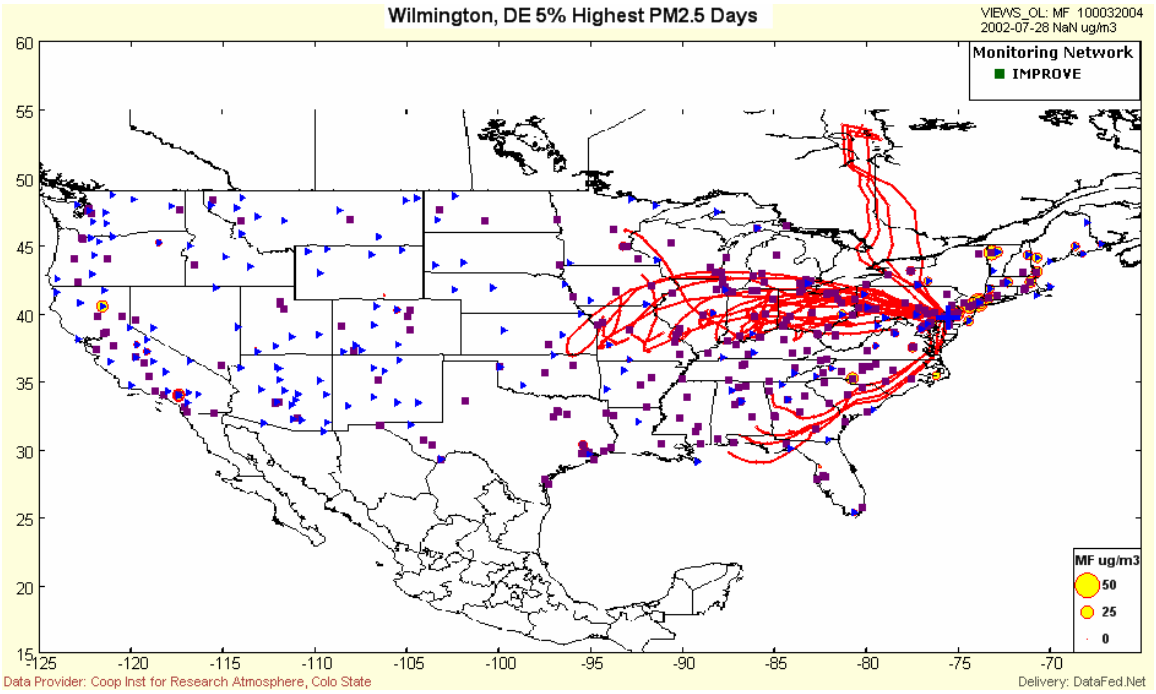

Figure 5-150 Wilmington, DE, Back Trajectories for the Five Percent Dirtiest Days

Table 5-53 lists the five percent dirtiest days and the total mass concentration measured by the speciation monitor on that day.

Table 5-53 Wilmington, DE, Five Percent Highest Days

Date	$PM_{2.5}$ Mass ($\mu g/m^3$)
6/12/2001	54.0
6/25/2002	43.7
7/7/2002	113
7/19/2002	58.9
6/26/2003	69.1
8/13/2003	38.4

6 Key Findings and Future Directions

This report provides background information on the $PM_{2.5}$ speciation monitoring program, describes the $PM_{2.5}$ monitoring network in the Mid-Atlantic Region, and provides information about the operation and configuration of $PM_{2.5}$ speciation samplers in the region. To aid analysts interested in exploring speciation data, the report presents a step-by-step guide to processing data from the speciation program. The report compares the five major species that contribute to $PM_{2.5}$ mass at eleven sites using data collected between September 10, 2001 and October 12, 2003. The report also provides detailed analysis of the speciated data collected at twelve monitoring sites in the Mid-Atlantic Region. Financial support for this report was provided by EPA Region III. MARAMA expresses its appreciation for that financial support and for the technical assistance it received from state and local agency staff, EPA staff, contractors, and academic researchers.

The following paragraphs summarize the findings and recommendations of this analytical effort.

6.1 Regional Comparison of the Major Constituents of $PM_{2.5}$ Mass

Since 90 percent or more of the $PM_{2.5}$ mass measured at a monitoring site could be attributed to five major species, these five major species were the focus of MARAMA's analysis. The five species were ammonium, elemental carbon, organic carbon mass, sulfate, and nitrate.

Given the application of an OM/OC ratio of 1.6, over the 2001-2003 period, on average, organic carbon mass was the largest contributor to $PM_{2.5}$ mass at seven of the eleven sites studied. Organic carbon mass concentration averaged 5.41 $\mu g/m^3$ over the eleven sites studied. The highest average concentration, 6.93 $\mu g/m^3$, occurred at the Elizabeth, NJ monitoring site, a site strongly affected by mobile source emissions and nearby industrial activity. While the Elizabeth site produced the highest average organic carbon mass concentration over the 2001-2003 period, Richmond was not far behind at 6.81 $\mu g/m^3$. Many large urban areas, namely Baltimore, Charlotte, Philadelphia, Pittsburgh, Washington, and Wilmington, had average organic carbon mass concentrations between 5.0 and 6.0 $\mu g/m^3$.

The rural sites at Arendtsville, PA, Dover, DE and Kinston, NC produced the lowest average organic carbon mass averages over 2001-2003. The relatively low organic carbon mass calculated at these sites, however, may be the result of applying too low an OM/OC ratio to the organic carbon data from these rural monitors. Applying a higher OM/OC ratio, that represents more "aged" (higher molecular weight) organic carbon species, would increase the concentration of organic carbon mass estimated at these rural sites. If the expectation holds true that rural sites exhibit higher OM/OC ratios than urban sites, applying site-specific OM/OC ratios would likely have the effect of increasing estimated rural concentrations and reducing estimated urban concentrations of organic carbon mass. This would decrease the disparity between estimated urban and rural concentrations of organic carbon mass to some extent.

Over the period, sulfate was the second largest contributor to average $PM_{2.5}$ mass and it was the largest contributor to $PM_{2.5}$ mass at most sites in the summer. If the average concentrations of sulfate and ammonium were added together, the combined specie concentration would have been the largest contributor to $PM_{2.5}$ mass at all sites averaged over 2001-2003. Sulfate concentration, averaged over the eleven sites studied, was 5.11 $\mu g/m^3$. The highest average concentration, 6.12 $\mu g/m^3$, occurred at Arendtsville, PA. The next highest average concentration occurred in Pittsburgh, PA (6.00 $\mu g/m^3$). Average sulfate concentrations were somewhat lower in Baltimore

(5.13 µg/m^3), Washington, DC (5.44 µg/m^3), and Wilmington, DE (5.24 µg/m^3). Four sites, Charlotte, NC, Dover, DE, Elizabeth, NJ, and Richmond, VA had values between 4.60 and 5.00 µg/m^3. The lowest concentration, 4.11 µg/m^3, was observed at the Kinston monitoring site in rural southeastern North Carolina.

Ammonium concentration, averaged over the eleven sites studied, was 2.01 µg/m^3. The highest average concentrations occurred in Arendtsville, PA (2.36 µg/m^3), Wilmington, DE (2.33 µg/m^3), and Pittsburgh, PA (2.28 µg/m^3). The lowest concentration, 1.51 µg/m^3 was observed at the Kinston monitoring site in rural southeastern North Carolina. The low average concentration of ammonium at Kinston was surprising given the monitor was located in an area of North Carolina known for Concentrated Animal Feeding Operations (CAFOs). In general, average ammonium concentrations varied little among the eleven monitors analyzed over 2001-2003.

Nitrate concentration, averaged over the eleven sites studied, was 1.76 µg/m^3. The highest average concentration, 2.48 µg/m^3, occurred in Wilmington, DE. The lowest concentration, 0.94 µg/m^3, was observed in Charlotte, NC. Relatively low values were also measured in Kinston, NC (1.10 µg/m^3) and Richmond, VA (1.20 µg/m^3). For the data analyzed, nitrate concentrations appeared correlated with wintertime conditions that favor the formation of solid phase nitrate species.

Elemental carbon concentration, averaged over the eleven sites studied, was 0.75 µg/m^3. Average concentrations ranged from a high of 1.82 µg/m^3 in Elizabeth, NJ to lows of 0.39 and 0.36 µg/m^3 at Arendtsville, PA and Kinston, NC, respectively. Arendtsville, PA and Kinston, NC were two of the most rural sites in the analysis. The high elemental carbon concentration at the Elizabeth, NJ monitoring site was likely associated with the monitor's proximity to heavy mobile source emissions and industrial sources. The Elizabeth site produced average elemental carbon concentrations about four to five times the average concentration of a rural site and more than twice the average concentration of other urban sites. Large urban areas such as Baltimore, Philadelphia, Pittsburgh, Washington, DC and Wilmington exhibited average concentrations between 0.73 and 0.85 µg/m^3, about twice the concentration of the most rural sites. Elemental carbon appeared strongly correlated with population.

6.2 Seasonal Variation in the Major Constituents of $PM_{2.5}$ Mass

The major constituents of $PM_{2.5}$ mass vary season to season. In the process of analyzing seasonal variability, MARAMA followed the convention of placing June, July and August in the summer season so all quarters are offset from calendar quarters by one month.

Averaged across the entire region, the average concentration of the five major constituents of $PM_{2.5}$ mass was highest in the summer at about 18.53 µg/m^3. A secondary peak in average concentration occurred in winter at about 15.38 µg/m^3. Spring and fall were characterized by lower concentrations of 12.91 and 14.19 µg/m^3, respectively.

Sulfate was an important contributor to $PM_{2.5}$ mass regardless of season. Sulfate exhibited strong seasonal behavior, however. It was the largest contribution to $PM_{2.5}$ mass at eight sites in the spring and summer. Averaged regionally, sulfate concentration peaked in summer at 7.71 µg/m^3 and reached its lowest level in winter at 3.34 µg/m^3. Average spring and fall concentrations were 4.48 µg/m^3 and 4.32 µg/m^3. While summer sulfate concentration averaged 7.7 µg/m^3 over the entire region, summer sulfate measurements on a particular day at a particular monitoring site reached 30 µg/m^3 or more. Sulfate concentrations are much more variable in summer than at other times of the year. In summer, they appear episodic in nature.

At an OM/OC ratio of 1.6, organic carbon mass was also an important contributor to $PM_{2.5}$ mass regardless of season. It was the dominate specie at most sites in the winter and fall and was the largest contributor to $PM_{2.5}$ mass at some sites in summer and spring as well. Organic carbon mass concentrations were quite variable throughout the study period. Averaged over the region, organic carbon mass concentration peaked during the summer at 6.65 $\mu g/m^3$. A secondary "peak" in regionally averaged organic carbon mass concentration occurred in winter at 5.85 $\mu g/m^3$. Average organic carbon mass concentration was 5.15 $\mu g/m^3$ in the fall and at its lowest level, 3.98 $\mu g/m^3$ in the spring. This seasonal pattern was often observed at specific monitoring sites. Seasonal swings in organic carbon mass concentration probably would be even more pronounced if seasonal, site-specific OM/OC ratios were developed for speciation monitors in the Mid-Atlantic Region.

Ammonium ion is a modest but important contributor to $PM_{2.5}$ mass in all seasons. Across the seasons, the average regional ammonium concentration was about 2.01 $\mu g/m^3$. Over 2001-2003, ammonium showed some seasonal variation. The regionally averaged ammonium concentration was 2.58 $\mu g/m^3$ in the summer, 1.58 $\mu g/m^3$ in the fall, 1.98 $\mu g/m^3$ in the winter, and 1.87 $\mu g/m^3$ in the spring. High ammonium values in the summer were episodic in nature and very often associated with high sulfate concentrations.

Nitrate species also showed strong seasonal behavior. Unlike sulfate species and organic carbon mass that peak during the summertime, nitrate species peaked during the winter. While an important contributor to winter $PM_{2.5}$ concentrations, nitrate concentrations were relatively modest when compared to the contributions made by organic carbon mass and sulfate species. Averaged regionally, nitrate concentration peaked in winter at 3.37 $\mu g/m^3$. Spring and fall concentrations were 1.88 $\mu g/m^3$ and 1.39 $\mu g/m^3$ respectively. In the summer, when nitrogen species were for the most part partitioned into the gas phase, average particulate matter nitrate concentration was only 0.92 $\mu g/m^3$.

Elemental carbon does not exhibit the strong seasonal variability seen with organic carbon mass and nitrate and sulfate species. At most sites, this contributor to $PM_{2.5}$ mass appeared to be consistently present at relatively low concentration season-to-season. Increased concentrations were often observed in late fall and/or winter.

6.3 Findings

Speciation data is valuable in understanding the nature and composition of fine particle pollution. Without these data, developing effective air quality control programs for $PM_{2.5}$ pollution would be much more difficult. These data are critically important for air quality planning activities. They provide basic information about what species contribute most strongly to a PM nonattainment problem in a specific area or across an entire region. They can be used to characterize local effects and are routinely used as input data for source apportionment analyses. Speciation data is rich and complex however and a lot of pre-processing and quality assurance is needed before the data can be used in analyses.

The following paragraphs summarize the major findings of this analytical effort.

- Speciation data is very valuable in understanding the nature and composition of fine particle pollution. The analysis of these data will help air quality planners develop appropriate and effective air quality control programs for fine particle pollution.

- The speciation monitoring network is producing data that will help assess the impacts of programs such as CAIR that are expected to reduce the concentration of $PM_{2.5}$ precursors between now, 2009, and thereafter.
- The analysis of speciation data is complex and requires increased knowledge of the nature and limitations of the data. State, local and regional air quality agencies will need training and practice to reap the full benefits of these data.
- Currently, a data analyst must gather information on how to process and analyze speciation data from a wide range of sources including EPA, regional associations, university researchers, contractors, etc.
- Averaging organic carbon blanks is a viable method for blank correcting organic carbon data from the STN/SLAMS speciation monitor network.
    - In this study, the average organic carbon blank value, averaged across all sites and seasons, was 1.27 $\mu g/m^3$. The highest average blank value was measured at Charlotte, NC at 1.56 $\mu g/m^3$; the lowest average blank value was measured at Baltimore, MD at 0.94 $\mu g/m^3$.
    - Average organic carbon blank values varied site-to-site and season-to-season. MARAMA applied averaged, site-specific organic blank corrections in its analysis. Seasonal organic carbon blank corrections were not applied.
- The OM/OC ratios used to convert organic carbon measurements from the speciation network into estimates of organic carbon mass have raised in recent years as research scientists improve the measurement of organic carbon species in the atmosphere. Higher OM/OC ratios increase the amount of mass attributed to organic carbon species.
    - Sensitivity analyses indicate 1.6 is a reasonable approximation of the OM/OC ratio at many urban monitoring sites in the MARAMA Region for the 2001-2003 period.
    - Sensitivity analyses indicate 1.9 or higher OM/OC ratios are appropriate for use at many rural monitoring sites in the MARAMA Region for the 2001-2003 period.
- Organic carbon mass and sulfate were the largest contributors to $PM_{2.5}$ mass at all sites for the period from September 10, 2001 through October 12, 2003.
    - Using an OM/OC ratio of 1.6, organic carbon mass was the largest contributor to $PM_{2.5}$ mass at seven of the eleven sites analyzed. Sulfate was the largest average contributor to $PM_{2.5}$ mass at the other four sites.
    - The average organic carbon mass concentration, averaged regionally over 2001-2003 was 5.41 $\mu g/m^3$. Average organic carbon mass levels ranged from a high of 6.93 $\mu g/m^3$ in Elizabeth, NJ to a low of 3.63 $\mu g/m^3$ in Dover, DE. At most sites, organic carbon mass concentrations were highest in summer and lowest in the spring.
    - Empirically determined site-specific and/or site-specific and season-specific OM/OC values would greatly improve estimates of organic carbon mass at monitoring sites in the MARAMA Region.

  - More needs to be known about organic carbon mass, since it constitutes a large part of total $PM_{2.5}$ mass in the MARAMA Region. More work is needed to determine or better understand: which organic carbon species are present and in what concentration, how do organic carbon mass species vary over time and place, are the organic carbon mass species the result of anthropogenic or biogenic emissions, and what constituents and processes are important to secondary organic aerosol formation, etc.

- Sulfate was a strong contributor to $PM_{2.5}$ mass at all sites and was the largest contributor to $PM_{2.5}$ mass at four of the eleven sites analyzed.
  - Sulfate concentrations were highest in summer, were often episodic in nature, and were correlated well with ammonium concentrations.
  - If the average concentrations of sulfate and ammonium are added together, the combined concentration was the largest contributor to $PM_{2.5}$ mass at all sites averaged over 2001-2003.
  - The average sulfate concentration, averaged regionally over 2001-2003 was 5.11 $\mu g/m^3$. Average sulfate levels ranged from a high of 6.12 $\mu g/m^3$ in Arendtsville, PA to a low of 4.11 $\mu g/m^3$ in Kinston, NC.
- Nitrate species made a much smaller contribution to $PM_{2.5}$ mass than organic carbon mass and sulfate species. The average nitrate concentration, averaged regionally over 2001-2003 was 1.76 $\mu g/m^3$. Average nitrate levels ranged from a high of 2.48 $\mu g/m^3$ in Wilmington, DE to a low of 0.94 $\mu g/m^3$ in Charlotte, NC. Nitrate concentrations peaked in the winter and were low in the summer. Nitrate concentrations appear linked to winter/cold weather conditions that produce solid phase nitrate species (Wittig et al., 2004). Lower average nitrate concentrations occurred in the southern part of the MARAMA Region and higher average nitrate concentrations occurred in northern areas.
- Ammonium species also made a much smaller contribution to $PM_{2.5}$ mass than organic carbon mass and sulfate species. The average ammonium concentration, averaged regionally over 2001-2003 was 2.01 $\mu g/m^3$. Average ammonium levels ranged from a high of 2.36 $\mu g/m^3$ in Arendtsville, PA to a low of 1.51 $\mu g/m^3$ in Kinston, NC. Ammonium concentrations were fairly uniform across the MARAMA Region. In many cases, urban sites produced higher ammonium concentrations than rural sites.
- Elemental carbon concentrations were generally small relative to other $PM_{2.5}$ mass constituents. Despite this, elemental carbon particles are important from a human health perspective, since they are considered air toxins and are associated with increased risk of cancer and other disease.
  - The average elemental carbon concentration, averaged regionally over 2001-2003 was 0.75 $\mu g/m^3$. Average elemental carbon levels ranged from a high of 1.82 $\mu g/m^3$ in Elizabeth, NJ to a low of 0.36 $\mu g/m^3$ in Kinston, NC.
  - Elemental carbon concentration was strongly correlated with population; higher concentrations occurred in urban sites and lower concentrations in rural areas.
- Over the period studied, $PM_{2.5}$ concentrations often rose and fell sympathetically across much of the MARAMA Region.

- Many back trajectories for days when $PM_{2.5}$ concentrations were low originated in relatively "clean" areas and moved quickly over great distances from western or central Canada or northern states to receptor sites in the MARAMA Region. In contrast to back trajectories associated with high $PM_{2.5}$ concentrations, these "clean day" trajectories did not remain or re-circulate over air pollution source regions.
- Many back trajectories for days when $PM_{2.5}$ concentrations were high were tracks of air masses that spent the last five days over the continental U.S. In many cases, the air circulated or re-circulated through air pollution source regions in the Midwest, Mid-Atlantic, Northeast and South. Many "dirty day" trajectories passed through the Ohio River Valley.
- Speciation data can be used to characterize air quality at a particular site as well as to provide information about regional conditions.
- Speciation data can be used to analyze and confirm exceptional events like forest fires and other phenomena.
- The uncertainty of many trace element measurements in the speciation program is poorly known.
- Many trace element measurements in the speciation program are below the Method Detection Limit (MDL) of the analytical equipment used to make these measurements.

6.4 Future Directions

During the course of this analysis, numerous potential follow-up activities were identified. MARAMA encourages EPA and other agencies to give serious consideration to the following:

- Continue the speciation monitoring program in order to produce data to help understand the sources and effects of $PM_{2.5}$.
- Develop a web site or other forum to share information on how to process and analyze speciation data to facilitate the use of these important data.
- Provide training to help analysts and researchers access and use speciation data expeditiously and with proper consideration of its strengths and weaknesses.
- Focus increased attention organic carbon since it constitutes a large part of $PM_{2.5}$ mass in the MARAMA Region. Conduct studies and analyses to determine:
    - OM/OC ratios in urban and rural areas, especially in $PM_{2.5}$ nonattainment areas,
    - Which organic carbon species are present and in what concentration,
    - How organic carbon mass species vary over time and place,
    - Whether organic carbon mass species are the result of anthropogenic or biogenic emissions, and
    - What constituents and processes are important to secondary organic aerosol formation.
- Update this analysis with 2004-2005 data, and include more sites to:
    - Improve comparisons between samplers on a 1-in-3 day sampling schedule and a 1-in-6 day sampling schedule,

- Confirm regional differences, and
- Confirm seasonal patterns.

In the future, analyses could be used to track $PM_{2.5}$ trends and assess the affects of air quality control measures.

- Conduct studies to assess the accuracy and precision of speciation measurements especially trace element measurements.
- Conduct studies to evaluate the analytes frequently measured beneath the minimum detection limit. Determine whether these measurements are needed in the program. If they are needed, determine how they can be improved. If they are not needed, suspend collection of these data.
- If trace element measurements are deemed important to source identification and/or source apportionment analyses, develop new sampling equipment and methods that would improve trace element measurements. New equipment and methods might include larger sample filters, higher sample volumes, longer sampling times, etc.
- Explore new ways of calculating "urban excess" mass using data from rural speciation monitors sited after 2003 and urban speciation monitors and by comparing data from the rural IMPROVE network and urban speciation monitors.
- Conduct analyses or studies at specific sites to examine/determine:
  - Differences between ridge-top and valley floor $PM_{2.5}$ mass constituents,
  - Whether combined animal feeding operations (CAFOs) or other animal husbandry or agricultural activities contribute to elevated $PM_{2.5}$ levels, or
  - How speciation data can be used in air quality forecasting.
- Assess the correlation of locally determined meteorological parameters and specie concentration to help identify sources of air pollution upwind of monitoring sites and to support air quality forecasting. This task will require the accurate measurement of parameters such as temperature, relative humidity, wind speed, and wind direction at a monitoring site. The general quality and quality assurance of meteorological data collected at monitoring sites needs to be improved. Rigorous auditing programs are needed to ensure high quality meteorological data is collected at monitoring sites.
- Since meteorological parameters change over very brief periods of time and current speciation measurements are made over 24-hours, install continuous speciation monitors and accurate meteorological instrumentation at selected sites and analyze collected data to correlate meteorological parameters with $PM_{2.5}$ concentration. This work would help determine the causes of high $PM_{2.5}$ concentrations and aid air quality forecasters.
- Analyze the meteorology and back trajectories for "non-episodic" days, days when concentrations are neither at their highest or lowest, to better understand behavior of $PM_{2.5}$ mass constituents on these days.

7 References

El-Zanan, H. S., Lowenthal, D. H., Zielinska, B., Chow, J. C., Kumar, N., Determination of the organic aerosol mass to organic carbon ratio in IMPROVE samples, Chemosphere 60 485-496 (2005).

Frank, N., 2005. U.S. Environmental Protection Agency, Research Triangle Park, NC, private communication with Neal Frank.

Kim, E., Hopke, P. K., Qin, Y., Estimation of Organic Carbon Blank Values and Error Structures of the Speciation Trends Network Data for Source Apportionment, J. Air & Waste Management Association, 55: 1190-1199 (2005).

Kiss, G., Varga, B., Galambos, I., Ganszky, I., Characterization of water-soluble organic matter isolated from atmospheric fine aerosol, J. Geophys. Res, 107, D21, 8339, doi.: 10.1029/2001JD000603 (2002).

NESCAUM, 2004, 2002: A Year in Review. Northeast States for Coordinated Air Use Management, Boston, MA.

Neter, J., Kutner, M. H., Nachtsheim, C. J., Wasserman, W., 1996. Applied Linear Statistical Models, Fourth Edition, Chapter 3, WCB McGraw Hill, Boston, pp. 95-151.

Poirot, R. L., Wishinski, P. R., Hopke, P. K., Polissar, A.V., Comparative Application of Multiple Receptor Methods to Identify Aerosol Sources in Northern Vermont, Environmental Science and Technology 35: 4622-4636 (2001).

Polidori, A., Characterizing the Origins and Polarity of Organic Aerosol, Ph.D. Dissertation, Rutgers University, New Brunswick, NJ, 08901 (2005).

Solomon, P. Organic Carbon Artifacts, MARAMA conference call presentation, (2004).

Takegawa, N., Miyazaki, Y., Kondo, Y., Komazaki, Y., Miyakawa, T., Jimenez, J.L., Jayne, J.T., Worsnop, D.R., Allan, J.D., Weber, R.J., Characterization of an Aerodyne Aerosol Mass Spectrometer (AMS): Intercomparison with other aerosol instruments, Aerosol Science and Technology, 39 (8): 760-770 (2005).

Tolocka, M. P., Solomon, P. A., Mitchell, W., Norris, G. A., Gemmill, D. B., Wiener, R. W., Vanderpool, R. W., Homolya, J. B., Rice, J., East versus West in the US: Chemical Characteristics of $PM_{2.5}$ during the Winter of 1999, Aerosol Science and Technology, 34:88-96 (2001).

Tropp, R., 2004. Desert Research Institute, Reno, NV, private communication with Richard Tropp.

Turpin, B. J., Lim, H. J., Species Contributions to PM2.5 Mass Concentrations: Revisiting Common Assumptions for Estimating Organic Mass, Aerosol Science and Technology 35: 602-610 (2001).

Turpin, B. J., Saxena, P., Andrews, E., Measuring and simulating particulate organics in the atmosphere: problems and prospects, Atmospheric Environment 34 2983-3013 (2000).

Wittig A.E., Pandis S.N., Hering S.V., Kirby B.W., Khlystov A.K., Takahama S., Davidson C. (2004). Semi-continuous $PM_{2.5}$ inorganic composition measurements during the Pittsburgh Air Quality Study. *Atmos. Environ.* 38: 3201-3213.

Zhang, Q., Worsnop, D. R., Canagaratna, M. R., Jimenez, J. L., Hydrocarbon-like and oxygenated organic aerosols in Pittsburgh: insights into sources and processes of organic aerosols, Atmos. Chem. Phys., 5, 3289-3311, 2005.

Appendix A: Speciation Analytes

Analytes in the EPA Chemical Speciation Program			
AIRS Parameter Code	**Analyte**	**Symbol**	**Analytical Method**
88301	Ammonium	NH_4^+	Ion Chromatography, Cations
88302	Sodium	Na^+	Ion Chromatography, Cations
88303	Potassium	K^+	Ion Chromatography, Cations
88306	Nitrate[1]	NO_3^+	Ion Chromatography, Nitrate
88309	Nitrate (Volatile NO_3^+; URG samplers only)[2]	NO_3^+	Ion Chromatography, Nitrate
88310	Nitrate (Non-volatile NO_3^+; URG samplers only)[3]	NO_3^+	Ion Chromatography, Nitrate
88403	Sulfate	SO_4^{2+}	Ion Chromatography, Sulfate
88101	Particulate Matter	$PM_{2.5}$	Gravimetric Mass
88102	Antimony	Sb	EDXRF (Trace Elements)
88103	Arsenic	As	EDXRF (Trace Elements)
88104	Aluminum	Al	EDXRF (Trace Elements)
88107	Barium	Ba	EDXRF (Trace Elements)
88109	Bromine	Br	EDXRF (Trace Elements)
88110	Cadmium	Cd	EDXRF (Trace Elements)
88111	Calcium	Ca	EDXRF (Trace Elements)
88112	Chromium	Cr	EDXRF (Trace Elements)
88113	Cobalt	Co	EDXRF (Trace Elements)
88114	Copper	Cu	EDXRF (Trace Elements)
88115	Chlorine	Cl	EDXRF (Trace Elements)
88117	Cerium	Ce	EDXRF (Trace Elements)
88118	Cesium	Cs	EDXRF (Trace Elements)
88121	Europium	Eu	EDXRF (Trace Elements)
88124	Gallium	Ga	EDXRF (Trace Elements)
88126	Iron	Fe	EDXRF (Trace Elements)
88127	Hafnium	Hf	EDXRF (Trace Elements)
88128	Lead	Pb	EDXRF (Trace Elements)
88131	Indium	In	EDXRF (Trace Elements)
88132	Manganese	Mn	EDXRF (Trace Elements)
88133	Iridium	Ir	EDXRF (Trace Elements)
88134	Molybdenum	Mo	EDXRF (Trace Elements)
88136	Nickel	Ni	EDXRF (Trace Elements)
88140	Magnesium	Mg	EDXRF (Trace Elements)
88142	Mercury	Hg	EDXRF (Trace Elements)
88143	Gold	Au	EDXRF (Trace Elements)
88146	Lanthanum	La	EDXRF (Trace Elements)
88147	Niobium	Nb	EDXRF (Trace Elements)

Analytes in the EPA Chemical Speciation Program			
AIRS Parameter Code	**Analyte**	**Symbol**	**Analytical Method**
88152	Phosphorus	P	EDXRF (Trace Elements)
88154	Selenium	Se	EDXRF (Trace Elements)
88160	Tin	Sn	EDXRF (Trace Elements)
88161	Titanium	Ti	EDXRF (Trace Elements)
88162	Samarium	Sm	EDXRF (Trace Elements)
88163	Scandium	Sc	EDXRF (Trace Elements)
88164	Vanadium	V	EDXRF (Trace Elements)
88165	Silicon	Si	EDXRF (Trace Elements)
88166	Silver	Ag	EDXRF (Trace Elements)
88167	Zinc	Zn	EDXRF (Trace Elements)
88168	Strontium	Sr	EDXRF (Trace Elements)
88169	Sulfur	S	EDXRF (Trace Elements)
88170	Tantalum	Ta	EDXRF (Trace Elements)
88172	Terbium	Tb	EDXRF (Trace Elements)
88176	Rubidium	Rb	EDXRF (Trace Elements)
88180	Potassium	K	EDXRF (Trace Elements)
88183	Yttrium	Y	EDXRF (Trace Elements)
88184	Sodium	Na	EDXRF (Trace Elements)
88185	Zirconium	Zr	EDXRF (Trace Elements)
88186	Wolfram (Tungsten)	W	EDXRF (Trace Elements)
88305	Organic Carbon STN	OC_TOT	OC/EC TOT
88307	Elemental Carbon STN	EC_TOT	OC/EC TOT
88332	PK1_OC STN	PK1_OC	OC/EC TOT
88333	PK2_OC STN	PK2_OC	OC/EC TOT
88334	PK3_OC STN	PK3_OC	OC/EC TOT
88335	PK4_OC STN	PK4_OC	OC/EC TOT
88336	PYROLC STN	PKYROLC	OC/EC TOT
88320	Organic Carbon IMPROVE [4]	IMPROVE	OC/EC TOR
88321	Elemental Carbon IMPROVE[4]	IMPROVE	OC/EC TOR
88322	OH IMPROVE (High Temperature OC)[4]	OH	OC/EC TOR
88323	EH IMPROVE (High Temperature EC) [4]	EH	OC/EC TOR
88324	O1 IMPROVE[4]	O1	OC/EC TOR
88325	O2 IMPROVE[4]	O2	OC/EC TOR
88326	O3 IMPROVE[4]	O3	OC/EC TOR
88327	O4 IMPROVE[4]	O4	OC/EC TOR
88328	OP IMPROVE[4]	OP	OC/EC TOR
88329	E1 IMPROVE[4]	E1	OC/EC TOR
88330	E2 IMPROVE[4]	E2	OC/EC TOR
88331	E3 IMPROVE[4]	E3	OC/EC TOR

Notes:

[1] Analyte 88306, nitrate ion, is reported for all samplers. For University Research Glass (URG) samplers, 88306 is the sum of analyte 88309, volatile nitrate and analyte 88310, non-volatile nitrate.

[2] Analyte 88309 is a measure of volatile nitrate from the nylon filters used in URG samplers.

[3] Analyte 88310 is a measure of non-volatile nitrate from the Teflon filters used in URG samplers.

[4] Analyses using IMPROVE methods are not typically performed in the speciation program (analytes 88320 through 88331). Data has been collected for these analytes during special studies, however.

Appendix B: FRM Time Series, 2001-2003

Shortly after beginning the process of analyzing $PM_{2.5}$ speciation data in the Mid-Atlantic Region, MARAMA plotted time series of the total mass measured by $PM_{2.5}$ FRM monitors around the region to gain an understanding of how $PM_{2.5}$ mass varies over time and space in the MARAMA Region. Figures B-1 through B-12 reproduce these time series. Each plot covers a calendar quarter beginning with the first quarter of 2001 and ending with the fourth quarter of 2003. As one would expect, mass measurements made on the same day and different locations places do not always agree. What is striking, however, is how frequently they do agree or are similar. As the figures show, $PM_{2.5}$ FRM monitors often move in unison or sympathetically around the region. Peaks of high concentration and troughs of low concentration are often experienced at roughly the same time throughout the region. This highlights the regional nature of fine particle pollution.

Table B-1 Daily $PM_{2.5}$ FRM Monitors in the MARAMA Region, 2001-2003

AIRS Site ID	Site Name	City, State
100032004	Martin Luther King Jr. Avenue	Wilmington, DE
110010041	River Terrace School	Washington DC
110010043	McMillan Reservoir	Washington DC
240053001	Essex	Baltimore, MD
245100035	FMC A	Baltimore, MD
245100040	Old Town	Baltimore, MD
340390004	Elizabeth Lab	Elizabeth, NJ
370630001	Durham	Durham, NC
370670022	Winston-Salem Hattie Avenue	Winston-Salem, NC
370810009	Greensboro EB	Greensboro, NC
371190010	Charlotte Fire Station #10	Charlotte, NC
371190041	Charlotte Garinger	Charlotte, NC
371190042	Charlotte Montclaire	Charlotte, NC
371830014	Raleigh Millbrook	Raleigh, NC
420010001	Arendtsville	Arendtsville, PA
420270100	State College	State College, PA
420430401	Harrisburg	Harrisburg, PA
420490003	Erie	Erie, PA
420692006	Scranton	Scranton, PA
420770004	Allentown	Allentown, PA
420791101	Wilkes-Barre	Wilkes-Barre, PA
420850100	Farrell	Farrell, PA
420950025	Freemansburg	Freemansburg, PA
421255001	Florence	Florence, PA
421010004	AMS Laboratory	Philadelphia
421010136	Elmwood	Philadelphia, PA
510590030	Lee District Park	Fairfax, VA
515500012	Oscar Smith Stadium	Chesapeake, VA

Figures B-1 through B-12 were developed from daily (24-hour, midnight to midnight) data from $PM_{2.5}$ FRM monitors in Delaware, the District of Columbia, Maryland, New Jersey, North Carolina, Pennsylvania, Philadelphia, and Virginia. Daily $PM_{2.5}$ FRM data were not available for West Virginia over 2001-2003. Table B-1 list the monitors plotted in the time series.

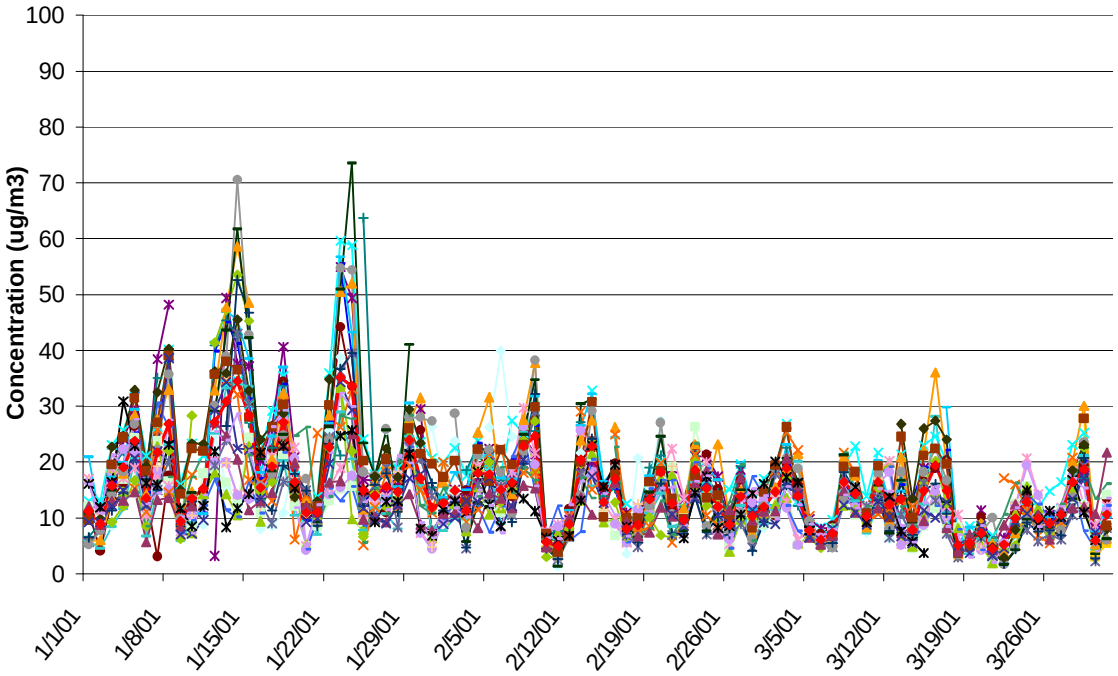

Figure B-1 Daily $PM_{2.5}$ FRM Time Series, January-March 2001

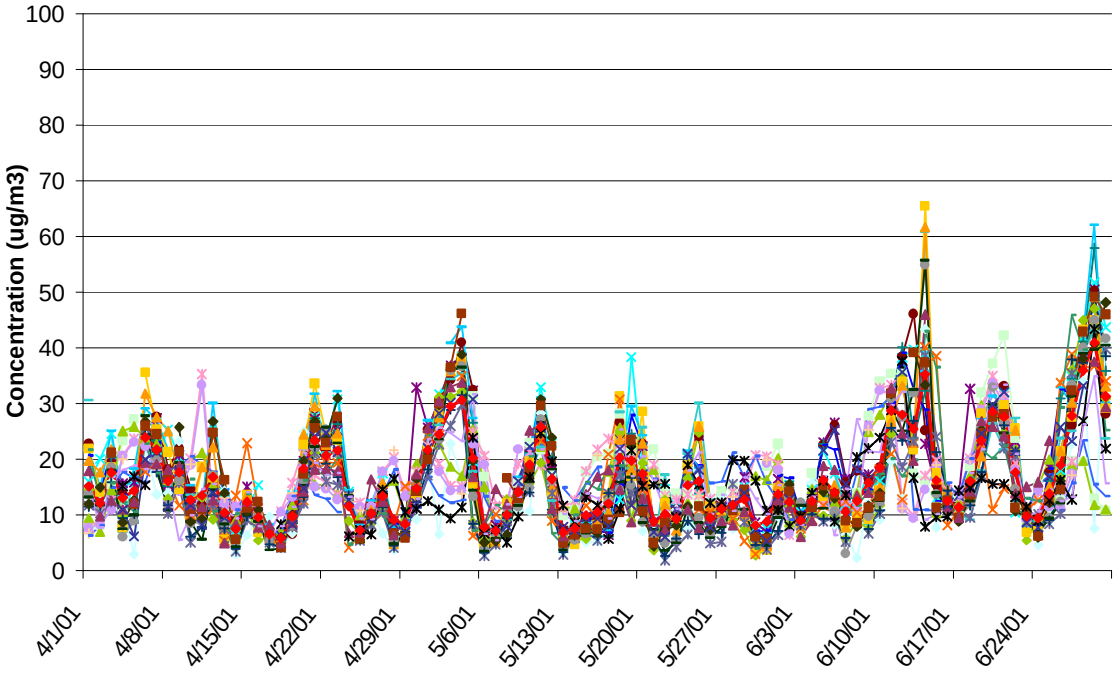

Figure B-2 Daily $PM_{2.5}$ FRM Time Series, April-June 2001

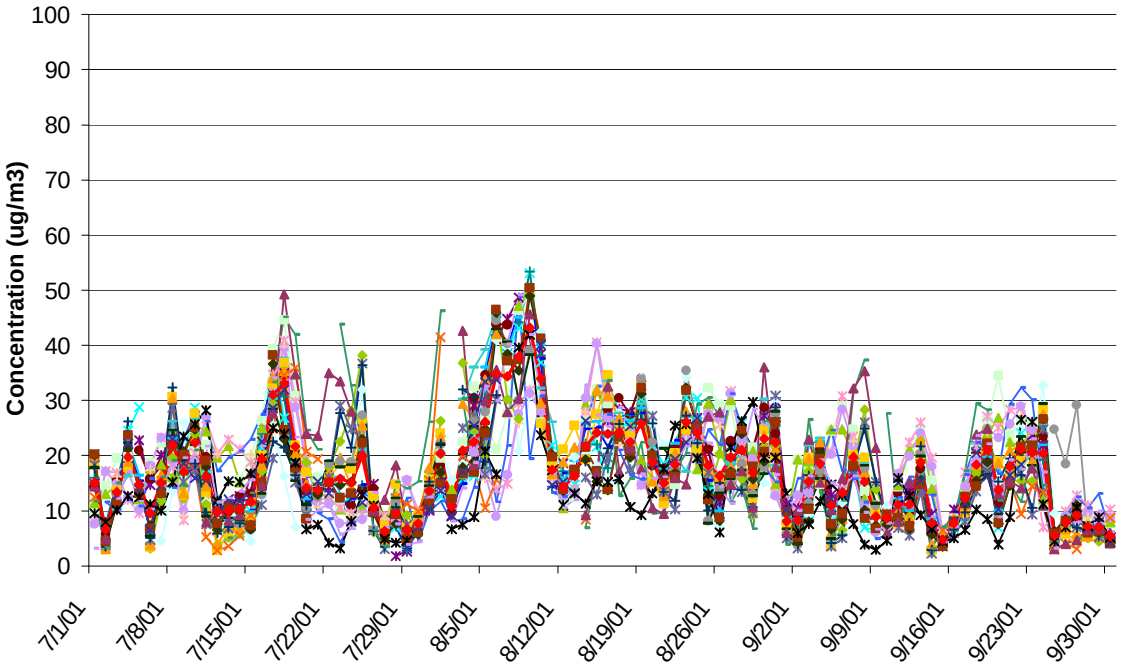

Figure B-3 Daily $PM_{2.5}$ FRM Time Series, July-September 2001

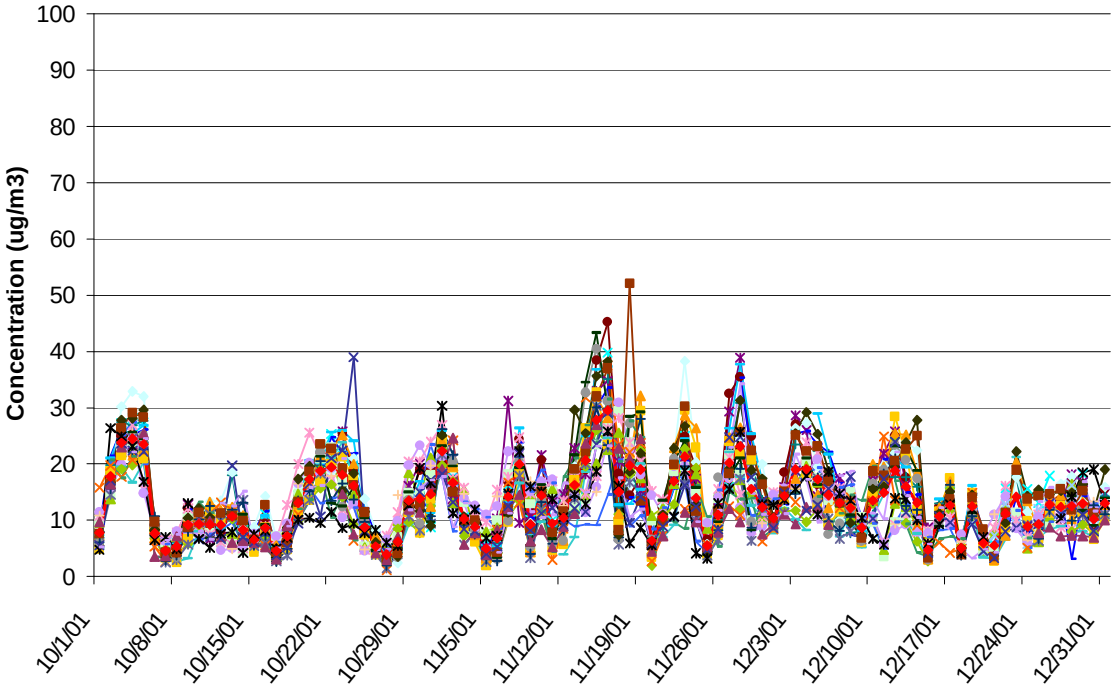

Figure B-4 Daily $PM_{2.5}$ FRM Time Series, October-December 2001

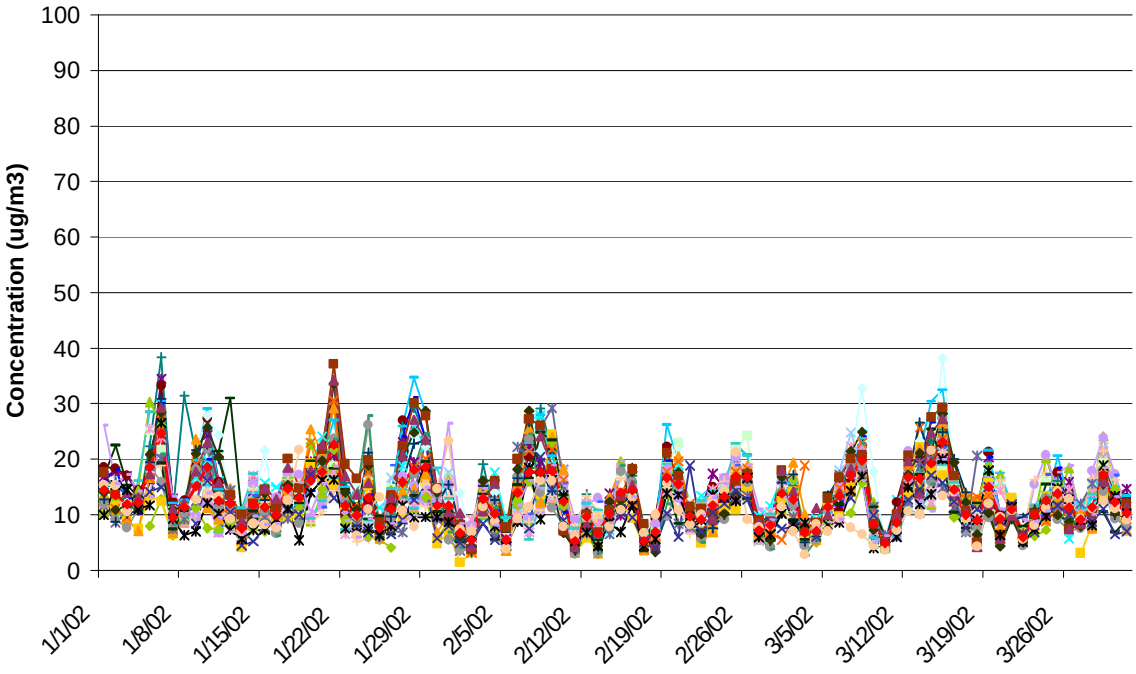

Figure B-5 Daily $PM_{2.5}$ FRM Time Series, January-March 2002

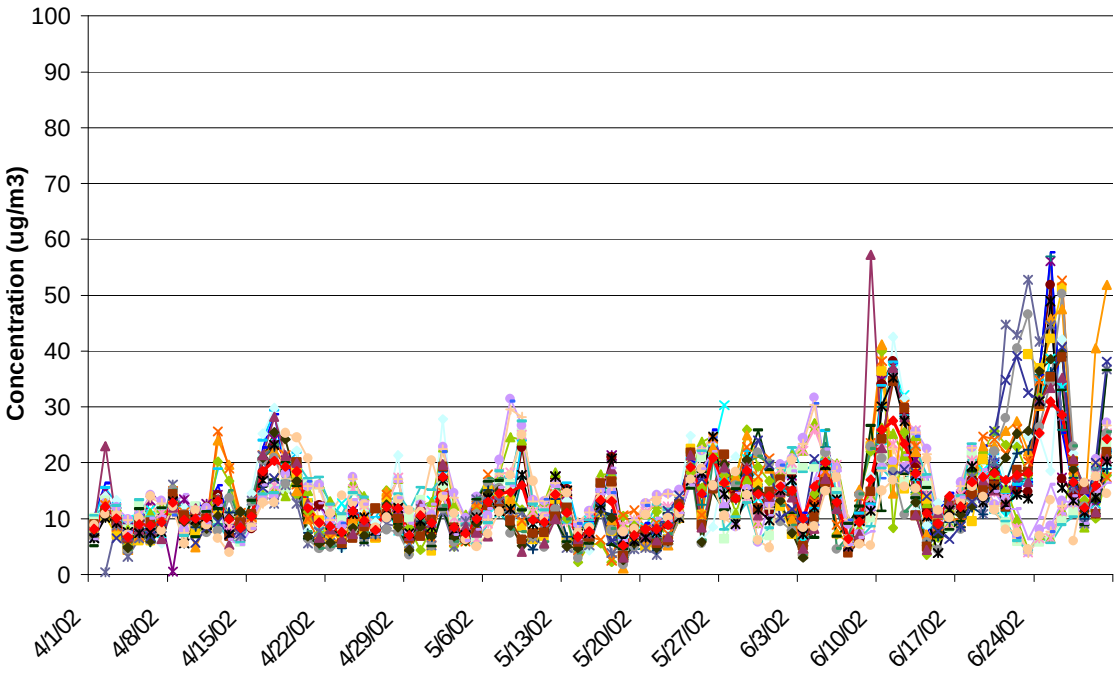

Figure B-6 Daily $PM_{2.5}$ FRM Time Series, April-June 2002

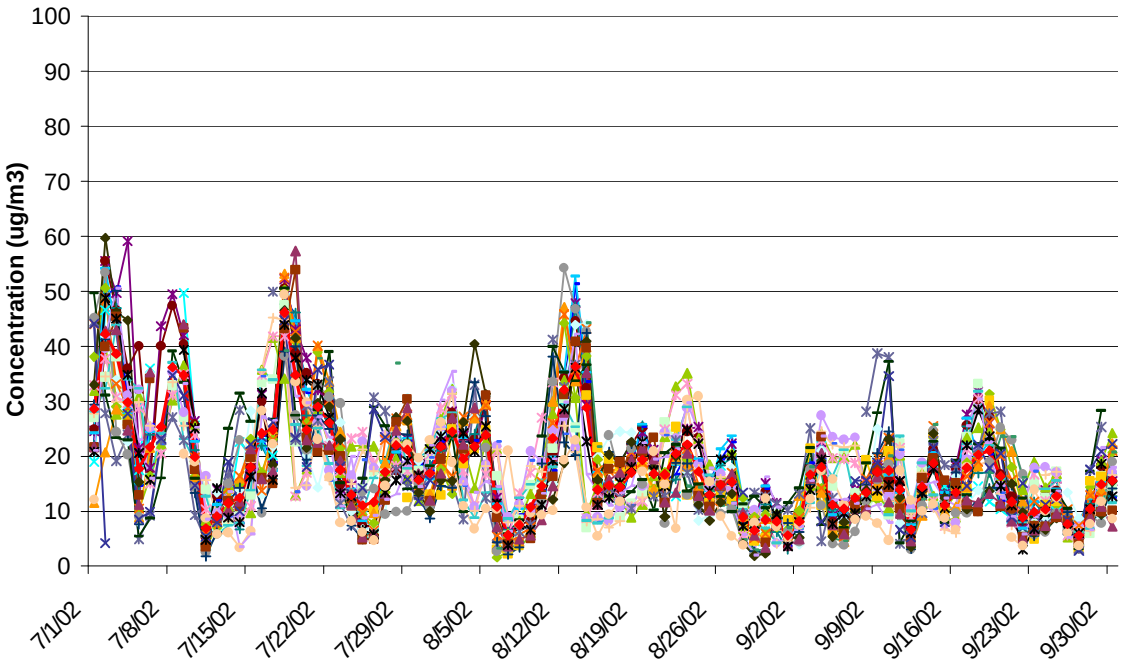

Figure B-7 Daily $PM_{2.5}$ FRM Time Series, July-September 2002

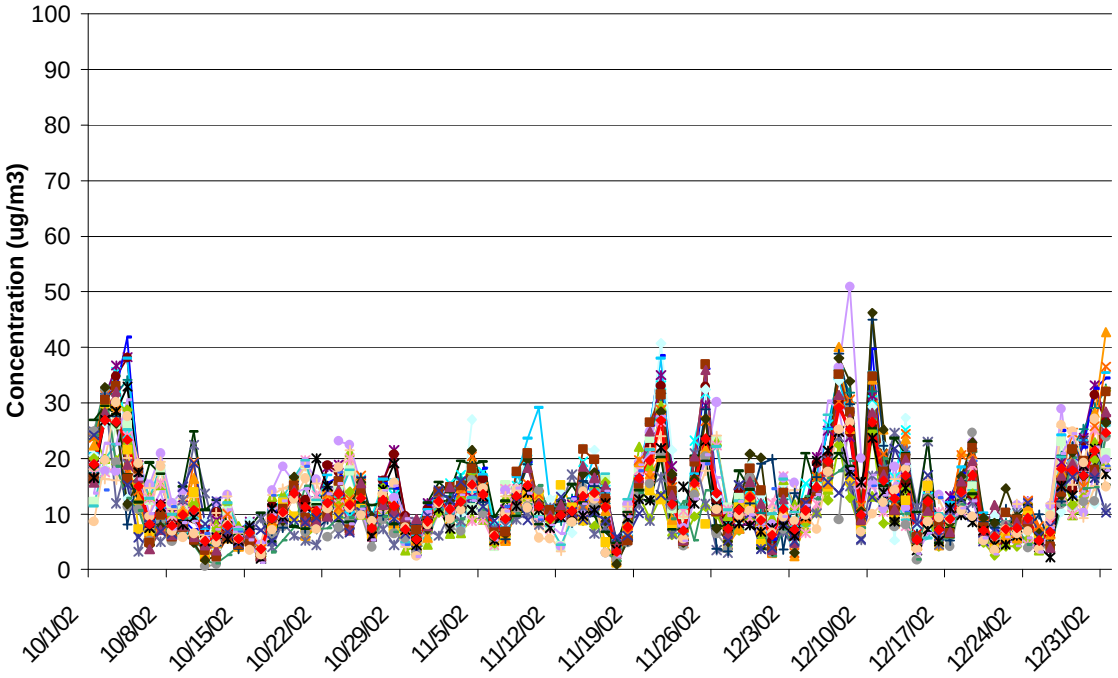

Figure B-8 Daily $PM_{2.5}$ FRM Time Series, October-December 2002

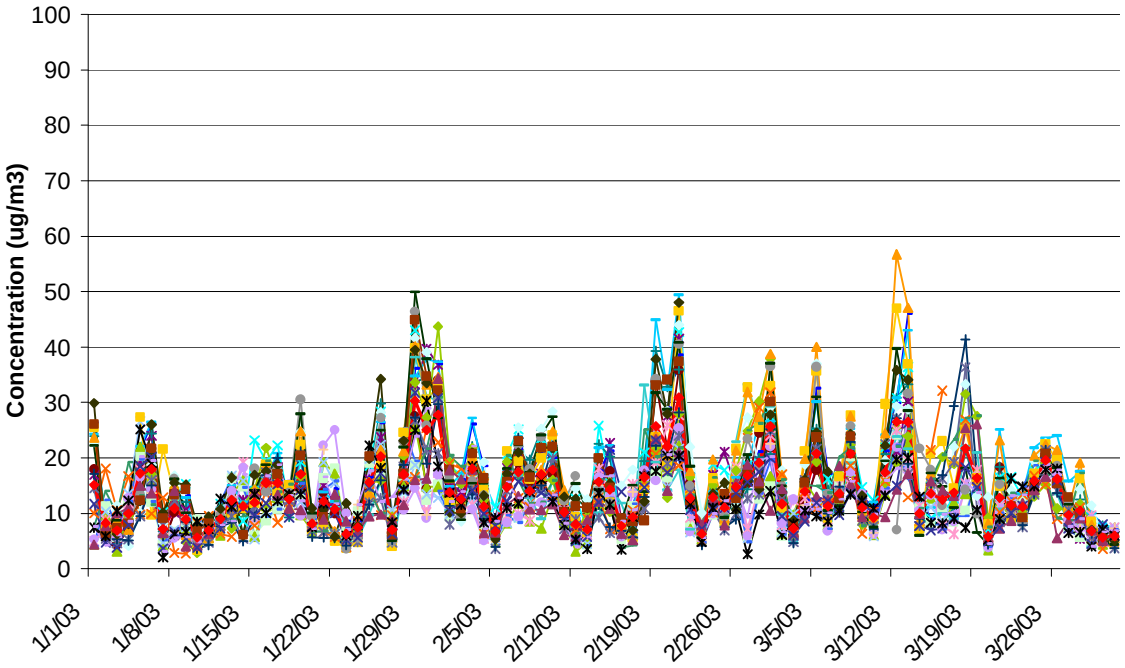

Figure B-9 Daily $PM_{2.5}$ FRM Time Series, January-March 2003

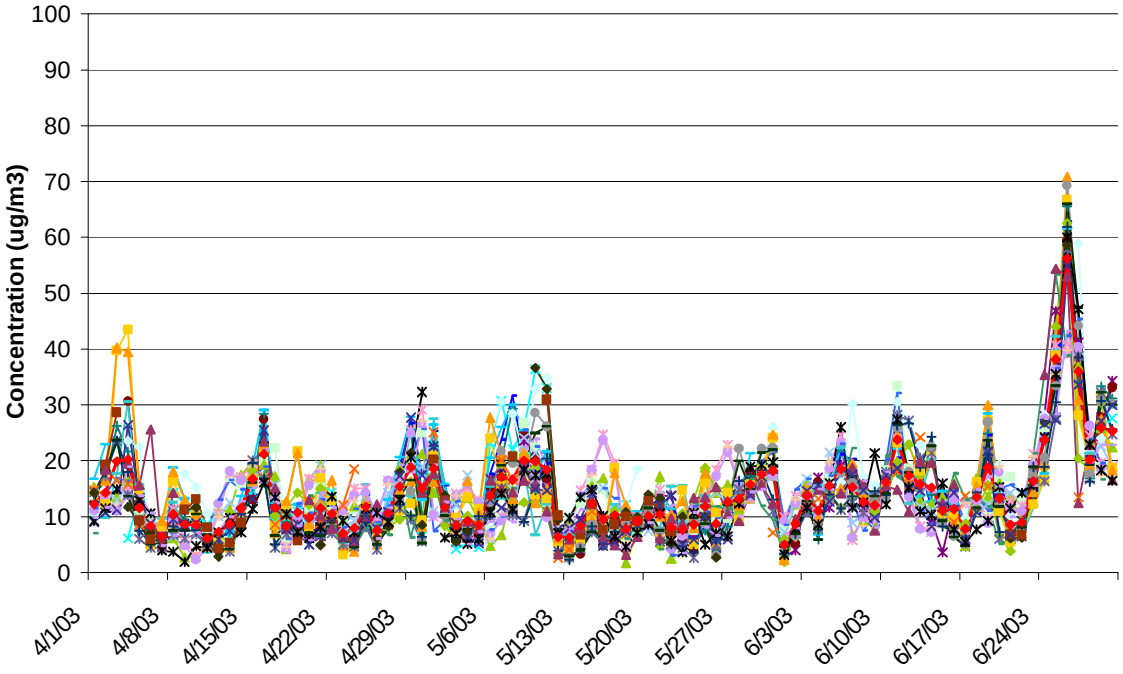

Figure B-10 Daily $PM_{2.5}$ FRM Time Series, April-June 2003

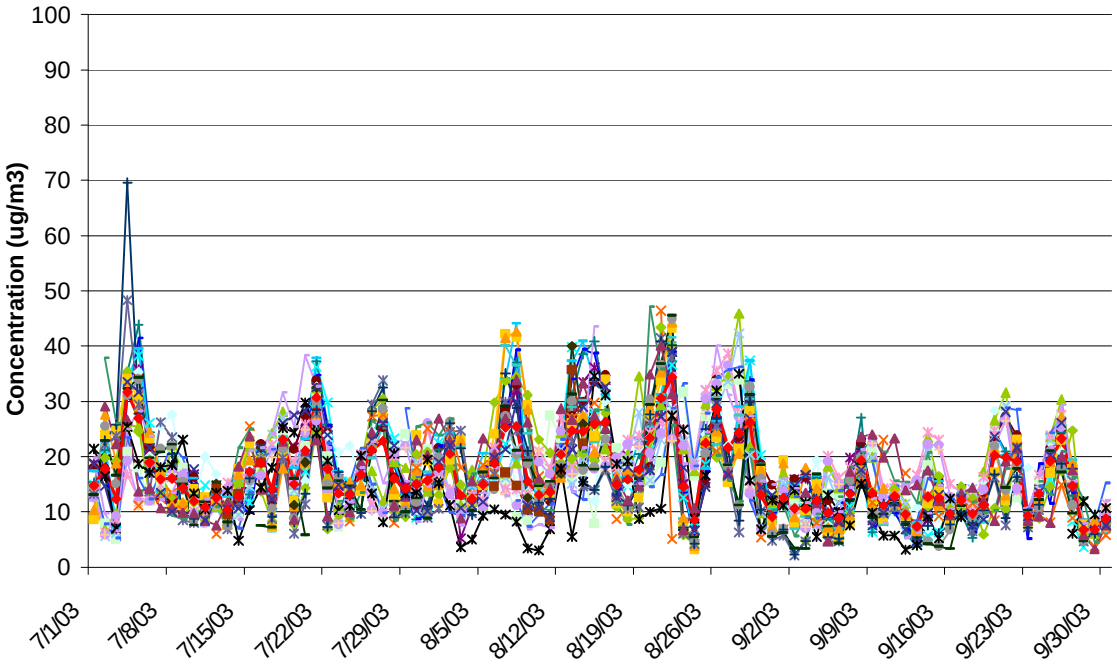

Figure B-11 Daily $PM_{2.5}$ FRM Time Series, July-September 2003

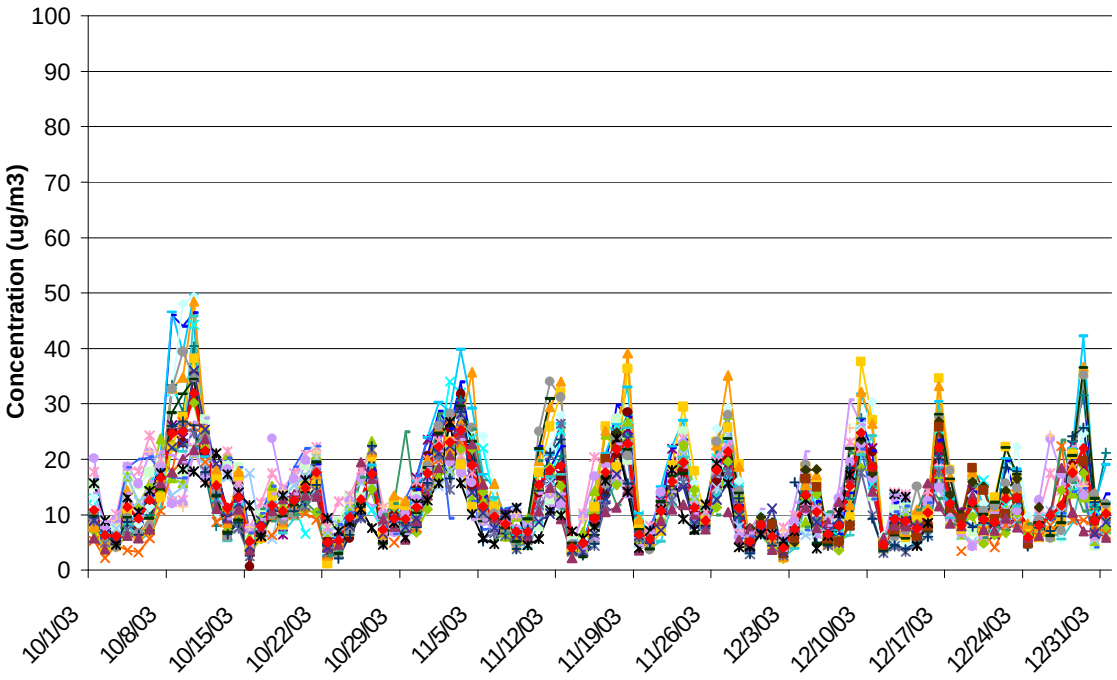

Figure B-12 Daily $PM_{2.5}$ FRM Time Series, October-December 2003

Appendix C: Null and Flagged Data Analysis

This appendix provides basic information about the number of flagged and null data found in the data analyzed for this report. This appendix also provides information about the predominate flag found in the data analyzed. The tables below present information for the period from January 1, 2001 through December 31, 2003 if data was available through this entire period. As noted in the tables, in many cases, samplers were put in operation after January 1, 2001. In these cases, information on flagged and null data is presented for the period when the monitor was brought on-line through December 31, 2003. The data used to make regional comparisons in this report covered the period from September 10, 2001 through October 12, 2003.

Table C-1 provides a summary of the null and flagged data for the eleven sites used in the regional comparisons. The table lists:

- The site name and state,
- The sample collection frequency for the site,
- The date the speciation sampler was put in operation,
- The total number of raw data records for all analytes from January 1, 2001 (or the day the monitor was put in operation, if later) to December 31, 2003,
- The percent of records that were null (no value reported),
- The percent of records that were flagged (any flag)
- The percent of flagged records flagged as "outlier, cause unknown."

As the table shows, the average percent null data across all sites was 6.3 percent. The percentage of null data ranged from a high in Charlotte, NC at 10.2 percent to a low of 4.0 percent in Philadelphia, PA. Average percent flagged data across all sites was 6.7 percent. By far the most frequent flag was "5," the flag defined as "outlier, cause unknown."

Table C-1 Percent of Null and Flagged Records

Site Name and State	Collection Frequency (Days)	Date Monitoring Started	Total Number of Raw Records	Null Records (%)	Flagged Records (%)	Percent of Flagged Data Flagged as "Outlier" (%)
Arendtsville, PA	6	07/01/01	8,158	5.6	8.2	91.7
Baltimore, MD	3	10/01/00	16,827	8.3	3.7	14.1
Charlotte, NC	3	10/01/00	17,365	10.2	5.4	52.9
Dover, DE	6	02/11/99	8,878	5.2	6.9	87.5
Elizabeth, NJ	3	05/13/01	15,064	4.3	6.6	79.3
Kinston, NC	6	01/01/02	6,982	7.4	9.4	56.0
Philadelphia, PA	3	02/04/99	18,893	4.0	6.0	67.8
Pittsburgh, PA	3	06/30/01	18,721	8.1	2.8	64.0
Richmond, VA	3	03/02/01	16,077	4.1	7.6	78.4
Washington, DC	3	03/26/01	16,082	6.1	12.1	16.2
Wilmington, DE	6	02/14/99	8,998	7.0	5.4	84.6
Averages				6.4	6.7	63.0

The assignment of flags is briefly discussed in this report in the section titled, Methodology and Data Handling Techniques for Speciation Data. A more complete discussion of the data

validation process and the assignment of flags is described in the RTI publication, *"Data Validation Process for the $PM_{2.5}$ Chemical Speciation Network"* which is available at: http://www.epa.gov/ttn/amtic/specdat.html.

Tables C-2 through C-6 present the percentage of records that were null or flagged for the five major species used in the regional analysis. The "Number of Dates in Raw Dataset" column is the number of records found for the specie over 2001-2003.

Table C-2 Percent of Null and Flagged Sulfate Records

Sulfate						
Site Name	**Collection Frequency**	**Date Monitoring Started**	**Number of Dates in Raw Dataset**	**Flagged Records (%)**	**Null Records (%)**	**Remaining Data (%)**
Arendtsville, PA	6	07/01/01	142	8.5	4.2	87.3
Baltimore, MD	3	10/01/00	296	6.4	8.8	84.8
Charlotte, NC	3	10/01/00	304	9.2	8.9	81.9
Dover, DE	6	02/11/99	155	11.0	5.2	83.9
Elizabeth, NJ	3	05/13/01	263	14.8	5.3	79.8
Kinston, NC	6	01/01/02	121	14.0	7.4	78.5
Philadelphia, PA	3	02/04/99	330	14.2	3.0	82.7
Pittsburgh, PA	3	06/30/01	320	5.0	8.1	86.9
Richmond, VA	3	03/02/01	281	22.1	5.7	72.2
Washington, DC	3	03/26/01	281	13.9	6.8	79.4
Wilmington, DE	6	02/14/99	157	7.0	6.4	86.6

Table C-3 Percent of Null and Flagged Organic Carbon Records

Organic Carbon						
Site Name	**Collection Frequency**	**Date Monitoring Started**	**Number of Dates in Raw Dataset**	**Flagged Records (%)**	**Null Records (%)**	**Remaining Data (%)**
Arendtsville, PA	6	07/01/01	142	8.5	6.3	85.2
Baltimore, MD	3	10/01/00	296	3.4	7.8	88.9
Charlotte, NC	3	10/01/00	304	5.6	9.5	84.9
Dover, DE	6	02/11/99	155	6.5	5.2	88.4
Elizabeth, NJ	3	05/13/01	263	5.7	5.7	89.0
Kinston, NC	6	01/01/02	121	9.1	6.6	84.3
Philadelphia, PA	3	02/04/99	330	5.2	2.4	92.4
Pittsburgh, PA	3	06/30/01	320	1.6	8.4	90.0
Richmond, VA	3	03/02/01	281	6.8	3.9	89.3
Washington, DC	3	03/26/01	281	12.1	7.1	80.8
Wilmington, DE	6	02/14/99	157	5.1	7.0	87.9

Table C-4 Percent of Null and Flagged Ammonium Records

Ammonium						
Site Name	**Collection Frequency**	**Date Monitoring Started**	**Number of Dates in Raw Dataset**	**Flagged Records (%)**	**Null Records (%)**	**Remaining Data (%)**
Arendtsville, PA	6	07/01/01	142	8.5	4.2	87.3
Baltimore, MD	3	10/01/00	296	5.4	8.8	85.8
Charlotte, NC	3	10/01/00	304	8.2	8.9	82.9
Dover, DE	6	02/11/99	155	9.7	5.2	85.2
Elizabeth, NJ	3	05/13/01	263	13.3	5.3	79.8
Kinston, NC	6	01/01/02	121	10.7	7.4	81.8
Philadelphia, PA	3	02/04/99	330	8.5	3.0	88.5
Pittsburgh, PA	3	06/30/01	320	4.4	8.1	87.5
Richmond, VA	3	03/02/01	281	8.9	5.7	85.4
Washington, DC	3	03/26/01	281	13.5	6.8	79.7
Wilmington, DE	6	02/14/99	157	7.0	6.4	86.6

Table C-5 Percent of Null and Flagged Nitrate Records

Nitrate						
Site Name	**Collection Frequency**	**Date Monitoring Started**	**Number of Dates in Raw Dataset**	**Flagged Records (%)**	**Null Records (%)**	**Remaining Data (%)**
Arendtsville, PA	6	07/01/01	142	8.5	4.2	87.3
Baltimore, MD	3	10/01/00	296	5.4	8.8	85.8
Charlotte, NC	3	10/01/00	304	8.2	8.9	82.9
Dover, DE	6	02/11/99	155	9.7	5.2	85.2
Elizabeth, NJ	3	05/13/01	263	13.3	5.3	79.8
Kinston, NC	6	01/01/02	121	10.7	7.4	81.8
Philadelphia, PA	3	02/04/99	330	8.5	3.0	88.5
Pittsburgh, PA	3	06/30/01	320	4.4	8.1	87.5
Richmond, VA	3	03/02/01	281	8.9	5.7	85.4
Washington, DC	3	03/26/01	281	13.5	6.8	79.7
Wilmington, DE	6	02/14/99	157	7.0	6.4	86.6

Table C-6 Percent of Null and Flagged Elemental Carbon Records

Elemental Carbon						
Site Name	**Collection Frequency**	**Date Monitoring Started**	**Number of Dates in Raw Dataset**	**Flagged Records (%)**	**Null Records (%)**	**Remaining Data (%)**
Arendtsville, PA	6	07/01/01	142	8.5	6.3	85.2
Baltimore, MD	3	10/01/00	296	3.4	7.8	88.9
Charlotte, NC	3	10/01/00	304	5.6	9.5	84.9
Dover, DE	6	02/11/99	155	6.5	5.2	88.4
Elizabeth, NJ	3	05/13/01	263	5.7	5.3	89.0
Kinston, NC	6	01/01/02	121	10.7	7.4	81.8
Philadelphia, PA	3	02/04/99	330	5.2	2.4	92.4
Pittsburgh, PA	3	06/30/01	320	1.6	8.4	90.0
Richmond, VA	3	03/02/01	281	6.8	3.9	89.3
Washington, DC	3	03/26/01	281	12.1	7.1	80.8
Wilmington, DE	6	02/14/99	157	5.1	7.0	87.9

Appendix D: Organic Carbon Blank Analysis

Since blank measurements were not made every time an organic carbon measurement was made, MARAMA estimated organic carbon blank corrections that were applied to the data by averaging the field and trip blanks collected at a site. Table D-1 summarizes the average organic carbon blank values used to adjust organic carbon data in this analysis. Figures D-1 through D-12 are time series showing how field and trip blanks varied over time at each monitoring site analyzed.

Table D-1 Average Organic Carbon Blank Concentration by Monitoring Site

Site	Average Organic Carbon Blank ($\mu g/m^3$)	Number of Blanks Used to Calculate Average	Time Period
Arendtsville, PA	1.24	16	7/14/01 to 10/12/03
Baltimore, MD	0.90	112	1/28/2002 to 9/21/03
Charleston, WV	1.16	11	6/2/04 to 9/7/05
Charlotte, NC	1.47	88	1/31/01 to 9/15/03
Dover, DE	1.42	21	6/12/01 to 10/12/03
Elizabeth, NJ	1.41	87	5/25/01 to 4/30/03
Kinston, NC	1.49	16	1/2/02 to 10/12/03
Philadelphia, PA	0.99	58	1/31/01 to 1/30/03
Pittsburgh, PA	1.22	57	7/14/01 to 10/3/03
Richmond, VA	1.31	98	3/14/01 to 9/21/03
Washington, DC	1.05	84	4/1/01 to 9/21/03
Wilmington, DE	1.42	29	6/12/01 to 9/30/03
Regional Average	1.26		

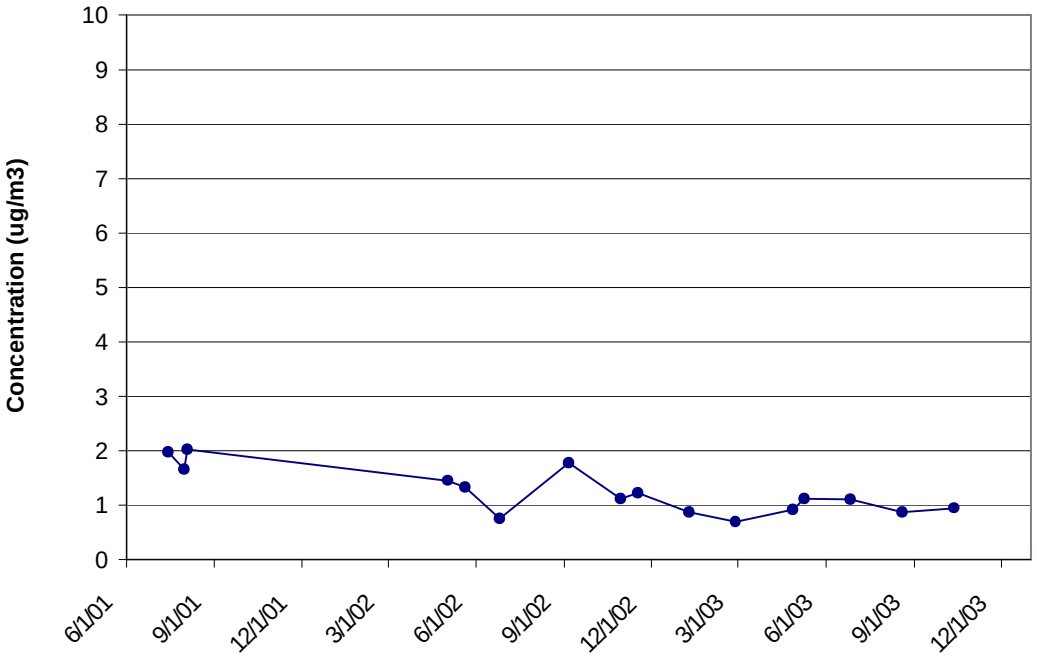

Figure D-1 Organic Carbon Blank Concentration, Arendtsville, PA

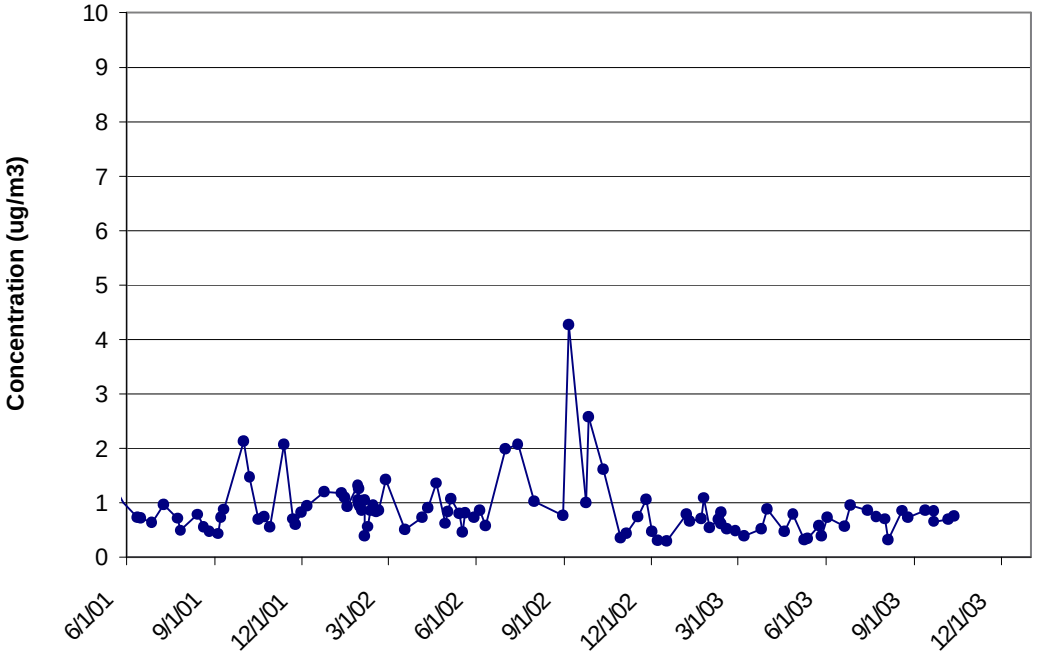

Figure D-2 Organic Carbon Blank Concentration, Baltimore, MD

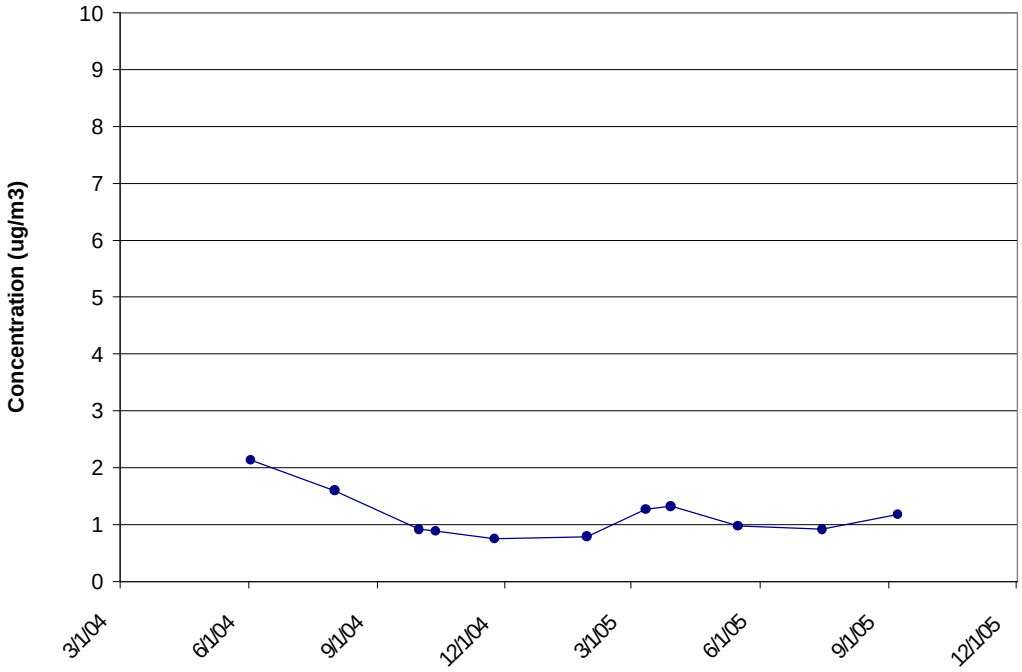

Figure D-3 Organic Carbon Blank Concentration, Charleston, WV

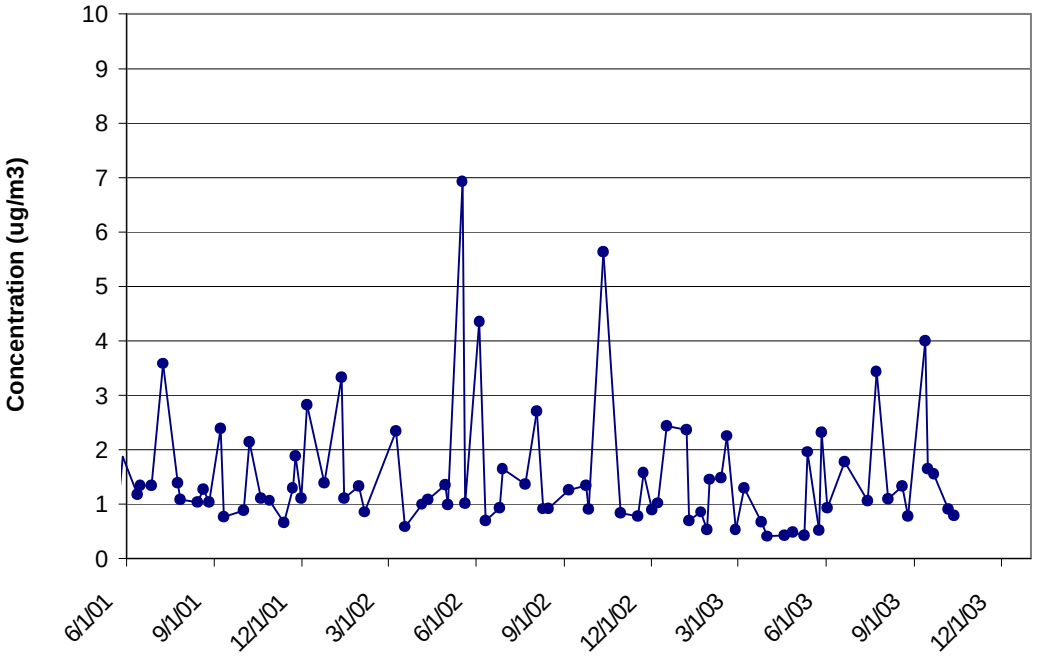

Figure D-4 Organic Carbon Blank Concentration, Charlotte, NC

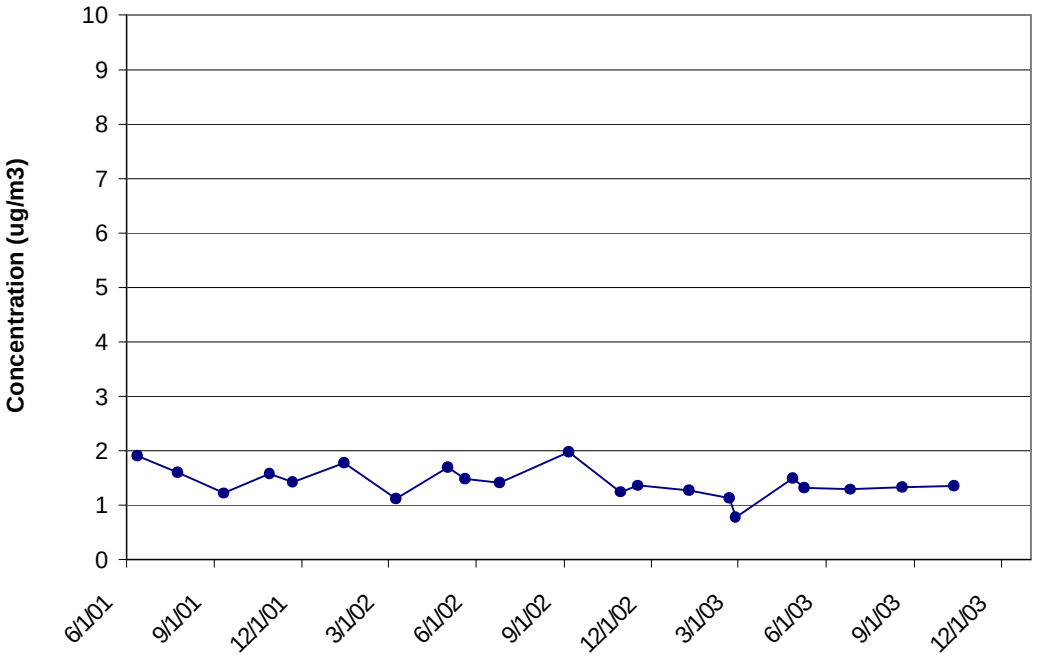

Figure D-5 Organic Carbon Blank Concentration, Dover, DE

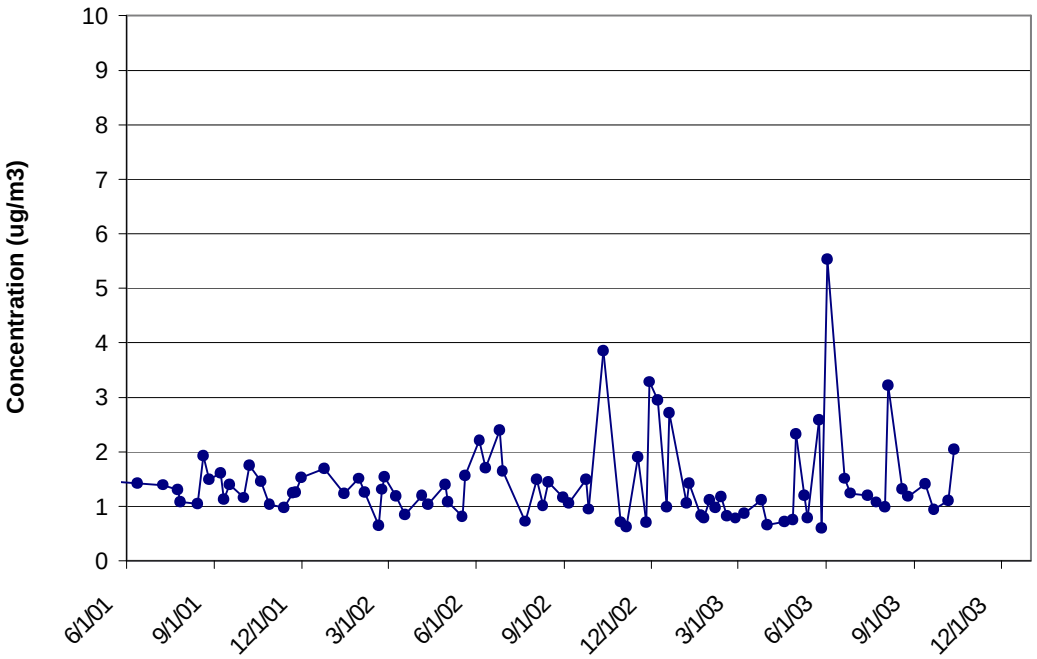

Figure D-6 Organic Carbon Blank Concentration, Elizabeth, NJ

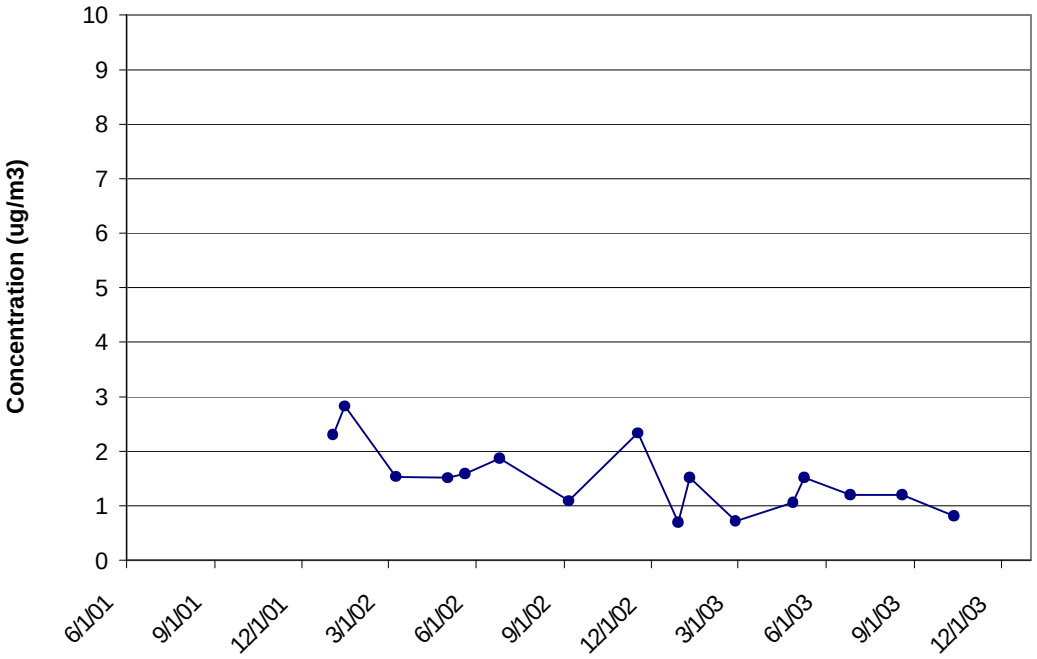

Figure D-7 Organic Carbon Blank Concentration, Kinston, NC

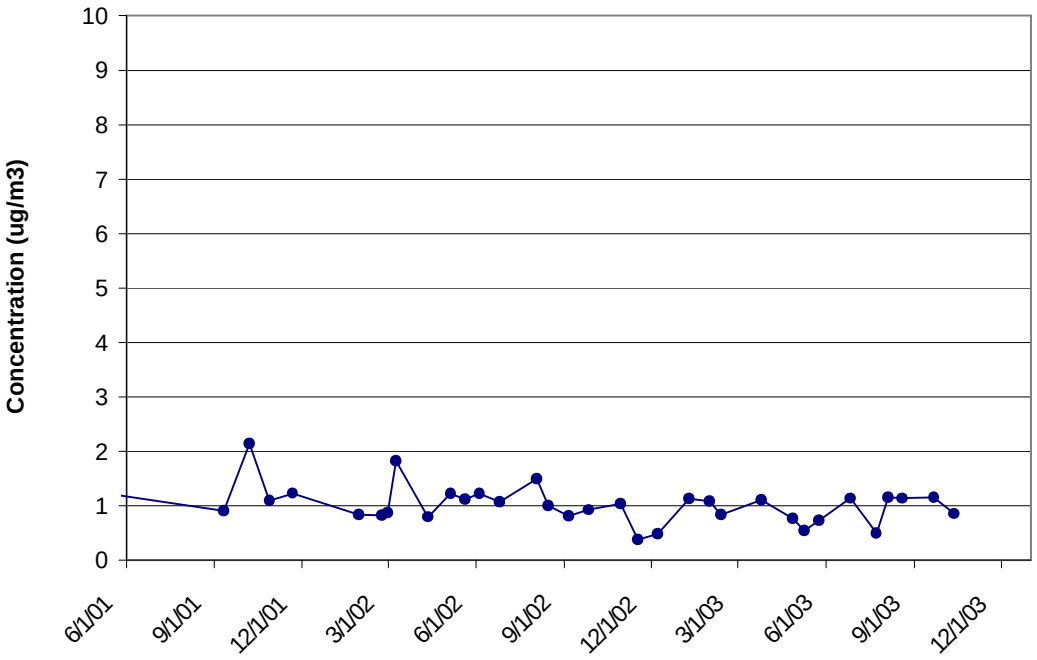

Figure D-8 Organic Carbon Blank Concentration, Philadelphia, PA

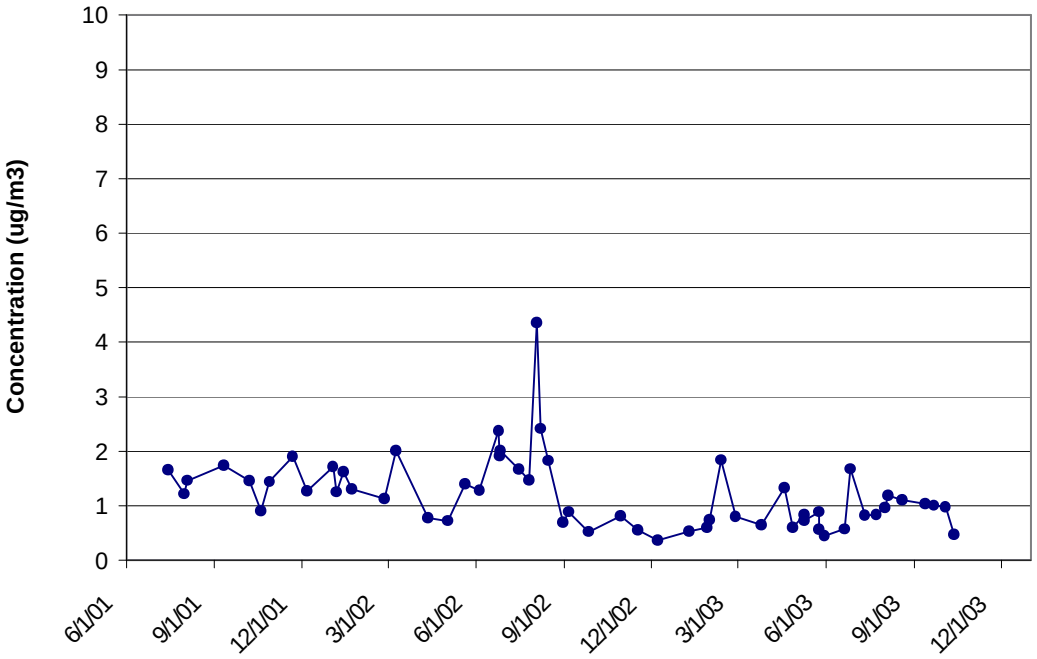

Figure D-9 Organic Carbon Blank Concentration, Pittsburgh, PA

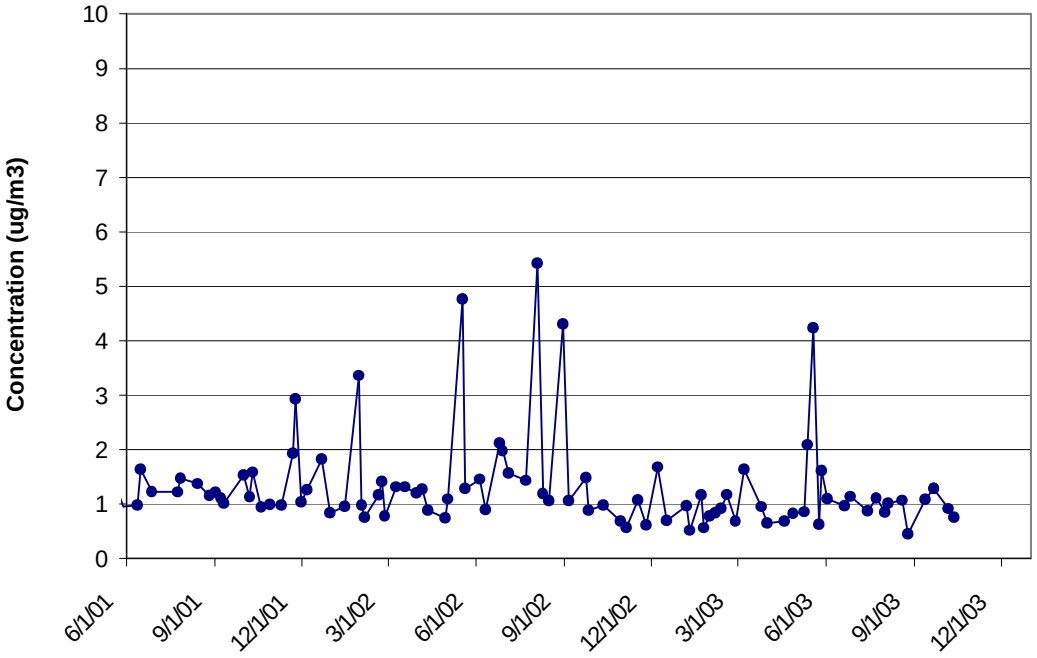

Figure D-10 Organic Carbon Blank Concentration, Richmond, VA

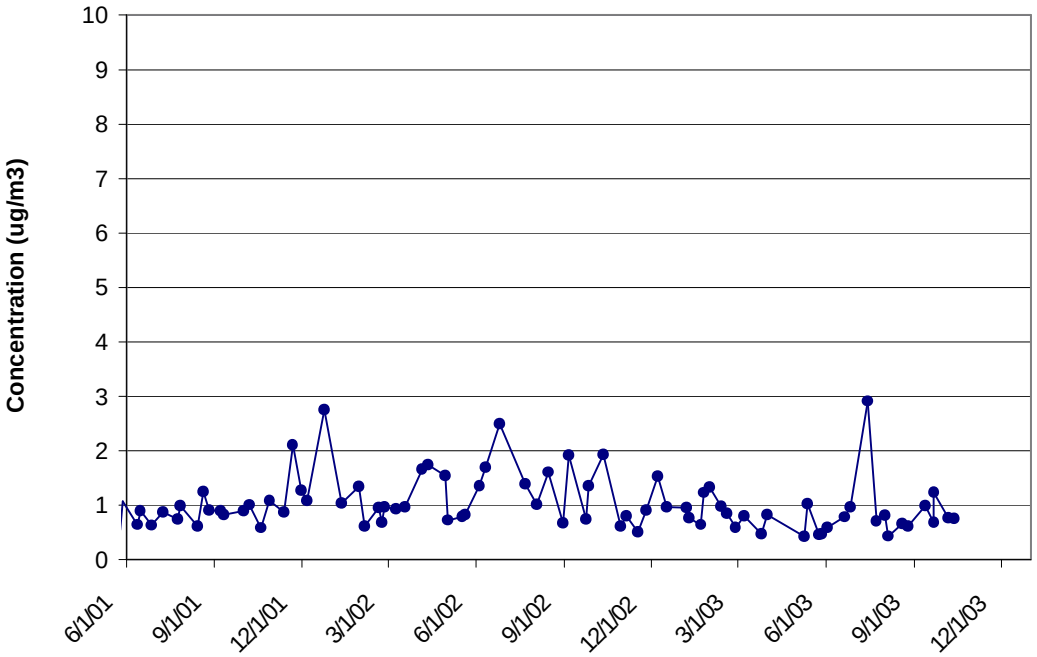

Figure D-11 Organic Carbon Blank Concentration, Washington, DC

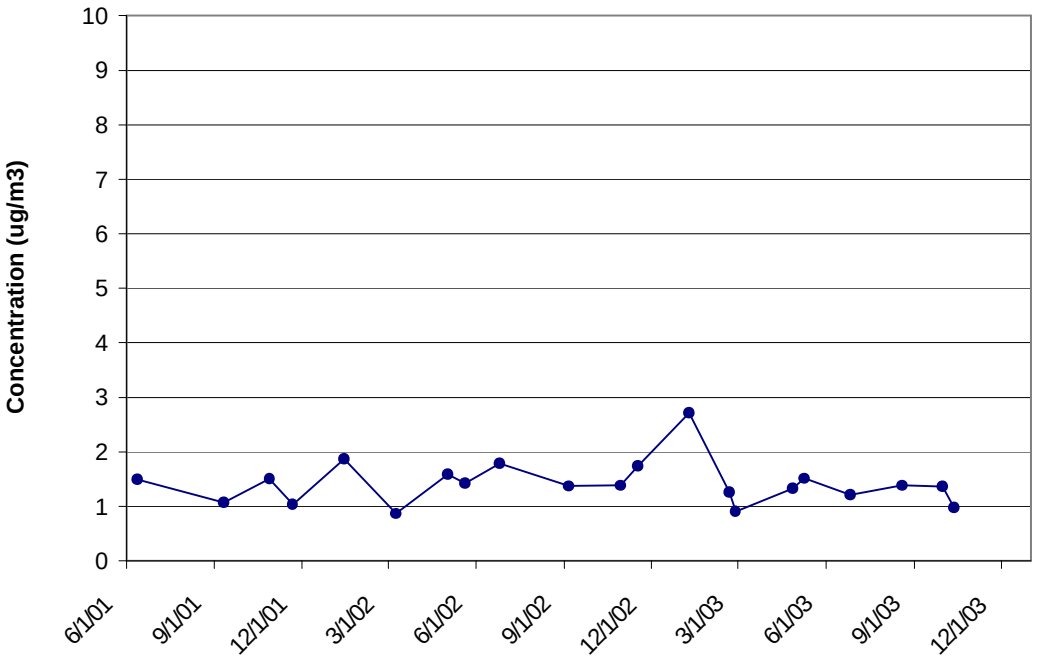

Figure D-12 Organic Carbon Blank Concentration, Wilmington, DE

Appendix E: Method Detection Limit Analysis

MARAMA's analysis of speciation data focused on the five major components of $PM_{2.5}$ mass: ammonium, elemental carbon, nitrate, organic carbon, and sulfate. The analysis focused on these species because they often make up 90 percent or more of measured $PM_{2.5}$ mass. To explore whether these species were being measured above the Method Detection Limit (MDL) of the analytical laboratories that process speciation filters, MARAMA evaluated the speciation data collected at the Martin Luther King Jr. monitoring site in Wilmington, DE (AIRS number 10-003-2004). In evaluating the data, MARAMA was also interested in determining if a large number of trace element measurements were being made at or below the MDL.

Table E-1 summarizes MDL and measurement information for each analyte measured at the Wilmington monitor. The Table provides:

- Estimates of the high and low MDL, expressed in units of ug/filter and ug/m^3,
- The number of measurements made from June 12, 2001 to December 29, 2003,
- The percent of measurements that were zero,
- The percent of measurements that were less than or equal to the high MDL and not zero, and
- The percent of measurements that were less than or equal to the high MDL and zero.

As the table shows, all measurements of the five major species at Wilmington were not zero and all measurements, except a few for elemental carbon, were above the high MDL. This is encouraging and provides analysts with some level of confidence that the data are valid. Many measurements of trace elements were zero or below the high MDL, however. This raises concerns about the quality and validity of these measurements. Further work needs to be done to determine if trace element measurements, both above and below the MDL, are valid and useful in source apportionment and other analyses. If trace element measurements are not valid or useful, collection of these data should be suspended, saving time, money and resources.

Trace element measurements are made by two XRF instruments at the RTI lab in Research Triangle Park, NC and by two XRF instruments at the Chester lab in Tigard, OR. Samples from the MARAMA Region are randomly assigned to both labs. Since samples could have been analyzed by any of the four instruments and MDLs vary by instrument and lab, Table E-1 reports a "high" MDL, the highest MDL of all four instruments and the "low" MDL, the lowest MDL of all four instruments. The highest MDL was used to estimate the number of measurements above and below the MDL because it is not clear in speciation datasets which instrument made the analysis. Applying the high MDL provides a conservative estimate of the number of measurements above and below the MDL.

Table E-1 Speciation Measurements Made at or Below the MDL, Wilmington, DE

Analyte	$PM_{2.5}$ Gravimetric Mass	Antimony	Arsenic	Aluminum
Analyte Number	88101	88102	88103	88104
High MDL (ug/filter)	7.2	0.267	0.037	0.219
Low MDL (ug/filter)	7.2	0.158	0.014	0.157
High MDL (ug/m^3)	0.7463	0.0277	0.0038	0.0227
Low MDL (ug/m^3)		0.0164	0.0015	0.0163
Number of Measurements	136	138	138	138
Percent of Measurements Equal to Zero	0.0%	52.9%	31.2%	44.9%
Percent of Measurements <=HMDL but not Zero	0.0%	42.8%	62.3%	37.7%
Percent of Measurements <=HMDL or Zero	0.0%	95.7%	93.5%	82.6%

Analyte	Barium	Bromine	Cadmium	Calcium	Chromium
Analyte Number	88107	88109	88110	88111	88112
High MDL (ug/filter)	0.85	0.031	0.152	0.071	0.023
Low MDL (ug/filter)	0.099	0.011	0.095	0.044	0.019
High MDL (ug/m^3)	0.0881	0.0032	0.0158	0.0074	0.0024
Low MDL (ug/m^3)	0.0103	0.0011	0.0098	0.0046	0.0020
Number of Measurements	138	138	138	138	138
Percent of Measurements Equal to Zero	24.6%	4.3%	44.9%	0.0%	12.3%
Percent of Measurements <=HMDL but not Zero	72.5%	45.7%	51.4%	1.4%	67.4%
Percent of Measurements <=HMDL or Zero	97.1%	50.0%	96.4%	1.4%	79.7%

Analyte	Cobalt	Copper	Chlorine	Cerium	Cesium
Analyte Number	88113	88114	88115	88117	88118
High MDL (ug/filter)	0.02	0.024	0.132	1.242	0.533
Low MDL (ug/filter)	0.014	0.019	0.078	0.08	0.097
High MDL (ug/m^3)	0.0021	0.0025	0.0137	0.1287	0.0552
Low MDL (ug/m^3)	0.0015	0.0020	0.0081	0.0083	0.0101
Number of Measurements	138	138	138	138	138
Percent of Measurements Equal to Zero	65.2%	2.2%	41.3%	47.1%	55.8%
Percent of Measurements <=HMDL but not Zero	33.3%	7.2%	28.3%	52.9%	44.2%
Percent of Measurements <=HMDL or Zero	98.6%	9.4%	69.6%	100.0%	100.0%

Analyte	Europium	Gallium	Iron	Hafnium	Lead
Analyte Number	88121	88124	88126	88127	88128
High MDL (ug/filter)	0.162	0.071	0.028	0.378	0.085
Low MDL (ug/filter)	0.036	0.026	0.02	0.155	0.027
High MDL (ug/m^3)	0.0168	0.0074	0.0029	0.0392	0.0088
Low MDL (ug/m^3)	0.0037	0.0027	0.0021	0.0161	0.0028
Number of Measurements	138	138	138	138	138
Percent of Measurements Equal to Zero	77.5%	68.8%	0.0%	72.5%	18.8%
Percent of Measurements <=HMDL but not Zero	18.8%	31.2%	0.0%	27.5%	71.0%
Percent of Measurements <=HMDL or Zero	96.4%	100.0%	0.0%	100.0%	89.9%

1 Analyte	Indium	Manganese	Iridium	Molybdenum	Nickel
Analyte Number	88131	88132	88133	88134	88136
High MDL (ug/filter)	0.163	0.033	0.165	0.085	0.018
Low MDL (ug/filter)	0.108	0.015	0.04	0.069	0.015
High MDL (ug/m^3)	0.0169	0.0034	0.0171	0.0088	0.0019
Low MDL (ug/m^3)	0.0112	0.0016	0.0041	0.0072	0.0016
Number of Measurements	138	138	138	138	138
Percent of Measurements Equal to Zero	46.4%	18.1%	54.3%	48.6%	0.7%
Percent of Measurements <=HMDL but not Zero	52.9%	49.3%	45.7%	50.7%	16.7%
Percent of Measurements <=HMDL or Zero	99.3%	67.4%	100.0%	99.3%	17.4%

Analyte	Magnesium	Mercury	Gold	Lanthanum	Niobium
Analyte Number	88140	88142	88143	88146	88147
High MDL (ug/filter)	0.427	0.065	0.127	1.004	0.067
Low MDL (ug/filter)	0.175	0.033	0.037	0.083	0.033
High MDL (ug/m^3)	0.0443	0.0067	0.0132	0.1041	0.0069
Low MDL (ug/m^3)	0.0181	0.0034	0.0038	0.0086	0.0034
Number of Measurements	138	138	138	138	138
Percent of Measurements Equal to Zero	77.5%	44.9%	42.0%	62.3%	60.1%
Percent of Measurements <=HMDL but not Zero	20.3%	55.1%	58.0%	37.7%	39.1%
Percent of Measurements <=HMDL or Zero	97.8%	100.0%	100.0%	100.0%	99.3%

Analyte	Phosphorous	Selenium	Tin	Titanium	Samarium
Analyte Number	88152	88154	88160	88161	88162
High MDL (ug/filter)	0.102	0.033	0.258	0.048	0.089
Low MDL (ug/filter)	0.056	0.025	0.131	0.03	0.041
High MDL (ug/m^3)	0.0106	0.0034	0.0267	0.0050	0.0092
Low MDL (ug/m^3)	0.0058	0.0026	0.0136	0.0031	0.0042
Number of Measurements	138	138	138	138	138
Percent of Measurements Equal to Zero	72.5%	13.8%	30.4%	2.9%	74.6%
Percent of Measurements <=HMDL but not Zero	20.3%	71.7%	66.7%	39.1%	24.6%
Percent of Measurements <=HMDL or Zero	92.8%	85.5%	97.1%	42.0%	99.3%

Analyte	Scandium	Vanadium	Silicon	Silver	Zinc
Analyte Number	88163	88164	88165	88166	88167
High MDL (ug/filter)	0.035	0.031	0.178	0.151	0.025
Low MDL (ug/filter)	0	0.021	0.098	0.082	0.017
High MDL (ug/m^3)	0.0036	0.0032	0.0184	0.0157	0.0026
Low MDL (ug/m^3)	0.0000	0.0022	0.0102	0.0085	0.0018
Number of Measurements	138	138	138	138	138
Percent of Measurements Equal to Zero	68.8%	1.4%	0.0%	42.0%	1.4%
Percent of Measurements <=HMDL but not Zero	31.2%	19.6%	3.6%	56.5%	6.5%
Percent of Measurements <=HMDL or Zero	100.0%	21.0%	3.6%	98.6%	8.0%

Analyte	Strontium	Sulfur	Tantalum	Terbium	Rubidium
Analyte Number	88168	88169	88170	88172	88176
High MDL (ug/filter)	0.036	0.204	0.282	0.109	0.031
Low MDL (ug/filter)	0.017	0.085	0.074	0.042	0.014
High MDL (ug/m^3)	0.0037	0.0211	0.0292	0.0113	0.0032
Low MDL (ug/m^3)	0.0018	0.0088	0.0077	0.0044	0.0015
Number of Measurements	138	137	138	138	138
Percent of Measurements Equal to Zero	45.7%	0.0%	43.5%	79.7%	56.5%
Percent of Measurements <=HMDL but not Zero	52.2%	0.0%	48.6%	18.8%	42.8%
Percent of Measurements <=HMDL or Zero	97.8%	0.0%	92.0%	98.6%	99.3%

Analyte	Potassium	Yttrium	Sodium (XRF)	Zirconium	Wolfram
Analyte Number	88180	88183	88184	88185	88186
High MDL (ug/filter)	0.106	0.044	1.58	0.054	0.208
Low MDL (ug/filter)	0.049	0.021	0.526	0.027	0.059
High MDL (ug/m^3)	0.0110	0.0046	0.1638	0.0056	0.0216
Low MDL (ug/m^3)	0.0051	0.0022	0.0545	0.0028	0.0061
Number of Measurements	138	138	138	138	138
Percent of Measurements Equal to Zero	0.0%	58.0%	51.4%	53.6%	46.4%
Percent of Measurements <=HMDL but not Zero	2.2%	41.3%	31.2%	44.2%	53.6%
Percent of Measurements <=HMDL or Zero	2.2%	99.3%	82.6%	97.8%	100.0%

Analyte	Ammonium	Sodium (IC)1	Potassium	Organic Carbon (TOT)2	Nitrate
Analyte Number	88301	88302	88303	88305	88306
High MDL (ug/filter)	0.16	0.29	0.134	2.352	0.084
Low MDL (ug/filter)	0.16	0.29	0.134	2.352	0.084
High MDL (ug/m^3)	0.0166	0.0301	0.0139	0.2438	0.0087
Low MDL (ug/m^3)	0.0166	0.0301	0.0139	0.2438	0.0087
Number of Measurements	136	120	136	138	136
Percent of Measurements Equal to Zero	0.0%	2.5%	72.1%	0.0%	0.0%
Percent of Measurements <=HMDL but not Zero	0.0%	5.8%	0.0%	0.0%	0.0%
Percent of Measurements <=HMDL or Zero	0.0%	8.3%	72.1%	0.0%	0.0%

[1] Sodium by ion chromatography, [2] Organic carbon determined by thermal optical transmittance.

Analyte	Elemental Carbon (TOT)3	Sulfate		
Analyte Number	88307	88403		
High MDL (ug/filter)	2.352	0.12		
Low MDL (ug/filter)	2.352	0.12		
High MDL (ug/m^3)	0.2438	0.0124		
Low MDL (ug/m^3)	0.2438	0.0124		
Number of Measurements	138	136		
Percent of Measurements Equal to Zero	0.0%	0.0%		
Percent of Measurements <=HMDL but not Zero	0.7%	0.0%		
Percent of Measurements <=HMDL or Zero	0.7%	0.0%		

[3] Elemental carbon determined by thermal optical transmittance.

Contributions to Regional Haze in the Northeast and Mid-Atlantic United States

Mid-Atlantic/Northeast Visibility Union (MANE-VU) Contribution Assessment

Prepared by NESCAUM
For the Mid-Atlantic/Northeast Visibility Union (MANE-VU)

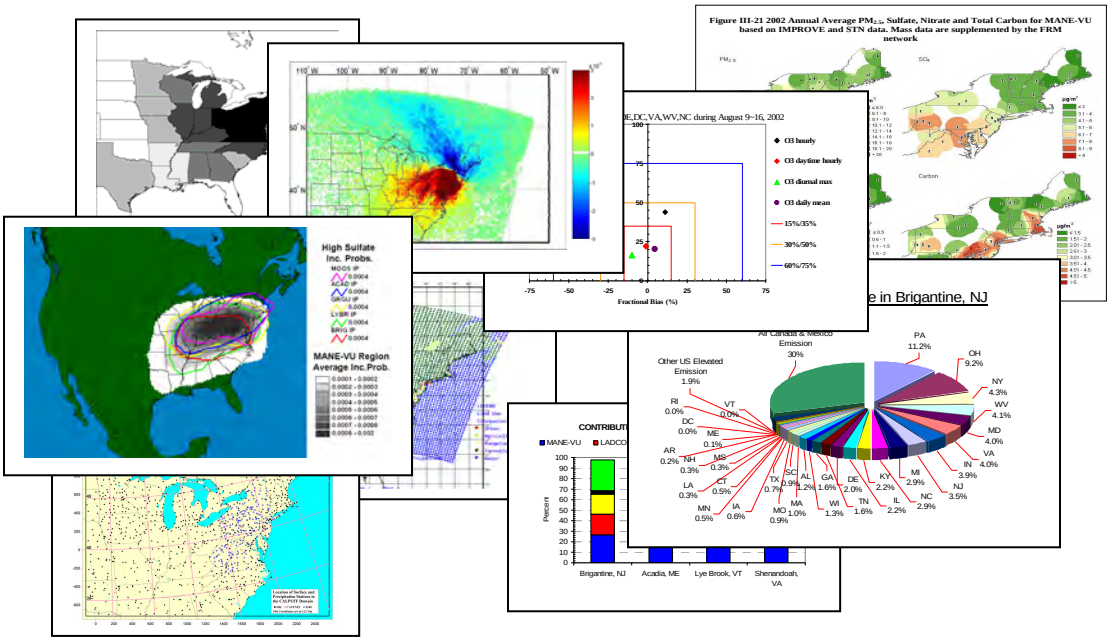

August 2006

Members of NESCAUM Board

Arthur Marin, Executive Director
NESCAUM

Anne Gobin, Bureau Chief
Connecticut Department of Environmental Protection, Bureau of Air Management

James P. Brooks, Bureau Director
Maine Department of Environmental Protection, Bureau of Air Quality

Barbara Kwetz, Director
Massachusetts Department of Environmental Protection, Bureau of Waste Prevention

Robert Scott, Director
New Hampshire Department of Environmental Services, Air Resources Division

William O'Sullivan, Director
New Jersey Department of Environmental Protection, Office of Air Quality Management

David Shaw, Director
New York Department of Environmental Conservation, Division of Air Recourses

Stephen Majkut, Chief
Rhode Island Department of Environmental Management, Office of Air Resources

Richard A. Valentinetti, Director
Vermont Department of Environmental Conservation, Air Pollution Control Division

Contributions to Regional Haze in the Northeast and Mid-Atlantic United States

Mid-Atlantic/Northeast Visibility Union (MANE-VU) Contribution Assessment

Prepared by
NESCAUM

August 2006

Contributions to Regional Haze in the Northeast and Mid-Atlantic United States

Mid-Atlantic/Northeast Visibility Union (MANE-VU) Contribution Assessment

Project Director

Gary Kleiman, NESCAUM

Program Officer

Marcia Spink, U.S. EPA

Editors

John Graham, NESCAUM
Gary Kleiman, NESCAUM
Marika Tatsutani, NESCAUM
Paul Miller, NESCAUM

Principle Contributors (listed alphabetically by chapter)

Chapter 1:	Gary Kleiman, NESCAUM
Chapter 2:	Gary Kleiman, NESCAUM
Chapter 3:	George Allen, John Graham, Alan Leston, NESCAUM
Chapter 4:	Michael Borucke, John Graham, NESCAUM, Serpil Kayin, MARAMA, Jung-Hun Woo, NESCAUM
Chapter 5:	Serpil Kayin, MARAMA Iyad Kheirbek, Gary Kleiman, NESCAUM, Rich Poirot, VT DEC.
Chapter 6:	John Graham, Shan He, Emily Savelli, Jung-Hun Woo, NESCAUM
Chapter 7:	Mark Garrison, ERM, Dan Riley, Paul Wishinski, VT DEC
Chapter 8:	All of the above
Chapter 9:	Gary Kleiman, NESCAUM

Acknowledgments

NESCAUM gratefully acknowledges the support of the United States Environmental Protection Agency. Funding for this report was provided through the Mid-Atlantic/Northeast Visibility Union (MANE-VU) Regional Planning Organization (Grant No. X-983799-01-0) to the Ozone Transport Commission.

This report is the result of a joint effort by staff of the MANE-VU and its member states.

NESCAUM also thanks the following individuals and organizations for providing comments on this report:

Tom Downs, Maine Department of Environmental Protection
VISTAS
MOG
Dominion Power
AMC
Ann McWilliams, EPA Region 1

Printed: October 2006

TABLE OF CONTENTS

FIGURES

TABLES

Units, Symbols, Acronyms

Acronyms

AGL – Above Ground Level
ATAD – Atmospheric Transport and Diffusion Model
ARL – Air Resources Laboratory (NOAA)
BART – Best Available Retrofit Technology
BEIS – Biogenic Emission Inventory System
BRAVO - Big Bend Regional Aerosol and Visibility Observational study
CAIR – Clean Air Interstate Rule
CALMET – Meteorological model for developing input data for CALPUFF
CALPUFF – Lagrangian dispersion model developed by EarthTech, Inc.
CAMNET – Northeast Visibility Camera Network
CASTNet – Clean Air States and Trends Network
CEMS – Continuous Emissions Monitoring System
CENRAP – Central Regional Air Planning Association
CFR – Code of Federal Regulations
CMAQ – Community Multi-scale Air Quality Model
CMB – Chemical Mass Balance
CMU – Carnegie Mellon University
CTM – Chemical Transport Model
CWP – Clustered Weighted Probability
EDAS – Eta Data Assimilation System
EFIG – USEPA Emission Factor and Inventory Group
EGU – Electricity Generating Unit
EMAD – Emissions, Monitoring and Analysis Division
ERM – Environmental Resources Management, Inc.
FASTNET – Fast Aerosol Sensing and Tools for Natural aErosol Tracking
FNL – FiNaL run of the Global Data Assimilation System
FRM – Federal Reference Method
GIS – Geographic Information System
IMPROVE – Interagency Monitoring of Protected Visual Environments
IP – Incremental Probability
HAPS – Hazardous Air Pollutants
HYSPLIT – Hybrid Single-Particle Langrangian Integrated Trajectory model
MANE-VU – Mid-Atlantic/Northeast Visibility Union
MARAMA – Mid Atlantic Region Air Management Association
MDE – Maryland Department of the Environment
MDNR – Maryland Department of Natural Resources
MM5 – Fifth Generation Mesoscale Model
MOBILE – Mobile Source Emission Factor Model (USEPA)
MWRPO – Midwest Regional Planning Organization
NAAQS – National Ambient Air Quality Standards
NARSTO – North American Research Strategy for Tropospheric Ozone
NCAR – National Center for Atmospheric Research
NEI – National Emissions Inventory
NESCAUM – Northeast States for Coordinated Air Use Management
NET – National Emissions Trends (EPA)
NOAA – National Oceanic and Atmospheric Administration
NRC – National Research Council
NTI – National Toxics Inventory
NWS – National Weather Service
OAQPS – USEPA Office of Air Quality Planning and Standards

OAR – USEPA Office of Air and Radiation
OTC – Ozone Transport Commission
PCA – Principle Component Analysis
PM – Particulate Matter
PMF – Positive Matrix Factorization
PSCF – Potential Source Contribution Function
RAIN – Real Time Aerosol Intensive Network
REMSAD – Regulatory Modeling System for Aerosols and Deposition
RH – Relative Humidity
RPO – Regional Planning Organization
RTA – Residence Time Analysis
SIP – State Implementation Plan
SMOKE – Sparse Matrix Operator Kernel Emissions model
STN – Speciation Trends Network
TLD – Transport Layer Depth
TSC – Technical Support Committee
UMD – University of Maryland
UNMIX – Mathematical receptor model used for source attribution studies
USEPA – United States Environmental Protection Agency
USFS – United States Forest Service
USFWS – United States Fish and Wildlife Service
USNPS – United States National Park Service
VISTAS - Visibility Improvement State and Tribal Association of the Southeast
VT DEC – Vermont Department of Environmental Conservation
WRAP-Western Regional Air Partnership

Chemical Species

BC – Black Carbon
CM – coarse mass
CO – carbon monoxide
EC – elemental carbon
HC – hydrocarbons
H_2SO_4 – sulfuric acid
HNO_3 – nitric acid
NO_X – oxides of nitrogen (NO_2 and NO)
NO – nitric oxide
NO_2 – nitrogen dioxide
NO_3^- – nitrate
NH_3 – ammonia
NH_4 – ammonium
NH_4HSO_4 – ammonium bisulfate
$(NH_4)_2SO_4$ – ammonium sulfate
(NH_4NO_3) – ammonium nitrate
O_3 – ozone
OC – organic carbon
OMC – organic mass from carbon
$PM_{2.5}$ – particle matter up to 2.5 μm in size
PM_{10} – particle matter up to 10 μm in size
Se – selenium
SOA – secondary organic aerosol
SO_2 – sulfur dioxide
SO_4^{2-} – sulfate
VOC – volatile organic compounds

Symbols

b_{ext} – light extinction coefficient (Mm^{-1})
C_i – constant for wind sector i
d – distance
E x UP – emissions times upwind probability
f(RH) – relative humidity adjustment factor
I – impact
Q – annual emissions
R^2 – correlation coefficient

Units

Length

m – meter
μm – micrometer (0.000001m; 10^{-6}m)
km – kilometer (1,000 x m; 10^{3} m)
Mm – Megameter (1,000,000 x m; 10^{6} m)

Area

m^2 – square meter
km^2 – square kilometer

Volume

L – liter
m^3 – cubic meter

Concentration

$\mu g/m^3$ – micrograms per cubic meter
ng/m^3 – nanograms per cubic meter
ppb – parts per billion
ppm – parts per million

Scattering Efficiency

m^2/g – square meters per gram

Visibility

dv – deciview

Executive Summary

Regional haze State Implementation Plans (SIPs) due in December 2007 must include a contribution assessment and pollution apportionment analysis as part of the long-term emissions management strategy for meeting visibility improvement objectives in Class I areas subject to USEPA's 1999 Regional Haze Rule. The Mid-Atlantic/Northeast Visibility Union (MANE-VU) Technical Support Committee (TSC) has adopted a weight-of-evidence approach as a first step toward meeting these obligations and in an effort to better understand the causes of visibility impairment at Class I areas within the MANE-VU region. The weight-of-evidence approach relies on several independent methods for assessing the contribution of different emissions sources and geographic source regions to regional haze in the northeastern and mid-Atlantic portions of the United States.

The preliminary findings described in this report draw from the considerable body of work that has already been developed concerning the nature and extent of visibility impairment in the MANE-VU region. This work has produced a conceptual model of regional haze in which sulfate emerges as the most important single constituent of haze-forming fine particle pollution and the principle cause of visibility impairment across the region. Sulfate alone accounts for anywhere from one-half to two-thirds of total fine particle mass on the 20 percent haziest days at MANE-VU Class I sites. Even on the 20 percent clearest days, sulfate generally accounts for the largest fraction (40 percent or more) of total fine particle mass in the region. Sulfate has an even larger effect when one considers the differential visibility impacts of different particle constituents. It typically accounts for 70–82 percent of estimated particle-induced light extinction at northeastern and mid-Atlantic Class I sites.

While substantial visibility impairment is common across the region, it is most severe in the southern and western portions of MANE-VU that are closest to large power plant sources of sulfur dioxide (SO_2) emissions located in the Ohio River and Tennessee Valleys. Summertime visibility is driven almost exclusively by the presence or absence of regional sulfate, whereas wintertime visibility depends on a combination of regional *and* local influences coupled with local meteorological conditions (inversions) that can lead to the concentrated build-up of emissions from local sources.

These findings suggest that an effective emissions management approach would rely heavily on broad-based regional SO_2 control efforts in the eastern United States aimed at reducing summertime fine particulate matter ($PM_{2.5}$) concentrations. MANE-VU is investigating additional measures to reduce in-region emissions of SO_2 and organic carbon (OC), which is typically the next most important contributor to overall fine particle mass throughout the region. Nearby SO_2 reductions can help reduce wintertime PM concentrations, while OC reductions can help reduce total PM concentrations year-round. For areas with high wintertime PM levels, strategies aimed at reducing ambient levels of nitrogen oxides (NO_X) may also be effective.

Available monitoring data provide strong evidence that regional SO_2 reductions have yielded, and will continue to yield, reductions in ambient secondary sulfate levels with subsequent reductions in regional haze and associated light extinction. They indicate that reductions in anthropogenic primary particle emissions will also result in visibility

improvements, but that these will not have a zone of influence as large as those of the secondary aerosols.

Given the dominant role of sulfate in the formation of regional haze in the Northeast and Mid-Atlantic region — and the likelihood that SO_2 reductions will therefore need to play a central role in achieving near-term visibility improvements — this report focuses on early efforts to assess the regional sulfate contribution to ambient fine particle levels experienced at the (primarily rural) MANE-VU Class I areas. The primary objective of this report is to identify and describe the suite of analytical tools and techniques that are presently available for: (1) understanding the causes of sulfate-driven visibility impairment at Class I areas in MANE-VU and nearby regions, as well as the relative contribution of various emissions sources and geographic source regions; and (2) describe how these tools and techniques will be applied in future MANE-VU SIP work.

The analytical and assessment tools discussed in this report include Eulerian (grid-based) source models, Lagrangian (air parcel-based) source dispersion models, as well as a variety of data analysis techniques that include source apportionment models, back trajectory calculations, and the use of monitoring and inventory data. A range of methodological approaches characterize these tools, which Table ES-1 summarizes. The tools rely on different data sources and entail varying degrees of sophistication and uncertainty. Thus, it is important to emphasize that these methods have been extensively reviewed, updated, and refined over the past year to ensure that the highest quality results are now available for the SIP development process. The overall coherence and consistency of results that emerges from application of these tools and techniques suggest that what is known about the causes of sulfate pollution in the MANE-VU region is sufficiently robust to provide a useful and appropriate basis for design of future control programs and for consultations between different regional organizations charged with planning for compliance with the Regional Haze Rule.

Figure ES-1 provides one illustration of the high degree of correspondence in the results. The figure shows rankings of state contributions to sulfate mass at Brigantine Wilderness Area in New Jersey derived from several of the techniques listed in Table ES-1.[1] There is substantial consistency across a variety of analysis methods using techniques based on disparate chemical, meteorological and physical principles. Taken together, these findings create a strong weight-of-evidence case for the preliminary identification of the most significant contributors to visibility impairment in the MANE-VU Class I areas.

Similar results for other sites demonstrate that highly simplified, empirical approaches for identifying source contributions are consistent with more sophisticated approaches. Therefore, a firm basis exists for addressing contributions to regional transport of sulfate, and the range of variability between these techniques suggests the precision of these estimates.

[1] As described in Chapter 8, REMSAD is the only analysis platform used to quantify "out of domain" contributions to sulfate. Thus, the REMSAD calculated contribution for the "out of domain" sources (17% at Brigantine, NJ) was used to calculate the percent contribution shown in Figure ES-1 for all other methods.

We have further aggregated these results by regional planning organization (RPO) using state-by-state sulfate mass contributions (in μg/m^3) derived by the REMSAD, CALPUFF, emissions/distance, and emissions times (×) upwind probability methods.[2] Figure ES-2 shows these results in terms of their absolute contribution (displayed within the bars shown in the graphic) and in terms of their proportional contribution relative to other RPOs.[1]

Table ES-1. Summary of technical approaches for attributing state contributions to observed sulfate in MANE-VU Class I areas.

Analytical technique	Approach
Emissions/distance	Empirical
Incremental probability	Lagrangian trajectory technique
Cluster-weighted probability	Lagrangian trajectory technique
Emissions × upwind probability	Empirical/trajectory hybrid
Source apportionment approaches	Receptor model/trajectory hybrid
REMSAD tagged species	Eulerian source model
CALPUFF with MM5-based meteorology	Lagrangian source dispersion model
CALPUFF with observation-based meteorology	Lagrangian source dispersion model

Figure ES-1. Comparison results using different techniques for ranking state contributions (in units of percent of in-domain contribution) to sulfate levels at Brigantine Wilderness Area, New Jersey.

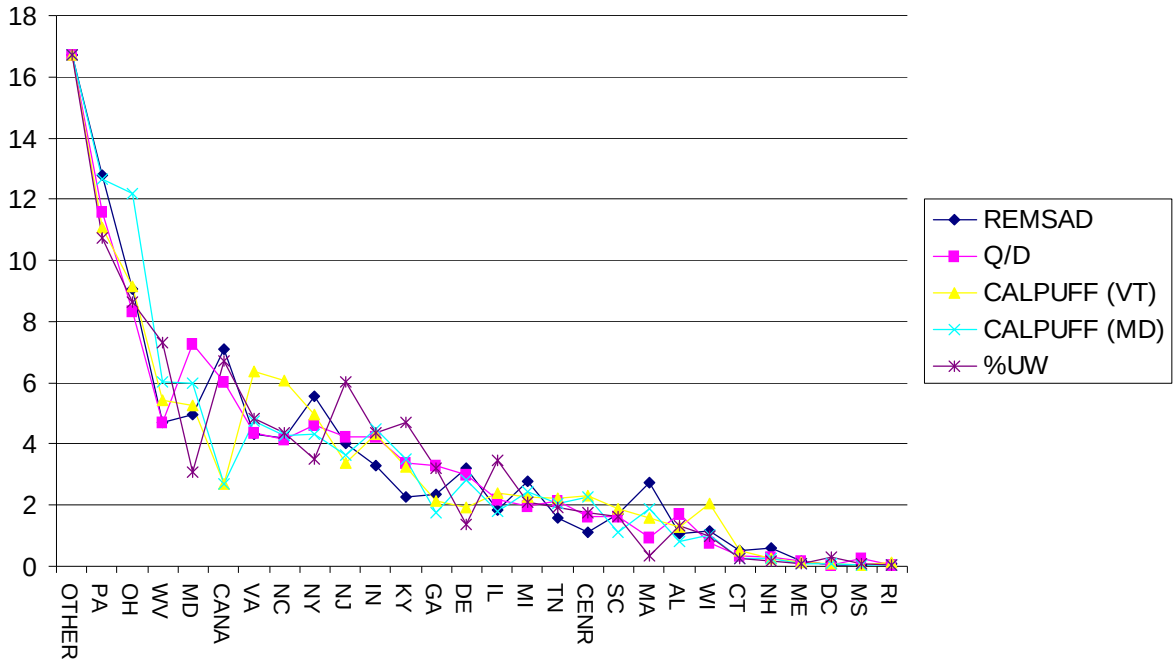

[2] See Chapter 4 for an explanation of how the emissions divided by distance technique is expressed as a sulfate mass concentration and the associated assumptions for the emissions × upwind probability method.

Notwithstanding small differences in precisely which states were included within each assessment technique, estimates obtained from averaging over the five quantitative assessment techniques indicate that MANE-VU states account for about 25-30 percent of the sulfate in the Acadia, Brigantine, and Lye Brook Class I areas. The Midwest RPO (MWRPO) and Visibility Improvement State and Tribal Association of the Southeast (VISTAS) states each account for about 15 percent of the total sulfate contribution at Acadia and about 25 percent each at Brigantine and Lye Brook. The Central states Regional Air Partnership (CENRAP) states, Canada, and an "out of domain" contribution add the remainder.[3] Although variation exists across estimates of contributions for different sites and using different techniques, the overall pattern is generally consistent.

Figure ES-2. Estimated RPO contributions to sulfate concentrations at Class I areas using different assessment techniques

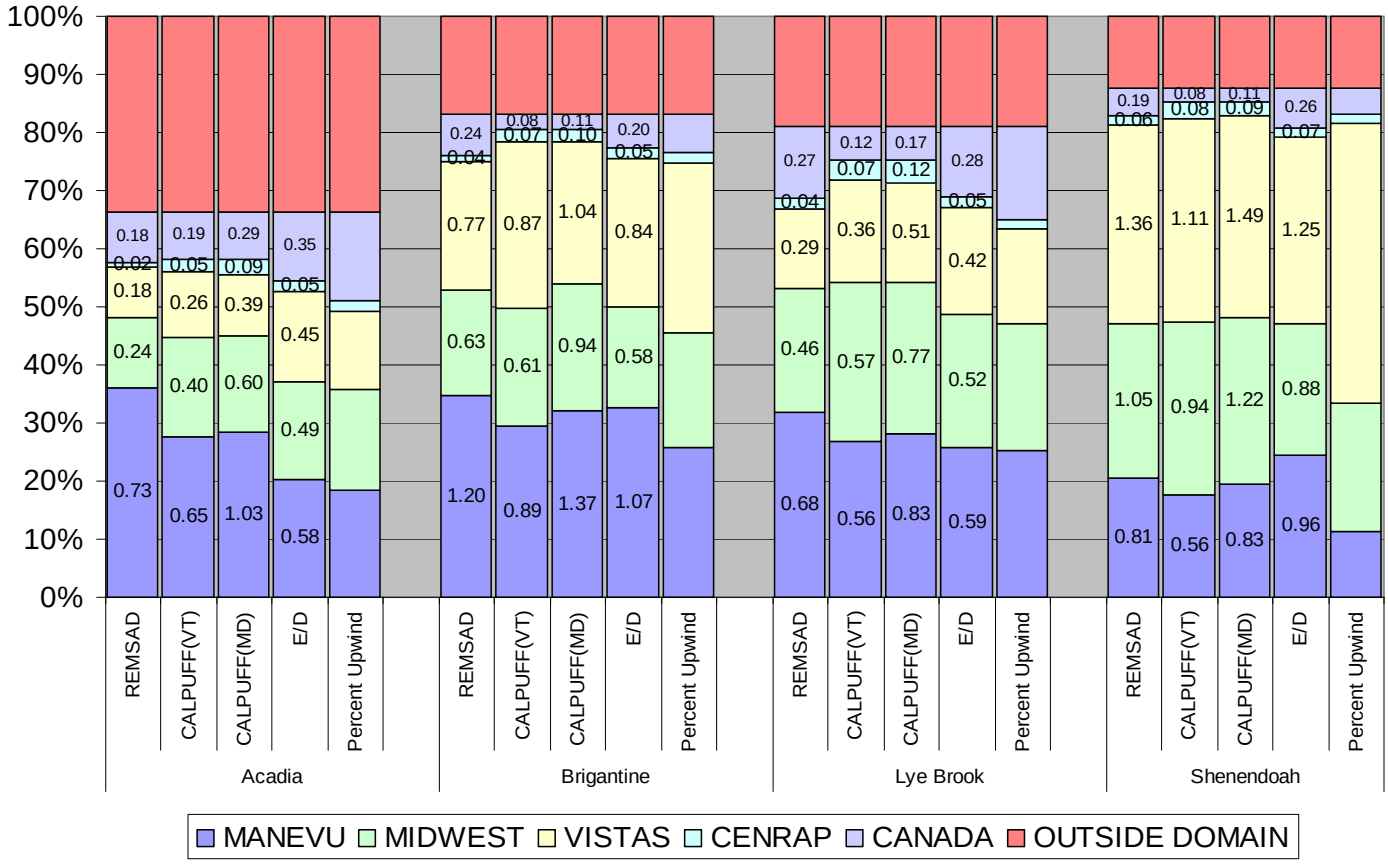

Shenandoah National Park, Virginia, which is a VISTAS Class I area, has a somewhat reversed order of relative contributions. There, VISTAS and MWRPO states account for roughly 30 percent of overall sulfate each, with MANE-VU states contributing roughly 15-20 percent and CENRAP states, Canada and "out of domain" accounting for the remainder.

[3] Note here that the contribution representing out of domain sources was – in all cases – derived solely by the REMSAD platform and that this value has been applied to the other analysis techniques to provide a consistent estimate of the total contributions to sulfate pollution at each site.

Other qualitative analysis methods have been developed that reinforce the findings shown above. These include trajectory methods and source apportionment techniques. These receptor-based methods provide compelling support for the more quantitative attribution methods discussed previously. Figure ES-3 (left panel) shows the source region associated with a "coal combustion/secondary sulfate" source profile observed at Brigantine Wilderness in New Jersey and (right panel) the predominant meteorological pathways associated with the highest sulfate observations at Brigantine. The meteorological transport regime most common during high sulfate observations (shown on the right) directly connects the most likely source region with the receptor site (shown on the left), which reinforces the large quantitative contributions of source states determined for the Brigantine receptor in Chapter 8.

Finally, we note that while sulfate is the most important particle constituent for designing near-term control strategies, reductions in other local and distant pollutant emissions are important. Additional measures will be necessary in the long term to address public health impacts of ambient fine particle concentrations and to achieve long-term regional haze goals to restore pristine visibility conditions year-round in the nation's Class I wilderness areas. This is especially true during winter months, when planners need to give particular consideration to reducing urban and mobile sources of NO_X and OC as well as sources of SO_2.

Figure ES-3. Geographic regions associated with "coal combustion/secondary sulfate" sources (left) and sulfate transport (right) for Brigantine Wilderness Area, NJ.

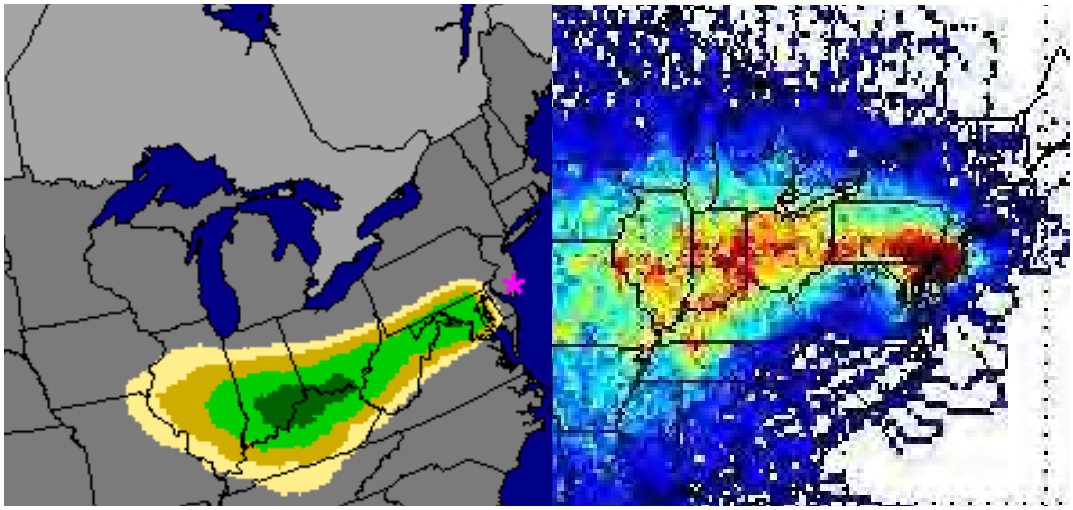

Note: This figure is the consistency of interpretation between the "coal-combustion/secondary sulfate" source region and receptor site shown in the left hand panel being directly connected by the predominant meteorological transport pathway on high observed sulfate days at Brigantine, shown in the right hand panel.

1. INTRODUCTION

The 1999 Regional Haze Rule (hereafter, the Haze Rule) requires States and Tribes to submit State Implementation Plans (SIPs) to the U.S. Environmental Protection Agency (USEPA) for approval by January 2008 at the latest. The haze SIPs must include a "contribution assessment" to identify those states or regions that may be influencing specially protected federal lands known as Federal Class I areas.[4] These states or regions would then be subject to the consultation provisions of the Haze Rule. The Haze Rule also requires a "pollution apportionment" analysis as part of the long-term emissions management strategy for each site.

In 2004, Congress harmonized the timeline for SIP submissions, including SIPs for meeting federal fine particulate matter ($PM_{2.5}$) and regional haze requirements.[5] One effect of this change is that the "regional planning SIP" or "committal SIP" — originally due one year after PM designations — will now be due along with all other SIP products in late 2007 or early 2008.

The Haze Rule originally would have applied a very low threshold test to determine whether a state would be part of a regional planning process, As a result of the congressional harmonization, however, the requirement for a contribution assessment is now, in effect, part of the "pollution apportionment" analysis used to determine which sources must be included in a long-term emissions management strategy. This is subject to a somewhat higher threshold of evidence since it forms the basis for judging whether long-term strategies are adequately addressing the causes of haze in protected areas.

To adequately determine the degree to which specific geographic regions or areas are contributing to visibility impairment at MANE-VU Class I areas, the MANE-VU Technical Support Committee (TSC) has adopted a weight-of-evidence approach that relies on several independent methods of attribution. These include Eulerian (grid-based) source models, Lagrangian (air pollution-based) source dispersion models, and a variety of data analysis techniques that include source apportionment models, back trajectory calculations, and the use of monitoring and inventory data.

---

[4] The Class I designation applies to national parks exceeding 6,000 acres, wilderness areas and national memorial parks exceeding 5,000 acres, and all international parks that were in existence prior to 1977. In the MANE-VU area, this includes: Acadia National Park, Maine; Brigantine Wilderness (within the Edwin B. Forsythe National Wildlife Refuge), New Jersey; Great Gulf Wilderness, New Hampshire; Lye Brook Wilderness, Vermont; Moosehorn Wilderness (within the Moosehorn National Wildlife Refuge), Maine; Presidential Range – Dry River Wilderness, New Hampshire; and Roosevelt Campobello International Park, New Brunswick.

[5] In the Omnibus Appropriations Act of 2004 [Consolidated Appropriations Act for Fiscal Year 2004, Pub. L. 108–199, January 23, 2004], Congress harmonized both designations and regional haze SIP deadlines. EPA promulgated $PM_{2.5}$ designations for all areas of each state on December 17, 2004. The Omnibus Appropriations Act provides that regional haze SIPs for each state as a whole are then due not later than three years after promulgation of the $PM_{2.5}$ designations. Thus, all components of the regional haze SIPs are now due no later than December 17, 2007 (three years after the USEPA issued the official designations). The USEPA has suggested informally that they will accept Regional Haze SIPs in April 2008 when $PM_{2.5}$ SIPs are due.

While we already know much about visibility impairment and its causes in the MANE-VU region (see NESCAUM, 2001; NESCAUM, 2002), significant gaps in understanding remain with respect to the organic component of fine particulate pollution. While we expect continuing research activities to substantially benefit future SIP efforts, the MANE-VU members have determined that sufficient information exists to design effective emission control strategies to meet visibility goals through 2018.

Reducing sulfur emissions offers particular leverage for achieving near-term visibility goals. It is the sulfate fraction of airborne fine particle matter that dominates light extinction on the 20 percent worst visibility days in the Northeast and Mid-Atlantic region. This is important because improving visibility on the 20 percent worst days is a near-term regulatory objective under the Regional Haze rule. In addition, many tools are available for assessing sulfate contributions. Therefore, this document focuses to a large extent on assessing sources and source regions for the sulfate fraction of haze-causing particles.

To lay a foundation for the analyses described in later chapters of this report, Chapter 2 provides a conceptual model of visibility impairment in the eastern United States. Chapter 3 presents a summary of available monitoring data and observations that we use to support the conceptual model and to validate models and data analyses. In fact, measured data — far from being used merely to support modeling analyses — serve as the primary basis for several of the receptor techniques presented in later chapters. There is thus no substitute for a robust monitoring network to understand the causes of fine particle pollution and visibility impairment.

Later chapters reinforce the notions introduced in Chapters 2 and 3 in using emission inventories (Chapter 4), receptor-based approaches including the use of back trajectories, trajectory clustering techniques and source apportionment models (Chapter 5), Eulerian chemical transport models (Chapter 6), and Lagrangian dispersion models (Chapter 7). We synthesize and interpret these various techniques in Chapter 8 and present conclusions in Chapter 9. We discuss technical aspects of the analyses in several of these later chapters in greater detail in a series of appendices.

As a general matter throughout this report, the focus is on assessing the contribution of all sources within broad geographical areas (i.e., whole states) whose combined emissions are likely to contribute to regional haze. As cited in Watson (2002), the National Research Council (NRC) has concluded that:

> (1) "…a program that focuses solely on determining the contribution of individual emission sources to visibility impairment is doomed to failure. Instead, strategies should be adopted that consider many sources simultaneously on a regional basis, although assessment of the effect of individual sources will remain important in some situations;" (2) "…there are (and will probably continue to be) considerable uncertainties in ascertaining a precise relationship between individual sources and the spatial pattern of regional haze;" and (3) "…the best approach for evaluating emission sources is a nested progression from simpler and more direct models to more complex and detailed methods" (Watson, 2002).

Watson (2002) goes on to point out that, "Part of the modeling conundrum is the focus of modeling efforts on demonstrating attainment rather than gaining a better understanding of the situation. Although USEPA emphasizes the construction of a conceptual model and evaluation of the weight of evidence in its introduction, the modeling details contained in the guidance are business as usual: seeking a quantitative comparison of present and future design values with a numerical goal."

Consistent with the NRC's admonition and USEPA's stated desire to incorporate weight-of-evidence approaches to improve conceptual models, MANE-VU has attempted wherever possible to incorporate qualitative analyses in sensible ways so as to increase confidence in its quantitative estimates of the contribution of various emissions sources and source regions to regional haze.

References

NESCAUM, *Regional Haze and Visibility Impairment in the Northeast and Mid-Atlantic United States*, Northeast States for Coordinated Air Use Management, Boston, MA, January, 2001.

NESCAUM, *Updated Visibility Statistics for the MANE-VU Region Technical Memorandum #1*, Northeast States for Coordinated Air Use Management, Boston, MA February, 2002.

Watson, J., "Visibility: Science and Regulation," *JAWMA* 52:628-713, 2002.

2. CONCEPTUAL MODEL OF REGIONAL HAZE IN THE MANE-VU REGION

Developing a conceptual model of regional haze requires combining experience and atmospheric-science expertise with multiple data sources and analysis techniques. This includes measured data on ambient pollutant concentrations as well as emission inventory and meteorological data, chemical transport modeling, and observationally based models (NARSTO, 2003). Here, we begin with a conceptual model based on the existing scientific literature concerning fine particles and their effect on visibility. This includes numerous review articles and reports on the subject. Most past assessments of fine particle pollution and visibility impairment have tended to be national in scope. For purposes of this discussion, we have selectively reviewed the literature in order to present a distinctly Eastern focus.

Because the uncertainties involved in any particular method of analysis are usually large or ill-defined, it is preferable to develop visibility and fine particle management strategies with inputs from multiple analyses using multiple approaches. The MANE-VU TSC has adopted this approach, which leads to the diversity of data analyses and model results that follow. Later chapters of this report use original contributions and analyses developed by MANE-VU researchers to bolster and support the concepts presented in these introductory chapters. MANE-VU has combined the outputs and integrated them into a final conceptual model that explains the formation and transport mechanisms for fine particulate matter in the eastern United States.

2.1. Visibility Effects of Particulate Matter (PM)

Visibility impairment in the eastern United States is largely due to the presence of light-absorbing and light-scattering fine particles in the atmosphere. The USEPA has identified visibility impairment as the best understood of all environmental effects of air pollution (Watson, 2002). A long-established physical and chemical theory relates the interaction of particles and gases in the atmosphere with the transmission of visual information along a sight path from object to observer.

Visibility-impairing particle-light interactions are sensitive to the chemical composition of the particles involved, and also depend strongly on ambient relative humidity. Secondary particles, which form in the atmosphere through chemical reactions, tend to fall within a size range that is most effective at scattering visible light (NARSTO, 2003). These particles are generally smaller than one micrometer (µm) or one one-millionth of a meter. The particles that contribute most to visibility impairment also are a concern under the health-based National Ambient Air Quality Standard (NAAQS) for fine particulate matter, defined as including all particles with an aerodynamic diameter less than 2.5 µm ($PM_{2.5}$).

2.2. Chemical Composition of Particulate Matter in MANE-VU

Sulfate alone accounts for anywhere from one-half to two-thirds of total fine particle mass on the 20 percent haziest days at all MANE-VU Class I sites. Even on the 20 percent clearest days, sulfate generally accounts for the largest fraction (40 percent or more) of total fine particle mass in the region (NESCAUM, 2001). Sulfate accounts for a

major fraction of $PM_{2.5}$, not only in the Northeast but across the eastern United States (NARSTO, 2003).

After sulfate, organic carbon (OC) consistently accounts for the next largest fraction of total fine particle mass. Its contribution typically ranges from 20 to 30 percent of total fine particle mass on the haziest days. The fact that the contribution from organic carbon can be as high as 40 percent at the more rural sites on the 20 percent clearest days is likely indicative of the role played by organic emissions from vegetation (so-called "biogenic hydrocarbons" (HC)). Relative contributions to overall fine particle mass from nitrate (NO_3), elemental carbon, and fine soil are all smaller (typically under 10 percent), but the relative ordering among the three species varies with location. Nitrate plays a noticeably more important role at urban sites compared to northeastern and mid-Atlantic Class I locations, perhaps reflecting a greater contribution from vehicles and other urban pollution sources (NESCAUM, 2001).

Almost all particle sulfate originates from sulfur dioxide (SO_2) oxidation and typically associates with ammonium (NH_4) in the form of ammonium sulfate ($(NH_4)_2SO_4$), 95 percent of SO_2 emissions are from anthropogenic sources (primarily from fossil fuel combustion), while the majority of ammonium comes from agricultural activities and, to a lesser extent, from transportation sources in some areas (NARSTO, 2003).

Two major chemical pathways produce sulfate from SO_2 in the atmosphere. In the gas phase, production of sulfate involves the oxidation of SO_2 to sulfuric acid (H_2SO_4), ammonium bisulfate (NH_4HSO_4), or ammonium sulfate, depending on the availability of ammonia (NH_3). In the presence of small wet particles (typically much, much smaller than rain drops or even fog), a highly efficient aqueous phase process can oxidize SO_2 to sulfate extremely quickly (~10 percent per hour).

Not only is sulfate the dominant contributor to fine particle mass in the region, it accounts for anywhere from 60 percent to almost 80 percent of the difference between fine particle concentrations on the clearest and haziest days at northeastern and mid-Atlantic Class I sites. Notably, at urban locations such as Washington, DC, sulfate accounts for only about 40 percent of the difference in average fine particle concentrations for the 20 percent most versus least visibility impaired days (NESCAUM, 2001). We discuss this further in the next section of this chapter.

Some of the dominant components of total fine particle mass have an even larger effect when considering the differential visibility impacts of different particle species. Sulfate typically accounts for over 70 percent of estimated particle-induced light extinction at northeastern and mid-Atlantic Class I sites. Organic carbon continues to be the second most important contributor to particle-induced light extinction at rural sites on the most impaired days, but slips to third behind nitrate in Washington, DC (NESCAUM, 2001).

2.3. Geographic Considerations and Attribution of PM/Haze Contributors

In the East, an accumulation of particle pollution often results in hazy conditions extending over thousands of square kilometers (km^2) (NARSTO, 2003). Substantial

visibility impairment is a frequent occurrence in even the most remote and pristine areas of the Northeast and Mid-Atlantic region (NESCAUM, 2001).

Both annual average and maximum daily fine particle concentrations are highest near heavily industrialized areas and population centers. Not surprisingly, given the direct connection between fine particle pollution and haze, the same pattern emerges when one compares measures of light extinction on the most and least visibility impaired days at parks and wilderness areas subject to the Haze Rule in the Northeast and Mid-Atlantic region (NESCAUM, 2001).

Contributions to fine particle mass concentrations at rural locations include long-range pollutant transport as well as non-anthropogenic background contributions. Urban areas generally show mean $PM_{2.5}$ levels exceeding those at nearby rural sites. In the Northeast, this difference implies that local urban contributions are roughly 25 percent of the annual mean urban concentrations, with regional aerosol contributing the remaining, and larger, portion (NARSTO, 2003).

This rural versus urban difference in typical concentrations also emerges in a source apportionment analysis of fine particle pollution in Philadelphia (Chapter 10, NARSTO, 2003) using two different mathematical models, UNMIX and Positive Matrix Factorization (PMF). (We describe these models in greater detail in Chapter 5 and Appendix B.) This analysis provides additional insight concerning sources of fine particle pollution in urban areas of the densely populated coastal corridor between Washington D.C. and New England. Specifically, this analysis found the following apportionment of $PM_{2.5}$ mass in the study area:

- Local SO_2 and sulfate: ~ 10 percent
- Regional sulfate: ~ 50 percent
- Residual oil: 4-8 percent
- Soil: 6–7 percent
- Motor vehicles: 25–30 percent

The analysis does not account for biogenic sources, which most likely are embedded in the motor vehicle fraction (NARSTO, 2003). The Philadelphia study suggests that both local pollution from near-by sources and transported "regional" pollution from distant sources contribute to the high sulfate concentrations observed in urban locations along the East Coast on an annual average basis. Summertime sulfate and organic carbon are strongly regional in eastern North America. Typically 75–95 percent of the urban sulfate concentrations and 60–75 percent of the urban OC concentrations arise from cumulative region-wide contributions (NARSTO, 2003).

While these statistics provide some preliminary context for attributing responsibility for the region's particulate matter and visibility problems, they say nothing about the relative efficiency of a state's or region's emissions in causing or contributing to the problem. It is clear that distance from the emissions source matters. Local, near-by sources are exceedingly important and sources within about 200 kilometers (km) are much more efficient (on a per ton emitted basis) at producing pollution impacts at eastern Class I sites such as Shenandoah National Park than emissions sources farther away (USNPS, 2003). In general, the "reach" of sulfate air pollution resulting from SO_2

emissions is longest (650-950 km). The reach of ammonia emissions or reduced nitrogen relative to nutrient deposition is the shortest (around 400 km), while oxides of nitrogen and sulfur — in terms of their impacts with respect to acidic deposition — have a reach between 550–650 km and 600–700 km, respectively (USNPS, 2003).

Monitoring evidence indicates that non-urban visibility impairment in eastern North America is predominantly due to sulfate particles, with organic particles generally second in importance (NARSTO, 2003). This makes sense, given the "long reach" of SO_2 emissions once they are chemically transformed into sulfate and given the ubiquitous nature of OC sources in the East.

The poorest visibility conditions occur in highly industrialized areas encompassing and adjacent to the Ohio and Tennessee River Valleys. These areas feature large coal-burning power stations, steel mills, and other large emissions sources. Average visibility conditions are also poor in the highly populated and industrialized mid-Atlantic seaboard but improve gradually northeast of New York City (Watson, 2002).

A review of source apportionment and ensemble trajectory analyses conducted by USEPA (2003) found that all back trajectory analyses for Eastern sites associated sulfate with the Ohio River Valley area. Studies also frequently associated other types of industrial pollutants with known source areas. Several studies in the USEPA review noted transport across the Canadian border, specifically sulfates from the midwestern United States into Canada, and smelter emissions from Canada into the northeastern United States.

A recent, comprehensive analysis of air quality problems at Shenandoah National Park conducted by the U.S. National Park Service (USNPS, 2003) focused on contributions to particulate pollution and visibility impairment south of the MANE-VU region. In descending order of importance, the National Park Service analysis determined that Ohio, Virginia, West Virginia, Pennsylvania, and Kentucky comprise the top five of thirteen key states contributing to ambient sulfate concentrations and haze impacts at the park. West Virginia, Ohio, Virginia, Pennsylvania, and Kentucky comprise the top five contributing states with respect to sulfur deposition impacts at the park. Finally, Virginia, West Virginia, Ohio, Pennsylvania, and North Carolina were found to be the top five states contributing to deposition impacts from oxidized nitrogen at the park (USNPS, 2003).

In summary, the National Park Service found that emission sources located within a 200 kilometer (125 mile) radius of Shenandoah cause greater visibility and acidic deposition impacts at the park, on a per ton basis, than do more distant emissions sources (USNPS, 2003). When mapping deposition and concentration patterns for all three pollutants using contour lines, the resulting geographic pattern shows a definite eastward tilt in the area of highest impact. This is the result of prevailing wind patterns, which tend to transport most airborne pollutants in an arc from the north-northeast to the east.[6] The Park Service found, for example, that emissions originating in the Ohio River Valley end up three times farther to the east than to the west (USNPS, 2003).

[6] The prevailing winds are eastward to northeast. This leads to greater pollution transport to the east-northeast relative to other directions.

We note that several MANE-VU states may themselves be contributing to fine particle mass concentrations observed at Shenandoah. According to the Park Service analysis, sources in Pennsylvania contribute on the order of 10 percent of observed ambient sulfate mass at the park, while sources in Maryland, New York and Delaware contribute 3.5, 1.7 and 0.5 percent respectively (USNPS, 2003).

2.4. Seasonal differences

Eastern and western coastal regions of the United States and Canada show marked seasonality in the concentration and composition of fine particle pollution, while central interior regions do not (NARSTO, 2003). While the MANE-VU domain extends inland as far as the Pennsylvania and Ohio border, the majority of Class I areas in MANE-VU cluster along the East Coast and thus typically show strong seasonal influences. Maximum $PM_{2.5}$ concentrations occur during the summer over most of the Northeast, with observed summer values for rural areas in the region, on average, twice those of winter. Winter nitrate concentrations, however, are generally higher than those observed in summer and, as mentioned above, urban concentrations typically exceed rural concentrations year-round. In addition, local mobile source carbon grows in importance during wintertime. Hence, in some large urban areas such as Philadelphia and New York City, peak concentrations of $PM_{2.5}$ can occur in winter.

The conceptual models that explain elevated regional $PM_{2.5}$ peak concentrations in the summer differ significantly from models that explain the largely urban peaks observed during winter. On average, summertime concentrations of sulfate in the northeastern United States are more than twice that of the next most important fine particle constituent, OC, and more than four times the combined concentration of nitrate and black carbon (BC) constituents (NARSTO, 2003). Episodes of high summertime sulfate concentrations are consistent with stagnant meteorological flow conditions and the accumulation of airborne sulfate (via atmospheric oxidation of SO_2) through long-range transport of sulfur emissions from industrialized areas within and outside the region.

National assessments (NARSTO, 2003) have indicated that in the winter, sulfate levels in urban areas are almost twice as high as background sulfate levels across the eastern U.S., indicating that the local urban contribution to wintertime sulfate levels is comparable in magnitude to the regional sulfate contribution from long-range transport. MANE-VU's network analysis for the winter of 2002 suggests that the local enhancement of sulfate in urban areas of the OTR is somewhat less with ranges from 25 to 40% and that the long range transport component of PM sulfate is still the dominant contributor in most eastern cities.

In the winter, urban OC and sulfate each account for about a third of the overall $PM_{2.5}$ mass concentration observed in Philadelphia and New York City. Nitrate also makes a significant contribution to urban $PM_{2.5}$ levels observed in the northeastern United States during the winter months. Wintertime concentrations of OC, sulfate, and NO_3 in urban areas can be twice the average regional concentrations of these pollutants, indicating the importance of local source contributions (NARSTO, 2003). This is likely because winter conditions are more conducive to the formation of local inversion layers that prevent vertical mixing. Under these conditions, emissions from tailpipe, industrial

and other local sources become concentrated near the Earth's surface, adding to background pollution levels associated with regionally transported emissions.

It is worth noting that while sulfate plays a significant role in episodes of elevated particle pollution during summer and winter months, the processes by which sulfate forms may vary seasonally. Nearly every source apportionment study reviewed by USEPA (2003) identified secondary sulfate originating from coal combustion sources as the largest or one of the largest contributors to overall fine particle mass in the region. It often accounted for more than 50 percent of $PM_{2.5}$ mass at some locations during some seasons. In a few cases, source apportionment studies identified a known local source of sulfate, but most assessments (in conjunction with back trajectory analysis) have pointed to coal-fired power plants in the Midwest as an important source for regional sulfate. Studies with multiple years of data have also tended to identify a distinguishable chemical "signature" for winter versus summer sources of sulfate, with the summer version typically accounting for a greater share of overall fine particle mass. Researchers have speculated that the two profiles represent two extremes in the chemical transformation processes that occur in the atmosphere between the source regions where emissions are released and downwind receptor sites. We note that while coal combustion is often referred to as the "sulfate source" because of the dominance of its sulfate contribution, coal combustion is usually the single largest source of selenium (Se) and other heavy metal trace elements (USEPA, 2003).

Visually, hazy summer days in the Northeast can appear quite different from hazy winter days. The milky, uniform visibility impairment shown in Figure 2-1 is typical of summertime regional haze events in the Northeast. During the winter, by comparison, reduced convection and the frequent occurrence of shallow inversion layers often creates a layered haze with a brownish tinge, as shown in Figure 2-2. This visual difference suggests seasonal variation in the relative contribution of different gaseous and particle constituents during the summer versus winter months (NESCAUM, 2001). Rural and inland areas tend not to experience these layered haze episodes as frequently due to the lack of local emission sources in most rural areas (valleys with high wood smoke contributions are an exception).

Overall (regional) differences in summer versus winter particle mass concentrations and corresponding visibility impairment (as measured by light extinction) are largely driven by seasonal variation in sulfate mass concentrations. This is because winter meteorological conditions are less conducive to the oxidation of sulfate from SO_2 (as borne out by the previously cited source apportionment studies). In addition, seasonal differences in long-range transport patterns from upwind SO_2 source regions may be a factor.

The greater presence of nitrate during the cold season is a consequence of the chemical properties of ammonium nitrate. Ammonia bonds more weakly to nitrate than it does to sulfate, and ammonium nitrate tends to dissociate at higher temperatures. Consequently, ammonium nitrate becomes more stable at lower temperatures and hence contributes more to overall light extinction during the winter months (NESCAUM, 2001).

Figure 2-1. Summer time at Mt Washington

Clean Day **Typical Haze Event**

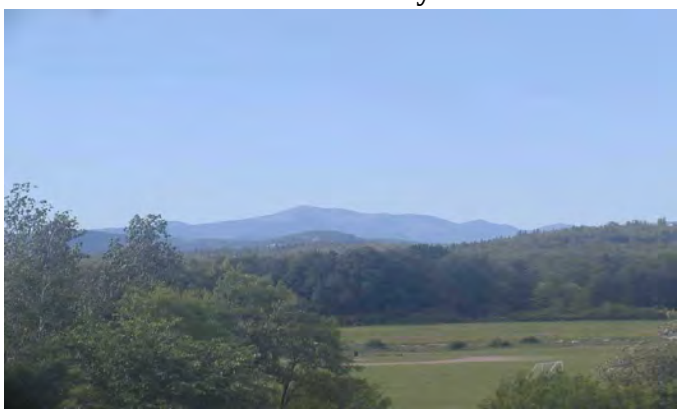

Figure 2-2. Wintertime in Boston

Clean Day **Typical Haze Event**

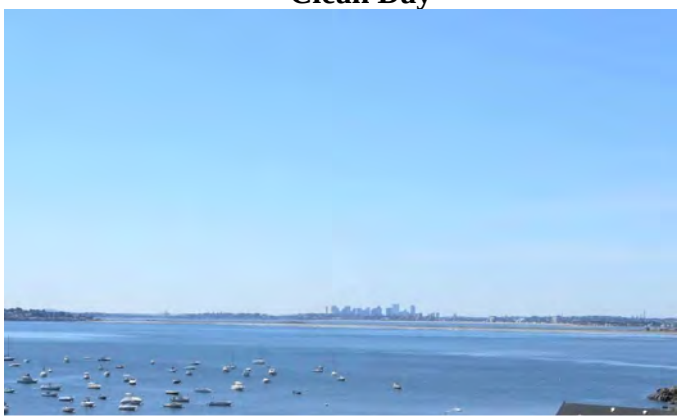

2.5. Implications for control strategies

A 2003 assessment of fine particulate matter by NARSTO[7] notes that, "[c]urrent air-quality management approaches focusing on reductions of emissions of SO_2, NO_X, and VOCs are anticipated to be effective first steps towards reducing $PM_{2.5}$ across North America, noting that in parts of California and some eastern urban areas VOC (volatile organic compounds) emissions could be important to nitrate formation."

This conclusion seems to be well supported by the historical record, which documents a pronounced decline in particulate sulfate concentrations across the eastern United States during the 1990s. The timing of this observed decline suggests that this is linked to reductions in SO_2 emissions resulting from controls implemented under the federal Acid Rain Program beginning in the early to mid 1990s. From 1989 to 1998, SO_2

[7] NARSTO was formerly an acronym for the "North American Research Strategy for Tropospheric Ozone." More recently, the term NARSTO became simply a wordmark signifying a tri-national, public-private partnership for dealing with multiple features of tropospheric pollution, including ozone and suspended particulate matter. For more information on NARSTO see http://www.cgenv.com/Narsto/.

emissions in the eastern half of the country — that is, including all states within a region defined by the western borders of Minnesota and Louisiana — declined by about 25 percent. This decline in SO_2 emissions correlated with a decline of about 40 percent in average SO_2 and sulfate concentrations, as measured at Clean Air States and Trend Networks (CASTNet) monitoring sites in the same region over the same time period. In fact, at prevailing levels of atmospheric SO_2 loading, the magnitudes of the emissions and concentration changes were not statistically different. This finding suggests that regional reductions in SO_2 emissions have produced near-proportional reductions of particulate sulfate in the eastern United States (NARSTO, 2003). Reductions since 1990 in precursor SO_2 emissions are likely also responsible for a continued decline in median sulfate concentrations in the northeastern United States. Nevertheless, the fact that episodes of high ambient sulfate concentrations (with peak levels well above the regional median or average) continue to occur, especially during the summertime when regional transport from the Ohio River Valley is also at its peak, suggests that further reductions in regional and local SO_2 emissions would provide significant further air quality and visibility benefits (NARSTO, 2003).

For urban areas of the northeastern and southeastern United States, an effective emissions management approach may be to combine regional SO_2 control efforts aimed at reducing summertime $PM_{2.5}$ concentrations with local SO_2 and OC control efforts. Local SO_2 reductions would help reduce wintertime PM concentrations, while OC reductions can help reduce overall PM concentrations year-round. For areas with high wintertime PM levels, strategies that involve NO_X reductions may also be effective (NARSTO, 2003).

Further support for this general approach may be found in a review of several studies by Watson (2002) that concluded SO_2 emission reductions have in most cases been accompanied by statistically significant reductions in ambient sulfate concentrations. One study (Husar and Wilson, 1993) shows that regionally averaged light extinction closely tracks regionally averaged SO_2 emissions for the eastern United States from 1940 through the mid-1980s. Another study by Malm et al. (2002) shows that regionally averaged emissions and ambient concentrations decreased together from 1988 through 1999 over a broad region encompassing the states of Connecticut, Delaware, Illinois, Indiana, Kentucky, Maine, Massachusetts, Maryland, Michigan, New Hampshire, New Jersey, New York, Ohio, Pennsylvania, Rhode Island, Vermont, Virginia, Wisconsin, and West Virginia (Watson, 2002).

These studies and available data from the IMPROVE (Interagency Monitoring of Protected Visual Environment) monitoring network provide strong evidence that regional SO_2 reductions have yielded, and will continue to yield, reductions in ambient secondary sulfate levels with subsequent reductions in regional haze and associated light extinction. They indicate that reductions in anthropogenic primary particle emissions will also result in visibility improvements, but that these will not have a zone of influence as large as those of the secondary aerosols (Watson, 2002).

Watson (2002) notes that during the 65 years in which the regional haze program aims to reach its final visibility goals, several opportunities to revise this basic control approach will arise through the decadal SIP cycle. This enables new scientific results to continue to exert a positive influence as states implement new regulatory control

programs for SO_2, NO_X and VOCs, and as ambient concentrations of these pollutants change relative to each other and relative to ambient ammonia levels. As these relationships between species change, atmospheric chemistry may dictate a revised control approach to those previously described. Further research on these issues should be a priority for supporting 2018 SIP submissions. They include the possibility that:

- Reduction of sulfate in a fully neutralized atmosphere (excess ammonia) could encourage ammonium nitrate formation.
- Ever greater emissions reductions could be required to produce a given level of improvement in ambient pollutant concentrations because of non-linearities in the atmospheric formation of sulfate.
- Changes in ambient conditions favoring the aqueous oxidation of sulfate (this pathway largely accounts for the non-linearity noted above) may have implications for future emissions control programs. Causes of changing ambient conditions could include, for example, climate change.

West et al. (1999) examine a scenario for the eastern United States where $PM_{2.5}$ mass decreases linearly with ammonium sulfate until the latter is fully neutralized by ammonia. Further reductions would free ammonia for combination with gaseous nitric acid that, in turn, would slightly increase $PM_{2.5}$ until all of the nitric acid is neutralized. At that point, further sulfate reductions would once again be reflected in lower $PM_{2.5}$ mass. This is an extreme case that is more relevant to source areas (e.g., Ohio) where nitric acid (HNO_3) is more abundant than in areas with lower emissions (e.g., Vermont) (Watson, 2002).

In most situations with non-neutralized sulfate (typical of the eastern United States), ammonia is a limiting agent for the formation of nitrate but will not make any difference until sulfate is reduced to the point where it is completely neutralized. At that point, identifying large sources of ammonia emissions will be important. This point is likely to be many years in the future, however (Watson, 2002).

Based on analyses using the Community Multi-Scale Air Quality (CMAQ) model, the aqueous phase production of sulfate in the Northeast appears to be very oxidant limited and hence non-linear. Thus, conditions that are conducive to a dominance of the gas-phase production pathway drive the summer peaks in ambient sulfate levels. Nonetheless, the expected reduction in ambient sulfate levels resulting from a given reduction in SO_2 emissions is less than proportional overall due to the non-linearity introduced by the aqueous pathway for sulfate formation (NARSTO, 2003). These non-linearity effects are more pronounced for haze than for sulfate deposition, especially at higher sulfate air concentrations (USNPS, 2003).

Finally, we note that because visibility in the clearest areas is sensitive to even minute increases in particle concentrations, strategies to preserve visibility on the clearest days may require stringent limits on emissions growth. In this context, even the dilute emissions from distant sources can be important (NARSTO, 2003).

2.6. Summary

The presence of fine particulate matter in ambient air significantly obscures visibility during most parts of the year at sites across the MANE-VU region. Particle pollution generally, and its sulfate component specifically, constitute the principle driver for regional visibility impacts. While the broad region experiences visibility impairment, it is most severe in the southern and western portions of MANE-VU that are closest to large power plant SO_2 sources in the Ohio River and Tennessee Valleys.

The presence or absence of regional sulfate almost exclusively drives summer visibility impairment, whereas winter visibility depends on a combination of regional and local influences coupled with local meteorological conditions (inversions) that lead to the concentrated build-up of pollution.

Sulfate is the key particle constituent from the standpoint of designing control strategies to improve visibility conditions in the northeastern United States. Significant further reductions in ambient sulfate levels are achievable, though they will require more than proportional reductions in SO_2 emissions.

Long-range pollutant transport and local pollutant emissions are important, especially along the eastern seaboard, so one must also look beyond the achievement of further sulfate reductions. During the winter months, in particular, consideration also needs to be given to reducing urban sources of SO_2, as well as NO_X and OC (NARSTO, 2003).

References

Husar, R.B. and Wilson, W.E., "Haze and Sulfur Emission Trends in the Eastern United States," *Environ. Sci. Technol. 27* (1), 12-16, 1993.

NARSTO, *Particulate Matter Science for Policy Makers: A NARSTO Assessment*, EPRI 1007735, February, 2003.

NESCAUM, *Regional Haze and Visibility Impairment in the Northeast and Mid-Atlantic United States*, Northeast States for Coordinated Air Use Management, Boston, MA, January, 2001.

Malm, W. C., Schichtel, B. A., Ames, R.B., and Gebhart, K.A., "A 10-year spatial and temporal trend of sulfate across the United States," *J. Geophys. Res. 107(D22):4627*, doi:10.1029/2002JD002107, 2002.

USEPA, *COMPILATION OF EXISTING STUDIES ON SOURCE APPORTIONMENT FOR $PM_{2.5}$, Second Draft*, Emissions, Monitoring, and Analysis Division, Office of Air Quality Planning and Standards, Research Triangle Park, NC, August, 2003.

USNPS, *Assessment of Air Quality and Related Values in Shenandoah National Park*, Technical Report NPS/NERCHAL/NRTR-03/090, U.S. Department of the Interior, National Park Service, Northeast Region, Philadelphia, Pennsylvania, May, 2003.

Watson, J., "Visibility: Science and Regulation," *JAWMA* 52:628-713, 2002.

West, J.J., Ansari, A.S., and Pandis, S.N., "Marginal $PM_{2.5}$: Nonlinear Aerosol Mass Response to Sulfate Reductions in the Eastern United States," *JAWMA* 49:1415-1424, 1999.

3. OVERVIEW OF MONITORING RESULTS

SIP developers use monitoring data in three important ways to support regional haze SIP activities. Section 3.1 presents measurements from the IMPROVE network needed in establishing SIP requirements. Following USEPA guidance (USEPA, 2003a; USEPA, 2003b), we use these data to preview the uniform progress goals that SIP developers must consider for each Class I area.

Section 3.2 reviews a recent NESCAUM report (NESCAUM, 2004b) to demonstrate how available monitoring data support and validate the conceptual model presented in Chapter 2.

Section 3.3 presents early results from the MANE-VU Real-Time Aerosol Intensive Network (RAIN). These suggest some of the ways MANE-VU is preparing to extend and improve understanding of visibility issues across the region. We anticipate this aspect of the MANE-VU monitoring strategy to be critical for future status reports and SIP updates.

3.1. Baseline Conditions

The Haze Rule requires states and tribes to submit plans that include calculations of current and estimated baseline and natural visibility conditions. They will use monitoring data from the IMPROVE program as the basis for these calculations. Table 3-1 presents the five-year average[8] of the 20 percent worst day mass concentrations in six Class I areas. Five of these areas are in MANE-VU and one (Shenandoah) is nearby but located in a neighboring regional planning organization (RPO) region.[9] Table 3-2 gives the corresponding worst day contributions to particle extinction for the six Class I areas. Each of these tables show the relative percent contribution for all six Class I sites. Sulfate and organic carbon dominate the fine mass, with sulfate even more important to particle extinction.

To guide the states in calculating baseline values of reconstructed extinction and for estimating natural visibility conditions, USEPA released two documents in the fall of 2003 outlining recommended procedures (USEPA 2003a; USEPA 2003b). These proposed methods were used, along with the data in Table 3-1 and Table 3-2 to create Table 3-3, which provides detail on the 20 percent worst conditions for the six Class 1 areas.

The first column of data in the Table 3-3 gives the default natural background levels for the worst visibility days at these six sites. Although debate continues with regard to some assumptions underlying the USEPA default approach for estimating natural background visibility conditions, MANE-VU has decided to use this approach, at least initially, for 2008 SIP planning purposes (NESCAUM, 2004a). The second column shows the baseline visibility conditions on the 20 percent worst visibility days. These values are based on IMPROVE data from the official five-year baseline period (2000-

[8] Great Gulf calculations are based on four years of data (2001-2004).

[9] Note that values presented for Shenandoah, a Class I area in the Visibility Improvement State and Tribal Association of the Southeast (VISTAS) region, are for comparative purposes only. VISTAS will determine uniform rates of progress for areas within its region.

2004). Using these baseline and natural background estimates, we derive the uniform rate of progress shown in the third column.[10] The final column displays the interim 2018 progress goal based on 14 years of improvement at the uniform rate.

Table 3-1. Fine mass and percent contribution for 20% worst days

20% Worst-day fine mass ($\mu g/m^3$) / % contribution to fine mass					
Site	SO_4	NO_3	OC	EC	Soil
Acadia	6.3 / 60%	0.8 / 8%	2.5 / 23%	0.4 / 4%	0.5 / 5%
Brigantine	11.5 / 59%	1.8 / 9%	4.5 / 23%	0.7 / 4%	1.0 / 5%
Great Gulf	7.3 / 63%	0.3 / 3%	2.9 / 25%	0.4 / 3%	0.6 / 5%
Lye Brook	8.5 / 62%	1.1 / 8%	3.0 / 22%	0.5 / 3%	0.6 / 5%
Moosehorn	5.7 / 58%	0.7 / 7%	2.6 / 27%	0.4 / 4%	0.4 / 4%
Shenandoah	13.2 / 72%	0.7 / 4%	3.3 / 18%	0.6 / 3%	0.7 / 4%

Table 3-2. Particle extinction and percent contribution for 20% worst days

20% Worst-day particle extinction (Mm^{-1}) / % contribution to extinction						
Site	SO_4	NO_3	OC	EC	Soil	CM
Acadia	66.0 / 73%	8.1 / 9%	10.1 / 11%	4.4 / 5%	0.5 / 1%	1.8 / 2%
Brigantine	106.2 / 69%	16.1 / 10%	18.3 / 12%	7.1 / 5%	1.0 / 1%	5.2 / 4%
Great Gulf	66.5 / 76%	3.0 / 3%	10.6 / 13%	3.8 / 4%	0.5 / 1%	2.9 / 3%
Lye Brook	76.7 / 73%	9.3 / 9%	12.1 / 11%	4.7 / 5%	0.7 / 1%	1.8 / 2%
Moosehorn	56.1 / 70%	6.3 / 8%	10.5/ 13%	4.4 / 5%	0.4 / 0%	2.1 / 3%
Shenandoah	132.5 / 82%	5.8 / 4%	13.2 / 8%	5.7 / 4%	0.8 / 0%	2.6 / 2%

Table 3-3. Natural background and baseline calculations for select Class I areas

Site	Natural Background (dv)	Baseline 2000-04 (dv)	Uniform Rate (dv/year)	Interim Progress Goal 2018 (dv)
Acadia	11.45	22.34	0.18	19.80
Brigantine	11.28	27.60	0.27	23.97
Great Gulf	11.30	22.25	0.18	19.69
Lye Brook	11.25	23.70	0.21	20.80
Moosehorn	11.36	21.18	0.16	18.89
Shenandoah	11.27	27.88	0.28	24.00

The regional haze rule calls for steady improvement of visibility on the 20 percent worst visibility days. States are to consider this uniform rate of progress, and if reasonable measures can be identified to meet or exceed this rate while ensuring no degradation of visibility on the best days, then it should be adopted as a Federal Class I

[10] We calculate the rate of progress as (baseline – natural background)/60 to yield the annual deciview (dv) improvement needed to reach natural background conditions in 2064, starting from the 2004 baseline.

area's *reasonable* progress goal. A number of instructive analyses are presented below using each area's uniform progress goal as an example, but these should not be interpreted as constituting MANE-VU recommendations on reasonable progress goals.

As a practical means of analyzing uniform progress goals, we have examined the components of observed fine particle pollution that substantially contribute to visibility degradation. This analysis shows that certain species dominate the extinction budget while others play virtually no role on the worst haze days.

As demonstrated in Table 3-2, the inorganic constituents of fine particles (sulfates and nitrates) are the dominant contributors to visibility impairment, accounting for about 80 percent of total particle extinction. Within the MANE-VU sites, the relative split between these two components is about eight to one sulfate to nitrate (at Shenandoah, the average 20 percent worst day contribution of sulfates is even more dominant). Carbonaceous components account for the bulk of the remaining particle extinction, ranging from 12 to nearly 20 percent, mostly in the form of organic carbon. The remaining components add little to the extinction budget on the worst days, with a few percent attributable to coarse mass and around a half percent from fine soil.

One approach to designing control strategies for achieving reasonable progress goals is to reduce all components of $PM_{2.5}$ in equal proportion. Achieving the 2018 uniform progress goals (expressed in Mm^{-1} in the second column of Table 3-4) requires between a 29 and 36 percent reduction in each component of the six haze components of fine particle extinction if their relative percent contributions to the current worst baseline conditions are kept constant (see the third column of Table 3-4). Given the dominant role of sulfate and nitrate, however, and the difficulty in obtaining 29 to 36 percent reductions in some of the other categories such as soil or course mass, sulfate- and nitrate-based control programs are likely to offer more reasonable emission reduction opportunities.

Table 3-4. Percent particle B_{ext} reduction needed to meet uniform progress[11]

Site	Particle Extinction Decrease (Mm^{-1})	Uniform Reduction (%)	Sulfate/Nitrate Reduction (%)	OC/EC Reduction (%)
Acadia	27.7	31	38	194
Brigantine	55.3	36	46	218
Great Gulf	30.6	33	42	195
Lye Brook	35.4	34	41	210
Moosehorn	23.4	29	38	158
Shenandoah	57.1	36	42	303

[11] We derive the information in this table from the results of Table 3-3. First, we converted the baseline and interim goal levels from dv to Mm^{-1} units, thus avoiding the logarithmic nature embedded into the deciview calculations. The first column of the table gives the difference between baseline and interim goal. The ratio of this difference to the baseline yields the uniform rate of reduction tabulated in the second column. We generate the paired species reduction percentages by using the wet and dry aerosol extinction coefficients. We determine f(RH) values by dividing the five-year B_{ext} average by the dry extinction coefficient, giving a weighted average value of the f(RH) during the worst 20% of days. Similarly, in Table 3-5, we calculate mass values using the relative contributions of the species to be reduced and their wet and dry efficiencies.

The fourth column of Table 3-4 displays the results if a sulfate and nitrate focused control approach were taken to meet uniform progress goals. For these two inorganic species, a greater reduction would be necessary on the 20 percent worst days if the other four components showed no change relative to baseline levels. The last column shows that the contribution of the carbonaceous species is too small to meet the entire required 2018 progress goal on its own (i.e. the percent reduction is greater than 100) if a carbon-only control approach were attempted.

Since it is easier to understand the implications of requisite mass reductions, rather than extinction, Table 3-5 tabulates the corresponding mass changes required for meeting uniform progress goals on the 20 percent worst days. On an absolute mass basis, the changes across sites are more varied than they are when viewed from a percentage change perspective. That in part is a function of the relative pollution levels at each site, in addition to the logarithmic nature of the deciview (dv). This table (along with Table 3-6) can aid planners to gauge the potential impact that meeting uniform progress goals under the Regional Haze program will have on regional fine particle mass levels.

Table 3-5. Mass reductions required on 20% worst days based on extinction estimates in Table 3-4

	20% Worst Day Mass Reduction ($\mu g/m^3$)							
	Uniform Percent Change All Species				Only Inorganic		Only Carbonaceous	
Site	SO_4	NO_3	OC	EC	SO_4	NO_3	OC	EC
Acadia	1.95	0.25	0.76	0.13	2.38	0.31	4.80	0.85
Brigantine	4.14	0.65	1.64	0.26	5.22	0.82	9.92	1.56
Great Gulf	2.42	0.11	0.97	0.13	3.06	0.14	5.74	0.76
Lye Brook	2.85	0.36	1.02	0.16	3.49	0.44	6.36	1.00
Moosehorn	1.68	0.20	0.77	0.13	2.14	0.26	4.12	0.69
Shenandoah	4.78	0.24	1.19	0.21	5.57	0.28	9.94	1.74

Table 3-6 provides an estimate of mass decreases that might be expected on an average day. It assumes using either a uniform rate of change in *all* species, or a uniform rate of change in the *sulfate and nitrate* component of fine particulate, to achieve the progress toward the 2018 goals, respectively. These values are likely a lower bound to the annual average change at Class I areas anticipated from current conditions to 2018 as they are based on the assumption that on the best days, no change occurs and the percent reduction on the middle days is half of what is predicted on the worst.[12]

[12] We derived the values tabulated in Figure 3-6 as follows: We multiplied half of the percentage change expected on the worst 20% of days by the average mass concentration of each species for the middle 20% of days. Note that if we apply a 25% reduction on the cleaner remaining quintile and 75% reduction on the dirtier remaining quintile, the annual average reduction would presumably be greater than that on the middle days given the skew in the distribution of all days. For example, in the inorganic-only case at Acadia, the average of the worst 20% change and best 20% is (2.69 + 0)/2 or 1.35 $\mu g/m^3$, which is nearly four times greater than the middle day. Further, given the large reduction on the worst days, it is reasonable to expect some small improvement on the best days.

Table 3-6. Estimated Mass Reduction on an Average Day

	Estimated Average Day Mass Reduction ($\mu g/m^3$)					
	Uniform Percent Change All Species				Only Inorganic	
Site	SO_4	NO_3	OC	EC	SO_4	NO_3
Acadia	0.25	0.05	0.16	0.02	0.31	0.06
Brigantine	0.80	0.19	0.38	0.08	1.01	0.25
Great Gulf	0.28	0.04	0.19	0.03	0.36	0.05
Lye Brook	0.29	0.07	0.17	0.03	0.36	0.09
Moosehorn	0.25	0.05	0.19	0.03	0.32	0.06
Shenandoah	0.79	0.24	0.28	0.05	0.92	0.28

3.1.1. Preview of revised IMPROVE Algorithm for aerosol extinction

Recently, the IMPROVE Steering Committee accepted an alternative approach for calculating visibility metrics based on measured aerosol concentrations. The new algorithm improves the correspondence between the reconstructed extinction and directly measured light scattering at the extremes of the visibility range. These extremes form the basis for determining the uniform progress "glide path."

The new equation revises or adds to the original version. The most significant changes include:

- revision of the dry aerosol extinction coefficients for sulfate, nitrate and organic carbon,
- splitting sulfate, nitrate and organic mass into small and large size fractions based on total species mass,
- revised f(RH) curves for inorganic species,
- inclusion of sea salt mass and associated f(RH) growth factor,
- use of a *site-specific* Rayleigh scattering term, and
- revision of the organic mass multiplier.

The VIEWS website provides the revised dataset for all IMPROVE data, allowing the calculation of the baseline period with the new algorithm. Natural background calculation methods that mirror many of the changes adopted as an alternative for baseline calculations have been suggested; however, none have been formally adopted by the IMPROVE Steering Committee at this time.

As a first step toward assessing the implications of the algorithm revisions, we compare the baseline visibility levels from the old and new approaches. The new calculation approach results in between one and two deciview increase in the 20 percent worst visibility conditions during the baseline period for the six sites considered. Extinction changes are observed for all components, with increases ranging from 6 to 42 percent depending on species. The greatest overall percentage change occurs for organic

carbon and the least for fine soil. Changes in the baseline 20 percent best days were much less with the absolute contribution of a component to visibility degradation increasing in some cases and decreasing in others. On average, the values decrease by 0.1 deciview. Table 3-7 and Table 3-8 summarize the species-specific changes for worst and best days' aerosol extinction.

Table 3-7. Aerosol extinction by specie for 20% worst days

20% worst-day particle extinction (Mm^{-1}) New Algorithm / Old Algorithm							
Site	SO_4	NO_3	OC	EC	Soil	Coarse	Salt
Acadia	76.4 / 66	8.6 / 8.1	12.5 / 10.1	4.8 / 4.4	0.6 / 0.5	2.1 / 1.8	1.4 / 0
Brigantine	134.2 / 106.2	18.1 / 16.1	25.9 / 18.3	7.9 / 7.1	1.0 / 1.0	6.5 / 5.2	0.7 / 0
Great Gulf	79.6 / 66.5	3.4 / 3.0	14.8 / 10.6	4.3 / 3.8	0.6 / 0.5	3.1 / 2.9	0.1 / 0
Lye Brook	94.4 / 76.7	10 / 9.3	17.1 / 12.1	5.3 / 4.7	0.7 / 0.7	2.1 / 1.8	0.1 / 0
Moosehorn	64 / 56.1	7 / 6.3	13.4 / 10.5	5.1 / 4.4	0.4 / 0.4	2.5 / 2.1	1.1 / 0
Shenandoah	169.6 / 132.5	7.9 / 5.8	18.2 / 13.2	6.5 / 5.7	0.8 / 0.8	3.0 / 2.6	0.1 / 0

Table 3-8. Aerosol extinction by specie for 20% best days

20% best-day particle extinction (Mm^{-1}) New Algorithm / Old Algorithm							
Site	SO_4	NO_3	OC	EC	Soil	Coarse	Salt
Acadia	6.8 / 7.4	1.1 / 1.2	2.3 / 2.4	0.9 / 0.9	0.1 / 0.1	0.7 / 0.7	0.4 / 0
Brigantine	5.7 / 6.2	1.0 / 1.1	2.0 / 2.1	0.9 / 0.9	0.1 / 0.1	0.9 / 0.7	0.2 / 0
Great Gulf	5.7 / 6.2	1.0 / 1.1	2.0 / 2.1	0.9 / 0.9	0.1 / 0.1	0.9 / 0.7	0.2 / 0
Lye Brook	4.5 / 5.0	1.2 / 1.2	1.3 / 1.4	0.6 / 0.6	0.1 / 0.1	0.5 / 0.5	0.0 / 0
Moosehorn	6.8 / 7.3	1.0 / 1.2	3.1 / 3.1	1.0 / 1.0	0.1 / 0.1	1.1 / 1.1	0.3 / 0
Shenandoah	11.4 / 12.8	4.2 / 4.4	2.9 / 3.0	1.6 / 1.6	0.2 / 0.2	1.1 / 1.1	0.1 / 0

Figure 3-1and Figure 3-2 graphically compare the old and new algorithm for six sites. The left-hand side of the figures presents the old contribution of aerosol extinction while the right-hand side shows the new calculations. Relatively small differences are apparent, with slight relative decreases in sulfate contribution offset by small increases in nitrate, organic carbon and the addition of sea salt.

The potential impact of these changes on the uniform rate of progress slope cannot be determined at this time, since revisions in natural background calculations remain incomplete. A preliminary assessment, however, suggests that natural background estimates for MANE-VU may increase by about 10 percent. This translates to a change of just over one deciview. This estimate combined with the average increase of 1.5 deciview in baseline conditions would not likely change the slope of the uniform progress curve in any significant way. Nonetheless, the actual mass reductions required could change given the logarithmic nature of the haze index, where marginal mass changes are larger at higher deciview levels. It is not a straightforward exercise to estimate the potential effect of such changes given the increased complexity of the new algorithm relative to the old equation.

Figure 3-1. Comparison of Old and New Algorithms for Baseline Worst Days

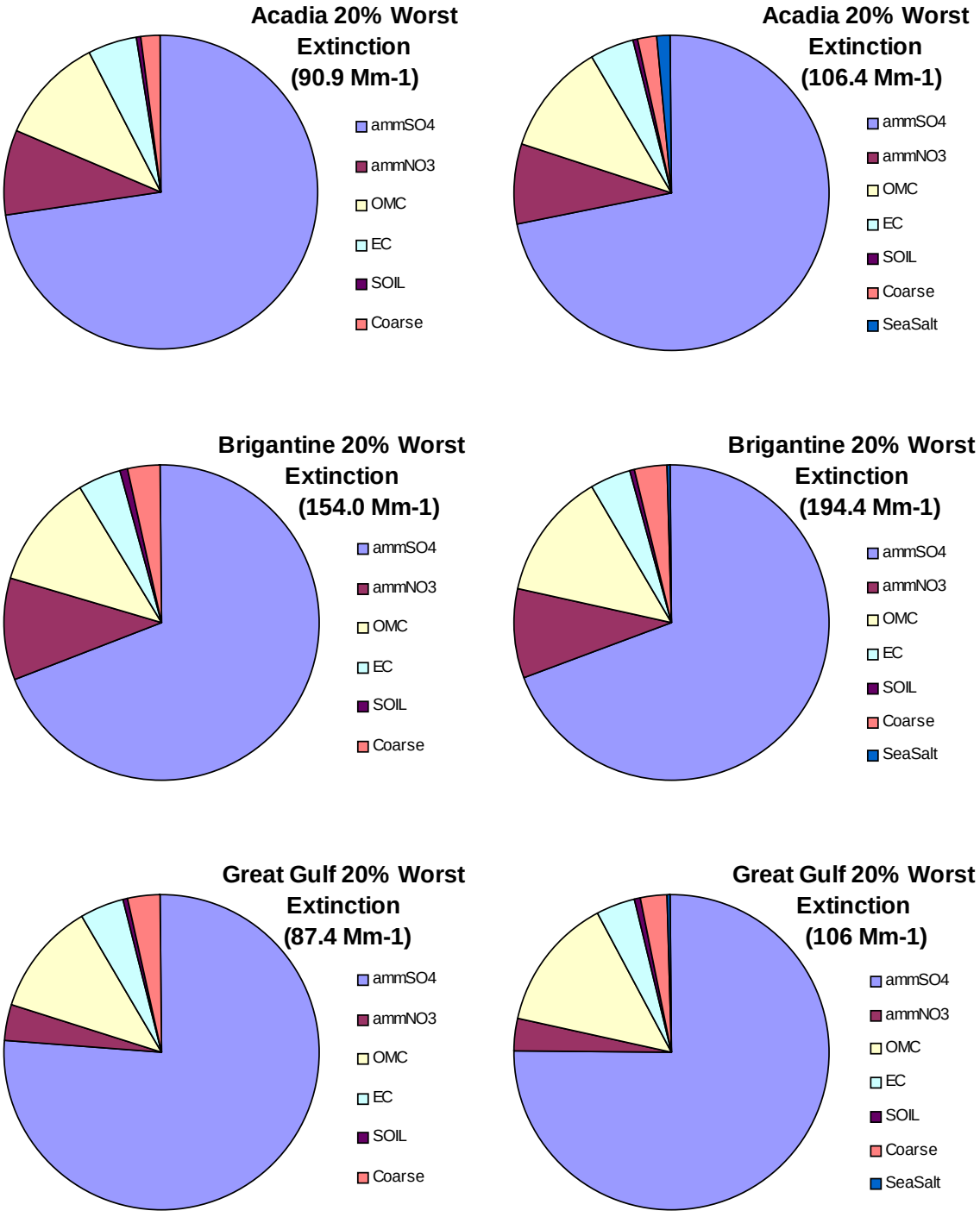

Figure 3-2. Comparison of Old and New Algorithms for Baseline Worst Days

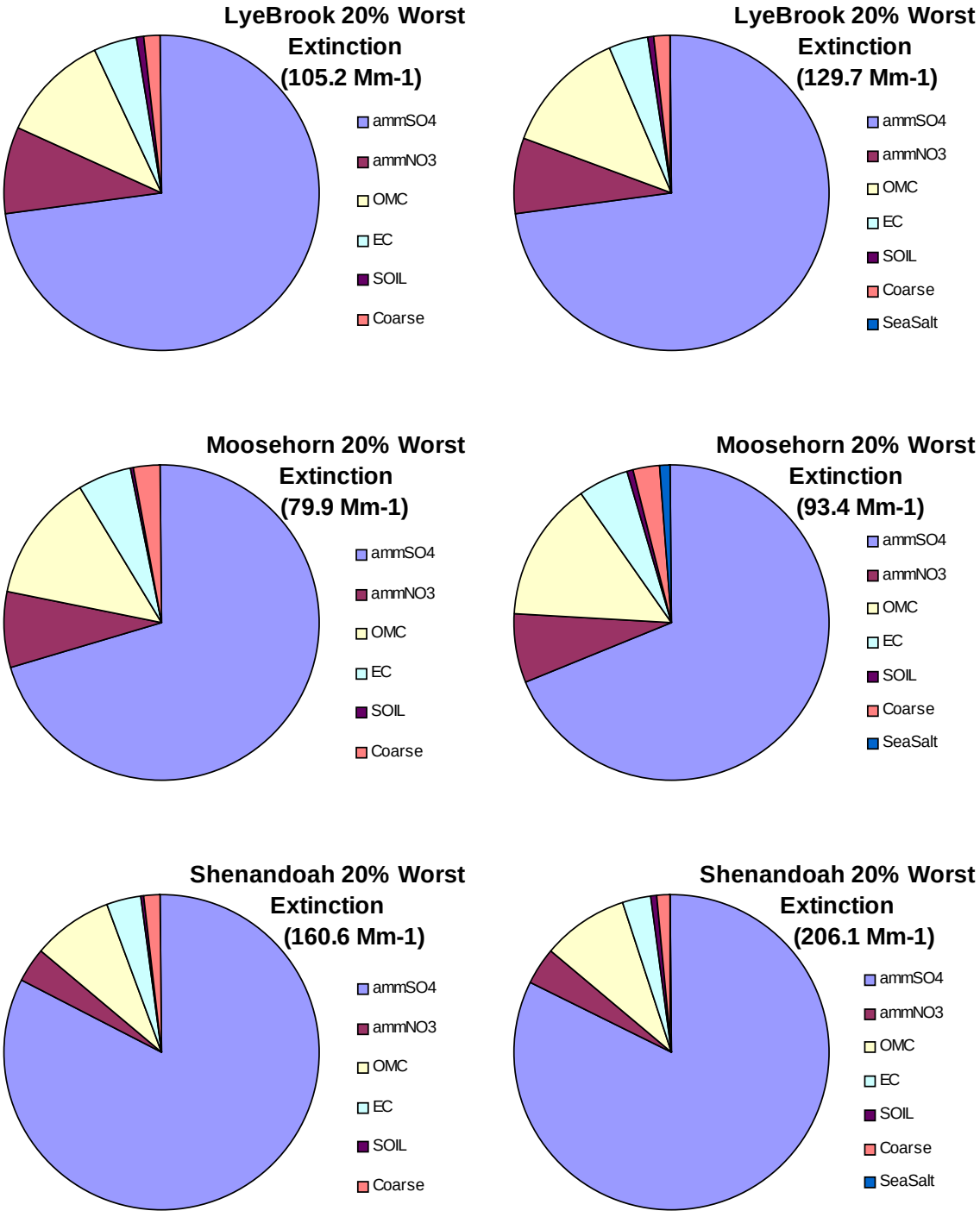

3.2. 2002 Monitoring Data

The recent MANE-VU report "2002 Year in Review" (NESCAUM, 2004b) provides a comprehensive review of monitoring data available to support SIP development in the MANE-VU region, including data on fine particle composition, as well as temporal and spatial distributions. The data in this study support the conceptual model in several important ways. They show that: (1) the single largest component of fine particle mass is sulfate; (2) the largest sulfate-generating emissions sources that affect the MANE-VU region lie to the south and west of the region; (3) fine particle concentrations are bi-modal with peaks in the summer and winter; and (4) summer and winter peak concentrations are generally caused by different chemical and physical processes in the atmosphere (i.e., summer peaks are strongly related to regional sulfate transport whereas winter peaks result from the sum of regionally-generated sulfate and locally generated sulfate, as well as organics and nitrate that build up during local stagnation events).

3.2.1. Sulfate

Data from several monitoring programs indicate that sulfate (on an annual basis) is the single largest component of fine particle mass in the MANE-VU region. Figure 3-3 displays sample data from two Speciation Trends Network (STN) sites in New Jersey. This shows that sulfate accounts for roughly half of fine particle mass on an annual average basis at background sites and about a third at the urban site. During summer, sulfate comprises over half the fine particle mass at rural background sites and two-fifths of fine particle mass at the urban site. When considering the different light-extinguishing properties of various fine particle constituents, sulfate is responsible for an even greater fraction of visibility impairment. It accounts for between three-quarters and four-fifths of overall light extinction on the 20 percent worst- visibility days (Table 3-2).

Figure 3-3. New Jersey Urban Area Compared to an Upwind Background Site

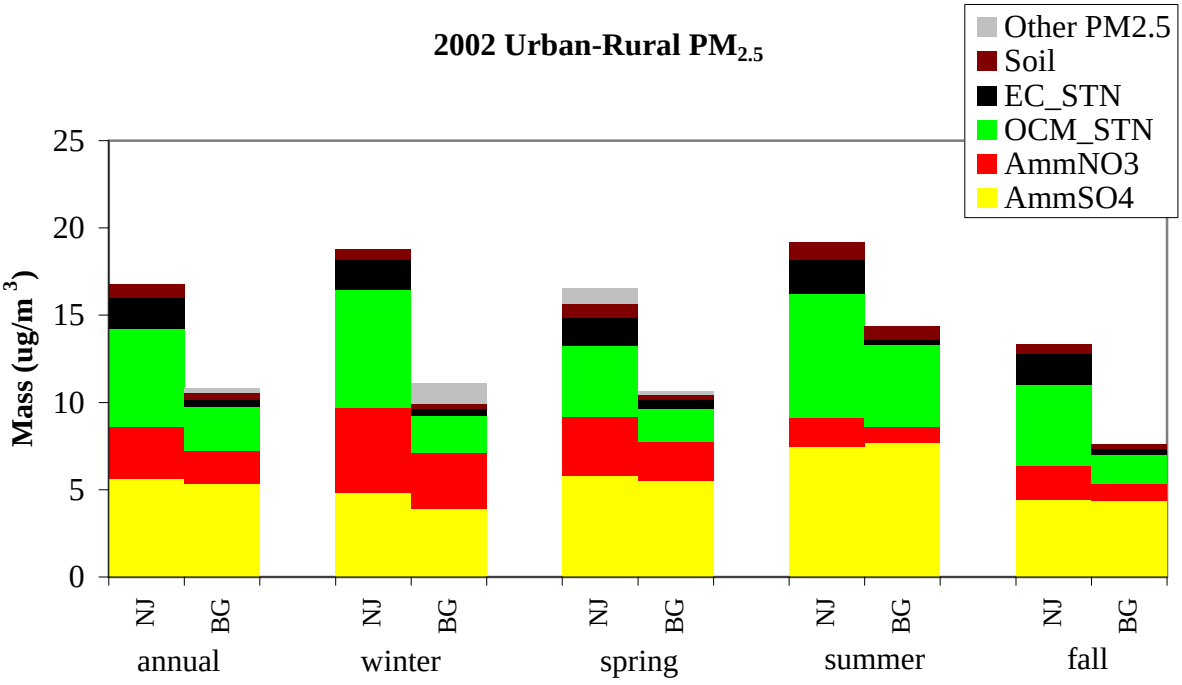

3.2.2. Southwest-Northeast Gradient

Figure 3-4 shows that $PM_{2.5}$ mass declines fairly steadily along a southwest to northeast transect of MANE-VU. This decline is consistent with the existence of large fine particle emissions sources (both primary and secondary) to the south and west of the MANE-VU region.

This trend in $PM_{2.5}$ mass is primarily due to a marked southwest-to-northeast gradient in ambient sulfate concentrations during three seasons of the year as illustrated in Figure 3-5. Wintertime concentrations, by contrast, are far more uniform across the entire region. Figure 3-6 shows that on an annual basis, both total PM and sulfate mass are highest in the southwestern portions of MANE-VU (note the different scales for each pollutant). High concentrations of nitrate and organic particle constituents, which play a role in localized wintertime PM episodes, tend to be clustered along the northeastern urban corridor and in other large urban centers.

Sulfate is a secondary pollutant, meaning that it forms in the atmosphere from precursor emissions. The formation of sulfate from SO_2 emissions requires time in an oxidizing environment. Therefore, it is likely that a substantial portion of the sulfate observed in the MANE-VU region is from sulfur emitted from south and west of the region. Modeled meteorological (trajectory) data presented in Chapter 5 support this conclusion by showing that the dominant wind direction over the MANE-VU region during periods of high sulfate concentrations is from the southwest.

Figure 3-4. MANE-VU FRM $PM_{2.5}$ statistics along a southwest to northeast axis

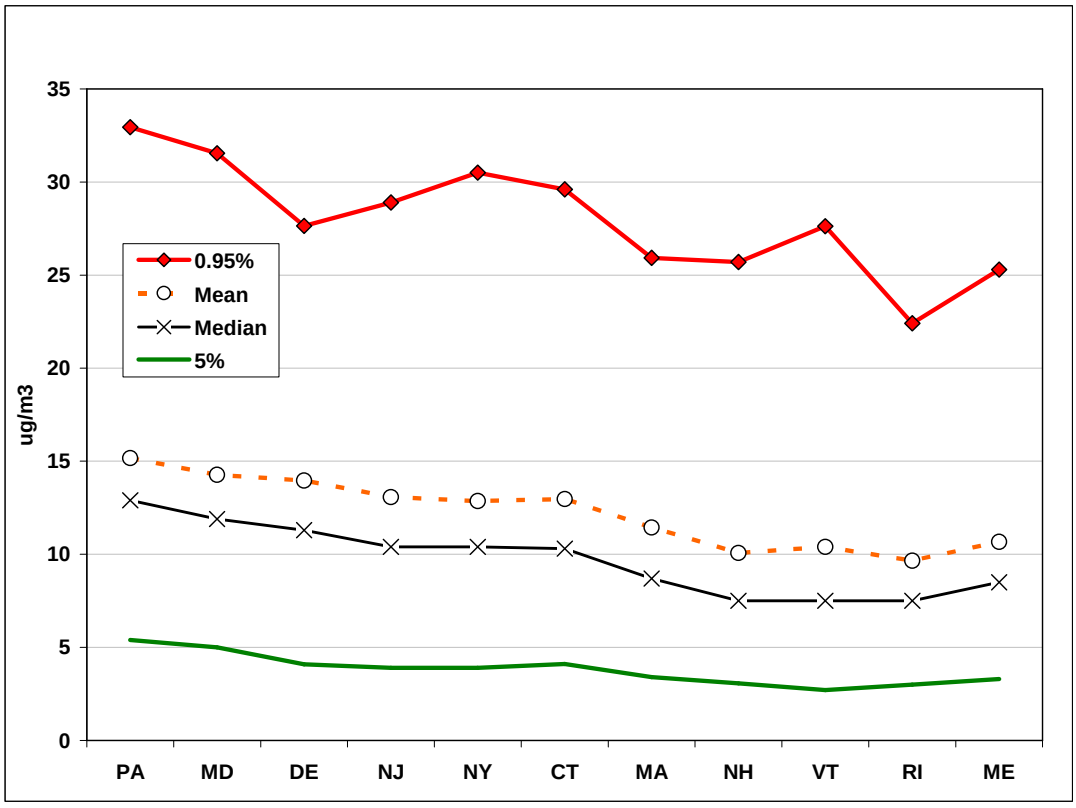

Figure 3-5. 2002 Seasonal average SO4 based on IMPROVE and STN data

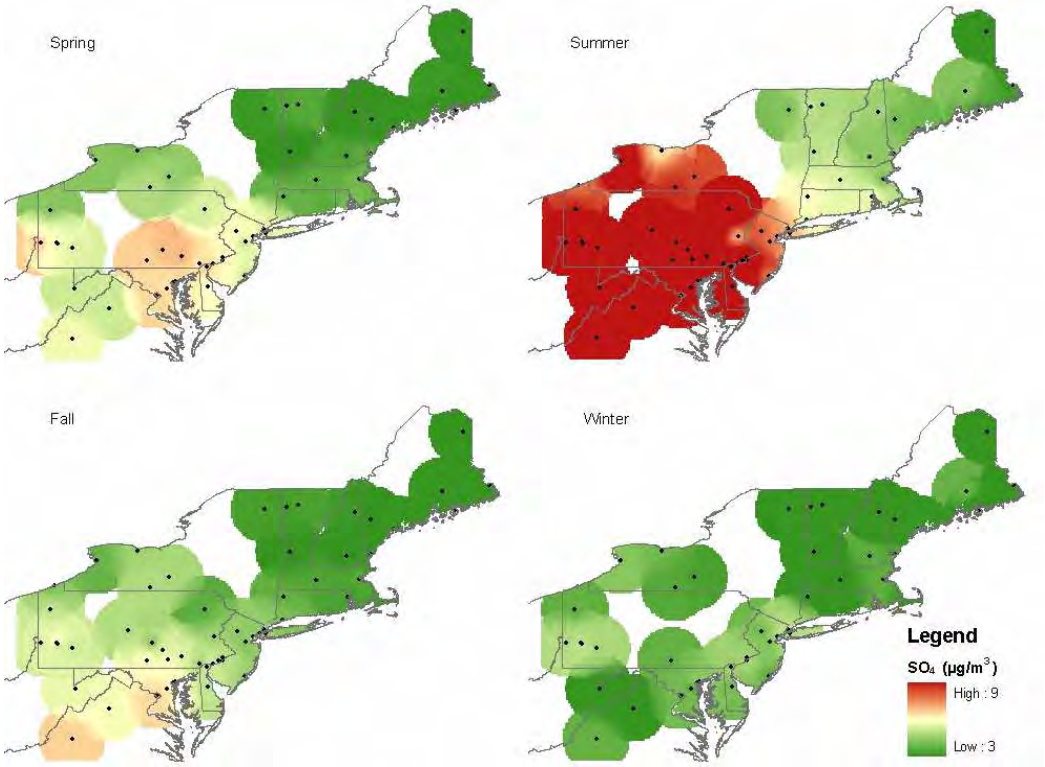

Figure 3-6. 2002 Annual average $PM_{2.5}$, sulfate, nitrate and total carbon for MANE-VU based on IMPROVE and STN data. Mass data are supplemented by the FRM network.

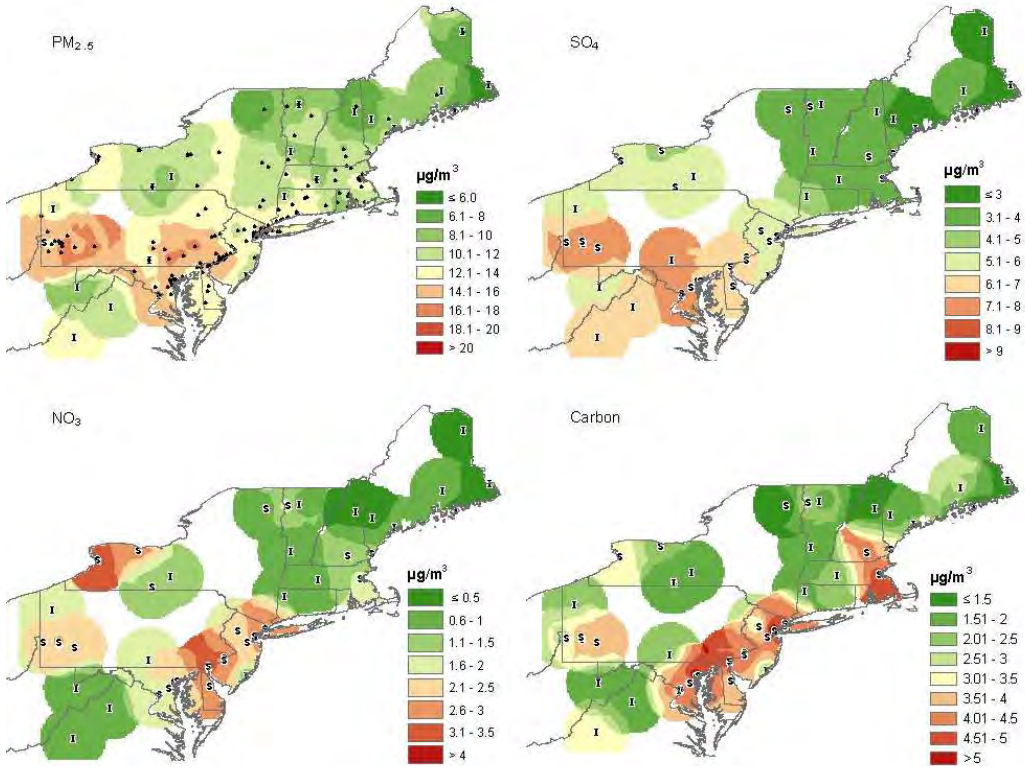

3.2.3. Seasonality

In general, fine particle concentrations in MANE-VU are highest during the warmest (summer) months but also exhibit a secondary peak during the coldest (winter) months. This bimodal seasonal distribution of peak values is readily apparent in Figure 3-7. The figure shows the smoothed 60-day running average of fine particle mass concentrations using continuous monitoring data from two northeastern cities over a period of several years.

Figure 3-7. Moving 60-day average of fine aerosol mass concentrations based on long-term data from two northeastern cities

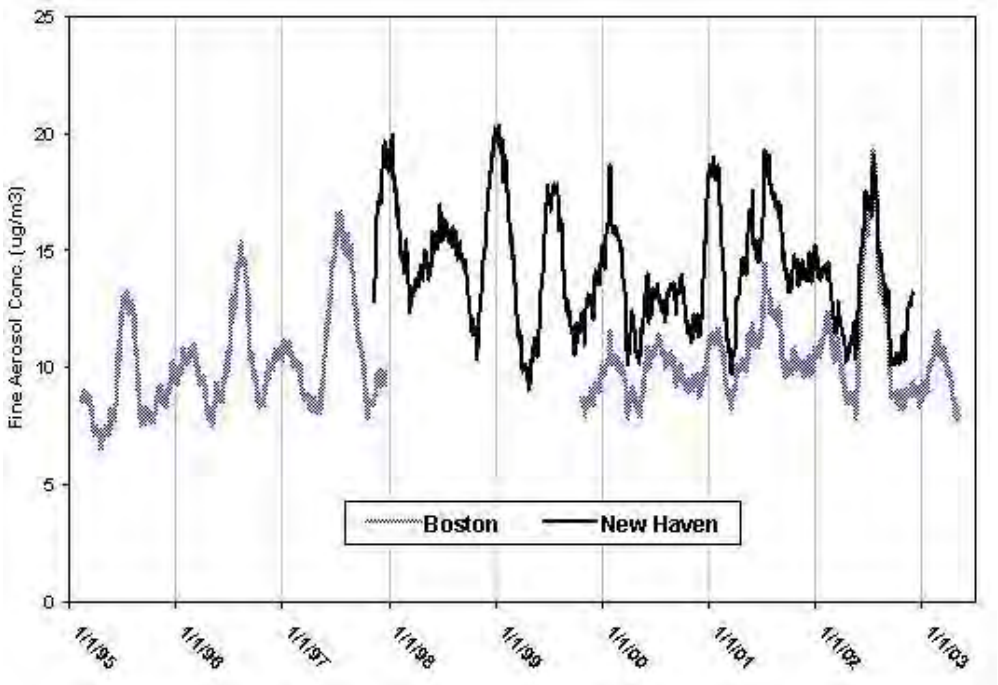

Figure 3-8. 30-day average fine aerosol mass concentrations from eight northeastern cities

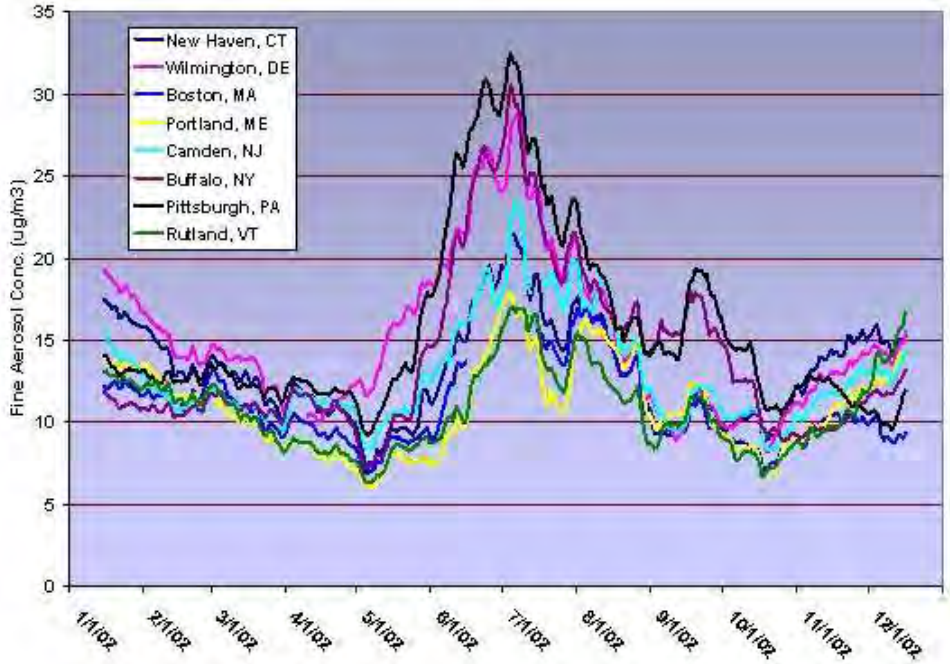

Although the patterns exhibited by these monitoring data include occasional anomalies (as in the summer of 2000), summer peak concentrations in both cities of Figure 3-7 are generally much higher than the surrounding winter peaks. Figure 3-8 also demonstrates this bimodal pattern. Though slightly more difficult to discern in just a single year's worth of data, a "W" pattern does emerge at almost all sites across the region during 2002 with the winter peak somewhat lower than the summer peak at most sites. Urban monitors in Wilmington, Delaware and New Haven, Connecticut have wintertime peak values approaching those of summer.

3.2.4. Seasonal Mechanisms

In the summertime, MANE-VU sites repeatedly experience sulfate events due to transport from regions to the south and west. During such events, rural and urban sites throughout the MANE-VU region record high (i.e., >15 $\mu g/m^3$) daily average $PM_{2.5}$ concentrations. Meteorological conditions during the summer frequently allow for summer "stagnation" events when very low wind speeds and warm temperatures allow pollution levels to build in an air mass as it is slowly transported across the continent. During these events, atmospheric ventilation is poor and local emission sources add to the burden of transported pollution with the result that concentrations throughout the region (both rural and urban) are relatively uniform. Generally there are enough of these events to drive the difference between urban and rural sites down to less than 1 $\mu g/m^3$ during the warm or hot months of the year. As a result, concentrations of fine particles aloft will often be higher than at ground-level during the summertime, especially at rural monitoring sites. Thus, when atmospheric "mixing" occurs during summer[13] mornings (primarily 7 to 11 a.m.), fine particle concentrations at ground-level can actually increase (see Hartford, CT or Camden, NJ in Figure 3-9).

During the wintertime, strong inversions frequently trap local emissions overnight and during the early morning, resulting in elevated urban concentrations. These inversions occur when the earth's surface loses thermal energy by radiating it into the atmosphere (especially on clear nights). The result is a cold, stable layer of air near the ground. At sunrise, local emissions (both mobile and stationary) begin increasing in strength and build-up in the stable ground layer (which may extend only 100 meters or less above-ground). Increasing solar radiation during the period between 10 a.m. and noon typically breaks this cycle by warming the ground layer so that it can rise and mix with air aloft. Because the air aloft during wintertime is typically less polluted than the surface layer, this mixing tends to reduce ground-level particle concentrations (see Figure 3-10). This diurnal cycle generally drives wintertime particle concentrations, although the occasional persistent temperature inversion can have the effect of trapping and concentrating local emissions over a period of several days, thereby producing a significant wintertime pollution episode.

[13] Here we define summer as May, June, July and August.

Figure 3-9. Mean hourly fine aerosol concentrations during the summer season

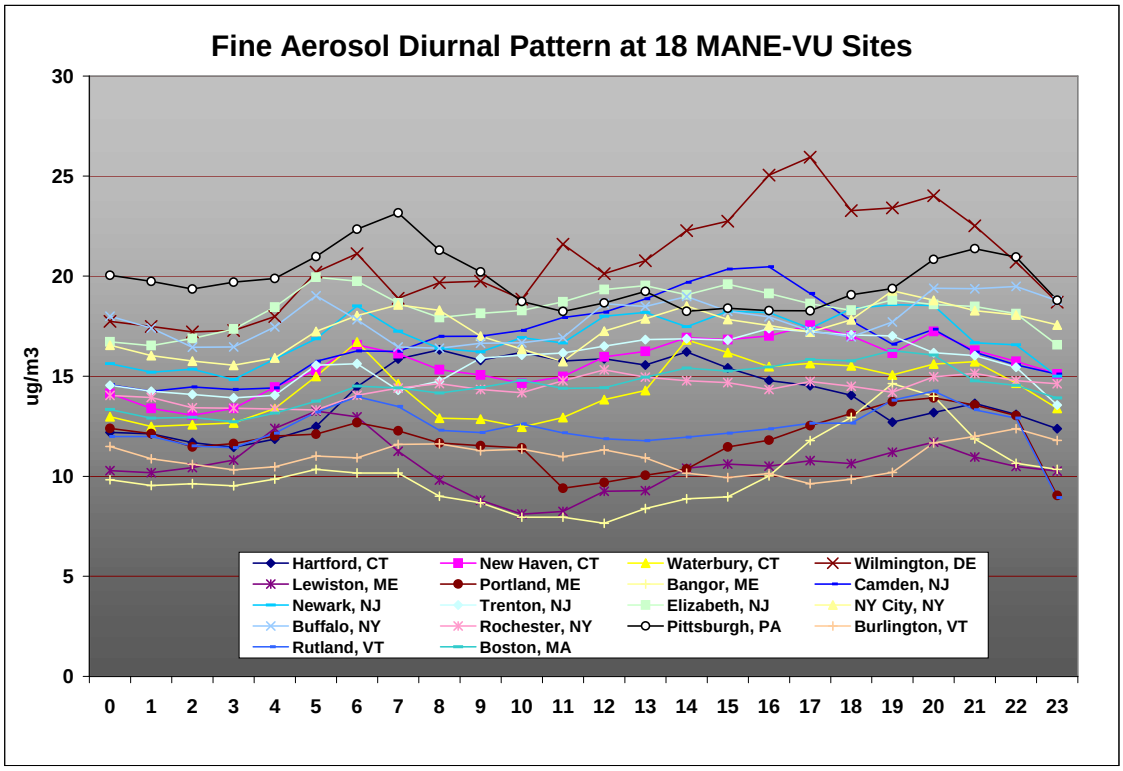

Figure 3-10. Mean hourly fine aerosol concentrations during the winter season

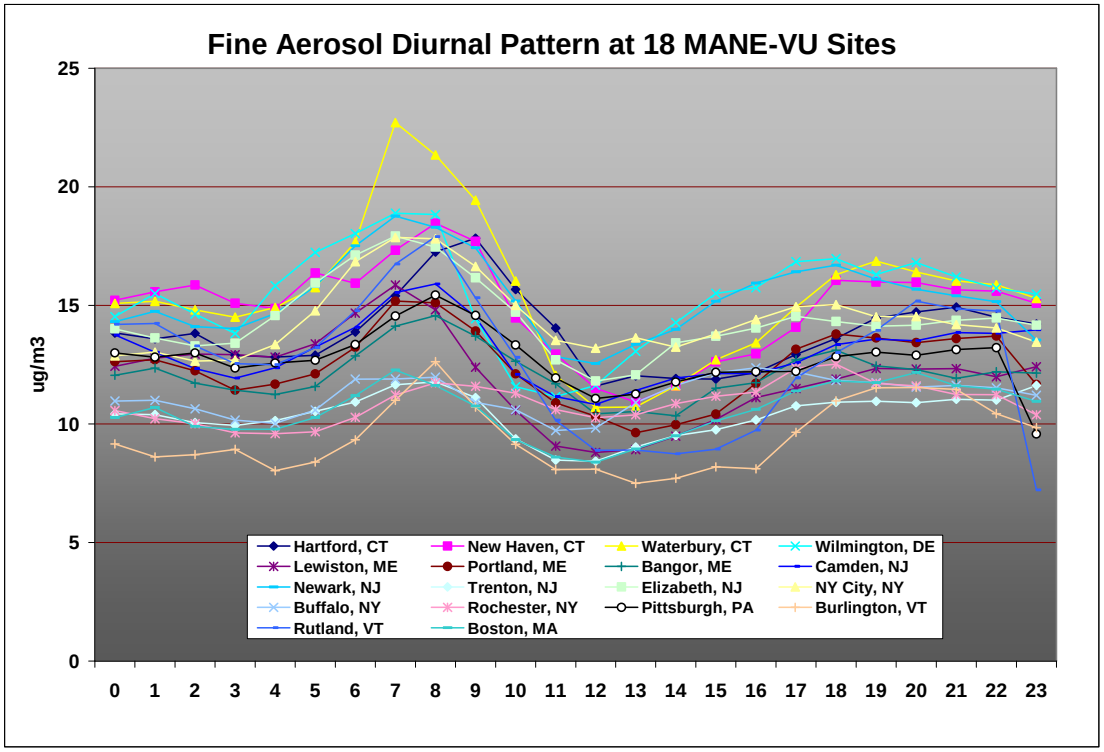

Rural areas experience the same temperature inversions but have relatively fewer local emissions sources so that wintertime concentrations in rural locations tend to be lower than those in nearby urban areas. Medium and long-range fine particle transport events do occur during the winter but to a far lesser extent than in the summertime. In sum, it is the interplay between local and distant sources together with seasonal meteorological conditions that drives the observed 3–4 $\mu g/m^3$ wintertime rural versus urban difference in PM concentrations.

3.3. RAIN data

Routine monitoring networks operated by USEPA, the National Park Service or state monitoring agencies collected much of the monitoring data shown so far. We anticipate that these data will continue to provide crucial information on the nature and extent of visibility impairment across the region. In addition, MANE-VU is also developing a network of enhanced monitoring sites capable of providing continuous data on the concentration, composition, and visibility impacts of fine particles. These data will be critical for understanding the more complex issues associated with organic carbon as well as any tradeoffs between sulfate and nitrate control. This Rural Aerosol Intensive Network (RAIN), which was first deployed in 2004, is therefore likely to play a prominent role in future visibility control programs and in the development of regional haze SIPs due in 2018.

NESCAUM coordinates the RAIN effort as a cooperative effort of the MANE-VU member state air agencies. The network covers the region from western Maryland (near large sulfur sources in the Ohio River Valley) through northwestern Connecticut to Acadia National Park in Maine. The initial network consists of these three rural, moderate elevation (700 to 2,500 feet) sites in a southwest to northeast line, all with detailed PM and visibility related measurements. The network design includes highly time resolved (1-2 hour) aerosol mass, composition, and optical property measurements. These provide enhanced insight into regional aerosol generation and source characterization, which are factors that drive short term visibility, and aerosol model performance and evaluation. In addition to these three sites, as of 2006 the NY-DEC/SUNY-Albany intensive measurement site at Pinnacle State Park (Addison, NY, seven miles southwest of Corning, NY, and seven miles north of the Pennsylvania border) has most of the RAIN parameters and methods other than visibility; efforts are underway to bring that site into the RAIN program (to ensure consistent method operation) and to add visibility measurements.

The RAIN sites use the Sunset Laboratory Model 3 field carbon analyzer and the new Thermo Environmental Model 5020 sulfate analyzer. This is the first use of these methods in routine, ongoing state-run networks. Combined with other more routine measurements such as IMPROVE aerosol, NGN-2 (wet) nephelometers, continuous $PM_{2.5}$, trace SO_2, ozone, meteorology, and automated digital visibility cameras (CAMNET), these methods make up the core RAIN monitoring lineup. Some of the RAIN sites will have additional related measurements, including "true" trace CO, NO_X, dry scattering (NGN-3a nephelometer), and other measurements. An Air and Waste

Management Association conference proceedings paper provides more information on the design of the network and examples of data from the summer of 2004.[14]

A longer term goal of RAIN is to enhance the network with other measurements and sites in future years. A National Weather Service ASOS visibility sensor at a RAIN site would allow the large network of existing ASOS data to be "tethered" to visibility measurements we understand well. Strong aerosol acidity, nitric acid, and ammonia are measurements that would be desirable on either an integrated or real-time basis. There are no continuous nitrate measurements in RAIN at this time because available methods suitable for routine deployment in state networks are not yet sufficiently robust.[15] Lack of continuous nitrate data is not a significant issue for this analysis since nitrate is not (yet) a major visibility factor at these rural sites. We expect that most of the continuous method data from RAIN to be available in real-time to web data resources like VIEWS, FASTNET and AIRNowTech by the end of 2006.

Measurements similar to those in RAIN done towards the west and south borders of the MANE-VU domain (Ohio and Virginia for example) would greatly enhance our understanding of the impact of the large sulfur source region in and around the Ohio River Valley on regional visibility. We encourage agencies and RPOs in those areas to develop intensive sites to complement the RAIN data.

As an initial test of the RAIN network, we examined visibility and related particle information for the third quarter of 2004 to determine how well the data from one (or both) of two recently installed semi-continuous monitors could reproduce the visibility data reported by existing NGN-2a nephelometers. The relevant data came from two monitors of interest: the Thermo Model 5020 (for sulfate) and the Sunset Labs (Model 3) semi-continuous analyzer for elemental and organic carbon. In addition, a Rotronic sensor (Model MP-101A, with active aspiration) measured relative humidity (RH) data on-site in order to supply a correction factor - f(RH) - for estimating the light scattering associated with various fine particle constituents.

Because ammonium sulfate is the major component of haze-producing particulate pollution in the northeastern United States, we examined sulfate data first. The Thermo Model 5020 reports sulfate and the IMPROVE algorithm for calculating visibility parameters assumes that all sulfate is in the form of ammonium sulfate. During high sulfate events in the rural Northeast this is not always the case, although it is still a reasonable first assumption.

The Thermo sulfate method has been shown to consistently under-report sulfate relative to IMPROVE sulfate measurements at the RAIN sites, but not at some other sites. Since the correlation with IMPROVE sulfate is high at all RAIN sites, the hourly RAIN sulfate data can be corrected to be "IMPROVE"-like with reasonable confidence. A RAIN technical memorandum describes this issue in more detail.[16] For the Acadia sulfate data used here, the daily correlation coefficient (R^2) between IMPROVE and

[14] http://www.nescaum.org/documents/allen-awma_haze-rain-paper-oct-2004_proceedings.pdf/
[15] See the EPA method evaluation report at http://www.epa.gov/ttn/amtic/semicontin.html for more information.
[16] "Rural Aerosol Intensive Network (RAIN) Preliminary Data Analysis," available at: http://www.nescaum.org/documents/2006-05-memo8-rain.pdf/

Thermo sulfate is 0.95 (based on third and fourth quarter 2004 data). A correction factor of 1.30 is applied to the Thermo sulfate data based on the linear regression of IMPROVE and Thermo sulfate 24-hour samples for the third and fourth quarters of 2004 data; this correction makes the Thermo sulfate data consistent with the IMPROVE sulfate data.

We need three types of data to relate direct measures of atmospheric light scattering to a re-constructed or calculated estimate of light scattering based on observed sulfate levels: (1) direct measurements of light scattering (via nephelometer); (2) sulfate measurements; and (3) relative humidity measurements. The three RAIN sites in the northeastern United States measure each of these variables. Of these sites, however, only the McFarland Hill site at Acadia National Park in Maine is within a Class I area. Therefore, we selected data from the McFarland Hill site for the preliminary analysis we describe below.

Given the highly non-linear relationship between relative humidity and ammonium sulfate particle size and the limitations of relative humidity (RH) sensor accuracy at very high values of RH, we excluded from this analysis data collected when relative humidity was equal to or greater than 95 percent. Of the 2,208 hourly observations recorded from June 1 through September 30, this relative humidity 'exclusion' removed 525 hours. Data for an additional 92 hours were not available due to missing measurements from either the sulfate monitor or the nephelometer. We excluded a further 35 hours due to flagged nephelometer performance (such flags could be triggered by excess noise or rate-of-change in the signal). This left 1,556 hourly observation pairs for the third quarter, equivalent to a data capture rate of 70 percent - still a substantial sample given the nature of the emerging technology employed at the RAIN sites.

We multiplied sulfate concentrations from the Thermo 5020 by 1.37 to convert them to a mass equivalent for ammonium sulfate (this is the same factor IMPROVE uses). This new variable (SULFATE) is the strongest driver of light extinction in the Northeast because of the extreme size-dependent nature of ammonium sulfate light scattering, which in turn is highly (and very non-linearly) dependent on atmospheric relative humidity. Next, we converted the hourly RH values to a relative humidity function "f(RH)" by using a conversion table adopted by IMPROVE.[17] Then we applied a "dry specific scattering" coefficient of "3"[18] to the hourly SULFATE values. The final equation is shown below:

Reconstructed Sulfate Scattering = 3 * f(RH) * (SULFATE)

When we compared this reconstructed estimate of hourly light scattering to the IMPROVE NGN-2a nephelometer data (via a least-squares linear regression), we obtained an R^2 of 0.888. When two apparent outlier hours are removed (both of which occurred during periods when relative humidity was over 87 percent and changing rapidly) the regression slope is 0.846, the intercept is -5, and R^2 increases to 0.942. This

[17] See: http://vista.cira.colostate.edu/improve/Tools/humidity_correction.htm; this is the original f(RH) table, not the new one.

[18] Described at http://vista.cira.colostate.edu/improve/Tools/ReconBext/reconBext.htm

implies that sulfate alone is responsible for approximately 85 percent of the light scattering (and visibility degradation) for this period of measurement.

Because elemental carbon absorbs light much more strongly than it scatters light, we added only the "light-scattering carbon" (OC) detected by the Sunset Model 3 to this reconstruction. The IMPROVE program uses the following equation to describe the impact of light-scattering carbon:

Reconstructed Carbon Scattering = 4 * f_{org}(RH) * [OMC]

where the dry scattering coefficient of this carbon fraction is set at "4," the relative humidity factor is set at unity (due to the weak hygroscopicity of organic carbon), and OMC represents "organic mass by carbon." The IMPROVE Steering Committee has recently adopted 1.8 as an alternative organic mass multiplier (rather than 1.4) for calculating OMC values for use in reconstructed extinction as described in section 3.1. We have also used 1.8 for the analysis presented below.

Because the RAIN sites collect carbon data over two-hour periods, we averaged the McFarland Hill sulfate (Thermo-5020), scattering (NGN-2) and RH (Rotronic) hourly data into two-hour, whole number blocks in order to bring the data from Sunset Labs into the reconstruction equation. In addition, we subtracted a "filter blank" value for the Sunset OC data of 0.5 $\mu g/m^3$ (empirically derived from user experience of the Model 3) from the OC data prior to their use in the reconstruction calculation (OMC = (Sunset OC – 0.5) x 1.8). See Figure 3-11 for results of these reconstructed estimates of visibility using both sulfate and carbon measurements.

As indicated by Figure 3-11, adding the organic carbon data to the sulfate data significantly improves the agreement between reconstructed estimates of aerosol scattering and direct visibility measurements at the McFarland Hill site. Specifically, it appears that these two components of the ambient aerosol generally explain about 94 percent of the observed scattering at Acadia during the summer, with a very high correlation coefficient even at 2-hour intervals. This is excellent agreement considering that scattering from nitrate and crustal aerosol components is not included in this reconstruction.

These data demonstrate that the highly time-resolved nature of RAIN data is invaluable in examining short-term variations (i.e., on the order of days to weeks) in haze production and transport. The sulfate, carbon and other monitoring capabilities emerging from the RAIN project will provide another valuable tool to state and tribal authorities in seeking to understand the sources of regional haze and to craft effective control strategies. A more detailed analysis of RAIN data is available in a recently released MANE-VU technical memorandum.[19]

[19] "Rural Aerosol Intensive Network (RAIN) Preliminary Data Analysis," available at: http://www.nescaum.org/documents/2006-05-memo8-rain.pdf/

Figure 3-11. 2-Hour Reconstructed scattering at Acadia, Maine using semi-continuous SO_4 and OC data for the third quarter of 2004

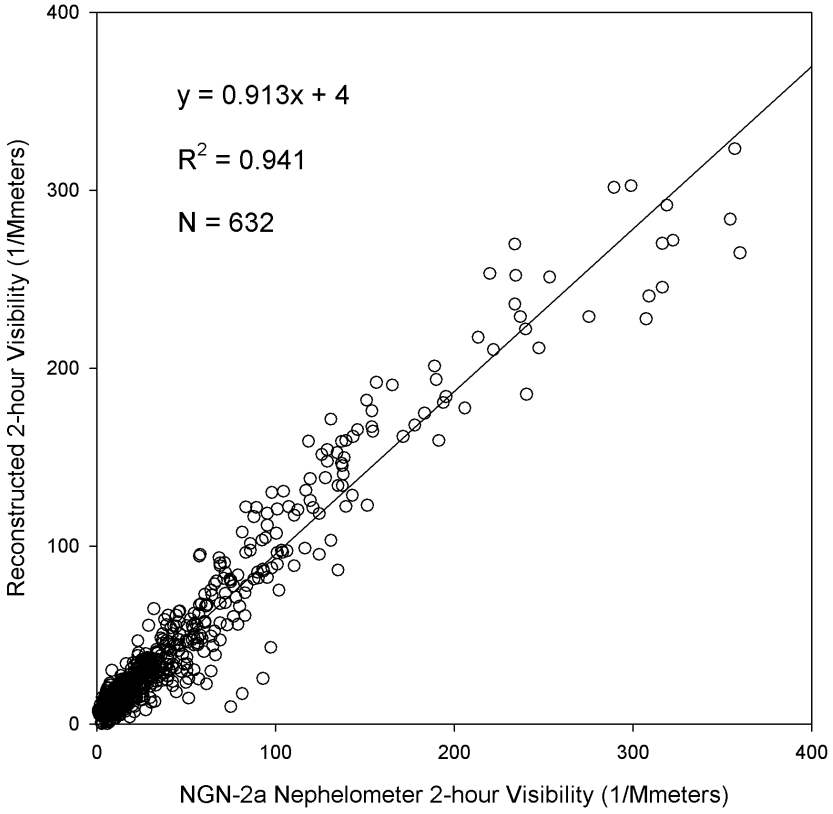

References

NESCAUM, "Natural Background Visibility Conditions: Considerations and Proposed Approach to the Calculation of Natural Background Visibility Conditions at MANE-VU Class I Areas," Northeast States for Coordinated Air Use Management, Boston, MA, June 2004a.

NESCAUM, "2002: A Year in Review," Northeast States for Coordinated Air Use Management, Boston, MA, December, 2004b.

USEPA, "Guidance for Tracking Progress under the Regional Haze Rule," EPA-454/B-03-004 September 2003a.

USEPA, "Guidance for Estimating Natural Visibility Conditions under the Regional Haze Program," EPA-454/B-03-005 September 2003b.

4. HAZE-ASSOCIATED POLLUTANT EMISSIONS

This chapter explores the origin and quantity of haze-forming pollutants emitted in the eastern and the mid-Atlantic United States. It also describes the procedures used to prepare emissions inventory data for use in chemical transport models (Chapter 6 describes in greater detail the models themselves).

The pollutants that affect fine particle formation, and thus contribute to regional haze, are sulfur oxides (SO_X), nitrogen oxides (NO_X), volatile organic compounds (VOC), ammonia (NH_3), and particles with an aerodynamic diameter less than or equal to 10 and 2.5 µm (i.e., primary PM_{10} and $PM_{2.5}$). The emissions dataset illustrated below is the 2002 MANE-VU Version 2 regional haze emissions inventory. The emission inventories include carbon monoxide (CO), but we do not consider that pollutant here as it does not contribute to regional haze. The MANE-VU regional haze emissions inventory version 3.0, released in April 2006, has superseded version 2 for modeling purposes. This inventory update was developed through the Mid-Atlantic Regional Air Management Association (MARAMA) for the MANE-VU RPO. The comparative observations among recent emission inventories presented here (the 1996 USEPA NET and 1999 NEI) would hold true were version 3.0 substituted for version 2.0. [20]

The first section of this chapter describes emission characteristics by pollutant and source type (e.g., point, area, and mobile). The second section describes on-going efforts to process emissions inventory data in support of air quality modeling. The final section provides source apportionment estimates for several MANE-VU Class 1 areas based on 2002 SO_2 inventory data.

4.1. Emissions Inventory Characteristics

4.1.1. Sulfur Dioxide (SO_2)

SO_2 is the primary precursor pollutant for sulfate particles. Sulfate particles commonly account for more than 50 percent of particle-related light extinction at northeastern Class I areas on the clearest days and for as much as or more than 80 percent

[20] EPA's Emission Factor and Inventory Group (EFIG) (USEPA/OAR (Office of Air and Radiation)/OAQPS (Office of Air Quality Planning and Standards)/EMAD (Emissions, Monitoring and Analysis Division) prepares a national database of air emissions information with input from numerous state and local air agencies, from tribes, and from industry. This database contains information on stationary and mobile sources that emit criteria air pollutants and their precursors, as well as hazardous air pollutants (HAPs). The database includes estimates of annual emissions, by source, of air pollutants in each area of the country on an annual basis. The NEI includes emission estimates for all 50 states, the District of Columbia, Puerto Rico, and the Virgin Islands. Emission estimates for individual point or major sources (facilities), as well as county level estimates for area, mobile and other sources, are available currently for years 1985 through 1999 for criteria pollutants, and for years 1996 and 1999 for HAPs. Data from the NEI help support air dispersion modeling, regional strategy development, setting regulation, air toxics risk assessment, and tracking trends in emissions over time. For emission inventories prior to 1999, the National Emission Trends (NET) database maintained criteria pollutant emission estimates and the National Toxics Inventory (NTI) database maintained HAP emission estimates. Beginning with 1999, the NEI began preparing criteria and HAP emissions data in a more integrated fashion to take the place of the NET and the NTI.

on the haziest days. Hence, SO_2 emissions are an obvious target of opportunity for reducing regional haze in the eastern United States. Combustion of coal and, to a substantially lesser extent, of certain petroleum products accounts for most anthropogenic SO_2 emissions. In fact, in 1998 a single source category — coal-burning power plants — was responsible for two-thirds of total SO_2 emissions nationwide (NESCAUM, 2001a).

Figure 4-1 shows SO_2 emissions trends in the MANE-VU states extracted from the NEI for the years 1996, 1999, and the 2002 MANE-VU inventory (USEPA, 2005; MARAMA, 2004). Most of the states (with the exception of Maryland) show declines in year 2002 annual SO_2 emissions as compared to 1996 emissions. Some of the states show an increase in 1999 followed by a decline in 2002 and others show consistent declines throughout the entire period. The upward trend in emissions after 1996 probably reflects electricity demand growth during the late 1990s combined with the availability of banked emissions allowances from initial over-compliance with control requirements in Phase 1 of the USEPA Acid Rain Program. This led to relatively low market prices for allowances later in the decade, which encouraged utilities to purchase allowances rather than implement new controls as electricity output expanded. The observed decline in the 2002 SO_2 emissions inventory reflects implementation of the second phase of the USEPA Acid Rain Program, which in 2000 further reduced allowable emissions and extended emissions limits to more power plants. Figure 4-2 shows the percent contribution from different source categories to overall, annual 2002 SO_2 emissions in the MANE-VU states. The chart shows that point sources dominate SO_2 emissions, which primarily consist of stationary combustion sources for generating electricity, industrial energy, and heat. Smaller stationary combustion sources called “area sources” (primarily commercial and residential heating) are another important source category in the MANE-VU states. By contrast, on-road and non-road mobile sources make only a relatively small contribution to overall SO_2 emissions in the region (NESCAUM, 2001a).

4.1.2. Volatile Organic Compounds (VOC)

Existing emission inventories generally refer to “volatile organic compounds” (VOCs) for hydrocarbons whose volatility in the atmosphere makes them particularly important from the standpoint of ozone formation. From a regional haze perspective, we are concerned less with the volatile organic gases emitted directly to the atmosphere and more with the secondary organic aerosol (SOA) that the VOCs form after condensation and oxidation processes. Thus the VOC inventory category is of interest primarily from the organic carbon perspective of $PM_{2.5}$. After sulfate, organic carbon generally accounts for the next largest share of fine particle mass and particle-related light extinction at northeastern Class I sites. The term organic carbon encompasses a large number and variety of chemical compounds that may come directly from emission sources as a part of primary PM or may form in the atmosphere as secondary pollutants. The organic carbon present at Class I sites almost certainly includes a mix of species, including pollutants originating from anthropogenic (i.e., manmade) sources as well as biogenic hydrocarbons emitted by vegetation. Recent efforts to reduce manmade organic carbon emissions have been undertaken primarily to address summertime ozone formation in urban centers. Future efforts to further reduce organic carbon emissions may be driven by programs that address fine particles and visibility.

Figure 4-1. State Level Sulfur Dioxide Emissions

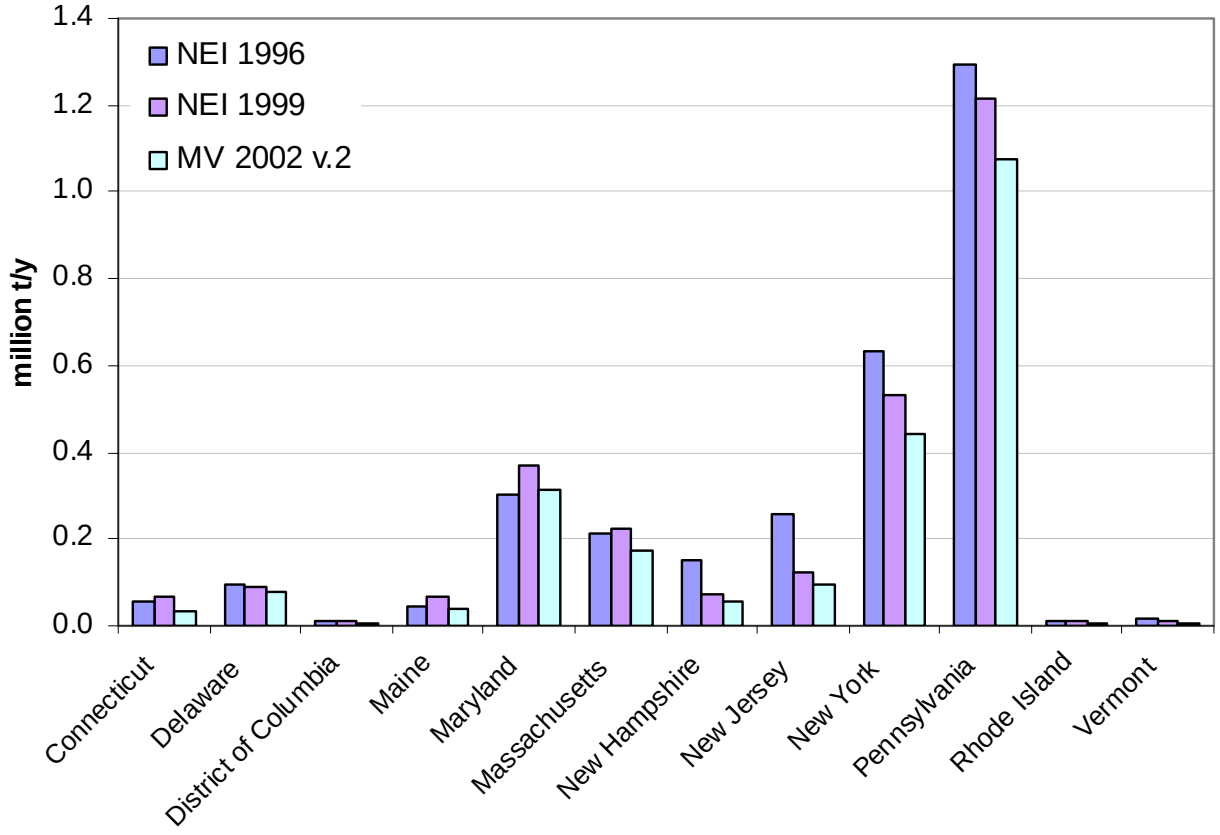

Figure 4-2. SO_2 (Bar graph: Percentage fraction of four source categories, Circle: Annual emissions amount in 10^6 tons per year)

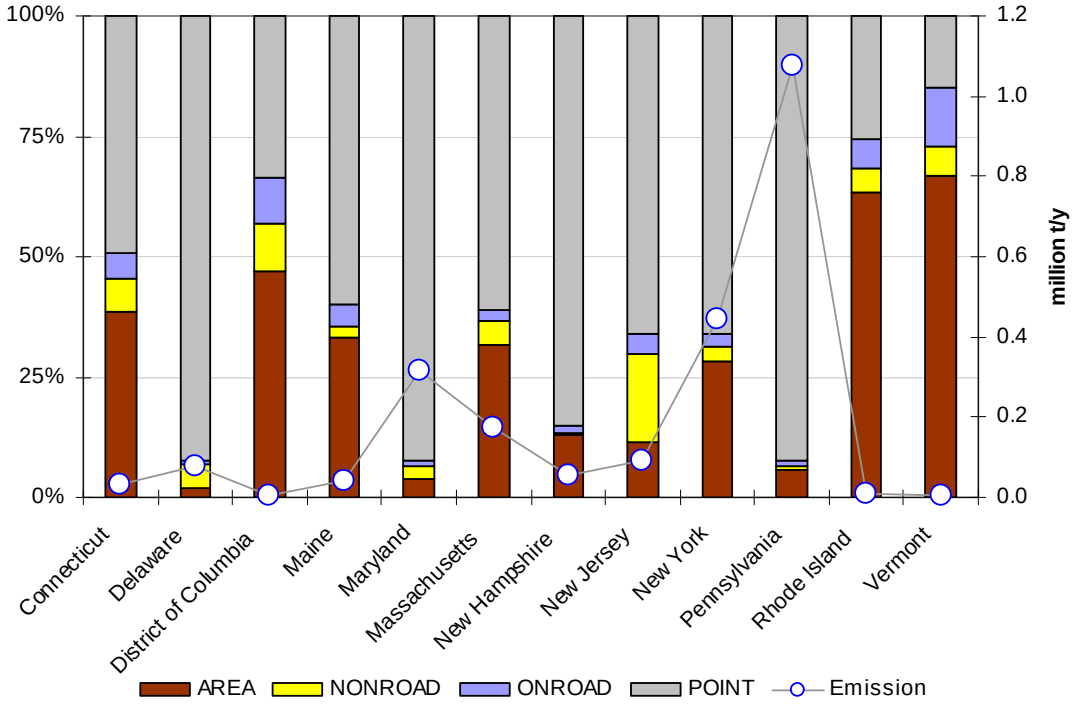

Understanding the transport dynamics and source regions for organic carbon in northeastern Class I areas is likely to be more complex than for sulfate. This is partly because of the large number and variety of OC species, the fact that their transport characteristics vary widely, and the fact that a given species may undergo numerous complex chemical reactions in the atmosphere. Thus, the organic carbon contribution to visibility impairment at most Class I sites in the East is likely to include manmade pollution transported from a distance, manmade pollution from nearby sources, and biogenic emissions, especially terpenes from coniferous forests.

As shown in Figure 4-3, the VOC inventory is dominated by mobile and area sources. On-road mobile sources of VOCs include exhaust emissions from gasoline passenger vehicles and diesel-powered heavy-duty vehicles as well as evaporative emissions from transportation fuels. VOC emissions may also originate from a variety of area sources (including solvents, architectural coatings, and dry cleaners) as well as from some point sources (e.g., industrial facilities and petroleum refineries).

Biogenic VOCs may play an important role within the rural settings typical of Class I sites. The oxidation of hydrocarbon molecules containing seven or more carbon atoms is generally the most significant pathway for the formation of light-scattering organic aerosol particles (Odum et al., 1997). Smaller reactive hydrocarbons that may contribute significantly to urban smog (ozone) are less likely to play a role in organic aerosol formation, though we note that high ozone levels can have an indirect effect on visibility by promoting the oxidation of other available hydrocarbons, including biogenic

Figure 4-3. VOC (Bar graph: Percentage fraction of four source categories, Circle: Annual emissions amount in 10^6 tons per year)

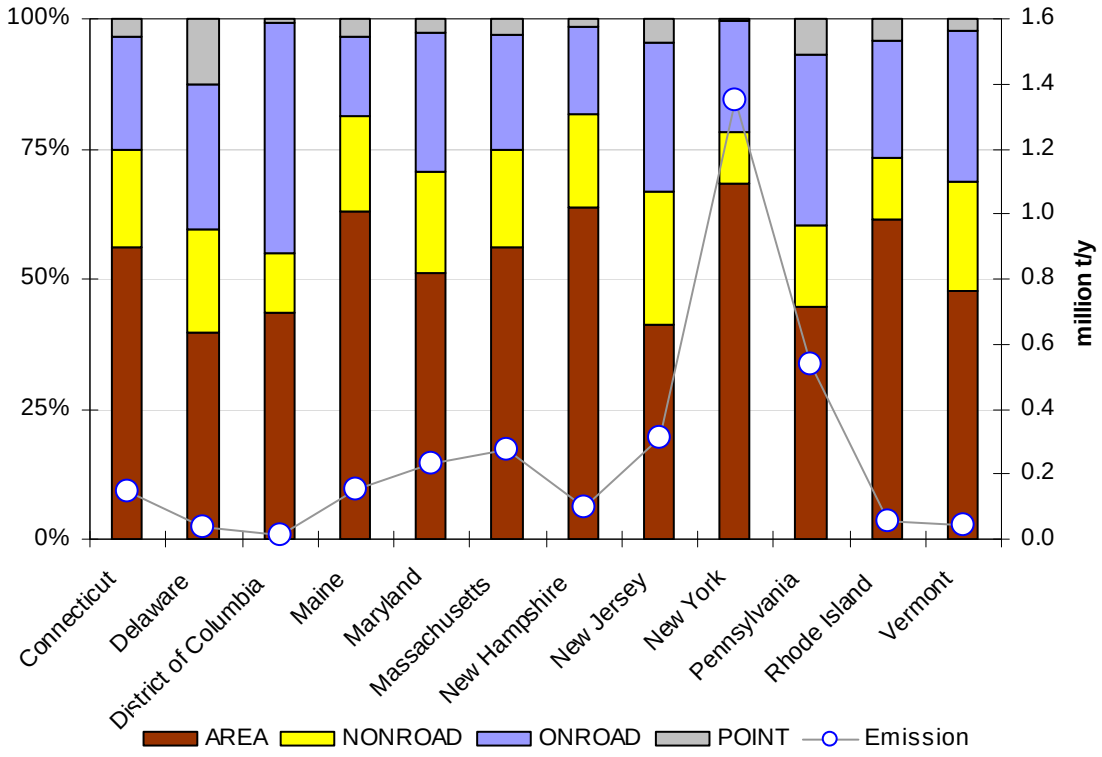

emissions (NESCAUM, January 2001). In short, we need further work to characterize the organic carbon contribution to regional haze in the Northeast and Mid-Atlantic states and to develop emissions inventories that will be of greater value for visibility planning purposes.

4.1.3. Oxides of Nitrogen (NO_X)

NO_X emissions contribute directly to visibility impairment in the eastern U.S. by forming light-scattering nitrate particles. Nitrate generally accounts for a substantially smaller fraction of fine particle mass and related light extinction than sulfate and organic carbon at northeastern Class I sites. Notably, nitrate may play a more important role at urban sites and in the wintertime. In addition, NO_X may have an indirect effect on summertime visibility by virtue of its role in the formation of ozone, which in turn promotes the formation of secondary organic aerosols (NESCAUM 2001a).

Figure 4-4 shows NO_X emissions in the MANE-VU region at the state level. Since 1980, nationwide emissions of NO_X from all sources have shown little change. In fact, emissions increased by 2 percent between 1989 and 1998 (USEPA, 2000a). This increase is most likely due to industrial sources and the transportation sector, as power plant combustion sources have implemented modest emissions reductions during the same time period. Most states in the MANE-VU region experienced declining NO_X emissions from 1996 through 2002, except Massachusetts, Maryland, New York, and Rhode Island, which show an increase in NO_X emissions in 1999 before declining to levels below 1996 emissions in 2002.

Power plants and mobile sources generally dominate state and national NO_X emissions inventories. Nationally, power plants account for more than one-quarter of all NO_X emissions, amounting to over six million tons. The electric sector plays an even larger role, however, in parts of the industrial Midwest where high NO_X emissions have a particularly significant power plant contribution. By contrast, mobile sources dominate the NO_X inventories for more urbanized Mid-Atlantic and New England states to a far greater extent, as shown in Figure 4-5. In these states, on-road mobile sources — a category that mainly includes highway vehicles — represent the most significant NO_X source category. Emissions from non-road (i.e., off-highway) mobile sources, primarily diesel-fired engines, also represent a substantial fraction of the inventory. While there are fewer uncertainties associated with available NO_X estimates than in the case of other key haze-related pollutants — including primary fine particle and ammonia emissions — further efforts could improve current inventories in a number of areas (NESCAUM, 2001a).

In particular, better information on the contribution of area and non-highway mobile sources may be of most interest in the context of regional haze planning. First, available emission estimation methodologies are weaker for these types of sources than for the large stationary combustion sources. Moreover, because SO_2 and NO_X emissions must mix with ammonia to participate in secondary particle formation, emissions that occur over large areas at the surface may be more efficient in secondary fine particulate formation than concentrated emissions from isolated tall stacks (Duyzer, 1994).

Figure 4-4. State Level Nitrogen Oxides Emissions

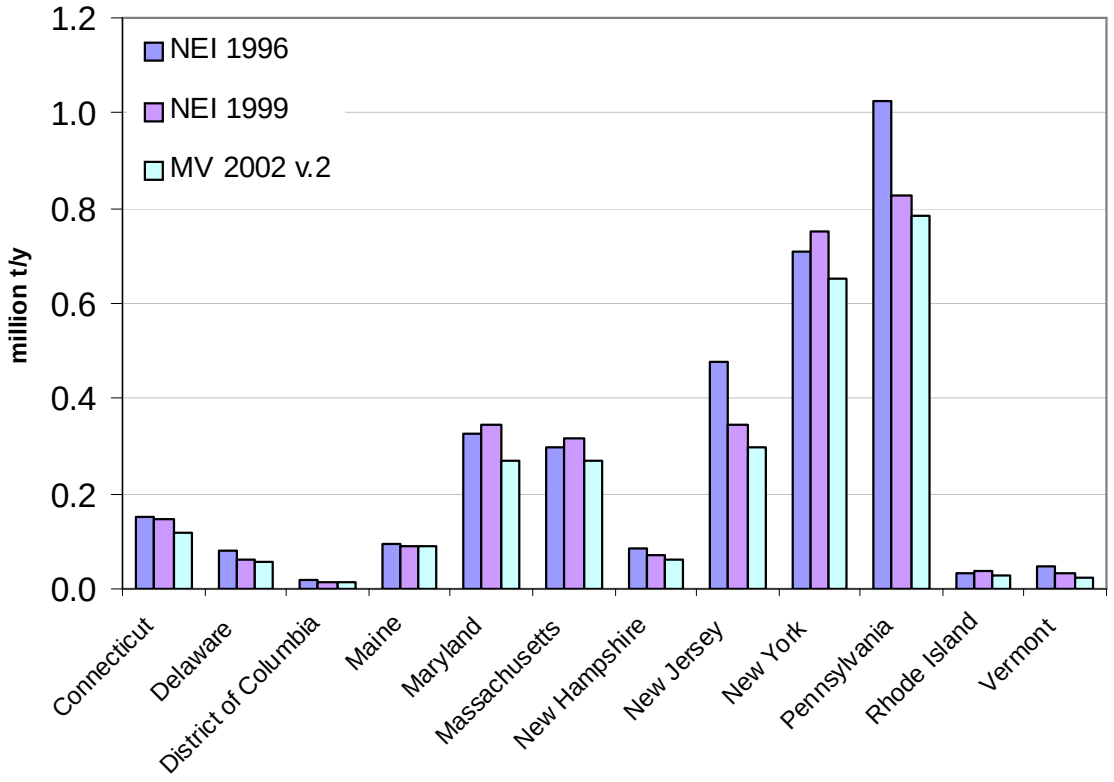

Figure 4-5. NO_X (Bar graph: Percentage fraction of four source categories, Circle: Annual emissions amount in 10^6 tons per year)

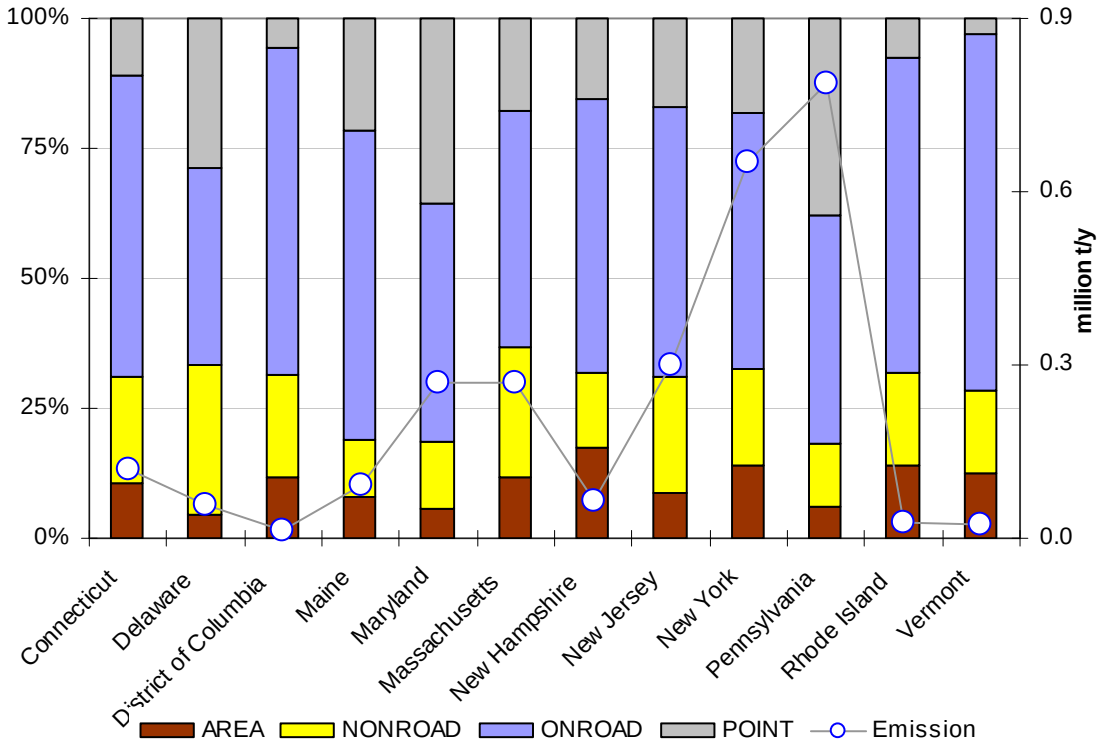

4.1.4. Primary Particulate Matter (PM_{10} and $PM_{2.5}$)

Directly-emitted or "primary" particles (as distinct from secondary particles that form in the atmosphere through chemical reactions involving precursor pollutants like SO_2 and NO_X) can also contribute to regional haze. For regulatory purposes, we make a distinction between particles with an aerodynamic diameter less than or equal to 10 micrometers and smaller particles with an aerodynamic diameter less than or equal to 2.5 micrometers (i.e., primary PM_{10} and $PM_{2.5}$, respectively).

Figure 4-6 and Figure 4-7 show PM_{10} and $PM_{2.5}$ emissions for the MANE-VU states for the years 1996, 1999, and 2002. Note that for PM_{10} the inventory values are drawn from the 2002 NEI. Most states show a steady decline in annual PM_{10} emissions over this time period. By contrast, emission trends for primary $PM_{2.5}$ are more variable.

Crustal sources are significant contributors of primary PM emissions. This category includes fugitive dust emissions from construction activities, paved and unpaved roads, and agricultural tilling. Typically, monitors estimate PM_{10} emissions from these types of sources by measuring the horizontal flux of particulate mass at a fixed downwind sampling location within perhaps 10 meters of a road or field. Comparisons between estimated emission rates for fine particles using these types of measurement techniques and observed concentrations of crustal matter in the ambient air at downwind receptor sites suggest that physical or chemical processes remove a significant fraction of crustal material relatively quickly. As a result, it rarely entrains into layers of the atmosphere where it can transport to downwind receptor locations. Because of this discrepancy between estimated emissions and observed ambient concentrations, modelers typically reduce estimates of total $PM_{2.5}$ emissions from all crustal sources by applying a factor of 0.15 to 0.25 before including in modeling analyses.

From a regional haze perspective, crustal material generally does not play a major role. On the 20 percent best-visibility days during the baseline period (2000-2004), it accounted for six to eleven percent of particle-related light extinction at MANE-VU Class 1 sites. On the 20 percent worst-visibility days, however, crustal material generally plays a much smaller role relative to other haze-forming pollutants, ranging from two to three percent. Moreover, the crustal fraction includes material of natural origin (such as soil or sea salt) that is not targeted under the Haze Rule. Of course, the crustal fraction can be influenced by certain human activities, such as construction, agricultural practices, and road maintenance (including wintertime salting) — thus, to the extent that these types of activities are found to affect visibility at northeastern Class I sites, control measures targeted at crustal material may prove beneficial.

Experience from the western United States, where the crustal component has generally played a more significant role in driving overall particulate levels, may be helpful to the extent that it is relevant in the eastern context. In addition, a few areas in the Northeast, such as New Haven, Connecticut and Presque Isle, Maine, have some experience with the control of dust and road-salt as a result of regulatory obligations stemming from their past non-attainment status with respect to the NAAQS for PM_{10}.

Figure 4-6. State Level Primary PM_{10} Emissions

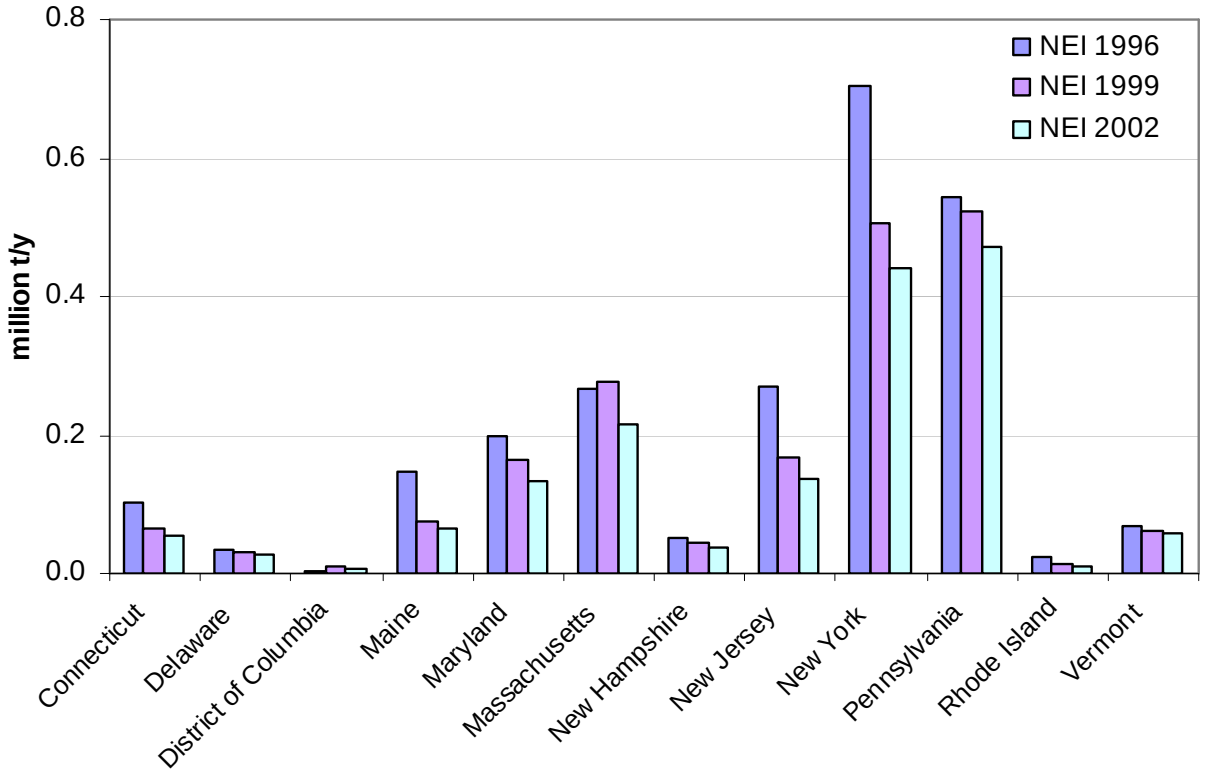

Figure 4-7. State Level Primary $PM_{2.5}$ Emissions

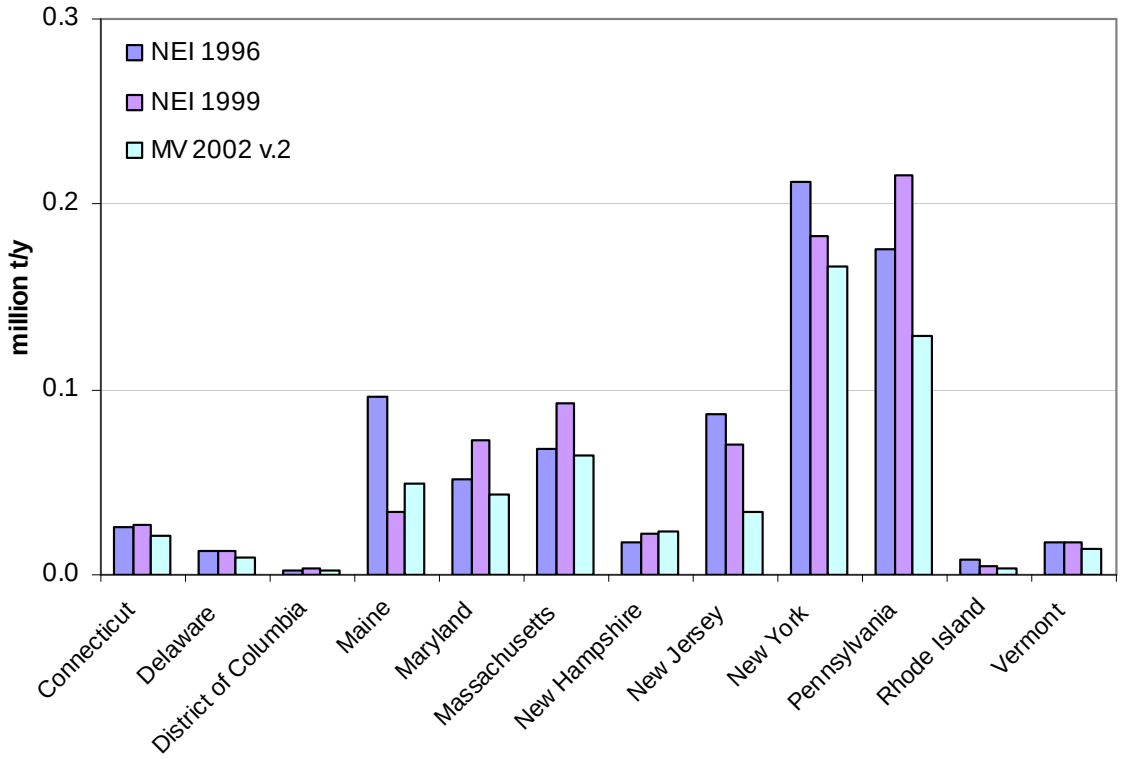

Current emissions inventories for the entire MANE-VU area indicate residential wood combustion represents 25 percent of primary fine particulate emissions in the region. This implies that rural sources can play an important role in addition to the contribution from the region's many highly populated urban areas. An important consideration in this regard is that residential wood combustion occurs primarily in the winter months, while managed or prescribed burning activities occur largely in other seasons. The latter category includes agricultural field-burning activities, prescribed burning of forested areas and other burning activities such as construction waste burning. Limiting burning to times when favorable meteorological conditions can efficiently disperse resulting emissions can manage many of these types of sources.

Figure 4-8 and Figure 4-9 show that area and mobile sources dominate primary PM emissions. (The NEI inventory categorizes residential wood combustion and some other combustion sources as area sources.) The relative contribution of point sources is larger in the primary $PM_{2.5}$ inventory than in the primary PM_{10} inventory since the crustal component (which consists mainly of larger or "coarse-mode" particles) contributes mostly to overall PM_{10} levels. At the same time, pollution control equipment commonly installed at large point sources is usually more efficient at capturing coarse-mode particles.

4.1.5. Ammonia Emissions (NH_3)

Knowledge of ammonia emission sources will be necessary in developing effective regional haze reduction strategies because of the importance of ammonium sulfate and ammonium nitrate in determining overall fine particle mass and light scattering. According to 1998 estimates, livestock agriculture and fertilizer use accounted for approximately 86 percent of all ammonia emissions to the atmosphere (USEPA, 2000b). We need, however, better ammonia inventory data for the photochemical models used to simulate fine particle formation and transport in the eastern United States. Because the USEPA does not regulate ammonia as a criteria pollutant or as a criteria pollutant precursor, these data do not presently exist at the same level of detail or certainty as for NO_X and SO_2.

Ammonium ion (formed from ammonia emissions to the atmosphere) is an important constituent of airborne particulate matter, typically accounting for 10–20 percent of total fine particle mass. Reductions in ammonium ion concentrations can be extremely beneficial because a more-than-proportional reduction in fine particle mass can result. Ansari and Pandis (1998) showed that a one $\mu g/m^3$ reduction in ammonium ion could result in up to a four $\mu g/m^3$ reduction in fine particulate matter. Decision makers, however, must weigh the benefits of ammonia reduction against the significant role it plays in neutralizing acidic aerosol.[21]

[21] SO_2 reacts in the atmosphere to form sulfuric acid (H_2SO_4). Ammonia can partially or fully neutralize this strong acid to form ammonium bisulfate or ammonium sulfate. If planners focus future control strategies on ammonia and do not achieve corresponding SO_2 reductions, fine particles formed in the atmosphere will be substantially more acidic than those presently observed.

Figure 4-8. Primary PM_{10} (Bar graph: Percentage fraction of four source categories, Circle: Annual emissions amount in 10^6 tons per year)

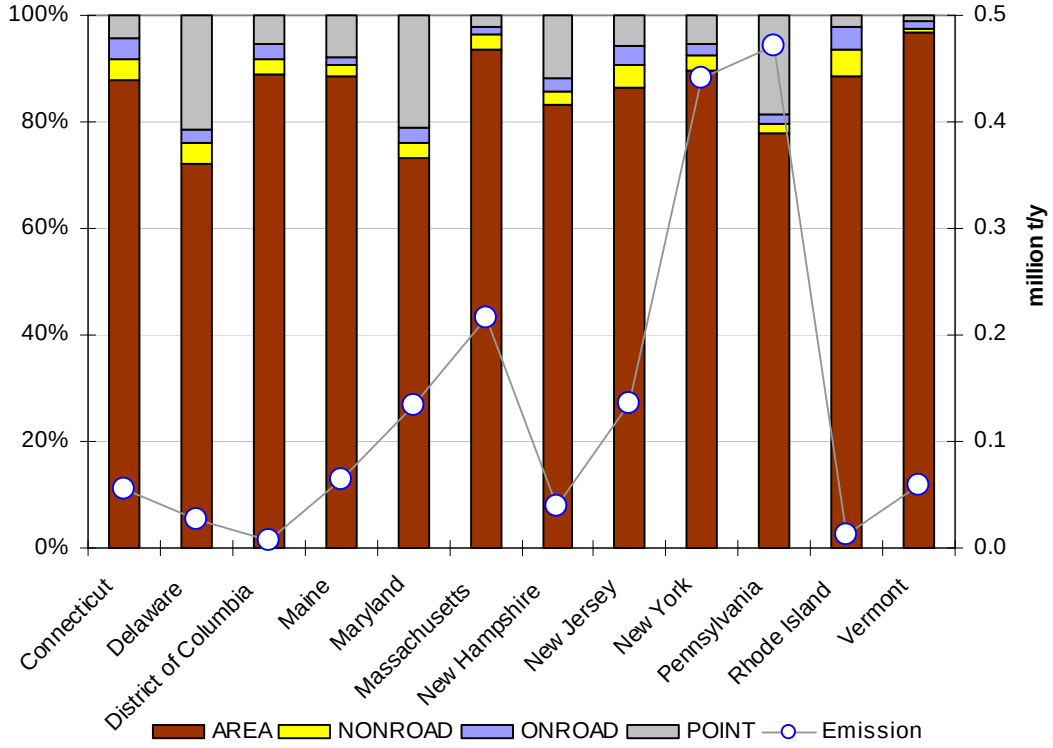

Figure 4-9. Primary $PM_{2.5}$ (Bar graph: Percentage fraction of four source categories, Circle: Annual emissions amount in 106 tons per year)

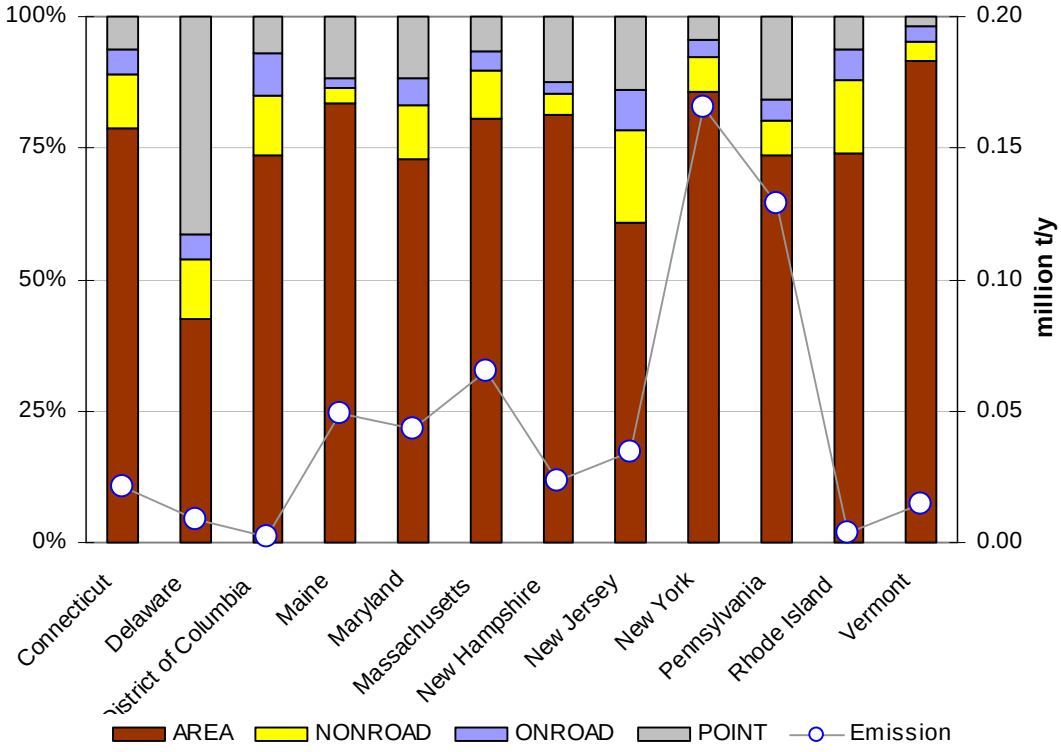

To address the need for improved ammonia inventories, MARAMA, NESCAUM and USEPA funded researchers at Carnegie Mellon University (CMU) in Pittsburgh to develop a regional ammonia inventory (Davidson et al., 1999). This study focused on three issues with respect to current emissions estimates: (1) a wide range of ammonia emission factor values, (2) inadequate temporal and spatial resolution of ammonia emissions estimates, and (3) a lack of standardized ammonia source categories.

The CMU project established an inventory framework with source categories, emissions factors, and activity data that are readily accessible to the user. With this framework, users can obtain data in a variety of formats[22] and can make updates easily, allowing additional ammonia sources to be added or emissions factors to be replaced as better information becomes available (Strader et al., 2000; NESCAUM, 2001b).

Figure 4-10 shows that estimated ammonia emissions were fairly stable in the 1996, 1999, and 2002 NEI for MANE-VU states, with some increases observed for Massachusetts, New Jersey and New York. Area and on-road mobile sources dominate the ammonia inventory, according to Figure 4-11. Specifically, emissions from agricultural sources and livestock production account for the largest share of estimated ammonia emissions in the MANE-VU region, except in the District of Columbia. The two remaining sources with a significant emissions contribution are wastewater treatment systems and gasoline exhaust from highway vehicles.

Figure 4-10. State Level Ammonia Emissions

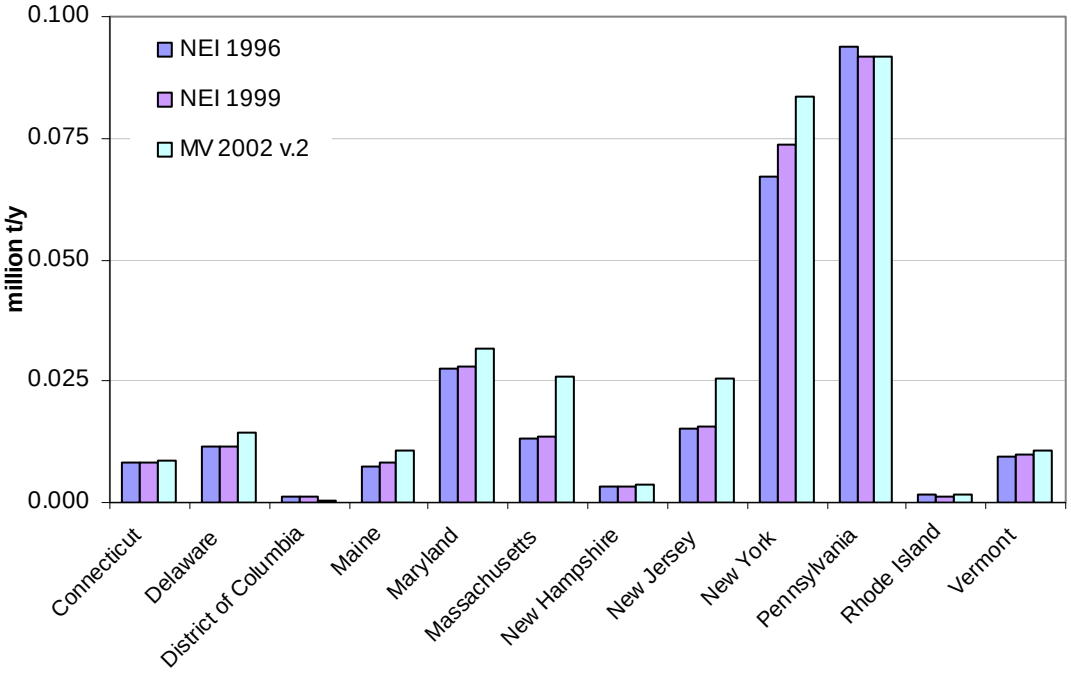

[22] For example, the user will have the flexibility to choose the temporal resolution of the output emissions data or to spatially attribute emissions based on land-use data.

Figure 4-11. NH_3 (Bar graph: Percentage fraction of four source categories, Circle: Annual emissions amount in 10^6 tons per year)

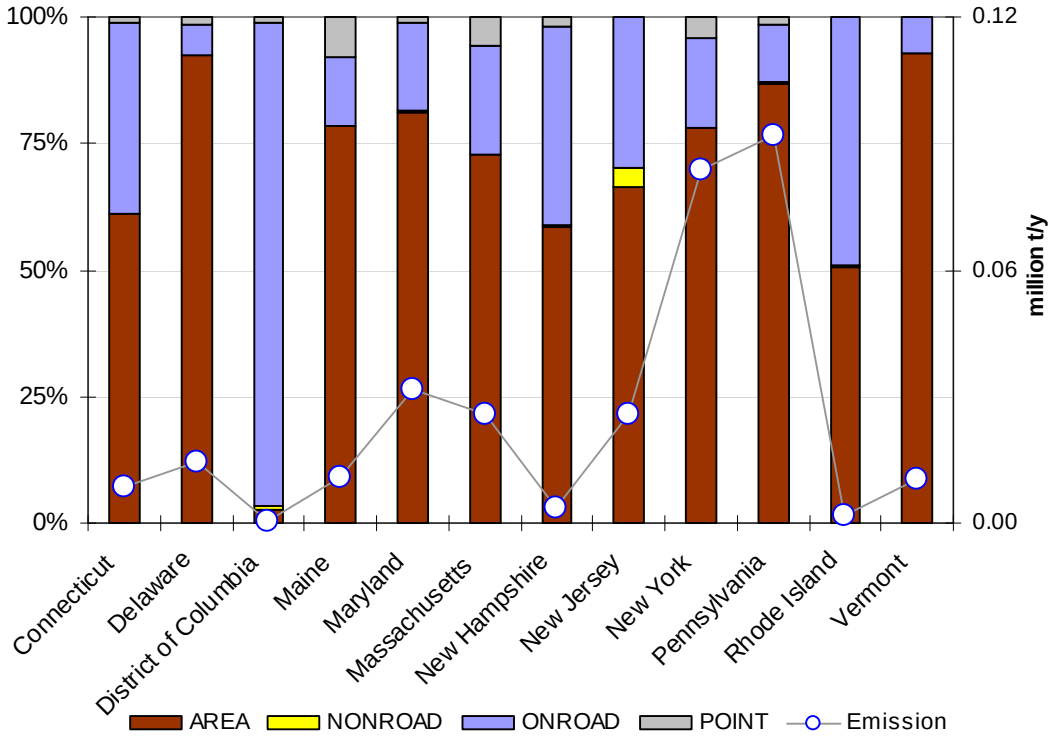

4.2. Contribution Assessments Based on Emissions Inventories

Two data analysis methods have been developed that directly combine emission inventory data with meteorological data in order to provide first-order contributions to observed sulfate from individual states. The first approach, known as "Q/d," evaluates the state contribution as a proportion of the ratio of the total SO_2 emissions from that state and the distance from the state to the receptor. States and sources are assigned wind sectors to account for prevailing wind patterns in establishing contributions. The second approach, known as "Emissions times Upwind Probability," evaluates the state contribution through the use of ensemble back trajectories (See Appendix A for a more detailed description of trajectory methods). The back trajectory-derived residence times of air parcels have been mapped onto a grid to create a "residence time probability field," which is then multiplied by an SO_2 emissions field to obtain estimated source contributions. The results of the two approaches are compared for receptor sites in and around the MANE-VU region.

4.2.1. Sulfur Dioxide Emissions Divided by Distance

Aggregated over long periods of time and large geographic areas, the total atmospheric sulfate contribution from a specific source, state, or region should be approximately proportionate to its SO_2 emissions. For specific receptor locations, like a Class 1 visibility area, relative impacts decrease with increasing distance from the source. Impacts diminish over distance as pollutants are dispersed in the atmosphere and removed through deposition. For non-reactive primary pollutant emissions, the

relationship between atmospheric concentrations and distance (d) can be approximated as a function of $1/d^2$. For secondary pollutants like sulfate, reductions in ambient concentrations that occur as a result of dispersion and deposition mechanisms are partially offset by the formation of secondary aerosol such that an increasing fraction of the remaining downwind sulfur is converted to aerosol sulfate. In these cases, the effects of distance are better characterized by the function 1/d. During regional sulfate episodes when sulfur conversion rates are enhanced by the presence of gas and aqueous-phase oxidants, pollutant concentrations decline even less rapidly with distance as accelerated aerosol formation rates work to both generate more sulfate and reduce the remaining sulfur available for deposition (deposition rates are roughly an order of magnitude slower for sulfate than for SO_2).

One simple technique for deducing the relative impact of emissions from specific point sources on a specific receptor site involves calculating the ratio of annual emissions (Q) to source-receptor distance (d).[23] This empirical relationship is reasonable based on simple dispersion assumptions. Results from SO_2 modeling using the CALPUFF (California Puff) model (EarthTech, 2004) further bolster its validity by showing a strong relationship between emissions and distance. In fact, this extremely simple method of estimating impact can be significantly improved to account for some aspects of meteorology by scaling results according to the extremely linear relationships between CALPUFF and Q/d values within specific wind sectors.

The geographic domain of the sources included in the Q/d study consisted of U.S. states in the CENRAP, MANE-VU, VISTAS, and MIDWEST RPO regions. Canadian provinces in the lower eastern region were also included. The categories of SO_2 emission sources included in this analysis were area sources (e.g., residential boilers and heaters), non-road mobile sources (e.g., tractors and construction vehicles), and point sources (e.g., industrial smokestacks and power generation facilities).[24] Results were calculated for seven receptors including: Acadia National Park, Brigantine Wilderness in the Forsythe Wildlife Preserve, Dolly Sods Wilderness, Lye Brook Wilderness, Moosehorn Wilderness, Presidential Range-Dry River Wilderness, and Shenandoah National Park.

The empirical formula that relates emission source strength and estimated impact can be expressed through the equation $I=C_i*Q/d$. In this equation, the strength of an emission source, Q, is linearly related to the impact, I, that it will have on a receptor located a distance, d, away. The effect of meteorological prevailing winds can be factored into this approach by establishing the constant, C_i, as a function of the sectors relative to the receptor site. This relationship can be established by comparing Q/d values to modeled impacts, which are also dependent on prevailing wind patterns at the site of impact. By establishing a different constant for each sector, based on prior modeling results – in this case, CALPUFF results – we are in effect "scaling" Q/d results

[23] We calculated distances using the Haversine formula, which uses spherical geometry to calculate the distance between two points on the surface of a sphere. Because the Earth is not an exact sphere, use of this formula introduces a small amount of error — on the order of 0.5% — in the distance calculations for any two locations on the Earth's surface (see http://mathforum.org/library/drmath for further details).

[24] On-road mobile sources contribute about 2% of the SO_2 inventory nationally (See Figure 4-2 for regional breakdown) and were not considered significant enough to include in this analysis, which does not provide results to that level of precision.

by CALPUFF-calculated source impacts. The absolute impacts produced are then dependent on the CALPUFF results, however the relative contributions of each source within a wind sector is established completely independent of the CALPUFF calculation, yielding a quasi-independent method of apportionment to add to our weight-of-evidence approach.

To determine the appropriate constant for each wind sector relative to a given receptor, a linear regression analysis was performed on 778 sources in the eastern U.S. with emissions data available from the continuous emissions monitoring system (CEMS) for 2002. The Q/d values were calculated for these sources and compared with their modeled source impacts from the CALPUFF model (see Phase I modeling discussed in Appendix D). The sites were grouped by angle into "wind sectors" such that each wind sector had a best-fit line with as high a correlation coefficient (R^2) value as possible. Most sectors had an R^2 above or near 0.90. The slopes of the resulting best-fit lines were used as the constants in the above equation.[25]

To calculate the impact that each state had on a given receptor, the area and non-road SO_2 emission sources were summed across the entire state, and the distance to the receptor site for those emission sources was calculated based on that state's geographic center, adjusted for population density.[26] In this way, the area and non-road emissions were treated as a single point source located at the population-weighted center of each state. These impacts were then added to the impact of the point sources that were calculated individually. The sum of area, non-road, and point source impacts for each state was used to compare the contributions relative to other states in the eastern U.S. and parts of Canada.

The principal contributors to the MANE-VU receptors, according to this method, include the midwestern states of Indiana and Ohio, as well as Pennsylvania and New York. This is due not only to the large emissions from these states, but also to the predominantly westerly winds that carry Midwest pollution eastward (the Midwest was located in the wind sector with the highest C_i-value, five times that of the lowest Ci-value). Table 4-1 shows the relative contribution of eastern states and Canadian provinces on several receptor sites in the region. Figure 4-12 and Figure 4-13 show the corresponding Q/d rankings across a set of northern and southern Class I areas in or near MANE-VU.

---

[25] The analysis resulted in best-fit lines that did not always go through the origin. By forcing the regression lines through the origin, we ensure that a source with zero emissions would correspond to zero impact at the receptor. After having forced the best-fit lines through the origin, R^2 values remained greater than 0.77 and changed less than 0.01 from the original regression. The changes to the slope were considered insignificant, with an average change of 4%, ranging from -11% to 16%; the extremes occurred for plots with relatively few points and on the low end of R-squared correlations. Some angle ranges were not associated with a wind sector because of insufficient data for that angle range. For example, there was a lack of data for Lye Brook Wilderness receptor in the 0-144^o angle range. This angle sector and similar sectors lacking adequate data were assigned the lowest C_i-value amongst the other wind sectors of the same receptor site. The impact of this decision should be small given the relatively few sources in these directions and their tendency to be downwind of the receptor.

[26] Calculations using county-level emissions and distance to county centroid to receptor were compared to the approach used here. This added complexity, however, did not substantially change the predicted impacts nor the relative rankings among states.

Table 4-1. 2002 SO_2 CALPUFF-scaled Emissions over Distance Impact ($\mu g/m^3$)

STATE	ACADIA	LYE BROOK	BRIGANTINE	SHENANDOAH	EMISSIONS
Pennsylvania	0.19	0.30	0.38	0.43	1,090,562
Ohio	0.19	0.23	0.27	0.46	1,273,755
West Virginia	0.08	0.09	0.16	0.32	573,136
Maryland	0.05	0.06	0.24	0.21	292,970
New York	0.12	0.15	0.15	0.13	341,493
Indiana	0.11	0.11	0.14	0.18	914,039
North Carolina	0.07	0.06	0.14	0.26	510,452
Virginia	0.06	0.04	0.14	0.17	309,709
Georgia	0.07	0.07	0.11	0.14	605,040
Kentucky	0.06	0.06	0.11	0.14	521,583
Michigan	0.08	0.08	0.06	0.10	432,166
Illinois	0.07	0.07	0.07	0.10	642,264
Tennessee	0.04	0.04	0.07	0.09	423,705
New Jersey	0.02	0.02	0.14	0.07	64,437
Alabama	0.05	0.05	0.07	0.08	548,054
Texas	0.04	0.04	0.05	0.06	849,831
Florida	0.04	0.03	0.06	0.07	537,327
Massachusetts	0.08	0.02	0.03	0.05	123,754
South Carolina	0.04	0.02	0.05	0.07	262,867
Delaware	0.02	0.02	0.10	0.04	83,549
Missouri	0.04	0.04	0.05	0.05	361,911
Wisconsin	0.03	0.03	0.03	0.04	263,040
Maine	0.05	<0.01	<0.01	0.01	39,423
Kansas	0.01	0.01	0.01	0.01	136,104
New Hampshire	0.03	<0.01	0.01	0.01	53,772
Minnesota	0.01	0.01	0.01	0.01	124,151
Mississippi	0.01	0.01	0.01	0.02	126,456
Iowa	0.01	0.01	0.01	0.01	230,676
Connecticut	0.01	0.01	0.01	0.01	41,093
Oklahoma	0.01	0.01	0.01	0.01	139,327
Louisiana	0.01	0.01	0.01	0.02	346,170
Arkansas	<0.01	<0.01	0.01	0.01	140,096
Nebraska	0.01	<0.01	<0.01	0.01	46,074
Rhode Island	<0.01	<0.01	<0.01	<0.01	2,531
Vermont	<0.01	<0.01	<0.01	<0.01	1,575
Dist. of Columbia	<0.01	<0.01	<0.01	<0.01	1,715
Ontario	0.01	0.24	0.12	0.15	5,010
New Brunswick	0.15	0.01	0.02	0.02	1,261
Quebec	0.09	0.02	0.03	0.05	6,567
Nova Scotia	0.08	0.01	0.02	0.02	7,566
Newfoundland	0.01	<0.01	<0.01	0.01	15,287
Prince Edward Is.	<0.01	<0.01	<0.01	<0.01	10,157

Figure 4-12. Ranked state percent sulfate contributions to Northeast Class I receptors based on emissions divided by distance (Q/d) results

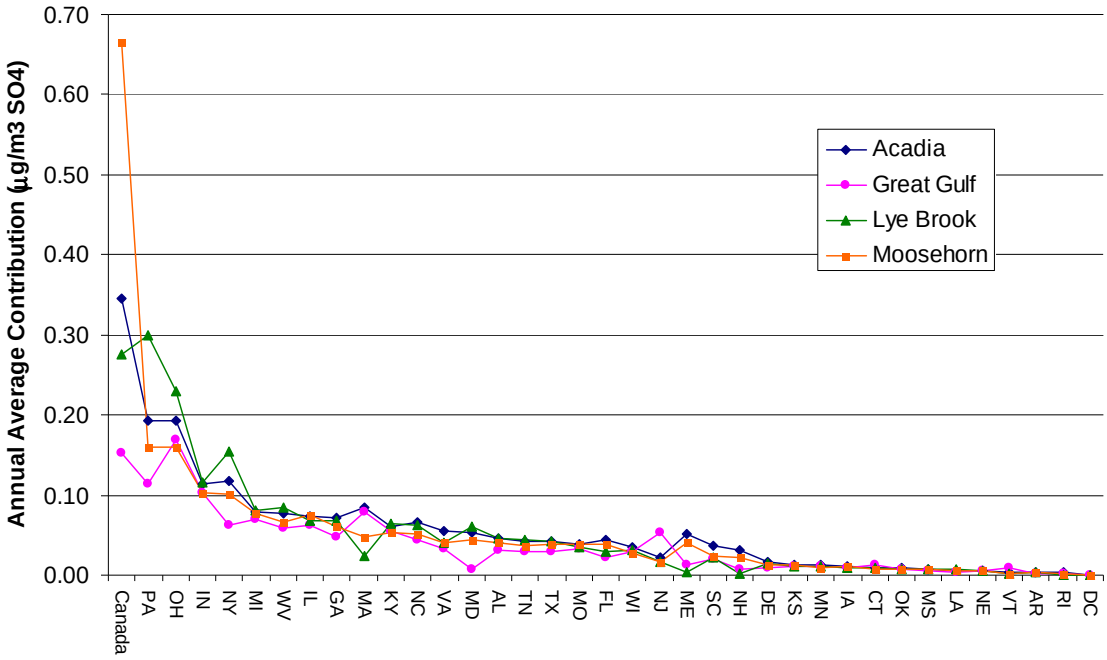

Figure 4-13. Ranked state percent sulfate contributions to Mid-Atlantic Class I receptors based on emissions divided by distance (Q/d) results

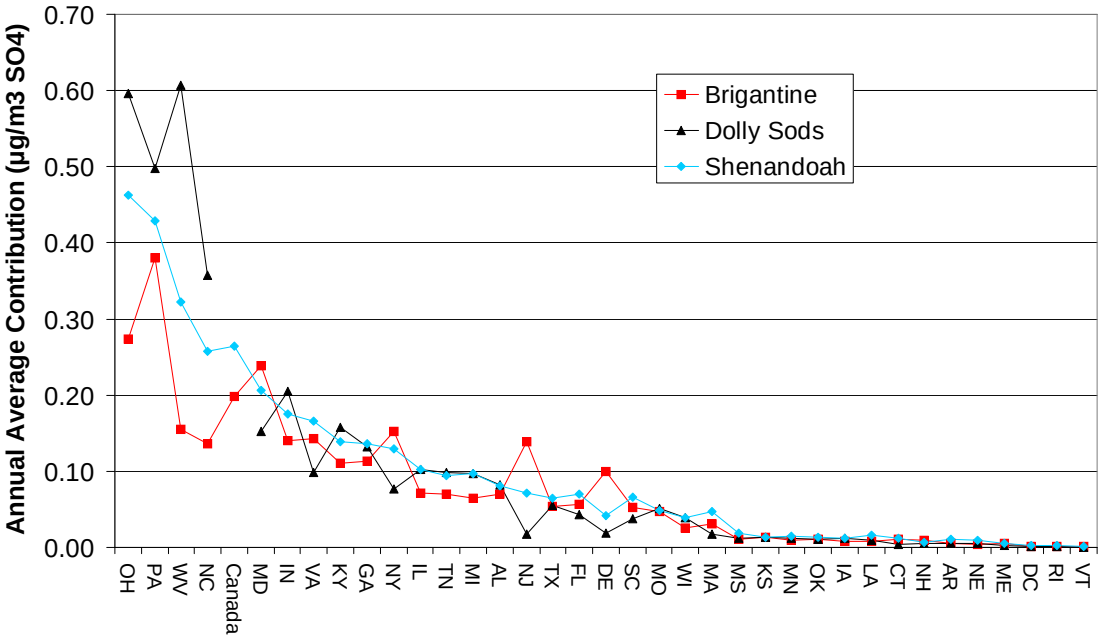

It is difficult to draw firm conclusions from what is essentially an empirical relationship between emission source strength, distance and observed impacts at receptor sites, but the addition of the CALPUFF-derived scale factors to this approach yields important insights as to the abilities of fairly simple screening techniques to accurately predict potential contributions to downwind receptors. This is borne out by the high degree of correspondence between the relative contributions of regions as identified by this and other techniques shown in Chapter 8.

4.2.2. Emissions times Upwind Probability

The Emissions times Upwind Probability method of assessing contribution to pollution involves multiplying the back-trajectory calculated residence time probability for a grid cell with the total emissions – over the same time period – from that grid cell. The product is an emissions-weighted probability field that can be integrated within state boundaries to calculate relative probabilities of each state contributing to pollution transport.

A back trajectory is the path that a parcel of air is calculated to have taken prior to its arrival at a given receptor (See Chapter 5). The back trajectories used in this study were calculated by the HYSPLIT system (Draxler, 1997 and 1998). Five years of back trajectories, calculated eight times per day results in 14,600 back trajectories. The back trajectories are 72-hours in length and have calculated endpoints, or locations, at hourly intervals that specify the air mass path. The endpoints from all trajectories are mapped into a matrix of residence times spent in individual grid cells over the five year period. The resulting sum expresses the likelihood that air spent time in a particular quarter degree longitude by quarter degree latitude grid cell over a domain between 25^o and 57^o latitude and -110^o to -50^o longitude. These residence times are then multiplied by the MANE-VU base year SO_2 emission inventory that has been allocated to a 12 km horizontal grid based on a Lambert Conformal projection.[27] The resulting product matrix contains the SO_2-weighted residence times that are then numerically integrated within the boundaries of each state to define a "contribution" for each state. This provides a relative ranking of contribution by state that can be used to compare with other methods of attribution.[28]

The area of analysis included states from Maine to Mississippi. Several states lie on the periphery of our available SO_2 emissions field and were used in the study despite an incomplete inventory of SO_2 emissions for the far edges of each state; these included

[27] Since the latitude-longitude projection of the residence time grid is different than the Lambert conformal projection of the emissions grid, there is not a one-to-one mapping. We therefore interpolated each residence time grid cell to increase the spatial resolution to $1/20^o$ latitude by $1/20^o$ longitude. Each residence time cell was then associated with the nearest SO_2 emission cell to ensure that each SO_2 emission component of the inventory was associated with the approximate residence time that was spent in nearest proximity to the emissions region. A distance of one-quarter degree between associated grid cells was used as a cutoff for the analysis. In other words, the product of a particular SO_2 cell and residence time cell would not be used if the geographical distance between them was greater than one-quarter degree (latitude or longitude).

[28] Note that the absolute units are expressed as nmole/hr, which represent a fractional contribution of a grid cell's emission rate that is likely to influence a downwind receptor. The physical meaning of this contribution is not clear, so this has been used in a relative sense only.

Missouri, Arkansas, Mississippi, Alabama, and Georgia.[29] Canada has significant SO_2 emissions in the domain of the SO_2 grid, hence contributions have been calculated for portions of Ontario, Quebec and New Brunswick that were within the SO_2 emission grid. Table 4-2 provides a ranking of state contributions and Figure 4-14 and Figure 4-15 show the ranked contribution for two groupings of Class I sites in or near MANE-VU.

Table 4-2. 2002 SO_2 Upwind Probability (percent contribution)

	ACADIA	LYEBROOK	BRIGANTINE	SHENANDOAH
West Virginia	0.06	0.07	0.09	0.19
Ohio	0.09	0.11	0.10	0.12
Pennsylvania	0.09	0.13	0.13	0.07
Kentucky	0.04	0.05	0.06	0.09
Indiana	0.05	0.05	0.05	0.06
New York	0.07	0.11	0.04	0.02
Virginia	0.03	0.02	0.06	0.06
North Carolina	0.02	0.01	0.05	0.07
Illinois	0.06	0.05	0.04	0.04
Georgia	0.02	0.02	0.04	0.05
Michigan	0.04	0.04	0.02	0.02
Tennessee	0.02	0.01	0.02	0.04
Maryland	0.02	0.02	0.04	0.03
New Jersey	0.02	0.02	0.07	0.01
Alabama	0.01	0.01	0.02	0.02
South Carolina	0.01	0.01	0.02	0.02
Wisconsin	0.02	0.02	0.01	0.01
Missouri	0.01	0.01	0.01	0.01
Delaware	<0.01	0.01	0.02	<0.01
Massachusetts	0.02	0.01	<0.01	<0.01
New Hampshire	0.02	0.01	<0.01	<0.01
Minnesota	0.01	0.01	<0.01	<0.01
Connecticut	0.01	0.01	<0.01	<0.01
Maine	0.02	<0.01	<0.01	<0.01
Iowa	0.01	<0.01	<0.01	<0.01
Dist. of Columbia	<0.01	<0.01	<0.01	<0.01
Arkansas	<0.01	<0.01	<0.01	<0.01
Mississippi	<0.01	<0.01	<0.01	<0.01
Vermont	<0.01	<0.01	<0.01	<0.01
Louisiana	<0.01	<0.01	<0.01	<0.01
Rhode Island	<0.01	<0.01	<0.01	<0.01
Texas	<0.01	<0.01	<0.01	<0.01
Canada	0.23	0.20	0.08	0.05

[29] These states still had significant areas that were not covered by the SO_2 grid. Thus only a fraction of these states' emissions were included in the total state contribution. The following are estimates of the area *not* covered by the SO_2 grid: MO-20%, AR-10%, MS-25%, AL-20%, GA-5%.

Figure 4-14. Ranked state percent sulfate contributions to Northeast Class I receptors based on emissions times upwind probability (E x UP) results

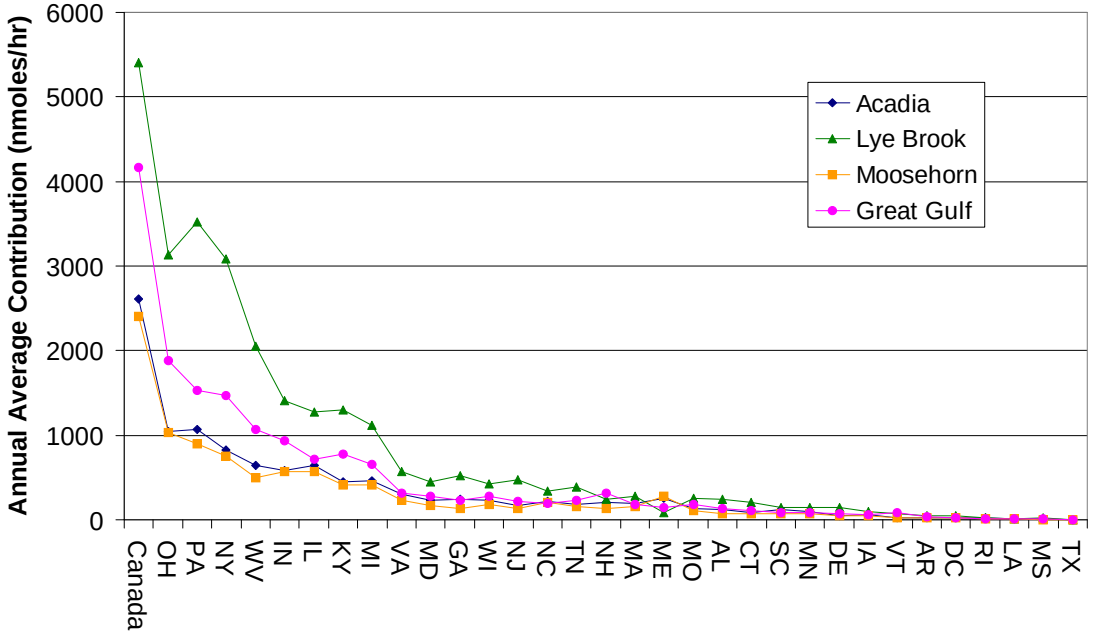

Figure 4-15. Ranked state percent sulfate contributions to Mid-Atlantic Class I receptors based on emissions times upwind probability (E x UP) results

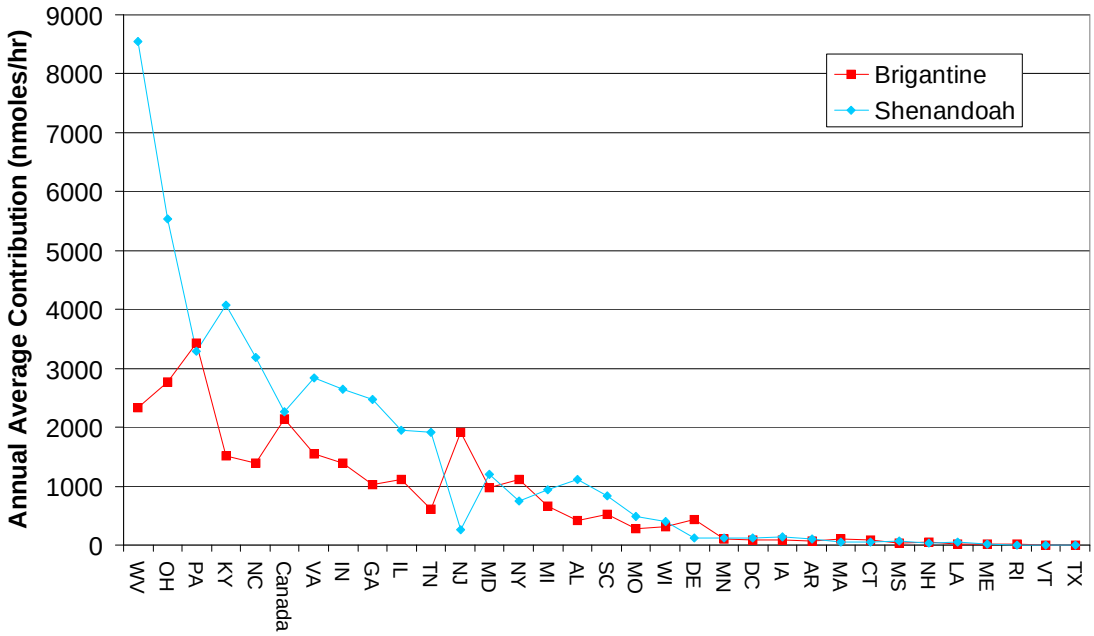

References

Ansari, A. S., and Pandis, S.N., "Response of inorganic PM to precursor concentrations," *Environ. Sci. Technol.*, 32, 2706-2714, 1998.

Davidson, C., Strader, R., Pandis, S., and Robinson, A., *Preliminary Proposal to MARAMA and NESCAUM: Development of an Ammonia Emissions Inventory for the Mid-Atlantic States and New England*. Carnegie Mellon University, Pittsburgh, PA. 7-Jan. 1999.

Draxler, R.D. and Hess, G.D., "Description of the HYSPLIT-4 Modeling System," *NOAA Technical Memorandum ERL, ARL-224*, Air Resources Laboratory, Silver Springs, Maryland, 24 pgs., 1997.

Draxler, R.D. and Hess, G.D., "An Overview of the HYSPLIT-4 Modeling System for Trajectories, Dispersion, and Deposition," *Australian Meteorological Magazine*, 1998, 47, 295-308.

Duyzer, J., "Dry Deposition of Ammonia and Ammonium Aerosols over Heathland," *J. Geophys. Res.*, 99(D9):18,757 – 18,763, 1994.

EarthTech, 2004, http://src.com/calpuff/calpuff1.htm

MARAMA 2004, http://www.marama.org/visibility/2002%20NEI/index.html

NESCAUM, "Regional Haze and Visibility in the Northeast and Mid-Atlantic States," January 2001a.

NESCAUM, "Development of an Improved Ammonia Emissions Inventory for the United States," December 2001b.

NESCAUM, "2002: A Year in Review," December, 2004.

Odum, J.R., Jungkamp, T.P.W., Griffin, R.J., Flagan, R.C., and Seinfeld, J.H., "The Atmospheric Aerosol-forming Potential of Whole Gasoline Vapor," *Science*, 276, 96-99, 1997.

Strader, R., Anderson, N., and Davidson, C., *Development of an Ammonia Inventory for the Mid-Atlantic States and New England, Progress Report, October 18, 2000*, available online: http://marama.org/rt_center/MARAMAprogress10-18-00.pdf, 2000.

USEPA, *National Air Quality and Emission Trends Report, 1998*, EPA 454/R-00-003, available online: http://www.epa.gov/oar/aqtrnd98/, 2000a.

USEPA, *National Air Pollutant Trends, 1900 – 1998*, EPA 454/R-00-002, available online: http://www.epa.gov/ttn/chief/trends/trends98/trends98.pdf, 2000b.

USEPA 2005, http://www.epa.gov/ttn/chief/eiinformation.html.

5. DATA ANALYSIS TECHNIQUES

Trajectory analyses have historically been used to trace the path of polluted air masses prior to their arrival at a given receptor site. Such analyses, by linking downwind measurements of ambient air quality with specific geographic areas upwind, can be very helpful in exploring the relative contribution of transported emissions from potential source regions on high and low pollution days. As with all of the tools and modeling techniques discussed in this report, trajectory analysis is not without some uncertainties and limitations. One such limitation is the fact that these analyses are typically unable to distinguish emission contributions from one point along the length of the trajectory from a different point along the path. In addition, the accuracy of any individual back trajectory calculation for a single observation or episode may be compromised by inherent limitations in the underlying Lagrangian trajectory models, which tend to become less accurate as the calculation progresses further back in time. Fortunately, a variety of techniques are available to mitigate these uncertainties and enhance confidence in the results obtained using trajectory analysis. These include techniques for triangulating results across multiple sites, ensemble techniques that combine the results of large numbers of back trajectories, clustering algorithms that group similar trajectories based on their spatial characteristics, and techniques for combining trajectory analyses with source apportionment models. All of these strategies can be useful in improving and refining traditional trajectory analyses.

This chapter describes the results of back trajectory analyses that have been conducted to date for key pollutant species observed at MANE-VU and nearby receptor sites. In addition, we explore novel techniques for improving the accuracy of individual trajectories by grouping meteorologically similar back-trajectories into trajectory "clusters" and examining the relationship between the transport pathways defined by these clusters and downwind air quality observations. We then turn to source apportionment models which can be used to group available monitoring data for various components of $PM_{2.5}$ in logical combinations that best explain the variation in observed species concentrations in terms of specific "source profiles." These source profiles are used to distinguish the emissions from common pollution sources (e.g., mobile sources, coal combustion). The information obtained through source apportionment analysis can then be used in combination with back trajectory analysis to link specific geographic source regions with downwind air quality conditions and to establish the relative contribution of different source regions to visibility impacts at the receptor site.

This chapter provides further description of several trajectory analysis techniques, before proceeding to a review of the insights gained to date by applying these techniques to analyze source regions for particulate pollution in the MANE-VU region. Preliminary results and interpretation are presented and used to support and bolster the basic conceptual model of regional haze outlined in Chapter 2.

5.1. Trajectory Analysis

The Hybrid Single Particle Lagrangian Integrated Trajectory (HYSPLIT) model (Draxler, 1997 and 1998) was used to calculate back trajectories for 13 sites in the northeastern United States. Most of these sites are located in Class I areas that are

subject to the Haze Rule, but several others are located in areas where potential nonattainment with the $PM_{2.5}$ NAAQS warrant analysis. Back trajectories were calculated eight times per day for starting heights of 200, 500, and 1,000 meters above ground level using meteorological wind fields for the five-year period from 2000 through 2004. Meteorological data from the National Oceanic and Atmospheric Administration (NOAA) Air Resources Laboratory (ARL) archives were used. These include wind fields from the Eta Data Assimilation System (EDAS), which cover North America with an 80 km spatial resolution and are based on 3-hourly variational analyses (Rolph, 2003). For the analyses presented here, we exclusively used the 500 meter EDAS trajectories from the baseline period (2000-2004).

Each trajectory was matched with corresponding monitoring data collected as close in time as possible to the "start" time of the back trajectory calculation. The analysis included ambient measurements for $PM_{2.5}$ and ozone (O_3), as well as all particulate matter constituents that are routinely measured as part of the IMPROVE program.

The resulting database of air quality monitoring results and associated back trajectories was used to develop several statistical measures of the probability or likelihood that a given upwind source region is associated with good or poor air quality at the receptor sites analyzed. Appendix A provides a detailed description of the metrics that were developed for this purpose and how they were calculated using both traditional trajectory analysis and cluster analysis techniques. This appendix also provides site-specific results.

5.1.1. Incremental Probability

The incremental probability (IP) field represents a measure of the likelihood that a given source region contributes more than "average" to high concentrations of a particular pollutant at a downwind receptor site (see Appendix A for a more complete definition). This technique can also be used to identify locations that are *less* likely to contribute to poor air quality at a given receptor site, thus allowing for more robust conclusions to be drawn about likely source regions for individual fine particle constituents.

Calculating IP fields for a subset of back trajectories within a complete sample can help further illuminate the different roles of different source regions. For example, it is interesting to note distinct differences between the IP field for back trajectories corresponding to the 10 percent highest observed sulfate values in the Northeast (three sites are shown that bracket the MANE-VU region's Class I sites) and the IP field for trajectories corresponding to the lowest sulfate values in the Northeast (specifically, sulfate values in the lowest 10^{th} percentile). Figure 5-1 and Figure 5-2 illustrate the IP fields for each set of observations, respectively.

In Figure 5-1 and Figure 5-2, note that the red color indicates areas with greater probability of contributing to transport on the selected days. These show that the very highest observed sulfate values across the region are strongly associated with transport from a source region that encompasses the Ohio River Valley, western Pennsylvania, and

the urban East Coast corridor. On the days with the lowest measured sulfate, transport is associated with northwesterly winds from Canada and weather patterns off the Atlantic.

Figure 5-1. Incremental Probability (Top 10% Sulfate) at Acadia, Brigantine and Lye Brook 2000-2004

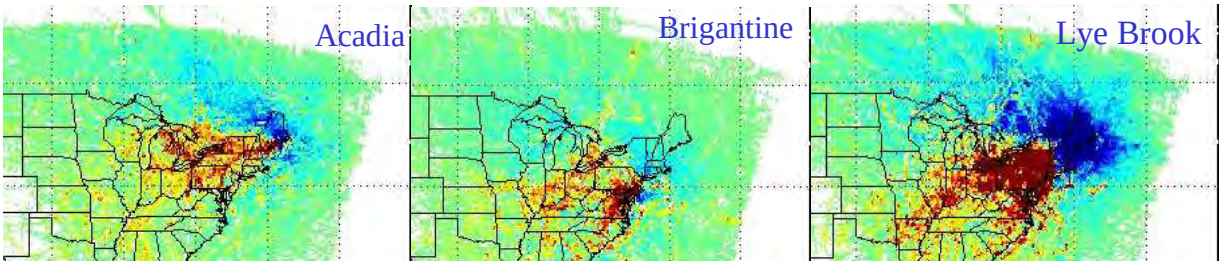

Figure 5-2. Incremental Probability (Bottom 10% Sulfate) at Acadia, Brigantine and Lye Brook 2000-2004

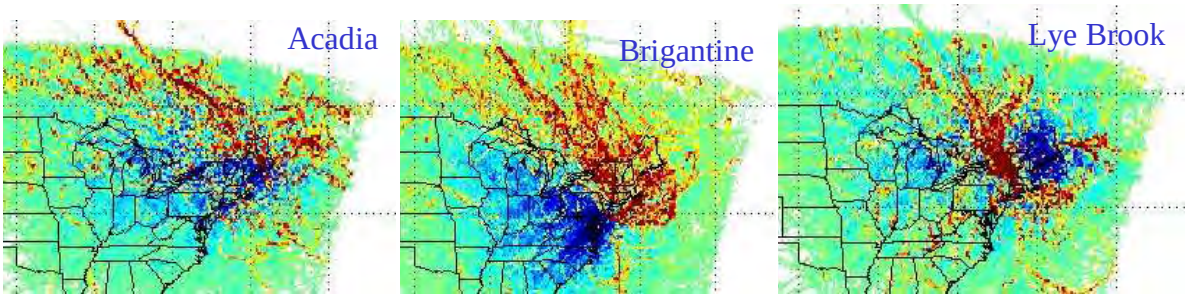

5.1.2. Clustered Back-Trajectories

Each of the IP fields shown in Figure 5-1 or Figure 5-2 incorporate results from over 14,000 back trajectories over the five-year period analyzed. In cases like these, where IP fields are calculated from a very large set of data points, the error in the calculation of any individual trajectory — which can be as high as 30 percent or more of the total transport distance involved in a given trajectory — is not likely to affect the overall result. Assuming that such errors are randomly distributed (i.e., no systematic bias exists in the calculations used by the trajectory model to calculate wind speed or direction), the use of large numbers of individual trajectories will effectively ensure that the random errors cancel out. To further minimize the effect of any errors with respect to individual trajectories, it is also possible to cluster large numbers of back trajectories according to their three-dimensional similarity (see Appendix A for a detailed description of several methodologies used). Figure 5-3 shows residence-time probability fields for clusters of similar back trajectories grouped according to their proximity to unique meteorological pathways. This metric yields probabilistic representations of the meteorological pathways which were most likely to be associated with the highest observed sulfate concentrations at the receptor site. Such probabilistic representations reduce the reliance on any one back trajectory and ensure that the general pattern used to associate a transport pathway with a downwind receptor site is more likely to be accurate.

Figure 5-3. Proximity based cluster with the highest associated sulfate value for three sites in the MANE-VU region, Acadia (sulf=3.19 μg/m^3), Brigantine (sulf=6.79 μg/m^3), and Lye Brook (sulf=3.92 μg/m^3)

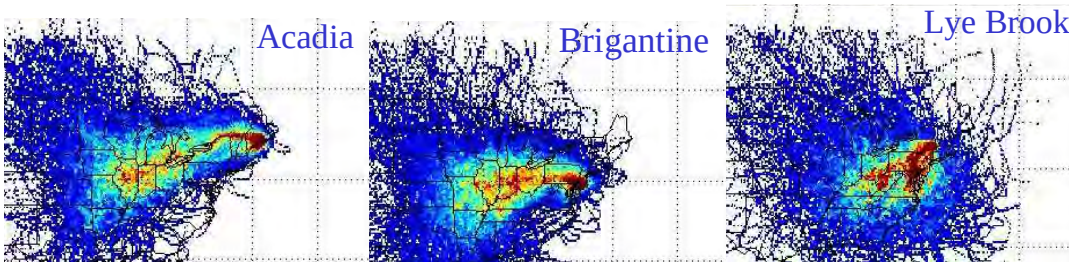

5.1.3. Cluster-Weighted Probability

The clusters derived above can be used individually or combined in an "ensemble cluster" approach similar to how individual trajectories are combined to develop the IP metric. This second method for associating transport patterns with downwind pollution measurements involves using all clusters generated by the clustering algorithms described in the preceding section (and in detail in Appendix A) and weighting them by their average observed sulfate value. Simply averaging the residence-time probability of all clusters would yield the "everyday" probabilities that are used in calculating IP fields. Instead, weighting each cluster *before* the averaging process serves to highlight transport patterns that are associated with high sulfate levels at the receptor site, while downplaying patterns that are associated with low values. Figure 5-4 shows the resulting cluster-weighted probability (CWP) field. Results are similar to those obtained using the incremental probability metric described previously, but they now include all clusters, not just the high-day values.

A noteworthy feature of the clustering process is that while it reduces uncertainty about prevailing transport patterns, it is not helpful in taking advantage of weather variations to identify specific source regions. Thus, results for a particular site should be interpreted as showing that observed air quality conditions have an increased probability of being associated with the transport of a specific pollutant, as opposed to being associated with a particular source region for a given pollutant. Put another way, it is difficult to make an association with a specific point along the pathway defined by a cluster. As with the IP approach described earlier, however, multi-site averaging can address this ambiguity by making it possible to triangulate on regions that are associated with the transport of pollution to multiple sites in different locations, as shown in Figure 5-4.

Both trajectory-based approaches (i.e., IP and CWP) have also been applied to Class I receptor sites in the nearby VISTAS region, which includes the Dolly Sods and Otter Creek Wilderness Areas in West Virginia as well as Shenandoah National Park and the James River Face Wilderness Area in Virginia. Results for the VISTAS Class I sites are presented at the conclusion of Appendix A.

Figure 5-4. Cluster Weighted Probability at Acadia, Brigantine and Lye Brook 2000-2004

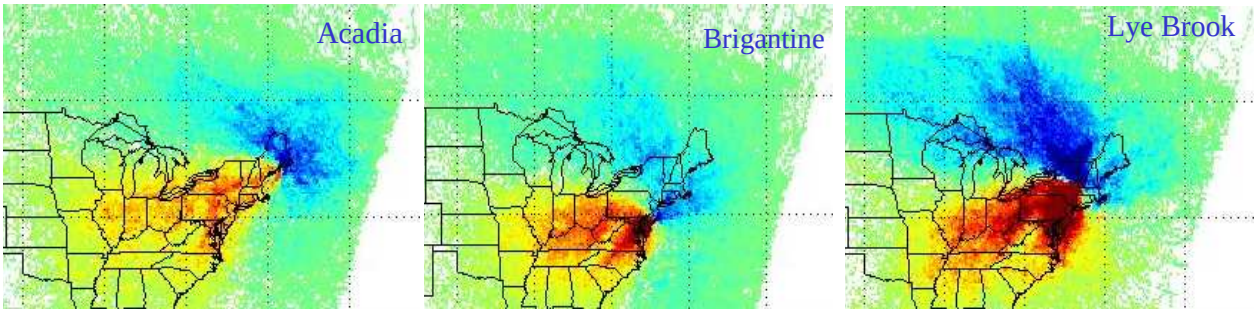

5.2. Source Apportionment Models and Ensemble Trajectory Analysis of Source Apportionment Results

Previous sections of this chapter have discussed a category of receptor-based assessment techniques known more generally as ensemble trajectory analysis. The latter category includes residence time analysis (RTA) as well as potential source contribution function (PSCF) and cluster analysis (see also Appendix A). In this section we turn to multivariate mathematical models for analyzing source contributions, such as chemical mass balance (CMB) models, principal component analysis (PCA), positive matrix factorization (PMF), and UNMIX.

Receptor-based models begin with ambient air quality measurements at one or more receptor locations and work "backward" to identify logical combinations of pollutant species that best fit a "source profile." Sources matching that profile are assumed to have contributed to the ambient pollutant concentrations historically observed at the receptor locations. These models are typically driven by variations in PM constituent concentrations across multiple observations at one or more sites. An advantage of PCA, PMF, and UNMIX is that source profiles do not need to be known in advance; however, this does mean that the results must be subjectively interpreted to identify and distinguish likely sources.

Because of these complexities and because the multivariate models typically rely entirely on measurements of PM constituents without regard to meteorology, it can be extremely useful to consider results obtained through the ensemble trajectory techniques (which rely on meteorology only) when interpreting or evaluating the outputs from a multivariate modeling exercise.

Appendix B provides details of numerous source apportionment and associated ensemble back trajectory analyses. These details cover results obtained for many of the most significant components of fine particulate mass and resulting light extinction. Here we focus on the "secondary sulfate" or "coal" source profile that was identified at nearly every site in the eastern United States. Secondary sulfate typically accounts for 30–60 percent of overall fine particle mass and 60–80 percent of visibility impairment on the haziest days in the Northeast.

Figure 5-5 shows results from one of the broadest studies conducted to date of sulfate sources and characteristics at nine eastern IMPROVE sites. The bars on the left

show the fraction of total sulfate measured at each site that is contributed by the "sulfate/coal" source profile as determined by the source apportionment models. The bars on the right show the fraction of each "sulfate/coal" source profile that is composed of sulfate. Figure 5-5 suggests that: (1) large sources contribute 70–90 percent of the total sulfate measured at these sites, and (2) that the contribution from these large sources consists of 50–90 percent sulfate.

Figure 5-5. Sulfate characteristics of "secondary sulfate" (coal) sources identified at eastern sites

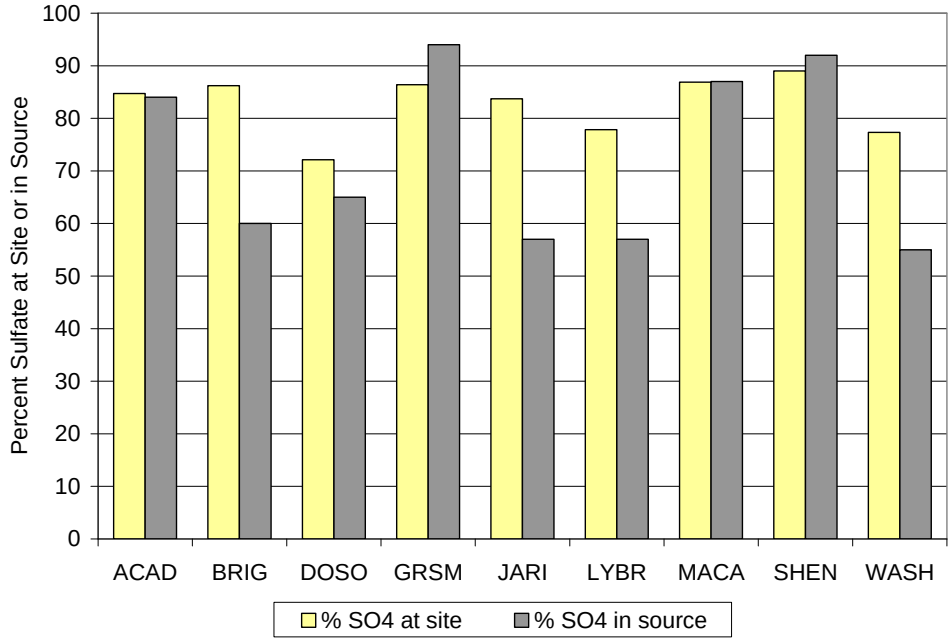

When large sulfate sources are associated with upwind states or regions through the use of back trajectories (Figure 5-6), it becomes clear that many Class I and urban sites in MANE-VU and adjoining areas are influenced by a common source region. These findings suggest that reductions in coal-related SO_2 emissions would have substantial benefits in terms of improved visibility and reduced PM concentrations over a large part of the eastern United States and eastern Canada.

This conclusion is further reinforced by comparing regions with significant emissions that match the "source profiles" generated by available mathematical modeling tools to regions identified through trajectory analysis as having a high probability of being upwind on days with high sulfate levels and high reconstructed extinction values. As shown in Figure 5-6, the degree of correspondence between these regions is substantial. This indicates that the "secondary sulfate/coal combustion" source profile prominent at several eastern sites is strongly linked to regions associated with the highest 10 percent of recorded sulfate and reconstructed extinction values. It is noteworthy that the upwind regions identified in Figure 5-7 are derived from measurements spanning the entire IMPROVE network, suggesting that the source region for "secondary sulfate/coal combustion," which is a dominant contributor to visibility impairment in parts of the eastern United States, is also a major contributor to observed sulfate and extinction outside the MANE-VU region.

Figure 5-6. Incremental Probabilities for "Secondary Sulfate" (Coal) Sources in Eastern U.S.

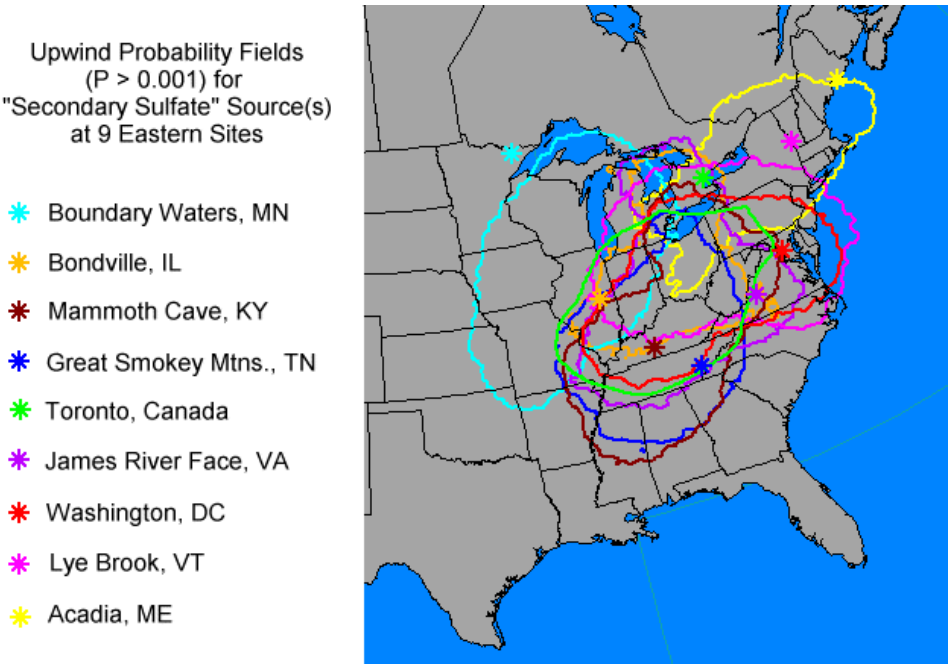

5.3. Trajectory Model Evaluation and Future Work

The geographical correspondence exhibited in Figure 5-7 extends to the multi-site average IP fields calculated for the MANE-VU region and shown previously in Figure 5-1. It also extends to the multi-site average IP field calculated using the ATAD model and shown in Figure B-30 in Appendix B. Essentially, both figures are versions of the same thing, but they do exhibit some subtle differences. These differences are highlighted in Figure 5-8 which compares the results of ATAD and HYSPLIT IP calculations for the top 10 percent of sulfate, selenium, and nickel observations at Lye Brook, Vermont. Sulfate is a secondary pollutant that tends to peak in the summer, whereas nickel and selenium are primary pollutants that typically peak in the wintertime. Ni and Se serve as excellent markers for residual oil and coal combustion respectively. The figure indicates strong agreement between the two models in terms of

Figure 5-7. Comparison of probability fields for observed sulfate, "sulfate" source profiles for seven eastern sites and reconstructed deciviews

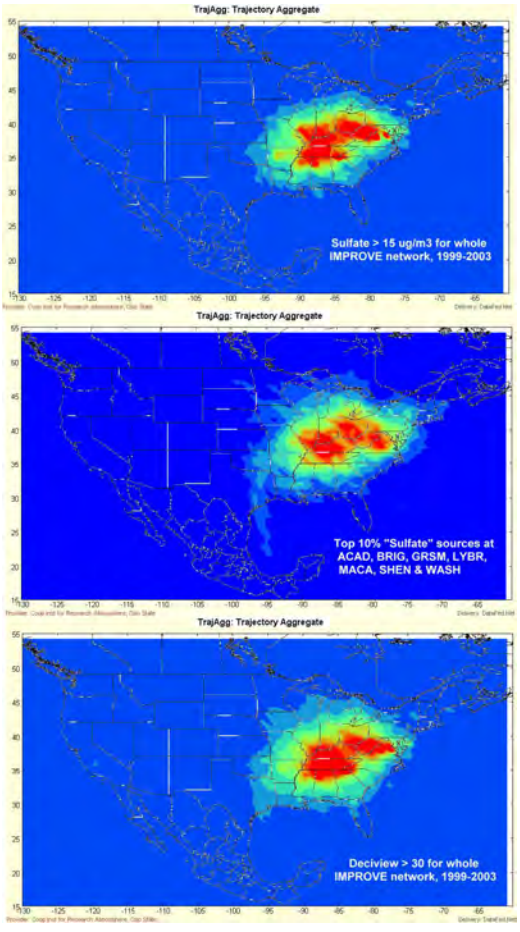

the IP fields they calculate for nickel, suggesting that — during wintertime — primary pollutants are tracked well by both techniques. There is less agreement between the IP fields for sulfate, suggesting either a southerly bias to the HYSPLIT calculations for this secondary pollutant, or a westerly bias to the ATAD results.

Seasonal differences in the meteorology that affects Lye Brook and other East Coast sites during the summer versus during the winter may help to explain these model discrepancies. Some of the largest absolute differences between the ATAD and HYSPLIT estimates occur for the highest sulfate days. While there are many differences between the models, one key difference is in their trajectory start heights. The HYSPLIT trajectories all start at 500 meters above ground level while the ATAD model first estimates a "transport layer depth" (TLD) and then initiates the trajectory (while constraining subsequent trajectory endpoints) at a point roughly half way between ground level and the TLD. During summer, when the largest sulfate events occur, the resulting ATAD start heights are roughly twice as high as the 500 m HYSPLIT start heights (see Figure 5-9). Hence the ATAD calculations tend to extend over a greater distance to the west, while the summer HYSPLIT trajectories may be more reflective of flows that are nearer the surface and more frequently east of the Appalachian Mountains. Both flow regimes are important. In fact, Blumenthal et al. (1997) have observed that the highest ozone concentrations in the Northeast (which often coincide with episodes of high sulfate concentrations) tend to occur when surface flows up the Northeast urban corridor combine with synoptic flows over the Appalachian Mountains from the west, a pattern that is often accompanied by lower level nocturnal jets along the Northeast corridor and through gaps in the Appalachians.

Figure 5-8. Comparison of IP contours generated by ATAD and HYSPLIT (both EDAS and FNL) for sulfate, nickel and selenium at Lye Brook

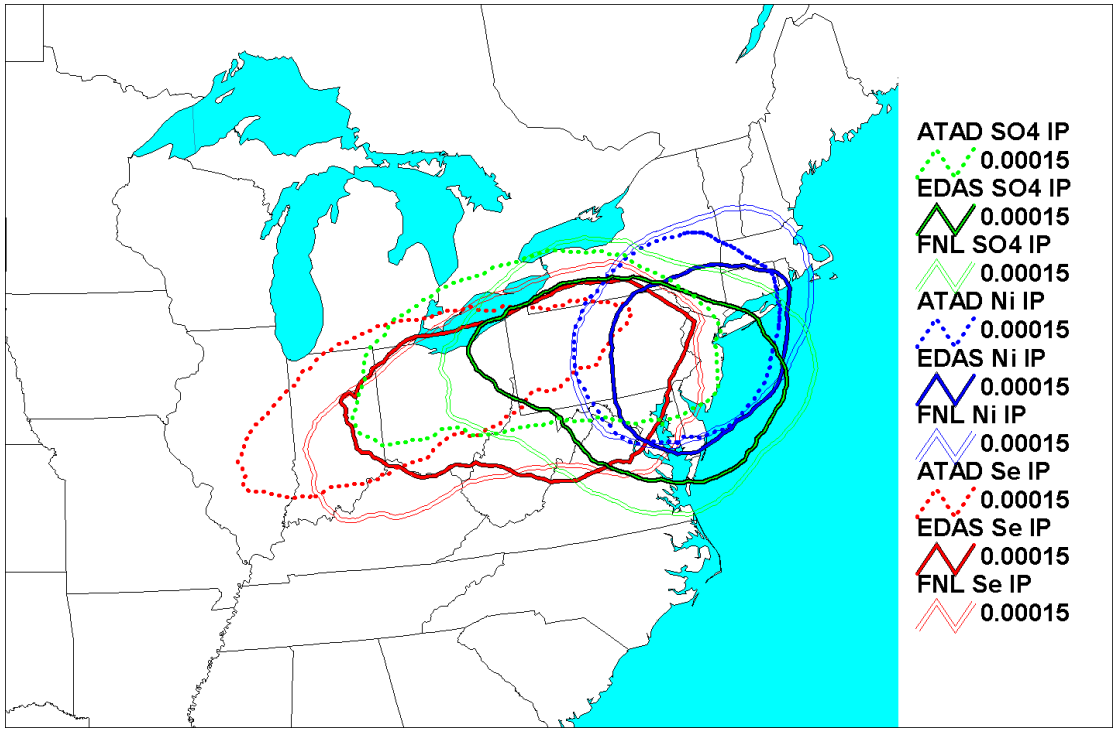

An extensive evaluation of the performance of HYSPLIT, ATAD, and Capita Monte Carlo trajectory models using a variety of different meteorological drivers, ensemble trajectory techniques, and performance tracers was recently conducted as part of the Big Bend Regional Aerosol and Visibility Observational (BRAVO) study (Pitchford et al., 2004). No one model consistently out-performed the others at that site, hence results from these and more sophisticated photochemical grid models (REMSAD and CMAQ) were merged to produce a best-estimate, "consensus" apportionment of sulfate in the BRAVO study.

MANE-VU is using all available trajectory models, trajectory-related metrics, and improved understanding of transport phenomena to further explore and support the development of emission control strategies for reducing regional haze.

Figure 5-9. ATAD Transport Layer Depth (TLD) by month. Color indicates the length of time prior to arriving at the receptor.

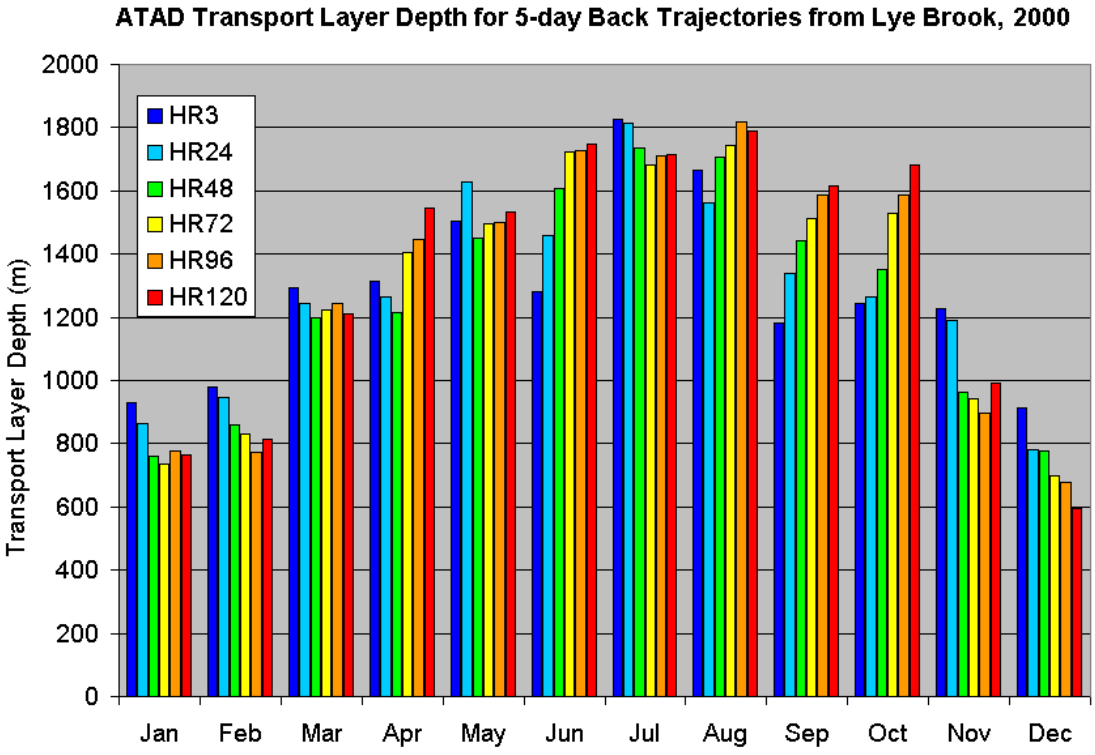

References

Blumenthal, D.L., Lurmann, F.W., Kumar, N., Ray, S.E, Korc, M.E., Londergan, R., Moore, G., Transport and mixing phenomena related to ozone exceedances in the Northeast U.S. Working Draft No. 1.1 prepared for Ozone Transport Assessment Group Air Quality Analysis Workgroup by Sonoma Technology, Inc., Santa Rosa, CA and Earth Tech, Concord, MA, STI-996133-1710-WD1.1, February 1997.

Draxler, R.D. and Hess, G.D., "Description of the HYSPLIT-4 Modeling System," *NOAA Technical Memorandum ERL, ARL-224*, Air Resources Laboratory, Silver Springs, Maryland, 24 pgs., 1997.

Draxler, R.D. and Hess, G.D., "An Overview of the HYSPLIT-4 Modelling System for Trajectories, Dispersion, and Deposition," *Australian Meteorological Magazine*, 47, 295-308, 1998.

Pitchford, M.L., Schichtel, B.A., Gebhart, K.A., Barna, M.G., Malm, W.C., Tombach, I.H., and Knipping, E.M., "Causes of Haze at Big Bend National Park – Results of the BRAVO Study and More" Regional and Global Perspectives on Haze: Causes, Consequences and Controversies – Visibility Specialty Conference, Air & Waste Management Association, Asheville, NC October 25-29, 2004.

Rolph, G.D., Real-time Environmental Applications and Display sYstem (READY) Website (http://www.arl.noaa.gov/ready/hysplit4.html). NOAA Air Resources Laboratory, Silver Spring, MD., 2003.

6. CHEMICAL TRANSPORT MODELS

Eulerian or "grid" models have traditionally served as the workhorse of air quality planning programs. These tools strive to be comprehensive in accounting for emissions, meteorological dynamics, chemical production, transformation, and destruction as well as wet and dry deposition and microphysical processes. With this degree of sophistication comes attendant uncertainty. Many of the more complex processes (e.g., cloud processes and boundary layer dynamics) are handled through parameterizations that attempt to approximate the real atmosphere at an appropriate level of detail. Chemical transport models for ozone and fine particles have improved markedly over the past several years as various groups have developed competing models and as the different strengths and weaknesses of these models help to shed light on various aspects of the underlying science.

Two regional-scale air quality models have been evaluated and used by NESCAUM to perform air quality simulations. These are the Community Multi-scale Air Quality modeling system (CMAQ)[30] and the Regional Modeling System for Aerosols and Deposition (REMSAD).[31] Appendix C provides detailed descriptions of these models and of their use by NESCAUM, together with performance evaluations and preliminary results. A brief overview of the two modeling platforms in terms of their relevance to future SIP work is provided here, along with highlights of the findings.

6.1. Chemical Transport Model (CTM) platforms – Overview

Both REMSAD and CMAQ are being used with a 12 km grid[32] in the eastern U.S. domain (see Figure 6-1(b)). Air quality is modeled on 22 vertical layers with hourly temporal resolution for the entire calendar year 2002. REMSAD has simplified chemistry but allows for emissions tracking of sulfate, nitrate, and mercury through a tagging feature that calculates the contribution of specific sources to ambient concentrations, visibility impacts, and wet or dry deposition. REMSAD has shown good performance when reproducing annual or seasonal statistics for sulfate and mercury chemistry, while CMAQ has shown good performance for multiple species. A new release of CMAQ (version 4.5) may improve performance for sulfate, nitrate and organics over what Appendix C presents and will be used with the quality-assured meteorology and emission inventory inputs described below for final SIP submissions in 2007 or 2008.

Meteorological inputs have been developed by the University of Maryland (UMD) using the Fifth-Generation Pennsylvania State University/National Center for Atmospheric Research (NCAR) Mesoscale Model (MM5) system.[33] A modified Blackadar boundary layer scheme is used as well as physics options including explicit representations of cloud physics with simple ice microphysics (no mixed-phase processes) and the Kain-Fritsch cumulus parameterization.

---

[30] See Byun and Ching, 1999.
[31] See ICF/SAI, 2002.
[32] 12 km grid describes a 12 by 12 km grid cell
[33] http://www.mmm.ucar.edu/mm5/

The New York Department of Environmental Conservation and NESCAUM are processing emissions inputs using the Sparse Matrix Operator Kernel Emissions (SMOKE) Modeling System. To model biogenic emissions, SMOKE uses the Biogenic Emission Inventory System, version 2.3 (BEIS2) and version 3.09 and 3.12 (BEIS3). SMOKE has also been integrated with the MOBILE6 model for on-road emissions. MANE-VU has developed a quality-assured 2002 emissions inventory which is being merged with the regional inventories for other RPOs in order to provide a comprehensive emissions inventory for the entire Northeast domain shown in Figure 6-1(b).

A dynamic 3-dimensional boundary condition feeds ambient concentration fields in at the domain boundaries which are representative of actual concentrations during 2002. This dynamic boundary condition was developed by applying the output of a global model run (Park et al., 2004) with 4 degree longitude by 5 degree latitude horizontal resolution at the boundaries of the 36 km grid domain shown in Figure 6-1(a). The results of this annual simulation are then applied at the boundary of our 12km grid domain, ensuring acceptable representation of the general trends and sulfate patterns that were present during the simulation period.

Figure 6-1. Modeling domains used in NESCAUM air quality modeling studies. (a) Domain 1: 36 km National US grid domain with location of 12 km grid domain highlighted; (b) Domain 2: 12km Northeast US grid domain. The gridlines are shown at 180 km intervals (5 x 5 36 km cells or 15 x 15 12 km cells).

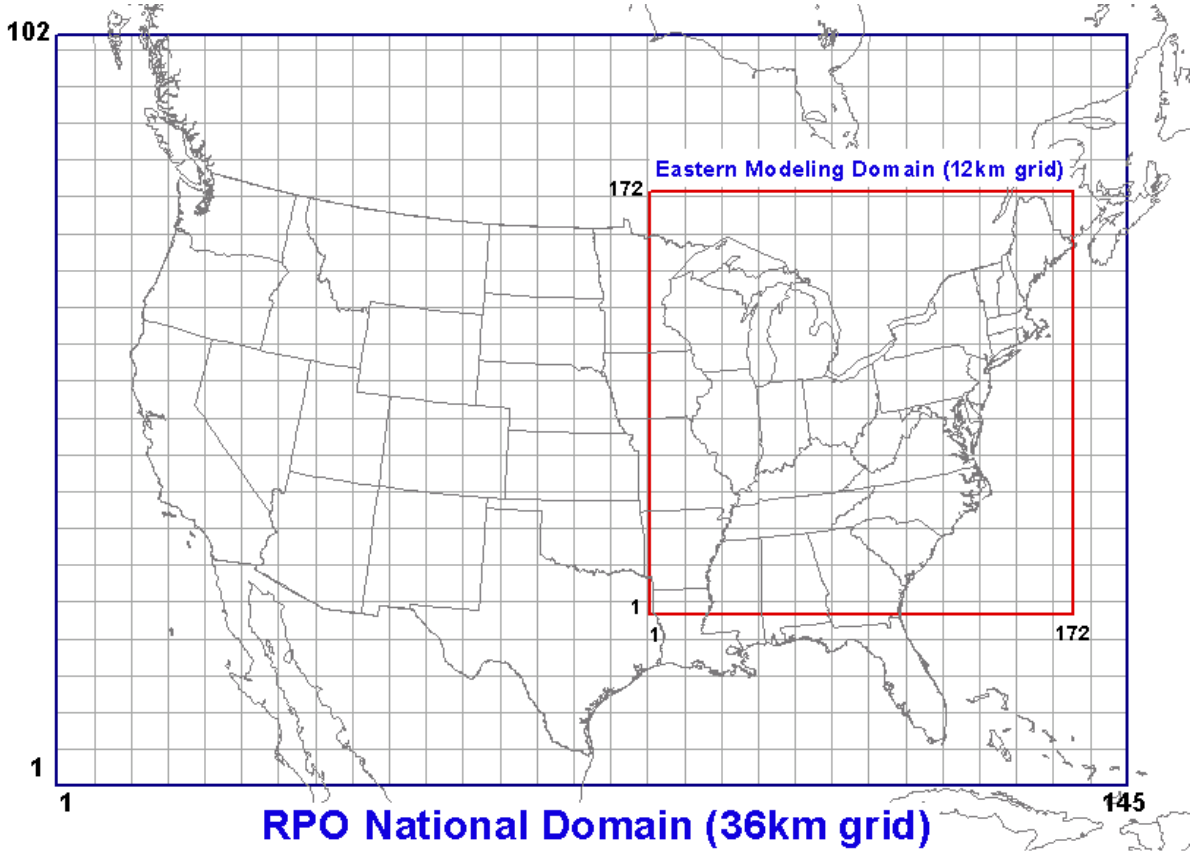

6.2. Preliminary Results

CMAQ has been run for a complete set of baseline simulations including 2002, 2009 and 2018. These preliminary runs are described in greater detail in Appendix C, but include inventory and meteorological drivers which will be updated for final SIP submissions. Nonetheless, these preliminary results suggest that implementation of existing regulations (including USEPA's Clean Air Interstate Rule, or CAIR) will continue to yield significant improvements in visibility over the next decade, primarily as a result of regional sulfate reductions (See Figure 6-2 a and b below for visibility improvement and see Figure C-27 in Appendix C for sulfate mass reductions). Despite these potential improvements, not all MANE-VU Class I areas are anticipated to achieve uniform progress goals as described by current USEPA guidance.[34] Brigantine Wilderness Area in New Jersey is projected to fall about a half deciview short of the uniform rate under existing emission reduction plans.

A significant difference between the CMAQ and the REMSAD results presented here is that NESCAUM has taken the additional step of reprocessing the SO_2 emission sources from each state such that these model inputs are formatted to take advantage of

Figure 6-2(a) and (b): CMAQ Integrated SIP Modeling Platform simulation results for 2002, 2009 and 2018 relative to Uniform Progress Goals calculated according to current USEPA guidance for (a) Northeast Class I sites in MANE-VU and (b) Mid-Atlantic Class I sites in or near MANE-VU.

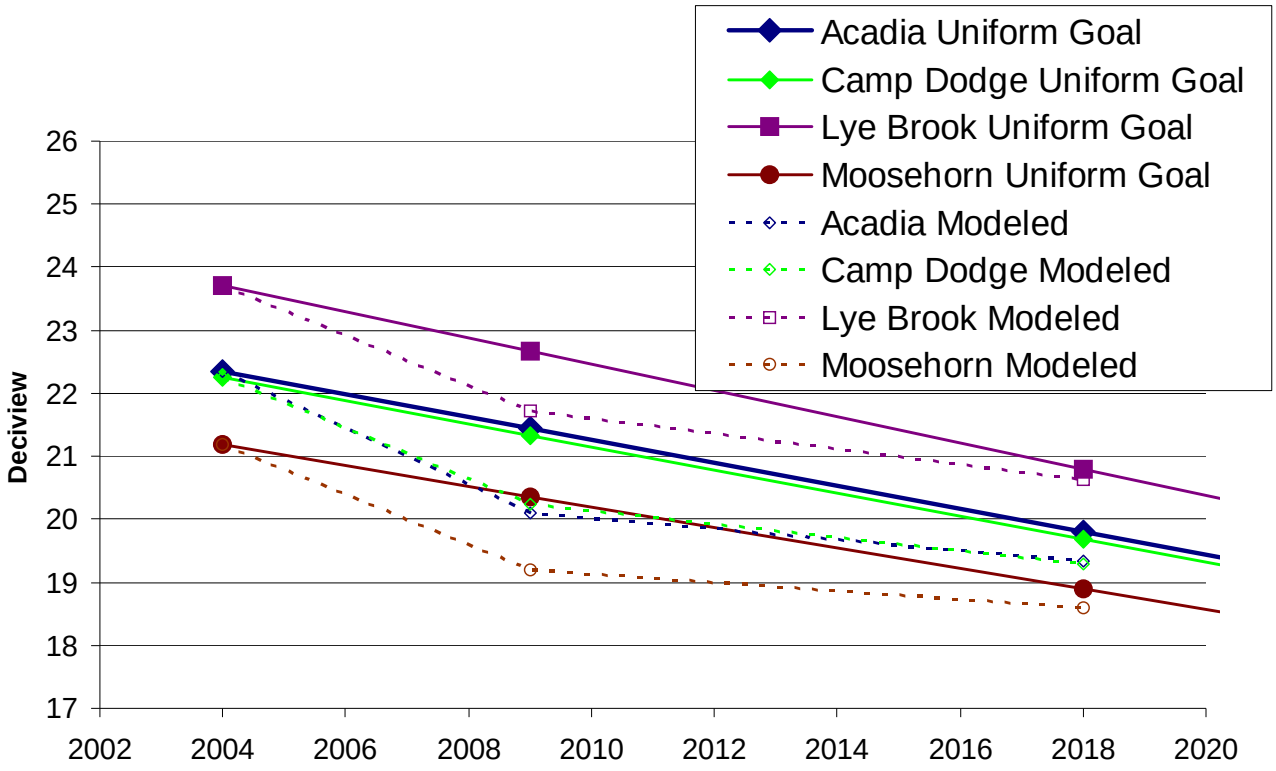

[34] We note that uniform progress goals do not necessarily dictate visibility levels required by statute, but do represent a point of comparison for states when establishing *reasonable* progress goals toward our national visibility goal of no anthropogenic visibility impairment by 2064.

Figure 6-2(b).

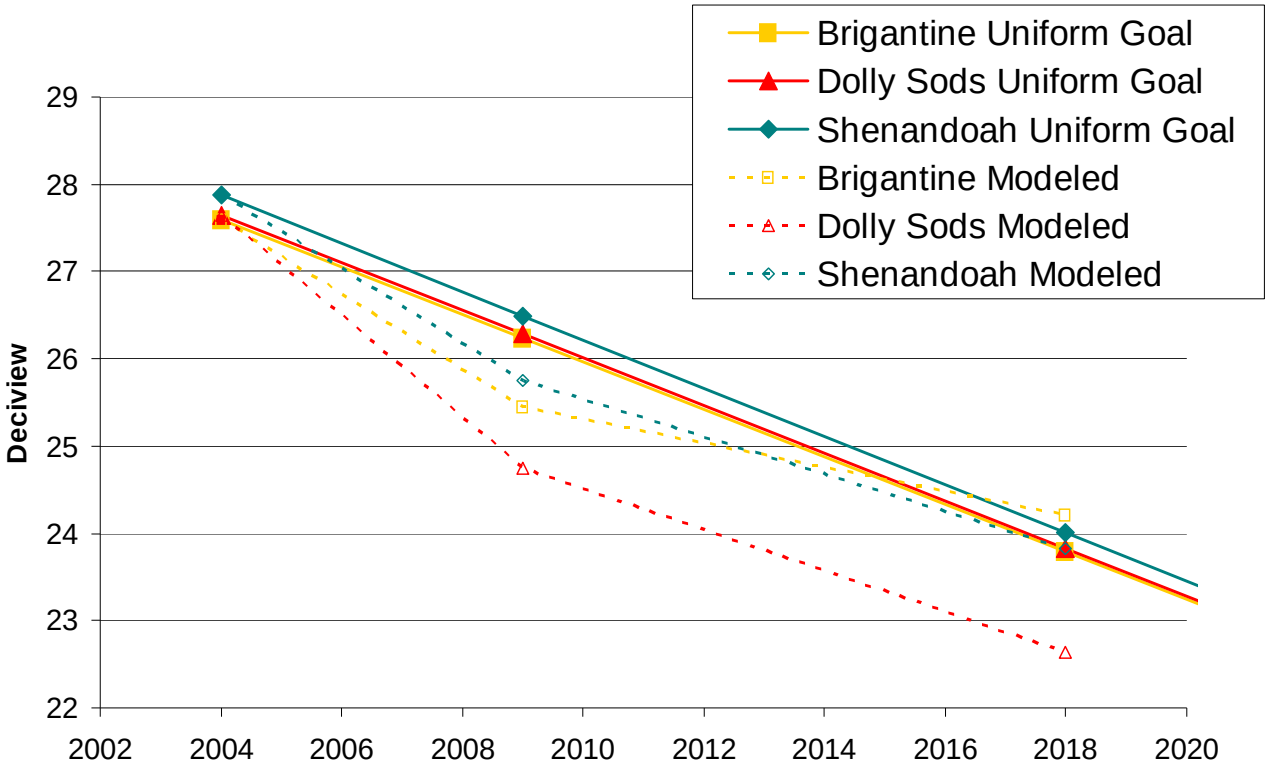

REMSAD's tagging capabilities. Thus, all SO_2 emissions included in the model for the eastern half of the country, Canada and the boundary conditions have been tagged according to state of origin. This allows for a rough estimation of the total contribution from elevated point sources in each state to simulated sulfate concentrations at eastern receptor sites. The tagging scheme employed for this analysis is illustrated in Figure 6-3. Using identical emission and meteorological inputs to those prepared for the Integrated SIP (CMAQ) platform, REMSAD was used to simulate the annual average impact of each state's SO_2 emission sources on the sulfate fraction of $PM_{2.5}$ over the northeastern United States.

Results of these tagged runs indicate that elevated point sources in Pennsylvania, Ohio, and New York contribute significantly, on an annual basis, to sulfate concentrations at all MANE-VU sites. Northern sites (e.g., Acadia) are more influenced by sources in upper midwestern states (e.g., Wisconsin and Michigan) whereas southern sites like Brigantine are more influenced by sources in more southerly states such as West Virginia, Maryland, and Virginia. Shenandoah, a VISTAS Class I site appears to be most strongly influenced by sources in Ohio, Pennsylvania, and West Virginia, followed by other nearby Southeast and Midwest states. Figure 6-4 through Figure 6-7 present these results showing the breakout of sulfate by individual tag. Note that the large "other" fraction of sulfate includes all sources outside the analysis domain, which includes some portions of the VISTAS and CENRAP RPO, Northern and Western Canada in addition to all other (i.e., inter-continental) sources of SO_2. Figure 6-8 shows similar results summarized by RPO for the 20% worst days.

Figure 6-3. REMSAD modeling tagging schemes.
(black: group 1, red: group 2, and blue: group 3)

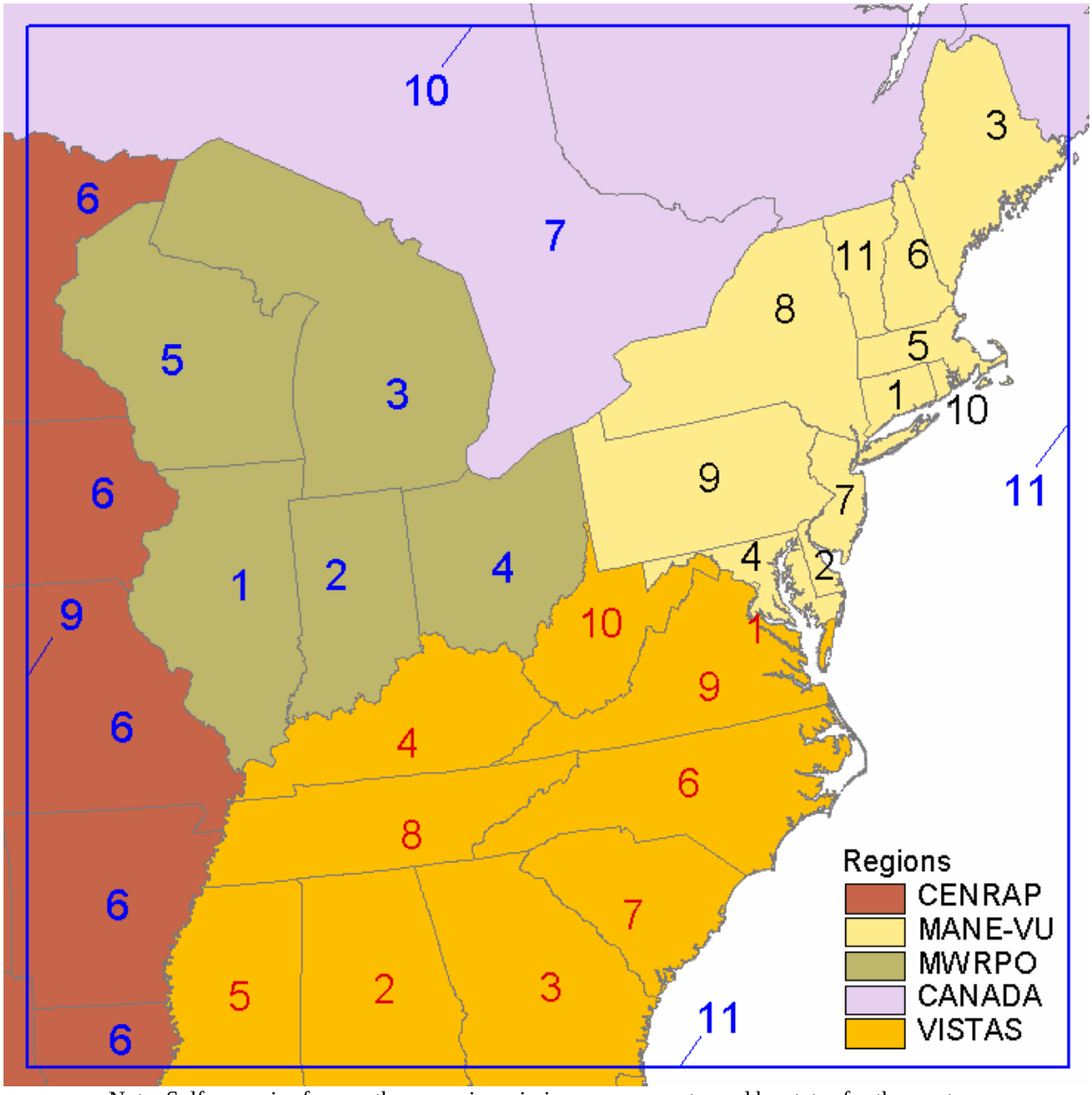

Note: Sulfur species from anthropogenic emission sources are tagged by states for three sets of tags. Tag group 3 also includes boundary conditions. The color of the numbers represents tag groups (black: group 1, red: group 2, and blue: group 3)

Figure 6-4. 2002 Eastern states' contribution to annual PM sulfate in Acadia, ME

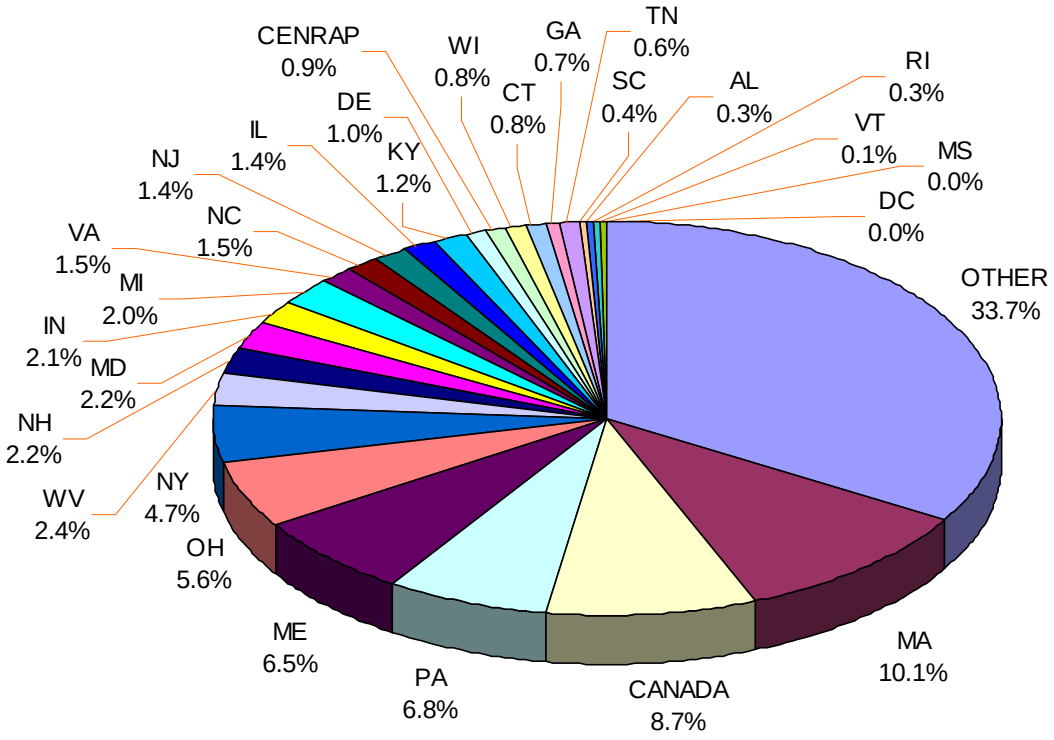

Figure 6-5. 2002 Eastern states' contribution to annual PM sulfate in Brigantine, NJ

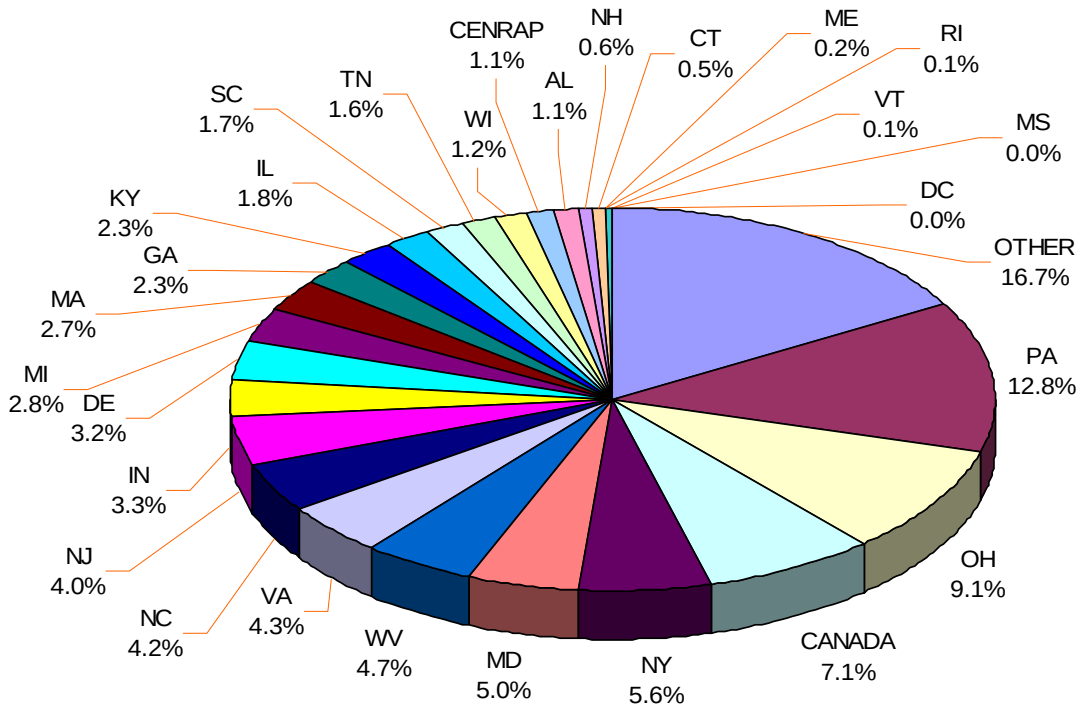

Figure 6-6. 2002 Eastern states' contribution to annual PM sulfate in Lye Brook, VT

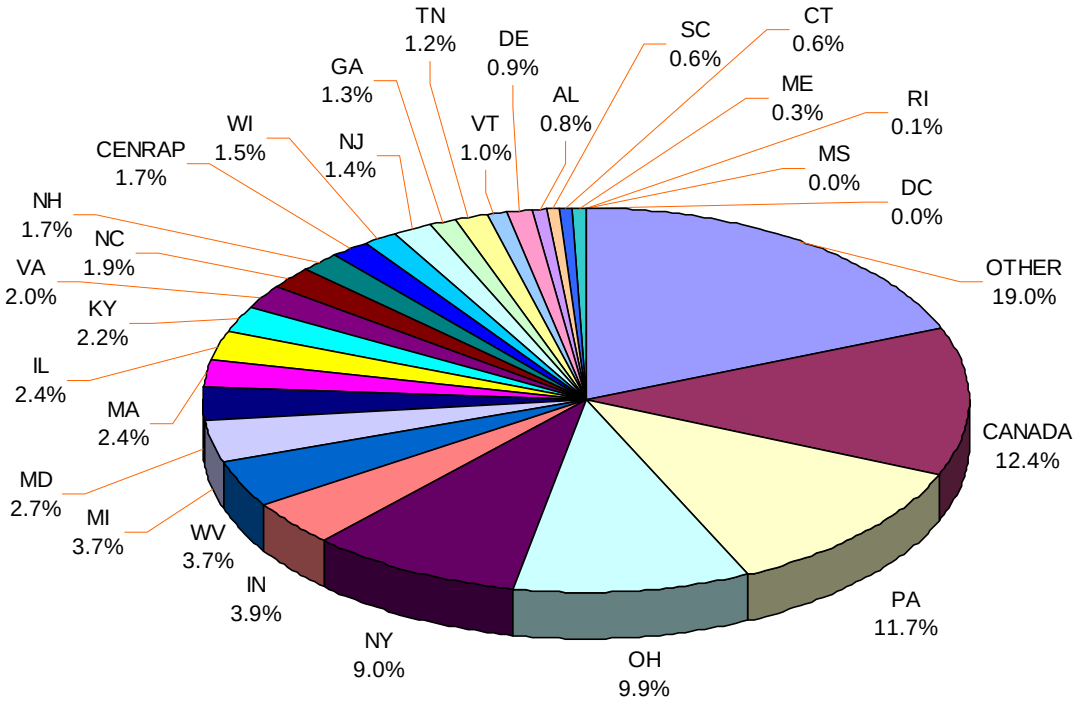

Figure 6-7. 2002 Eastern states' contribution to annual PM sulfate in Shenandoah, VA

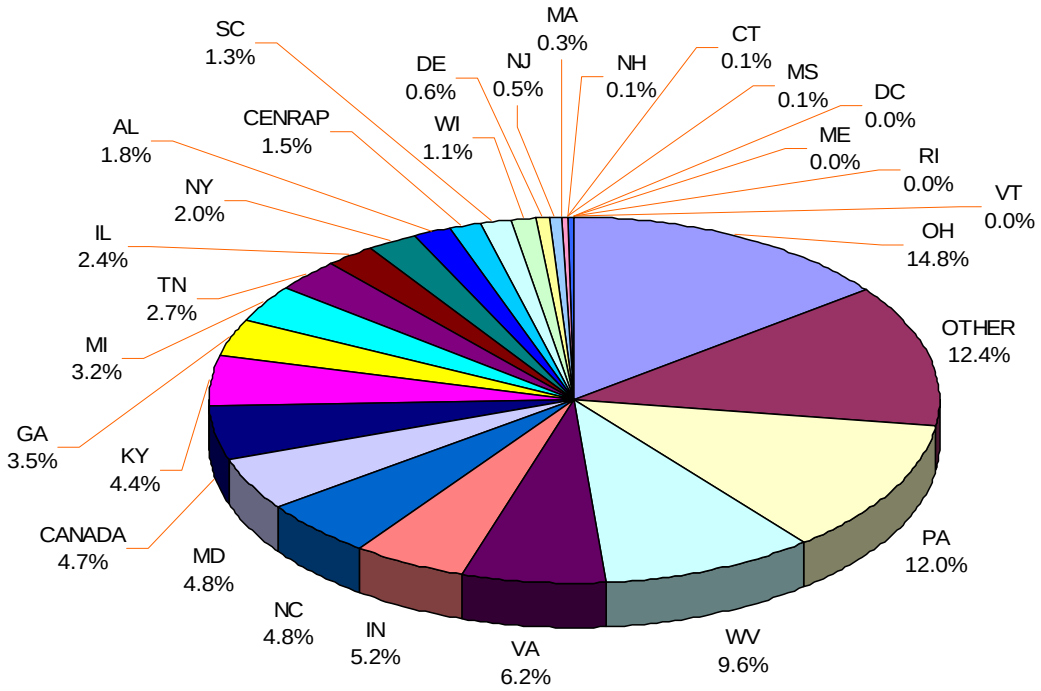

Figure 6-8. Comparison of Sulfate Extinctions on 20% Worst Visibility Days

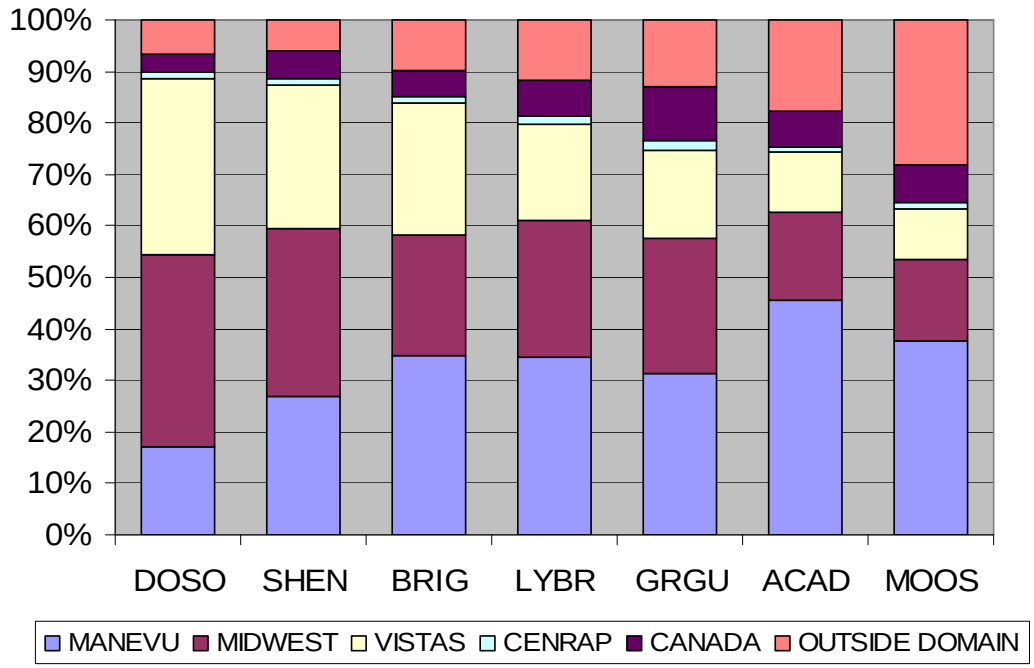

References

Byun, D.W., and Ching, J.K.S., *Science Algorithms of the EPA Models-3 Community Multiscale Air Quality (CMAQ) Modeling System*, EPA/600/R-99/030, March 1999.

Park, R. J., Jacob, D. J., Field, B. D., Yantosca, R. M., and Chin, M., *Natural and transboundary pollution influences on sulfate-nitrate-ammonium aerosols in the United States: implications for policy* , J. Geophys. Res., D15204, 10.1029/2003JD004473, 2004.

SAI, *User's Guide to the Regional Modeling System for Aerosols and Deposition (REMSAD), Version 7*, ICF Consulting/SAI, San Francisco, CA, 2002.

7. LAGRANGIAN DISPERSION MODELS

Dispersion models are commonly used to study the impacts of pollutant plumes or specific point source emissions on surrounding areas. The scale of these models has traditionally been limited to a few hundred kilometers because of a perceived lack of ability to accurately reproduce horizontal dispersion beyond these distances. Recent advances in the CALPUFF system (USEPA, 2006) — including enhancements to its horizontal diffusion and dispersion algorithms as well as the addition of chemical transformation parameterizations — have resulted in improved performance over much greater distances. In fact, the most recent proposed guidance for implementing the BART (Best Available Retrofit Technology) requirements of the Regional Haze Rule provide for the use of CALPUFF to analyze dispersion over distances exceeding 200 km as long as a detailed modeling protocol is included for approval by the appropriate reviewing authority (40 CFR Part 51, pg. 25194, May 5, 2004).

Appendix D provides specific information related to two CALPUFF platforms that have been developed for a large domain (see Figure 7-1) by the Vermont Department of Environmental Conservation (VT DEC) Air Pollution Control Branch and by the State of Maryland's Department of the Environment (MDE) and Department of Natural Resources (MDNR) with contract assistance provided by Environmental Resources Management (ERM). Appendix D contains detailed descriptions of the two platforms; the processing and evaluation of both MM5- and National Weather Service (NWS)-based meteorological data; the processing and evaluation of CEMS (Continuous Emissions Monitoring System)- and 2002 RPO-based emissions data; performance evaluations of

Figure 7-1. CALPUFF modeling domain utilized by MANE-VU

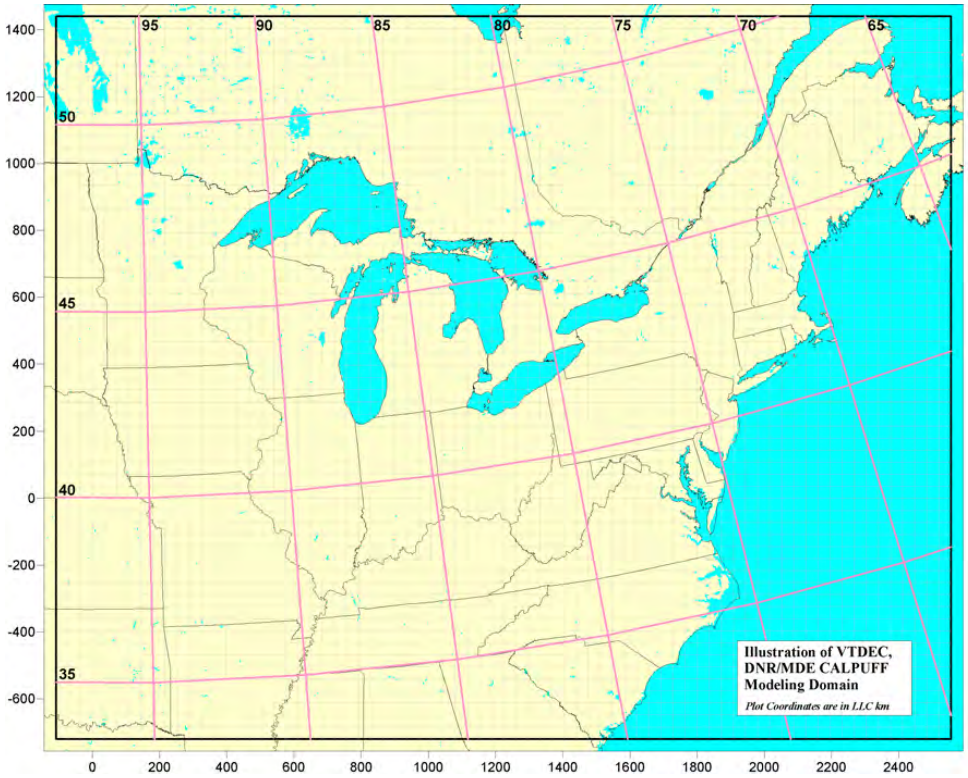

the overall modeling system; preliminary results of modeling to determine annual average and maximum 24-hour impact by individual unit and by state; and discussion of the future application of these platforms to the BART program. This chapter provides an overview of the two modeling platforms, a summary of initial results, and a brief analysis of the differences between the two platforms.

While CALPUFF will certainly play a role in helping MANE-VU assess potential visibility impacts for BART-eligible sources, the development of twin CALPUFF platforms utilizing both MM5-based and NWS-based meteorological drivers further expands the suite of analytical tools available for assessing contributions — at both the facility and state level — to downwind visibility impairment in the MANE-VU region.

7.1. Platform Overview

The VT DEC developed meteorological inputs for CALPUFF using observation-based inputs (i.e., rawinsonde and surface measurements) from the NWS and by applying CALMET. VT DEC also developed hourly emissions and exhaust flow data from the Acid Rain Program's CEMS data files for 869 large electric generating units (EGUs). These emissions data were utilized as inputs to CALPUFF, along with emissions data for four additional source sectors: non-EGU point sources, mobile (on-road), mobile (off-road), and general area sources. The emission inputs for these source sectors were derived from the 2002 RPO inventories.

The MDNR and MDE developed meteorological inputs for CALPUFF using MM5 data developed by the University of Maryland for the MANE-VU and Ozone Transport Commission SIP modeling work. The Maryland agencies utilized the CEMS data files developed by VT DEC, and independently developed emissions and source parameters for the other four source sectors based on the same inter-RPO 2002 inventories.

Both platforms were used to model the entire calendar year 2002. These simulations have been configured to provide estimates for both individual source impacts and cumulative state impacts and to allow for inter-platform comparisons. The modeling domain has been designed to be consistent with the other modeling systems described in this report (e.g., REMSAD, CMAQ), so that conclusions regarding the most significant sources of sulfate-related visibility impacts in MANE-VU can be compared. Consistency across a broad range of approaches will add credibility to the conclusions reached in the overall contribution assessment.

7.2. CALPUFF Modeling Results for Individual Sources

To explore differences between the two CALPUFF modeling platforms, each was used to create a ranked list of the 100 emissions sources that contribute most to ambient sulfate levels at each of several eastern Class I sites. Of the 100 top sources identified for the Brigantine Wilderness Area, 70 sources appeared on the lists generated by both platforms. At Acadia, Lye Brook, and Shenandoah, there was even more agreement between the model results, with both platforms identifying 78, 76, and 85 out of 100 of the same top sources for each of these sites, respectively. Figure 7-2 shows the correlation between estimated annual average impacts for the sources that were identified by both platforms as among the top 100 sulfate contributors. While the

NWS/rawindsonde-based meteorology consistently produced slightly lower estimates of impact than the MM5-based platform, the correlations are relatively robust, ranging from 0.89 at Brigantine to 0.93 at Lye Brook.

Overall, the CALPUFF modeling results to date demonstrate reasonably good comparability between the two platforms (as illustrated by Figure 7-2 and Table 7-1), but they also suggest a consistent pattern of under prediction for one platform relative to the other.

7.3. CALPUFF Modeling Results Overview

Table 7-1 provides further comparisons of the results of CALPUFF modeling utilizing the two different platforms described earlier in this chapter: VT DEC (NWS/rawinsonde-based meteorology) and Maryland (MM5-based meteorology).[35] The table summarizes annual average sulfate concentrations by source category for each of the two platforms relative to observed concentrations.

Table 7-1. CALPUFF Overall Modeling Summary

	Annual Average SO_4 Ion Concentration ($\mu g/m^3$)								
	NWS/Rawinsonde-based Meteorology				**MM5-based Meteorology**				**Observed**
	CEMS EGU	**Non-CEMS Point**	**Area/Mobile**	**Total**	**CEMS EGU**	**Non-CEMS Point**	**Area/Mobile**	**Total**	
Shenandoah	2.271	0.412	0.106	2.789	2.98	0.46	0.22	3.66	4.61
Brigantine	1.847	0.421	0.257	2.526	2.6	0.51	0.38	3.48	4.06
Acadia	0.965	0.385	0.218	1.569	1.42	0.42	0.28	2.13	1.86
Lye Brook	1.178	0.342	0.178	1.698	1.65	0.36	0.25	2.26	2.17

Generally, the NWS/rawinsonde platform predicts lower sulfate ion concentrations than the MM5 platform. On an annual average basis, the concentrations predicted using the MM5 platform are much closer to observed values than the concentrations predicted using the NWS/rawindsonde platform.

7.4. CALPUFF Results for Ranked State Sulfate Contributions

This section focuses on the ranked contribution of emissions from individual states to overall sulfate levels at specific receptor sites (additional results are summarized in a number of different ways in Appendix D). The rankings were calculated by summing impacts from EGUs included in the 2002 data base for each state. State contributions are then sorted by total annual impact. Predicted annual average sulfate ion concentrations from other source sectors were added to these data in Table 7-2(a-d) for both platforms. As in previous chapters, estimated contributions to receptor impact by state (using the results presented in Table 7-2) are depicted graphically in Figure 7-3 and Figure 7-4 for the observation-based and MM5-based platforms, respectively. States are ranked along the horizontal axis by averaging the individual results calculated for each state using the two CALPUFF platforms.

[35] The Maryland Department of the Environment is contributing toward this work through the Maryland Department of Natural Resources and their contractor ERM, Inc. who have developed the MM5-based meteorology and CALPUFF platform.

Figure 7-2. Correlation between MM5-based source contributions (Maryland/ERM) and NWS/rawindsonde-based source contributions (VT DEC) for common EGUs modeled at four receptor sites in or near MANE-VU

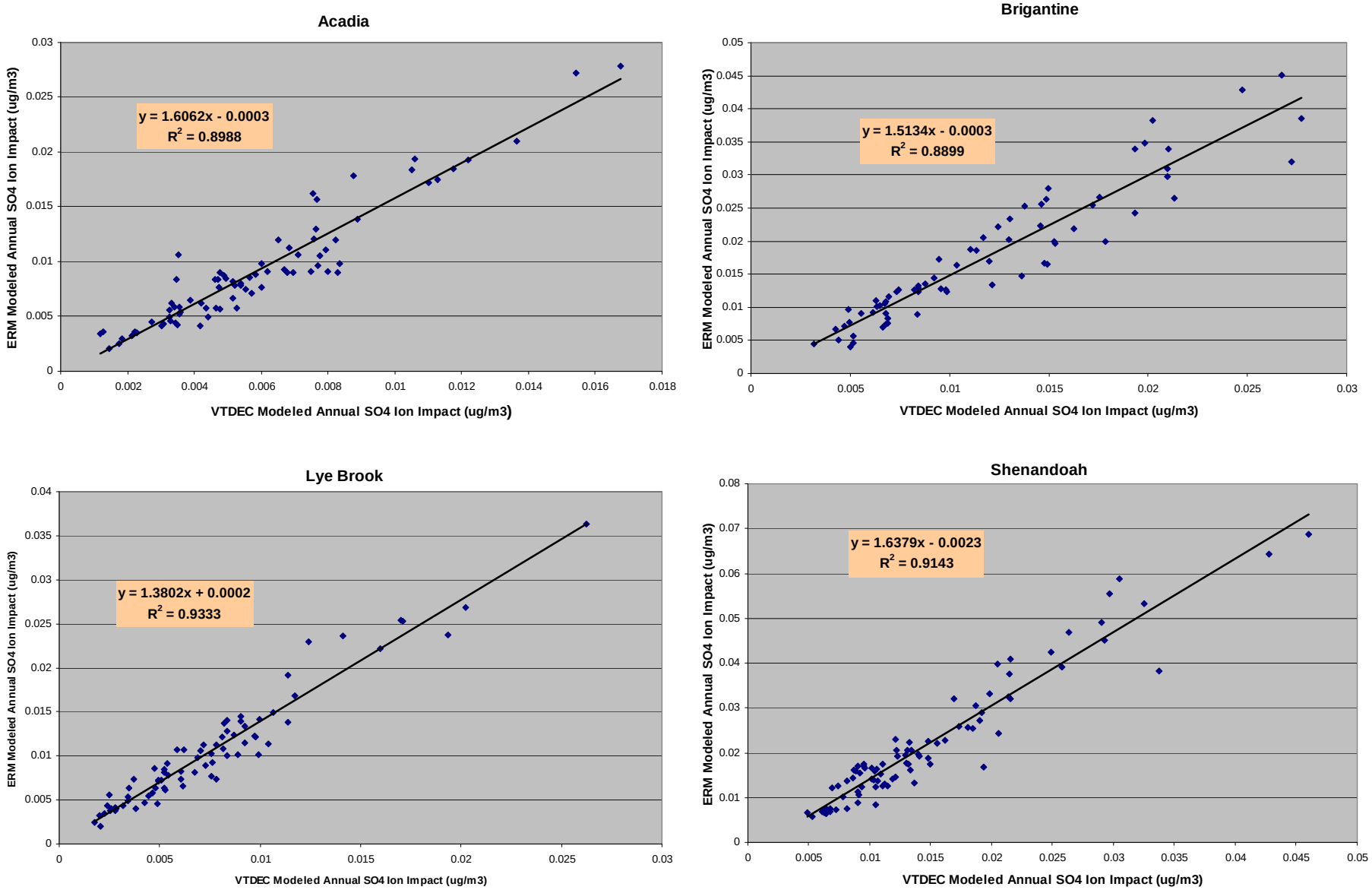

Table 7-2a. Sulfate Ion Impacts by State (Annual Average)
Acadia National Park

	NWS-based Meteorology (VT DEC) µg/m^3				MM5-based Meteorology (MDE/MDNR) µg/m^3			
STATE	**CEM PT**	**Non-CEM PT**	**Area/ Mobile**	**TOTAL PT**	**CEM PT**	**Non-CEM PT**	**Area/ Mobile**	**TOTAL**
AL(a)	0.0086	0.0013	0.0003	0.0102	0.0139	0.0009	0.0011	0.0159
AR(a)	0.0039	0	0	0.0039	0.0054	0.0020	0.0010	0.0083
CT	0.0041	0.0012	0.0085	0.0138	0.0074	0.0011	0.0072	0.0156
DC	0.0001	0.0001	0.0002	0.0004	6.9E-05	0.0001	0.0003	0.0005
DE	0.0087	0.002	0.0008	0.0115	0.0093	0.0109	0.0018	0.0219
GA(a)	0.0142	0.0008	0.0005	0.0155	0.0259	0.0009	0.0019	0.0287
IA	0.0097	0.0122	0.0001	0.0219	0.0149	0.0120	0.0030	0.0299
IL	0.0342	0.0157	0.0004	0.0504	0.0486	0.0172	0.0034	0.0693
IN	0.0758	0.0103	0.001	0.087	0.1089	0.0119	0.0099	0.1307
KS(a)	0.0081	0	0	0.0081	0.0137	0.0012	0.0010	0.0159
KY	0.0411	0.0054	0.0023	0.0487	0.0632	0.0038	0.0069	0.0740
MA	0.0653	0.0127	0.0579	0.136	0.0860	0.1544	0.0773	0.3176
MD	0.0398	0.0019	0.0034	0.0451	0.0780	0.0062	0.0040	0.0882
ME	0.0032	0.0243	0.0294	0.057	0.0030	0.0356	0.0236	0.0622
MI	0.0611	0.0083	0.0031	0.0726	0.0656	0.0095	0.0093	0.0844
MN	0.0089	0.0043	0.0005	0.0137	0.0107	0.0022	0.0023	0.0151
MO	0.014	0	0	0.014	0.0215	0.0115	0.0041	0.0371
MS(a)	0	0.0002	0.0002	0.0003	0	0.0002	0.0002	0.0004
NC	0.0342	0.0081	0.0014	0.0437	0.0554	0.0057	0.0019	0.0630
ND(a)					0	0.0009	0.0012	0.0021
NE(a)	0.0017	0	0	0.0017	0.0028	0	0.0009	0.0037
NH	0.0386	0.0022	0.0071	0.0479	0.0666	0.0020	0.0065	0.0750
NJ	0.013	0.0025	0.0076	0.0232	0.0187	0.0033	0.0133	0.0354
NY	0.0577	0.0118	0.0505	0.12	0.0736	0.0363	0.0578	0.1677
OH	0.1402	0.0081	0.0013	0.1496	0.2248	0.0457	0.0055	0.2759
OK(a)	0.0059	0	0	0.0059	0.0071	0.0015	0.0006	0.0092
PA	0.1383	0.0196	0.0126	0.1706	0.2354	0.0214	0.0156	0.2725
RI	0	0	0.0074	0.0074	5.9E-06	0.0007	0.0043	0.0050
SC	0.0092	0.003	0.001	0.0132	0.0134	0.0036	0.0012	0.0182
SD(a)	0.0009	0	0	0.0009	0.0012	2.8E-05	0.0009	0.0022
TN	0.0192	0.0045	0.0024	0.0261	0.0286	0.0076	0.0031	0.0393
TX(a)	0	0	0	0	1.1E-05	0	2.3E-05	3.5E-05
VA	0.0319	0.0082	0.0007	0.0407	0.0389	0.0081	0.0029	0.0499
VT	0	0.0004	0.0169	0.0173	4.0E-06	0.0004	0.0026	0.0030
WI	0.0152	0.0196	0.0005	0.0353	0.0254	0.0085	0.0019	0.0358
WV	0.0583	0.0053	0.0006	0.0642	0.0865	0.0086	0.0016	0.0966
Canada(b)	0	0.1914	0	0.1914				
Totals	**0.96511**	**0.3854**	**0.21832**	**1.5688**	**1.45**	**0.44**	**0.28**	**2.17**

Notes:

(a) Only sources in that portion of the state within the RPO modeling domain were modeled.

(b) 52 Canadian point sources > 250 tons/yr SO_2 emissions during 2002 (from Canadian NPRI).

Table 7-2b. Sulfate Ion Impacts by State (Annual Average)
Brigantine Wilderness Area

	NWS-based Meteorology (VT DEC) µg/m^3				MM5-based Meteorology (MDE/MDNR) µg/m^3			
STATE	**CEM PT**	**Non-CEM PT**	**Area/ Mobile**	**TOTAL PT**	**CEM PT**	**Non-CEM PT**	**Area/ Mobile**	**TOTAL**
AL(a)	0.0317	0.0055	0.0011	0.0383	0.0304	0.0017	0.0020	0.0341
AR(a)	0.0047	0	0	0.0047	0.0088	0.0032	0.0017	0.0137
CT	0.0041	0.0013	0.0099	0.0153	0.0044	0.0009	0.0063	0.0116
DC	0.0009	0.0004	0.0008	0.0021	0.0012	0.0005	0.0013	0.0030
DE	0.0395	0.0111	0.0073	0.0579	0.0524	0.0549	0.0138	0.1211
GA(a)	0.0576	0.0044	0.0030	0.0649	0.0672	0.0024	0.0057	0.0753
IA	0.0156	0.0176	0.0001	0.0333	0.0152	0.0137	0.0032	0.0321
IL	0.0521	0.0192	0.0005	0.0719	0.0535	0.0190	0.0043	0.0768
IN	0.1165	0.0125	0.0011	0.1302	0.1632	0.0162	0.0128	0.1921
KS(a)	0.0113	0	0	0.0113	0.0107	0.0009	0.0008	0.0124
KY	0.0846	0.0098	0.0039	0.0982	0.1285	0.0076	0.0135	0.1496
MA	0.0240	0.0049	0.0191	0.0480	0.0234	0.0406	0.0168	0.0808
MD	0.1351	0.0073	0.0165	0.1589	0.2191	0.0228	0.0210	0.2630
ME	0.0004	0.0017	0.0016	0.0037	0.0002	0.0017	0.0011	0.0030
MI	0.0579	0.0077	0.0028	0.0685	0.0810	0.0110	0.0120	0.1040
MN	0.0120	0.0056	0.0007	0.0183	0.0114	0.0025	0.0027	0.0166
MO	0.0179	0	0	0.0179	0.0202	0.0108	0.0036	0.0346
MS(a)	0	0.0006	0.0003	0.0009	0	0.0006	0.0005	0.0012
NC	0.1414	0.0360	0.0060	0.1835	0.1609	0.0160	0.0054	0.1823
ND(a)					0	0.0011	0.0015	0.0026
NE(a)	0.0031	0	0	0.0031	0.0025	0	0.0009	0.0035
NH	0.0064	0.0004	0.0012	0.0080	0.0100	0.0003	0.0010	0.0113
NJ	0.0426	0.0081	0.0518	0.1024	0.0625	0.0124	0.0805	0.1553
NY	0.0658	0.0120	0.0719	0.1497	0.0810	0.0307	0.0779	0.1896
OH	0.2611	0.0130	0.0017	0.2757	0.4297	0.0836	0.0088	0.5221
OK(a)	0.0068	0	0	0.0068	0.0077	0.0014	0.0007	0.0098
PA	0.2538	0.0460	0.0339	0.3336	0.4407	0.0553	0.0461	0.5421
RI	0	0	0.0042	0.0042	2.1E-06	0.0003	0.0016	0.0019
SC	0.0362	0.0139	0.0042	0.0542	0.0341	0.0101	0.0032	0.0475
SD(a)	0.0011	0	0	0.0011	0.0012	3.4E-05	0.0012	0.0024
TN	0.0477	0.0138	0.0049	0.0664	0.0630	0.0188	0.0061	0.0879
TX(a)	0	0	0	0	2.5E-07	0	2.9E-05	3.0E-05
VA	0.1442	0.0447	0.0035	0.1924	0.1577	0.0331	0.0119	0.2027
VT	0	0.0002	0.0033	0.0035	1.5E-06	0.0001	0.0006	0.0008
WI	0.0216	0.0312	0.0007	0.0535	0.0315	0.0106	0.0026	0.0447
WV	0.1499	0.0118	0.0016	0.1633	0.2340	0.0202	0.0046	0.2588
Canada(b)	0	0.0807	0	0.0807				
Totals	**1.84732**	**0.42121**	**0.25746**	**2.526**	**2.61**	**0.51**	**0.38**	**3.49**

Notes:

(a) Only sources in that portion of the state within the RPO modeling domain were modeled.

(b) 52 Canadian point sources > 250 tons/yr SO_2 emissions during 2002 (from Canadian NPRI).

Table 7-2c. Sulfate Ion Impacts by State (Annual Average)
Lye Brook Wilderness Area

	NWS-based Meteorology (VT DEC) µg/m^3				MM5-based Meteorology (MDE/MDNR) µg/m^3			
STATE	**CEM PT**	**Non-CEM PT**	**Area/ Mobile**	**TOTAL PT**	**CEM PT**	**Non-CEM PT**	**Area/ Mobile**	**TOTAL**
AL(a)	0.0151	0.0023	0.0005	0.0179	0.0209	0.0013	0.0015	0.0238
AR(a)	0.0053	0	0	0.0053	0.0072	0.0029	0.0015	0.0116
CT	0.0015	0.0004	0.0038	0.0057	0.0024	0.0006	0.0045	0.0075
DC	0.0001	0.0002	0.0003	0.0005	7.9E-05	0.0002	0.0004	0.0006
DE	0.0045	0.0017	0.0007	0.0068	0.0076	0.0123	0.0020	0.0219
GA(a)	0.0270	0.0016	0.0011	0.0296	0.0351	0.0012	0.0029	0.0392
IA	0.0151	0.0175	0.0001	0.0326	0.0184	0.0158	0.0041	0.0383
IL	0.0473	0.0173	0.0005	0.0651	0.0550	0.0208	0.0047	0.0805
IN	0.1039	0.0120	0.0011	0.1170	0.1369	0.0148	0.0128	0.1645
KS(a)	0.0115	0	0	0.0115	0.0167	0.0016	0.0013	0.0195
KY	0.0647	0.0075	0.0031	0.0753	0.0820	0.0047	0.0099	0.0967
MA	0.0106	0.0040	0.0125	0.0270	0.0161	0.0291	0.0203	0.0655
MD	0.0452	0.0025	0.0040	0.0518	0.0686	0.0088	0.0052	0.0826
ME	0.0001	0.0020	0.0017	0.0038	0.0003	0.0024	0.0018	0.0044
MI	0.0841	0.0113	0.0041	0.0995	0.0798	0.0121	0.0120	0.1039
MN	0.0130	0.0062	0.0007	0.0200	0.0147	0.0031	0.0035	0.0213
MO	0.0191	0	0	0.0191	0.0253	0.0140	0.0052	0.0445
MS(a)	0	0.0004	0.0002	0.0006	0	0.0006	0.0004	0.0011
NC	0.0424	0.0088	0.0016	0.0528	0.0680	0.0058	0.0022	0.0760
ND(a)					0	0.0014	0.0020	0.0035
NE(a)	0.0027	0	0	0.0027	0.0032	0	0.0012	0.0044
NH	0.0072	0.0007	0.0020	0.0098	0.0137	0.0008	0.0023	0.0167
NJ	0.0071	0.0017	0.0051	0.0139	0.0128	0.0029	0.0115	0.0272
NY	0.0637	0.0289	0.0586	0.1511	0.0985	0.0613	0.0842	0.2440
OH	0.2108	0.0112	0.0016	0.2237	0.2963	0.0649	0.0078	0.3690
OK(a)	0.0086	0	0	0.0086	0.0097	0.0020	0.0009	0.0127
PA	0.1918	0.0255	0.0169	0.2342	0.3050	0.0288	0.0219	0.3558
RI	0	0	0.0013	0.0013	1.4E-06	0.0002	0.0010	0.0012
SC	0.0088	0.0037	0.0013	0.0138	0.0133	0.0040	0.0014	0.0187
SD(a)	0.0014	0	0	0.0014	0.0017	4.3E-05	0.0014	0.0031
TN	0.0281	0.0065	0.0032	0.0378	0.0407	0.0098	0.0042	0.0546
TX(a)	0	0	0	0	8.4E-06	0	3.2E-05	4.0E-05
VA	0.0295	0.0088	0.0008	0.0391	0.0454	0.0104	0.0037	0.0596
VT	0	0.0006	0.0499	0.0505	4.0E-06	0.0017	0.0083	0.0100
WI	0.0229	0.0293	0.0007	0.0529	0.0351	0.0116	0.0028	0.0495
WV	0.0852	0.0079	0.0009	0.0939	0.1232	0.0121	0.0023	0.1375
Canada(b)	0	0.1211	0	0.1211				
Totals	**1.1780**	**0.3416**	**0.1781**	**1.6977**	**1.65**	**0.36**	**0.25**	**2.27**

Notes:

(a) Only sources in that portion of the state within the RPO modeling domain were modeled.

(b) 52 Canadian point sources > 250 tons/yr SO_2 emissions during 2002 (from Canadian NPRI).

Table 7-2d. Sulfate Ion Impacts by State (Annual Average)
Shenandoah National Park

	NWS-based Meteorology (VT DEC) µg/m^3				MM5-based Meteorology (MDE/MDNR) µg/m^3			
STATE	**CEM PT**	**Non-CEM PT**	**Area/ Mobile**	**TOTAL PT**	**CEM PT**	**Non-CEM PT**	**Area/ Mobile**	**TOTAL**
AL(a)	0.0521	0.0084	0.0018	0.0623	0.0504	0.0029	0.0034	0.0567
AR(a)	0.0074	0	0	0.0074	0.0087	0.0035	0.0019	0.0141
CT	0.0005	0.0002	0.0011	0.0018	0.0007	0.0001	0.0009	0.0017
DC	0.0004	0.0004	0.0008	0.0016	8.1E-05	0.0003	0.0009	0.0013
DE	0.0101	0.0029	0.0011	0.0141	0.0086	0.0136	0.0021	0.0243
GA(a)	0.0879	0.0056	0.0040	0.0975	0.0963	0.0032	0.0079	0.1073
IA	0.0192	0.0181	0.0001	0.0374	0.0152	0.0130	0.0036	0.0318
IL	0.0646	0.0222	0.0006	0.0874	0.0561	0.0189	0.0045	0.0794
IN	0.1782	0.0156	0.0015	0.1952	0.1907	0.0181	0.0155	0.2243
KS(a)	0.0137	0	0	0.0137	0.0091	0.0007	0.0006	0.0104
KY	0.1273	0.0135	0.0057	0.1465	0.1741	0.0106	0.0184	0.2031
MA	0.0036	0.0005	0.0020	0.0060	0.0029	0.0047	0.0023	0.0098
MD	0.1045	0.0116	0.0118	0.1280	0.1365	0.0373	0.0109	0.1847
ME	0	0.0004	0.0003	0.0007	2.8E-05	0.0003	0.0002	0.0006
MI	0.0830	0.0082	0.0036	0.0948	0.0860	0.0100	0.0125	0.1085
MN	0.0148	0.0055	0.0007	0.0210	0.0109	0.0023	0.0028	0.0160
MO	0.0255	0	0	0.0255	0.0180	0.0104	0.0034	0.0318
MS(a)	0	0.0009	0.0004	0.0013	0	0.0010	0.0007	0.0017
NC	0.1669	0.0251	0.0050	0.1970	0.2257	0.0148	0.0062	0.2467
ND(a)					0	0.0011	0.0016	0.0027
NE(a)	0.0038	0	0	0.0038	0.0023	0	0.0009	0.0032
NH	0.0010	0.0001	0.0002	0.0012	0.0013	5.3E-05	0.0002	0.0016
NJ	0.0102	0.0018	0.0046	0.0166	0.0119	0.0022	0.0071	0.0212
NY	0.0350	0.0027	0.0141	0.0519	0.0468	0.0141	0.0167	0.0776
OH	0.4678	0.0256	0.0027	0.4960	0.6483	0.1088	0.0114	0.7685
OK(a)	0.0080	0	0	0.0080	0.0081	0.0016	0.0009	0.0105
PA	0.2774	0.0354	0.0214	0.3342	0.4517	0.0318	0.0247	0.5082
RI	0	0	0.0004	0.0004	3.1E-07	2.9E-05	0.0002	0.0002
SC	0.0242	0.0117	0.0041	0.0401	0.0232	0.0093	0.0035	0.0359
SD(a)	0.0011	0	0	0.0011	0.0011	4.0E-05	0.0014	0.0025
TN	0.0781	0.0207	0.0073	0.1061	0.0929	0.0304	0.0086	0.1319
TX(a)	0	0	0	0	1.7E-07	0	3.2E-05	3.2E-05
VA	0.1102	0.0398	0.0047	0.1547	0.1124	0.0469	0.0263	0.1856
VT	0	0	0.0006	0.0007	3.6E-07	2.6E-05	0.0001	0.0002
WI	0.0259	0.0311	0.0007	0.0577	0.0289	0.0096	0.0026	0.0410
WV	0.2691	0.0259	0.0045	0.2995	0.4657	0.0402	0.0111	0.5170
Canada(b)	0	0.0781	0	0.0781				
Totals	**2.271**	**0.412**	**0.106**	**2.789**	**2.98**	**0.46**	**0.22**	**3.66**

Notes:

(a) Only sources in that portion of the state within the RPO modeling domain were modeled.

(b) 52 Canadian point sources > 250 tons/yr SO_2 emissions during 2002 (from Canadian NPRI).

Figure 7-3a. Ranked state percent sulfate contributions to Northeast Class I receptors based on observation-based (VT) CALPUFF results

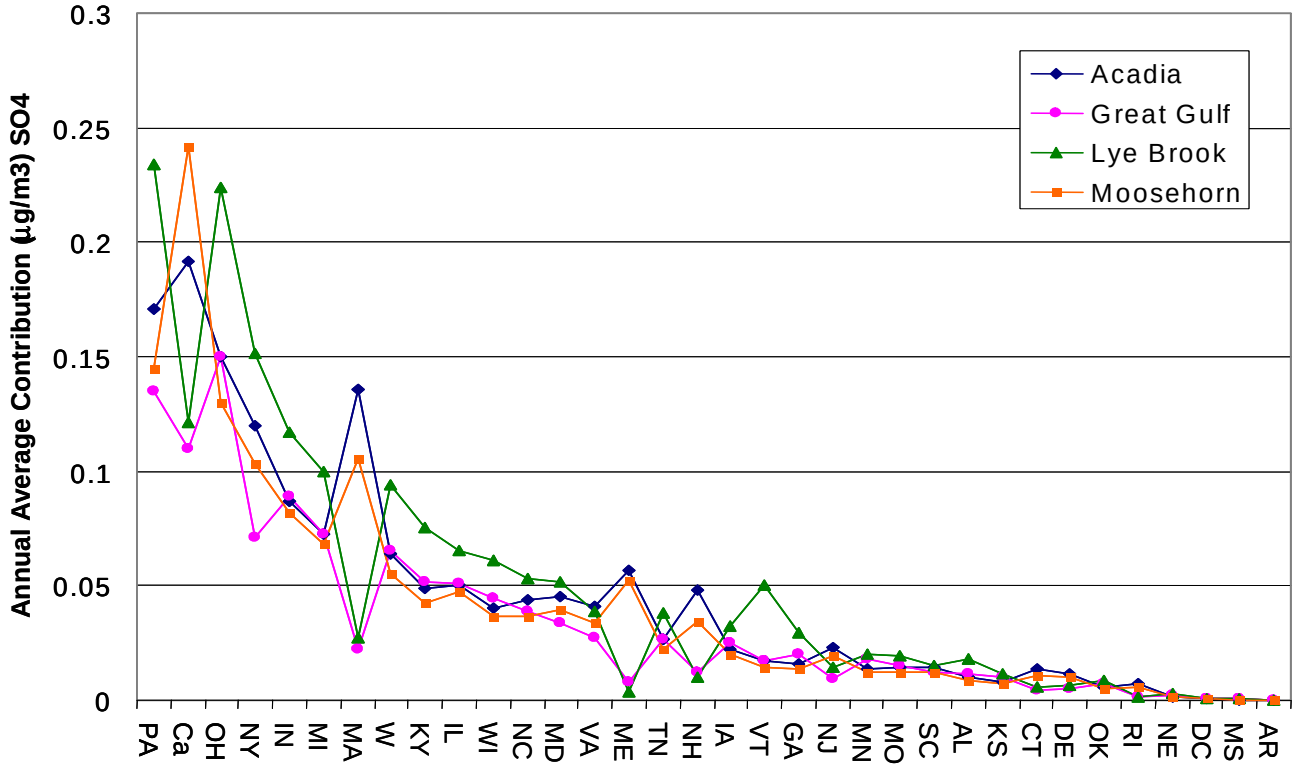

Figure 7-3b. Ranked state percent sulfate contributions to Mid-Atlantic Class I receptors based on observation-based (VT) CALPUFF results

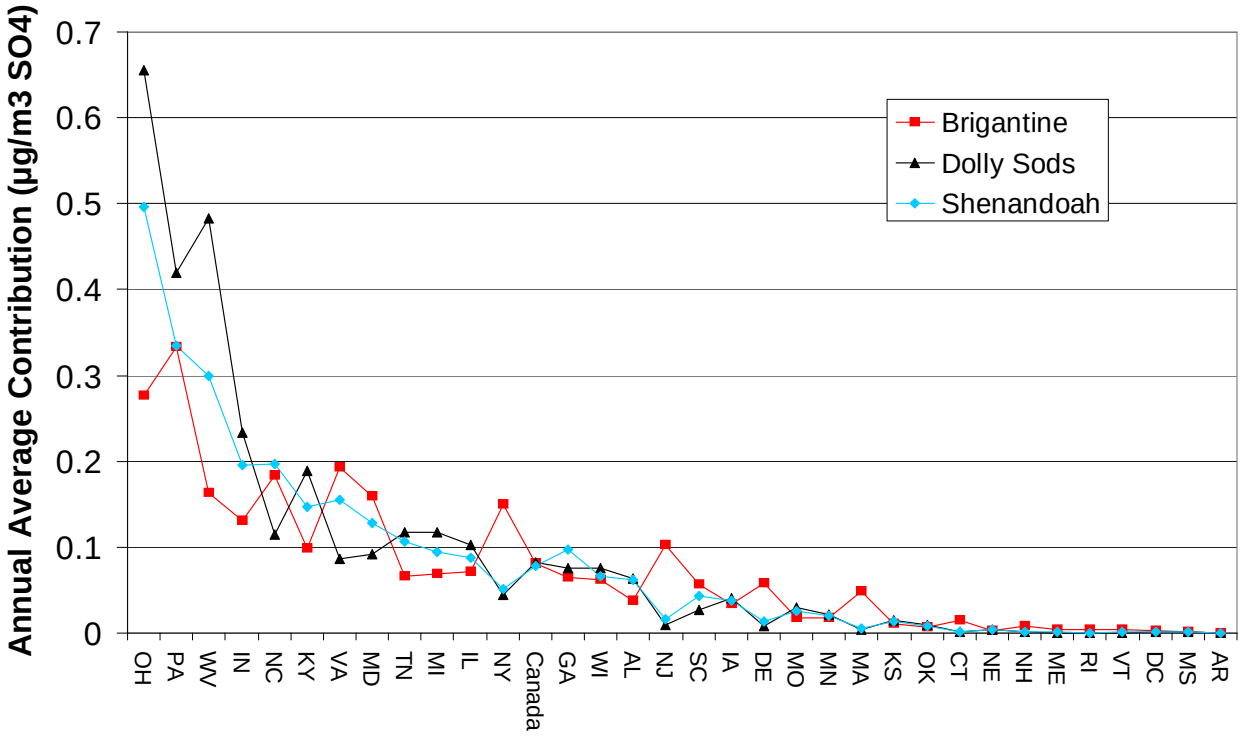

Figure 7-4a. Ranked state percent sulfate contributions to Northeast Class I receptors based on MM5-based (MD) CALPUFF results

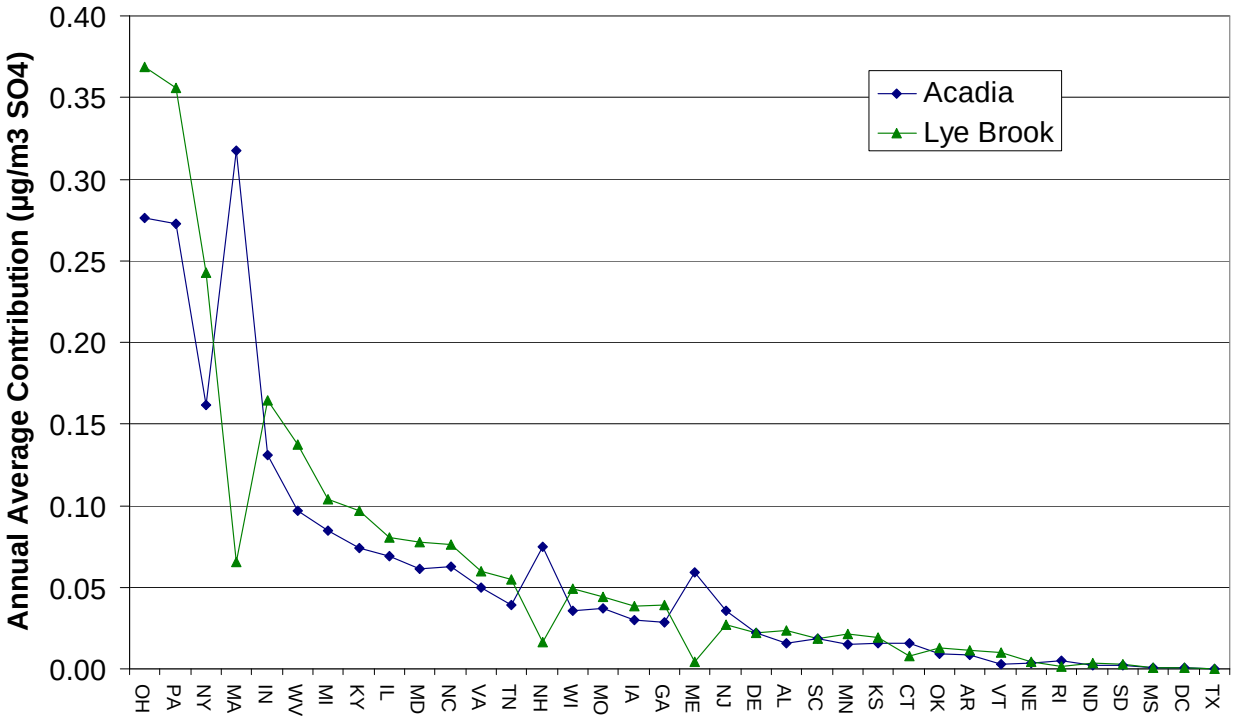

Figure 7-4b. Ranked state percent sulfate contributions to Mid-Atlantic Class I receptors based on MM5-based (MD) CALPUFF results

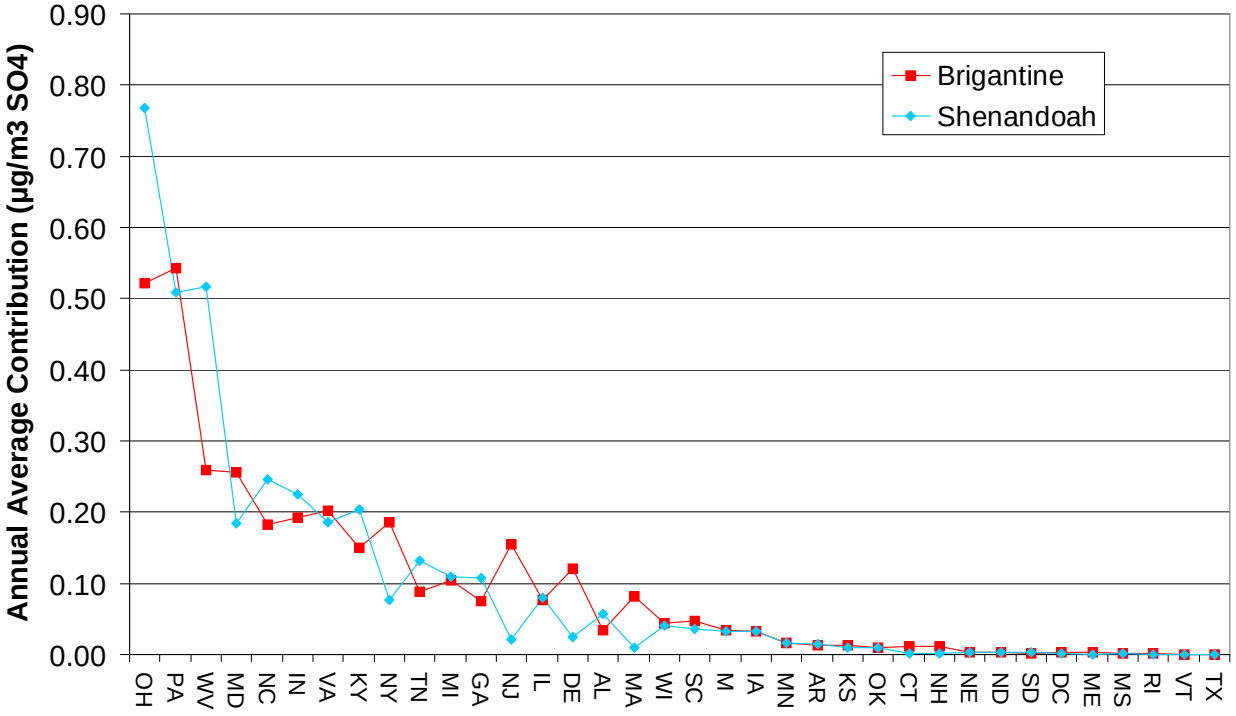

7.5. Future work and potential uses of CALPUFF results for BART determinations

Modeling efforts to date have provided a solid basis for contributing to a weight-of-evidence assessment of state contributions. In addition, the two CALPUFF platforms can be used to evaluate the relative contributions to fine PM and visibility impacts of individual sources in the MANE-VU region. It is anticipated that MANE-VU will provide all states with a consistent set of modeling results from each of these platforms to serve as a preliminary basis for BART visibility determinations and states will have several options with regard to how these results are used:

- States may accept the MANE-VU modeling as an adequate basis for determining whether BART controls at a facility are justified by its contribution to visibility degradation.

- States may conduct additional modeling on their own to determine whether BART controls at a facility are justified by its contribution to visibility degradation.

- States may require a source to conduct additional modeling to determine whether BART controls at a facility are justified by its contribution to visibility degradation.

These options and the use of modeling results for BART determinations are discussed in more detail in the *MANE-VU BART Resource Book* (NESCAUM, 2006), and the reader is referred to that resource for additional information.

References

NESCAUM, *BART Resource Guide*, Northeast States for Coordinated Air Use Management, 2006.

USEPA, CALPUFF Modeling System, Available at: http://www.epa.gov/ttn/scram, 2006.

8. SYNTHESIS OF RESULTS USING DIFFERENT SOURCE ASSESSMENT TECHNIQUES

By synthesizing results from a variety of data sources and analysis techniques MANE-VU has taken a first step toward identifying sources of visibility impairment in the Northeast generally, and toward understanding the role of transported sulfate in particular. The variety of approach and complexity of analytical tools utilized for this purpose provides numerous metrics and means of comparison into how SO_2 emissions are chemically transformed, transported and combined with various local constituents of fine particle pollution in the MANE-VU region. Beyond reviewing these results, additional sections of this chapter describe opportunities for further synthesizing the available data to solidify a weight-of-evidence approach to implementing the contribution assessment and pollution apportionment requirements of the Haze Rule

8.1. Ranked Contribution

Chapter 4 of this report describes two crude methods of ranking state contributions based on the ratio of source emissions to source-receptor distance as well as the gridded product of emissions and upwind residence time probability. Chapter 5 describes the qualitative evidence available from several different trajectory-based techniques and source apportionment studies. These include source region comparisons, source profile examinations, and the development of other techniques and metrics to support the more quantitative ranking techniques. Chapter 6 describes results obtained using Eulerian grid models such as the Regulatory Modeling System for Aerosols and Deposition (REMSAD) and the Community Multi-scale Air Quality (CMAQ) model. Ultimately these types of models are likely to yield the most definitive assessments of contribution from different sources. Chapter 7 explores the use of lagrangian puff dispersion models such as CALPUFF for estimating source contributions and compares two related but distinct versions of the CALPUFF modeling system that demonstrate the sensitivity of this tool to emissions and meteorology inputs.

In Table 8-1 through Table 8-5 (and graphically in Figure 8-1), we have normalized the results obtained using five techniques for assessing state contribution by calculating the percentage contribution and plotted them on a common graph. The figure shows substantial consistency across a variety of independent analyses using techniques that are themselves based on the application of disparate chemical, meteorological and physical principles. Together, these findings create a strong weight-of-evidence case for identifying the most significant contributors to visibility impairment in MANE-VU Class I areas.

In Figure 8-1, several features of the normalized results bear notice. First, we note that the apparent perfect agreement among the techniques for the “other” contribution that represents all emissions from outside the domain of study is a result of having substituted the REMSAD calculated “other” contribution for all of the other methods. REMSAD is the only method that has a means of developing a comprehensive estimate of the total out-of-domain contribution because the boundary condition used was derived from a global model run using global SO_2 emissions estimates. It is also worth noting how high the “other,” or out-of-domain, contribution is to observed sulfate at

Acadia National Park. This is not surprising given how close Acadia is to the domain boundaries on both the northern and eastern edge. There may be some recirculation of in-domain SO_2 emissions that leave the modeling domain and re-enter through the dynamic boundary condition, but lose their tag in the process.

It is also worth noting the differences between the methods for certain states and Canada, such as Massachusetts and Maine in the case of Acadia, Maryland and Canada for Brigantine, Canada for Lye Brook, and Ohio and West Virginia for Shenandoah. Those states and Canada that are directly upwind a large fraction of the time, either because they are very large geographically or because they are very nearby, are likely to be treated differently by the percent-time-upwind method relative to the other methods. In addition, the CALPUFF models appear to underestimate the contribution from Canada relative to other methods. This is likely to result from an incomplete characterization of the total SO_2 inventory for Canada relative to other methods that are based on the entire MANE-VU Canadian inventory.

Table 8-1. Annual Average Sulfate Impact from REMSAD (%)

RPO	STATE	ACADIA	BRIGANTINE	DOLLY SODS	GREAT GULF	LYE BROOK	MOOSEHORN	SHENANDOAH
CANADA		**8.69**	**7.11**	**3.90**	**14.84**	**12.43**	**7.85**	**4.75**
CENRAP		**0.88**	**1.12**	**1.58**	**1.65**	**1.67**	**0.82**	**1.48**
MANE-VU		**36.17**	**34.83**	**14.81**	**27.83**	**31.78**	**30.08**	**20.59**
MANE-VU	Connecticut	0.76	0.53	0.04	0.48	0.55	0.56	0.08
	Delaware	0.96	3.20	0.30	0.63	0.93	0.71	0.61
	District of Columbia	0.01	0.04	0.01	0.01	0.02	0.01	0.04
	Maine	6.54	0.16	0.01	2.33	0.31	8.01	0.02
	Maryland	2.20	4.98	2.39	1.92	2.66	1.60	4.84
	Massachusetts	10.11	2.73	0.18	3.11	2.45	6.78	0.35
	New Hampshire	2.25	0.60	0.04	3.95	1.68	1.74	0.08
	New Jersey	1.40	4.04	0.27	0.89	1.44	1.03	0.48
	New York	4.74	5.57	1.32	5.68	9.00	3.83	2.03
	Pennsylvania	6.81	12.84	10.23	8.30	11.72	5.53	12.05
	Rhode Island	0.28	0.10	0.01	0.11	0.06	0.19	0.01
	Vermont	0.13	0.06	0.00	0.41	0.95	0.09	0.01
MIDWEST		**11.98**	**18.16**	**30.26**	**20.10**	**21.48**	**10.40**	**26.84**
MIDWEST	Illinois	1.37	1.82	2.56	2.52	2.42	1.30	2.47
	Indiana	2.13	3.29	5.40	3.94	3.93	2.02	5.23
	Michigan	2.02	2.77	3.24	3.88	3.67	1.74	3.20
	Ohio	5.62	9.11	17.98	8.33	9.96	4.62	14.87
	Wisconsin	0.85	1.16	1.08	1.42	1.49	0.72	1.07
VISTAS		**8.49**	**21.99**	**36.75**	**12.04**	**13.65**	**6.69**	**33.86**
VISTAS	Alabama	0.32	1.07	2.13	0.65	0.81	0.25	1.77
	Georgia	0.67	2.32	3.71	1.27	1.31	0.56	3.47
	Kentucky	1.17	2.22	4.89	1.99	2.22	0.98	4.34
	Mississippi	0.01	0.04	0.08	0.03	0.04	0.01	0.07
	North Carolina	1.45	4.19	4.29	1.88	1.89	1.14	4.78
	South Carolina	0.43	1.69	1.04	0.64	0.56	0.36	1.30
	Tennessee	0.61	1.56	3.41	1.11	1.23	0.50	2.73
	Virginia	1.48	4.30	2.82	1.52	1.95	1.13	6.20
	West Virginia	2.35	4.59	14.38	2.96	3.64	1.75	9.19
OTHER		**33.79**	**16.78**	**12.70**	**23.54**	**18.99**	**44.17**	**12.48**
TOTAL ($\mu g/m^3$)		**2.026**	**3.444**	**3.867**	**1.780**	**2.137**	**1.767**	**3.919**

Table 8-2. Annual Average Sulfate Impact from Q/D (%)

RPO	STATE	ACADIA	BRIGANTINE	DOLLY SODS	GREAT GULF	LYE BROOK	MOOSEHORN	SHENANDOAH
CANADA		**11.91**	**6.01**	**0.00**	**8.97**	**12.00**	**18.77**	**6.76**
CENRAP		**1.74**	**1.64**	**1.59**	**2.33**	**1.99**	**1.35**	**1.72**
CENRAP	Arkansas	0.13	0.15	0.13	0.08	0.17	0.09	0.26
	Iowa	0.29	0.19	0.24	0.40	0.32	0.24	0.24
	Louisiana	0.02	0.03	0.02	0.02	0.03	0.02	0.04
	Minnesota	0.22	0.13	0.16	0.30	0.24	0.13	0.19
	Missouri	1.08	1.15	1.03	1.53	1.23	0.87	1.00
MANE-VU		**20.13**	**32.53**	**20.10**	**21.48**	**25.69**	**12.84**	**24.50**
MANE-VU	Connecticut	0.34	0.33	0.11	0.74	0.38	0.21	0.31
	Delaware	0.59	3.01	0.46	0.51	0.67	0.36	1.07
	District of Columbia	0.01	0.05	0.02	0.01	0.02	0.01	0.09
	Maine	1.74	0.15	0.08	0.71	0.15	1.13	0.15
	Maryland	1.83	7.26	3.86	0.43	2.67	1.27	5.27
	Massachusetts	2.89	0.95	0.46	4.61	1.06	1.33	1.22
	New Hampshire	1.07	0.30	0.14	0.42	0.08	0.60	0.18
	New Jersey	0.76	4.22	0.43	3.11	0.75	0.48	1.82
	New York	4.02	4.61	1.93	3.67	6.71	2.83	3.30
	Pennsylvania	6.64	11.57	12.58	6.62	13.07	4.50	11.00
	Rhode Island	0.12	0.05	0.02	0.08	0.04	0.06	0.06
	Vermont	0.10	0.03	0.02	0.57	0.10	0.07	0.04
MIDWEST		**16.99**	**17.48**	**26.30**	**25.38**	**22.84**	**12.49**	**22.46**
MIDWEST	Illinois	2.53	2.16	2.60	3.64	2.98	2.11	2.61
	Indiana	3.94	4.24	5.17	6.01	5.01	2.91	4.50
	Michigan	2.69	1.95	2.46	4.08	3.50	2.16	2.49
	Ohio	6.63	8.34	15.06	9.94	9.98	4.51	11.85
	Wisconsin	1.19	0.79	1.00	1.71	1.38	0.80	1.01
VISTAS		**15.44**	**25.55**	**39.32**	**18.30**	**18.48**	**10.39**	**32.08**
VISTAS	Alabama	1.24	1.69	1.66	1.45	1.60	0.91	1.65
	Georgia	2.36	3.28	3.18	2.62	2.82	1.63	3.30
	Kentucky	2.07	3.36	3.99	3.18	2.79	1.50	3.54
	Mississippi	0.19	0.24	0.22	0.22	0.24	0.14	0.37
	North Carolina	2.27	4.16	9.03	2.59	2.69	1.44	6.60
	South Carolina	1.29	1.62	0.95	1.14	0.94	0.70	1.69
	Tennessee	1.45	2.14	2.49	1.74	1.92	1.06	2.40
	Virginia	1.93	4.36	2.49	1.97	1.78	1.12	4.25
	West Virginia	2.64	4.71	15.33	3.39	3.71	1.88	8.27
OTHER[36]		**33.79**	**16.78**	**12.70**	**23.54**	**18.99**	**44.17**	**12.48**
TOTAL ($\mu g/m^3$)		**1.920**	**2.740**	**3.455**	**1.305**	**1.858**	**1.977**	**3.417**

[36] OTHER is % from REMSAD result; Florida is considered within OTHER

Table 8-3. Annual Average Sulfate Impact from CALPUFF (NWS Observations) (%)

RPO	STATE	ACADIA	BRIGANTINE	DOLLY SODS	GREAT GULF	LYE BROOK	MOOSEHORN	SHENANDOAH
CANADA		**8.07**	**2.65**	**2.30**	**7.22**	**5.77**	**9.45**	**2.45**
CENRAP		**2.76**	**2.98**	**3.34**	**5.06**	**4.50**	**2.30**	**3.42**
CENRAP	Iowa	0.93	1.09	1.13	1.65	1.55	0.80	1.17
	Kansas	0.34	0.37	0.41	0.64	0.55	0.28	0.43
	Louisiana	0.00	0.00	0.00	0.00	0.00	0.00	0.00
	Minnesota	0.58	0.60	0.62	1.16	0.95	0.49	0.65
	Missouri	0.59	0.59	0.81	1.00	0.91	0.49	0.80
	Nebraska	0.07	0.10	0.11	0.14	0.13	0.06	0.12
	Oklahoma	0.25	0.22	0.26	0.47	0.41	0.20	0.25
MANE-VU		**27.41**	**29.17**	**16.21**	**20.91**	**26.52**	**21.11**	**17.47**
MANE-VU	Connecticut	0.58	0.50	0.03	0.26	0.27	0.41	0.06
	Delaware	0.48	1.90	0.21	0.31	0.32	0.38	0.44
	District of Columbia	0.02	0.07	0.02	0.03	0.02	0.02	0.05
	Maine	2.40	0.12	0.01	0.53	0.18	2.04	0.02
	Maryland	1.90	5.22	2.54	2.19	2.47	1.55	4.01
	Massachusetts	5.73	1.58	0.12	1.44	1.29	4.13	0.19
	New Hampshire	2.02	0.26	0.02	0.79	0.47	1.36	0.04
	New Jersey	0.98	3.37	0.28	0.63	0.67	0.75	0.52
	New York	5.06	4.92	1.24	4.67	7.20	4.03	1.63
	Pennsylvania	7.19	10.97	11.71	8.86	11.16	5.65	10.48
	Rhode Island	0.31	0.14	0.01	0.08	0.06	0.22	0.01
	Vermont	0.73	0.12	0.01	1.13	2.41	0.56	0.02
MIDWEST		**16.85**	**19.99**	**33.09**	**26.68**	**26.98**	**14.21**	**29.46**
MIDWEST	Illinois	2.12	2.37	2.86	3.36	3.11	1.84	2.74
	Indiana	3.67	4.28	6.52	5.83	5.57	3.19	6.11
	Michigan	3.06	2.25	3.28	4.74	4.74	2.67	2.97
	Ohio	6.31	9.07	18.33	9.82	10.66	5.07	15.55
	Wisconsin	1.69	2.03	2.10	2.93	2.90	1.44	2.09
VISTAS		**11.12**	**28.43**	**32.35**	**16.59**	**17.24**	**8.76**	**34.72**
VISTAS	Alabama	0.43	1.26	1.77	0.77	0.85	0.32	1.96
	Georgia	0.65	2.13	2.12	1.30	1.41	0.52	3.06
	Kentucky	2.05	3.23	5.29	3.39	3.59	1.64	4.59
	Mississippi	0.01	0.03	0.04	0.03	0.03	0.01	0.04
	North Carolina	1.84	6.03	3.20	2.52	2.51	1.42	6.18
	South Carolina	0.61	1.87	0.75	0.80	0.71	0.49	1.33
	Tennessee	1.10	2.19	3.27	1.72	1.80	0.86	3.33
	Virginia	1.72	6.33	2.42	1.80	1.86	1.32	4.85
	West Virginia	2.71	5.37	13.49	4.26	4.48	2.17	9.39
OTHER[36]		**33.79**	**16.78**	**12.70**	**23.54**	**18.99**	**44.17**	**12.48**
TOTAL ($\mu g/m^3$)		**1.571**	**2.533**	**3.125**	**1.167**	**1.701**	**1.429**	**2.793**

Table 8-4. Annual Average Sulfate Impact from CALPUFF (MM5) (%)

RPO	STATE	ACADIA	BRIGANTINE	DOLLY SODS	GREAT GULF	LYE BROOK	MOOSEHORN	SHENANDOAH
CANADA		**8.05**	**2.65**			**5.76**		**2.46**
CENRAP		**3.26**	**2.85**			**5.08**		**2.74**
CENRAP	Arkansas	0.23	0.32			0.39		0.33
	Iowa	0.82	0.75			1.28		0.74
	Kansas	0.43	0.29			0.65		0.24
	Louisiana							
	Minnesota	0.41	0.39			0.71		0.37
	Missouri	1.01	0.80			1.48		0.74
	Nebraska	0.10	0.08			0.15		0.07
	Oklahoma	0.25	0.23			0.42		0.24
	Texas	0.00	0.00			0.00		0.00
MANE-VU		**28.09**	**31.83**			**27.69**		**19.31**
MANE-VU	Connecticut	0.43	0.27			0.25		0.04
	Delaware	0.01	0.07			0.02		0.03
	District of Columbia	0.60	2.81			0.73		0.57
	Maine	1.62	0.06			0.14		0.01
	Maryland	1.68	5.95			2.59		4.27
	Massachusetts	8.67	1.87			2.18		0.23
	New Hampshire	2.05	0.26			0.56		0.04
	New Jersey	0.97	3.60			0.91		0.49
	New York	4.41	4.30			8.08		1.79
	Pennsylvania	7.44	12.57			11.86		11.83
	Rhode Island	0.14	0.04			0.04		0.00
	Vermont	0.08	0.02			0.33		0.00
MIDWEST		**16.28**	**21.79**			**25.58**		**28.43**
MIDWEST	Illinois	1.89	1.78			2.68		1.85
	Indiana	3.57	4.46			5.48		5.22
	Michigan	2.30	2.41			3.47		2.53
	Ohio	7.53	12.11			12.30		17.88
	Wisconsin	0.98	1.04			1.65		0.95
VISTAS		**10.53**	**24.10**			**16.90**		**34.57**
VISTAS	Alabama	0.43	0.79			0.79		1.32
	Georgia	0.78	1.74			1.30		2.50
	Kentucky	2.02	3.47			3.22		4.73
	Mississippi	0.01	0.03			0.04		0.04
	North Carolina	1.72	4.23			2.53		5.74
	South Carolina	0.50	1.10			0.62		0.84
	Tennessee	1.07	2.04			1.82		3.07
	Virginia	1.36	4.70			1.99		4.32
	West Virginia	2.64	6.00			4.58		12.03
OTHER[36]		**33.79**	**16.78**	**12.70**	**23.54**	**18.99**	**44.17**	**12.48**
TOTAL (µg/m^3)		**2.424**	**3.589**			**2.430**		**3.761**

Table 8-5. Annual Average Sulfate Impact from percent time upwind method (%)

RPO	STATE	ACADIA	BRIGANTINE	DOLLY SODS	GREAT GULF	LYE BROOK	MOOSEHORN	SHENANDOAH
CANADA		**15.24**	**6.70**		**19.29**	**15.91**	**13.45**	**4.33**
CENRAP		**1.89**	**1.77**		**1.73**	**1.66**	**1.52**	**1.72**
CENRAP	Arkansas	0.12	0.24		0.15	0.15	0.15	0.20
	Iowa	0.38	0.27		0.27	0.28	0.28	0.25
	Kansas	0.00	0.00		0.00	0.00	0.00	0.00
	Louisiana	0.04	0.08		0.06	0.04	0.04	0.09
	Minnesota	0.56	0.33		0.38	0.44	0.44	0.22
	Missouri	0.80	0.85		0.87	0.75	0.62	0.95
	Texas	0.00	0.00		0.00	0.00	0.00	0.00
MANE-VU		**18.33**	**25.83**		**20.64**	**25.38**	**15.23**	**11.38**
MANE-VU	Connecticut	0.51	0.27		0.52	0.59	0.40	0.10
	Delaware	0.30	1.36		0.34	0.42	0.28	0.24
	District of Columbia	0.12	0.29		0.11	0.14	0.12	0.24
	Maine	1.49	0.08		0.68	0.26	1.53	0.05
	Maryland	1.32	3.06		1.31	1.31	0.96	2.29
	Massachusetts	1.10	0.33		0.86	0.81	0.90	0.12
	New Hampshire	1.21	0.17		1.48	0.72	0.77	0.06
	New Jersey	1.02	6.01		0.99	1.39	0.78	0.49
	New York	4.80	3.49		6.80	9.08	4.23	1.44
	Pennsylvania	6.21	10.71		7.10	10.36	5.07	6.33
	Rhode Island	0.11	0.05		0.08	0.08	0.09	0.02
	Vermont	0.14	0.03		0.37	0.23	0.10	0.01
MIDWEST		**17.35**	**19.55**		**20.67**	**21.63**	**15.56**	**22.03**
MIDWEST	Illinois	3.79	3.47		3.31	3.74	3.22	3.76
	Indiana	3.37	4.36		4.33	4.13	3.21	5.08
	Michigan	2.73	2.07		3.03	3.27	2.34	1.80
	Ohio	6.10	8.65		8.73	9.23	5.77	10.64
	Wisconsin	1.36	1.00		1.28	1.25	1.02	0.76
VISTAS		**13.40**	**29.37**		**14.14**	**16.43**	**10.07**	**48.06**
VISTAS	Alabama	0.72	1.32		0.63	0.71	0.39	2.14
	Georgia	1.40	3.21		1.06	1.54	0.72	4.73
	Kentucky	2.65	4.71		3.59	3.83	2.31	7.82
	Mississippi	0.04	0.10		0.06	0.06	0.03	0.12
	North Carolina	1.29	4.35		0.92	0.99	1.18	6.11
	South Carolina	0.72	1.64		0.42	0.41	0.44	1.62
	Tennessee	1.05	1.91		1.04	1.16	0.86	3.67
	Virginia	1.80	4.83		1.48	1.67	1.32	5.45
	West Virginia	3.74	7.31		4.94	6.05	2.81	16.39
OTHER[36]		**33.79**	**16.78**	**12.70**	**23.54**	**18.99**	**44.17**	**12.48**

MANE-VU will continue to explore these differences, but it remains encouraging that the use of different platforms and approaches results in more agreement across the various techniques than difference. With the few, specific exceptions mentioned above, it is relatively easy — using the normalized results from multiple techniques shown in Figure 8-1(a-d) — to identify those states that have the largest influence on sulfate levels at each Class I site. MANE-VU believes that this information can provide a solid basis for initiating consultation and planning efforts between upwind and downwind states and RPOs.

Figure 8-1(a-d). Comparison of normalized (percent contribution) results using different techniques for ranking state contributions to sulfate levels at the MANE-VU Class I sites (a) Acadia National Park, ME, (b) Brigantine Wilderness Area, NJ, (c)Lye Brook Wilderness Area, VT, and (d) Shenandoah National Park, VA.

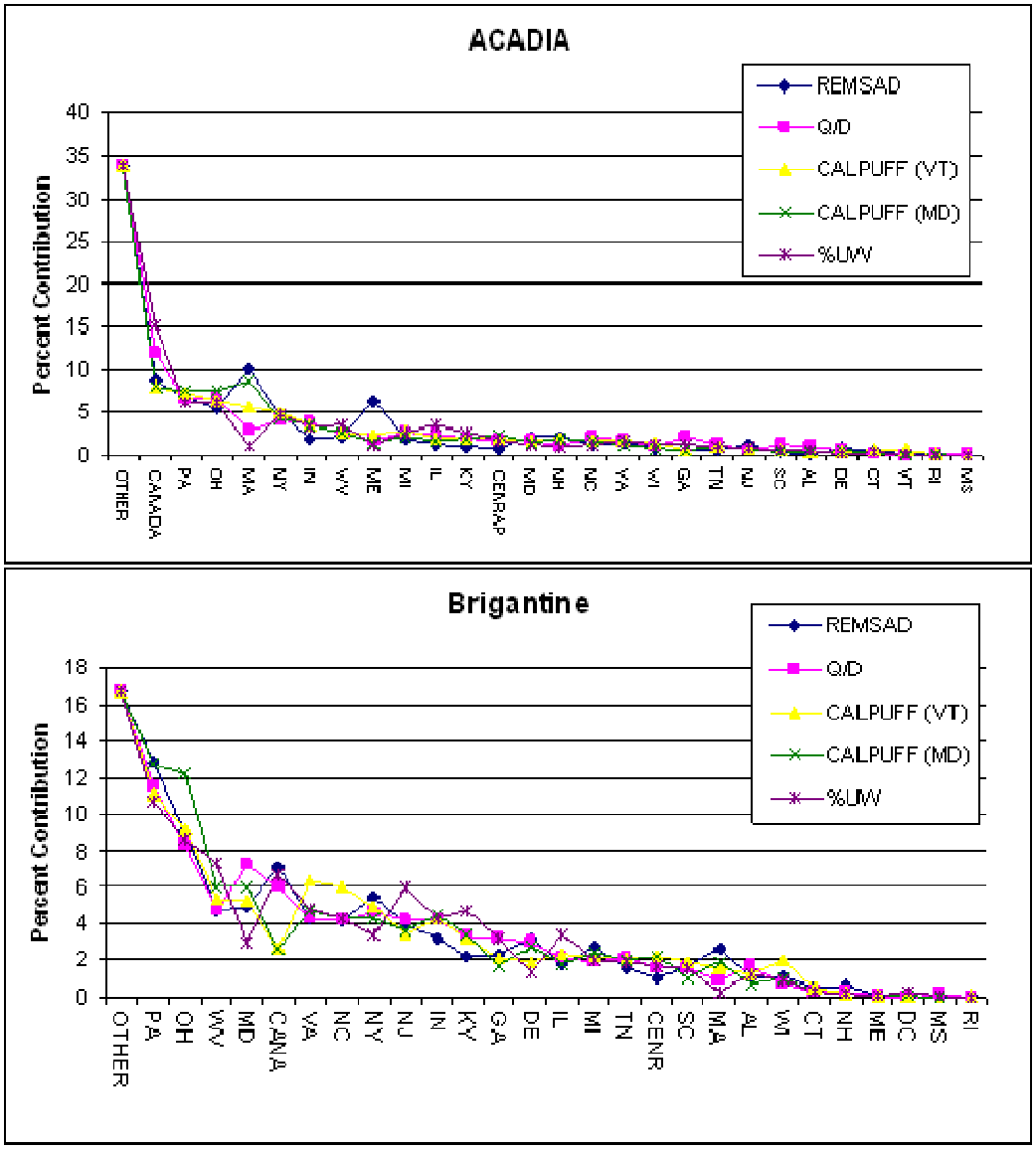

Figure 8-1(a-d). Continued

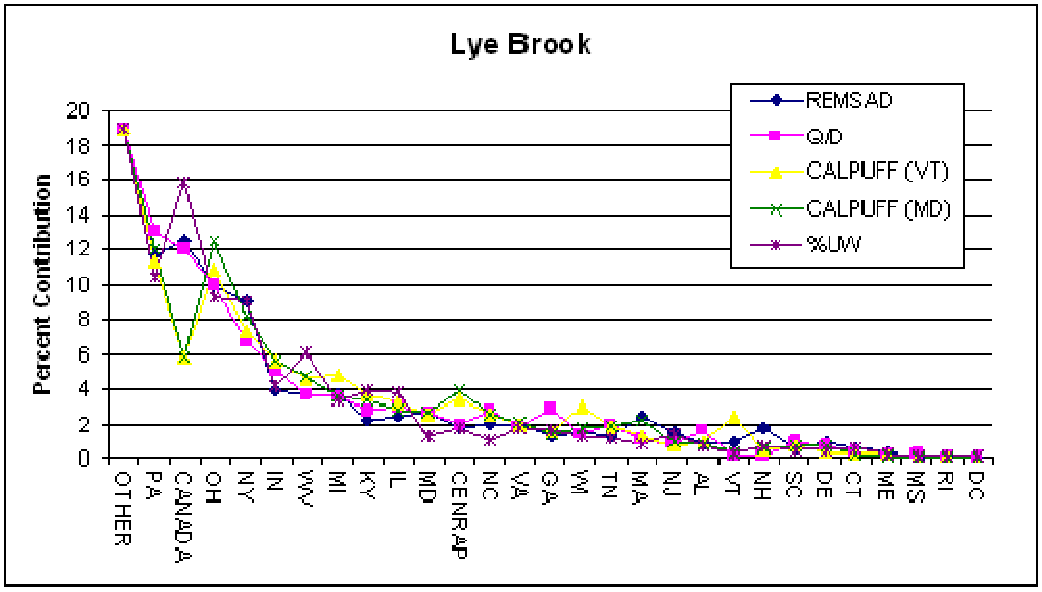

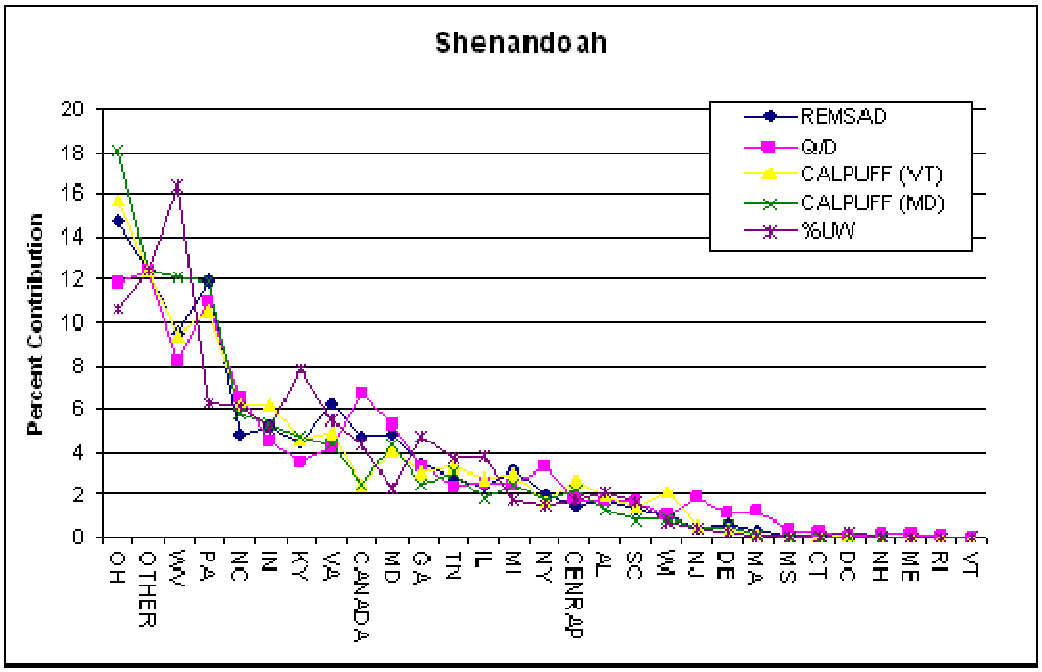

An alternative means of displaying the above results is in Table 8-6, which shows the individual state rankings produced by different assessment techniques for Acadia National Park, Maine. In the left-side column of Table 8-6, states are colored according to their average ranking across the different assessment methods. Those states that are ranked in the top five on average, across all techniques are colored red, while states ranked in the top six through ten are colored magenta, and so on for each group of five going down the left-side column. Through this color scheme, one can see how the states' average ranking compares to their rankings under each individual assessment method given in the other columns of the table. The fact that all techniques tend to come to

consistent conclusions about which states are top contributors provides some confidence that the source regions with the most influence on sulfate levels at MANE-VU Class I sites can be correctly identified. Note that the CENRAP states and several other states along the border of the analysis domain represent only partial state contributions.

Table 8-6. Ranked Contributing States to Acadia Sulfate

Average	REMSAD	Q/d	CALPUFF (VT)	CALPUFF (MD)	E x RTP
CANADA	MA	CANADA	CANADA	MA	CANADA
PA	CANADA	PA	PA	CANADA	PA
OH	PA	OH	OH	OH	OH
MA	ME	NY	MA	PA	NY
NY	OH	IN	NY	NY	IL
IN	NY	MA	IN	IN	WV
WV	WV	MI	MI	WV	IN
ME	NH	WV	WV	CENRAP	MI
MI	MD	IL	ME	MI	KY
IL	IN	GA	IL	NH	CENRAP
KY	MI	NC	CENRAP	KY	VA
CENRAP	VA	KY	KY	IL	ME
MD	NC	VA	NH	NC	GA
NH	NJ	MD	MD	MD	WI
NC	IL	CENRAP	NC	ME	MD
VA	KY	ME	VA	VA	NC
WI	DE	TN	WI	TN	NH
GA	CENRAP	SC	TN	WI	MA
TN	WI	AL	NJ	NJ	TN
NJ	CT	WI	VT	GA	NJ
SC	GA	NH	GA	DE	AL
AL	TN	NJ	SC	SC	SC
DE	SC	DE	CT	AL	CT
CT	AL	CT	DE	CT	DE
VT	RI	MS	AL	RI	VT
RI	VT	RI	RI	VT	DC
MS	MS	VT	DC	DC	RI
DC	DC	DC	MS	MS	MS

Yet one more way of combining the ranked contributions is shown in Figure 8-2, which summarizes the relative contributions of four RPOs, Canada, and "outside domain" regions to ambient sulfate concentrations at several Class I areas using four different assessment techniques. The techniques considered here include: tagged REMSAD modeling, two CALPUFF platforms (MM5-based meteorology used by MDE and NWS observation-based meteorology used by VT DEC), the empirical emissions divided by distance approach (Q/d), and emissions times residence time probability. The estimates of state-by-state sulfate mass contributions ($\mu g/m^3$) from each method have been aggregated by RPO, both in terms of their absolute contribution (these values are displayed within the bars shown in the graphic) and in terms of their proportional contribution relative to other RPOs. It should be noted that the "outside domain"

contribution shown for each analysis method was derived exclusively from the REMSAD result. Averaging estimated impacts at the Acadia, Brigantine, and Lye Brook sites over the four assessment techniques utilized, MANE-VU states account for about 20 to 30 percent of sulfate impacts in these three MANE-VU Class I areas, while the Midwest RPO and VISTAS states each account for about 20 to 25 percent of the total sulfate contribution at Brigantine and Lye Brook and about 10 to 15 percent each at Acadia. The CENRAP states, Canada and "outside domain" add the remainder. Although variation exists across estimates of contribution for different sites and using different techniques, the overall pattern is generally consistent. Relative contributions are somewhat reversed at Shenandoah, which is a VISTAS Class I area. There, VISTAS states and Midwest RPO states account for roughly 20 to 30 percent of overall sulfate impacts, with MANE-VU states contributing roughly 15 to 20 percent.

Figure 8-2. Estimated RPO contributions to sulfate concentrations at Class I areas using different assessment techniques

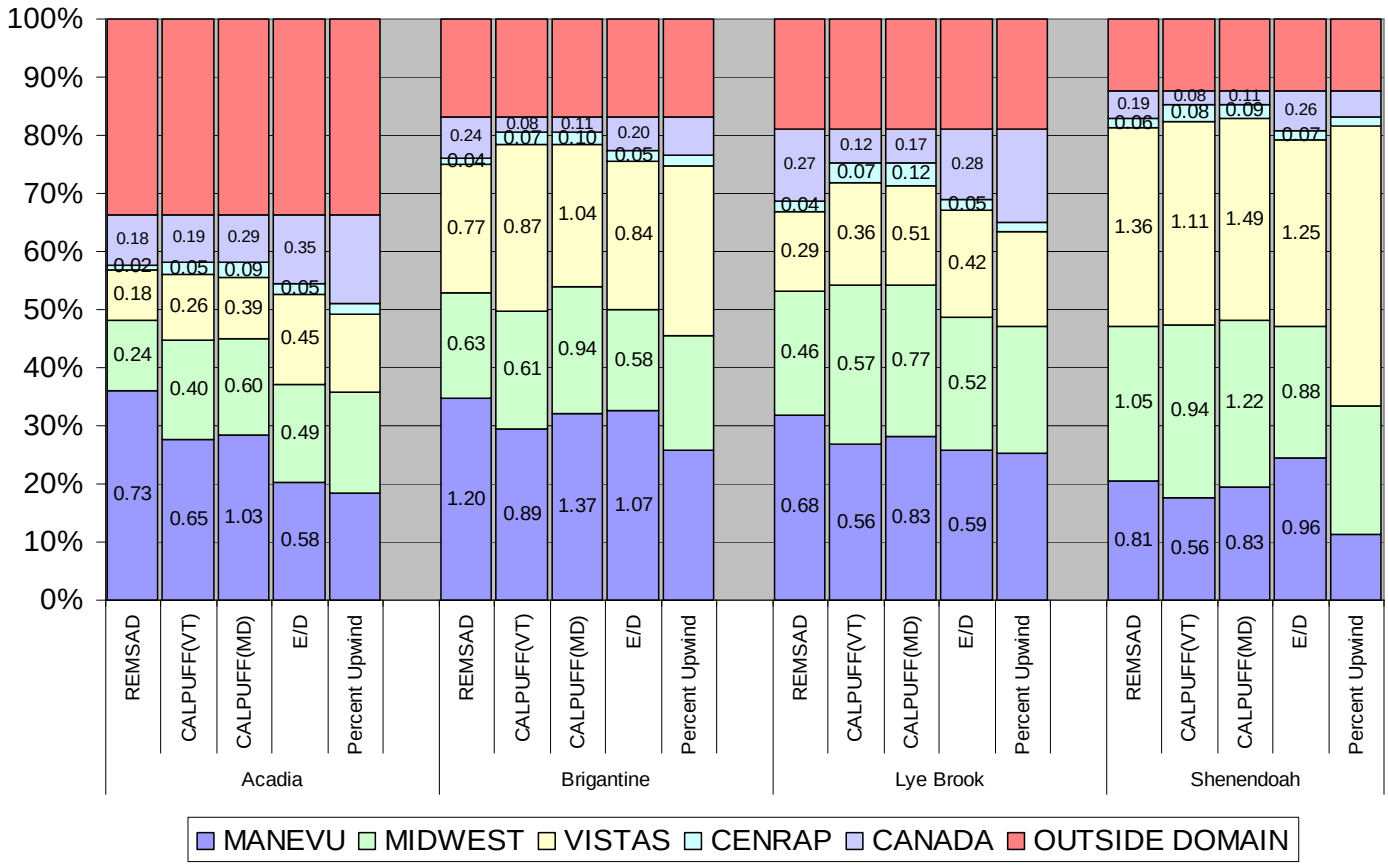

While the foregoing discussion has focused on quantitative methods for comparing contributions from individual states and regions, additional analyses have been conducted to verify and support these results using more qualitative means of identifying "regions of influence" for each Class I area. One such qualitative approach to synthesizing and interpreting the results obtained through different assessment techniques is illustrated in Figure 8-3 and Figure 8-4 below, which show a series of maps shaded to indicate different levels of contribution from different states and regions as determined by the analysis platforms already discussed. In these maps, states are shaded darker the higher they rank in terms of percent contribution to sulfate at a Class I site. For example, in Figure 8-3, states in a line from Indiana through Massachusetts are calculated to have the greatest impact on sulfate at Acadia. Overlaid on top of these maps are contours of

Figure 8-3. Ranked contributions of states to ambient sulfate concentrations at Acadia National Park, Maine.

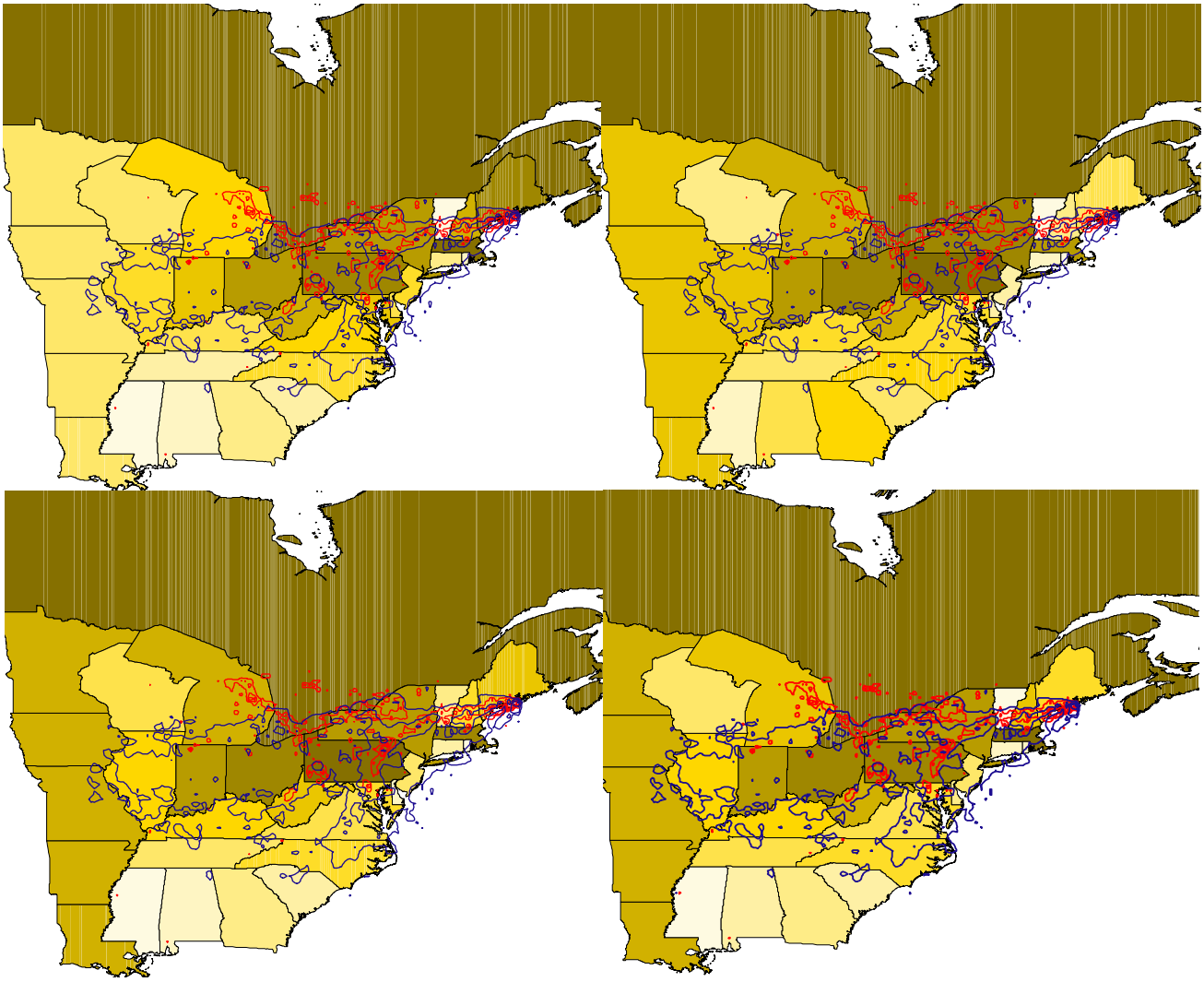

Note: Shaded maps show contributions as estimated by REMSAD, Emissions divided by Distance, CALPUFF VT, and CALPUFF MD. Red and blue contours representing regions of high incremental probability (IP) and high cluster-weighted probability (CWP) are overlaid onto the shaded state maps to indicate similarity of regional contributions as calculated by these independent receptor-based methods.

Incremental Probability (red) and Cluster Weighted Probability (blue) of contributing to sulfate on the highest days. The substantial consistency in the patterns support and bolster the quantitative results. The importance of this finding is that the receptor-based results portrayed by the contours rely on methods that are completely independent of the source-based modeling approaches used to calculate the underlying ranks. This sort of internal consistency among approaches gives considerable strength to the weight-of-evidence approach that MANE-VU has adopted for identifying sulfate source regions.

Figure 8-4. Ranked contributions of states to ambient sulfate concentrations at Brigantine Wilderness Area, New Jersey.

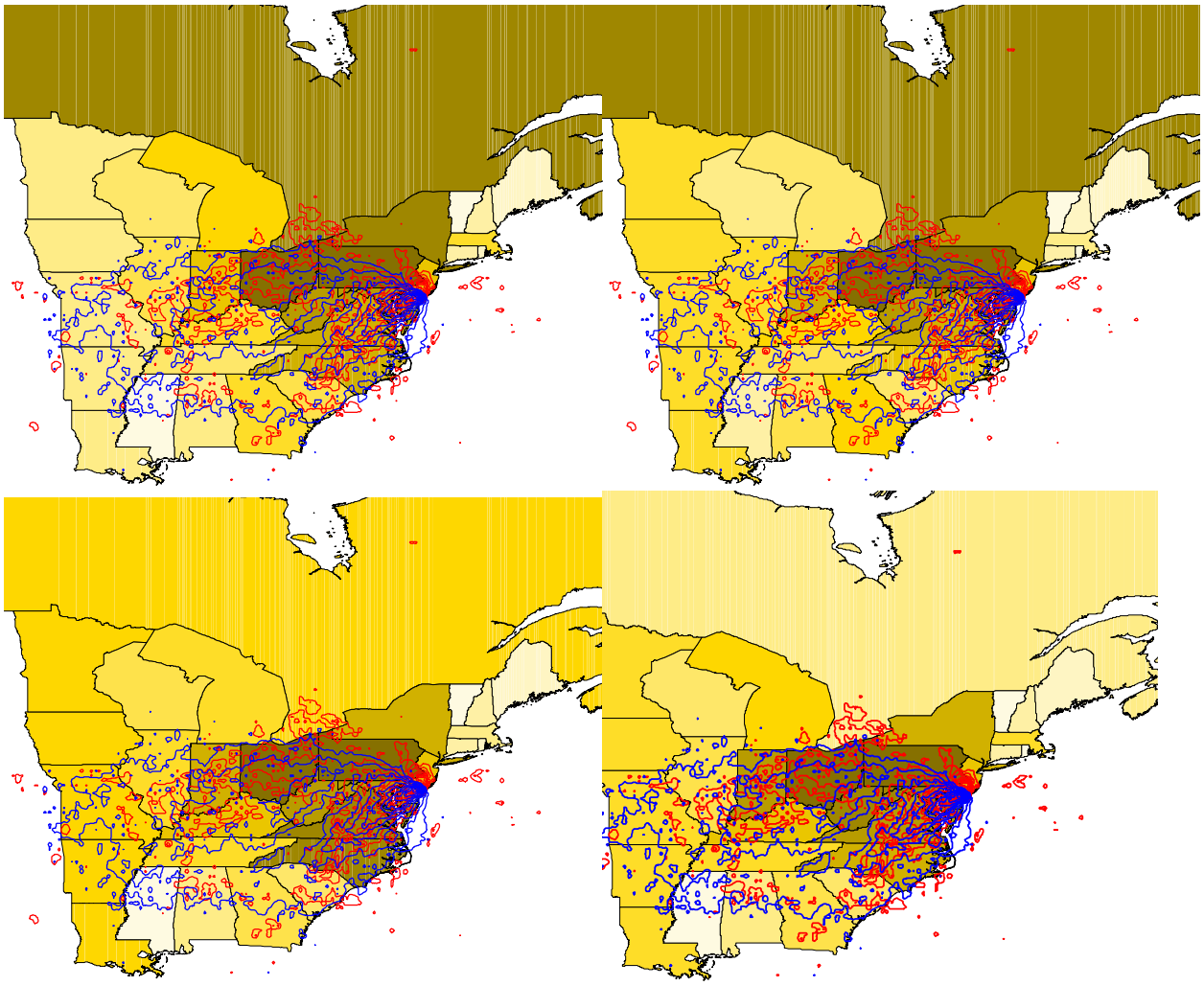

Note: Shaded maps show contributions as estimated by REMSAD, Emissions divided by Distance, CALPUFF VT, and CALPUFF MD. Red and blue contours representing regions of high incremental probability (IP) and high cluster-weighted probability (CWP) are overlaid onto the shaded state maps to indicate similarity of regional contributions as calculated by these independent receptor-based methods.

9. CONCLUSION

As MANE-VU prepares to implement the requirements of the Regional Haze Rule, a significant technical effort has focused on developing multiple analysis tools for assessing contributions to fine particle pollution and thus visibility impairment at Class I areas in the eastern United States. These analysis tools span the discipline of atmospheric science and include traditional Eulerian "source" or "grid" models, Lagrangian dispersion models, back trajectory receptor techniques, source apportionment models, and simple approximations based on empirical relationships between emissions and geography.

A review of the literature and of recent monitoring data has yielded a conceptual model of visibility impairment in the MANE-VU region that attributes a dominant role, on the worst visibility days, to the sulfate component of fine particle matter. This model in turn suggests that the most effective near-term strategy for reducing fine particle pollution and visibility impairment in the East is to continue reducing anthropogenic emissions of SO_2. Reductions in both NO_X and VOCs should also be considered. Given that sulfate, in particular, plays a dominant role in causing visibility impairment throughout the East, MANE-VU has focused on multiple methods of apportioning the sulfate mass found in ambient air at Class I sites to contributing states and regions. This weight-of-evidence approach is intended to overcome large uncertainties that would otherwise undermine confidence in the results obtained using any one modeling or analysis technique in isolation.

The assessment techniques described in this report use numerous approaches to develop ranked lists of individual state contributions to sulfate levels in MANE-VU Class I areas. When these results are normalized and compared, we find broad general agreement concerning the top contributing states at each site as well as some differences that suggest the magnitude of uncertainty inherent in these results.

The conclusions that emerge from this report regarding the relative contributions of different upwind RPOs to downwind sulfate concentrations at MANE-VU Class I areas appear quite robust and the modest differences presented here relative to the preliminary results presented in Spring of 2005 are a further indication that the general patterns of contribution presented here are unlikely to change due to further refinements of the emissions and meteorological inputs. This suggests that the MANE-VU findings are sufficiently robust to serve as a basis for inter-RPO consultations and the regional haze planning process. Given that as much as 30 to 50 percent of the ambient sulfate found at northeastern Class I sites on hazy days appears to originate within neighboring RPOs, coordination and consultation is likely to be critical if MANE-VU is to achieve its visibility goals for 2018 and beyond.

Appendix A: Application of Trajectory Analysis Methods to Sulfate Source Attribution Studies in the Northeast U.S.

Appendix B: Source Attribution by Receptor-Based Methods

Appendix C: Chemical Transport Model Results for Sulfate Source Attribution Studies in the Northeast U.S.

Appendix D: Development of Parallel CALPUFF Dispersion Modeling Platforms for Sulfate Source Attribution Studies in the Northeast U.S.

Appendix D: Development of Parallel CALPUFF Dispersion Modeling Platforms for Sulfate Source Attribution Studies in the Northeast U.S.

Mark Garrison, Environmental Resources Management
[on behalf of] Maryland Department of the Environment/Maryland Department of Natural Resources (MDE/MDNR)
Baltimore, Maryland

Dan Riley, Paul Wishinski
Vermont Department of Environmental Conservation (VT DEC)
Waterbury, VT

ABSTRACT

The CALPUFF Lagrangian dispersion model was run on two different, largely independent platforms – developed and implemented by two different groups participating in this study – which were used to simulate sulfate production and transport in the MANE-VU and nearby regions. Most of the techniques and approaches for both platforms (including model versions) were consistent if not identical. The primary difference involved the source, and processing, of meteorological data with CALMET. An additional difference included a different focus for each group on the development of emissions and source parameters. The Vermont Department of Environmental Conservation (VT DEC) developed meteorological inputs for CALPUFF through the use of observation-based inputs (i.e., rawinsonde and surface measurements) from the National Weather Service (NWS) and application of CALMET. VTDEC furthermore developed hourly emissions and exhaust flow data from the Acid Rain Program's continuous emissions monitoring system (CEMS) data files for large electric generating units, and created and utilized these inputs for the CALPUFF modeling, along with emissions data for non-EGU point sources from the 2002 NEI inventory. The Maryland Department of Natural Resources and the Maryland Department of the Environment (DNR/MDE) developed a second CALMET/CALPUFF platform with contractor assistance provided by ERM. Meteorological inputs for CALPUFF on the DNR/MDE platform were developed through the use of MM5 data developed for 2002 by the University of Maryland on a 12-km grid. This MM5 data set was used to update the DNR/MDE modeling which had been conducted for Phase I using a 36-km MM5 data set developed by the CENRAP RPO. DNR/MDE focused on the development of emissions and source parameters through the use of the 2002 NEI. Phase II model results for sulfate ion predications are presented, in an evaluation mode (comparing model predictions with measurements) and an application mode (ranking states and individual EGUs), along with comparison of results between platforms. Additionally, the DNR/MDE modeling included an evaluation of model performance based on nitrate aerosol predictions and measurements.

APPENDIX D: DISPERSION MODEL TECHNIQUES

This appendix deals with Lagrangian models, specifically the CALPUFF modeling system (USEPA, 2006). In contrast to the Eulerian grid models referenced and utilized in other sections of this report, a Lagrangian model simulates atmospheric transport, transformation, and dispersion through the treatment of air pollutant emissions from stacks or area sources as a series of discrete puffs. Each puff is tracked individually by the model until it leaves the modeling domain, and the contribution of each puff to receptor concentrations (or deposition fluxes) is calculated separately and can be used to create individual source impacts, or summed in different ways to create total impacts over source groups based on the users' choices. The CALPUFF modeling system includes numerous related programs used to create inputs for the model and to extract and analyze model outputs. One key related program is CALMET, which is the meteorological processor that creates three-dimensional wind fields for the dispersion model CALPUFF. Another key related program is CALPOST, which performs a number of post-processing functions including the calculation of visibility impacts from model-predicted particulate concentrations (including particulate sulfate, particulate nitrate, and direct emissions of $PM_{2.5}$).

This appendix is devoted to describing two specific applications of the CALPUFF system to the simulation of particulate sulfate concentrations, and corresponding visibility impacts, at a number of receptors in the MANE-VU region.[1] Two different, largely independent platforms – developed and implemented by two different groups participating in this study – were used for the modeled simulations described here. Most of the techniques and approaches for both platforms (including model versions) were consistent if not identical. The primary difference involved the source, and processing, of meteorological data with CALMET. An additional difference included a different focus for each group on the development of emissions and source parameters.

The Vermont Department of Environmental Conservation (VTDEC) developed meteorological inputs for CALPUFF through the use of observation-based inputs (i.e., rawinsonde and surface measurements) from the National Weather Service (NWS) and application of CALMET. VTDEC furthermore developed hourly emissions and exhaust flow data from the Acid Rain Program's continuous emissions monitoring system (CEMS) data files for large electric generating units, and created and utilized these inputs for the CALPUFF modeling, along with emissions data for non-EGU point sources from the 2002 NEI inventory.

The Maryland Department of Natural Resources and the Maryland Department of the Environment (DNR/MDE) developed a second CALMET/CALPUFF platform with contractor assistance provided by ERM. Meteorological inputs for CALPUFF on the DNR/MDE platform were developed through the use of MM5 data developed by the University of Maryland on a 12-km grid. This MM5 data set was used to update the DNR/MDE Phase I modeling, which had been conducted using a 36-km MM5 data set

[1] While CALPUFF is capable of estimating concentrations of particulate nitrate and of primary PM2.5, estimates of these pollutants are not included here (except for an evaluation of nitrate ion predictions compared to measurements with the DNR/MDE platform) due to the importance of sulfate contributions to visibility impairment in the MANE-VU region .

developed by the CENRAP RPO. DNR/MDE focused on the development of emissions and source parameters through the use of the 2002 NEI, incorporating five different source sectors: EGUs, non-EGU point sources, mobile (on-road), mobile (off-road), and general area sources. The hourly data files developed by VTDEC based on CEMS data for large EGUs were used directly with the MM5 platform.

Both platforms were used to model the entire calendar year 2002. In this section, reference is made to Phase I and Phase II of the CALPUFF modeling; generally, Phase I was the initial effort designed to provide reasonably complete estimates of particulate sulfate impacts at a set of receptors in the MANE-VU region based on the two different modeling platforms. These estimates have been configured to provide individual source and cumulative state impacts to provide inter-platform comparisons. The modeling domain has been designed to be consistent with the other modeling approaches included in this report (e.g. REMSAD, CMAQ), so that conclusions regarding the most significant sources and states to sulfate visibility impacts in MANE-VU can be compared. Consistency across a broad range of approaches will add credibility to the conclusions reached in the overall contribution assessment.

The rest of this appendix provides a brief description of the CALPUFF modeling system; describes the application of CALPUFF in this Phase I assessment on both the VTDEC and the DNR/MDE platforms including a description of model input development and data evaluations; provides the results of evaluations of the performance of CALPUFF compared to measured particulate sulfate concentrations; and provides the results of the Phase I contribution assessment modeling based on both platforms.

D.1. The CALPUFF Modeling System Description and Background

The CALPUFF modeling system is included in EPA's Guideline on Air Quality Models (GAQM) as a recommended model for long-range transport, specifically to address the impacts of emissions from Prevention of Significant Deterioration (PSD) sources in Class I areas. CALPUFF has recently seen wide use across the US, providing estimated concentration and visibility impacts in Class I areas for numerous PSD applications for new power plants and other PSD sources. The use of CALPUFF for regional modeling at the scale of this contribution assessment (where transport distances exceed 1000 kilometers in some cases) has not been as wide-spread, and its performance at distances beyond 300 kilometers is subject to some uncertainty. The Interagency Workgroup on Air Quality Modeling (IWAQM) Phase II Report (USEPA, 1998) suggested, based on an analysis of the CAPTEX tracer study, that under-prediction of horizontal dispersion at greater than 300 kilometer transport distances could lead to an over prediction of surface concentrations using CALPUFF. For the present study, this uncertainty is addressed through the emphasis on model performance (compared to measured data) and by the context in which the CALPUFF model results are used. This context is that the CALPUFF results are used to contribute to a weight of evidence assessment that considers the results of many different modeling approaches.

The CALPUFF modeling system was developed by Earth Tech, and is publicly available. Model and support program executables, a graphical user interface, model and support program source code, examples, and users guides are available either through a link provided on EPA's web site www.epa.gov/ttn/scram or directly from Earth Tech at

www.src.com/calpuff/calpuff1.htm. Two beta-test versions of CALPUFF have been released since the GAQM version was released on April 17, 2003: one dated July 11, 2003, and one dated July 16, 2004. Additional updates to the modeling system have been released by Earth Tech, most notably the version recommended by the VISTAS RPO for BART modeling and Version 6 that includes the capability to model with sub-hourly time steps (latest updates released on April 14, 2006). The model versions identified as V5.711 030625 and V5.711 040716 are being used in this analysis as opposed to the GAQM version, since they correct bugs found in the GAQM version that affect the use of data files (e.g. the hourly emissions and point source parameter file for incorporating CEMS data) that are important for this analysis. The latest model versions (VISTAS, Version 6) were not available at the time that this work was being performed and were therefore not used.

D.1.1. CALMET

The CALMET meteorological processor is a key component of the CALPUFF modeling system. Its primary purpose is to prepare meteorological inputs for running CALPUFF, consisting nominally of three-dimensional wind fields, two-dimensional gridded derived boundary layer parameter fields (e.g. mixing depth, friction velocity, Monin Obukhov length, etc.), and two-dimensional gridded fields of surface measurements and precipitation rates (for use in calculating wet deposition fluxes).

The wind field generated by CALMET is based on a diagnostic wind field model. An initial guess wind field is adjusted for the effects of terrain to produce a step 1 wind field. Observations are then used to adjust the step 1 wind field to produce a final step 2 wind field based on interpolation that is written to the CALMET output data file. The CALMET model differs from the family of prognostic meteorological models, such as the Penn State/NCAR Meteorological Model (MM5), that solve basic conservation equations to generate a modeled atmosphere and which can be used in a forecast mode.

Inputs to CALMET consist of geophysical data (land use, terrain) and observations in the form of surface measurements, precipitation rates, and upper air rawinsonde soundings. The output from MM5 can also be used as input to CALMET. Depending on the relationship of the MM5 grid to the CALMET grid, the MM5 data can be introduced in one of three places: as the initial guess field, as the step 1 wind field, or as pseudo-observations. The latest version of CALMET allows for a “no observations” mode for cases where the prognostic model grid is similar in resolution to the CALMET grid. This option allows for maximum reliance on the prognostic model meteorological fields. The no observations mode can be configured to rely entirely on MM5 data, or to combine surface observations with MM5 data.

The CALMET model contains numerous options regarding both the wind field and micrometeorological parameters. Further descriptions of the development of inputs, the selection of options and application of CALMET, and the evaluation of CALMET inputs and outputs can be found in the appropriate sections below for the observation-based platform (VTDEC) and the MM5-based platform (DNR/MDE).

The domain utilized for both of these platforms is identical, and is based on a Lambert Conformal Conic projection consistent with the RPO projection; namely, an

origin of 40.0 degrees N and 97.0 degrees W and matching parallels of latitude at 33.0 and 45.0 degrees N. The vertical extent of the domain is set at approximately 3 km with different resolution depending on the platform. Grid resolution for the VTDEC platform was set at 36 kilometers, which resulted in a grid size of 74 by 61 cells. Grid resolution for the DNR/MDE platform was set at 12 km, which resulted in a grid size of 222 by 180 cells. A depiction of the domain utilized in these analyses is shown in Figure D-1.

Figure D-1. CALPUFF modeling domain.

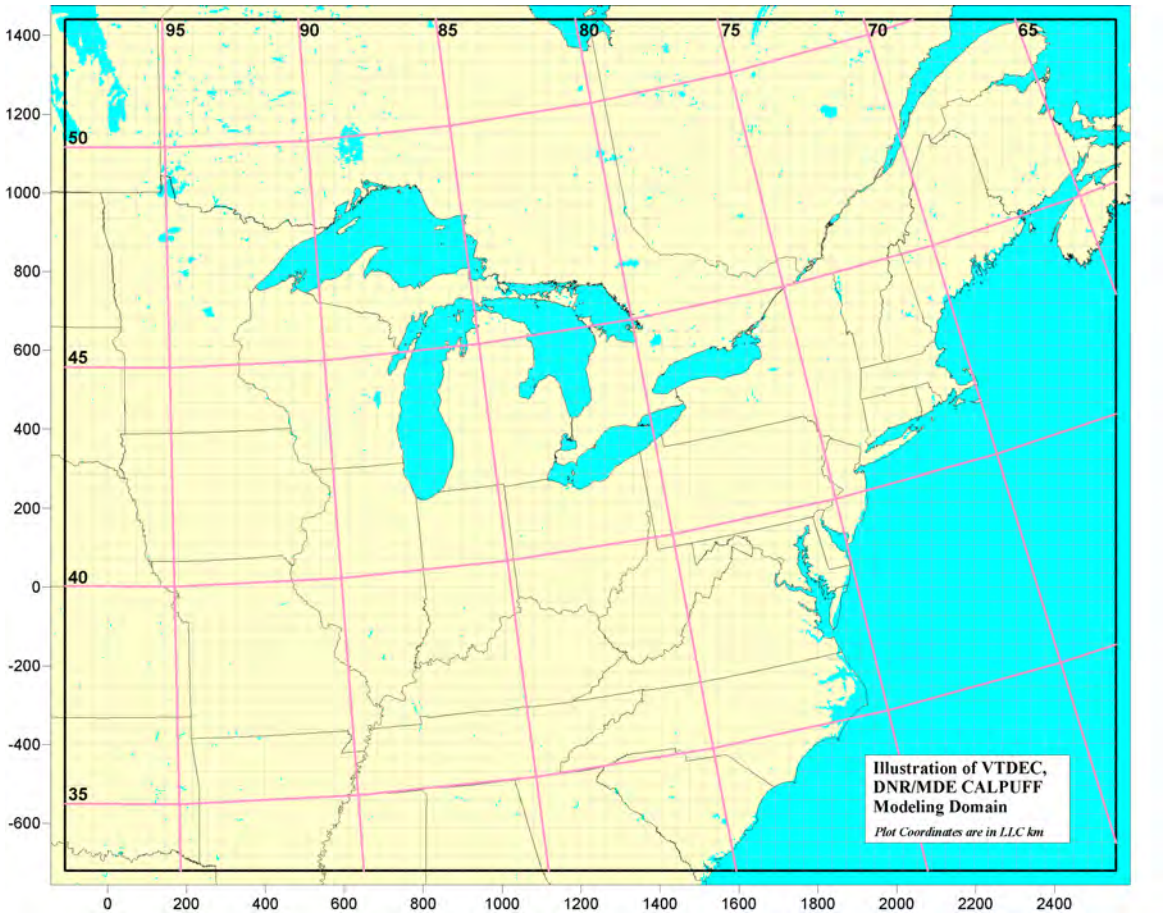

D.1.2. CALPUFF

For this modeling effort, the focus is on the prediction of sulfate aerosol at a number of receptors in and near the MANE-VU RPO. Visibility impacts are also presented based on the application of the default extinction efficiency coefficient for SO_4 from the CALPOST program. The present visibility calculations are based on monthly-averaged relative humidity coefficients.

CALPUFF initiates the simulation of point source plumes with a calculation of buoyant plume rise. Based on the effective plume height (stack height plus plume rise), transport winds are extracted from the meteorological data file. For near-field effects, the height of the plume in transition to the final plume height is taken into account. The puff release rate is calculated internally, based on the transport speed and the distance to the

closest receptor; for the present analysis, source-receptor distances are such that in most cases, the puff release rate is one per hour. As the puff is transported downwind, it grows due to dispersion and wind shear and the trajectory is determined by transport winds at the puff location and height at each time step. The pollutant mass within each puff is initially a function of the emission rate from the original source. The pollutant mass is subject to chemical transformation based on model user choices and removal by both wet and dry processes. Chemical transformation and removal are calculated based on a one-hour time step.

The chemical transformation scheme chosen for this analysis is the "MESOPUFF-II" scheme available with CALPUFF, described in the CALPUFF user's guide as a "pseudo first-order chemical reaction mechanism". This scheme involves five species: SO_2, SO_4, NO_X, HNO_3, and particulate nitrate. CALPUFF calculates the rate of transformation of SO_2 to SO_4, and the rate of transformation of NO_X to NO_3, based on environmental conditions including the ozone concentration, atmospheric stability, solar radiation, relative humidity, and the plume NO_X concentration. For SO_2, the primary subject of this modeling, the following expression is used to calculate the SO_2 to SO_4 transformation rate (equation 2-253 in the CALPUFF user guide):

$$k_1 = 36\,[R]^{0.55}\,[O_3]^{0.71}\,S^{-1.29} + k_{1(aq)}$$
$$k_{1(aq)} = 3 \times 10^{-8} \times [RH]^{4.0}$$

where,

k_1	is the SO_2 to SO_4 transformation rate (percent/hour)
R	is the total solar radiation intensity (kw/m^2)
$[O_3]$	is the background ozone concentration (ppm)
S	is a stability index ranging from 2 (unstable) to 6 (stable)
$k_{1(aq)}$	is a parameterization of the aqueous phase component of the SO_2 conversion rate
RH	is the relative humidity (percent)

At night, the transformation rate defaults to a constant value of 0.2% per hour. At present, CALPUFF does not have a mechanism for estimating aqueous SO_2 transformation that can occur in clouds. Calculations based on these formulas show that the transformation rate can reach about 3 percent per hour at noon on a cloudless day with 100 ppb of ozone.

For NO_X, the transformation rates are calculated by the following (equations 2-254 and 2-255 in the CALPUFF user guide):

$$k_2 = 1206\,[O_3]^{1.5}\,S^{-1.41}\,[NO_X]^{-0.33}$$
$$k_3 = 1261\,[O_3]^{1.45}\,S^{-1.34}\,[NO_X]^{-0.12}$$

where,

k_2	is the NO_X to $HNO_3 + RNO_3$ transformation rate (percent/hour)
k_3	is the NO_X to HNO_3 (only) transformation rate (percent/hour)
$[O_3]$	is the background ozone concentration (ppm)
S	is a stability index ranging from 2 (unstable) to 6 (stable)
$[NO_X]$	is the plume NO_X concentration (ppm)

In the NO_X transformation scheme, RNO_3 represents organic nitrates and is a sink for NO_X since the transformation is irreversible – RNO_3 does not react further in this scheme, and is not subject to wet or dry deposition. At night, the NO_X transformation rate defaults to a constant value of 2.0% per hour. After HNO_3 (nitric acid) is formed from the oxidation of NO_X, the MESOPUFF-II mechanism estimates the formation of particulate nitrate by the reaction of nitric acid and ammonia. This reaction is reversible and is a function of temperature and relative humidity.

The CALPUFF model does not simulate the interaction of puffs; in other words, each puff does not "know" about the number or characteristics of other puffs from other sources that may be nearby. The puff is informed of the state of the atmosphere during transport through the specification of ozone concentrations (used in the transformation rate equations) and background concentrations of ammonia. Ammonia concentrations are used to calculate the equilibrium between nitric acid and particulate nitrate. For the Phase I and Phase II modeling, both platforms used hourly surface ozone concentrations, derived from AIRS data, as input to CALPUFF to calculate transformation rates.

The availability of ammonia to react with both SO_4 and NO_3 to form fine particulate matter is an issue that requires special consideration. CALPUFF first assumes that ammonia reacts preferentially with sulfate, and that there is always sufficient ammonia to react with all of the sulfate present within a single puff. Once particulate sulfate has been formed, CALPUFF performs a calculation to determine how much ammonia remains and is available for reaction with NO_3 within the puff. Subsequent formation of particulate nitrate is limited by the amount of available ammonia. In situations where significant puff overlap can occur (such as the multi-source modeling conducted here), the individual puff computation can result in the over-prediction of particulate nitrate formation since available ammonia may not be sufficient to react with the total quantity of nitrate due to the combined impacts of many sources. The POSTUTIL program, part of the CALPUFF modeling system, is capable of re-partitioning the nitric acid/particulate nitrate split to address situations that may be ammonia-limited. Its use is recommended in the CALPUFF sections of BART modeling protocols for other RPOS (e.g. VISTAS, CENRAP). The latest version of POSTUTIL (released April 14, 2006) is currently being evaluated for application in MANE-VU.

Both wet and dry deposition fluxes are calculated by CALPUFF, based on a full resistance model for dry deposition and the use of precipitation rate-dependent scavenging coefficients for wet deposition. Pollutant mass is removed from the puff due to deposition at each time step.

CALPUFF has numerous options to control the way in which transformation, deposition, and concentrations are calculated. It also contains a complex terrain module based on the CTDMPLUS treatment of terrain. For the present modeling analyses, most options were set at "default" values, including the MESOPUFF II transformation scheme and the treatment of terrain. Several sensitivity studies were carried out with the VTDEC platform to examine the performance of different approaches to calculating the SO_2 to SO_4 transformation rate, including the use of user-defined diurnal variations. As described further in Section D.2.1.1, the overall effect of different chemistry approaches showed did not appear to be significant enough, or the underlying basis of the approach

was not well established enough, to depart from the defaults used for the model runs that are reported in this appendix.

Additional, platform-specific details of the implementation of CALPUFF are contained in the following sections.

D.2. VT DEC CALMET/CALPUFF Platform

CALPUFF_v5.711_030625 BETA version was downloaded and compiled for use on the domain shown in Figure D-1 which contains some or all of 34 states in the eastern U.S and portions of southeastern Canada. The model source code had to be re-compiled using Lahey Fortran 95 after changing parameter settings. These changes allowed large numbers of emission sources to be modeled together, hourly ozone inputs from more than 500 ozone monitoring sites to be used, input of hourly met data from a comprehensively large number of surface met stations (ASOS), and data from more than 1000 precipitation stations to be used. As finally configured for Phase I modeling which was conducted during 2004, the VT CALPUFF platform was able to handle up to 2,000,000 puffs on the domain simultaneously. However, soon after the initiation of modeling runs during Phase I it was found to be counter-productive to model very large sets of sources together in one run due to the run-time involved. It also proved to be impossible for the model to handle the complete set of all sources, even with 2,000,000 puffs allowed on the domain at one time, since during summertime periods when transport across the domain is less rapid than at other times, more than that number of puffs remained on the large domain being used. Consequently, a procedure was developed by which all EGU point sources modeled were modeled as individual sources in separate runs, and groups of smaller point sources, groups of area sources (based on county boundaries or on 20 km sized area source squares), and groups of area sources representing on-road and non-road mobile emission patterns by county were modeled on a state-by-state run basis. The post-processing software (CALSUM) available for use with CALPUFF output was used to combine impacts from all source categories. This procedure was also used in the follow-up Phase II modeling carried out during 2005.

Aside from the 3-dimensional meteorological fields required to run CALPUFF (described in the CALMET discussion above and detailed for the VT application below), the primary inputs needed by CALPUFF are the temporal and spatial emissions data for all air pollutants to be modeled, as well as information related to the stationary point, mobile, and area categories of sources that emit these pollutants. In addition, the transformation, deposition and dispersion parameter settings and flags mentioned above needed to be selected. Discussion of the platform-specific parameters and settings used for these CALPUFF runs is included in section D.2.1 describing the emissions used in the CALPUFF dispersion modeling and section D.2.2 describing data validation and settings used in the CALMET meteorological modeling.

D.2.1. VT DEC Emissions Preparations

This section describes the development of the emissions input information used by VT DEC in both the Phase I and Phase II CALPUFF modeling. The objective of the VT DEC modeling with CALPUFF is specifically to quantify and rank the relative impact on the sulfate component of regional haze attributable to sulfur dioxide emissions

from individual large stationary point sources and from collective emissions of sulfur dioxide from individual states at specific receptor locations in the MANE-VU RPO. Achieving this modeling objective was planned as a 2-Phase modeling exercise. The year 2002 was chosen for modeling since it represents a year for which extensive measurement data is available (NESCAUM, 2004), it is within the five-year time period being used to characterize regional haze baseline levels at Class I areas in MANE-VU, and several other contribution assessment techniques are focused on this time period. The ultimate objective involves running CALPUFF with all sulfur dioxide emissions as accurately represented as possible within the domain for the entire year of 2002 and through comparison of ambient measured sulfate (possibly also deposited sulfur) to predicted impacts, to establish that the platform is producing acceptable overall results. Once this "validation" of the modeling system is established, impacts from the individual stationary point sources and from the individual states can be calculated.

Because quality-assured 2002 emissions data for all categories of sulfur dioxide emissions was not yet available in early 2004 when this modeling exercise was initiated, a Phase I modeling objective was established. This objective was to create a working, semi-validated CALPUFF modeling platform using actual 2002 hourly continuous emissions monitoring system (CEMS) data for the large electric generating units (EGUs) in the domain and utilizing 1999 National Emissions Inventory (NEI) data for all other stationary point sources as a surrogate until 2002 NEI data became available. The CEMS data is more time-resolved (hourly average rates) than the NEI data (annual average hourly rate). In the Phase I modeling, only stationary point sources of sulfur dioxide were included in the Vermont CALPUFF runs and, as noted, emissions used were not contemporaneous with the actual year 2002 for all these sources. During Phase II, which began in February 2005, contemporaneous 2002 sulfur dioxide emissions data was used for all source categories, including small stationary point sources, "area sources" and "mobile sources" of sulfur dioxide and nitrogen oxides extracted from the regional planning organization emission inventories developed under the auspices of the RPOs in MANE-VU, MWRPO, and VISTAS. Phase II modeling also involved the utilization of slightly adjusted NWS-based meteorological fields (particularly the first quarter met fields were re-produced with some adjusted assumptions in CALMET).

In addition to more general sensitivity runs exploring model input assumptions applied to the full set of CEMS emission sources on the domain, sensitivity runs were conducted on only a few representative CEMS sources in the initial stages of Phase II modeling by VTDEC. These selected source runs included a sensitivity check on the use of different dispersion settings. The default dispersion setting from the CALPUFF model is utilized when the parameter MDISP is set equal to 3. This causes the PG dispersion coefficients for rural areas (computed using the ISCST multi-segment approximation) and the MP coefficients for urban areas to be used. This was the setting used in Phase I modeling. An additional run was done for a selection of representative CEMS sources using the setting MDISP set equal to 4. This causes the CALPUFF model to calculate dispersion coefficients for rural areas by using the MESOPUFF II equations, and otherwise uses the same MP coefficients for urban portions of the domain. It was found that using MESOPUFF II dispersion coefficients did not show appreciable changes in impacts at the 72 standardized receptor locations identified for model evaluation, therefore subsequent to these initial sensitivity runs, only the setting MDISP=3 was

utilized in the Phase II modeling conducted by VTDEC. Other aspects of the sensitivity runs conducted on the entire set of CEMS emission sources are discussed below under the CEMS data section of this report.

D.2.1.1. CEMS Data

EGUs subject to the reporting requirement for hourly CEMS data for sulfur dioxide contained in Title IV of the Clean Air Act Amendments of 1990 (Acid Rain Program) have been submitting data since 1995. The raw data files submitted to EPA in fulfillment of this requirement on a quarterly basis are routinely made available to the public via the internet. The data files may be found at the following URL:

http://www.epa.gov/airmarkets/emissions/raw/index.html

Submission of the hourly data is in what is called EDR format. The EDR format has undergone some changes over time. For year 2002 data, the format utilized is generally EDR Version 2.1 which was required for all "Acid Rain Program" facilities beginning on April 1, 2000. Some additional CEMS reporting EGUs may not have begun using EDR Version 2.1 until after May 1, 2002 based on requirements for units subject to the NO_X SIP call and NO_X Model Trading Rule, before which EDR Version 1.3 may have been used. The changes and/or additions to requirements between these versions generally do not complicate the extraction of sulfur dioxide hourly data from the database. Differences involved relate primarily to the nitrogen oxides emissions reporting. For extracting emissions data from the Acid Rain CEMS database files, VTDEC created procedures which extracted both the sulfur dioxide and the nitrogen oxides emissions information along with unit and facility stack parameters (as available in the database).

Important constraints exist to running sequential quarterly variable hourly emissions data with the CALPUFF model. The CALPUFF model can accept two forms of input emissions data: (1) constant average hourly data which is input into the model through lines of entry within the "control file" for each stack emission point where each entry has a constant emission rate for all hours during the modeling period (VT chose to run separate runs for each quarter during 2002), and (2) variable hourly data which is input into the model through an entirely separate file structured to allow each hour during the time period to have a different emission rate and a different stack velocity. These separate files for variable hourly emissions will be referred to as "PTEMARB" files after the default name given in the model's guidance document. VTDEC determined through some sensitivity testing, that in random cases tested, use of an average hourly emission rate for the entire time period modeled does not always produce the same maximum short-term (hourly or 24-hourly) impact at a random receptor than use of variable actual hourly emissions during the time period. For this reason VTDEC decided that it wanted to utilize the variable hourly CEMS data for any stationary point sources for which it was available from the Acid Rain CEMS database. The hourly variability of the set of CEMS EGU sources modeled in Phase I for the year 2002 can be seen in Figure D-2.

Figure D-2. CEMS EGU SO_2 Emission Hourly Variability during 2002

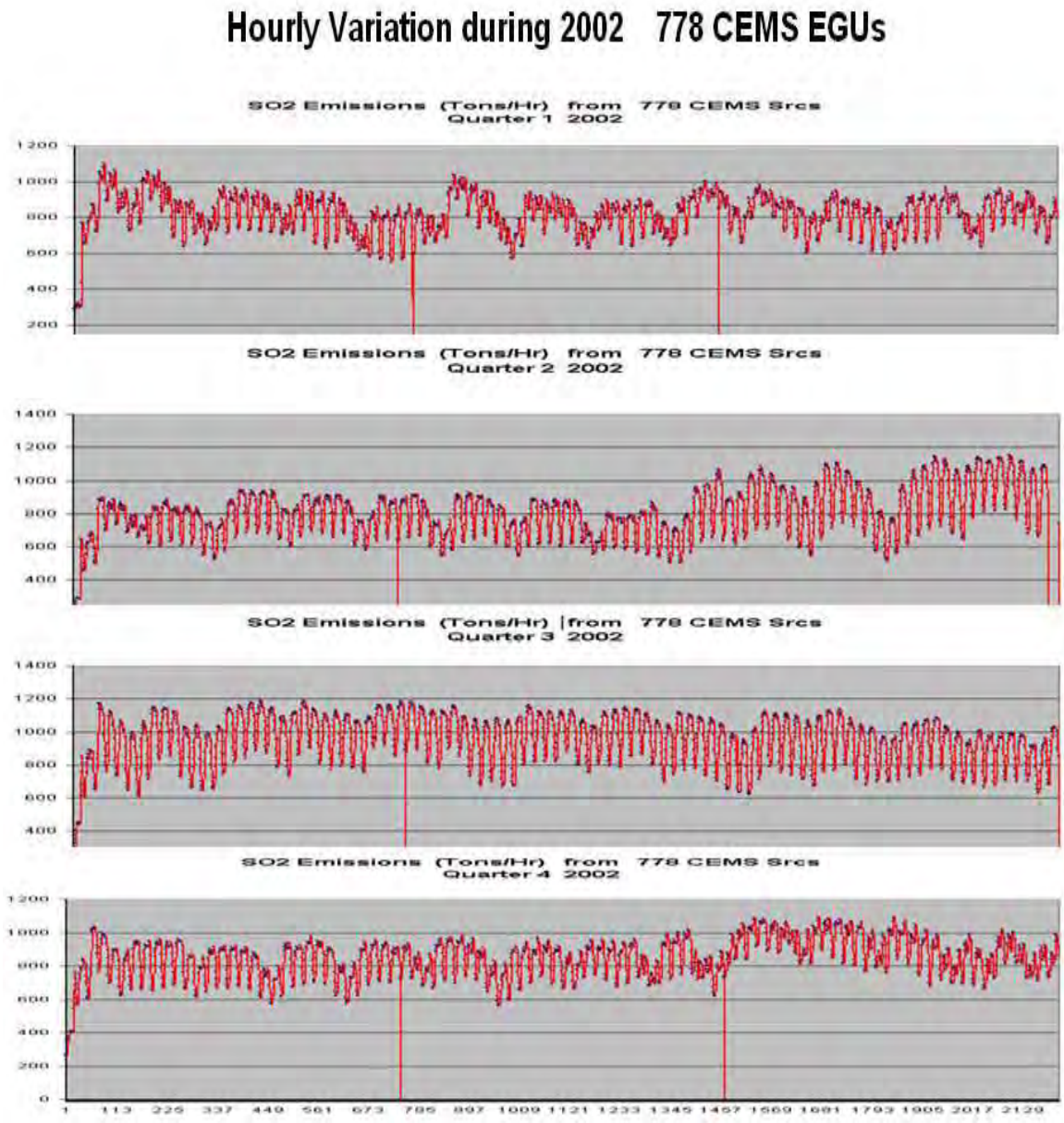

In order for output from multiple sequential modeling periods (4 quarters for example) to be as complete as possible, without ramp up between each of the periods modeled, CALPUFF has a feature which allows preservation of the "state" of all puffs on the entire domain at the end of each modeled period. This allows the model to continue running sequentially, with the initial puff state for the next period the same as the end puff state of the last period's run. Model output for all hours of the entire year covered by four quarters run separately is usable for evaluation in this mode. However, in order to utilize hourly variable emission inputs with this feature, because the puff "state" depends on puffs associated with each source and each hour, the number of sources with hourly data contained in each PTEMARB file for each of the quarters involved must

remain exactly the same. Also, it was found by VTDEC that utilization of the CALPUFF BETA version dated June 25, 2003 was necessary if input of hourly variable CEMS emission rates using a PTEMARB file was desired.

During Phase I, VTDEC first examined the entire listing of EGUs in the CEMS database for each quarter of 2002 to determine a common set of units reporting for all four quarters. We also removed those units which were not located within the domain. An examination of the 2002 CEMS data on the EPA website indicates that for the entire U.S., quarter 1 has 2646 data files, quarter 2 has 3161, quarter 3 has 3340, and quarter 4 has 3017. However, after applying the constraints listed above and limiting selection to those sources which had non-zero SO_2 emissions during at least one hour in each quarter, 778 common units (or combined units as reported) were identified and extracted. During Q/A on the source emission files, the initial procedure used was determined to be somewhat too restrictive in that it missed 8 additional EGUs which had reasonably significant SO_2 emissions in only three or less of the quarters. Hourly variable emission PTEMARB files for these eight additional EGUs were included in the final stages of Phase I modeling. As Phase II modeling was initiated, it became clear that a further error in the extraction routine related to nitrogen oxide emitting EGUs was discovered and the final set of EGUs for which CEMS data was used to develop inputs for Phase II CALPUFF modeling included a total of 869 different electric generating units.

In most cases, the CEMS information being reported by a source applies to a single EGU at a facility associated with a single stack or emission point. In many cases, however, the reported information represents the combined emissions for between one and five EGUs at a facility. In these cases emissions for each unit are reported separately, but some of the stack or emission point information is common. We extracted the reported hourly SO_2 and NO_X emissions data for each of the combined units and created an hourly sum from all the units included in the raw data file. Thus for more than 200 of the 869 modeled points (represented by a stack), the mass emission of pollutants modeled is actually the sum of emissions from a combination of two or more EGUs at a facility.

Information characterizing how the emission occurs at each emission point (stack height, stack diameter, stack exit velocity, stack temperature, and stack base elevation) are necessary inputs required by CALPUFF. The CEMS database generally has data fields allowing calculation of all but the stack temperature. A default stack temperature of 422 degrees K was used for VTDEC modeling during Phase I. This assumed stack temperature was also used for all CEMS points modeled during Phase II. This assumption affects the height of plume transport in the long range transport situations being modeled. In cases where there were missing values in the reported data for stack exit velocity, a default value which was the average of all the reported values in the CEMS database extracted was used (14.67 m/sec based on 3,785,000 values reported in the data for the initial 778 EGUs extracted during Phase I). In cases where stack height or diameter was missing, a two step process was followed. First, a database comprised of Utility ORIS codes and 1990 National Emissions Data with stack parameters was searched to match the ORIS code and extract the information if available. If this did not produce a usable stack height or stack diameter, 150m was used for stack height and 6m was used for stack diameter.

Stack base elevations were determined from the model terrain created by CALMET pre-processors and the lat/lon location of the EGU point which was always available in the CEMS database.

To rank the individual stationary point sources with the largest ambient sulfate impact at receptors, it proved useful to structure modeling input files in a way such that a single source's impacts could be distinguished separately from all others. Post-processing routines available for use with CALPUFF output (CALSUM) allow individual output files to be combined into composite output files providing combined impacts at the receptors. This post-processing works properly if there is compatibility between the model results running all sources together with summing the model results from many individual source runs. For the sulfur chemistry involved, this assumption is entirely reasonable. Although nitrogen chemistry does not prove so amenable to this assumption, there are ways to post-process the results to obtain more realistic partitioning of nitrogen compounds predicted. As previously mentioned, the primary objective of the Vermont modeling study is to evaluate sources of sulfur emissions and their influence on ambient sulfate concentrations at Class I areas, therefore we were not so concerned about the predictions for ambient nitrogen at these receptors. While sulfur will utilize available ammonia preferentially, leaving only excess ammonia available for nitrogen reactions, sensitivity runs using an assumed background ammonia concentration of 1 ppb for all 12 months of year did not show any significant difference in the sulfate modeled when sources were run together versus when they were run individually.

Sensitivity Runs Conducted Prior to Final Phase II Model Runs

Prior to Phase II final runs, a relatively comprehensive sensitivity and validation process was conducted examining several potential variations in CALPUFF input file assumptions about rate of conversion from gaseous sulfur dioxide to particulate sulfate forms. Sensitivity to diurnal variability in percent conversion rates was tested. In addition to these diurnal variability sensitivity runs, a single run was conducted which assumed only domain boundary conditions and no sources internal to the domain. This allowed us to test the sensitivity of results in various portions of the domain to background SO_4 values transported into the domain and temporal changes in these.

Sensitivity runs were only conducted for the CEMS variable hourly emission EGUs modeled individually which were then summed to show combined impacts for the total of all 869 stack points. For Phase I modeling it had been concluded that running individual sources in separate CALPUFF runs and combining the results together using CALSUM processing routines provided by EarthTech (the developers of the CALPUFF system) was appropriate for the ambient sulfate assessment which is the primary objective of this VTDEC modeling work. The additional sensitivity runs conducted during Phase II did not change our conclusion in this regard.

The most comprehensive aspect of the sensitivity runs conducted during Phase II related to how the assumptions estimating rate of chemical conversion from sulfur dioxide gas to sulfate particle form affected the predicted impacts at the receptors. Five different scenarios were utilized. The first scenario (ORIGc) used the standard default assumptions from CALPUFF's January 2000 User's Guide. The default assumes a constant conversion rate at night throughout the entire time period of the run (0.2% per

hour) and daytime rates based on MESOPUFF II chemistry. This initial Phase II version of the modeling runs for CEMS sources (ORIGc) was essentially the same as the Phase I run except for the fact that instead of leaving the night-time conversion rate at 0.2% for all four quarters of the year, scenario ORIGc changed the default rate in each quarter. 1st quarter rate was set at 0.1% per hour, 2nd quarter rate at 0.2%, 3rd quarter rate at 0.3%, and 4th quarter rate at 0.2%. Other differences between this base run for Phase II and the Phase I run were the result of an increase in the number of CEMS sources from 778 to 869 and a revised Quarter 1 CALMET wind-field treatment which corrected a bias in the 750 mb wind speeds for the 1st Quarter that was discovered while analyzing Phase I runs.

Four other scenarios were run. Three of these incorporated user-specified SO_2 to SO_4 conversion rates which were input into the model through an external file. These three runs also added an estimate of direct SO_4 emissions for the CEMS sources. A direct sulfate emission rate for each of the EGUs, estimated to be 3% of the total mass of SO_2 emission each hour was incorporated into the input files for each CEMS source. The fourth run involved only the addition of direct SO_4 emissions, with no change to the conversion rate chemistry. The direct SO_4 emission added was thought to be a reasonable estimate based on a number of papers in the literature concerning power plant plume studies using aircraft and theoretical quantification of sulfite (SO_3) and H_2SO_4 in exhaust streams exiting power plant stacks. The 2nd thru 5th sensitivity runs were labeled DIRso4, CHEM2, CHEM3, and finally CHEM4, run in that order. The DIRso4 run was comparable to the ORIGc run except for addition of the direct SO_4 emissions. For the three runs labeled CHEM2, CHEM3, and CHEM4, flags were set to cause CALPUFF to read the appropriate user-supplied CHEM.DAT file which contained diurnal variation in hourly chemical conversion rates which were the same for each day during a quarter but changed by quarter.

In the first of the three user-specified diurnal rate variation scenarios (CHEM2), rates were based on information contained in informal guidance included with the HYSPLIT4 SO_2/SO_4 Chemistry Module developed as part of an experimental package by NOAA Air Resources Laboratory staff (Draxler, 29 August 2003 Readme.txt file which was attached to the downloaded software). The CHEM3 scenario used similar diurnal patterns for rates of conversion as CHEM2 but roughly doubled the rates uniformly. In all three of these scenarios exploring the effect of hourly conversion rate the same assumptions for direct SO_4 emissions were incorporated as were included in the DIRso4 scenario. The last scenario run (CHEM4) used rates of conversion roughly halfway between the CHEM2 and CHEM3 scenarios. Table D-1 below shows the diurnal hourly SO_2 to SO_4 conversion rates in percent per hour for these sensitivity runs.

Table D-1. Transformation Rates of gaseous SO_2 to particulate form SO_4 used in VTDEC Sensitivity Run Scenarios

Diurnal %/Hour Rates of Conversion of SO_2 to SO_4 used in VTDEC CALPUFF Phase II Sensitivity Runs																									
Scenario	**Hr 01**	**Hr 02**	**Hr 03**	**Hr 04**	**Hr 05**	**Hr 06**	**Hr 07**	**Hr 08**	**Hr 09**	**Hr 10**	**Hr 11**	**Hr 12**	**Hr 13**	**Hr 14**	**Hr 15**	**Hr 16**	**Hr 17**	**Hr 18**	**Hr 19**	**Hr 20**	**Hr 21**	**Hr 22**	**Hr 23**	**Hr 24**
Quarter 1																								
ORIGc	**Default CALPUFF setting: MESOPUFF II transformation rates used in Day-time Night-time rate constant 0.1**																							
DIRso4	**Default CALPUFF setting: MESOPUFF II transformation rates used in Day-time Night-time rate constant 0.1**																							
CHEM2	0.1	0.1	0.1	0.1	0.1	0.1	0.1	0.2	0.4	0.6	0.7	0.8	0.8	0.8	0.7	0.6	0.4	0.2	0.1	0.1	0.1	0.1	0.1	0.1
CHEM3	0.2	0.2	0.2	0.2	0.2	0.2	0.2	0.4	0.8	1.2	1.4	1.6	1.6	1.6	1.4	1.2	0.8	0.4	0.2	0.2	0.2	0.2	0.2	0.2
CHEM4	.15	.15	.15	.15	.15	.15	.15	0.3	0.6	0.9	1.0	1.2	1.2	1.2	1.0	0.9	0.6	0.3	.15	.15	.15	.15	.15	.15
Quarter 2																								
ORIGc	**Default CALPUFF setting: MESOPUFF II transformation rates used in Day-time Night-time rate constant 0.2**																							
DIRso4	**Default CALPUFF setting: MESOPUFF II transformation rates used in Day-time Night-time rate constant 0.2**																							
CHEM2	0.2	0.2	0.2	0.2	0.2	0.2	0.2	0.4	0.8	1.2	1.6	2.0	2.0	2.0	1.6	1.2	0.8	0.4	0.2	0.2	0.2	0.2	0.2	0.2
CHEM3	0.4	0.4	0.4	0.4	0.4	0.4	0.4	0.8	1.6	2.4	3.2	4.0	4.0	4.0	3.2	2.4	1.6	0.8	0.4	0.4	0.4	0.4	0.4	0.4
CHEM4	0.3	0.3	0.3	0.3	0.3	0.3	0.3	0.6	1.2	1.8	2.4	3.0	3.0	3.0	2.4	1.8	1.2	0.6	0.3	0.3	0.3	0.3	0.3	0.3
Quarter 3																								
ORIGc	**Default CALPUFF setting: MESOPUFF II transformation rates used in Day-time Night-time rate constant 0.3**																							
DIRso4	**Default CALPUFF setting: MESOPUFF II transformation rates used in Day-time Night-time rate constant 0.3**																							
CHEM2	0.3	0.3	0.3	0.3	0.3	0.3	0.3	0.6	1.3	2.0	2.6	3.0	3.0	3.0	2.6	2.0	1.3	0.6	0.3	0.3	0.3	0.3	0.3	0.3
CHEM3	0.6	0.6	0.6	0.6	0.6	0.6	0.6	1.2	2.6	4.0	5.4	7.0	7.0	7.0	5.4	4.0	2.6	1.2	0.6	0.6	0.6	0.6	0.6	0.6
CHEM4	.45	.45	.45	.45	.45	.45	.45	0.9	2.0	3.0	4.0	5.3	5.3	5.3	4.0	3.0	2.0	0.9	.45	.45	.45	.45	.45	.45
Quarter 4																								
ORIGc	**Default CALPUFF setting: MESOPUFF II transformation rates used in Day-time Night-time rate constant 0.2**																							
DIRso4	**Default CALPUFF setting: MESOPUFF II transformation rates used in Day-time Night-time rate constant 0.2**																							
CHEM2	0.2	0.2	0.2	0.2	0.2	0.2	0.2	0.4	0.7	1.0	1.3	1.5	1.5	1.5	1.3	1.0	0.7	0.4	0.2	0.2	0.2	0.2	0.2	0.2
CHEM3	0.4	0.4	0.4	0.4	0.4	0.4	0.4	0.8	1.4	2.0	2.6	3.0	3.0	3.0	2.6	2.0	1.4	0.8	0.4	0.4	0.4	0.4	0.4	0.4
CHEM4	0.3	0.3	0.3	0.3	0.3	0.3	0.3	0.6	1.0	1.5	2.0	2.3	2.3	2.3	2.0	1.5	1.0	0.6	0.3	0.3	0.3	0.3	0.3	0.3

A PTEMARB input file was created for each quarter of 2002 for each of the 869 CEMS emission points. The emission points are identified by an ID created from the EGU ORIS facility code and a descriptor of the unit or units for which the hourly emission applied. These individual 869 CEMS EGU emission points were run separately for the full year 2002 (it takes 4 minutes per CEMS emission point to complete the full year run on a 3.2 Ghz PC with 1 GB RAM). In testing the sensitivity to the different rates of conversion, each of these EGU input files was run for the complete year of 2002 a total of five times. All other groups of small point sources, area sources, and mobile sources modeled were only run one time using the default (ORIGc) sensitivity conditions. A sixth set of results was independently produced by incorporating transport into the domain using an hourly estimate of sulfate formed external to the domain boundaries. A variable boundary file was produced by examining measurements along the boundaries and wind directions indicated by the CALMET meteorological fields. Results from this "background SO_4" estimate could be added to any of the sensitivity runs for the CEMS sources. As of the writing of this report, final evaluation of these sensitivity runs is still being conducted and there may be further refinement of some of these scenarios in the future. After our initial interpretation of the comparative results obtained for the various sensitivity runs, we concluded that the differences between them was either relatively minor at almost all locations in the domain, or the assumptions used in the sensitivity scenario were not well enough documented to support utilization of those results over the base case (ORIGc) run results.

In Phase II, the Vermont modeling included small points and most "area" and mobile source categories of emissions whereas these were not modeled during Phase I.

In addition to the CEMS point EGU results, the Phase II results include these additional sources of sulfur dioxide, nitrogen oxides, and $PM_{2.5}$ for most of the states in the domain (inventories for these emissions for some source categories in states on the western boundary of the domain were not complete enough by the time the modeling was conducted.). In making a decision as to the appropriateness of the ORIGc assumptions over others tested for the CEMS point EGU sources, an evaluation was conducted to examine how well the model reproduced the 24-hr sulfate measurements at 22 sites in the northeastern quadrant of the domain when run with all the sources included.

As seen in Figure D-3 and Figure D-4, there were some clear differences between some of the sensitivity runs, primarily in the magnitude of impacts predicted at various receptors. However, the regression of modeled 24-hr SO_4 impact against monitored ambient SO_4 at ground level did not show obvious improvement from the base ORIGc scenario when evaluated at the 22 evaluation sites chosen from the northeastern quadrant of the domain, based on either paired 24-hr comparisons individually or the quarterly averages of those paired 24-hr values at each site (Figure D-5 and Figure D-6). As of the date of this report, the analysis has not been completed adequately to cause us to currently determine that anything other than the default (ORIGc) run was any better at reproducing measured SO_4 ion at the discrete receptors overall. Therefore the results of Phase II modeling with the Vermont CALPUFF platform are being presented based on the ORIGc scenario results which were produced using essentially all default settings for the CALPUFF inputs. There is some potential that this decision could be revised as we have more time to carefully examine the huge volume of information that all the Phase II modeling produced.

Figure D-3. Acadia National Park Modeled 24-Hr SO_4 Ion Comparison to Measurements

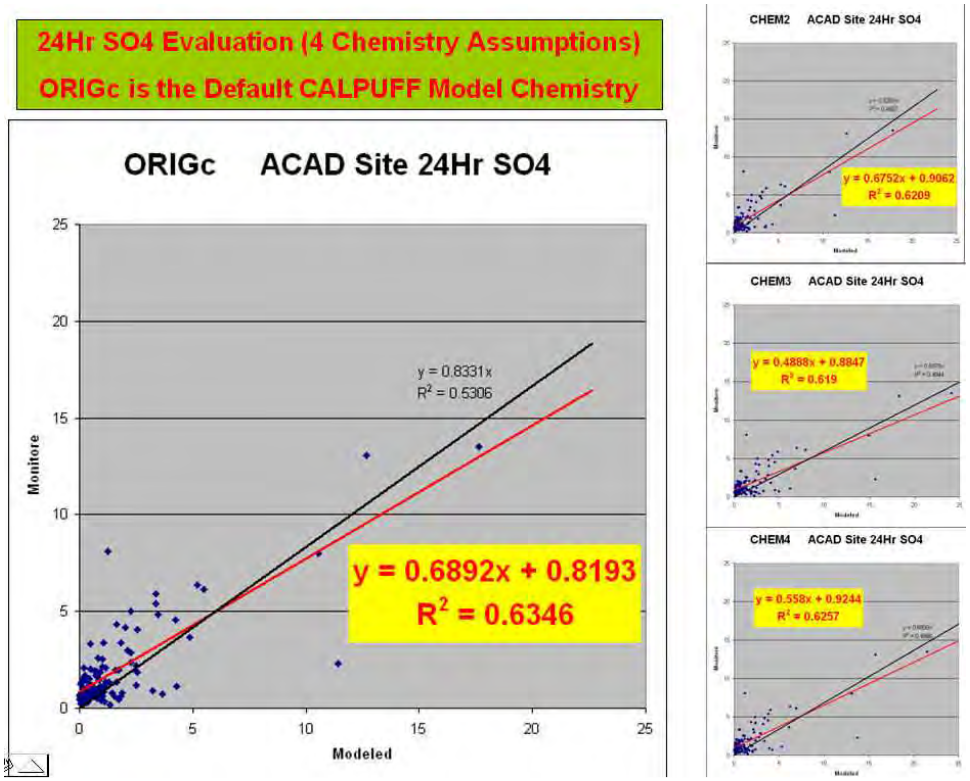

Figure D-4. Lye Brook Wilderness Area Modeled 24-Hr SO_4 Ion Comparison to Measurements

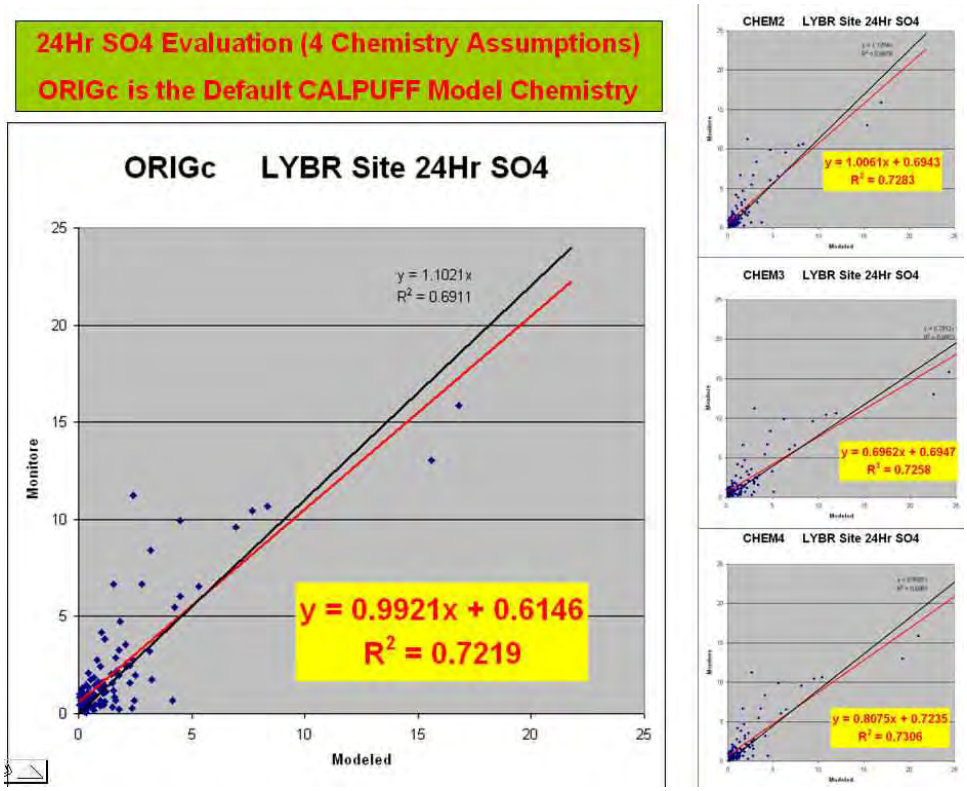

Figure D-5. 22 Northeastern Site Modeled 24-Hr SO_4 Ion Comparison to Measurements

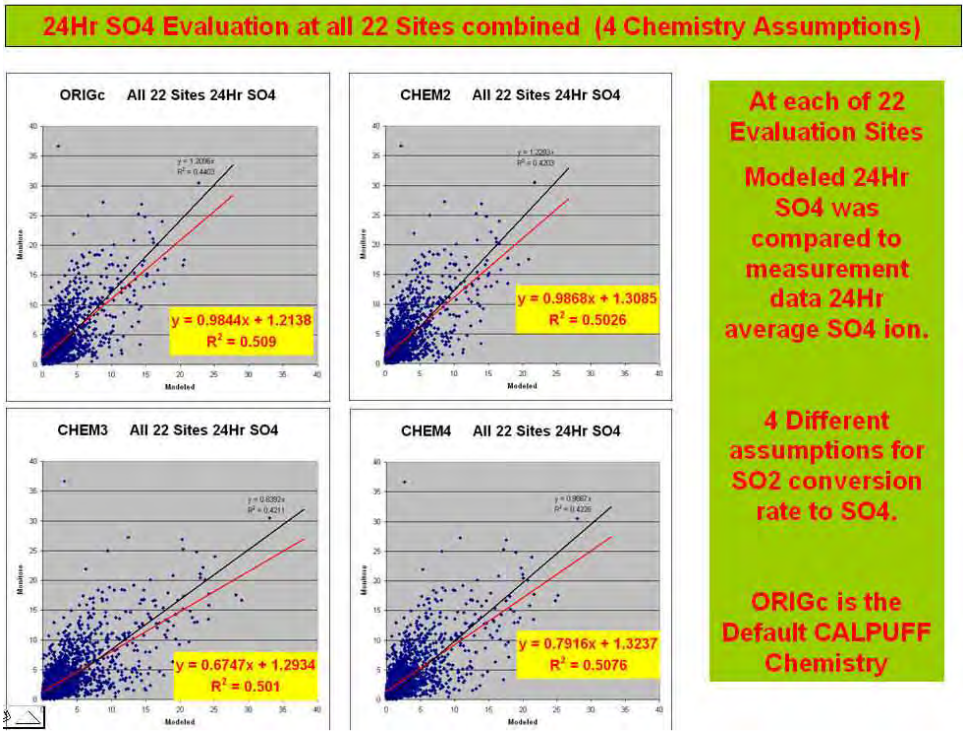

Figure D-6. 22 Northeastern Site Modeled Quarterly Average SO4 Ion Comparison to Measurements

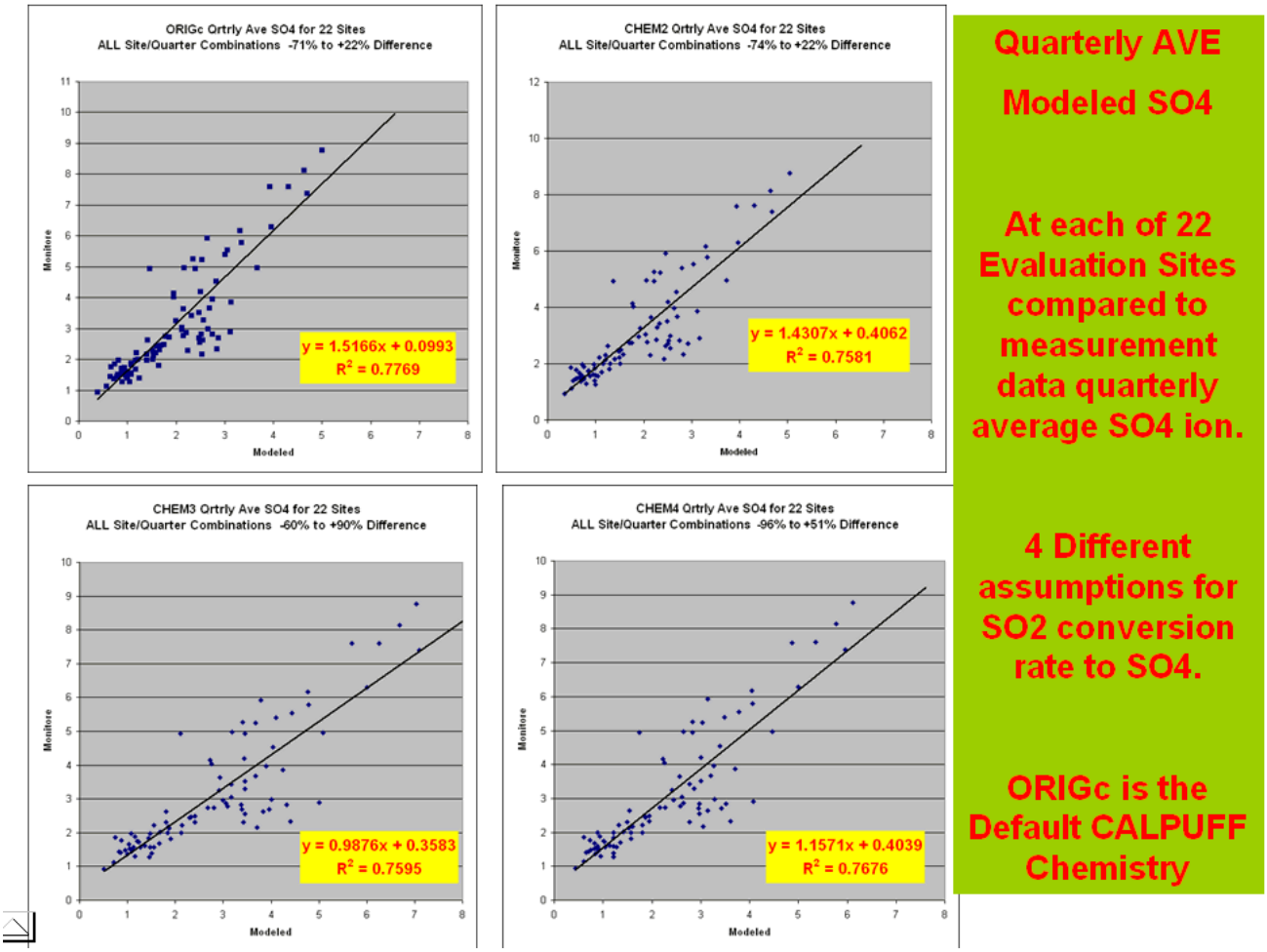

D.2.1.2. RPO Modeling Inventories and NEI Data Used for Non-CEMS Sources

The most complete source of emission data available from states is generally the National Emission Inventory (NEI) which is updated and maintained by EPA on a three-year cycle. The most recent quality-assured data available at the initiation of Phase I modeling was for calendar year 1999. At the end of 2005, year 2002 NEI data was still being reviewed and quality assured. Data incorporated in the NEI for any given year is data that has been submitted to EPA by the individual state regulatory air programs. It routinely includes annual average emissions for sulfur dioxide, nitrogen oxides, and fine particulate matter from both EGUs and non-EGUs located in each state. Data in the NEI may also include emission data for time periods less than annual, such as rates applicable only to several months of the year or typical summer day emissions. The average long-term emission data in NEI includes entries for the same EGUs that are also reporting detailed hourly variable emissions to the EPA maintained CEMS database.

For Phase I CALPUFF point source modeling conducted by VTDEC, the 1999 NEI version 3 (files dated 11/20/03) data was used to supplement CEMS data described

above. Data was downloaded from the EPA website in mid-December 2003. A revised version of 1999 NEI version 3 (dated 3/3/04) was posted at some point in 2004, however that updated version was not used in Phase I modeling by VTDEC. The 1999 NEI version 3 data consisted of zipped files with emission data for point sources, area sources, on-road sources, and non-road sources. Phase I modeling by VTDEC was focused on the point source component therefore only the 1999 point source NEI file data was used for the modeling performed by VTDEC during Phase I of the project.

The record structure used for 1999 NEI is NIF version 2. Fortran executable code was developed to extract records from the point source data files based on the file formats specified in NIF version 2. The code was designed to also create text files which placed the NEI data extracted into lines of input formatted to be compatible with CALPUFF control file Input Group 13 format (for large point sources) or Input Group 14 format (aggregated small point sources into area sources). The code repeatedly searched the record files contained in the file "99v3pointascii.zip" which contain stack parameter ("erpoint.txt"), emissions ("empoint.txt"), and facility id ("sipoint.txt") data. The extracted facility and emission point identification information was compared to a target listing of identification codes for EGUs for which variable hourly emissions of sulfur oxides and nitrogen oxides already had been extracted from the CEMS database. Several output files were generated for each of 34 states in the domain. Each output file comprised a subset of emission and stack data formatted in CALPUFF control file input format. The extracted subsets produced during Phase I VTDEC modeling (and later reproduced using RPO databases during Phase II) are described below:

FOR EACH STATE IN THE DOMAIN

1. A subset of NEI sources whose ID matched a CEMS EGU point. Only the $PM_{2.5}$ emissions information was included in the formatted "POINT source" input file, the NEI sulfur oxide and nitrogen oxide emission information was ignored in preference to the CEMS data.

2. A subset of NEI sources with ANNUAL SO_2 emissions greater than 100 Tons for 1999 whose ID did not match any CEMS EGU point. In this case all three pollutant emissions ($PM_{2.5}$, SO_2, and NO_X) were included in the formatted "POINT source" input file.

3. A subset of NEI sources with DAILY SO_2 emissions specifically identified at different rate at the start of the 3rd quarter time period whose ID did not match any CEMS EGU point. In this case all three pollutant emissions ($PM_{2.5}$, SO_2, and NO_X) were included in the formatted "POINT source" input file. When annual CALPUFF run was done, for the 3rd quarter this subset of inputs was substituted for the inputs in subset 2 or subset 4 that were used for the other three quarters in the annual run.

4. A subset of NEI sources with ANNUAL SO_2 emissions greater than 10 Tons for 1999 and located within 100 km of any of 51 receptors identified for the MANE-VU RPO whose ID did not match any CEMS EGU point. In this case all three pollutant emissions ($PM_{2.5}$, SO_2, and NO_X) were included in the formatted "POINT source" input file.

5. A subset of NEI sources with ANNUAL SO_2 emissions less than 100 Tons for 1999 and also not within 100 km of any of the 51 receptors whose ID did not match any CEMS EGU point. In this case all three pollutant emissions ($PM_{2.5}$, SO_2, and NO_X) were aggragated in a formatted "20km x 20km AREA Source" input file appropriate for the location of the point source.

When combined with the 2002 CEMS emission data for SO_2 and NO_X from EGUs, these subsets of emission points derived from the 1999 NEI data represented a reasonable surrogate for all the remaining 2002 non-CEMS point source emissions of SO_2, NO_X, and $PM_{2.5}$ in the domain being modeled. For Phase I CALPUFF runs, each of the state-specific subsets was run in a single run to produce the NEI large point source impacts and the NEI small point source impacts (pseudo area sources) from each state on each of 72 chosen receptors in the domain. The pseudo area sources were run with an assumed initial sigma-z of 5.0 meters and a default emission height of 25.0 meters. In cases where the NEI data permitted the computation of an average stack height for the small sources incorporated into the pseudo area source, the average stack height was used for that area source.

For Phase II modeling, the VTDEC initially intended to utilize the quality assured version of the 2002 NEI. This would have meant that the same software developed to extract non-CEMS source input data from the 1999 NEI could have been used to extract similar data from the 2002 NEI. At the beginning of the Phase II modeling effort (March 2005) there was still no quality assured NEI for 2002; only a draft version was available. In the same time period, each of the regional haze planning organizations (RPOs) had already created draft versions of the RPO inventories that would be used for base-year 2002 CMAQ or other grid-based modeling efforts needed for ozone SIPs (as well as $PM_{2.5}$ and regional haze SIPs) required by states in the eastern U.S. VTDEC decided to re-configure its emission data extraction program codes to be able to access the various RPO emission inventory data files. RPO inventories were accessed from RPO web-sites identified by the MARAMA organization which is coordinating the production of SIP quality emission inventories for states in the MANE-VU and OTC regions and also coordinating exchange of these inventories with other RPOs. Inventories are always being upgraded and changed, so it is likely that the actual inventory files accessed to create modeling inputs used by VTDEC may differ from the latest versions of those inventories. VTDEC believes that the conclusions that can be drawn about sources and relative source and state impacts on visibility in eastern Class I areas due to sulfate aerosol formed secondarily from sulfur dioxide emissions in the domain modeled would not change dramatically should more current non-CEMS RPO source emissions be substituted for modeling inputs used by VTDEC in its Phase II CALPUFF modeling.

Source categories modeled during Phase II were expanded from those modeled during Phase I. In addition to utilizing the expanded set of 869 CEMS EGU hourly source emission inputs, the Phase II VTDEC modeling included all subsets of stationary sources extracted from the RPO inventories in a manner similar to that described above for extraction and identification of non-CEMS point sources modeled under Phase I. On-road and non-road mobile sources and area sources aggregated at the county level were also modeled during Phase II, although in some cases data was not available from

particular states in the domain covered by the CALPUFF modeling. Only the largest SO_2 point sources located in portions of Canada within the modeling domain were included. The Canadian sources modeled had to be modeled using reasonable assumptions with regard to stack height and stack exit flow conditions due to inability to obtain this information. The state-by-state emissions of sulfur dioxide, nitrogen oxides, and $PM_{2.5}$ modeled by VTDEC during Phase II are summarized in Table D-2 through Table D-4. Canadian source emissions modeled are summarized on the line labeled CN in these tables.

Table D-2. Summary of SO_2 Emission Inputs for Phase II VT CALPUFF runs

2002 SO2 Emissions Modeled (12,163,466 Tons)

STATE	EGUs using CEMS	RPO Large PT as PT	RPO Small PT 20kmx20km AREA	MOBILE ON-ROAD as CNTY km**2	MOBILE NON-ROAD as CNTY km**2	RPO Area as CNTY km**2
AL	301,262	28,977	31,374	not modeled	4,153	14,725
CT	10,131	1,905	287	1,534	8,149	11,489
DC	1,073	967	20	1,599	1,677	7,940
DE	31,144	5,000	4,043	2,942	18,180	5,744
GA	497,490	18,467	21,107	not modeled	9,074	29,014
IA	125,460	183,377	1,247	not modeled	4,429	not modeled
IL	342,762	142,501	5,329	not modeled	360,917	77,362
IN	720,890	87,818	8,593	not modeled	11,976	98,268
KY	462,012	30,688	34,362	not modeled	80,477	67,317
MA	90,194	11,219	3,416	3,338	9,776	40,421
MD	248,407	34,687	2,634	22,835	121,496	103,098
ME	1,923	20,610	718	2,682	6,620	10,689
MI	319,673	60,963	5,154	not modeled	6,736	23,069
MN	93,895	65,046	5,844	not modeled	5,701	3,990
MS	8	7,914	9,041	not modeled	10,071	176
NC	442,505	54,048	60,887	not modeled	51,775	8,625
NH	41,425	1,923	678	479	3,591	4,416
NJ	46,791	7,820	1,019	5,815	44,682	16,800
NY	216,112	30,184	6,971	9,781	38,960	117,584
OH	1,073,526	59,200	680	not modeled	83,946	22,961
PA	788,130	90,457	22,339	19,417	58,309	112,610
SC	189,252	55,119	60,482	not modeled	21,802	10,134
TN	302,876	84,652	5,607	not modeled	79,963	28,677
VA	224,375	20,362	56,178	not modeled	38,166	35,895
VT	5	874	36	515	25,580	2,322
WI	187,937	61,458	3,367	not modeled	5,616	2,065
WV	489,823	15,775	41,121	not modeled	106,622	71,793
RI	5	0	0	350	5,715	3,795
MO	179,396	not modeled	not modeled	not modeled	not modeled	not modeled
OK	103,734	not modeled	not modeled	not modeled	not modeled	not modeled
KS	125,918	not modeled	not modeled	not modeled	not modeled	not modeled
AR	70,009	not modeled	not modeled	not modeled	not modeled	not modeled
NE	30,536	not modeled	not modeled	not modeled	not modeled	not modeled
TX	39	not modeled	not modeled	not modeled	not modeled	not modeled
SD	11705	not modeled	not modeled	not modeled	not modeled	not modeled
CN	Modeled as PT	592,073	not modeled	not modeled	not modeled	not modeled
	7,770,423	**1,774,084**	**392,534**	**71,287**	**1,224,159**	**930,979**

Table D-3. Summary of NO_X Emission Inputs for Phase II VT CALPUFF runs

2002 Nox Emissions Modeled (18,068,578 Tons)

STATE	EGUs using CEMS	RPO Large PT as PT	RPO Small PT 20kmx20km AREA	MOBILE ON-ROAD as CNTY km**2	MOBILE NON-ROAD as CNTY km**2	RPO Area as CNTY km**2
AL	109,435	17,072	39,769	0	46,530	9,213
CT	5,144	6,141	1,169	63,490	22,916	11,751
DC	402	769	40	52,556	16,453	9,669
DE	9,574	2,067	2,366	72,166	54,509	10,192
GA	139,613	7,729	27,656	not modeled	111,016	18,904
IA	77,015	84,596	122,089	not modeled	41,026	not modeled
IL	167,937	37,988	96,931	not modeled	3,406,188	720,994
IN	241,542	37,336	76,498	not modeled	122,347	44,933
KY	176,107	12,033	38,186	not modeled	618,504	60,897
MA	27,421	15,592	4,543	90,378	50,739	23,217
MD	69,625	22,642	3,351	684,914	255,726	109,333
ME	734	17,905	1,659	39,805	10,671	5,820
MI	109,169	33,434	85,526	not modeled	77,698	23,348
MN	72,834	76,365	105,786	not modeled	59,794	15,136
MS	4,455	3,821	20,316	not modeled	91,412	951
NC	137,313	28,950	56,472	not modeled	590,772	not modeled
NH	6,430	2,261	864	20,687	6,323	6,867
NJ	26,154	17,943	4,177	236,710	103,467	40,161
NY	64,318	33,897	7,130	306,829	131,190	93,606
OH	325,887	9,415	22,666	not modeled	866,257	67,647
PA	174,127	84,165	14,056	607,150	130,801	84,112
SC	79,314	28,244	46,529	not modeled	235,457	14,608
TN	133,278	42,923	73,250	not modeled	747,932	17,289
VA	77,061	25,145	45,621	not modeled	246,970	196,212
VT	228	500	58	11,978	3,785	1,809
WI	87,239	433	36,932	not modeled	63,292	6,807
WV	197,459	15,976	32,954	not modeled	1,418,683	76,908
RI	290	0	0	13,716	4,074	3,185
MO	122,373	not modeled	not modeled	not modeled	not modeled	not modeled
OK	74,219	not modeled	not modeled	not modeled	not modeled	not modeled
KS	84,686	not modeled	not modeled	not modeled	not modeled	not modeled
AR	40,891	not modeled	not modeled	not modeled	not modeled	not modeled
NE	21,978	not modeled	not modeled	not modeled	not modeled	not modeled
TX	2,156	not modeled	not modeled	not modeled	not modeled	not modeled
SD	14,503	not modeled	not modeled	not modeled	not modeled	not modeled
CN	Modeled as PT	147,250	not modeled	not modeled	not modeled	not modeled
	2,880,912	**812,592**	**966,594**	**2,200,379**	**9,534,532**	**1,673,569**

Table D-4. Summary of $PM_{2.5}$ Emission Inputs for Phase II VT CALPUFF runs

2002 PM2.5 Emissions Modeled (3,091,089 Tons)

STATE	EGUs using CEMS	RPO Large PT as PT	RPO Small PT 20kmx20km AREA	MOBILE ON-ROAD as CNTY km**2	MOBILE NON-ROAD as CNTY km**2	RPO Area as CNTY km**2
AL	Modeled as RPO PT	0	13,066	not modeled	3,044	12,873
CT	Modeled as RPO PT	928	678	959	2,705	15,116
DC	Modeled as RPO PT	211	48	900	1,270	8,200
DE	Modeled as RPO PT	207	540	8,998	7,133	15,246
GA	Modeled as RPO PT	0	5,736	not modeled	10,212	25,546
IA	Modeled as RPO PT	0	13,108	not modeled	4,737	not modeled
IL	Modeled as RPO PT	0	1,242	not modeled	354,094	432,882
IN	Modeled as RPO PT	0	12,560	not modeled	12,060	174,177
KY	Modeled as RPO PT	0	4,823	not modeled	38,749	58,087
MA	Modeled as RPO PT	3,540	3,155	8,129	8,080	39,238
MD	Modeled as RPO PT	2,186	4,749	12,701	108,798	235,600
ME	Modeled as RPO PT	10,144	979	10,870	6,161	36,959
MI	Modeled as RPO PT	0	2,701	not modeled	8,056	5,634
MN	Modeled as RPO PT	0	1,159	not modeled	7,019	31,478
MS	Modeled as RPO PT	0	2,666	not modeled	5,495	10,358
NC	Modeled as RPO PT	0	10,736	not modeled	52,353	52,438
NH	Modeled as RPO PT	631	437	349	2,745	11,910
NJ	Modeled as RPO PT	2,396	2,274	3,965	21,792	34,711
NY	Modeled as RPO PT	3,129	3,123	5,642	31,617	120,295
OH	Modeled as RPO PT	166	1,861	not modeled	76,598	29,696
PA	Modeled as RPO PT	12,128	13,938	9,993	55,721	165,612
SC	Modeled as RPO PT	0	13,263	not modeled	18,583	19,289
TN	Modeled as RPO PT	0	27,818	not modeled	52,588	31,248
VA	Modeled as RPO PT	5,567	7,777	not modeled	30,553	118,368
VT	Modeled as RPO PT	309	131	273	2,634	7,621
WI	Modeled as RPO PT	0	40	not modeled	7,364	6,979
WV	Modeled as RPO PT	14,505	3,785	not modeled	106,251	79,642
RI	Modeled as RPO PT	68	116	1,484	417	2,170
MO	not modeled	not modeled	not modeled	not modeled	not modeled	not modeled
OK	not modeled	not modeled	not modeled	not modeled	not modeled	not modeled
KS	not modeled	not modeled	not modeled	not modeled	not modeled	not modeled
AR	not modeled	not modeled	not modeled	not modeled	not modeled	not modeled
NE	not modeled	not modeled	not modeled	not modeled	not modeled	not modeled
TX	not modeled	not modeled	not modeled	not modeled	not modeled	not modeled
SD	not modeled	not modeled	not modeled	not modeled	not modeled	not modeled
CN	not modeled	not modeled	not modeled	not modeled	not modeled	not modeled
	0	**56,115**	**152,509**	**64,263**	**1,036,829**	**1,781,373**

D.2.2. VT DEC Meteorological Preparations

The VT DEC CALPUFF Modeling System uses the 2003 'beta test' version of the CALMET Model on the domain shown in Figure D-1 and described earlier. The vertical grid structure for the VT platform consisted of 8 levels, specified to allow accurate representation of atmospheric conditions in the surface level, transition level, and the free atmosphere.

CALMET runs performed by the VT DEC utilized *National Weather Service meteorological observations only* (i.e. radiosonde measurements for the upper atmospheric representation, Automated Surface Observing Station (ASOS) for the surface, and precipitation observers' measurements). Usage of the meteorological fields computed for this domain are acceptable for transport scenarios which occur above the surface layers, or, as defined by the EPA, long range transport events of greater than 50 kilometers. For these CALMET runs, the geographical processing to produce terrain heights and land use represented in the model was performed per Scire et al. (2000).

D.2.2.1. CALMET model input settings

A progressive model validation procedure (PMVP) – involving repetitive comparison of modeled to measured meteorological quantities as CALMET was run iteratively – was utilized to optimize CALMET model performance. In the following discussion the option settings are divided between 'invariable' settings which were constant throughout (e.g. grid size), and 'variable' settings which are indeterminate until the PMVP is complete. A list of the variable settings is provided below.

The 'Variable' CALMET Settings

The final meteorological fields produced by CALMET for this analysis resulted from comparison of the CALMET output meteorological fields to observations in the progressive model validation procedure. Thus comparison of CALPUFF predicted to monitored concentrations of sulfate was used to select optimal CALMET switch settings. The 'variable' settings primarily control the radial interpolation of meteorological observations as well as the distances at which terrain effects are estimated. The following 'variable' option settings were determined through the progressive model validation procedure discussed in section D.2.2.3:

IEXTRP - Defines extent to which surface wind observations are extrapolated to upper layers.

LVARY - Defines radial interpolation methods of observational inputs, where all observations within a specified radius may be utilized in estimation of wind field at a grid point, or just the nearest observation beyond a specified radial distance from the grid point.

R1,R2 - Defines the relative weighting of the first guess field and observations at each grid point in the domain, where R1 is the distance from an observational station at which the observation and first guess field are equally weighted.

TERRAD – Defines the radius of influence of terrain features in the generation of the first guess field at each grid point within the domain.

D.2.2.2. Production of CALMET Model Inputs

Meteorological data inputs consisted of 684 surface stations, 27 radiosonde stations for upper air representation, 1037 precipitation measurement sites, and 5 overwater (buoy) sites (see Figure D-7).

The surface stations were extracted from the integrated surface hourly observations (ISHO) dataset compiled by the National Climatic Data Center (NCDC). This data set also includes over-water stations, supplementing the 5 buoy site data acquired from a separate database. From all of these sources, 2002 data was extracted and processed in four quarters to allow for reasonable run times. For each meteorological data set, data format conversion and data filling was necessary. The following sections discuss procedures for each data set.

Figure D-7. Surface (ASOS), and Upper Air (Radiosonde), Stations used in the CALMET runs.

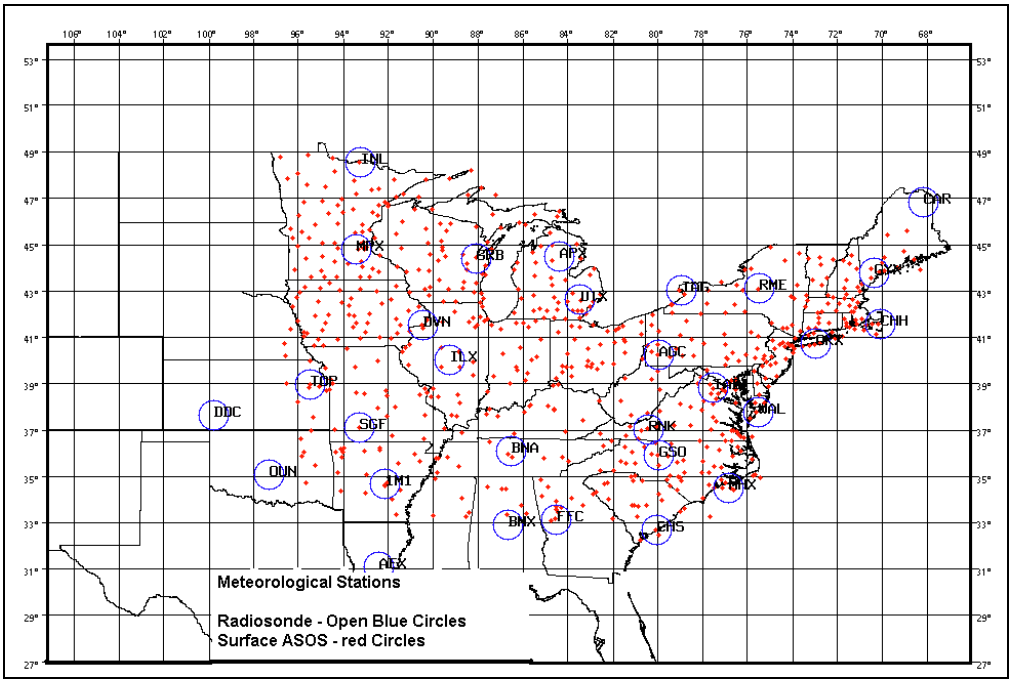

Upper Air Radiosonde Data

In order to develop a continuous dataset, a data substitution routine is required in order to fill-in missing radiosonde data. A routine was established to maximized the use of radiosonde data, given that the CALMET model does not always accept radiosonde measurements. If a sounding has a missing level within one of the lowest defined vertical model levels, CALMET will not accept the sounding. To correct this problem, wind or temperature data is taken from the closest level above where data *does* exist and substitutes for the missing datum (usually the lowest 200 meters of the atmosphere). This

method is preferable to substituting an entire sounding from a different location. When too much data was missing from a sounding, or the sounding was missing entirely, the surrounding stations were used for substitution.

Surface Meteorological Data

The ISHO surface meteorological observations is a compilation of the automated surface observing stations (ASOS), across North America. Variables that CALMET requires as inputs for the surface level are wind speed, wind direction, ceiling height, opaque sky cover, air temperature, relative humidity, station pressure and precipitation code. Given the parameters available in the ISHO dataset, it was necessary to compute relative humidity. This was done using following the National Weather Service guidance method (NWS, 2006).

Precipitation Data

Because of the large number of precipitation stations and the required format in CALMET input files, preprocessing and preparation of this data set can be time-consuming. For the precipitation data, the flag indicating data validity had to be recoded before the data could be read in by the EarthTech preprocessors.

Geographical Data

Using a set of programs for preprocessing geographical data (available from Earth Tech including terrel, ctgproc, ctgcomp, and makegeo) the land use and terrain elevations for the chosen domain were developed (Shown in Figure D-8 and Figure D-9). From this information CALMET then produces related physical fields that are necessary for the CALPUFF pollutant predictions including surface roughness, albedo, bowen ratio, soil heat flux, and leaf area index. Figure D-10 and Figure D-11 portray fields of friction velocity and the leaf area index for the domain.

Figure D-8. Smoothed Terrain Heights Utilized by VT DEC CALMET.

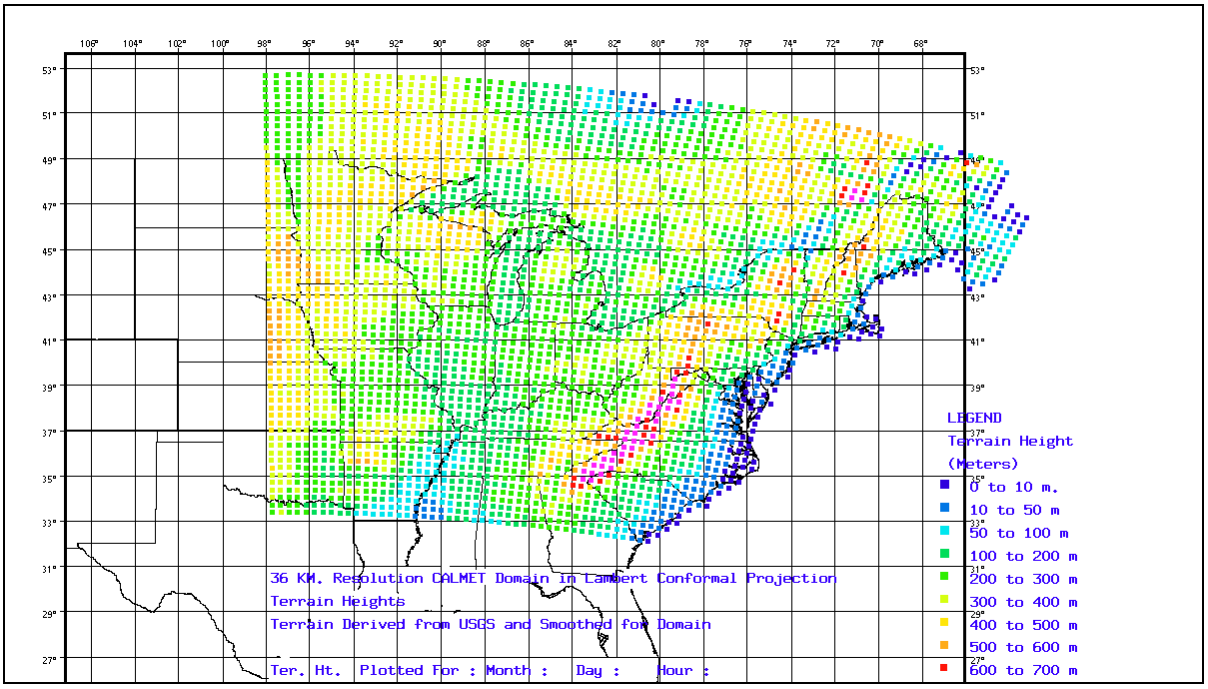

Figure D-9. Land Use Utilized by VT DEC CALMET.

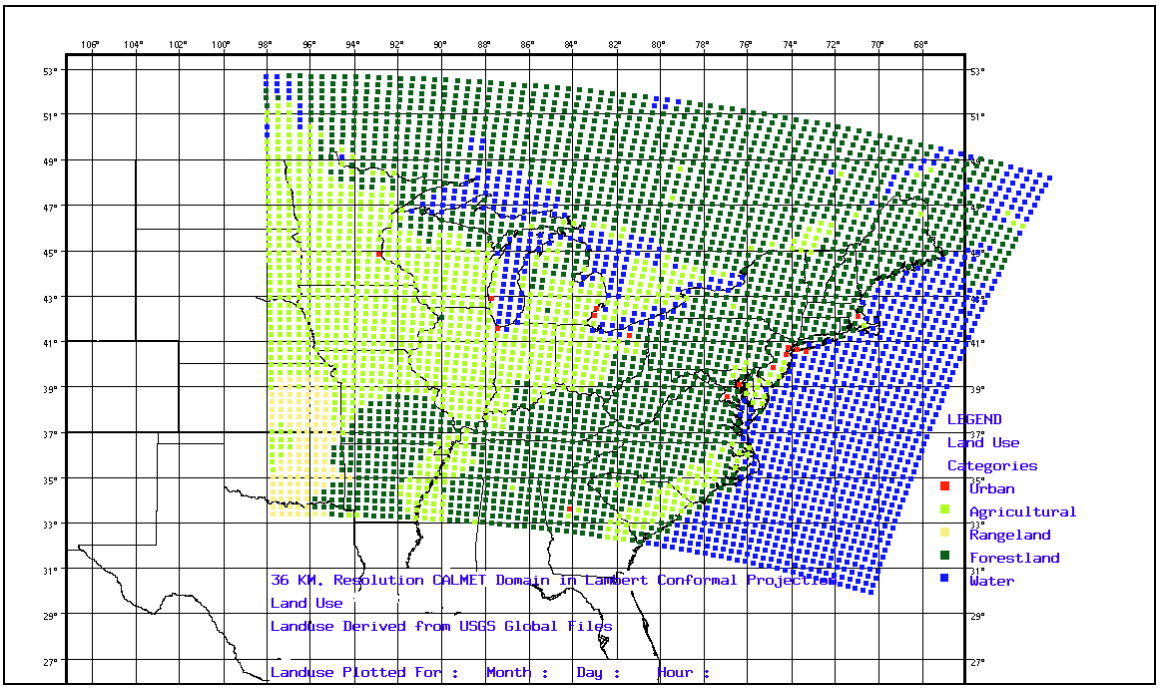

Figure D-10. Friction Velocity Field Produced by VT DEC CALMET.

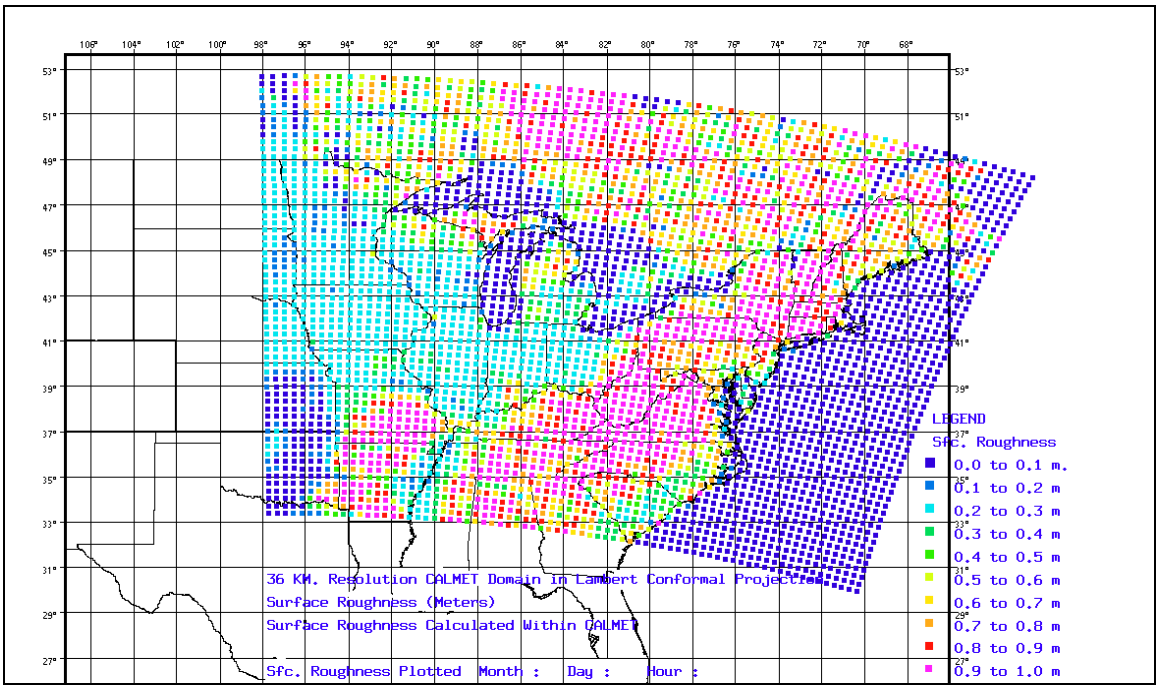

Figure D-11. Indexed Leaf Area Field Produced by VT DEC CALMET.

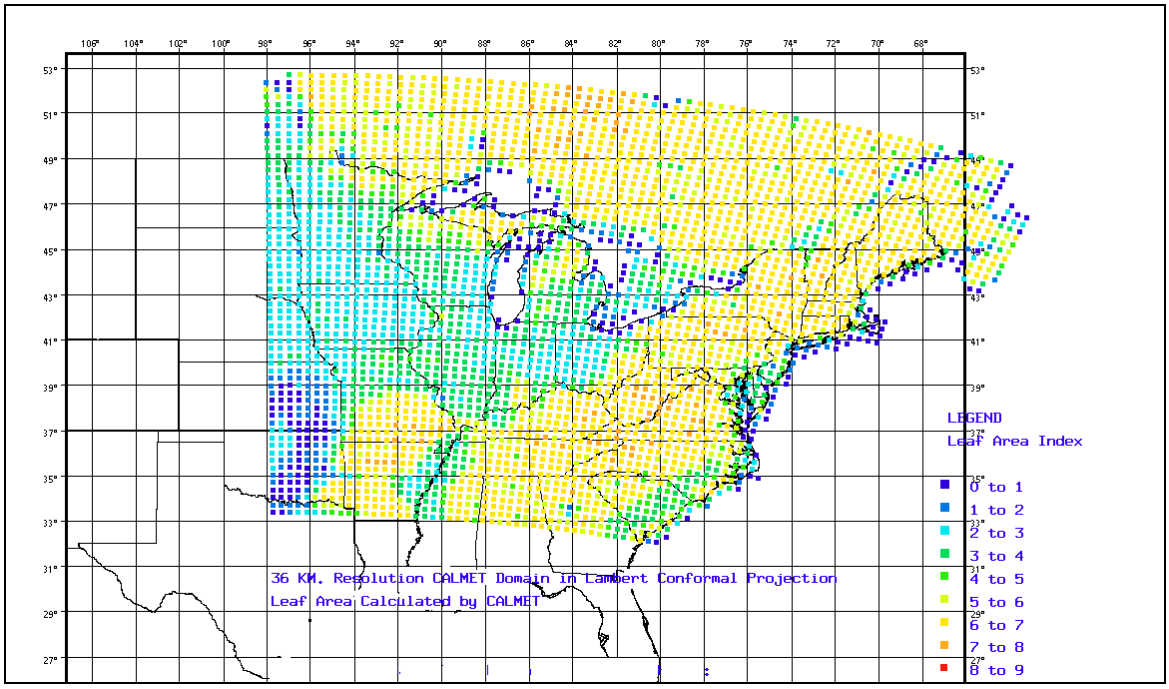

D.2.2.3. Data Validation

An iterative data validation/optimization process was used to determine the best mode to run CALMET in, and will be used for verification of the accuracy of the final meteorological fields produced to run CALPUFF during Phase II. Phase I data validation procedures involves only comparison of CALMET predicted meteorological fields to observations.

Validation Method Used to Determine Optimum CALMET Parameter Settings

The fundamental physical processes affecting long-range transport of air pollutants related to CALMET option settings are:

- Transport
- Dispersion
- Chemistry (not evaluated for CALMET usage).

With respect to long-range transport, model performance on the order of 200 kilometers or more, is most important. Therefore the CALMET runs must be able to accurately simulate transport above the surface layer. Thus, in order to minimize geographical effects on surface wind flows simulated in the production of the “Step One” windfield in CALMET option settings were intended to minimize CALMET physics and

produce wind fields by interpolating measured data from the NWS meteorological observations. A major concern for this application, where a very large domain was employed, was accurate representation of the meteorological fields at the domain edges, such as over water and over Canada.

When utilizing 'observations only' (i.e., no prognostic model inputs) mode for CALMET, 'variable' option settings must be set uniquely for each application. These option settings primarily involve interpolation of the observations, defining the 'weighting' of the observations in relation to the first guess field, and defining the extent to which surface observations may be weighted at levels above the surface. These settings include IEXTRP, LVARY, R1,R2, and TERRAD which were defined previously. The validation procedures consisted of a *visual examination* of these fields for ten day periods during each quarter of the year *prior* to the progressive model validation procedure involving comparison to observations. Visual examination also occurred as a final verification of fields produced to be utilized by CALPUFF. Figure D-12 and Figure D-13 are snapshots of the wind fields examined in movie form for a daytime and nighttime wind field for a summer day.

In the progressive model validation procedure, comparison to observations and quantification of accuracy were performed. Because this evaluation examines wind fields above the surface layer, radiosonde data was utilized. A radiosonde station located at 38.9 North Latitude and 77.5 West Longitude was chosen in a region of the domain where its exclusion would be acceptable because of the density other nearby radiosonde stations. This station then comprised the observational data set for the evaluation. Wind data at 925 millibars pressure level from the radiosonde was compared to CALMET output for level 4, whose center level elevation was 750 meters. The radiosonde was *excluded* from the CALMET runs for which the validation procedures were performed.

Figure D-12. Example noontime wind field at 750 meters for VT DEC CALMET.

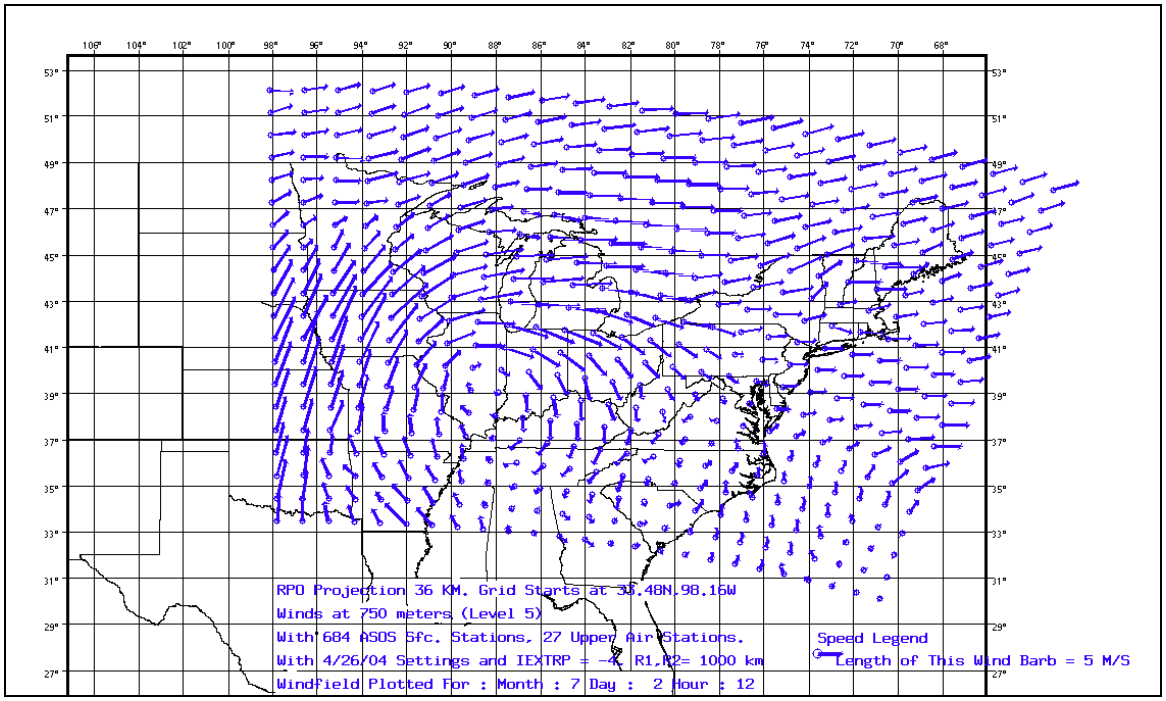

Figure D-13. Example midnight wind field at 750 meters for VT DEC CALMET.

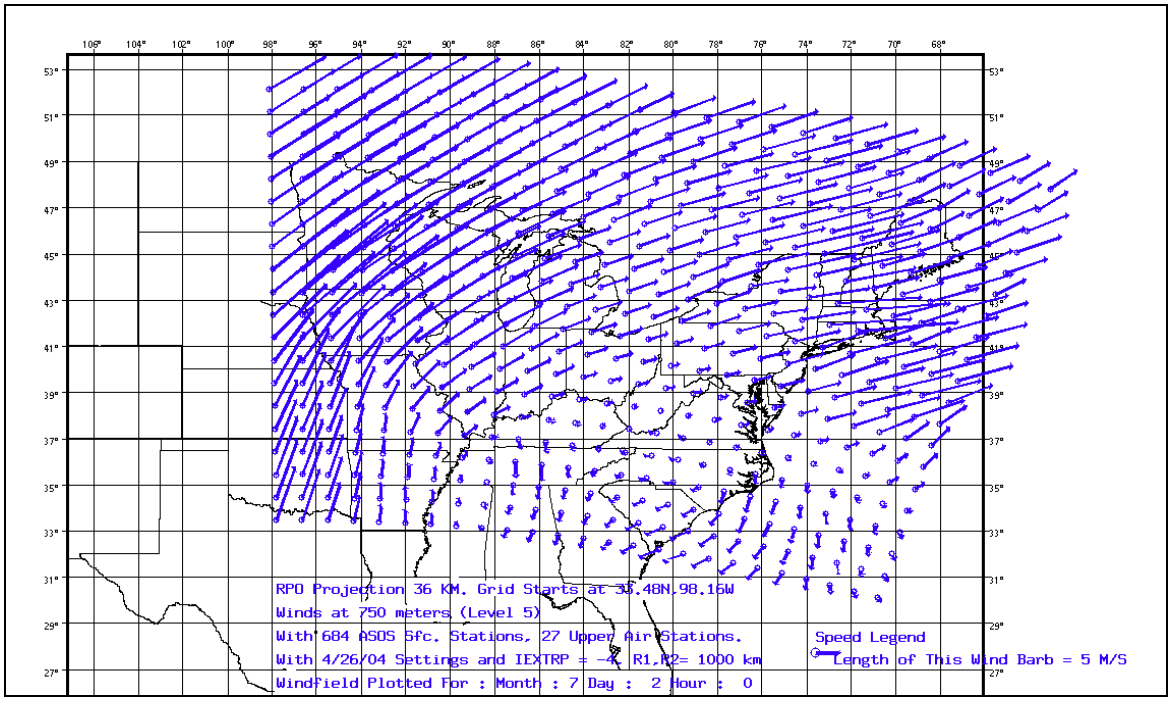

Wind field calculations produced by CALMET were then extracted for the grid point nearest the geographical location of the radiosonde station.

The first method involving comparison of CALMET wind fields to observations was paired in space and time and involves the estimation of 'bias' and 'absolute error' measures for wind speed and direction, where the 'bias' is computed as the average of the difference between modeled and measured values for each data pair accounting for the sign. The 'absolute error' estimates are identical to the bias estimate method, except the sign is not accounted for in the averaging. Table D-5 and Table D-6 give summaries of these results since the option settings mentioned above were varied to ascertain best model performance in this application.

The progressive model validation procedure runs performed in Table D-5 represent the final runs in the procedure. Early in this process it was established that a setting of 100 km for TERRAD and LVARY = T produced best results. In the runs tabulated in Table D-5, the R1 and R2 settings were varied by orders of magnitude over a reasonable range of settings, and also set at the horizontal grid resolution. The IEXTRP setting, which controls the vertical extrapolation of the surface wind to upper layers, was set for the several alternatives governing its effect on wind field production. Note that variation of the Option settings from run to run has significant effect on the four quantities calculated. It was decided that the most important quantities in this procedure, which was validating CALPUFF usage for an annual averaging application of pollutant impacts, were the bias estimates. In Table D-5 the first three runs have comparable values for the composite bias measure, which represents the product of the speed and directional bias. Therefore choice of these sensitive option settings for the final CALMET runs was narrowed to these three alternatives. An unrelated issue regarding domain accuracy was selecting the best representation of the wind field for large areas of

the domain with no observations (i.e. Canada). For these areas, it was decided that geographic effects should be minimized and reliance on interpolated observations should occur to the greatest extent possible. The default setting for IEXTRP for the CALMET model version used for this study, is to use similarity theory to perform vertical extrapolation from the surface wind to upper layers (IEXTRP = -4).

Table D-5. A summary of observed to modeled wind fields in the progressive model evaluation procedure for CALMET for summer. Sorted by Composite Bias Measure

Summer or Winter	Radiosonde Location	WD Bias	WD Error	WS Bias	WS Error	Notes Regarding Switch Settings	Composite bias measure
summer	IAD	-1.93	40.6	-0.5	5.44	IEXTRP = 4, R1,R2 = 1000 km	0.97
summer	IAD	-2.01	40.52	-0.51	5.43	IEXTRP = -4, R1,R2 = 1000 km	1.03
summer	IAD	-2.01	40.52	-0.51	5.43	IEXTRP =-4, R1,R2 = 100 km	1.03
summer	IAD	-1.26	40.12	-2.31	4.66	IEXTRP=-4, R1,R2 = 36 km	2.91
summer	IAD	2.82	22.84	-3.26	4.02	IEXTRP =1, R1,R2 = 100 km	9.19
summer	IAD	4.58	24.57	-3.82	4.25	With ETA upper air	17.5
summer	IAD	21.06	44.9	-5.86	6.11	IEXTRP =2, R1,R2 = 1000 km	123.41

Table D-6. A summary of observed to modeled wind fields in the progressive model evaluation procedure for CALMET for all other seasons. Sorted by Wind Direction Bias

Summer or Winter	Radiosonde Location	WD Bias	WD Error	WS Bias	WS Error	Notes Regarding Switch Settings
spring	IAD	-1.57	37.65	0.77	7.2	IEXTRP = -4, R1,R2 = 1000 km
winter	IAD	-3.85	23.88	-0.63	6.46	IEXTRP=4,R1,R2=36 km
winter	IAD	-4.12	16.21	-2.17	4.31	IEXTRP =1, R1,R2 = 1000 km
winter	IAD	4.94	25.52	-4.31	5.7	With ETA upper air
winter	IAD	-5.19	25.95	7.16	10.04	IEXTRP = -4, R1,R2 = 1000 km
winter	IAD	-8.08	23.47	12.16	12.96	IEXTRP=4,R1,R2=1000 km
fall	IAD	8.82	20.81	-4.43	5.74	With ETA upper air
spring	IAD	12.02	24.75	-4.24	5.13	With ETA upper air
winter	IAD	17.47	30.2	-11.81	11.86	IEXTRP =2, R1,R2 = 1000 km

The first priority in determination of the optimized settings was based on the summer season, because the maximum sulfate events occur during the summer. Based on this consideration, and the progressive model validation procedure for summer, the following settings were utilized for the final runs for all of the year except the winter season.

R1, R2 = 1000 km
IEXTRP = -4

LVARY = T
TERRAD = 100 km.

Note that for all results there are significant seasonal variations. In particular, it was noted that the effect of the IEXTRP setting on wind field accuracy during the winter at 750 meters elevation was significant. Therefore it was necessary to decide whether CALMET would be run with the sensitive option settings varied for different seasons, or to utilize option settings fixed over the entire year. There was no guidance on this subject available. Because a significant level of accuracy improvement can be obtained for the winter period by using the IEXTRP setting of 1, it was decided to rely on this non-default setting for the first quarter of the year. Table D-7 is a representation of the progressive model validation procedure for January in which the switch settings for quarter 2 through 4 are compared to the optimum switch settings for the winter period (i.e., with IEXTRP turned off). Table D-8 is a representation of same bias and error measures for January and July with the final switch settings for both winter and summer at 750 meters and 3000 meters elevation.

Table D-7. Progressive Model Validation Procedure for January

Month of 2002	Calmet Vertical Level (M)	Rad. Pres. Lvl (Mb)	WD Bias	WD Error	WS bias (kts)	WS Error (kts)	composite bias measure	Notes Regarding Switch Settings
January	750	925	-6.8	22.5	8.23	9.4	56.3	iextrp=-4,R1,R2=1000 km,LVARY=T
January	750	925	-1.2	16.7	-0.75	3.92	0.92	iextrp=1,R2=1000km, LVARY=T
January	3000	700	-1.3	11.1	2.51	6.65	3.26	iextrp=-4,R1,R2=1000 km,LVARY=T
January	3000	700	1.84	8.44	0.84	5.2	1.5	iextrp=1,R2=1000km, LVARY=T

Table D-8. Bias and Error measures for January and July

Summer or Winter	Calmet Vertical Level (M)	Rad. Pres. Lvl (Mb)	WD Bias	WD Error	WS bias (kts)	WS Error (kts)	composite bias measure	Notes Regarding Switch Settings
January	3000	700	1.84	8.44	0.84	5.2	1.5	iextrp=1,R2=1000km,LVARY=T
January	750	925	-1.2	16.74	-0.75	3.92	0.92	iextrp=1,R2=1000km,LVARY=T
July	3000	700	3.35	21	1.78	3.9	5.96	iextrp=-4,R1,R2=1000 km,LVARY=T
July	750	925	-2.3	39.5	1.86	7.5	4.28	iextrp=-4,R1,R2=1000 km,LVARY=T

In a *time independent* evaluation, wind roses were produced for each quarter's CALMET run and compared to windroses produced from the radiosonde location. Figure D-14 shows the wind rose plots by season using the final option settings chosen in the analysis described above.

Figure D-14. Comparison of observed(top) and CALMET calculated (bottom) wind roses for four quarters of 2002.

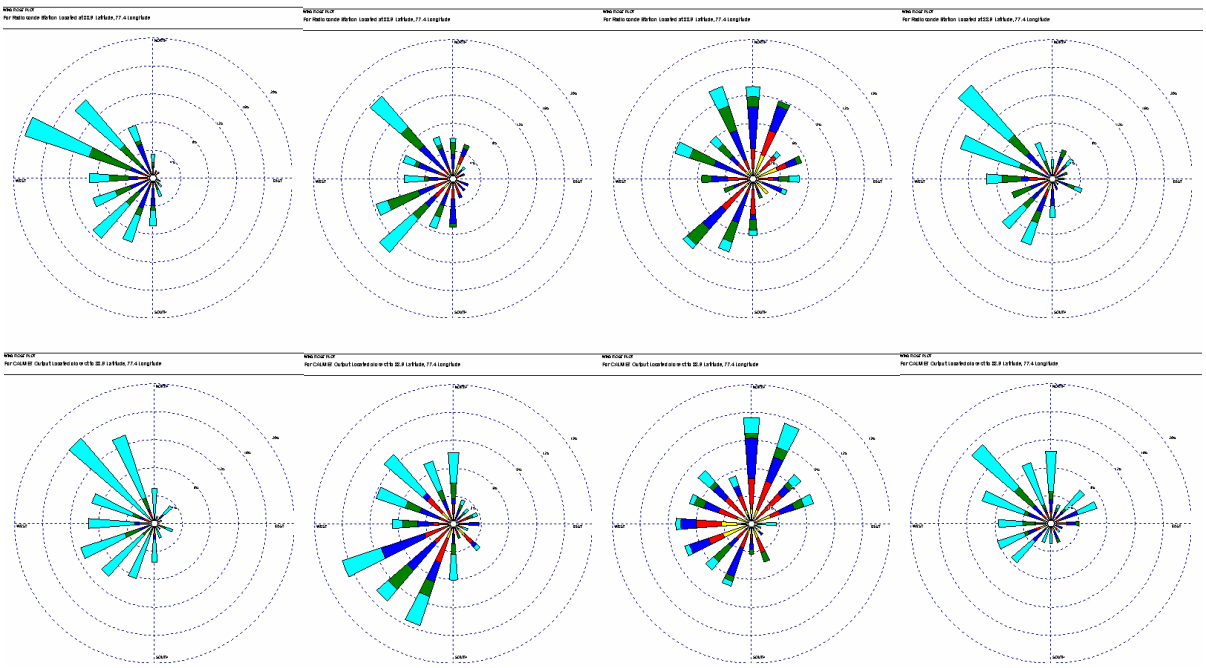

First Second Third Fourth

Validation Method Used to Determine Optimum CALMET Parameter Settings for Other physical processes

Other physical processes – including lateral and vertical pollutant dispersion, chemical conversion of SO_2 to sulfate, and mechanisms to reduce airborne concentrations of sulfur compounds, including dry deposition of SO_2 and wet deposition of sulfate – must be properly handled by CALPUFF, and all of these are greatly affected by the meteorological fields CALMET produces.

The choice of calculation method *for lateral pollutant dispersion* is made in the CALPUFF option settings, where several alternatives are available. A sensitivity analysis was performed using the CALPUFF SO_4 fields in comparison to monitored SO_4 values. For Gaussian dispersion methods, *ground level stability estimates* dictate the amount of lateral spread in CALPUFF. Stability, as a function of thermal and mechanical mixing, is calculated within CALMET. Figure D-15 and Figure D-16 show stability fields which were used for visual examination of diurnal variability.

Figure D-15. VT DEC Daytime PGT Stability Classifications During Summer.

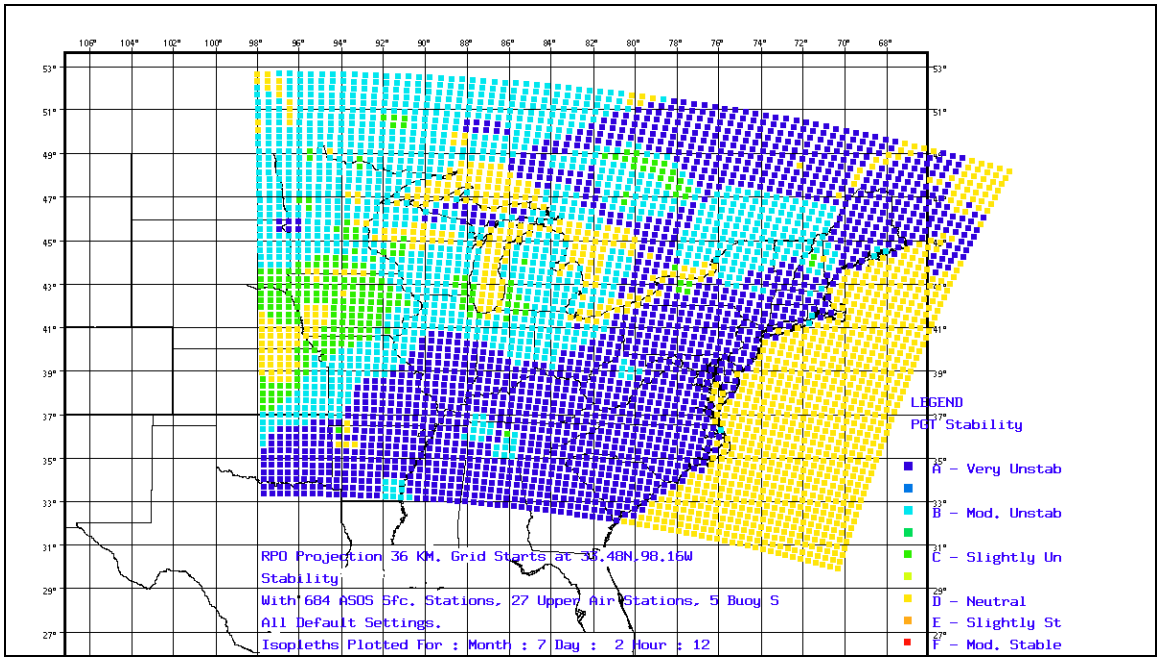

Figure D-16. VT DEC Morning Transition PGT Stability Classifications During Summer.

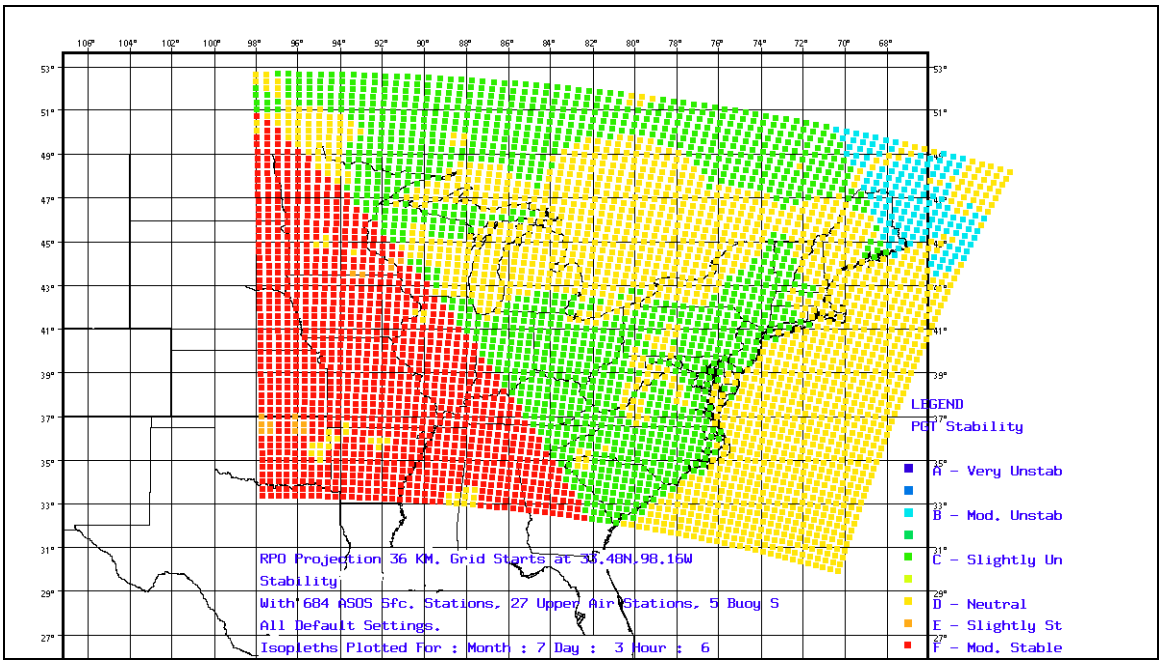

Vertical Pollutant Dispersion is largely a function of *mixing height*. Mixing heights are estimated by CALMET. Therefore validation procedures were performed to examine the reasonableness of the stability and temperature fields produced by CALMET, since the mixing height calculations are based on these fields, and the mixing heights themselves for reasonableness. This validation, then, consisted of a *visual examination* of the aforementioned fields for ten day periods during each quarter of the year. Figure D-17 and Figure D-18 illustrate examples of mixing height fields during a fair weather period in July.

Figure D-17. Mixing Height Calculations from CALMET for a summer day.

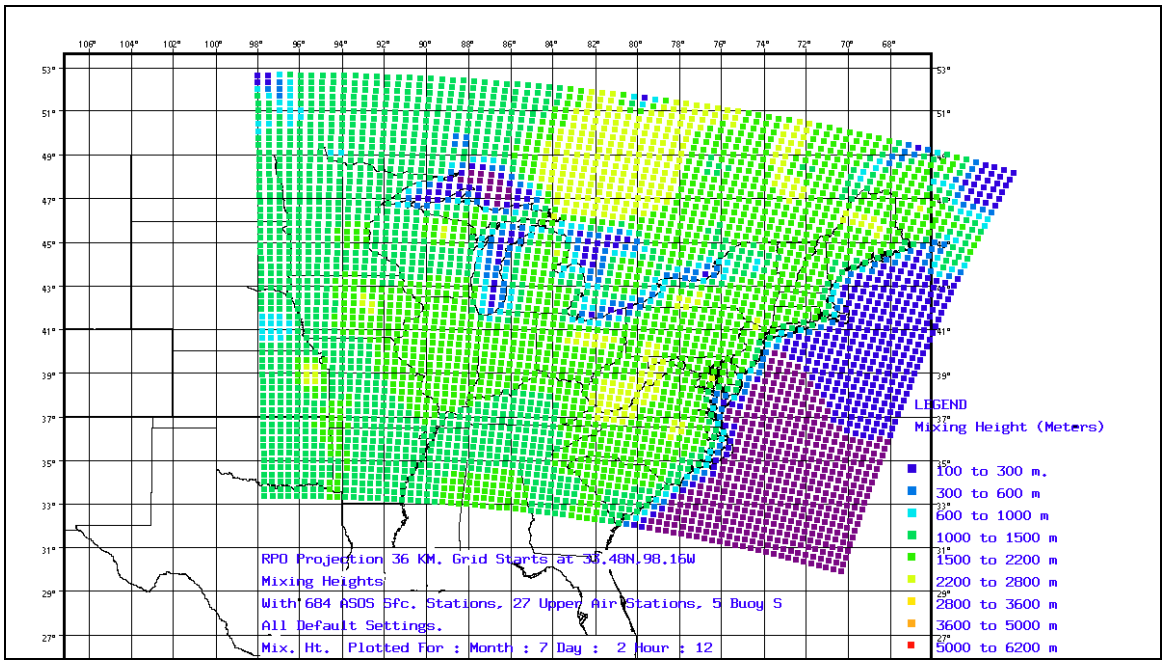

Figure D-18. Mixing Height Calculations from CALMET for a summer night.

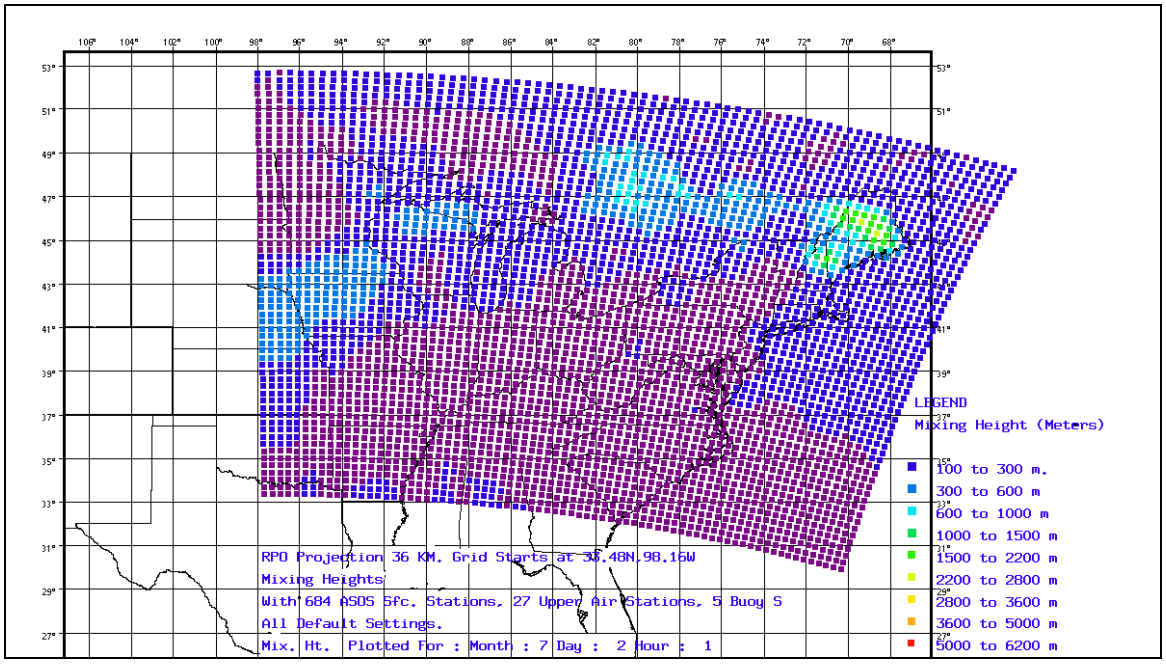

Chemical Conversion of SO_2 to H_2SO_4 in CALPUFF is strongly dependent on surface *temperature* and *relative humidity fields* produced by CALMET. Therefore these fields were subject to a *visual examination* for ten day periods during each quarter of the year, where CALMET was run in different modes to effect their estimation. Part of the temperature field evaluation involved inspection of the predicted fields when ISURFT, which defines which surface observational site input to CALMET is used to produce the first guess temperature field, was varied, Figure D-19 and Figure D-20 illustrate examples of the final surface temperature fields during a fair weather period in July.

Figure D-19. Surface Temperature from CALMET for a summer day.

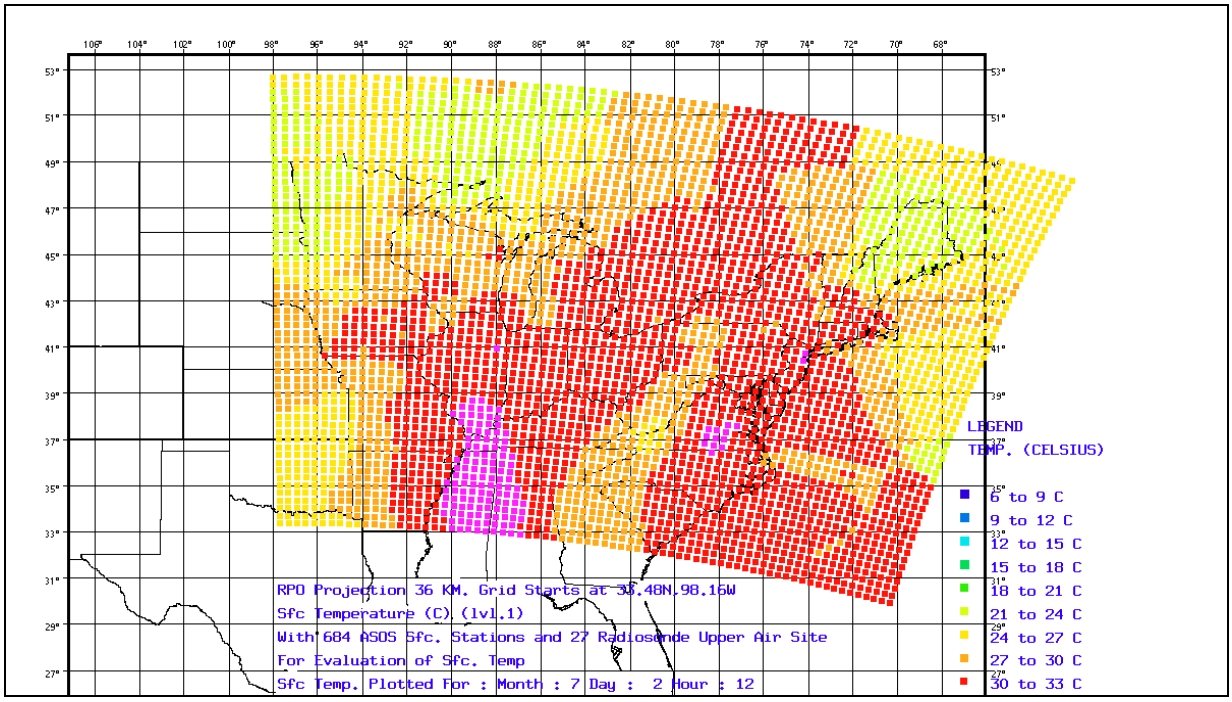

Figure D-20. Surface Temperature from CALMET for a summer night.

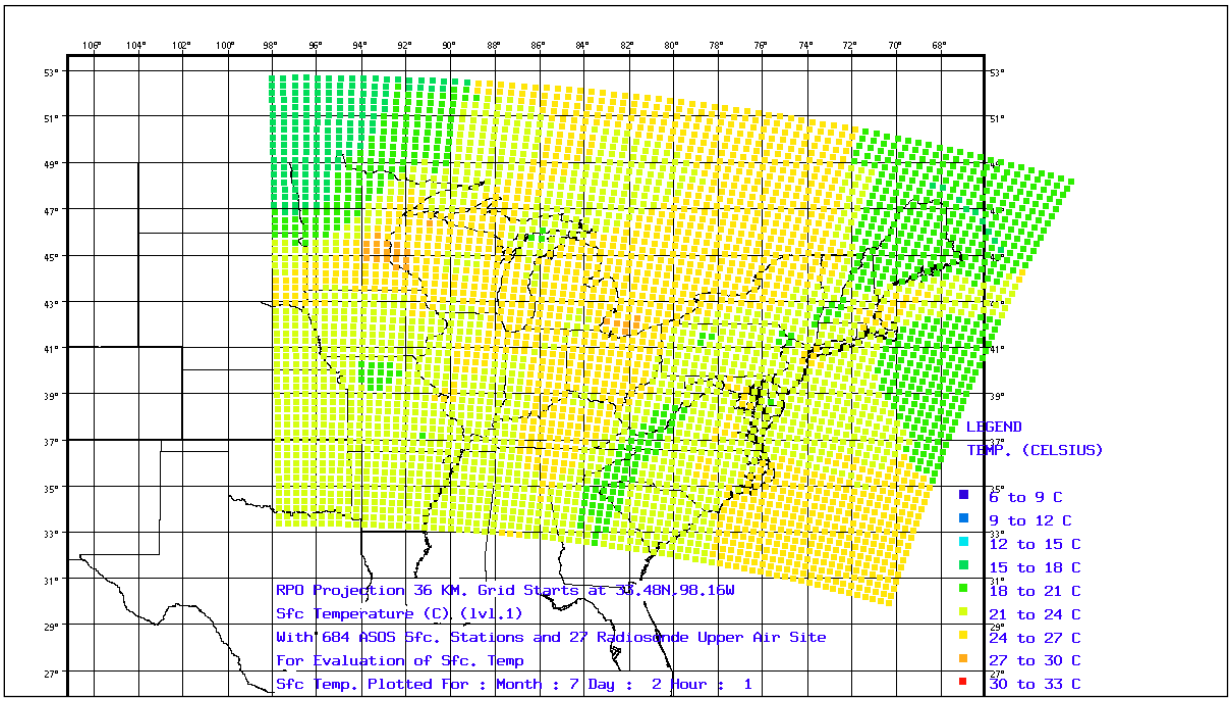

Dry Deposition estimates by CALPUFF are sensitive to the original geographical representation of certain variables for the domain (eg leaf area). See Figure D-11 for a plot of the leaf area index values. Parameters in equations for dry deposition rates may also be altered in CALPUFF. CALPUFF runs will be performed in Phase II of this effort to assess effect of different dry deposition algorithms.

Wet deposition is primarily influenced by representation of precipitation fields, as well as parameters in equations for dry deposition rates within CALPUFF. Therefore, for wet deposition handling by CALMET, precipitation fields were examined for reasonableness. Some modifications will be performed in CALPUFF runs in Phase II. for wet deposition, as well as additional CALMET reruns.altering initial production of the precipitation fields. Figure D-21 illustrates an example of a precipitation field for one hour. Fields were compared to National Weather Service maps to verify accurate representation of precipitation events.

Figure D-21. Example of a Precipitation Field Snapshot produced by CALMET.

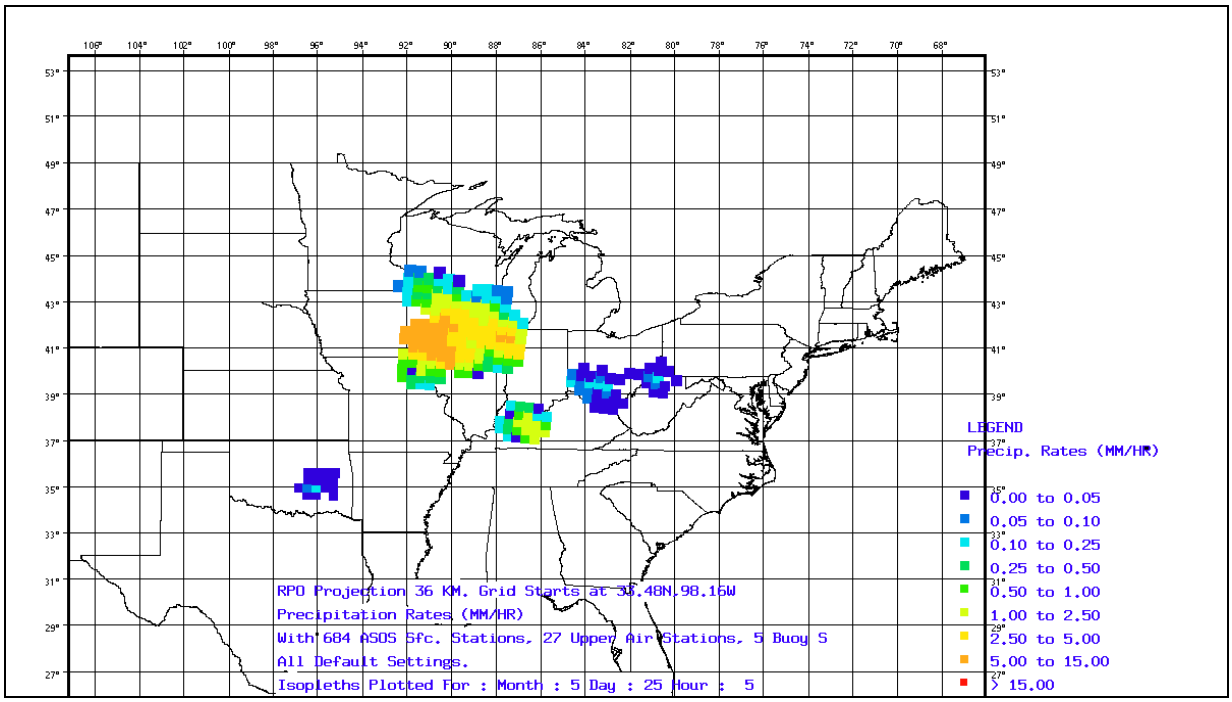

D.2.3. CALPUFF Phase II Modeling Results Using NWS-derived Wind Fields

We note again that these Phase II VTDEC CALPUFF results for year 2002 are based on emissions reported in the CEMS raw data files and data from RPO emission inventories which include only sulfur dioxide, nitrogen oxides, and $PM_{2.5}$. The sulfate component of visibility affecting aerosol is the only model output component that has been evaluated against measurement data. Direct emissions of $PM_{2.5}$ from all source categories modeled (including the CEMS EGU point sources) were estimated using data from the RPO modeling inventories available in the October 2005 time period. However, we have not evaluated the model results for all regional haze affecting species that the

EGUs, other point sources, and area/mobile sources may be emitting. Direct emissions of $PM_{2.5}$ or VOC may affect visibility at Class I areas. An estimate of direct $PM_{2.5}$ emissions from some of the sources has been included in the CALPUFF runs completed under Phase II of the project, but there was no attempt to evaluate direct $PM_{2.5}$ visibility impacts or to incorporate any organics effects on visibility in the CALPUFF modeling which Vermont has conducted thru Phase II. As of the end of 2005, it has not been possible to spend the time to do a complete analysis of all the outputs generated by the modeling. The ambient sulfate component of impacts affecting haze has been examined in some detail for a number of the Class I areas in the northeastern portion of the domain.

CALPUFF was run on the VT DEC platform for each quarter sequentially, using the restart option of the CALPUFF switch settings. Ramp-up was confined to several days at the beginning of January 2002. Six chemical species were specified to be modeled. In the Vermont CALPUFF modeling presented in these Phase II results, only three of these species were emitted, these being SO_2, NO_X, and $PM_{2.5}$. Calculation of ambient concentration for SO_4, HNO_3, and NO_3 was also performed in addition to that for the emitted species. In some of the sensitivity runs tested during Phase II, direct emissions of SO_4 from the CEMS EGUs were also estimated as 3% of the hourly SO_2 emission rate, but these emissions were not included in the reported Phase II results. Phase II modeling evaluation was limited to the sulfate ion concentration output. Because the nitrogen chemistry in the model is dependant on partitioning of the chemical transformation products properly under available ammonia conditions, the direct concentration and deposition results for nitrogen compounds obtained in Phase II modeling would need to be post-processed in a more complex way using a utility called POST-UTIL. Post-processing with POST-UTIL has not yet been carried out with the Phase II results. The option to post-process results obtained for $PM_{2.5}$, nitrogen compounds and overall visibility impacts remains available

During Phase I, CALPUFF was also run selectively using a dense set of gridded receptors (117 x 117 @ 18 km spacing) for short periods of time with all point sources and for annual periods with small groups of sources. These output results were used to visually observe the time series of hourly predictions being produced by the model. This process proved helpful in identifying time periods when episodic levels of sulfate were predicted in the MANE-VU region and for which monitoring patterns could also be matched in time. Modeling on sets of gridded receptors was not conducted during Phase II modeling.

Phase II CALPUFF Results compared to observations

VTDEC modeled predictions for SO_4 ion concentration at 72 discrete receptors in the eastern U.S. produced during Phase II CALPUFF modeling were available for comparison to SO_4 ion measurements available at these same locations. Modeled emissions from the comprehensive set of SO_2 source categories which have been identified in Table D-2 through Table D-4 in Section D.2.1.2.are estimated to represent at least 95% of the SO_2 emissions which occurred in the domain during calendar year 2002. A comparison of predicted impacts from the modeling with actual measurements of SO_4 ion at these receptors was done for both quarterly average impacts and for 24-hour

average impacts during the entire year, based on predictions and measurements paired in space and time.

During Phase I we had identified the entire set of pertinent calendar year 2002 measurements from within the domain for use in performing a validation of the CALPUFF model platform for the most significant regional haze affecting component (SO_4 ion) in the northeast. These measurements comprise a very substantial dataset that is spatially and temporally dense for this purpose. Both ambient concentration measurements and deposition measurements may eventually be utilized to perform this validation on Phase II modeling results. The discussion to follow focuses only on a comparison of Phase II CALPUFF modeled ambient SO_4 ion to measurements of ambient SO_4 ion. 24-hr fine particulate matter ($PM_{2.5}$) measurements for the modeled time period are available at many locations (in some cases on a daily basis) in the domain covered by the modeling. However, because Phase II VTDEC CALPUFF modeling results have not yet been post-processed to accurately represent secondary nitrate particulate matter impacts at the receptors, it did not seem productive to do comparisons between modeled and measured $PM_{2.5}$ until the Phase II results can be post-processed to account for nitrogen partitioning more appropriately.

SO_4 Ion Measurements used for Model Validation

The modeling domain includes 41 monitoring locations which utilize IMPROVE-type monitors. These operate on a one-in-three day schedule (every third day) which is the same for each of the monitor locations. Each 24-hr ambient air sample collected has been analyzed for a large number of compounds and elemental concentrations, including SO_4 ion. This network of monitors operated throughout 2002 and measurements obtained at all 41 of these sites were available for comparison to VTDEC CALPUFF modeled predictions of SO_4 ion at these specific discrete receptor locations. 22 of these IMPROVE-type measurement sites are in the northeastern quadrant of the domain, that portion most frequently upwind of other portions. One of the sites (WASH) is located in the urban area of Washington D.C. so although it is being used in the model validation, it is a site somewhat different than the rural sites used and measurements may include the influence of locally important sources not appropriately accounted for in the modeling. Two of these 22 sites (AREN & QUCI) were not included in the initial Phase I validation process. The remaining 19 sites in the other three quadrants are close to boundaries of the domain from which direction the prevailing air flow over the domain frequently occurs (south and west). Information about emission sources outside the domain in those directions was not accounted for in a completely satisfactory way during the Phase II modeling. A sensitivity test run which attempted to account for transport of sulfate aerosol across these boundaries did show a definite ability to improve the results close to the western and southern boundaries of the domain. In the evaluation described below, the 19 IMPROVE-type monitoring sites outside the northeast quadrant were not considered as primary sites for model validation, but comparisons for them were also produced.

Figure D-22 shows the locations of all ambient SO_4 ion concentration monitoring sites available for model validation purposes. The RED circles shown are the 20 IMPROVE-type monitoring sites used in the preliminary validation of SO_4 ion predicted

during Phase I modeling. These primary receptor sites plus the AREN and QUCI (green squares) sites were used to validate SO_4 ion predictions using Phase II model results. BLUE triangles show 31 FRM sites which could be used in the future with Phase II modeling results for $PM_{2.5}$ validation. The remaining GREEN squares show the 19 additional IMPROVE-type monitor locations outside the northeast quadrant, some of which may be considered for expanded SO_4 ion and NO_3 ion comparison. It would be very useful to conduct further validation analysis if there is future enhancement of Phase II results by incorporating improved transport representation of ambient SO_4 and NO_3 ion concentrations being carried into the domain across its western, southern, and northern boundaries. All of these sites could be considered for use when an evaluation of the particulate matter and nitrate components of visibility affecting aerosol can more appropriately be performed following post-processing to properly partition the nitrogen compound results.

Figure D-22. Ambient SO_4 ion concentration monitors

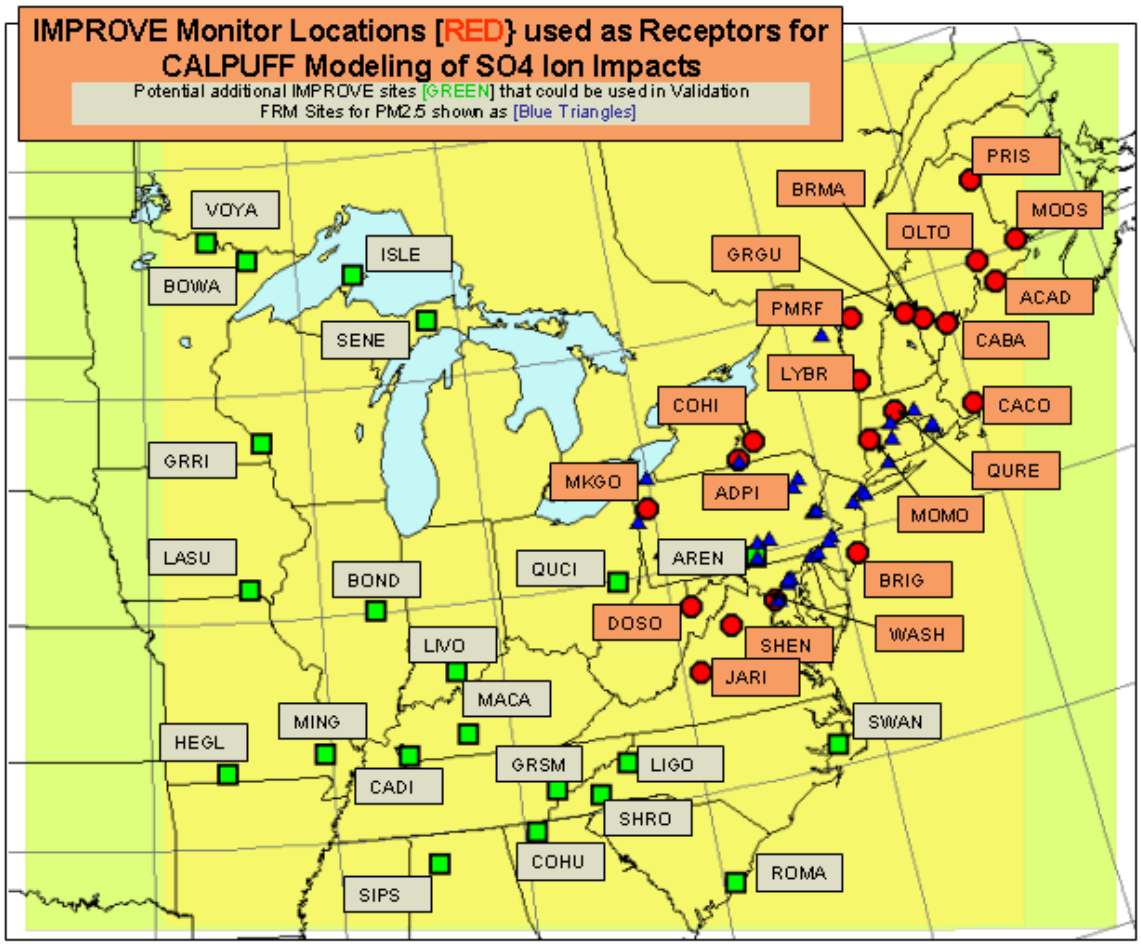

Model Validation Results (Quarterly Averages of Coincident 24HrAve)

Table D-9 shows a comparison of average long-term (quarterly) SO_4 ion impacts obtained during Phase II modeling showing predicted values at the 22 IMPROVE site

locations versus the monitored average values when only the dates with monitored SO_4 ion were included in both sets of average value calculations.

This table indicates that in the configuration being run for Phase II the model is under-predicting the long-term (quarterly average) impacts for SO_4 Ion by at least 30% for 22 of the 88 site/quarter combinations in the northeastern portion of the domain. Most of these under-predictions occurred during the first two quarters of the year. This seems to indicate that, based on the patterns and magnitudes of under-prediction seen, the overall conversion of SO_2 to SO_4 during transport and/or the deposition and removal during transport may not be optimized appropriately in the model during these seasons. In the winter (1st quarter) most of the sites under-predicted are located in the extreme northeastern portion of the domain, the furthest from the primary known large sources of SO_2. However during the spring (2nd quarter) many of the sites under-predicted are located closer to the primary source regions for SO_2.

Table D-9. Phase II Evaluation of Average SO_4 ion CALPUFF Predictions

COMPARISON of IMPROVE Monitored Ave Qrtrly SO4 vs CALPUFF Modeled Ave Qrtrly SO4
Coincident 24-Hr periods paired in Space & Time used for averaging

SO4 Ion Values in ug/m3 DIFF given is Modeled minus Monitored

	QUARTER 1 Ave SO4 Ion				QUARTER 2 Ave SO4				QUARTER 3 Ave SO4				QUARTER 4 Ave SO4			
Site	Monitor	Model	DIFF	%DIFF	Monitor	Model	DIFF	%DIFF	Monitor	Model	DIFF	%DIFF	Monitor	Model	DIFF	%DIFF
ACAD	1.53	1.19	-0.34	-22.27	1.57	1.83	0.26	16.46	2.54	3.08	0.54	21.17	1.56	1.86	0.30	19.19
ADPI	2.47	1.63	-0.84	-33.87	4.04	2.78	-1.26	-31.16	5.55	6.47	0.91	16.46	2.44	2.79	0.36	14.70
AREN	2.96	2.22	-0.73	-24.82	5.93	3.08	-2.86	-48.12	7.18	6.65	-0.54	-7.49	3.25	3.23	-0.02	-0.61
BRIG	2.13	1.56	-0.57	-26.87	4.54	2.87	-1.68	-36.92	4.86	6.05	1.19	24.52	2.78	2.90	0.12	4.35
BRMA	1.67	1.12	-0.55	-32.65	1.44	1.07	-0.37	-25.80	3.21	2.23	-0.98	-30.58	1.45	1.43	-0.02	-1.62
CABA	1.89	1.22	-0.67	-35.54	1.74	1.78	0.03	1.99	2.53	2.75	0.22	8.87	1.61	1.76	0.15	9.31
CACO	1.82	1.92	0.10	5.35	1.99	2.12	0.12	6.26	2.65	4.05	1.39	52.44	2.00	2.29	0.30	14.84
COHI	2.48	1.73	-0.75	-30.36	4.15	2.89	-1.26	-30.38	5.17	5.95	0.79	15.24	2.32	2.80	0.47	20.28
DOSO	2.33	3.74	1.41	60.19	5.26	2.96	-2.30	-43.76	4.81	4.95	0.13	2.79	2.16	3.76	1.60	74.36
GRGU	1.52	1.10	-0.42	-27.81	1.77	1.32	-0.44	-25.01	3.27	1.99	-1.28	-39.23	1.37	1.34	-0.03	-2.15
JARI	2.73	2.52	-0.21	-7.61	4.94	1.99	-2.95	-59.72	7.68	6.65	-1.04	-13.47	2.98	3.60	0.62	20.81
LYBR	1.39	1.31	-0.08	-5.85	1.83	1.91	0.08	4.13	3.13	2.91	-0.22	-7.00	1.27	1.60	0.33	26.25
MKGO	2.83	2.74	-0.09	-3.27	4.94	3.42	-1.52	-30.69	5.67	7.63	1.96	34.46	2.74	3.78	1.05	38.31
MOMO	2.30	1.63	-0.67	-29.08	2.63	2.36	-0.27	-10.28	3.56	4.92	1.36	38.35	2.22	2.04	-0.17	-7.82
MOOS	1.47	1.03	-0.44	-30.02	1.29	1.83	0.53	41.20	2.45	2.60	0.15	6.21	1.58	1.72	0.14	8.89
OLTO	1.86	0.77	-1.09	-58.76	0.93	0.56	-0.36	-39.29	2.86	2.17	-0.70	-24.28	1.52	1.38	-0.14	-9.42
PMRF	1.58	1.00	-0.58	-36.57	1.98	1.46	-0.52	-26.31	3.80	2.70	-1.10	-28.86	1.72	1.83	0.11	6.32
PRIS	1.41	0.75	-0.66	-46.81	1.13	0.95	-0.18	-16.29	2.08	1.29	-0.80	-38.27	1.69	1.81	0.12	6.81
OUCI	2.90	3.60	0.70	24.13	5.24	2.82	-2.41	-46.11	6.77	9.96	3.19	47.11	3.04	3.71	0.66	21.87
OURE	1.98	1.46	-0.51	-25.92	2.21	2.14	-0.07	-3.16	3.38	3.96	0.58	17.21	2.01	1.84	-0.17	-8.49
SHEN	2.30	2.87	0.57	24.84	4.97	2.11	-2.86	-57.60	7.17	6.52	-0.66	-9.16	2.63	3.51	0.87	33.13
WASH	3.29	2.75	-0.54	-16.49	5.40	2.85	-2.55	-47.17	8.55	8.52	-0.02	-0.28	3.96	3.88	-0.07	-1.83

	Model was OVER-Predicting the quarterly average by more than 30% primarily during 3rd and 4th quarters	9 of 88 Averages
	Model was UNDER-Predicting the quarterly average by more than 30% primarily during 1st and 2nd quarters	22 of 88 Averages
	Maximum OVER-PREDICTIONS are found for IMPROVE site within the most significant known SO2 source region	

Figure D-23 and Figure D-24 represent a graphic depiction of the tendency for the model to under-predict ambient SO_4, especially during the 1st and 2nd quarters. In the first of these figures D-23 the set of 22 sites is repeated in the same sequence for each of the four quarters of the year while in the following Figure D-24 the site/quarter average values are ordered from highest monitored quarterly value to lowest (left to right). From Figure D-24 it seems appropriate to conclude that model over-prediction is most likely to occur at locations measuring mid-range quarterly average SO_4 ion values (i.e. not the

highest quarterly averages nor the lowest for the northeastern part of domain). At these same mid-range measurement value locations, the model also appears to be least likely to under-predict.

Figure D-23. Quarter-by-Quarter Under-prediction & Over-prediction at 22 Sites

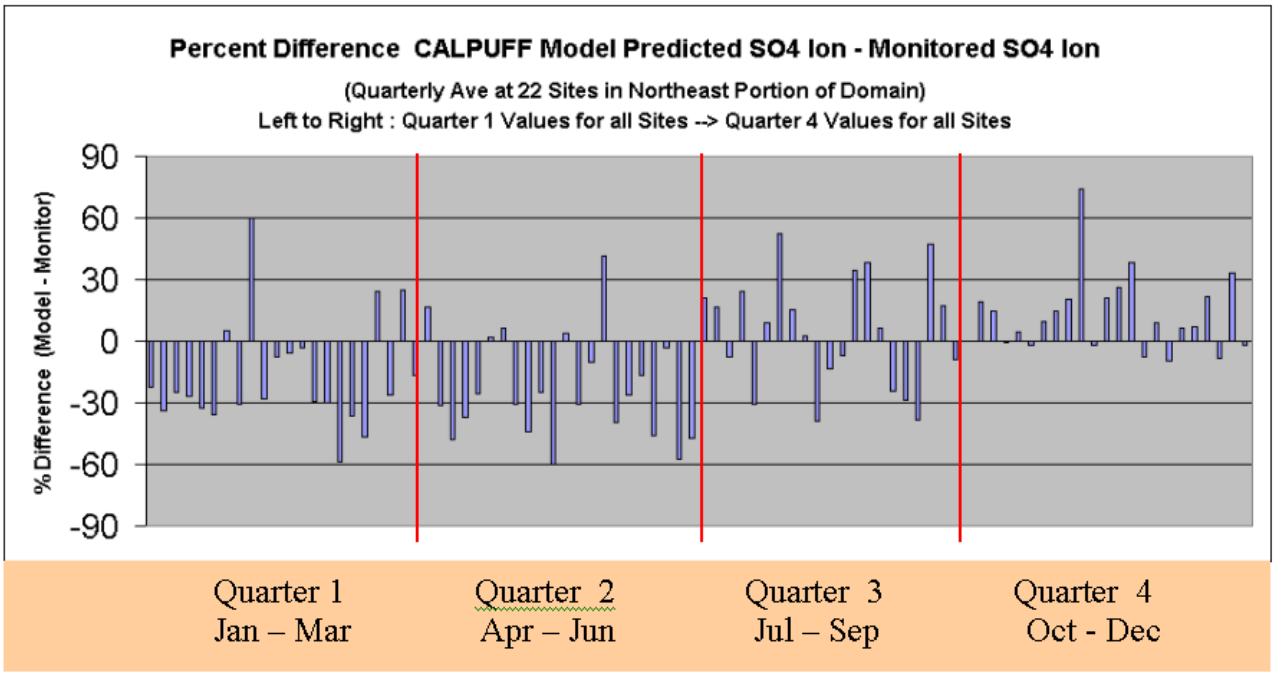

Figure D-24. Under-prediction & Over-prediction at 22 Sites relative to Measured Quarterly Values

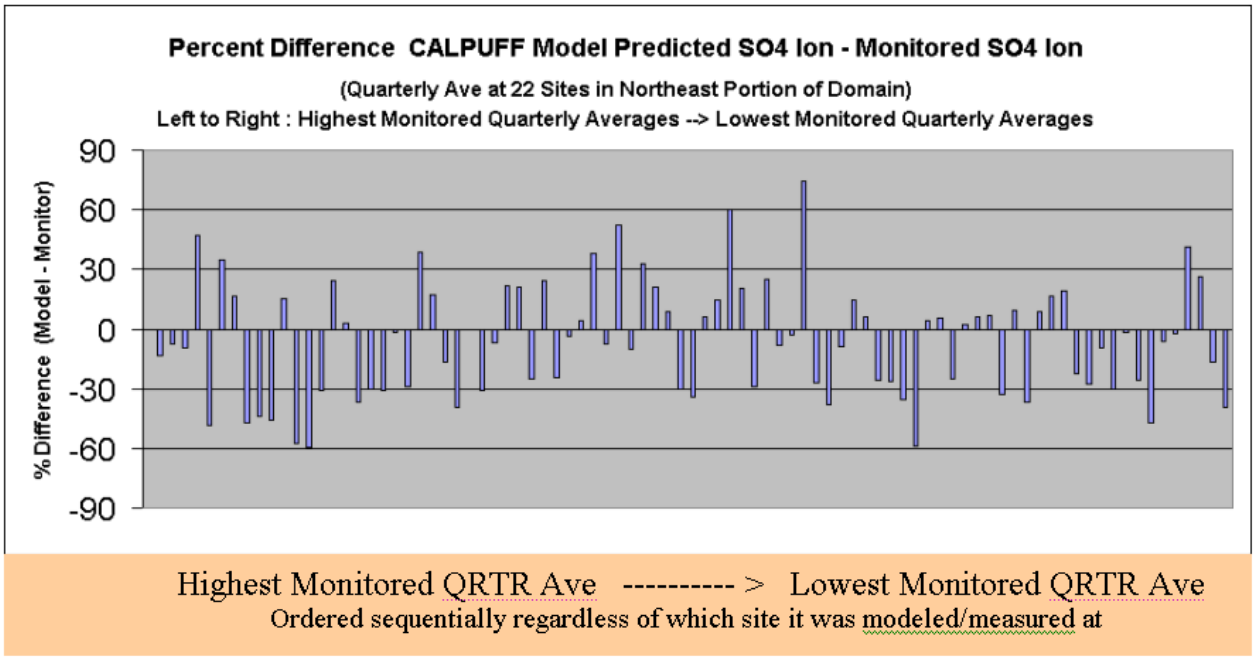

Examining the quarterly average SO_4 ion predictions at these 22 sites in yet another way is also informative as to the potential for the regional modeling platform to produce very robust results at subsets of the receptors being used in the validation. Figure D-25 indicates that by gradually removing the outlier site/quarter averages from the regression of receptor measurements vs modeled predictions, very close agreement of the model to measurement at a more limited set of receptors may be demonstrated. Figure D-25 is included in this report to simply illustrate that there may be a subset of receptors (either spatially consistent with model settings or appropriately located relative to most significant SO_2 emission regions) for which model performance is greatly improved.

Figure D-25. Regression of Modeled vs Monitored Quarter-by-Quarter SO_4 Ion at 22 Sites: Gradually Removing Outliers

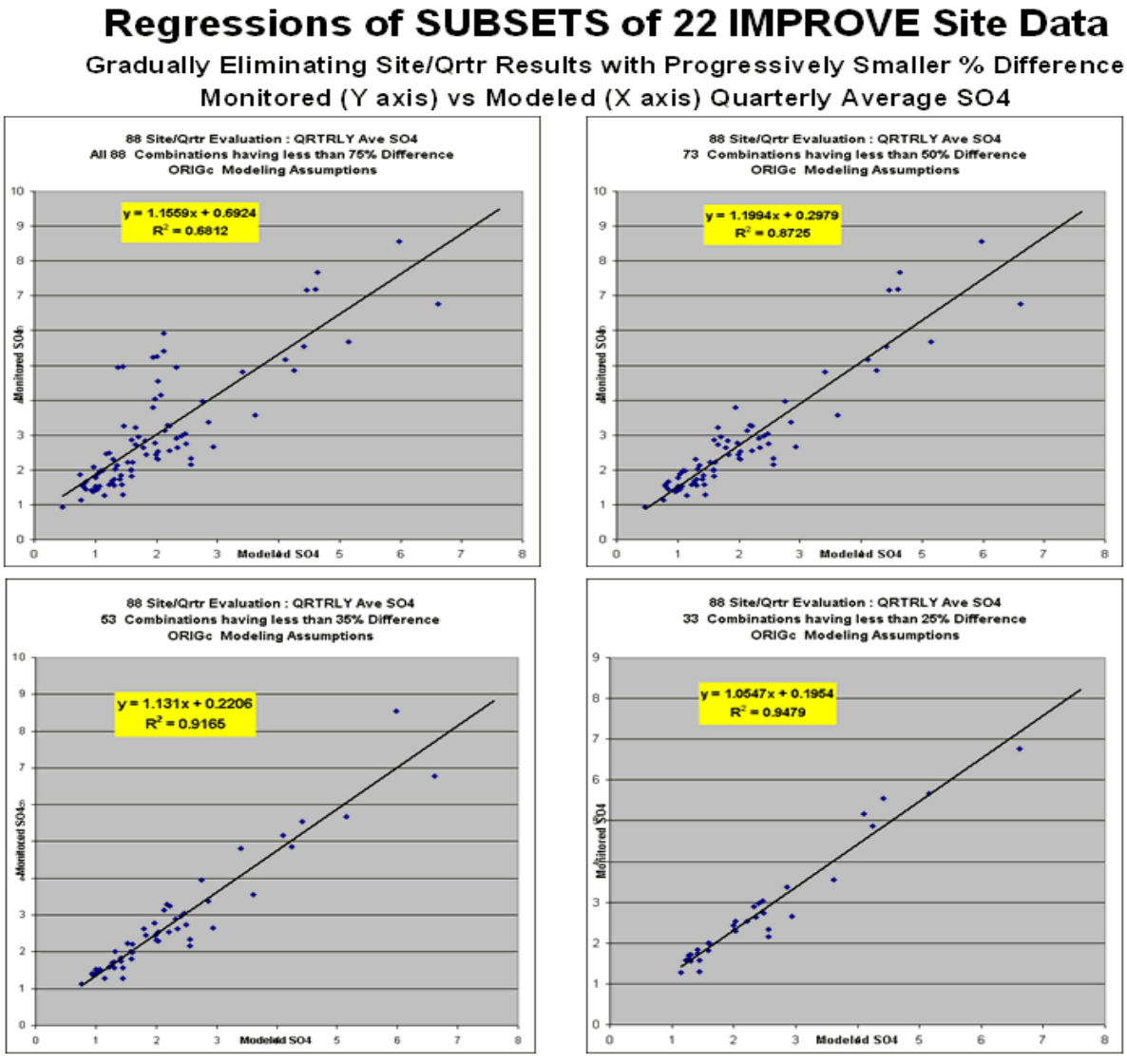

If, rather than only the 22 upwind northeastern sites, 40 of the available IMPROVE sites are used in this type of analysis of the long-term predictive ability of the VTDEC modeling platform, results are surprisingly good even though several of these sites are located near the extreme south-western or north-western portions of the domain modeled. By including these sites, which are most likely not seeing enough modeled SO_4 ion transport from outside domain boundaries, it was not expected that model performance would be very good. When average quarterly modeled impacts were regressed against measurement at these 40 sites it is clear that some sites are not at all well predicted. However, if those quarters which produced the greatest percent difference in predicted vs measured quarterly averages are sequentially removed, predictive agreement for the site/quarter combinations which remain improves significantly. The following Figure D-26, Figure D-27, and Figure D-28 show the relationship when 7, 27, and 57 of the greatest percent difference outliers are removed.

Figure D-26. Modeled vs Monitored Quarter-by-Quarter SO_4 Ion at 40 Sites: Quarterly %Differences Ordered with best 150 Site/Quarter Values Regressed

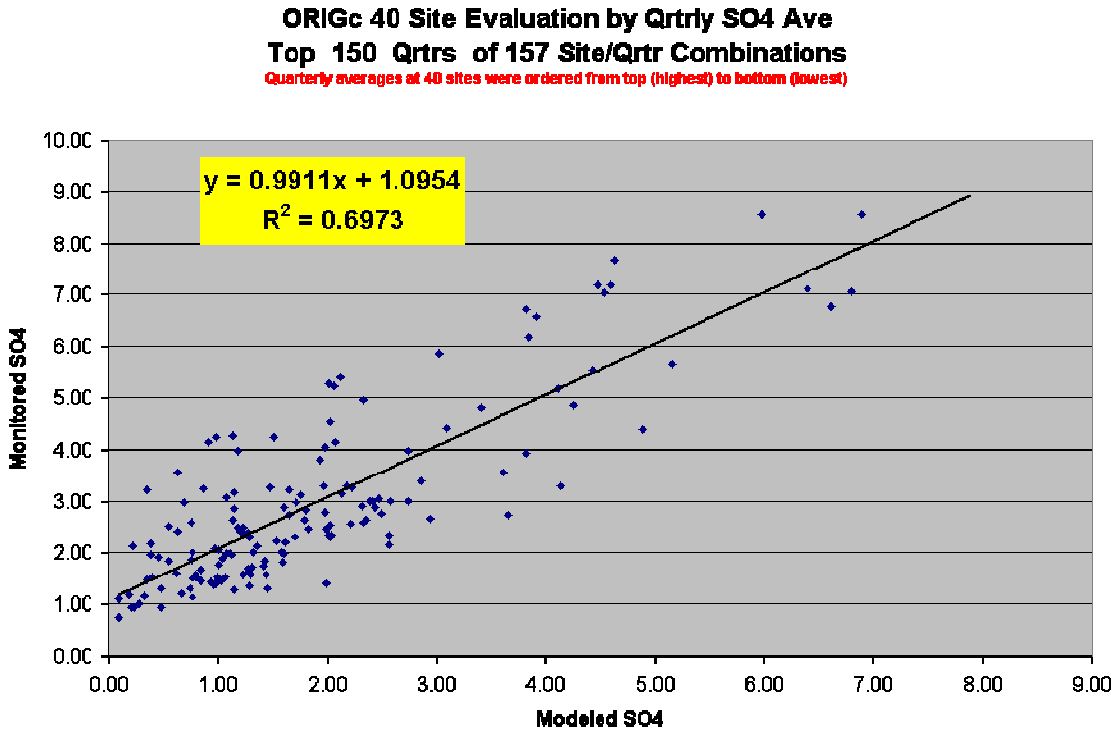

Figure D-27. Modeled vs Monitored Quarter-by-Quarter SO_4 Ion at 40 Sites: Quarterly %Differences Ordered with best 140 Site/Quarter Values Regressed

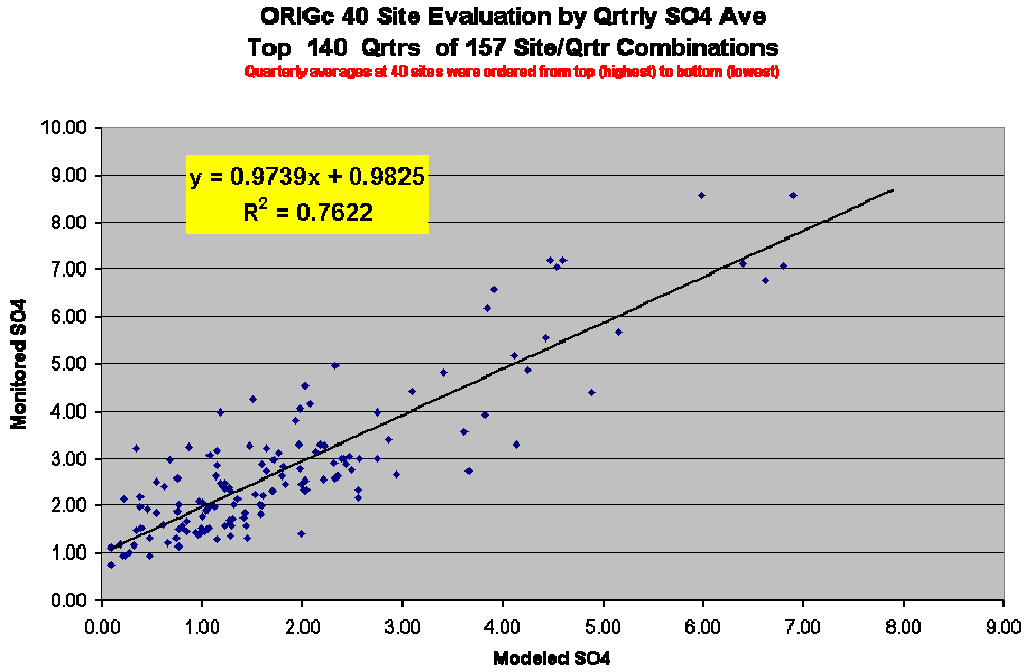

Figure D-28. Modeled vs Monitored Quarter-by-Quarter SO_4 Ion at 40 Sites: Quarterly %Differences Ordered with best 100 Site/Quarter Values Regressed

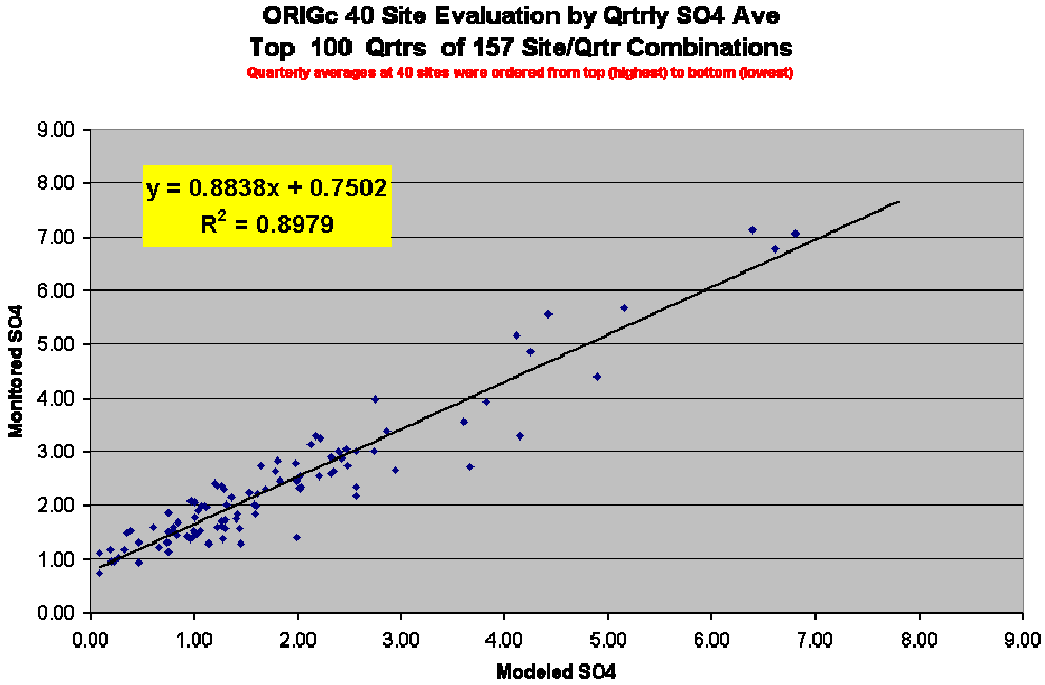

Model Validation Results (24 Hour Averages of Hourly Predictions)

Quarterly average validation of the VTDEC CALPUFF platform for 22 sites (and even the set of 40 sites) was quite encouraging in that regression models relating the modeled to measured quarterly averages generally show that the average over-prediction or under-prediction balances out on that time scale at sites in the domain. Comparisons of 24-hr ambient SO_4 Ion concentrations monitored and modeled at the 22 IMPROVE sites were also produced for the full year of 2002 modeling. The modeled predictions and the monitored 24-hr measurements were paired in both space and time for these comparisons. When we examined the 24-hr predictions versus the measurements the results are not quite so encouraging as they are for quarterly averages. For an averaging period of 24 hours, the model does not appear well able to match the variability of SO_4 ion formation that is taking place over the spatial scale of the domain. There is more scatter in the data than desired, although the overall linear model does not seriously over or under predict on average. Figure D-29 shows the relationship between monitored and modeled 24-hr SO_4 ion for the 22 northeastern IMPROVE sites generally upwind of the major source regions of SO_2.

Figure D-29. Modeled vs Monitored 24-Hr Average SO_4 Ion at 22 Sites

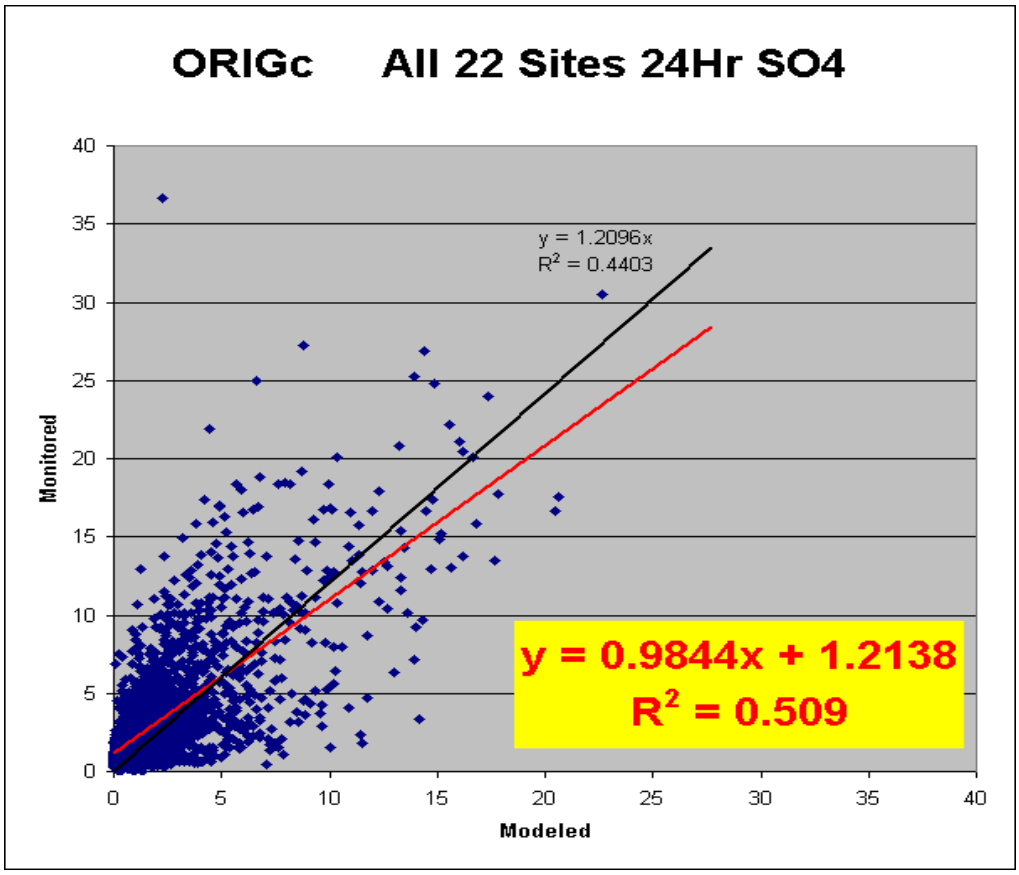

Figure D-30 shows further evidence that the model is generally under-predicting SO_4 ion for the highest actual monitored values measured across the northeast portion of the domain. As a percent of under or over-prediction, the plot indicates that for these 22

mostly downwind receptor sites, for dates when the highest SO_4 ion was measured (24Hr SO_4 ion measurements in the range of 10 $\mu g/m^3$ to 36 $\mu g/m^3$ occurred 151 times at the 22 IMPROVE sites during 2002) **only 14 dates were over-predicted**. The performance of the model in predicting 24-hr SO_4 ion appears to be biased toward under-prediction for those sites generally directly downwind of the major source regions. Given that a very large percentage of the SO_2 emissions have been incorporated in the modeling, this implies that model predictions represent a lower limit to the influence of these sources on the receptor areas.

Figure D-30. Percent Difference between Modeled and Monitored 24Hr Avg of SO_4 Ion

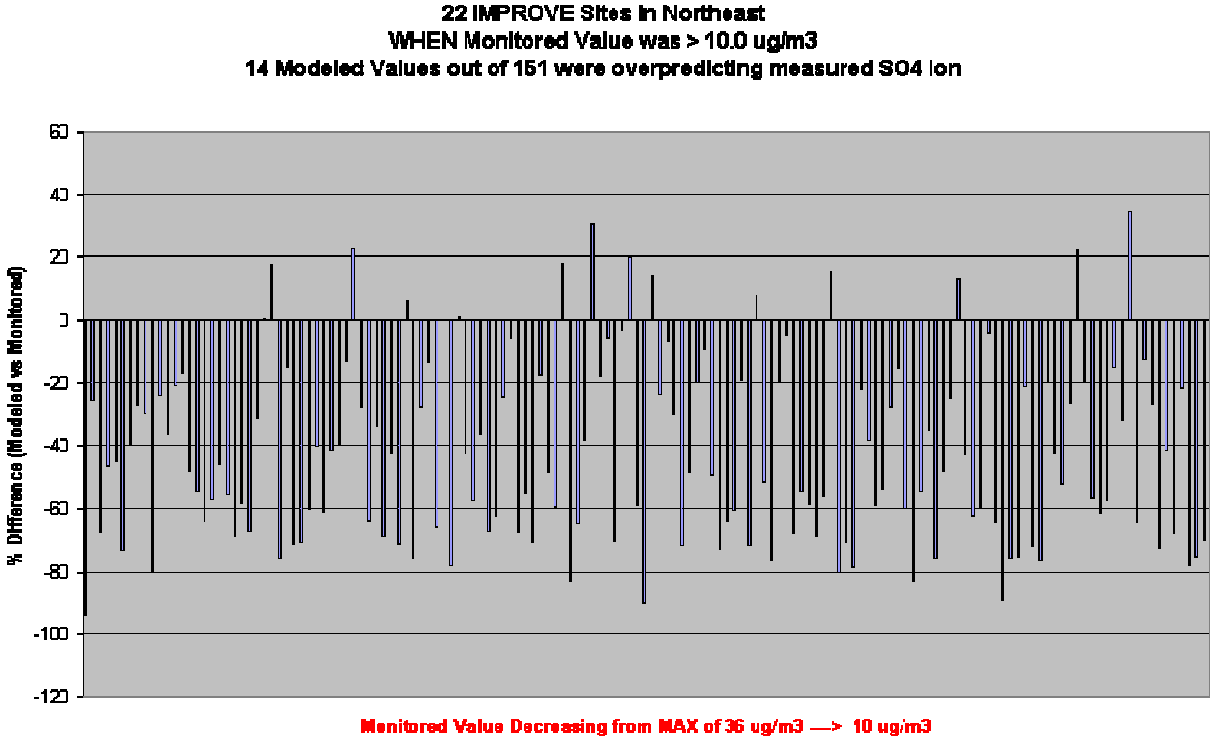

Looking at the performance of the model for smaller subsets of receptor sites allows us to identify how well the model platform is representing the combined processes of transport, chemical conversion, removal, and dispersion to predict SO_4 ion concentration at sites similar to each other in some characteristic way, but different from other subsets. Figure D-31a-c show model performance summaries of the variability and success or lack of success the model had in predicting 24-hr SO_4 ion in the distribution of values modeled for the year 2002 meteorology. The three subsets of sites are characteristically different from each other mostly by their location in the domain, representing either coastal New England, interior New England, or locations closer to the western boundary of the MANE-VU region

In these three figures, the smoother blue line is the monitored 24-hr SO_4 ion and the variable red line shows the corresponding modeled value, where the distribution of monitored values for the subset of sites is ordered from highest to lowest going from left to right on the figure.

Figure D-31a. Four Coastal New England IMPROVE Sites

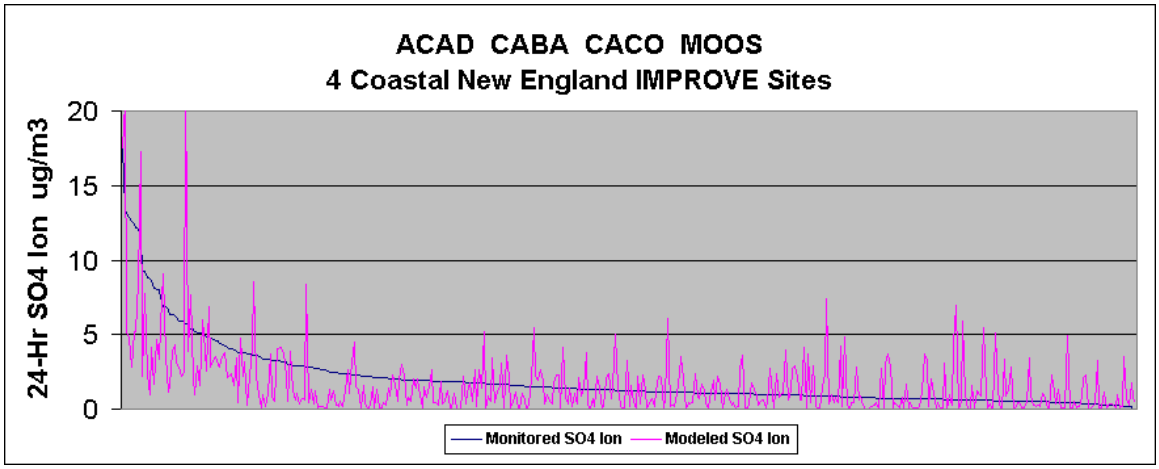

Figure D-31b. Four IMPROVE Sites in Western Portion of MANE-VU

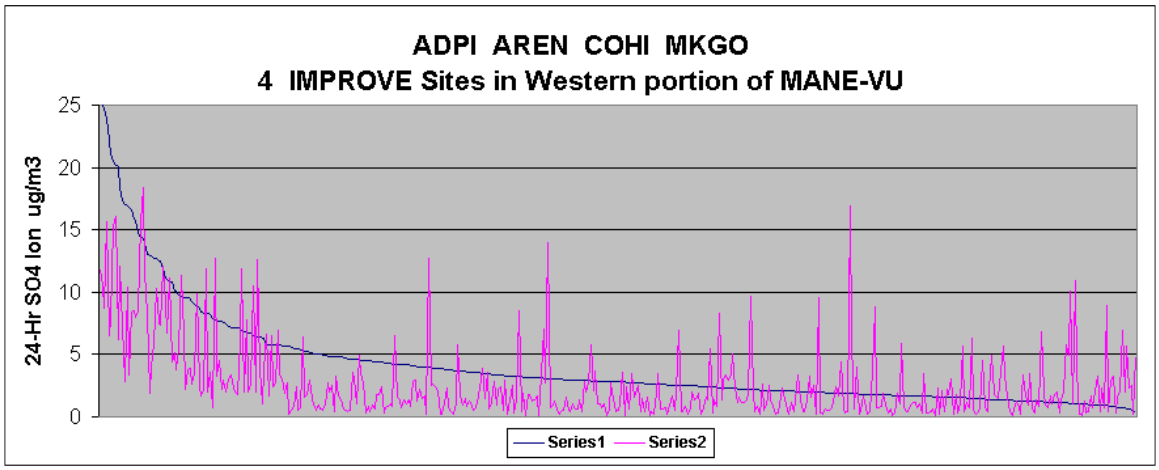

Figure D-31c. Six Interior New England IMPROVE Sites

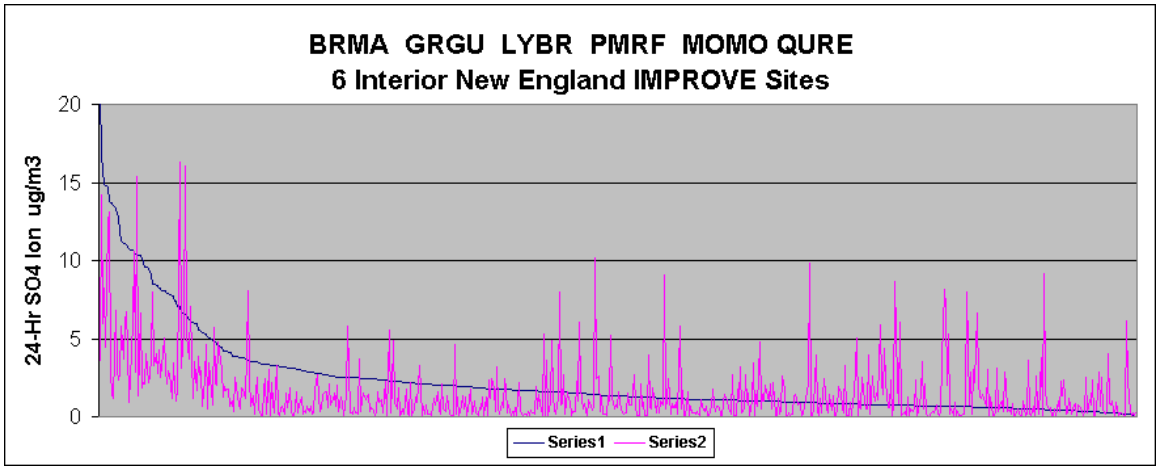

Note: **BLUE LINE shows the monitored 24-hr SO4 ion** and the **RED LINE shows the corresponding modeled value**, where the distribution of monitored values for the subset of sites is ordered from **HIGHEST → LOWEST** going from left to right on the figure.

For all three of these subsets it is still clear that for the highest values monitored (especially those greater than about 5.0 ug/m3) at each of the sites in that subset, there is under-prediction of the 24-hr ambient SO_4 ion. This under-prediction appears to be least in the subset comprised of coastal Maine and Massachusetts sites which are furthest from the primary SO_2 emitting source regions in the domain. For sites on the western edge of the MANE-VU region which is closer to the primary SO_2 emitting sources contributing to domain wide precursors of SO_4 ion the magnitude of the under-prediction appears to increase in absolute value. Under-prediction at sites in interior New England appears to fall between that seen for the other two subsets. For all the sites in the northeastern portion of the domain (generally downwind of the most significant SO_2 emission areas) it is clear that the model is not producing enough SO_4 ion for the meteorological and emission representations used in the model during periods of highest measured SO_4 ion. This could mean that the chemistry is not adequately being modeled or that missing emissions are coming into play. Based on a relatively good understanding of the sources of SO_2 precursor emissions, and the belief that the inventories of emissions used in the Phase II modeling were very good representations of the actual emissions pattern during 2002, these results seem to indicate that a more robust chemical conversion rate from gaseous SO_2 to aerosol form SO_4 ion needs to be incorporated in the model, perhaps through better representation of the aqueous phase chemistry which is currently not accounted for well in CALPUFF.

Apportioning the Contribution of States and Individual EGU Sources of SO_2

Based on a reasonable conclusion that the VTDEC CALPUFF modeling platform appears to be performing well enough to be used at least in a relative sense, the following Figure D-32a and Figure D-32b summarize the contribution to annual ambient SO_4 ion at all of the Class I areas in the northeastern portion of the domain due to modeled SO_2 emissions originating in the four RPOs and portions of Canada located either entirely or partially in the domain.

Figure D-32a. Contribution to SO_4 Ion at ACAD LYBR BRIG SHEN

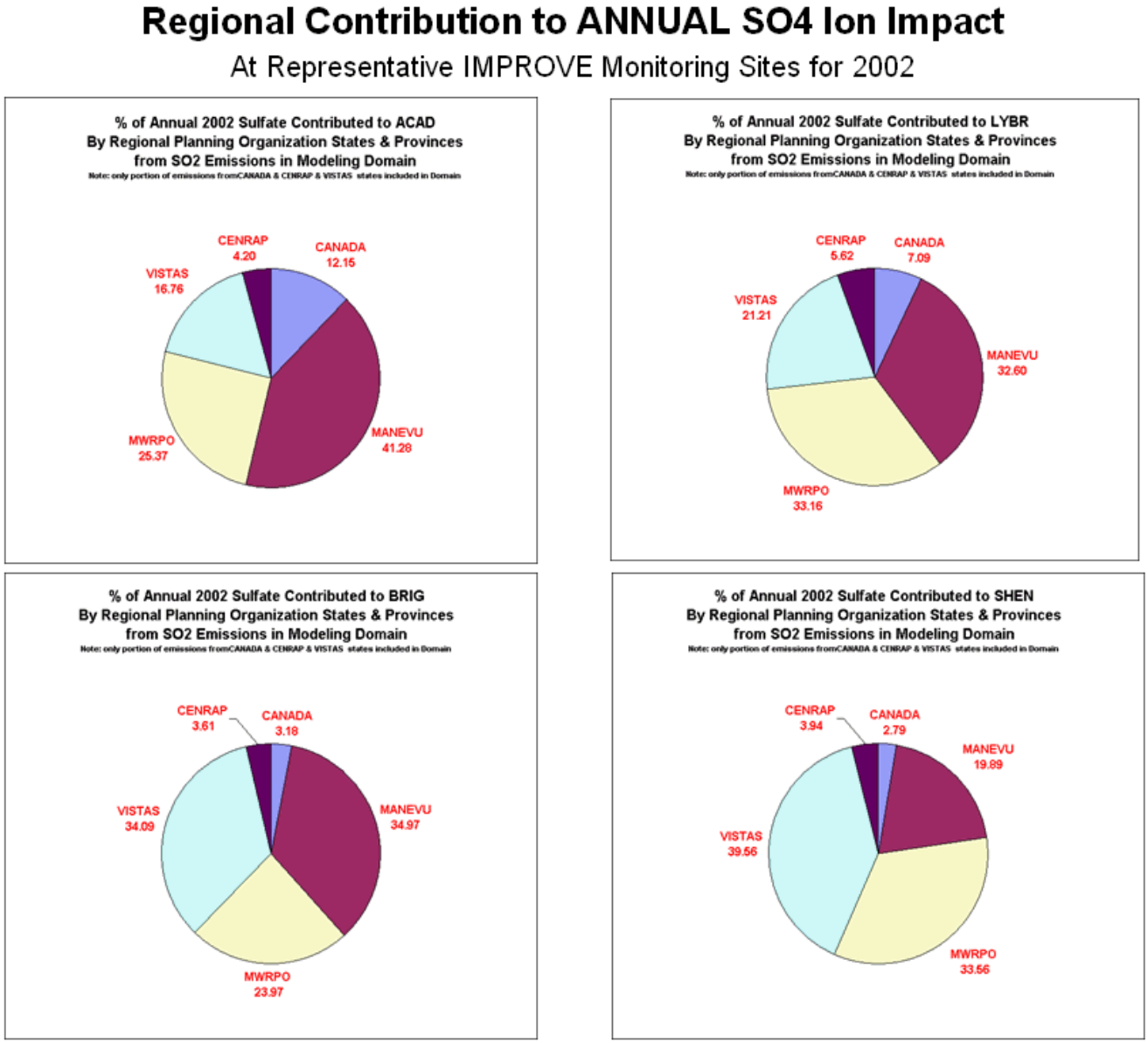

Figure D-32b. Contribution to SO_4 Ion at MOOS GRGU JARI DOSO

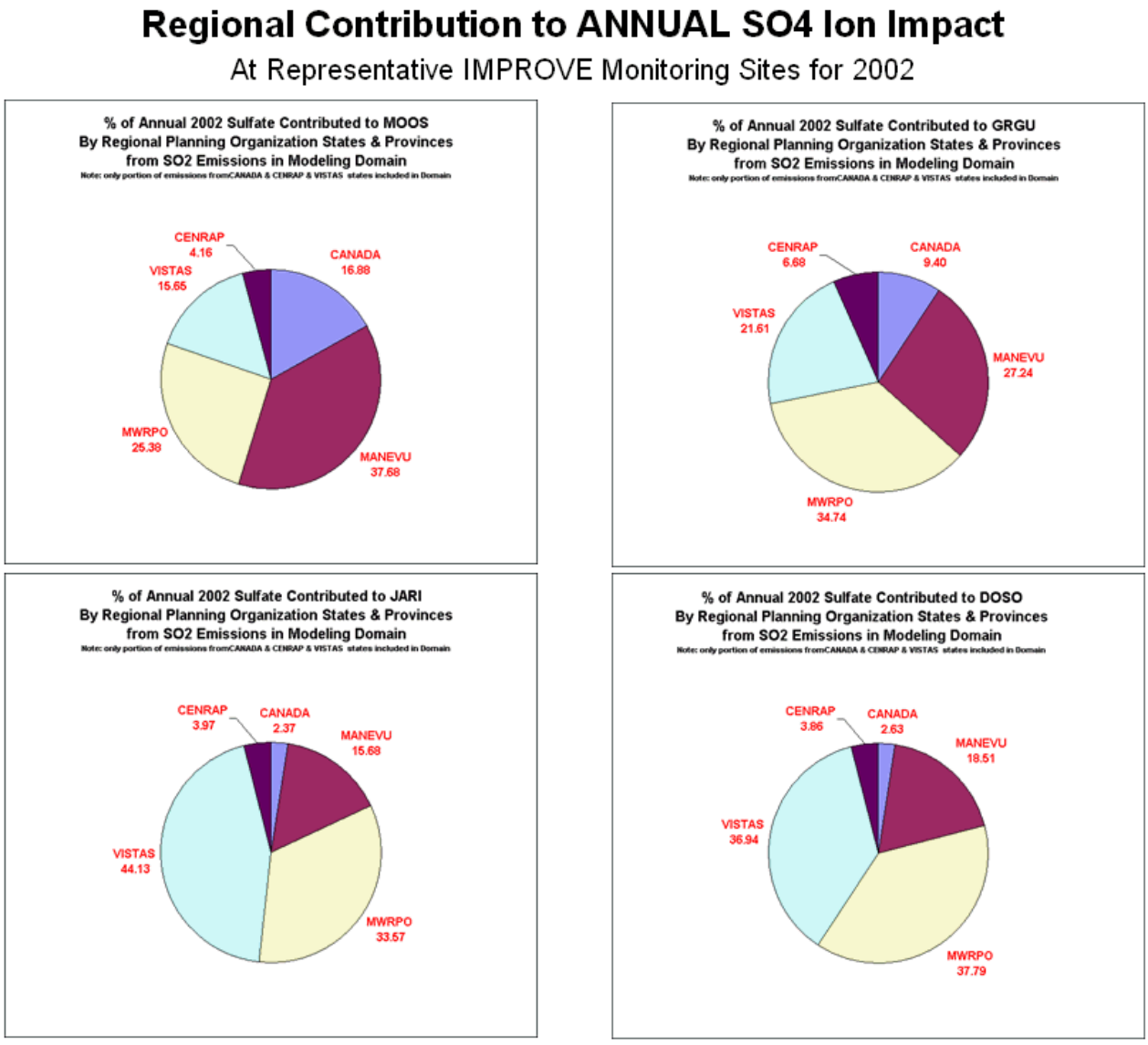

State-by-State Results Summary: VTDEC NWS-Based Meteorology

Figure D-33(a-d, for different Class I areas) shows the contribution from individual states and from Canada to the SO_4 Ion concentrations predicted for 2002 at four of the Class I areas in the northeastern portion of the domain modeled.

Figure D-33a. State by State Contributions to Ambient SO_4 Ion at Acadia National Park

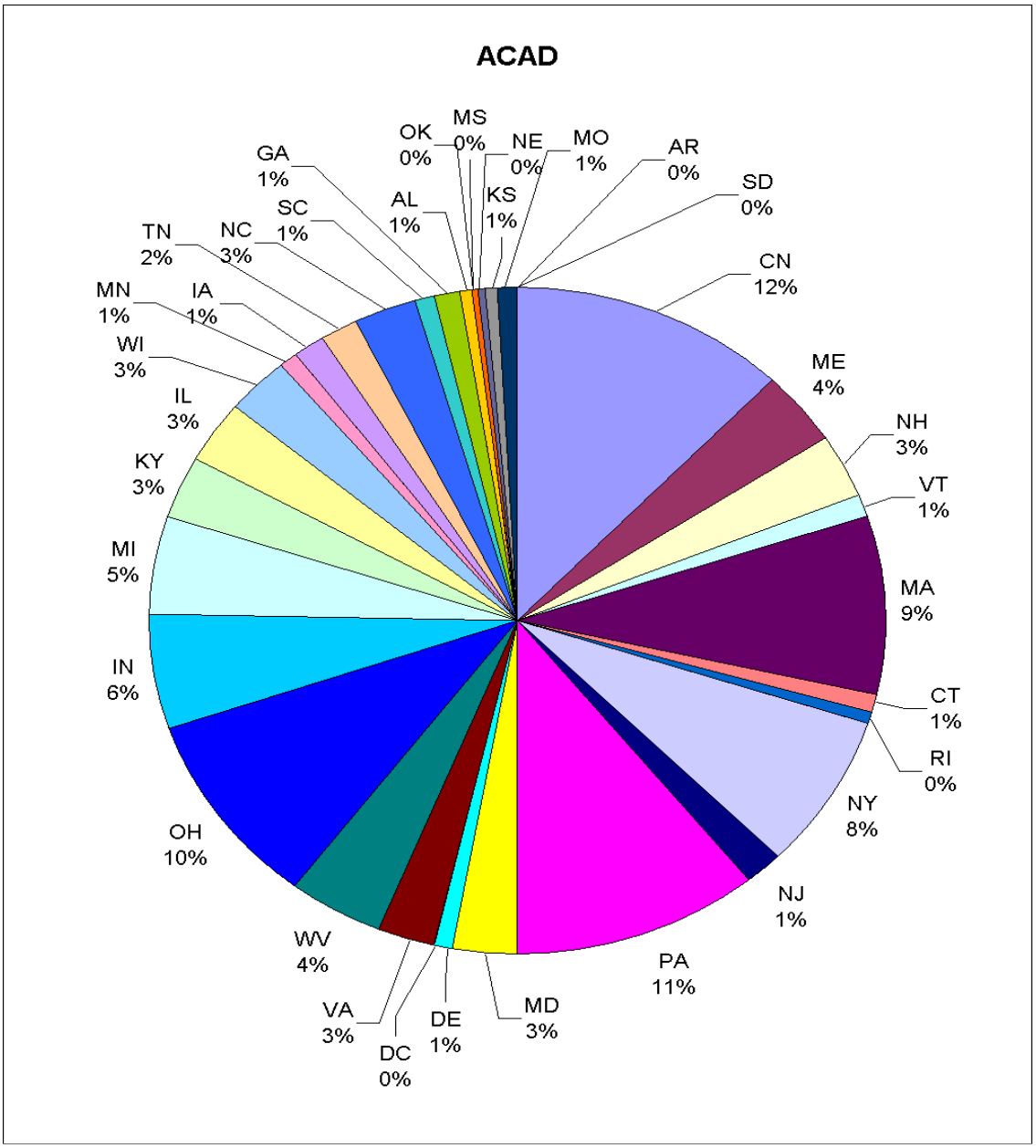

Figure D-33b State by State Contributions to Ambient SO_4 Ion at Lye Brook Wilderness Area

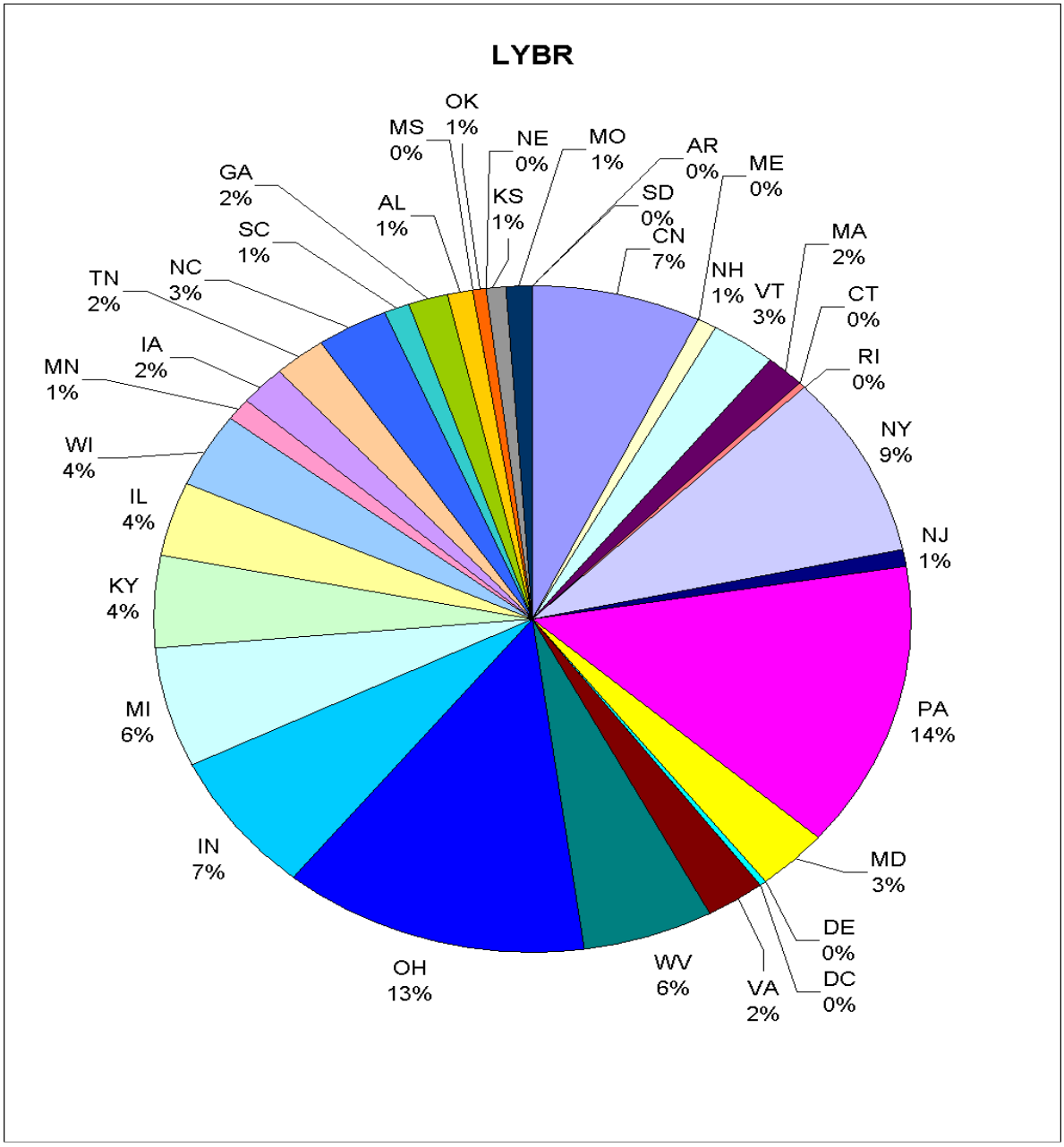

Figure D-33c. State by State Contributions to Ambient SO_4 Ion at Brigantine National Wildlife Refuge

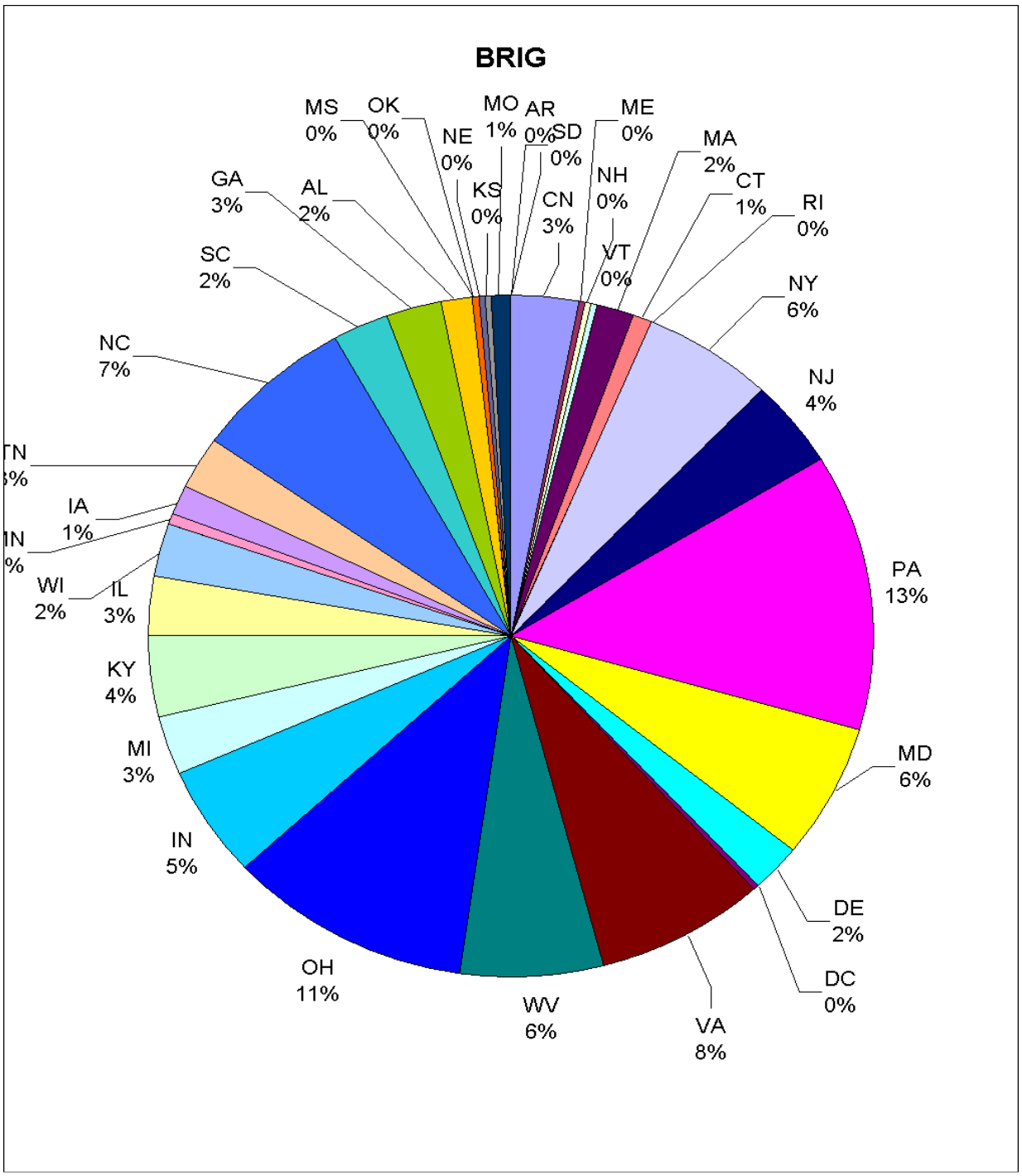

Figure D-33d. State by State Contributions to Ambient SO_4 Ion at Shenandoah National Park

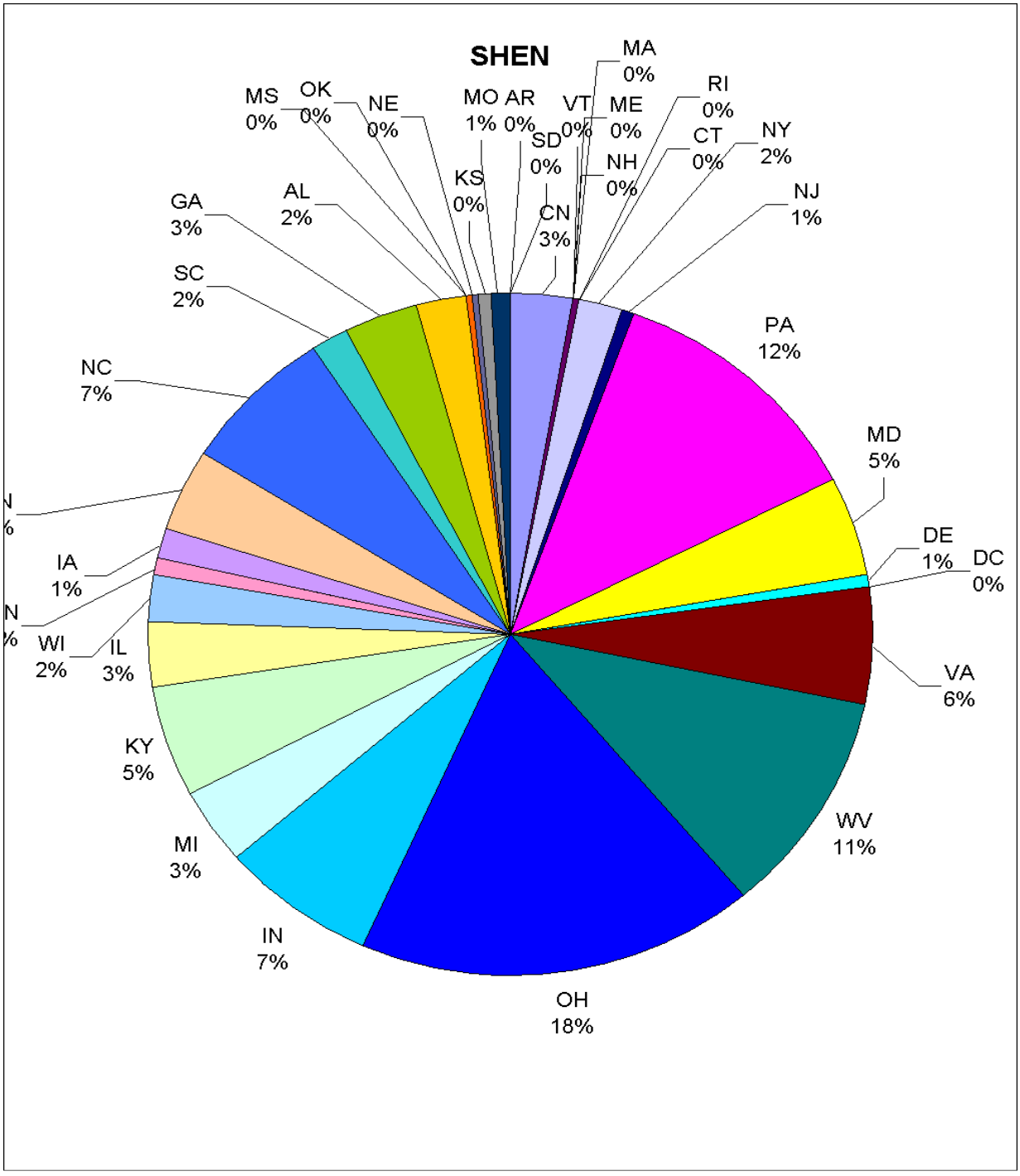

Table D-10(a-d, for different Class I areas) provides a summary of individual EGU impacts. These tables represent the 100 highest predicted 24-hr average sulfate ion concentrations at each site. Additional information shown includes the unit identification code from the CEMS data base, the State where the unit is located, the date of the 24-hr prediction, the predicted annual average sulfate ion concentration for the unit (and the

rank of the annual average concentration), total tons of SO_2 emitted in 2002, the stack height, and the distance from the source to the Class I area.

Table D-10a. VT DEC CALPUFF MODELING RESULTS

Acadia National Park								
RANK	**CEMS SOURCE**	**STATE**	**24-Hr Max SO4 Ion Impact (~µg/m^3)**	**24Hr Date**	**Annual SO_4 Ion Impact (~µg/m^3)**	**2002 SO_2 (Tons)**	**Modeled StkHt (Meters)**	**Distance (Kms)**
1	D028404	OH	0.541	08/14/02	0.01364	87723.73	245.4	1207.2
2	D031361	PA	0.498	08/13/02	0.01677	87357.00	243.8	992.3
3	D031362	PA	0.473	08/13/02	0.01176	62791.27	243.8	992.3
4	D031222	PA	0.429	08/13/02	0.01050	55167.46	243.8	990.5
5	D031492	PA	0.394	07/23/02	0.01102	50232.01	347.2	776.2
6	D031221	PA	0.394	08/13/02	0.00887	45713.85	243.8	990.5
7	D02876C01	OH	0.392	08/15/02	0.00793	72528.72	243.8	1294.7
8	D031491	PA	0.368	08/13/02	0.01220	60188.24	347.2	776.2
9	D028281	OH	0.336	08/14/02	0.00650	37274.20	251.5	1111.4
10	D03179C01	PA	0.319	08/14/02	0.01128	79564.81	150.0	1080.3
11	D03406C10	TN	0.311	10/03/02	0.00696	104430.60	150.0	1875.4
12	D080421	NC	0.299	08/16/02	0.00472	57768.69	182.9	1337.1
13	D03948C02	WV	0.294	08/14/02	0.00823	55355.96	167.6	1146.4
14	D016193	MA	0.270	07/23/02	0.01060	19307.64	107.3	378.9
15	D080422	NC	0.270	08/16/02	0.00388	45255.73	182.9	1337.1
16	D028667	OH	0.268	08/14/02	0.00670	33571.62	259.1	1095.9
17	D023642	NH	0.259	08/13/02	0.01541	19435.42	159.7	291.3
18	D037976	VA	0.239	08/16/02	0.00540	40533.88	127.7	1086.1
19	D02872C04	OH	0.235	08/14/02	0.00877	83060.23	150.0	1223.3
20	D0283612	OH	0.220	08/14/02	0.00777	41395.14	182.9	1161.8
21	D082261	PA	0.217	08/13/02	0.00683	40231.91	228.6	1033.1
22	D039432	WV	0.215	08/14/02	0.00620	45808.91	167.6	1088.3
23	D039431	WV	0.209	08/14/02	0.00564	42347.54	167.6	1088.3
24	D01733C12	MI	0.207	08/14/02	0.00799	46039.95	137.2	1249.4
25	D016264	MA	0.199	09/20/02	0.00345	2877.66	152.4	294.1
26	D01733C34	MI	0.199	01/31/02	0.00769	39326.85	152.4	1249.4
27	D015992	MA	0.194	05/31/02	0.00353	8971.48	151.8	341.6
28	D028327	OH	0.190	08/15/02	0.00600	46949.57	243.8	1482.6
29	D00988U4	IN	0.189	01/31/02	0.00570	45022.27	122.8	1488.3
30	D01353C02	KY	0.189	08/15/02	0.00477	41507.88	243.8	1375.6
31	D03131CS1	PA	0.188	08/13/02	0.00476	22323.74	150.0	901.2
32	D01010C05	IN	0.182	10/03/02	0.00836	60693.13	122.8	1662.7
33	D039353	WV	0.181	08/15/02	0.00527	42174.31	274.9	1299.5
34	D031403	PA	0.177	08/13/02	0.00600	38766.62	269.1	837.4
35	D03298WL1	SC	0.177	08/16/02	0.00114	25147.74	121.9	1614.4
36	D015991	MA	0.176	07/29/02	0.00756	13002.46	151.8	341.6
37	D02712C03	NC	0.176	08/16/02	0.00327	30749.26	150.0	1260.2
38	D028306	OH	0.175	01/30/02	0.00358	30438.59	137.2	1451.0
39	D027274	NC	0.174	08/16/02	0.00183	27284.07	85.3	1447.9

Acadia National Park								
RANK	**CEMS SOURCE**	**STATE**	**24-Hr Max SO4 Ion Impact (~µg/m^3)**	**24Hr Date**	**Annual SO_4 Ion Impact (~µg/m^3)**	**2002 SO_2 (Tons)**	**Modeled StkHt (Meters)**	**Distance (Kms)**
40	D027273	NC	0.173	08/16/02	0.00176	26305.45	85.3	1447.9
41	D027122	NC	0.170	08/16/02	0.00303	29310.41	121.9	1260.2
42	D03935C02	WV	0.170	05/29/02	0.00677	63009.75	274.3	1299.5
43	D03809CS0	VA	0.169	08/16/02	0.00417	21200.55	98.8	1048.1
44	D06166C02	IN	0.168	10/03/02	0.00554	51662.69	304.8	1715.4
45	D027215	NC	0.167	08/16/02	0.00145	19128.20	152.4	1527.9
46	D03140C12	PA	0.166	07/23/02	0.00514	29709.17	259.1	837.4
47	D01571CE2	MD	0.164	07/23/02	0.00711	48522.41	335.3	950.7
48	D06113C03	IN	0.162	08/15/02	0.00828	71118.81	150.0	1748.0
49	D062641	WV	0.161	08/15/02	0.00514	42719.38	335.3	1276.8
50	D015731	MD	0.156	08/16/02	0.00521	36790.12	213.4	983.0
51	D02554C03	NY	0.155	09/11/02	0.00748	30124.51	150.0	916.5
52	D038093	VA	0.154	08/16/02	0.00140	10467.61	149.0	1048.1
53	D015732	MD	0.153	08/16/02	0.00435	30760.70	213.4	983.0
54	D02866C01	OH	0.153	08/14/02	0.00419	24627.17	153.6	1095.9
55	D0099070	IN	0.151	10/03/02	0.00411	29774.44	172.2	1559.5
56	D02864C01	OH	0.146	08/14/02	0.00473	35161.71	259.1	1141.4
57	D023641	NH	0.145	04/17/02	0.00766	9347.83	131.7	291.3
58	D062491	SC	0.145	08/16/02	0.00093	17919.56	123.1	1550.3
59	D06250C05	NC	0.144	08/16/02	0.00273	27370.73	243.8	1245.7
60	D067054	IN	0.139	10/03/02	0.00442	40082.21	152.4	1738.5
61	D027133	NC	0.139	08/16/02	0.00116	14460.20	167.6	1391.2
62	D03947C03	WV	0.137	08/14/02	0.00489	38540.84	150.0	1145.8
63	D031782	PA	0.133	08/13/02	0.00339	16468.79	307.2	988.8
64	D02549C01	NY	0.132	08/14/02	0.00671	25320.03	150.0	869.6
65	D028502	OH	0.132	08/15/02	0.00328	28672.85	213.4	1425.8
66	D016192	MA	0.131	09/20/02	0.00757	8881.31	107.3	378.9
67	D028501	OH	0.131	08/15/02	0.00354	30770.84	213.4	1425.8
68	D03297WT1	SC	0.131	08/16/02	0.00089	17670.72	91.4	1577.2
69	D02866C02	OH	0.130	08/14/02	0.00429	25999.24	153.6	1095.9
70	D06113C04	IN	0.129	01/31/02	0.00348	27823.32	213.4	1748.0
71	D01356C02	KY	0.129	01/30/02	0.00343	25622.89	225.9	1519.4
72	D02712C04	NC	0.128	08/16/02	0.00227	22941.29	150.0	1260.2
73	D02840C02	OH	0.128	08/14/02	0.00333	22770.56	172.2	1207.2
74	D080021	NH	0.126	08/14/02	0.00461	5028.40	133.2	247.0
75	D000475	AL	0.125	10/03/02	0.00110	27218.75	152.4	1975.2
76	D025945	NY	0.125	08/15/02	0.00084	1746.53	213.4	668.5
77	D028504	OH	0.124	08/15/02	0.00327	27318.93	213.4	1425.8
78	D016263	MA	0.122	09/20/02	0.00494	4966.05	132.6	294.1
79	D01572C23	MD	0.121	08/13/02	0.00464	32159.23	121.9	950.3
80	D016191	MA	0.118	09/20/02	0.00763	9244.07	107.3	378.9
81	D023781	NJ	0.118	03/14/02	0.00351	9737.90	144.8	770.2
82	D028665	OH	0.117	08/14/02	0.00330	19778.82	304.8	1095.9

Acadia National Park								
RANK	**CEMS SOURCE**	**STATE**	**24-Hr Max SO4 Ion Impact (~µg/m^3)**	**24Hr Date**	**Annual SO_4 Ion Impact (~µg/m^3)**	**2002 SO_2 (Tons)**	**Modeled StkHt (Meters)**	**Distance (Kms)**
83	D03297WT2	SC	0.117	08/16/02	0.00075	17199.39	91.4	1577.2
84	D00709C02	GA	0.115	08/16/02	0.00090	47548.54	121.9	1788.7
85	D02866M6A	OH	0.115	08/14/02	0.00335	19546.42	304.8	1095.9
86	D028375	OH	0.113	07/03/02	0.00712	35937.73	182.9	1111.1
87	D03407C15	TN	0.113	08/16/02	0.00213	37274.48	152.4	1660.6
88	D037975	VA	0.113	08/16/02	0.00265	19602.10	61.0	1086.1
89	D07253C01	OH	0.112	08/15/02	0.00369	30949.43	213.4	1224.2
90	D033194	SC	0.111	08/16/02	0.00056	11838.20	91.4	1591.7
91	D017437	MI	0.110	09/12/02	0.00359	15804.84	182.9	1154.7
92	D028725	OH	0.110	08/14/02	0.00355	30052.41	252.1	1223.3
93	D060191	OH	0.109	08/15/02	0.00244	21495.65	174.6	1452.5
94	D038034	VA	0.109	08/15/02	0.00211	10806.45	61.0	1078.6
95	D007034LR	GA	0.106	08/16/02	0.00128	40973.96	304.8	1818.2
96	D00861C01	IL	0.105	07/24/02	0.00540	42318.01	152.4	1838.3
97	D024032	NJ	0.105	03/09/02	0.00582	18768.40	152.1	621.5
98	D03407C69	TN	0.105	10/03/02	0.00223	38610.70	150.0	1660.6
99	D007033LR	GA	0.104	08/16/02	0.00118	43029.15	304.8	1818.2
100	D013783	KY	0.102	05/26/02	0.00309	46660.04	243.8	1749.3

Table D-10b. VT DEC CALPUFF MODELING RESULTS

Brigantine National Wildlife Refuge								
RANK	**CEMS SOURCE**	**STATE**	**24-Hr Max SO_4 Ion Impact (~µg/m^3)**	**24Hr Date**	**Annual SO_4 Ion Impact (~µg/m^3)**	**2002 SO_2 (Tons)**	**Modeled StkHt (Meters)**	**Distance (Kms)**
1	D03935C02	WV	0.580	06/26/02	0.02133	63009.75	274.3	643.2
2	D028404	OH	0.560	06/11/02	0.02024	87723.73	245.4	636.0
3	D037976	VA	0.511	06/27/02	0.02723	40533.88	127.7	343.0
4	D01571CE2	MD	0.504	08/14/02	0.02772	48522.41	335.3	217.5
5	D080421	NC	0.454	08/14/02	0.01933	57768.69	182.9	603.1
6	D02872C04	OH	0.453	07/20/02	0.01933	83060.23	150.0	616.7
7	D031491	PA	0.435	03/15/02	0.02096	60188.24	347.2	258.4
8	D03179C01	PA	0.424	07/19/02	0.02476	79564.81	150.0	468.3
9	D02876C01	OH	0.396	06/26/02	0.01982	72528.72	243.8	660.6
10	D080422	NC	0.389	08/14/02	0.01531	45255.73	182.9	603.1
11	D039353	WV	0.386	06/26/02	0.01527	42174.31	274.9	643.2
12	D015731	MD	0.380	07/03/02	0.02099	36790.12	213.4	249.5
13	D015732	MD	0.372	07/03/02	0.01753	30760.70	213.4	249.5
14	D031361	PA	0.371	07/16/02	0.02671	87357.00	243.8	435.1
15	D023781	NJ	0.367	07/02/02	0.01627	9737.90	144.8	25.0
16	D038034	VA	0.363	08/13/02	0.01059	10806.45	61.0	338.7
17	D03809CS0	VA	0.362	08/13/02	0.01787	21200.55	98.8	303.9
18	D062641	WV	0.354	06/26/02	0.01298	42719.38	335.3	643.2
19	D031362	PA	0.352	07/16/02	0.02101	62791.27	243.8	435.1
20	D031492	PA	0.338	07/04/02	0.01719	50232.01	347.2	258.4
21	D005944	DE	0.318	08/05/02	0.00987	7383.72	121.9	118.5
22	D028327	OH	0.315	06/26/02	0.00920	46949.57	243.8	886.4
23	D027122	NC	0.308	08/13/02	0.01213	29310.41	121.9	520.7
24	D02712C03	NC	0.307	08/13/02	0.01365	30749.26	150.0	520.7
25	D03954CS0	WV	0.291	01/22/02	0.00613	20111.54	225.9	413.0
26	D01353C02	KY	0.289	06/26/02	0.01479	41507.88	243.8	718.2
27	D037975	VA	0.289	06/27/02	0.01494	19602.10	61.0	343.0
28	D01010C05	IN	0.282	06/26/02	0.00842	60693.13	122.8	1106.0
29	D038093	VA	0.273	08/13/02	0.00839	10467.61	149.0	303.9
30	D028281	OH	0.268	07/19/02	0.01137	37274.20	251.5	533.3
31	D039432	WV	0.268	07/20/02	0.01378	45808.91	167.6	466.6
32	D039431	WV	0.264	07/20/02	0.01305	42347.54	167.6	466.6
33	D03406C10	TN	0.258	07/30/02	0.01199	104430.60	150.0	1214.5
34	D00988U4	IN	0.256	07/20/02	0.00843	45022.27	122.8	891.4
35	D06250C05	NC	0.253	08/13/02	0.01148	27370.73	243.8	505.3
36	D03948C02	WV	0.244	07/20/02	0.01490	55355.96	167.6	543.4
37	D03298WL1	SC	0.236	08/15/02	0.00499	25147.74	121.9	870.8
38	D031221	PA	0.228	07/16/02	0.01247	45713.85	243.8	420.4
39	D027215	NC	0.225	08/15/02	0.00515	19128.20	152.4	795.8
40	D028306	OH	0.225	06/26/02	0.00555	30438.59	137.2	844.8

Brigantine National Wildlife Refuge								
RANK	**CEMS SOURCE**	**STATE**	**24-Hr Max SO_4 Ion Impact (~µg/m^3)**	**24Hr Date**	**Annual SO_4 Ion Impact (~µg/m^3)**	**2002 SO_2 (Tons)**	**Modeled StkHt (Meters)**	**Distance (Kms)**
41	D028667	OH	0.224	07/19/02	0.01036	33571.62	259.1	536.7
42	D082261	PA	0.224	07/19/02	0.01106	40231.91	228.6	467.9
43	D06113C03	IN	0.221	06/26/02	0.00955	71118.81	150.0	1152.2
44	D005943	DE	0.215	08/05/02	0.00681	4681.50	117.3	118.5
45	D01572C23	MD	0.213	07/03/02	0.01459	32159.23	121.9	259.4
46	D031403	PA	0.213	09/05/02	0.01465	38766.62	269.1	203.1
47	D02712C04	NC	0.210	06/12/02	0.00998	22941.29	150.0	520.7
48	D027273	NC	0.210	08/15/02	0.00660	26305.45	85.3	713.7
49	D028502	OH	0.210	06/26/02	0.00672	28672.85	213.4	798.7
50	D024032	NJ	0.209	08/03/02	0.00984	18768.40	152.1	145.4
51	D027274	NC	0.207	08/15/02	0.00688	27284.07	85.3	713.7
52	D028504	OH	0.206	06/26/02	0.00648	27318.93	213.4	798.7
53	D028501	OH	0.204	06/26/02	0.00695	30770.84	213.4	798.7
54	D005935	DE	0.201	08/05/02	0.00316	2135.69	83.8	121.1
55	D038033	VA	0.201	08/13/02	0.00843	9493.00	61.0	338.7
56	D016193	MA	0.199	03/20/02	0.00664	19307.64	107.3	369.7
57	D07253C01	OH	0.194	06/11/02	0.00877	30949.43	213.4	604.0
58	D007034LR	GA	0.188	03/08/02	0.00678	40973.96	304.8	1099.1
59	D027121	NC	0.187	08/13/02	0.00519	12020.17	121.9	520.7
60	D02832C06	OH	0.186	06/26/02	0.00489	23673.32	213.4	886.4
61	D03297WT1	SC	0.186	08/15/02	0.00392	17670.72	91.4	832.3
62	D028503	OH	0.184	06/26/02	0.00636	27943.53	213.4	798.7
63	D02864C01	OH	0.181	06/11/02	0.00947	35161.71	259.1	542.5
64	D007033LR	GA	0.180	03/08/02	0.00690	43029.15	304.8	1099.1
65	D00861C01	IL	0.180	06/26/02	0.00553	42318.01	152.4	1279.5
66	D03407C15	TN	0.178	08/14/02	0.00792	37274.48	152.4	965.0
67	D06170CS1	WI	0.175	07/20/02	0.00533	32737.32	182.9	1172.4
68	D010012	IN	0.174	06/26/02	0.00427	25992.39	152.4	1103.3
69	D03140C12	PA	0.174	09/05/02	0.01169	29709.17	259.1	203.1
70	D0099070	IN	0.168	06/26/02	0.00472	29774.44	172.2	1000.8
71	D081021	OH	0.166	06/26/02	0.00493	18190.75	253.0	659.3
72	D060191	OH	0.166	06/26/02	0.00472	21495.65	174.6	840.5
73	D03297WT2	SC	0.166	08/15/02	0.00351	17199.39	91.4	832.3
74	D005942	DE	0.165	08/05/02	0.00524	3759.93	152.4	118.5
75	D00709C02	GA	0.163	05/14/02	0.00616	47548.54	121.9	1050.5
76	D01733C34	MI	0.163	07/19/02	0.00804	39326.85	152.4	792.7
77	D060312	OH	0.162	06/26/02	0.00496	19500.08	274.3	779.6
78	D081022	OH	0.161	06/26/02	0.00404	12322.44	253.0	659.3
79	D0393851	WV	0.161	06/26/02	0.00402	12936.25	183.8	642.4
80	D01733C12	MI	0.160	07/19/02	0.00823	46039.95	137.2	792.7
81	D06166C02	IN	0.158	06/26/02	0.00742	51662.69	304.8	1098.7
82	D062491	SC	0.158	08/15/02	0.00407	17919.56	123.1	807.9
83	D06113C04	IN	0.156	06/26/02	0.00443	27823.32	213.4	1152.2

Brigantine National Wildlife Refuge								
RANK	**CEMS SOURCE**	**STATE**	**24-Hr Max SO_4 Ion Impact (~µg/m^3)**	**24Hr Date**	**Annual SO_4 Ion Impact (~µg/m^3)**	**2002 SO_2 (Tons)**	**Modeled StkHt (Meters)**	**Distance (Kms)**
84	D013783	KY	0.156	06/26/02	0.00630	46660.04	243.8	1112.4
85	D019151	MN	0.155	12/17/02	0.00329	21855.00	239.0	1620.5
86	D007031LR	GA	0.153	03/08/02	0.00619	38486.16	304.8	1099.1
87	D033194	SC	0.153	08/15/02	0.00215	11838.20	91.4	847.5
88	D01356C02	KY	0.151	06/26/02	0.00505	25622.89	225.9	911.1
89	D0283612	OH	0.151	07/19/02	0.00841	41395.14	182.9	677.8
90	D037974	VA	0.150	06/27/02	0.00687	9293.00	61.0	343.0
91	D03407C69	TN	0.149	08/14/02	0.00828	38610.70	150.0	965.0
92	D031222	PA	0.148	08/20/02	0.01496	55167.46	243.8	420.4
93	D000265	AL	0.147	02/01/02	0.00515	53015.27	228.6	1271.8
94	D03938C04	WV	0.145	06/26/02	0.00672	26427.11	121.9	642.4
95	D005941	DE	0.144	08/05/02	0.00488	3742.48	152.4	118.5
96	D02866C01	OH	0.141	07/19/02	0.00679	24627.17	153.6	536.7
97	D027093	NC	0.139	08/15/02	0.00375	9389.76	91.4	553.7
98	D03936C02	WV	0.138	06/26/02	0.00557	15466.69	304.8	616.2
99	D01355C03	KY	0.136	09/05/02	0.00736	38069.95	150.0	905.3
100	D033193	SC	0.136	08/15/02	0.00221	11045.11	91.4	847.5

Table D-10c VT DEC CALPUFF MODELING RESULTS

Lye Brook Wilderness								
RANK	**CEMS SOURCE**	**STATE**	**24-Hr Max SO_4 Ion Impact (~µg/m^3)**	**24Hr Date**	**Annual SO_4 Ion Impact (~µg/m^3)**	**2002 SO_2 (Tons)**	**Modeled StkHt (Meters)**	**Distance (Kms)**
1	D031361	PA	0.764	06/24/02	0.02622	87357.00	243.8	580.4
2	D031362	PA	0.689	06/24/02	0.01933	62791.27	243.8	580.4
3	D028404	OH	0.680	08/13/02	0.02024	87723.73	245.4	794.3
4	D03179C01	PA	0.598	08/13/02	0.01709	79564.81	150.0	671.2
5	D031492	PA	0.576	06/23/02	0.01598	50232.01	347.2	371.2
6	D031491	PA	0.557	06/23/02	0.01699	60188.24	347.2	371.2
7	D03948C02	WV	0.543	08/13/02	0.01175	55355.96	167.6	735.3
8	D028281	OH	0.539	08/13/02	0.00996	37274.20	251.5	699.1
9	D082261	PA	0.470	06/24/02	0.01067	40231.91	228.6	621.0
10	D02876C01	OH	0.463	08/14/02	0.01137	72528.72	243.8	884.6
11	D031222	PA	0.444	08/13/02	0.01239	55167.46	243.8	579.5
12	D039432	WV	0.409	08/13/02	0.00903	45808.91	167.6	680.2
13	D039431	WV	0.405	08/13/02	0.00834	42347.54	167.6	680.2
14	D031221	PA	0.402	08/13/02	0.01137	45713.85	243.8	579.5
15	D02872C04	OH	0.377	08/13/02	0.01413	83060.23	150.0	811.6
16	D028667	OH	0.370	08/13/02	0.00976	33571.62	259.1	683.1
17	D01010C05	IN	0.321	07/03/02	0.00817	60693.13	122.8	1251.9
18	D031403	PA	0.312	06/23/02	0.00871	38766.62	269.1	448.1
19	D00988U4	IN	0.311	07/03/02	0.00834	45022.27	122.8	1075.3
20	D028327	OH	0.282	08/14/02	0.00891	46949.57	243.8	1069.6
21	D03935C02	WV	0.282	03/17/02	0.00972	63009.75	274.3	892.6
22	D01733C12	MI	0.267	07/10/02	0.01042	46039.95	137.2	845.4
23	D03140C12	PA	0.262	06/23/02	0.00757	29709.17	259.1	448.1
24	D02864C01	OH	0.257	08/13/02	0.00705	35161.71	259.1	730.1
25	D03947C03	WV	0.255	08/13/02	0.00720	38540.84	150.0	734.6
26	D039353	WV	0.238	05/28/02	0.00757	42174.31	274.9	892.6
27	D01733C34	MI	0.227	07/10/02	0.00991	39326.85	152.4	845.4
28	D01571CE2	MD	0.205	07/23/02	0.00922	48522.41	335.3	590.0
29	D01353C02	KY	0.200	08/14/02	0.00784	41507.88	243.8	967.9
30	D02866C01	OH	0.199	08/13/02	0.00604	24627.17	153.6	683.1
31	D060041	WV	0.197	08/13/02	0.00493	21561.93	304.8	785.8
32	D01572C23	MD	0.194	07/23/02	0.00676	32159.23	121.9	566.1
33	D07253C01	OH	0.193	08/13/02	0.00571	30949.43	213.4	813.5
34	D080421	NC	0.190	08/15/02	0.00587	57768.69	182.9	961.3
35	D0283612	OH	0.189	07/23/02	0.00906	41395.14	182.9	752.6
36	D028725	OH	0.188	08/13/02	0.00522	30052.41	252.1	811.6
37	D0099070	IN	0.184	06/12/02	0.00449	29774.44	172.2	1148.0
38	D015731	MD	0.181	07/15/02	0.00690	36790.12	213.4	620.2
39	D015732	MD	0.180	07/15/02	0.00604	30760.70	213.4	620.2
40	D062641	WV	0.177	08/14/02	0.00728	42719.38	335.3	867.0

Lye Brook Wilderness								
RANK	**CEMS SOURCE**	**STATE**	**24-Hr Max SO_4 Ion Impact (~µg/m^3)**	**24Hr Date**	**Annual SO_4 Ion Impact (~µg/m^3)**	**2002 SO_2 (Tons)**	**Modeled StkHt (Meters)**	**Distance (Kms)**
41	D06113C03	IN	0.172	03/07/02	0.00924	71118.81	150.0	1335.3
42	D013783	KY	0.172	06/13/02	0.00615	46660.04	243.8	1337.1
43	D03406C10	TN	0.171	10/03/02	0.00820	104430.60	150.0	1464.8
44	D024032	NJ	0.170	03/16/02	0.00341	18768.40	152.1	276.9
45	D028501	OH	0.170	08/14/02	0.00466	30770.84	213.4	1014.1
46	D028502	OH	0.170	08/14/02	0.00444	28672.85	213.4	1014.1
47	D01008C01	IN	0.169	06/13/02	0.00383	24087.17	228.6	1193.7
48	D016061	MA	0.168	06/21/02	0.00197	5249.48	112.8	105.0
49	D080422	NC	0.168	08/15/02	0.00476	45255.73	182.9	961.3
50	D02866C02	OH	0.168	08/13/02	0.00590	25999.24	153.6	683.1
51	D02554C03	NY	0.167	09/11/02	0.00835	30124.51	150.0	510.9
52	D01355C03	KY	0.165	06/27/02	0.00509	38069.95	150.0	1139.9
53	D028665	OH	0.160	08/13/02	0.00494	19778.82	304.8	683.1
54	D028504	OH	0.160	08/14/02	0.00477	27318.93	213.4	1014.1
55	D01008C02	IN	0.154	06/13/02	0.00388	23827.97	307.2	1193.7
56	D028282	OH	0.154	08/13/02	0.00433	20579.94	251.5	699.1
57	D06166C02	IN	0.150	06/27/02	0.00761	51662.69	304.8	1302.5
58	D02866M6A	OH	0.150	08/13/02	0.00476	19546.42	304.8	683.1
59	D01356C02	KY	0.149	06/13/02	0.00521	25622.89	225.9	1106.5
60	D060191	OH	0.146	08/14/02	0.00386	21495.65	174.6	1039.9
61	D017459A	MI	0.144	07/10/02	0.00487	18324.29	171.3	826.8
62	D00861C01	IL	0.139	07/03/02	0.00541	42318.01	152.4	1428.1
63	D02840C02	OH	0.139	08/13/02	0.00495	22770.56	172.2	794.3
64	D02832C06	OH	0.137	08/14/02	0.00466	23673.32	213.4	1069.6
65	D03131CS1	PA	0.137	06/24/02	0.00619	22323.74	150.0	489.3
66	D037976	VA	0.135	08/16/02	0.00536	40533.88	127.7	731.9
67	D03954CS0	WV	0.133	11/22/02	0.00249	20111.54	225.9	672.2
68	D007032LR	GA	0.129	10/03/02	0.00226	37255.59	304.8	1424.5
69	D028306	OH	0.129	07/03/02	0.00521	30438.59	137.2	1038.2
70	D028375	OH	0.128	06/12/02	0.00811	35937.73	182.9	702.1
71	D00709C02	GA	0.125	08/16/02	0.00175	47548.54	121.9	1411.5
72	D02549C01	NY	0.125	07/03/02	0.00781	25320.03	150.0	470.3
73	D067054	IN	0.123	08/14/02	0.00528	40082.21	152.4	1325.6
74	D000265	AL	0.121	10/03/02	0.00201	53015.27	228.6	1592.6
75	D007031LR	GA	0.121	10/03/02	0.00242	38486.16	304.8	1424.5
76	D03407C15	TN	0.121	08/15/02	0.00320	37274.48	152.4	1258.5
77	D00988C03	IN	0.119	08/14/02	0.00303	15946.48	85.3	1075.3
78	D02712C03	NC	0.119	08/16/02	0.00345	30749.26	150.0	893.4
79	D039423	WV	0.119	08/13/02	0.00218	10126.02	68.6	675.6
80	D028283	OH	0.118	06/24/02	0.00253	15372.27	274.3	700.2
81	D031782	PA	0.118	08/13/02	0.00460	16468.79	307.2	576.1
82	D027274	NC	0.117	08/15/02	0.00261	27284.07	85.3	1070.2
83	D06113C04	IN	0.116	07/03/02	0.00426	27823.32	213.4	1335.3

Lye Brook Wilderness								
RANK	**CEMS SOURCE**	**STATE**	**24-Hr Max SO_4 Ion Impact (~µg/m^3)**	**24Hr Date**	**Annual SO_4 Ion Impact (~µg/m^3)**	**2002 SO_2 (Tons)**	**Modeled StkHt (Meters)**	**Distance (Kms)**
84	D027273	NC	0.116	08/15/02	0.00253	26305.45	85.3	1070.2
85	D027215	NC	0.116	08/15/02	0.00204	19128.20	152.4	1146.7
86	D02963C10	OK	0.114	12/16/02	0.00278	34232.90	182.9	2050.3
87	D023642	NH	0.112	07/26/02	0.00371	19435.42	159.7	134.1
88	D080062	NY	0.112	06/22/02	0.00086	2839.86	79.2	187.9
89	D007034LR	GA	0.110	08/15/02	0.00278	40973.96	304.8	1424.5
90	D060312	OH	0.110	08/14/02	0.00303	19500.08	274.3	995.4
91	D03407C69	TN	0.110	08/15/02	0.00344	38610.70	150.0	1258.5
92	D060042	WV	0.110	03/17/02	0.00388	20531.62	304.8	785.8
93	D080061	NY	0.109	06/22/02	0.00103	3816.50	79.2	187.9
94	D007033LR	GA	0.107	08/15/02	0.00238	43029.15	304.8	1424.5
95	D081021	OH	0.107	03/17/02	0.00281	18190.75	253.0	882.6
96	D01702C09	MI	0.106	06/27/02	0.00154	4565.21	91.4	864.7
97	D0393851	WV	0.106	08/14/02	0.00225	12936.25	183.8	867.0
98	D060412	KY	0.104	08/14/02	0.00347	20472.77	245.7	1019.3
99	D006022	MD	0.103	07/23/02	0.00426	19263.13	211.8	523.1
100	D006021	MD	0.102	06/24/02	0.00436	19995.88	211.8	523.1

Table D-10d. VT DEC CALPUFF MODELING RESULTS

Shenandoah National Park								
RANK	**CEMS SOURCE**	**STATE**	**24-Hr Max SO_4 Ion Impact (~µg/m^3)**	**24Hr Date**	**Annual SO_4 Ion Impact (~µg/m^3)**	**2002 SO_2 (Tons)**	**Modeled StkHt (Meters)**	**Distance (Kms)**
1	D03179C01	PA	1.281	07/04/02	0.04605	79564.81	150.0	194.9
2	D028404	OH	0.950	07/16/02	0.03373	87723.73	245.4	347.2
3	D03954CS0	WV	0.868	10/14/02	0.01228	20111.54	225.9	103.7
4	D02872C04	OH	0.757	12/13/02	0.04278	83060.23	150.0	302.6
5	D01353C02	KY	0.711	06/26/02	0.01905	41507.88	243.8	365.1
6	D02876C01	OH	0.684	07/19/02	0.03050	72528.72	243.8	321.6
7	D01571CE2	MD	0.658	06/21/02	0.02057	48522.41	335.3	151.3
8	D03948C02	WV	0.635	07/16/02	0.02926	55355.96	167.6	250.0
9	D039353	WV	0.631	06/11/02	0.02051	42174.31	274.9	293.3
10	D03935C02	WV	0.609	06/26/02	0.02967	63009.75	274.3	293.3
11	D039432	WV	0.581	01/02/02	0.02901	45808.91	167.6	182.0
12	D060041	WV	0.577	03/15/02	0.01345	21561.93	304.8	249.8
13	D039431	WV	0.576	07/04/02	0.02634	42347.54	167.6	182.0
14	D060042	WV	0.556	03/15/02	0.01311	20531.62	304.8	249.8
15	D028281	OH	0.517	07/04/02	0.01871	37274.20	251.5	269.0
16	D031361	PA	0.498	09/19/02	0.03253	87357.00	243.8	250.4
17	D028667	OH	0.464	07/04/02	0.01554	33571.62	259.1	290.5
18	D031222	PA	0.462	09/19/02	0.02149	55167.46	243.8	231.7
19	D031221	PA	0.459	09/19/02	0.01982	45713.85	243.8	231.7
20	D01010C05	IN	0.455	07/19/02	0.01123	60693.13	122.8	779.6
21	D015731	MD	0.446	06/21/02	0.01614	36790.12	213.4	127.6
22	D080421	NC	0.443	02/01/02	0.02574	57768.69	182.9	286.2
23	D02864C01	OH	0.443	01/21/02	0.01917	35161.71	259.1	253.5
24	D015732	MD	0.442	06/21/02	0.01401	30760.70	213.4	127.6
25	D03407C15	TN	0.435	08/13/02	0.01102	37274.48	152.4	609.5
26	D03947C03	WV	0.424	03/15/02	0.02157	38540.84	150.0	251.3
27	D037976	VA	0.422	10/01/02	0.01934	40533.88	127.7	155.9
28	D031362	PA	0.419	09/19/02	0.02489	62791.27	243.8	250.4
29	D07253C01	OH	0.417	03/15/02	0.01732	30949.43	213.4	281.3
30	D031491	PA	0.415	08/31/02	0.01328	60188.24	347.2	319.0
31	D03406C10	TN	0.413	07/29/02	0.01808	104430.60	150.0	856.8
32	D062641	WV	0.412	06/11/02	0.02153	42719.38	335.3	306.0
33	D031492	PA	0.407	08/31/02	0.01222	50232.01	347.2	319.0
34	D080422	NC	0.382	06/25/02	0.02137	45255.73	182.9	286.2
35	D006022	MD	0.375	08/28/02	0.00817	19263.13	211.8	178.7
36	D006021	MD	0.364	08/28/02	0.00902	19995.88	211.8	178.7
37	D03407C69	TN	0.360	08/13/02	0.01147	38610.70	150.0	609.5
38	D0283612	OH	0.342	10/24/02	0.01406	41395.14	182.9	449.9
39	D06113C03	IN	0.339	07/20/02	0.01362	71118.81	150.0	809.1
40	D082261	PA	0.337	01/21/02	0.01687	40231.91	228.6	251.1

Shenandoah National Park								
RANK	**CEMS SOURCE**	**STATE**	**24-Hr Max SO_4 Ion Impact (~µg/m^3)**	**24Hr Date**	**Annual SO_4 Ion Impact (~µg/m^3)**	**2002 SO_2 (Tons)**	**Modeled StkHt (Meters)**	**Distance (Kms)**
41	D02866C01	OH	0.336	07/04/02	0.01060	24627.17	153.6	290.5
42	D028504	OH	0.336	07/20/02	0.00920	27318.93	213.4	454.7
43	D01572C23	MD	0.335	08/28/02	0.01845	32159.23	121.9	112.8
44	D00988U4	IN	0.329	07/19/02	0.01314	45022.27	122.8	556.8
45	D031403	PA	0.327	08/28/02	0.01494	38766.62	269.1	229.4
46	D028375	OH	0.316	12/13/02	0.01332	35937.73	182.9	433.0
47	D027122	NC	0.315	02/01/02	0.01298	29310.41	121.9	232.4
48	D02712C04	NC	0.303	02/01/02	0.01066	22941.29	150.0	232.4
49	D007034LR	GA	0.300	08/14/02	0.00905	40973.96	304.8	755.7
50	D037975	VA	0.300	02/01/02	0.01047	19602.10	61.0	155.9
51	D038044	VA	0.298	09/09/02	0.00720	10441.80	46.9	99.8
52	D007033LR	GA	0.294	08/14/02	0.00911	43029.15	304.8	755.7
53	D03936C02	WV	0.288	08/13/02	0.00872	15466.69	304.8	261.3
54	D039543	WV	0.286	02/08/02	0.00284	2919.63	181.7	103.7
55	D028725	OH	0.285	10/04/02	0.01477	30052.41	252.1	302.6
56	D02866C02	OH	0.281	07/04/02	0.01109	25999.24	153.6	290.5
57	D028502	OH	0.280	07/19/02	0.00960	28672.85	213.4	454.7
58	D01733C34	MI	0.277	07/05/02	0.01049	39326.85	152.4	557.5
59	D06250C05	NC	0.276	02/01/02	0.01214	27370.73	243.8	224.3
60	D015543	MD	0.272	08/28/02	0.00525	10075.06	109.7	178.6
61	D039462	WV	0.266	03/15/02	0.00676	10320.05	65.8	263.5
62	D028501	OH	0.262	07/19/02	0.00950	30770.84	213.4	454.7
63	D028665	OH	0.261	07/04/02	0.00863	19778.82	304.8	290.5
64	D03396M1A	TN	0.261	08/13/02	0.00641	20011.21	228.6	574.6
65	D00050C16	AL	0.260	08/14/02	0.00645	24955.19	304.8	764.0
66	D02712C03	NC	0.259	02/01/02	0.01483	30749.26	150.0	232.4
67	D00709C02	GA	0.255	08/14/02	0.00677	47548.54	121.9	734.0
68	D027274	NC	0.254	06/26/02	0.01018	27284.07	85.3	393.3
69	D007032LR	GA	0.251	08/14/02	0.00777	37255.59	304.8	755.7
70	D028283	OH	0.249	07/04/02	0.00681	15372.27	274.3	268.7
71	D027273	NC	0.246	06/26/02	0.01031	26305.45	85.3	393.3
72	D028503	OH	0.246	07/19/02	0.00883	27943.53	213.4	454.7
73	D01733C12	MI	0.243	07/05/02	0.01091	46039.95	137.2	557.5
74	D03140C12	PA	0.242	10/14/02	0.01188	29709.17	259.1	229.4
75	D015522	MD	0.241	09/10/02	0.00574	14261.70	107.6	199.0
76	D007031LR	GA	0.238	08/14/02	0.00805	38486.16	304.8	755.7
77	D028327	OH	0.238	06/26/02	0.01296	46949.57	243.8	552.4
78	D01384CS1	KY	0.237	08/13/02	0.00670	21817.18	61.0	563.9
79	D081021	OH	0.234	02/08/02	0.00899	18190.75	253.0	320.8
80	D03938C04	WV	0.234	07/19/02	0.01213	26427.11	121.9	304.8
81	D010012	IN	0.232	07/19/02	0.00565	25992.39	152.4	783.8
82	D01355C03	KY	0.231	06/26/02	0.00952	38069.95	150.0	551.9
83	D028282	OH	0.230	07/04/02	0.01013	20579.94	251.5	269.0

Shenandoah National Park								
RANK	**CEMS SOURCE**	**STATE**	**24-Hr Max SO_4 Ion Impact (~µg/m^3)**	**24Hr Date**	**Annual SO_4 Ion Impact (~µg/m^3)**	**2002 SO_2 (Tons)**	**Modeled StkHt (Meters)**	**Distance (Kms)**
84	D06166C02	IN	0.229	07/20/02	0.01037	51662.69	304.8	749.9
85	D03809CS0	VA	0.220	10/05/02	0.00728	21200.55	98.8	225.0
86	D015521	MD	0.213	08/28/02	0.00610	17766.58	107.6	199.0
87	D060312	OH	0.213	07/19/02	0.00690	19500.08	274.3	436.3
88	D00710C01	GA	0.205	08/14/02	0.00553	27865.05	213.4	749.5
89	D000265	AL	0.203	08/14/02	0.00628	53015.27	228.6	927.1
90	D000508	AL	0.203	07/28/02	0.00279	9823.53	152.4	763.5
91	D02840C02	OH	0.202	07/04/02	0.00932	22770.56	172.2	347.2
92	D010011	IN	0.196	07/19/02	0.00550	28850.75	152.4	783.8
93	D027215	NC	0.196	06/12/02	0.00675	19128.20	152.4	469.2
94	D039423	WV	0.195	03/15/02	0.00738	10126.02	68.6	148.5
95	D017437	MI	0.194	08/26/02	0.00442	15804.84	182.9	578.5
96	D017436	MI	0.194	08/26/02	0.00361	11172.85	129.5	578.5
97	D027121	NC	0.192	02/01/02	0.00490	12020.17	121.9	232.4
98	D02866M6A	OH	0.184	07/04/02	0.00811	19546.42	304.8	290.5
99	D02549C01	NY	0.179	10/18/02	0.00542	25320.03	150.0	493.8
100	D028306	OH	0.179	07/19/02	0.00742	30438.59	137.2	508.1

Figure D-34a-v. State-by-State Apportionment of Annual SO4 Ion at all 22 IMPROVE-type Monitoring Sites in the Northeastern Portion of Domain

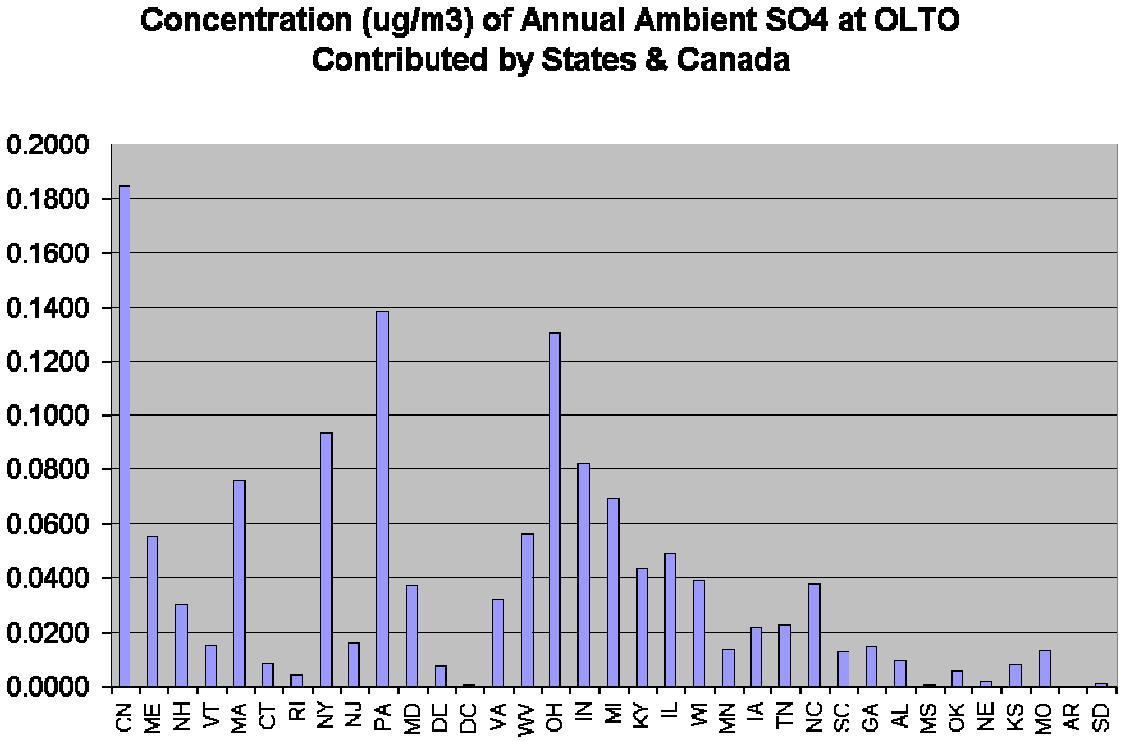

a.

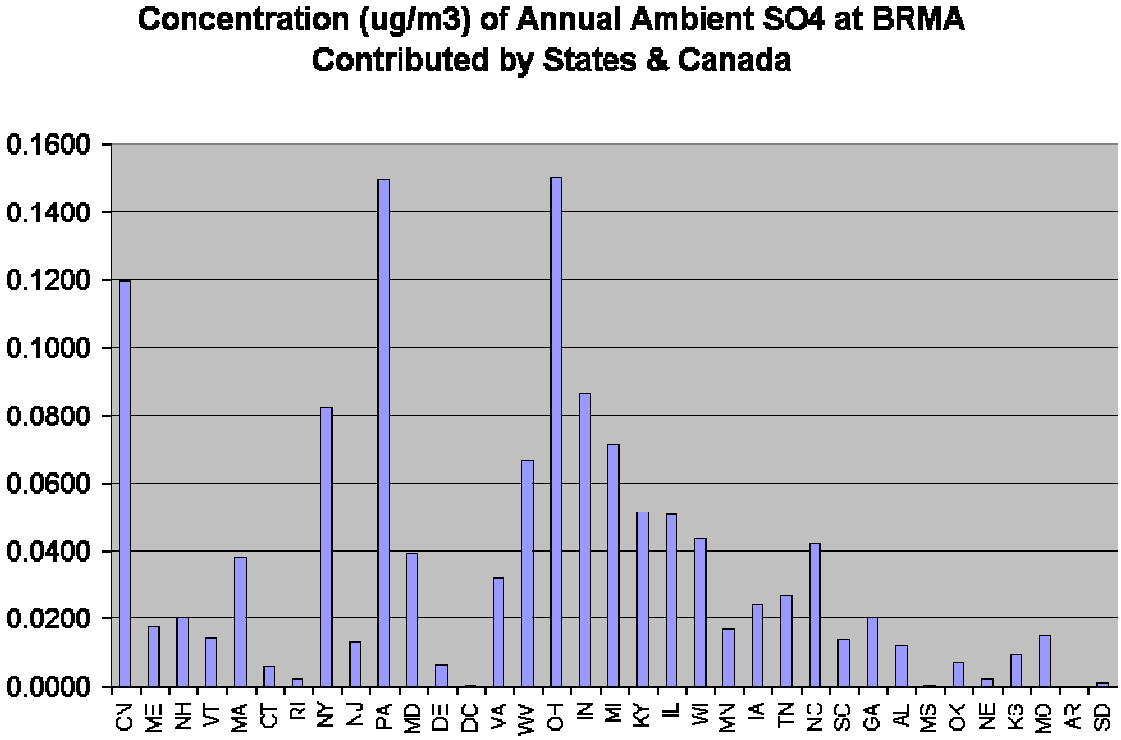

b.

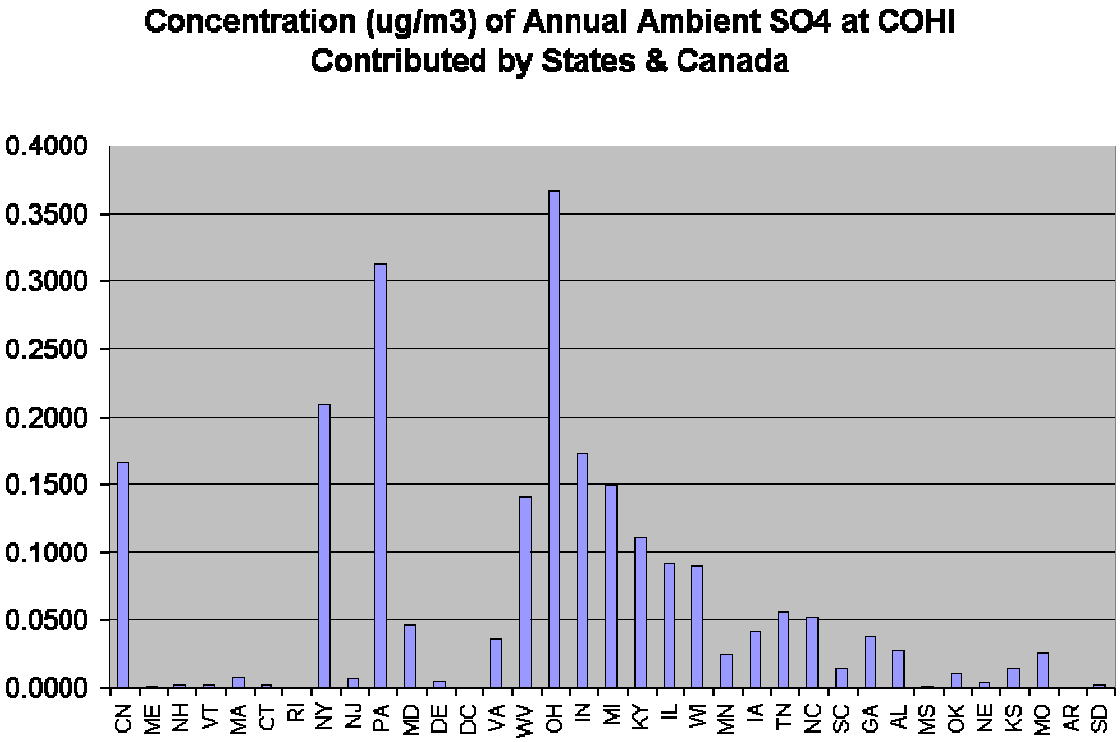
Concentration (ug/m3) of Annual Ambient SO4 at COHI
Contributed by States & Canada
0.4000
0.3500
0.3000
0.2500
0.2000
0.1500
0.1000
0.0500
0.0000
CN ME NH VT MA CT RI NY NJ PA MD DE DC VA WV OH IN MI KY IL WI MN IA TN NC SC GA AL MS OK NE KS MO AR SD

c.

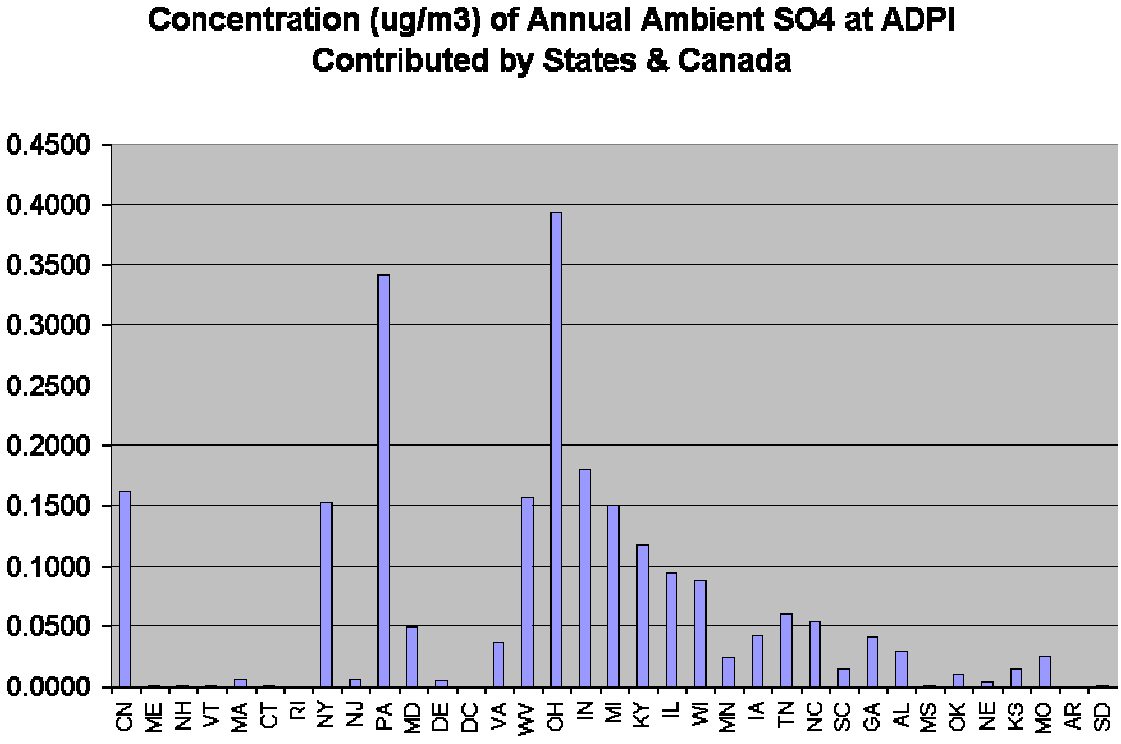
Concentration (ug/m3) of Annual Ambient SO4 at ADPI
Contributed by States & Canada
0.4500
0.4000
0.3500
0.3000
0.2500
0.2000
0.1500
0.1000
0.0500
0.0000
CN ME NH VT MA CT RI NY NJ PA MD DE DC VA WV OH IN MI KY IL WI MN IA TN NC SC GA AL MS OK NE KS MO AR SD

d.

Concentration (ug/m3) of Annual Ambient SO4 at MOMO
Contributed by States & Canada

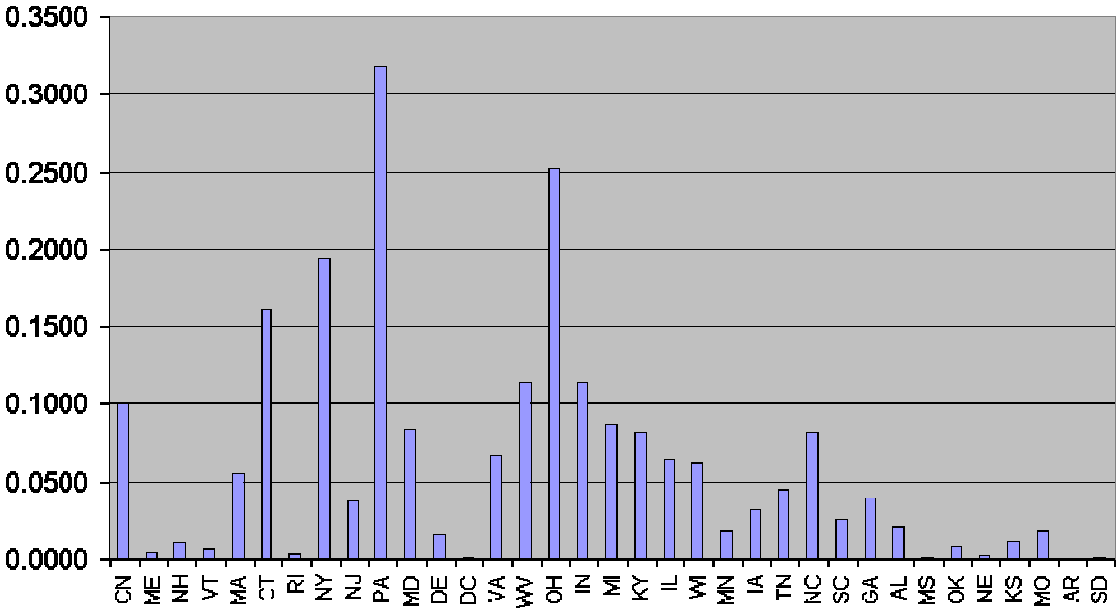

e.

Concentration (ug/m3) of Annual Ambient SO4 at QURE
Contributed by States & Canada

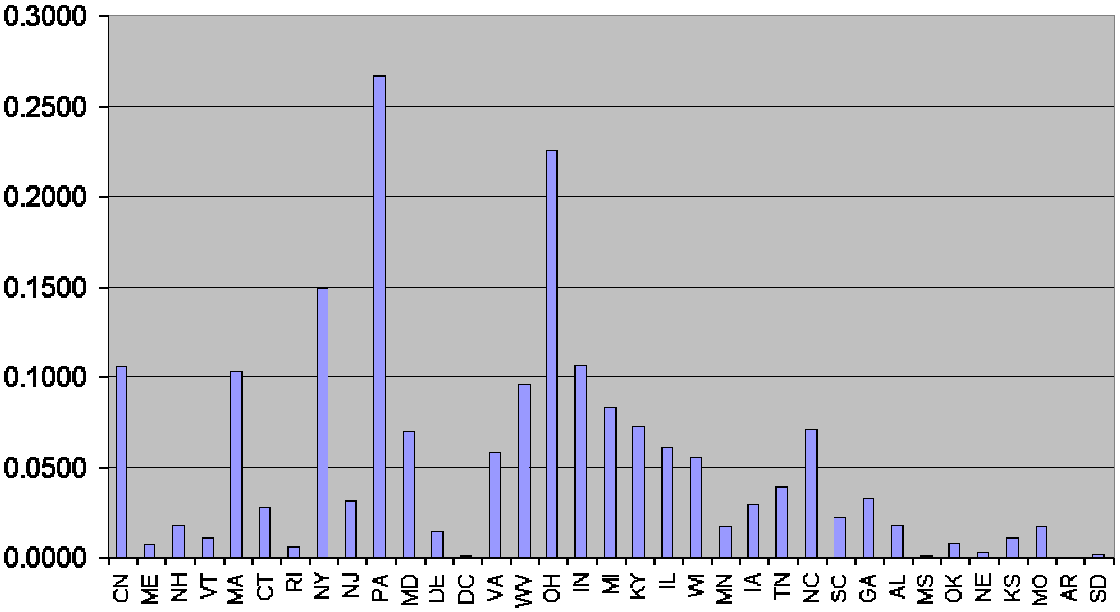

f.

Concentration (ug/m3) of Annual Ambient SO4 at CABA
Contributed by States & Canada

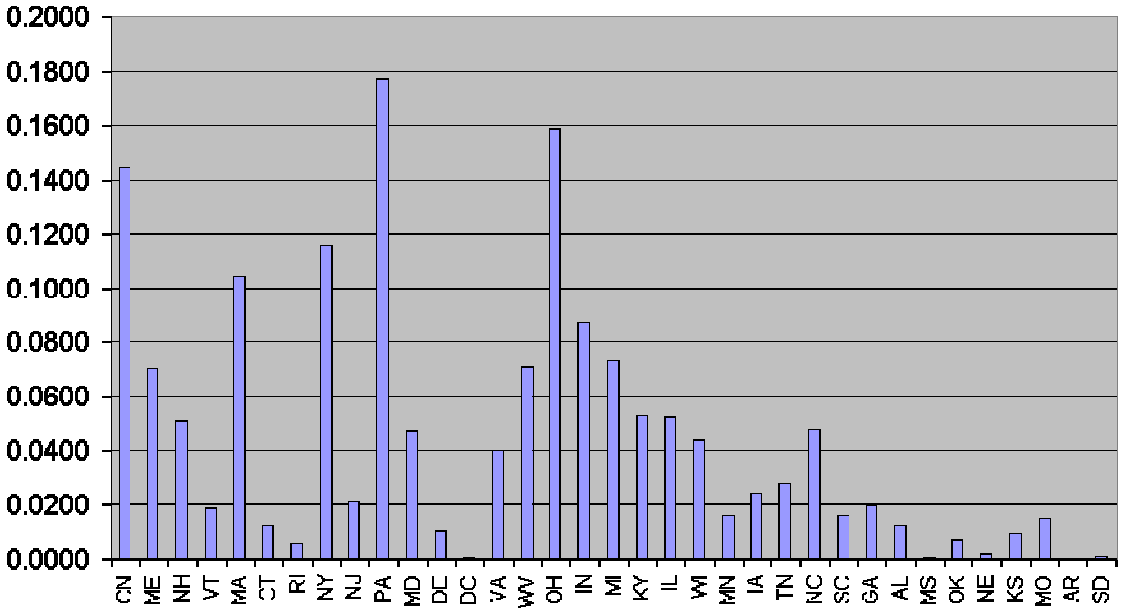

g.

Concentration (ug/m3) of Annual Ambient SO4 at PMRF
Contributed by States & Canada

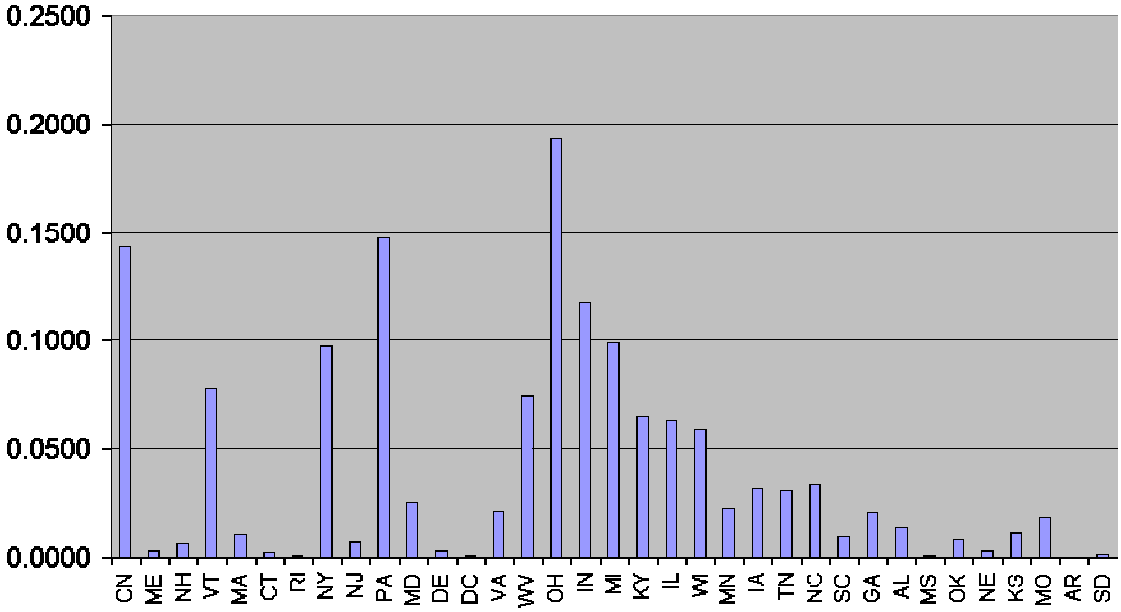

h.

Concentration (ug/m3) of Annual Ambient SO4 at PRIS
Contributed by States & Canada

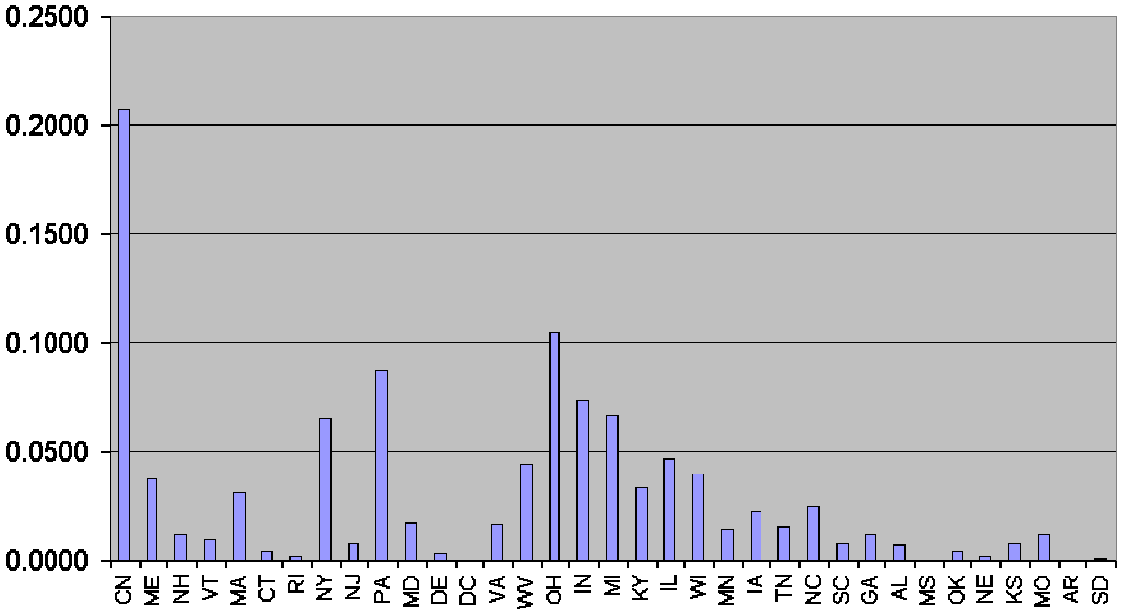

i.

Concentration (ug/m3) of Annual Ambient SO4 at CACO
Contributed by States & Canada

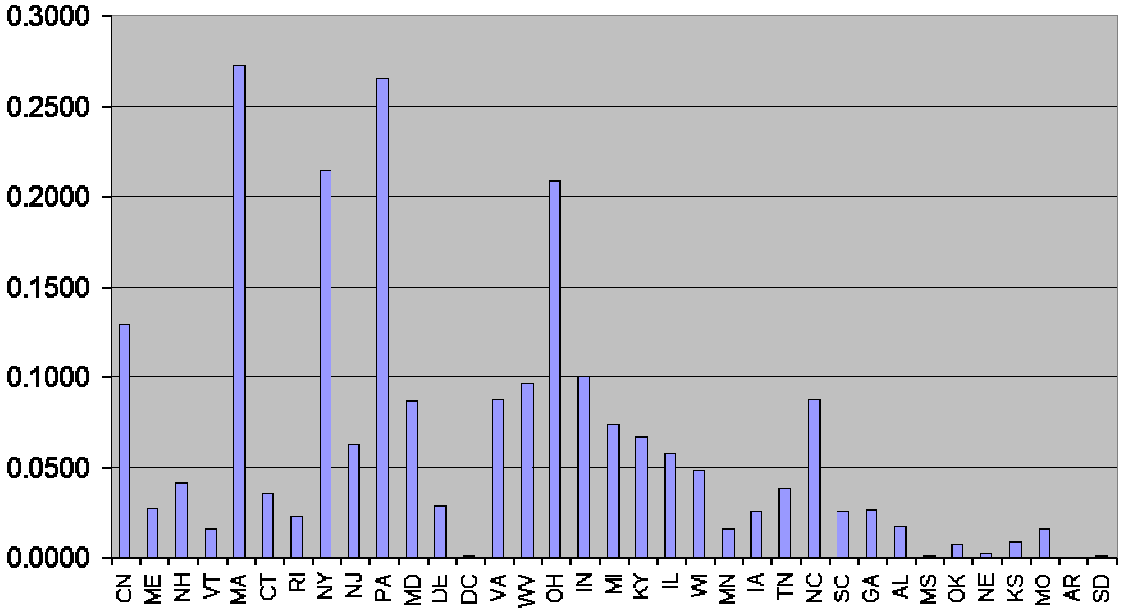

j.

Concentration (ug/m3) of Annual Ambient SO4 at MKGO
Contributed by States & Canada

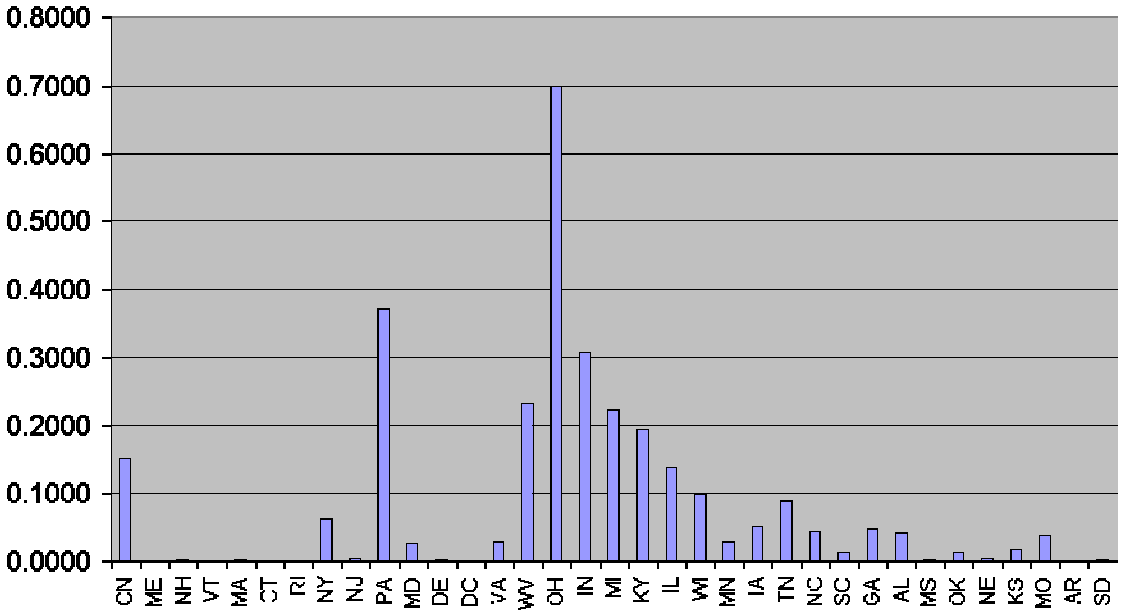

k.

Concentration (ug/m3) of Annual Ambient SO4 at QUCI
Contributed by States & Canada

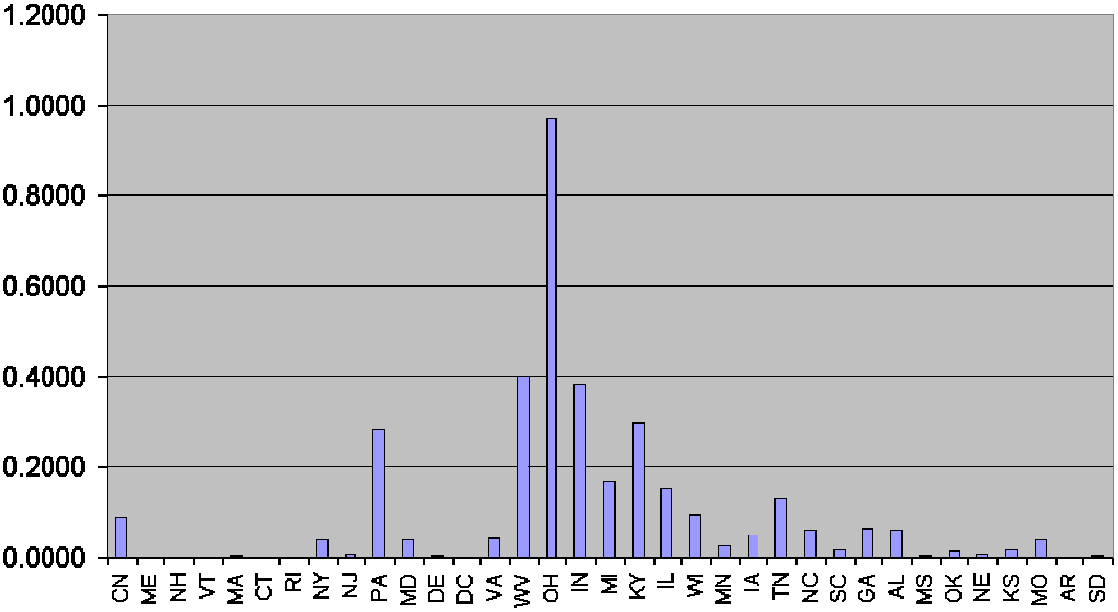

l.

Concentration (ug/m3) of Annual Ambient SO4 at WASH
Contributed by States & Canada

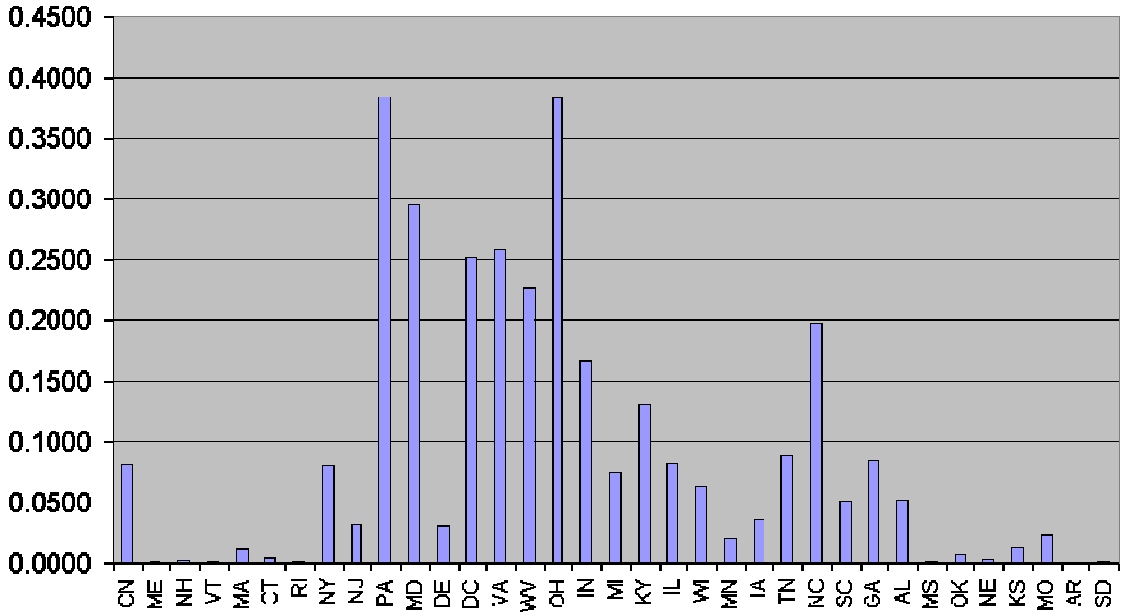

m.

Concentration (ug/m3) of Annual Ambient SO4 at AREN
Contributed by States & Canada

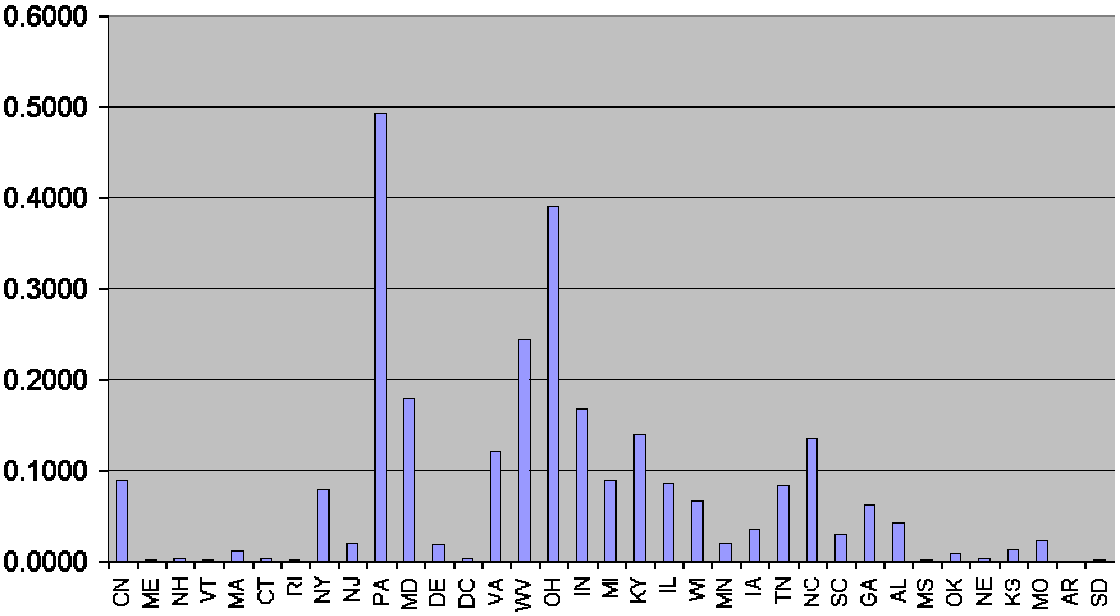

n.

Concentration (ug/m3) of Annual Ambient SO4 at DOSO
Contributed by States & Canada

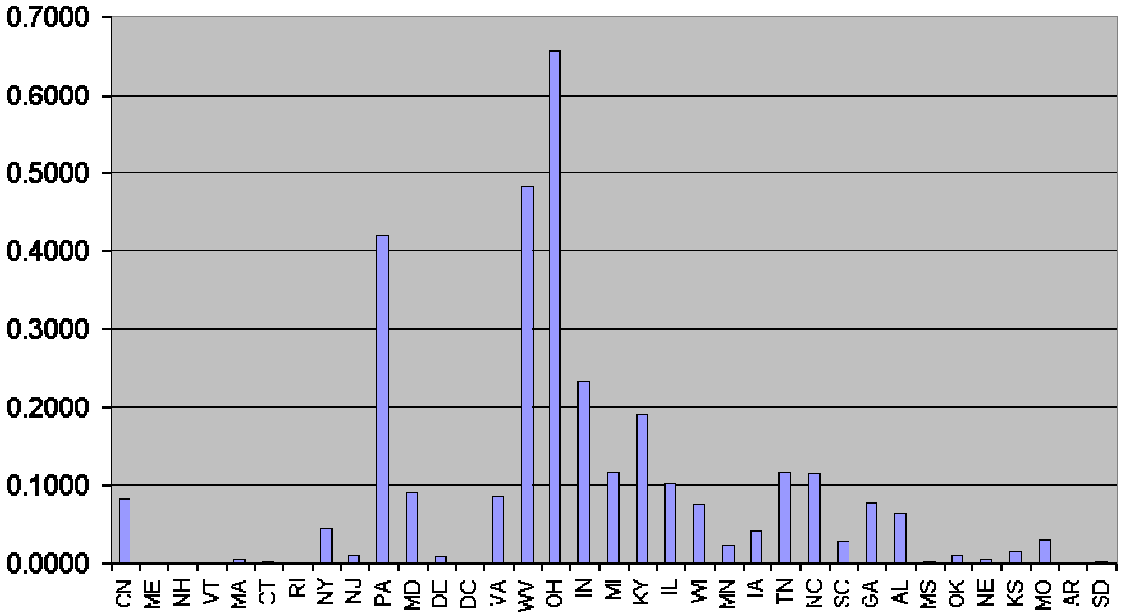

o.

Concentration (ug/m3) of Annual Ambient SO4 at MOOS
Contributed by States & Canada

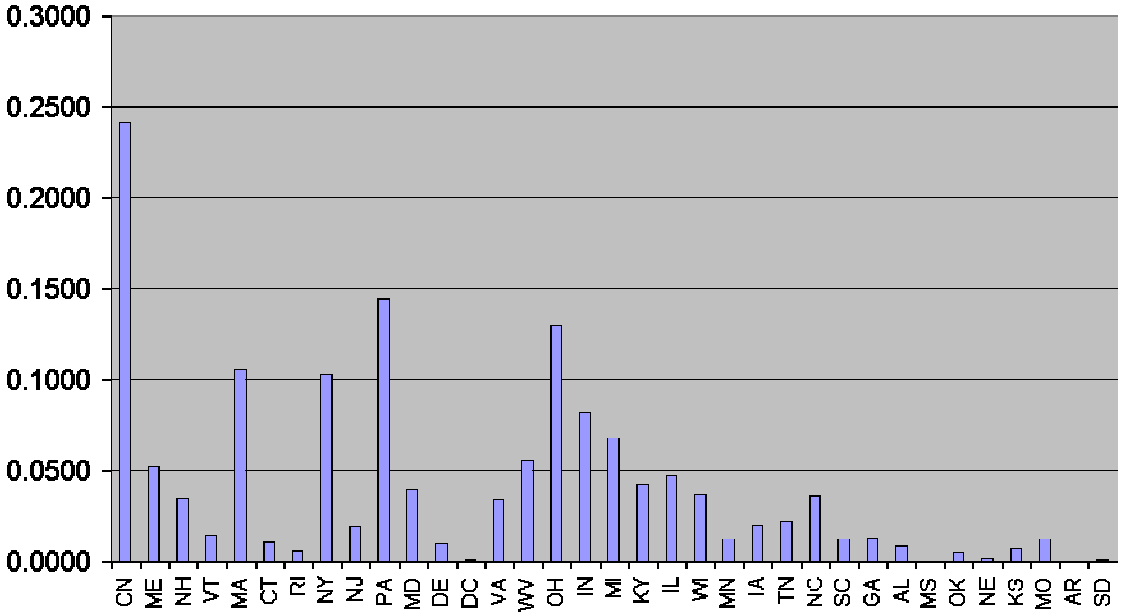

p.

Concentration (ug/m3) of Annual Ambient SO4 at GRGU
Contributed by States & Canada

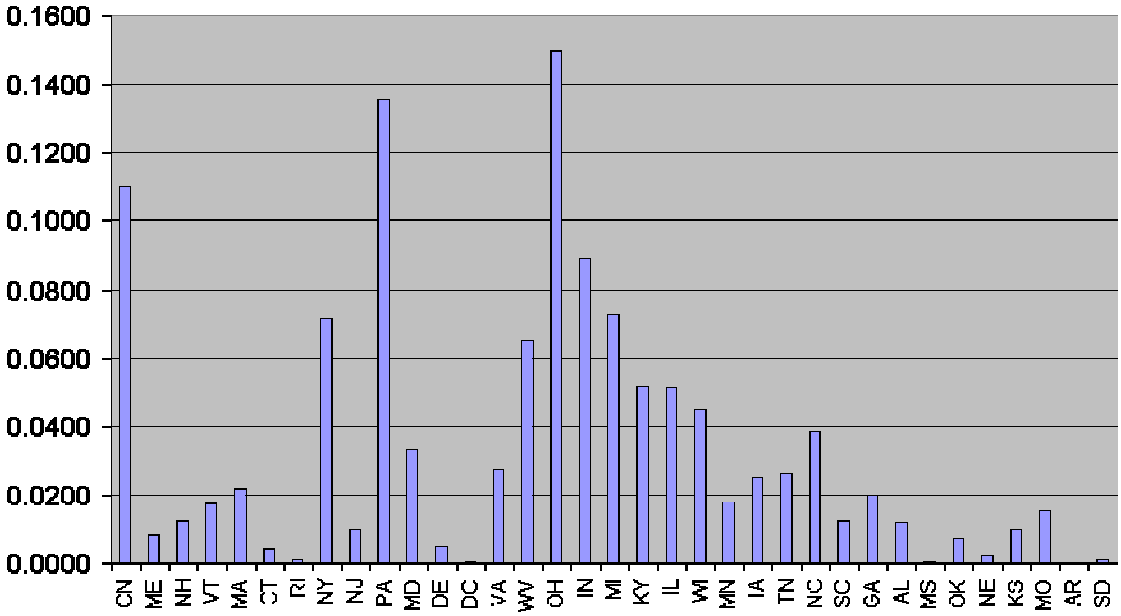

q.

Concentration (ug/m3) of Annual Ambient SO4 at JARI
Contributed by States & Canada

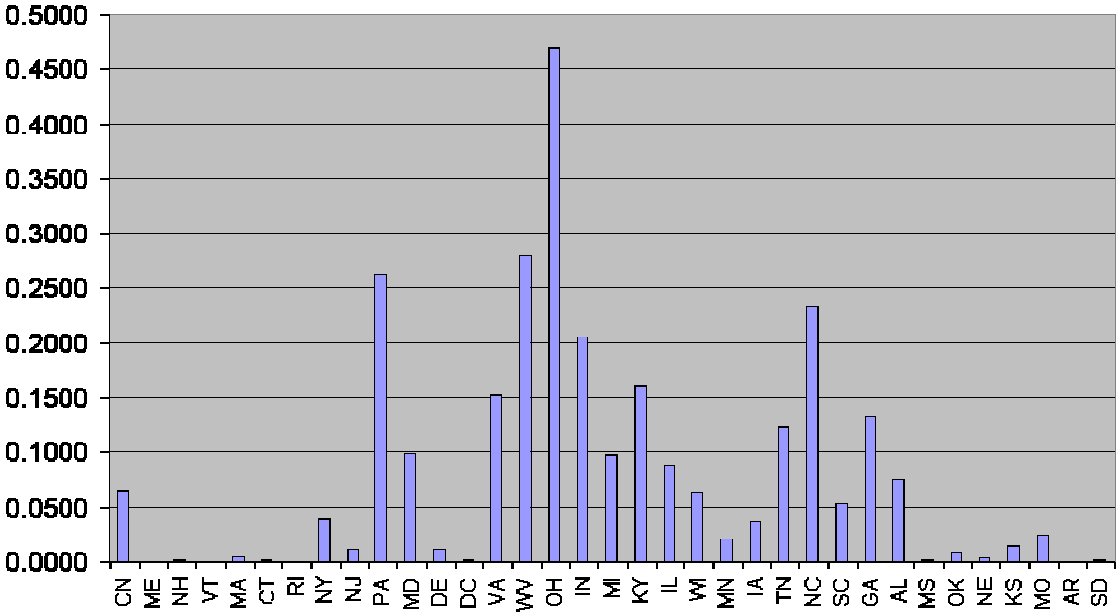

r.

Concentration (ug/m3) of Annual Ambient SO4 at SHEN
Contributed by States & Canada

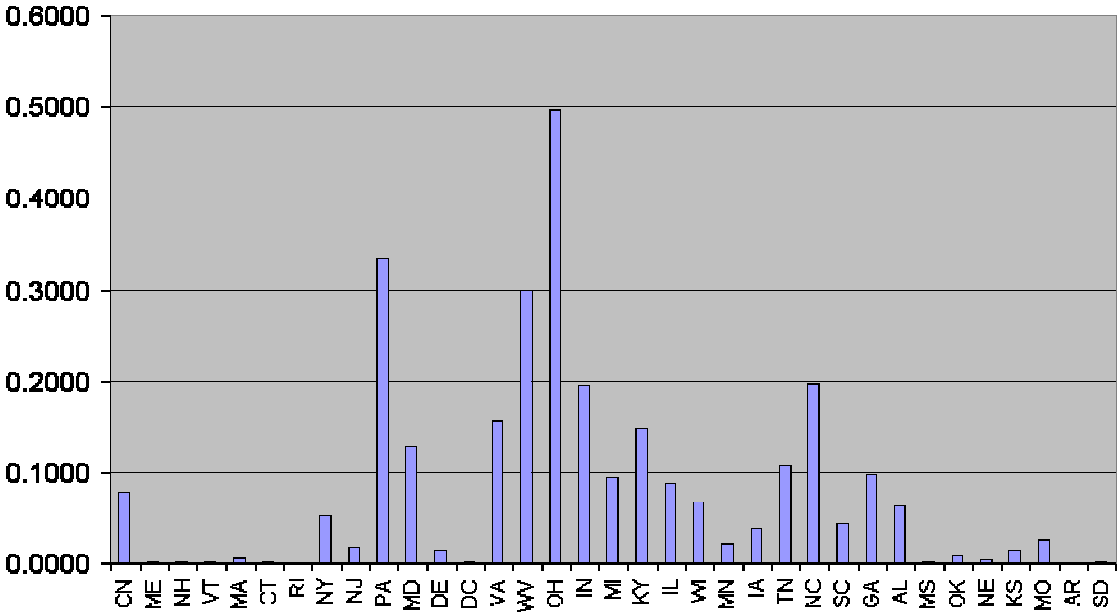

s.

Concentration (ug/m3) of Annual Ambient SO4 at BRIG
Contributed by States & Canada

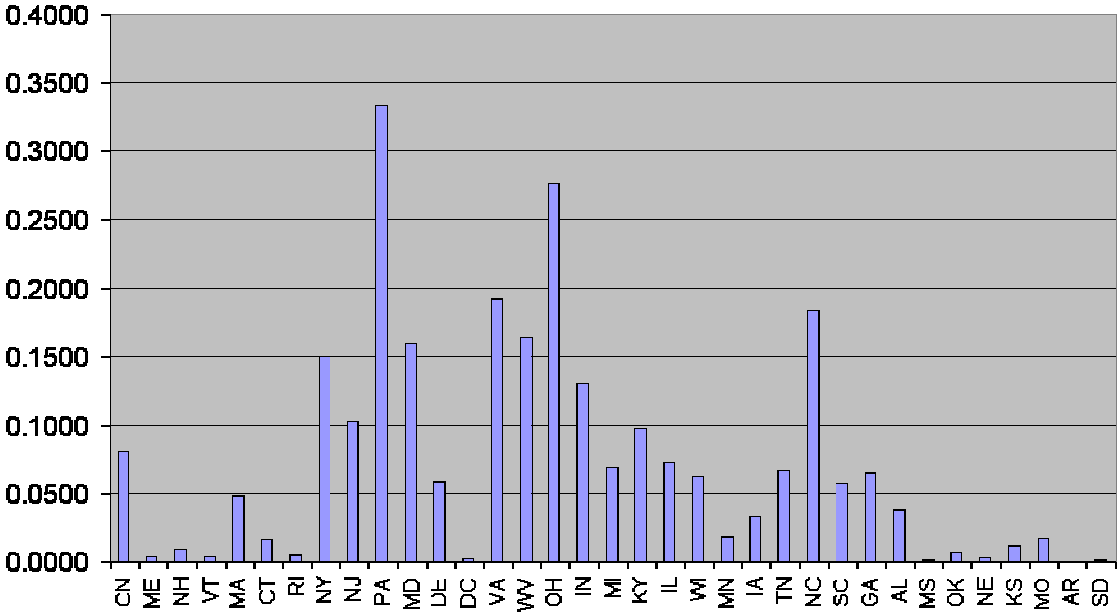

t.

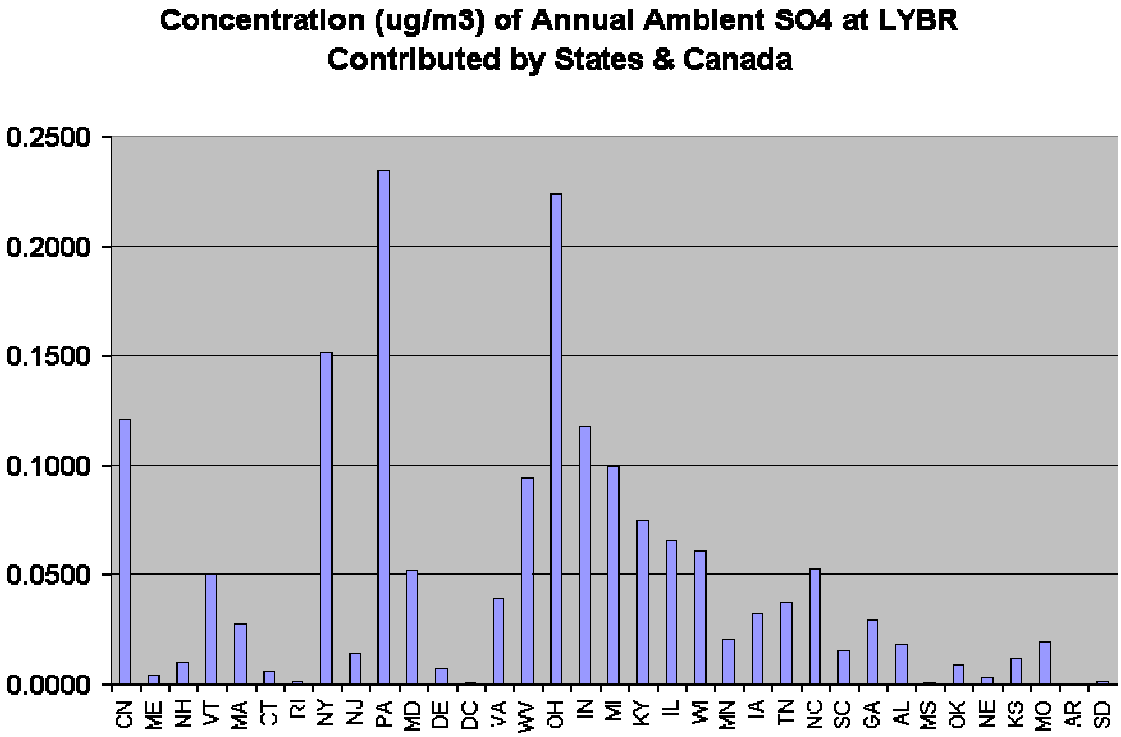
Concentration (ug/m3) of Annual Ambient SO4 at LYBR
Contributed by States & Canada
0.2500
0.2000
0.1500
0.1000
0.0500
0.0000
CN ME NH VT MA CT RI NY NJ PA MD DE DC VA WV OH IN MI KY IL WI MN IA TN NC SC GA AL MS OK NE KS MO AR SD

u.

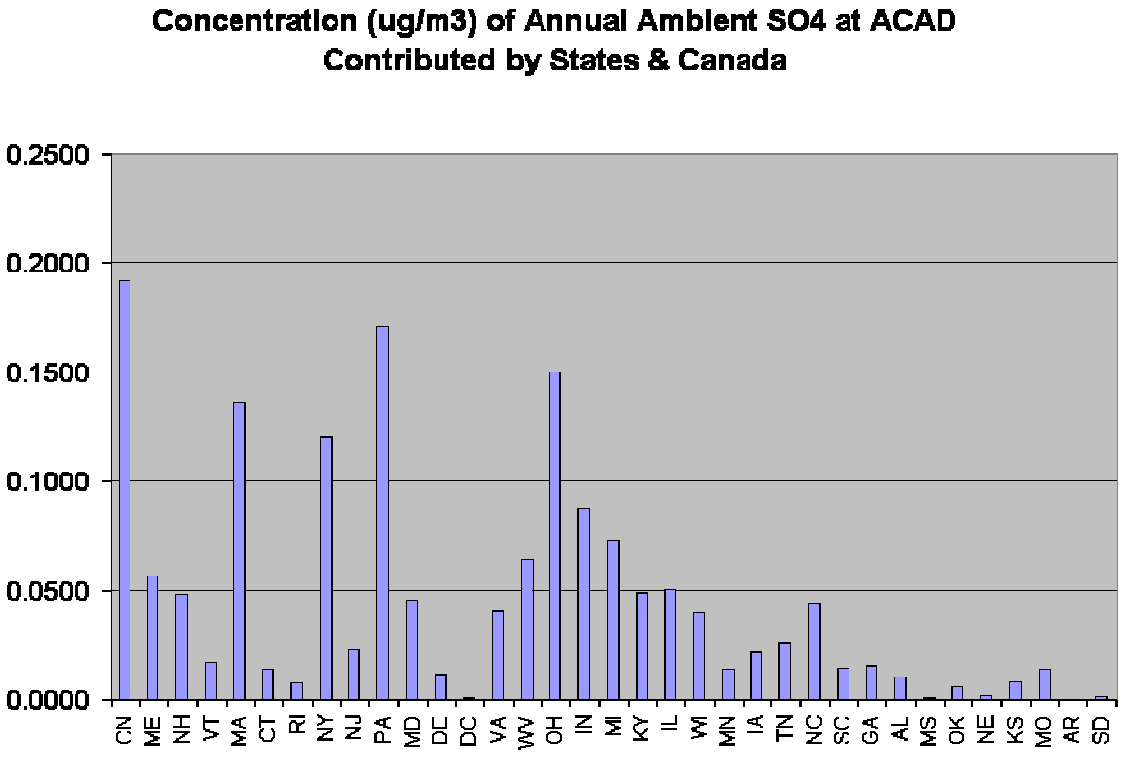
Concentration (ug/m3) of Annual Ambient SO4 at ACAD
Contributed by States & Canada
0.2500
0.2000
0.1500
0.1000
0.0500
0.0000
CN ME NH VT MA CT RI NY NJ PA MD DC DC VA WV OH IN MI KY IL WI MN IA TN NC SC GA AL MS OK NE KS MO AR SD

v.

State-by-State Apportionment of Annual SO_4 Ion Impact by Source Type at Selected Class I Areas

Table D-11(a-d) provides a different type of summary. Impacts from EGUs in the 2002 data base were summed by state, and then sorted by annual impact. Predicted annual average sulfate ion concentrations from the other source sectors were added to this table, and SO_2 emissions totals for the source categories and states shown were added for comparison. The last part of this table shows the relative contribution of each state and source sector to the total predicted sulfate ion concentration.

Table D-11a. VT DEC CALPUFF Modeling Results
Acadia National Park
Phase II Modeling States --- Ranked by Annual Impact

STATE	Annual SO_4 Ion (~ µg/m^3)							CEMS PT % of Total
	CEMS PT	Non-CEMS PT	Small PT	On-Road	Non-Road	Area	TOTAL	
CN	0.00000	0.19135	0.00000	0.00000	0.00000	0.00000	0.19135	0.00
PA	0.13834	0.01618	0.00343	0.00073	0.00247	0.00942	0.17057	81.10
OH	0.14017	0.00805	0.00008	0.00000	0.00101	0.00027	0.14957	93.72
MA	0.06530	0.00967	0.00307	0.00179	0.00642	0.04970	0.13595	48.03
NY	0.05771	0.00976	0.00205	0.00202	0.00708	0.04140	0.12003	48.08
IN	0.07575	0.00957	0.00071	0.00000	0.00011	0.00087	0.08701	87.06
MI	0.06114	0.00769	0.00065	0.00000	0.00071	0.00240	0.07261	84.20
WV	0.05834	0.00203	0.00326	0.00000	0.00035	0.00021	0.06418	90.90
ME	0.00318	0.02323	0.00111	0.00287	0.00782	0.01875	0.05696	5.58
IL	0.03422	0.01525	0.00049	0.00000	0.00034	0.00007	0.05037	67.94
KY	0.04106	0.00272	0.00264	0.00000	0.00113	0.00116	0.04871	84.29
NH	0.03864	0.00143	0.00076	0.00028	0.00195	0.00484	0.04790	80.67
MD	0.03978	0.00166	0.00027	0.00029	0.00101	0.00206	0.04508	88.24
NC	0.03420	0.00412	0.00398	0.00000	0.00119	0.00018	0.04367	78.31
VA	0.03185	0.00173	0.00646	0.00000	0.00034	0.00034	0.04071	78.24
WI	0.01521	0.01936	0.00024	0.00000	0.00032	0.00013	0.03525	43.15
TN	0.01922	0.00430	0.00022	0.00000	0.00172	0.00068	0.02613	73.56
NJ	0.01304	0.00219	0.00029	0.00060	0.00407	0.00297	0.02315	56.33
IA	0.00970	0.01209	0.00008	0.00000	0.00007	0.00000	0.02194	44.21
VT	0.00000	0.00041	0.00002	0.00027	0.01507	0.00154	0.01731	0.00
GA	0.01418	0.00041	0.00041	0.00000	0.00012	0.00039	0.01551	91.42
MO	0.01401	0.00000	0.00000	0.00000	0.00000	0.00000	0.01401	0.00
CT	0.00413	0.00105	0.00012	0.00054	0.00267	0.00525	0.01376	30.01
MN	0.00887	0.00394	0.00035	0.00000	0.00030	0.00019	0.01365	64.98
SC	0.00919	0.00158	0.00143	0.00000	0.00061	0.00036	0.01318	69.73
DE	0.00871	0.00107	0.00090	0.00007	0.00042	0.00032	0.01148	75.87
AL	0.00862	0.00066	0.00059	0.00000	0.00006	0.00023	0.01016	84.84
KS	0.00806	0.00000	0.00000	0.00000	0.00000	0.00000	0.00806	100.00
RI	0.00000	0.00000	0.00000	0.00020	0.00349	0.00375	0.00744	0.00
OK	0.00590	0.00000	0.00000	0.00000	0.00000	0.00000	0.00590	100.00
AR	0.00391	0.00000	0.00000	0.00000	0.00000	0.00000	0.00391	100.00
NE	0.00169	0.00000	0.00000	0.00000	0.00000	0.00000	0.00169	100.00
SD	0.00088	0.00000	0.00000	0.00000	0.00000	0.00000	0.00088	100.00
DC	0.00011	0.00011	0.00000	0.00001	0.00001	0.00015	0.00039	28.21
MS	0.00000	0.00008	0.00010	0.00000	0.00016	0.00000	0.00034	0.00
TX	0.00000	0.00000	0.00000	0.00000	0.00000	0.00000	0.00000	0.00
TOTALS	**0.96511**	**0.35169**	**0.03371**	**0.00967**	**0.06102**	**0.14763**	**1.56881**	

Notes: 52 Canadian Point Sources > 250 Tons/Yr SO_2 Emission during 2002 (from Canadian NPRI) and sources that were within the RPO Modeling Domain were modeled.

Table D-11b. VT DEC CALPUFF Modeling Results
Brigantine National Wildlife Refuge
Phase II Modeling --- States Ranked by Annual Impact

STATE	Annual SO_4 Ion (~ µg/m^3)							CEMS PT % of Total
	CEMS PT	Non-CEMS PT	Small PT	On-Road	Non-Road	Area	TOTAL	
PA	0.25376	0.03810	0.00785	0.00219	0.00623	0.02549	0.33363	76.06031
OH	0.26112	0.01284	0.00011	0.00000	0.00131	0.00035	0.27573	94.70134
VA	0.14417	0.00794	0.03678	0.00000	0.00172	0.00182	0.19244	74.91686
NC	0.14144	0.01819	0.01783	0.00000	0.00521	0.00079	0.18347	77.09162
WV	0.14990	0.00419	0.00756	0.00000	0.00100	0.00059	0.16325	91.82236
MD	0.13513	0.00584	0.00146	0.00136	0.00560	0.00949	0.15888	85.05161
NY	0.06578	0.01034	0.00169	0.00283	0.01051	0.05856	0.14971	43.93828
IN	0.11649	0.01166	0.00087	0.00000	0.00013	0.00101	0.13015	89.50442
NJ	0.04258	0.00661	0.00149	0.00374	0.03034	0.01767	0.10243	41.56985
KY	0.08456	0.00486	0.00489	0.00000	0.00168	0.00217	0.09815	86.15385
CN	0.00000	0.08067	0.00000	0.00000	0.00000	0.00000	0.08067	0.00000
IL	0.05214	0.01864	0.00060	0.00000	0.00044	0.00009	0.07190	72.51739
MI	0.05793	0.00708	0.00062	0.00000	0.00065	0.00219	0.06846	84.61876
TN	0.04767	0.01324	0.00059	0.00000	0.00343	0.00149	0.06642	71.77055
GA	0.05755	0.00218	0.00220	0.00000	0.00073	0.00222	0.06488	88.70222
DE	0.03951	0.00510	0.00596	0.00066	0.00407	0.00259	0.05788	68.26192
SC	0.03615	0.00724	0.00663	0.00000	0.00270	0.00150	0.05422	66.67281
WI	0.02161	0.03084	0.00038	0.00000	0.00050	0.00020	0.05353	40.36989
MA	0.02400	0.00376	0.00111	0.00066	0.00214	0.01629	0.04796	50.04170
AL	0.03165	0.00283	0.00265	0.00000	0.00024	0.00089	0.03825	82.74510
IA	0.01564	0.01746	0.00012	0.00000	0.00010	0.00000	0.03332	46.93878
MN	0.01195	0.00509	0.00049	0.00000	0.00044	0.00029	0.01825	65.47945
MO	0.01786	0.00000	0.00000	0.00000	0.00000	0.00000	0.01786	100.00000
CT	0.00405	0.00120	0.00014	0.00065	0.00279	0.00644	0.01526	26.53997
KS	0.01130	0.00000	0.00000	0.00000	0.00000	0.00000	0.01130	100.00000
NH	0.00643	0.00026	0.00011	0.00004	0.00029	0.00083	0.00796	80.77889
OK	0.00676	0.00000	0.00000	0.00000	0.00000	0.00000	0.00676	100.00000
AR	0.00474	0.00000	0.00000	0.00000	0.00000	0.00000	0.00474	100.00000
RI	0.00000	0.00000	0.00000	0.00012	0.00194	0.00212	0.00418	0.00000
ME	0.00038	0.00166	0.00006	0.00013	0.00034	0.00111	0.00370	10.27027
VT	0.00000	0.00015	0.00000	0.00007	0.00289	0.00037	0.00348	0.00000
NE	0.00306	0.00000	0.00000	0.00000	0.00000	0.00000	0.00306	100.00000
DC	0.00094	0.00041	0.00001	0.00005	0.00006	0.00064	0.00211	44.54976
SD	0.00107	0.00000	0.00000	0.00000	0.00000	0.00000	0.00107	100.00000
MS	0.00000	0.00029	0.00034	0.00000	0.00028	0.00000	0.00091	0.00000
TX	0.00000	0.00000	0.00000	0.00000	0.00000	0.00000	0.00000	0.00000
TOTALS	**1.84732**	**0.31867**	**0.10254**	**0.01250**	**0.08776**	**0.15720**	**2.52597**	

Notes: 52 Canadian Point Sources > 250 Tons/Yr SO_2 Emission during 2002 (from Canadian NPRI) and sources that were within the RPO Modeling Domain were modeled.

Table D-11c. VT DEC CALPUFF Modeling Results
Lye Brook Wilderness
Phase II Modeling -- States Ranked by Annual Impact

STATE	Annual SO_4 Ion (~ µg/m^3)							CEMS PT % of Total
	CEMS PT	Non-CEMS PT	Small PT	On-Road	Non-Road	Area	TOTAL	
PA	0.19176	0.02092	0.00462	0.00097	0.00349	0.01239	0.23416	81.89
OH	0.21083	0.01114	0.00010	0.00000	0.00129	0.00034	0.22370	94.25
NY	0.06369	0.02643	0.00243	0.00280	0.01110	0.04466	0.15110	42.15
CN	0.00000	0.12108	0.00000	0.00000	0.00000	0.00000	0.12108	0.00
IN	0.10387	0.01112	0.00083	0.00000	0.00012	0.00100	0.11695	88.82
MI	0.08405	0.01042	0.00089	0.00000	0.00094	0.00315	0.09945	84.51
WV	0.08523	0.00305	0.00480	0.00000	0.00053	0.00032	0.09393	90.74
KY	0.06466	0.00378	0.00373	0.00000	0.00149	0.00161	0.07528	85.89
IL	0.04731	0.01678	0.00054	0.00000	0.00041	0.00008	0.06512	72.65
WI	0.02285	0.02897	0.00037	0.00000	0.00048	0.00019	0.05286	43.23
NC	0.04239	0.00443	0.00438	0.00000	0.00133	0.00023	0.05276	80.34
MD	0.04519	0.00223	0.00030	0.00037	0.00118	0.00249	0.05176	87.31
VT	0.00000	0.00060	0.00001	0.00103	0.03579	0.01306	0.05050	0.00
VA	0.02949	0.00256	0.00627	0.00000	0.00040	0.00038	0.03910	75.42
TN	0.02807	0.00620	0.00031	0.00000	0.00229	0.00093	0.03780	74.26
IA	0.01505	0.01735	0.00012	0.00000	0.00009	0.00000	0.03261	46.15
GA	0.02700	0.00077	0.00078	0.00000	0.00026	0.00080	0.02960	91.22
MA	0.01055	0.00323	0.00079	0.00061	0.00166	0.01018	0.02702	39.05
MN	0.01304	0.00567	0.00052	0.00000	0.00044	0.00029	0.01996	65.33
MO	0.01911	0.00000	0.00000	0.00000	0.00000	0.00000	0.01911	100.00
AL	0.01506	0.00121	0.00112	0.00000	0.00011	0.00043	0.01793	83.99
NJ	0.00707	0.00154	0.00020	0.00040	0.00268	0.00204	0.01394	50.72
SC	0.00882	0.00191	0.00183	0.00000	0.00078	0.00051	0.01384	63.73
KS	0.01153	0.00000	0.00000	0.00000	0.00000	0.00000	0.01153	100.00
NH	0.00716	0.00052	0.00013	0.00007	0.00060	0.00134	0.00982	72.91
OK	0.00858	0.00000	0.00000	0.00000	0.00000	0.00000	0.00858	0.00
DE	0.00448	0.00096	0.00070	0.00006	0.00034	0.00026	0.00680	65.88
CT	0.00149	0.00039	0.00005	0.00026	0.00106	0.00244	0.00569	26.19
AR	0.00533	0.00000	0.00000	0.00000	0.00000	0.00000	0.00533	100.00
ME	0.00012	0.00188	0.00007	0.00015	0.00037	0.00122	0.00382	3.14
NE	0.00273	0.00000	0.00000	0.00000	0.00000	0.00000	0.00273	0.00
SD	0.00137	0.00000	0.00000	0.00000	0.00000	0.00000	0.00137	100.00
RI	0.00000	0.00000	0.00000	0.00004	0.00057	0.00069	0.00129	0.00
MS	0.00000	0.00019	0.00021	0.00000	0.00022	0.00000	0.00063	0.00
DC	0.00011	0.00015	0.00000	0.00002	0.00002	0.00022	0.00052	21.15
TX	0.00000	0.00000	0.00000	0.00000	0.00000	0.00000	0.00000	0.00
TOTALS	**1.17799**	**0.30548**	**0.03610**	**0.00678**	**0.07004**	**0.10125**	**1.69767**	

Notes: 52 Canadian Point Sources > 250 Tons/Yr SO_2 Emission during 2002 (from Canadian NPRI) and sources that were within the RPO Modeling Domain were modeled.

Table D-11b. VT DEC CALPUFF Modeling Results
Shenandoah National Park (10/26/04v)
Phase II Modeling -- States Ranked by Annual Impact

STATE	Annual SO_4 Ion (~ µg/m^3)							CEMS PT % of Total
	CEMS PT	Non-CEMS PT	Small PT	On-Road	Non-Road	Area	TOTAL	
OH	0.46778	0.02542	0.00017	0.00000	0.00209	0.00057	0.49604	94.30
PA	0.27738	0.03016	0.00523	0.00129	0.00405	0.01608	0.33420	83.00
WV	0.26914	0.01024	0.01566	0.00000	0.00280	0.00170	0.29953	89.85
NC	0.16692	0.01270	0.01235	0.00000	0.00420	0.00081	0.19698	84.74
IN	0.17820	0.01454	0.00103	0.00000	0.00016	0.00129	0.19523	91.28
VA	0.11024	0.01697	0.02286	0.00000	0.00221	0.00244	0.15472	71.25
KY	0.12733	0.00670	0.00676	0.00000	0.00247	0.00327	0.14653	86.90
MD	0.10452	0.01074	0.00090	0.00110	0.00338	0.00732	0.12796	81.68
TN	0.07812	0.01981	0.00086	0.00000	0.00499	0.00235	0.10614	73.60
GA	0.08786	0.00277	0.00286	0.00000	0.00099	0.00299	0.09747	90.14
MI	0.08299	0.00747	0.00075	0.00000	0.00083	0.00280	0.09484	87.51
IL	0.06458	0.02152	0.00071	0.00000	0.00050	0.00010	0.08740	73.89
CN	0.00000	0.07814	0.00000	0.00000	0.00000	0.00000	0.07814	0.00
AL	0.05209	0.00437	0.00405	0.00000	0.00038	0.00145	0.06233	83.57
WI	0.02589	0.03066	0.00039	0.00000	0.00052	0.00021	0.05765	44.91
NY	0.03504	0.00207	0.00063	0.00060	0.00219	0.01132	0.05185	67.58
SC	0.02424	0.00587	0.00583	0.00000	0.00248	0.00163	0.04005	60.52
IA	0.01915	0.01799	0.00013	0.00000	0.00010	0.00000	0.03737	51.24
MO	0.02552	0.00000	0.00000	0.00000	0.00000	0.00000	0.02552	100.00
MN	0.01477	0.00498	0.00048	0.00000	0.00044	0.00029	0.02096	70.47
NJ	0.01022	0.00165	0.00017	0.00033	0.00260	0.00166	0.01663	61.46
DE	0.01005	0.00142	0.00149	0.00009	0.00059	0.00044	0.01408	71.38
KS	0.01372	0.00000	0.00000	0.00000	0.00000	0.00000	0.01372	100.00
OK	0.00803	0.00000	0.00000	0.00000	0.00000	0.00000	0.00803	100.00
AR	0.00735	0.00000	0.00000	0.00000	0.00000	0.00000	0.00735	100.00
MA	0.00355	0.00043	0.00011	0.00008	0.00022	0.00166	0.00604	58.77
NE	0.00379	0.00000	0.00000	0.00000	0.00000	0.00000	0.00379	100.00
CT	0.00053	0.00013	0.00002	0.00007	0.00028	0.00074	0.00177	29.94
DC	0.00036	0.00042	0.00001	0.00006	0.00006	0.00069	0.00161	22.36
MS	0.00000	0.00043	0.00048	0.00000	0.00039	0.00001	0.00131	0.00
NH	0.00095	0.00004	0.00001	0.00001	0.00004	0.00012	0.00117	81.20
SD	0.00112	0.00000	0.00000	0.00000	0.00000	0.00000	0.00112	100.00
ME	0.00003	0.00035	0.00001	0.00003	0.00007	0.00019	0.00068	4.41
VT	0.00000	0.00003	0.00000	0.00001	0.00054	0.00007	0.00065	0.00
RI	0.00000	0.00000	0.00000	0.00001	0.00015	0.00019	0.00035	0.00
TX	0.00000	0.00000	0.00000	0.00000	0.00000	0.00000	0.00000	0.00
TOTALS	**2.27146**	**0.32802**	**0.08395**	**0.00368**	**0.03972**	**0.06239**	**2.78921**	

Notes: 52 Canadian Point Sources > 250 Tons/Yr SO_2 Emission during 2002 (from Canadian NPRI) and sources that were within the RPO Modeling Domain were modeled.

D.3. The MDNR/MDE CALMET/CALPUFF Platform

D.3.1. CALMET: Meteorological Inputs and Processing

As described for the VTDEC CALMET platform, several different types of inputs are needed to create the meteorological data file for CALPUFF: geophysical, surface, precipitation, and upper air winds and temperatures. The inputs as they were prepared and used to develop the MD CALMET data are described in the following sections.

D.3.1.1. Geophysical Data

The geophysical data required by CALMET consists of information about land use and terrain elevations. A data file is prepared with this information through the use of several preprocessors. TERREL is used to read raw terrain data and to calculate the average elevation for each cell. CTGCOMP and CTGPROC compress and then process land use data, respectively, and create a file containing the fractional land use in each model cell for 38 categories. MAKEGEO combines the output from TERREL and CTGPROC to create a single geophysical data file for CALMET input, referred to as the GEO.DAT file. The GEO.DAT file contains values for each grid cell of the predominant land use category (14 categories), terrain elevation, surface parameters (roughness length, albedo, Bowen ratio, soil heat flux parameter, and leaf area index), and anthropogenic heat flux (kept as a category but for practical purposes, negligible compared to other sources of heat flux). Fractional land use based on the original 38 categories are used by MAKEGEO to estimate weighted values of the surface parameters for inclusion in the geophysical data file. The modeling domain used in this analysis extends well into Canada. High resolution land use and terrain files were obtained from USGS and used for the U.S.; less highly resolved global files were used to define land use and terrain characteristics for the part of the domain located in Canada.

D.3.1.2. Surface Data

The primary source of surface data for input to CALMET (winds, temperature, relative humidity, pressure, cloud cover and ceiling height) was the Integrated Surface Hourly (ISH) data set. ISH data consists of worldwide surface weather observations from about 12,000 stations, collected for sources such as the Automated Weather Network (AWN), Global Telecommunications System (GTS), Automated Surface Observing System (ASOS), and data keyed from paper forms. The ISH data for 2002 was obtained from the National Climatic Data Center (NCDC) on two cd-roms, one for the U.S. and one for Canada. The availability of hourly observations depends on the station type, location and instrumentation. Since the publicly available CALMET processors do not accept the ISH format, software was developed to read the raw data, test data quality codes, generate summaries of data availability, test for outliers, and create a surface data file (SURF.DAT) for input to CALMET. Although CALMET contains routines for handling missing values, a minimum data capture of 50% for winds was imposed to accept a station for inclusion in the SURF.DAT file. The software also performed other functions normally done with the standard processors, including making adjustments for time zone of the surface station. Surface stations located within 200 kilometers of the modeling domain were included, to improve CALMET processing in cells close to the

domain boundary. A total of 959 ISH surface stations were incorporated into the surface data file.

The Clean Air Status and Trends Network (CASTNET) program includes stations throughout the U.S. (and one site in Ontario, Canada) that measure weekly concentrations of sulfate, nitrate, and ammonium aerosols, and sulfur dioxide and nitric acid. The stations also record hourly meteorological parameters including winds, relative humidity, temperature, and precipitation. Location of the CASTNET sites at relatively rural and in many cases elevated locations provide a good complement to the set of ISH stations. Data from 55 CASTNET sites were incorporated into the CALMET surface data file.

D.3.1.3. Precipitation

Hourly precipitation is an important input to CALPUFF: it utilizes precipitation intensity and type to estimate wet deposition of both particulate and gaseous species. Removal by wet deposition (as well as removal by dry deposition) is an important process in modeling on this scale, even when the main focus is on ambient concentrations. CALMET utilizes interpolation routines to create gridded precipitation fields in the meteorological data file for CALPUFF; no physical processes are modeled to fill in the gaps between measurement stations.

Hourly precipitation quantities were obtained from the ISH stations within, and up to 200 kilometers of the edge of the domain. As with the surface data processing, software was developed to read the raw data, test data quality codes, generate summaries of data availability, test for outliers, and create a precipitation data file (PRECIP.DAT) for input to CALMET. Many of the ISH stations in Canada reported precipitation data as accumulations over six hours instead of hourly. Rather than reject these data, the software was programmed to divide the six-hour total by three and assign the resulting value to hours 2, 3, and 4 of the period. Additional hourly precipitation data were obtained from coop stations (in the "3240" format) for states from Virginia to New York. Finally, precipitation data from CASTNET sites were analyzed and incorporated. Data from a total of 748 ISH stations, 227 3240 coop stations, and 55 CASTNET sites passed data quality checks and were included in the precipitation data file.

A further observation was that many of the stations that were analyzed reported annual total precipitation in a range that appeared reasonable for the station location, but reported missing data for a significant portion of the year. Although CALMET has routines for handling missing hourly precipitation data, experimentation with the interpolation routines revealed that erroneous gridded fields could be produced in regions where significant numbers of stations reported high percentages of missing data. A selective process was used to identify stations with reasonable annual totals and a large amount of missing data, and data that was coded as "missing" at these stations was filled with zero values. The resulting gridded precipitation field appeared to almost eliminate areas where this anomaly initially occurred.

Figure D-35 shows the location of the ISH, 3240, and CASNET measurement sites that were used for both surface and precipitation data input to CALMET.

Figure D-35. Location of the ISH, 3240, and CASNET measurement sites that were used for both surface and precipitation data input to CALMET.

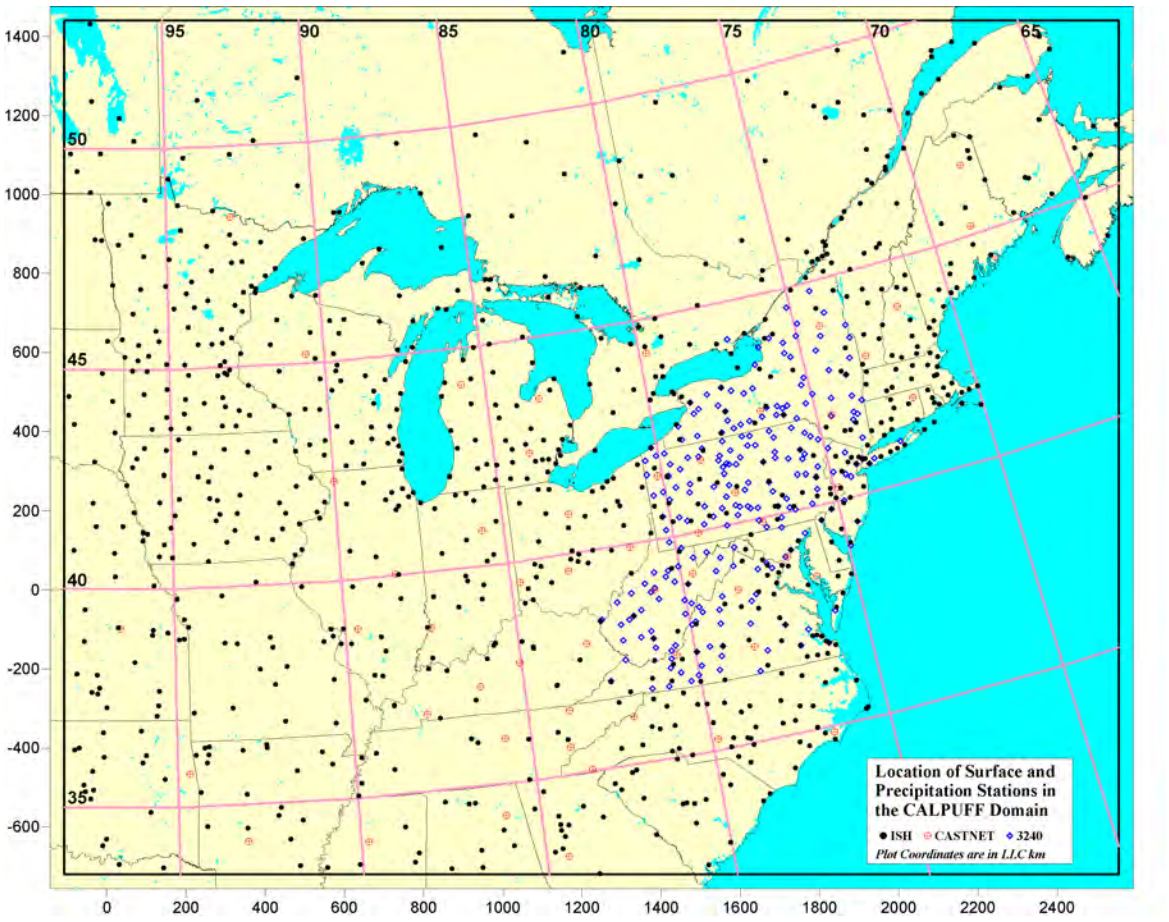

D.3.1.4. CENRAP 2002 MM5

The modeling conducted in Phase I utilized a continental scale, 36-kilometer, full year meteorological data set for calendar year 2002 created by the Iowa DNR for the Central Regional Air Planning Association (CENRAP) RPO. The Penn State/NCAR Meteorological Model (MM5) version 3.5 was used in this effort. Development of the data set is described in the protocol, available at www.iowadnr.com/air/prof/progdev/regionmod.html. CALMET has the option to utilize prognostic model (e.g., MM5) output as input to CALMET. CALMET has the capability to account for local scale effects created by terrain, and can be used to "refine" the prognostic model outputs through the use of a much finer grid. In the present case, the domain has been designed to be consistent with the projection and the location of the MM5 grid, including the 36-kilometer grid spacing. The objective of CALMET processing in Phase I, therefore, was to maximize reliance on the MM5 wind fields. The only introduction of additional observational data for the creation of the CALMET meteorological data set was to utilize the surface and precipitation data developed as described above in place of the MM5 surface and precipitation data.

The MM5 data for 2002 were provided to DNR/MDE on two external, 300-GB drives. In order to be used as input to CALMET, processing was required that extracted data for the CALMET domain and re-formatted the data for input to CALMET. This is normally accomplished with the CALMM5 processor, part of the CALPUFF modeling system. The CALMM5 processor was not publicly available at the time, however, was programmed to process MM5 version 2 inputs, and modifications were required to process version 3+ data. Utility programs were obtained from the MM5 Community Model home page to aid in this process. Numerous tests were run both during and after processing to ensure that data were being read correctly. For a small number of time periods during the 2002 calendar year, data were not readable from the original files and substitutions were made to fill in the entire calendar year.

Twenty-four MM5 files were created for input to CALMET, each consisting of one-half months'data (e.g., January 1-15 and 16-31). This setup was necessary due to the 4GB file size limit for PCs. Further information on the development of the original MM5 data can be found in the protocol (see the link above); further information on the MM5 model can be found at the MM5 Community model home page at www.mmm.ucar.edu/mm5.

D.3.1.5. University of Maryland 12 km MM5

The University of Maryland created a continental scale, 36-kilometer, full year meteorological data set for calendar year 2002 and a 12-kilometer, full year meteorological data set for a smaller domain covering most of the CALPUFF domain. The extent of the 12-kilometer UMd domain is shown in Figure D-36. The Phase II modeling used the UMd MM5 data on a 12-kilometer grid. As seen in Figure D-36, The 12-kilometer data did not completely cover the CALPUFF domain in border areas to the west, north and east. In order to maintain the domain that is consistent with the Phase I modeling, these border areas were handled by utilizing the UMd 36-kilometer grid and creating pseudo-12-kilometer MM5 data by duplicating the 36-kilometer data for surrounding cells.

Slightly different processing steps were taken with the 12-kilometer MM5 data. A more recent version of CALMM5 was used that is designed to read version 3+ MM5 files. The files generated by CALMM5 for input to CALMET occupied approximately 1GB per day. Since it was not practical to generate and archive the CALMET-ready files, CALMM5 was used to generate MM5 files on a daily basis for each month. After the daily files for each full month were created, CALMET was run and the files were over-written for the next month processed.

Figure D-36. Extent of 12-km MM5 Domain

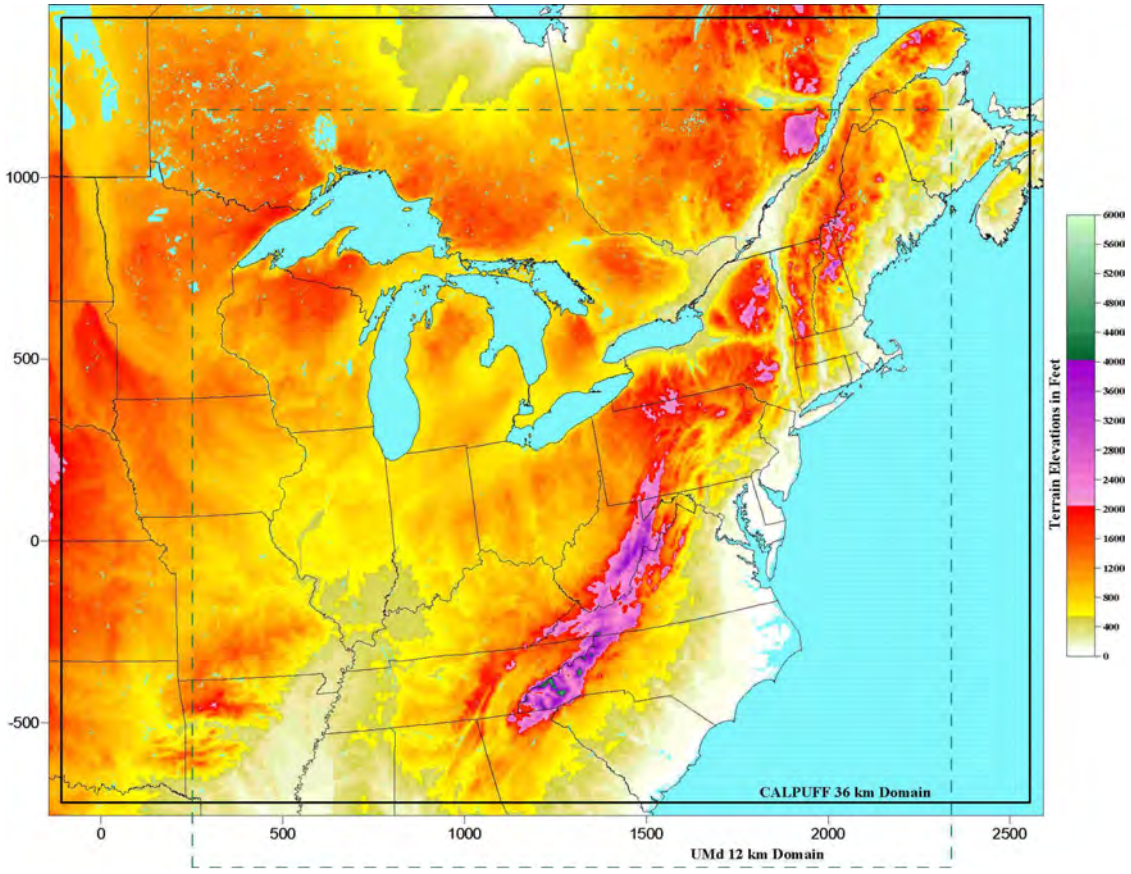

D.3.1.6. CALMET Options and Execution

The CALMET model inputs were developed as described above, and the CALMET processor was used to create 12 meteorological data files, one for each month, for input to CALPUFF (the original CENRAP processing created a total of 24 files, based on a half month each) . Running CALMET requires the selection of many processing options; some of these, including sensitivity studies as to the effect of different options on the creation of wind fields from rawinsonde data, are described in the section of this report on the Vermont DEC platform. In keeping with the goal of maximizing reliance on MM5 wind fields, options were selected for use on this platform that minimized wind field modifications by CALMET (with the exception of surface and precipitation data). Key parameter option choices were as follows:

"NOOBS" was set to a value of 2, which instructs CALMET to use MM5 data for wind fields, including surface winds. The only external data that was incorporated into the CALMET files was the hourly precipitation values developed from ish, CASTNE, and 3240 files;
"IWFCOD" was set to a value of 0, which results in excluding any diagnostic wind field processing;
"IPROG" was set to a value of 13, which causes CALMET to treat MM5 winds as the Step 1 windfield;

Eleven vertical layers were specified; the "face heights" of the layers (ZFACE) were set at 0, 20, 80, 220, 380, 620, 980, 1420, 1860, 2300, 2740, and 3180 meters. These values were chosen to reflect the vertical layers in MM5 up to about 3 kilometers; however, above about 400 meters the CALMET layers were deeper than the MM5 layers.

Evaluations of the meteorological data used by, and created by, CALMET can be found in the next section. These evaluations include a comparison of MM5 12-kilometer winds to profiler-measured winds, comparison of MM5 12-kilometer winds to the 36-kilometer CENRAP winds, and domain-wide summaries of winds and other derived parameters calculated by CALMET.

D.3.2. Evaluation of Meteorological Fields

The process of evaluating the three-dimensional, time-varying winds and other meteorological fields produced by CALMET is an important but difficult step. Comparison to observations can be problematical, since in many cases observations were used to generate the CALMET meteorology; furthermore, the CALMET modeled meteorology is much more detailed both in space (e.g., every 12 kilometers in this application, and 11 vertical layers) and time (every hour) than observational data sets. For the present analysis, the evaluation focused on three components: comparison of wind fields with available measured data from wind profilers; comparison of predicted weekly precipitation totals for locations that represent the location of NADP measurement stations; and finally, examination of the patterns of derived boundary layer parameters that are important inputs to CALPUFF. These evaluations are described in the following sections.

D.3.2.1. Wind Fields: Comparison to Profiler Data

The NOAA Profiler Network web site provides information about, and data access to, NOAA's own profiler network and also participating Cooperative Agency Profiler (CAP) sites (see http://www.profiler.noaa.gov/jsp/capSiteLocations.jsp). The site information at this link was examined for sites with data availability during the summer of 2002. Three sites were selected to use for the CALMET/MM5 comparisons: Fort Meade, MD (FMEMD, sponsored by MDE); New Brunswick, New Jersey (RUTNJ, sponsored by Rutgers University and the New Jersey Department of Environmental Protection (NJDEP)); and Stow, Massachusetts (STWMA, sponsored by the Massachusetts Department of Environmental Protection, Air Assessment Branch).

Data from these three sites was downloaded and processed to extract winds for three months in 2002 (June through August). The wind profiles were further processed by linearly interpolating measured levels to a set of elevations above ground that were selected to provide a common vertical profile for comparison. Wind profiles were also extracted from the CALMET files created with MM5 data (MDNR/MDE platform) and with NWS inputs (VTDEC platform), and linearly interpolated to the common vertical levels.

Wind profile comparisons were made in three different ways. First, plots were created that illustrate the geographic surroundings of each of the profiler sites and that also display wind roses representing the three different wind profiles (Profiler, CALMET-MM5 and CALMET-NWS) at 100, 500, 1000, and 3000 meters above ground. The wind

roses were developed based on three months (June-August) of data from 2002. These plots are shown in Figure D-37 through Figure D-39 for the Fort Meade, Rutgers, and Stowe sites respectively. Although there are some similarities between the three profiles at all levels, generally the MM5-based wind roses appear to more closely match the profiler-based wind roses at the upper levels, while the NWS-based wind roses appear to more closely match the profiler-based wind roses at the lower levels. One limitation of these plots is that, especially at the upper levels, data capture on the profilers is somewhat limited (ranging from 33% to 54% at the three sites, as shown on the figures), while the meteorological models have wind estimates at all levels 100% of the time.

Wind profile comparisons were also made by calculating statistics that express the degree of bias between different sets of profiles for the three months June-August 2002. The statistics were developed by calculating the difference in wind direction and speed at each level, for each hour with available data, for three combinations: MM5 vs. Profiler, MM5 vs. NWS, and NWS vs. Profiler. The bias for speed and wind direction are presented in Table D-12. In general, the MM5-based winds compared more favorably against the profiler winds for this time period, for the three profiler locations.

Figure D-37. Comparison of wind roses based on observed profiler data, MM5-based CALMET (MD) and NWS observation-based CALMET (VT) for Fort Meade, MD.

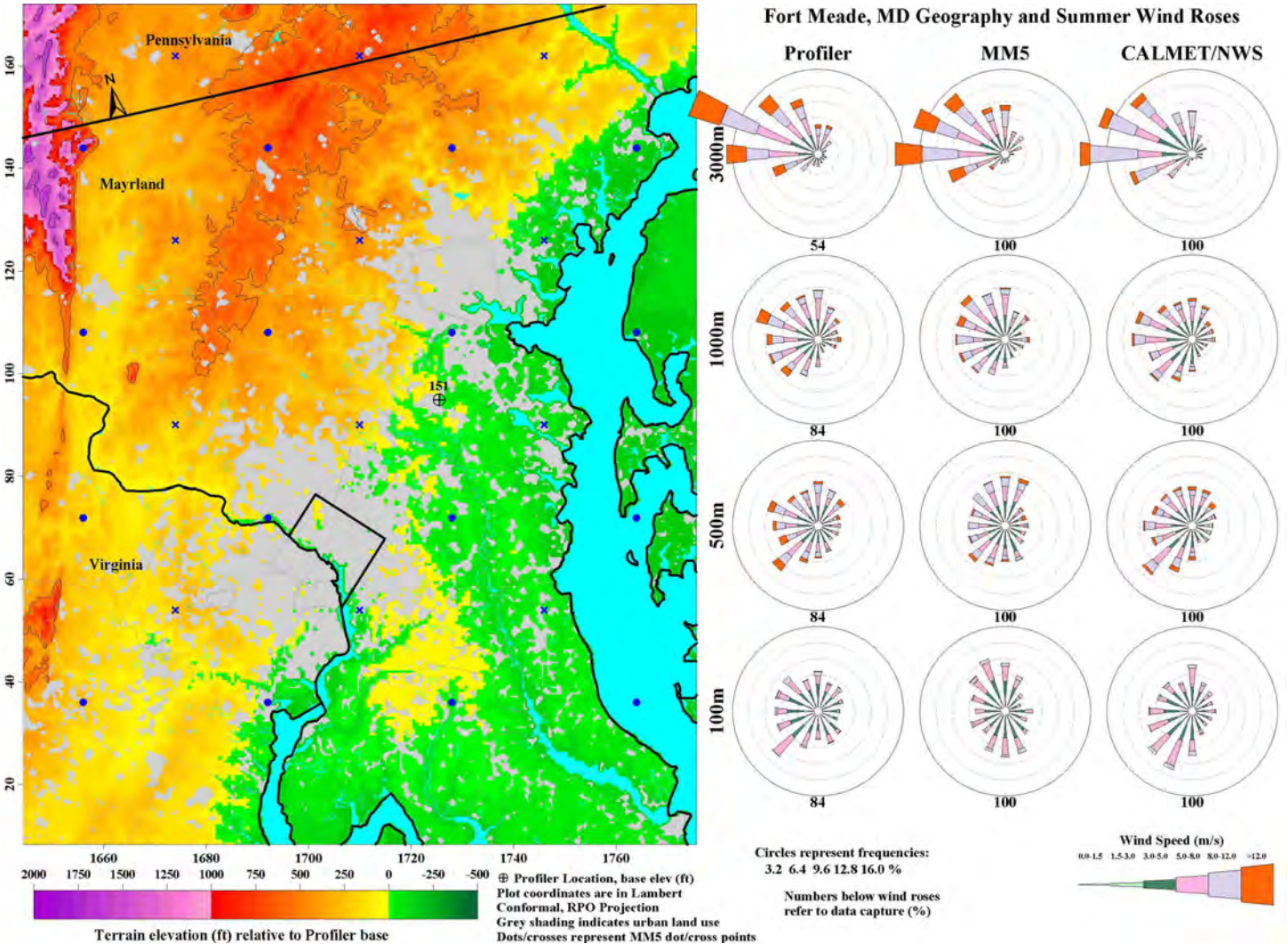

Figure D-38. Comparison of wind roses based on observed profiler data, MM5-based CALMET (MD) and NWS observation-based CALMET (VT) for Rutgers, NJ.

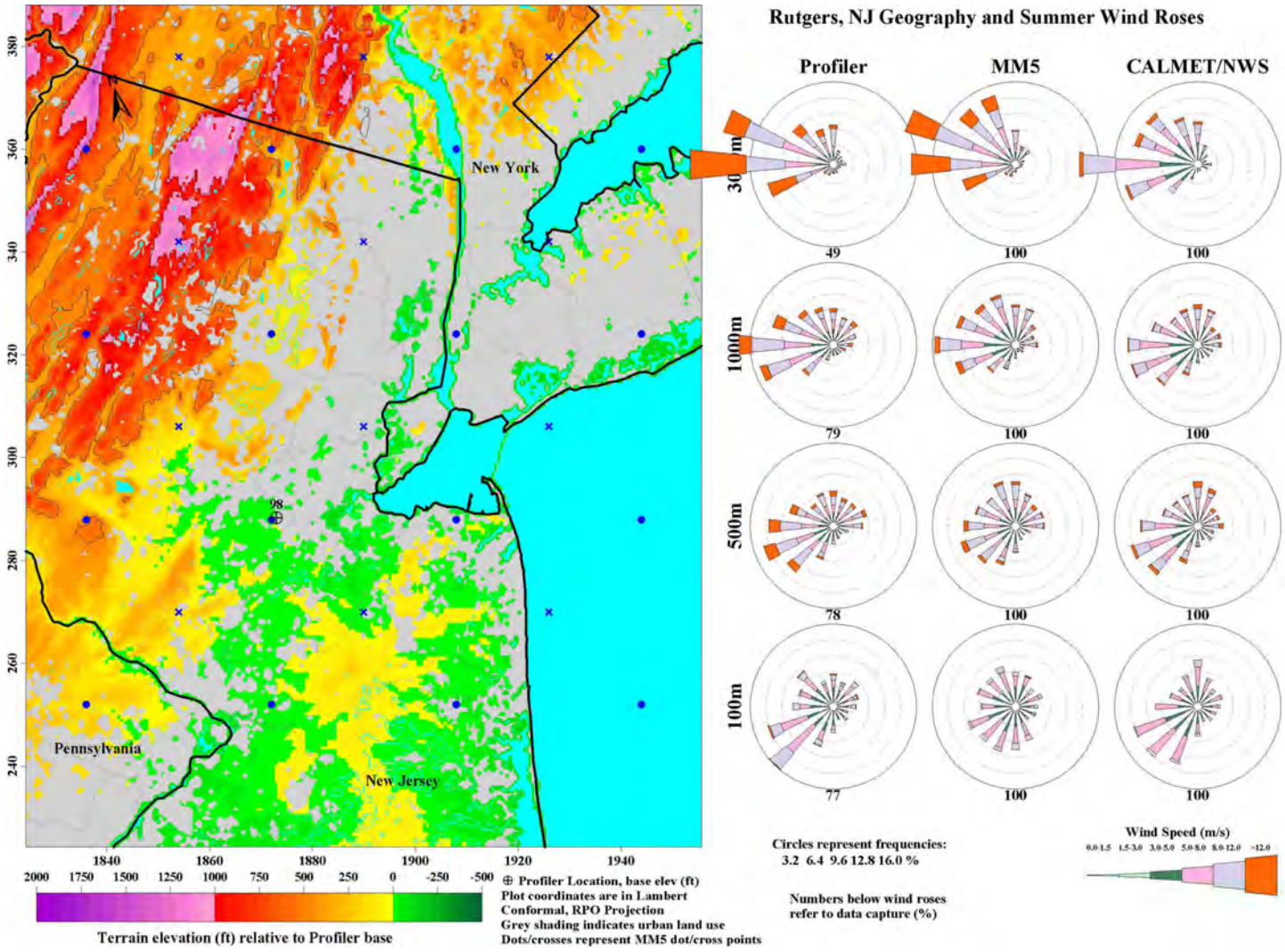

Figure D-39. Comparison of wind roses based on observed profiler data, MM5-based CALMET (MD) and NWS observation-based CALMET (VT) for Stowe, MA.

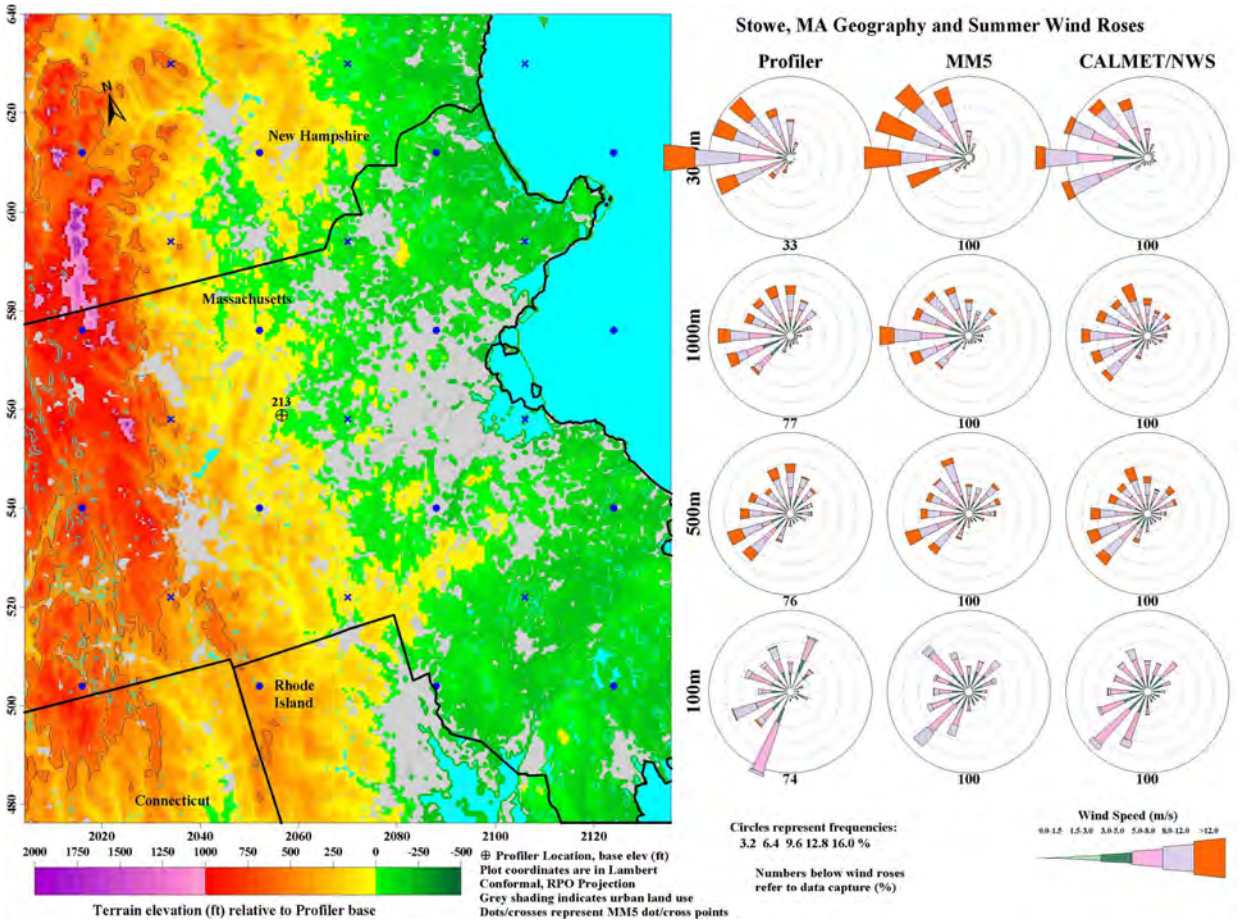

Table D-12. Wind Speed and Direction Bias at Three Profiler Sites.

Site	Elevation (m)	Wind Speed Bias (m/s)			Wind Direction Bias (degrees)		
		mm5_pro	mm5_nws	nws_pro	mm5_pro	mm5_nws	nws_pro
Fort Meade	100	0.23	0.02	0.15	3.44	8.51	-4.29
Fort Meade	500	-0.88	-0.19	-0.78	-6.42	1.55	-3.58
Fort Meade	1000	-0.75	0.07	-0.88	-5.31	10.35	-11.08
Fort Meade	3000	-0.71	1.11	-1.67	-1.99	1.64	-8.28
Rutgers	100	-0.14	0.20	-0.40	-6.19	6.86	-13.32
Rutgers	500	-0.77	0.23	-1.03	-3.38	8.37	-10.16
Rutgers	1000	-0.86	0.48	-1.37	0.38	21.81	-19.87
Rutgers	3000	-0.57	3.08	-3.25	3.56	17.83	-19.89
Stowe	100	0.39	0.15	0.34	1.89	7.75	-6.27
Stowe	500	-0.15	-0.70	0.56	8.94	7.44	1.79
Stowe	1000	-0.23	-0.63	0.52	8.53	12.93	-1.06
Stowe	3000	-0.23	2.72	-2.93	6.45	17.27	-7.93

Comparison codes:

mm5_pro: MM5-based CALMET winds vs. profiler winds

mm5_nws: MM5-based CALMET winds vs. NWS-based CALMET winds

nws_pro: NWS-based CALMET winds vs. profiler winds

Two time periods in the summer of 2002, namely, July 4-12 and August 7-15, were used to develop a third type of comparison between wind profiles. These comparisons were based on visualizations of the vertical profiles of wind speed and direction, and are presented in Figure D-40a-c for the July time period and in Figure D-41a-c for the August time period. These figures show a representation of the vertical winds from 100 to 3000 meters above ground, and use arrow symbols to represent wind vectors and a color scale to represent wind speed. Generally, the MM5-based wind profiles appear to provide a better representation of the measured profiles.

One point that is clear from these comparisons is that fine details of wind fields are difficult to represent accurately at each point in space and time, although the broad patterns appear to be reasonably well simulated, especially with the MM5-based profiles. It is instructive to recall that these comparisons represent only three locations in a much larger domain.

Figure D-40a. Comparison of vertical components of wind fields from observed profiler data, MM5-based CALMET (MD) and NWS observation-based CALMET (VT) for Ft. Meade, MD during July, 2002.

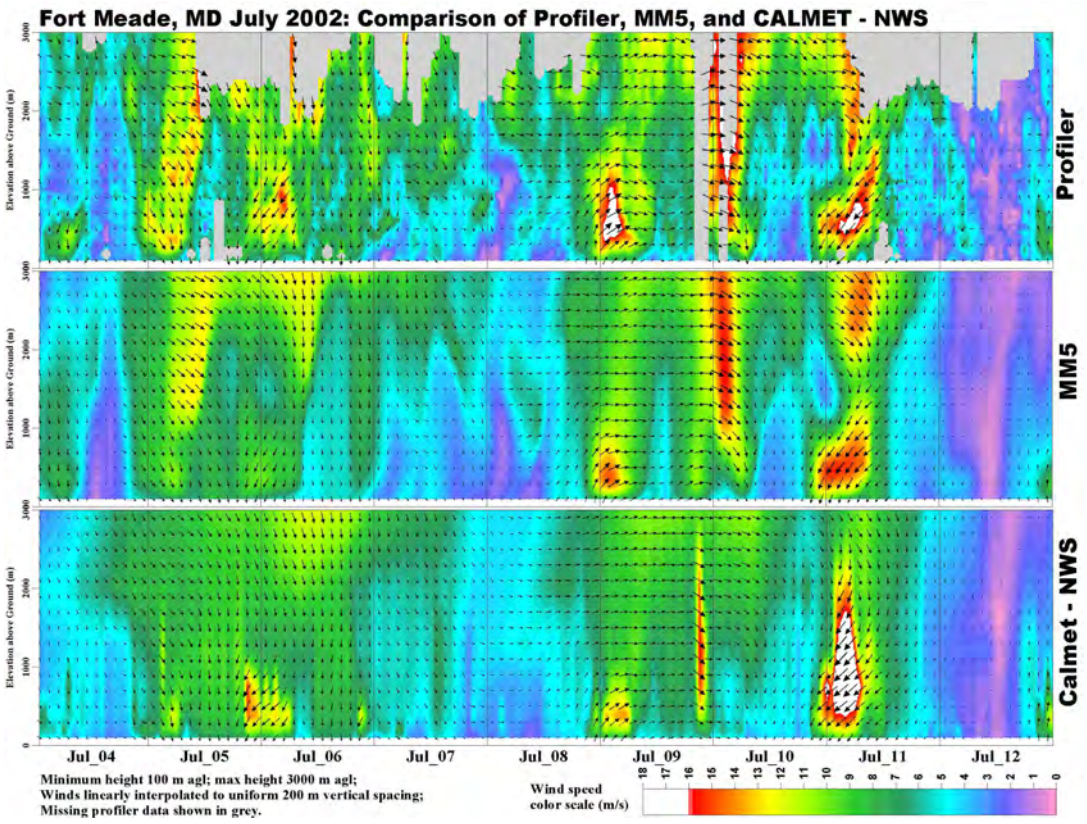

Figure D-40b. Comparison of vertical components of wind fields from observed profiler data, MM5-based CALMET (MD) and NWS observation-based CALMET (VT) for Rutgers, NJ during July, 2002.

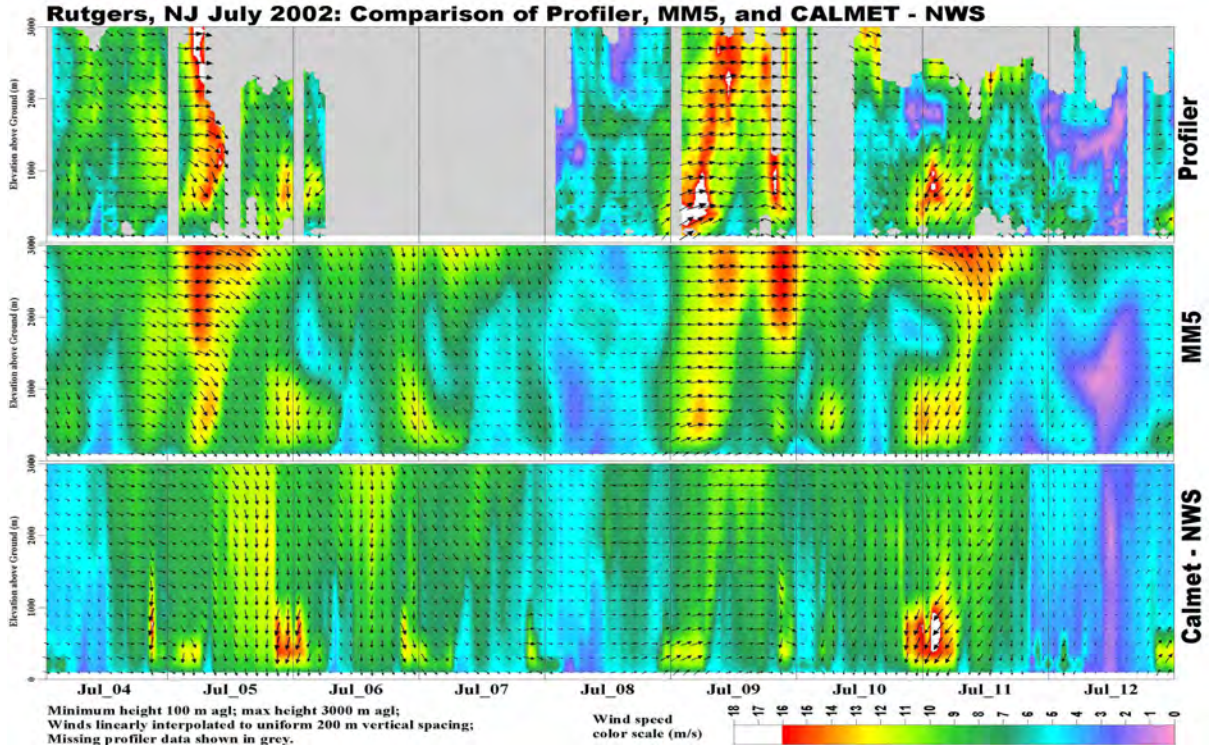

Figure D-40c. Comparison of vertical components of wind fields from observed profiler data, MM5-based CALMET (MD) and NWS observation-based CALMET (VT) for Stowe, MA during July, 2002.

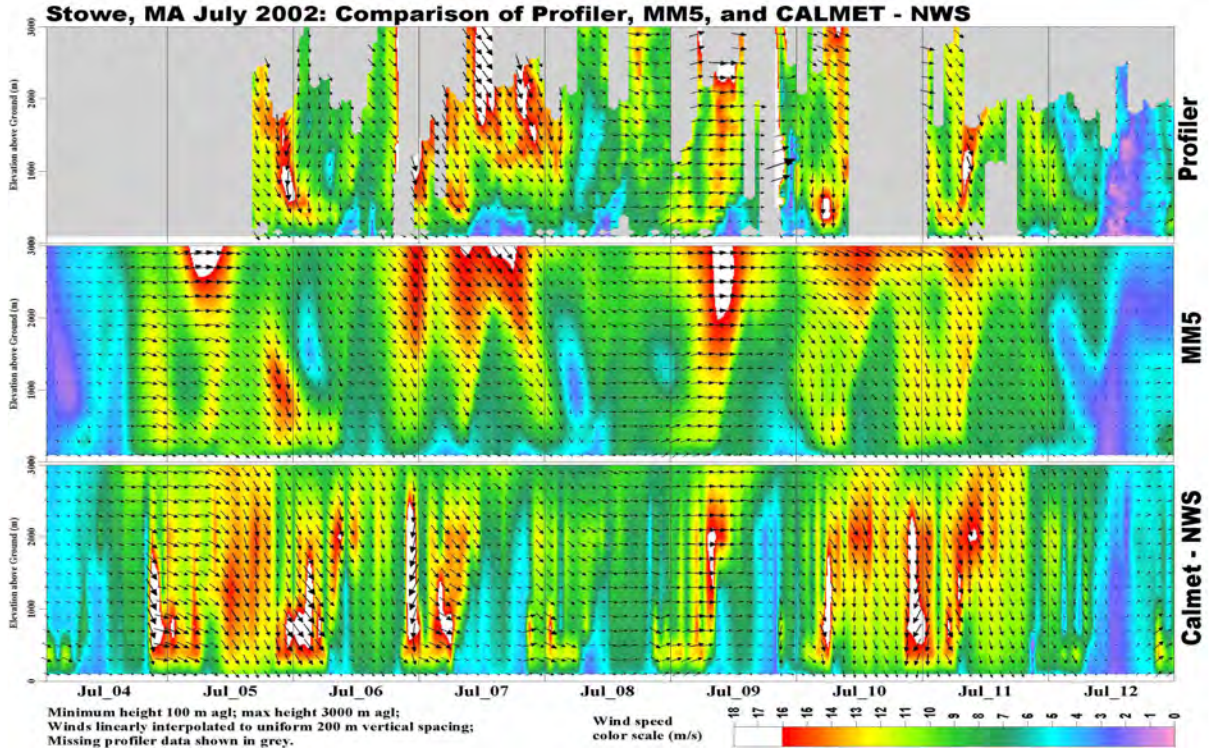

Figure D-41a. Comparison of vertical components of wind fields from observed profiler data, MM5-based CALMET (MD) and NWS observation-based CALMET (VT) for Ft. Meade, MD during August 2002.

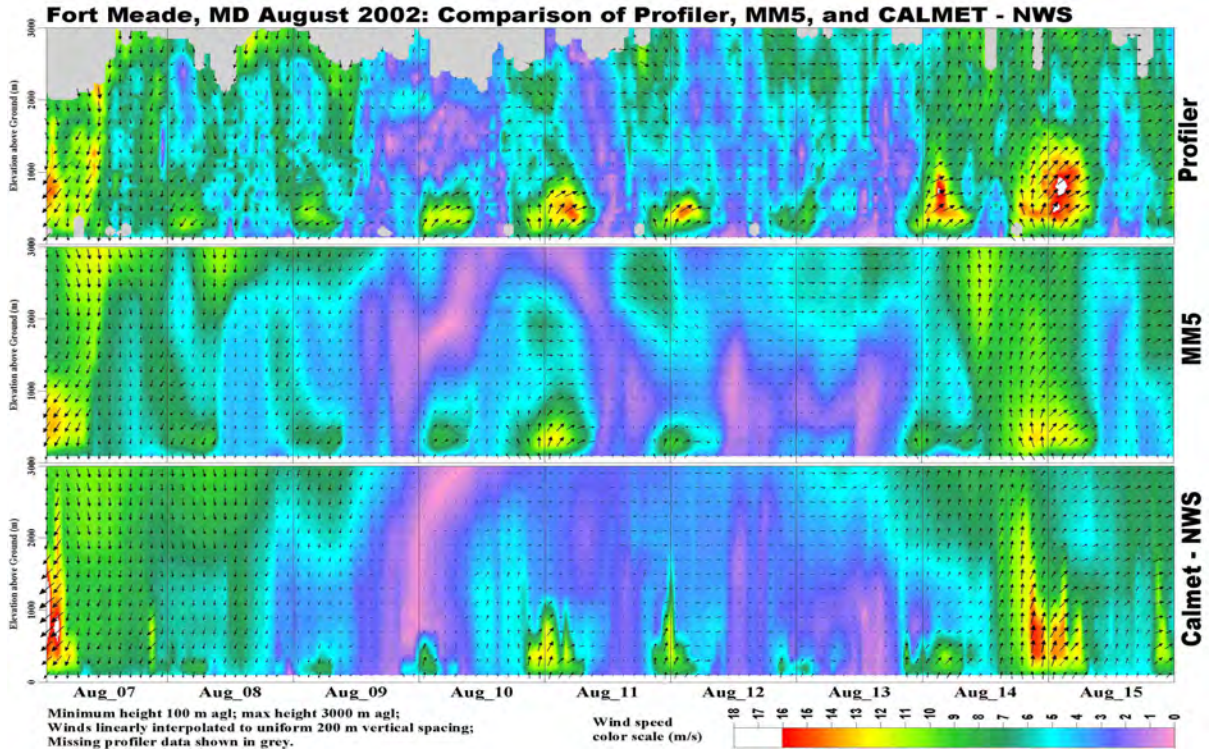

Figure D-41b. Comparison of vertical components of wind fields from observed profiler data, MM5-based CALMET (MD) and NWS observation-based CALMET (VT) for Rutgers, NJ during August 2002.

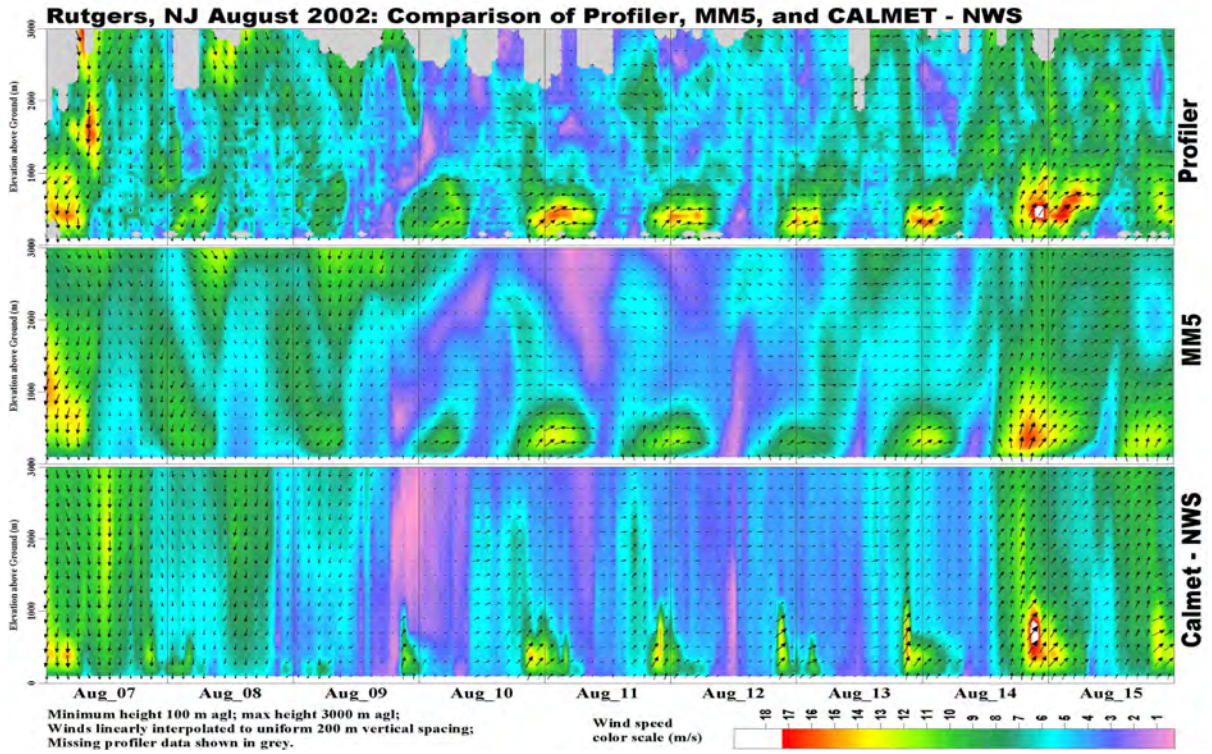

Figure D-41c. Comparison of vertical components of wind fields from observed profiler data, MM5-based CALMET (MD) and NWS observation-based CALMET (VT) for Stowe, MA during August 2002.

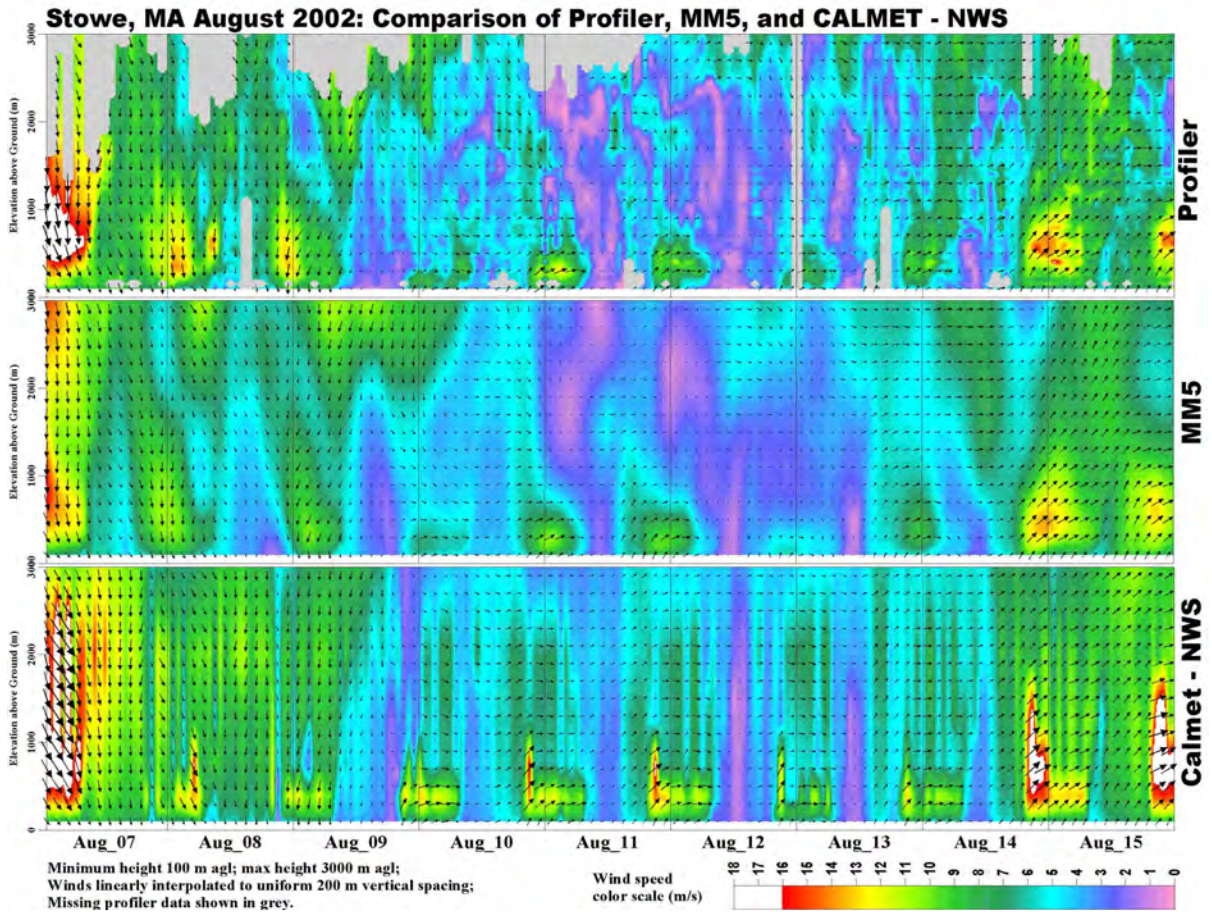

D.3.2.2. Precipitation

The hourly gridded precipitation fields were developed as discussed previously. In order to evaluate the gridding carried out by CALMET, the annual average precipitation at National Acid Deposition Program (NADP) sites in the domain were compared to the annual average precipitation predicted by CALMET in the model cell where the NADP site is located. In some cases, a CASTNET site is co-located with the NADP site. In these cases, the hourly data recorded at the CASTNET site was used in the gridding process and the comparison is less meaningful than comparisons at locations where measurement stations were more distant from the grid cell (NADP sites record precipitation as weekly totals, not hourly values, and so these data were not input to CALMET).

Figure D-42 displays the results of the comparison of gridded vs. measured annual precipitation within the domain. Points representing NADP sites with collocated CASTNET stations are shown separately from NADP sites with no collocated CASTNET station. The CALMET predictions for cells with NADP sites that have collocated CASTNET stations are, as expected, closer to observations than other cells. Even though most predictions are within a factor of two of the observations, these

Figure D-42. Comparison of gridded vs. measured annual precipitation within the CALPUFF domain

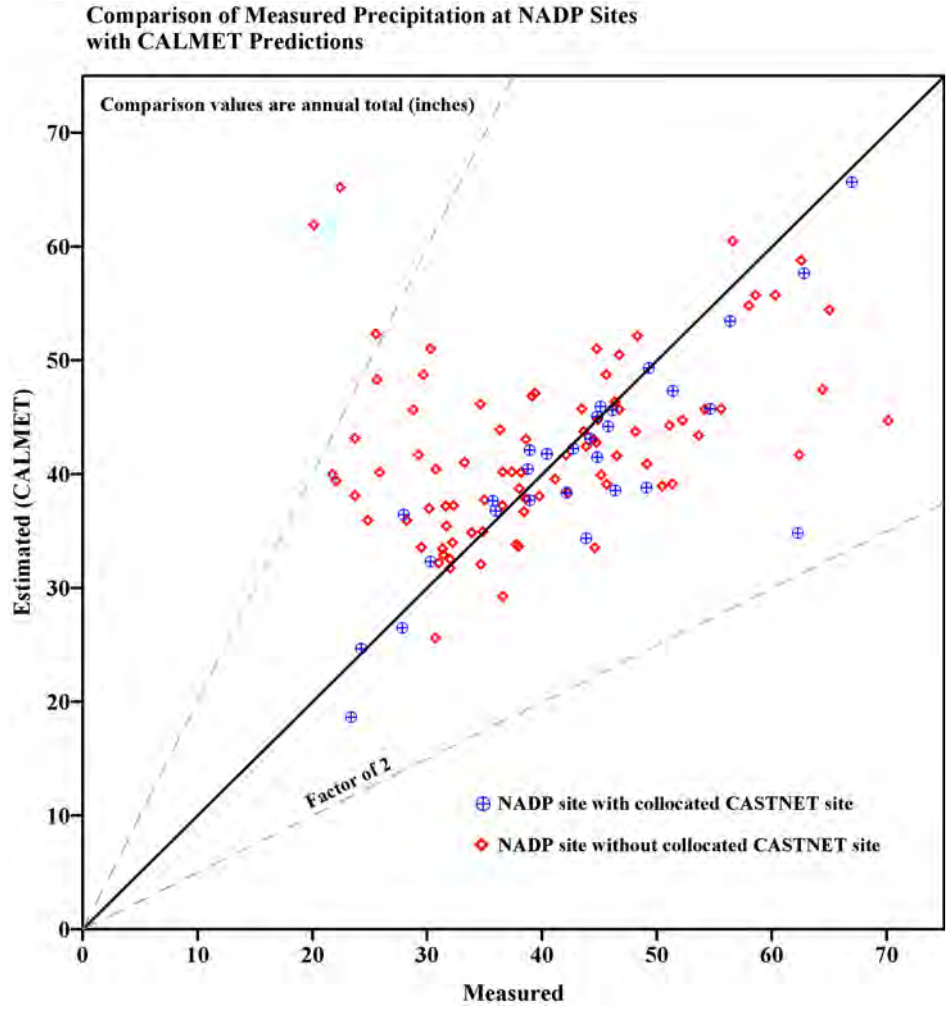

differences should be considered when comparing CALPUFF predictions of wet deposition at NADP stations.

D.3.2.3. Other Evaluations

Additional evaluations of the meteorological fields produced by CALMET were carried out. This set of evaluations was not based on comparisons to observations; rather, data summaries were prepared that allowed for an evaluation of ranges and averages of parameters (including derived boundary layer parameters) and of interrelationships between these parameters and other features such as land use and terrain. Table D-13 illustrates the relationship of the derived parameters of friction velocity, convective velocity scale, and heat flux with land use type by month. Table D-14 displays the maximum daily and average night-time mixing depths by land use type and by month; and Table D-15 illustrates the relationship of average wind speed with height, season, and land use type.

Table D-13. Derived Boundary Layer Parameters

	Land Use	# Cells	Overall	Jan	Feb	Mar	Apr	May	Jun	Jul	Aug	Sep	Oct	Nov	Dec
Parameter Friction Velocity m/s (ustar)	All Land	29546	0.39	0.37	0.45	0.46	0.45	0.46	0.38	0.34	0.34	0.35	0.35	0.38	0.41
	Urban	199	0.37	0.38	0.44	0.45	0.42	0.41	0.34	0.32	0.31	0.31	0.33	0.39	0.39
	Agriculture	12465	0.37	0.38	0.45	0.45	0.44	0.41	0.34	0.30	0.30	0.30	0.31	0.36	0.38
	Forest	16882	0.41	0.37	0.46	0.47	0.46	0.49	0.40	0.37	0.37	0.39	0.37	0.39	0.43
	Water	9919	0.22	0.26	0.27	0.24	0.21	0.21	0.17	0.16	0.15	0.18	0.20	0.25	0.29
	Other	495	0.33	0.31	0.36	0.40	0.38	0.39	0.36	0.30	0.31	0.30	0.29	0.30	0.31
	All LU Cats	39960	0.35	0.34	0.41	0.41	0.39	0.39	0.33	0.29	0.29	0.31	0.31	0.35	0.38
Convective Velocity m/s (wstar)	All Land	29546	0.59	0.27	0.39	0.53	0.70	0.84	0.92	0.92	0.81	0.64	0.46	0.32	0.24
	Urban	199	0.58	0.29	0.41	0.52	0.68	0.79	0.88	0.89	0.78	0.63	0.45	0.33	0.26
	Agriculture	12465	0.60	0.29	0.41	0.54	0.70	0.83	0.93	0.92	0.81	0.66	0.47	0.34	0.26
	Forest	16882	0.58	0.25	0.37	0.53	0.70	0.84	0.92	0.92	0.81	0.62	0.45	0.30	0.22
	Water	9919	0.00	0.00	0.00	0.00	0.00	0.00	0.00	0.00	0.00	0.00	0.00	0.00	0.00
	Other	495	0.55	0.27	0.38	0.50	0.63	0.76	0.86	0.85	0.77	0.62	0.43	0.31	0.24
	All LU Cats	39960	0.44	0.20	0.29	0.40	0.52	0.63	0.69	0.69	0.61	0.48	0.34	0.24	0.18
Heat Flux w/m2	All Land	29546	201.9	92.9	133.9	185.6	244.2	291.2	321.6	320.1	281.1	218.5	145.5	103.5	80.9
	Urban	199	210.1	102.0	146.3	191.6	250.9	294.3	327.5	327.5	288.1	230.5	153.5	113.3	91.9
	Agriculture	12465	210.0	102.6	143.7	193.1	248.1	294.0	329.3	326.9	287.8	230.8	154.9	114.5	90.6
	Forest	16882	195.9	85.6	126.6	180.0	241.2	289.2	315.9	315.0	276.0	209.3	138.6	95.3	73.7
	Water	9919	210.2	101.4	138.4	194.8	253.4	299.2	324.2	324.4	288.6	234.0	165.8	106.5	87.4
	Other	495	210.2	104.7	148.2	196.0	246.3	293.4	329.3	320.0	287.9	228.6	154.9	116.7	93.1
	All LU Cats	39960	204.1	95.1	135.2	188.0	246.5	293.2	322.3	321.2	283.0	222.5	150.7	104.4	82.7

Table D-14. Mixing Depths

Land Use	# Cells	Overall	Jan	Feb	Mar	Apr	May	Jun	Jul	Aug	Sep	Oct	Nov	Dec
Average of maximum daily mix height														
All Land	29546	1415	2204	785	965	1267	1430	1697	1746	1786	1657	1362	1119	896
Urban	199	1334	2037	847	1001	1209	1366	1526	1596	1652	1562	1234	1024	910
Agriculture	12465	1417	2193	801	981	1235	1413	1666	1786	1811	1662	1422	1081	890
Forest	16882	1414	2215	772	953	1291	1444	1722	1718	1770	1654	1320	1149	900
Water	9919	600	1089	688	641	649	559	582	471	458	435	475	534	619
Other	495	1348	2104	756	896	1147	1282	1490	1656	1787	1691	1433	1039	839
All LU Cats	39960	1212	1926	760	884	1112	1212	1418	1429	1456	1354	1143	973	827
Average of night-time mix heights														
All Land	29546	759	418	588	736	893	1093	1159	1131	993	774	578	482	447
Urban	199	720	445	608	706	856	972	1056	1056	925	701	535	489	444
Agriculture	12465	756	436	606	729	889	1071	1175	1132	984	782	556	473	425
Forest	16882	763	405	574	742	897	1110	1149	1132	1001	769	595	488	463
Water	9919	383	426	456	423	384	389	325	309	287	321	352	421	472
Other	495	713	390	524	672	802	981	1108	1120	1020	794	538	425	368
All LU Cats	39960	665	420	554	658	766	917	951	927	818	662	521	466	452

Table D-15. Domain-wide wind speed averages

By elevation above ground and land use (m/s)							
Elevation (m)	**All_Land**	**Urban**	**Agriculture**	**Forest**	**Water**	**Other**	**All_LU_Cats**
10	3.07	3.05	3.38	2.84	5.68	3.54	3.72
50	4.72	4.63	4.96	4.55	6.49	5.18	5.17
150	6.15	5.95	6.34	6.02	7.35	6.61	6.46
300	7.37	7.14	7.51	7.28	8.00	7.78	7.54
500	8.17	7.95	8.21	8.13	8.40	8.47	8.23
800	8.72	8.52	8.64	8.79	8.67	8.83	8.71
1200	9.38	9.16	9.15	9.56	9.13	9.11	9.32
1640	10.25	10.11	9.90	10.51	9.97	9.54	10.17
2080	11.27	11.27	10.84	11.59	11.01	10.24	11.19
2520	12.35	12.48	11.86	12.71	12.10	11.11	12.28
2960	13.48	13.69	12.94	13.88	13.21	12.07	13.40
By season and land use (surface speeds; m/s)							
Season	**All_Land**	**Urban**	**Agriculture**	**Forest**	**Water**	**Other**	**All_LU_Cats**
Annual	3.07	3.05	3.38	2.84	5.68	3.54	3.72
Winter	3.42	3.48	3.94	3.04	6.78	3.80	4.26
Spring	3.37	3.27	3.72	3.10	5.52	4.01	3.91
Summer	2.57	2.46	2.64	2.52	4.48	3.10	3.05
Fall	2.94	3.01	3.24	2.72	6.00	3.25	3.70

D.3.3. CALPUFF: Development and Evaluation of Model Inputs

The CALPUFF model requires the development of several different types of inputs. Meteorological data files (12 files for the full year) based on MM5 upper air wind fields were developed using CALMET and associated processors as described in Sections D.3.1 and D.3.2. For this analysis, hourly ozone concentrations were required based on CALPUFF option selections. Development of the ozone data file, and source and emissions data processing and inputs, are described below.

For the MM5 platform, a total of 22 receptor locations were selected and modeled.. These receptors correspond to the location of 11 Clean Air Status and Trends Network (CASTNET) sites, 7 IMPROVE monitor sites, and 5 sites that have collocated CASTNET and IMPROVE measurement station. The locations of these receptors are shown in Figure D-43, and Table D-16 provides further identification of the receptor sites.

Figure D-43. Location of Receptors Modeled with the DNR/MDE MM5 Platform

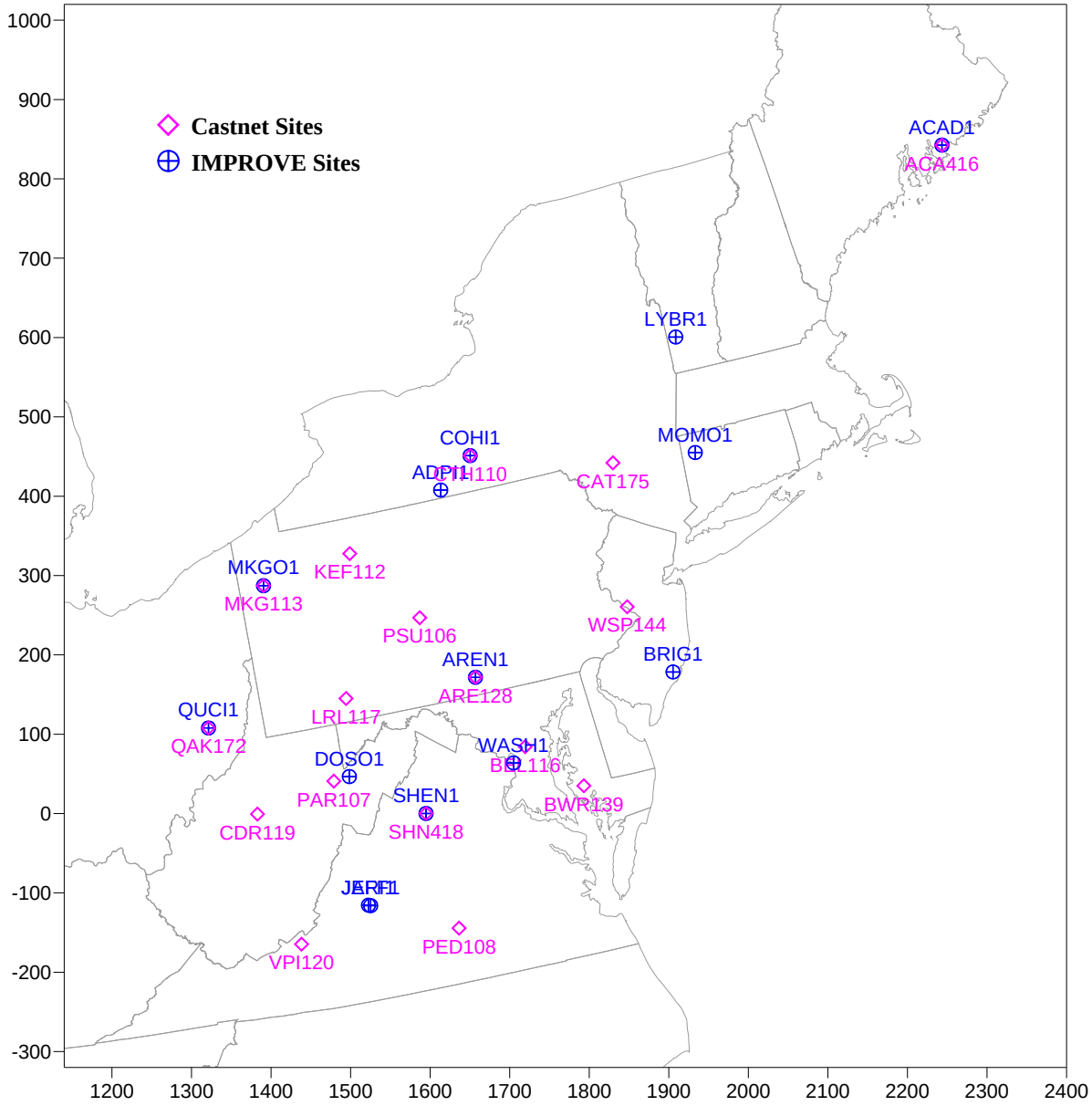

Table D-16. Identification of Receptors Modeled with DNR/MDE MM5 Platform

Site	State	CASTNET ID	IMPROVE ID
Arendtsville	PA	ARE128	AREN1
Kane Experimental Forest	PA	KEF112	-
Horton's Station	VA	VPI120	-
Prince Edward	VA	PED108	-
Shenandoah National Park-Big Meadows	VA	SHN418	SHEN1
Cedar Creek State Park	WV	CDR119	-
Parsons	WV	PAR107	-
Beltsville	MD	BEL116	-
Blackwater NWR	MD	BWR139	-
Claryville	NY	CAT175	-
Connecticut Hill	NY	CTH110	COHI1
Laurel Hill	PA	LRL117	-
M.K. Goddard	PA	MKG113	MKGO1
Penn State	PA	PSU106	-
Quaker City	OH	QAK172	QUCI1
Wash. Crossing	NJ	WSP144	-
Addison Pinnacle	NY	-	ADPI1
Brigantine National Wildlife Refuge	NJ	-	BRIG1
Dolly Sods /Otter Creek Wilderness	WV	-	DOSO1
James River Face	VA	-	JARI1
Mohawk Mt.	CT	-	MOMO1
Washington D.C.	DC	-	WASH1

D.3.3.1. Ozone Data

Hourly ozone data sets for calendar year 2002 were downloaded from EPA's Technology Transfer Network Air Quality System (http://www.epa.gov/ttn/airs/airsaqs/detaildata/downloadaqsdata.htm). Approximately 1,500 stations within the modeling domain had at least some data available for 2002. These data were read and processed were downloaded for calendar year 2002. Processing consisted of identifying the model grid location of each station, averaging hourly concentrations for each hour for all stations located within one grid cell, and creating the CALPUFF hourly ozone file based on the averages within the grid cells (i.e., grid cell centers were essentially identified as pseudo-ozone stations). This process resulted in a data file that included 1,077 such pseudo-ozone stations for use in the modeling.

D.3.3.2. NEI 2002

The National Emissions Inventory (NEI) for criteria pollutants, 1999 version 3 (as of March, 2004) was used to develop emissions and source characteristics for EGUs, for

non-EGU point sources, and general area, non-road mobile, and onroad mobile sources for the Phase I modeling effort. As stated in the Phase I report, use of the 1999 inventory was considered temporary until the 2002 inventory was available. The final 2002 inventory was released by EPA in February, 2006 and there have been several updates including the latest in April, 2006. At the time when the work for this modeling was being conducted, a final 2002 inventory was not available; therefore, individual RPO inventories were obtained from web postings and processed for modeling with CALPUFF. The VISTAS (Base F) and Midwest (Base J) RPO inventories were downloaded from http://www.rpodata.org/. The MANE-VU Version 2 inventory was downloaded from ftp://manevu.org. Emissions of SO_2, NO_X, and PM were extracted from three inventories for the non-EGU point, area, and nonroad mobile source categories. The VISTAS and Midwest RPO inventories did not have emissions calculated for onroad mobile sources, so for these states emissions for this category were obtained from the 2002 draft NEI dated February 2005; onroad mobile source emissions were available from the MANE-VU Version 2 inventory, and these were processed and used in the modeling. For states outside of the MANE-VU, VISTAS, and Midwest RPO, emissions were obtained from the 2002 draft NEI dated February 2005 For EGU sources, the VTDEC hourly CEMS file was utilized in the MM5 platform modeling, so that at least for this source category, the emissions and stack parameter inputs were identical between the two platforms.

Emissions from mobile (onroad and nonroad) and area sources are reported in the NEI and in the RPO inventories on a county total basis, and each county was modeled as a single area source with some exceptions. Some counties with low emissions and that were distant (greater than 200 kilometers) from any of the model receptors were combined and modeled as large state-wide area source instead of being modeled as individual counties. This process of developing input files for CALPUFF resulted in a slightly different total number of sources modeled: 1,104 mobile/onroad sources; 684 mobile/nonroad sources, and 617 area sources.

The RPO and draft 2002 NEI point source inventories were also used to extract emissions and stack information to develop model inputs for industrial (non-EGU) facilities. The distinction between EGU and non-EGU sources was made based on the listed SIC code in the inventory; a small number of obvious mistakes in the listed SIC code were made to ensure that no EGUs were in this category.

Stack parameters and emission rates were extracted from the NEI point source text files. Thes files contained entries for a large number of individual release points, far more than could be modeled individually with CALPUFF. For this modeling effort, a single stack was selected for each facility (generally, the stack with the highest total of SO_2 plus NO_X emissions). Further processing was undertaken to reduce the number of sources to model, based on the total annual facility SO_2 + NO_X emissions and the closest distance to any of the modeled receptors. Facilities with emissions greater than specified distance-dependent thresholds were modeled as individual stacks; emissions from all other facilities were added to county-wide “industrial cateogry” sources. Most of these counties were modeled as area sources; some with low total emissions were combined into state-wide area sources. This process resulted in a modeling inventory of 545 stacks and 349 county-wide area sources.

D.3.3.3. CEMS Data

The VTDEC "PTEMARB" files, based on the CEMS data and including hourly stack parameters and SO_2 and NO_X emissions, were used with the DNR/MDE MM5 modeling platform. The individual files were combined into three files covering the entire year for approximately one-third of the total number of sources in each file. For the EGU category, therefore, the only differences in model predictions are related to meteorology. CALPUFF was modified to allow for writing predicted values from each source modeled to a separate external output file. In this way, the impacts of individual sources were retained as well as the total impacts.

D.3.3.4. Emissions Summary

Table D-17 and Table D-18 provide a summary of the 2002 emissions of SO_2 and NO_X, respectively, that were modeled with the DNR/MDE platform.

Table D-17. Summary of SO_2 Emissions from 2002 NEI and CEMS

FIPS	STATE	TOTAL	CEM PT (2002)	Non-EGU Point TOTAL	AREA	ONROAD	NONROAD
39	OH	1,417,975	1,074,480	277,438	32,334	12,641	21,082
42	PA	974,532	786,467	82,098	80,590	8,459	16,918
18	IN	925,837	741,918	86,664	74,252	8,525	14,477
13	GA*	605,137	497,931	23,919	59,137	9,640	14,510
21	KY	594,149	462,425	31,619	74,928	5,736	19,442
54	WV	565,597	489,511	52,809	16,299	2,345	4,633
37	NC	548,019	440,989	55,828	24,199	9,923	17,080
17	IL	496,469	322,682	124,606	23,526	7,392	18,263
26	MI	473,952	319,958	59,184	61,528	13,476	19,806
36	NY	469,507	193,088	85,653	154,343	14,594	29,188
47	TN	465,533	303,145	88,087	47,762	8,670	17,869
1	AL*	371,342	301,530	28,233	30,208	4,024	7,347
29	MO	333,707	173,391	95,453	44,523	8,154	12,186
24	MD	331,351	269,265	34,162	27,402	7,505	15,010
51	VA	329,896	224,577	58,181	25,054	6,653	15,431
55	WI	295,847	188,108	72,176	17,743	6,439	11,382
45	SC	278,838	189,419	52,390	22,420	5,088	9,520
19	IA	271,742	125,575	102,956	31,323	3,714	8,174
25	MA	267,251	63,543	106,056	72,015	8,546	17,092
27	MN	169,783	93,980	29,110	27,955	6,332	12,406
20	KS*	163,660	124,451	15,989	11,751	2,948	8,521
40	OK*	161,220	103,827	30,471	13,255	4,923	8,744
5	AR*	159,937	70,056	47,868	27,853	3,677	10,483
34	NJ	151,617	46,833	9,874	44,403	16,836	33,671
10	DE	92,718	30,138	40,979	9,593	4,003	8,005
33	NH	52,497	41,463	2,519	7,649	289	578
31	NE*	52,200	30,564	0	14,188	1,643	5,805
38	ND*	48,675	0	16,958	28,727	411	2,579
23	ME	37,891	1,170	20,713	14,760	806	1,612
9	CT	36,142	10,137	2,234	16,959	2,271	4,541
46	SD*	33,256	11,716	647	17,588	635	2,670
28	MS*	23,053	0	10,073	5,791	1,701	5,488
44	RI	7,384	6	956	5,304	373	745
50	VT	6,780	6	874	4,811	363	726
11	DC	4,445	1,074	616	1,903	284	568
48	TX*	2,952	40	0	1,285	524	1,103
TOTAL		**11,220,887**	**7,733,461**	**1,747,389**	**1,173,361**	**199,543**	**397,655**
Percent			**68.9%**	**15.6%**	**10.5%**	**1.8%**	**3.5%**

Emissions by source category in tons per year
States are sorted by total emissions
* indicates a stat that was only partially inculded in the domain

Table D-18. Summary of NO_X Emissions from 2002 NEI and CEMS

FIPS	STATE	TOTAL	CEM PT (2002)	Non-EGU Point TOTAL	AREA	ONROAD	NONROAD
39	OH	1,655,416	326,181	126,123	456,215	327,821	419,076
26	MI	1,325,288	109,102	60,242	435,058	324,986	395,900
17	IL	1,296,175	164,341	75,575	421,454	260,786	374,019
47	TN*	1,237,292	133,398	72,466	385,111	279,034	367,283
37	NC*	1,229,497	137,215	50,794	403,521	278,341	359,626
18	IN	1,122,064	245,511	71,973	309,277	216,202	279,101
13	GA	1,098,553	139,740	31,580	348,219	259,890	319,124
51	VA	953,642	77,132	58,751	326,623	216,498	274,638
21	KY	926,067	176,267	36,481	310,825	150,649	251,845
29	MO	900,576	120,322	24,949	288,952	215,990	250,364
27	MN	841,563	72,900	64,497	296,037	171,628	236,501
42	PA*	827,834	170,989	81,573	258,658	105,538	211,076
36	NY*	800,498	52,839	45,232	336,224	122,568	245,135
55	WI*	781,618	87,320	41,296	249,565	175,864	227,573
45	SC	669,276	79,289	39,762	211,882	145,793	192,550
40	OK	618,634	74,190	36,520	205,560	129,920	172,444
19	IA	539,457	77,087	42,584	173,081	102,693	144,012
1	AL	526,963	109,534	38,449	148,947	96,005	134,028
5	AR	526,790	40,719	21,984	200,413	99,530	164,144
54	WV	495,954	195,221	45,472	105,013	57,920	92,328
20	KS	477,806	84,221	14,422	156,534	79,248	143,381
25	MA	438,255	20,562	48,242	166,595	67,619	135,237
34	NJ*	398,923	24,791	18,298	158,296	65,846	131,692
24	MD	279,131	74,828	21,633	84,673	34,499	68,997
31	NE	260,450	21,998	0	102,934	44,427	91,091
28	MS	237,014	0	31,083	80,804	46,043	79,084
9	CT	144,756	4,145	6,578	61,226	24,269	48,538
46	SD	111,342	14,516	463	41,508	17,897	36,958
10	DE*	99,250	8,082	7,080	35,200	16,296	32,593
38	ND	87,990	0	1,657	41,648	11,669	33,016
23	ME*	66,201	414	17,362	23,951	8,296	16,592
33	NH	64,602	6,436	1,768	29,135	9,088	18,175
48	TX*	57,386	2,158	0	21,040	13,849	20,339
44	RI*	29,478	290	590	13,765	4,944	9,889
50	VT	23,801	229	386	11,192	3,998	7,996
11	DC	16,452	403	476	7,212	2,787	5,574
TOTAL		**21,165,984**	**2,852,370**	**1,236,336**	**6,906,348**	**4,188,431**	**5,989,919**
Percent			**13.5%**	**5.8%**	**32.6%**	**19.8%**	**28.3%**

Emissions by source category in tons per year
States are sorted by total emissions
* indicates a stat that was only partially inculded in the domain

D.3.4. Phase I CALPUFF Results Using MM5-Derived Wind Fields

CALPUFF modeling was conducted utilizing the meteorological, source, ozone, and receptor inputs developed as described previously. Modeled concentrations of sulfate and nitrate ion were extracted from output files and summarized. Comparisons of total predicted sulfate and nitrate ion concentrations to measurements at the 22 modeled CASTET and IMPROVE stations, and summaries of model predictions by source and by state, are discussed in the following sections.

D.3.4.1. Evaluation of CALPUFF Sulfate and Nitrate Predictions

Tables D19(a-c) display the results of CALPUFF modeling with MM5 meteorological inputs, compared to observations at CASTNET and IMPROVE locations. Table D19(a) displays a comparison of predicted and observed sulfate ion concentrations. There is a distinct tendency to under predict annual average sulfate ion concentrations at nearly all of the sites modeled, with slight overprediction at Acadia and Lye Brook. The maximum predicted 24-hr sulfate ion concentrations display a wider range of predicted to observed ratios, ranging from a low of 0.58 at Dolly Sods to 1.87 at Acadia. Table D-19(b) displays similar comparisons with nitrate aerosol ion concentrations at IMPROVE and CASTNET sites. Both annual average and 24-hr maximum nitrate aerosol ion concentrations are over-predicted substantially. Table D-19(c) displays model comparisons for total nitrate ion at CASTNET sites, where the total nitrate ion is calculated as the sum of nitric acid and nitrate aerosol. CALPUFF still overpredicts, but not as substantially as with the nitrate aerosol ion alone (IMPROVE sites do not report nitric acid, therefore comparisons of total nitrate ion could not be made at IMPROVE sites). The CALPUFF algorithms, as described in Section D.1.2, partition available nitrate between nitric acid and nitrate aerosol as a function of temperature, relative humidity, and available ammonia. The results shown in Tables 19(b) and 19(c) show that the nitrate partitioning is clearly biased towards forming too much nitrate aerosol, and that this may be due to limitations on available ammonia that are not simulated directly by CALPUFF. The POSTUTIL program, also discussed in Section D.1.2, can be applied to effectively correct for limited ammonia availability; however, the results shown here do not reflect the application of POSTUTIL. The nitrate ion predictions based on using this modeling platform should therefore be considered to be conservative estimates.

Table D-19a. Summary of Model Performance for Sulfate Ion: MM5 Meteorology

Annual Averages (ug/m3) CASTNET and IMPROVE Sites						
				Source Category Contributions		
Location	Total Modeled	Observed	Predicted/ Obs Ratio	EGU CEMS	Industry Point	Mobile/ Area
Arendtsville	3.81	5.00	0.76	3.03	0.51	0.28
Shenandoah National Park-Big Meadows	3.66	4.61	0.79	2.99	0.46	0.22
Connecticut Hill	2.81	3.76	0.75	2.16	0.42	0.24
M.K. Goddard	3.30	4.29	0.77	2.61	0.47	0.22
Quaker City	4.06	4.90	0.83	3.28	0.57	0.21
Addison Pinnacle	2.80	3.90	0.72	2.17	0.41	0.22
Brigantine National Wildlife Refuge	3.50	4.06	0.86	2.63	0.51	0.38
Dolly Sods	3.33	4.23	0.79	2.75	0.42	0.18
James River Face	3.16	4.84	0.65	2.54	0.44	0.19
Mohawk Mt.	2.88	2.88	1.00	2.09	0.43	0.37
Washington D.C.	4.07	5.27	0.77	3.22	0.52	0.35
Acadia NP	2.19	1.86	1.18	1.48	0.44	0.28
Lye Brook Wilderness	2.27	2.17	1.05	1.66	0.36	0.25
Kane Experimental Forest	3.08	4.25	0.72	2.44	0.43	0.20
Horton's Station	2.86	4.69	0.61	2.26	0.44	0.17
Prince Edward	3.58	4.48	0.80	2.92	0.45	0.22
Cedar Creek State Park	3.48	4.36	0.80	2.84	0.47	0.19
Parsons	3.23	4.72	0.68	2.65	0.41	0.17
Beltsville	4.04	4.73	0.85	3.20	0.53	0.33
Blackwater NWR	3.82	4.53	0.84	2.98	0.52	0.32
Claryville	2.66	3.31	0.80	2.02	0.38	0.26
Laurel Hill	3.84	5.08	0.76	3.17	0.47	0.22
Penn State	3.60	4.74	0.76	2.90	0.46	0.25
Wash. Crossing	3.51	4.18	0.84	2.61	0.50	0.41
24-hr Maxima (ug/m3) IMPROVE Sites Only						
				Source Category Contributions		
Location	Total Modeled	Observed	Predicted/ Obs Ratio	EGU CEMS	Industry Point	Mobile/ Area
Arendtsville	23.01	24.97	0.92	19.28	3.07	0.66
Shenandoah National Park-Big Meadows	20.54	19.20	1.07	16.68	2.42	1.44
Connecticut Hill	21.76	22.17	0.98	16.76	3.20	1.80
M.K. Goddard	18.00	25.22	0.71	16.30	1.28	0.42
Quaker City	22.04	18.82	1.17	18.05	3.35	0.65
Addison Pinnacle	18.96	24.83	0.76	14.30	2.87	1.79
Brigantine National Wildlife Refuge	21.16	26.87	0.79	18.04	2.36	0.76
Dolly Sods	21.23	36.61	0.58	17.15	3.07	1.01
James River Face	23.15	16.95	1.37	18.95	2.83	1.37
Mohawk Mt.	17.51	14.86	1.18	14.49	2.14	0.88
Washington D.C.	24.59	25.31	0.97	20.90	2.71	0.98
Acadia NP	25.23	13.51	1.87	18.04	3.84	3.34
Lye Brook Wilderness	17.37	15.87	1.09	11.74	3.91	1.72

Table D-19b. Summary of Model Performance for Nitrate Aerosol Ion: MM5 Meteorology

Annual Averages (ug/m3) CASTNET and IMPROVE Sites						
				Source Category Contributions		
Location	Total Modeled	Observed	Predicted/ Obs Ratio	EGU CEMS	Industry Point	Mobile/ Area
Arendtsville	3.01	1.51	1.99	0.89	0.37	1.75
Shenandoah National Park-Big Meadows	2.95	0.71	4.15	1.02	0.32	1.61
Connecticut Hill	2.31	0.94	2.45	0.71	0.26	1.33
M.K. Goddard	3.06	1.28	2.39	0.87	0.32	1.88
Quaker City	3.35	0.98	3.41	0.96	0.42	1.97
Addison Pinnacle	2.29	0.91	2.53	0.74	0.27	1.29
Brigantine National Wildlife Refuge	2.71	0.92	2.94	0.70	0.31	1.71
Dolly Sods	2.39	0.44	5.47	0.99	0.28	1.12
James River Face	2.60	0.62	4.20	0.78	0.30	1.52
Mohawk Mt.	2.77	0.65	4.26	0.67	0.31	1.79
Washington D.C.	3.16	1.39	2.28	0.87	0.32	1.97
Acadia NP	1.77	0.36	4.94	0.45	0.26	1.07
Lye Brook Wilderness	2.02	0.48	4.19	0.54	0.24	1.25
Kane Experimental Forest	2.54	0.58	4.36	0.87	0.29	1.38
Horton's Station	2.41	0.34	7.01	0.77	0.28	1.36
Prince Edward	2.66	0.33	8.17	0.78	0.33	1.55
Cedar Creek State Park	2.67	0.28	9.52	0.88	0.36	1.44
Parsons	2.27	0.49	4.61	0.88	0.27	1.12
Beltsville	3.00	0.71	4.23	0.85	0.33	1.82
Blackwater NWR	2.53	1.12	2.26	0.79	0.30	1.45
Claryville	2.17	0.47	4.65	0.66	0.24	1.26
Laurel Hill	2.79	0.40	7.03	1.06	0.33	1.41
Penn State	2.76	1.18	2.33	0.88	0.33	1.55
Wash. Crossing	3.16	1.22	2.59	0.72	0.35	2.10
24-hr Maxima (ug/m3) IMPROVE Sites Only						
				Source Category Contributions		
Location	Total Modeled	Observed	Predicted/ Obs Ratio	EGU CEMS	Industry Point	Mobile/ Area
Arendtsville	16.93	10.59	1.60	6.45	1.81	8.66
Shenandoah National Park-Big Meadows	19.14	3.10	6.18	7.25	2.48	9.42
Connecticut Hill	23.94	5.61	4.27	8.92	2.36	12.66
M.K. Goddard	13.36	5.83	2.29	3.12	1.11	9.13
Quaker City	16.66	5.27	3.16	7.87	2.40	6.39
Addison Pinnacle	21.72	4.85	4.48	7.46	2.06	12.20
Brigantine National Wildlife Refuge	13.93	5.70	2.44	4.01	1.65	8.27
Dolly Sods	15.64	1.78	8.81	5.04	1.65	8.96
James River Face	16.86	3.26	5.17	6.59	2.00	8.27
Mohawk Mt.	17.80	3.86	4.61	4.86	1.68	11.26
Washington D.C.	22.15	7.44	2.98	2.98	0.97	18.20
Acadia NP	22.76	2.56	8.89	6.61	2.93	13.22
Lye Brook Wilderness	16.99	3.68	4.62	6.26	1.92	8.81

Table D-19c. Summary of Model Performance for Total Nitrate Ion: MM5 Meteorology

Annual Averages (ug/m3) CASTNET Sites Only						
				Source Category Contributions		
Location	Total Modeled	Observed	Predicted/ Obs Ratio	EGU CEMS	Industry Point	Mobile/ Area
Kane Experimental Forest	3.17	2.35	1.35	1.13	0.39	1.66
Horton's Station	3.25	2.68	1.21	1.02	0.46	1.78
Prince Edward	3.97	1.92	2.07	1.21	0.49	2.27
Cedar Creek State Park	3.60	1.69	2.13	1.28	0.50	1.83
Parsons	2.93	1.83	1.60	1.20	0.35	1.38
Beltsville	4.74	2.96	1.60	1.37	0.51	2.86
Blackwater NWR	3.79	3.55	1.07	1.17	0.45	2.17
Claryville	2.65	2.58	1.03	0.81	0.30	1.55
Laurel Hill	3.73	2.25	1.66	1.50	0.43	1.80
Penn State	3.57	3.31	1.08	1.22	0.42	1.93
Wash. Crossing	4.71	3.74	1.26	1.05	0.52	3.14

D.3.4.2. Results Summary: MM5-Based Meteorology

Table D-20(a-d, for different Class I areas) provides a summary of individual EGU impacts. These tables represent the 100 highest predicted 24-hr average sulfate ion concentrations at each site. Additional information shown includes the unit identification code from the CEMS data base, the State where the unit is located, the date of the 24-hr prediction, the predicted annual average sulfate ion concentration for the unit (and the rank of the annual average concentration), total tons of SO_2 emitted in 2002, the stack height, and the distance from the source to the Class I area.

Table D-21(a-d, for different Class I areas) provides a different type of summary. Impacts from EGUs in the 2002 data base were summed by state, and then sorted by annual impact. Predicted annual average sulfate ion concentrations from the other source sectors were added to this table, and SO_2 emissions totals for the source categories and states shown were added for comparison. The last part of this table shows the relative contribution of each state and source sector to the total predicted sulfate ion concentration.

Table D-20 and Table D-21 provide an overall summary of the modeling with MM5 meteorology. This summary can be used to compare with results from other platforms to evaluate commonalities and differences.

Table D-20a. Individual Unit Sulfate Ion Impact Summary: MM5 Meteorology

Acadia National Park

RANK	CEMS Unit	STATE	24-HR Max Impact ~ µg/m^3	24Hr Date	Annual ~ µg/m^3	Annual Rank	2002 SO_2 Tons	Modeled StkHt Meters	Distance Kms
1	D023642	NH	0.693	28_Jan_028	0.0272	2	19,452.6	159.7	291.4
2	D023641	NH	0.672	29_Jan_029	0.0157	12	9,356.2	131.7	291.4
3	D028404	OH	0.663	29_Jan_029	0.0210	3	87,801.2	245.4	1207.3
4	D016193	MA	0.569	12_Aug_224	0.0194	4	19,324.8	107.3	378.9
5	D015991	MD	0.546	03_Aug_215	0.0162	11	13,014.0	151.8	341.6
6	D02872C04	OH	0.494	29_Jan_029	0.0178	8	83,133.5	150.0	1223.4
7	D015992	MD	0.476	03_Aug_215	0.0106	20	8,979.5	151.8	341.6
8	D031361	PA	0.452	16_Mar_075	0.0278	1	87,434.3	243.8	992.3
9	D031222	PA	0.424	07_Mar_066	0.0184	7	55,216.4	243.8	990.5
10	D03406C10	TN	0.414	29_Jan_029	0.0090	33	104,522.6	150.0	1875.4
11	D031221	PA	0.401	07_Mar_066	0.0139	13	45,754.3	243.8	990.5
12	D000265	AL	0.399	29_Jan_029	0.0024	174	53,062.0	228.6	1988.9
13	D080421	NC	0.396	16_Mar_075	0.0084	41	57,819.7	182.9	1337.1
14	D00988U4	IN	0.388	30_Jan_030	0.0071	50	45,062.0	122.8	1488.3
15	D031492	PA	0.385	12_Aug_224	0.0172	10	50,276.3	347.2	776.2
16	D03179C01	PA	0.384	16_Mar_075	0.0175	9	79,635.0	150.0	1080.3
17	D03935C02	WV	0.369	16_Mar_075	0.0090	32	63,065.5	274.3	1299.6
18	D031362	PA	0.364	12_Aug_224	0.0185	6	62,846.8	243.8	992.3
19	D031491	PA	0.363	15_Jul_196	0.0193	5	60,241.6	347.2	776.2
20	D028504	OH	0.354	29_Jan_029	0.0056	69	27,343.1	213.4	1425.9
21	D01355C03	KY	0.349	29_Jan_029	0.0059	62	38,103.8	150.0	1550.8
22	D01384CS1	KY	0.343	29_Jan_029	0.0035	121	21,836.6	61.0	1591.4
23	D080422	NC	0.335	16_Mar_075	0.0065	54	45,295.8	182.9	1337.1
24	D028502	OH	0.331	29_Jan_029	0.0046	85	28,698.3	213.4	1425.9
25	D082261	PA	0.312	29_Jan_029	0.0113	18	40,267.5	228.6	1033.2
26	D028503	OH	0.311	29_Jan_029	0.0053	74	27,968.3	213.4	1425.9
27	D01733C34	MI	0.305	30_Jan_030	0.0096	25	39,361.7	152.4	1249.5
28	D00861C01	IL	0.302	30_Jan_030	0.0078	45	42,355.4	152.4	1838.3
29	D028281	OH	0.299	29_Jan_029	0.0120	16	37,307.2	251.5	1111.5
30	D06113C03	IN	0.296	30_Jan_030	0.0090	30	71,181.7	150.0	1748.1
31	D031403	PA	0.294	01_Oct_274	0.0098	24	38,800.9	269.1	837.5
32	D016264	MA	0.291	12_Aug_224	0.0084	40	2,880.2	152.4	294.2
33	D02554C03	NY	0.281	18_Jan_018	0.0091	29	30,151.1	150.0	916.6
34	D067054	IN	0.275	30_Jan_030	0.0050	78	40,117.7	152.4	1738.6
35	D016192	MA	0.270	28_May_148	0.0121	15	8,889.3	107.3	378.9
36	D028501	OH	0.269	29_Jan_029	0.0052	76	30,798.1	213.4	1425.9
37	D016191	MA	0.261	28_May_148	0.0130	14	9,252.3	107.3	378.9
38	D01353C02	KY	0.260	16_Mar_075	0.0057	67	41,544.5	243.8	1375.7
39	D03405C34	TN	0.259	16_Mar_075	0.0023	176	19,368.2	150.0	1519.9
40	D02876C01	OH	0.259	18_Jan_018	0.0111	19	72,592.9	243.8	1294.7
41	D039353	WV	0.255	16_Mar_075	0.0058	66	42,211.5	274.9	1299.6

Acadia National Park

RANK	CEMS Unit	STATE	24-HR Max Impact ~ µg/m^3	24Hr Date	Annual ~ µg/m^3	Annual Rank	2002 SO_2 Tons	Modeled StkHt Meters	Distance Kms
42	D01571CE2	MD	0.252	13_Mar_072	0.0106	21	48,565.5	335.3	950.8
43	D01010C05	IN	0.244	30_Jan_030	0.0098	23	60,746.6	122.8	1662.8
44	D06113C04	IN	0.242	30_Jan_030	0.0042	98	27,847.9	213.4	1748.1
45	D080021	NH	0.238	08_Sep_251	0.0084	39	5,032.9	133.2	247.1
46	D028306	OH	0.237	30_Jan_030	0.0054	73	30,465.5	137.2	1451.1
47	D03775C02	VA	0.234	16_Mar_075	0.0022	184	16,673.8	307.2	1428.4
48	D03407C69	TN	0.228	16_Mar_075	0.0036	119	38,645.0	150.0	1660.7
49	D01733C12	MI	0.221	29_Dec_363	0.0091	27	46,080.6	137.2	1249.5
50	D039432	WV	0.221	16_Mar_075	0.0091	28	45,849.5	167.6	1088.4
51	D039431	WV	0.220	16_Mar_075	0.0086	36	42,385.1	167.6	1088.4
52	D03140C12	PA	0.217	01_Oct_274	0.0082	43	29,735.6	259.1	837.5
53	D060412	KY	0.214	29_Jan_029	0.0039	108	20,491.0	245.7	1431.4
54	D03131CS1	PA	0.213	12_Aug_224	0.0090	31	22,343.5	150.0	901.2
55	D0283612	OH	0.212	30_Jan_030	0.0105	22	41,431.8	182.9	1161.9
56	D02712C03	NC	0.211	16_Mar_075	0.0050	80	30,776.4	150.0	1260.3
57	D028667	OH	0.210	07_Mar_066	0.0093	26	33,601.3	259.1	1096.0
58	D03948C02	WV	0.203	18_Jan_018	0.0120	17	55,404.9	167.6	1146.5
59	D015732	MD	0.200	13_Mar_072	0.0058	65	30,788.0	213.4	983.0
60	D06250C05	NC	0.198	16_Mar_075	0.0045	90	27,395.0	243.8	1245.7
61	D060411	KY	0.194	29_Jan_029	0.0036	118	18,374.6	245.4	1431.4
62	D06166C02	IN	0.193	30_Jan_030	0.0075	49	51,708.4	304.8	1715.4
63	D024032	NJ	0.189	28_Jul_209	0.0088	34	18,785.1	152.1	621.5
64	D03407C15	TN	0.186	16_Mar_075	0.0032	128	37,307.5	152.4	1660.7
65	D028327	OH	0.179	30_Jan_030	0.0077	47	46,991.1	243.8	1482.6
66	D037976	VA	0.178	13_Mar_072	0.0080	44	40,569.8	127.7	1086.1
67	D015731	MD	0.177	13_Mar_072	0.0078	46	36,822.7	213.4	983.0
68	D03954CS0	WV	0.174	21_Nov_325	0.0036	116	20,129.5	225.9	1073.0
69	D007034LR	GA	0.172	29_Jan_029	0.0036	117	41,010.3	304.8	1818.3
70	D02864C01	OH	0.172	18_Jan_018	0.0077	48	35,193.0	259.1	1141.5
71	D007033LR	GA	0.170	29_Jan_029	0.0034	126	43,067.2	304.8	1818.3
72	D007032LR	GA	0.166	29_Jan_029	0.0029	140	37,288.5	304.8	1818.3
73	D01572C23	MD	0.163	16_Mar_075	0.0058	64	32,187.7	121.9	950.3
74	D028725	OH	0.160	29_Jan_029	0.0059	61	30,079.1	252.1	1223.4
75	D062641	WV	0.160	16_Mar_075	0.0067	53	42,757.1	335.3	1276.9
76	D013783	KY	0.157	06_Jan_006	0.0043	95	46,701.2	243.8	1749.4
77	D031782	PA	0.156	28_Jan_028	0.0059	63	16,483.5	307.2	988.9
78	D015074	ME	0.154	14_Aug_226	0.0030	136	1,170.0	128.3	166.6
79	D007031LR	GA	0.152	29_Jan_029	0.0030	137	38,520.3	304.8	1818.3
80	D00026CAN	AL	0.152	29_Jan_029	0.0012	287	33,723.4	150.0	1988.6
81	D00026CBN	AL	0.150	29_Jan_029	0.0012	300	35,099.1	121.9	1988.6
82	D027122	NC	0.147	16_Feb_047	0.0041	103	29,336.5	121.9	1260.3
83	D060182	KY	0.143	30_Jan_030	0.0025	160	12,083.1	198.1	1497.4
84	D02840C02	OH	0.143	18_Jan_018	0.0062	58	22,790.7	172.2	1207.3
85	D016261	MA	0.142	18_Jun_169	0.0067	52	3,430.0	132.6	294.2

Acadia National Park

RANK	CEMS Unit	STATE	24-HR Max Impact ~ µg/m^3	24Hr Date	Annual ~ µg/m^3	Annual Rank	2002 SO_2 Tons	Modeled StkHt Meters	Distance Kms
86	D03947C03	WV	0.141	07_Mar_066	0.0087	35	38,575.0	150.0	1145.8
87	D06170CS1	WI	0.141	29_Dec_363	0.0046	88	32,766.4	182.9	1591.1
88	D02712C04	NC	0.139	16_Mar_075	0.0035	123	22,961.7	150.0	1260.3
89	D027274	NC	0.137	16_Mar_075	0.0030	138	27,308.3	85.3	1448.0
90	D006021	MD	0.137	16_Mar_075	0.0046	87	20,013.7	211.8	892.8
91	D016263	MA	0.137	21_Jun_172	0.0085	38	4,970.6	132.6	294.2
92	D06705C02	IN	0.137	30_Jan_030	0.0033	127	27,895.4	121.9	1738.6
93	D01356C02	KY	0.137	30_Jan_030	0.0044	93	25,645.7	225.9	1519.5
94	D016138	MA	0.134	18_Jun_169	0.0065	55	4,376.3	73.8	374.2
95	D010012	IN	0.133	29_Dec_363	0.0041	102	26,015.5	152.4	1645.3
96	D03809CS0	VA	0.133	15_Sep_258	0.0041	101	21,219.4	98.8	1048.1
97	D02866C01	OH	0.132	29_Jan_029	0.0062	59	24,649.0	153.6	1096.0
98	D027215	NC	0.132	10_Nov_314	0.0021	196	19,145.2	152.4	1527.9
99	D006022	MD	0.132	13_Mar_072	0.0045	89	19,280.3	211.8	892.8
100	D027273	NC	0.131	16_Mar_075	0.0025	161	26,328.9	85.3	1448.0

Note: Top 100 Based on ranking of maximum 24-hr Sulfate Ion Impact

Table D-20b. Individual Unit Sulfate Ion Impact Summary: MM5 Meteorology

Brigantine National Wildlife Refuge

RANK	CEMS Unit	STATE	24-HR Max Impact ~ µg/m^3	24Hr Date	Annual ~ µg/m^3	Annual Rank	2002 SO_2 Tons	Modeled StkHt Meters	Distance Kms
1	D01571CE2	MD	0.920	23_Jun_174	0.0386	3	48,565.5	335.3	217.5
2	D023781	NJ	0.687	26_Aug_238	0.0219	22	9,746.6	144.8	25.1
3	D02876C01	OH	0.685	12_Aug_224	0.0348	5	72,592.9	243.8	660.7
4	D031361	PA	0.567	18_Jul_199	0.0451	1	87,434.3	243.8	435.2
5	D03179C01	PA	0.566	24_Jun_175	0.0429	2	79,635.0	150.0	468.3
6	D028404	OH	0.546	18_Jul_199	0.0383	4	87,801.2	245.4	636.0
7	D037976	VA	0.531	25_Nov_329	0.0320	8	40,569.8	127.7	343.0
8	D031362	PA	0.526	18_Jul_199	0.0339	7	62,846.8	243.8	435.2
9	D031403	PA	0.481	15_Jul_196	0.0256	15	38,800.9	269.1	203.1
10	D015732	MD	0.476	12_Aug_224	0.0267	12	30,788.0	213.4	249.5
11	D013783	KY	0.447	25_Mar_084	0.0110	61	46,701.2	243.8	1112.4
12	D01010C05	IN	0.445	19_Jul_200	0.0124	56	60,746.6	122.8	1106.0
13	D02872C04	OH	0.431	14_Mar_073	0.0340	6	83,133.5	150.0	616.7
14	D06113C03	IN	0.423	04_Feb_035	0.0128	47	71,181.7	150.0	1152.3
15	D01353C02	KY	0.408	12_Aug_224	0.0167	35	41,544.5	243.8	718.2
16	D015731	MD	0.406	12_Aug_224	0.0309	9	36,822.7	213.4	249.5
17	D03948C02	WV	0.402	13_Aug_225	0.0264	14	55,404.9	167.6	543.4
18	D080421	NC	0.400	02_Oct_275	0.0243	18	57,819.7	182.9	603.2
19	D03809CS0	VA	0.388	25_Nov_329	0.0199	25	21,219.4	98.8	304.0
20	D039431	WV	0.380	13_Aug_225	0.0234	19	42,385.1	167.6	466.6

Brigantine National Wildlife Refuge

RANK	CEMS Unit	STATE	24-HR Max Impact ~ µg/m^3	24Hr Date	Annual ~ µg/m^3	Annual Rank	2002 SO_2 Tons	Modeled StkHt Meters	Distance Kms
21	D031492	PA	0.376	06_Dec_340	0.0255	16	50,276.3	347.2	258.5
22	D039432	WV	0.369	13_Aug_225	0.0253	17	45,849.5	167.6	466.6
23	D081021	OH	0.368	01_Mar_060	0.0097	75	18,207.0	253.0	659.4
24	D03954CS0	WV	0.366	21_Jan_021	0.0093	76	20,129.5	225.9	413.0
25	D024032	NJ	0.358	30_Aug_242	0.0126	51	18,785.1	152.1	145.4
26	D031221	PA	0.357	15_Jul_196	0.0221	21	45,754.3	243.8	420.4
27	D03406C10	TN	0.351	25_Nov_329	0.0169	34	104,522.6	150.0	1214.5
28	D039353	WV	0.351	09_Jul_190	0.0199	26	42,211.5	274.9	643.2
29	D006022	MD	0.347	28_Jul_209	0.0164	37	19,280.3	211.8	181.5
30	D06166C02	IN	0.347	29_Dec_363	0.0126	52	51,708.4	304.8	1098.7
31	D028281	OH	0.343	24_Jun_175	0.0186	29	37,307.2	251.5	533.3
32	D080422	NC	0.338	02_Oct_275	0.0196	27	45,295.8	182.9	603.2
33	D082261	PA	0.338	18_Jul_199	0.0188	28	40,267.5	228.6	468.0
34	D067054	IN	0.332	29_Dec_363	0.0078	91	40,117.7	152.4	1124.2
35	D031491	PA	0.332	06_Dec_340	0.0298	10	60,241.6	347.2	258.5
36	D031132	PA	0.330	26_Aug_238	0.0125	53	14,293.8	121.9	168.4
37	D031222	PA	0.326	19_Mar_078	0.0280	11	55,216.4	243.8	420.4
38	D006021	MD	0.326	28_Jul_209	0.0170	33	20,013.7	211.8	181.5
39	D028501	OH	0.318	13_Aug_225	0.0116	59	30,798.1	213.4	798.8
40	D028502	OH	0.309	13_Aug_225	0.0106	67	28,698.3	213.4	798.8
41	D02549C01	NY	0.305	26_Nov_330	0.0092	78	25,342.5	150.0	538.0
42	D028667	OH	0.304	18_Jul_199	0.0163	38	33,601.3	259.1	536.7
43	D03935C02	WV	0.296	12_Aug_224	0.0265	13	63,065.5	274.3	643.2
44	D037975	VA	0.282	25_Nov_329	0.0165	36	19,619.6	61.0	343.0
45	D028504	OH	0.282	13_Aug_225	0.0103	69	27,343.1	213.4	798.8
46	D010012	IN	0.281	19_Jul_200	0.0067	110	26,015.5	152.4	1103.4
47	D01572C23	MD	0.275	24_Jun_175	0.0223	20	32,187.7	121.9	259.4
48	D0283612	OH	0.270	18_Jul_199	0.0130	46	41,431.8	182.9	677.8
49	D03140C12	PA	0.270	18_Aug_230	0.0205	23	29,735.6	259.1	203.1
50	D062641	WV	0.263	12_Aug_224	0.0203	24	42,757.1	335.3	643.3
51	D01355C03	KY	0.247	11_Jun_162	0.0123	57	38,103.8	150.0	905.4
52	D00988U4	IN	0.242	31_Jan_031	0.0132	45	45,062.0	122.8	891.5
53	D010011	IN	0.241	19_Jul_200	0.0064	117	28,876.3	152.4	1103.4
54	D027122	NC	0.241	31_Dec_365	0.0134	44	29,336.5	121.9	520.7
55	D03947C03	WV	0.233	13_Aug_225	0.0181	31	38,575.0	150.0	543.8
56	D028375	OH	0.231	19_Mar_078	0.0114	60	35,969.5	182.9	638.9
57	D02712C03	NC	0.230	31_Dec_365	0.0148	40	30,776.4	150.0	520.7
58	D07253C01	OH	0.228	13_Aug_225	0.0136	42	30,976.8	213.4	604.1
59	D028327	OH	0.221	28_Dec_362	0.0145	41	46,991.1	243.8	886.5
60	D024082	NJ	0.220	27_Aug_239	0.0087	84	5,674.9	99.1	82.6
61	D02864C01	OH	0.220	13_Aug_225	0.0173	32	35,193.0	259.1	542.5
62	D02554C03	NY	0.218	04_Jul_185	0.0124	54	30,151.1	150.0	528.6
63	D015521	MD	0.215	03_Sep_246	0.0185	30	17,782.4	107.6	164.4
64	D038093	VA	0.213	07_Feb_038	0.0090	81	10,476.9	149.1	304.0

Brigantine National Wildlife Refuge

RANK	CEMS Unit	STATE	24-HR Max Impact ~ µg/m^3	24Hr Date	Annual ~ µg/m^3	Annual Rank	2002 SO_2 Tons	Modeled StkHt Meters	Distance Kms
65	D016193	MA	0.213	21_Jul_202	0.0070	107	19,324.8	107.3	369.6
66	D060041	WV	0.211	13_Aug_225	0.0109	64	21,581.2	304.8	570.6
67	D060312	OH	0.211	13_Aug_225	0.0078	92	19,517.4	274.3	779.6
68	D015522	MD	0.209	03_Sep_246	0.0158	39	14,274.4	107.6	164.4
69	D005944	DE	0.208	23_Jun_174	0.0124	55	7,390.4	121.9	118.5
70	D028306	OH	0.207	31_Jan_031	0.0091	79	30,465.5	137.2	844.8
71	D03148C12	PA	0.203	26_Aug_238	0.0127	48	17,214.2	228.6	157.0
72	D028503	OH	0.201	29_Dec_363	0.0101	71	27,968.3	213.4	798.8
73	D01008C01	IN	0.198	29_Dec_363	0.0067	109	24,108.5	228.6	988.8
74	D007033LR	GA	0.195	26_May_146	0.0076	98	43,067.2	304.8	1099.1
75	D06705C02	IN	0.195	29_Dec_363	0.0051	135	27,895.4	121.9	1124.2
76	D000265	AL	0.195	02_Oct_275	0.0046	151	53,062.0	228.6	1271.8
77	D015543	MD	0.195	28_Jul_209	0.0099	72	10,084.1	109.7	181.6
78	D028725	OH	0.194	13_Aug_225	0.0134	43	30,079.1	252.1	616.7
79	D03131CS1	PA	0.194	06_Dec_340	0.0126	50	22,343.5	150.0	376.3
80	D01733C12	MI	0.191	28_Oct_301	0.0126	49	46,080.6	137.2	792.8
81	D013644	KY	0.191	29_Dec_363	0.0024	255	7,184.7	182.9	999.8
82	D031131	PA	0.190	26_Aug_238	0.0076	96	9,674.3	121.9	168.4
83	D027274	NC	0.189	28_Jan_028	0.0083	87	27,308.3	85.3	713.8
84	D005943	DE	0.188	23_Jun_174	0.0091	80	4,685.7	117.4	118.5
85	D03403C34	TN	0.186	29_Dec_363	0.0056	130	20,314.4	183.8	1035.6
86	D007034LR	GA	0.186	14_Mar_073	0.0075	99	41,010.3	304.8	1099.1
87	D027215	NC	0.184	14_Aug_226	0.0057	127	19,145.2	152.4	795.9
88	D060042	WV	0.184	13_Aug_225	0.0103	68	20,549.8	304.8	570.6
89	D007032LR	GA	0.184	29_Jan_029	0.0065	113	37,288.5	304.8	1099.1
90	D005935	DE	0.184	04_Aug_216	0.0045	157	2,137.6	83.8	121.2
91	D060412	KY	0.182	13_Aug_225	0.0077	94	20,491.0	245.7	808.2
92	D02866C02	OH	0.182	23_Oct_296	0.0109	65	26,022.4	153.6	536.7
93	D02866C01	OH	0.182	18_Jul_199	0.0109	63	24,649.0	153.6	536.7
94	D03298WL1	SC	0.174	27_May_147	0.0040	172	25,170.1	121.9	870.9
95	D024081	NJ	0.173	30_Aug_242	0.0093	77	8,075.5	99.1	82.6
96	D025163	NY	0.172	27_Aug_239	0.0042	166	7,359.0	182.9	186.4
97	D06113C04	IN	0.171	29_Dec_363	0.0050	139	27,847.9	213.4	1152.3
98	D01008C02	IN	0.170	29_Dec_363	0.0067	111	23,849.1	307.2	988.8
99	D023642	NH	0.168	31_Jan_031	0.0050	140	19,452.6	159.7	476.3
100	D0099070	IN	0.167	28_Dec_362	0.0071	106	29,800.8	172.2	1000.8

Note: Top 100 Based on ranking of maximum 24-hr Sulfate Ion Impact

Table D-20c. Individual Unit Sulfate Ion Impact Summary: MM5 Meteorology

Lye Brook Wilderness Area

RANK	CEMS Unit	STATE	24-HR Max Impact ~ µg/m^3	24Hr Date	Annual ~ µg/m^3	Annual Rank	2002 SO_2 Tons	Modeled StkHt Meters	Distance Kms
1	D031491	PA	0.744	14_Jul_195	0.0254	3	60,241.6	347.2	371.2
2	D028404	OH	0.719	12_Aug_224	0.0268	2	87,801.2	245.4	794.3
3	D031492	PA	0.708	14_Jul_195	0.0222	8	50,276.3	347.2	371.2
4	D03406C10	TN	0.663	30_Jan_030	0.0137	17	104,522.6	150.0	1464.9
5	D03179C01	PA	0.584	01_Oct_274	0.0253	4	79,635.0	150.0	671.2
6	D031361	PA	0.519	22_Jun_173	0.0363	1	87,434.3	243.8	580.4
7	D00988U4	IN	0.495	30_Jan_030	0.0100	36	45,062.0	122.8	1075.4
8	D031362	PA	0.441	22_Jun_173	0.0237	5	62,846.8	243.8	580.4
9	D03948C02	WV	0.419	12_Aug_224	0.0168	10	55,404.9	167.6	735.3
10	D080421	NC	0.398	15_Mar_074	0.0107	30	57,819.7	182.9	961.3
11	D03935C02	WV	0.391	01_Oct_274	0.0123	21	63,065.5	274.3	892.6
12	D028306	OH	0.377	29_Jan_029	0.0085	42	30,465.5	137.2	1038.2
13	D031222	PA	0.365	11_Aug_223	0.0229	7	55,216.4	243.8	579.5
14	D039432	WV	0.349	01_Oct_274	0.0139	15	45,849.5	167.6	680.3
15	D080422	NC	0.341	15_Mar_074	0.0086	41	45,295.8	182.9	961.3
16	D039431	WV	0.341	01_Oct_274	0.0128	19	42,385.1	167.6	680.3
17	D031221	PA	0.340	11_Aug_223	0.0192	9	45,754.3	243.8	579.5
18	D031403	PA	0.323	14_Jul_195	0.0124	20	38,800.9	269.1	448.1
19	D02872C04	OH	0.320	06_Jan_006	0.0236	6	83,133.5	150.0	811.7
20	D01571CE2	MD	0.309	26_Feb_057	0.0134	18	48,565.5	335.3	590.0
21	D02712C03	NC	0.304	15_Mar_074	0.0063	68	30,776.4	150.0	893.4
22	D06113C03	IN	0.301	29_Dec_363	0.0115	24	71,181.7	150.0	1335.3
23	D03954CS0	WV	0.289	01_Oct_274	0.0056	77	20,129.5	225.9	672.3
24	D028281	OH	0.288	12_Aug_224	0.0142	13	37,307.2	251.5	699.2
25	D03140C12	PA	0.280	14_Jul_195	0.0103	33	29,735.6	259.1	448.1
26	D01733C34	MI	0.278	30_Jan_030	0.0101	35	39,361.7	152.4	845.4
27	D02554C03	NY	0.270	09_Sep_252	0.0140	14	30,151.1	150.0	511.0
28	D023642	NH	0.269	22_Nov_326	0.0074	53	19,452.6	159.7	134.0
29	D0283612	OH	0.258	30_Jan_030	0.0145	12	41,431.8	182.9	752.7
30	D02876C01	OH	0.251	28_Jan_028	0.0138	16	72,592.9	243.8	884.7
31	D01010C05	IN	0.237	22_Jan_022	0.0108	29	60,746.6	122.8	1251.9
32	D03131CS1	PA	0.237	11_Aug_223	0.0107	31	22,343.5	150.0	489.3
33	D06166C02	IN	0.234	22_Jan_022	0.0093	38	51,708.4	304.8	1302.5
34	D037976	VA	0.233	19_Dec_353	0.0091	39	40,569.8	127.7	732.0
35	D028375	OH	0.230	28_Dec_362	0.0121	23	35,969.5	182.9	702.1
36	D082261	PA	0.230	24_Jan_024	0.0149	11	40,267.5	228.6	621.1
37	D06250C05	NC	0.230	15_Mar_074	0.0054	81	27,395.0	243.8	880.6
38	D000265	AL	0.226	29_Jan_029	0.0032	139	53,062.0	228.6	1592.7
39	D060182	KY	0.221	29_Jan_029	0.0035	129	12,083.1	198.1	1084.4
40	D024032	NJ	0.220	19_Sep_262	0.0054	80	18,785.1	152.1	276.9
41	D028667	OH	0.212	12_Aug_224	0.0122	22	33,601.3	259.1	683.1
42	D02549C01	NY	0.210	05_Aug_217	0.0113	26	25,342.5	150.0	470.4
43	D02832C06	OH	0.207	30_Jan_030	0.0058	75	23,694.3	213.4	1069.6

Lye Brook Wilderness Area

RANK	CEMS Unit	STATE	24-HR Max Impact ~ µg/m^3	24Hr Date	Annual ~ µg/m^3	Annual Rank	2002 SO_2 Tons	Modeled StkHt Meters	Distance Kms
44	D067054	IN	0.204	30_Jan_030	0.0061	70	40,117.7	152.4	1325.6
45	D01733C12	MI	0.196	22_Jul_203	0.0114	25	46,080.6	137.2	845.4
46	D00861C01	IL	0.194	07_Feb_038	0.0078	50	42,355.4	152.4	1428.1
47	D02712C04	NC	0.193	15_Mar_074	0.0044	103	22,961.7	150.0	893.4
48	D028327	OH	0.191	26_Jun_177	0.0101	34	46,991.1	243.8	1069.6
49	D02864C01	OH	0.189	12_Aug_224	0.0106	32	35,193.0	259.1	730.1
50	D01356C02	KY	0.185	29_Jan_029	0.0064	65	25,645.7	225.9	1106.6
51	D015732	MD	0.175	19_Dec_353	0.0073	54	30,788.0	213.4	620.3
52	D00983C01	IN	0.174	30_Jan_030	0.0047	90	19,922.4	150.0	1136.0
53	D00047C14	AL	0.171	29_Jan_029	0.0024	180	22,492.0	107.3	1568.0
54	D00983C02	IN	0.169	30_Jan_030	0.0046	96	18,130.8	153.6	1136.0
55	D013783	KY	0.168	06_Jan_006	0.0066	62	46,701.2	243.8	1337.1
56	D015731	MD	0.167	19_Dec_353	0.0098	37	36,822.7	213.4	620.3
57	D03947C03	WV	0.165	24_Jan_024	0.0113	27	38,575.0	150.0	734.6
58	D01384CS1	KY	0.165	28_Jan_028	0.0036	128	21,836.6	61.0	1183.6
59	D081021	OH	0.162	02_Mar_061	0.0040	113	18,207.0	253.0	882.6
60	D007034LR	GA	0.161	28_Jan_028	0.0041	110	41,010.3	304.8	1424.5
61	D007032LR	GA	0.159	28_Jan_028	0.0035	131	37,288.5	304.8	1424.5
62	D03809CS0	VA	0.158	15_Jan_015	0.0049	88	21,219.4	98.8	714.3
63	D007033LR	GA	0.156	28_Jan_028	0.0043	106	43,067.2	304.8	1424.5
64	D039353	WV	0.154	26_Jun_177	0.0077	51	42,211.5	274.9	892.6
65	D015991	MD	0.154	08_Mar_067	0.0029	151	13,014.0	151.8	262.7
66	D027274	NC	0.154	15_Mar_074	0.0040	115	27,308.3	85.3	1070.3
67	D03407C15	TN	0.153	09_Nov_313	0.0044	101	37,307.5	152.4	1258.5
68	D01355C03	KY	0.153	26_Jun_177	0.0072	55	38,103.8	150.0	1139.9
69	D01572C23	MD	0.152	15_Mar_074	0.0081	49	32,187.7	121.9	566.1
70	D02963C10	OK	0.150	29_Dec_363	0.0038	120	34,263.2	182.9	2050.3
71	D024804	NY	0.148	19_Sep_262	0.0045	97	7,719.9	72.5	187.7
72	D00008CAN	AL	0.148	29_Jan_029	0.0014	295	17,650.8	150.0	1673.7
73	D06113C04	IN	0.148	22_Jan_022	0.0047	91	27,847.9	213.4	1335.3
74	D015992	MD	0.147	08_Mar_067	0.0020	226	8,979.5	151.8	262.7
75	D027273	NC	0.147	15_Mar_074	0.0038	122	26,328.9	85.3	1070.3
76	D017459A	MI	0.145	09_Jul_190	0.0046	93	18,340.6	171.3	826.9
77	D062641	WV	0.144	01_Oct_274	0.0089	40	42,757.1	335.3	867.0
78	D02526C03	NY	0.144	20_Nov_324	0.0109	28	14,929.0	150.0	259.0
79	D016193	MA	0.144	18_Mar_077	0.0037	127	19,324.8	107.3	224.3
80	D025276	NY	0.142	13_Aug_225	0.0084	43	12,650.2	69.2	291.4
81	D02840C02	OH	0.142	12_Aug_224	0.0071	58	22,790.7	172.2	794.3
82	D03407C69	TN	0.141	09_Nov_313	0.0049	89	38,645.0	150.0	1258.5
83	D060041	WV	0.140	12_Aug_224	0.0072	56	21,581.2	304.8	785.8
84	D03148C12	PA	0.139	20_Sep_263	0.0068	59	17,214.2	228.6	307.7
85	D01353C02	KY	0.139	14_Aug_226	0.0074	52	41,544.5	243.8	967.9
86	D037975	VA	0.138	19_Dec_353	0.0046	94	19,619.6	61.0	732.0
87	D013782	KY	0.137	29_Jan_029	0.0035	130	20,244.8	182.9	1337.1

Lye Brook Wilderness Area

RANK	CEMS Unit	STATE	24-HR Max Impact ~ µg/m^3	24Hr Date	Annual ~ µg/m^3	Annual Rank	2002 SO_2 Tons	Modeled StkHt Meters	Distance Kms
88	D028504	OH	0.136	29_Jan_029	0.0063	67	27,343.1	213.4	1014.1
89	D00709C02	GA	0.135	10_Nov_314	0.0025	177	47,590.6	121.9	1411.5
90	D028725	OH	0.134	13_Aug_225	0.0081	48	30,079.1	252.1	811.7
91	D02642CS2	NY	0.132	26_Nov_330	0.0081	47	14,086.2	150.0	364.1
92	D02866C01	OH	0.131	12_Aug_224	0.0082	46	24,649.0	153.6	683.1
93	D031132	PA	0.129	19_Dec_353	0.0063	66	14,293.8	121.9	295.3
94	D027122	NC	0.127	15_Aug_227	0.0053	84	29,336.5	121.9	893.4
95	D06170CS1	WI	0.126	18_Jul_199	0.0066	63	32,766.4	182.9	1201.2
96	D06705C02	IN	0.124	30_Jan_030	0.0040	112	27,895.4	121.9	1325.6
97	D027215	NC	0.124	15_Aug_227	0.0020	221	19,145.2	152.4	1146.7
98	D028502	OH	0.120	29_Jan_029	0.0055	79	28,698.3	213.4	1014.1
99	D02549C02	NY	0.120	06_Dec_340	0.0053	83	12,317.4	150.0	470.4
100	D01008C01	IN	0.119	26_Jun_177	0.0040	116	24,108.5	228.6	1193.7

Note: Top 100 Based on ranking of maximum 24-hr Sulfate Ion Impact

Table D-20d. Individual Unit Sulfate Ion Impact Summary: MM5 Meteorology

Shenandoah National Park

RANK	CEMS Unit	STATE	24-HR Max Impact ~ µg/m^3	24Hr Date	Annual ~ µg/m^3	Annual Rank	2002 SO_2 Tons	Modeled StkHt Meters	Distance Kms
1	D039432	WV	1.505	02_Jan_002	0.0491	6	45,849.5	167.6	181.9
2	D02876C01	OH	1.100	12_Aug_224	0.0587	3	72,592.9	243.8	321.5
3	D080421	NC	1.077	21_Nov_325	0.0391	12	57,819.7	182.9	286.1
4	D080422	NC	1.020	21_Nov_325	0.0324	16	45,295.8	182.9	286.1
5	D03948C02	WV	0.896	25_Jun_176	0.0450	8	55,404.9	167.6	250.0
6	D03935C02	WV	0.785	14_Mar_073	0.0555	4	63,065.5	274.3	293.2
7	D028404	OH	0.764	19_Mar_078	0.0382	13	87,801.2	245.4	347.2
8	D02872C04	OH	0.738	23_Oct_296	0.0643	2	83,133.5	150.0	302.5
9	D062641	WV	0.734	27_Dec_361	0.0409	10	42,757.1	335.3	305.9
10	D03179C01	PA	0.688	31_Jan_031	0.0687	1	79,635.0	150.0	194.9
11	D028281	OH	0.685	17_Sep_260	0.0305	19	37,307.2	251.5	269.0
12	D03938C04	WV	0.681	14_Mar_073	0.0229	26	26,450.6	121.9	304.7
13	D031361	PA	0.671	03_Jan_003	0.0533	5	87,434.3	243.8	250.4
14	D031221	PA	0.640	04_Dec_338	0.0332	15	45,754.3	243.8	231.7
15	D031362	PA	0.635	03_Jan_003	0.0425	9	62,846.8	243.8	250.4
16	D015732	MD	0.630	24_Dec_358	0.0197	34	30,788.0	213.4	127.6
17	D015731	MD	0.623	24_Dec_358	0.0227	27	36,822.7	213.4	127.6
18	D02864C01	OH	0.623	25_Jun_176	0.0289	20	35,193.0	259.1	253.4
19	D031492	PA	0.590	02_Aug_214	0.0206	31	50,276.3	347.2	319.1
20	D039353	WV	0.580	14_Mar_073	0.0398	11	42,211.5	274.9	293.2
21	D031222	PA	0.579	04_Dec_338	0.0376	14	55,216.4	243.8	231.7

Shenandoah National Park

RANK	CEMS Unit	STATE	24-HR Max Impact ~ µg/m^3	24Hr Date	Annual ~ µg/m^3	Annual Rank	2002 SO_2 Tons	Modeled StkHt Meters	Distance Kms
22	D031491	PA	0.544	02_Aug_214	0.0224	29	60,241.6	347.2	319.1
23	D028667	OH	0.543	17_Sep_260	0.0220	30	33,601.3	259.1	290.5
24	D01572C23	MD	0.541	01_Sep_244	0.0254	24	32,187.7	121.9	112.9
25	D03406C10	TN	0.533	23_Aug_235	0.0257	23	104,522.6	150.0	856.7
26	D01353C02	KY	0.531	13_Aug_225	0.0272	21	41,544.5	243.8	365.0
27	D01571CE2	MD	0.508	05_Dec_339	0.0244	25	48,565.5	335.3	151.3
28	D039431	WV	0.507	25_Jun_176	0.0469	7	42,385.1	167.6	181.9
29	D03947C03	WV	0.505	25_Jun_176	0.0320	18	38,575.0	150.0	251.3
30	D007034LR	GA	0.479	25_Mar_084	0.0113	75	41,010.3	304.8	755.6
31	D082261	PA	0.474	12_Dec_346	0.0321	17	40,267.5	228.6	251.1
32	D03954CS0	WV	0.458	20_Jan_020	0.0192	36	20,129.5	225.9	103.7
33	D027122	NC	0.451	30_Dec_364	0.0176	39	29,336.5	121.9	232.4
34	D01355C03	KY	0.447	10_Jun_161	0.0175	41	38,103.8	150.0	551.8
35	D081021	OH	0.439	14_Mar_073	0.0170	45	18,207.0	253.0	320.7
36	D028327	OH	0.429	23_Oct_296	0.0195	35	46,991.1	243.8	552.3
37	D007033LR	GA	0.426	25_Mar_084	0.0107	77	43,067.2	304.8	755.6
38	D013783	KY	0.394	03_Sep_246	0.0130	65	46,701.2	243.8	758.2
39	D007032LR	GA	0.391	25_Mar_084	0.0101	82	37,288.5	304.8	755.6
40	D03407C15	TN	0.386	11_Aug_223	0.0125	68	37,307.5	152.4	609.4
41	D02712C03	NC	0.386	20_Sep_263	0.0187	38	30,776.4	150.0	232.4
42	D01733C12	MI	0.378	16_Jul_197	0.0152	55	46,080.6	137.2	557.4
43	D028501	OH	0.378	12_Aug_224	0.0170	44	30,798.1	213.4	454.6
44	D028502	OH	0.377	12_Aug_224	0.0166	47	28,698.3	213.4	454.6
45	D06166C02	IN	0.372	12_Aug_224	0.0159	52	51,708.4	304.8	749.9
46	D028282	OH	0.366	17_Sep_260	0.0166	48	20,598.2	251.5	269.0
47	D01733C34	MI	0.354	16_Jul_197	0.0123	70	39,361.7	152.4	557.4
48	D015521	MD	0.349	05_Dec_339	0.0068	111	17,782.4	107.6	199.1
49	D03407C69	TN	0.347	11_Aug_223	0.0127	66	38,645.0	150.0	609.4
50	D0283612	OH	0.347	16_Jul_197	0.0192	37	41,431.8	182.9	449.9
51	D031403	PA	0.343	31_Jan_031	0.0175	42	38,800.9	269.1	229.5
52	D01008C01	IN	0.343	12_Aug_224	0.0093	89	24,108.5	228.6	642.0
53	D038093	VA	0.342	26_Mar_085	0.0036	183	10,476.9	149.1	225.0
54	D00988U4	IN	0.340	18_Jul_199	0.0175	40	45,062.0	122.8	556.8
55	D07253C01	OH	0.335	23_Oct_296	0.0258	22	30,976.8	213.4	281.3
56	D03140C12	PA	0.335	31_Jan_031	0.0142	58	29,735.6	259.1	229.5
57	D006022	MD	0.335	27_Aug_239	0.0076	101	19,280.3	211.8	178.8
58	D028375	OH	0.330	26_Nov_330	0.0162	51	35,969.5	182.9	433.0
59	D028725	OH	0.328	23_Oct_296	0.0226	28	30,079.1	252.1	302.5
60	D006021	MD	0.323	27_Aug_239	0.0089	94	20,013.7	211.8	178.8
61	D028504	OH	0.319	12_Aug_224	0.0154	54	27,343.1	213.4	454.6
62	D02866C01	OH	0.305	26_Nov_330	0.0164	49	24,649.0	153.6	290.5
63	D01008C02	IN	0.305	12_Aug_224	0.0092	90	23,849.1	307.2	642.0

Shenandoah National Park

RANK	CEMS Unit	STATE	24-HR Max Impact ~ µg/m^3	24Hr Date	Annual ~ µg/m^3	Annual Rank	2002 SO_2 Tons	Modeled StkHt Meters	Distance Kms
64	D037976	VA	0.303	18_Sep_261	0.0167	46	40,569.8	127.7	156.0
65	D027274	NC	0.301	31_Dec_365	0.0142	59	27,308.3	85.3	393.2
66	D02866C02	OH	0.301	26_Nov_330	0.0174	43	26,022.4	153.6	290.5
67	D06250C05	NC	0.295	26_Mar_085	0.0146	56	27,395.0	243.8	224.3
68	D01010C05	IN	0.293	03_Nov_307	0.0131	64	60,746.6	122.8	779.6
69	D060041	WV	0.289	10_Jun_161	0.0205	33	21,581.2	304.8	249.8
70	D067054	IN	0.288	12_Aug_224	0.0085	97	40,117.7	152.4	775.6
71	D060312	OH	0.278	12_Aug_224	0.0122	71	19,517.4	274.3	436.2
72	D06113C03	IN	0.275	01_May_121	0.0132	63	71,181.7	150.0	809.0
73	D02712C04	NC	0.274	30_Dec_364	0.0138	61	22,961.7	150.0	232.4
74	D03396M1A	TN	0.268	11_Aug_223	0.0075	103	20,029.0	228.6	574.5
75	D060521	GA	0.268	25_Mar_084	0.0061	127	39,071.2	304.8	817.9
76	D060042	WV	0.267	10_Jun_161	0.0206	32	20,549.8	304.8	249.8
77	D027215	NC	0.256	26_May_146	0.0069	109	19,145.2	152.4	469.1
78	D027273	NC	0.254	31_Dec_365	0.0140	60	26,328.9	85.3	393.2
79	D02963C10	OK	0.254	29_Dec_363	0.0030	206	34,263.2	182.9	1530.7
80	D02866M6A	OH	0.248	17_Sep_260	0.0137	62	19,563.8	304.8	290.5
81	D015543	MD	0.247	05_Dec_339	0.0058	133	10,084.1	109.7	178.7
82	D000265	AL	0.245	02_Oct_275	0.0067	112	53,062.0	228.6	927.0
83	D037964	VA	0.245	30_Dec_364	0.0094	88	8,098.0	61.0	90.9
84	D03936C02	WV	0.243	13_Aug_225	0.0162	50	15,480.4	304.8	261.2
85	D01356C02	KY	0.243	09_Jul_190	0.0107	76	25,645.7	225.9	570.4
86	D037975	VA	0.243	10_Feb_041	0.0084	98	19,619.6	61.0	156.0
87	D060522	GA	0.238	25_Mar_084	0.0046	150	34,085.1	304.8	817.9
88	D00709C02	GA	0.236	25_Mar_084	0.0076	102	47,590.6	121.9	734.0
89	D038044	VA	0.231	21_Apr_111	0.0072	107	10,451.1	46.9	99.9
90	D00050C16	AL	0.230	11_Aug_223	0.0065	121	24,977.3	304.8	763.9
91	D02840C02	OH	0.225	19_Mar_078	0.0124	69	22,790.7	172.2	347.2
92	D02554C03	NY	0.225	07_Jan_007	0.0106	78	30,151.1	150.0	445.6
93	D03405C12	TN	0.221	28_Jan_028	0.0081	100	14,994.6	150.0	463.0
94	D028665	OH	0.219	17_Sep_260	0.0144	57	19,796.4	304.8	290.5
95	D027121	NC	0.216	30_Dec_364	0.0066	116	12,030.9	121.9	232.4
96	D081022	OH	0.213	14_Mar_073	0.0095	87	12,333.4	253.0	320.7
97	D0393851	WV	0.211	27_Dec_361	0.0104	80	12,947.7	183.8	304.7
98	D028503	OH	0.209	06_Feb_037	0.0159	53	27,968.3	213.4	454.6
99	D028306	OH	0.202	19_Mar_078	0.0126	67	30,465.5	137.2	508.1
100	D03775C02	VA	0.197	14_Mar_073	0.0115	74	16,673.8	307.2	373.2

Note: Top 100 Based on ranking of maximum 24-hr Sulfate Ion Impact

Table D-21a. State Total Annual Average Sulfate Ion Impact Summary: MM5 Meteorology, Acadia

	SO_4 Ion Impact (Annual Average)				Percent of Total Modeled			
STATE	CEM PT (2002)	Non-CEM PT (2002)	Area/ Mobile (2002)	TOTAL	CEM PT (2002)	Non-CEM PT (2002)	Area/ Mobile (2002)	TOTAL
MA	0.2248	0.0457	0.0055	0.2759	10.36%	2.10%	0.25%	12.71%
OH	0.0865	0.0086	0.0016	0.0966	3.98%	0.40%	0.07%	4.45%
PA	0.2354	0.0214	0.0156	0.2725	10.85%	0.99%	0.72%	12.55%
NY	0.0554	0.0057	0.0019	0.0630	2.55%	0.26%	0.09%	2.90%
IN	0.1089	0.0119	0.0099	0.1307	5.02%	0.55%	0.46%	6.02%
WV	0.0632	0.0038	0.0069	0.0740	2.91%	0.18%	0.32%	3.41%
MI	0.0389	0.0081	0.0029	0.0499	1.79%	0.37%	0.14%	2.30%
NH	0.0780	0.0062	0.0040	0.0882	3.59%	0.29%	0.18%	4.06%
KY	0.0286	0.0076	0.0031	0.0393	1.32%	0.35%	0.14%	1.81%
IL	0.0656	0.0095	0.0093	0.0844	3.02%	0.44%	0.43%	3.89%
NC	0.0259	0.0009	0.0019	0.0287	1.19%	0.04%	0.09%	1.32%
MD	0.0486	0.0172	0.0034	0.0693	2.24%	0.79%	0.16%	3.19%
ME	0.0736	0.0363	0.0578	0.1677	3.39%	1.67%	2.66%	7.73%
VA	0.0139	0.0009	0.0011	0.0159	0.64%	0.04%	0.05%	0.73%
TN	0.0254	0.0085	0.0019	0.0358	1.17%	0.39%	0.09%	1.65%
MO	0.0134	0.0036	0.0012	0.0182	0.62%	0.17%	0.05%	0.84%
WI	0.0215	0.0115	0.0041	0.0371	0.99%	0.53%	0.19%	1.71%
NJ	0.0149	0.0120	0.0030	0.0299	0.69%	0.55%	0.14%	1.38%
IA	0.0093	0.0109	0.0018	0.0219	0.43%	0.50%	0.08%	1.01%
GA*	0.0187	0.0033	0.0133	0.0354	0.86%	0.15%	0.61%	1.63%
DE	0.0107	0.0022	0.0023	0.0151	0.49%	0.10%	0.10%	0.70%
SC	0.0054	0.0020	0.0010	0.0083	0.25%	0.09%	0.05%	0.38%
KS*	0.0071	0.0015	0.0006	0.0092	0.33%	0.07%	0.03%	0.42%
AL*	0.0137	0.0012	0.0010	0.0159	0.63%	0.06%	0.05%	0.73%
CT	0.0860	0.1544	0.0773	0.3176	3.96%	7.11%	3.56%	14.64%
MN	0.0028	0	0.0009	0.0037	0.13%	0%	0.04%	0.17%
OK*	0	0.0009	0.0012	0.0021	0%	0.04%	0.06%	0.10%
AR*	0.0012	2.8E-05	0.0009	0.0022	0.06%	0.00%	0.04%	0.10%
RI	0	0.0002	0.0002	0.0004	0%	0.01%	0.01%	0.02%
NE*	0.0074	0.0011	0.0072	0.0156	0.34%	0.05%	0.33%	0.72%
VT	0.0666	0.0020	0.0065	0.0750	3.07%	0.09%	0.30%	3.46%
SD*	0.0001	0.0001	0.0003	0.0005	0.00%	0.01%	0.01%	0.02%
ND*	0.0030	0.0356	0.0236	0.0622	0.14%	1.64%	1.09%	2.87%
DC	5.9E-06	0.0007	0.0043	0.0050	0.00%	0.03%	0.20%	0.23%
MS*	4.0E-06	0.0004	0.0026	0.0030	0.00%	0.02%	0.12%	0.14%
TX*	1.1E-05	0	2.3E-05	3.5E-05	0.00%	0%	0.00%	0.00%
Total	**1.454**	**0.436**	**0.280**	**2.170**	**67.0%**	**20.1%**	**12.9%**	**100.0%**

Note: States sorted by annual average SO_4 Ion Impact (2002 CEMs)

* indicates a state that was only partially included in the domain

Table D-21b. State Total Annual Average Sulfate Ion Impact Summary: MM5 Meteorology, Brigantine

STATE	SO_4 Ion Impact (Annual Average)				Percent of Total Modeled			
	CEM PT (2002)	Non-CEM PT (2002)	Area/ Mobile (2002)	TOTAL	CEM PT (2002)	Non-CEM PT (2002)	Area/ Mobile (2002)	TOTAL
PA	0.4297	0.0836	0.0088	0.5221	12.31%	2.40%	0.25%	14.96%
OH	0.2340	0.0202	0.0046	0.2588	6.70%	0.58%	0.13%	7.42%
WV	0.4407	0.0553	0.0461	0.5421	12.63%	1.58%	1.32%	15.53%
MD	0.1609	0.0160	0.0054	0.1823	4.61%	0.46%	0.16%	5.22%
VA	0.1632	0.0162	0.0128	0.1921	4.67%	0.46%	0.37%	5.50%
IN	0.1285	0.0076	0.0135	0.1496	3.68%	0.22%	0.39%	4.29%
NY	0.1577	0.0331	0.0119	0.2027	4.52%	0.95%	0.34%	5.81%
NC	0.2191	0.0228	0.0210	0.2630	6.28%	0.65%	0.60%	7.54%
NJ	0.0630	0.0188	0.0061	0.0879	1.81%	0.54%	0.18%	2.52%
KY	0.0810	0.0110	0.0120	0.1040	2.32%	0.32%	0.34%	2.98%
DE	0.0672	0.0024	0.0057	0.0753	1.93%	0.07%	0.16%	2.16%
MI	0.0535	0.0190	0.0043	0.0768	1.53%	0.54%	0.12%	2.20%
TN	0.0810	0.0307	0.0779	0.1896	2.32%	0.88%	2.23%	5.43%
MA	0.0304	0.0017	0.0020	0.0341	0.87%	0.05%	0.06%	0.98%
IL	0.0315	0.0106	0.0026	0.0447	0.90%	0.30%	0.07%	1.28%
GA*	0.0341	0.0101	0.0032	0.0475	0.98%	0.29%	0.09%	1.36%
SC	0.0202	0.0108	0.0036	0.0346	0.58%	0.31%	0.10%	0.99%
WI	0.0152	0.0137	0.0032	0.0321	0.44%	0.39%	0.09%	0.92%
MO	0.0524	0.0549	0.0138	0.1211	1.50%	1.57%	0.39%	3.47%
AL*	0.0625	0.0124	0.0805	0.1553	1.79%	0.35%	2.31%	4.45%
IA	0.0114	0.0025	0.0027	0.0166	0.33%	0.07%	0.08%	0.48%
MN	0.0088	0.0032	0.0017	0.0137	0.25%	0.09%	0.05%	0.39%
AR*	0.0077	0.0014	0.0007	0.0098	0.22%	0.04%	0.02%	0.28%
KS*	0.0107	0.0009	0.0008	0.0124	0.31%	0.03%	0.02%	0.35%
CT	0.0234	0.0406	0.0168	0.0808	0.67%	1.16%	0.48%	2.31%
NH	0.0025	0	0.0009	0.0035	0.07%	0%	0.03%	0.10%
OK*	0	0.0011	0.0015	0.0026	0%	0.03%	0.04%	0.07%
NE*	0.0012	3.4E-05	0.0012	0.0024	0.03%	0.00%	0.03%	0.07%
DC	0	0.0006	0.0005	0.0012	0%	0.02%	0.01%	0.03%
ME	0.0044	0.0009	0.0063	0.0116	0.12%	0.03%	0.18%	0.33%
ND*	0.0100	0.0003	0.0010	0.0113	0.29%	0.01%	0.03%	0.32%
SD*	0.0012	0.0005	0.0013	0.0030	0.04%	0.01%	0.04%	0.09%
RI	0.0002	0.0017	0.0011	0.0030	0.01%	0.05%	0.03%	0.09%
MS*	2.1E-06	0.0003	0.0016	0.0019	0.00%	0.01%	0.05%	0.05%
VT	1.5E-06	0.0001	0.0006	0.0008	0.00%	0.00%	0.02%	0.02%
TX*	2.5E-07	0	2.9E-05	3.0E-05	0.00%	0%	0.00%	0.00%
Total	**2.607**	**0.505**	**0.378**	**3.490**	**74.7%**	**14.5%**	**10.8%**	**100.0%**

Note: States sorted by annual average SO_4 Ion Impact (2002 CEMs)

* indicates a state that was only partially included in the domain

Table D-21c. State Total Annual Average Sulfate Ion Impact Summary: MM5 Meteorology, Lye Brook

STATE	SO_4 Ion Impact (Annual Average)				Percent of Total Modeled			
	CEM PT (2002)	Non-CEM PT (2002)	Area/ Mobile (2002)	TOTAL	CEM PT (2002)	Non-CEM PT (2002)	Area/ Mobile (2002)	TOTAL
OH	0.2963	0.0649	0.0078	0.3690	13.05%	2.86%	0.34%	16.25%
PA	0.1232	0.0121	0.0023	0.1375	5.43%	0.53%	0.10%	6.06%
NY	0.3050	0.0288	0.0219	0.3558	13.43%	1.27%	0.96%	15.67%
IN	0.0680	0.0058	0.0022	0.0760	2.99%	0.26%	0.10%	3.35%
WV	0.1369	0.0148	0.0128	0.1645	6.03%	0.65%	0.56%	7.24%
MI	0.0820	0.0047	0.0099	0.0967	3.61%	0.21%	0.44%	4.26%
KY	0.0454	0.0104	0.0037	0.0596	2.00%	0.46%	0.16%	2.62%
IL	0.0686	0.0088	0.0052	0.0826	3.02%	0.39%	0.23%	3.64%
MD	0.0407	0.0098	0.0042	0.0546	1.79%	0.43%	0.19%	2.41%
NC	0.0798	0.0121	0.0120	0.1039	3.51%	0.53%	0.53%	4.58%
MA	0.0351	0.0012	0.0029	0.0392	1.55%	0.05%	0.13%	1.73%
VA	0.0550	0.0208	0.0047	0.0805	2.42%	0.92%	0.21%	3.54%
TN	0.0985	0.0613	0.0842	0.2440	4.34%	2.70%	3.71%	10.75%
WI	0.0209	0.0013	0.0015	0.0238	0.92%	0.06%	0.07%	1.05%
MO	0.0351	0.0116	0.0028	0.0495	1.54%	0.51%	0.13%	2.18%
GA*	0.0133	0.0040	0.0014	0.0187	0.59%	0.18%	0.06%	0.82%
IA	0.0253	0.0140	0.0052	0.0445	1.11%	0.62%	0.23%	1.96%
NJ	0.0184	0.0158	0.0041	0.0383	0.81%	0.69%	0.18%	1.69%
AL*	0.0076	0.0123	0.0020	0.0219	0.33%	0.54%	0.09%	0.97%
DE	0.0128	0.0029	0.0115	0.0272	0.57%	0.13%	0.51%	1.20%
MN	0.0147	0.0031	0.0035	0.0213	0.65%	0.14%	0.15%	0.94%
KS*	0.0072	0.0029	0.0015	0.0116	0.32%	0.13%	0.07%	0.51%
SC	0.0097	0.0020	0.0009	0.0127	0.43%	0.09%	0.04%	0.56%
NH	0.0167	0.0016	0.0013	0.0195	0.73%	0.07%	0.06%	0.86%
OK*	0.0161	0.0291	0.0203	0.0655	0.71%	1.28%	0.89%	2.88%
AR*	0.0032	0	0.0012	0.0044	0.14%	0%	0.05%	0.19%
VT	0	0.0014	0.0020	0.0035	0%	0.06%	0.09%	0.15%
CT	0.0017	4.3E-05	0.0014	0.0031	0.07%	0.00%	0.06%	0.14%
NE*	0	0.0006	0.0004	0.0011	0%	0.03%	0.02%	0.05%
ME	0.0024	0.0006	0.0045	0.0075	0.11%	0.03%	0.20%	0.33%
ND*	0.0137	0.0008	0.0023	0.0167	0.60%	0.04%	0.10%	0.74%
SD*	0.0001	0.0002	0.0004	0.0006	0.00%	0.01%	0.02%	0.03%
RI	0.0003	0.0024	0.0018	0.0044	0.01%	0.10%	0.08%	0.19%
MS*	1.4E-06	0.0002	0.0010	0.0012	0.00%	0.01%	0.04%	0.05%
DC	4.0E-06	0.0017	0.0083	0.0100	0.00%	0.07%	0.36%	0.44%
TX*	8.4E-06	0	3.2E-05	4.0E-05	0.00%	0%	0.00%	0.00%
Total	**1.654**	**0.364**	**0.253**	**2.271**	**72.8%**	**16.0%**	**11.1%**	**100.0%**

Note: States sorted by annual average SO_4 Ion Impact (2002 CEMs)

* indicates a state that was only partially included in the domain

Table D-21d. State Total Annual Average Sulfate Ion Impact Summary: MM5 Meteorology, Shenandoah National Park

STATE	SO_4 Ion Impact (Annual Average)				Percent of Total Modeled			
	CEM PT (2002)	Non-CEM PT (2002)	Area/ Mobile (2002)	TOTAL	CEM PT (2002)	Non-CEM PT (2002)	Area/ Mobile (2002)	TOTAL
OH	0.6483	0.1088	0.0114	0.7685	17.70%	2.97%	0.31%	20.99%
WV	0.4657	0.0402	0.0111	0.5170	12.72%	1.10%	0.30%	14.12%
PA	0.4517	0.0318	0.0247	0.5082	12.33%	0.87%	0.68%	13.88%
NC	0.2257	0.0148	0.0062	0.2467	6.16%	0.40%	0.17%	6.74%
IN	0.1907	0.0181	0.0155	0.2243	5.21%	0.49%	0.42%	6.13%
KY	0.1741	0.0106	0.0184	0.2031	4.75%	0.29%	0.50%	5.55%
VA	0.1124	0.0469	0.0263	0.1856	3.07%	1.28%	0.72%	5.07%
MD	0.1365	0.0373	0.0109	0.1847	3.73%	1.02%	0.30%	5.04%
TN	0.0929	0.0304	0.0086	0.1319	2.54%	0.83%	0.24%	3.60%
MI	0.0860	0.0100	0.0125	0.1085	2.35%	0.27%	0.34%	2.96%
GA*	0.0963	0.0032	0.0079	0.1073	2.63%	0.09%	0.21%	2.93%
IL	0.0561	0.0189	0.0045	0.0794	1.53%	0.52%	0.12%	2.17%
NY	0.0468	0.0141	0.0167	0.0776	1.28%	0.39%	0.46%	2.12%
AL*	0.0504	0.0029	0.0034	0.0567	1.38%	0.08%	0.09%	1.55%
WI	0.0289	0.0096	0.0026	0.0410	0.79%	0.26%	0.07%	1.12%
SC	0.0232	0.0093	0.0035	0.0359	0.63%	0.25%	0.09%	0.98%
MO	0.0180	0.0104	0.0034	0.0318	0.49%	0.28%	0.09%	0.87%
IA	0.0152	0.0130	0.0036	0.0318	0.42%	0.35%	0.10%	0.87%
DE	0.0086	0.0136	0.0021	0.0243	0.24%	0.37%	0.06%	0.66%
NJ	0.0119	0.0022	0.0071	0.0212	0.33%	0.06%	0.19%	0.58%
MN	0.0109	0.0023	0.0028	0.0160	0.30%	0.06%	0.08%	0.44%
AR*	0.0087	0.0035	0.0019	0.0141	0.24%	0.10%	0.05%	0.39%
OK*	0.0081	0.0016	0.0009	0.0105	0.22%	0.04%	0.02%	0.29%
KS*	0.0091	0.0007	0.0006	0.0104	0.25%	0.02%	0.02%	0.28%
MA	0.0029	0.0047	0.0023	0.0098	0.08%	0.13%	0.06%	0.27%
NE*	0.0023	0	0.0009	0.0032	0.06%	0%	0.02%	0.09%
ND*	0	0.0011	0.0016	0.0027	0%	0.03%	0.04%	0.07%
SD*	0.0011	4.0E-05	0.0014	0.0025	0.03%	0.00%	0.04%	0.07%
MS*	0	0.0010	0.0007	0.0017	0%	0.03%	0.02%	0.05%
CT	0.0007	0.0001	0.0009	0.0017	0.02%	0.00%	0.02%	0.05%
NH	0.0013	0.0001	0.0002	0.0016	0.04%	0.00%	0.00%	0.04%
DC	0.0001	0.0003	0.0009	0.0013	0.00%	0.01%	0.03%	0.04%
ME	2.8E-05	0.0003	0.0002	0.0006	0.00%	0.01%	0.01%	0.02%
RI	3.1E-07	2.9E-05	0.0002	0.0002	0.00%	0.00%	0.00%	0.01%
VT	3.6E-07	2.6E-05	0.0001	0.0002	0.00%	0.00%	0.00%	0.00%
TX*	1.7E-07	0	3.2E-05	3.2E-05	0.00%	0%	0.00%	0.00%
Total	**2.985**	**0.462**	**0.216**	**3.662**	**81.5%**	**12.6%**	**5.9%**	**100.0%**

Note: States sorted by annual average SO_4 Ion Impact (2002 CEMs)

* indicates a state that was only partially included in the domain

D.4. CALPUFF Phase I Modeling Results Overview

Previous sections have described in some detail the results of CALPUFF modeling of sulfate ion impacts at receptor locations, including IMPROVE and CASNET sites, in the northeast U.S. These results have been presented and discussed for two different modeling platforms, namely, the VTDEC/rawinsonde platform and the DNR-MDE/MM5 platform. A limited number of comparisons were provided comparing nitrate ion predictions to measurements at both IMPROVE and CASTNET sites.

Table D-22 and Table D-23 address the comparability between the results created by the two platforms. Table D-22 displays the rank of each state included in the modeling, based on annual averages, for the two platforms, and also shows the difference in the ranking. These differences show fairly close comparability between the two platforms, with only a small number of exceptions. Differences in ranking for the states with the highest total impacts are smaller than differences for states that have smaller total impacts.

Table D-23 shows how the two platforms compare on the basis of 24-hr maximum predicted sulfate ion concentrations. This table is divided into three parts, representing comparability of the top 10, top 50, and top 100 EGUs respectively. The average concentration at each Class I area for these three groups is displayed, along with the number of "common" units between the two platforms, i.e. the number of units within the group that is in that group for both platforms. For the top 10 units, a significant percentage (from 3 at Acadia to 7 at Lye Brook) are identified by both platforms. For the top 50 and 100 units, comparability is much better: 32 out of 50 at Lye Brook to 36 out of 50 at Brigantine, and 70 out of 100 at Brigantine to 85 out of 100 at Shenandoah. This comparability is an improvement over the same metrics presented in the Phase I report. Overall, reasonably good comparability has been demonstrated between the two platforms.

Several conclusions can be drawn from this Phase II CALPUFF modeling.

- The meteorological data for both platforms appears to be well-represented, based on comparisons that were made to profiler and other available data for comparison. Sensitivity tests conducted by VTDEC of selected choices aided in choosing the best options within CALMET.
- The results for both platforms showed an ability to predict the highest 24-hour sulfate ion concentrations reasonably well, although an examination of the top 24-hour rankings by VTDEC indicated that underprediction occurred for many days out of the year. Annual averages were underpredicted by both platforms. In contrast to the Phase I results, the DNR-MD/MM5 platform predicted generally higher sulfate concentrations than the VTDEC platform. The DNR-MDE/MM5 results showed a tendency to predict high sulfate concentrations in the wintertime, which is not consistent with observations.
- Sensitivity tests conducted by VTDEC suggested that the default chemistry transformation scheme in CALPUFF may not produce enough sulfate, and the lack of a complete aqueous phase transformation within the CALPUFF scheme may contribute to the underprediction.

- Particulate nitrate ion concentrations predicted by the DNR-MDE/MM5 platform overpredicted measured concentrations substantially. When total nitrate (particulate nitrate plus nitric acid) predicted concentrations are compared to measurements at CASTNET sites, some overprediction is still evident but to a much lesser degree than for particulate nitrate. This result indicates the importance of applying an ammonia-limiting technique, such as implemented in the POSTUTIL program, if particulate nitrate is an important factor in visibility impacts.
- The two model platforms show good comparability for sulfate ion predictions, which indicates a degree of robustness in CALPUFF's ability to simulate this important component of visibility impairment in the northeast U.S.
- Although some issues (sulfate transformation, wintertime sulfate, ammonia-limiting conditions) need to be investigated further, CALPUFF has shown a reasonably good capability to reproduce sulfate ion concentrations in the northeast U.S. This evaluation of the model using two different meteorological platforms and comparing predictions to observations should provide further support for its use in assessing visibility impacts in the MANE-VU region, particularly when used to complement the use of other modeling and analysis tools.

Table D-22. CALPUFF Overall Modeling Summary

State	Rawinsonde-Based Meteorology				MM5-Based Meteorology				Differences in Ranking			
	Shen	Brig	Acad	LyeB	Shen	Brig	Acad	LyeB	Shen	Brig	Acad	LyeB
OH	1	2	2	1	1	2	2	2	0	0	0	-1
WV	2	3	6	5	3	5	7	6	-1	-2	-1	-1
PA	3	1	3	2	2	1	1	1	1	0	2	1
NC	4	8	11	10	4	4	13	10	0	4	-2	0
IN	5	6	5	4	5	8	5	4	0	-2	0	0
KY	6	10	9	7	7	10	10	7	-1	0	-1	0
VA	7	5	14	12	6	3	14	13	1	2	0	-1
MD	8	4	12	9	8	6	12	11	0	-2	0	-2
TN	9	13	15	13	9	13	16	14	0	0	-1	-1
MI	10	12	7	6	11	12	6	5	-1	0	1	1
GA*	11	16	20	16	10	14	20	16	1	2	0	0
IL	12	15	10	8	12	11	9	8	0	4	1	0
NY	13	7	4	3	15	7	4	3	-2	0	0	0
AL*	14	20	24	19	13	19	26	20	1	1	-2	-1
WI	15	18	17	14	14	17	15	9	1	1	2	5
SC	16	17	22	23	16	16	24	22	0	1	-2	1
MO	17	19	16	15	18	22	21	19	-1	-3	-5	-4
IA	18	21	19	17	17	20	18	15	1	1	1	2
DE	19	11	21	20	21	15	25	26	-2	-4	-4	-6

State	Rawinsonde-Based Meteorology				MM5-Based Meteorology				Differences in Ranking			
	Shen	Brig	Acad	LyeB	Shen	Brig	Acad	LyeB	Shen	Brig	Acad	LyeB
NJ	20	9	18	18	20	9	17	21	0	0	1	-3
MN	21	22	26	21	19	21	23	18	2	1	3	3
AR*	22	23	28	26	24	27	30	28	-2	-4	-2	-2
OK*	23	27	27	25	23	26	29	25	0	1	-2	0
KS*	24	24	23	22	22	24	27	23	2	0	-4	-1
MA	25	14	1	11	25	18	3	17	0	-4	-2	-6
NE*	26	28	30	29	26	31	31	30	0	-3	-1	-1
SD*	27	31	32	31	31	33	32	31	-4	-2	0	0
MS*	28	33	34	33	29	34	34	33	-1	-1	0	0
CT	29	25	25	28	27	23	22	27	2	2	3	1
NH	30	26	8	24	30	25	11	24	0	1	-3	0
DC	31	29	33	34	28	32	33	34	3	-3	0	0
ME	32	30	13	30	32	29	8	29	0	1	5	1
RI	33	32	29	32	34	28	28	32	-1	4	1	0
VT	34	34	31	27	33	30	19	12	1	4	12	15
TX*	35	35	35	35	35	35	35	35	0	0	0	0

Note: State Ranking: Annual Average SO_4 Ion Concentration

Table D-23. CALPUFF Overall Modeling Summary

Top 10

	NWS	MM5	Number in Common
Shenandoah	0.778	0.931	6
Brigantine	0.471	0.598	5
Acadia	0.414	0.540	3
Lye Brook	0.588	0.569	7

Top 50

	NWS	MM5	Number in Common
Shenandoah	0.483	0.578	35
Brigantine	0.318	0.397	36
Acadia	0.245	0.350	32
Lye Brook	0.310	0.324	32

Top 100

	NWS	MM5	Number in Common
Shenandoah	0.361	0.424	85
Brigantine	0.242	0.299	70
Acadia	0.185	0.257	78
Lye Brook	0.218	0.235	76

Note: Averages of EGU 2002 CEMS (24-hr SO_4 Ion Concentrations)

References

NESCAUM, "2002: A Year in Review," Northeast States for Coordinated Air Use Management, Boston, MA, December, 2004.

NWS, National weather service guidance method can be found at this website: http://www.srh.weather.gov/bmx/tables/rh.html, 2006.

Scire, J. et al., A User's guide for the CALMET Meteorological Model (version 5), Earth Tech, Inc., 196 Baker Avenue, Concord, MA, January 2000.

USEPA, CALPUFF Modeling System, Available at: http://www.epa.gov/ttn/scram, 2006.

USEPA, Inter-agency Working Group on Air Quality Modeling (IWAQM) Phase II report, U.S. Environmental Protection Agency, Research Triangle Park, NC, 1998.

Abstract

Title of Document:	A CHEMICAL CLIMATOLOGY OF LOWER TROPOSPHERIC TRACE GASES AND AEROSOLS OVER THE MID-ATLANTIC REGION
	Jennifer Carrie Hains, Doctor of Philosophy, 2007
Directed By:	Professor Russell R. Dickerson, Department of Atmospheric and Oceanic Science

Ozone and aerosols affect air quality, visibility and human health. The University of Maryland research aircraft conducted flights over the Mid-Atlantic region between 1995 and 2005 to characterize pollution events. I developed a chemical climatology of trace gases and aerosols that can be used to validate and improve models. O_3 and SO_2 measured aboard the aircraft were compared with O_3 and SO_2 generated with the Community Multiscale Air Quality (CMAQ). In general, CMAQ under-estimates O_3 above 500 m and over-estimates O_3 below 500 m (possible reasons for this include chemistry not being properly represented in the model). A sensitivity test of the rate of photolysis of NO_2 was performed and improving the photochemistry did improve the modeled O_3. CMAQ over-predicts the SO_2 column content by about 50%, possibly because the model gives SO_2 too long a lifetime. To test this theory I developed a method for calculating the SO_2 lifetime using *in-situ* measurements. The mean SO_2 lifetime was 19 ± 7 hours for measurements made in the daytime in the summer in the Mid-Atlantic region with in-

cloud processes responsible for ~80% of the removal. I made comparisons of three aerosol sampling systems and found the uncertainty of $PM_{2.5}$, sulfate, and ammonium measured with the Speciation Trends Network is larger than what has been reported and is at least 20%. I have developed clustering methodologies to group back trajectories associated with aircraft profiles as well as group trace gas and aerosol profiles by size and shape. The first clustering method produced eight distinct meteorological regimes associated with pollution and haze events. I quantified the amount of O_3 transported for each meteorological regime. Using the second method, I found a strong correlation between O_3 profiles and point source NOx emissions. The comparisons of model and measured profiles, comparisons of surface measurements, and clustering methods are used to explain sources, sinks and distributions of trace gases and aerosols in the mid-Atlantic thus improving the understanding of the lower atmospheric composition in this area.

A CHEMICAL CLIMATOLOGY OF LOWER TROPOSPHERIC TRACE GASES AND AEROSOLS OVER THE MID-ATLANTIC REGION

By

Jennifer Carrie Hains

Dissertation submitted to the Faculty of the Graduate School of the
University of Maryland, College Park, in partial fulfillment
of the requirements for the degree of
Doctor of Philosophy
2007

Advisory Committee:

Professor Russell R. Dickerson, Chair
Professor Neil Blough
Professor Douglas English
Professor John M. Ondov
Professor Robert Hudson

Dedication

To Julie, Peter, Brendan, Miss Elisabeth and Cindy Rollo. Thank you for all of your love and support.

Acknowledgements

Funding for this work was provided in part by the Maryland Department of the Environment and Constellation Energy Group, Baltimore Gas and Electric Company and Potomac Electric Power Company through the Electric Power Research Institute and Maryland Industrial Partnership. Work related to GOME was supported by the University of Bremen. Special thanks to Russell Dickerson for infinite patience and inspiring creativity. Also many thanks to Brett Taubman, Jeff Stehr, Lung-Wen Chen, Charles Piety and Lackson Marufu for great ideas and support. Many thanks to Dale Allen the IDL master. Also many thanks to Bruce Doddridge, Mian Chin, Andreas Richter, Annette Ladstätter-Weißenmayer, John Burrows, Anne Thompson, Peter Mueller, Robert Hudson, Tad Aburn, Diane Franks, Matthew Seybold, David Krask, Can Li, Pedro Bueno, Zahra Chaudry, Bryan Bloomer, and Rob Levy.

Table of Contents

List of Tables

List of Figures

Chapter 5

Chapter 6.

Appendix A.

Appendix B

Chapter 1: Introduction

1.1 Background

Numerous locations in the Mid-Atlantic US do not comply with National Ambient Air Quality Standards (NAAQS) for O_3 (80 ppb eight hour standard, formerly 120 ppb one hour standard) and $PM_{2.5}$ (15 $\mu g/m^3$ annual average standard and 35 $\mu g/m^3$ daily average standard). Figures1 and 2 show counties in the Mid-Atlantic that violate the NAAQS eight hour O_3 standard and the annual $PM_{2.5}$ air quality standards.

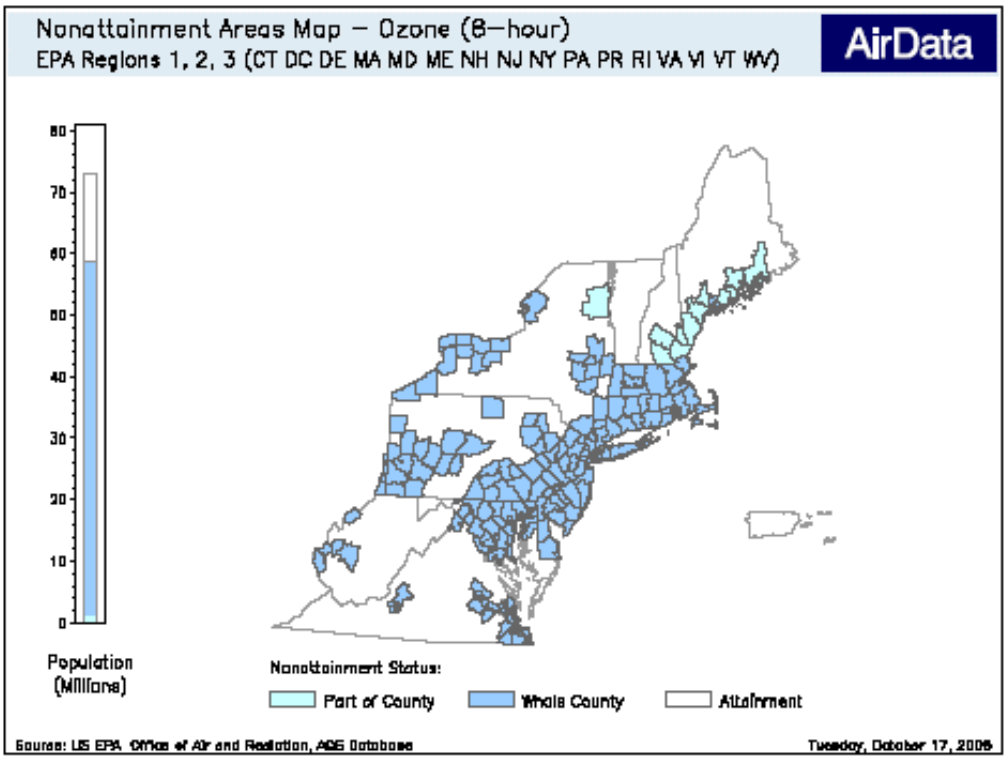

Figure 1. Counties in the Mid-Atlantic Region out of compliance with NAAQS 8-hr O_3 standards.

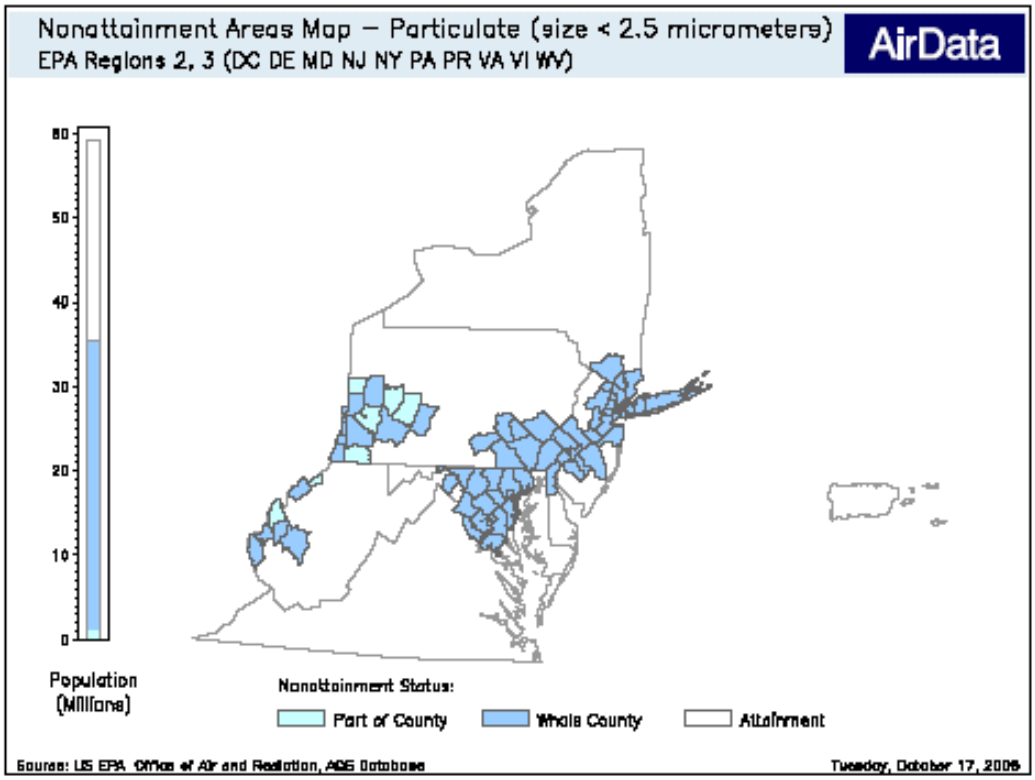

Figure 2. Counties in the Mid-Atlantic Region out of compliance with NAAQS annual $PM_{2.5}$ standards.

Asthma hospitalizations (Buchdahl et al., 2000; White et al., 1994; Wong et al., 2001), reduced lung function in children (Frischer et al., 1999; Gauderman et al., 2002) and acute myocardial infarcation (Ruidavets et al., 2005) have been associated with exposure to large O_3 concentrations. Fine particulate matter ($PM_{2.5}$ with an aerodynamic diameter ≤ 2.5 μm) alters the radiative balance of the Earth, decreases visibility and acts as cloud condensation nuclei (CCN). Increases in the CCN concentration can impact the global climate (IPCC, 2001). These increases in CCN lead to smaller cloud droplets which make clouds brighter and more reflective. Recent studies (Laden et al., 2000; Schwartz and Neas, 2000; Peters et al, 2001a)

have shown that elevated levels of $PM_{2.5}$ are associated with cardiovascular and respiratory problems and even increased mortality rates. SO_2 is a major precursor of fine particulate matter in the Mid-Atlantic region of the United States and accounts for 30-60% of $PM_{2.5}$ mass (Chen et al., 2002; Malm et al., 2004; Rees et al., 2004; Schwab et al., 2004; Frank et al., 2006; Ondov et al., 2006).

1.2 Chemical Transport Models

Models are used to predict pollution events and can be used in regulatory measures (such as when to issue warnings to the public to not drive, pump gas, paint, run electrical appliances, etc.) in order to reduce the pollution impact on the area. To achieve good predictions, accurate initial conditions are needed. A chemical climatology of the vertical and horizontal distribution of trace gases and aerosols can be used to improve model initial conditions and determine how well models generate these three-dimensional distributions.

The Community Multiscale Air Quality (CMAQ) system was developed by the EPA to improve predictions of pollution events associated with O_3, $PM_{2.5}$ and reactive nitrogen species. The CMAQ modeling system incorporates outputs from meteorological modeling systems and emissions databases into a chemical transport model. Hogrefe et al. (2004) describe comparisons between O_3 surface measurements and CMAQ model results for 5 years of data (1993-1997) in the Eastern US. They found that CMAQ tends to overestimate small values of one and eight –hour maximum O_3, and underestimate large values of 1-hr maximum O_3. They also found that CMAQ captures the higher eight-hr maximum O_3. Tesche et al. (2006) compared daily CMAQ sulfate with surface measurements made using six

different networks in the United States in 2002. They found that the monthly averages of daily CMAQ simulations overestimated sulfate in the summer and fall and underestimate sulfate in the winter and spring with a fractional bias ≤ 30%. I found the opposite, in summary, CMAQ overestimates SO_2 (and likely underestimates sulfate) when compared with aircraft profiles (presented in Chapter 5). Levy (2007) found that CMAQ underestimates $PM_{2.5}$ in Maryland. Because sulfate accounts for 30-60% of $PM_{2.5}$ (Chen et al., 2002; Malm et al., 2004; Rees et al., 2004; Schwab et al., 2004; Frank et al., 2006;Ondov et al., 2006) it is likely that CMAQ underestimates sulfate. Mueller et al. (2006) also found that CMAQ underestimates sulfate. Mueller et al. (2006) found that CMAQ consistently underestimates cloud cover for model simulations in summertime episodes of 1992, 1993 and 1995 in the Eastern US. They also compared surface SO_2 and sulfate measurements to CMAQ model results and they found that CMAQ typically over-estimated SO_2 and underestimated sulfate. They concluded that this is likely because CMAQ does not properly account for in-cloud oxidation of SO_2.

The Georgia Tech/ Goddard Global Ozone Chemistry Aerosol Radiation and Transport (GOCART) model was developed to simulate the atmospheric sulfur cycle (Chin et al., 2000a). Chin et al., (2000b) compared daily surface measurements of SO_2 in the US and Europe with GOCART simulations for 1989 and 1990. They found that GOCART was able to capture daily variations in SO_2 and sulfate, but the model overestimates SO_2 in the summer (by more than a factor of two) and underestimates measured maximum sulfate for the US.

1.3 Meteorology Associated with Elevated O_3

Understanding the relationship between meteorology and pollution events can improve forecasting of these events. In the Mid-Atlantic region voluntary measures such as car-pooling, public transportation, refueling after dark, and limiting electrical usage are encouraged on days when pollution events are predicted. These measures can help reduce pollution levels and their effectiveness is determined in part by how well pollution levels can be predicted. Elevated levels of O_3 are generally associated with high pressure systems and weak winds (Vukoich, 1994). Vukovich et al. (1999) and Ryan et al. (1998) found that larger O_3 levels are generally associated with areas with high pressure systems just above the surface as well as high pressure systems to the west or northwest. These high pressure systems are generally associated with little cloud cover, weak winds, subsidence and low-level inversions that allow for local O_3 accumulation. These conditions are also conducive for transport of O_3 and O_3 pre-cursors from the industrialized Mid-West. Vukovich et al. (1999) found that the most O_3 exceedences occur in July. These O_3 exceedences can be reduced if energy saving programs are implemented during this time period. The development of a chemical climatology and determination of meteorological conditions associated with pollution events can aid in the improvement of model predictions and forecasting these events as well as improve the understanding of transport over source regions.

1.4 O_3 Chemistry

O_3 is formed from oxides of nitrogen (NOx) and volatile organic compounds (VOC). O_3 is produced by the following reaction of NO_2 and light

$$NO_2 + h\nu\ (\lambda < 430\ nm) \rightarrow NO + O \quad (1)$$

$$O + O_2 + M \rightarrow O_3 + M \quad (2)$$

However, the NO formed in Reaction 1, readily reacts with O_3 to form NO_2 as shown below:

$$NO + O_3 \rightarrow NO_2 + O_2 \quad (3)$$

This results in a steady state between O_3 and NO_2. O_3 production is driven by reactions with the hydroxyl radical (OH) and organic compounds that provide a sink for NO, shown in equations 4-7 below:

$$OH + RCH_2R + O_2 \rightarrow H_2O + RCOOHR \quad (4)$$

$$RCOOHR + NO \rightarrow NO_2 + RCHOR \quad (5)$$

$$RCHOR + O_2 \rightarrow RCOR + HO_2 \quad (6)$$

$$HO_2 + NO \rightarrow NO_2 + OH \quad (7)$$

Here R represents a portion of the organic compound C_nH_m, where n and m are integers. The major sources of OH include photodissociation of O_3.

$$O_3 + h\nu\ (\lambda > 340nm) \rightarrow O(^1D) + O_2 \quad (8)$$

$$O(^1D) + H_2O \rightarrow 2OH \quad (9)$$

In polluted areas, sources can include photodissociation of nitrous acid (HONO) and hydrogen peroxide (H_2O_2). The reaction between the hydroperoxyl radical (HO_2) and NO can also form OH. Sources of NOx (NO and NO_2) in the United States include transportation (56% for 2002, EPA, 2003) and fuel combustion (37% for 2002, EPA,

2003). Though the sources of NOx are generally at or near the surface the peak in O_3 production does not occur at the surface because the amount of light needed for NO_2 photodissociation increases with altitude (Kelley et al., 1995, Taubman et al., 2004a).

1.5 SO_2 Chemistry

Annual emissions of SO_2 for 2000 in the US were 1.65 x 10^7 kg (EPA, 2003). Fuel combustion accounted for 86%, industrial processes accounted for 9% and transportation sources accounted for 5%. SO_2 is the pre-cursor for most sulfate; Rees et al.(2004) found that sulfate accounts for 38% of $PM_{2.5}$ annually in Pittsburgh, PA, Frank et al. (2006) found that sulfate accounts for 44-53% of $PM_{2.5}$ annually in Bronx, NY, Schwab et al. (2004) found that sulfate accounts an average of 30% of $PM_{2.5}$ in the summer, at six sites in NY; Ondov et al. (2006) found sulfate accounts for 32-40% of $PM_{2.5}$ mass in Baltimore, MD, and Malm et al. (2004) found it accounts for 50-60% of $PM_{2.5,}$ and Chen et al.(2002) found it accounts for 35% of $PM_{2.5}$. SO_2 is a short lived species that is oxidized quickly with the OH radical to form sulfate; other loss processes include dry and wet deposition. The reaction with OH proceeds as follows:

$$OH^{\cdot} + SO_2 + M \rightarrow HOSO_2 + M \quad (10)$$

$$HOSO_2 + O_2 \rightarrow HO_2 + SO_3 \quad (11)$$

When sufficient water vapor is available, SO_3 is converted to H_2SO_4

$$SO_3 + H_2O + M \rightarrow H_2SO_4 + M \quad (12)$$

Typical atmospheric concentrations of OH give rise to an atmospheric lifetime for SO_2 of about a week. Seinfeld and Pandis (1998) suggest that by accounting for a typical dry deposition velocity of 1 cm s^{-1} and a boundary layer of 1km, the lifetime

of SO_2 is about one day. I have found that the lifetime of SO_2 is 19 ± 7 hours (presented in Chapter 5) for the Mid-Atlantic for summertime and daytime conditions. The oxidation of SO_2 with OH (determined from CMAQ) accounts for about 11% of SO_2 removal. This lifetime was determined from profiles made when fair weather cumulus clouds were common. The reaction between SO_2 and aqueous H_2O_2 (found in fair weather cumulus clouds) also account for a significant amount of SO_2 oxidation. Using the calculated SO_2 lifetime (presented in Chapter 5) and assuming OH and H_2O_2 contribute significantly to the SO_2 loss, it appears that the Seinfeld and Pandis (1998) theoretical estimate of SO_2 dry deposition velocity is too fast for the Mid-Atlantic in the summer during daylight hours.

Global model calculations have shown the SO_2 lifetime to vary from, 0.6 – 2.6 days (Pham *et al*., 1995; Chin *et al*., 1996; Rested *et al*., 1998; Koch *et al*., 1999; Roelofs *et al*., 1998; Berglen *et al*., 2004). SO_2 in the gas phase can also dissolve in water to form the following species depending on the pH:

$$SO_2 + H_2O \rightarrow SO_2 \cdot H_2O \quad (13)$$

$$SO_2 \cdot H_2O \rightarrow HSO_3^- + H^+ \quad (14)$$

$$HSO_3^- \leftarrow \rightarrow H^+ + SO_3^{2-} \quad (15)$$

Here the bisulfite (HSO_3^-) form is most often produced at a pH of 2-6, common for atmospheric droplets. SO_2 can also be oxidized by H_2O_2 in clouds and fogs at a pH less than 4.5 (Finlayson-Pitts and Pitts, 2000).

$$HSO_3^- + H_2O_2 \leftarrow \rightarrow SO_2OOH^- + H_2O \quad (16)$$

$$SO_2OOH^- + H^+ \rightarrow H_2SO_4 \quad (17)$$

Edgerton et al. (2006) measured hourly SO_2, sulfate and other trace gases and aerosols at surface stations in the Southeast US in early spring 2002 (as part of the Southeastern Aerosol Research and Characterization Study, SEARCH). Using back trajectories and pollutant ratios they calculated SO_2 to sulfate conversion rates in SO_2 plumes (generally from coal-fired power plants, in the first 10 hours of transit time from the source) corresponding to an e-folding lifetime of 500- 40 hours.

1.6 Determination of Meteorological Influences on Pollution Episodes: Clustering Back Trajectories

In order to effectively reduce pollution, major sources and meteorological conditions associated with pollution events need to be accurately determined. Clustering, a statistical technique to group data in space has been used to assess the impacts of emissions and meteorology on pollutant concentrations at receptor sites. This technique has been employed to group back trajectories into different meteorological regimes (Moody and Galloway, 1988; Dorling *et al*., 1992a; Dorling *et al*., 1992b; Lee *et al*., 1994; Moy *et al*., 1994; Dorling and Davies, 1995; Moody *et al*., 1995; Harris and Oltmans, 1997; Brankov *et al*., 1998; Moody *et al*., 1998; Cape *et al*., 2000; Eneroth *et al*., 2003; Berto *et al*., 2004; Jorba et al., 2004; Russell *et al*., 2004). The clustered back trajectories can then be used to determine source regions and synoptic regimes that support the regional transport of different atmospheric constituents. The studies listed above differ mainly in methods used to calculate the trajectories and the different techniques used to cluster the trajectories.

A major limitation of the published studies cited above arises from the fact that all of the receptor sites were surface-based. This restricts the amount of

information available on regional transport and the influences of lower atmospheric dynamics on the pollution measured at the surface. Eneroth et al. (2003) and Jorba *et al*. (2004) clustered trajectories at multiple altitudes to better describe the general circulation patterns in the troposphere, but the measurements were still fixed at the surface. Taubman et al. (2006) improved upon the previous studies by using similar statistical techniques to analyze several years of data collected from aircraft.

Aircraft provide a horizontally and vertically mobile sampling platform. The horizontal mobility allows for deployment to specific areas of interest, while the vertical mobility provides insight into boundary layer dynamics, and allows for measurements representative of a larger area. The ability to deploy to specific locations enables the investigation of multi-day haze and O_3 episodes, the influences of regionally transported pollution on urban and rural areas as well as the impacts large metropolitan areas have on Mid-Atlantic air quality. The vertical profile information presents a more complete picture of the composition and dynamics of the lower atmosphere, and this allows for the investigation of factors influencing the transport and chemical transformations of air pollutants and their precursors. Specifically, the nocturnal emissions from elevated sources and transport of pollution in the residual layer can be calculated from vertical profiles taken before the stable, nocturnal boundary layer has eroded and the pollution mixed down to the surface. The identification of transported pollution allows for a more accurate assessment of the effects of mixed layer development on surface pollution as well as local emissions and photochemical production.

The Regional Atmospheric Measurement Modeling and Prediction Program (RAMMPP) (http://www.atmos.umd.edu/~RAMMPP/) was formed to address problems with air pollution over the Mid-Atlantic US. To perform long term air quality studies and analyze tran-boundary pollution transport RAMMPP uses – measurements (ground-based and airborne), chemical transport modeling (Models-3/CMAQ), meso-scale modeling (MM5), and air quality forecasting. The airborne measurements have been conducted by the University of Maryland since 1992 with an instrumented light aircraft outfitted for atmospheric research. The aim of the aircraft analyses thus far has been to answer specific questions regarding lower atmospheric CO (Dickerson *et al*., 1995; Doddridge *et al*., 1998), pollutant transport and boundary layer dynamics during individual, Mid-Atlantic haze and O_3 episodes (Ryan *et al*., 1998; Taubman *et al*., 2004a), and the air quality and radiative impacts of smoke in the Mid-Atlantic from Canadian forest fires (Taubman *et al*., 2004b). Additionally, a fortuitous experiment demonstrated the regional air quality benefits of the 2003 North American blackout (Marufu *et al*., 2004). In Chapter 3 a chemical climatology of trace gases and aerosols (some of which was published in Taubman et al., 2006) that answers some of the overarching questions not yet addressed by these case studies will be presented.

Typical clustering analyses clustered back trajectories ending at a single location. However, there were limited individual locations over which enough flights were performed to provide statistical meaning using this typical analysis. Furthermore, narrowly focusing on a few locations would fail to take advantage of the regional coverage offered by the dataset. For these reasons I have developed a novel

approach to clustering the data using multiple spatially heterogeneous receptor locations (presented in Taubman et al., 2006). Ozone events have long been identified as regional in nature with variability expected on scales of hundreds of km (Logan, 1985), so the use of multiple receptor locations is justified. I modified the standard distance calculation to account for spatial variability in the cluster algorithm. A detailed description of the methods is presented in Chapter 3. The statistical analysis of vertical profiles that I have developed is inherently different from analyses of single measurements at surface-based receptor sites. Using these techniques we were able to quantify the impacts of source regions and transport patterns on Mid-Atlantic air quality.

The measurements from this study overlap in time with those from the Mid-Atlantic EPA Supersites in Baltimore, New York, and Pittsburgh. Because of the regional nature of the study, the results presented in Chapter 3 will complement the investigations from those sites, aiding in measurement comparisons, model validation, and understanding the processes that control regional pollutant transport to and between the individual sites. The analyses should also be useful for air quality forecasting and modeling of pollution episodes as well as pollution control strategies.

1.7 Determining the influence of Point Source on Pollution Episodes: Clustering species profiles

Methods that clarify the influence of meteorology and emissions on the vertical distribution of trace gases and aerosols can improve modeling and prediction of pollution events. I developed a method for clustering vertical profiles of trace gases and aerosols to group distinct profile shapes that may be associated with

different meteorological patterns or various transport regimes. This complements the previous section that clustered back trajectories and then formed associated trace gas and aerosol profiles. Many previous studies (Dorling *et al*., 1992a; Dorling *et al*., 1992b; Lee *et al*., 1994; Moy *et al*., 1994; Dorling and Davies, 1995; Moody *et al*., 1995; Harris and Oltmans, 1997; Brankov *et al*., 1998; Moody *et al*., 1998; Cape *et al*., 2000; Eneroth *et al*., 2003; Berto *et al*., 2004; Jorba *et al*., 2004; Russell *et al*., 2004, Taubman *et al*., 2006) were devoted to clustering back trajectories to describe meteorological patterns associated with different trace gas and aerosol values. Moy *et al*. (1994), Brankov *et al*. (1998), and Taubman *et al*. (2006) were able to use back trajectory clusters to describe meteorological patterns associated with smog events. The converse of this method, clustering by O_3 profiles to identify different transport patterns, has been applied to ozonesonde and aircraft data (Diab *et al*., 2003; Diab *et al*., 2004, Colette *et al*., 2005 a; Colette *et al*., 2005 b).

Models used to predict O_3 and $PM_{2.5}$ levels have limited ability to describe lower tropospheric transport within the planetary boundary layer (Seigneur, 2001; Mebust *et al*., 2003; Zhang *et al*., 2004; Hodzic, *et al*., 2005). There is inadequate information on the planetary boundary layer distribution of trace gases and aerosols to improve the models. The University of Maryland has conducted summertime aircraft measurement campaigns since 1993 to gain a better understanding of the chemistry and dynamics of the lower troposphere including (Dickerson et al., 1995; Doddridge et al., 1998; Ryan et al., 1998; Taubman et al., 2004a; 2004b; 2006). Species measured aboard the University of Maryland research aircraft include O_3, SO_2, CO, particle light absorption at 565 nm, and total particle scattering at 450, 550, and 700

nm. I have clustered vertical profiles of the species by shape and absolute value to improve understanding of meteorological and emissions influences on trace gases and aerosols in the lower troposphere.

Taubman *et al*. (2006) grouped 48 hr back trajectories associated with 550 of the University of Maryland profiles into eight distinct meteorological regimes and used these clusters of back trajectories to describe differences among morning and afternoon profiles of O_3, SO_2, CO, particle scattering, Ångström exponent (α) calculated from the 450/700 nm ratio of particle scattering, and particle absorption. In Chapter 4, I will introduce a method for clustering these same profiles by their shape and magnitude (mixing ratio and scattering and absorption coefficients). This allows for separation of profiles based on small-scale structure and these differences may be ascribable to other factors such as emissions. The characterization of the planetary boundary layer and the lower free tropospheric composition of trace gases and aerosols can be used to evaluate and improve chemical transport modeling of these species, and aid in the forecasting of pollution events. It can also improve understanding of the relationship between the meteorology and chemistry of the lower troposphere.

1.8 Surface Measurements

The EPA has developed a Speciation Trends Network (STN) which has measured aerosols at the surface for 54 sites in the US since 1999. Precise measurements are critical for $PM_{2.5}$ source apportionment tasks based on chemical mass balance and/or multivariate receptor models (Hopke, 1984; Watson et al., 1984; Kim and Hopke, 2005; Kim et al., 2005; Ogulei et al., 2005).

NAAQS calls for the use of a Federal Reference Method, FRM, (Code of Federal Regulations (CFR), 1997) for the measurement of filter-based gravimetric $PM_{2.5}$ mass to determine compliance. However, other sampling and analytical protocols have been used extensively in air quality monitoring projects, such as the Speciation Trends Network –STN (US EPA, 1999), the Interagency Monitoring and Protective Visual Environment network –IMPROVE (Malm et al., 1994; Ames et al., 2001; Malm et al., 2002; 2004; 2005) and the California Regional $PM_{10}/PM_{2.5}$ air quality study (Chow et al., 2006). Equivalence of $PM_{2.5}$ mass determined with different protocols is currently under evaluation (Peters et al., 2001b; Watson and Chow, 2002; Solomon et al., 2003; Chow et al., 2005a). A FRM for $PM_{2.5}$ speciation has not yet been established by the United States Environmental Protection Agency.

I collected $PM_{2.5}$ samples during the 2002 intensive sampling periods at Fort Meade, Maryland (FME). I have used the samples to evaluate the STN speciation samplers and filter analyses under typical and elevated $PM_{2.5}$ events. FME, a suburban site located in the Baltimore-Washington urban corridor, approximately 3 km east of the Baltimore-Washington Parkway (I-295) and 10 km east of Interstate 95, was the anchor site for the Maryland Aerosol Characterization (MARCH-Atlantic) study (Chen et al., 2002) and part of the nationwide Speciation Trends Network (STN). It also served as one of the satellite sites for the Baltimore Supersite experiment during 2001 – 2003 (Lake et al., 2003; Harrison et al., 2004; Lee et al., 2005a; Ogulei et al., 2005; Park et al., 2005a; Park et al., 2005b; Ondov et al., 2006). Previous studies indicate that FME observations often reflect regional haze episodes and local accumulation under stagnant conditions. The annual mean $PM_{2.5}$

concentration at FME is around 13 $\mu g/m^3$, and is influenced by local and regional sulfate, wood smoke, industry, mobile sources and secondary nitrate (Chen et al., 2001; 2002; 2003).

During January and July 2002, $PM_{2.5}$ speciation monitors from two different protocols (Speciation Trends Network-STN and Desert Research Institute-DRI) were installed at FME to concurrently measure atmospheric aerosol on a 24-h basis. Two Sequential Filter Samplers (SFS, Desert Research Institute, Reno, NV) from DRI were deployed in both January and July, while a Reference Ambient Air Sampler (RAAS $PM_{2.5}$, Thermo Scientific, Waltham, MA) and a Met One Speciation Air Sampling System (SASS, Met One Instruments Inc., Grants Pass, OR) represented the STN operation in January and July, respectively. The change of STN sampling systems (from January to July) was made with the understanding that both samplers had been equally approved by EPA for the STN application (US EPA, 1999). However their performances are not the same with respect to the DRI sampler. The SFS samples were analyzed by DRI and the RAAS and SASS samples were analyzed at the Research Triangle Institute (RTI, Research Triangle Park, NC) using methods described in Chow et al. (1996) and US EPA (1999). I will refer to the SFS samplers as DRI_F and the RAAS and SASS samplers as STN_R and STN_S (STN_{RS} denotes both instruments) hereafter. Components quantified by both DRI and RTI include gravimetric $PM_{2.5}$ mass, 35 trace elements, elemental carbon (EC), organic carbon (OC), total carbon (TC), and water soluble ions such as sulfate, nitrate and ammonium. DRI and RTI often used different techniques and instruments for the

analyses. Continuous measurements of $PM_{2.5}$ mass were made in July with a Tapered Element Oscillating Microbalance (TEOM 1400a, Thermo Scientific, Waltham, MA).

Field performance of the STN_R and performance of the STN_{RS} size-selective inlet was assessed during the early stage of STN_{RS} development (Peters et al., 2001b, 2001c), but up-to-date evaluations of the STN_{RS} speciation data under real-world operation are rather limited. I will compare the STN_{RS} data from FME with collocated DRI measurements and investigate the $PM_{2.5}$ chemical composition and mass closure within the context of uncertainty analysis. Approaches and conclusions presented in Chapter 6 can be tested in other studies facilitating a weight of evidence approach (e.g., Burton et al., 2002; Weed, 2005) to improve the design of ambient $PM_{2.5}$ networks. The objective and results of this study are coordinated with others in the region including Lee et al., (2005a, 2005b), Flanagan et al., (2006) and the EPA-sponsored Eastern Supersites program (Solomon et al., 2003; Rees et al., 2004; Ondov et al., 2006).

1.9 Overview

The chemical climatology was developed with 10 years of summertime measurements of trace gases and aerosols made aboard the UMD research aircraft. Chapter 2 will provide specifics on instrumentation used aboard the aircraft. Most flights were made in the Mid-Atlantic region and Chapter 2 will present locations and times when flights were made.

An introduction to the chemical climatology with statistics of trace gas and aerosol measurements will be presented in Chapter 3. Diurnal variations in measurements will also be discussed. I performed a cluster analysis of back

trajectories associated with the aircraft flights in order to describe different meteorological regimes associated with the profiles. Results from this cluster analysis will be presented in Chapter 3, and some results from this Chapter were published in Taubman et al. (2006). The typical flight pattern consisted of flying upwind of pollution centers in the morning and downwind of the centers in the afternoon. This allowed for quantification of transported lower tropospheric O_3. A description of how transported O_3 was calculated and which meteorological regimes were associated with the most transport is presented in Chapter 3.

I developed of a methodology to cluster profiles of trace gases and aerosols to separate extreme events and to better understand meteorological and point source influences on aircraft profiles. This clustering methodology is presented in Chapter 4 along with the relationship between trace gas and aerosol profiles with point source emissions of SO_2 and NOx.

To better understand how well models predict trace gases in the Mid-Atlantic I have compared O_3, SO_2, and CO with a regional model (CMAQ) presented in Chapter 5. I have also compared aircraft measured SO_2 with a global model (GOCART). The SO_2 column content generated from CMAQ and GOCART was 50% larger than that measured aboard the University of Maryland aircraft. As described in Chapter 4 the SO_2 profiles were not well correlated with SO_2 emissions encountered along a 48 hour back trajectory. These findings support the hypothesis that the lifetime of SO_2 in the Mid-Atlantic region in the summer is less than 48 hours. I developed a method for calculating the SO_2 lifetime using the UMD research

aircraft profiles and the EPA's SO_2 emissions database. This lifetime calculation is presented in Chapter 5.

In 2002 I collected surface filter samples of aerosols with two different American sampling systems. Comparisons of surface $PM_{2.5}$ measurements made and the uncertainties associated with the sampling systems will be presented in Chapter 6. A summary of the research and recommendations for future work will be presented in Chapter 7.

Chapter 2: Sampling Platform and Instrumentation

2.1 Introduction

The chemical climatology was developed with 10 years of aircraft measurements of trace gases and aerosols. These measurements were made aboard the UMD research aircraft, mostly in the Mid-Atlantic region during regional haze and O_3 episodes. This Chapter will give specifics on where flights were made and how they were made. It will also provide details on the instruments used to collect trace gases O_3, SO_2 and CO as well as aerosol scattering and absorption.

2.2 Aircraft

A twin engine Piper Aztec was used to collect vertical profiles of trace gases and aerosols. Instruments were housed inside the aircraft and the sampling inlets were attached to the upper fuselage. On the upper fuselage there was an aft facing inlet that was attached to the trace gas instruments. There was also a forward facing isokinetic inlet that sampled aerosols. There were line losses of particles due to impaction on the side walls of the forward facing inlet and for this reason only submicron particles (< 1μm) were sampled. Flights were made mostly in the Mid-Atlantic region from 1995-2005. Spirals from 3 m above the surface to about 3000 m were made at small airports shown in Figure 1.

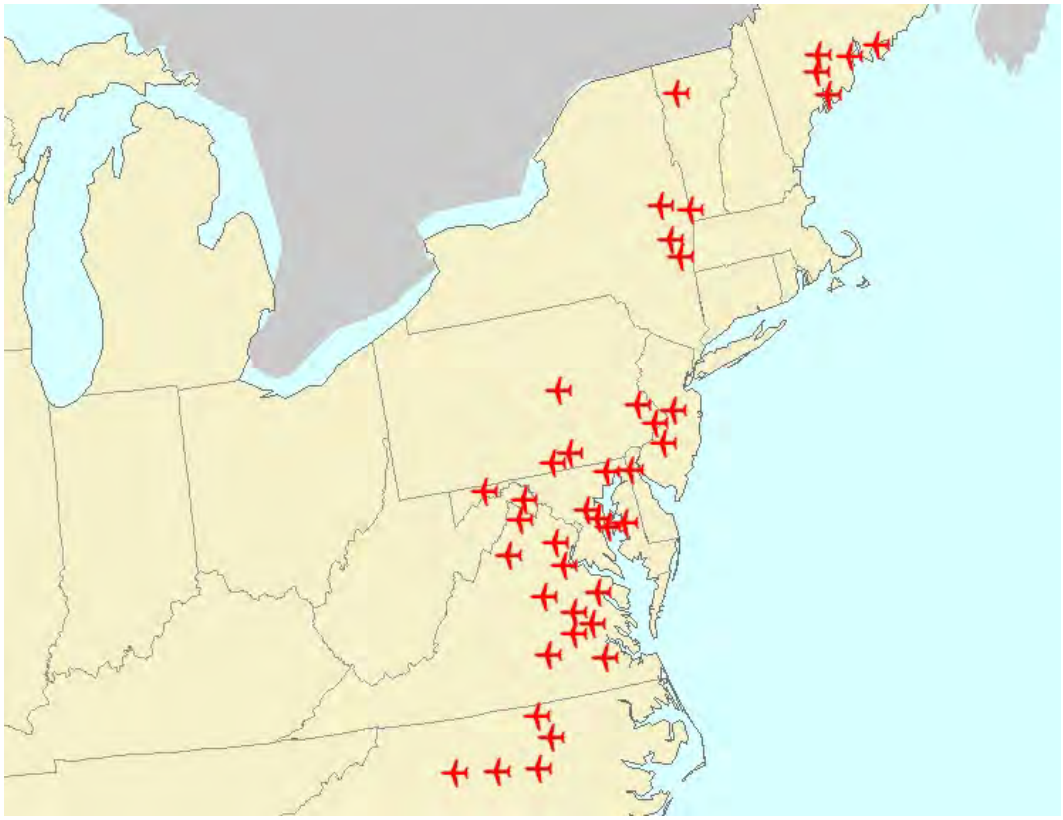

Figure 1. Locations of University of Maryland research aircraft flights made in the Eastern US between 1995 and 2005.

Spirals were completed within 30 minutes at a vertical climb rate of 100 m min^{-1}. Flight patterns were generally chosen to capture transport of pollutants to areas downwind of urban areas, and so flights conducted in the morning (before 12 noon EST) were upwind of urban areas in the Mid-Atlantic, while flights conducted in the afternoon (after 12 noon EST) were downwind of urban areas. The full instrument suite was not used every year and Table 1 shows the years in which new instruments were added to the suite. I collected samples aboard the aircraft for 12 of the flights (30 profiles) in 2005.

	O_3	CO	SO_2	PSAP	Nephelometer
1996	X				
1997	X				
1999	X	X			
2000	X	X	X	X	
2001	X	X	X	X	X
2002	X	X	X	X	X
2003	X	X	X	X	X
2004	X	X	X	X	X
2005	X	X	X	X	X

Table 1. Years when O_3, CO, SO_2, absorption with the PSAS and scattering with the nephelometer were sampled.

2.3 SO_2

Thermo Scientific SO_2 analyzer (43C, Franklin, MA) measures SO_2 fluorescence from a pulsating UV light. SO_2 absorbs radiation in three wavelength regions, 1) 390-340 nm, 2) 320-250nm and 3) 230-190 nm. SO_2 absorbs weakly in region 1 and is quenched rapidly. SO_2 is also quenched rapidly by O_2 and N_2 in region 2. SO_2 is quenched least in region 3. In this region SO_2 absorbs a quantum of energy ($h\nu_1$) and forms an electronically excited molecule

$$SO_2 + h\nu_1 \rightarrow SO_2^* \quad (1)$$

The light intensity absorbed by SO_2, I_a, is a function of the incident light, I_o, the absorption coefficient, a, the path length, x, and the SO_2 concentration (SO_2) and described by beer's law:

$$I_a = I_o^*\{1 - \exp\text{-}[a^*x^*(SO_2)]\} \quad (2)$$

The electronically excited SO_2 molecule can release the excess energy in three ways: fluorescence, quenching and dissociation. Fluorescence of SO_2 can be written as:

$$SO_2^* \rightarrow SO_2 + h\nu_2 \quad (3)$$

Here the quantum of energy released, $h\nu_2$, is at a lower frequency than the quantum of energy absorbed, $h\nu_1$. Reaction 3 proceeds with a rate constant k_f. Quenching of the excited SO_2 can be written as

$$SO_2^* + M \rightarrow SO_2 + M \qquad (4)$$

Here M is a molecule of air that absorbs the excess energy. The rate constant for Reaction 4 is *kq*. Dissociation of SO_2 can be written as:

$$SO_2^* \rightarrow SO + O \qquad (5)$$

Dissociation occurs with a rate constant of k_d. The fluorescent intensity measured by the detector, *F*, can be written as

$$F = [G*k_f*Io*\{1 - \exp-[a*x*(SO_2)]\}] / (k_f + k_d + k_q*[M]) \qquad (6)$$

Here *G* accounts for the geometry of the fluorescent chamber design. Assuming the SO_2 concentration and path length are small, this equation reduces to:

$$F = [G*k_f*Io*a*x*(SO_2)] / (k_f + k_d + k_q*[M]) \qquad (7)$$

The reaction rates (k_f, k_d and k_q) are relatively constant over a wide range of temperatures and pressures. The incident light *Io* can be engineered to remain constant, and *G* and *x* are also constants so the fluorescent intensity is directly proportional to the SO_2 concentration. This direct proportionality between fluorescent intensity and SO_2 concentration is the basis of the SO_2 instrument.

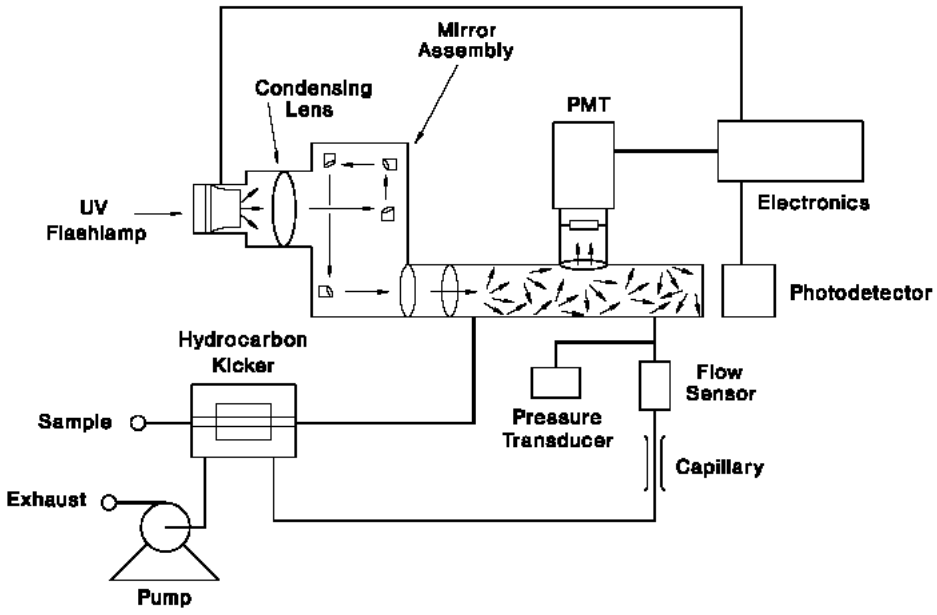

Figure 2. Schematic of flow diagram for SO_2 pulsed fluorescence monitor (Thermo Scientific, 2004a).

Figure 2 shows a schematic of gas flow through the SO_2 monitor. The monitor draws air in through a sample port at a rate of 0.5 L/min. Air then moves through a Nafion hydrocarbon kicker. The hydrocarbon kicker is used because there are significant interferences from polynuclear aromatic hydrocarbons (PAH); the most common of these being naphthalene. The hydrocarbon kicker is a semi permeable membrane, allowing only hydrocarbons through. A differential pressure is established by passing the sample air through a capillary tube. SO_2 enters a fluorescence chamber and is excited to a higher energy state. The excited SO_2 emits in 3 wavelength ranges with the 190-230 nm range being the most easily measured. The instrument runs on a switch able zero or measure mode. During the zero modes sampled air is run through a K_2CO_3 filter to remove SO_2. The zero modes are averaged and subtracted from the measure mode to decrease background noise (Thermo Scientific, 2004a).

In order to reduce the effects of non-methane hydrocarbons (NMHC) an extra PFA Teflon canister packed with activated charcoal was added to the kicker. The addition of the canister helps to reduce the partial pressure of the NMHCs in the sampling device and increases their diffusion out of the semi-permeable membrane (Luke, 1997). These modifications make interferences from most hydrocarbons negligible, though there are still interferences from NO_x that can only be removed through zeroing.

A UV lamp source is used to generate light in the 230-190 nm region. The light passes through a condensing lens (to focus the beam) and a series of reflective bandpass filters to stabilize and intensify the beam. The beam is passed through a relay lens and a circular baffle to remove stray light. The beam then enters the reaction volume, which contains the ambient air. The detector is perpendicular to the incident beam of light. Before the fluorescent light reaches the photo multiplier tube, the beam passes through a condensing lens and then a bandpass filter to ensure only light from SO_2 fluorescence enters the detector.

Luke (1997) approximated the detection limit to be around 0.3 ppb during the 1994 National Science Foundation-sponsored Gas-Phase Sulfur Intercomparison Experiment. I calculated the detection limit in 2005 for the SO_2 monitor used aboard the Maryland Research aircraft. I measured zero mode SO_2 1-minute averages for 30 minutes. I assume that the detection limit is two times the standard deviation of the zeros and this was 0.25 ppb. Luke (1997) approximated the uncertainty of the instrument to be 16% (at the 95% confidence level) when sampling mixing ratios were greater than 0.5 ppb.

2.4 CO

A modified (Dickerson and Delany, 1988) Thermo Scientific CO infrared filter correlation analyzer (43C, Franklin, MA) was used to measure CO. An IR source of 4.6 μm wavelength radiation is used because CO absorbs in this region. Figure 3 shows the schematic of the instrument.

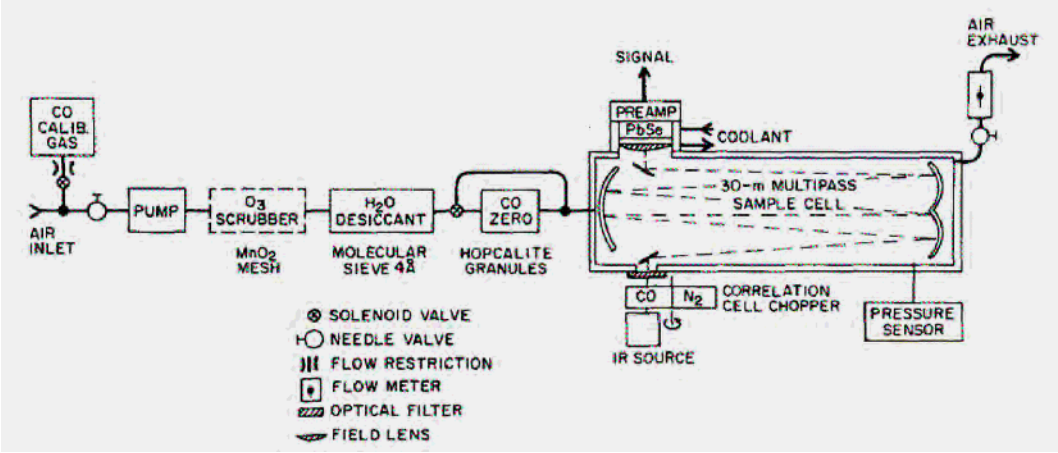

Figure 3. Flow schematic for the CO detector (Dickerson and Delany, 1988). Modifications include a collecting lens, cooling chamber, dessicant, chemical zero, and operation at positive pressure.

The air sample is drawn into the instrument and enters the sample chamber. The source is chopped and then travels through a gas filter wheel. Half of the filter wheel contains high concentrations of CO and the other half contains N_2. N_2 does not absorb in this IR region and so light that passes through this half of the wheel becomes the measure beam. The high concentration of CO in the other half of the wheel absorbs all the IR radiation and this produces a reference beam. Both beams pass through the sample cell, with a 30 m effective path length. The CO concentration being measured is derived from the relative intensity of the measure

and reference beam (Thermo Scientific, 2004b). The instrument is capable of a 2-5% precision determined from a 1-min mean of 10 s data.

2.5 O_3

Ozone is measured with a Thermo Scientific UV photometric analyzer (49, Franklin, MA). This analyzer operates on the Beer-Lambert law by measuring the attenuation of light due to O_3 absorption at 254 nm. The source is a low pressure mercury vapor lamp, which has 95% output at 254 nm. The detector is a solar blind vacuum photodiode sensitive to UV light only. Figure 4 gives a schematic of the instrument. The sample enters the instrument and is split into two gas streams. One of the streams is scrubbed of O_3, which allows it to be the reference beam, I_o. The reference beam then passes onto the sample solenoid valve. The other gas stream flows directly to the sample solenoid and is the measure beam, I. The solenoid switches the instrument between zero and measure modes (sampling from the I and I_o beam). The ratio of I/I_o is directly proportional to the concentration of O_3.

$$I/I_o = \exp^{-KlC} \qquad (8)$$

Where $K = 308\ cm^{-1}\ atm^{-1}$ at 0^oC and 1 atm, l is the length of the cell (38 cm), and C is the O_3 partial pressure in atm. In order to register a change of 1ppb concentration, the instrument must be able to detect a change in I/I_o of 2 parts in 10^5. It takes about 10 seconds to measure I and I_o, and the source must be stable to 2 parts in 10^5. Because this stability is difficult to reach, a second detector is used to monitor and correct the changes in light intensity. The instrument employs 2 photometers with a single light source and two absorption cells and detector systems. These photometers operate synchronously but out of phase so that when one is in measure mode, the

other is in zero mode. A flush time of about 7 seconds is used to remove the ambient air from the sample cell, and then the measurement is made during the next 3 seconds. By taking the average of the 2 photometer readings, the fluctuations of the lamp intensity are cancelled out. The instrument is capable of 1 ppb precision for 10 s data.

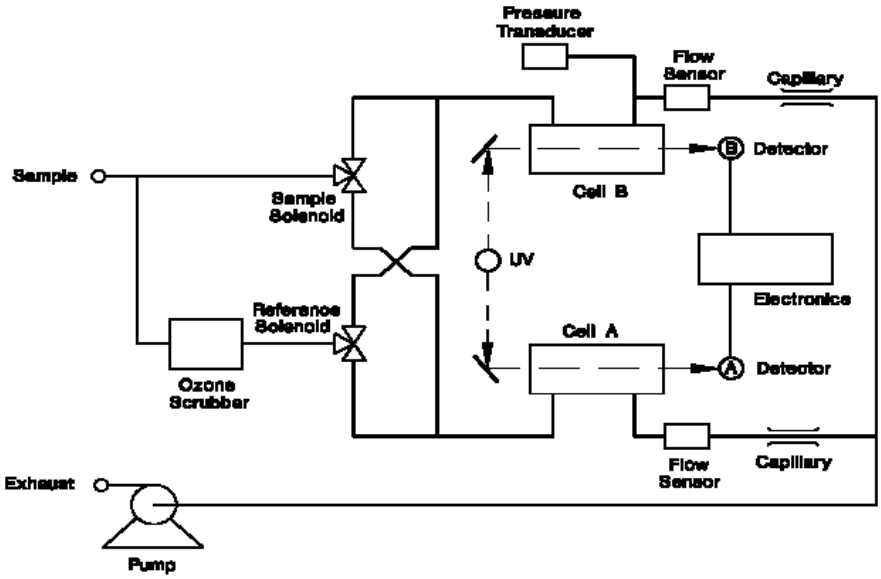

Figure 4. Flow schematic for U.V. photometric O_3 analyzer (Thermo Scientific, 2004c).

2.6 Aerosol Absorption

A Particle Soot Absorption Photometer (PSAP; Radiance Research, Seattle, WA) was used to measure near real-time aerosol absorption on a filter. An LED light source shines 567 nm light through an opal glass and onto a Pallafax filter. The PSAP measures the absorption coefficient, σ_{ap} ($Mm^{-1} = 10^6\ m^{-1}$), with an integrating technique. The absorption coefficient is determined from the volume of air sampled during an averaging time using Beers law:

$$\sigma_{ap} = A/V * \ln (I_o/I) \quad (9)$$

Where *A* is the area of the filter exposed to the light beam, *V* is the average volume of air sampled by the instrument, I_o is the average filter transmittance for averaging time j and *I* is the average filter transmittance for averaging time j + 1. The σ_{ap} is then corrected for filter nonlinearities including filter loading and filter characteristics. This correction can be written as:

$$\sigma_{ap} = \sigma_{ap}\, f(Tr) \quad (10)$$

Where f(Tr) is a transfer function based on filter loading (or transmittance, which is recorded by the instrument), for Pallafex filters. Figure 5 shows a diagram of the air flow. Ambient air flows through the first filter (measurement filter), where all particles are removed. The particle-free air then flows through the reference filter. The transmission of light through the filter is measured with a photodiode. A second filter, adjacent to the first is used to ensure that changes in the change in intensity results from buildup of particles on the filter and not fluctuations in the LED source.

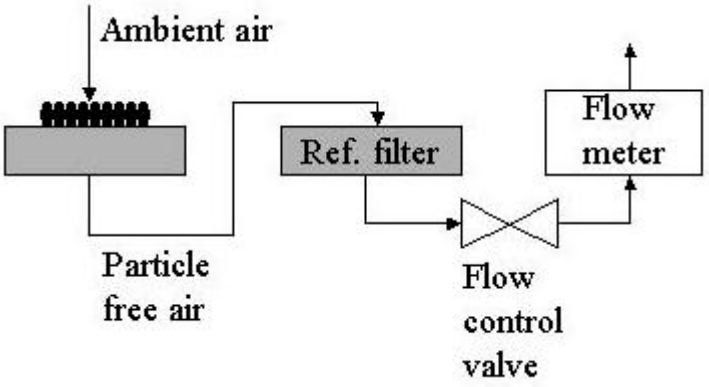

Figure 5. Flow diagram for PSAP (http://www.cmdl.noaa.gov/aero/instrumentation/psap_desc.html).

The detection limit is 0.9x10-6 m^{-1} (95% confidence level) when 1-min measurement averages are used (Bond et al., 1999). Bond et al. (1999) has recommended corrections for differences in flow rates, spot size, and exaggerations of absorption due to scattering, and these have been applied to PSAP measurements.

2.7 Scattering

The TSI integrating nephelometer (Model 3563, TSI, St. Paul, MN) was used to measure light scattering of atmospheric particles at 450, 550, and 700 nm. Figure 6 show a diagram of the instrument.

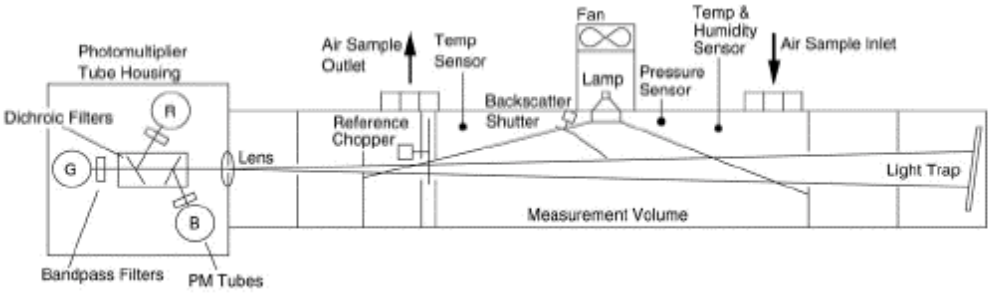

Figure 6. Flow schematic for the integrating nephelometer.

The light source travels through a diffuser plate, ensuring a lambertian source. A photomultiplier tube detector is positioned parallel to the incoming light and measures scattering over 7° to 170°. The light source flux that reaches the detector is defined by the following:

$$B = I_o / y \int_{\phi_1}^{\phi_2} \beta(\phi) \sin(\phi) d\phi \qquad 11$$

where *Io* is the intensity of the incident light, *y* is the distance between the source and the detector, ϕ is angle between the light reaching the source and the incident light, and $\beta(\phi)$ is the angular scattering function (TSI, 1997). Integrating the scattering function from $\phi_1 = 0$ to $\phi_2 = \pi$ gives:

$$B = (I_o / y) * (\sigma_{scat} / 2\pi) \qquad (12)$$

Where σ_{scat} is the scattering coefficient (TSI, 1997).

A chopper is used to generate an AC signal. The light passes through three different filters to correct for interferences. The first filter lets through all light for the full signal measurement. The second filter is used to remove the dark signal from the photomultiplier. The third filter measures the light source to monitor the lamp stability (TSI, 1997). Corrections were made for truncation errors (where forward

scattered light at angles less than 7^o is blocked) and nonlambertian errors as suggested by Anderson and Ogren (1998).

The inlet airstream was dried to an RH < 20%. To account for hydroscopic particle growth an estimated growth factor, F(RH), was calculated. F(RH) is the ratio of scattering from ambient particles to scattering from dried particles

$$F(RH) = \sigma_{sp}(\lambda, RH) / \sigma_{sp}(ref) = \{(1-RH_{amb})/(1-RH_{ref})\}^{-\gamma} \quad (13)$$

Here $\sigma_{sp}(\lambda, RH)$ represents light scattering from the ambient particles, $\sigma_{sp}(ref)$ represents light scattering from the dried particles, RH_{amb} is the ambient RH, RH_{ref} is the RH inside the nephelometer, and γ is derived from parallel nephelometers. A γ value of 0.35 was used, similar to that in Remer et al. (1997), because the region of their study is similar to those presented here. The detection limits for scattering are 0.44×10^{-6}, 0.17×10^{-6} and 0.26×10^{-6} m for scattering at 450, 550, and 700 nm. The instrument is calibrated with CO_2 for Raleigh scattering

Chapter 3: Determination of Meteorological Influences on Pollution Episodes: Clustering Back Trajectories.

3.1 Introduction.

This chapter will address the two questions: 1) Is there a statistical link between characteristic regional transport patterns in the Mid-Atlantic US during summertime haze and O_3 episodes and specific pollution loadings? 2) Can the local O_3 contributions be differentiated from regionally imported O_3; if so, are the regional contributions quantifiable? Much of the work in this chapter was published in Taubman et al. (2006). In this chapter I will present statistics of trace gasses and aerosols from all flights made in June-August for 1995-2005. I collected measurements aboard the aircraft for 12 of the flights (36 profiles) in 2005. I calculated statistics for morning (before 12 noon EST) and afternoon (after 12 noon EST) profiles. Most morning flights were made upwind of pollution centers and most afternoon flights were made downwind of pollution centers. I clustered back trajectories for flights from 1997-2003 to determine meteorological regimes associated with the flights. The method for clustering back trajectories will be described and the resulting meteorological regimes determined by the clusters will be analyzed. I calculated statistics for profiles of trace gases and aerosols associated with the meteorological regimes and will discuss the results. I also calculated transported O_3 using *in-situ* measurements. The method and the amount of transport associated with each of the meteorological regimes will be discussed.

3.2. Observations

3.2.1 Measurements

All flights analyzed for this study were conducted in the summertime (June, July, and August) and were specifically designed to characterize episodic pollution events. The observations reported herein represent polluted periods, not background values. Statistics for all flights made between 1995 and 2005 are presented first. The flight locations for statistics of all flights are presented in Figure 1 in Chapter 2.

From 1995 through 2005, there were 658 summertime flights, which included 305 morning spirals (before noon EST, average time 09:30 EST) and 353 afternoon spirals (after noon EST, average time 13:30 EST). The median profiles for the morning and afternoon O_3, CO, SO_2, scattering at 550 nm and absorption at 550 nm are shown in Figure 1. The single scattering albedo represents the relative contribution of scattering from particles and was calculated using:

$$\text{single scattering albedo} = \sigma_{550} / (\sigma_{550} + \text{abs}_{550}) \quad (1)$$

Where σ_{550} is the scattering coefficient at 550 nm and abs_{550} is absorption coefficient at 550 nm. The Ångström exponent (α) represents the relative size of particles and was calculated using:

$$A = [\log(\sigma_{450}) - \log(\sigma_{700})] / [\log(450) - \log(700)] \quad (2)$$

Here $\sigma_{450}$and σ_{700} are the scattering coefficients at 450 and 700 nm respectively. Statistics for the single scattering albedo and α are also presented in Figure 1. The profiles shown were generated by calculating the median value at each altitude layer from all of the measured profiles.

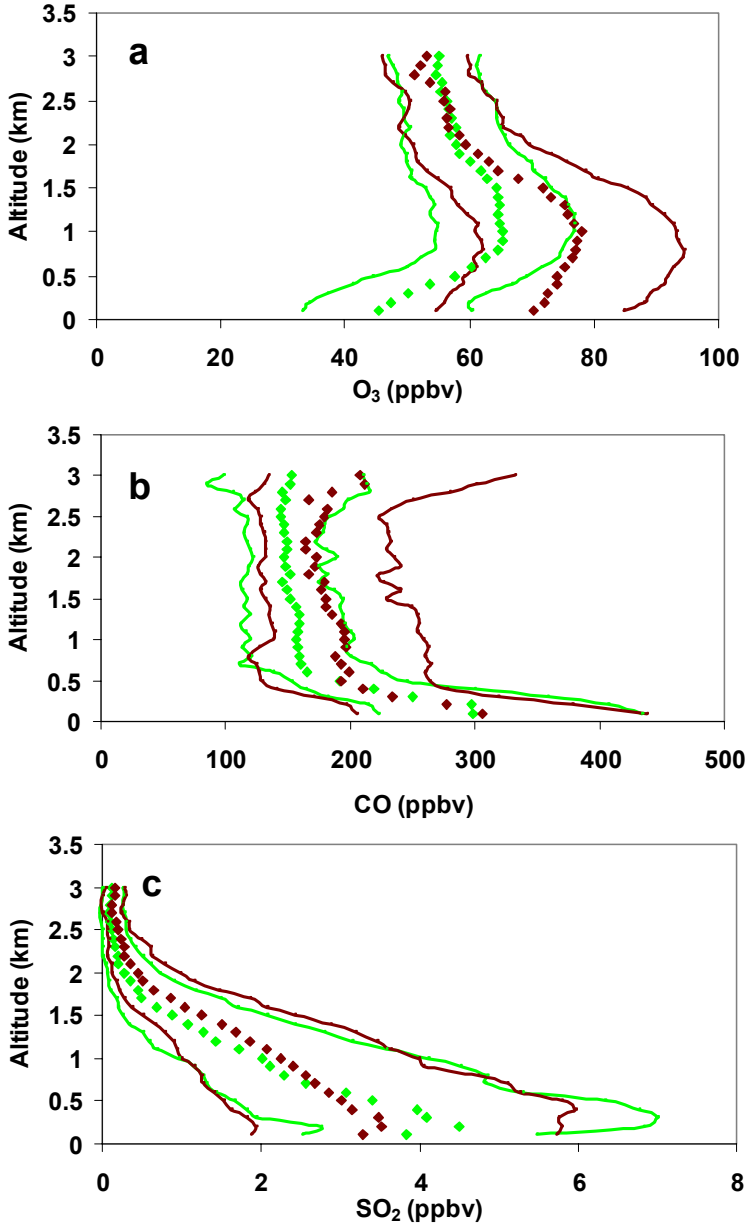

Figures 1a-c. Median values calculated every 100 m from all morning (green diamonds, before 12:00 EST) and afternoon (red diamonds, after 12:00 EST) profiles for a) O_3 (305 morning profiles, 353 afternoon profiles), b) CO (134 morning profiles, 178 afternoon profiles), and c) SO_2 (234 morning profiles, 254 afternoon profiles). The solid lines represent the 25th and 75th percentiles.

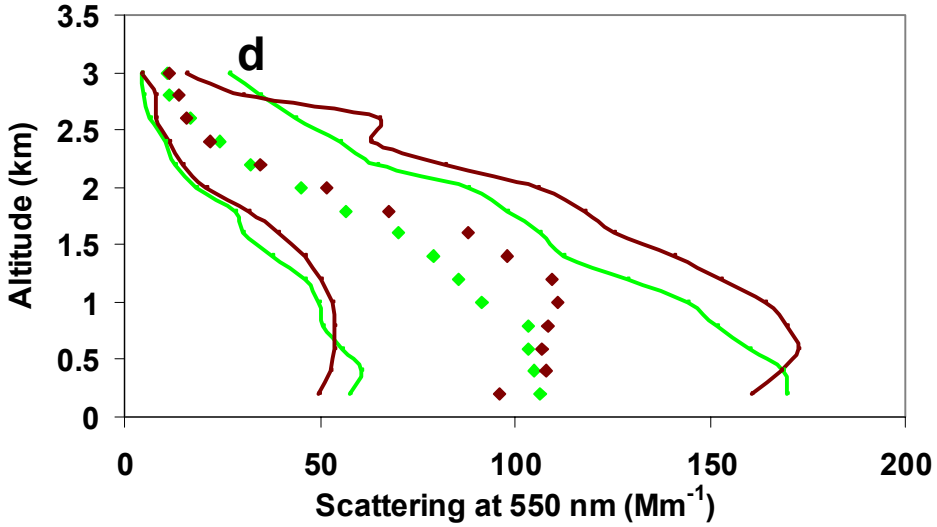
d
Altitude (km)
3.5
3
2.5
2
1.5
1
0.5
0
0
50
100
150
200
Scattering at 550 nm (Mm-1)

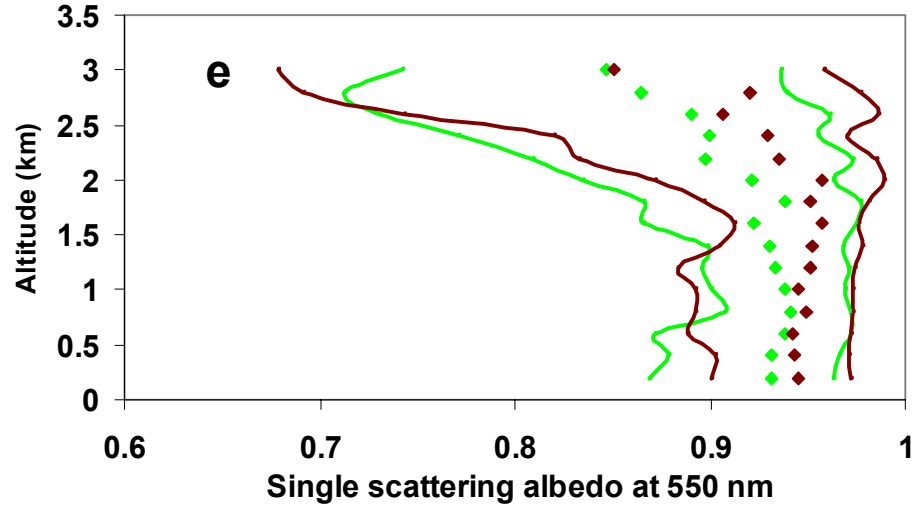
e
Altitude (km)
3.5
3
2.5
2
1.5
1
0.5
0
0.6
0.7
0.8
0.9
1
Single scattering albedo at 550 nm

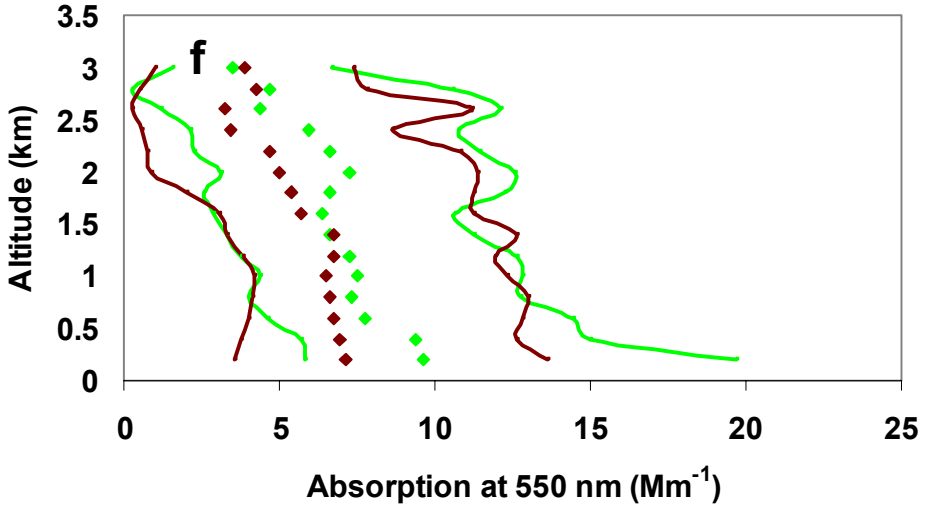
f
Altitude (km)
3.5
3
2.5
2
1.5
1
0.5
0
0
5
10
15
20
25
Absorption at 550 nm (Mm-1)

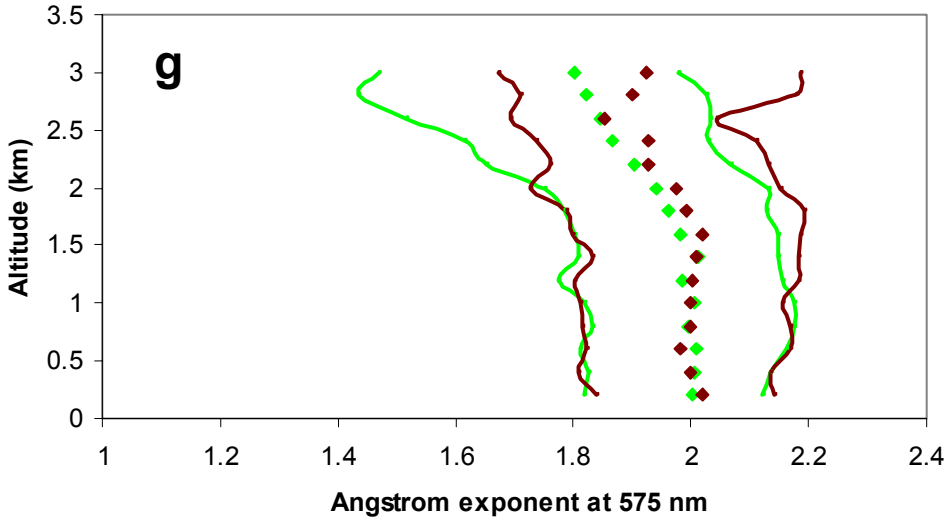

Figure 1d-g. Median values calculated every 100 m from all morning (green, before 12:00 EST) and afternoon (red, after 12:00 EST) profiles for d) scattering at 550 nm (189 morning profiles, 185 afternoon profiles), e) single scattering albedo at 550 nm (132 morning profiles, 153 afternoon profiles), f) absorption at 550 nm (175 morning profiles, 214 afternoon profiles), and g) Ångström exponent (189 morning profiles, 185 afternoon profiles). The solid lines indicate the 25th and 75th percentiles.

The morning O_3 profile (Figure 1a) shows relatively small values (~45-55 ppbv) within the nocturnal boundary layer (roughly the lowest 500 m), with considerably more O_3 in the residual layer above. This results from surface deposition and titration with freshly emitted NO within the nocturnal boundary layer combined with night-time regional transport from upwind sources within the residual layer. Solar heating induces a more thoroughly mixed afternoon O_3 profile with photochemical production adding to that which was transported overnight. Above approximately 2 km, the morning and afternoon values are nearly identical (~55 ppbv), indicating a summertime continental background value.

The morning and afternoon CO profiles (Figure 1b) are nearly identical below ~1 km, with large values near the surface that fall off with altitude. The shape of the

vertical profiles is similar to those presented by Dickerson *et al*. (1995) for spring, although the absolute values presented herein are slightly greater than in the previous study. Above 1 km, the afternoon values are slightly larger than the morning, indicating convective outflow from the boundary layer, the preamble to long range transport.

The SO_2 profiles (Figure 1c) show little difference between the morning and afternoon. The afternoon profile shows somewhat smaller values near the surface, likely the result of oxidation to sulfate. There is also evidence of vertical mixing in the afternoon; however, both profiles show greater values near the surface that decrease sharply with altitude. Sulfur dioxide is a fairly short-lived species, typically less than a day in summertime (Seinfeld and Pandis, 1998), with sources generally elevated slightly above the surface.

The afternoon scattering profiles (Figure 1d) are somewhat larger than the morning profiles between 200 and 2000 m and this may be explained by SO_2 oxidation to sulfate, the primary scattering component in fine particles over the eastern U.S. There is a maximum in the afternoon single scattering albedo near the top of the boundary layer where RH is also at a maximum. Both profiles decrease considerably above 2 km. The single scattering albedo profiles are similar to the scattering profiles and the single scattering albedo in the afternoon boundary layer average is greater than that in the morning profile (0.94 ± 0.01 vs. 0.93 ± 0.01) (Figure 1e). This increase of single scattering albedo in the afternoon is presumably the result of SO_2 oxidation and RH changes due to the planetary boundary layer growth. The absorption was relatively invariant with altitude (Figure 1f), so the

decline in single scattering albedo with altitude is driven by a decrease in scattering values. These observations are consistent with those of Novakov *et al*. (1997), who reported an increase in the relative amounts of carbonaceous to sulfate species with altitude over the Eastern U.S. coastline. No diurnal pattern in Ångström exponent was observed (Figure 1g); however a slight decrease with altitude is apparent in both the morning and afternoon profiles. The presence of larger particles aloft may be due to particle growth through preferential aging in the lower free troposphere as articulated in Taubman *et al*. (2004a).

3.2.2 Trajectory Calculations

Back trajectories are a standard tool for determining the source regions and transport patterns of air parcels observed at receptor sites. While they may not represent the exact transport path of an air parcel, back trajectories are good representations of the general 3-dimensional wind flow and are useful in identifying particular synoptic situations. The accuracy and errors associated with the different estimations of air parcel trajectories have been quantified (Stohl *et al*., 1995; Stunder, 1996; Stohl, 1998). Individual trajectories may be subject to errors; however, clustering multiple trajectories together minimizes errors and uncertainties.

I calculated 48 hour, 3-dimensional kinematic back-trajectories ending at the time and location of each aircraft spiral (made from 1997 – 2003 with the UMD research aircraft) using the NOAA Air Resources Laboratory (ARL) HYbrid Single-Particle Lagrangian Integrated Trajectory (HY-SPLIT) model (Version 4) (R. R. Draxler and G. D. Rolph, 2003, http://www.arl.noaa.gov/ready/hysplit4.html) and 80 km Eta Data Assimilation System (EDAS) 3-hourly archive data. Kinematic back

trajectories were used because, due to improvements to the accuracy of the vertical wind component, they have been shown to be more accurate than other methods (e.g., isentropic and isobaric) (Stohl *et al*., 1995; Stohl, 1998; Jorba *et al*., 2004). Two-day back trajectories were long enough to capture regional transport patterns and short enough to keep trajectory errors, which accumulate with simulation time, to acceptable levels. The air parcel latitudes, longitudes, and pressures were recorded at 1 h intervals. Trajectories were calculated ending at 1, 2, and 3 km (above ground level). Back trajectories associated with 550 flights made from 1997-2003 were used in the clustering analysis.

3.2.3. Cluster Analysis

I performed a separate cluster analysis for back trajectories ending at 1, 2, and 3 km. These ending altitudes describe the vertical range over which the aircraft vertical survey spirals were performed. By clustering the trajectories at each of the three altitudes, any variations in the atmospheric circulation patterns in the lower atmosphere and the impacts on regional transport could be identified. The results of the cluster analysis for the three altitudes were similar. The 2 km trajectory cluster results were used for the remainder of the analysis because this altitude is near the middle of the aircraft spirals and most representative of the entire spiral.

The trajectories trace a 3-dimensional path through time to the receptor site. To determine the similarity among individual trajectories, the total variability between each trajectory pair must be quantified. The variability may be calculated as a scalar distance between trajectories. At each time step, the position of the air parcel is defined by its latitude, longitude, and pressure. These data were converted to

Cartesian coordinates by treating the Earth as a sphere and calculating their position in 3-dimensional space. The x, y and z distances in km are given as:

$$x = (r_e + alt_i)*\cos(\pi/180 * lon_i)* \sin(\pi /2 - \pi /180*lat_i) \quad (3)$$

$$y = (r_e + alt_i)*\sin(\pi /180 * lon_i)* \sin(\pi /2 - \pi /180*lat_i) \quad (4)$$

$$z = (r_e + alt_i)* \cos(\pi /2 - \pi /180*lat_i) \quad (5)$$

Where r_e is the radius of the earth (approximated at 6378 km), alt_i, lat_i, and lon_i are the altitude, latitude and longitude at a specific hour i, in the back trajectory.

Vertical variability along the trajectory paths may have a large impact on transport and hence, pollution levels, but the spatial distances described by the variability in the vertical wind component are typically less than the horizontal spatial distances covered by the air parcels. Thus, without normalizing the data, the vertical variability may not have an equal impact on the cluster analysis when examining the similarity among trajectories. To account for this inconsistency I calculated the mean value and standard deviation for each coordinate at every time step (x_{avg}, y_{avg}, z_{avg} and x_{stdev}, y_{stdev}, z_{stdev}). I then subtracted the mean value from the individual coordinates and normalized them with the standard deviation.

$$x^* = (x - x_{avg}) / x_{stdev} \quad (6)$$

Normalized differences (like x*) were also calculated for y and z. In this way, the coordinates were all converted to a standardized distance from the mean value of that particular coordinate and equal weighting was given to all three coordinates in the cluster analysis.

The Euclidean distance, D, between each trajectory pair was calculated according to the equation:

$$D_{ij} = \sqrt{\sum_{k=1}^{n} (x^*_{ik} - x^*_{jk})^2 + (y^*_{ij} - y^*_{jk})^2 + (z^*_{ik} - z^*_{jk})^2} \qquad (7)$$

In the above equation, D is the 3-dimensional distance between the two trajectories under comparison, represented here by the subscripts i and j. The variables x^*, y^*, and z^* represent the normalized distances from the means of the Cartesian coordinates. The number of time steps used in the analysis is given by k (48 for hourly time steps over 2 days). However, the first six time steps back from the receptor site were given zero weighting to account for the spatial heterogeneity of the aircraft spiral locations. To further discount the spatial variability of the receptor locations and place the emphasis on the source regions, the trajectory time steps were weighted linearly back in time, increasing the weighting for each hour after the initial six zero-weighted time steps.

After the distances between individual trajectories were calculated I clustered the trajectories using an agglomerative, hierarchical clustering algorithm in Matlab. The algorithm used an average linkage function, where the average distances between all pairs of objects in clusters i and j are calculated, to determine the distances between the trajectories making up the clusters. Average linkage minimizes the within-cluster variance while maximizing between-cluster variance and has been identified as an effective method for categorizing different synoptic situations (Kalkstein *et al*., 1987). Newly formed clusters were linked to other trajectories to create successively larger clusters until all of the trajectories were connected by a hierarchical dendrogram. The algorithm has no inherent mechanism for identifying an appropriate terminus for this iterative process. Barring manual intervention, all

objects are eventually grouped into one cluster. So, the final number of clusters was specified arbitrarily from 1 to 15 clusters.

To determine the appropriate number of clusters I first calculated an "average" trajectory, or trajectory center, for each cluster. The root mean square deviation (RMSD) of each trajectory within a cluster from the cluster center was quantified. The RMSDs were then summed to give the total root mean square deviation (TRMSD). The percent change in the TRMSD was plotted against the total number of clusters (e.g., Cape *et al*., 2000; Brankov *et al*., 1998) (Figure 2). Large changes were interpreted as the merging of significantly different trajectories into the same cluster. Accordingly, the appropriate number of clusters would be found just prior to the large percent change in TRMSD. While this technique lends objectivity to the analysis, a subjective interpretation of the optimal number of clusters based on the meteorology and pollutant profiles as well as what value constitutes a large enough percent change in TRMSD is still required. When eight clusters were merged into fewer clusters the change in TRMSD remained consistently high (~10%) and grew larger upon further agglomeration. After reviewing the meteorology and pollutant profiles associated with each cluster, eight was determined to be the appropriate number of clusters

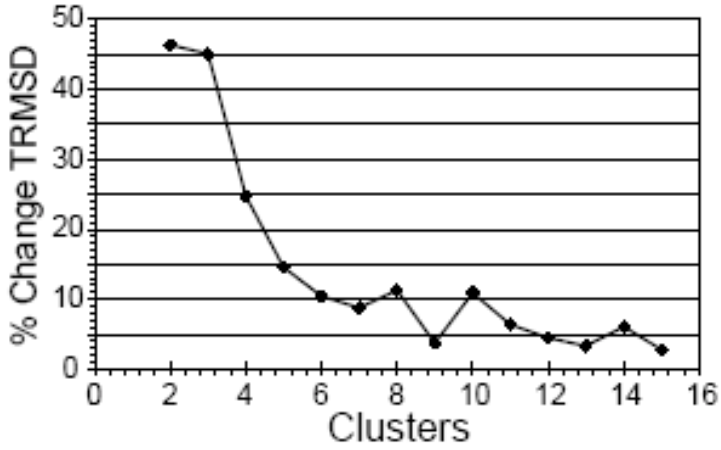

Figure 2. Percent change in the total root mean square deviation (TRMSD) calculated by summing the root mean square deviation of each cluster versus the number of total clusters.

3.3. Results and Discussion

3.3.1 Cluster Solution

The eight cluster solution is shown in Figure 3 with trajectory "spaghetti" plots of each cluster. The relative density of air parcel locations in each cluster, however, is better described by trajectory density plots, given in Figure 4. A linear interpolation method was used to generate values between the original trajectory latitude and longitude points and smooth the density plots. The locations of the largest (top 0.3%) annual NO_x and SO_2 emitters in the eastern U.S. (EPA AirData Facility Emissions Report – Criteria Air Pollutants 1999, http://www.epa.gov/air/data/) are overlaid on the trajectory density maps. The trajectory densities represent the relative amount of time the air parcels from every trajectory in a cluster spent over the areas defined by the spaghetti plots before reaching the receptor location. This is a technique based on the "residence time

analysis" (Ashbaugh, 1983) and it will be shown below that it is an effective means of determining downwind pollutant loadings.

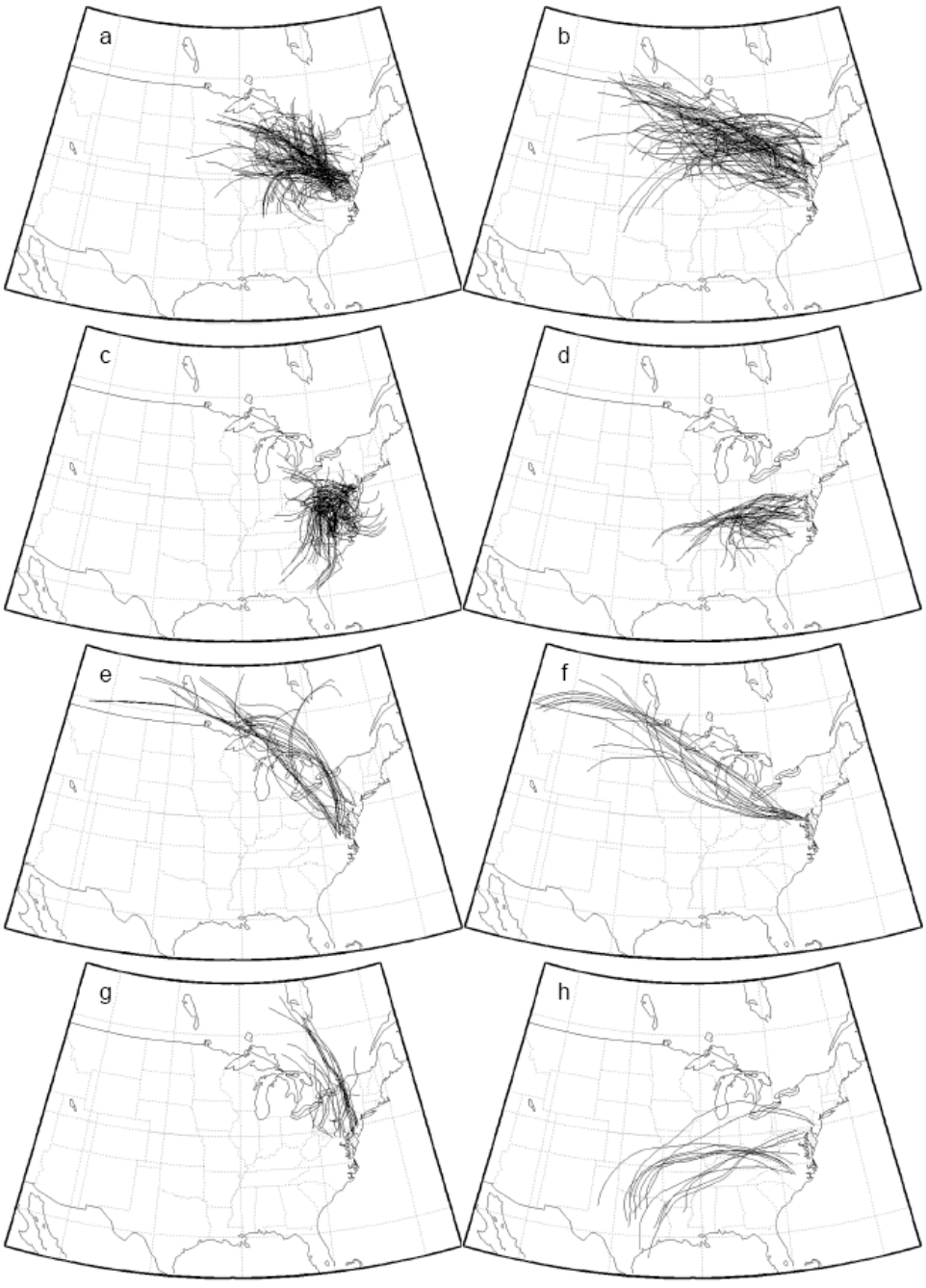

Figure 3. Spaghetti plots of the 48 hr HY-SPLIT back trajectories ending at 2km altitude that make up a) Cluster 1, b) Cluster 2, c) Cluster 3, d) Cluster 4, e) Cluster 5, f) Cluster 6, g) Cluster 7, and h) Cluster 8.

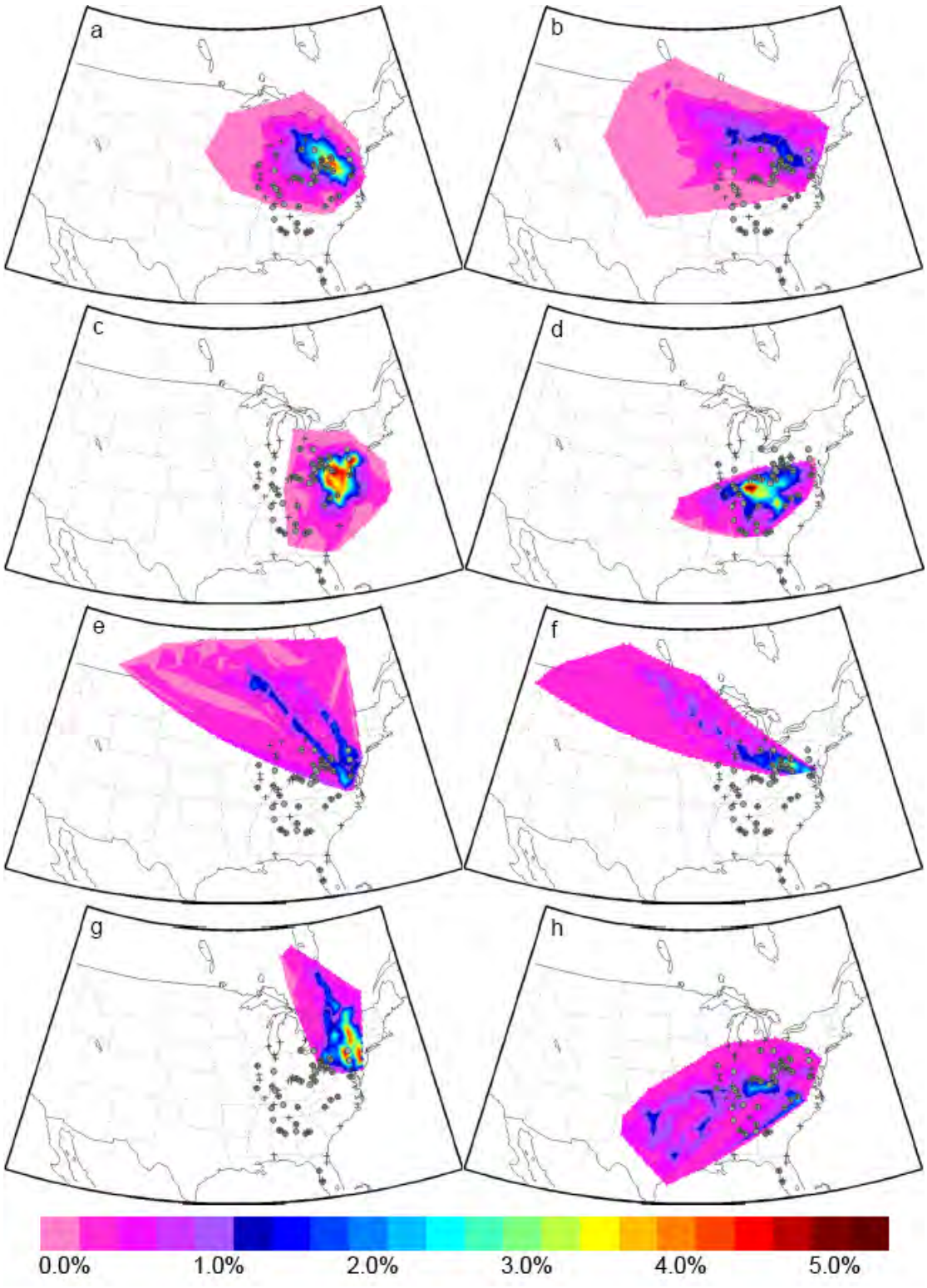
a
b
c
d
e
f
g
h
0.0%
1.0%
2.0%
3.0%
4.0%
5.0%

Figure 4. Trajectory density maps for a) Cluster 1, b) Cluster 2, c) Cluster 3, d) Cluster 4, e) Cluster 5, f) Cluster 6, g) Cluster 7, and h) Cluster 8. The plots were generated using a linear interpolation method between the trajectory end points. They indicate the relative density (%) of air parcels over the total area described by the spaghetti plots. Also pictured are the locations of the top 0.3% emitters annually of NO_x (diamonds) and SO_2 (crosses) in the eastern U.S.

To determine the statistical difference between the constituents associated with each cluster I first subdivided the clusters into morning and afternoon profiles according to the aforementioned criteria. For all trace gas profiles but morning O_3, I calculated the boundary layer (defined here as the layer between 100 m and 2000 m) column content (in matm-cm). For morning O_3, the residual layer (defined here as the layer between 500 m and 2000 m) column content (also in matm-cm) was quantified to capture the impacts of regionally transported pollution on the receptor locations. For the aerosol profiles I calculated the extinction weighted single scattering albedo column average, aerosol optical depth at 550 nm between the surface and 3 km (AOD), and scattering weighted α. The cluster median values were then determined. The cluster median ranks are given in Table 1 and the cluster median values for the extinction weighted single scattering albedo and AOD are given in Table 2.

Table 1. Cluster median profile ranks, % O_3 transported, and cluster median column content SO_2/CO ratios for the morning (upper number) and afternoon (lower number). Values in parentheses under the cluster number are the total profiles that went into that cluster (left) and the percent of the total profiles (right). The grey area indicates insufficient data to calculate statistical values for Cluster 8.

clusters	Median O_3 rank	% O_3 transported	Median CO rank	Median SO_2 rank	SO_2/CO	Median ω_{0550} rank	Median AOD rank	Median α rank
1 (107,26.3)	1 / 2	67 ± 4[a]	4 / 7	4 / 2	0.014 / 0.017	2 / 1	1 / 1	6 / 7
2 (77,19.0)	4 / 5	67 ± 6	8 / 8	5 / 4	0.015 / 0.016	1 / 2	2 / 2	7 / 6
3 (108,26.6)	3 / 1	54 ± 8	3 / 3	7 / 3	0.009 / 0.011	3 / 4	3 / 4	4 / 4
4 (39,9.6)	6 / 8	82 ± 8	7 / 2	8 / 6	0.010 / 0.006	4 / 3	5 / 3	2 / 5
5 (24,5.9)	5 / 3	62 ± 16	5 / 6	3 / 7	0.015 / 0.008	5 / 5	6 / 7	1 / 1
6 (15,3.7)	2 / 4	73 ± 17	2 / 4	1 / 1	0.026 / 0.016	6 / 7	4 / 5	3 / 3
7 (23,5.7)	8 / 7	56 ± 16	6 / 5	6 / 8	0.013 / 0.008	7 / 6	7 / 6	5 / 2
8 (13,3.2)	7 / 6	55 ± 11	1 / 1	2 / 5	0.008 / 0.006			

[a] error estimated by adding in quadrature $1\sigma/\sqrt{n}$ from the residual layer and afternoon boundary layer mean values.

Table 2. Cluster median profile values for the morning and afternoon aerosol extinction weighted ω_{0550} and AOD.

clusters[a]	**am** ω_{0550}	**pm** ω_{0550}	**am AOD**	**pm AOD**
1	0.91 ± 0.05[b]	0.95 ± 0.04	0.37 ± 0.19	0.35 ± 0.30
2	0.91 ± 0.06	0.94 ± 0.05	0.31 ± 0.23	0.31 ± 0.25
3	0.90 ± 0.06	0.93 ± 0.04	0.30 ± 0.28	0.26 ± 0.12
4	0.88 ± 0.06	0.94 ± 0.03	0.22 ± 0.06	0.29 ± 0.07
5	0.87 ± 0.08	0.91 ± 0.05	0.17 ± 0.10	0.15 ± 0.10
6	0.82 ± 0.09	0.85[c]	0.25 ± 0.08	0.25[c]
7	0.81 ± 0.17	0.85 ± 0.12	0.15 ± 0.12	0.20 ± 0.12

[a] there were not enough data to calculate statistical values for Cluster 8
[b] the error represents 1σ of the cluster mean value
[c] no error is given because there was only one profile that went into the Cluster 6 pm ω_{0550} and AOD values

Using the individual profile values, I calculated the statistical difference between the cluster medians using a multiple comparison procedure with statistical values generated from the Kruskal-Wallis test. This test is similar to the standard one-way analysis of variance, but is a non-parametric version. The one-way analysis of variance requires data to be normally distributed whereas in the Kruskal-Wallis test the data must only be continuously distributed. The test ranks the values and performs an analysis of variance on the ranks rather than the values themselves. For this study, the cutoff for the probability value (p-value) was set to 0.05. When the p-value was less than this limit, the null hypothesis was rejected and the cluster medians were declared statistically different with greater than 95% confidence. The results are summarized in Table 3.

Table 3. Statistical difference among cluster morning and afternoon profile median values. The > (<) signifies that the median value for the cluster is statistically greater (less) than, with 95% confidence, the median values of the cluster numbers listed after the symbol. Grey areas indicate no statistical difference.

Clusters								
	1	**2**	**3**	**4**	**5**	**6**	**7**	**8**
am O_3	>7,8		>8			>8	<1	<1,3,6
pm O_3	>4	<3	>2,4,7	<1,3			<3	
am CO		<8		<8				>2,4
pm CO								
am SO_2			<6	<6		>3,4		
pm SO_2								
am ω_{0550}								
pm ω_{0550}								
am AOD	>4,5			<1	<1			
pm AOD	>5	>5			<1,2			
am α	<5	<5			>1,2,7		<5	
pm α	<5,7				>1		>1	

3.3.2 Pollution Profiles

Figures 5 and 6 show the morning and afternoon median vertical profiles, respectively, for each constituent. Cluster 1, associated with large amounts of O_3, a

large SO_2/CO ratio, large, highly scattering particles, and a large AOD (see Figures 5, 6, and Tables 1, 2), shows moderate northwesterly flow. These values are indicative of aged point source pollution. The greatest trajectory density lies over the northern Ohio River Valley where there are several large NO_x and SO_2 sources (see Figure 4). Fresh NO_x and SO_2 emissions from these sources have had ample opportunity under a moderate flow regime to produce O_3 and secondary aerosols en route to the Mid-Atlantic.

Cluster 2 shows similar wind direction to Cluster 1, but with higher wind speeds (see Figure 3). The greatest trajectory density also lies mainly over the northern Ohio River Valley and extends into the Great Lakes region. The particles are also large and highly scattering, but the AOD is lower. The CO is even less than in Cluster 1, the SO_2/CO ratio is large, and the O_3 values, particularly in the afternoon, are small (see Figures 5, 6, and Tables 1, 2). These values are all consistent with northwesterly flow similar to Cluster 1 that brings northern Ohio River Valley point source pollution, but with higher wind speeds, so that there is less time for local, photochemical O_3 production or mixing with urban, mobile source pollution. Figure 4 shows that, in fact, the greatest trajectory density intersects many large NO_x and SO_2 sources.

Cluster 3 is typified by stagnant conditions with light, southerly flow (see Figure 3). The greatest air parcel density is found over the central Mid-Atlantic region. Ozone values, particularly in the afternoon, are large, as are CO values, whereas SO_2 values, especially in the morning, are small. Hence, the SO_2/CO ratio is small. The particle property values are moderate (see Figures 5, 6, and Tables 1, 2).

These values, together with the stagnant conditions associated with Cluster 3, indicate local, urban, mobile source-dominated pollution. Figure 4 shows that there are few large NO_x and SO_2 sources in the area of greatest trajectory density. Presumably, because there is less hygroscopic sulfate available for particle growth, the particles are smaller and less scattering than in the first two clusters.

The transport pattern identified by Cluster 4 is characterized by moderate southwesterly flow and the greatest trajectory density lies over the southern Ohio River Valley (see Figures 3, 4). For the most part, this cluster is associated with little pollution loading and the SO_2/CO ratio is small (see Figures 5, 6, and Tables 1, 2), suggesting that there are fewer point sources located farther south along the Ohio River. Figure 4 shows no large NO_x or SO_2 sources in the area of greatest trajectory density, although many do encircle this area. Also, the afternoon O_3 values are particularly small, and not much larger than the morning values (see Figures 5, 6, and Table 1), indicating there was little photochemical production during the air parcels transport.

Cluster 5 shows fairly fast north-northwesterly flow over the northern Great Lakes region into the Mid-Atlantic region (see Figure 3). Generally, this flow pattern seems to transport little pollution into the region. However, the O_3 values are large below ~1200 m in the morning and ~1500 m in the afternoon and only fall off to lower values aloft (see Figures 5, 6). The areas of greatest trajectory density do intersect large NO_x and SO_2 sources (see Figure 4), a fact corroborated by a high SO_2/CO ratio in the morning (Table 1), but the wind speeds, particularly aloft, are too great to allow for pollution to accumulate in the Mid-Atlantic region. The fast wind

speeds are also not conducive to particle growth, so the smallest particles are found in this cluster.

The wind direction of the trajectories in Cluster 6 is northwesterly as in Clusters 1 and 2, with still faster wind speeds than in Cluster 2 (see Figure 3). The greatest trajectory density again lies over the northern Ohio River Valley and several large NO_x and SO_2 sources (see Figure 4). The pollution loadings of this cluster are also consistent with these sources, but because of the higher wind speeds, the pollution appears to be relatively fresher. The O_3 values are moderately large, with smaller values in the afternoon, the CO values are moderate, and the SO_2 values are very large, so that the SO_2/CO ratio is also very large (see Figures 5, 6, and Table 1). The SO_2 apparently did not have much opportunity for oxidation before entering the Mid-Atlantic region. The particles were smaller and less scattering and the AOD was smaller than in Clusters 1 and 2 (see Figures 5, 6, and Tables 1, 2).

Overall, Cluster 7 is associated with the least pollution of any of the clusters (see Figures 5, 6, and Tables 1, 2). The flow is out of the north, bringing relatively cool, dry, continental air to the Mid-Atlantic region. There are no major urban centers, nor are there many NO_x or SO_2 sources in the area of greatest trajectory density (see Figure 4).

Cluster 8 comprises very few trajectories. The flow is fast and from the southwest, originating near Texas (see Figure 3). There were not enough particle data to generate any statistical values. The O_3 values are small, the SO_2 values are moderate, and the CO is very large (see Figures 5, 6, and Table 1). The areas of greatest trajectory density do no intersect many large NO_x or SO_2 sources (see Figure

4). Despite the fast wind speeds, the air parcels appear to be picking up a local, mobile source, indicated by the large CO values, small SO_2/CO ratio, and trajectory densities. Figure 7 summarizes the transport from the areas of greatest trajectory density into the Mid-Atlantic region as a percent of the total number of profiles examined in this study.

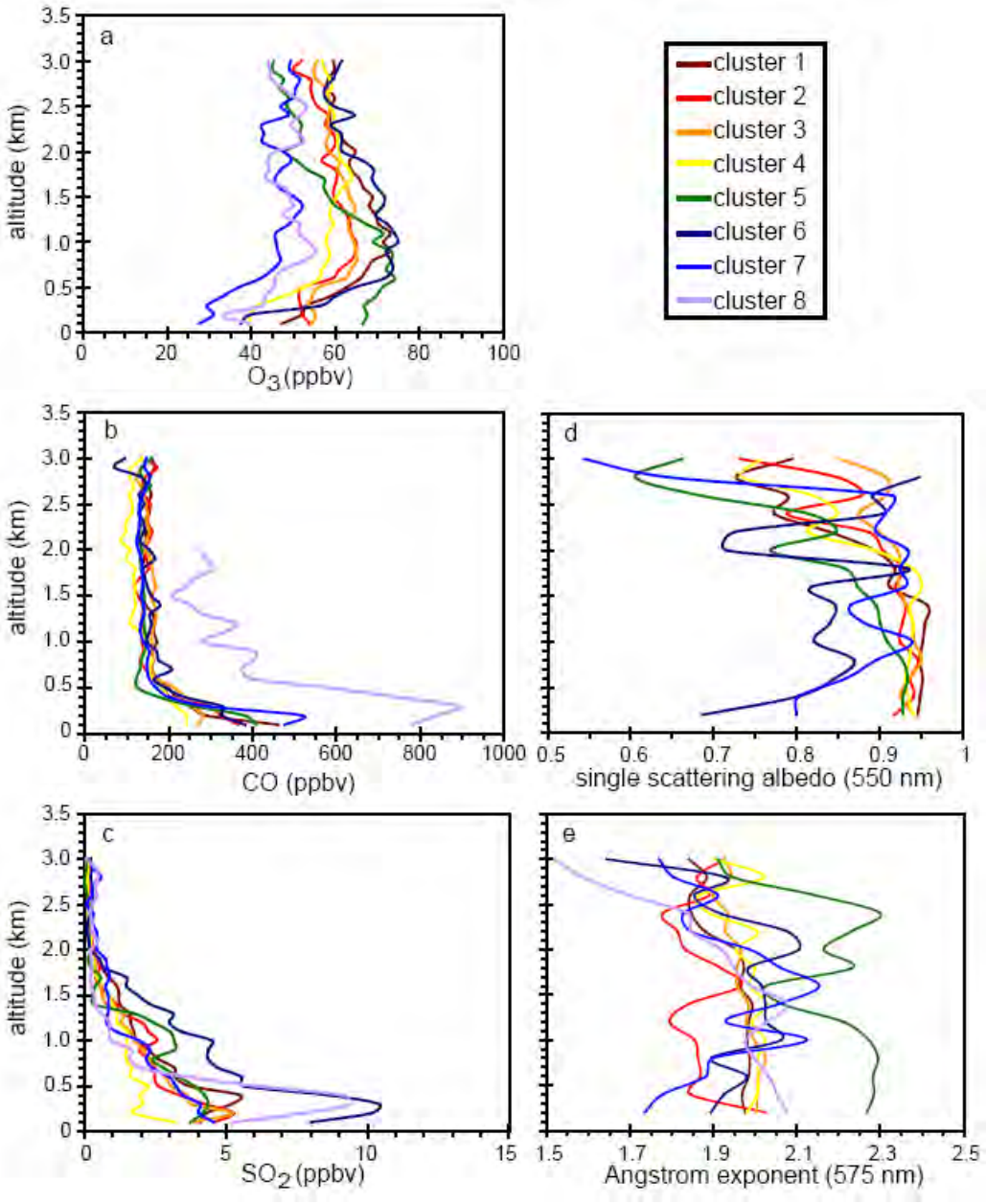

Figure 5. The median morning profiles for Clusters 1 (brown), 2 (red), 3 (orange), 4 (yellow), 5 (green), 6 (dark blue), 7 (blue), and 8 (violet) of a) O_3, b) CO, c) SO_2, d) single scattering albedo (550 nm), and e) Ångström exponent (575 nm).

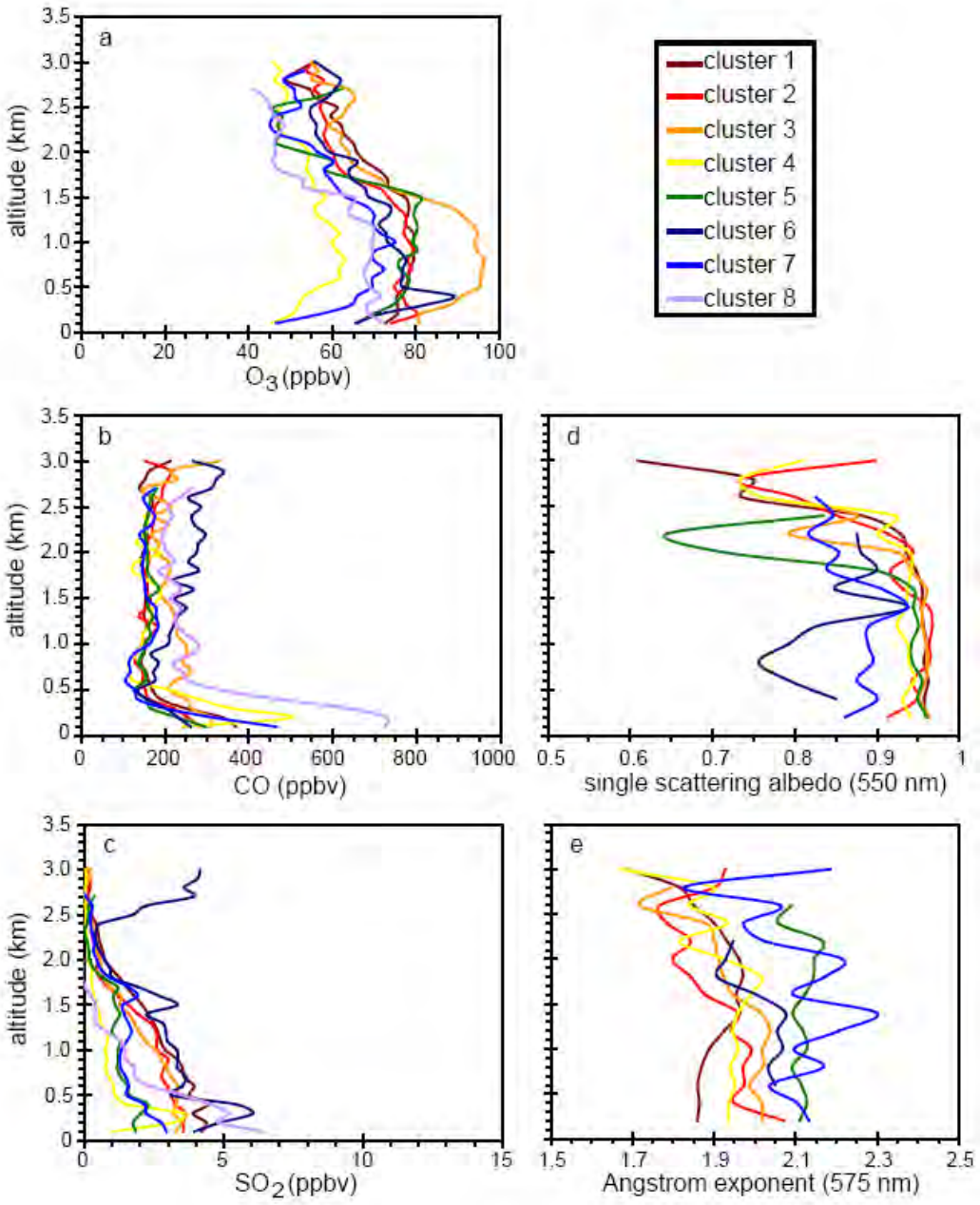

Figure 6. The median afternoon profiles for Clusters 1 (brown), 2 (red), 3 (orange), 4 (yellow), 5 (green), 6 (dark blue), 7 (blue), and 8 (violet) of a) O_3, b) CO, c) SO_2, d) single scattering albedo (550 nm), and e) Ångström exponent (575 nm).

3.3.3 O_3 Transport

Thus far, the first of the two original questions posed has been addressed. Namely, a statistical link between characteristic regional transport patterns into the Mid-Atlantic during summertime haze and O_3 episodes and specific pollution loadings has been established. In this section I will quantify the contribution of regionally transported O_3 to afternoon boundary layer O_3 over the Mid-Atlantic.

The percent of the afternoon O_3 boundary layer column content for each cluster that can be accounted for by regional transport was estimated with the following equation:

$$\%\ O_3\ transported = \left(\frac{RL}{MBL}\right) \times \left(\frac{MBL}{ABL}\right) \times 100, \qquad (2)$$

where *RL* is the residual layer column content, *MBL* is the morning boundary layer column content, and *ABL* is the afternoon boundary layer column content. The equation simplifies to the ratio of *RL*/*ABL* after the *MBL*s cancel out. The accuracy of this method depends upon the Lagrangian nature of the morning and afternoon profiles from each cluster. Because flight plans were designed in a Lagrangian manner, where morning flights were upwind of afternoon flights, the estimate should be accurate. The results are shown in Table 1 and Figure 7. The amount of afternoon O_3 that can be accounted for by regional transport ranges from a low of 55% to a high of 82%. One of the smallest contributions from transport (58%) corresponds to Cluster 3. This cluster shows the most stagnant conditions so that transport would not be expected to contribute as much to the afternoon totals (the weak winds allow for transport of only a few hundreds of km in a 24 hr period). The largest contributions from regional transport are seen in Clusters 1(70%), 2(69%), 4(82%) and 6(73%).

The trajectory density plots (see Figure 4) show that their greatest air parcel densities are over the Ohio River Valley. Those of Cluster 4 lie over the southern Ohio River Valley whereas those of the other three Clusters all lie over the northern portion of the Ohio River. While the pollution loadings associated with Cluster 4 are relatively small, those in Clusters 1, 2, and 6, particularly with respect to O_3, SO_2, and particle pollution, are large. In general, the greatest regional O_3 transport was from the Ohio River Valley, while some of the least transport occurred during clean, northerly flow (Cluster 7) and when stagnant conditions persisted and photochemical production was highest (Cluster 3). Our analysis neglected O_3 produced locally from precursors transported from upwind and may thus be an under-estimate of the role of transport.

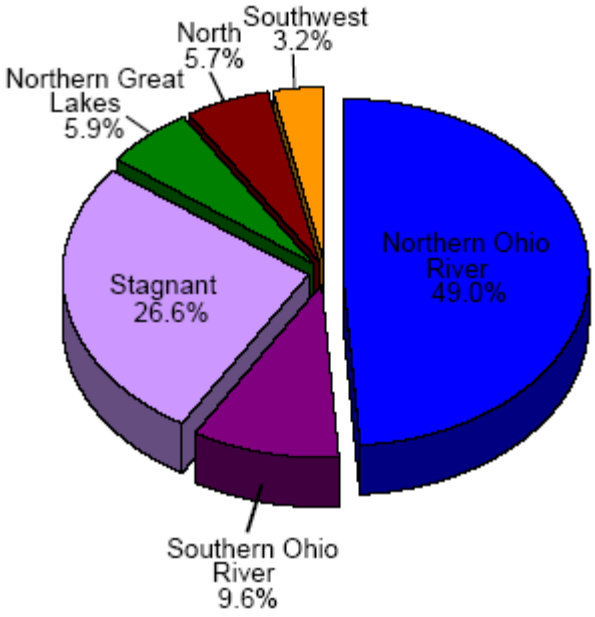

Figure 7. Pie chart showing the transport from the particular areas, as defined by the trajectory densities in each cluster, into the Mid-Atlantic region as a percent of the total number of profiles examined in the study. The Northern Ohio River slice comprises Clusters 1, 2, and 6.

3.4. Conclusions

Several years of episodic, summertime aircraft vertical profile trace gas and aerosol data collected as part of the Regional Atmospheric Measurement, Modeling, and Prediction Program (RAMMPP) were analyzed in this study. The data were divided into morning and afternoon profiles to identify diurnal patterns. Little diurnal variation was observed in the CO, SO_2, or Ångström exponent but O_3 values were greater in the afternoon than the morning. O_3 above the planetary boundary layer in the lower free troposphere, amenable to long range transport, was consistently ~55 ppbv. The single scattering albedo was larger in the afternoon than the morning, likely the result of VOC and SO_2 oxidation to secondary organic aerosols and sulfate, respectively. A decrease in the single scattering albedo above 2000 m was due to invariant absorption values with altitude combined with scattering values that declined with altitude. This phenomenon could have a large-scale radiative impact, although the aerosol extinction in the lower free troposphere may be too low to have any significant effects. Even so, this occurrence merits further investigation.

Characteristic transport patterns and source regions during summertime haze and O_3 episodes were analyzed with an agglomerative hierarchical cluster analysis of back trajectory data. Eight clusters were identified, which were then divided into morning and afternoon profiles. The median profile values were calculated and statistical differences were determined using a nonparametric procedure. When the greatest trajectory density lay over the northern Ohio River Valley and large NO_x and SO_2 sources, the result was large O_3 values, a large SO_2/CO ratio, large, scattering particles, and high AOD over the Mid-Atlantic U.S. In contrast, relatively clean

conditions over the Mid-Atlantic occurred when the greatest trajectory density lay over the southern Ohio River Valley and nearly missed many large NO_x and SO_2 sources. The greatest afternoon O_3 occurred during periods of near stagnation (when the average wind speed was 4.4m s^{-1} at 2km) that were most conducive to photochemical production. The least pollution occurred when flow from the north-northwest was too fast for pollution to accumulate and when flow was from the north, where there are few urban or industrial sources.

O_3 transport over several hundred kilometers into the Mid-Atlantic U.S. was estimated by calculating the ratio of the residual layer O_3 in the upwind morning profiles to the downwind afternoon boundary layer values. The greatest O_3 transport (69-82%) occurred when the maximum trajectory density lay over the southern and northern Ohio River Valley (~59% of the total profiles). The least O_3 transport (55-58%) was associated with fast southwesterly flow (~3% of the total profiles), clean northerly flow (~6% of the total profiles), and stagnant, polluted conditions (~27% of the total profiles). Altogether, about 64% of the O_3 during an episode is already present as the air enters the Baltimore/Washington area from the West.

In summary, this investigation demonstrated the ability to identify important statistical differences among pollution profiles that resulted from seemingly minor variations of the typical summertime, polluted meteorological regime. When trajectory density plots were overlaid on maps with the largest annual NO_x and SO_2 emitters, specific source regions were identified. The results indicate that the areas of maximum trajectory density together with wind speed are effective predictors of regional pollutant loadings. Additionally, due to the Lagrangian nature of the dataset,

the regionally transported contribution to the total afternoon boundary layer column O_3 content in each cluster could be quantified.

Chapter 4: Cluster Analysis of Pollutant Profiles.

4.1 Introduction

4.1.1 Background

Understanding the influences of meteorology and emissions on the vertical distribution of trace gases and aerosols can improve modeling and prediction of pollution events. Some work presented in this chapter is from Hains et al. (2007a). I have developed a method to cluster vertical profiles of trace gases and aerosols. I then examined meteorological conditions as indicated by back trajectories associated with each cluster. Results from this cluster analysis are used to explain meteorological and emission influences on the vertical distribution of trace gases and aerosols. I have clustered over 150 profiles of O_3, CO, SO_2, absorption, scattering, and Ångström exponent (α) collected between 1997-2003 in June, July and August. I developed a method for integrating point source emission sources (from the EPA's AirData database) encountered by a 48-hr back trajectory. I have employed this method to explain the relationship between point source emissions and the different clustered profiles.

4.1.2 Cluster Analysis

Statistical cluster analysis involves determining the differences between the objects being analyzed, and clustering those objects with the smallest differences. The trace gases presented in Chapter 3 showed distinctive profiles; for example, most of the SO_2 was found below 500 m throughout the day, while O_3 was most concentrated

above 500 m in the morning and was more uniform from the surface to 2000 m in the afternoon (the largest values in the profile were found near the 1100 m level).

For this work, the raw data were averaged into altitude layers of 100 m (gases) or 200 m (aerosols) and then the layers were grouped into bins shown in Table 1. The slope and correlation of the points in each pair of profiles under comparison were considered as well as the total difference in values between the two profiles within each altitude bin. The following equation was used to calculate the differences among the aircraft profiles:

$$Dij = \sum_{k=1}^{k=4} \left\{ \left(\sum_{a=1}^{a=n_k} abs(c_{ia} - c_{ja}) \right)^2 * \left(1 + [1 - r] + [1 - \exp(-(s-1)^2]\right) \right\} \qquad (1)$$

Here, k is the index for the four different altitude bins for the profiles and a is an index for the n_k layers within the k^{th} bin (Table 1). The species value is represented by c for the i^{th} and j^{th} profile. In each altitude bin, k, there are at least four layers of trace gas or aerosol data. A regression was made to obtain the slope, s, and the correlation coefficient, r, for each pair of profiles using the mixing ratio (or aerosol coefficient) within the k bins. The first part of Equation 1 determines the square of the sum of the differences between values at each altitude bin, k. The second part of the equation multiplies the difference by one plus differences associated with the correlation and slope. When the correlation is small or negative the profiles are very different and the 1- r portion increases, which increases the total difference D_{ij}. As the correlation coefficient approaches unity the 1-r portion approaches zero, and this decreases the total difference D_{ij}. The exponent of the slope portion is used to account for the slope between the pairs of profiles. A slope near unity suggests that the profiles are similar and thus should add little to the total difference. The exponent

of the slope was used to guarantee that slopes much different from unity will make the exponential term small and thus increase the total difference. Once the difference between each pair of profiles has been calculated, the profiles with the smallest differences are clustered. These clusters are constructed from hierarchical cluster trees generated with an average linkage algorithm in Matlab (described in Chapter 3 section 3.2.3).

k bin	Altitude bins for trace gases	Number of layers in bin (m_k)	Altitude bins for aerosols	Number of layers in bin (m_k)
1	151-650 m	5	100-900 m	4
2	651-1150 m	5	901-1700 m	4
3	1151-1650 m	5	1701-2500 m	4
4	1651-2450 m	8		

Table 1. Altitude bins for trace gases and aerosols used in Equation 1.

4.2 Results

4.2.1 O_3

Figure 1 shows the median profiles for each of the six O_3 clusters calculated in the above manner. The clustering technique identified a small group of outliers, Cluster 6, with large values of O_3 above 2000 m altitude. These profiles were made on 8 and 9 July 2002 when smoke from Canadian forest fires impacted the Mid-Atlantic region (*Colarco et al.*, 2004; *Taubman et al.*, 2004a). The transported O_3 can be seen in the peak (up to 150 ppb) above 2000 m. This shows that the statistical technique employed can separate anomalous episodes. The quartiles for the six clusters rarely overlap, which further exemplifies how the method was able to separate distinct events.

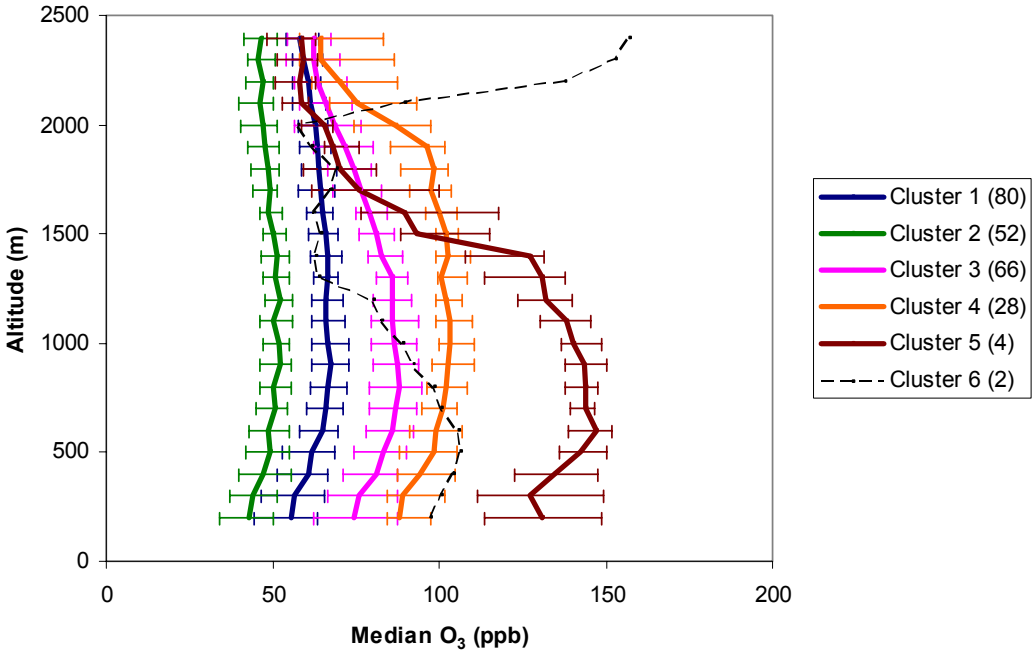

Figure 1. Median O_3 profiles for each cluster. Error bars represent the 25th and 75th percentiles. The number of profiles in each cluster is shown in parentheses in the key. Clusters 1 and 2 show the smallest O_3 values, while Clusters 3, 4 and 5 show the largest. Cluster 6 profiles were made when the Canadian forest fires impacted the region and the peak above 2000 m shows their influence.

I calculated two-day HYSPLIT back trajectories for each spiral, ending at an altitude of 1, 2 and 3 km, at the latitude and longitude of the spiral and at the time the spiral was made. Back trajectories were similar at all altitudes and so I chose those ending at 1 km because these are most likely to be closer to point source emissions. Profiles from Clusters 3, 4 and 5 had large O_3 values and the back trajectory density plots (Figure 2) show passage over the Northern Ohio River Valley, where there is a higher concentration of NO_x sources. Taubman et al. (2006) found a similar relationship between back trajectories concentrated over the Northern Ohio River Valley and large mixing ratios of O_3 and suggested that the large concentration of

power plants in this region contributes to the O_3 in the Mid-Atlantic region. The back trajectory density plots for Clusters 3-5 also show larger densities around the I-95 corridor, which is suggestive of stagnation events that lead to higher O_3 values. Cluster 2 has back trajectories that pass over the Atlantic Ocean, which may explain the smaller O_3 values associated with this cluster. Cluster 1 has the second smallest O_3 values (Cluster 1 column content is 19% less than that of Cluster 3), even though the back trajectories associated with Cluster 1 are similar to those of Cluster 3. To address this discrepancy, the integrated NO_x point source emissions along the back trajectories were examined.

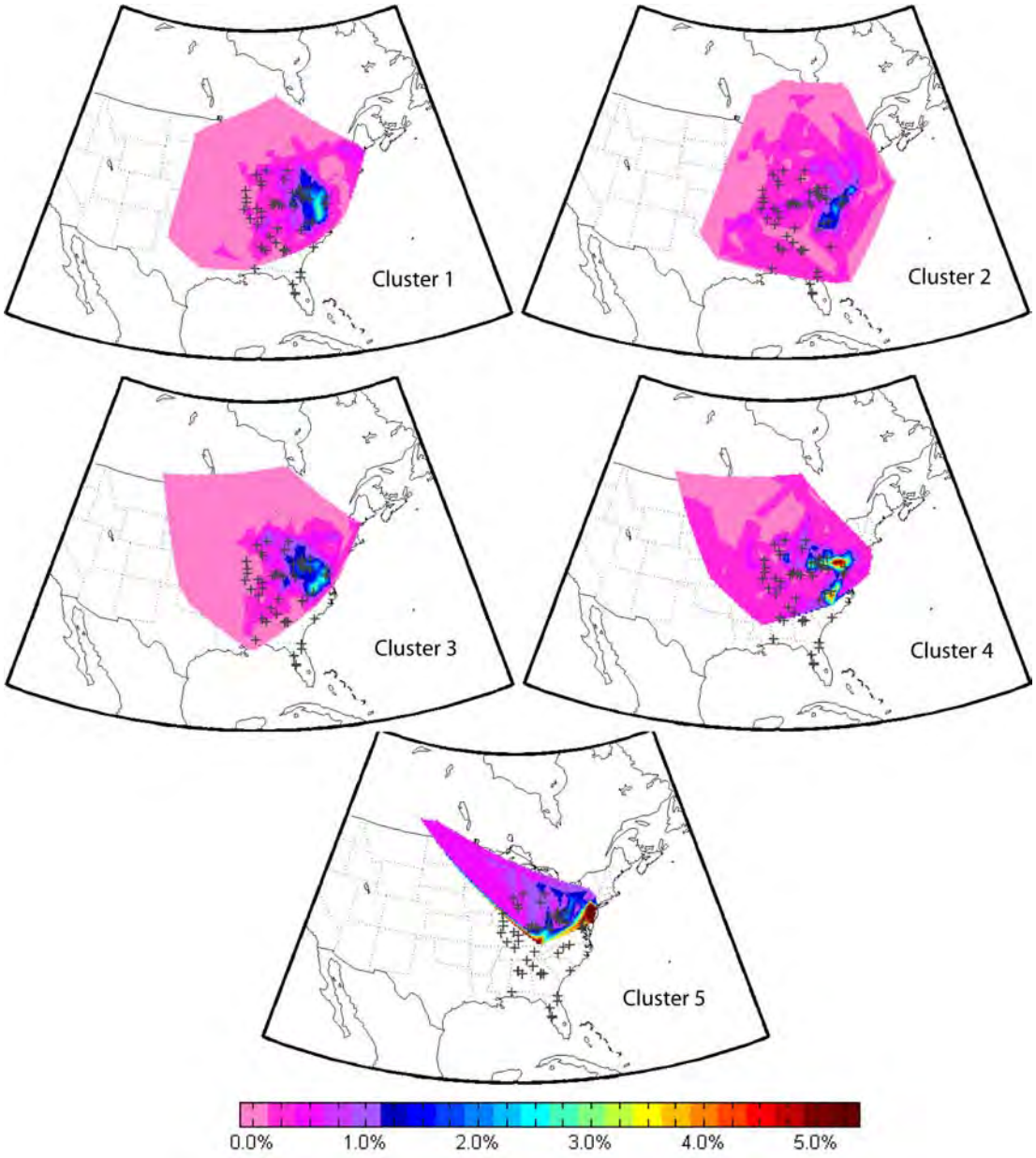

Figure 2. Back trajectory density plots for O_3 Clusters 1-5. The top 0.3% NOx sources are shown with a + symbol. Clusters 3, 4 and 5 associated with larger O_3 values show larger densities near point sources as well as along the I-95 corridor, suggestive of stagnation. Cluster 5 also has an unusual flow pattern from the northeast. Clusters 1-2, with smaller O_3 values are associated with more variable winds.

I integrated the NO_x emissions along each back trajectory to explain the influence of upwind emissions on upwind ozone mixing ratios. Emissions from the daily EPA Clean Air Market unit level emissions database (http://cfpub.epa.gov/gdm/index.cfm?fuseaction=emissions.wizard) were used in this study. I drew a circle, centered at each back trajectory position for each hour of the two day back trajectory (Figure 3). The radius of the circle was 80 km to account for uncertainties associated with the back trajectory position and the influence of eddy diffusion and mixing processes. The emissions within each circle were summed. The sum of the emissions for each circle was divided by the area of the circle. I used emissions from the day on which the back trajectory crossed a circle for the date of each back trajectory position. The summed emissions will be referred to as integrated emissions. Statistics (median, 5^{th}, 25^{th}, 75^{th} and 95^{th} percentiles) for the integrated NO_x emissions for each O_3 cluster are shown in Figure 4.

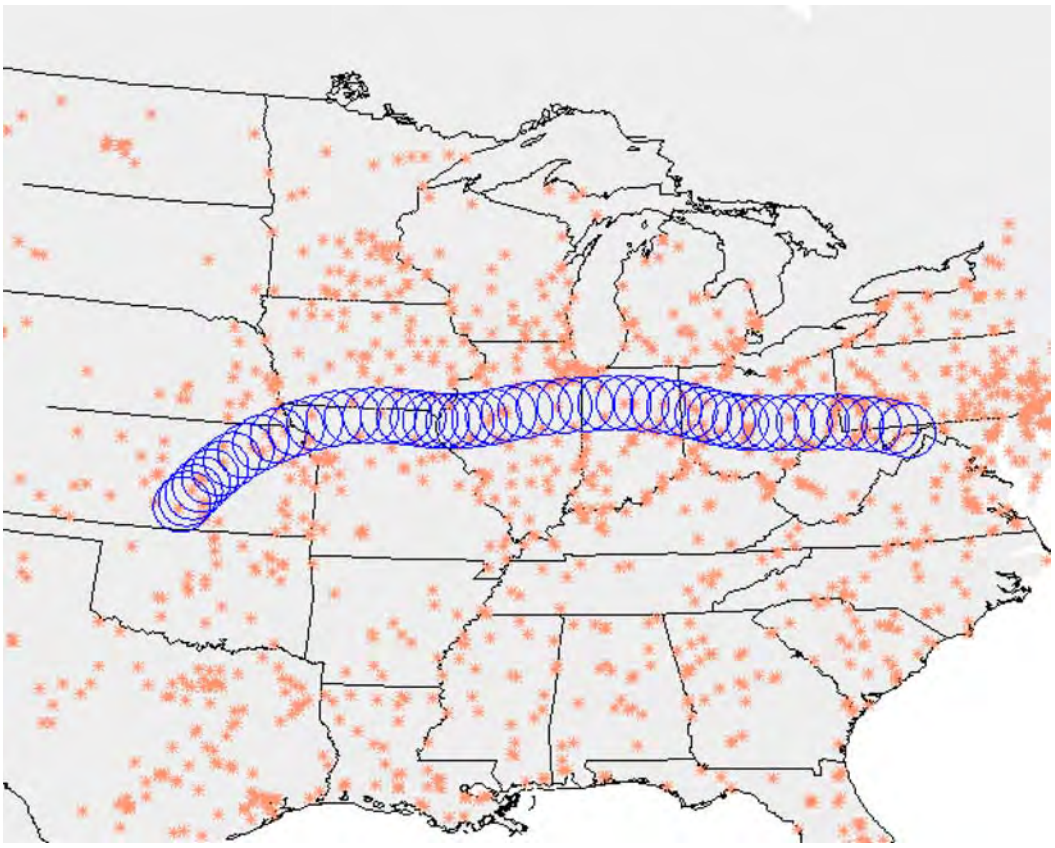

Figure 3. Circles drawn around an example back trajectory. The emissions contained in each circle were summed and divided by the area of the circle. Then emissions from each circle were summed. The pink * represent point source locations.

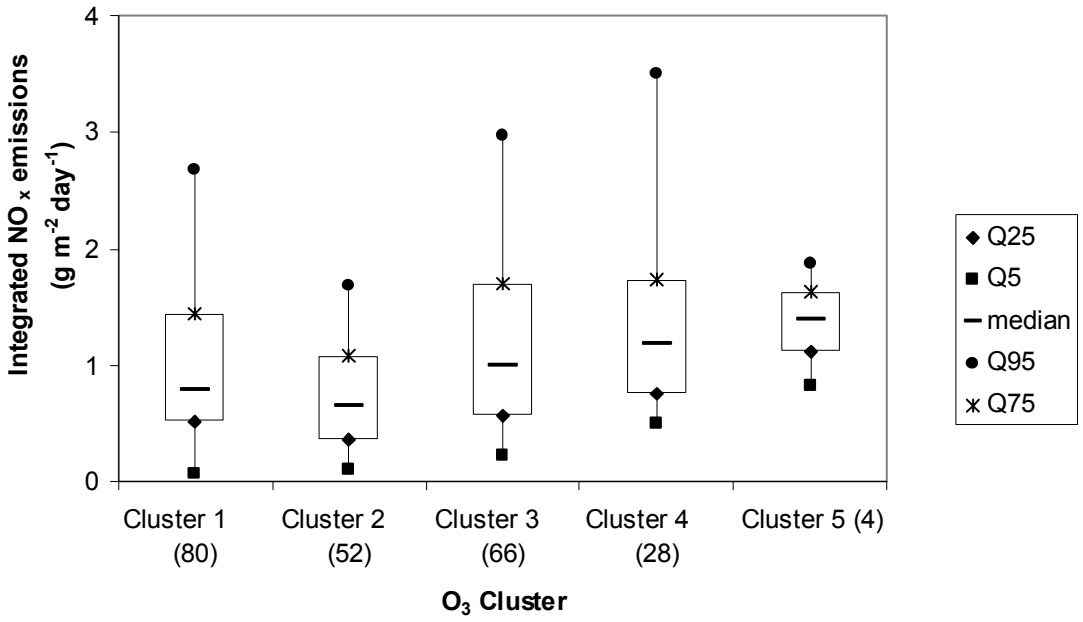

Figure 4. Statistics for NOx emissions encountered by back trajectories for each O_3 cluster. The NOx emissions are sums of all emissions (g day^{-1}) encountered by a back trajectory divided by the area of the circle drawn around the back trajectory point (m^2). Clusters 1 and 2, with the smallest O_3 values are also associated with the smallest NOx emissions. Clusters 3, 4 and 5, with the largest O_3 values are associated with the largest NOx emissions.

Clusters 3, 4 and 5 have the largest O_3 column contents and the largest NO_x emissions, while Clusters 1 and 2 have the smallest O_3 column contents and the smallest NO_x emissions. Even though back trajectory density maps for Clusters 1 and 3 are similar, Cluster 1 is associated with 21% less integrated NOx emissions, explaining the 18% smaller O_3 values. The median O_3 column content and integrated NO_x emissions for Clusters 1 through 5 show a positive relationship (Figure 5), suggesting that NO_x emissions from point sources play an important role in downwind O_3 production.

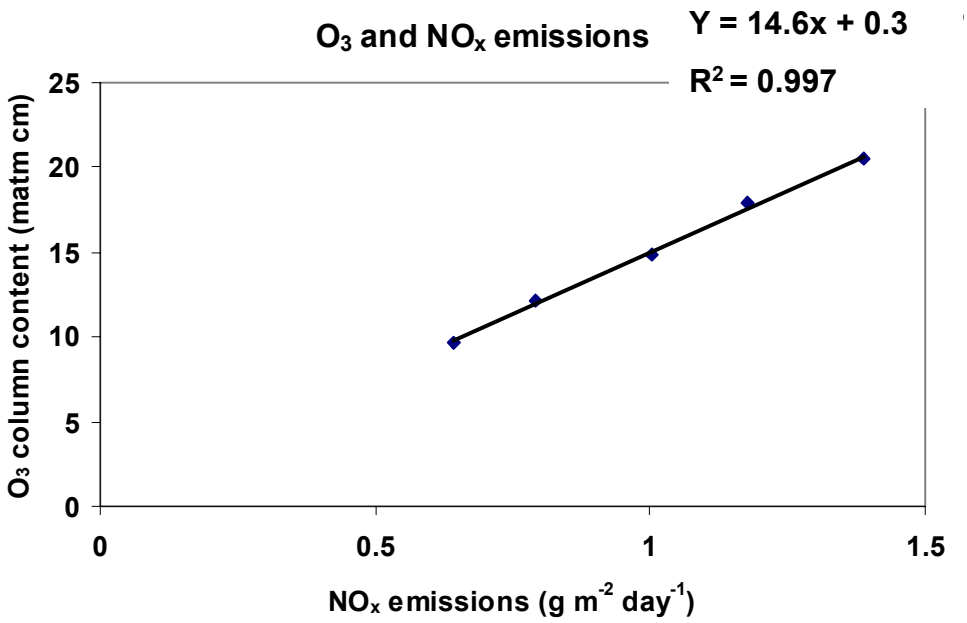

Figure 5. Median O_3 column content and median integrated NOx emissions (from point sources) for O_3 Clusters 1 through 5. The O_3 is positively correlated with integrated NOx emissions.

Profiles were also analyzed by time of day, where morning profiles are defined as those made before 12 noon EST and afternoon as profiles made after 12 noon EST. Sixty-one and sixty-eight percent of the profiles in Clusters 3 and 4 were measured in the afternoon, whereas only 38% and 46% of the profiles in Clusters 1 and 2 were measured in the afternoon. Greater O_3 values in Clusters 3 and 4 may be partly explained by the increased number of afternoon profiles which were generally made downwind of urban centers, and had more time for O_3 production.

4.2.2 SO_2

I also clustered the SO_2 profiles and generated three distinct SO_2 profile clusters (Figure 6). Of the 192 profiles analyzed, 170 (89%) fell into the relatively clean Cluster 3. The other clusters reflect large values of SO_2 at altitudes from near

the surface (Cluster 2) to 1000 m (Cluster 1). Back trajectories associated with Cluster 3 show a broader area of origin than the more heavily polluted Clusters 1 and 2 (Figure 7). The median SO_2 profile from Cluster 2 shows large values near the surface that decrease above 500 m. Profiles in Cluster 1 show large values near the surface that do not drop off as rapidly as those in Cluster 1, indicating better mixing in the lower troposphere.

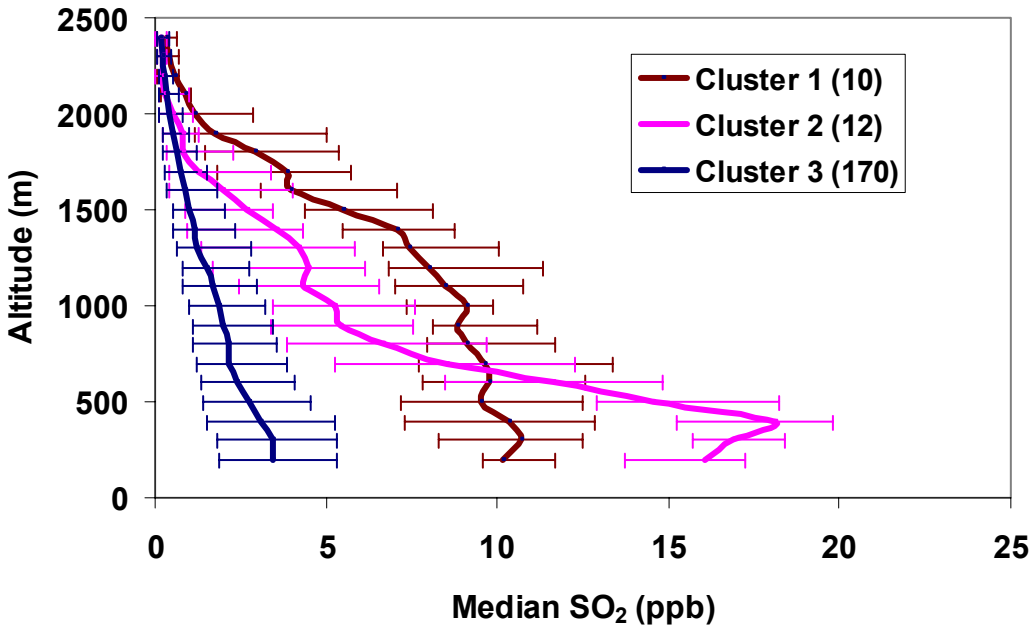

Figure 6. Median SO_2 profiles for each cluster. Error bars represent the 25th and 75th percentiles. The number of profiles in each cluster is shown in parentheses in the key. Cluster 3 is the background Mid-Atlantic summertime SO_2 profile, representing the majority of SO_2 profiles measured. Clusters 1 and 2 represent profiles impacted by chance plume encounters.

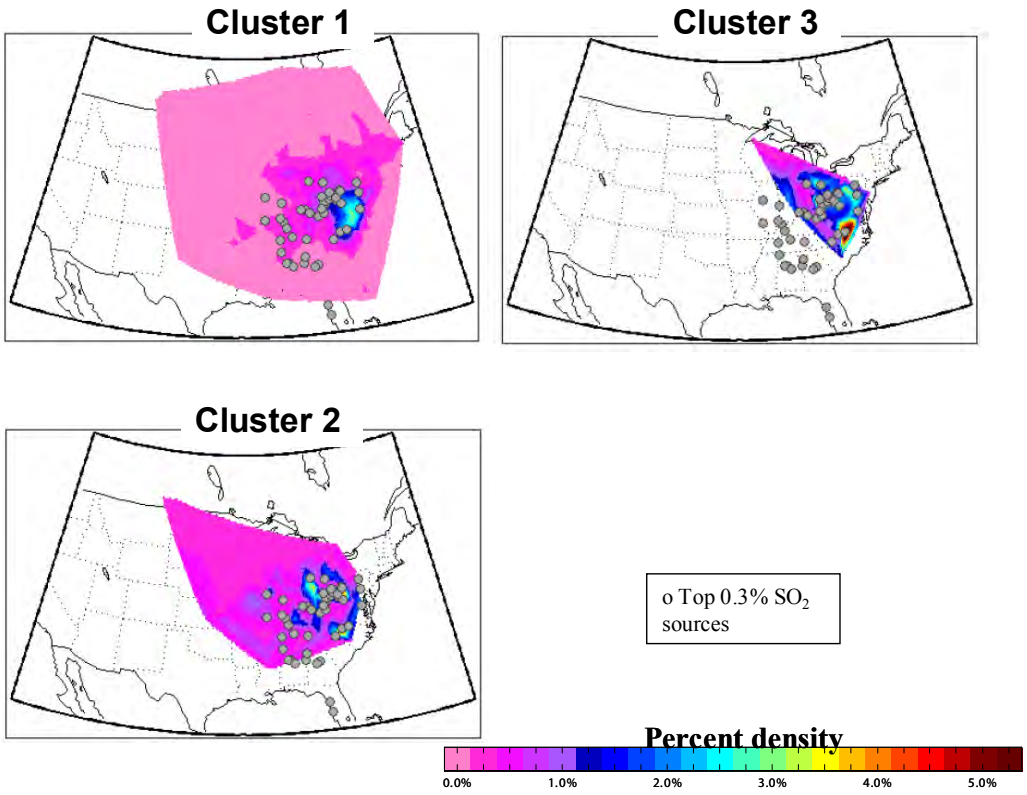

Figure 7. Back trajectory density plots for SO_2 Clusters 1-3. The top 0.3% SO_2 sources are shown with a circle. Back trajectories associated with Clusters 2 and 3 show more density over SO_2 sources while the back trajectories associated with Cluster 1 show more variable origins.

The integrated SO_2 emissions along each back trajectory and statistics for each SO_2 cluster were calculated (Figure 8). The SO_2 emissions do not show as much range as the NO_x emissions. The lack of relationship between emissions and the SO_2 profiles, and the small number of meaningful SO_2 clusters generated, suggests profiles with larger values are likely the result of chance encounters with fresh plumes, and that the lifetime of SO_2 in the summer is shorter than 48 hours. The lifetime of SO_2 is addressed in Chapter 5.

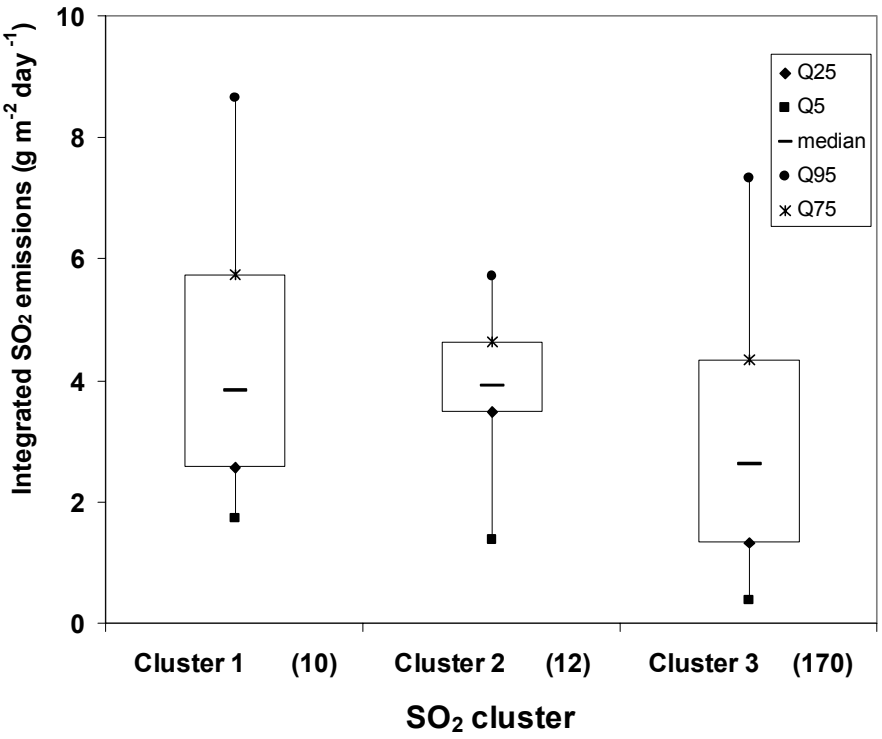

Figure 8. Statistics for SO_2 emissions encountered by back trajectories for each SO_2 cluster. The SO_2 emissions are sums of all emissions (g day^{-1}) encountered by a back trajectory divided by the area of the circle drawn around the back trajectory point (m^2). The SO_2 emissions show little relationship with the profiles.

4.2.3 Particle Scattering

Figure 9 shows the median scattering coefficients (in units of m^{-1}) for all flights conducted between 2001 and 2003 (June through August). The clustering methodology produced four scattering clusters, but two are sparsely populated (Clusters 3 and 4) and associated with the Canadian forest fire episode (Figure 9). The median scattering profile for Cluster 1 is similar to the median profile of all flights. Cluster 1, with 125 profiles, has smaller values than Cluster 2, with 48 profiles (Figure 9). Back trajectories associated with profiles from Cluster 2 show winds from the Northern Ohio River Valley, while Cluster 1 has back trajectories

with more variable winds and greater mean wind speeds (Figure 10). Slower wind speeds or stagnant conditions allow time for the conversion of SO_2 to sulfate. Figure 11 shows statistics of integrated SO_2 emissions for each cluster. The median SO_2 emissions for Cluster 2 are almost a factor of two greater than those for Cluster 1. This suggests that the aerosol loading reflects the SO_2 emitted into the air parcel over the previous 48 hours.

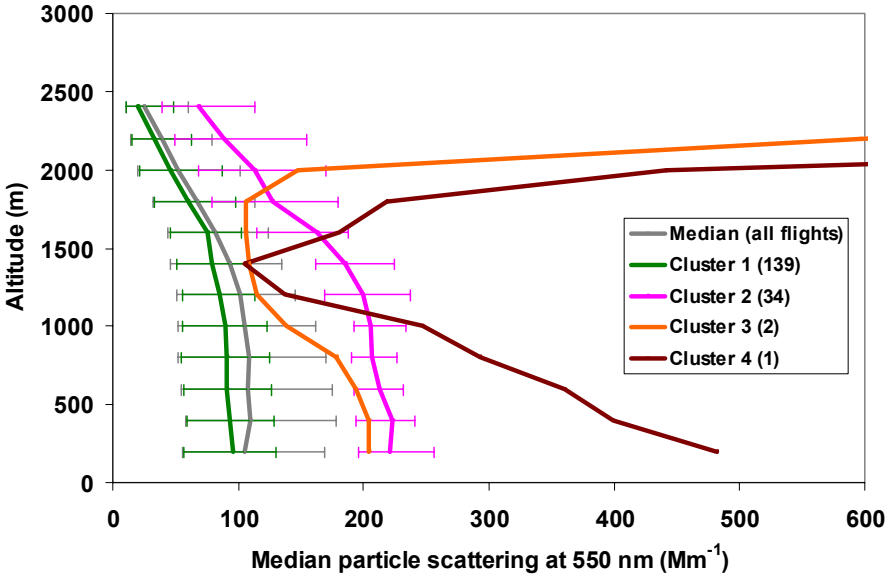

Figure 9. Median scattering profiles for each cluster. Error bars represent the 25th and 75th percentiles. The number of profiles in each cluster is shown in parentheses in the key. Cluster 2 has profiles with twice the scattering value as Cluster 1. Profiles from Clusters 3 and 4 were measured when the Canadian forest fires impacted the region.

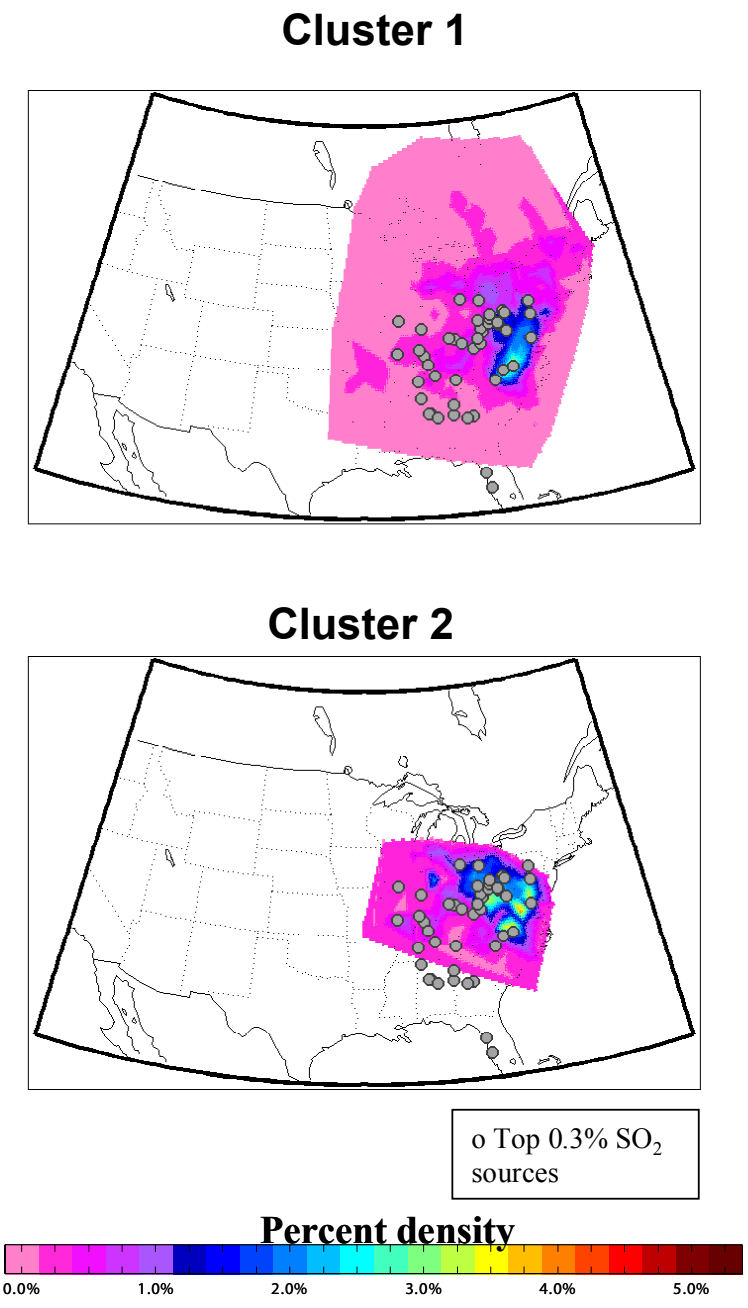

Figure 10. Back trajectory density plots for scattering Clusters 1and 2. The top 0.3% SO_2 sources are shown with a circle. Back trajectories associated with Clusters 2 show more density over SO_2 sources while the back trajectories associated with Cluster 1 show more variable origins.

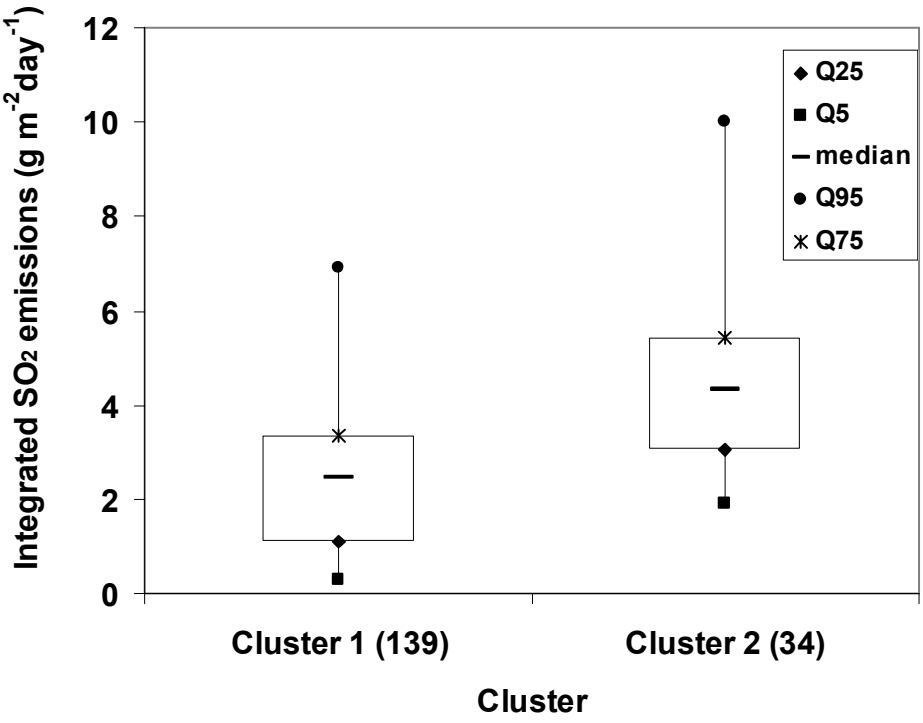

Figure 11. Statistics for SO_2 emissions encountered by back trajectories for each scattering cluster. The SO_2 emissions are sums of all emissions (g day^{-1}) encountered by a back trajectory divided by the area of the circle drawn around the back trajectory point (m^2). Cluster 2 is associated with almost double the emissions of Cluster 1, explaining why cluster 2 profiles have double the scattering values as Cluster 1 (Figure 9).

The conversion from SO_2 to sulfate in the summer is so rapid that there is little discernable relationship between SO_2 emissions from the Ohio River Valley and SO_2 values in the Mid-Atlantic. There is a positive relationship between SO_2 emissions in the Northern Ohio River Valley and particle scattering in the Mid-Atlantic, indicating an important source of sulfate aerosols is from Northern Ohio River Valley coal fired power plants (e.g., Taubman et al. 2006). The stronger relationships between emissions and SO_2 and aerosol profiles suggest that the lifetime of sulfate is longer than 48 hours.

4.2.4 Angstrom Exponent

The clustering methodology produced four distinct α clusters (Figure 12). The median profile for Cluster 1 has relatively small α values and thus represents larger particles. The back trajectories associated with Clusters 1 and 2 are concentrated over point sources in the Northern Ohio River Valley (Figure 13). Cluster 1 back trajectories however, are slower allowing more time for particle growth. Profiles from Cluster 1 are associated with larger integrated SO_2 emissions than the other clusters (Figure 14). Profiles in Cluster 4 have the largest α values and the least integrated SO_2 emissions. The α values are calculated from scattering measurements, explaining why they show a relationship similar to that between SO_2 emissions and scattering. Profiles in Cluster 3 decrease sharply above 2000 m and represent large particles. Four of the profiles in Cluster 3 were measured during the Canadian forest fires and one profile was measured on the 4th of July, when large particles would also be expected.

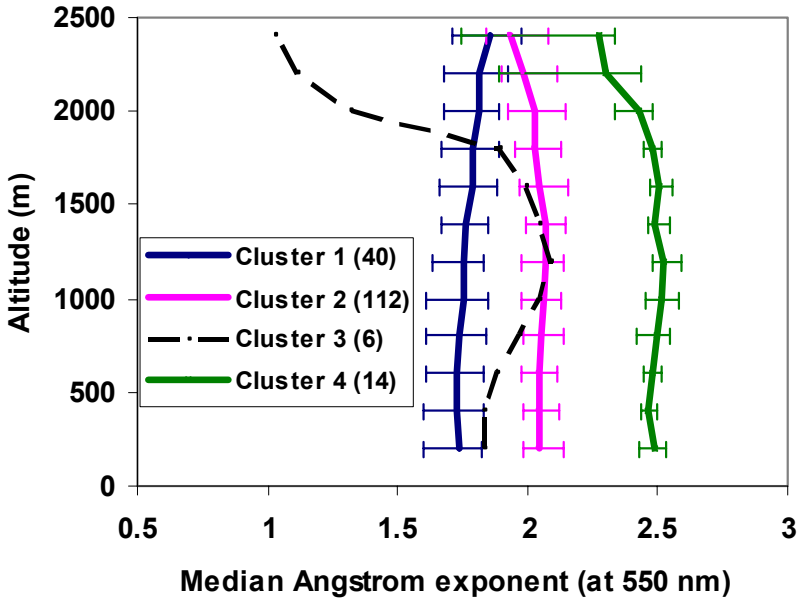

Figure 12. Median Angstrom exponent profiles for each cluster. Error bars represent the 25th and 75th percentiles. The number of profiles in each cluster is shown in parentheses in the key. Clusters 1 and 3 have the smallest angstrom exponents (largest particles), while Clusters 2 and 4 have the largest angstrom exponents (smallest particles). Profiles in Cluster 3 were measured when Canadian forest fires impacted the region, bringing in large particles aloft (above 2000 m).

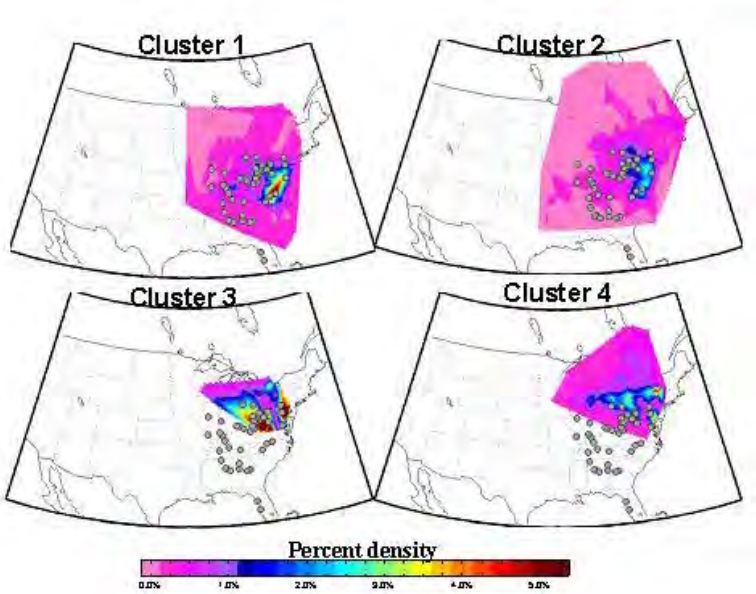

Figure 13. Back trajectory density plots for Angstrom exponent Clusters 1-4. The top 0.3% SO_2 sources are shown with a circle. Back trajectories associated with Clusters 1 and 2 show density over SO_2 sources, however back trajectories associated with Cluster 1 has the weakest winds allowing for more particle growth.

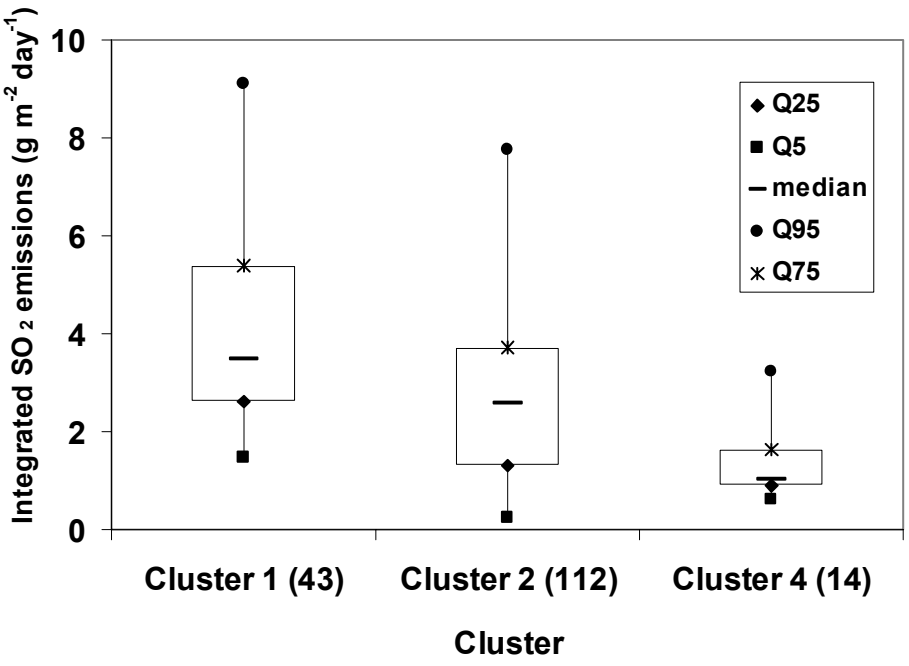

Figure 14. Statistics for SO_2 emissions encountered by back trajectories for each Angstrom exponent cluster. The SO_2 emissions are sums of all emissions (g day^{-1}) encountered by a back trajectory divided by the area of the circle drawn around the back trajectory point (m^2). Cluster 1 is associated with the largest SO_2 emissions, while Clusters 2 and 4 emissions are much smaller. This explains the larger particles seen in Cluster 1 profiles (Figure 12).

4.2.5 CO

The clustering methodology produced three CO clusters (Figure 15). Cluster 3 had only one profile which was measured during the Canadian forest fire episode of 2002 and shows the signature peak in CO values above 2000 m (Taubman *et al.*, 2004a). Cluster 1, with 87% of the profiles, represents the background CO measured in the summer months in the Mid-Atlantic region. Cluster 2 values are about twice as large as Cluster 1 values. The back trajectories for Cluster 2 are short and concentrated around the I-95 corridor (a source for CO); while the back trajectories for Cluster 1 are more diffuse (Figure 16). This may explain the difference in CO

values between Clusters 1 and 2. Many of the profiles in Cluster 2 were made near Philadelphia and Baltimore, where the urban environments likely added to CO values. Most of the other flight locations for Cluster 2 were downwind of the I-95 corridor between Virginia and Pennsylvania. Cluster 2 not only has larger peaks near the surface but also larger values aloft. This suggests that the Eastern US is a major source for regional CO.

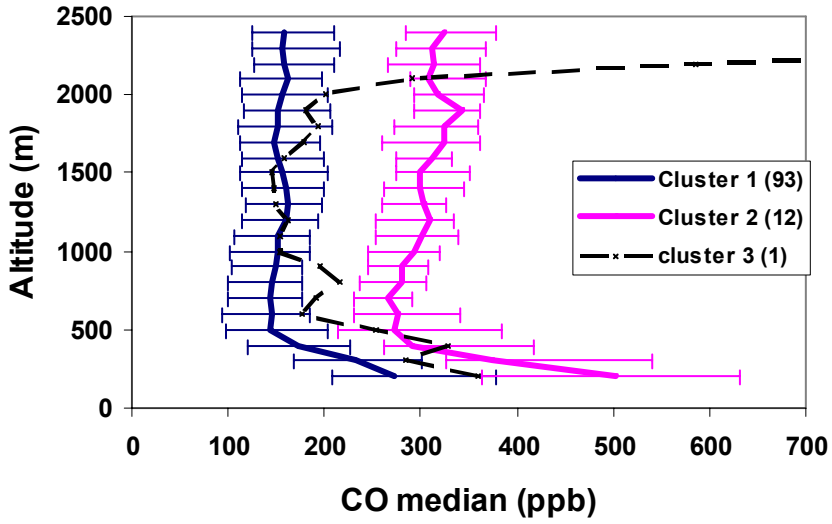

Figure 15. Median CO profiles for each cluster. Error bars represent the 25th and 75th percentiles. The number of profiles in each cluster is shown in parentheses in the key. Cluster 3 profiles have double the CO values in Cluster 1. Profiles in Cluster 4 were made when Canadian forest fires impacted the region.

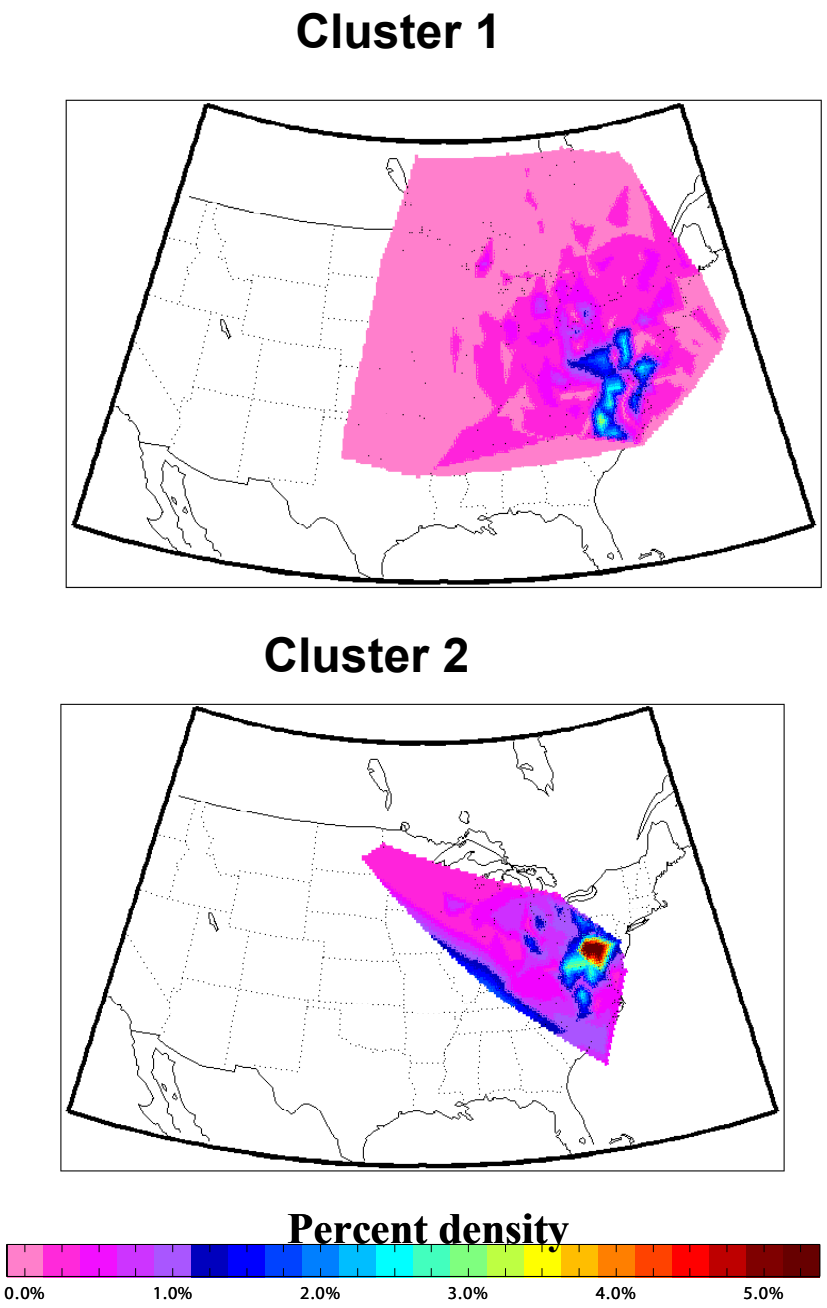

Figure 16. Back trajectory density plots for CO Cluster1 (clean profile) and Cluster 2 (polluted profile). Back trajectories for Cluster 2 are short and concentrated around the I-95 corridor (a source for CO); while the back trajectories for Cluster 1 are more diffuse.

4.2.6 Particle Absorption

The clustering methodology produced three absorption clusters and the associated median profiles are shown in Figure17 along with the median of all flights made between 2000 and 2003 (June through August). The median profile for Cluster 2 represents 77% of the profiles and is similar to the median of all flights made. The median profile for Cluster 1 has on average twice the absorption values of Cluster 2, and is greater than the 75th percentile of the median of all profiles. The back trajectory densities for Clusters 1 and 2 both show northwesterly winds, however, Cluster 1 winds are slightly faster (Figure 18). These faster back trajectories associated with Cluster 1 may bring in air from the industrialized Midwest to mix with local, mobile emissions. Cluster 3 contains only profiles measured during the Canadian forest fires and shows the characteristic peak above 2000 m (Taubman *et al.*, 2004a).

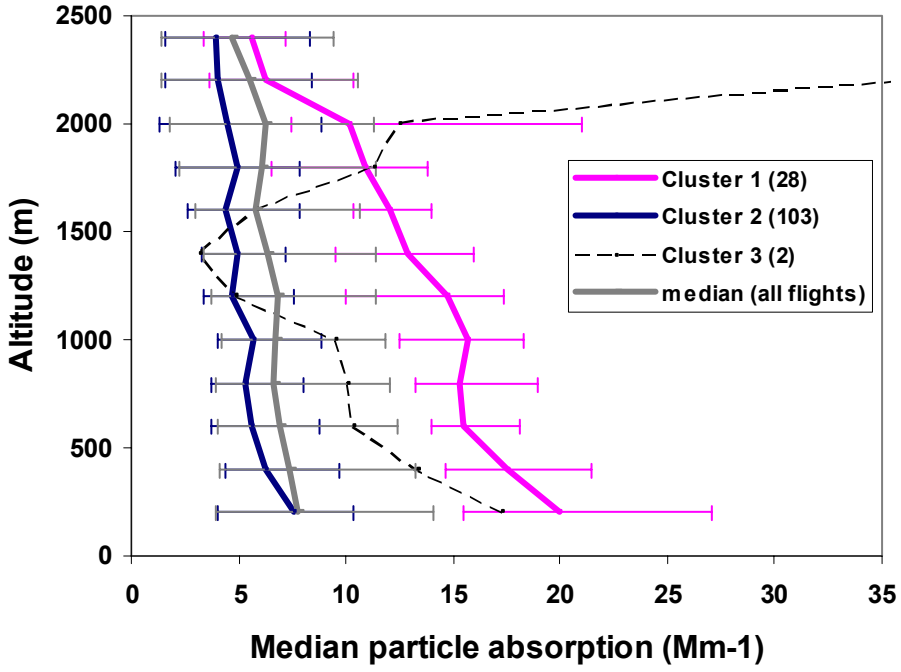

Figure 17. Median absorption profiles for each cluster. Error bars represent the 25th and 75th percentiles. The number of profiles in each cluster is shown in parentheses in the key. Absorption values in Cluster 1 are double those in cluster 2 below 1200 m. Profiles in Cluster 3 were made when Canadian forest fires impacted the region.

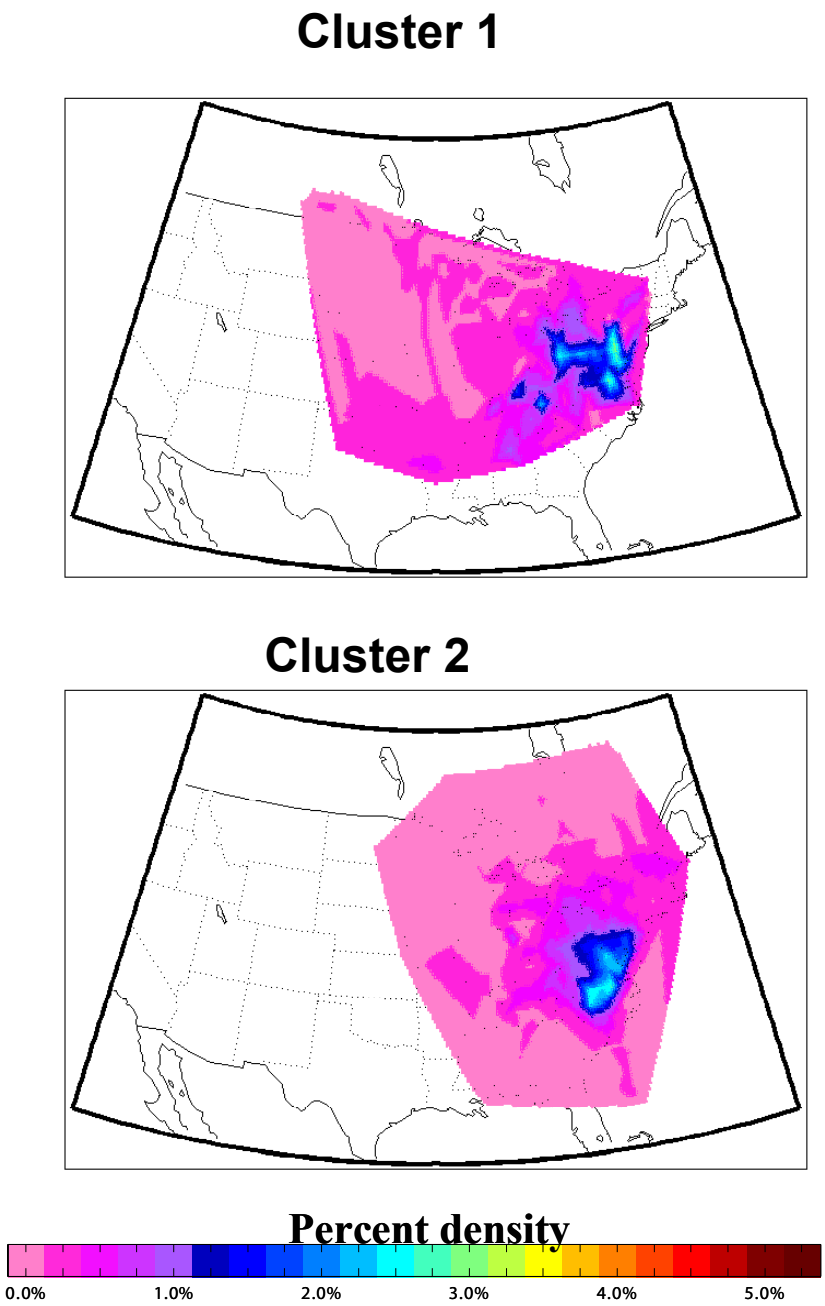

Figure 18. Back trajectory density plots for absorption Clusters 1 and 2. The back trajectory densities for clusters both show northwesterly winds, however, Cluster 1 winds are slightly faster. These faster back trajectories associated with Cluster 1 may bring in air from the industrialized Midwest to mix with local, mobile emissions.

4.3 Discussion

In order to better understand the chemistry associated with each O_3 cluster, the median profiles for SO_2, particle scattering and CO measured simultaneously with the O_3 profiles from each of the clusters (herein referred to as matching species profiles) were examined (Figure 19). The clusters with the least O_3 (Clusters 1 and 2) are associated with the least SO_2 and scattering particles, while the clusters with more O_3 (Clusters 3 and 4) are associated with the most SO_2 and scattering particles (measurements of scattering and SO_2 were not made for Cluster 5). The SO_2/CO ratio (Table 2) was also used to determine whether mobile or point source pollution was most influential on the O_3 values. The larger SO_2/CO ratio for Clusters 3 and 4, with large O_3 values, suggests that these clusters were impacted most by point source emissions. CO profiles were similar for Clusters 1-4, but very large CO was measured in Cluster 5 (only one CO profile was measured for this small cluster), suggesting that localized pollution from mobile sources may affect these profiles.

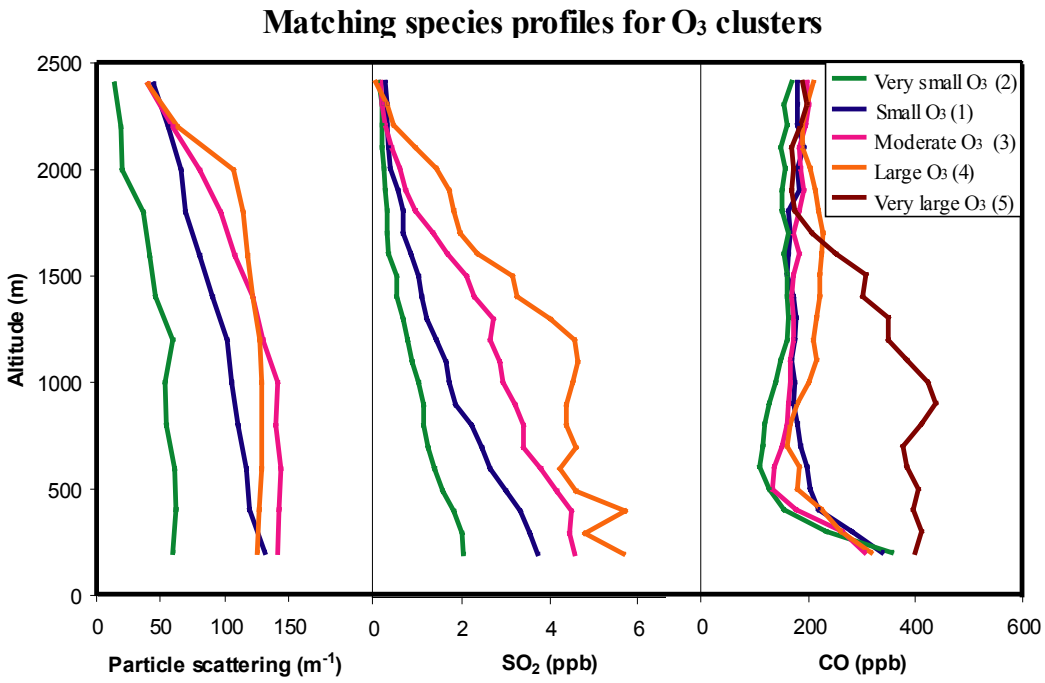

Figure 19. Matching species profiles for O_3 clusters. The O_3 cluster number is in parentheses in the key. Profiles with the smallest O_3 values are associated with the smallest scattering and SO_2 values, while profiles with larger O_3 values are associated with more SO_2 and scattering. The profile with the largest O_3 is associated with the most CO, suggesting that this cluster was influenced by mobile sources.

Table 2. SO_2/CO ratios for O_3 Clusters 1-4. Clusters 3 and 4, with large O_3 values also have large SO_2/CO ratios, suggesting that they are most heavily influenced by point source emissions.

Cluster	SO_2/CO ratio	n
1	0.010528	38
2	0.005548	18
3	0.014472	25
4	0.019471	10

Median matching profiles of SO_2, O_3 and α were examined for the scattering clusters (Figure 20). Cluster 2, with the most scattering particles, was also associated with the most O_3 and SO_2, as well as the largest particles (small α values). This suggests that days with more aerosol pollution are often associated with conditions conducive to O_3 production and is consistent with the idea the NOx from elevated sources is more effective at producing O_3 than NOx from mobile sources.

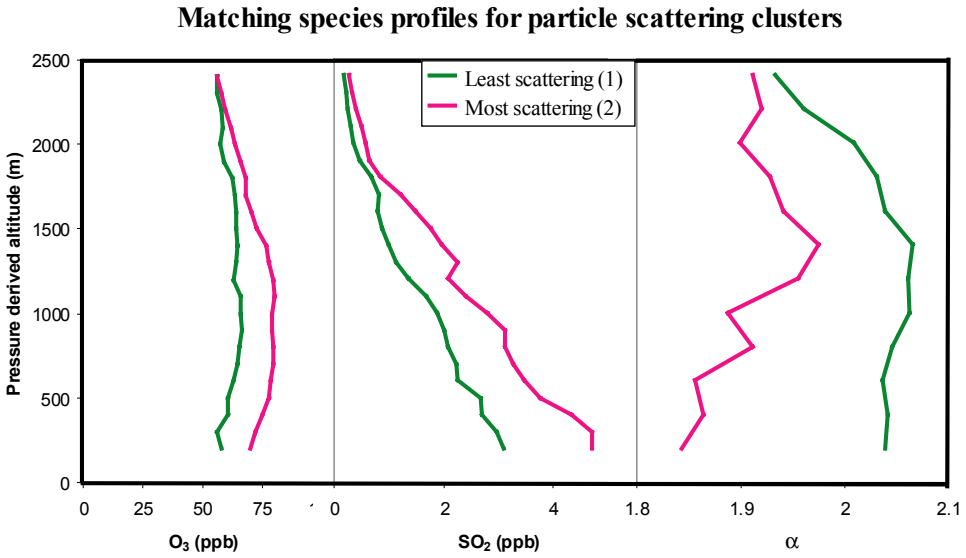

Figure 20. Matching species profiles for particle scattering clusters. Profiles with the most particle scattering are associated with the most O_3 and SO_2 as well as the largest particles (smallest a values).

Median matching species of CO were examined for the absorption clusters (Figure 21). Cluster 1 profiles, that are twice as absorbing as Cluster 2 profiles, have matching species profiles of CO that are on average 30% larger. This relationship between absorption and CO suggests that increased levels of absorbing species are likely the result of mobile emissions.

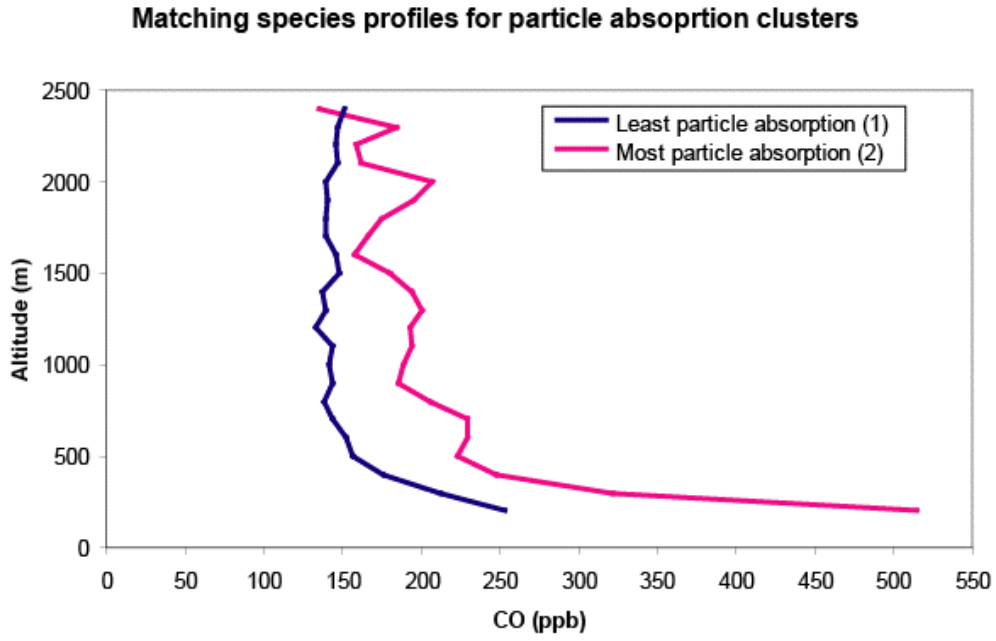

Figure 21. Matching species profiles for particle absorption clusters. The profile with the most particle absorption is associated with the most CO.

4.4 Conclusions

Clustering profiles of species allows for separation of distinct pollution events from a large collection of profiles, enabling a better understanding of how meteorology and chemistry affect the shape and size of the profiles. Profiles with the largest O_3 values were associated with larger integrated NO_x emissions from point sources. The clustering methodology also separated profiles affected by Canadian forest fires. SO_2 profiles were less influenced by regional emissions than local emissions. The amount of SO_2 emitted into an air parcel over the previous 48 hours did not correlate well with observed SO_2 values. The product of SO_2 oxidation, as evidenced by particle light scattering, does correlate with SO_2 emissions integrated

over the previous 48 hours. This suggests the sulfate lifetime is longer than 48 hours. Particle size, calculated using scattering values, shows a similar relationship to emissions as scattering. Profiles with the largest CO values were made downwind of urban regions, and so these profiles appear to be characteristic of local/mobile sources. Profiles with highly absorbing particles are likely representative of urban scale pollution and are strongly influenced by mobile sources because they are associated with increased CO concentrations.

Chapter 5: Comparisons of University of Maryland Aircraft and Trace Gas Profiles with Models CMAQ and GOCART

5.1 Introduction

5.1.1 Background

I compared O_3 measured aboard the University of Maryland Research aircraft in the summer of 2002 with the EPA Models-3 Community Multiscale Air Quality (CMAQ) modeling system. I examined differences among individual profiles as well as the statistical spread of all profiles. The standard CMAQ algorithm does not account for aerosols in the photochemistry of NO_2. A revised version of CMAQ was run to account for aerosol effects (typically found in the Mid-Atlantic US) on NO_2 photochemistry. I compared O_3 from the standard and revised model run and results are presented below. Emissions of NO_x are expected to be reduced by 2018 because of improved technology in motor vehicles and EPA imposed restrictions on power plant emissions. I have investigated how these reductions would be impacted by including aerosol effects in the photochemistry of NO_2 in CMAQ.

I compared SO_2 from the aircraft to CMAQ and the Georgia Tech/Goddard Global Ozone Chemistry Aerosol Radiation and Transport (GOCART) model output; both models over-predict the SO_2. This suggests the models assume a lifetime that is too long. A method for calculating the lifetime of SO_2 from *in-situ* measurements is described below as well as results from the calculation.

5.1.2 Description of Models

CMAQ uses the PSU/NCAR Mesoscale Model (MM5) for meteorological modeling. The MM5 uses a non-hydrostatic model with sigma coordinates that follow the terrain (http://www.mmm.ucar.edu/mm5/). CMAQ uses the Sparse Matrix Operator Kernel Emissions (SMOKE) to represent natural and anthropogenic emissions. There are four processors that account for chemistry in the model; these include the Meteorology-Chemistry Interface Processor (MCIP), the Photolysis rate processor (JPROC), the Initial Conditions Processor (ICON) and the Boundary Conditions Processor (BCON). Transport of emissions is modeled with the CMAQ Chemical Transport Model (CCTM). CMAQ has 172 × 172 grid cells and the size of each grid cell is 12 km × 12 km. There are 16 vertical layers in the lower tropospheric boundary layer from the surface to 3400 m. The temporal resolution is 1 hour.

The GOCART model uses assimilated meteorology from the Goddard Earth Observing System Data Assimilation System (GEOS-DAS; Schubert *et al.*, 1993). This is an online model which allows for daily results to be compared with measurements. GOCART has a spatial resolution of 2^{o} latitude by 2.5^{o} longitude. The GEOS DAS meteorological data uses 30 vertical layers from the surface to 80 km and 7 layers between the surface and 1.8 km. GOCART has a temporal resolution of 6 hours and calculates three dimensional SO_2, dimethylsulfide, sulfate and methanesulfonic acid. Anthropogenic emissions used in GOCART emissions are from the Emission Database for Global Atmospheric Research (EDGAR) and include DMS from the ocean, SO_2 and sulfate from anthropogenic sources, SO_2 from biomass

burning, aircraft, and volcanoes. The anthropogenic emissions include industrial processes (81%), residential and commercial fuel consumption (12%), and transportation (road, rail, shipping, 7%), with an annual rate of 72.8 Tg S yr^{-1}. Anthropogenic emission rates over the United States are assumed constant for the year for the US (Chin et al., 2000a).

Chemical reactions for SO_2 in the GOCART model include oxidation by OH in air and H_2O_2 in cloud to form sulfate. It is assumed that H_2O_2 is regenerated to prescribed values every 3 hours. Dry deposition is represented as a function of aerodynamic resistance, sublayer resistance, and surface resistance. Dry deposition velocities of SO_2 over land are usually 0.2-0.4 cm s^{-1}. In-cloud and below-cloud precipitation are also accounted for (Chin et al., 2000a).

I compared CMAQ trace gases from the lowest 16 layers (around 10, 24, 68, 116, 185, 282, 398, 544, 727, 949, 1212, 1523, 1886, 2312, 2820, 3393 m above ground level) of the model to aircraft measurements made in 2002. The CMAQ layers were converted to meters above sea level, by adding the surface elevation of each grid point. The model output was extracted at the location and time closest to the aircraft measurements. SO_2 was interpolated in altitude and time to match aircraft measurements. The same extraction process was performed for CMAQ O_3.

The resolution of GOCART SO_2 is 2^o latitude by 2.5^o longitude, with the first seven altitude layers around 118, 223, 377, 590, 880, 1265, 1768 m above ground level for the Mid-Atlantic US for June-August. GOCART has a 6 hour temporal resolution at 6, 12, 18, and 24 UT. Aircraft SO_2 profiles measured within the latitude longitude box and within the 6 hour time period were compared with GOCART SO_2.

Generally, only one aircraft profile was compared with GOCART model output (70% of the time) although in some cases, up to five aircraft profiles were averaged.

5.2 Comparisons Between Models and Measurements

5.2.1 O_3 Comparisons

Figure 1 shows the median aircraft measured and CMAQ O_3 profiles with the 25^{th} and 75^{th} percentiles for 136 profiles made in 2002. CMAQ is 10% (~6 ppb) smaller than aircraft O_3 between 600 and 2600 m. The ratio of the CMAQ/Aircraft O_3 mixing ratio is shown in Figure 2 and this shows that CMAQ under-predicts O_3 above 600 m and over-predicts O_3 below 600m. The CMAQ O_3 column content is 3% smaller than the aircraft column content (Table 1).

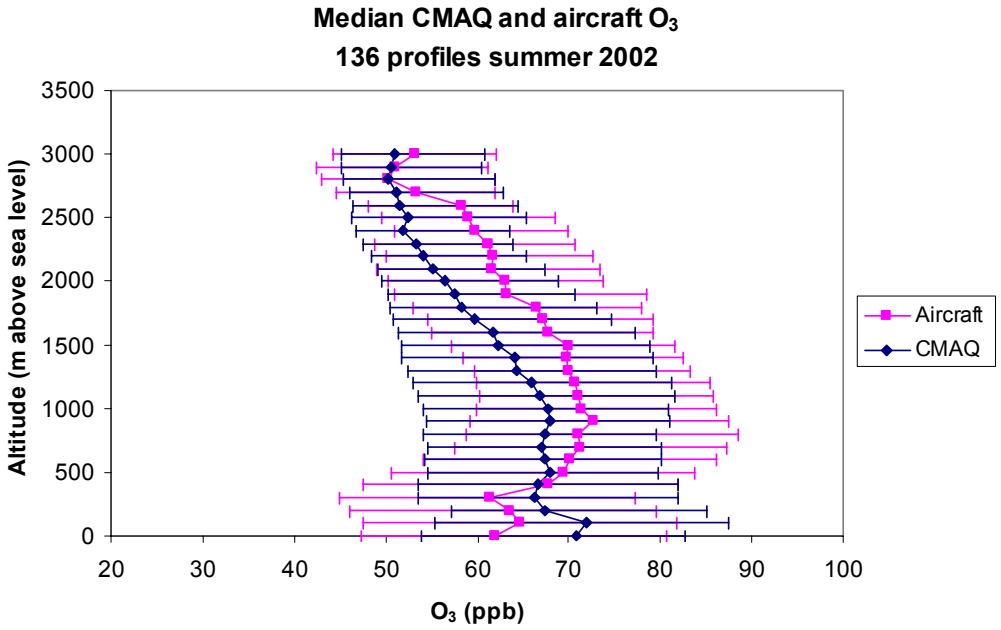

Figure 1. Median CMAQ and aircraft O_3 profiles from 2002 (June –August). The median was obtained from 136 profiles. The error bars represent the 25th and 75th percentiles. Though the error bars overlap, CMAQ under-predicts O_3 by 10% between 600 and 2600m.

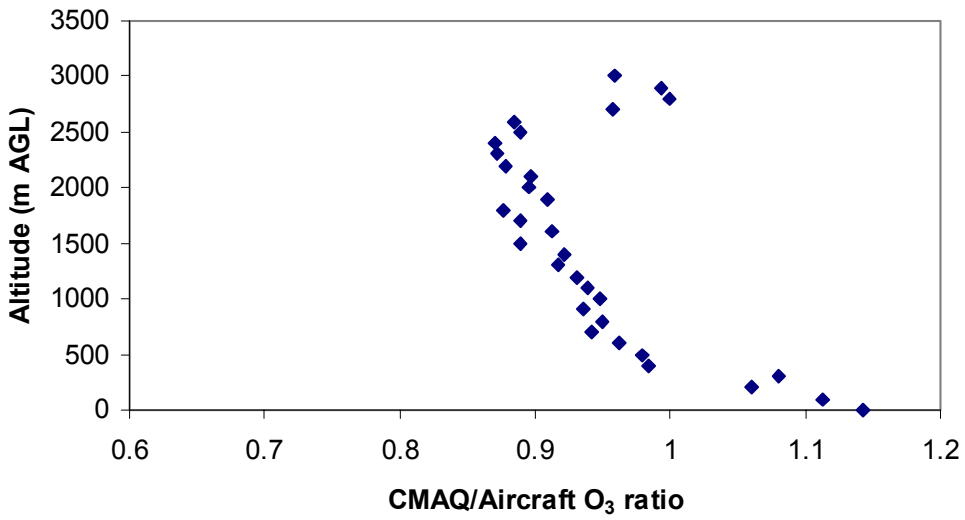

Figure 2. The ratio of CMAQ/Aircraft O_3 as a function of altitude. Below 600 m CMAQ over-predicts O_3, above 600 m CMAQ under-predicts O_3.

Column content (g m^{-2})	Aircraft	CMAQ
average	0.29	0.28

Table 1. CMAQ and aircraft O_3 column contents calculated from near the surface (~3 m above ground level) to the top of the aircraft spiral (~ 2500 m). The CMAQ column content is 3% smaller than the aircraft column content.

I also compared individual profiles to better understand the relationship between aircraft and CMAQ profiles. I have developed a method to look at these profiles in an objective manner by sorting the differences (between profiles) into three categories, the smallest, median and largest differences. This method is described below.

The differences between aircraft and model profiles were calculated accounting for shape (location of minima and maxima in the profiles) as well as size (absolute differences in mixing ratio). All aircraft spirals and matching CMAQ modeled outputs were initially averaged into 100 m altitude levels. This allowed for consistent comparisons between each pair of modeled and measured O_3 profiles. The difference between modeled and measured O_3 at each altitude bin accounted for the size. The profiles were examined at four altitude bins (250 – 650 m, 651-1150 m, 1151-1650 m, and 1651-2150 m). In each altitude bin there were at least five altitude layers examined. A linear regression was made between the O_3 mixing ratios of the two profiles being compared at these altitude layers. The slope and correlation coefficient were used to account for the shapes of the profiles being compared. The difference equation from Chapter 4 (Equation 2) was used.

The differences were sorted and profiles associated with three of the 5^{th} percentile (smallest) differences, three of the median differences and three of the 95^{th} percentile (largest) differences were examined. Figure 3 shows the three modeled and measured profiles with the 5^{th} percentile smallest differences. I examined profiles in the grid cell closest to where the airplane flew (the center cell) as well as the profiles in the 8 grid cells surrounding this center cell. Figure 3 shows the CMAQ profiles associated with the center cell in dark blue as well as the smallest and largest profiles from the surrounding grid cells. There are some jumps in the CMAQ profiles as shown for the Louisa, VA profile at 1200 m. The aircraft profiles have a diameter of about 1 km, and sometimes they crossed two different CMAQ grid cells. CMAQ O_3 for the closest grid cell was used for the difference calculation and sometimes

more than one grid cell was used in a profile. Figure 4 shows three of the modeled and measured profiles with median differences. The differences between profiles were calculated between 250 and 2150 m and the portions of the profile not included in this calculation are shown in grey. On July 8, 2002 Canadian forest fires impacted the region, and the aircraft profile over Easton, MD shows the signature peak of O_3 above 2200 m. Below the forest fire peak the aircraft profile compared reasonably well with CMAQ O_3. This example presents a limitation of the difference method. Figure 5 shows three of the modeled and measured profiles with the 95th percentile largest differences. The comparison of CMAQ and aircraft O_3 over Winchester, VA shows that the model does not always under-predict O_3 aloft. The differences between profiles seem to be independent of altitude and the shape of the profiles. Also shown in Figures 3-5 are the 24 hour back trajectories ending at the location of the aircraft spiral (at 1000, 2000, and 3000 m) for each of the CMAQ-aircraft comparisons. The differences between profiles also seem to be independent of wind speed and direction (from back trajectories).

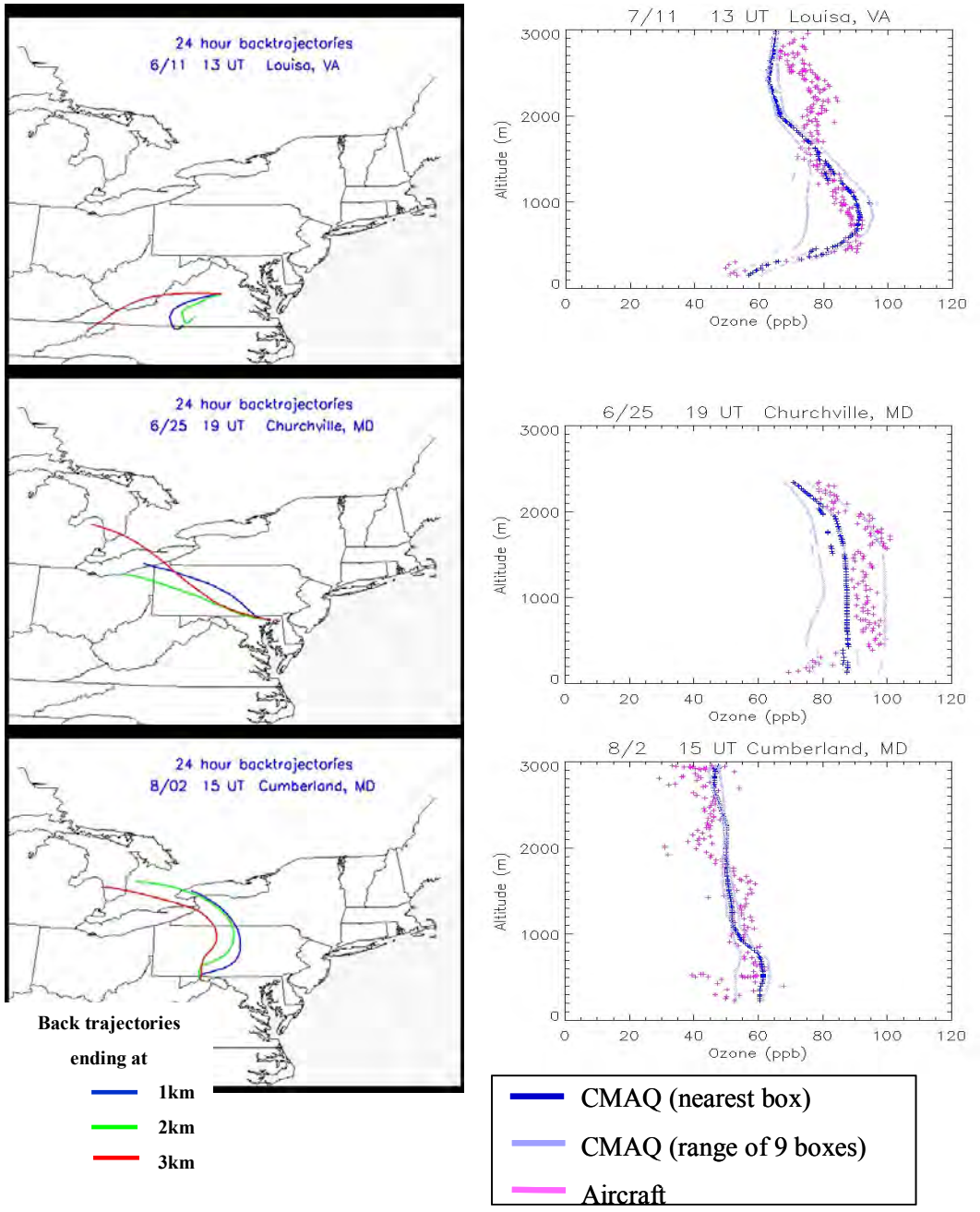

Figure 3. CMAQ and aircraft O_3 profiles associated with the 5th percentile smallest differences (the best agreement). The dark blue profiles represent CMAQ O_3 from the closest (center) grid cell. The light blue profiles represent the smallest and largest O_3 from the surrounding 8 grid cells. There are some jumps in the Louisa, VA CMAQ profile. The aircraft profiles have a diameter of about 1 km, and sometimes they crossed two different CMAQ grid cells. CMAQ O_3 for the closest grid cell was used in the difference calculation and sometimes more than one grid cell was used in a profile. Back trajectories at three altitudes are also shown.

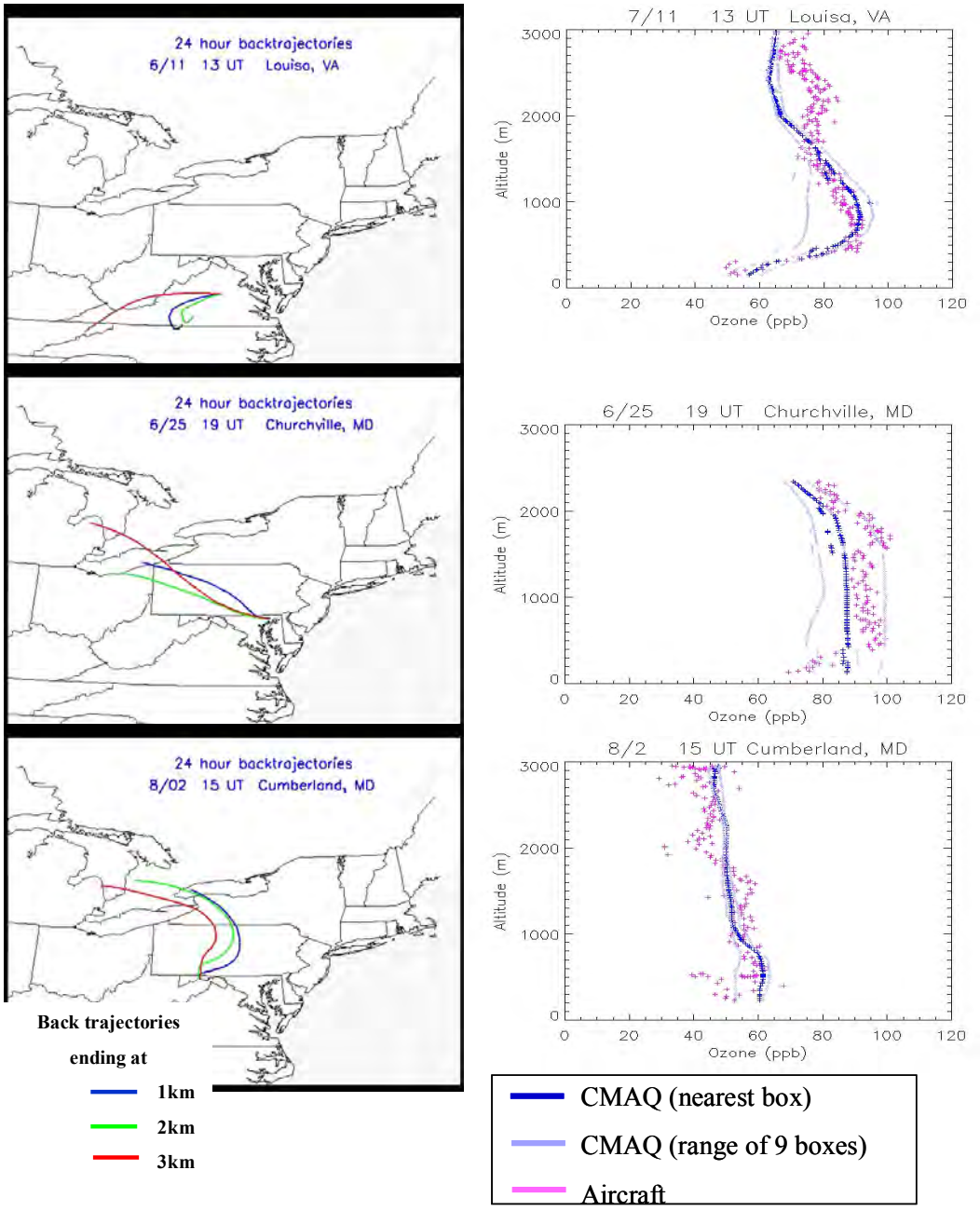

Figure 4. CMAQ and aircraft O_3 profiles associated with the median differences. The dark blue profiles represent CMAQ O_3 from the closest (center) grid cell. The light blue profiles represent the smallest and largest O_3 from the surrounding 8 grid cells. Canadian forest fires impacted the region on July 8, and this is seen in the aircraft O_3 profile over Easton. The differences were calculated between 250 and 2150 m and so the influence of the fires was not accounted for in the equation. This shows a limitation of the method.

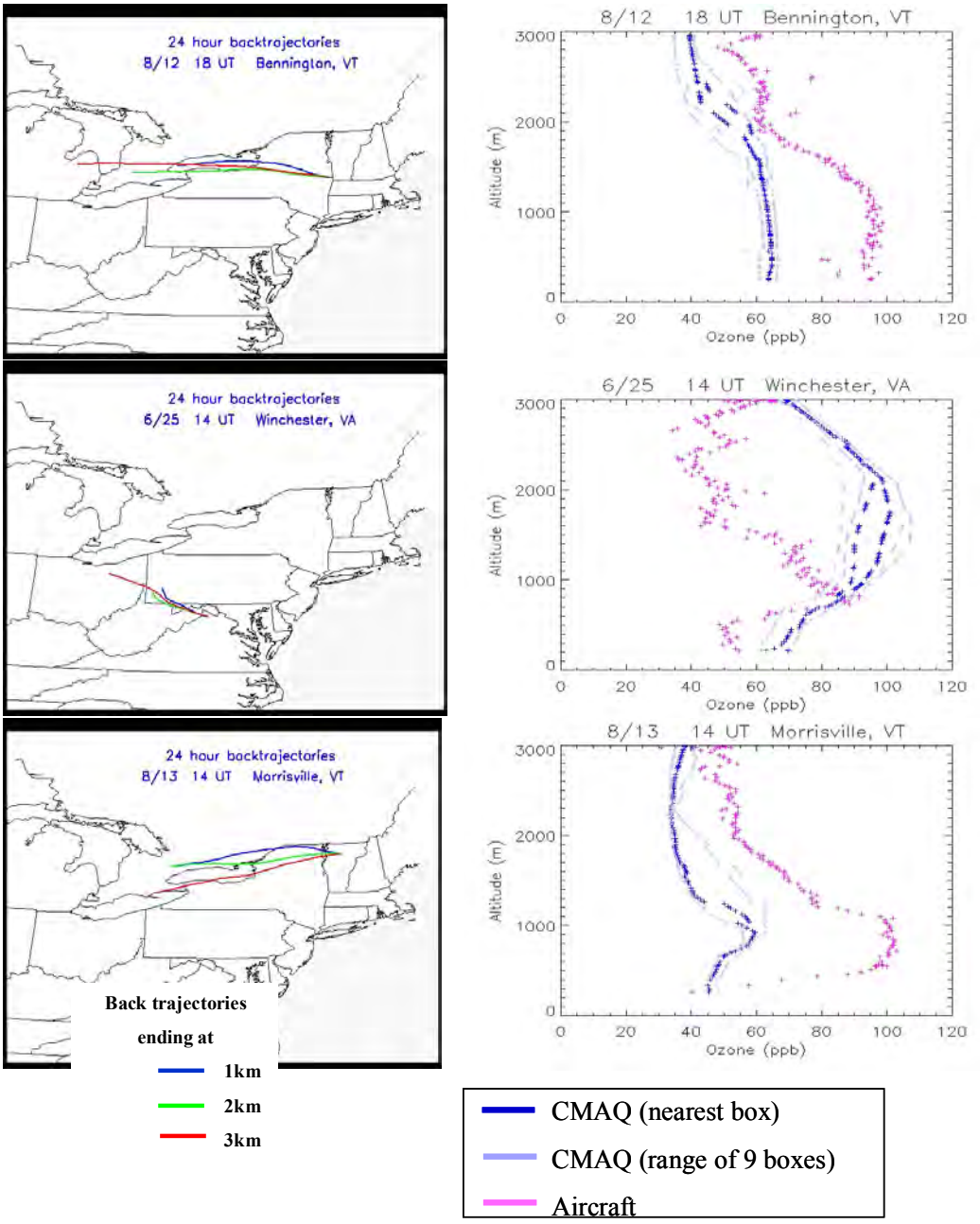

Figure 5. CMAQ and aircraft O_3 profiles associated with the 95th percentile largest differences (the worst agreement). The dark blue profiles represent CMAQ O_3 from the closest (center) grid cell. The light blue profiles represent the smallest and largest O_3 from the surrounding 8 grid cells. The comparison at Winchester shows that CMAQ sometimes over-predicts O_3 aloft.

5.2.2 The Effects of Aerosols on the Photolysis Rate of NO_2 and the Production of O_3

In general CMAQ under-predicts O_3 aloft. Reasons for this under-prediction include problems with emissions inventories as well as problems with meteorology, cloud cover, and CMAQ's ability to describe transport. The NO_2 photolysis rates that CMAQ uses also impact how much O_3 is produced by the model. The reaction rate coefficient for the photolysis of NO_2 (hereafter referred to as j-NO_2 value) used by the standard version of CMAQ assumes no aerosol loading. Dickerson et al. (1997) show that an increase of aerosols from an optical depth of 0 to 2 increases the j-NO_2 values by 30% above the boundary layer (1000 m). Park (2001) performed a sensitivity test of CMAQ using j-NO_2 values associated with CMAQ aerosols. He used the aerosol properties generated by CMAQ to develop a program to modify the j-NO_2 values accordingly, and then compared the O_3 generated with the modified CMAQ run to surface measurements. He found that the effects on O_3 production were variable, and there were still numerous disagreements between modeled and measured O_3. Aerosols generated with CMAQ are often under-predicted (Mebust et al., 2003; Mueller et al., 2006; Tesche et al., 2006) and this may partly explain the mixed results Park (2001) found. I performed a sensitivity study using j-NO_2 values associated with typical aerosols measured in the Mid-Atlantic from July 15-18, 2002 using the Park (2001) program that allows for adjustment of the Angstrom slope and intercept defined in the Angstrom equation:

$$\tau = \beta \lambda^{-\alpha} \quad (1)$$

Here, τ is the aerosol optical depth, α is the Angstrom slope (Angstrom exponent) that represents the size of aerosols, λ is the wavelength in μm, and β is the intercept related to the amount of aerosols present in the atmosphere. The Angstrom coefficient intercept can be assigned a value of 0, 0.1, 0.2, 0.3, 0.4, or 0.5. The Angstrom coefficient slope can be assigned a value between 0.5, 1.0, 1.5, 2.0, or 2.5. Figure 6 shows the median of Angstrom exponent measurements made during July 15-18, 2002 for 20 aircraft profiles. Of the values allowed in the Park (2001) model, the median Angstrom exponent (Angstrom slope) is closest to 2.0. The Park (2001) model also allows for the adjustment of single scattering albedo, asymmetry parameter and aerosol layer depth.

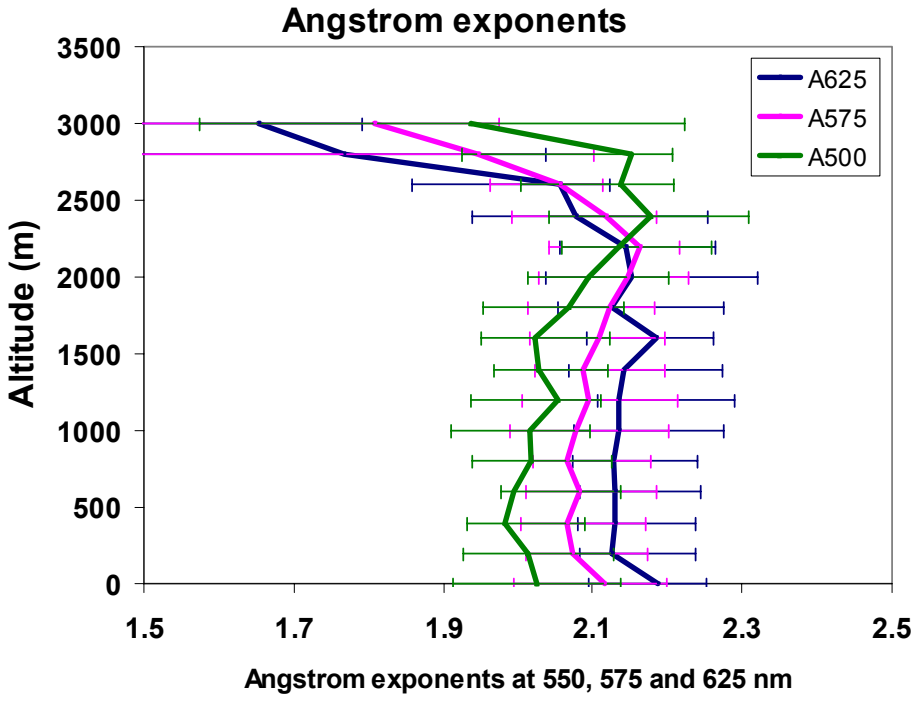

Figure 6. The median Angstrom exponent calculated with the ratio of scattering at 450 and 550 nm (A500), 450 and 700 nm (A575), and 550 and 700 nm (A625) for flights made between July 15-18, 2002. The error bars represent the 25th and 75th percentile. The Angstrom exponent measured aboard the aircraft is closest to the 2.0 input for the Park (2001) model.

	Aerosol optical depth	
	550 nm	380 nm
average	0.31	0.68
median	0.28	0.63
minimum	0.12	0.26
maximum	0.66	1.41

Table 2. Statistics for aerosol optical depth calculated at 550 nm and 380 nm for 17 flights made between July 15-18, 2002.

Table 2 shows that the average optical depth at 550 nm is 0.31. Because the photolysis of NO_2 occurs at wavelengths of 380 nm and not at wavelengths of 550 nm (where the aircraft made measurements), I interpolated the aerosol properties to the 380 nm wavelength. The absorption coefficient (*abs*, with units of m^{-1}) can be approximated at different wavelengths, λ, using the relationship (from Bodhaine, 1995):

$$abs = c_a/\lambda \quad (2)$$

Here c_a is a constant. From Equation 2, abs_{380} can be solved using:

$$abs_{380} = abs_{550} \times 550/380 \quad (3)$$

I also converted the scattering coefficient (with units of m^{-1}) at 550 nm to the scattering coefficient at 380 nm, *scat380*, using the relationship (from Bodhaine, 1995):

$$Scat_{550} = c_s/550^{A550} \quad (4)$$

$$Scat_{380} = c_s/380^{A380} \quad (5)$$

Here c_s is a constant. From Equation 5, $scat_{380}$ can be solved using:

$$Scat_{380} = Scat_{550} * 550^{A550}/380^{A380} \quad (6)$$

Here A_{550} represents the Angstrom exponent calculated from the ratio of scattering measurements at two different wavelengths (as shown in Equation 2 in Chapter 3) where the average wavelength is 550 nm. A_{380} is just the Angstrom exponent calculated from the ratio of scattering at two different wavelengths where the average wavelength is 380 nm. Figure 6 shows the Angstrom exponent calculated from the ratio of scattering at 450 and 550 nm (A500), 450 and 700 nm (A575), and 550 and 700 nm (A600). There is little variability among the Angstrom exponents calculated from different wavelength ratios and so I assumed that A_{550} and A_{380} (from Equation 6) are equal. I then calculated aerosol optical depth at 380 nm (Table 2). Using the optical depth at 380 nm or 550 nm in Equation 1, results in an Angstrom intercept closest to 0.1. The Park (2001) model allows values of single scattering albedo of 0.92, 0.96 and 1.0. Figure 7 shows the median profile for single scattering albedo at 550 nm measured during July 15-18, 2002 and composed of 17 profiles. For the values allowed in the Park (2001) model the median single scattering albedo is closest to 0.96.

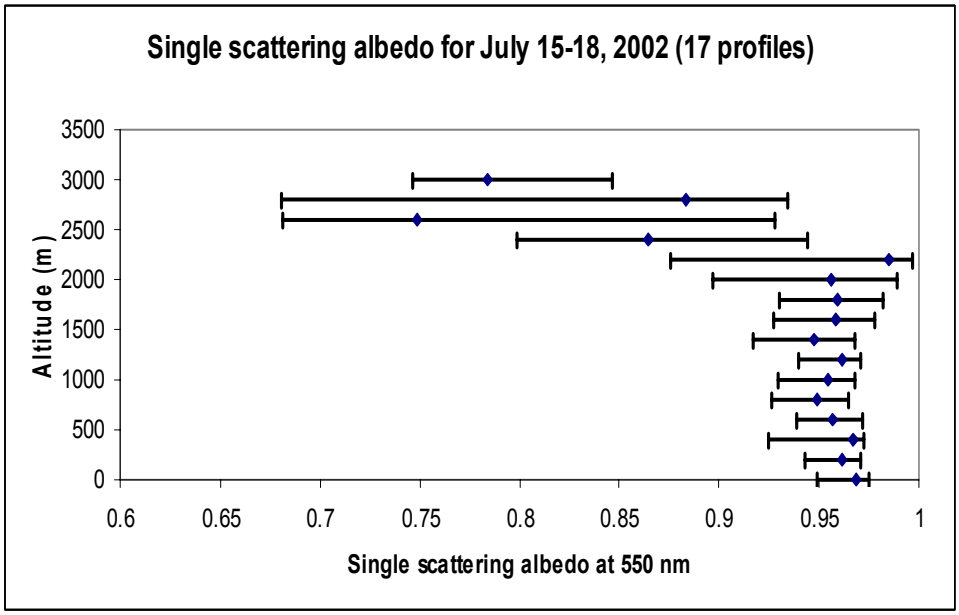

Figure 7. The median single scattering albedo at 550 nm for flights made between July 15-18. The error bars represent the 25th and 75th percentile. The single scattering albedo measured aboard the aircraft is closest to the 0.96 input for the Park (2001) model

The model allows values of asymmetry parameter to be 0.6, 0.7, or 0.8. The asymmetry parameter is calculated from the backscatter to total scattering ratio using the equation

$$g = -2x + 1 \quad (7)$$

Where g is the asymmetry parameter and x is the backscatter to total scattering ratio. The aircraft did not make measurements of backscatter to total scattering in 2002, but measurements were made in 2003-2005. Figure 8 shows the asymmetry parameter for 139 flights measured in 2003-2005. For the values allowed in the Park (2001) model the median profile of asymmetry parameter is closest to 0.8. The Park (2001) model allows for aerosol layer depths to be 0.5, 1.5, or 2.5 km. Figures 1d and 1f in Chapter 3 show the median scattering and absorption profiles for all flights made in the Mid-Atlantic region. The depth of the aerosol layer for these profiles is closest to

1.5. These aerosol values were used in the Park (2001) model and the resultant j-NO_2 values are shown in Figure 9. Above 1000 m the j-NO_2 values calculated with aerosols were 25% larger than those with no aerosols.

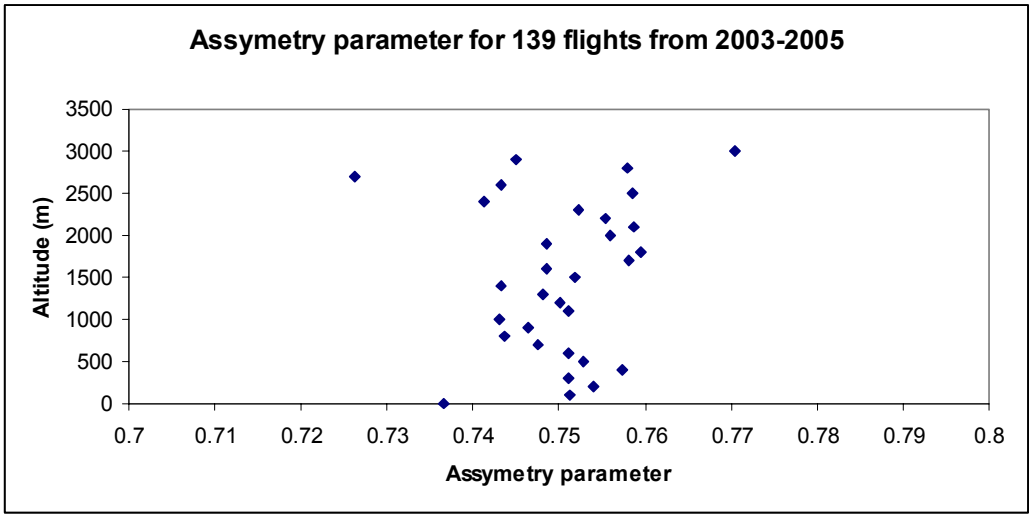

Figure 8. The median asymmetry parameter at 550 nm for 139 flights made between 2003 and 2005. The error bars represent the 25th and 75th percentile. The asymmetry parameter measured aboard the aircraft is closest to the 0.8 input for the revised CMAQ run.

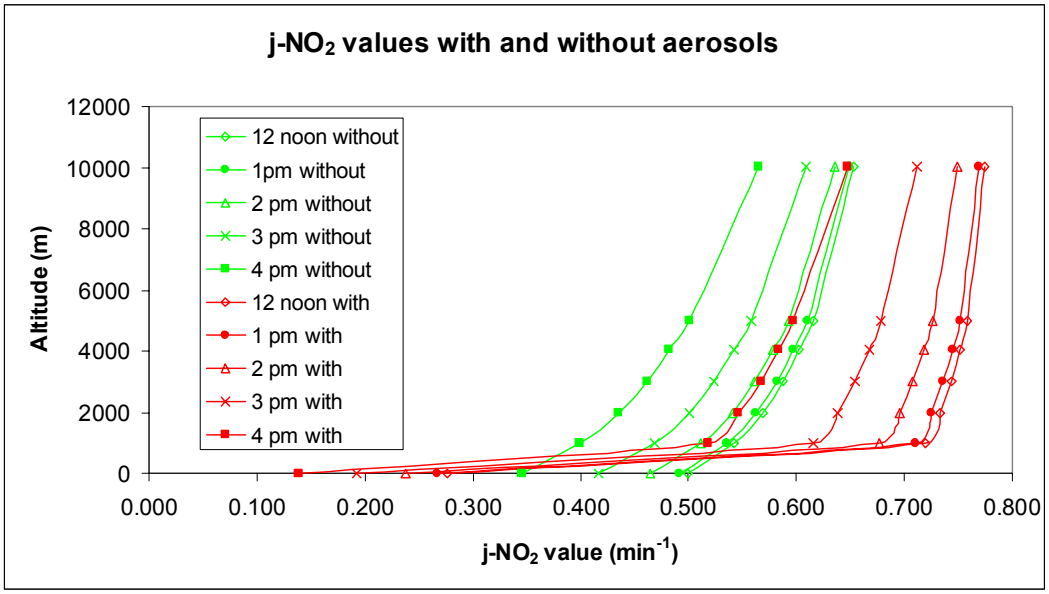

Figure 9. Standard and revised j-NO_2 values used in CMAQ (at 0, 1, 2, 3, 4.05, 5 and 10 km). The standard j-NO_2 values assume there are no aerosols (without) and the revised j-NO_2 values (with) were calculated using aerosol properties presented in Figures 6,7 and 8 and Table 2. The different symbols represent the j-NO_2 values at different times of the day.

I ran CMAQ from July 15-18, 2002 with the standard j-NO_2 values (assuming no aerosol) and revised j-NO_2 values (assuming aerosol typical for the episode). The same aerosol values were used throughout the domain. The aircraft flies downwind of urban and suburban areas with large optical depths, and also rural areas with small optical depths. Using the average optical depth from all of the flights should be a reasonable approximation of the Mid-Atlantic average optical depth. Levy (2007) found a correlation coefficient (r^2) of 0.26 between MODIS satellite retrievals and aircraft calculated aerosol optical depth. Two emissions scenarios were used; one with 2002 emissions and one with 2018 emissions that are substantially lower than those from 2002. This resulted in four model runs for comparison:

- 2002 emissions with standard j-NO_2 values (2002, standard)
- 2002 emissions with revised j-NO_2 values (2002, revised)
- 2018 emissions with standard j-NO_2 values (2018, standard)
- 2018 emissions with revised j-NO_2 values (2018, revised).

CMAQ O_3 values were generated during a previous run by the New York State Department of Environmental Quality (NYDEQ) using the standard j-NO_2 values. The NYDEQ runs used TOMS data to determine the stratospheric O_3 influence on radiative forcing and on boundary layer O_3 production. I did not have access to the TOMS data, so I performed the four runs using CMAQ default overhead O_3 (generated from Nicolet et al., 1982). The O_3 I generated from the CMAQ run using 2002 emissions and j-values with no aerosols correlated well with the NYDEQ runs using the same emissions and j-values (but different overhead O_3). However, the O_3 generated from my CMAQ run was up to 5 ppb smaller than that generated from the NYDEQ run. In order to make meaningful comparisons between aircraft O_3 and O_3 generated with the revised CMAQ run (2002, revised), I adjusted the CMAQ O_3 using the following:

$$O_{3\ (2002,\ revised)} = O_3\ (NYDEQ) * \frac{O_{3\ (2002,\ revised\ without\ TOMS\ O3)}}{O_{3\ (2002,\ standard\ with\ TOMS\ O3)}} \qquad (8)$$

Figures 10a-e show O_3 generated by CMAQ using the standard j-NO_2 values, O_3 generated using the revised j-NO_2 values (adjusted using Equation 8) and O_3 from the aircraft. The revised CMAQ run generated more O_3 (~1 ppb) above 500 m than the standard run. The revised CMAQ run generated less O_3 (1-4 ppb) below 500 m than the standard run. The revised run did not eliminate measurement/model differences, but brought the CMAQ output closer to observations. Figures 10a-e are

limited in space because they only represent a few grid cells. Figure 11 shows the median differences in O_3 between revised and standard runs (revised CMAQ–standard CMAQ) for the 16 profiles. Table 3 compares the average O_3 column contents among the aircraft, standard CMAQ runs, and revised CMAQ runs for the July 15-18, 2002 episode. CMAQ O_3 column content from the standard and the revised runs were ~7% smaller than the aircraft O_3. The O_3 column content from the revised run was 0.3% larger than the O_3 column content from the standard run.

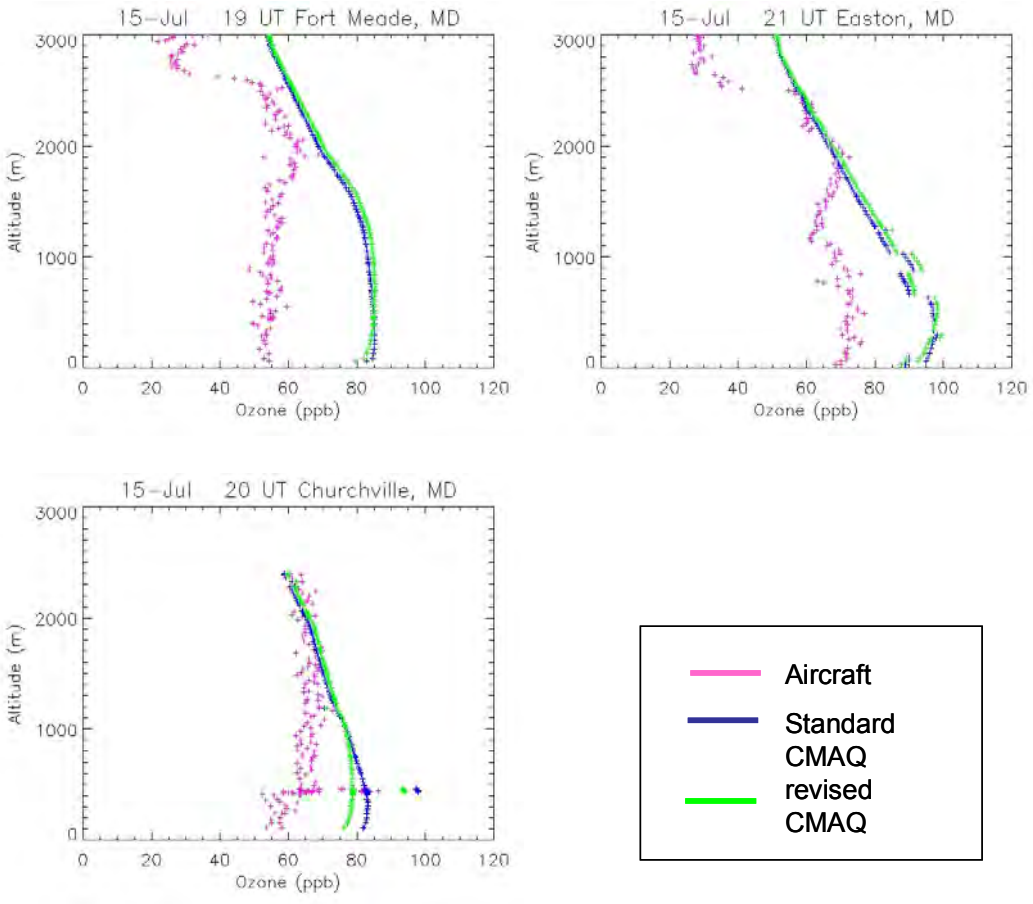

Figure 10a. O_3 profiles from the aircraft (pink), standard CMAQ runs (shown in blue), and revised CMAQ runs (shown in green) for July 15, 2002. Above 500 m the revised CMAQ profiles are about 1 ppb larger than the standard CMAQ profiles shown in blue. Below 500 m the revised CMAQ O_3 is smaller than the standard CMAQ O_3.

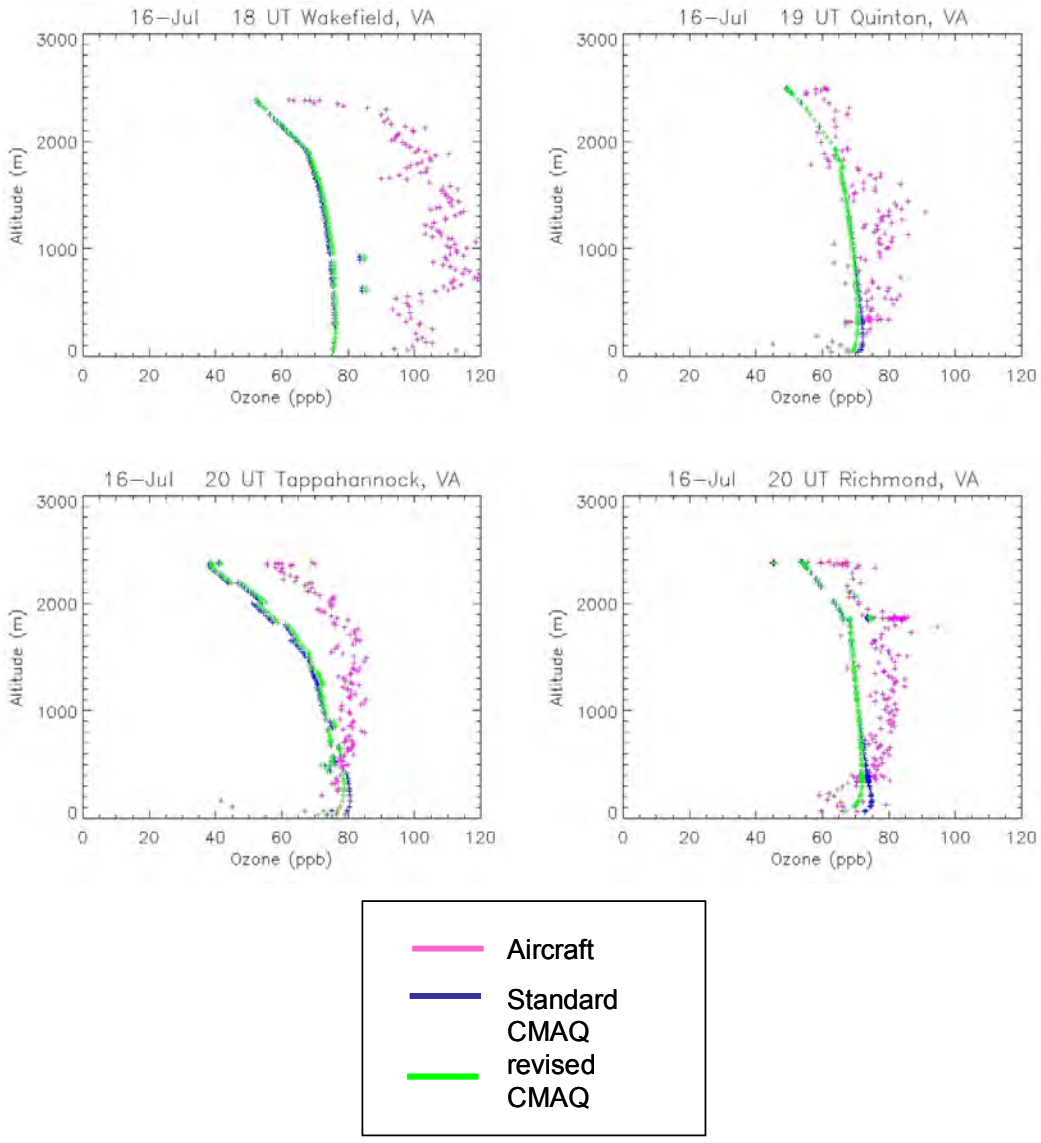

Figure 10b. O_3 profiles from the aircraft (pink), standard CMAQ runs (shown in blue), and revised CMAQ runs (shown in green) for the morning of July 16, 2002. Above 500 m the revised CMAQ profiles are about 1 ppb larger than the standard CMAQ profiles shown in blue. Below 500 m the revised CMAQ O_3 is smaller than the standard CMAQ O_3.

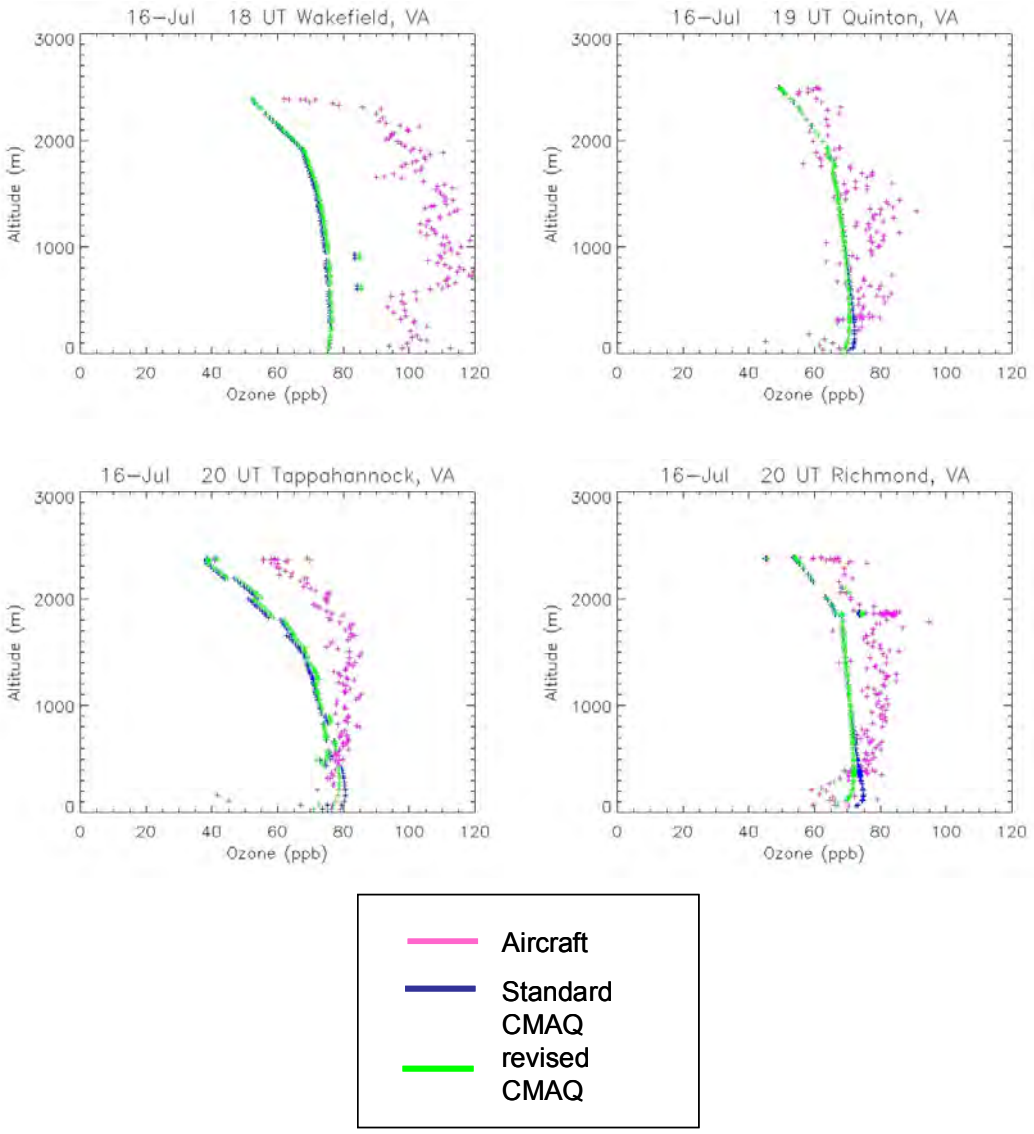

Figure 10c. O_3 profiles from the aircraft (pink), standard CMAQ runs (shown in blue), and revised CMAQ runs (shown in green) for the afternoon of July 16, 2002. Above 500 m the revised CMAQ profiles are about 1 ppb larger than the standard CMAQ profiles shown in blue. Below 500 m the revised CMAQ O_3 is smaller than the standard CMAQ O_3.

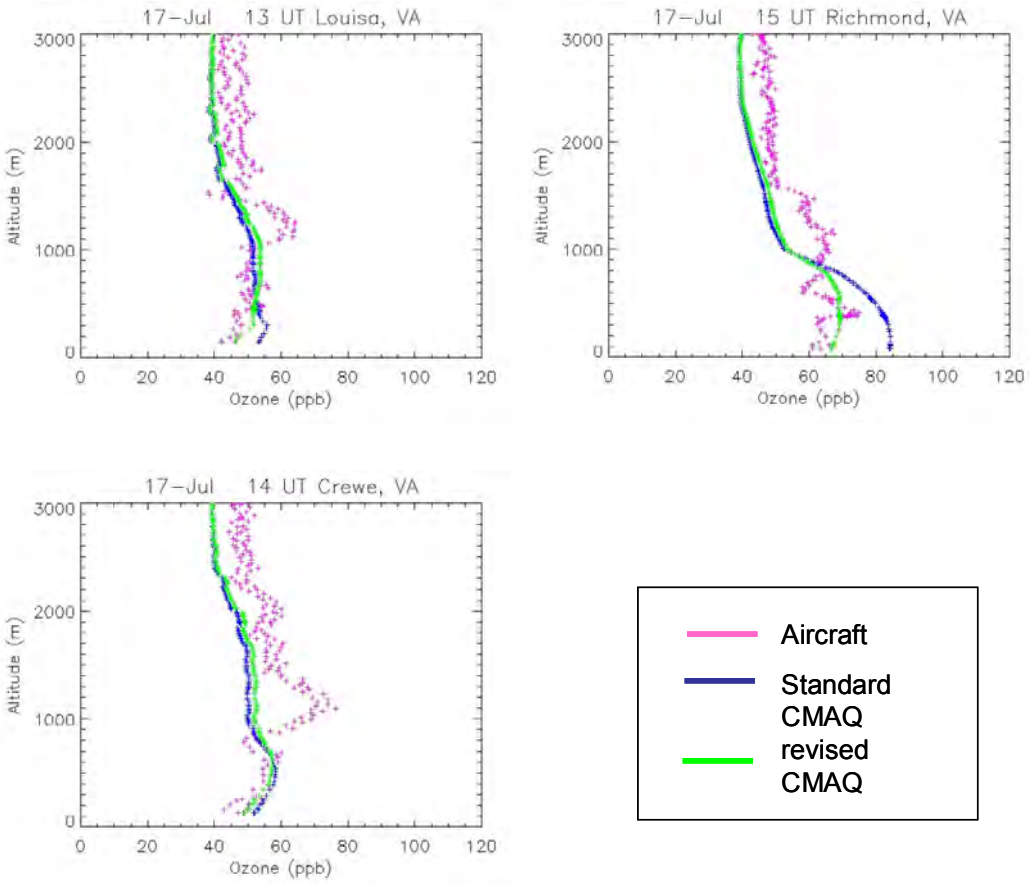

Figure 10d. O_3 profiles from the aircraft (pink), standard CMAQ runs (shown in blue), and revised CMAQ runs (shown in green) for July 17, 2002. Above 500 m the revised CMAQ profiles are about 1 ppb larger than the standard CMAQ profiles shown in blue. Below 500 m the revised CMAQ O_3 is smaller than the standard CMAQ O_3.

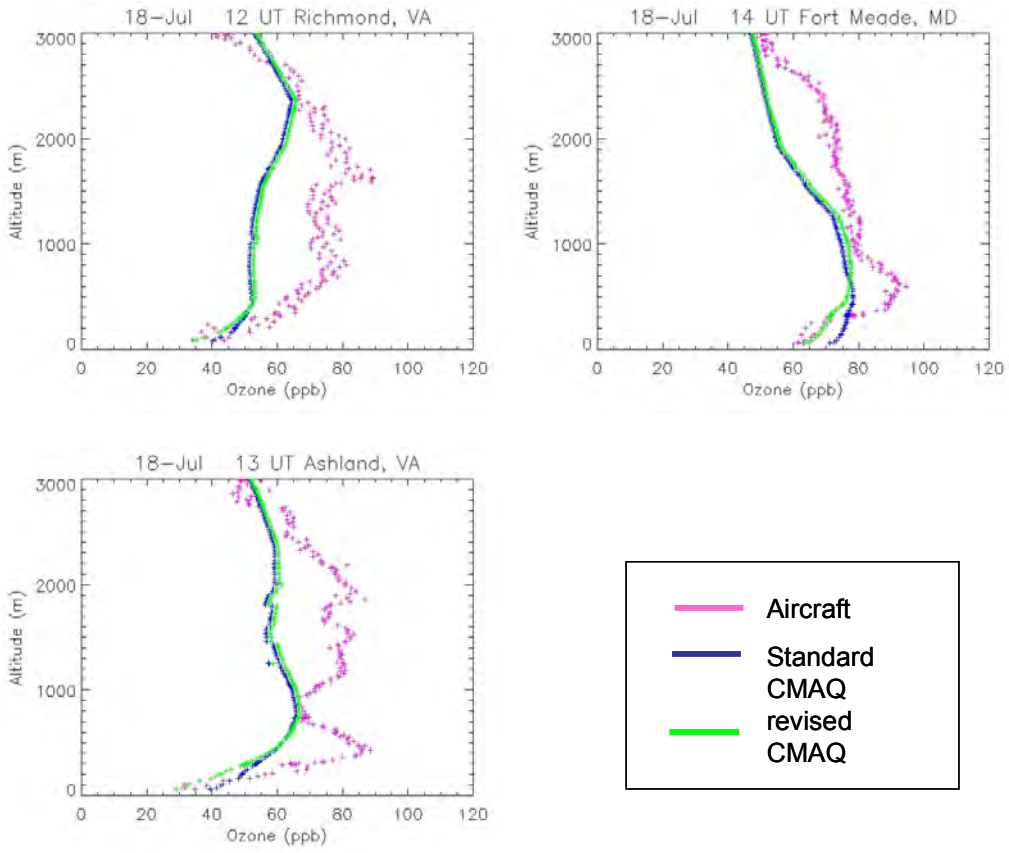

Figure 10e. O_3 profiles from the aircraft (pink), standard CMAQ runs (shown in blue), and revised CMAQ runs (shown in green) for July 18, 2002. Above 500 m the revised CMAQ profiles are about 1 ppb larger than the standard CMAQ profiles shown in blue. Below 500 m the revised CMAQ O_3 is smaller than the standard CMAQ O_3.

	Average O_3 column content ($g\ m^{-2}$)
Aircraft	0.3093
CMAQ 2002 (standard run)	0.2885
CMAQ 2002 (revised run)	0.2888
CMAQ 2018 (standard run)	0.2561
CMAQ 2018 (revised run)	0.2555

Table 3. Median O_3 column contents for the July 15-18, 2002 episode (for locations sampled by the aircraft) from the aircraft, standard CMAQ 2002 run, revised CMAQ 2002 run, standard CMAQ 2018 run, and revised CMAQ 2018 run.

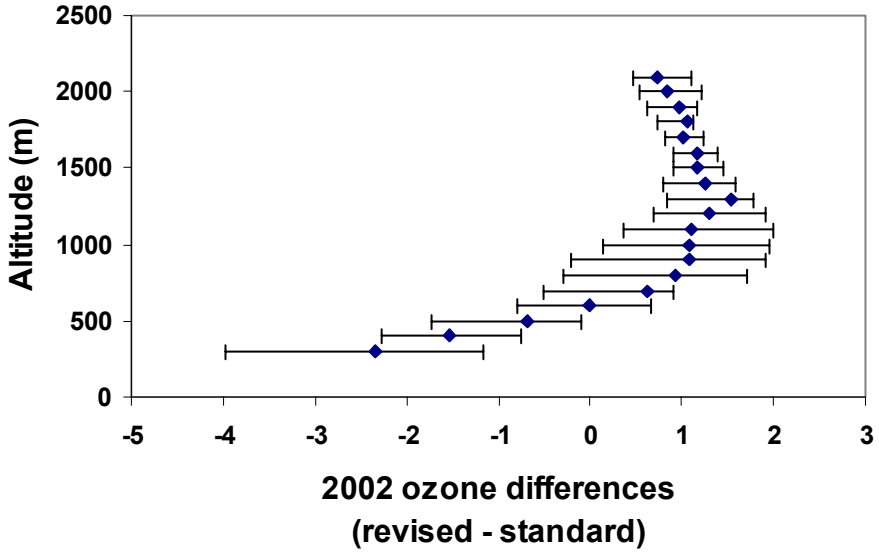

Figure 11. Median CMAQ O_3 differences (standard – revised) for 16 profiles generated between July 15-18, 2002. Error bars represent the 25th and 75th percentiles. Near the surface the revised CMAQ run generates less O_3 than the standard CMAQ run. Above 500 m the revised CMAQ run generates more O_3 than the standard run.

Figure 12 shows the difference between revised CMAQ and standard CMAQ runs for three different levels (1, 8, and 16 that are approximately at the surface, 500, and 2000m) for the Eastern US at 14 UT and 18 UT. The largest O_3 production generally occurs within these times. Here negative values, when the revised CMAQ run generates less O_3 than the standard CMAQ run, are shown with cooler colors. These differences, of up to 10 ppb, are seen mainly at the surface. Positive values, when the revised CMAQ run generates more O_3 than the standard run, are shown with warm colors. These differences, of up to 1 ppb, generally occur above 500 m.

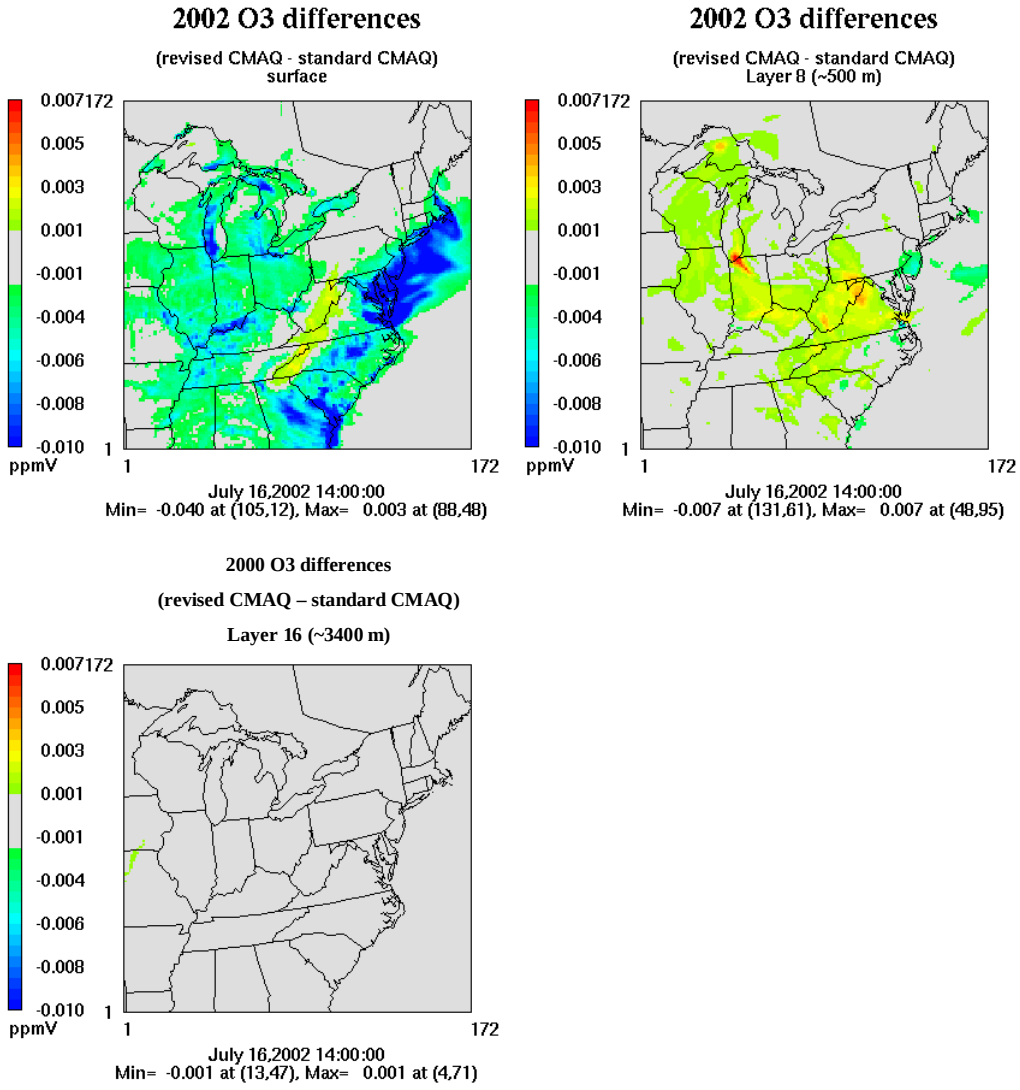

Figure 12a. Differences between revised and standard CMAQ O_3 (revised-standard) for a July 2002 smog and haze episode. These plots are for 14 UT (10 EST). The differences are negative at the surface meaning that the revised CMAQ run generates less O_3 than the standard run. Above 500 m the differences are positive and the revised CMAQ run produces more O_3 than the standard CMAQ.

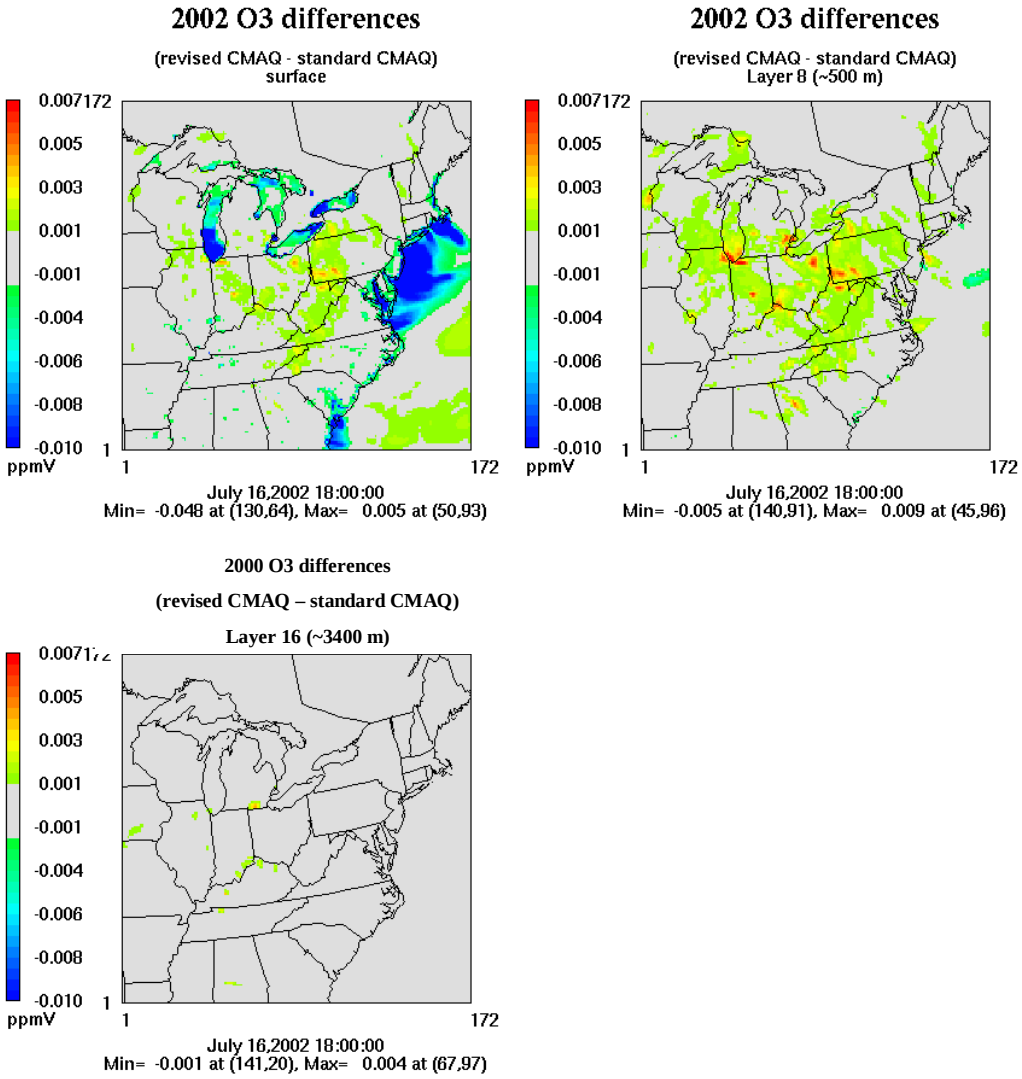

Figure 12b. Differences between revised and standard CMAQ O_3 (revised-standard) for a July 2002 smog and haze episode. These plots are for 18 UT (14 EST). The differences are negative at the surface meaning that the revised CMAQ run generates less O_3 than the standard run. Above 500 m the differences are positive and the revised CMAQ run produces more O_3 than the standard CMAQ.

A curtain plot (Figure 13) was used to examine the diurnal variation in the first 16 layers of CMAQ showing the differences in O_3 generated from:

Revised CMAQ - standard CMAQ (9)

The x-axis represents a swath made one grid cell wide (East and West) extending from the southernmost grid cell to the northernmost grid cell in the Eastern US shown in Figure 14. The y-axis represents the first 16 layers of CMAQ. Six time periods of 3, 7, 11, 15, 19 and 23 UT are shown for July 17, 2002. In the early morning (from 3 to 11 UT) there are positive differences (where the revised CMAQ generated O_3 is larger than the standard CMAQ O_3) above 500 m that are mixed down to the surface. At 15 and 23 UT, right after rush hour, there are negative differences (where the revised CMAQ O_3 is smaller than the standard CMAQ O_3) near the surface.

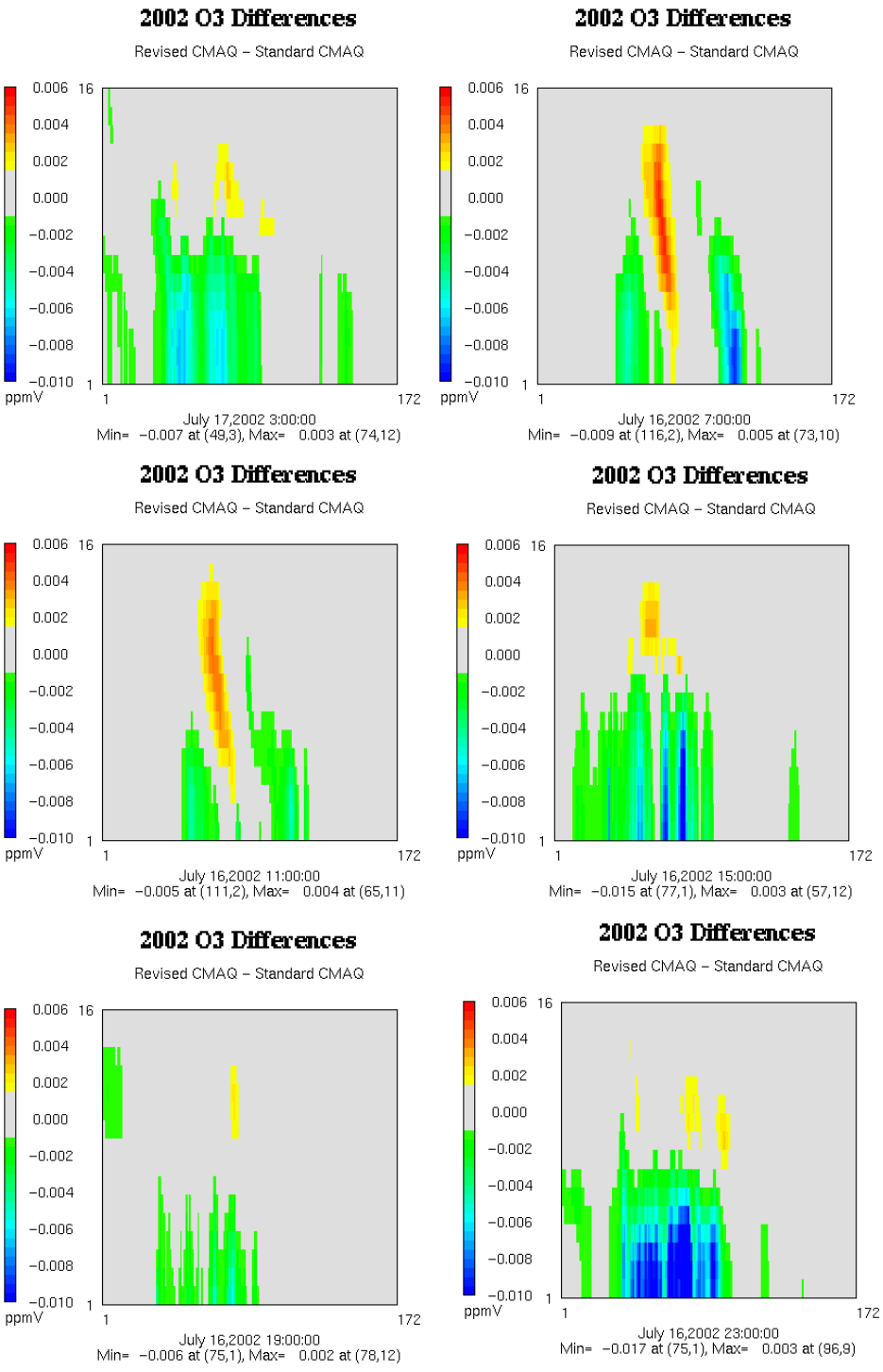

Figure 13. O_3 differences (revised-standard) for a single swath in the CMAQ grid. The y-axis represents the first16 altitude layers used in CMAQ. The x-axis represents a swath of the grid cells examined (Figure 14), where 1 is the Southernmost grid cell and 172 is the Northernmost grid cell. Here negative differences mean that O_3 generated with the revised CMAQ is smaller than the standard CMAQ O_3 and these are seen closer to the surface.

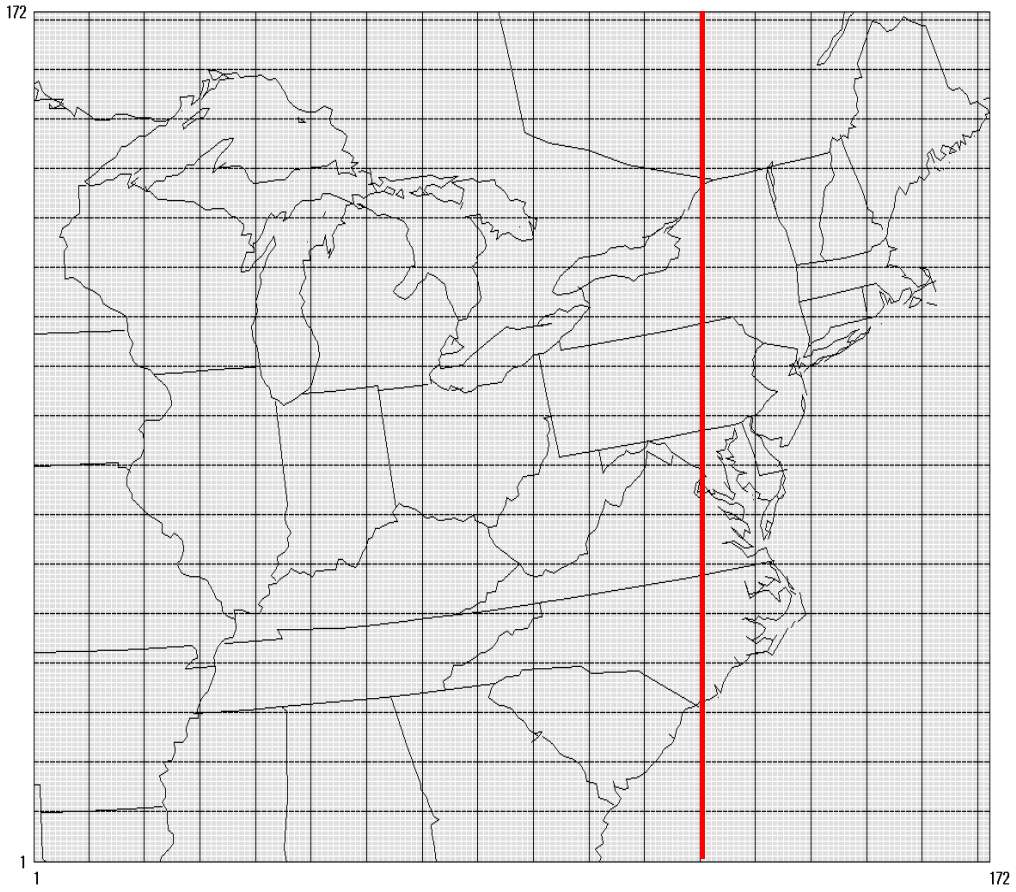

Figure 14. The curtain plot in Figure 13 was made from a vertical swath, shown in red. This swath represents the x-axis in Figure 13.

I also examined how the emissions reductions scenario, expected for 2018, would be impacted by incorporating aerosols into CMAQ. Figures 15 a and b show the CMAQ O_3 reductions (CMAQ 2018 – CMAQ 2002) for profiles made during the July15-18 episode (at locations where the aircraft made spirals) for the standard CMAQ runs (Figure 15 a) and the revised CMAQ runs (Figure 15 b). The revised CMAQ reductions and standard CMAQ reductions are similar, with the largest

reductions (10 ppb) near the surface and smaller reductions (7 ppb) at 2000 m. Figure 15 c shows the difference between:

[(2018 revised – 2002 revised) – (2018 standard – 2002 standard)] (10)

The differences between O_3 reductions using revised CMAQ and standard CMAQ (Equation 10) are small (Figure 15 c) for the locations where the UMD research aircraft made spirals. However, the revised reductions are smaller than the standard reductions, and this means the standard CMAQ run slightly overestimates reductions at the surface (by 0.6ppb). Above 1000 m the standard CMAQ run underestimates reductions. The column contents in Table 3 suggest that the reductions using the revised CMAQ runs are 3% larger than the reductions using the standard CMAQ runs.

a

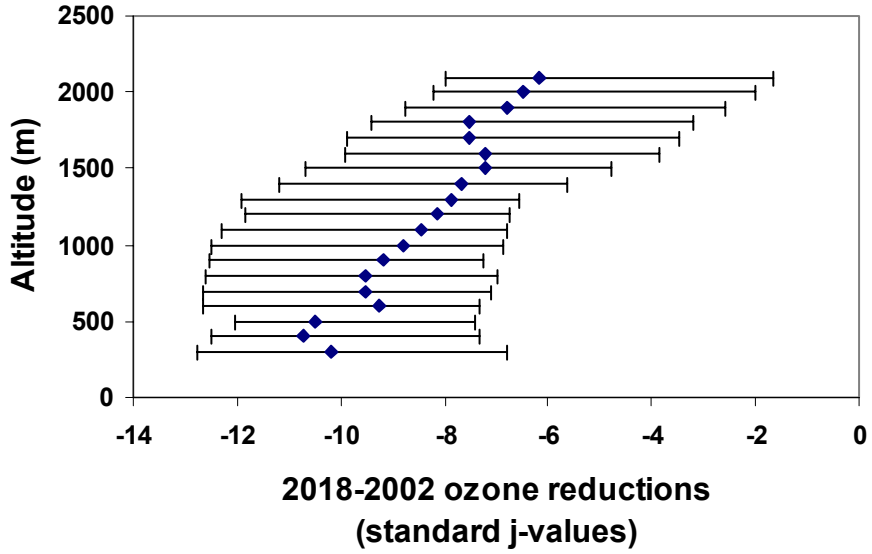

b

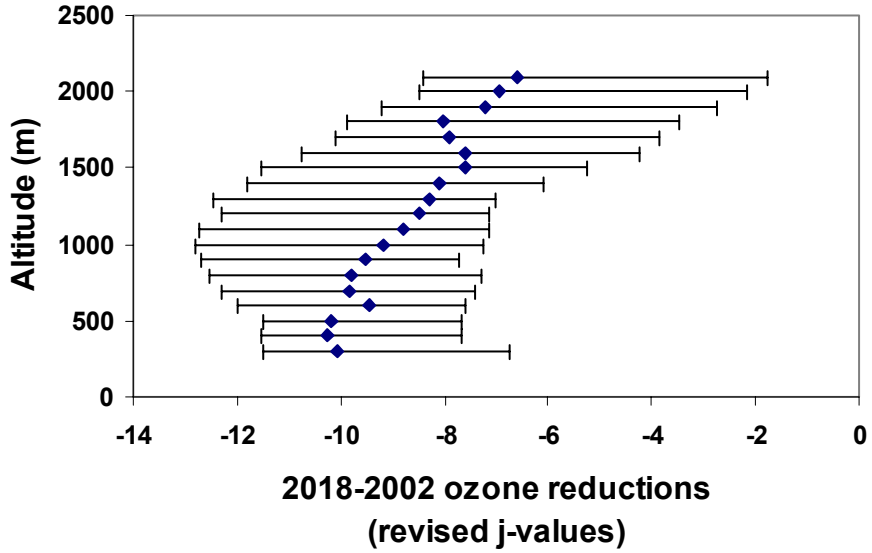

Figure 15 a b. Median CMAQ ozone reductions (CMAQ 2018 – CMAQ 2002) using a) standard j-values and b) revised j-values. Error bars represent the 25th and 75th percentiles. The largest reductions occur near the surface.

c

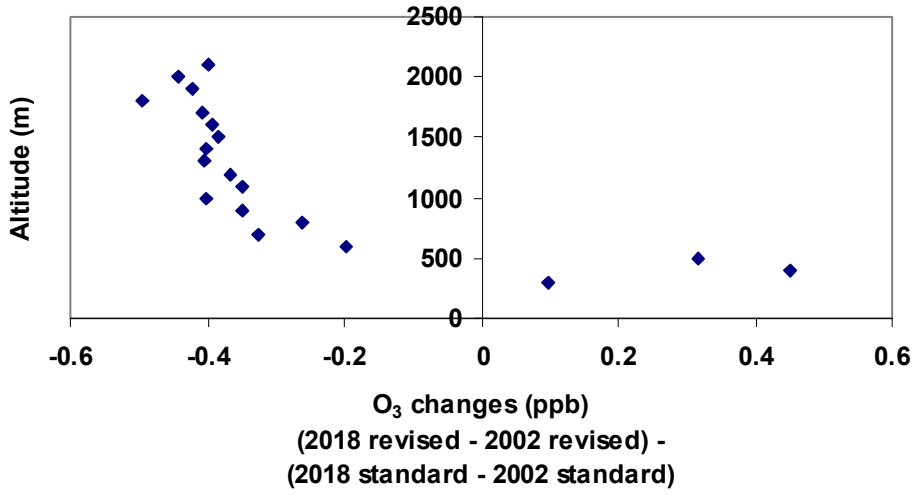

Figure 15 c. Changes in O_3 reductions of revised CMAQ– standard CMAQ. Near the surface standard CMAQ overestimates the reductions and above 500 m the standard CMAQ underestimates the reductions.

Figure 16 shows the results of Equation 10 (differences in O_3 reductions for revised and standard CMAQ runs) for the Eastern US. These differences are plotted at three levels (approximately the surface, 500 m and 3400 m) at 14 UT and 18 UT. The positive changes show that the standard model over-predicts O_3 reductions (because the revised CMAQ reductions are smaller than the standard CMAQ reductions) by up to 2 ppb near the surface. Above 500 m the standard model under-predicts O_3 reductions by up to 2 ppb.

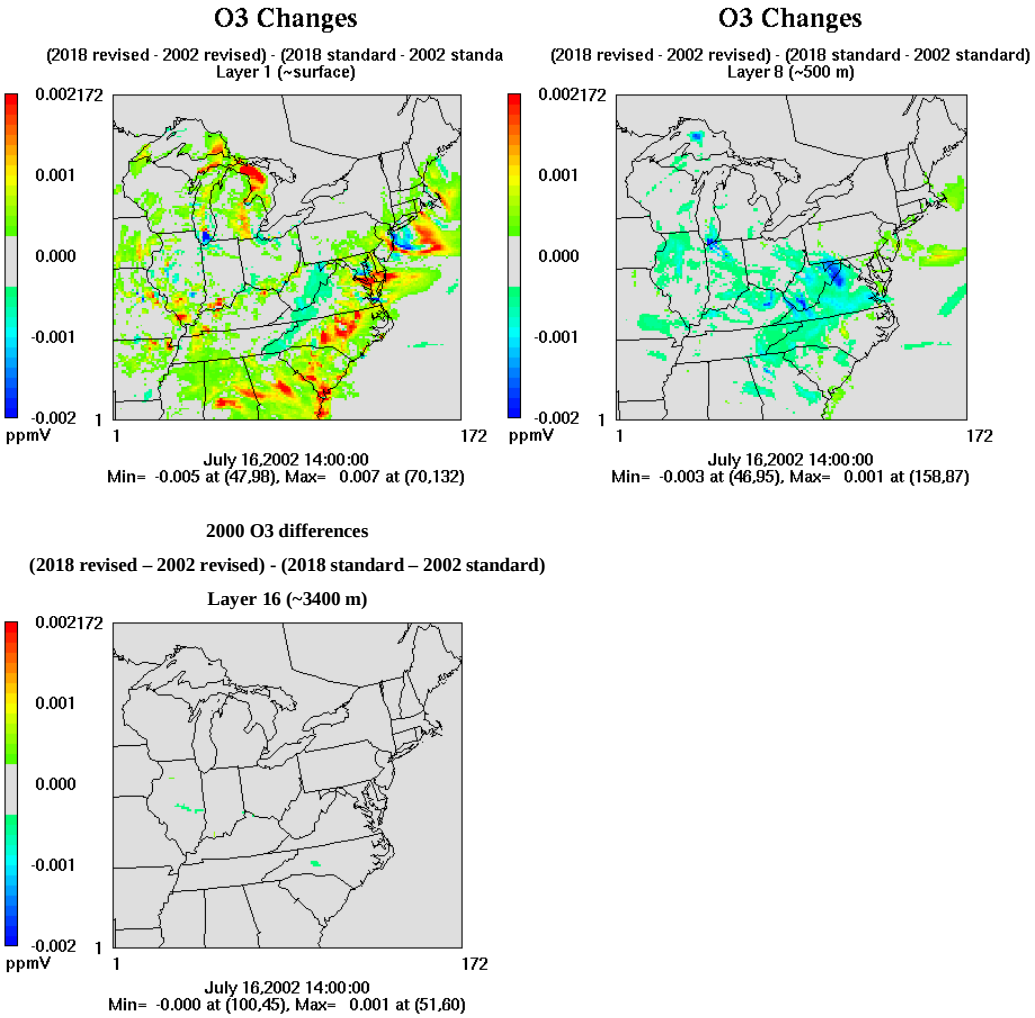

Figure 16a. O_3 differences of [(2018, revised – 2002, revised) – (2018, standard – 2002, standard)] for the 1st, 8th, and 16th layers at 14 UT. The standard CMAQ runs over-predict O_3 reductions near the surface (warm colors). Above 500 m the standard model under-predicts O_3 reductions.

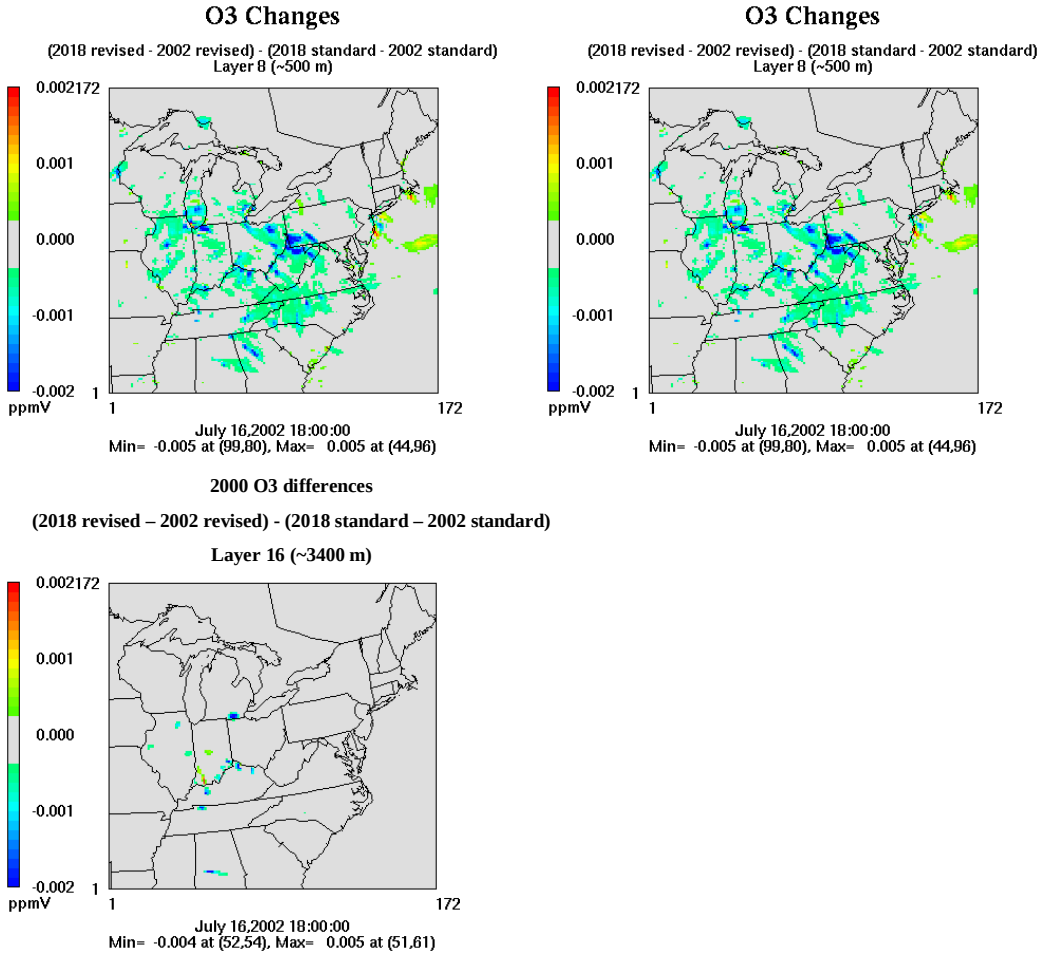

Figure 16b. O_3 differences of [(2018, revised – 2002, revised) – (2018, standard – 2002, standard)]. For the 1st, 8th, and 16th layers at 18 UT. The standard CMAQ runs over-predict O_3 reductions near the surface (warm colors). Above 500 m the standard model under-predicts O_3 reductions.

This study has important policy implications. The National Ambient Air Quality Standards (NAAQS) regulate surface O_3 and the EPA requires states to use the CMAQ model to determine future compliance, for surface sites. Above I have shown that accounting for aerosols in the photolysis rates of NO_2 decreases O_3 production near the surface. State agencies that are not in compliance with NAAQS O_3 standards can use this model bias to their advantage when developing the State

Implementation Plans. The reductions in O_3 (incurred by reductions point and mobile NOx emissions) generated with the standard CMAQ model are overestimated at the surface. This must be accounted for when state agencies develop plans to reduce O_3.

5.2.3 SO_2 Comparisons

Modeled SO_2 from CMAQ and GOCART was compared to aircraft profiles. Figure 17 shows the median of 118 CMAQ and aircraft SO_2 profiles (ppb) for 2002 (June – August), with error bars representing the 25th and 75th percentiles. These profiles were made in the area contained by 37.18 to 44.53^{o} latitude and -79.44 to -68.36^{o} longitude. CMAQ over-predicts SO_2 by a factor of 1.2 at 200 m and by a factor of 4.6 at 2300 m (Figure 18). CMAQ over-predicts the column content by 55% (Table 4).

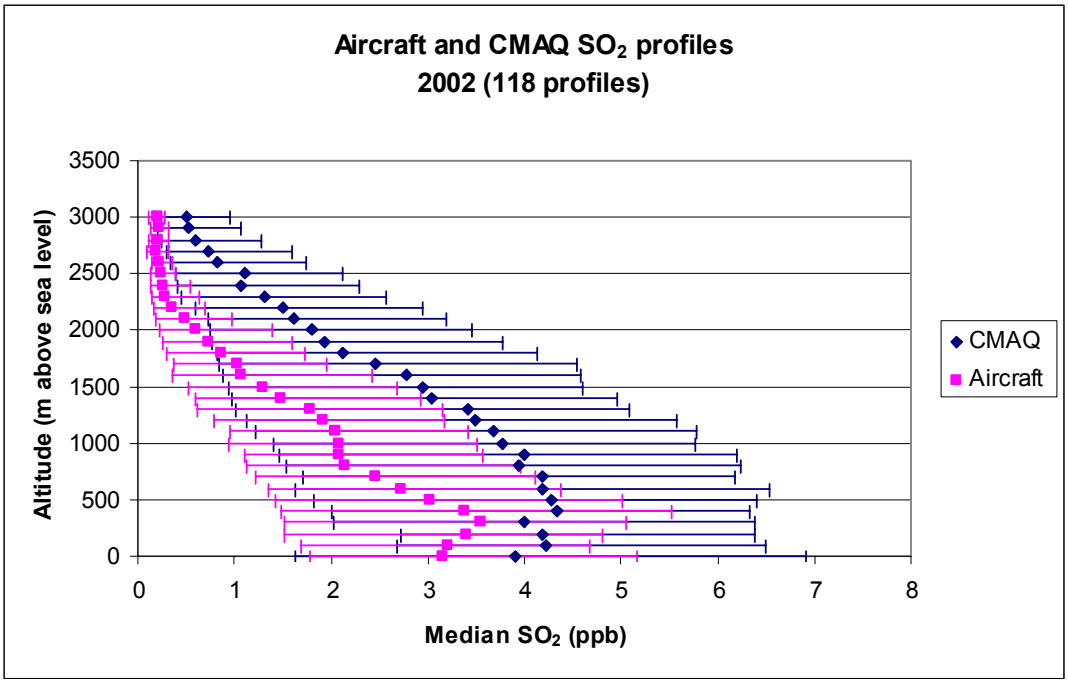

Figure 17. Median CMAQ and aircraft profiles of SO_2 from 2002 (June –August). The median was obtained from 118 profiles. The error bars represent the 25th and 75th percentiles. Though the error bars overlap, CMAQ over-predicts SO_2 throughout the profile.

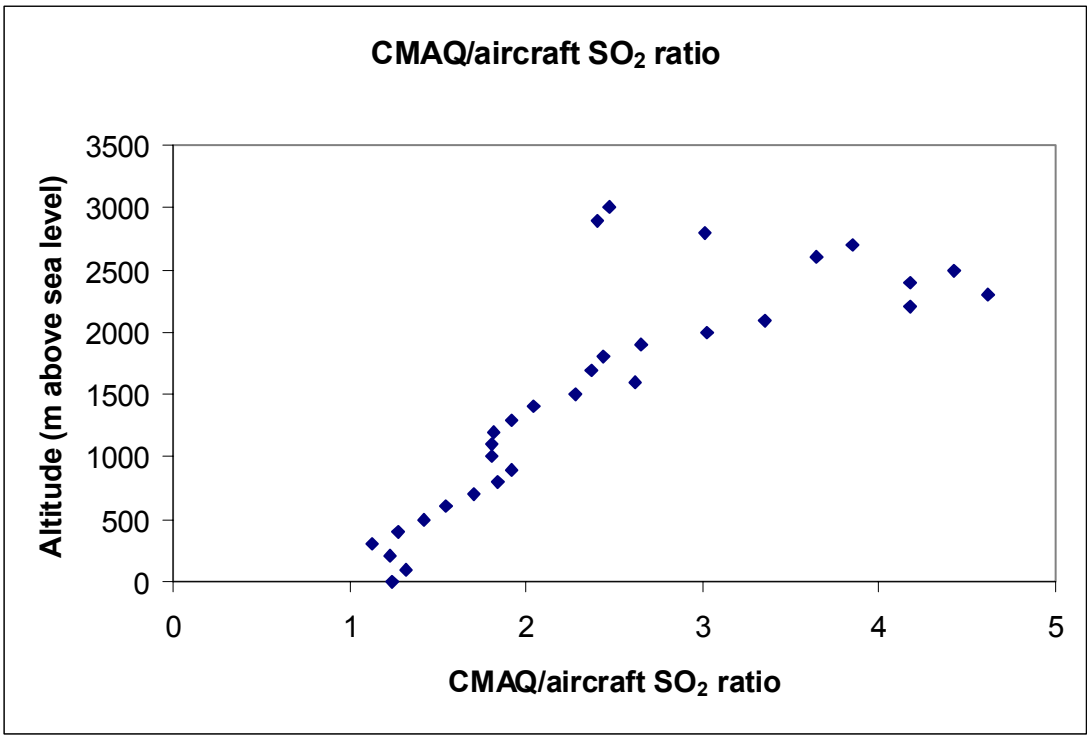

Figure 18. The ratio of median CMAQ SO_2 mixing ratios divided by median aircraft SO_2 mixing ratios. CMAQ over-predicts SO_2 by a factor of 1.2 at 200 m and a factor of 4.6 at 2300 m.

Column content (g m^{-2})	Aircraft	CMAQ
average	0.009	0.014

Table 4. The average aircraft and CMAQ SO_2 column content (g m^{-2}) for 118 profiles. The average CMAQ column content is 55% larger than the average aircraft column content.

Figure 19 shows median SO_2 profiles ($\mu g/m^3$) from 223 GOCART and aircraft averaged profiles for 2000 to 2003 (April – August) with error bars representing the 25th and 75th percentiles. These profiles were made in the area contained by 34 to 44^{o}

latitude and -82.5 to -67.5° longitude. Figure 20 shows the ratio of GOCART/aircraft SO_2 at each of the seven altitudes examined. GOCART over-predicts SO_2 by a factor of 1.4 at 100 m and by a factor of 2 at 1250 m. The GOCART column content is 50% larger than the aircraft column content (Table 5). Although CMAQ and GOCART are representative of different times and locations and are not strictly comparable with each other, they show a consistent high bias relative to observations.

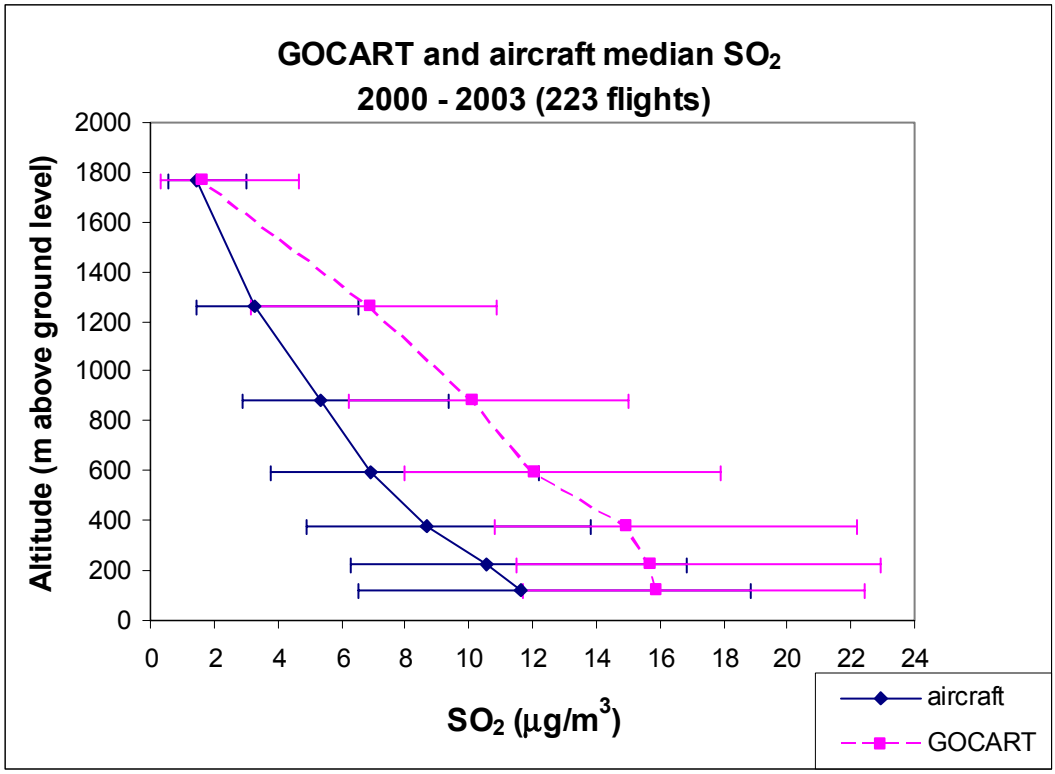

Figure 19. Median GOCART and aircraft profiles of SO_2 from 2000-2002 (April –August). The median was obtained from 223 profiles. The error bars represent the 25th and 75th percentiles. Though the error bars overlap, GOCART over-predicts SO_2 up to 1800 m.

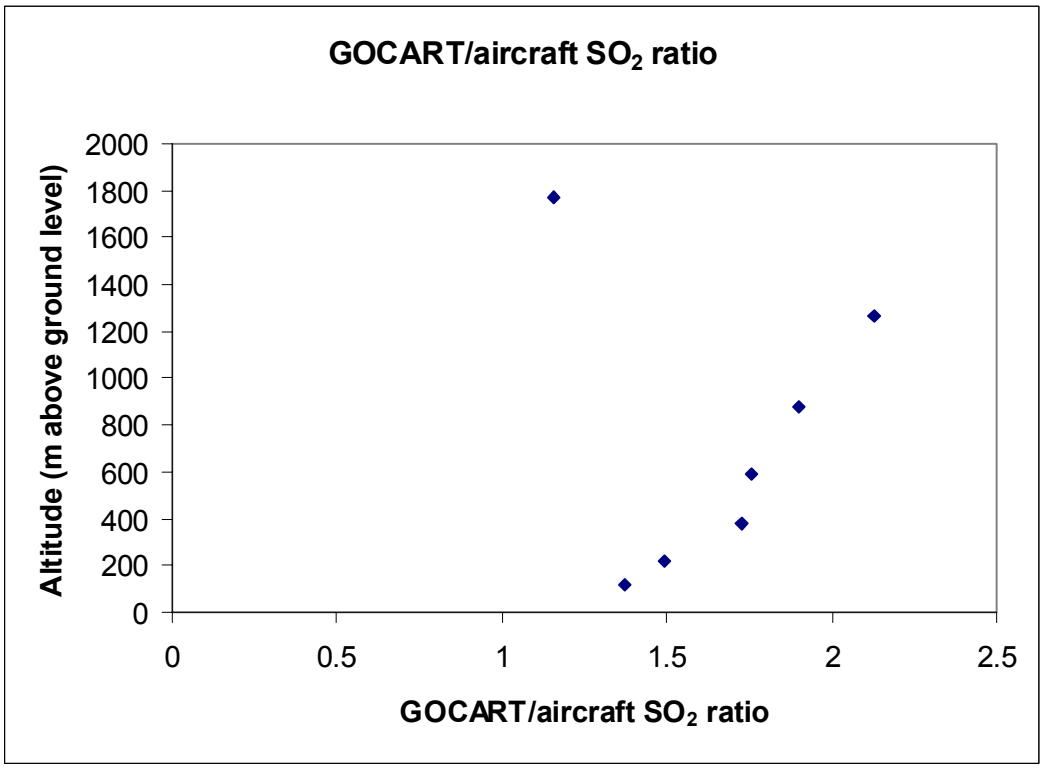

Figure 20. The ratio of median GOCART SO_2 mixing ratios divided by median aircraft SO_2 mixing ratios. GOCART over-predicts SO_2 by a factor of 1.4 at 100 m and a factor of 2 at 1250 m.

Column content ($g\ m^{-2}$)	Aircraft	GOCART
average	0.012	0.018

Table 5. The average aircraft and GOCART SO_2 column content ($g\ m^{-2}$) for 223 profiles. The average GOCART column content is 50% larger than the average aircraft column content.

Differences between CMAQ and measured SO_2 were calculated and sorted as those for O_3. The profile differences are smallest for SO_2 with small mixing ratios (around 2 ppb at the surface). Figures 21-23 show CMAQ and aircraft profiles with the 5th percentile smallest differences, median differences and 95th percentile largest

differences. Back trajectories (from HYSPLIT) are also shown. Profiles associated with the median differences show that the model over-predicts SO_2 above 1500 m. The profile over Easton, MD on June 25, 2002 shows that the model does under-predict SO_2 sometimes. Profiles associated with the 95^{th} percentile largest differences show that the model over-predicts SO_2 by a factor of two to five throughout the profile. There does not appear to be a relationship among wind speeds and direction and SO_2 profiles.

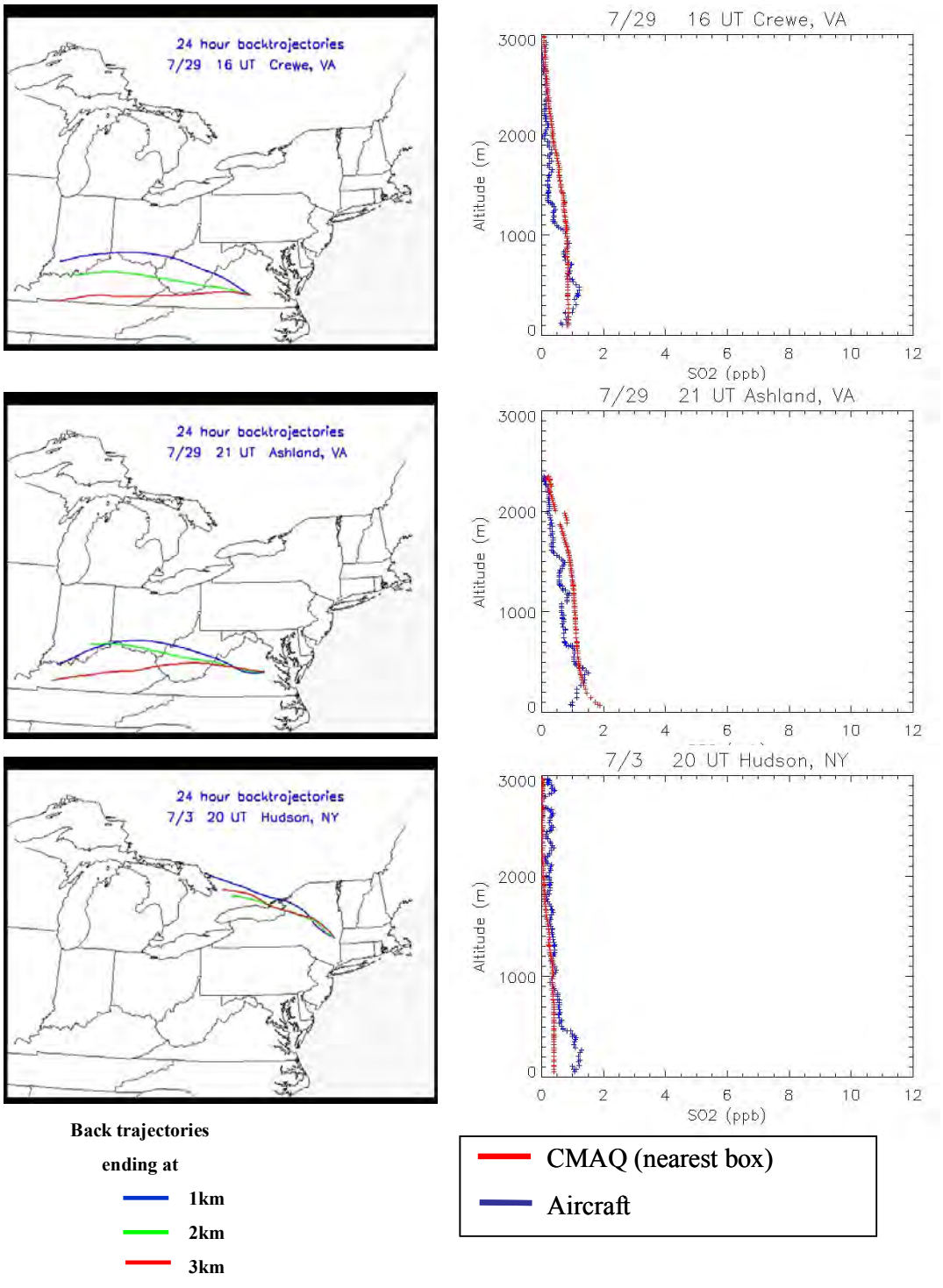

Figure 21. CMAQ and aircraft SO_2 profiles associated with the 5th percentile smallest differences (best agreement). The red profiles represent CMAQ SO_2 from the closest (center) grid cell. In general CMAQ over-predicts SO_2. Back trajectories at 3 altitudes are also shown.

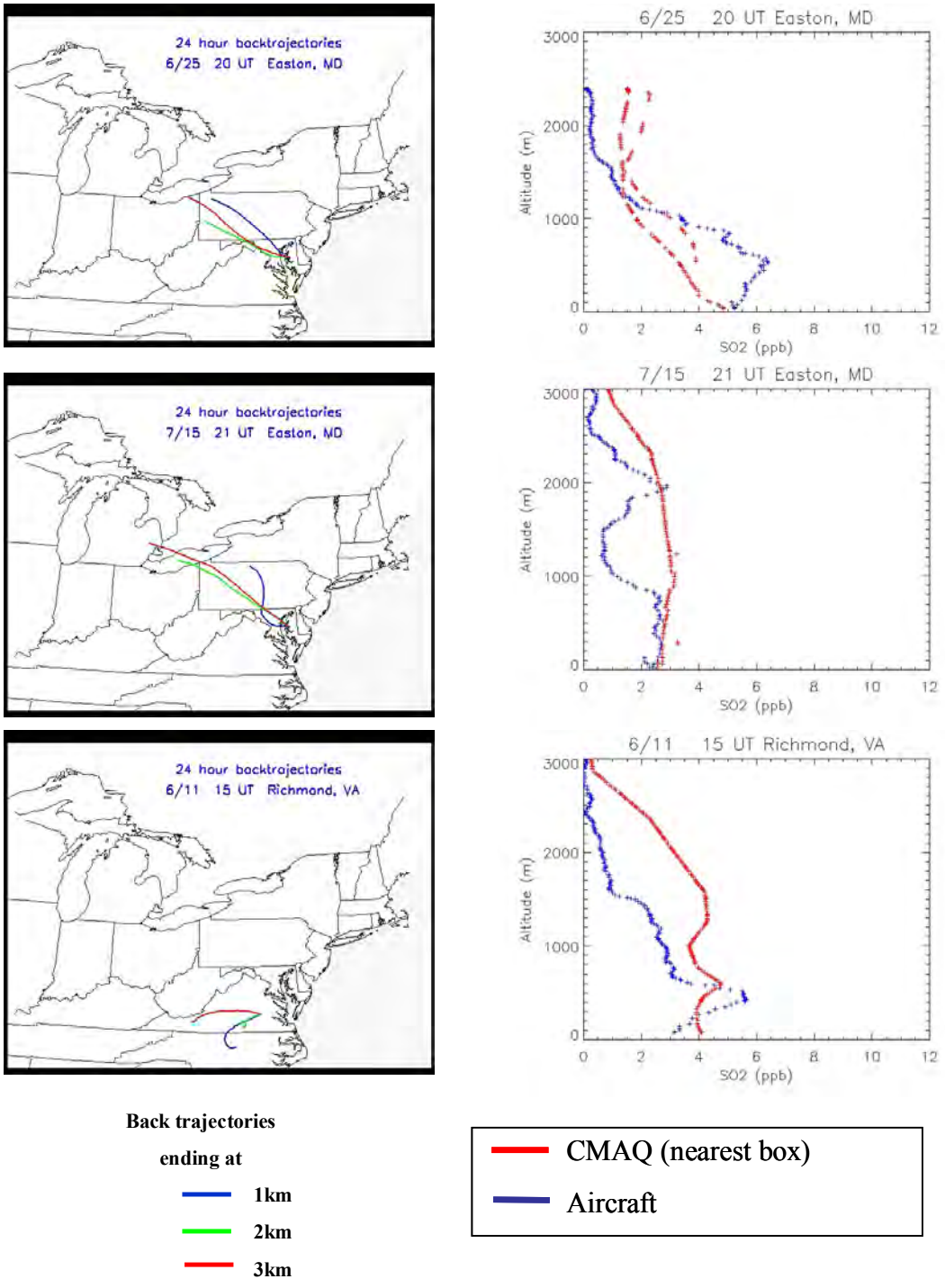

Figure 22. CMAQ and aircraft SO_2 profiles associated with the median differences. The red profiles represent CMAQ SO_2 from the closest (center) grid cell.

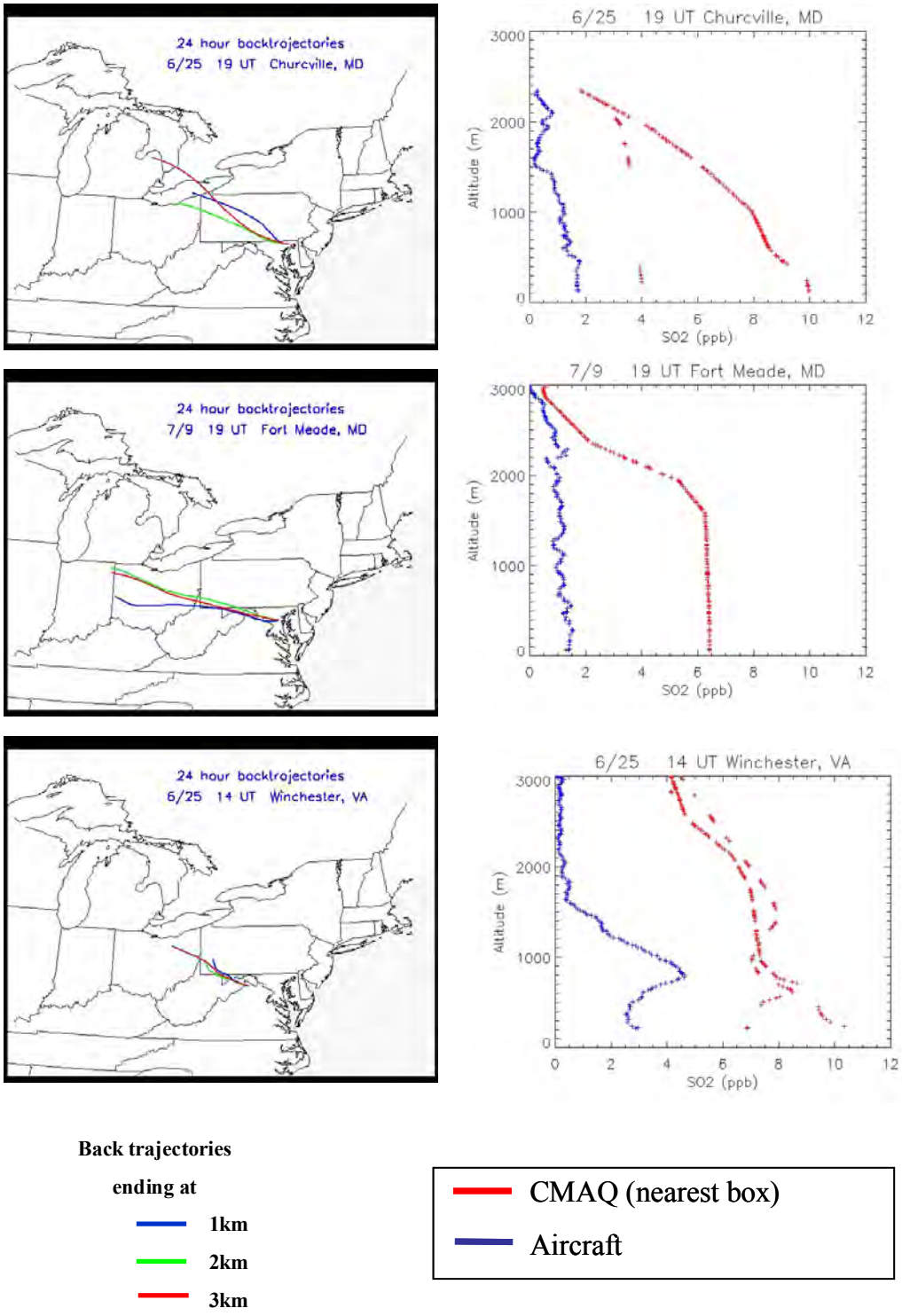

Figure 23. CMAQ and aircraft SO_2 profiles associated with the 95th percentile largest differences (worst agreement). The red profiles represent CMAQ SO_2 from the closest (center) grid cell.

Differences between GOCART simulations and aircraft observations of SO_2 were calculated in a manner similar to the differences between CMAQ and aircraft. GOCART has coarse vertical resolution and there were only seven altitude layers to compare with the aircraft profiles. For this reason only one altitude bin with the seven layers (k=1 from Equation 1 in chapter 4) was analyzed for differences. Figures 24-26 show profiles associated with the 5^{th} percentile smallest differences, median differences, and 95^{th} percentile largest differences. Profiles associated with the median differences show that the model tends to over-predict SO_2, however profiles associated with the 95^{th} percentile largest differences show the model sometimes over-predicts and sometimes under-predicts SO_2.

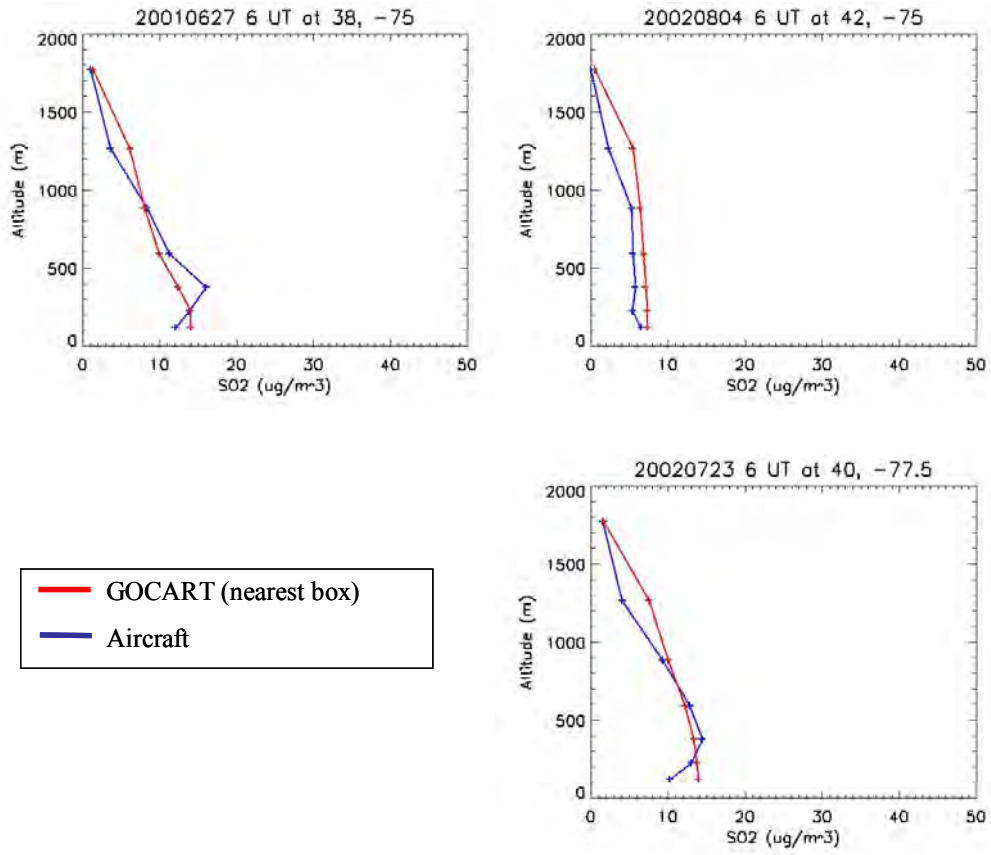

Figure 24. GOCART and aircraft SO_2 profiles associated with the 5th percentile smallest differences (best agreement). The red profiles represent GOCART SO_2 from the closest (center) grid cell.

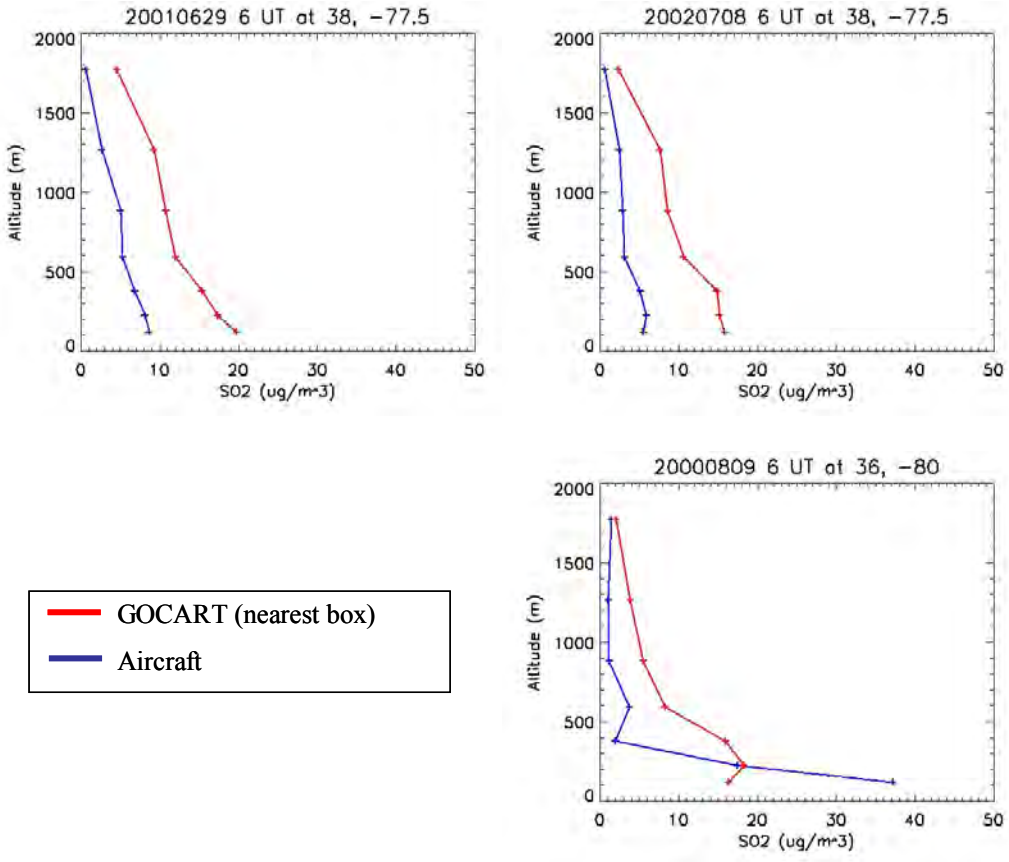

Figure 25. GOCART and aircraft SO_2 profiles associated with the median differences. The red profiles represent GOCART SO_2 from the closest (center) grid cell. GOCART gets the right shape, but the magnitude is too large.

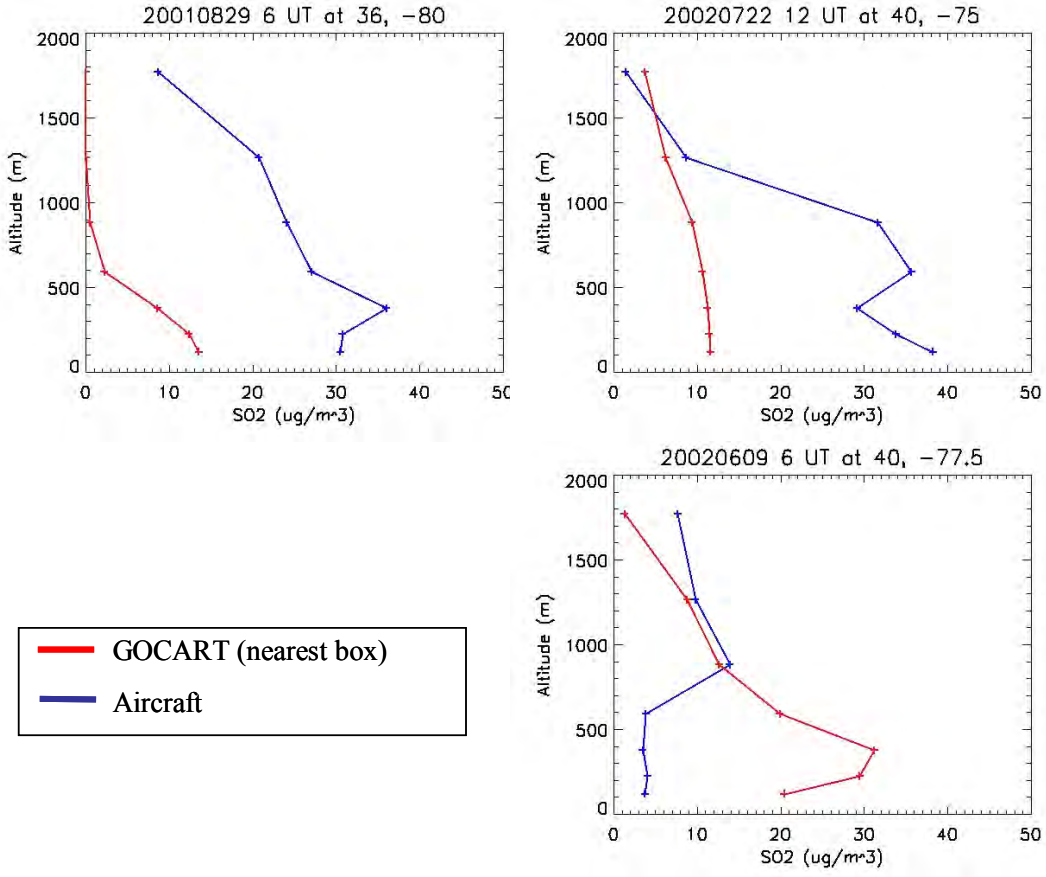

Figure 26. GOCART and aircraft SO_2 profiles associated with the 95th percentile largest differences (worst agreement). The red profiles represent GOCART SO_2 from the closest (center) grid cell. GOCART gets the right shape, but the magnitude is too large.

The model over-prediction could be a result from:

1. Emissions that are too large, with losses modeled correctly.
2. Correct emissions, but the loss in the model is too slow.

To test possibility 1 (that the emissions are too large), I calculated the flux of SO_2 using national inventories of point and area SO_2 sources (area sources are composed of mobile emissions) as well as accounting for a small contribution from biogenic sources. I compared these SO_2 fluxes with those used in GOCART. For my SO_2 flux

calculation I used the EPA's AirData (http://epa.gov/air/data/geosel.html) database for the United States point and area SO_2 sources (emissions are in g/hr).

I used the National Pollutant Release Inventory (NPRI) database for Canadian point source emissions. The NPRI database does not report area emissions and therefore I estimated them from the EPA's AirData database. I calculated the slope between the US state populations – x-axis, (ESRI data and maps 2000) and US state area SO_2 emissions- y-axis, by forcing the line through zero (Figure 27). This slope of area emissions/population was used to approximate area emissions from Canadian municipalities using Canadian populations (ESRI data and maps 2000). I also estimated the small contribution of SO_2 from biogenic sources using sulfur fluxes presented in Wayne (2000); the biogenic contribution of SO_2 is 0.7% of the contribution from anthropogenic emissions. I calculated the total flux of SO_2 for half of the United states and some Canadian municipalities by adding the point and area source emissions for each state (or municipality) to the biogenic contribution and dividing this by the total area of the state (or municipality). Figure 28 shows a comparison of the SO_2 fluxes I calculated from the national databases and the SO_2 flux used in the GOCART model. The average flux from the national inventories (Figure 28 a) is 2.8 $x10^{-4}$ g m^{-2} hr^{-1} and the average flux from GOCART (Figure 28 b) is 2.5 $x10^{-4}$ g m^{-2} hr^{-1}, only 16% smaller than the average flux from the national inventories. The SO_2 emissions used in CMAQ were generated with SMOKE which converts the resolution of the national inventories into a resolution that can be used in CMAQ. Because the SO_2 fluxes from the models (CMAQ and GOCART) are similar to those I calculated using the national inventories, it is unlikely that model emissions

are too large by a substantial amount. The likely explanation for why the model SO_2 is larger than measured is that the model removal of SO_2 is too slow.

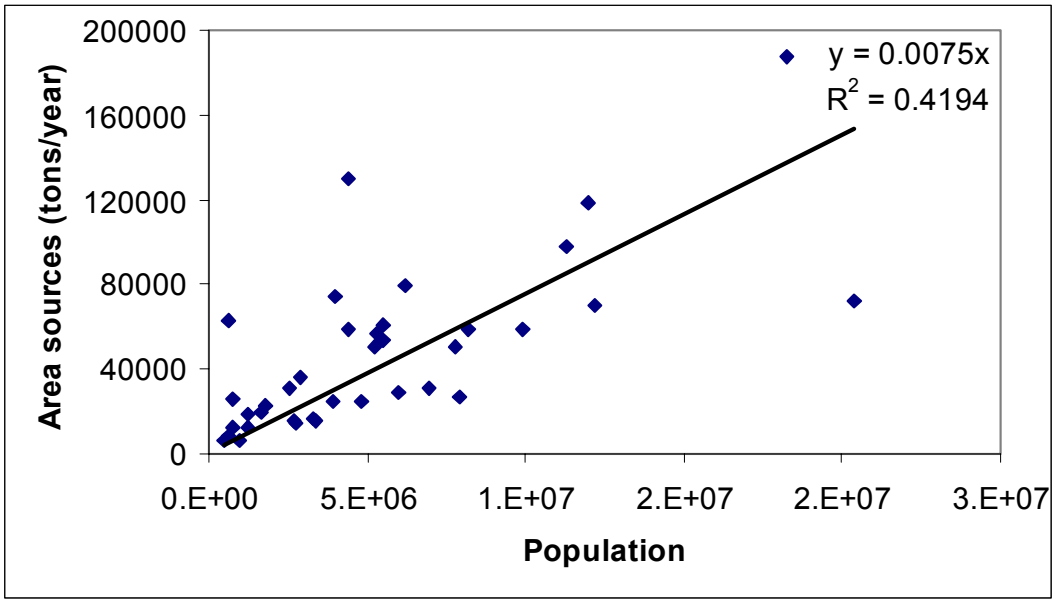

Figure 27. US state population and area sources of SO_2.

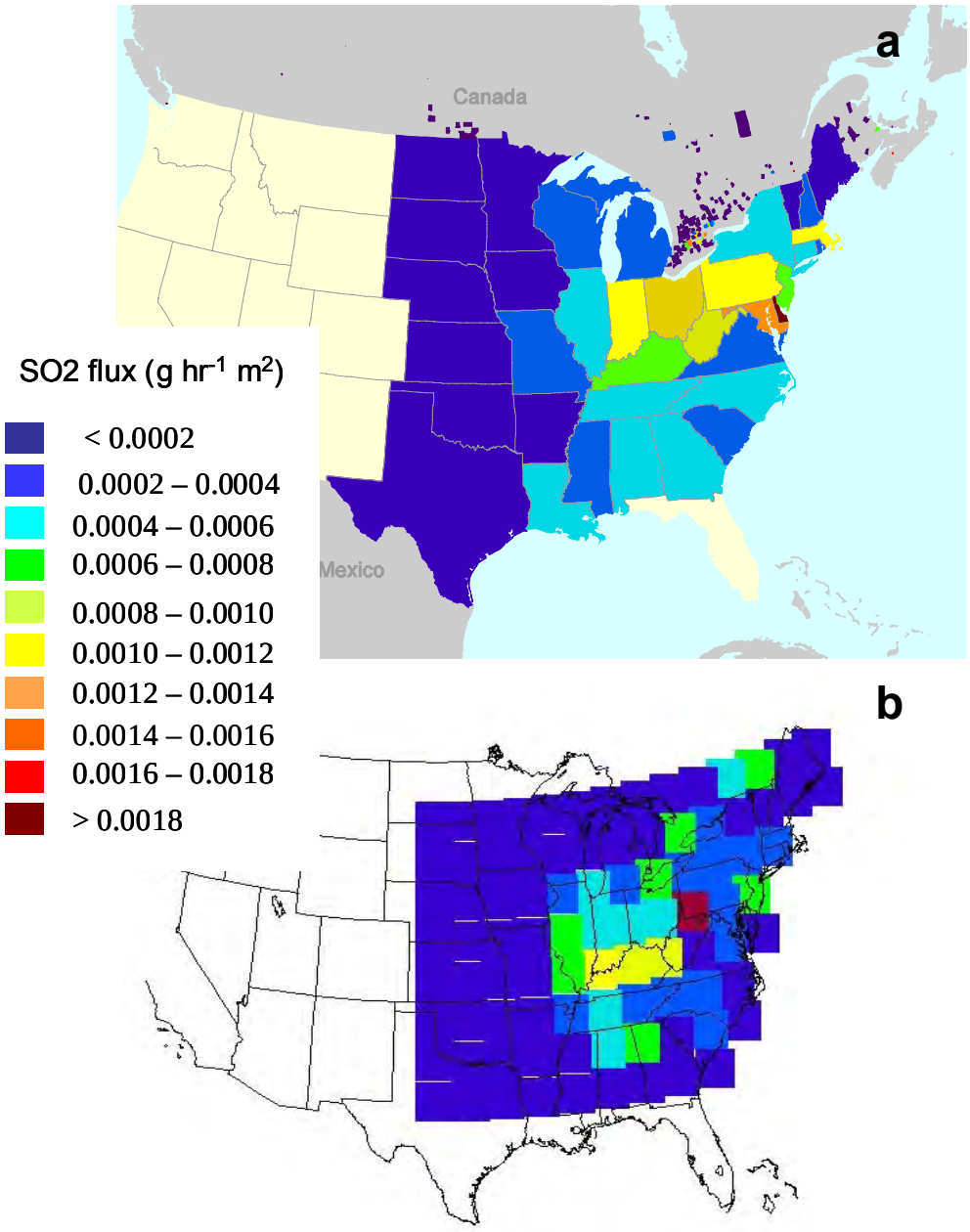

Figure 28. a) The SO_2 flux (g hr^{-1} m^{-2}) calculated using national emission inventories and b) the SO_2 (g hr^{-1} m^{-2}) flux used by GOCART.

The model may underestimate reactions that oxidize SO_2 to sulfate properly and this could explain a model loss of SO_2 that is too slow (possibility 2). SO_2 oxidation to sulfate via H_2O_2 in clouds is well understood and in the Mid-Atlantic region with an acidic environment this is the most probable reaction pathway for

sulfate formation (Seinfeld and Pandis, 1998). Figure 29 shows the mixing ratio of H_2O_2 over the average CMAQ domain and at a specific rural location (Big Meadows, VA) for July 1, 2002. H_2O_2 is 2-4 times greater than SO_2, from 1000 – 2000 m, (Figure 17) and large enough to oxidize completely the SO_2 to sulfate. It is therefore likely that the model generates enough H_2O_2 to react with SO_2. Heterogeneous oxidation on mineral aerosols is not as well understood (Detener et al., 1996; Zhang et al., 2006), and may be more difficult to account for in the models. The models may also not fully account for wet and dry deposition in the Mid-Atlantic region, thus increasing the lifetime of SO_2. The models may also under-represent clouds (as described by Mueller et. al., 2006), where SO_2 is oxidized to sulfate with H_2O_2 and therefore produce an SO_2 lifetime that is too long. There are no NAAQS exceedences of SO_2 in the Mid-Atlantic region, but there are exceedences of $PM_{2.5}$ for which sulfate (with an SO_2 precursor) is a major component, accounting for 30% of $PM_{2.5}$ mass (Rees et al., 2004; Schwab et al., 2004; Frank et al., 2006; Ondov et al., 2006).

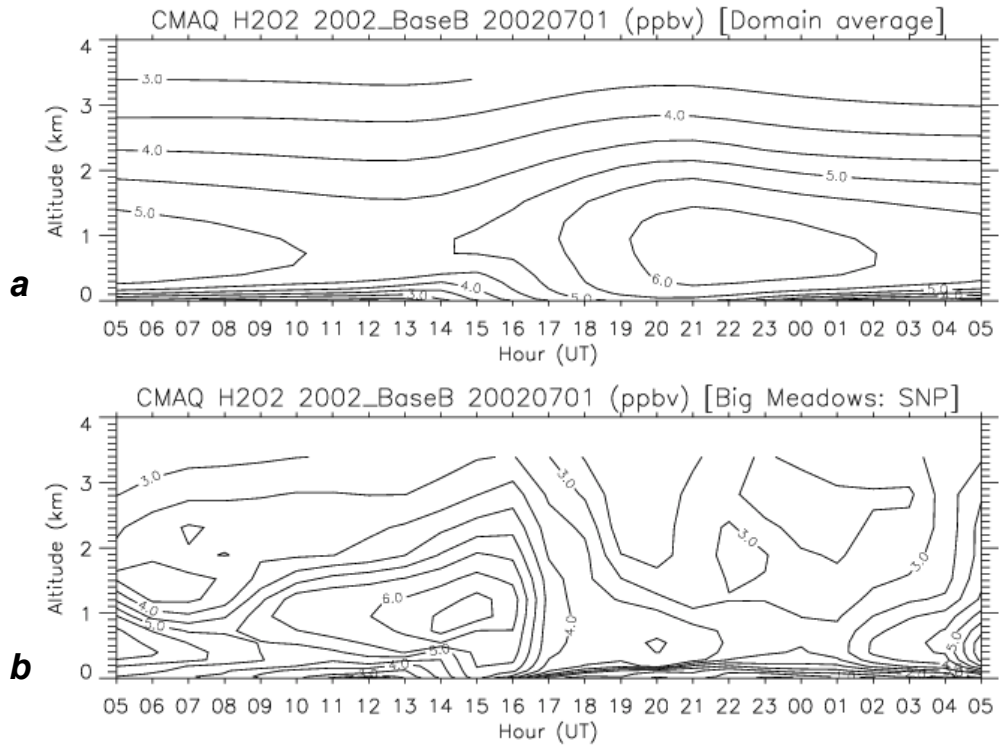

Figure 29. The CMAQ domain average H_2O_2 (ppbv) for a day in July 2002 (a) and the CMAQ H_2O_2 for a rural site (Big Meadows at Shenandoah National park) for the same day. The H_2O_2 is 2-4 times greater than CMAQ SO_2 (from Figure 17) at 1000-2000 m. The altitudes presented are above ground level.

5.2.4 Lifetime Calculation

The CMAQ and GOCART overestimation of SO_2 in the atmosphere suggests that the models do not properly simulate the lifetime of SO_2; specifically the models usually overestimate the lifetime. I have calculated the SO_2 lifetime for the conditions when aircraft observations were made (in the daytime for June through August in the Mid-Atlantic region see Figure 1 in Chapter 2 for map of locations). The mean profile of SO_2 shows a rapid decrease in mixing ratio with increasing altitude. This shows that SO_2 is destroyed on time scales fast relative to mixing in the planetary boundary layer. If SO_2 is on average destroyed before it is advected away

from the source region, the Eastern US, then we can assume that the rate of emissions into the atmosphere is equal to the rate of loss in the atmosphere (i.e., production equals loss). For an air column the production is the flux, F, in g m^{-2} s^{-1}. Because the steady state approximation can be applied to the system the rate of loss (L g m^{-2} s^{-1}) of SO_2 in an air column is

$$L = \int_0^\infty k'[SO_2]dz \tag{11}$$

Where k' is the effective first order rate constant, s^{-1}, $[SO_2]$ is the concentration of SO_2 in g m^{-3} as a function of altitude, z. The product of k' and $[SO_2]$ must be integrated to an altitude where the concentration of SO_2 is much less than at the surface. At steady state the flux is equal to the loss and can be written as:

$$F = \int_0^\infty k'[SO_2]dz \tag{12}$$

The effective first order rate constant is the sum of all losses, including dry deposition, attack by OH, and oxidation by H_2O_2 in cloud droplets. Equation 12 can be rearranged to separate the integral of the effective first order rate constant k' that is the inverse of the mean lifetime, τ (s).

$$\tau = \frac{1}{k'} = \frac{1}{F}\int_0^\infty [SO_2]dz \tag{13}$$

5.2.5 Verification of Lifetime Equation and Results

If Equation 13 is valid then we can use it to calculate the lifetime from measurements of SO_2 made aboard the UMD research aircraft. I developed a method to test Equation 13 using the Gaussian plume equation multiplied by a lifetime factor ($\exp^{-t/\tau}$, where τ is a user-defined lifetime) to generate SO_2 profiles from a known

source. I calculated the average lifetime by averaging the integrated profiles and dividing them by the source flux. If the lifetime I calculated using Equation 13 was the same as the user-defined lifetime then Equation 13 is valid. The Gaussian plume equation is:

$$C(x,y,z) = \frac{q}{2\pi\mu\sigma_y\sigma_z}\exp(-\frac{y^2}{2\sigma_y^2})\left[\exp(-\frac{(z-h)^2}{2\sigma_z^2}) + \exp(-\frac{(z+h)^2}{2\sigma_z^2}\right] \qquad (14)$$

Here C is the concentration at an altitude z, a distance x downwind of a source and a distance y that is perpendicular to the x-axis. The emission rate is given by q, μ represents the wind speed and was assumed to be 6 m s^{-1} (the average wind speed for all 48 hr back trajectories ending at 1 km, associated with flights the UMD research aircraft made in 2002), h represents the effective stack height, assumed to be 200 m, and σ_y and σ_z are functions of x and represent the standard deviation of the plume distribution in the horizontal and vertical directions respectively. To determine the σ_y and σ_z values I assumed that the stability class was D, which is a neutral stability class and associated with winds greater than 6 m s^{-1} and moderate incoming solar radiation during the day (Schnelle and Dey, 2000). The equations for σ_y and σ_z are given below:

$$\sigma_y = ax^b \qquad (15)$$

$$\sigma_z = cx^d \qquad (16)$$

Where a = 44 and b = 0.51 for stability class D (Schnelle and Dey, 2000) and c = 68 and d= 0.89 for stability class D (Seinfeld and Pandis, 1998). The effective stack height, h from Equation 14, is the sum of the actual height of the stack, H plus the plume rise Δh. The plume rise can be calculated using the Holland plume rise

formula (Schnelle and Dey, 2000), however, for simplicity, I assumed that all stack heights were 200 m.

To test the method for determining SO_2 lifetime (using Equation 13) I generated SO_2 profiles from a single source of $4.5x10^7$ g/day, in 14400 grid cells of 0.01^o latitude by 0.01^o longitude at 24 altitude levels from 0 – 30 km. To account for the lifetime (due to chemical or physical removal of SO_2) I multiplied the Gaussian plume dispersion Equation 13 by $\exp^{-t/\tau}$, where t is the time it takes to get to the sampling point from the source and τ is a user-defined input lifetime. Figure 30 shows the SO_2 column contents in this box generated from this one source. The flux of SO_2 from the one source was $1.35\ x10^{-4}$ g $m^{-2}day^{-1}$ for the chosen domain. US EPA (2003) states that 86% of SO_2 is generated from fuel combustion and the rest (14%) is generated from transportation and industrial sources. To account for these transportation and industrial sources I added 509 g day^{-1} to each grid cell. This added a $2.2x10^{-5}$ g day^{-1} m^{-2} to the flux and $2.5x10^{-5}$ gm^{-2} was added to the column content in each grid cell.

Figure 30 shows the SO_2 column contents generated by one SO_2 source. In order to calculate the lifetime, the column contents are divided by the flux (the emission rate/ area of the box). Sampling any single point will probably not return the lifetime that is input into the model. However, an average of lifetimes from all sampling points in the box must equal the lifetime put into the model.

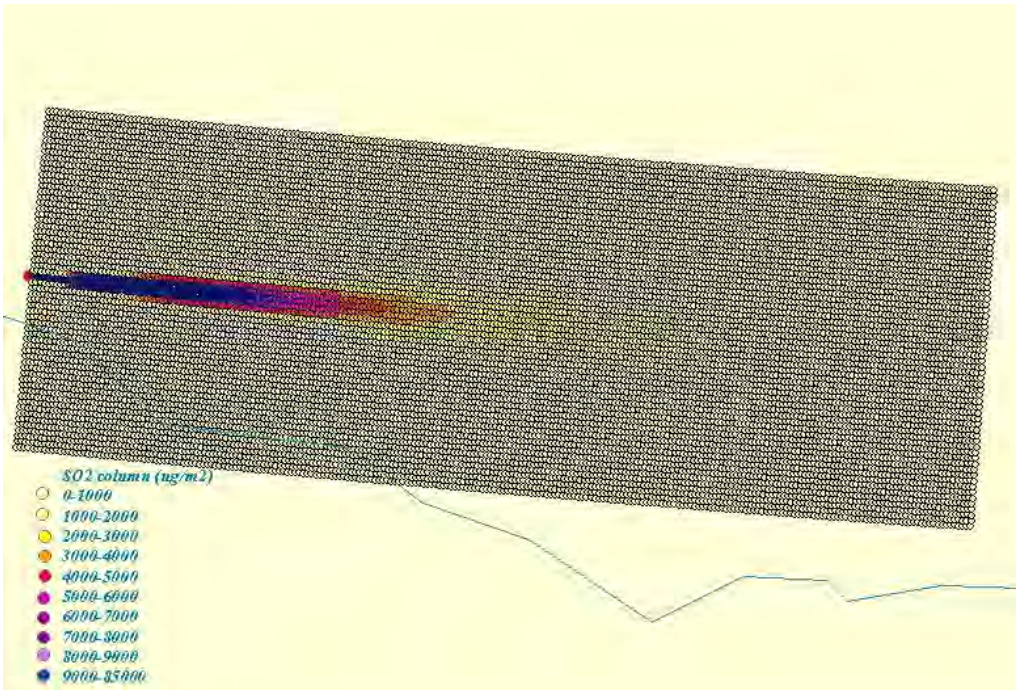

Figure 30. SO_2 column contents generated using a Gaussian plume dispersion model with one source.

To calculate the lifetime of SO_2 from UMD aircraft profiles I am limited to the locations over which the aircraft flew; the number of locations is a small fraction of the 14400 grid of 0.01^o latitude by 0.01^o longitude described above. I performed a test to determine if the locations and number of spirals made by the UMD research aircraft were sufficient to calculate the average lifetime using Equation 13. In 2002 the UMD airplane flew at 17 different locations and made a total of 90 different spirals sampling SO_2. Even though there were only 17 locations, the SO_2 profiles were independent because the winds changed between sampling days. To represent these locations in the model the 17 locations were shifted by 0.1 degree latitude or longitude, North, South, East, and West for a total of 85 sampling points. To test the effects of nudging the points on lifetime, the 85 points were shifted 0.15 degrees latitude or longitude, North, South, East, and West. This resulted in 5 sets of 85

samples that should have similar average lifetimes. Figure 31 shows the locations of these 425 sampling points (5 x 85) with sources of SO_2 in green. The sampling locations are represented by pink circles.

I also adjusted the area of the box used to calculate the flux in order to determine how that affected the resulting lifetime. Lifetimes of 8, 16, 24 and 32 hours were tested using three different sized boxes to calculate the flux of SO_2. Figure 32 shows the boxes used in this study and Table 6 gives the locations of the boxes and the distances and times between the westernmost sampling point and the western edge of the box.

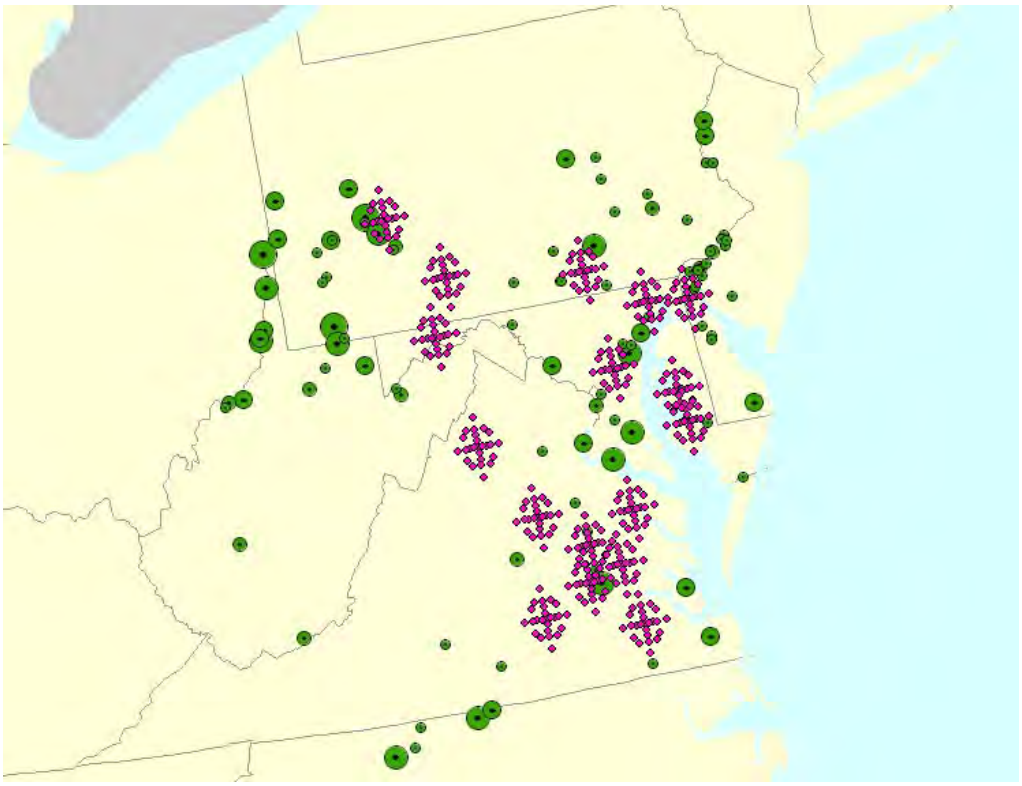

Figure 31. The locations of the 425 sampling points to be used in the simplified Gaussian plume dispersion model are shown in pink. The green circles represent power plants emitting SO_2 and the size of the circle represents the relative size of SO_2 emissions.

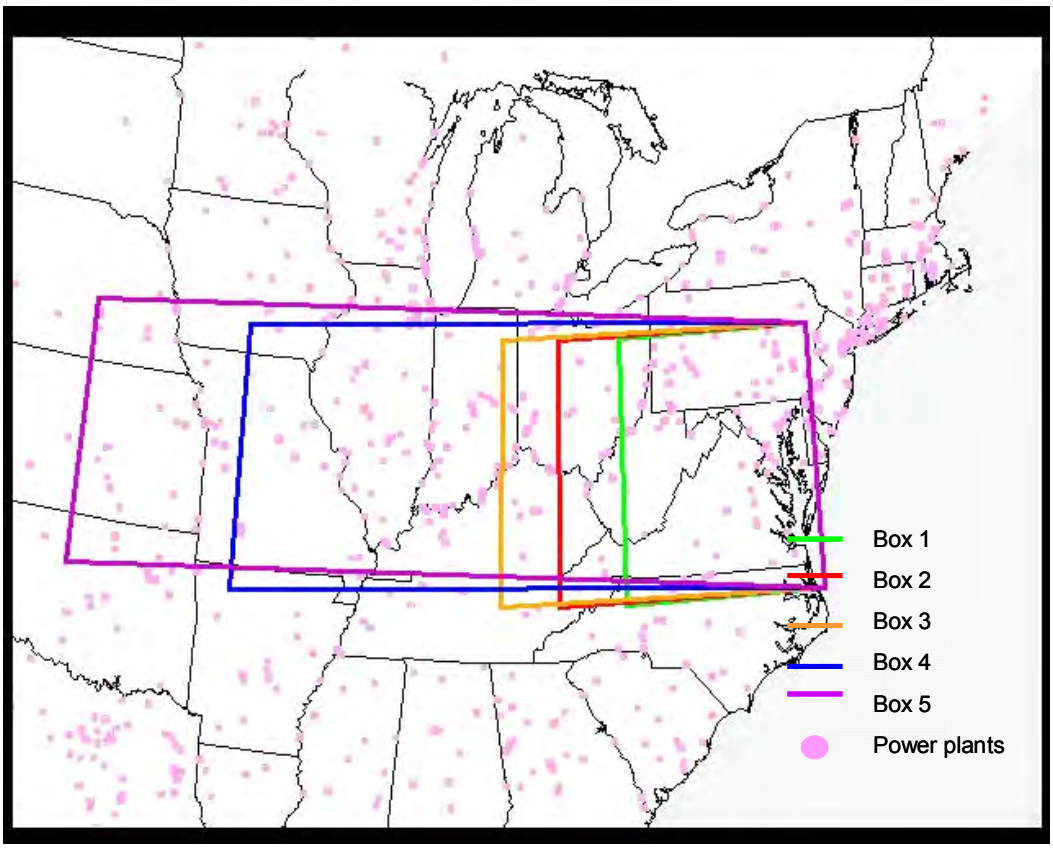

Figure 32. Boxes used to determine SO_2 flux from point sources.

	Box 1	Box 2	Box 3	Box 4	Box 5
Initial latitude	36.1	36.1	36.1	36.1	36.1
Final latitude	41.2	41.2	41.2	41.2	41.2
Initial longitude	-83.5	-85.3	-88.5	-93.5	-98.5
Final longitude	-75.5	-75.5	-75.5	-75.5	-75.5
Distance from western most sample point (m) to western edge of box	3.6E+05	5.3E+05	8.0E+05	1.2E+06	1.7E+06
Time (hours) from western most sample point to western edge of box	16.7	24.7	36.8	6.9	77.0

Table 6. Location of box edges (from Figure 32) in degrees latitude and longitude. Also shown is the time needed for sources from the western most

points of the box to arrive at the western most sampling point.

Table 7a shows the lifetimes generated using an input lifetime of 8 hours and using 3 different fluxes (from Box 1, Box 2 and Box 3) and 5 different sets of 85 sampling locations for a total of 15 groups of 85 measurements of lifetimes. The lifetimes and SO_2 column contents appear to be lognormally distributed (Figure 33). The mean μ_x and variance σ_x^2 for a lognormal distribution are given by the following (Wilks, 1995)

$$\mu_x = \exp[\mu_y + 0.5*\sigma_y^2/2] \quad (17)$$

$$\sigma_x^2 = (\exp[\sigma_y^2] - 1) * \exp[2\mu_y + \sigma_y^2] \quad (18)$$

Where μ_y and σ_y^2 are the mean and variance of the transformed variable y = ln(x). The lognormal statistics for each of the sets of lifetimes calculated with different fluxes (from Box 1, Box 2 and Box 3) are shown in Table 7b. Table 7c shows the average lifetime of all 15 groups with the standard deviation and the standard error (the standard deviation / $\sqrt{15}$). Statistics for lifetimes calculated using inputs of 16, 24 and 32 hours are shown in Tables 8-10. I calculated the 2-σ uncertainty associated with the lifetimes generated using the method, by accounting for the accuracy (the difference between the median and the 95th percentile of the 15 average lifetimes) and the precision (the standard error). I added these in quadrature and determined there was a 30% uncertainty associated with the method assuming a normal distribution, the uncertainty associated with the method assuming a lognormal distribution was 20%.

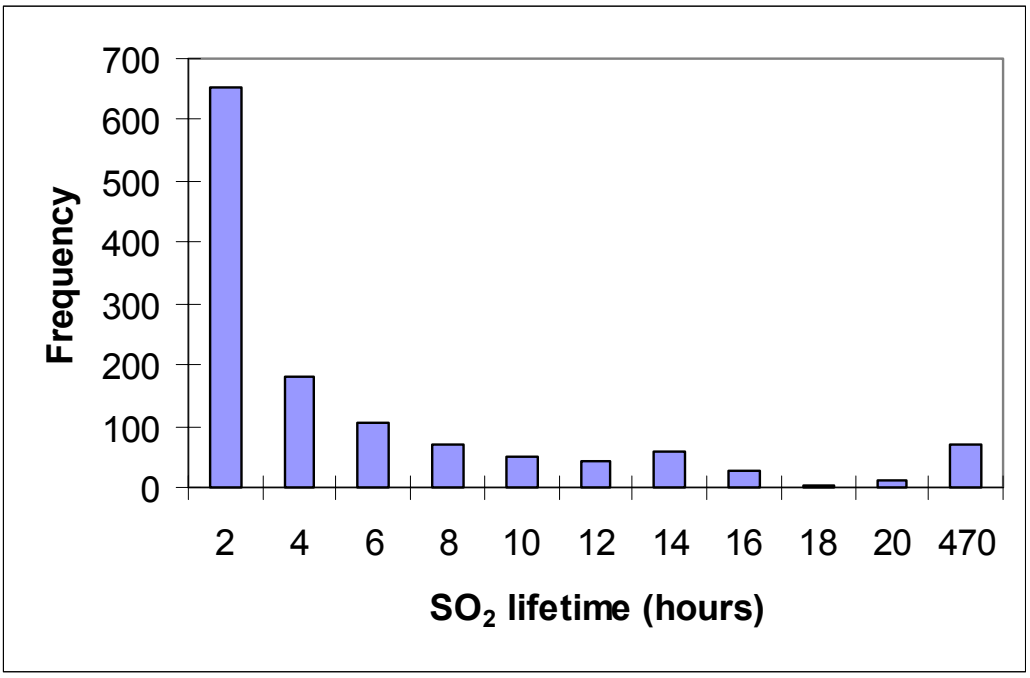

Figure 33. Histogram of SO_2 lifetimes calculated using Gaussian plume dispersion model and an input lifetime of 8 hours.

A

Box 1	Center	North	South	West	East
Mean	9.43	6.65	7.09	5.35	5.87
Standard Error	5.12	2.70	3.59	0.93	1.52
Standard Deviation	47.22	24.86	33.14	8.53	14.05
Box 2	Center	North	South	West	East
Mean	10.74	7.76	8.28	6.34	7.08
Standard Error	5.37	2.82	3.77	0.97	1.60
Standard Deviation	49.48	26.03	34.74	8.97	14.77
Box 3	Center	North	South	West	East
Mean	11.31	8.22	8.75	6.74	7.55
Standard Error	5.53	2.91	3.88	1.00	1.65
Standard Deviation	50.99	26.82	35.79	9.22	15.22

B

Box 1	Center	North	South	West	East
Mean	5.87	5.33	4.69	6.98	5.49
Standard Error	3.19	2.60	2.12	4.06	2.96
Standard Deviation	29.41	23.95	19.58	37.46	27.26
Box 2	Center	North	South	West	East
Mean	7.70	6.87	6.42	8.13	7.53
Standard Error	3.15	2.56	2.35	3.20	3.06
Standard Deviation	29.07	23.57	21.65	29.49	28.17
Box 3	Center	North	South	West	East
Mean	7.99	7.19	6.74	8.05	7.79
Standard Error	2.78	2.32	2.18	2.59	2.64
Standard Deviation	25.60	21.37	20.06	23.87	24.36

C

	Normal Distribution	Log-normal Distribution
Mean	7.32	6.25
Standard Error	0.44	0.29
Standard Deviation	1.70	1.11

Table 7. a) Statistics of SO_2 lifetimes (hours) from profiles generated using a Gaussian plume model assuming a lifetime of 8 hours for boxes 1, 2 and 3 for a) an assumed normal distribution b) an assumed lognormal distribution. c) The average lifetime for all sets (Center, North, South, West and East) for boxes 1, 2 and 3 as well as the standard deviation and standard error (standard deviation / $\sqrt{15}$).

A

Box 3	Center	North	South	West	East
Mean	16.88	13.78	14.49	12.25	13.04
Standard Error	5.90	3.33	4.18	1.45	2.05
Standard Deviation	54.43	30.67	38.52	13.38	18.93
Box 4	Center	North	South	West	East
Mean	18.54	15.30	16.09	13.72	14.62
Standard Error	6.08	3.42	4.30	1.50	2.11
Standard Deviation	56.05	31.53	39.62	13.82	19.44
Box 5	Center	North	South	West	East
Mean	22.71	18.80	19.76	16.89	17.99
Standard Error	7.35	4.13	5.19	1.82	2.55
Standard Deviation	67.72	38.11	47.88	16.73	23.50

B

Box 3	Center	North	South	West	East
Mean	15.14	14.16	15.51	14.55	14.75
Standard Error	3.86	3.40	4.52	3.45	3.71
Standard Deviation	35.58	31.34	41.71	31.79	34.18
Box 4	Center	North	South	West	East
Mean	15.39	14.41	16.57	14.85	15.02
Standard Error	2.65	2.34	3.58	2.47	2.52
Standard Deviation	24.46	21.56	32.99	22.74	23.24
Box 5	Center	North	South	West	East
Mean	18.63	17.50	18.45	18.03	18.10
Standard Error	3.00	2.67	3.23	2.82	2.80
Standard Deviation	27.67	24.62	29.75	25.96	25.82

C

	Normal Distribution	Log-normal Distribution
Mean	15.30	14.76
Standard Error	0.74	0.42
Standard Deviation	2.87	1.63

Table 8 a) Statistics of SO_2 lifetimes (hours) from profiles generated using a Gaussian plume model assuming a lifetime of 16 hours for boxes 3, 4 and 5 for a) an assumed normal distribution b) an assumed lognormal distribution. c) The average lifetime for all sets (Center, North, South, West and East) for boxes 3, 4 and 5 as well as the standard deviation and standard error (standard deviation / $\sqrt{15}$).

A

Box 3	Center	North	South	West	East
Mean	20.56	17.51	18.34	15.84	16.65
Standard Error	6.06	3.52	4.31	1.70	2.28
Standard Deviation	55.86	32.43	39.71	15.69	20.98
Box 4	Center	North	South	West	East
Mean	23.73	20.52	21.49	18.77	19.76
Standard Error	6.22	3.60	4.41	1.76	2.33
Standard Deviation	57.37	33.19	40.64	16.22	21.46
Box 5	Center	North	South	West	East
Mean	29.58	25.68	26.86	23.59	24.81
Standard Error	7.52	4.36	5.33	2.14	2.82
Standard Deviation	69.35	40.15	49.15	19.72	26.01

B

Box 3	Center	North	South	West	East
Mean	19.72	18.66	21.70	18.71	19.19
Standard Error	4.52	4.03	6.21	3.99	4.37
Standard Deviation	41.68	37.20	57.22	36.77	40.25
Box 4	Center	North	South	West	East
Mean	21.15	20.01	24.64	20.08	20.66
Standard Error	3.00	2.65	4.95	2.74	2.87
Standard Deviation	27.69	24.46	45.62	25.22	26.45
Box 5	Center	North	South	West	East
Mean	25.94	24.68	26.33	24.81	25.14
Standard Error	3.31	2.97	3.72	3.08	3.06
Standard Deviation	30.52	27.42	34.26	28.39	28.23

C

	Normal Distribution	Log-normal Distribution
Mean	20.23	20.71
Standard Error	1.04	0.73
Standard Deviation	4.01	2.82

Table 9. a) Statistics of SO_2 lifetimes (hours) from profiles generated using a Gaussian plume model assuming a lifetime of 24 hours for boxes 3, 4 and 5 for a) an assumed normal distribution b) an assumed lognormal distribution. c) The average lifetime for all sets (Center, North, South, West and East) for boxes 3, 4 and 5 as well as the standard deviation and standard error (standard deviation / $\sqrt{15}$).

A

Box 4	Center	North	South	West	East
Mean	27.58	24.40	25.48	22.50	23.56
Standard Error	6.30	3.71	4.47	1.93	2.48
Standard Deviation	58.10	34.18	41.21	17.83	22.83
Box 5	Center	North	South	West	East
Mean	34.86	30.99	32.30	28.72	30.04
Standard Error	7.62	4.49	5.41	2.36	3.01
Standard Deviation	70.28	41.41	49.88	21.76	27.75
Box 6	Center	North	South	West	East
Mean	41.35	36.80	38.34	34.16	35.70
Standard Error	8.95	5.28	6.36	2.79	3.54
Standard Deviation	82.52	48.65	58.60	25.68	32.67

B

Box 4	Center	North	South	West	East
Mean	25.44	24.19	30.80	23.95	24.84
Standard Error	3.30	2.91	6.03	2.96	3.16
Standard Deviation	30.43	26.87	55.63	27.29	29.16
Box 5	Center	North	South	West	East
Mean	31.54	30.21	32.28	30.01	30.50
Standard Error	3.58	3.23	4.07	3.32	3.29
Standard Deviation	33.03	29.80	37.56	30.57	30.36
Box 6	Center	North	South	West	East
Mean	37.46	35.89	38.16	35.65	36.23
Standard Error	4.22	3.81	4.73	3.89	3.88
Standard Deviation	38.91	35.14	43.64	35.89	35.75

C

	Normal Distribution	Log-normal Distribution
Mean	29.17	28.67
Standard Error	1.48	1.26
Standard Deviation	5.75	4.88

Table 10. a) Statistics of SO_2 lifetimes (hours) from profiles generated using a Gaussian plume model assuming a lifetime of 32 hours for boxes 3, 4 and 5 for a) an assumed normal distribution b) an assumed lognormal distribution. c) The average lifetime for all sets (Center, North, South, West and East) for boxes 3, 4 and 5 as well as the standard deviation and standard error (standard deviation / $\sqrt{15}$).

The above study was used to determine the uncertainty associated with the method. I calculated the actual lifetime of SO_2 for 180 daytime profiles made in June, July and August from 2000-2003 in the Mid-Atlantic region using equation 13. I integrated all aircraft profiles of SO_2 from the lowest altitude where measurements were made (usually 3 m above ground) to 5000 m. The aircraft generally measured SO_2 up to 3000 m. I assumed SO_2 was 0.07 ppb between 5000 m and the highest altitude the aircraft sampled (Thornton et al. 1987; Andronache et al. 1997). Extrapolating the SO_2 to 5000 m added 9% on average to the column measured by the aircraft. I calculated the flux using national inventories and an estimate of the biogenic contribution as described in section 5.2.3. Back trajectories of 12, 24, 32, 40 and 48 hours (with one hour interval outputs) were used to determine which states to include in the flux calculation. The flux associated with each state (or municipality) was weighted by the number of back trajectory points in the state divided by the total number of back trajectory points. The weighted fluxes were then summed. Figure 34 shows 24 hr back trajectories for all 180 profiles.

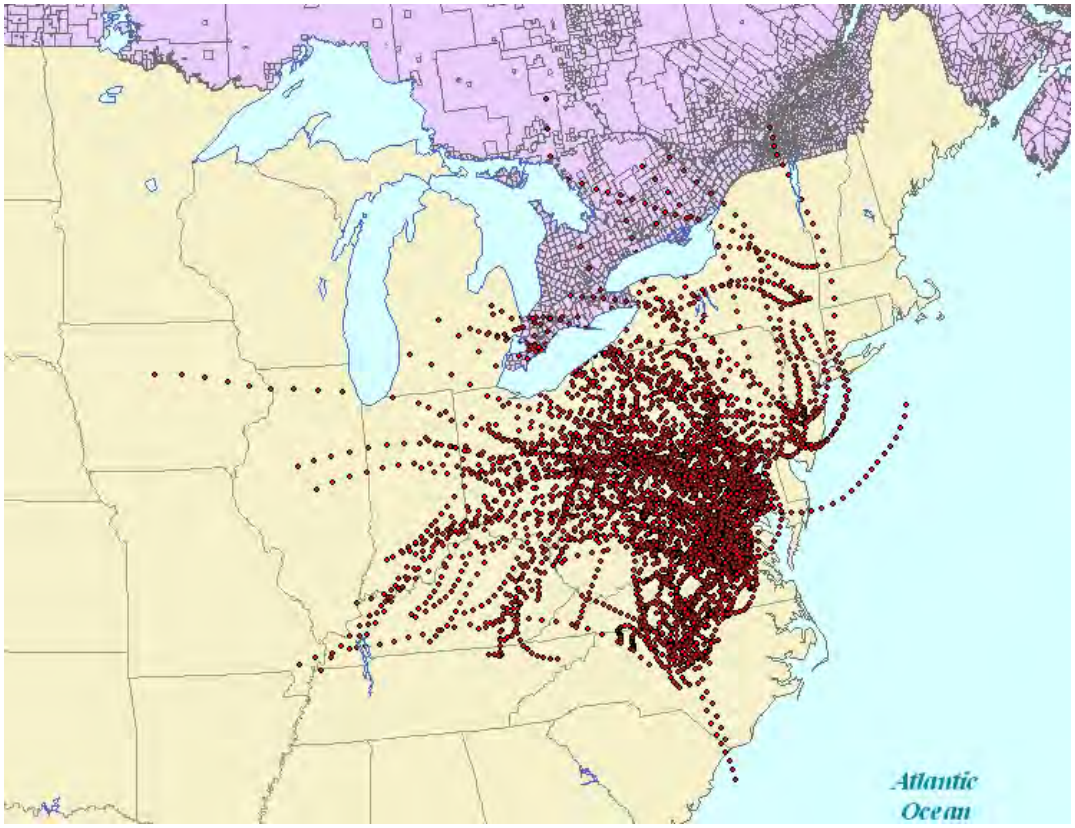

Figure 34. Back trajectories of 24 hr (with one hr intervals) associated with the 180 SO_2 profiles used to calculate the SO_2 lifetime.

Statistics for lifetimes are shown in Table 11 and a histogram of the lifetimes is shown in Figure 35. The fluxes used to calculate the lifetime were determined using 24 hour back trajectories. I calculated the uncertainty associated with the lifetime by accounting for four factors:

1. The uncertainty associated with the method (Equation 13), determined from the simplified Gaussian plume model to be 30% assuming a normalized distribution (the uncertainty associated with the method was 20% assuming a lognormal distribution).

2. The standard error (Table 11), calculated from the standard deviation of all 180 lifetimes and divided by the square root of the number of independent days flights made (in this case 60 days).
3. Uncertainties associated with area and point source emissions (area source emission uncertainties were estimated to be 50% and point source emission uncertainties were estimated to be 16% using the Luke et al. (1997) reported uncertainty).
4. Uncertainties associated with SO_2 measured aboard the University of Maryland research aircraft (assumed to be 16% from Luke et al. (1997)).

To determine the uncertainty associated with area sources I recalculated the lifetime assuming a 50% uncertainty associated with area source emissions and this resulted in a 6% uncertainty associated with the lifetime. I also recalculated the lifetime assuming a 16% uncertainty associated with the point source emissions and this resulted in a 14% uncertainty associated with the lifetime. Therefore the total uncertainty associated with emissions was 20% (14% + 6%). I then added the four factors listed above in quadrature to get the 2-σ uncertainty of 7 hours. The average lifetime is 19 ± 7 hours (at the 95 percent confidence level). The lognormal average lifetime is 20 ± 6 hours. These lifetimes are within the range of model results (for the global average SO_2 lifetime) of 0.6 to 2.6 days (Pham *et al*., 1995; Chin *et al*., 1996; Rested *et al*., 1998; Koch *et al*., 1999; Roelofs *et al*., 1998; Berglen *et al*., 2004) and are on the shorter side of the lifetime estimates.

	Lifetime statistics (hours)
Mean	19
Standard Error	1.7
Median	17
Standard Deviation	13
Minimum	1.5
Maximum	63
Count	180

lognormal distribution	Lifetime statistics (hours)
Mean	20
Standard Deviation	17
Standard Error	2.2

Table 11. Statistics for SO_2 lifetime. The standard error is the standard deviation divided by the square root of 60 (the number of days sampled).

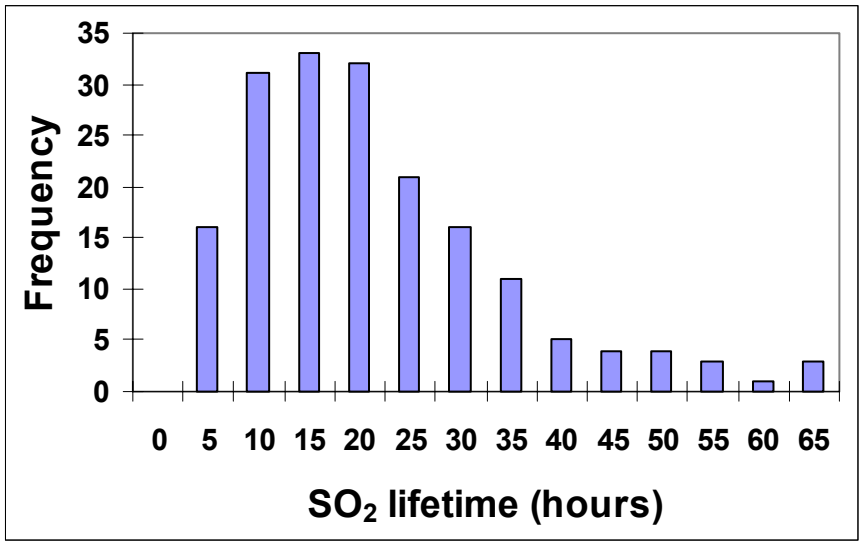

Figure 35. Histogram of SO_2 lifetimes calculated using 24 hour back trajectories to weight the flux. These lifetimes were calculated from 180 profiles measured in the daytime in the summer from 2000-2003.

As discussed above, GOCART uses similar emissions to that presented in national inventories and CMAQ emissions are derived from these national inventories. Therefore it is unlikely that the models over-estimate SO_2 because the emissions of SO_2 are too large. The model over-prediction is likely explained by inadequate oxidation of SO_2 to sulfate in clouds. Mueller et al. (2006) found the CMAQ has difficulty generating typical cloud cover, and reduced cloud cover results in less oxidation of SO_2 by H_2O_2. UMD CMAQ runs may also underestimate cloud cover. Future work should include a verification of CMAQ and GOCART cloud cover.

To investigate the effects of OH on the lifetime of SO_2, the EPA's Community Multi-scale Air Quality (CMAQ) was used to generate OH. CMAQ version 4.5.1 was used with CBIV chemistry, 2002 base year emissions supplied by a regional planning organization, and MM5 version 3 meteorology that was nudged back to observations using data assimilation (Zhang and Anthes, 1982; Grell et al., 1995; Zhang and Zheng, 2004). We have examined OH profiles (from the surface to 645 mbar) from CMAQ for days in 2002 when the University of Maryland Research aircraft made spirals. The CMAQ OH profiles along 24-hr Hysplit back trajectories (ending at 1 km and the location of the UMD aircraft spiral) were averaged to get the 24 hour average OH profile. All of the 24 hour average OH profiles associated with aircraft profiles (made in June through August 2002) were then averaged. This average OH profile represents the daily average OH likely encountered by the SO_2 plumes measured aboard the University of Maryland Research aircraft in 2002. The effective second order rate constant, for the SO_2 + OH reaction, changes by only 2%

between the surface and 645 mbar and so it can be approximated with the high pressure rate constant of 9.5×10^{-13} molecules cm^{-3} s^{-1} (JPL, 2006). The approximate lifetime of SO_2 (with respect to OH oxidation), τ_{OH} (seconds), can be calculated as shown below:

$$\tau_{OH} = (k_{OH} \times [OH])^{-1} \quad (5)$$

Here k_{OH} is the high pressure rate constant (molecules cm^{-3} s^{-1}) and *[OH]* is the concentration of OH (molecules cm^{-3}). The approximate average SO_2 lifetime, with respect to OH oxidation, for days and locations where the University of Maryland research aircraft made flights is shown as a function of altitude in Figure 36. The average SO_2 lifetime (with respect to OH oxidation) between the surface and 950 mbar, is seven days, and this suggests that OH accounts for only 11% of SO_2 removal.

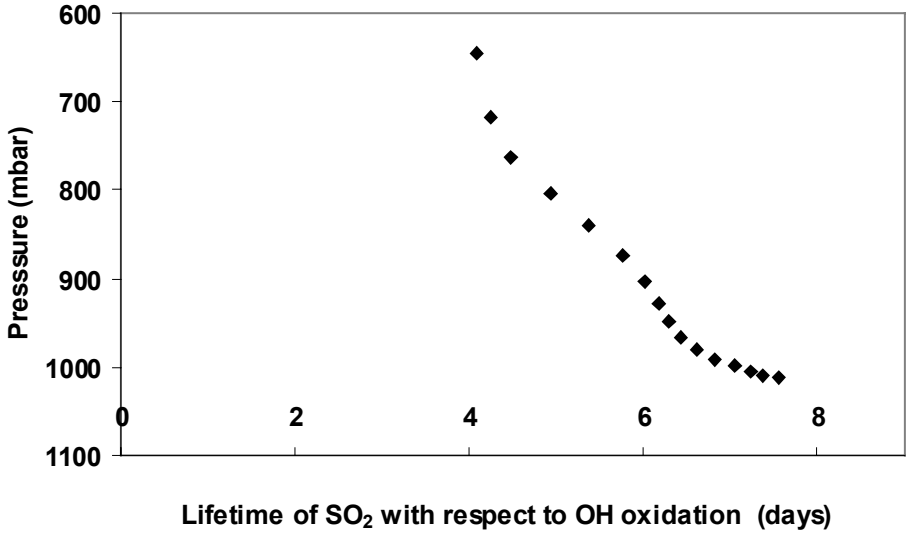

Figure 36.
The lifetime of SO_2 with respect to OH oxidation, where OH was generated from CMAQ. Between the surface and 950 mbar the average lifetime of SO_2 (with respect to OH oxidation) is seven days.

5.3 Conclusions

Aircraft measurements of O_3 were compared with CMAQ. CMAQ over-predicts O_3 from the surface to 600 m, and under-predicts O_3 by 10% between 600 and 2600 m. The CMAQ column content is 3% smaller than the aircraft column content. Possible explanations for the modeled and measured differences include misrepresentation of clouds and aerosols, especially in how they affect photchemistry. I made adjustments in the photochemistry of CMAQ by accounting for aerosol properties measured during a four day event in July 2002. The aerosol properties affected the photolysis of NO_2 and this affected the O_3 production. In general the revised CMAQ model runs over-predicted O_3 above 500 m (~1 ppb) and under-

predicted O_3 below 500 m (1-4 ppb). O_3 reductions are expected for 2018 because stricter regulations on power plant emissions will be implemented and motor vehicles should have cleaner emissions. I tested how the expected decreases in O_3 would be affected if CMAQ accounted for aerosol properties in the NO_2 photochemistry. At the surface, I found that the standard CMAQ runs over-predict O_3 reductions up to 2 ppb and above 500 m the standard CMAQ runs under-predict O_3 reductions up to 2 ppb.

SO_2 from CMAQ and GOCART were also compared with aircraft profiles. The models tend to over-predict the SO_2 column content by 50-55% (GOCART and CMAQ respectively). This over-prediction may result from an over-prediction of the lifetime by either including too large emission sources of SO_2 or not accounting for destruction processes properly. I calculated the summertime lifetime of SO_2 in the Mid-Atlantic region to be 19 ±7 hours from *in-situ* measurements of SO_2. This is on the short side of typical global model estimates of the SO_2 lifetime. The emissions used in CMAQ and GOCART do not appear to be overestimated and thus it is likely that these models underestimate the rate of removal of SO_2. I examined the CMAQ profiles of OH to determine the lifetime of SO_2 with respect to oxidation by OH. Oxidation by OH roughly accounts for 25% of the SO_2 lifetime. This suggests that CMAQ underestimates oxidation of SO_2 in clouds.

Chapter 6: A Side by Side Comparison of Filter-based $PM_{2.5}$ Measurements at a Suburban Site: A Closure Study

6.1 Introduction

6.1.1 Background

As shown in Chapter 1, numerous counties in the Mid-Atlantic region violated the NAAQS $PM_{2.5}$ standards. Models can be effective tools to determine sources and methods for reducing $PM_{2.5}$, but this requires accurate measurements of $PM_{2.5}$. In this Chapter I will give results from ambient measurements an uncertainty analysis of $PM_{2.5}$ samplers used in the Speciation Trends Network. There are no NAAQS standards for speciated mass; however, understanding the $PM_{2.5}$composition can aid states in determining sources of $PM_{2.5}$. This is one reason why data is collected from monitors in the Speciation Trends Network. Accurate and precise measurements of the speciated mass are necessary to determine sources and develop strategies to reduce $PM_{2.5}$. Some work presented in this chapter is from Hains et al. (2007b).

A part of the Maryland Aerosol Research and Characterization study (MARCH- Atlantic) was conducted in Maryland in the Baltimore-Washington corridor. Experiments were carried out during 2002 at a suburban site in Maryland, United States, where two samplers from the U.S. Environmental Protection Agency (USEPA) Speciation Trends Network: Met One Speciation Air Sampling System – STN_S and Thermo Scientific Reference Ambient Air Sampler – STN_R, two Desert Research Institute Sequential Filter Samplers – DRI_F, and a continuous TEOM monitor (Thermo Scientific Tapered Element Oscillating Microbalance, 1400a), all run in parallel. These monitors differ not only in sampling configuration but also in

protocol-specific sample analysis procedures. I will present statistics for $PM_{2.5}$ mass and speciated mass as well as an uncertainty analysis for the different samplers. This Chapter addresses $PM_{2.5}$ concentration and composition as a function of time for summer and winter and the uncertainty associated with $PM_{2.5}$ measurements.

6.1.2 Experiment

STN_{RS} and DRI_F differ in filter types used to collect aerosol as well as flow rates required by the specific cyclone to maintain a stable cut-point at 2.5 μm. Figure 1 illustrates all the sampler configurations and Table 1 summarizes the specifications of the samplers along with analytical methods for determining all species reported. STN_R samplers are considered FRM equivalent (Solomon et al., 2003) and have been compared with other samplers (Peters et al., 2001b, 2001c; Solomon et al., 2003), while DRI_F has been successfully deployed in many air quality studies since 1988 (Chow et al., 1992, 1996; Chen et al., 2002; Watson and Chow, 2002).

	DRI analysis *	RTI analysis **
$PM_{2.5}$	mass gravimetry	mass gravimetry
Trace elements	x-ray fluorescence	x-ray fluorescence
Sulfate	ion chromatography	ion chromatography
Nitrate	ion chromatography	ion chromatography
Ammonium	automated colorimetry	ion chromatography
Chloride	ion chromatography	chlorine is measured with XRF
Sodium ion	atomic absorption	ion chromatography
Potassium ion	atomic absorption	ion chromatography
EC	thermal optical reflectance (IMPROVE)	thermal optical transmittance (NIOSH***)
OC	thermal optical reflectance (IMPROVE)	thermal optical transmittance (NIOSH***)

	Instrument specifications		
	DRI_F	**STN_R**	**STN_S**
Flow (L min^{-1})	20 ± 0.8	16.7 ± 0.3 (mass and elements) 7.3 ± 0.1(ions and carbon)	6.7 ± 0.1
Cyclone	Bendex 240	AN 3.68	SC 2.141
Nitric acid denuder coating	Aluminum oxide	Magnesium oxide	Magnesium oxide
Sample inlet height (m)	10	15	15
Filter diameter (mm)	47	47	47

Table 1. Analytical methods for species collected by DRI_F (analyzed by DRI) and STN_{RS} (analyzed by RTI) and instrument specifications. Flow rate uncertainties are ± 1-σ.
* DRI operating procedure, 1990; Chow et al., 1993c; Chow et al., 2001.
** US EPA, 2001; Thermo Anderson, 2001.
*** National Institute for Occupational Safety and Health.

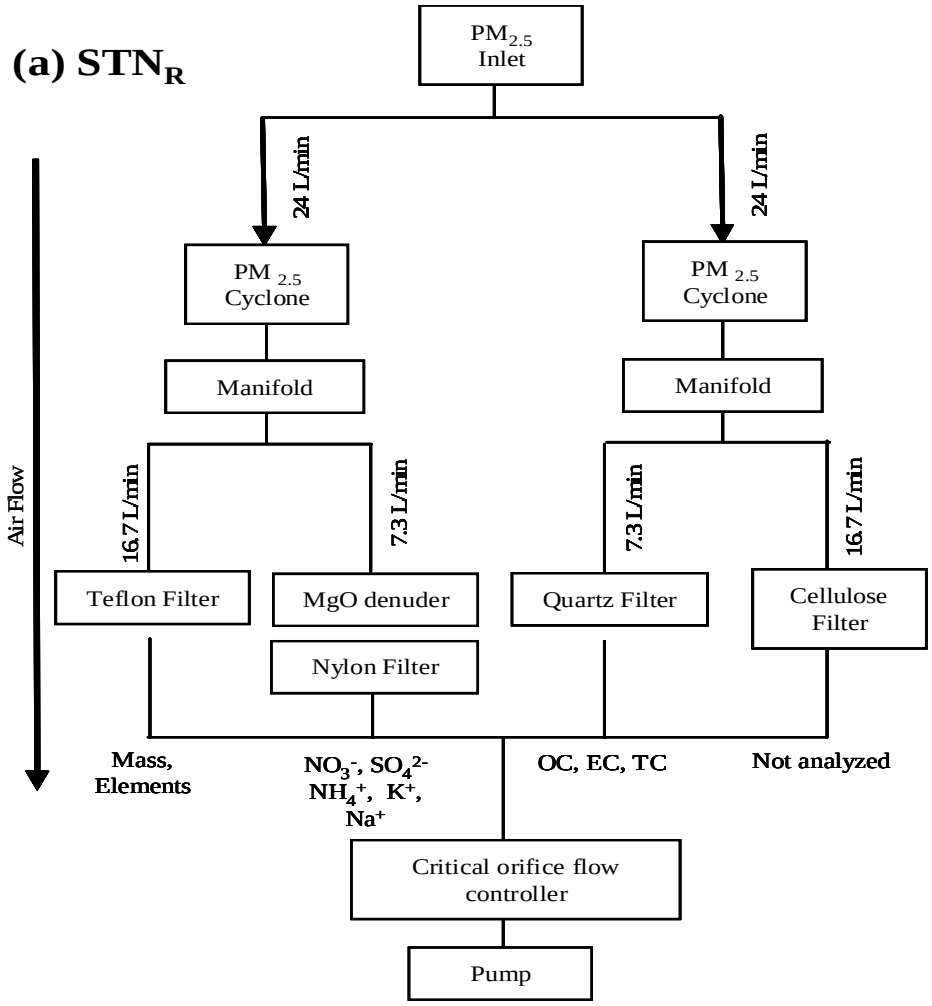
(a) STN$_R$
PM$_{2.5}$ Inlet
24 L/min
24 L/min
PM $_{2.5}$ Cyclone
PM $_{2.5}$ Cyclone
Manifold
Manifold
Air Flow
16.7 L/min
7.3 L/min
7.3 L/min
16.7 L/min
Teflon Filter
MgO denuder
Quartz Filter
Cellulose Filter
Nylon Filter
Mass, Elements
NO_3^-, SO_4^{2-} NH_4^+, K^+, Na^+
OC, EC, TC
Not analyzed
Critical orifice flow controller
Pump

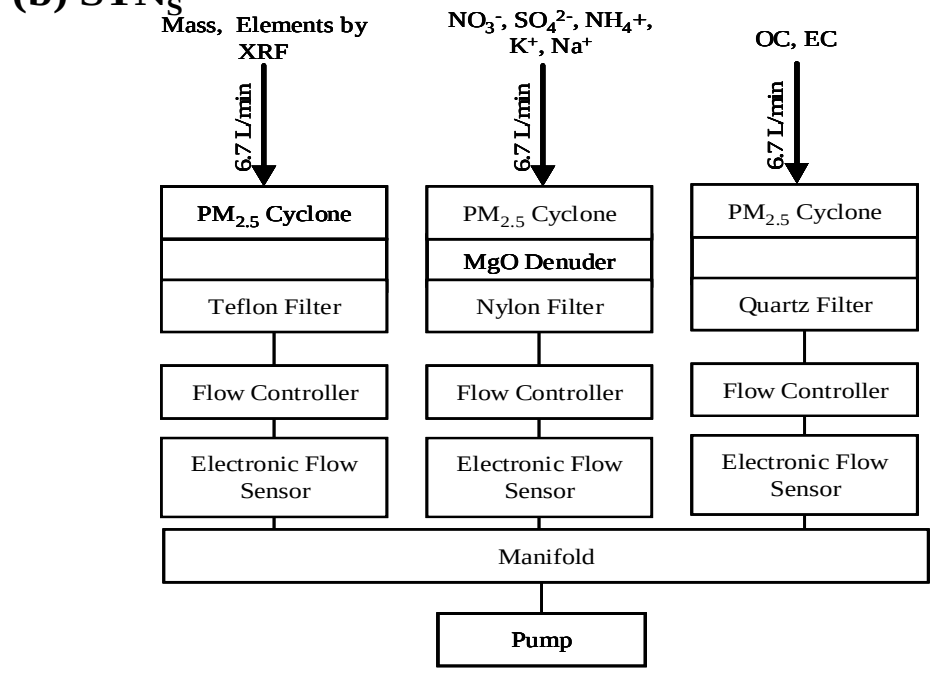
(b) STN$_S$
Mass, Elements by XRF
NO_3^-, SO_4^{2-}, NH_4^+, K^+, Na^+
OC, EC
6.7 L/min
6.7 L/min
6.7 L/min
PM$_{2.5}$ Cyclone
PM$_{2.5}$ Cyclone
PM$_{2.5}$ Cyclone
MgO Denuder
Teflon Filter
Nylon Filter
Quartz Filter
Flow Controller
Flow Controller
Flow Controller
Electronic Flow Sensor
Electronic Flow Sensor
Electronic Flow Sensor
Manifold
Pump

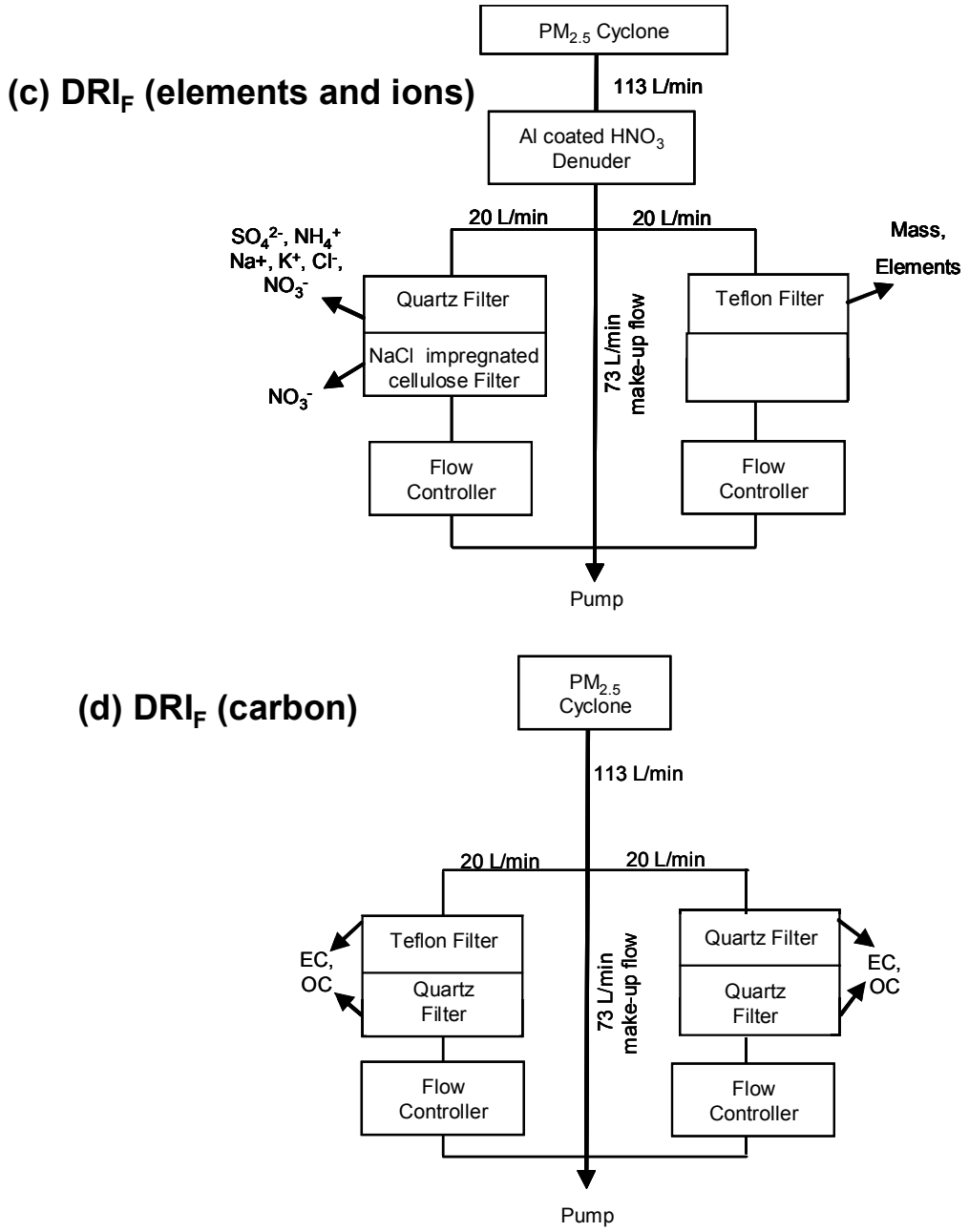

Figure 1. Sampler configuration for a) STN_R (Anderson RAAS) b) STN_S (Met-One SASS) c) DRI_F for elements and ions d) DRI_F for carbonaceous material.

STN_{RS} use a critical orifice to set the flow rate and monitors it with a mass flow sensor. STN_{RS} record ambient temperature and pressure and this is used to convert the mass flow to volumetric flow. The average volumetric flow rate and total volume sampled are recorded for every 24-hr sampling period (Thermo Anderson,

2001; US EPA, 2001). The STN_R flow was calibrated with a flow audit device (BGI deltaCal) and the STN_S flow was calibrated with a bubble meter (Sensidyne/Gilian Gilibrator 2). The DRI_F also uses a critical orifice to maintain constant flow, but the flow was measured and adjusted only once every third day using a rotameter (calibrated against a NIST-traceable Roots meter). The flow rate is recorded before and after each three-day sampling period for the DRI_F, and it can drop by 4% due to buildup of water and particles on the filter. DRI uses the average flow rate (from the initial and final flow) to calculate the total volume sampled and the resultant mass concentration. STN_{RS} record the total volume sampled, which is calculated from the mass flow sensor, temperature and pressure readings.

The sample flow rates for $PM_{2.5}$ mass were 20, 16.7, and 6.7 L min^{-1} in DRI_F, STN_R, and STN_S, respectively. Since all the samplers used 47-mm filters, DRI_F imposed an approximately 17% larger face velocity than the STN_R and an 82% larger face velocity than the STN_S around the filter. The STN_R sample flow rate was 7.3 L/min for ions and carbon (similar to the STN_S) and the DRI_F imposed a 64% larger face velocity than the STN_R.

Cyclones used by STN_R and STN_S (Table 1) exhibit different size-selection curves at their specified flow, but Peters et al. (2001c) found that only sites dominated by crustal material had significantly different $PM_{2.5}$ mass collected by the two samplers. Chen et al. (2002) showed a minor crustal material contribution at FME, ~3% of $PM_{2.5}$ mass on average, and therefore strong biases resulting from imperfect size cut are not expected in this study. There may also be diffusion losses of ultrafine particles between the sampler inlet and filter which vary with the different flow rates

used by DRI_F, STN_R and STN_S. Ultrafine particles (< 0.1 μm in diameter) typically contribute little to $PM_{2.5}$ mass in this environment (e.g., Tolocka et al., 2005; Ondov et al., 2006) and strong biases resulting from diffusion losses are unlikely.

The DRI_F used a front quartz-fiber filter with a sodium-chloride-impregnated cellulose backup filter to collect nitrate. The backup filter captured nitrate volatized from the front filter (Zhang and McMurry, 1992). These filters were located behind a bundle of aluminum-oxide-coated denuders to remove gaseous nitric acid. Specifications of the denuders are described in Chow et al. (1993a). The STN_R and STN_S collected nitrate particles behind a magnesium-oxide denuder on a single nylon filter (Figure 1). Specifications of the denuders are described in Research Triangle Institute (2000). Frank (2006) found that denuded nylon filters captured more nitrate than undenuded Teflon filters. The different denuders and filter types used by the STN_{RS} and DRI_F in this study likely affect the nitrate collection efficiency as suggested by Solomon et al. (2003) and Frank (2006).

Quartz-fiber filters were used in all the samplers to collect carbonaceous material, and DRI_F used backup filters to account for known sampling artifacts from volatile organic compounds (McDow and Huntzicker, 1990; Turpin et al., 1994; Chow et al., 1996; Chow et al., 2001). For carbon analysis, RTI adopted the Speciation Trends Network-Thermal Optical Transmission (STN-TOT) method (Peterson and Richards, 2002; OC/EC Laboratory, 2003), while DRI used the Interagency Monitoring of Protected Visual Environments-Thermal Optical Reflectance (IMPROVE-TOR) method (Chow et al., 1993b). The IMPROVE-TOR and STN-TOT differ in temperature steps used to extract OC and EC and in optical

charring corrections. They usually yield equivalent total carbon (TC) but different OC and EC concentrations (Chow et al., 2001; Schmid et al., 2001; Chow et al., 2004; Subramanian et al., 2004; Chow et al., 2005a). The IMPROVE-TOR method generally assigns less OC and more EC to a filter sample than the STN-TOT method.

DRI quantified water-soluble potassium (K^+) and sodium (Na^+) with atomic absorption spectroscopy (AAS) and RTI quantified the species with ion chromatography (IC). AAS has a lower detection limit (Chow et al., 1993c; Technology Transfer Network Air Quality System, 2006). There were also differences in blank collection. A field blank was collected every third day for the DRI_F sampler and once every two weeks for the STN_S sampler. Only one field blank was collected for the STN_R sampler. DRI corrected for field blanks as part of their analysis (Watson et al., 1989a; 1989b), but RTI did not. To correct STN_{RS} samples for field blanks, we averaged all STN_{RS} blank values, converted them from mass/filter to mass/m^3 using the volume sampled by the instrument, and then subtracted the blanks from the mass measurement.

Sample recovery was scheduled for different time periods. The DRI_F filters were collected from the site every three days, so that used filters remained in the sampler for up to 2.5 days (an average of 1.5 days). The STN_R filters were collected every day, immediately after the sampling finished, so that used filters remained in the sampler for less than 30 minutes. The STN_S filters were collected every other day, so that used filters remained in the sampler for about 12 hours. Chen (2002) performed an audit experiment in summer 2001 at FME with the DRI_F samplers, to determine how filters left in the sampler may be affected by volatile losses and/or

passive collection. He found that OC and TC mass (measured on the front quartz-fiber filters) decreased (by 38% and 29%, respectively) during a 2.5-day period after sampling. Total $PM_{2.5}$ mass and sulfate mass varied less than their respective uncertainties.

A TEOM measures near real-time continuous $PM_{2.5}$ mass. The TEOM at FME drew ambient air in at 3 L/min through a $PM_{2.5}$ cyclone inlet. A constant volumetric flow was achieved using a mass flow controller corrected for ambient temperature and pressure. The air stream was heated to 50°C to maintain a low, relatively constant relative humidity. This heating likely increased volatilization of nitrate and semi-volatile organic compounds. The TEOM measurements were adjusted with scaling factors of 1.03 × TEOM mass + 3.0 to account for loss of semi-volatile material and to be compatible with FRM measurements as recommended by Patashnick and Rupprecht (1991). The mean mass concentration was recorded every 30 minutes, every hour, and every eight hours. All one-hour measurements made in a day were averaged to compare with the DRI_F and STN_S data.

6.2 Results and Discussion

6.2.1 Uncertainty Analysis

Uncertainties associated with flow control and sample analysis need to be accounted for to determine the uncertainty in total $PM_{2.5}$ and each reported species concentration. For STN_{RS}, the species concentration (with units of mass m^{-3} at ambient temperature and pressure) is calculated using the equation below:

$$\text{Species concentration} = m \times (t \times \text{mass flow} \times MM^{-1} \times R \times T \times P^{-1})^{-1} \quad (1)$$

Here m is the mass of a given species on the filter, t is the time over which sampling occurred, mass flow has units of mass time^{-1}, MM is the molar mass of the air sampled, R is the gas constant (0.08314 L atm K^{-1} mol^{-1}), T is ambient temperature and P is the ambient pressure. Uncertainties in the calculated concentration reflect uncertainties in the laboratory analysis, the mass flow sensor reading, the temperature reading and the pressure reading. Uncertainties associated with the integration time appear to be less than 1% and are therefore not included in the error analysis. US EPA (2001) states that STN_{RS} temperature readings must be within ±4 K of the actual temperature and pressure readings must be within ±0.013 atm of the actual pressure. These ranges represent part of the uncertainty associated with the measurements. The precision associated with a commercial mass flow sensor for the maximum allowable mass flow, i.e., ±2% at the 1-σ level, is used as an estimate of the mass flow sensor uncertainty (Table 1). Flanagan et al. (2006) report the percentage difference in laboratory replicates of $PM_{2.5}$ and speciated masses. I adopted their values of laboratory uncertainty to calculate the total uncertainty. The resultant ±2-σ uncertainty, u, (i.e., the 95% confidence level) associated with $PM_{2.5}$ mass, sulfate, ammonium, OC or elemental concentration is given by:

$$u = \text{mass concentration} \times [(\delta A/A)^2 + (\delta mf/mf)^2 + (\delta T/T)^2 + (\delta P/P)^2]^{1/2} \quad (2)$$

Here δA/A represents fractional uncertainty associated with the laboratory determination of the mass of a species (uncertainties from Flanagan et al., 2006 were used), δmf/mf represents the fractional uncertainty associated with the mass flow meter measurements, and δT/T and δP/P represent the fractional uncertainty

associated with temperature and pressure measurements, respectively. RTI did not report uncertainties for samples analyzed in 2002, however they did report uncertainties for samples measured in the U.S. in 2005 to the EPA's Air Quality System database (AQS, Technology Transfer Network Air Quality System, 2006). The uncertainties reported by RTI include laboratory analysis (±1-σ uncertainty) and a 5% uncertainty associated with flow control and shipment of the samples (RTI, 2004). Using their uncertainties associated with concentrations that were similar to (within ±1% of) the FME samples, and multiplying them by two to obtain the ±2-σ uncertainties, I found the resultant uncertainties are on average 2.5 times larger than those calculated from Equation (2) for most species except $PM_{2.5}$ mass (Table 2). For this Chapter I adopt the RTI reported ±2-σ uncertainties. Kim et al., (2005) report fractional uncertainty associated with measurements made in New York, New Jersey and Vermont. Uncertainties they reported for sulfate, ammonium and calcium agreed within 20% of the uncertainties used in this paper.

	Calculated 2 σ uncertainty (%)	RTI reported 2 σ uncertainty (%)
$PM_{2.5}$	10	10
OC	12	27
Sulfate	9	16
Ammonium	4	14
Iron	6	16

Table 2. Comparison of 2-σ uncertainty in concentration calculated using Equation 2 and RTI reported 2-σ uncertainty (from 2005 AQS database).

The DRI_F measures the flow rate using a pressure drop across a critical orifice. Ambient temperature and pressure can alter this flow rate. DRI calculates the uncertainty for each measurement by accounting for the variability between the initial

and final flow tests through 24-hr sampling (typically ±4%), as well as precision in laboratory analyses (Chow et al., 1993c). The monthly average concentration of species and the average uncertainty (i.e., the average of all 2-σ uncertainty values for the month) for STN_{RS} versus DRI_F are shown in Table 3 along with the signal-to-MDL (minimum detection limit) ratio, where the MDL was obtained from Chow et al. 1993c) for the DRI samplers and the median of all 2005 MDL values reported by RTI (to the EPA's AQS database) for the STN samplers. The signal-to-noise ratio for each species can be calculated from Table 3 by dividing the species average by the 2-σ uncertainty.

	Deming Slope	Deming Intercept	Correlation (r)	Average Difference (STN_R-DRI_F)	RMS Difference	STN_R species average (± 2σ uncertainty)	STNR Signal-to-MDL	DRI_F Signal-to-MDL	DRI_F species average (± 2σ uncertainty)
$PM_{2.5}$	0.76	0.62	0.98	1.47	1.66	8.77 ± 0.94	11.9	8.58	7.30 ± 0.98
Sulfate	0.89	-0.01	0.94	0.28	0.35	2.32 ± 0.40	193	240	2.04 ± 0.27
Ammonium	0.98	-0.03	0.92	0.05	0.14	1.02 ± 0.14	60.2	115	0.98 ± 0.12
Nitrate (with backup*)	0.80	-0.22	0.97	0.52	0.57	1.49 ± 0.29	171	115	0.97 ± 0.11
Nitrate (no backup)	0.89	-0.71	0.93	0.88	0.93	1.49 ± 0.29	171	72	0.61 ± 0.04
OC	0.68	0.72	0.80	-0.12	0.73	1.88 ± 0.63	7.82	58.7	2.00 ± 0.53
EC	2.72	-0.20	0.65	-0.40	0.49	0.35 ± 0.45	1.45	22.2	0.75 ± 0.18
TC	0.91	0.60	0.80	-0.52	0.97	2.23 ± 0.78	9.28	80.7	2.74 ± 0.61
Bromine	0.66	1.62	0.88	-0.61	1.10	2.95 ± 1.52	5.46	21.0	3.56 ± 1.66
Calcium	0.75	1.25	0.85	3.20	4.72	17.8 ± 4.79	2.40	19.2	14.6 ± 9.40
Potassium	0.92	5.46	0.97	-1.59	5.06	47.4 ± 7.94	6.59	64.5	49.0 ± 10.5
Iron	0.82	3.45	0.95	4.78	9.51	46.4 ± 6.68	22.12	245.1	41.7 ± 5.63
Silicon	2.06	-25.01	0.50	-6.72	16.71	29.9 ± 12.7	2.98	24.4	36.6 ± 10.7
Titanium	0.71	-0.25	0.48	1.08	1.95	2.84 ± 2.72	0.57	3.5	1.76 ± 52.2

Table 3a. January average concentrations and uncertainties for $PM_{2.5}$, sulfate, ammonium, nitrate, OC, EC, TC, bromine, calcium, potassium, iron, silicon and titanium measured with the STNRS and DRIF. The ±2-σ uncertainty is just the average of all uncertainties for the month. Deming slope, intercept, correlation coefficient, monthly average difference and RMS difference for species measured with STN_R and DRI_F in January and STN_S and DRI_F in July are presented. Slopes and intercepts were calculated with the y-axis = DRI_F and the x-axis = STN_{RS}. Bromine, calcium, potassium, iron, silicon and titanium are reported in units of ng/m^3 and shaded in grey. All other species are reported in units of $\mu g/m^3$.

*Only DRI_F collected nitrate with a front and backup filter.

	Deming Slope	Deming Intercept	Correlation (r)	Average Difference (STN_S-DRI_F)	RMS Difference	STN_S species average (± 2σ uncertainty)	STN_S Signal-to-MDL	DRI_F Signal-to-MDL	DRI_F species average (± 2σ uncertainty)
$PM_{2.5}$	0.88	-0.50	0.96	3.75	5.59	27.8 ± 2.82	37.62	28.3	24.4 ± 1.29
Sulfate	0.89	-0.20	0.97	1.29	2.28	9.72 ± 1.43	810.10	992	8.44 ± 0.43
Ammonium	1.08	0.10	0.95	-0.32	0.73	2.61 ± 0.36	153.51	344	2.93 ± 0.24
Nitrate (with backup*)	0.62	0.17	0.54	0.06	0.25	0.60 ± 0.17	68.89	63.5	0.54 ± 0.05
Nitrate (no backup)	0.01	0.03	0.13	0.57	0.63	0.60 ± 0.17	68.89	3.5	0.03 ± 0.04
OC	0.93	-0.14	0.99	0.64	1.14	6.97 ± 1.35	29.05	186	6.33 ± 0.63
EC	2.02	0.03	0.58	-0.51	0.62	0.47 ± 0.48	1.98	29.0	0.98 ± 0.33
TC	0.97	0.12	0.98	0.13	1.03	7.45 ± 1.45	31.03	215	7.32 ± 0.72
Bromine	0.82	1.06	0.88	-0.42	1.15	3.58 ± 1.45	6.63	23.5	4.00 ± 0.52
Calcium	0.79	-2.92	0.89	14.95	26.73	56.1 ± 8.39	7.57	54.1	41.1 ± 3.79
Potassium	0.92	3.00	0.94	7.51	54.82	135 ± 12.3	18.87	168.9	128 ± 7.64
Iron	0.98	-6.39	0.88	7.85	44.62	91.0 ± 15.7	43.35	489.3	83.2 ± 5.85
Silicon	0.84	9.51	0.88	19.61	148.55	175 ± 26.7	17.65	104.6	157 ± 17.0
Titanium	0.45	1.47	0.58	2.73	8.68	7.68 ± 3.21	1.54	9.7	4.95 ± 18.6

Table 3 b

Same as Table 3 a, but for July.

6.2.2 Gravimetric Mass Comparisons

Comparisons of daily STN_R and STN_S $PM_{2.5}$ with DRI_F $PM_{2.5}$ are shown in Figure 2 and their error bars (representing the ± 2-σ uncertainty) overlap only part of the time. Table 3 shows the Deming slope and intercept, which reduces variance in both independent (x) and dependant (y) variables (Cornbleet and Gochman, 1979), as well as the correlation coefficient, monthly average difference and monthly RMS difference between the two pairs of measurements. Good correlations ($r \sim 0.95$) are found between STN_R and DRI_F and between STN_S and DRI_F with respect to $PM_{2.5}$ mass, though both the STN_R and STN_S measurements are generally larger than the DRI_F measurements. The percentage differences ($[STN_{RS}\text{-}DRI_F] / [STN_{RS} + DRI_F]/2 \times 100$) ranged from 8 to 31% between daily $PM_{2.5}$ from STN_R and DRI_F and from -38 to 67% between STN_S and DRI_F. To determine whether the daily differences were statistically significant I calculated the z-test values for each day using the standard formula (Wilks, 1995):

$$z = \{(xbar_1 - xbar_2) - E[xbar_1 - xbar_2]\} / (s_1^2/n_1 + s_2^2/n_2)^{1/2} \quad (3)$$

Here $xbar_1$ and $xbar_2$ are the individual measurement of $PM_{2.5}$ from STN_{RS} and DRI_F, respectively. The $s_{1(2)}$ represents the STN_{RS} (DRI_F) ±1-σ uncertainty value for the specified day. It is assumed that $n = 1$ and the expected value of the difference between $xbar_1$ and $xbar_2$, i.e., $E[xbar_1 - xbar_2]$, is zero. A z-value less than 1.96 indicates the two measurements are significantly different at the 95% confidence level. Table 4 shows the percentage of days when the paired measurements were significantly different under this test. In January 62% of the daily measurements of

$PM_{2.5}$ were significantly different, and in July this percentage was lowered slightly to 50%.

	Percentage of significantly different values January	Percentage of significantly different values July
$PM_{2.5}$	62%	50%
Nitrate	100%	0%
Sulfate	15%	33%
Ammonium	15%	38%
OC	36%	8%
EC	NA	NA
TC	69%	8%
Bromine	0%	5%
Calcium	NA	65%
Potassium	0%	26%
Iron	15%	29%
Silicon	29%	30%
Titanium	NA	NA

Table 4. Percentage of days when the species measured with STN_{RS} and DRI_F were significantly different at the 95% confidence level. Only species with concentrations greater than three times the MDL were compared. Comparisons could not be made for EC, calcium (January), nitrate (July) or titanium because over half of the measurements were too small.

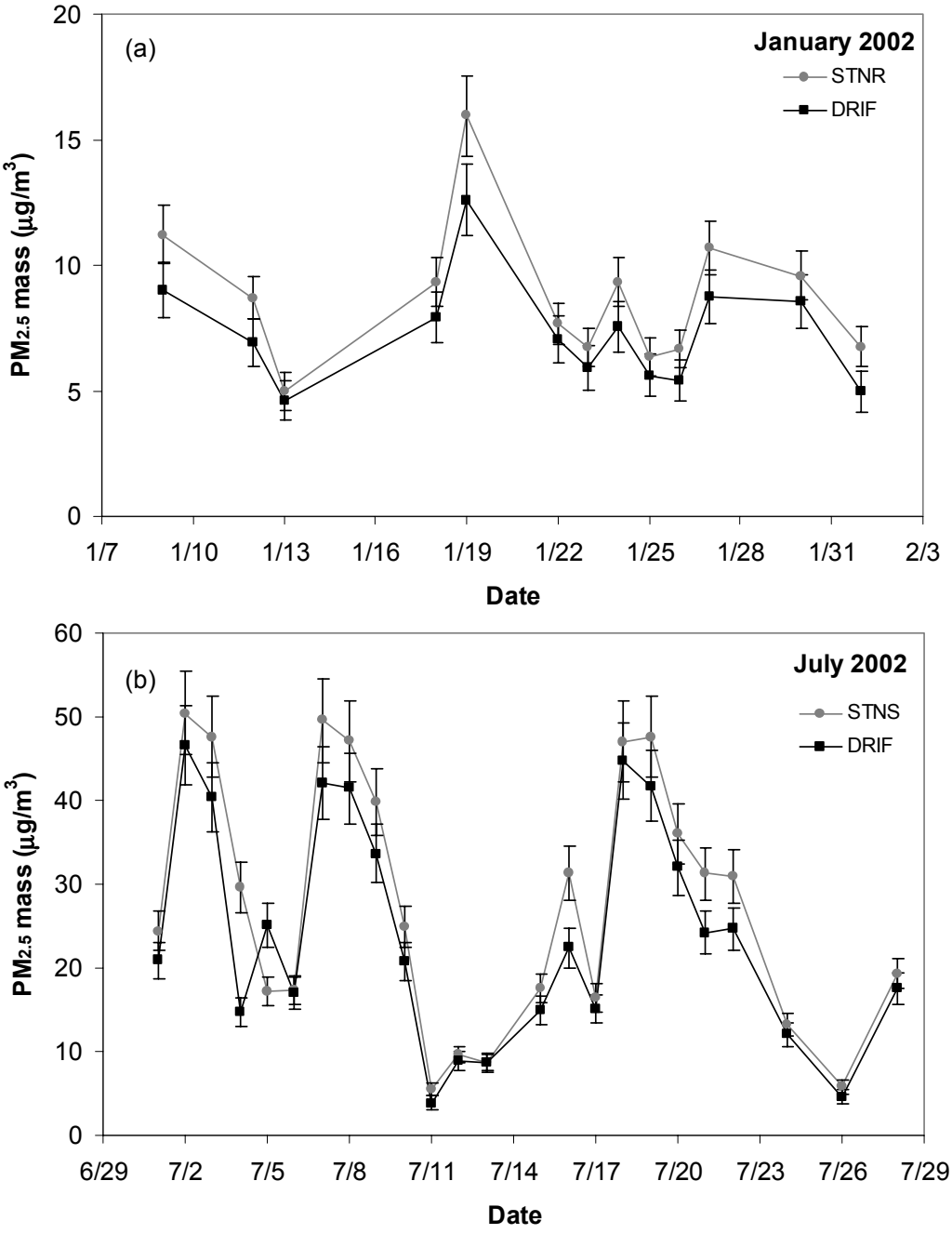

Figure 2. Time series of $PM_{2.5}$ concentrations measured with STN_{RS} and DRI_F for January (a) and July (b). Error bars represent ±2-σ uncertainty.

Watson and Chow (2002) compared mass concentrations obtained with the STN_R and DRI_F (both analyses were performed at DRI) and found similar results.

They attribute the discrepancies between the DRI_F and the STN_R to different instrument inlet designs, flow controls, and resulting cyclone cutoff efficiencies. As discussed in the experimental section above, large particle intrusion is not expected to be a major issue at FME despite the uncertainty in the flow and size cut. Other reasons for the inter-sampler discrepancies include differences in face velocity which may result in losses of volatile material. For submicrometer particles, the overall filter collection efficiency decreases with increasing face velocity (Liu et al. 1983; Lippmann 1995; McDow and Hutzicker, 1990). The overall efficiency of membrane filters, however, is close to 100% for particles larger than the pore size (Lippmann 1995), which is ~0.2 μm in this study.

The TEOM data are available for half of July 2002, and comparisons were made between it and the DRI_F and STN_S. The DRI_F and STN_S versus TEOM have r-values of 0.95 and slopes within 11% of unity (Table 5). These results agree with prior studies (Chen et al., 2003; Rees et al., 2004; Lee et al., 2005a; Lee et al., 2005b). The RMS difference is greater for STN_S-TEOM than DRI_F-TEOM. The STN_S - TEOM average difference is positive and about half of the RMS difference, while the DRI_F -TEOM average difference is slightly negative and about 1/8 of the RMS difference (Table 5). The magnitude of these differences indicates a systematic bias (in addition to random noise) between the STN_S and TEOM measurements. In contrast, deviations between the DRI_F and TEOM appear to be random in nature (Figure 3a) and generally fall within 10% of the Deming regression line. Chen (2002) and Chen et al. (2003) found similar results when comparing the DRI_F to the TEOM in summer months from 1999-2001. The addition of the 3.0 $\mu g/m^3$ offset added to

TEOM measurements may not fully compensate for volatile losses from the heated inlet.

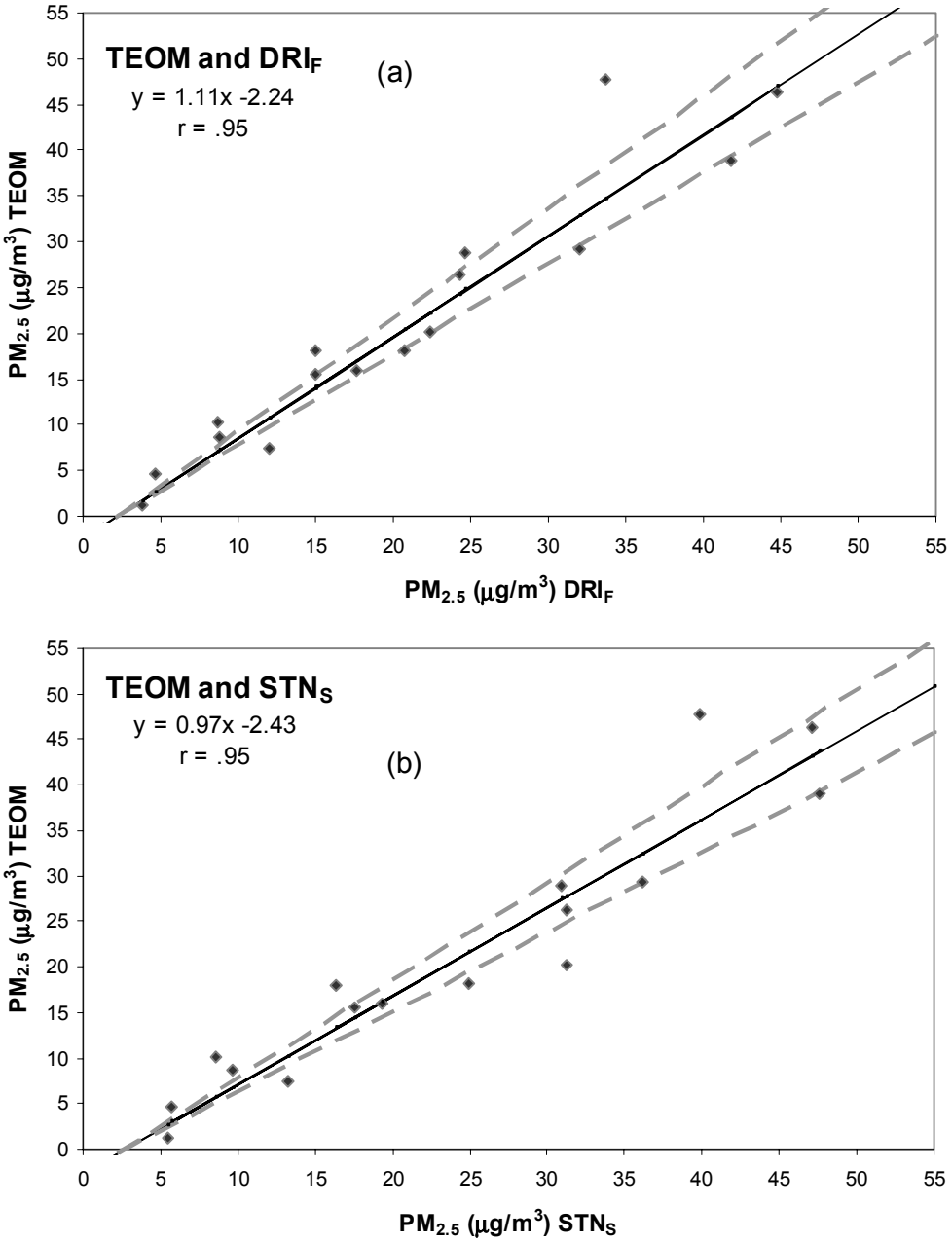

Figure 3. Comparisons of $PM_{2.5}$ total mass between TEOM and (a) DRI_F and (b) STN_S. Deming regression line shown in black, ±10% (of the regression line) shown in broken grey. The TEOM and DRI_F generally agree within experimental error.

x	y	Slope	Intercept	Correlation (r)	N	Average Difference (x-y)	RMS Difference	Monthly Average x	Monthly Average y
STN_S	TEOM	0.97	-2.64	0.95	16	2.96	5.35	24.06	21.10
DRI_F	TEOM	1.11	-2.24	0.95	16	-0.48	4.28	20.62	21.10

Table 5. Deming slope, intercept, correlation, and average and RMS difference ($\mu g/m^3$) for the STN_S versus TEOM, and the DRI_F versus TEOM as well as N, number of days comparisons were made. The averages ($\mu g/m^3$) for each sampler for the 2nd half of July are also given.

6.2.3 Chemical Compositions

Besides gravimetric mass, Tables 3 and 4 include the statistics and comparisons of major contributing species to $PM_{2.5}$ including sulfate, ammonium,

nitrate, OC, EC, TC, bromine and potassium as well as crustal mass made of calcium, iron, silicon and titanium. In January, 15% of the paired sulfate measurements were found to be significantly different, but in July this fraction increased to 33%. Although sulfate measurements from the different instruments are well correlated with r-values greater than 0.94, the STN_{RS} consistently report higher values than the DRI_F. Since the average deviation is 14 to 17% for both $PM_{2.5}$ and sulfate (Table 3), there appears to be a bias in the flow control, allowing more or less sample volume than specified. It should be noted that sulfate concentration is not sensitive to a small difference in the size cut. Chen (2002) show that sulfate mass from DRI_F increases by 4% when filters are exposed for 72 hours after sampling while total mass may either increase (by 1%) or decrease (by 3%). This suggests that the different filter exposure times may have minimal effects on the differences between DRI_F and STN_{RS} for sulfate and mass.

DRI_F and STN_{RS} measure nitrate on different filter substrates behind different denuder configurations (Figure 1). Comparisons between the front only DRI_F filters and front plus backup DRI_F filters with STN_{RS} have both been made. The nitrate concentrations are well correlated in the winter (without or with backup filter concentrations added), although DRI_F measures only 3 to 65% of the average STN_R nitrate (without or with backup filter concentration added; see Table 3). All differences were found statistically significant (Table 4). The nylon filters used by STN_R appear to retain much more nitrate than single quartz-fiber filters. Moreover, the DRI_F filters remained in the field for up to 2.5 days longer, and this led to more nitrate loss through volatilization. The DRI_F July average nitrate (on the front filter)

is below its 2-σ uncertainty and most of the nitrate (above the 2-σ uncertainty) was found on the backup filter. The July measurements of nitrate do not correlate well (r = 0.13 front filter only, r = 0.54 front and backup filter), and the DRI_F nitrate accounts for 6 to 90% of the STN_S (without or with backup filters added). When the DRI_F front and backup nitrate are compared with STN_S, there are no significant differences (Table 4).

Ammonium shows good inter-sampler correlation with r-values greater than 0.92, and significant differences in 15 to 38% of the daily measurements in January and July. In January the average difference as well as the RMS difference between the DRI_F and the STN_R measured ammonium is negligible. In July the DRI_F monthly average is slightly greater than the STN_S average, but within 11% (Table 3). Like nitrate, ammonium can also be volatilized readily (Appel and Tokiwa, 1981; Appel et al., 1984; Chow et al., 2005b; Pathak et al., 2004). Pathak et al., 2004 found that there were substantially less losses of ammonium than nitrate on filter samplers possibly resulting from chemical reactions on the filter.

For total carbon (TC) that is independent of thermal/optical method, the STN_S concentration is similar to that of the DRI_F. The STN_R concentration is less than DRI_F, but within 20%. Inter-sampler differences of TC were significant 8% of the time in July and 69% in January (Table 4). Correlation between the DRI_F and STN_S is good in July with an r-value of 0.98, much better than the r-value of 0.80 between the DRI_F and STN_R in January. Since the TC concentration was low in January (<1/3 of that in July) and close to the MDL, more scatter could be expected. The OC/EC ratio was 5.4 in -January, compared with 14.8 in July (based on STN_{RS}). This reflects

larger secondary organic aerosol contributions in the summer (Polidori et al., 2006). OC correlation was similar to that of TC with an r-value of 0.99 in July and an r-value of 0.80 in January. OC is the dominant fraction of TC in both seasons and this explains the similar relationship. EC correlation is poor between the paired measurements both in winter and summer and the STN_{RS} EC are generally only ~50% of the DRI_F EC, likely because of the different ways STN-TOT and IMPROVE-TOR define EC (Chow et al., 1993b; Peterson and Richards, 2002; OC/EC Laboratory, 2003). STN_{RS} EC concentrations were generally less than 3 times the MDL and for this reason the z-test comparison was not performed.

McDow and Hutzicker (1990) demonstrate that increases in face velocity increase volatilization of organic species. The DRI_F and STN_{RS} all use 47-mm filters. Assuming that the filter holder has negligible effects on the area of the filter impacted by the flow, the face velocity can be approximated by the flow rates such that the DRI_F has the largest face velocity (with a flow rate of 20 L min^{-1}) for OC collection, followed by STN_R and STN_S (with flow rates of ~ 7 L min^{-1}). In July the average DRI_F OC and TC are smaller than the STN_S, and these differences may be partly attributed to the effects of face velocity. The higher temperatures in July might facilitate OC volatilization, especially from the DRI_F filters that were left in the field for a longer time period. However, in January the DRI_F TC is larger than the STN_R. This is explained neither by flow control differences nor by face velocity. A problem specific to the TC and OC measurement is the blank correction and the only field blank collected for the STN_R sampler showed relatively high OC. The STN_R field blank OC was on average 50% of the non-blank corrected OC, while the STN_S and

DRI_F field blank OC was on average 20% of the non-blank corrected OC. The winter STN_R TC and OC might have been overcorrected. The quantification of OC mass might also be affected by different thermal analysis protocols that define the OC and EC split differently.

Inter-sampler comparisons of crustal species, including silicon (in July), calcium and iron, as well as trace elemental species that are > 3 times the MDL (bromine and potassium) all have r-values greater than 0.85. STN_S generally reports larger crustal species concentrations than DRI_F does, consistent with the situation for $PM_{2.5}$ mass and sulfate. The smaller DRI_F concentration could be reflected by either a small DRI_F/STN_S slope (< 1) or a negative intercept (Table 3). STN_{RS} and DRI_F differences for silicon, calcium, iron and potassium concentrations were significant 0 to 30% of the time in January and 25 to 65% of the time in July. Calcium (in January), and Titanium, were below three times the MDL and thus the z-test was not performed for these species.

6.2.4 Mass Closure

Reconstructed mass from the sum of individual species determines the degree to which the gravimetrically measured total mass is explained by the measured species (Chow et al., 1996; Andrews et al., 2000; Malm et al., 2005; Frank et al., 2006). To reconstruct the $PM_{2.5}$ mass, the crustal mass, organic mass and mass of all other species are added together. The crustal mass is the sum of silicon, calcium, iron and titanium multiplied by factors to account for oxygen associated with them (Frank, 2006) as shown below:

$$\text{Crustal mass} = 3.73 \times \text{silicon} + 1.63 \times \text{calcium} + 2.42 \times \text{iron} + 1.94 \times \text{titanium} \quad (4)$$

There is much debate over what factor should be used to determine the oxygen, nitrogen and hydrogen associated with organic carbon, and this factor can range from 1.2 to 2.5 (Turpin and Lim 2001; Rees et al., 2004; El-Zanan et al., 2005). We multiply the organic carbon by a factor of 1.8, similar to Rees et al. (2004), because the area is highly influenced by regional sources. Front and backup filter nitrate are included in the DRI_F reconstructed mass.

The reconstructed mass from the DRI_F samplers is well correlated with the measured gravimetric mass in both January and July ($r = 0.94 – 0.99$, see Table 6), and a good correlation is also found for STN_S. The July DRI_F reconstructed $PM_{2.5}$ mass overestimates the gravimetric mass by 6% while the STN_S reconstructed mass underestimates the gravimetric mass by just 3%. For STN_R in January, the average measured and reconstructed mass differ by less 2%, although their correlation is not as good ($r = 0.80$). Histograms of the difference between the gravimetric and reconstructed masses (i.e., the residuals) are shown in Figure 4. In January, the DRI_F residuals are shifted negatively from the normal distribution, with a mode at -1 $\mu g\ m^{-3}$. The STN_R residuals have a mode at zero and an apparent outlier, which explains the poorer correlation. There is better overlap between the DRI_F and STN_S residuals in July, but the DRI_F residuals are still less than STN_S residuals.

	Average gravimetric mass	Average reconstructed mass	RMS difference	Average difference (gravimetric - reconstructed)	Slope	Intercept	Correlation (r)
January							
DRI_F	7.3	8.8	1.7	-1.5	1.2	0.38	0.94
STN_R	8.8	8.9	1.7	-0.12	0.93	0.73	0.80
July							
DRI_F	24.1	25.5	2.1	-1.4	0.99	1.5	0.99
STN_S	27.8	27.3	3.2	0.57	0.99	-0.37	0.98

Table 6. Average reconstructed mass for STN_{RS} and DRI_F for January and July (units are in $\mu g/m^3$). Also shown is the Deming slope, intercept, and correlation for the gravimetric (x-axis) and reconstructed mass (y-axis). The DRI reconstructed mass is generally larger than the gravimetric mass and the STN reconstructed mass is generally smaller than the gravimetric mass.

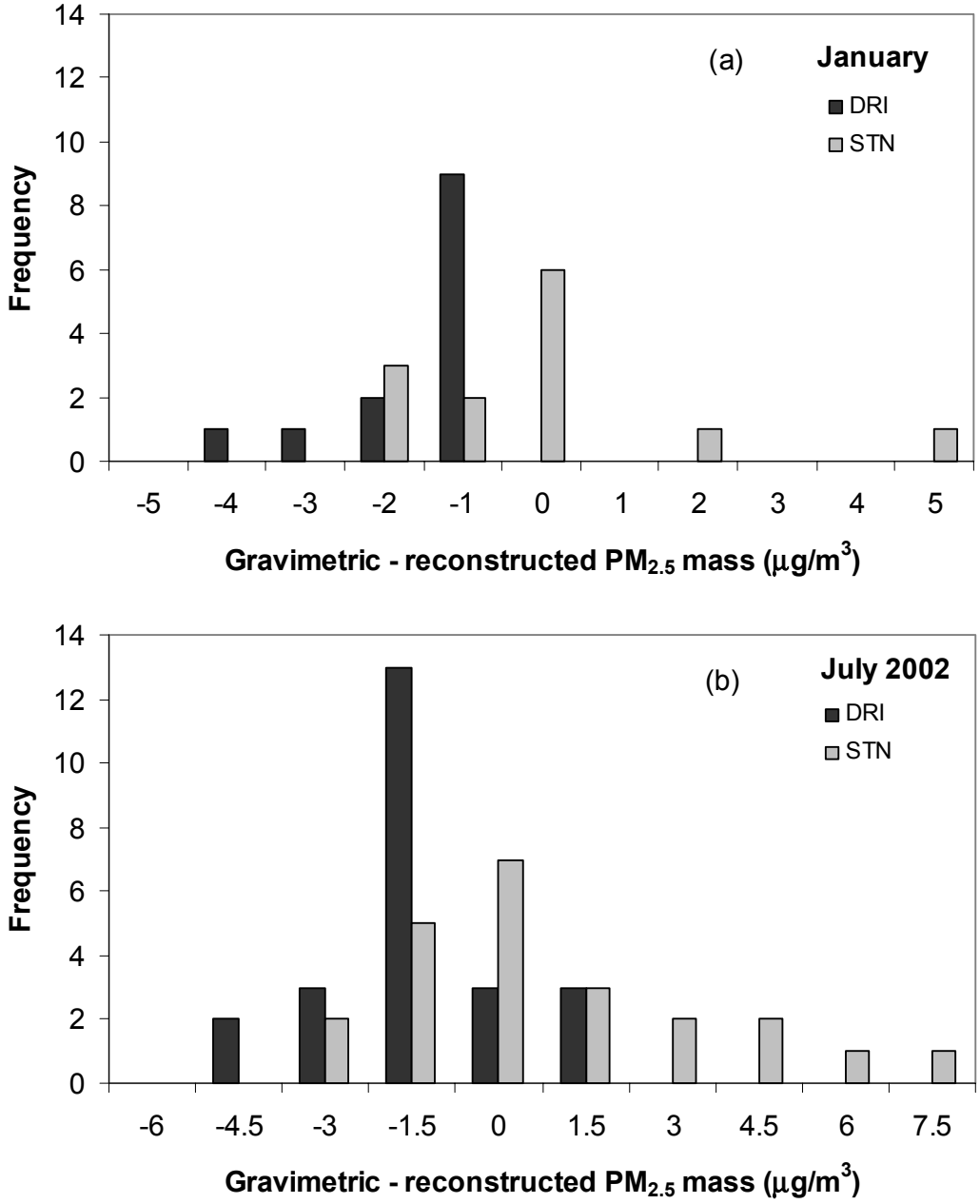

Figure 4. Frequency distribution of gravimetric – reconstructed differences (residuals), for January DRI_F and STN_R and July DRI_F and STN_S.

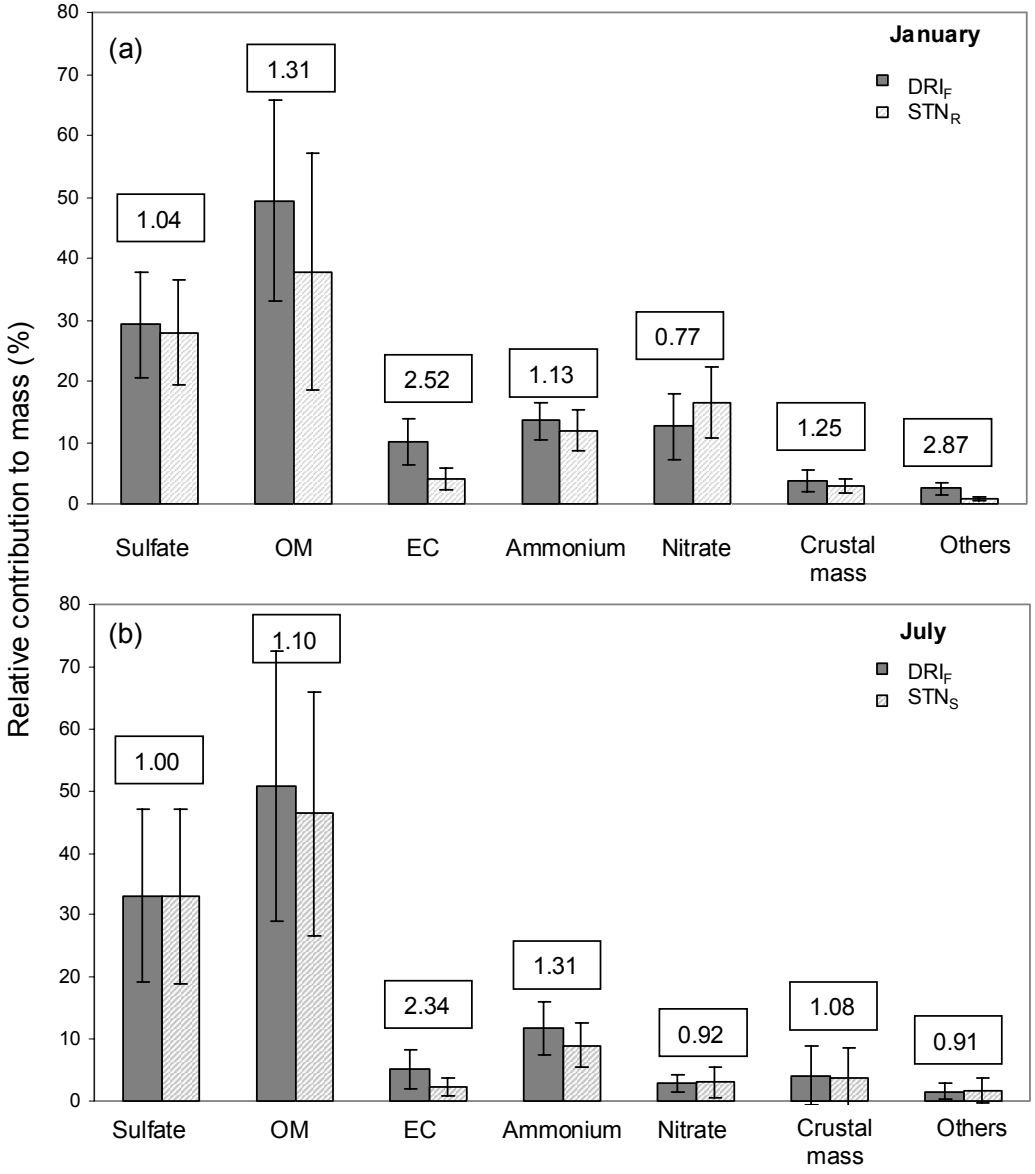

Figure 5. Contributions of individual species to $PM_{2.5}$ mass (relative contribution) for (a) January and (b) July. Numbers in boxes are the DRI_F relative contribution divided by STN_{RS} relative contribution. Error bars represent the standard deviation of the relative contributions.

Figure 5 shows the contributions of sulfate, organic matter (OM = OC × 1.8), EC, ammonium, nitrate, crustal mass and the sum of all other species, to total mass (the relative contribution) as well as the ratios of DRI_F/STN_{RS} relative contribution.

Here nitrate from the front and backup filter of DRI_F was used. In January and July STN_{RS} report larger sulfate concentrations, but the relative contribution of sulfate to total mass is similar for STN_{RS} and DRI_F (shown by the ratios of relative contribution [DRI_F/STN_{RS}] being close to unity in Figure 5). A systematic bias could explain why the difference between the sulfate concentrations does not show up in the relative contributions. This bias can result from differences in how the two instruments record volume as described in the experimental section. In January DRI_F reports more OM concentration than STN_R and the relative contribution of OM to total mass from DRI_F is greater than that from STN_R. In July DRI_F reports less OM concentration than STN_S and the relative contribution of OM to total mass from DRI_F is greater than that from STN_S. This should not negate the above argument that there is a systematic bias between the two instruments. The relative contribution of OM to total mass is affected by artifacts in both mass and OC measurements. The differences in OM relative contribution are not the same as the differences in sulfate relative contribution because of issues related to organic sampling artifacts, blank correction and analysis protocols. The mass closure of DRI_F usually exceeds 100%, consistent with an uncorrected positive organic sampling artifact. For STN_R, however, the problem associated with organic sampling artifacts has been offset by a relatively high blank subtraction in this study. The organic sampling artifact is a major issue regarding $PM_{2.5}$ mass closure, particularly for low PM-loaded samples.

6.3 Conclusions

Measurements from the DRI and RTI analyzed samplers (DRI_F versus STN_R and DRI_F versus STN_S) at Fort Meade, MD were generally well correlated.

- $PM_{2.5}$, sulfate, OC, TC and ammonium all had r-values in excess of 0.8.

- The STN method reported larger $PM_{2.5}$ mass than the DRI method by 14 – 17% and generally showed larger concentrations than the DRI_F.

- Possible causes for the bias between STN_{RS} and DRI_F include different flow monitoring strategies, DRI_F losses of volatile species because used filters remained in the field for a longer time and/or because face velocities were larger than those for the STN_{RS}.

- With the current state of ambient monitoring it is reasonable to expect uncertainties of at least 20% (at the 95% confidence level) for $PM_{2.5}$, sulfate, ammonium, and organic matter.

Even though the $PM_{2.5}$ mass measurements were well correlated, differences between the measurements were statistically significant more than 50% of the time under the current uncertainty estimates. The uncertainty associated with $PM_{2.5}$ mass must be raised from 10% to 20% for January measurements, and from 10% to 28% for July measurements, to make the differences statistically significant only 5% of the time (using a z-test and assuming only random errors). Even though the measurements of speciated mass were well correlated, the differences between the samplers are statistically significant at the 95% confidence level from 5 to 100% of the time. Particularly, measurements of EC did not compare well. Two different analysis methods, IMPROVE-TOR and STN-TOT, were used, and these two methods are known to define EC differently. Nitrate correlated well between the two samplers in January, however the DRI_F measurements were substantially smaller than those

from the STN_R and all the measurements were significantly different using a z-test. In July the nitrate correlation was weaker, possibly because of the increased volatility and lower concentration of the nitrate aerosol. It is likely that the STN_{RS} nylon filters retained more nitrate than the DRI_F quartz filters (e.g. Frank 2006). At FME this problem was mitigated somewhat because DRI_F used backup filters. Residuals of gravimetric – reconstructed mass were generally small and negative for both DRI_F and STN_{RS}. The differences possibly result from the organic sampling artifact and/or conversion factor between the mass of organic carbon and organic matter.

Overall, the error estimates used in the current STN network (i.e., from AQS) may be too low to account for the actual uncertainty in the measurements, and to some extent this may impact the conclusions of trend analyses and receptor modeling based on the STN data. With the current state of ambient monitoring it is reasonable to expect uncertainties of at least 20% (at the 95% confidence level) for $PM_{2.5}$, sulfate, ammonium, and organic matter and larger uncertainties for EC and nitrate. Further evaluation for these sampling systems is recommended through side-by-side measurements at multiple locations for longer periods of time.

Chapter 7: Conclusions

7.1 Summary

In Chapters 3-6 I presented work from clustering back trajectories and profiles of trace gases and aerosols, comparisons of model and measured profiles of trace gases and surface comparisons of aerosols to explain sources, sinks and distributions of aerosols and trace gases in the Mid-Atlantic region. From 1995 - 2002, airborne measurements of O_3, CO, SO_2, and aerosol properties were made during summertime air pollution episodes over the Mid-Atlantic U.S. (34.7˚ to 44.6˚N, 68.4˚ to 81.6˚W) as part of the Regional Atmospheric Measurement, Modeling, and Prediction Program (RAMMPP). In Chapter 3, I presented statistics for all profiles made. Little diurnal variation was identified in the CO, SO_2, and Ångström exponent profiles, although the Ångström exponent profiles decreased with altitude. Boundary layer O_3 was greater in the afternoon, while lower free tropospheric O_3 was invariant at ~55 ppbv. The single scattering albedo increased from morning to afternoon (0.93 ± 0.01 - 0.94 ± 0.01); however, both profiles decreased with altitude. A cluster analysis of back trajectories in conjunction with the vertical profile data was used to identify source regions and characteristic transport patterns during summertime pollution episodes. When the greatest trajectory density lay over the northern Ohio River Valley, the result was large O_3 values, large SO_2/CO ratios, highly scattering particles, and large aerosol optical depths. Maximum trajectory density over the southern Ohio River Valley resulted in little pollution. The greatest afternoon O_3 values occurred during periods of stagnation. North-northwesterly and northerly flow brought the least pollution overall. The contribution of regional transport to

afternoon boundary layer O_3 was quantified. When the greatest cluster trajectory density lay over the Ohio River Valley (~59% of the profiles), transport accounted for 69-82% of the afternoon boundary layer O_3. Under stagnant conditions (~27% of the profiles), transport only accounted for 58% of the afternoon boundary layer O_3. On average transported O_3 accounts for 64% of the O_3 measured in the aircraft profiles (this is a weighted averaged shown in Table 1). This transported O_3 may be an underestimate because we were unable to account for O_3 precursors produced by upwind sources. The results from this study provide a description of regional chemical and transport processes that will be valuable to investigators from the Baltimore, New York, and Pittsburgh EPA Supersites.

Cluster	% of flights made for this cluster	% O_3 transported	weighted % O_3 transported
1	26	67	18
2	19	67	13
3	27	54	14
4	10	82	8
5	6	62	4
6	4	73	3
7	6	56	3
8	3	55	2
		weighted average	64

Table 1. The percent of O_3 transported for each back trajectory cluster and the weighted average of O_3 transported from upwind sources for all clusters.

Upwind emission sources of NO_x and SO_2 play a crucial role in the amount of O_3 and aerosols in the lower troposphere in the Mid-Atlantic region. In Chapter 4 a hierarchical clustering method was used to separate distinct chemical and meteorological events from over 150 aircraft vertical profiles in the lower troposphere

measuring O_3, SO_2, CO, and particle absorption and scattering in the Mid-Atlantic US. Forty-eight-hour back trajectories were run for each profile and the integrated NO_x and SO_2 point source emissions encountered by each trajectory were calculated using data from the EPA Clean Air Market Division's database. Greater integrated point source NO_x emissions along the back trajectories were correlated with greater O_3 mixing ratios measured during the flights, indicating that O_3 mixing ratios are strongly influenced by and can be predicted with point source emissions. The amount of CO observed depended on where the profiles were made, and larger CO values were found in areas with larger mobile source emissions. Profiles with greater particle absorption were associated with greater CO values.

There is a pervasive "background" SO_2 profile over the eastern US with mixing ratios decreasing smoothly from about 3.5 ppb near the surface to 0.2 ppb at 2400 m. Most SO_2 measured fit this clean profile, but there were exceptions and the clustering method was able to separate these profiles with larger SO_2 values. Profiles with larger, more scattering particles, were correlated with greater integrated SO_2 emissions. The clustering technique also separated profiles made during the 2002 Canadian forest fires.

The UMD aircraft measurements of O_3 have also been compared with EPA's Community Multiscale Air Quality (CMAQ) model. CMAQ under-predicts O_3 by 10% above 500 m altitude. I performed a sensitivity test of the model to determine how including aerosols with NO_2 photolysis rate coefficients affected O_3 production using a revised CMAQ run. These adjustments of the chemistry had modest impacts on CMAQ calculated profiles. In general the revised CMAQ run generated more O_3

above 500 m (~1 ppb), and generated less O_3 (1-4 ppb) below 500 m and brought them into closer agreement with observations. Improvements in the model's ability to describe clouds might increase the oxidation of SO_2 to sulfate and thereby bring the modeled O_3 in closer agreement with measurements.

The UMD aircraft SO_2 measurements were also compared with CMAQ and GOCART. Both models over-predicted SO_2 aloft by ~50%. Possible reasons for this include problems with the emissions inputs and the difficulty the models have resolving clouds. Because the models over-predict SO_2, they likely over-predict the lifetime of SO_2. This has far-reaching policy implications on the ability of the models to describe the oxidation product of SO_2 (sulfate) and the ability of the models to describe $PM_{2.5}$ accurately. Some locations in the Mid-Atlantic are not in compliance with $PM_{2.5}$ standards, and improvement of the models ability to replicate the oxidation of sulfate will aid in the development of state implementation plans for the reduction of $PM_{2.5}$.

Assessing the effects of air quality on public health and the environment requires reliable measurement of $PM_{2.5}$ mass and the individual chemical components of fine aerosols. In Chapter 6 $PM_{2.5}$ measurements that are part of a newly-established national network were compared with more conventional sampling systems. Experiments were carried out during 2002 at a suburban site in Maryland, United States, where two samplers from the U.S. Environmental Protection Agency Speciation Trends Network: Met One Speciation Air Sampling System – STN_S and Thermo Scientific Reference Ambient Air Sampler – STN_R, two Desert Research Institute Sequential Filter Samplers – DRI_F, and a continuous TEOM monitor

(Thermo Scientific Tapered Element Oscillating Microbalance, 1400a) were sampling air in parallel. These monitors differ not only in sampling configuration but also in protocol-specific sample analysis procedures. Measurements of $PM_{2.5}$ mass and major contributing species were well correlated among the different methods with r-values > 0.8. Despite the good correlations, daily concentrations of $PM_{2.5}$ mass and major contributing species were significantly different at the 95% confidence level from 5 to 100% of the time. Larger values of $PM_{2.5}$ mass and individual species were generally reported from STN_R and STN_S. The January STN_R average $PM_{2.5}$ mass (8.8 $\mu g\ m^{-3}$) was 1.5 $\mu g\ m^{-3}$ larger than the DRI_F average mass. The July STN_S average $PM_{2.5}$ mass (27.8 $\mu g\ m^{-3}$) was 3.8 $\mu g\ m^{-3}$ larger than the DRI_F average mass. These differences can only be partially accounted for by known random errors. Variations in flow control, face velocity, and sampling artifacts possibly influence the measurement of $PM_{2.5}$ speciation and mass closure. Statistical tests indicate that the current uncertainty estimates used in the STN network may underestimate the actual uncertainty.

7.2 Recommendations for Future Work

The chemical climatology has been used to evaluate modeled O_3 and SO_2. In Chapter 5, I showed that CMAQ modeled O_3 responds to radiative changes due to aerosols and so CMAQ would likely also respond to changes in clouds. A rigorous analysis of how well MM5 and CMAQ represent cloud cover should be performed. Model improvements would be useful. A determination of how changes in cloud cover affect O_3 and aerosol production would be enlightening. A detailed comparison

of measured aerosols with those generated by CMAQ would also be useful for improving forecasting of $PM_{2.5}$ events.

Appendix A presents comparisons between aircraft and surface measurements of trace gases made for morning and afternoon flights carried out over Ft. Meade, Maryland (1999-2002). Morning aircraft measurements were averaged from 100 – 500 m and afternoon measurements were averaged from 100 – 2000 m. O_3 measurements compared better in the afternoon, likely because O_3 is better mixed in the atmosphere later in the day. CO and SO_2 measurements compared better in the morning. They both have peaks below 500m which is consistent with the expectation of CO coming from ground level combustions and SO_2 emissions from point sources. Extension of this work to all EPA surface sites near aircraft profiles may prove interesting.

Satellites can be powerful tools to monitor the movement of atmospheric pollutants and may have future uses in the prediction of pollution events. Appendix B shows results from comparisons of the Global Ozone Monitoring Experiment (GOME) satellite with UMD aircraft profiles of SO_2. Because of the coarse resolution of GOME and high level of noise, the comparison was poor. This provides an understanding of the limitations of satellite measurements of SO_2. The chemical climatology presented here can be used for validation and improvement of other satellite measurements.

Appendix A

Surface and Aircraft Measurements

Understanding sources of pollution can aid in prevention of pollution events. The transport of pollutants can often been seen in vertical profiles (made with aircraft) as described in Chapter 3. Vertical profiles are expensive and are limited in space and time. Surface networks measuring trace gases and aerosols on a continuous or near-continuous basis have been set up by the EPA throughout the US to monitor pollution levels.

I compared surface measurements of O_3, SO_2, and CO with average columns measured aboard the UMD research aircraft to assess how well surface measurements represent the mixed layer and how they might be influenced by transported pollutants. During the 1999 –2002 intensive sampling period at Fort Meade, the University of Maryland research aircraft made flights over Fort Meade measuring O_3, SO_2, and CO. The shapes of O_3 profiles are affected by the breakdown of the nocturnal boundary layer and to account for this I divided the flights into morning and afternoon. Morning flights were flown between 6:00 and 12:00 EST, with an average time of 9:30 EST. Afternoon flights were flown between 12:00 and 19:00 EST, with an average time of 14:30 EST. In order to compare the aircraft measurements with surface measurements I assumed the afternoon boundary layer extended from 100 m to 2000 m and I calculated a boundary layer average for all of the trace gases in this layer. For morning flights I assumed that the residual nocturnal boundary layer was

between 500 m and 2000 m, and I calculated an average below that, from 100 - 500 m, to compare with surface measurements. I used a three-hour average of the surface measurements around the time of the flight to compare with aircraft measurements.

Comparisons between surface and aircraft measurements of O_3, SO_2, and CO, for morning and afternoon flights, are shown in A.1-A.3. O_3 measurements compare better in the afternoon ($r^2 = 0.6$) than in the morning ($r^2 = 0.5$). The average difference (surface – aircraft) is smaller in the afternoon (8 ppb) than in the morning (9 ppb) and the RMS difference is also smaller in the afternoon than in the morning (A4). In the afternoon the profile is generally well mixed and this explains the better correlation and smaller differences between surface and aircraft measurements in the afternoon. SO_2 measurements compared better in the morning, when the comparison was made between the surface and the aircraft 100 – 500 m average, than in the afternoon when the comparison was made between the surface and the aircraft 100 - 2000 m average. Morning SO_2 comparisons had an r^2 of 0.8 and this dropped to 0.5 in the afternoon. The average difference (surface – aircraft) increased from 0.4 to 1.6 ppb between morning and afternoon, though the RMS difference was similar (3 ppb). The SO_2 generally peaks below 500 m (at elevations where it is emitted) and concentrations drop off substantially above this level, so the average SO_2 from 100 m to 2000 m is smaller than the average SO_2 from 100 to 500 m. Afternoon surface SO_2 was compared with aircraft average SO_2 from 100 – 500 m (A.2.c) and the r^2 of 0.7 was better than that from A.2.b which had an r^2 of 0.5.

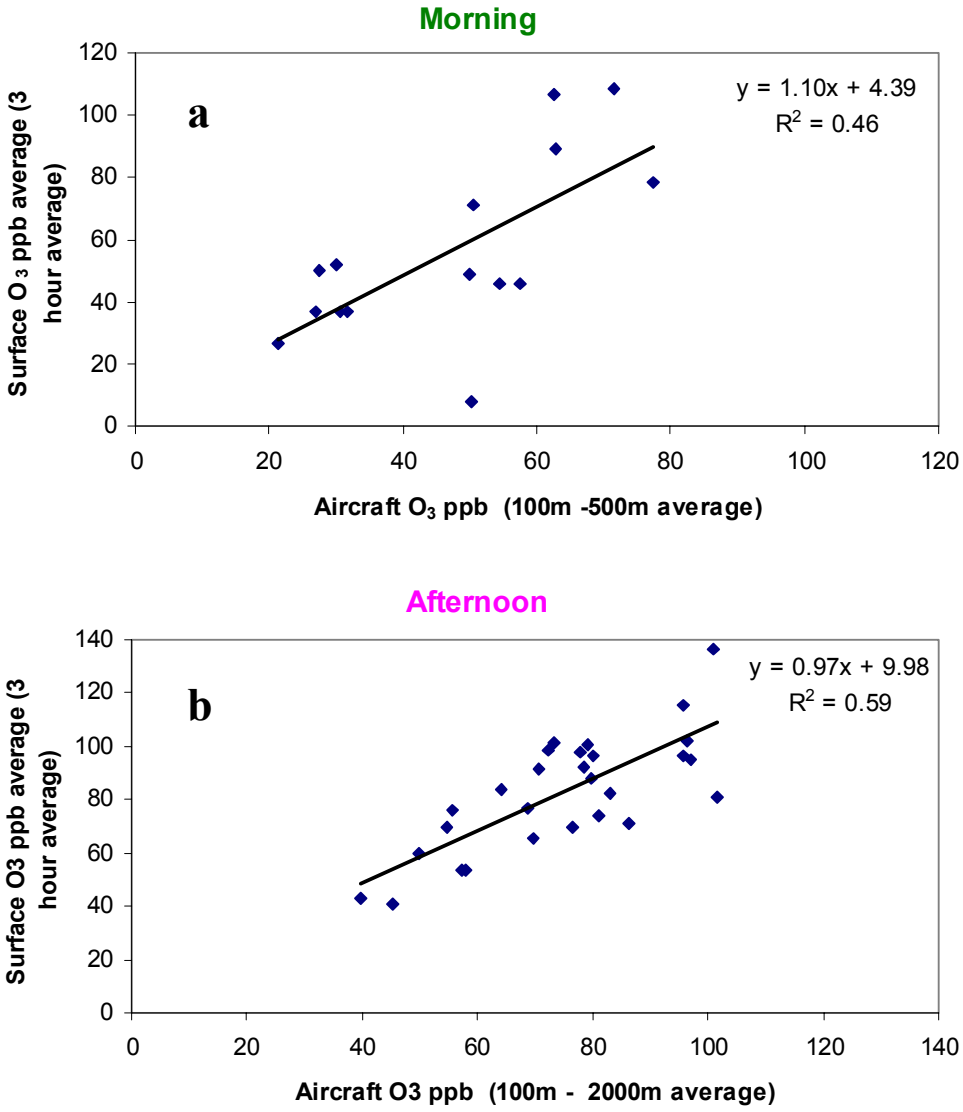

A.1. Comparison of aircraft and surface measurements of O_3 for a) morning and b) afternoon flights. The afternoon shows better correlation between surface and measurements aloft, likely due to improved mixing in the afternoon.

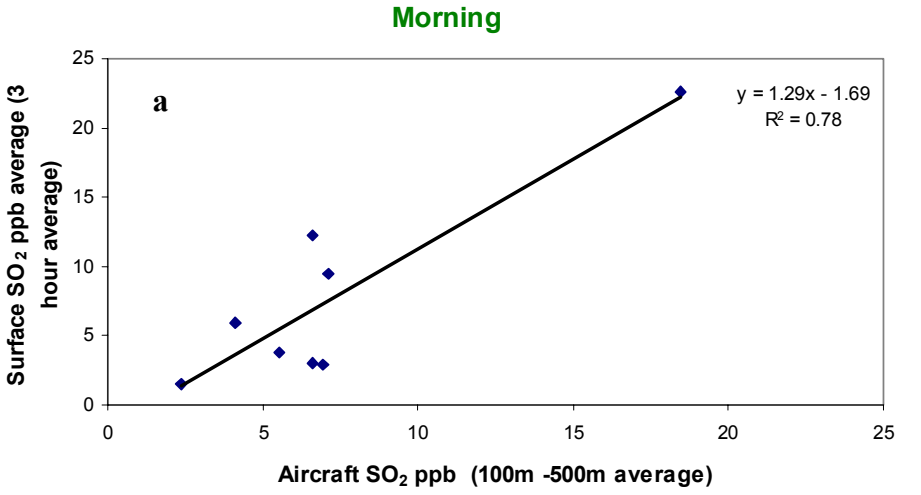
Morning
a
y = 1.29x - 1.69
R² = 0.78
Surface SO2 ppb average (3 hour average)
Aircraft SO2 ppb (100m -500m average)
0
5
10
15
20
25

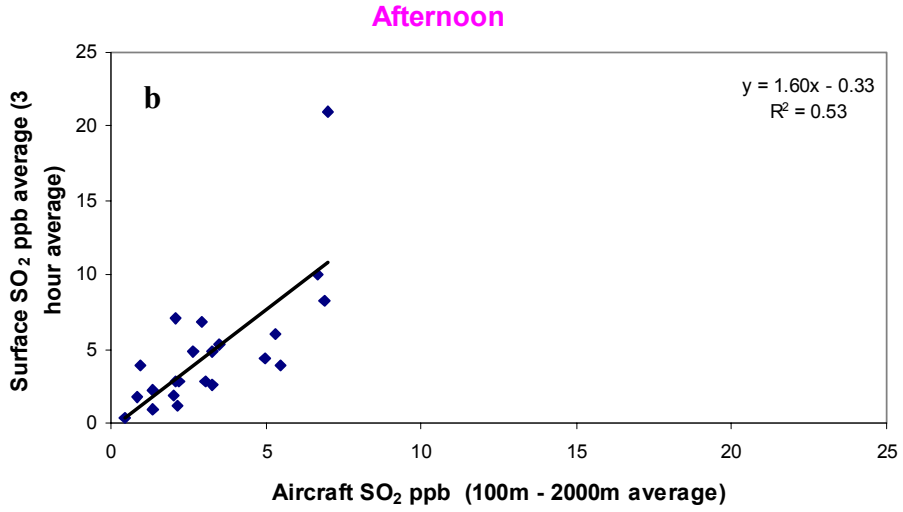
Afternoon
b
y = 1.60x - 0.33
R² = 0.53
Surface SO2 ppb average (3 hour average)
Aircraft SO2 ppb (100m - 2000m average)
0
5
10
15
20
25

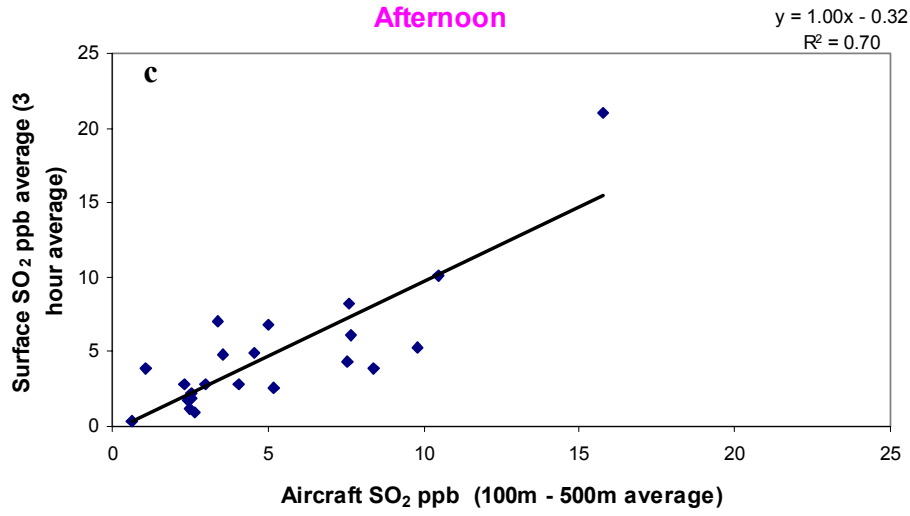
Afternoon
y = 1.00x - 0.32
R² = 0.70
c
Surface SO2 ppb average (3 hour average)
Aircraft SO2 ppb (100m - 500m average)
0
5
10
15
20
25

A.2. Comparison of aircraft and surface measurements of SO_2 for a) morning and b) afternoon flights (with aircraft averages from 100 -2000 m) and b) afternoon flights (with aircraft averages from 100 – 500 m). Surface measurements compare well with aircraft averages in the lower boundary layer (100 -500 m).

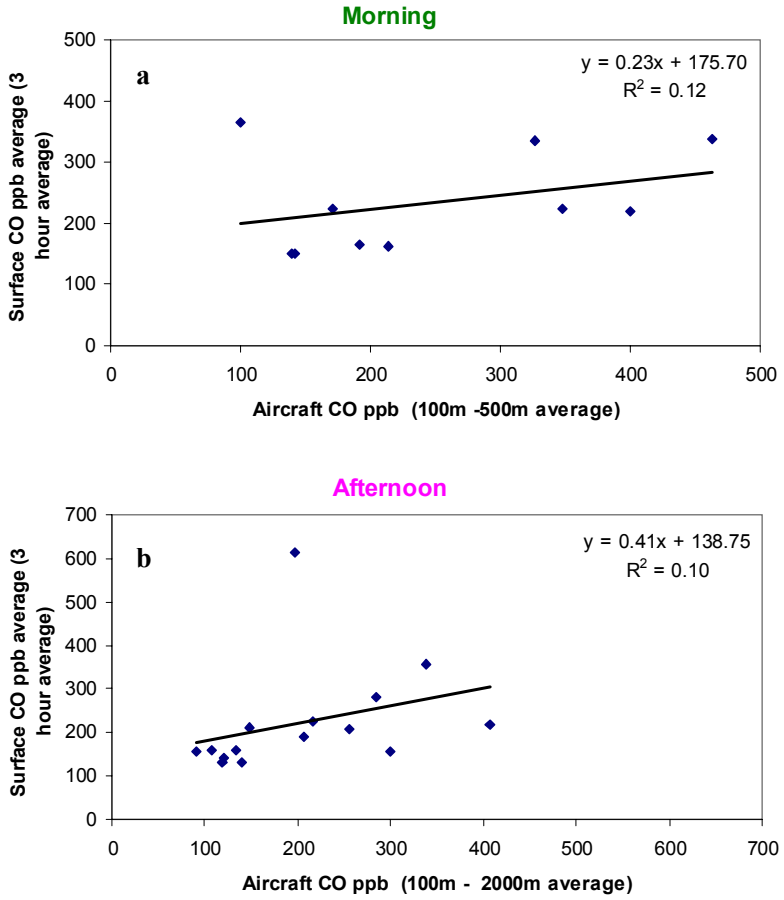

A.3. Comparison of aircraft and surface measurements of CO for a) morning and b) afternoon flights. Both morning and afternoon show poor correlation and this could be because of spikes in surface CO data.

	Aircraft column average (ppb)	Aircraft standard deviation (ppb)	Surface 3-hr average (ppb)	Surface standard deviation (ppb)	RMS difference (ppb)	Average difference (surface-aircraft) (ppb)
O_3 am	47.0	17.8	56.1	29.0	22.6	9.1
O_3 pm	74.6	17.0	82.5	21.6	15.8	8.0
SO_2 am	7.2	4.8	7.7	7.0	3.4	0.4
SO_2 pm	3.2	2.0	4.8	4.4	3.5	1.6
CO am	250	125	233	83	118	-16.2
CO pm	204	95	222	124	127	17.7

A.4. Comparisons of O_3, SO_2, and CO aircraft column averages with surface measurements. Morning aircraft measurements were averaged between 100-500 m and afternoon aircraft measurements were averaged between 100-2000 m. The RMS difference, average difference (surface – aircraft), and standard deviation is also shown. All data have units of ppb.

CO morning and afternoon aircraft measurements do not compare well with surface measurements (A.3). This is likely because of some peaks at the surface not seen aloft. When one outlier (June 24, 1999) is removed from the morning data, the correlation between morning surface and aircraft measurements improves from an r^2 of 0.1 to an r^2 of 0.6 (A.5a). The June 24, 1999 spiral was made at 6:00 EST, and shows CO around 100 ppb, from the surface to 3km. The small CO values are seen at nearby locations of Gaithersburg, MD and Manassas, VA. O_3 is also extremely low below 150 m (around 30 ppb for all three locations). The CO surface measurement shows 300-400 ppb from 5:00 to 7:00 EST, with a standard deviation of 64 ppb (for this specific day, this differs somewhat from the standard deviation for all days in the analysis shown in A.4). No peaks like this are seen in the aircraft profile, even below 100 m, suggesting that this is a very local plume (perhaps a vehicle was idling near

the instrument). The RH is about 90% at the surface and drops off to 50% at 300 m, suggesting that the lower level aircraft measurements were made in the inversion layer. When an outlier is removed from the afternoon measurements (A.5.b) the correlation improves from an r^2 of 0.1 to an r^2 of 0.5. This outlier occurred on June 24, 2002. The aircraft made a spiral at 15:00 pm EST, and shows 400 ppb of CO at 200 m, which decreases quickly aloft. The surface measurements show a three-hour average CO of 611 ppb, with at standard deviation of 66 ppb. Since this was an afternoon profile, I calculated the average from 100 m to 2000 m, and the peak near the surface was washed out. Though the correlation did improve when the outliers were removed, the correlation was still not as good as that for O_3 and SO_2. Thus, surface CO measurements may not be representative of the mixed layer measurements.

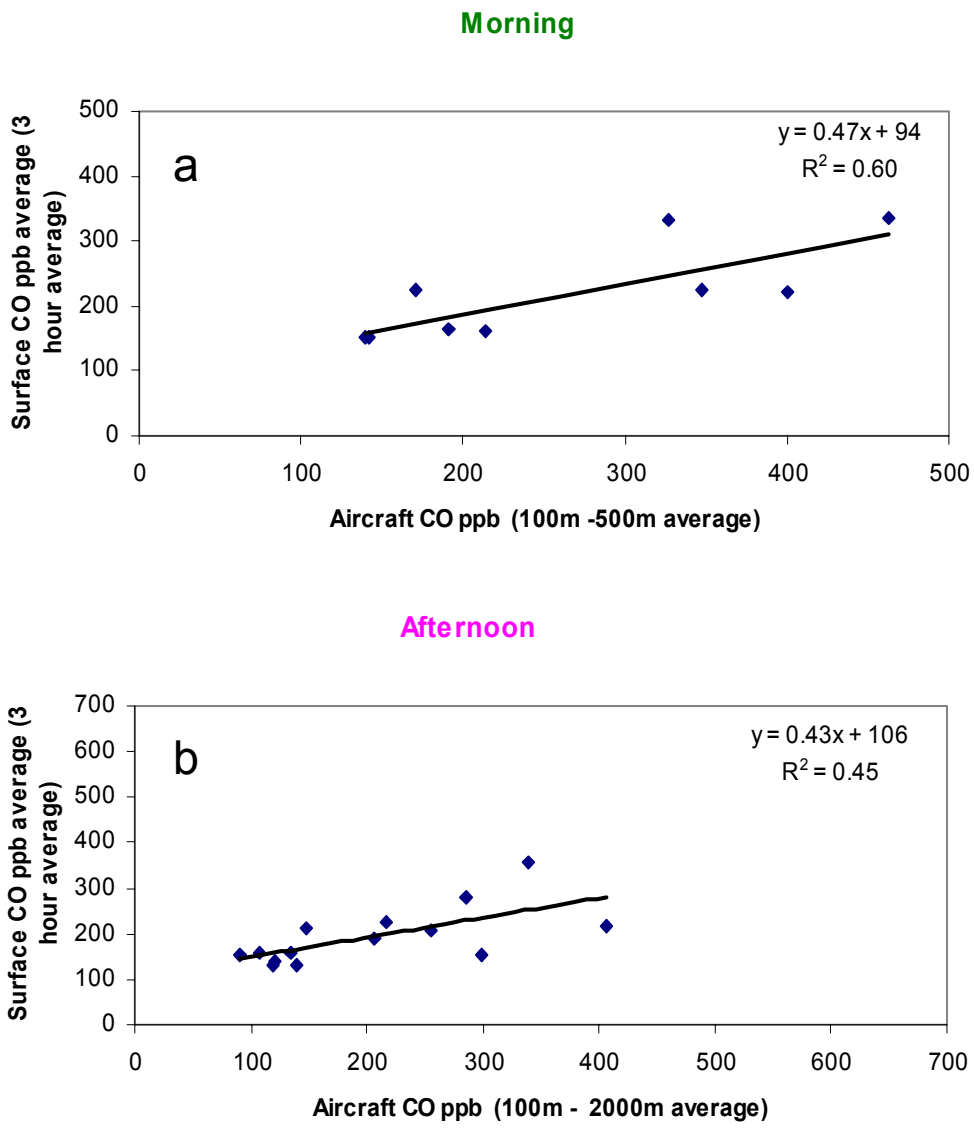

A.5. Comparison of aircraft and surface measurements of CO for a) morning and b) afternoon flights with outliers removed. The correlation improves when the outliers are removed, however the correlation is not as good as that for O_3 and SO_2.

Appendix B

Satellite Measurements

Surface measurements can be made continuously to show the diurnal and seasonal variability of SO_2. A network of surface stations like those in the Sulfate Regional Experiment and the Atmospheric Integrated Research Monitoring Network provide information about regional SO_2 distributions (EPRI, 1981; Hicks, 2001) but this can be expensive and difficult to implement everywhere. Aircraft measurements provide altitude profiles and some spatial information including possible transport of pollutants. However, aircraft observations are also expensive and very limited in space and time. Satellites show SO_2 distributions around the world year round. These measurements are usually taken once daily and thus do not offer information on the diurnal variability of SO_2; nor do they provide information about the vertical distribution of SO_2. Because of their spatial coverage, satellites are great tools to monitor mesoscale and synoptic scale atmospheric events. A combination of surface, aircraft, and satellite measurements can be a powerful tool for describing the SO_2 distribution. Satellites could also be used in conjunction with models to predict and characterize pollution events. Understanding the uncertainty in satellite measurements is a key step in the advancement of satellites into the tropospheric air quality monitoring ensemble. In this Appendix I will present comparisons of SO_2 from the UMD research aircraft with those retrieved from The Global Ozone Monitoring Experiment (GOME) instrument aboard the European Research Satellite (ERS-2).

GOME Instrumentation

GOME measures scattered and reflected light from the Earth and the atmosphere. Data collected in the wavelength range of 315.5-327 nm are used to determine SO_2 column content with Differential Optical Absorption Spectroscopy (DOAS) (Eisinger et al. 1998). Beer's law enables the quantification of the concentration of a species from the absorption spectrum using measurements of attenuated and unattenuated light. It is difficult to measure the true unnattenuated light, I_o, coming from the Earth because of Mie and Rayleigh scattering, as well as absorption by atmospheric species that attenuate light. B.1 shows the absorption cross section of SO_2 in the wavelength region from 317 to 325. There is more structure in the spectrum in the smaller wavelength region of 318 to 320. DOAS fits a curve to the absorption spectrum in the larger wavelength region (317 to 325 nm) to describe the "unattenuated" beam I_o'. This "unattenuated" beam is only unattenuated by SO_2 and accounts for the difficult to measure attenuation from scattering and other atmospheric species (Platt, 1994). The differential absorption, D' is just I_o' – I.

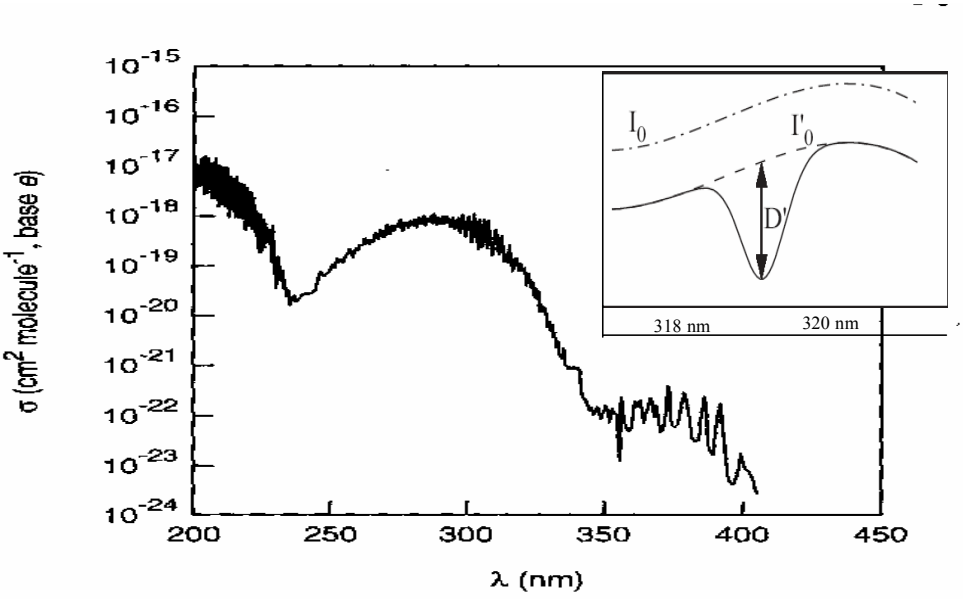

B.1. SO_2 absorption cross section. In the smaller box I_o is the true unattenuated beam of light that cannot be measured because of atmospheric scattering and absorption. I_o' is fit over the larger wavelength region (317-325) and is only attenuated by the species of interest. The differential absorption (D') is then just I_o' – I (Finlayson-Pitts and Pitts, 2000; Platt, 2003).

GOME measures trace gasses with a nadir scanning double monochromator. The resolution of the monochromator is 0.17-0.33 nm. The incoming light is split into 4 channels and is recorded with a 1024 reticon photodiode array. SO_2 absorbs at 317 to 325, and the monochromator channel corresponding to this region detects the gas. The SO_2 integrated column content is then calculated using a differential optical absorption spectrometry algorithm (Eisinger et. al. 1998).

There is an overlap in the absorption signal between SO_2 and O_3 from the Huggins bands in the 300-360 nm region (Finlayson-Pitts and Pitts, 2000). This O_3 interference can be removed from the GOME data by subtracting the SO_2 signal in areas with little SO_2 (like areas over the ocean) from the SO_2 signal in an area of interest.

Comparisons between In-situ and Satellite Measurements: Implications for Revisions to the Air Mass Factor.

I have compared the aircraft column contents of SO_2 with those measured with GOME to test the sensitivity of GOME SO_2 measurements. B.2 shows a map of GOME SO_2 retrievals over North America. Plumes of SO_2 are visible over Mexico City as well as the Eastern and Midwestern US. Plumes in these areas are most likely located in the troposphere.

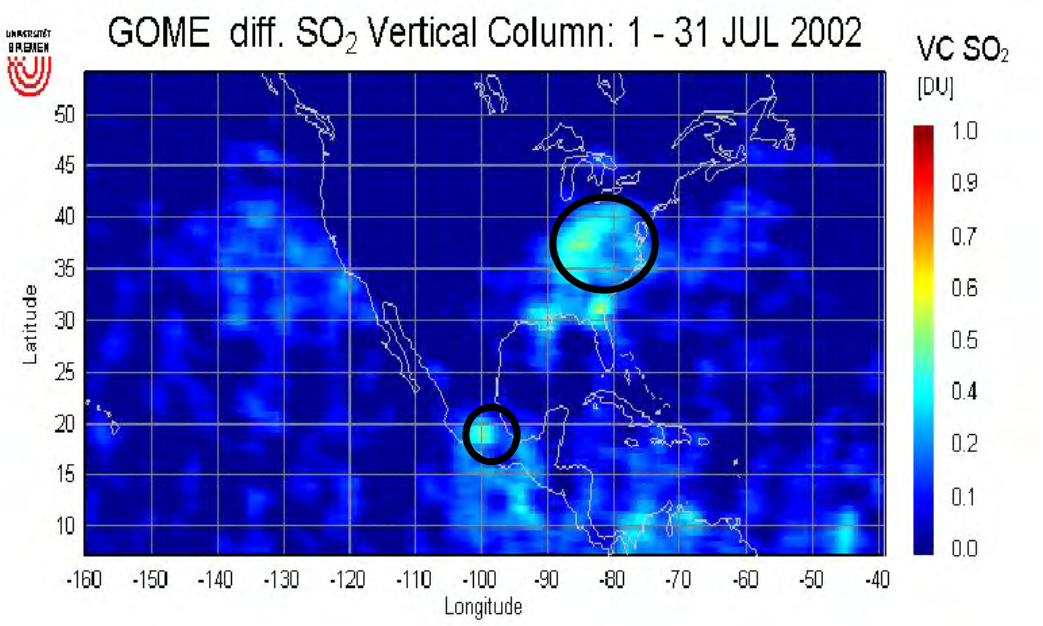

B.2. Map of GOME SO_2. The SO_2 plume over the Eastern US and Mexico City can clearly be seen with a column content of about 0.4 DU.

B.3 shows comparisons I made between the default GOME retrievals and aircraft column contents. The correlation between GOME and aircraft measurements is poor and GOME retrieves much less SO_2 than the aircraft measures. To improve the GOME retrievals I used *in-situ* data to modify the Air Mass Factor (AMF) used in

the GOME retrieval algorithm. The AMF is used to convert the measured slant columns of trace gases into vertical columns and can be written as:

$$\text{AMF} = \tau_{\text{slant}} / \tau_{\text{vert}} \quad (1)$$

Where τ_{slant} is the optical density along the slant path (this is what is measured by GOME) and τ_{vert} is the optical density along the vertical path. To determine the AMF, a radiative transfer model is run with and without the absorbing species to calculate respective intensites $I(\lambda)^{w}$ and $I(\lambda)^{w/o}$ along the slant path s_s.

$$\ln (I(\lambda)^{w/o} / I(\lambda)^{w}) = \int_0^{TOA} \sigma_x(s_s, \lambda) C_x(s_s) ds_s \quad (2)$$

Here x is some absorbing species, s_s is the slant path length, σ_x is the extinction cross section, and C_x is the concentration of the species of interest. The left side of Equation 2 is the slant optical density. The vertical optical density, τ_{vert}, can be calculated as:

$$\tau_{vert} = \int_0^{TOA} \sigma_x(s_v, \lambda) C_x(s_v) ds_v \quad (3)$$

Here s_v is the vertical path length. The air mass factor can be written as:

$$\text{AMF} = \ln (I(\lambda)^{w/o} / I(\lambda)^{w}) / \int_0^{TOA} \sigma_x(s_v, \lambda) C_x(s_v) ds_v \quad (4)$$

(Perliski et al., 1993). The extinction cross section can be measured in the lab or determined from literature. The radiative transfer model SCIATRAN solves the following equation to determine $I(\lambda)^{w}$ and $I(\lambda)^{w/o}$.

$$\mu \frac{dI(z,\mu,\varphi)}{dz} = -c(z) I(z,\mu,\varphi) + \frac{b(z)}{4\Pi} \int_0^{2\pi} \int_{-1}^{1} p(z,\mu,\mu',\varphi,\varphi') I(z,\mu',\varphi') d\mu' d\varphi' \quad (5)$$

Here μ and μ' denote the cosine of the zenith angle, z represents altitude, φ and φ' represent the azimuthal angles in relation to the line-of-site projection on the earth's

surface, *c* is the total extinction coefficient, *b* is the total scattering coefficient (the sum of the trace gas and particle scattering coefficients), and *p* is the total scattering phase function (Rozonov et al., 1997).

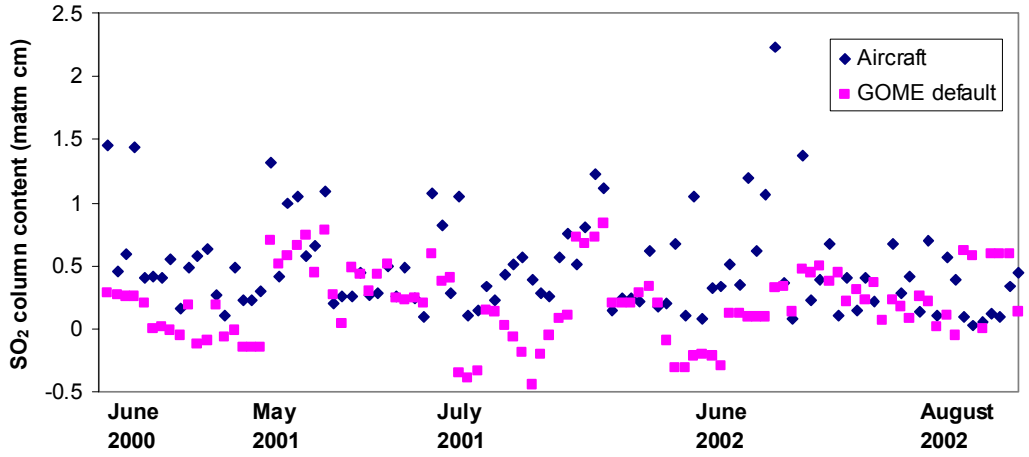

B.3. Comparison between default GOME SO_2 and UMD aircraft SO_2 (matm cm). GOME SO_2 is smaller than that measured aboard the aircraft and the correlation between the measurements is poor ($r^2 = 0.20$).

The AMF depends on the altitude of the absorbing species of interest and where the most absorption and scattering occur in a vertical column. B.4 shows how light is scattered when the absorbing and scattering layers are near the surface (Example 1) and when the absorbing and scattering layers are at higher altitudes (Example 2). Light at 320 nm is mostly attenuated by the time it reaches the surface. The path length is smaller in example 1 than in example 2 and thus the intensity reaching the satellite in example 1 will be greater than in example 2. Because the intensity is greater, the AMF for example 1 will be smaller than that for example 2. The default AMF calculation assumes the column concentration of SO_2 has a peak

above the boundary layer. I have recalculated the AMF using SO_2 profiles measured aboard the UMD research aircraft. B.5 shows results of the comparison between aircraft SO_2 columns and GOME SO_2 when a revised AMF was used. These adjustments to the AMF made the GOME retrieved SO_2 larger but did not improve the correlation between the aircraft and GOME.

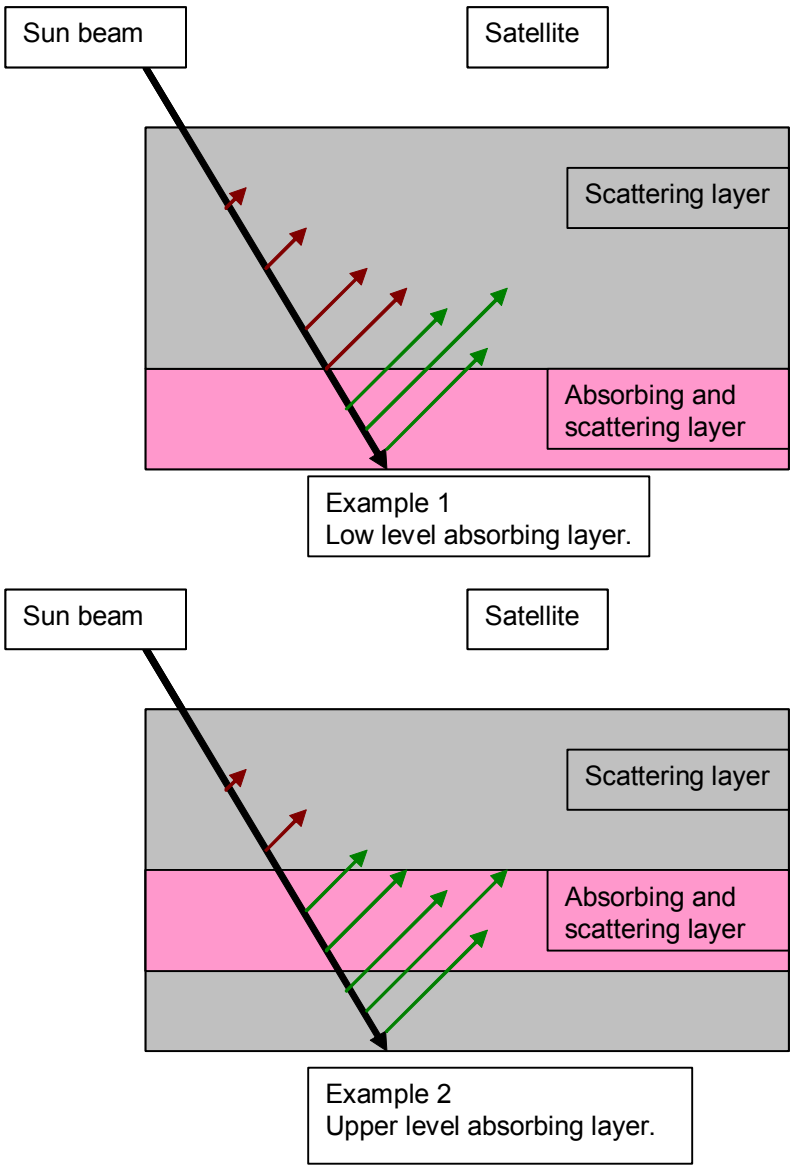

B.4. Light is scattered differently when an absorbing and scattering layer is near the surface (example 1) than when the layer is above the planetary boundary layer (example 2). Red arrows denote light that is not scattered through the absorbing layer and green arrows denote light that is scattered through the absorbing layer. The length and space between the arrows represent the generalized degree of scattering (as altitude increases there are less scattering species). There is more scattering when the layer is above the planetary boundary layer (example 2) than when the layer is near the surface. This is because the light scatters on its way to the surface and then again on its way to the satellite for example 2.

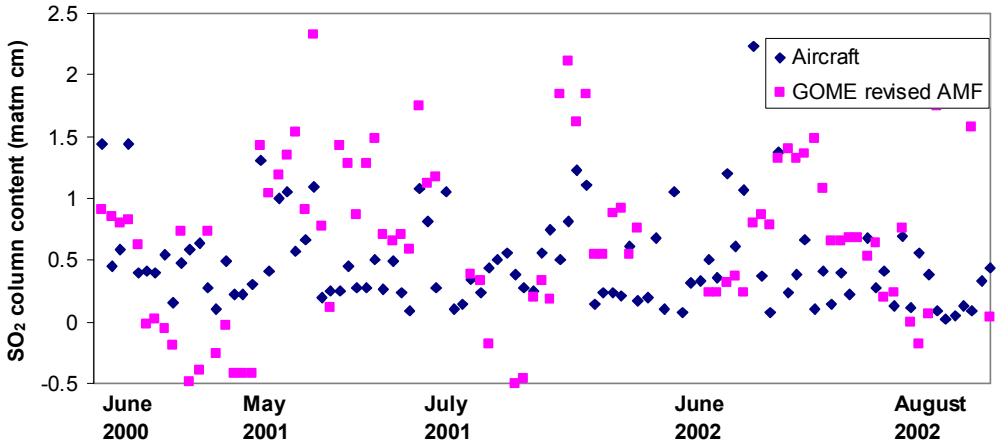

B.5. Comparison between GOME SO_2, using a revised AMF, and UMD aircraft SO_2 (matm cm). The revised AMF made the retrieved GOME SO_2 larger than the default retrieval but the correlation between the measurements is poor (r^2 = 0.16).

GOME Interference Corrections

Because the SO_2 and O_3 absorption band overlap in the UV, GOME SO_2 retrievals must be corrected for O_3 interference (this process will be referred to as an O_3 correction). The default O_3 correction subtracts SO_2 retrieved columns over the Pacific Ocean (where SO_2 should be small) from the SO_2 column at the point of interest. To account for the latitudinal gradient of O_3, only the ocean SO_2 at latitudes matching that of the point of interest are used in the correction. For annual averages this correction works well but for daily GOME retrievals this correction sometimes gives negative SO_2. I have developed a method to improve the O_3 correction and this is described below.

The method to improve the O_3 correction involves finding regions over the ocean with O_3 column contents similar to those over the area of interest and is

diagrammed in B.6. For this method I first generated a map of O_3. Because O_3 has a shape different from SO_2 I had to use a different AMF. For O_3 a good approximation of the AMF can be made with the solar zenith angle (*SZA*):

$$AMF = 1 + 1/\cos(SZA) \quad (6)$$

I made a grid of 1^o latitude by 1^olongitude and averaged the O_3 in each grid box. I then searched for an O_3 box over the ocean that was within 5% of the O_3 box over the area of interest (Steps 1 and 2 in B.6). The latitude and longitude of this box over the ocean was saved. Next I made a map of SO_2 using the revised AMF, described in the previous section, and found the SO_2 at the area of interest and the SO_2 at the same location as the ocean box (Steps 3 and 5). To correct for the O_3 interference at an area of interest I subtracted the SO_2 at the ocean box (that had O_3 that matched O_3 over the area of interest) from the SO_2 over the area of interest. B.7 shows a comparison of SO_2 from the aircraft with GOME retrieved SO_2 (using the revised AMF and O_3 correction). The revised O_3 correction did decrease the number of negative values, but the correlation between aircraft and GOME SO_2 is still poor. In Chapter 5 I calculated the average lifetime of SO_2 in the summer in the daytime in the Mid-Altantic to be short, ~ 19 hours (Chapter 5, Table 11). GOME has coarse spatial resolution, and only makes measurements once a day. The short lifetime and the coarse resolution partly explain why the correlation between aircraft and GOME SO_2 was poor. The SO_2 in the Mid-Atlantic may also be below the GOME detection limit. This analysis provides an understanding of the limitations of the GOME SO_2 retrievals.

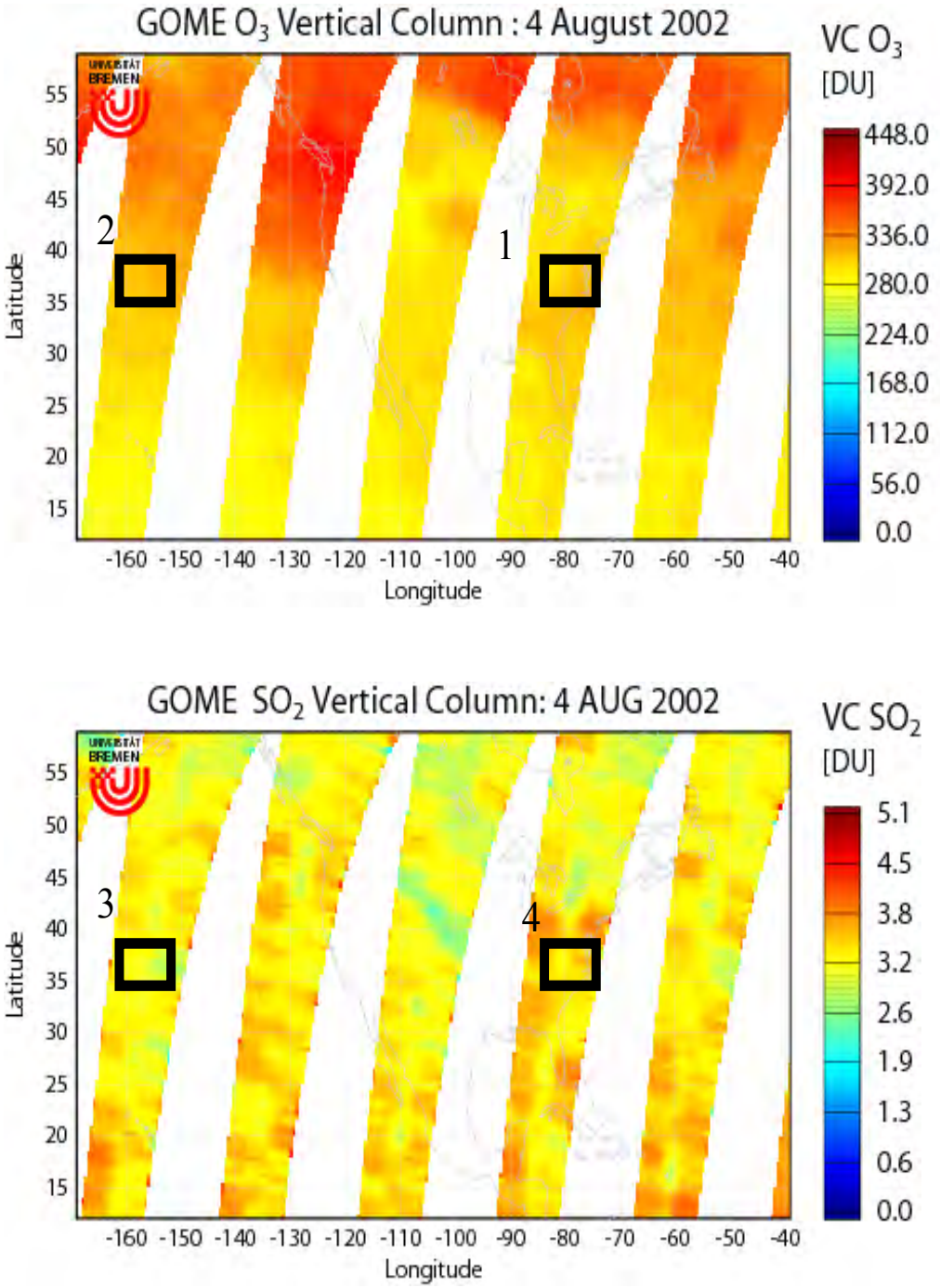

B.6. Diagram of the steps used to calculate the revised O_3 correction. 1.) Find O_3 over area of interest. 2.) Find matching O_3 over ocean (where SO_2 is minimal). 3).Find SO_2 in same location as in 2. 4). Find SO_2 column (over spiral location with no O_3 correction. 5.) Subtract SO_2 in step 4 from SO_2 in step 3.

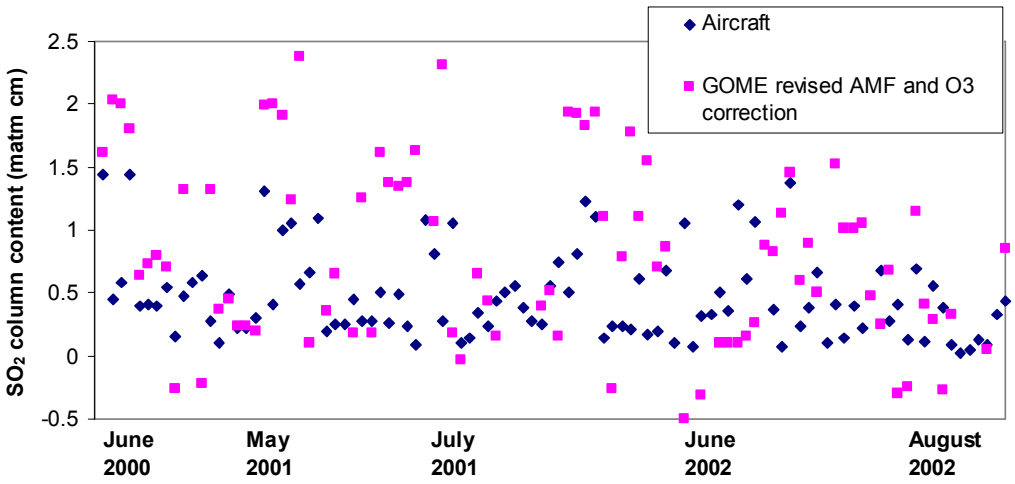

B.7. Comparison between UMD aircraft SO_2 (matm cm) GOME SO_2, using a revised AMF and revised O_3 corrections. The revised O_3 corrections decreased the number of negative GOME retrievals but the correlation between the measurements is still poor ($r^2 = 0.15$).

Bibliography

Andronache, C., W.L. Chameides, D.D. Davis, B.E. Anderson, R.F. Pueschel, A.R. Bandy, D.C.Thornton, R.W. Talbot, P. Kasibhatla, and C.S. Kiang, Gas-to-particle conversion of tropospheric sulfur as estimated from observations in the western North Pacific during PEM-West B. *J.Geo. Phys. Res., 102,* 28511-28538, 1997.

Appel, B.R. and Y.Tokiwa, Atmospheric particulate nitrate sampling errors due to reactions with particulate and gaseous strong acids. *Atmos. Environ., 15*, 1087-1089, 1981.

Appel, B.R., Y. Tokiwa, M. Haik, and E.L. Kothny, Artifact particulate sulfate and nitrate formation on filter media. *Atmos. Environ.,* 18, 409-416, 1984.

Anderson, T.L., and J.A. Ogren, Determining aerosol radiative properties using the TSI 3563 Integrating Nephelometer, *Aerosol Sci. Technol.*, *29*, 57-69, 1998

Andrews, E., P. Saxena, S. Musarra, L.M. Hildemann, P. Koutrakis, P.H. McMurry, I. Olmes, and W.H. White, Concentration and composition of atmospheric aerosols from the 1995 SEAVS experiment and a review of the closure between chemical and gravimetric measurements. *J. Air & Waste Manage. Assoc., 50*, 648-664, 2000.

Ames R.B. and W.C. Malm, Comparison of sulfate and nitrate particle mass concentrations measured by IMPROVE and the CDN. *Atmos. Environ.,* 35, 905-916, 2001.

Ashbaugh, L.L., A statistical trajectory technique for determining air pollution source regions, *J. Air Pollut. Control Ass.*, *33*, 1096-1098, 1983.

Berglen, T.F., T.K. Berntsen, S.A. Isaksen, and J.K. Sundet, A global modle of the coupled sulfur/oxidant chemistry in the troposphere: The sulfur cycle, *J. Geophys. Res., 109,* D19310, doi:10.1029/2003JD003948, 2004.

Berto, A., A. Buzzi, and D. Zardi, Back-tracking water vapour contributing to a precipitation event over Trentino: a case study, *Meteorol. Z.*, *13*(3), 189-200, 2004.

Bond, T.C., T.L. Anderson, and D. Campbell, Calibration and intercomparison of filter-based measurements of visible light absorption by aerosols, *Aerosol Sci. Technol.*, *30*, 582-600, 1999.

Bodhaine, B.A., Aerosol absorption measurements at Barrow, Mauna Loa and the south pole, *J. Geophys. Res.,* 100, 8967-8975, 1995.

Brankov, E., S.T. Rao, and P.S. Porter, A trajectory-clustering-correlation methodology for examining the long-range transport of air pollutants, *Atmos. Environ.*, *32*(9), 1525-1534, 1998.

Buchdahl R, C.D. Willems, M, Vander, and A. Babiker Associations between ambient ozone, hydrocarbons, and childhood wheezy episodes: a prospective observational study in south east London. *Occup. Environ. Med., 57*, 86–93, 2000.

Burton, G.A., G.E. Batley, P.M. Chapman, V.E. Forbes, E.P. Smith, T. Reynoldson, C.E. Schlekat, P.J. den Besten, A.J. Bailer, A.S. Green, and R.L. Dwyer, A weight-of-evidence framework for assessing sediment (or other) contamination: Improving certainty in the decision-making process. *Human Eco. Risk Assess., 8*, 1675-1696, 2002.

Cape, J.N., J. Methven, and L.E. Hudson, The use of trajectory cluster analysis to interpret trace gas measurements at Mace Head, Ireland, *Atmos. Environ.*, *34*, 3561-3663, 2000

Chen, L.-W. A., B.G. Doddridge, R. R. Dickerson, P. K. Mueller, J. C. Chow, and W.A. Butler, Seasonal variations in elemental carbon aerosol, carbon monoxide, and sulfur dioxide: Implications for sources. *Geophys. Res. Let., 28*, 1711-1714, 2001.

Chen, L.-W.A., Urban fine particulate matter: Chemical composition and possible origins. Doctoral dissertation, Chemical Physics, University of Maryland, College Park, 2002.

Chen, L.-W.A., B.G. Doddridge, R.R. Dickerson, J.C. Chow, and R.C. Henry, Origins of fine aerosol mass in the Baltimore-Washington corridor: implications from observation, factor analysis, and ensemble air parcel back trajectories. *Atmos. Environ.,* 36, 4541-4554, 2002.

Chen, L.-W. A., J.C. Chow, B. G. Doddridge, R. R. Dickerson, W. F. Ryan, and P.K. Mueller, Analysis of a summertime PM2.5 and Haze Episode in the Mid-Atlantic Region. *J. Air & Waste Manage. Assoc., 53*, 946-956, 2003.

Chin, M., D. J. Jacob, G. M. Gardner, M. S. Foreman-Fowler, P. A. Spiro, and D. L. Savoie, A global three-dimensional model of tropospheric sulfate, *J. Geophys. Res*., 101, 18,667–18,690, 1996.

Chin, M., R.B. Rood, S.J. Lin, J.F. Muller, and A.M. Thomson, Atmospheric sulfur cycle simulated in the global model GOCART: Model description and global properties, *J. Geophys. Res*., 105(D20), 24671-24687, 2000a.

Chin, M., D.L., Savoie, B.J. Huebert, A.R. Bandy, D.C. Thornton, T.S.Bates, P.K. Quinn, E.S. Saltzman, and W.J. DeBruyn, Atmospheric sulfur cycle simulated in the global model GOCART: Comparison with field observations and regional budgets. *J. Geophys. Res*., 105, 24689-24712, 2000b.

Chow, J.C., J.G. Watson, D.,H. Lowenthal, P.A. Solomon, K.L. Magliano S.D. Ziman, and L.W. Richards, PM10 Source Apportionment in California San-Joaquin Valley. *Atmos. Environ.,* 26, 3335-3354, 1992.

Chow, J.C., J.G. Watson, J.L. Bowen, C.A. Frazier, A.W. Gertler, K.F. Kochy, D. Landis, and L. Ashbaugh, A sampling system for reactive species in the Western United States. In Sampling and analysis of airborne pollutants, Winegar, E.D., Keith, L.H. eds, 212-214, 1993a.

Chow, J.C., Watson, J.G., Pritchett, L.C., Pierson, W.R., Frazier, C.A., Purcell, R.G., The DRI thermal/optical reflectance carbon analysis system: Description, evaluation, and applications in U.S. air quality studies. *Atmos. Environ.,* 27, 1185-1201, 1993b.

Chow, J.C., J.G. Watson, D.H. Lowenthal, P.A.. Solomon, K.L. Magliano, S.D. Ziman, and L.W. Richards, PM10 and PM2.5 Compositions in California's San Joaquin Valley. *Aerosol Sci. and Tech.,* 18, 105-128, 1993c.

Chow, J.C., J.G. Watson, Z.Q. Lu, D.H. Lowenthal, C.A. Frazier, P.A. Solomon, R.H. Thullier, and K. Magliano, Descriptive Analysis of PM2.5 and Pm10 at Regionally Representative Locations during SJVAC/AUSPEX. *Atmos. Environ.,* 30, 2079-2112, 1996.

Chow, J.C., J.G. Watson, D. Crow, D.H. Lowenthal, and T. Merrifield, Comparison of IMPROVE and NIOSH carbon measurements. *Aerosol Sci. and Tech.,* 34, 23-34, 2001.

Chow, J.C., J.G. Watson, L.-W.A. Chen, W.P. Arnott, and H. Moosmuller,. Equivalence of elemental carbon by thermal/optical reflectance and transmittance with different temperature protocols. *Enviro. Sci. and Tech.,* 38, 4414-4422, 2004

Chow, J.C., J.G. Watson, L.-W.A. Chen, G. Paredes-Miranda, M.C.O. Chang, D. Trimble, K.K. Fung, H. Zhang, and J.Z. Yu, Refining temperature measures in thermal/optical carbon analysis. *Atmos. Chem. Phys. 5*, 4477-4505, 2005a.

Chow, J.C., J.G. Watson, D.H. Lowenthal, and K.L Magliano, Loss of $PM_{2.5}$ nitrate from filter samples in central California. *J. Air & Waste Manage. Assoc.,* 55, 1158-1168, 2005b.

Chow, J.C., L.-W.A. Chen, J.G. Watson, D.H. Lowenthal, K.A. Magliano, K. Turkiewicz, and D.E. Lehrman, PM2.5 chemical composition and spatiotemporal variability during the California Regional PM10/PM2.5 Air Quality Study (CRPAQS). *J. Geophys. Res. Let. 111*, D10S04, 2006.

Code of Federal Regulations (CFR), National Primary and Secondary Ambient Air Quality Standards, Final Rules, Title 40, Parts 50-53 and 58, 18 July 1997.

Colarco, P.R., M.R. Schoeberl, B.G. Doddridge, L.T. Marufu, O. Torres, and E.J. Welton, Transport of smoke from Canadian forest fires to the surface near Washington, D.C.: Injection height, entrainment, and optical properties, *J. Geophys. Res*., 109, D06203, 2004.

Colette, A., G. Ancellet, and F. Borchi, Impact of vertical transport processes on the tropospheric ozone layering above Europe. Part I: Study of air mass origin using multivariate analysis, clustering and trajectories, *Atmos. Environ., 39*, 5409-5422, 2005a.

Colette, A., and G. Ancellet, Impact of vertical transport processes on the tropospheric ozone layering above Europe. Part II: Climatological analysis of the past 30 years, *Atmos. Environ., 39*, 5423-5435, 2005b.

Cornbleet, P., and N. Gochman, Incorrect least-squares regression coefficients in method-comparison analysis. *Clin. Chem.*, 25, 432-438, 1979.

Dentener, F. J., G.R. Carmichael, Y. Zhang, J. Lelieveld, and P.J. Crutzen, Role of mineral aerosol as a reactive surface in the global troposphere, *J. Geophys.Res.,101* (D17), 22869-22889, 1996.

Diab, R.D., A. Raghunandan, A.M. Thompson, and V.Thouret, Classification of tropospheric ozone profiles over Johannesburg based on mosaic aircraft data, *Atmos. Chem. Phys., 3*, 713-723, 2003.

Diab, R.D., A.M., Thompson, K. Mari, L. Ramsay, and G.J.R. Coetzee, Tropospheric ozone climatology over Irene, South Africa, from 1990 to 1994 and 1998 to 2002, *J. Geophys. Res., 109,* D20301, 2004.

Dickerson, R.R., and A.C. Delany, Modification of a commercial gas filter correlation CO detector for increased sensitivity, *J. Atmos. Oceanic Technol.*, *5*(3), 424-431, 1988.

Dickerson, R.R., B.G. Doddridge, P.K. Kelley, and K.P.Rhoads, Large-scale pollution of the atmosphere over the North Atlantic Ocean: Evidence from Bermuda, *J.Geophys. Res., 100(5),* 8945-8952, 1995.

Dickerson, R.R., S. Kondragunta, G. Stenchikov, K.L. Civerolo, B.G. Doddridge, and B.N. Holben, The impact of aerosols on solar ultraviolet radiation and photochemical smog. *Science 278*, 827- 830, 1997.

Doddridge, B.G., R.M. Morales, K.P. Rhoads, J.T. Merrill, P.C. Novelli, R.R. Dickerson, V.S. Connors, and H.G. Reichle, Jr, Ground-based and airborne observations of carbon monoxide during NASA/MAPS missions SRL-1 and SRL-2, *J. Geophys. Res.*, *103*, 19305-19316, 1998.

Dorling, S.R., T.D. Davies, and C.E. Pierce, Cluster Analysis: A technique for estimating the synoptic meteorological controls on air and precipitation chemistry – method and applications, *Atmos. Environ.*, *26A*(14), 2575-2582, 1992a.

Dorling, S.R., T.D. Davies, and C.E. Pierce, Cluster Analysis: A technique for estimating the synoptic meteorological controls on air and precipitation chemistry – results from Eskdalemuir, S. Scotland, *Atmos. Environ.*, *26A*(14), 2583-2602, 1992b.

Dorling, S.R., and T.D. Davies, Extending cluster analysis – synoptic meteorology links to characterise chemical climates at six northwest European monitoring stations, *Atmos. Environ.*, *29*(2), 145-167, 1995.

Draxler, R.R., and G.D. Rolph, HYSPLIT (HYbrid Single-Particle Lagrangian Integrated Trajectory) Model access via NOAA ARL READY website (http://www.arl.noaa.gov/ready/hysplit4.html), NOAA Air Resources Laboratory, Silver Spring, MD, 2003.

DRI Operating Procedure, Sequential Filter Sampler: Operation, Maintenance, and Field Calibration. Desert Research Institute, 1990.

Edgerton, E.S., B.E. Hartsell, R.D. Saylor, J.J. Jansen, D.A. Hansen, and G.M. Hidy, The Southeastern Aerosol Research and Characterization study, part 3: Continuous measurements of fine particulate matter mass and composition, *J. Air & Waste Manage. Assoc.,56*, 1325-1341, 2006.

Eisinger, M. and J. P. Burrows, Tropospheric sulfur dioxide observed by the ERS-2 GOME instrument, *Geophys. Res. Lett.*, 25, 4177-4180, 1998.

El-Zanan, H.S., D.H. Lowenthal, B. Zielinska, J.C. Chow, and N. Kumar, Determination of the organic aerosol mass to organic carbon ratio in IMPROVE samples. *Chemosphere* 60, 485-496, 2005.

Eneroth, K., E. Kjellstrom, and K. Holmen, A trajectory climatology for Svalbard; investigating how atmospheric flow patterns influence observed tracer concentrations, *Phys. Chem. Earth*, *28*, 1191-1203, 2003.

EPRI, Aircraft Measurements of Pollutants and Meteorological Parameters During the Sulfate Regional Experiment (SURE) Program: Research Triangle Institute, Inc., 1981.

ESRI Data and Maps, Arcview 8.0, 2000.

Finlayson-Pitts, B., and J. Pitts, Chemistry of the Upper and Lower Atmosphere, Academic Press, San Diego, 2000.

Galloway, J. N. and D. M. Whelpdale, An Atmospheric Sulfur Budget for Eastern North-America, *Atmos. Environ.,* **14**(4): 409-417, 1980.

Flanagan, J., R. Jayanty, E. Rickman, and M. Peterson, PM2.5 Speciation Trends Network: Evaluation of whole-system uncertainties using data from sites with collocated samplers. *J. Air & Waste Manage. Assoc.,* 56, 492-499, 2006.

Frank, N. H., Retained nitrate, hydrated sulfates, and carbonaceous mass in Federal Reference Method fine particulate matter for six Eastern U.S. cities. *J. Air & Waste Manage. Assoc.,* 56, 500-511, 2006.

Frischer T, M. Studnicka, C. Gartner, E. Tauber, F .Horak, A. Veiter, J. Spengler, J. Kuhr, and R. Urbanek, Lung function growth and ambient ozone: a 3-year population study in schoolchildren. *Am. J. Respir. Crit. Care Med.*,160, 390–396, 1999.

Gauderman W.J., G.F.Gilliland, H .Vora, E. Avol, D. Stram, R. McConnell, D. Thomas, F. Lurmann, H.G. Margolis, E.B. Rappaport, K. Berhane, and J.M., Peters, Association between air pollution and lung function growth in southern California schoolchildren: results from a second cohort. *Am. J. Respir. Crit. Care Med.*,166, 76–84, 2002.

Grell, G. A., J. Dudhia, and D. R. Stauffer, A description of the fifth-generation Penn State/NCAR Mesoscale Model (MM5). NCAR Tech. Note NCAR/TN-398 STR, 1995.

Hains, J.C., B.F. Taubman, A.M. Thompson, L.T. Marufu, B.G. Doddridge, J.W. Stehr, D.Allen, and R.R. Dickerson, Origins of chemical pollution derived from Mid-Atlantic aircraft profiles using a clustering technique, J. Geophys. Res., submitted 2007a.

Hains, J.C., L.W.A. Chen, B.F. Taubman, B.G. Doddridge, and R.R. Dickerson, A side by side comparison of filter-based PM2.5 measurements at a suburban site: A closure study, *Atmos. Environ*., in press 2007b.

Harris, J.M., and S.J. Oltmans , Variations in tropospheric ozone related to transport at American Samoa, *J. Geophys. Res.*, *102*(D7), 8781-8791, 1997.

Harrison, D., S.S. Park, J. Ondov, T. Buckley, S.R. Kim, and R.K.M. Jayanty, Highly time resolved fine particle nitrate measurements at the Baltimore Supersite. *Atmos. Environ.,* 38, 5321-5332, 2004.

Hicks, B. B., T. P. Meyers, R.P. Hosker, R.S. Artz, Climatological features of regional surface air quality from the Atmospheric Integrated Research Monitoring Network (AIRMoN) in the USA , *Atmos. Environ*., 35(6): 1053-1068, 2001.

Hodzic, A., R. Vautard, B. Bessagnet, M. Lattuaati, F. Moreto, Long-term urban aerosol simulation versus routine particulate matter observations, *Atmos. Environ*., 39, 5851-5864, 2005.

Hogrefe, C., J. Biswas, B.Lynn, K. Civerelo, J.Y. Ku, J. Rosenthal, C. Rosenzweig, R. Goldberg, and P.L. Kinney, Simulating regional-scale ozone climatology over the eastern United States: model evaluation results, *Atmos. Environ, 38,* 2627-2638, 2004.

Hopke, P.K., Receptor models in air-pollution. *Trac-Trends in Analytical Chemistry* 3, R6-R7, 1984.

IPCC Climate Change 2001: The scientific Basis, 2001.

Jorba, O., C. Perez, F. Rocadenbosch, and J.M. Baldasano, Cluster analysis of 4-day back trajectories arriving in the Barcelona area, Spain, from 1997 to 2002, *J. Appl. Meteor.*, *43*(6), 887-901, 2004

JPL Publication, Chemical kinetics and photochemical data fro use in atmospheric studies. Evaluation Number 15, JPL Publication 06-2, 2006.

Kalkstein, L.S., G. Tan, and J.A. Skindlov, An evaluation of three clustering procedures for use in synoptic climatological classification, *J. Appl. Meteor.*, *26*, 717-730, 1987.

Kelley, P., R.R. Dickerson, W.T. Luke, and G.L, Kok, Rate of NO2 photolysis from the surface to 7.6-km altitude in clear-sky and clouds, *Geophys. Res. Lett.,* 22, 2621-2624, 1995.

Kim, E., and P.K. Hopke, Identification of fine particle sources in mid-Atlantic US area. *Water Air and Soil Poll. 168*, 391-421, 2005.

Kim, E., P.K. Hopke, and Y. Qin, Estimation of organic carbon blank values and error structures of the speciation trends network data for source apportionment. Journal *J. Air & Waste Manage. Assoc.,* 55, 1190-1199, 2005.

Koch, D., D. J. Jacob, I. Tegen, D. Rind, and M. Chin , Tropospheric sulfur simulation and sulfate direct radiative forcing in the Goddard Institute for Space Studies general circulation model, *J. Geophys. Res.,104*, 23,799– 23,822, 1999.

Laden, F., L.M. Neas, D.W. Dockery, and J. Schwartz, Association of fine particulate matter from different sources with daily mortality in six US cities. *Enviro. Health Perspect.* 108, 941-947, 2000.

Lake D.A., M.P. Tolocka, M.V., Johnston, and A.S. Wexler, Mass spectrometry of individual particles between 50 and 750 nm in diameter at the Baltimore supersite. *Enviro. Sci. & Tech. 37*, 3268-3274, 2003.

Lee, G., J.T. Merrill, and B.J. Huebert, Variation of free tropospheric total nitrate at Mauna Loa Observatory, Hawaii, *J. Geophys. Res.*, *99*(D6), 12821-12831, 1994.

Lee, J.H., P.K. Hopke, T.M. Holsen, A.V. Polissar, D.W. Lee, E.S. Edgerton, J.M. Ondov, and G. Allen, Measurement of fine particle mass concentrations using continuous and integrated monitors in eastern US cities. *Aerosol Sci. and Tech.,* 39, 261-275, 2005a.

Lee, J.H., P.K. Hopke, T.M. Holsen, and A.V. Polissar, Evaluation of Continuous and filter-based methods for measuring PM2.5 mass concentration. *Aerosol Sci. and Tech.,* 39, 290-303, 2005b.

Levy, R.C., Second generation retrieval of tropospheric aerosol properties over land from inversion of visible and near-infrared spectral reflectance: Application over Maryland, Doctoral Dissertation, Atmospheric and Oceanic Science, University of Maryland, 2007.

Lippmann M., Filters and filter holders. In: Cohen BS, Hering SV, eds. Air sampling instruments for evaluation of atmospheric contaminants, 8th ed. Cincinnati, OH: American Conference of Governmental Industrial Hygienists, Inc., pp. 247-279. 1/15/98 110 NIOSH Manual of Analytical Methods, 1995.

Liu B.Y.H., D.Y.H. Pui, and K.L. Rubow, Characteristics of air sampling filter media. In: Marple VA, Liu BYH, eds. Aerosols in the mining and industrial work environments, vol. 3, instrumentation. Ann Arbor, MI: Ann Arbor Science, pp. 989-1038, 1983.

Logan, J.A., Tropospheric ozone: Seasonal behavior trends and anthropogenic influence, *J. Geophys. Res.*, *90*, 10,463-10,482, 1985.

Luke, W.T., Evaluation of a commercial pulsed fluorescence detector for the measurement of low-level SO_2 concentrations during the Gas-Phase Sulfur Intercomparison Experiment, *J. Geophys. Res.*, *102*(D13), 16255-16265, 1997.

Malm, W.C., J.F. Sisler, D. Huffman, R.A. Eldred, and T.A. Cahill, Spatial and seasonal trends in particle concentration and optical extinction in the United States. *J. Geophys. Res.*, 99, 1347-1370, 1994.

Malm, W.C., B.A. Schichtel, R.B. Ames, and K.A. Gebhart, A 10-year spatial and temporal trend of sulfate across the United States. *J. Geophys. Res.*, 107, 4627, 2002.

Malm, W.C., B.A. Schichtel, M.L. Pitchford, L.L. Ashbaugh, and R.A. Eldred, Spatial and monthly trends in speciated fine particle concentration in the United States. *J. Geophys. Res.*, 109, D03306, 2004.

Malm, W.C., D.E. Day, C. Carrico, S.M. Kreidenweis, J.L. Collett, G. McMeeking, T. Lee, J. Carrillo, and B. Schichtel, Intercomparison and closure calculations using measurements of aerosol species and optical properties during the Yosemite Aerosol Characterization Study. *J. Geophys. Res.*, 110, D14302, 2005.

Marufu, L.T., B.F. Taubman, B. Bloomer, C.A. Piety, B.G. Doddridge, and R.R. Dickerson, The 2003 North American electrical blackout: An accidental experiment in atmospheric chemistry, *Geophys. Res. Lett.*, *31*, L13106, doi:10.1029/2004GL019771, 2004

McDow, S.R., and J.J. Huntzicker, Vapor adsorption artifact in the sampling of organic aerosol : Face velocity effects. *Atmos. Environ.,* 24, 2563-2571, 1990.

Mebust, M., B. Eder, F. Binhowski, and S. Roselle, Models-3 Community Multiscale Air Qualtiy (CMAQ) model aerosol component 2. Model evaluation, *J.Geophys. Res*., 108(D6), 4184, doi:10.1029/2001JD001410, 2003.

Moody, J.L., and J.N. Galloway, Quantifying the relationship between atmospheric transport and the chemical composition of precipitation on Bermuda, *Tellus 40B*, 463-479, 1988.

Moody, J.L., J.W. Munger, A.H. Goldstein, D.J. Jacob, and S.C.Wofsy, Harvard Forest regional-scale air mass composition by Patterns in Atmospheric Transport History (PATH), *J. Geophys. Res.*, *103*(D11), 13181-13194, 1998

Moody, J.L., S.J. Oltmans, H. Levy II, and J.T. Merrill, Transport climatology of tropospheric ozone: Bermuda, 1988-1991, *J. Geophys. Res.*, *100*(D4), 7179-7194, 1995

Moy, L.A., R.R. Dickerson, and W. F. Ryan, Relationship between back trajectories and tropospheric trace gas concentrations in rural Virginia, *Atmos. Environ., 28*(17), 2789-2800, 1994.

Mueller, S.F., E.M. Bailey, T.M. Cook, and Q. Mao, Treatment of clouds and the associated response of atmospheric sulfur in the Community Multiscale Air Quality (CMAQ) modeling system, *Atmos. Environ., 40,* 6804-6820, 2006.

Nicolet, M. R.R. Meier, and D.E. Anderson, Radiation field in the troposphere and stratosphere-II. Numerical Analysis. *Planet. Space. Sci.,* 30, 935-983, 1982.

Novakov, T., D.A. Hegg, and P.V. Hobbs, Airborne measurements of carbonaceous aerosols on the East Coast of the United States, *J. Geophys. Res., 102*, 30,023–30,030, 1997.

OC/EC Laboratory Environmental and Industrial Sciences Division, Research Triangle Institute, Standard Operating Procedure for the Determination of Organic, Elemental, and Total Carbon in Particulate Matter Using a Thermal/Optical Transmittance Carbon Analyzer, 2003.

Ogulei, D., P.K. Hopke, L.M. Zhou, P. Paatero, S.S. Park, and J. Ondov, Receptor modeling for multiple time resolved species: The Baltimore supersite. *Atmos. Environ.,* 39, 3751-3762, 2005.

Ondov, J.M., T.J. Buckley, P.K. Hopke, D. Ogulei, M.B. Parlange, W.F. Rogge, K.S. Squibb, M.V. Johnston, and A.S. Wexler, Baltimore Supersite Highly time- and size-resolved concentrations of urban PM2.5 and its constituents for resolution of sources and immune responses. *Atmos. Environ.,* 40, S224-A237, 2006.

Park, R., The interaction of regional- and global-scale atmospheric chemistry, transport, and climate processes. Doctoral dissertation, Meteorology, University of Maryland, College Park, 2001.

Park S.S., D. Harrison, J.P. Pancras, and J.M. Ondov. Highly time-resolved organic and elemental carbon measurements at the Baltimore Supersite in 2002. *J. Geophys. Res.*, 110, D07S06, 2005a.

Park S.S., J.M. Ondov, D. Harrison, and N.P. Nair, Seasonal and shorter-term variations in particulate atmospheric nitrate in Baltimore. *Atmos. Environ.,* 39, 2011-2020, 2005b.

Patashnick, H. and E.G. Rupprecht, Continuous PM10 measurement using the Tapered Element Oscillating Microbalance. *J. Air & Waste Manage. Assoc.,* 41, 1079-1083, 1991.

Pathak, R.K., X. Yao, and C.K .Chan, Sampling artifacts of acidity and ionic species in $PM_{2.5}$. *Enviro. Sci. & Tech.,* 38, 254-259, 2004.

Perliski, L. and S. Solomon, On the Evaluation of Air Mass Factors for Atmospheric Near-Ultraviolet and Visible Absorption Spectroscopy. *J. Geophys. Res.,* 98 (D6) 10363-10374, 1993.

Peterson, M.R., and M.H. Richards, Thermal-Optical-Transmittance Analysis for Organic, Elemental, Carbonate, Total Carbon, and OCX2 in PM2.5 by the EPA/NIOSH Method. RTI Conference proceedings, 2002.

Peters, A., D.W. Dockery, J.E. Muller, and M.A. Mittleman,. Increased particulate air pollution and the triggering of myocardial infarction. *Circulation* 103, 2810-2815, 2001a.

Peters, T.M., G.A. Norris, R.W. Vanderpool, D.B.Gemmill, R.W.Wiener, R.W. Murdoch, F.F. McElroy, and M. Pitchford, Field performance of PM2.5 Federal Reference Method samplers. *Aerosol Sci. and Tech.,* 34, 433-443, 2001b.

Peters, T.M., R.A. Gussman, L.C. Kenny, and R.W. Vanderpool,. Evaluation of PM2.5 size selectors used in speciation samplers. *Aerosol Sci. and Tech.,* 34, 422-429, 2001c.

Pham, M., J.F. Muller, G. Brasseur, C. Granier, and G. Megie, A three-dimensional study of the tropospheric sulfur cycle, *J. Geophys. Res., 100*, 26061-26092, 1995.

Platt, U., Differential Optical Absorption Spectroscopy (DOAS) in *Air Monitoring by Spectroscopic Techniques* (M.W. Sigrist. Ed.), *Chemical Analysis Series*, Vol 127, pp.27-84, Wiley, New York, 1994.

Platt, U., Recent Developments in DOAS: an Overview. Poster presentation, Second International DOAS Workshop 2003.

Polidori, A., B.J. Turpin, H-J. Lim, J.C. Cabada, R. Subramanian, S.N. Pandis, and A.L. Robinson, Local and regional secondary organic aerosol: Insights from a year of semi-continuous carbon measurements at Pittsburgh. *Aerosol Sci. and Tech.,* 40, 861-872, 2006.

Rees, S.L., A.L. Robinson, A. Khlystov, C.O. Stanier, and S.N. Pandis, Mass balance closure and the Federal Reference Method for PM2.5 in Pittsburgh, Pennsylvania. *Atmos. Environ.,* 38, 3305-3318, 2004.

Remer, L.A., S.Gasso, D.A. Heff, Y.J. Kaufmann, and B.N. Holben, Urban/industrial aerosol: Ground gased Sun/sky radiometer and airborne in-situ measurements, *J. Geophys. Res.,* 102, 16849-46859, 1997.

Research Triangle Institute, Final data summary report for year 1 of the chemical speciation of PM2.5 filter samples project, 2000.

Restad, K., I. S. A. Isaksen, and T. K. Berntsen, Global distribution of sulfate in the troposphere: A three-dimensional model study, *Atmos. Environ., 32*, 3593–3609, 1998.

Roelofs, G.-J., J. Lelieveld, and L. Ganzeveld, Simulation of global sulfate distribution and the influence on effective cloud drop radii with a coupled photochemistry-sulfur cycle model, *Tellus, Ser. B*, 50, 224– 242, 1998

Rozanov,V.V., D. Diebel, R.J.D. Spurr, and J.P. Burrows, GOMETRAN: A radiative transfer model for the satellite project GOME, the plane parallel version, *J. Geophys. Res.,* 102(D14):16683-16695, 1997.

Ruidavets J.B., M.Cournot, S. Cassadou, M.Giroux, M. Meybeck, and J.Ferrieres, Ozone air pollution is associated with acute myocardial infarction. *Circulation,* 111, 563–569, 2005.

Russell, A., G.R. McGregor, and G.J. Marshall, An examination of the precipitation delivery mechanisms for Dolleman Island, eastern Antarctic Peninsula, *Tellus 56A*, 501-513, 2004

RTI, Quality Assurance Projects Plan Chemical Speciation of PM2.5 Filter Samples. Research Triangle Park, NC, 2004.
http://www.epa.gov/ttn/amtic/files/ambient/pm25/spec/rtiqap.pdf

Ryan, W.F., B.G. Doddridge, R.R. Dickerson, R.M. Morales, K.A. Hallock, P.T. Roberts, D.L. Blumenthal, J.A. Anderson, and K.L. Civerolo, Pollutant transport during a regional O_3 episode in the Mid-Atlantic states, *J. Air & Waste Manage. Assoc.*, *48*, 786-797, 1998.

Schmid, H., L. Laskus, H.J. Abraham, U. Baltensperger, V. Labanchy, M. Bizjak, P. Burba, H. Cachier, D. Crow, J. Chow, T. Gnauk, A. Even, H.M. Brink, K.P. Giesen, R. Hitzenberger, E. Hueglin, W. Maenhaut, C. Pio, A. Carvalho, J.P. Putaud, D.Toom-Sauntry, and H. Puxbaum,. Results of the "carbon conference" international aerosol carbon round robin test stage I. *Atmos. Environ.,* 35, 2111-2121, 2001.

Schnelle, K.B., and Dey, P.R., Atmospheric dispersion modeling compliance guide, New York: McGraw-Hill, 2000.

Schubert, S.D., R.B. Rood, and J. Pfaendtner, An assimilated data set for earth science applications, *Bul. Am. Met. Soc. 74*, 2331-2342, 1993.

Schwab, J., H. Felton, and K. Demerjian, Aerosol chemical composition in New York state from integrated filter samples: Urban/rural and seasonal contrasts *J. Geophys. Res.*, 109,(D16) D16S05, 2004.

Schwartz, J. and L.M. Neas, Fine particles are more strongly associated than coarse particles with acute respiratory health effects in schoolchildren. *Epidemiology,* 11, 6-10, 2000.

Seigneur, C., Current Status of air quality models for particulate matter, *J. Air & Waste Manage. Assoc.,* 51, 1508-1521, 2001.

Seinfeld, J.H. and S.N. Pandis, Atmospheric chemistry and physics: From air pollution to climate change, John Wiley and Sons, Inc. New York, 1998.

Solomon, P., K.Baumantt, E. Edgerton, R. Tanner, D. Eatough, W. Modey, H. Maring, D. Savoie, S. Natarajan, M.B. Meyer, and G. Norris, Comparison of integrated samplers for mass and composition during the 1999 Atlanta Supersites project. *J. Geophys. Res. 108*, 8423, 2003.

Stohl, A., G. Wotawa, P. Seibert, and H. Kromp-Kolb, Interpolation errors in wind fields as a function of spatial and temporal resolution and their impact on different types of kinematic trajectories, *J. Appl. Meteor.*, *34*, 2149-2165, 1995.

Stohl, A., Computation, accuracy and applications of trajectories – a review and bibliography, *Atmos. Environ.*, *32*(6), 947-966, 1998.

Stunder, B.J.B, An assessment of the quality of forecast trajectorie,. *J. Appl. Meteor.*, *35*, 1319-1331, 1996.

Subramanian, R., A.Y. Khlystov, J.C. Cabada, and A.L. Robinson, Evaluation of measurement methods: Positive and negative artifacts in particulate organic carbon measurements with denuded and undenuded sampler configurations. *Aerosol Sci. and Tech.,* 38, 27-48, 2004.

Taubman, B.F., L.T. Marufu, C.A. Piety, B.G. Doddridge, J.W. Stehr, and R.R. Dickerson, Airborne characterization of the chemical, optical, and meteorological properties, and origins of a combined ozone/haze episode over the eastern U.S., *J. Atmos. Sci.*, *61*(14), 1781-1793, 2004a.

Taubman, B.F., L.T. Marufu, B.L. Vant-Hull, C.A. Piety, B.G. Doddridge, R.R. Dickerson, and Z. Li, Smoke over haze: Aircraft observations of chemical and optical properties and the effects on heating rates and stability, *J. Geophys. Res.*, *109*, D02206, doi:10.1029/2003JD003898, 2004b.

Taubman, B.F., J.C. Hains, A.M. Thompson, L.T. Marufu, B.G. Doddridge, J.W. Stehr, C.A. Piety, and R.R. Dickerson, Aircraft vertical profiles of trace gas and aerosol pollution over the mid-Atlantic United States: Statistics and meteorological cluster analysis, *J. Geophys. Res.*, 111, D10S07, 2006

Technology Transfer Network Air Quality System, 2006. http://www.epa.gov/ttn/airs/airsaqs/detaildata/downloadaqsdata.htm

Tesche, T.W., R. Morris, G. Tonnesen, D. McNally, J. Boylan, and P. Brewer, CMAQ/CAMx annual 2002 performance evaluation over the eastern US, *Atmos. Envrion., 40*, 4906-4919, 2006.

Thermo Anderson, RAAS Operator's Manual. Chemical speciation monitor, 2001.

Thermo Scientific, Model 43C Pulsed fluorescence SO_2 analyzer instruction manual, 2004a.

Thermo Scientific, Model 48C UV gas filter correlation CO analyzer instruction manual, 2004b.

Thermo Scientific, Model 49C UV photometric O_3 analyzer instruction manual, 2004c.

Thornton, D.C., A.R. Bandy, A.R. Drieger, Sulfur dioxide over the western Atlantic ocean. *Global Biogeochem. Cycles,* 1, 317-328, 1987.

Tolocka, M.P., D.A. Lake, V. Johnston, and A.S. Wexler, Size-resolved fine and ultrafine particle composition in Baltimore, Maryland. *J. Geophys. Res.*, 110, D07S04, 2005.

TSI, Model 3550/3560 Series Integrating nephelometer, Instruction manual, 1997.

Turpin, B.J., J.J. Huntzicker, and S.V. Hering, Investigation of organic aerosol sampling artifacts in the Los Angeles Basin. *Atmos. Environ.,* 28, 3061-3071, 1994.

Turpin, B. J. and H. Lim, Species contributions to PM2.5 mass concentrations: Revisiting common assumptions for estimating organic mass. *Aerosol Sci. and Tech.,* 35, 602-610, 2001.

US EPA Emissions Monitoring and Analysis Division Monitoring & Quality Assurance Group, Strategic plan. Development of the Particulate Matter (PM2.5) quality system for the chemical speciation monitoring trends sites, 1999.

US EPA Office of Air Quality and Planning Standards, National Air Pollution Emission Trends, 2000.

US EPA, Model SASS & SuperSASS PM2.5 Ambient Chemical Speciation Samplers Field Operation Manual, 2001.

US EPA, National air quality and emissions trends report. 2003 Special Studies Edition, 2003.

Vukovich, F.M., Boundary-layer ozone variations in the eastern United-States and their association with meteorological variations – long-term variations, *J. Geophys. Res.*, 99, 16839-16850, 1994.

Vukovich, F.M., R. Wayland, and J.Sherwell, Characteristics of ozone in the Baltimore-Washington area as established from one-hour average concentrations, *J. Air & Waste Manage. Assoc., 49,* 794-803, 1999.

Watson, J. G., J.A. Cooper, and J.J. Huntzicker, The Effective Variance Weighting for Least-Squares Calculations Applied to the Mass Balance Receptor Model. *Atmos. Environ.,* 18, 1347-1355, 1984.

Watson, J.G., J.L. Bowen, J.C. Chow, C.F. Rogers, M.G. Ruby, M.J. Rood, and R.T. Egami, High volume measurements of size classified suspended particulate matter, in: Methods of Air Sampling and Analysis 3rd edition (J.P. Lodge), Lewis Publishers, Inc., Chelsea, MI, 1989a.

Watson, J.G., P.J. Lioy, and P.K. Mueller, The measurements process: Precision, accuracy, and validity in: Air sampling instruments for evaluation of atmospheric contaminants 7th edition, (S.V. Hering), American Conference of Governmental Industrial Hygienists, Cincinnati, OH, pp. 51-57, 1989b.

Watson, J.G. and J.C. Chow, Comparison and evaluation of in situ and filter carbon measurements at the Fresno Supersite. *J. Geophys. Res.107*, 8341, 2002.

Wayne, R.P., Chemistry of Atmospheres Third Edition, Oxford University Press, New York, 2000.

Weed, D.L., Weight of evidence: A review of concept and methods. *Risk Analysis 25*, 1545-1557. 2005.

White, M.C., R.A. Etzel, W.D. Wilcox, and C. Lloyd, Exacerbations of childhood asthma and Ozone pollution in Atlanta. *Environ Res., 65*, 56–68, 1994

Wilks, Daniel, Statistical Methods in the Atmospheric Sciences. Academic Press, San Diego, 1995.

Wong G.W., F.W. Ko, T.S.Lau, S.T. Li, D. Hui, S.W. Pang, R.Leung, T.F. Fok, and C.K.W. Lai, Temporal relationship between air pollution and hospital admissions for asthmatic children in Hong Kong. *Clin Exp. Allergy, 31*, 565–569, 2001.

Zhang, D. and R.A. Anthes, A high-resolution model of the planetary boundary layer - Sensitivity tests and comparisons with SESAME-79 data. *J.App. Meteo., 21*, 1594-1609, 1982.

Zhang, X. Q., and P.H. McMurry, Evaporative Losses of Fine Particulate Nitrates During Sampling. *Atmos. Environ.,* 26, 3305-3312, 1992.

Zhang, Y., B. Pun, S. Wu, K. Vijayaraghavan, and C. Seigneur, Application and evaluation of two air quality models for particulate matter for a Southeastern U.S. episode. *J. Air & Waste Manage. Assoc., 54*, 1478-1493, 2004.

Zhang, D.-L. and W.-Z. Zheng, Diurnal cycles of surface winds and temperatures as simulated by five boundary-layer parameterizations, *J.App. Meteo., 43*, 157-169, 2004.

Zhang, X., G. Zhuang, J. Chen, Y. Wang, X. Wang, Z. An, and P. Zhang, Heterogeneous reactions of sulfur dioxide on typical mineral particles, *J. Phys. Chem. B, 110*, 12588-12596, 2006.

ABSTRACT

Title of Document: SECOND GENERATION RETRIEVAL OF TROPOSPHERIC AEROSOL PROPERTIES OVER LAND FROM INVERSION OF VISIBLE AND NEAR-INFRARED SPECTRAL REFLECTANCE: APPLICATION OVER MARYLAND

Robert Carroll Levy, Doctor of Philosophy, 2007

Directed By: Professor Russell R. Dickerson, Department of Atmospheric and Ocean Sciences, and Dr. Lorraine A. Remer, NASA-Goddard Space Flight Center

Aerosols are major components of the Earth's global climate system, affecting the radiation budget and cloud processes of the atmosphere. When located near the surface, high aerosol concentrations lead to poor air quality, lowered visibility, increased health problems and generally reduced quality of life for the human population. This is especially true during along the U.S. mid-Atlantic region in the summertime. Satellites, such as the MODerate Imaging Spectrometer (MODIS), from their vantage point above the atmosphere, provide unprecedented global and regional views of aerosol properties that are useful for many applications. Since MODIS' first view nearly eight years ago, an incredible amount of data has been collected, each observation containing the radiative signature of global aerosol. As a result of exhaustive data validation and analyses, it became clear that much of the original

algorithm should be replaced. This dissertation describes the development of the 'second-generation' operational algorithm for retrieval of global tropospheric aerosol properties over dark land surfaces, from MODIS -observed spectral reflectance. New understanding about global aerosol properties, land surface reflectance characteristics, and radiative transfer properties were learned in the process. This new operational algorithm performs a simultaneous inversion of reflectance in two visible channels (0.47 and 0.66 μm) and one shortwave infrared channel (2.12 μm), thereby utilizing the 2.12μm channel's sensitivity to coarse aerosol. Inversion of the three channels retrieves the aerosol optical depth (τ) at 0.55 μm, the percentage of non-dust (fine model) aerosol (η) and the surface reflectance at 2.12 μm. This algorithm is applied globally and over the U.S. East Coast, retrieving τ that is highly correlated ($y = 0.02 + 1.0x$, $R=0.9$) with ground based sunphotometer retrievals. Over Maryland, specifically, retrievals of τ (a column property) are related with measurements of surface $PM_{2.5}$ concentration, using aircraft measurements and the Community Multi-scale Air Quality Model (CMAQ) model, thus characterizing the relationship of optical depth and surface aerosol properties in the region.

SECOND GENERATION RETRIEVAL OF TROPOSPHERIC AEROSOL PROPERTIES OVER LAND FROM VISIBLE AND NEAR-INFRARED SPECTRAL REFLECTANCE: APPLICATION OVER MARYLAND

By

Robert Carroll Levy

Dissertation submitted to the Faculty of the Graduate School of the
University of Maryland, College Park, in partial fulfillment
of the requirements for the degree of
Doctor of Philosophy,
Atmospheric and Ocean
Science
2007

Advisory Committee:
Professor Russell Dickerson, Chair
Dr. Lorraine Remer
Professor Zhanqing Li
Professor Rachel Pinker
Professor Raymond Hoff
Professor Shunlin Liang

Preface

If needed.

Foreword

If needed.

Dedication

For Deborah, Samantha and Jordan

To Yoram Kaufman

Acknowledgements

Lots of ‘em

To Deborah, Samantha and Jordan for their patience, their support and their love (even if Samantha, at age 3, managed to drag my entire dissertation into the ‘trash’). I love you! My parents, Ronald and Rosalind Levy, for taking the kids over weekends. Lorraine Remer and Russell Dickerson for their direction and patience. SSAI for allowing me the freedom to work on this dissertation (and pay me!) To committee members for advice and then taking the time to get through ‘the beast.’ Pete Colarco and Mian Chin for help with modeling, aerosol theory, and coding. To Jennifer Hains for letting me hang out in the Chem Lab, for putting up with all my questions, and handing me perfectly working codes! Charles Ichoku, Rich Kleidman, Santiago Gasso, Shana Mattoo for your advice, providing ears. Etc… To Alan Weinstein for his mentorship since judging my barometer building and weather forecasting ability (for 7th grade science fair); he has always pushed me toward the three letter (PhD). To Yoram Kaufman for your inspiration and the idea for the retrieval in the first place. Without your suggestion, I never would have considered going back to school.

.

Table of Contents

This Table of Contents is automatically generated by MS Word, linked to the Heading formats used within the Chapter text.

List of Tables

If needed.

List of Figures

If needed.

Chapter 1: Background and Scope of the Dissertation

1.1: Why this research?

Tropospheric aerosols significantly influence global climate, by changing the radiative energy balance [Kaufman and Chou, 1993; Hansen et al., 1997; Haywood and Boucher, 2002; Hignett et al., 2002; Jacobson et al., 2001; Ghan et al., 2002; Yu, 2006] and clouds and the hydrological cycle [IPCC, 2001; Ramanathan et al., 2001; Rosenfeld, 2000; Kaufman and Koren, 2005]. Spanning from nanometers to tens of micrometers (μm) in radius, aerosols are efficient at scattering solar radiation back to space. Their hygroscopic properties enable them to act as cloud condensation nuclei (CCN), which in turn influence cloud/precipitation processes (Toon, 2000; Rosenfeld, 2000) and global albedo [Twomey, 1977]. Also known as suspended airborne particles, or particulate matter (PM), aerosols are a component of smog and air pollution [e.g. USEPA, 2003; Chen et al., 2002; Dickerson et al, 1997] and on the list of the EPA's (recently revised) regulated criteria air pollutants (e.g. http://www.epa.gov/oar/particlepollution/naaqsrev2006.html). Aerosols reduce aesthetic visibility [Malm, 1994; Watson, 2002; Hand et al., 2000] and those less than about 2.5 micrometers (μm) in diameter (known as $PM_{2.5}$) can adversely affect human health by being ingested into lungs [Samet et al., 2000; Prospero, 1999b] or accompany disease [Mims et al., 1997].

Unlike greenhouse gases, aerosols are not well mixed in the atmosphere. They are spatially and temporally inhomogeneous, and usually concentrated near Earth's surface. Their scale height is on the order of 2-3 km, compared to the

standard 8 km atmospheric scale height. Depending on their source, their size, and their ability to react within the atmosphere, aerosols can be found near or far from their sources. Dust arising from the Saharan desert is commonly observed in the Caribbean Sea [e.g. Prospero, 1996; Levy et al., 2003], and urban aerosols from the U.S. East Coast are observed far out into the Atlantic Ocean [e.g. Dickerson et al., 1995; Fraser et al., 1972].

Over the Washington/Baltimore corridor and the rest of the U.S. mid-Atlantic region, poor surface air quality (for particulate matter) is prevalent during the summer [Kaufman and Fraser, 1981; US EPA, 2003]. These heavy aerosol events often are associated with high surface temperatures, high humidity and poor surface ozone air quality. Numerous counties in the region have annual average surface $PM_{2.5}$ concentration greater than 15 $\mu m/m^3$, meaning that they are considered in 'non-attainment' of National Ambient Air Quality Standards (NAAQS) required by the U.S. Environmental Protection Agency's (EPA). These same areas may exceed 35 $\mu m/m^3$ for 24-hour periods, also exceeding EPA requirements (revised as of September 2006). As part of the EPA's State Implementation Program (SIP), states in non-attainment (including Maryland) are required to develop plans for reducing pollution and coming into compliance with the NAAQS. The Maryland Department of the Environment (MDE; http://www.mde.state.md.us) is responsible for the effort in Maryland.

Due to their ability to scatter and absorb solar radiation, high concentrations of aerosols near the surface reduce visibility. The Interagency Monitoring of Protected Visual Environments (IMPROVE; http://vista.cira.colostate.edu/improve/)

program aims at evaluating the aesthetic impacts of pollution in our national parks. In addition, aerosols lend themselves to be studied by passive and active remote sensing techniques. The AErosol Robotic NETwork (AERONET, [Holben et al., 1998]) is a federated network of global ground-based sunphotomers, that when properly calibrated, use a simple application of the Beer-Bouger-Lambert law to measure spectral (multiple wavelengths) aerosol extinction, directly retrieving spectral τ to expected accuracies of ±0.02. Passive satellite sensors, from their vantage point above the atmosphere, provide the means for the assessment of global τ distribution [e.g. Kaufman et al., 1997a], by analyzing scattered radiation. Remotely sensed measurements of aerosol optical depth (AOD or τ) during these heavy aerosol events are on the order of 1.0 or higher (at 0.55 μm) in the region. During these events, observed visibilities may be reduced to a few miles or less.

Combining sensors and information helps to characterize aerosols on all scales, from the global radiative budget [e.g Yu et al., 2006], aerosol interactions with clouds and the hydrologic cycle [e.g. Kaufman and Koren, 2005], and with air quality and visibility at the surface. Given recent success of passive sensors to characterize global aerosols, satellite products may be able to monitor aerosols related to poor surface air quality, both globally and over the U.S. mid-Atlantic. In fact, products from both GEOstationary Satellites (GOES, [Knapp et al., 2005]) sensors and polar-orbiting (e.g. Advanced Very High Resolution Radiometer (AVHRR, [Higurashi et al., 2000; Mischenko et al., 1997; Stowe et al., 1997]) sensors can be linked to pollution events in the mid-Atlantic region [e.g. Al-Saadi et al., 2005].

However, it was not until the launch of the MODerate Imaging Spectroradiometer (MODIS, [Salomonson et al., 1989; King et al., 1993]) sensors aboard NASA's *Terra* (in 1999; [Kaufman et al, 1998]) and *Aqua* (in 2002; [Parkinson et al,. 2003]) satellites, that any expectation was made to the accuracy of products over land [e.g. Kaufman et al., 1997b]. In particular, the spectral and spatial resolution of the MODIS instrument provided significant potential for assessing both global and regional columnar aerosol properties over land. The over-land algorithm described by Kaufman et al., [1997b], in combination with an over-ocean algorithm [Tanré et al., 1996; Tanré et al., 1997] became the basis for an *operational* algorithm (near real time processing) for retrieving global aerosol properties. The products are free and available to any investigator. Not only have MODIS aerosol products been used to answer scientific questions about radiation and climate [e.g. IPCC, 2001; Yu et al., 2006], they are being used for applications not previously intended. From operational products, studies such as Chu et al., [2003], Al-Saadi et al., [2005], Engel-Cox et al., [2006] demonstrated that MODIS –derived aerosol optical depth (τ) product has the potential to monitor air quality, by estimating surface $PM_{2.5}$ concentration ($\{PM_{2.5}\}$), globally and in the mid-Atlantic region.

By 2004, enough MODIS data had been collected to enable extensive statistical evaluation of the aerosol products, both globally and regionally [Remer et al., 2005]. One facet of this analysis was comparison of MODIS-derived τ over land with τ retrieved from AERONET. Regression of this comparison (shown in Fig. 1.1) showed correlation R=0.80, and that 68% (about one standard deviation) of

τ retrieved by MODIS (τ_{MODIS}) was within expected error bars (τ_{ε}) of ground-truth (sunphotometer –observed τ_{true}), defined by Remer et al., [2005] as

$$\tau_{\varepsilon} = \pm 0.05 \pm 0.15\,\tau_{true} \qquad (1.1)$$

The quality of the comparison was said to have *validated* the MODIS τ product. However, the same analysis also showed that MODIS tended to be biased high in low τ conditions, and biased low for high τ, such that

$$\tau_{MODIS} = 0.07 + 0.78\,\tau_{true} \qquad (1.2)$$

at 0.55 μm wavelength. The regression equation was poorer for the eastern United States, such that only about 64% of MODIS τ fell within the expected error, with y-offset over 0.1. I found a similar poor regression equation as compared to a (nearly) independent set of sunphotometer data, collected during the summer of 2001 over the region [Fig. 1.2; Levy et al., 2005]. These analyses suggested that the MODIS algorithm could use some improvement.

As a first step in studying regional aerosols and their link to regional and urban-scale quality over the U.S. mid-Atlantic, it is imperative to start with MODIS products that are unbiased and show better comparison to ground truth (sunphotometer) data. Only after the MODIS products are defined properly, should they be applied to problems such as climate forcing or regional air quality. In the case of regional air quality in the mid-Atlantic, the MODIS retrievals and surface measurements may be linked through use of a chemical transport or air quality model.

1.2: Objectives of this research

I understood that globally, the MODIS aerosol algorithm over land worked remarkably well. MODIS-retrieved τ correlated with ground truth τ measured from sunphotometer, and about two-thirds (one standard deviation) of the points fall within expected error bars defined by Eq. 1.1. Yet MODIS tended to over-estimate τ for low aerosol loadings, while under-estimate for high loadings. These problems seem to be worse in many regions, including the eastern U.S. I believe it is imperative to evaluate why the algorithm fails in certain conditions, and to apply necessary changes before proceeding to any sort of application.

The original intent of this dissertation was to fix (likely by tuning) the MODIS algorithm for use over the mid-Atlantic only, and then to apply the products to help characterize aerosols in the region. However, during the process of evaluating the algorithm over the mid-Atlantic, it became clear how one might improve the *global* operational algorithm for performance over the entire globe. Therefore, the first goal of my work was to develop an algorithm that retrieves global aerosol properties over land, with low bias, and to the accuracy suggested by Eq. 1.1 [Remer et al., 2005].

Even though I am developing a global algorithm, I still require the products to be accurate over the mid-Atlantic. Therefore, I also expect to demonstrate regional accuracy by comparing to regional sunphotometer data. Only then can I feel comfortable enough to use MODIS products to help characterize the aerosol in the region.

I correlate the products of the new algorithm with surface measurements at selected sites in Maryland. For some understanding of the vertical properties of the aerosol, I look to the aircraft measurements made by the University of Maryland-

College Park's (UMCP) Piper Aztec [e.g. Taubman et al., 2004]. Finally, the measurements are compared with those calculated from results from the Community Multi-scale Air Quality Model (CMAQ) [Byun and Ching, 1999] air quality forecast model, for July and August 2002.

1.3: Organization of the dissertation

This dissertation is organized as follows. Chapter 2 introduces the fundamental physical and optical properties of aerosols, provides an overview of in-situ and remote sensing aerosol methods, and summarizes current knowledge about global aerosol and aerosol over the U.S. mid-Atlantic. MODIS, AERONET, and the physics of aerosol remote sensing are introduced in Chapter 3. Chapter 4 describes the Collection 4 aerosol algorithm and its biases globally and over the mid-Atlantic. Chapter 5 suggests some steps that would improve the MODIS retrieval, which are developed in Chapters 6 and 7. Chapter 6 concentrates on global aerosol optical models, whereas Chapter 7 introduces the assumptions of surface reflectance and inversion of spectral reflectance. Global validation is presented in Chapter 7. Chapter 8 evaluates MODIS in the context of $PM_{2.5}$ in the U.S. mid-Atlantic, combining remote sensed and in-situ measurements, from surface, aircraft and satellite, all in the context of developing 3-dimensional aerosol climatology in the region. For a specific two-month period (July and August 2002), known to have many interesting aerosol events, the CMAQ model results are analyzed in the context of the measurements. The last chapter is dedicated to conclusions and suggestions of future work.

CHAPTER 1 FIGS.

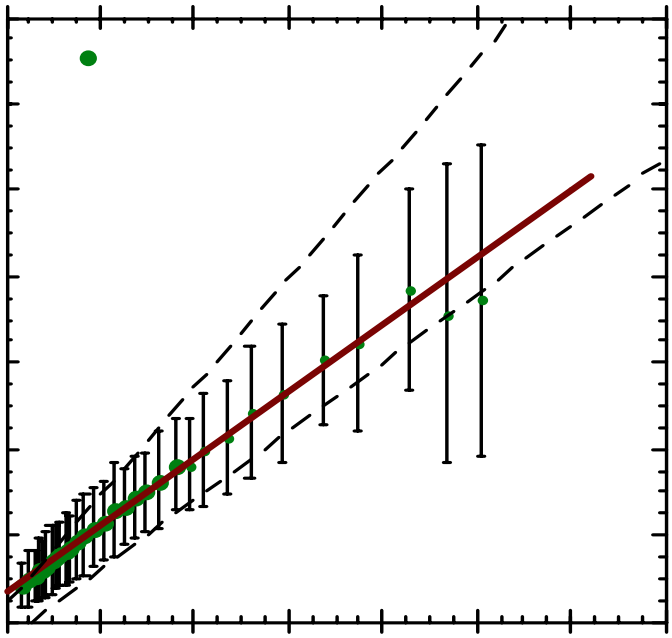

Fig. 1.1: MODIS τ (AOT) retrievals over land at 0.55 μm as a function of AERONET observations co-located in space and time. The data were sorted according to AERONET aerosol optical thickness and averaged for every 100 points. At higher optical thickness where the data become sparser, fewer points are used in the average (as indicated). The standard deviation of the MODIS – derived τ each bin is shown by the error bars. The regression (red line) equation given at the top of the plot was calculated from the full scatter plots before binning. The solid black line is the 1:1 line and the dashed lines denote the expected uncertainty calculated pre-launch. (Reproduced from Fig. 8b of [Remer et al., 2003]).

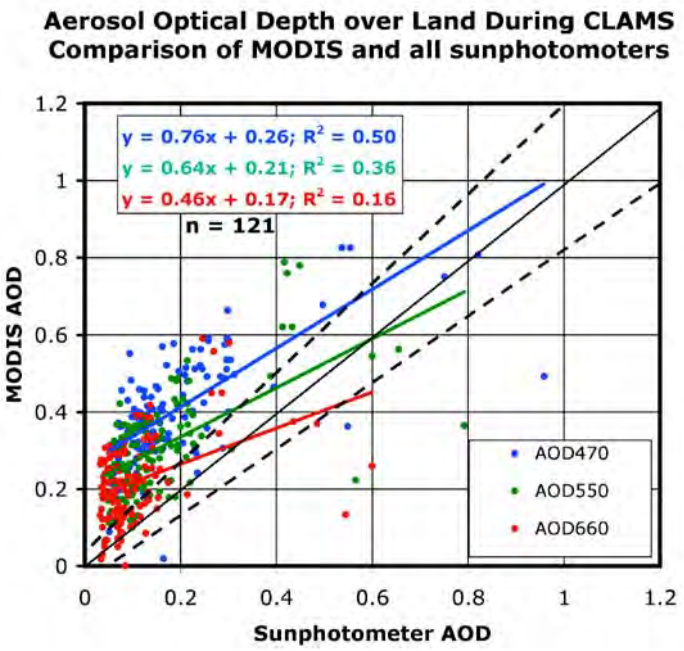

Fig. 1.2: Scatterplot of MODIS (Terra) versus sun-photometer –derived τ (AOD) over the land during the CLAMS experiment (July-August 2001 over the mid-Atlantic) for three MODIS land wavelengths (0.47, 0.55 and 0.66 μm). All sunphotometer measurements were included in this plot. MODIS data are averages for 5x5 boxes, centered on the sunphotometer site. Sunphotometer data are within ±0.5 hour of MODIS overpass. The MODIS expected error is marked by the black dashed lines, and the 1:1 line is solid black. (Reproduced from [Levy et al., 2005]).

Chapter 2: Properties of aerosols

2.1: Physical properties of aerosols

An aerosol is a system of particles, solid or liquid, in gaseous suspension. Unlike ozone or other atmospheric gases, aerosols are a mixture of particles of different sizes, shapes, compositions, and chemical, physical, and thermodynamic properties. They range in size from a few nanometers to nearly 100 μm, spanning from molecular aggregates to cloud droplets. Aerosols between about 0.1 μm and $_{2.5}$ μm in radius are of main interest to climate, precipitation, visibility, and human health studies. Most aerosols of interest are found in the troposphere and concentrated toward the Earth's surface (having a scale height of about 2-3 km).

Aerosols are normally either defined by their source or their size. The IPCC in its climate change report [IPCC, 2001] identified a number of major aerosol types, including: soil dust, sea salt, carbonaceous (both organic and black/elemental carbon), sulfate and nitrate. Much of the carbonaceous, sulfate and nitrate aerosols are produced directly from human activities (e.g. biomass burning, heating/cooking, agriculture, electricity generation and transportation). Others, such as soil dust, may be in part related to human activities as well (e.g. agriculture, land use change). Conveniently, nature has determined that aerosol sources are directly responsible for determining aerosol physical and chemical properties. *Very fine* aerosols (radius < 0.1 μm) are also known as *Aitken* particles or *ultrafine* aerosols, and are primarily formed by gas to particle conversion (*nucleation)* in oxidizing environments. The concentration of these very fine aerosols depends on numerous factors, including the

proximity of emissions, presence of reactive/oxidizing species, and atmospheric conditions (humidity, temperature, solar radiation). Very fine aerosols coagulate and combine to form *fine* aerosols between 0.1 and 1.0 μm. Aerosols in this size range may also be produced by incomplete burning during combustion processes (such as biomass or coal burning). Finally, aerosols larger than about 1.0 μm are known as *coarse* particles. These aerosols are mainly produced by mechanical erosion of the Earth's surface, including sea salt and soil dust lifted by winds. Because of their larger size (and mass), coarse particles are usually quickly settled out of the atmosphere by gravity and are concentrated close to their sources. However, if they have been lifted by convection into the prevailing winds, they may be transported far from their sources.

Ambient aerosol distributions contain all three size ranges [Whitby, 1978]. Particles in the coarse mode are small in number but contain the largest portion of aerosol mass (or volume). In contrast, the nuclei (very fine) mode encompasses the largest number, but the smallest volume (e.g. Hegg and Kaufman [1998]). The fine mode contains the largest portion of aerosol surface area. Also known as the *accumulation* mode, the fine mode has the longest residence time (days to weeks) because it neither efficiently settles nor coagulates on its own. In terms of health, fine aerosols are the most efficient at penetrating deep into the lung.

Many aerosols are *hygroscopic*, meaning that they have the ability to attract and absorb water vapor [e.g. Day and Malm, 2001; Hand et al., 2000; Malm et al., 1994; Kotchenruther et al., 1999; Gassó et al., 2003]. As water vapor is added to the aerosol, they grow until they become activated. It turns out that the size change is not

a linear function of relative humidity (RH), and that the functional dependence differs whether the RH is increasing or decreasing. Because of this hygroscopicity, the residence time for aerosols is on the same order as water vapor in the atmosphere, usually about four to fourteen days.

Generally, more hygroscopic aerosols (known as hydrophilic, e.g. sulfate or sea salt) are spherical in shape, whereas those less hygroscopic (e.g. hydrophobic, e.g. soot or dust) may be non-spherical. Non-spherical aerosols may be clumplike (soot) or crystalline (certain dusts). Fig. 2.1 displays some size and shape properties of commonly observed aerosols.

2.2: Properties of aerosol size distributions

For any size distribution of spherical particles, the number distribution as a function of radius, *N(r)*, (or more simply *N*) is related to the volume *V* and area *A* distributions by:

$$\frac{dN}{d\ln r} = \frac{3}{4\pi r^3}\frac{dV}{d\ln r} = \frac{1}{\pi r^2}\frac{dA}{d\ln r}, \qquad (2.1)$$

such that N_0, V_0, and A_0 are the amplitudes of the corresponding distributions, i.e.

$$V_0 = \int_0^\infty \frac{dV}{d\ln r} d\ln r \quad N_0 = \int_0^\infty \frac{dN}{d\ln r} d\ln r \quad A_0 = \int_0^\infty \frac{dA}{d\ln r} d\ln r \qquad (2.2)$$

and $dN/d\ln r$ is the number size distribution with r denoting radius (in μm). Note that whereas the *in-situ* community defines in terms of diameter (for example [Seinfeld and Pandis, 1998]), the remote sensing community defines as function of radius. For a single lognormal mode (e.g. [Remer and Kaufman, 1998]), the median radius of the number distribution (r_g) is related to the median radius of the volume (or mass) distribution (r_v) by

$$r_g = r_v \exp(-3\sigma^2), \tag{2.3}$$

such that the number size distribution is

$$\frac{dN}{d\ln r} = \frac{N_0}{\sigma\sqrt{2\pi}} \exp\left(-\frac{\ln(r/r_g)^2}{2\sigma^2}\right)$$

and . (2.4)

$$N_0 = V_0 \frac{3}{4\pi r_g^3} \exp\left(-\frac{9}{2}\sigma^2\right)$$

Note that within the remote sensing community, the width of the size distribution (σ) is the log of the quantity defined within the *in-situ* community. The moments of order *k*, M^k are defined as

$$M^k = \int_0^\infty r^k \frac{dN}{d\ln r} d\ln r = (r_g)^k \exp(0.5k^2\sigma^2). \tag{2.5}$$

The effective radius r_{eff} in [μm] of a lognormal mode is

$$r_{eff} = \frac{M^3}{M^2} = \frac{\int_0^\infty r^3 \frac{dN}{d\ln r} d\ln r}{\int_0^\infty r^2 \frac{dN}{d\ln r} d\ln r} = \frac{3}{4}\frac{V_0}{A_0} = r_g \exp(\frac{5}{2}\sigma^2). \tag{2.6}$$

For aerosols composed of two or more modes, integration must be over both size bin and mode. For example, if there are two modes, (i.e. modes 1 and 2), r_{eff} is

$$r_{eff} = \frac{\int_0^\infty r^3 \frac{(dN_1 + dN_2)}{d\ln r} d\ln r}{\int_0^\infty r^2 \frac{(dN_1 + dN_2)}{d\ln r} d\ln r}. \tag{2.7}$$

2.3: Aerosol optical properties

Aerosols are important to Earth's climate and radiation because of their size. Mie theory (more properly Lorenz-Mie-Debye theory: e.g. Mie, [1908]; Chandresekhar, [1950]) states that particles most strongly affect the radiation field

when their size is most similar to the wavelength of the radiation. Aerosols in the fine mode (0.1 to 1.0 μm) are similar in size to the wavelengths of solar radiation within the atmosphere, and are also the largest contributors to aerosol surface area (Fig. 2.1). Radiation incident on aerosols may be absorbed, reflected or transmitted, depending on the chemical composition (complex refractive index, *m*) and orientation (if non-spherical) of the aerosol particles. Scattering and absorption quantities [Thomas and Stamnes, 1999] may be represented as functions of path distance (the scattering/absorption *coefficients,* β_{sca}/β_{abs}, each in units of [per length]), column number (the scattering/absorption *cross sections,* $\sigma_{sca}/\sigma_{abs}$, each in units of [area]) or mass (the scattering/absorption *mass coefficients,* B_{sca}/B_{abs}, each in units of [area per mass]). The use of symbols is inconsistent within the literature, so symbols are defined for this dissertation like that of Liou, [2002]. *Extinction* (coefficient/cross section/mass coefficient) is the sum of the appropriate absorption and scattering (coefficients/cross sections/mass coefficients), e.g.,

$$\sigma_{ext}(\lambda) = \sigma_{sca}(\lambda) + \sigma_{abs}(\lambda). \qquad (2.8)$$

for the cross sections. These properties define the amount of radiation 'lost' from the radiation field, per unit of material loading, in the beam direction. Note all of the parameters are dependent on the wavelength λ. The ratio of scattering to extinction (e.g. β_{sca}/β_{ext}) is known as the single scattering albedo (SSA or ω_0). As most aerosols are nearly non-absorbing in mid-visible wavelengths (except for those with large concentrations of organic/black carbon), extinction is primarily by scattering (ω_0>0.90 at 0.55 μm). Black or elemental carbon (soot) can have ω_0<0.5 [Bond and Bergstrom, 2006] especially near sources. Mineral dusts are unique in that they have

a spectral dependence of absorption, such that they are absorbing in the short visible and UV wavelengths (λ<0.47 μm) and nearly non-absorbing at longer wavelengths.

Properties of extinction (scattering and absorption) are related to the ambient size number distribution (*N(r)*), chemical composition, and physical shape of the aerosols, as well as the wavelength of radiation. For a single spherical aerosol particle with radius (*r*), interacting with radiation of wavelength (λ), the *Mie size parameter, X*, describes the ratio of size to wavelength, $X=2\pi r/\lambda$. Finally, assuming the complex refractive index (*m+ki)*, Mie formulae yield expressions for the scattering and extinction cross sections (e.g. σ_{sca} and σ_{ext}), representing the interaction of a photon with the 'face' of the aerosol. The scattering/extinction *efficiencies* are defined per unit aerosol as:

$$Q_{sca} = \sigma_{sca} / \pi r^2 \text{ and } Q_{ext} = \sigma_{ext} / \pi r^2. \quad (2.9)$$

The scattered photons have an angular pattern, known as the *scattering phase* ($P_\lambda(\Theta)$), which is a function of the scattering angle (Θ) and wavelength. In other words, the Mie quantities describe whether an incoming photon is displaced by an aerosol, whether it is scattered, and towards which direction relative to the incoming path.

For a distribution of aerosol particles, one is concerned with the scattering by all particles within a space. In general, since the average separation distance between aerosols is so much greater than particle radius, particles are considered independent of each other. This means that if the unit volume contains *N* particles of varying *r*, the integrated cross sections are

$$\sigma_{ext} = \int \sigma_{ext}(r)N(r)dr \text{ and } \sigma_{sca} = \int \sigma_{sca}(r)N(r)dr. \quad (2.10)$$

The scattering/extinction efficiencies for a representative single aerosol are calculated by dividing by the total integrated cross section ($\int \pi r^2 N(r) dr$) of the distribution (Q_{sca} and Q_{ext}).

Light scattering by aerosols is a function of the wavelength, the aerosol size distribution, and the aerosol composition [Fraser, 1975]. Fig. 2.2 demonstrates the spectral response of aerosol scattering for a number of idealized aerosol types. Calculating the scattering properties at two or more wavelengths provides information about the aerosols' size. The Ångstrom exponent (α) [Ångstrom, 1929; Eck et al., 1999] relates the spectral dependence of the scattering at two wavelengths, $\lambda 1$ and $\lambda 2$:

$$\alpha_{\lambda 1,\lambda 2} = \frac{-\log(\sigma_{sca,p,\lambda 1} / \sigma_{sca,p,\lambda 2})}{\log(\lambda 1 / \lambda 2)}, \qquad (2.11)$$

where are two wavelengths (defined in the visible or near-infrared, for example, 0.47 and 0.66 μm or 0.87 μm). Aerosol size is inversely proportional to α, such that aerosol distributions dominated by fine aerosols have $\alpha \geq 1.6$, whereas those dominated by coarse aerosols have $\alpha \leq 0.6$. Modified Ångstrom exponents, that are quadratic fits to more than two wavelengths [e.g., O'Neill et al., 2001], can provide additional size information, such as the relative weighting of fine mode aerosol to the total (known as Fine Weighting, FW, or η).

The asymmetry parameter, g, represents the degree of asymmetry of the angular scattering, and is defined as:

$$g_\lambda = \frac{1}{2} \int_0^\pi P_\lambda(\Theta) \cos\Theta \sin\Theta d\Theta \qquad (2.12)$$

Values of g range from -1 for entirely backscattered light to +1 for entirely forward scattering. Due to the phase function's dependence on aerosol size, the asymmetry parameter also is related to aerosol size. Andrews et al., [2006] showed that aerosols at a site in Oklahoma typically have values of g (at 0.55μm) ranging between 0.6 and 0.7, the lower values in dryer conditions. They also found a strong relationship between the accumulation mode size distribution and g.

The aerosol (scattering) optical depth (AOD or τ) is the integral of the aerosol scattering or extinction coefficients over vertical path through the atmosphere, i.e.

$$\tau(\lambda) = \int_0^{TOA} \beta_{ext,p}(\lambda, z)dz \qquad (2.13)$$

where the subscript *p* is the contribution from the particles (to be separated from molecular or Rayleigh optical depth). Typically, aerosol optical depths (at 0.55 μm) range from 0.05 over the remote ocean to 1.0, 2.0 or even 5.0, during episodes of heavy pollution, smoke or dust. The sun is obscured to a ground observer when τ is greater than about 3.0. The optical depth is the fundamental aerosol quantity that can be retrieved by remote sensing.

An additional effect of aerosol scattering is on photochemistry and ozone production in the atmosphere. Dickerson et al., [1997] demonstrated how increased optical depth leads to increased photolysis, suggesting that multiple scattering due to the presence of many aerosols (with ω_0 near 1.0, like sulfate) increases the chance of photolyzation. However, absorbing aerosols (with low ω_0) will inhibit photolysis.

2.4: Aerosol Mass and Relative Humidity dependence on aerosol properties

As discussed in the previous section, the *mass extinction coefficient*, B_{ext}, represents the area extinction for a unit mass of the aerosol (literature usually reports units of [m^2/g]). It is related to the extinction efficiency Q_{ext}, effective radius, r_{eff}, and aerosol density ρ. For a distribution of aerosols, the mass extinction coefficient is defined as:

$$B_{ext} = \frac{3Q_{ext}}{4\rho r_{eff}}. \qquad (2.14)$$

[e.g. Chin et al., 2002]. Therefore, τ can be calculated by multiplying B_{ext} by the columnar aerosol mass per unit area, *M*.

Many aerosols are hygroscopic, however, so that the extinction properties of aerosols are modified by the addition of water. Observational studies show that aerosols grow with humidity [e.g. Malm, 1994], thus increasing r_{eff}. The increase is minimal at low relative humidity (i.e. < ~30%), slow and linear between 30% and 80%, and nearly exponential at RH > 80%. At RH~98%, depending on the aerosol type, that the size ratio, $r_{eff}/r_{eff,dry}$ ~2.0. Corresponding ratios of light scattering, (f_{RH}) at 0.55 μm, in humid versus dry conditions (RH~30%), range from f_{RH}~2 for RH~80% to f_{RH}~15 or more for RH~98% [e.g. Malm et al., 1994; Kotchenruther et al., 1999; Gassó et al., 2003]. Fig. 2.3 plots the f_{RH} curve assumed for sulfate aerosol within the IMPROVE program (e.g. [Malm et al., 1994; IMPROVE, 2006]). Empirical fits to the f_{RH} curve suggest something like

$$f_{RH} = \left(\frac{1 - RH_{amb}}{1 - RH_{dry}} \right)^{-\gamma} \quad (2.15)$$

where γ is a fitting exponent (on the order of 0.2-0.7, depending on aerosol type). For, example, Remer et al., [1997] suggested values of 0.35-0.50, which was later adopted by Taubman [2004] for estimating dry mass from aircraft scattering measurements.

Köpke et al., [1997] describes how one might parameterize observed f_{RH} in a chemical transport or general circulation model. Eq. 2.14 requires additional terms (relating to aerosol growth as a function of humidity) if B_{ext} should represent ambient aerosol mass extinction. For example, the aerosol mass, *M* contains both dry aerosol mass, M_{dry}, and water mass. The particle density is a linear combination of dry aerosol density and water, assuming that the volume of the water and the dry particle are additive in the solution droplets [Köpke et al., 1997], i.e.

$$\rho = \rho_{water} + (\rho_{dry} - \rho_{water}) \frac{r_{g,dry}^3}{r_g^3}. \quad (2.16)$$

Complex refractive indices used for calculating Q can be combined the same way [Köpke et al., 1997; Chin et al., 2002]. This means that ambient B_{ext} may also be represented by

$$B_{ext} = \frac{3 Q_{ext} M}{4 \rho r_{eff} M_{dry}}. \quad (2.17)$$

[e.g. Chin et al., 2002]. Q_{ext}, r_{eff}, and ρ are properties of the ambient aerosol. Optical depth (τ) can be calculated by simply multiplying by the dry aerosol mass, $M_{dry,}$ i.e [Chin et al., 2002],

$$\tau = B_{ext} M_{dry}. \quad (2.18)$$

Note that also,

$$B_{ext} = f_{RH} B_{ext,dry}. \quad (2.19)$$

2.5: Linking aerosol physical and optical properties: closure

An aerosol 'closure' study is where one attempts to characterize ambient conditions using multiple independent measurements of different aerosol properties. Some may be optical measurements (e.g. aerosol extinction or optical depth), whereas others may be physical measurements (e.g. aerosol mass or concentration). In theory, combining measurements from enough different types of aerosol measurements will completely characterize the ambient aerosol field. Yet all current instrument platforms have strengths and limitations. Therefore, appropriate models must be used to link measurement from multiple vantage points, and customized to the intended application. Applications for climate, visibility, and human health each require knowledge of different aerosol properties.

As an example, satellite retrievals of ambient (relative humidity) column τ (intended as a 'climate' product) have been shown to relate to measurements of dried (to low relative humidity) surface particulate matter (PM) concentrations ('air quality' products). Under normal (for the U.S. mid-Atlantic during the summertime) conditions where the bulk of aerosol is found within the boundary layer, τ correlates with surface $PM_{2.5}$ concentration (dry aerosol less than 2.5 μm in diameter). In fact numerous papers have empirically calculated formulas to relate the two quantities (e.g. [Chu et al., 2003; Al-Saadi et al., 2005; Engel-Cox et al., 2006]), and use as a basis for developing algorithms for monitoring and forecasting surface air quality from satellite.

While it is beneficial to note empirical correlations, it is more scientifically interesting to develop appropriate models to link optical and physical aerosol properties. For example, physically converting τ to surface $PM_{2.5}$ concentration $\{PM_{2.5}\}$ begins with understanding the mass extinction coefficient described in Eq. 2.17. To finish converting from τ to $\{PM_{2.5}\}$, one also must know the effect of measurement size cutoff compared to the theoretical (Mie) size distribution. Thus, the full conversion looks something like:

$$[PM_{2.5}] = \frac{\tau}{\Delta Z_{PBL} B_{ext}^{'}} \qquad (2.20)$$

where B_{ext}' is mass extinction coefficient appropriate for a measured (truncated) size distribution (ambient RH), which in case of $PM_{2.5}$ means aerosols less than 2.5 μm in diameter ($r < 1.25$ μm). ΔZ_{PBL} is the thickness of the surface aerosol layer (usually taken to be the boundary layer). Note the necessity of performing correct unit conversion to get $\{PM_{2.5}\}$ in units of [$\mu g/m^3$]. In a later section this calculation will be performed explicitly, linking satellite-derived τ and $PM_{2.5}$ over the U.S. mid-Atlantic.

2.6: Abridged summary of global and US mid-Atlantic aerosol properties

A quick search of the ISI's Science Citation Index (Thomson Scientific; http://www.thomsonisi.com/) yields thousands of articles relating to 'aerosol', suggesting an exhaustive survey of all aerosol-related literature is impossible. This section, however, provides a very, very short summary of global and U.S. mid-Atlantic aerosol properties in the literature.

2.6.1 Global aerosol properties

The IPCC [IPCC, 2001] determined that aerosols that interact with climate and radiation include sulfate, nitrate, carbonaceous (both organic carbon and elemental/black carbon), sea salt and dust. Globally, the largest 'emitter' of aerosols is the ocean's surface, emitting on the order of 5000 Tg (Tg = 10^{12} grams) per year [e.g. Chin et al., 2002]. However, these are primarily coarse sized aerosols, such that they are immediately returned to the ocean. Therefore, their number concentration ($<500 m^{-3}$) and total optical depth (< 0.15) are much smaller in magnitude than values over continents. From the continents, dust aerosol emitted mass is a distant second to sea salt, on the order of 1600 Tg/year [Chin et al., 2002]. However, as dust arises from much more concentrated sources (primarily topographic depressions in deserts), its concentrations and optical depths can be much, much higher. Values of $\tau > 2.0$ are not uncommon over areas near and downwind of major dust sources (e.g. Cape Verde Islands off the coast of the Sahara desert in Africa). Like sea-salt, dust aerosols are primarily coarse in size ($r > 1.0$ μm). Sea salt is hydrophilic, while most dusts are generally hydrophobic. Single scattering albedos for sea-salt are generally agreed to be nearly unity, whereas there is debate among the values for dust. Most recent

literature suggests that most dust shows ω_0 spectral dependence, from $\omega_0<0.90$ in the ultraviolet and deep blue ($\lambda < 0.47$ μm), to $\omega_0>0.95$ in visible and near-infrared wavelengths, although it depends on the specific source and aging of the dust. Visually, some dust is yellow, where others are orange, or brown in color, suggesting variability of its optical properties.

Among the aerosol types considered to be clearly influenced or dominated by anthropogenic processes, organic aerosols come next on the list for global emitted mass [Chin et al. 2002], about 100-120 Tg/year. These include emissions from biomass burning (forest clearing for agriculture) in the tropics, and local and regional emissions from transportation and industry. These are often separated into *organic* carbon (OC) and *elemental* (*black*) carbon (EC or BC), as they represent aerosols with very different refractive indices, densities and hygroscopic properties. OC aerosols generally have ω_0~0.95 or more, are hydrophilic, and result from complete combustion processes. BC, often found in soot, arise from incomplete fuel combustion processes (e.g. wood or oil heating, cooking, diesel combustion, flaming combustion). BC may have $\omega_0<0.5$ or even $\omega_0<<0.5$, depending on the measurement [Bond et al., 2006], and are usually hydrophobic. Most of the OC and BC mass is contained as fine-sized aerosols. Biomass burning aerosols close to the source can be very dense, having $\tau > 2.0$ or even more. In special cases, due to the extreme heating within a burning area, these aerosols may be lofted high enough into the atmosphere to be transported long distances.

Finally, also dominated by fine mode, are the sulfate and nitrate aerosols. Primarily formed by oxidation of SO_2 and NO_2, respectively, sulfate and nitrate are

primarily the result of manmade activities. Except for emissions from biological processes in the ocean, and emissions from low altitude volcanoes, most tropospheric sulfate and nitrate are related to electrical generation (coal fired power plants), industry, and agriculture (fertilizing processes). These aerosols are emitted globally at the rate of ~40 Tg/year [Chin et al., 2002]. Easily combined with ammonium, as ammonium sulfate or ammonium nitrate, these hydrophilic aerosols ($f_{RH} > 2$ in RH > 80% conditions) have similar scattering properties (ω_0>0.95). As these aerosols age, in is not uncommon to observe $\tau > 1.0$ in polluted conditions. In fact, much of the particle pollution in the Eastern U.S. and Western Europe are compounds of sulfate and nitrate.

Of course, aerosols representative of a region may be transported into other regions. Fraser et al., [1984] attempted to measure aerosol mass transported from the U.S. into the Atlantic, using Geostationary Satellite (GOES) satellites. Saharan dust is found in the Caribbean Sea [e.g. Prospero, 1996; Levy et al., 2003; Colarco et al., 2003], whereas Asian dust and pollution is found over the United States [e.g. Chin et al., 2003; Heald et al., 2006]. Also, depending on meteorology, aerosol types may be mixed with each other, thus eliminating most distinguishing optical and physical features. For example, eastern Asia can be a soup of dust, pollution and smoke. Choudhary et al., [submitted 2007] found that fine aerosols over Xianghe (southeast of Beijing, China) during the early spring were characteristic of pollution mixed with soot, whereas coarse aerosols indicated dust mixed with soot. They measured bulk ω_0 ~ 0.80, but varied widely on a daily basis.

Global simulations of aerosol in climate transport models suggest that the largest optical depth values ($\tau > 0.5$ on a monthly basis) are persistent over Saharan Northern Africa and directly downwind into the eastern Atlantic Ocean. These high values are dominated by dust. Other 'hotspots' of elevated τ include: over and downwind of the Eastern U.S. and Europe (primarily sulfate), Southern Africa and South America (OC and BC), eastern Asia (a mix of everything: dust, sulfate and carbon), and the Indian Ocean (the 'Asian Brown Cloud' [e.g. Ramanathan et al., 2003]). Fig. 2.4 displays a simulation of monthly averaged τ for July 2002, provided by the Georgia Tech-Goddard Global Ozone Chemistry Aerosol Radiation and Transport model (GOCART; [Chin et al., 2002]). Shown are the optical depths contributed by each major aerosol type (dust, seasalt, OC, BC, sulfate and the grand total).

2.6.2 U.S. mid-Atlantic aerosol properties

In the eastern U.S., aerosols are dominated by hydrophilic sulfate (~50%; e.g. [Russell et al., 1999]), with f_{RH} (80% vs 30%) on the order of two or more (e.g. Kotchenruther, [1999]; Malm et al., [1994]; Gassó et al., [2003]). Deviations from this growth factor are due to the history of the aerosol field, owing to the interaction between sulfate with clouds as well as other aerosols. Carbonaceous (BC and OC) represents most of the remaining aerosol fraction (e.g. Novakov et al., [1999]; Chen et al., [2002]), with relatively small contributions from dust and seasalt. Total annually averaged $PM_{2.5}$ concentrations are on the order of 13-15 $\mu g\ m^{-3}$, depending

mainly on urban density near the monitoring site. There is some indication that total PM loadings in the region may be dropping [US EPA, 2003].

The EPA has designated areas in the mid-Atlantic as *PM supersites*, including Baltimore, Maryland. This is an ambient monitoring research program intended to address the scientific uncertainties associated with fine particulate matter. Most of the research concentrates on highly time resolved surface filter measurements for mass and chemical apportionment for source determination (e.g. Ondov et al., [2006]; Frank, [2006] and Lake et al., [2003]).

Chen et al., [2002; 2003] performed analysis and speciation of fine aerosol ($PM_{2.5}$) mass at Fort Meade, Maryland (FME, about halfway between Baltimore, MD and Washington, D.C.) during 2000, and found that sulfate dominates in summer (>50%), but drops to 30% in the winter and spring. Carbonaceous aerosols (both OC and BC) accounted for 30-45% of the aerosol mass, whereas seasalt and dust accounted for less than 5%. Through back-trajectory and chemical analyses, Chen et al., [2002] determined that most of the sulfate is aged and regional, arising from upwind sources, whereas the carbonaceous aerosols are locally produced, the result of wood burning and transportation. During heavy haze episodes, $PM_{2.5}$ concentrations can reach 45 $\mu g\ m^{-3}$ or greater, such that water within the aerosol contributes >40% to the total extinction [e.g. Chen et al., 2003]. Hains et al., [submitted, 2007] continued analysis of speciated and total $PM_{2.5}$ at FME. Another set of measurements at Wallops Island, Virginia during the summer of 2001 [Castanho et al., 2005] suggested that out of total measured fine particle mass at the ground, on average ~55% was sulfate, ~3% was BC, ~6% was dust, and the most of the rest was likely

composed of OC. However, sulfate can contribute nearly 70% of fine aerosol mass during heavy regional pollution, like that observed on July 17, 2001 at Wallops Island.

Coordinated regional intensive experiments, such as the Tropospheric Aerosol Radiative Forcing Operational Experiment (TARFOX, [Russell et al., 1997]), the Chesapeake Lighthouse and Aircraft Measurements for Satellites (CLAMS, [Smith Jr. et al., 2005]) have shown that the bulk of aerosol is found in the planetary boundary layer (PBL). The thickness of the PBL is governed by the strength of convection, and it varies diurnally. During the peak of afternoon heating in the summer time, the bulk of aerosol over mid-Atlantic is found in a PBL that is on the order of 2-3km (e.g. [Redemann et al., 2000; Gasso et al., 2003]). In most cases, there is some variability of the aerosol size and aerosol complex refractive index in the aerosol layer [Redemann et al., 2000], suggesting that the composition of the aerosol changes with altitude. Regular aircraft measurements, as part of the Regional Atmospheric Measurement Modeling and Prediction Program (RAMMPP, [http://www.atmos.umd.edu/~RAMMPP], have been made over many years, further characterizing the vertical structure of aerosol physical and optical properties [e.g. Taubman et al., 2006]. Fig. 2.5 displays a photo of a haze layer, taken aboard the University of Maryland's (UMD) Piper Aztec. Fig. 2.6 is adapted from Taubman's dissertation [2004], displaying the statistics of the vertical structure of ω_0 and α measured in the mid-Atlantic (biased toward polluted conditions).

In heavily polluted (sulfate dominated) conditions, aerosol optical depths may be $\tau>1.0$. Fig. 2.7 shows a time series (June 2002-June 2003) of daily averaged τ (at

0.55 μm) from (Level 2; quality controlled) data collected from AERONET sunphotometers at the Maryland Science Center (MD_Science_Center) in Baltimore, compared with daily averaged surface $\{PM_{2.5}\}$ measured by an EPA Federal Reference Monitor (FRM) also in Baltimore (Old_Town). There is a strong seasonal dependence of τ, with maximum τ during the summer time. These values are also associated with highest values of columnar water vapor (>4.0 cm) as derived by AERONET [e.g. Holben et al., 2001]. Derived 440 μm -870 μm Ångstrom exponents show large spectral dependence on average ($\alpha \sim 1.55$) indicating dominance of fine sized aerosols. There is a seasonal dependence of α, ranging from $\alpha \sim 1.8$ in the summertime to $\alpha \sim 1.2$ in the spring. Presumably, the springtime minimums are associated with the presence of transported Asian coarse dust aerosols [e.g. Chin et al., 2003]. Derived fine aerosol fractions (also from AERONET) also indicate seasonal dependence, ranging from ~90% in the summertime to ~70% in the spring. The seasonal dependence of surface $\{PM_{2.5}\}$ is also present, although it is much noisier. Annual averaged values of τ and $\{PM_{2.5}\}$ (for one year; June 2002-May 2003) are 0.24 and 16.7 $\mu m \cdot m^{-3}$ (above NAAQS), respectively.

While the average and normal variability of aerosol properties is well characterized in the region, there are cases with unexpected aerosol properties. During CLAMS, Castanho et al., [2005] observed that dust contributed 40% of the total fine aerosol mass at Wallops Island during an incursion of Saharan dust between July 24 and 26, 2001. At other times, smoke from biomass burning in Canada can flow into the region by strong northwesterly winds. For example, during July 6 and 9, 2002, extremely dense smoke was transported at high altitudes (> 3km) from northern

Quebec [e.g. Taubman et al., 2004; Vant-Hull et al., 2005; Colarco et al., 2005]. This episode was marked by extremely high optical depth ($\tau > 5.0$), slightly lower than normal ω_0 (~0.90) and except for one day, very little evidence for it at surface PM monitors. As part of RAMMPP, the UMD aircraft flew during the episode, and demonstrated that this heavy aerosol event was not a result of a stagnant summertime air mass, the usual environment for buildup of the mid-Atlantic's soup of sulfate and organic carbon.

In contrast to heavy aerosol events, the UMD aircraft also has flown through unusually light aerosol events. On August 15, 2003, much of the Eastern United States was affected by a near total blackout of the electrical grid. This 2003 electrical blackout event later became known as the 'accidental experiment in atmospheric chemistry' [Marafu et al., 2004], providing a unique opportunity to evaluate the contribution of power plant emissions to regional haze. With the UMD aircraft, they measured vertical profiles of the aerosol at two locations. Marafu et al., [2004] found that without the normal burden of power plant emissions, the relative scattering and extinction properties of the aerosol column were substantially lower than would be expected in similar meteorological conditions. Yet absorption remained normal. This suggested that since local source contributions to PM (transportation and the like) were unaffected by the blackout, carbonaceous aerosol, not sulfate, was dominating the measured aerosol signal.

CHAPTER 2 FIGS.

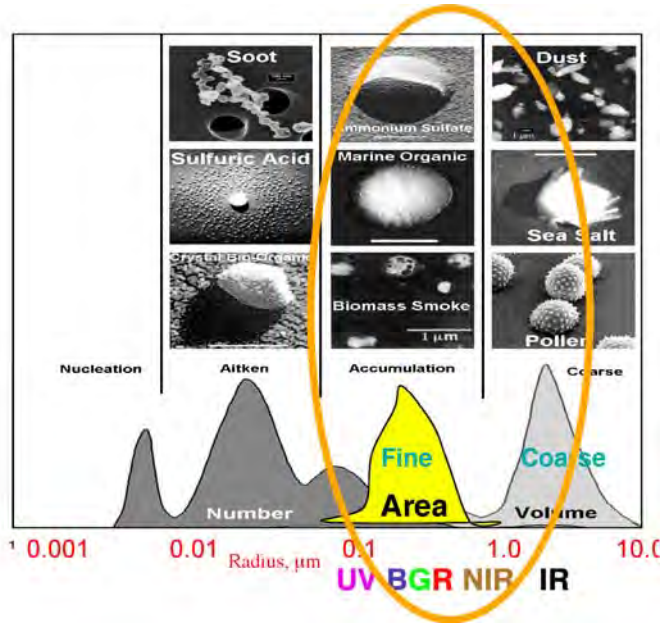

Fig. 2.1: Properties of some global aerosol types, from physical and optical perspectives. Electron microscope pictures of aerosol shape binned by their approximate radius. The orange oval encompasses the aerosol types that interact with solar radiation with wavelengths listed below the x-axis. The moments of 'number', 'area' and 'volume' represent which particle size dominates in that distribution; the 'area' distribution dominates the shortwave signal. Within the remote sensing community, 'fine' and 'coarse' aerosol are roughly analogous to the 'accumulation' and 'coarse' modes known within the in-situ community. This figure is modified from the Figure 1 of Heintzenberg et al., [2000].

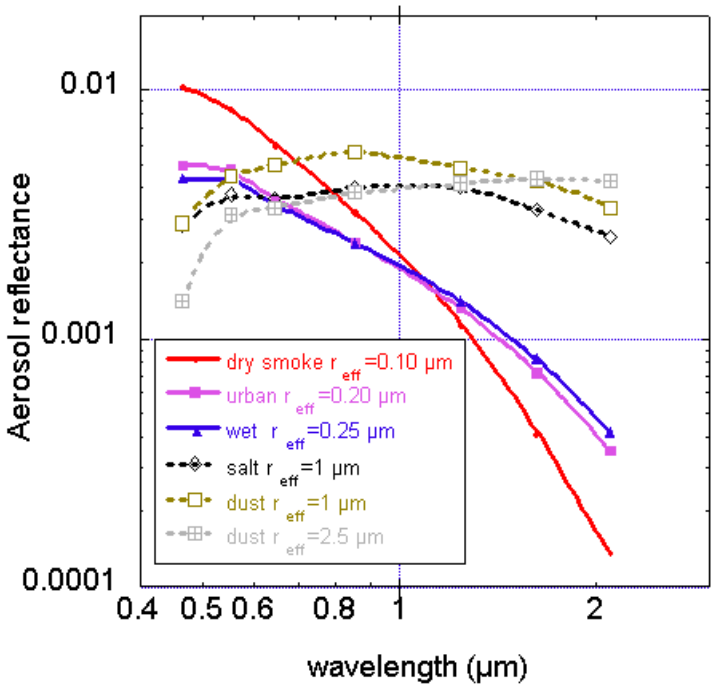

Fig. 2.2: Spectral dependence of selected aerosol types viewed from the top of the atmosphere. (Fig. reproduced from Yoram Kaufman)

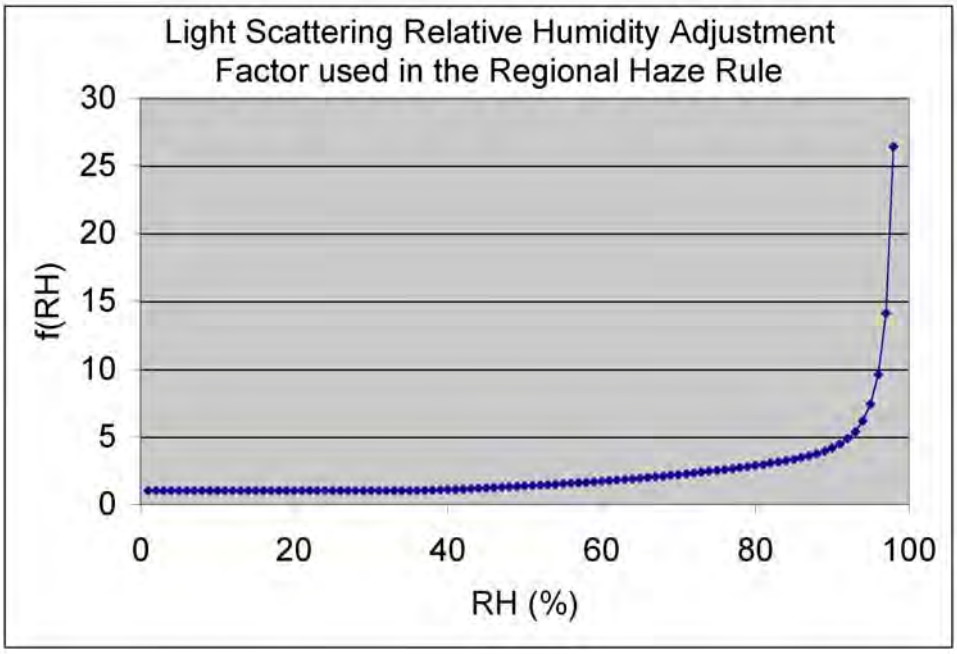

Fig. 2.3: Relative humidity dependence of the scattering coefficient used in the regional haze rule (IMPROVE). Fig. adapted from that on the IMPROVE web site.

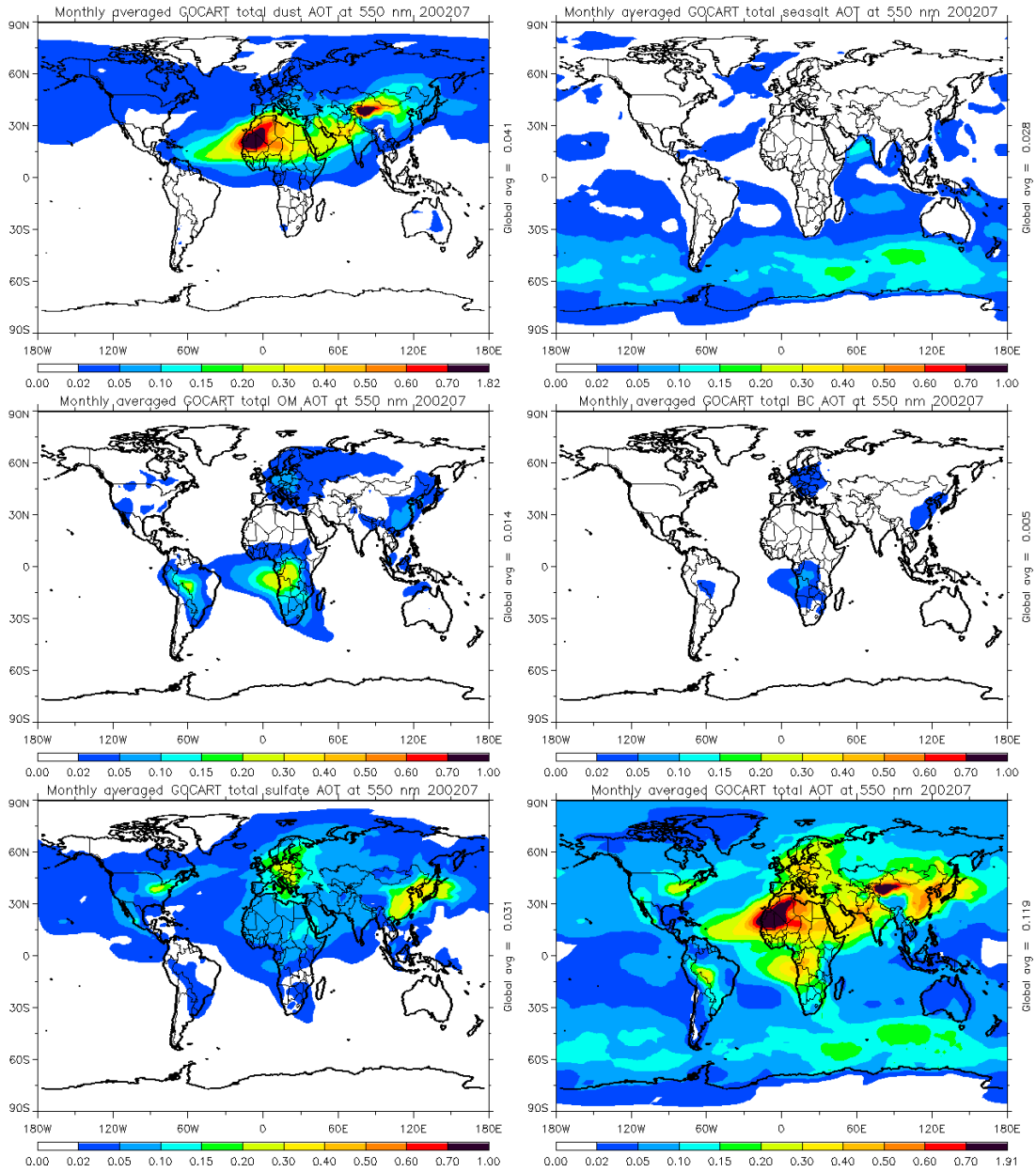

Fig. 2.4: Monthly averaged τ (AOT), under all sky conditions, simulated by GOCART for July 2002. Simulated are τ for dust, seasalt, organic matter (OM), black carbon (BC), sulfate and total.

Fig. 2.5: Photograph of mid-Atlantic haze taken aboard the UMD Piper Aztec. Marafu, Doddridge, Taubman et al.,

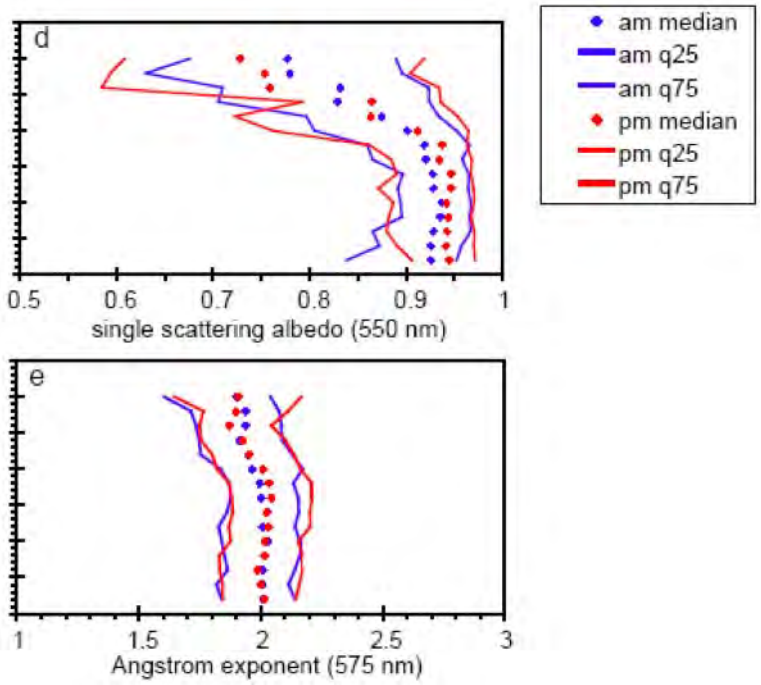

Fig. 2.6: Median values calculated every 100 m from all morning (blue, before Noon Local Standard Time, LST) and afternoon (red, after Noon LST) profiles for d) single scattering albedo at 0.55 μm (122 morning profiles, 138 afternoon profiles), and e) Angstrom exponent at 0.575 μm (142 morning profiles, 153 afternoon profiles). The solid lines indicate the 1st and 3rd quartiles for the morning (blue) and afternoon (red) profiles. Fig. adapted from Taubman et al., [2005].

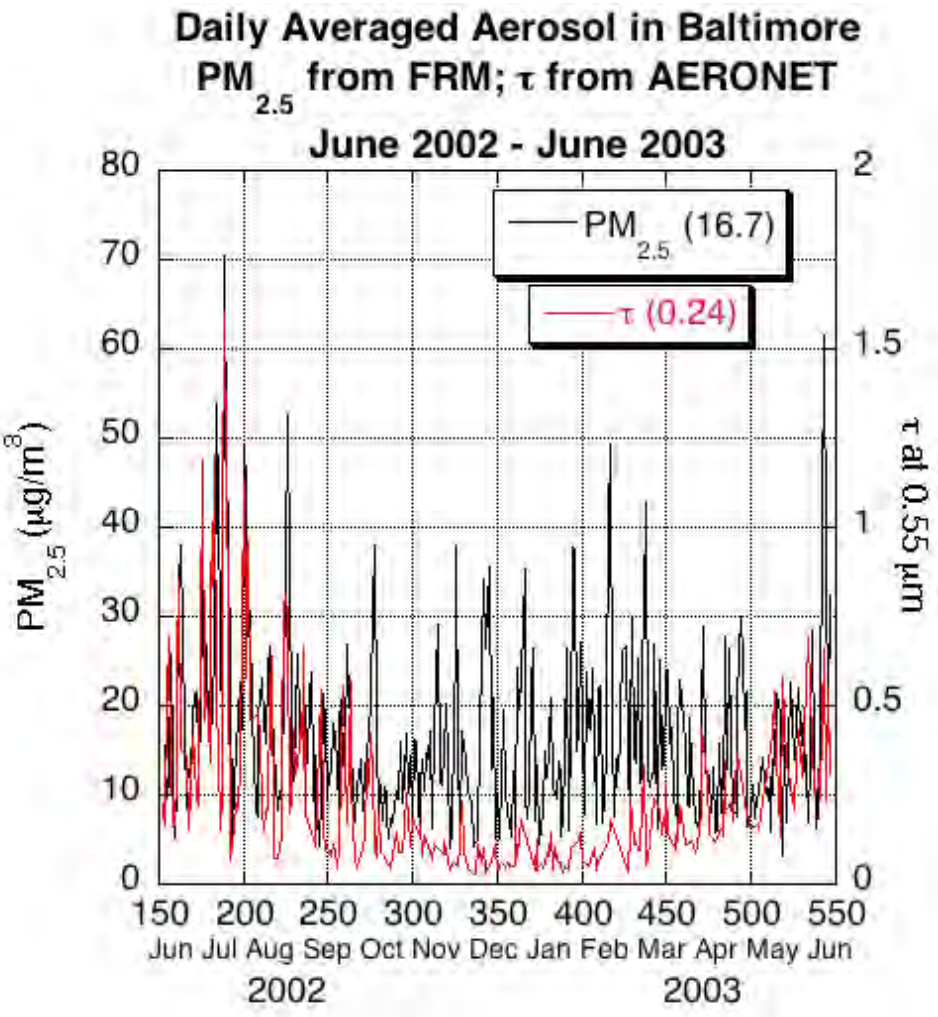

Fig. 2.7: Daily average τ (at 0.55 μm) observed by AERONET sunphotometer (red), compared with daily {$PM_{2.5}$} from the EPA-FRM monitor (black), in Baltimore, between June 2002 and June 2003. The yearly mean (June-May) of each dataset are given in parentheses in the legend. The AERONET data are Level 2 (quality controlled).

Chapter 3: Aerosol measurement techniques

3.1: Aerosol measurement overview

Numerous techniques are used to observe and quantify aerosol physical and chemical properties [e.g., Seinfeld and Pandis, 1998], either *in-situ* or by remote sensing. Each of these techniques may be passive (operating under ambient conditions) or active (perturbing the conditions in some way). Combined surface and airborne measurements provide profiles of aerosol properties such as loading, size distribution, and chemistry. For example, aerosol mass concentrations at the surface may be measured by weighing filters before and after aerosol collection. In fact, the EPA calls for the use of the Federal Reference Method (Code of Federal Regulations (CFR), 1997) for the measurement of filter based, gravimetric $PM_{2.5}$ mass to determine compliance to NAAQS. Aerosol size distributions are determined by setting filter sizes to selectively collect aerosols of certain diameters (e.g. 2.5 μm) Subsequent laboratory analyses can be used to determine chemical properties. Different protocols have been used extensively in other non-NAAQS air quality monitoring projects, such as the Speciation Trends Network (STN), [US EPA, 1999], and the Interagency Monitoring and Protective Visual Environment network (IMPROVE), [Ames and Malm., 2001; Malm et al., 2004]).

Other in-situ techniques measure extinction of radiation, by measuring the optical properties to infer aerosol properties. These active instruments emit radiation into a container or filter of aerosols, collected by pumping (usually warmed and dried) air (containing aerosols) through an inlet. In fact, both types of instruments

were present aboard the UMD research aircraft. A nephelometer [e.g. Anderson et al., 1996] attempts to retrieve part of the aerosol scattering phase function at one or more wavelengths (nominally 0.45, 0.55 and 0.70 μm), by shining light into a cavity, and measuring the signal at specific angles. The Particle/Soot Absorption Photometer (PSAP, Radiance Research, Seattle, WA) attempts to retrieve aerosol absorption properties by measuring the absorption of an emitted 0.565 μm light beam as it passes through a filter subjected to ambient aerosol deposition. In either case, the aerosols must be brought into the instrument and may be dried, de-iced, or otherwise modified before measurement. While these *in-situ* instruments are appropriate for measuring properties of dry aerosols, they may not represent the properties of ambient aerosol.

Remote sensing techniques measure the ambient (undisturbed) aerosol field. Like in-situ techniques, remote sensing also includes ground based and airborne measurements. Radiometers of various types measure different components of the solar radiation field. The simplest technique is sunphotometry [Volz, 1959], where the solar disc is observed through a collimator. When calibrated and pointed properly, the sunphotometer applies the Beer-Bouger-Lambert law to accurately measure extinction at one or more wavelengths. Water vapor, ozone and Rayleigh effects can be removed to yield the aerosol optical depth (to within expected error of ±0.02). Fig. 3.1 displays a schematic of the sunphotometer measurement, using a Cimel Electonique (Cimel) instrument. Spectral dependence of τ (or α) can then be related to aerosol size distribution. Examples include the global automated Cimel instruments of the AERosol Robotic Network (AERONET) [Holben et al., 1998; Holben et al., 2001], the accurate portable handheld Microtops instruments [Morys et

al., 2001; Ichoku et al., 2002b], and the Automated Airborne Tracking Sunphotometer (AATS) [Ehasani et al., 1988; Redemann et al., 2005]. Scattered sky radiance measurements from AERONET have been used to determine aerosol size distributions [Kaufman et al., 1994; Nakajima et al., 1996; Dubovik and King, 2000; Dubovik et al., 2003]. Yet, like the *in-situ* techniques, most sunphotometer measurements lack spatial and temporal representation. They do not operate at night. Sunphotometer –derived τ is not necessarily representative of surface concentrations or profiles (except when measured directly by the AATS). Also, sunphotometers cannot determine aerosol properties in between sites.

Passive satellite sensors are uniquely able to retrieve aerosol information on a regional and global scale [Kaufman et al., 1997a; King et al., 1999; Kaufman et al., 2002]. Using measurements of the spectral radiance exiting the Earth system, properties of atmospheric aerosols can be inferred, especially at certain wavelengths, where the surface contribution or other atmospheric contributions can be neglected or assumed. Aerosol properties are retrieved by comparing the observed radiance with a lookup table (LUT) of radiance values simulated by radiative transfer (RT) codes. Whitby [1978] showed that in-situ aerosol size distributions are accurately modeled by three *log-normal* distributions with appropriate parameters. O'Neill et al., [2001] showed that remote sensed aerosol distributions also are log-normal, convenient for creating the satellite LUTs. Troposopheric aerosol properties have been operationally retrieved from passive (non-emitting), nadir-viewing, polar-orbiting satellite sensors, such as the Advanced Very High Resolution Radiometer (AVHRR) [Stowe et al., 1997; Husar et al., 1997; Higurashi et al., 2000], and the Total Ozone Mapping

Sensor (TOMS) [Herman et al., 1997; Torres et al., 1998; Torres et al., 2002], both of which have been flown on a variety of satellites over the past two decades. Other passive sensors that are or have been used to retrieve aerosol properties, operationally, include the family of polarization sensing instruments (e.g. the POLarizaiton and Directionality of the Earth's Reflectance – POLDER, [Deuze et al., 1997]), the family of geostationary sensors [e.g. Global Aerosol and Smoke Product – GASP, e.g. Knapp et al., [2005]), and multi-angle instruments such as MISR [Diner et al., 1998]. These sensors are not ideal, however, because they lack the temporal, spatial and/or spectral resolution necessary for deriving global and regional scale aerosol properties.

LIght Detection And Ranging (LIDAR or lidar) is an example of 'active' remote sensing capable of detecting aerosol properties. Instead of using ambient radiation, a lidar transmits light out to a target. The light that is reflected / scattered back to the instrument includes aerosol signal. Lidars are usually ground-based (e.g. Micro-Pulse Lidar – MPL [Welton et al., 2001] or Raman Lidar, http://ramanlidar.gsfc.nasa.gov/), but may be deployed on aircraft or in space (like the Cloud-Aerosol Lidar and Infrared Pathfinder Satellite Observation (CALIPSO); http://www-calipso.larc.nasa.gov/). Lidars present a unique view of the vertical structure of the aerosol, but their measurements are usually limited to a single thin horizontal column (no spatial resolution).

Measurements from all instruments should all be considered for understanding the 4-dimensional (including time) properties of aerosol, globally, regionally and locally (e.g. Kim et al., [2006]). Ideally, these measurements should be evaluated and

compared within a modeling framework to understand the physical and chemical processes that occur with aerosols. This thesis, however, focuses on passive remote sensing as the central to the aerosol characterization effort.

3.2: Passive aerosol remote sensing

Passive remote sensing of ambient tropospheric aerosol properties operates on the concept that solar radiation is modified as it interacts with the atmosphere (by gases and aerosols) and the surface [e.g. Kaufman et al., 1997b]. The simplest conceptual measurement is derivation of the optical depth via observation of the direct beam of solar radiation through a collimated radiometer (known as a sunphotometer) in clear skies [e.g. Volz, 1957]. This measurement assumes that the radiation has had little or no interaction with the surface or clouds, and that there is minimal (or known) gas absorption in the chosen wavelength, λ. In other words, sunphotometry is a basic application of the Beer-Bougeur-Lambert law, in the form of:

$$L_\lambda(\theta_0) = F_{0,\lambda}(\theta_0, d)\exp[-\tau^t_\lambda m^t(\theta_0)] \qquad (3.1)$$

where L, F_0, d, θ_0, τ^t, and m are the measured solar radiance, extra-terrestial solar irradiance (irradiance outside the atmosphere), ratio of the actual and average Earth/Sun distance, solar zenith angle, total atmospheric optical depth, and total relative optical air mass, respectively. The factor $\tau^t m^t$ is the only unknown (the other parameters can be calculated), and it can be further broken down as:

$$\tau^t_\lambda m^t = \tau^R_\lambda m^R + \tau^a_\lambda m^a + \tau^g_\lambda m^g \qquad (3.2)$$

where the superscripts t, R, a and g refer to total, molecular (Rayleigh scattering), aerosol and gas absorption (variably distributed gases such as H_2O, O_3, NO_2, etc). The relative optical air masses of each component differ due to differing vertical distributions. The molecular portions of Eq. 3.2 are dependent only on the altitude of

the surface target, and can be accurately calculated (e.g. Bodhaine et al., [2003]) and the gas absorption portion, while less spatially homogenous can be reasonably estimated. Therefore, since errors are well defined, estimation of aerosol optical depth (τ^a, or hereby simplified as τ) is straightforward from a sunphotometer. Except for instrument calibration and uncertainties due to cloud screening, estimates of τ from sunphotometer should be within ±0.02 [e.g. Holben et al., 1998]. When made at more than one wavelength, sunphotometers retrieve spectral (wavelength dependent) τ, which in turn can be used to characterize the relative size of the ambient aerosol [e.g. Eck et al., 1999; O'Neill et al., 2003].

Instead of pointing directly at the sun, collimated radiometers can be pointed at discrete points in the sky to observe scattered sky radiance. Requiring additional assumptions as to aerosol shape, interaction with the surface and multiple scattering processes, properties of aerosol size distribution and scattering/extinction properties can be retrieved from these sky radiance measurements (e.g. Nakajima et al., 1996; Dubovik et al., 2000; Dubovik et al., 2002b). In essence, this technique boils down to retrieval of the spectral aerosol scattering phase function, $P_\lambda(\Theta)$, from measurements of the scattering angle dependence of the sky radiance. The scattering angle, Θ, is defined as:

$$\Theta = \cos^{-1}(-\cos\theta_0 \cos\theta + \sin\theta_0 \sin\theta \cos\phi), \qquad (3.3)$$

where θ_0, θ and ϕ are the solar zenith, target view zenith and relative solar/target relative azimuth angles, respectively (illustrated in Fig. 3.2).

Tropospheric aerosol properties may also be retrieved from satellite measurements of backscattered radiation [Kaufman et al., 1997a]. Instead of radiance,

satellite algorithms make use of normalized spectral solar radiance, or *reflectance,* ρ_λ, defined by

$$\rho_\lambda = L_\lambda \frac{\pi}{F_{0,\lambda} \cos(\theta_0)}. \qquad (3.4)$$

Because the backscattered radiation includes multiple contributions from the atmosphere and surface, reasonable assumptions must be made to separate them. The upward spectral reflectance observed by a satellite at the top of the atmosphere (TOA) is a function of successive orders of radiation interactions within the coupled surface-atmosphere system. The observed spectral reflectance results in a combination of processes, including: scattering of radiation within the atmosphere without interaction with the surface (known as the 'atmospheric path reflectance'), the reflection of radiation off the surface that is directly transmitted to the TOA (the 'surface function'), and the reflection of radiation from outside the sensor's field of view (the 'environment function'). The environment function is neglected so that to a good approximation, the angle dependent TOA reflectance at a wavelength λ is described by:

$$\rho^*_\lambda(\theta_0, \theta, \phi) = \rho^a_\lambda(\theta_0, \theta, \phi) + \frac{F_{d,\lambda}(\theta_0) T_\lambda(\theta) \rho^s_\lambda(\theta_0, \theta, \phi)}{1 - s_\lambda \rho^s_\lambda(\theta_0, \theta, \phi)} \qquad (3.5),$$

where $\rho^a{}_\lambda$ represents the atmospheric path reflectance, including aerosol and molecular contributions, $F_{d\lambda}$ is the 'normalized downward flux' for zero surface reflectance, T_λ represents 'upward total transmission' into the satellite field of view, s_λ is the 'atmospheric backscattering ratio' (reflectance of the atmosphere for isotropic light leaving the surface), and $\rho^s{}_\lambda$ is the angular 'surface reflectance' [Kaufman et al., 1997a]. Except for the surface reflectance, each term on the right

hand side of Eq. 3.5 is a function of the aerosol type (chemical composition, size distribution) and its columnar loading τ. Assuming well-defined spectral surface reflectance, accurate measurements of TOA spectral reflectance can lead to retrievals of spectral τ and reasonable estimates of one or more aerosol size parameters [e.g. Tanré et al., 1996]. Note that in the context of satellite observations, the 'target' angles (defined in Eq. 3.5) are referred to as 'sensor' angles or 'view' angles. In any case, the Earth's surface is considered the vantage point.

In order to reduce the computational cost of difficult radiative transfer calculations at every satellite observed pixel, most, if not all operational aerosol retrievals from satellite make use of a lookup table (LUT). The LUT is a simulation of the atmospheric contribution to the TOA reflectance, namely the non-surface terms in Eq. 3.5. The LUT must be sufficiently representative of all reasonably likely atmospheric scenarios and satellite observations.

3.3: Aerosol remote sensing from AERONET

3.3.1 AERONET retrievals of spectral τ from direct sun

Although sunphotometers have been used for decades, the products provided by AERosol Robotic NETwork (AERONET, [Holben et al., 1998]), are considered the state-of-the-art for consistent, calibrated and useful spectral aerosol depth data. Operating at hundreds of sites globally, the AERONET sunphotometers (produced by Cimel Electonrique in France) have been reporting at some sites since 1993 (e.g. http://climate.gsfc.nasa.gov). 'Sun' products are retrievals of spectral τ at several wavelengths (0.34, 0.38, 0.44, 0.67, 0.87 and 1.02 μm, and possibly others depending

on instrument), resulting from application of Eq. 3.1 to the observations of spectral extinction of the direct sunbeam. In addition to spectral τ, AERONET provides retrievals of columnar water vapor (*PW*) from a water vapor absorbing channel. Approximately every 15 minutes during the daytime, the sunphotometer points directly at the sun, taking spectral measurements in triplicate during a 1.5 minute span. Transmitted to GSFC in real time, averages and standard deviations of these triplets are calculated. Cloud screening [Smirnov et al., 2001] is performed by limiting the variability within each triplet and compared to prior and subsequent triplets.

Level 1 (raw data averages) and Level 1.5 (cloud screened data) are provided in near real time to the user community. Level 2 data is considered calibrated, quality assured data, meaning that the instrument has been corrected for optical drift and the products meet certain requirements. Since the upgrade to Level 2 requires the instrument to be taken from the field and re-calibrated, it may not be available for months or years after Level 1.5 is available.

3.3.2 AERONET retrievals of aerosol properties from sky radiance

In addition to the direct 'sun' measurements, the AERONET instruments are programmed to observe angular distribution of sky radiance, approximately every hour during the daytime. These 'sky' measurements are made in the almucantur (a circle made with constant zenith angle equal to solar zenith angle), and the principle plane (line of constant azimuth angle) in at least at four wavelengths (0.44, 0.67, 0.87 and 1.02 μm), in order to observe aerosol spectral scattering. These observations are controlled for quality, through rigorous cloud screening and requirements of

angularly symmetric radiance. To ensure large enough signal, use of sky radiance requires ambient optical depth, retrieved by 'sun' observation, to be at least 0.4 at 0.44 μm.

These sky measurements are used to retrieve size distribution and scattering/extinction properties of the ambient aerosol field using spherical aerosol assumptions [Nakajima and King, 1990; Kaufman et al., 1994; Dubovik and King, 2000a], and more recently, non-spherical assumptions [e.g. Dubovik et al., 2002b]. By assuming the ambient aerosol to be a homogenous ensemble of poly-disperse spheres and randomly oriented spheroids [Dubovik et al., 2006], the algorithm retrieves the volume distribution ($dV/dlnR$) for 22 radius size bins and spectral complex refractive index (at wavelengths of sky radiances observations) that correspond to the best fit of both sun-measured τ and almucantur sky radiances. The non-spherical fraction is modeled with distribution of aspect ratios retrieved [Dubovik et al. 2006)] that fit scattering matrices of mineral dust measured in the laboratory [Volten et al. 2001]. In either case, the modeling is performed using kernel lookup tables of quadrature coefficients employed in the numerical integration of spheroid optical properties over size and shape. These kernel look-up tables were generated using exact T-Matrix code [Mishchenko and Travis, 1994] and approximated geometric-optics-integral Eq. method of Yang and Liou [1996], that was used for size or shape parameters exceeded convergence limits of T-Matrix code. As a result the kernels cover wide range of sizes ($\sim 0.12 \leq 2\pi R/\lambda \leq \sim 625$) and axis ratios ε ($0.3 \leq \varepsilon \leq 3$). The usage of kernel look-up table allows quick and accurate simulations of optical properties of spheroids and therefore it allows using model of randomly oriented

spheroids (introduced by [Mishchenko et al. 1997] for desert dust) in AERONET operational retrievals.

The retrieved size distribution and complex refractive index uniquely determine the aerosol radiative properties of phase function (P) and single scattering albedo (ω_0), also provided as retrieved products. In addition, AERONET derives optical properties (τ, P and ω_0) and integral parameters of size distribution (volume concentration C_v volume median radius r_v and σ - standard deviation from r_v), separately for fine mode ($r \leq 0.6$ μm) and coarse mode ($r > 0.6$ μm) of the retrieved aerosol. Such representation of AERONET retrievals is based on the fact that majority of observed aerosol is bi-modal and it is convenient for validation of satellite retrieval products, such as that of MODIS. Whereas the parameters C_v, r_v, σ are simulated for each mode without assuming any particular shape of size distribution (see formulation in [Dubovik et al. 2002a]), they are analogous to corresponding parameters of log-normal size distributions described in Section 2.1 (V_0, r_v, σ). In fact, the assumption of log-normality allows accurate reproduction of aerosol optical properties in most cases, suggesting that these parameters represent log-normal properties of AERONET climatology [Dubovik et al. 2002a].

Retrievals from both sun and sky AERONET measurements are controlled by rigorous calibration and cloud screening processes. The results are also constrained by the criteria identified in sensitivity studies [Dubovik et al. 2000]. As discussed by Dubovik et al. [2002a] these selections yield more accurate retrieval results that can be used as ground-truth estimates (for certain aerosol properties). These products are known as Level 2 AERONET products, and within this dissertation are designated as

'L2A' products. Finally, it should be noted the AERONET team is performing a re-processing the entire dataset, known as 'Version 2' (http://aeronet.gsfc.nasa.gov), but was not available at the time I began this dissertation.

3.4: Aerosol remote sensing from MODIS

3.4.1 Characteristics of the MODIS instrument

The MODerate resolution Imaging Spectro-radiometer (MODIS) is one of the first passive satellite radiometers to be designed with aerosols in mind [King et al., 1993]. From polar-orbit, approximately 700 km above the surface and a ±55° view scan, MODIS views the earth with a swath about 2330 km (schematic in Fig 3.3), thereby observing nearly the entire globe on a daily basis (**Fig. 3.3**), and repeating orbits every 16 days. MODIS measures radiance in 36 wavelength bands, ranging from 0.41 to 14.235 μm [Salomonson et al., 1989], with on-ground spatial resolutions between 250 meters and 1km. Its measurements are organized into 5 minute sections, known as *granules*, each ~2300 km long. MODIS actually flies on two NASA satellites, *Terra* and *Aqua*. Terra has a *descending* orbit (southward), passing over the equator about 10:30 local sun time, whereas Aqua is in *ascending* orbit (northward), so that it passes over the equator about 13:30 local sun time.

The over-land algorithm described by Kaufman et al., [1997a], in combination with an over-ocean algorithm [Tanré et al., 1996; Tanré et al., 1997] became the basis for an *operational* algorithm for retrieving global aerosol properties from MODIS observations. The operational algorithms are maintained by the MODIS Data Processing System (MODAPS) at NASA Goddard Space Flight Center (GSFÇ) in Greenbelt, Maryland. The MODIS Aerosol Science Team (MAST; also at NASA-

GSFC) is responsible for *validation* of the aerosol products and for updating the 'science' of the algorithm when necessary. The products are free and available to any investigator.

The aerosol retrieval uses the seven wavelength bands (listed in Table 1.1), which are all in atmospheric 'windows' (little or no absorption by gases). Included in Table 3.1 are estimates of the central wavelength in each band (obtained by integration of the channel-averaged response functions). To keep in line with common references in the literature, MODIS channels 1, 2, 3, 4, 5, 6 and 7 are known in this document as the 0.66, 0.86, 0.47, 0.55, 1.24, 1.64 and 2.12 μm channels, respectively. In addition, the aerosol algorithms make use of radiance in other MODIS bands to help with cloud and surface screening.

TABLE 3.1: CHARACTERISTICS OF MODIS CHANNELS USED IN THE AEROSOL RETRIEVAL

Band #	**Bandwidth (μm)**	**Weighted Central Wavelength (μm)**	**Resolution (m)**	**NeΔρ ($x10^{-4}$)**	**Max ρ**	**Required SNR**	**Rayleigh optical depth**
1	0.620 - 0.670	0.646	250	3.39	1.38	128	0.0520
2	0.841 - 0.876	0.855	250	3.99	0.92	201	0.0165
3	0.459 - 0.479	0.466	500	2.35	0.96	243	0.1948
4	0.545 - 0.565	0.553	500	2.11	0.86	228	0.0963
5	1.230 – 1.250	1.243	500	3.12	0.47	74	0.0037
6	1.628 – 1.652	1.632	500	3.63	0.94	275	0.0012
7	2.105 – 2.155	2.119	500	3.06	0.75	110	0.0004

Note: NeΔρ corresponds to the sun at zenith ($\theta = 0°$)

The MODIS instrument is spectrally stable and is sufficiently sensitive to changes in aerosol properties (e.g. Guenther et al., [2002]; Xiong et al., [2003]). The spectral

stability for each instrument is better than 2 nm (0.002 μm). The *Noise equivalent Differential Spectral Reflectance* (*Neρ*) represents the sensitivity to changes in the signal, and is an inherent property of the instrument. *Signal to Noise Ratio* (*SNR*) is defined as the ratio of the *typical scene reflectance* (ρ^{ts}) and NeΔρ. The NeΔρ and the SNR specifications are given in Table 3.1. To be understood in the framework of aerosol remote sensing, the definition of SNR should be based on the expected aerosol signal. Therefore, the *Noise Equivalent Differential optical depth* (*Neτ)* can be defined, where:

$$Ne\Delta\tau = \pi Ne\Delta\rho \frac{4\cos(\theta_0)\cos(\theta_v)}{\omega_0 P(\Theta)} \qquad (3.6)$$

where ω_0 is the aerosol single scattering albedo. The least sensitivity to aerosol scattering optical depth (largest noise) is expected when both sun and satellite are at nadir views ($\theta_0 = \theta_v = 0.0$), the aerosol and Rayleigh phase functions are minimum ($\Theta \sim 120°$) and the channel used is the least sensitive (channel 7, at 2.12 μm). With a typical phase function value of 0.08 at 120°, a typical aerosol has $Ne\tau \sim 1.5\text{x}10^{-2}$. The 2.12 μm channel is also where the 'typical scene τ' is (τ^{ts}) is 0.01 or less. Therefore the SNR ratio defined by the ratio of $\tau^{ts}/Ne\tau$ is about 0.66. This means that single 500 m pixels are insufficiently sensitive to characterize aerosol.

However, if individual pixels are aggregated to larger areas, say to a grid of 10x10 km^2 (20 x 20 500 m pixels), then the noise is reduced by a factor of 20. Instead of 0.66, the SNR becomes 13. Since SNR>10, 10x10 km^2 boxes are used as the default retrieval size [Tanré et al., 1996].

3.4.2 Introduction to the MODIS aerosol algorithm

Since MODIS' launch aboard *Terra* (in late 1999) and aboard *Aqua* (in early 2002), MODIS spectral reflectance observations have led to retrievals of spectral τ and a measure of aerosol size, known as the fine weighting (FW or η), each with 10 km resolution (at nadir). Separate algorithms derive aerosol properties over ocean and land [e.g. Remer et al., 2005], necessitated by different surface optical properties. While this dissertation focuses on over-land aerosol retrievals, MODIS also retrieves aerosol products over water. Because of better constrained ocean-surface optical properties, the algorithm used over ocean [Tanré et al., 1997; Levy et al., 2003; Remer et al., 2005] has more sensitivity to aerosol. Later sections of this dissertation discuss concepts of the over-ocean inversion technique that are applied to the retrieval over land.

For either over-land or over-water retrieval, the algorithm must ensure that the target is free of clouds, snow, ice and extreme surface variability. A number of tests are performed to separate water bodies and land surfaces [see Remer et al. 2005] and to select appropriate pixels for retrieval. Over either surface, some of the brightest and darkest pixels (within the 10 km box) are removed, in order to reduce residual cloud and surface contamination effects (such as shadowing or adjacency effects).

For both over-land and over-water, the MODIS algorithm uses a lookup table (LUT). The LUT is derived by a radiative transfer (RT) code, to simulate the radiative effects of a small set of aerosol types, loadings, and geometry that presumably span the range of global aerosol conditions [e.g. Kaufman et al., 1997b]. The goal of the algorithm is to select which of the LUT's simulated scenarios best matches the

MODIS-observed spectral reflectance. To retrieve realistic aerosol properties, it is essential that the LUT represent realistic scenarios.

The original MODIS retrieval algorithms were formulated for over dark land by Kaufman et al. [1997a] and for over water by Tanre et al., [1997]. By MODIS launch aboard *Terra* (in December, 1999), the algorithm had been already revised in order to align with actual MODIS specifications and operational needs. The operational algorithms and products have been continuously evaluated for self-consistency and comparability to other datasets, including AERONET [e.g. Remer et al., 2005]. MODIS algorithms are organized by 'versions' (e.g. vX.Y.Z, where X represents major 'science' update, Y represents minor updates, and Z represents bug fixes or otherwise presumably small updates; see http://modis-atmos.gsfc.nasa.gov/MOD04/history), whereas products are arranged as 'collections' (e.g. c00X, where X represents major science updates or reprocessing). After initial review by the MODIS science team, the products were released to the public as Collection 003. Chu et al., [2002] and Remer et al., [2002] evaluated c003 products over land and ocean, respectively. Soon after *Aqua* was launched (in June 2002), the algorithm was applied to both MODIS instruments, beginning the product dataset known as Collection 004. In theory, the entire c004 would be derived by a static algorithm. However, while the fundamental science assumptions remained in place, the c004 algorithm continued to evolve. Updates were necessary due to changes in MODIS instrument calibration, operational processing environments, and new science (for example improved cloud masking). Remer et al., [2005] describe v4.2.2

of the algorithm, (c004), which are used in this dissertation to provide baselines for the algorithm and products.

3.4.3 MODIS aerosol retrieval: Collection 4 algorithms

As explained in the previous section, Kaufman et al., [1997b] introduced the MODIS aerosol retrieval algorithm from MODIS. Its major assumptions and methodology were unchanged through v4.2.2 [Remer et al., 2005] and the processing of c004. This section summarizes the major assumptions of the c004 family of algorithms, highlighting the assumptions that were revised during c005 algorithm development and for this dissertation. While the focus of this dissertation is on over-land aerosol retrieval of aerosol properties, I also include a short section outlining the basic assumptions of the algorithm over ocean.

Processing of the MODIS data begins with collecting raw data (known as *Level 0*), and cutting them into 5-minute chunks (known as *granules*) as *Level 1A*. Each granule is converted into calibrated radiance/reflectance and geo-location data (known as *Level 1B* or *L1B*). The aerosol retrieval uses calibrated reflectance data from the seven MODIS bands listed in Table 1. These reflectance data are first corrected (by about 1-2%) for trace gas and water vapor columns, using 'ancillary' data from NCEP (National Centers for Environmental Prediction) analysis [MAST, 2006]. They are organized into 10 km x 10 km boxes (e.g., 40x40 of 250 m data, 20x20 of 500m data and 10x10 of 1 km data), and separated into land and ocean pixels. Depending on the relative dominance of either surface, the appropriate

algorithm is assigned. Near coastlines, if any of the observed pixels are considered land, then the over-land algorithm is followed.

Primary products for each algorithm include the total optical depth (τ) at 0.55 μm and an estimate of the fine aerosol weighting (η) to the total optical depth. At the conclusion of either algorithm, these primary products are evaluated and given Quality Assurance (QA) values, ranging from 0 (not to be trusted) to 3 (trustworthy). The MODIS products include trusted and non-trusted products, it is up to the user to determine which QA level, he or she should use. It is also noted here, that whereas the definitions of τ are the same, the definitions of η are different for land and ocean. This difference is explained more in detail as it relates within the dissertation.

3.4.3.1 MODIS c004 over ocean

The main premise of the over-ocean algorithm is that the ocean reflectance is generally close to zero at red (0.66 μm) and longer wavelengths, providing a dark background to view aerosol. If all pixels in the 10km x 10km box are identified as water pixels, the ocean algorithm is chosen. First, obstructed pixels (cloudy-or otherwise unsuitable for retrieval) are removed, including: those within the glint mask (within 40° of the specular reflection angle), those flagged as cloudy [Platnick et al., 2003; Martins et al., 2002; Gao et al., 2003], and those that contain suspended river or other sediments [Li et al., 2003]. The remaining good pixels are sorted by their 0.86 μm brightness. Of these, the darkest and brightest 25% are removed, thereby eliminating residual cloud and or surface contamination. If at least 10 pixels remain in the 10km x 10km box, then reflectance statistics for all seven channels are calculated and used for the inversion.

As introduced by Tanré et al. [1997] and updated by Levy et al., [2003] and finally by Remer et al., [2005] for c004, the MODIS inversion attempts to minimize the difference between the observed spectral radiance in six MODIS channels and radiance pre-computed in a LUT. The ocean LUT models the total reflectance observed by satellite, which includes not only aerosol contributions, but also spatially and temporally constant atmospheric (Rayleigh) and ocean surface (chlorophyll, foam, whitecaps and sunglint) contributions. The c004 LUT is computed by vector RT (to include polarization effects on the radiance) for 2304 sun/surface/satellite geometries and five total aerosol loadings, for four fine modes and five coarse modes [Remer et al., 2005]. The inversion first interpolates the LUT to match the sun/surface/satellite geometry of the observation. The major assumption is that the total aerosol contribution is composed of a single fine and single coarse mode. For each combination of fine and coarse modes (20 combinations) the inversion determines the total spectral τ and the *fine mode weighting* (η) to the total τ that minimizes the least squares difference error (ε) between the modeled and observed spectral reflectance. The fine/coarse mode combination providing the smallest ε is the final solution. A variety of other aerosol parameters are inferred, including the effective radius of the aerosol size distribution.

3.4.3.2 MODIS c004 over land

Land surfaces do not provide the same uniform surface signal as the ocean. Land surfaces are much more variable in their reflectance properties and therefore the algorithm must include additional steps to estimate the land surface contribution to the satellite -observed signal. If the surface is well-behaved (i.e. it is either completely

dark or its reflectance can be accurately modeled or assumed), the atmospheric signal may be sufficiently decoupled from the combined surface/atmosphere signal.

The aerosol retrieval over land uses spectral reflectance in four of the channels listed in Table 3.1, specifically the 0.66, 0.86, 0.47 and 2.12 μm channels. In cloud-free regions, these bands are sensitive primarily to molecular, aerosol and surface scattering. Preliminary steps of the retrieval include testing the spectral observations to screen the 10 km box for clouds [e.g. Martins et al., 2002; Gao et al., 2002], snow and ice [Li et al., 2005], and sub-pixel water bodies such as ponds or swamps [Remer et al., 2005]. The pixels that remain are sorted by their relative reflectance (at 0.66 μm), such that the 20% of the darkest pixels and 50% of the brightest pixels are removed. The remaining pixels are expected to represent dark surface targets with the least amount of contamination from clouds (including cloud shadowing) as well as surface inhomogenieties. This means that at most, 120 pixels remain from the original 400.

The retrieval can proceed if least 12 pixels (10%) remain. These remaining pixels are averaged, yielding one set of spectral (0.47, 0.66 and 2.12 μm) reflectance values that are used to the retrieve 10 km products. The first key assumption is that surface reflectance in the visible channels (0.47 and 0.66 μm) are each fixed ratios of the surface reflectance at 2.12 μm [Kaufman et al., 1997a; Remer et al., 2005], which are denoted here as the 'VISvs2.12' ratios. Specifically, the c004 VISvs2.12 ratios are assumed as 0.25 for 0.47vs2.12 and 0.50 for 0.66vs2.12. These empirically derived relationships [Kaufman and Remer, 1994] represent the relationship of liquid water absorption and chlorophyll reflectance in healthy vegetation [Kaufman et al.,

2002], meaning that they are expected to be valid only in vegetated and semi-vegetated regions.

Even in conditions of large numbers of coarse aerosols (such as in dust-dominated regions), aerosols are assumed to be transparent to radiation at 2.12 μm [Kaufman et al., 1997a]. This means that the surface reflectance in the visible channels can be calculated from the observed reflectance at 2.12 μm, via the VISvs2.12 ratios. Therefore, any difference between the satellite reflectance (observed) and visible surface reflectance (estimated via the ratios) is due to the radiative impacts of the impeding atmosphere (including the aerosol).

According to Remer et al. [2005], the c004 LUT contains simulations for five aerosol types (known as 'Continental', 'Urban/Industrial', 'Moderate Smoke/Developing World', 'Absorbing Smoke', and 'Dust') at 2304 angle combinations, six τ loadings (plus $\tau = 0$; molecular conditions), and for two channels (0.47 and 0.66 μm). The c004 LUT was simulated with scalar radiative transfer (RT) code, meaning that any polarization effects on the reflectance were neglected.

The procedure begins by performing linear interpolation upon the LUT, so that the LUT represents the exact geometry of the MODIS observation. The algorithm selects the 'Continental' model [Lenoble and Brogniez, 1984] to derive an initial estimate of the spectral τ. τ is retrieved in the two visible channels (0.47 and 0.66 μm) independently, such that the difference to the observed reflectance (the fitting error, ε) is minimized. From the spectral dependence of τ, the two channel Ångstrom exponent (α) is calculated, which in turn is used to derive the relative contribution of fine aerosol to the total τ (η) [Chu et al. 2002].

The algorithm then works to fine tune its initial estimate of spectral τ. It selects the appropriate fine-dominated aerosol type (choice of the 'Urban/Industrial', 'Moderate Smoke/Developing World' or 'Absorbing Smoke') characteristic of the region and season being observed [Remer et al., 2005]. The choice of aerosol type is mixed with 'Dust' using the previously derived fraction η. Again τ is retrieved independently for the two visible channels (based on minimum ε). This revised retrieval of spectral τ is known as the 'Corrected Optical Depth.' If the surface is elevated (e.g. a mountain), the 'Corrected Optical Depth' is further corrected by adding (in the 0.47 μm channel only), the difference in Rayleigh optical depth between the elevated surface and a sea level surface. The final products of the over land algorithm include the spectral τ (at 0.47, 0.66 and interpolated to 0.55 μm), as well as the Fine Weighting (the fine fraction), η. Again, it is noted the difference in land and ocean η definitions; while over ocean η refers to *fine mode* weighting, over land it refers to *fine model* weighting or non-dust weighting.

There are additional details of pixel selection and dark target criteria not described here, but the reader is referred to Remer et al., [2005] and MAST, [2006] for more discussion.

3.5: Summary

Aerosols are complicated beasts that require a variety of measurement techniques from all different platforms (vantage points). Measurements of mass and optical properties can be made *in situ* with high temporal resolution, but are only representative of aerosol properties at that site. In addition, many *in situ*

measurements must collect the aerosol onto a filter or into a cavity, thus modifying the aerosol characteristics. Since the EPA regulates dry aerosol concentrations, the aerosols must be dried, thus further distancing from ambient aerosol conditions. Remote sensing techniques do not modify the physical characteristics of the aerosol, thus they have the advantage that they observe ambient aerosol conditions. However, remote sensing products represent aerosol properties integrated over a distance (e.g. the atmospheric column), so that they may not represent the portion of aerosol (say near the surface) that effects human health and is regulated by the EPA.

Remote sensing techniques, however, should and do make use of *in situ* measurements to constrain their algorithms and understand their results. Retrieval algorithms from measurements of reflected sky radiance (sunphotometer) and reflected light to space (satellites) use the physical understanding brought by other datasets to relate the aerosol's optical properties with the physical characteristics that affect our lives on earth's surface.

CHAPTER 3 FIGS.

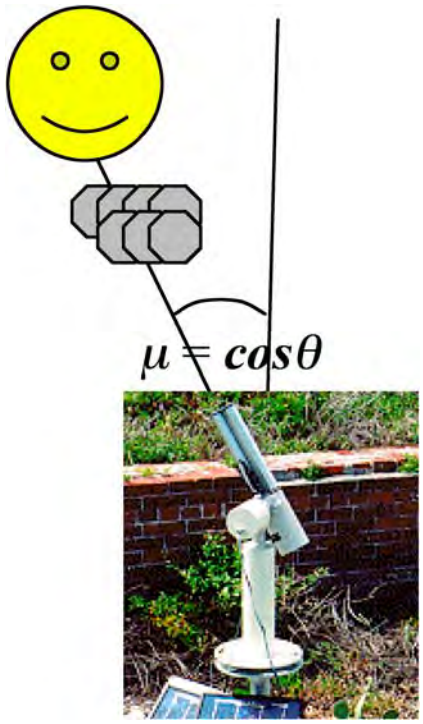

Fig. 3.1: Schematic of a sunphotometer direct measurement of extinction of solar radiation through the atmosphere. The instrument illustrated is the Cimel instrument used for AERONET.

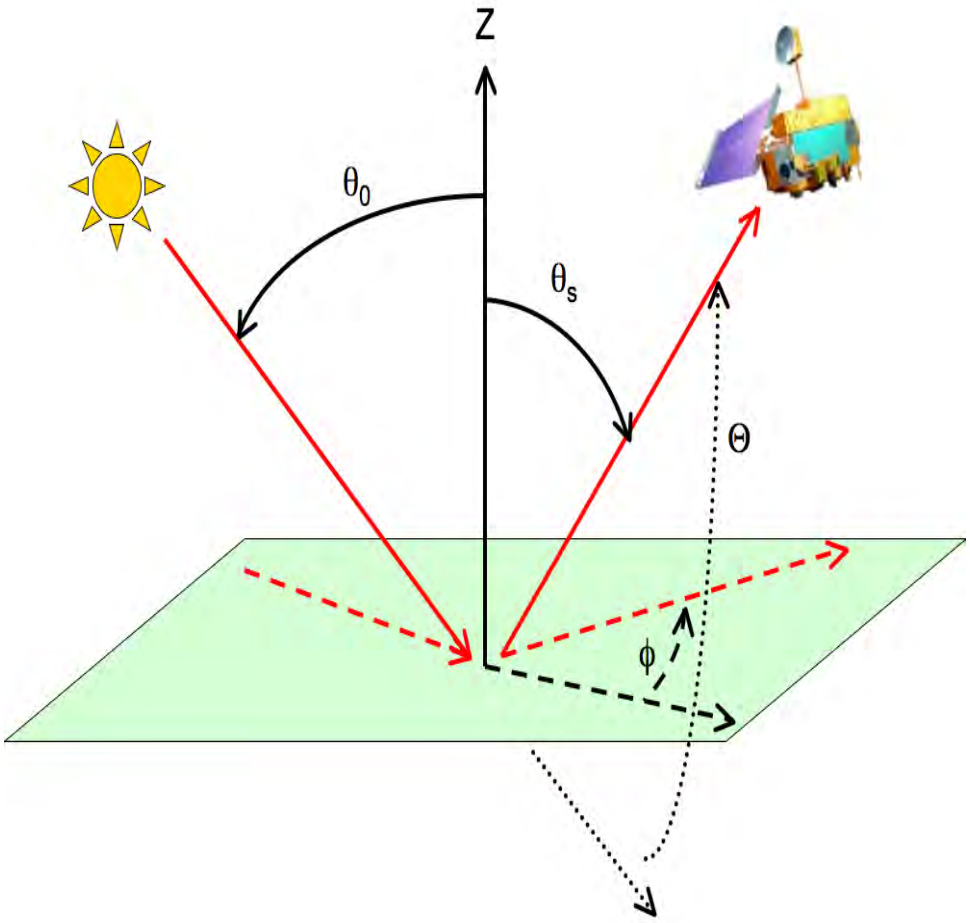

Fig. 3.2: Schematic of sun/surface/satellite remote sensing geometry, defining the angles as viewed from the surface target. The solid lines (and curves) represent solar zenith θ_0 and satellite view zenith θ angles (measured from the zenith, Z). The dashed lines (and curves) represent the relative azimuth angle ϕ (measured from the extension of the solar azimuth), whereas the dotted lines (and curves) represent the scattering angle Θ (measured from the extension of the direct beam). The Terra satellite icon is from the Earth Observatory (http://earthobservatory.nasa.gov).

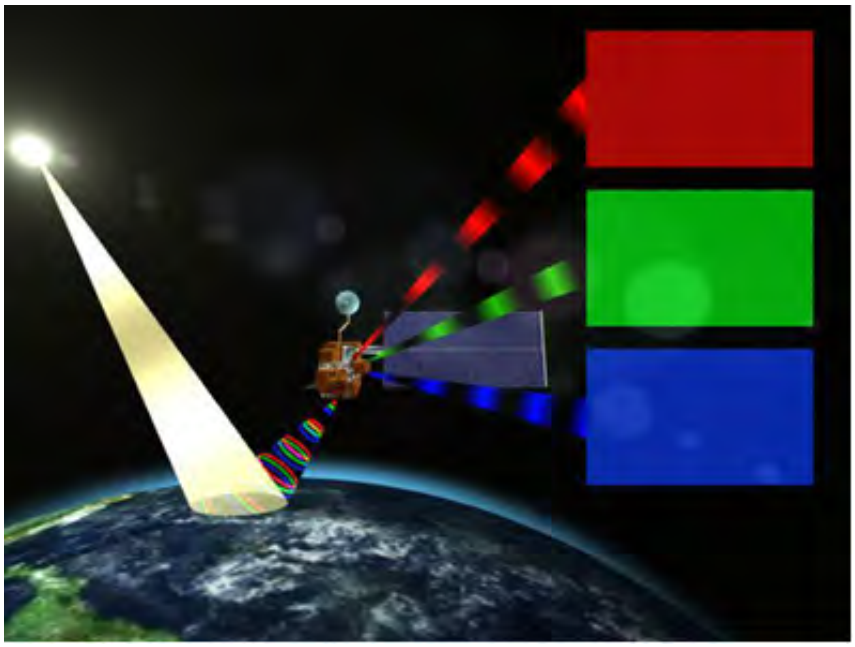

Fig. 3.3: Schematic of satellite remote sensing of the Earth, using Terra as an example. (Figure from Earth Observatory, http://earthobservatory.nasa.gov)

Fig. 3.4: Example of a composite MODIS 'RGB' image for a whole day, April 1, 2001. Images are known as 'RGB' or 'True-Color', created by merging MODIS observations in 0.47, 0.55 and 0.66 μm.

Chapter 4: Evaluation of MODIS c004 products as motivation

Evaluation of a satellite (or any) dataset refers to the exercise of understanding the quality of the data under all measurement conditions. Validation implies quantitative assessment of the measurement uncertainty. The validation process asks questions about the precision, accuracy and consistency of the derived data products. This dissertation focuses on consistency (Do the products represent physical quantities with no artificial boundaries?), precision (Do the products capture increments of physical quantities?) and accuracy (Can the products be matched with reference standards?).

The total aerosol optical depth (τ) is a physical quantity, resulting from the interaction of a particular wavelength of radiation with a particular composition and amount of aerosol within the atmospheric column. All remote sensing techniques are essentially attempting to measure the same defined physical quantity. If one assumes that sunphotometry provides the most simple and direct measurement of this quantity, then satellite derivations of τ should be directly compared to them.

The fine weighting (FW or η) is defined differently by AERONET and by each MODIS algorithm. By the technique of AERONET almucantur inversions [Dubovik and King, 2000], η is a 'volume fine weighting' or fraction of the total volume (size) distribution contributed by fine aerosol (defined as all aerosol of radius, $r < 0.6$ μm). By the technique of spectral deconvolution of AERONET sun measurements [O'Neill et al., 2003], η is the 'τ fine weighting', or the fraction of total τ resulting from fine (r

< 0.6 μm) aerosol (for wavelength of 0.55 μm). MODIS over land defines η to be a 'τ fine model weighting', or the fraction of τ contributed by fine-dominated *model*, where the model is comprised of multiple lognormal modes (for example, fraction of urban/industrial aerosol to the total aerosol, or non-dust fraction). Finally, the MODIS over ocean algorithm defines η to be a true 'τ fine mode weighting', the fraction of the total optical depth contributed by the fine (lognormal) *mode*. While the definitions of η vary across products, the physical meaning of η is similar enough that it is reasonable to compare them directly.

Unlike comparisons of MODIS and AERONET -derived τ and η, (which are essentially the same physical quantity), comparisons of remotely sensed products with most other aerosol measurements are not usually as straightforward. For example, much recent research has focused on using MODIS -derived τ products to monitor surface concentrations of dry $PM_{2.5}$ mass concentration {$PM_{2.5}$}, which are two completely different physical quantities. Yet, since there are situations in which they should be comparable (when the bulk of the aerosol column is located in the boundary layer near the surface), and much can be gained by exploiting this relationship, regulatory agencies (e.g. the EPA) are developing the tools to use satellite -derived τ (including MODIS) for $PM_{2.5}$ monitoring and forecasting.

4.1: Global validation of c004 products; comparison to AERONET

Remer et al. [2005] performed a global validation of the spectral τ products contained in c004. They showed that the MODIS yielded physically reasonable

values in a variety of conditions, and that that there was sufficient sensitivity to differentiate relative aerosol load. The bulk of their validation study was comparison with reference ground based sunphotometers (AERONET) at over a hundred global sites.

Remer et al [2005] demonstrated accuracy of the MODIS derived τ, both over ocean and over land. Specifically, they applied the spatial-temporal technique of Ichoku et al. [2002a], such that the average of a 50 km x 50 km area of MODIS products centered at the AERONET site (a 5 x 5 box of 10 km retrievals) was compared to the average of the AERONET direct-sun measurements within one hour of satellite overpass (normally four or five measurements). Fig. 4.1 illustrates the validation process. Concentrating on cloud-free conditions (MODIS must have at least 5 out of 25 pixels, and AERONET must have at least 2 measurements during the hour, out of a possible 4) and on quality assured data (MODIS QA=3, cloud screened AERONET L15), Remer et al. [2005] demonstrated that MODIS retrieves τ to within the error bars over land (Eq. 1.1) expected before launch. Over ocean, they found that MODIS performed to within more stringent expected errors, except in dust regions (previously found by Levy et al., [2003]).

While MODIS over-land retrievals and AERONET compared within pre-launch expectations, Remer et al., [2005] found that MODIS generally over-estimated τ for low aerosol loadings, and under-estimated for high loadings (e.g. Eq. 1.2). Over ocean, they found no such consistent bias (except in conditions of dust aerosol).

Global, long term scatterplots are informative, but they may hide systematic errors pertaining to certain regions. Remer et al., [2005] separated the global

scatterplot into a number of large regions, presumably each region representing a given aerosol regime. The algorithm performed in similar fashion in most regions, some better, some worse. Some of the poorest MODIS/AERONET comparisons were over the land along the East Coast of the United States, where less than 60% of the retrievals fell within expected error bars over land (between 2000 and 2002). Retrievals over the nearby ocean were much closer, falling within the more stringent over ocean error bars.

Kleidman et al. [2005] evaluated the MODIS fine weighting (η) products (over ocean) in context of those retrieved from AERONET data. Generally, they found that aerosol product over ocean has higher values (by about 0.2) than those estimated by AERONET. Anderson et al., [2006] evaluated the retrievals of η over land and ocean separately, in the vicinity of Japan, by comparing to in-situ profiles (from nepholometers, PSAPs and AATS) of spectral dependence (e.g. Ångstrom exponent, α) and sub-micrometer fraction (SMF) of τ. The MODIS ocean retrievals were systematically higher than SMF by about 0.2, suggesting that in situ measurements indicate a systematically different relationship between fine fraction and α than what is assumed from satellite. Over land, Anderson et al., [2006] found very little significance to MODIS reported η values.

4.2: Evaluation of c004 over the U.S. East Coast during CLAMS

Based on global and regional studies of MODIS derived τ over land, the land algorithm is not performing as well as one might hope, especially over the U.S. East

Coast. Retrievals of η over land are almost meaningless. I began the process of evaluating the MODIS algorithm for use over the region, and determine how the algorithm could be improved. The Chesapeake Lighthouse Aircraft Measurements for Satellites (CLAMS) took place from July 10 to August 2, 2001, in a combined ocean/land region that included the Chesapeake Lighthouse (COVE) and the Wallops Flight Facility (WFF), both along coastal Virginia [Smith Jr. et al. 2005]. This experiment was designed mainly for validating instruments and algorithms aboard Terra, including MODIS. Held in July and August 2001, it was expected that CLAMS would showcase the heavy aerosol loadings common to the U.S. East Coast during the summer.

I was deployed at CLAMS, along with other members of the MAST. One of our objectives was to set up a network of handheld Microtops [Morys et al. 2001; Ichoku et al. 2002b] sunphotometers, that measure spectral τ in conjunction with baseline AERONET instruments located at Wallops and COVE, two independent robotic instruments [Ehsani et al., 1998] at NASA's Langley Research Center (LaRC), and the Ames Airborne Tracking 14 Channel Sunphotometer (AATS-14; [Redemann et al., 2005]). This network was designed primarily to test spatial variability of aerosol properties, but also to evaluate the performance of longer wavelength (1.6 and 2.l μm) sunphotomers (AATS-14 and Microtops) over ocean. All sun-photometers used in this study were pre- and/or post- calibrated, and were expected to measure optical depths with accuracy of ±0.03 or better [Holben et al., 1998; Ichoku et al., 2002b; Russell et al., 1993; Ehsani et al., 1998]. Thus, I chose to consider all sunphotometer measurements as one large dataset.

Over the ocean, MODIS retrieved τ at seven wavelengths and an estimate of the aerosol size. Over the land, MODIS retrieved τ at three wavelengths, plus very qualitative estimates of the aerosol size. As most CLAMS sunphotometer data were obtained near the coastline, in many cases there were both ocean and land retrievals from MODIS that could be separately compared with sunphotometer. This experiment was productive for the MAST, resulting in numerous papers within the CLAMS 'special section' published in the *Journal of Atmospheric Sciences* [Smith, Jr. et al., 2005], including my paper [Levy et al., 2005].

4.2.1 Comparison of MODIS-derived τ with sunphotometer

As most CLAMS sunphotometer data were obtained near the coastline, in many cases there were both ocean and land retrievals from MODIS to be compared with sunphotometer measurements. Over the nearby ocean, MODIS -derived τ (at 0.55 μm) correlated well with sun-photometer measurements, such that nearly 86% of the ocean points lay within ocean expected error bars, with correlation coefficients $R > 0.9$ and nearly one-to-one fit. Over land, however, the correlation is weak, and a majority of MODIS retrievals are outside the expected error (Eq. 1.1). Like the global results seen by Remer et al. [2005], MODIS over-estimates τ for low aerosol loadings and under-estimates for higher τ. At 0.55 μm, the linear least square regression was $y=0.64x + 0.21$, with correlation coefficient, $R=0.6$ (e.g. Fig. 1.2).

Fig. (4.2) shows a case where there is pronounced discontinuity of the MODIS-derived τ. Even though retrievals may not match at the coastline, the lack of match is extreme. Fig. 4.3 shows τ comparisons for AERONET sites during CLAMS, both

over ocean and over land. The black symbols represent ocean and land separately, whereas the red shapes display τ in cases that MODIS retrieved both ocean and land. The AERONET sites along the coastline were better represented by the ocean retrieval. In all cases, the retrieved land values were much larger (often more than double) the ocean values. I focused on determining the cause of the poor over-land retrievals.

4.2.2 Comparison of MODIS-derived η with sunphotometer

As noted above, the fine weighting (FW or η) is defined differently for different retrieval techniques. Nonetheless, I tried to evaluate the retrievals by comparing the size distributions implied by η and the choice of aerosol models (or modes) from MODIS to those retrieved by AERONET. These results were included in Levy et al., [2005].

The MODIS over ocean algorithm retrieves between two and three pieces of information [Tanré et al., 1996]. These products include the total τ, which fine and coarse modes were chosen, and η. One can infer a relative aerosol size distribution that created these products. While these 'optically equivalent' modes have no direct conversion to size distribution units (such as $\mu m^3/\mu m^2$), they can be normalized to yield understanding of the relative maxima and standard deviations of the bi-modal size distribution.

The MODIS over land algorithm retrieves τ and the relative weighting η of dust and non-dust (urban/industrial in the U.S. mid-Atlantic). While each multi-modal

aerosol model has physical size distribution units, the total retrieved size distribution can also be normalized to understand the relative maxima and standard deviations.

Finally, for this experiment, I chose to compare the normalized ocean size distributions against the size distributions retrieved by inverted AERONET almucanturs. Again, even though the AERONET size distributions represent physical (with units) size distributions, they can be normalized as well. By assuming that all three techniques observed similar aerosol conditions, I compared relative mean radius and radius standard deviations from all three techniques.

Using results from spatio-temporal MODIS/AERONET matches [Ichoku et al., 2002a], I derived a relative aerosol size distribution that represented 50 km x 50 km boxes over AERONET sites. Averaging across all matches, I obtained the MODIS-derived unitless aerosol size distribution from CLAMS. Fig 4.4a visually shows CLAMS averaged aerosol size distributions independently retrieved by the over-ocean (blue curve) and over-land (green curve) algorithms from MODIS, and from AERONET almucantar radiance inversions (red curve). The size distributions show significant differences. Although all three have fine mode peaks at approximately 0.15 μm, the AERONET fine mode peak has much smaller width or standard deviation. The contribution to the total volume is larger for ocean than for land near the inflection point (fine/coarse mode split at 0.6 μm), but smaller as the radius increases over 1 μm. Because the AERONET retrievals are split into fine and coarse mode at a radius of 0.6 μm, radii bins near 0.6 μm are not well represented.

The scattering effects of aerosols are best explained by estimating surface area distributions. Fig. 4.4b is analogous to Fig. 4.4a, but plots surface area distribution,

such that each area distribution curve encloses the same total aerosol unitless surface area. For CLAMS, the aerosol fine mode clearly dominated the area size distribution, presumably dominating aerosol scattering. There is, however, a small contribution from the coarse mode (just above 0.6 μm), especially as retrieved by the ocean retrieval.

One way to compare the size distributions is to compute the modal radius r_v, standard deviation of the modal radius σ, and the effective radius r_{eff}. We used the strategy prescribed by AERONET (splitting at 0.6 μm) to define fine and coarse mode. Table 4.1 shows the results of calculating average CLAMS effective radii, modal radii and standard deviation. The AERONET and the MODIS over-ocean algorithm's fine mode effective radii are similar, while the MODIS over-land algorithm represents smaller values. On the other hand, the over land's coarse mode effective radius agrees better with AERONET. For the total effective radius, all three values are close, with the land and ocean retrievals are nearly identical. AERONET retrieves slightly larger total effective radius. The largest differences are in the fine mode standard deviation, σ_f.

4.3: Summary

The MODIS aerosol algorithm was formulated well before the launch of the first MODIS sensor (aboard Terra) in December of 1999. It is actually composed of two separate algorithms (over land and over ocean) that have been updated since launch.

Table 4.1: CLAMS-averaged total, coarse mode and fine mode modal radius, standard deviation σ, and effective radius r_{eff} calculated from MODIS over ocean, over land and by AERONET.

PARAMETER MODE	r_V(μm)	σ	r_{eff}
Ocean algorithm			
Fine	0.178	0.718	0.136
Coarse	1.870	0.724	1.498
Total	0.327	1.258	**0.178**
Land algorithm			
Fine	0.143	0.746	0.108
Coarse	6.166	1.137	3.334
Total	0.708	2.081	**0.183**
AERONET			
Fine	0.149	0.410	0.138
Coarse	3.657	0.696	2.849
Total	0.493	1.638	**0.214**

CHAPTER 4 FIGS.

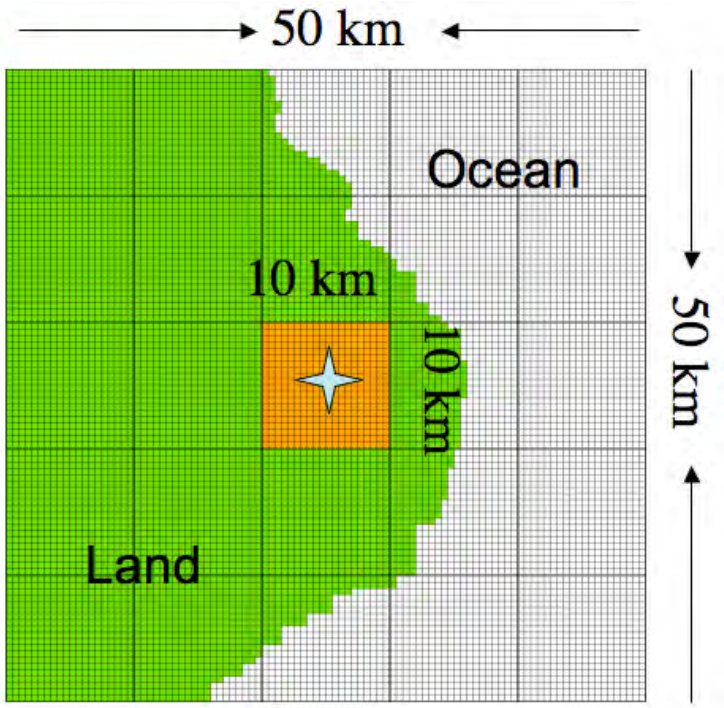

Fig. 4.1: Illustration of Ichoku et al., [2002a] spatial/temporal validation technique over a coastal AERONET site (star). The orange box is the 10 km x 10 km MODIS retrieval containing the site. Since both MODIS over-land and over-ocean retrievals are performed in this case, both are averaged over the 50 km x 50 km domain, and will be compared with the AERONET measurements. Any 10 km MODIS retrieval containing land is derived as land, whereas 100% water is necessary for deriving as ocean. The tiny boxes represent the 20 x 20 original 500 m MODIS pixels within each 10 km.

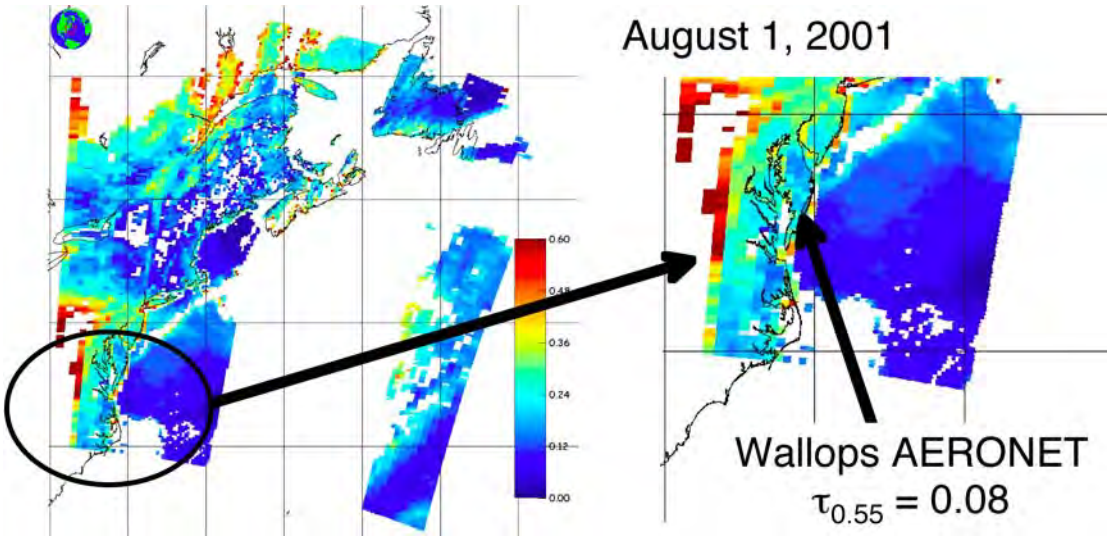

Fig. 4.2: Illustration (and blowup) of discontinuity between MODIS over-land and over-ocean $\tau_{0.55}$ retrievals for 1 August 2001 (CLAMS). The AERONET value at Wallops ($\tau_{0.55}$ =0.08) is placed for comparison.

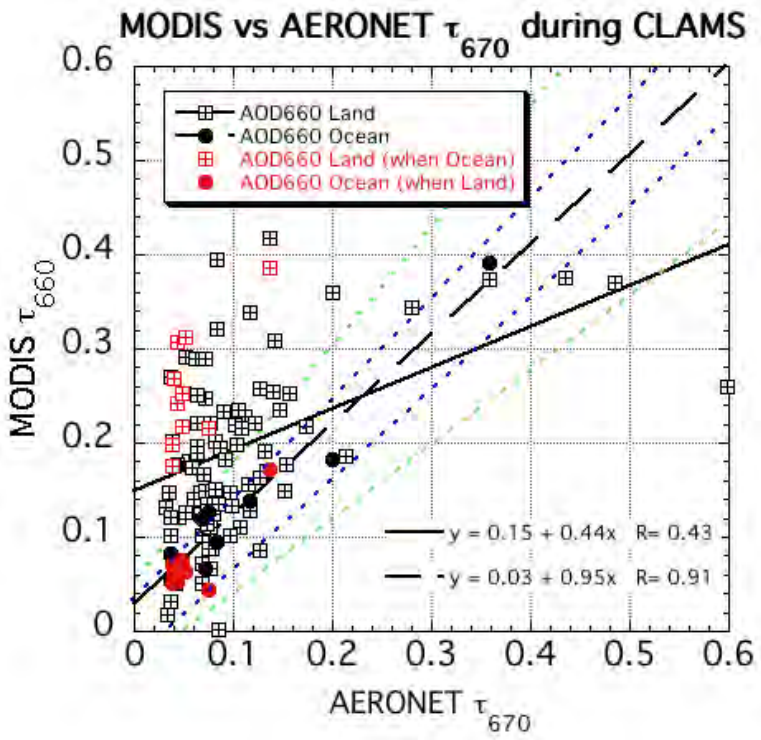

Fig. 4.3: Comparison of MODIS over-land and over-ocean retrieved τ (at 0.66 μm) with AERONET (only). The open squares are for over-land, where the closed dots are for over-ocean. Black shapes denote land and ocean retrievals independent of whether the other is performed. Their regression lines are given. Red shapes represent cases when both land and ocean retrievals were performed for a site. Land and ocean expected errors are the green and blue dashed lines, respectively. (Fig. reproduced from [Levy et al,. 2005].

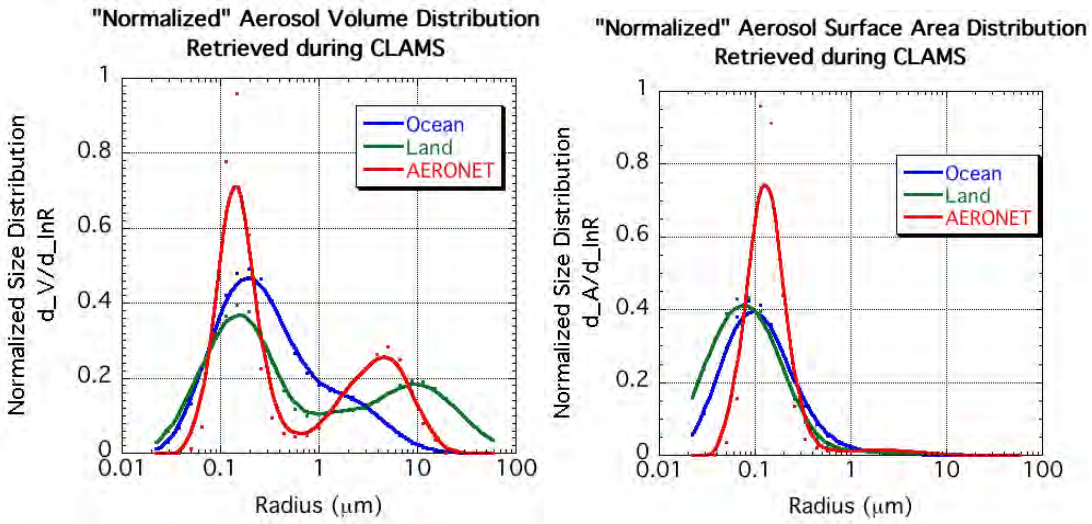

Fig. 4.4: CLAMS-averaged 'equal total volume' aerosol volume distribution (a) and 'equal total area' aerosol area distribution (b) from MODIS over ocean and land separately, and from AERONET inversions. (Fig. reproduced from [Levy et al., 2005].

Chapter 5: Strategies for improving aerosol retrieval over land

Globally, regionally, and specifically for CLAMS, the MODIS c004 / sun-photometer τ correlation equations over land showed significant positive offsets and slopes less than one. The y-offset (MODIS retrieves τ when in fact there is none) implies errors induced by assuming inappropriate surface reflectance. On the other hand, the less than one slope implies errors in the aerosol models. For Levy et al., [2005], I used CLAMS data to address each of these problems and introduced possible solutions. In a previous work [Levy et al., 2004], I had determined that the simplified scalar RT code used to derive the c004 LUT neglected effects of atmospheric polarization that could also lead to retrieval errors. This chapter summarizes some of the main reasons that the over-land algorithm may be performing at a subpar level, and strategies for correcting the problems.

5.1: New aerosol models for improving the slope

Ichoku et al., [2003] showed that c003 MODIS retrieval errors for smoke over Southern Africa could be significantly reduced by decreasing the assumed single scattering albedo (ω_0) from ~0.90 to ~0.85. This 'absorbing' model was added for c004 and improved MODIS retrievals in Africa. However, fixing single scattering albedo is not the correct strategy in all parts of the world. For example, the assumed ω_0 (~0.96) for the c004 urban/industrial model of Remer and Kaufman [1998] is

appropriate over the U.S. mid-Atlantic [e.g Vant-Hull et al., 2005; Taubman et al., 2004]. Therefore, for this region (and possibly others), a different strategy must be prescribed.

The c004 dynamical urban/industrial aerosol model [RK-model; Remer and Kaufman, 1998] was derived from data collected from 5 AERONET sites along the U.S. East Coast, during the Sulfates Clouds and Radiation – Atlantic (SCAR-A) experiment of summer 1993. After cloud screening and almucantur symmetry determination, the method of Nakajima et al., [1996] was used to retrieve aerosol size volume distributions from 125 sky radiance measurements. Remer and Kaufman [1998] noted a dependence of τ that explained 60% of the variance in the shift (growth) of the aerosol modes and the total volume distribution.

Using eight years of AERONET data obtained at the GSFC site, Dubovik et al., [2002a] developed a dynamical urban/industrial aerosol model based on Dubovik and King's [2000] almucantur inversion technique. Like the RK-model, this so-called 'D-model' [Levy et al., 2005], describes a size distribution that is a dynamical function of the τ. Unlike the RK-model, a tri-modal distribution, the D-model is modeled as a combination of two lognormal distributions. Particles with radius less than 0.6 μm belong to the fine mode and larger than 0.6 μm belong to the coarse mode.

Figs. 5.1a and 5.1b show size distributions (as a function of τ at 0.44 μm) of the RK-model and D-model, respectively. There are substantial differences between the two models. The fine mode for the D-model has a peak at a slightly smaller radius, with narrower curvature (smaller σ). The RK-model's coarse mode (centered

around 9 μm) lack of τ dependence looks unphysical compared to direct observations, but the D-model's is more realistic and better defined. The refractive indices (*m*) differ as well. The RK-model uses *m* = 1.43 +0.0035i for the accumulation modes, 1.43 + 0.0i for the marine (salt) mode, and 1.53 + 0.008i for the coarse (dust) mode. For both fine and coarse modes, the D-model's refractive index is a function of τ, i.e. $m = 1.41 - 0.03\tau_{440} + 0.003i$, where τ_{440} is the τ at 0.44 μm. For the τ ranges displayed in Fig. 5.1, this means the real part m_r ranges between about 1.41 and 1.38, which is closer to that of water (m_r=1.33) than used for the RK-model.

For Levy et al., [2005], I attempted to correct the less-than-one slope, by replacing the RK-model by the D-model. I created two lookup tables, one for each aerosol model. Using a single value of solar/surface/satellite geometry and spectral surface albedo for both tables, I ran the Second Simulation of the Satellite Signal in the Solar Spectrum (6S) radiative transfer code [Vermote et al., 1997b] to simulate apparent (satellite) reflectance as a function of τ. Fig. 5.2 [Levy et al., 2005] plots apparent reflectance in three MODIS wavelengths (0.47, 0.66 and 2.1 μm) for an example of solar/surface/satellite geometry, observed during CLAMS. Empirical conversion from one aerosol model to another is also illustrated in Fig. 5.2. A line of constant apparent reflectance (ρ = 0.16 in the example), describes different values of τ for the two models. In this example, τ of 0.5 for the RK-model is equivalent to 0.7 for the D-model. In essence, updating the assumed aerosol model increases the MODIS-derived τ.

Fig. 5.3 (from [Levy et al., 2005]) demonstrates how updating to the D-model could apply to the entire CLAMS dataset. The red (at 0.66 μm) and blue (0.47 μm)

solid lines are of the regression fitted by CLAMS c004 data. Assuming that all geometry behaves like the example of Fig. 5.2, conversion from the RK-model to the D-model results in the red and blue dashed lines. The slopes for the dashed lines are increased (from 0.76 to 1.23 in the blue and from 0.46 to 0.58 in the red). While not plotted, the slope of 0.55 μm would increase from 0.64 to something much closer to one. Note that the offsets are unchanged, due to the same reflectance for both models at zero τ. This suggests that the D-model is better than the RK-model for CLAMS. Note however, that the assumption of a single geometry for all CLAMS is questionable, and inclusion of angle dependence could have changed the plot drastically. This exercise, nonetheless, demonstrated that the retrieval is sensitive to the assumed aerosol models, and that updating aerosol models can improve MODIS products. It also suggested that AERONET derived products have potential for introducing new information into the MODIS retrieval algorithm.

5.2: Surface reflectance correction for improving the y-offset

Both measurements [Kaufman and Remer 1994; Kaufman et al., 1997c] and theoretical studies [Kaufman et al., 2002)] demonstrated a relationship between visible and IR surface reflectance ρ_λ, for certain vegetated surfaces throughout the globe. These are known as the c004 VISvs2.12 surface ratios, and were assumed to be 0.25 for 0.47 μm vs 2.12 μm (0.47vs2.12) and 0.5 for 0.66 μm vs 2.12 μm (0.66vs2.12), and assumed globally for the operational MODIS retrieval over land [Kaufman et al., 1997a].

Yet it is known that these ratios vary over vegetation types and exact viewing geometry. Remer et al. [2001] measured surface reflectance aboard a low flying aircraft, and found that the VISvs2.12 relationship depends on geometry. Generally, the 0.66vs2.12 ratio was less than 0.5 for backscattering view angles, and greater than 0.5 for forward scattering. They also found seasonal differences that were weakly correlated with changes in the degree of vegetation ('greenness') of the surface (such as might be associated with the Normalized Differential Vegetation Index (NDVI; e.g. Tucker, [1979])). The blue channel (0.47 μm) exhibited even greater deviations from assumed ratios when viewed from the aircraft. Also from aircraft, Gatebe et al., [2001] demonstrated a bi-directional reflectance function (BRDF) to the surface reflectance relationships.

The landscape along the U.S. East Coast is heterogeneous, containing urban areas, forests, and grassy/agricultural fields. Due to ample rainfall and proximity to the ocean, small land water bodies (such as puddles or swamps) are also ubiquitous and may be underneath the tree canopy. While the MODIS over land algorithm attempts to mask even the most shallow water bodies, puddles and swamps are not always completely masked out. Because water is nearly black (near zero reflectance) at 2.12 μm, assuming the standard VISvs2.12 ratios would result in over-estimating the aerosol path reflectance, contributing to the y-offsets. Indeed, some of the outlying very high VIS/IR points displayed in Remer et al. [2001] were measured over swamps or puddles in forests.

5.2.1 Atmospheric correction of CLAMS data

What was the actual spectral surface reflectance relationship over the U.S. mid-Atlantic during CLAMS or over another region at a different time period? One strategy is to assume that clean aerosol conditions lead to surface reflectance retrievals with small atmospheric contamination. Operational MODIS surface land products [Vermote et al., 1997a] employ this strategy to provide land reflectance products from MODIS, by searching for the cleanest cases in eight or sixteen-day periods, and assuming appropriately low τ to assume. However, the exact spectral τ can be measured from sunphotometer, as was done during CLAMS.

Atmospheric correction [Kaufman and Sendra, 1998; Kaufman, 1999] is the process of determining the surface reflectance that would be measured if there were no atmosphere [Kaufman et al., 1997b]. Vermote et al., [1997a] describes how the atmospheric correction could be applied to MODIS over land. Using the MODIS spectral reflectance data as the primary input, the satellite reflectance can be corrected for Rayleigh scattering, aerosol scattering, and coupling between the atmospheric and surface reflectance functions. The 6S RT code includes a module for performing atmospheric correction with MODIS data [Vermote et al., 1997b], which includes trace gas and ozone assumptions.

I performed atmospheric correction on some CLAMS data to determine whether the global c004 VISvs2.12 ratios were appropriate [Levy et al., 2005]. On August 1, the AERONET instruments at both Wallops and Oyster reported very clean (τ~0.08 at 0.55 μm) and dry (PW~2.4 cm) conditions. Assuming the U.S. standard [1976] mid-latitude profile for temperature, ozone gas climatology, and near zero τ at 2.1μm, 6S was used to perform atmospheric correction on Level 1B (reflectance)

MODIS reflectance data over the CLAMS area (small box in Fig. 5.4a). Figs. 5.4b,c and d show the resulting atmospherically corrected surface reflectance at 0.47, 0.66 and 2.12 μm respectively, on a 500 m resolution. Figs 5.4e and 5.4f show the resulting 0.47vs2.12 and 0.66vs2.12 reflectance ratios over the same region. Note the bright clouds (that would be masked by the MODIS algorithm) in Fig. 5.4a that carry over to Fig. 5.4b-d as high reflectance and to Figs. 5.4e and 5.4f as high ratios. Over much of the grassy and open agricultural regions (central peninsula), the VISvs2.12 ratios are generally lower than assumed, about 0.13 and 0.45, for 0.47vs2.12 and 0.66vs2.12, respectively. Toward the coastline, however, sandy beach shores (bright in the visible) alternate with swampy forests (very dark at 2.12μm), both would greatly increase the VISvs2.12 ratios, to 0.7 and 0.8, respectively. These ratios, much higher than the assumed values, would introduce significant offsets into retrieved τ.

I also performed atmospheric correction on the lower resolution co-located (Ichoku et al. [2002a] algorithm) MODIS/AERONET data from the clean August 1 case. Even on this much larger scale, the VISvs2.12 ratios were higher than assumed by the retrieval algorithm, about 0.45 and 0.63 for 0.47vs2.12 and 0.66vs2.12 respectively.

5.2.2 Application of CLAMS-derived surface reflectance relationship

Fig. 5.5 displays images of both the operational (c004) retrieval (a) and that retrieved by simply increasing the assumed VISvs2.12 ratios to 0.45 and 0.63, respectively (b). Clearly, the use of the derived CLAMS ratios removes much of the τ discontinuity over the coastline. Applying the CLAMS ratios to all CLAMS

MODIS/AERONET comparisons (where the bulk of the AERONET sites are located near the coastline) cuts the regression y-offset in half. However, Fig. 5.5 also shows that some of the pixels far from the coastline are not retrieved when the CLAMS ratios are applied. Presumably, these increased ratios caused the algorithm to over-correct for the surface and retrieve $\tau < 0.0$ (which is screened as an unphysical value). Thus, from this exercise, it was clear that while a new VISvs2.12 surface reflectance assumption improves the regression of MODIS and AERONET during CLAMS (Fig. 5.6), the CLAMS -derived ratios are not applicable everywhere.

5.3: Use of vector RT code for simulating polarization effects

As described previously, MODIS uses two separate algorithms to retrieve clear sky (non-cloudy) τ over ocean and land. Both algorithms make use of lookup tables (LUT), wherein TOA spectral reflectance (in %) is simulated by RT calculations. Included within the RT are assumptions about the surface reflectance, molecular scattering and aerosol scattering/absorption (functions of assumed aerosol chemical and size parameters). I suspected that one reason for differences in the performance of retrievals over land versus over ocean had to do with the treatment of atmospheric polarization within the RT codes used for the LUTs. The over-ocean algorithm employs a vector radiative transfer code [Ahmad et al., 1982] that includes polarization within the atmosphere, whereas the over-land algorithm assumes a scalar RT [Dave, 1970] that neglects this effect. Under conditions of Rayleigh (molecular) optical depth (ROD) greater than 0.1, (characteristic of wavelengths < 0.55 μm) polarization within the atmosphere will modifies the TOA radiance by 2% or more [Mishchenko et al., 1994]. At 0.47 μm, the sea-level ROD is nearly 0.2, introducing

errors of 4% or more [Fraser et al., 1989] The addition of at least moderate τ (say 0.2) induces multiple scattering of the Rayleigh induced polarization. While aerosols tend to depolarize radiation (reducing the relative error from neglecting polarization), however, the increased AOT increases the TOA radiance, resulting in larger *absolute* errors in scalar assumed radiance. It is the absolute error in reflectance, not the relative error that introduces error into the retrieval of τ.

To fully describe electromagnetic radiation at the TOA, one must use the Stokes vector, I, composed of four Stokes parameters,

$$\mathbf{I} = \{I, Q, U, V\}, \tag{5.1}$$

where the scalar I represents the intensity (radiance in units of W/m^2), or reflectance (normalized radiance), and Q, U and V describe the polarization state of the radiation. Incoming sunlight at the TOA is unpolarized, such that $\boldsymbol{I} = \{I,0,0,0\}$. However, due to interaction with the surface and the atmosphere, reflected light at the TOA generally becomes polarized (Q, U, and/or V are nonzero). The degree of polarization, P, is defined as

$$P = (Q^2 + U^2 + V^2)^{1/2} / I \tag{5.2}$$

This means that radiation with polarization P, can be decomposed into unpolarized and polarized components such that [e.g. Liou, 2002; Van de Hulst, 1984]:

$$\mathbf{I} = \mathbf{I}_{\text{Unpol}} + \mathbf{I}_{\text{Pol}} = [I(1\text{-}P),0,0,0] + [IP,Q,U,V], \tag{5.3}$$

and that intensity itself is

$$I = I_{Unpol} + I_{Pol} = I(1\text{-}P) + IP. \tag{5.4}$$

If P is assumed equal to zero, this is known as the *scalar approximation* of RT transfer, and results in estimating I by I_{Unpol}. In many applications of remote sensing,

the scalar approximation is considered to be sufficient. If P is large, however, substantial errors will be introduced by equating I with I_{Unpol}. It was first shown by Chandresekhar [1950] that radiance errors introduced by the scalar approximation can exceed 10% for Rayleigh scattering. Mishchenko et al., [1994] provided expanded discussion and formal analysis of Rayleigh scattering errors in a plane-parallel atmosphere above a Lambertian surface. Their study showed that the relative error of the TOA intensity decreased with increasing depolarization (arising from multiple scattering for example), and/or increasing surface albedo. For Rayleigh single scattering albedo of 1.0 (conservative scattering), maximum relative errors were observed at (Rayleigh) optical depth near one and at scattering angles near 0° and 90°. These findings were attributed to the unique qualities of Rayleigh scattering. The Mishchenko et al., [1994] study did not include aerosols, nor did they address how errors of the estimated intensity would lead to errors in remote sensing applications, such as retrieval of τ.

For Levy et al., [2004], I employed the polarized atmospheric radiative transfer model (RT3) of Evans and Stephens [1991]. This plane-parallel, adding/doubling code allows for polarization to be turned on or off by changing only one line within an input file. Thus, it was easy to determine differences in reflectance due only to polarization. The other inputs, including the wavelength, aerosol parameters, surface reflectance and atmospheric profiles, were kept constant in both representations. Like Colarco et al., [2002], I used the Mie Vector (MIEV) code [Wiscombe et al., 1980] to compute aerosol optical properties, to be used as input to RT3. Results are presented in the following subsections.

5.3.1 Errors in TOA spectral reflectance

For Levy et al., [2004], I simulated the 'Continental' aerosol model [Lenoble and Brogniez, 1984; Kaufman et al., 1997a], composed of three lognormal modes. Mie outputs (from MIEV), included the extinction and scattering coefficients, and coefficients of the scattering phase matrix (calculated for 750 moments). For the atmospheric profile (temperature, pressure, humidity), I assumed the U.S. Mid-latitude summer profile [1976], at 36 levels between the surface and TOA. Aerosols were placed within this model atmosphere as an exponential distribution, having a scale height of 2km. I assumed the land surface to be Lambertian and very dark vegetation (as may be found around Washington, D.C), with spectral reflectance of 0.04 and 0.08 for 0.47 μm 0.66 μm, respectively. The RODs (at sea level) are about 0.194 and 0.051 for the two wavelengths, respectively (Table 3.1). Within each layer of the atmosphere, aerosol and molecular extinctions were combined to spectral τ and phase matrices, for seven discrete values of τ between 0.0 and 5.0.

The TOA spectral reflectance was calculated by both the scalar and the vector implementations of the RT3 code, for a set of 3069 sun/surface/satellite geometrical conditions. Plotted in Fig. 5.6 are the 0.47 μm and 0.66 μm differences (vector – scalar) in TOA reflectance, for eight geometries representative of MODIS geometry in the tropics and midlatitudes (Table 5.1).

TABLE 5.1
SOLAR/SURFACE/SATELLITE GEOMETRY FOR EIGHT EXAMPLES

Reference	Solar Zenith Angle	View Zenith Angle	Relative Azimuth Angle	Scattering Angle
A	12.00	6.97	60.00	163.40
B	12.00	52.84	60.00	120.53
C	12.00	6.97	120.00	169.59
D	12.00	52.84	120.00	132.35
E	36.00	6.97	60.00	140.12

F	36.00	52.84	60.00	104.74
G	36.00	6.97	120.00	147.00
H	36.00	52.84	120.00	136.29

All units are degrees

At large optical depths, the magnitude of the vector-scalar reflectance at 0.47 μm (~0.003) is about double that at 0.66 μm (~0.0015). However, in more normal aerosol loadings ($\tau = 0.25$), the differences at 0.47 μm (~ 0.004) may be more than eight times than that at 0.66 μm (~0.0008).

Fig. 5.6 also demonstrates that the sign of the vector/scalar reflectance difference can be either positive or negative. This is mainly a result of the scattering angle Θ, a result of the relative positions of the sun, surface and satellite (Eq. 2.5). Fig. 5.7 displays contour plots of the vector/scalar difference as a function of solar and view zenith geometry, for two separate relative azimuth angles ($\phi = 30°$ and 150°). Scattering angles are also plotted as contours. Generally, vector-scalar reflectance is positive when $\Theta > 135°$ and negative when $\Theta < 135°$. Magnitudes of the differences increase toward 180° and 90°, similar as would be expected from simulating a purely Rayleigh atmosphere (e.g. Lacis et al., [1998]). However, the contours are not necessarily parallel. Because upward and downward radiation paths are asymmetric, all angles must be considered, not just the scattering angle. Due to the orbit of a polar orbiting satellite such as MODIS, passing the equator close to noon, scattering angles less than 90° are rare.

5.3.2 Errors in τ retrieval

For the above examples of solar and satellite geometry, absolute vector-scalar reflectance differences at 0.47 μm are often greater than 0.01, and may be as high as 0.03 for very large solar zenith angles. For the eight selected geometrical conditions described in Table 5.1, I integrated the vector-scalar reflectance differences into the MODIS algorithm. Fig. 5.8 plots the change in retrieved τ as a function of input τ, at 0.47 μm (a) and 0.66 μm (b). Positive differences in reflectance lead to negative errors in the retrieved τ. In other words, if at a particular input τ, the new (polarized) reflectance value is larger than the old (scalar) value, the retrieved τ must be lower.

In most cases, the magnitude of the τ error is about ten times the magnitude of the reflectance error. However, at some geometries and optical depths, the ratio can be even larger. Some examples include geometries 'F' and 'B' at 0.47 μm, where the τ error is thirty times the reflectance difference at input $\tau = 3.0$, and for geometries 'G' and 'A', where the error is more than twenty times the difference at $\tau = 0.25$. The "kinks" in Fig. 5.8 are a result of numerical instability in the MODIS algorithm's interpolation.

Whereas the neglect of polarization can induce large errors (either positive or negative) upon individual aerosol retrievals, it is not clear how neglecting polarization will affect retrievals of aerosol climatology. Fig. 5.9 displays the extreme, median and quartile values of vector-scalar differences of TOA reflectance, for the entire set of simulated τ and geometrical conditions. Whereas the magnitude of vector-scalar differences can be greater than 0.03 at 0.47 μm, more than half of our simulations result in differences of 0.004 or less at this wavelength. This translates into errors of approximately 0.04 in retrieved τ (assuming a ratio of ten to one), which is not so

extreme. At 0.66 μm, maximum vector-scalar differences are 0.01, but most are less than 0.002. Also plotted in Fig. 5.9 are the maximum (magnitude) reflectance differences that would still yield τ within expected MODIS uncertainty over land, defined in this plot as $\tau_\varepsilon = \pm 0.05 \pm 0.2\tau_{true}$ [Chu et al., 2002], assuming that a 0.01 error in reflectance leads to 0.1 error in derived τ. In more than half the simulations, the neglect of polarization does not lead to extreme errors in retrieved τ, even at 0.47 μm.

Finally, Fig. 5.9 also plots the median vector-scalar reflectance difference for the set of simulated geometry, –0.0008 for 0.47 μm and –0.0002 for 0.66 μm. These errors would introduce approximately +0.008 and +0.002 errors upon the retrieved τ in the two wavelengths, respectively. These are small relative to typical τ~0.2 (over the continents).

Next, I compared the simulated geometry to the statistics of MODIS observation geometry over long-term and global scales. MODIS-atmosphere global data (Level 3 Daily) includes scattering angle histogram data, that can be aggregated into a year-long histogram. [http://modis-atmos.gsfc.nasa.gov] that includes over two billion observations (Fig. 5.10). MODIS from Terra and MODIS from Aqua are plotted separately as well as together. The Figure shows that the simulated geometry is similar to the observed geometry, and may even over represent extreme angles, suggesting that TOA reflectance errors from neglecting polarization would introduce only a small error (~ 0.008) into a global, long term value of MODIS derived τ over land. This means while a vector code is not required for deriving aerosol climatology,

including polarization is necessary if MODIS is used to monitor individual aerosol events, such as in application to air quality.

5.4: Additional strategies for improving MODIS aerosol retrieval over land

The first three subsections in this chapter describe several approaches for improving aerosol retrieval from MODIS. These were all investigated based on my original intent to improve the algorithm for specific application over the U.S. mid-Atlantic. These approaches should be generally and universally applicable regionally and globally. However, there are a number of other concepts that should be addressed, including:

- Consistency of the assumed wavelengths compared to response function of the MODIS channels. The assumed wavelengths for the MODIS c004 over-land algorithm differ from those assumed over ocean, in some channels, by up to 10 nm.
- Assumption of sea-level Rayleigh optical depth (ROD) as a function of the 'correct' MODIS channel wavelength. For the 0.47 μm channel, the over-ocean algorithm assumes 0.466 μm, whereas the over-land algorithm assumes 0.470 μm. This amounts to differences in assumed ROD of ~0.008.
- Correction for (lower) Rayleigh optical depth in elevated terrain. The MODIS over-land algorithm makes a correction for elevated terrain, by simply adding the difference from assumed sea-level ROD, and in the 0.47 μm channel only. Differences in Rayleigh versus aerosol phase functions may introduce errors.

- Cloud masking and selection of statistically appropriate pixels to be used in a 10 x 10 km framework.
- Implementation of a MODIS aerosol retrieval on a finer (urban?) scale.

The last two points were not considered for this dissertation.

5.5: A new paradigm for MODIS aerosol retrieval.

Yoram Kaufman challenged me to find a way to estimate the land surface reflectance with higher accuracy, such that one could separate aerosol and land surface signals based on the observed spectral dependence including that in the 2.12 μm channel. One major theoretical flaw of the c004 algorithm is that aerosol is assumed to have no interaction with the 2.12 μm radiation. In other words, τ at 2.12 μm is assumed zero for all aerosols. For a fine-dominated aerosol such as urban/industrial aerosol (either the Remer and Kaufman, [1998] or Dubovik et al, [2002a] models), $\tau = 0.50$ at 0.55 μm translates into $\tau \sim 0.05$ at 2.12 μm. Surface reflectance ratios of ¼ for the 0.47 μm channel and ½ for the 0.66 μm channel, produce errors in retrieved τ of approximately 0.0125 and 0.025, respectively for the two channels. However, for coarse-dominated dust aerosol, with much lower spectral dependence, $\tau \sim 0.3$, such that there much larger scattered reflectance at 2.12 μm (Fig. 2.2). This is a significant source of the observed signal at 2.12 μm that, if neglected, can lead to significant errors in retrieved visible τ (e.g. $\tau \sim 0.15$ at 0.66 μm). This is a bias that is correctable, and provides the major incentive for development of the second-generation operational algorithm, described in the next two chapters.

CHAPTER 5 FIGS.

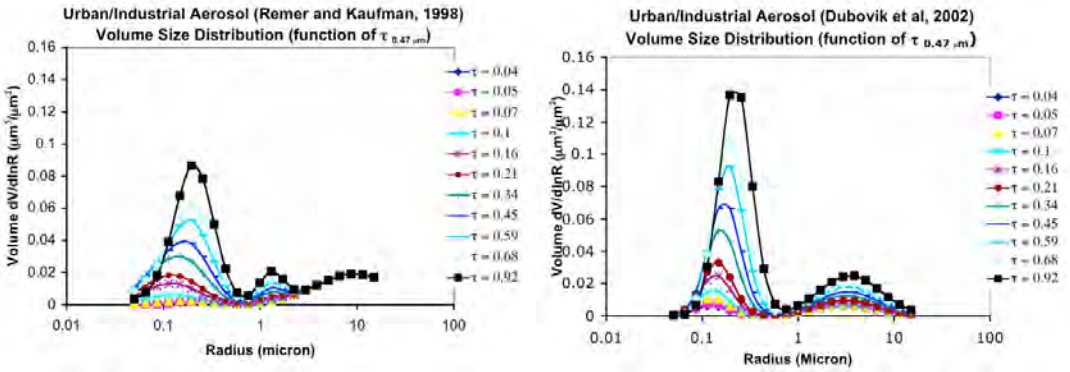

Fig. 5.1: Volume size distributions for the dynamic urban/industrial models of Remer and Kaufman [1998] ('RK-model') and Dubovik et al., [2002a] ('D-model). Curves are monotonically increasing functions of τ at 0.44 μm. (Fig. reproduced from [Levy et al., 2005]). Note the 0.44 μm channel was selected to be consistent with the AERONET derivations

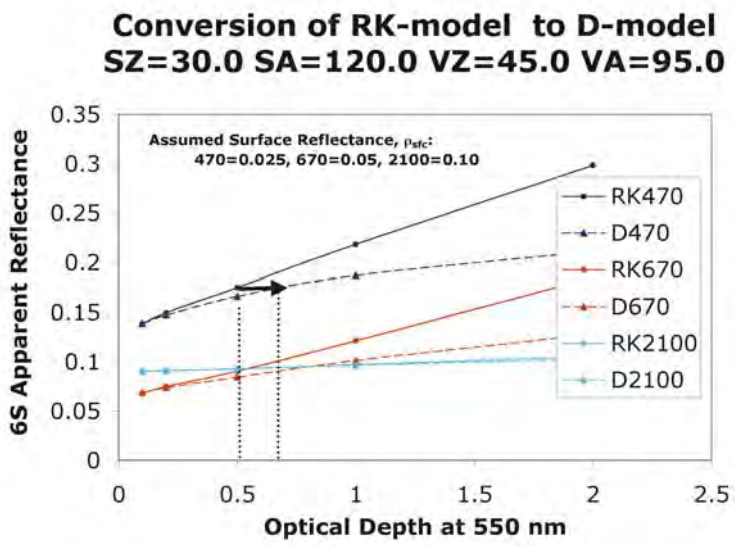

Fig. 5.2: Conversion from the RK-model to the D-model. Apparent (satellite) reflectance has been calculated using 6S code. Black arrow shows conversion for a given apparent reflectance. SZ is the solar zenith angle, SA is the solar azimuth angle, VZ is the satellite view zenith angle and VA is the satellite view azimuth angle, all in degrees. (Fig. reproduced from [Levy et al., 2005]).

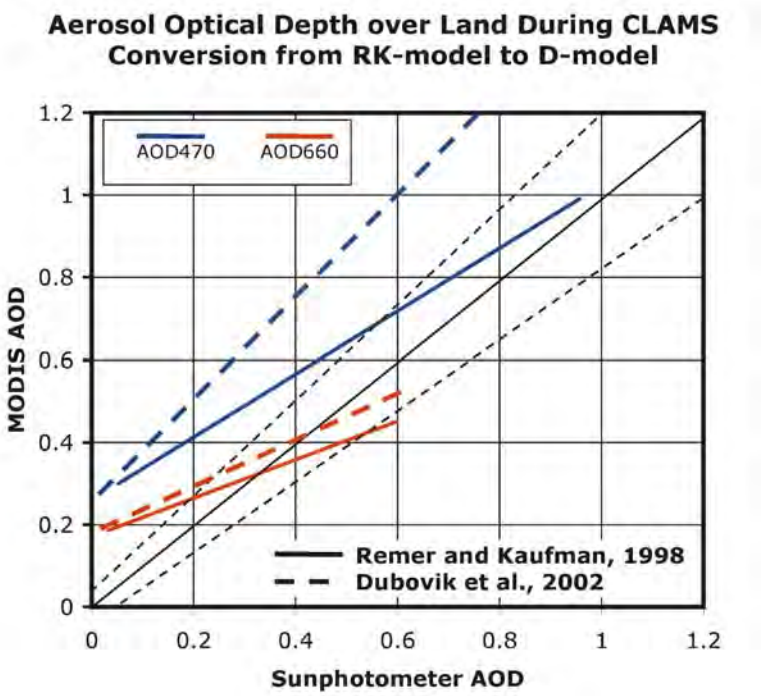

Fig. 5.3: Empirically corrected τ (AOD) over land. Solid red and blue lines are the regression lines from Fig. 1.2. The red and blue dashed lines are the corrected optical depths. The black lines are the expected errors plotted in Fig. 1.2. (Fig. reproduced from [Levy et al., 2005])

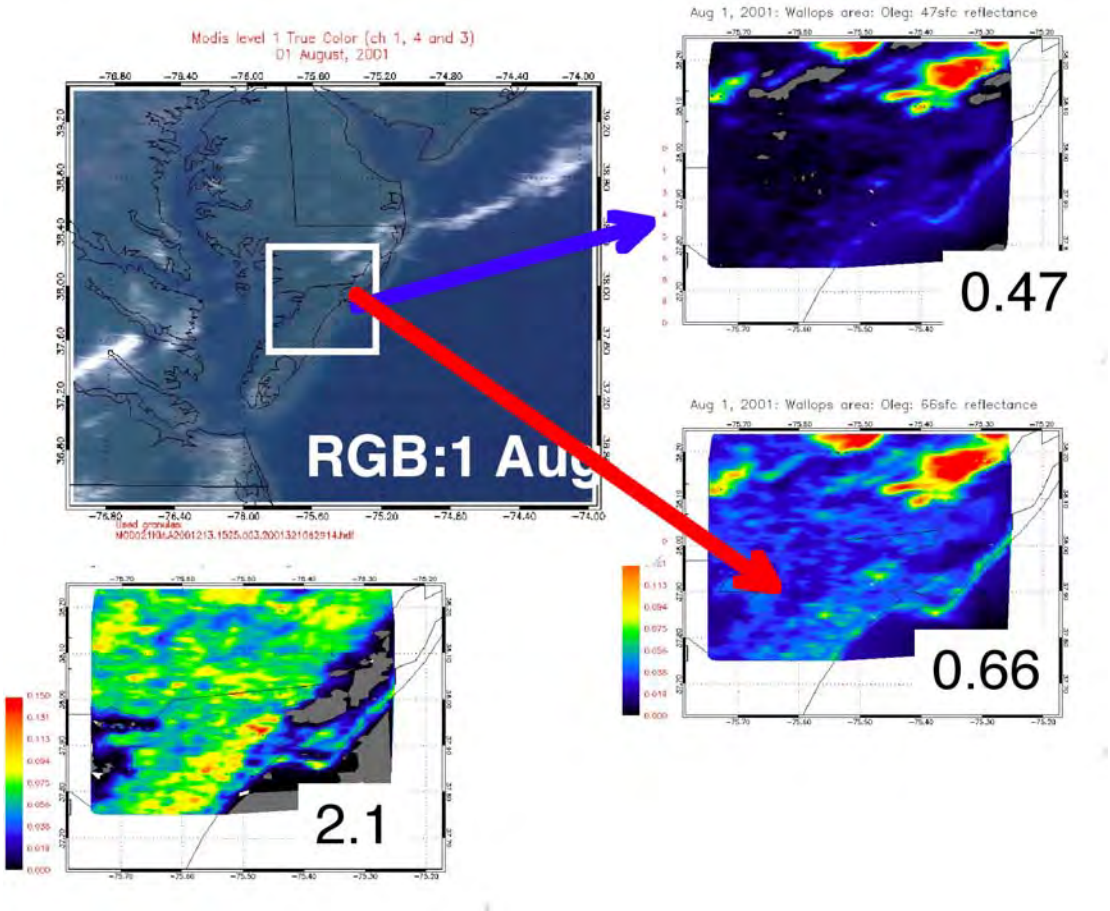

Fig. 5.4: Atmospherically corrected surface reflectance a) at 0.47 µm; b) at 0.66 µm; and c) at 2.1 µm, for a small portion of the August 1, 2001 granule shown in the RGB image. The clouds have high reflectance in the visible wavelengths, but are not as distinct at 2.12 µm. (Fig. reproduced from [Levy et al., 2005]).

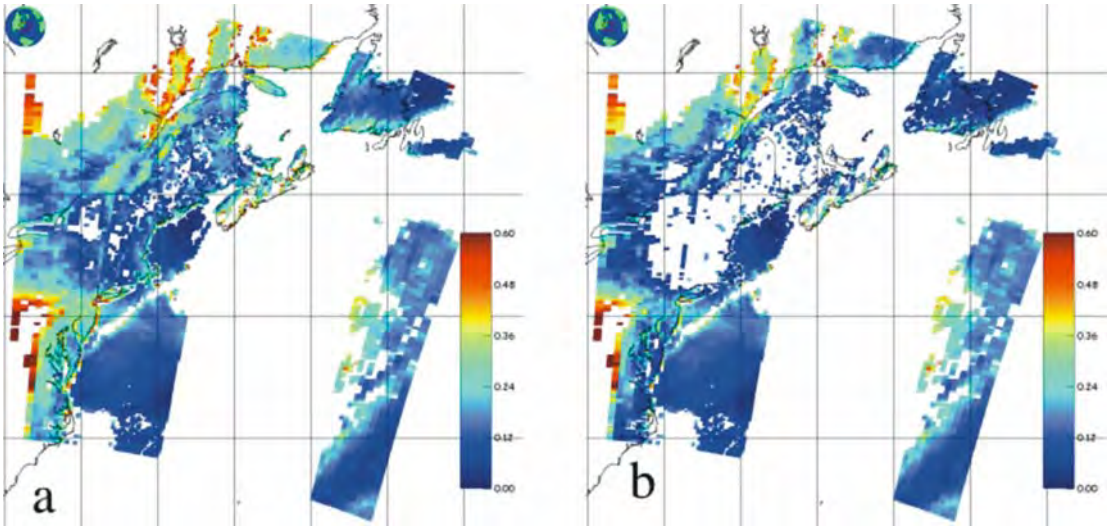

Fig. 5.5: τ at 0.55 μm for the August 1 case retrieved a) using the c004 assumed VISvs2.12 surface reflectance ratios and b) using the CLAMS-derived VISvs2.12 ratios. The discontinuities along the coastline in a) that were mostly removed in b). Note that some of the τ retrievals in New England are now missing.

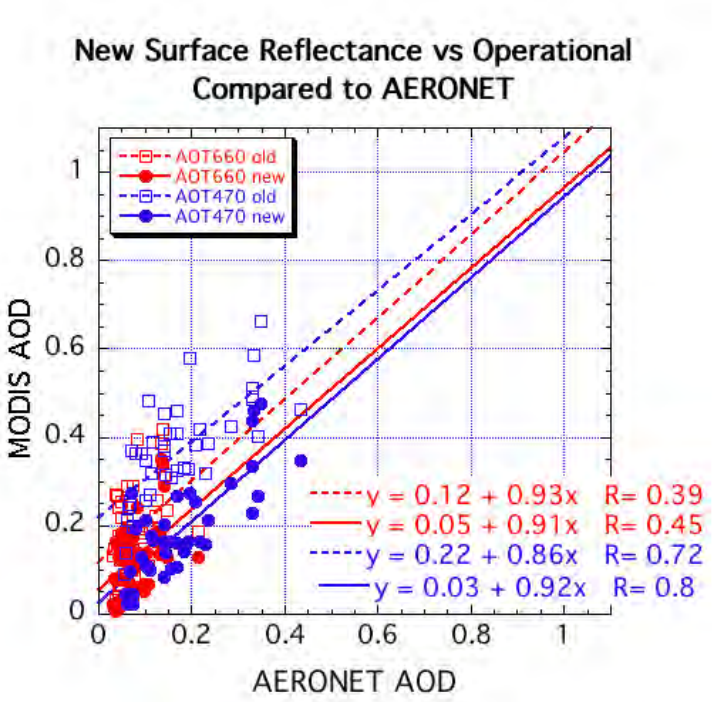

Fig. 5.6: Comparison of τ (at 0.47 and 0.66 μm) retrieved by MODIS-land and by AERONET. The open symbols and dashed lines represent retrievals using the c004 VISvs2.12 surface reflectance ratios, whereas the filled symbols and solid lines represent retrievals using the CLAMS-derived surface reflectance ratios. (Fig. reproduced from [Levy et al., 2005]).

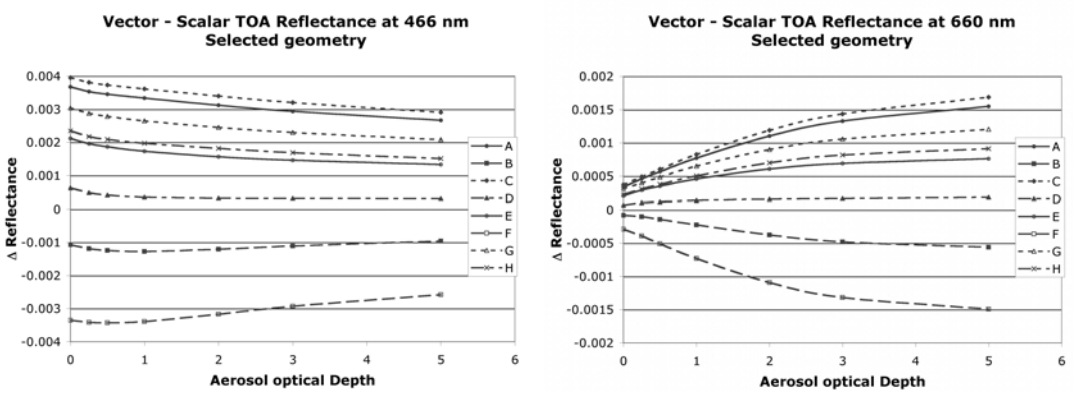

Fig. 5.6: Difference between vector and scalar derived reflectance at the TOA, for eight example sun/surface/satellite geometries, as a function of τ. a) At 0.466 μm, where the ROD = 0.194. b) At 0.66 μm, where the ROD = 0.051. Details of the eight geometries are given in Table 5.1. (Fig. reproduced from Levy et al., [2004]).

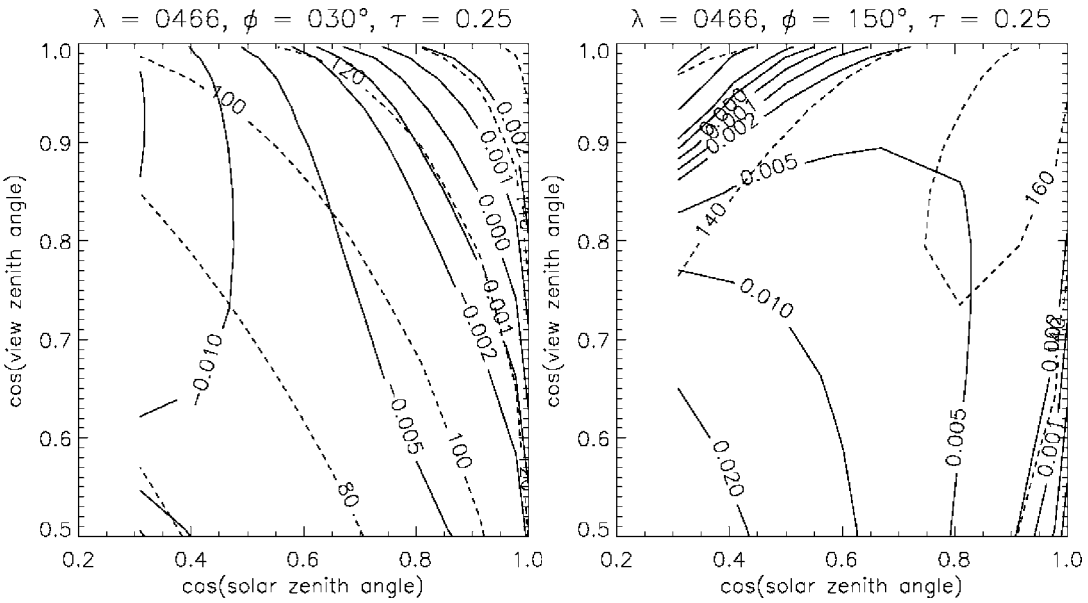

Fig. 5.7: Contour plots of the reflectance difference (vector – scalar) between RT3 calculations of TOA 0.466 μm reflectance, as a function of view and solar zenith angles for two different relative azimuths. Contours of scattering angle are also plotted. τ= 0.25 and ROD = 0.194. a) ϕ = 30°, b) ϕ = 150°. Note the signs of the contours. (Fig. reproduced from Levy et al., [2004].

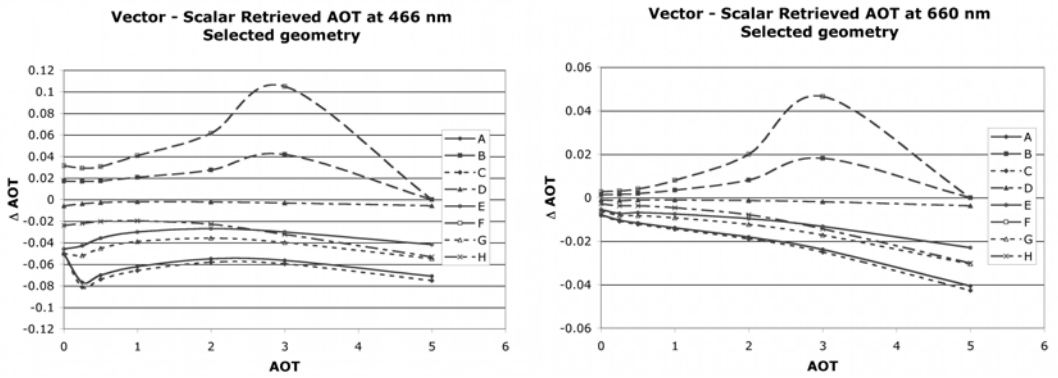

Fig. 5.8: Errors in retrieved τ (AOT), as a function of input τ, due to the neglect of polarization in the RT formulation, for each of the sample geometries listed in Table 5.1. a) 0.466 μm; b) 0.660 μm. (Fig. reproduced from [Levy et al., 2004]).

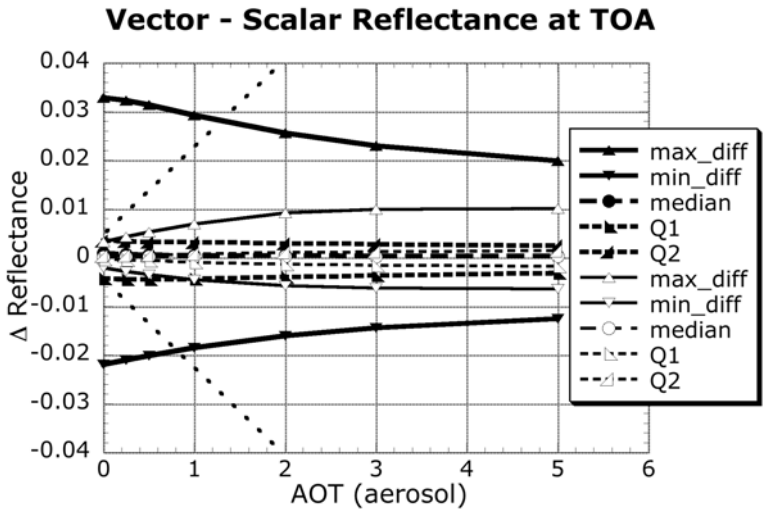

Fig. 5.9: Maximum, minimum, median and quartile values of the difference between vector and scalar TOA reflectance, plotted as a function of τ. Thick curves and closed symbols represent 0.47 μm whereas thin curves and open symbols depict 0.66 μm MODIS channels. The black dotted lines approximate the maximum difference in reflectance that would yield τ retrieved within the expected τ error ($\Delta\rho \sim ((0.05 + 0.2\tau) / 10)$. (Figure reproduced from [Levy et al., 2004]).

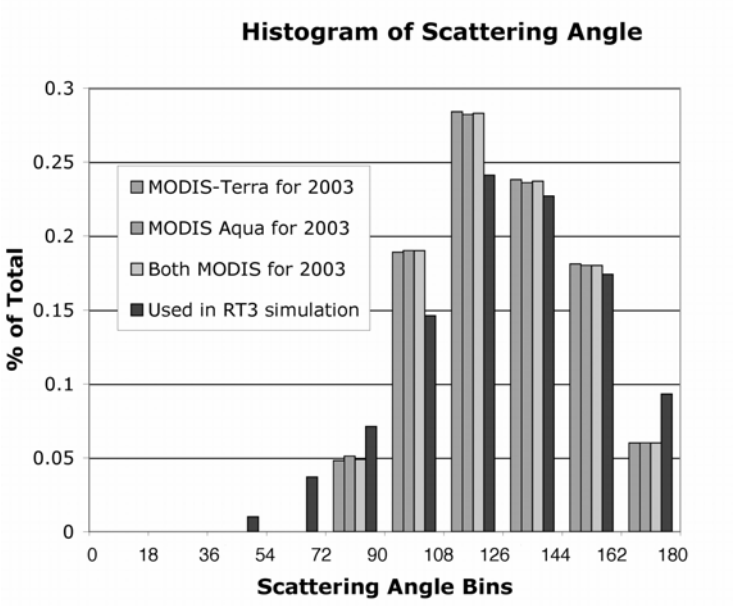

Fig. 5.10: Histograms of scattering angles simulated by our set of geometry compared to scattering angles observed by MODIS throughout the course of 2003. Terra and Aqua are plotted separately and together. (Fig. reproduced from [Levy et al., 2004]).

Chapter 6: Global aerosol models for the second-generation algorithm

Chapter 5 examined some of the sources of error in the global MODIS aerosol retrieval (c004). The next two chapters summarize the development of the second-generation algorithm, expanding the concepts introduced in Chapter 5. This chapter summarizes my derivation of new global aerosol models and optical properties [e.g. Levy et al., 2007a]; Chapter 7 details the mathematical implementation of a new algorithm, including parameterization of surface reflectance [e.g. Levy et al., 2007b].

6.1: Motivation

The limited wavelengths used in the MODIS algorithm over land provide rough information about aerosol size, and can be used to estimate η (non-dust fraction). However, since the MODIS over-land retrieval suffers from surface and other contaminations, it is not sufficiently sensitive to aerosol ω_0 or details of the size distribution within each size range (fine or coarse). Therefore, the algorithm must select the aerosol model *apriori* of the retrieval.

As described by Remer et al., [2005], the c004 over-land aerosol algorithm selects the aerosol type (model) appropriate for a given region and season. For many regions around the world, there were little or no data for our decisions were made. In other words, some of the model assignments were essentially guesses. The assumed optical properties (size and refractive index) used for creating the LUTs were also based on very limited information. For example, the 'Urban/Industrial' model, derived by Remer and Kaufman [1998], was derived from fewer than 150 AERONET almucantur measurements at six sites along the East Coast of the U.S, during the

summertime only. The model's optical properties were calculated using early versions of the almucantur retrieval algorithm (e.g. [Nakajima and King, 1990; Kaufman et al., 1994]). Even though aerosol properties are different in the winter (less water), in Europe (more absorbing) and the U.S. Midwest (larger particles), the Remer and Kaufman [1998] East Coast summertime aerosol model was assumed not only for the East Coast U.S. during all seasons, but to the entire Eastern half of the U.S. and to Europe!

Since the original development of the MODIS aerosol algorithm, and even since the advent of c004 products, much has been learned about global and regional aerosols' physical and optical properties. Dubovik et al. [2002] analyzed AERONET almucantur inversions at selected sites around the globe, where each site presumably represented a different aerosol regime. Their study resulted in derivation of bi-lognormal aerosol models for each of these sites, which included descriptions of their size and optical properties. For Levy et al. [2005], I applied the Dubovik et al. [2002] version of the Urban/Industrial aerosol model derived at GSFC, and found that the model improved retrievals of U.S. mid-Atlantic aerosol during the summer of 2001. While these studies found unique aerosol types at each site, they did not account for seasonal variation, nor were they necessarily representative of all AERONET sites.

Omar et al., [2005] attempted to interpret all almucantur retrievals from all AERONET sites to determine global aerosol climatology. They performed a cluster analysis of AERONET data and found that six aerosol models (listed as desert dust, biomass burning, background/rural polluted continental, marine, and dirty pollution) represented the global AERONET dataset. These models varied mainly by their ω_0

and size parameters. Two models were representative of clean conditions (marine and background/rural $\tau < 0.1$). One of the remaining models (dust) was dominated by coarse mode, whereas three were dominated by fine mode. The three fine-dominated models varied mainly by their ω_0 (biomass burning, polluted continental, and dirty pollution). While their study determined which models were observed over each AERONET site, it did not try to assign unique aerosol type to each site. Because of the similarity (in physics) of remotely sensed measurements from AERONET and satellite, the following section uses the AERONET data to distinguish regional aerosol types.

6.2: Cluster analysis of AERONET data

Cluster analysis encompasses a number of different algorithms and methods for grouping objects of similar kind into respective categories. A general question facing researchers in many areas of inquiry is how to organize observed data into meaningful structures. In other words cluster analysis is an exploratory data analysis tool which aims at sorting different objects into groups in a way that the degree of association between two objects is maximal if they belong to the same group and minimal otherwise. Therefore, cluster analysis can be used to discover structures in data without providing an explanation for why they exist at all. It is up to the investigator to provide this explanation based on his or her theoretical understanding of the matter. For air quality studies, clustering has been used to organize wind backtrajectories for understanding the interaction of sources and meteorology that contributes to polluted conditions along the U.S. mid-Atlantic (e.g. [Taubman et al., 2006; Hains et al., submitted 2007]).

The goal here is to discover patterns in AERONET data in order to determine the properties of aerosol at a given site. For the purpose of a constrained satellite algorithm, where the aerosol type must be known *apriori* to the retrieval, the final goal is to assign an aerosol model that is appropriate in a given region. Thus, the Omar et al., [2005] study, while it provides meaningful interpretation to aerosol optical models, does not assign a particular model at a particular site. Therefore, I performed a sort of 'forced' cluster analysis, thereby limiting the number of potential clusters. I used the cluster analysis routines provided with the IDL (Interactive Display Language) software version 6.1.

There were about 136,000 AERONET almucantur retrievals that were processed as of February 2005. At that time, the AERONET retrievals did not determine non-spherical fraction [e.g. Dubovik et al., 2006], instead assuming that either aerosol is 100% spherical or 100% spheroid mixture. About 13,496 spherical and 5128 spheroid retrievals (~14%) met the minimum quality parameters suggested by the AERONET team, including: $\tau_{0.44} > 0.4$, $\theta_0 > 45°$, 21 symmetric left/right azimuth angles, and radiance retrieval error less than 4%. Quadratic fit to the spectral τ [e.g. Eck et al., 1999], yielded τ at 0.55 μm ($\tau_{0.55}$) associated with each almucantur retrieval. In order to extract expected dependence on τ, (e.g. [Remer and Kaufman 1998]), the retrievals were separated into ten equal bins of τ (having $\tau_{0.55}$ medians ranging between 0.28 and 1.33). Note that while AERONET requires $\tau_{0.44}>0.40$, because of the strong spectral dependence of most aerosol, the minimum bin for $\tau_{0.55}$ is around $\tau_{0.55}=0.28$. This is only slightly higher than the lowest τ index within the

operational c004 MODIS LUT (τ=0.25), so no significant aerosol information is lost. We cluster each τ bin separately to keep track of dynamic properties.

Knowing that MODIS is incapable of separating similar sized aerosol types over land, I chose to limit the number of possible aerosol types, to represent 'low', 'medium' and 'high' in some parameter space. Thus, the cluster analysis is allowed to find only three clusters. It is assumed that clusters from separate τ bins can be recombined in some way, to collectively describe the dynamical properties of a particular aerosol type.

Omar et al., [2005] showed that other than τ, unique aerosol types are identified by parameters that represent aerosol size and absorption. Therefore, I chose to cluster with respect to only two optical parameters: SSA (ω_0) at 0.67 μm and the asymmetry parameter (ASYM or g) at 0.44 μm, assuming that one absorption parameter (ω_0) and one size parameter (g) is sufficient to represent the entire aerosol parameter space. Separate wavelengths were chosen to reduce the chance for finding an artificial dust cluster due to its near-ultraviolet 0.44 μm absorption (ω_0), while noting that larger-sized aerosols are be better separated by phase function asymmetry at the shortest wavelength (0.44 μm).

Since I 'forced' the cluster analysis to retrieve three distinct aerosol clusters, I desired that each cluster would comprise about a third (plus or minus) of the entire AERONET population. However, the results included two clusters with significant fraction and a third with only 11 points. This eleven-point cluster included points with unusually low $\omega_0 < 0.6$, and/or $g < 0.5$, indicating either retrieval errors or true (physically unlikely) outliers. Upon removing these points and re-clustering, there are

now three clusters each having a similar number of points. Averaging the optical parameters within each cluster yields three distinct spherical fine-dominated aerosol optical models.

At each AERONET site, and for each season, Fig. 6.1 (a-d) displays pie-plots showing the percentage of the retrievals attributed to each cluster. To remove poor statistics, only shown are pie plots at sites having at least 10 observations (per season) during the history of AERONET, excluding the many sites that have few retrievals of $\tau_{0.44} > 0.4$ ($\tau_{0.55} > \sim 0.28$). Green pie segments represent the non-absorbing $\omega_0 \sim 0.95$ model (presumably urban/industrial aerosol, dominated by sulfate and OC), blue segments are the moderately absorbing $\omega_0 \sim 0.90$ model (presumably generic, forest smoke and developing world aerosol), and red segments designate the highly absorbing $\omega_0 \sim 0.85$ model (presumably savanna/grassland smoke aerosol). At most sites and most seasons, the aerosol type is as expected. Non-absorbing aerosol (green) dominates the U.S. East Coast and far western Europe, whereas highly absorbing aerosol (red) dominates the savannas of South America and Africa. Most other sites are either dominated by moderately absorbing aerosol (blue) or are a mix of all clusters.

There are some surprises, however. Southeast Asia seems to be primarily non-absorbing aerosols, as opposed to more absorbing type assumed by Remer et al., [2005]. Recent studies (e.g. Eck et al., [2005]) confirm that aerosol in urban areas in far Southeast Asia are primarily non-absorbing ($\omega_0 \sim 0.95$). A few sites in Western Europe have large fractions of absorbing aerosol, possibly a result of heavy diesel use.

A similar cluster analysis was performed for the spheroid retrievals, resulting in that a single cluster is sufficient for describing the spheroid-based almucantur inversions [Dubovik et al., 2006]. Since the sites contributing to spheroid data are primarily those known to be in dust regions, the spheroid model presumably represents coarse-dominated (dust) aerosol.

6.3: Regional assignment of aerosol type

Since the MODIS aerosol retrieval over land is not sufficiently sensitive to ω_0, the expected aerosol type must be assigned *a priori* to the retrieval. Remer et al., [2005] described how assumed aerosol type was assigned to region and season for the c004 algorithm, even where little was known about the prevailing aerosol type. For example, MODIS assigned the same moderately absorbing smoke properties in regions of forest fire burning (both tropical and high latitude forest) and developing industrial regions in Eastern Europe and most of Asia. Whether the c004 boundaries are appropriate can be evaluated by determining the dominant aerosol type represented at each AERONET site (Fig. 6.1), and within regions.

Keeping in mind our goal of dividing the world into plausible aerosol types, a MODIS algorithm requires that each site should have an assumed aerosol type attached to it. The moderately absorbing aerosol type is set as the default, overwritten only if clear dominance of one of the other two aerosol types is observed. If either the non-absorbing or the absorbing aerosol occupies more than 40% of the pie, while the other occupies less than 20%, the site is assigned to the dominant aerosol type. For example, GSFC (39°N, 77°W) during the summer months (JJA), is 87% non-

absorbing and 13% moderately absorbing, meaning the non-absorbing type is assigned.

Fig. 6.2 (a-d) displays the aerosol types assigned at each site. As in Fig. 6.2, green represents non-absorbing, blue represents moderately absorbing and red designates absorbing aerosol types. Most site designations seem reasonable and expected. North America during the summer (JJA) is split between non-absorbing and moderately absorbing aerosol types at approximately 100°W longitude, similar to that assumed in Remer et al., [2005]. Southern Africa during the winter season (DJF) is solidly designated as absorbing aerosol (like was found by Ichoku et al., [2003]). Even though Western Europe is evenly split between non-absorbing and moderately absorbing (except for two absorbing sites), the entire region was assigned to 'non-absorbing', deferring to that assumed by the MODIS c004 algorithm.

Fig. 6.3 plots the final assignment of aerosol types around the globe, as a function of season. Note that where possible the shapes correspond with the clustering of AERONET sites over land. At some regions, however, some subjectivity was needed to connect areas and draw lines. Over southeastern Asia, high mountains are boundaries between two aerosol regimes. Over Brazil, the boundary is near the border of Amazon forest and grasslands. Even though insufficient data exists for Africa north of the equator, the known surface types and seasonal cycles suggest that heavy absorbing aerosol would be produced during the biomass-burning season [Pinker et al., XXXX?]. Red designates regions where the absorbing aerosol is chosen, whereas green represents non-absorbing aerosol. The moderately absorbing (ω_0~ 0.90) model is assumed everywhere else. These images were mapped onto a 1°

longitude x 1° latitude grid, such that a fine aerosol type is assumed for each grid point, and each season. As new information becomes available (e.g. [Mi et al., submitted 2007]), these maps can be easily updated.

6.4: Physical and optical properties of the aerosol models

As indicated in section 6.2, my 'forced' AERONET clustering produced three spherical, fine-dominated models (moderately absorbing, absorbing and non-absorbing), and one spheroid, coarse-dominated type (dust). I considered these to represent the range of expected global aerosol. By averaging the properties within each aerosol type cluster, the physical properties of each aerosol 'model' are determined. These models can be compared with the well-known 'Continental' model (Lenoble and Brogniez, 1984) that is used in many satellite applications, including over-land applications of MODIS (e.g. [MAST, 2006] for aerosol and http://modis-land.gsfc.nasa.gov for MODIS land surface products).

Fig. 6.4 shows the size distributions for the four AERONET-derived models as a function of τ. Note the strong dynamic nature of the size properties of the non-absorbing model, consistent with urban/industrial aerosol models (e.g. Dubovik et al., [2002]; Remer and Kaufman [1998]). While the primary product of the AERONET almucantur inversion is the complex refractive index and the volume size distribution *dV(r)/dln(r)* in 22 bins of equal log size (*dlnr*), the AERONET retrieval reports the set of two lognormal modes that represent the size distribution.

Table 6.1a displays the lognormal size parameters and refractive indices for the four AERONET-derived models, as well as the 'Continental' model. For each lognormal mode, r_v is the median radius of the volume size distribution, σ is the

standard deviation of the radius, and V_0 is the volume of particles per cross section of the atmospheric column (i.e. the amplitude of the lognormal size distribution).

Theoretical scattering and absorption properties of aerosols are explained in Chapter 2, and are defined as a function of wavelength, aerosol size and composition (which establishes the complex refractive index). Calculation of extinction and scattering efficiencies are accomplished by using a Mie computer program (MIEV, [Wiscombe, 1980]). Assuming the size distribution is normalized (N_0=1), Q_{ext}, Q_{sca} and $P(\Theta)$ for the particle population are defined by integrating the single particle properties over the size distribution. This requires a sufficient number of Mie size parameter ($X=2\pi r/\lambda$) bins (such as 300 or more that cover $0.02 < X < 2000$). The actual number of bins depends on how many are needed to represent a given accuracy (say 99.99%) of the area distribution described by the theoretical distribution. For non-spherical aerosol particles, a code (such as a complete or approximate T-matrix code; [Mischenko et al., 1994, Dubovik et al., 2006] is required.

Mass and extinction properties are related through the mass extinction coefficient, B_{ext}. For the purpose of columnar mass M estimation, the *mass concentration coefficient* (M_c) can be defined as:

$$M_c = \frac{1}{B_{ext}} \tag{6.1}$$

so that

$$M = \tau M_c. \tag{6.2}$$

In reality, since the aerosol lognormal properties are dependent on τ, the extinction parameters and thus M_c is also a weak function of τ. Table 6.2 lists the extinction,

scattering and mass conversion factors for the four AERONET-derived aerosol models, along with the Continental model for comparison. In each case, $\tau_{0.55}$=0.5.

Fig. 6.5 plots numerous properties of the four AERONET-derived aerosol models, along with the Continental model for comparison. Figs. 6.5-d are plotted for $\tau_{0.55}$ = 0.5, where Fig. 6.5b plots the spectral dependence of τ, 6.5a plots phase function at 0.55 μm, 6.5c plots the spectral dependence of ω_0, and 6.5d plots the spectral dependence of *g*. Note that even though the three fine-dominated models have similar τ spectral dependence, they differ in other properties. The coarse model (spheroid-dust) has much smaller spectral dependence than any of the fine-dominated models, and nearly flat phase function in the 90°-180° scattering angle range observable by MODIS.

Fig. 6.6 compares the phase function of each of the models (also for $\tau_{0.55}$ = 0.5) as compared to the analogous models from the MODIS c004 algorithm. Differnences are minimal (especially for the 90°-180° scattering angle range) for the non-absorbing (urban) and absorbing (heavy smoke) aerosol types. A possibly significant change is seen in the moderately absorbing (developing world/moderate smoke) phase function. The largest change is for the 'dust' model, due to assuming spheroids instead of spheres. The differences are primarily in the MODIS-observable scattering angle ranges, which will have a significant effect within the aerosol retrieval. The quality of these aerosol models is evaluated in the next section.

6.5: Simulation of spectral τ with model optical properties.

How well do the assigned aerosol models represent ambient aerosol at specific AERONET sites? The time series of Level 2 'sun' (extinction of direct solar radiation) retrieved products from AERONET are independent of the 'sky' retrieved products. The sun measurements cannot evaluate the assumed absorption properties, but can validate the resulting spectral dependence of the aerosol optical depth.

Fig. 6.5b showed the spectral τ dependence of each model for $\tau_{0.55}$ =0.5. Similar plots could be made from the spectral dependence indexed by other $\tau_{0.55}$ values. For each AERONET site, the sun-retrievals were divided into three-month seasons (winter = DJF, spring = MAM, summer = JJA, fall = SON). The *N* (number of) observations within each season were sorted according to $\tau_{0.55}$, where $\tau_{0.55}$ was calculated by fitting a quadratic to the observed spectral τ. For given indexed value of $\tau_{0.55}$ (τ = 0.25, 0.5, 1.0, 2.0), I determined which AERONET observation contained $\tau_{0.55}$ closest in magnitude to the indexed value. This location was considered the 'central' (C) index of the bin and all observations indexed between C-N/20 and C+N/20 determined all observations considered 'close' to the indexed $\tau_{0.55}$ value. The spectral optical thickness for each bin was calculated by averaging the spectral optical thickness for the set of observations within the bin.

Fig. 6.7 compares spectral dependence of the aerosol models with spectral dependence at selected AERONET sites, for indexed $\tau_{0.55}$ = 0.5. Since MODIS observes at many wavelengths (including 0.47, 0.55, 0.66, 0.86 and 2.12 μm bands), the AERONET spectral τ observations (4 to 8 bands between 0.34 and 1.02 μm, depending on site) were interpolated to the same wavelengths. Extrapolation of AERONET to 2.12 μm was not performed because of the great distance from 1.02

μm. Different seasons (for AERONET) are represented by different line styles. At least one fine-dominated model, plus dust, are plotted for each site.

At Alta Floresta (9°S, 56°W), the spectral dependence in the visible wavelengths agrees well with either the moderately absorbing or absorbing models. The AERONET spectral dependence varies with season, and is seen most clearly at 0.86 μm. During the summer and fall, the AERONET dependence is slightly closer to the absorbing model than the moderately absorbing, and during the winter and spring, the moderately absorbing model provides a slightly better match to sun-derived spectral τ. Therefore, the distribution of models includes this seasonal dependence at this location.

At Cape Verde (16°N, 22°W), although the moderately absorbing fine-dominated model is assumed all year, coarse (dust) is expected to dominate. Plotted for Cape Verde is the AERONET spectral τ compared with the modeled dust. Even though the dust model is improved from that assumed by MODIS c004, my modeled spectral dependence is still too large to properly represent dust over Cape Verde. This means that my global dust properties may not be specifically appropriate for Cape Verde and that separate dust models may be required at different sites. Yet, errors between modeled and observed spectral dependence are smaller than for c004.

The non-absorbing model ($\omega_0 \sim 0.95$) shows remarkable match to observations at GSFC (39°N, 77°W). The only difference is seen during the winter and spring for the lowest τ value (0.25), where the particles are known to be larger (have less spectral dependence) than the rest of the year. Mongu (15°S, 23°E) is another site that is well represented by its assumed aerosol type (absorbing).

Beijing (39°N, 116°E) and Venice (45°N, 12°E) are interesting because dominant aerosol type is known to vary. Both sites are influenced by dust transport, so that the averaged AERONET spectral dependence should lie somewhere between the fine-dominated and coarse-dominated (dust) models. It is clear that Beijing is mixed, and is more coarse-dominated during the winter and spring. Venice is less often in the path of dust (from Africa) but its averaged spectral dependence shows the addition of coarse aerosol not represented by a fine-dominated model.

The derivation of the new set of aerosol models provides important information on characterizing the global aerosol system. Details about their derivation are important for comparison with measurements from other sensors and with models. These models have been implemented within the new aerosol algorithm described in Chapter 7 [Levy et al., 2007], and are improving the accuracy of the aerosol retrieval over land.

CHAPTER 6 TABLES

TABLE 6.1: OPTICAL PROPERTIES OF THE AEROSOL MODELS USED FOR THE V5.2 OVER-LAND LOOKUP TABLE

Model	Mode	r_v (μm)	σ	V_0 ($\mu m^3/\mu m^2$)	Refractive Index: k
Continental					
	Water Solub	0.176	1.09	3.05	1.53 - 0.005i; 1 1.53 - 0.006i; 2 1.53 - 0.006i; 3 1.42 - 0.01i; 4
	Dust	17.6	1.09	7.364	1.53 - 0.008i; 1 1.53 - 0.008i; 2 1.53 - 0.008i; 3 1.22 - 0.009i; 4
	Soot	0.050	0.693	0.105	1.75 - 0.45i; 1 1.75 - 0.44i; 2 1.75 - 0.43i; 3 1.81 - 0.50i; 4
Moderately absorbing/ Developing					
	Accum	$0.0203\tau + 0.145$	$0.1365\tau + 0.374$	$0.1642\ \tau^{0.775}$	$1.43 - (-0.002\tau+0.008)i$
	Coarse	$0.3364\tau + 3.101$	$0.098\tau + 0.729$	$0.1482\ \tau^{0.684}$	$1.43 - (-0.002\tau+0.008)i$
Absorbing/ Smoke					
	Accum	$0.0096\tau + 0.134$	$0.0794\tau + 0.383$	$0.1748\ \tau^{0.891}$	$1.51 – 0.02i$
	Coarse	$0.9489\tau + 3.448$	$0.0409\tau + 0.743$	$0.1043\ \tau^{0.682}$	$1.51 – 0.02i$
Non-absorb/ Urban-Ind					
	Accum	$0.0434\tau + 0.160$	$0.1529\tau + 0.364$	$0.1718\ \tau^{0.821}$	$1.42 - (-0.0015\tau+0.007)i$
	Coarse	$0.1411\tau + 3.325$	$0.1638\tau + 0.759$	$0.0934\ \tau^{0.639}$	$1.42 - (-0.0015\tau+0.007)i$
Spheroid/ Dust					
	Accum	$0.1416\ \tau^{-0.052}$	$0.7561\ \tau^{0.148}$	$0.0871\ \tau^{1.026}$	$1.48\tau^{—0.021} – (0.0025\tau^{0.132})i$; 1 $1.48\tau^{—0.021} – 0.002i$; 2 $1.48\tau^{—0.021} – (0.0018\tau^{-0.08})i$; 3 $1.46\tau^{—0.040} – (0.0018\tau^{-0.30})i$; 4
	Coarse	2.2	$0.554\ \tau^{-0.052}$	$0.6786\ \tau^{1.057}$	$1.48\tau^{—0.021} – (0.0025\ \tau^{0.132})i$; 1 $1.48\tau^{—0.021} – 0.002i$; 2 $1.48\tau^{—0.021} – (0.0018\tau^{-0.08})i$; 3 $1.46\tau^{—0.040} – (0.0018\tau^{-0.30})i$; 4

Listed for each model are the individual lognormal modes, and the final SSA at different wavelengths. Listed for each mode are the volume modal radius r_v, standard deviation σ of the volume distribution, and total volume of the mode, V_0. The complex refractive index is assumed for all wavelengths (1,2,3 and 4 for 0.47, 0.55. 0.66 and 2.1 μm, respectively), unless otherwise noted. The Absorbing and Moderately absorbing model parameters (r_v, σ and k) are defined for $\tau \leq 2.0$; for $\tau > 2.0$, we assume $\tau = 2.0$. Likewise, the Non-absorbing and Spheroid model parameters are defined for $\tau \leq 1.0$. V_0 (for all models) is defined for all τ.

TABLE 6.2: EXTINCTION/MASS PROPERTIES OF THE AEROSOL MODELS

Model	ω_0	Q_{ext} [ ]	r_{eff} [μm]	B_{ext} [m^2/g]	M_c [$\mu g/cm^2$]
Continental	0.886	0.621	0.293	1.5910	62.8600
Moderately Absorbing / Developing World	0.920	1.018	0.261	2.9220	34.2230
Absorbing / Smoke	0.869	0.977	0.256	3.5330	28.3070
Non-absorbing / Urban-Industrial	0.947	1.172	0.207	3.4310	29.1460
Spheroid / Dust	0.953	1.339	0.680	1.4770	67.6960

Listed for each model are the single scattering albedo, extinction efficiency, effective radius, mass extinction coefficient and mass concentration conversion factor. These parameters are calculated at 0.55 μm, for $\tau_{0.55} = 0.5$. The particle density is assumed to be 1 g /cm^3.

CHAPTER 6 FIGS.

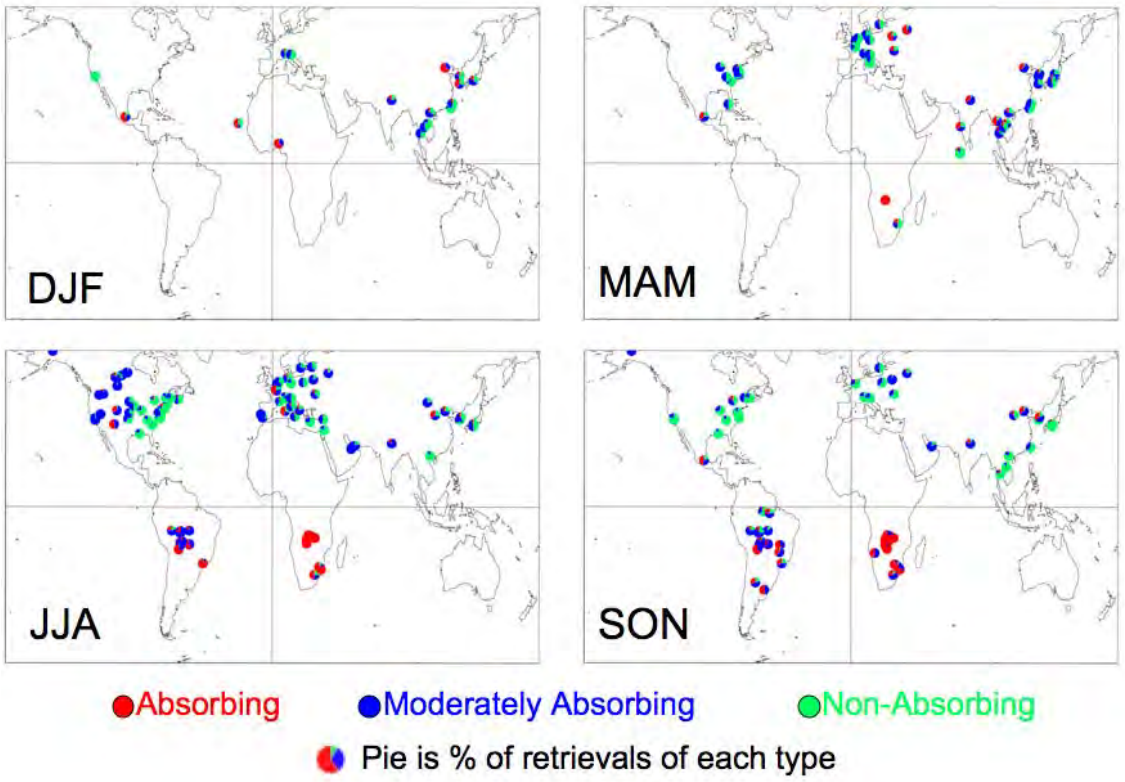

Figure 1: Percentage (pie charts) of spherical aerosol model type (from cluster analysis) observed at each AERONET site per season. Colors represent absorbing (ω_0~0.85), moderately absorbing (ω_0~0.90) and non-absorbing (ω_0~0.95), respectively.

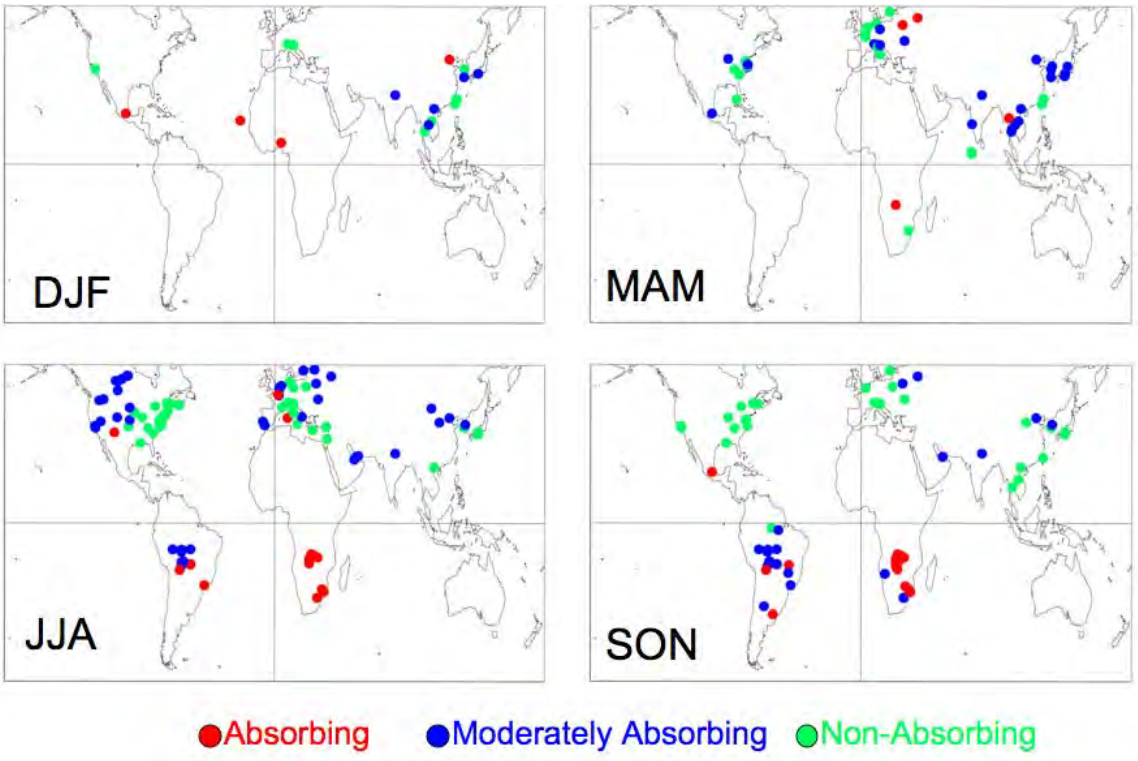

Figure 2: Final spherical aerosol model type designated at each AERONET site per season. Colors represent absorbing (ω_0~0.85), moderately absorbing (ω_0~0.90) and non-absorbing (ω_0~0.95), respectively.

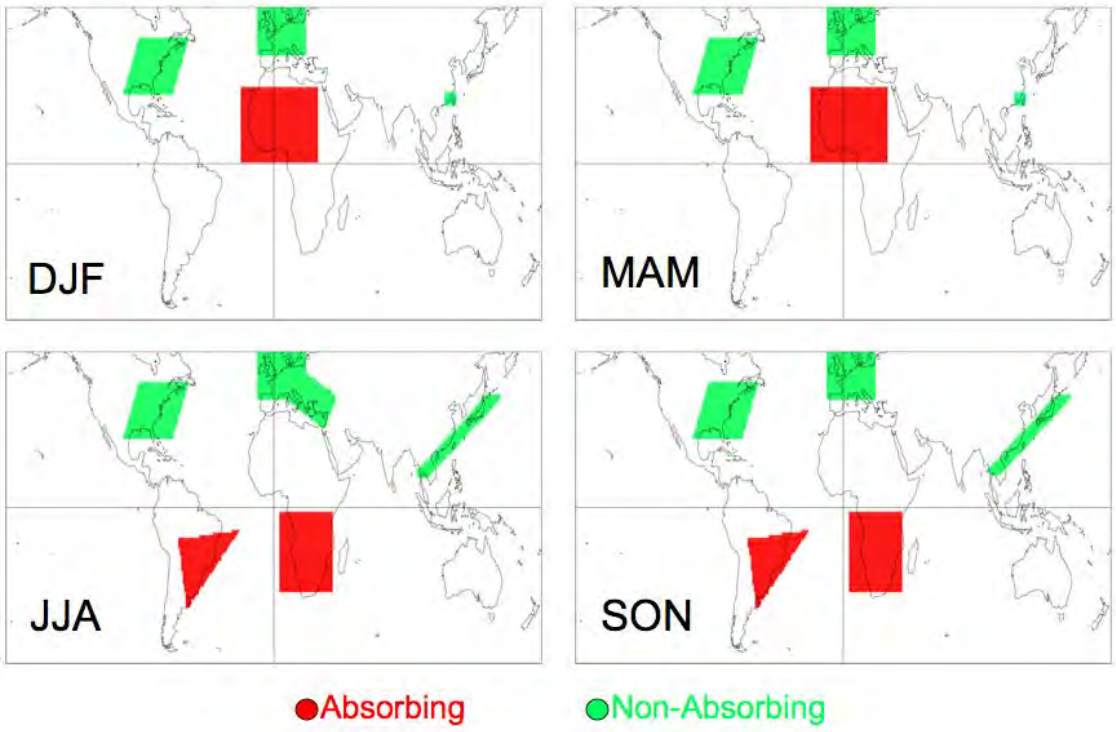

Figure 3: Final spherical aerosol model type designated at 1° x 1° gridbox per season. Red and green represent absorbing (ω_0~0.85) or non-absorbing (ω_0~0.95) models, respectively. Moderately absorbing (ω_0~0.90) is assumed everywhere else.

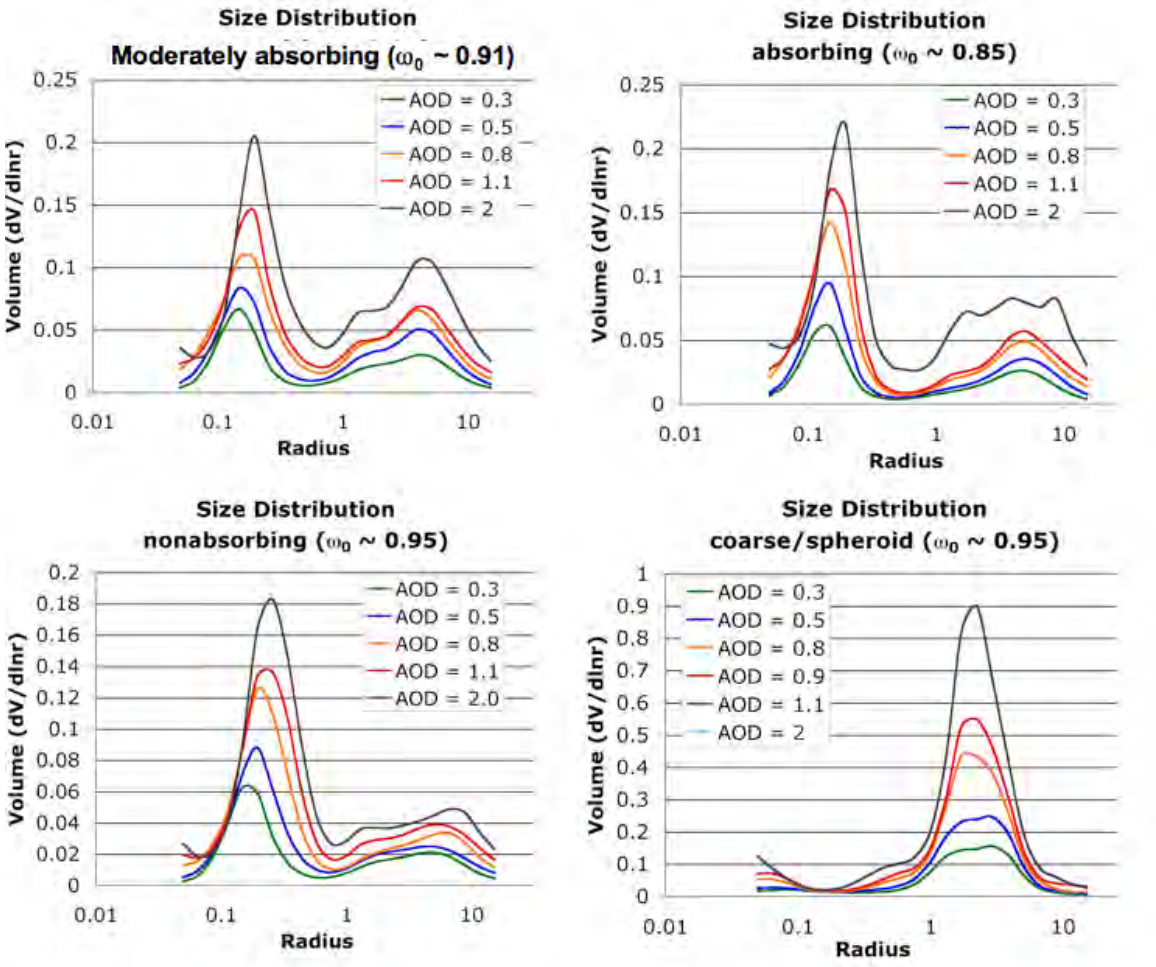

Figure 4: Aerosol size distribution as a function of τ (AOD) bin for the three spherical (moderately absorbing, absorbing and non-absorbing) and spheroid (dust) models identified by clustering of AERONET.

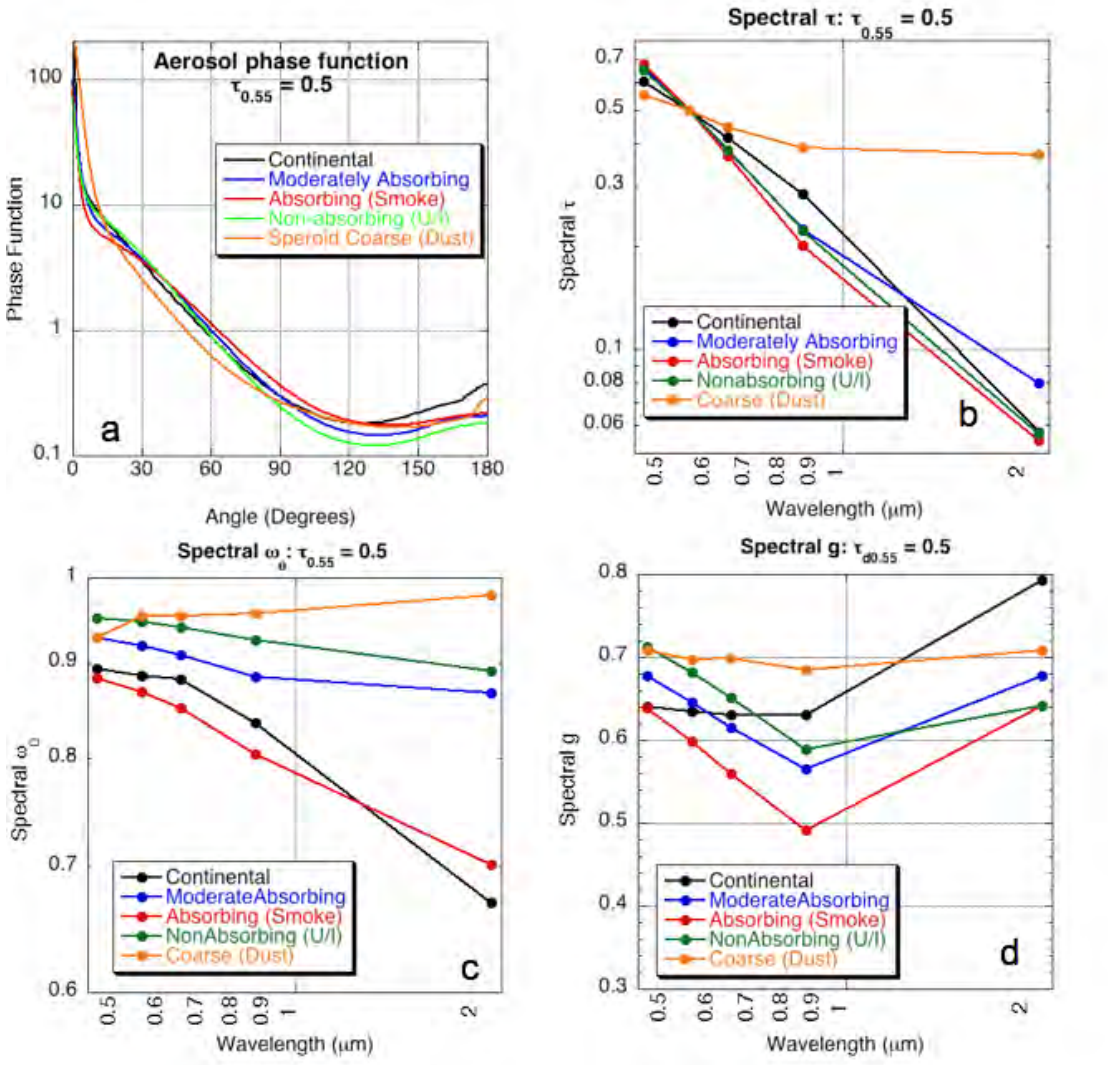

Figure 5: Optical properties of the AERONET-derived models, compared with the Continental model for $\tau_{0.55}$ = 0.5. The phase function at 0.55 μm is plotted in (a), whereas the spectral dependence of the optical depth, single scattering albedo and asymmetry parameter are plotted in (b-d), respectively.

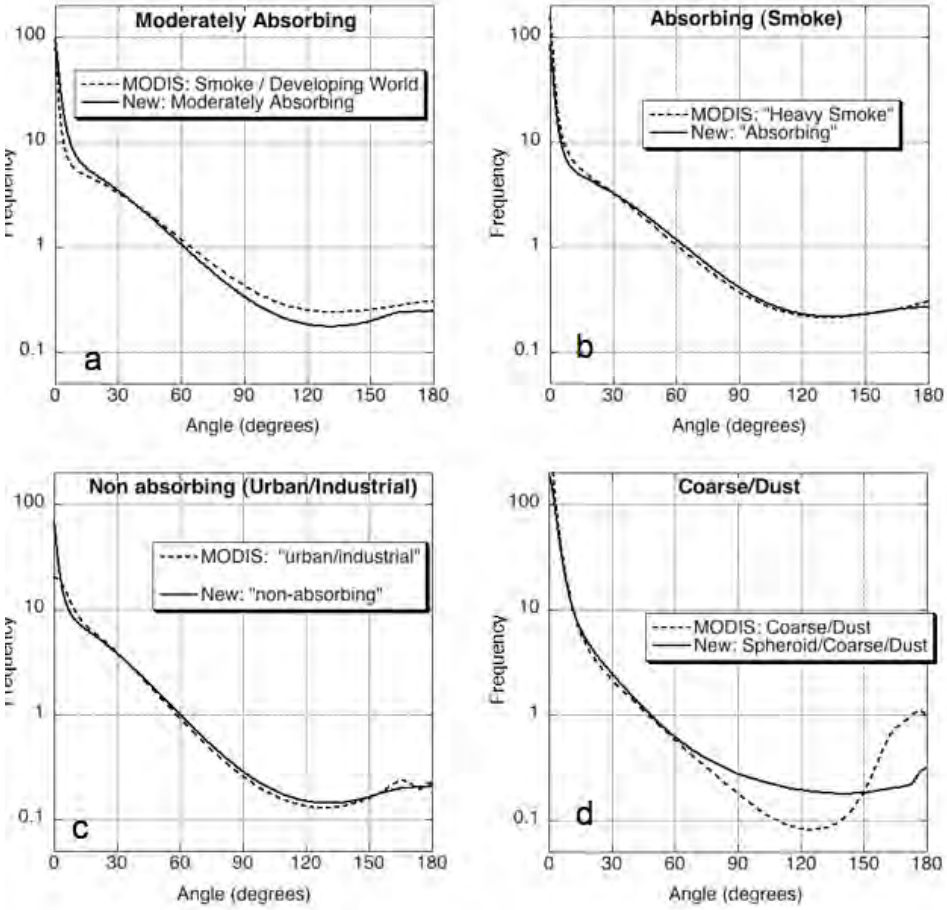

Figure 6: Comparison of phase function (at 0.55 μm) between new (solid curves) and analogous MODIS (dotted curves) aerosol models. Models are moderately absorbing (a), absorbing (b), nonabsorbing (c), and dust (d). For all plots, $\tau_{0.55}$ = 0.5.

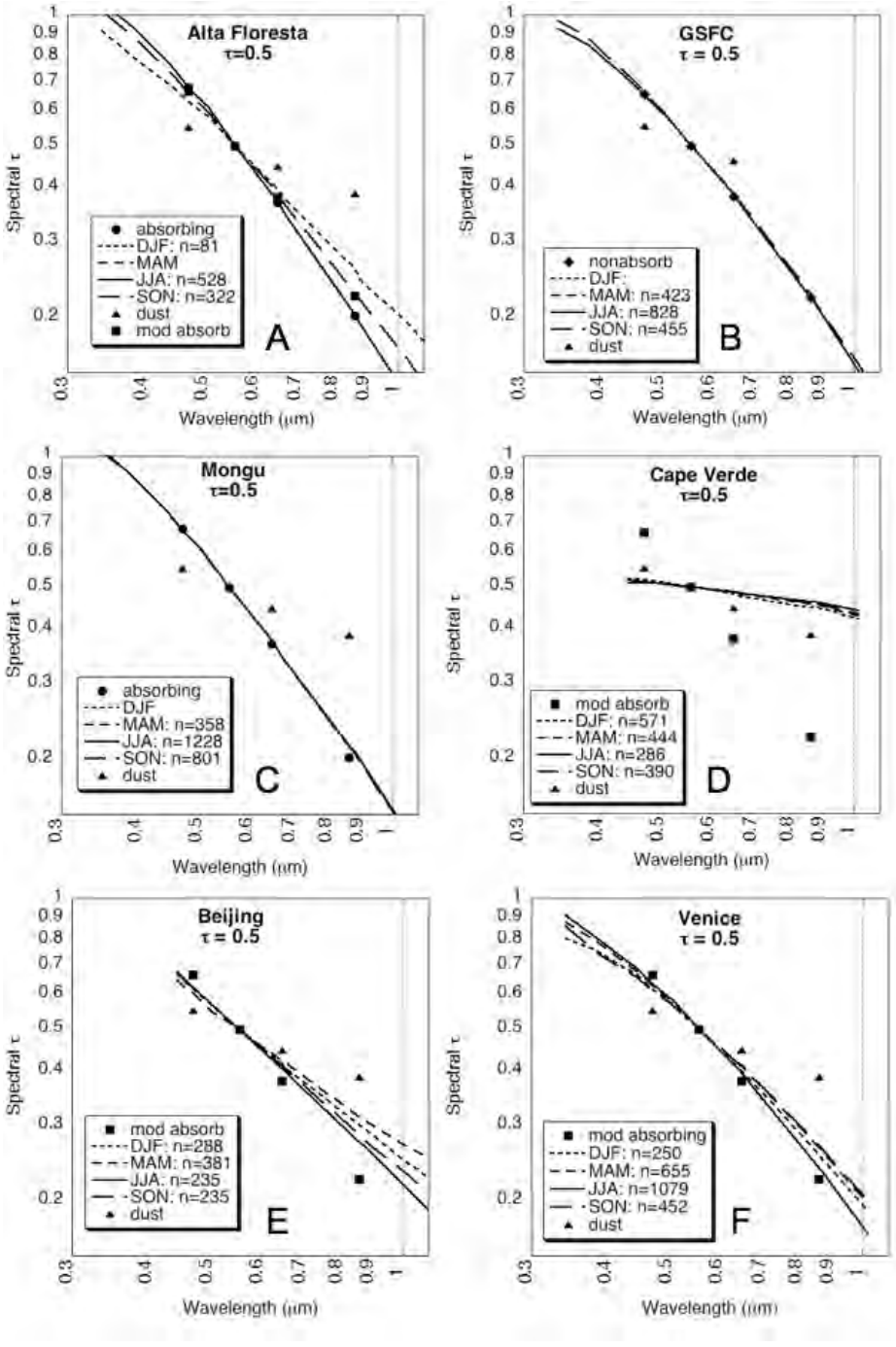

Figure 7: Comparison of spectral τ between new models (filled shapes) and averages of AERONET 'sun' measurements (dotted curves) at selected sites and seasons, for $\tau_{0.55}$ = 0.5. Different curves represent AERONET data during different seasons. The number of observations (*n*) used to create each curve is displayed in the legend. Note that there are at least two aerosol types displayed (at least one fine-dominated type plus dust). Sites plotted are Alta Floresta (A), GSFC (B), Mongu (C), Cape Verde (D), Beijing (E) and Venice (F).

Chapter 7: The second-generation MODIS aerosol algorithm over land.

7.1: Motivation

Kaufman et al., [1997a] introduced the strategy for retrieving aerosol over land from MODIS, based on Eq. 3.5. Except for the surface reflectance, each term on the right hand side is a function of the Rayleigh scattering, aerosol type and aerosol loading (τ). While Eq. 3.5 is technically valid for a uniform, Lambertian surface, the bi-directional properties of the surface reflectance can be approximated by the value of the surface reflectance for the relevant solar and satellite viewing geometry [Kaufman et al., 1997a]. Assuming that a small set of aerosol types and loadings can describe the range of global aerosol, the algorithm relies on a LUT to determine the conditions that best mimic the MODIS-observed spectral reflectance ρ^m_λ, and retrieve the associated aerosol properties (including τ and η). The key to maximal accuracy lies in making the most appropriate assumptions about both the surface and atmospheric contributions.

Since launch, the aerosol products have been monitored for quality, so that the algorithm has been continuously improved and updated for bug fixes, cloud masking and pixel selection. However, comparisons with ground truth sunphtometer observations indicated deficiencies in the algorithm that were correctable (discussed in Chapter 5). Chapter 6 derived a set of new global aerosol models that are applicable to a MODIS-type retrieval algorithm. This chapter describes the essential

components of the second-generation algorithm and demonstrates under what conditions it is useful.

7.2: MODIS and AERONET datasets

This work made extensive use of both MODIS and AERONET data products. Aerosol products have been derived from Terra reflectance observations since 2000 and since 2002 from Aqua. As of early 2005, most MODIS observations of reflectance ('Level 1') through 2004 had been processed or re-processed into 'Level 2' products (L2) using consistent retrieval algorithms, creating the set of products known collectively as c004. Data products include the averaged gas-corrected spectral reflectance (10 km x 10 km) used within the retrieval, the resulting spectral optical depth τ_λ and fine aerosol weighting, η. This amounts to ~10^8 retrievals over-land during the period.

At some sites, AERONET has been reporting since 1993, and as of early 2005, most of the AERONET data have been re-processed and quality assured by the AERONET team. These products are known as Level 2 AERONET (L2A) products (http://aeronet.gsfc.nasa.gov).

Sunphotometer data includes direct 'sun' measurements of spectral τ in four or more wavelengths (at least including 0.44, 0.67, 0.87 and 1.02 μm) and columnar water vapor *w* (precipitable water in units of [cm]). The AERONET direct sun measurements are made approximately every 15 minutes during mid-day and more often during sunrise and sunset. These data go through rigorous calibration and cloud screening processes to be assigned to Level 2. O'Neill et al. [2003] developed a method for retrieving fine aerosol weighting (η) from the direct sun measurements of

spectral τ. I modified the de-convolution code [O'Neill et al., 2005] to provide easy comparison with MODIS wavelengths and products.

AERONET data also includes the products retrieved via indirect measurements of 'sky' radiance in the almucantur [e.g. Holben et al., 1998]. These data, also are put through rigorous calibration and cloud screening processes. The AERONET sky radiance measurements are made less often (about once per hour), and are inverted simultaneously either assuming spherical aerosol particles [Dubovik and King, 2000] and/or spheroid particles [Dubovik et al., 2002b; Dubovik et al., 2006]. The choice of spheres or spheroids depends on the quality of the sky radiance fitting. Under either particle assumption, the fundamental derived parameters include spectral τ, spectral complex refractive index, the volume size distribution as a function of 22 radius size bins (dV(r)/dln(r)), and fitting error to the radiance measurements. Derived parameters include Ångstrom exponents, properties of bi-modal lognormal (fine and coarse mode) aerosol distributions, spectral single scattering albedo (*SSA* or ω_0) and asymmetry parameter (g) of the lognormal modes.

Although the actual products provided by MODIS and AERONET are not necessarily physically identical, in many cases they are comparable. For example, by fitting a quadratic equation through the logarithms of τ and wavelength, AERONET τ can be interpolated to 0.55 μm [Eck et al., 1999] to match directly with the MODIS retrieval. Comparison of η is trickier. Over land, MODIS considers η to be the contribution of the fine-dominated model (the non-dust model) to the total τ, the AERONET sky retrievals designate η to be the volume contribution from aerosol below a radius of 0.6 μm, whereas the O'Neill method separates fine and coarse

aerosol by spectral behavior. Practically, however, the definitions of η are similar enough so that they should be correlated [Kleidman et al., 2005; Anderson et al., 2005; Chu et al. 2005].

Over 15,000 pairs of MODIS and AERONET 'sun' data, at over 200 global sites, have been co-located in time via the technique of Ichoku et al., [2002a]. A valid MODIS/AERONET match is considered when there at least five (out of a possible 25) MODIS retrievals (10 km x 10 km resolution) within the box, and at least two (out of a possible five) AERONET observations within the hour. The co-location retrieves the spatial average of MODIS and the temporal average of AERONET, as well as the values of the nearest pixel and temporal scan. Some of this co-located data set was used for studies of surface reflectance and with others used for validation of the new algorithm.

7.3: Creating the new LUT

The derivation of new aerosol models was discussed in Chapter 6. Cluster analysis yielded three fine-dominated, spherical, models including: a 'non-absorbing' aerosol model (ω_0~0.95), presumably corresponding to urban/industrial aerosol in the industrialized Northern Hemisphere, an 'absorbing' (ω_0~0.85) aerosol model found in the known sooty and/or savanna-burning regions of South America and Africa, and a 'moderately absorbing' aerosol model representative of biomass burning and incomplete fossil fuel burning in the developing world. Similar cluster analysis of spheroid assumed retrievals yielded only one model, a coarse-dominated model that presumably represented global dust aerosol. Each aerosol 'model' is comprised of

two lognormal modes, either dominated by the fine mode (the three spherical models) or the coarse mode (the spheroid model). For each model, the spectral dependence of τ and optical properties (scattering and extinction) were calculated via Mie code or T-matrix code (depending on spherical or spheroid assumptions). Based on the dominant aerosol type found during clustering, an aerosol type was 'assigned' to each AERONET site (as a function of season) and then extrapolated to include the surrounding region. These regions were mapped onto a 1° longitude x 1° latitude grid, such that a fine aerosol type is assigned for each grid point, globally. As more information becomes available (for example, studies like [Mi et al., submitted 2007]), it should be easy to update this map.

7.3.1 Choice of radiative transfer code, assumed wavelengths and Rayleigh optical depths

The c004 (and previous MODIS over-land) LUTs were calculated using 'SPD', the scalar version of the RT code written by Dave et al., [1970], a code that is a standard in the remote sensing community. However, as discussed in Chapter 5, Fraser et al [1989] suggested and I demonstrated [Levy et al., 2004], that under some geometries, neglecting polarization would lead to significant errors in top of atmosphere reflectance, further leading to significant errors (> 10% or > 0.1) in τ retrieval. Dave also provided a vector (polarized) option to the code (VPD), although the code had not been kept up to date, and was unusable. Therefore, the choice of vector code should be well understood and suitable for creating the LUT. In scalar mode, the RT code should be consistent with the Dave benchmark. Also, it should

reasonably match the Ahmad et al., [1982] calculations used for the over ocean aerosol retrieval [Remer et al., 2005]. Since I had used RT3 [Evans and Stephens [1991] for my polarization study [Levy et al., 2004], I was familiar with compiling and executing the code, as well as analyzing its products. This plane-parallel adding/doubling code allows for polarization to be turned on or off, by changing only one line within an input file. Thus, it was easy to compare the results to the Dave code's scalar mode, and then upgrade to vector mode to include polarization effects. Under most geometries and optical depths, differences between the two RT codes are less than 0.001 (which is about 1%).

As noted in Chapter 6, the aerosol scattering phase function elements and extinction efficiencies (that are inputs to RT3) are calculated by integrating (over size distribution) the results of Mie code (MIEV - Wiscombe et al., 1980) or T-matrix kernel code (Dubovik et al., 2002b; Dubovik et al., 2006) depending on spherical or spheroid assumptions. Assuming a Rayleigh atmosphere and realistic layering of the aerosol, I computed the Legendre moments of the combined Rayleigh and aerosol, for each layer of a US Standard Atmosphere [U.S. Government, 1976]. These moments were fed into RT3 to calculate TOA reflectance and total fluxes.

While Table 3.1 represents best estimates of MODIS central wavelengths and expected Rayleigh optical depth (ROD) for each channel, the c004 algorithm over land used different values. For example, the MODIS 0.47 μm band (channel 3) stretches between 0.459 and 0.479 μm (http://modis.gsfc.nasa.gov). The sea-level Rayleigh optical depth (*ROD* or τ_R) drops drastically over this channel, from about 0.203 at 0.459 μm to 0.170 at 0.479 μm [Bodhaine et al., 1999]. Therefore, the

choice of 'center' wavelength to model and its associated ROD is crucial to obtaining unbiased aerosol retrieval. This is also an issue for the 0.66 μm channel (channel 1: 0.620 - 0.670 μm), but since the RODs are only about one-quarter of those at 0.47 μm, any error is much less crucial. In c004, the assumed ROD was 0.186 for channel 3 and 0.048 for channel 1. The 6S RT code [Vermote et al., 1997] models the MODIS channel filter functions, and suggests that the ROD values should be more like 0.193 and 0.051, respectively for the two channels. The MODIS aerosol over ocean algorithm [Tanre et al., 1997, Ahmad et al., 1982] assumes the RODs for the channels as 0.195 and 0.052, respectively. The assumptions for other channels (Table 3.1) are also consistent with those assumed over ocean.

7.3.2 Structure of the LUT

As introduced in Chapter 5, it is desirable that a new aerosol algorithm should include aerosol information in the longer wavelengths (e.g. 2.12 μm). Therefore the LUT is computed at four wavelengths (λ of 0.466, 0.553, 0.644 and 2.119 μm) representing the MODIS channels 3, 4, 1 and 7. The aerosol model-dependent parameters of Eq. 3.5 are calculated for several values of aerosol total loadings (indexed by τ at 0.55 μm), and for a variety of geometry. Each of the spherical aerosol models (Continental, moderately absorbing, absorbing and non-absorbing) and the one spheroid model (dust) are represented within the LUT.

The scattering and reflectance parameters are calculated for seven aerosol loadings ($\tau_{0.55}$ = 0.0, 0.25, 0.5, 1.0, 2.0 3.0, and 5.0). TOA reflectance is calculated for 9 solar zenith angles (θ_0 = 0.0, 6.0, 12.0, 24.0, 36.0, 48.0, 54.0, 60.0 and 66.0), 16

sensor zenith angles (θ = 0.0 to 65.8, approximate increments of 6.0, based on Lobatto quadrature with 8 abscissa points (e.g. http://mathworld.wolfram.com/LobattoQuadrature.html)), and 16 relative azimuth angles (ϕ = 0.0 to 180.0 increments of 12.0). All of these parameters are calculated assuming a surface reflectance of zero. These are similar to the indices and geometry calculated for c004 LUT.

When surface reflectance is present, the second term in Eq. 3.5 is nonzero. The flux is a function only of the atmosphere, however, the atmospheric backscattering term, *s*, and the transmission term, *T*, are functions of both the atmosphere and the surface. Therefore, RT3 is run two additional times with distinct positive values of surface reflectance.

$$s = (1/\rho_1^s)(1-(F_d T \rho_1^s/(\rho^* - \rho^a)))$$
$$\text{and} \qquad (7.1)$$
$$s = (1/\rho_2^s)(1-(F_d T \rho_2^s/(\rho^* - \rho^a)))$$

Here, values of 0.1 and 0.25 were chosen for the surface reflectances ρ^s_1 and ρ^s_2. These two Eq.s can be solved for the two unknowns, *s* and *T*. These values of F_d, *s*, and *T* are included within the LUT, for each τ index.

7.4: VISvs2.12 surface reflectance

When performing atmospheric retrievals from MODIS or any other passive satellite sensor, the major challenge is separating the total observed reflectance into atmospheric and surface contributions (e.g. Eq. 3.4), and then defining the aerosol contribution. Over the open ocean, the surface reflectance is nearly zero in the 0.66 μm and longer wavelength channels, so that assuming negligible surface reflectance

in these channels is a good approximation. Moving from coastline onto land, however, the surface reflectance in 0.66 μm and longer channels can be far from zero and vary over surface type. As the land surface and the atmospheric signals are comparable, errors of 0.01 in assumed surface reflectance can lead to errors on the order of 0.1 in τ retrieval [Kaufman et al., 1997b]. Errors in multiple wavelengths can lead to poor retrievals of spectral τ, which in turn would be useless for estimating size parameters.

As discussed in Chapter 5, a single set of VISvs2.12 ratios is not globally applicable. Some surfaces exhibit strong bi-directional reflectance functions (BRDF). Gatebe et al., [2001] flew the Cloud Absorption Radiometer at low altitudes over different vegetated surfaces and found not only did VISvs2.12 vary by surface type, but also as a function of angle. In fact VISvs2.12 ratios often greatly differed from the one-to-four and one-to-two values assumed by the c004 algorithm. Also, Remer et al., [2001] noted that VISvs2.12 varied as a function of scattering geometry. Thus, an improved global aerosol retrieval algorithm requires estimates of surface reflectance that include surface type and angular variability.

Application of modeled surface type and global maps of measured spectral albedo (like those described by [Moody et al., 2004]) were explored, but they are not necessarily representative of the directional surface reflectance. Yet, the combined MODIS/AERONET data sets, developed since 2000, contain information that can be used for developing empirical surface reflectance relationships. Before Terra launch such data were unavailable. In the following section, I perform atmospheric

correction of MODIS/AERONET co-locations to derive new surface reflectance models.

7.4.1 Atmospheric correction of c004 MODIS/AERONET co-located products

Atmospheric correction [Kaufman and Sendra, 1988)] attempts to calculate the optical properties of the surface, by theoretically subtracting the effects of the atmosphere from the satellite-observed radiation field. One needs to assume the optical properties of the intervening atmosphere, including all aerosol and non-aerosol components. In addition to knowing or assuming all atmospheric components, accurate radiative transfer (RT) is also required. The atmospherically corrected surface reflectance ρ^{s}_{λ} is calculated by re-arranging Eq. 3.5.

In order to minimize errors arising from multiple scattering by the aerosol, the atmospheric corrections should be limited to conditions of low τ (e.g. $\tau<0.2$). Out of the original 15,000 co-located MODIS/AERONET points (described in section 2), there were over 10,000 collocations with low τ ($\tau_{0.55} < 0.2$). The archive included the 'gas absorption corrected' MODIS-Level 2 observed reflectance (average over 50 x 50 km as well as the 10km box nearest the AERONET site), as well as AERONET-observed (L2A) spectral τ_{λ} and column water vapor depth (both averages over 1 hour, and observation nearest in time to MODIS overpass). The closest 10 km MODIS box and nearest AERONET observation were used for atmospheric correction. The molecular properties of the atmosphere were assumed those of the U.S. standard atmosphere [1976], with the Rayleigh optical depth (ROD) values scaled from sea level values, according to the elevation/air pressure of the sunphotometer.

The relationship between the satellite-measured reflectance and the surface reflectance is a complicated function of the atmospheric effects of scattering and absorption by the aerosol. Previous atmospheric correction exercises often assumed some form of the Continental aerosol model (e.g. Vermote et al. [1997]), to describe both the scattering and absorption properties. While this model may provide reasonable simulations in channels near to 0.55 μm (such as 0.47 and 0.66 μm), it cannot be expected to provide accurate simulations at 2.12 μm, even for low τ. For example, for $\tau_{0.55} = 0.2$, $\tau_{2.12}$ ranges from 0.03 to 0.16, depending on whether fine or coarse dominated aerosol is assumed. Thus, assuming the wrong aerosol size in the correction procedure will lead to errors in estimating 2.12 μm surface reflectance.

Therefore, the AERONET-derived Ångstrom exponent (α) was used to decide which aerosol type to assume. In the 4200 cases where $\alpha > 1.6$, the atmospheric correction assumed a fine-dominated model, specifically the 'moderately absorbing' model ($\omega_0 \sim 0.9$). When $\alpha < 0.6$ (400 cases), the correction procedure assumed the coarse-dominated model. Co-locations where $0.6 < \alpha < 1.6$ (about 6000 cases) were not used due to uncertainties of aerosol mixing.

The atmospheric correction resulted in two datasets: surface reflectance at three wavelengths (0.47, 0.66, 2.12 μm) for each of the two regimes (fine and coarse-dominated). Separate comparison of 0.66μm versus 2.12μm and 0.47μm versus 2.12μm, for each regime indicated that their regressions differed by less than 10% (both slope and y-offset values), suggesting to combine the two surface reflectance datasets into one.

7.4.2 Mean values of VISvs2.12 surface reflectance relationships

Atmospheric correction was performed on the 4600 MODIS/AERONET co-locations having AERONET-observed $\tau_{0.55} < 0.2$ and either $\alpha < 0.6$ or $\alpha > 1.6$. Fig. 7.1a plots the regressions of corrected 0.47 μm and 0.66 μm surface reflectance, each versus the corrected 2.12 μm surface reflectance. Note both slope and y-offset. The presence of the y-offset is important, because even in the darkest, most water-laden vegetation, zero reflectance at 2.12 μm does not imply zero surface reflectance in the visible channels (e.g. Kaufman et al., [2002]).

Correlation (*R*) values are 0.93 for the 0.66vs2.12 μm channel regression, but only about 0.75 for 0.47vs2.12. For 0.47vs2.12, including the offset (about +0.011) yields a slope close to one-quarter (0.258). For 0.66vs2.12, the offset is near zero, but the slope is greater than one-half (0.55). Thus in a mean sense, atmospheric correction of MODIS data yields VISvs2.12 surface reflectance relationships that differ from the assumed c004 VISvs2.12 ratios.

The relationship of 0.47 to 0.66 μm ('0.47vs0.66') may be stronger than 0.47vs2.12 because it has higher correlation (R = 0.87) and less scatter (Fig. 7.1b). This suggests that the 0.47 μm surface reflectance should be estimated indirectly via 0.66 μm, rather than directly from 2.12 μm. In other words, the algorithm should first estimate 0.66 μm from 2.12 μm, then estimate 0.47 μm from 0.66 μm, i.e.

$$\begin{aligned} \rho^s_{0.66} &= f(\rho^s_{2.12}) \\ \rho^s_{0.47} &= g(\rho^s_{0.66}) \end{aligned}, \qquad \textbf{(7.2)}$$

where f() and g() are different relationships. To test whether the relationships shown in Fig. 7.1 are dependent on the formulation data set, similar regressions were performed on a subset of the data where AERONET-measured $\tau < 0.1$ (2508 cases). The results show differences in both slope and y-offset of less than 1%, suggesting that the average VISvs2.12 relationship (displayed in Fig. 7.1) is robust.

7.4.3 Variability of VISvs2.12 surface reflectance relationships: Angle

However, Fig. 7.1 shows that the VISvs2.12 surface reflectance relationship displays large scatter. For example, if surface reflectance is 0.15 at 2.12 μm, applying the regressed relationships of 0.66vs2.12 and 0.47vs0.66 results in estimates of surface reflectance of 0.083±0.03 at 0.66 μm and 0.050±0.03 at 0.47 μm. Obviously, this could result in very large errors in retrieved τ, on the order of 0.3 or more. Therefore, to reduce the scatter we look for dependencies on other parameters to refine the relationships.

A number of papers suggest that the VISvs2.12 surface reflectance relationships are angle dependent (e.g. Remer et al., 2001; Gatebe et al., 2001; Lypustin et al., 2001). Out of different possible angle parameters (solar zenith angle, sensor zenith angle, glint angle or scattering angle) we found that the scattering angle had the largest influence on the VISvs2.12 relationship.

The Fig. 7.1 data were sorted according to scattering angle and put into 20 groups of equal size (about 230 points for each scattering angle bin). Fig. 7.2a displays the median values of surface reflectance in each bin as a function of scattering angle, and shows a definite relationship at 2.12 μm, less at 0.66 μm, and nearly none at 0.47 μm.

Since Fig. 7.1 noted a slope and y-offset for both VISvs2.12 relationships, I suspected that slope and offset might depend on scattering angle. Fig. 7.2 (b-d) plots the slope, y-offset and correlation of the surface reflectance relationships calculated in each scattering angle bin and plotted as a function of scattering angle. The 0.66vs2.12 regression slope (r0660 in the Figure) shows dependence on scattering angle, whereas the 0.47vs0.66 regression slope (rVIS in the Figure) shows nearly none. Both y-intercepts show strong dependence on scattering angle.

7.4.4 Variability of VISvs2.12 surface reflectance relationships: Surface type and $NDVI_{SWIR}$

Because AERONET sites are located in different surface type regimes, it could be expected that the VISvs2.12 surface relationships will vary based on surface type and/or season. Using the International Geosphere/Biosphere Programme's (IGBP) scene map of USGS surface types and formatted for MODIS validation (http://edcdaac.usgs.gov/modis/mod12c1v4.asp), scene type of the MODIS/AERONET validation box was determined. Urban and non-urban retrievals were separated and grouped into season (winter or summer) and into general location (mid-latitude or tropical). Different surface types display different VISvs2.12 relationships. Generally, more vegetated surfaces (midlatitude summer sites both urban and nonurban) have higher 0.66vs2.12 surface reflectance ratios (ratio > 0.55) than winter sites or tropical savannas and grasslands (ratio < 0.55). Except for the urban sites during summer (ratio ~ 0.766), the 0.47vs0.66 surface reflectance ratio is relatively consistent (ratio ~ 0.52). The relationship of the surface reflectance ratios to

known surface condition suggests a relationship to its vegetation amount/condition or 'greenness.'

Except for urban areas, most surfaces seem to have VISvs2.12 surface reflectance relationships that may be related to a vegetation index (VI). The well-known Normalized Difference Vegetation Index (NDVI), defined as a function of the red (0.66 μm – channel 1) and near-IR (0.86 μm – channel 2), are influenced by aerosol, negating its usefulness for determining surface type. We attempted to work with other VIs (such as described by Karnieli et al., [2000]) that have different sensitivity to atmospheric (aerosol) conditions, and found the most promising to be the $NDVI_{SWIR}$, defined as:

$$NDVI_{SWIR} = (\rho^m_{1.24} - \rho^m_{2.12})/(\rho^m_{1.24} + \rho^m_{2.12}) \quad \textbf{(7.3)}$$

where $\rho_{1.24}$ and $\rho_{2.12}$ are the MODIS-measured reflectances of the 1.24 μm channel (MODIS channel 5) and the 2.12 μm channel (channel 7). These longer wavelengths are much less influenced by aerosol (except for heavy aerosol or dusts), and thus are potentially most useful for estimating surface condition. This VI is also known as $NDVI_{MIR}$ (Mid-InfraRed) (e.g. Karnieli et al., [2000]). In aerosol free conditions $NDVI_{SWIR}$ is highly correlated with regular *NDVI.* A value of $NDVI_{SWIR} > 0.6$ is relative to more active vegetation, whereas $NDVI_{SWIR} < 0.2$ is representative of dormant or sparse vegetation. Fig. 7.3 plots the relationship of the 0.66 μm channel and 2.12 μm channel (atmospherically corrected) surface reflectance relationship for non-urban sites, as a function of low, medium and high values of $NDVI_{SWIR}$. As the $NDVI_{SWIR}$ increases, the ratio between 0.66 μm and 2.12 μm surface reflectance increases.

7.4.5 Final parameterization of VISvs2.12 surface reflectance relationships

Results of the global atmospheric correction exercise imply that not only do the VISvs2.12 surface relationships differ from the ratios assumed by the c004 algorithm, they also have a strong dependence on both geometry and surface type. Therefore, the VISvs2.12 surface reflectance relationship is parameterized as a function of both $NDVI_{SWIR}$ and scattering angle Θ, such that Eq. (7.2) can be expanded into:

$$\begin{aligned} \rho^s_{0.66} &= f(\rho^s_{2.12}) = \rho^s_{2.12} * slope_{0.66/2.12} + yint_{0.66/2.12} \\ &\text{and} \\ \rho^s_{0.47} &= g(\rho^s_{0.66}) = \rho^s_{0.66} * slope_{0.47/0.66} + yint_{0.47/0.66} \end{aligned} \quad \textbf{(7.4)}$$

where

$$\begin{aligned} slope_{0.66/2.12} &= slope^{NDVI_{SWIR}}_{0.66/2.12} + 0.002\Theta - 0.27, \\ yint_{0.66/2.12} &= -0.00025\Theta + 0.033, \\ slope_{0.47/0.66} &= 0.49, \text{and} \\ yint_{0.47/0.66} &= 0.005 \end{aligned} \quad \textbf{(7.5)}$$

where in turn

$$\begin{aligned} slope^{NDVI_{SWIR}}_{0.66/2.12} &= 0.48; NDVI_{SWIR} < 0.25, \\ slope^{NDVI_{SWIR}}_{0.66/2.12} &= 0.58; NDVI_{SWIR} > 0.75 \\ slope^{NDVI_{SWIR}}_{0.66/2.12} &= 0.48 + 0.2(NDVI_{SWIR} - 0.25); 0.25 \le NDVI_{SWIR} \le 0.75 \end{aligned} \quad \textbf{(7.6)}$$

If the relationships described by Fig. 7.1 are considered global average relationships, then the above parameterization describes perturbations for angle and land type. Note that while the parameterization is based on the results of Figs. 7.4,7.5 and 7.6, the coefficients are not identical to those shown in the Figures. Even though the atmospheric corrected data set is the broadest and most comprehensive representation of global surface reflectance relationships, it is limited to AERONET site locations, which in turn are mostly concentrated in certain geographical regions (http://aeronet.gsfc.nasa.gov). Trial and error was used to modify the basic results from the AERONET-based atmospheric correction, to give more realistic MODIS retrievals globally, (especially in places were few or no AERONET sites are located). The parameterization derives more accurate estimates of surface reflectance on average, than those estimated using fixed ratios.

7.4.6 Notes on VISvs2.12 surface reflectance relationship errors

Note that even with the surface reflectance parameterization, there still will be errors in estimating surface reflectance. According to the MODIS Land Surface Reflectance Homepage (http://modis-sr.ltdri.org/html/prodacc.htm), improper aerosol model assumptions can lead to errors in atmospherically corrected reflectance on the order of 0.002 in the 0.47 and 0.66 μm channels, and 0.006 at 2.12 μm. The errors are especially large at 2.12 μm due to potentially choosing a fine-dominated model instead of a coarse-dominated model (or vice-versa). However, since this study pre-determined the choice of fine or coarse-dominated aerosol models via the AERONET-observed Ångstrom exponent, errors at 2.12 μm should be much less, dependent on the choice of fine-dominated aerosol model. For $\tau_{0.55}$=0.5, the

difference in spectral optical thickness between the moderately absorbing model (ω_0~0.90) and absorbing model (ω_0~0.85) is about 0.02, 0.02 and 0.002, respectively in the 0.47, 0.66 and 2.12 μm channels (e.g. Fig. 6.5b). On average, this would be equivalent to errors of about 0.002, 0.002 and 0.0002, respectively in surface reflectance, but would vary according to the differences in phase function. Regardless, the error at 2.12 μm is small enough so that the derived surface reflectance relationship should be reasonably robust, even when a model with wrong ω_0 was assumed.

Of course, other errors may creep into the surface reflectance parameterization. These include, but are not limited to additional surface BRDF effects lost during averaging over scattering angle and errors due to MODIS instrument calibration. These errors can cause reflectance errors that are similar in magnitude to those caused by improper aerosol model assumptions.

7.5: Inversion of spectral reflectance, including 2.12 μm

A major limitation of the c004 algorithms was that aerosol is assumed transparent in the 2.12 μm channel. Under a dust aerosol regime, aerosol transparency is an extremely poor assumption. Even in a fine aerosol dominated regime, τ is not zero. For the moderately absorbing aerosol model (ω_0~0.90), $\tau_{0.55} = 0.5$ corresponds to $\tau_{2.12} \sim 0.05$, corresponding to an error in 2.12 μm path reflectance of about 0.005. Via the VISvs2.12 reflectance relationship, the path reflectance error at 0.66 μm is on the order of 0.003, leading to ~ 0.03 error in retrieved τ. As a percentage of the actual

τ, the error is not very large. However, combined with errors at 0.47 μm, the resulting error in spectral dependence leads to error in estimating η.

In the spirit of the MODIS aerosol over ocean algorithm [Tanré et al., 1997], an over-land multi-channel reflectance inversion is developed. Analogous to the ocean algorithm's combination of fine and coarse aerosol *modes*, the new land algorithm attempts to combine fine-dominated and coarse-dominated aerosol *models* (each bi-modal) to match with the observed spectral reflectance. The 2.12 μm channel is assumed to contain both surface and aerosol information, and the visible surface reflectance is a function of the VISvs2.12 surface reflectance relationships derived in section 7.4. Simultaneously inverting the aerosol and surface information in the three channels (0.47 μm, 0.66 μm and 2.12 μm) yields something greater than 2 pieces of information. With some assumptions, three parameters can be derived: $\tau_{0.55}$, $\eta_{0.55}$ and the surface reflectance ($\rho^s_{2.12}$).

Eq. 3.5 can be rewritten, noting that the calculated spectral total reflectance ρ^*_λ at the top of the atmosphere is the weighted sum of the spectral reflectance from a combination of fine and coarse –dominated aerosol models, i.e.

$$\rho^*_\lambda = \eta\rho^{*f}_\lambda + (1-\eta)\rho^{*c}_\lambda \qquad \textbf{(7.7)}$$

where ρ^{*f}_λ and ρ^{*c}_λ are each composites of surface reflectance ρ^s_λ and atmospheric path reflectance of the separate aerosol models. That is:

$$\rho^{*f}_\lambda = \rho^{af}_\lambda + F^f_{d\lambda}T^f_\lambda\rho^s_\lambda/(1-s^f_\lambda\rho^s_\lambda)$$
$$\text{and} \qquad \textbf{(7.8)}$$
$$\rho^{*c}_\lambda = \rho^{ac}_\lambda + F^c_{d\lambda}T^c_\lambda\rho^s_\lambda/(1-s^c_\lambda\rho^s_\lambda)$$

where ρ^{af}_{λ} and ρ^{ac}_{λ} are the fine and coarse model atmospheric path reflectance, $F^{f}_{d\lambda}$ and $F^{c}_{d\lambda}$ are normalized downward fluxes for zero surface reflectance, T^{f}_{λ} and T^{c}_{λ} represent upward total transmission into the satellite field of view, and s^{f}_{λ} and s^{c}_{λ} are atmospheric backscattering ratios. The weighting parameter, η of Eq. 7.7 is defined for λ = 0.55 μm. Remer et al. [2005] explains how this parameter also represents the fraction of the total optical thickness at 0.55 μm contributed by fine (non-dust) aerosol. Note the angular and τ dependence of some of the terms: $\rho^{a}=\rho^{a}(\tau, \theta_0,\theta,\phi)$, $F=F(\tau,\theta_0)$, $T=T(\tau,\theta)$, $s = s(\tau)$ and $\rho^{s}=\rho^{s}(\theta_0,\theta,\phi)$. Whereas the other terms are a function of the aerosol properties (not aerosol amount or geometry) and are contained within the LUT. The surface reflectance is independent of the aerosol, but dependent on the geometry. In practical terms, we parameterize the surface reflectance using the VISvs2.12 surface reflectance relationships, which assumes it is a function of scattering angle and vegetation index.

Due to the limited set of aerosol optical properties in the lookup table, the Eq.s may not have exact solutions, and solutions may not be unique. In order to reduce the possibility of non-unique retrievals the algorithm attempts to fit with discrete values of η. Upon completion, the retrieval is assigned a Quality Assurance 'confidence' (QAC) value that ranges from 0 (bad quality) to 3 (good quality). This QAC flag is used for creation of Level 3 (gridded) products and for combining land retrievals with concurrent over-ocean aerosol retrievals into 'joint products' (see [MAST, 2006] and [Hubanks et al., 2005] for more details).

7.5.1 Selection of "dark pixels"

Fig. 7.4 illustrates the main steps of the second-generation land algorithm. The procedure collects Level 1 B (L1B) spectral reflectance in eight wavelength bands (Table 3.1, plus 1.37 μm) at their finest spatial resolutions, as well as associated geo-location information. These L1B reflectance values are corrected for water vapor, ozone, and carbon dioxide obtained from ancillary NCEP analysis data files. Details of this gas correction and cloud masking are found online [MAST, 2006]. Basically, the high resolution (20 x 20 at 500 m resolution) pixels in the 10 km x 10 km box are evaluated pixel by pixel to identify whether the pixel is suitable for aerosol retrieval. Clouds [Martins et al., 2002], snow/ice [Li et al., 2004] and inland water bodies (via NDVI tests) are considered not suitable and are discarded.

The non-masked pixels are checked for their brightness. Pixels having measured 2.12 μm reflectance between 0.01 and 0.25 are grouped and sorted by their 0.66 μm reflectance. The brightest (at 0.66 μm) 50% and darkest 20% are discarded, in order to reduce cloud and surface contamination and scale towards darker targets. If there are at least 12 pixels remaining (10% of 30% of the original 400), then the reflectance in each channel is averaged, yielding the "MODIS-measured" spectral reflectance $\rho^m_{0.47}$, $\rho^m_{0.66}$, $\rho^m_{2.12}$, and $\rho^m_{1.24}$. These reflectance values are used for Procedure A. If less then 12 pixels remain, then Procedure B (described later) is followed.

7.5.2 Correcting the LUT for elevation

A major change from the c004 algorithm concerns how the algorithm corrects for elevated surface targets. The sea-level Rayleigh optical depth (*ROD*, $\tau_{R,\lambda}$) at a wavelength λ (in μm) can be approximated over the visible range [e.g. Dutton et al., 1994; Bodhaine et al., 1999] by:

$$\tau_{R,\lambda} = 0.00877\lambda^{-4.05} \qquad \textbf{(7.9)}$$

When not at sea level (pressure = 1013 mb), the ROD is a function of pressure (or height, *z*) so that it can be approximated by:

$$\tau_{R,\lambda}(z = Z) = \tau_{R,\lambda}(z = 0)\exp(\frac{-Z}{8.5}) \qquad \textbf{(7.10)}$$

where Z is the height (in kilometers) of the surface target and 8.5 km is the exponential scale height of the atmosphere. The difference between ROD at z=0 and z=Z is $\Delta\tau_{R,\lambda}$.

In c004, the algorithm (too) simply corrected the retrieved τ product by adding the optical depth that was neglected by assuming sea level for the retrieval, (i.e. $\tau_{\lambda}(z = Z) = \tau_{\lambda}(z = 0) + \Delta\tau_{R,\lambda}$). However, this correction can give poor results because of the large differences between molecular and aerosol phase functions. Instead, the new algorithm makes use of the procedure described in Fraser et al., [1989], adjusting the lookup table to simulate different ROD by adjusting the wavelength. Substitution of Eq. 7.10 into Eq. 7.9 yields

$$\lambda(z = Z) = \lambda(z = 0)\exp(\frac{Z}{34}). \qquad \textbf{(7.11)}$$

For example, at Z = 0.4 km, λ increases by about 1.2%. For the blue 0.47 μm channel, (centered at 0.466 μm) this means that $\tau_{R,\lambda}(z=0)=0.194$, $\tau_{R,\lambda}(z=0.4)=0.185$ and $\lambda(z=0.4)=0.471$ μm. In other words, the algorithm simulates a 0.4 km elevated surface by adjusting the blue channel's wavelength to 0.471 μm. Assuming that gases and aerosols are optically well mixed in altitude, the parameter values of a 0.471 μm LUT can be acquired by interpolating (linearly as functions of log wavelength and log parameter) between the 0.47 μm (0.466 μm) and the 0.55 μm (0.553 μm) entries. Similar interpolations are performed for the other channels (for example, 0.55 μm would be adjusted to 0.559 μm). For the 0.4 km case, this means that lower values of TOA atmospheric path reflectance and higher values of transmission are chosen to represent a given aerosol model's optical contribution. However, also note that since the 0.55 μm channel has also been adjusted, the associated values of the τ indices have been adjusted accordingly. In other words, the algorithm retrieves aerosol optical depth at the adjusted wavelength, which is equivalent to retrieving τ down to the surface elevation height. For highly elevated terrain (e.g. Z = 4 km), ROD decreases by 40%, resulting in a channel equivalent wavelength increase of 10%.

Whereas most global land surfaces are at sea level or above, a few locations are below sea level (Z < 0). In these cases, the algorithm is allowed to extrapolate below 0.466 μm. Since the extrapolation is at most for a hundred meters or so, this is not expected to introduce large errors, and these cases can still be retrieved. Note also that due to the extremely low ROD in the 2.12 μm channel, little is gained by adjusting this channel.

7.5.3 Procedure A: Inversion for dark surfaces

If following Procedure A (for dark surfaces), the QAC is initially set to a value between 0 (bad quality) and 3 (good quality), depending on the number of dark pixels remaining. In Procedure A, the algorithm assigns the fine aerosol model, based on the location and season. From the lookup table, ρ^a, F, T and s (for the fine model and coarse model separately) are interpolated for angles (θ_0, θ and ϕ), resulting in six values for each parameter, each one corresponding to a different aerosol loading (indexed by τ at 0.55 μm).

The 2.12 μm path reflectance is a non-negligible function of the τ, so that the surface reflectance is therefore also a function of the τ. For discrete values of η between -0.1 and 1.1 (intervals of 0.1), the algorithm attempts to find the τ at 0.55 μm and the surface reflectance at 2.12 μm that exactly matches the MODIS measured reflectance at 0.47 μm. There will be some error, ε, at 0.66 μm. The solution is the one where the error at 0.66 μm is minimized. In other words,

$$\rho^m_{0.47} - \rho^*_{0.47} = 0$$

$$ABS(\rho^m_{0.66} - \rho^*_{0.66}) = \varepsilon \qquad \textbf{(7.12abc)}$$

$$\rho^m_{2.12} - \rho^*_{2.12} = 0$$

where

$$\rho^*_{2.12} = \eta(\rho^{fa}_{2.12} + F^f_{d,2.12}T^f_{2.12}\rho^f_{2.12}/(1 - s^f_{2.12}\rho^s_{2.12})) + (1-\eta)(\rho^{ca}_{2.12} + F^c_{d,2.12}T^c_{2.12}\rho^s_{2.12}/(1 - s^c_{2.12}\rho^s_{2.12}))$$

$$\rho^*_{0.66} = \eta(\rho^{fa}_{0.66} + F^f_{d0.66}T^f_{0.66}f(\rho^s_{2.12})/(1 - s^f_{0.66}f(\rho^s_{2.12}))) + (1-\eta)(\rho^{ca}_{0.66} + F^c_{d,0.66}T^c_{0.66}f(\rho^s_{2.12})/(1 - s^c_{0.66}f(\rho^s_{2.12})))$$

and

$$\rho^*_{0.47} = \eta(\rho^{fa}_{0.47} + F^f_{d0.47}T^f_{0.47}g(\rho^s_{0.66})/(1 - s^f_{0.47}g(\rho^s_{0.66}))) + (1-\eta)(\rho^{ca}_{0.47} + F^c_{d,0.47}T^c_{0.47}g(\rho^s_{0.66})/(1 - s^c_{0.47}g(\rho^s_{0.66}))),$$

(7.13abc)

where in turn, $\rho^a=\rho^a(\tau)$, $F=F(\tau)$, $T=T(\tau)$, $s = s(\tau)$ are each functions of τ indexed within the lookup table, calculated for separate fine and coarse models. The surface reflectance relationships, $f(\rho^s_{2.12})$ and $g(\rho^s_{0.66})$ are described by Eqs. 7.4-7.6. The algorithm actually tries non-physical values of η (-0.1 and 1.1) to allow for the possibility of imperfect assumptions in either aerosol models or surface reflectance. Again, the primary products are $\tau_{0.55}$, $\eta_{0.55}$, and the surface reflectance ($\rho^s_{2.12}$). The fitting error ε is also noted.

Once the solution is found, a number of secondary products can also be calculated. These include the fine and coarse mode optical depths $\tau^f_{0.55}$ and $\tau^c_{0.55}$:

$$\tau^f_{0.55} = \tau_{0.55}\eta_{0.55} \quad \text{and} \quad \tau^c_{0.55} = \tau_{0.55}(1-\eta_{0.55}) \qquad \textbf{(7.14)}$$

the columnar mass concentration, *M:*

$$M = M^f_c\,\tau^f_{0.55} + M^c_c\,\tau^c_{0.55} \qquad \textbf{(7.15)}$$

the spectral total and model optical thicknesses τ_λ, $\tau^f_{\lambda,}$ and τ^c_λ:

$$\tau_\lambda = \tau^f_\lambda + \tau^c_\lambda \qquad \textbf{(7.16)}$$

where

$$\tau^f_\lambda = \tau^f_{0.55}(Q^f_\lambda / Q^f_{0.55}) \quad \text{and} \quad \tau^c_\lambda = \tau^c_{0.55}(Q^c_\lambda / Q^c_{0.55}), \qquad \textbf{(7.17)}$$

The Ångstrom Exponent α:

$$\alpha = \ln(\tau_{0.47} / \tau_{0.66}) / \ln(0.466/0.644) \qquad \textbf{(7.18)}$$

and the spectral surface reflectance $\rho^s_{\lambda,,}$. M^f_c and M^c_c are mass concentration coefficients for the fine and coarse mode, whereas Q^f_λ and Q^c_λ represent model

extinction efficiencies at wavelength, λ. If the resulting products are inconsistent, then the QAC value initially assigned to the pixel is changed to 0 ('bad quality').

7.5.4 Procedure B: Alternative Retrieval for Brighter surfaces

The derivation of aerosol properties is still possible when the 2.12 μm reflectance is brighter than 0.25, but is expected to be less accurate [Remer et al., 2005], due to increasing errors in the VISvs2.12 relationship. However, if Procedure A is not possible, but there are at least 12 cloud-screened, non-water pixels that satisfy

$$0.25 < \rho_{2.12}^{m} < 0.25G < 0.40 \qquad \textbf{(7.19)}$$

where

$$G = 0.5((1/\mu) + (1/\sqrt{\mu_0})) \text{ ,} \qquad \textbf{(7.20)}$$

then Procedure B is attempted. In this relationship μ_0 is the cosine of the solar zenith angle, $\cos(\theta_o)$, and μ is cosine of the satellite view angle, $\cos(\theta)$. Eq. 7.20 represents the slant path of the radiation. The concept is that at oblique angles, as the photon path increases, the atmospheric signal dominates over that from the land surface. The contribution from the surface reflectance becomes less important, and the retrieval can tolerate higher surface reflectance [Remer et al., 2005]. In procedure B, the QAC is automatically set to 0 ("bad quality").

Procedure B is analogous to "Path B" of the c004 algorithm described in Remer et al., [2005]. Like in c004, the Continental aerosol model is assumed. Unlike c004, the VISvs2.12 surface reflectance assumptions are those described by Eqs. 7.4-

7.6, and the Continental aerosol properties are indexed to 0.55 μm. In other words,η=1.0). The primary products for Procedure B are τ ($\tau_{0.55}$) and the surface reflectance ($\rho^{s}_{2.12}$). The error ε is also saved. Since Procedure B was followed, the only secondary products calculated are *M* and $\tau_{0.47}$, and the QAC is set to 0. The other products in are left undefined.

7.5.5 Low and negative optical depth retrievals

A major philosophical for the second-generation algorithm is that negative τ retrievals are allowed. Given that there is both positive and negative noise in the MODIS observations, and that surface reflectance and aerosol properties may be under or over-estimated depending on the retrieval conditions, it is statistically imperative to allow retrieval of negative τ. In fact it is necessary for creating an unbiased dataset from any instrument. Without negative retrievals the τ dataset is biased by definition. However, a large negative retrieval indicates a situation outside the algorithm's solution space and should not be reported. The trick is to determine the cutoff between a retrieved τ that is essentially the same as zero, and a retrieved τ that is truly wrong. MODIS should retrieve with the expected error defined by Eq. 1.1, then values down to -0.05 are essentially the same as a zero retrieval and are reported as retrieved. Allowing for slightly higher uncertainty, the algrorithm include τ retrievals down to -0.10 (twice the expected error in pristine aerosol conditions), but report these values as -0.05 and lower the QAC value. Note that all retrievals with $-0.05 < \tau < 0$ are reported with high QAC value = 3, unless identified as poor quality for some other reason. Some of the products that are retrieved or derived (such as

η or Ångstrom Exponent) are set to zero or reported as not defined for negative retrievals. In cases of low τ (τ < 0.2), η is too unstable to be retrieved with any accuracy. Therefore, η is reported as un-defined even though other parameters (such as Ångstrom exponent and Fine τ) may be reported.

7.5.6 Sensitivity study

Because it uses MODIS channels with wide spectral range, and assigns expected aerosol type, the algorithm (Procedure A) should be able to retrieve τ with robustness, and have some sensitivity to the size parameter η. Following the lead of Tanré et al [1997], I tested the sensitivity of Procedure A by applying the following exercises: (1) simulation of conditions that are included within the LUT, (2) and simulations for conditions that include one or more errors.

Exercise 1: Whereas the study of Tanré et al, [1997] tested the algorithm on a single geometrical combination, this experiment simulated the 720 reasonable geometrical combinations in the LUT ($0° \leq \phi \leq 180°$, $\theta \leq 60°$, $\theta_0 \leq 48°$). The fine-dominated aerosol model was set as the moderately absorbing ($\omega_0 \sim 0.9$) aerosol model, with the coarse-dominated model set as the spheroid (dust) model (Chapter 6). For each combination of geometry, and for each MODIS channel, I extracted the fine and coarse mode values of atmospheric path reflectance ρ^a_λ, backscattering ratio s_λ, downward flux F_d and transmission T_λ. I assumed that the 2.12 μm surface reflectance $\rho^s_{2.12} = 0.15$, and the c004 VISvs2.12 surface reflectance ratios (i.e, $\rho^s_{0.66} = 0.5\ \rho^s_{2.12}$ and $\rho^s_{0.47} = 0.5\rho^s_{0.66}$). TOA reflectance ρ^*_λ was simulated for 5 discrete

values of η (η = 0.0, 0.25, 0.5, 0.75 and 1.0). Therefore, for each value of τ in the LUT, there are 720 x 5 = 3600 attempts to retrieve that τ.

For smaller τ ($\tau \leq 1$), the τ was retrieved within $\Delta\tau < 0.01$ for all 3600 combinations. As τ increases, however, computational instabilities lead to a less exact solution. Still, though, the retrieved τ is certainly within 10% and in most cases to within $\Delta\tau<0.1$. When τ=0.5 with η either 0.0 or 1.0 simulated, both τ and η are retrieved exactly.

Figs. 7.5 and 7.6 provide a way of assessing the retrieved MODIS products. Fig. 7.5 plots retrieved τ, surface reflectance and fitting error as a function of either air mass (top) or scattering angle (bottom), given that the input conditions are $\tau_{0.55}$=0.5, η=0.5 and $\rho^{s}_{2.12}$=0.15. In this case, all of the 720 geometrical combinations in the LUT were plotted. The retrieval never exactly matches the input reflectances, although the errors are very small (less than 0. 1%). Note that the retrieval uses an under-estimated surface reflectance to balance the over-estimated optical depth. Fortunately, though, most errors are small, and are well within any expected error bars. Fig. 7.6 is similar, but for η=0.25, and plotted only for the air mass dependence. The errors are much larger (up to 1%), but τ is still well within expected error.

Exercise 2. The same combination of radiative transfer codes used to create the operational LUT (MIEV + RT3) was used to simulate additional values of aerosol loading ($\tau_{0.55}$ = 0.35, 1.5 and 6.0). This "extended" LUT simulates the same 720 geometrical combinations and same values of η (as in exercise 1). On average the retrieval is very close to the expected value, however, the standard deviation over all geometry is larger than for τ in the normal LUT. A notable exception is the attempt at

retrieving $\tau_{0.55}$ = 6.0, where the algorithm does a poor job of extrapolating. In the operational algorithm, we constrain the maximum possible τ to be 5.0. As for retrieving values of η not included in the LUT, the algorithm is successful. The η=0.5 retrieval is well behaved. All attempts at retrieving either η=0.25 or η=0.75 led to retrieving η=0.20 and η=0.70. Although it is impossible for an exact retrieval, due to the algorithm choosing between 0.1 intervals, it is interesting that no retrievals of η=0.30 or η= 0.80 are produced.

Exercise 3. This exercise studied the impact of different types of errors that could creep into the retrieval process. Potential errors include (but are not limited to) random, systematic or spectrally dependent errors that arise from issues like sensor calibration, assuming the wrong aerosol model at a given location, coarse input topography mapping, or wrong estimates of the VISvs2.12 surface reflectance relationships. These errors are expressed by adding random or systematic errors in the spectral reflectance measurements, geometrical conditions or other input boundary conditions. Table 7.1 lists some prescribed errors, for the same set of eight geometries listed in Table 5.1. Table 7.2 shows the results when attempting to retrieve conditions of $\tau_{0.55}$=0.5, η=0.5 and $\rho^{s}_{2.12}$=0.15, for the eight sample geometries. Table 7.2adisplays the retrieved values of $\tau_{0.55}$ for each case. Table 7.2b shows the Mean Squared Error (MSE) for each retrieved product, computed over all eight geometries. For any case of prescribed errors/geometry, one or more products may be over-estimated or under-estimated. If all geometry leads to either one direction or the other, the MSE value is designated by (+) or (-). For example, when retrieving with no additional errors ('LUTinput'), τ is never retrieved exactly, but is over-estimated

by an average MSE of 0.0011 (+). In balance, $\rho^s_{2.12}$ is consistently underestimated (MSE of 0.0004 (-)), with a nonzero fitting error, ε. This is simply a result of computer round off error.

Under most conditions, introducing minor calibration or random errors does not destroy the retrieval of τ. For most individual errors, the retrieved τ is accurate to within 0.02. However, even when errors are combined (model error, random error, surface error, calibration error and geometrical error), the algorithm still retrieves τ=0.5 with MSE = 0.10, thus retrieving within the expected error of Δτ=0.125. Retrieval of surface reflectance seems to be robust. Retrieval of η is much more unstable. For simple calibration and geometrical errors, the MSE for η is < 0.1. Combinations of errors lead to large MSE (>0.2) for η retrieval, meaning that η is not a stable product. Yet, even though the η parameter is sensitive to errors, it can give qualitative indication of particle size.

7.6: Preliminary validation

Examples of the three primary aerosol products ($\tau_{0.55}$, η and $\rho^s_{2.12}$) are shown in Fig. 7.9, along with a color composite of the L1B reflectances (RGB image; 0.47, 0.55 and 0.66 μm channels). This image was taken on May 4, 2001 over the U.S. East Coast, and is the same image used by King et al., [2003]. There is continuity of τ from land to ocean, and that the retrieval of η and surface reflectance seem reasonable. Note that η is not plotted over land when τ < 0.2.

The primary means of MODIS validation is by comparing the products with equivalent measurements from AERONET or other aerosol measurements. In this

way, the standard products of c004 were *validated* [e.g. Remer et al., 2005], meaning that their uncertainties are quantified. In the case of the land products (through V4.2), this meant that ~60% (slightly less than one standard deviation) of the AERONET-measured τ values were retrieved by MODIS to the expected error described by Eq. 1.1. The other land parameters were either not yet validated, or are diagnostic parameters that cannot be validated. In addition to validation by AERONET, it is important to perform qualitative analyses based on visual inspection and global statistics.

Since the algorithm was described by Remer et al., [2005], it has continued through minor updates. The last update to the c004 family was known as Version 5.1 ('V5.1'). V5.1 updated the snow mask [Li et al., 2005] and cleaned up confusing information in the output files. However, V5.1 never became operational, as there was the opportunity to replace it with the algorithm described in this Chapter. In this work [Levy et al., 2007] V5.1 is used to bridge from c004 algorithms to the second-generation algorithm, known in operation as V5.2.

7.6.1 Direct comparison of V5.2 and V5.1

Fig. 7.8 plots retrieved τ at 0.55 μm from both V5.1 and V5.2, over small areas of a MODIS granule over the Western U.S. on Sep 30, 2003. V5.1 (OLD) is presented in (a), whereas V5.2 (NEW) is shown in (b). The V5.2 aerosol retrieval adds more valid retrievals over very low τ areas (coastal Oregon and northern California). V5.2 reports these areas as having near zero or slightly negative τ, where V5.1 would have reported fill values (no retrieval). In areas farther from the coastline, V5.2 tends to

clean up contamination presumably caused by clouds, elevation, and inhomogeneous surface properties, and produces a more reasonable picture of τ.

7.6.2 Statistics of V5.2 versus V5.1

Of most interest to the climate community will be the changes in the statistics of the aerosol products. These include the global mean values and the distribution (histogram) of the values. For the set of MODIS granules listed in Table 7.3 (about 6300 granules of both Terra and Aqua), the mean 0.55 μm τ is reduced from 0.28 to 0.21. This is a significant reduction that can be compared with model estimates.

Fig. 7.9 plots the histograms of retrieved τ at 0.55 μm from both V5.1 and V5.2. These histograms include 141 individual Terra and Aqua granules that are known as the MODIS "test_bed", and twelve days of global data – all listed in Table 7.3. The use of global data is especially important for determining how the retrieval behaves in regions not selected for algorithm development. Of course, the obvious change in the V5.2 product is that small magnitude negative τ retrievals are valid. About 10-11% of the total τ retrievals are now retrieved as below zero, of which only about 3% are below -0.05. This promising result indicates that V5.2 has reasonable ability to detect very clean conditions within the expected error of $\pm$0.05. Also Fig. 7.9 shows that the fraction of retrieved medium to medium high τ ($0.2 < \tau < 0.75$) is reduced, while the fraction of high τ ($\tau > 0.75$) remains about the same.

7.6.3 Comparison of V5.2 to V5.1 and with AERONET

As of 1 April 2006, the V5.2 algorithm was run on nearly 6300 granules, including one full month (August 2001), fifteen entire days (listed in Table 7.3) and about 141 individual granules that are known as the MODIS "test_bed." These granules include observations from both Terra and Aqua, and are seasonally and yearly representative of the MODIS time series. For comparison, both V5.1 and V5.2 were run on the same set of granules. Note that the database used to derive the land surface relationships (350,000 Aqua and Terra data from 2000-2004) has a small overlap with our 6300 granule-testbed. In that way, the comparison to AERONET shown in this section is not entirely independent of the formulation database. However, the data used in this section includes all values of τ and α, while the formulation database was limited to specific ranges of these variables. Also, the data used here represent a comparison of spatio-temporal statistics, while in the formulation data base only the individual match between sunphotometer location and satellite overpass were used. Thus, the plots shown here, while not entirely independent, offer a test of the new retrieval in more general conditions than in the specific formulation data. Figs. 7.10 and 7.11 plot the comparisons of both V5.1 and V5.2 with the AERONET data, via the spatio-temporal co-location method of Ichoku et al., [2002a]. (NOTE THAT 7.11 SHOULD BE REPLOTTED WITH 4th VERSION OF O'NEILL ALGORITHM)

Fig. 7.10 plots the retrieved MODIS τ against AERONET τ, both at 0.55 μm. The data have been sorted by AERONET τ and averaged into bins with equal numbers of observations in each bin. The mean and standard deviation of each bin are calculated and plotted in Fig. 7.10 as a solid dot and error bars. The correlation is

calculated from the freely plotted points before binning, although the cloud of points is not shown in the plot. The regression equation has improved tremendously compared to V5.1, from "y=0.097+0.91x" to "y=0.029+1.01x." Correlation R is also improved, from R=0.847 to R=0.894. It should be noted that slight differences in the number of points arise due to different selection of valid dark pixels and allowance of below zero τ retrievals.

Fig. 7.11a plots MODIS η against AERONET η, where I calculated AERONET η from sun observations of spectral τ, using the 4^{th} version of the O'Neill et al., [2003] spectral de-convolution algorithm. Keep in mind that unlike MODIS/AERONET comparisons of τ, MODIS and AERONET do not retrieve the same quantity labeled as η. The AERONET retrieval assumes one fine mode and one coarse mode. Thus, AERONET η is the weighting between *modes*. The MODIS land η is a weighting between bi-modal *models*, where fine-dominated models also contain a coarse mode and vice-versa. The improvement to the MODIS η product is mainly its correlation to AERONET. Note that η is defined only when $\tau > 0.2$. Figs 7.11b and c show comparisons for derived products, including the Ångstrom Exponent (defined by 0.47 and 0.66 μm), and Fine optical depth (i.e. $\tau^f = \tau \times \eta$), respectively. For Fine τ, the correlation and slopes are nearly unchanged between V5.1 and V5.2; however, the offset decreases from +0.051 to -0.031. The result is that nearly two-thirds of all V5.2 MODIS Fine τ fall within expected errors defined by Eq. 1.1. Note again that the difference in the number of points is due to different selection of dark pixels and treatment of negative τ retrievals. The Ångstrom exponent has little improvement from V5.1 to V5.2, except for slightly better but still poor correlation

with the AERONET measured quantities. In general, the changes to the MODIS aerosol retrieval algorithm described here have resulted in a much less biased τ and τ^f products than the previous algorithm. MODIS η and other size parameters correlate better with AERONET, although it still leaves room for improvement.

7.6.4 Other validation efforts

As of April 2006, the second-generation algorithm went into operational production. By the end of 2006, the entire MODIS mission was expected to be reprocessed using the new algorithm. Since the products are easily accessible to any investigator, certain studies have been brought to my attention. In most cases, the c005 results look good, however, in certain regions under certain conditions, the products are not as accurate as would be hoped.

For example, Mi et al., [submitted, 2007] present a validation of MODIS retrieved aerosol τ over two AERONET sites in Northern and Southern China, and compare the results of c005 with c004. The uncertainties of surface estimation have been singled out from other error sources by replacing the c004 reflectance ratios with atmospherically corrected reflectance. The difference between the aerosol models used in c004 and c005 algorithm is also investigated, in terms of the effects on the quality of τ retrieval at the two sites. As might have been expected, the performance of MODIS τ retrievals differs in Northern and Southern China, where the surface ecosystem and climate are quite different. Like previous validation studies, Mi et al., [2007] showed generally overestimation of τ at both sites by MODIS c004, attributing to the assumptions of VISvs2.12 surface reflectance ratio

and single scattering albedo of the aerosol fine model. Although the second-generation algorithm tackled both issues, resulting in generally improved retrieval of τ, uncertainties in aerosol models still dominate retrieval errors. Some of the largest retrieval errors occur at the northern site, primarily due to the presence of complex aerosol compositions, including mixtures of dust with sulfate aerosol, organic and black carbon.

TABLE 7.1: LIST OF PRESCRIBED ERRORS FOR V5.2 SENSITIVITY STUDY (ADAPTED FROM LEVY ET AL., [2008])

Reference	Error Name	Description
1	LUTinput	LUT input: Use the LUT with no prescribed errors
2	ModError	Aerosol model error: We tried to retrieve with the Non-absorbing fine model LUT
3	RndError	Random Error: All channels have random reflectance error of up to ±0.002
4	SfcError	Surface Error: 10% error in assumed 0.66/2.12 surface reflectance relationship
5	CalError	Calibration Error: All channels have random error of up to ±1%
6	ElvError	Elevation Error: Elevation is 1km instead of assumed sea level
7	GeoError	Geometry Error: All angles have random error of up to ±5 degrees
8	AllError	Combination of 2,3,4,5,6 and 7.

TABLE 7.2: RESULTS OF SENSITIVITY STUDY USING PRESCRIBED ERRORS (ADAPTED FROM LEVY ET AL., [2008])

Geometry Error Name	LUTinput	RndError	CalError	GeoError	ModError	ElvError	SfcError	AllError
A	0.501	0.4786	0.5242	0.5143	0.5015	0.6068	0.5402	0.6963
B	0.501	0.4887	0.5242	0.4977	0.4993	0.6035	0.5422	0.6677
C	0.501	0.5227	0.5227	0.4657	0.4835	0.5104	0.4955	0.4809
D	0.5011	0.5104	0.4995	0.4761	0.5014	0.5228	0.498	0.4892
E	0.5008	0.4754	0.502	0.4893	0.4866	0.5211	0.4877	0.5737
F	0.501	0.5135	0.5029	0.4922	0.5035	0.531	0.488	0.5536
G	0.5014	0.4973	0.5199	0.4698	0.4811	0.5097	0.488	0.427
H	0.5016	0.4961	0.5001	0.4744	0.5198	0.5299	0.4939	0.5106

A: Retrieved τ at 0.55 μm (expected τ=0.5)

Product Error Name	LUTinput	RndError	CalError	GeoError	ModError	ElvError	SfcError	AllError
τ	0.0011(+)	0.0159	0.0162	0.0215	0.0123	0.0561(+)	0.0221	0.1006
η	0.0000	0.0000	0.0707	0.1000	0.0707	0.4243 (+)	0.1323 (+)	0.4912 (+)
ρ	0.0004 (-)	0.0008	0.0022	0.0025	0.0031 (-)	0.0067	0.0020 (+)	0.0074 (+)
ε	0.0010	0.0021	0.0037	0.0028	0.0020	0.0025	0.0035	0.0052

B: MSE of retrieved τ,η,ρ^{σ} and ε (expected τ=0.5, η=0.5, ρ^{σ}=0.15 and ε=0.0). Entries designated with (+) mean that the product was over-estimated for all 8 geometries, whereas those with a (-) means it was under-estimated for all geometries.

TABLE 7.3: Description of Data used in V5.2 Provisional Validation (adapted from Levy et al., [2008])

Date of MODIS Observations	Terra/Aqua	Why interesting?
August 2001 (full month: 4138 granules)	Terra and Aqua	
7 July 2002 (full day: 132 granules)	Aqua	Quebec Smoke in NE US
8 July 2002 (full day: 136 granules)	Aqua	Quebec Smoke in NE US
6 Mar 2004 (full day: 132 granules)	Aqua	Asian Dust
7 Mar 2004 (full day: 138 granules)	Aqua	Asian Dust
Eight days in 2003 (full days: 1070 granules)	Aqua	Yearly Cycle
14 Nov 2005 (full day: 138 granules)	Terra	Low AOD globally
22 Apr 2001 (full day: 136 granules)	Terra	ACE-Asia
26 Jun 2002 (full day: 138 granules)	Terra	Summer time haze
Test_bed_Aqua: (39 granules)	Aqua	Test bed of interesting Aqua data
Test_bed_Terra: (102 granules)	Terra	Test bed of interesting Terra data

Total granules = 6299

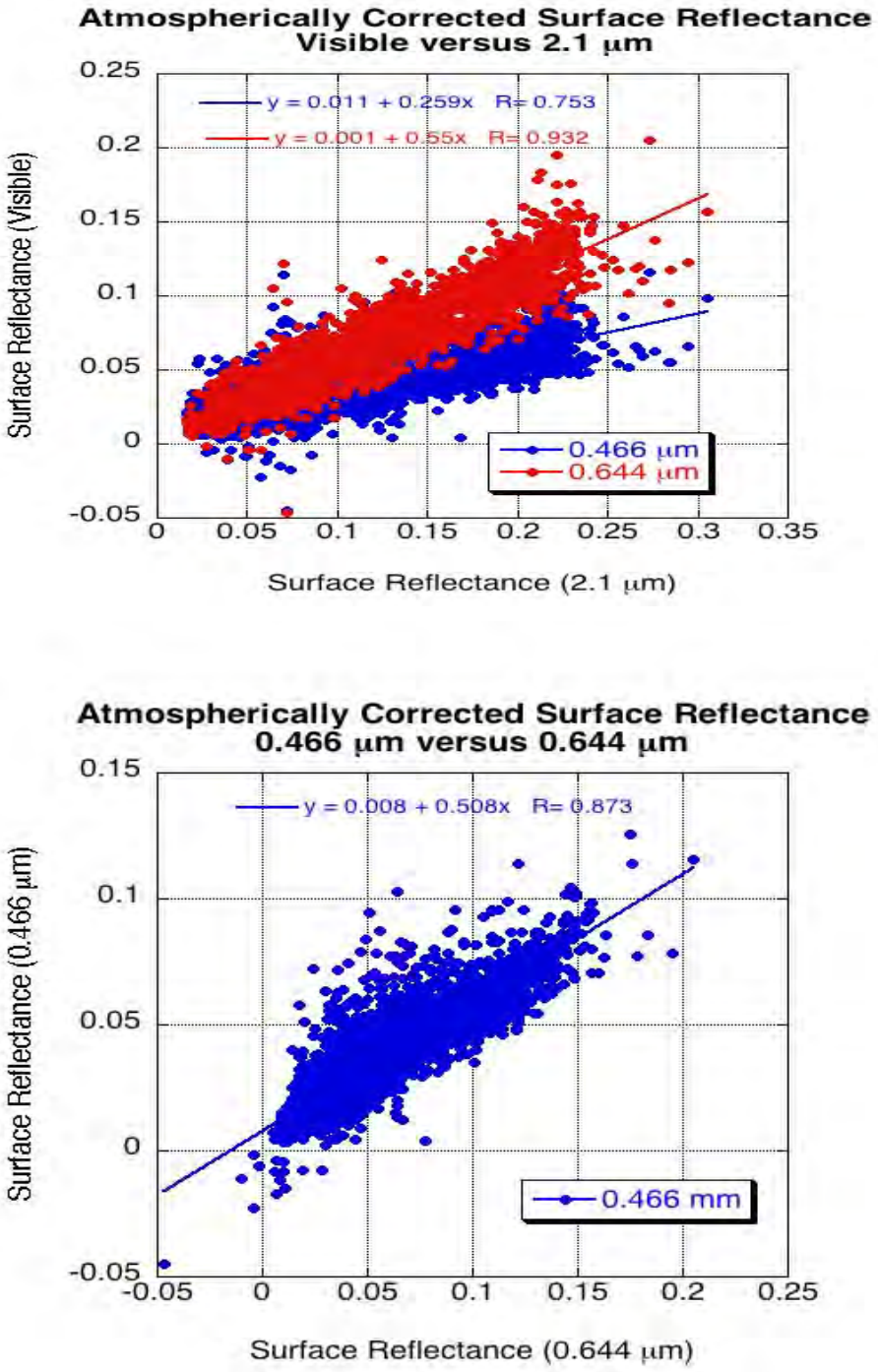

Figure 7.1: Atmospherically corrected surface reflectance in the visible (0.47 and 0.66 μm channels) compared with that in the 2.12 μm SWIR channel (a), and the 0.47μm compared with that in the 0.66 μm channel (b). (adapted from Levy et al., [2007])

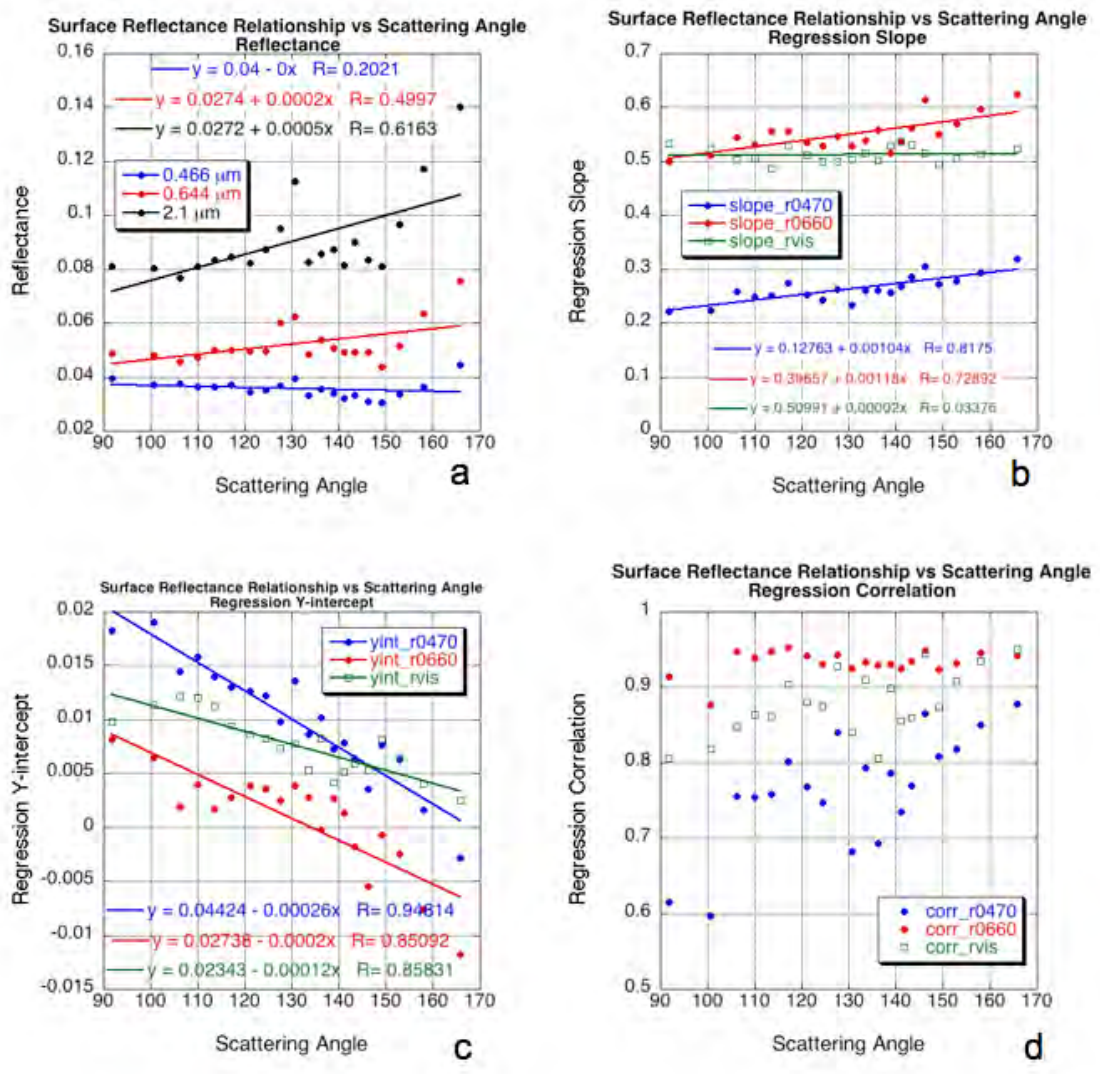

Figure 7.2: VISvs2.12 surface reflectance relationships as a function of scattering angle. The data were sorted according to scattering angle and put into 20 groups of equal size (about 230 points for each scattering angle bin). On all subplots, each point is plotted for the median value of scattering angle in the bin. Part (a) plots median values of reflectance at each channel as a function of the scattering angle. Linear regression was calculated for the 230 points in each group. The slope of the regression (for each angle bin) is plotted in (b), the y-intercept is plotted in (c) and the regression correlation is plotted in (d). Note for (b), (c) and (d) that 0.47 µm vs 2.12 µm (r0470) is plotted in blue, 0.66 µm vs 2.12 µm (r0660) is plotted in red and 0.47 vs 0.66 µm (rvis) is plotted in green. (adapted from Levy et al., [2007])

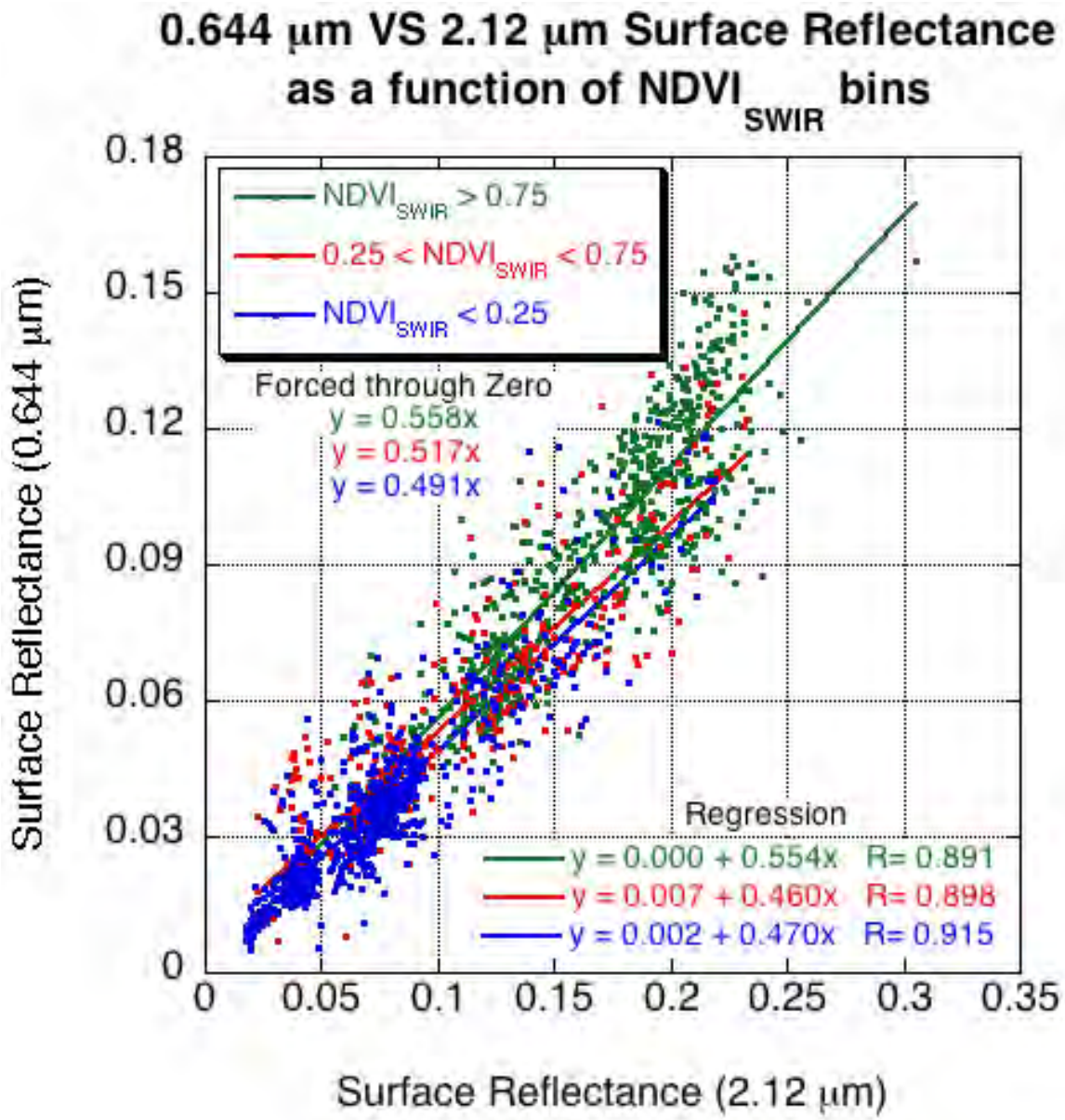

Figure 7.3: 0.66 μm versus 2.12 μm surface reflectance as a function of bins of *$NDVI_{SWIR}$* values. The standard regression is plotted, with regression Eq.s given in the lower right hand corner. The ratios (if forced through zero) are given beneath the legend. Blue refers to low *$NDVI_{SWIR}$*, red to medium and green to high values. (Fig. adapted from Levy et al., [2007])

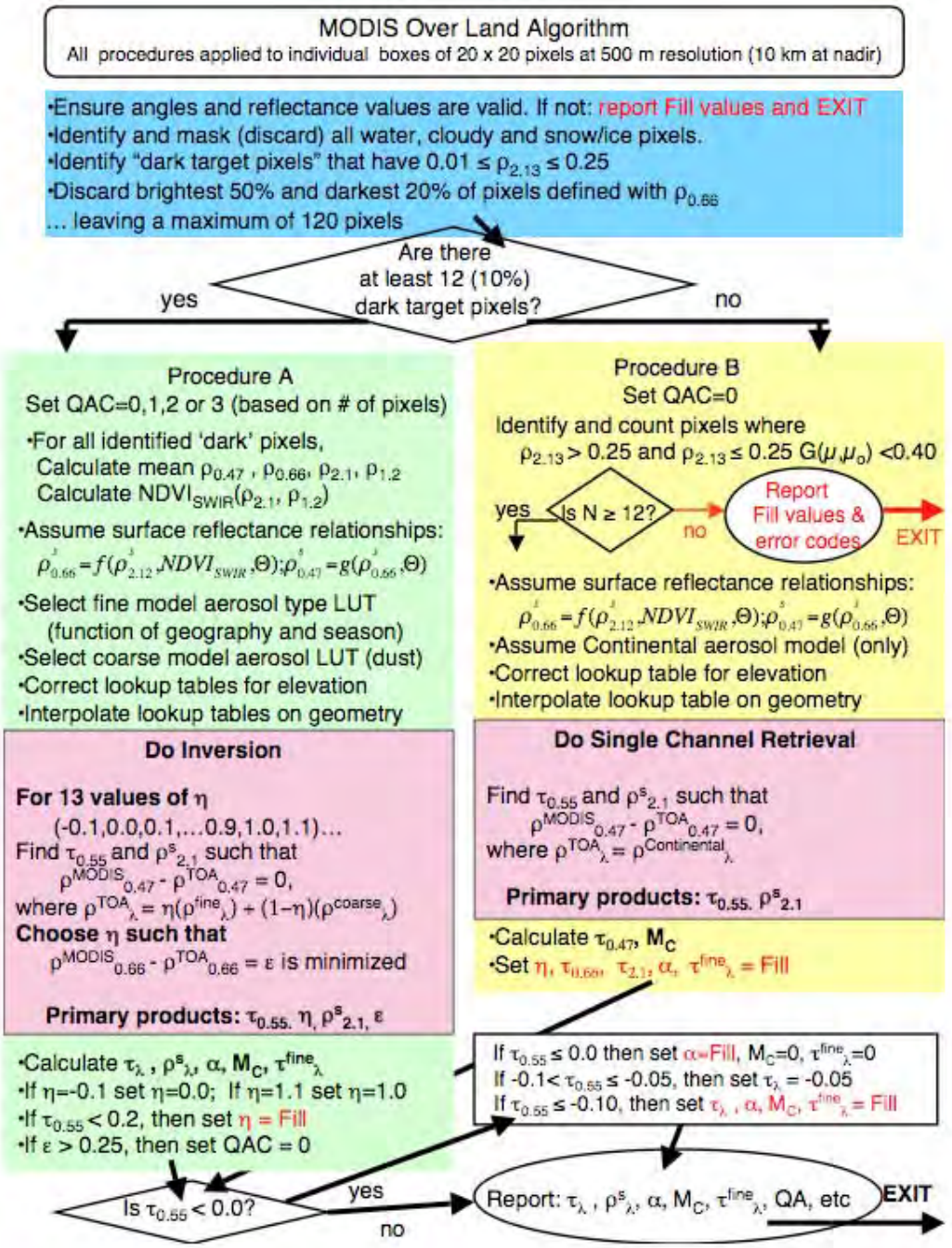

Figure 7.4: Flowchart illustrating the derivation of aerosol over land for the new algorithm. (Fig. adapted from Levy et al., [2007])

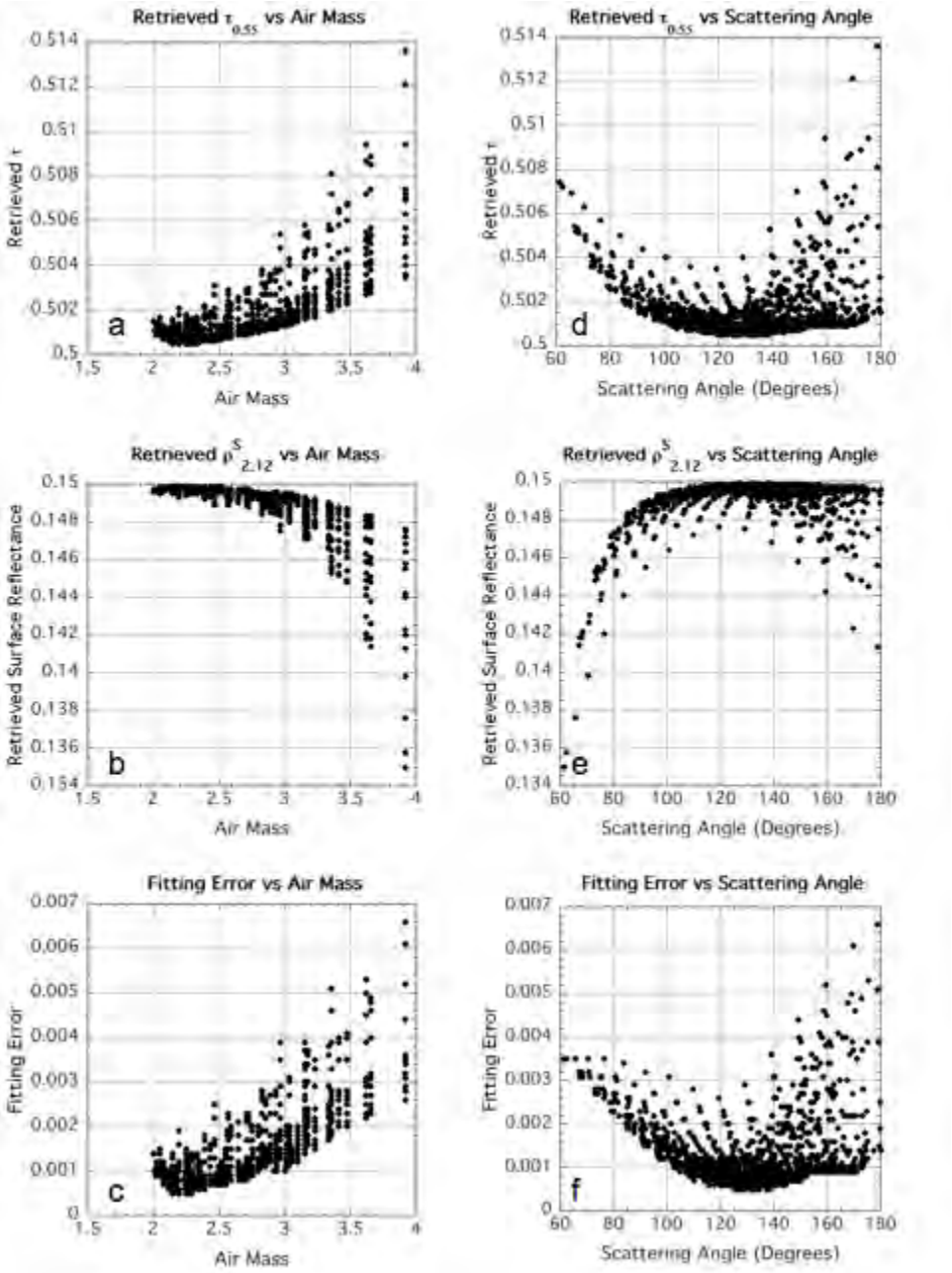

Figure 7.5: Retrieved MODIS products as a function of Air Mass (a-c) and Scattering Angle (d-f) for inputted atmospheric conditions (τ=0.5, η=0.5 and $\rho^{s}_{2.12}$=0.15) and 720 LUT geometrical combinations. The retrieved τ is plotted in (a) and (d), the 2.12 μm surface reflectance in (b) and (e) and the fitting error is plotted in (c) and (f). Note that in all cases, the η value of 0.5 was retrieved exactly. (Fig. adapted from Levy et al., [2007])

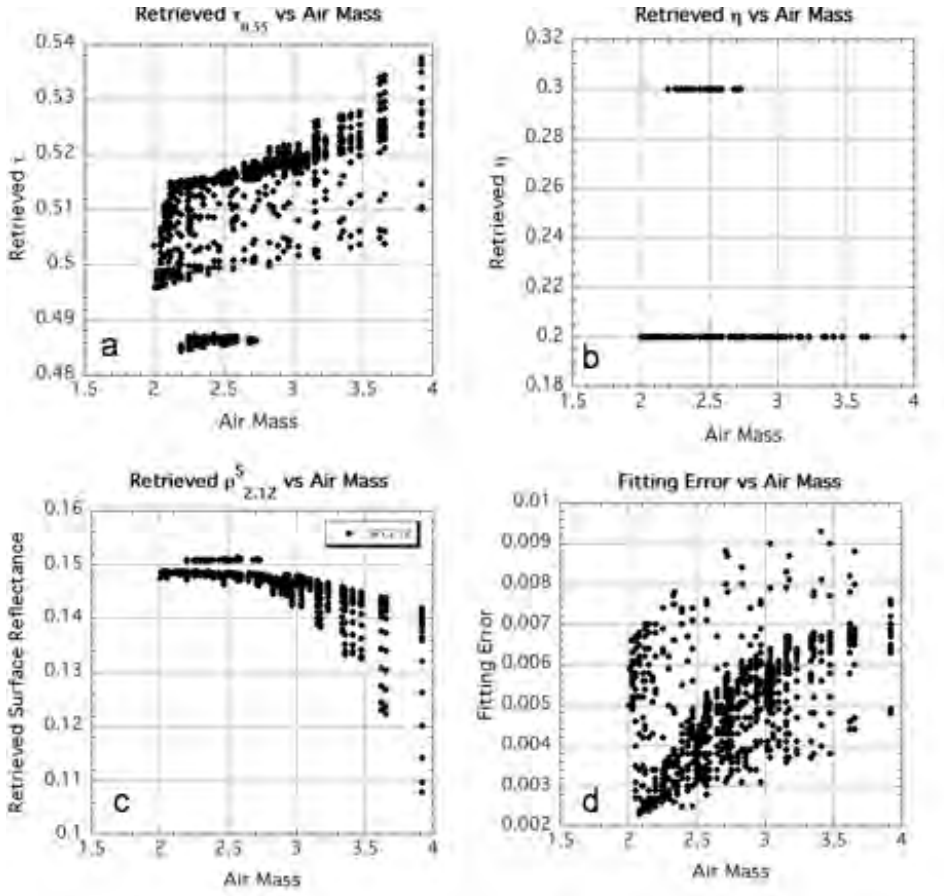

Fig. 7.6: Retrieved MODIS products as a function of Air Mass for inputted atmospheric conditions (τ=0.5, η=0.25 and $\rho^{s}_{2.12}$=0.15) and 720 LUT geometrical combinations. The retrieved τ is plotted in (a), retrieved η in (c), the 2.12 μm surface reflectance in (c) and the fitting error is plotted in (d). (Fig. adapted from Levy et al., [2007])

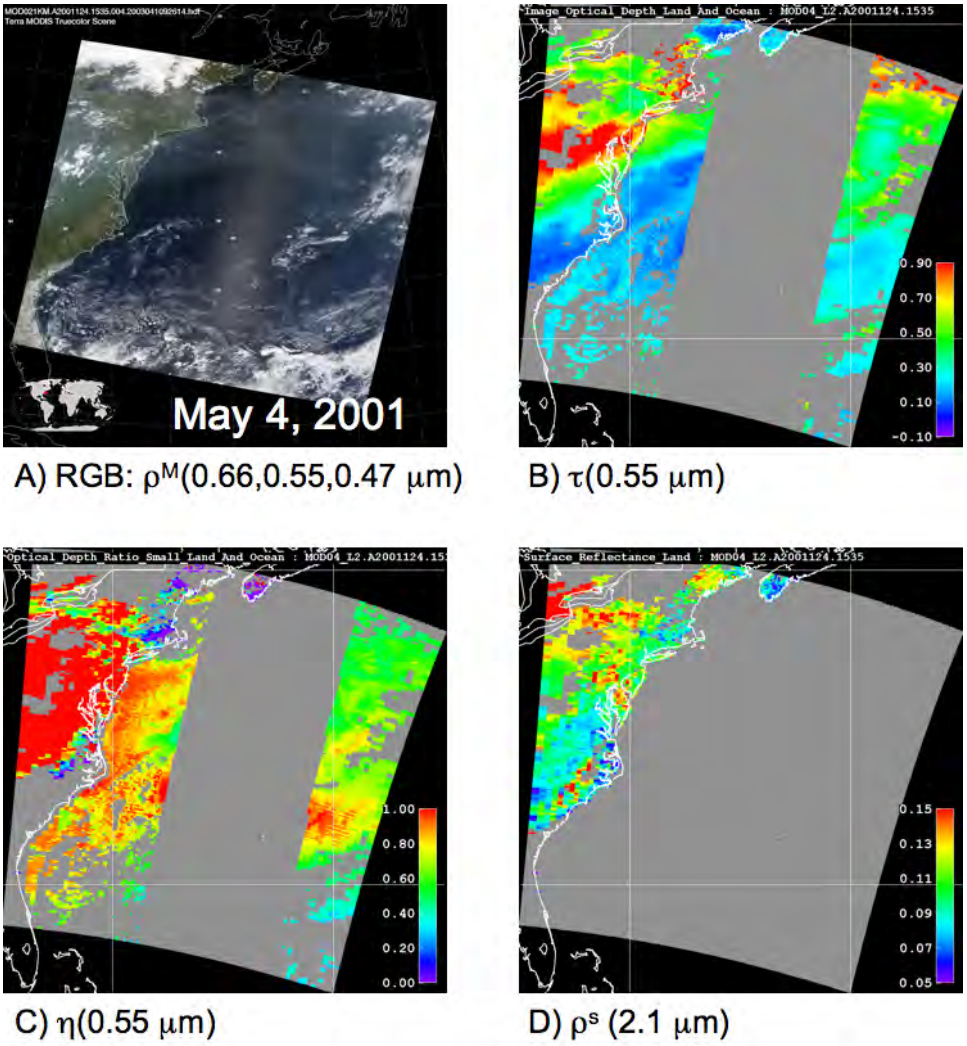

Fig. 7.7: Retrieved aerosol and surface properties over the Eastern U.S. on May 4, 2001. This Fig. can be compared with that plotted in King et al., (2003). Panel A) is a 'true-color' composite image of three visible channels, showing haze over the mid-Atlantic. Panels B) and C) show retrieved τ and η, showing that the heavy aerosol (τ ~ 1.0) is dominated by fine particles. The transport of the aerosol into the Atlantic is well represented with good agreement between land and ocean. Note that over-land η is not reported when τ < 0.2. Panel D) shows the retrieved surface reflectance. (Fig. adapted from Levy et al., [2007])

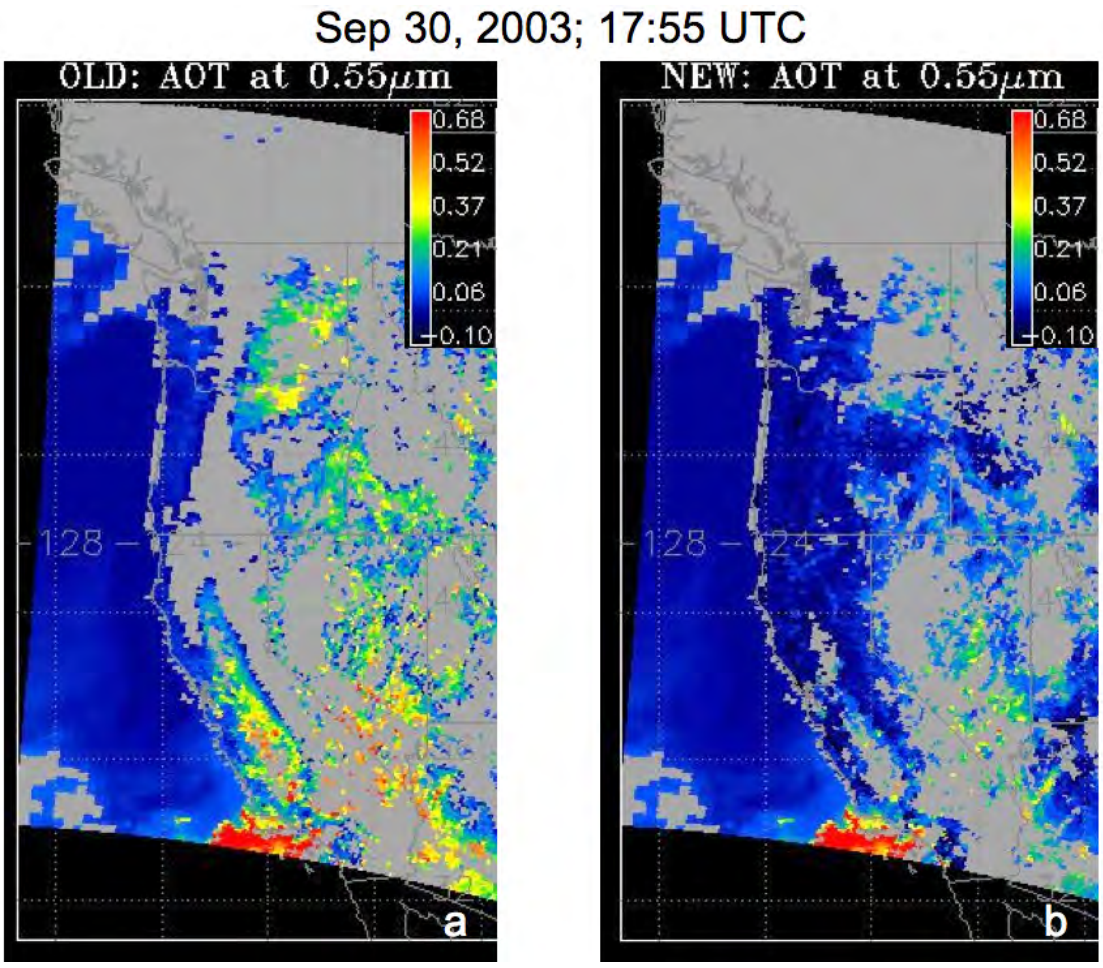

Fig. 7.8: Retrieved τ (AOT) at 0.55 μm for Old V5.1 (a) and New V5.2 (b) over California for 30 September 2003. The color scale is the same for both plots. Note the increase in the retrieval spatial coverage and reduction in surface contamination for V5.2. (Fig. adapted from Levy et al., [2007])

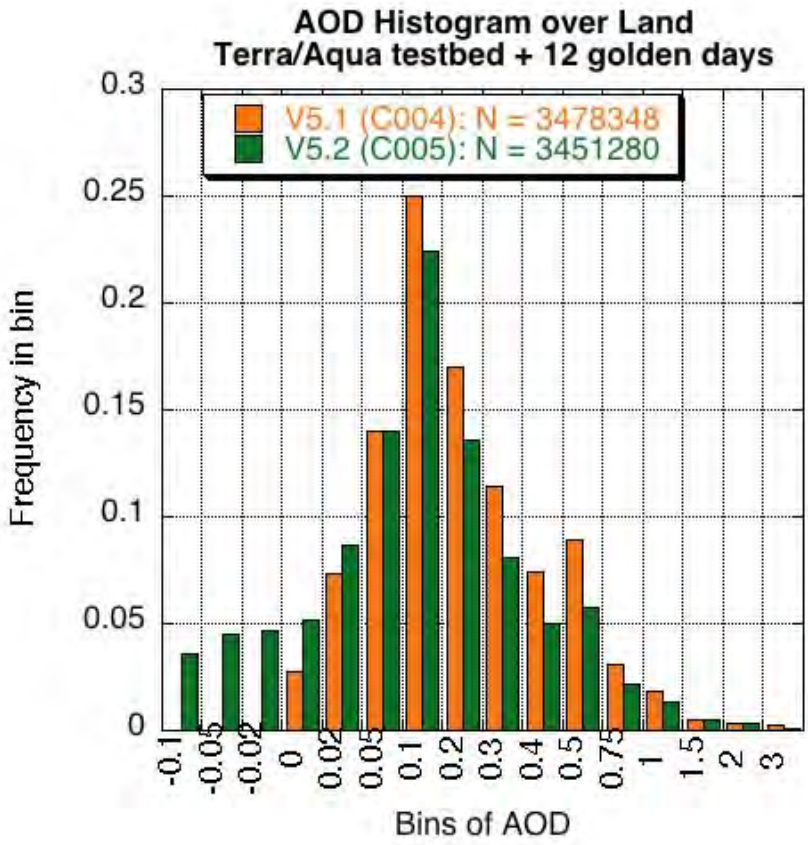

Fig. 7.9: Histogram of retrieved τ (AOD) over land, from V5.2 (c005) in green, compared to V5.1 (c004) in orange. The data include the 141 granules of the Terra and Aqua "test_bed" as well as twelve complete days. The value of each bin refers to the minimum value of the bin (the max value would be the value of the next bin). Note that the general lognormal nature of the retrievals is preserved, except now there are some negative values. (Fig. adapted from Levy et al., [2007])

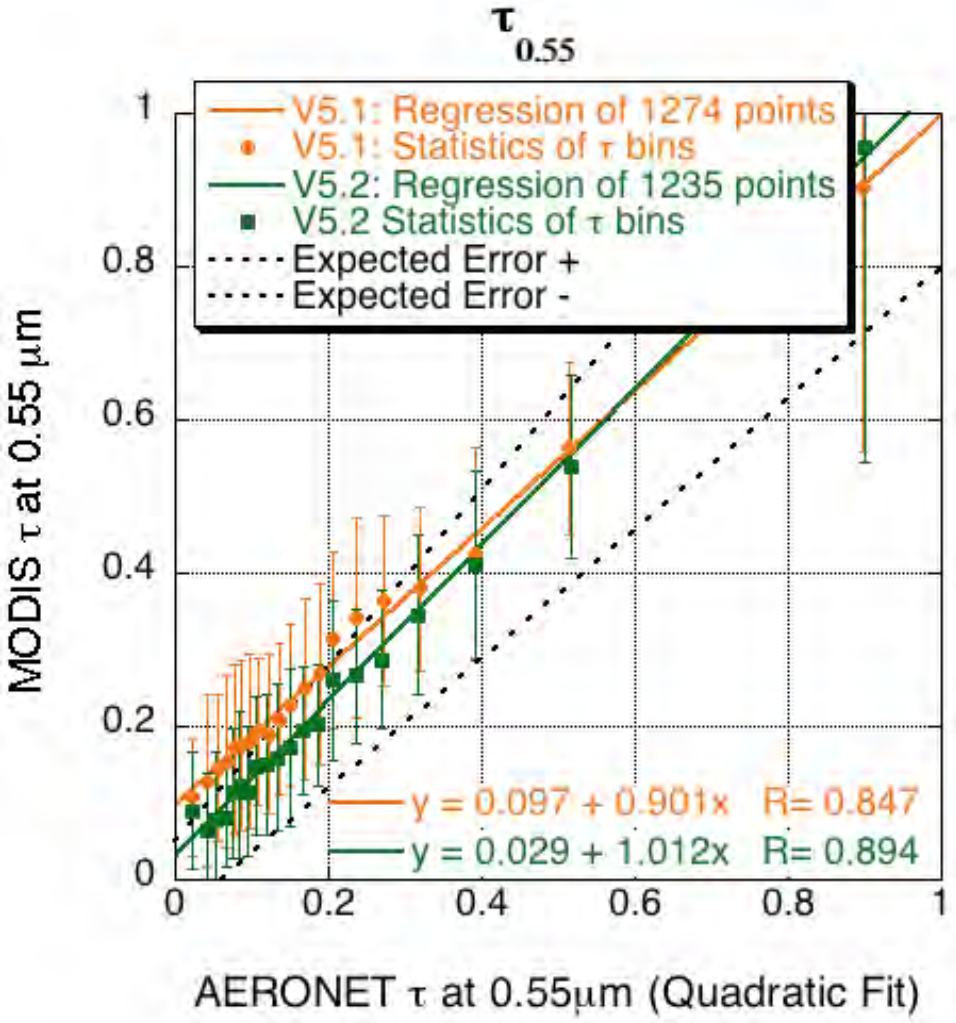

Fig. 7.10: MODIS τ over land retrieved at 0.55 μm, compared with AERONET τ interpolated to 0.55 μm. The solid shapes and error bars represent the mean and standard deviation of the MODIS retrievals, in 20 bins of AERONET-derived τ. Both the retrievals from V5.1 (orange) and V5.2 (green) are shown. The regressions (solid lines) are for the cloud of all points before binning (not shown). The expected errors for MODIS (±0.05 ±0.15τ) are also shown (dashed lines). (Fig. adapted from Levy et al., [2007])

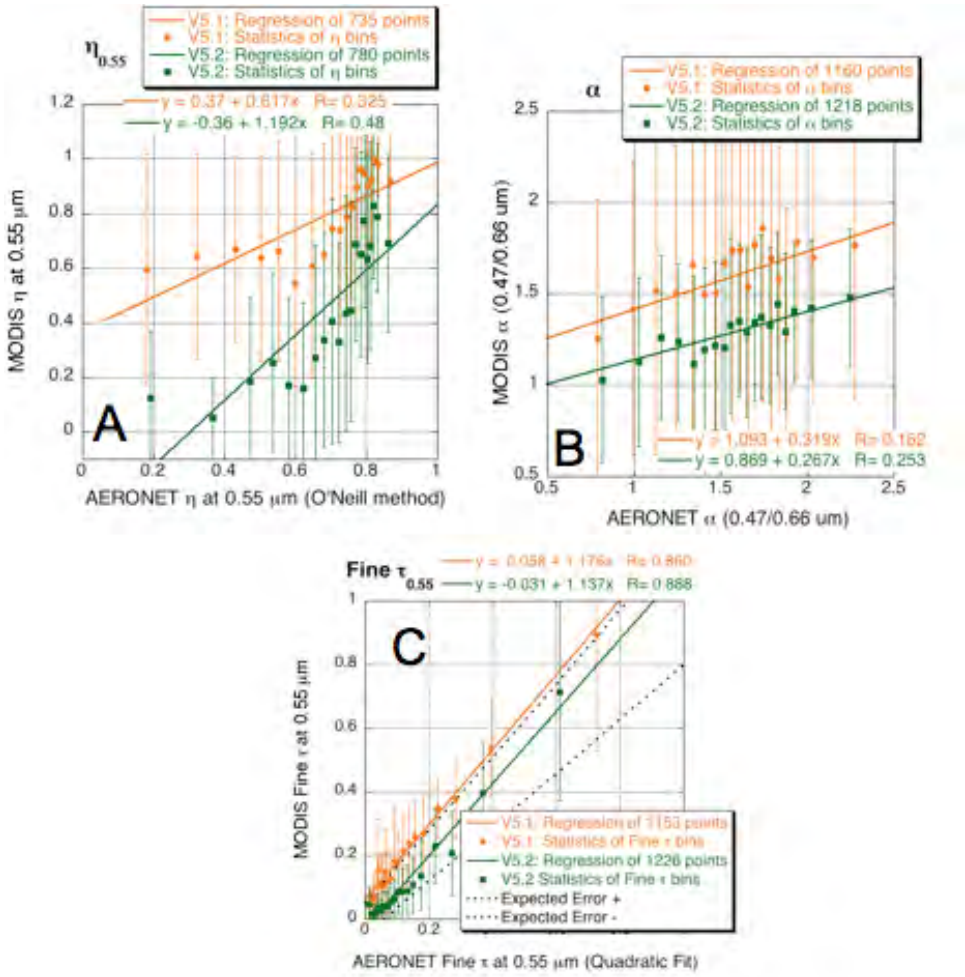

Fig. 7.11: MODIS aerosol size retrievals compared with AERONET derived products. The solid shapes and error bars represent the mean and standard deviation of the MODIS retrievals, in 20 bins of AERONET-derived product. Both the retrievals from V5.1 (orange) and V5.2 (green) are shown. The regressions (solid lines) are for the cloud of all points (not shown). A) η over land retrieved at 0.55 μm, compared with AERONET η retrieved by the O'Neill (2003) method. Note that η is defined differently for MODIS and AERONET and that we only show results for τ > 0.20. B) MODIS-derived α (0.466/0.644 μm) over land with AERONET α interpolated to the same wavelengths. C) MODIS Fine τ over land retrieved at 0.55 μm, compared with AERONET Fine τ interpolated to 0.55 μm by quadratic fitting and the O'Neill method. The expected errors for MODIS (±0.05 ±0.15τ) are also shown (dashed lines). (Fig. adapted from Levy et al., [2007])

Chapter 8: Using MODIS for evaluating modeled relationship between τ and surface $\{PM_{2.5}\}$ over the U.S. mid-Atlantic

Chapters 6 and 7 introduced the principles of the second-generation algorithm, which was validated (preliminarily) by comparing to global AERONET data. Once the performance of the new MODIS algorithm is evaluated, the products can be applied to answer scientific questions. While the primary goal of the MODIS retrieval is to characterize the global and regional aerosol properties and their effects on climate, investigators have used the MODIS products for various other applications. One hot topic is the effort to relate the column-averaged aerosol properties to properties of aerosol near the Earth's surface that impact air quality and human health.

This Chapter concentrates on MODIS retrievals over the U.S. mid-Atlantic, and how they can be used to further the understanding of aerosols in the region. Since the University of Maryland has been tasked with evaluating the CMAQ model results in the region for 2002, this Chapter evaluates during this time period (specifically July and August, 2002).

The primary goal is to understand the relationship of columnar ambient optical depth and surface dry aerosol concentration in the region. The previous Chapters developed the new MODIS algorithm that retrieves integrated ambient aerosol optical properties (c005) that are realistic and accurate on a global scale. First, the c005 products are validated over the mid-Atlantic during the summer of 2002, by comparing to sunphotometer. Then the products are compared against measurements

of surface {$PM_{2.5}$} in the region. Chapter 2 (e.g. Eq. 2.20) suggested that when the conditions are appropriate (aerosol column concentrated in the boundary layer), the two quantities should be related. Wind analyses, lidar, and aircraft measurements performed during the summer 2002 period all will help to evaluate this assumption in specific cases; however this dissertation concentrates on some of the relevant RAMMPP aircraft profiles. For the sake of understanding the effect of chemical processes and meteorological impacts on aerosol properties, model output from the (baseline version) CMAQ regional air quality model provides statistics of the τ / $PM_{2.5}$ relationship over the region.

8.1: Historical perspective of estimating {$PM_{2.5}$} from MODIS

In order to capture the variability of aerosols within their short lifetime, it is necessary to measure them with high spatial and temporal coverage. While it is desirable to measure them on hourly and urban scales for climate applications, it is imperative to measure them on these scales for air quality (and human exposure) assessment. Some of the highest concentrations of hourly surface {$PM_{2.5}$} measurement sites are located in the U.S. mid-Atlantic region, yet that concentration is only on the order of 1 site per 1000 km^2. Considering that most of the world does not support regular PM measurements, evaluating the measurements we do have will go a long way to knowing how to fill in the gaps.

Satellites have the vantage point to observe the whole picture, and the operational MODIS algorithm provides data on 10 km x 10 km resolution. While not ideal for urban scale aerosol monitoring, they are certainly an improvement on any

existing $PM_{2.5}$ observing network. Since satellites can observe plumes, they can help to determine whether they are a result of local emissions or long-range transport. Thus, they can help determine 'who is to blame' in cases of NAAQS violations in the mid-Atlantic region (e.g. Engel-Cox et al., [2005]). However, passive sensors (such as MODIS) are only sensitive to the column-integrated properties of the aerosol (τ and possibly size information). For there to be a relationship between τ and $\{PM_{2.5}\}$, the aerosol must be 'correctly' vertically distributed, that is, the bulk of the aerosol loading must be near the surface. Also, the aerosol properties (size, shape, composition) must be truly representative of the column.

Given these caveats, Chu et al., [2003] demonstrated that satellite –derived τ (from MODIS) can be applied to global, regional, metropolitan, and even local/urban air pollution events. They designed three case studies around the world, representing regional (~24000 km^2 over northern Italy), metropolitan (~5000 km^2 over greater Los Angeles) and urban scales (~900 km^2 over urban Beijing) and found that MODIS derived τ was comparable to sunphotometer measurements (AERONET and non-AERONET) on all of these spatial scales.

Experiments such as that described by Engel-Cox et al., [2004] took MODIS derived τ one step further, specifically comparing MODIS to hourly $\{PM_{2.5}\}$ measurements from EPA surface sites. They found correlations on the order of R~0.5-0.6 over much of the Eastern half of the U.S., with much lower (even negative) correlations over the Western half. These and other results encouraged Al –Saadi et al., [2005] to elaborate on this concept, describing a joint EPA/NOAA/NASA concept of using MODIS and other satellite products to monitor and help forecast surface PM

on a national scale. For August and September 2003, they found generally correlations of R~0.6 over the Eastern half of the U.S., but R<0.4 over most of the west. Over the eastern U.S., surface $\{PM_{2.5}\}$ (in $[\mu g \cdot m^{-3}]$) could be approximated by

$$\{PM_{2.5}\} \approx 60[\mu g \cdot m^{-3}] \times \tau_{0.55}$$

Other studies have focused on τ/{PM} correlations over global cities (e.g. Gupta et al., [2006]), and specific regions (e.g. Wang et al., [2004]), all suggesting that the two quantities are correlated when the aerosol is well behaved in the vertical.

Engel-Cox et al., [2006] investigated the MODIS-τ versus $\{PM_{2.5}\}$ correlation over Baltimore during the summer of 2004. On average, they found that

$$\{PM_{2.5}\} \approx 30[\mu g \cdot m^{-3}] \times \tau_{0.55} + 5[\mu g \cdot m^{-3}],$$

whether $\{PM_{2.5}\}$ represented observations by a continuous aerosol mass monitor $\{PM_{2.5}\}_{hourly}$ or a Federal Reference Monitor (FRM;), $\{PM_{2.5}\}_{daily}$. Correlation values of R~0.6 were found for ~20 matches in either case. Note the presence of a slope and offset. Then they used ~100 cases of lidar (at any time during the day) measurements of total τ and τ in the PBL (τ_{PBL}), also comparing with either $\{PM_{2.5}\}_{hourly}$ or $\{PM_{2.5}\}_{daily.}$ For hourly $PM_{2.5}$, correlations were higher when regressing to τ_{PBL} (R=0.64) than to total τ (R=0.56), but the main difference was the regression Eq.. Like that reported for MODIS τ, slopes for the total τ were 25-30 $\mu g \cdot m^{-3}$. When regressing to τ_{PBL}, however, the slope was 48 $\mu g \cdot m^{-3}$. For daily $PM_{2.5}$, both correlations were R~0.75, and slopes rose to 40 and 65 $\mu g \cdot m^{-3}$ for τ and τ_{PBL}, respectively. This suggested that vertical apportionment of aerosol depth (like that can be measured from lidar) explains (case by case) whether a τ/{PM} correlation should exist [Engel-Cox et al., 2006; Chaw et al., 2006] When there is significant

high altitude aerosol (for example high altitude smoke transport), the correlation between the two properties will be reduced.

Statistical analysis of the vertical apportionments will lead to better quantification of the correlation. Obviously, understanding of the meteorological conditions that precede specific 3-D aerosol configurations would lead towards improved ability to monitor and even forecast aerosol events at the surface. Van Donkelaar et al., [2006] evaluated the relationship by simulating meteorology and vertical profiles using a global chemical transport model, and concluded that temporal variation of τ in the vertical is the dominant variable for determining the τ/PM relationship.

8.2: Observed aerosol properties over the mid-Atlantic during July-August 2002

The Mid-Atlantic Regional Air Management Association, Inc. (MARAMA; http://www.marama.org) is a voluntary, non-profit association of ten state and local air pollution control agencies, including those in Delaware, the District of Columbia, Maryland, New Jersey, North Carolina, Pennsylvania, Virginia and West Virginia. For the purpose of this dissertation, the mid-Atlantic region is defined by this area. MARAMA recognizes pollution as a regional problem, thus encompassing the work of the MDE.

8.2.1 Datasets

A number of aerosol datasets were collected during July and August of 2002 over the mid-Atlantic. MODIS observations from Aqua began in early July, thus this

was the first two months of both Terra and Aqua observations. AERONET data were collected at nine sites in the mid-Atlantic region: CCNY (40N,73W), Columbia_SC (34N,81W), COVE (36N,75W), GISS (40N,73W), GSFC (38N,76W), MD_Science_Center (39N,76W), Norfolk_State_Univ (36N,76W), SERC (38N,76W), and Wallops (37N,75W). Backtrajectories at multiple levels, from NASA Global Modeling and Assimilation Office (GMAO) assimilated gridded data, are available for most of the AERONET sites. The EPA collected speciated, daily and/or hourly average aerosol concentrations at several sites in the region. RAMMPP sponsored 22 measurements of extinction/scattering profiles from the University of Maryland's aircraft, along with intensive measurements of PM at Fort Meade, Maryland (FME) [Hains et al., submitted 2007]. Finally observations from the Micropulse LIDAR (MPL: http:mplnet.gsfc.nasa.gov) were available during the period. In this chapter, I utilize retrievals of τ from MODIS and AERONET, hourly surface $\{PM_{2.5}\}$ from the EPA's continuous monitors, and scattering and absorption coefficients measured by the three-wavelength nepholometer and the PSAP onboard the UMD Piper-Aztec aircraft. Each of these products are inter-compared and compared with that simulated by the CMAQ model during the period.

8.2.2 Summary of events

Fig. 8.1 shows a plot of daily averaged τ and surface $\{PM_{2.5}\}$ measured in Baltimore, during July-August 2002. The period was marked by periods of heavy aerosol loadings evident in both the column and at the surface. In most cases, the events tracked together, with a $\tau = 1.0$ representing approximately 40 $\mu g \cdot m^{-3}$ (matching that found by Engel-Cox et al., [2006]. Days 187-189 (July 6-8) are

marked by extreme loadings in both the column and the surface, and is known to be a result of heavy smoke transported into the region from fires in Quebec (e.g. Taubman et al., [2004]; Vant-Hull et al., [2005]; Colarco et al., [2004]). It is worth noting the correlation of the aerosol at Baltimore, as the studies suggested that smoke was transported at elevation and did not reach the surface at all locations in the region. Other interesting events are days 198-204 (July 16-22), which was a 'garden variety' episode of summer pollution, marked by stagnant conditions and buildup of local and regional sulfate based pollution. This was seen at both satellite and surface at all sites. Days 225-226 (August 13-14) is likely another episode of smoke transport from Canada, but this time, also includes some regional pollution as well.

8.2.3 Comparisons of datasets

This section provides scatterplots of comparison between datasets. They provide some understanding of the variability in measurement techniques and vertical distribution within the MARAMA region.

Fig. 8.2a is a comparison of MODIS with AERONET in the region, providing a validation of the MODIS over land product in the region. The correlation is high ($R = 0.93$) with nearly a one-to-one fit. There are some outliers though, which should be explained. Overall, however, this plot indicates the quality of the MODIS τ retrieval and that it can be trusted. This is a relief, because this suggests that all the work that went into creating the global algorithm was worthwhile for over the U.S. mid-Atlantic. Plotted in (Fig. 8.2b) is the comparison of η retrieved by MODIS and AERONET (O'Neill method). There is some correlation ($R=0.42$), but it is obvious that the MODIS product is not yet robust.

Fig. 8.3 plots the two hourly-averaged surface {$PM_{2.5}$} against the MODIS – derived τ in a 5 x 5 (~50 x 50 km) box. Plotted in red are all co-locations during July-August 2002. Since (except for at Baltimore site), it is known that the July 6-8 smoke did not make it to the surface in all locations, overplotted in black are the same points but without those dates. Without the smoke data, the correlation is much higher (R = 0.719) and the relationship is (as expected) similar to that found by Engel-Cox et al., [2006].

In support of the MDE, the UMD Piper Aztec aircraft measured 22 profiles of scattering coefficient during the period [Taubman, 2004], concentrating on the interesting events described in section 8.2.2. Jennifer Hains analyzed each flight and calculated τ (from the scattering) at 0.55 μm. Fig. 8.4 compares the values, derived from these profiles, to the averaged MODIS τ in a 5x5 (25 values) box centered at the profiled airport. Data are plotted if either Terra or Aqua passed over the site within 2 hours of the profile, and there were sufficient MODIS statistics (5 within the 25 possible); thus, only 10 matches were made. Nonetheless, the regression shows correlation (R = 0.51) with offset (0.05) and slope (1.28) not too different from a one-to-one line. Since τ derived from the aircraft included only scattering, reasonable choice of ω_0 would increase those τ values, thus helping the regression. Also, the aircraft profiles usually topped out around 3km, so any aerosol above that would not included in calculation of τ.

8.3: Modeling aerosol properties using CMAQ

For the purpose of aerosol modeling and air quality forecasting it is necessary to evaluate the models that are used for these purposes. Are they realistic in their treatment of aerosol processes? Do they give reasonable results that can be validated by observations, if not in magnitude, at least in a relative sense? Kinne et al., [2006] describes a project (known as AeroCom) that is assessing aerosols within global chemical transport models (CTM) and general circulation models (GCM). In general, large scale models demonstrate agreement in total aerosol optical depth (compared to remote sensing from AERONET and satellite), but completely disagree in deriving component masses and optical depths. Much of the differences stem from individual model assumptions, including their assumed aerosol properties, their processing and their size binning.

While there are coordinated efforts to evaluate aerosol in global models, there is little mention in the literature about evaluating aerosol properties in regional chemical models, such as are used in air quality forecasting. As the CMAQ model was developed for the EPA, MDE is using the CMAQ model to evaluate scenarios for meeting NAAQS compliance in Maryland. Therefore, this section evaluates results provided by the Models-3/CMAQ air quality model for the impacts of PM in the region during July-August 2002.

8.3.1 Introduction to CMAQ

The Models-3 Emission Projection and Processing System (MEPPS) is a flexible software framework that encompasses the Community Multi-scale Air Quality Model (CMAQ; Byun and Ching, [1999]). Designed and used by the USEPA

to model the chemistry and physical processes leading to poor air quality, Models-3/CMAQ addresses applications ranging from regulatory issues to scientific studies. The CMAQ system can simulate tropospheric ozone, acid deposition, visibility, surface $PM_{2.5}$ and other constituents of air pollution. The Models-3 framework consists of the Fifth generation Penn State University/National Center for Atmospheric Research Mesoscale Model (MM5), the MEPSS emission system, and the CMAQ chemical transport model (CCTM). The Models-3/CMAQ system is an open source collection of computer modules that can be accessed and modified for a user's specific purpose.

One of the major advantages of CMAQ is its high resolution. The 'baseline' version of CMAQ run for the University of Maryland produces hourly output for 22 vertical levels (p-sigma coordinates), at 12 km x 12 km horizontal resolution within a 172 x 172 grid box (~2000 km^2). This high resolution is comparable to MODIS 10 km x 10 km resolution and is adequate for studying aerosol variability on a regional scale. Chandresekar et al., [2002] evaluated the MM5 model for a pollution event over Philadelphia, and concluded that the model was generally successful at predicting the meteorology.

The aerosol component of the CMAQ system is described in general by Byun and Ching, [1999], with the most version described by Binkowski and Roselle, [2003]. It is designed to be an efficient and economical depiction of aerosol dynamics that includes processes of direct emission, new (from gas) particle formation, coagulation, deposition and activation into cloud droplets. The model includes the primary emissions of elemental (black) carbon, organic carbon, dust, sea salt and

other species (from the 1995 USEPA emission inventory, plus assumed size distributions), as well as secondary (produced) species like sulfate, ammonium, nitrate and organics. CMAQ uses a 'modal approach', such that it considers the particle size distribution as a superposition of three lognormal modes (Aitken, accumulation and coarse) that are allowed to grow in size (diameter) and in concentration (loading) at every time step. Hygroscopic growth is also considered. Aerosol is allowed to jump from one mode to another. The properties of the size distribution for each mode and each species are calculated at each time step: the total particle number, surface area and mass concentrations. Binkowski and Roselle [2003] list the component modes of each aerosol species modeled in CMAQ, as well as a number of diagnostic parameters that represent other properties of the aerosol.

Mebust et al., [2003] evaluated the speciation of the CMAQ air quality model against IMPROVE observations, finding that the model consistently under-predicts the aerosol concentrations of each species (except for sulfate) by ~30-40%. Smyth et al., [2006] found similar behavior (under-prediction of mass) of CMAQ over a domain in Western Canada. However, there was excellent temporal agreement between the model and observations, suggesting that some of the aerosol processes simulated within the model are appropriate.

8.3.2 Computation of τ from CMAQ output

CMAQ uses a modal approach to represent the aerosol size distribution [Binkowski and Roselle, 2003], such that the properties of the size distribution for each mode are calculated at each time step. Along with the surface PM concentration, another parameter monitored by the EPA is the visibility, defined as a function of the

extinction coefficient, β_{ext} (in units of km^{-1}). CMAQ calculates the extinction coefficient in two different ways.

A theoretical method for computing extinction is to perform full Mie calculations at each time step, integrating over the size distributions and refractive indices of each individual species and mode. This is computationally expensive, and is not necessarily representative of extinction coefficients measured in-situ. In his PhD dissertation, Park [2001] described a method for calculating aerosol optical properties, by interpolating to a LUT of previously simulated aerosol models. Unfortunately, while this method is now used within CMAQ for computing photolysis rates at each level, the individual calculations at each layer are not saved into output files.

The alternative method is introduced in Malm et al., [1994] and is known as the 'reconstructed mass extinction.' This a fit to observations from the IMPROVE network, and is calculated empirically:

$$\beta_{ext} = 3.0 * f_{RH} * (\{\text{ammonium}\} + \{\text{nitrate}\} + \{\text{sulfate}\}) + 4.0 * \{\text{OC}\} + 10.0 * \{\text{BC}\} + 1.0 * \{\text{fine soil}\} + 0.6 * \{\text{coarse}\} \quad (8.1)$$

where the units of the mass extinction coefficients (the constants) are $[m^2 \cdot g^{-1}]$, the curly braces represent aerosol species dry mass concentrations (sum of all modes) in $[\mu g \cdot m^{-3}]$, and the f_{RH} is from a lookup table [Malm et al., 1994] (plotted in Fig. 3.3). Mebust et al., [2003] evaluated the visibility component of the CMAQ and found that in general, CMAQ over-predicts visibility by 25-35%, consistent with the under-prediction of aerosol mass.

While the above equation is intended for computing surface extinction, it can be applied at any level within the CMAQ atmosphere. Therefore, the optical depth is

simply the integral of the extinction coefficient at the center of each layer, multiplied by the layer thickness (in km).

Due to constraints of computer space, a CMAQ model end-user (like myself) has access only to the information contained in the {} of Eq. 8.1, not the size distribution, modal components, and extinction properties of each species. This means that Eq. 8.1 and reconstructed mass extinction is really the only appropriate way to calculate τ from CMAQ output. However, given the knowledge that has been learned about aerosol properties in the region, it may be interesting to play with the assumptions of species mass extinction coefficients in the equation.

8.4: Evaluation of MODIS/PM relationship in CMAQ

The CMAQ 'baseline' version outputs from July-August 2002 are available on the University of Maryland's computer system. The 'concentration' files contain total speciated PM concentrations (sums of all three modes), as well as pollutant gas concentrations, at 12 km x 12 km horizontal resolution, in 16 p-sigma (p_σ) layers, at every hour during the two month period. Additional files are outputted by CMAQ to include latitude, longitude, elevation and urban surface percentage in each horizontal box, as well as information about thickness, pressure, temperature, water vapor, liquid water, ice and snow mixing ratios at each level in the atmosphere.

In p-sigma coordinates, (pressure normalized to surface level pressure; $p_\sigma = p_{layer}/p_{sfc}$, where p_{layer} is the pressure and p_{sfc} is the pressure at the land surface), the values for each layer (bottom of layer) are p_σ = 1.0, 0.9974, 0.9940, 0.9890, 0.9820, 0.9720, 0.9590, 0.9430, 0.9230, 0.8990, 0.8719, 0.8390, 0.8030, 0.7630, 0.7180,

0.6680 and 0.5680. These values correspond to layer middle heights (km above the surface) of approximately 0.010, 0.024, 0.068, 0.116, 0.185, 0.282, 0.398, 0.544, 0.727, 0.949, 1.212, 1.523, 1.886, 2.312, 2.820 and 3.393 km, depending on the elevation of the surface, pressure and temperature. The 16 layers are a subset of the 22 layers modeled by CMAQ, truncated on assumption that little tropospheric air pollution is contained above about 3.6 km (and that comparable Piper Aztec measurements are limited in the vertical by aircraft design).

In each layer, and at each grid box, I calculate the relative humidity from the CMAQ outputs of vapor mixing ratio [w in kg vapor per kg dry air], using the parameterization from Rogers and Yau [1989], e.g.

$$RH = \frac{w}{w_s}$$

where the saturation mixing ratio (w_s) is

$$w_s = 0.622\left(\frac{6.112\exp[17.67T/(T+243.5)]}{p}\right),$$

a function of the temperature (T) in deg C and pressure (p) in millibars. Note that the numerator in the parentheses is the saturation vapor pressure (e_s), and that 0.622 is the ratio of water vapor and dry air specific heats. This relative humidity is in turn, used to calculate f_{RH} for specific aerosol species.

For all comparisons to data described in this section ({$PM_{2.5}$} monitors, MODIS, AERONET), I calculated statistics of the CMAQ data on 5x5 grid boxes (60 km x 60 km) centered on the comparison data. Thus I assume that the spatial/temporal behavior of CMAQ and observations is similar to that described by Ichoku et al., [2002a].

I began by comparing CMAQ estimates of total surface $\{PM_{2.5}\}$ at each hour, to that observed by the continuous $\{PM_{2.5}\}$ monitors in the region within one hour of the CMAQ model hour. Fig. 8.5 shows that CMAQ consistently under-predicts total $\{PM_{2.5}\}$. When the heavy smoke event (July 6-8) is removed the correlation is R=0.57, with a slope of 0.349. I did not compare the speciated mass concentrations.

8.4.1 Calculating τ with the Malm reconstructed mass extinction

Using the Malm et al., [1994] reconstructed extinction coefficient equation (Eq 8.1), I computed the aerosol optical depth at each of the 172x172 points in the CMAQ domain, for each daylight hour (9:00 to 23:00 UTC, 5:00 AM to 9:00 PM Eastern Daylight Time). Relative humidity dependence of the optical properties was computed from relative humidity, which was calculated from model temperature, pressure and water vapor mixing ration at each layer.

Fig. 8.6a compares CMAQ derived τ with MODIS -observed τ, centered at and closest in hour with MODIS overpass. Both datasets are averaged over a 5 x 5 boxes (~50 x 50 km for MODIS; 60 x 60 km for CMAQ). No comparison is made when either MODIS detects a cloud, or there is RH>98% or liquid water present within any layer of the CMAQ output. When the known smoke days are taken out, there is a surprisingly good correlation (R = 0.66), however the slope is 0.235 (CMAQ represents only 24% of the total τ!). Obviously the CMAQ optical depth retrieval would be poor, but what about the apportionment of the optical depth to the surface? Fig. 8.6b correlates the CMAQ surface $\{PM_{2.5}\}$ with derived τ. Compared to MODIS/monitor observations, CMAQ has better internal correlation (R=0.8),

which is consistent with it having no knowledge of elevated aerosol transport. The slope is nearly 58 $\mu g \cdot m^{-3} \cdot \tau^{-1}$, which is much higher than observed slope (~30 $\mu g \cdot m^{-3} \cdot \tau^{-1}$). This result suggests that the Malm extinction equation may need to be updated; either the f_{RH} or the assumed mass extinction coefficients of the dry aerosol.

8.4.2 Calculating τ using GOCART models for reconstructed mass extinction

Chin et al., [2002] describes the size and optical characteristics of the aerosol assumed within the GOCART model. While they not one to one matched with the aerosol types used by CMAQ, she suggested to me that I try using them to represent the CMAQ aerosol types. I assumed the sulfate model for the union of sulfate, nitrate and ammonium, the OC model for organic carbon, the BC model for elemental carbon, and dust modes B and E for fine mode and coarse mode dusts respectively. I also used the GOCART formulations for f_{RH}, different for sulfate, organic and black carbon aerosol types (e.g. [Köpke et al., 1997]). Since the optical properties for the GOCART models [Chin et al., 2002] are presented for a wavelength of 0.50 μm, and that fine mode aerosol is assumed to be smaller than r<0.5 μm, I re-calculated the Mie optical properties (using MIEV; Wiscombe, 1980), for 0.55 μm wavelength and assumed r<1.25 μm for $PM_{2.5}$. I used the listed values [Chin et al., 2002] for aerosol density, except for BC, which I updated (as per [Bond and Bergstrom, 2006]) to 1.8 $g \cdot cm^{-3}$.

Figs. 8.7a and 8.7b are analogous to Figs. 8.6a and 8.6b, except for using the GOCART properties instead of the Malm mass coefficients (Eq. 8.1) for

reconstructing the extinction. The correlations are nearly the same as those using the Malm coefficients, but slope is raised to 0.374 for the τ comparison. The slope of the CMAQ internal τ/{PM} equation is lowered to 39 $\mu g \cdot m^{-3} \cdot \tau^{-1}$, suggesting that the GOCART models provide better representation of aerosol optical properties. For the fun of it, I also co-located CMAQ with AERONET (Fig. 8.8), resulting in a slope and correlation similar to Fig. 8.6a.

8.4.3 Calculating τ using c005 LUT models for reconstructed mass extinction

As a final exercise in CMAQ τ calculation, I assumed the extinction properties calculated via the new MODIS (c005) LUT, appropriate for the region. However, instead of using values retrieved from Table 6.2, I re-calculated mass extinction for a truncated size distribution ($r < 1.25$ μm) and appropriate values of dry density (sulfate; 1.8 $g \cdot m^{-3}$). The resulting non-absorbing model mass extinction (~4.1 $m^2 \cdot g^{-1}$) was applied to the sum of all $PM_{2.5}$ components (e.g. sulfate + ammonium + nitrate + organic carbon + elemental carbon + fine soil), while the dust model mass extinction (0.5 $m^2 \cdot g^{-1}$) and density (2.6 $g \cdot m^{-3}$) was assumed for coarse mass only.

Because the aerosol models derived in Chapter 6 are considered to represent 'ambient' aerosol properties, the non-absorbing model mass extinction does not represent 'dry' mass as does the GOCART [Chin et al., 2002] and Malm [IMPROVE, 2006] modeled values.

For f_{RH}, I assumed the formula suggested by Kotchenruther et al., [1999] with values of the exponent (γ=0.35) suggested by Taubman [2004] in his dissertation.

The results turned out to be similar to those using the Malm mass extinction assumptions, so they are not plotted here.

8.5: Spatial comparison between MODIS and CMAQ derived τ.

Since the best simulations of τ itself, as well as τ to $\{PM_{2.5}\}$, were realized when using the GOCART models for optical properties, I selected the GOCART models for creating images of CMAQ versus MODIS derived τ. Figs. 8.9a and 8.9b provide examples for cases when the spatial match was good (July 16) and poor (July 7). As noted before, July 16 is a case of typical summer buildup of regional, sulfate dominated haze, whereas July 7 is an atypical case of dense smoke transported into the region.

For the July 7 case, the spatial distribution and the relative magnitudes of the aerosol plume is captured very well by CMAQ. In general CMAQ underestimates MODIS by about 20%, but the location of maximum τ in Kentucky area is confirmed by MODIS. CMAQ is less cloudy than MODIS, but this is at least partially due to having CMAQ data only to 3.6 km. High (cirrus) clouds that are observed by MODIS cannot be determined from the truncated CMAQ vertical profiles.

The July 16 case shows no similarity between the two datasets. This is the case of heavy smoke transport, of which CMAQ is not privy to such information outside of its domain. Therefore, CMAQ cannot be expected to simulate this smoke.

8.6: CMAQ τ and vertical profiles compared to UMD Aircraft.

As might be expected, the relationship of CMAQ –derived τ and aircraft –derived τ is similar to CMAQ compared to either MODIS or AERONET. Figure 8.10a is a scatter plot of this comparison, for all matches during July-August, as well as when excluding the smoke episode of July 6-8. When excluding the smoke event, the slope is ~0.365, with correlation (R=0.5).

Finally, both CMAQ and the aircraft profiles provide estimates about the vertical structure of extinction. Figure 8.10b displays averaged (throughout the entire period) of CMAQ and aircraft –derived extinction coefficients. The aircraft extinction profiles are the sum of scattering and extinction at 0.1 km altitude increments, provided by Jennifer Hains. Overall, there is some similarity between the two profiles, especially when considering the standard deviations during the period (displayed by the error bars). Although not plotted, when the smoke days (July 6-9) are excluded, the mean values are nearly unchanged, with slightly smaller standard deviations.

Following the two specific aerosol events compared by the MODIS/CMAQ imagery of Fig. 8.9, I compare extinction profiles from the same two dates in Fig. 8.11. As might be expected, CMAQ shows some skill at simulating the vertical profile of typical pollution on July 16, but fails miserably at capturing any of the smoke observed on July 8 over Easton, Maryland (also analyzed by [Colarco et al., 2004]).

8.7: Summary

Increasing research relates to the possibility of using MODIS -derived τ products to help to monitor and forecast periods of high surface $PM_{2.5}$ concentrations

and poor air quality. However, if MODIS is to be used to address policy issues related to poor air quality (for example, withdrawal of federal funds to states or counties in non-attainment of NAAQS), it should be well understood and its products be of high accuracy. This Chapter demonstrated that MODIS τ is of high quality (compared to AERONET over a 50 km x 50 km box) in the region, and that it can be considered.

The next step was to determine whether (column integrated) τ should even be expected to relate to measurements of surface $\{PM_{2.5}\}$. Scatterplots of the two products (different units) showed that there is a general correlation between the two, but that in some cases (e.g. elevated aerosol layers resulting from long range transport), columnar aerosol properties are unrelated to what is measured by a monitor at the surface.

I evaluated the relationship of τ and surface aerosol concentrates as simulated by the baseline run of the CMAQ air quality model. Three different lookup tables and f_{RH} corrections were used to calculate τ from the model, showing that the use of the GOCART models and relative humidity corrections [Chin et al., 2002] provided the best fit to observed τ from AERONET, MODIS and integration of aircraft measured extinction profiles. The GOCART LUT also provided the best simulation of the τ to $\{PM_{2.5}\}$ relationship observed by the combination of remote sensing and surface monitors. However, while the τ to $\{PM_{2.5}\}$ relationship was well simulated within the model, both quantities were only ~40% of the magnitudes of the observed values. As for vertical profiles, again CMAQ estimated only a portion (~40%) of the extinction in each layer.

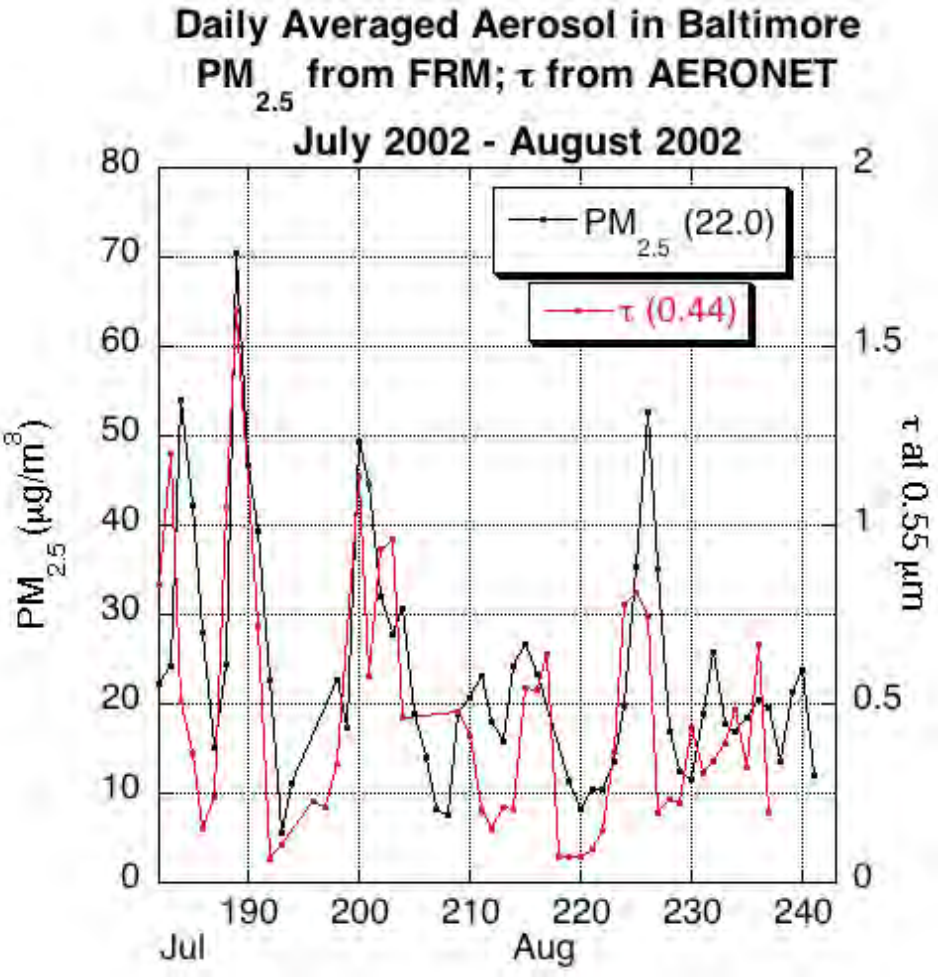

Fig. 8.1: Daily average τ (at 0.55 μm) observed by AERONET sunphotometer (red), compared with daily {$PM_{2.5}$} from the EPA-FRM monitor (black), in Baltimore, between July and August 2002. The mean of each dataset are given in parentheses in the legend. The AERONET data are Level 2 (quality controlled).

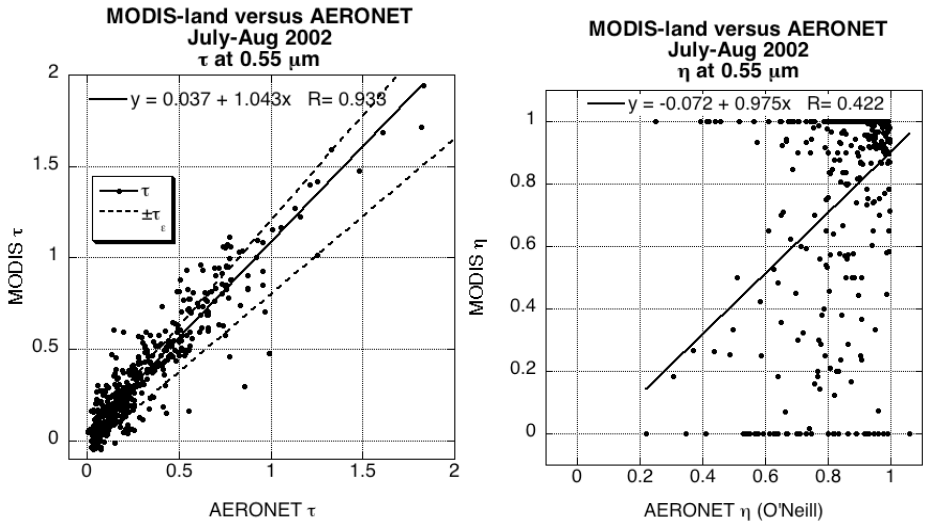

Fig. 8.2: Comparison of MODIS-land and AERONET derived τ(a) and η (b) over the mid-Atlantic region during July-August 2002. The τ expected error is given by the dashed lines in (a). For AERONET, η is derived using the O'Neill method.

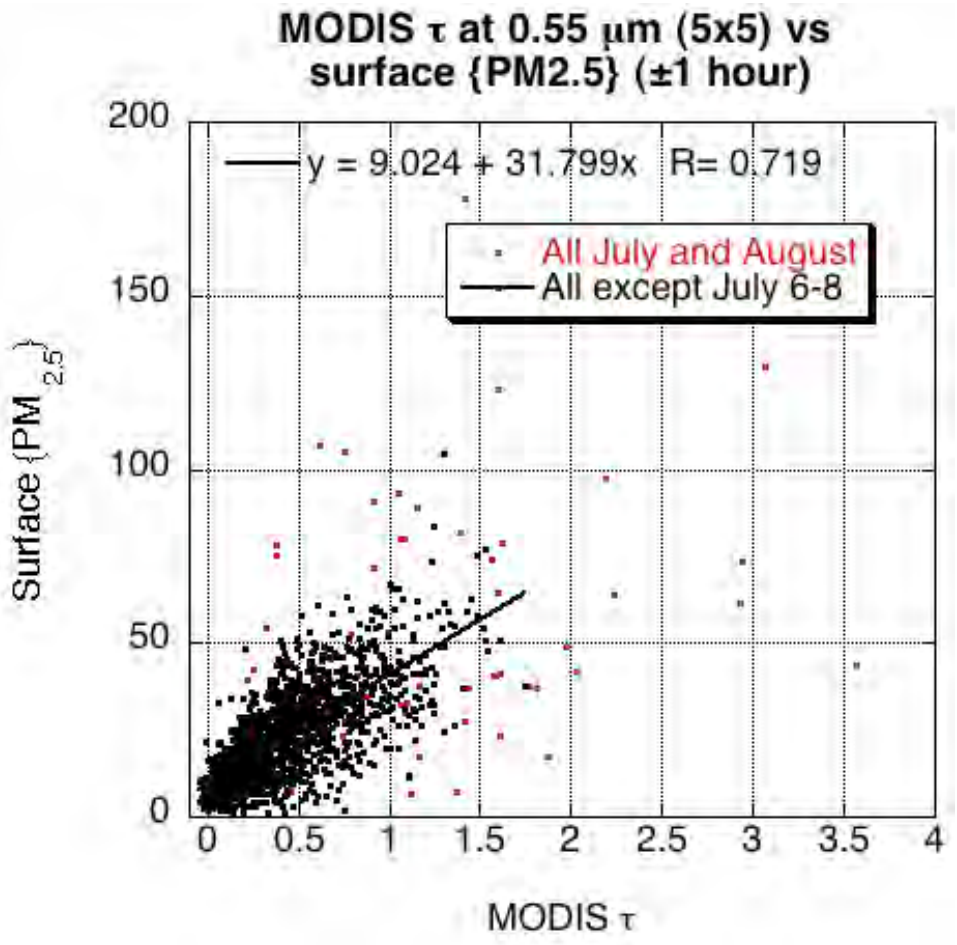

Fig. 8.3: Comparison of two-hourly averaged measured surface {PM2.5} with 5x5 box averaged MODIS over land –derived τ for July and August 2002 in the mid-Atlantic (red). The three days of the heavy smoke episode (July 6-8) are removed (black), and the correlation is displayed.

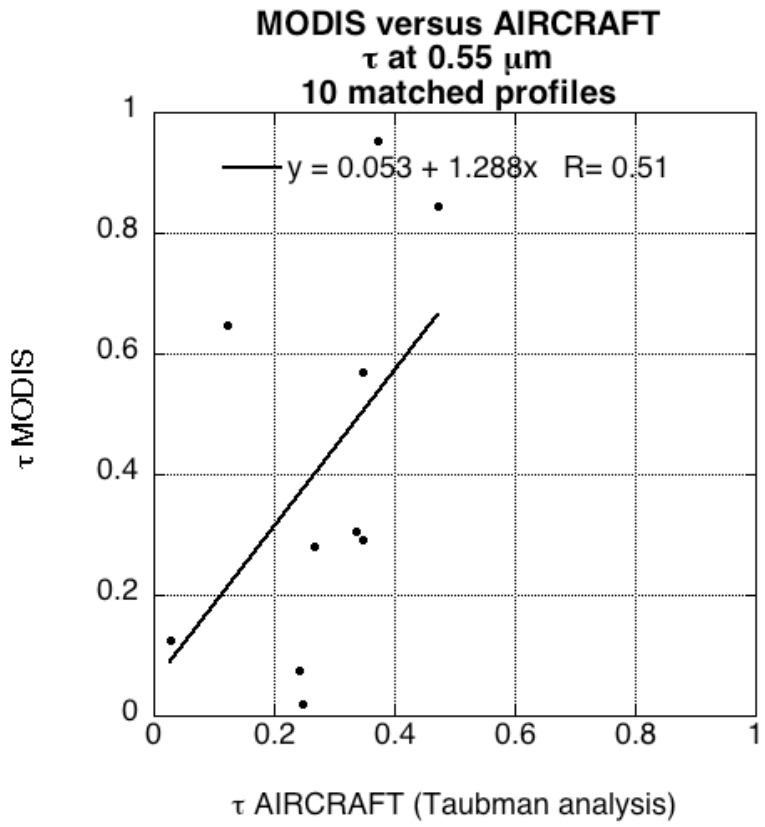

Fig. 8.4: Comparison (and regression) of MODIS derived τ (either Terra or Aqua) if observed within two hours of aircraft measured profile. Aircraft τ values were provided by Jennifer Hains.

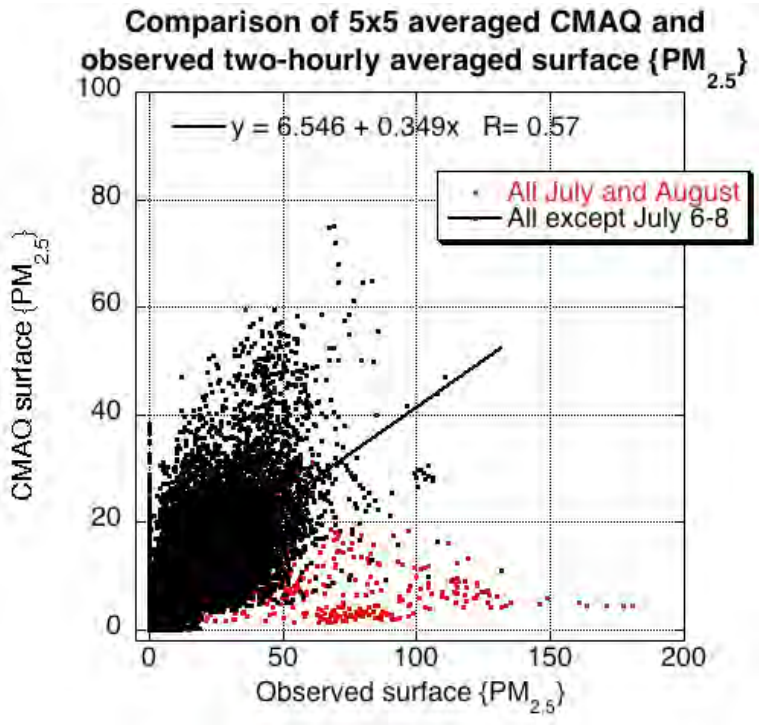

Fig. 8.5: Comparison of CMAQ 5x5 box averages (60 km) of surface {$PM_{2.5}$} with observed two-hourly averaged {$PM_{2.5}$} from continuous monitors. The red points are all collocations during July and August 2002, whereas the black points (and regression) exclude the smoke episode (July 6-8).

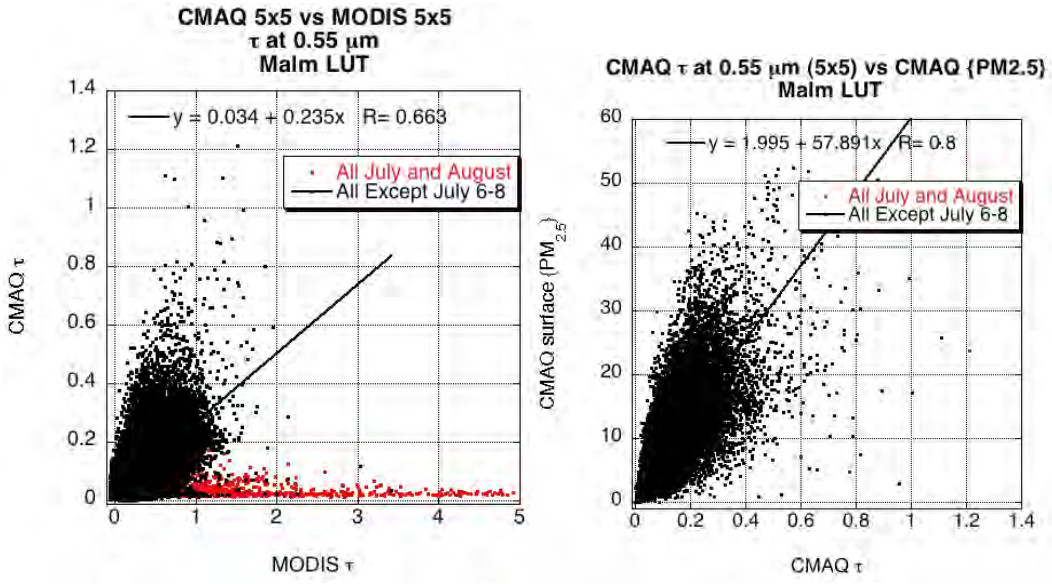

Fig. 8.6: A) CMAQ 5x5 (60 x 60 km) box averaged τ derived with the Malm (IMPROVE) LUT compared with MODIS 5x5 box averages (between 50-80 km depending on view angle). B) CMAQ 5x5 box averages (60 km) of surface {$PM_{2.5}$} compared with CMAQ-derived τ (Malm LUT). The red points are all co-locations during July and August 2002, whereas the black points (and regressions) denote exclusion of the three days of the heavy smoke episode (July 6-8).

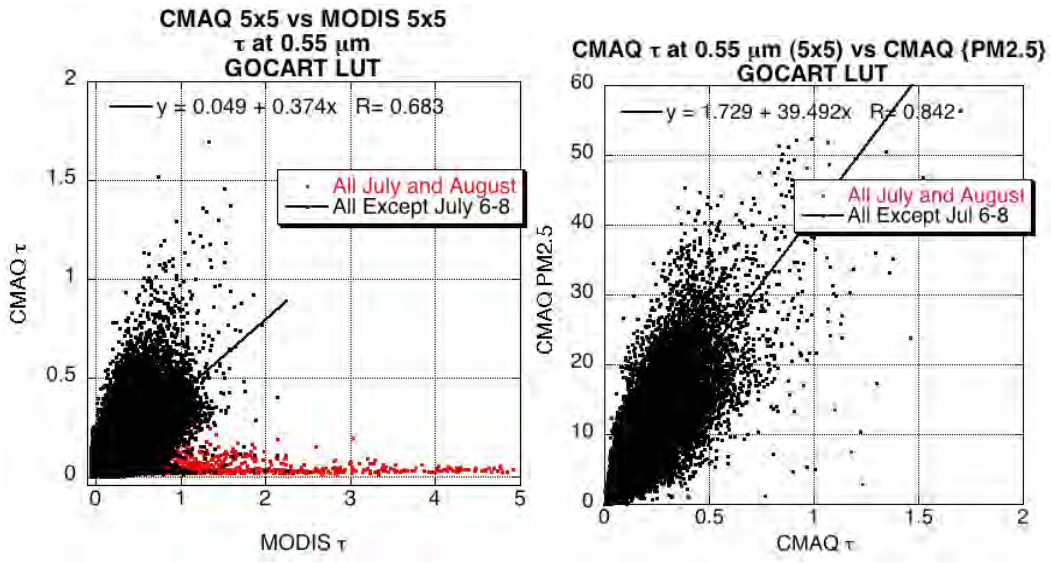

Fig. 8.7: A) CMAQ 5x5 (60 x 60 km) box averaged τ derived with the GOCART LUT compared with MODIS 5x5 box averages (between 50-80 km depending on view angle). B) CMAQ 5x5 box averages (60 km) of surface {$PM_{2.5}$} compared with CMAQ-derived τ (GOCART LUT). The red points are all co-locations during July and August 2002, whereas the black points (and regressions) denote exclusion of the three days of the heavy smoke episode (July 6-8).

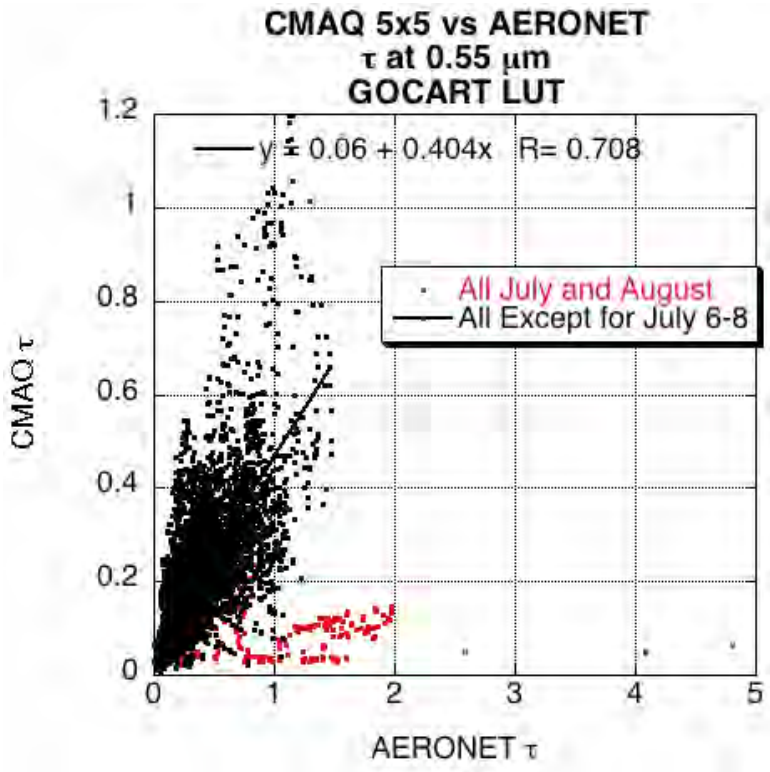

Fig. 8.8: Comparison of CMAQ 5x5 box averages (60 km) of computed τ (GOCART LUT) with observed two-hourly averaged AERONET observations. The red points are all collocations during July and August 2002, whereas the black points (and regression) exclude the smoke episode (July 6-8).

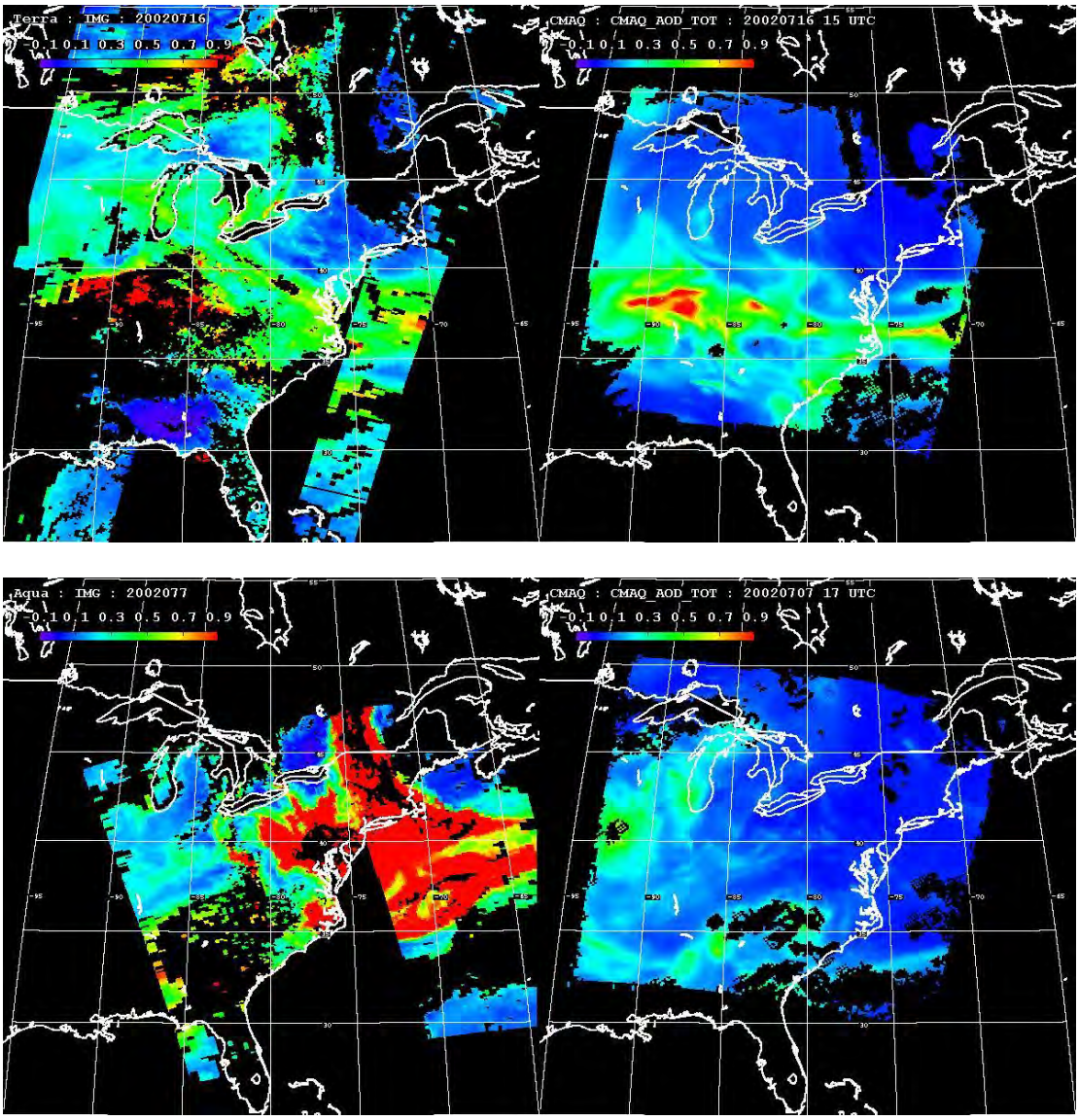

Fig. 8.9: Comparison of CMAQ (GOCART LUT) to MODIS retrievals of τ at 0.55 μm. The top panel is for a day of garden variety sulfate pollution (July 16, 2001) where the model matches the satellite. The bottom panel is from an unusually heavy infusion of Canadian smoke at high altitudes (July 7, 2001), where the model does captures very little of satellite measured τ.

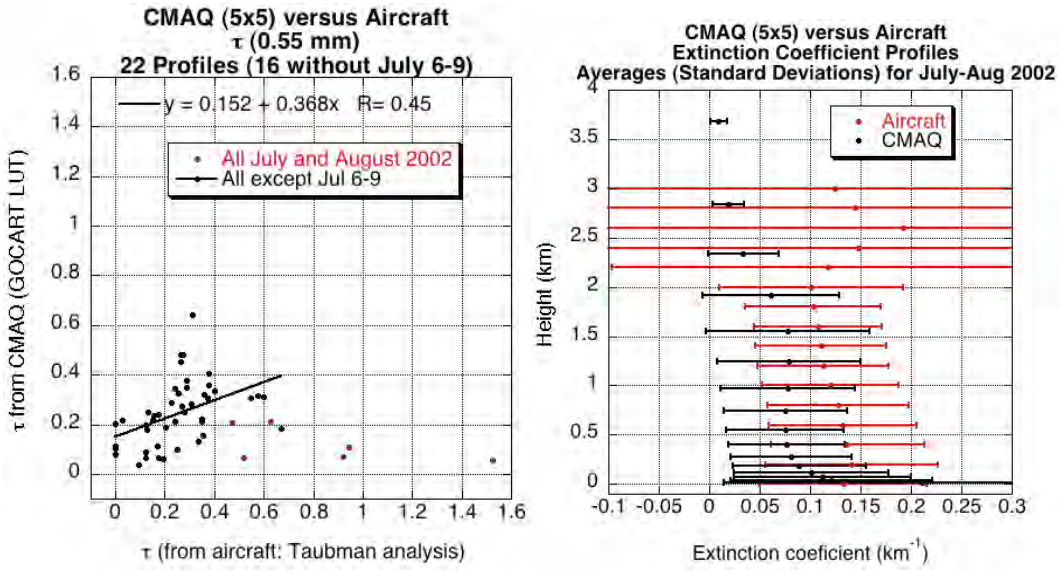

Fig. 8.10: A) Comparison of CMAQ derived τ (GOCART LUT) to derived τ from aircraft profiles. The red points are for all profiles during the July-August 2002, whereas the black points (regressed) exclude the smoke event of July 6-9, 2002. B) Comparison of average CMAQ derived extinction profiles (GOCART LUT) and averaged aircraft extinction profiles for the entire July-August 2002 period. The error bars are the standard deviations for each data set. The CMAQ data are 5x5 boxes centered at and hours closest to aircraft profiles. Aircraft profiles were provided by Jennifer Hains, using data measured and assumptions from Taubman, [2004].

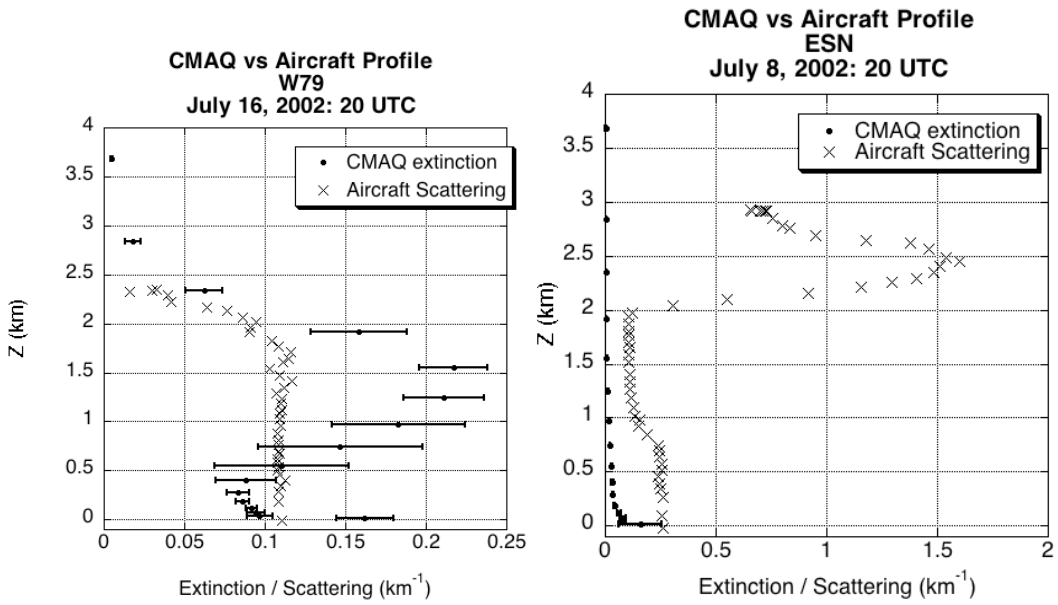

Fig. 8.11: Comparison of CMAQ extinction (GOCART LUT) to specific UMD aircraft profiles of scattering over airports (both at 0.55 μm). The left panel is for a day of typical sulfate pollution (July 16, 2001) where the model reasonably matches the profile. The bottom panel is from an unusually heavy infusion of Canadian smoke at high altitudes (July 7, 2001), where the model does captures very little of the aircraft measured extinction. The error bars for the model represent the standard deviation within a 5x5 box (60 x 60 km) around the airport.

Chapter 9: Conclusion: Summary and Further Study

9.1: Summary

Aerosols are recognized as major components of the Earth's atmosphere/surface climate system, influencing the radiative budget, clouds and precipitation processes and the health of organisms on the planet (including humans). A significant fraction of emitted aerosol is anthropogenic, so that they are monitored by the USEPA and other international agencies that regulate pollution. However, unlike long-lived spatially homogenous gas pollutants (such as carbon dioxide), aerosols' short lifetimes (~ 1 week), complicated chemical compositions, and tendency to interact with clouds and precipitation processes, make them impossible to monitor on all scales from only one instrument.

Therefore, aerosol characterization must be performed from multiple sensors, both *in-situ* and remotely, from surface, aircraft and satellite. It is imperative to understand each measurement technique and how it relates to others. Otherwise, aerosol properties gleaned from one instrument may seem contradictory to another set of measurements.

In this dissertation, I concentrated on remote sensing of aerosols from space, specifically from the MODIS sensors aboard NASA's polar-orbiting Terra and Aqua satellites. Although the MODIS operational aerosol retrievals had been validated in the past, it was becoming apparent that the MODIS products were suffering biases and other inaccuracies that could be fixed. By comparing with other remote sensing techniques (e.g both sun and sky sunphotometery, I developed a new algorithm that reduced the bias and uncertainty in retrievals of global τ, over dark land surfaces.

This second-generation operational algorithm was put into operation in early 2006 and, providing a complete mission 'Collection 5' product dataset by the end of 2006.

In the processes of developing the algorithm, I determined a set of aerosol optical models that characterized the range of commonly observed aerosol properties (by AERONET). Also, using the technique of atmospheric correction, I found that land surface reflectance in two visible wavelengths (0.47 and 0.66 μm) could be parameterized as a function of 2.12 μm, scattering angle and surface type ($NDVI_{SWIR}$). I tapped the 2.12 μm channel to provide coarse aerosol optical information as part of a simultaneous inversion. In previous MODIS algorithms over land, the 2.12 μm channel was presumed to have none. Finally, I implemented a better correction for elevated surfaces with more sophisticated radiative transfer that includes atmospheric polarization.

I applied the new algorithm to a subset (the testbed) of MODIS observations and showed that the retrieved τ correlated better, with lower bias, as compared to ground-truth sunphotometer measurements. Globally, histograms and statistics suggested that the new MODIS algorithm retrieves average global τ of ~0.21, as compared to the previous version's estimate of 0.28.

Although I worked to create a new global aerosol retrieval algorithm, for this thesis, I intended to apply MODIS products to problems of poor air quality and surface $\{PM_{2.5}\}$ non-attainment in the U.S. mid-Atlantic region. As the University of Maryland was funded to evaluate the year 2002 in support of the state of Maryland's mission to put together an 'attainment' plan, I concentrated on the most active two months of the year (July and August 2002), where both surface {PM} and column τ

reached high levels (as seen by EPA's continuous monitors and AERONET sites). In addition to typical sulfate-dominated pollution episodes (e.g. July 16-22), the period was characterized by infusions of transported smoke from Canada (e.g. [Taubman et al., 2004; Vant-Hull et al., 2005; Colarco et al., 2004]), including a three day period (July 6-8) with daily averaged τ>2.0 as seen by AERONET.

I began by evaluating the MODIS products (both τ and η) and demonstrated that the τ product was within expected error bars, as compared to (ground-truth) AERONET sites in the region (regression: $\tau_{MODIS} = 0.037 + 1.043\tau_{true}$, with correlation R=0.935). The η product was somewhat correlated (R=0.422), but cannot be considered validated. Therefore, I was justified in using the MODIS –derived τ for comparison with other datasets.

MODIS derived τ in 5 x 5 boxes (~ 50 x 50 km) centered at surface $PM_{2.5}$ continuous monitors was compared with the measured surface $\{PM_{2.5}\}$ within ± 1 hour of overpass, in Maryland and the surrounding MARAMA region. Like had been found by previous studies (e.g. [Engel-Cox et al., 2006]), τ was correlated with $\{PM_{2.5}\}$. When I eliminated the three smoke days (July 6-8) from the comparison, the regression improved to ($\{PM_{2.5}\} = 9.024 + 31.799\ \tau_{MODIS}$; R = 0.719).

As part of EPA's Maryland regulatory plan, the CMAQ model is being used to evaluate the processes that lead up to surface PM non-attainment. I analyzed the products from the 'baseline' CMAQ model runs for the period. The major task was deriving 'ambient' optical depth from speciated dry aerosol mass concentrations. This required assumptions about the mass extinction coefficients and dependence on relative humidity for each species, such that I could integrate the extinction as a

function of relative humidity and layer thickness over the entire column. As the CMAQ model outputs did not include such extinction information, I was forced to make assumptions. I tried three different sets of extinction/humidity assumptions, including those assumed by IMPROVE (IMPROVE web site), by GOCART model [Chin et al., 2002], and by modifying the dust and non-absorbing aerosol models derived for the new MODIS algorithm. The use of the GOCART models provided the best match to observed τ (from either AERONET or MODIS), as well as the most similar $\tau/\{PM_{2.5}\}$ to that observed by MODIS and surface monitors. However, CMAQ magnitudes of each property were only about 40% of those observed, indicating that CMAQ is under-predicting aerosol consistently throughout the column.

For cases of 'typical' summertime pollution (e.g. July 16), CMAQ produced a regional picture of τ that compared very well to that observed by MODIS. For cases of atypical pollution (e.g. July 7) marked by transported smoke, CMAQ has no knowledge of emissions outside the regional domain, resulting in no similarities between the two images.

Finally, I compared both MODIS and CMAQ with the measured scattering and extinction profiles as well as total derived total τ characterized by the UMD aircraft flights during July and August 2002 (originally processed by B. Taubman for this thesis and again by Jennifer Hains). MODIS and aircraft τ were reasonably correlated, especially when considering appropriate single scattering albedo and that the aircraft profiles did not represent aerosol above 3.5 km. Similar to the performance at estimating surface aerosol, CMAQ values of extinction and total

aerosol optical depth were on average only about 40% of those observed aboard the Piper-Aztec, with little or no correlation for the atypical smoke event.

9.2: Further study

As a researcher, I realize that there is still incredible amount of work that should be performed, both in creating algorithms for satellite sensors, as well as in characterizing aerosols globally and within the mid-Atlantic region. Here, I consider possibilities only for the immediate future.

The MODIS instruments do not provide the only observations of aerosol properties. Previous and current lower resolution satellite sensors (such as TOMS, AVHRR and GOES) have value in evaluating decadal aerosol trends, especially when calibrated with MODIS (e.g. [Ignatov et al., 2005]). Newer and future passive instruments (such as MISR, Caliop, and OMI) provide quality information in different wavelengths as well as directional and polarization information, which can be fused with information from MODIS to determine more of the climatic and distributional characteristics of aerosol. In fact, numerous proposals have been submitted through NASA agencies (including GSFC and the MAST) for providing such fusion.

The next significant step forward in global and regional aerosol research is from active sensors such as those from the Calipso satellite-borne and various surface borne lidar instruments. These instruments, while focused only on narrow swaths or in discrete locations, provide information about the vertical distribution that represents the same physics (light extinction by aerosols) as measurements from passive sensors. Thus, they should be used in combination, each measurement

constraining the others. For example, Anderson et al., [2005] presents a strategy for combining the instruments from the "A-Train" of satellite instruments. The REALM group at University of Maryland-Baltimore County (http://alg.umbc.edu/usaq/) is using lidar data in national and regional applications (e.g. [Engel-Cox et al., 2006]). These applications are slowly becoming quantitative.

This does not mean that *in situ* measurements of aerosols will become obsolete. They are representative of discrete locations and times, and provide direct measurements of the aerosol properties most important in our daily lives, e.g. the number and mass concentrations that affect our ability to breathe, to fly safely, and to enjoy our daily lives.

Appendices

If needed.

Glossary (of symbols and acronyms)

Very much needed.

{$PM_{2.5}$} – concentration of Particulate Matter less than 2.5 μm in diameter

AATS – Ames Airborne Tracking Sunphotometer

AERONET – AErosol RObotic NETwork

ATBD – Algorithm Theoretical Basis Document

B_{ext}, B_{sca} – Mass extinction/scattering coefficients

CLAMS – Chesapeake Lighthouse and Aircraft Measurements for Satellites (experiment)

CMAQ – Community Mesoscale Air Quality model

EC/BC/OC – Elemental/Black/Organic Carbon

FRM – Federal Reference Monitor

LUT – LookUp Table

MARAMA – Mid-Atlantic Regional Air Management Association

MAST – MODIS Aerosol Team

MODAPS – MODIS Adaptive Processing System

MODIS – MODerate resolution Imaging Spectro-radiometer

N(r), V(r) - Number, Volume size distribution as a function of radius (r).

NAAQS – National Ambient Air Quality Standards

NASA-GSFC: National Aeronautical and Space Administration – Goddard Space Flight Center (in Greenbelt, MD)

P(Θ) – Phase function (as a function of scattering angle)

RAMMPP - Regional Atmospheric Measurement Modeling and Prediction Program

r_{eff} – effective radius of size distribution

r_g, r_v – median (geometric) radius of number size distribution, median radius of volume (mass) size distribution

subscripts: s = surface, λ = wavelength, a = atmospheric

superscripts: * = top of atmosphere.

TARFOX – Tropospheric Aerosol Radiation FOrcing eXperiment

TOA – Top Of Atmosphere

UMCP – University of Maryland, College Park (sometimes also written as UMD)

UMD-Piper Aztec – Aircraft used by the University of Maryland.

USEPA – United States Environmental Protection Agency

VISvs2.12, 0.47vs0.66, 0.47vs2.12, 0.66vs2.12 – Visible versus 2.12 μm surface reflectance relationship, 0.47 μm verus 0.66 μm, etc

w_s, w – saturated, ambient water vapor mixing ratio

X – Mie size parameter

α – Ångstrom exponent

β_{ext}, B_{sca} – extinction/scattering coefficients

η – fine (aerosol) weighting (exact definition in context)

Θ, θ, θ_0, ϕ - Scattering, view zenith, solar zenith, relative azimuth angles

λ – wavelength

ρ – reflectance (normalized radiance). May have subscripts or superscripts

ρ – particle density

σ – width of size distribution

σ_{ext} σ_{sca}, σ_{abs} – extinction, scattering, absorbing cross section

τ – optical depth (usually taken to mean 'aerosol' optical depth, AOD or optical thickness, AOT). May have subscripts to symbolize wavelength or measured by which instrument (e.g. $\tau_{0.55}$ or τ_{MODIS})

ω_0 – single scattering albedo (SSA)

Bibliography

Ahmad, Z., and R.S. Fraser, (1982), An Iterative Radiative Transfer Code For Ocean-Atmosphere Systems***,*** *J. Atmos. Sci., **39***, 656-665.

Al-Saadi, J., J. Szykman, R. B. Pierce, C. Kittaka, D. Neil, D. A. Chu, L. Remer, L. Gumley, E. Prins, L. Weinstock, C. MacDonald, R. Wayland, F. Dimmick, and J. Fishman (2005), Improving National Air Quality Forecasts with Satellite Aerosol Observations. *Bull. Am. Met. Soc., 86* (9), 1249-1261.

Ames R.B. and W.C. Malm, (2001), Comparison of sulfate and nitrate particle mass concentrations measured by IMPROVE and the CDN. *Atmos. Environ. **35***, 905-916.

Anderson, T.L., et al., (2005), An "A-Train" strategy for quantifying direct climate forcing by anthropogenic aerosols, *Bull. Am. Met. Soc., **86***(12), 1795-1809, doi: 10.1175/BAMS-86-12-1795.

Anderson, T.L., D.S. Covert, S.F. Marshall, M.L. Laucks, R.J. Charlson, A.P. Waggoner, J.A. Ogren, R. Caldow, R.L. Holm, F.R. Quant, G.J. Sem, A. Wiedensohler, N.A. Ahlquist, and T.S. Bates (1996), Performance characteristics of a high-sensitivity, three- wavelength, total scatter/backscatter nephelometer, J. Atmos. Oceanic Technol., 13, 967-986.

Anderson, T.L., Y. Wu, D.A. Chu, B.Schmid, J. Redemann and O. Dubovik (2006), Testing the MODIS satellite retrieval of aerosol fine-mode fraction, *J.Geophys.Res., **110***(D18204), doi: 10.1029/2005JD005978.

Andreae, M.O., The dark side of aerosols, (2001), *Nature, **409*** (6821), 671-672.

Andrews, E., Sheridan, P J., Fiebig, M., McComiskey, A., Ogren, J.A., Arnott, P., Covert, D., Elleman, R., Gasparini, R., Collins, D., Jonsson, H., Schmid, B., and Wang, J. (2006): Comparison of methods for deriving aerosol asymmetry parameter. *J. Geophys. Res., **111*** (D05S04), DOI 10.1029/2004JD005734.

Ångstrom, A., 1929; On the atmospheric transmission of sun radiation and on dust in the air. *Geograf. Ann. Deut.*, ***11***, 156 - 166.

Asrar, G., (1989) Theory and applications of optical remote sensing, xiv, 734 pp., Wiley, New York.

Binkowski, F.S., Roselle, S.J., (2003), Models-3 Community Multiscale Air Quality (CMAQ) model aerosol component 1. Model description. *J. Geophys. Res.*, ***108***(D6), 4183, doi:10.1029/2001JD001409.

Bodhaine, B. A., N. B. Wood, et al. (1999), On Rayleigh optical depth calculations, *J. Atmos. Ocean. Tech. 16*(11), 1854-1861.

Bond, T.C. and R. W. Bergstrom (2006), Light Absorption by Carbonaceous Particles: An Investigative Review, *Aerosol Sci Tech.*, ***40***(1), 27-47, 2006

Brown, O.B., R.H. Evans, J.W. Brown, H.R. Gordon, R.C. Smith, and K.S. Baker, (1985), Phytoplankton Blooming Off the United-States East Coast - a Satellite Description, *Science*, ***229*** (4709), 163-167.

Byun, D. W., and J. K. S. Ching (Eds.), 1999: Science algorithms of the EPA Models-3 Community Multiscale Air Quality (CMAQ) Modeling System. EPA-600/R-99/030, Office of Research and Development, U.S. Environmental Protection Agency, Washington, D.C. [Available from U.S. EPA, ORD, Washington, D.C. 20460.]

Castanho, A. D. A., J. V. Martins, P. V. Hobbs, P. Artaxo, L. Remer, and M. Yamasoe, 2005: Chemical characterization of aerosols on the East Coast of the United States using aircraft and ground-based stations during the CLAMS experiment. *J. Atmos. Sci*., 62, 934–946.

Chandresekhar, S, (1950), *Radiative Transfer*, Clarendon Press, London.

Chandrasekar, A., B.G. Doddridge, C.R. Philbrick, R.D. Clark, and P.G. Georgopoulous, (2003), A Comparative Study of Prognostic MM5 Meteorological Model With Aircraft, Wind Profiler, Lidar, Tethered Balloon and RASS Data Over Philadelphia During a 1999 Summer Episode, *Journal of Environmental Fluid Mechanics*,

Chaudry, Z., J.V. Martins, Z. Li, S-C. Tsay, C. Li, T. Wen, H. Chen, P. Wang, and R.R. Dickerson (2007), In situ measurements of aerosol mass concentration and radiative properties in Xianghe, SE of Beijing, submitted to *J. Geophys. Res.*, (EAST-AIRE special issue).

Chen, L. W. A., B. G. Doddridge, R. R. Dickerson, J. C. Chow and R. C. Henry, 2002: Origins of fine aerosol mass in the Baltimore-Washington corridor: Implications from observation, factor analysis, and ensemble air parcel back trajectories. *Atmos. Environ.*, **36**, 28, 4541-4554.

Chen, L.-W. A., Chow, J.C., Doddridge, B. G., Dickerson, R. R., Ryan, W. F., Mueller, P. K., 2003. Analysis of a summertime PM2.5 and Haze Episode in the Mid-Atlantic Region. *J. Air and Waste Management* **53**, 946-956.

Chen, L.-W.A., 2002. Urban fine particulate matter: Chemical composition and possible origins. Doctoral dissertation, Chemical Physics, University of Maryland, College Park.

Chen, L.-W.A., Doddridge, B.G., Dickerson, R.R., Chow, J.C., Henry, R.C., 2002. Origins of fine aerosol mass in the Baltimore-Washington corridor: implications from observation, factor analysis, and ensemble air parcel back trajectories. *Atmos. Environ.* ***36***, 4541-4554.

Chin, M., D. A. Chu, R. Levy, L. Remer, Y. Kaufman, B. Holben, T. Eck, P. Ginoux, and Q. Gao (2004): Aerosol distribution in the Northern Hemisphere during ACE-Asia: Results from global model, satellite observations, and Sun photometer measurements. *J. Geophys. Res.*, ***109*** (D23), doi: 10.1029/2004GL02014.

Chin, M., P. Ginoux, et al. (2002), Tropospheric aerosol optical thickness from the GOCART model and comparisons with satellite and Sun photometer measurements, *J. Atmos. Sci., 59*(3), 461-483.

Chow, J.C., J.D. Bachmann, S.S.G. Wierman, C.V. Mathai, W.C. Malm, W.H. White, P.K. Mueller, N. Kumar, and J.G. Watson, Visibility: Science and regulation - Discussion, Journal of the Air & Waste Management Association, 52 (9), 973-999, 2002.

Chu, D. A., L. A. Remer, Y. J. Kaufman, B. Schmid, J. Redemann, K. Knobelspiesse,

J. D. Chern, J. Livingston, P. B. Russell, X. Xiong, and W. Ridgway (2005), Evaluation of aerosol properties over ocean from Moderate Resolution Imaging Spectroradiometer (MODIS) during ACE-Asia. *J. Geophys. Res., 110* (D07308), doi: 10.1029/2004/JD005208.

Chu, D. A., Y. J. Kaufman, et al. (2002), Validation of MODIS aerosol optical depth retrieval over land, *Geophys, Res. Lett. 29*(12): art. no.-1617.

Chu, D. A., Y. J. Kaufman, G. Zibordi, J. D. Chern, J. Mao, C. Li, and B. N. Holben, (2003), Global monitoring of air pollution over land from EOS- Terra MODIS, *J. Geophys. Res, 108* (D21), 4661, doi: 10.1029/2002JD003179.

Code of Federal Regulations (CFR), 18 July 1997, National Primary and Secondary Ambient Air Quality Standards, Final Rules, Title 40, Parts 50-53 and 58.

Colarco, P.R., M.R. Schoeberl, B.G. Doddridge, L.T. Marafu, O.Torres and E.J. Welton, (2004), Transport of smoke from Canadian forest fires to the surface near Washington, D.C.: Injection height, entrainment and optical properties, *J. Geophys. Res., **109***(D06203), doi: 10.1029/2003JD004248.

Colarco, P.R., O. B. Toon, O. Torres, and P. J. Rasch, (2002), Determining the UV imaginary index of refraction of Saharan dust particles from Total Ozone Mapping Spectrometer data using a three-dimensional model of dust transport, *J. Geophys. Res.*,***107***(D16), , doi: 10.1029/2001JD000903.

Dave, J. V. (1970), Intensity and Polarization of Radiation Emerging from a Plane-Parallel Atmosphere Containing Monodispersed Aerosols, *App. Optics, 9*(12): 2673-2687.

Day, D.E., and W.C. Malm, Aerosol light scattering measurements as a function of relative humidity: a comparison between measurements made at three different sites, Atmospheric Environment, 35 (30), 5169-5176, 2001.

Deuze, J.L., F.M. Breon, C. Devaux, P. Goloub, M. Herman, B. Lafrance, F. Maignan, A. Marchand, F. Nadal, G. Perry, and D. Tanre, Remote sensing of aerosols over land surfaces from POLDER- ADEOS-1 polarized measurements, Journal of Geophysical Research-Atmospheres, 106 (D5), 4913-4926, 2001.

Dickerson, R. R., S. Kondragunta, G. Stenchikov, K. L. Civerolo, B. G. Doddridge

and B. N. Holben, 1997: The impact of aerosols on solar ultraviolet radiation and photochemical smog. *Science*, **278**, 5339, 827-830.

Dickerson, R.R., B.G. Doddridge, P.K. Kelley, and K.P. Rhoads (1995), Large-scale pollution of the atmosphere over thGeophys. Res., ***100***(5), 8945-8952.

Diner, D.J., J.C. Beckert, T.H. Reilly, C.J. Bruegge, J.E. Conel, R. Kahn, J.V. Martonchik, T.P. Ackerman, R. Davies, S.A.W. Gerstl, H.R. Gordon, J-P. Muller, R. Myneni, R.J. Sellers, B. Pinty, and M.M. Verstraete (1998). Multi-angle Imaging SpectroRadiometer (MISR) description and experiment overview. *IEEE Trans. Geosci. Rem. Sens.*, ***36*** (4). 1072-1087.

Draxler, R.R., and G.D. Rolph (2003), HYSPLIT (HYbrid Single-Particle Lagrangian Integrated Trajectory): Model access via NOAA ARL READY website (http://www.arl.noaa.gov/ready/hysplit4.html), NOAA Air Resources Laboratory, Silver Spring, MD.

Dubovik, O. and M. D. King (2000), A flexible inversion algorithm for retrieval of aerosol optical properties from Sun and sky radiance measurements, *J. Geophys. Res, 105*(D16), 20673-20696.

Dubovik, O., A. Sinyuk, T. Lapyonok, B. N. Holben, M. Mishchenko, P. Yang, T. F. Eck, H. Volten, O. Munoz, B. Veihelmann, van der Zander, M Sorokin, and I. Slutsker, (2006) Application of light scattering by spheroids for accounting for particle non-sphericity in remote sensing of desert dust, *J. Geophys. Res., 111*(D11208), doi: 10.1029/2005JD006619.

Dubovik, O., A. Smirnov, B. N. Holben, et al. (2000), Accuracy assessments of aerosol optical properties retrieved from AERONET sun and sky radiance measurements, *J. Geophys. Res.*, *105*, 9791-9806.

Dubovik, O., B. N. Holben, et al. (2002a), Variability of absorption and optical properties of key aerosol types observed in worldwide locations, *J. Atmos. Sci. 59*(3), 590-608.

Dubovik, O., B. N. Holben, et al. (2002b), Non-spherical aerosol retrieval method employing light scattering by spheroids, *Geophys, Res. Lett. 29*(10): art. no.-1415.

Durkee, P.A., K.E. Nielsen, P.J. Smith, P.B. Russell, B. Schmid, J.M. Livingston, B.N. Holben, C. Tomasi, V. Vitale, D. Collins, R.C. Flagan, J.H. Seinfeld, K.J. Noone, E. Ostrom, S. Gasso, D. Hegg, and L.M. Russell, Regional aerosol optical depth characteristics from satellite observations: ACE-1, TARFOX and ACE-2 results, *Tellus* Series B-Chemical and Physical Meteorology, 52 (2), 484-497, 2000.

Eck, T. F., B. N. Holben, et al. (1999), Wavelength dependence of the optical depth of biomass burning, urban, and desert dust aerosols, *J. Geophys. Res., 104*(D24), 31333-31349.

Eck, T. F., B. N. Holben, et al. (2005), Columnar aerosol optical properties at AERONET sites in central eastern Asia and aerosol transport to the tropical mid-Pacific, *J. Geophys. Res., 110*(D6).

Ehsani, A.R., J.A. Reagan, and W.H. Erxleben, 1998: Design and performance analysis of an automated 10-channel solar radiometer instrument, *J. Atmos. Oceanic Tech.,* **15**, 697-707.

Engel-Cox, J., C. Holloman, B. Coutant, and R. Hoff, (2004), Qualitative and quantitative evaluation of MODIS satellite sensor data for regional and urban scale air quality, *Atmospheric Environment*, ***38*** (16), pp. 2495-2509.

Engel-Cox, J., G. Young, and R. Hoff, (2005), Application of satellite remote sensing data for source analysis of fine particulate matter transport events, *Journal of Air and Waste Management*, ***55***(9), pp. 1389-1397.

Engel-Cox, J., R. Hoff, R. Rogers, F. Dimmick, A. Rush, J. Szykman, J. Al-Saadi, D. Chu, and E. Zell (2006), Using particulate matter concentration and lidar and satellite optical depth to build a 3-dimensional integrated air quality monitoring capability, *Atmospheric Environment*, in press.

Evans, K.F., and G.L. Stephens, A New Polarized Atmospheric Radiative-Transfer Model, (1991), Q*uant. Spect. . Rad. Trans.*, ***46***(5), pp. 413-423.

Ferrare, R., S. Ismail, E. Browell, V. Brackett, S. Kooi, M. Clayton, P.V. Hobbs, S. Hartley, J.P. Veefkind, P. Russell, J. Livingston, D. Tanre, and P. Hignett, Comparisons of LASE, aircraft, and satellite measurements of aerosol optical properties and water vapor during TARFOX, Journal of Geophysical Research-Atmospheres, 105 (D8), 9935-9947, 2000.

Frank, Neil, H., 2006. Retained nitrate, hydrated sulfates, and carbonaceous mass in Federal Reference Method fine particulate matter for six Eastern U.S. cities. *Journal of Air and Waste Management Association* ***56***, 500-511.

Fraser, R.S., (1975), Degree of Inter-dependence among Atmospheric Optical Thicknesses in Spectral Bands between 0.36-2.4 microns, *J. Applied Meteorology*, ***14*** (6), 1187-1196.

Fraser, R.S., Ferrare, R.A., Kaufman, Y.J., and Mattoo, S. (1989). Algorithm for Atmospheric Corrections of Aircraft and Satellite Imagery. NASA Technical Memorandum 100751. Greenbelt, MD USA, NASA Goddard Space Flight Center.

Fraser, R.S., Y.J. Kaufman and R.L. Mahoney (1984), Satellite measurements of aerosol mass and transport, *Atmos. Env.*, ***18***(12), 2577-2584.

Gao, B.-C., Y.J. Kaufman, D. Tanré and R.-R. Li, 2002: Distinguishing tropospheric aerosols from thin cirrus clouds for improved aerosol retrievals using the ratio of 1.38-µm and 1.24-µm channels. *Geophys. Res. Lett.*, **29**, 1890, doi:10.1029/2002GL015475.

Gao, B.C., Y.J. Kaufman, D. Tanre, and R.R. Li, Distinguishing tropospheric aerosols from thin cirrus clouds for improved aerosol retrievals using the ratio of 1.38-mu m and 1.24-mu m channels, Geophysical Research Letters, 29 (18), art. no.-1890, 2002.

Gasso, S., and D. A. Hegg, (2003), On the retrieval of columnar aerosol mass and CCN concentration by MODIS. *J. Geophys. Res., 108* (D1), 4010, doi: 10.1029/2002JD002382.

Gasso, S., (2001), Retrieval of Aerosol Properties from Space: Studies from an In-Situ Perspective, PhD thesis, University of Washington, Seattle.

Gatebe, C. K., M. D. King, et al. (2001). Sensitivity of off-nadir zenith angles to correlation between visible and near-infrared reflectance for use in remote sensing of aerosol over land, *IEEE Trans. Geosci. Remote Sens. 39*(4), 805-819.

Ghan, S.J., R.C. Easter, E.G. Chapman, H. Abdul-Razzak, Y. Zhang, L.R. Leung, N.S. Laulainen, R.D. Saylor, and R.A. Zaveri, A physically based estimate of radiative forcing by anthropogenic sulfate aerosol, Journal of Geophysical Research-Atmospheres, 106 (D6), 5279-5293, 2001.

Guenther, B., X. Xiong, V.V. Salomonson, W.L. Barnes and J. Young, (2002), On orbit performance of the Earth Observing System Moderate Resolution Imaging Spectroradiometer: First year of data. *Rem. Sens. Environ.*, ***83*** , pp. 16-30.

Gupta, P. S.A. Christopher, J. Wang, R. Gehrig, Y. Lee and N. Kumar, (2006). Satellite remote sensing of particulate matter and air quality assement over global cities, *Atmos Env., **40**,* 5880-5892.

Hains, J.C., L-W. A. Chen, B.F. Taubman, B.G. Doddridge and R.R. Dickerson (2007), A side by side comparison of filter-based $PM_{2.5}$ measurements at a suburban site: a closure study, in preparation.

Hand, J.L., R.B. Ames, S.M. Kreidenweis, D.E. Day, and W.C. Malm, Estimates of particle hygroscopicity during the Southeastern Aerosol and Visibility Study, Journal of the Air & Waste Management Association, 50 (5), 677-685, 2000.

Hansen, E. H., and L. D. Travis, 1974: Light scattering in planetary atmospheres. *Space. Sci. Rev., **16**,* 527–610.

Haywood, J., and O. Boucher, (2000), Estimates of the direct and indirect radiative forcing due to tropospheric aerosols: A review, Reviews of Geophysics, 38 (4), 513-543.

Heald, C.L., D.J. Jacob, R.J. Park, B. Alexander, T.D.Fairlie, D.A. C hu, R.M. Yantosca, (2006), Transpacific transport of Asian anthropogenic aerosols and it s impact on surface air quality in the United States, *J. Geophys. Res., **111***, D14310, doi:10.1029/2005JD006847.

Hegg, D.A., and Y.J. Kaufman, Measurements of the relationship between submicron aerosol number and volume concentration, Journal of Geophysical Research-Atmospheres, 103 (D5), 5671-5678, 1998.

Heintzenberg, J., F. Raes, and S. Schwartz (Lead Authors) et al., (2000), Chapter 4: Tropospheric Aerosols (Draft, Oct, 2000). The IGAC (International Global Atmospheric Chemistry) Integration and Synthesis Report, 2001, available online from: http://www-nacip.ucsd.edu/NACIPreferencelibrary.html.

Hess, M., P. Koepke, and I. Schult (1998): Optical Properties of Aerosols and clouds: The software package OPAC, *Bull. Am. Met. Soc*., ***79***, 831-844.

Hignett, P., J.P. Taylor, P.N. Francis, and M.D. Glew, (1999), Comparison of observed and modeled direct aerosol forcing during TARFOX, Journal of Geophysical Research-Atmospheres, 104 (D2), 2279-2287.

Higurashi, A., T. Nakajima, B.N. Holben, A. Smirnov, R. Frouin, and B. Chatenet, (2000), A study of global aerosol optical climatology with two-channel AVHRR remote sensing, Journal of Climate, 13 (12), 2011-2027.

Holben, B. N., D. Tanre, A. Smirnov, T. F. Eck, I. Slutsker, N. Abuhassan, W. W. Newcomb, J. S. Schafer, B. Chatenet, F. Lavenu, Y. J. Kaufman, J. V. Castle, A. Setzer, B. Markham, D. Clark, R. Frouin, R. Halthore, A. Karnieli, N. T. O'Neill, C. Pietras, R. T. Pinker, K. Voss, and G. Zibordi (2001): An emerging ground based aerosol climatology: Aerosol optical depth from AERONET. *Geophys. Res. Lett.*, ***106***, 12067-12097.

Holben, B. N., T. F. Eck, et al. (1998), AERONET - A federated instrument network and data archive for aerosol characterization, *Remote Sens. Environ. 66*(1), 1-16.

Hubanks, P. A. (2005), MODIS Atmosphere QA Plan for Collection 005. Greenbelt, MD USA, NASA Goddard Space Flight Center**,** 57 pages.

Husar, R.B, J.M. Holloway and D.E. Patterson (1981), Spatial and temporal pattern of Eastern U.S. haziness; a summary, *Atmos. Environ.*, ***15***, 1919-1928.

Ichoku, C., D. A. Chu, et al. (2002a), A spatio-temporal approach for global validation and analysis of MODIS aerosol products, *Geophys. Res. Lett.*,

29(12): art. no.-1616.

Ichoku, C., R. Levy, Y. J. Kaufman, L. A. Remer, R. R. Li, V. J. Martins, B. N. Holben, N. Abuhassan, I. Slutsker, T. F. Eck and C. Pietras, 2002b: Analysis of the performance characteristics of the five-channel Microtops II Sun photometer for measuring aerosol optical thickness and precipitable water vapor. *J. Geophys. Res.-Atmos.*, **107**, D13, art. no.-4179.

Ichoku, C., L. A. Remer, et al. (2003), MODIS observation of aerosols and estimation of aerosol radiative forcing over southern Africa during SAFARI 2000, *J. Geophys. Res., 108*(D13): art. no.-8499.

Ignatov A., L.Stowe, S.Sakerin, G.Korotaev, (1995), Validation of the NOAA/NESDIS satellite aerosol product over the North Atlantic in 1989.*"* *J.Geophys.Res., **100***(D3), pp. 5123-5132,

Ignatov, A., and N.R. Nalli, Aerosol retrievals from the multiyear multisatellite AVHRR Pathfinder Atmosphere (PATMOS) dataset for correcting remotely sensed sea surface temperatures, Journal of Atmospheric and Oceanic Technology, 19 (12), 1986-2008, 2002.

Ignatov, A., P. Minnis, N. Loeb, B. Wielicki, W. Miller, S. Sun-Mack, D. Tanré, L. Remer, I. Laszlo, and E. Geier (2005), Two MODIS Aerosol Products over Ocean on the Terra and Aqua CERES SSF Datasets, *J. Atm. Sci., 62*, 1008-1031.

Intergovernmental Panel on Climate Change (IPCC), 2001, Climate Change 2001: The Scientific Basis, J. T. Houghton, Y. Ding, D.J. Griggs, M. Noguer, P. J. van der Linden and D. Xiaosu (Eds.), Cambridge University Press, UK. pp 944.

Jacobson, M.Z., (2001), Global direct radiative forcing due to multicomponent anthropogenic and natural aerosols, Journal of Geophysical Research-Atmospheres, 106 (D2), 1551-1568.

Jiang, W., S. Smyth, E. Giroux, H. Roth and D. Yin (2006), Differences between CMAQ fine mode particle and PM2.5 concentrations and their impact on model performance evaluation in the lower Fraser valley, *Atmos Environ. **40**,* 4973-4985, doi: 10.10106/j.atmosenv.2005.10.069.

Karnieli, A., Y. J. Kaufman, L. A. Remer, and A. Wald, (2001) AFRI-aerosol free vegetation index. *Remote Sens. Environ.*, ***77***(1), 1-21.

Kaufman, Y. J. and L. A. Remer, 1994: Detection of Forests Using Mid-Ir Reflectance - an Application for Aerosol Studies. IEEE Trans. *Geosci. Remote Sensing*, **32**, 3, 672-683.

Kaufman, Y. J. and R. S. Fraser, 1983: Light Extinction by Aerosols during Summer Air Pollution. *Journal of Climate and Applied Meteorology*, **22**, 10, 1694-1706.

Kaufman, Y. J., A. E. Wald, L. A. Remer, B. C. Gao, R. R. Li and L. Flynn, (1997c): The MODIS 2.1-mu m channel - Correlation with visible reflectance for use in remote sensing of aerosol. *IEEE Trans. Geosci. Remote Sensing*, ***35***, 5, 1286-1298.

Kaufman, Y. J., A. Gitelson, A. Karnieli, E. Ganor, R. S. Fraser, T. Nakajima, S. Mattoo, and B. N. Holben, (1994), Size distribution and scattering phase function of aerosol particles retrieved from sky brightness measurements. *J. Geophys. Res.*, ***99***, 10341-10356.

Kaufman, Y. J., and C. Sendra, (1988), Algorithm for atmospheric corrections of visible and Near IR satellite imagery, *Int. J. Rem. Sens., 9,* 1357-1381.

Kaufman, Y. J., D. Tanré, et al. (1997a), Operational remote sensing of tropospheric aerosol over land from EOS moderate resolution imaging spectroradiometer. *J. Geophys. Res, 102*(D14), 17051-17067.

Kaufman, Y. J., D. Tanre, H. R. Gordon, T. Nakajima, J. Lenoble, R. Frouin, H. Grassl, B. M. Herman, M. D. King, and P. M. Teillet, (1997b), Passive remote sensing of tropospheric aerosol and atmospheric correction for the aerosol effect. *J. Geophys. Res. 102*(D14), 16815-16830.

Kaufman, Y. J., N. Gobron, B. Pinty, J. L. Widlowski and M. M. Verstraete, (2002), Relationship between surface reflectance in the visible and mid-IR used in MODIS aerosol algorithm – theory, *Geophys, Res. Lett.* ***29***(23), art. no.-2116.

Kaufman, Y. J., O. Boucher, et al. (2005), Aerosol anthropogenic component estimated from satellite data, *Geophys, Res. Lett. 32*(17).

Kaufman, Y.J., 1989: The atmospheric effect on remote sensing and its correction. In *Theory and Applications of Optical Remote Sensing, John Wiley & Sons, New York*, G. Asrar, editor, 336-428.

Kaufman, Y.J., and M.D. Chou, Model Simulations of the Competing Climatic Effects of SO2 and CO2, Journal of Climate, 6 (7), 1241-1252, 1993.

Kaufman, Y.J., and R.S. Fraser, Light Extinction by Aerosols during Summer Air Pollution, Journal of Climate and Applied Meteorology, 22 (10), 1694-1706, 1983.

Kaufman, Y.J., D. Tanre, and O. Boucher, (2002), A satellite view of aerosols in the climate system, *Nature*, ***419***(6903) , pp. 215-223.

Kaufman, Y.J., D.D. Herring, K.J. Ranson, and G.J. Collatz, Earth Observing System AM1 mission to earth, (1998), *IEEE Trans. Geosci. Remote Sens*, ***36*** (4), 1045-1055.

Kim, S.-W., S.-C. Yoon, J. Kim and S-Y. Kim, (2006), Seasonal and monthly variations of columnar aerosol optical properties over east Asia determined from multi-year MODIS, LIDAR and AERONET sun/sky radiometer measurements, *Atmos. Environ.*, doi: 10.1016/j.atmosenv.2006.10.044.

King, M. D., W. P. Menzel, Y. J. Kaufman, D. Tanre, B.-C. Gao, S. Platnick, S. A. Ackerman, L. A. Remer, R. Pincus, and P. A. Hubanks (2003), Cloud and aerosol properties, precipitable water, and profiles of temperature and humidity from MODIS. *IEEE Trans. Geosci. Remote Sens.*, ***41***, 442-458.

King, M. D., Y. J. Kaufman, W. P. Menzel and D. Tanre, 1992: Remote-Sensing of Cloud, Aerosol, and Water-Vapor Properties From the Moderate Resolution Imaging Spectrometer (Modis). *IEEE Trans. Geosci. Remote Sensing*, **30**, 1, 2-27.

King, M.D., Y.J. Kaufman, D. Tanre, and T. Nakajima, (1999), Remote sensing of tropospheric aerosols from space: Past, present, and future, *Bull. Am. Met. Soc.*, ***80***(11), pp. 2229-2259.

Kinne, S., M. Shulz, C. Textor, et al., (2006), An AeroCom initial assessment – optical properties in aerosol component modules of global models, *Atmos.*

Chem. Phys., 6, 1–20.

Kleidman, R. G., N. T. O'Neill, et al. (2005), Comparison of moderate resolution Imaging spectroradiometer (MODIS) and aerosol robotic network (AERONET) remote-sensing retrievals of aerosol fine mode fraction over ocean, *J. Geophys. Res, 110*(D22), Art. No. D22205.

Knapp, K., R. Fourin, S. Kondragunta, A. Prados, (2005),Toward aerosol optical depth retrievals over land from GOES visible radiances: Determining surface reflectance, *Int. J. of Remote Sensing*,

Köpke, P., M. Hess, I. Schult, and E.P. Shettle (1997), Global Aerosol Data Set, Report No. 243, Max-Planck-Institut für Meteorologie, Hamburg, ISSN 0937-1060.

Kotchenruther, R.A., P. V. Hobbs, and D. A. Hegg, (1999), Humidification factors for aerosols off the mid-Atlantic coast of the United States, *J. Geophys. Res.*, ***104***(D2).

Kovacs, Thomas (2006), Comparing MODIS and AERONET aerosol optical depth at varying separation distances to assess ground-based validation strategies for spaceborne lidar, *J. Geophys. Res., Vol.* ***111***, D24203 doi. 10.1029/2006JD007349.

Lacis, A.A., J. Chowdhary, M.I. Mishchenko, and B. Cairns, (1998), Modeling errors in diffuse-sky radiation: Vector vs. scalar treatment, *Geophys. Res. Lett.*, ***25***(2) pp. 135-138.

Lake D.A., Tolocka M.P., Johnston M.V., Wexler, A.S., 2003. Mass spectrometry of individual particles between 50 and 750 nm in diameter at the Baltimore supersite. *Environmental Science and Technology* ***37***, 3268-3274.

Lenoble, J. and C. Brogniez, (1984), A comparative review of radiation aerosol models, *Beitr. Phys. Atmos.*, ***57***(l), l-20.

Levy, R. C., L. A. Remer, et al. (2004), Effects of neglecting polarization on the MODIS aerosol retrieval over land, *IEEE Trans. Geosci. Remote Sens 42*(11), 2576-2583.

Levy, R. C., L. A. Remer, et al. (2005), Evaluation of the MODIS aerosol retrievals over ocean and land during CLAMS, *J. Atmos. Sci., 62*(4), 974-992.

Levy, R.C., L.A. Remer and O. Dubovik et al. (in review, 2007), Global aerosol optical properties and application to MODIS aerosol retrieval over land, submitted to JGR.

Levy, R.C., L.A. Remer, D. Tanré, Y.J. Kaufman, C. Ichoku, B.N. Holben, J.M. Livingston, P.B. Russell and H. Maring, 2003: Evaluation of the MODIS retrievals of dust aerosol over the ocean during PRIDE. *J. Geophys. Res.*, **108 (**D14), 10.1029/2002JD002460

Levy, R.C., L.A. Remer, S. Mattoo, E. Vermote, Y.J. Kaufman, (in review, 2007), The second generation operational algorithm for retrieving aerosol properties over land from MODIS spectral reflectance., *J. Geophys. Res.*

Li, R. R., L. Remer, et al. (2005). Snow and ice mask for the MODIS aerosol products." *IEEE Geo. and Rem. Sens. Lett., 2*(3), 306-310.

Li, R. R., Y. J. Kaufman, B. C. Gao and C. O. Davis, 2003: Remote sensing of suspended sediments and shallow coastal waters. *IEEE Trans. Geosci. Remote Sensing*, **41**, 3, 559-566.

Liou, K.-N., (2002), *An Introduction to Atmospheric Radiation 2nd Edition*, Academic Press, San Diego, , 577 pps.

Lyapustin, A.I., and Y.J. Kaufman, (2001), Role of adjacency effect in the remote sensing of aerosol, *Journal of Geophysical Research-Atmospheres*, ***106*** (D11), 11909-11916.

Malm, W. C., 1992: Characteristics and Origins of Haze in the Continental United-States. *Earth-Sci. Rev.*, **33**, 1, 1-36.

Malm, W.C., B.A. Schichtel, R.B. Ames, and K.A. Gebhart, (2002), A 10-year spatial and temporal trend of sulfate across the United States, Journal of Geophysical Research-Atmospheres, 107 (D22), art. no.-4627.

Malm, W.C., J.F. Sisler, D. Huffman, R.A. Eldred, and T.A. Cahill, Spatial and Seasonal Trends in Particle Concentration and Optical Extinction in the United-States, Journal of Geophysical Research-Atmospheres, 99 (D1), 1347-1370, 1994.

Martins, J.V., D. Tanré, L.A. Remer, Y.J. Kaufman, S. Mattoo and R. Levy, 2002: MODIS Cloud screening for remote sensing of aerosol over oceans using spatial variability. *Geophys. Res. Lett.*, **29**(12), 10.1029/2001GL013252.

Marufu, L.T., B.F. Taubman, B. Bloomer, C.A. Piety, B.G. Doddridge, and R.R. Dickerson (2004), The 2003 North American electrical blackout: An accidental experiment in atmospheric chemistry, *Geophys. Res. Lett.*, ***31***, L13106, doi:10.1029/2004GL019771.

Mebust, M.R., B.K. Eder, F.S. Binkowski and S.J. Roselle, (2003), Models-3 Community Air Quality (CMAQ) model aerosol component: 2. Model evaluation, , *J. Geophys. Res.*, ***108****(D6)*, 4184, doi: 1029/2001JD001410.

Mi, W., Z. Li, X. Xia, B.N. Holben, R.C. Levy and H. Chen, (submitted 2007) Evaluation of the MODIS Aerosol Retrievals at Two AERONET Stations in China, To be submitted to the EAST-AIRE special issue in Journal of Geophysical Research – Atmosphere.

Mims, F.M., B.N. Holben, T.F. Eck, B.C. Montgomery, and W.B. Grant, Smoky skies, mosquitoes, and disease, *Science*, ***276*** (5320), 1774-1775, 1997.

Mishchenko, M. I., A. A. Lacis, and L. D. Travis, (1994), Errors induced by the neglect of polarization in radiance calculations for Rayleigh-scattering atmospheres, *J. Quant. Spectrosc. Radiat. Transfer*, ***51***, pp.491-510.

Mishchenko, M. I., and L. D. Travis (1994), *T*-matrix computations of light scattering by large spheroidal particles, *Opt. Commun.*, 109, 16-21.

Mishchenko, M. I., L. D. Travis, R. A. Kahn, et al. (1997), Modeling phase functions for dustlike tropospheric aerosols using a shape mixture of randomly oriented polydisperse spheroids, *J. Geophys. Res.*, *102*, 16831-16847.

Mie, G. (1908) A contribution to the optics of turbid media: Special colloidal metal solutions (in German: Beitrage zur Optik trüber Medien speziell kolloidaler Metallösungen). *Ann. Phys*. ***25***: 377-445.

MAST-MODIS Aerosol Science Team (2006), Algorithm Theoretical Basis Document (ATBD): Algorithm for Remote Sensing of Tropospheric Aerosol from MODIS, available from http://modis-atmos.gsfc.nasa.gov/MOD04_L2.

Moody, E. G., M. D. King, S. Platnick, C. B. Schaaf, and F. Gao, 2005: Spatially complete global spectral surface albedos: Value-Added datasets derived from Terra MODIS land products. *IEEE Trans. Geosci. Remote Sens.*, ***43***, 144-158.

Morys, M., F.M Mims III, S. Hagerup, S.E. Anderson, A. Baker, J. Kia, T. Walkup, 2001: Design, calibration and performance of Microtops II handheld ozone monitor and Sun photometer, *Geophysical Research-Atmospheres*, **106,** D13, 14573-14582.

Myhre, G., F. Stordal, M. Johnsrud, D. J. Diner, I. V. Geogdzhayev, J. M. Haywood, B. Holben, T. Holzer-Popp, A. Ignatov, R. Kahn, Y. J. Kaufman, N. Loeb, J. Martonchik, M. I. Mishchenko, N. R. Nalli, L. A. Remer, M. Schroedter-Homscheidt, and et. al, (2005): Intercomparison of satellite retrieved aerosol optical depth over ocean during the period September 1997 to December 2000. *Atm. Chem. Physic*s ***5***, 1697-1719.

Nakajima, T., and M. D. King, (1990). Determination of the optical thickness and effective particle radius of clouds from reflected solar radiation measurements. Part I: Theory. *J. Atmos. Sci., 47*, 1878-1893.

Nakajima, T., G. Tonna, R. Z. Rao, P. Boi, Y. Kaufman and B. Holben, 1996: Use of sky brightness measurements from ground for remote sensing of particulate polydispersions. *Appl. Optics*, **35**, 15, 2672-2686.

Novakov, T., D. A. Hegg, and P. V. Hobbs, 1997: Airborne measurements of carbonaceous aerosols on the East Coast of the United States. *J. Geophys. Res.*, ***102*** (D25), 30 023–30 030.

Omar, A. H., J. G. Won, et al. (2005), Development of global aerosol models using cluster analysis of Aerosol Robotic Network (AERONET) measurements, *J Geophys. Res., 110*(D10).

Ondov, J.M., Buckley, T.J., Hopke, P.K., Ogulei, D., Parlange, M.B., Rogge, W.F., Squibb, K.S., Johnston, M.V., Wexler, A.S., 2006. Baltimore Supersite Highly time- and size-resolved concentrations of urban PM2.5 and its constituents for resolution of sources and immune responses. *Atmospheric Environment*, ***40***, S224-A237.

O'Neill, N. T., Eck, T. F., Smirnov, A., Holben, B. N. and Thulasiraman, S. (2003),

Spectral discrimination of coarse and fine mode optical depth, *J Geophys. Res., 108*, doi:10.1029/2002JD002975.

O'Neill, N. T., Smirnov, A., Holben, B., and Thulasiraman, S. (2005), Spectral Deconvolution algorithm: Technical memo.

O'Neill, N.T., A. Ignatov, B.N. Holben, and T.F. Eck, (2000), The lognormal distribution as a reference for reporting aerosol optical depth statistics; Empirical tests using multi-year, multi-site AERONET sunphotometer data, *Geophys Res. Lett.*, ***27*** *(*20), 3333-3336.

O'Neill, N.T., O. Dubovik, and T.F. Eck, Modified angstrom exponent for the characterization of submicrometer aerosols, *Applied Optics, 40* (15), 2368-2375, 2001.

Park, R.J., (2001), The interaction of regional- and global-scale atmospheric chemistry, transport and climate processes, PhD Thesis, University of Maryland, College Park, 232 pages.

Park, R.J., G.L. Stenchikov, K.E. Pickering, R.R. Dickerson, D.J. Allen, and S. Kondragunta, (2001), Regional air pollution and its radiative forcing: Studies with a single-column chemical and radiation transport model, *J. Geophys. Res*, 106 (D22), 28751-28770.

Parkinson, C. L., 2003: Aqua: An earth-observing satellite mission to examine water and other climate variables. *IEEE Trans. Geosci. Remote Sensing*, **41**, 2, 173-183.

Platnick, S., M.D. King, S.A. Ackerman, W.P. Menzel, B.A. Baum, J.C. Riedi, and R.A. Frey, (2003), The MODIS cloud products: Algorithms and examples from Terra, *IEEE Trans. Geosc. Remote Sens****, 41*** (2), 459-473.

Prospero, J.M., (1996), Saharan dust transport over the North Atlantic Ocean and Mediterranean: And overview, in The *Impact of Desert Dust Across the Mediterranean*, edited by S. Guerzoni and R. Chester, pp. 133-151, Kluwer Acad., Dordrecht, The Netherlands.

Prospero, J.M., (1999) Assessing the impact of advected African dust on air quality and health in the eastern United States, Human and Ecological Risk Assessment, 5 (3), 471-479.

Prospero, J.M., (1999), Long-term measurements of the transport of African mineral dust to the southeastern United States: Implications for regional air quality, *J. Geophys. Res*, 104 (D13), 15917-15927.

Ramanathan, V., P.J. Crutzen, J.T. Kiehl, and D. Rosenfeld, (2001), Atmosphere - Aerosols, climate, and the hydrological cycle, *Science*, ***294*** (5549), 2119-2124.

Ramanathan, V. and P. J. Crutzen, (2003), New Directions: Atmospheric Brown "Clouds". *Atmos. Env.*, ***37***, 4033-4035.

Redemann, J., B. Schmid, J. A. Eilers, R. Kahn, R. C. Levy, P. B. Russell, J. M. Livingston, P. V. Hobbs, W. L. Smith Jr., B. N. Holben, 2004: Suborbital measurements of spectral aerosol optical depth and its variability at sub-satellite grid scales in support of CLAMS, 2001, *J. Atmos. Sci.*, **CLAMS special issue**.

Redemann, J., R.P. Turco, K.N. Liou, P.B. Russell, R.W. Bergstrom, B. Schmid, J.M. Livingston, P.V. Hobbs, W.S. Hartley, S. Ismail, R.A. Ferrare, and E.V. Browell, (2000), Retrieving the vertical structure of the effective aerosol complex index of refraction from a combination of aerosol in situ and remote sensing measurements during TARFOX, *J. Geophys. Res.*, **105** (D8), 9949-9970.

Remer, L. A. and Y. J. Kaufman (1998), Dynamic aerosol model: Urban/industrial aerosol, *J Geophys. Res.*, ***103***(D12): 13859-13871.

Remer, L. A., A. E. Wald, et al. (2001), Angular and seasonal variation of spectral surface reflectance ratios: Implications for the remote sensing of aerosol over land, *IEEE Trans. Geosci. Remote Sens., 39*(2), 275-283.

Remer, L. A., S. Gasso, D. A. Hegg, Y. J. Kaufman, and B. N. Holben, 1997: Urban/industrial aerosol: Ground-based sun/sky radiometer and airborne in situ measurements. *J. Geophys. Res.*, ***102***, 16849-16859.

Remer, L. A., Y. J. Kaufman, and B. N. Holben, (1999), Interannual variation of ambient aerosol characteristics on the East Coast of the United States. *J. Geophys. Res*. (TARFOX special issue), ***104***, 2223-2231.

Remer, L. A., Y. J. Kaufman, et al. (2005), The MODIS aerosol algorithm, products, and validation, *J. Atmos. Sci., 62*(4), 947-973.

Rogers, R.R., and M.K. Yau, A short course in cloud physics, xiv, 293 pp., Pergamon Press, Oxford ; New York, 1989.

Rosenfeld, D., Suppression of rain and snow by urban and industrial air pollution, Science, 287 (5459), 1793-1796, 2000.

Russell, P. B., J. M. Livingston, E. G. Dutton, R. F. Pueschel, J. A. Reagan, T. E. Defoor, M. A. Box, D. Allen, P. Pilewskie, B. M. Herman, S. A. Kinne, and D. J. Hofmann, 1993: Pinatubo and pre-Pinatubo optical-depth spectra: Mauna Loa measurements, comparisons, inferred particle size distributions, radiative effects, and relationship to lidar data. *J. Geophys. Res*., **98**, 22,969-22,985.

Russell, P.B., J.M. Livingston, P. Hignett, S. Kinne, J. Wong, A. Chien, R. Bergstrom, P. Durkee, and P.V. Hobbs, (1999), Aerosol-induced radiative flux changes off the United States mid-Atlantic coast: Comparison of values calculated from sunphotometer and in situ data with those measured by airborne pyranometer, *J. Geophys. Res*, ***104*** (D2), 2289-2307.

Russell, P.B., P.V. Hobbs, and L.L. Stowe, (1999), Aerosol properties and radiative effects in the United States East Coast haze plume: An overview of the Tropospheric Aerosol Radiative Forcing Observational Experiment (TARFOX), *J. Geophys. Res*, ***104*** (D2), (D2), 2213-2222.

Ryan, W.F., B.G. Doddridge, R.R. Dickerson, R.M. Morales, K.A. Hallock, P.T. Roberts, D.L. Blumenthal, and J.A. Anderson, Pollutant transport during a regional O-3 episode in the mid-Atlantic states, Journal of the Air & Waste Management Association, 48 (9), 786-797, 1998.

Salomonson, V.V., W. L Barnes, P.W. Maymon, H.E. Montgomery, and H. Ostrow, (1989), MODIS, Advanced facility instrument for studies of the Earth as a system,*" IEEE Trans. Goesci, Remote Sens*., ***27***, pp. 145-153.

Samet, J. M., F. Dominici, F. C. Curriero, I. Coursac and S. L. Zeger, 2000: Fine particulate air pollution and mortality in 20 US Cities, 1987-1994. *N. Engl. J. Med.*, **343**, 24, 1742-1749.

Samet, J.M., F. Dominici, F.C. Curriero, I. Coursac, and S.L. Zeger, Fine particulate air pollution and mortality in 20 US Cities, 1987-1994, New England Journal of Medicine, 343 (24), 1742-1749, 2000.

Seinfeld, J.H., and S.N. Pandis, Atmospheric chemistry and physics: From air pollution to climate change, xxvii, 1326 pp., John Wiley, New York, 1998.

Shettle E.P. and Fenn R.W. (1979), Models for the aerosols of the lower atmosphere and the effects of humidity variations on their optical properties, AFCRL-TR-79-0214, *Air Force Research Papers*, L.G. Hanscom Field, Bedford, MA USA.

Smirnov, A., B. N. Holben, T. F. Eck, O. Dubovik and I. Slutsker, (2000), Cloud-screening and quality control algorithms for the AERONET database. *Remote Sens. Environ.*, **73**, 3, 337-349.

Smirnov, A., B.N. Holben, T.F. Eck, I. Slutsker, B. Chatenet, and R.T. Pinker, Diurnal variability of aerosol optical depth observed at AERONET (Aerosol Robotic Network) sites, Geophysical Research Letters, 29 (23), art. no.-2115, 2002.

Smith, Jr.W.L, T.P. Charlock, R. Kahn, J.V. Martins and L. Remer: EOS-TERRA aerosol and radiative flux validation (2005), An overview of the Chesapeake Lighthouse and Aircraft Measurements for Satellites (CLAMS) experiment, *J. Atmos. Sci.*, **CLAMS special issue**.

Smyth, S.C., W. Jiang, D. Yin, H. Roth and E. Giroux, (2006), Evaluation of CMAQ O3 and PM25 performance using Pacifac 2001 measurement data, *Atmos Env, **40***, 2735-2749.

Stowe, L.L., A.M. Ignatov, and R.R. Singh, (1997), Development, validation, and potential enhancements to the second-generation operational aerosol product at the national environmental satellite, data, and information service of the

national oceanic and atmospheric administration, *J. Geophys. Res*., ***102***(D14) pp. 16923-16934.

Tanré, D., M. Hermon, and Y. J. Kaufman, (1996), Information on aerosol size distribution contained in solar reflectance spectral radiances, *J Geophys. Res., 101*(D14), 19043-19060.

Tanré, D., Y. J. Kaufman, et al. (1997), Remote sensing of aerosol properties over oceans using the MODIS/EOS spectral radiances, *J Geophys. Res., 102*(D14), 16971-16988.

Taubman, B., 2004, Airborne Characterization of Regional Aerosol Origins and Optical Properties, PhD thesis, University of Maryland, College Park, MD, 242 pages.

Taubman, B.F., J.C. Hains, A.M. Thompson, L.T. Marufu, B.G. Doddridge, J.W. Stehr, C.A. Piety, and R.R. Dickerson, (2006), Aircraft Vertical Profiles of Trace Gas and Aerosol Pollution over the Mid-Atlantic U.S.: Statistics and Meteorological Cluster Analysis, *J. Geophys. Res., **111***(D10), doi: 2005JD006196.

Taubman, B.F., L.T. Marufu, B.L. Vant-Hull, C.A. Piety, B.G. Doddridge, R.R. Dickerson, and Z. Li (2004b), Smoke over haze: Aircraft observations of chemical and optical properties and the effects on heating rates and stability, J. Geophys. Res., ***109***(D2), D02206, doi:10.1029/2003JD003898.

Taubman, B.F., L.T. Marufu, C.A. Piety, B.G. Doddridge, J.W. Stehr, and R.R. Dickerson (2004a), Airborne characterization of the chemical, optical, and meteorological properties, and origins of a combined ozone/haze episode over the eastern U.S., J. Atmos. Sci., ***61***(14), 1781-1793.

Thomas, G.E., and K. Stamnes, (1999), Radiative transfer in the atmosphere and ocean, xxvi, 517 pp., Cambridge University Press, New York.

Toon, O.B., (2000), Atmospheric science - How pollution suppresses rain, *Science*, ***287*** (5459), 1763-.

Torres O., P.K. Bhartia, J.R. Herman and Z. Ahmad, (1998), Derivation of aerosol properties from satellite measurements of backscattered ultraviolet radiation. Theoretical Basis, *J. Geophys. Res.*, ***103***, 17099-17110.

Torres, O., P.K. Bhartia ,J.R. Herman, A. Sinyuk and B. Holben, (2002), A long term record of aerosol optical thickness from TOMS observations and comparison to AERONET measurements, *J. Atm. Sci.,**59***, 398-413.

Tucker, C. J. (1979), Red and photographic infrared linear combinations monitoring vegetation, *Remote Sens. Environ.*, *8*, 127-150.

Twomey, S., 1977: Atmospheric Aerosols. Elsevier. 251 pp.

U.S. Environmental Protection Agency (USEPA), (2003), National Air Quality and Emissions Trends Report, EPA 454/R-03-005, Research Triangle Park, NC, (http://www.epa.gov/airtrends)

U.S. Government Printing Office, (1976), U.S. Standard Atmosphere, Washington, D.C.

Van de Hulst, H.C., (1984), *Light Scattering by Small Particles*, Dover Publications, New York, 470 pps.

van Donkelaar, A., R. V. Martin, and R. J. Park (2006), Estimating ground-level PM2.5 using aerosol optical depth determined from satellite remote sensing, *J. Geophys. Res.*, ***111***, D21201, doi:10.1029/2005JD006996.

Vant-Hull, B., Z. Li, B. F. Taubman, R. Levy, L. Marufu, F.-L. Chang, B. G. Doddridge, and R. R. Dickerson, (2005), Smoke over haze: Comparative analysis of satellite, surface radiometer, and airborne in situ measurements of aerosol optical properties and radiative forcing over the eastern United States. *J. Geophys. Res.*, ***110***, D10S21, doi:10.1029/2004JD004518.

Vermote, E. F., D. Tanré, et al. (1997a), Second Simulation of the Satellite Signal in the Solar Spectrum, 6S: An overview, *IEEE Trans. Geosci. Remote Sens.*, *35*(3), 675-686.

Vermote, E. F., N. ElSaleous, C. O. Justice, Y. J. Kaufman, J. L. Privette, L. Remer, J. C. Roger and D. Tanre (1997b): Atmospheric correction of visible to middle-infrared EOS-MODIS data over land surfaces: Background, operational algorithm and validation. *J. Geophys. Res.-Atmos.*, **102**, D14,

17131-17141.

Vermote, E.F., N.Z. El Saleous, and C.O. Justice, Atmospheric correction of MODIS data in the visible to middle infrared: first results, Remote Sensing of Environment, 83 (1-2), 97-111, 2002.

Volten H., O. Munoz, E. Rol, J. F de Haan., W. Vassen., J. W. Hovenier., K. Muinonen, and T. Nousiainen (2001), Scattering matrices of mineral aerosol particles at 441.6 nm and 632.8 nm, *J. Geophys. Res*., *106*, 17375-17401.

Wang, J. and S. Christopher (2003), Intercomparison between satellite-derived aerosol optical thickness and PM2.5 mass: Implications for air quality studies, *Geophys Res Lett,*. ***30*** (21), 2095, doi:10.1029/2003GL018174.

Watson, J.G., Visibility: Science and regulation, Journal of the Air & Waste Management Association, 52 (6), 628-713, 2002.

Welton, E. J., J. R. Campbell, J. D. Spinhirne, and V. S. Scott, 2001: Global monitoring of clouds and aerosols using a net- work of micropulse lidar systems, *Proc. Lidar Remote Sensing for Industry and Environmental Monitoring*, Sendai, Japan, SPIE, ***4153***, pp151–158.

Whitby, K. T., (1978): The physical characteristics of sulfur aerosols. *Atmos. Environ*., ***12***, 135–159.

Wiscombe, W. J. (1981), Improved Mie scattering algorithms, *Appl. Opt.*, *19*, 1505-1509.

Volz, F.E., (1959), Photometer mit Selen-photoelement zurspektralen Messung der Sonnenstrahlung und zer Bestimmung der Wallenlangenabhangigkeit der Dunsttrubung. *Arch. Meteor. Geophys Bioklim*. ***B10***:100-131.

Volz, F.E., (1974) Economical multispectral sun photometer for measurements of aerosol extinction from 0.44 μm to 1.6 μm and precipitable water. *Appl. Opt.*, ***13***, 1732–1733.

Yang P., and K. N. Liou (1996), Geometric-optics-integral-Eq. method for light scattering by nonspherical ice crystals, *Appl. Opt.*, *35*, 6568-6584.

Yu, H., Y. J. Kaufman, M. Chin, G. Feingold, L. Remer, T. Anderson, Y. Balkanski, N. Bellouin, O. Boucher, S. Christopher, P. DeCola, R. Kahn, D. Koch, N.

Loeb, M. S. Reddy, M. Schulz, T. Takemura, and M. Zhou (2006), A review of measurement-based assessments of aerosol direct radiative effect and forcing, *Atmos. Chem . Phys., 6,* 613-666.

Xiong X, Sun J, Esposito J, Guenther, and Barnes WL, (2003), MODIS Reflective Solar Bands Calibration Algorithm and On-orbit Performance, *Proceedings of SPIE Optical Remote Sensing of the Atmosphere and Clouds* ***III****,* 4891, 95-104.

ABSTRACT

Title of Dissertation: **Airborne Characterization of Regional Aerosol Origins and Optical Properties**

Brett F. Taubman, Doctor of Philosophy, 2004

Dissertation Directed By: **Professor Russell R. Dickerson, Department of Meteorology**

The ubiquity of air pollution in the Mid-Atlantic and northeastern U.S. is a major concern for human and ecological health as well as the climate. Between February 2001 and February 2004, 160 flights on a light aircraft outfitted for atmospheric research were conducted over the region to characterize the factors that lead to severe air pollution episodes and how the pollutants impact the radiation budget. One salient discovery was that the chemistry and physics of multi-day haze and ozone episodes over the Mid-Atlantic and northeastern U.S. may be accurately represented by a two-reservoir system composed of the planetary boundary layer (PBL) and the lower free troposphere (LFT). Primary pollutants are typically emitted in the PBL, where they are subject to greater humidification effects and surface deposition. Pollutants in the LFT are not subject to direct deposition and photochemical processes are accelerated, which appears to play a larger role in particle growth processes than relative humidity. Measurements of a smoke plume from Canadian forest fires showed that the plume was separated from the underlying

layer by a morning subsidence inversion. Absorption of solar radiation within the optically thick plume nearly equaled the total amount attenuated at the surface, creating a feedback loop that sustained the vertical stability and protracted the lifetime of the plume. Satellite reflectances were used to calculate the optical depth of the smoke plume with two sets of inputs; AERONET retrieved optical properties and optical properties measured aboard the aircraft. The optical depths calculated using the AERONET optical properties were the lowest, while retrievals using the in-situ values were 22-43% larger, due to greater absorption measured in-situ. Radiative forcings calculated with the in-situ optical properties matched surface and TOA measurements more closely than those calculated with the AERONET retrievals. Measurements made downwind of power plants during the North American electrical blackout showed reductions in SO_2 (>90%), O_3 (~50%), and light scattered by particles (~70%). These observations indicate the central role power plants play in regional air quality. Finally, statistical analyses of all flights point to the dominance of photochemical and meteorological processes in determining aerosol optical properties.

AIRBORNE CHARACTERIZATION OF REGIONAL AEROSOL ORIGINS AND OPTICAL PROPERTIES

By

Brett F. Taubman

Dissertation submitted to the Faculty of the Graduate School of the
University of Maryland, College Park, in partial fulfillment
of the requirements for the degree of
Doctor of Philosophy
2004

Advisory Committee:
Professor Russell R. Dickerson, Chair
Professor Neil V. Blough
Res. Assoc. Prof. Bruce G. Doddridge
Professor Robert Hudson
Professor Alice C. Mignerey
Professor John M. Ondov

Dedication

To Julie, Sam, and Matthew for your love, support, and above all, your patience.

Acknowledgements

Funding for this work was provided by the Maryland Department of Environment (MDE), the Mid-Atlantic and Northeast – Visibility Union (MANE-VU), and the US Department of Energy's Atmospheric Radiation Measurement (ARM) program, grant DEFG0201ER63166. I gratefully acknowledge the NOAA Air Resources Laboratory (ARL) for the provision of the HYSPLIT transport and dispersion model and/or READY website (http://www.arl.noaa.gov/ready.html) used in this publication. The author would like to thank the Center for Ocean-Land-Atmosphere Studies (COLA), Institute of Global Environment and Society, Calverton, MD for the use of Grid Analysis and Display System (GrADS). I am eternally grateful to the AERONET team and to Paul Ricchiazzi and the SBDART code. Finally, a special thanks for their support and contributions goes to George “Tad” Aburn, George Allen, Bryan Bloomer, Pedro Bueno, Kevin Civerolo, Tom Downs, Jennifer Hains, Daniel Kirk-Davidoff, Al Leston, Zanqhing Li, Lackson Marufu, Charles Piety, Rich Poirot, Matt Seybold, Gopal Sistla, Jeff Stehr, Jeff Underhill, and Brian Vant-Hull.

Table of Contents

List of Tables

List of Figures

Chapter 1: Introduction

1.1. Background

Air pollution impacts human health, global climate, and the environment (McClellan, 2002, Gent *et al*., 2003, USEPA, 2003(b), IPCC, 2001). However, the current scientific understanding of trace gas pollution is greater than for aerosols (IPCC, 2001). Trace gases and aerosols may both have deleterious effects on human health and agriculture, but the impacts on the climate are largely competing. Many trace gases have a warming effect, and have thus been classified as greenhouse gases. Conversely, aerosols have a net cooling effect (IPCC, 2001). Trace gases often have lifetimes that are quite long and, therefore, have global consequences. Aerosols, on the other hand, are generally thought to have lifetimes on the order of one week, due to precipitation cycles, and as a result may be limited to a regional scale. Nevertheless, aerosols have been found in areas of the globe that were hitherto thought to be pristine with no regional emission sources, such as the Arctic (e.g., Rosen *et al*., 1981). Discoveries such as this reinforce the fact that our current understanding of aerosol chemistry, physics, and overall impacts is rudimentary at best.

Surface observations over the last several decades seem to indicate a contradiction in solar heating and surface temperatures. Namely, solar heating has decreased while surface temperatures have increased (Liepert *et al*., 2004). Index trends and modeling studies show that the increasing temperatures, at least in North

America, are unlikely the result of natural climate variation (Karoly *et al.*, 2003). The competing effects of greenhouse species and the direct and indirect effects of atmospheric aerosols explain the apparent paradox. Contrary to the effect of greenhouse gases, the net effect of atmospheric aerosols, either directly or through cloud interactions, is to cool the climate by reducing solar radiation at the surface. Specifically, anthropogenic aerosols either directly reflect incoming solar radiation or enhance cloud reflectivity by increasing the number concentration of cloud droplets. The indirect effect accounts for no small portion of the total radiative forcing either. The globally averaged radiative forcing of the aerosol direct effect over the ocean, as determined by satellite observations, was estimated to be –0.4 W m^{-2}, while the aerosol indirect effect was found to be –0.6 to –1.2 W m^{-2} (Sekiguchi *et al.*, 2003). However, a lot of uncertainty remains as to an accurate net forcing value.

Sulfate-dominated aerosols are primarily responsible for the direct and indirect cooling effects attributed to aerosols in general. Much of the climate forcing uncertainty stems from a lack of understanding of humidification effects on sulfate aerosols as well as mixing processes with other chemical species. Black carbon (BC), the primary absorbing compound in particulate matter (PM), warms the atmosphere and may in fact be the second most important greenhouse species after CO_2 (excluding water vapor) (Jacobson, 2001). The type and degree of mixing of BC with sulfate particles is one of the processes that generates a large portion of the climate forcing uncertainty (Haywood and Boucher, 2000; Jacobson, 2000; Jacobson, 2001; Chung and Seinfeld, 2002; Lesins *et al.*, 2002).

1.1.1. Chemistry

Ozone (O_3) formation in the troposphere occurs in the presence of carbon-containing species (represented here with the simplest atmospheric carbon-containing species, CO), NO_x ($NO + NO_2$), and sunlight via the following reaction pathway:

$$CO + OH\ (+O_2) \rightarrow CO_2 + HO_2$$

$$HO_2 + NO \rightarrow NO_2 + OH$$

$$NO_2 + h\nu \rightarrow NO + O$$

$$O + O_2 + M \rightarrow O_3 + M$$

$$O_3 + h\nu \rightarrow O_2 + O(^1D)$$

$$O(^1D) + H_2O \rightarrow 2OH$$

where $h\nu$ represents a photon and M is a third body needed to stabilize the O_3 molecule (typically either N_2 or O_2). Ozone may subsequently regenerate NO_2 through reaction with NO:

$$O_3 + NO \rightarrow O_2 + NO_2$$

Thus, concentrations of O_3 are highly dependent upon NO_x concentrations (Crutzen, 1971). When the sun goes down and NO_2 cannot be photolyzed, O_3 is no longer produced. Ozone captured in the stable nocturnal boundary layer is then destroyed through reaction with NO or surface deposition. The lifetime of this O_3 is several hours. When O_3 remains in the free troposphere, however, it is no longer subject to deposition and its lifetime may be as long as several weeks.

The chemical and optical properties of transported pollutants may be very different from those locally emitted. Air pollution originating in the Midwest is dominated by power plant emissions, with high levels of SO_2 (but not CO) that lead

to secondary aerosol formation and a highly scattering, sulfate-dominated haze (Malm, 1992). Sulfates are formed in the gas phase by means of the following reactions:

$$OH + SO_2 + M \rightarrow HOSO_2 + M$$

$$HOSO_2 + O_2 + M \rightarrow HO_2 + SO_3 + M$$

$$SO_3 + H_2O \rightarrow\rightarrow H_2SO_4$$

and in the aqueous phase through reaction with hydrogen peroxide:

$$SO_2 + H_2O_2 \rightarrow H_2SO_4.$$

Under cloud free conditions, the lifetime of SO_2 is dependent upon the gas phase reaction with the OH radical and dry deposition. At typical atmospheric concentrations of OH, the lifetime of SO_2 is roughly one week. The dry deposition velocity of SO_2 is ~1 cm s^{-1}, so in a 1 km deep boundary layer, the lifetime due to dry deposition is only ~1 d. When SO_2 is transported out of the boundary layer, however, dry deposition is no longer a factor.

Mobile sources, predominant in urban centers in the eastern U.S., emit significantly more black carbon (BC) and CO than stationary point sources (Chen *et al.*, 2001). Black carbon results from biomass burning or the incomplete combustion of fossil fuels and is graphitic in nature, but is generally found as an amalgam with organic matter as well. The lifetime of CO is on the order of several weeks and it is therefore considered a fairly stable tracer species, whereas the lifetime of BC, as with other particulate species, is thought to depend on the frequency of precipitation.

1.1.1. Meteorology

Variability in the concentrations of fine particulate matter ($PM_{2.5}$, particles with aerodynamic diameters $\leq 2.5\mu m$) and O_3 in the lower atmosphere is controlled by local and regional emissions, chemistry, meteorology, and dynamics. When emissions are held relatively constant, however, the meteorology and dynamics assume a major role in determining air quality. The daytime mixed layer is known to be a reservoir of local emissions and regionally transported emissions that are entrained as it deepens (Berkowitz and Shaw, 1997; Banta *et al.*, 1998; Luke *et al.*, 1998; Ryan *et al.*, 1998; Zhang and Rao, 1999; Baumann *et al.*, 2000; Fast *et al.*, 2002). The lower free troposphere (LFT), roughly defined here as the narrow layer just above the planetary boundary layer (PBL), may also act as a reservoir of photochemically aged air parcels that are not subject to deposition, particularly during multi-day stagnation events (Taubman *et al.*, 2004(a)).

The synoptic meteorology associated with O_3 episodes over the eastern U.S. has been investigated in a number of studies (Vukovich, 1995; Zelenka, 1997; Ryan *et al.*, 1998; Zhang *et al.*, 1998; Kleinman *et al.*, 2000; Seaman and Michelson, 2000; Sistla *et al.*, 2001; Vukovich, 2002; Rao *et al.*, 2003) and is reasonably well understood. Regional high O_3 events often occur when the Bermuda high strengthens and extends west into the eastern U.S. Subsidence east of the ridge induces clear skies, high temperatures, atmospheric stability, and stagnant winds. These factors enhance photochemistry and inhibit vertical mixing, thereby contributing to increased local concentrations of O_3. Circulation around the ridge results in westerly transport of O_3 and O_3 precursors from the Midwest to the eastern U.S., where they combine

with local emissions. In the eastern U.S., hazy conditions often occur during periods of high O_3, but not always (Chen, 2002). The meteorological conditions that support high concentrations of regional $PM_{2.5}$ are not as well characterized as for O_3. However, recent studies have shown that transport of $PM_{2.5}$ from the south and west into the region plays a role (Malm, 1992; Chen *et al.*, 2002; Civerolo *et al.*, 2003).

Two meso-scale meteorological phenomena often associated with air pollution events in the eastern U.S. are the Appalachian lee trough (APLT) and the nocturnal low-level jet (LLJ). The synoptic flow typical during these events is orthogonal to the Appalachian mountain range. As the air descends over the eastern ridge of the mountains it is adiabatically heated, creating a column of hot air. In response to the increased buoyancy of the air parcel, surface pressures drop and a mesoscale trough forms (Seaman and Michelson, 2000). To conserve absolute vorticity, the winds turn cyclonically across the trough. The APLT is associated with approximately 70% of the high O_3 episodes in the Mid-Atlantic (Pagnotti, 1987).

The LLJ in this region occurs between approximately 00:00 and 06:00 EST and is a south-southwesterly wind maximum in the residual layer, generally observed between ~300-1000 m. The wind speeds are typically ~10-20 m s^{-1} and are greater than those in the underlying nocturnal boundary layer and those just above it. The nocturnal boundary layer provides a low friction surface over which the jet can travel. This phenomenon also seems to be orographically derived, possibly resulting from the differential heating and pressure gradients associated with sloping terrain (e.g., Parish *et al.*, 1988). Pollutant transport via the LLJ is disproportionately important during periods of stagnation when geostrophic winds are light.

1.1.2. Contributions from Biomass Burning

Biomass burning can have significant impacts on regional air quality and the radiative balance of the earth. Large amounts of trace gases, including CO, NO_x, and O_3, are typically associated with biomass combustion plumes (Evans *et al.*, 1977; Crutzen *et al.*, 1979; Stith *et al.*, 1981; Delmas, 1982; Crutzen and Andreae, 1990; Andreae and Merlet, 2001). O_3 is photochemically produced downwind of fires in the presence of NO_x, NMHCs (non-methane hydrocarbons), CO, and UV light (Evans *et al.*, 1977; Stith *et al.*, 1981; McKeen *et al.*, 2002). Combustion temperatures generated from biomass burning are not high enough to fix atmospheric nitrogen; rather the reactive nitrogen generated from biomass burning results from the nitrogen content of the species burned (Andreae and Merlet, 2001). Most of the species also contain S, but little SO_2 is normally observed downwind of biomass burning (Stith *et al.*, 1981).

Particles generated from burning vegetation are dominated by organic carbon (OC) and BC (Crutzen and Andreae, 1990; Martins *et al.*, 1998) that reduce the flux at the surface by scattering and absorbing solar radiation (Penner *et al.*, 1992; Hobbs *et al.*, 1997; Remer *et al.*, 1998; Eck *et al.*, 1998; Li, 1998; Li and Kou, 1998). This is in contrast to sulfate particles, prevalent over the eastern U.S., that predominantly scatter solar radiation and cool both the atmosphere and the surface (Charlson *et al.*, 1991; Ramanathan *et al.*, 2001). The degree of absorptivity of carbonaceous smoke particles depends largely on fuel type (dictated by region and vegetation), age of the particles, and the phase of burning (i.e., flaming vs. smoldering) (Dubovik *et al.*, 2001). Emissions from North American boreal forest fires have been shown to be

less absorptive than those of African savannah and South American cerrado fires and commensurate with those of Amazonian forest fires (Dubovik *et al.*, 2001). This is largely due to a protracted smoldering phase in forest fires that produces less absorptive particles. Chemical and physical transformations may, however, occur downwind of the source. In an aged plume, particle coagulation, gas-to-particle conversion, heterogeneous reactions, and cloud processing influence the trace gas concentrations and the size distribution and optical properties of the smoke particles (Reid *et al.*, 1998(a); Reid *et al.*, 1999, Wong and Li, 2002). Near source and downwind *in-situ* measurements are thus necessary to provide constraints on remote sensing retrieval algorithms as well as for validations of numerical based model simulations.

The scattering Ångström exponent, α, a measure of the wavelength (λ) dependence of the scattering coefficient, is inversely related to particle size, and thereby provides information on the source and age of the observed particles:

$$\alpha = \frac{-\log(\sigma_{sp\lambda 1}/\sigma_{sp\lambda 2})}{\log(\lambda_1/\lambda_2)} \qquad (1)$$

The single-scattering albedo (ω_o) is the ratio of particle scattering (represented by the scattering coefficient, σ_{sp}) to total extinction due to particle scattering and absorption (represented by the absorption coefficient, σ_{ap}), and represents the probability that a photon encountering the particle will be scattered:

$$\omega_o = \frac{\sigma_{sp}}{(\sigma_{sp} + \sigma_{ap})} \qquad (2)$$

Smoke particles reportedly become less absorptive with age (Reid *et al.*, 1998(a)). In optically thick smoke plumes, small changes in ω_o can have profound

impacts on the radiative budget (Reid *et al.*, 1999). The energy balance of the surface-atmosphere system is thus altered according to the degree of scattering and absorption (Eck *et al.*, 1998). A more absorbing aerosol can heat the atmosphere and cool the surface, generating greater stability in the lower atmosphere and impacting the hydrological cycle (Ramanathan *et al.*, 2001). This in turn affects the vertical mixing of the aerosols and potential removal mechanisms (e.g., Park *et al.*, 2001).

The direct effect of aerosols upon this energy balance is quantified through calculations of aerosol direct radiative forcing. Top of the atmosphere forcing (ΔF TOA) is a measure of the reflectivity of the atmosphere (after accounting for surface albedo), while surface forcing (ΔF sfc) gives the total attenuation of solar flux at the surface, both driven by aerosols in this case. If the two are equal, then the aerosols are completely scattering. If the attenuation at the surface is greater than the reflected flux at the top of the atmosphere, then the aerosols have absorbed some of the solar radiation. Aerosol direct radiative forcing depends upon the aerosol optical depth (AOD, τ), ω_0, and the asymmetry parameter (g) of the particles. Aerosol optical depth is defined as the extinction coefficient, σ_{ext}, integrated from the surface (sfc) to the top of the atmosphere (TOA):

$$\tau(\lambda, RH) = \int_{sfc}^{TOA} \sigma_{ext}(\lambda, RH)\, dz \tag{3}$$

The extinction coefficient is the sum of the scattering and absorption coefficients and τ can therefore be represented as the sum of their vertical integrals:

$$\tau(\lambda, RH) = \int_{sfc}^{TOA} \sigma_{sp}(\lambda, RH)\, dz + \int_{sfc}^{TOA} \sigma_{ap}(\lambda, RH)\, dz \tag{4}$$

The asymmetry parameter represents the degree of asymmetry of the angular scattering and is defined as:

$$g = \frac{1}{2}\int_0^{\pi} \cos\theta P(\theta)\sin\theta d\theta \quad (5)$$

where θ is the scattering angle and P is the phase function, the scattered intensity at angle θ relative to the incident beam.

1.1.3. Discrepancies Between Remotely Sensed and In-Situ Measurements

Aerosol optical depth is a quantity that is used for column closure studies as well as the calculation of aerosol radiative forcing. In most areas of the western hemisphere, light is primarily scattered by particles. The contribution of particle light absorption to the aerosol optical depth is small. As a result, uncertainties in absorption values are often overlooked. Because of the large contribution of scattering to the aerosol optical depth, a reasonable agreement in scattering values typically leads to a reasonable agreement in optical depth values. However, significant disparities in optical depth or forcing values may arise when there are large discrepancies in absorption values used as inputs to satellite algorithms and in calculations of aerosol radiative forcing, respectively (Vant-Hull *et al.*, 2004).

Absorption measured in-situ is almost invariably lower than that determined through remotely sensed techniques (e.g. sun photometry) (Hegg *et al.*, 1997; Hartley *et al*., 2000; Dubovik *et al*., 2001; Taubman *et al.*, 2004(b)). For example, in-situ aircraft measurements of ω_0 during SCAR-B and INDOEX were consistently lower than sun photometer observations (Dubovik *et al.*, 2001; Ramanathan *et al*., 2001(b)). Better agreement, however, was achieved during the SAFARI campaign (Haywood *et*

al., 2003, Magi *et al.*, 2003). In the LACE-98 campaign (Bundke *et al*., 2002) measurement conformity was only achieved after the introduction of a variable liquid layer used to theoretically envelop the carbonaceous core of aged smoke particles.

Whether or not one measurement technique is more accurate than the other, both have inherent advantages and disadvantages. The important advantage of satellites is that they offer global coverage, a necessity when studying climate variability (Kaufman *et al*., 2002). However, satellites, as well as most other passive remote sensing techniques, cannot resolve vertical layers within the column and only retrieve column-averaged properties. Also, while the surface albedo naturally varies, the satellite observational angle is fixed for a particular pixel. These factors preclude the possible retrieval of all of the aerosol optical properties. Rather, one or more of the optical properties are assumed and the rest are derived from the measured reflectances (Kaufman *et al.*, 1990; Wang *et al*., 2003).

Sun photometers that measure solar radiance at the surface, such as those used in the AErosol RObotic NETwork (AERONET) (Holben *et al*., 1998), make observations over a large range of scattering angles through a constant aerosol profile to retrieve many column-averaged aerosol optical properties (Dubovik *et al*., 2000). Previous studies that used sun photometers to retrieve certain aerosol optical properties (size distribution, phase function, optical depth) incorporated algorithms with fixed values for the remaining ones (index of refraction, single scattering albedo) (Kaufman *et al.*, 1998; Russell *et al.*, 1999(b)). Currently, a more sophisticated and exhaustive algorithm is used for sun photometer retrievals that provides a comprehensive suite of estimated optical properties (Dubovik *et al.*, 2000; Dubovik *et al*., 2001). A distinct advantage of remote sensing techniques in general is that they

do not physically alter the aerosols measured. However, the veracity of the measurements depends upon the assumptions used in the retrievals (Remer *et al.*, 1997; Dubovik *et al*., 2000).

Unlike remote sensing techniques, in-situ measurements can resolve the vertical layers within an atmospheric column. However, measurement errors may arise through the physical interaction of the instrument with the measured aerosols (Remer *et al.*, 1997; Bond *et al*., 1999). A comprehensive laboratory calibration of the PSAP (Particle/Soot Absorption Photometer) showed that when using the integrating plate method to measure absorption, filter interferences are a significant source of error (Bond *et al.*, 1999). Despite the potential problems, both in-situ and sun photometer measurements of aerosol optical properties are currently used in satellite algorithms (Bundke *et al.*, 2002; Kaufman *et al.*, 1998).

The natural variability in biomass burning aerosol optical properties exacerbates the existing discrepancy between in-situ and remote sensing techniques. Biomass burning aerosol optical properties vary depending on the type of vegetation burned, whether the fire is flaming or smoldering, and the age of the particles (Kaufman *et al.*, 1998; Reid *et al.*, 1999; Wong and Li, 2002). Measurements of smoke particles in Brazil showed a range of single scattering albedos at 550 nm (ω_{0550}) of 0.6 to 0.91, depending on the age (Kaufman *et al*., 1998; Reid *et al.*, 1998(b)). Canadian smoke had ω_{0550} values from 0.70 to 0.98 for similar reasons (Miller and O'Neill, 1997; Li and Kou, 1998). The ω_{0550} from burning pine needles, measured in a controlled environment, varied between 0.66 and 0.97 according the burning mode (smoldering or flaming) (Miller and O'Neill, 1997).

1.1.4. Contributions from Power Plants

Fossil fuel burning power plants are responsible for more than half of the electrical energy production in the U.S., but also ~22% of the NO_x and ~69% of the SO_2 emissions (USEPA, 2003(a)). As detailed above, nitrogen oxides combine with volatile organic compounds (VOCs) in the presence of sunlight to produce O_3, the principal component of photochemical smog. Likewise, SO_2 may be oxidized to produce sulfate (SO_4^{2-}), the primary constituent of $PM_{2.5}$ in the northeastern U.S. (IMPROVE, 2000). In summertime, under high pressure systems with westerly transport, emissions of NO_x and SO_2 in the northeastern U.S. induce severe smog and haze events, primarily comprising O_3 and sulfate-dominated fine particles (Ryan *et al.*, 1998, Sistla *et al.*, 2001, Taubman *et al.*, 2004(a)). Both pollutants have been linked to adverse health effects, degradation of the environment, and global climate change (McClellan, 2002, Gent *et al.*, 2003, USEPA, 2003(b), IPCC, 2001).

Despite improvements made to air quality in the U.S. over the past 20 years, approximately 146 million people live in counties where the monitored air in 2002 was deemed unhealthy (USEPA, 2003(a)). Unacceptably high levels of either O_3 or PM or both were the primary reason for the unhealthy classification. Of all the air pollutants routinely monitored, ground level O_3 has been the most challenging to reduce. Some metropolitan areas have shown improvements, but the 8-hour average O_3 levels have increased in many national parks (USEPA, 2003(b)). This is apparently the result of region-specific responses to VOC versus NO_x reductions. In the past 20 years, VOC emissions have decreased by ~40% while NO_x emissions

have decreased by only ~15% (USEPA, 2003(b)). Except for urban centers, which are VOC limited, the majority of the U.S. is NO_x limited (Fiore *et al*., 1998).

The impact of transported point source pollution on regional air quality depends upon emissions, meteorology, and non-linear chemical responses. Thus far, quantification of these impacts has been based on multi-year measurement and modeling studies (Solomon *et al*., 2000) and the results of long-term emissions reduction scenarios (Malm *et al*., 2002). Not until the work reported herein has there been an opportunity to make direct air quality measurements during a large scale-back of one pollution source.

1.2. Overview of the Research

Between February 2001 and February 2004, 160 research flights were conducted to investigate the chemical, meteorological, and dynamical factors that influence regional air pollution episodes in the Mid-Atlantic and northeastern U.S. Most of these flights were performed in the summertime; however, three mini-campaigns were conducted in the winters of 2001, 2003, and 2004. Measurements were made using a light aircraft outfitted for atmospheric research. Details of the experimental methods and sampling platform will be covered in the next chapter. One of the main foci of the research was climatically relevant: an investigation of the optical property characteristics of the aerosols and their impact on the regional radiation budget. Another area of interest was more policy relevant: the source attribution of the pollution through an examination of the chemical and optical characteristics of the pollutants.

1.3. Organization

The next chapter details the experimental methods used for this work, including the sampling platform, trace gas analyzers, and particle instruments. Chapter 3 discusses the formulation of the two-reservoir conceptual model, a new paradigm for describing the chemistry and physics of the lower atmosphere during multi-day air pollution episodes. The two subsequent chapters describe the measurements made of an optically thick smoke plume from Canadian forest fires that was advected over the eastern U.S. in early July 2002. The radiative impacts of the plume are quantified and comparisons are made between the in-situ measurements of aerosol optical properties and AERONET values when used as inputs to a satellite algorithm to calculate optical depth. Chapter 6 describes the measurements made downwind of power plants that were tripped during the North American electrical blackout in August 2003 and the subsequent analyses. Finally, Chapter 7 gives an overview of the statistical analyses of aerosol optical properties over the three-year time period described above during which research flights were conducted. Following the statistical overview is a summary of all the work described herein as well as the climate and policy implications and recommendations for the future.

Chapter 2: Experimental Methods

2.1. Sampling Platform

The sampling platform used for this research was a twin engine Piper Aztec-E PA-23-250 research aircraft (owned and operated by Advanced Helicopter Concepts, Figure 1). The aircraft is outfitted with a suite of trace gas and aerosol instruments, the inlets for which are on the upper fuselage. There is an aft-facing inlet plumbed to the trace gas instruments while a forward facing, isokinetic inlet feeds the aerosol instruments. Due to apparent inlet sampling line impaction losses of particles larger than 1 μ m (diameter), reported measurements are of sub-μ m particles only. A meteorological probe is nestled between these two inlets. Geographic position is measured and stored using a Global Positioning System, GPS (Garmin GPS-90), with 10 s resolution, and verified several times per flight relative to known geographic reference points. Data acquisition for the continuous meteorological and trace gas instruments at 10 s resolution is performed using a Rustrak Ranger II (EIL Instruments Inc., Hunt Valley, MD) data logger. Aerosol data are logged every 10 s on the aircraft PC based system using commercial and custom data acquisition software.

Figure 1. Photograph of the Piper Aztec-E PA-23-250 research aircraft.

2.2. Meteorological Measurements

Temperature and relative humidity (RH) were measured using a thermistor and capacitive thin film, respectively, with a regularly calibrated Rustrak RR2-252 RH probe (EIL Instruments Inc., Hunt Valley, MD). The instrument is capable of 0.5^{o} C temperature precision and 2% humidity precision at a 30 s response time.

2.2.1. Pressure Altitude

Static pressure was measured inside the unpressurized cabin of the aircraft using a Rosemount Model 2008 pressure transducer, capable of 5 mb precision, and calibrated regularly with a laboratory standard. To calculate pressure altitude, the average static pressures before takeoff and after landing as recorded by the pressure transducer are calculated. Altimeter readings reported by the Automated Weather Observation System (AWOS) at the airports are recorded before takeoff and after landing for every flight. The altimeter reading before takeoff is converted to millibars (mb) and subtracted from the average static pressure value before takeoff. The same

procedure is then followed for the altimeter reading and average static pressure value after landing. The two differences are averaged together. The average value is then subtracted from the static pressure values recorded during the flight and the resultant pressures in mb are converted to pressure altitude (*palt*) using the 1976 standard atmosphere equation:

$$palt = 8303.951372 \times \ln(1013.25 / pressure) \quad (6)$$

The altitude of the airport at takeoff is added to the resulting pressure altitudes. Likewise, the altitude of the airport at landing is added to the resulting pressure altitudes. The two sums are then averaged to give the final pressure altitude values. Adding in quadrature the uncertainty from the altimeter readings and the static pressure measurements, the estimated uncertainty of the pressure altitude values is ± 50 m (95% confidence).

2.3. Trace Gas Measurements

2.3.1. Ozone

Ozone data were acquired with a commercial instrument based on the principle that O_3 absorbs UV light at 254 nm (Thermo Environmental, TEI Model 49, Franklin, MA). The amount of absorption is directly related to the O_3 mixing ratio as described by the Beer-Lambert Law:

$$\frac{I}{I_o} = e^{-axc} \quad (7)$$

where:

a = molecular absorption coefficient, 308 cm^{-1} (STP)

x = path length, 38 cm

c = O_3 mixing ratio (ppbv)

I = UV light intensity with O_3 (sample gas)

I_o = UV light intensity without O_3 (reference gas)

The sample is drawn into the inlet and split into two streams (Figure 2). One of the streams is passed through an O_3 scrubber to become the reference gas (I_o) and continues on to the reference solenoid valve. The other gas stream (I) goes to the sample solenoid valve. The solenoid valves alternate the flow of sample and reference streams to the two cells, A and B, every 10 s. The UV light intensity is measured in each cell by detectors A and B. The difference between the sample and reference cells is the O_3 mixing ratio. This instrument is routinely compared to an in-house primary O_3 calibrator (TEI Model 49PS) and is capable of 1 ppb precision for 10 s data.

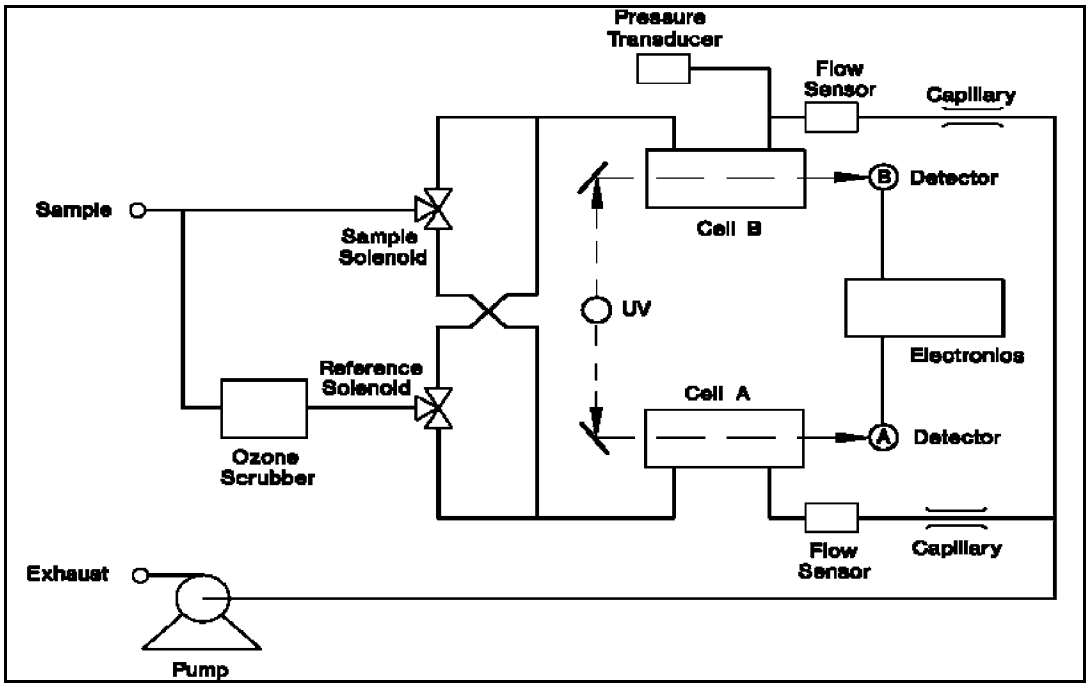

Figure 2. Schematic of the TEI model 49.

2.3.2. Carbon Monoxide

For observations of CO, a high-performance, modified (Dickerson and Delany, 1988) commercial (TEI Model 48) non-dispersive infrared gas filter correlation analyzer was used. The instrument operates on the principle that CO absorbs IR at 4.6 μm. The sample gas stream is drawn into the instrument and flows through the optical bench (see Figure 3). Infrared radiation is chopped, passed through gas filters alternating between CO and N_2, and then directed through a bandpass interference filter to the optical bench where it is absorbed by the sample gas. The remaining radiation exits the optical bench and falls on the detector. The CO gas filter fully absorbs the IR so that there is no further attenuation by the sample gas, thereby creating the reference beam. The N_2 does not absorb the IR, thus allowing absorption by CO in the sample cell. Alternating between the two gas filters effects a modulation of the chopped detector signal. Any interference by other gases is precluded by the fact that modulation of the detector signal occurs equally for the measure and reference beams. Thus, the amplitude of the signal is directly related to the concentration of CO in the sample gas.

The instrument is calibrated regularly using CO working standards (1.9 ppmv CO in nitrogen), in turn referenced to a National Institute of Standards and Technology (NIST) Standard Reference Material (1677c 9970 ppbv CO in nitrogen, certified; NIST, Gaithersburg, Maryland). This instrument is capable of ~2-5% precision determined for a 1-min mean of 10 s data. The CO instrument has

undergone formal international calibrations (Novelli et al., 1998) under a WMO protocol (Doddridge, 1995).

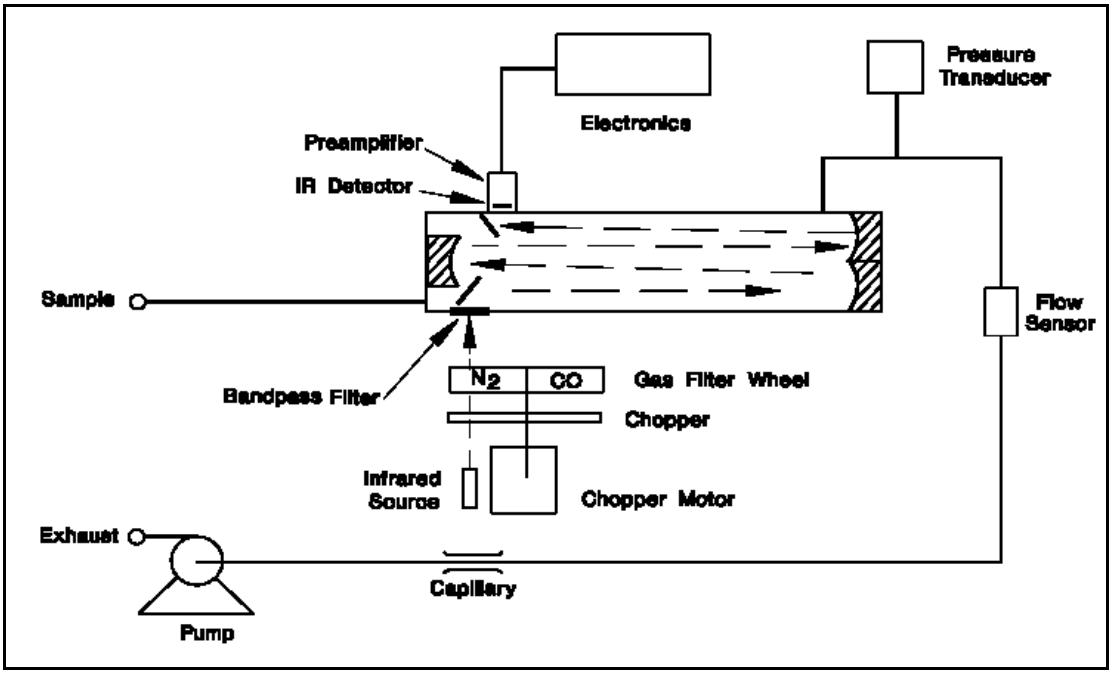

Figure 3. Schematic of the TEI model 48.

2.3.3. Sulfur Dioxide

A modified, commercial, pulsed-fluorescence detector (TEI Model 43C, see Figure 4) is used for measurements of ambient SO_2 (Luke, 1997). This instrument is based on the principle that SO_2 absorbs a pulsed UV light source in the 190 – 230 nm range and is promoted to an excited state. The excited molecule may then decay back to the ground state through one of three pathways: fluorescence, quenching, or dissociation.

Fluorescence:

$SO_2 + h\nu_1 \rightarrow SO_2^* \xrightarrow{k_f} SO_2 + h\nu_2$

Quenching:

$SO_2 + h\nu_1 \rightarrow SO_2^* + M \xrightarrow{k_q} SO_2 + M^*$

Dissociation:

$SO_2 + h\nu_1 \rightarrow SO_2^* \xrightarrow{k_d} SO + O$

where:

$h\nu_1$ = a photon of light at absorption frequency (1)

$h\nu_2$ = a photon of light at a different frequency of fluorescence (2)

M = any molecule available in the ambient air

k_f, k_q, k_d = the rate constants of the respective processes

Considering the above processes, an expression may be derived to represent the fluorescent intensity at the detector:

$$F = \frac{Gk_f I_o[1 - e^{-[ax(SO_2)]}]}{k_f + k_d + k_q[M]} \qquad (8)$$

In this equation, G is a geometric factor related to the design of the fluorescent chamber, a is the absorption coefficient of SO_2 and x is the path length. However, when the SO_2 concentration is relatively low and the path length is short, the expression may be simplified to:

$$F = \frac{Gk_f I_o ax(SO_2)}{k_f + k_d + k_q[M]} \qquad (9)$$

This expression can then be simplified further because k_f, k_q, and k_d remain mostly constant over a wide range of temperatures and background atmospheres. The

intensity of the impingent light (I_o) is also constant as are the geometric factor and path length. The equation may then be rewritten as a direct proportionality:

$$F = K(SO_2) \qquad (10)$$

Thus, the fluorescent radiation that reaches the detector is directly proportional to the SO_2 concentration.

Based upon this principle of operation, the sample air is drawn into the instrument and directed through a hydrocarbon "kicker" (Figure 4). Many interferents, most notably aromatic hydrocarbons, mimic the fluorescent activity of SO_2. The "kicker" removes hydrocarbons from the sample by forcing the molecules to permeate the tube wall. The unaffected SO_2 then enters the fluorescence chamber where it is excited by pulsed UV light that has been wavelength selected by the mirror assembly. As the excited SO_2 molecules decay, the bandpass filter only allows the emitted radiation to reach the photomultiplier tube. In this way, the concentration of trace levels of ambient SO_2 is measured. The instrument has a detection limit of ~140 pptv (S:N=1:1 for $\pm 2\sigma$ noise) for a 1-min mean of 10 s data and is calibrated regularly using SO_2 working standards.

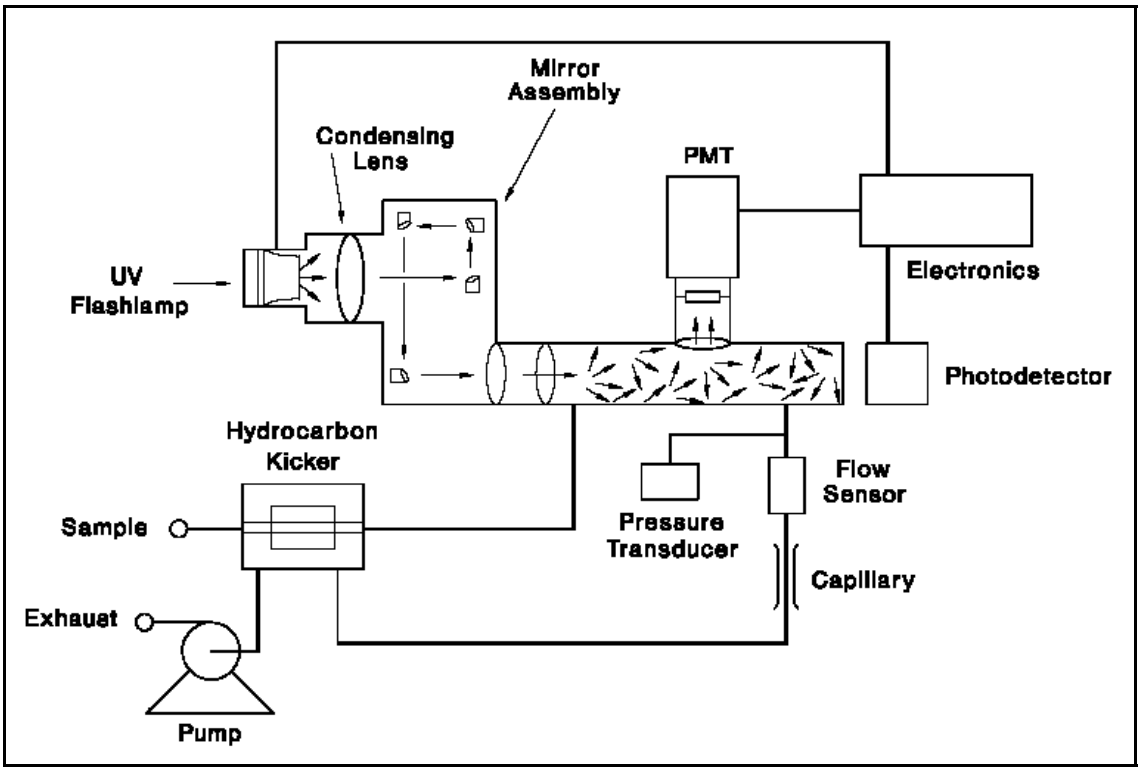

Figure 4. Schematic of the TEI model 43.

2.4. Aerosol Measurements

2.4.1. PSAP

Particle light absorption is measured using a Particle/Soot Absorption Photometer (PSAP, Radiance Research, Seattle, WA). The operational principle is based on the integrating plate technique whereby the intensity of 565 nm light is measured after passing through a filter subjected to ambient aerosol deposition. The transmissivity of the filter is related to the light absorption coefficient of the particles according to Beers Law:

$$A = \ln(I_o/I) \qquad (11)$$

where:

A = the absorbance

I_o = the original intensity of impingent light

I = the intensity of transmitted light

The absorption coefficient of the particles (σ_{ap}) can be calculated according to the volume of sample air during the specified averaging time:

$$\sigma_{ap} = (A/V)\ln(I_o/I) \quad (12)$$

where:

A = the area of the sample spot (varies according to the instrument)

V = volume of the air sampled in the averaging period

I_o = the average filter transmittance for averaging period, j

I = the average filter transmittance for averaging period, j + 1

The absorption coefficient is corrected for filter nonlinearity such that:

$$\sigma_{ap,\,corr} = \sigma_{ap} f(Tr) \quad (13)$$

In this equation, *f(Tr)* is a transfer function specific to filter loading of Pallflex filters. The particles are filtered out of the sample stream when it passes through the sample filter. The remaining stream (reference stream) is then passed through a reference filter (Figure 5). The reference filter, which is adjacent to the sample filter, measures the constancy of the LED light source (Figure 6).

The detection limit (95% confidence level) for S:N=1 is 0.9×10^{-6} m^{-1} (Anderson *et al.*, 1999, Bond *et al.*, 1999) when 1-min measurement averages are used. Further corrections to absorption values were made for differences in flow rate (as measured by the instrument and an electronic bubble flow meter) and spot size, instrumental variation, noise, and exaggerations of absorption due to scattering and

non-scattering influences (Bond *et al.*, 1999). The estimated instrumental uncertainty for the absorption values is 25% with 95% confidence.

Variations in RH have been shown to cause measurement inaccuracies in the PSAP (Anderson *et al.*, 2002), which operates under ambient conditions. For this reason, the commercial instrument was modified at the University of Miami. There, a heater and insulator were added to the optical bench portion of the PSAP so that the sample air would be dried before absorption measurements were made. In theory, this should have removed the uncertainty caused by variations in the RH, but introduced new uncertainty in converting dry absorption measurements to ambient conditions. However, the modification was ineffective; a RH dependence in the absorption measurements was still apparent after the modification was made.

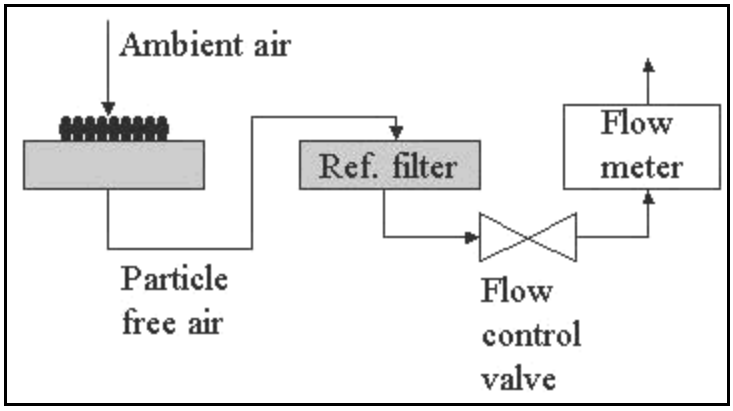

Figure 5. Flow diagram of the PSAP showing the sample filter (left) and reference filter (right).

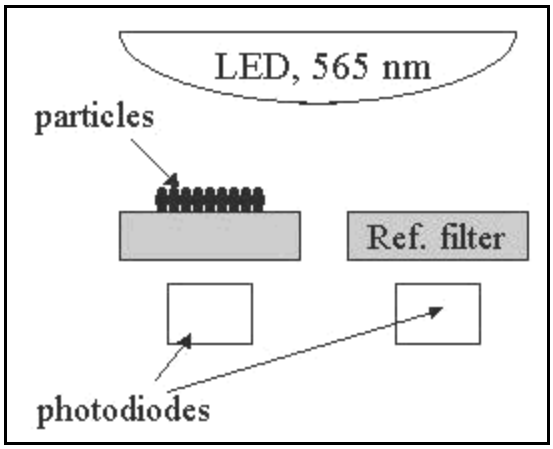

Figure 6. Schematic showing light absorption by the sample filter (left) and reference filter (right).

2.4.2. Nephelometer

Particle light scattering is quantified using an integrating nephelometer (TSI Model 3563) that measures the particle scattering coefficient (σ_{sp}) at 450, 550, and 700 nm after correcting for light scattered by the walls of the measurement chamber, the sample gas, and any electronic noise (Anderson *et al.*, 1996) (Figure 7). Total scattering is measured by integrating the scattered light over an angular range of 7 – 170°. Backscatter may also be measured through the use of the backscatter shutter, which adjusts the integrated range to 90 – 170°.

The instrument operates based on principles described by the Beer-Lambert Law:

$$\frac{I}{I_o} = e^{-\sigma_{ext}x} \tag{14}$$

where:

$$\sigma_{ext} = \sigma_{scat} + \sigma_{abs} \tag{15}$$

$$\sigma_{scat} = \sigma_{rg} + \sigma_{sp} \quad (16)$$

$$\sigma_{abs} = \sigma_{ag} + \sigma_{ap} \quad (17)$$

In these equations, σ_{rg} represents Rayleigh scattering by gases, σ_{sp} represents particle scattering, σ_{ag} represents absorption by gases, and σ_{ap} represents particle absorption. The instrument measures σ_{scat} and calculates σ_{sp} by also measuring and then subtracting σ_{rg} from σ_{scat}.

The nephelometer is calibrated with CO_2 and particle-free air, and corrected as necessary. At an averaging time of 5 minutes, detection limits for S:N=2 are: $\sigma_{sp450} = 0.44\times10^{-6}$ m^{-1}, $\sigma_{sp550} = 0.17\times10^{-6}$ m^{-1}, and $\sigma_{sp700} = 0.26\times10^{-6}$ m^{-1}. Corrections were made to the measurements to account for forward scattering angular truncation and nonlambertian distribution of illumination intensity within the nephelometer. A wavelength dependent correction factor (C_{ts}) was calculated assuming a linear relationship between C_{ts} and the scattering Ångström exponent (α), such that $C_{ts} = a + b\ \alpha$, where a and b are constants used for sub-μm particles and $\alpha_{450/550}$, $\alpha_{450/700}$, and $\alpha_{550/700}$ are used for 450, 550, and 700nm, respectively (Anderson and Ogren, 1998). The estimated instrumental uncertainty for values of total scattering is 10% with 95% confidence.

Measurements of light scattering were made after the sample airflow was dried from ambient conditions to an RH of < 20%. This necessitated the estimation of a growth factor, $F(RH)$, to account for hygroscopic particle growth. $F(RH)$ is the ratio of ambient light scattering, $\sigma_{sp}(\lambda, RH)$, to dry light scattering, $\sigma_{sp}(ref)$:

$$F(RH) = \frac{\sigma_{sp}(\lambda, RH)}{\sigma_{sp}(ref)} \tag{18}$$

$F(RH)$ was calculated using the following relationship between particle scattering coefficients at two values of RH:

$$\frac{\sigma_{sp}(\lambda, RH)}{\sigma_{sp}(ref)} = \left(\frac{1-RH_{amb}}{1-RH_{ref}}\right)^{-\gamma}, \tag{19}$$

where RH_{amb} is the ambient RH, RH_{ref} is the RH inside the nephelometer, and γ is an empirically derived constant. Parallel nephelometers were not used in this study, so γ had to be estimated. In polluted conditions, such as those on the east coast of the U.S., typical values of γ range from 0.20-0.50. For this research a value of 0.35 was chosen as per Remer *et al.* (1997) because of the similarities in both the sampling platforms and the regions of the studies.

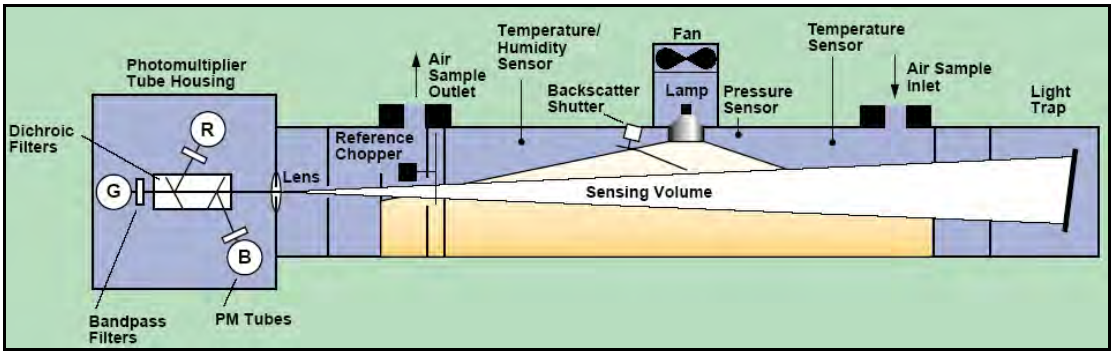

Figure 7. Schematic of the TSI model 3563 three-wavelength integrating nephelometer.

2.4.3. Particle Counts

Information on the total number of particles with optical diameters between 0.01 and 1.0 μm was obtained using a condensation particle counter (TSI Model 3007

CPC) (Figure 8). An internal pump draws the sample air stream through a saturator tube where isopropyl alcohol saturates the sample stream. The air stream then passes through a cooled condenser tube. The alcohol vapor becomes supersaturated and condenses onto any particles larger than 10 nm in diameter. The particles exit the condenser and are passed through a laser. The scattered light is collected and focused onto a photodetector where it is converted to an electrical signal and recorded as a particle count. The frequency of this instrument can be as great as particles s^{-1} and the concentration range is 0 – 100,000 particles cm^{-3}.

Number concentrations for particles with optical diameters between 0.30 and 1.0 μm (nDp) were collected using an optical particle counter (Met One Model 9012). The basic operation of this instrument is the same as the condensation particle counter, but there is no pre-optics condensation process. The internal pump draws the sample stream into the instrument where a laser-diode based optical sensor is used to convert scattered light to numbers of particles in particular size ranges. The pre-specified size ranges were 0.30-0.40 μm, 0.40-0.491 μm, 0.491-0.60 μm, 0.60-0.701 μm, 0.701-0.80 μm, and 0.80~1.0 μm.

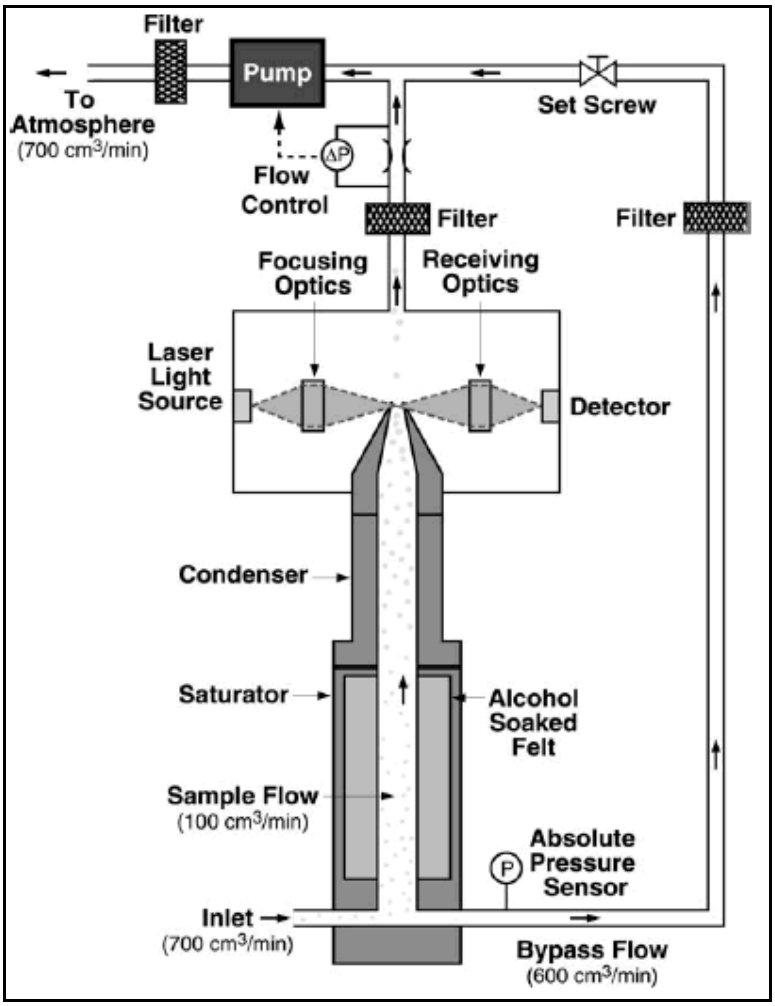

Figure 8. Schematic of the TSI Model 3007 Condensation particle counter.

Chapter 3: The Two-Reservoir Conceptual Model

3.1. Introduction

This chapter investigates the hypothesis that the chemistry and physics of multi-day haze and O_3 episodes over the Mid-Atlantic and northeastern U.S. may be treated as a simple two-reservoir model, comprising the LFT and PBL. Conclusions are based on aircraft measurements made during a constant altitude transect from Manchester, New Hampshire (42.9º N, 71.4º W) to College Park, Maryland (39.0º N, 76.9º W) on August 14, 2002, the last day of a multi-day haze and O_3 episode, and subsequent analyses of air parcel age, source apportionment, and boundary layer chemistry and dynamics.

The flight began in Manchester, NH at 21:45:02 UTC on August 14, 2002 and ended in College Park, MD at 00:30:23 UTC, just after sunset (Figure 9). An altitude of 800 m above mean sea level (MSL) was attained at 21:50:41 UTC and maintained until 00:20:00 UTC. Takeoff and landing are excluded from all time series plots for clarity.

Investigation of the aforementioned hypothesis begins with a brief meteorological analysis of the three-day episode, including new data on the impact of the LLJ on Mid-Atlantic and Northeast haze and O_3 episodes. A statistical analysis is used in order to garner information about source apportionment and air parcel age. Potential temperature (θ) is used as a proxy for altitude above ground level to investigate the chemical and physical signatures of air parcels as they vary with

height. The results described in this chapter are based on work published in the Journal of the Atmospheric Sciences (Taubman *et al*., 2004(a)).

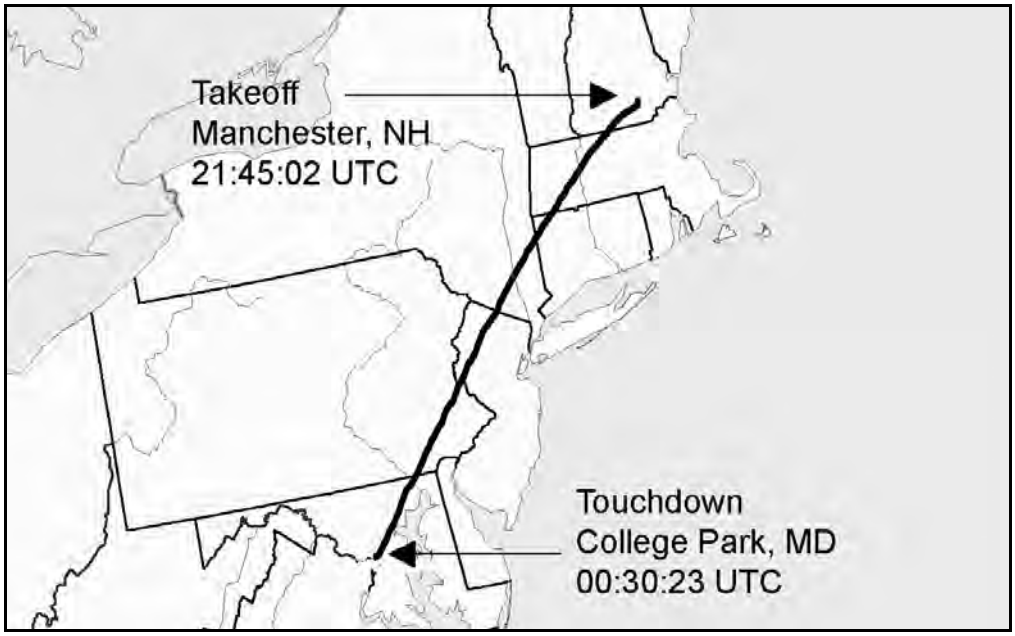

Figure 9. Flight track that began in Manchester, New Hampshire at 21:45:02 UTC and ended in College Park, Maryland at 00:30:23 UTC. Except for initial ascent and final descent, the altitude was constant at 800 m above mean sea level (Taubman *et al.*, 2004(a)).

3.2. Meteorology

On August 10, 2002, a slow moving upper level ridge positioned itself over the Great Lakes while a surface high-pressure system, lying below the region of convergence in the downwind upper level trough, blanketed the eastern seaboard. By August 12, at 850 mb, a trough over the Great Lakes, together with a ridge over the northeastern U.S., created an isobaric gradient normal to an axis lying along the U.S.-Canadian border. Surface analyses on August 12 at 00:00 UTC and 12:00 UTC show a parallel, albeit weaker, isobaric pattern (Figures 10, 11). This general pattern

persisted through the 14th and resulted in prevailing southwesterly winds over the Midwest and Northeast. Stagnant conditions predominated over the Mid-Atlantic throughout the episode. Figures 10 and 11 also indicate the presence of an APLT that augmented southerly flow up the urban corridor. Surface temperatures in the Mid-Atlantic and Northeast rose steadily between the 10th and the 14th.

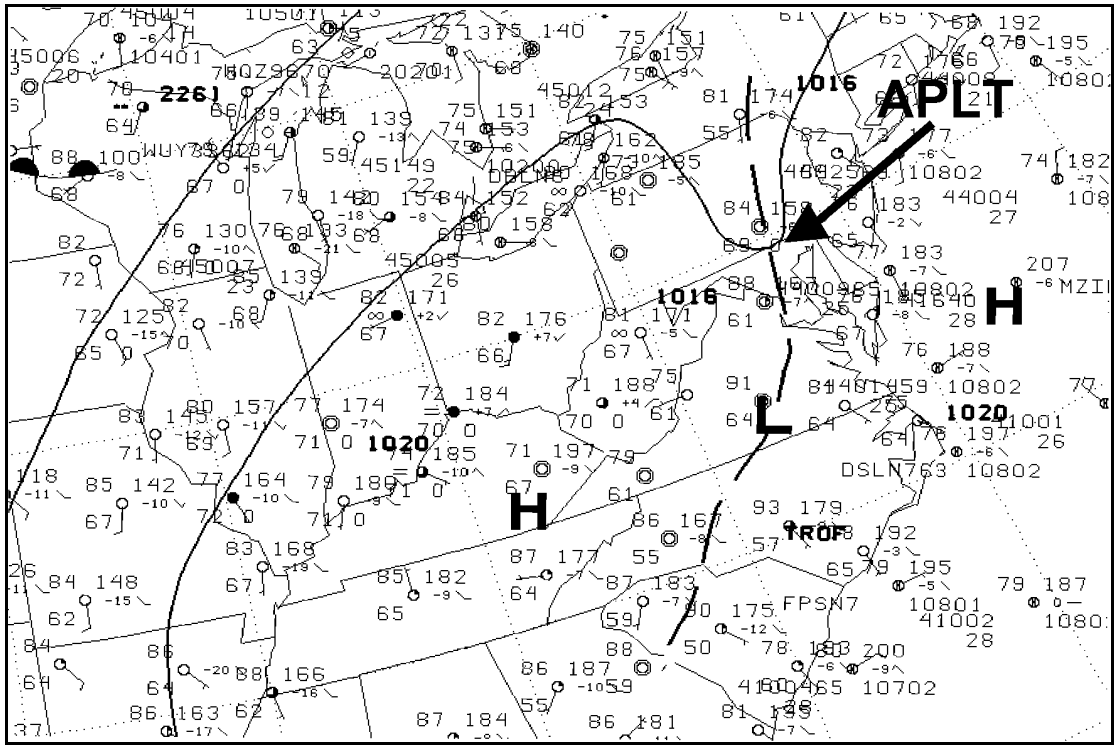

Figure 10. National Center for Environmental Prediction surface analysis for 00:00 UTC 12 August 2002 shows a weak isobaric gradient normal to the U.S.-Canadian border as well as the Appalachian Lee Trough (APLT) (Taubman *et al.*, 2004(a)).

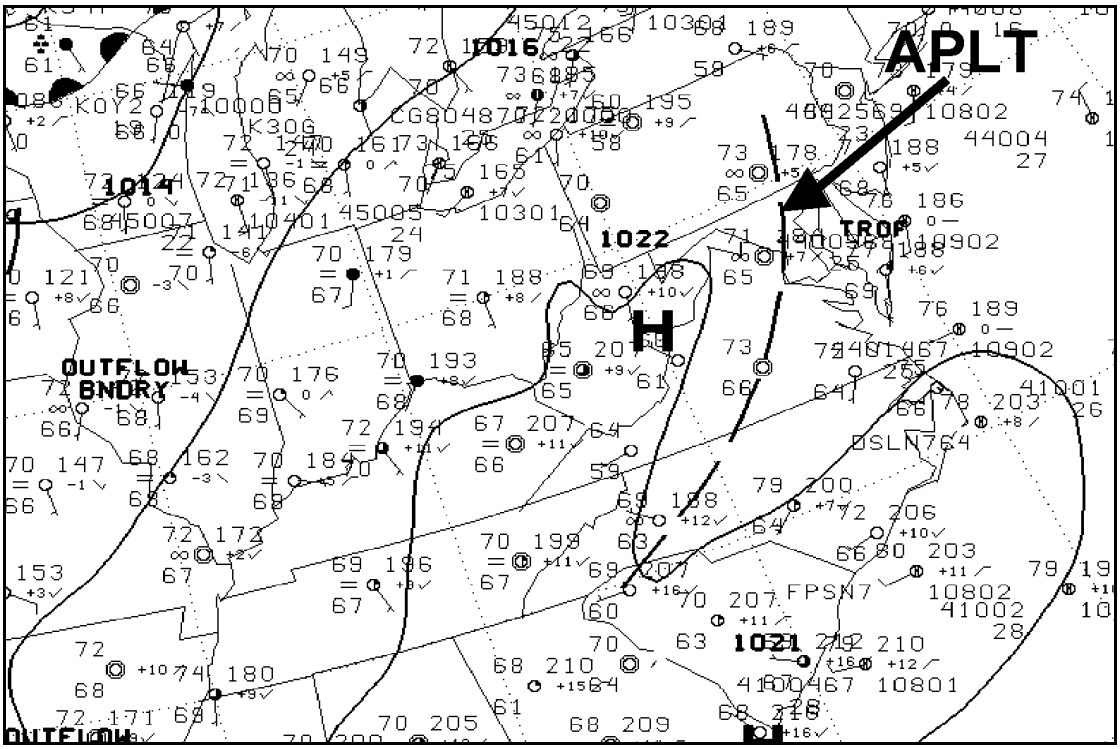

Figure 11. National Center for Environmental Prediction surface analysis for 12:00 UTC 12 August 2002 shows a weak isobaric gradient normal to the U.S.-Canadian border as well as the Appalachian Lee Trough (APLT) (Taubman *et al.*, 2004(a)).

A LLJ was observed every morning between ~01:00 UTC and 07:00 UTC at Ft. Meade, MD from the 11th through the 14th (Figure 12). The wind speed maximum appears to be between ~200 – 800 m AGL, indicating that the nocturnal stable boundary layer was quite shallow, with a maximum depth of only ~200 m AGL. The horizontal extent and magnitude of the jet on the 12th is shown in Figure 13, a time series plot of the Mid-Atlantic and Northeast generated using Rapid Update Cycle-2 (RUC-2) data (Benjamin *et al.*, 1998). The wind vectors in both the observed and analysis data show south-southwesterly flow during times of the jet maximum. At the indicated wind speeds and duration, an air parcel in the LLJ could travel >200 km up

the eastern seaboard overnight to mix with the local air under the jet once the nocturnal inversion eroded and vertical mixing ensued during the daytime.

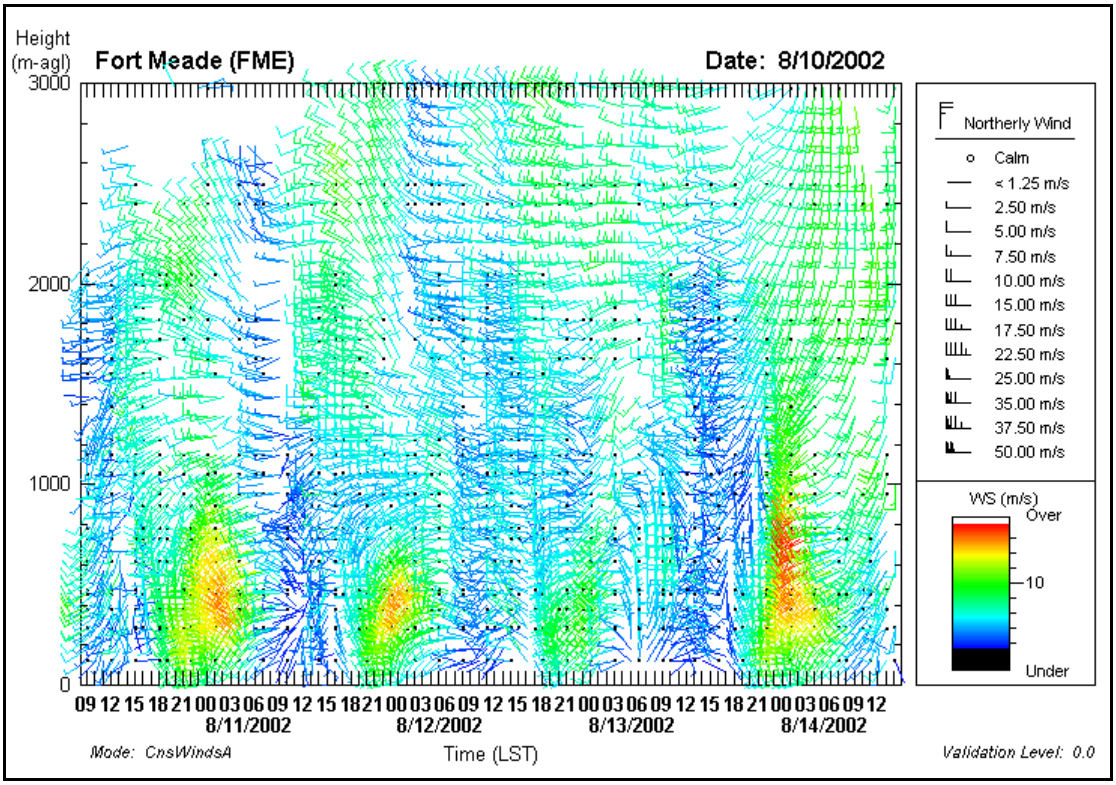

Figure 12. Wind profiler data (30 min average) from Ft. Meade, Maryland from 09:00 LST 10 August to 15:00 LST 14 August 2002 showing south-southwesterly flow in the jet with a maximum between 200 – 800 m AGL (Taubman *et al.*, 2004(a)).

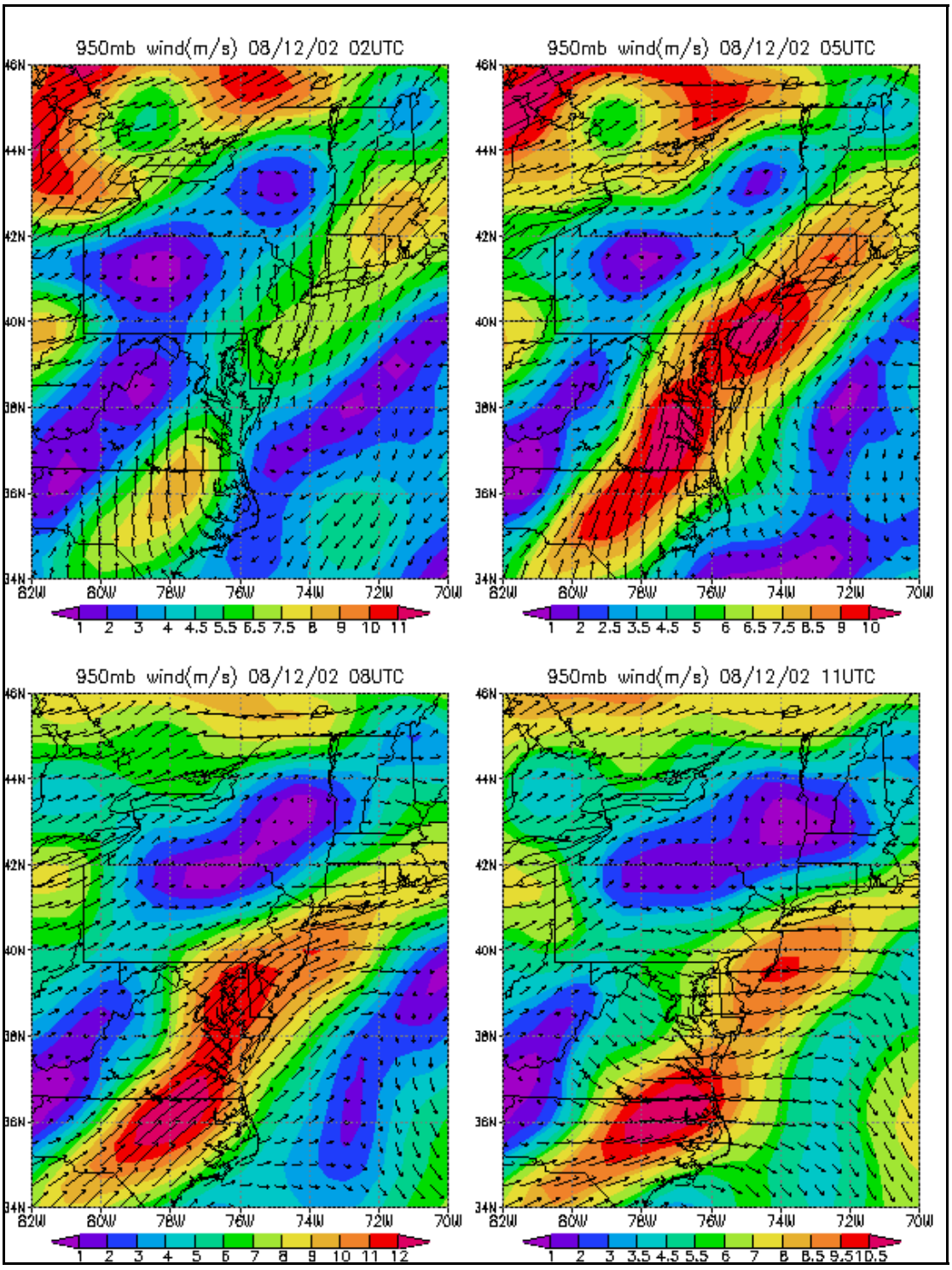

Figure 13. A time series plot of the 950 mb (the approximate altitude of the LLJ) wind speed and direction over the Mid-Atlantic and Northeast from 02:00 to 11:00 UTC 12 August 2002 generated using RUC-2 data (Taubman *et al.*, 2004(a)).

3.3. Observations and Analyses

3.3.1. Trajectory Analysis

A backward trajectory analysis of the entire flight track was performed utilizing the NOAA ARL HYbrid Single-Particle Lagrangian Integrated Trajectory (HYSPLIT) model (Version 4) (Draxler and Rolph, 2003) and Eta Data Assimilation System (EDAS) meteorological fields (with a 3 h temporal resolution). The 72 h model vertical velocity backward trajectories ending at 500, 1000, and 1500 m above ground level (AGL) came primarily from the south-southwest and intersected many of the urban centers in the Mid-Atlantic and Northeastern U.S (e.g., Figure 14). There was little difference in the source regions or transport direction of the parcels analyzed. However, a significant difference was seen in the vertical motions of the air parcels that culminated in southern upstate New York near the Hudson River Valley (Figure 14). A transition from downward vertical motion to upward vertical motion in this area appears to have occurred at ~23:00 UTC.

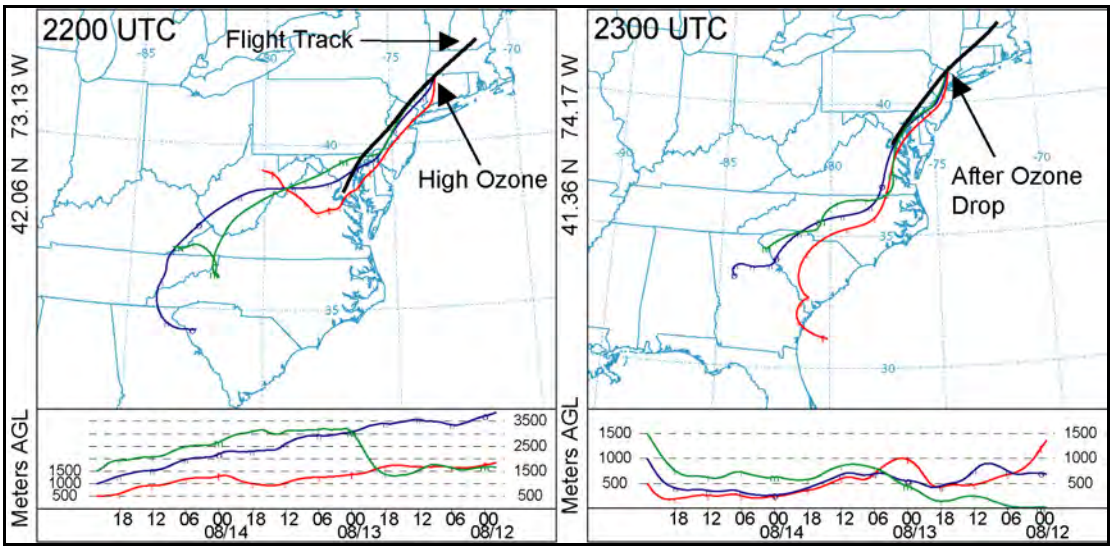

Figure 14. Sample NOAA ARL EDAS model vertical velocity 72 hour backward trajectories for air parcels at 500, 1000, and 1500 m AGL on 14 August 2002 at 42.06° N, 73.13° W, 22:00 UTC (left), where the highest O_3 was measured, and 41.36° N, 74.17° W, 23:00 UTC (right) after a steep decline in O_3 concentration. There is no noticeable distinction in transport direction between the trajectories, but there is a manifest conversion from subsidence (left) to upward vertical motion (right) (Taubman *et al.*, 2004(a)).

3.3.2. Trace Gases

Correlations among the chemical and physical properties observed during the flight allow for insight into source apportionment, photochemical age, and the dynamical structure of the lower atmosphere. To estimate the number of independent air parcels (i.e., the number of degrees of freedom associated with each time series plot), autocorrelation tests were performed that correlated measured variables with themselves over successive time intervals. The threshold for autocorrelation (non-randomness between the two points) was $r > 0.50$ (95% confidence). Any value below this threshold indicated that there was no statistically significant relationship between the points after this time lag, thereby suggesting the presence of a discrete air

parcel. The number of independent air parcels was then calculated from dividing the sampling period by the autocorrelated time lag. Approximately 10 discrete air parcels were positively identified in this manner (the exact value varied slightly according to the variable tested). The statistical significance of each correlation was determined according to the number of degrees of freedom (discrete air parcels) and reported along with the correlation coefficients (Table 1).

Table 1. Correlation coefficients, r, for trace gases, meteorological and dynamic parameters, and particle properties. The number in parenthesis is the p value (the probability that the statistical relationship occurred by random chance) for the regression. If two sets of correlation coefficients and p values are given, the top one is for the regression until 22:56:00 UTC and the bottom is for the period between 22:56:10 and 23:10:00 UTC (Taubman *et al.*, 2004(a)).

	O_3 (ppbv)	CO (ppbv)	σ_{sp450} (m^{-1})	σ_{ap} (Mm^{-1})	$\alpha_{450/700}$
CO (ppbv)	0.70(0.08) -0.84(0.02)				
SO_2 (ppbv)	0.70(0.08) -0.67(0.10)	0.71(0.02)			
σ_{sp450} (m^{-1})	0.90(0.00)				
σ_{sp550} (m^{-1})	0.89(0.00)			0.79(0.03) 0.10(0.87)	
σ_{sp700} (m^{-1})	0.88(0.00)				
nDp (dm^{-3}) 0.30- 0.40 μm	0.76(0.01)			0.50(0.25) -0.45(0.31)	
nDp (dm^{-3}) 0.40-0.49 μm	0.90(0.00)		0.96(0.00)		
TPC (cm^{-3})	0.67(0.10) -0.63(0.13)			0.79(0.00)	
σ_{ap} (Mm^{-1})	0.68(0.09) -0.73(0.16)				
RH (%)					0.82(0.00)
θ (K)	0.56(0.09)				-0.86(0.00)
BC (μg m^{-3})		0.57(0.09)			
ω_b	-0.58(0.17) 0.77(0.04)				

CO and SO_2 were positively correlated throughout the flight and early positive correlations were found between O_3 and CO and O_3 and SO_2 (Table 1, Figure 15), suggestive of a combination of mobile and point source emissions. The initial correlation between O_3 and CO had a regression slope ($\Delta O_3/\Delta CO$) of 0.31 ± 0.04. This value agrees with previous examples of polluted, North American, boundary layer air (Chin *et al.*, 1994, Daum *et al.*, 1996, Dickerson *et al*., 1995). CO decreased at ~22:40:00 UTC and no longer showed a strong positive correlation with O_3 (Table 1,

Figure 15), whereas SO_2 remained positively correlated with O_3 until O_3 declined at ~22:56:00 UTC (Table 1, Figure 15). This suggests a shift from mixed mobile and point source influences to point source dominated ones.

When the O_3 concentration decreased at ~22:56:00 UTC near the Hudson River Valley, CO and SO_2 concentrations increased and became anti-correlated with O_3 (Table 1, Figure 15). This transition corresponds to the shift in the backward trajectories from downward to upward vertical motion. The increase in CO and SO_2 suggests the influence of mixed sources again, while the sudden decrease in O_3 could be explained by NO_x titration in the middle of a combination mobile and point source plume.

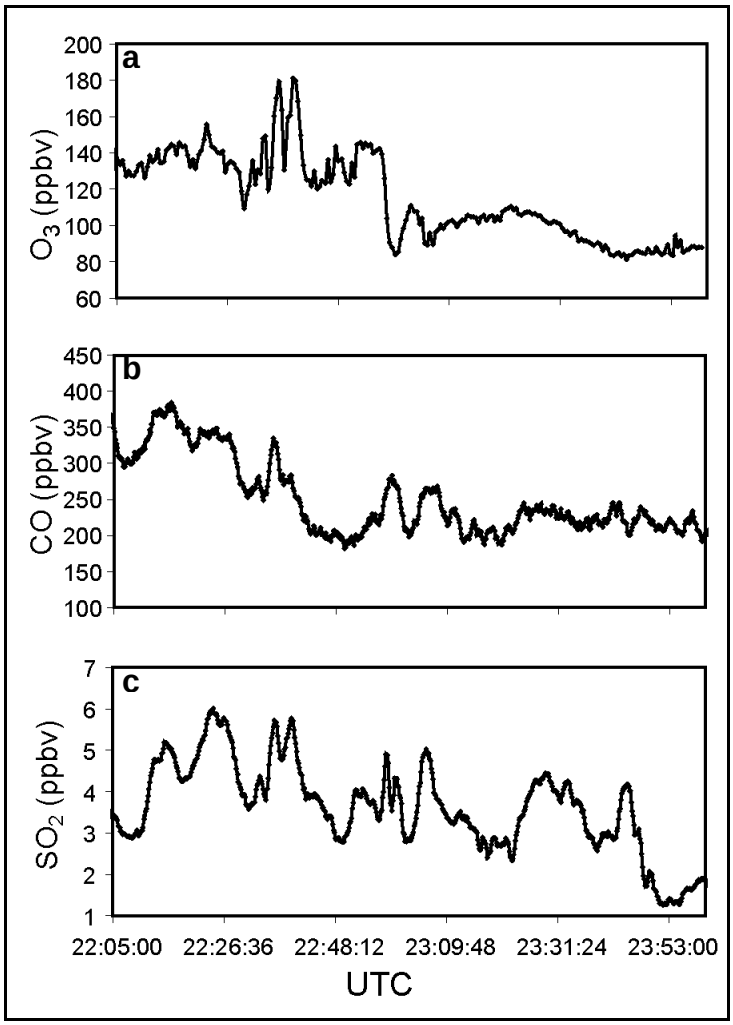

Figure 15. 10 s ozone mixing ratios (a) and running 1 min. mean CO (b) and SO2 (c) mixing ratios measured during the flight (Taubman *et al.*, 2004(a)).

3.3.3. Aerosols

O_3 and nDp (especially particles with diameters between 0.40-0.491 μm), as well as O_3 and σ_{sp}, were positively correlated throughout the entire flight (Table 1, Figures 15, 16). O_3 and total particle counts between 0.01 and 1.0 μm (TPC) along with O_3 and σ_{ap} were initially positively correlated (Table 1, Figures 15, 16). However, these profiles became anti-correlated at ~22:56:00 UTC, when the O_3

concentration rapidly declined (Table 1, Figures 15, 16). Thus, O_3 remained correlated with particles between ~0.30 and 1 μm in diameter, but when the O_3, nDp, and σ_{sp} profiles decreased at ~22:56:00 UTC, there was a significant increase in the number of absorptive particles < 0.30 μm in diameter. This is evidence of primary BC particles emitted from a local, mobile source that had insufficient time to mix with the sulfate-dominated haze of the region. When nDp, σ_{sp} , and σ_{ap} were correlated (before 22:56:00 UTC), greater absorption occurred despite the presence of fewer total sub-micrometer particles. Assuming that the air parcels contained internally mixed BC and sulfate particles at that time, this suggests that the internal mixture was more absorptive than the external one.

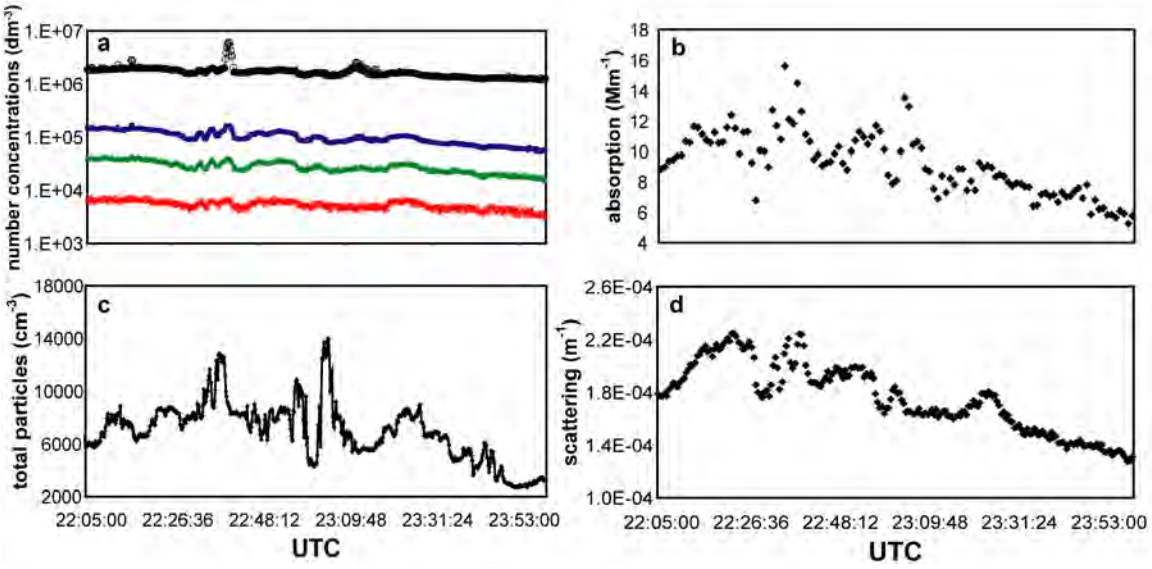

Figure 16. Particle number concentrations measured during the flight (a) for the following size ranges: 0.30-0.40 mm (black), 0.40-0.491 mm (blue), 0.491-0.60 (green), and 0.60-0.701 (red). σ_{ap} corrected to 550 nm (b); total sub-micrometer particle count (c); and σ_{sp} at 550 nm (d) all measured during the flight (Taubman *et al.*, 2004(a)).

The BC concentration was calculated from σ_{ap} assuming BC is the primary absorber in atmospheric aerosols. Despite apparent differences in degrees of mixing, an average mass absorption efficiency of 7 m^2 g^{-1} was assumed in accordance with prior, regional surface and aircraft studies (Novakov *et al.*, 1997; Chen *et al.*, 2001). A regression analysis of BC and CO was performed and a correlation (r = 0.57) was found between the two (Table 1), with a slope of $\Delta BC/\Delta CO = 0.0034 \pm 0.0007$. Chen e*t al.* (2001) found a similar value (0.0034 ± 0.0013) for the annual average at Fort Meade, MD. They scaled this number by the North American CO emissions value to compute a BC emission rate of 0.32 Tg yr^{-1}. The results of this flight support that estimate.

The aerosols measured during the flight were largely scattering. The mean value for ω_b at 550 nm over the entire flight was 0.95 ± 0.01 (see Figure 17), in agreement with previous aircraft observations over the east coast of the U.S. (e.g., Hartley *et al.*, 2000; Hegg *et al.*, 1997) and AERONET observations at NASA Goddard Space Flight Center between 1993 and 2000 (ω_b at 440 and 670 nm equal to 0.98 ± 0.02 and 0.97 ± 0.02, respectively) (Dubovik *et al.*, 2001). Nevertheless, the variations in ω_b were driven by the absorption in this study since σ_{ap} varied by as much as a factor of three, while σ_{sp} varied by less than a factor of two.

Before ~22:56:00 UTC, ω_b was anti-correlated to O_3, while after this time, O_3 and ω_b positively correlated (Table 1). Thus, initially, absorption was highest when the O_3 mixing ratio was highest. Total scattering also peaked at this time, but absorption was relatively stronger, leading to a smaller ω_b. After ~22:56:00 UTC, the greatest absorption was observed with the least O_3. There was a large influx of small,

absorptive particles during this time, and since σ_{sp} dropped off with O_3, ω_0 decreased accordingly.

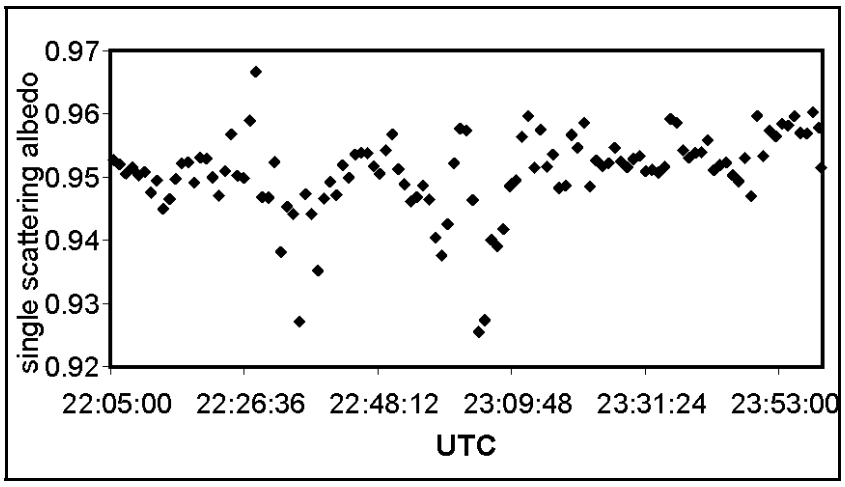

Figure 17. Aerosol single scattering albedo at 550 nm, calculated from flight data. The mean value for the flight was 0.95+0.01 (Taubman *et al.*, 2004(a)).

3.3.4. Thermodynamic Analysis

The flight under investigation was conducted at a constant altitude above mean sea level. Thus, the elevation above the surface increased or decreased according to the local terrain. Because the dynamic structure of the lower atmosphere tends to follow the surface features, the flight continually traversed through different dynamic altitudes. To investigate the dynamical structure of the lower atmosphere and the associated chemistry and physics, the potential temperature (θ) was calculated from the flight measurements of temperature and pressure. Figure 18 shows an inverse relationship between θ, calculated along a portion of the flight path, and the surface elevation, generated using a digital elevation model. This is the

expected result in a stable lower atmosphere, where θ is at a minimum and relatively constant in the daytime mixed layer, with a steep, positive gradient in the interfacial layer, and a smaller positive gradient in the LFT. Thus, as the surface elevation decreases, flight elevation above ground level increases, as does θ if the altitude is at or above the interfacial layer.

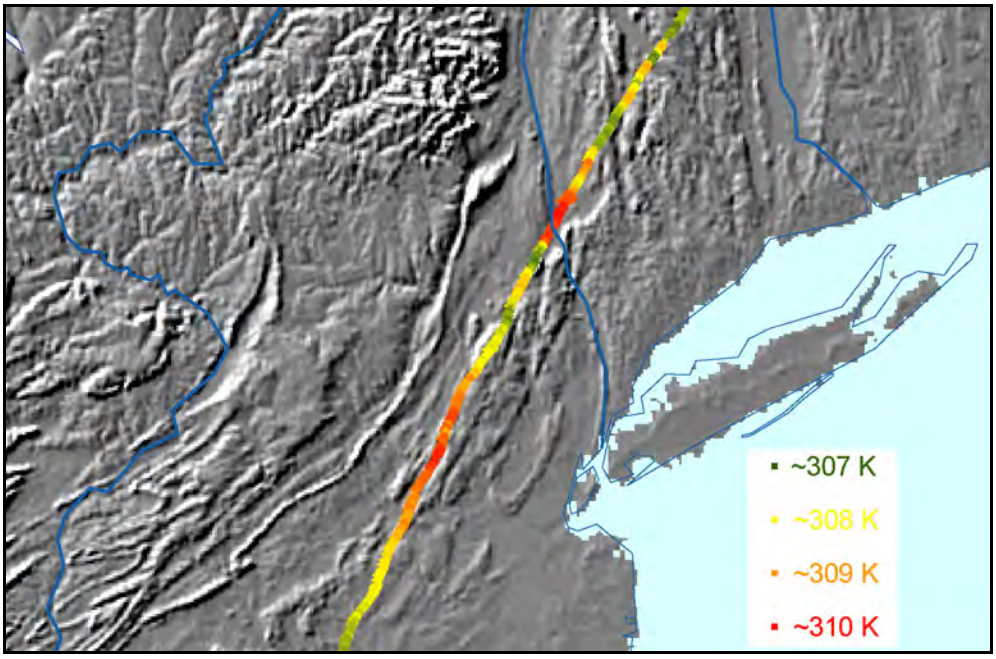

Figure 18. Potential temperature (θ) plotted with color-coded values (provided in the key) along a portion of the flight track. These values are overlaid on a shaded relief digital elevation model of the northeastern U.S. Darker shading signifies lower elevations and lighter shading, higher elevations. The blue lines indicate rivers. The one in the middle is the Hudson River. This region shows the most obvious inverse relationship between θ and surface elevation (Taubman *et al.*, 2004(a)).

It follows, then, that the chemical and physical nature of the atmosphere should vary with altitude, particularly between the PBL and the LFT. To investigate this hypothesis, statistical analyses with θ and representative chemical and physical values were performed. Ozone and θ were positively correlated throughout the flight

(Figure 19a, Table 1). Because θ is constant and at a minimum in the mixed layer, any increase would indicate a transition into the interfacial layer and beyond into the LFT. Likewise, O_3 concentrations should be fairly constant in the mixed layer, and because of the positive correlation with θ, any increases indicate more O_3 in the LFT relative to the PBL. Exceptions to this rule result from the spatially and temporally dynamic nature of the atmosphere and the platform, but the consistency of the correlation supports the argument.

Throughout the flight, α was positively correlated with RH and anti-correlated with θ (Figures 19b,c, Table 1). Within an individual air parcel, α and RH would be expected to anti-correlate because of the covariance of particle size and RH. Thus, the correlation between RH and α was due to the observation of distinct air parcels at discrete altitudes above the surface that contained particles of different sizes and unique optical properties. It can be reasonably assumed that particles in the LFT, where RH was lower and θ was higher, were more aged than those in the PBL. The photochemical processing of these particles would, therefore, be enhanced because of longer lifetimes as well as increased actinic flux in the LFT. This would explain why, despite the lower RH, the particles in the LFT were larger than those in the PBL. Conversely, particles in the PBL, where RH was higher and θ was lower, were relatively fresher and less subject to photochemical processing and hence, were smaller.

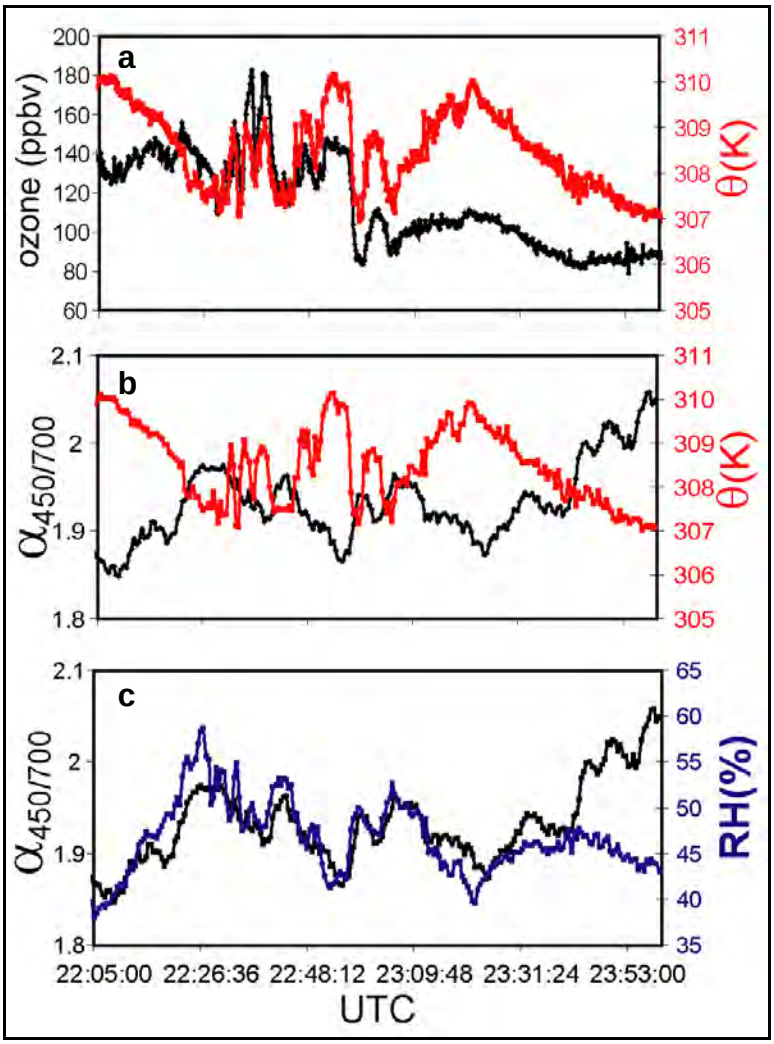

Figure 19. 10 s O_3 mixing ratios (black) recorded during the flight and potential temperature, θ, (red) derived from flight data (a); θ (red) and scattering Ångström exponent, α, (black) calculated from the ratio of total particle scattering, 450/700 (in nm), measured during the flight (b); relative humidity, RH, (blue) and α (black) calculated from flight data (c) (Taubman *et al.*, 2004(a)).

3.4. Discussion

The thermodynamic analysis indicates that the observed chemical and optical properties varied according to altitude, specifically whether the observations were made in the PBL or the LFT. Drier, more aged air parcels were observed in the LFT

where the protracted lower atmospheric stability allowed them to persist for multiple days without being subjected to vertical mixing, dilution, and deposition. These air parcels were more photochemically processed and contained higher concentrations of O_3 and larger particles that scattered and absorbed visible light efficiently. The relatively fresh parcels in the PBL had less O_3 and smaller particles that scattered light less efficiently, but were highly absorptive. Variations in the concentrations of CO and SO_2 seemed to vary less according to altitude *per se*. Rather, the source region and photochemical age of the air parcels in which they resided played more important roles.

The change in vertical winds between the trajectories shown in Figure 4 could be the result of upsloping winds on the windward side of the western ridge of the Hudson River Valley. The associated shift from positive to negative correlations between several species of interest is likely due to observations of the difference between air with more regional characteristics above the LFT to more local air in the PBL. As mentioned before, the absolute accuracy of such a conclusion is questionable because of the spatially and temporally dynamic nature of the study. The fact that the study was performed in the late afternoon, however, reduces the incidence of thermally driven convective eddies. Turbulent eddies would add to the variations in θ, according to the associated heat flux, but would be on a much smaller scale than θ fluctuations due to terrain characteristics.

The current foci of numerical model simulations of severe air pollution episodes are on the composition of the lower atmosphere, including especially the structure of the inversion layer, and the chemical and physical processes that drive the

events. This study provides a characterization of the chemistry and physics that occur during multi-day episodes in the Mid-Atlantic and Northeast that should prove useful in these simulations. The chemical and physical structure of the lower atmosphere could be conceptualized as a simple, two-reservoir model, comprising the PBL and LFT (Figure 20). Of particular importance is the realization that the LFT does not contain clean, background air during these episodes. This not only has direct consequences on model simulations of these episodes, but may have indirect ones as well. Photochemical mechanisms are accelerated in the LFT, but these mechanisms are also operating on air parcels with different chemical and physical characteristics than those in the PBL. Therefore, modeled photochemical mechanisms that work in the PBL would not be appropriate for the LFT. Numerical model simulations of multi-day haze and ozone episodes over the Mid-Atlantic and Northeast therefore must account for the unique chemistry and physics of the two reservoirs. However, future aircraft studies that specifically investigate the small-scale dynamical processes that drive the mixing between the two reservoirs are still necessary. These studies will allow for the more accurate simulation of transfer across the boundary separating the PBL and LFT.

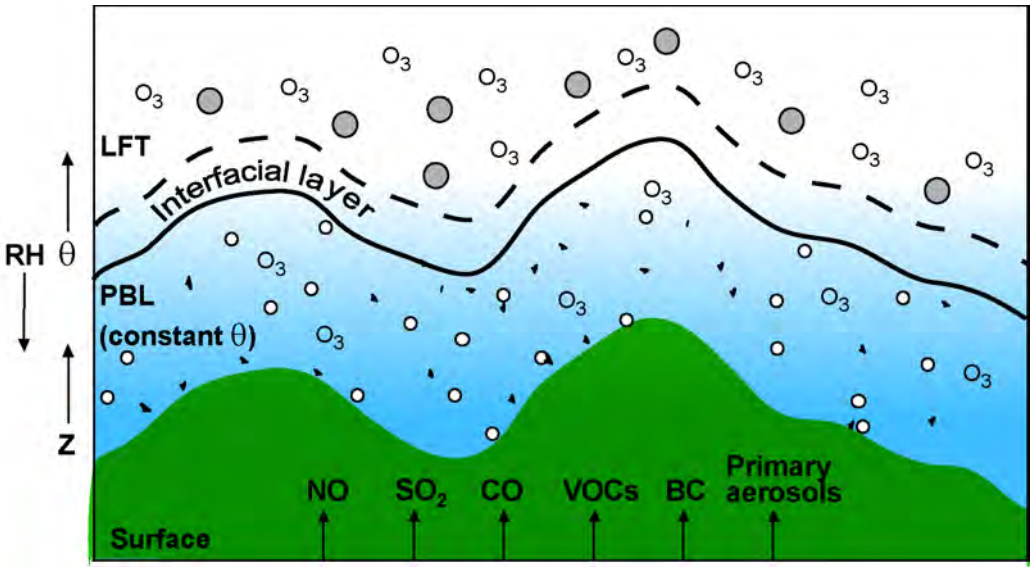

Figure 20. A schematic of the two-reservoir system during the daytime. The vertical and horizontal axes represent altitude and distance, respectively. The shape of the inversion layer that delineates the PBL from the LFT mimics the variations in surface elevation (green). The inversion layer is shown here with an interfacial layer of finite thickness. The upward arrows with the chemical species along the surface represent the injection of emissions into the PBL. The blue to white gradient represents greater RH in the PBL relative to the LFT. Potential temperature (θ) is shown as constant in the mixed layer and increasing with altitude from the interfacial layer. The small white circles and black flecks in the PBL represent sulfate particles and BC particles, respectively. They are shown as an external mixture in the PBL. The larger grey circles in the LFT represent internally mixed sulfate and BC particles. The O_3 represents molecules of ozone. There are more particles in the PBL than the LFT, but more molecules of ozone in the LFT (Taubman *et al.*, 2004(a)).

The observations reported herein may have broader implications as well. Absorbing aerosols heat the atmosphere and alter atmospheric stability (e.g., Park *et al.*, 2001; Menon *et al.*, 2002). During a stagnation event such as this one, when stable layers of air pollution have discrete aerosol optical properties, preexisting atmospheric stability may be augmented if more absorptive aerosol layers are juxtaposed above more scattering layers. This could in turn create a positive feedback loop, inhibiting vertical mixing and dilution and ultimately delaying the

termination of the episode. Such a distribution of aerosol optical properties could also have a significant impact on the solar radiation budget and therefore the accuracy of climate modeling studies.

A specific question regarding absorbing aerosols is the nature and extent of mixing between BC and sulfate particles. Although the aerosols encountered during this study primarily scattered solar radiation, there were manifest fluctuations in their absorptive nature, reflected in the calculated values of ω_b. Two noticeable deviations from the mostly invariant mean value of ω_b were during the periods of highest observed O_3 concentrations (between ~22:30:00 and ~22:40:00 UTC) and lowest observed O_3 concentrations (from ~22:56:00 to ~23:10:00 UTC). During these times, ω_b dropped to a minimum value of ~0.92, with a mean value of 0.94. Given the analytical uncertainty, a value of 0.94 is not statistically different from the overall mean, but does indicate greater relative absorption at these times. During the period of highest O_3, the drop in ω_b may be attributed to two factors: a greater degree of internal mixing between BC and sulfate particles due to the age and photochemical processing of the air parcels in question, and a larger influx of absorptive BC particles due to transport up the eastern seaboard urban corridor. The influence of the APLT and LLJ during this episode redirected the westerly synoptic flow in a more southerly direction during the day and evening, respectively. As a result, air that had been transported from the industrialized Midwest then mixed with the urban plumes of the eastern seaboard.

Another question of great scientific interest involves the mechanism and time scale for particle formation. The strong correlation between O_3 and nDp may provide

evidence for the link between O_3 and secondary organic aerosol formation through the oxidation of hydrocarbons (Andreae and Crutzen, 1997). Greater atmospheric oxidizing potential through increased concentrations of OH and H_2O_2 concomitantly with O_3 would also lead to the production of SO_4^{2-} from SO_2 and thereby secondary aerosol formation. Further explanation for the correlation may lie in the oxidation of SO_2 by dissolved O_3 (Hoffman and Calvert, 1985), but this is unlikely since there were few clouds during the episode and the acidity of Mid-Atlantic and Northeastern aerosols would inhibit such a reaction. The correlation between O_3 and σ_{sp} is likely a secondary result of the O_3 and nDp correlation since the particles with diameters commensurate to visible wavelengths scatter that light most efficiently. Although, highly scattering particles, such as the ones encountered in this study, also increase the flux of diffuse UV radiation and may, therefore, increase the photochemical production of O_3 as well (Dickerson *et al*., 1997), especially in the LFT.

3.5. Summary

The salient discovery of this study is that the chemistry and physics of severe, multi-day haze and ozone episodes over the Mid-Atlantic and northeastern U.S. may be simply and accurately represented by two reservoirs, comprising the PBL and LFT. These conclusions are drawn from observations during a constant altitude flight from Manchester, New Hampshire to College Park, Maryland on August 14, 2002, the last day of a multi-day haze and ozone episode. Most precursor species are injected into the PBL, where surface deposition may occur. When these precursors escape into the LFT, however, deposition is no longer a factor, and chemical lifetimes

are protracted. Photochemical processes are also accelerated in the LFT and air parcels age photochemically with greater rapidity. As a result, more O_3 and larger particles that scattered visible light more efficiently were observed in the LFT than in the PBL. An accurate numerical model simulation of photochemical smog processes over the Mid-Atlantic and Northeast should incorporate the existence of these two reservoirs, and simulate or at least parameterize the role of mixing between them in multi-day smog events.

Chapter 4: Smoke over Haze

4.1. Introduction

In early July of 2002, a pall of smoke, the result of forest fires in Quebec, blanketed the Mid-Atlantic and northeastern U.S. A cutoff upper level low-pressure system centered over Maine, together with a high amplitude ridge to the west, caused long range funneling of northern continental air to the Mid-Atlantic region beginning on July 5, 2002 and continuing through the morning of the 8th (Figure 21). This meridional flow is normally associated with cool, dry, and relatively clean air. However, smoke from forest fires burning in northern Quebec traveled south over 1000 km to cover the Mid-Atlantic and northeastern U.S. Diffluence downstream of the upper level trough caused the plume to fan out over the region. Figure 22 is a Moderate Resolution Imaging Spectroradiometer (MODIS) visible image of the plume and several active fire detections (red dots) on the 7th that shows how the diffluent flow caused such a regional impact.

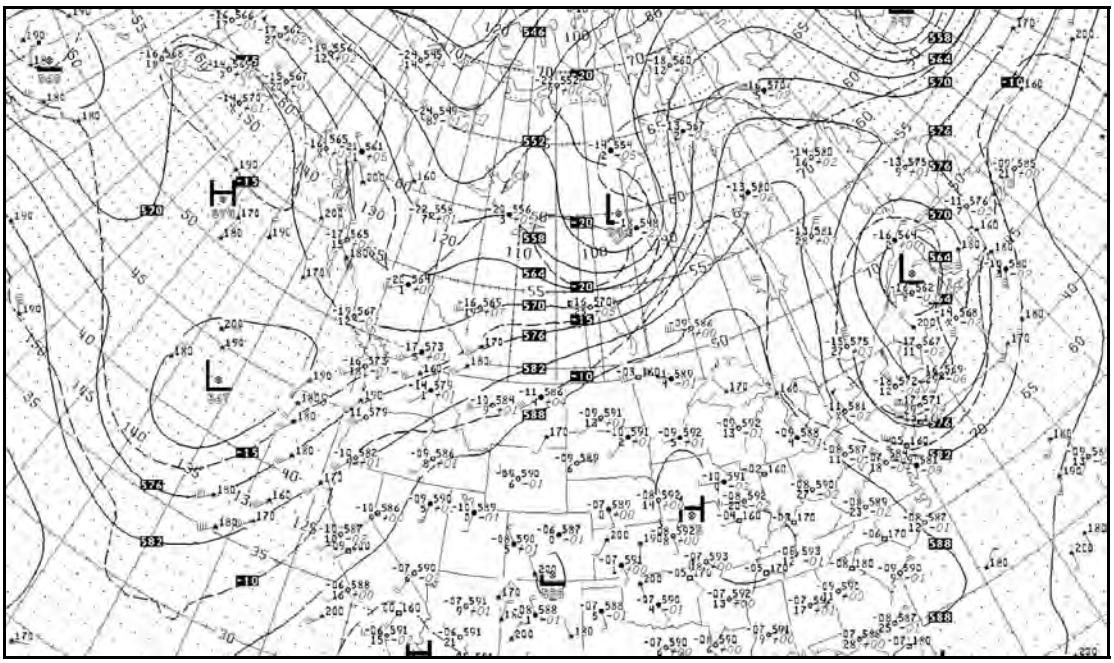

Figure 21. National Center for Environmental Prediction analysis of geopotential height fields at 500 mb for 12:00 UTC 6 July 2002 (adapted from Taubman *et al.*, 2004(b)).

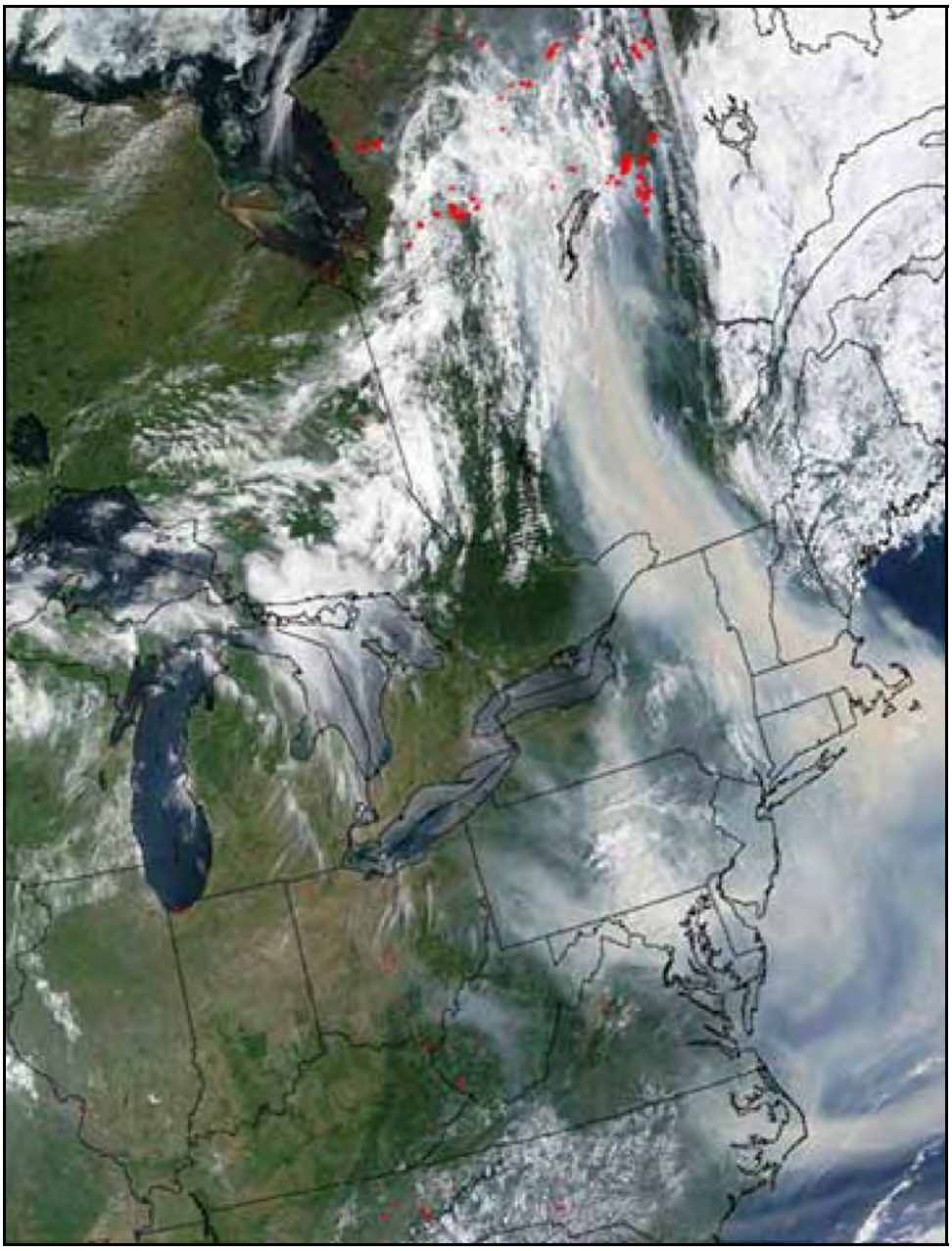

Figure 22. Moderate Resolution Imaging Spectroradiometer (MODIS) visible image from the Terra satellite on 7 July 2002. Active fire detections are shown as red dots east of James Bay. Diffluence downstream of the upper level trough caused the smoke plume to fan out over the eastern U.S. (Taubman *et al.*, 2004(b)).

On July 8, the upper level trough filled and migrated east, resulting in a wind shift to the west. This began to push the plume out over the Atlantic Ocean. By the

9th the majority of the plume was advected offshore. For a more complete analysis of the meteorology associated with this event, go to http://www.atmos.umd.edu/~forecaster/summary_2002.htm

Two research flights, one in the morning and one in the afternoon, were conducted on July 8, 2002 (Figure 23). The dark black circles on the figure indicate ascending or descending fixed location vertical survey spirals performed at ~100 vertical m min^{-1} between ~5 m AGL to ~3 km MSL. The first spiral was made over Luray, Virginia (38.70ºN, 78.48ºW) beginning at ~13:00 UTC. After a short transect to the northeast, the second spiral was performed over Winchester, Virginia (39.15ºN, 78.15ºW) commencing at ~14:00 UTC. The final spiral of the morning, over Cumberland, Maryland (39.60ºN, 78.70ºW) was initiated at ~15:00 UTC. The afternoon spirals were performed over Harford County (Harford), Maryland (39.56ºN, 76.18ºW) and Easton, Maryland (38.80ºN, 76.06ºW) beginning at ~19:00 and 20:00 UTC, respectively. Evidence of the smoke plume was strongest over Luray, Winchester, Harford, and Easton. The spiral over Cumberland showed little evidence of the smoke plume.

Results of aircraft measurements of trace gas and particle concentrations as well as particle optical properties on July 8, 2002 over Maryland and Virginia are reported herein. The AOD, aerosol direct radiative forcing, and heating rates associated with the smoke plume are calculated. This chapter also investigates the impacts that absorptive heating within the plume had on atmospheric stability. The results described in this chapter are based on work published in the Journal of

Geophysical Research (Taubman *et al*., 2004(b)) (reproduced by permission of American Geophysical Union).

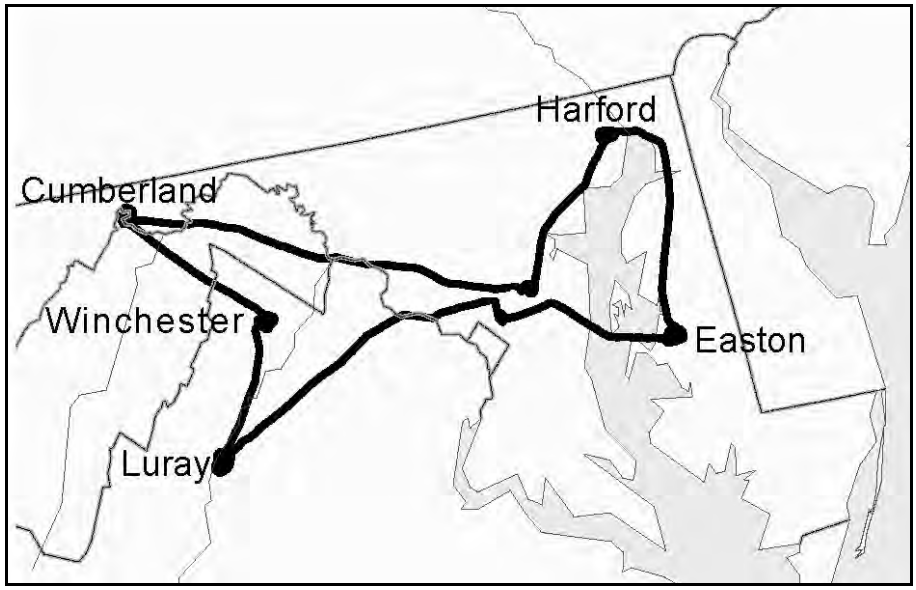

Figure 23. Flight track for 8 July 2002, consisting of a morning and an afternoon flight. Luray, VA (38.70ºN, 78.48ºW), Winchester, VA (39.15ºN, 78.15ºW), and Cumberland, MD (39.60ºN, 78.70ºW) (in that order chronologically) were the locations of the morning flight spirals. Harford, MD (39.56ºN, 76.18ºW) and Easton, MD (38.80ºN, 76.06ºW) (in that order chronologically) were the locations of the afternoon flight spirals (Taubman *et al.*, 2004(b)).

4.2. Results and Discussion

Vertical profiles of the temperature and RH measured over the five locations are given in Figure 24. The three morning profiles (Luray, Winchester, and Cumberland) show a nocturnal radiance inversion around 500 m that erodes by the time of the later profiles. A persistent inversion around 2 km is evident in all of the profiles, delineating the upper limits of the PBL and the dichotomy between the two regimes observed in this study. This particular study investigates the hypothesis that

absorption of solar radiation within the layer between ~2 and 3 km led to the protraction of this temperature inversion, initiated by morning subsidence, through the afternoon.

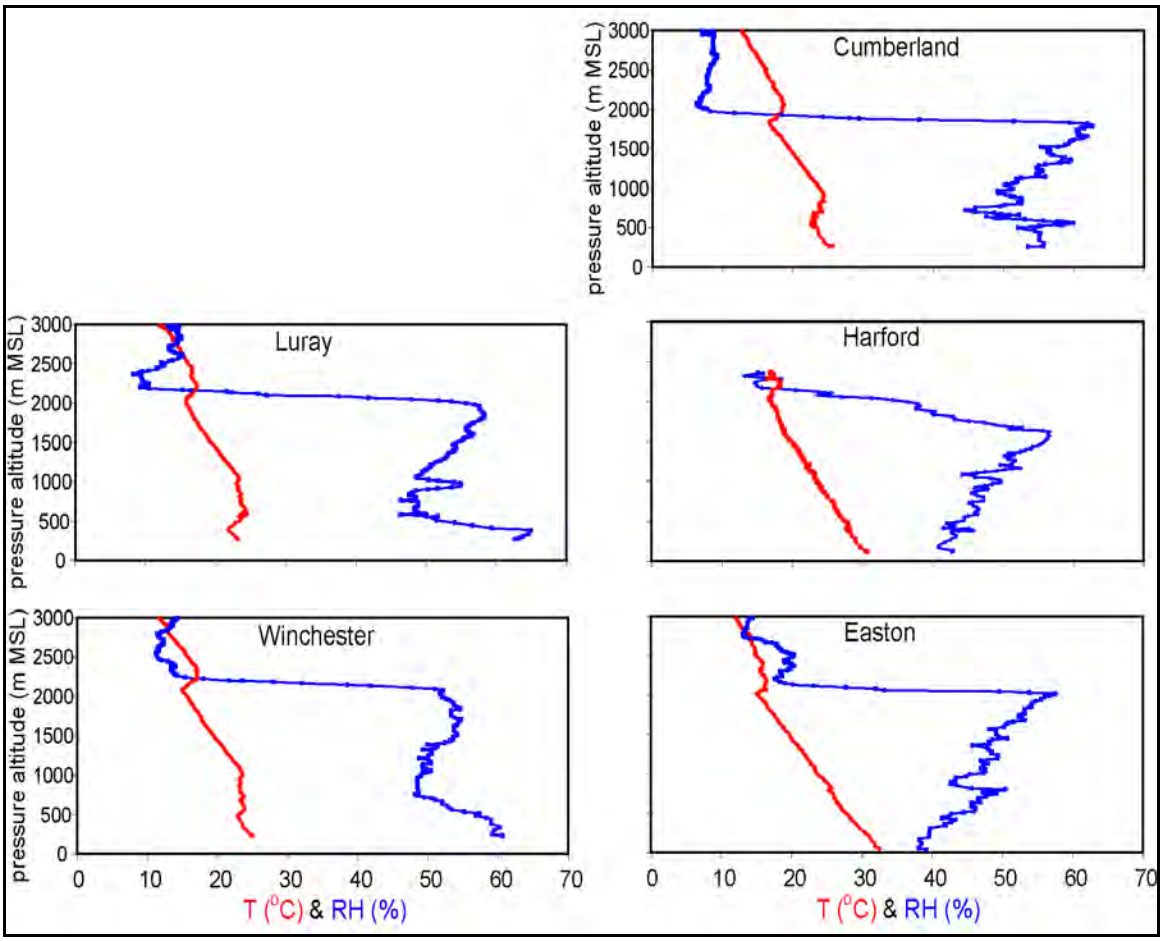

Figure 24. Measured temperature (red) and relative humidity (blue) over Luray, VA, Winchester, VA, Cumberland, MD, Harford, MD, and Easton, MD (adapted from Taubman *et al.*, 2004(b)).

4.2.1. Trajectory Analysis

A backward trajectory analysis utilizing the NOAA Air Resources Laboratory (ARL) HYbrid Single-Particle Lagrangian Integrated Trajectory (HYSPLIT) model

(Version 4) (Draxler and Rolph, 2003) and Eta Data Assimilation System (EDAS) meteorological fields was performed at each of the five locales addressed in this study (Figure 25). The 72-hour model vertical velocity backward trajectories were commenced at altitudes of 1000, 2000, and 3000 m MSL to shed light on observations made within the PBL and the observed free tropospheric pall. The upper-level trajectories all show advection from the north and northwest, indicating that the observations between 2 and 3 km MSL were of the Canadian forest fire smoke. The meteorological and trajectory analyses suggest that air parcels were lifted near the fires and then transported in the lower free troposphere. The lower level trajectories also show northerly advection, however the observations made in this study suggest a vertical separation between PBL air and that in the free troposphere.

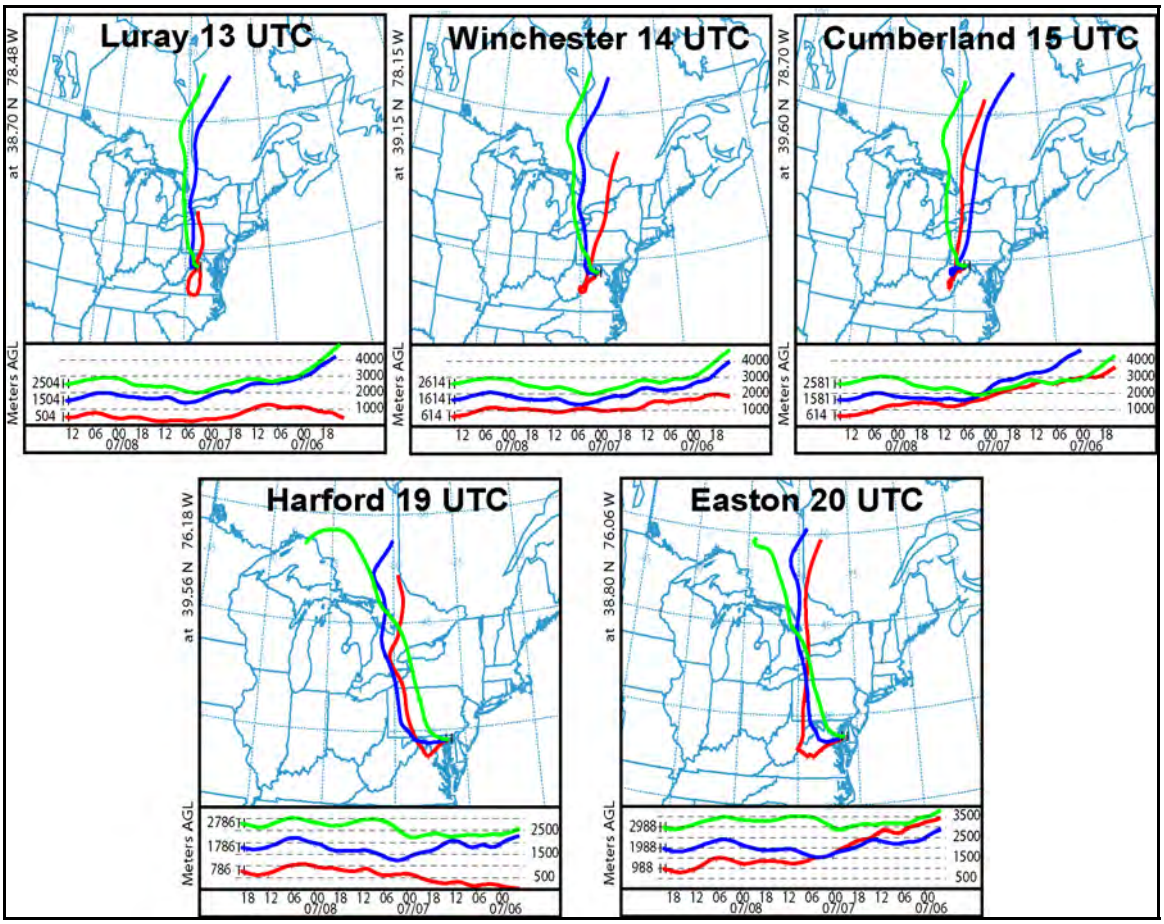

Figure 25. NOAA HYSPLIT 4 ARL EDAS model vertical velocity 72-hour backward trajectories for air parcels at 1000, 2000, and 3000 m MSL on 8 July 2002 over Luray, VA, Winchester, VA, Cumberland, MD, Harford, MD, and Easton, MD (Taubman *et al.*, 2004(b)).

4.2.2. Trace Gases

The mixing ratios for O_3, CO, and SO_2 measured over the five locations are provided in Figures 26, 27, and 28, respectively. Luray, Winchester, Harford, and Easton displayed similar trends: high O_3 and CO mixing ratios between 2 and 3 km with little SO_2 observed within this altitude range. Ozone mixing ratios exceeded 160 ppbv at this altitude and the mixing ratios in the layer aloft consistently exceeded those in the PBL by 40 – 60 ppbv. Carbon monoxide mixing ratios approached 1600

ppbv in the layer aloft, and were upwards of 1000 ppbv greater than those in the PBL. These observations are indicative of a photochemically aged smoke plume. Large amounts of SO_2 were observed near the surface in the three later profiles, including Cumberland. This enhanced SO_2, routinely observed during regular air pollution survey flights conducted in this area (Ryan *et al.*, 1998), could be the result of westerly transport from a point source, observed in the later profiles because of the wind shift from the north to the west.

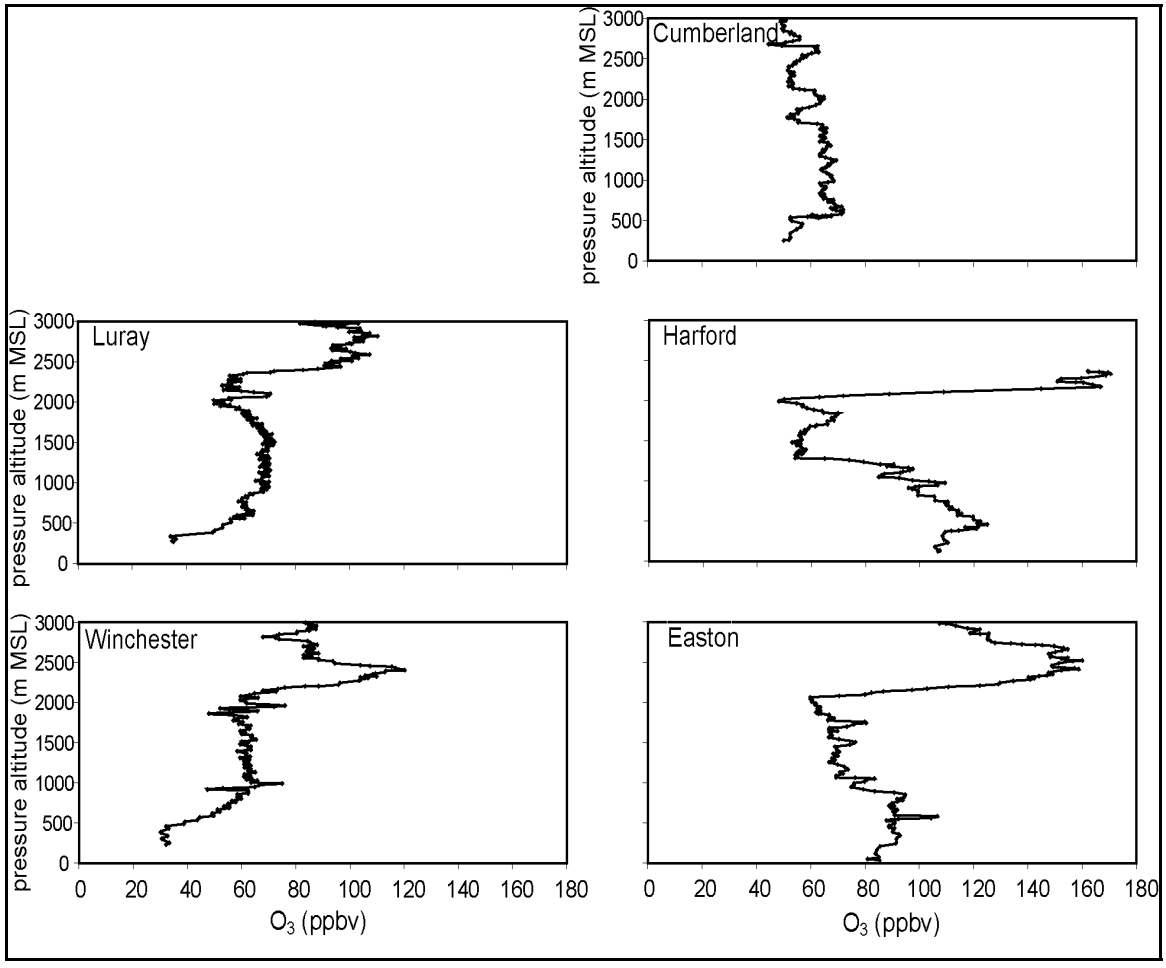

Figure 26. 10-s ozone measured during the vertical survey spirals over Luray, VA, Winchester, VA, Cumberland, MD, Harford, MD, and Easton, MD (adapted from Taubman *et al.*, 2004(b)).

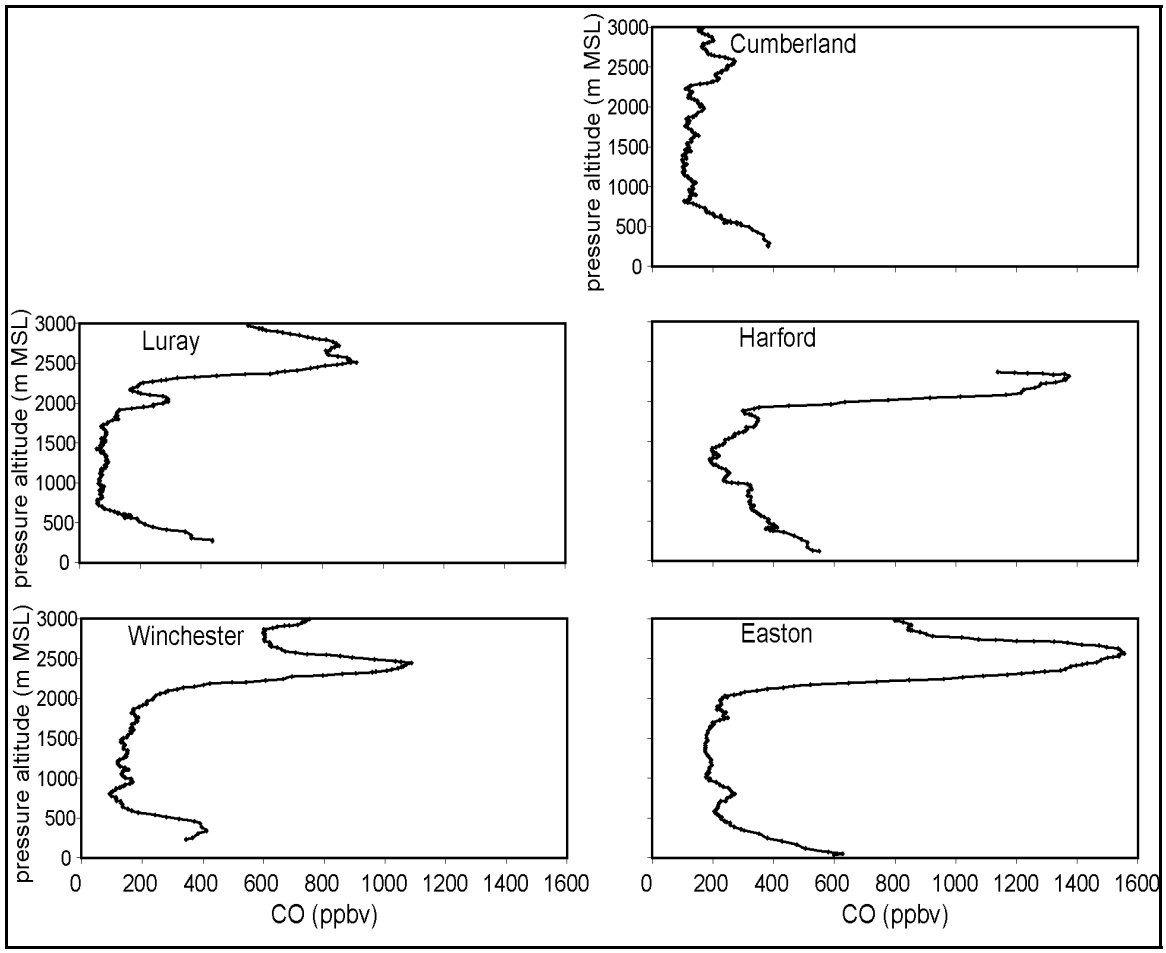

Figure 27. Running 1-min mean CO measured during the vertical survey spirals over Luray, VA, Winchester, VA, Cumberland, MD, Harford, MD, and Easton, MD (adapted from Taubman *et al.*, 2004(b)).

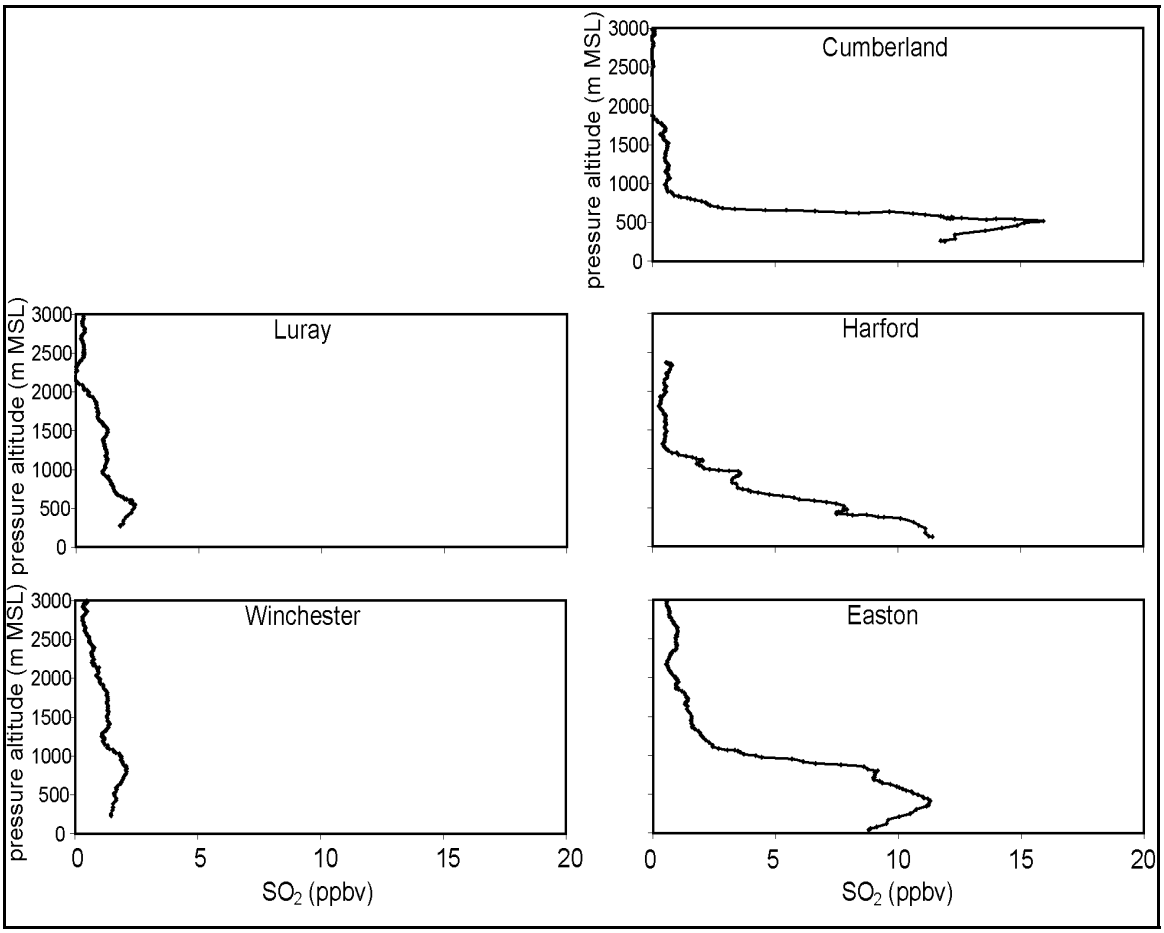

Figure 28. Running 1-min mean SO_2 measured during the vertical survey spirals over Luray, VA, Winchester, VA, Cumberland, MD, Harford, MD, and Easton, MD (adapted from Taubman *et al.*, 2004(b)).

4.2.3. Aerosol Properties

Particle light scattering at 450, 550, and 700 nm, absorption at 550 nm, and particle concentrations in the six accumulation mode size bins over the five locations are provided in Figures 29, 30, and 31, respectively. The absorption values were extrapolated from 565 to 550 nm, based on the assumption that $\sigma_{ap} \propto 1/\lambda$ (Bodhaine, 1995), to calculate the AOD and single-scattering albedo at this wavelength. Methods used to extrapolate measured optical properties across the solar spectrum

will be addressed later in this section. Total scattering at 450, 550, and even at 700 nm over Harford and Easton exceeded 10^{-3} m^{-1} between 2 and 3 km. Particle absorption at 550 nm approached 100 Mm^{-1} in this vertical layer over each location and even surpassed this value at Easton. The greatest numbers of particles were observed in the 0.30 – 0.60 μm diameter range. Particles larger than this may not have been collected efficiently due to inlet line losses. There were at least as many particles in the 0.40 – 0.491 μm range as in the smallest size bin observed over each location (except Cumberland and Harford) at ~2.5 km, roughly the vertical center of the smoke plume. At Luray and Winchester, particles with diameters between 0.491 – 0.60 μm were also as numerous as those in the smallest size bin. These observations are rare in a typical plume of anthropogenic origin. In such cases, the particles with diameters between 0.30 – 0.40 μm are far more numerous than the larger particles, as can be seen in the PBL in the morning profiles.

A large increase in the number of particles between 0.30 – 0.40 μm was seen at roughly 500 m above Cumberland. This increase corresponded to an increase in SO_2 at the same altitude over Cumberland. Despite the fact that similar increases in SO_2 were measured at low altitudes over Harford and Easton, no increase in the number of 0.30 – 0.40 μm particles was observed. The optically thick layer of smoke covering Harford and Easton may have inhibited the photochemical oxidation of SO_2 to SO_4^{2-} and thereby secondary aerosol formation. Over Cumberland, where there was less solar attenuation, gas to particle conversion would not have been hindered. This may have resulted in the observed increase in small particles. Unfortunately, there was no speciation data to confirm this supposition.

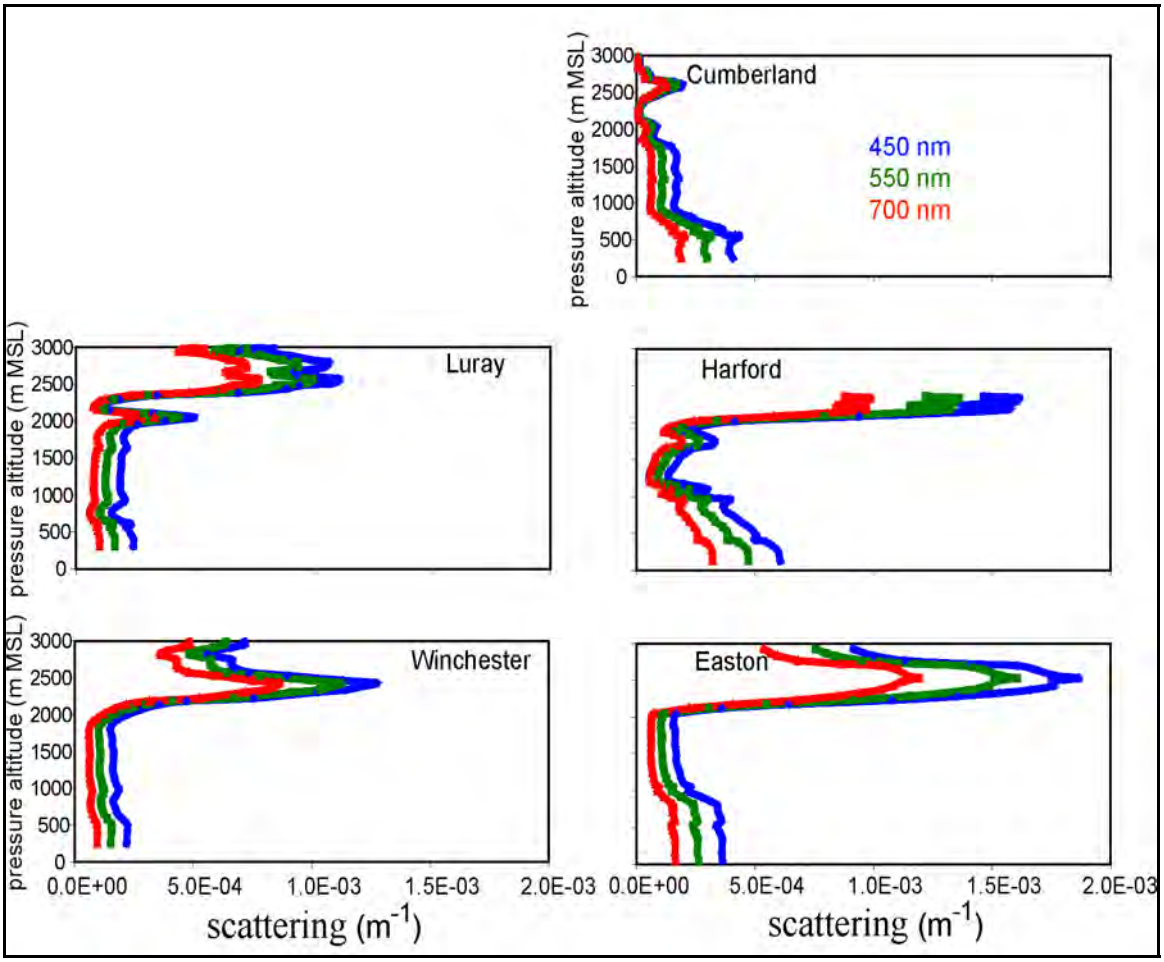

Figure 29. σ_{sp} **at 450 nm (blue), 550 nm (green), and 700 nm (red) measured during the vertical survey spirals over Luray, VA, Winchester, VA, Cumberland, MD, Harford, MD, and Easton, MD (adapted from Taubman *et al.*, 2004(b)).**

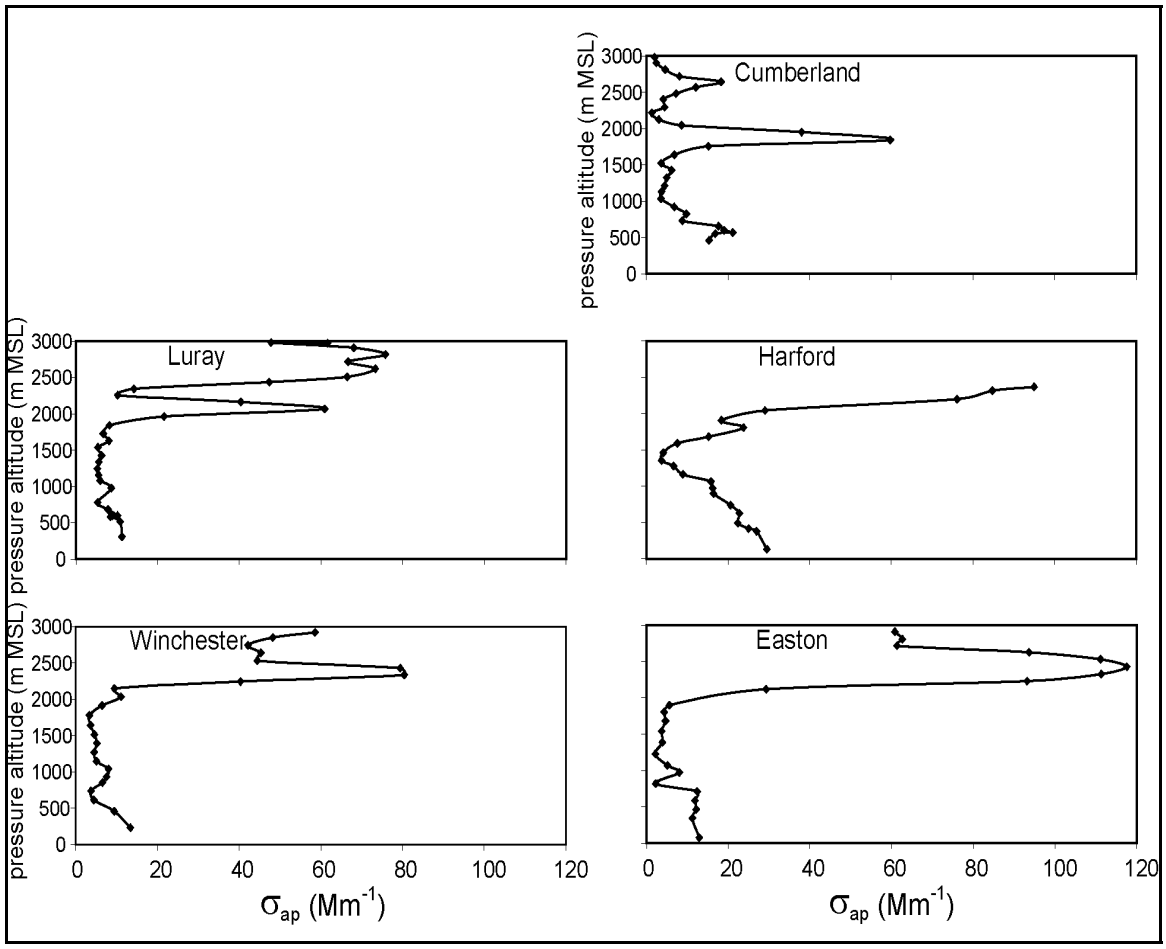

Figure 30. σ_{ap} at 550 nm, extrapolated from σ_{ap} at 565 nm that was measured during the vertical survey spirals over Luray, VA, Winchester, VA, Cumberland, MD, Harford, MD, and Easton, MD (adapted from Taubman *et al.*, 2004(b)).

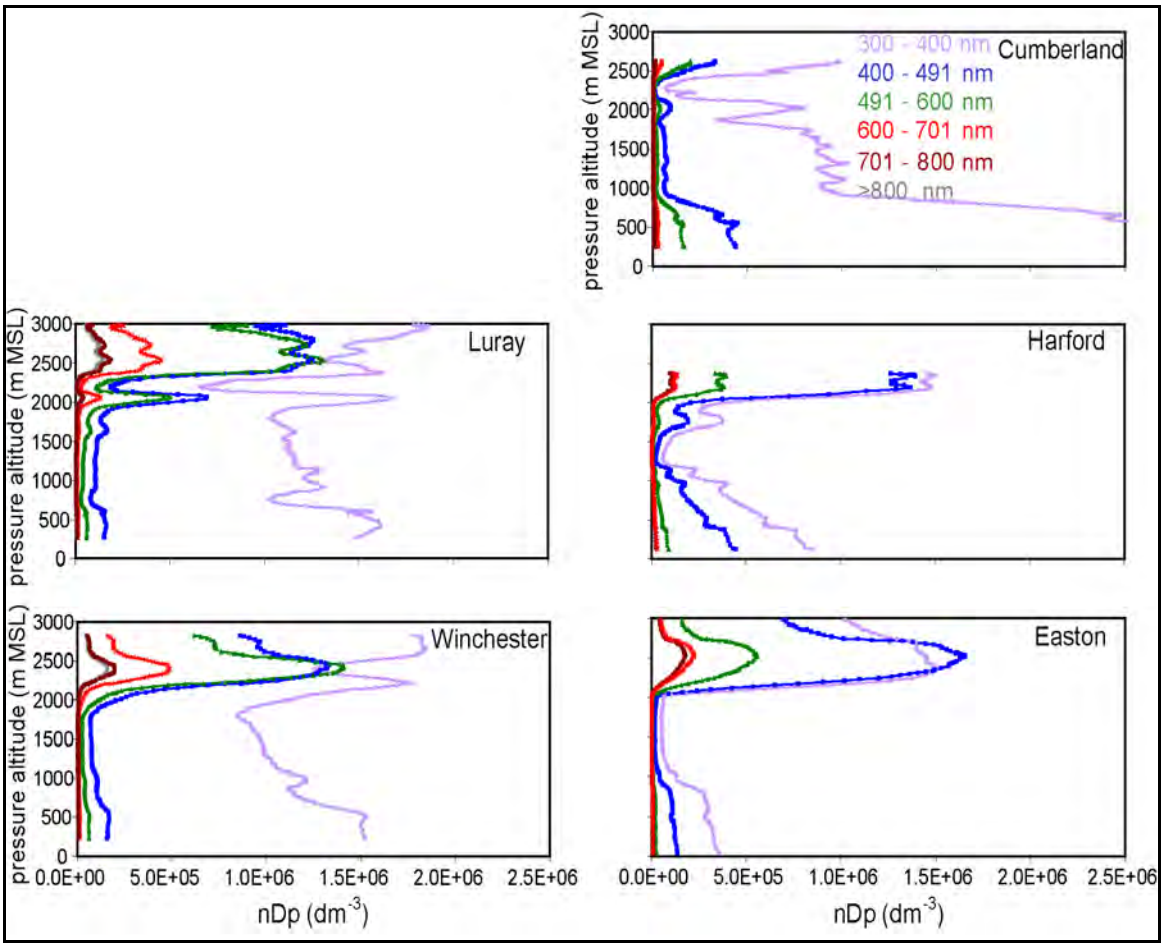

Figure 31. Number of particles in six discrete particle diameter size bins measured during the vertical survey spirals over Luray, VA, Winchester, VA, Cumberland, MD, Harford, MD, and Easton, MD: 0.30-0.40 μm (violet), 0.40-0.491 μm (blue), 0.491-0.60 μm (green), 0.60-0.701 (red), 0.701-0.80 (maroon), 0.80~1.0 μm (gray) (adapted from Taubman *et al.*, 2004(b)).

Calculations of α were made using the following ratios of the total scattering at 450, 550, and 700 nm: 450/550, 450/700, and 550/700. Figure 32 shows $\alpha_{450/700}$ over the five locations. Table 1 gives the average values of α for the smoke layer and the PBL at each location. The average values of α in the PBL are larger than those in the smoke layer, indicating smaller particles in the PBL and larger ones aloft. This is consistent with relatively fresh anthropogenic particles lying below an aged

smoke plume that had traveled over 1000 km (Reid *et al.*, 1998(a)). Even the Cumberland profile, despite showing a weak overall smoke signature, is consistent with this trend.

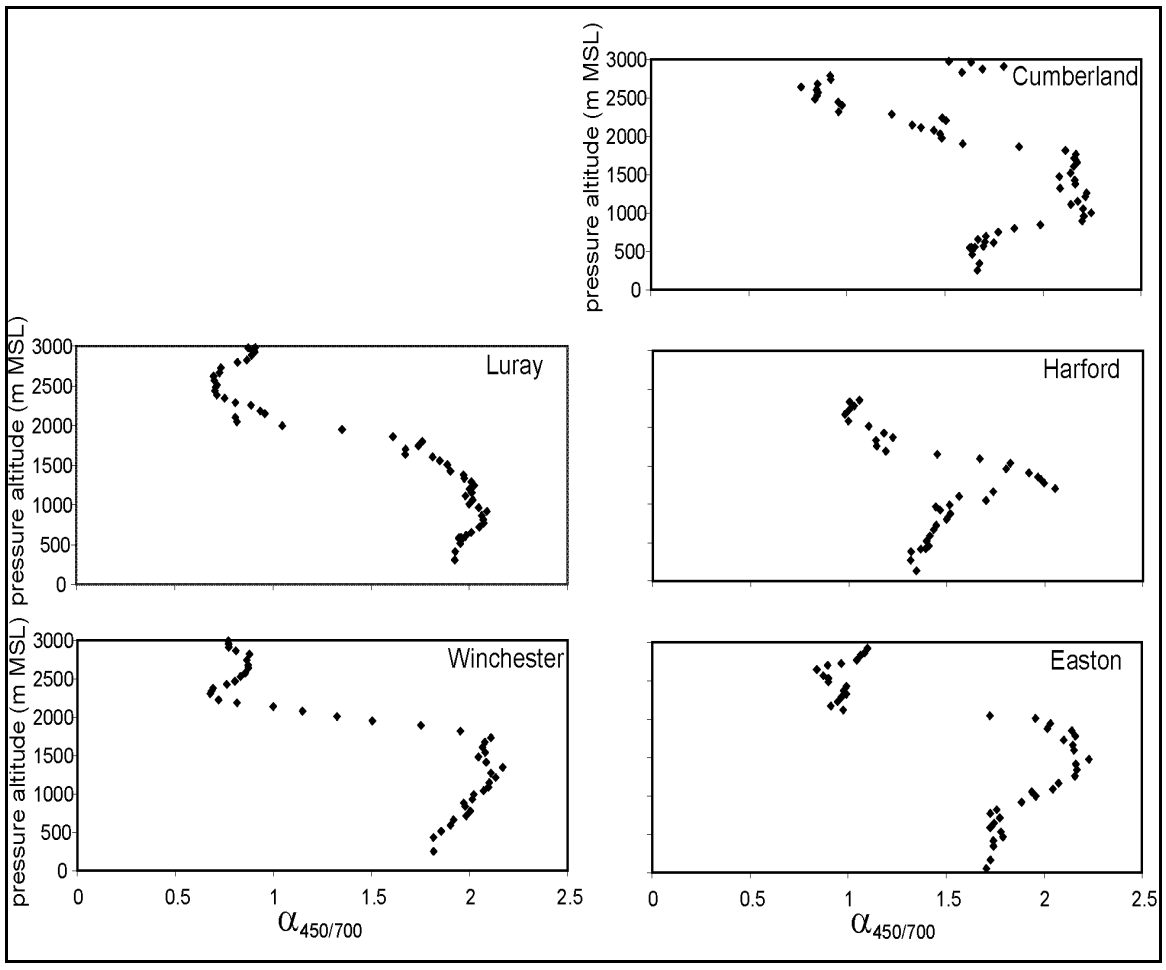

Figure 32. The scattering Ångström exponent, α , (450/700) calculated from flight data measured during the vertical survey spirals over Luray, VA, Winchester, VA, Cumberland, MD, Harford, MD, and Easton, MD (adapted from Taubman *et al.*, 2004(b)).

Table 2. Ångström exponents calculated for the smoke layer and PBL at vertical survey spiral locations during flights on 8 July 2002 (Taubman *et al.*, 2004(b)).

	Smoke $\alpha_{450/550}$	**Smoke** $\alpha_{450/700}$	**Smoke** $\alpha_{550/700}$	**PBL** $\alpha_{450/550}$	**PBL** $\alpha_{450/700}$	**PBL** $\alpha_{550/700}$
Luray	0.57±0.18	0.83±0.15	1.04±0.11	1.84±0.42	1.92±0.38	1.99±0.34
Winchester	0.60±0.44	0.85±0.32	1.05±0.22	1.90±0.34	1.99±0.32	2.06±0.30
Cumberland	1.17±0.64	1.23±0.38	1.29±0.30	1.85±0.26	1.96±0.22	2.05±0.21
Harford	0.87±0.10	1.09±0.09	1.26±0.09	1.45±0.33	1.59±0.30	1.70±0.29
Easton	0.71±0.10	0.97±0.09	1.18±0.09	1.83±0.19	1.94±0.19	2.03±0.16

Uncertainties represent 1 σ deviation about the mean.

Because of the measurement of dry light scattering, $\sigma_{sp}(ref)$, the calculation of AOD had to be modified to account for the difference between $\sigma_{sp}(ref)$ and $\sigma_{sp}(\lambda, RH)$:

$$\tau(\lambda, RH) = \int_{sfc}^{TOA} \sigma_{sp}(ref) F(RH) dz + \int_{sfc}^{TOA} \sigma_{ap}(\lambda, RH) dz \qquad (20)$$

However, the correction factor, $F(RH)$, was only applied to total scattering measurements made within the PBL. The smoke plume was presumably less hygroscopic than the sulfate dominated anthropogenic aerosols of the Mid-Atlantic U.S. and was observed in the free troposphere, where the RH was already below 20%. The corrections for angular non-idealities, on the other hand, were applied to all of the measurements.

The vertical survey spirals covered roughly the bottom 3 km of the atmosphere, from ~5 m AGL (z_1) to ~3 km MSL (z_2). Because of the small temporal and horizontal spatial scale of the individual spirals, atmospheric homogeneity was assumed in both horizontal composition and time. Based on this assumption, AOD for the vertical column at a single time was calculated. Measurements of extinction (as the sum of scattering and absorption) were made every minute and roughly every

100 m to give approximately 30 measurements per spiral. These extinction measurements were then integrated vertically and the AOD reported herein was calculated as such:

$$\tau(\lambda, RH) = \int_{z_1}^{z_2} \sigma_{sp}(ref) F(RH) dz + \int_{z_1}^{z_2} \sigma_{ap}(\lambda, RH) dz \quad (21)$$

The smoke plume was observed in the lower free troposphere at a minimum altitude of ~2 km MSL and extended somewhat beyond 3 km MSL. Therefore, the entire smoke plume was not accounted for in these calculations. AOD at 550 nm (τ_{550}) is given in Table 3. The uncertainty in these values was calculated by adding in quadrature the uncertainties in the particle scattering and absorption. A 25% uncertainty was assigned to the absorption values according to the instrumental error. A 15% uncertainty was estimated for the scattering values after adding in quadrature the 10% instrumental error and an additional 11% sensitivity to the possible range of γ values in the humidification factor.

Table 3. AOD calculated from ~5 m AGL to ~3 km MSL at 550 nm at vertical survey spiral locations during flights on 8 July 2002 (Taubman *et al.*, 2004(b)).

	Luray	Winchester	Cumberland	*Harford	Easton
τ_{550}	1.01±0.14	0.98±0.14	0.42±0.06	1.05±0.15	1.53±0.21

*AOD only to ~2.5 km MSL

The profiles of ω_b at 550 nm (ω_{b550}) over the five locations are given in Figure 33. The average values of ω_{b550} in the PBL and smoke layer aloft at each location are given in Table 4. The particles in the smoke plume were consistently more absorbing than the particles in the PBL. The mean values in the smoke plume and the PBL at 550 nm were 0.93±0.02 and 0.95±0.01, respectively. Calculation of the mean smoke value excluded Cumberland. A weak smoke signature was observed over this location, and inclusion would bias the calculation toward a value uncharacteristic of the smoke plume measured over the other sites. These ω_{b550} values are consistent with those reported by Dubovik *et al*. (2001) for North American boreal forest fires and at NASA GSFC. The smoke plume values also fall within the range of satellite-based retrieval values for smoke from boreal forest fires (Ferrare *et al.*, 1990; Li and Kou, 1998). The uncertainty in ω_b was calculated according to the aforementioned uncertainties in the absorption and scattering values with the following equation:

$$\frac{|\Delta\omega_b|}{\omega_b} = (1-\omega_b)\left\{\left(\frac{\Delta\sigma_{sp}}{\sigma_{sp}}\right)^2 + \left(\frac{\Delta\sigma_{ap}}{\sigma_{ap}}\right)^2\right\}^{1/2} \qquad (22)$$

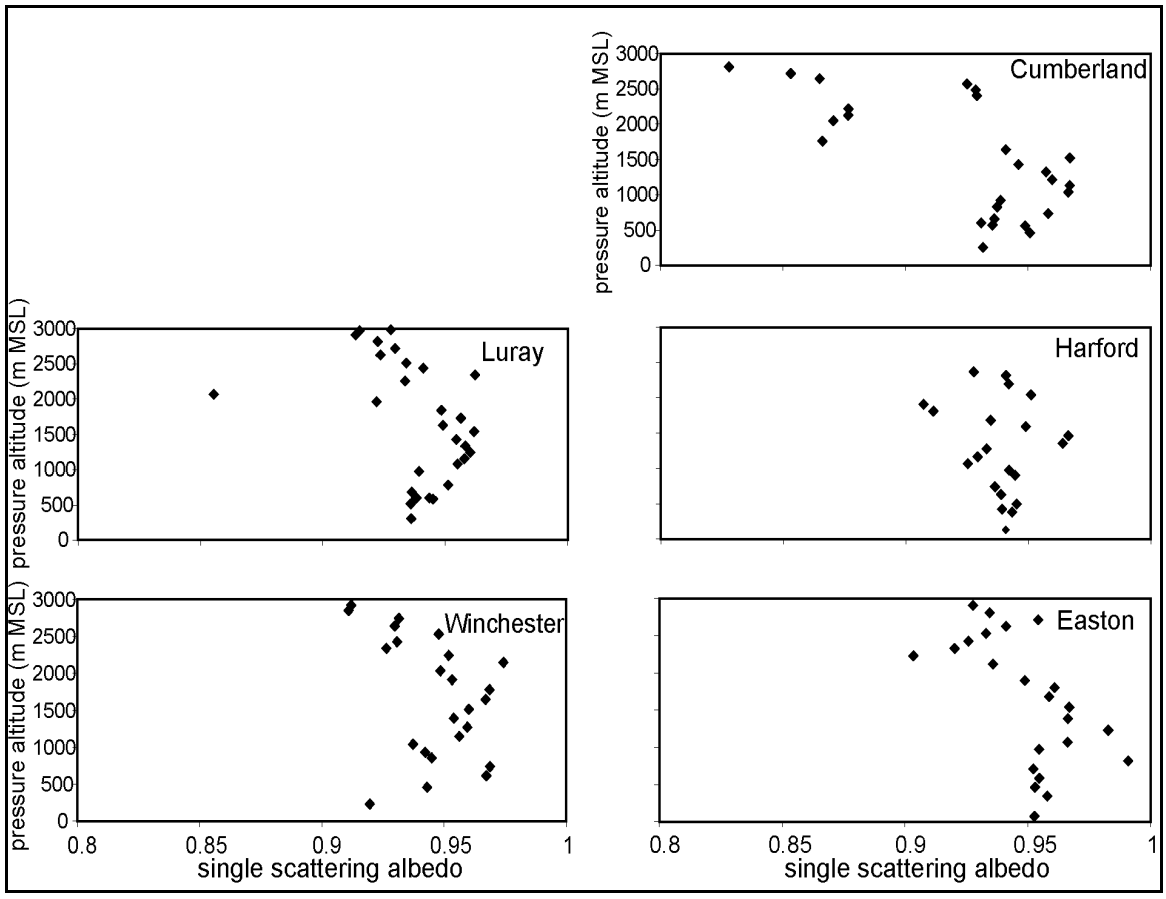

Figure 33. The single-scattering albedo, ω_b , at 550 nm calculated from flight data measured during the vertical survey spirals over Luray, VA, Winchester, VA, Cumberland, MD, Harford, MD, and Easton, MD (adapted from Taubman *et al.*, 2004(b)).

Table 4. Single-scattering albedo at 550 nm calculated for the smoke layer and PBL at vertical survey spiral locations during flights on 8 July 2002 (Taubman *et al.*, 2004(b)).

	Luray	Winchester	Cumberland	Harford	Easton
Smoke ω_{b550}	0.91±0.03	0.93±0.02	0.81±0.06	0.93±0.02	0.93±0.02
PBL ω_{b550}	0.95±0.01	0.95±0.01	0.94±0.02	0.94±0.02	0.96±0.01

The wavelength dependent index of refraction and particle size distribution were necessary to extrapolate optical properties at the measured wavelengths over the solar spectrum using Mie theory (Mishchenko *et al.*, 2002). The real index of refraction at 550 nm was determined assuming the column integrated AERONET (Holben *et al.*, 1998) value at 550 nm (1.56, interpolated from the wavelengths measured) on July 8, 2002 represented a weighted average of two discrete values, one for the PBL plume and one for the smoke plume. The value assigned to the PBL plume was 1.43 according to a 7-year average from NASA GSFC in Greenbelt, MD (Dubovik *et al.*, 2001). A value of 1.58 was therefore assigned to the smoke plume, slightly larger than the column integrated value. This refractive index was then scaled according to the wavelength dependence of the AERONET values. The imaginary index of refraction was calculated assuming absorption was solely the result of particle BC content. The wavelength dependence was then considered to be proportional to that measured for BC (Chang and Charalampopolous, 1990), adjusted so the ω_b value calculated at 550 nm matched the in-situ value.

The measured particle concentrations were over a limited size range. Thus, size distributions were determined using the measured Ångström exponents and the

assumed complex index of refraction at 550 nm. The lognormal distributions were adjusted so that the measured Ångström exponents matched those calculated by Mie theory for adjustable lognormal distributions (Mishchenko *et al*., 2002). Figure 34 shows the lognormal curves of the size distributions for the smoke and PBL layers derived from the Ångström exponents, together with data points from the MET-One measured size distributions as a consistency check. The AERONET retrieval is given for comparison. Though the lognormal curve for the AERONET distribution was based directly on statistics from the data, the volume-weighted curve does not appear to fit the data well. Optical properties (ω_0, phase functions) at other wavelengths were then calculated based on the size distributions and wavelength dependent complex index of refraction.

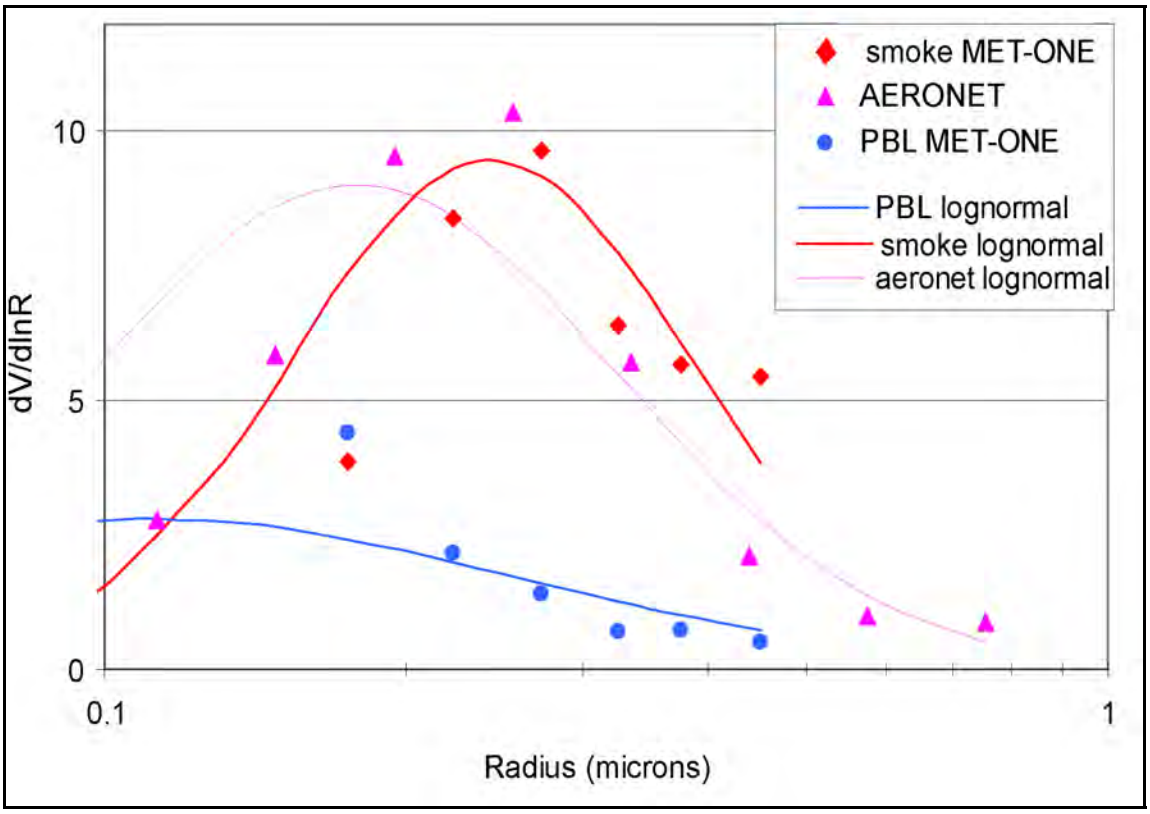

Figure 34. Population per cubic centimeter: Met-One smoke data points (diamonds), Met-One PBL aerosol data points (circles), and AERONET retrievals (triangles). The solid lines are lognormal fits to scattering Ångström exponents from in-situ data. The dotted line is based on statistics from the AERONET retrieval. The amplitude of each lognormal curve was adjusted to fit the points (adapted from Vant-Hull *et al.*, 2004).

4.2.4. Aerosol Direct Radiative Forcing

The clear sky aerosol direct radiative forcing (ΔF) at each location was calculated using the Santa Barbara DISORT Radiative Transfer (SBDART) code (Ricchiazzi *et al.*, 1998). AOD is proportional to the sum of the scattering and absorption cross sections calculated from Mie theory, allowing measured values to be extrapolated to any wavelength. The calculated values of AOD and ω_0 at 0.30, 0.40, 0.55, 0.70, 1.0, 2.0, and 3.0 μm in ~100 m vertical layers from roughly the surface to

3 km (depending on the vertical survey spiral at each location) were used as inputs to the code. Measured temperature, pressure, water vapor, and O_3 values were also input for the lowest 3 km. Surface albedo between $0.47\,\mu m - 2.1\,\mu m$ was taken from the MODIS land team 8 d surface reflectance product (Vermote and Vermuelen, 1999), derived from satellite measurements during a low aerosol period 2-3 weeks after this study. Outside of this wavelength range, CERES (Clouds and the Earth's Radiant Energy System) mixed vegetation albedos were used (Charlock *et al*., 2002). These values were chosen because of consistency with the MODIS land team surface reflectance at the specified sites.

ΔF TOA, ΔF sfc, and atmospheric absorption (Atmos) were calculated at each location. To determine the effects of the smoke layer at each location, the program was run with the smoke layer intact and after removal of the layer. The difference between the two sets of outputs was the direct effect of the smoke plume (Table 5). The PBL forcing was compared to a zero aerosol background and was, therefore, not the anthropogenic forcing. Since no background was assumed, a more accurate value for the smoke forcing was obtained. Because the smoke signature was weak at Cumberland and the majority of the plume was not measured at Harford, the values reported for these locations are not necessarily representative of the situation being described.

Table 5. ΔF TOA, ΔF sfc, and Atmos calculated with the PBL and smoke layers (Total forcing), with just the PBL layer (PBL), and the difference between the two (Smoke) at vertical survey spiral locations during flights on 8 July 2002 (Taubman *et al.*, 2004(b)).

	Total forcing			**PBL**			**Smoke**		
	ΔF TOA Wm^{-2}	Atmos Wm^{-2}	ΔF sfc Wm^{-2}	ΔF TOA Wm^{-2}	Atmos Wm^{-2}	ΔF sfc Wm^{-2}	ΔF TOA Wm^{-2}	Atmos Wm^{-2}	ΔF sfc Wm^{-2}
Luray	-47±7	115± 17	-162± 24	-26±4	30±5	-56± 8	-21±3	85± 13	-106± 16
Winchester	-50±8	108± 16	-168± 25	-20±3	23±3	-43± 6	-30±5	85± 13	-115± 17
Cumberland	-25±4	57± 9	-82± 12	-27±4	36±5	-63± 9	2±1	21± 3	-19± 3
Harford	-42±6	124± 19	-166± 25	-31±5	57±9	-88± 13	-11±2	67± 10	-78± 12
Easton	-57±9	167± 25	-224± 34	-29±4	29±4	-58± 9	-28±4	138± 21	-166± 25

Sources of error in the values calculated using the radiative transfer code resulted from uncertainties in the AOD at 550 nm and the extrapolation to other wavelengths using Mie theory. The AOD at 550 nm was found to be linearly proportional with the calculated forcing values, and the uncertainty in the forcing values was therefore assumed to be proportional to the uncertainty in AOD. The extrapolation uncertainty was calculated using sensitivity tests in which the real index of refraction was varied by 0.04 (a value greater than the AERONET uncertainty of 0.03) (Dubovik *et al.*, 2000) and the Ångström exponents used to calculate the size distributions were varied by one standard deviation. These sources of error were then added in quadrature to give the uncertainties listed in Table 5.

Calculations of the effect of the smoke plume indicated that the forcing at the TOA was small relative to the surface forcing. The values for atmospheric absorption were, therefore, nearly equal to the attenuation at the surface. This indicates that

multiple scattering of solar radiation within the optically thick plume typically ended in photon absorption. The fact that the smoke overlaid more scattering, smaller particles also increased the absorption within the smoke layer. The net effect was to cool the surface and heat the air aloft, thereby increasing the vertical stability of the lower atmosphere.

To quantify this effect, the calculated heating rates at each spiral location were integrated from sunrise to the time of observation. These values were then used to generate vertical heating profiles. Observed temperature profiles from the surface to ~2 km (below the temperature inversion) were extrapolated to 3 km to provide a temperature profile that did not include the observed inversion. The extrapolated temperature profiles were then subtracted from the measured temperature profiles. The resulting temperature difference was compared to the integrated heating profiles to determine the impact of the absorptive heating on the observed temperature profiles (Figure 35).

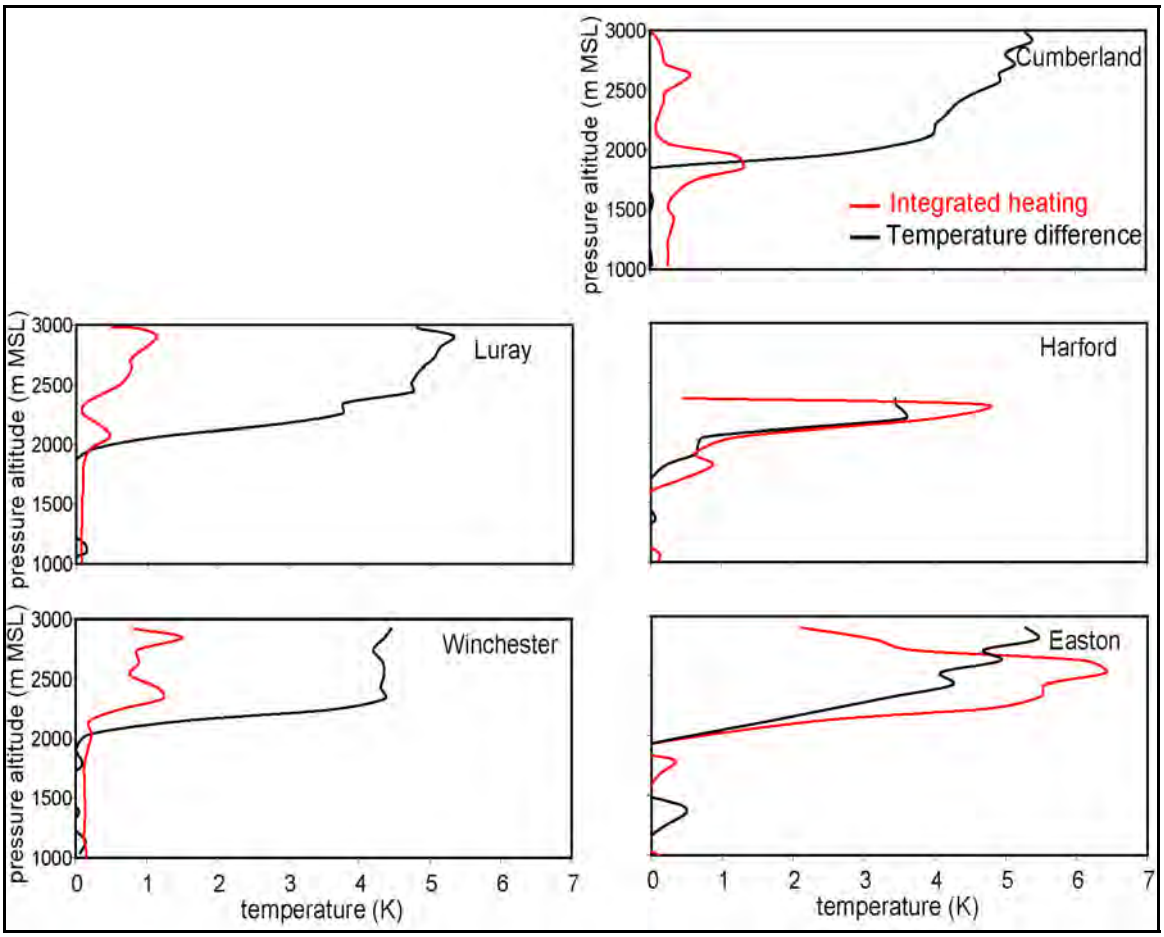

Figure 35. The temperature differences between the temperature measured during the vertical survey spirals over Luray, VA, Winchester, VA, Cumberland, MD, Harford, MD, and Easton, MD and temperature profiles extrapolated from 2 to 3 km as if there were no temperature inversions are shown with the black lines. The integrated heating profiles calculated with the radiative transfer code and integrated from sunrise to the time of each observation spiral are given with the red lines (adapted from Taubman *et al.*, 2004(b)).

The integrated heating for the morning profiles underestimated the observed temperature difference while the afternoon profiles overestimated the amount of heating. The spatially and temporally dynamic nature of the smoke plume would naturally affect the accuracy of this calculation. However, there was also more smoke above the highest measurements made in the aircraft, which was unaccounted

for in the heating rate calculations. Solar attenuation from this unaccounted for smoke would reduce the calculated absorption, and thereby the heating rates, at lower altitudes. This would decrease the amplitude and width of the resulting heating rate profiles. Although these explanations could account for the discrepancy in the afternoon profiles, heating in the smoke layer did not seem to account for the morning inversion.

Figure 36 is the NOAA ARL EDAS meteogram of pressure vertical velocity from 900 – 700 mb, which shows weak subsidence on the morning of the 8th. Hence, adiabatic heating of the descending air may have initially capped the mixed layer and positioned the smoke plume in a thin layer just above it, where heating of the absorptive smoke layer strengthened the inversion. The meteogram shows negative vertical velocity beginning at ~15:00 UTC, indicating upward vertical motion. If the modeled vertical velocity was correct, the subsidence inversion should have dissipated by the afternoon. However, the measured temperature showed an inversion after 20:00 UTC. Thus, the initial subsidence inversion may have acted to sequester the smoke in a thin enough layer above the PBL where it heated the layer and stabilized the atmosphere enough to create a positive feedback loop for its own sequestration. This prevented vertical mixing and dilution and ultimately increased the regional impact of the plume.

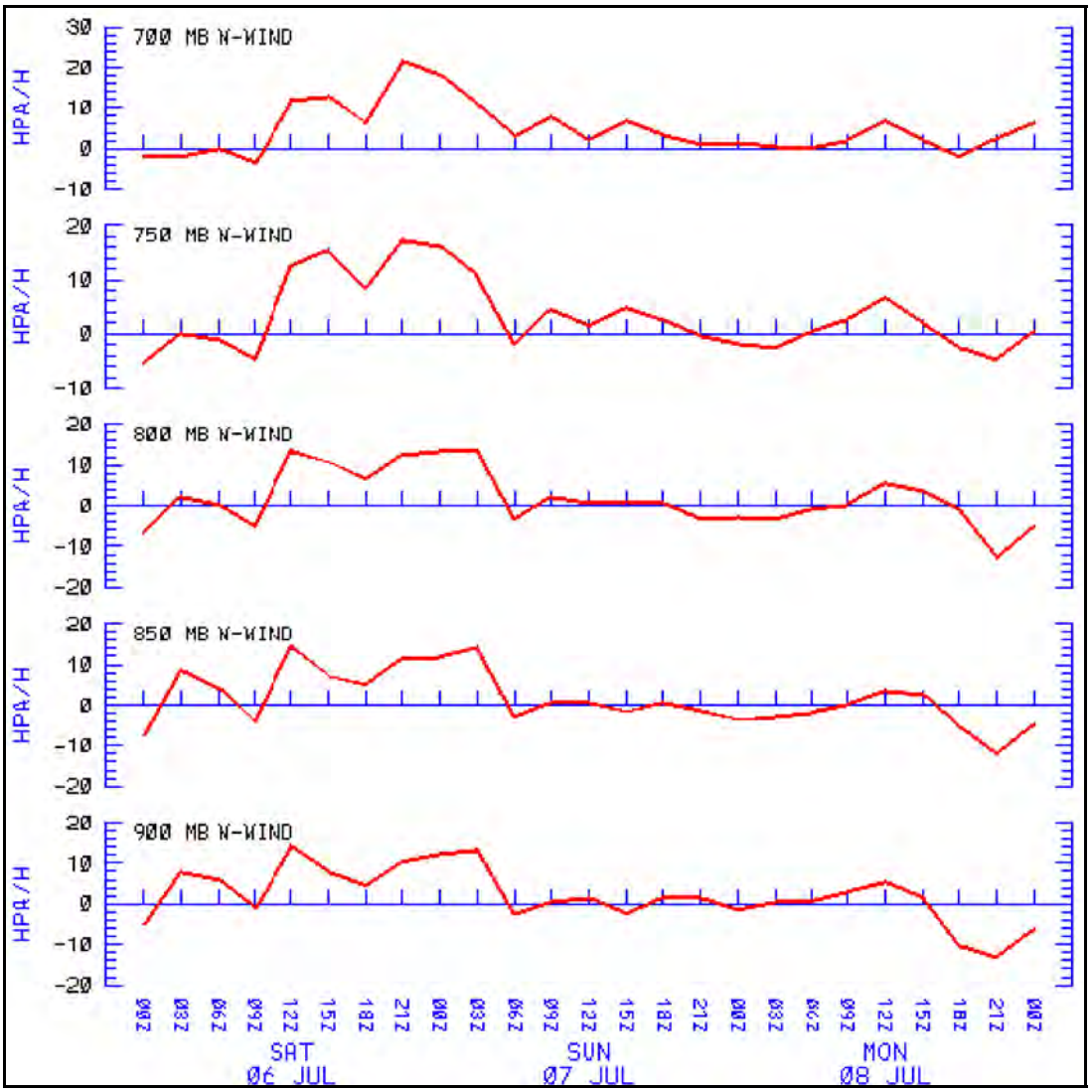

Figure 36. NOAA ARL EDAS meteogram of the pressure vertical velocity at 39.18°N, 76.67°W for 6 July – 8 July 2002. The morning of the 8th shows downward vertical motion. By the afternoon of the 8th, there is upward vertical motion (Taubman *et al.*, 2004(b)).

4.3. Summary

Measurements were made of trace gas and particle concentrations as well as particle optical properties associated with the smoke plume advected ~1500 km to the Mid-Atlantic from the Quebec forest fires. Large increases in CO and O_3 mixing

ratios, total particle scattering and absorption, as well as in the number of particles with optical diameters between 0.30 ~1.0 μm were observed between ~2 and 3 km. However, very little SO_2 (less than 0.1% of the CO) was observed at this altitude.

The more absorptive smoke particles had a mean single-scattering albedo value of 0.93±0.02 at 550 nm while the underlying PBL particles had a mean value of 0.95±0.01 at 550 nm. The scattering Ångström exponents of the larger, aged smoke particles were between 0.83±0.15 and 1.23±0.38 while the smaller, PBL particles had values between 1.59±0.30 and 1.99±0.32 for $\alpha_{450/700}$. Calculated Aerosol Optical Depths (550 nm) from just above the surface to ~3 km ranged from 0.42±0.06 above Cumberland to 1.53±0.21 above Easton.

Clear sky aerosol direct radiative forcing was calculated at each location using the SBDART code. Absorption of solar radiation within the smoke plume nearly equaled that which was attenuated at the surface, acting to cool the surface and heat the air aloft. Due to a morning subsidence inversion, the smoke plume was positioned in a thin layer above the PBL between ~2 and 3 km. The heating of this layer was concentrated enough to maintain the temperature inversion through the afternoon. This created a positive feedback loop that prevented vertical mixing and dilution, thereby protracting the lifetime of the plume and the regional radiative impacts.

Chapter 5: Regional Forcing and Uncertainty Analysis

5.1. Introduction

This chapter details the calculation of the regional radiative forcing from the Canadian forest fire smoke plume investigated in the previous chapter and examines the uncertainty involved in measurements of aerosol optical properties when used as inputs to satellite retrieval algorithms. AERONET and aircraft in-situ measurements were made on July 8, 2002 when the plume traversed Maryland and Virginia. The two independent measurements of aerosol optical properties were used as inputs to a standard satellite algorithm to calculate the aerosol optical depth. The optical depth was extrapolated across the solar spectrum to estimate the broadband, regional radiative forcing due to the optically thick smoke plume. Column closure was evaluated by comparing the calculated values of optical depth and radiative forcing at the TOA and surface with measurements from space using CERES and at the surface with SURFRAD (SURFace RADiation network of radiometers) and ISIS (Integrated Surface Irradiance Study). A comprehensive uncertainty analysis of the retrieved smoke optical depth and radiative forcing is detailed, including the possible reasons for disparity between the two measurement techniques.

The results described in this chapter are based on work that I co-authored, in press in the Journal of Geophysical Research (Vant-Hull *et al.*, 2004) (reproduced by permission of American Geophysical Union). Brian Vant-Hull, the first author, performed the radiative forcing calculations and used the standard satellite algorithm,

while I collected and analyzed the in situ data and assisted in all other calculations and analyses.

5.2. Results

5.2.1. In-situ Measurements

The sampling platform used to acquire the in-situ data for this study, flight track, and meteorology during the event were detailed in the previous chapter. Two atmospheric layers with discrete aerosol properties were observed in the study. The aerosols within the PBL (surface to ~2 km) were of local origin, stemming from fossil fuel combustion emissions. The LFT, between ~2 and 3 km, was dominated by smoke that was transported from the Canadian forest fires. The larger, more absorptive smoke particles were sequestered in this thin layer by a subsidence inversion. Radiative heating of the smoke protracted the thermal inversion, thereby preventing the vertical mixing and dilution of the plume (Taubman *et al*., 2004(b)). The distinct aerosol characteristics of the two layers allowed for their independent treatment in subsequent calculations.

Observations over Cumberland, MD showed a weak smoke signature in the LFT and inconsistent aerosol properties within the PBL as compared to the other sites. Therefore, the data from this location were excluded from calculations of layer averages.

5.2.2. AERONET Measurements

AERONET is an automated network of ground-based sun photometers that measure the direct solar irradiance at eight wavelengths (340, 380, 440, 500, 670, 870, 940 and 1020 nm) as well as the sky radiance at four wavelengths (440, 670, 870, and 1020 nm). After accounting for attenuation due to Rayleigh scattering and absorption by O_3 and trace gas pollutants, optical depth at each of the wavelengths, $\tau(\lambda)$, is calculated from extinction of the direct solar beam according to the Beer-Bouguer Law:

$$K(\lambda)\downarrow_{dir} = K(\lambda)_{\infty} e^{-\tau(\lambda)} \qquad (23)$$

where:

$K(\lambda)\downarrow_{dir}$ = the wavelength dependent direct beam flux at the surface

$K(\lambda)_{\infty}$ = the wavelength dependant solar radiation at the TOA.

By observing sky radiance over many scattering angles through a constant aerosol profile, particle size distributions and phase functions are retrieved.

Three AERONET sites coincided geographically with the aircraft measurements: The GSFC site in Greenbelt, MD (39.02ºN, 76.87ºW), the Smithsonian Environmental Research Center (SERC) site located on the edge of the Chesapeake Bay in Edgewater, MD (38.88°N, 76.50°W), and the Maryland Science Center (MDSC) site located in downtown Baltimore in the inner harbor (39.27°N, 76.62°W). The observed optical depths at all three of the AERONET sites on July 8, 2002 were fairly high; values representative of an optically thick smoke plume. Values at the GSFC site varied between 1.3 and 2.2, the SERC site fluctuated

between 1.8 and 2.2, while the MDSC site recorded optical depths ranging from 1.3 to 1.8 for the day.

In contrast to the optically thick values in the LFT, aircraft measurements in the PBL indicated a regional average value of 0.34 ± 0.10 (the uncertainty represents the variability about this mean value). Because the smoke layer values were roughly five times greater, the AERONET retrievals were probably dominated by the smoke optical properties. However, the PBL aerosol was closer to the instrument and would still exert an influence. Table 6 compares aerosol properties retrieved at the GSFC AERONET site with those measured in-situ aboard the aircraft on July 8, 2002. As mentioned earlier, the aircraft inlet system was unable to collect coarse mode aerosols. According to the AERONET almucantar retrievals, however, the coarse mode only accounted for ~3% of the total optical depth at 550 nm. There are two AERONET asymmetry parameter values given in Table 6. The first one, g = 0.65, is the value provided by AERONET. The second one, g = 0.62, was calculated using Mie theory and the retrieved index of refraction and size distribution (Mishchenko *et al.*, 2002). The satellite retrieved optical depth (see section 5.2.3) was virtually identical whether using the Mie theory phase function (corresponding to the lower asymmetry parameter) or the Henyey-Greenstein phase function (with the larger asymmetry parameter). To be consistent, the Mie theory calculated values were used in the study. The ω_0 and asymmetry parameter values retrieved from the MDSC site were higher than the GSFC values, perhaps due to the propinquity to the water. Whatever the reason, the MDSC values were not considered representative of the entire plume and were excluded from the analysis. The SERC site retrieved only

optical depth. Thus, the AERONET ω_0 and asymmetry parameter values used in this study came solely from the GSFC site.

The column averaged AERONET ω_0 value on July 8, 2002, interpolated to 550 nm (ω_{0550}), was 0.964. The GSFC climatological value (from 1993-2000) of ω_{0550} is ~0.98 ± 0.02 (Dubovik *et al*., 2001). It was assumed that this climatological value is representative of the regional, fossil fuel combustion-dominated PBL aerosols. The ω_0 retrieval on July 8, 2002, on the other hand, must have been a weighted column average of PBL fossil fuel combustion and LFT smoke aerosols. Because the smoke layer had approximately five times the optical thickness as the underlying layer, the smoke ω_{0550} value would have been ~0.962. This value, however, is nearly equivalent to the column averaged value of 0.964. Therefore, the column averaged value was used to represent the particles in the smoke layer.

Table 6. Averaged aerosol parameters for the three optical models. Wavelength dependent quantities are given for 550 nm. AERONET values represent a total column average, interpolated to 550 nm, with algorithm uncertainties given for ω_0. Instrumental (but not statistical) uncertainties are given for the aircraft values of ω_0. The uncertainties for g are a composite of instrumental uncertainties and assumptions made in calculating the index of refraction (Vant-Hull *et al.*, 2004).

	Effective radius r_e	variance $\delta(\ln r)$	Refractive index (n+ik)	single scattering albedo ω_0	asymmetry parameter g
AERONET GSFC	0.15 μm	0.61	1.56 + 0.0067i	0.964 ± .03	0.65/0.62
Aircraft smoke	0.22 μm	0.46	1.58 + 0.015i	0.930 ± .02	0.66 ± .04
Aircraft PBL	0.08 μm	0.86	1.43 + 0.006i	0.949 ± .02	0.62 ± .04

5.2.3. Satellite Retrieval of Optical Depth

The in-situ measurements at the four spiral locations (excluding Cumberland, MD) and the retrievals from the three AERONET sites were mostly invariant about the respective mean values, given instrumental and statistical uncertainties. The mean values were therefore considered to be representative of the region defined by Figure 37. Given the synoptic scale of the meteorological system during this event (see Figure 21), the region was extended to include the SurfRad site as well.

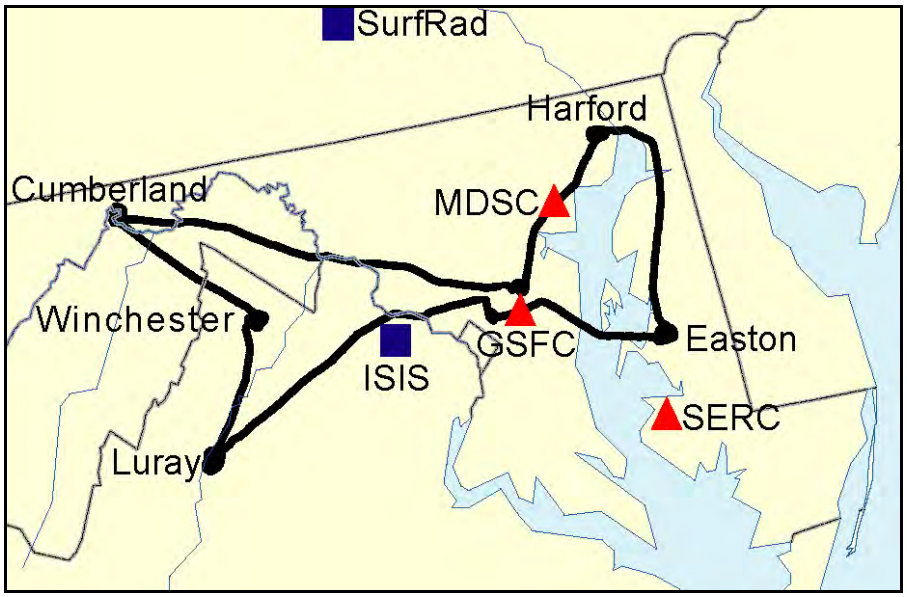

Figure 37. Flight track and locations of measurement spirals on July 8, 2002. The AERONET sites are indicated by red triangles, the SurfRad and ISIS sites by blue squares (adapted from Vant-Hull *et al.*, 2004).

A two-layer system with discrete optical properties in each layer was assumed. The PBL, defined here as the altitude range between the surface and 2 km, made up the bottom layer of the system, while the LFT, between 2 and 3 km, was the upper layer (Figure 38). The aerosol properties within the PBL were assumed to be fixed. The values used were the regional averages (as measured by the aircraft or calculated from measured values) of optical depth (0.34 ± 0.10), ω_{0550} (0.95 ± 0.01), and asymmetry parameter (0.62). The ω_{0550} and asymmetry parameter values used within the smoke layer were either the regional average aircraft values (ω_{0550} = 0.93 ± 0.02, g = 0.66) or the values derived from the AERONET retrievals (ω_{0550} = 0.964, g = 0.62). To retrieve optical depth using the satellite algorithm, the PBL aerosol optical depth was assumed to be invariant, while the smoke optical depth was varied until the calculated and measured radiances at the TOA were equal.

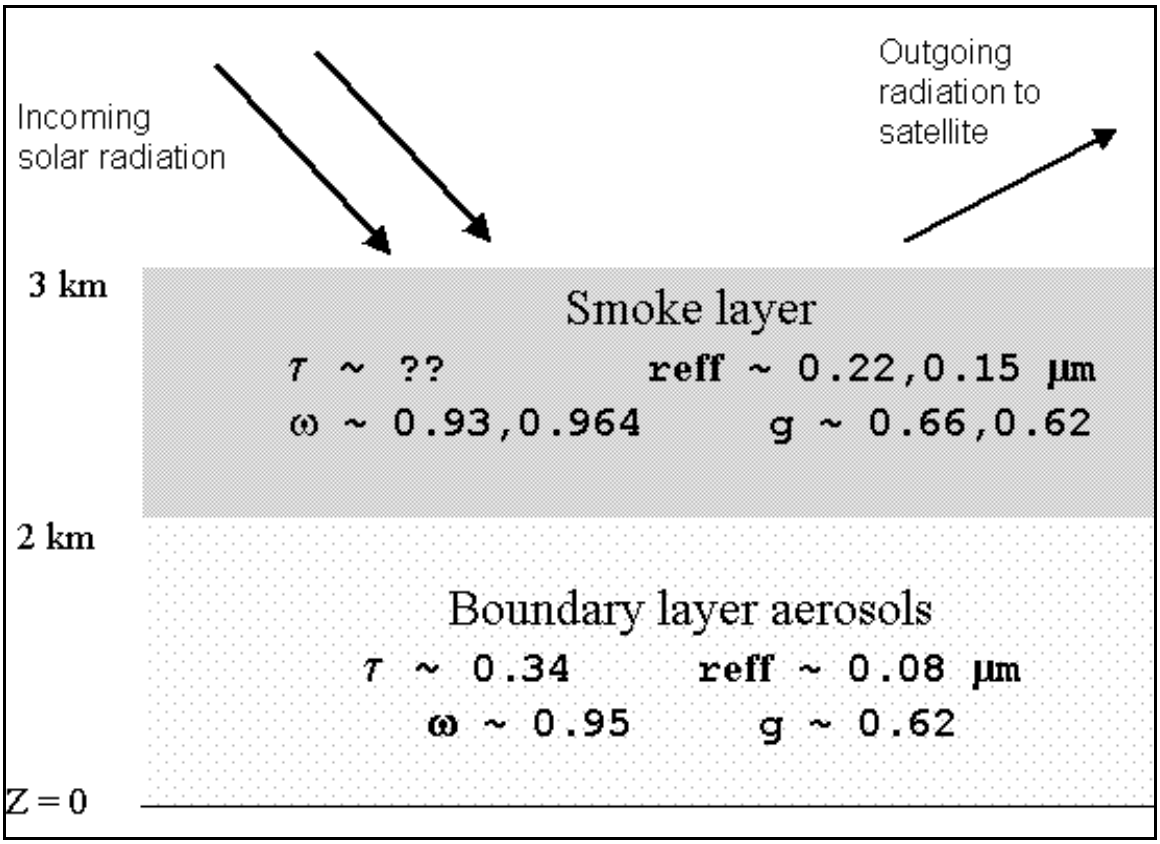

Figure 38. Two layer model in which the smoke layer optical depth was adjusted until the outgoing radiance matched that observed by satellite. The smoke parameters came either from the aircraft in-situ measurements or from AERONET, respectively (adapted from Vant-Hull *et al*., 2004).

TOA radiances at 550 nm (5 km resolution) were measured from the MODIS instrument during the Terra overpass from 1540 to 1545 UTC. The pixels under review were cloud screened to ensure that there was no interference from clouds. Distinguishing between smoke and clouds in the visible wavelengths can be difficult. However, cloud droplet diameters are commensurate to near IR wavelengths while smoke particle diameters are in the sub-micrometer range. Thus, reflectivity in the near IR may be used to distinguish between the two (Kaufman *et al*., 1990(b)). Cloud screening in this manner indicated that the area under review was cloud free.

The satellite retrieved optical depth was calculated from two primary optical models: one employing the AERONET column average values, and one utilizing the layered structure measured by the aircraft, with disparate properties in each layer (Table 7). Two mixed models were also used to retrieve the optical depth. Both mixed models used a layered system, with the PBL layer and different combinations of aircraft and AERONET ω_0 and phase function values in the smoke layer (Table 7). The satellite retrievals of optical depth were compared to the AERONET measurements of optical depth (interpolated from 440 and 670 nm to 550 nm as well interpolated in time to match the satellite overpass) at each of the three sites within the study region (Table 7). The interpolations added estimated uncertainties of ± 0.02 to the algorithm uncertainty for the AERONET observations (Holben, 1998). To make the comparison, the data from four satellite pixels that fell within a 0.1° box centered on each sun photometer were averaged. Some of the data over SERC were rejected due to abnormally high surface reflectance over the Chesapeake Bay.

Table 7. Comparison of aerosol optical depth retrievals. The first three rows show the satellite retrieved optical depth added to the assumed optical depth of the PBL aerosol, the fourth row is a satellite retrieval of the total aerosol column based on AERONET derived properties. The source of the optical parameters used as inputs are listed on the left. Uncertainties denote the variation in retrieved values from surrounding pixels only, and do not reflect instrument or algorithm errors. The fifth row lists the optical depths observed by AERONET interpolated to the time of the satellite overpass, with instrumental and interpolation uncertainties included. The last two rows list the MODIS retrieval with the smoke model used in the western U.S., and the operational retrieval, with algorithmic uncertainties included (Vant-Hull *et al*., 2004).

Single Scattering Albedo	Scattering Phase Functions	GSFC (4 pixels)	SERC (3 pixels)	MDSC (4 pixels)
In-situ + PBL	In-situ + PBL	2.25 ± .10	2.18 ± .26	1.92 ± .08
AERONET + PBL	In-situ + PBL	1.71 ± .07	1.67 ± .21	1.46 ± .06
AERONET+ PBL	AERONET+ PBL	1.55 ± .06	1.51 ± .19	1.33 ± .05
Pure AERONET	Pure AERONET	1.54 ± .06	1.50 ± .19	1.31 ± .05
AERONET Observations		*1.68 ± .04*	*1.79 ± .03*	*1.34 ± .04*
MODIS standard smoke model		*2.02 ± .45*	*1.93 ± .44*	- - -
MODIS operational Eastern US model		1.*69 ± .39*	*1.64 ± .38*	- - -

Satellite retrievals of optical depth using the aircraft optical properties were the highest (Figure 39a), while those using the AERONET optical properties were the lowest (Figure 39b). The mixed models generated optical depths between the two extremes and identified the sensitivity of the satellite retrievals to variations in absorption values and size distributions. Figure 39c shows the optical depth ratio when using in-situ versus AERONET optical properties. The optical depth calculated with the in-situ optical properties was roughly 30% higher than the optical depth calculated with the AERONET optical properties, due mainly to the disparity in ω_0

values between the two models. However, a 30% disparity in optical depth values is inconsistent with a 3.5% divergence in ω_0. This apparent contradiction is explained by multiple scattering effects in optically thick media (Bohren, 1987). Specifically, despite the high probability that each individual encounter leads to a scattering event (dictated by the high ω_0 value), multiple scattering creates greater opportunities for photon absorption. As a result, when optical depths are large, the TOA reflectance becomes a nonlinear function of the single scattering albedo (Wong and Li, 2002).

The MODIS retrieval is given to provide a comparison to an operational satellite algorithm (Figure 39d). MODIS optical depth was retrieved using the smoke model for western U.S. biomass burning and the eastern U.S. operational retrieval with the cloud screening function deactivated (Table 7). Figure 39d shows the retrieval using the eastern U.S. algorithm. The values of ω_0 (0.96) and g (0.66) used in the MODIS retrieval algorithm were nearly identical to the AERONET values. Consequently, the optical depth generated by the MODIS retrieval was very similar to the value determined by AERONET (Figure 39b).

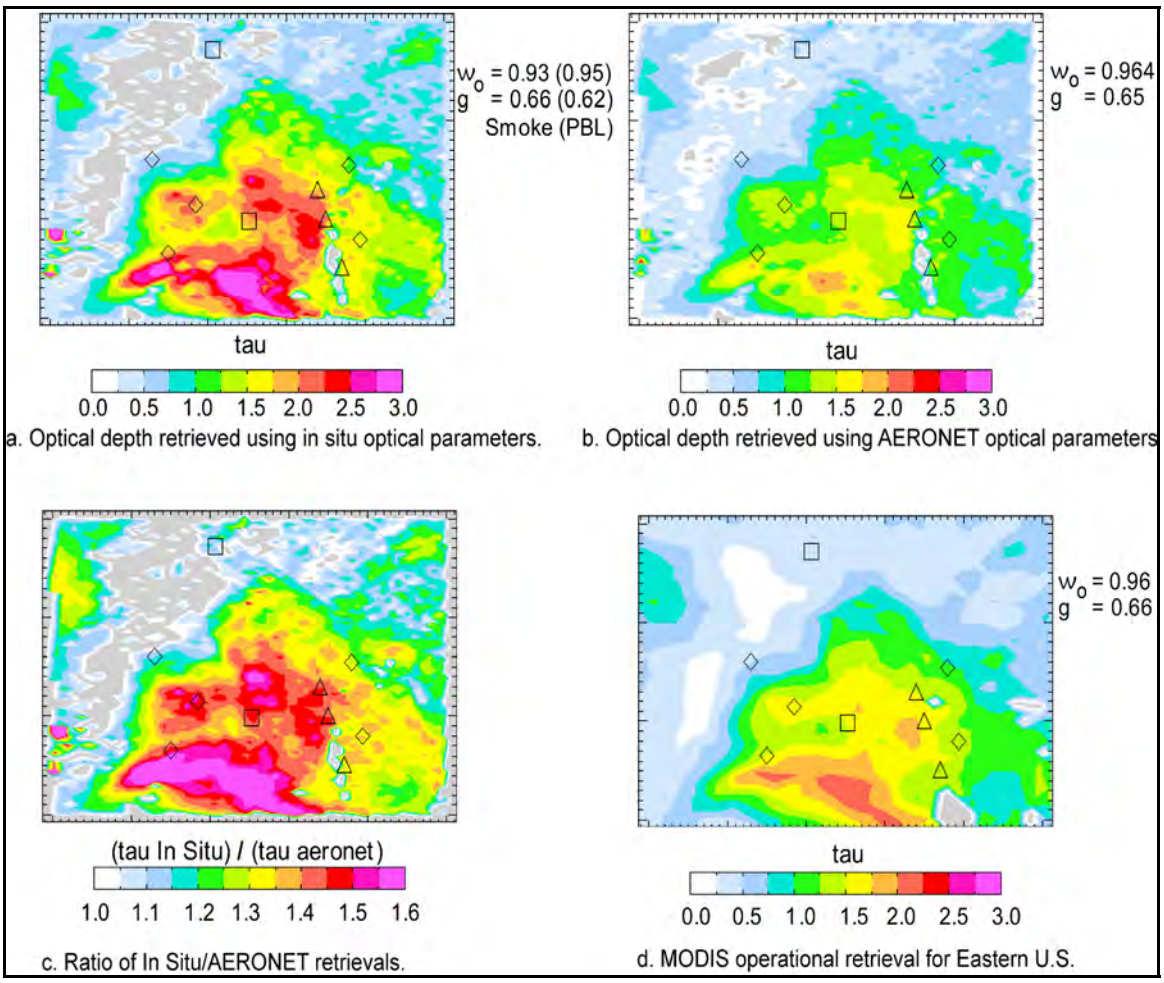

Figure 39. Comparison of optical depth retrievals via satellite. Diamonds show the locations of aircraft spirals, triangles denote AERONET locations, and squares indicate surface radiometer sites. The color scale ranges from 1 to 3. The panels show optical depth retrieved using in-situ optical parameters (a), optical depth retrieved using AERONET optical parameters (b), the ratio of In-situ/AERONET retrievals (c), and the MODIS operational retrieval for the Eastern U.S. (d) (Vant-Hull *et al.*, 2004).

There were portions of the region in which the optical depth retrieval was performed where the calculated reflectance was greater than that measured by the satellite. The areas where this occurred are denoted by the gray color in Figure 39. The large area in the northwestern corner of Figure 39a indicates vicinities lying

outside of the smoke plume where the optical depth must have been lower than the assumed regional average of 0.34. Cumberland, MD is seen to lie right on the edge of this region, confirming that this locale was mostly devoid of smoke at the time of observation. The small gray areas between the two southernmost AERONET sites represent portions of the Chesapeake Bay where the surface reflectance product generated artificially large values. The cloud-screening function in the algorithm may be responsible for any of the other scattered gray areas.

As mentioned earlier, the veracity of satellite retrievals of optical depth are dependent upon the accuracy of the assumed aerosol optical properties used as inputs to the retrieval algorithm. This comparison exhibits the range of possible retrieval values when using different optical properties as inputs. Some of the optical depth retrievals were nearly twice as large when using in-situ measurements of optical properties as compared to retrievals using AERONET optical properties. Because it is unknown which values are the correct ones, the range of retrieval values represents the uncertainty surrounding satellite retrievals of optical depth.

5.2.4. Aerosol Radiative Forcings

The regional aerosol radiative forcings were calculated using the satellite retrievals of optical depth together with the in-situ and AERONET aerosol optical properties. To test column closure of the aerosol optical properties, the radiative forcing calculations were compared to surface broadband flux measurements taken by the Pennsylvania SurfRad and Virginia ISIS radiometers as well as TOA fluxes measured by the CERES satellite radiometer. All radiative forcing calculations were

performed with the SBDART code (Ricchiazi *et al*., 1998), using the LOWTRAN-7 solar spectrum and sixteen streams.

The SurfRad and ISIS surface forcing measurements (clear sky spectrally integrated flux minus spectrally integrated flux with smoke) were compared to the forcing calculations using the four aforementioned optical models (Table 8). Some of the data were interpolated temporally to coincide with the satellite overpass. The SurfRad site was largely smoke-free (see Figure 39, Table 8). Conversely, the ISIS site was enshrouded in smoke (see Figure 39, Table 8). Nevertheless, for both situations, the value calculated using the aircraft in-situ optical properties came closest to the surface measurements. The calculated value was ~10% less than the value measured at the SurfRad site, and ~20% greater than the measured value at the ISIS site (Table 8). The radiative forcing values calculated with the AERONET optical properties, on the other hand, were significantly less than the measured values. Specifically, the calculated values were roughly 50% and 33% lower than the values measured at the SurfRad and ISIS sites, respectively.

Table 8. Broadband surface radiative forcing at the two radiometer sites. The top four rows are calculations based on satellite retrievals of optical depth whereas the bottom row gives the actual measurements. Uncertainties indicate spatial variation between pixels surrounding the site for the satellite retrievals and temporal interpolation uncertainty for radiometers (adapted from Vant-Hull *et al*., 2004).

Single scattering albedo	Scattering phase functions	SurfRad 1541 Z		ISIS 1541 Z	
		Tau	Forcing (W/m^2)	Tau	Forcing (W/m^2)
In-situ + PBL	In-situ + PBL	$0.57 \pm .12$	-102 ± 19	$1.93 \pm .09$	-297 ± 11
AERONET + PBL	In-situ + PBL	$0.53 \pm .09$	-87 ± 12	$1.47 \pm .04$	-193 ± 4
AERONET + PBL	AERONET+ PBL	$0.51 \pm .08$	-88 ± 12	$1.33 \pm .03$	-188 ± 3
Pure AERONET	Pure AERONET	$0.45 \pm .12$	-58 ± 17	$1.32 \pm .03$	-166 ± 3
Measured Forcing			***-113*** $\pm$ *11*		***-246*** $\pm$ *8*

The greater optical depths generated with the in-situ optical properties were largely the reason for the larger surface forcings calculated with the in-situ values. The lower forcing values calculated with the AERONET optical properties are more difficult to justify. Using only the fine-mode aerosol retrievals may be partly to blame. Larger particles account for greater percentages of the optical depth as the wavelength increases to become commensurate with the particle diameter. However, coarse mode aerosols only accounted for 10% of the AERONET retrievals of optical depth at $1.02\,\mu m$. Even if the radiative forcing at longer wavelengths were due primarily to coarse mode aerosols, these wavelengths only account for a small portion of the overall forcing. Rather, the lower radiative forcing values are probably the result of the narrow AERONET size distribution within the region of greatest solar intensity. Broadband radiative forcing is calculated by integrating the forcing at each wavelength. Aerosols with a narrow size distribution are only spectrally active over a

narrow range of wavelengths. Conversely, aerosols with broader size distributions (e.g., the aircraft in-situ derived size distribution) are spectrally active across a greater wavelength range and result in a larger broadband radiative forcing.

The CERES instrument, on the same Earth Observing System (EOS) satellite as MODIS, measures both solar-reflected and Earth-emitted radiation. The CERES team uses an ERBE-like (Earth Radiation Budget Experiment) inversion of measured radiance to calculate instantaneous TOA flux (Green and Robbins, 1997). This process uses angular dependence models (ADMs) that account for the anisotropy of the radiation field due to geotype (e.g., ocean, land, snow, desert, coast) and cloud cover. The CERES TOA flux was compared to the TOA flux calculated with the in-situ and AERONET optical properties (Figure 40). The calculated TOA fluxes are both larger than the flux retrieved by CERES, although the flux calculated with the in-situ optical properties is closer to the CERES value. This is despite the fact that the optical depth retrieved using the AERONET optical properties was lower than that retrieved with the in-situ values. Thus, the larger flux calculated with the AERONET optical properties must be due entirely to the aerosol optical properties. The smaller, more scattering particles scattered more light in the backward direction, thereby increasing the calculated TOA flux. The measured and calculated flux values were also used to estimate TOA forcing. Figure 41 shows the forcing at the TOA, the surface, and within the atmosphere calculated using the in-situ and AERONET optical properties. The fluxes measured at the surface and the TOA were all closer to the fluxes calculated with the in-situ optical properties. Therefore, the aerosol radiative forcing calculated with the in-situ values may be more accurate.

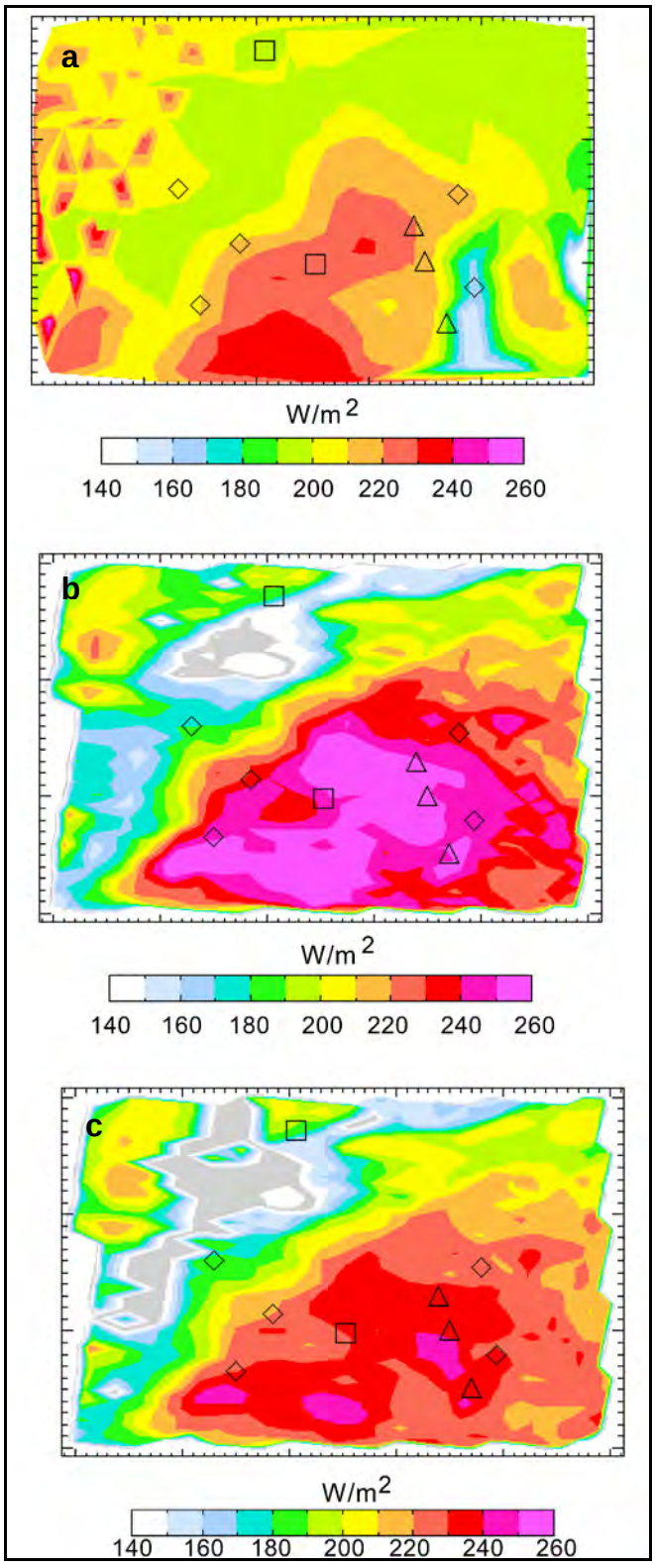

Figure 40. Comparisons of TOA flux measurements to calculations from the two primary optical models. For symbol definitions see figure 39. The gray areas are undefined data. The three panels indicate: TOA flux retrieved by CERES

(a), TOA flux calculated from the AERONET model (b), and TOA flux calculated from the in-situ model (c) (Vant-Hull *et al.*, 2004).

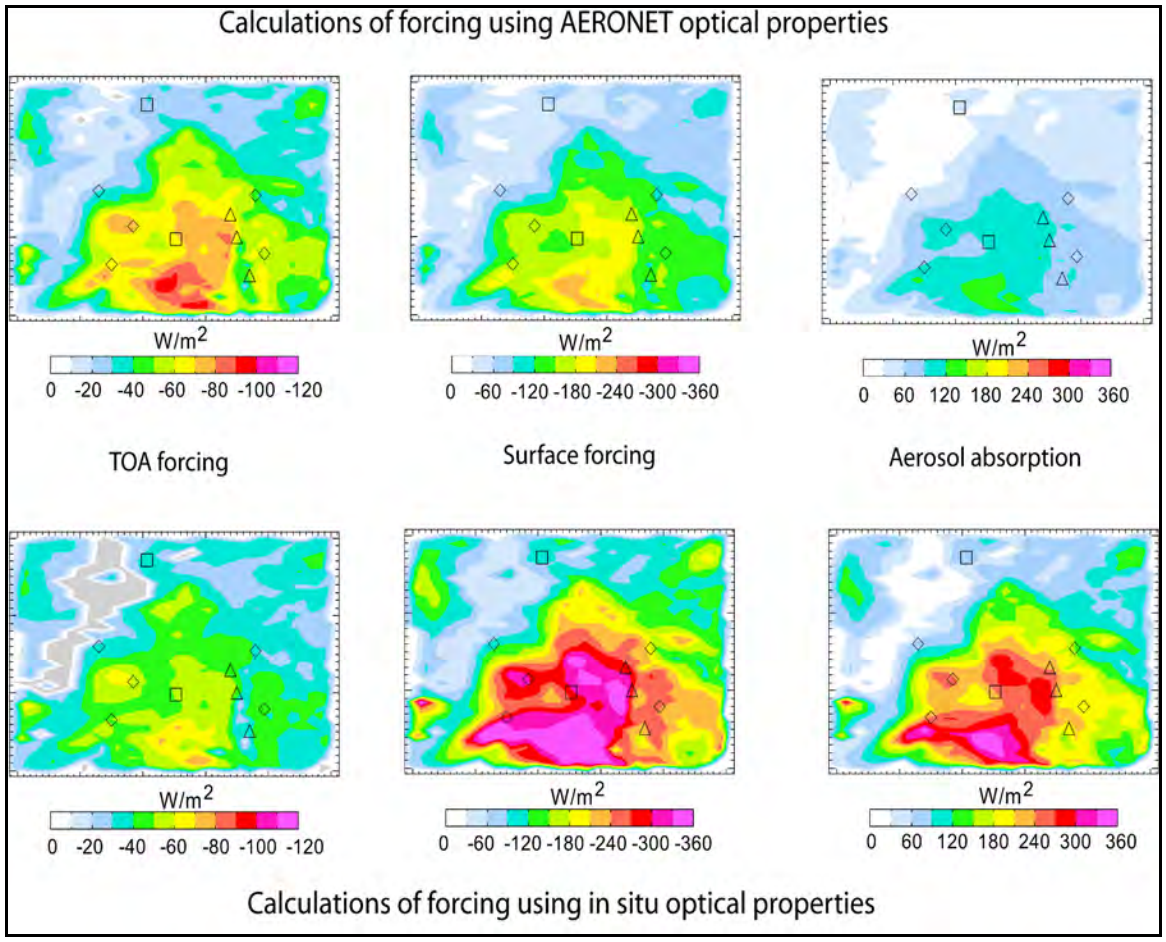

Figure 41. Radiative forcing maps calculated from the optical depth retrievals and optical models. The top row is based on AERONET, the bottom row is based on in-situ data. For symbol definitions see figure 39. Gray areas are undefined data. The color scale ranges from 0 - 120 W/m^2 for TOA forcing, 0 - 360 W/m^2 for the absorption and surface forcing (Vant-Hull *et al.*, 2004).

5.2.5. Uncertainty in Optical Depth Retrievals

When the TOA reflectance is fixed, minor fluctuations in the single scattering albedo produce large, contrary changes in the satellite derived optical depth (Figure 42). The curve may be roughly described by the following relationship:

$$\Delta\tau \approx -(5\tau^{5/2})\Delta\omega_o \qquad (24)$$

Thus, for an optical depth, τ = 2, a small decrease in the single scattering albedo of 0.01 would increase the optical depth by ~0.28 or 14%.

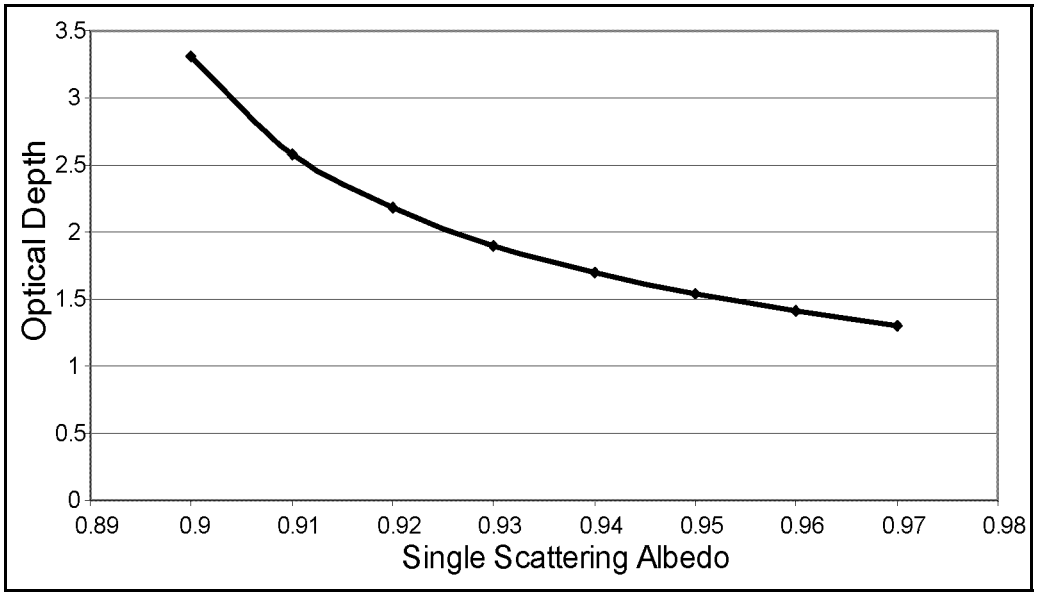

Figure 42. Retrieved optical depth as a function of single scattering albedo for a fixed TOA radiance (Vant-Hull *et al.*, 2004).

When the measured radiance is fixed, changes in the surface albedo produce contrary changes in the retrieved optical depth. To test the sensitivity of the retrieved optical depth to the surface albedo, a point was selected in the middle of the study area as representative of the typical sun-satellite geometry used in the retrievals. Figure 43 shows "isorads", or lines of constant radiance, in 5 W m^{-2} increments. The slopes of the isorads decrease with increasing optical depths. This indicates that the optical depth becomes less sensitive to the surface reflectance as it becomes larger. At an optical depth close to 2 (reasonable with regard to this study), an uncertainty in

surface reflectance of ± 0.02 (typical for mid-latitude, summertime, mixed vegetation land cover) would create an optical depth uncertainty of ± 0.1. This would be, for example, approximately a 5% uncertainty for the optical depths retrieved over the AERONET sites.

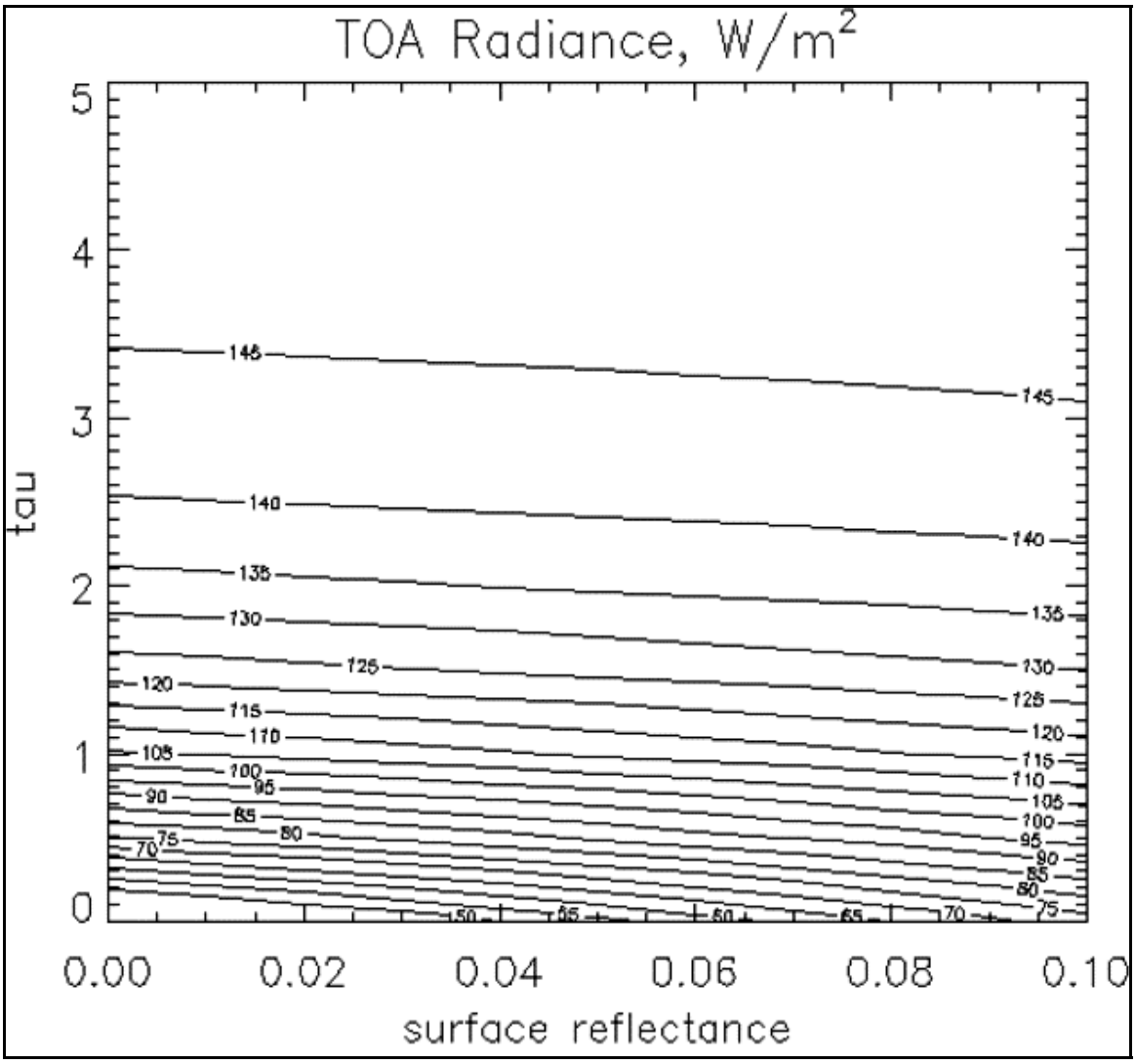

Figure 43. Satellite observed radiance (contours) as a function of optical depth and surface reflectance (Vant-Hull *et al*., 2004).

The measured scattering Ångström exponents ($\alpha_{450/550}$ and $\alpha_{550/700}$) were used to calculate the phase functions. For the purpose of this study, the scattering Ångström exponents were assumed to vary no more than one standard deviation about the mean values. A sensitivity analysis was performed to determine the effect of these possible fluctuations on the retrieved optical depth. The results are given in Table 9. The asymmetry parameters are also shown to provide a measure of the impact of the perturbations on calculated optical properties. The optical properties were affected less by the absolute values of the Ångström exponents than by the distance between the values. Thus, when the two Ångström exponents were altered by one standard deviation about their respective mean values, but in opposite directions, the optical depth changed by ~20% (see the last two rows, Table 9).

Table 9. Retrieved optical depth of smoke as a function of the scattering phase functions derived from scattering Ångström exponents measured in-situ. Note that optical depth does not include PBL (Vant-Hull *et al*., 2004).

	Angstrom Exponents	g	Tau GSFC
"average"	$\alpha_{450/550} + 0$, $\alpha_{550/700} + 0$	**0.662**	**1.90**
"high"	$\alpha_{450/550}$ + s.d., $\alpha_{550/700}$ + s.d.	0.656	1.87
"low"	$\alpha_{450/550}$ - s.d., $\alpha_{550/700}$ - s.d.	0.667	1.94
"tight"	$\alpha_{450/550}$ + s.d., $\alpha_{550/700}$ - s.d.	0.638	1.60
"wide"	$\alpha_{450/550}$ - s.d., $\alpha_{550/700}$ + s.d.	0.691	2.33

The calculated phase functions (and hence the optical depth) are also impacted by the real part of the complex index of refraction. The retrieval is mostly invariant when $1.54 < n < 1.62$. When the real index of refraction falls below this range, however, the impacts to the retrieved optical depth become substantial. AERONET reports an uncertainty in real index of refraction values of ± 0.03 (Dubovik *et al*., 2000). An estimated real index of refraction value of 1.58 ± 0.03 for this study falls within the above stable range, making the contribution to retrieved optical depth uncertainty minimal.

The PBL aerosol optical depth was fixed at 0.34 ± 0.1 (the regional average determined by the aircraft profiles, with the uncertainty representing the variation about the mean value) to isolate the radiative impacts of the smoke. However, the optical depth, in reality, must have varied across the study area at the time of satellite overpass. As a result, the retrieved smoke optical depth must counterbalance the unaccounted for variance in the PBL. The uncertainty of the PBL aerosol (0.1) was therefore added to the uncertainty of the retrieved optical depth in the smoke layer.

When all of the individual uncertainties, including the instrumental uncertainty with scattering and absorption measurements addressed in chapter 2, were added in quadrature, a total uncertainty of $\pm 22\%$ for satellite retrieved optical depths close to 2 resulted. An uncertainty of this magnitude accounts for the assortment of values calculated with the different optical models. Therefore, given the current instrumental uncertainties, the in-situ and AERONET optical properties used in this study may be said to be equivalent.

5.2.6. Uncertainty in Forcing Calculations

Calculations of surface forcing are sensitive to the retrieved optical depth values. In fact, for the optical depth values reported in this study, multiple scattering effects did not play a dominant role and the surface forcing was proportional to the optical depth. The relationship between uncertainties in the optical depth and single scattering albedo is described in equation 24. For an uncertainty in ω_0 of ± 0.02 (the approximate instrumental uncertainties for the range of single scattering albedo values measured during this study), the optical depth uncertainties at the SurfRad and ISIS sites would be 0.5% and 16%, respectively. Equivalent uncertainties in the surface forcing values at these two sites would then be expected.

As mentioned before, the optical depth over multiple wavelengths is affected by the size distribution, the calculation of which is affected by the real part of the index of refraction. Within the aforementioned stable range of real index of refraction values, the effect on surface forcing values was minimal, but once this threshold was breached, the effect was quite large (Table 10). The SurfRad site is not given because the optical depth there was too low to show significant effects. The

width of the size distribution is also inversely related to the numerical distance between scattering Ångström exponents. However, changes to the size distribution may not result in concomitant variations in the retrieved optical depth at a single wavelength and broadband TOA forcing. In fact, altering the size distribution may even create an inverse impact on optical depth at 550 nm and TOA forcing (Table 10). The forcing values represent the integrated forcing over many wavelengths and the impacts felt at a single wavelength may not reflect the overall variability.

The uncertainties in the optical depth and size distribution were added in quadrature and the overall uncertainties in the calculated surface forcing values at the SurfRad and ISIS sites were determined to be ~6% and ~19%, respectively. These uncertainties account for the disparity between the measured values and the values calculated with the in-situ optical properties, but not for the values calculated with the AERONET optical properties. Because it was measured by satellite, the TOA forcing was determined for the entire region. However, the spectral variability of the surface reflectance is complicated to estimate. Not to mention the fact that the uncertainties associated with the aerosol characteristics alone contributed ~11% to the total uncertainty. Regardless, the TOA forcing calculated with the in-situ data matched the CERES values (within uncertainty ranges), while the TOA forcing calculated with the AERONET optical properties did not.

Table 10. Effects of varying the scattering Ångström exponents and real index of refraction on retrieved radiative forcing. Refer to table 9 for the explanation of the types of variations in the two values. The PBL aerosol layer was not varied (adapted from Vant-Hull *et al*., 2004).

	Tau (550 nm) ISIS (Sterling, VA)	Surface Forcing (Watts/m^2)	TOA Forcing (Watts/m^2)
Average properties: Total	**1.93**	**-297**	**-50**
properties: PBL	**0.34**	**-64**	**-25**
Ångström exponent variations			
"tight"	1.66	-279	-54
"wide"	2.28	-324	-44
"low"	1.96	-299	-49
"high"	1.90	-295	-51
Index of refraction variations			
n = 1.50	2.45	-345	-43
n = 1.54	1.97	-299	-49
n = 1.62	1.92	-298	-50

5.3. Discussion

In-situ measurements of aerosol optical properties used as inputs to a satellite algorithm generated greater optical depth values than when AERONET derived optical properties were used. Because the optical depth was large, due to the thick pall of smoke, the absorption, though relatively small compared to the scattering, played a more vital role in the retrieval. Further, the radiative forcing calculated at the surface and TOA did not correlate with the retrieved optical depth.

The single scattering albedo was the primary source of uncertainty in the satellite retrieval of optical depth. The difference between the AERONET derived single scattering albedo and that measured in-situ cannot be attributed to the column averaged retrieval performed by AERONET. The values were equivalent given the

statistical and instrumental uncertainties; however, the difference between the two had a large impact on the radiative calculations that were based upon them.

The in-situ ω_{0550} value of 0.93, as compared to the AERONET value of 0.964, indicates that either the in-situ absorption was twice as large or the in-situ scattering was twice as small as the AERONET value. This disparity also arises in an evaluation of the GSFC AERONET climatological average ω_{0550} value of 0.975 (Dubovik *et al.*, 2001) and the in-situ measurement value of 0.95 (Hartley *et al.*, 2000). The notion that in-situ scattering measurements are responsible for the discrepancy of ω_{0550} values is unlikely. Scattering typically (this study included) makes up more than 90% of the total extinction by particles. Multiple column closure studies have demonstrated conformity in optical depth values (the vertically integrated extinction by particles) measured in-situ by aircraft and using sun photometer retrievals (Hegg *et al.*, 1997; Remer *et al.*, 1997; Russell *et al.*, 1999; Ross *et al.*, 1998; Kato *et al.*, 2000; Fiebig *et al.*, 2003; Haywood *et al.*, 2003; Magi *et al.*, 2003). Considering the large scattering/absorption ratio seen in these studies, the scattering values must also have agreed.

The above studies set the bar for conformity at values within 20% and a few percent for the optical depth and ω_0, respectively. When column closure tests are based upon the optical depth, little information is gained in regards to the absorption, which is relatively small compared to the scattering, and could vary considerably while having little impact on the optical depth and ω_0. It is imperative, however, when dealing with optically thick plumes such as the one encountered in this study, to achieve greater confidence in ω_0 values. The MODIS retrieval uncertainty is given

as $\pm(0.2\tau + .05)$ (Kaufman and Tanre, 1998), or 35% for an optical depth of 1.5. That seems quite large until one realizes that, according to the results of this study, if the uncertainty in ω_{o550} was ± 0.03, the uncertainty for an optical depth of 1.5 would surpass that quoted for the MODIS retrieval (see Figure 42 and equation 24).

There was a consistent difference in the measured optical properties as observed by the two platforms used for this study. Smoke optical properties have been observed to change as the optical depth of the plume changed (Remer *et al*., 1998; Dubovik *et al*., 2001; Wong and Li, 2002). However, there was no spatial trend observed in either the aircraft or the AERONET measurements of the smoke optical properties. Therefore, the offset cannot be attributed to a compositional difference in the smoke particles observed by the two platforms.

The absorption, then, must be the reason behind the discrepancy between the two measurement platforms. The PSAP is a simple and widely used instrument for measuring in-situ particle absorption, particularly on aircraft platforms (Hegg *et al*., 1997; Reid *et al*., 1998(b); Hartley *et al*., 2000; Taubman *et al*., 2004(a); Taubman *et al*., 2004(b)). Nevertheless, it is a filter based measurement technique that naturally introduces measurement error. The laboratory calibration on which the corrections to the PSAP values in this study and most others since 1999 were based (Bond *et al*., 1999) used a single, solid, standard absorptive hydrocarbon aerosol. However, different particles react differently to variability in heating and humidity as well as to filter interactions. For example, the recommended corrections to account for scattering effects were based solely on the calibration aerosol (n = 1.67 at 550 nm), but different aerosols would cause different scattering effects depending on the

ambient aerosol index of refraction. Because scattering is so dominant relative to absorption, this is not an insignificant source of uncertainty either. Also, many particles are largely liquid and, therefore, may deform when collected on the filter. The calibration was based upon a non-deformable solid aerosol, whereas aged smoke particles (such as the ones observed in this study) are thought to be a solid core enveloped by liquid (Bundke *et al*., 2002).

The radiative forcing values calculated with the in-situ optical properties were closer to the SURFRAD, ISIS, and CERES measurements than those calculated using the AERONET optical properties. In apparent contradiction to these results is the fact that the satellite retrieved optical depth using the AERONET optical properties was closer to observed values than when the in-situ values were used as inputs. The AERONET area-weighted size distribution consisted of an incomplete multimodal distribution. The effective radius used in the radiative calculations was based on an area-weighted average, although it was difficult to estimate a value for the incomplete multimodal distribution, a potential source of error. The multiple assumptions and steps necessary to complete the radiative forcing calculations may have introduced a systematic bias that favored the higher optical depths generated with the in-situ values. Further, the conversion of CERES radiance measurements to TOA flux is based on multiple assumptions of radiation anisotopries due to different surface characteristics and cloud cover, creating uncertainties that are challenging to quantify. Despite the uncertainty surrounding the calculations, the results of this study suggest that optical depth values at a single wavelength may not correspond to radiative forcing values that are integrated over the entire solar spectrum.

5.4. Summary

The optical depth of the smoke plume from Canadian forest fires was calculated using satellite reflectances as well as AERONET retrieved and in-situ aircraft measured optical properties. Different combinations of the AERONET and in-situ values were also used. The optical depths calculated using the pure AERONET optical properties were the lowest, while the retrievals using pure in-situ values were the highest. The larger optical depths retrieved using the in-situ optical properties were due to the fact that the in-situ measurement of absorption was twice as large as that derived by AERONET. However, given the algorithmic, instrumental, and statistical uncertainties of the results, the retrieved values of optical depth could be said to be equivalent.

The broadband radiative forcings at the surface and TOA were calculated using the satellite retrieved optical depth at a single wavelength by extrapolating the value across the solar spectrum according to the particle size distributions. Forcings calculated using the in-situ optical properties matched surface and TOA measurements more closely than those determined using the AERONET optical properties. This is in apparent contradiction with the fact that optical depth retrievals using AERONET optical properties matched the AERONET observations more closely than the retrievals using the in-situ optical properties and merits further investigation.

Measuring absorption by particles in the atmosphere is a relatively new focus in the aerosol community. Despite Herculean efforts, achieving consistency between

disparate measurement techniques has proven a formidable challenge. Satellites provide the most spatially efficacious means of observing aerosols, but the accuracy of their retrievals depends upon the veracity of the aerosol optical properties used as inputs. Calculations of radiative forcing are even more involved than optical depth retrievals and are, thereby, more prone to inaccuracy. This phenomenon is demonstrated by the fact that the optical properties measured in-situ and by AERONET and the retrieved optical depths calculated with these two inputs were equivalent, given instrumental uncertainty, but the radiative forcing values based on these inputs diverged considerably. The disparities between the two measurement platforms observed in this study were exacerbated by the optical thickness of the smoke plume. Because typical aerosol loading is considerably lower than that observed in this study, this issue has garnered little interest in the past.

Chapter 6: The Blackout

6.1. Introduction

The August 14, 2003 electrical blackout was the largest in North American history. It affected roughly 50 million people in a 24,000 km^2 area that stretched from New York through Connecticut, Massachusetts, and Vermont to Ottawa and Toronto, Canada west to Detroit, Michigan, and south through Ohio, Pennsylvania, and New Jersey. Within minutes after 16:00 EST on August 14, 2003, 21 power plants were tripped in the United States. In all, over 100 power plants were significantly scaled back for varying amounts of time, ranging from hours to days. Figure 44 shows a nighttime satellite view of the evening prior to the blackout, August 13. Figure 45 shows the same view on the evening of the blackout, August 14. Note the loss of evening illumination throughout most of the northeastern U.S. and southeastern Canada. Power was gradually restored to the region over the next several days.

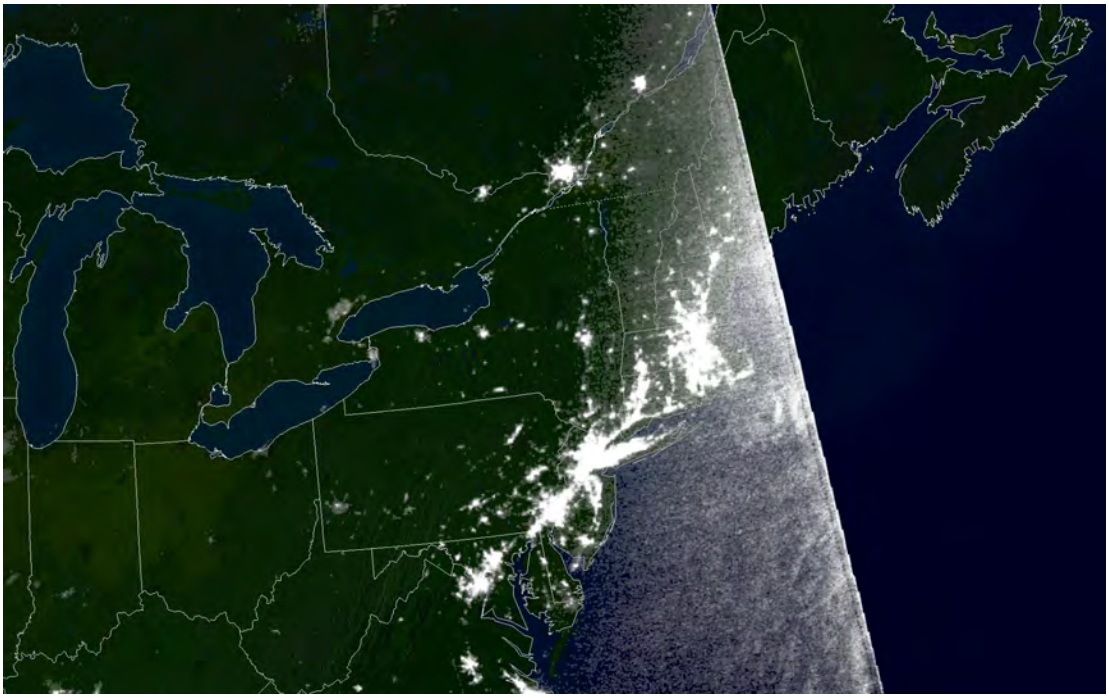

Figure 44. Satellite image of the northeastern US taken Aug. 13, 2003, at 21:21 EDT (NOAA processed the data from the Defense Meteorological Satellite Program).

Figure 45. Satellite image of the northeastern US taken Aug. 14, 2003, at 21:03 EDT (NOAA processed the data from the Defense Meteorological Satellite Program).

Airborne measurements were made over Maryland and Virginia (outside the blackout area) and Pennsylvania (downwind of the blackout area) on August 15, 2003, ~24 h into the blackout. The data were compared to those from the previous summer in the same locations and under similar meteorological conditions when upwind power plants were operating normally. Emissions data were examined in conjunction with back trajectories to determine the contribution of power plants to the observed air quality. The results enabled the quantification of the impact of reduced SO_2 and NO_x emissions, with all other factors held relatively constant, on air quality in the northeastern U.S. The results described in this chapter are based on work that I co-authored, published in Geophysical Research Letters (Marufu *et al.*, 2004) (reproduced by permission of American Geophysical Union). I was the mission

scientist aboard the flights used in this study. I also performed most of the subsequent analyses and contributed extensively to the written manuscript.

6.2. Results and Discussion

Two flights were conducted on August 15, 2003. During the first flight, three vertical survey spirals (surface - 3 km) were performed over Luray (38.70ºN, 78.48ºW) and Winchester (39.15ºN, 78.15ºW) in Virginia and Cumberland, Maryland (39.60ºN, 78.70ºW) at ~14:00, 15:00, and 15:30 UTC, respectively. Two spirals were performed over Selinsgrove, Pennsylvania (40.82ºN, 76.86ºW) at ~19:00 and 20:00 UTC during the second flight.

The morning spirals (outside the blackout region) revealed trace gas mixing ratios and particle properties typical of those routinely observed on previous flights (Dickerson *et al*., 1995; Ryan *et al*., 1998; Taubman *et al*., 2004(a)). Observations over Luray, for example, showed maxima in SO_2 and O_3 mixing ratios in a thin layer at ~1 km MSL (Figures 46a,b). A corresponding peak in particle light scattering was also seen at this altitude; but scattering values increased again below 500 m MSL (Figure 46c), corresponding to a maximum in CO (Figure 46d). These observations indicate a stable nocturnal boundary layer with a maximum depth of 500 m MSL. Above this altitude, NO_x and SO_2 from power plants produced O_3 and SO_4^{2-}, respectively, which were transported in the residual layer. Below 500 m, the pollution was most likely of local origin. Particles observed in the nocturnal boundary layer may have been largely organics, the products of vehicle exhaust and

home heating and cooking, which can scatter visible light efficiently (Malm *et al.*, 1994).

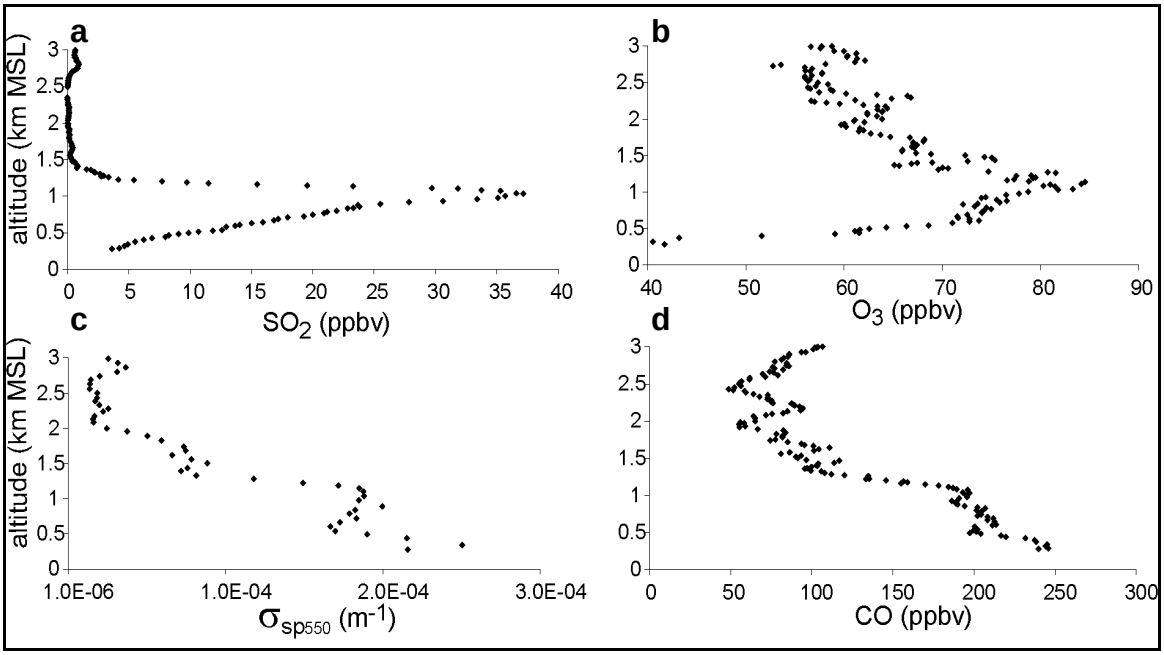

Figure 46. Running 1 min mean SO_2 mixing ratios (a); 10 s O_3 mixing ratios (b); particle light scattering at 550 nm (c); and running 1 min mean CO mixing ratios (d) over Luray, Virginia (outside blackout area) at 1500 UTC (10:00 LST) 15 Aug, 2003 (Marufu *et al.*, 2004).

Observations from the afternoon flight were different. Spirals over Selinsgrove, Pennsylvania revealed very little O_3, SO_2, and PM relative to the morning flight and areas to the south (Figures 47a-c). CO concentrations were within 0.5 σ of the 1992 median August and September values over Baltimore, Maryland and vicinity (Dickerson *et al.*, 1995), and remained fairly constant throughout the afternoon, apparently only varying with altitude (Figure 47d). Linear regressions between O_3 and SO_2 measured during the flight showed that O_3 over Selinsgrove was not correlated with SO_2 ($r = -0.13$), while it was elsewhere ($r = 0.80$) (Figures 48a,b).

The observations over Selinsgrove are consistent with reductions in power plant emissions but no corresponding changes in vehicle emissions.

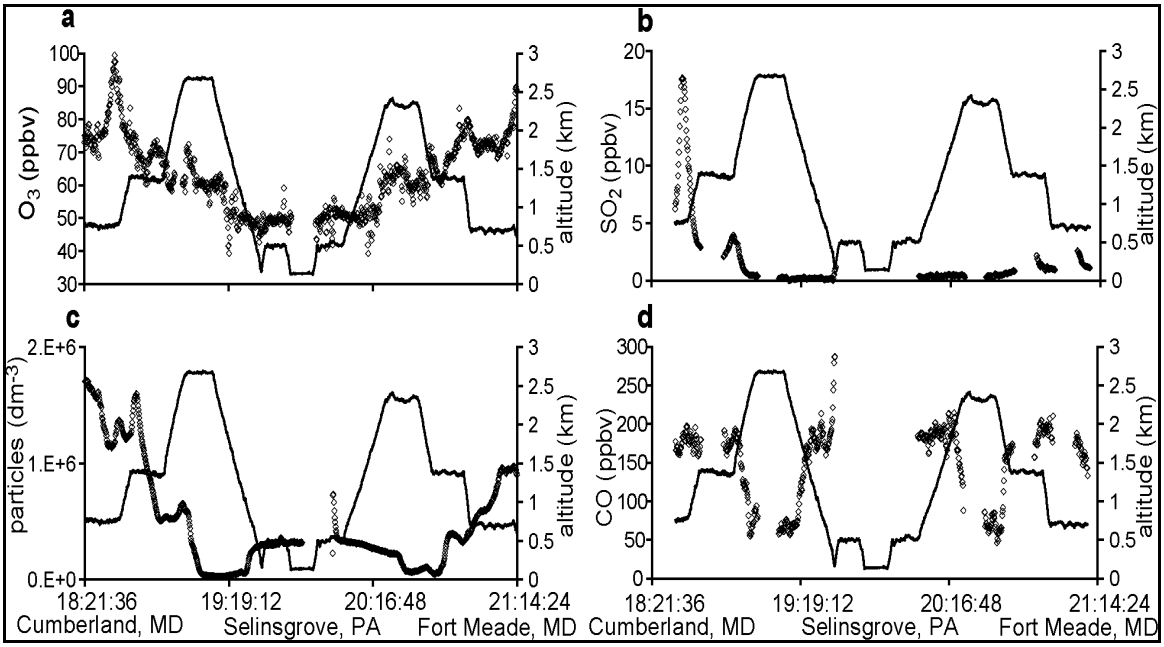

Figure 47. Second flight on August 15, 2003 showing altitude (solid black lines), time (UTC), as well as takeoff, landing and spiral locations. Open diamonds represent 10 s O_3 mixing ratios (a); running 1 min mean SO_2 mixing ratios (b); sub-micrometer particle counts (c); and running 1 min mean CO mixing ratios (d) (Marufu *et al.*, 2004).

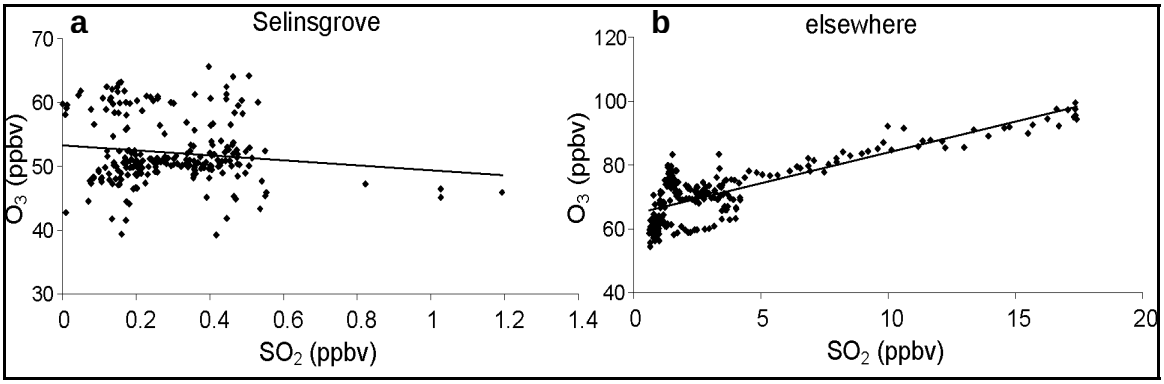

Figure 48. Linear regressions of SO_2 and O_3 over Selinsgrove, PA (r = -0.13) (a) and elsewhere (r = 0.80) (b) during the second flight on August 15, 2003.

To investigate whether the improvement in air quality over Selinsgrove was due to reductions in upwind power plant emissions, 24 h backward trajectories were run from Selinsgrove at 500, 1500, and 2500 m AGL using the NOAA ARL HYbrid Single-Particle Lagrangian Integrated Trajectory (HYSPLIT) model (Version 4) (Draxler and Rolph, 2003) and EDAS meteorological fields (Figure 49a). A 100 km wide swath was then assigned to the trajectory paths to account for uncertainties. Hourly NO_x and SO_2 emissions data (USEPA, 2003, Personal Communication) for U.S. power plants falling within the swaths were integrated over the 24 h period preceding the measurements (Table 11), thus enabling a comparison between the upwind emissions data and the wind trajectory analysis. A large source of uncertainty in this approach is the lack of emissions data from Canada.

Table 11. 24 h integrated SO_2 and NO_x emissions from upwind power plants that fell within back trajectory source regions for Selinsgrove on 15 Aug, 2003 and 4 Aug, 2002 (normal day), and Cumberland on 15 Aug, 2003(outside blackout area). Also shown are percentage emissions reductions upwind of Selinsgrove on 15 Aug, 2003 relative to 4 Aug, 2002 and Cumberland on 15 Aug, 2003 (Marufu *et al.*, 2004).

	Selinsgrove 15 Aug, 2003	**Selinsgrove 4 Aug, 2002**	**Cumberland 15 Aug, 2003**	**Emissions reduction upwind of Selinsgrove on 15 Aug, 2003 relative to:**	
	Blackout Day	*Normal Day*	*Blackout Day*	*Selinsgrove on 4 Aug, 2002*	*Cumberland on 15 Aug, 2003*
SO_2 tons/day	2424.1	7227.9	7033.9	66 %	66%
NO_x tons/day	309.2	1565.0	1219.9	80%	75%

The same back trajectory and emissions procedure was followed for Selinsgrove, PA on August 4, 2002 (prior to blackout) and Cumberland, MD on August 15, 2003 (out of blackout area) to provide a comparison with emissions from power plants that were operating normally. On August 4, 2002, the synoptic meteorological patterns over Selinsgrove were similar to those on August 15, 2003. Regional mean surface temperatures were ~33^{o}C on both days, winds and relative humidity were similar (Figure 49b), and both days were mostly cloud free but for some high clouds. Also, downwelling flux measured by the SurfRad site in central Pennsylvania revealed little difference between the two days. This analysis yielded large differences in upwind power plant emissions (Table 11). SO_2 and NO_x emissions upwind of Selinsgrove on August 15, 2003 were reduced to 34% and 20% of normal and to 34% and 25% of that observed upwind of Cumberland, respectively (Table 11).

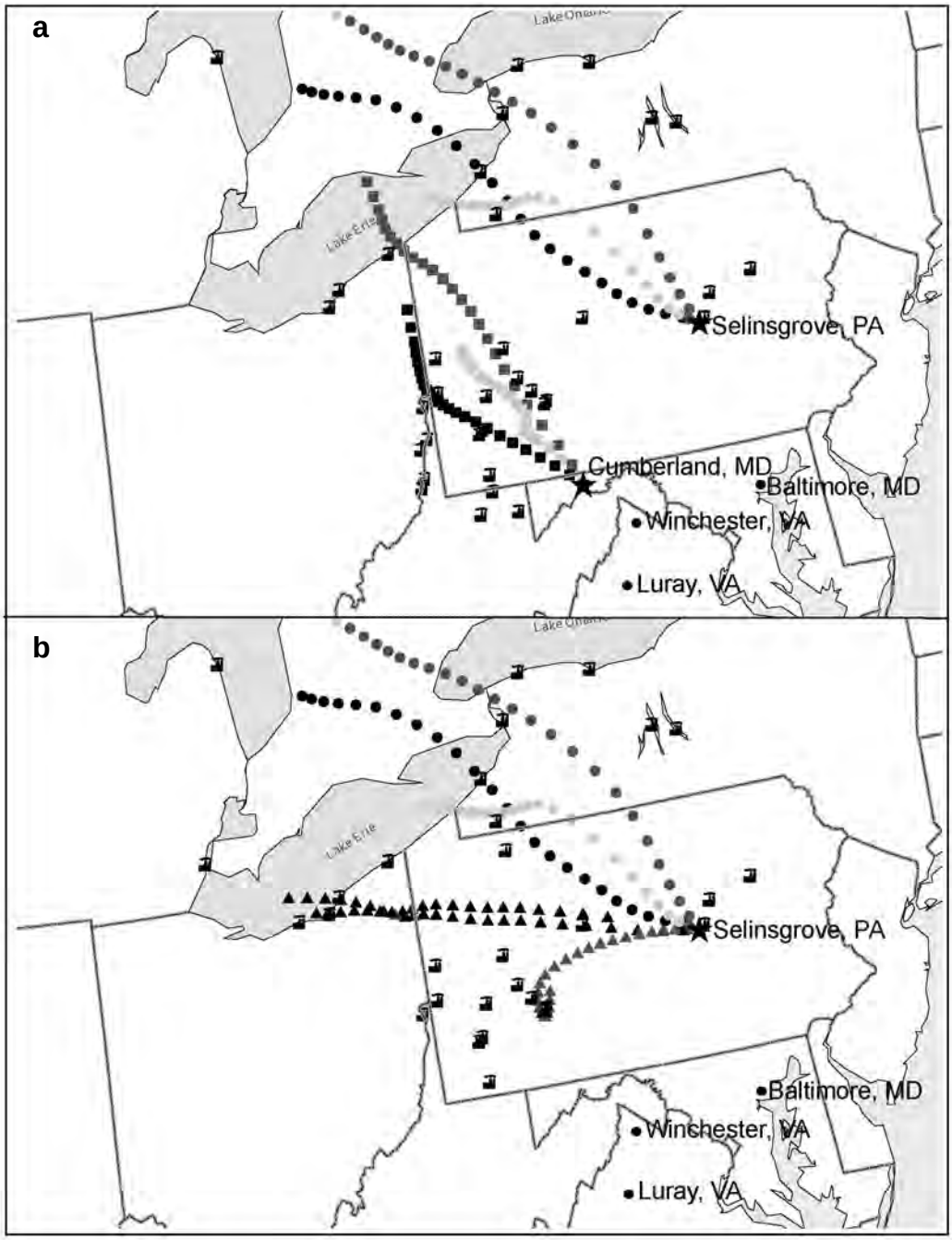

Figure 49. Map of northeastern U.S. showing modeled back trajectories (24 h) from Cumberland, MD and Selinsgrove, PA on 15 Aug, 2003 at 1500 and 2000 UTC, respectively (a); and Selinsgrove, PA on 15 Aug, 2003 (circles) and on 4 Aug, 2002 (triangles) at 2000 and 2100 UTC, respectively (b). Light gray represents 0-500 m, dark gray 500-1500 m, and black 1500-2500 m AGL. Icons represent power plants that fall within trajectory buffers regardless of size or extent of down scaling during the blackout (Marufu *et al*., 2004).

The impact of this emissions disparity on downwind air quality is illustrated in Figure 50. Sulfur dioxide, O_3, and light scattered by particles measured over Selinsgrove in 2003 were reduced by >90%, ~50%, and ~70%, respectively, relative to 2002 observations (Figures 50a-c). Defining visual range as the 98% extinction point, the reduction in aerosol extinction corresponds to an increase in visual range of > 40 km. The concomitant decreases in SO_2 and particle light scattering suggest that improvements in visibility resulted directly from reduced power plant SO_2 emissions. Reductions in O_3, apparently the result of decreased NO_x emissions, were greatest near the surface (~38 ppbv) and fell off at higher altitudes where large-scale processes play a more dominant role in the O_3 budget. As with CO concentrations, however, light absorption by particles shows a less dramatic difference (Figure 50d). In fact, absorption was higher in 2003 than in 2002, suggesting little or no reduction in mobile emissions during the blackout relative to typical values. The single scattering albedo was 0.95 on the normal day, but fell to 0.85 during the blackout because of the reduced scattering. Electricity generation produces very little CO or absorbing aerosols; instead, they are mainly emitted by mobile sources that continued to operate during the blackout. No discernible changes in road vehicular traffic activity could be observed near or upwind of the study area during the blackout (Szekeres, 2004).

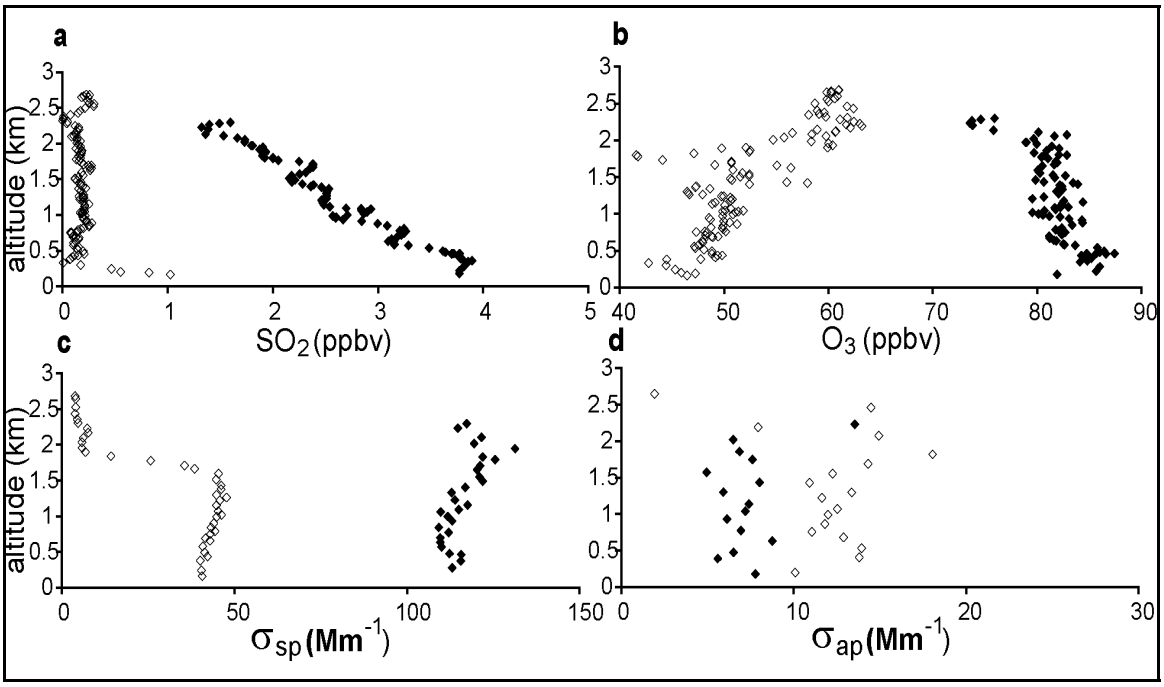

Figure 50. Comparison of running 1 min mean SO_2 mixing ratios (a); 10 s O_3 mixing ratios (b); particle light scattering at 550 nm (c); and particle light absorption at 565 nm (d) measured on 15 Aug, 2003 (open diamonds) and 4 Aug, 2002 (filled diamonds) over Selinsgrove, Pennsylvania (Marufu *et al.*, 2004).

Twenty-four hour forward trajectories using the NOAA ARL HYSPLIT model (Version 4) (Draxler and Rolph, 2003) and EDAS meteorological fields run from Selinsgrove at 21:00 UTC from 500, 1500, and 2500 m AGL reach Baltimore, Philadelphia, and New York, depending on the altitude (Figure 51). Based on these results, the improvement in air quality depicted in Figure 50 was likely experienced over several major eastern cities. This is corroborated by the fact that O_3 concentrations in the Baltimore non-attainment area were forecasted to be 115 ppbv but reached only 80 ppbv (Maryland Department of Environment, 2003). Because the median and RMS forecast errors are 10 and 22 ppbv, respectively, the bulk of this overestimation has been attributed to the reduction in power plant emissions.

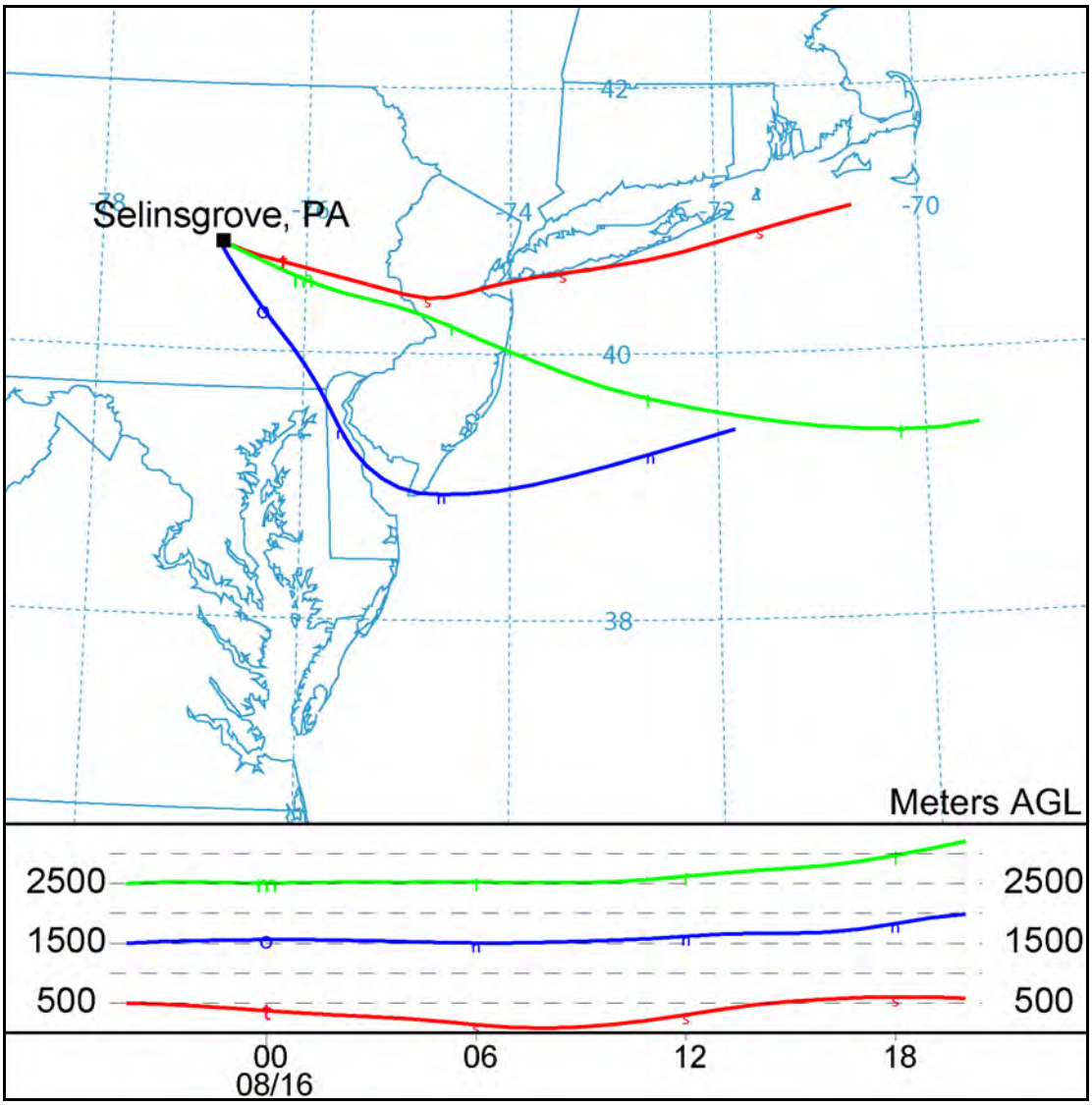

Figure 51. 24 h forward trajectories using the NOAA ARL HYSPLIT model (Version 4) and EDAS meteorological fields run from Selinsgrove, PA at 21:00 UTC 15 August 2003 from 500, 1500, and 2500 m AGL traverse Baltimore, Philadelphia, and New York.

6.3. Summary

Airborne measurements over central Pennsylvania on August 15, 2003, ~24 hours into one of the largest electrical blackouts in North American history, showed large reductions in SO_2 (>90%), O_3 (~50%), and light scattered by particles (~70%) relative to observations over western Maryland earlier in the day and over the same

location the year before. This translated into a reduction in low level O_3 of ~38 ppbv and an improvement in visual range of > 40 km. Forward trajectories show that these improvements in air quality benefited much of the eastern U.S. Carbon monoxide and particle light absorption values did not change much, however, suggesting that mobile emissions were largely unaffected during the blackout. Reported power plant SO_2 and NO_x emissions upwind of central Pennsylvania on August 15, 2003 were 34% and 20% of normal, respectively. Thus, the decreases in SO_2, O_3, and particle light scattering appear to be predominantly due to reductions in power plant emissions hundreds of km upwind of the study area. The observed reductions exceed expectation based on estimated relative contribution of power plants to these pollutants and their precursors (NO_x ~22%, SO_2 ~69%, and PM ~ 8%) (USEPA, 2003(a)). This apparent paradox may be the result of an underestimation of emissions from power plants, inaccurate representation of power plant effluent in emissions models, or unaccounted for atmospheric chemical reaction(s). These unique observations will provide a valuable resource for determining whether air quality models can accurately reproduce the contributions of specific pollution sources to regional air quality.

Chapter 7: Overview and Conclusions

7.1. Statistical Overview

The previous chapters highlight investigations of the most interesting events captured while performing the aircraft measurements. However, as described in the introduction, between February 2001 and February 2004, 160 research flights were conducted over the Mid-Atlantic and northeastern U.S. In an attempt to ascertain seasonal or annual trends in the aerosol optical properties measured during the flights, a statistical analysis was undertaken.

For each month during which flights were conducted, the fixed position, vertical survey spirals were grouped according to location and time of day. If more than one spiral per month was performed near the same time (but on a different day) at a given location, the mean, median, standard deviation, minimum and maximum values as well as the 1st and 3rd quartile values were calculated for temperature, relative humidity, O_3, SO_2, CO, σ_{sp} (at 450, 550, and 700 nm), backscatter ratio (at 450, 550, and 700 nm when available), σ_{ap} (corrected to 550 nm), and particle counts (for particles with diameters between 0.01 and 1.0 μm as well as diameters between 0.3 and 1.0 μm). Figure 52 shows the flight tracks for the flights with vertical survey spirals that were analyzed. The stars represent the locations where the vertical survey spirals were performed. The three character codes given at the spiral locations are the airport identifiers. The airport names, latitudes, and longitudes are provided in Appendix 1.

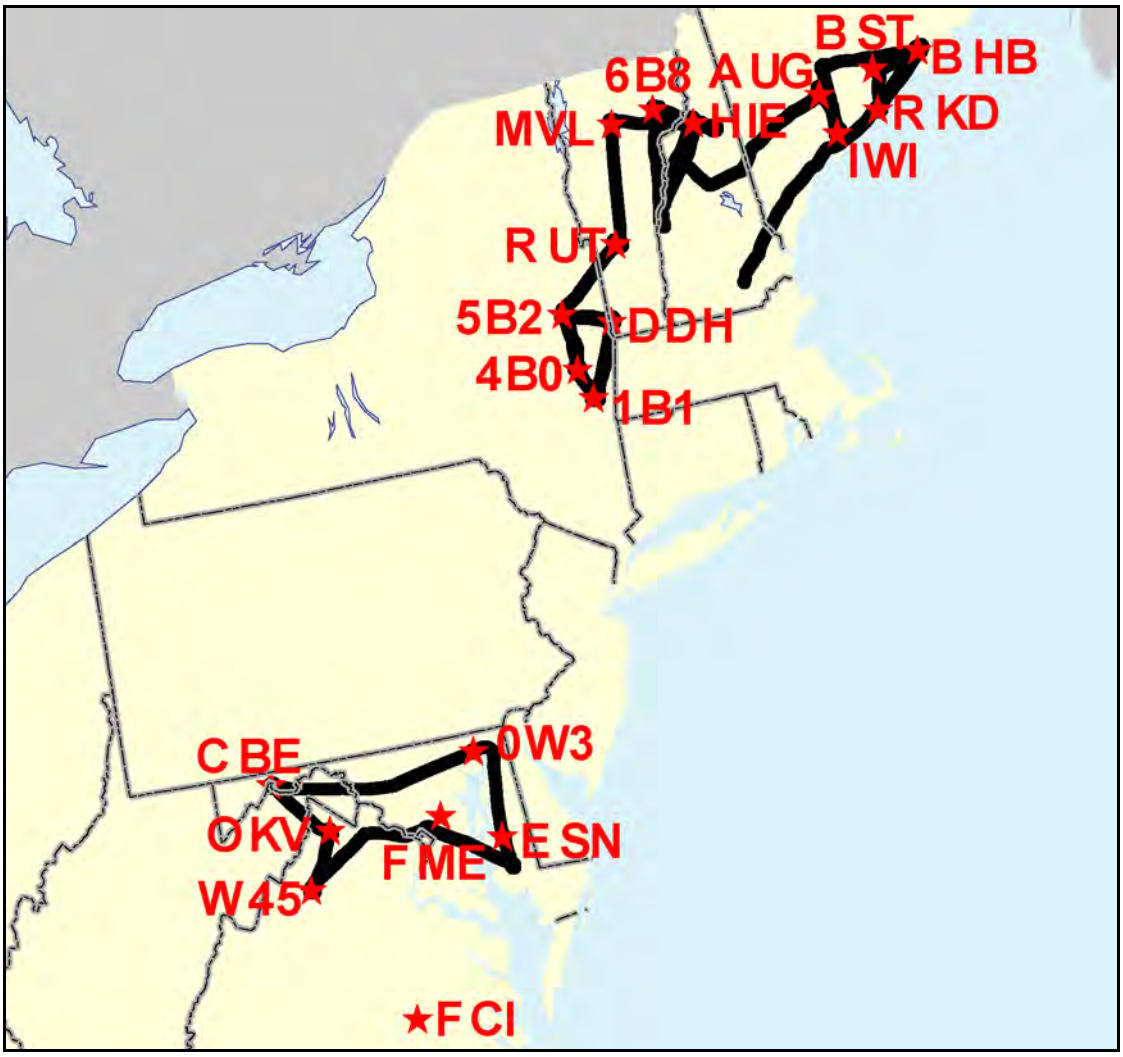

Figure 52. Map of the Mid-Atlantic and northeastern US. Solid black lines denote flight tracks. Red stars show locations of vertical survey spirals with the three character identifiers also given in red.

The statistical data were calculated at 100 m intervals beginning at the surface and culminating at 3 km. Data were collected at different frequencies depending on the instruments and the particular flights. Likewise, as detailed previously, vertical survey spirals were conducted as closely to 100 m min^{-1} as possible, although strict adherence to this rate of climb was sometimes impossible. As a result, there was often more than one value in a 100 m interval. In these cases, the values were

averaged so that only one value was reported for every 100 m. Conversely, there was frequently little or no data collected near the top of the 3 km column, depending on the flight time (morning spirals were typically performed from the surface to 3 km whereas the afternoon flights usually only went to 2.5 km) and the weather conditions (the inlet system and instrumentation are not designed for sampling within clouds). Also, because pressure altitude is calculated as meters above mean sea level, there was often a lack of data near the surface (depending on surface altitude above mean sea level).

Plots of the optical property statistical values are given in Appendix II. The 2001 and 2002 data show the single scattering albedo at 550 nm. The winter 2003 data show the particle counts (for particles with diameters between 0.01 and 1.0 and 0.30 and 1.0 μm) since the PSAP was being modified during that campaign. The subsequent data include these values as well as the asymmetry parameter at 550 nm. The asymmetry parameter data are available due to the use of the backscatter shutter on the nephelometer. By measuring scattering from 90 – 170^{o} (the nephelometer is limited in its scattering angles; data are corrected for this angular truncation, see chapter 2), the backscatter to total scatter ratio was calculated. This ratio was converted to the asymmetry parameter with the equation:

$$g = -2x + 1 \qquad (25)$$

where x represents the backscatter to total scatter ratio. The plots shown in Appendix II are the median values with the horizontal error bars representing the 1st and 3rd quartile values.

Seventy-two hour backward wind trajectories at 250 and 1500 m above ground level (AGL) using the NOAA ARL HYSPLIT model (Version 4) (Draxler and Rolph, 2003) and EDAS meteorological fields were run from each spiral location used in the calculation of the statistical data beginning at the times the individual spirals were performed. Therefore, there are twice as many trajectories as there are spirals that went into the calculation of the statistical data (one at 250 m and one at 1500 m above each spiral location for every time a spiral was performed). The 250 m altitude was chosen to characterize the transport path of the air parcels ultimately observed within the daytime mixed layer. The 1500 m altitude was chosen to characterize the transport path of the air parcels observed near the maximum depth of the daytime mixed layer. The seventy-two hour time frame was chosen to illustrate the regional origins of the pollutants. The trajectories that correspond to the statistical data are given in Appendix III. Each point along the trajectories represents an hour in the path of the air parcel. The individual points are color coded according to altitude (color bar shown in the Appendix). The end of each trajectory is labeled with the research flight designation (ymmddflight#) and beginning altitude. Some endpoints are not shown because the trajectory path continues outside the regional area of the plots. While the back trajectories do not provide a quantitative insight into the statistical analysis, they do allow for a qualitative examination of whether the monthly statistical values are representative of specific transport regimes.

7.1.1. Summary of Results

The calculated asymmetry parameters in the summer of 2003 and winter of 2004 (Appendix 2) show a distinct inter-seasonal trend. The values in summer are

larger than those in winter, providing evidence that photochemical processes dominate over RH as the determining factor in particle growth. The larger a particle is relative to the wavelength of impingent radiation, the more it will scatter light in the forward direction. This leads to a smaller backscatter ratio and a higher asymmetry parameter. Relative humidity is generally higher in winter due to the decreased temperatures, but the amount of solar radiation reaching the lower atmosphere is much less than in the summertime. Consequently, the oxidation potential of the atmosphere is increased and photochemical processes are accelerated in the summertime. The primary constituent of $PM_{2.5}$ in the eastern U.S. is SO_4^{2-} (Malm, 1992). Sulfate is largely a secondary pollutant, resulting from the oxidation of SO_2 (see Chapter 1). When the oxidation potential is diminished (as in the wintertime), SO_2 cannot be oxidized as rapidly as in the summertime. When this is the case, less SO_4^{2-} is produced and particle growth decreases. With less SO_4^{2-} available, the RH is irrelevant, as it will only play a role when enough soluble material is readily available. All this, however, is only true assuming that emissions and transport of SO_2 are relatively constant between summer and winter.

Further evidence of photochemical processes playing the dominant role over RH in determining particle growth is the tendency for the asymmetry parameter to increase slightly above the PBL. The PBL in this case was defined as the point where the RH began to rapidly decrease with altitude. Thus, the RH is lower above the PBL than within it. At the same time, however, larger asymmetry parameters mean larger particles that scatter light predominantly in the forward direction. The actinic flux is greater above the PBL and photochemical processes are accelerated. Also, particles

are less subject to deposition and rainout above the PBL and may persist for longer periods, thereby allowing more time for growth. The same phenomenon (larger particles above the PBL than within and photochemical processes playing a dominant role over RH in particle growth processes) was observed through independent analytical techniques and described in detail in Chapter 3.

There are three interesting trends associated with the calculated single scattering albedo values at 550 nm. First, the ω_{0550} values appear to decrease with altitude. Hartley *et al*. (2000) also observed this phenomenon during the TARFOX experiment. Their explanation was twofold: that it was due to decreasing RH with altitude and/or an increase in the relative amounts of carbonaceous to sulfate species with altitude. The first explanation is unlikely given the fact that particle growth seems to be dominated by photochemical processes rather than RH. The latter is the more likely scenario and is corroborated by evidence presented herein. However, the reality may be somewhat more complex.

The statistical analysis showed that scattering tends to decrease with altitude while absorption, although a small fraction of total particle light extinction, remains fairly constant with altitude. Sulfate is the primary light scattering species in $PM_{2.5}$ in the eastern U.S. It is also highly soluble and consequently subject to rain out, a possible reason for the decrease in scattering with altitude. Black carbon is the primary light absorbing species in $PM_{2.5}$. Black carbon is not soluble and would be less subject to rain out prior to mixing. This may explain the constancy of absorption with altitude as well as the decrease in ω_{550} with altitude. It would also support the

hypothesis that the relative amounts of carbonaceous to sulfate species increase with altitude. There are more factors at work though.

In Chapter 3, it was shown that the extent of internal mixing between sulfate-dominated particles and BC particles determines the degree of absorptivity of the resulting mixture. When BC and sulfate-dominated particles were internally mixed, the absorption was greater than the corresponding external mixture. Thus, the increase in absorption with altitude is not solely due to an increase in the relative amounts of carbonaceous species. It is also due to a change in the degree of mixing between predominantly absorbing and predominantly scattering particles with altitude.

The second noticeable trend associated with ω_{0550} (now defined as the extinction weighted column average) is a diurnal increase. Single scattering albedo values at 550 nm were seen to increase in time between the morning and afternoon. This was due primarily to the fact that scattering generally increased over the course of a day while absorption remained largely constant. This finding also supports the predominance of photochemical processes over RH in particle growth. Relative humidity typically decreases diurnally while photochemical processes increase due to increased solar radiation. The oxidation of SO_2 to SO_4^{2-} is the rate limiting step in the particle growth process since the SO_2 must be converted to SO_4^{2-} before RH can play a role. Nonetheless, at the moderate RH values typically encountered during the flights, the rate limiting step also appears to be the dominant one.

The final observable trend in ω_{0550} is a weak seasonal increase, which may possibly follow a photochemical argument similar to the other observable trends.

Absorption remained relatively constant from the beginning of the summer to the end, while scattering increased as the season progressed. Once again, this could be explained through an increase in photochemical processes; this time, however, more as a result of increased temperatures and reaction rates than an increase in actinic flux, which should peak near the summer solstice. Another explanation may lie in increased power consumption (due to increased use of air conditioning), although this is unlikely; SO_2 emissions tend to be relatively constant seasonally and annually.

Another interesting observation in the ω_{0550} data is a decline in the 2003 values as compared to the previous two years (Figure 53). The 2004 winter data are also lower than any of the summer values (including 2003), but unfortunately there are no other winter data with which to compare them. Again, the reason for the decline can be explained by variable scattering values and fairly constant absorption values. Scattering values were lower in 2003 relative to the previous two years while absorption values changed little between the years. The summer of 2003 was considerably cooler and wetter than the previous two summers. The synoptic scale meteorological patterns were often such that a large upper air ridge was positioned over the Great Plains with a low centered over the eastern third of the country. This created large scale funneling of continental polar air from Canada to the Mid-Atlantic and Northeast, bringing with it cooler, more pristine conditions. There is very little industry or electricity generation due north of the Mid-Atlantic and Northeast. Most industrial facilities and power plants lie to the west and northwest. Also, recirculation of the air around the Western Atlantic Ridge entrained moisture from the Atlantic Ocean and Gulf of Mexico, which encouraged greater than average precipitation. As

noted before, rain out would reduce the amounts of soluble SO_4^{2-} in the atmosphere. Hydrophobic BC, however, would be largely undisturbed by increased precipitation amounts. Thus, to a large degree the drop in ω_{o550} values in the summer of 2003 can be attributed to the anomalous meteorological patterns. The monthly average ω_{o550} values at the GSFC AERONET site also show a slight decrease in the summer of 2003 relative to the previous two summers (Figure 53). Although these decreases are not statistically significant as the values in question are all within analytical uncertainty. On the other hand, the AERONET and aircraft values do disagree despite analytical uncertainty. The optical depth values measured by the two platforms, however, agree during the summer of 2003 (Figure 54). Given that the scattering makes up ~90% or more of the total extinction, the scattering values most likely agree also. Once again, the absorption values are seen as the reason for the disagreement between the two platforms. Higher absorption measured aboard the aircraft has little effect on optical depth values, but does impact the single-scattering albedo. The same inconsistencies are seen between the two platforms for February 2004 (Figures 53, 54).

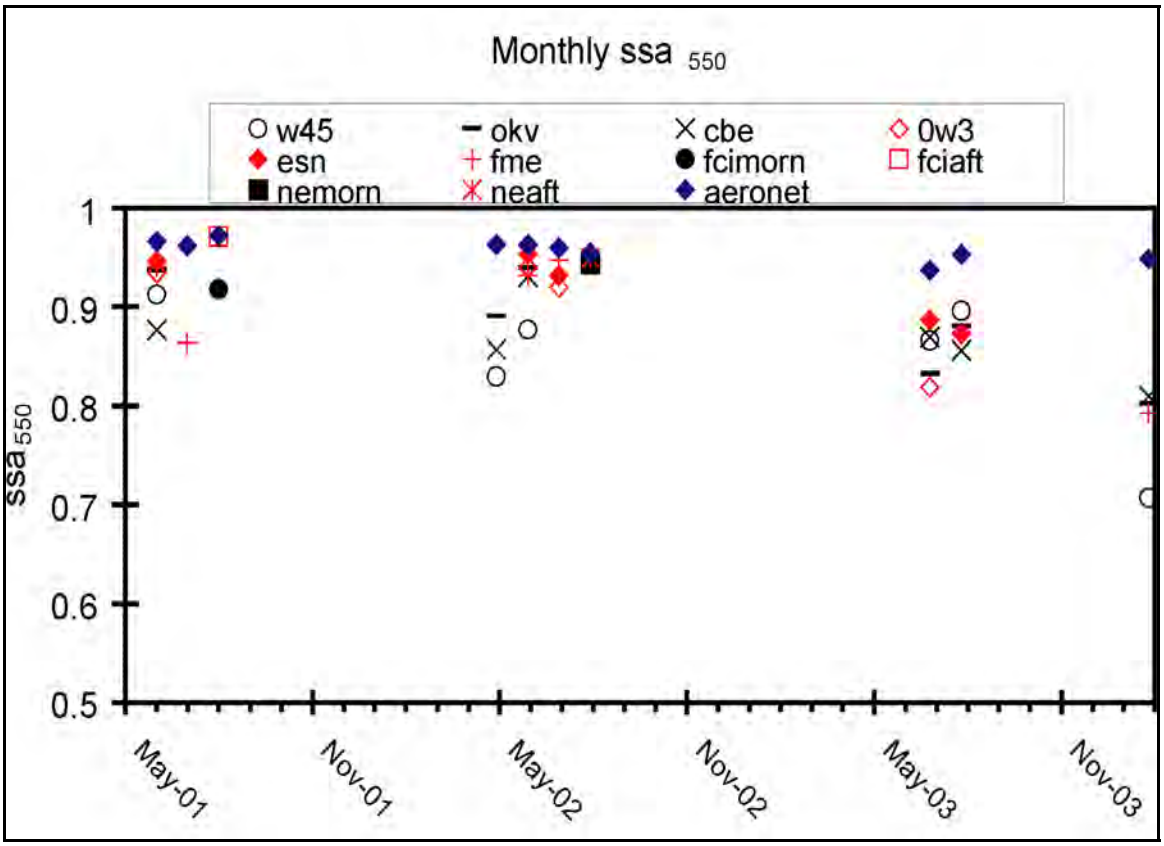

Figure 53. Monthly median single scattering albedo values at 550 nm measured by the aircraft and monthly average values determined by AERONET. The symbols are identified in the key. The aircraft measurement locations are described by the airport identifiers. Fcimorn and fciaft denote the median value from all spirals performed in that particular month over the airport FCI in the morning (fcimorn) and afternoon (fciaft). Nemorn and neaft denote the median values of all flight spirals performed in the Northeast between August 12 and August 14, 2002 in the morning (nemorn) and afternoon (neaft). See Appendix IV.1 for uncertainty estimates.

The statistical data show a general propensity for the scattering values to be perturbed while the absorption values remain largely invariant. Potential problems do exist with the measurement technique used aboard the aircraft that were discussed thoroughly in previous chapters and will not be revisited here other than to say that they may contribute to an overestimation of low absorption values. Also discussed above is the fact that selective rain out of soluble SO_4^{2-} species over insoluble BC

may engender the phenomenon. There is another possibility as well. Sulfate dominated particles are largely secondary pollutants that result from point source emissions of SO_2. By definition, point sources are geographically fixed and happen to be largely concentrated in the Ohio River Valley and to a lesser degree the Great Lakes region. Thus, the impact of this pollution source on the air quality in the eastern U.S. is dependent upon certain meteorological conditions. BC on the other hand is predominantly the product of vehicular emissions and is, therefore, more ubiquitous with respect to geographical variations. The impact of these emissions would not be as dependent upon meteorological conditions.

The August 2002 data were analyzed in a different manner from the rest of the data. All the flights that went into the analysis for this month were part of a multi-day campaign in the northeastern U.S. during a sustained haze episode in that region. Chapter 3 describes the study based on measurements made during the transect between New Hampshire to Maryland on the last day of the campaign. Rather than grouping spirals conducted over the same locations, as per the other months, all morning spirals during the three-day campaign were grouped together for statistical analysis. The same was done for the afternoon spirals. This was performed to investigate the regional nature of the pollution episode and, specifically, the hypothesis that optical property values should be mostly invariant both spatially and temporally. The results exceeded expectations.

The winds were mainly from the west during the campaign and only shifted to the southwest toward the end of the campaign (Appendix III.22-27). Thus, most of the emissions that were transported to the measurement locations were from power

plants in the Great Lakes region. There is not a lot of vehicular activity in the area of the study or in the transport paths of the trajectories compared to the large metropolitan areas in the Mid-Atlantic and Northeast. As a result, scattering values were relatively high and absorption values were average to low (Appendix II.9). The consistency of the values (denoted by the small error bars on the plots) points to the regional nature of the episode and the impact of transported pollutants on the regional air quality. Further corroboration of the regional nature of the episode is seen in the comparison of average GSFC AERONET optical depth and single scattering albedo values for the days of the episode to values calculated from flight measurements (Figures 53, 54). The similarity of both the optical depth and single scattering albedo values as observed by the disparate sampling platforms hundreds of km away argues against the likelihood of this being coincidental. Interestingly, though, while the aircraft values of single scattering albedo were relatively high (presumably due to the predominance of sulfates and lack of soot), the AERONET values were low (within uncertainty ranges though) compared to climatological data (Dubovik *et al*., 2001). Even so, accounting for the analytical uncertainty of both sets of measurements, the aircraft values agree with the AERONET climatological values. This does not explain, however, the lower values observed by AERONET during this period. Given the synoptic scale of the episode, westerly and southwesterly winds would traverse the Ohio River Valley and areas to the south before reaching the GSFC site. These areas have some of the highest concentrations of elemental carbon according to the Interagency Monitoring of Protected Visual Environments (IMPROVE) network of surface observation stations (Malm *et al*., 2004). The relatively large

concentrations of absorptive particles would explain the lower single-scattering albedos observed by AERONET during this period.

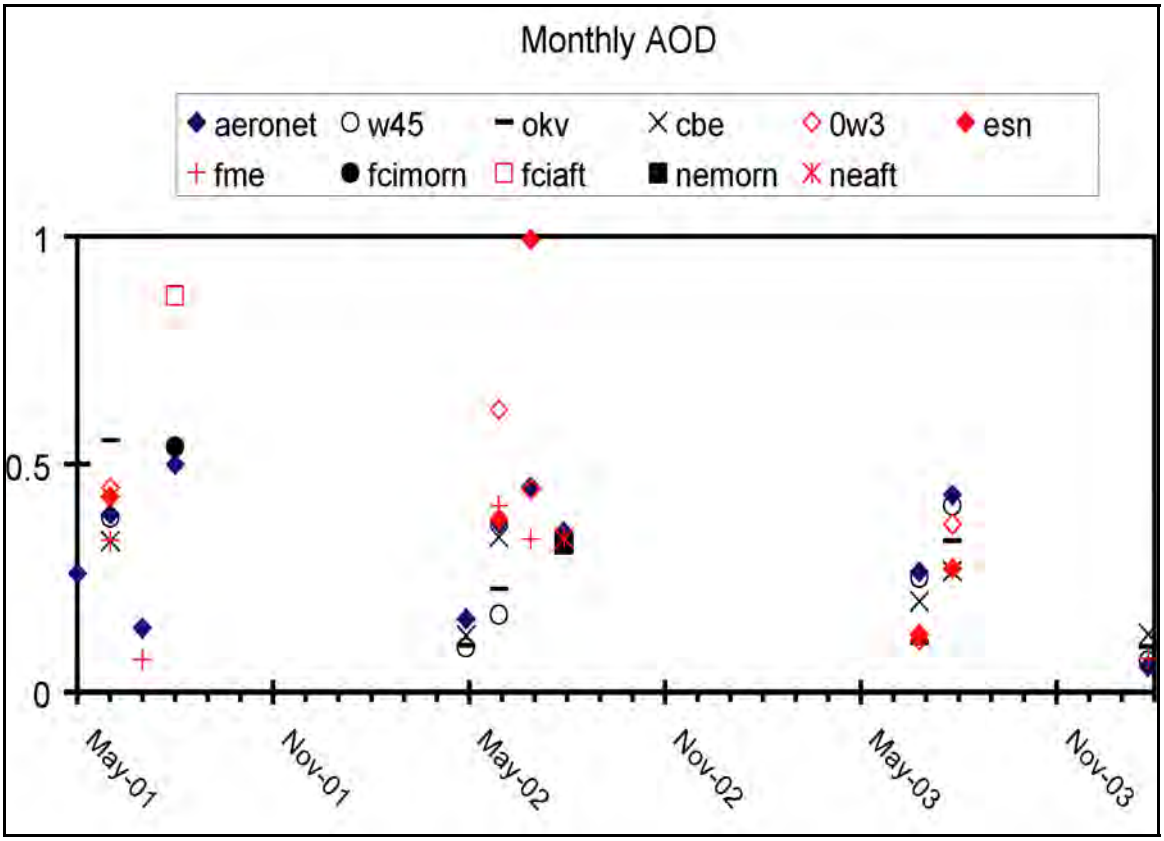

Figure 54. Monthly median values of aerosol optical depth at 550 nm calculated from aircraft measurements of extinction and monthly averages as determined by AERONET. See Figure 53 for an explanation of the symbology. See Appendix IV.2 for uncertainty estimates.

There are some general conclusions that may be drawn from the wind trajectory analyses. Namely, wind speed and direction seem to have an impact on the aerosol optical properties observed over the eastern U.S. As noted earlier, the largest effect is seen in the scattering values. Absorption values, once again, were largely unperturbed by the wind speed and direction. As a result, the variability in the single-

scattering albedo was mainly due to the variability in scattering values. Also, because scattering makes up ~90% or more of the extinction, changes in aerosol optical depth were the result of fluctuations in scattering values. This finding would hold true under most circumstances given the typical ratio of scattering to absorption. Winds from the west and northwest brought the highest scattering aerosols and thus, the highest single-scattering albedo and optical depth values. Areas to the west and northwest of the eastern U.S. are dominated by coal-fired power plants, the likely explanation for this occurrence. Southerly winds brought slightly lower scattering values and as a result, the single-scattering albedo and optical depth values were lower as well. Areas to the south lack the power plants of the Midwest, but biogenic emissions of organic species are much higher. Particles dominated by organics also scatter light efficiently (Malm *et al*., 1994). Winds from the north, where there is little in the way of pollution sources or biogenic emissions, were associated with lower scattering values and, therefore, single-scattering albedo and optical depth values. Wind speed also affected these values though. Higher wind speeds, translated into longer trajectories, were always associated with lower scattering and even absorption values. Greater dispersion of pollution does not allow it to accumulate in one spot. Thus, when wind speeds were greater, the optical depth declined, whereas the single-scattering albedo was largely unaffected since scattering and absorption were equally impacted.

Particle number data are unavailable until the winter of 2003 and so only the data will from that point on will be discussed. There is little difference seen in the number of total sub-micrometer particles ($0.01 - 1.0\,\mu m$) in the boundary layer

between the summer and winter data (Appendix II). There are, however, fewer accumulation mode particles ($0.3 – 1.0\,\mu m$) in the boundary layer in the winters of 2003 and 2004 as compared to the summer of 2003. There appears to be as many primary particles in the boundary layer during the winter as there are in the summer. The difference, then, is in the formation of secondary particles between the seasons. This provides further evidence that photochemical processes play the predominant role in particle growth. If there are roughly the same amounts of primary particles in the boundary layer regardless of the season, the difference in haze episodes stems largely from the photochemical processes that drive them. However, this conclusion presupposes equivalent amounts of particles that are subject to photochemical processes (i.e., SO_2 or organics) during both seasons. The requisite meteorology must therefore be present to transport the emissions of primary photochemically active species.

There is also a general decline seen in summertime and wintertime of particle numbers with altitude. However, the decline in the wintertime occurs at much lower altitudes than in the summertime. This is due to the decreased surface heating during the wintertime. Surface heating drives the vertical mixing of air parcels. In the wintertime, vertical mixing is decreased and particles are seldom able to reach the lower free troposphere.

Comparisons between in-situ aircraft measurements and AERONET observations have already been discussed in detail. Therefore, the only further comment will be a substantiation of previous comparisons through the statistical analyses. When the monthly average AERONET values of optical depth and single-

scattering albedo (both interpolated to 550 nm) were compared to the monthly median values calculated using aircraft measurements, the optical depth values agreed nicely while the AERONET values of single-scattering albedo were consistently higher (Figures 53, 54). Once again, because scattering makes up ~90% or more of the total extinction, this shows that the scattering values are most likely in agreement, while the absorption values measured aboard the aircraft are significantly higher than those determined by AERONET.

7.2. Conclusions

7.2.1. Summary

Chapter 3 details the investigation that led to the inception of the two reservoir conceptual model, the theory that the chemistry and physics of multi-day haze and ozone episodes over the Mid-Atlantic and northeastern U.S. may be accurately represented by two reservoirs, the PBL and LFT. Measurements were made during a constant altitude flight at the maximum height of the PBL from New Hampshire to Maryland on the last day of a multi-day haze and ozone episode in early August 2002. Precursor species are typically emitted in the PBL, where they are subject to surface deposition. When these precursors reach the LFT, however, deposition is no longer a factor, and their lifetimes are protracted. The acceleration of photochemical processes in the LFT causes air parcels to undergo chemical changes more rapidly. As a result, there were greater concentrations of O_3 and larger particles that scattered (and absorbed) visible light more efficiently in the LFT than in the PBL.

Chapters 4 and 5 describe the measurements and subsequent analyses of the smoke plume from Canadian forest fires that was advected over the eastern U.S. Observations of the smoke plume were made aboard the aircraft on July 8, 2002. On this day, the smoke was contained in a layer between 2 and 3 km and distinct from the local haze pollution below. Large O_3 and CO mixing ratios were found in the smoke layer together with many sub-micrometer particles that scattered and absorbed the solar radiation efficiently. The smoke particles had a mean single-scattering albedo value of 0.93±0.02 at 550 nm while the underlying PBL particles had a mean value of 0.95±0.01 at 550 nm. The scattering Ångström exponents of the larger, aged smoke particles were between 0.83±0.15 and 1.23±0.38 while the smaller, PBL particles had values between 1.59±0.30 and 1.99±0.32 for $\alpha_{450/700}$. Calculated Aerosol Optical Depths (550 nm) from just above the surface to ~3 km ranged from 0.42±0.06 to 1.53±0.21 depending on the location.

According to radiative transfer calculations, absorption of solar radiation within the smoke plume nearly equaled the total amount attenuated at the surface. This demonstrates a cooling at the surface coupled with a warming of the air aloft. A morning subsidence inversion was posited as the cause of the delineation of the smoke from the underlying layer. Solar heating of the smoke layer then maintained the temperature inversion through the afternoon. This is an example of a positive feedback loop that prevented vertical mixing and dilution, thereby protracting the lifetime of the plume and the regional radiative impacts.

Satellite reflectances were used to calculate the optical depth of the smoke plume with two sets of inputs, AERONET retrieved optical properties and in-situ

aircraft measured optical properties. Different combinations of AERONET and in-situ measured optical properties were also used to retrieve the optical depth. The optical depths calculated using the pure AERONET optical properties were the lowest, while retrievals using the pure in-situ values produced optical depths 22-43% larger, due to the lower reflectivity (greater absorption) of the measured aerosol. In fact, the in-situ measurement of absorption was twice as large as that derived by AERONET. Even so, the optical depth retrievals using the different inputs were equivalent given the total uncertainty of the results.

To calculate broadband regional radiative forcings, the optical depth values (550 nm) were extrapolated across the entire solar spectrum according to the particle size distributions. The radiative forcing at the surface and TOA calculated using the in-situ optical properties came closer to surface and TOA measurements than those calculated with the AERONET optical properties.

Finally, Chapter 6 details airborne measurements made over central Pennsylvania on August 15, 2003, ~24 hours into the largest electrical blackout in North American history. The observations included large reductions in SO_2 (>90%), O_3 (~50%), and light scattered by particles (~70%) relative to observations over western Maryland earlier in the day and over the same location (central Pennsylvania) the year before. Ground level O_3 dropped by ~38 ppbv and visibility improved by >40 km. Carbon monoxide and absorption values were unaffected by the blackout. Forward trajectories illustrate that the cleaner air resulting from the blackout benefited much of the eastern U.S., including Philadelphia, New York, and Baltimore.

Reported power plant SO_2 and NO_x emissions upwind of central Pennsylvania on August 15, 2003 were 34% and 20% of normal, respectively. The decreases in SO_2, O_3, and particle light scattering appear to be mainly due to reduced power plant emissions hundreds of km upwind of the study area, an observation that exceeds expectations based on the estimated relative contributions of power plants to these pollutants and their precursors (NO_x ~22%, SO_2 ~69% and PM ~ 8%) (USEPA, 2003(a)). This apparent inconsistency may be the result of an underestimation of power plant emissions, inaccurate representation of power plant effluent in emissions models, or unaccounted for atmospheric chemical reactions. These unique observations will provide a valuable resource for determining whether air quality models can accurately reproduce the contributions of specific pollution sources to regional air quality.

7.2.2. Policy Implications

The 2003 North American electrical blackout provided a unique opportunity to enhance our understanding of the complex interplay of factors contributing to air pollution in the Mid-Atlantic and northeastern U.S. Transport of point source pollution over hundreds of kilometers, particularly into large urban areas, makes it difficult to quantify the effects power plants have on regional air quality. Measurements made during the blackout are likely inimitable because of the suddenness and magnitude of the scale back. A multiplicity of power plants was tripped while all other variables, atmospheric and chemical, were held relatively constant. The blackout also rendered inoperable many surface stations in the region normally capable of making measurements of such a phenomenon. Likewise, high

clouds prevented satellites from contributing much data to the investigation. As a result, the aircraft measurements were a valuable source of data for this unique event.

The regulation of electrical generation facilities and adoption of sound environmental policies that benefit the consumer without deleterious effects to the producer are contentious issues. Determining the direct impact of power plant emissions on regional pollution levels aids in the formulation of effective mitigation strategies. The evidence from the aircraft measurements shows that power plants may play a more dominant role in regional air quality than previously suspected. In fact, the observed reductions in air pollutants exceed expectations based on the estimated relative contributions of power plants to these pollutants and their precursors (see section 7.2.1). Regardless, the results from the blackout study should aid in parameterizing future modeling studies that investigate the impact of power plants and other pollution sources on regional air quality as well as guide in the formulation of future mitigation strategies.

The regulation of power generation facilities and air pollution is not just a North American problem. These issues have global import. In fact, Asian NO_x emissions surpassed those in North America and Europe in the last decade and will most likely continue to do so for the foreseeable future (Akimoto, 2003). International initiatives to mitigate global air pollution are not only necessary but call for involvement from both developed and developing countries.

7.2.3. Climate Implications

The two-reservoir conceptual model provides a characterization of the chemistry and physics that occur during multi-day air pollution episodes in the Mid-

Atlantic and Northeast. The existence of a layer aloft comprising large, absorptive particles and high concentrations of O_3 is a product of the vertical stability of these multi-day episodes. An accurate numerical model simulation of photochemical smog processes over the Mid-Atlantic and Northeast should incorporate the existence of these two reservoirs, and simulate or at least parameterize the role of mixing between them in multi-day smog events.

The smoke plume from Canadian forest fires allowed for the characterization of the optical properties and radiative impacts of a boreal forest fire plume that had been transported over 1000 km. The results of this study further our understanding of the chemical transformations of transported smoke particles and the role absorbing aerosols play in the global climate. The presence of a discrete, optically thick, absorptive layer of smoke overlying a more scattering plume provided a rare opportunity to quantify the climatic impacts of this type of vertical stratification. The results also reinforce the importance of in-situ aircraft measurements of aerosol optical properties. Remote sensing platforms that collect column-integrated aerosol optical properties cannot provide the requisite vertical information for the investigation of the climatic impacts of stratified layers of aerosols with different radiative properties.

A common theme that reoccurred throughout this research was the presence of an absorptive aerosol layer overlying a more scattering one. The presence of such a layer may have profound impacts on the global climate. Despite the fact that the absorptive layer was optically thin the majority of the time (except during the forest fire smoke plume), the underlying scattering layer would exacerbate the absorptive

nature of the layer aloft. Because of multiple scattering effects, each photon would have a greater probability of being absorbed than if the absorptive layer existed independently. Plus, because the scattering layer lies below the absorptive one, the reflectivity of this layer is diminished. If this phenomenon of an absorptive layer overlying a scattering layer is as ubiquitous as this study suggests (which is reasonable considering the meteorological and chemical explanations put forward in this chapter), then it may serve to decrease the modeled estimates of the net global cooling effects of scattering aerosols and increase estimates of the net warming effects of absorbing aerosols that are based on column-averaged and surface measurements.

7.3. Recommendations

Aerosol optical depth, the vertically integrated sum of aerosol light scattering and absorption, is a quantity that is used for column closure studies and the calculation of aerosol radiative forcing. In most areas of the western hemisphere, light is primarily scattered by particles. The contribution of particle light absorption to the aerosol optical depth is small. As a result, uncertainties in absorption values are often overlooked. Because of the large contribution of scattering to the aerosol optical depth, a reasonable agreement in scattering values typically leads to a reasonable agreement in optical depth values. However, radiative forcing calculations are more complex than optical depth retrievals and are more prone to inaccuracy. This particular phenomenon was demonstrated in Chapter 5, where optical depth retrievals using two sets of inputs were equivalent to within uncertainty,

but the radiative forcing values based upon the two inputs were significantly different.

The degree of particle absorption as well as the vertical distribution of absorptive particles can have profound impacts on the energy balance of the surface-atmosphere system, the stability of the lower atmosphere, the hydrological cycle, and ultimately the global climate. Therefore, it is imperative that the experimental community improves the uncertainty surrounding the quantification of particle light absorption. Absorption measured in-situ is consistently lower than that determined through remotely sensed techniques (e.g. sun photometry). Also, while there are readily available instruments for measuring particle light scattering at multiple wavelengths, very few exist for the measurement of absorption at multiple wavelengths. Thus, to extrapolate absorption measurements to wavelengths other than those measured, one must rely on laboratory measurements of the refractive indices of light absorbing species that may be quite different than the observed ambient species. Similarly, the calibrations of field deployable particle light absorption measuring instruments have been largely based on laboratory measurements of standardized light absorbing spherical particles. Increasing the accuracy of particle light absorption measurements and decreasing the uncertainty range of such measurements would be extremely beneficial to both satellite retrievals of atmospheric aerosols and numerical model simulations of climate change.

One area of concern that has recently garnered the attention of the experimental community is the need for a validation, calibration, and standardization process for particle inlets on instrumented aircraft. Because of the spatial and

temporal variability of atmospheric particles, remote sensing, especially by satellites, provides the most efficacious means of observation. However, remotes sensors cannot directly measure the particle optical and physical properties, and must rely on certain assumptions. In-situ measurements are thereby required as a means of validation. Aircraft measurements in particular supply the requisite vertical distribution information. The accuracy of these measurements, however, is limited by knowledge of the particle inlet system sampling efficiency. The efficiency is impacted by the positioning of the inlet relative to the aircraft boundary layer, the isokineticity of the inlet, diffusional loss of small particles, and sedimentation, inertial losses, and turbulent deposition of larger particles. The chemical composition and size distributions of the particles may also be affected by direct or indirect heating of the sample. Currently available low-turbulence inlets that prevent the loss of large particles are only suitable for large aircraft because of space and power requirements. We are currently working on the design of an efficient aerosol inlet system for light aircraft that may allow for the measurement of super-micrometer particles. The new inlet, if successful, would greatly enhance the ability of the scientific community to accurately characterize the chemical and optical properties of aerosol columns on a regular basis.

Appendix I

Spiral	Airport	Town	Lat	Long	Elevation (m)
0W3	Harford County	Churchville, MD	39.57ºN	76.20ºW	400
19N	Camden County	Berlin, NJ	39.78ºN	74.95ºW	150
1B1	Columbia County	Hudson, NY	42.29ºN	73.71ºW	197
1N7	Blairstown	Blairstown, NY	40.97ºN	75.00ºW	372
2G2	Jefferson County	Stubenville, OH	40.36ºN	80.70ºW	1194
3G6	Tri-City	Sebring, OH	40.91ºN	81.00ºW	1188
4B0	South Albany	South Bethlehem, NY	42.56ºN	73.83ºW	196
5B2	Saratoga County	Saratoga Springs, NY	43.05ºN	73.86ºW	433
5W5	Triple W	Raleigh, NC	35.62ºN	78.70ºW	244
5W8	Siler City Municipal	Siler City, NC	35.70ºN	79.51ºW	614
6B8	Caledonia County	Lyndonville, VT	44.57ºN	72.02ºW	1188
8G2	Corry-Lawrence	Corry, PA	41.91ºN	79.64ºW	1766
8G6	Harrison County	Cadiz, OH	40.24ºN	81.01ºW	1174
9G1	West Penn/Rock	Tarentum, PA	40.60ºN	79.82ºW	1125

AKQ	Wakefield	Wakefield, VA	36.99ºN	77.00ºW	113
ANP	Lee	Annapolis, MD	38.94ºN	76.57ºW	30
AOO	Altoona Blair County	Altoona, PA	40.30ºN	78.32ºW	1504
AUG	Augusta St.	Augusta, ME	44.32ºN	69.80ºW	352
AXQ	Clarion County	Clarion, PA	41.23ºN	79.44ºW	1458
BHB	Hancock County Bar Harbor	Bar Harbor, ME	44.45ºN	68.36ºW	83
BST	Belfast Municipal	Belfast, ME	44.41ºN	69.01ºW	195
CBE	Cumberland Regional	Cumberland, MD	39.62ºN	78.76ºW	776
CGE	Cambridge Dorchester	Cambridge, MD	38.54ºN	76.03ºW	19
CGS	College Park	College Park, MD	38.98ºN	76.92ºW	50
DDH	William H. Morse State	Bennington, VT	42.89ºN	73.25ºW	826
EHO	Shelby Municipal	Shelby, NC	35.26ºN	81.60ºW	847
ERI	Erie International	Erie, PA	42.08ºN	80.18ºW	733
ESN	Easton Newman	Easton, MD	38.80ºN	76.07ºW	74
EVY	Summit	Middletown, DE	39.52ºN	75.72ºW	45
FCI	Chesterfield County	Richmond, VA	37.41ºN	77.53ºW	237

FDK	Frederick	Frederick, MD	39.42°N	77.37°W	303
FME	Tipton AFB	Fort Meade, MD	39.08ºN	76.76ºW	145
HIE	Mount Washington Regional	Whitefield, NH	43.37ºN	71.54ºW	1074
HMZ	Bedford County	Bedford, PA	40.09ºN	78.51ºW	1161
HNZ	Henderson-Oxford	Henderson, NC	36.36ºN	78.53ºW	527
IDI	Indiana County Jimmy Stewart	Indiana, PA	40.63ºN	79.11ºW	1405
ITH	Tompkins County	Ithaca, NY	42.49ºN	76.46ºW	1099
IWI	Wiscasset	Wiscasset, ME	43.96ºN	69.71ºW	70
JNX	Johnson County	Smithfield, NC	35.54ºN	78.39ºW	165
JQF	Concord Regional	Concord, NC	35.39ºN	80.71ºW	690
LEB	Lebanon Municipal	Lebanon, NH	43.63ºN	72.30ºW	604
LHZ	Franklin County	Louisburg, NC	36.02ºN	78.33ºW	369
LKR	Lancaster County McWhirter County	Lancaster, SC	34.72ºN	80.85ºW	486
LKU	Louisa County Feeman	Louisa, VA	38.01ºN	77.97ºW	493
MHT	Manchester	Manchester, NH	42.93ºN	71.44ºW	242

MRB	Eastern WV Regional Shepherd	Martinsburg, WV	39.40ºN	77.98ºW	557
MRN	Morganton Lenoir	Morganton, NC	35.82ºN	81.61ºW	1270
MVL	Morisville-Stowe State	Morrisville, VT	44.53ºN	72.61ºW	732
N03	Cortland County Chase	Cortland, NY	42.59ºN	76.21ºW	1198
N23	Sidney Municipal	Sidney, NY	42.30ºN	75.42ºW	1027
N27	Bradford County	Towanda, PA	41.74ºN	76.45ºW	730
N38	Grand Canyon State	Wellsboro, PA	41.73ºN	77.40ºW	1899
N70	Pennridge	Perkasie, PA	40.39ºN	75.29ºW	568
N87	Trenton Robbinsville	Robbinsville, NJ	40.21ºN	74.60ºW	119
OFP	Hanover County Municipal	Ashland, VA	37.71ºN	77.44ºW	205
OKV	Winchester Regional	Winchester, VA	39.14ºN	78.14ºW	727
P53	Rostraver	Monongahela, PA	40.21ºN	79.83ºW	1228
PNE	Northeast Philadelphia	Philadelphia, PA	40.08ºN	75.01ºW	121
RKD	Knox County Regional	Rockland, ME	44.53ºN	72.95ºW	787
RUT	Rutland State	Rutland, VT	43.06ºN	69.10ºW	55

SEG	Penn Valley	Selinsgrove, PA	40.82ºN	76.86ºW	450
SVH	Statesville Municipal	Statesville, NC	35.77ºN	80.96ºW	965
THV	York	York, PA	39.92ºN	76.87ºW	480
VUJ	Stanly County	Albemarle, NC	35.42ºN	80.15ºW	609
W00	Freeway	Mitchellville, MD	38.94ºN	76.77ºW	168
W29	Bay Bridge	Stevensville, MD	38.98ºN	76.33ºW	15
W45	Luray Caverns	Luray, VA	38.67ºN	78.50ºW	902
W79	Tappahannock Municipal	Tappahannock, VA	37.93ºN	76.87ºW	31
W81	Crewe Municipal	Crewe, VA	37.18ºN	78.10ºW	420
W96	New Kent County	Quinton, VA	37.50ºN	77.13ºW	123
WVL	Waterville Robert Lafleur	Waterville, ME	44.53ºN	69.68ºW	333

Appendix II

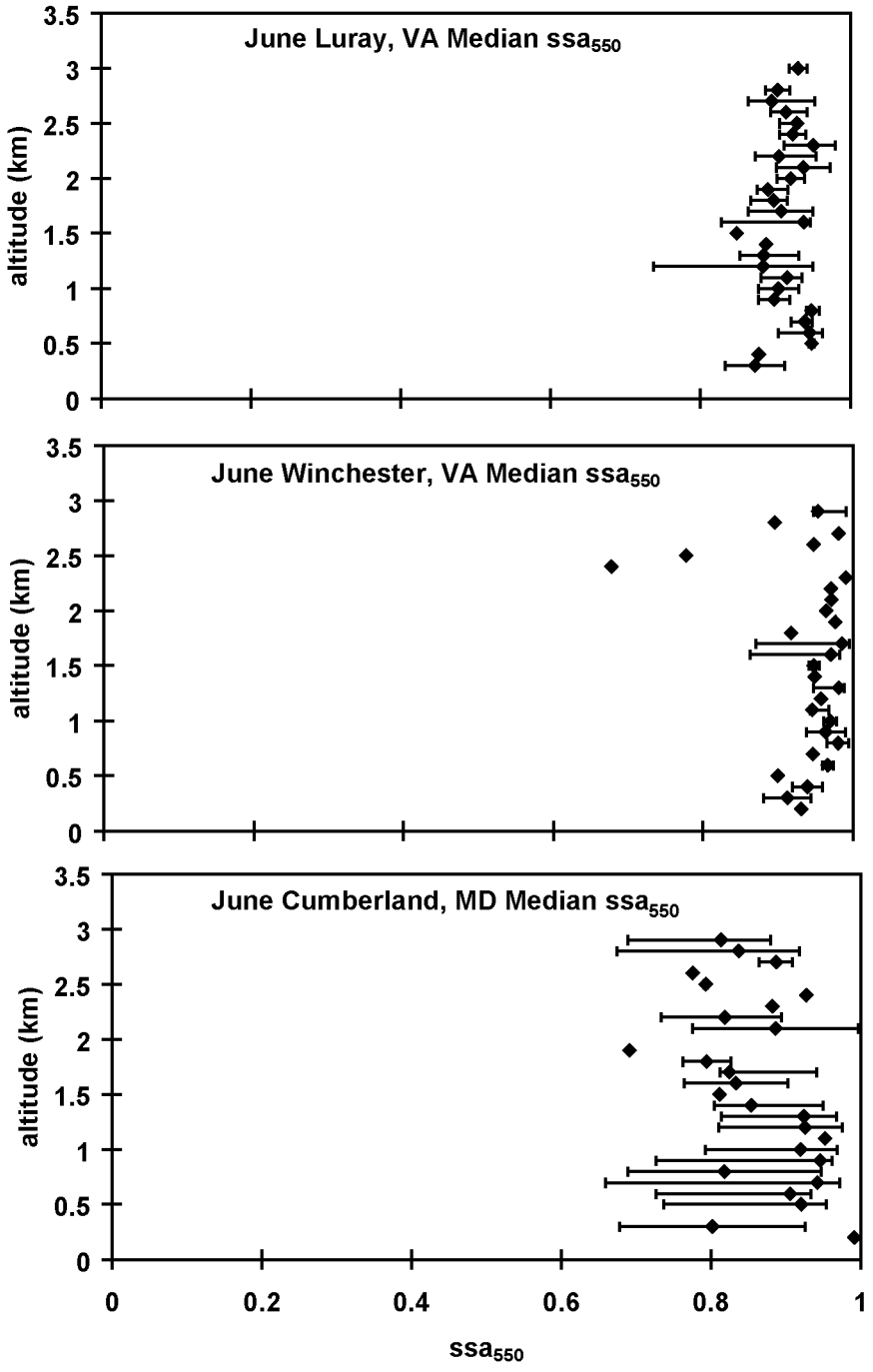

Appendix II.1. June 2001 morning profile median single scattering albedo (550 nm). The error bars represent the 1st and 3rd quartile values.

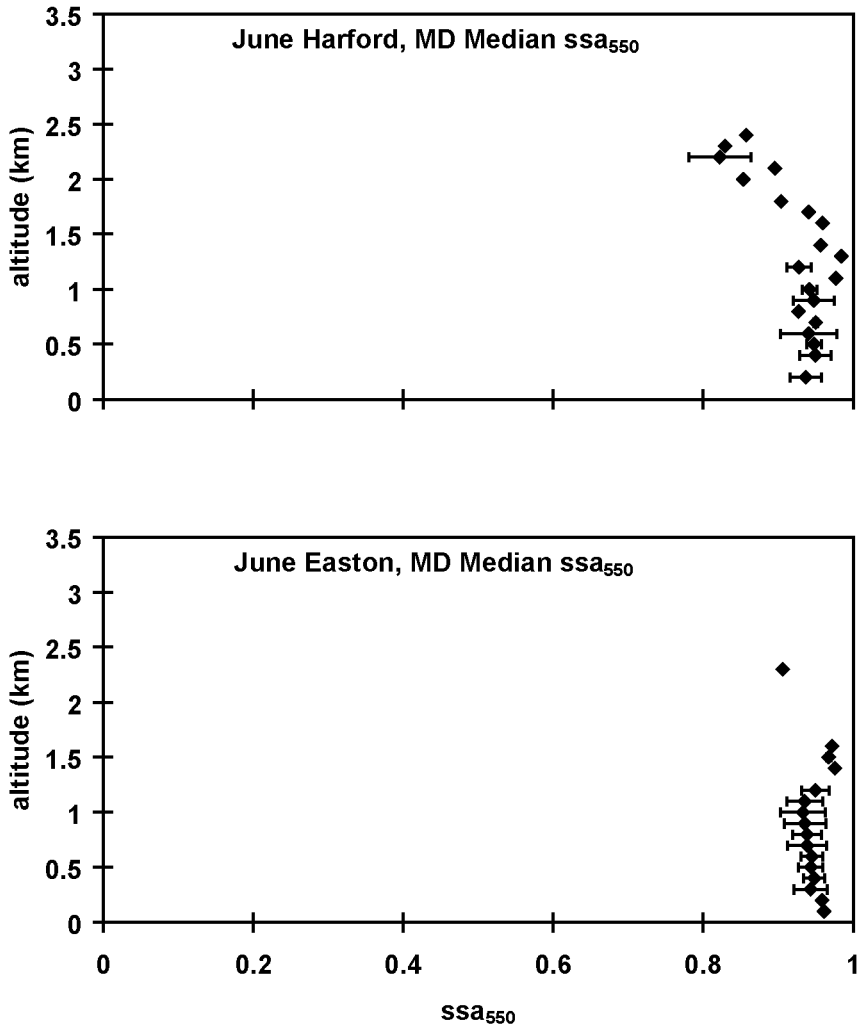

Appendix II.2. June 2001 afternoon profiles median single scattering albedo (550 nm).

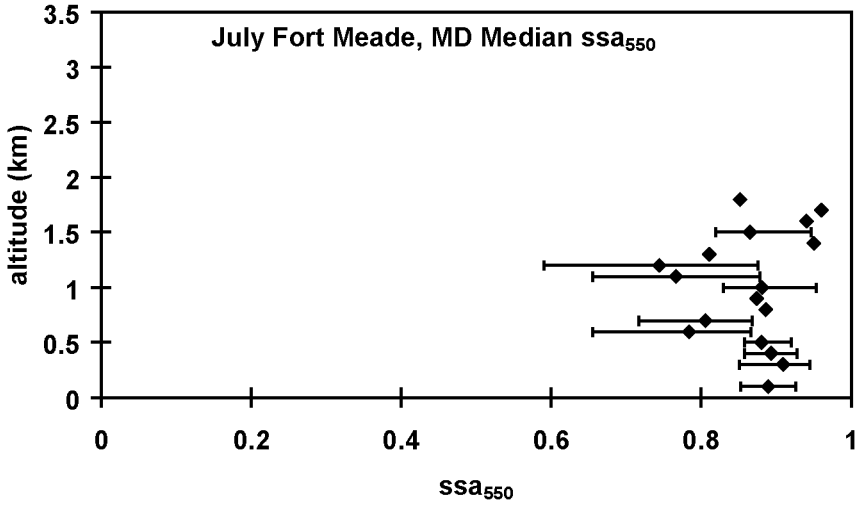

Appendix II.3. July 2001 afternoon profiles median single scattering albedo (550 nm).

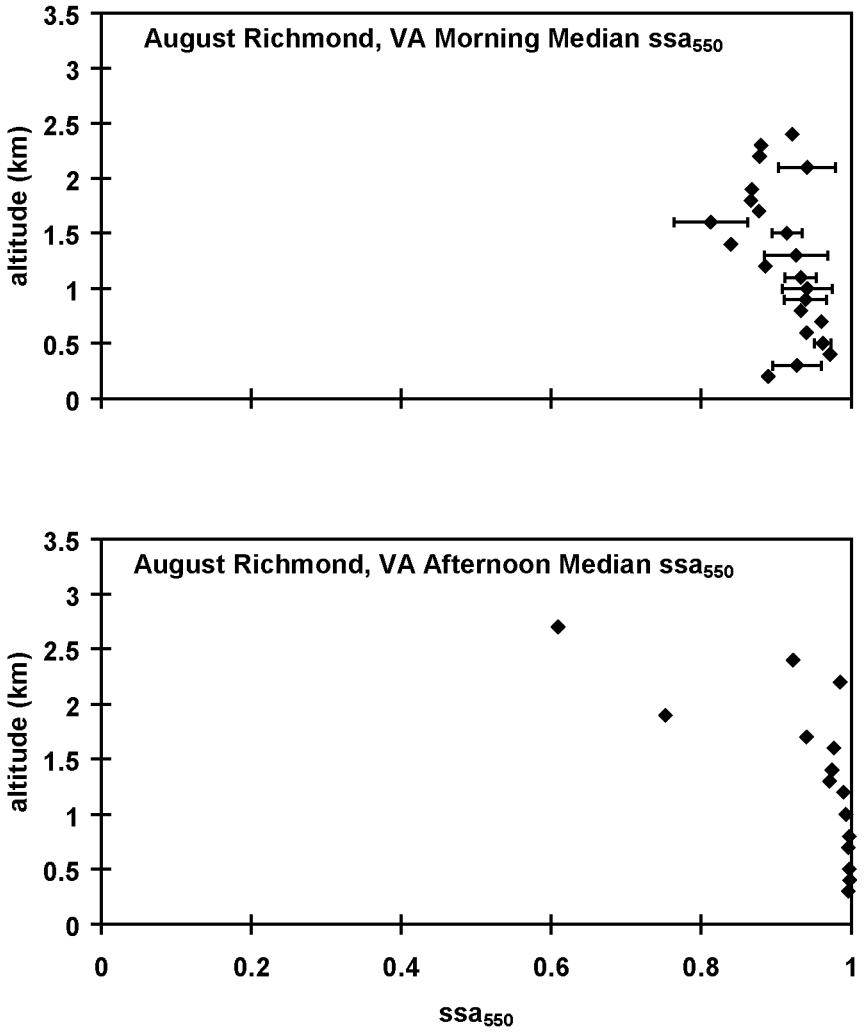

Appendix II.4. August 2001 morning and afternoon profiles median single scattering albedo (550 nm).

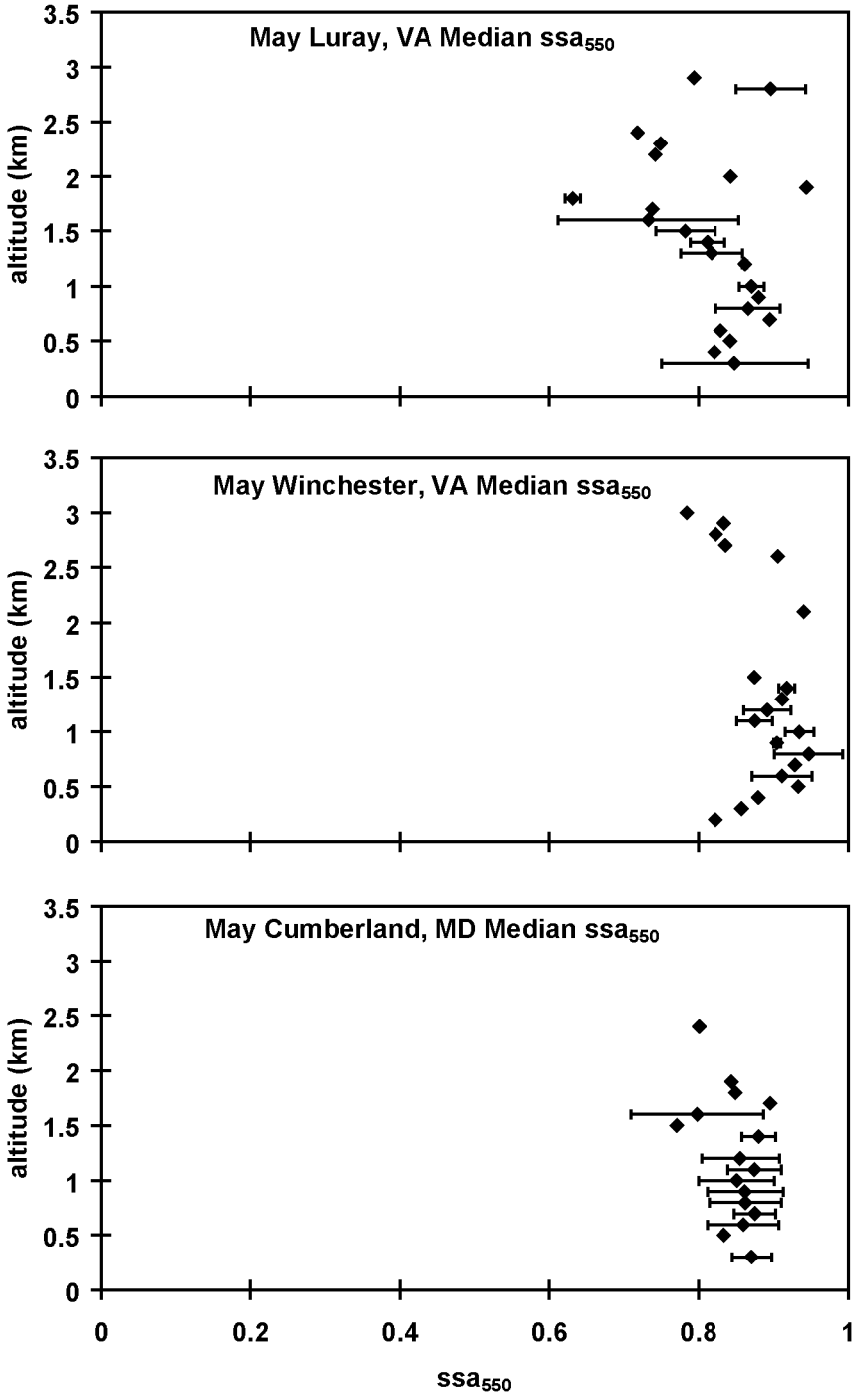

Appendix II.5. May 2002 morning profiles median single scattering albedo (550 nm).

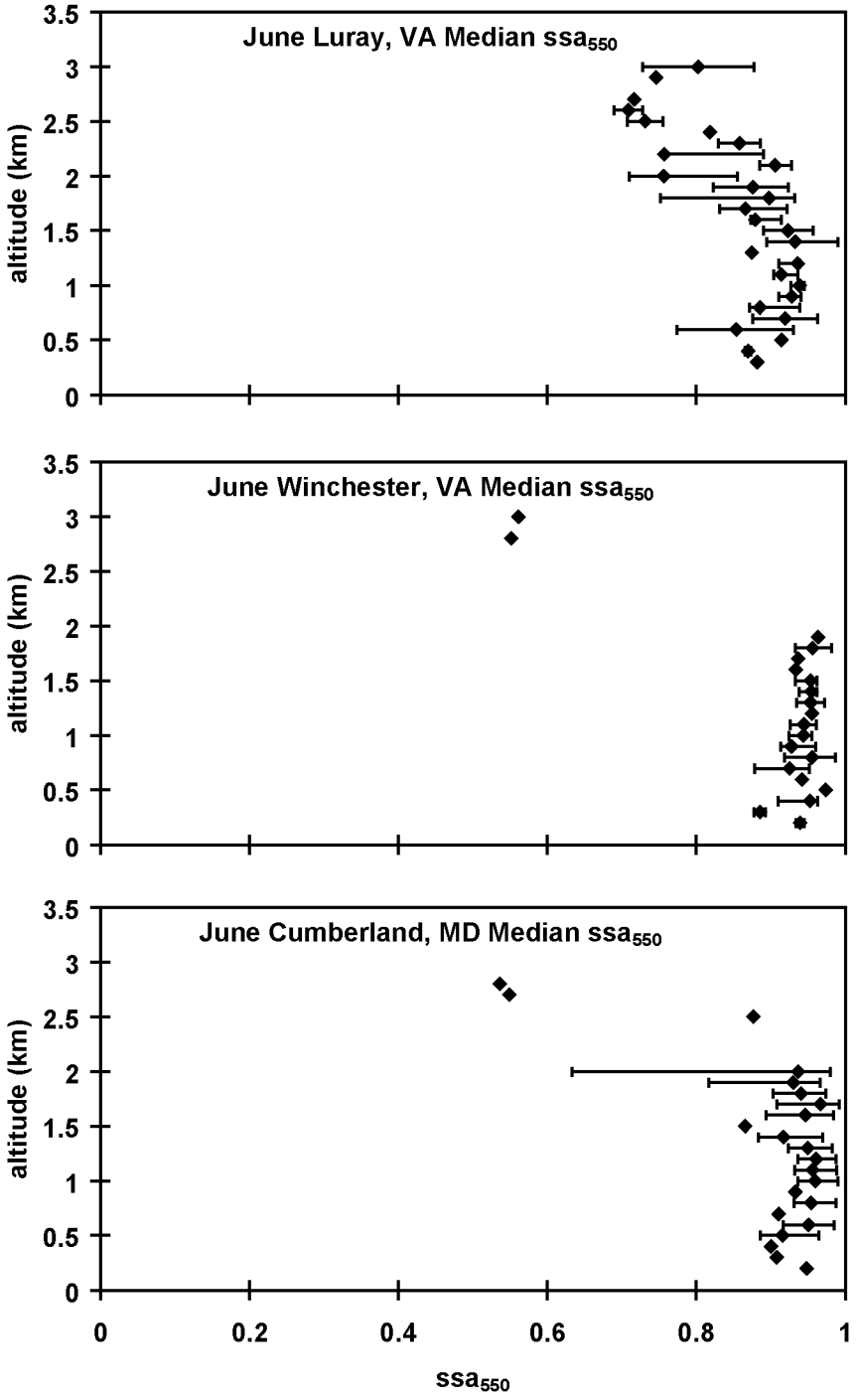

Appendix II.6. June 2002 morning profiles median single scattering albedo (550 nm).

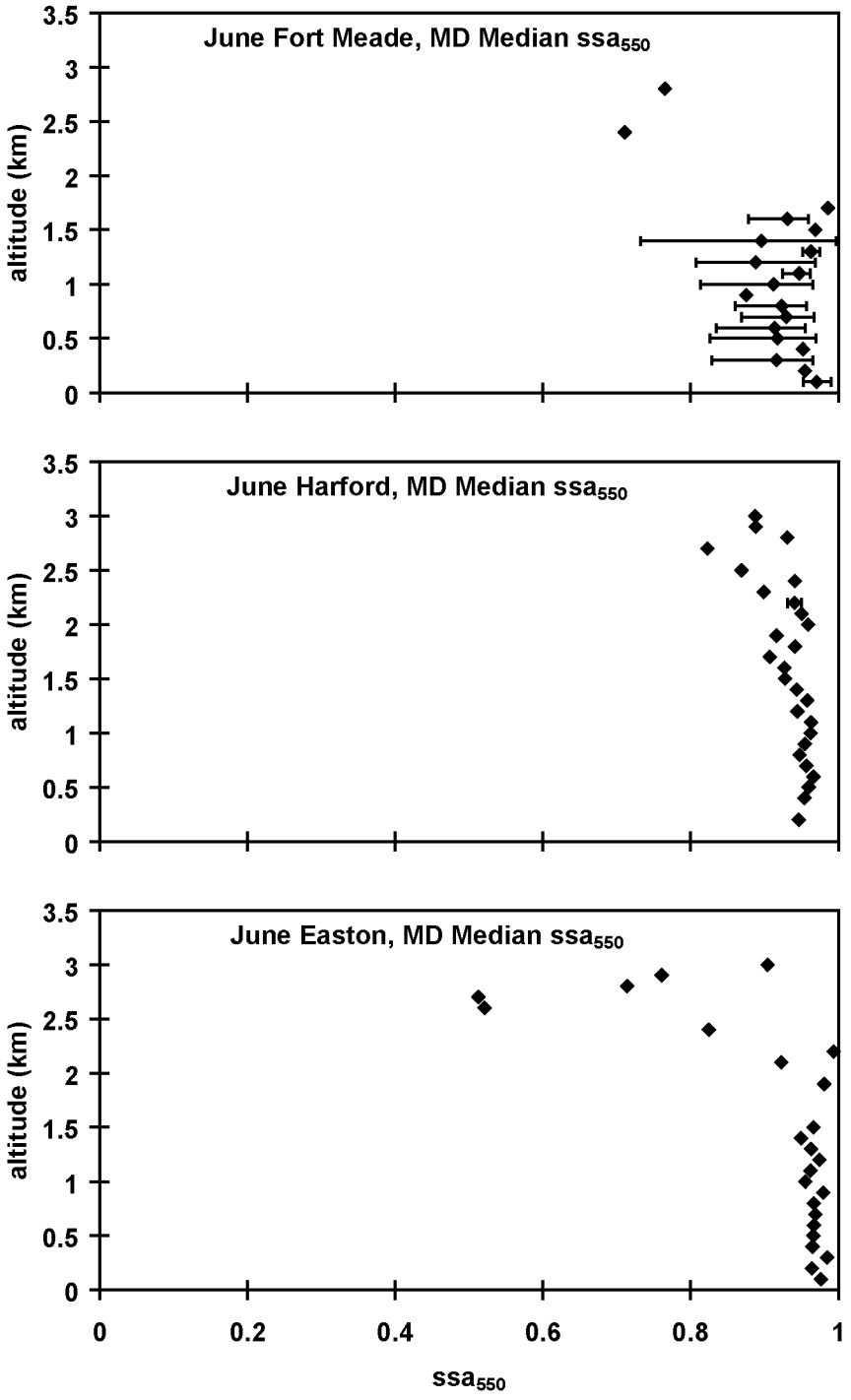

Appendix II.7. June 2002 afternoon profiles median single scattering albedo (550 nm).

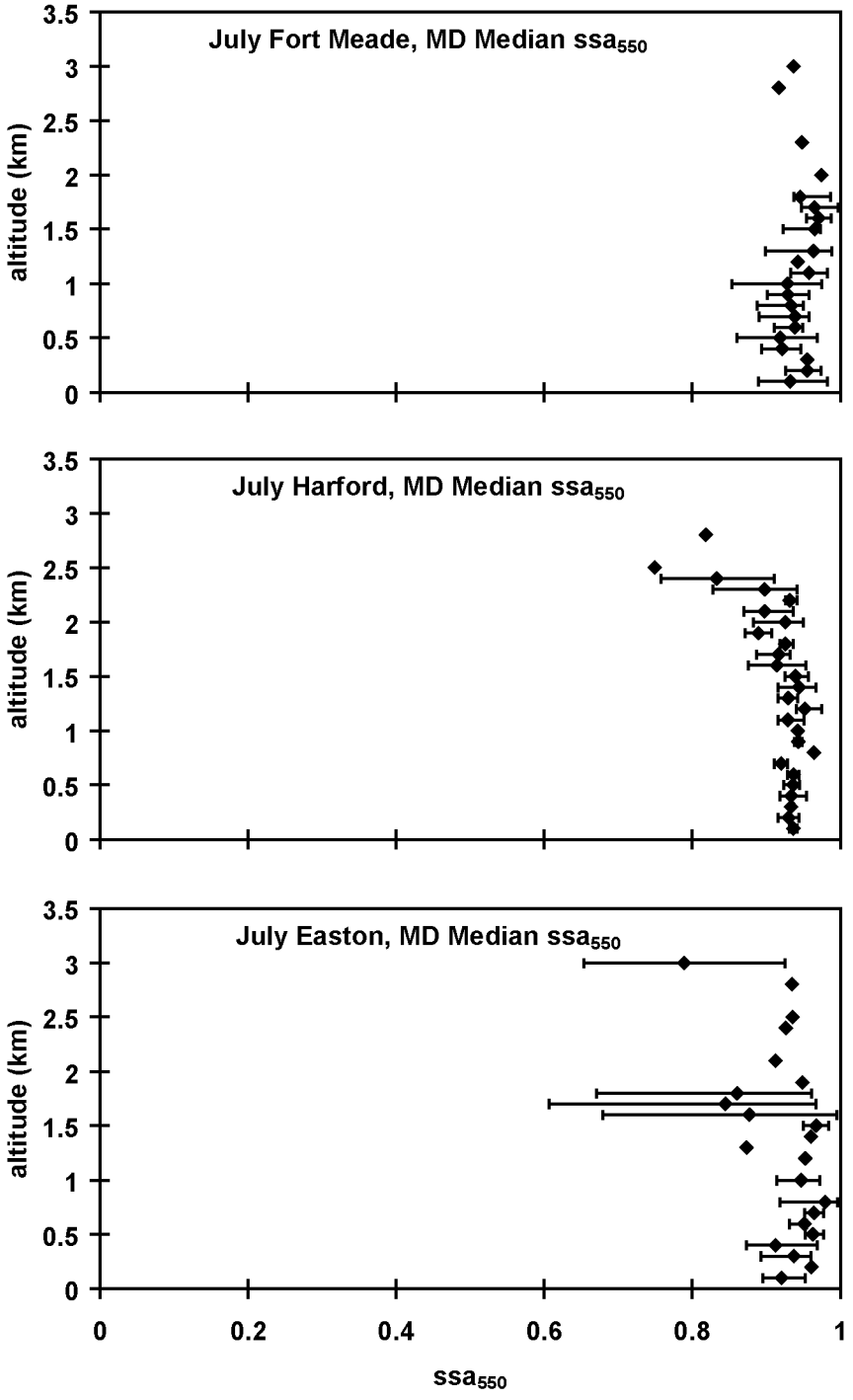

Appendix II.8. July 2002 afternoon profiles median single scattering albedo (550 nm).

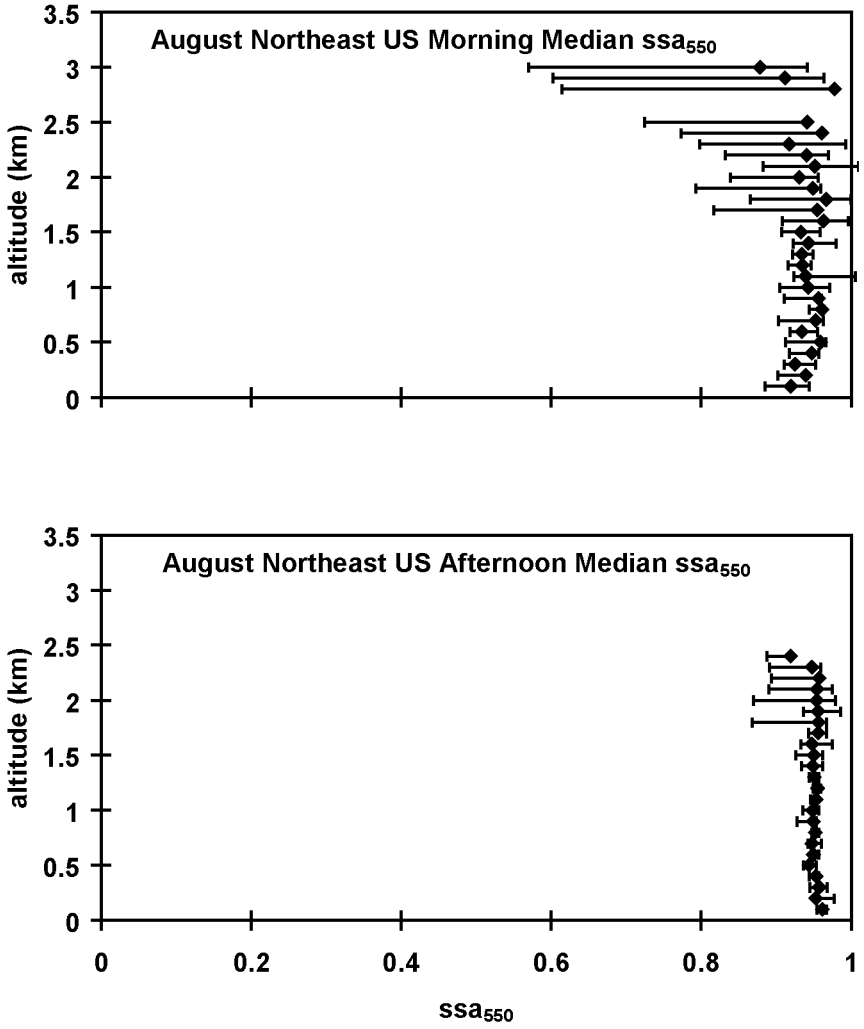

Appendix II.9. August 2002 morning and afternoon profiles over northeastern US median single scattering albedo (550 nm).

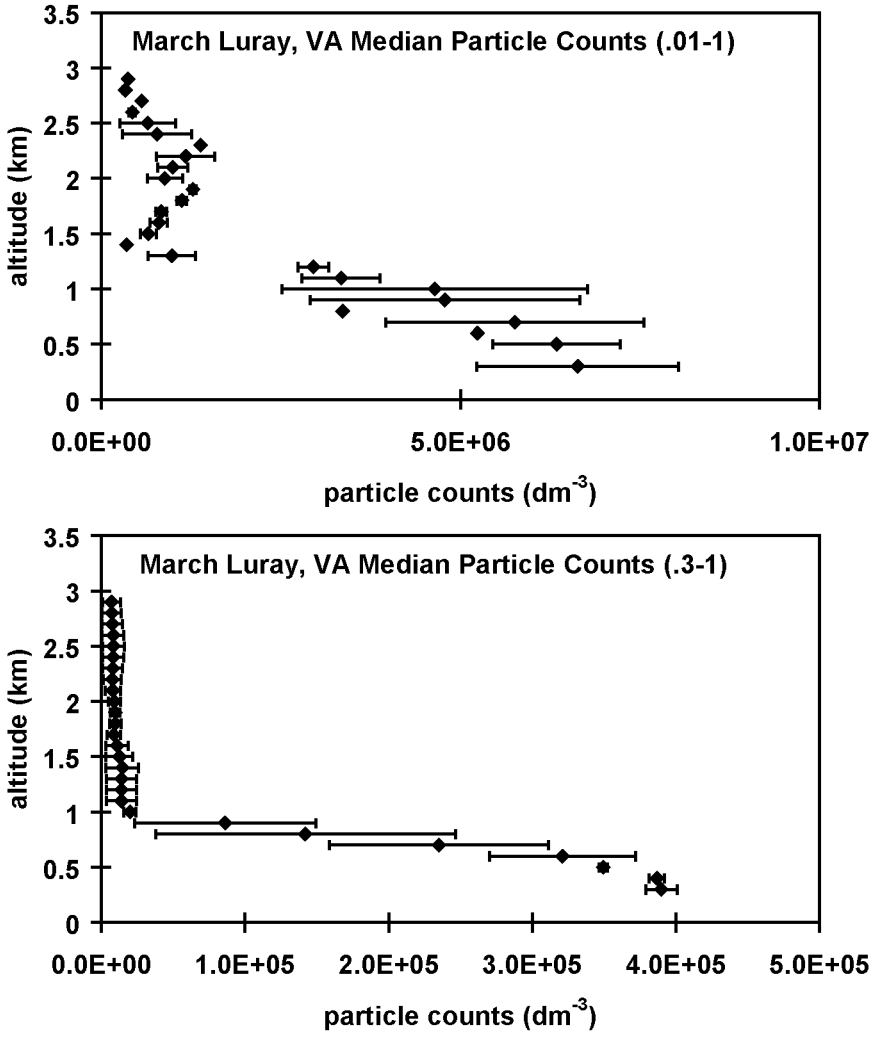

Appendix II.10. March 2003 Luray, VA profiles median particle counts [0.01 - 1 μm (above), 0.3 - 1 μm (below)].

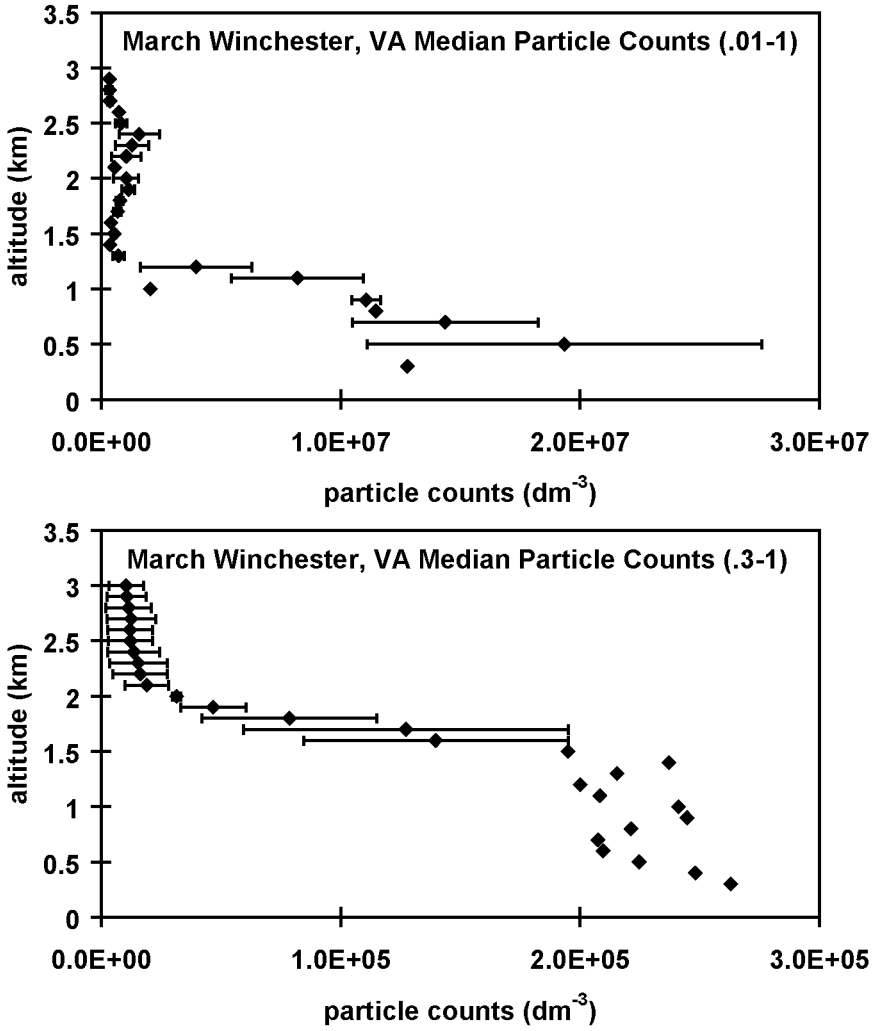

Appendix II.11. March 2003 Winchester, VA profiles median particle counts [0.01 - 1 μm (above), 0.3 - 1 μm (below)].

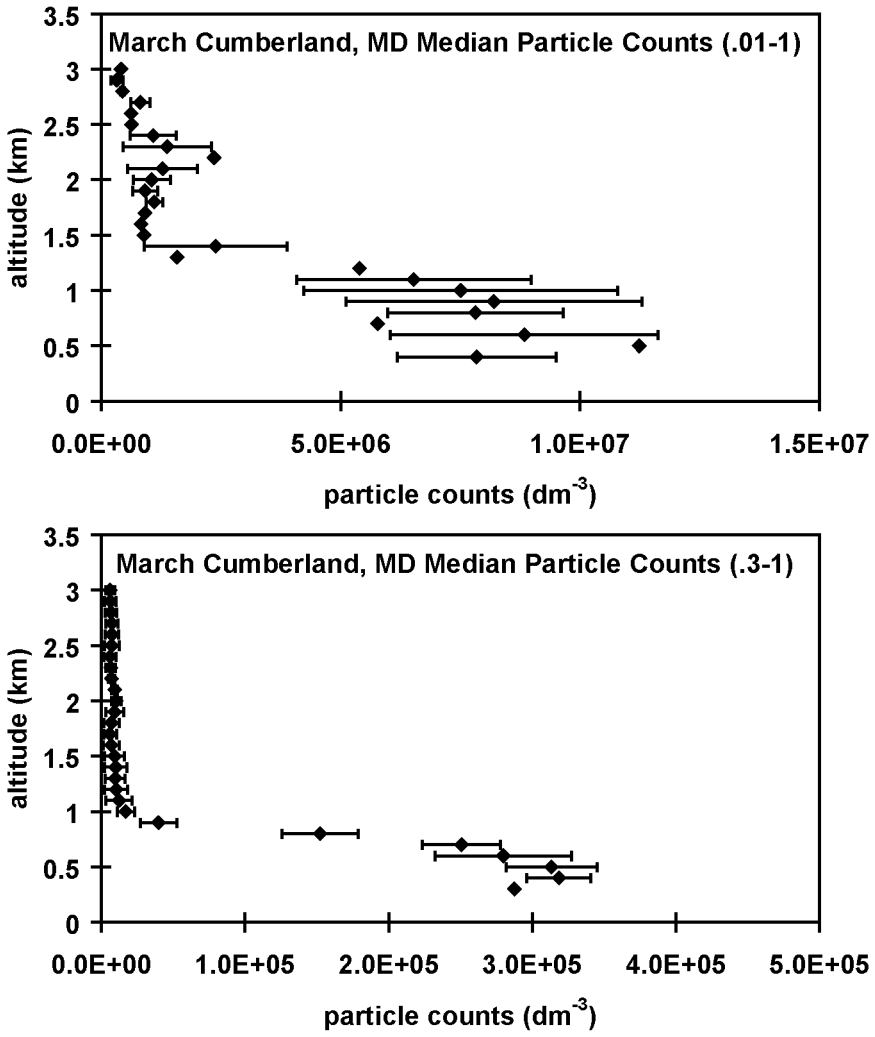

Appendix II.12. March 2003 Cumberland, MD profiles median particle counts [0.01 - 1 μm (above), 0.3 - 1 μm (below)].

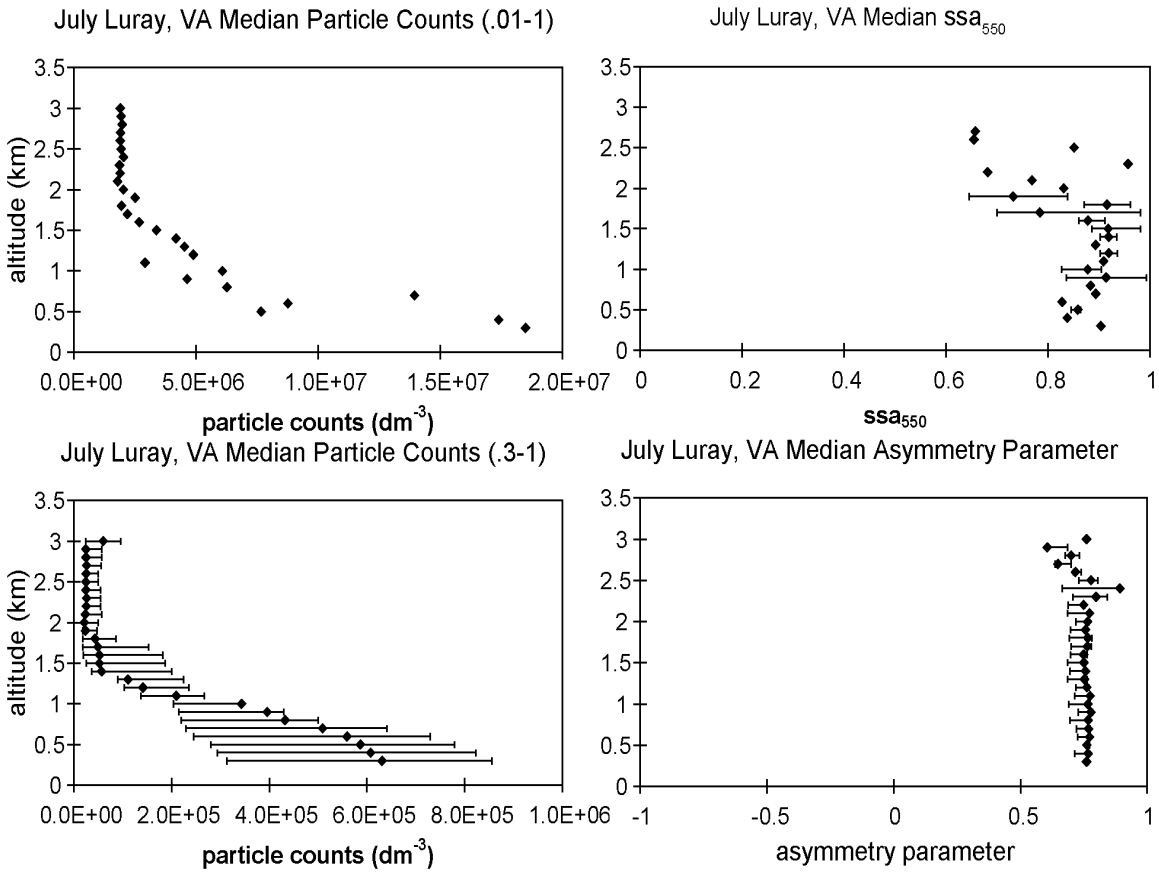

Appendix II.13. July 2003 Luray, VA profiles median particle counts (0.01 - 1 μm and 0.3 - 1 μm), single scattering albedo (550 nm), and asymmetry parameter (550 nm).

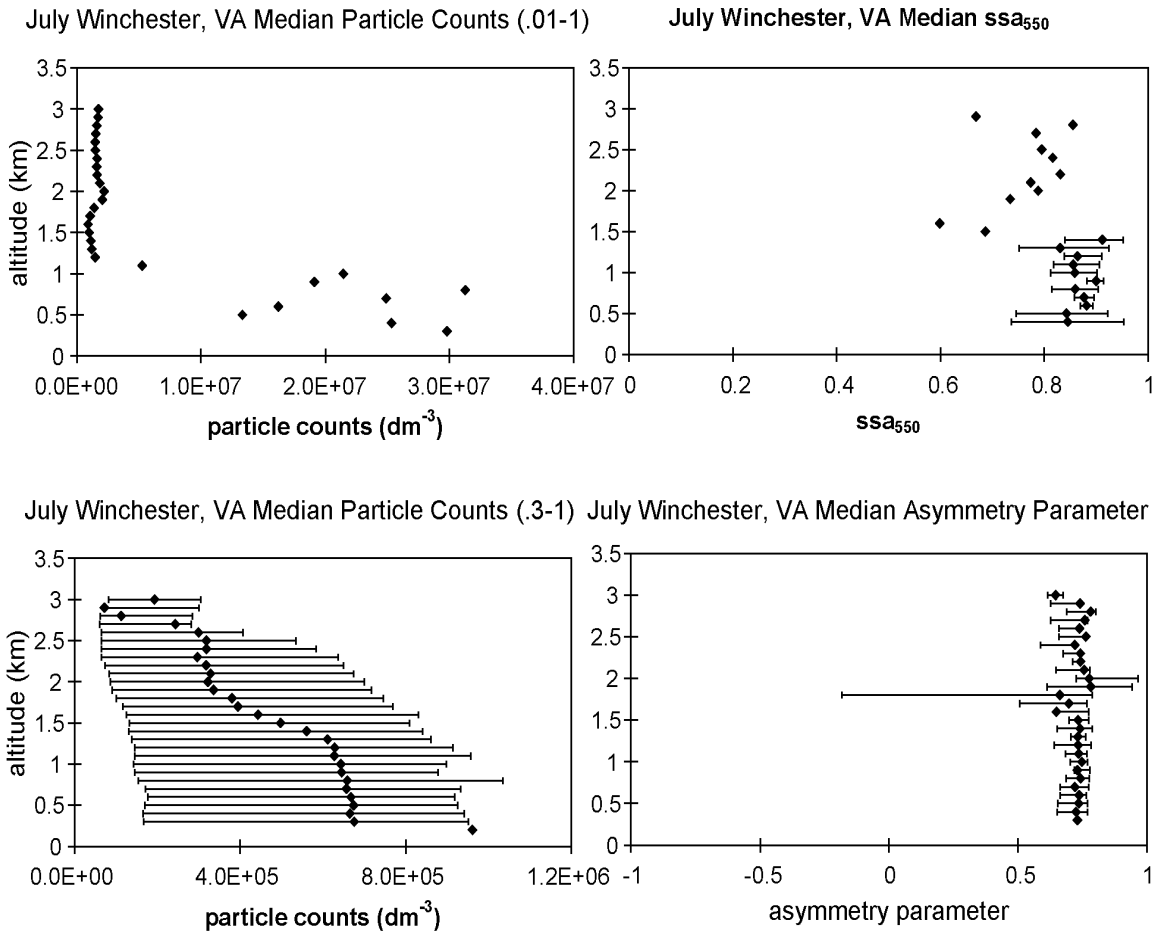

Appendix II.14. July 2003 Winchester, VA profiles median particle counts (0.01 - 1 μm and 0.3 - 1 μm), single scattering albedo (550 nm), and asymmetry parameter (550 nm).

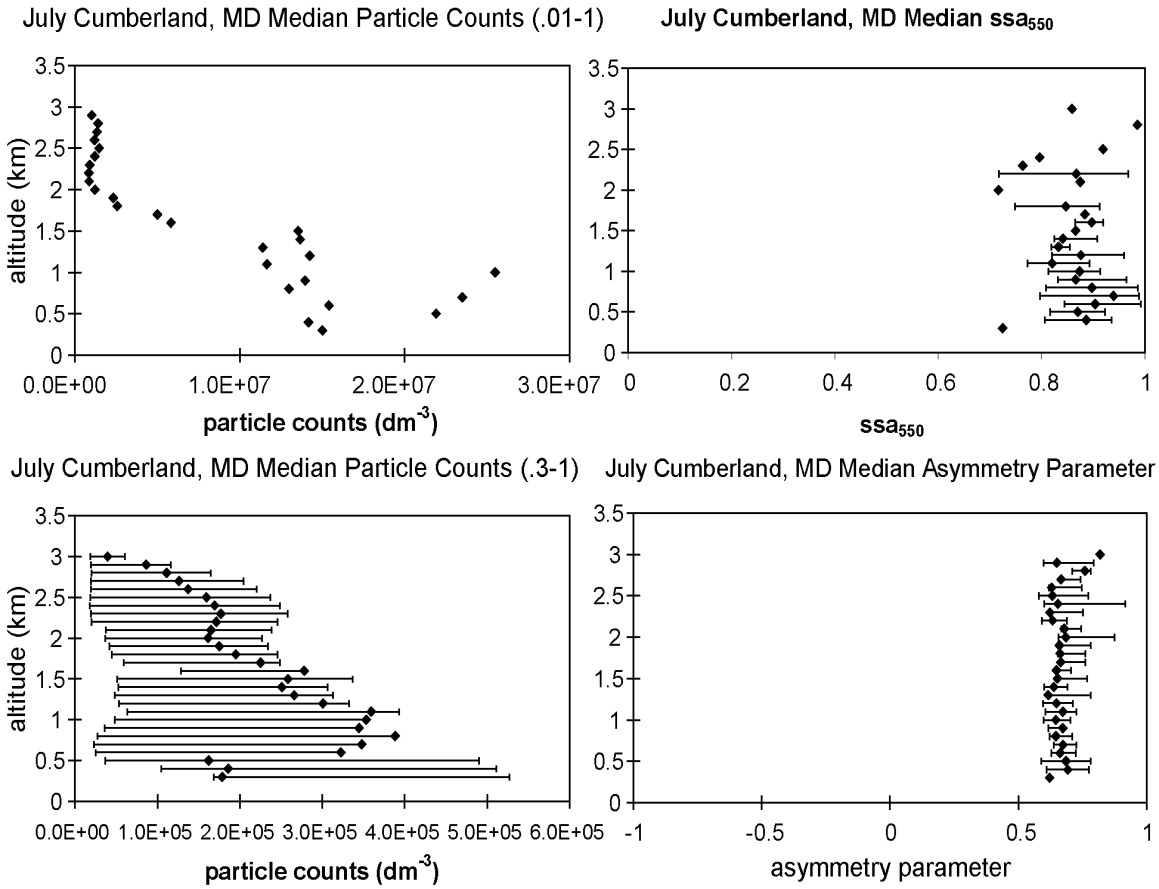

Appendix II.15. July 2003 Cumberland, MD profiles median particle counts (0.01 - 1 μm and 0.3 - 1 μm), single scattering albedo (550 nm), and asymmetry parameter (550 nm).

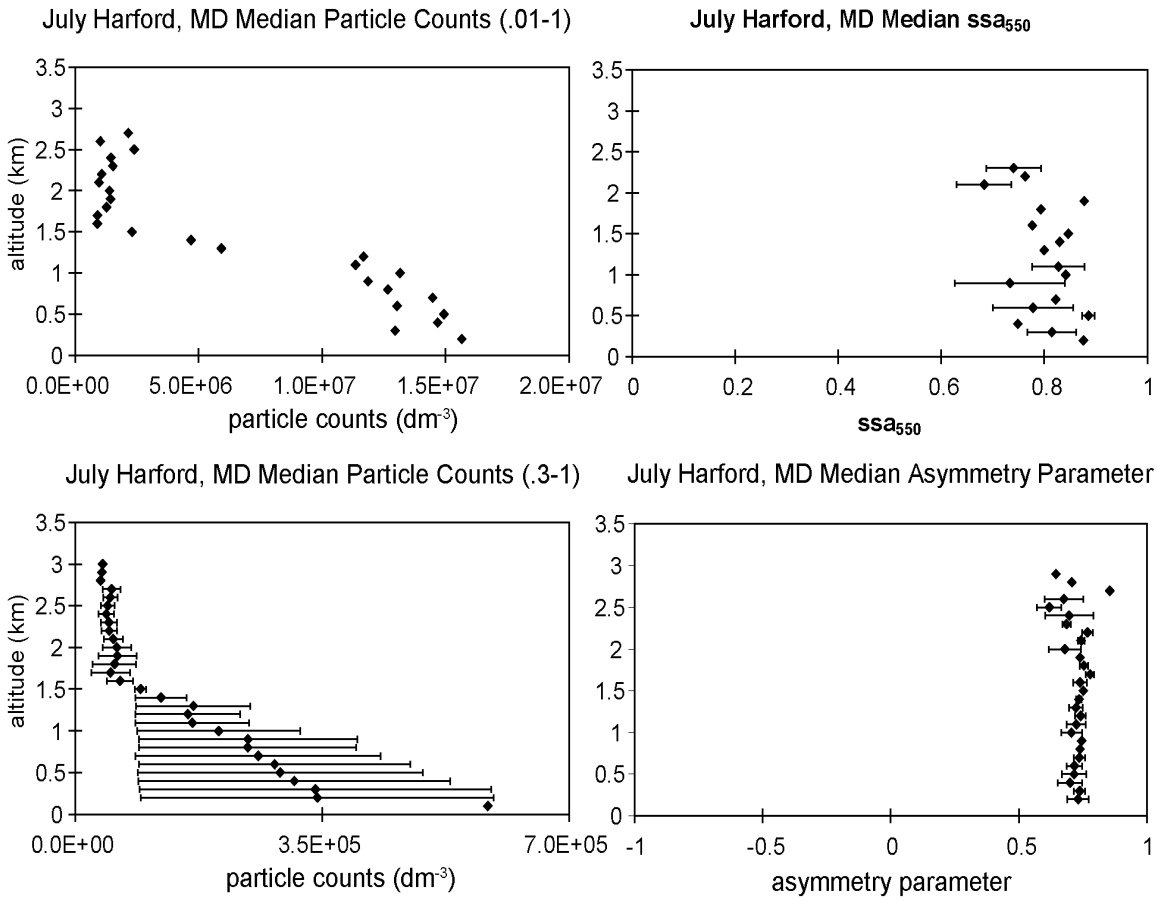

Appendix II.16. July 2003 Harford County, MD profiles median particle counts (0.01 - 1 μm and 0.3 - 1 μm), single scattering albedo (550 nm), and asymmetry parameter (550 nm).

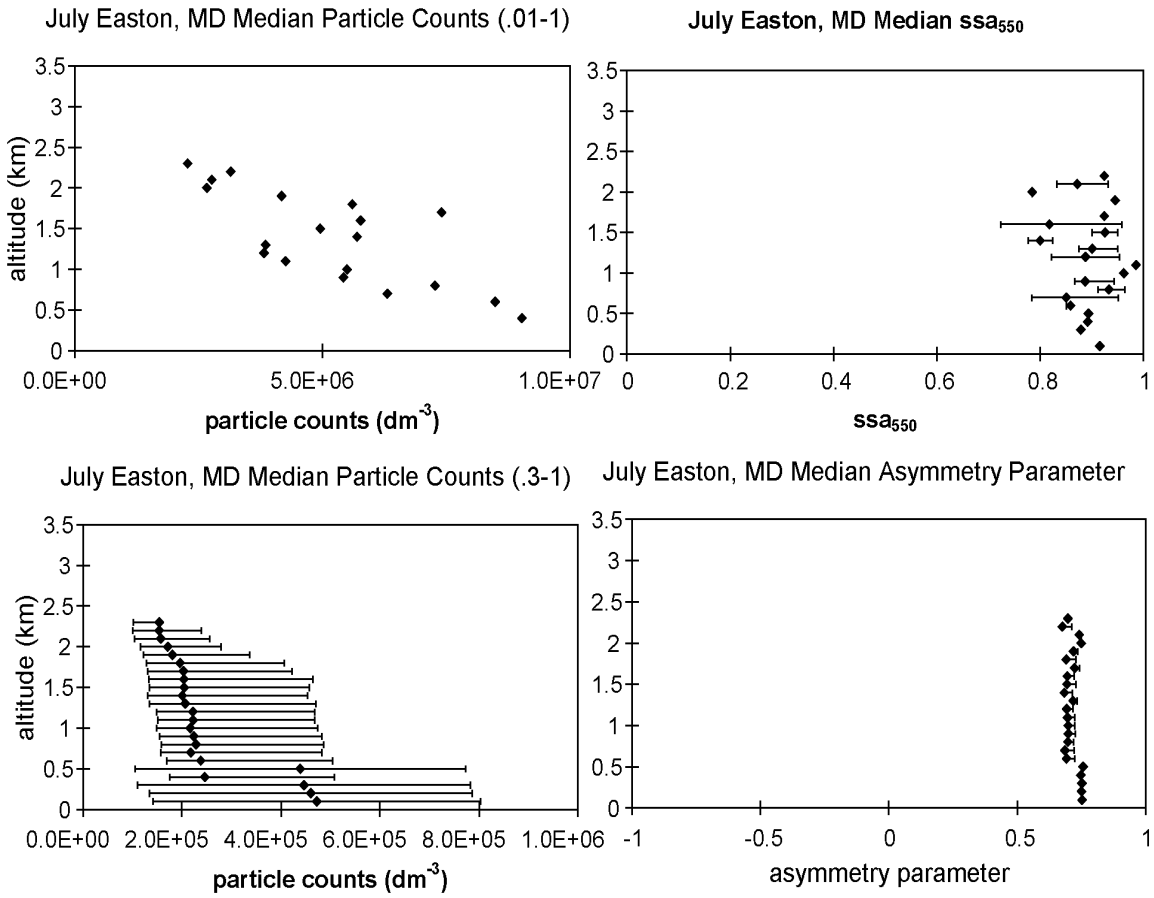

Appendix II.17. July 2003 Easton, MD profiles median particle counts (0.01 - 1 μm and 0.3 - 1 μm), single scattering albedo (550 nm), and asymmetry parameter (550 nm).

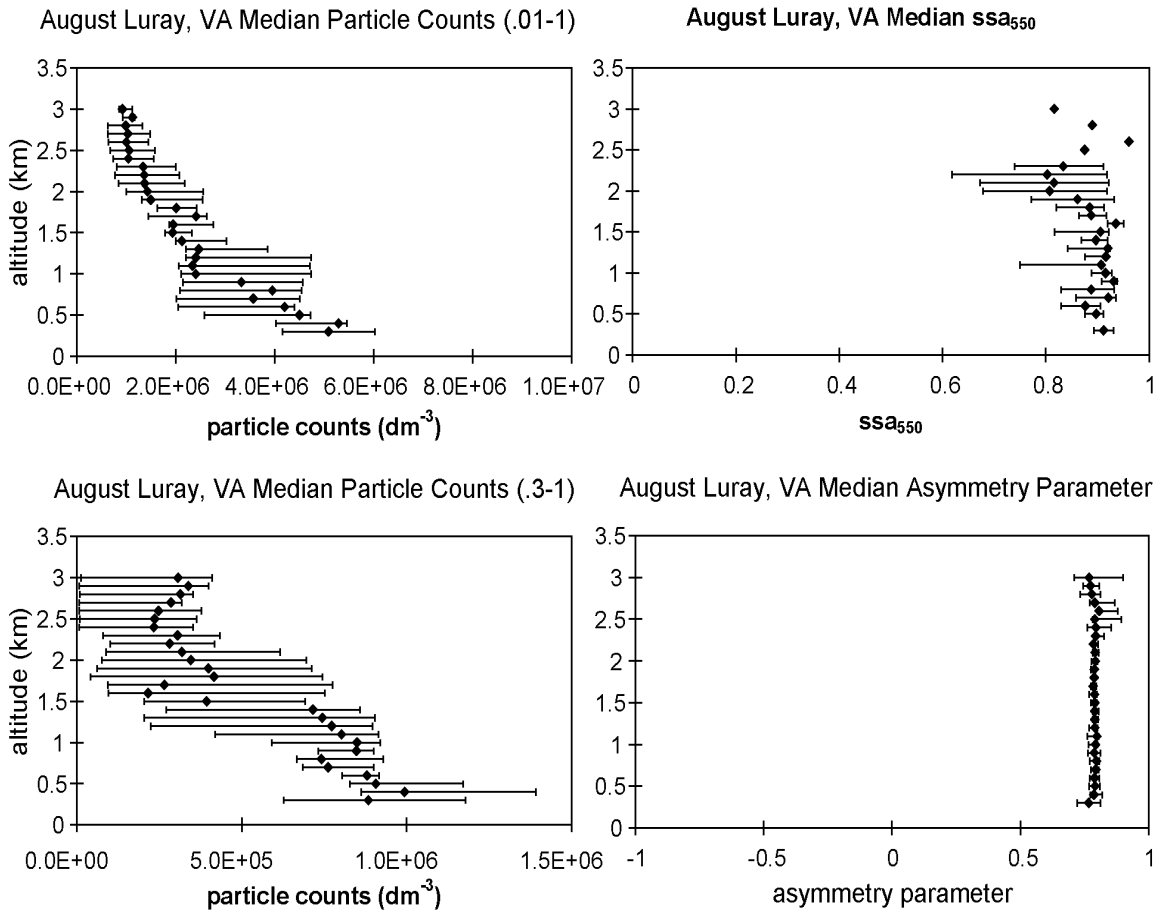

Appendix II.18. August 2003 Luray, VA profiles median particle counts (0.01 - 1 μm and 0.3 - 1 μm), single scattering albedo (550 nm), and asymmetry parameter (550 nm).

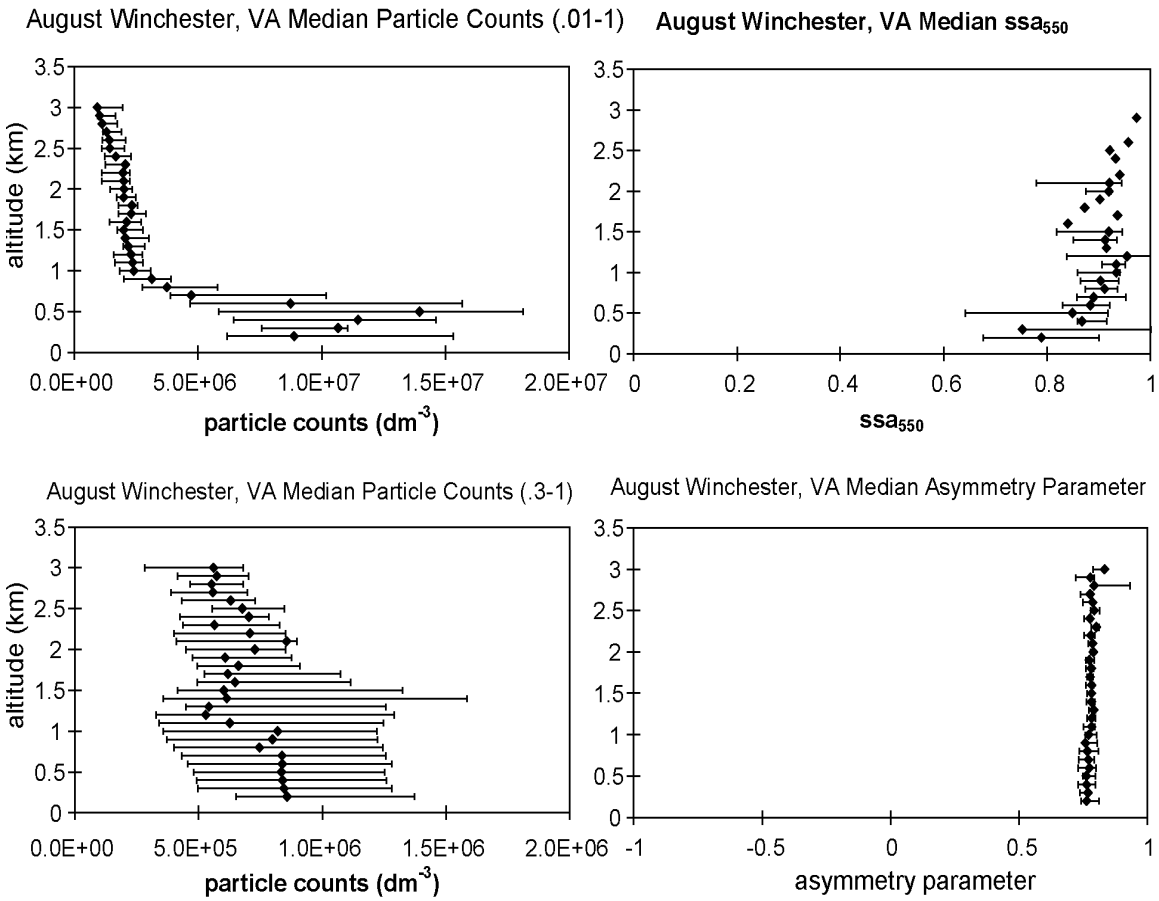

Appendix II.19. August 2003 Winchester, VA profiles median particle counts (0.01 - 1 μm and 0.3 - 1 μm), single scattering albedo (550 nm), and asymmetry parameter (550 nm).

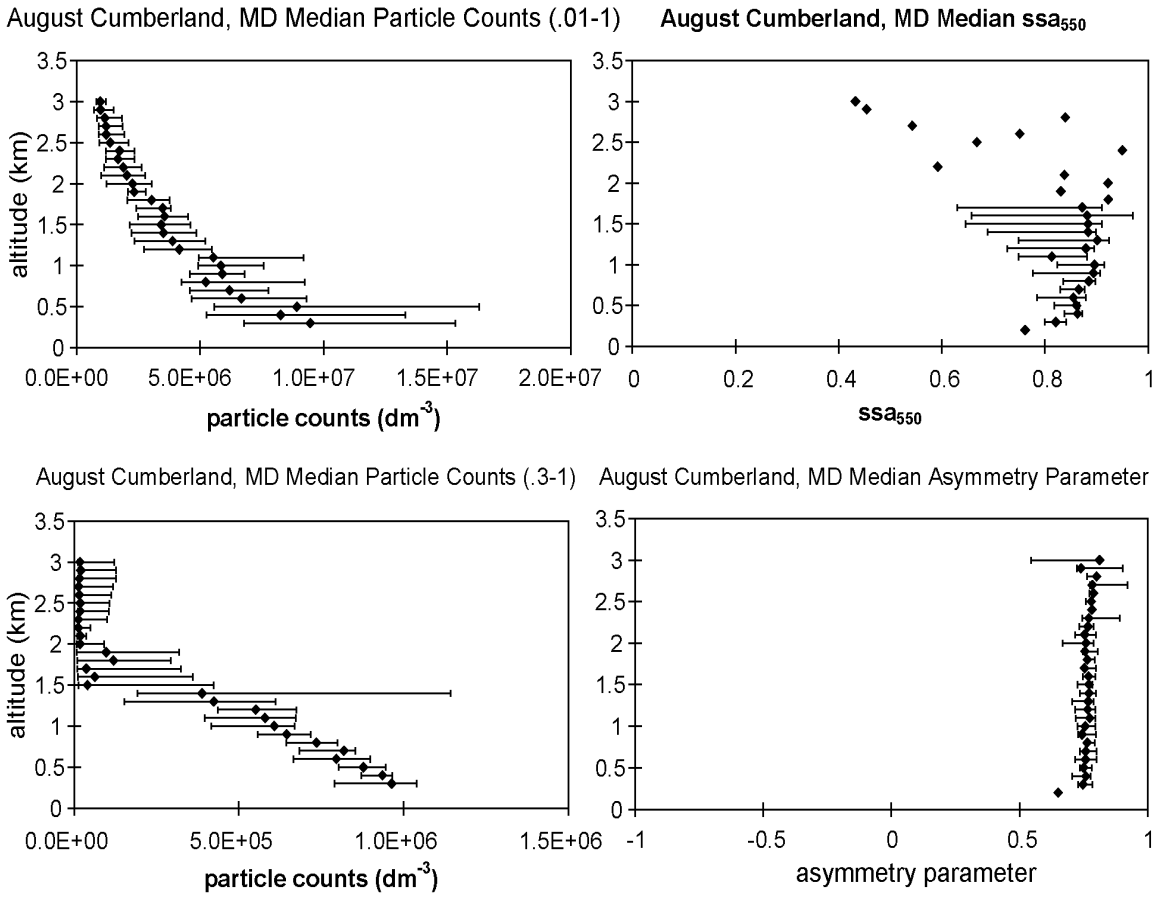

Appendix II.20. August 2003 Cumberland, MD profiles median particle counts (0.01 - 1 μm and 0.3 - 1 μm), single scattering albedo (550 nm), and asymmetry parameter (550 nm).

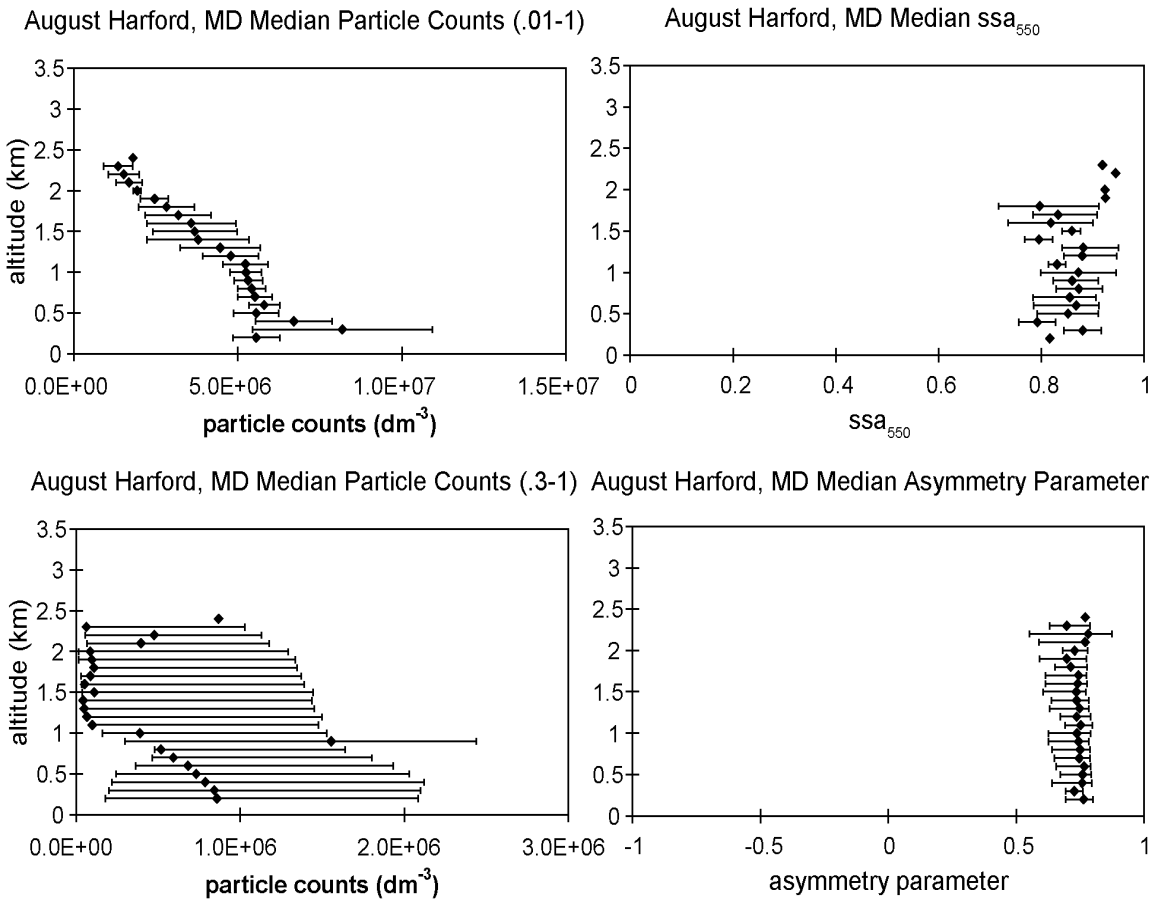

Appendix II.21. August 2003 Harford County, MD profiles median particle counts (0.01 - 1 μm and 0.3 - 1 μm), single scattering albedo (550 nm), and asymmetry parameter (550 nm).

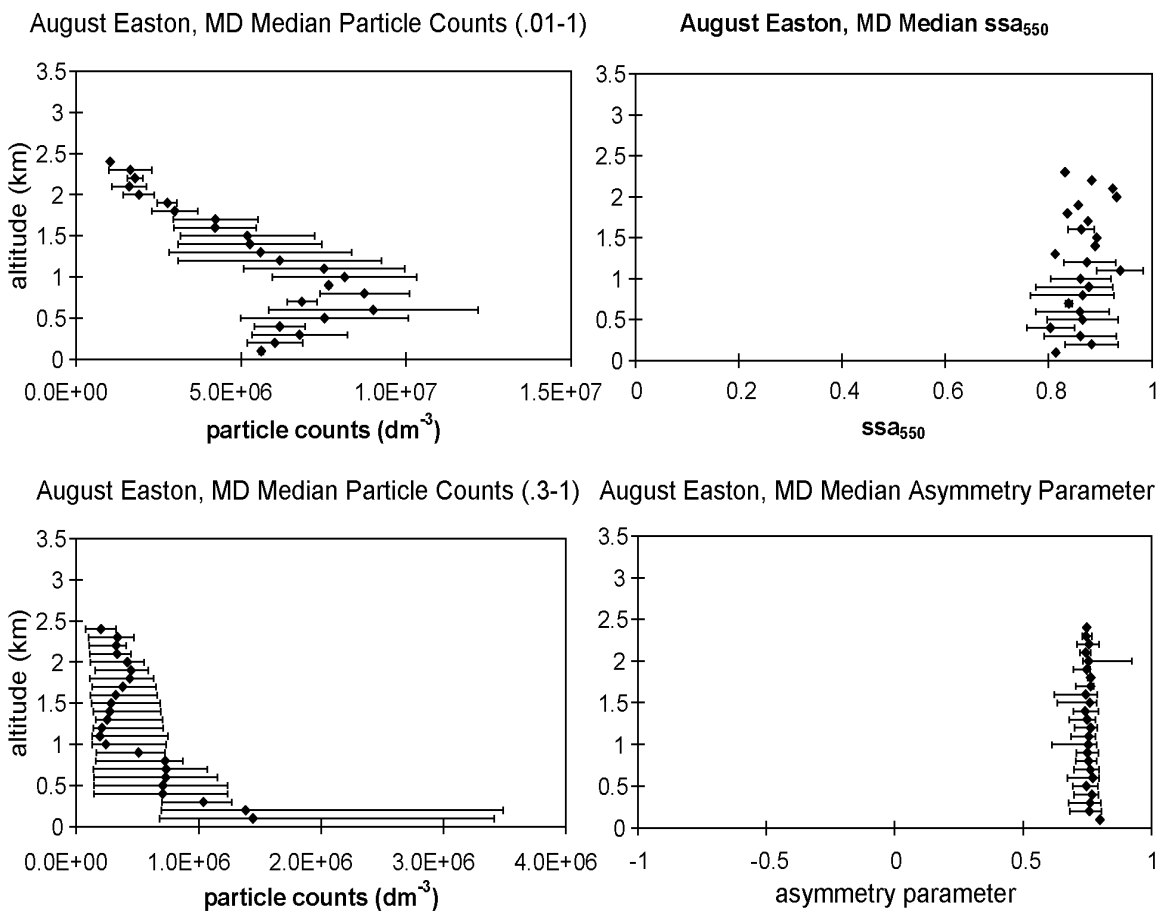

Appendix II.22. August 2003 Easton, MD profiles median particle counts (0.01 - 1 μm and 0.3 - 1 μm), single scattering albedo (550 nm), and asymmetry parameter (550 nm).

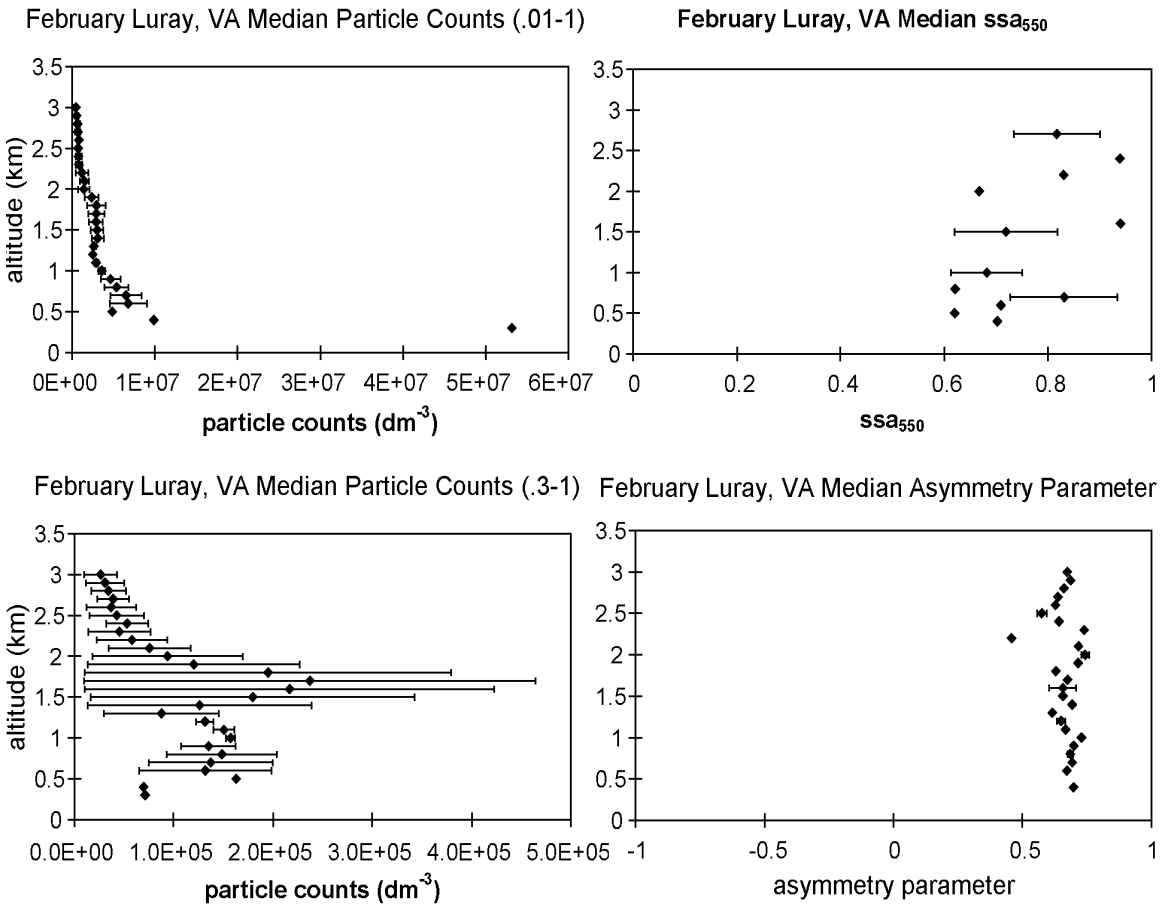

Appendix II.23. February 2004 Luray, VA profiles median particle counts (0.01 - 1 μm and 0.3 - 1 μm), single scattering albedo (550 nm), and asymmetry parameter (550 nm).

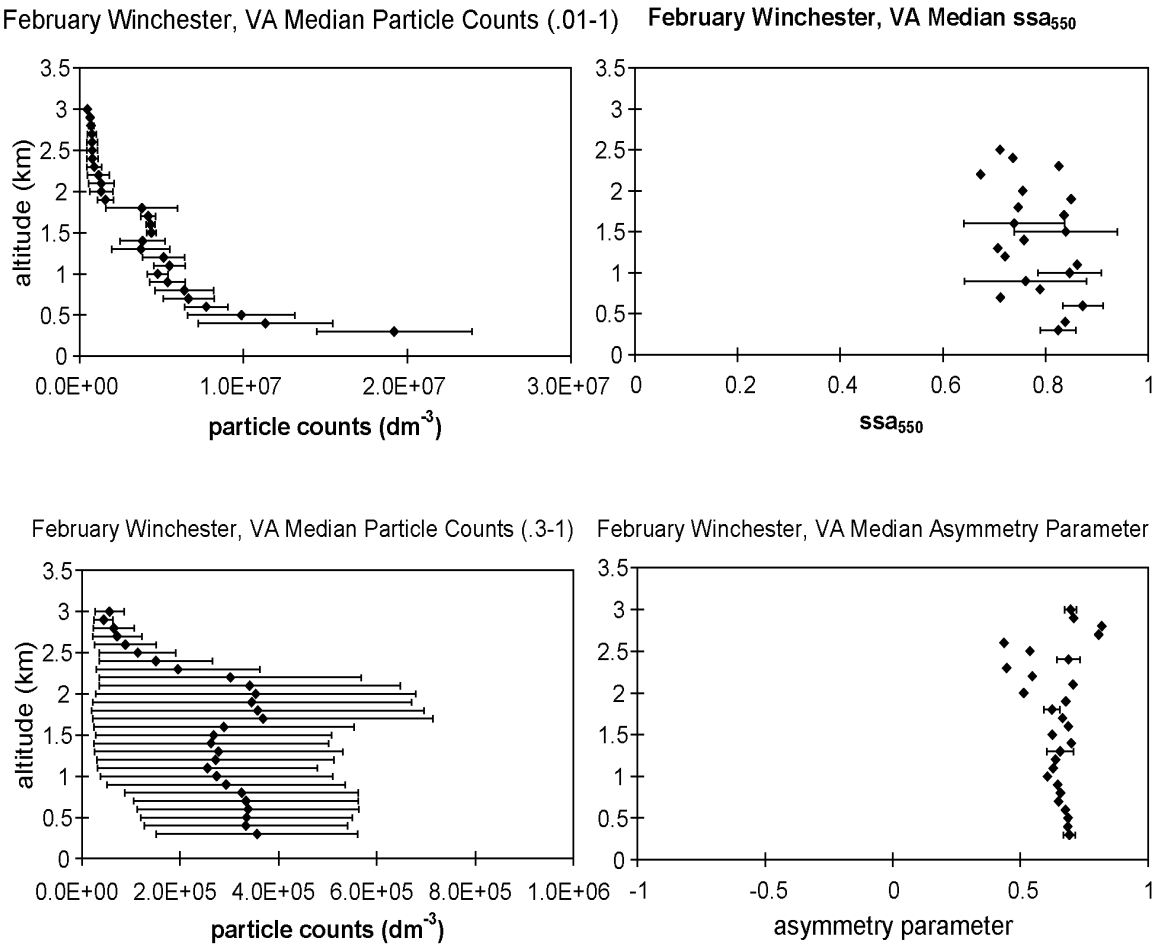

Appendix II.24. February 2004 Winchester, VA profiles median particle counts (0.01 - 1 μm and 0.3 - 1 μm), single scattering albedo (550 nm), and asymmetry parameter (550 nm).

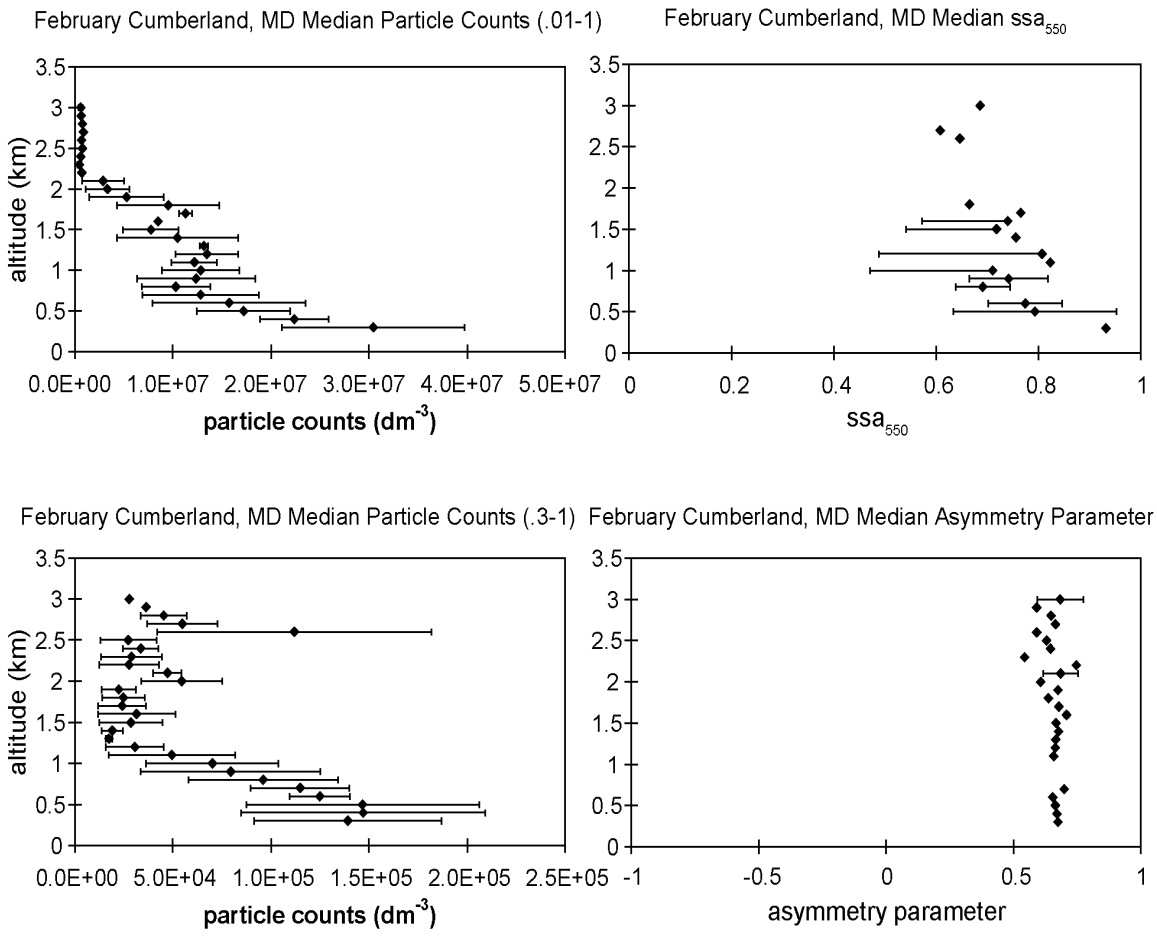

Appendix II.25. February 2004 Cumberland, MD profiles median particle counts (0.01 - 1 μm and 0.3 - 1 μm), single scattering albedo (550 nm), and asymmetry parameter (550 nm).

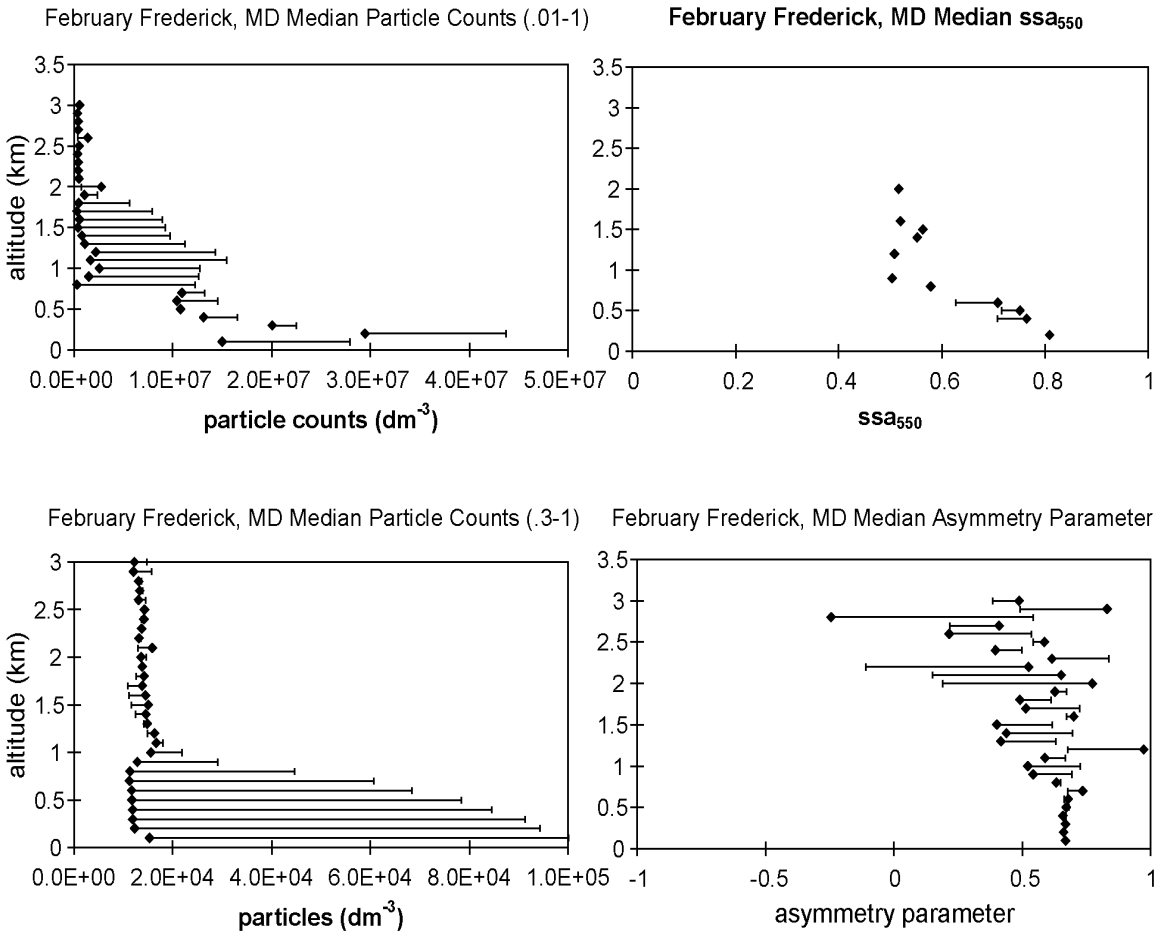

Appendix II.26. February 2004 Frederick, MD profiles median particle counts (0.01 - 1 μm and 0.3 - 1 μm), single scattering albedo (550 nm), and asymmetry parameter (550 nm).

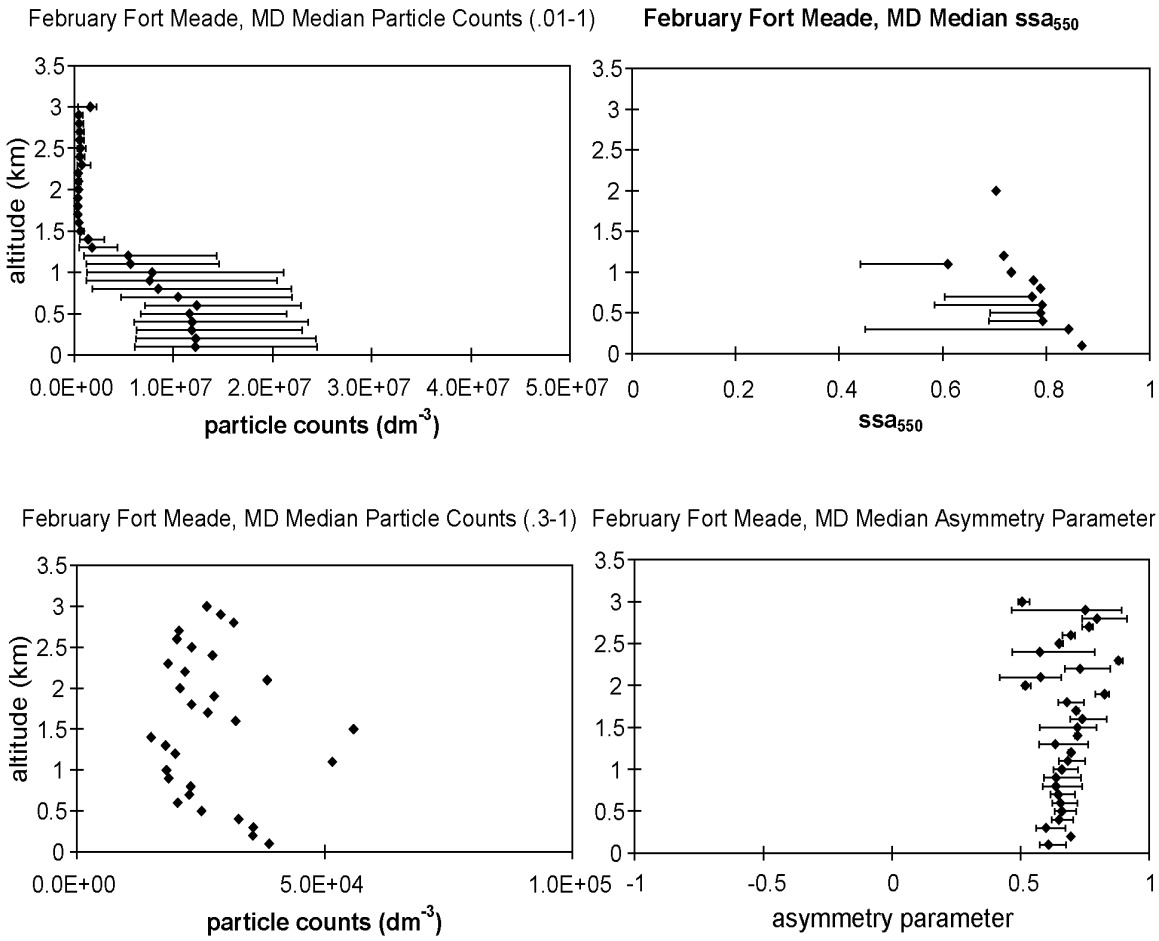

Appendix II.27. February 2004 Fort Meade, MD profiles median particle counts (0.01 - 1 μm and 0.3 - 1 μm), single scattering albedo (550 nm), and asymmetry parameter (550 nm).

Appendix III

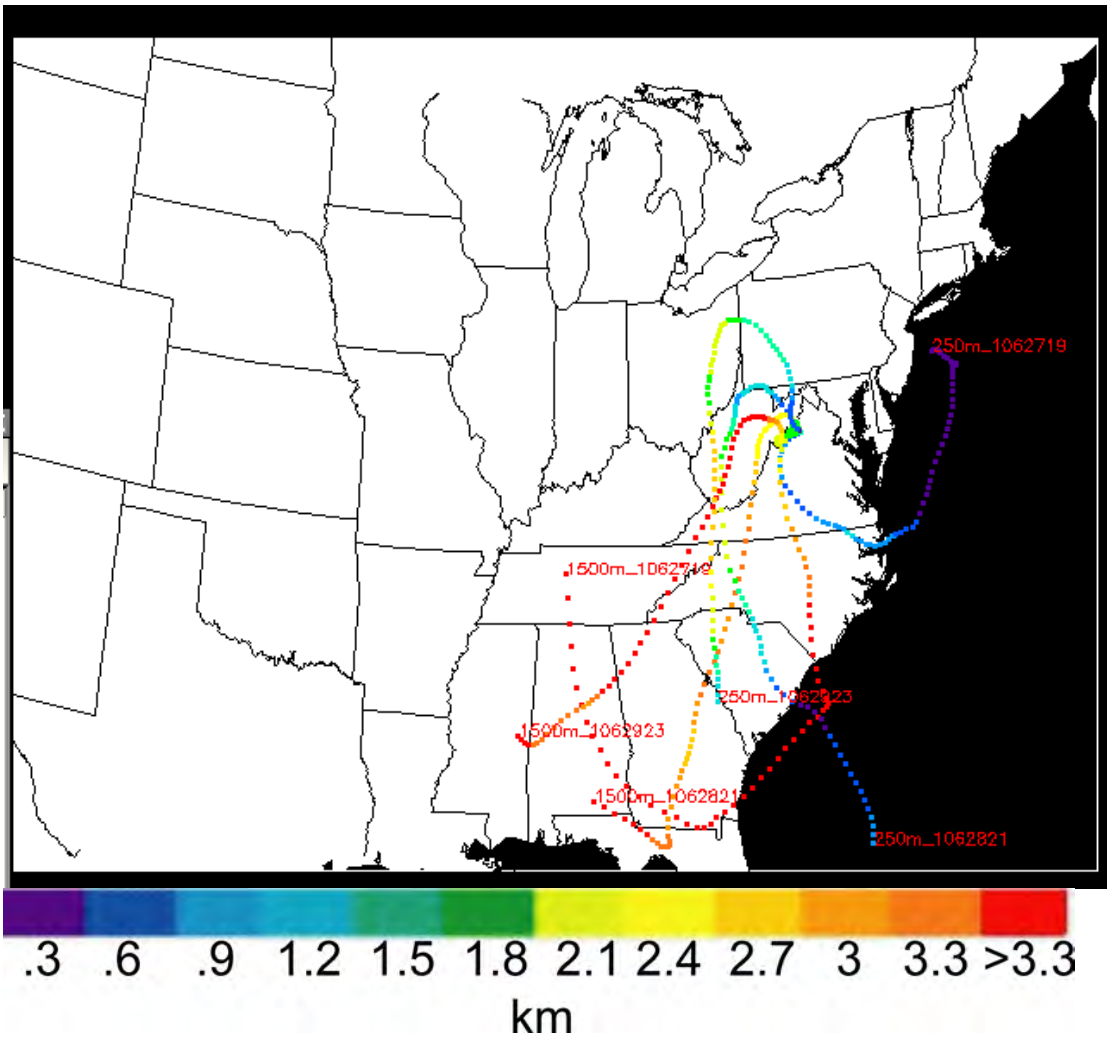

Appendix III.1. June 2001 W45 72 h backward trajectories

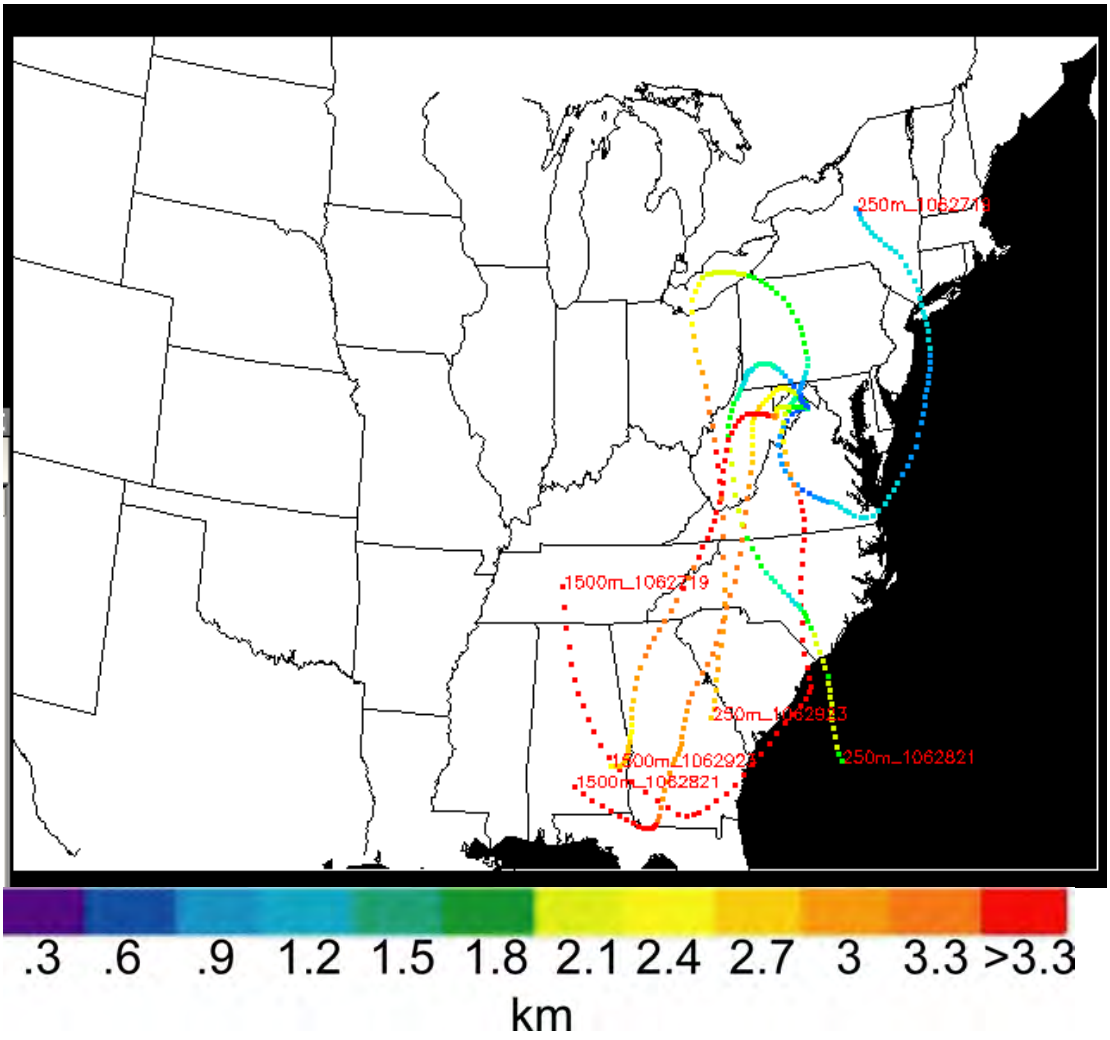

Appendix III.2. June 2001 OKV 72 h backward trajectories

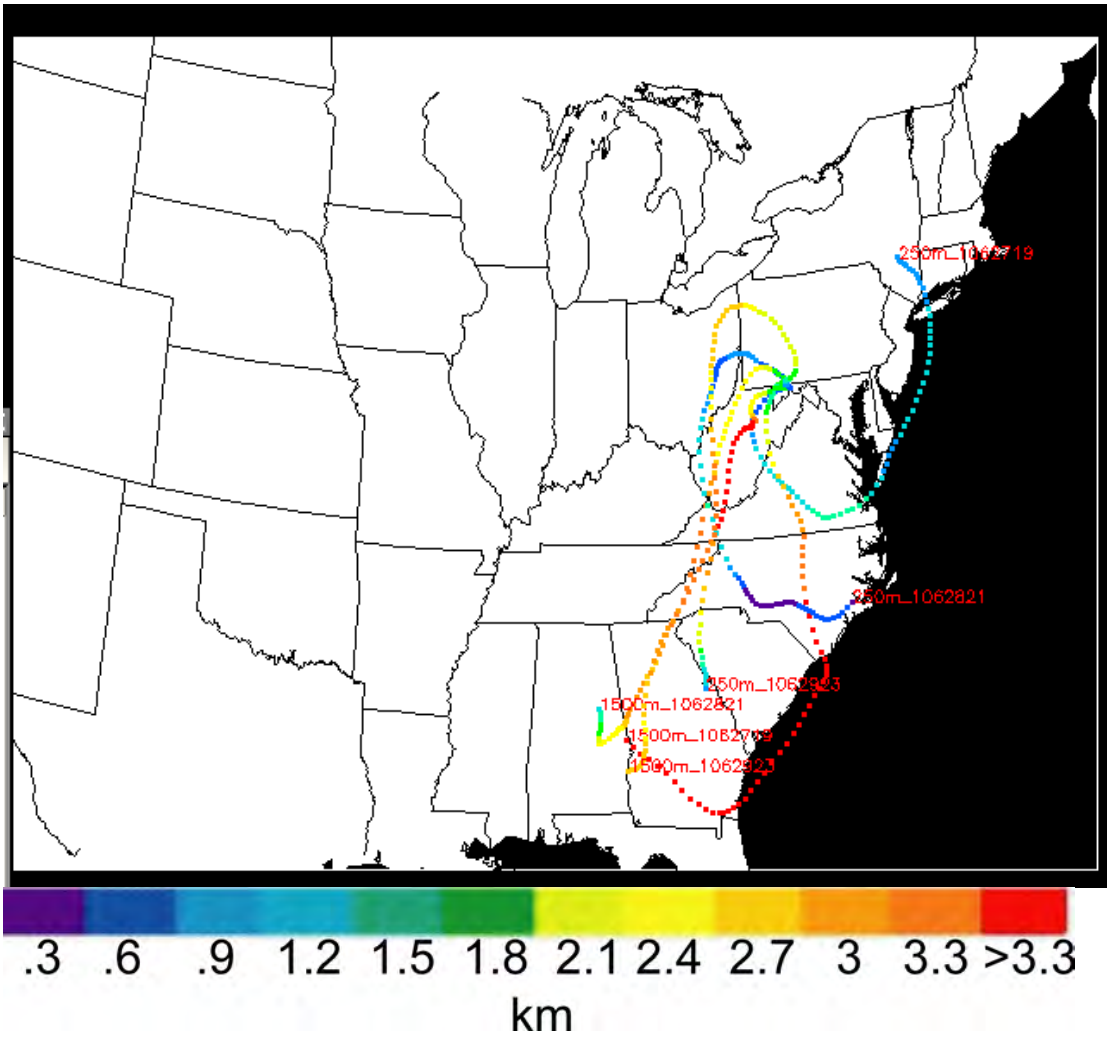

Appendix III.3. June 2001 CBE 72 h backward trajectories

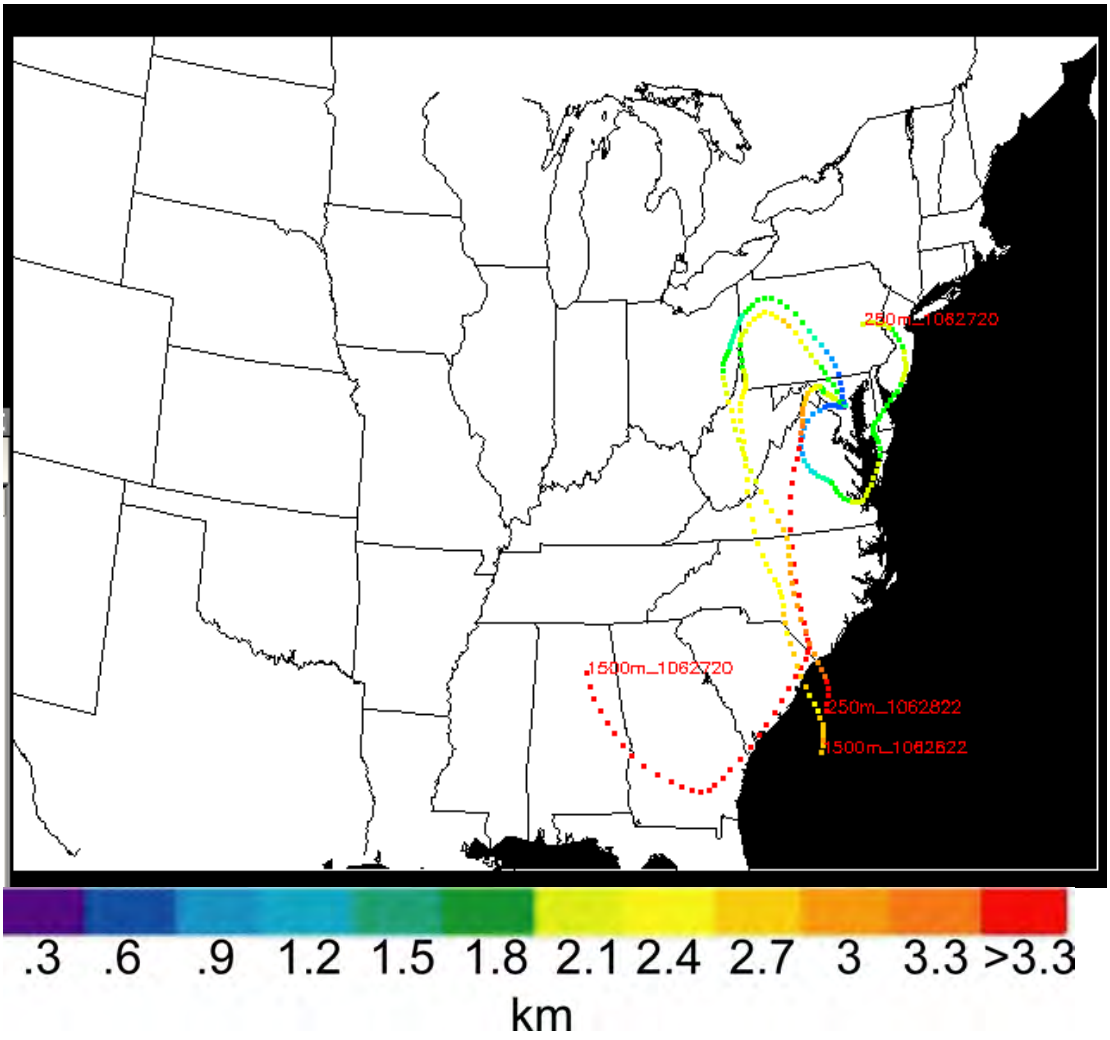

Appendix III.4. June 2001 FME 72 h backward trajectories

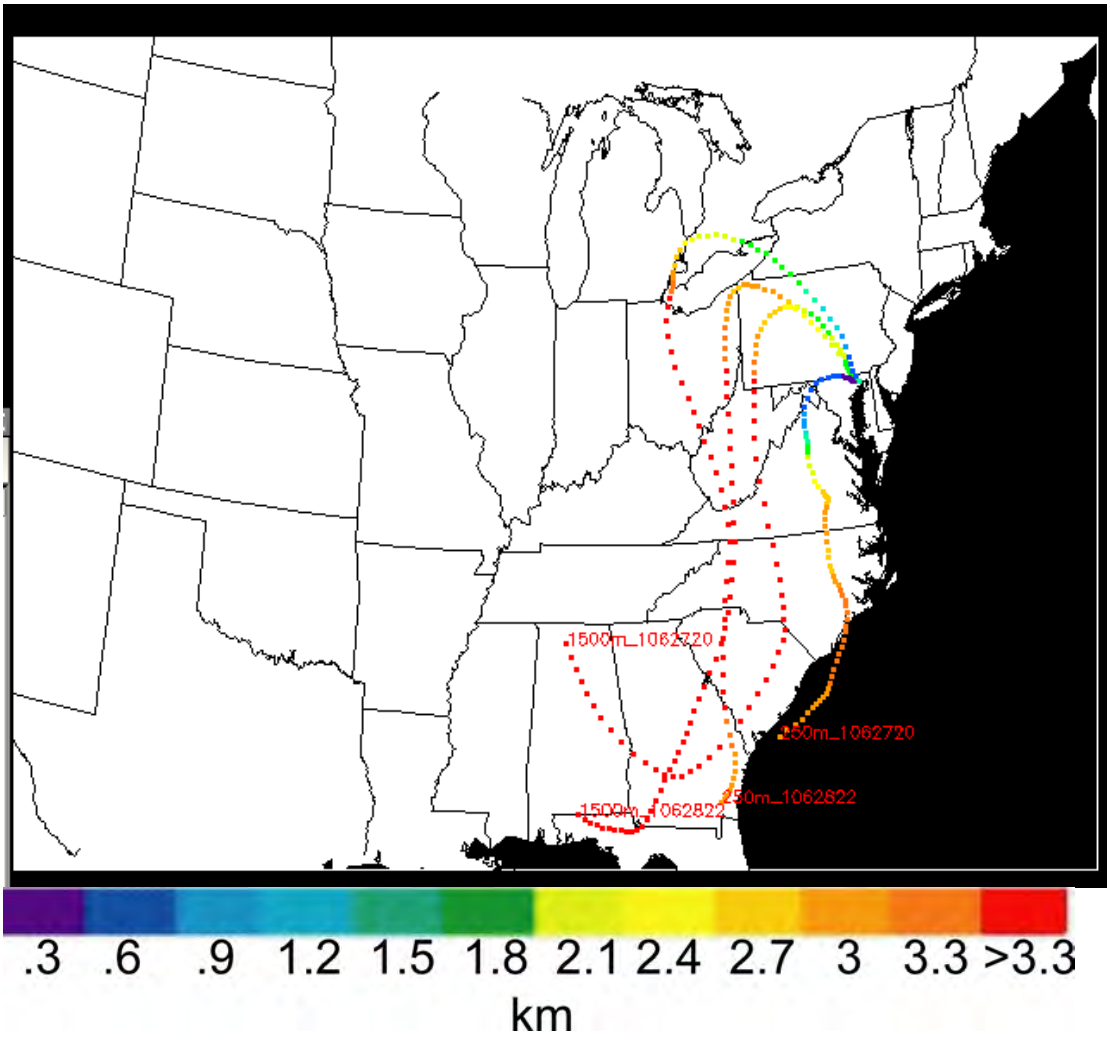

Appendix III.5. June 2001 0W3 72 h backward trajectories

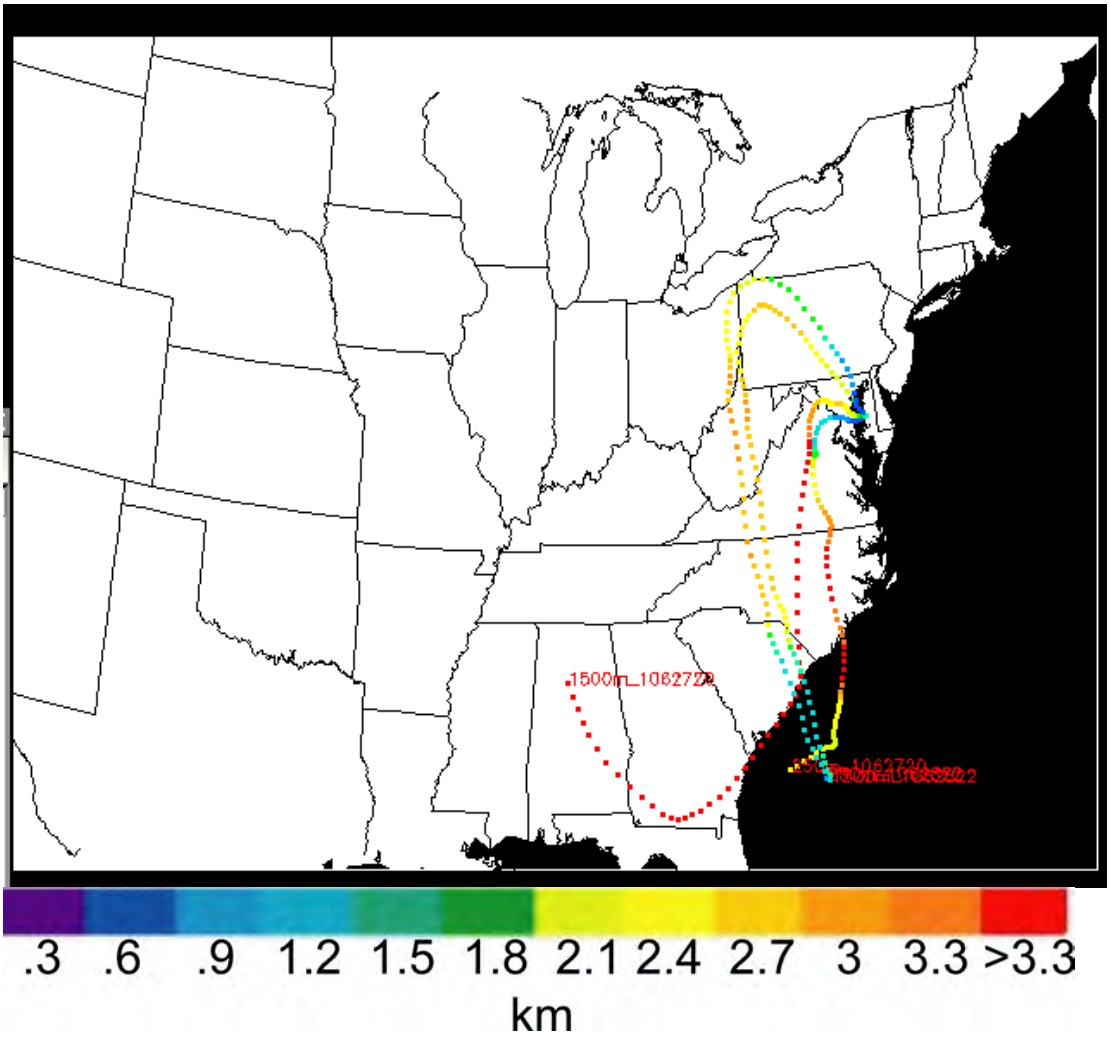

Appendix III.6. June 2001 ESN 72 h backward trajectories

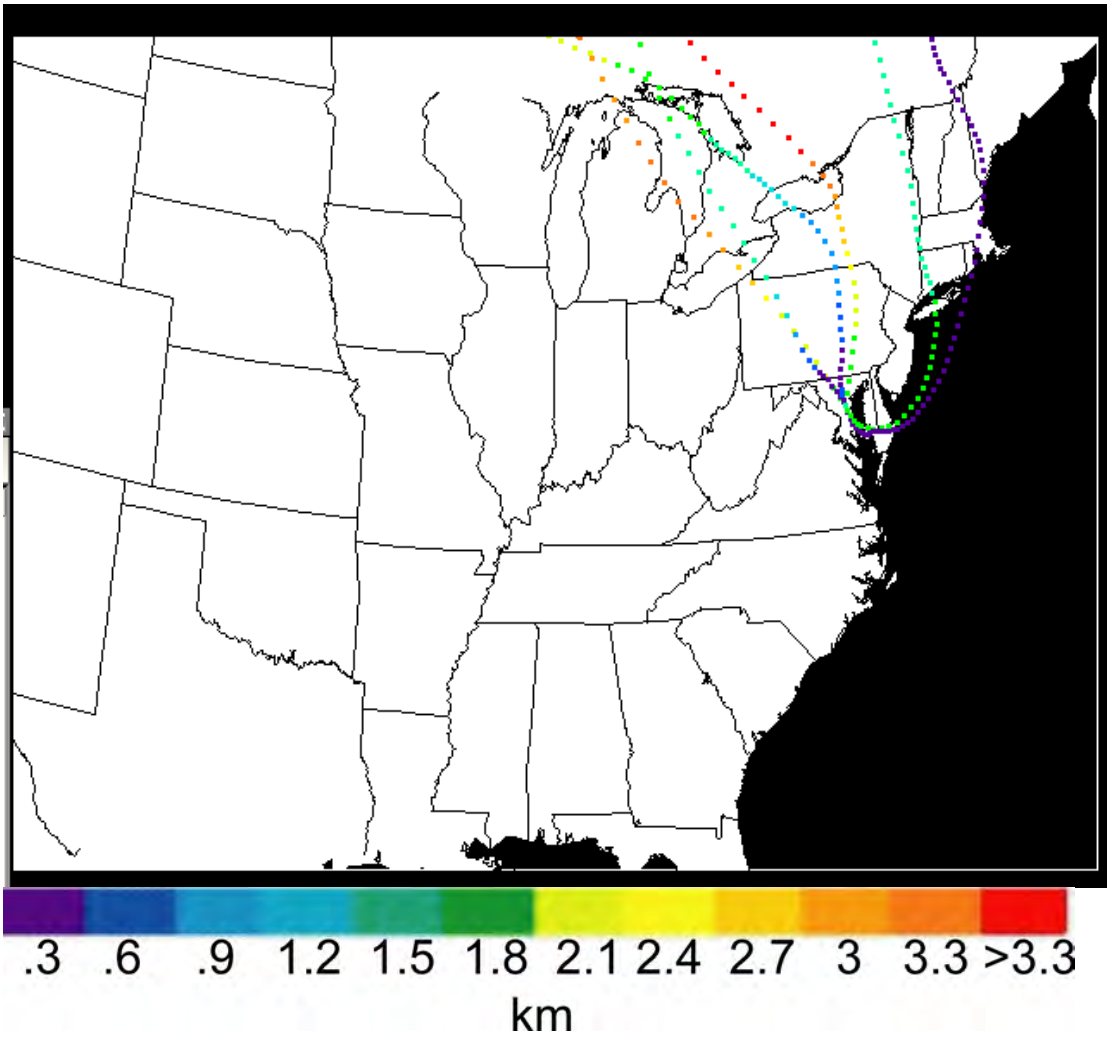

Appendix III.7. July 2001 FME 72 h backward trajectories

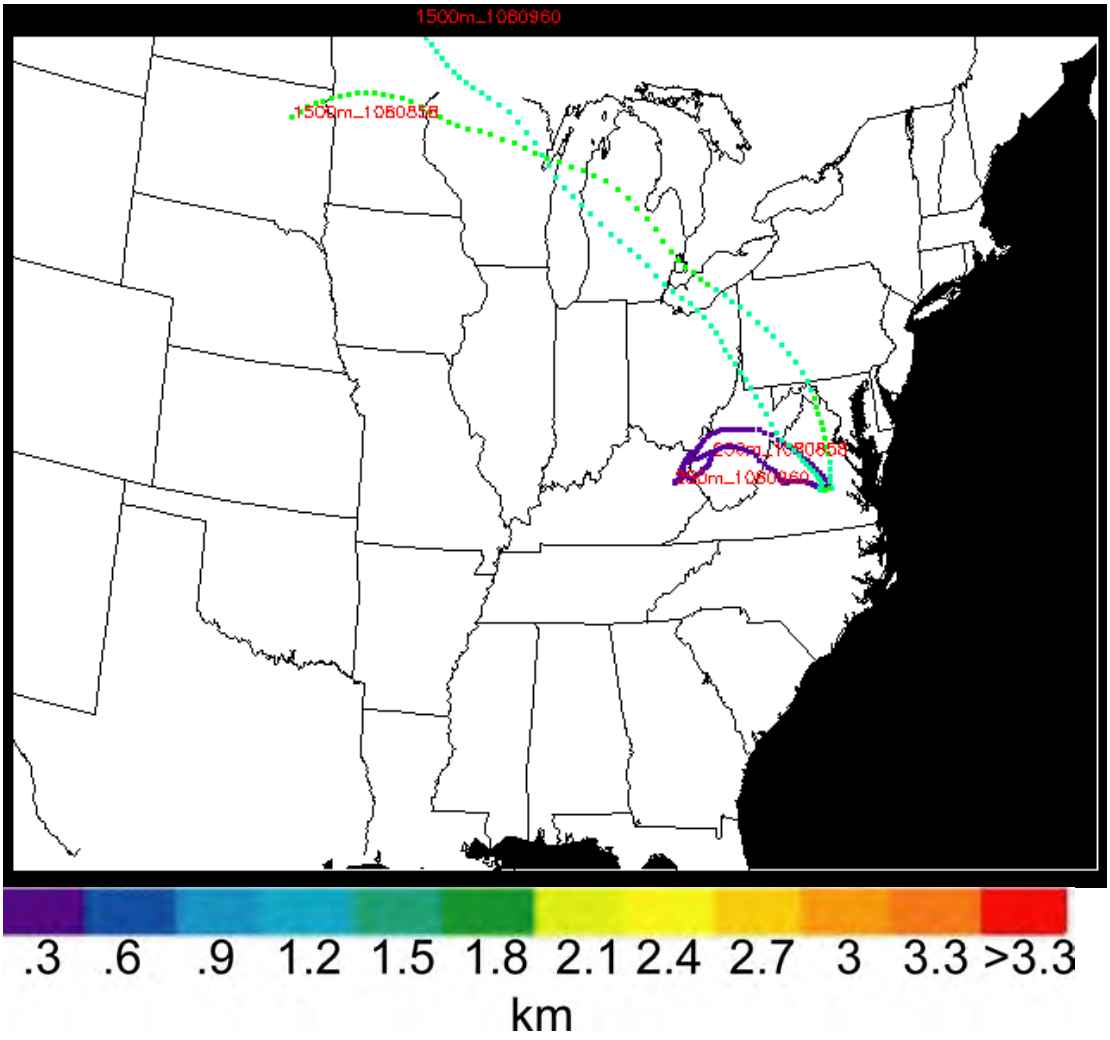

Appendix III.8. August 2001 FCI morning 72 h backward trajectories

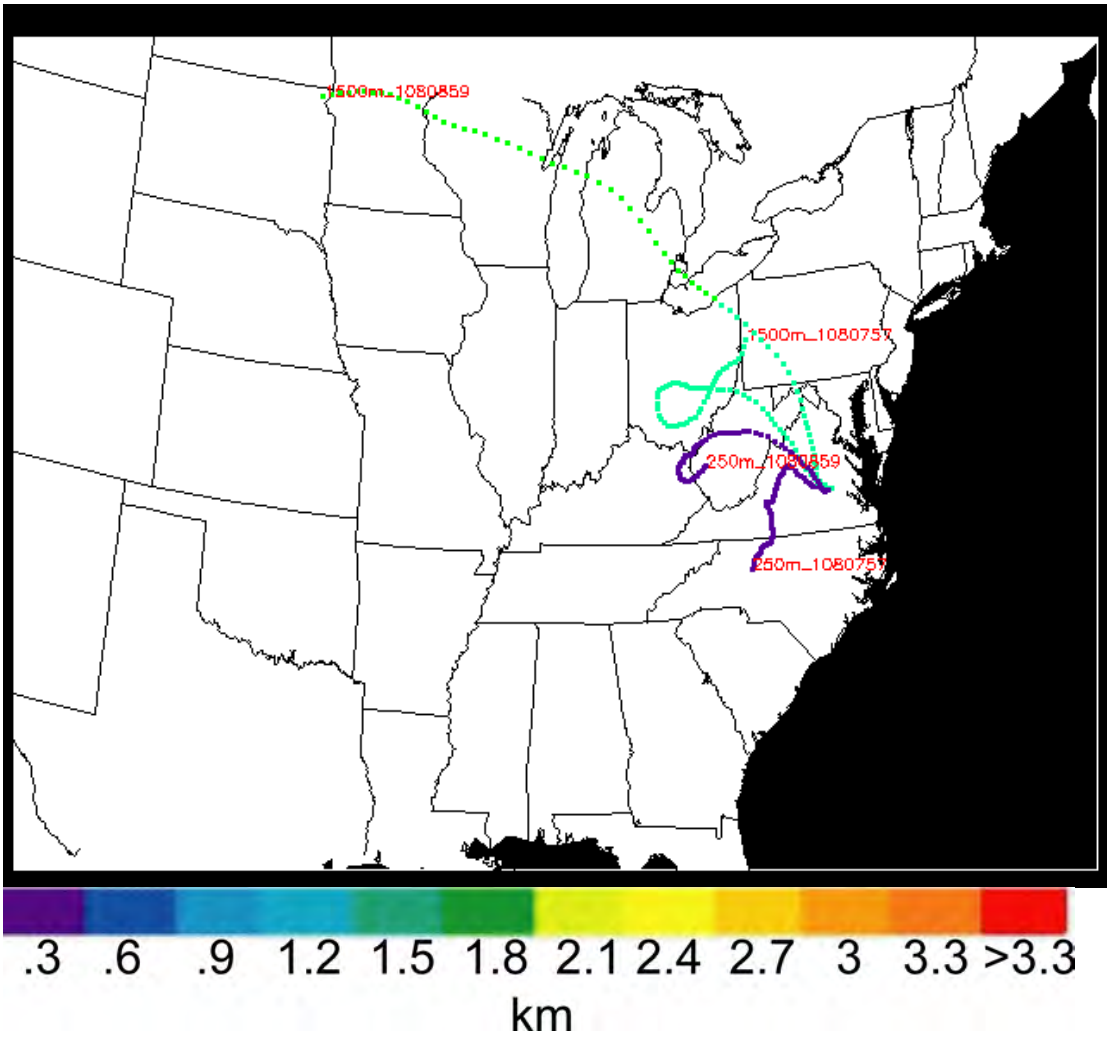

Appendix III.9. August 2001 FCI afternoon 72 h backward trajectories

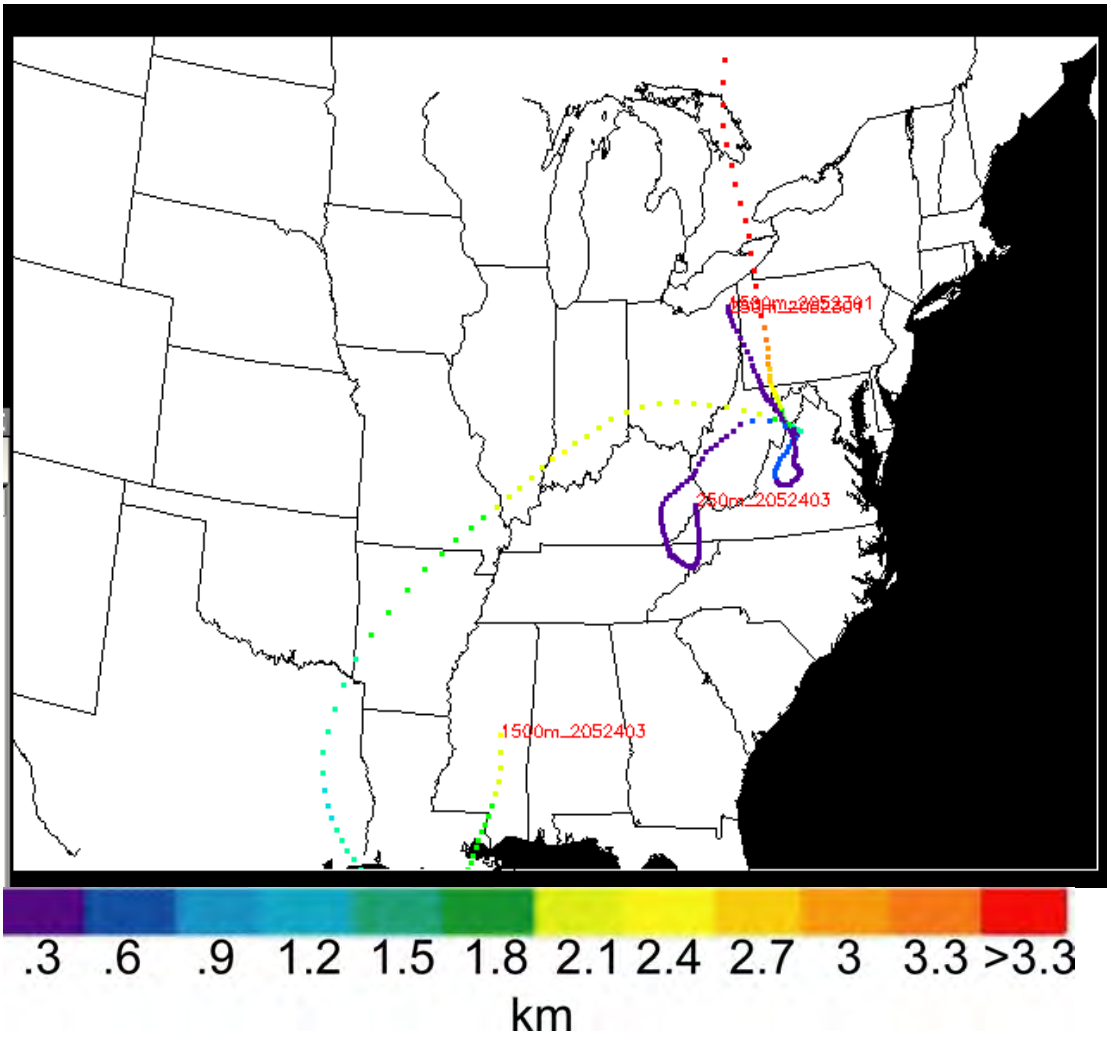

Appendix III.10. May 2002 W45 72 h backward trajectories

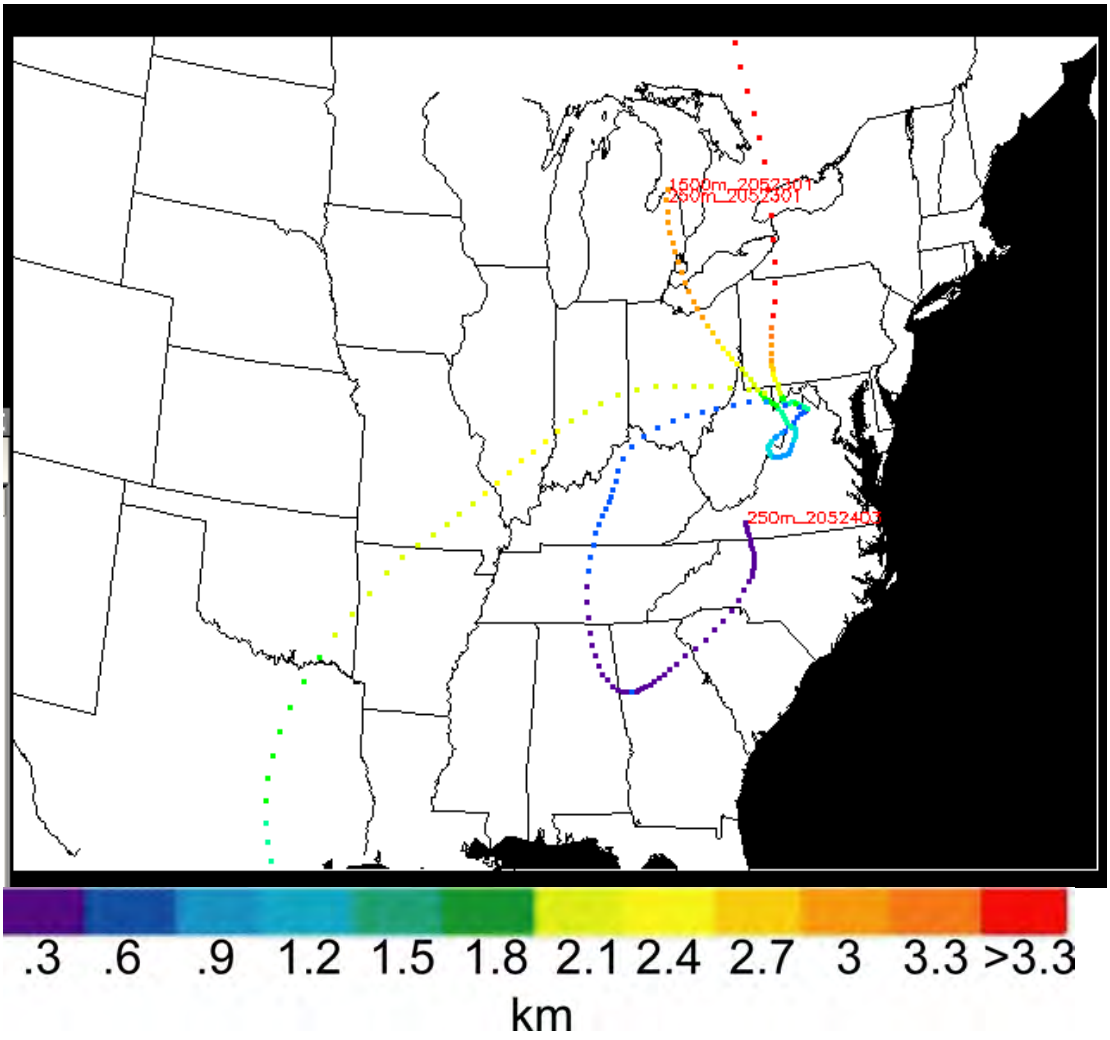

Appendix III.11. May 2002 OKV 72 h backward trajectories

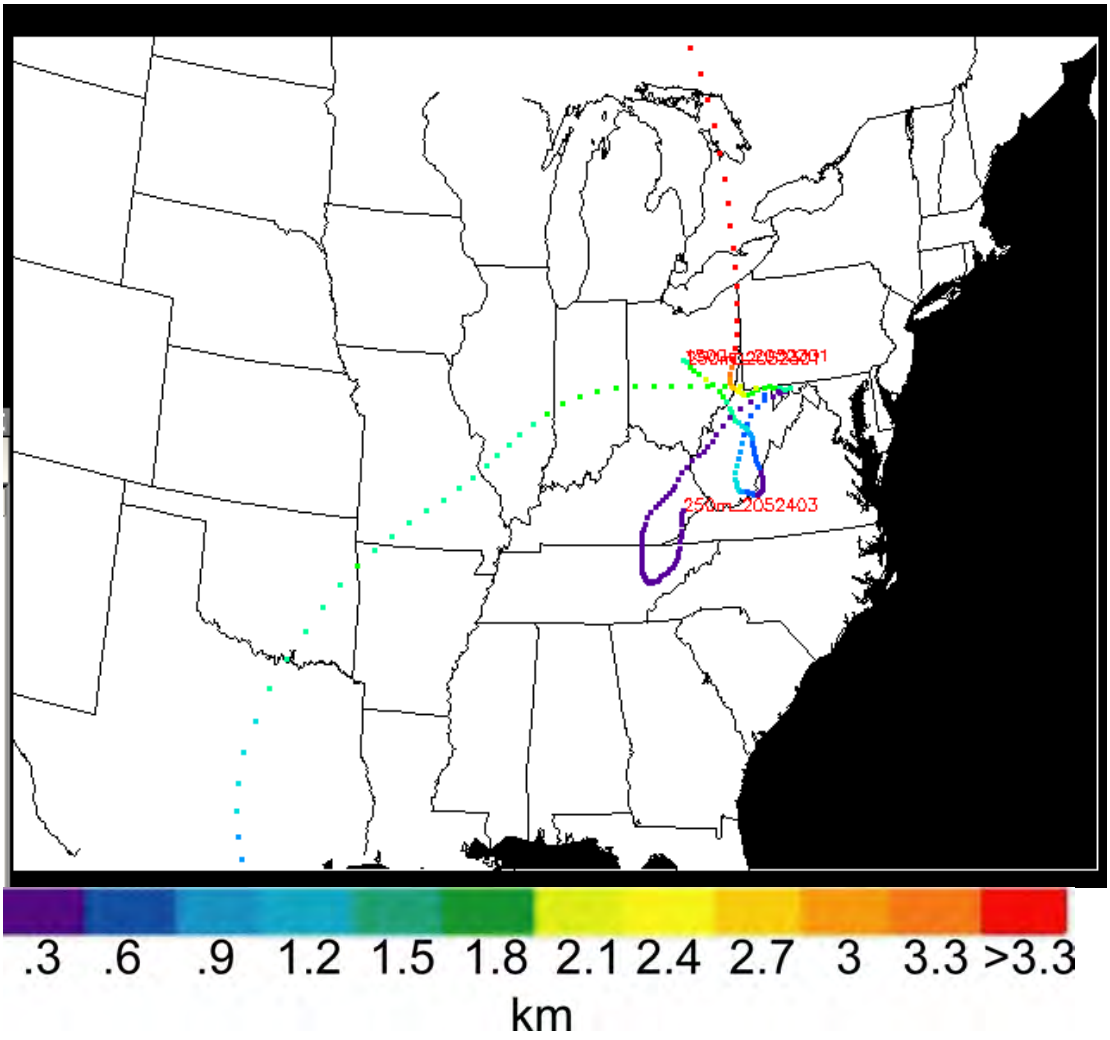

Appendix III.12. May 2002 CBE 72 h backward trajectories

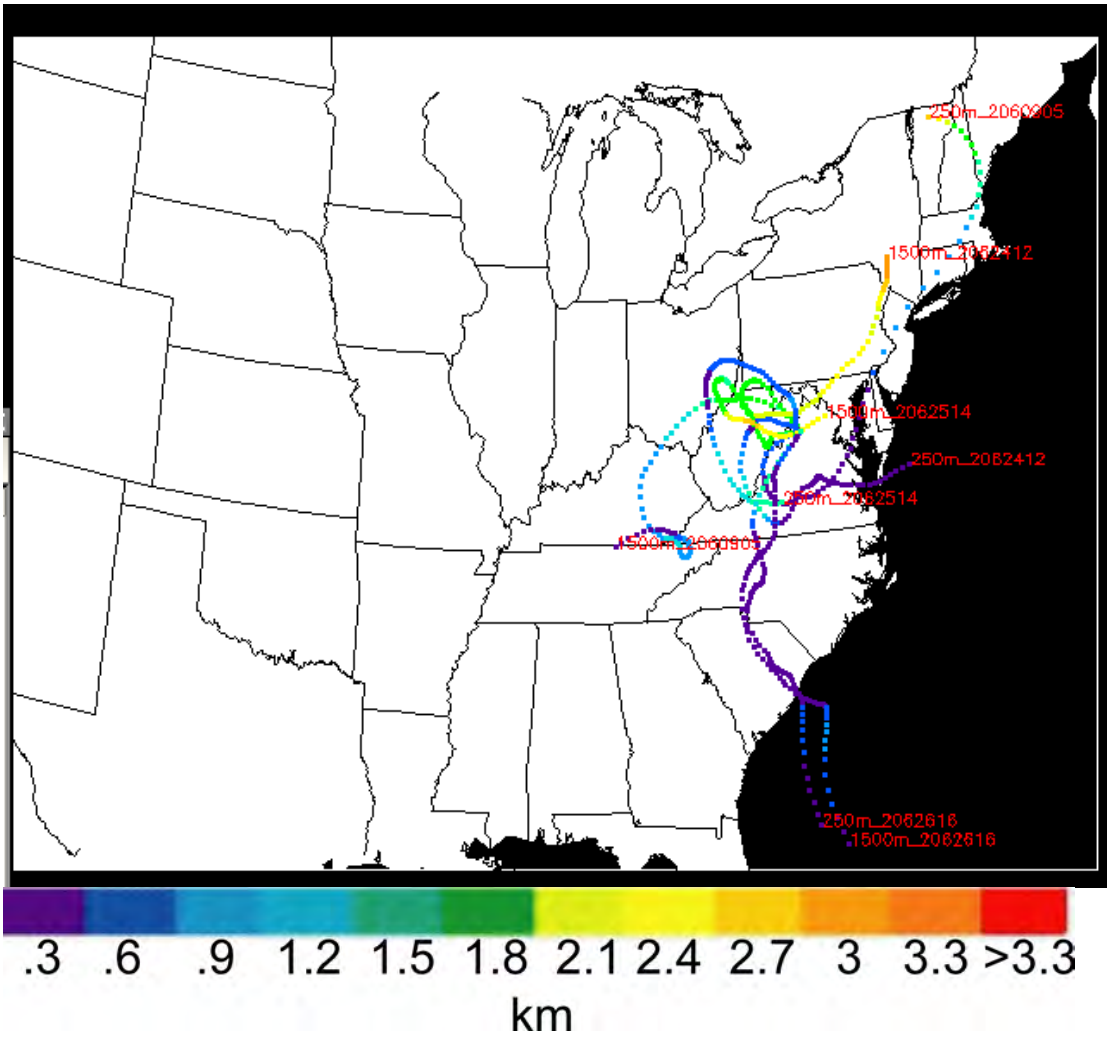

Appendix III.13. June 2002 W45 72 h backward trajectories

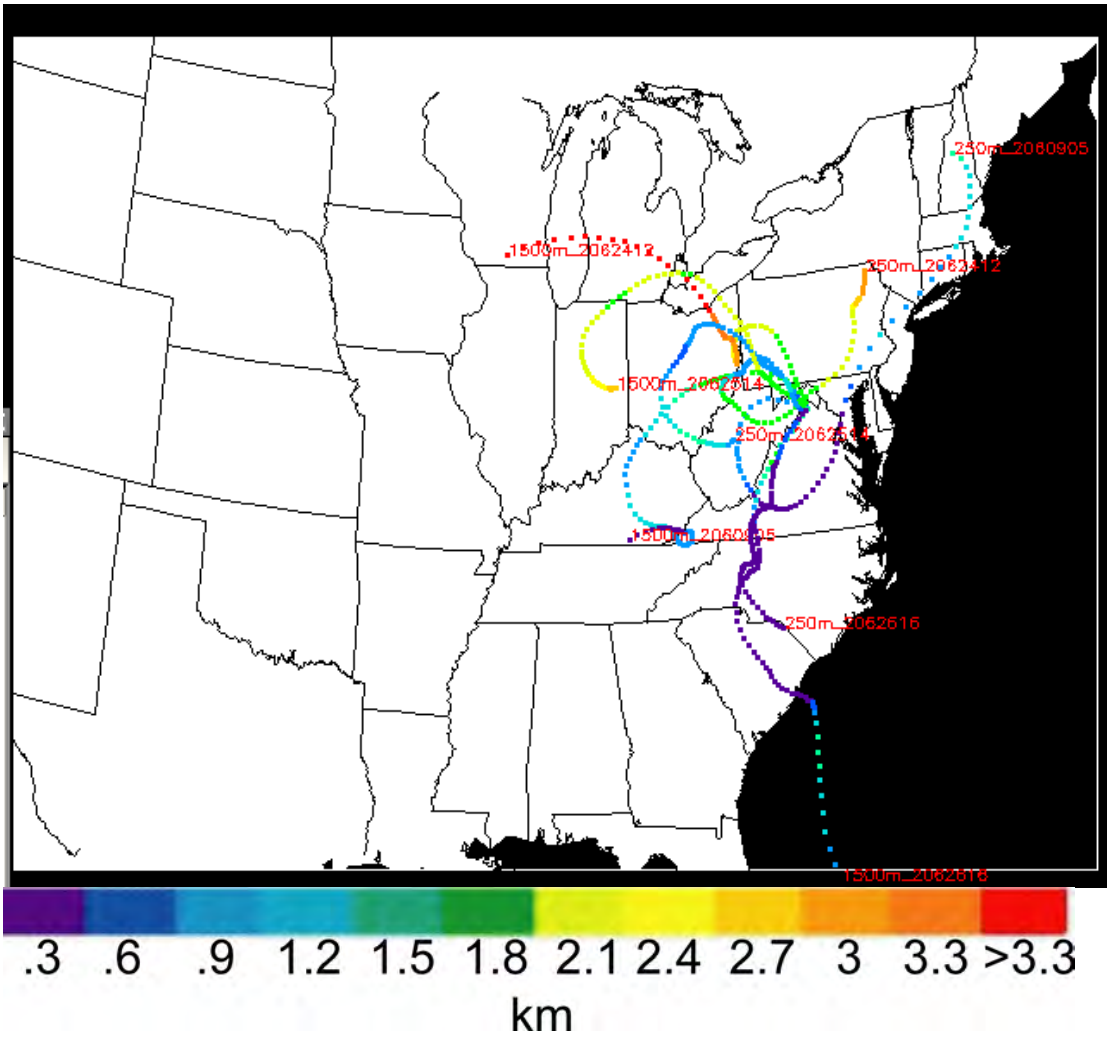

Appendix III.14. June 2002 OKV 72 h backward trajectories

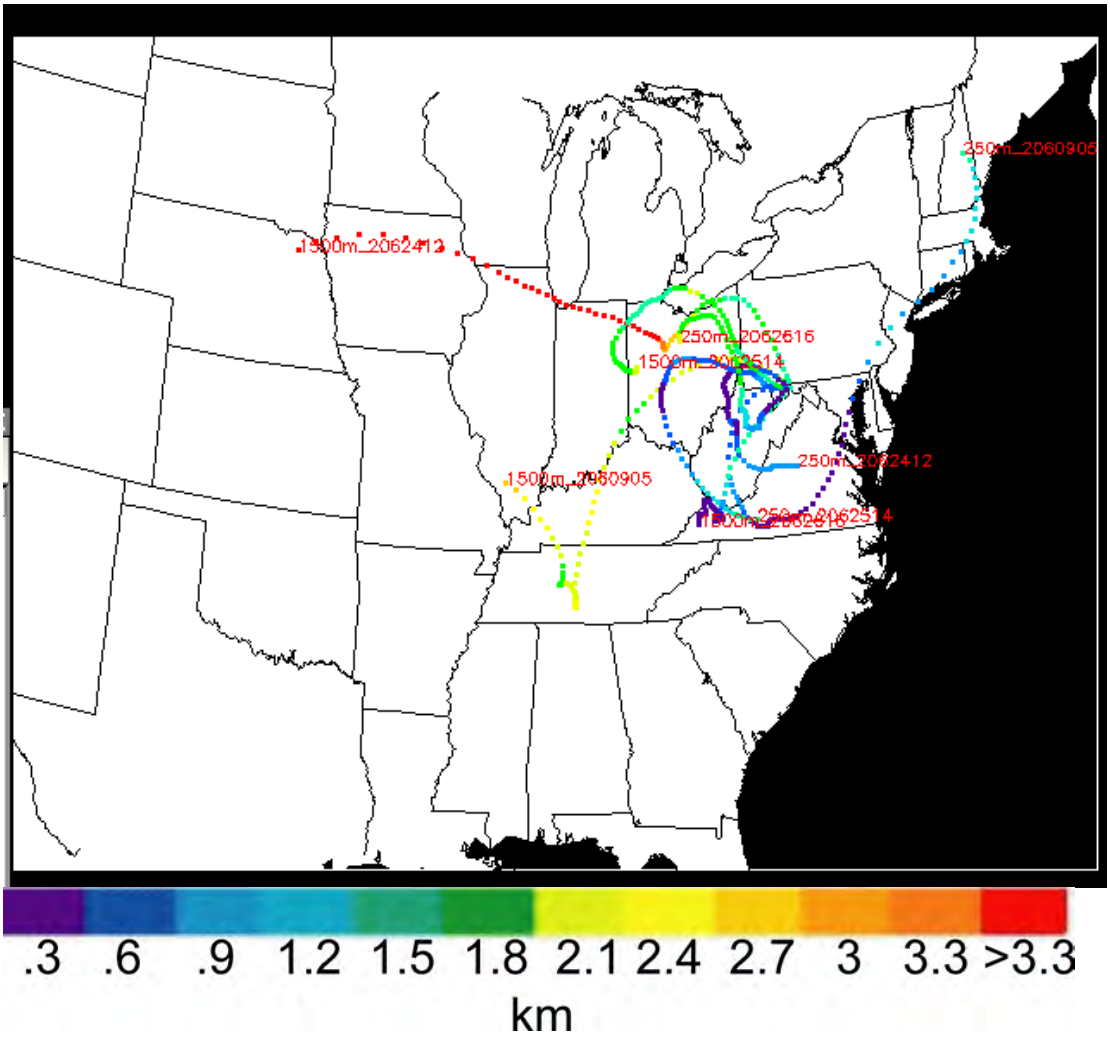

Appendix III.15. June 2002 CBE 72 h backward trajectories

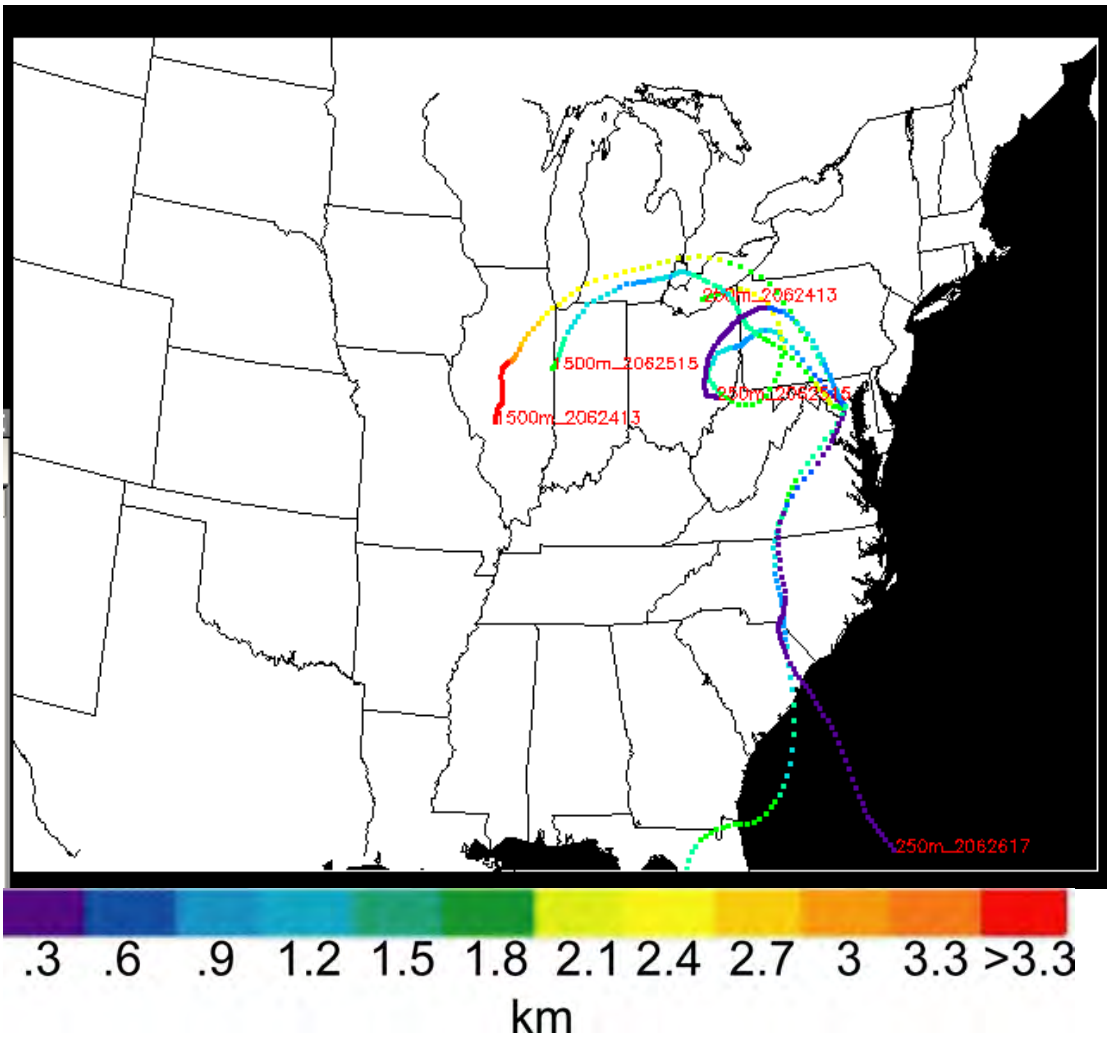

Appendix III.16. June 2002 FME 72 h backward trajectories

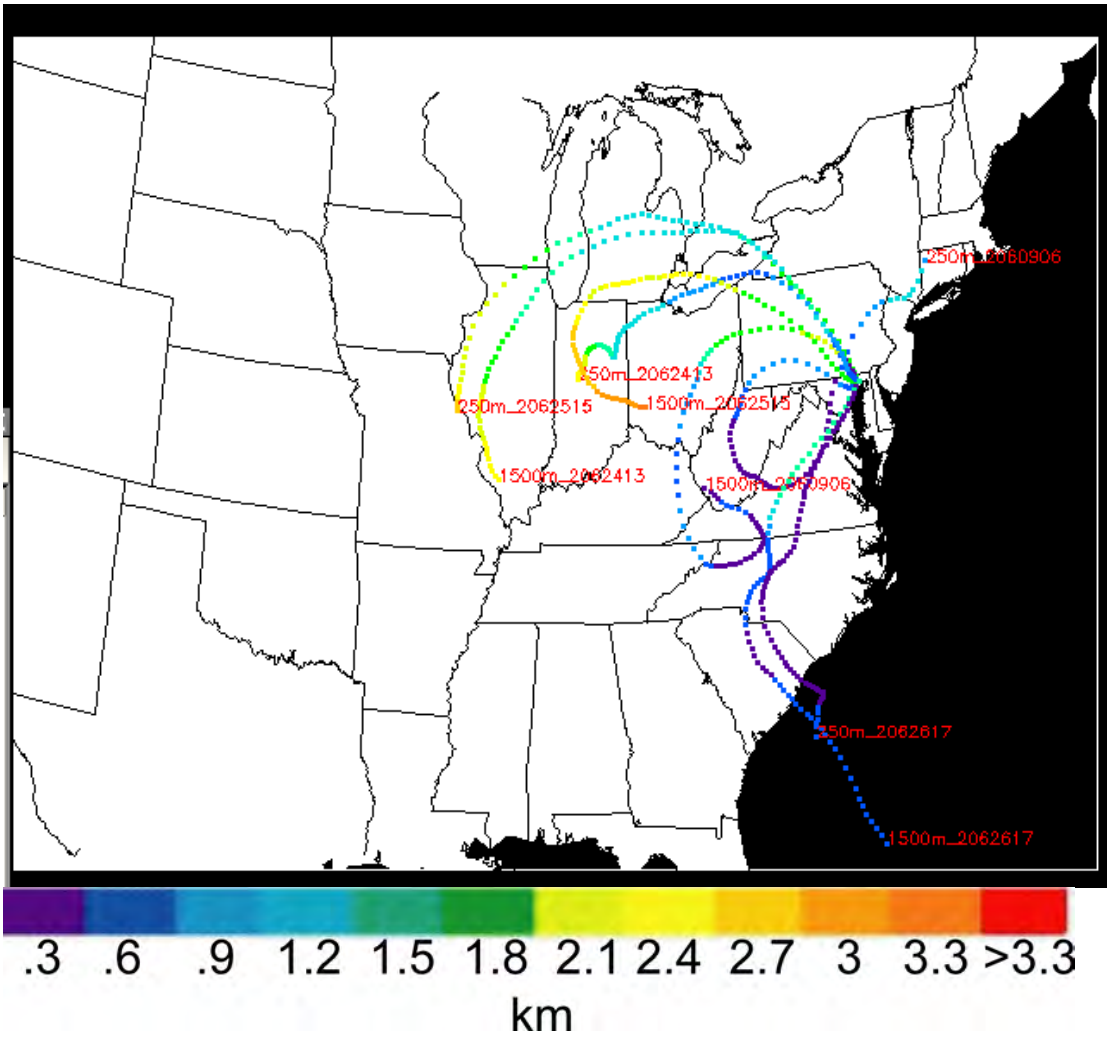

Appendix III.17. June 2002 0W3 72 h backward trajectories

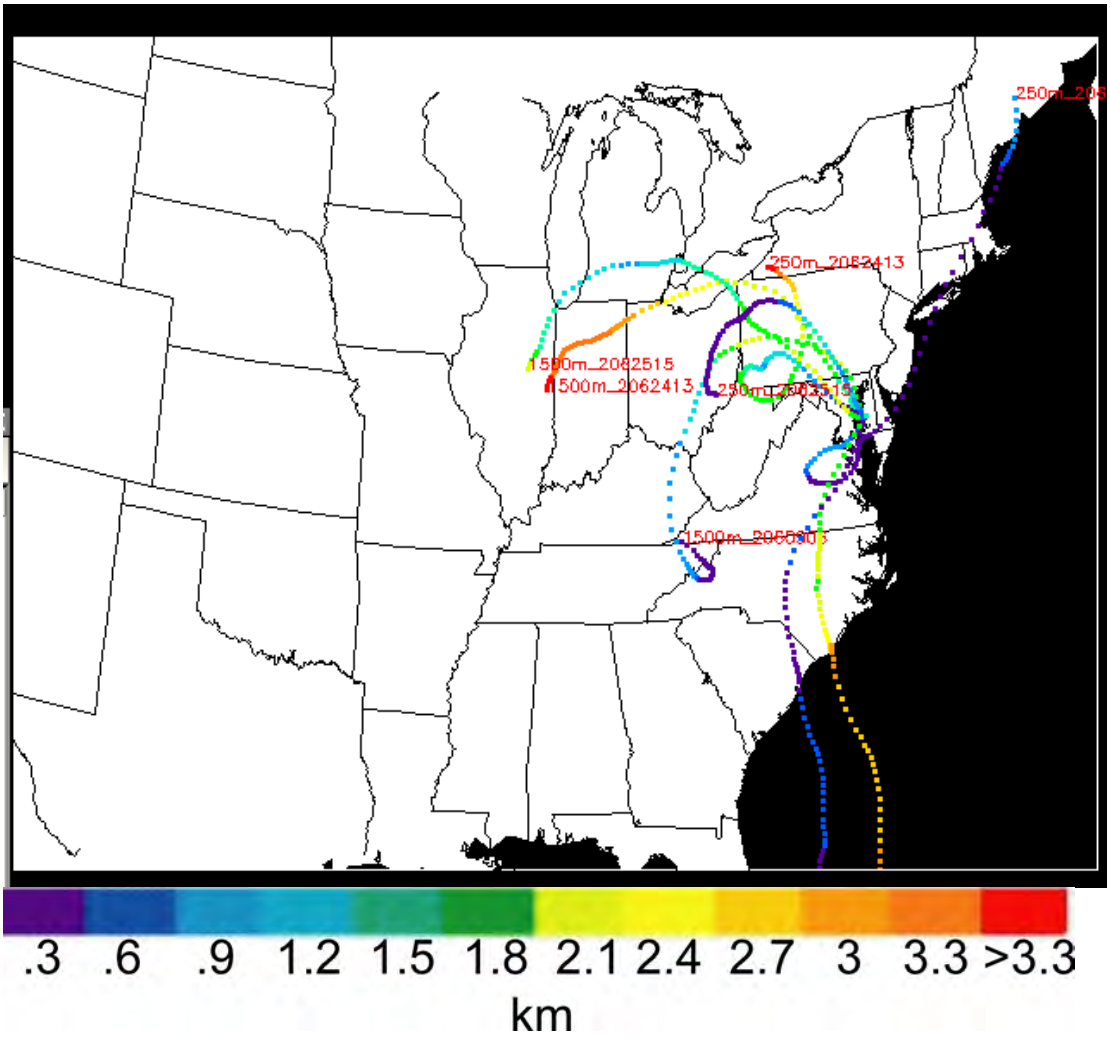

Appendix III.18. June 2002 ESN 72 h backward trajectories

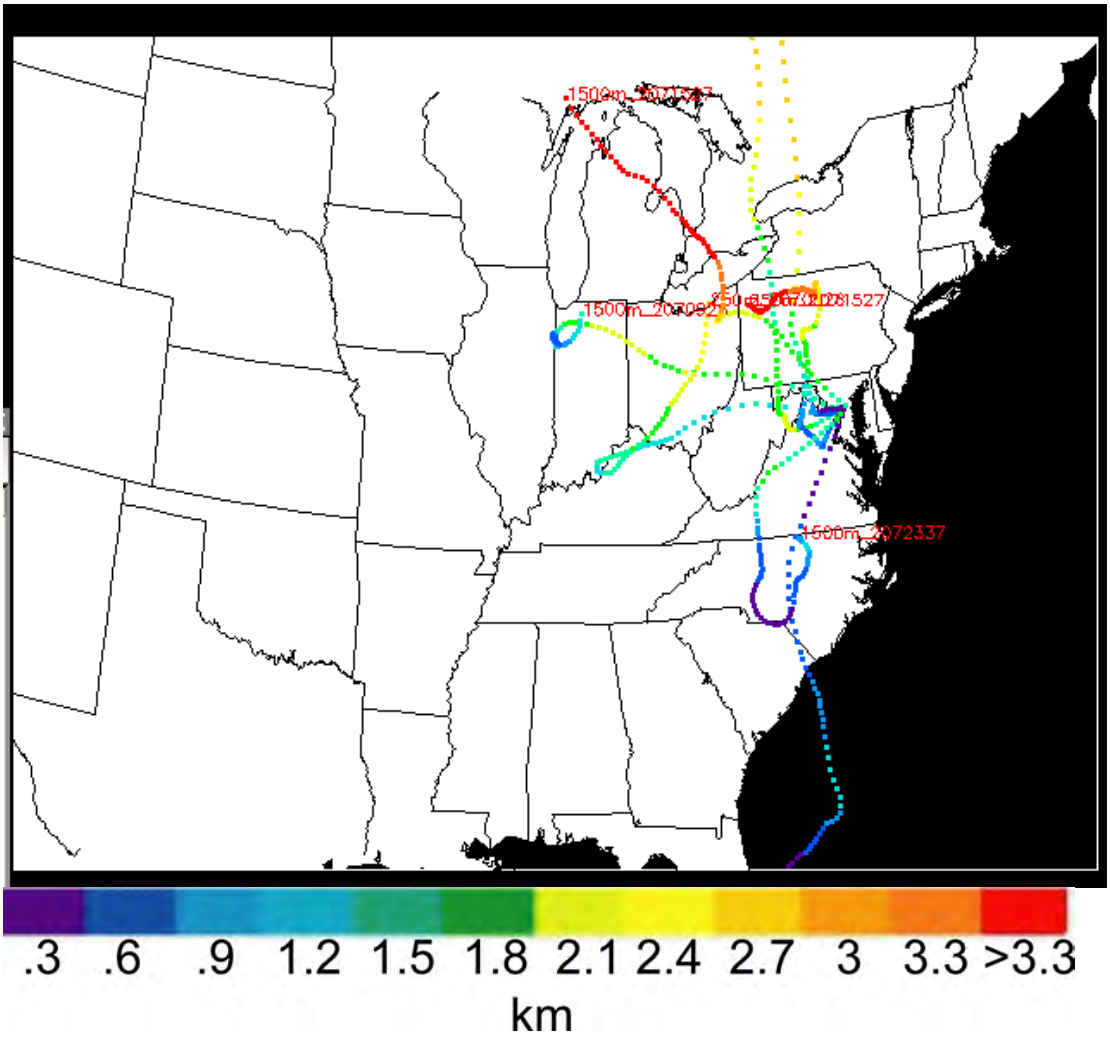

Appendix III.19. July 2002 FME 72 h backward trajectories

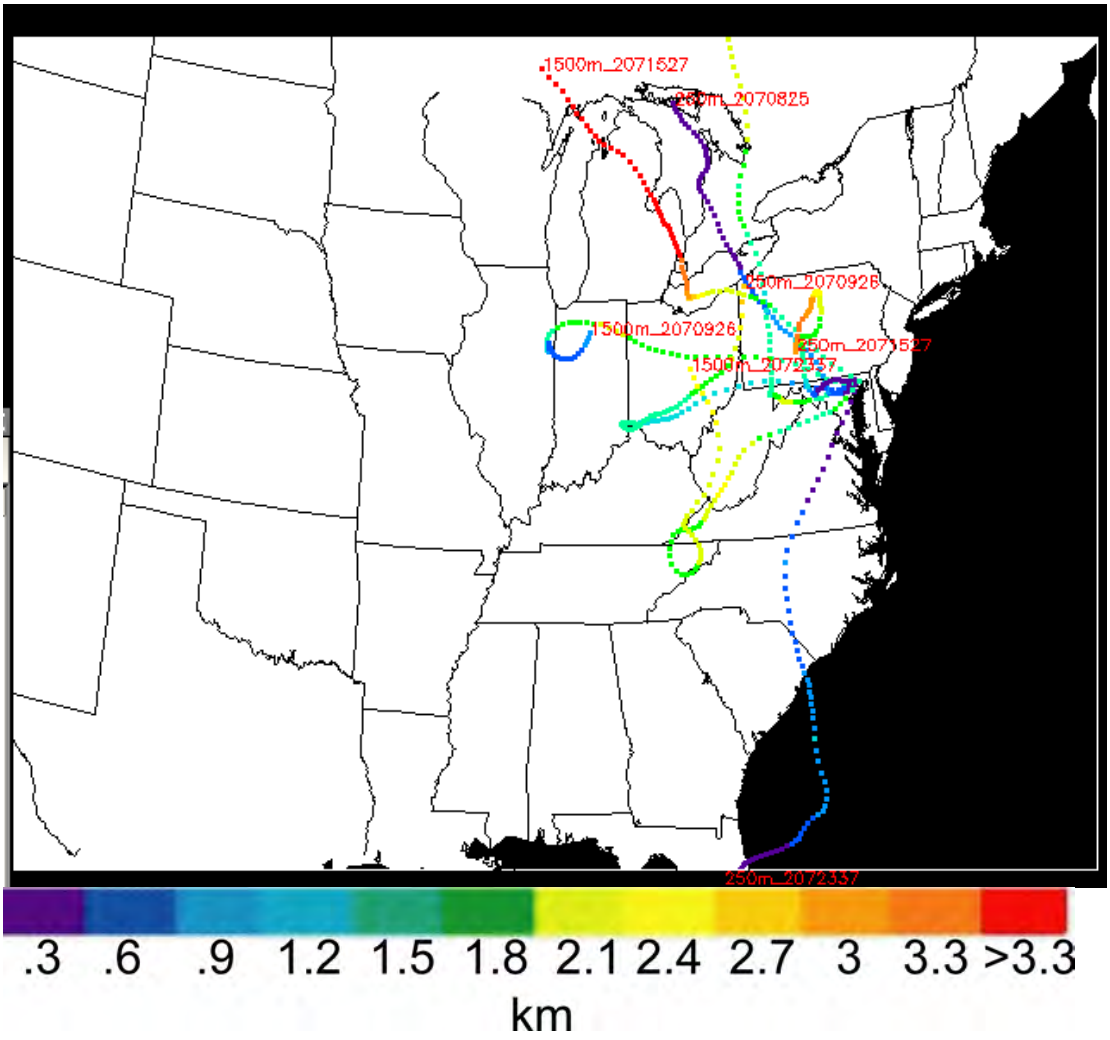

Appendix III.20. July 2002 0W3 72 h backward trajectories

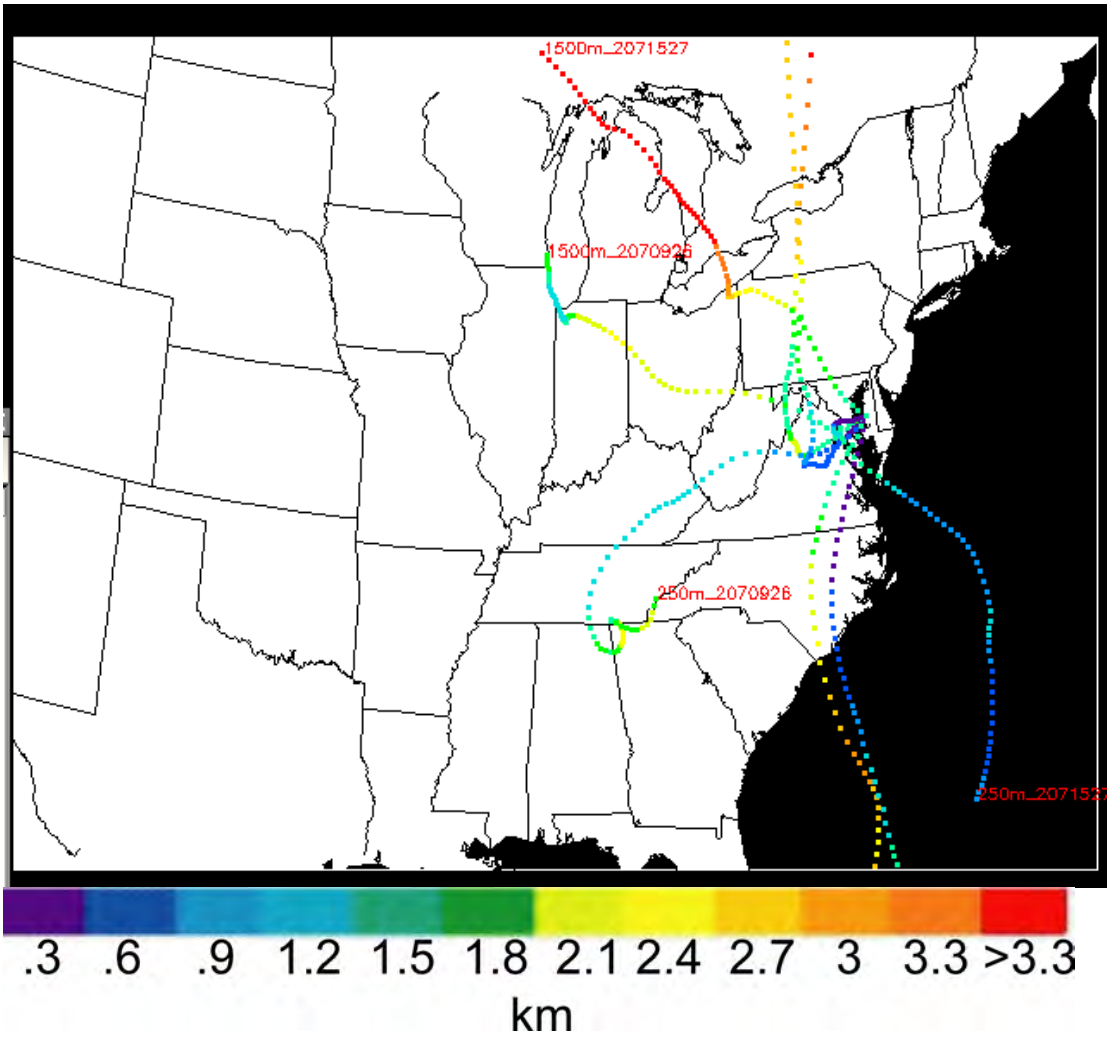

Appendix III.21. July 2002 ESN 72 h backward trajectories

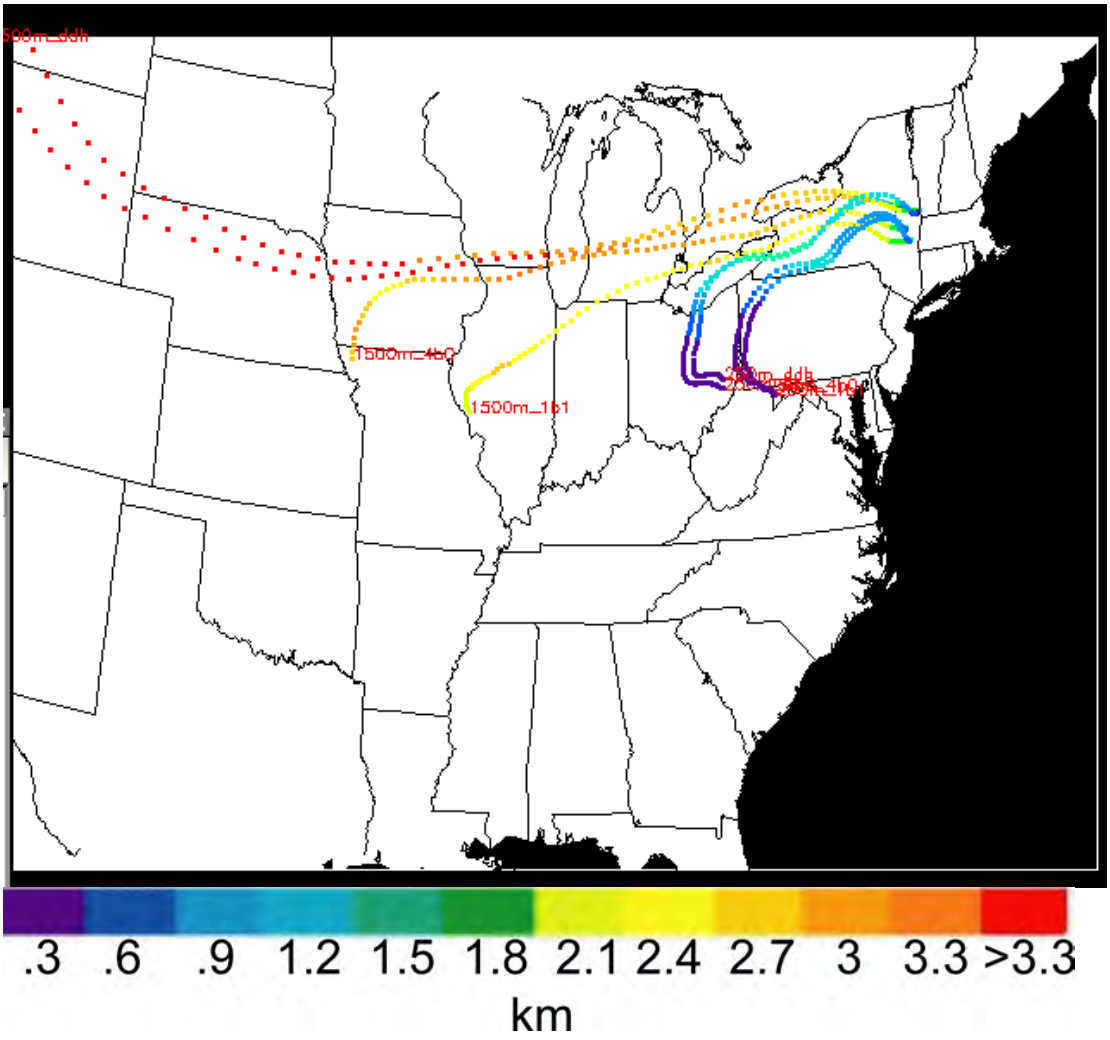

Appendix III.22. 12 August 2002 Northeast morning 72 h backward trajectories

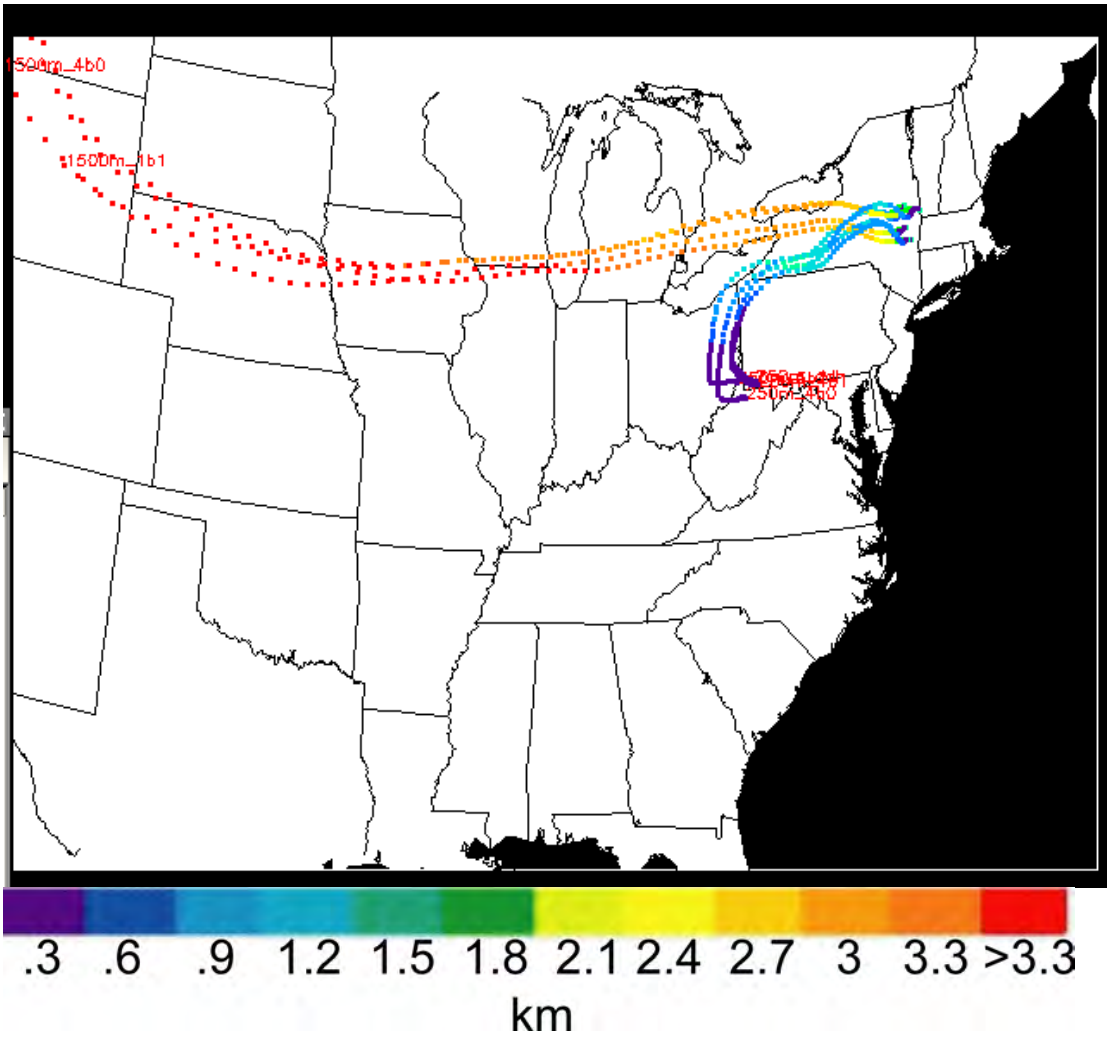

Appendix III.23. 12 August 2002 Northeast afternoon 72 h backward trajectories

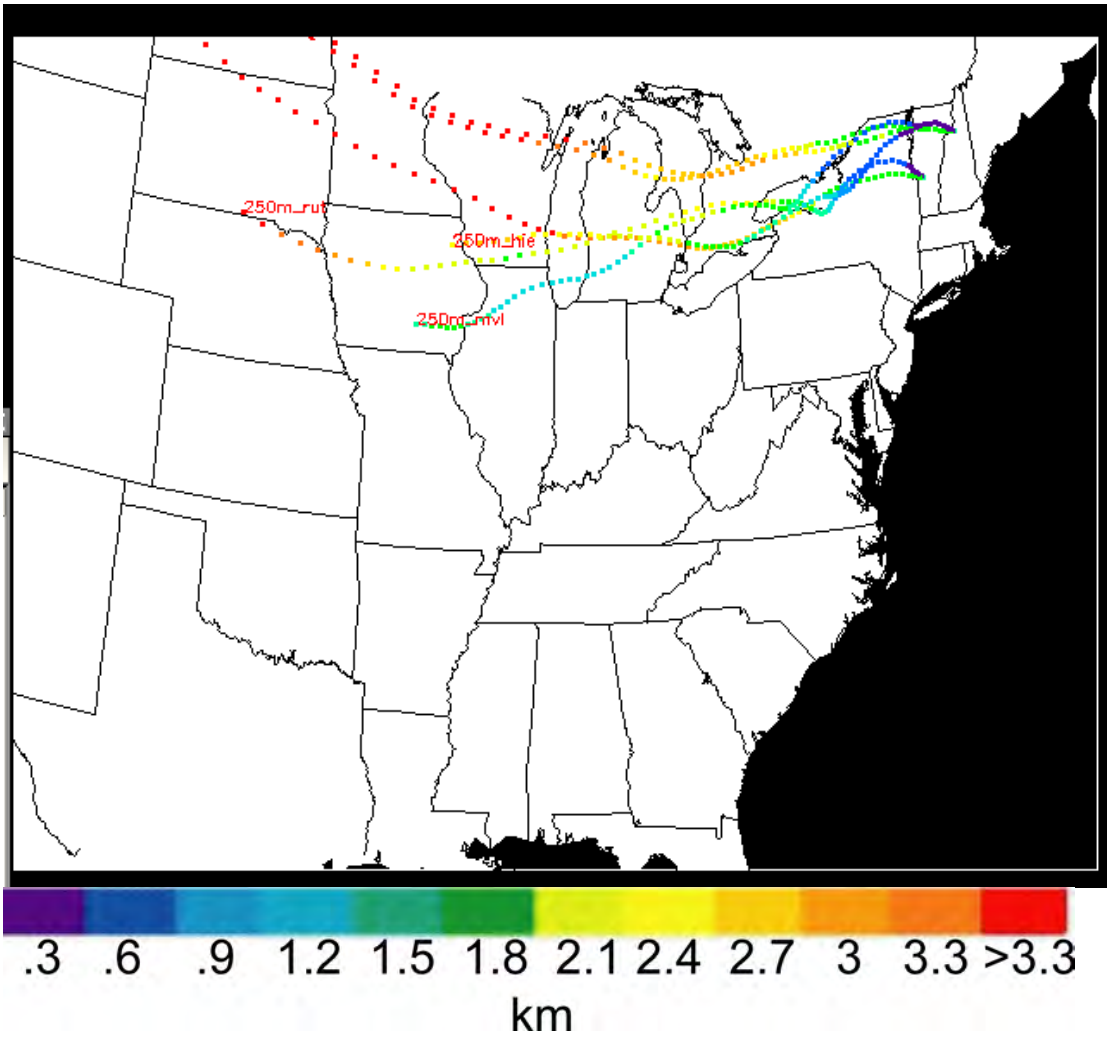

Appendix III.24. 13 August 2002 Northeast morning 72 h backward trajectories

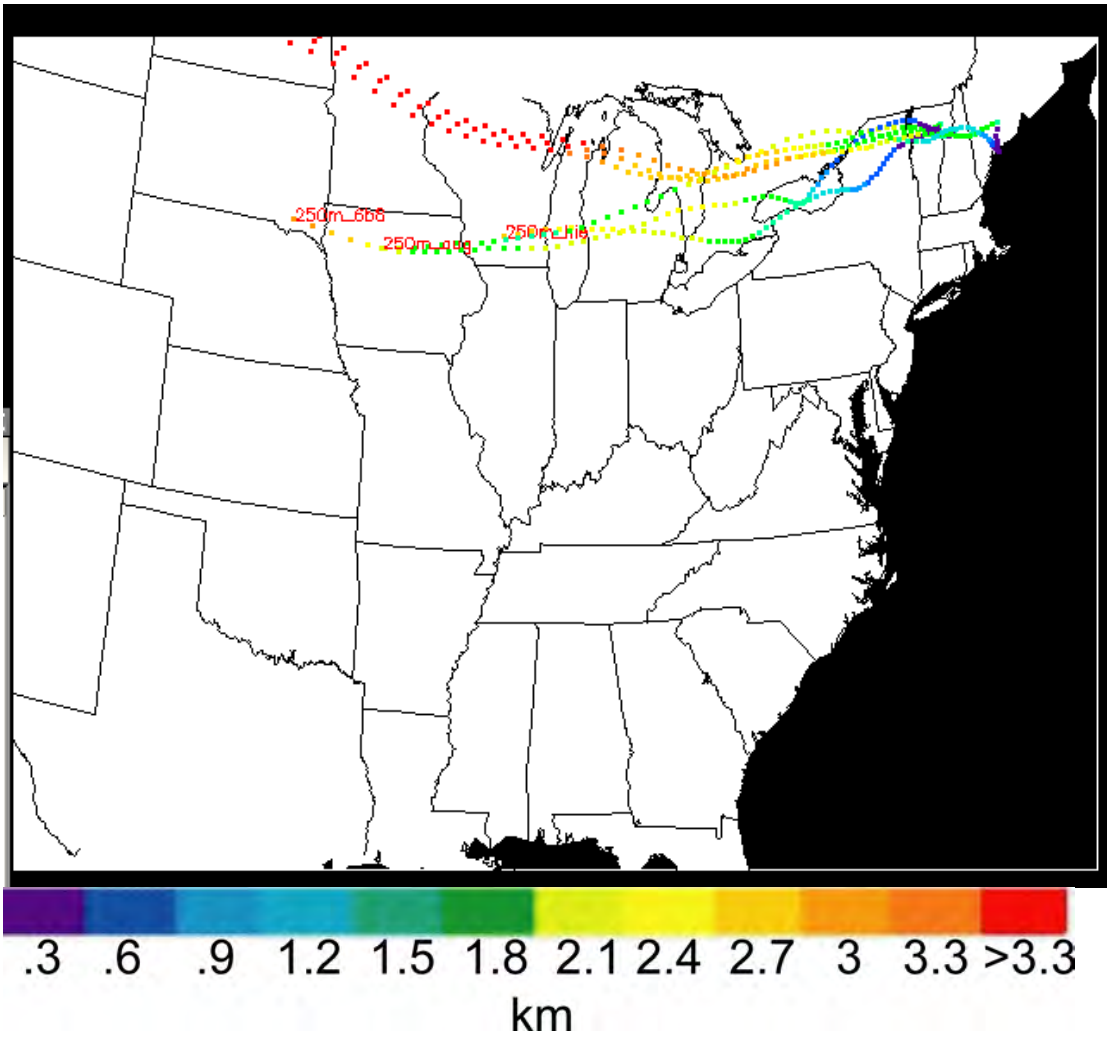

Appendix III.25. 13 August 2002 Northeast afternoon 72 h backward trajectories

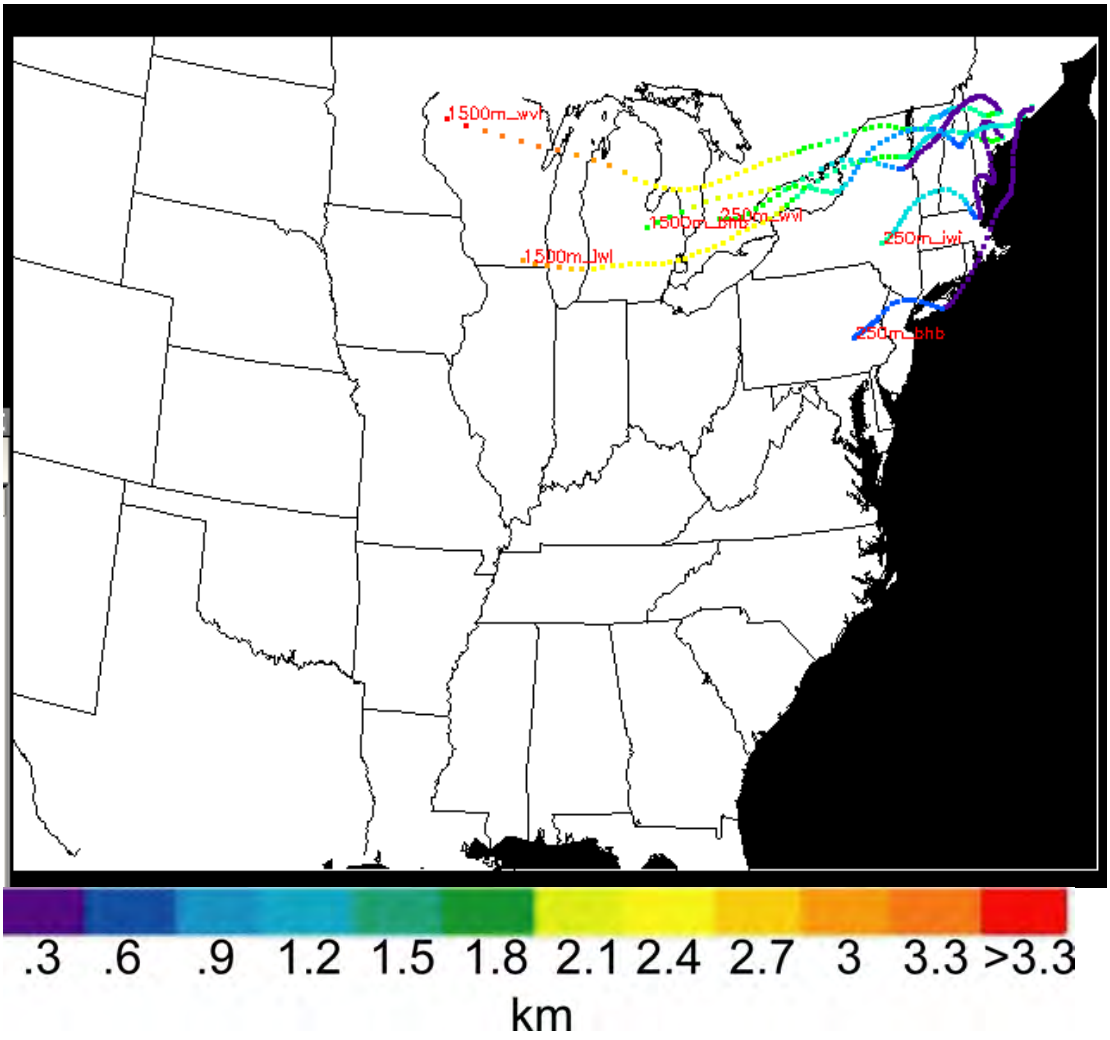

Appendix III.26. 14 August 2002 Northeast morning 72 h backward trajectories

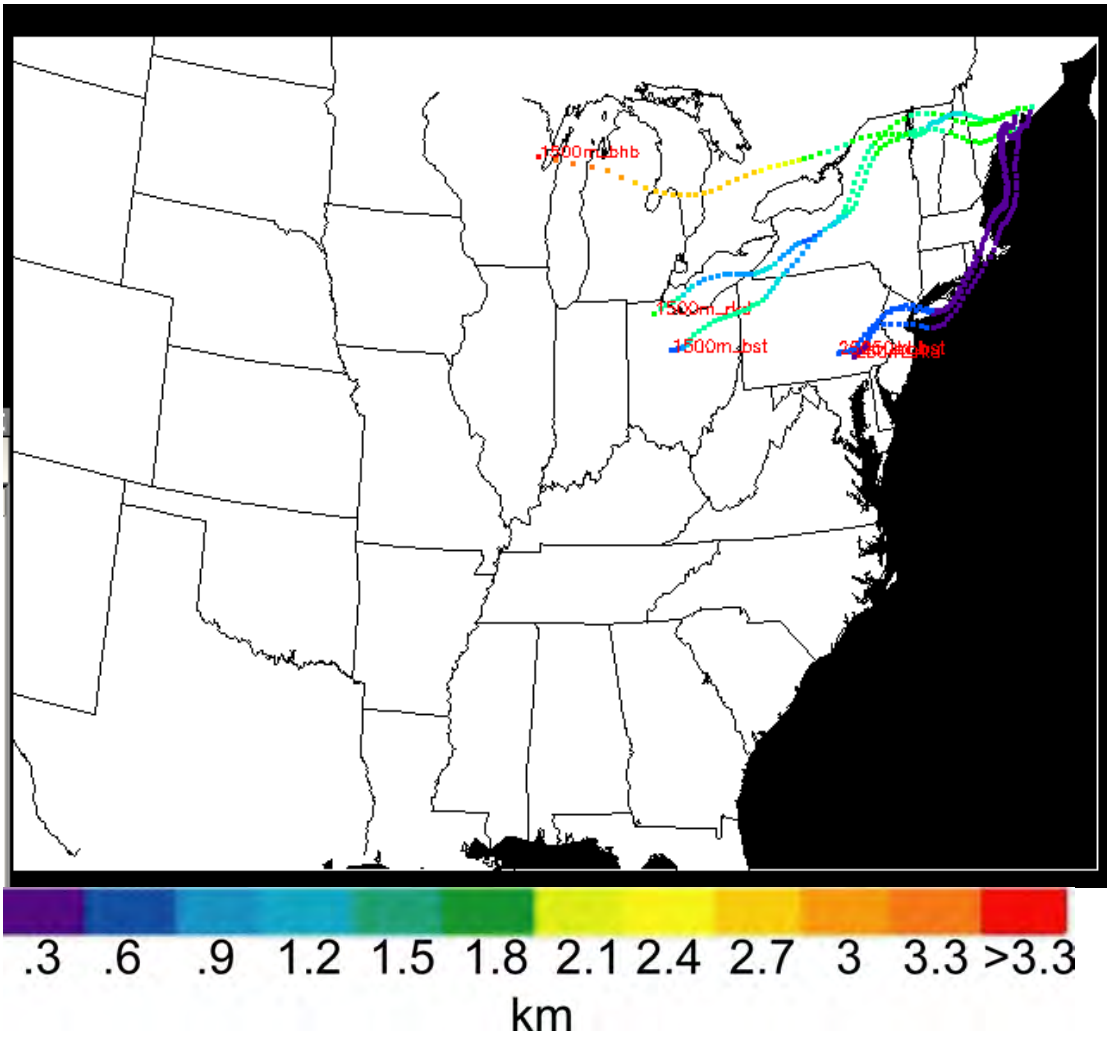

Appendix III.27. 14 August 2002 Northeast afternoon 72 h backward trajectories

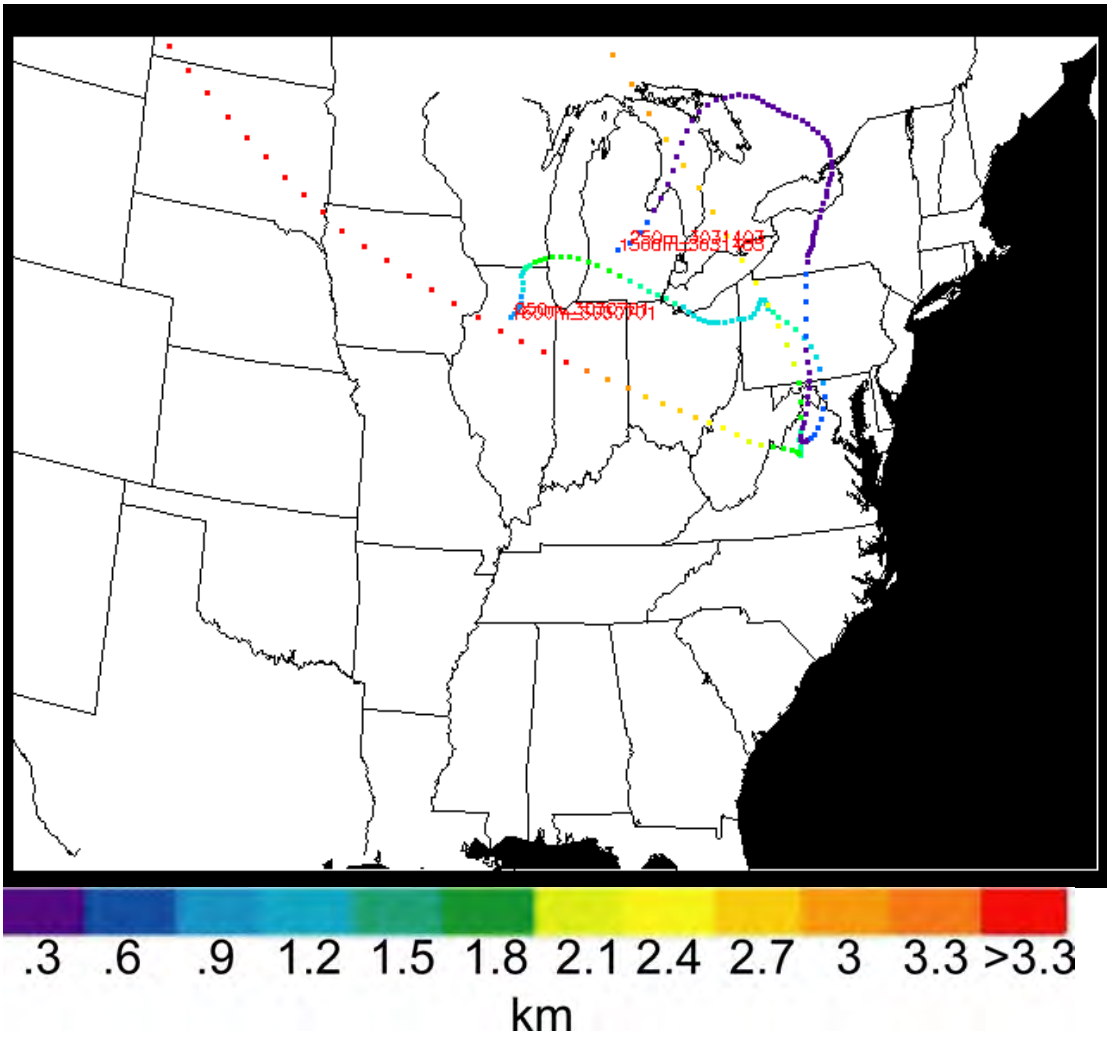

Appendix III.28. March 2003 W45 72 h backward trajectories

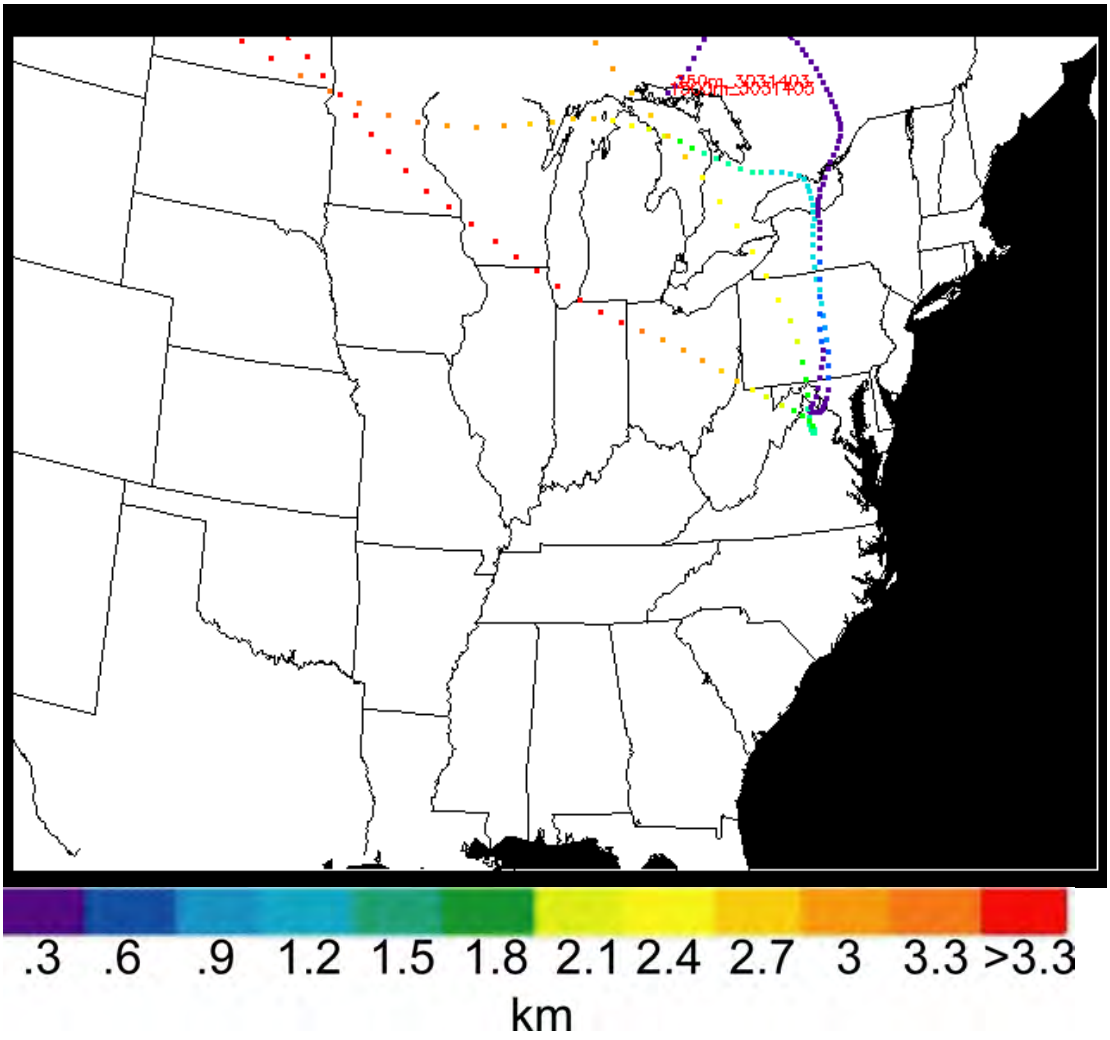

Appendix III.29. March 2003 OKV 72 h backward trajectories

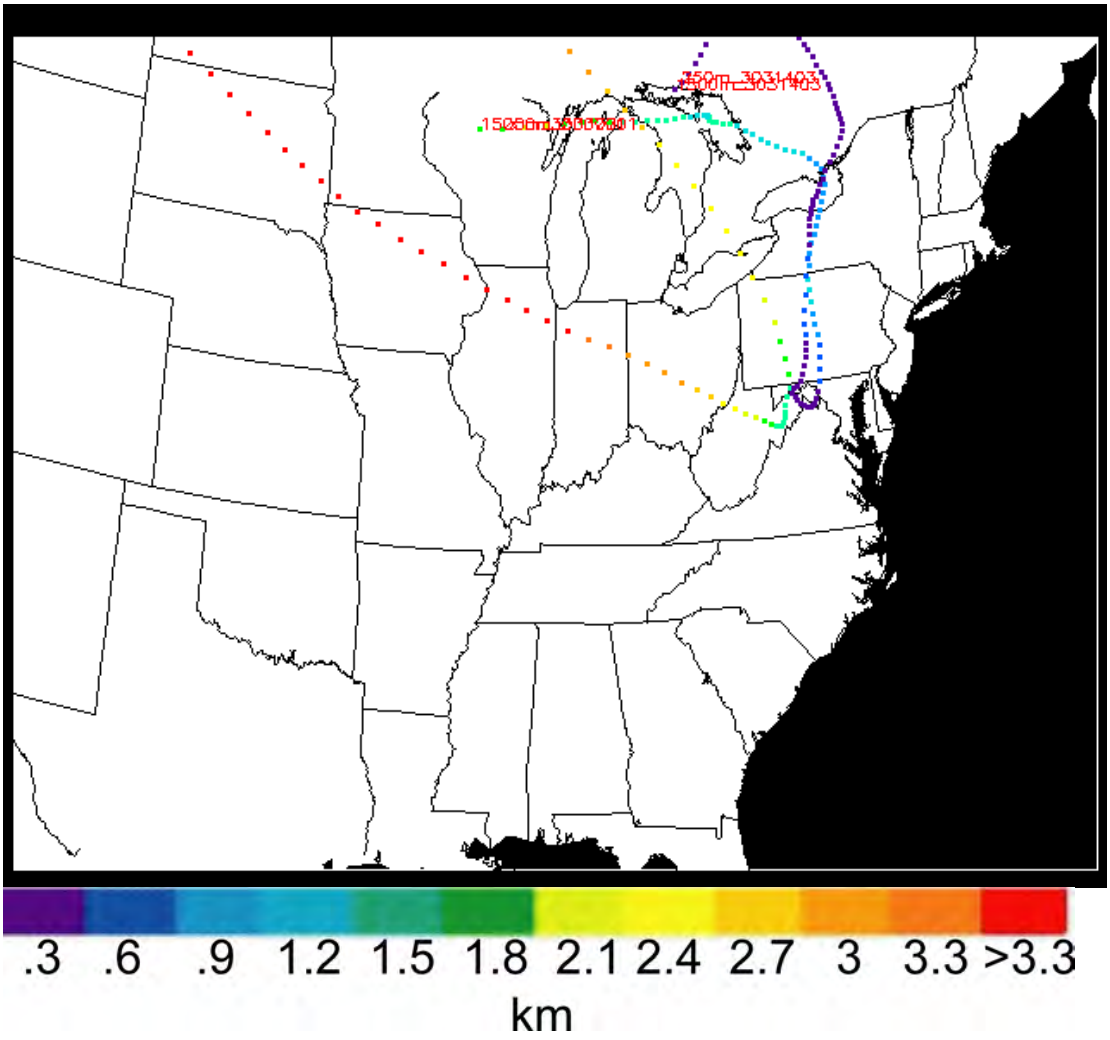

Appendix III.30. March 2003 CBE 72 h backward trajectories

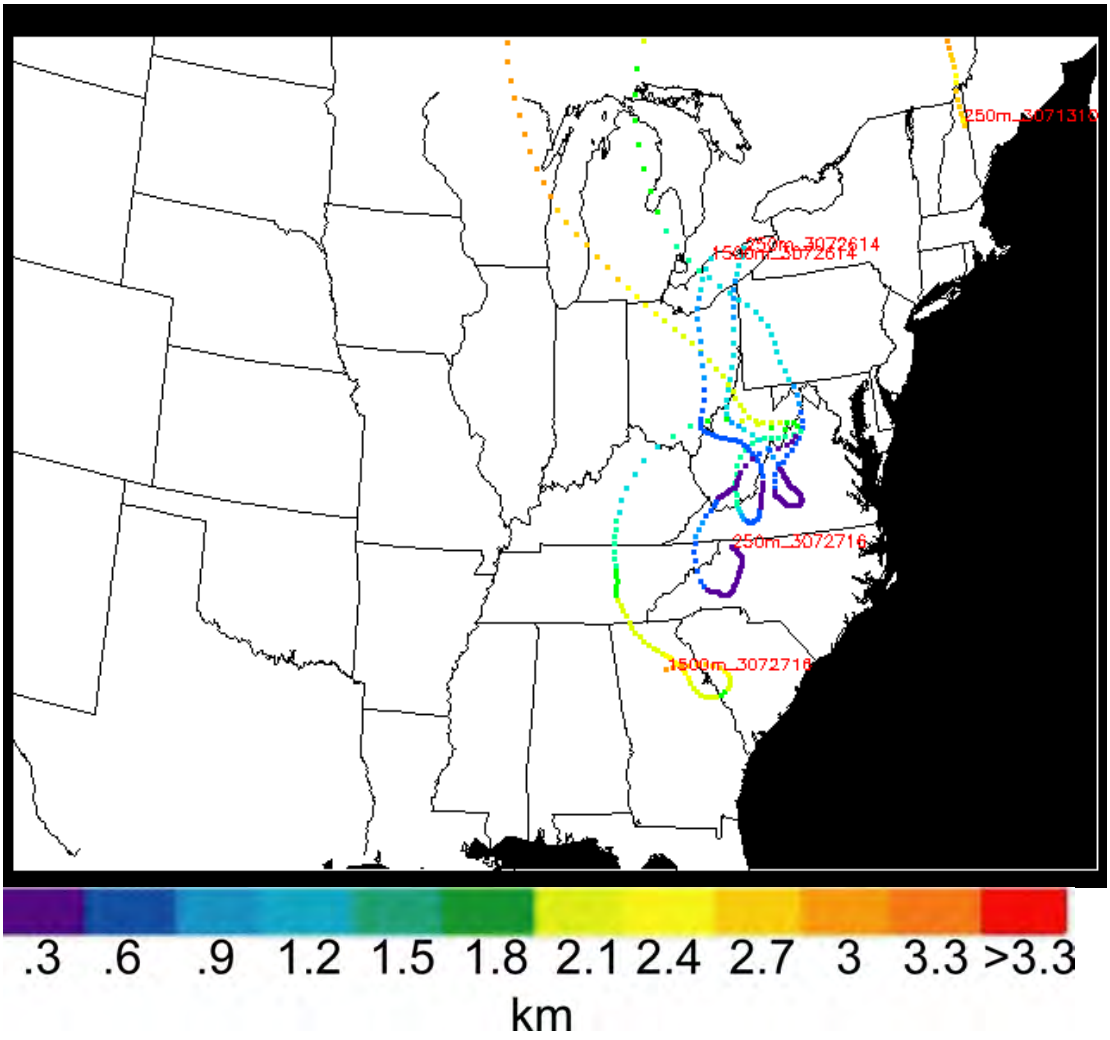

Appendix III.31. July 2003 W45 72 h backward trajectories

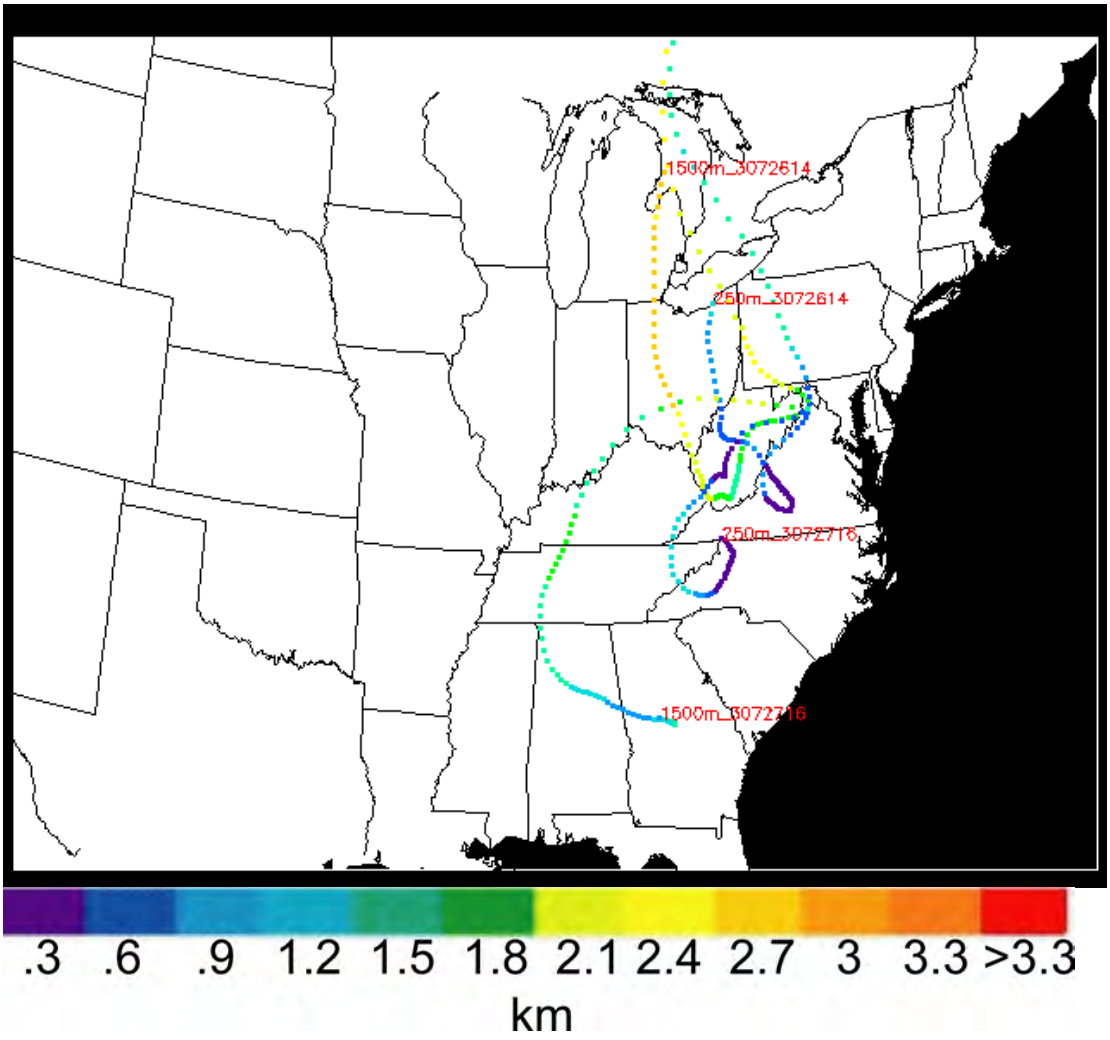

Appendix III.32. July 2003 OKV 72 h backward trajectories

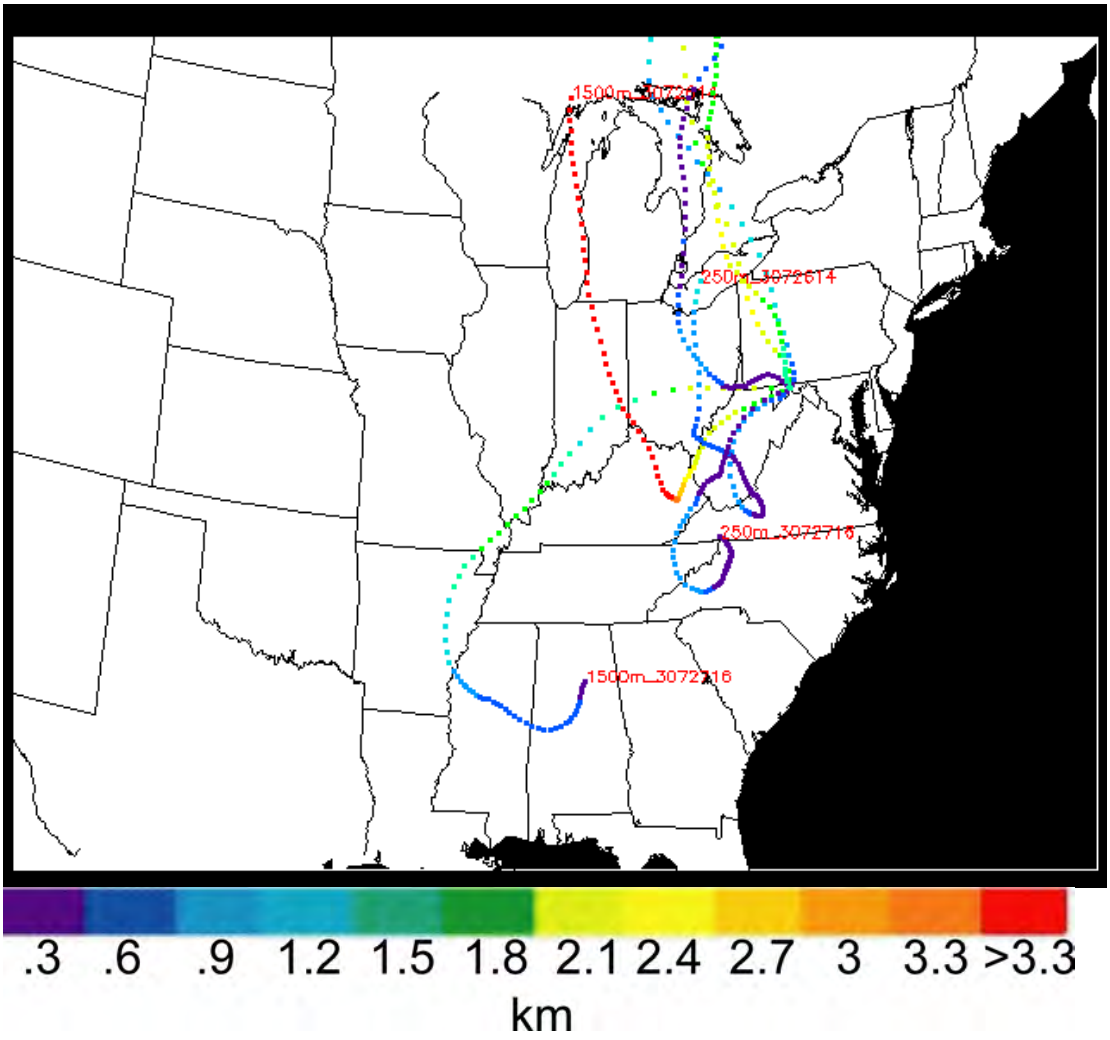

Appendix III.33. July 2003 CBE 72 h backward trajectories

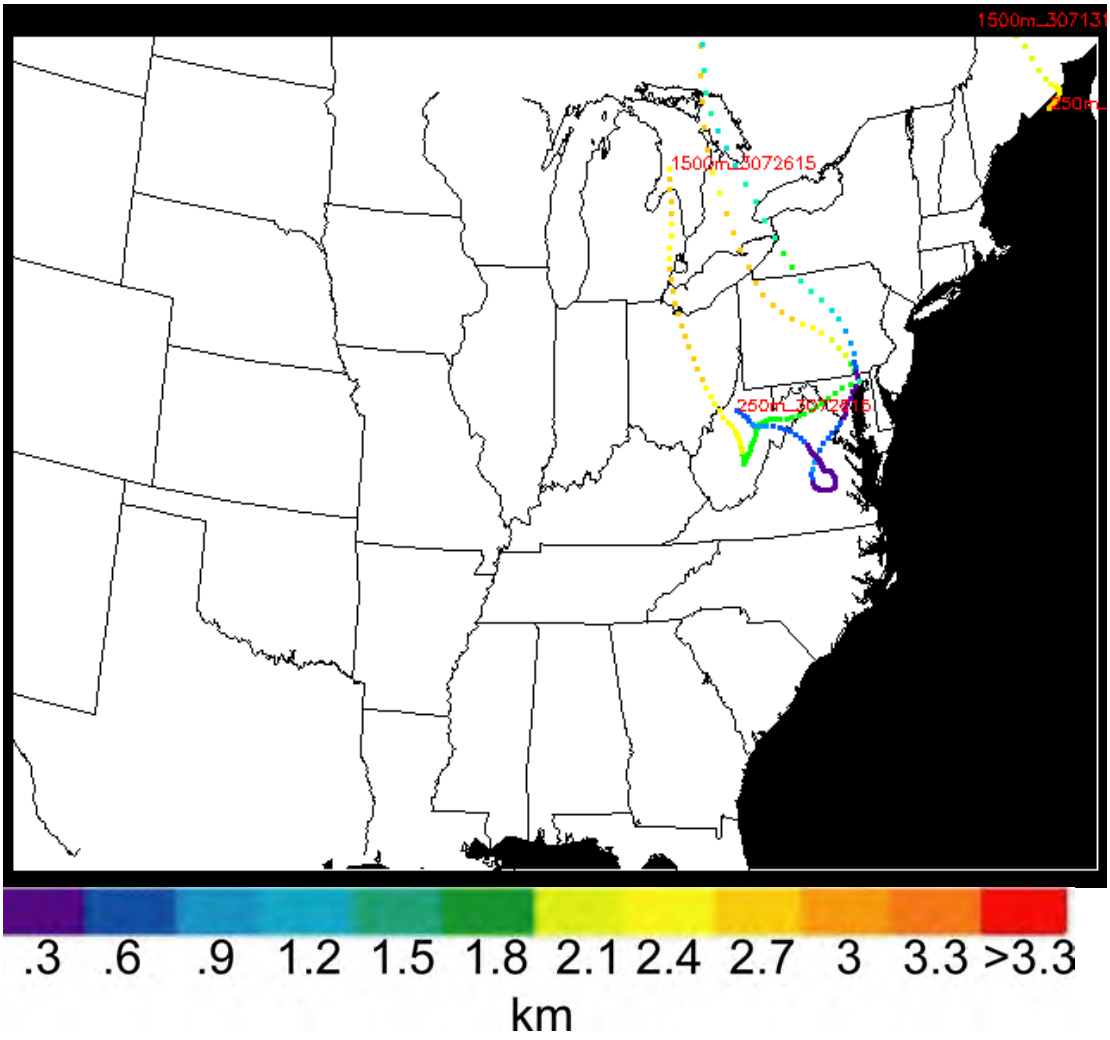

Appendix III.34. July 2003 0W3 72 h backward trajectories

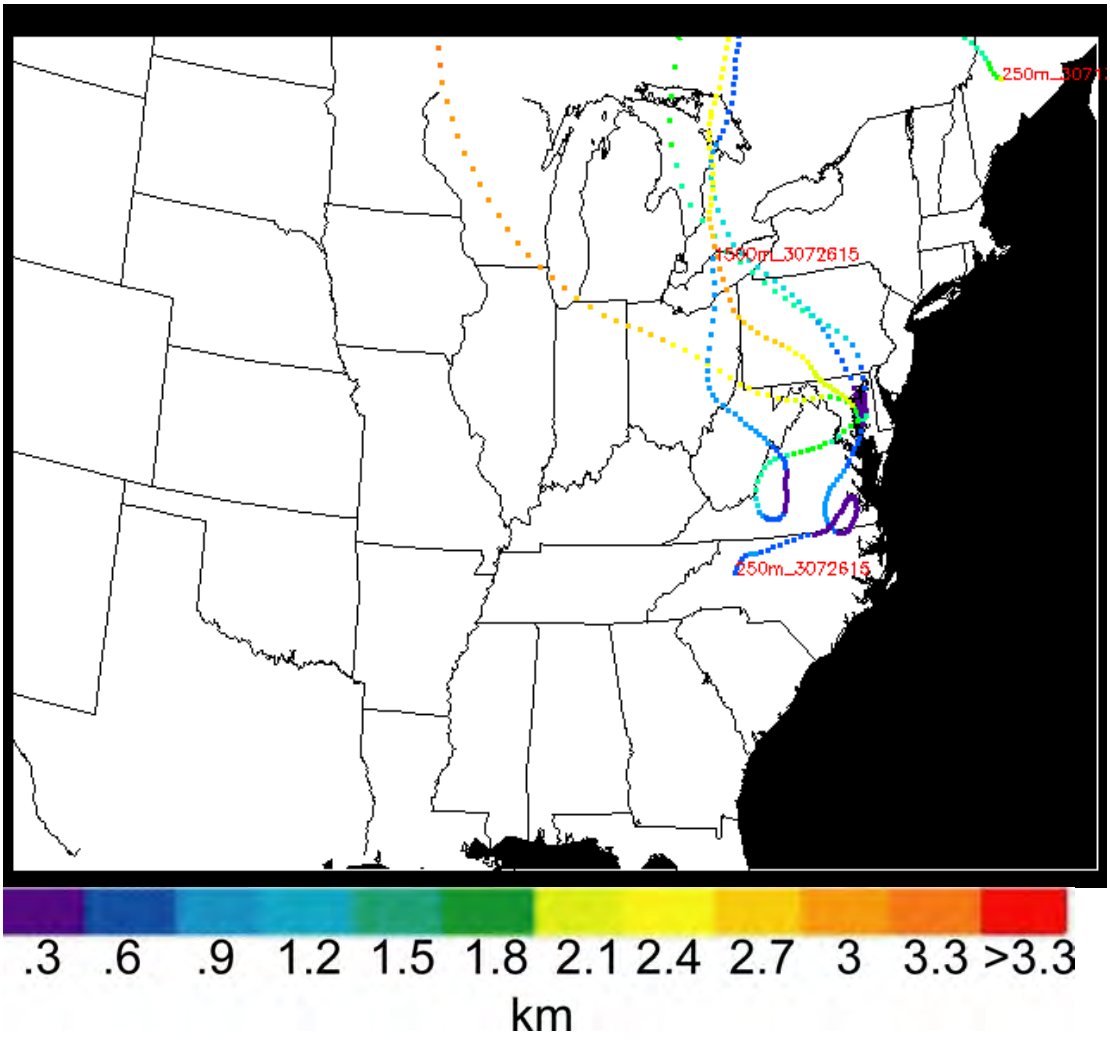

Appendix III.35. July 2003 ESN 72 h backward trajectories

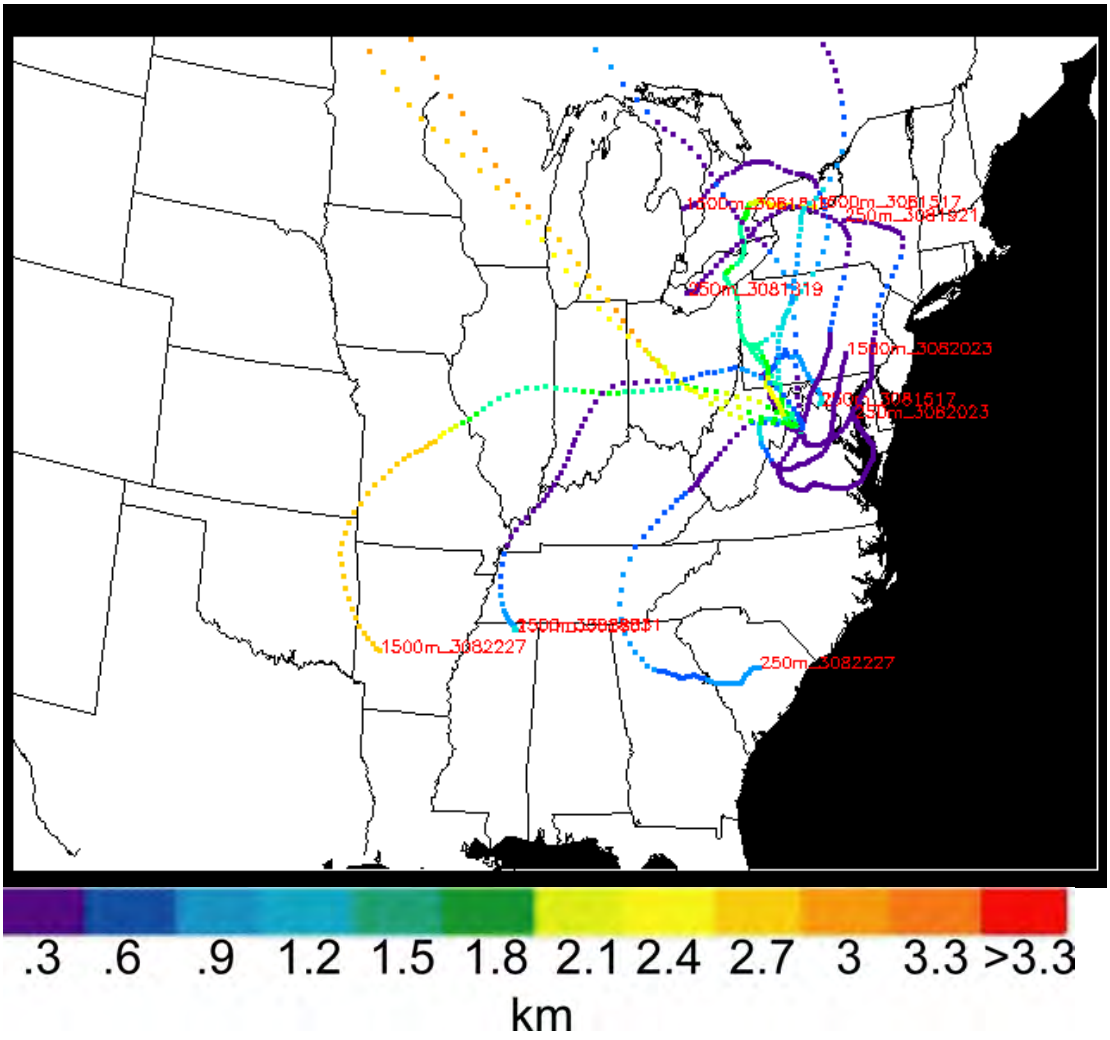

Appendix III.36. August 2003 W45 72 h backward trajectories

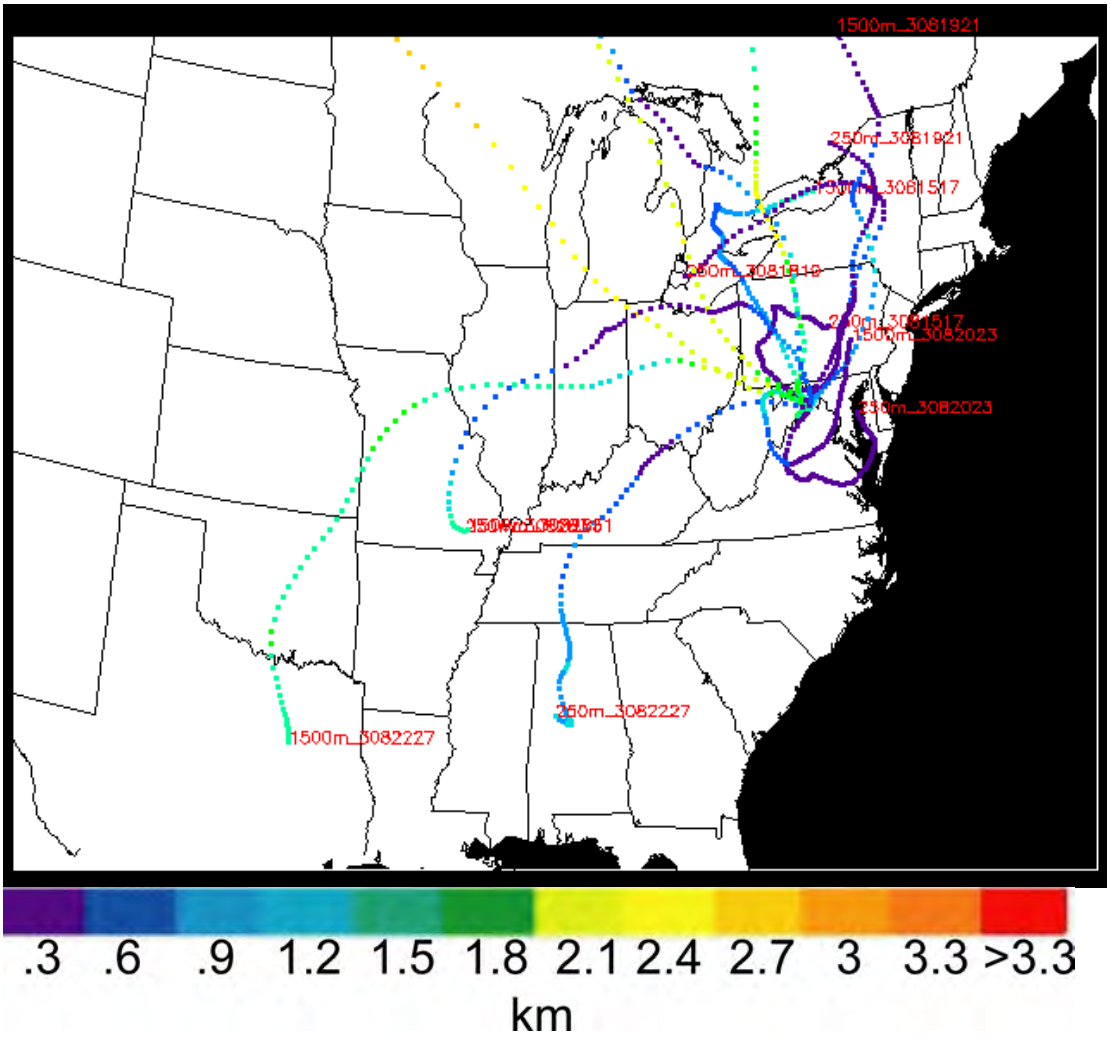

Appendix III.37. August 2003 OKV 72 h backward trajectories

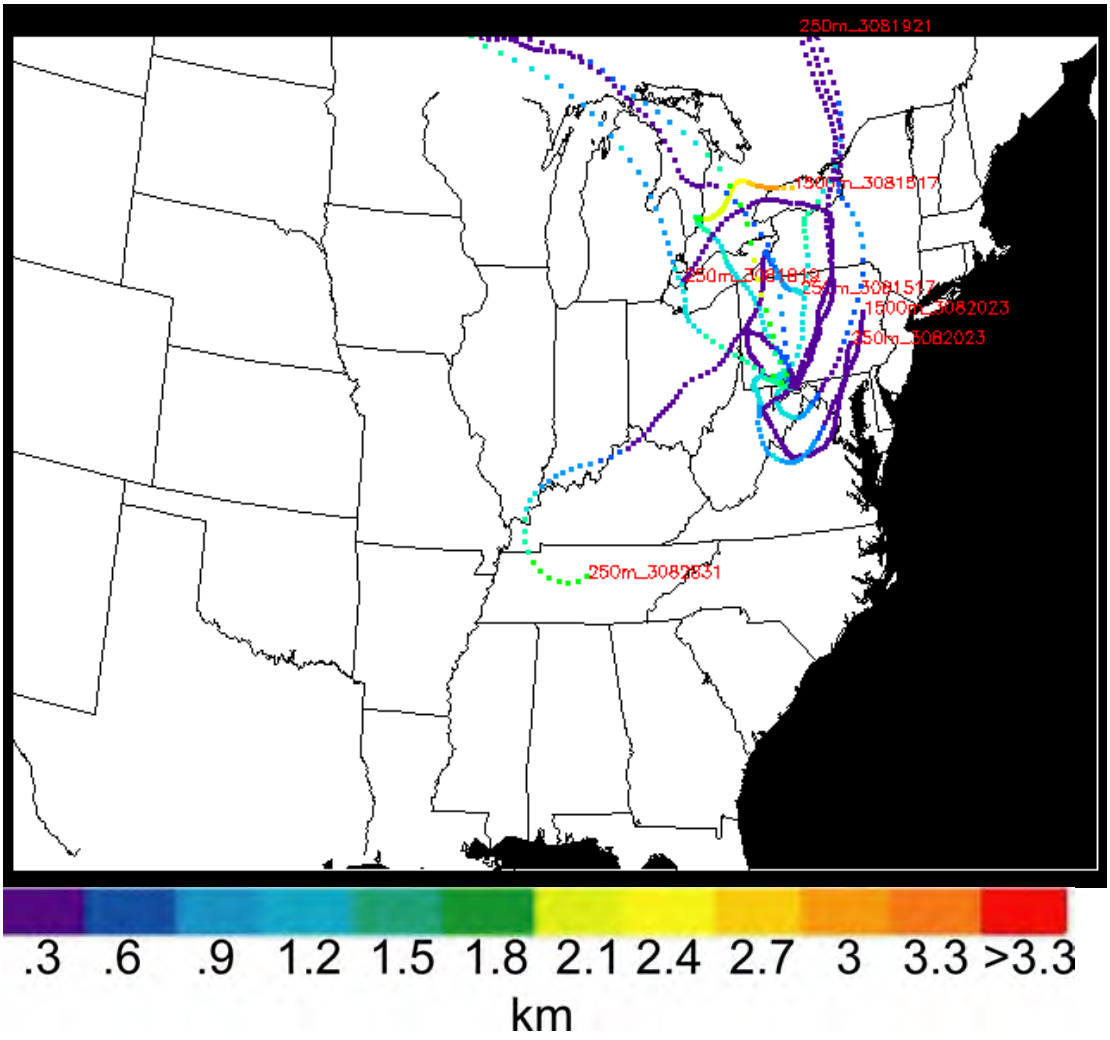

Appendix III.38. August 2003 CBE 72 h backward trajectories

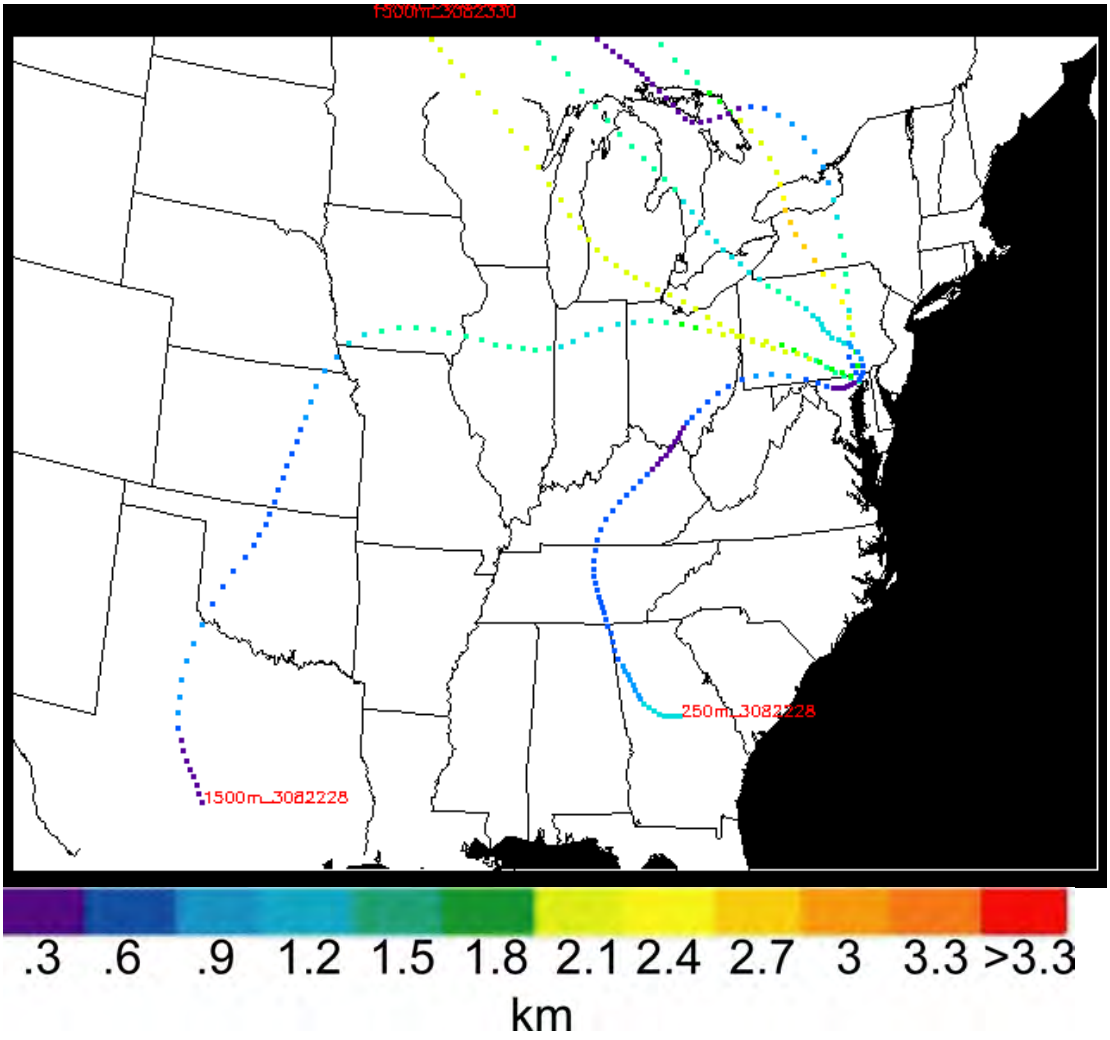

Appendix III.39. August 2003 0W3 72 h backward trajectories

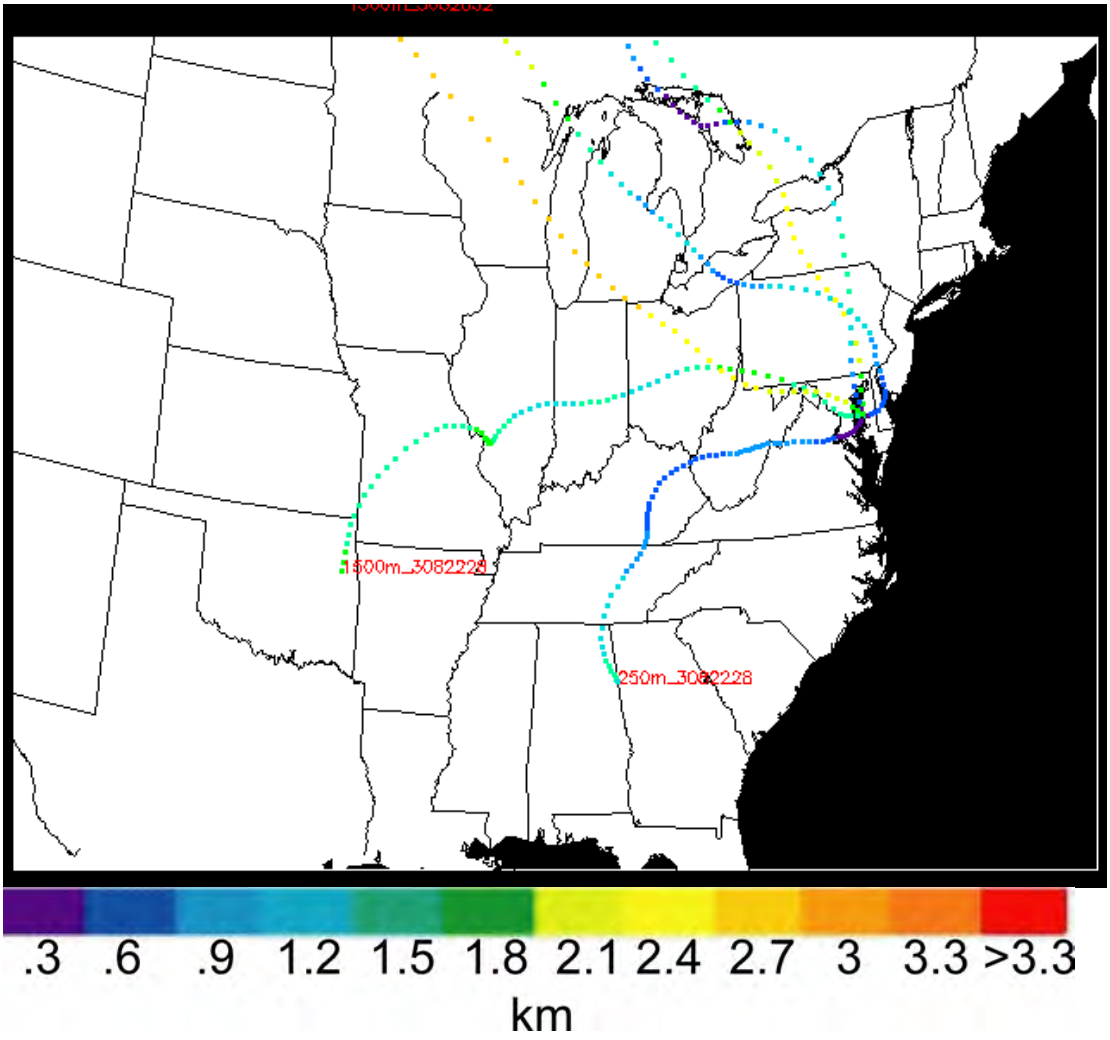

Appendix III.40. August 2003 ESN 72 h backward trajectories

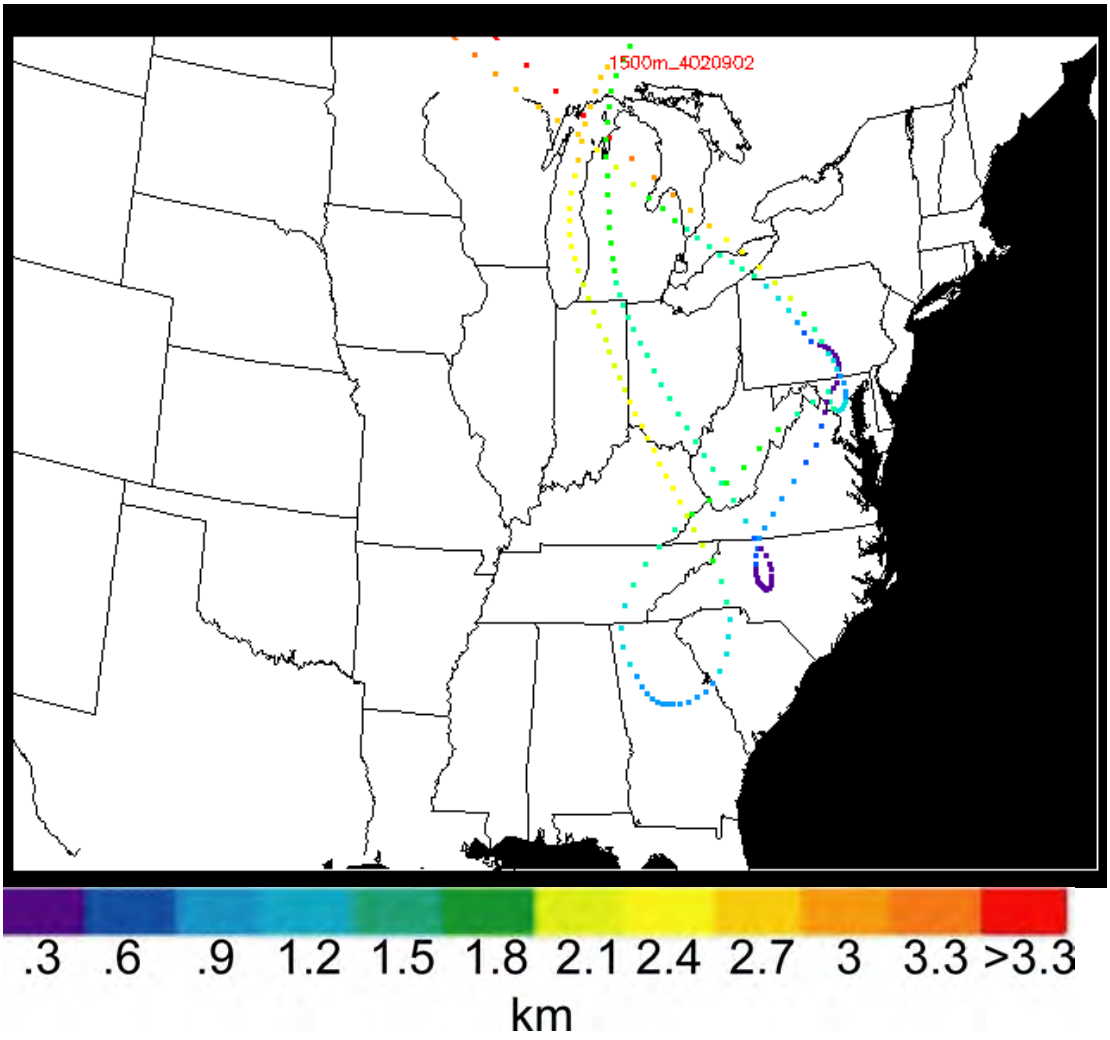

Appendix III.41. February 2004 FDK 72 h backward trajectories

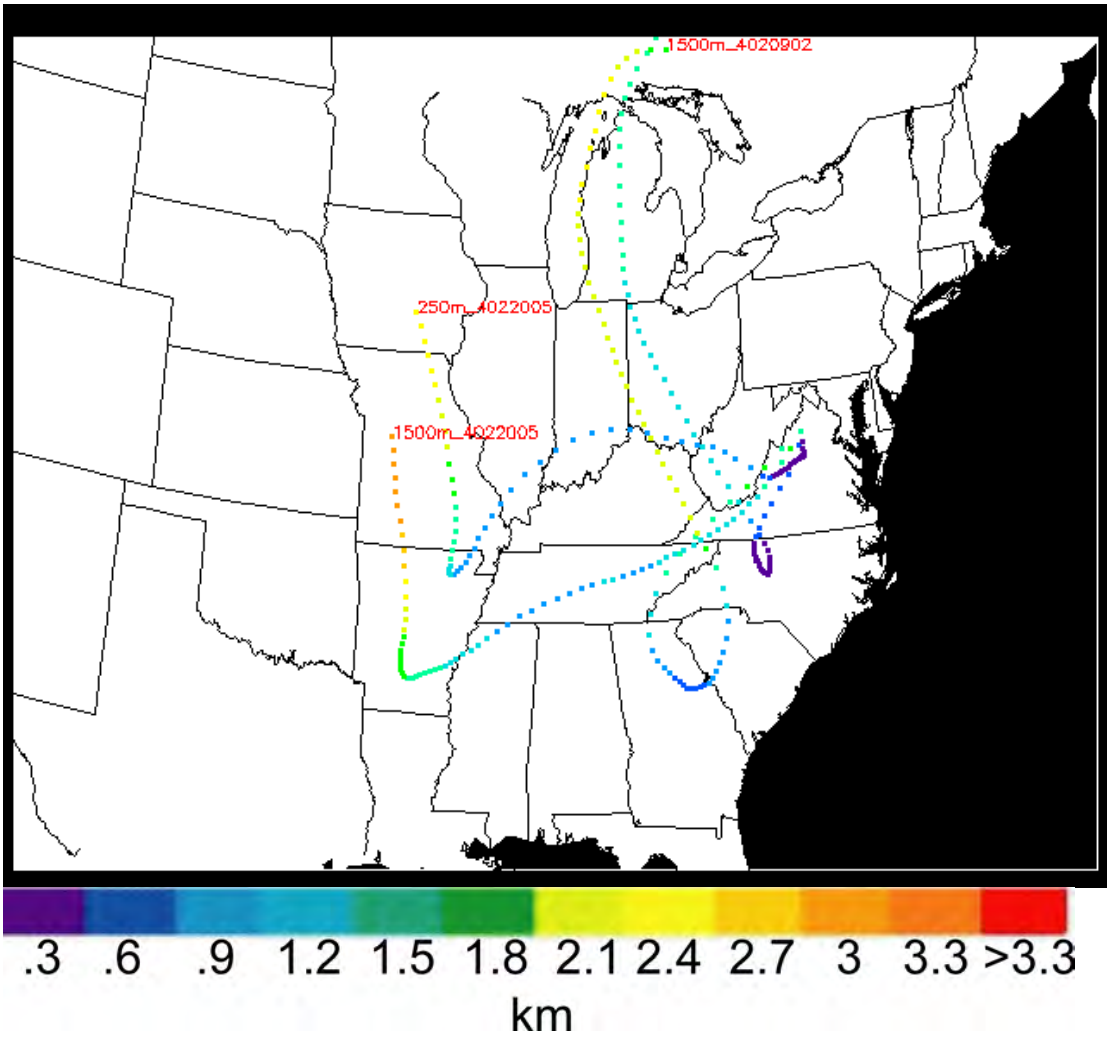

Appendix III.42. February 2004 W45 72 h backward trajectories

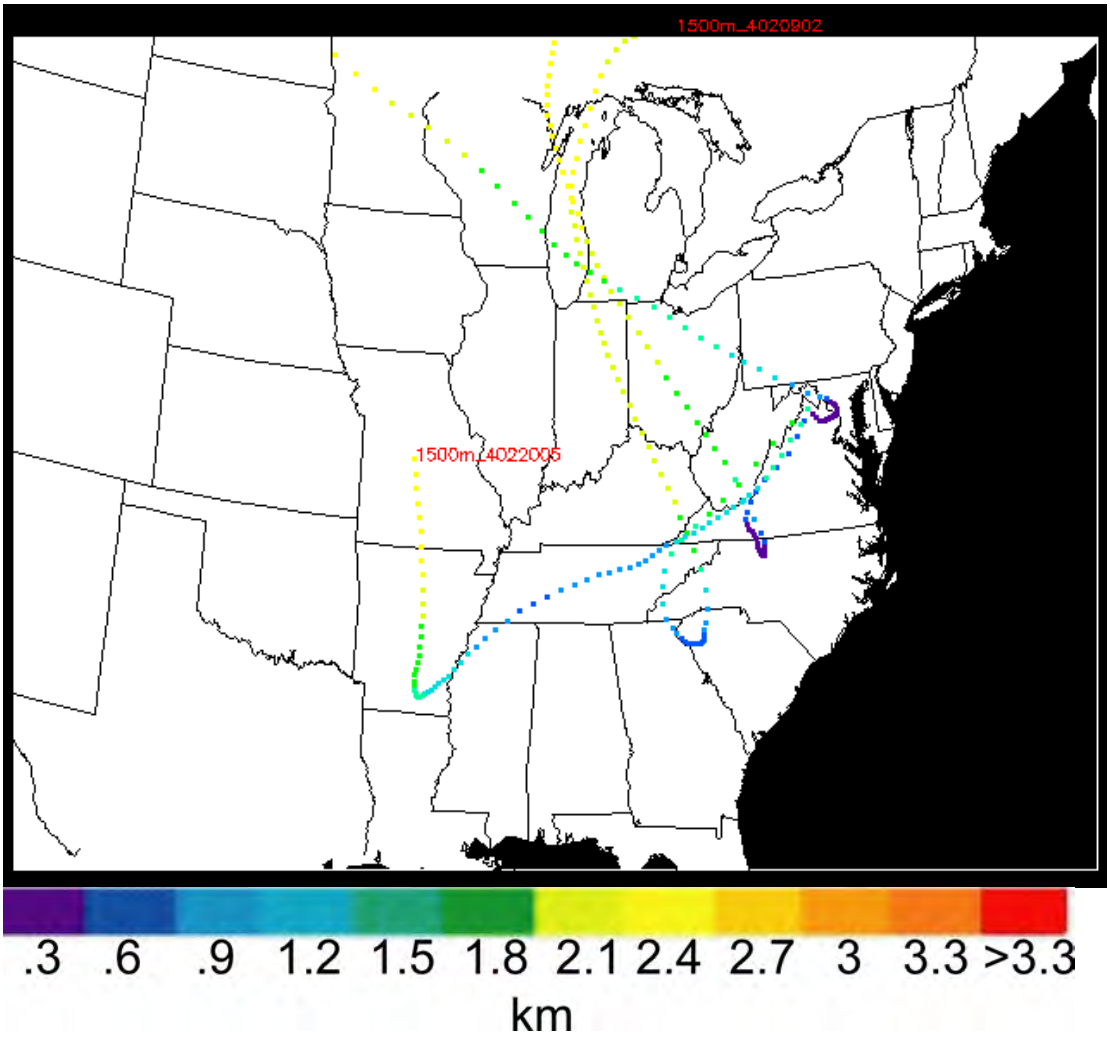

Appendix III.43. February 2004 OKV 72 h backward trajectories

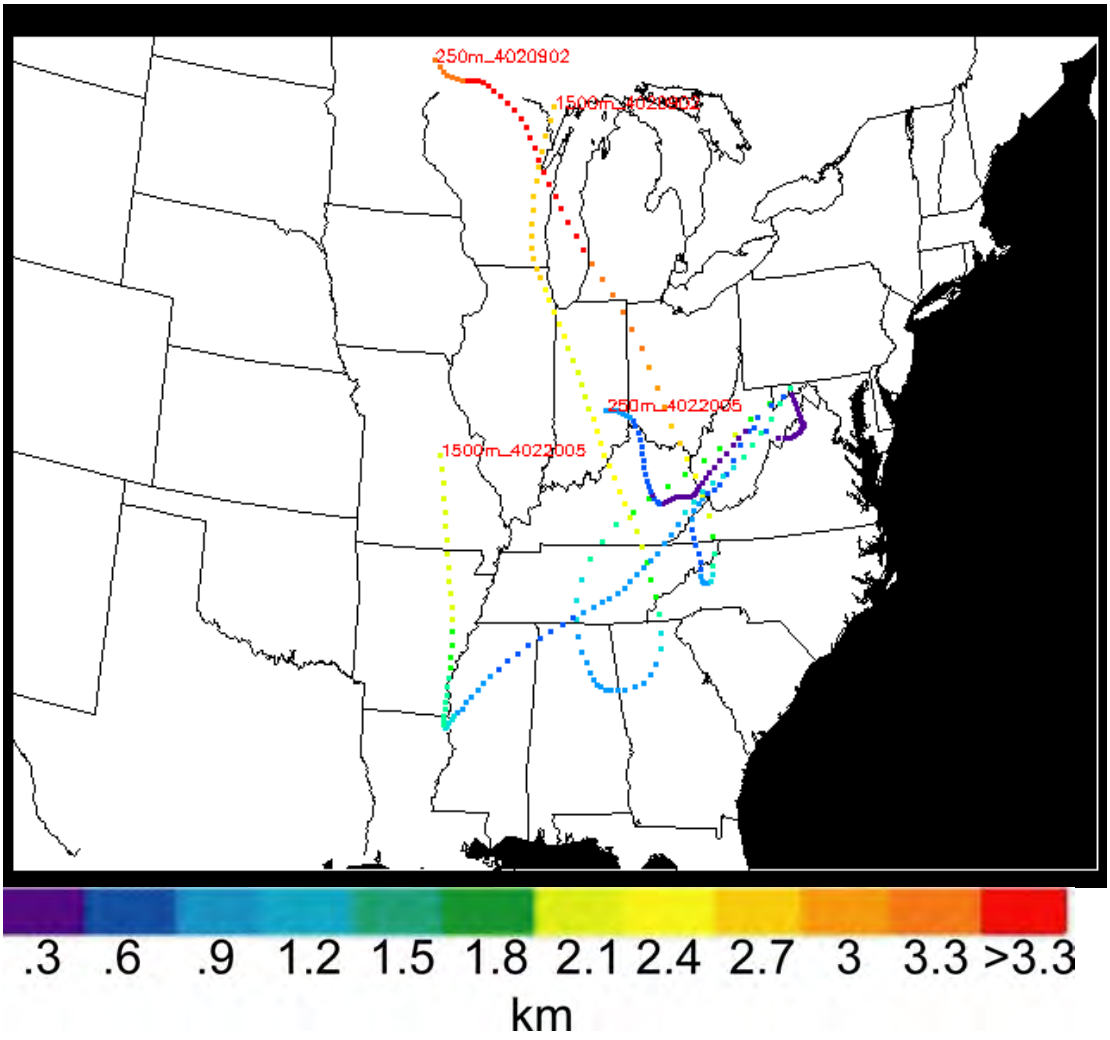

Appendix III.44. February 2004 CBE 72 h backward trajectories

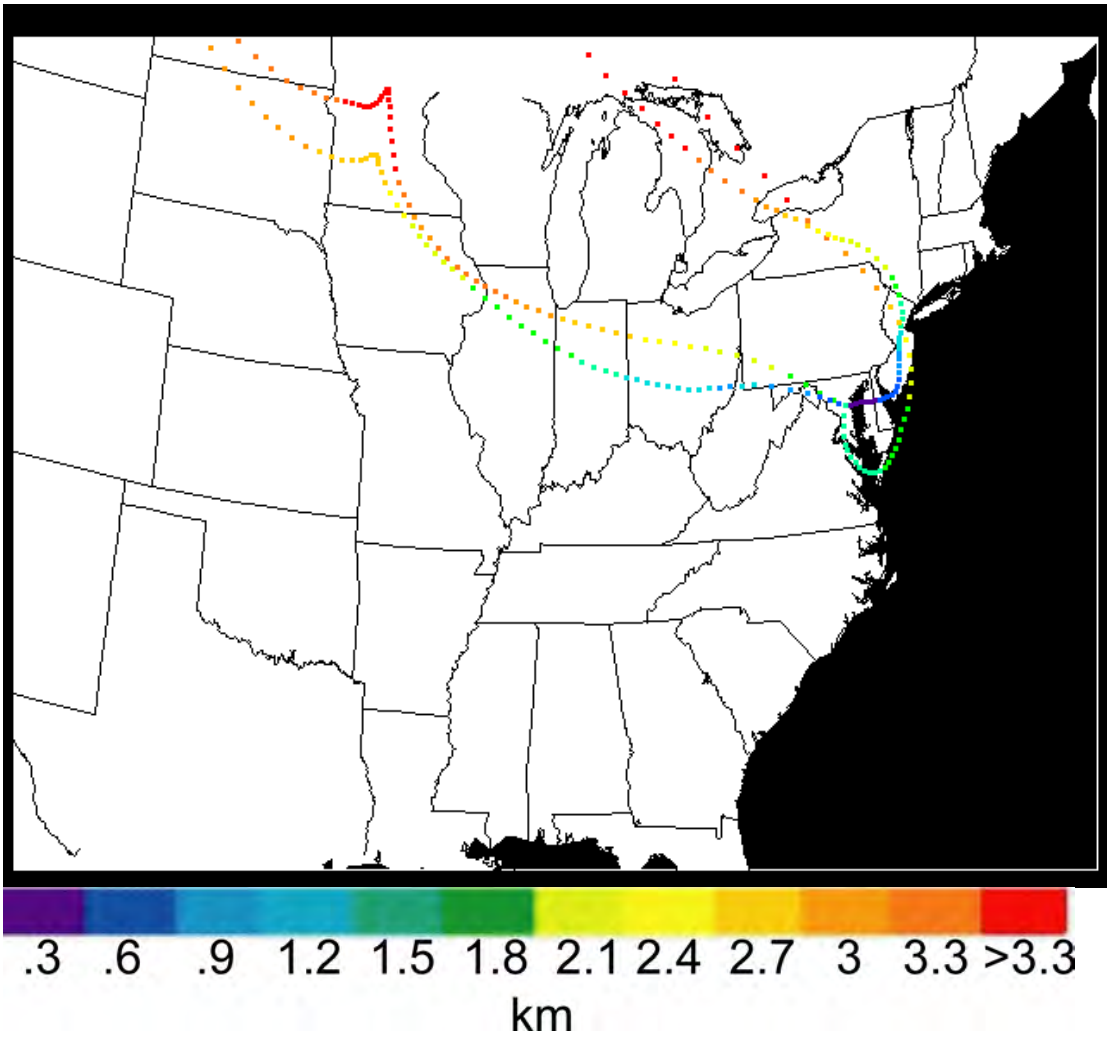

Appendix III.45. February 2004 FME 72 h backward trajectories

Appendix IV

Appendix IV.1. Monthly average AERONET ω_{o550} values and monthly median, extinction weighted, column averaged ω_{o550} aircraft in-situ values (see also Figure 53). The "minus" and "plus" represent the uncertainty. The AERONET uncertainty is estimated from that reported by Dubovik *et al*. (2001). The aircraft uncertainty represents the variability of the 1st and 3rd quartiles about the median values. See Figure 53 for symbology.

	Jun 01	Jul 01	Aug 01	May 02	Jun 02	Jul 02	Aug 02	Jul 03	Aug 03	Feb 04
AERONET	0.97	0.96	0.97	0.96	0.96	0.96	0.95	0.94	0.95	0.95
minus	0.02	0.02	0.02	0.02	0.02	0.02	0.02	0.02	0.02	0.02
plus	0.02	0.02	0.02	0.02	0.02	0.02	0.02	0.02	0.02	0.02
W45	0.91			0.83	0.88			0.87	0.90	0.71
minus	0.03			0.03	0.02			0.02	0.05	0.01
plus	0.02			0.03	0.03			0.02	0.03	0.01
OKV	0.94			0.89	0.94			0.83	0.88	0.80
minus	0.01			0.01	0.02			0.06	0.05	0.03
plus	0.01			0.01	0.01			0.06	0.05	0.03
CBE	0.88			0.86	0.93			0.87	0.86	0.81
minus	0.09			0.03	0.03			0.05	0.08	0.08
plus	0.05			0.03	0.02			0.05	0.02	0.03
0W3	0.93				0.94	0.92		0.82	0.87	
minus	0.01				0.00	0.02		0.02	0.03	
plus	0.01				0.00	0.02		0.02	0.04	
ESN	0.95				0.95	0.93		0.89	0.87	
minus	0.01				0.00	0.02		0.01	0.04	
plus	0.01				0.00	0.02		0.02	0.04	
FME	0.94	0.86			0.93	0.95				0.79
minus	0.02	0.04			0.05	0.03				0.16
plus	0.02	0.04			0.03	0.02				0.00
FCIm			0.92							
minus			0.01							
plus			0.01							
FCIa			0.97							
minus			0.00							
plus			0.00							
NEm							0.94			
minus							0.05			
plus							0.02			
NEa							0.95			
minus							0.02			
plus							0.01			

Appendix IV.2. Monthly average AERONET AOD values and monthly median, AOD aircraft in-situ values (see also Figure 54). The "minus" and "plus" represent the uncertainty. The AERONET uncertainty is estimated from that reported by Dubovik *et al*. (2001). The aircraft uncertainty represents the variability of the 1st and 3rd quartiles about the median values. See Figure 54 for symbology.

	Jun 01	Jul 01	Aug 01	May 02	Jun 02	Jul 02	Aug 02	Jul 03	Aug 03	Feb 04
AERONET	0.39	0.14	0.50	0.16	0.37	0.45	0.35	0.26	0.43	0.06
minus	0.03	0.03	0.03	0.03	0.03	0.03	0.03	0.03	0.03	0.03
plus	0.03	0.03	0.03	0.03	0.03	0.03	0.03	0.03	0.03	0.03
W45	0.38			0.10	0.17			0.25	0.41	0.07
minus	0.18			0.02	0.06			0.08	0.16	0.01
plus	0.20			0.02	0.10			0.06	0.20	0.01
OKV	0.55			0.10	0.23			0.11	0.33	0.10
minus	0.14			0.03	0.08			0.05	0.19	0.03
plus	0.08			0.02	0.13			0.09	0.19	0.03
CBE	0.33			0.12	0.34			0.20	0.27	0.13
minus	0.14			0.06	0.09			0.11	0.17	0.01
plus	0.20			0.05	0.22			0.09	0.20	0.01
0W3	0.45				0.62	0.44		0.11	0.37	
minus	0.13				0.08	0.16		0.06	0.20	
plus	0.13				0.08	0.82		0.06	0.12	
ESN	0.43				0.38	0.99		0.13	0.27	
minus	0.12				0.05	0.69		0.00	0.16	
plus	0.12				0.05	0.90		0.04	0.21	
FME	0.33	0.07			0.41	0.34				0.07
minus	0.08	0.04			0.21	0.17				0.02
plus	0.07	0.06			0.11	0.22				0.02
FCIm			0.54							
minus			0.07							
plus			0.07							
FCIa			0.87							
minus			0.01							
plus			0.01							
NEm							0.32			
minus							0.08			
plus							0.16			
NEa							0.34			
minus							0.11			
plus							0.21			
FDK										0.05
minus										0.00
plus										0.03

Bibliography

Akimoto, H., Global air quality and pollution, *Science, 302*, 1716-1719, 2003.

Anderson, T.L., D.S. Covert, S.F. Marshall, M.L. Laucks, R.J. Charlson, A.P. Waggoner, J.A. Ogren, R. Caldow, R.L. Holm, F.R. Quant, G.J. Sem, A. Wiedensohler, N.A. Ahlquist, and T.S. Bates, Performance characteristics of a high-sensitivity, three-wavelength, total scatter/backscatter nephelometer, *J. Atmos. Oceanic Technol.*, *13*, 967-986, 1996.

Anderson, T.L., D.S. Covert, J.D. Wheeler, J.M. Harris, K.D. Perry, B.E. Trost, and D.J. Jaffe, Aerosol backscatter fraction and single scattering albedo: measured values and uncertainties at a coastal station in the Pacific NW, *J. Geophys. Res.*, *104*, 26,793-26,807, 1999.

Anderson, T.L., and J.A. Ogren, Determining aerosol radiative properties using the TSI 3563 Integrating Nephelometer, *Aerosol Sci. Technol.*, *29*, 57-69, 1998.

Anderson, T.L., S.J. Masonis, D.S. Covert, N.C. Ahlquist, S.G. Howell, A.D. Clarke, and C.S. McNaughton, Variability of aerosol optical properties derived form in-situ aircraft measurements during ACE-Asia, *J. Geophys. Res.*, *108*(D23), 8647, 10.1029/2002JD003247, 2003.

Andreae, M.O., and P.J. Crutzen, Atmospheric aerosols: Biogeochemical sources and role in atmospheric chemistry. *Science*, 276, 1052-1058, 1997.

Andreae, M.O., and P. Merlet, Emission of trace gases and aerosols from biomass burning, *Global Biogeochem. Cycles, 15*, 955-966, 2001.

Banta, R.M., C.J. Senff, A.B. White, M. Trainer, R.T. McNider, R. J. Valente, S.D. Mayor, R.J. Alvarez, R.M. Hardesty, D. Parrish, and F.C. Fehsenfeld. Daytime buildup and nighttime transport of urban ozone in the boundary layer during a stagnation episode. *J. Geophys. Res.*, *103*, 22,519-22,544, 1998.

Baumann, K., E.J. Williams, W.M. Angevine, J.M. Roberts, R.B. Norton, G.J. Frost, F.C. Fehsenfeld, S.R. Springston, S.B. Bertman, and B. Hartsell. Ozone production and transport near Nashville, Tennessee: Results from the 1994 study at New Hendersonville. *J. Geophys. Res.*, *105*, 9137-9153, 2000.

Benjamin, S.G., J.M. Brown, K.J. Brundage, B.E. Schwartz, T.G. Smirnova, and T.L. Smith. The operational RUC-2. Preprints, *16th Conference on Weather Analysis and Forecasting*, Phoenix, AZ, Amer. Meteor. Soc., 249-252, 1998.

Bergstrom, R.W., P.B. Russell, and P. Hignett. Wavelength dependence of the absorption of black carbon particles: Predictions and results from the TARFOX experiment and implications for the aerosol single scattering albedo, *J. Atmos. Sciences, 59*, 567-577, 2002.

Berkowitz, C.M., and W.J. Shaw. Airborne measurements of boundary layer chemistry during the southern oxidant study: A case study, *J. Geophys. Res., 102*(D11), 12,795-12,804, 1997.

Bodhaine, B.A., Aerosol absorption measurements at Barrow, Mauna Loa, and the South Pole, *J. Geophys. Res., 100*, 8967-8975, 1995.

Bohren, C.F., Multiple scattering of light and some of its observable consequences, *Am. J. Phys., 55*(6), 524-533, 1987.

Bond, T.C., T.L. Anderson, and D. Campbell, Calibration and intercomparison of filter-based measurements of visible light absorption by aerosols, *Aerosol Sci. Technol., 30*, 582-600, 1999.

Bundke, U., et al, Aerosol optical properties during the Lindenberg Aerosol Characterization Experiment (LACE 98), *J. Geophys. Res. 107*, 10.1029/2000JD000188, 2002.

Chang, H., and T. Charalampopolous, Determination of the wavelength dependence of refractive indices of flame soot, *Proc. Roy. Soc. London., 430*, 577-591, 1990.

Charlock, T. *et al.*, CERES/SARB Surface properties, Surface and Radiation Budget working group web page, http://snowdog.larc.nasa.gov/pub/surf/pages/explan.html, 2002.

Charlson, R.J., J. Langner, H. Rodhe, C.B. Leovy, and S.G. Warren, Perturbation of the northern-hemisphere radiative balance by backscattering from anthropogenic sulfate aerosols, *TellusA, 43*, 152-163, 1991.

Chen, L.W.A., B.G. Doddridge, R.R. Dickerson, J.C. Chow, P.K. Mueller, J. Quinn, and W.A. Butler. Seasonal variations in elemental carbon aerosol, carbon monoxide, and sulfur dioxide: Implications for sources. *Geophys. Res. Lett., 28*, 1711-1714, 2001.

Chen, L.W.A. Urban fine particulate matter: Chemical composition and possible origins. *Ph.D. Dissertation*, Department of Chemical Physics, University of Maryland, 2002.

Chin, M., D.J. Jacob, J.W. Munger, D.D. Parrish, and B.G. Doddridge. Relationship of ozone and carbon monoxide over North America. *J. Geophys. Res., 99(D7)*, 14,565-14,573, 1994.

Chung, S.H., and J.H. Seinfeld. Global distribution and climate forcing of arbonaceous aerosols. *J. Geophys. Res., 107(D19):* art. no. 4407, 2002.

Civerolo, K.L., H. Mao, and S.T. Rao. The airshed for ozone and fine particulate pollution in the eastern United States. *Pure Appl. Geophys., 160,* 81-105, 2003.

Crutzen, P.J. Ozone production rates in an oxygen-hydrogen-nitrogen oxide atmosphere. *J. Geophys. Res., 76*(30), 7311, 1971.

Crutzen, P.J., and M.O. Andreae, Biomass burning in the tropics – impact on atmospheric chemistry and biogeochemical cycles, *Science, 250,* 1669-1678, 1990.

Crutzen, P.J., L.E. Heidt, J.P. Krasnec, W.H. Pollock, and W. Seiler, Biomass burning as a source of atmospheric gases CO, H_2, N_2O, NO, CH_3CL and COS, *Nature, 282,* 253-256, 1979.

Daum, P.H., L.I. Kleinman, L. Newman, W.T. Luke, J. Weinstein-Lloyd, C.M. Berkowitz, and K.M. Busness. Chemical and physical properties of plumes of anthropogenic pollutants transported over the North Atlantic during the North Atlantic Regional Experiment. *J. Geophys. Res., 101*(D22), 29,029-29,042, 1996.

Delmas, R., On the emission of carbon, nitrogen and sulfur in the atmosphere during bushfires in intertropical savannah zones, *Geophys. Res. Lett., 9,* 761-764, 1982.

Dickerson, R.R., and A.C. Delany, Modification of a commercial gas filter correlation CO detector for increased sensitivity, *J. Atmos. Oceanic Technol., 5*(3), 424-431, 1988.

Dickerson, R.R., B.G. Doddridge, P. Kelley, and K.P. Rhoads, Large-scale pollution of the atmosphere over the remote Atlantic Ocean: Evidence from Bermuda, *J. Geophys. Res., 100*(D5), 8945-8952, 1995.

Dickerson, R.R., S. Kondragunta, G. Stenchickov, K.L. Civerolo, B.G. Doddridge, and B.N. Holben. The impact of aerosols on solar ultraviolet radiation and photochemical smog. *Science, 278,* 827-830, 1997.

Doddridge, B.G., P.C. Novelli, and R.M. Rosson, WMO meeting of experts on global carbon monoxide measurements, *Rapporteur's Report of the Working Session on Measurement Techniques and Standards,* pp. 8-11, 1995.

Draxler, R.R., and G.D. Rolph. HYSPLIT (HYbrid Single-Particle Lagrangian Integrated Trajectory) Model access via NOAA ARL READY website (http://www.arl.noaa.gov/ready/hysplit4.html). NOAA Air Resources Laboratory, Silver Spring, MD, 2003.

Dubovik, O., B. Holben, Y. Kaufman, M. Yamaxoe, A. Smirnov, D. Tanre, I. Slutsker, Single-scattering albedo of smoke retrieved from the sky radiance and solar transmittance measured from the ground, *J. Geophys. Res. 103,* 31,903-31,923, 1998.

Dubovik, O., B.N. Holben, T.F. Eck, A. Smirnov, Y.J. Kaufman, M.D. King, D. Tanre, and I. Slutsker. Variability of absorption and optical properties of key aerosol types observed in worldwide locations. *J. Atmos. Sciences, 59,* 590-608, 2001.

Dubovik, O., A. Smirnov, B.N. Holben, M.D. King, Y.J. Kaufman, T.F. Eck, and I. Slutsker, Accuracy assessments of aerosol optical properties retrieved from Aerosol Robotic Network (AERONET) sun and sky radiance measurements, *J. Geophys. Res., 105*, 9791-9806, 2000.

Eck, T., B. Holben, J. Reid, O. Dubovik, A. Smirnov, N. O'Neill, I Slutsker, S. Kinne, Wavelength dependence of the optical depth of biomass burning, urban, and desert dust aerosols. *J. Geophys. Res. 104*, 31,333-31,349, 1999.

Eck, T.F., B.N. Holben, I. Slutsker, and A. Setzer, Measurements of irradiance attenuation and estimation of aerosol single scattering albedo for biomass burning aerosols in Amazonia, *J. Geophys. Res., 103,* 31,865-31,878, 1998.

Evans, L.F., I.A. Weeks, A.J. Eccleston, and D.R. Packham, Photochemical ozone in smoke from prescribed burning of forests, *Environ. Sci. Technol., 11,* 896-900, 1977.

Fast J.D., R.A. Zaveri, R.X. Bian, E.G. Chapman, and R.C. Easter. Effect of regional-scale transport on oxidants in the vicinity of philadelphia during the 1999 NE-OPS field campaign. *J. Geophys. Res., 107*(D16), 10.1029/2001JD000980, 2002.

Ferrare, R.A., R.S. Fraser, and Y. Kaufman, Satellite measurement of large-scale air-pollution: measurements of forest fire smoke, *J. Geophy. Res., 95*(D7), 9911-9925, 1990.

Fieberg, M., A Petzold, U. Wandinger, M. Wendisch, C. Kiemle, A. Stifter, M. Ebert, T. Rother, U. Leiterer, Optical Closure for an aerosol column: Method, accuracy, and inferable properties applied to a biomass-burning aerosol and its radiative forcing. *J. Geophys. Res. 107*, web correction, 2003.

Fiore A.M., D.J. Jacob, J.A. Logan, and J.H. Yin, Long-term trends in ground level ozone over the contiguous United States, 1980-1995, *J. Geophys. Res., 103*(D1), 1471-1480, 1998.

Gent J.F., E.W. Triche, T.R. Holford, K. Belanger, M.B. Bracken, W.S. Beckett, and B.P. Leaderer, Association of low-level ozone and fine particles with respiratory symptoms in children with asthma, *J. Amer. Med. Assoc., 290*(14), 1859-1867, 2003.

Green, R. and Robbins, J., ERBE-like inversion to instantaneous TOA flux, *Clouds and the Earth's Radiant Energy System (CERES) Algorithm Theoretical Basis Document 03*, 37 pages, 1997.

Hartley, W.S., P.V. Hobbs, J.L. Ross, P.B. Russell, and J.M. Livingston. Properties of aerosols aloft relevant to direct radiative forcing off the Mid-Atlantic coast of the United States. *J. Geophys. Res.*, *105*(D8), 9859-9885, 2000.

Hansen, J., and L. Travis, Light-scattering in planetary atmospheres, *Space Sci. Rev.*, *16*, 527-610, 1974.

Haywood, J., and O. Boucher. Estimates of the direct and indirect radiative forcing due to tropospheric aerosols: A review. *Geophys. Rev.*, *38*(4), 513-543, 2000.

Hegg, D.A., J. Livingston, P.V. Hobbs, T. Novakov, and P. Russell. Chemical apportionment of aerosol column optical depth off the Mid-Atlantic coast of the United States. *J. Geophys. Res.*, *102*(D21), 25,293-25,303, 1997.

Hobbs, P.V., J.S. Reid, R.A. Kotchenruther, R.J. Ferek, and R. Weiss, Direct radiative forcing by smoke from biomass burning, *Science*, *275*, 1776-1778, 1997.

Hoffman, M.R., and J.G. Calvert. Chemical transformation modules for Eulerian acid deposition models, volume 2, the aqueous-phase chemistry. EPA/600/3-85/017, 1985.

Holben, B., et al, AERONET – a federeated instrument network and data archive for aerosol characterization, *Remote Sens. Env.*, *66*, 1-16, 1998.

Interagency Monitoring of Protected Visual Environments (IMPROVE), Spatial and Seasonal Patterns and Temporal Variability of Haze and its Constituents in the Unite States: Report III, ISSN: 0737-5352-47, 2000.

IPCC: Climate Change 2001: The Scientific Basis, Contribution of Working Group 1 to the Third Assessment Report of the Inter-governmental Panel on Climate Change [Houghton *et al.* (eds.)], Cambridge University Press, Cambridge, United Kingdom and New York, NY, USA, 881pp, 2001.

Jacobson, M.Z. A physically-based treatment of elemental carbon optics: Implications for global direct forcing of aerosols. *Geophys. Res. Lett.*, *27*(2), 217-220, 2000.

Jacobson, M.Z. Strong radiative heating due to the mixing state of black carbon in atmospheric aerosols. *Nature*, *409*, 695-697, 2001.

Jin, Z., Radiative transfer modeling of ocean surface albedo for CERES SARB. *23rd CERES team meeting*, http://www-cagex.larc.nasa.gov/jin/Papers/Jin23CERES.pdf, 2001.

Karoly, D.J., K. Braganza, P.A. Stott, J.M. Arblaster, G.A. Meehl, A.J. Broccoli, and K.W. Dixon, Detection of a human influence on North American climate, *Science, 302*, 1200-1203, 2003.

Kato, S., M. Bergin, T. Ackerman, T. Charlock, E. Clothiaux, R. Ferrare, R. Halthore, N. Laulainen, G. Mace, J. Michalsky, D. Turner, A comparison of the aerosol thickness derived from ground-based and airborne measurements, *J. Geophys. Res.*, *105*(D11), 14,701-14,717, 2000.

Kaufman, Y. J. et al: Smoke, Clouds, and Radiation-Brazil (SCAR-B) Experiment. *J. Geophys. Res. 103*(D24), 31,783-31,808, 1998.

Kaufman, Y. J., R. Fraser, R. Ferrare, Satellite Measurements of Large-Scale Pollution: Methods, *J. Geophys. Res. 95*, 9895-9909, 1990.

Kleinman, L.I., P.H. Daum, D.G. Imre, J.H. Lee, Y.N. Lee, L.J. Nunnermacker, S.R. Springston, J. Weinstein-Lloyd, and L. Newman. Ozone production in the New York City urban plume. *J. Geophys. Res.*, *105*(D11), 14,495-14,511, 2000.

Lesins, G., P. Chylek, and U. Lohmann. A study of internal and external mixing scenarios and its effect on aerosol optical properties and direct radiative forcing. *J. Geophys. Res.*, *107*(D10), art. no. 4094, 2002.

Li, Z., 1998, Influence of absorbing aerosols on the inference of solar surface radiation budget and cloud absorption, *J. Climate*, *11*, 5-17, 1998.

Li, Z., and L. Kou, 1998, Atmospheric direct radiative forcing by smoke aerosols determined from satellite and surfase measurements, *Tellus (B)*, *50*, 543-554, 1998.

Liepert, B.G, J. Feichter, U. Lohmann, and E. Roeckner, Can aerosols spin down the water cycle in a warmer and moister world?, *Geophys. Res. Lett.*, *31*, 10.1029/2003GL019060, 2004.

Luke, W.T., Evaluation of a commercial pulsed fluorescence detector for the measurement of low-level SO_2 concentrations during the Gas-Phase Sulfur Intercomparison Experiment, *J. Geophys. Res.*, *102*(D13), 16,255-16,265, 1997.

Luke, W.T., T.B. Watson, K.J. Olszyna, R.L. Gunter, R.T. McMillen, D.L. Wellman, and S.W. Wilkison. A comparison of airborne and surface trace gas measurements during the Southern Oxidants Study (SOS). *J. Geophys. Res.*, *103*(D17), 22317-22337, 1998.

Malm, W.C. Characteristics and origins of haze in the continental United States. *Earth-Science Review, 33*, 1-36, 1992.

Malm, W.C., B.A. Schichtel, R.B. Ames, and K.A. Gebhart, A 10-year spatial and temporal trend of sulfate across the United States, *J. Geophys. Res.*, *107*(D22), 10.1029/2002JD002107, 2002.

Malm, W.C., J. F. Sisler, D. Huffman, R. A. Eldred, and T. A. Cahill, Spatial and seasonal trends in particle concentration and optical extinction in the United States, *J. Geophys. Res.*, *99*(D1), 1347-1370, 1994.

Malm, W.C., B.A. Schichtel, M.L. Pitchford, L.L. Ashbaugh, and R.A. Eldred, Trends in speciated fine particle concentration in the United States, *J. Geophys. Res.*, *109*, 10.1029/2003JD003739, 2004.

Martins, J.V., P. Artaxo, C. Liousse, J.S. Reid, P.V. Hobbs, and Y.J. Kaufman, Effects of black carbon content, particle size, and mixing on light absorption by aerosols from biomass burning in Brazil, *J. Geophys. Res.*, *103*, 32,041-32,050, 1998.

Marufu, L.T., B.F. Taubman, B. Bloomer, C.A. Piety, B.G. Doddridge, and R.R. Dickerson, The 2003 North American electrical blackout: An accidental experiment in atmospheric chemistry, *Geophys. Res. Lett*., *31*, 10.1029/2004GL019771, 2004.

Maryland Department of Environment, http://www.mde.state.md.us/Air/air_quality/ozone_forecast.asp, 2003.

McClellan, R.O., Setting ambient air quality standards for particulate matter, *Toxicology*, *181*, 329-347, 2002.

McKeen, S.A., G. Wotawa, D.D. Parrish, J.S. Holloway, M.P. Buhr, G. Hubler, F.C. Fehsenfel, and J.F. Meagher, Ozone production from Canadian wildfires during June and July of 1995, *J. Geophys. Res.*, *107*, art. no. 4192, 2002.

Menon, S., J. Hansen, L. Nazarenko, and Y.F. Luo. Climate effects of black carbon aerosols in China and India. *Science*, *297*(5590), 2250-2253, 2002.

Mishchenko, M. I., L. D. Travis, and A. A. Lacis, *Scattering, Absorption, and Emission of Light by Small Particles*, Cambridge University Press, Cambridge. 2002.

Novakov, T., D.A. Hegg, and P.V. Hobbs, Airborne measurements of carbonaceous aerosols on the East Coast of the United States, *J. Geophys. Res.*, *102*(D25), 30,023-30,030, 1997.

Novelli, P.C., V.S. Connors, H.G. Reichle, Jr., B.E. Anderson, C.A.M. Brenninkmeijer, E.G. Brunke, B.G. Doddridge, V.W.J.H. Kirchoff, K.S. Lam, K.A. Masarie, T. Matsou, D.D. Parrish, H.E. Scheel, and L.P. Steele, An internally constistent set of globally distributed atmospheric carbon monoxide mixing ratios developed using results from an intercomparison of measurements, *J. Geophys. Res.*, *103*, 19,285-19,293, 1998.

Pagnotti, V. A mesoscale meteorological feature associated with high ozone concentrations in the northeastern United States. *J. Air Pollut. Control Assoc., 37,* 720-722, 1987.

Parish, T.R., A.R. Rodi, and R.D. Clark. A case study of the summertime Great Plains low level jet. *Mon. Wea. Rev., 116*, 94-105, 1988.

Park, R.J., G.L. Stenchikov, K.E. Pickering, R.R. Dickerson, D.J. Allen, and S. Kondragunta, Regional air pollution and its radiative forcing: Studies with a single-column chemical and radiation transport model, *J. Geophys. Res., 106*(D22), 28,751-28,770, 2001.

Penner, J.E., R.E. Dickinson, and C.A. O'Neill, Effects of aerosol from biomass burning on the global radiation budget, *Science*, *256*, 1432-1434, 1992.

Ramanathan, V., P.J. Crutzen, J.T. Kiehl, and D. Rosenfeld, Aerosols, climate, and the hydrological cycle, *Science*, *294*, 2119-2123, 2001.

Ramanathan, V. et al, Indian Ocean Experiment: An integrated analysis of the climate forcing and effects of the great Indo-Asian haze, *J. Geophys. Res. 106*, 28,371-28,398, 2001.

Rao, S.T., J.Y. Ku, S. Berman, K. Zhang, and H. Mao. Summertime characteristics of the atmospheric boundary layer and relationships to ozone levels over the eastern United States. *Pure Appl. Geophys., 160*, 21-55, 2003.

Reid, J.S., P.V. Hobbs, R.J. Ferek, D.R. Blake, J.V. Martins, J.V. Dunlap, and C. Liousse, Physical, chemical, and optical properties of regional hazes dominated by smoke in Brazil, *J. Geophys. Res., 103*, 32,059-32,080, 1998(a).

Reid, J.S., T.F. Eck, S.A. Christopher, P.V. Hobbs, and B. Holben, Use of the Ångstrom exponent to estimate the variability of optical and physical properties of aging smoke particles in Brazil, *J. Geophys. Res., 104*, 27,473-27,489, 1999.

Reid, J.S., P. Hobbs, C. Liousse, J Martins, R. Weiss, T. Eck, Comparisons of techniques for measuring shortwave absorption and black carbon content of aerosols from biomass burning in Brazil, *J. Geophys. Res. 103*, 32,031-32,040, 1998(b).

Remer, L.A., S. Gasso, D.A. Hegg, Y.J. Kaufmann, and B.N. Holben. Urban/industrial aerosol: Ground based Sun/sky radiometer and airborne in-situ measurements. *J. Geophys. Res, 102*, 16,849-16,859, 1997.

Remer, L.A., Y.J. Kaufman, B.N. Holben, A.M. Thompson, and D. McNamara, Biomass burning aerosol size distribution and modeled optical properties, *J. Geophys. Res., 103*, 31,879-31,891, 1998.

Ricchiazzi, P., S. Yang, D Gautier, and D. Sowle, SBDART: a research and teaching software tool for plane-parallel radiative transfer in the Earth's atmosphere, *Bull. Amer. Met. Soc., 79,* 2101- 2114, 1998.

Rosen, H., T. Novakov, and B. Bodhaine, Soot in the Arctic, *Atmos. Environ., 15,* 1371-1374, 1981.

Ross, J.L., P. Hobbs, B. Holben, Radiative Characteristics of regional hazes dominated by smoke from biomass burning in Brazil: Closure tests and direct radiative forcing, *J.Geophys. Res. 103,* 31,925-31,941, 1998.

Russell, P.B., J. Livingston, P. Hignett, S. Kinne, J. Wong, A. chien, R. Bergstrom, P. Durkee, P. Hobbs, Aerosol-induced radiative flux changes off the United States Mid-Atlantic Coast: Comparison of values calculated from sunphotometer and in-situ data with those measured by airborne pyranometer. *J. Geophys. Res. 104,* 2289-2307, 1999(a).

Russell, P.B., P. Hobbs, L. Stowe, Aerosol properties and radiative affects in the United States East Coast haze plume: an overview of the Tropospheric Aerosol Radiative Forcing Observational Experiment (TARFOX), *J. Geophys. Res. 104,* 2213-2222, 1999(b).

Ryan, W.F., B.G. Doddridge, R.R. Dickerson, R.M. Morales, K.A. Hallock, P.T. Roberts, D.L. Blumenthal, J.A Anderson, and K.L. Civerolo, Pollutant transport during a regional O_3 episode in the Mid-Atlantic states, *J. Air & Waste Manage. Assoc., 48,* 786-797, 1998.

Seaman, N.L., and S.A. Michelson. Mesoscale meteorological structure of a high-ozone episode during the 1995 NARSTO-Northeast study. *J. Appl. Met., 39*(3), 384-398, 2000.

Sekiguchi, M., T. Nakajima, K. Suzuki, K. Kawamoto, A. Higurashi, D. Rosenfeld, I. Sano, and S. Mukai, A study of the direct and indirect effects of aerosols using global satellite data sets of aerosol and cloud parameters, *J. Geophys. Res., 108*(D22), 10.1029/2002JD003359, 2003.

Sistla, G., W. Hao, J.Y. Ku, G. Kallos, K. Zhang, H. Mao, and S. T. Rao, An operational evaluation of two regional-scale ozone air quality modeling systems over the eastern United States, *Bull. Amer. Meteor. Soc., 82*(5), 945-964, 2001.

Solomon P., E. Cowling, G. Hidy, and C. Furiness, Comparison of scientific findings from major ozone field studies in North America and Europe, *Atmos. Environ., 34* (12-14), 1885-1920, 2000.

Stehr, J.W., R.R. Dickerson, K.A. Hallock-Waters, B.G. Doddridge, and D. Kirk. Observations of NO_y, CO, and SO_2 and the origin of reactive nitrogen in the eastern United States. *J. Geophys. Res.*, *105*(D3), 3553-3563, 2000.

Stephens, G., Remote Sensing of the Lower Atmosphere, Oxford University Press, New York, 1994.

Stith, J.L., F.R. Lawrence, and P.V. Hobbs, Particle emissions and the production of ozone and nitrogen-oxides from the burning of forest slash, *Atmos. Environ.*, *15*, 73-82, 1981.

Szekeres, D., Traffic counts data, Pennsylvania Department of Transportation (PDOT), Bureau of Planning and Research, 2004.

Taubman, B.F., L.T. Marufu, C.A. Piety, B.G. Doddridge, J.W. Stehr, and R.R. Dickerson, Airborne characterization of the chemical, optical, and meteorological properties, and origins of a combined ozone/haze episode over the eastern U.S., *J. Atmos. Sci.*, *61*(14), 1781-1793, 2004(a).

Taubman, B.F., L.T. Marufu, B.L. Vant-Hull, C.A. Piety, B.G. Doddridge, R.R. Dickerson, and Z. Li, Smoke over haze: Aircraft observations of chemical and optical properties and the effects on heating rates and stability, *J. Geophys. Res.*, *109*(D2), 10.1029/2003JD003898, 2004(b).

United States Environmental Protection Agency, *Personal Communication*, 2003.

United States Environmental Protection Agency, *EPA Acid Rain Program 2002 Progress Report*, EPA-430-R-03-011, November 2003(a).

United States Environmental Protection Agency, *Latest Findings on National Air Quality 2002 Status and Trends*, EPA 454/K-03-001, August 2003(b).

Vant-Hull, B.L., Z. Li, B.F. Taubman, R. Levy, L.T. Marufu, B.G. Doddridge, and R.R. Dickerson, Smoke over haze: Comparison of satellite, surface and in-situ measurements of aerosol optical properties and radiative forcing of forest fire smoke over the eastern U.S., *J. Geophys. Res.*, In Press, 2004.

Vermote, E., E. Vermuelen, Atmospheric correction algorithm: Spectral reflectances (MOD09). NASA Algorithm Theoretical Basis Document, http://modis.gsfc.nasa.gov/data/atbd/atbd_mod08.pdf, 1999.

Vukovitch, F.M. Regional scale boundary layer ozone variations in the eastern United States and their association with meteorological variations. *Atmos. Environ.*, *29*, 2259-2273, 1995.

Vukovich, F.M., and J. Sherwell. Comparison of fine particles and the relationship between particle variation and meteorology at an urban site and a remote site in the eastern United States. *J. Air Waste Manage. Assoc., 52* (5), 573-584, 2002.

Wong, J., and Z. Li, Retrieval of optical depth for heavy smoke aerosol plumes: uncertainties and sensitivities to the optical properties, *J. Atmos. Sci., 59*, 250-261, 2002.

Zelenka, M.P., 1997: An analysis of the meteorological parameters affecting ambient concentrations of acid aerosols in Uniontown, Pennsylvania. *Atmos. Environ., 31* (6), 869-878, 1997.

Zhang, J., S.T. Rao, and S.M. Daggupaty. Meteorological processes and ozone exceedances in the northeastern United States during the 12-16 July 1995 episode. *J. Appl. Met., 37*, 776-789, 1998.

Zhang, J., and S.T. Rao. The role of vertical mixing in the temporal evolution of ground-level ozone concentrations. *J. Appl. Met., 38*, 1674-1691, 1999.

ABSTRACT

Title of Dissertation: A STUDY OF GROUND-LEVEL OZONE OVER THE BALTIMORE/WASHINGTON OZONE NONATTAINMENT AREA

Yu-Jin Choi, Doctor of Philosophy, 2004

Dissertation directed by: Associate Professor Sheryl H. Ehrman
Professor Richard V. Calabrese
Department of Chemical Engineering
Professor Russell R. Dickerson
Department of Meteorology

Surface ozone is a persistent problem in U.S.A. and Europe as well as developing countries. A key prerequisite to identifying effective approaches to meeting an ozone air quality standard is to understand the relationship between VOC and NOx, the significance of biogenic emissions, and the contribution of long-range transport.

The Baltimore/Washington area is an EPA-designated severe ozone non-attainment area. In this study, the characteristics of ozone events over this area were investigated to develop a possible control strategy. Both observational and computational modeling approaches were employed, and it was divided into three parts. The first part was to investigate sources of VOC emissions in the Baltimore area using highly time resolved measurements, and to investigate possible relationships between each VOC source category and episodes of elevated ozone concentrations.

The results showed that biogenic emissions contribute significantly to local ozone production in this area. The second part was emissions inventory evaluation, focused on VOC emissions inventory because VOC estimates are commonly assumed to be more uncertain than NOx estimates. The results indicated a possibility of overestimation of solvent VOC emissions. Photochemical simulations with reduction of solvent VOC emissions did not affect ozone prediction, but affected significantly secondary organic aerosol prediction. Lastly, photochemical ozone simulations were performed to find an effective control strategy for this area. The simulation results showed that long-range transport of ozone was responsible for 20-90 ppb of ozone concentration in the state of Maryland, Northern Virginia, and D.C. area, displaying a decreasing contribution as it approached to the Baltimore/Washington area. Local emissions contributed considerably to high ozone occurrences in this area. Moreover, the contribution of biogenic VOC emissions in this region was responsible for much of the local ozone production, which was a consistent result from the part one. Accordingly, the results indicated that NOx emissions reductions would probably mitigate high ozone occurrences in this area, and this was confirmed through several simulations with emissions reductions. However, our results suggested that control of only local NOx emissions might not be sufficient to comply with the 8 hr ozone standard because of the importance of long-range transported ozone.

A STUDY OF GROUND-LEVEL OZONE OVER THE BALTIMORE/WASHINGTON OZONE NONATTAINMENT AREA

by

Yu-Jin Choi

Dissertation submitted to the Faculty of the Graduate School of the
University of Maryland, College Park in partial fulfillment
of the requirements for the degree of
Doctor of Philosophy
2004

Advisory Committee:
Associate Professor Sheryl H. Ehrman, Chair/Advisor
Professor Richard V. Calabrese, Coadvisor
Professor Russell R. Dickerson, Coadvisor
Professor Robert D. Hudson
Assistant Professor Srinivasa R. Raghavan

Acknowledgements

I would like to greatly acknowledge the enthusiastic supervision of my advisors, Professor Sheryl H. Ehrman, Professor Richard V. Calabrese, and Professor Russell R. Dickerson, during this work. This work cannot be completed without their encouragement, invaluable advice, continuous support, and patience through the many years.

I am grateful to Dr. Jeffrey W. Stehr for sharing lots of good ideas, and providing many helpful comments and suggestions. I thank Michael Mitchell for his great efforts to teach me UNIX and SMOKE. Special thanks to all my friends for being the surrogate family during the many years I have stayed here.

I have been supported financially by the Maryland Department of Environment. For this assistance I am very grateful.

Lastly, and most importantly, I wish to thank my family, and especially my parents, for their love, support and absolute confidence in me.

Table of Contents

List of Tables

List of Figures

Chapter 1: Introduction

1.1 Objectives and organization

Human exposure to high concentrations of ozone continues to bother many areas of the United States, despite the implementation of government-mandated emissions control strategies (Roselle et al., 1991). Persistent ozone problems also exist in parts of Western Europe, Mexico, Brazil, and other developing countries (Winner and Cass, 2000).

The task of developing control strategies for ozone is more difficult than controlling primary pollutants emitted directly from emissions sources. In case of the primary pollutants, a reduction in emissions results in an approximately proportional reduction of pollutants. However, ozone, a secondary pollutant, which is formed from primary pollutants and other chemical species in the atmosphere, does not necessarily respond in a proportional manner to reductions in precursor emissions (Finlayson-Pitts and Pitts, 2000).

Key prerequisites to identifying effective approaches to meeting ozone air quality standards at a given area are to understand the relationship between VOC and NOx, the significance of biogenic emissions, and the contribution of long-range transport.

The Baltimore/Washington area is classified as a severe ozone non-attainment area by the U. S. EPA. In this study, the characteristics of ozone events in this area are investigated to develop a possible control strategy leading to ozone reduction. For that reason, both an observation-based approach and an emission-based air quality modeling approach are employed, and the study is divided into three parts (Chapters 3, 4, and 5). Chapter 2 addresses background information about ground-level ozone, air quality models, and observational approaches to the ozone study. In Chapter 3, we investigate sources of VOC emissions in the Baltimore area using highly time resolved measurements, and possible relationships between each VOC source category and episodes of elevated ozone concentrations. In particular, the contribution of biogenic VOC emissions to high ozone occurrences in this area is compared to that of anthropogenic VOC emissions.

Several studies have been performed to predict ozone concentrations over the eastern U.S with coarse grid resolutions (36 km x 36 km, 18.5 km x 18.5 km) using various modeling systems such as Urban Airshed Model with Variable Grid (UAM-V), San Joaquin Valley Air Quality Model (SAQM), Urban and Regional Model (URM), Regional Oxidant Model (ROM) (Sistla et al., 2001; Roselle et al., 1995; Milford et al., 1994; Possiel et al. 1993). Kumar et al. (1996) pointed out that, by using coarse resolution over the whole domain, one could lose detail of the pollutant dynamics that can only be captured by using finer scales. Even though there are several studies focusing on smaller regions in a finer grid (Arunachalam et al., 2001; Smith et al., 2001; Hanna et al., 1996; Kumar et al., 1996), there has been little research into ozone formation with a fine grid resolution for the Baltimore/Washington

ozone non-attainment area. Hence, the next two parts (Chapters 4 and 5) are related to modeling of this area with a fine grid resolution. Chapter 4 describes an emissions inventory evaluation before a further photochemical ozone modeling study is performed, for it has been pointed out that the uncertainty of emissions inventory greatly affects the performance of a photochemical modeling. The focus of the evaluation is placed on the VOC emissions inventory because VOC estimates are commonly assumed to be more uncertain than NOx estimates. Several methods of evaluation of emissions are implemented to come to solid conclusions.

Chapter 5 is a photochemical ozone modeling study to determine an effective control strategy for the Baltimore/Washington ozone non-attainment area. The first simulations are focused on investigating the relative impact of long-range transport of ozone and precursors versus local emissions on high ozone occurrences in the Baltimore/Washington ozone non-attainment area. Russell and Dennis (2000) reported in their work that most studies were first done for urban applications, but more recently studies are progressing to regional scales because of the significance of long distance transport of pollutants including ozone precursors. Also, several studies based on observations stressed a significant role of long-range transport of pollutants on ozone events (Ryan et al., 1998; 2000; Zhang and Rao, 1999). Hence, the relative contribution of transport and local emissions is investigated by controlling boundary conditions obtained from multi-nesting technique. In the second group of simulations, the relative role of anthropogenic VOC emissions versus biogenic VOC emissions in high ozone occurrences is studied. Lastly, several simulations with emissions

reductions are carried out in order to identify a possible ozone control strategy leading toward ozone mitigation for the Baltimore/Washington ozone non-attainment area.

Finally, a summary of results and overall conclusions obtained from this study, and recommendations for future work are presented in Chapter 6.

1.2 Implications and impacts of the study

In this study, using observation-based and emissions-based air quality modeling approaches, we tried to identify and quantify each contribution of long-range transport, local anthropogenic emissions, and local biogenic emissions to ozone occurrences. Here, the issues associated with biogenic and long-range transport contributions to ozone events have been critical subjects of debate. The findings presented in the following chapter suggest that local anthropogenic NOx and biogenic VOC emissions play a significant role in high ozone occurrences over the Baltimore/Washington ozone non-attainment area, while the role of anthropogenic VOC in ozone formation is not as critical. This conclusion about the role of biogenic VOC in high ozone formation was consistent in both observation-based and air quality modeling-based approaches, even though the observation-based approach was limited to a Baltimore observation site. Also, the results suggest that lowering anthropogenic NOx emissions may lead to a decrease in high ozone concentration occurrences over the Baltimore/Washington ozone non-attainment area. However, a considerable contribution of long-range transport was also observed when considering a wider area encompassing the Baltimore/Washington region, hence the need for regulation of

ozone at upwind areas to accompany local reductions in order to meet the 8 hr ozone standard over this study region.

Even though this study was focused on the Baltimore/Washington ozone non-attainment area, the procedure we used in order to identify the characteristics of high ozone events and to develop an optimal control strategy can be applied to other regions.

Chapter 2: Background

2.1 Ground level ozone

The earth's atmosphere is divided into four distinct layers based on the vertical temperature profile: the troposphere, stratosphere, mesosphere, and thermosphere. The tops of these layers are called the tropopause, stratopause, mesopause, and thermopause, respectively. The troposphere is the atmosphere between the earth's surface and 10 to 18 km in altitude, where the temperature normally decreases with increasing altitude. The troposphere accounts for more than 80% of the mass and nearly all of the water vapor, clouds, and precipitation in the earth's atmosphere. The portion of the atmosphere between the tropopause and approximately 50 km altitude is the stratosphere, whose temperature increases with altitude. Beyond the stratosphere are the mesosphere and thermosphere (Wallace and Hobbs, 1977; Jacobson, 2002).

Ozone, a reactive oxidant gas, is found in the lower two layers of the atmosphere. Most of the earth's atmospheric ozone is found in the stratosphere, and stratospheric ozone prevents the sun's harmful ultraviolet rays in the wavelength range of 200-300 nm from reaching the lower atmosphere and the earth's surface. On the other hand, ozone in the troposphere is an air pollutant and a major component of urban smog.

Increased ground level ozone concentrations can negatively affect human health as well as damage forest systems, reduce agricultural yields, and degrade

sensitive materials. Repeated exposures to ozone can make people more susceptible to respiratory infection, result in lung inflammation, and aggravate pre-existing respiratory diseases such as asthma. The U.S. Environmental Protection Agency (EPA) estimates that 5% to 20% of the total U.S. population is especially susceptible to the harmful effects of ozone air pollution. Ozone also affects vegetation and ecosystems, leading to reduced growth and survivability of tree seedlings, and increased plant susceptibility to disease, pests, and other environmental stresses (DNREC Division of Air & Waste Management, 2001; Jacobson, 2002).

Ozone is a secondary air pollutant. It is not emitted directly into the air, but rather formed by the reaction of volatile organic compounds (VOC) and nitrogen oxides (NOx) in the presence of sunlight. Ground level ozone has an atmospheric lifetime of the order of days to weeks, generally longer than its precursors, and then once formed, it can be transported over much wider regions. Moreover, the precursors emitted from elevated sources such as power plant stacks can be also transported great distances, and ozone is often found outside of major urban centers and rural areas (Baumann et al., 2000). Consequently, the ground level ozone problem is not only a concern at urban sites that are the center of emissions, but also rural locations because ozone is wide-ranging as well as persistent.

Anthropogenic emissions of NOx and VOC have decreased over the last decade in Europe and North America (Jonson et al., 2001). Elkins et al. (2000) report that over the past 20 years, ambient ozone levels decreased 20% based on 1-hour average measurements, and 12% based on 8-hour average measurements. According to U.S. EPA emissions estimates, between 1980 and 1999, the emissions of VOC have

decreased 33%, and the emissions of NOx have increased 1%. For the more recent 10-year period (1990-1999), urban sites showed decreases in ozone of approximately 6% and suburban sites showed 4% decreases of ozone. However, rural sites in the eastern United States showed increases in 8-hour ozone levels over the last 10 years (Elkins et al., 2000). Also, many regions in the eastern United States still exceed the 1-hour ozone National Ambient Air Quality Standard (0.12 ppm) (NAAQS) in summer time. In addition, the shift to the 8-hour ozone standard (0.08 ppm; USEPA, 1997) is expected to increase the number of non-attainment areas (Sistla et al., 2001). That is because the 8-hour ozone standard is in most cases stricter than the 1-hour standard, and ozone levels in Mid-Atlantic States exceeding the 8-hour standard are more widespread than the 1-hour standard (Wierman, 2003).

2.2 Ozone chemistry in troposphere

In 1950s, Haagen-Smit and co-workers discovered the key roles of NOx and VOCs in ground-level ozone formation (Haagen-Smit and Fox, 1954). The discovery was observed from a study of production of ozone with NOx and VOCs in the laboratory (NRC, 1991; Jacobson, 2002). Since then, the chemical mechanism of ozone formation has been improved, and well established.

Ozone is present in the natural, unpolluted troposphere. The sources of ozone in the natural troposphere are a downward transport of ozone from the stratosphere, and in-situ photochemical production from reactions of natural organic compounds (e.g., CH_4, CO, and other organic carbons), NOx, and sunlight. These sources of

tropospheric ozone are balanced by in-situ photochemical destruction and by dry deposition at the earth's surface. Ozone mixing ratios at clean remote sites at ground level are in the range of 10 to 40 ppb, and tend to increase with increasing altitude (NRC, 1991; Atkinson, 2000). However, as human activities accompanying emissions of ozone precursors are increased, the balance of destruction and formation of ozone becomes broken, and accordingly the accumulation of ozone takes place.

In the troposphere, the first step in ozone formation is the production of OH radicals by initiation reactions, primarily photolysis of ozone. Water vapor collides with an excited oxygen atom to produce OH radical, which reacts with most trace species in the atmosphere, and leads to cycles of reactions, resulting in the photochemical degradation of organic compounds of anthropogenic and biogenic origin, the enhanced formation of ozone, and the atmospheric formation of acidic compounds (NRC, 1991).

$$O_3 + h\nu \rightarrow O(^1D) + O_2 \ (\lambda < 335 \text{ nm})$$

$$O(^1D) + H_2O \rightarrow 2OH$$

The production of OH radicals through the reactions above is the major process in the lower troposphere where water vapor mixing ratios are high, but in some continental environments, other sources like peroxides, acetone, and formaldehyde may be sources of OH (Seinfeld and Pandis, 1998). The next step in the chemical process of ozone formation occurs through reaction sequences involving VOC, CO and NOx, which

result in the conversion of NO to NO_2 through reactions below. The hydrocarbons and intermediate organics emitted directly are collectively referred to as VOC. The reaction sequences are almost always initiated by the reactions of OH radicals with reactive hydrocarbons (RH) (Sillman, 1999).

$$RH + OH + O_2 + M \rightarrow RO_2 + H_2O + M \quad (1)$$

$$CO + OH + O_2 + M \rightarrow HO_2 + CO_2 + M \quad (2)$$

where M represents a third body such as N_2 or O_2, which removes the energy of the reaction and stabilizes O_3. This is followed by the reaction of RO_2 and HO_2 radicals with NO

$$RO_2 + NO + O_2 \rightarrow RCHO + HO_2 + NO_2 \quad (3)$$

$$HO_2 + NO \rightarrow OH + NO_2 \quad (4)$$

where RCHO represents intermediate organic species, typically carbonyl compounds.

$$NO_2 + h\nu \rightarrow NO + O(^3P) \; (\lambda < 420nm) \quad (5)$$

$$O_2 + O(^3P) + M \rightarrow O_3 + M \quad (6)$$

Apparently, the reaction sequence initiated by RH, equation (1), leads to greater ozone formation per OH radical than the reaction sequence initiated by CO, equation (2), which otherwise dominates in the remote troposphere (Sillman, 1999). That is, the

lifetime of CO against breakdown by reaction (2) in tropospheric air is 28-110 days, and so the rate of ozone production by this sequence is low (Jacobson, 1999). Additionally, methane (CH_4) has been traditionally precluded from the consideration as a precursor to regional O_3 pollution episodes because of its long lifetime (8 to 9 years). Therefore, in case of the urban or regional ozone problem the extent of contribution of CO and CH_4 is small. However, on the global scale, reactions of OH with CO and CH_4 become major source of tropospheric background. Furthermore, recent studies have shown an important role of these pollutants on regional O_3 episodes causing increase of hemispheric background O_3 concentrations (Fiore et al., 2003).

2.3 Organic compounds and oxides of nitrogen

NOx is released into troposphere from a variety of biogenic and anthropogenic sources. It is emitted from the combustion of fossil fuels such as vehicle emissions and fossil-fueled power plants, which leads to emission directly into the planetary boundary layer (PBL), mainly in the form of NO (Jenkin et al., 2000). The four major natural sources of NOx are soil in which nitrification, denitrification, and the decomposition of nitrite contribute to NO production, lightning, natural fires, and the oxidation of NH_3 by photochemical processes in oceans and by some terrestrial plants (Finlayson-Pitts and Pitts, 2000). The natural sources are reported to be 3 to 6% of the total (Trainer et al., 2000). The estimated US and worldwide emissions of NOx are 1 million tons/yr, and 10 million tons/yr, respectively, for natural sources. Also, NOx

emissions from anthropogenic sources for the US and worldwide are estimated to be around 6 million tons/yr, and 40 million tons/yr, correspondingly (Atkinson, 2000).

Organic compounds are also emitted from natural and anthropogenic sources. Vehicles and gasoline-burning engines are large anthropogenic sources of VOC. VOC also comes from consumer products such as paints, insecticides, and cleaners as well as industrial operations, solvent usage, landfills, and waste facilities, petroleum refining, and chemical manufacturing. The estimates of US and worldwide emissions of anthropogenic VOC amount to 20 million tons/yr, and 60-140 million tons/yr, respectively (Atkins, 2000). Additionally, large quantities of VOC are emitted from vegetation. About 98% of the estimated total natural VOC emissions are from vegetation. Other natural emission sources are soil and biomass burning. Many of these species from biogenic sources such as isoprene, and terpenes are extremely photochemically reactive. Hence, it is expected that they exert a strong influence upon photochemical ozone production in regions where their emissions are localized (Trainer et al., 2000; Guenther et al., 2000). Isoprene is emitted typically from deciduous trees, and its emissions are ambient temperature and light dependent. On the other hand, terpenes such as α-pinene and β-pinene, whose emissions vary with ambient temperature, are emitted from conifers (Seinfeld and Pandis, 1998). Literature estimates of US and worldwide emissions of biogenic VOC are 29 million tons/yr, and 1150 million tons/yr, respectively (Atkins, 2000).

2.4 Air quality modeling

The U.S. EPA requires that areas not meeting the ozone NAAQS demonstrate an appropriate planning process showing that adequate steps, such as reductions in anthropogenic emissions of ozone precursors, will be undertaken to reduce the ozone problem (Sistla et al, 2001). Many studies have been conducted to understand the physicochemical characteristics of ozone formation, in order to determine adequate steps for mitigating the ozone problem. These include how pollutants are produced, what kinds of processes are most important, and how pollutant interactions occur. As a tool to perform these studies, air quality modeling has been used. That is, photochemical models can simulate the complex physical and chemical processes associated with the production and removal of ozone.

Air quality models are used mainly for two purposes. The first is for making regulatory or policy decisions. Model simulations are needed to identify the sources of a problem, contributing factors, and methods of controlling or alleviating pollutant emissions, in order to understand the causes of air pollution and alternative means of reducing it. Models are necessary to test the relative effectiveness of different controls and potential effects of the proposed strategies. Typically, an air quality model would be used to simulate a variety of alternative scenarios in a comparative manner to help the regulatory user arrive at recommendations. The second purpose is for improving our understanding of the physicochemical system, how pollutants are produced, what processes are most important, and how pollutant interactions occur. The models help

scientists understand how human and natural activities cause pollution problems in both rural and urban environments (Dennis et al., 1996).

Modern air quality models are actually a system of models or submodels. Each submodel performs a function when needed. A meteorological model, which in and of itself is a collection of models, characterizes the mean and turbulent physical properties of the atmosphere. A dispersion model estimates how a cloud of emissions expands as it moves downwind. A chemistry model simulates chemical transformations. A wet deposition model estimates removal by rainfall, and a dry deposition model estimates removal to the ground and vegetation. Most of the current air quality models are formulated in the Eulerian reference frame. In particular, multidimensional grid-based air quality models with several vertical layers are potentially the most powerful, and involve the least restrictive assumptions, but are also the most computationally intensive (Russell and Dennis, 2000).

First-generation models have first-order chemistry with only a few primary reactions simulated. The transport and dispersion calculations are based upon steady-state approximations in time and space. Second-generation models typically add removal processes, increase the level of sophistication in the parameterizations and chemistry simulations, and allow transport and dispersion to vary as a function of time and space. Third-generation models, called “next-generation” models, consist of select processes coupled together so that interactions and feedbacks can be investigated (Irwin, 2003).

A variety of air quality models have been applied to both urban and regional scales, and they have been improved and updated with the rapid development of

computer systems, and with continued research into the chemistry and meteorology related to air pollution. The Urban Airshed Model-version IV (UAM-IV), California Air Resources Board Grid model (CALGRID), California/Carnegie Institute of Technology model (CIT) and the Gas and Aerosol Transport and Reaction model (GATOR) are examples of urban scale photochemical air quality models. The Regional Acid Deposition Model (RADM), Regional Oxidant Model (ROM), European Air Dispersion Model (EURAD) and the Long Term Ozone Simulation model (LOTOS) are known as regional scale photochemical air quality models. As multiscale/nested models, providing the needed boundary conditions to the smaller model, SARMAP Air Quality Model (SAQM), Multiscale Air Quality Simulation Program (MAQSIP), European Air Dispersion Model (EURAD), Urban Airshed Model-Variable (UAM-V), and Community Multiscale Air Quality model (CMAQ) are used (Russell and Dennis, 2000). They have many things in common, but depending on the formulation of meteorological fields, numerical algorithms, and parameterization schemes used in simulating the ozone formation process, these models could give different results for modeled ozone concentrations that may affect the efficacy of emission control strategies based on model results (Sistla et al., 2001).

As shown in Figure 2.1, air quality modeling is composed of three main parts: chemistry and transport, meteorology, and emissions. The chemistry and transport model (CTM) simulates the chemical reactions that take place among chemical species in the atmosphere, and the movement of these components. To drive this, a meteorology model is needed to predict atmospheric conditions such as the wind fields, humidity, temperature and pressure. An emissions component of the model

should provide the information regarding sources of pollution, derived from inventories of known emissions sources of both manmade and natural origins.

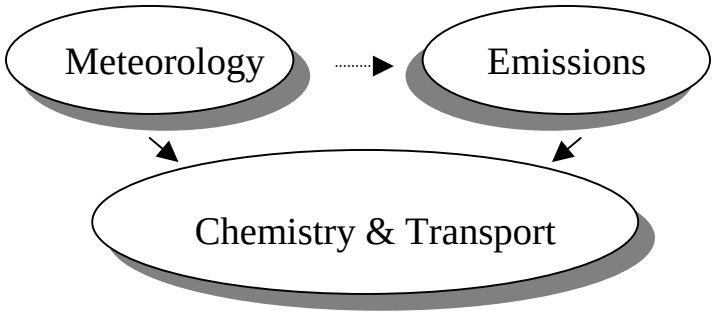

Figure 2.1: Air quality modeling system.

In this study, CMAQ, which has been developed to investigate scientific and regulatory concerns related to acid deposition, tropospheric ozone, and particulate matter over scales ranging from urban to intercontinental by the U.S. EPA, was used to simulate ozone formation on a regional scale (Ching and Byun, 1999). The CMAQ modeling system is composed of the CMAQ Chemical Transport Modeling system (CCTM) as a chemistry and transport model, the Pennsylvania State University-National Center for Atmospheric Research Mesoscale Model Version 5 (MM5) as a meteorology model, the Sparse Matrix Operator Kernel Emissions (SMOKE) as an emission preprocessing model, and interface processors to incorporate the outputs of the meteorology processors and to prepare the requisite information for initial conditions, boundary conditions and photolysis rates for the CCTM. Figure 2.2 illustrates the relationship to show the flow of data through the modeling system.

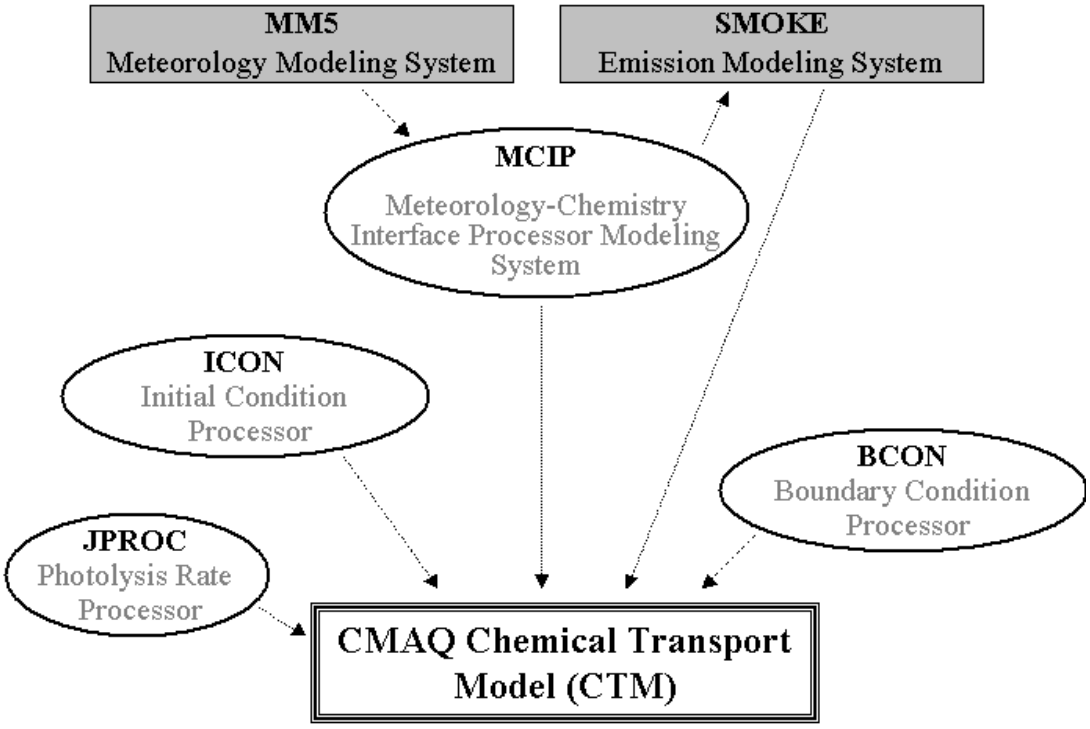

Figure 2.2: CMAQ modeling system. Schematic is based on the CMAQ manual (EPA-III, 1999).

2.4.1 MM5

MM5 has been developed in cooperation with Penn State and the University Corporation for Atmospheric Research (UCAR), and is continuously being improved by contributions from users at several universities and government laboratories. It was evolved from the model used by Anthes and Warner in the early 1970s. The model is a limited-area, nonhydrostatic (or hydrostatic), terrain-following sigma-coordinate model designed to simulate or predict mesoscale and regional-scale atmospheric circulation. In the hydrostatic model, the variables are explicitly predicted. In the

non-hydrostatic model, pressure, temperature and density are defined in terms of a reference state and perturbations from the reference state. MM5 is non-mass conserving in the non-hydrostatic mode (UCAR, 2003; Otte, 1999).

The model is supported by several auxiliary programs, which are referred to collectively as the MM5 modeling system. Terrestrial and isobaric meteorological data are horizontally interpolated from a latitude-longitude grid to a variable high-resolution domain on either a Mercator, Lambert conformal, or polar stereographic projection (programs TERRAIN and REGRID). Since the interpolation does not provide mesoscale detail, the interpolated data may be enhanced with observations from the standard network of surface and rawinsonde stations (program LITTLE_R/RAWINS). A subprogram performs the vertical interpolation from pressure levels to the sigma coordinate system of MM5 (program INTERF). The vertical coordinate is terrain following meaning that the lower grid levels follow the terrain while the upper surface is flat. Intermediate levels progressively flatten as the pressure decreases toward the chosen top pressure (UCAR, 2003).

MM5 is used to calculate the wind speed, which is especially critical for determining transport and residence times of pollutants, and estimates the turbulent diffusion coefficients and dry deposition velocities. Also, it provides temperature, relative humidity, mixing depth, and UV radiation (Seinfeld and Pandis, 1998).

2.4.2 SMOKE

SMOKE (Version 1.4), which employs matrix-vector multiplication for efficient emissions processing, has been developed by the North Carolina Supercomputing Center (NCSC). The main goal of an emission pre-processing model is to convert the source-level emissions (county total emissions) reported on a yearly basis to spatially resolved, hourly emissions, with detailed speciation information. Such conversions consist of multiplying emissions of various sources by several factors in steps called temporalization, speciation, and gridding. These steps are the main components of emissions pre-processing, and they are typically performed separately for point, area, mobile, and biogenic sources. At each step, a processing model uses profile tables and cross-reference tables to convert the emissions from county wide, yearly emissions to hourly emissions with finer spatial resolution. The cross-reference tables assign the profiles to each source (Houyoux et al., 2000). Figure 2.3 shows the SMOKE main programs and data flow.

In the temporalization step (TEMPORAL), SMOKE creates an hourly pollutant emissions inventory by applying the monthly, weekly, and diurnal profiles based on the source characteristics, using the cross-reference table to match the profile to the source type. If there is no temporal profile given in the cross-reference table for a particular source, the user must define a temporal profile for that source. In the speciation step (SPCMAT), it creates a speciation matrix containing conversion factors, used to convert total VOC concentration to the concentrations of specific compounds. In the same manner as in the temporal processing step, if the speciation matrix for a

particular source is not specified in the cross-reference table, the user must define the speciation matrix to be used by that source. In the gridding or spatial allocation step (GRDMAT), SMOKE uses a gridding surrogate to create a matrix containing conversion factors, used to transform county level aggregate emissions to emissions in each grid cell. A gridding surrogate is a dataset developed from geographic information (e.g. population or land use) at a finer spatial gridding resolution than the initial emissions data, and it is used to spatially allocate the emissions to the grid cells.

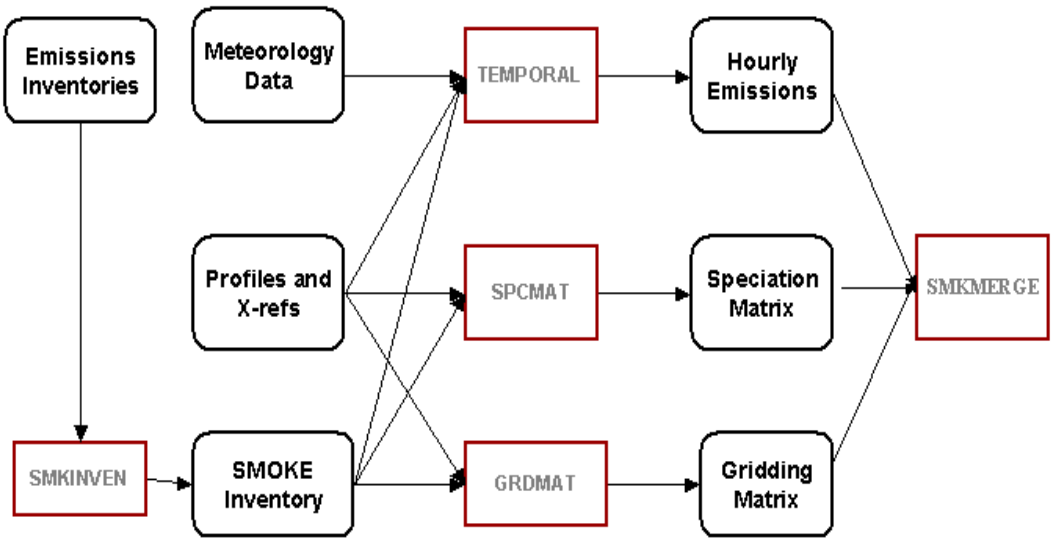

Figure 2.3: SMOKE main programs and dataflow.

The following surrogates are used for SMOKE processing: county area, population, urban, rural, and major highways. Surrogates based on the density of households, agriculture land use and forest type can also be used. After the spatial allocation step, if the spatial gridding surrogate contains zero values for an entire county, the default spatial gridding surrogate will be assigned to that source. The spatial allocation step is then repeated, and if the default spatial gridding surrogate for the source is still zero, this source is dropped from the final inventory.

SMOKE processes each source category slightly differently. For area source emissions, after importing the raw inventory, SMOKE allocates the county-level emissions to each grid cell using spatial surrogate files. Then SMOKE splits inventoried pollutants into model species using speciation profiles that contain the assumed pollutant-to-species factors. Following speciation, SMOKE assigns monthly, weekly, and diurnal temporal profiles to each source. Through these procedures SMOKE generates speciated, gridded, and hourly emissions data.

For mobile sources, SMOKE applies different procedures and requires different supplementary data depending on type of raw inventory: pollutant emissions or daily vehicle miles traveled (VMT). If pollutant emissions data are available, SMOKE processes mobile source data in the same manner as area source information. Otherwise, SMOKE converts VMT data into emissions data using the internal module MOBILE5b. The subsequent steps of speciation, gridding, and temporalization are the same as for area source processing.

SMOKE also applies the speciation and temporal profiles to process point source emissions. The gridding surrogates are not required since point sources contain

the latitude and longitude information that allow the direct allocation of emissions to each grid cell. While SMOKE treats area and mobile source emissions as occurring at the surface (2-D data), it calculates plume rise, which depends on ambient temperature, boundary layer height, pressure, and wind direction and speed. Those meteorological parameters were generated with the MM5 model and reformatted before inputting into SMOKE using the Meteorology-Chemistry Interface Processor (MCIP).

SMOKE determines biogenic source emissions based on emission factors and land-use data reflecting the types and quantities of vegetation represented in each grid cell. Specifically, the Biogenic Emissions Inventory System 2 (BEIS2), contained in SMOKE, converts land-use data into standard emissions by applying emissions factors. SMOKE then conducts the gridding process in the same manner as for area and mobile sources. Biogenic emissions are functions of temperature and solar radiation. SMOKE accounts for this by incorporating meteorological information in the emission estimation. Finally, SMOKE merges area, biogenic, mobile, and point source emissions to generate the three-dimensional total emissions for each grid cell (SMKMERGE) (Tao et al., 2003).

2.4.3 CMAQ CTM (CCTM)

The formation and transport of chemically reacting atmospheric species is described by the mass conservation equation.

$$\frac{\partial C_i}{\partial t} = -\nabla \bullet (\mathbf{u} C_i) + \nabla \bullet (K_e \nabla C) + R_i + E_i - S_i$$

where C is the concentration of the species of interest; **u** is the velocity vector at each grid point within the model domain; K_e is the eddy diffusivity used to parameterize the subscale turbulent fluxes of species; R is the net rate of chemical production; E is the emissions rate; and S represents removal fluxes from processes such as dry deposition and cloud scavenging (Ching and Byun, 1999; Seinfeld and Pandis, 1998; Tao et al., 2003). Generally, K-theory is used to determine the K_e values, which are expressed as a function of atmospheric stability and mixing height following some parameterization (Russell and Dennis, 2000).

The equation is a set of time-dependent, nonlinear, coupled partial differential equations. Several methods have been proposed to solve the full equation. The most popular technique for the solution is the operator splitting technique. The basic idea is to solve independently the pieces of the problem corresponding to the various processes and then couple the various changes resulting from the separate partial calculations, instead of solving the full equation at once. Hence, the chemical transport model solves chemical species equations in the general form

$$\frac{\partial C_i}{\partial t} = \left(\frac{\partial C_i}{\partial t}\right)_{adv} + \left(\frac{\partial C_i}{\partial t}\right)_{diff} + \left(\frac{\partial C_i}{\partial t}\right)_{cloud} + \left(\frac{\partial C_i}{\partial t}\right)_{dry} + \left(\frac{\partial C_i}{\partial t}\right)_{aeros} + E_i + R_i$$

where $(\partial C_i/\partial t)_{adv}$, $(\partial C_i/\partial t)_{diff}$, $(\partial C_i/\partial t)_{cloud}$, $(\partial C_i/\partial t)_{dry}$, and $(\partial C_i/\partial t)_{aeros}$ are the rates of change of C_i due to advection, diffusion, cloud processes (cloud scavenging,

evaporation of cloud droplets, aqueous-phase reactions, wet deposition, etc.), dry deposition, and aerosol processes (transport between gas and aerosol phases, aerosol dynamics, etc), respectively (Seinfeld and Pandis, 1998). As the equation above indicates, the CCTM contains modules representing advection, eddy diffusion, air chemistry, aerosol physics, in-cloud, precipitation processes, and sources and sinks such as dry deposition and emission. Thus, chemical transport models are characterized by the following science process classes (Seinfeld and Pandis, 1998; Ching and Byun, 1999):

HADV : Horizontal advection operator

VADV : vertical advection operator

HDIFF : Horizontal diffusion operator

VDIFF : Vertical diffusions operator

CHEM : Gas-phase chemistry operator

CLOUD : Cloud operator

AERO : Aerosol operator

S : Source and sink operator

If $\mathbf{C}(x,y,z;t)$ is the concentration vector at time t, then its value at the next time step ($t + \Delta t$) will be the net result of the simultaneous applications of all operators

$$\mathbf{C}(x,y,z;t + \Delta t) = \mathbf{C}(x,y,z;t) + [\, HADV(\Delta t) + VADV(\Delta t) + HDIFF(\Delta t) + VDIFF(\Delta t) + CEHM(\Delta t) + CLOUD(\Delta t) + AERO(\Delta t) + S(\Delta t) \,]\, \mathbf{C}(x,y,z;t)$$

This method greatly shortens solution times and improves numerical accuracy because more accurate and efficient numerical algorithms are used to treat the different processes (Russell and Dennis, 2000). For example, in order to calculate the rate of advection, finite difference, finite element, or finite volume techniques can be employed. As for gas-phase chemistry, the Euler method, Tayler series, or Gear method can be introduced.

One of the major components of a photochemical model is its description of atmospheric chemistry. Interactions in the gas-phase are represented by means of chemical mechanisms, which are a collection of reactions that transform reactants into products, including important intermediates. Since a number of reactions take place in the atmosphere, and the chemistry of even relatively simple organics can be quite complex, it is impossible for a photochemical model to accommodate the complete reactions and species. Hence, chemical mechanisms developed for air quality modeling are highly condensed to substantially reduce the number of organic reactions, and these are parameterized representations of a true chemical mechanism. The manner in which the grouping of organic compounds is carried out typically distinguishes one mechanism from another. There are several chemical mechanisms commonly used: the Carbon Bond IV (CB-IV) mechanism, the Regional Acid Deposition Mechanism 2 (RADM2), and the SAPRC mechanism (Ching and Byun, 1999).

The CB-IV mechanism described by Gery et al. (1989) is a lumped structure type, and the CMAQ implementation of the CB-IV mechanism includes 46 species and 96 reactions, including aerosol and aqueous chemistry. Table 2.1 shows the 46 species

including ten primary organic species emitted directly to the atmosphere, used in the CB-IV mechanism. The ten primary organic species includes three single compounds, ETH (ethene), ISOP (isoprene), and FORM (formaldehyde), and six aggregated compounds, PAR (single carbon bond), OLE (double carbon bond), TOL (seven carbon aromatics), XYL (eight carbon aromatics), ALD2 (higher molecular weight aldehydes), TERP (terpenes), and NR (non-reactive carbon atom) (Ching and Byun, 1999).

The RADM2 mechanism described by Stockwell (1990) is a lumped species type that uses a reactivity-weighting scheme to adjust for lumping. It contains 65 modeling species and 161 reactions. In the RADM2, the primary organics are represented by 15 mechanism species with five single compounds, methane, ethane, ethen, isoprene, and formaldehyde, and ten aggregated compounds based on their reactivity with the hydroxyl radical (OH) and their molecular weights (Ching and Byun, 1999).

The latest version of the SAPRC mechanism designated as the SAPRC99 (Carter, 2000) represents a complete update of the SAPRC90 mechanism. The mechanism has assignments for 400 types of VOCs, and can be used to estimate reactivities for 550 VOC categories. A total of 24 model species are used to represent the reactive organic product species. The SAPRC99 mechanism used in the CMAQ consists of 72 species in 198 reactions (Jimenez et al., 2003).

The CB-IV mechanism is widely used in research and regulatory air quality models, and it is the mechanism used in this study.

Table 2.1: CB-IV mechanism species list

	Symbol	Description
Nitrogen Species	NO	Nitric oxide
	NO2	Nitrogen dioxide
	HONO	Nitrous acid
	NO3	Nitrogen trioxide
	N2O5	Nitrogen pentoxide
	HNO3	Nitric acid
	PNA	Peroxynitric acid
Oxidants	O3	Ozone
	H2O2	Hydrogen peroxide
Sulfur species	SO2	Sulfur dioxide
	SULF	Sulfuric acid
Atomic species	O	Oxygen atom (triple)
	O1D	Oxygen atom (singlet)
Odd hydrogen species	OH	Hydroxyl radical
	HO2	Hydroperoxy radical
Carbon oxides	CO	Carbon monoxide
Hydrocarbons	PAR	Paraffin carbon bond (C-C)
	ETH	Ethene (CH_2=CH_2)
	OLE	Olefine carbon bond (C=C)
	TOL	7 carbon aromatics
	XYL	8 carbon aromatics
	ISOP	Isoprene
Carbonyls and phenols	FORM	Formaldehyde
	ALD2	Acetaldehyde and higher aldehydes
	MGLY	Methyl glyoxal ($CH_3C(O)C(O)H$)
	CRES	Cresol and higher molecular weight phenol
Organic nitrogen	PAN	Peroxyacyl nitrate ($CH_3C(O)OONO_2$)
	NTR	Organic nitrate
Organic radicals	C2O3	Peroxyacyl radical ($CH_3C(O)OO\cdot$)
	ROR	Secondary organic oxy radical
	CRO	Methylphenoxy radical
Operators	XO2	NO-to-NO2 operation
	XO2N	NO-to-nitrate operation
Products of organics	TO2	Toluene-hydroxyl radical adduct
	OPEN	High molecular weight aromatic oxidation ring fragment
	ISPD	Products of isoprene reactions

Table 2.1 (continued)

	Symbol	Description
Species for aerosol	SULAER	Counter species for H_2SO_4 production
	TOLAER	Counter species for toluene reaction
	XYLAER	Counter species for xylene reaction
	CSLAER	Counter species for cresol reaction
	TERPA	Counter species for terpene reaction
	TERP	Monoterpenes
Species for aqueous chemistry	FACD	Formic acid
	AACD	Acetic and higher acids
	PACD	Peroxy acetic acid
	UMHP	Upper limit of methylhydroperoxide

2.4.4 CMAQ Interface Processors

The CMAQ modeling system includes several interface processors to incorporate the outputs of the meteorology processor and to prepare the required information for initial and boundary conditions and photolysis rates to the CCTM. Since most meteorological models including MM5 are not built for air quality modeling purposes, the outputs cannot be implemented directly to air quality models. The MCIP program translates and processes model output from the MM5 model for the CCTM and the SMOKE processor. The MCIP handles data format transformation, conversions of units of parameters, extraction of data for appropriate window domains, collapsing of metrological profile data if coarse vertical resolution data are required, computation of clouds parameters, surface and PBL parameters, and species-specific dry deposition velocities. The programs Initial Condition (ICON) and Boundary Condition (BCON) provide the concentration fields for individual chemical species for the beginning of a simulation and for the grids surrounding the modeling domain,

respectively. The photolysis processor (JPROC) creates look-up table of clear-sky photolysis rates depending on the chemical scheme, latitude, altitude, and hour angles. Then, a module in CCTM interpolates and adjusts the photolysis rates for each grid cell location and modeling time considering the presence of clouds. For example, the below cloud photolysis rate will be lower than the clear-sky value due to the reduced transmission of radiation through cloud. The above cloud values will be enhanced, and within cloud photolysis rates will be interpolated from the below cloud values and above cloud values (Ching and Byun, 1999).

2.5 Observation-based approaches to understanding the ozone problem

Emission-based approaches such as CMAQ air quality models, which use emissions inventories and a numerical representation for transport and photochemistry, play a central role in determining relationship between ozone precursors and the production and accumulation of ozone within a given area, and in developing a strategy for ozone abatement within the area. However, there can be significant uncertainties in the many aspects of emission-based models associated with emissions inventories, meteorological fields and parameterization (Cardelino and Chameides, 1995, 2000). For this reason, observation-based approaches have been developed to provide complimentary method for assessing ozone precursor relationships. Since they are based on observations, inaccurate and incomplete observations can result in misleading conclusions as well. Also, they are a diagnostic rather than prognostic and cannot be used in predicting ozone to determine the exact amount of precursor

reduction needed to bring an area into attainment. Hence, the observation-based approaches should be viewed as a complement to more sophisticated gridded, emission-based models (Cardelino and Chameides, 1995; 2000).

Observation-based methods can be divided into two broad categories: methods based on ambient VOC, NOx and CO; and methods based on secondary reaction products, usually involving reactive nitrogen and peroxides (Sillman, 1999). Chameides et al. (1992) and Rappengluck et al. (1998) used reactivity-weighted ambient VOC/NOx ratios to obtain information about NOx-VOC sensitivity to ozone occurrences for area of interest. Some examples for the latter case are O_3/NOy (NOy = NOx + PAN + HNO_3 + N_2O_5 + other nitrates), O_3/NOz (NOz = NOy – NOx), H_2O_2/HNO_3, etc (Sillman, 1999). That is, ambient measurements of those ratios can be used to interpret NOx-VOC sensitivity.

In this study, we attempted to interpret characteristics of high ozone occurrences over an area of interest, using ambient VOC and NOx measurements and implementing a receptor model. The results obtained from the observation-based approach were compared with that of emissions-based air quality model to corroborate our conclusions. Here, receptor models are focused on elucidating sources and source contributions to pollution in the ambient environment from analysis of measurements at the point of impact (Hopke, 1991). Receptor models have been applied to air quality data, providing useful insight into sources of gaseous hydrocarbons and speciated aerosols since the late 1960's (Thurston and Spengler, 1985; Miller et al., 1972; Billford and Meeker, 1967). The details about the receptor model implemented in this study are described in Chapter 3.

Chapter 3: Investigation of Sources of Volatile Organic Carbon in the Baltimore Area Using Highly Time Resolved Measurements

3.1 Introduction

Since nitrogen oxides (NOx) and volatile organic compounds (VOCs) were uncovered as key precursors of ground level ozone formation by Haagen-Smit, and co-worker in the1950s (Haagen-Smit and Fox, 1954), many studies have been focused on determining effective strategies for ozone reduction. The complex relationship between ozone and its precursors, and the strong dependence of ozone formation on meteorological conditions are the major difficulties associated with the study of ground-level ozone. Though meteorological conditions and transport are important variables for ozone formation and accumulation, anthropogenic VOC and NOx emissions are the primary focus of ozone reduction programs in that only they are controllable.

Most NOx emissions are from combustion related sources such as motor vehicles and fossil-fueled power plants in urban and suburban areas. On the other hand, VOCs are emitted from wide variety of sources, both anthropogenic and biogenic. In the United States, it is estimated that the amount of VOC emissions from biogenic sources is of the same order of magnitude as the total emissions of anthropogenic VOCs (Watson et al., 2001; Atkinson, 2000; Trainer et al., 2000).

Guenther et al. (2000) concluded that over 98% of total biogenic VOCs in North America are from vegetation. Biogenic VOCs are composed primarily of isoprene (35%), terpenoid compounds (25%) and non-terpenoid compounds (40%).

Lagrangian and Eulerian models have been used extensively to predict the change of ozone to controls of NOx and VOC. Several modeling studies have shown that, in general, VOC controls may be effective in reducing the ozone levels in urban and suburban areas, which are most strongly impacted by anthropogenic emissions (Hanna et al., 1996; Possiel and Cox, 1993; McKeen et al., 1991). In addition, a simple rule, based on a modeling study, that morning VOC (ppbC) /NOx (ppb) ratios less than 10 indicate VOC-sensitive peak ozone, and morning VOC/NOx ratios more than 20 indicate NOx-sensitive peak ozone has been used to justify NOx-VOC sensitivity prediction and policies (Sillman, 1999). Therefore, a reduction of VOC emissions in VOC-sensitive regions may be effective in reducing ozone, while a reduction of NOx emissions in NOx-sensitive regions may lead to ozone reduction. However, the emissions from biogenic sources have been reported to be most likely underestimated in past modeling studies, and several analyses of observed measurements have suggested a significant role of biogenic hydrocarbon emissions in many urban and suburban locations in ozone formation (Chameides et al., 1992, 1988; Cardelino and Chameides, 2000, 1995). Thus, it cannot easily be determined whether reducing VOC emissions or NOx emissions or both is the most effective strategy for ozone reduction for a given area, using a simple rule based on modeling studies conducted for only a few specific areas (Sillman, 1999).

The development of an effective ozone reduction strategy in a given urban or suburban area requires an accurate understanding of three key ozone precursor relationships: the relative concentrations of NOx and VOC in the area, the importance of natural VOC relative to anthropogenic VOC in the atmosphere (Piety et al., 2003, Trainer et al. 2000, Cardelino and Chameides, 1995), and the significance of long range transport as compared to local emissions of ozone precursors. While the importance of long range transport versus local emissions can only be resolved using photochemical and meteorological modeling, source apportionment of VOC can be expected to give insight into the importance of natural VOC relative to anthrogenic VOC in the atmosphere for a given area.

In this work, hourly ambient surface measurements of the concentrations of 55 VOC species, taken from a Photochemical Assessment Monitoring Stations (PAMS) site in Baltimore County in the state of Maryland during the summer months of 1996 ~ 1999, are used to investigate the relationships between ozone and its natural and anthropogenic precursors. To identify and apportion VOC sources, the UNMIX receptor model is used. Specific focus is placed on analysis of the observed diurnal variation in concentrations as well as source contributions. These phenomena have been investigated for VOC in other geographical regions, for example, Seoul, Korea (Na et al., 2003) and the Paso del Norte region of the Texas – Mexico border (Fujita, 2001). VOC emissions can vary greatly from region to region, and in contrast to the above-mentioned regions, biogenic emissions at the location under study here are significant. With the receptor modeling results, a study of the contribution of the identified source categories to episodes of high ozone concentrations is conducted.

The results of this study will be useful in the development of effective ozone control strategies in this and similar regions.

3.2 VOC source identification and apportionment using a receptor model

3.2.1 Receptor models

There are several different approaches to receptor model analysis that have been successfully applied including the chemical mass balance (CMB) and multivariate receptor models.

CMB models require that the compositions of emissions from all the contributing source types be known. That is, the source profile (the mass fraction of a chemical in the emissions from each source type) must be known before the analysis. Several libraries of VOC source profiles have been assembled from original measurements at sources and a combination of published and unpublished laboratory test results. Even though CMB is widely accepted, the need for accurate profiles is a limitation associated with its usage; available profiles represent older technology and fuels that may be different today, and some of profiles may be regionally specific. An alternative is the use of multivariate receptor models, which do not require *a priori* knowledge of detailed source profiles, requiring only ambient measurement data and known source tracers to interpret the factors (Kavouras et al., 2001; Kumar et al., 2001; Dillon and Goldstein, 1984).

Several multivariate receptor models have been applied to air pollution studies including absolute principal component analysis (PCA), target transformation factor

analysis, and factor analysis followed by multiple linear regression (Hopke, 1991). However, interpreting results from traditional factor analysis is problematic. Use of traditional factor analysis can produce many different solutions, which are statistically sound, but which may be physically invalid (Poirot et al., 2001; Henry, 2001). There have been some improvements in multivariate receptor models such as positive matrix factorization (PMF) and UNMIX. These models have recently been introduced to air pollution source apportionment and their utility for this purpose has been evaluated (Miller et al., 2002; Chen et al., 2002; Larson et al., 2002;Wu and Pratt, 2002; Poirot et al., 2001).

In this study, the UNMIX version 2.4 receptor model developed by Henry (2001) was used to determine possible sources and source contributions to ambient concentrations of VOC. The UNMIX process starts with the normalization of data to a mean of one by dividing each measurement for a given species by the mean of all measurements of that species, in order to put all measurements on the same scale. In UNMIX, unlike other factor analysis routines, a centering about the mean, or z-score transformation, is not done because there is no appropriate method to un-center the results. The normalized data is analyzed in order to reduce the dimensionality, or the number of sources, of the data space using the singular value decomposition (SVD) matrix operation. The SVD operation produces an abstract mathematical solution. Factor analysis routines such as PCA typically use either a transformation method such as an orthogonal transformation that keeps the statistical independence of the factors, or an oblique transformation that allows the factors to be co-dependent, in order to derive meaningful factors (Hopke, 1991), but those solutions may still contain many

negative loadings and lead to negative concentrations. In contrast, UNMIX incorporates user specified non-negativity constraints and edge finding algorithms in order to derive a single, physically reasonable solution from the abstract mathematical solution (Wu and Pratt, 2002; Poirot et al., 2001; Henry, 2001, 2002). Further details regarding the model can be found in Henry (2001, 2002). The final outputs of the UNMIX model are the estimates of the number of sources, the source composition, the average source contribution, and source contribution to each sample.

3.2.2 Ambient monitoring measurements

In accordance with the 1990 Clean Air Act Amendments, the U.S. EPA initiated the Photochemical Assessment Monitoring Stations (PAMS) program for 1hr ozone nonattainment areas with persistently high ozone levels (mostly large metropolitan areas). The objective of the PAMS program is to develop a large database of ambient air measurements for important pollutants associated with ozone, which will be used to test complicated photochemical air quality models (Lewis et al., 1998).

The U.S. EPA has determined that the network should consist of five different site types to provide information sufficient to satisfy important monitoring objectives. Type 1 sites are located in the predominant morning upwind direction, with the purpose of characterizing upwind background and transported ozone and its precursor concentrations entering the area. Type 2 sites are located immediately downwind of areas with significant ozone precursor emissions. Type 2A sites may be required

depending on the size of the area, and are placed in the downwind area of the second-most predominant morning wind direction. Type 3 sites are located 10 to 30 miles from the boundary of the urban area. These sites are intended to monitor maximum ozone concentrations occurring downwind from the area of maximum precursor emissions. Type 4 sites are used for extreme downwind monitoring of transported ozone and for measurements of its precursor concentrations exiting the area (Demerjian, 2000).

The sampling frequency varies among regions, states, and sites. Of the five PAMS sites located in the state of Maryland, only the Essex site, located in a parking lot northeast of downtown Baltimore as shown in Figure 3.1, belongs in the Type 2 site category. The samples are collected and analyzed hourly using an on site gas chromatograph equipped with a flame ionization detector. See EPA-I (1998) for further details about the analysis method.

The Essex site is surrounded by residential and commercial areas with several gas station facilities within 500 m of this site, and several industrial point sources distributed around this site within a few kms.

The concentrations of 55 hydrocarbons, total nonmethane organic carbon species (TNMOC), ozone, oxides of nitrogen, as well as meteorological conditions such as temperature, wind direction, wind speed, and radiation are monitored at the Essex site. Using these continuous hourly measurements gathered by Maryland Department of Environment (MDE) personnel, we investigated source and receptor relationships of VOCs during the summer months of 1996, 1997, 1998 (June to September), and 1999 (June to July). The summary is shown in Table 3.1.

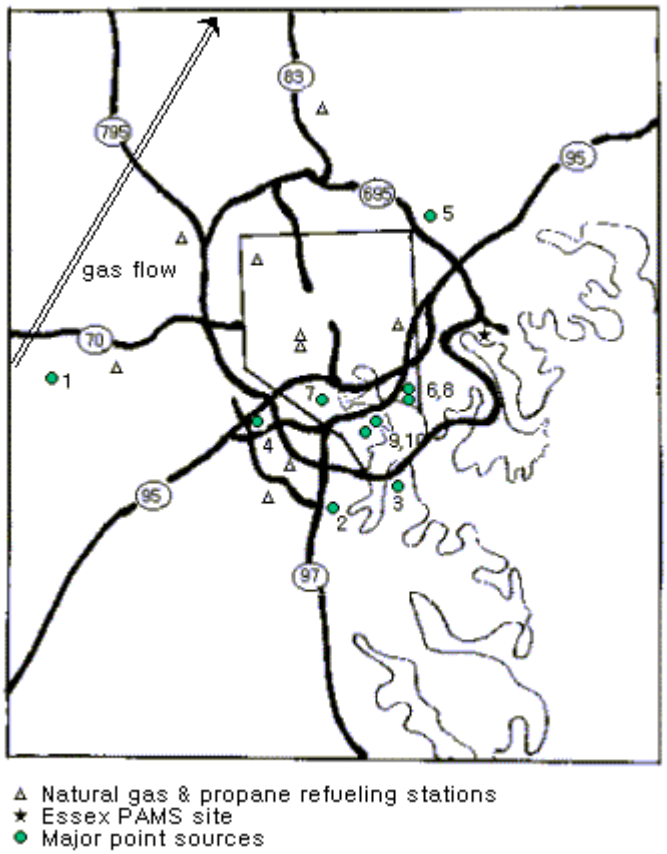

	Description of major point sources	VOC (tons/yr)
1	Natural gas transmission	228
2	Commercial printing	330
3	Electric services	104
4	Food manufacture (distilled & blended liquors)	186
5	Food manufacture (bread)	172
6	Food manufacture	249
7	Paint manufacture	237
8	Automobile surface coating operations	816
9	Petroleum bulk stations and terminals	123
10	Prepared feeds	172

Figure 3.1: Map of region surrounding the PAMS measurement site, Essex, MD (Point sources information based on the1996 EPA National emission trends database).

Table 3.1: Summary of measurement data used in the study

Year	1996	1997	1998	1999
Period of measurement	June 6 to September 30	June 6 to September 30	June 4 to September 14	June 1to July 31
Number of measurements	2683	2833	2206	1284

3.2.3 Methods

Figure 3.2 shows the box plots for several compounds selected to provide a representative summary of the variation in the observed concentrations. For comparison purposes, concentrations or mixing ratios are reported in units of ppb on a carbon basis. The black line across the box denotes the mean, and the median is shown as a gray line across the box. The lower and upper boundaries of box are defined as the 25^{th} percentile and the 75^{th} percentile, respectively. The bottom and top lines extending from box denote the 10^{th} and 90^{th} percentiles, respectively. Isoprene, which is expected to be a marker of biogenic emissions, shows much larger variation during daytime than during nighttime, while the other species show the reverse behavior.

Source apportionment of hydrocarbons was conducted using measurement data from all four years. 37 chemical species were selected from the 55 measured species based upon several considerations; either they made up the majority of the TNMOC mass emissions (Hopke, 1991), their lifetimes were greater than that of toluene (Fujita,

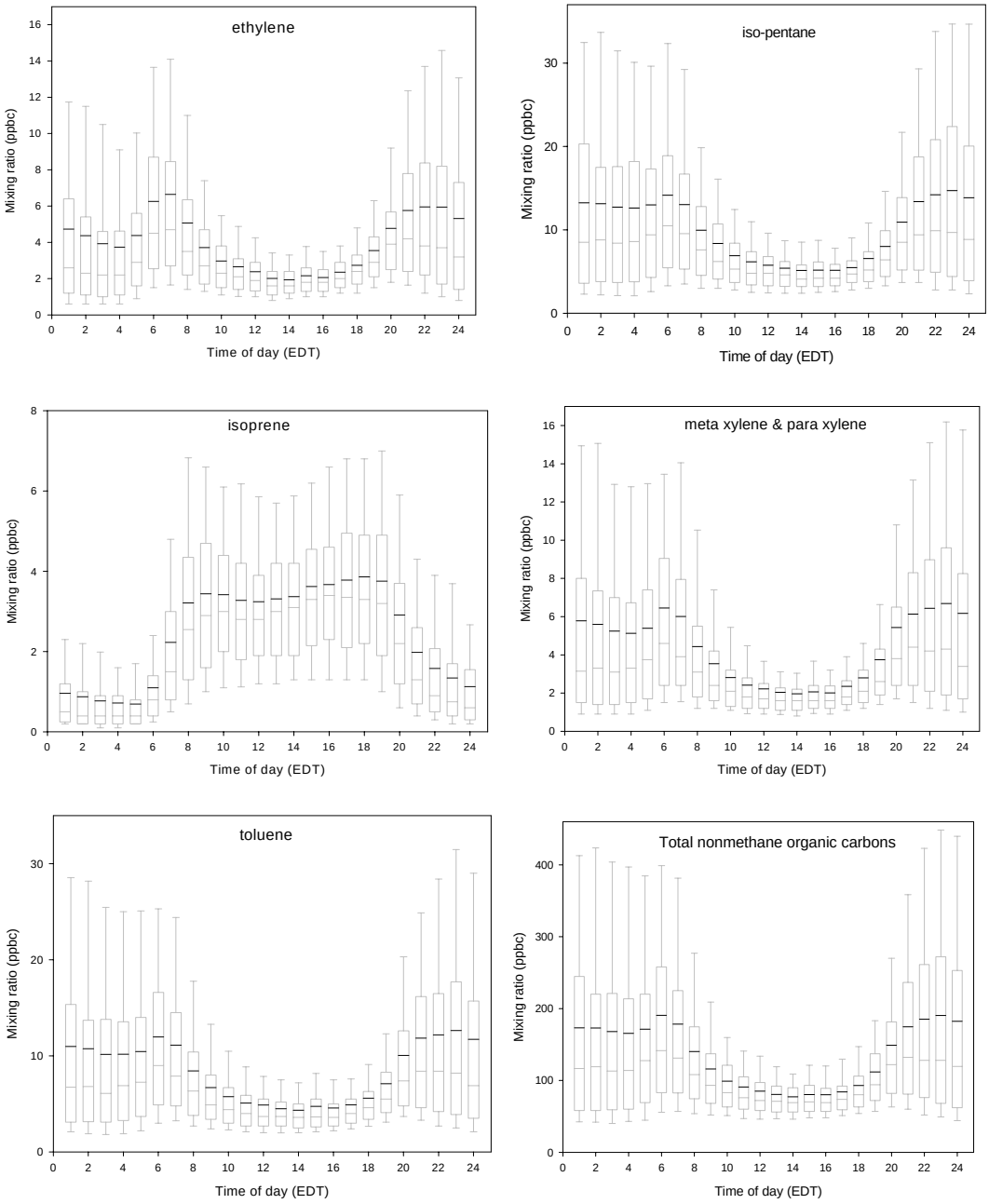

Figure 3.2: Box plots of selected species to show distribution of observed concentrations by hour of day. The black line across the box denotes the mean value, and the gray line across the box denotes the median value. The lower and upper boundaries of box are defined as the 25th percentile and the 75th percentile, respectively. The bottom and top lines extending from box denote the 10th and 90th percentiles, respectively. The EDT represents eastern daylight time.

2001), or these species have been used as tracer species in previous studies. The number of species was reduced using the UNMIX overnight option, in which multiple numbers of possible combinations of input variables are tried with the goals of maximizing the number of input variables and of generating physically reasonable and interpretable results (Poirot et al., 2001). After this optimization, 23 species and 8975 observations were employed by UNMIX to identify sources of total hydrocarbons. The 23 species are given in Table 3.2.

To investigate yearly trends of hydrocarbon sources, we applied the UNMIX model to each year of 1996, 1997 and 1998. The year 1999 was not used to investigate yearly trends because only June and July measurements were available. 25 species and 2673 observations for 1996, 25 species and 2812 observations for 1997, and 25 species and 2203 observations for 1998 were employed by UNMIX. Refer to Appendix 2.

3.2.4 UNMIX receptor model results

Six possible source categories of hydrocarbons for the 1996-1999 combined set of measurements were identified using the UNMIX receptor model. Table 3.2 gives the mean contributions and compositions of each source category, and their one-sigma errors as estimated by the so-called 'bootstrap method' (Henry, 2001). Isoprene is predominantly associated with the first source category, suggesting the source is biogenic in origin. The mass fraction of iso-pentane in this source is a little over 0.05, with ethane and toluene showing mass fractions just under 0.05. Considering that

Table 3.2: Source compositions (mass fraction) and apportionment results for the combined set, 1996~1999, of measurements

Estimated source category	Source 1 biogenic	Source 2 liquid gasoline	Source 3 Surface coatings	Source 4 natural gas	Source 5 vehicle exhaust	Source 6 Gasoline vapor
Species						
Ethane	0.038 ± 0.003	0.038 ± 0.005	0.009 ± 0.007	**0.270** ± 0.061	**0.056** ± 0.002	0.037 ± 0.005
Ethylene	0.015 ± 0.001	0.023 ± 0.002	0.018 ± 0.002	0.010 ± 0.005	**0.059** ± 0.001	0.022 ± 0.001
Propane	0.030 ± 0.004	**0.057** ± 0.005	0.018 ± 0.003	**0.259** ± 0.074	0.048 ± 0.003	-0.002 ± 0.004
Propylene	0.010 ± 0.001	0.013 ± 0.001	0.009 ± 0.001	0.014 ± 0.002	0.029 ± 0.001	0.008 ± 0.001
Acetylene	0.010 ± 0.001	0.005 ± 0.002	0.003 ± 0.002	0.015 ± 0.003	0.038 ± 0.001	0.008 ± 0.001
n-butane	0.029 ± 0.001	0.018 ± 0.002	0.020 ± 0.003	**0.079** ± 0.018	0.024 ± 0.001	0.025 ± 0.003
iso-butane	0.009 ± 0.001	0.014 ± 0.001	0.009 ± 0.001	**0.055** ± 0.011	0.019 ± 0.001	0.013 ± 0.001
n-pentane	0.017 ± 0.001	**0.220** ± 0.018	0.011 ± 0.001	0.022 ± 0.002	0.024 ± 0.001	0.023 ± 0.001
iso-pentane	**0.056** ± 0.004	**0.071** ± 0.003	0.042 ± 0.005	**0.071** ± 0.010	**0.070** ± 0.002	**0.107** ± 0.004
3-methylpentane	0.008 ± 0.001	0.017 ± 0.001	0.008 ± 0.001	0.006 ± 0.004	0.016 ± 0.000	0.023 ± 0.001
n-hexane	0.008 ± 0.002	0.018 ± 0.001	0.013 ± 0.001	0.003 ± 0.007	0.018 ± 0.001	0.030 ± 0.001
Isoprene	**0.153** ± 0.012	0.003 ± 0.000	0.000 ± 0.000	-0.002 ± 0.001	0.004 ± 0.000	0.002 ± 0.000
3-methylhexane	0.008 ± 0.001	0.010 ± 0.001	0.011 ± 0.001	-0.002 ± 0.005	0.011 ± 0.000	0.018 ± 0.001
2,2,4-trimethylpentane	0.010 ± 0.002	0.016 ± 0.001	0.011 ± 0.002	-0.011 ± 0.011	0.024 ± 0.001	0.037 ± 0.002
2,3,4-trimethylpentane	0.003 ± 0.001	0.007 ± 0.000	0.005 ± 0.001	-0.005 ± 0.005	0.010 ± 0.000	0.015 ± 0.001
2-methylhexane	0.005 ± 0.001	0.008 ± 0.000	0.009 ± 0.001	-0.003 ± 0.005	0.009 ± 0.000	0.016 ± 0.001
2,3-dimethylbutane	0.008 ± 0.000	0.007 ± 0.000	0.002 ± 0.001	0.006 ± 0.001	0.010 ± 0.000	0.013 ± 0.000
2-methylpentane	0.013 ± 0.002	0.023 ± 0.001	0.010 ± 0.002	0.012 ± 0.006	0.027 ± 0.001	0.036 ± 0.001
M&p xylene	0.010 ± 0.002	0.025 ± 0.002	**0.117** ± 0.013	0.007 ± 0.007	0.028 ± 0.001	0.025 ± 0.001
Benzene	0.012 ± 0.001	0.014 ± 0.001	0.012 ± 0.001	0.009 ± 0.003	0.028 ± 0.001	0.018 ± 0.001
Toluene	0.042 ± 0.004	**0.052** ± 0.003	**0.084** ± 0.007	0.018 ± 0.018	**0.065** ± 0.002	**0.086** ± 0.003
Ethylbenzene	0.007 ± 0.000	0.007 ± 0.001	0.034 ± 0.004	0.003 ± 0.002	0.008 ± 0.000	0.008 ± 0.000
o-xylene	0.006 ± 0.001	0.010 ± 0.001	0.035 ± 0.003	0.001 ± 0.003	0.011 ± 0.000	0.011 ± 0.000
Total NMOC(ppbc)	14.4 ± 0.8	11.5 ± 0.9	15.9 ± 2.1	17.0 ± 3.1	39.0 ± 1.7	35.5 ± 2.6
% of total NMOC	11	9	12	13	29	26

Bold values indicate mass fractions > 0.05. The errors are based on one sigma.

isoprene is likely underestimated because of its high reactivity, the mass fraction of isoprene in reality may be much higher. Therefore, the relative importance of the other compounds would be reduced. However, it should be noted that some studies report that alkanes are emitted from vegetation, and that aromatics are emitted from microbial decomposition of leaves litter (Guenther et al., 2000; Isidorov et al., 2002). Moreover, as shown in Figure 3.3, Source 1 follows very different diurnal patterns from the other sources. During nighttime when photosynthesis ceases, the concentration of Source 1 falls to a much lower value, and a rapid increase in concentration is observed with sunrise. This pattern is typical of isoprene, the principal biogenic VOC (Trainer et al., 2000). Thus, this source category is identified as biogenic in origin. Even though highly reactive species are not typically included to perform source apportionment, isoprene is included as a modeling species because it is a marker of biogenic emissions and a major precursor to ozone. Hence, the source contribution estimate is likely to be low compared to actual biogenic contributions, as noted by other researchers (Fujita, 2001; Lawrimore and Aneja, 1997; Fujita et al., 1995).

According to several previously reported source profiles, sources related to gasoline such as vehicle exhaust, liquid gasoline and gasoline vapor show high loadings of iso-pentane, n-pentane and toluene (Lawrimore and Aneja, 1997; Fujita et al., 1994). Here, the gasoline vapor category stands for headspace emissions from service stations and bulk terminals, and some evaporative emissions from vehicles such as diurnal emissions, and resting loss, characterized by an enrichment of high

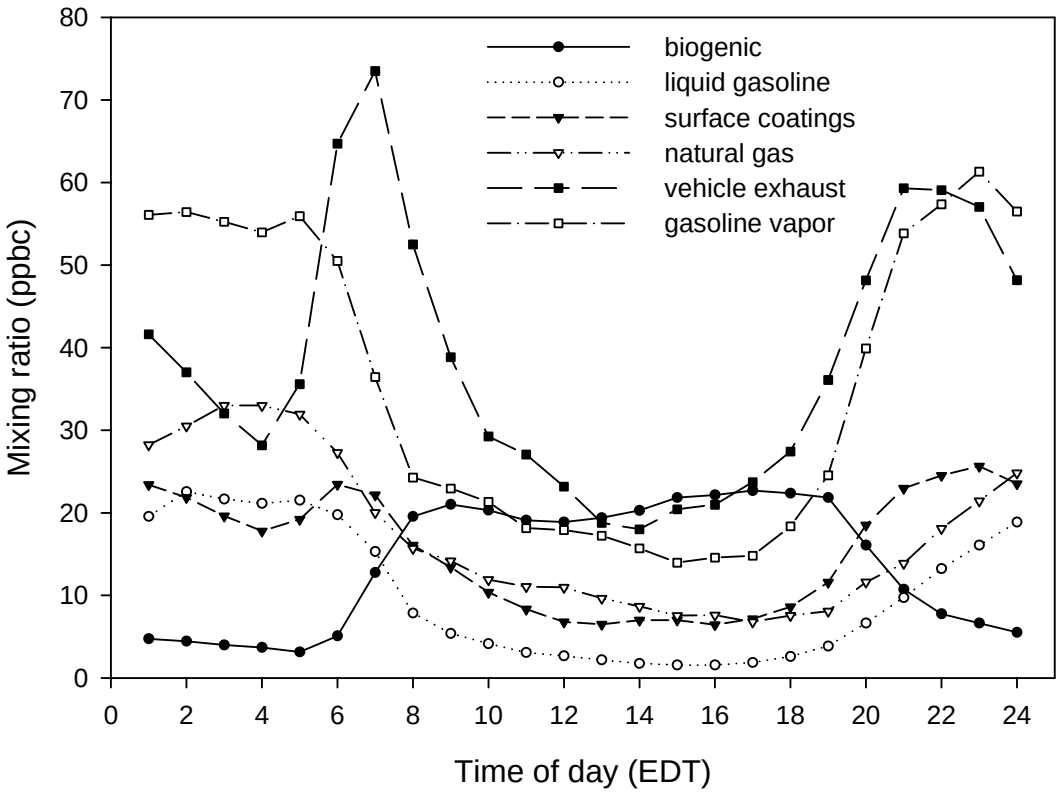

Figure 3.3: Average diurnal patterns of each source type of VOC, estimated from hourly source apportionment using summer measurements taken over four years from 1996 to 1999.

volatility species. The liquid gasoline category represents whole gasoline emissions having a composition resembling liquid gasoline itself, which can arise from spillage, leakage, and vehicle operations such as running loss and hot soak (Scheff et al., 1996). Hence, the origins of Source 2, Source 5, and Source 6 were regarded as gasoline-related sources, and each of them was interpreted based upon previously reported source profiles.

Source 5 shows higher loadings of ethene and acetylene than the other two sources. Source profiles reported in several studies indicated that high ethene and acetylene loadings were associated with automotive emissions (Vega et al., 2000; Lawrimore and Aneja, 1997; Scheff et al., 1996; Kenski et al., 1995; Fujita et al., 1994; Wadden et al., 1994). Also, as shown in Figure 3.4, Source 5 exhibits significantly different weekday and weekend diurnal behaviors; during weekdays the peak in VOC concentration resulting from Source 5 takes place at around 7 am, during heavy commuting traffic time, while on weekends this sharp peak around 7 am is not observed. This is consistent with different diurnal activity levels for automotive sources on weekends versus weekdays. Therefore, Source 5 is recognized as a vehicle exhaust source category. As far as Source 6 and Source 2 are concerned, their diurnal patterns do not show significant differences between weekends versus weekdays. Even though the liquid gasoline and gasoline vapor source categories include contributions from motor vehicle activity, they include other contributions that may not be directly related to commuter traffic patterns such as losses during handling of bulk gasoline. The only difference was that Source 6 had slightly higher loadings of iso-pentane and toluene while Source 2 had a higher loading of n-pentane. Several

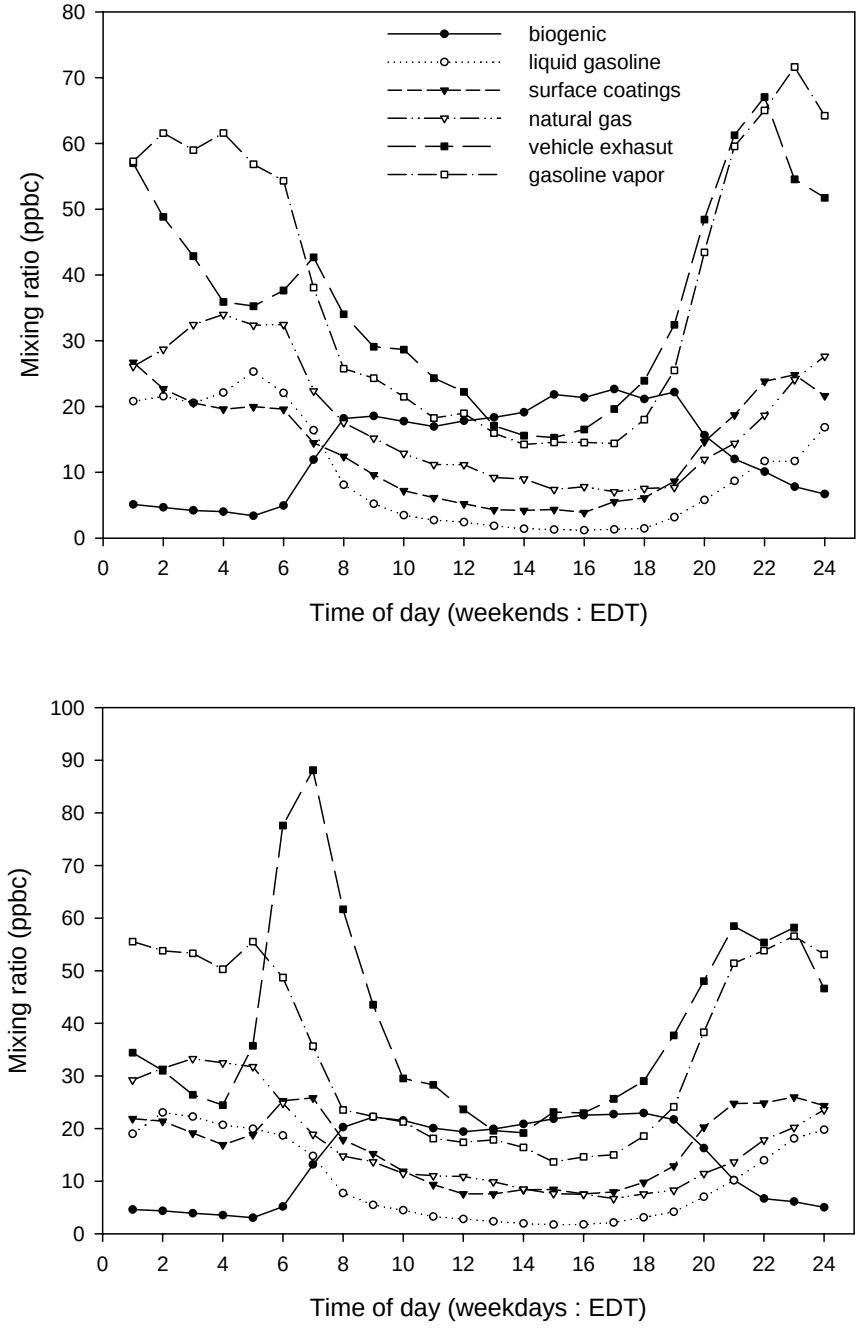

Figure 3.4: Comparison of average diurnal pattern of weekdays with that of weekends, estimated from hourly source apportionment using the summer measurements taken over four years from 1996 to 1999.

studies showed that iso-pentane is especially abundant in gasoline vapor, and iso-pentane has higher vapor pressure than n-pentane. Thus, Source 6 and Source 2 were regarded as gasoline vapor and liquid gasoline source categories, respectively (Watson et al., 2001; Lawrimore and Aneja, 1997; Scheff et al., 1996; Fujita et al., 1994).

The greater proportion of the lower molecular weight paraffin hydrocarbons such as ethane and propane in Source 4 suggests a natural gas source category. The natural gas source may result from possible leakage in the transmission system, or refueling stations of natural gas and propane around the sampling site as the Figure 3.1 shows (Mukund et al., 1996; Derwent et al., 1995; Fujita et al., 1994). Source 3 was considered to be related to surface coating sources because it was primarily composed of xylene and toluene (Fujita, 2001; Lawrimore and Aneja, 1997; Mukund et al., 1996), and local point sources such as paint manufacture and automobile surface coating operations were located around the measurement site as shown in Figure 3.1.

The relationship between surface wind direction and source category concentrations was examined for each source category, in order to try to further resolve specific sources. However, no correlations were observed, likely because of the significant hour-to-hour variation in surface wind direction observed at the sampling location.

Figure 3.5 shows the overall mean hourly absolute source contributions and percentage source contributions for each year and for four years, respectively. In the single year analyses, 6 source categories for 1996 and 1997, and 5 source categories for 1998 were identified using UNMIX (Appendix 2). Source compositions for each

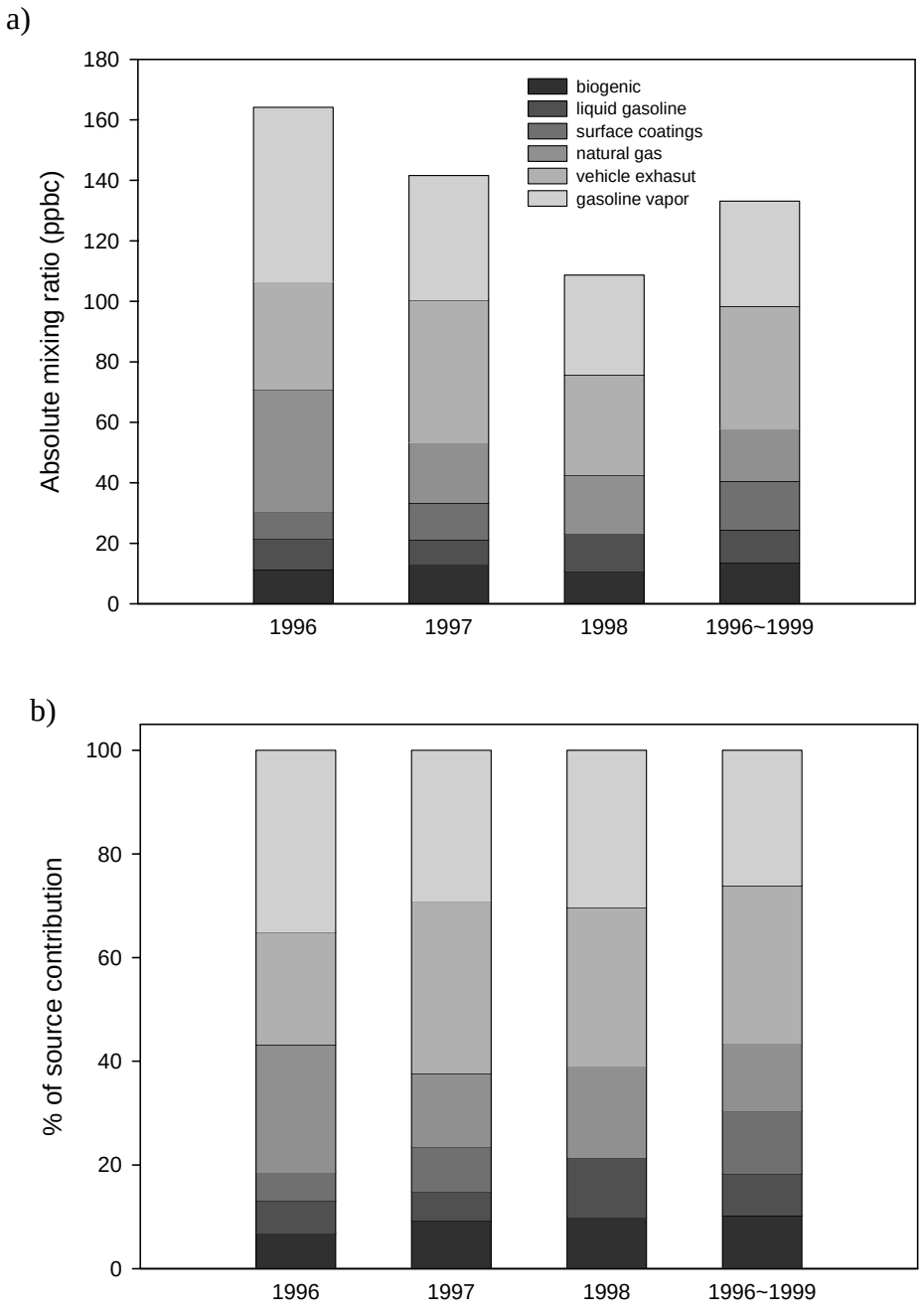

Figure 3.5: Yearly trend of each source contribution to average hourly total VOC in terms of a) both absolute mixing ratio in ppbC as well as b) percent contribution.

year showed the same characteristics as those of four-year data analysis, and thus each source category was identified in the same way as explained above. The surface coating source category was not identified as a distinct source for 1998, but high loadings of xylene and toluene were seen in the vehicle exhaust and gasoline vapor source categories.

The contribution of the natural gas source category in terms of absolute concentration is significantly greater in 1996 than in subsequent years. The possible cause of the difference may be increased handling of natural gas, particularly injection and release from underground storage wells, reported for 1996 as compared to subsequent years (DOE, 2001).

Generally, gasoline vapor and vehicle exhaust source categories explain more than half of contributions to total hydrocarbons for all cases. Also, a downward trend in total VOC concentrations is observed.

As mentioned by Watson et al. (2001) in a recent review of VOC source apportionment by the chemical mass balance receptor model approach, gasoline vehicle exhaust, liquid gasoline, and gasoline vapor typically contribute more than 50% of ambient VOC in urban areas in the United States. Results presented for VOC source apportionment using the UNMIX receptor model in the Baltimore area suggest that around 60% of total hydrocarbons came from gasoline-related source categories such as vehicle exhaust, gasoline vapor and liquid gasoline. Biogenic emissions, natural gas and surface coating source categories explained the remaining 40% of total hydrocarbons. Considering that the sampling site is located in a parking lot close to

the city of Baltimore, near heavily traveled roads and several industrial/commercial sites as shown in Figure 3.1, the source apportionment results seem reasonable.

3.3 Identification of characteristics of source patterns during high ozone episodes

During the time period of the PAMS measurements between 1996 and 1999, ozone levels at Essex, Maryland exceeded the 8-hour ozone standard of 80 ppb on 47 out of a total of 400 days according to hourly ozone measurements. NOx, meteorological variables such as wind speed, and temperature as well as the hourly contribution of each source category were split into high ozone days and low ozone days based on this criteria.

Figure 3.6 shows the diurnal patterns of hourly mean mixing ratios on high ozone days and low ozone days for total hydrocarbons and NOx. The horizontal arrow bars in the figures indicate the times which can be considered as having significantly different mean mixing ratios based upon a two-tailed t-test at the 95% confidence interval. As shown in Figure 3.6, the mean mixing ratios of total hydrocarbons during afternoon of both high and low ozone days are not significantly different, while the difference during nighttime between both days is distinct. UNMIX apportions total hydrocarbons to each source category, and Figure 3.7 shows the diurnal patterns of hourly mean mixing ratios on high ozone days and low ozone days for each source category obtained from the UNMIX outputs. We can see only the biogenic source category has a significant difference in mean mixing ratios between high and low

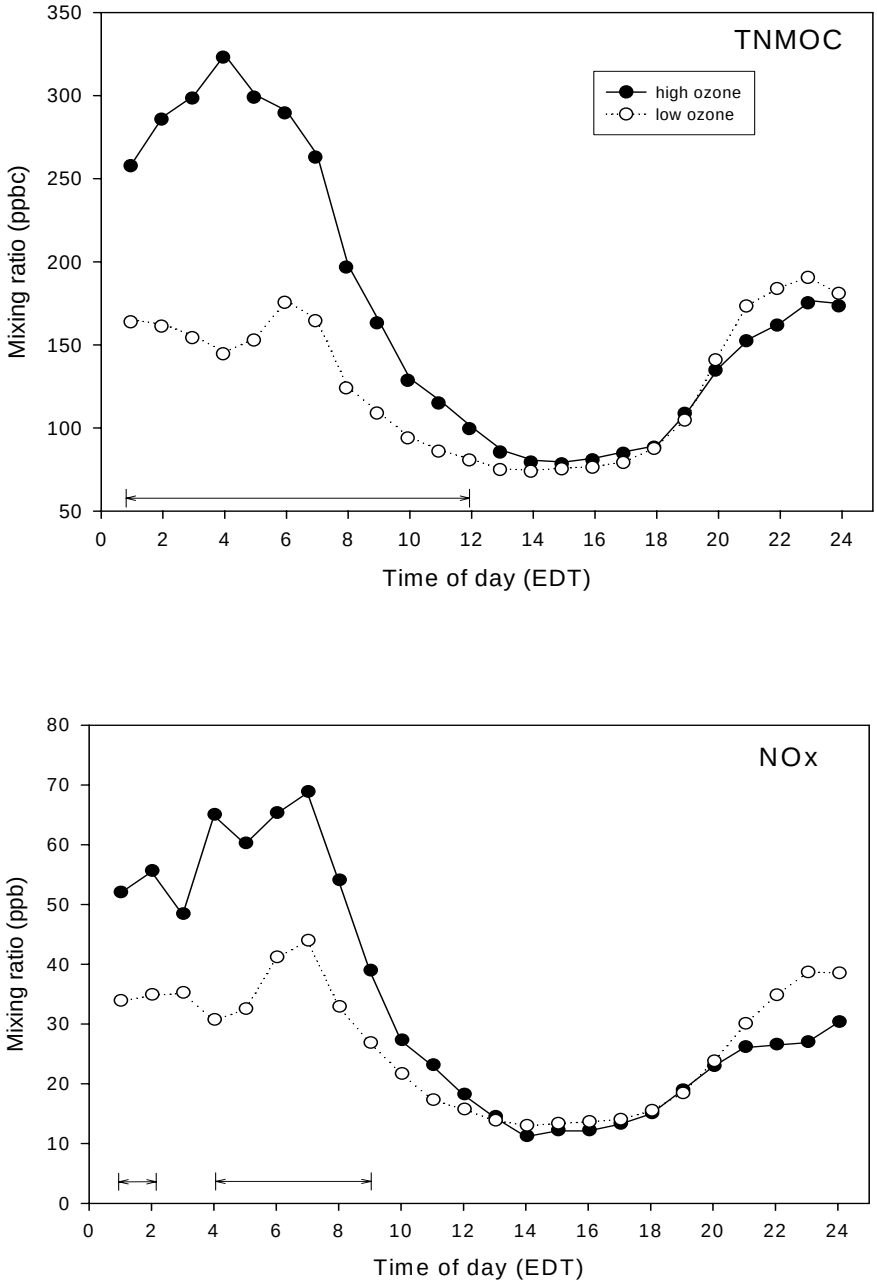

Figure 3.6: Comparisons of diurnal pattern of average mixing ratios of NOx and total nonmethane organic carbon (TNMOC) between high ozone days and low ozone days. The bars indicate the times that can be considered as having significantly different mean mixing ratios between both days based upon a two-tailed t-test at the 95% confidence interval.

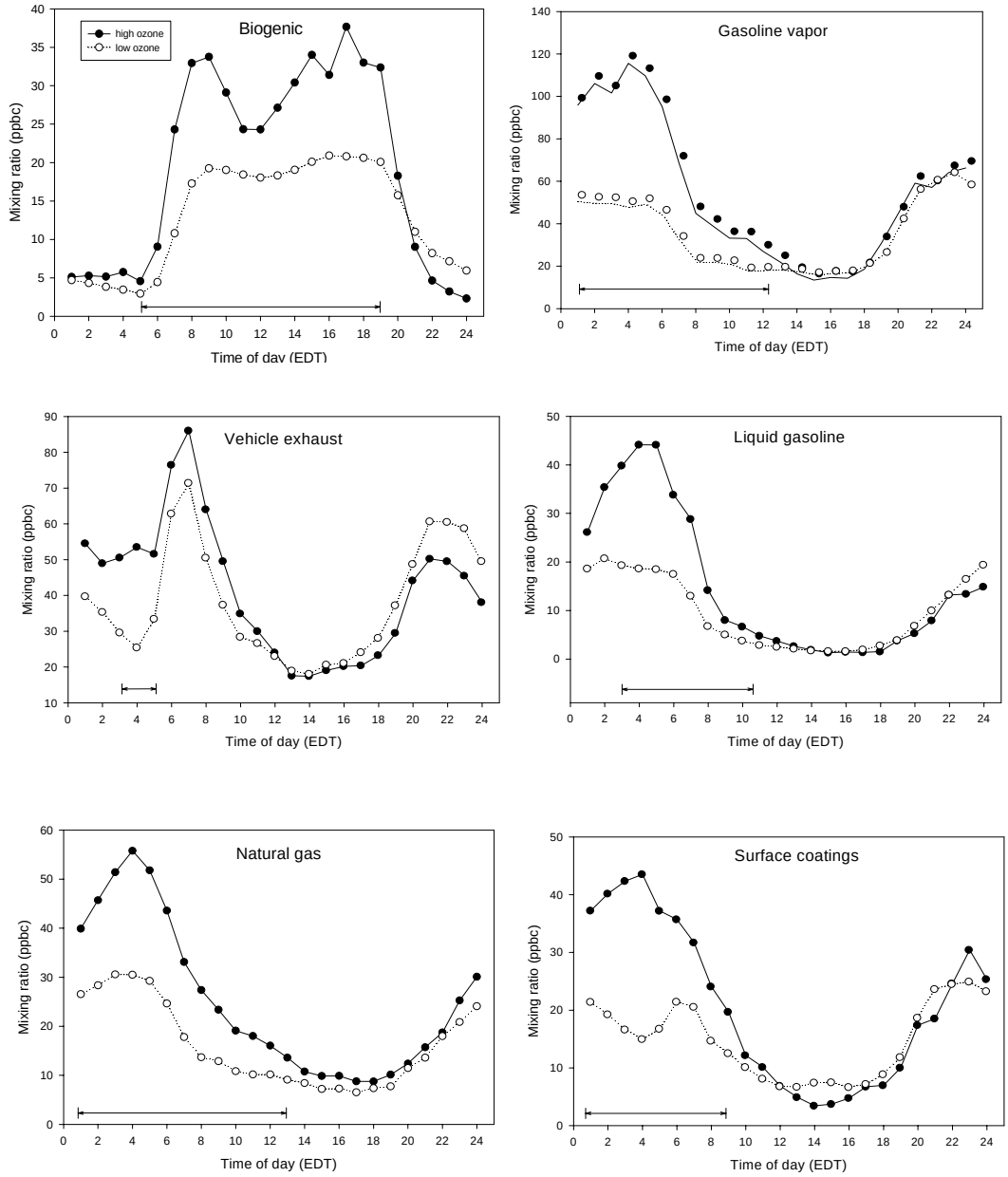

Figure 3.7: Comparisons of diurnal pattern of average mixing ratio of each VOC emission source between high ozone days and low ozone days. The bars indicate the times that can be considered as having significantly different mean mixing ratios between both days based upon a two-tailed t-test at the 95% confidence interval.

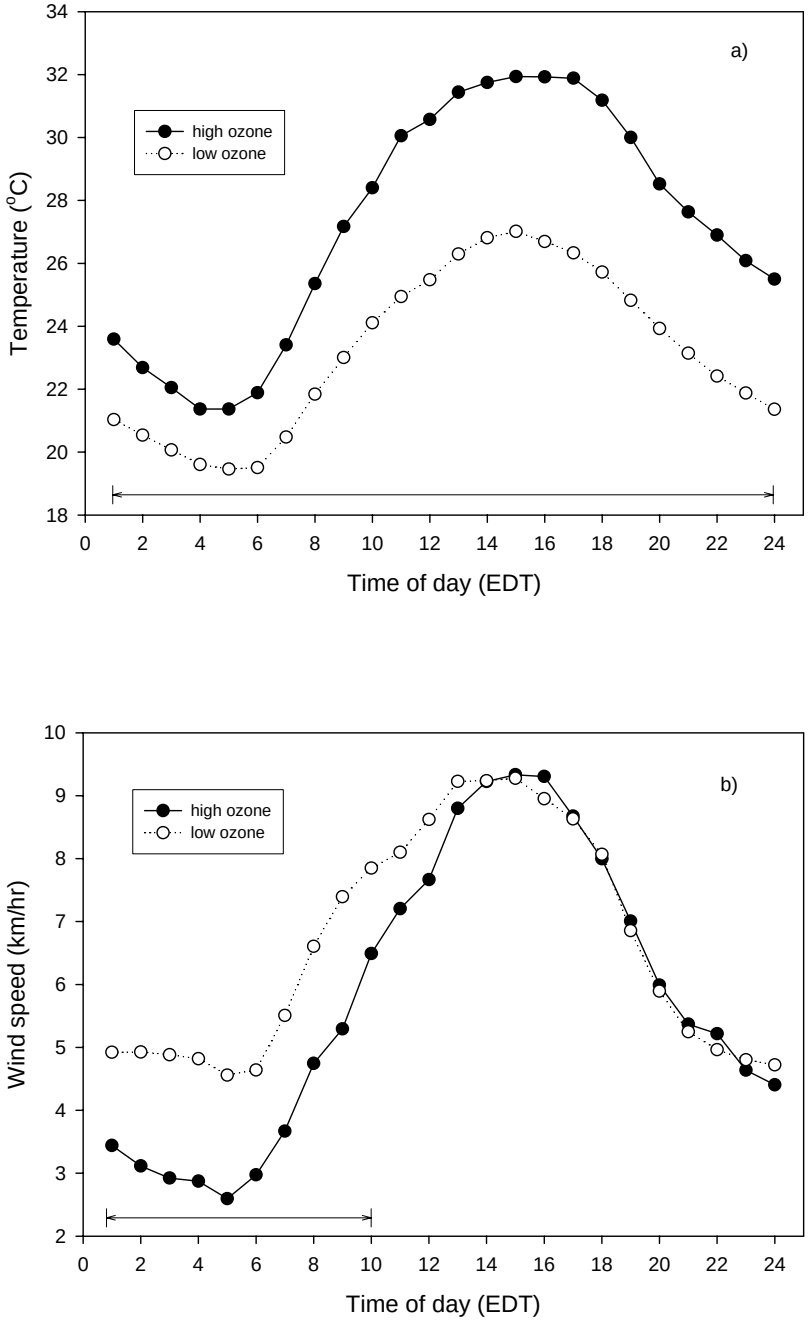

Figure 3.8: Comparisons of diurnal patterns of a) average temperature and b) average wind speed between high ozone days and low ozone days. The bar indicates the times which can be considered as having significantly different mean temperatures and wind speeds between both days based upon a two-tailed t-test at the 95% confidence interval.

ozone days during the afternoon. During the afternoon on high ozone days, the contribution of the biogenic source category to the total hydrocarbon mixing ratio is twice as high as that during the afternoon of low ozone days, while other source categories show no significantly different mixing ratios for both days. As shown in Figure 3.8a, higher contributions from biogenic sources during high ozone episodes may have resulted from higher temperatures (by 4~5 ^{o}C) during daytime, as the emission activity of biogenic sources tends to increase exponentially with temperature (Guenther et al., 2000).

On the other hand, during nighttime, the VOC mixing ratios resulting from anthropogenic source categories during high ozone days show similar patterns, about 1.5 ~2 times as high as those during low ozone days. Generally, the natural gas source is expected to show a constant emissions rate, and so differences in the mixing ratio associated with the source categories are most likely from variations of the mixing height in the atmosphere with time (Derwent et al., 1995). At night, the air is stably stratified because of the warmer air above the colder ground, and the effect of shear stress becomes dominant in maintaining turbulent flow, leading to mixing of pollutants from surface sources. During daytime the effect of buoyancy is predominant resulting in relatively vigorous and rapid vertical mixing. Under circumstances corresponding to very low wind speeds at night, shear is minimal and stratification becomes dominant, leading to poor mixing of pollutants from surface sources (Seinfeld and Pandis, 1998). As a result, the mixing height becomes relatively thin, and emissions from surface sources are concentrated. As shown Figure 3.7, the difference of natural gas mixing

ratios by a factor of two between both types of days likely suggests a difference in mixing height in the late evening and early morning between the two types of days.

To determine if the differences between two types of days during nighttime result from different emissions from sources or from poor atmospheric mixing during nighttime, we took a closer look at meteorological variables for both types of days. Figure 3.8b gives the diurnal patterns of average wind speed for both types of days, and during nighttime on high ozone days the average wind speed was less than that during nighttime on low ozone days by about 1.5 km/hr. A scatter plot of wind speed vs. total hydrocarbons and NOx from 1 am to 6 am shown in Figure 3.9, illustrates the inverse relationship between them. Also, hourly average temperatures, as shown in Figure 3.8a, were significantly higher on high ozone days. Therefore, we can explain the higher mixing ratios of anthropogenic sources on high ozone days at night by increased stratification caused by higher temperatures, and weaker shear stress caused by weaker wind speed rather than an increase in emissions from surface sources.

Accordingly, our focus is on the daytime differences. As mentioned earlier, the only difference during daytime between two types of days is seen in the biogenic source category, which shows the highest afternoon mixing ratios among source categories during high ozone days as shown in Figure 3.7. In the Baltimore region, a reactivity weighted source apportionment analysis of VOC for the summer time of 1993 and 1995 revealed biogenic sources to be the most significant source category with respect to ozone formation (Morales-Morales, 1998). Additionally, Cardelino and Chameides (2000), in a study of hydrocarbons measured at PAMS sites in Washington, DC and Bronx, NY in the summer of 1995, showed that during some

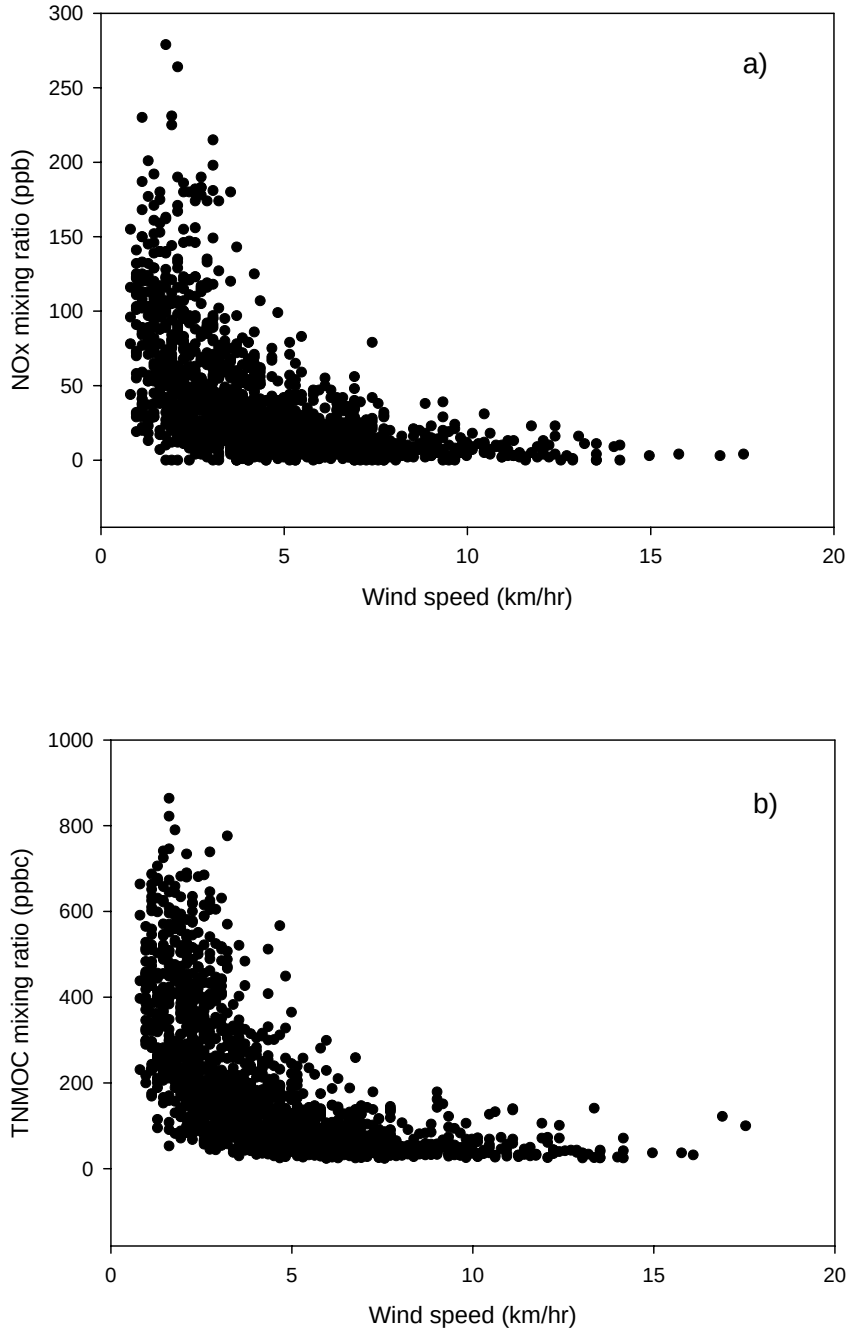

Figure 3.9: Scatter plots of wind speed vs. a) NOx and b) TNMOC for observations between 1 am to 6 am.

ozone episodes, the reactivity-based average concentrations of natural hydrocarbons from 7 am to 7 pm were greater than those of anthropogenic hydrocarbons. Even at these two sites, which are categorized as urban/central city commercial, natural hydrocarbons appear to be an important emission source in ozone formation.

To investigate contributions of each source category based on reactivity, we assumed that the 23 chemical species, shown in Table 3.2, account for 100 % of the mass fraction of each source category, and we estimated source contributions during daytime from 7 am to 7 pm. The reactivity-weighted mixing ratios of each source category were calculated by multiplying mixing ratios of each species by the maximum incremental relativities (MIR) scale (moles O_3 formed/moles C). The MIR scale developed by Carter et al. (1989) is defined as the change in ozone caused by adding a small amount of a VOC species, and has been used to quantify a species ability to produce ozone (Carter et al., 1994). It should be noted that this rough estimate of reactivity-weighted source contribution contains substantial uncertainty because of the assumption that emissions from each source category are composed solely of the 23 species.

Table 3.3 shows the reactivity–based comparison of mixing ratios for each source category. As indicated in Table 3.3, the reactivity-weighted mixing ratio of the biogenic source category shows the same order of reactivity-weighted mixing ratio of vehicle exhaust source category. Also, the biogenic and surface coating source categories are likely to be more reactive towards ozone production than the other four source categories because the mixing ratios of the former two categories show similar values for both reactivity based and absolute mass based contributions, while those of

the latter source categories show significantly reduced contributions in the reactivity-weighted scale.

Table 3.3: Source mixing ratios (ppbc) based on reactivity and on absolute mass, obtained from daytime (7 am to 7 pm) source contributions

	Absolute mixing ratio	Reactivity-weighted mixing ratio
Biogenic emissions	20.1	23.7
Liquid gasoline	4.3	2.3
Surface coatings	10.3	10.8
Natural gas	10.9	3.1
Vehicle exhaust	32.2	23.5
Gasoline Vapor	20.2	12.4
Total TNMOC	98.0	75.8

In addition, in terms of the morning VOC/NOx ratio used to justify NOx-VOC sensitivity to peak ozone in the past, this area would fall into the VOC-sensitive category, for which VOC reduction results in a decrease of ozone formation. However, the method of determining VOC or NOx sensitivity using the morning VOC/NOx ratio does not incorporate the impact of the biogenic source identified as a significant source in this study and other studies (Sillman, 1999; Milford et al., 1994). As indicated in Figure 3.10, the average ratios of VOC/NOx during 6 am to 9 am are the same for both types of days, and are much lower than 10, the criteria for VOC sensitivity. High ozone episodes in this area took place when the biogenic contribution was elevated, while average NOx mixing ratios as well as the average mixing ratios of other emission sources remained at the same levels.

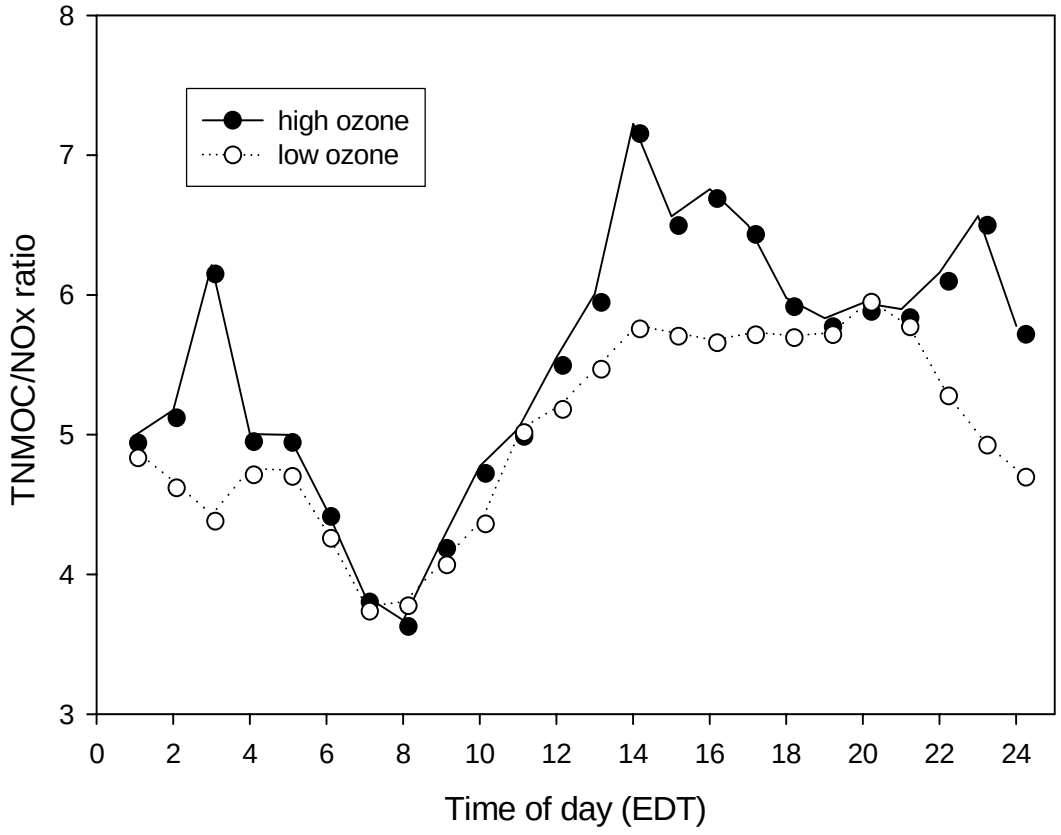

Figure 3.10: Comparison of diurnal pattern of average ratio of TNMOC to NOx between high ozone days and low ozone days.

As Ryan et al. (1998) indicated, the most severe ozone events in the Baltimore/Washington area occurred when the regional-scale transport of ozone and its precursors was significant. Thus, long-range transport of ozone and its precursors is likely an important contributor to ozone episodes in this area. With receptor models, techniques developed to assess contributions from various sources based on observations at receptor sites, the impacts of long-range transport on the contributions of a particular source cannot be resolved without additional meteorological input. For this reason, it is not possible to gauge the impact of regional transport and local ozone production on ozone episodes, including mild ozone events, in this area. Considering the short lifetime of compounds of biogenic origin such as isoprene, compared to compounds from other sources, the results presented here suggest that biogenic emissions play an important role in local ozone production in this area. Hence, if only local ozone production is considered, simply decreasing the emission of anthropogenic VOC by a small amount may not result in local ozone reduction in this area if weather conditions are conducive to high levels of biogenic emissions.

3.4 Summary and conclusions

Hourly hydrocarbon mixing ratios measured at Essex, Maryland, for the summers of 1996 to 1999 were analyzed to identify possible VOC sources using the UNMIX receptor model. Gasoline-related sources such as vehicle exhaust, gasoline vapor, and liquid gasoline explained more than half of total VOC mixing ratio, which is typical for VOC found in urban/suburban areas in United States. Natural gas,

surface coatings, and biogenic source categories each accounted for 13, 12 and 11 % of the total VOC, respectively, when all measurements were considered.

Even though the hourly average contribution of biogenic sources in quantity did not appear to be significant, the comparisons of diurnal patterns of high-ozone days with those of low-ozone days and rough reactivity-weighted daytime source apportionment results suggested that biogenic emissions contribute significantly to local ozone production for high ozone episodes at this site.

At this point, without a help of air quality modeling, we cannot conclude whether VOC control or NOx control or both controls will be effective in reducing violations of National Ambient Air Quality Standard (NAAQS) for ozone in this area. However, if the focus is on the reduction of high ozone occurrences coming from local ozone production in which weather conditions are conducive to high biogenic emissions, NOx reduction, which must be significant enough to offset increased biogenics, may be more effective, because NOx reduction creates NOx limited conditions, and highly reactive biogenic VOCs cannot proceed to react to form ozone. However, the NOx reduction may not lead to ozone reduction under weather conditions unfavorable to increased biogenic emissions. On the other hand, if the focus is on the general reduction of ozone for all summer days, a substantial reduction of anthropogenic VOC sources such as automobile exhaust may lead to ozone reduction. These strategies can be resolved through the use of a well-evaluated photochemical air quality model taking into account long-range transport of ozone and its precursors, deposition of pollutants, and chemical reactions. This practice using an air quality model was performed, and the results were described in the Chapter 5.

Chapter 4: Evaluation of a VOC Emissions Inventory by Comparison to Ambient Measurements

4.1 Introduction

Air quality models, composed of meteorology, chemistry and emissions, have been widely implemented to simulate the chemistry and physics of the atmosphere, and to understand the cause-effect relationships between pollutants and their precursors. Potential control measures for target air pollutants have been determined, based on those modeling results. Hence, inaccurate results from air quality modeling can lead to negative impacts both economic and environmental in nature. The usefulness of the output of air quality models is largely dependent on the quality of their inputs. Hanna et al. (1998), Placet et al. (2000), and Solomon et al. (2000) indicate that the uncertainties in atmospheric model results may originate mainly from the uncertainties in the emission inventories.

Previous studies described in detail the limitations and difficulties associated with evaluation of emission inventories resulting from the intrinsically different nature of inventory estimates and ambient monitoring measurements (Fujita et al., 1992; Harley et al., 1992; Funk et al., 2001; Mannschreck et al., 2002; Slemr et al., 2002; Houyoux et al., 2000; EPA-II, 1996; LADCO, 1998; Stoeckenius et al., 2000). Such comparisons are limited to ratios of VOC species or VOC species groups (abundance

of a given species or species group relative to that of another species group) since the emissions estimates in units of mass flux per area cannot be converted directly into concentrations without the application of a suitable dispersion model or a chemical transport model. In addition, the chemical mechanisms commonly used in photochemical models aggregate chemical species, and this constrains the comparisons to a few individual species and species groups. Furthermore, since estimates from emissions processing models do not demonstrate the impact of chemical reactions and transport, the comparison is often limited to the early morning hours of the day when these impacts tend to be minimal.

Because of the above limitations, two approaches in terms of ratio comparisons have been employed to evaluate emissions inventories. In one approach, VOC/NOx or CO/NOx ratios and weight fractions of individual VOC species are compared to ambient measurements during the early morning (6:00 a.m.-10:00 a.m.) (Fujita et al., 1992; Funk et al., 2001; Houyoux et al., 2000; LADCO, 1998; Stoeckenius et al., 2000). In another approach, receptor-modeling techniques are used to compare emissions estimates for specific source categories (Harley et al., 1992; EPA-II, 1996; Hidy, 2000). Receptor models take ambient measurements of speciated organic compounds and allocate VOCs to various source categories through complex statistical manipulations.

Even though the ratio comparisons can give some insight into the uncertainty in an emissions inventory, care is needed to avoid reaching misrepresentative and possibly misleading conclusions. For example, the same values modeled and observed VOC/NOx ratios do not indicate that the absolute amounts of VOC and NOx are the

same in both the simulation and the observation. For that reason, a dispersion model has been employed in several studies. Fujita et al. showed the comparisons of measured CO/NOx and NMOG (non-methane organic gas)/NOx and CO, NMOG, and NOx concentrations with air quality model prediction using the UAM model (Fujita et al., 1992). Recently, Mannschreck et al. and Kuhlwein et al. adopted a Gaussian dispersion model to calculate pollutant concentrations of individual hydrocarbons for comparison with measured concentration ratios (Mannschreck et al., 2002; Kuhlwein et al., 2002). Slemr et al. (2002) performed a comparison of the results from a CTM (chemistry and transport model) with observations as a part of their study.

This study focuses on emissions inventory evaluation. As NOx is a direct product of combustion, while VOCs are emitted by both combustion and non-combustion sources, NOx emission estimates are generally assumed to be more accurate than VOC estimates (Funk et al., 1992; Watson et al., 2001). In addition, Hanna et al. (1998) concluded, in a study of estimates of uncertainties in predictions by a photochemical grid model, that anthropogenic VOC area source emissions had the most influence on the variations in the 50% of peak ozone concentrations. Therefore, the evaluation of the emissions inventory here is mainly focused on VOC.

Since the use of several evaluation methods and inter-comparison between the results from each method will lead to more solid conclusions, we investigate both ratio comparisons of each VOC source contribution from a source apportionment model and CB-IV VOC groups relative to NOx or CO at the emissions modeling level (EPA-II, 1996). Furthermore, the CMAQ model, a photochemical air quality model including the effects of chemistry and transport, is employed to compare the ratios of CB-IV

VOC groups to NOx or CO, and effectively to put values from the emissions inventory into concentration units so they may be compared with observations.

4.2 Modeling and monitoring data

4.2.1 Overview of emissions inventory and modeling

An aggregated emissions inventory was obtained from the Mid-Atlantic Regional Air Management Association (MARAMA). This is an improved emission inventory for 1997 to support studies of regional ozone in the Mid-Atlantic and Northeastern states. Average daily VOC, NOx, and CO emissions for area and point sources and average daily Vehicle Mileage Traveled (VMT) were compiled at the county level. It was based upon EPA's 1996 National Emission Trends (NET) inventory.

Additionally, a gridded land use assessment, prepared by the New York State Department of Environmental Conservation (NYDEC), was used for biogenic source processing. Even though the focus of our evaluation is on the anthropogenic emissions inventory, it is necessary to process biogenic emissions in conjunction with anthropogenic emissions since the ambient measurements include the contributions from biogenic sources and biogenics lead to ozone.

We employed the SMOKE version 1.4, an emissions pre-processing model, to convert the source-level emissions (county total emissions) to gridded, speciated, and temporally allocated emissions.

As described in Chapter 2, the temporal allocation step creates an hourly pollutant emissions inventory based on the characteristics of each source. In the spatial allocation step, a gridding surrogate is used to create a matrix containing conversion factors, used to transform county level aggregate emissions into emissions in each grid cell. For example, emissions from major on-road mobile sources are allocated in each grid cell according to the distribution of roads. In the speciation step, SMOKE creates a speciation matrix containing conversion factors, to convert VOC emissions into emissions of specific compounds. In this study, the speciation is based on the CB-IV chemical mechanism (Gery et al., 1989). Actual VOCs are converted to 10 modeling species: ETH (ethene), ISOP (isoprene), PAR (paraffin group, molecules containing single carbon bond groups), OLE (olefin group, molecules containing double carbon bond groups), TOL (toluene group, 7-carbon rings), XYL (xylene group, 8-carbon rings), ALD (aldehyde group), FORM (formaldehyde), NR (non reactive VOC group), and TERP (terpene group). The final gridded, chemically speciated hourly emission estimates are produced by multiplication of the matrices developed in the main processing steps. For biogenic sources, in order to convert land use information to normalized emissions values, the BEIS2 is embedded in SMOKE. For mobile sources, MOBILE5b, also embedded in SMOKE, generates emission factors, which are multiplied by VMT in order to get emissions values (Houyoux et al., 2000).

CMAQ version 4.3 used in this study has been designed to approach air quality as a whole by including state-of-the-science capabilities for modeling multiple air quality subjects. The CMAQ modeling system simulates various chemical and physical processes that are thought to be important for understanding atmospheric

trace gas transformation and distribution such as dispersion, chemical reactions, and surface deposition (EPA-III, 1999). More details are described in Chapter 2.

Meteorological variables, required to process biogenic, mobile, and point sources in SMOKE, and CMAQ, were simulated using the MM5 by the Department of Meteorology, University of Maryland. The simulations were performed with a modified Blackadar PBL scheme and a standard nudging process (Sistla et al., 2002; Zhang and Zheng, 2004). The meteorological variables for 4 km grid resolution were extracted and interpolated from the meteorological variables for 12 km grid resolution using the MCIP version 2.2.

The simulation was performed for the period July 5-July 20 of 1997 using multi-nesting techniques for boundary conditions. As shown in Figure 4.1, the detailed 4 km study domain, nested within the outer domains, covers the whole state of Maryland, and parts of Virginia, West Virginia, Delaware, New Jersey, and Pennsylvania. The innermost domain has 108 columns by 78 rows with 4 km horizontal grid cell resolution, and 16 vertical layers. The outer domains have horizontal grid cell resolutions of 36 km, and 12 km, respectively. The comparison to observations was done from July 8-July 20 of 1997, allowing for three days of spin-up time to minimize the impact of initial conditions on the CMAQ simulation.

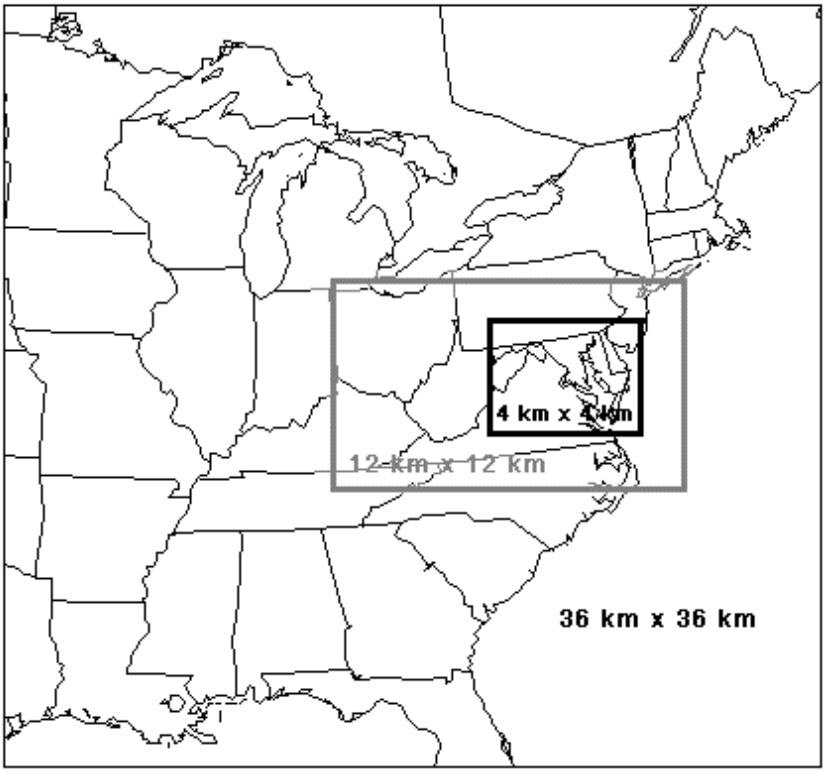

Figure 4.1: Map of CMAQ modeling domain.

4.2.2 Overview of ambient measurements

The PAMS network consists of five different site types to provide information sufficient to satisfy important monitoring objectives. Type 2 sites are located immediately downwind of areas with significant ozone precursor emissions. It is reasonable to compare ambient measurements and emissions estimates only in situations where the local ozone precursor concentrations are dominated by local sources because emissions estimates and ambient measurements are two fundamentally different quantities. Emissions estimates represent the amount of a given pollutant released by a particular source. Ambient measurements represent the concentration of these pollutants in the atmosphere at a particular location and time. It is best to use monitoring measurements from sites where local emissions dominate such as PAMS type 2 sites (LADCO, 1998; Stoeckenius et al., 2000). We obtained the measurements for three PAMS sites (McMillan reservoir in DC, Essex in MD, Camden in NJ), categorized as type 2 sites. Table 4.1 contains a summary of the PAMS measurements and Figure 4.2 shows the site locations. The concentrations of 55 hydrocarbons, total nonmethane organic carbon (TNMOC), ozone, oxides of nitrogen, as well as surface meteorological conditions such as temperature, wind direction, wind speed, and radiation are monitored at the sites. At the Camden site, CO was measured instead of NOx.

Table 4.1: Summary of PAMS observations

	Essex, MD	McMillan Reservoir, DC	Camden, NJ
Period of obs.	Jun. 1 -Sep. 30,1997	Jun. 1 -Sep. 24,1997	Jun. 1 -Aug. 31,1997
# of hourly obs. for 6:00 am-9:00 am	387	359	269
Total # of hourly obs.	2812	2152	1680

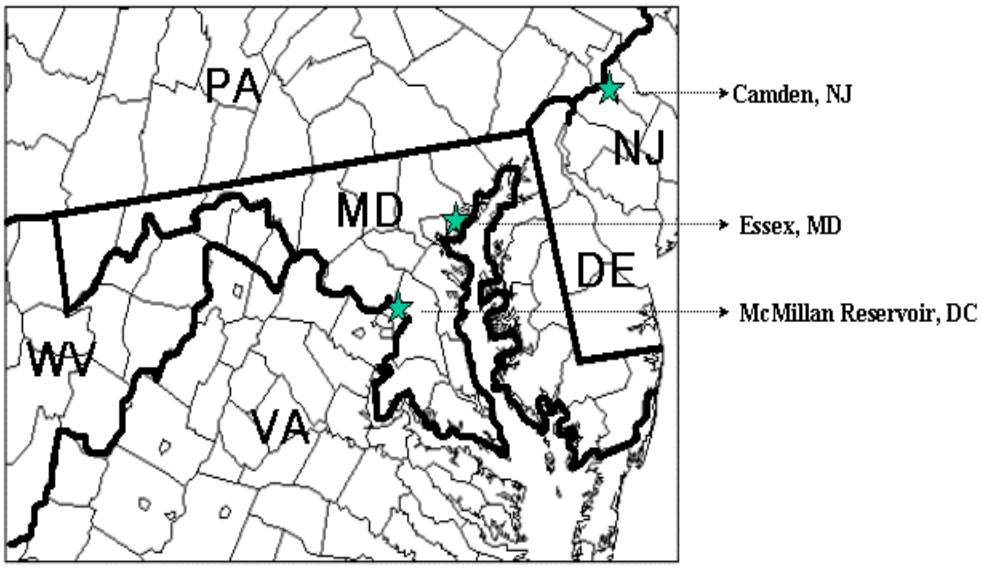

Figure 4.2: Map of PAMS locations used in this study. DE (Delaware), MD (Maryland), NJ (New Jersey), PA (Pennsylvania), VA (Virginia), WV (West Virginia).

The 55 individual hydrocarbons observed by PAMS were lumped into categories for comparison with emissions estimates using the VOC categories in the CB-IV chemical mechanism. There is a limitation associated with this conversion. TERP, FORM, and ALD2 are not included in the 55 PAMS species. ETH and ISOP in the CB-IV mechanism are the only single species measured by PAMS. Also, the 55 PAMS hydrocarbons accounted for only 70-90% of the TNMOC for the three sites, with the remainder unidentified. The unidentified portion of TNMOC might be volatile hydrocarbons of C2 through C12 such as terpenes, and oxygenated hydrocarbons (EPA-IV, 1998). Therefore, the concentrations of the lumped species such as PAR, OLE, TOL, XYL, and NR, estimated from only 55 species measured at PAMS sites, may be lower than actual concentrations of these lumped species in ambient air. For example, dodecane, not included in the 55 PAMS species, may be in a measurement of TNMOC, and 1 ppb of this species is converted to 12 ppb of PAR (12 ppbC) in terms of modeling species. Hence, a concentration of PAR converted from only 55 PAMS species may under-represent the actual concentration of PAR in the ambient air. Therefore, the concentrations of PAR, OLE, TOL, and XYL obtained from the 55 PAMS observed species are considered a lower limit of the actual concentrations in ambient air.

4.3 Approach

Two types of comparisons between observation and estimation were performed. One is the comparison of CB-IV VOC groups both in an absolute and a relative

manner. The other is a ratio comparison of each VOC source contribution, obtained from a source apportionment model, relative to NOx (or CO for the Camden PAMS site). As far as the ratio comparisons are concerned, they are based on NOx or CO rather than VOC, because NOx or CO likely has less uncertainty in both measurement and emissions modeling than VOC (Funk et al., 2001; Watson et al., 2001). In addition, the definitions of VOC categories in modeling and measurements are not the same. As described above, TNMOC observations include nonmethane hydrocarbons and oxygenated hydrocarbons, while the calculated total VOC from the emissions model stands for total organic gas (TOG) including methane. The morning time period from 6:00 a.m. to 9:00 a.m. was investigated to minimize the impact of chemical reactions and transport on comparisons with ambient measurements.

When it comes to comparing absolute concentrations of CB-IV VOC groups by employing the CMAQ photochemical model, there are some additional issues to be noted. The photochemical air quality model is a complicated system composed of a meteorological modeling system for the description of atmospheric states and motions, emission models for man-made and natural emissions injected into the atmosphere, and a chemistry-transport modeling system. Hence, the results from an air quality model reflect uncertainties in the meteorology and chemistry, in addition to uncertainty in the emission estimation. Even though the comparisons are performed during the morning period from 6:00 a.m. to 9:00 a.m. when the impacts of chemistry and transport are minimized, there still exists a possibility of errors in concentration predictions originating from meteorological parameters such as mixing height.

4.4 Results and discussion

4.4.1 Comparison of CB-IV VOC categories

ETH (ethene), TOL (toluene group), and XYL (xylene group) were considered for this comparison. Isoprene was excluded because this species is not appropriate for this comparison - short-lived isoprene is at a minimum in early morning hours, the time frame in which we focus. Considering the limitations mentioned earlier, TOL and XYL were included in this comparison, as toluene and xylenes are known as tracer species for both vehicle exhaust and solvent sources. Ethene is known as a tracer species for vehicle exhaust (Wadden et al., 1994; Fujita et al., 1994; Kenski et al, 1995; Scheff et al., 1996; Lawrimore and Aneja, 1997; Vega et al., 2000). Even though this comparison is limited to a few species group, the result is expected to give insight into the emissions inventories of sources such as vehicle exhaust and solvent usage – major VOC sources in urban and suburban areas (Placet et al., 2000; Lawrimore and Aneja, 1997; Mukund et al., 1996).

Figure 4.3 shows the comparison of the estimated and observed average ratios of each species to NOx between 6:00 a.m. and 9:00 a.m. at Essex, Maryland (MD). Here, the estimated ratios from SMOKE were calculated for five different grid areas surrounding the monitoring site including: the cell containing the monitoring site with 16 km^2 area, extended areas of 3 x 3 cells, 5 x 5 cells, 7 x 7 cells, and 9 x 9 cells. That is because the estimates from SMOKE do not incorporate the impact of transport and chemistry, and comparing only at a corresponding grid cell to the monitoring site may be misleading. The ratios from CMAQ were the average values at the site cell

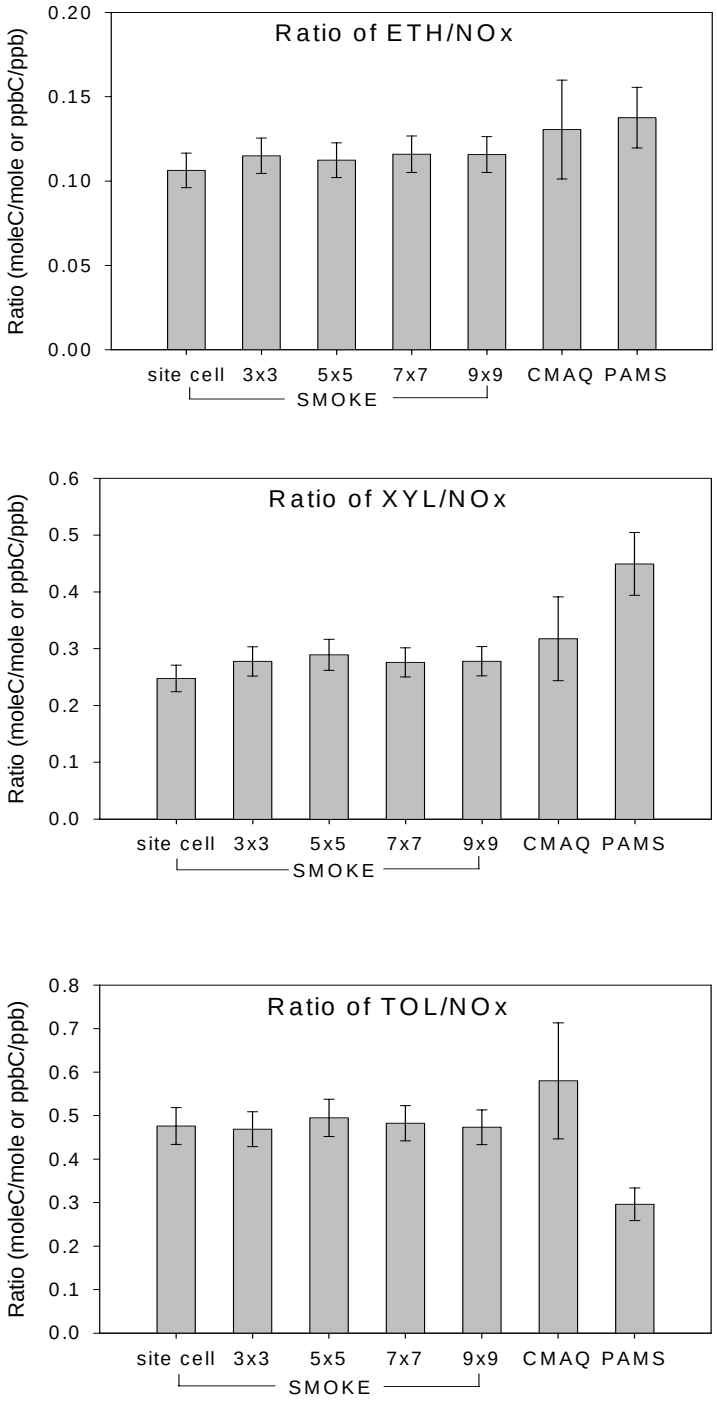

Figure 4.3: Comparison of average ratios between the estimated (SMOKE or CMAQ) and the observed values in the morning from 6:00 a.m. to 9:00 a.m. for Essex, MD. The error bars indicate the two-sigma standard errors of the means (95% confidence interval).

corresponding to the location of the PAMS monitoring station. The emission estimates from SMOKE show little diversity with respect to spatial distribution. The ratios from CMAQ and SMOKE show good agreement with each other for all species, suggesting that processes such as chemical evolution, transport, and deposition of pollutants during the morning period of 6:00 a.m. to 9:00 a.m. are relatively unimportant in the CMAQ simulation.

The estimated ratios of ETH to NOx from SMOKE and CMAQ are within an acceptable range of the corresponding observed ratio, taking into account the uncertainties associated with the averages. However, the model XYL/NOx ratio appears to be somewhat underestimated, while TOL/NOx seems considerably overestimated by a factor of 1.5 to 2.

Figure 4.4 compares the average concentration predicted by CMAQ to the observed values in the morning period from 6:00 a.m. to 9:00 a.m. at Essex, MD. The concentration of NOx predicted by CMAQ is a little higher than the observed NOx concentration. In addition, ETH and TOL show a trend similar to the ratio comparisons in Figure 4.3. On the other hand, the predicted XYL concentration is in good agreement with observed XYL.

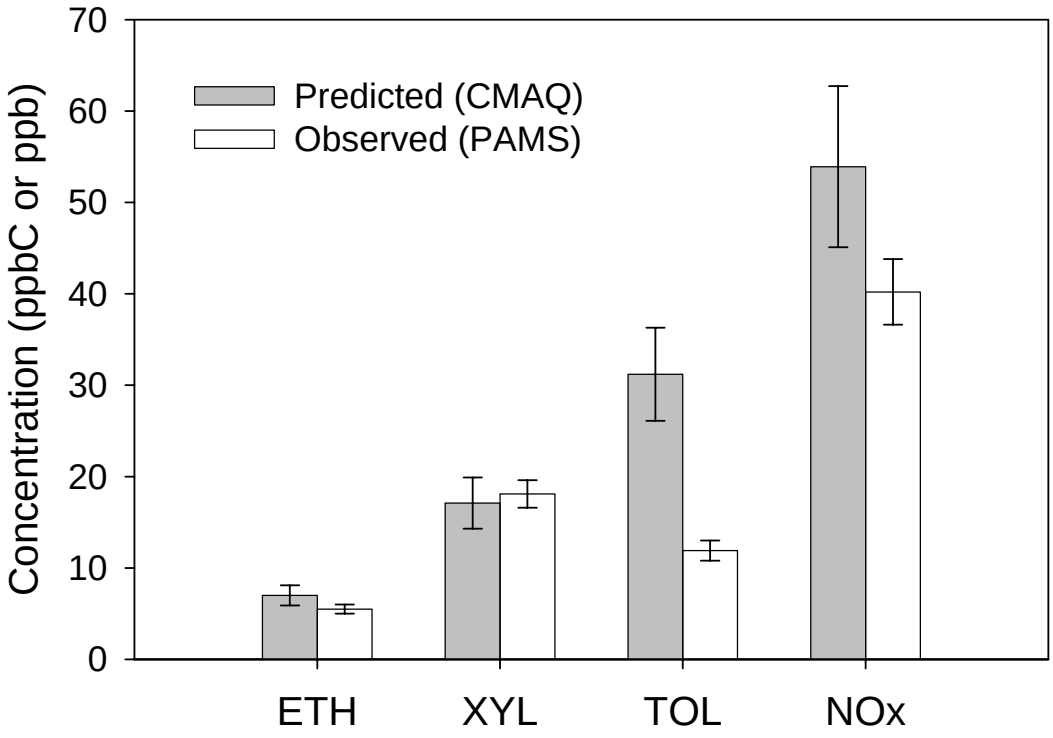

Figure 4.4: Comparison of average concentrations between the predicted (CMAQ) and the observed values in the morning from 6:00 a.m. to 9:00 a.m. for Essex, MD. The error bars indicate the two-sigma standard errors of the means (95% confidence interval).

To identify the major sources of TOL, XYL, and ETH in the estimates, SMOKE was run with only solvent and vehicle exhaust emissions. Table 4.2 shows the average percentage contribution of both emission sources to emission estimates of each modeling species in the morning period around the three observation sites. As indicated in Table 4.2, around 60% of estimated TOL in the vicinity of the Essex site is emitted from solvent sources, and 30% from vehicle exhaust. If the estimates of vehicle exhaust emissions are assumed to be acceptable as indicated by the favorable comparison between observed and estimated ETH/NOx ratios, an overestimate of emissions from solvent sources would be the likely cause for the overestimated TOL/NOx ratio.

Table 4.2: Average percentage contribution of sources to emission estimates of each species in the morning period by SMOKE

	Essex, MD		McMillan Reservoir, DC		Camden, NJ	
Grid cells	Solvent	Vehicle	Solvent	Vehicle	Solvent	Vehicle
			ETH (%)			
Site cell	3	62	1	88	5	93
3x3	5	62	2	70	8	68
5x5	5	62	5	74	11	53
7x7	5	56	6	76	12	49
9x9	5	56	6	78	11	50
			TOL (%)			
Site cell	63	31	58	37	54	42
3x3	60	34	58	35	57	36
5x5	63	34	58	34	63	31
7x7	59	30	57	35	65	28
9x9	59	31	55	36	64	29
			XYL (%)			
Site cell	35	57	28	61	29	64
3x3	33	56	29	54	32	57
5x5	35	54	30	51	37	50
7x7	33	52	29	53	37	45
9x9	32	53	28	54	38	47

At the McMillan reservoir site in Washington District of Columbia (DC), there is little variability in the spatial distribution of emission estimates of ETH/NOx, and TOL/NOx from SMOKE, as shown in Figure 4.5. For the XYL/NOx ratio, there is some spatial variability, but this is not a remarkable change. Also, the ratios from CMAQ and SMOKE show good agreement with each other for all species. While the XYL/NOx ratio shows good agreement with observation, ETH/NOx is slightly underestimated, and TOL/NOx is overestimated with statistical significance at 95% confidence interval. In Figure 4.6, the predicted NOx at the McMillan site is three times higher than observed NOx, and other species show similar patterns of overestimations. However, considering that the ratios from CMAQ in Figure 4.5 are similar to those from SMOKE, the consistent overestimation of concentrations from CMAQ implies that the incorrect estimates originated from a miscalculated mixing height rather than a problem with the ratios of emissions, and therefore the emissions inventory. From Table 4.2, more than 70% of the estimated ETH comes from vehicle exhaust. About 50% of the estimated XYL is emitted from vehicle exhaust with 30% from solvent sources. On the other hand, around 60% of the estimated TOL around this site is emitted from solvent sources while 35% comes from vehicle exhaust. The data suggest that solvent sources are significantly overestimated in this area.

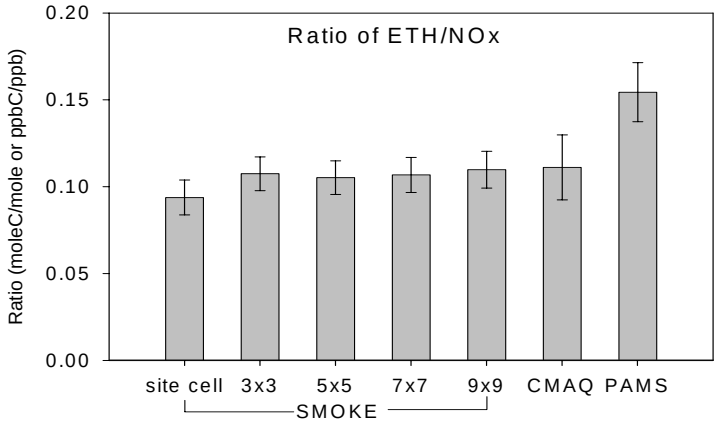

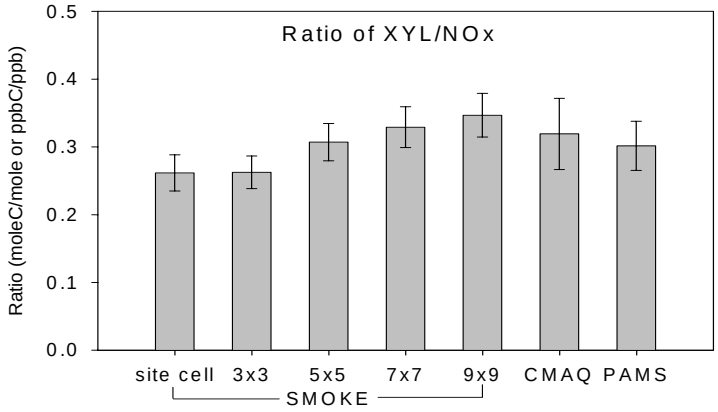

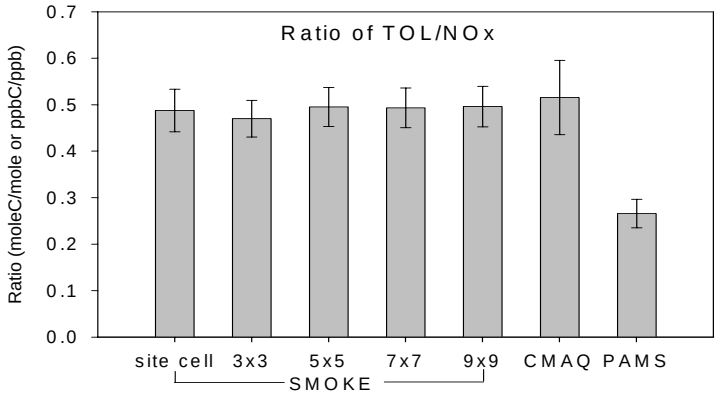

Figure 4.5: Comparison of average ratios between the estimated (SMOKE or CMAQ) and the observed values in the morning from 6:00 a.m. to 9:00 a.m. for McMillan reservoir, DC. The error bars indicate the two-sigma standard errors of the means (95% confidence interval).

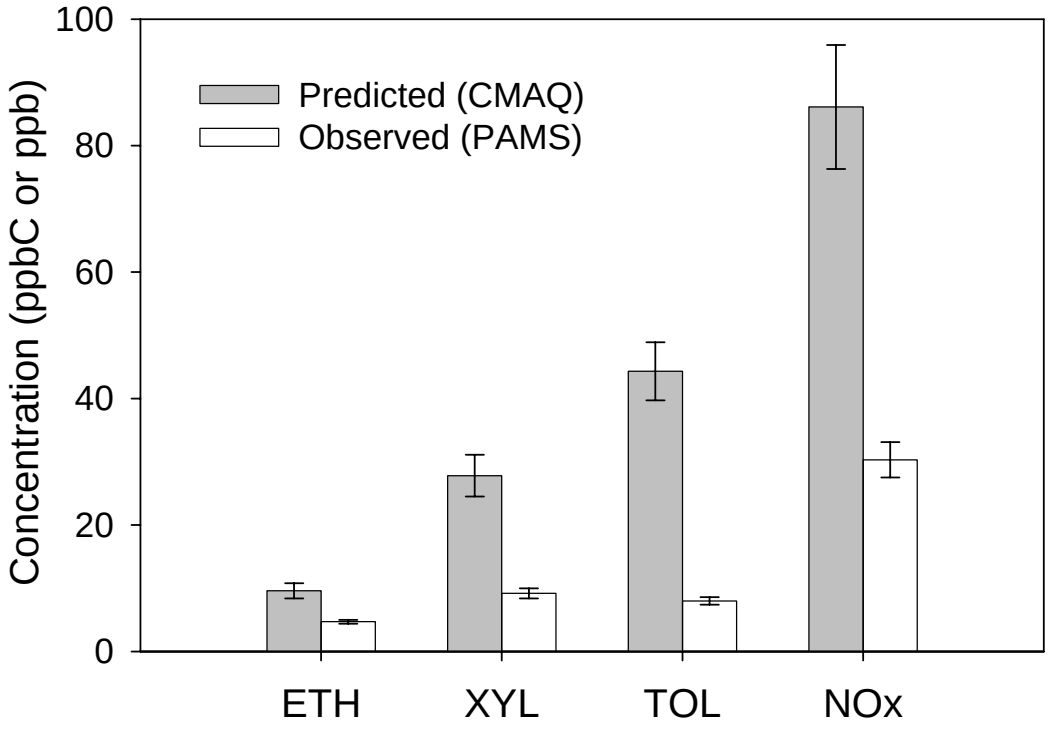

Figure 4.6: Comparison of average concentrations between the predicted (CMAQ) and the observed values in the morning from 6:00 a.m. to 9:00 a.m. for McMillan reservoir, DC. The error bars indicate the two-sigma standard errors of the means (95% confidence interval).

At the Camden site in New Jersey (NJ), the estimated emission ratios for the grid cells surrounding the site are spatially non-homogeneous with large emissions gradients observed among grid cells in the inventory. As shown in Figure 4.7, the ratios of all three species from CMAQ and SMOKE show overestimation. In particular, the estimated TOL/NOx ratio is two to three times higher than the observed ratio. The comparison of concentrations shows the same trend of overestimation, as indicated in Figure 4.8. Also, the relative contributions of sources to emission estimates are very similar to those at the other two PAMS sites.

In addition, we adjusted NOx or CO in the ratios in accordance with the comparison of CMAQ outputs and observations in order to look at whether the result would be affected if the NOx or CO estimations were wrong. Figure 4.9 shows the ratio comparison of TOL to adjusted NOx or CO for Essex, MD and Camden, NJ sites. The McMillan reservoir site in DC was excluded because of concern that the mixing height was wrong so that the estimated concentrations at this site did not reflect real values. As shown in Figures 4.4 and 4.8, NOx or CO is slightly overestimated. We can expect that the extent of overestimation in the ratios with the adjustment of NOx or CO to the ambient value will be larger than without adjustment. Hence, Figure 4.9 reveals the overestimate of TOL becomes larger after adjusting NOx or CO.

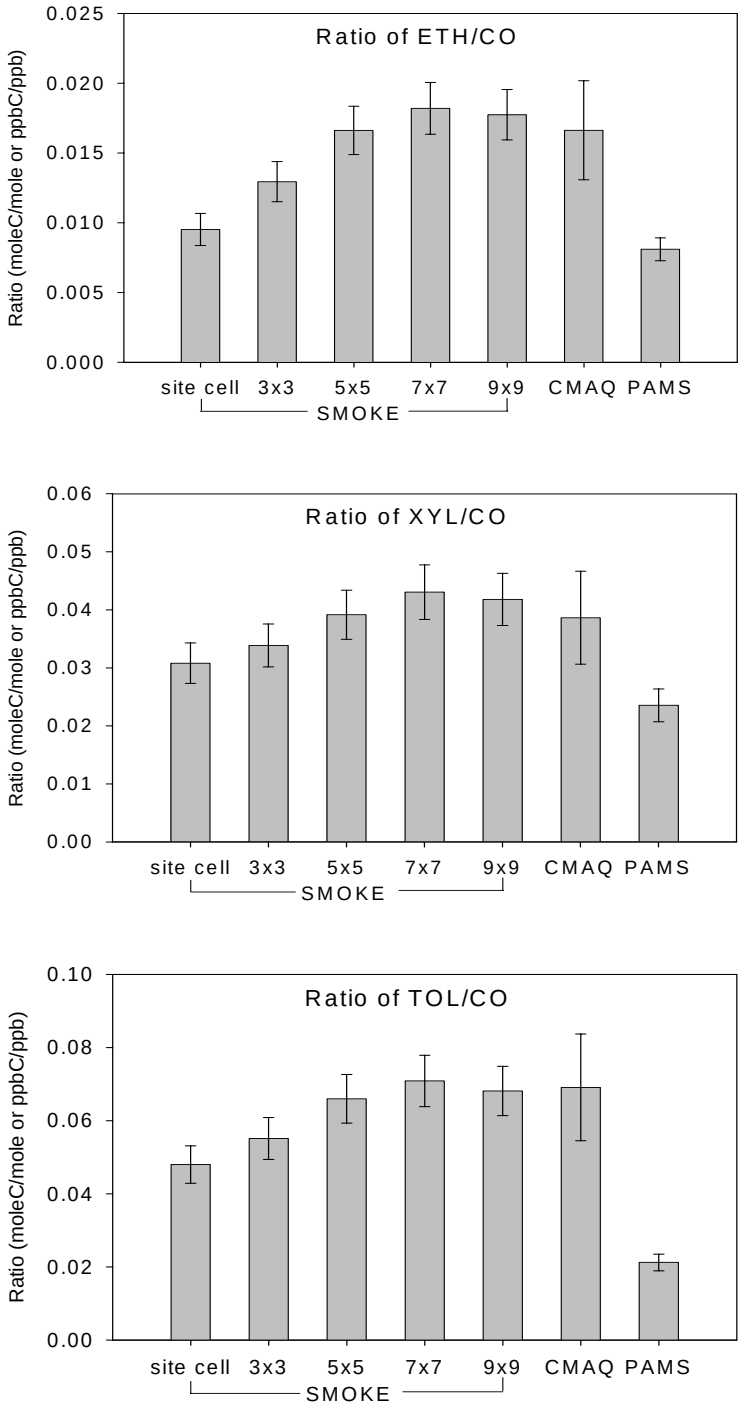

Figure 4.7: Comparison of average ratios between the estimated (SMOKE or CMAQ) and the observed values in the morning from 6:00 a.m. to 9:00 a.m. for Camden, NJ. The error bars indicate the two-sigma standard errors of the means (95% confidence interval).

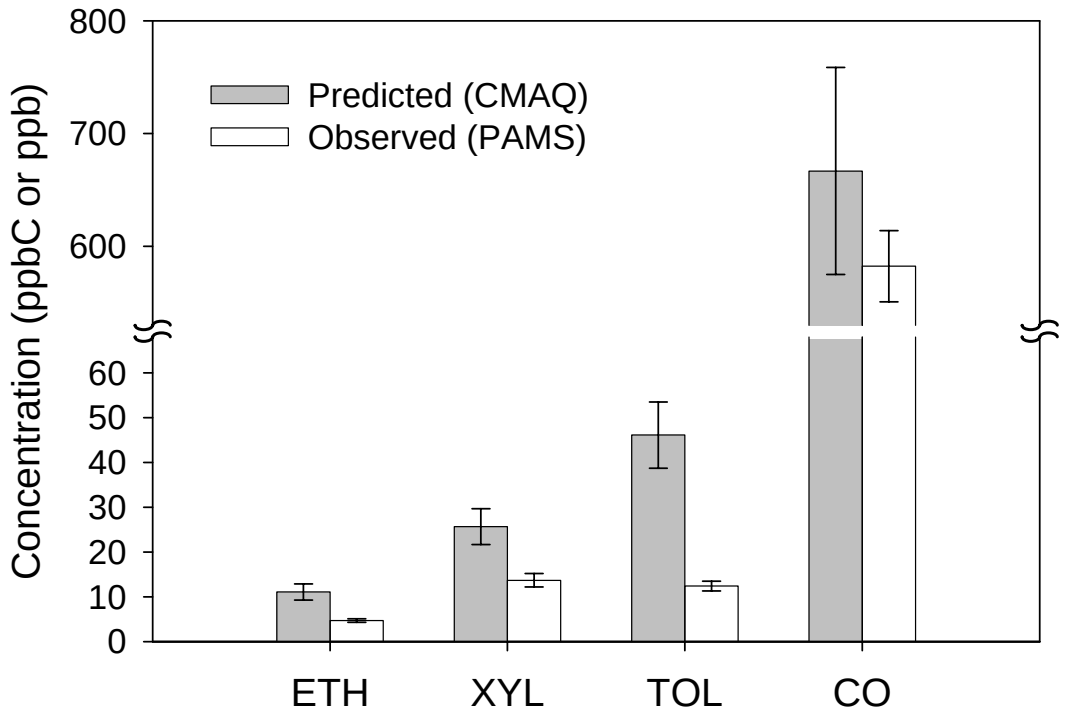

Figure 4.8: Comparison of average concentrations between the predicted (CMAQ) and the observed values in the morning from 6:00 a.m. to 9:00 a.m. for Camden, NJ. The error bars indicate the two-sigma standard errors of the means (95% confidence interval).

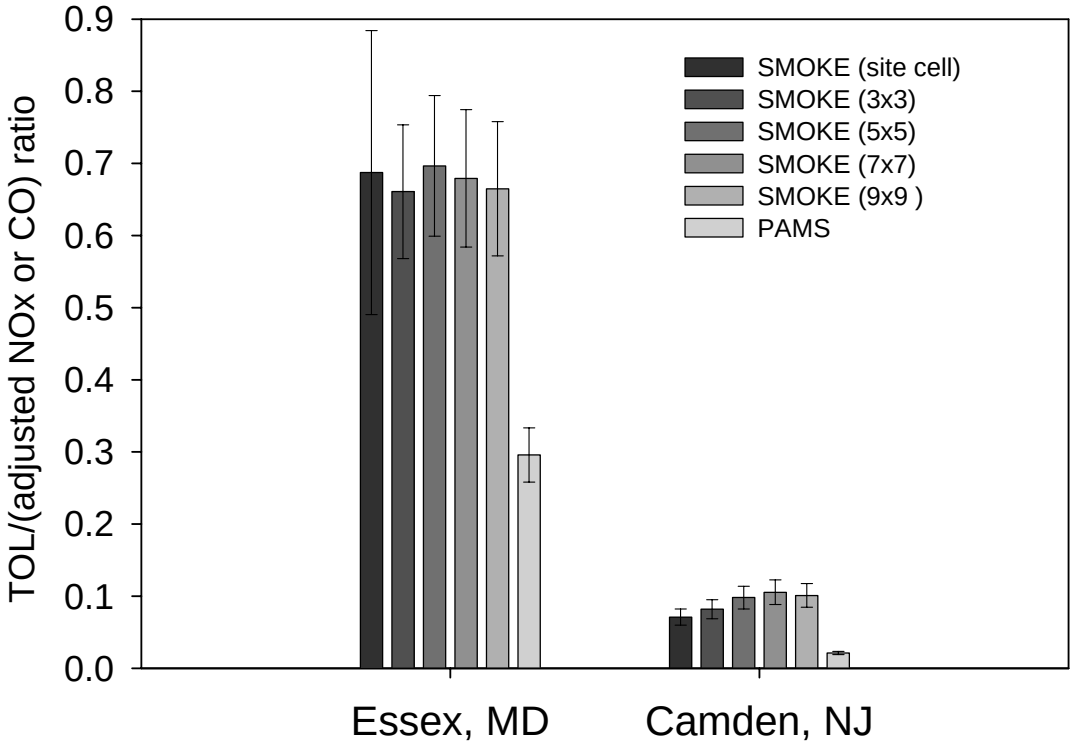

Figure 4.9: Comparison of average ratios of TOL to adjusted NOx or CO between the estimated (SMOKE) and the observed values in the morning period of 6:00 a.m. to 9:00 a.m. The error bars indicate the two-sigma standard errors of the means (95% confidence interval).

As stated above, the results for all three sites suggest a significant overestimate of solvent emissions while the estimates of emissions from vehicle exhaust differ depending on location. However, the observed TOL might under-represent the actual concentration because of the unidentified portion in PAMS observations as mentioned earlier; this result is very dependent upon the VOC speciation step in SMOKE. If the speciation of VOC does not represent reality, this comparison might lead to an erroneous conclusion. Therefore, we implemented another method of evaluation of emissions estimates from vehicle exhaust and solvent sources, a source apportionment technique. The next section describes the method and the results.

4.4.2 Comparison of ratios of VOC source categories using a source apportionment model

To identify and apportion VOC sources, the UNMIX 2.4 receptor model was used. The details about the UNMIX were described in the Chapter 3.

Using PAMS measurements from Essex, MD, six possible VOC emission sources were identified: vehicle exhaust, gasoline vapor, liquid gasoline, solvent, natural gas, and biogenics. The procedure of identification of source categories is described in the study of VOC emissions sources in the Baltimore area using PAMS measurements by Choi and Ehrman (2004). As for the DC and NJ measurements, we could not identify distinct solvent sources of VOC using UNMIX. The unexplained source categories, which may represent real sources or mixtures of real sources, were extracted by using UNMIX at the two sites. The composition of each of these source

categories showed a high portion of toluene, suggesting a possibility that a solvent source category may be mixed into other source categories instead of being separated out as a distinct category. Refer to Appendix 2 regarding source apportionment results. Hence, we focus here on the source apportionment results from the Essex site, MD, only.

Figure 4.10 shows a comparison of the average ratios of VOC source contributions to total NOx estimated from SMOKE and UNMIX at Essex, MD. The ratios for vehicle exhaust are underestimated. In contrast, the SMOKE solvent source contribution from SMOKE is three times higher than for the source apportionment. This overestimate of solvent sources is consistent with the results for the comparison of individual VOC species in the previous section. We could not perform the same comparison using the DC and NJ measurements, but the consistency of the results between VOC species comparison and VOC source contribution comparison at the Essex site suggests that the overestimate of emissions from solvent sources may also occur at the McMillan Reservoir in DC and the Camden in NJ sites.

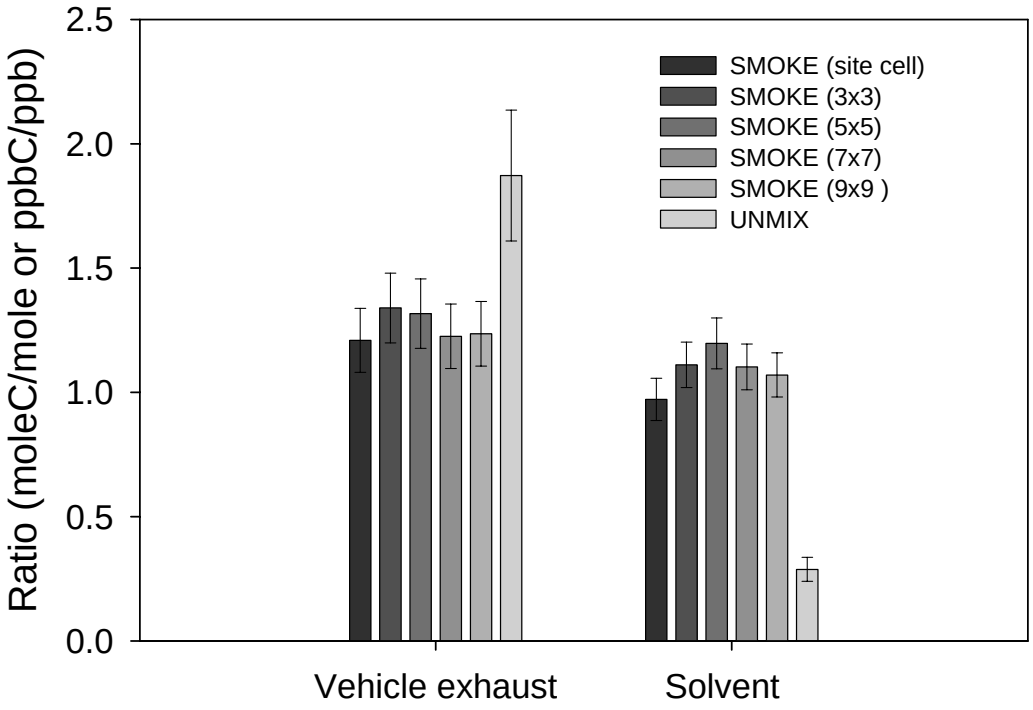

Figure 4.10: Comparison of average ratio of each VOC source contribution to NOx between estimates from SMOKE and UNMIX for Essex, MD in the morning from 6:00 a.m. to 9:00 a.m. The error bars indicate the two-sigma standard errors of the means (95% confidence interval).

4.4.3 Modeling the impact of VOC solvent source emissions reduction on ozone and anthropogenic secondary organic aerosol (SOA) concentrations

Parrish et al. and Demerjian pointed out the uncertainties associated with PAMS measurements (Parrish et al., 1998, 2000; Demerjian, 2000). According to an internal consistency test of PAMS measurements at several observation sites by Parrish et al. (1998), poor precision and systematic measurement errors were present in the PAMS measurements. Our study was based on PAMS measurements, and a certain degree of uncertainty may exist in the results. Nevertheless, there are several studies suggesting a result for solvent emissions similar to this study. Mannschreck et al. evaluated an emissions inventory for the city of Augsburg in Germany using an extensive comparison between individual hydrocarbons (HC_i) to total measured hydrocarbons (HC_{sum}), HC_i/CO, HC_{sum}/CO, and HC_{sum}/NO emission ratios from measured concentrations and modeled emissions (Mannschreck et al., 2002). Their results showed a possible overestimate of emissions from solvent sources. Mannschreck et al. suggested a further analysis from measurements including oxygenated and halogenated VOC, which are important solvent components, and implementation of a source apportionment model. In addition, Watson et al. reviewed VOC source apportionment using the CMB method in more than 20 urban areas, mainly in the United States, and pointed out that coatings and solvent contributions were much lower than the proportions attributed to these sources in current emissions inventories (Watson et al., 2001).

Even though we cannot perform further analysis using oxygenated and halogenated VOCs, use of two different approaches at the Essex, MD PAMS site - relative and absolute comparison of individual species, and relative comparison of source contribution to NOx - leads to a similar conclusion about the estimate of solvent source emissions. The other two sites also showed patterns of overestimates of TOL like those at the Essex site, suggesting that overestimation of solvent sources in urban and suburban areas may be a general phenomenon, as Watson et al. pointed in their review (Watson et al., 2001).

Based on the findings of this study and other studies, the impact of a reduction of solvent source VOC emissions on ozone and anthropogenic SOA concentrations in the study domain was investigated using a photochemical air quality model. VOC emissions from solvent sources throughout the study domain were reduced by 50 %, in line with the average overestimation at the three PAMS sites. This reduction corresponds to 16% reduction of total VOC emissions. A CMAQ simulation was performed with this modified emissions inventory. Figure 4.11 compares the frequency distributions of hourly surface ozone and anthropogenic SOA concentrations for the base case and the 50% reduction in solvent VOC emissions case. As for ozone, there is little difference between these cases. The maximum difference in ozone concentration between the two cases when time and space are paired was less than 10 ppb. The solvent emissions around the three PAMS sites are roughly speciated to 55% PAR, 25% TOL, 11% NR, and 8% XYL. According to a study of photochemical ozone creation potential (POCP) for organic compounds by Derwent et al. and a study of ozone reactivity scales for VOCs by Carter, TOL (toluene group)

shows one third to a half of the ozone forming potential of XYL (xylene group), which has approximately as high an ozone forming potential as isoprene (Derwent et al., 1998; Carter, 1994). Hence, the undetectable change of ozone after a solvent emissions reduction may result from solvent emissions being dominated by VOC species that do not have high ozone forming potentials. As another reason, it is speculated that this region has NOx-sensitive characteristics, such that VOC control does not result in a remarkable change of ozone concentration. When it comes to anthropogenic SOA, the difference between two cases is not substantial. However, we can see a noticeable decrease of SOA concentrations in with 50% solvent emissions reduction. TOL and XYL have been studied as precursors of secondary organic aerosol, and their aerosol yields are approximately similar (Bowman et al., 1995; Apndis et al., 1992).

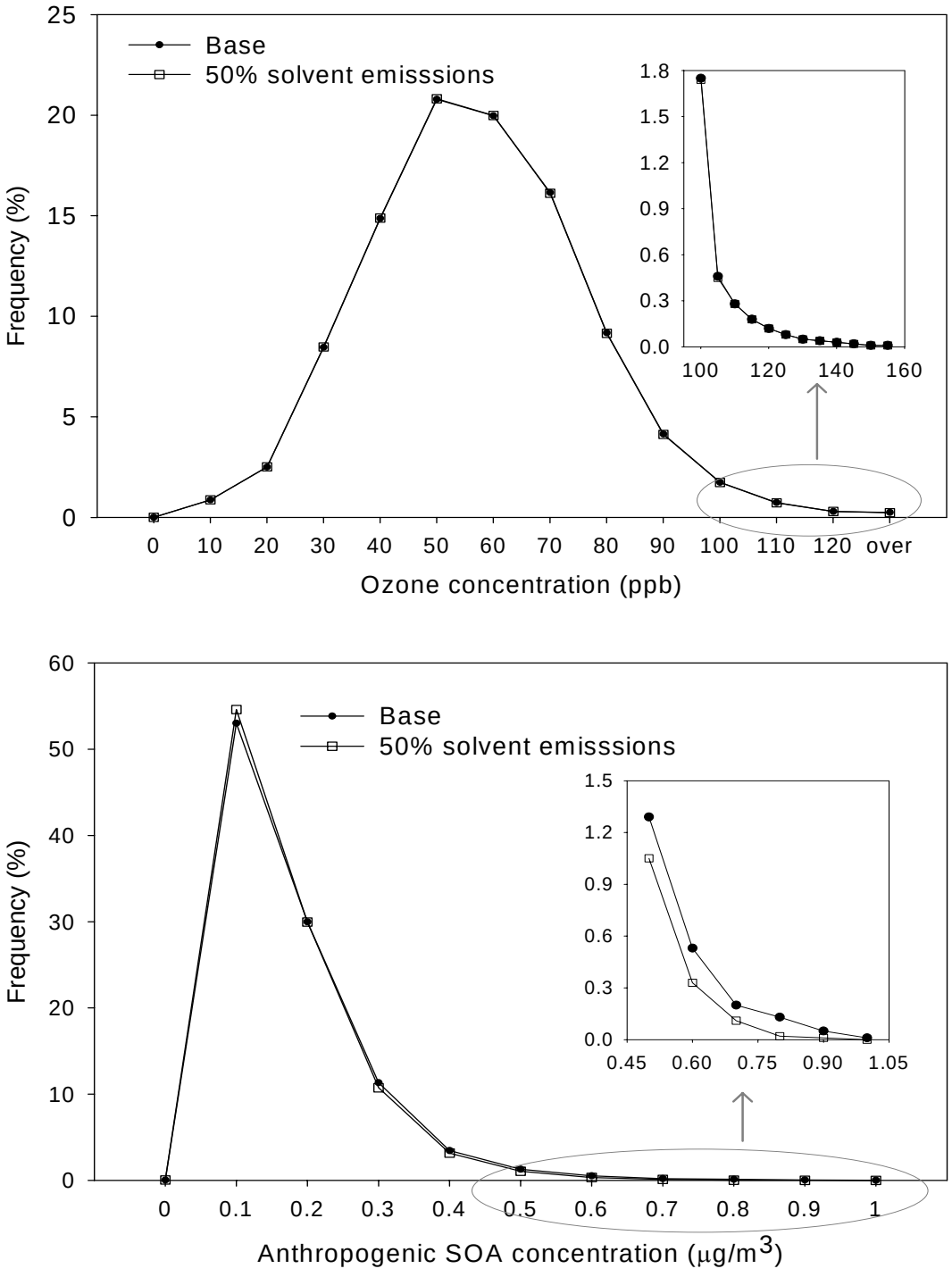

Figure 4.11: Comparison of the frequency distributions of hourly surface ozone and anthropogenic SOA concentrations between the base case and the case with 50% of the total solvent VOC emissions from July 8 to July 20, 1997, based on all grids in the modeling domain.

4.5 Conclusions

At the Essex, MD and McMillan reservoir, DC sites the comparisons of ETH/NOx and XYL/NOx ratios between estimates and measurements, and the comparisons of predicted ETH and XYL concentrations to the corresponding observed concentrations showed some differences between methods. However, the results for the Camden, NJ site demonstrated consistent results between comparison methods, implying a possible overestimate of vehicle exhaust. In terms of TOL, which is mainly emitted from solvent sources, the ratio of TOL to NOx as well as absolute concentrations of TOL and NOx revealed overestimates of solvent sources by a factor of 1.5 to 3 at all three sites. In addition, overestimates of solvent source emissions were corroborated by comparing ratios of VOC solvent source contribution to NOx to the ratio from SMOKE at the Essex, MD PAMS site. Other investigators also proposed that solvent sources were overestimated, implying the possibility of inaccurate emission factors in estimating VOC emissions from solvent sources. Hence, we recommend further investigation of the emissions inventory of solvent sources and their emission factors.

The photochemical model simulations did not show a perceptible change in ozone concentrations after the reduction of solvent VOC emissions, possibly because this region is NOx-sensitive, or because the solvent chemical species do not readily form ozone. However, a noticeable decrease of high SOA concentrations with 50% solvent emissions reduction was observed.

Chapter 5: Regional-scale Ozone Air Quality Modeling over the Baltimore/Washington Ozone Non-attainment Area: Characteristics of a Multi-day Ozone Event and Development of an Optimal Control Strategy

5.1 Introduction

The lifetime of ozone is longer in the free troposphere than near the surface, and meteorological processes play a critical role in transport and diffusion as well as chemical transformation (Jonson et al., 2001). Additionally, transport of pollutants on the order of 100 km-500 km across state boundaries has been reported within the northeastern U.S. (Samson and Shi, 1988; NRC, 1991; Solomon et al., 2000). Therefore, local emissions of ozone precursors cannot be entirely responsible for the ozone events in individual urban areas exceeding National Ambient Air Quality Standard (NAAQS).

Horizontal transport within the PBL is described in detail by Hidy (2000) and Solomon et al. (2000). For example, the PBL can be separated into three layers: a nocturnal surface boundary layer from the ground to about 400 m, an intermediate layer from 400-1000 m, and a sub-synoptic layer above 1000 m to the free atmosphere around 1.5 km. Note that the height of each layer varies greatly depending on time and geographical location. At night, the lower two layers are often decoupled, while

during daytime these two layers become mixed. Furthermore, all three layers are frequently well blended in the middle of the day. In the surface boundary layer, local dynamic processes such as surface friction are predominant. In the intermediate layer, local scale and mesoscale phenomena coexist. In the upper layer, synoptic scale phenomena dominate. Hence, the origins of winds in these three layers are most likely to be different. In the upper two layers of the PBL, usually called the nocturnal residual layer, pollutants can be transported during the night over long distances with faster winds than at the surface. In the morning as the ground starts to heat up, warm air above the ground ascends, forcing the growth of the mixing layer. As the mixing layer grows, pollutants trapped aloft in the nocturnal residual layer can be entrained downward into the mixing layer (Zhang and Rao, 1999). Based on this characteristic of the diurnal variation of the PBL, and subsequent vertical distribution of pollutant concentrations, most ozone events are a product of both long distance transport of pollutants and in-situ photochemical production.

There are several areas in the Northeastern United States with elevated ozone levels often exceeding the NAAQS. In particular, the highest ozone concentrations in the Northeastern U.S. occur across the Northeast Corridor of the United States, a relatively concentrated string of urban centers extending from Washington D.C. to Boston (Kumar and Russell, 1996). With a focus on the Baltimore-Washington (B-W) ozone non-attainment area, the extreme ozone events occur during multi-day episodes. These events can be regional in scale, with ozone concentrations exceeding the NAAQS at numerous locations along the East Coast. According to an analysis in the mid-Atlantic by Ryan et al. (2000), high ozone events are typically associated with a

slow moving, high-pressure system overhead or just west of the region and an upper air ridge to the west or northwest. The ridge maximizes the local potential for ozone formation by causing subsidence downstream of the ridge axis. The subsidence inhibits cloud formation and strengthens the low level inversion so that photochemistry is maximized and vertical mixing of low-level emissions is minimized. In addition, the upper air ridge to the west of the region leads to transport of air from heavily industrialized areas west and northwest of the Baltimore/Washington region (NRC, 1991; Ryan et al., 1998).

Ryan et al. (1998) showed the impact of significant regional scale transport of ozone and its precursors on an ozone event in July 1995 in this region through an analysis of observations and calculation of back trajectories. However, with only an observational analysis, we cannot reach a conclusion as to the relative impacts of long-range transport of ozone and its precursors versus local emissions on the ozone events in the region. For that reason, we employed a three dimensional photochemical model in order to study an ozone episode during July 1997, which showed a similar synoptic meteorological pattern to historically typical ozone events.

The focus of this modeling study is three-fold:1) to investigate the relative impact of long-range transport of ozone and precursors versus local emissions on high ozone occurrences in the Baltimore/Washington ozone non-attainment area, 2) to investigate the relative contribution of biogenic VOC emissions and anthropogenic VOC emissions to local ozone production during ozone events, and 3) to identify and apply control strategies leading towards ozone reduction. As stated earlier, ozone events are combinations of long-range transport and local generation. Hence, in order

to come to an effective control strategy for ozone reduction, it is necessary to identify the relative importance of long-range transport and local emissions. After that, we can focus on the dependence of ozone formation on local emissions. In this study, in particular, the relative impact of biogenic VOC emissions versus local anthropogenic VOC emissions on local ozone production was compared. Our motivation is that only anthropogenic emissions can be controlled, and a significant role of biogenic VOC in rural areas as well as in many urban and suburban locations in ozone formation has been reported based upon several observation-based studies (Chameides et al., 1988, 1992; Cardelino and Chameides, 1995, 2000; Morales-Morales, 1998; Choi and Ehrman, 2004). Several modeling studies have suggested that in general, VOC controls might be effective in reducing ozone levels in urban and suburban areas, which are most strongly impacted by anthropogenic emissions (McKeen et al., 1991; Possiel and Cox, 1993; Hanna, 1996). However, the biogenic emissions used in modeling studies in the past are now considered most likely underestimated (Guenter et al., 2000; Russell et al., 2000). Consequently, VOC control for certain urban and suburban areas might not lead to sufficient ozone reductions. Thus, modeling-based as well as observation-based studies of the importance of biogenic VOC emissions in ozone events for the region of interest are warranted, and the results should be consistent with each other. With this information, reliable control strategies for anthropogenic emissions for urban and suburban areas can be developed.

Morales-Morales (1998) and Choi and Ehrman (2004) suggested a significant contribution of biogenic VOC emissions to local ozone production in the Baltimore area based upon observed measurements. The second focus of this modeling study is

to investigate the relative contributions of local biogenic VOC emissions versus local anthropogenic VOC emissions on high ozone events. Finally, several local control scenarios were applied to identify a possible control strategy for reducing high ozone events in the Baltimore/Washington ozone non-attainment area.

5.2 Methods

5.2.1 Description of the modeling system

In this study, we implemented a three-dimensional modeling system that consists of MM5 version 3.3, the SMOKE version 1.4 and the CMAQ version 4.3. MM5 is used to provide meteorological input fields for the model simulation in SMOKE and CMAQ. The MM5 simulations, consisting of the two nested grid domains with resolutions of 36 km, and 12 km, were conducted with a modified Blackadar PBL scheme and standard nudging process by the Department of Meteorology, University of Maryland (Sistla et al., 2002; Zhang and Zheng, 2004). The meteorological variables were extracted using MCIP version 2.2. This program was also used to provide meteorological variables at the 4 km grid resolution by interpolating 12 km grid results. Figure 5.1 shows the modeling domain for three nested grids with 36 km, 12 km, and 4 km resolution. The detailed study domain, nested within the outer domains, covers the entire state of Maryland, and parts of Virginia, West Virginia, Delaware, New Jersey, and Pennsylvania. The detailed domain has 108 columns by 78 rows with 4 km horizontal grid cell resolution.

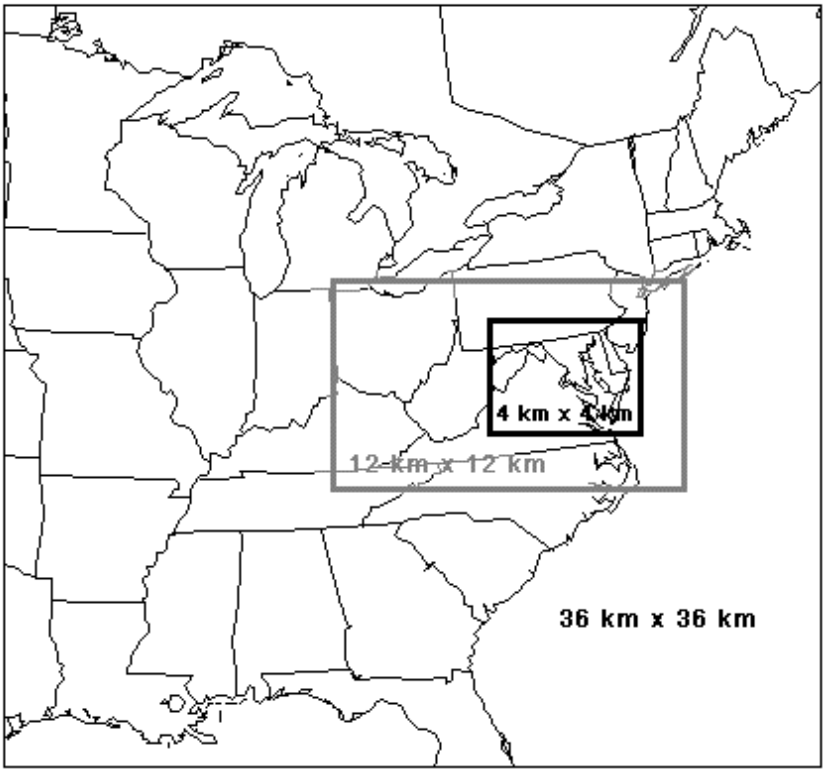

Figure 5.1: Map of CMAQ modeling domain.

There are 16 vertical layers extending from the surface to approximately 20 km above the ground. The vertical layers are unevenly distributed with higher resolution at lower levels to better resolve boundary layer phenomena. The total height of the lowest 8 layers is around 1.5 km, and the surface layer height is about 30 m.

In this study, an aggregated emissions inventory was obtained from the Mid-Atlantic Regional Air Management Association (MARAMA). SMOKE processing using this emissions inventory was described in the Chapter 4.

In the CMAQ chemistry and transport model, the Modified Euler Backward Iterative (MEBI) chemistry solver was used (Dolwick et al., 2001). The chemistry mechanism employed by CMAQ is based on CB-IV, a chemical kinetic mechanism for urban and regional photochemistry, and contains 37 species and 96 reactions (EPA-III, 1999).

5.2.2 Modeling period

Our simulation period begins on July 5 and ends on July 20 1997. This period includes the most extensive episode of 1997, which occurred from July 12 to July 17. The weather pattern associated with this episode was very similar to the July 1995 episode. Aloft, a ridge formed over the region, resulting in decreased vertical motion, limited cloud formation, and strong photochemistry. In addition, a surface high-pressure system with widely spaced isobars created weak winds and limited horizontal ventilation. Also, the clear skies led to radiational cooling at night, which produced a surface inversion, and caused an even greater buildup of pollutants near the surface.

At the beginning of the July 12 to July 17, 1997 episode, a ridge moved into position west of the region, and ozone exceedances were reported on July 12 in Pennsylvania and Maryland, and spread into New York and New Jersey on July 13. Region-wide exceedances (from Virginia to Connecticut) were reported on July 14 and 15 (NESCAUM, 1998).

5.3 Organization of simulations

In this study, the simulations were divided into three main categories based on different objectives. Firstly, five simulations including the base case were conducted with the objective of investigating the contribution of long-range transport of pollutants versus local emissions to ozone episodes in the Baltimore/Washington ozone non-attainment region. The simulations were performed mainly by controlling output variables from the Boundary Condition (BCON) processor in CMAQ. BCON is used to generate species concentrations for the cells immediately surrounding the modeling domain from the existing three dimensional, gridded, time-variant concentration files of a coarser grid (Ching and Byun, 1999). In this case, the boundary condition files for the base case, with 4 km grid resolution, were obtained from the concentration files with 12 km grid resolution. Table 5.1 lists the identification (RUN) code, which will be referred to in the subsequent discussion, and the conditions of operation for each simulation. The "NoEmis" case has no emissions from both anthropogenic and biogenic sources within the modeling domain with 4 km grid resolution, but the boundary conditions are the same as the base case. This case

Table 5.1: Simulation details

Run Code	Operation Conditions	
	Emissions	Boundary conditions
Base	Normal emissions (biogenic & anthropogenic pollutants)	Normal B.C. (obtained from the runs with 12 km rid resolution)
NoEmis	No emissions	Normal B.C.
CleanBC	Normal emissions	Without O_3 and precursors
CleanOZ	Normal emissions	Without O_3 but with precursors
CleanPRE	Normal emissions	Without precursors but with O_3
CleanBC_woAVOC	Without anthropogenic VOC emissions but with other emissions	Without O_3 and precursors
CleanBC_woBVOC	Without biogenic VOC emissions but with other emissions	Without O_3 and precursors
Half_Anox	With 50 % reduction of anthropogenic NOx emissions	Normal B.C.
Half_Avoc	With 50 % reduction of anthropogenic VOC emissions	Normal B.C.
Half_Anox_Avoc	With 50 % reduction of both anthropogenic NOx and VOC emissions	Normal B.C.
HalfozBC_baseEMI	Normal emissions	With 50% reduction of ozone in B.C.
HalfozBC_halfAnox	With 50 % reduction of anthropogenic NOx emissions	With 50% reduction of ozone in B.C.

was included to probe how transported pollutants would evolve in the modeling domain. The clean boundary conditions or "CleanBC" case has the same emissions as the base case, but there are no pollutants such as ozone and its precursors in the boundary conditions. Here, the precursors denote NOy and VOC in terms of the CB-IV chemical mechanism as listed in Table 5.2. From this case, we expect to get insight into the impact of local contributions on an ozone episode in the modeling domain. The clean ozone precursors in the boundary condition or "CleanPRE" case have the same emissions as the base case. However, the boundary conditions do not include ozone precursors, NOy and VOC, but do include transported ozone. This simulation can provide insight into the impact of transported ozone on the ozone episode in the modeling domain. The clean ozone in the boundary conditions or "CleanOZ" case has the same emissions as the base case, while the boundary conditions include not ozone, but ozone precursors, NOy and VOC. This simulation can provide insight into the impact of transported ozone precursors on an ozone episode within the modeling domain.

Secondly, two additional simulations were carried out in order to test the relative contributions of biogenic VOC and anthropogenic VOC to local ozone production. The first one, the clean boundary conditions without anthropogenic VOC emissions or "CleanBC_woAVOC" case, has the same boundary conditions as the "CleanBC" case, and the anthropogenic VOC emissions are excluded, but the biogenic VOC emissions and both anthropogenic and biogenic NOx emissions are included.

Table 5.2: NOy, and VOC species list in terms of CB-IV chemical mechanism (Ching and Byun, 1999)

Symbol		Description
NOy	NO	Nitric oxide
	NO2	Nitrogen dioxide
	HONO	Nitrous acid
	NO3	Nitrogen trioxide
	N2O5	Nitrogen pentoxide
	HNO3	Nitric acid
	PNA	Peroxynitric acid
	PAN	Peroxyacyl nitrate
	NTR	Organic nitrate
VOC	PAR	Paraffin carbon bond
	ETH	Ethene
	OLE	Olefinic carbon bond
	TOL	7 carbon aromatics
	XYL	8 carbon aromatics
	ISOP	Isoprene
	FORM	Formaldehyde
	ALD2	Acetaldehyde and higher aldehydes
	MGLY	Methyl glyoxal
	CRES	Cresol and higher molecular weight phenols

The clean boundary conditions without biogenic VOC emissions or "CleanBC_woBVOC" case is different in that it excludes only biogenic VOC emissions with the same boundary conditions as the "CleanBC" case.

Lastly, five simulations were performed in order to investigate possible control strategies towards ozone mitigation for the Baltimore/Washington ozone non-attainment area. A 50% reduction of anthropogenic NOx emissions or "Half_Anox" case is the same as the Base case except that the anthropogenic NOx emissions in the domain were reduced to 50% of their original emissions. The "Half_Avoc" case has 50% reduction of anthropogenic VOC emissions, and the "Half_Anox_Avoc" case has 50% reduction of both anthropogenic NOx and VOC emissions, with the other conditions the same as the Base case. In the remaining two simulations, ozone concentrations in the boundary conditions were reduced by 50% in order to look at a reduction effect of long-range transport of ozone on ozone concentrations in this area. In one simulation, normal emissions in the modeling domain were used (HalfozBC_baseEMI), while in the other a 50% reduction of anthropogenic NOx emissions in the modeling domain was incorporated (HalfozBC_halfAnox).

5.4 Results and discussion

5.4.1 Model performance

CMAQ model performance was evaluated based on 1-hr surface ozone measurements for 56 observation sites in the modeling domain for July 8-July 20, 1997, and aircraft data measured during University of Maryland (UM) research flights

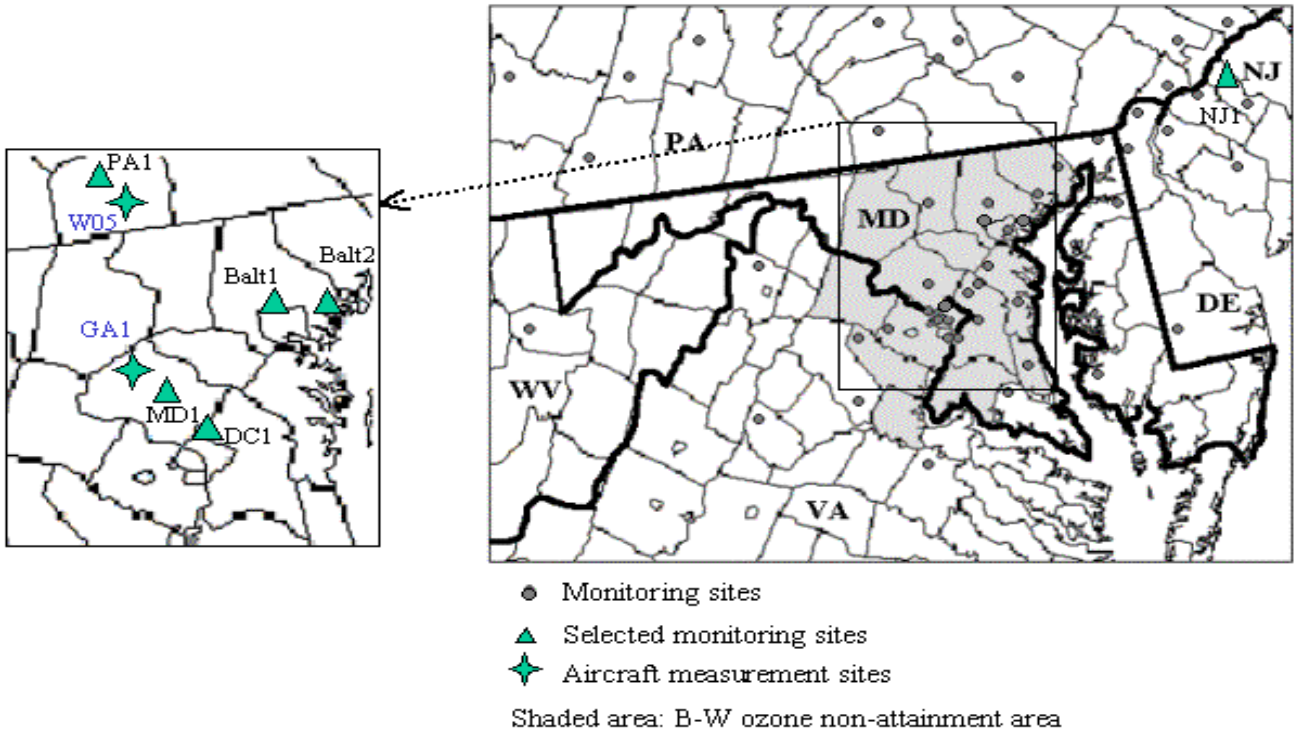

Figure 5.2: Map of the ozone monitoring sites. DE (Delaware), MD (Maryland), NJ (New Jersey), PA (Pennsylvania), VA (Virginia), and WV (West Virginia). Balt2 (Essex PAMS site), NJ1 (Camden PAMS site), and DC1 (McMillan reservoir PAMS site).

for July 12-July 17, 1997. Figure 5.2 shows the locations of the monitoring sites. The first three days are not included in the performance evaluation, and are considered model "spin-up" days.

Modeled ozone levels were statistically evaluated using measures, which are recommended by the U. S. EPA (EPA-V, 1991), for both a grid cell corresponding to the location of the observation sites and nine grid cells surrounding the observation sites. The statistical values for a grid cell and nine grid cells do not show a significant difference. The normalized bias is computed as the mean residual, where the residual is the predicted minus the observed concentration, divided by the corresponding observed concentration before averaging. Therefore, negative bias implies underprediction of observations by the model. Gross error is computed in the same manner as bias except that the absolute values of the residuals are used, so gross error is always positive. Note that underpredictions and overpredictions may offset one another in computing bias statistics. Whenever the observed ozone concentration is below the specified cutoff level of 60 ppb, the observed and predicted concentrations for that hour and location are not used in computing the performance statistics (McNair et al., 1996). It should be noted that even though the statistics have been extensively used for model evaluation, there is a concern that such statistical measures do not reveal model weaknesses. These recommendations were based on previous modeling studies, in which the models were tuned to improve the model performance. As such, use of these guidelines may not be appropriate for evaluation of more recently developed models (Russell and Dennis, 2000).

As shown in Table 5.3, the negative values of unpaired peak and normalized bias suggest a slight tendency toward underprediction, while normalized bias is somewhat over the EPA's guideline (Sistla et al., 2001; Yarwood et al., 2003). Figure 5.3 compares time series of modeled ozone to observed ozone at selected monitoring sites marked in Figure 5.2. The model prediction shows different results depending on the location of monitoring station. However, the model simulates well the times of the ozone peak within 2-3 hours during the ozone event days of July 12 to July 15 (Yarwood et al., 2003). In addition, we compared vertical ozone profiles observed and estimated at two aircraft measurement sites shown in Figure 5.2.

Table 5.3: Statistical analysis of model performance for ozone

Statistical measure	Model		Guidelines
	Site cell	Avg. for nine cells	
Unpaired peak (%)	-2.2	-5.4	< ±20
Normalized bias (%)	-21	-20	< ±15
Normalized gross error (%)	24	23	< 35
Correlation coefficient	0.75	0.76	

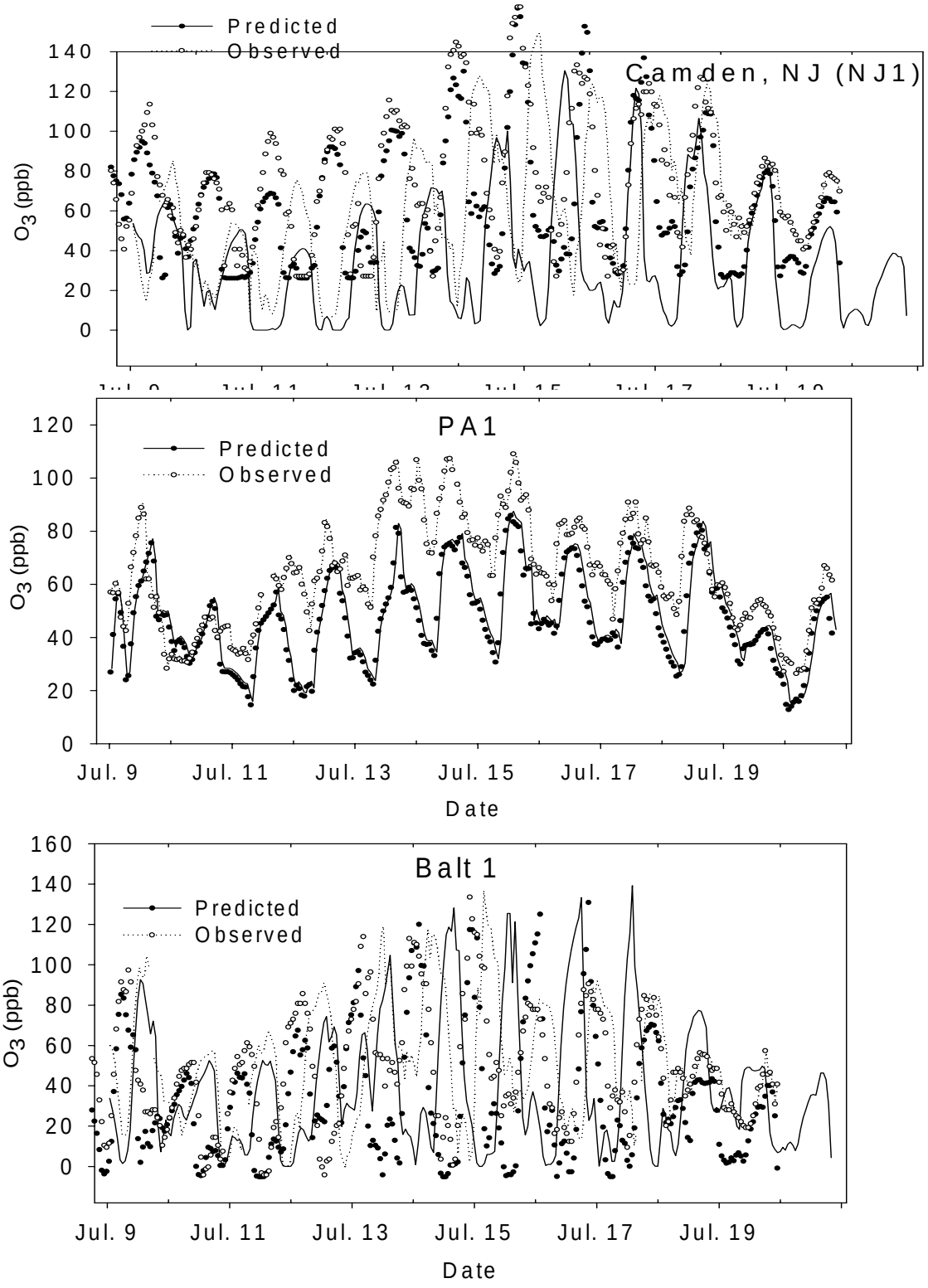

Figure 5.3: Time series of predicted (site grid cell) and observed ozone concentration for the selected sites for July 9 ~ 20, 1997.

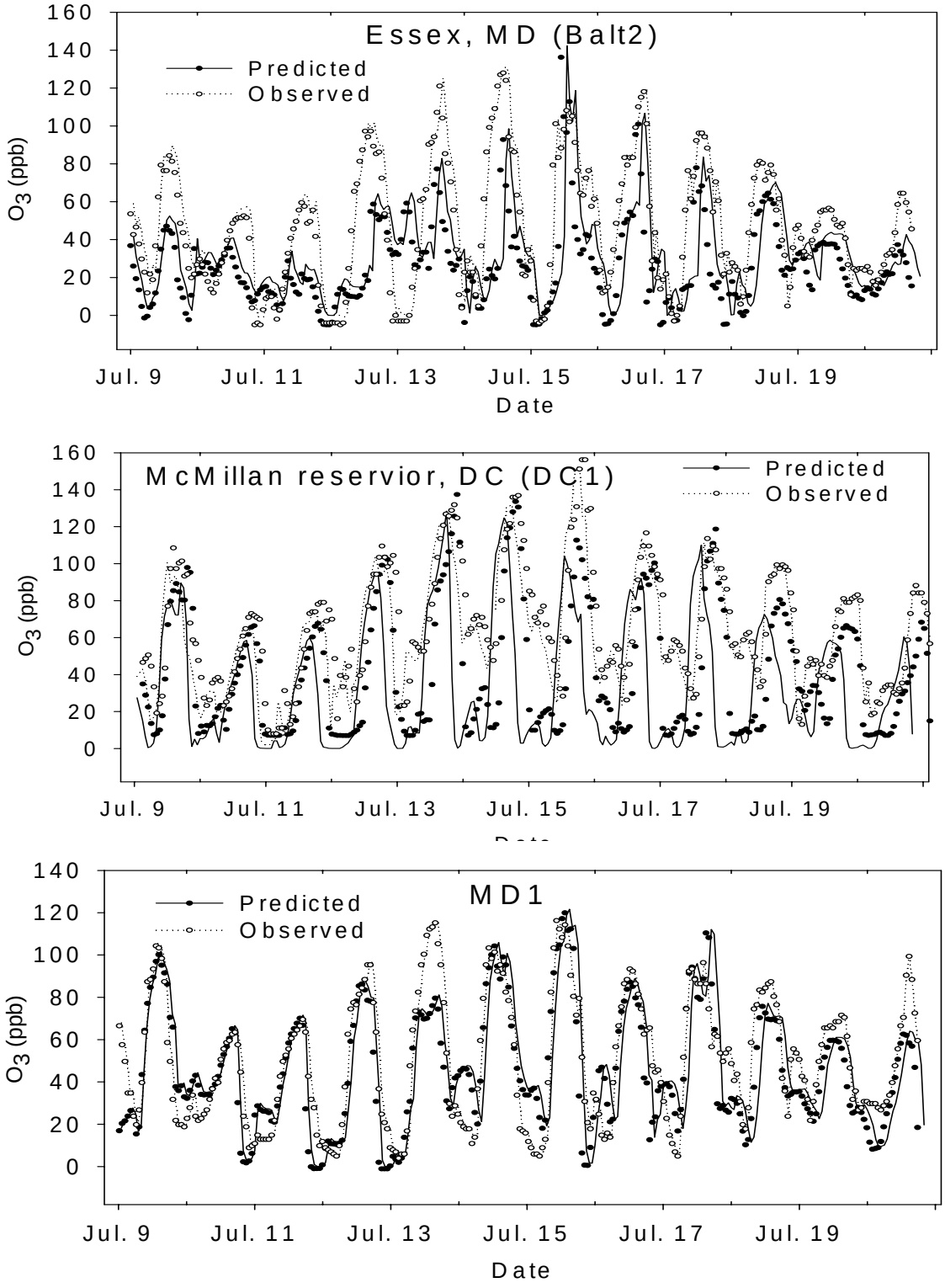

Figure 5.3: (continued)

Figures 5.4 and 5.5 show the comparison of predicted and observed vertical ozone profiles at two aircraft sites indicated in Figure 5.2. The CMAQ simulation of the morning of July 13 appears to underpredict the extraordinarily high ozone at about 0.8-1.5 km above the ground, which is within the nocturnal residual layer. Ozone contained in this layer can be a combination of the previous day's ozone by local photochemical generation and regional transport of ozone. Even under stagnant conditions at night near the surface, ozone can be transported by the nocturnal jet aloft (Aneja et al., 2000). Synoptic scale or mesoscale flow at this elevation is dominant during nighttime and just after sunrise, so that the underprediction of ozone at this elevation in the morning may suggest underprediction of long-range transport during the day. Hence, this seems linked to the negative normalized bias mentioned earlier, since the under-prediction of ozone aloft in the morning affects the surface ozone concentration after the mixing layer is fully developed. However, the measurements aloft are limited at these two sites, and the vertical ozone profiles on two later days (July 16 and 17) showed relatively good agreement between prediction and observation. Therefore, we cannot conclude that the CMAQ simulations in this study did not reproduce the long-range transport. Nevertheless, we should keep the possibility of under-prediction of long-range transport in mind in further analysis of the CMAQ simulation results. In particular, the significant underestimation of ozone concentrations in July 12 and 13 at the W05 site in Gettysburg, PA, is thought to be a combined result of underestimated emissions and underestimated transport. The two days are weekend days, and the SMOKE emission model allocates fewer emissions on weekends than weekdays.

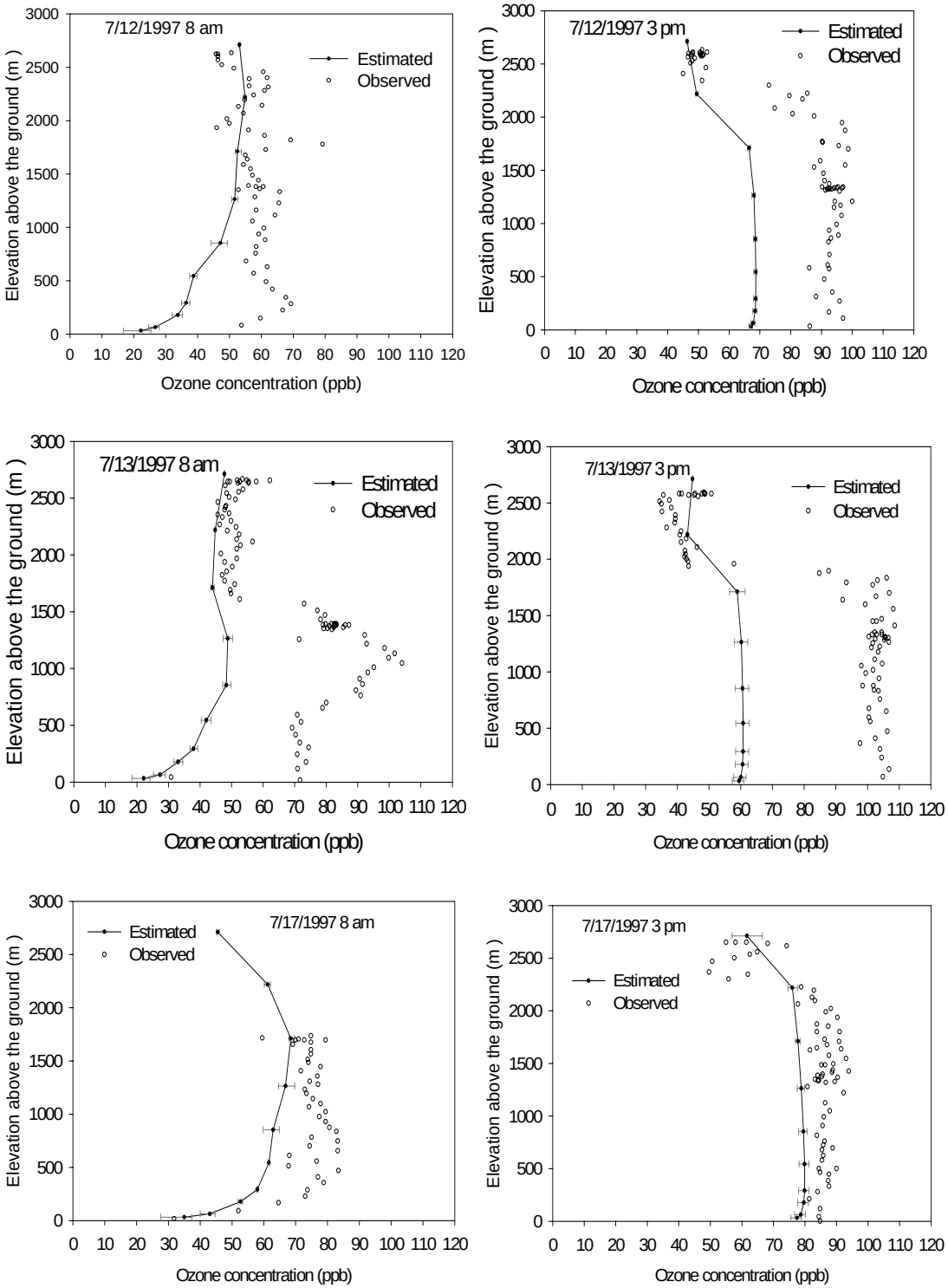

Figure 5.4: Comparison of estimated ozone (average of nine grid cells surrounding the observation site) with aircraft measurements at W05 (Gettysburg, PA). The horizontal bars indicate the minimum and maximum values in nine grid cells.

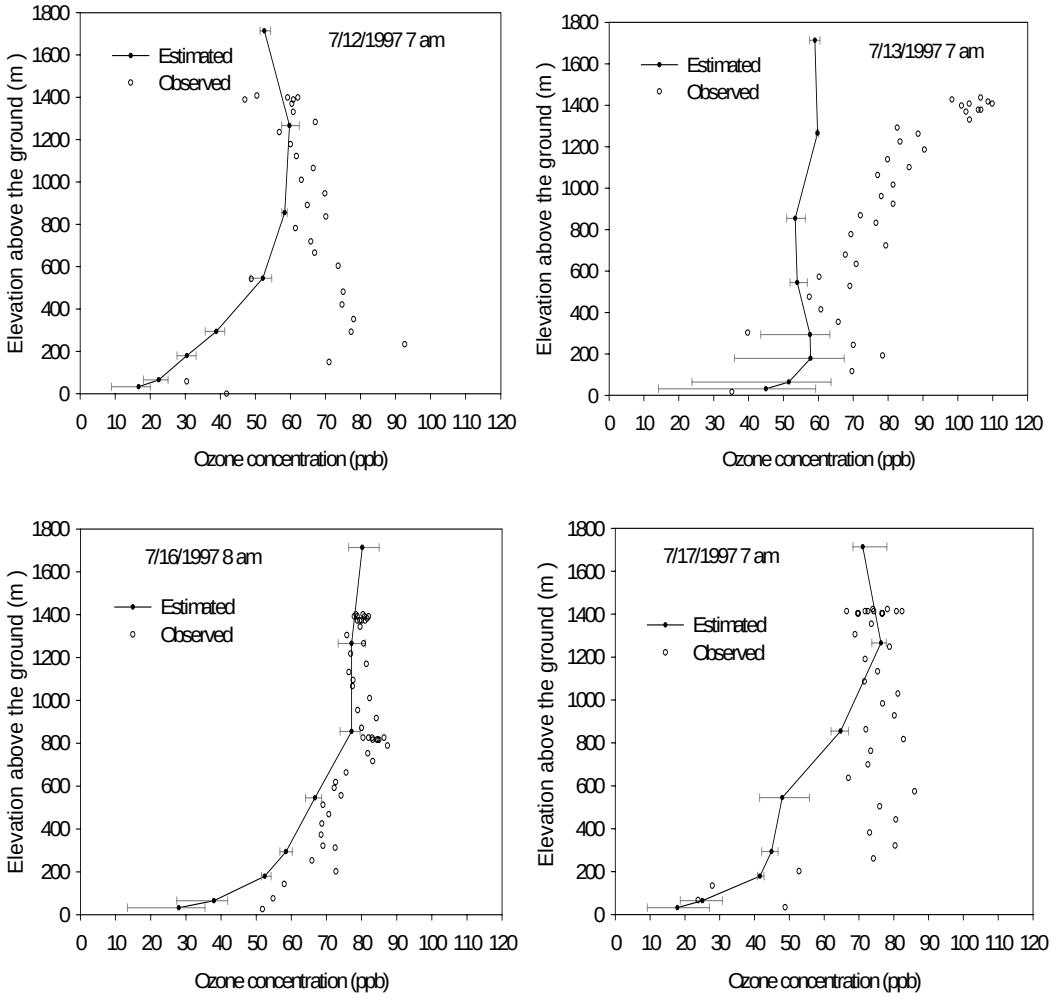

Figure 5.5: Comparison of estimated ozone (average of nine grid cells surrounding the observation site) with aircraft measurements at GAI (Montgomery, MD). The horizontal bars indicate the minimum and maximum values in nine grid cells.

The location is one of high weekend tourist activity in the summer, and SMOKE did not incorporate all possible extra activities at a specific location and a specific period with currently available temporal and spatial allocation factors.

The uncertainty of biogenic estimation remains an essential subject in the continuing debate on NOx versus VOC control, and we made a rough comparison of the estimated and observed isoprene at three PAMS sites located in urban/suburban areas that are shown in Figure 5.2. Taking into account that short-lived isoprene emissions are much more spatially heterogeneous than long-lived species, the comparison was done using the values at a site cell with 16 km^2 area and the average values for 3 cells x 3 cells surrounding the observation site. Figure 5.6 shows box plots of observed and estimated isoprene at the Essex site, MD for the site cell and 3 cells x 3 cells surrounding the Essex site. The black line across the box denotes the mean value, and the gray line across the box denotes the median value. The estimated isoprene concentrations agree with measured values better during the mid-day hours, when the atmosphere is well mixed and biogenic emissions are greatest, than during night. These differences during night are likely to be associated with problems with the modeled mixing height, nighttime chemistry representation, and/or deposition, rather than with emissions (Trainer et al., 2000; Pierce et al., 1998).

The isoprene emissions rates estimated using BEIS2, not shown here, were very small at night. When we take a closer look at the difference between the site cell comparison and nine cells comparison during daytime, the predictions show different behavior.

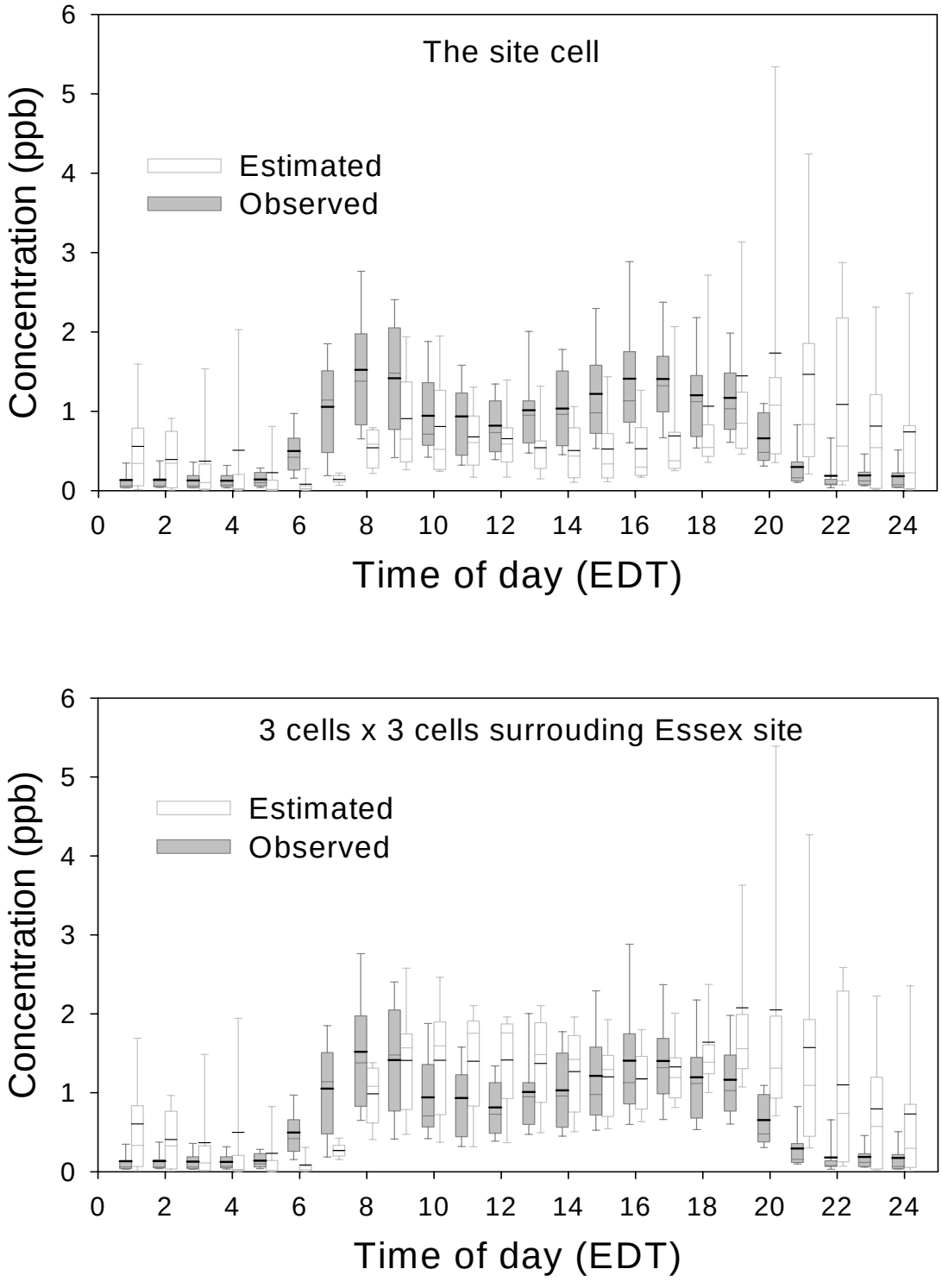

Figure 5.6: Comparison of observed and estimated isoprene during July 8 to July 20, 1997 at Essex site, MD for the site grid cell and 3 cells x 3 cells surrounding the Essex site (Balt2).

The predictions for the site cells are somewhat underpredicted, while those from the nine cells are slightly overestimated. In addition, the normalized bias using measured and predicted isoprene concentrations during daytime from 9 am to 6 pm at three PAMS sites was about + 40% for the nine cells comparison, and about –22% for the site cell comparison. Goldstein et al. (1998) found that BEIS2 underestimated the summer midday isoprene emission flux by at least 40% at Harvard forest, and Geron et al. (1997) pointed out that BEIS2 isoprene flux estimates are accurate to within about 50% from an analysis of published field flux studies. Our result seems consistent with those published studies.

There exist a wide variety of factors that could be responsible for isoprene overprediction or underprediction. These factors include chemical destruction rates, and horizontal advection, deposition, or vertical mixing in this modeling system (Pierce et al., 1998), as well as limitations associated with BEIS2. Andronache et al. (1994) recommended the use of measurements of isoprene concentration above at least 40 m rather than measurements near the surface because of the difficulties attributed to rapid and spatially heterogeneous processes of emissions, vertical diffusion, and surface chemistry (Pierce et al., 1998). Here, it is difficult to separate shortcomings originating from the complex modeling system from shortcomings from measurements. Since this analysis is limited to a few surface measurements located at urban/suburban sites, we are not confident about drawing conclusions regarding biogenic emissions modeling. However, assuming that land-use is well projected onto these fine grid cells, the site cell comparison might be more representative than the average of nine grid

cells. The underprediction of isoprene from the site cell comparison might be connected to the tendency for underprediction of ozone as mentioned earlier.

5.4.2 Investigation of transport vs. local contributions to ozone occurrences

Figures 5.7 through 5.10 show the surface ozone concentrations simulated for the ozone episode of July 1997, starting from July 12 to July 15 at the peak time of each day. From a comparison of the Base case, the NoEmis case and the CleanBC case (a, b, and c in Figures 5.7-5.10), it is seen that long-range transported pollutants, including ozone and its precursors (boundary conditions), have a significant influence on the ozone concentrations near the boundary cells, and the impact of long-range transport becomes less significant towards the center of the domain.

The Base case and the CleanPRE case (a and e in Figures 5.7-5.10) each show a similar distribution of ozone over the domain, while the CleanBC case and the CleanOZ case (c and d in Figures 5.7-5.10) look alike. These results imply that long-range transport of ozone has a more immediate influence on ozone concentration in the domain than transported ozone precursors. In addition, the contribution of transported ozone amounts to 40-90 ppb ozone for the area surrounding the Baltimore/Washington D.C ozone non-attainment area, while its contribution is less than 40 ppb for the Baltimore/Washington D.C. ozone non-attainment area.

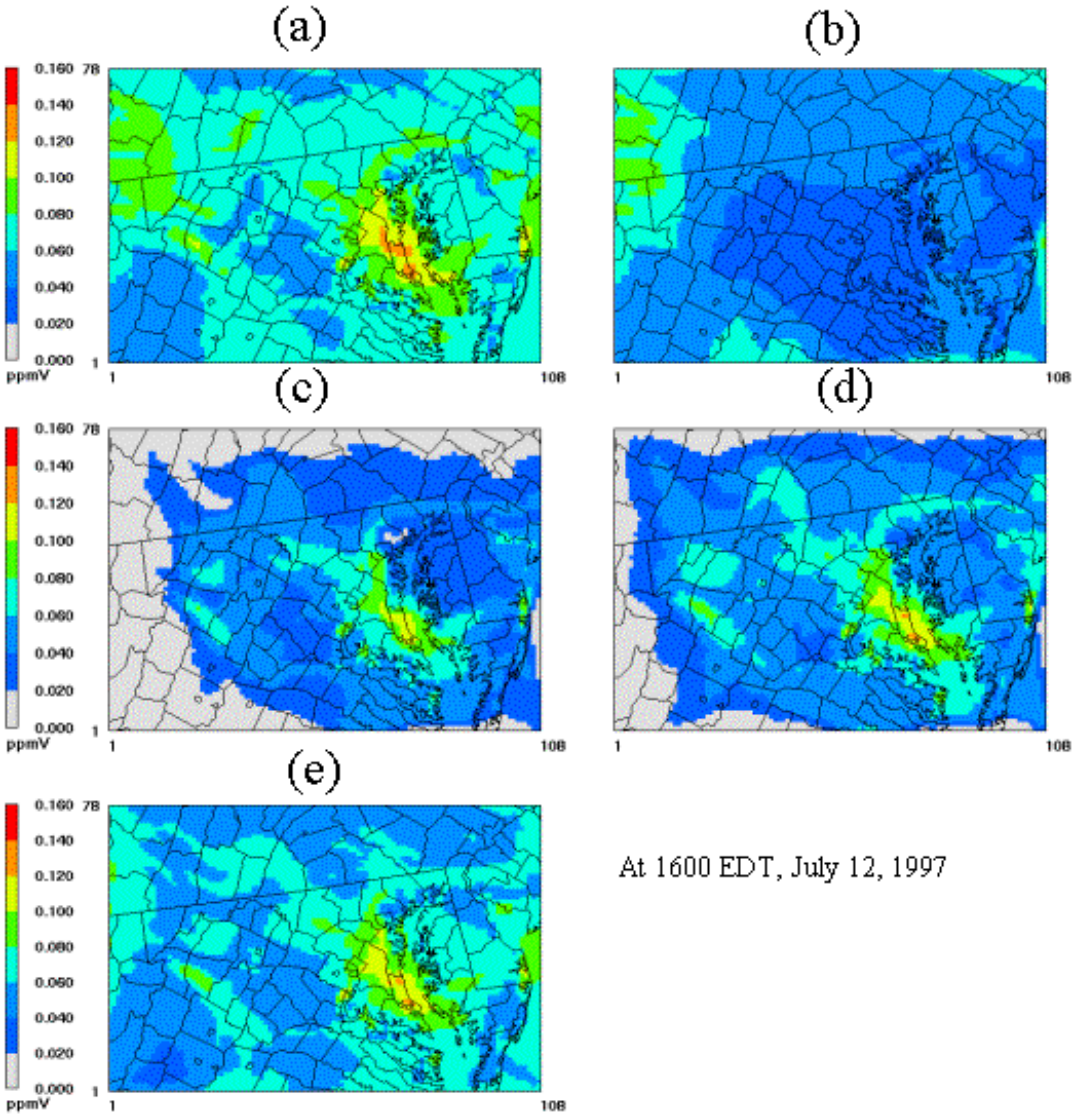

Figure 5.7: Surface ozone concentrations at 1600 EDT, July 12, 1997: (a) Base case, (b) NoEmis case, (c) CleanBC case, (d) CleanOZ case, and (e) CleanPRE case.

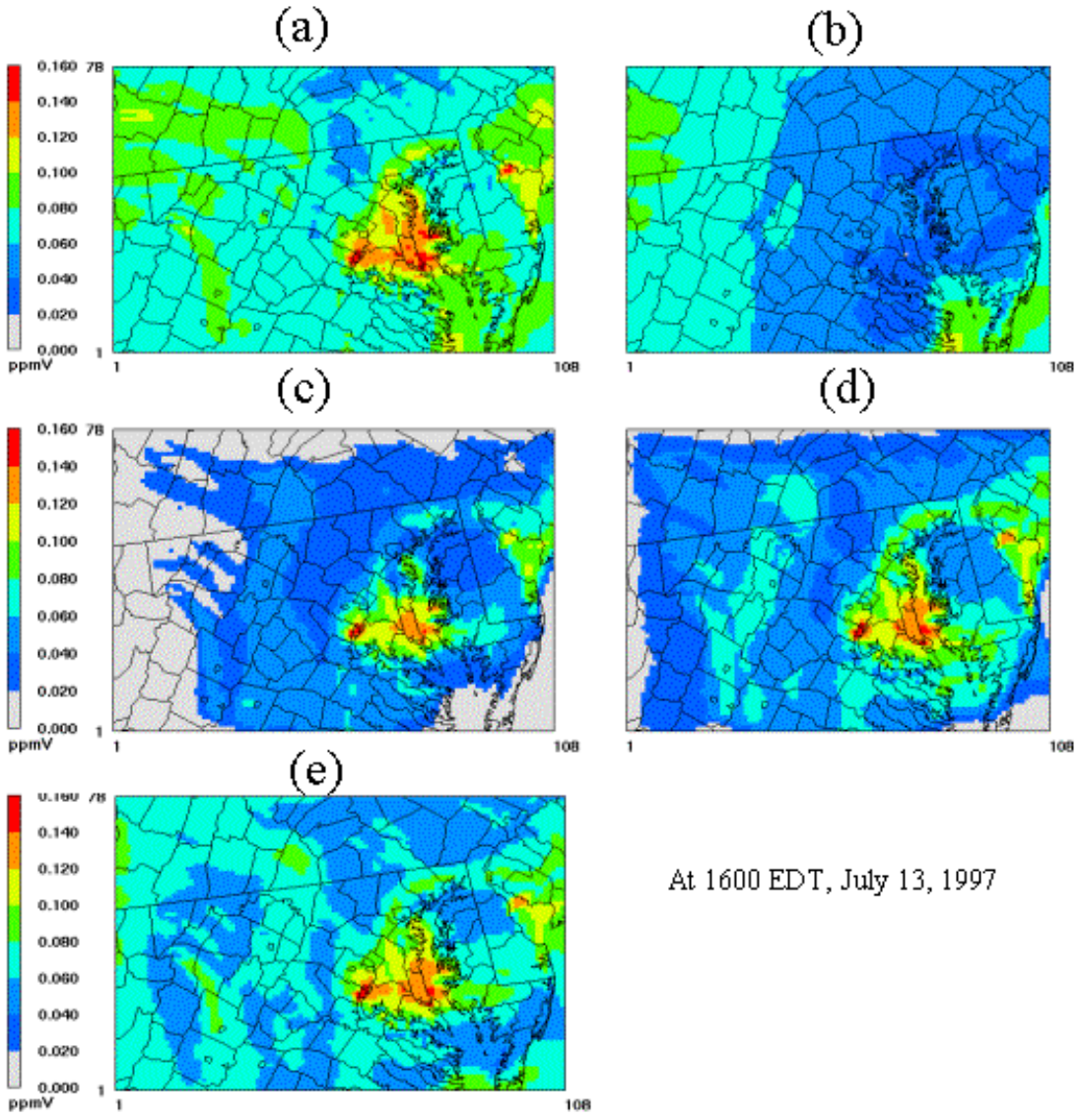

Figure 5.8: Surface ozone concentrations at 1600 EDT, July 13, 1997: (a) Base case, (b) NoEmis case, (c) CleanBC case, (d) CleanOZ case, and (e) CleanPRE case.

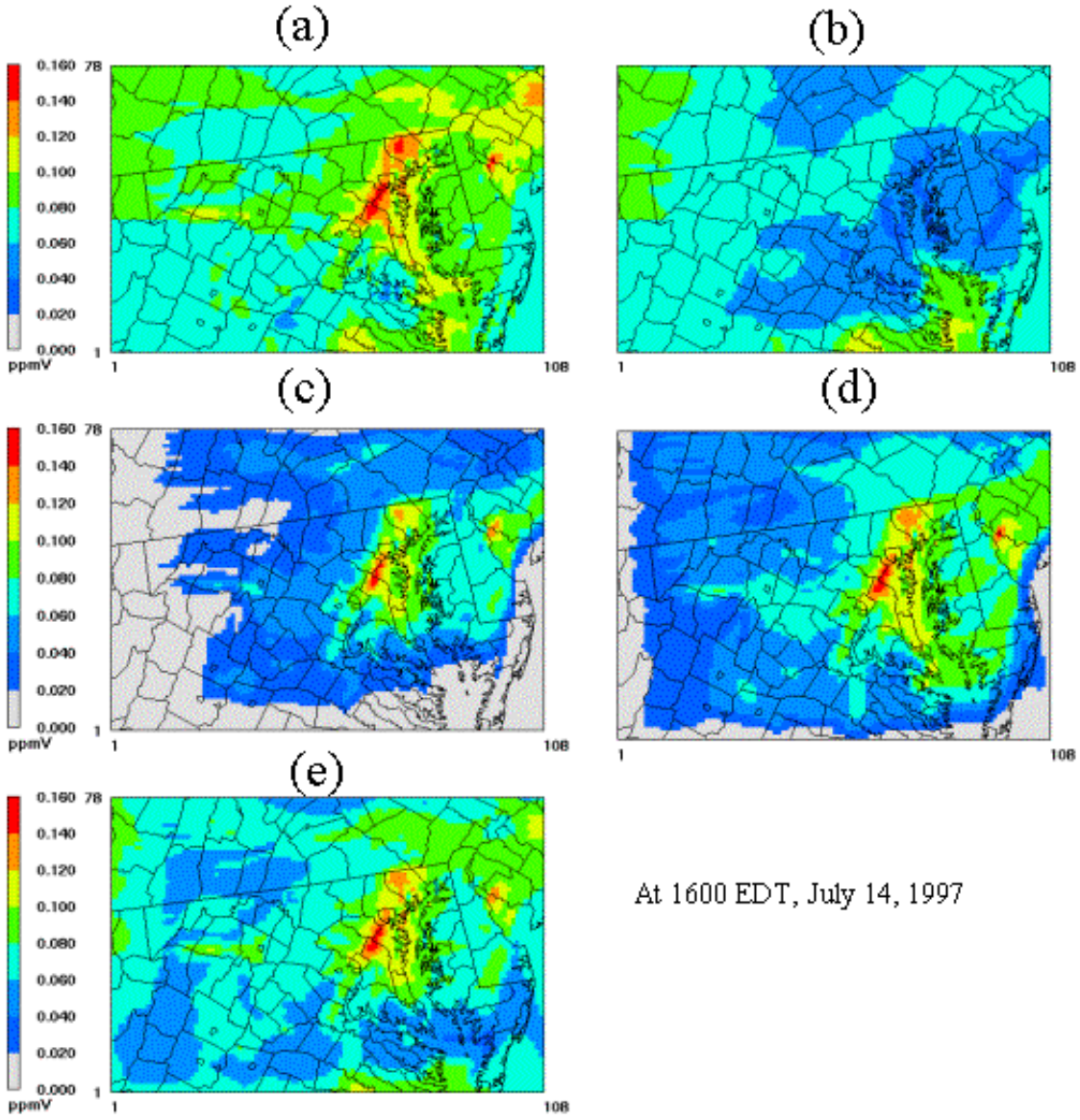

Figure 5.9: Surface ozone concentrations at 1600 EDT, July 14, 1997: (a) Base case, (b) NoEmis case, (c) CleanBC case, (d) CleanOZ case, and (e) CleanPRE case.

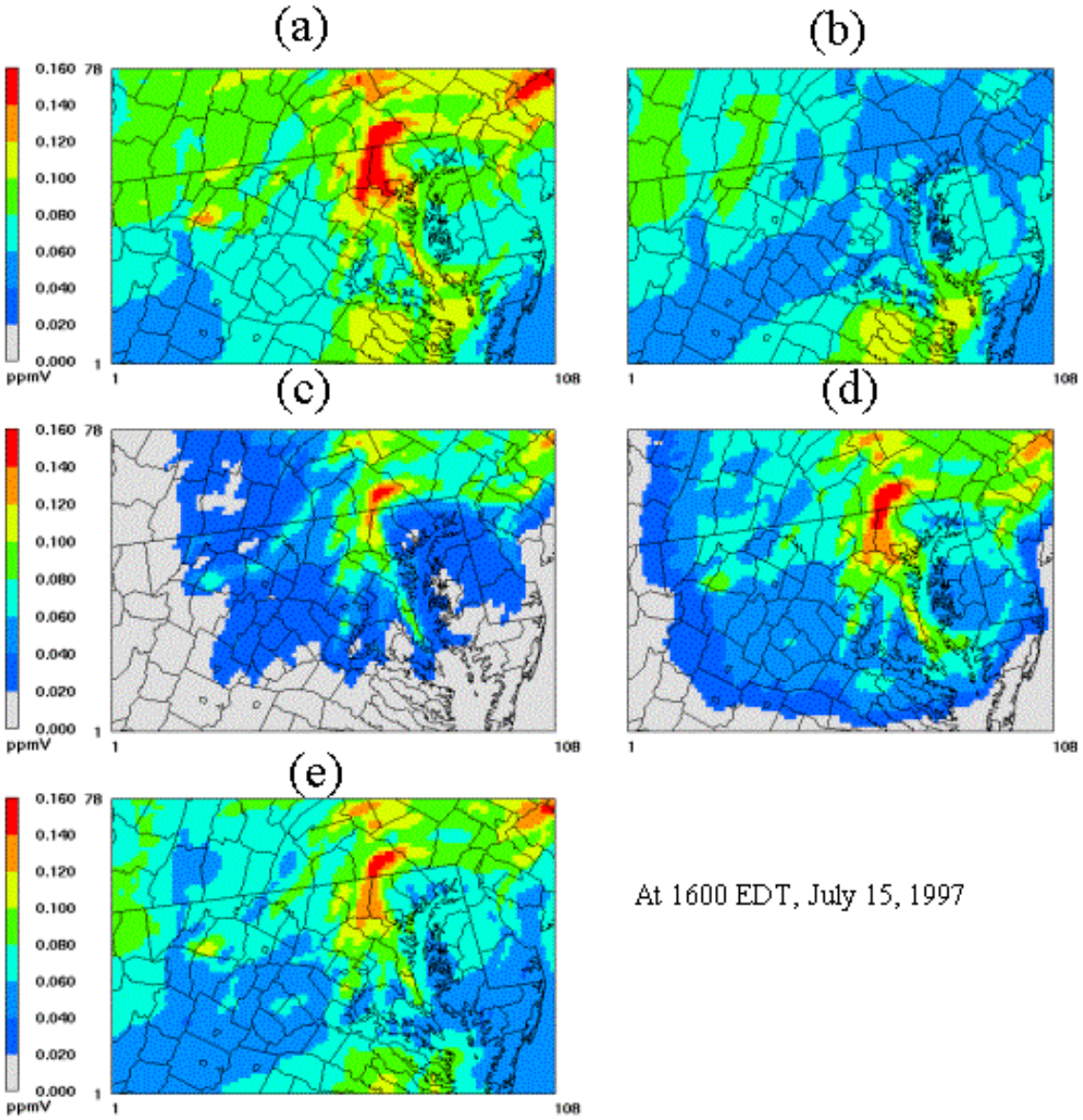

Figure 5.10: Surface ozone concentrations at 1600 EDT, July 15, 1997: (a) Base case, (b) NoEmis case, (c) CleanBC case, (d) CleanOZ case, and (e) CleanPRE case.

The remarkable point in these figures is that hot spots, areas with more than 100 ppb of ozone concentration, are seen in all cases but the NoEmis case. For each day, the peak concentration of ozone in the CleanBC case is less than the Base case by 10-20 ppb. In particular, on July 14 more than 120 ppb of ozone along the I-95 corridor connecting Washington D.C. and Baltimore is observed in the CleanBC case, while the NoEmis case shows lower concentration in this area than in the surrounding area. This suggests that local emissions contribute significantly to this high ozone episode in the Baltimore/Washington D. C. ozone non-attainment area. In general, transported pollutants appear to strengthen the intensity of ozone by about 10-20 ppb for the Baltimore/Washington D.C. area.

Figure 5.11 compares the frequency distributions of hourly surface ozone concentrations for the five cases. The CleanBC and the CleanOZ cases show very different characteristics from the other cases. More than half of the simulated grid hours show ozone concentrations less than 20 ppb. As shown in Figures 5.7 through 5.10, this results from effect of the boundary conditions on the grid cells near the boundaries. The NoEmis case and the CleanPRE case show a similar distribution with slightly increased occurrences of high ozone. As indicated earlier, transported pollutants seem to play a role, enhancing ozone by about 40-70 ppb in this area.

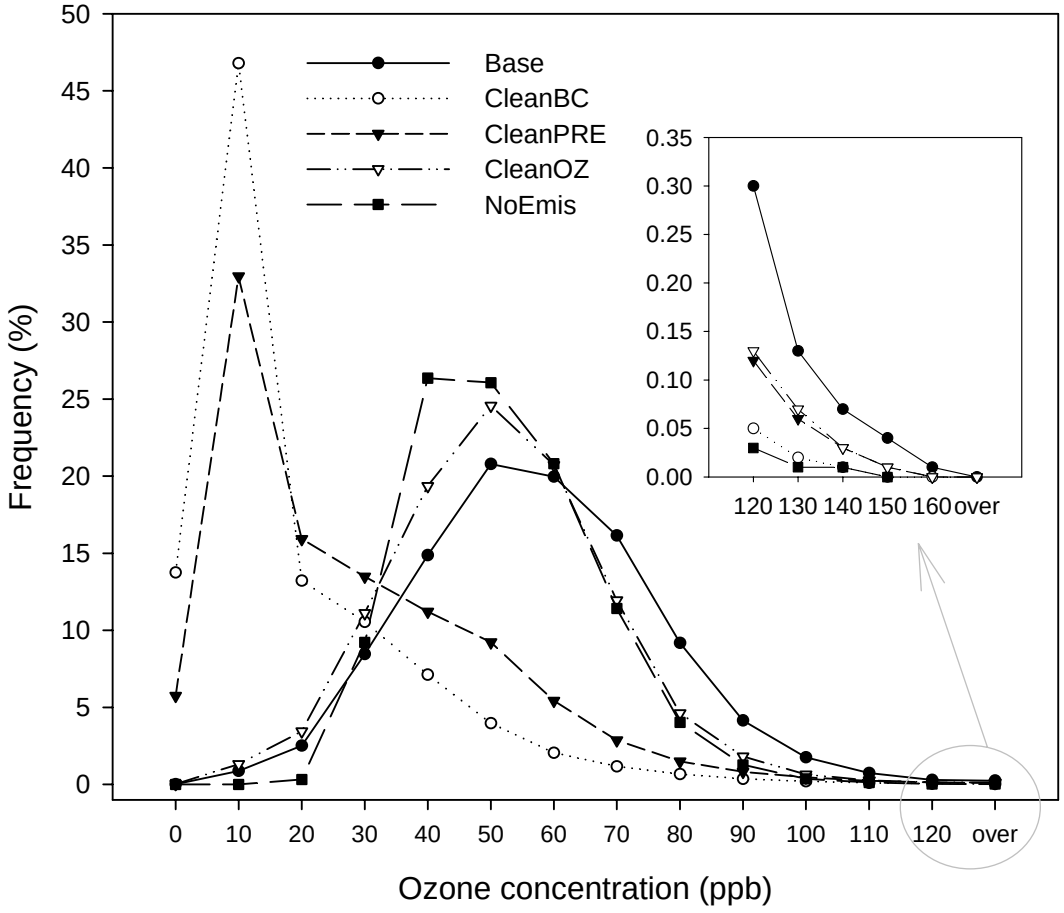

Figure 5.11: Comparison of frequency distributions of hourly surface ozone concentrations between July 8 and July 20, 1997, based on all grids in the modeling domain for the Base, the CleanBC, the CleanOZ, the CleanPRE, and NoEmis cases.

In summary, local emissions are mainly responsible for the 1 hour ozone standard exceedance in Baltimore/Washington D.C. area, while the long-range transport of ozone and/or precursors are most likely to contribute to the 8 hr ozone standard exceedance by adding to local emissions, leading to the occurrence of elevated concentrations over a wider area.

5.4.3 Investigation of the contribution of biogenic vs. anthropogenic VOC to local ozone production

Most NOx emissions are from combustion-related sources such as motor vehicles and fossil-fueled power plants in urban and suburban areas. On the other hand, VOCs are emitted from a wide variety of sources, both anthropogenic and biogenic. In the United States, it is estimated that the total amount of reactive VOC emissions from biogenic sources is approximately 1.4 times greater than emissions from anthropogenic VOC when it is averaged by land use over the continental US (Solomon et al., 2000). However, there are large variations of this ratio on a region-to region basis. According to the study by Guenther et al. (2000), over 98% of total biogenic VOCs in North America are from vegetation, and isoprene, with high ozone forming potential, accounts for 35% of the total VOCs emitted from vegetation.

In this section, we compare the relative contribution of anthropogenic VOC emissions versus biogenic VOC emissions to local ozone production. Figures 5.12 and 5.13 are the surface ozone distribution from the model at 1600 EDT, on July 13 and July 14, 1997. Compared to the CleanBC case with both anthropogenic and

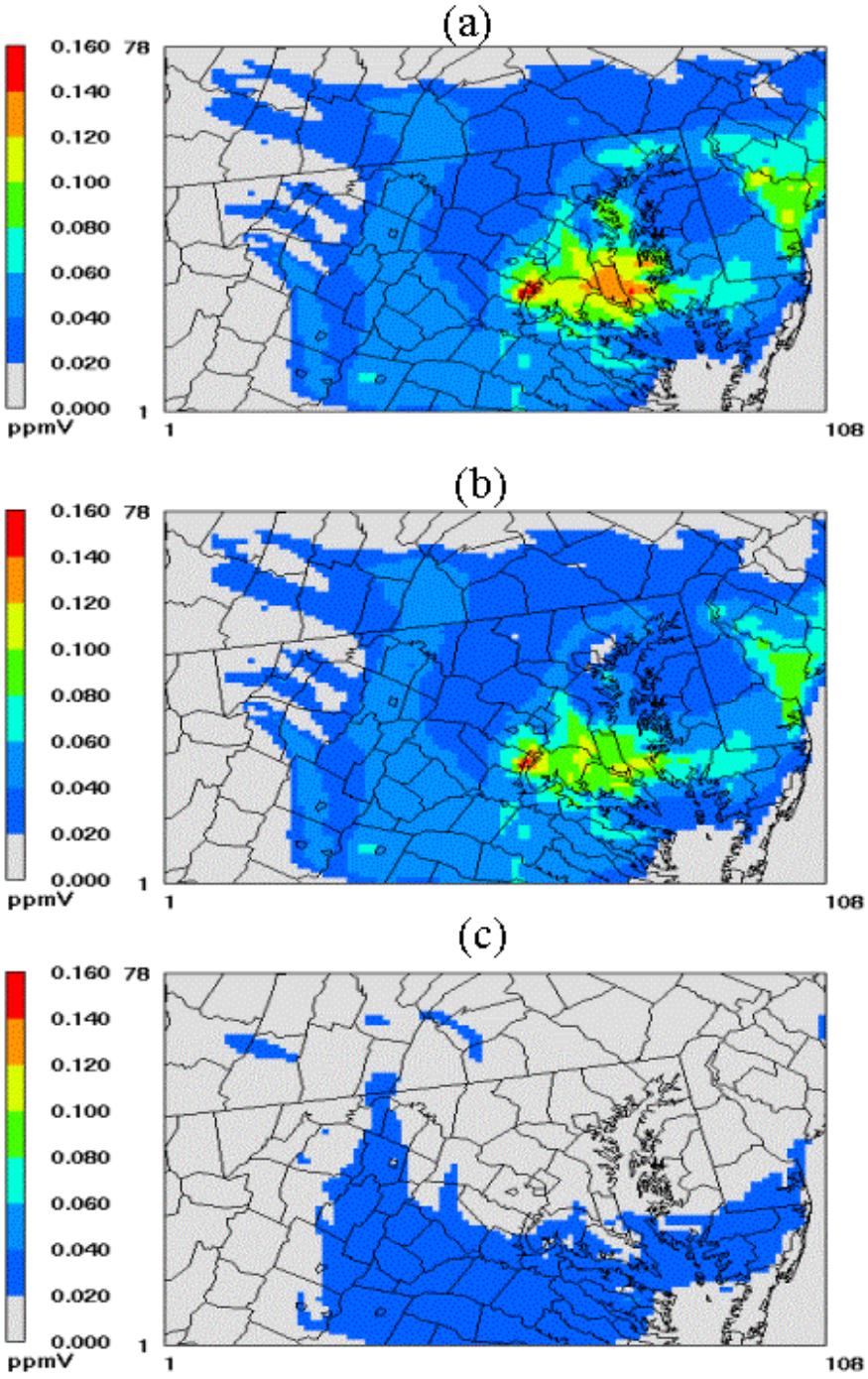

Figure 5.12: Surface ozone concentrations at 1600 EDT, July 13, 1997: (a) CleanBC case, (b) woAVOC case, and (c) woBVOC case.

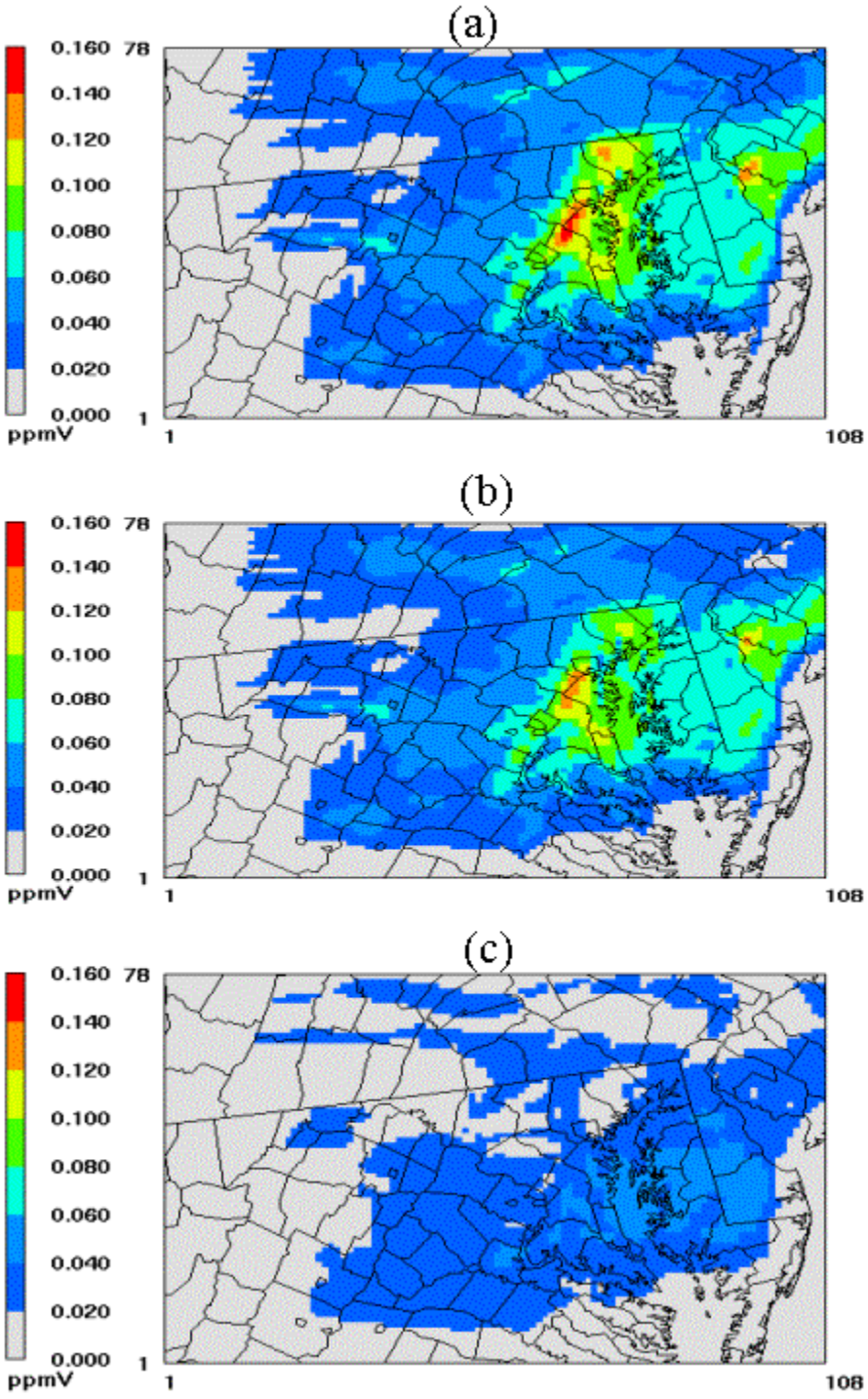

Figure 5.13: Surface ozone concentrations at 1600 EDT, July 14, 1997: (a) CleanBC case, (b) woAVOC case, and (c) woBVOC case.

biogenic emissions, the woAVOC case, which includes biogenic VOC emissions and not anthropogenic VOC emissions, displays a similar distribution of surface ozone. On the other hand, the woBVOC case, which has anthropogenic VOC emissions but not biogenic VOC emissions, shows a nearly homogeneous distribution of ozone below 60 ppb over the domain, except for the grid cells near the boundary. Moreover, the frequency distribution of surface ozone concentration shown in Figure 5.14 exhibits the same consequences. Hence, the results suggest that biogenic VOC emissions play a critical role in formation of local ozone in Baltimore/Washington D.C. region. These results are also in agreement with findings from observation-based analyses for the Baltimore area by Morales-Morales (1998) and in Chapter 3 of this dissertation.

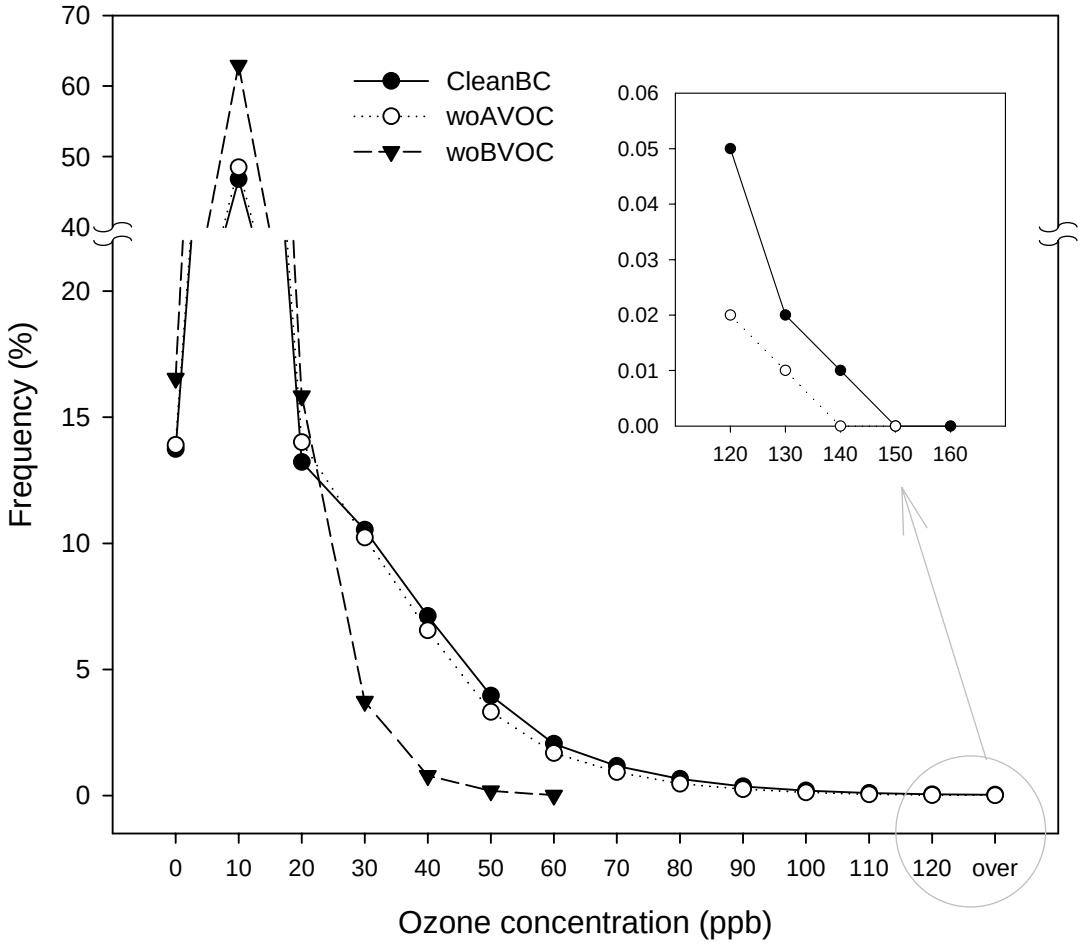

Figure 5.14: Comparison of frequency distribution of hourly surface ozone concentrations between July 8 and July 20, 1997, based on all grids in the modeling domain for the CleanBC, the woAVOC, and woBVOC cases.

5.4.4 Application of control scenarios

Three control scenarios were simulated: 50% anthropogenic NOx reduction (Half_Anox), 50% anthropogenic VOC reduction (Half_Avoc), and 50% anthropogenic NOx and VOC reduction (Half_Anox_Avoc) with the same boundary conditions as the Base case. Two additional scenarios with 50% reduction of ozone in the boundary conditions were performed. One was with normal emissions (HalfozBC_baseEMI), and the other was with 50% anthropogenic NOx reduction (HalfozBC_halfAnox).

The frequency distribution of ozone concentrations for the five control scenarios and the base case are compared in Figure 5.15. While the Half_Avoc case and the Base case show approximately the same distribution of ozone concentrations, the Half_Anox case and the Half_Anox_Avoc case show a similar pattern. Figures 5.16 and 5.17, which give the ozone distribution at selected times during the episode, show the same trend of ozone concentrations as was seen in the frequency comparison. These results suggest that anthropogenic NOx emissions control in the domain is more likely to lead to alleviation of high ozone occurrences, in contrast to anthropogenic VOC emissions control that rarely affects ozone reduction. As mentioned in the previous section, the contribution of transport is not negligible. When local NOx reduction accompanying reduced transport of ozone was simulated, we could observe improved results as indicated in Figures 5.16 and 5.17.

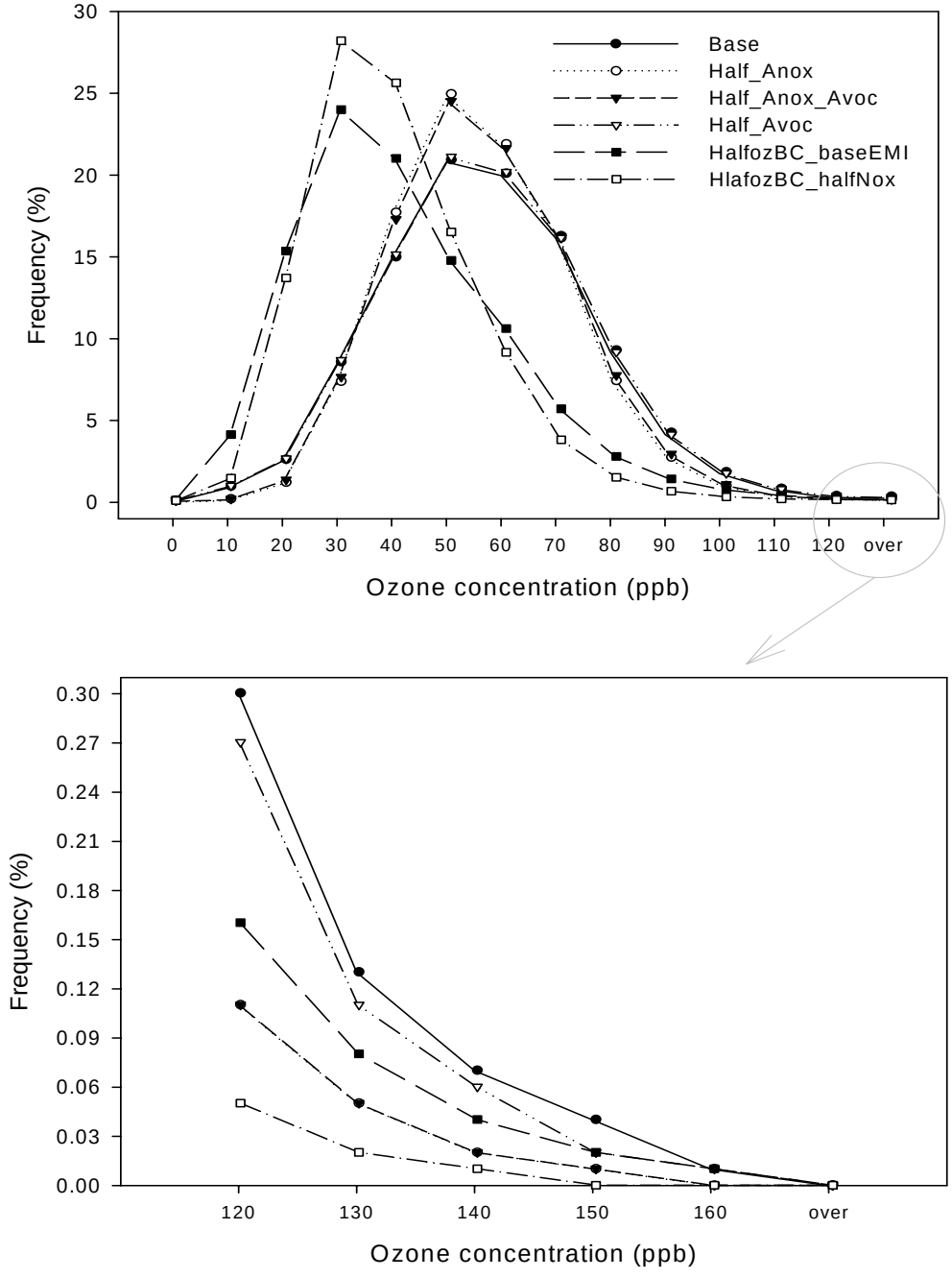

Figure 5.15: Comparison of frequency distribution of hourly surface ozone concentrations between July 8 and July 20, 1997, based on all grids in the modeling domain for the Base, Half_Anox, the Half_Anox_Avoc, the Half_Avoc, the HalfozBC_baseEMI, and the HalfozBC_halfAnox cases.

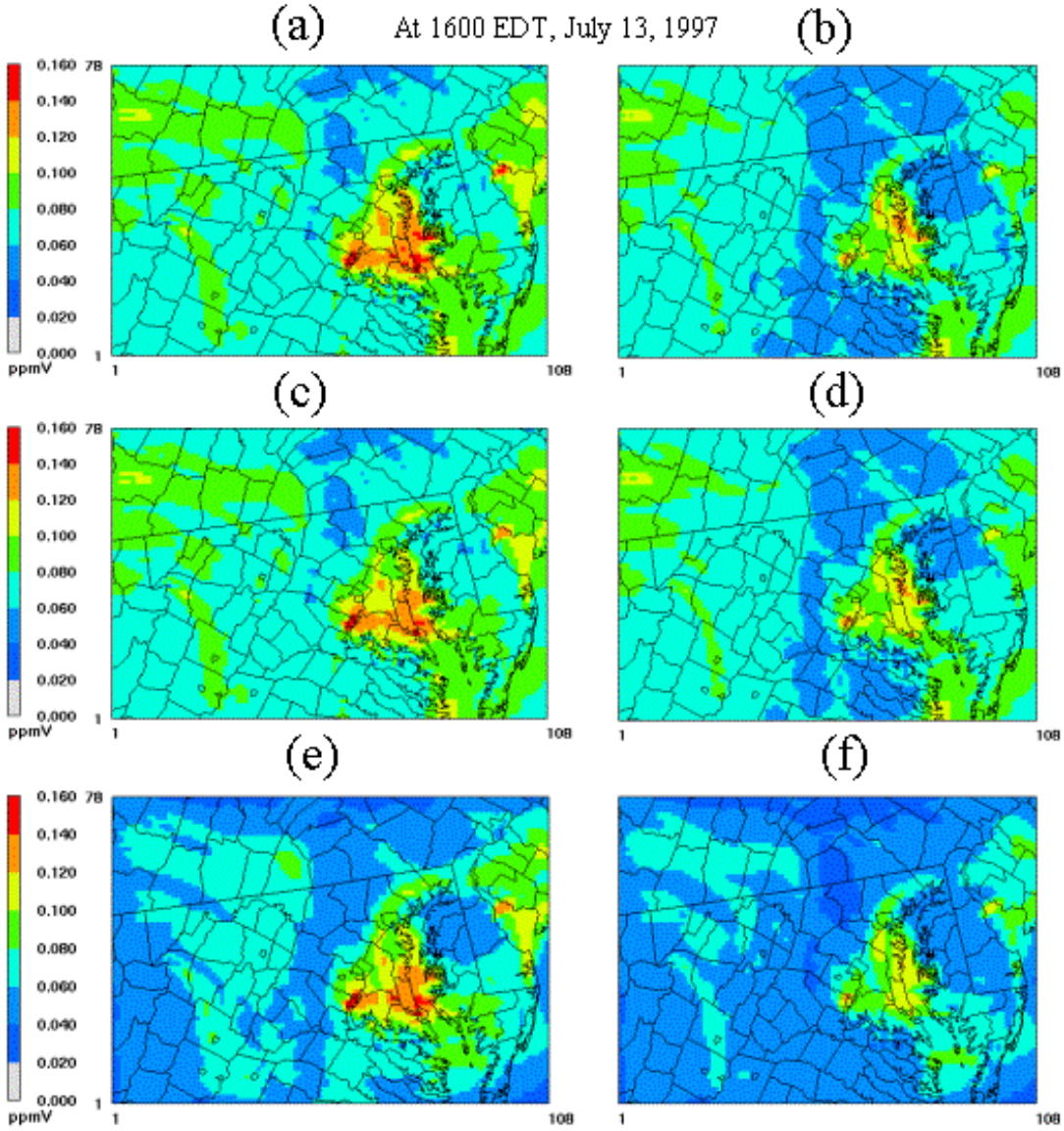

Figure 5.16: Surface ozone concentrations at 1600 EDT, July 13, 1997: (a) Base case, (b) Half_Anox case, (c) Half_Avoc case, (d) Half_Anox_Avoc case, (e) HalfozBC_baseEMI case, and (f) HalfozBC_halfAnox case.

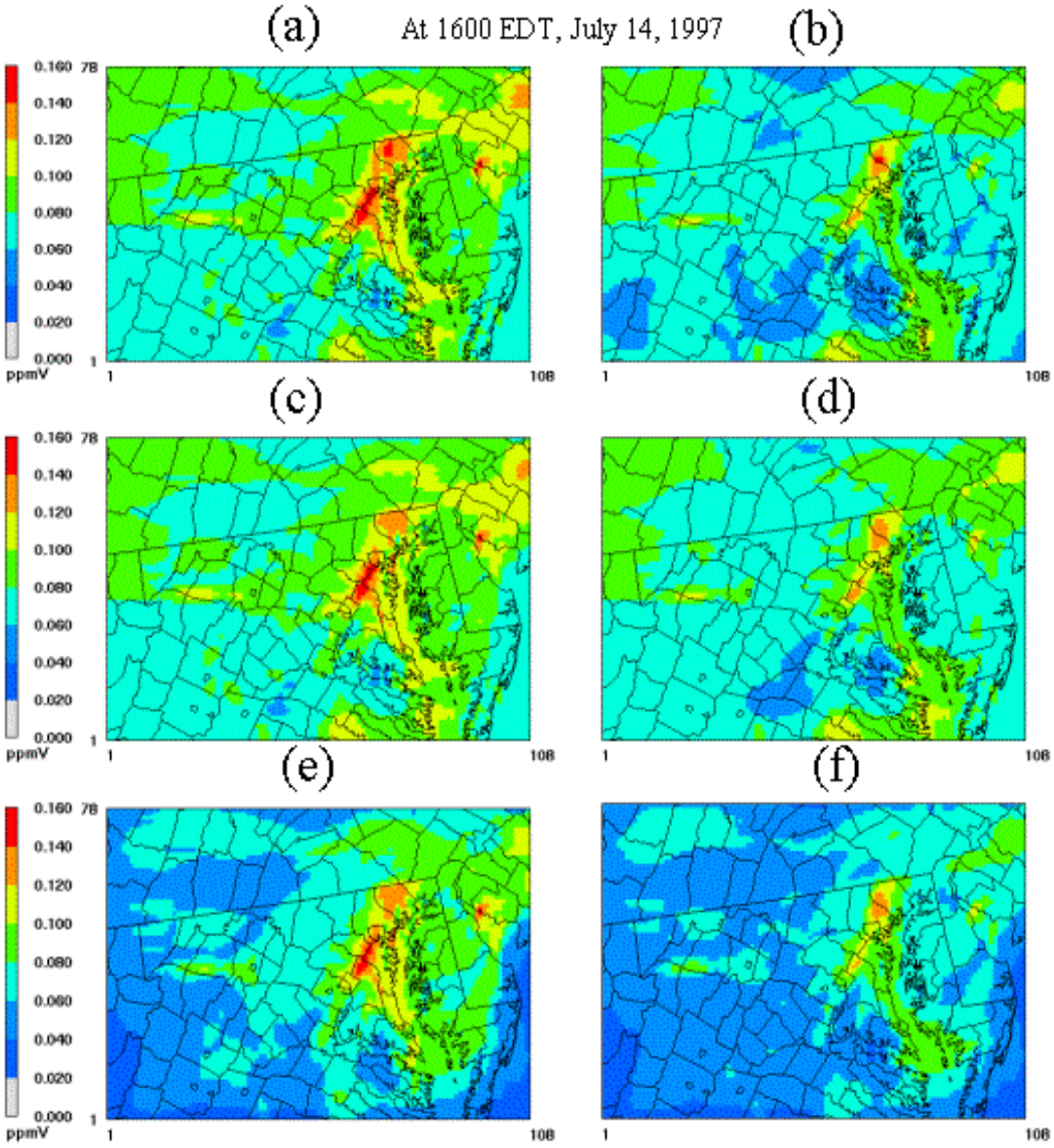

Figure 5.17: Surface ozone concentrations at 1600 EDT, July 14, 1997: (a) Base case, (b) Half_Anox case, (c) Half_Avoc case, (d) Half_Anox_Avoc case, (e) HalfozBC_baseEMI case, and (f) HalfozBC_halfAnox case.

5.5 Summary and conclusions

Photochemical simulations were performed of an ozone event in July 1997 to investigate both the relative contribution of long-range transport versus local emissions, and the relative impact of biogenic VOC emissions versus anthropogenic VOC emissions on local ozone production. Even though the simulations were limited to a single ozone event, the synoptic weather pattern was typical of high ozone occurrences. Therefore, the conclusions drawn from these simulations are more general.

From the first set of simulations, it appears that transported pollutants may be responsible for 20-90 ppb of ozone concentration in the domain, displaying a decreasing contribution as they pass through the Baltimore/Washington D.C. ozone non-attainment area. Simulations without including long-range transport of pollutants show a significant contribution of local emissions to high ozone occurrences in this region. Hence, the results imply that local emissions are mainly responsible for 1 hour ozone standard exceedances in the Baltimore/Washington D.C. area. However, transported ozone and its precursors play an important role in the violation of the 8 hr ozone standard, by adding to the local contribution and resulting in elevated concentrations over a wider area.

In the second set of simulations, the relative contribution of anthropogenic VOC emissions versus biogenic VOC emissions to local ozone production was investigated. The simulations suggest that biogenic VOC emissions in this region are responsible, to a great extent, for local ozone production. This conclusion is similar to

those obtained from observation based studies of the Baltimore area described in Chapter 3.

Finally, three control scenarios were applied to the region: 50% anthropogenic NOx reduction, 50% anthropogenic VOC reduction, 50% anthropogenic NOx and VOC reduction. The results show the potential for NOx emissions reduction for the mitigation of high ozone occurrences around the Baltimore/Washington area. This result supports a significant role for biogenic VOC emissions in ozone formation in this region, identified in the second set of simulations. That is, the role of biogenic VOCs in ozone formation will be limited due to a reduced concentration of NOx. On the other hand, the reduction of only anthropogenic VOCs, which has much less ozone-forming potential than biogenic VOCs, might not be able to effectively limit ozone formation as compared to NOx reduction. In addition, we observed an enhanced reduction when the contribution of ozone transported from outside the modeling domain was reduced, along with the reduction of local NOx emissions.

In conclusion, the simulations show significant roles for both transported and local emissions. Our results suggest controlling NOx emissions locally would be effective in alleviating extremely severe ozone events. However, considering that the 8 hr ozone standard needs to be attained as well, control of only local NOx emissions may not be satisfactory, because of the importance of long-range transport of ozone and its precursors. In the future, several emissions control scenarios for the upwind area outside the domain should be investigated through simulation, in order to determine the degree of ozone reduction that can be achieved through control of transported ozone and its precursors.

Chapter 6: Conclusions and Recommendations

6.1 Summary and conclusions

The Baltimore/Washington area has experienced severe ozone episodes in the past. In order to find a strategy for ozone reduction in a given area, it is essential to understand the complex chemistry between the precursors of ozone, VOC and NOx, to identify the role of biogenic VOC in local ozone formation, and to identify the impact of long-range transport on the ambient ozone concentration. Hence, three studies of ozone for Baltimore/Washington area were undertaken to identify and evaluate control strategies towards ozone alleviation for effectiveness.

The first study was to investigate sources of VOC emissions in the Baltimore area using highly time resolved measurements, and to investigate possible relationships between each VOC source category and episodes of elevated ozone concentrations. In this work, hourly ambient concentrations of 55 VOC species, measured at the Essex PAMS site in Baltimore County in the state of Maryland during the summer months of 1996 ~ 1999, were analyzed to investigate the relationships between ozone and its natural and anthropogenic precursors using the UNMIX receptor model. Gasoline-related sources such as vehicle exhaust, gasoline vapor, and liquid gasoline accounted for more than half of the total VOC mixing ratio, which is a typical result for VOC in urban/suburban areas in the United States. Natural gas, surface coatings, and biogenic source categories each explained 13, 12 and 11 % of the

total VOC, respectively. Even though the hourly average contribution of biogenic sources in quantity did not appear to be significant, comparisons of diurnal patterns of high-ozone days with those of low-ozone days and rough reactivity-weighted daytime source apportionment results implied that biogenic emissions might contribute considerably to local ozone production for episodes in which the National Air Quality 8-hour standard for ambient ozone was violated at this site.

The second part of this study consisted of an evaluation of an emissions inventory, an essential input to a photochemical air quality model. Emissions inventories significantly affect photochemical model performance, and thus development of effective control strategies. In this study, in order to evaluate a VOC emissions inventory, the ratios of CB-IV VOC groups to NOx or CO, and the ratios of VOC source contributions from a source apportionment technique to NOx or CO were compared with the corresponding ambient ratios at three observation sites located in Maryland, District of Columbia, and New Jersey. Furthermore, a photochemical air quality model was introduced to compare ratios of CB-IV VOC groups to NOx or CO, and the absolute concentrations of CB-IV VOC groups with the same ratios and concentrations from observations.

The comparisons of ETH(ethene)/NOx ratio, XYL(xylenes)/NOx ratio, ETH and XYL concentrations between estimates and measurements showed some differences, depending on the comparison approach, at the MD and DC sites. On the other hand, the consistent results at the NJ site were observed, implying a possible overestimation of vehicle exhaust. However, in the case of TOL(toluenes), which are emitted mainly from solvent sources, the ratios of TOL to NOx or CO as well as the

absolute concentrations revealed an overestimate of solvent sources by a factor of 1.5 to 3 at the three sites. In addition, the overestimate of solvent sources agreed with the comparisons of solvent source contributions relative to NOx from a source apportionment technique to the corresponding value of estimates at the MD site. Other researchers have also proposed the overestimation of solvent sources, implying a possibility of inaccurate emission factors in estimating VOC emissions from solvent sources.

The photochemical model simulations with 50% reduction of solvent VOC emissions did not show a perceptible change in ozone concentrations, possibly because this region is NOx-sensitive, or because the solvent chemical species do not readily form ozone. However, a noticeable decrease of secondary organic aerosol (SOA) concentrations with 50% solvent emissions reduction was observed.

The last part of this dissertation was to develop an effective control strategy for the Baltimore/Washington ozone non-attainment area, which requires an understanding of the relative impact of long-range transport of ozone and precursors versus local emissions on ozone events, and the contribution of biogenic VOC emissions to ozone production during ozone events in the area. In this study, ozone simulations for the Baltimore/Washington ozone non-attainment area were performed in order to investigate both the relative contribution of long-range transport versus local emissions to an ozone event which occurred in July 1997, to identify the relative impact of biogenic VOC emissions versus anthropogenic VOC emissions on local ozone production, and finally to test a possible control strategy for this area.

The simulation results showed that long-range transport of ozone was responsible for 20-90 ppb of ozone concentration in the state of Maryland, Northern Virginia, and D.C. area, displaying a decreasing contribution as it passed through the Baltimore/Washington D.C. area. Local emissions contributed considerably to high ozone occurrences in the Baltimore/Washington D.C. ozone non-attainment area. In particular, the contribution of biogenic VOC emissions in this region was responsible for the local ozone production to a great extent, which was consistent with the past studies based on observations for the Baltimore area including a result from the first part of my study. Accordingly, the results suggested that NOx emissions reduction rather than VOC emissions reduction might mitigate high ozone occurrences in the Baltimore/Washington ozone non-attainment area, and it was confirmed through several simulations with emissions reductions. However, our results suggested that a control of only local NOx emissions might not be sufficient to comply with the 8 hr ozone standard because of the importance of long-range transport of ozone and its precursors.

In conclusion, both observational-based and emissions-based air quality modeling studies consistently suggested a significant role of biogenic VOC emissions in high ozone formation over the Baltimore/Washington region. Also, control of anthropogenic NOx emissions may possibly lead to a decrease in high ozone occurrences.

6.2 Recommendations for future work

In this study, we employed a receptor model, UNMIX, to analyze observations and to induce meaningful conclusions from the analyses. As mentioned in the Chapter 3, in addition to the UNMIX receptor model, there are several receptor models such as PMF and Chemical Mass Balance (CMB) 8, recently refined and developed. In particular, it is important to obtain reliable results for topics related to policy-making, based on scientific findings and analyses. For that reason, we recommend introducing other well-evaluated receptor models to analyze the same observations in future.

In addition, the analysis here was limited to a single sampling site. However, there are a couple of observation stations with high time resolution around the study domain, and we can apply the same analysis approach to the observations. Since the stations are not close to each other, we can get some insight into atmospheric conditions over the sampling sites, and compare the characteristics between sites. Considering that the meteorological information such as wind speeds and wind directions are usually available at the sampling sites, we may be able to identify possible connections between emission source categories at upwind observation areas and those at downwind observation areas.

When it comes to air quality modeling studies, the simulations were based on a multi-day ozone episode and the synoptic weather during the episode followed a pattern typical of high ozone formation. Therefore, the transport from outside the region and biogenic emissions, which are highly dependent on meteorological parameters, and significant factors during high ozone occurrences over this region,

may not be considerably different from ozone episode to episode. However, the conclusions we drew in this study will be more reliable if simulations for other ozone episodes over this area are performed, and similar results are obtained. Hence, we recommend gathering reliable inputs into the modeling system and observations for evaluations for other ozone episodes, and following the same practice.

Appendix 1: CB-IV representations of PAMS 55 hydrocarbons

	ALD2	ETH	FORM	ISOP	OLE	PAR	TOL	XYL	NR
ethane						0.4			1.6
ethene		1							
propane						3			
propene					1	1			
i-butane						4			
butane						4			
acetylene						1			1
t-2-butane	2								
1-butene					1	2			
c-2-butane	2								
cyclopentane						5			
isopentane						5			
pentane						5			
t-2-pentene	2					1			
1-pentene					1	3			
c-2-pentene	2					1			
2,2-dimethylbutane						6			
2,3-dimethrylbutane						6			
2-methylpentane						6			
3-methylpentane						6			
isoprene				1					
2-methyl-1-pentene					1	4			
hexane						6			
methylcyclopentane						6			
2,4-dimethylpentane						7			
benzene						1			5
cyclohexane						6			
2-methylhexane						7			
2,3-dimethylpentane						7			
3-methylhexane						7			
2,2,4-trimethylpentane						8			
heptane						7			
methylcyclohexane						7			
2,3,4-trimethylpentane						8			
toluene							1		
2-methylheptane						8			
3-methylheptane						8			
octane						8			
ethylbenzene						1	1		
m&p-xylene								1	
styrene					1	1			5
o-xylene								1	
nonane						9			
isopropylbenzene						2	1		
propylbenzene						2	1		

	ALD2	ETH	FORM	ISOP	OLE	PAR	TOL	XYL	NR
1-ethyl-3-methylbenzene						1		1	
1-ethyl-4-methylbenzene						1		1	
1,3,5-trimethylbenzene						1		1	
1-ethyl-2-methylbenzene						1		1	
1,2,4-trimethylbenzene						1		1	
decane						10			
1,2,3-trimethylbenzene						1		1	
m-diethylbenzene						2		1	
p-diethylbenzene						2		1	
undecane						11			

Appendix 2: Source compositions (mass fraction) and apportionment results using UNMIX

A. Essex site, MD for 1996 summer measurements

Estimated source category	Source 1 Liquid gasoline	Source 2 Surface coatings	Source 3 biogenic	Source 4 Natural gas	Source 5 Vehicle exhaust	Source 6 Gasoline vapor
Species						
Ethane	0.0295	0.0086	0.0313	**0.1584**	**0.0628**	0.0295
Ethylene	0.0221	0.0117	0.0150	0.0187	**0.0723**	0.0200
Propane	**0.0856**	0.0193	0.0230	**0.1261**	**0.0719**	0.0006
Propylene	0.0136	0.0078	0.0086	0.0117	0.0372	0.0077
Acetylene	0.0013	0.0075	0.0215	0.0149	0.0467	0.0104
n-butane	0.0169	0.0047	0.0288	**0.0509**	0.0324	0.0209
iso-butane	0.0178	0.0040	0.0057	0.0323	0.0244	0.0089
n-pentane	**0.2794**	0.0048	0.0162	0.0227	0.0277	0.0189
iso-pentane	0.0715	0.0487	0.0534	0.0943	**0.0590**	**0.0932**
3-methylpentane	0.0149	-0.0004	0.0055	0.0149	0.0156	0.0166
n-hexane	0.0209	-0.0018	0.0026	0.0166	0.0129	0.0240
Isoprene	0.0051	0.0026	**0.2115**	0.0001	0.0026	0.0015
3-methylhexane	0.0094	0.0014	0.0073	0.0075	0.0086	0.0164
2,2,4-trimethylpentane	0.0102	-0.0014	0.0004	0.0110	0.0271	0.0261
2,3,4-trimethylpentane	0.0047	-0.0004	-0.0034	0.0042	0.0119	0.0108
Methylcyclopentane	0.0090	-0.0002	0.0019	0.0082	0.0084	0.0115
2-methylhexane	0.0078	-0.0016	0.0053	0.0057	0.0062	0.0133
2,3-dimethylbutane	0.0062	0.0005	0.0076	0.0095	0.0111	0.0089
2-methylpentane	0.0244	-0.0007	0.0078	0.0251	0.0275	0.0260
2,3-dimethylpentane	0.0048	-0.0000	-0.0038	0.0046	0.0116	0.0096
M&p xylene	0.0263	0.0126	0.0053	0.0162	0.0228	**0.0531**
Benzene	0.0169	0.0036	0.0114	0.0139	0.0305	0.0168
Toluene	**0.0573**	0.0120	0.0590	0.0427	**0.0556**	**0.0851**
o-xylene	0.0080	0.0042	0.0055	0.0068	0.0087	0.0175
1,2,4-trimethylbenzene	0.0176	**0.5004**	0.0034	0.0102	0.0284	0.0112
Total NMOC(ppbc)	10.3	8.9	11.3	40.4	38.7	57.6
% of total NMOC	6	5	7	24	23	34

B. Essex site, MD for 1997 summer measurements

Estimated source category	Source 1 Liquid gasoline	Source 2 biogenic	Source 3 Surface coatings	Source 4 Natural gas	Source 5 Vehicle exhaust	Source 6 Gasoline vapor
Species						
Ethane	0.0397	0.0434	0.0007	**0.2138**	**0.0542**	0.0267
Ethylene	0.0213	0.0194	0.0080	0.0109	**0.0553**	0.0247
Propane	**0.0636**	0.0382	-0.0046	**0.2344**	0.0408	0.0013
Propylene	0.0129	0.0116	0.0022	0.0171	0.0270	0.0089
Acetylene	0.0056	0.0115	0.0009	0.0089	0.0284	0.0091
n-butane	0.0077	0.0333	0.0248	**0.0674**	0.0163	0.0275
iso-butane	0.0090	0.0066	0.0074	0.0492	0.0168	0.0135
n-pentane	**0.3366**	0.0175	0.0127	0.0198	0.0223	0.0223
iso-pentane	**0.0521**	0.0495	**0.0607**	0.0472	**0.0610**	**0.1007**
3-methylpentane	0.0066	0.0082	0.0115	0.0055	0.0169	0.0213
n-hexane	0.0097	0.0107	0.0162	0.0130	0.0225	0.0261
Isoprene	0.0024	**0.1582**	0.0011	-0.0026	0.0032	0.0023
3-methylhexane	0.0055	0.0097	0.0106	0.0050	0.0128	0.0164
2,2,4-trimethylpentane	0.0038	0.0112	0.0210	-0.0031	0.0241	0.0348
2,3,4-trimethylpentane	0.0025	0.0028	0.0086	-0.0014	0.0106	0.0140
Methylcyclopentane	0.0040	0.0045	0.0080	0.0037	0.0102	0.0130
2-methylhexane	0.0042	0.0060	0.0086	0.0019	0.0108	0.0139
2,3-dimethylbutane	0.0030	0.0082	0.0062	0.0052	0.0087	0.0114
2-methylpentane	0.0102	0.0130	0.0187	0.0082	0.0255	0.0337
M&p xylene	0.0170	0.0097	**0.1671**	0.0022	0.0334	0.0278
Benzene	0.0092	0.0141	0.0081	0.0101	0.0268	0.0172
Toluene	0.0197	0.0317	**0.0808**	0.0439	**0.0658**	**0.0919**
Ethylbenzene	0.0054	0.0059	0.0495	0.0015	0.0108	0.0081
o-xylene	0.0086	0.0059	0.0466	0.0016	0.0139	0.0116
1,2,3-trimethylbenzene	0.0115	0.0142	0.0063	0.0105	0.0089	0.0074
Total NMOC(ppbc)	7.9	13.2	12.2	20.0	47.1	41.2
% of total NMOC	6	9	9	14	33	29

Bold values indicate mass fractions > 0.05.

C. Essex site, MD for 1998 summer measurements

Estimated source category Species	Source 1 biogenic	Source 2 Liquid gasoline	Source 3 Natural gas	Source 4 Gasoline vapor	Source 5 Vehicle exhaust
Ethane	0.0309	**0.0574**	**0.2293**	**0.0554**	0.0168
Ethylene	0.0142	0.0228	0.0143	0.0247	**0.0517**
Propane	0.0240	**0.0853**	**0.1842**	0.0133	0.0411
Propylene	0.0092	0.0128	0.0126	0.0092	0.0258
Acetylene	0.0194	0.0083	0.0108	0.0136	0.0253
n-butane	0.0359	0.0296	0.0483	0.0380	0.0185
iso-butane	0.0137	0.0188	0.0461	0.0166	0.0172
n-pentane	0.0175	**0.1903**	0.0175	0.0158	0.0186
iso-pentane	**0.0690**	**0.0910**	0.0330	**0.1189**	0.0483
3-methylpentane	0.0087	0.0163	0.0052	0.0231	0.0142
n-hexane	0.0045	0.0202	0.0074	0.0244	0.0166
Isoprene	**0.1899**	0.0017	0.0009	-0.0007	0.0026
3-methylhexane	0.0046	0.0102	0.0044	0.0148	0.0126
2,2,4-trimethylpentane	0.0094	0.0120	-0.0049	0.0357	0.0196
2,3,4-trimethylpentane	0.0030	0.0054	-0.0026	0.0146	0.0086
Methylcyclopentane	0.0038	0.0096	0.0033	0.0128	0.0086
2-methylhexane	0.0025	0.0085	0.0016	0.0127	0.0103
2,3-dimethylbutane	0.0108	0.0077	0.0037	0.0135	0.0072
2-methylpentane	0.0156	0.0258	0.0078	0.0371	0.0221
M&p xylene	-0.0076	0.0239	0.0176	0.0374	**0.0515**
Benzene	0.0103	0.0145	0.0128	0.0174	0.0240
Toluene	0.0288	**0.0594**	0.0205	**0.0882**	**0.0747**
Ethylbenzene	0.0016	0.0.079	0.0064	0.0119	0.0163
o-xylene	0.0009	0.0094	0.0048	0.0147	0.0184
1,2,4-trimethylbenzene	-0.0075	0.0129	0.0026	0.0145	0.0180
Total NMOC(ppbc)	10.6	12.5	19.2	33.0	33.2
% of total NMOC	10	12	18	30	31

Bold values indicate mass fractions > 0.05.

D. McMillan reservoir, DC for 1997 summer measurements

Estimated source category	Source 1 Unidentified	Source 2 Unidentified	Source 3 Natural gas	Source 4 Diesel exhaust	Source 5 Gasoline (Vehicle exhaust & evaporization)
Species					
Acetylene	0.0124	0.0131	0.0072	**0.0836**	0.0127
Ethylene	-0.0145	0.0037	0.0173	**0.1748**	0.0437
Ethane	-0.0172	**0.1179**	**0.3109**	**0.0835**	0.0295
Propylene	0.0069	-0.0054	0.0149	**0.0543**	0.0253
Propane	0.0086	**0.0541**	**0.1946**	0.0137	0.0251
iso-butane	-0.0072	0.0248	**0.0569**	0.0171	0.0215
n-butane	0.0453	0.0347	**0.0834**	0.0237	0.0294
iso-pentane	0.3419	0.0284	**0.1757**	**0.0972**	**0.0736**
n-pentane	**0.0707**	0.0120	**0.0534**	0.0339	0.0262
Isoprene	**0.4340**	0.0009	-0.0116	0.0058	0.0015
2,3-dimethylbutane	0.0167	0.0035	0.0124	0.0157	0.0111
2-methylpentane	**0.0240**	0.0080	0.0279	0.0358	0.0296
3-methylpentane	0.0156	0.0065	0.0158	0.0205	0.0191
n-hexane	-0.0001	0.0176	0.0019	0.0010	0.0203
Benzene	0.0071	0.0106	-0.0054	0.0246	0.0301
3-methylhexane	-0.0018	0.0097	-0.0055	-0.0008	0.0145
2,2,4-trimethylpentane	0.0014	0.0157	-0.0084	0.0280	0.0365
2,3,4-trimethylpentane	-0.0005	0.0059	-0.0054	0.0129	0.0158
Toluene	0.0319	**0.0594**	0.0199	**0.0657**	**0.0931**
Ethylbenzene	0.0109	0.0145	-0.0020	0.0084	0.0149
M&p xylene	0.0187	0.0437	-0.0076	0.0313	0.0479
o-xylene	0.0108	0.0169	-0.0031	0.0137	0.0185
1,2,4-trimethylbenzene	-0.0004	0.0220	-0.0047	0.0381	0.0174
n-decane	-0.0009	**0.0854**	-0.0028	-0.0063	0.0025
Total NMOC(ppbc)	4.4	9.4	14.5	9.4	47.9
% of total NMOC	5	11	17	11	56

Bold values indicate mass fractions > 0.05.

E. Camden, NJ for 1997 summer measurements

Estimated source category	Source 1 Unidentified	Source 2 Unidentified	Source 3 Biogenic	Source 4 Refinery	Source 5 Natural gas	Source 6 Vehicle exhaust	Source 7 Gasoline vapor
Species							
Acetylene	-0.0008	0.0013	0.0028	0.0018	0.0012	0.0221	-0.0030
Ethylene	0.0059	0.0136	0.0145	0.0110	0.0038	0.0482	0.0162
Ethane	0.0165	0.0435	0.030	0.0281	**0.0649**	**0.0890**	-0.0061
Propylene	0.0151	0.0058	-0.0030	**0.2443**	0.0077	0.0099	0.0033
Propane	**0.0811**	0.0462	0.0094	**0.1225**	**0.2260**	0.0430	-0.0338
iso-butane	0.0487	0.0096	0.0127	0.0447	**0.0879**	0.0254	-0.0225
n-butane	**0.0996**	0.0002	0.0078	**0.2032**	**0.1839**	0.0052	-0.0104
iso-pentane	-0.0667	**0.0677**	0.0292	**0.0860**	**0.1063**	**0.0812**	**0.0808**
n-pentane	-0.0784	0.0431	0.0139	0.0222	**0.0914**	0.0323	0.0065
Isoprene	-0.0032	-0.0012	**0.0754**	-0.0015	-0.0002	-0.0008	0.0001
Cyclopentane	**0.1649**	0.0000	-0.0001	-0.0003	-0.0007	-0.0000	0.0002
2-methylpentane	0.0217	-0.0063	0.0077	0.0225	0.0178	0.0265	0.0429
3-methylpentane	-0.0035	0.0161	0.0046	0.0076	0.0150	0.0136	0.0266
n-hexane	0.0290	0.0160	0.0042	0.0119	0.0261	0.0181	0.0250
Methylcyclopentane	0.0109	0.0029	-0.0015	0.0077	0.0109	0.0104	0.0131
Benzene	0.0136	0.0275	0.0086	0.0439	0.0047	0.0182	0.0195
2-methylhexane	0.0180	0.0082	0.0017	0.0052	0.0044	0.0046	0.0342
3-methylhexane	0.0336	0.0110	-0.0014	0.0028	0.0035	-0.0027	**0.0685**
2,2,4-trimethylpentane	0.0104	0.0114	0.0117	0.0096	0.0043	0.0290	0.0272
Toluene	0.0306	**0.0580**	0.0180	0.0128	0.0086	**0.0873**	**0.0683**
M&p xylene	0.0141	0.0238	0.0001	0.0102	0.0054	0.0499	0.0339
Isopropylbenzene	-0.0035	**0.1244**	-0.0002	-0.0002	0.0002	-0.0003	0.0000
1,2,3-trimethylbenzene	0.0005	0.0053	-0.0011	0.0011	0.0015	0.0149	0.0035
Total NMOC(ppbc)	5.0	5.7	21.3	16.9	60.4	39.8	25.3
% of total NMOC	3	3	12	10	35	23	15

Bold values indicate mass fractions > 0.05.

Bibliography

Anderson, M. J., Daly E. P., Miller, S. L., Milford, J. B., Source apportionment of exposures to volatile organic compound: II. Application of receptor models to TEAM study area. Atmospheric Environment 36, 3643-3658, 2002.

Andronache, C., Chameides, W., Rodgers, M., Martinez, J., Zimmerman, P., Greenberg, J., Vertical distribution of isoprene in the lower boundary layer of the rural and urban southern United States. Journal of Geophysical Research 99,16989-16999, 1994.

Aneja, V. P., Mathur, R., Arya, S. P., Li, Y., Murray, G. C., Manuszak, T. L., Coupling the vertical distribution of ozone in the atmospheric boundary layer. Environmental Science and Technology 34, 2324-2329, 2000.

Apndis, S. N., Harley, R. A., Cass, G. R., Seinfeld, J. H., Secondary aerosol formation and transport. Atmospheric Environment 26A, 2269-2282, 1992.

Arunachalam, S., Adelman, Z., Mathur, R., Olerud, D., Holland A., A comparison of Models3/CMAQ and MAQSIP modeling system for ozone modeling in North Carolina. 94th Annual meting of the Air and Waste Management Association, Orlando, Florida. Paper #989, 2001.

Atkinson, R., Atmospheric chemistry of VOCs and NOx. Atmospheric Environment 34, 2063-2101, 2000.

Baumann, K., Williams, E.J., Angevine, W.M., Roberts, J. M., Norton, R. B., Frost, G. J., Fehsenfeld, F. C., Springston, S. R., Bertman, S. B., Hartsell, B., Ozone production and transport near Nashville, Tennessee: Results from the 1994 study at New Hendersonville. Journal of Geophysical Research 105, 9137-9153, 2000.

Billford, P.D.E., Meeker, G. O., A factor analysis model of large scale pollution. Atmospheric Environment 1, 147-157, 1967.

Bowman, F. M., Pilinis, C., Seinfeld, J. H., Ozone and aerosol productivity of reactive organics. Atmospheric Environment 29, 579-589, 1995.

Cardelino, C. A., Chameides, W. L., An observation-based model for analyzing ozone precursor relationships in the urban atmosphere. Journal of Air & Waste Management Association 45, 161-180, 1995.

Cardelino, C. A., Chameides, W. L., The application of data from photochemical assessment monitoring stations to the observation-based model. Atmospheric Environment 34, 2325-2332, 2000.

Carter, W. P., Development of ozone reactivity scales for volatile organic compounds. Journal of Air and Waste Management Association 44, 881-899, 1994.

Carter, W.P.L., Documentation on the SAPRC-99 chemical mechanism for VOC reactivity assessment. Final Report to California Air Resources Board Contract No. 92-329 and 95-308, 2000.

Chameides, W. L., Lindsay, R. W., Richardson, J., Kiang, C. S., The role of biogenic hydrocarbons in urban photochemical smog: Atlanta as a case study. Science 241, 1473-1475, 1988.

Chameides, W. L., Fehsenfekd, D., Rodgers, M. O., Cardelino, C., Martinez, J., Parrish, D., Lonneman, W., Lawson, D. R., Ramussen, R. A., Zimmerman, P., Greenberg, J., Middleton, P., Wang, T., Ozone precursor relationships in the ambient atmosphere. Journal of Geophysical Research 97, 6037-6055, 1992.

Chen, L. W. A., Doddridge, B. G., Dickerson, R. R., Chow, J. C., Henry, R. C., Origins of fine aerosol mass in the Baltimore-Washington corridor: implications from observation, factor analysis, and ensemble air parcel back trajectories. Atmospheric Environment 36, 4541-4554, 2002.

Ching, J. K., Byun, D. W., Science algorithms of the EPA Models-3 Community multiscale Air Quality (CMAQ) modeling system.; U.S. EPA; Office of Research and Development; Washington D. C., EPA-600/R-99/030, 1999.

Choi, Y., Ehrman, S. H., Investigation of sources of volatile organic carbon in the Baltimore area using highly time resolved measurements. Atmospheric Environment 38, 775-791, 2004.

Cooter, E. J., Hutzell, W. T., A regional atmospheric fate and transport model for Atrazine. 1. Development and implementation. Environmental Science & Technology 36, 4091-4098, 2002.

Dennis, R. L, Byun, D. W., Nocak J. H., Galluppi, K. J., Coats, C. J., The next generation of integrated air quality modeling: EPA's models-3. Atmospheric Environment 30, 1925-1938, 1996.

Demerjian, K. L., A review of national monitoring networks in North America. Atmospheric Environment 34, 1861-1884, 2000.

Department of Energy (DOE) Document, Historical natural gas annual 1930 through 2000. DOE/EIS-E-0110(00), 2001.

Derwent, R. G., Middleton, D. R., Field, R. A., Goldstone, M. E., Lester, J. N., Perry, R., Analysis and interpretation of air quality data from an urban roadside location in central London over the period from July 1991 to July 1992. Atmospheric Environment 29, 923-946, 1995.

Derwent, R. G., Jenkin, M. E., Saunders, S. M., Pilling, M. J., Photochemical ozone creation potentials for organic compounds in Northwest Europe calculated with a master chemical mechanism. Atmospheric Environment 32, 2429-2441, 1998.

Dillon, W. R., Goldstein, M., Multivariate analysis, John Wiley & Sons Inc., 1984.

DNREC home page, http://www.dnrec.state.de.us. 2001

Dolwick, P., Jang, C., Possiel, N., Timin, B., Gipson, G. L., Godowitch, J., Summary of results from a series of Models-3/CMAQ simulations of ozone in the Western United States. Proceedings of the 94th Annual Meeting of the Air and Waste Management Association, Orlando, FL, June 24-28, 2001. Paper #957, 2001.

Elkins, J. B., Hemby J., Rao V., Mintz D., National air quality and emissions trends report, 1999. 94th Annual meting of the Air and Waste Management Association, Orlando, Florida. Paper #466, 2000.

EPA Document I, Technical Assistance Document (TAD) for Sampling and Analysis of Ozone Precursors. EPA/600-R-98/161, 1998.

EPA Document II, Evaluating emissions factors, models, and inventories with PAMS data. EPA-454/R-96-006, 1996.

EPA Document III, Science algorithms of the EPA Models-3 Community Multi-scale Air Quality (CMAQ) modeling system. EPA/600/R-99/030, 1999.

EPA Document IV, Technical assistance document for sampling and analysis of ozone precursors. EPA/600-R-98/161, 1998.

EPA Document V, Guideline for regulatory applications of the Urban Airshed Model. EPA-450/4-91-013, 1991.

Finlayson-Pitts, B. J., Pitts, J. N., Upper and lower atmosphere. Academic press, 2000.

Fiore, A., Holloway T., Hastings, M. G., A global perspective on air quality. EM December, 13-22, 2003.

Fujita, E. M., Croes, B. E., Bennerr C. L., Lawson, D. R., Comparison of emissions inventory and ambient concentration ratios of CO, NMOG, and NOx in California's south coast air basin. Journal of Air & Waste Management Association 42, 264-276, 1992.

Fujita, E. M., Watson, J. G., Chow, J. C., Lu, Z., Validation of the chemical mass balance receptor model applied to hydrocarbon source apportionment in the Southern California air quality study. Environmental Science and Technology 28, 1633-1649, 1994.

Fujita, E. M., Waston, J. G., Chow, J. C., Magliano, K. L., Receptor model and emissions inventory source apportionments of nonmethane organic gases in California's San Joaquin valley and San Francisco bay area. Atmospheric Environment 29, 3019-3035, 1995.

Fujita, E. M., Hydrocarbon source apportionment for the 1996 Paso del Norte ozone study. The Science of the Total Environment 276, 171-184, 2001.

Funk, T. H., Chinkin, L. R., Roberts, P. T., Saeger, M., Mulligan, S., Paramo Figueroa, V. H., Yarbrough, J., Compilations and evaluation of a Paso del Norte emission inventory. The Science of the Total Environment 276, 135-151, 2001.

Geron, C. D., Nie, D., Arnts, R. R., Sharkey, T. D., Singsaas, E. L., Vanderveer, P. J., Guenther, A., Sickles II, J. E., Kleindienst, T. E., Biogenic isoprene emissions: Model evaluatin in a southeastern Unites States bottomland deciduous forest. Journal of Geophysical Research 102, 18889-18901, 1997.

Gery, M.W.,m Whitten, G. Z., Killus, J. P., Dodge, M.C., A photochemical kinetics mechanism for urban and regional scale computer modeling. Journal of Geophysical Research, 94, 12925-12956, 1989.

Goldstein, A. H., Goulden, M. L., Munger, J. W., Wofsy, S. C., Geron, C. D., Seasonal course of isoprene emissions from a midlatitude deciduous forest. Journal of Geophysical Research 103, 31045-31056, 1998.

Guentehr, A., Geron, C., Pierce, T., Lamb, B., Harley, P., Fall, R., Natural emissions of non-methane volatile organic compounds, carbon monoxide, and oxides of nitrogen from North America. Atmospheric Environment 34, 2205-2230, 2000.

Haagen-Smit, A. J., Fox, M. M., Photochemical ozone formation with hydrocarbons and automobile exhaust. Journal of Air Pollution Control Association 4, 105-109, 1954.

Hanna, S.R., Moore, G.E., Fernau, M. E., Evaluation of photochemical grid models (UAM-IV, UAM-V, and the ROM/UAM-IV couple) using data from the Lake Michigan Ozone Study (LMOS). Atmospheric Environment 30, 3265-3279, 1996.

Hanna, S. R., Chang, J.C., Fernau, M.E., Monte Carlo estimates of uncertainties in predictions by photochemical grid model (UAM-IV) due to uncertainties in input variables. Atmospheric Environment 32, 3619-3628, 1998.

Harley, R. A., Hannlgan, M. P., Cass, G. R., Respeciation of organic gas emissions and detection of excess unburned gasoline in the atmosphere. Environmental Science & Technology 26, 2395-2408, 1992.

Henry, R. C., UNMIX version 2.4 Manual, 2001.

Henry, R. C., Multivariate receptor modeling by N-dimensional edge. Submitted to Journal of Chemometrics and Intelligent laboratory Systems, 2002..

Hidy, G. M., Ozone process insights from field experiments Part I: Overview. Atmospheric Environment 34, 2001-2022, 2000.

Hopke, P. K., Receptor modeling for air quality management, Elsevier Science Publishing Company Inc., 1991.

Houyoux, M.R., Vukovich, J. M., Coats, C. J., Emission inventory development and processing for the Seasonal Model for Regional Air Quality (SMRAQ) project. Journal of Geophysical Research 105, 9079-9090, 2000.

Irwin, J. S., A historical look at the development of regulatory air quality models. EM January, 22-29, 2003.

Isidorov, V., Jdanova, M., Volatile organic compounds from leaves litter. Chemosphere 48, 978-979, 2002.

Jacobson, M. Z., Fundamentals of Atmospheric Modeling, Cambridge University Press, 1999.

Jacobson, M. Z., Atmospheric pollution, Cambridge University Press., 2002.

Jenkin, M. E., Clemitshaw, K. C., Ozone and other secondary photochemical pollutants: Chemical processes governing their formation in the planetary boundary layer. Atmospheric Environment 34, 2499-2527, 2000.

Jonson, J. E., Sundet, J. K., Tarrason, L., Model calculations of present and future levels of ozone and ozone precursors with a global and a regional model. Atmospheric Environment 35, 525-537, 2001.

Jimenez, P, Baldasano, J. M., Dabdub, D., Comparison of photochemical mechanisms for air quality modeling. Atmospheric Environment 37, 4179-4194, 2003.

Jonson, J. E., Sundet, J. K., Tarrason, L., Model calculations of present and future levels of ozone and ozone precursors with a global and a regional model. Atmospheric Environment 35, 525-537, 2001.

Kavouras, I. G., Koutrakis, P., Tsapakis, M., Lagoudki, E., Stephanou, E. G., Baer, D. V., Oyola, P., Source apportionment of urban particulate aliphatic and polynuclear aromatic hydrocarbons (PAHs) using multivariate methods. Environmental Science and Technology 35, 2288-2294, 2001.

Kenski, D. M., Wadden, R. A., Scheff, P. A., Lonneman, W. A., Receptor modeling approach to VOC emissions inventory validation. Journal of Environmental Engineering 121, 483-491, 1995.

Kuhlwein, J., Wickert, B., Trukenmuller, A., Theloke, J., Friedrich, R., Emission-modeling in high spatial and temporal resolution and calculation of pollutant concentrations for comparisons with measured concentrations. Atmospheric Environment 36, S7-S18, 2002.

Kumar, N., Russell A. G., Multiscale air quality modeling of the northeastern United States Atmospheric Environment 30, 1099-1116, 1996.

Kumar, A. V., Patil, R. S., Nambi, K. S. V., Source apportionment of suspended particulate matter at two traffic junctions in Mumbia, India. Atmospheric Environment 35, 4245-4251, 2001.

LADCO report I, Comparison of ambient and emissions VOC and NOx data in the Lake Michigan region. (Available at http://www.ladco.org), 1998.

Lawrimore, J. H., Aneja, V. P., A chemical mass balance analyses of nonmethane hydrocarbon emissions in North Carolina. Chemosphere 35, 2751-2765, 1997.

Lewis, C. W., Henry, R. C., Shreffler, J. H., An exploratory look at hydrocarbon data from the photochemical assessment monitoring stations network. Journal of Air and Waste management Association 48, 71-76, 1998.

Mannschreck, K., Klemp, D., Kley, D., Friedrich, R., Huhlwein, J., Wickert, B., Matuska, P., Habram, M., Slemr, F., Evaluation of an emission inventory by comparisons of modeled and measured emission ratios of individual HCs, CO and NOx. Atmospheric Environment 36, S81-S94, 2002.

McKeen, S. A., Hsie, E. Y., Liu, S. C., A study of the dependence of rural ozone on ozone precursors in the Eastern United States. Journal of Geophysical Research 96, 15377-15394, 1991.

McNair, L. A., Harley, R. A., Russell, A. G., Spatial inhomogeneity in pollutant concentrations, and their implications for air quality model evaluation. Atmospheric environment 30, 4291-4301, 1996.

Milford, J. B., Gao D., Sillman S., Blossy P., Russell A.G., Total reactive nitrogen (NO_y) as an indicator of the sensitivity of ozone to reductions in hydrocarbon and NO_x emissions. Journal of Geophysical Research 99, 3533-3542, 1994.

Miller, M. S., Friedlander, S. K., Hidy, G. M., A chemical element balance for the Pasadena aerosol. Journal of Colloid and Interface Science 39, 165-176, 1972.

Miller, S. L., Anderson, M. J., Daly, E. P., Milford, J. B., Source apportionment of exposures to volatile organic compounds. I. Evaluation of receptor models using simulated exposure data. Atmospheric Environment 36, 3629-3641, 2002.

Miller, S. L., Anderson, M. J., Daly, E. P., Milford, J. B., Source apportionment of exposures to volatile organic compounds. II. Application of receptor models to REAM study data. Atmospheric Environment 36, 3643-3658, 2002.

Morales-Morales, R., Carbon monoxide, ozone, and hydrocarbons in the Baltimore metropolitan area. Ph.D. Thesis, University of Maryland, College Park, MD, USA, 1998.

Mukund, R., Kelly, T. J., Spicer, C. W., Source attribution of ambient air toxic and other VOCs in Columbus, Ohio. Atmospheric Environment 30, 3457-3470, 1996.

Na, K., Kim, Y. P., Moon, K. C., Diurnal characteristics of volatile organic compounds in the Seoul atmosphere. Atmospheric Environment 37, 733-742, 2003.

National Research Council (NRC), Rethinking the ozone problem in urban and regional air pollution. National Academy Press. Washington D.C., 1991.

NESCAUM, 1997 summer ozone season in the NESCAUM region. (http://www.nescaum.org/pdf/o3rpt_8a.PDF), 1998.

Parrish, D. D., Trainer, M., Young, V., Goldan, P. D., Kuster, W. C., Jobson, B. T., Fehsenfeld, F. C., Lonneman, W. A., Zika, R. D., Farmer, C. T., Riemer, D. D., Rodgers, M. O., Internal consistency tests for evaluation of measurements of anthropogenic hydrocarbons in the troposphere. Journal of Geophysical Research 103, 22339-22359, 1998.

Parrish, D. D., Fehsenfeld, F. C., Methods for gas-phase measurements of ozone, ozone precursors and aerosol precursors. Atmospheric Environment 34, 1921-1957, 2000.

Pierce, T., Geron, C., Bender, L., Dennis, R., Tonnesen, G., Guenther, A., Influence of increased isoprene emissions on regional ozone modeling. Journal of Geophysical Research 103, 25611-25629, 1998.

Placet, M., Mann, C. O., Gilbert, R. O., Niefer, M. J., Emissions of ozone precursors from stationary source: a critical review. Atmospheric Environment 34, 2183-2204, 2000.

Poirot, R. L., Wishinski, P. R., Hopke, P. K., Polissar, A.V., Comparative application of multiple receptor methods to identify aerosol sources in Northern Vermont. Environmental Science and Technology 35, 4622-4636, 2001.

Possiel, N.C., Cox, W. M., The relative effectiveness of NO_x and VOC strategies in reducing northeast US ozone concentrations. Water, Air and Soil Pollution 67, 161-179, 1993.

Rappengluck, B., Fabian, P., Kalabokas, P., Viras, L. G., Ziomas, I. C., Quasi-continuous measurements of non-methane hydrocarbons (NMHC) in the greater Athens area during MEDCAPHOT-TRACE. Atmospheric Environment 32, 2103-2121, 1998.

Roselle, S. J., Pierce, T. E., Schere, K. L., The sensitivity of regional ozone modeling to biogenic hydrocarbons. Journal of Geophysical Research 96, 7371-7394, 1991.

Roselle S. J., Schere K. L., Modeled response of photochemical oxidants to systematic reductions in anthropogenic volatile organic compound and NO_x emissions. Journal of Geophysical Research 100, 22929-22941, 1995.

Russell, A., Dennis, R., NARSTO critical review of photochemical models and modeling. Atmospheric Environment 34, 2283-2324, 2000.

Ryan, W. F., Doddridge, B. G., Dickerson, R. R., Morales, R. M., Hallock, K. A., Roberts, R. T., Blumenthal, D. L., Anderson, J.A., Civerolo, K. L., Pollutant transport during a regional O3 episode in the Mid-Atlantic States. Journal of Air and Waste Management Association 48, 786-797, 1998.

Ryan, W. F., Piety C. A., Luebehusen, E. D., Air quality forecasts in the mid-Atlantic region: Current practice and benchmark skill. Weather and Forecasting 15, 46-60, 2000.

Samson, P. J., Shi, B., A meteorological investigation of high ozone values in American cities. Report prepared for the United States Congress, Office of Technology assessment. Washington, D. C. : U.S. Government Printing Office, 1988.

Scheff, P. A., Wadden, R. A., Kenski, D. M., Chung, J., Receptor model evaluation of the southeast Michigan ozone study ambient NMOC measurements. Journal of Air and Waste Management Association 46, 1048-1057, 1996.

Seinfeld, J., Pandis, S. N., Atmospheric Chemistry and Physics, John Wiley & Sons, Inc., 1998.

Sillman, S., The relation between ozone, NO(x) and hydrocarbons in urban and polluted rural environments. Atmospheric Environment 33, 1821-1845, 1999.

Sistla, G., Hao W., Ku J., Kallos G., An operational evaluation of two regional scale ozone air quality modeling systems over the eastern United States. Bulletin of the American Meteorological Society 82, 945-964, 2001.

Sistla, G., Ku, M., Hao, W., An assessment of an MM5 simulation of July 6 to 19, 1997, in the Eastern United States. New York Department of Environment Conservation. (Available at http://www.otcair.org), 2002.

Slemr, F., Baumbach, G., Blank, P., Corsmeier, U., Fiedler, F., Fridrich, R., Habram, M., Kalthoff, N., Klemp, D., Kuhlwein, J., Mannschreck, K., Mollmann-coers, M., Nester, K., Pannitz, H.-J., Rabl, P., Slemr, J., Vogt, U., Wickert, B., Evaluation of modeled spatially and temporarily highly resolved emission inventories of photosmog precursors for the city of Augsburg: The experiment EVA and its major results. Journal of Atmospheric Chemistry 42, 207-233, 2002.

Smith, J.H., Durrenberger, P.E., Garrett, C., Control strategy modeling for the Huston-Galveston ozone nonattainment area. 94th Annual meeting of the Air and Waste Management Association, Orlando, Florida. Paper #987, 2001.

Solomon, P., Cowling, E., Hidy, G., Furiness, C., Comparison of scientific findings from major ozone field studies in North America and Europe. Atmospheric Environment 34, 1885-1920, 2000.

Stockwell, W. R., Middleton, P., Chnag, J.S., The second generation regional acid deposition model chemical mechanism for regional air quality modeling. Journal of Geophysical Research, 95, 16343-16367, 1990.

Stoeckenius, T., Jimenez, M., Reconciliation of an emissions inventory with PAMS ambient monitoring data in the Mid-Atlantic region: Final Report prepared for MARAMA, ENVIRON International corporation. 2000. (Available at http://www.marama.org/report), 2000.

Thurston, G. D., Spengler, J. D., A Quantitative assessment of source contributions to inhalable particulate matter pollution in metropolitan Boston. Atmospheric Environment 19, 9-25, 1985.

Trainer, M., Parrish, D.D., Goldan, P.D., Roberts, J., Fehsenfeld, F.C., Review of observation-based analysis of the regional factors influencing ozone concentrations. Atmospheric Environment 34, 2045-2061, 2000.

UCAR MM5 home page, http://www.mmm.ucar.edu/mm5/mm5-home.html, 2003.

Vega, E., Mugica, V., Carmona, R., Valencia, E., Hydrocarbon source apportionment in Mexico City using the chemical mass balance receptor model. Atmospheric Environment 34, 4121-4129, 2000.

Wadden, R.A., Scheff, P. A., Uni, I., Receptor modeling of VOCs-II. Development of VOC control functions for ambient ozone. Atmospheric Environment 28, 2507-2521, 1994.

Wallace, J. M., Hobbs, P. V., Atmospheric science, Academic Press, 1977.

Watson, J. G., Chow, J. C., Fujita, E. M., Review of volatile organic compound source apportionment by chemical mass balance. Atmospheric Environment 35, 1567-1584, 2001.

Wierman, S. S., Will the 8-hr ozone standard finally get off the ground, EM September, 20-28, 2003.

Winner, D. A., Cass, G. R., Effect of emissions control on the long-term frequency distribution of regional ozone concentrations. Environmental Science & Technology. 34, 2612-2617

Wu, C. Y., Pratt, G. C., 2002. UNMIX modeling assessment of gaseous organic compounds. 95th Annual Meeting, Baltimore, MD. Air and Waste Management association, Pittsburgh, PA, 2000.

Yarwood, G., Stoeckeninus, T. E., Heiken, J. G., Dunker, A. M., Modeling weekday/weekend ozone differences in the Los Angeles region for 1997. Journal of Air and Waste Management Association 53, 864-875, 2003.

Zhang, D., Zheng, W., Diurnal cycles of surface winds and temperature as simulated by five boundary layer parameterizations. Journal of Applied Meteorology 43, 157-169, 2004.

Zhang, J., Rao, S. T., The role of vertical mixing in the temporal evolution of ground-level ozone concentrations. Journal of Applied meteorology 38, 1674-1691, 1999.

URBAN FINE PARTICULATE MATTER:

CHEMICAL COMPOSITION AND POSSIBLE ORIGINS

by

Lung-Wen Antony Chen

Dissertation submitted to the Faculty of the Graduate School of the
University of Maryland, College Park in partial fulfillment
of the requirements for the degree of
Doctor of Philosophy
2002

Advisory Committee:

Professor Russell R. Dickerson, Chair/Advisor
Dr. Bruce G. Doddridge, Advisor
Professor John M. Ondov
Professor John H. Moore
Professor Sheryl H. Ehrman

ABSTRACT

Title of Dissertation: URBAN FINE PARTICULATE MATTER: CHEMICAL COMPOSITION AND POSSIBLE ORIGINS

Lung-Wen Antony Chen, Doctor of Philosophy, 2002

Thesis directed by: Dr. Bruce G. Doddridge
Professor Russell R. Dickerson

Department of Meteorology

Fine aerosol plays an important role in the atmosphere's radiative transfer. Elevated fine aerosol concentration in urban areas can result in visibility reduction and human respiratory diseases. To study the chemical composition and possible origins of fine particulate matter ($PM_{2.5}$) in the Baltimore-Washington (B-W) corridor, chemically speciated $PM_{2.5}$ and trace gases (including NH_3, HNO_3, CO, SO_2, NO_y) have been measured at Fort Meade (FME: 39.10°N, 76.74°W; elevation 46 m MSL), Maryland over a three-year period (1999-2002) including nine seasonally-representative months. FME is suburban, located in the middle of the B-W corridor, and generally downwind of the highly industrialized Midwest. The $PM_{2.5}$ shows an annual mean concentration of ~ 13 μg m^{-3}. On average, over 90% of the $PM_{2.5}$ mass can be attributed to sulfate, nitrate, ammonium, carbonaceous material, and crustal material. The $PM_{2.5}$ reconstructed mass is

found < ±15% different from its gravimetric mass. Ammonium sulfate dominates (> 50%) in the summertime high PM episodes while organic matter also contributes (~ 30%). By comparing the FME data with concurrent measurements at upwind and downwind sites, sulfate and crustal material are found to be more regional than other major components.

The inorganic fraction of fine aerosol is studied using a thermodynamic model, ISORROPIA. FME changes from an ammonia-poor environment in summer to an ammonia-rich environment in winter. ISORROPIA also estimates the aerosol water content; water can contribute to > 50% of the atmospheric extinction in the visible region on humid days.

The elemental carbon (EC)/CO ratio observed at FME is compared to those from individual vehicles, tunnel studies, and biomass burning to estimate the contribution from each potential source. Ambient temperature appears to influence emission factors. Based on a well-established CO emission inventory, the EC/CO ratio leads to an estimate of EC emission at 0.32 ± 0.12 Tg (EC) yr^{-1} for North America.

Using a factor analysis module, UNMIX, six factors that contribute to the $PM_{2.5}$ mass are resolved; these include regional sulfate, local sulfate, wood smoke, mobile, secondary nitrate, and copper/iron processing industry. The six factors are studied further using an ensemble back trajectory method to identify the possible source locations. Regional sulfate and wood smoke are more regional than other factors and associated with westerly and southerly transport, respectively. This study suggests that the local contribution to the $PM_{2.5}$ mass can vary from < 30% in summer to > 60% in winter.

ACKNOWLEDGEMENT

This work was supported by Baltimore Gas and Electric Company and Potomac Electric Power Company through Electric Power Research Institute and Maryland Industrial Partnerships. The United States Environmental Protection Agency provided additional support for data analysis through grant number R826373. The author thanks Maryland Department Environment for providing and maintaining the Fort Meade sampling site.

This work cannot be accomplished without substantive help from many people. The author thanks Dr. Bruce Doddridge and Dr. Russell Dickerson for their instruction and advisories in both theoretical and experimental aspects of this study. The author enjoyed working with Dr. Jeff Stehr, Charles Piety, and many others in the Air Chemistry Group in the Department of Meteorology. Dr. Peter Muller was the manager for the MARCH-Atlantic study and made great efforts ensuring the smooth progress of this project. Steven Kohl organized the excellent chemical analyses at the Desert Research Institute. G. Aburn, W. Butler, E. Gluth, F. Pluciennik, D. Preece, and J. Quinn all provided important contributions to this project.

Finally, the author would like to thank the Chemical Physics Program and Dr. Michael Coplan for the opportunity to study at University of Maryland. This has been an inspirational and delightful four years in my life.

TABLE OF CONTENTS

LIST of TABLES

LIST of FIGRURES

Chapter 1 Introduction

1.1 Background

Condensed-phase (liquid or solid) particles, referred to as aerosols (airborne particles), represent the greatest source of uncertainty in estimating global climate forcing and cause substantial environmental and health effects on the urban scale. Most of the aerosol particles stay in the troposphere, approximately the lowest 8 - 15 km of the atmosphere. Unlike gases, aerosols have a broad size distribution and complicated chemical composition. Aerosols play an important role in the Earth's energy balance. First, aerosol particles can effectively scatter incident short wavelength solar radiation (visible and ultraviolet) back to space and cause a direct cooling effect on the troposphere [*IPCC*, 2001; *Kiehl*, 1994, 1995]. Aerosol such as soot is light absorbing so that it may cause a warming effect as well [*Jacobson*, 2001]. Aerosols contain effective cloud condensation nuclei (CCN) that have significant impacts on the development of clouds and precipitation, essential in the Earth's climate system. A possibly larger but yet quantified indirect radiative forcing is caused by aerosols through modifying the coverage and reflectivity of cloud systems [*Jones et al.*, 1994; *Gillani et al.*, 1995]. Stratospheric aerosols, though at a much lower concentration, are crucially involved in the ozone depletion process over Antarctica in spring [*Molina*, 1991; *Portmann et al.*, 1996].

Since the industrial revolution in the late 19th century, along with increasing

anthropogenic and industrial activities, air pollution has been becoming a serious problem in both urban and remote areas. The Antarctic ozone hole, acidic precipitation, photochemical smog, and global warming are all related to the release of air pollutants, such as chlorofluorocarbons (CFC's), sulfur dioxide (SO_2), reactive nitrogen oxides (NO_x), hydrocarbons, and carbon monoxide (CO). Particles released from anthropogenic activities also increase so much that they may have significantly altered the concentration and chemical composition of nature aerosols. In addition to the potential climate impacts, there is a growing concern about the health and environmental effects of these anthropogenic aerosols in the last few decades. Certain aerosol components could be toxic. Also, small particles could risk the health of susceptible and elderly individuals through damaging their lung and respiratory functions. Epidemiological studies have demonstrated statistical associations between short-term increases in ambient aerosols and daily mortality/morbidity [e.g. *Dockery et al*., 1993; *Samet et al.*, 1995; *Kaiser*, 2000]. (Note that the correlation slope in *Samet et al.* [1995] might be a factor of 2 high [*USEPA*, 2002].) Elevated aerosol concentration is often linked to the haze or smog formation that causes light extinction, reducing visibility and influencing flight safety. In 1997, the United States Environment Protection Agency (USEPA) classified fine particulate matter as a criteria air pollutant and added new annual (15 $\mu g\ m^{-3}$) and 24-hr (65 $\mu g\ m^{-3}$) standards of ambient $PM_{2.5}$ (particles with aerodynamic mean diameters at or below 2.5 μm) mass concentration to the National Ambient Air Quality Standard (NAAQS).

The NAAQS took the first step toward the regulation of particle release. However, the particulate pollution problem is complicated by the diverse physical and chemical properties of aerosols. Typical aerosol samples have a size spectrum ranging from several

nanometers to tens of micrometers. Particles of different sizes usually result from different processes and have different atmospheric lifetime, optical properties, and health effects. Furthermore, aerosol particles are composed of various chemical compounds, including inorganic and organic species, in the form of internal or external mixtures (Internal mixtures: single particles of multi-components; external mixtures: a mixture of various types of pure particles). Aerosol chemical composition is found to have a strong spatial variation, reflecting the multiple origins of particles and short atmospheric lifetimes. Once in the air, aerosol size, shape, and chemical composition can evolve via physical (condensation, evaporation, coagulation, etc) process, chemical (oxidation, photo-dissociation, etc.) process, or both (e.g. cloud-smoke interactions). The situation is especially complex in urban areas where all sorts of pure particles and gases emitted quickly interact with one another to produce various mixtures. Designing effective pollution control strategies require a better knowledge of aerosol chemical composition and how the composition varies with time and space. The next step is to understand how emissions lead to aerosol ambient concentrations, environmental and health effects.

The Baltimore-Washington (B-W) corridor is one of the major metropolitan areas in the U.S. region, where serious haze and photochemical smog have been observed frequently during summertime [*Ryan et al*., 1998; *Russell et al.*, 1999]. The Maryland Aerosol Research and CHaracterization (MARCH-Atlantic) study was initiated in 1999 with the goal of investigating daily/seasonal variations of fine aerosol concentration and chemical composition in the urban corridor and determine possible sources and source regions. The technical approach includes installing equipment to sample $PM_{2.5}$ and its gaseous precursors every day during seasonally-representative months. The sampling site of this

study is chosen at Fort Meade (FME), Maryland, approximately in the middle of the Baltimore-Washington corridor. Data acquired are interpreted based on chemistry and meteorology. Using the data, we evaluate the aerosol-caused visibility reduction and investigate origins of aerosols. This study contributes to the understanding of particulate pollution and provides insights for pollution control.

1.2 Physical and Chemical Properties of Aerosols

1.2.1 Aerosol Size and Concentration

In quiescent air, the movement of a particle driven by gravity can be described by

$$m_p \frac{d\boldsymbol{v}}{dt} = m_p \boldsymbol{g} + \frac{3\pi\eta D_p}{C_c}(\boldsymbol{u} - \boldsymbol{v}) \qquad (1)$$

where m_p is the particle mass, $\boldsymbol{g}$ is the gravity, η is the gas viscosity, D_p is the particle diameter, and $\boldsymbol{v}$ **-** $\boldsymbol{u}$ represents the particle velocity relative to the air. C_c is the slip correction factor, which is particularly important for $D_p < 0.2$ μm [*Seinfeld and Pandis*, 1998, pp. 464]. The last term in the equation indicates the drag force acting on a smooth spherical particle due to the laminar flow of air over it. From (1) the aerosol terminal velocity (v_t) due to gravitational settling can be derived assuming that the particle has a density ρ_p:

$$v_t = \frac{D_p^2 \rho_p g C_c}{18\eta} \qquad (2)$$

v_t is proportional to the square of aerosol diameter. In most cases, particles are neither smooth nor spherical so that it is difficult to measure the actual particle diameter. The aerodynamic diameter (D_a) of a particle is defined as the diameter of a sphere of unit density (1 g cm^{-3}) that has the same terminal velocity in the air as the particle under consideration. D_a is given by equation:

$$D_a = D_g k \sqrt{\frac{\rho_p}{\rho_0}}$$

D_g is the geometric diameter, ρ_0 is the reference density (1 g cm^{-3}), and k is a shape factor, which is 1 for a sphere [*Finlayson-Pitts and Pitts*, 1999]. This effective diameter is particularly useful because it determine in part the particle's atmospheric lifetime against dry deposition. Throughout the paper, the term diameter is used with the understanding that it is the aerodynamic diameter of the particle.

Atmospheric aerosols consist of particles ranging from a few nanometers to tens or even hundreds of micrometers in size. Submicrometer particles settle extremely slowly, only a few centimeters per hour. These particles are easily lifted by wind and can stay in the atmosphere for weeks to months in the absence of other sinks. Particles around 10 μm settle with speed exceeding 10 m h^{-1} and therefore are expected to have a much short atmospheric residence time. Particles greater than 10 μm usually fall to the surface in one day and cannot travel far away from their sources.

The various processes that influence particle sizes are shown in an idealized schematic in Figure 1.2.1, which depicts the typical distribution of surface area of atmospheric aerosols. Airborne particles observed can often be divided into three modes: the nucleus mode, accumulation mode, and coarse particle mode. The nucleus mode, extending from

~ 5 nm to 0.1 μm diameter, is produced by the condensation of gas (e.g. soot) during combustion. Though the nucleus mode accounts for the preponderance of particles by number, nucleus-mode particles usually do not travel far away from sources of pollution before evolving into the accumulation mode. The accumulation mode, extending from 0.1 to ~ 2.5 μm, results from the coagulation of particles in nucleus mode, from condensation of vapors onto existing particles, and from the particles left behind when cloud drops evaporate (aqueous phase reaction). Accumulation mode particles are more aged in character and usually account for most of the aerosol surface area.

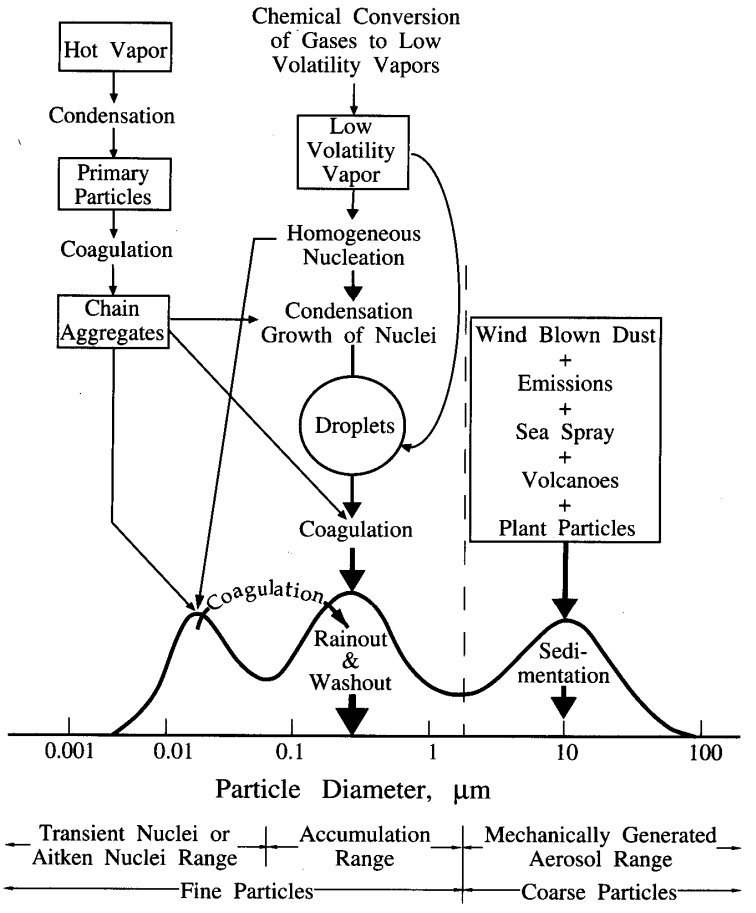

Figure 1.2.1 Idealized schematic of aerosol-size modes and relevant atmospheric processes. (Adapted from *Whitby and Cantrell*, [1976])

The coarse particle mode has diameter between 2.5 and ~ 10 μm, consisting of wind-blown dust, vegetation debris, sea salt, fly ash, etc. Coarse particles often dominate the aerosol mass. Conventionally, particles less than 2.5 μm in diameter are referred to as 'fine' particles in contrast to 'coarse' particles between 2.5 μm and 10 μm in diameter. Coarse and fine particles not only originate from different sources but also have distinct chemical composition, optical properties and deposition rates. They need to be treated separately in considering environmental and health effects of aerosols.

Three types of aerosol concentrations, number, surface area, and volume (mass) concentrations are often used. The number concentration indicates the total number of particles in a unit volume of air. One of the oldest but most convenient techniques for counting the number of aerosol particle is the Aitken nucleus counter. This instrument expands humid air adabatically to cool it and supersaturate it to several-hundred-percent relative humidity. Under this condition, water vapor condenses onto virtually all of the particles in the air to form small water droplets. The number concentration of particles can be determined by counting these droplets. The number concentration of aerosols is most concerned in considering aerosol-cloud interactions, especially if the aerosol is effective CCN.

When the aerosol radiative effects are considered, the surface area concentration is more useful. The spectral extinction efficiency (scattering plus absorption) of a single particle is defined as the ratio of total extinction cross section at a specific wavelength over the particle's cross section (e.g. see *Bohren and Huffman* [1983] for detailed discussions). Therefore, the surface area concentration of aerosols is essentially a measure of direct aerosol radiative forcing.

The aerosol volume or mass concentration, sometimes called the 'bulk' concentration, is a measure of total aerosol mass loading in the atmosphere. It is the aerosol mass concentration that enters the NAAQS. Aerosol mass concentration can be measured by weighting a filter through which a known volume of ambient air is drawn. So far most of the chemically speciated measurements, including this study, are made for the bulk aerosol since techniques for single-particle chemical analysis are still either immature or expensive.

The aerosol size distribution depends on the type of concentration used. The size-number distribution $n_N(D_p)$ is defined as follows:

$n_N(D_p)dD_p$ = the number of particles per unit volume of air having diameter in the range D_p *to* $D_p + dD_p$

The units of $n_N(D_p)$ usually $\mu m^{-1}\ cm^{-3}$ and the total number of particles per unit volume of air, N, is then just

$$\frac{dN}{dD_p} = n_N(D_p) \quad \text{or} \quad N = \int_0^\infty n_N(D_p)dD_p$$

Similarly, the size-resolved surface area concentration $n_S(D_p)$ and volume concentration $n_V(D_p)$ can be defined as follows:

$n_S(D_p)dD_p$ = the surface area of particles per unit volume of air having diameter in the range D_p *to* $D_p + dD_p$

$n_V(D_p)dD_p$ = the volume of particles per unit volume of air having diameter in the range D_p *to* $D_p + dD_p$

Assuming that all the particles are spherical and homogeneous, each of them would have cross section πD_p^2 and volume $\pi/6 D_p^3$. It is straightforward that

$$n_S(D_p) = \pi D_p^2 \, n_N(D_p)$$

$$n_V(D_p) = \pi/6 D_p^2 \, n_N(D_p)$$

and size-resolved mass concentration $n_M(D_p)$:

$$n_M(D_p) = \rho_p \, n_V(D_p)$$

where ρ_p is the density of particles.

A typical aerosol number, surface area, and mass distribution are shown in Figure 1.2.2 (size in log scale). The peaks around 0.02 μm and 0.1 μm in the size-number distribution correspond to the nucleus mode and the accumulation mode, respectively. The number concentration of coarse particles is too low to be distinguished. Though nucleus-mode particles are abundant, because of their small size, these particles rarely account for more than a few percent of the total aerosol mass. The accumulation mode is overwhelmingly responsible for the surface area concentration and likely for the aerosol radiative effects as well. The Aitken nucleus count near the Earth's surface varies strongly both spatially and temporally. Generally, the average aerosol number concentration is ~ 10^3 cm^{-3} over the oceans, ~ 10^4 cm^{-3} over rural areas, and can be much higher than 10^5 cm^{-3} in the highly polluted air. Coarser (super-micrometer) particles, though much fewer in number, contribute to substantial aerosol mass due to their large sizes. Near the Earth's surface, the typical aerosol mass concentration ranges from a few μg m^{-3} in remote areas to several tens μg m^{-3} in urbanized areas.

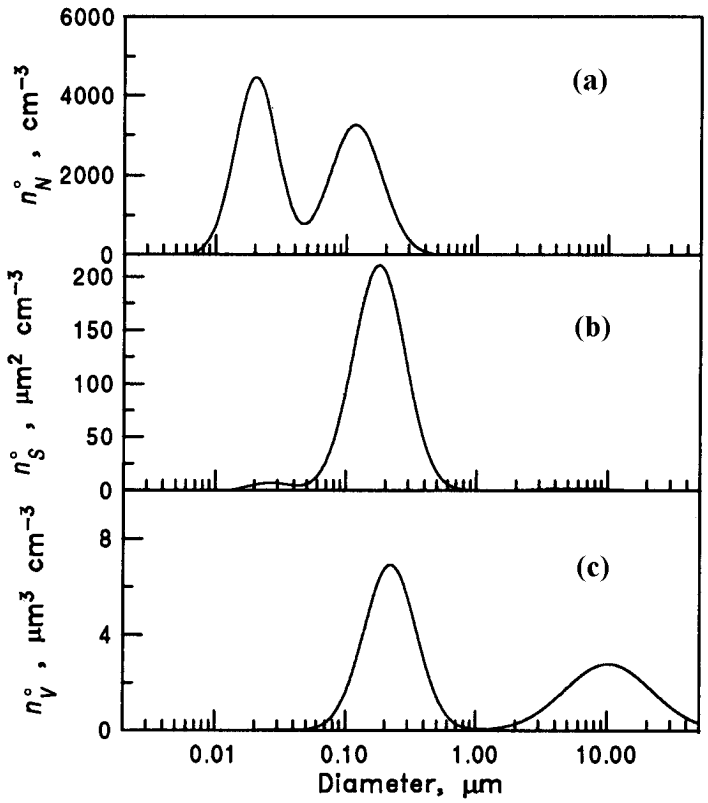

Figure 1.2.2 Typical aerosol number, surface and volume distributions in remote continents. (Adapted from *Seinfeld and Pandis*, [1998], pp. 436)

1.2.2 Aerosol Sources and Chemical Composition

Atmospheric aerosols originate from both natural and anthropogenic sources. Natural sources include the Earth's crust, oceans, and biosphere. Crustal material, in the forms of sand, ash, or soil dust, is generated from mechanical actions of wind and turbulence on the Earth's crust. On the global scale, deserts are the main origin of crustal particles while volcanic ashes could be the second important source. Most commonly seen elements in crustal material include O, Si, Al, Fe, Ca, Na, Mg, K, Ti, etc [*Mason and Moore*, 1982]. These crustal components tend to appear mainly in the coarse particle mode [e.g., *Artaxo et al.*, 1988] ranging from 1 to 100 μm in diameter. In the absence of long-range transport

from continents, aerosols over remote oceans are mostly of marine origin. Marine particles result from the evaporation of sea spray produced by bursting bubbles or wind-induced wave breaking, and they can be in both coarse and fine mode. Sea salt elements in the form of ions, such as Na^+, Cl^-, K^+, Ca^{2+} and SO_4^{2-}, are commonly found in the marine aerosols [e.g., *Fitzgerald et al.*, 1991]. Biogenic aerosols are emitted into the atmosphere from plants and animals. These aerosols includes coarse particles, such as seeds, pollens, and plant wax as well as fine particles, such as bacteria, algae, and viruses. Biogenic aerosols are mostly composed of organics, produced from both land and ocean. In remote areas, the biogenic fraction in the aerosol number concentration for particles with diameter < 2 μm can reach 50%; for coarse particles it is ~ 10%. Another important natural source of aerosol is wild forest fire caused by lightning. Smoke from forest fires contains significant fine-mode carbonaceous particles, including soot and various organics [*Cofer et al.*, 1988; *Artaxo et al.*, 1994].

The global input of anthropogenic aerosols is estimated at ~ 20% (by mass) of that from natural sources, but it is mostly in the fine-aerosol mode and highly concentrates in the urbanized areas. Wind-blown road dusts and construction debris contribute to coarse-mode particles. However, widely utilized fossil fuel and biofuel produce particles predominately in the sub-micrometer range and have become the core of modern particulate pollution problems. Activities involving fossil fuel or biofuel combustion, such as coal/oil burning power plants, industries, automobiles, and residential woodstoves/fireplaces directly emit elemental carbon (EC, also called black carbon or soot) and organic carbon (OC) particles into the atmosphere. In addition to direct particle emission, high temperature combustion processes cause the oxidation of nitrogen (N_2)

and release gaseous pollutant NO and NO_2. Burning fuels rich in sulfur (S) can produce sulfur dioxide (SO_2) gas. The gaseous NO_x ($NO + NO_2$) and SO_2 are subsequently converted to particles in the atmosphere, increasing the anthropogenic contribution to fine particulate matter.

Particles formed in the atmosphere through gas-to-particle conversion are called "secondary" in contrast to "primary" particles that are ejected directly from sources. Three commonly observed aerosol components, sulfate (SO_4^{2-}), nitrate (NO_3^-), and secondary organic carbon (secondary OC), are mostly formed through gas-to-particle conversion. SO_2 can be oxidized in both gaseous and aqueous phase. The mechanism in the gaseous phase usually involves hydroxyl radical (OH) and oxygen (O_2):

$$SO_2 + OH + M \rightarrow HSO_3 + M \quad (R1)$$

$$HSO_3 + O_2 \rightarrow HO_2 + SO_3 \quad (R2)$$

$$SO_3 + H_2O \rightarrow H_2SO_4 \quad (R3)$$

The reaction R1 has to involve a third body M, which could be any air molecule, for maintaining the conservation of momentum. The reaction R2 and R3 are so fast that the production rate of H_2SO_4 mostly depends on the OH concentration. H_2SO_4 has a low saturated vapor pressure over H_2SO_4-H_2O solution and condenses under all atmospheric conditions to form aqueous phase sulfate (SO_4^{2-}). The lifetime of SO_2 against oxidation by OH is 1 – 2 weeks, but the actual atmospheric lifetime of SO_2 appears to be much shorter. Researchers in the 1980's suggested that most of the atmospheric oxidation of SO_2 takes place in cloud and rain droplets [*Burkhard et al.*, 1994], where SO_2 is converted to HSO_3^-, which is then rapidly oxidized by H_2O_2 produced from self-reaction of HO_2:

$$SO_{2(g)} \rightarrow SO_2 \cdot H_2O \quad (R4)$$

$$SO_2 \cdot H_2O \rightarrow HSO_3^- + H^+ \quad (R5)$$

$$HSO_3^- + H_2O_{2(aq)} + H^+ \rightarrow SO_4^{2-} + 2H^+ + H_2O \quad (R6)$$

The sulfate particle formed after cloud water evaporates is usually in the accumulation mode, and its size depends on the amount of SO_2 dissolved and the ambient RH [e.g. *Ondov and Wexler*, 1998]. Ammonium (NH_4^+) serves as the main cation associated with sulfate in continental aerosols. On the global scale, ammonia (NH_3) is the only significant gaseous base in the atmosphere. It is produced primarily by livestock wastes and fertilizer; smaller amounts are believed to be generated by industrial activities, cars with catalytic converter [*Durbin et al.*, 2002], and natural processes in the soil [*Schlesinger and Hartley*, 1992]. Ammoniated sulfate is usually produced by NH_3 neutralizing H_2SO_4 in the condensed phase. Sulfate particles are hydroscopic and can uptake significant atmospheric water vapor (H_2O) at high relative humidity. Therefore, the mass of a sulfate particle at ambient conditions could be much larger than its dry mass.

Nitric acid (HNO_3) can be formed through high-temperature oxidation of atmospheric N_2 to reactive nitrogen oxides ($NO_x = NO + NO_2$) during combustion or lightning, followed by further oxidation of NO_x through

$$NO + O_3 \rightarrow NO_2 + O_2 \quad (R7)$$

$$NO_2 + OH + M \rightarrow HNO_3 + M \quad (R8)$$

or

$$NO_2 + O_3 \rightarrow NO_3 + O_2 \quad (R9)$$

$$NO_3 + NO_2 + M \rightarrow N_2O_5 + M \quad (R10)$$

$$N_2O_5 + H_2O_{(l)} \rightarrow 2HNO_3 \quad (R11)$$

R9 – R11 are enhanced at nighttime due to a higher concentration of NO_2. HNO_3 is highly soluble with respect to water, and in water it reacts with NH_3 to form NH_4NO_3. In a marine environment, reactions between HNO_3 and sea salt (e.g., NaCl) may occur to produce $NaNO_3$ [*De Haan et al.*, 1999]. Evaporation of cloud water is a major source of fine nitrate particles. HNO_3 has a higher vapor pressure than H_2SO_4 and can remain in the gaseous phase at ambient conditions. The gas-particle partitioning of a HNO_3-NO_3^- system at thermodynamic equilibrium depends on temperature, relative humidity, and the availability of SO_4^{2-} and NH_4^+ as well as other anions and cations (Cl^-, Na^+, K^+, etc.) [*Kim et al.*, 1993]. This will be discussed in Chapter 4.

Organic aerosol is usually the second most abundant component in $PM_{2.5}$ after sulfate. Unlike sulfate, organic aerosol covers a very wide range of molecular forms, solubilities, reactivities and physical properties (e.g., *Jacobson et al.* [2000]). Organic compounds generated from natural or anthropogenic sources consist of volatile, semi-volatile, and non-volatile components, separated according to their vapor pressure at ambient temperature. High vapor-pressure compounds, often referred to as volatile organic compounds (VOCs), include many short-chain alkanes and alkenes and always stay in gaseous phase. Semi-volatile organic compounds generally have a larger molecular size and lower vapor pressure. These molecules can either condense into particulate phase by themselves or onto surface of existing aerosols at a lower temperature. The definition of particulate organic carbon (OC) should include all of the non-volatile compounds and the particulate fraction of semi-volatile organics. Obviously, the amount of OC depends on ambient temperature.

It is also suggested that organic aerosols can be formed in the atmosphere through the oxidation of organic gas. The most effective oxidants include OH, O_3, and NO_3. Some of the products from oxidation of organic gases have low volatility and condense onto available nuclei to produce secondary organic carbon. *Grosjean and Seinfeld* [1989] suggested that secondary OC is formed only from the oxidation of hydrocarbon molecules containing seven or more carbon atoms. For example, the gas-to-particle conversion of α-Pinene is studied extensively in *Nadarajan* [2002]. In most cases, primary OC dominates, but the secondary OC contribution could exceed the primary OC during peak photochemical air pollution episodes [*Turpin and Huntzicker*, 1995].

Secondary particles, once formed, are in nucleus mode but can grow into accumulation mode rapidly. A recent estimate suggests that ~ 20% of fine aerosols in the global atmosphere are sulfate derived from oxidation of anthropogenic SO_2 [*Raes et al.*, 2000].

It is believed that fine-mode aerosols carry most of the threat to our health and environment because of their relatively long atmospheric lifetime and predominately combustion origin. Particles emitted from combustion sources usually contain toxic organics and metals (e.g., Hg, Pb, As, etc) that raise health risks related to particles. Highly industrialized North America is one of the largest fossil fuel consumers in the world. Coal burning power plants are operated across the United States, and according to the USEPA, ~ 80% of the SO_2 released in the U.S. comes from these point sources [*USEPA*, 1997]. A few previous field studies indicate that ammoniated sulfate generally accounts for about half of the $PM_{2.5}$ mass in the eastern U.S. [*Malm et al.*, 1994; *Hegg et al.*,1997; *USEPA* 1999; *IMPROVE*, 2000]. Particulate nitrate, possibly resulting from both point and mobile source, could play a greater role in the $PM_{2.5}$ mass on the U.S. west

coast [*Chow et al*., 1994; *IMPROVE*, 2000]. The rest of the $PM_{2.5}$ mass is mainly carbonaceous material. The carbonaceous material along with toxic organic gases like polycyclic aromatic hydrocarbons (PAHs) is certainly in the spotlight with respect to the $PM_{2.5}$ health issues.

1.2.3 Aerosols Sinks and Transport

Aerosol particles can be removed from the atmosphere through dry and wet processes. Dry processes include coagulation, sedimentation and collision with surfaces. Coagulation (i.e., fusion of two particles) is a very effective sink for nucleus mode particles near their sources. Once a particle grows into a size of ~ 10 μm in diameter, sedimentation (gravitational settling) drives the particle to the Earth's surface [*Slinn et al.*, 1978] rapidly. A detailed description of the dry deposition process and calculation of deposition velocity (V_d) can be found in Chapter 19, *Seinfeld and Pandis* [1998]. V_d depends on particle size and turbulent diffusion coefficient. Ambient relative humidity that determines the aerosol water content (e.g. *Ondov et al.* [1995] and Section 4.5) is found to influence V_d as well [*Quinn and Ondov*, 1998]. It is estimated that ~ 10 to 20% of the aerosol mass is removed from the atmosphere by sedimentation. Fine aerosols may be removed by impacting onto obstacles when brought close to a surface by winds or by turbulent air motions. Some surfaces have higher impaction efficiency that may increase the deposition rate of fine particles by 1 – 2 orders of magnitude.

The dry deposition of aerosols with diameter between ~ 0.2 μm and 2 μm (accumulation mode) is relatively weak, and the atmospheric lifetime of these particles

can reach hundreds of days if only dry processes are involved. However, wet processes, including cloud droplet absorption and precipitation scavenging, greatly reduce the atmospheric lifetime of aerosols in the middle and lower troposphere to that of water. CCNs take up water vapor to form cloud droplets, which can subsequently absorb nucleus-mode particles in their vicinity. Precipitation scavenging is usually very efficient for removing particles. Assuming that a raindrop collects and removes particles of all sizes in the volume it sweeps, the atmospheric lifetime of aerosols against precipitation scavenging would be in the same order of magnitude as the atmospheric lifetime of water vapor against precipitation, which is ~ 1 week on the global average. Figure 1.2.3 illustrates the aerosol cycle in the atmosphere, and Figure 1.2.4 shows the typical atmospheric lifetime of aerosol as a function of aerosol size. Near the tropopause wet processes are weak, and the accumulation mode aerosols can survive as long as 10^7 seconds (~100 days). In the mid troposphere (~ 7 km altitude) this is reduced to 10^6 seconds (~ 10 days). The lifetime of aerosols within the first 1 – 2 km of the troposphere is generally just several days.

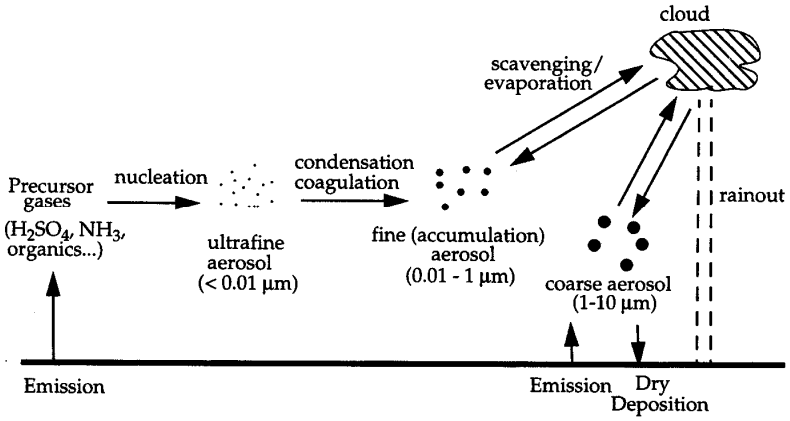

Figure 1.2.3 Production, growth, and removal of atmospheric aerosols. (Adapted from *Jacob*, [1999])

Once in the atmosphere, particles are carried by air motions and transported both horizontally and vertically. Horizontal transport is restricted by aerosol atmospheric lifetime and synoptic wind speed. Assuming a synoptic wind speed of ~ 2 m s^{-1}, an accumulation-mode particle having a lifetime ~ 5×10^5 s can travel ~ 1000 km (the regional scale) before settling down. However, intercontinental or even global transport of fine particles is possible during special events. For example, Saharan dust is transported to the America [*Prospero et al.*, 1987]. Vertical transport in the atmosphere is generally less efficient; the typical vertical mixing time in the troposphere is ~ 1 month in the absence of strong convection such as thunderstorm. The mass of aerosol mostly appears in the lower troposphere, reflecting the dominant sources near the surface and the short atmospheric lifetime that prevents a thorough vertical mixing.

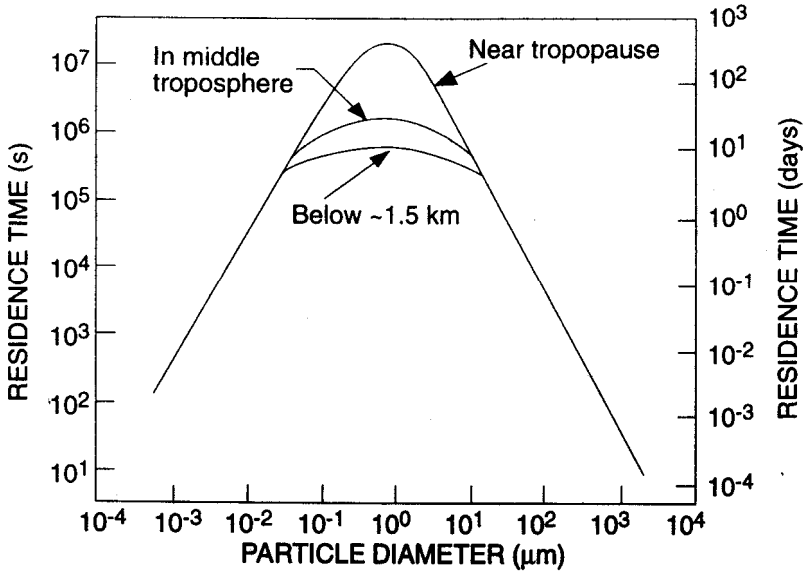

Figure 1.2.4 Estimates of the residence (atmospheric) lifetime of aerosol as a function of its diameter. (Adapted from *Hobbs*, [2000], pp. 103.)

Moreover, the vertical transport of pollutants released on the surface is largely confined within a so-called planetary boundary layer (PBL). The PBL is a layer of air that extends from the Earth's surface up to a height of 1 – 2 km. Normally, the troposphere have a positive lapse rate, where the temperature falls with altitude. Under such a lapse rate, warm air close to the surface rises and is replaced by cooler air from higher altitude, generating circulation in the troposphere. A thin inversion layer (temperature increases with altitude), however, defines the top of a PBL. The inversion is formed via two major mechanisms. The emission of infrared radiation after sunset causes rapid cooling of the Earth's surface and the layer of air immediately above it. An inversion layer forms when this cooling is sufficiently rapid that the layer of air adjacent to the surface becomes cooler than the air above. This type of inversion layer (radiation inversion) is usually quite shallow (< 500 m). Large scale sinking motion of air masses caused by, for example, anticyclones produces the 'subsidence' inversion. The sinking leads to the compression and heating of air immediately below, resulting in a change in the lapse rate and the formation of an inversion layer. A subsidence inversion layer is generally ~ 0.5 – 2 km thick. The formation of thermal inversions is one of the most important factors contributing to the air pollution problems in urban areas because it acts as a 'lid' on air masses. The cooler air beneath an inversion layer cannot rise through it. Therefore, pollutants trapped below the inversion layer are not mixed rapidly throughout the troposphere. In fact, pollutants released at the surface are generally well mixed by turbulence up to the PBL top but become much more dilute beyond that. The daytime PBL is deeper than the nighttime PBL since strong solar insolation after sunrise tends to weaken the radiation inversion built at night. This is illustrated in Figure 1.2.5. The

change in PBL depth could cause interesting diurnal variations in pollutant level. The summertime PBL is generally deeper than the wintertime PBL for the same reason. Strong and persistent subsidence inversions in urban regions can lead to accumulation of pollutants within the PBL over several days, resulting in severe air pollution episodes.

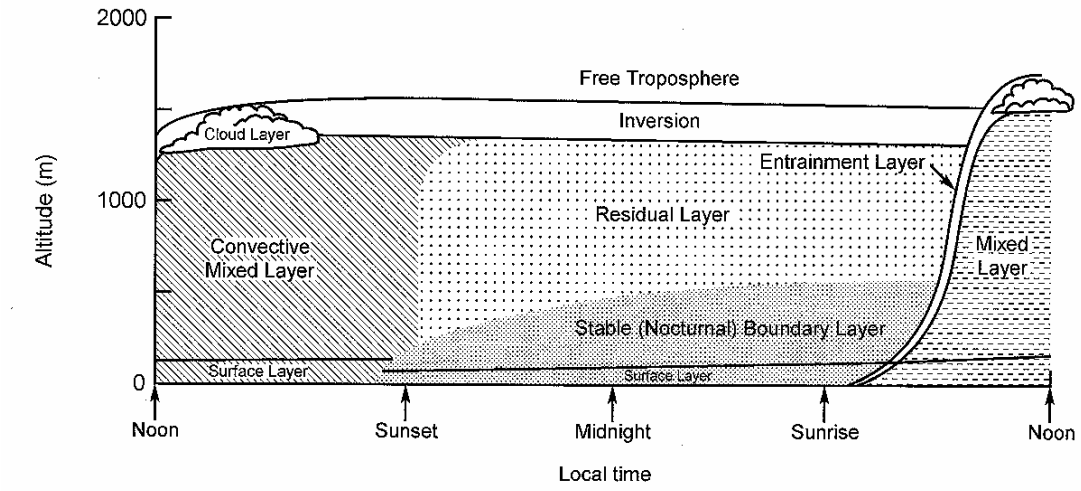

Figure 1.2.5 Schematic of mixing processes in atmosphere close to the Earth's surface as a function of time of day. (Adapted from *Stull* [1988].)

1.2.4 Urban Photochemical Smog and Regional Haze

Urban photochemical smog and regional haze are two air pollution problems involving fine aerosols. Urban photochemical smog was first reported in Los Angeles in the early 1950's and subsequently observed, in various degrees, in Houston, New York, Boston, and many major metropolitan areas in the United States. Chemicals from heavily contaminated plumes combine to produce fog-like pollution when subjected to sunlight

and stagnant meteorological conditions. The health hazards of smog are caused in part by particles but also by gaseous pollutants such as O_3, NO_x, CO, SO_2 and VOCs. Ozone is secondary, produced through photochemical reactions involving NO_x and VOCs. A detailed review of gaseous phase reactions in photochemical smog can be found in *Sillman* [1999]. Photochemical smog also results in visibility reduction, which is mostly due to the scattering and absorption of light by aerosols [*Charlson and Ahlquist*, 1969]. In Los Angeles-type smog, ozone has been proven to be the most difficult pollutant to bring into compliance with the air quality standard, and therefore it draws most of the public's attention. However, complex interactions between gases and particles occur in urban smog [*Meng et al.* 1997; *Dickerson et al.*, 1997] (Figure 1.2.6); it is impossible to solve the air pollution problem without considering gas and particle as a whole.

Visibility reduction is perhaps the most noticeable effect of air pollution. Visibility is a measure of our eyes' ability to distinguish an object from the surrounding background. In the absence of aerosols our visual range would be approximately 300 km, limited by air molecule scattering. Scattering of visible radiation by aerosols is the main process limiting visibility in the troposphere, but in a very polluted environment absorption by elemental (black) carbon particles can contribute up to 50% of the visibility reduction [*Groblicki et al.*, 1981]. The accumulation mode particles scatter visible light more efficiently since their size is of the same order as the wavelength of visible radiation. As shown earlier, fine aerosols account for most of the aerosol surface area and therefore are most responsible for the visibility reduction. Anthropogenic particles in an urban environment can reduce visibility to below 10 km. Severe visibility reduction is often observed with high relative humidity since aerosols swell by taking up water, and this

increase their scattering cross section. This is the phenomenon known as 'haze'. The formation of haze will be discussed further in Section 4.5.

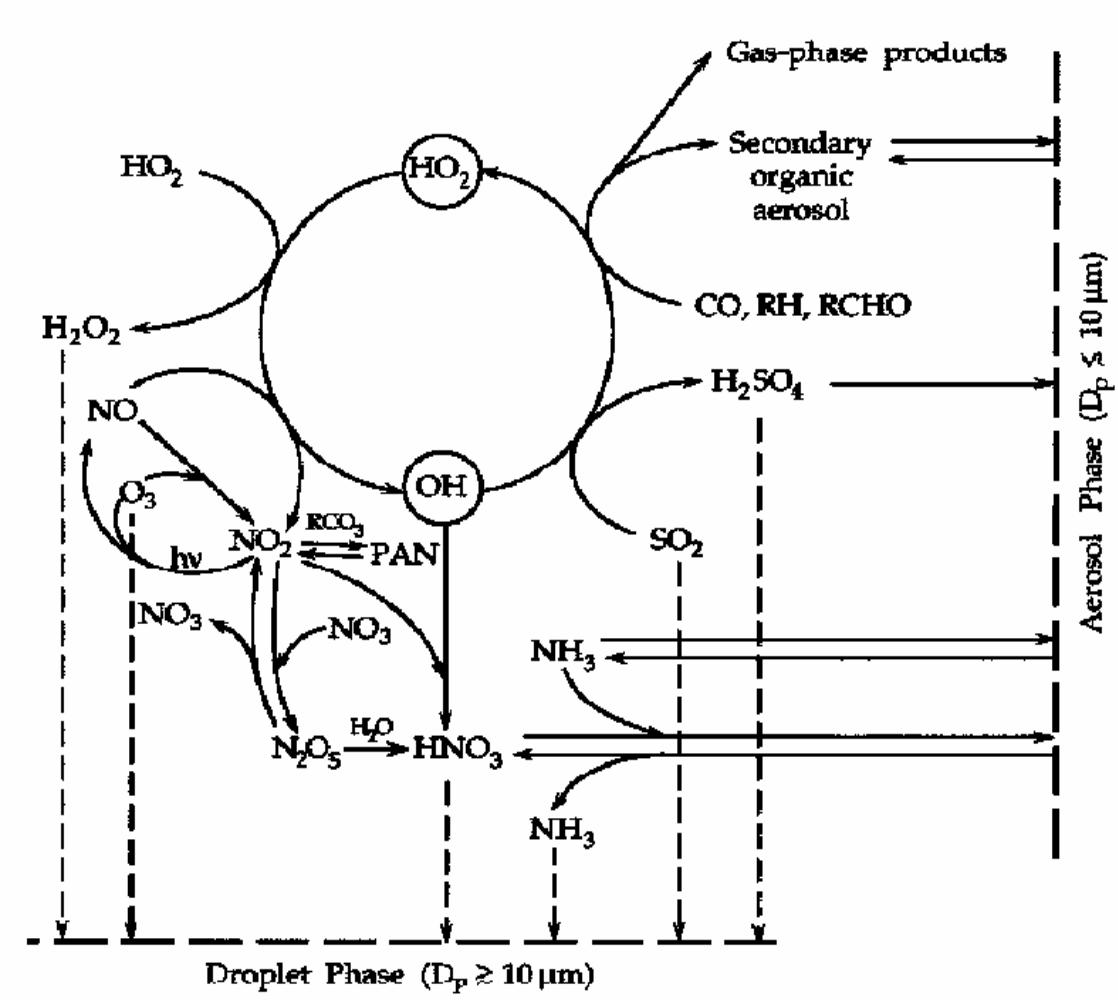

Figure 1.2.6 Chemical coupling in the tropospheric gas, particle, and aqueous phases. (Adapted from *Meng et al.* [1997]) Cycling in the OH-HO_2 system generates O_3 and H_2O_2, major oxidants of dissolved SO_2. In the gaseous phase, OH levels determine the rates of oxidation of SO_2 and NO_2 to H_2SO_4 and HNO_3, respectively, which are precursors to aerosol SO_4^{2-} and NO_3^-. OH (and O_3) attack on organic molecules containing seven or more carbon atoms can generate semi-volatile secondary organic aerosol. D_p is particle diameter and $h\nu$ is energy of a photon.

Haze pollution is not restricted within urban or suburban areas. It tends to be regional and appears in rural areas as well (Figure 1.2.7). In the United States, regional haze has caused serious visibility degradation in the National Parks [*IMPROVE*, 2000]. Along the U.S. northeast coast, haze is frequently reported in hot summer, blanketing a region ~ 1000 km in diameter. Regional haze remains a challenging problem for both scientific and pollution-control communities. Understanding how haze is related to ambient fine aerosol is a long-term goal of the MARCH-Atlantic study.

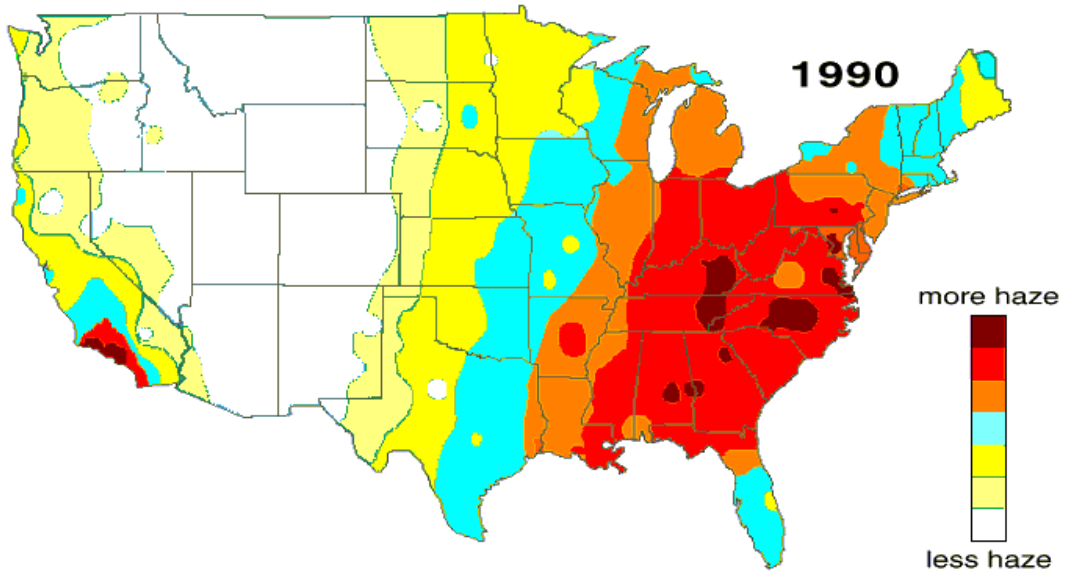

Figure 1.2.7 Annual mean visibility across the United States. (Adapted from *IMPROVE* [2000]). The higher haze level indicates lower visibility.

1.3 Overview of the Research

The northeastern coast is one of the most heavily populated regions in the nation. This region includes several major cities, from Boston, MA to Norfolk, VA, accommodating a

high density of industry and traffic. Maintaining air quality to prevent tens of millions of citizens from exposure to toxic pollutants challenges the government. In the last decade, the environmental and health threat of anthropogenic fine aerosol have developed substantially. Airborne fine particles are involved in the urban smog and regional haze. So far, most of the states in this region regularly violate the USEPA standard for photochemical smog (USEPA O_3 standards: 120 ppbv for 1-hr mean and 80 ppbv for 8-hr mean) in summer. The health effect of haze is uncertain, but it reduces visibility on a regional scale. There is an urgent need to understand the composition and origin of aerosols.

A few field studies carried out in the Mid-Atlantic region generally suggested that PM_{10} (particle diameter < 10 μm) contains significant amount of crustal material while $PM_{2.5}$ is dominated by sulfate and organics. These studies covered both rural [e.g. *Vossler et al.*, 1989] and urban areas [e.g. *Heller-Zeisler and Ondov*, 1999] but focused on summer when pollution episodes occur most frequently. However, it is difficult to achieve a full understanding of the problem without investigating the seasonal variation in the aerosol chemical composition. The Interagency Monitoring of PROtected Visual Environments (IMPROVE) network has been monitoring chemically-speciated $PM_{2.5}$ and visibility in the U.S. National Parks since 1988 [*Malm et al.*, 1994; *IMPROVE*, 2000]. Even though the network is operated year around, $PM_{2.5}$ measurement is only made once every 3 – 4 days. Smog and haze is known to be episodic, typically lasting for 2 – 5 days. The representativeness of the IMPROVE data is therefore questionable. Moreover, the IMPROVE network does not contain gas measurements such as CO, NO_y, and NH_3 which can provide crucial information regarding the phase transition in the atmosphere.

Bearing these concepts in mind, a multi-year project (7/1999-1/2002), the MARCH-Atlantic study, was initialized. To resolve the daily and seasonal variation, 24-hour average chemically-speciated $PM_{2.5}$ was sampled every day during July, October (except October 2001), January and April (except April 2001), chosen to represent summer, fall, winter and spring seasons. Gaseous precursors, HNO_3 and NH_3, were measured concurrently. A few different analytical techniques were employed to measure the $PM_{2.5}$ mass, and this provided additional quality assurance for our $PM_{2.5}$ data. Gaseous pollutant measurements were included in this study for various purposes. For example, automobiles produce both CO and carbonaceous material but little SO_2. Coal-burning power plants are the dominant source of SO_2 and sulfate but produce little CO. Therefore, CO and SO_2 are good tracers for mobile and utility emissions, respectively. At FME, CO, SO_2, NO_y, and O_3 were measured continuously, and therefore their diurnal variations can be resolved. Usually, the diurnal variation of these trace gases reveal not only their source locations but also information related to the PBL dynamics. All of the measurements are presented in Chapter 3, and they are interpreted based on meteorology and chemistry. Analyses of the $PM_{2.5}$ chemical composition, mass closure, degree of neutralization, etc. are discussed in Section 4.1 – 4.3.

The spatial distribution of $PM_{2.5}$ is investigated by comparing the FME data with concurrent measurements at other sites. The IMPROVE network operates a few sites in the Mid-Atlantic region both upwind and downwind of FME (Section 4.4). The spatial extent of various $PM_{2.5}$ components can be different because of their different source locations and atmospheric lifetimes. This study focuses on the urban aerosol in the Baltimore-Washington (B-W) corridor. Utility plants and industries in the city of

Baltimore and Washington, DC, traffic on the highways, and residential cooking/heating can all contribute to fine aerosols in the corridor. The local (< 100 km, roughly the B-W corridor) sources, however, may not fully explain the fine aerosol mass observed. For instance, it has been acknowledged that sources in the U.S. Midwest can contribute to sulfate over the downwind Mid-Atlantic region [*Ferman et al*., 1981; *Vossler et al*., 1989; *Malm*, 1992]. A recent SO_2 emission inventory for the U. S. (Figure 1.3.1) indicates strong source regions within the Midwest and Mid-Atlantic states. A high density of coal-burning electric utilities in the Ohio River Valley does generate substantial SO_2. The $PM_{2.5}$ observed at FME is expected to originate from both local and more distant sources.

Long-range transport is not limited to sulfate; carbonaceous particles and other trace elements can be transported downwind as well. Though particles of various types from various sources are mixed together when arriving at the receptor site, day-to-day and seasonal variations in the $PM_{2.5}$ chemical composition reflect changes in the contribution from each source. With suitable assumptions, chemically-speciated $PM_{2.5}$ data can be used to retrieve source emission profiles. In this study, a factor analysis tool, UNMIX, is utilized to characterize major potential sources (Chapter 5). Source contributions to the receptor site depend on meteorology, or to be more precise, depend on atmospheric transport and dispersion. Important meteorological parameters such as temperature, pressure, relative humidity, and wind speed/direction (both upper and lower level) are recorded at FME for data analysis. The PBL depth and wind speed are probably the most important factors modulating the concentration of pollutants released locally. Urban CO is a good example [*Glen et al.*, 1996]. For a pollutant originating from a distant source, the pollutant concentration at the receptor site could more depend on how long the air

parcels stay above the source region. In this study, an ensemble back trajectory technique is developed to estimate the spatially-resolved residence time of air parcels in the atmosphere (Chapter 5). Comparing the ensemble back trajectory of highly polluted episodes against the normal condition provides insights into the source region of the pollutant. This ensemble back trajectory approach is to be used to investigate the locations of sources derived by the UNMIX factor analysis. One of the interesting questions is whether we can estimate the relative contribution of local and more distant sources. This can be done by combining factor analysis and the ensemble back trajectory technique (Section 5.4).

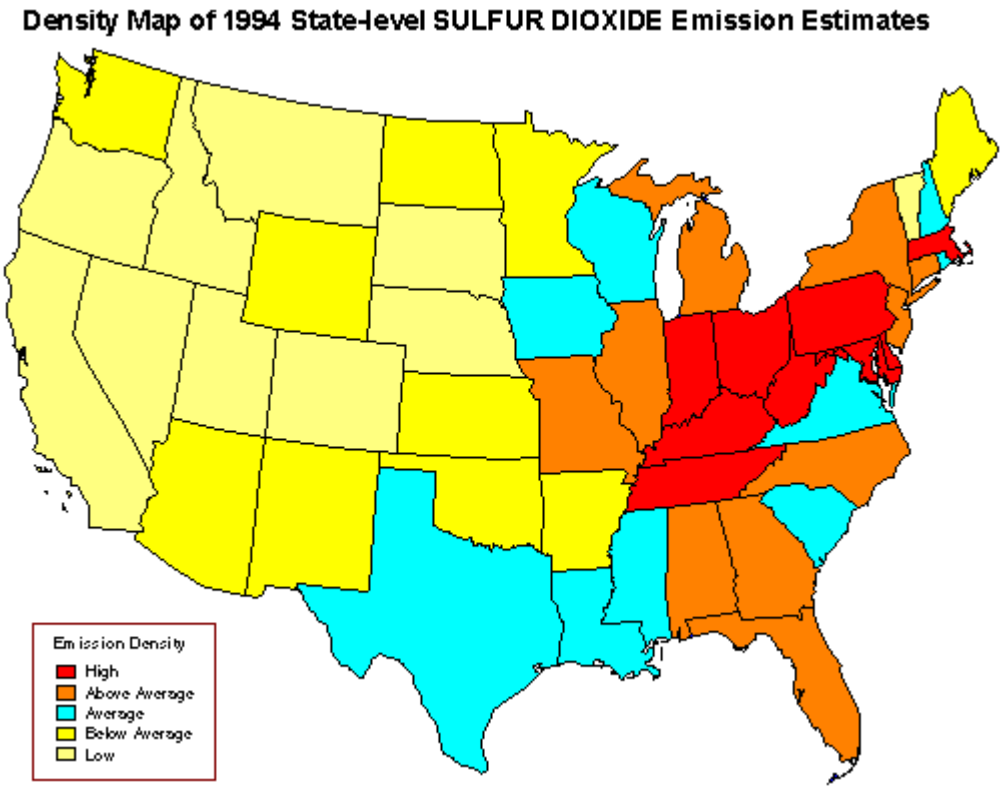

Figure 1.3.1 Density of state-level SO_2 emission across the U. S. in 1994 [*USEPA*, 1995].

Another goal of this study is to examine the role of $PM_{2.5}$ in visibility reduction. Hourly visibility measurement was made at the Baltimore-Washington International (BWI) airport (~ 15 km north of FME) with an Automated Surface Observing System (ASOS, see Section 4.5 or www.nws.noaa.gov/asos/ for more information). A special study of the aerosol optical properties was carried out in January 2002 using a Nephelometer and a Particle Soot/Absoprtion Photometer (See Chapter 2 for details of the instruments). Correlating the $PM_{2.5}$ and visibility data yields the aerosol extinction efficiency; it also suggests that relative humidity, besides aerosol concentration, is another important factor in the formation of regional haze. The aerosol optical depth (AOD, the attenuation of incoming solar radiation from space to the Earth's surface) is measured at nearby NASA Goddard Space Flight Center as part of the international AERONET system (see http://aeronet.gsfc.nasa.gov:8080/). AOD is more a measure of the aerosol column content. Comparing the AOD and surface aerosol concentration is one of the future projects.

Chapter 2 Sampling Techniques

2.1 Sampling Site

For a representative air quality in the B-W corridor, the sampling site in this study was chosen at FME (39.10°N, 76.74°W; elevation 46 m MSL), a suburban site ~ 30 km from both downtown Baltimore, MD and Washington, DC. There is no significant source within 1 km around the site. The FME site is one of the Photochemical Assessment Monitoring Stations (PAMS, see http://www.epa.gov/oar/oaqps/pams for a detailed description of the PAMS program) configured and operated by the Maryland Department of Environment (MDE). This site is at a secure location on the grounds of the Fort Meade army base. The fenced observatory station (Figure 2.1.1 and Figure 2.1.2) was set up in a broad open field, ~ 100 m from the closest minor roads and buildings. Two major highways (MD-295 and MD-32) run 4 km and 2 km to its west and south, respectively. Interstate 95 (I-95) and U.S. Route 1 run 6 km and 5 km to the west. MD-175 is about 1 km east of the sampling site.

Measurements made routinely at FME by MDE include continuous solar insolation, standard surface meteorology, upper layer meteorology (by a radar profiler with Radio Acoustic Sounding System), O_3, and NO_y. Also sampled at a 3-hr resolution are canisters for VOCs (every third day from May to September) and 24-hour PM_{10} and $PM_{2.5}$ mass

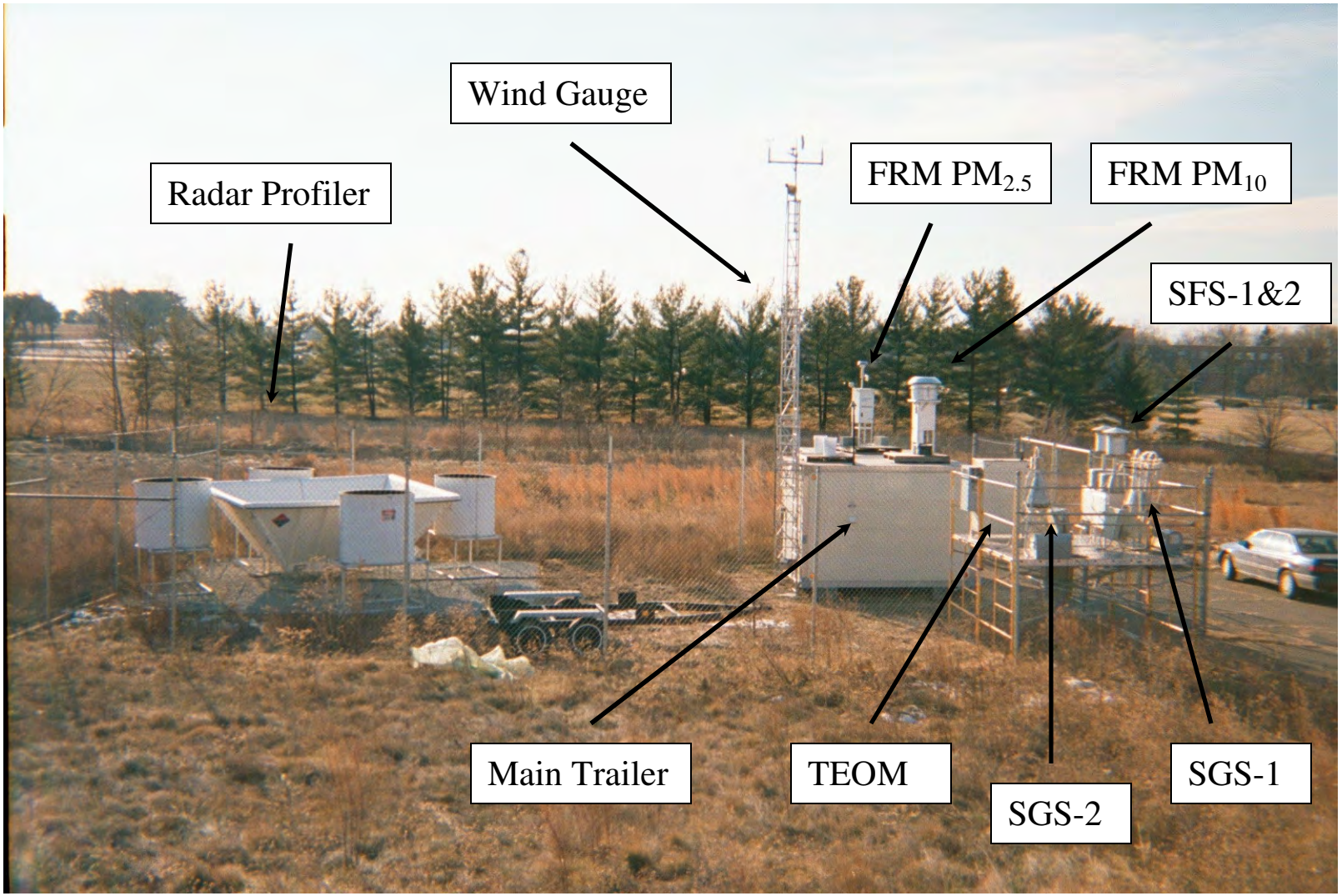

Figure 2.1.1 Overview of the FME sampling site. (Photo courtesy Dr. Bruce Doddridge)

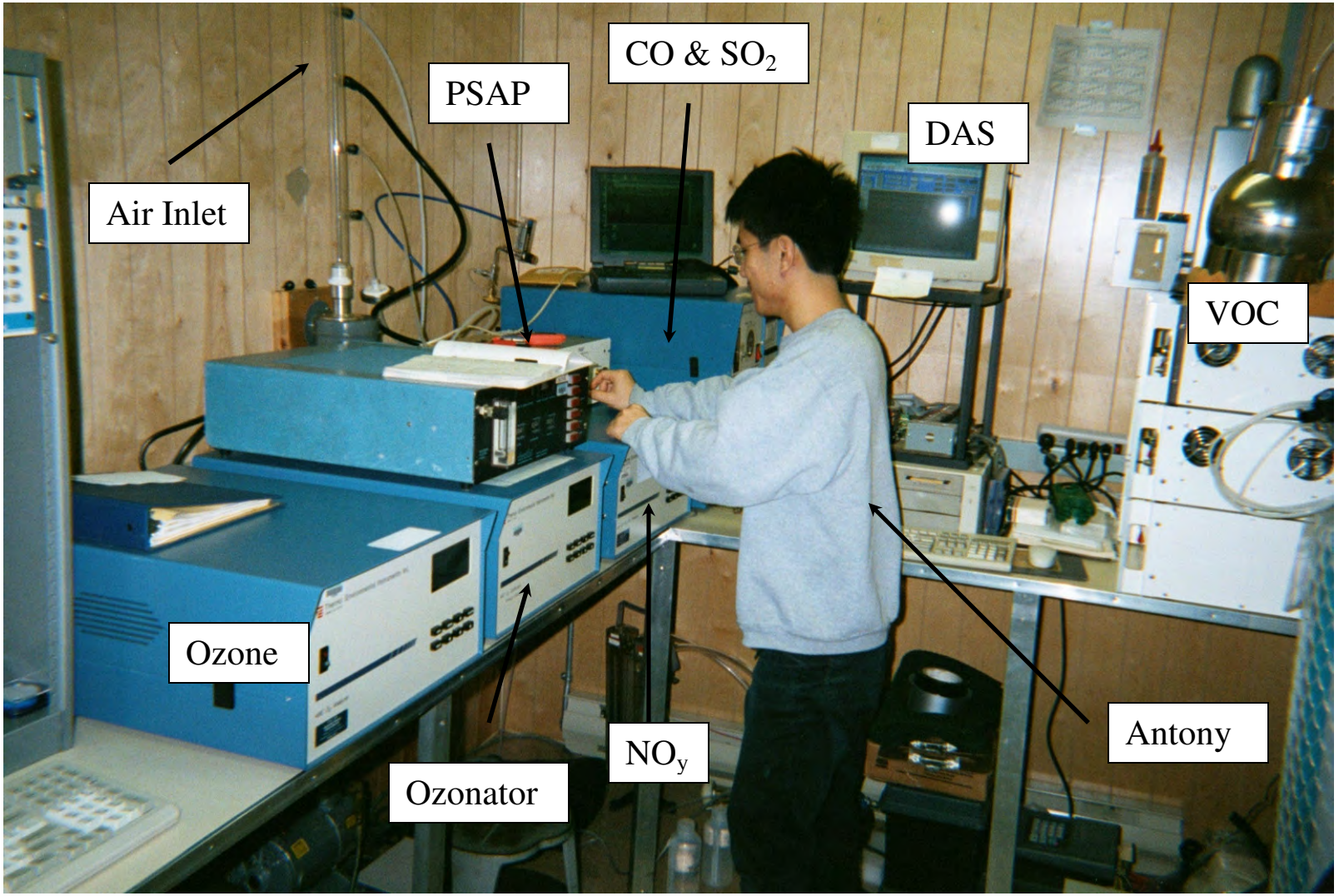

Figure 2.1.2 Inside the main trailer at FME (Photo courtesy Dr. Bruce Doddridge)

using the Federal Reference Method (FRM, see Section 2.4). The MARCH-Atlantic study installed $PM_{2.5}$ chemistry samplers, including two sequential filter samplers (SFS-1 and SFS-2) and two sequential gas samplers (SGS-1 and SGS-2) at FME. A Tapered Element Oscillating Microbalance (TEOM) was also employed to acquire the $PM_{2.5}$ mass concentration at a sub-hourly resolution. These instruments were setup on a platform ~ 1.5 m above the ground (Figure 2.1) with their sample air inlets above the fence (~ 3 m above the ground). Trace gas monitors, NO_y, O_3, CO, SO_2, and VOCs, were kept in a climate-controlled trailer (Figure 2.2). High-volume glass/Teflon sample tubing ran from the instruments to a common air inlet ~ 4 m above the ground. The field experiment took place over three years (June 1999 – February 2002). 1-min CO, SO_2, O_3, NO_y, and $PM_{2.5}$ mass (by TEOM) concentrations were measured continuously throughout the period, and their 1-hour averages were archived.

2.2 Sequential Filter and Gas samplers

The SFSs and SGSs utilized in this study were designed by the Desert Research Institute (DRI, Nevada, U.S.). Similar SFSs had been deployed in other field studies [*Chow et al*., 1994, 1996]. Each sampler has two channels, each of which contains a filter pack with one or two sampling filters through which air is drawn by a pump at a rate of 20 L min^{-1} to collect aerosols. The first SFS (SFS-1), equipped with a $PM_{2.5}$ size-selective inlet (Bendix/Sensidyne Model 240 cyclone) and an anodized-aluminum-coated HNO_3 denuder, uses a Teflon filter on one channel for determining dry $PM_{2.5}$ mass and elemental concentration. The second channel of the SFS-1 contains a quartz filter

followed by a sodium chloride impregnated cellulose backup filter. The quartz filter is used to determine the concentration of water-soluble ions (soluble SO_4^{2-}, NH_4^+, Na^+, K^+, Cl^- and NO_3^-). Since NO_3^- is highly volatile, the cellulose backup filter is used to capture the NO_3^- evaporating from the front quartz filter [*Zhang and McMurray*, 1992]. Aerosols greater than 2.5 μm in diameter are trapped in the cyclone before entering the instruments. The HNO_3 denuder put upstream of the filters removes gaseous HNO_3 that could interfere the particulate NO_3^- measurement once depositing on quartz filter surfaces. A schematic diagram of the SFS is shown in Figure 2.3.

The second SFS (SFS-2) was utilized to determine the $PM_{2.5}$ carbonaceous material, containing a flow system similar to SFS-1. SFS-2 uses two quartz filters in series on one channel, and a Teflon filter followed by quartz backup filter on the second channel. This design addresses known artifacts in the OC measurements [*Turpin et al*., 1994]. Gaseous HNO_3 concentration is measured using a SGS (SGS-1). Both channels of SGS-1 contain a quartz filter followed by a sodium chloride impregnated cellulose filter. One channel is equipped with an HNO_3 denuder (similar to that in SFS-1) upstream of the filters. The ambient HNO_3 concentration is determined from the difference between total nitrate (T-NO_3^-: $HNO_3 + NO_3^-$) collected by the two channels. A similar design is applied to the second SGS (SGS-2) used to determine gaseous NH_3 concentration. Both channels of SGS-2 contain a quartz filter followed by a citric acid impregnated cellulose filter while one of them has a NH_3 denuder made of critic-acid-coated parallel tubes upstream of the filters. The ambient NH_3 concentration is determined from the difference between total ammonium (T-NH_4^+: $NH_3 + NH_4^+$) collected by the two channels. Since the SGSs do not

contain a $PM_{2.5}$ size-selective inlet, the T-NO_3^- and T-NH_4^+ obtained are from total suspended particulate matter rather than just $PM_{2.5}$.

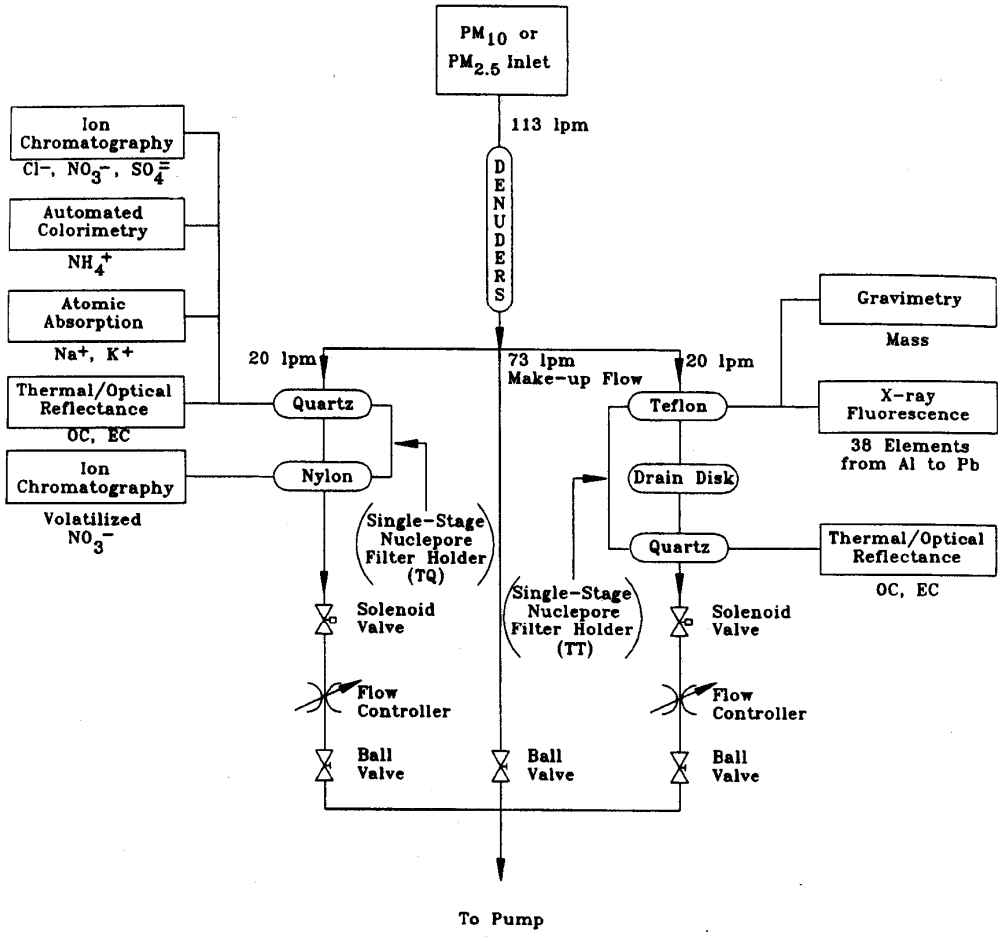

Figure 2.2.1 Schematic diagram of the $PM_{2.5}/PM_{10}$ sequential filter sampler designed by DRI [*Chow et al.*, 1996].

All of the SFSs and SGSs were programmed to sample air continuously for 24 hours with daily filter packs replaced manually every third day. The exposed filters, well sheltered, remained in the sampler for 0.5 to 2.5 days before being collected and shipped in coolers (at ~ 273 K) to DRI for chemical analysis. Blank filters were used to correct passive depositions occurring during and after sampling. The $PM_{2.5}$ mass concentration

was determined with a gravimetric method that weighs Teflon filter before and after sampling, and the concentrations of ~ 40 trace elements such as S, Al, Si, Ca, Fe, Ti, Pb, etc. were determined by X-ray fluorescence (XRF). Water-soluble anions (SO_4^{2-}, NO_3^-, Cl^-) were measured by ion chromatography (IC). Since NO_3^- appeared on both front quartz filter and backup cellulous filter due to volatilization, NO_3^- data used hereafter is the sum of those on front and backup filters. For cations, soluble Na^+ and K^+ are detected by atomic absorption spectrometry (AA) while NH_4^+ by automated colorimetry (AC).

The thermal optical reflectance method (TOR) was used to measure EC and OC (EC and OC) on quartz filters from SFS-2 [*Chow et al.*, 1993]. The analyses were done for front quartz filter (FQ), backup quartz filter behind quartz (BQ), and backup quartz filter behind Teflon (TBQ), but not for front Teflon filter (FT). EC detected on backup filters is usually negligible (below the detection limit) but OC can be significant. In this study, the OC measured on backup filter behind quartz (BQ) averages ~ 30% of that on front quartz filter (FQ), and the OC on backup filter behind Teflon (TBQ) can be as much as ~ 50% of that on front quartz filter. The OC on backup filter likely results from two possibilities: 1) semi-volatile OC that evaporates off the front filter and recaptured the backup filter [*Zhang and McMurry*, 1987], and 2) gaseous volatile organic compounds (VOCs) absorbed by front and backup quartz filters [*Warner et al.*, 2001]. The first possibility causes a negative bias while the second causes a positive bias if OC is determined solely using front quartz filters. The contribution from each of these possibilities, however, is highly uncertain. Extra caution needs to be exercised to interpret the OC measurement.

Measurement precisions of the SFSs and SGSs are estimated from flow rate performance tests and replicate analyses [*Watson et al.*, 1995; *Chow et al*., 1996]. The

analytical uncertainty in a single measurement is typically within ± 10% for a measured value that exceeds ten times the minimum detection limit (MDL). One of the major concerns is the stability of various species on the filters. Since the filters remained on site after sampling, deposition or evaporation could cause changes in the amount of material on the filters. To estimate the uncertainty, an audit experiment was carried out in July 2001. The design and result of this experiment as well as a more detailed description of the sampling detection limit and analytical uncertainty is presented in Section 4.0.

2.3 Tapered Element Oscillating Microbalance

Nearly-continuous measurement of $PM_{2.5}$ mass concentration was achieved by using a commercial Tapered Element Oscillating Microbalance (TOEM, R&P Company, Series 1400a, see http://www.rpco.com/products/ambprod/amb1400/ for description) equipped with a $PM_{2.5}$ inlet (cyclone inlet). The TEOM is an inertial-method instrument that draws ambient air through a filter at a constant flow rate (3 L m^{-1}), continuously weighing the filter and calculating near real-time mass concentrations. The core of TEOM is a mass transducer (Figure 2.3.1). A filter made of Teflon-coated borosilicate glass is placed on the top of the tapered element through which sample flow is drawn. The tapered element is essentially a hollow cantilever beam with an associated spring rate and moment of inertial. An automatic gain control circuit maintains the vibration at a constant amplitude. As in any spring-mass system, if additional mass, in this case the aerosol loading on the filter, is added, the frequency of vibration decreases. By monitoring the frequency change, TEOM determines the aerosol loading and subsequently the aerosol ambient

concentration. The period for each individual frequency measurement is 2 seconds. However, this raw data contain significant fluctuations. A smoothing technique [*Rupprecht & Patashnick*, 1996] is employed to compute total mass, and eventually 0.5-hr, 1-hr, 8-hr, and 24-hr average $PM_{2.5}$ mass concentrations are reported and archived.

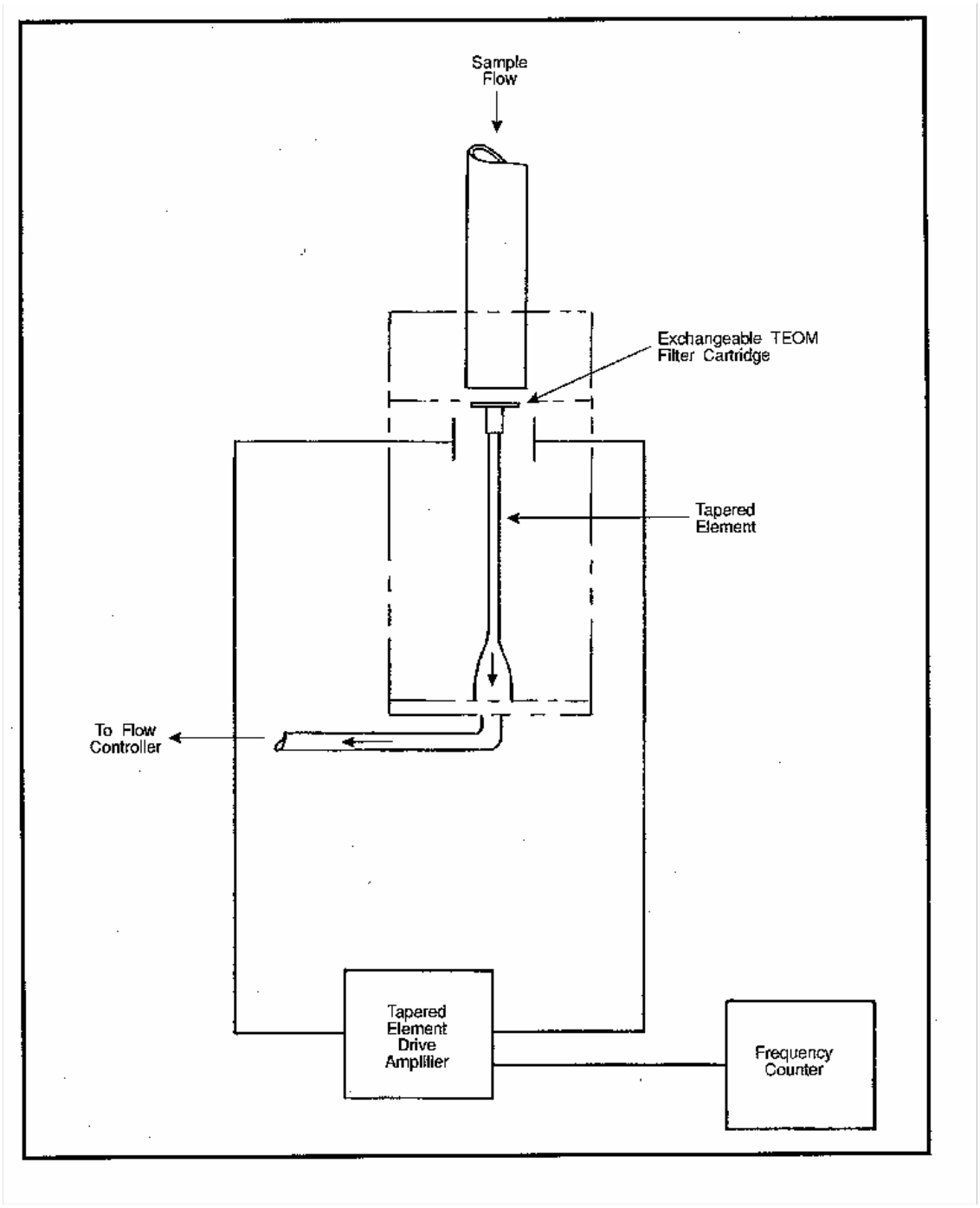

Figure 2.3.1 Diagram of the TEOM mass transducer [*Rupprecht & Patashnick*, 1996].

To prevent the uptake of water vapor by aerosol at high relative humidity biasing the aerosol mass, sample air is preheated to 50°C before drawn into the instrument to lower its relative humidity. Volatile species such as nitrate or OC, however, could gradually evaporate at such a high temperature. Occasional negative readings are observed likely due to the volatilization. The TEOM filter needs to be replaced regularly after one is saturated. The flow system is checked automatically but also requires a manual audit once a year.

Even though the TEOM is a Federal-Reference-Method equivalent instrument. Its performance remains to be examined in a robust manner. By comparing to the $PM_{2.5}$ measured by SFS-1, the TEOM at FME is found to have a least quantifiable limit (LQL) ~ 2 $\mu g\ m^{-3}$ in the 24-hr $PM_{2.5}$ mass concentration (Section 3.1). The TEOM data are particularly questionable in winter when ambient temperature is much lower than 50°C. In ~ 15% of the whole sampling period the TEOM data were not available due to malfunctions and an upgrade of the instrument.

2.4 Federal Reference Method for $PM_{2.5}$

In conjunction of the proposed $PM_{2.5}$ standard in NAAQS, the USEPA published the Federal Reference Method (FRM) for the $PM_{2.5}$ mass evaluation [e.g. *USEPA*, 1998]. The FRM is gravimetric, employing a sampler to draw a measured quantity of ambient air at a

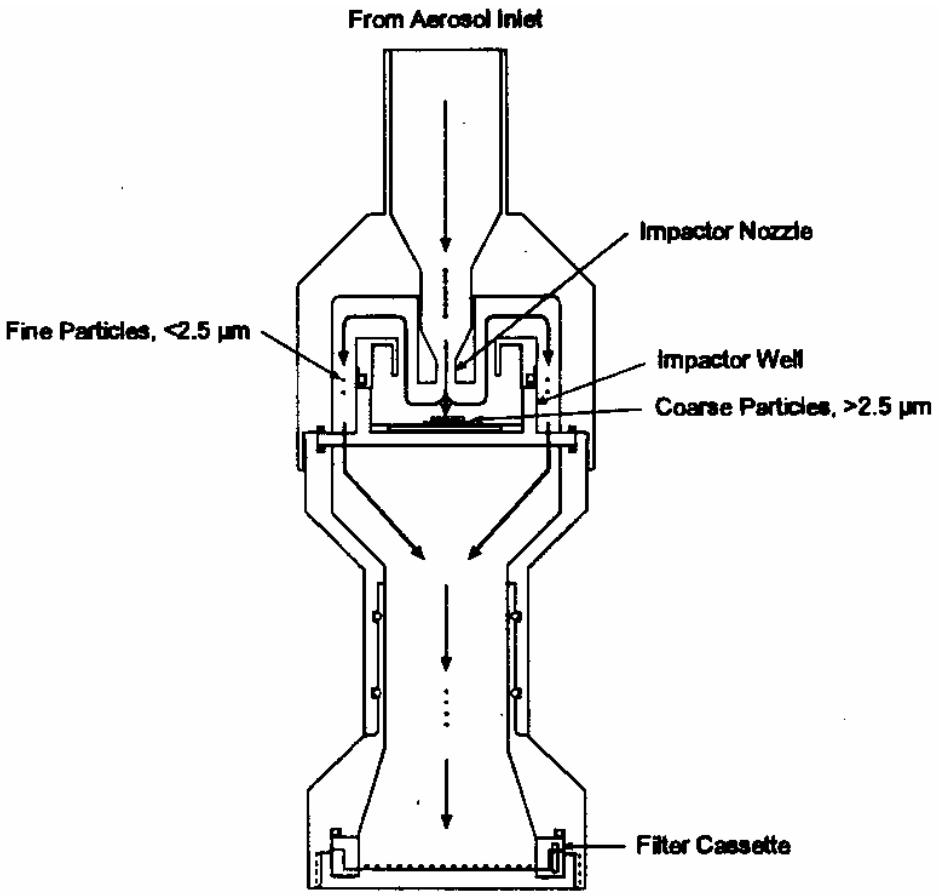

Figure 2.4.1 Air flow through FRM $PM_{2.5}$ impactor well and filter holder [*USEPA*, 1998].

constant volumetric flow rate (16.67 L min^{-1}) through a specially designed particle-size selective inlet. Particles in 2.5 µm or smaller size range ($PM_{2.5}$) are collected on a 46.2-mm diameter Teflon filter during the specified 23- to 25-hr sampling period. Each filter is weighed before use and after sampling. From these measurements, the mass of the collected $PM_{2.5}$ and average $PM_{2.5}$ ambient concentration can be calculated. At FME, MDE operated an Anderson RAAS 2.5 Model 300 under the guidance of FRM. The sampling period is 24 hours, and therefore the FRM data can be easily compared with those from SFS-1.

This FRM sampler is equipped with an impactor inlet rather than a cyclone. Figure 2.4.1 illustrates the impactor and filter holder assembly of the instrument. The impactor removes those coarse particles but allows particles < 2.5 μm in diameter to pass and be collected on a Teflon filter surface. Since the FRM sampler and SFS-1 do not utilize the same type of size-selective inlet, the size-cut for the sampled particles could be slightly different. The FRM sampler was calibrated and maintained by MDE. A 24-hr sampling was carried out every third day year around.

2.5 Particle/Soot Absorption Photometer

Aerosol is responsible for most of the light extinction in the atmosphere, including light scattering and absorption (see Chapter 4.5). Major light-absorbing species in the atmosphere are soot (EC) and dust. The atmospheric absorption coefficient (b_{ap}), usually in unit $m^2\ m^{-3}$ (or m^{-1}), is a measure of the total spectral absorption cross section of a unit volume of air. In an urban environment, b_{ap} often reflects the ambient concentration of soot. A Particle/Soot Absorption Photometer (PSAP, Radiance Research Inc.) was used to monitor the atmospheric absorption at FME during January 2001.

The PSAP draws ambient air through a specially designed filter at a constant flow rate (~ 1 L m^{-1}) and sends a laser beam (at 565 nm) to measure the attenuation of radiation by the filter. The direct calculation of atmospheric absorption is given by

$$b_{ap} = \frac{A}{V}\ln(\frac{I_0}{I})$$

where A is the area of the sample spot on the filter, V is the volume of air drawn through the filter during a given time period, and I_0 and I are the average filter transmittances during and prior time period and the time period, respectively. In practice, this time period is set to be 1 min. Internal errors resulting from the magnification of absorption by filter medium or non-linearity in the response of the unit have been calibrated by the manufacturer [*Bond et al.*, 1999]. Routine calibration of the PSAP is not applicable, and one has to rely on the manufacturer's calibration and the consistent performance of the instrument.

A major uncertainty in PSAP as well as any filter-based absorption measurement is their response to light scattering. The PSAP uses fiber filters that allow the particles to become partly or completely embedded in an optically diffusive environment in order to minimize the sensitivity to scattering. However, *Bond et al.* [1999] reported that PSAP still exhibits a significant response to non-absorbing aerosols and could overestimate absorption by as much as 20 – 30%. Extra caution should be exercised in interpreting the PSAP data. Besides, without knowledge of the particle size-number distribution and absorption efficiency, the EC concentration from PSAP can only be qualitative.

2.6 Total Scatter/Back Scatter Nephelometer

In a special study (Section 4.5), a three-wavelength Nephelometer (TSI, Inc., model 3560) was used to measure the atmospheric total scattering and backscattering (scatter angle > 90°) at FME. The Nephelometer performs a geometrical integration of the angular distribution of scattered intensity; this is achieved by using a combination of a

Lambertian light source and an orthogonal light detector. The theory of this technique is beyond the scope of this dissertation but can be found in *Anderson et al.* [1996]. This instrument measures six parameters, total scattering (m^{-1}) and backscattering (m^{-1}) at three wavelengths, 450, 550, and 700 nm.

The calibration was made in the laboratory using filtered clean air as low-span gas and pure CO_2 (99%) as high-span gas; the calibration factor remained unchanged in a 6-month period. At FME, air was drawn into the instrument through a 1 m Teflon tubing. No size-selective inlet or dryer was installed upstream of the instrument. Therefore, we were measuring the light scattering by particles of full size range at ambient condition (the chamber temperature was generally higher than ambient temperature by < 1 K). The averaging period was set to be five minutes but hourly averages were used for analysis. Due to measurement noises, the instrument's detection limit at 550 nm is ~ 2×10^{-7} m^{-1} (60-second average, 90% confidence level) [*Anderson and Ogren*, 1998].

2.7 Carbon Monoxide Detector

Carbon monoxide (CO) was measured at FME with a commercial non-dispersive infrared (NDIR) gas filter correlation (GFC) analyzer (Thermo Environment Instruments Model 48). This technique utilizes the infrared (IR) absorption of the 4.67 μm vibration-rotation band of CO. IR radiation from a glow-bar source is alternately passed through two gas-filled cells mounted on a correlation wheel before entering a chamber where it interacts with ambient air through an effective 30-m optical path (Figure 2.7.1). One cell filled with a high concentration of CO produces an IR beam that cannot be further

attenuated by ambient CO and provides reference intensity. The beam through the other cell, filled with high purity N_2 that does not absorb IR of 4.67 μm wavelength, remains sensitive to CO in the ambient air. A photoelectric detector (PbSe detector) is installed at the end of the optical path. Ideally, the difference between the reference and sample intensities is proportional to the number of CO molecules in the optical chamber. The instrument microprocessor corrects the output signal to calculate the CO ambient concentration based on internal transducer measurements of temperature and pressure.

Carbon dioxide (CO_2) and water vapor (H_2O) also absorb radiation at ~ 4.67 μm and therefore could interfere the CO measurement. *Dickerson and Delany* [1988] reported that changes in the ambient temperature could influence the CO detector and cause a base-line drift. To account for these potential errors, we installed a Pyrex tube (10 cm long × 1.5 cm diameter) containing palladium/alumina beads (Pd/Al_2O_3) upstream of the optical chamber [*Dickerson and Delany*, 1988; *Doddridge* et al., 1994; *Hallock-Waters et al.*, 1999]. The beads were heated to 250°C, effectively catalyzing the oxidation of CO to CO_2 to provide a chemical zero. The CO instrument was operated with a 30-minute cycle of 25 minutes in CO measure mode followed by 5 minutes in chemical zero mode. The switch was achieved by a timer-controlled 3-way solenoid valve (Figure 2.7.1). The CO concentration archived for analysis was derived from the difference between the measure and zero modes [*Hallock-Waters*, 2000]. A Nafion tube dryer (Model PD-625-12PS, Perma Pure, Inc.) and a Teflon filter (pore size 0.5 μm) were installed upstream of the instrument to remove water vapor and particles in the sample air, respectively. These modifications improved the sensitivity and selectivity of the CO measurement.

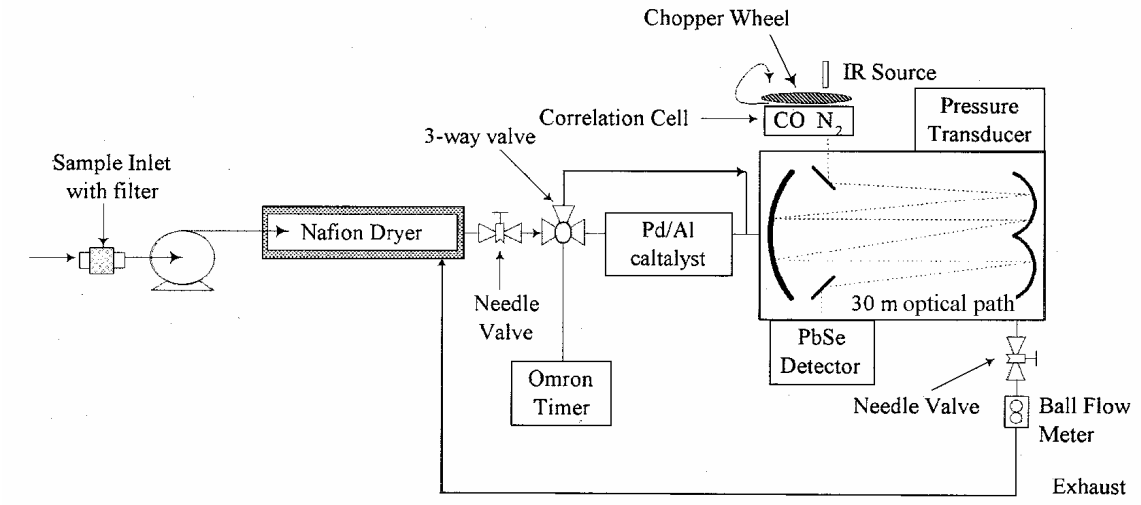

Figure 2.7.1 Schematic diagram of the modified CO detector deployed at FME. The circle after sample inlet filter indicates the pump. (Adapted from *Hallock-Waters* [2000].)

At FME, 20-sec average CO concentration was acquired, but hourly averages were used in most of the study. The instrument's status was checked 1 – 2 times a week and calibrations were made generally before and after each intensive period (or a period of ~ 3 months) in the laboratory using bottled standards traceable to the National Institute of Standards and Technology (NIST). The calibration factor varied by < 5% over a course of 2.5 years. The minimum detection limit of this instrument is ~ 10 ppbv CO (95% confidence at 1-min average). The instrumental noise for 60-min average of 1-min data with this technique is ~ 6 ppbv [*Doddridge*, et al., 1998]. Overall, uncertainty in the 1-hr CO data in this study is estimated at < 10%.

2.8 Sulfur Dioxide Detector

SO_2 molecule absorbs ultraviolet (UV) light in three wavelength regions, 340 – 390 nm, 250 – 320 nm, and 190 – 230 nm. Once a SO_2 molecule reaches an electronically excited state by absorbing a photon, it can rapidly return to the ground state through fluorescence emission or quenching (e.g. transfer energy to an air molecule). The fluorescence emission is the dominant process when SO_2 is activated by radiation in the 190 – 230 nm range [*Okabe et al.*, 1973]. Ambient SO_2 concentration was measured at FME with a commercial pulsed UV fluorescence analyzer (Thermo Environmental Instruments, Model 43A) that utilizes a xenon flash lamp pulsed at 10 Hz as the UV source and a photomultiplier tube as the fluorescence detector. A condensing lens focuses the source UV onto a series of eight mirrors arranged so that only UV of wavelengths in the 190 – 230 nm region can enter the fluorescence chamber in which the UV interacts with pressure-reduced ambient air (Figure 2.8.1). As excited-state SO_2 molecules return to the ground state they fluoresce in the 240 – 420 nm region with peak emission at ~ 320 nm. A condenser lens collects the fluorescent radiation onto a bandpass filter that limits the wavelengths reaching the photomultipilier to the SO_2 fluorescence region. In principle, the concentration of SO_2 in the ambient sample is proportional to the fluorescence intensity. Minor corrections due to nonlinear instrument responses were applied [*TEI*, 1992].

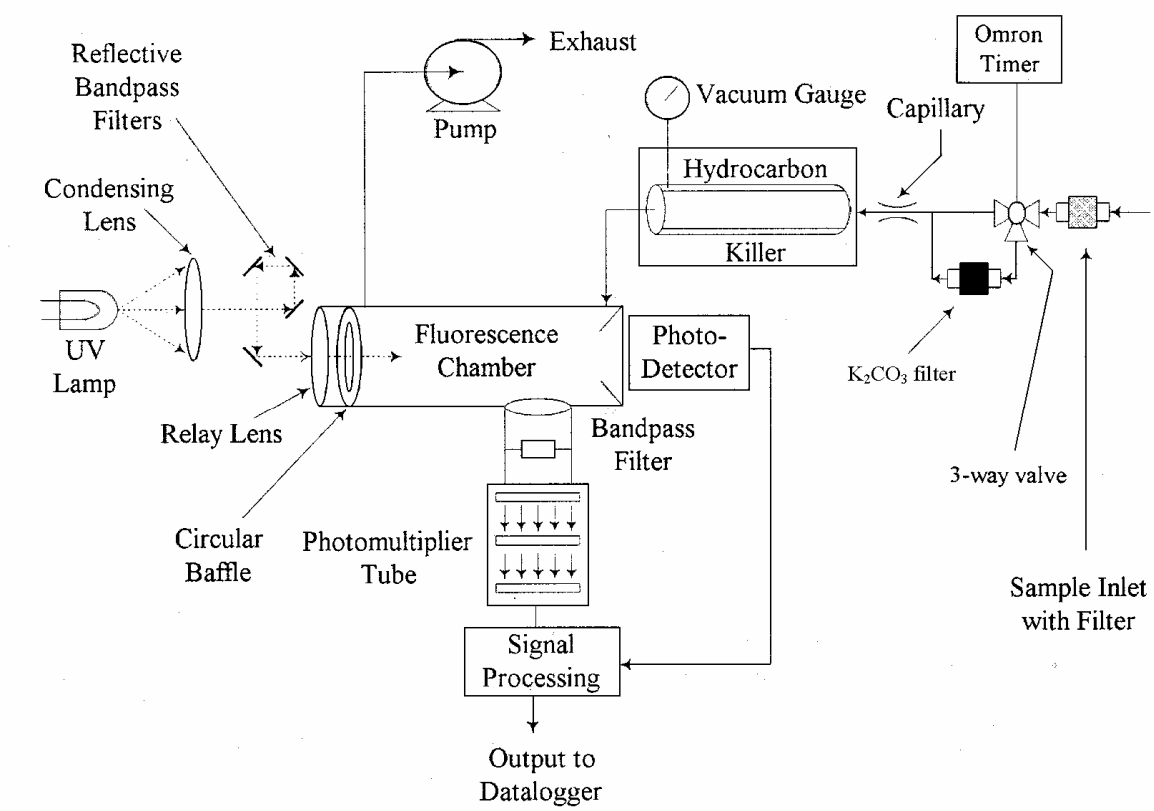

Figure 2.8.1 Schematic diagram of the SO_2 monitor deployed at FME. (Revised from *Hallock-Waters* [2000].)

Aromatic hydrocarbons response to the UV in a similar way and therefore could interfere the SO_2 measurement. A 'hydrocarbon kicker' made of a tubular semi-permeable membrane is installed upstream of the fluorescence chamber to remove hydrocarbons (Figure 2.8.1) [*Luke*, 1997]. Similar to the CO instrument, the change in the ambient environment such as temperature and relative humidity can cause a baseline drift in the SO_2 detector. To reduce the uncertainty, we added a potassium carbonate (K_2CO_3) impregnated filter upstream of the instrument. This filter can effectively remove SO_2 molecules as the sample air passes through it, and this produces a chemical zero for SO_2 measurement. At FME, the SO_2 detector was operated in a 60-min cycle of 50 minutes in SO_2 measure mode and 10 minutes in zero mode (bypassing ambient air to the zeroing

filter). The switch was achieved by a timer-controlled 3-way solenoid valve (Figure 2.8.1). The background level within each measure mode was derived by interpolating the zero mode readings before and after the measure period. The ambient SO_2 concentration was then determined from the difference between the measured and background levels. The SO_2 detector shared the same air inlet with the CO detector so that air was dehydrated by the Nafion tube dryer before entering the instrument.

20-sec average SO_2 concentration was measured at field, but hourly averages were used for analysis. The instrumental status was checked once or twice a week, and calibrations were conducted before and after each intensive period (once in ~ 3 months) in the laboratory using bottled standards (SO_2/N_2 mixture) traceable to the National Institute of Standards and Technology (NIST). The calibration factor varied by ~ 10% over a 2.5-year period. The detection limit of this instrument is ~ 0.1 ppbv SO_2 (95% confidence at 60-second average). The consistency of the SO_2 measurement was also examined by using another SO_2 monitor (Thermo Environmental Instruments, Model 43C) with the same configurations sampling concurrently in October 2000. Data from the two instruments agree within ± 10% (r^2 ~ 0.95). Overall, uncertainty of the 1-hr SO_2 data in this study is estimated at 10 – 15%.

2.9 Total Reactive Nitrogen Oxides Detector

Reactive nitrogen oxides were measured at FME with a commercial chemi-luminescence NO-NO_2-NO_x detector (Thermo Environmental Instruments, Model 42) configured and operated by MDE under the USEPA guidance. The theory of operation is

based on the rapid reaction between NO and O_3. O_3 is generated by the instrument with a high-voltage electrodes (ozonizers) that convert O_2 to O_3. The NO in the sample air reacts with O_3 in the reaction chamber producing NO_2 ($NO + O_3 \rightarrow NO_2 + O_2$). The O_3 reacts with more than 95% of the NO present in the reaction chamber producing NO_2 with ~ 10% of the NO_2 molecules in an electronically excited state [*Kley and McFarland*, 1980]. As the excited NO_2 molecules relax to the ground state a characteristic luminescence at wavelengths 600 – 3000 nm is emitted. The emitted photons are detected with a photomultiplier. Under reduced pressure in the reaction chamber, the lifetime of NO against O_3 oxidation is short relative to its residence time in the reaction chamber, and therefore the signal voltage in photomultiplier should be proportional to the NO concentration in the sample air [*Dickerson et al.*, 1984].

The measurement of NO_x ($NO + NO_2$) is achieved by activating a commercial molybdenum converter that reduces NO_2 in the sample air to NO before the air enters the reaction chamber (Figure 2.9.1). Previous studies indicated that surface converts that can convert NO_2 to NO also convert other reactive nitrogen oxides species, such as peroxyacetyl nitrate (PAN) and HNO_3 to NO [*Fehsenfeld et al.*, 1987]. Therefore, it is suggested that the quantity reported by the instrument is the concentration of total reactive nitrogen oxides (NO_y) that includes NO_x, HNO_3, particulate NO_3^-, HONO, N_2O_5, NO_3, HO_2NO_2, PAN, $RC(O)OONO_2 + RONO_2$, and $ROONO_2$. At FME, a ~ 3 m glass/Teflon tube used to sample ambient air and the stainless steel fittings could remove HNO_3 and NO_3^- before they entered the instrument [*Fehsenfeld et al.*, 1987]. The quantity reported as 'NO_y' in this study is then likely limited to the sum of NO, NO_2, and PAN. In an urban environment, NO_x is probably the most dominant species in NO_y, and

the uncertainty in the NO_y measurement due to line losses of nitrate is believed to be minor. It will be shown in Section 3.4 that NO_y can be underestimated by as much as 30% in this study.

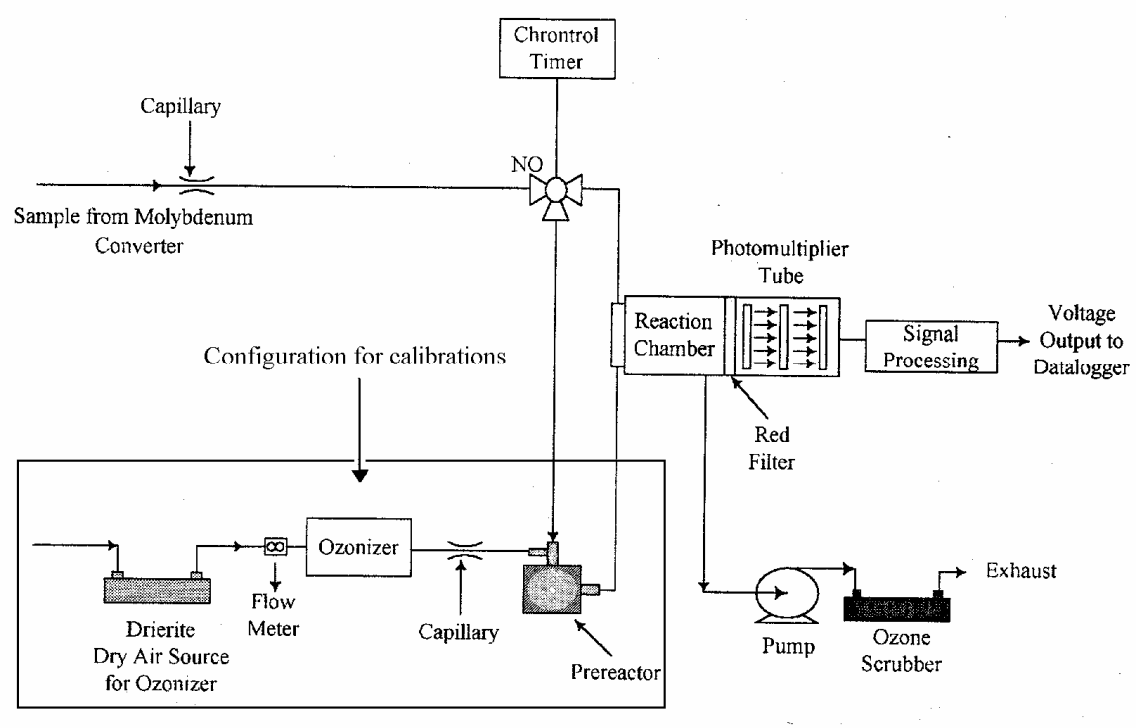

Figure 2.9.1 Schematic diagram of the NO_y detector deployed at FME. (Revised from *Hallock-Waters* [2000].)

At FME, 10-sec average NO_y concentration was measured, but hourly averages were used in this study. The detection limit of this instrument is ~ 0.05 ppbv for NO (95% confidence at 2-min average). Calibrations were made regularly (once in 2 – 3 months) at the site using dynamic dilution of NIST bottled standards in zero air. The dilution is achieved by utilizing an ozonator (Thermo Environmental Instruments, Model 49PS) with ozone lamp turned off. The calibration factor was used as a parameter feedback to the instrument.

Chapter 3 Seasonal and Diurnal Variations

3.0 Weather

How emissions lead to aerosol ambient concentration depends on both chemistry and meteorology. Meteorological parameters such as ambient temperature, relative humidity, and precipitation present seasonal and interannual variations. Long-term monitoring of temperature and precipitation has been conducted at the BWI airport since 1871, and the data can be used for calculating the climate norm in the B-W corridor. In this study, BWI weather data between June 1999 and February 2002 were analyzed and compared with the climate norm. This comparison determines how the weather during our field experiment deviates from the typical conditions. Temperature and relative humidity was also measured at FME. BWI is so close (~ 15 km) to FME that daily mean temperature at the two sites always agree with each other (r^2 ~ 0.97 and slope ~ 1 during our sampling period).

The seasonal variation of daily mean temperature is shown in Figure 3.0.1. The monthly norm shows a maximum and minimum in July and January, respectively. There were some abnormalities during the period of our study. For example, December 2000 was much colder than January 2001, and August 2001 was warmer than July 2001. The most noted interannual variation appeard in July 1999, 2000, and 2001. Unlike

temperature, monthly precipitation is dominated by a few rainy days and usually has much greater deviations from the normal condition. Figure 3.0.2(a) and 3.0.2(b) show the variation of monthly rainfall and snowfall, respectively, according to the daily totals measured at BWI. At least half of each month is rain-free. The monthly norms show little summer-winter contrast, indicating that precipitation is uniformly distributed in a year. There is no obvious dry or wet season in the Mid-Atlantic region. As shown in Figure 3.0.2, however, a dry summer occurred in 1999 while summer 2000 was very wet. The number of days that have significant precipitation rather than the total precipitation in a month determines the efficiency of precipitation scavenging of aerosols. The abnormality in weather pattern may impact the ambient concentration of aerosol and trace gases.

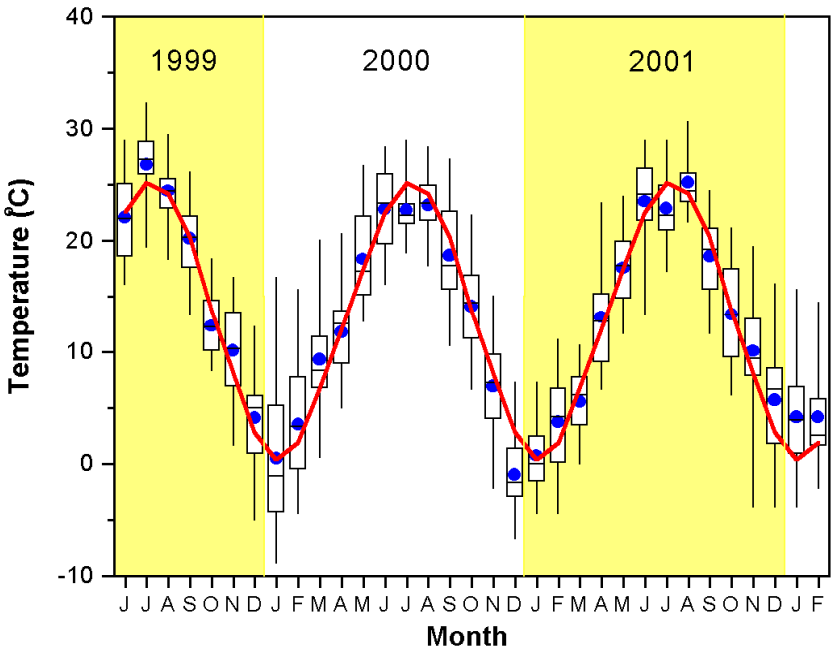

Figure 3.0.1 Seasonal variation of temperature at BWI. Monthly means are indicated by solid circles and median values by short dashes. Boxes indicate the quartiles and vertical bars indicate the maximum and minimum. The solid line indicates the climate norm based on a 40-year (1960 – 2000) average.

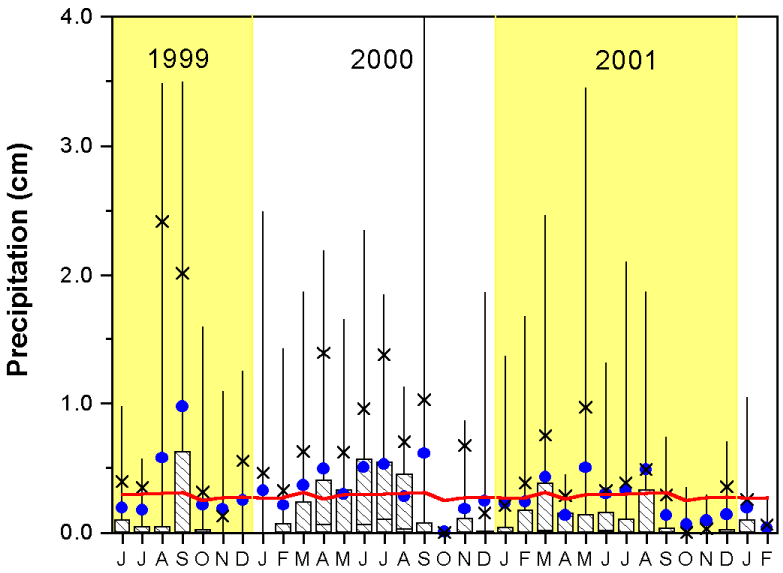

(a)

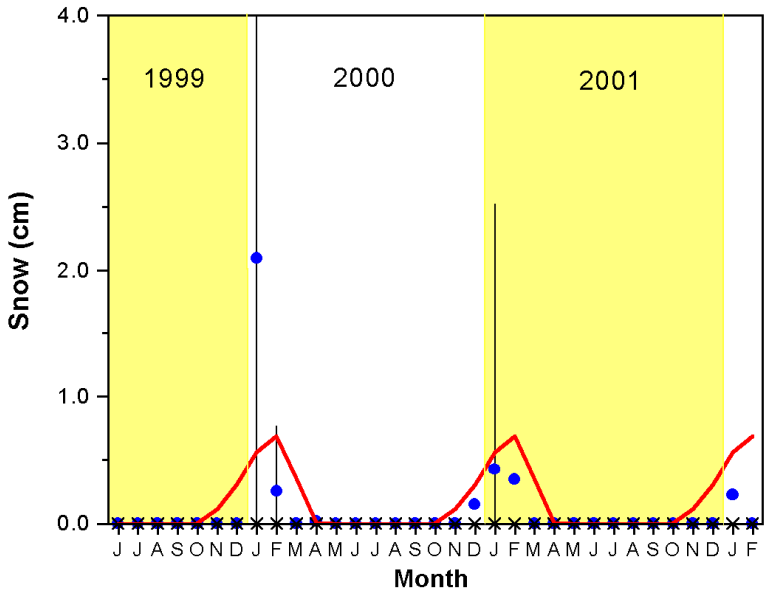

(b)

Figure 3.0.2 Seasonal variation of (a) precipitation (b) snow at BWI. Monthly means are indicated by solid circles. Vertical bars indicate the 95 percentiles and crosses indicate the 85 percentiles. The solid line indicates the climate norm based on a 40-year (1960 – 2000) average.

Therefore, it is a necessary to study the general features of weather in each month, especially our nine intensive sampling periods. These analyses are summarized in Table 3.0.1.

Table 3.0.1 Summary of temperature and precipitation in the Baltimore-Washington corridor during nine intensive sampling periods.

Sampling period	Climatological descriptions
Summer 1999 (7/1– 8/3)	Very hot and dry. Temperature was generally 2 - 4 °C higher than normal except during a cold front from 7/11 to 7/15. Precipitation was recorded in 10 days but 50% of it occurred on 7/22. Total precipitation was only ~ 50% of the normal.
Fall 1999 (9/30 – 11/2)	Cool and humid. The summer drought ended in September. Occasional heavy precipitation was distributed uniformly throughout this period, and the monthly mean relative humidity was above 80%. Temperature was generally lower than normal by 1 – 2 °C.
Winter 2000 (12/31 – 2/1)	Warm-cold mixed and snowy/windy. An unusual warm weather during the first half of the period was followed by a persistent cold and snowy conditions in the last half. Three storm systems hit the area providing snowfall three times than normal.
April 2000 (3/31 – 4/30)	Moderate and wet. It was the wettest April since 1983 and the pattern persisted throughout the month with 15 days of measurable rain. The temperature was slightly higher during the first 10 days of the period.
Summer 2000 (6/30 – 8/1)	Very cool and wet. It was a sharp contrast to summer 1999. Temperature was remarkably low with only 6 - 7 days of above-normal temperature. Total precipitation was almost twice of normal with ~ 70% of it occurring in the second half of the period.
Fall 2000 (9/30 – 10/31)	Moderate and extremely dry. It was the second driest October in 100 years with total precipitation generally lower than 2 mm in this area. Temperature was slightly above normal during the first 20 days but dropped down rapidly in the last week of the period.

Winter 2001 (12/31 – 1/31)	Slightly warm and dry. The persistent cold weather that dominated in December ended around 1/10 and was followed by generally warmer conditions. The total rain and snow were below normal and dominated by an event occurring between 1/18 – 1/20.
Summer 2001 (6/30 – 8/3)	Cool with normal rainfall. For the second consecutive July we had a persistent pattern of cool weather with only 8 days of above-normal temperature. Four thunderstorms produced an above-normal total precipitation, but it was sunny and dry for the rest of the time.
Winter 2002 (12/31-2/1)	Dry and very warm. Precipitation and snow are less than normal. Monthly mean temperature was 2 – 3 ºC above normal. Coldest weather appeared on the first few days of the month. Driest January since 1981. The first snowfall of the season occurred on 1/19/2002.

3.1 Carbon Monoxide: Implications for Boundary Layer Dynamics

Monthly statistics of 24-hr average CO concentration at FME between 6/1999 and 2/2002 are presented in Table A.2.1. CO is a good tracer for fossil fuel combustion and biomass burning, but a fraction of CO may be produced through oxidation of hydrocarbons in the air. CO is removed from the atmosphere primarily (~ 80%) through reacting with OH to become CO_2. Depending on the OH concentration, CO has an atmospheric lifetime ranging from 1 to 4 months. Because of its relatively long atmospheric lifetime, near urban centers with strong combustion sources the ambient CO concentration is influenced more by emission rate and meteorology than chemistry. Planetary boundary layer depth and wind speed that control the dilution and dispersion of CO released at the surface are the two major factors for ambient CO concentration [*Glen et al.*, 1999]. In remote areas, CO can serve as a tracer for long-range transport of

anthropogenic emissions because of its long atmospheric lifetime. Typical CO concentration over remote oceans (background level) is ~ 100 ppbv in northern hemisphere and ~ 50 ppbv in southern hemisphere [*Holloway et al.*, 2000]. This reflects the different degrees of industrial activity between the two hemispheres. CO level over rural parts of continents is usually higher than that over remote oceans by a few tens of ppbv.

Long-term CO monitoring has been made at the Shenandoah National Park (SNP), Virginia since 1989 [*Hallock-Waters et al.,* 1999]. The SNP site is rural, located at 1100 m elevation (MSL) and generally removed from any proximate CO sources. Therefore, CO at SNP may be considered representative for the CO background level in the Mid-Atlantic region. At SNP, CO shows an annual mean concentration of 160 - 180 ppbv; it features a weak diurnal variation (within 10%) and a spring maximum versus a fall minimum (within 50 ppbv difference) [*Hallock-Waters*, 2000]. Since the SNP site is generally at or above the PBL, influences of the PBL dynamics are believed to be minor. The OH concentration is usually higher in summer than in winter; the observed seasonal variation in CO may be modulated by the destruction of CO and production of CO through the OH chemistry on isoprene.

The FME site is generally downwind of SNP (Figure 4.4.1) and much more urban. As shown in Figure 3.1.1, the CO concentration at FME is usually higher than 180 ppbv. Strong diurnal variations of ~ 25% in summer and ~ 100% in winter are observed at FME (Figure 3.1.2(a)-(d)). The two peaks in the CO diurnal profile correspond to the morning and evening traffic rush hours, respectively. A mid-day low could reflect the stronger turbulent dilution into a deeper PBL in the early afternoon. The observations suggest a

strong influence from on-road vehicular emissions. CO is probably not well mixed vertically so that its surface level is sensitive to the PBL depth. Figure 3.1.3 illustrates the dilution process. The diurnal contrast is enhanced in fall and winter likely due to a shallower PBL that suppresses vertical dispersion during rush hours. In addition to solar insolation, synoptic and meso- scale meteorology such as subsidence and convection can influence the PBL depth as well (Section 1.2.3); this could be the cause for the difference between the CO diurnal profiles in fall and spring. In Figure 3.1.1, the quartiles of monthly CO are generally broader in winter. Summer CO may be less sensitive to large-scale meteorology because turbulent convection is strong enough to overcome the

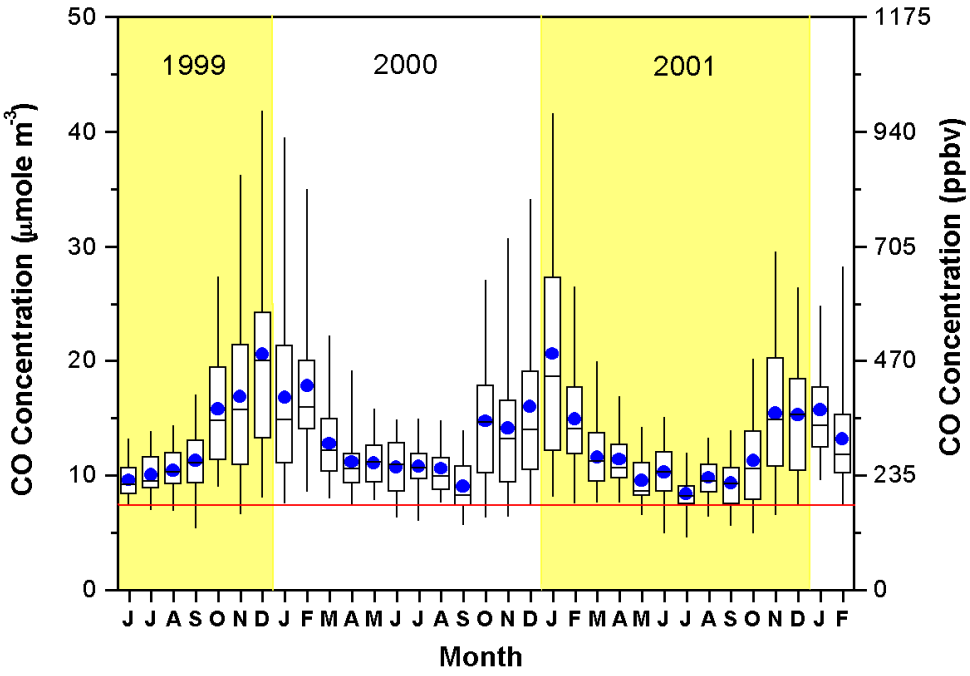

Figure 3.1.1 Seasonal variation of 24-hr CO concentration at FME. Monthly means are indicated by solid circles and median values by short dashes. Boxes indicate the quartiles and vertical bars indicate the maximum and minimum. The solid line indicates the mean CO concentration (1995-1997) at SNP.

subsidence and keep the surface CO concentration low. In winter, when solar insolation turns weaker, the PBL depth could more depend on large-scale meteorological systems.

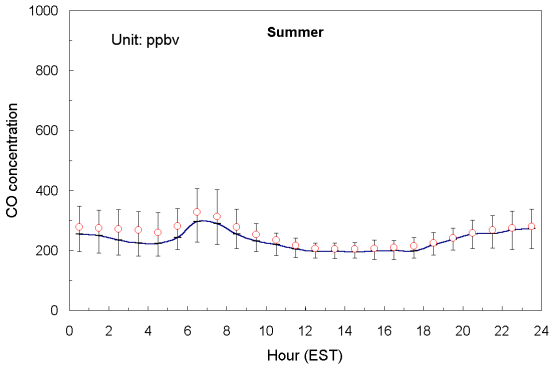

(a) Summer (Jun., Jul., and Aug.)

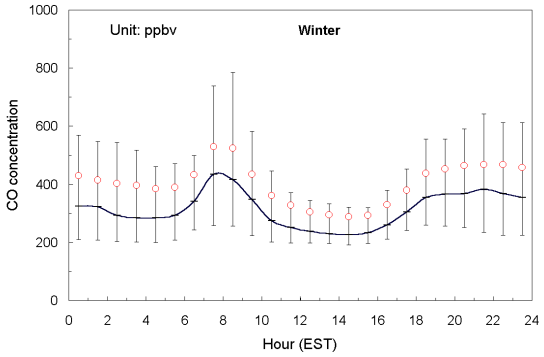

(c) Winter (Dec., Jan., and Feb.)

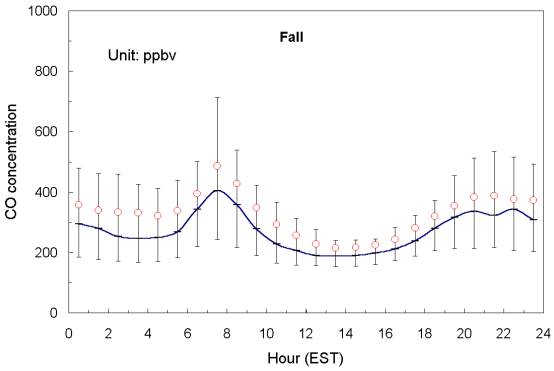

(b) Fall (Sep., Oct., and Nov.)

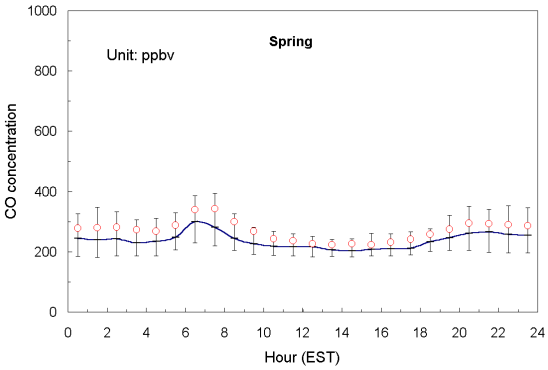

(d) Spring (Mar., Apr., and May)

Figure 3.1.2 Average diurnal variation of CO concentration at FME by season. Statistics is based on hourly averages collected from June 1999 to May 2001. Mean values are indicated by circles and median values by short dashes. Vertical bars indicate the quartiles.

Wind speed is another important factor that determines the dispersion efficiency of CO released. The relatively low CO in January 2000 (compared to those in December 1999 and February 2000) is believed to result from more frequent strong winds that enhance the removal of pollutants in the source region. According to the records of hourly-averaged wind speed at Baltimore-Washington International (BWI) airport, ~ 15 km northeast of FME, strong winds (wind speed > 5 m s^{-1}) are nearly twice as probable in January 2000 as in December 1999 and February 2000 (30% versus ~15%).

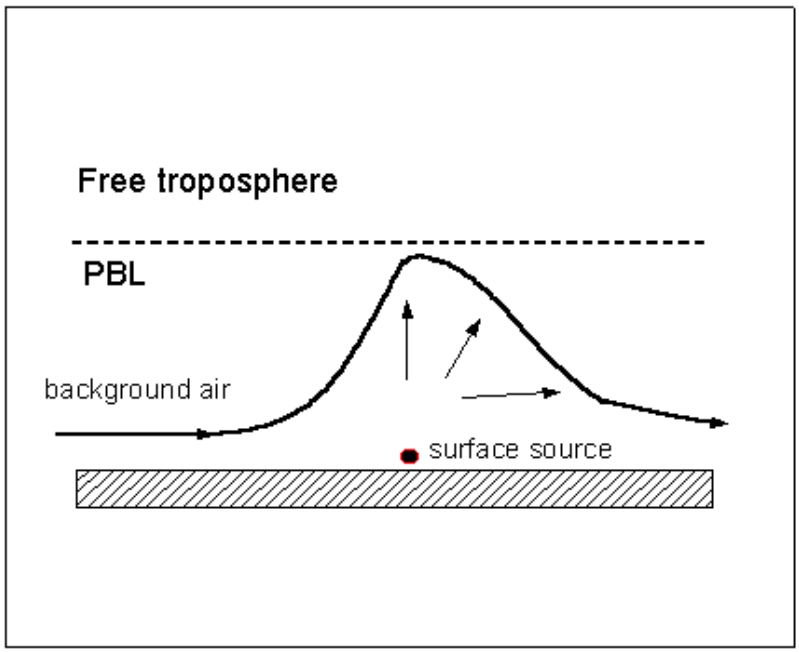

Figure 3.1.3 Schematic plot of transport and dispersion of CO in the planetary boundary layer.

3.2 Fine Particulate Mass

At FME, 24-hr $PM_{2.5}$ mass was measured by the DRI SFS-1 and FRM, and hourly $PM_{2.5}$ mass by TEOM. Seasonal variation of the $PM_{2.5}$ mass is shown in Figure 3.2.1. By looking at the SFS data, the $PM_{2.5}$ mass concentration is generally higher in summer and winter than in fall and spring. There are also significant interannual variations. For instance, July 1999 shows a mean $PM_{2.5}$ concentration ~ 50% higher than July 2000 and July 2001. $PM_{2.5}$ concentration in October 2000 has much broader quartiles than October 1999. Compared to CO, aerosol has a short atmospheric lifetime due to dry deposition and precipitation scavenging. July 1999 was warmer and drier than July 2000 and 2001, and October 2000 was the driest October in about a century. Dry and warm weather may lead to the higher ambient $PM_{2.5}$ concentration. Unlike CO, variability of the $PM_{2.5}$ mass seems to be strong in both summer and winter; the mechanisms that modulate CO and $PM_{2.5}$ levels (dispersion, source location, etc) are likely very different. Throughout the whole sampling period, only two monthly means (July 1999 and January 2001) exceed 15 $\mu g\ m^{-3}$, the USEPA annual standard. Statistics (mean, median, quartiles, etc) of the $PM_{2.5}$ data from SFS-1 are presented in Table A.1.1 – A.1.9.

The $PM_{2.5}$ mass measurement using the FRM instrument was made every third day. After the quality assurance process conducted by MDE, there are usually only 6 – 8 valid 24-hr data for each month, and therefore the FRM data are not considered suitable for monthly statistics calculation. Single FRM data are compared with concurrent SFS-1 measurements in Figure 3.2.2. Although the correlation is excellent (r^2 ~ 0.98), the FRM mass concentration is generally higher by ~ 10%. Since the FRM and SFS-1 are both

gravimetric methods and use similar sampling protocols (e.g. they both use Teflon filters and weigh the filters at 30% - 40% relative humidity), the 10% deviation probably results from using different size-selective inlets (impactor versus cyclone). Considering that the analytical uncertainty of the SFS mass is 5% – 10% (see Appendix 1), the FRM data are indeed a good verification of our $PM_{2.5}$ mass measurement.

Monthly mean $PM_{2.5}$ mass concentration from TEOM is generally lower but close to the SFS data except in winter when a significant deficit (> 40%) appears (Figure 3.2.1). As suggested in Section 2.3, this deficit could be due to the loss of volatile nitrate and organics when sample air is preheated to 50°C to achieve a lower relative humidity. The material loss is expected to more in winter because of a larger difference between temperatures of sample stream and ambient air. This explains the substantial deficit in the TEOM measurement in winter. A comparison of 24-hr average TEOM and SFS data is presented in Figure 3.2.3. As long as measurements acquired in winter (January) are excluded, the TEOM data generally agree with the SFS data (r^2 ~ 0.9, slope ~1, and intercept ~ -2 $\mu g\ m^{-3}$). These comparisons imply that 24-hr TEOM measurement is more reliable from April to October though a potential lower quantifiable limit (LQL) of 2 – 3 $\mu g\ m^{-3}$ may still apply.

Hourly TEOM data can be used to investigate the diurnal variation of $PM_{2.5}$ mass concentration. The diurnal profiles averaged over a 2-year period based on the TEOM data are shown, by season, in Figure 3.2.4(a)-(d). In summer, the diurnal variation is < 25%. High concentrations agreeing in time with the morning and evening rush hours do exist but are not as marked as those in the CO diurnal profile. The mid-day low due to vertical dispersion in the early afternoon also seems to be relatively weak. This can be

explained by assuming that fine particles and CO originate from different sources in summer. The vertical profile of aerosol concentration, if available, can help reveal the atmospheric transport and dispersion. The $PM_{2.5}$ diurnal profiles in fall and spring (Figure 3.2.4) look similar to the summer profile except a more distinguishable mid-day low. The $PM_{2.5}$ diurnal profile in winter is relatively similar to CO. This could mean that local sources that dominate the CO emission play greater roles in $PM_{2.5}$ concentration in winter. However, one has to exercise extra caution since TEOM can substantially underestimate $PM_{2.5}$ mass in winter.

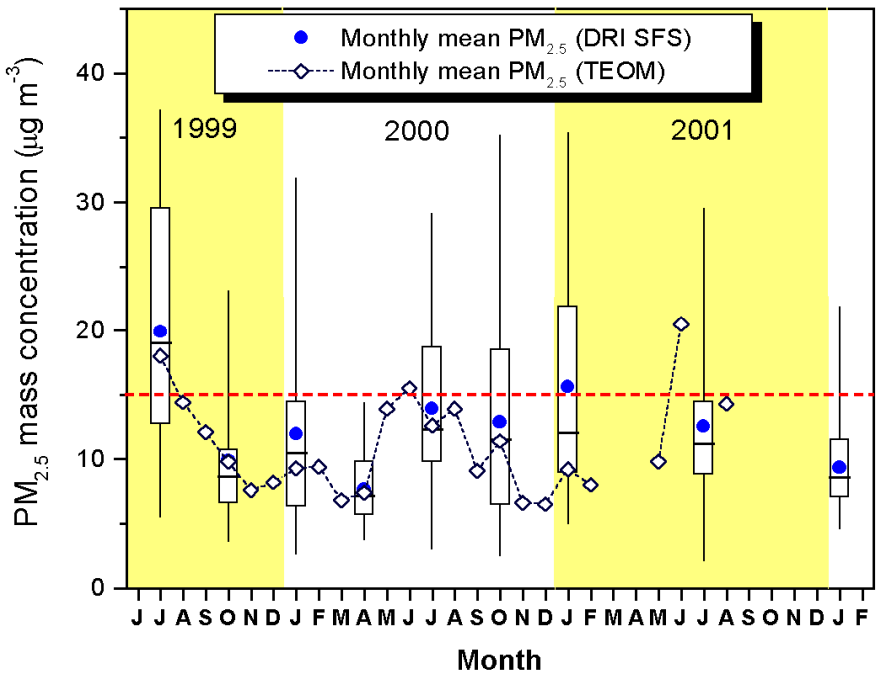

Figure 3.2.1 Seasonal variation of 24-hr $PM_{2.5}$ mass measured by SFS-1 at FME. Monthly means are indicated by solid circles and median values by short dashes. Boxes indicate the quartiles and vertical bars indicate the maximum and minimum. Monthly averaged $PM_{2.5}$ mass by TEOM are indicated by diamonds. The dashed line indicates the USEPA standard for annual mean $PM_{2.5}$ concentration.

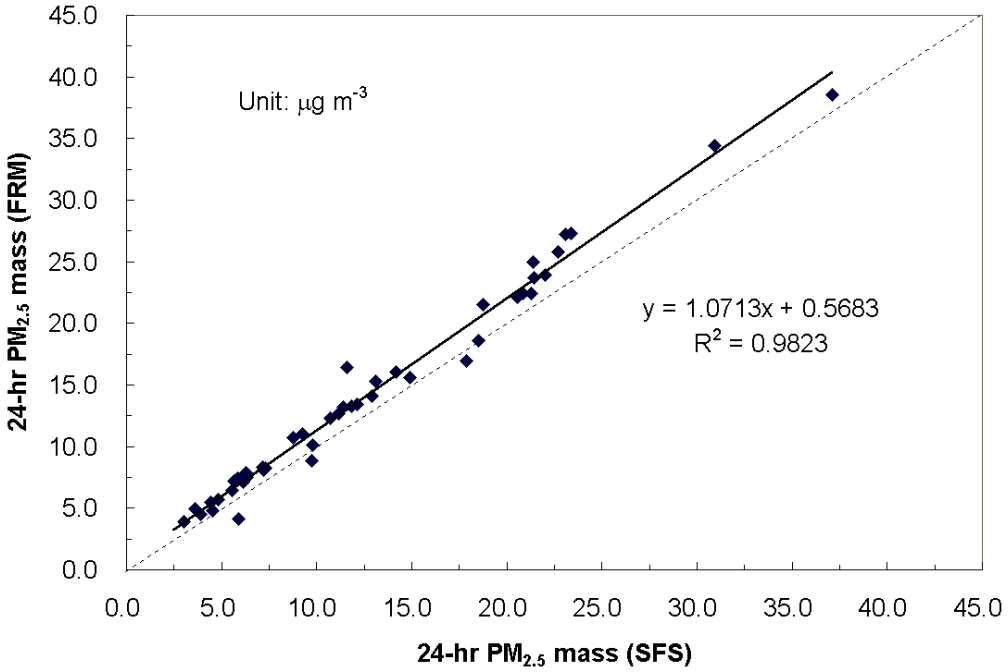

Figure 3.2.2 A comparison of 24-hr $PM_{2.5}$ mass measured by SFS-1 and FRM at FME during a 2-year period (1999 – 2001). The dotted line indicate the 1:1 line.

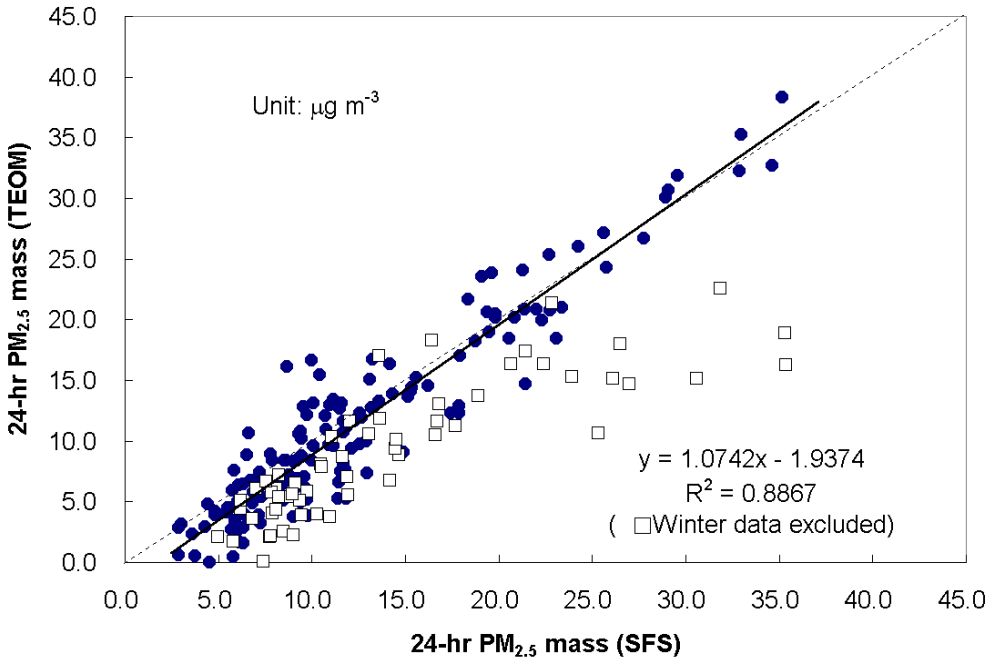

Figure 3.2.3 A comparison of 24-hr $PM_{2.5}$ mass measured by SFS-1 and TEOM at FME during a nearly 2-year period (1999 – 2001). Data acquired in winter are separated, indicated by squares, and excluded in the linear regression.

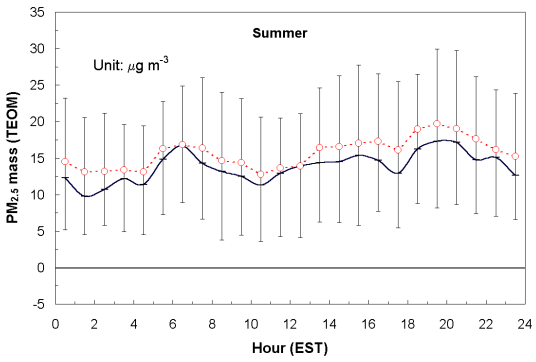

(a) Summer (Jun., Jul., and Aug.)

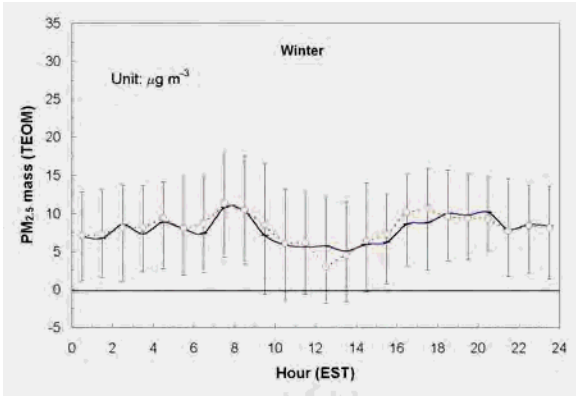

(c) Winter (Dec., Jan., and Feb.)

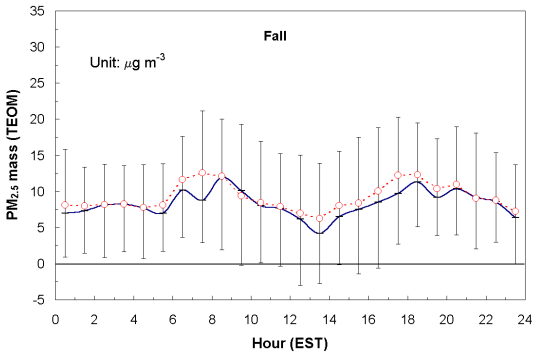

(b) Fall (Sep., Oct., and Nov.)

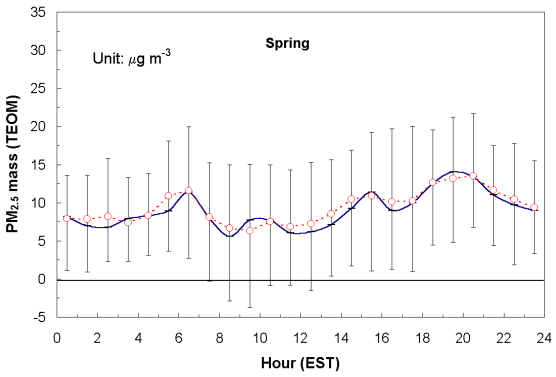

(d) Spring (Mar., Apr., and May.)

Figure 3.2.4 Average diurnal variation of $PM_{2.5}$ mass concentration at FME by season. Statistics is based on hourly means acquired by TEOM between July 1999 and June 2001. Mean values are indicated by circles and median values by short dashes. Vertical bars indicate the quartiles. The winter profile could underestimate the ambient $PM_{2.5}$ concentration due to a sampling artifact of TEOM.

3.3 Sulfate and Sulfur dioxide

Fine particulate sulfur (S) and sulfate (SO_4^{2-}) were measured by X-ray fluorescence and ion chromatography, respectively (see Appendix 1 for data). These two measurements agree closely with each other (Figure 3.3.1) despite that S is sampled on Teflon filter but SO_4^{2-} on quartz filter. Teflon and quartz filters function similarly in measuring SO_4^{2-}. Sulfate is certainly the dominant form of sulfur in the $PM_{2.5}$, and ~ 10% of the sulfate could be insoluble salts and cannot be detected by ion chromatography.

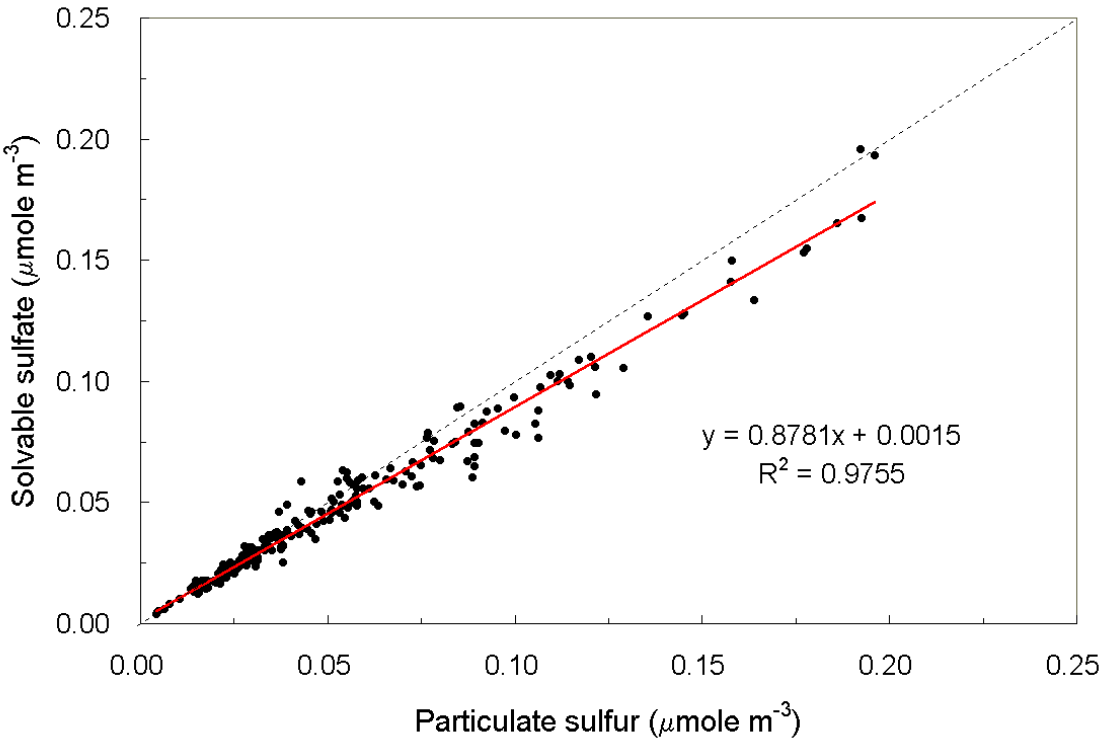

Figure 3.3.1 A comparison of 24-hr S and SO_4^{2-} measured by Teflon and quartz filters, respectively at FME during the first eight intensive sampling months. The dotted line indicates the 1:1 line.

The seasonal variation of SO_4^{2-} and SO_2 (precursor of SO_4^{2-}) are shown in Figure 3.3.2, and the monthly statistics of 24-hr SO_2 concentration are presented in Appendix 2. The two highest monthly mean SO_4^{2-} concentrations appear in July 1999 and July 2000, but SO_2 in winter is twice as high as that in summer. The SO_4^{2-}/SO_2 ratio is 2 - 4 times higher in summer than in winter. Long-term monitoring at Washington, DC, within 30 km from FME, also indicates higher sulfate concentration in summer [*Malm et al*., 1994; *IMPROVE*, 2000]. July 1999, which was extremely warm and dry compared to July 2000 and 2001, had the highest SO_4^{2-} concentration among the three summers. SO_4^{2-} is secondary, resulting from oxidation of SO_2 and removed primarily through dry and wet deposition. The relatively high SO_4^{2-} concentration in July 1999 could be explained by

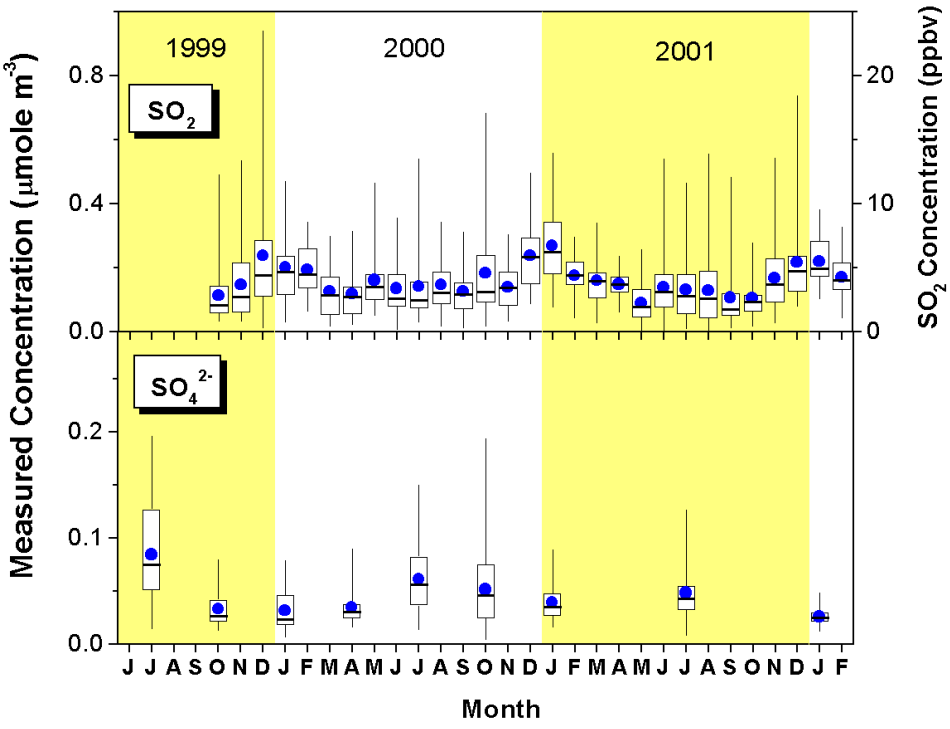

Figure 3.3.2 Seasonal variation of 24-hr SO_2 and $PM_{2.5}$ SO_4^{2-} at FME. Monthly means are indicated by solid circles and median values by short dashes. Boxes indicate the quartiles and vertical bars indicate the maximum and minimum.

a stronger SO_2-to-SO_4^{2-} conversion due to stronger solar insolation and/or a longer atmospheric lifetime of SO_4^{2-} because of the lack of precipitation.

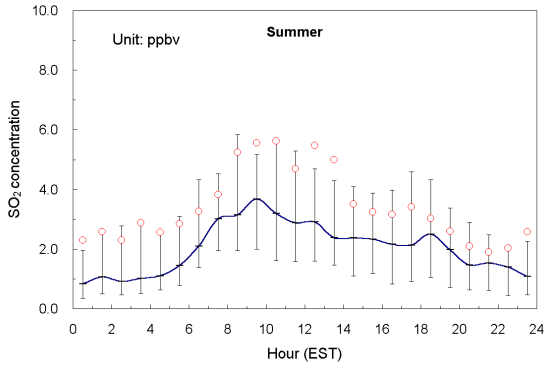

(a) Summer (Jun., Jul., and Aug.)

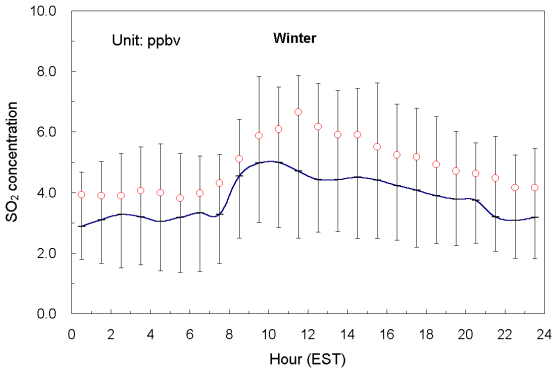

(c) Winter (Dec., Jan., and Feb.)

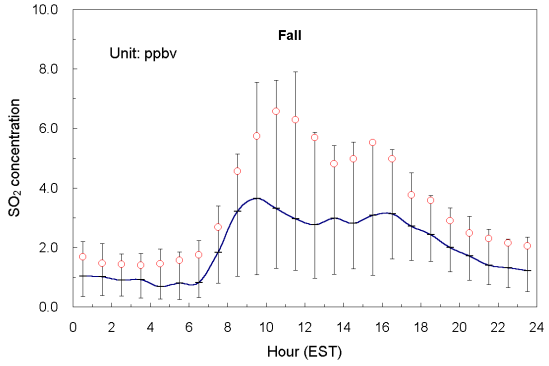

(b) Fall (Sep., Oct., and Nov.)

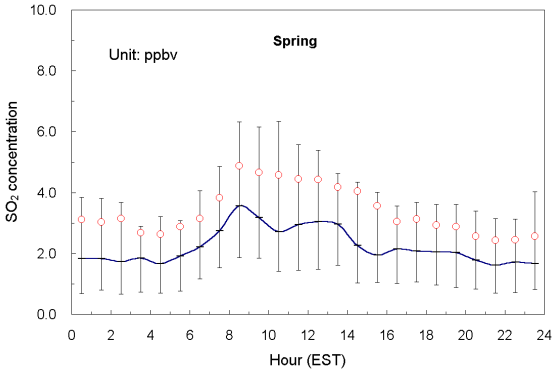

(d) Spring (Mar., Apr., and May.)

Figure 3.3.3 Average diurnal variation of SO_2 concentration at FME by season. Statistics are based on hourly means acquired between October 1999 and August 2001. Mean values are indicated by circles and median values by short dashes. Vertical bars indicate the quartiles.

Figure 3.3.3(a)-(d) shows the SO_2 diurnal profile in which a distinct mid-day maximum appears, especially in summer. This pattern is almost opposite to the CO diurnal profile. *Stehr et al.* [2000] observed a similar pattern at Wye River, MD and suggested that SO_2 originates from distant sources; more intensive turbulence around noon mixes SO_2 downward from aloft, increasing the surface SO_2 concentration. SO_2 is oxidized mostly by OH and H_2O_2 in the gaseous and aqueous phases. OH and H_2O_2 concentration are estimated to be several times higher in summer than in winter due to a stronger O_3 photolysis [*Spivakovsky et al.*, 1990; *Goldstein et al.*, 1995]. The lifetime of SO_2 against oxidation can have a significant seasonal variation [*Lusis et al.*, 1978]. A shorter atmospheric lifetime in summer may explain the stronger diurnal contrast in SO_2 concentration.

Long-range transport from the U.S. Midwest is believed to be a major source of SO_2 and SO_4^{2-} in the Mid-Atlantic region. However, the correlation between SO_4^{2-} and SO_2 is weak in any season ($r^2 < 0.2$), and the variation of SO_4^{2-} only explains ~ 20% of the SO_2 variation. Providing that long-range transport of SO_2 is not likely enhanced in winter, the high SO_2 concentration in winter implies not only a slower oxidation rate to SO_4^{2-} but also increased contributions from sources other than the U.S. Midwest. According to the SO_2 emission inventory (Figure 1.3.1), these could be local sources in the B-W corridor. More work related to the source apportionment of SO_2 and SO_4^{2-} is to be presented in Chapter 5.

3.4 Nitrate, Nitric acid, and Total Reactive Nitrogen Oxides

In an urban environment, total reactive nitrogen oxides (NO_y) is believed to be mostly NO_x (NO + NO_2) but may include nitric acid (HNO_3), nitrate (NO_3^-), and peroxyacetyl nitrates (PAN) as well. As shown in Figure 3.4.1, HNO_3 and NO_3^- account, on average, for less than 15% of the measured NO_y. Therefore, uncertainty due to line losses of nitrate (Section 2.9) should be minor and not alter the general diurnal and seasonal patterns of NO_y.

The NO_y concentration at FME is much higher than that in rural SNP (generally < 3 ppbv) [*Doddridge et al*., 1992; *Hallock-Waters,* 2000]. Despite the known uncertainty, two peaks and a mid-day low can be easily distinguished in the NO_y diurnal profile (Figure 3.4.2(a)-(d)). The two peaks approximately agree in time with the morning and evening rush hours. This diurnal profile is somewhat similar to CO and opposite to SO_2, suggesting that the surface NO_y concentration is strongly influenced by the on-road vehicle emissions, too. The correlation r^2 between 24-hr average NO_y and CO (using all data) is ~ 0.65. Considering the complex nature of NO_y and analytical uncertainty, this positive correlation is significant enough to further support a common origin of CO and NO_y, most likely traffic emission in the corridor. If so, the mid-day low again reflects the stronger turbulent dilution into a deeper PBL in the early afternoon.

The summer-winter contrast in the correlation of 24-hr average NO_y with CO is presented in Figure 3.4.3. The correlation becomes weaker when summer and winter data are separated. It is interesting that the NO_y/CO slope in summer is about 2 times higher than that in winter. Both NO_y and CO have a shorter atmospheric lifetime in summer due to stronger deposition and oxidation, respectively. However, in such a source-dominated environment, the higher NO_y/CO slope in summer more likely implies either stronger

NO_y (or NO_x) source strength in summer or stronger CO emission in winter. Similar relations are observed between CO and EC, and this will be discussed in Section 4.3.

Gaseous HNO_3, $PM_{2.5}$ NO_3^-, and total nitrate (T-NO_3^-, HNO_3 + all particulate NO_3^-) were measured separately at FME (Section 2.1). The HNO_3 and T-NO_3^- data in January 2000 contain untypical analytical uncertainties (likely due to the degradation of filters) and therefore are not used for analysis. Since the T-NO_3^- measurement includes particles of a full size range, the good agreements between T-NO_3^- and the sum of HNO_3 and $PM_{2.5}$ NO_3^- (Figure 3.4.4) suggests that most of the NO_3^- appears in fine particles; coarse-mode NO_3^- only accounts for as much as 10 - 20%. HNO_3 and NO_3^- are formed in the atmosphere predominantly through oxidation of NO_x (Section 1.2.2). The summer-winter contrast of the T-NO_3^- concentration is not significant despite that NO_y is ~ 100% higher in winter than in summer (Figure 3.4.1). The NO_x-to-NO_3^- conversion is weaker in winter due to lower concentrations of oxidants such as OH and O_3. This, however, could be compensated by a shallower PBL that keeps T-NO_3^- concentration high in winter. Note that the T-NO_3^- concentration in October 1999 is very low in comparison with that in October 2000, but the NO_y and CO concentrations in the two months show little differences.

In summer, > 90% of T-NO_3^- is HNO_3, but this fraction drops to < 50% in winter. The gas/particle partitioning of T-NO_3^- at thermodynamic equilibrium depends on many factors, including ambient temperature, relative humidity, availabilities of SO_4^{2-}, NH_4^+, Na^+, K^+ Cl^-, etc [*Kim et al.*, 1993]. At FME, temperature is lower in winter than in summer typically by 20 – 30 °C; the cooler weather favors the formation of particulate

nitrate that becomes a significant fraction of $PM_{2.5}$ in winter. This system is to be discussed in more detail in Section 4.2.

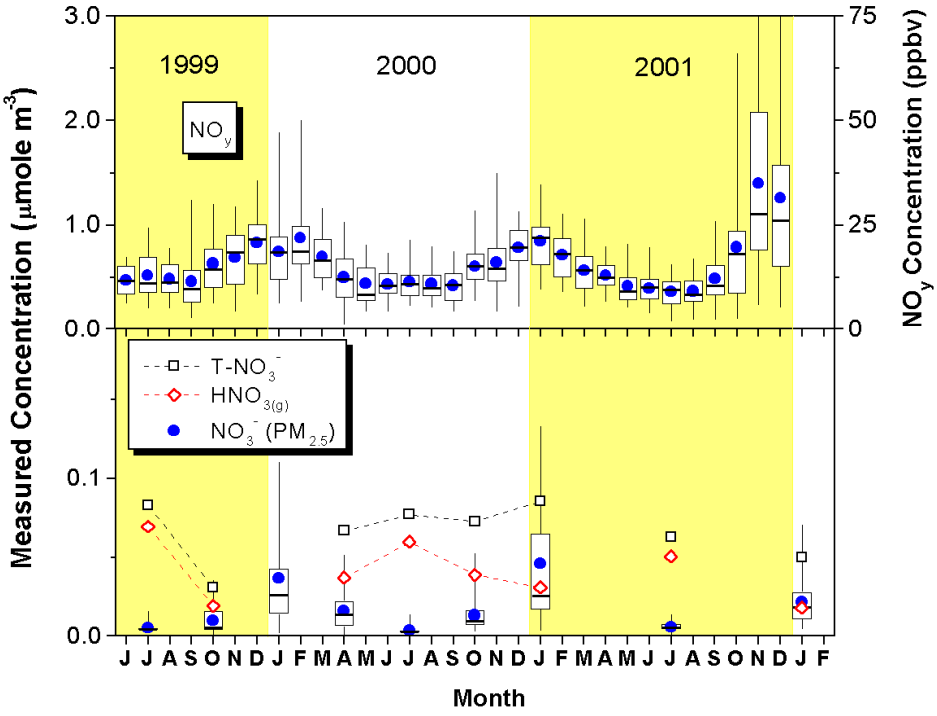

Figure 3.4.1 Seasonal variation of 24-hr NO_y, T-NO_3^-, HNO_3 and $PM_{2.5}$ NO_3^- at FME. Monthly means are indicated by circles, diamonds, and squares while median values by short dashes. Boxes indicate the quartiles and vertical bars indicate the maximum and minimum.

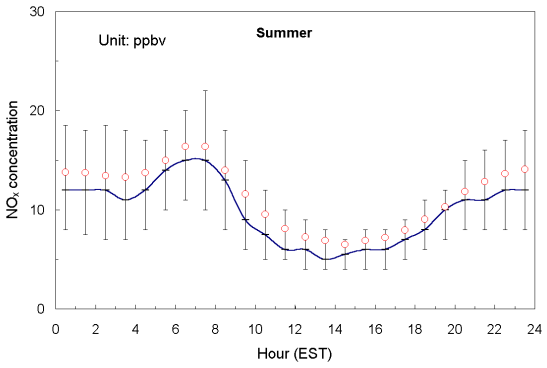

(a) Summer (Jun., Jul., and Aug.)

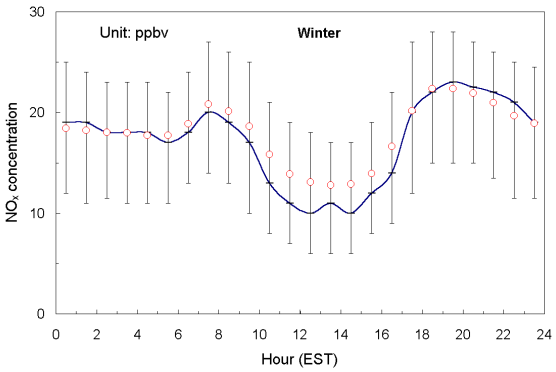

(c) Winter (Dec., Jan., and Feb.)

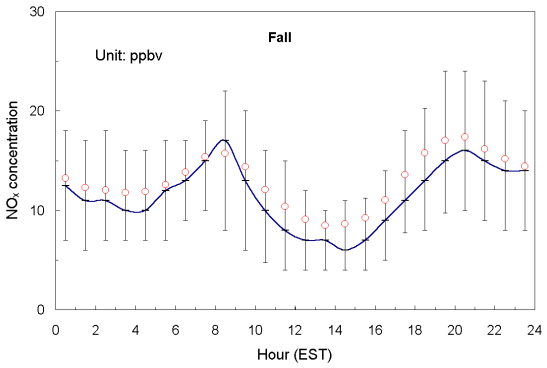

(b) Fall (Sep., Oct., and Nov.)

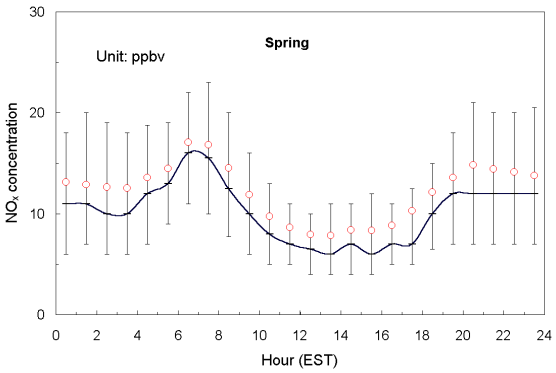

(d) Spring (Mar., Apr., and May.)

Figure 3.4.2 Average diurnal variation of NO_y concentration at FME by season. Statistics is based on hourly means acquired between June 1999 and June 2001. Mean values are indicated by circles and median values by short dashes. Vertical bars indicate the quartiles.

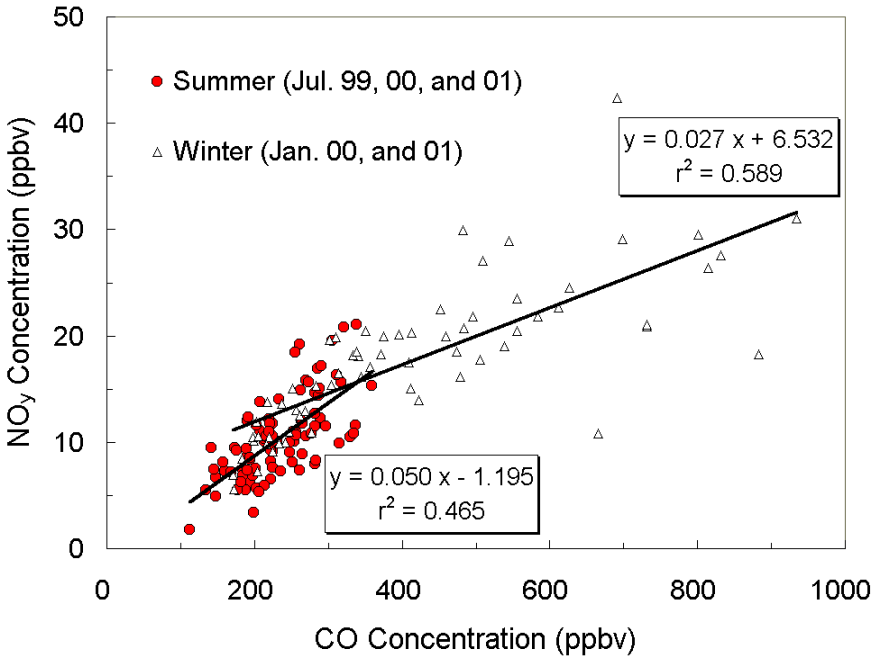

Figure 3.4.3 Seasonal variation of NO_y versus CO at FME.

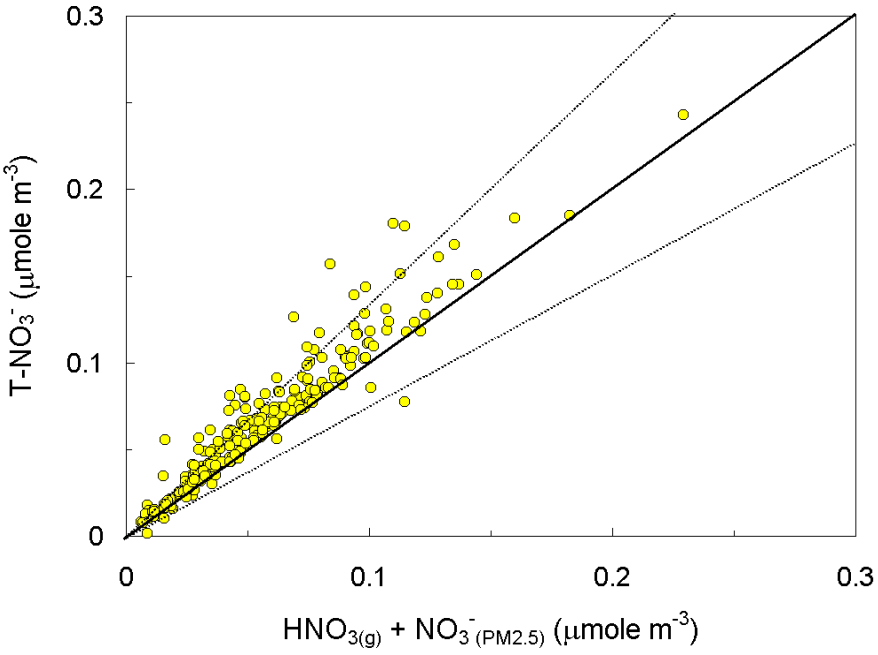

Figure 3.4.4 Comparison of T-NO_3^- and the sum of HNO_3 and $PM_{2.5}$ NO_3^- at FME. The solid line indicates the 1:1 line while the dashed lines indicate the ± 25% deviation. T-NO_3^- measurement includes particles of all size ranges.

3.5 Ammonia and Ammonium

Ammonia (NH_3) is the primary basic gas in the atmosphere. The most important sources of NH_3 include animal waste, ammonification of humus followed by losses of NH_3-based fertilizers from soils, and industrial emissions. Ammonium (NH_4^+) is one of the most abundant cations in the atmosphere. The seasonal variation of 24-hr $PM_{2.5}$ NH_4^+, NH_3, and total ammonium (T-NH_4^+, NH_3 + all particulate NH_4^+, measured by SGS-2) is shown in Figure 3.5.1 and their monthly statistics presented in Appendix 1. Generally, the analytical uncertainty of particulate NH_4^+ is ~ 10%. The analytical uncertainty of NH_3 is 20 – 30 % in summer, fall, and spring but increases to 60 – 80 % in winter. Actually, in winter, NH_3 concentration is frequently below the detection limit. The T-NH_4^+ is compared to the sum of NH_3 and $PM_{2.5}$ NH_4^+ in Figure 4.5.2, and they agree with each other within ± 25% most of the time. This suggests that NH_4^+ is mostly in the fine-aerosol mode. *Larsen* [2002] conducted a sub-hourly measurement of T-NH_4^+ at FME in July 2001 and acquired results in good agreement with this study.

The highest monthly mean NH_4^+ concentration was observed in July 1999 when SO_4^{2-} concentration also reached a maximum. In summer, the correlation between fine particulate NH_4^+ and SO_4^{2-} is very strong ($r^2 > 0.9$); thus, most of the NH_4^+ is associated with SO_4^{2-}. There is still significant gaseous NH_3 left in the atmosphere, coexisting with gaseous HNO_3 in summer, fall, and spring. In winter, however, NH_3 seems to be depleted, forming particulate NH_4NO_3 as the temperature decreases (Figure 3.5.1). The high NH_3 concentration in January 2002 (warm winter) was driven by a special two-day episode. The gas/particle partitioning of T-NH_4^+ also depends on ambient temperature

and relative humidity. The inorganic fraction of the fine aerosol at FME can generally be considered as an NH_4^+-SO_4^{+2}-NO_3^- system that requires further study (Section 4.2).

If the sulfate observed at FME is dominated by regional sources (e.g., long-range transport from the U.S. Midwest), certain amount of ammonium could enter the B-W corridor along with the sulfate. Long-range transport of gaseous ammonia is not probable because of its relatively short atmospheric lifetime against dry/wet deposition; local sources within the corridor can contribute to ammonia and ammonium as well. Based on limited days of measurement, *Larsen* [2002] generally observed a midday low in the T-NH_4^+ diurnal profile at FME. This possibly results from a stronger turbulent dispersion or deposition at noon, implying substantial local contributions.

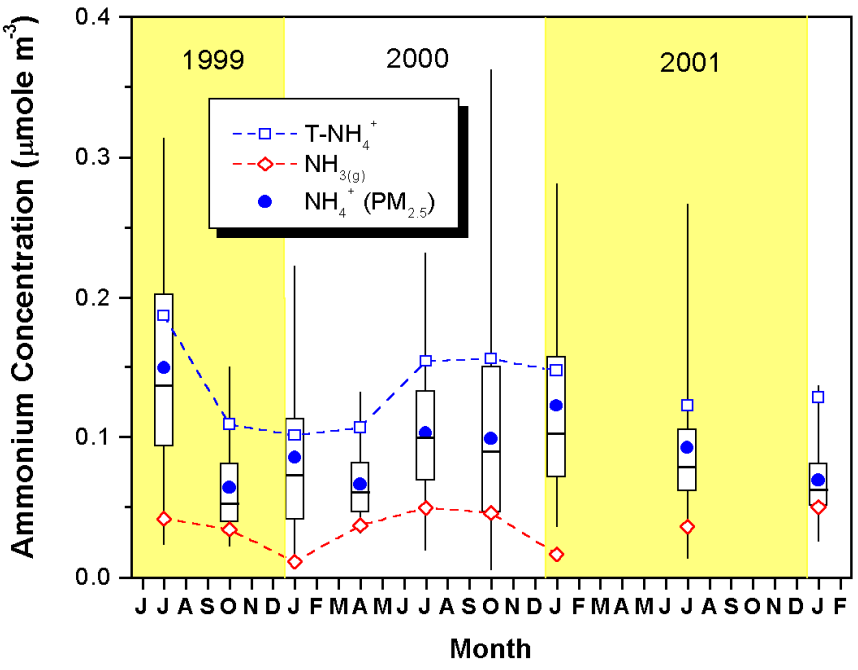

Figure 3.5.1 Seasonal variation of 24-hr T-NH_4^+, NH_3, and $PM_{2.5}$ NH_4^+ at FME. Monthly means are indicated by circles, diamonds, and squares while median values by short dashes. Boxes indicate the quartiles and vertical bars indicate the maximum and minimum.

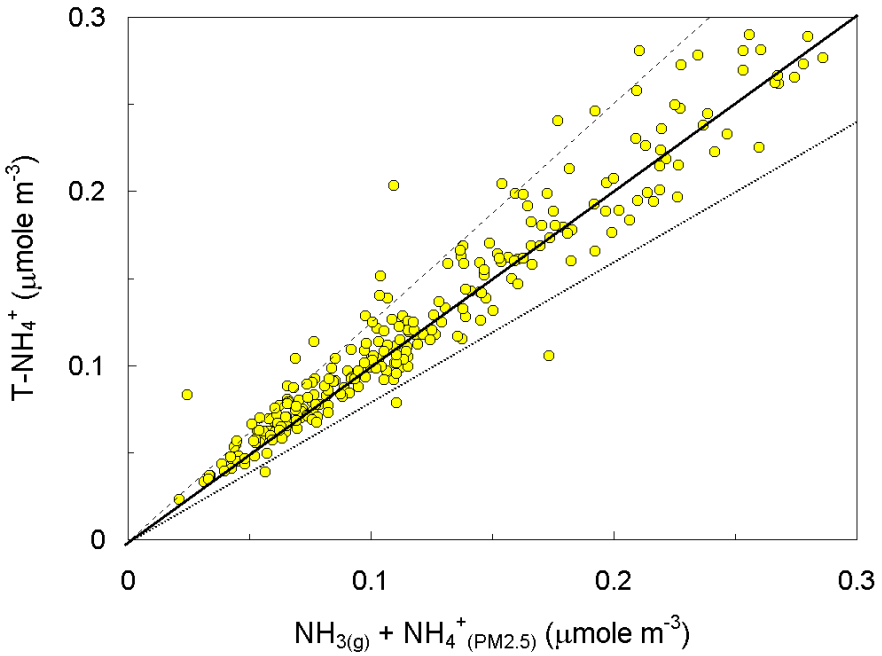

Figure 3.5.2 Comparison of T-NH_4^+ and the sum of NH_3 and $PM_{2.5}$ NH_4^+ at FME. The solid line indicates the 1:1 line while the dashed lines indicate the ± 25% deviation. T-NH_4^+ measurement includes particles of all size ranges.

3.6 Carbonaceous Material

Carbonaceous material is usually the second dominant species in fine aerosol mass after sulfate [*Malm et al*., 1994; *Tolocka et al*., 2001]. As mentioned in Section 2.1, elemental carbon (EC) and organic carbon (OC) in this study are determined by the Thermo-Optical-Reflectance method. However, the EC-OC separation could vary if different sampling substrates or analytical procedures are used [*Hering et al*., 1990; *Chow et al.*, 2001; *Neusüß et al*., 2001]. The measurement protocol followed in this study is similar to that in the IMPROVE network, the largest $PM_{2.5}$ sampling network in the U.S., in order to facilitate data comparisons (Section 4.4). The seasonal variation of EC, OC

(FQ), OC (BQ), and OC (TBQ) at FME are shown in Figure 3.6.1, and the monthly statistics can be found in Appendix 1. EC on backup filters is usually below the detection limit. Monthly mean EC and OC (FQ) concentrations do not show a clear seasonal cycle, but their 24-hr values have much broader distributions in winter than in summer (Figure 3.6.1). In other words, EC and OC (FQ) levels in winter are driven by fewer but stronger events. This pattern is similar to CO (Figure 3.1.1) and could partly be explained by boundary layer meteorology.

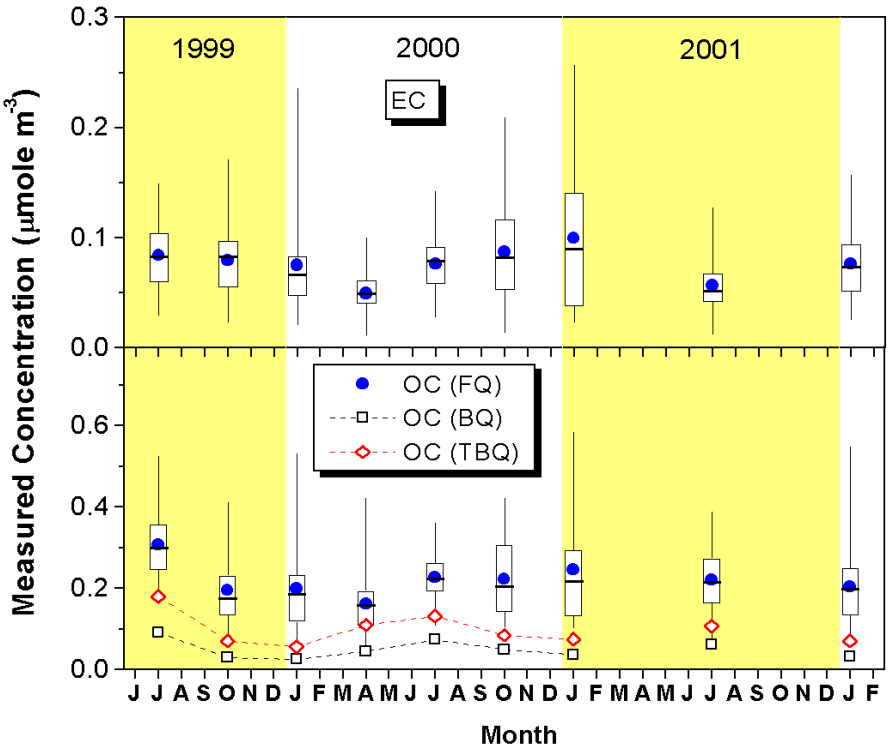

Figure 3.6.1 Seasonal variation of 24-hr EC, OC (FQ), OC (BQ), and OC (TBQ) at FME. Monthly means are indicated by circles, diamonds, and squares while median values by short dashes. Boxes indicate the quartiles and vertical bars indicate the maximum and minimum.

A direct observation of the EC diurnal variation is not available at FME. However, atmospheric absorption (b_{ap}) at 565 nm wavelength was measured with a PSAP (Section

2.5) in January 2001. Hourly-averaged b_{ap} was calculated and archived. Assuming that EC is the single most important light-absorbing spices in the atmosphere, b_{ap} can be considered equivalent to the *in-situ* EC concentration. Figure 3.6.2 shows the correlation of 24-hr average b_{ap} with EC in January 2001. The strong correlation of $r^2 \sim 0.87$ supports the earlier assumption while an absorption efficiency of ~ 7 m^2 $g(EC)^{-1}$ generally agrees with those previously suggested of ~ 10 m^2 $g(EC)^{-1}$ [*Liousse et al.*, 1993; *Petzold et al.*, 1997]. The average diurnal variation of b_{ap}, based on the hourly data, is somewhat similar to CO and NO_y, showing two peaks likely corresponding to the morning and evening rush hours (Figure 3.6.3). Emissions from vehicles, especially diesel, have been suggested to contribute to EC. At FME, EC is correlated to CO in every month ($r^2 \sim 0.50 – 0.84$) and better in winter (Section 4.3). Similar observations were reported at other sites, too. The relation of EC and CO is to be discussed in Section 4.3.

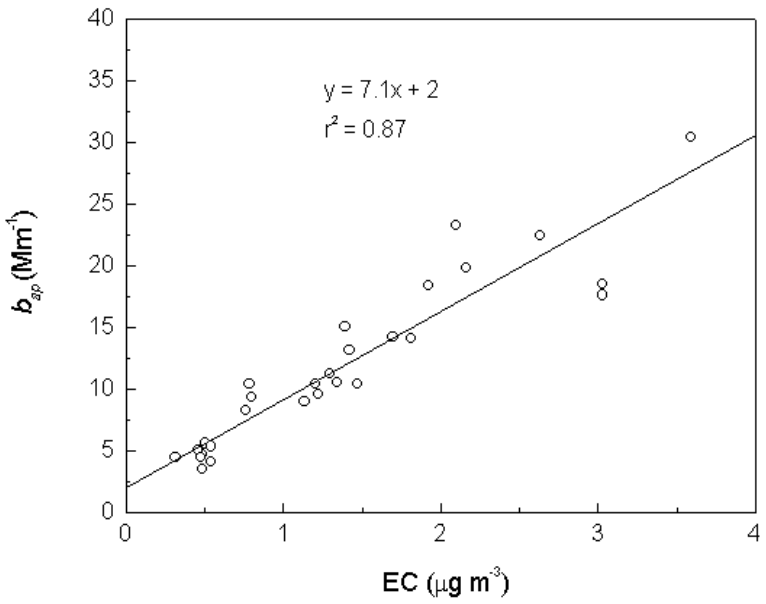

Figure 3.6.2 Scatter plot of 24-hr average atmospheric absorption (b_{ap}) versus EC concentration at FME in January 2001.

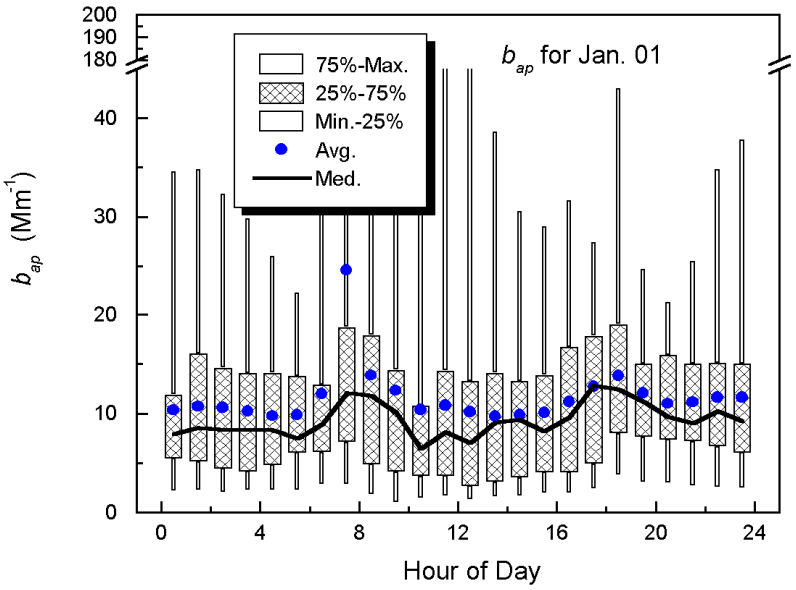

Figure 3.6.3 Average diurnal variation of atmospheric absorption (b_{ap}) at FME in January 2001. Statistics are based on hourly means. Mean values are indicated by circles and median values by short dashes. Boxes indicate quartiles and vertical bars indicate the maximum and minimum.

OC is more complicated than EC. It covers a very broad range of molecular forms, and the volatile fraction of OC varies with ambient temperature. At FME, the highest monthly mean OC (FQ) concentration appears in July 1999 (Figure 3.6.1), which was extremely warm and dry. The ratio of OC (BQ) or OC (TBQ) over OC (FQ) is lower in winter, and this could result from either the lower vapor pressure of semi-volatile OC or less VOC adsorption in winter. OC is positively correlated to EC with an overall $r^2 \sim 0.6$ and wintertime $r^2 \sim 0.85 – 0.9$. Mobile emissions, known to contribute to OC, EC, and CO [e.g. *Gertler et al.*, 2001], are believed to be a major source of carbonaceous particles at FME. A scatter plot of OC versus EC (Figure 3.6.4) indicates an OC/EC ratio ranging

from 2 to 6. The OC/EC ratio is suggested to be 0.5 – 4 for fossil fuel combustion and be higher for biomass burning [*Liousse et al.*, 1996; *Cooke et al.*, 1999]. The FME site does not seem to be dominated by biomass burning. Alternatively, this could also suggest a significant amount of OC produced by non-combustion sources (e.g., biogenic and secondary OC) especially in summer.

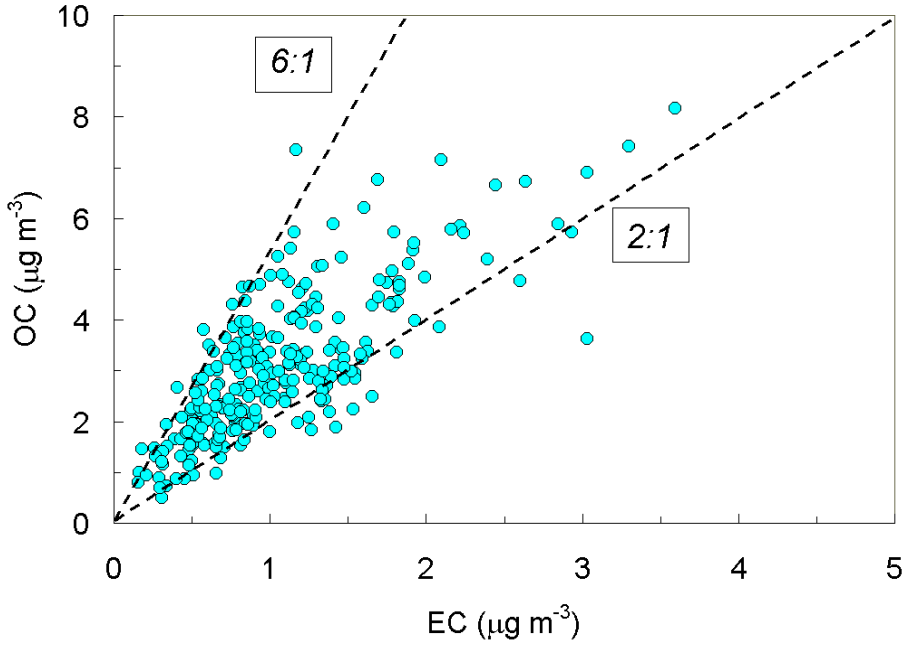

Figure 3.6.4 Scatter plot of 24-hr OC (FQ) versus EC at FME during the first eight intensive sampling months (7/1999 – 7/2001). The two dashed lines indicate 6:1 and 2:1 lines, respectively.

3.7 Crustal Material and Other Trace elements

At FME, more than 40 trace elements in $PM_{2.5}$ were analyzed using X-ray fluorescence (XRF), and Cl^-, K^+, and Na^+ ions were analyzed using ion chromatography and atomic absorption spectrometry. These results are summarized in Appendix 1. The concentration of some species is always low or below the detection limit and therefore contains significant uncertainty. More reliable measurements include Na^+, K^+, Al, Si, S, K, Ca, Mn, Fe, Ni, Cu, Zn, Se, Br, and Pb. S is known to be mostly SO_4^{2-}. Elements considered primarily of crustal origin include, in decreasing order of overall $PM_{2.5}$ mass fraction, Si (0.64%), Fe (0.49%), Al (0.25%), Ca (0.2%). K (0.53%) is also considered to be crustal, but K at FME contains 81% soluble K^+ that could originate from vegetative burning. Fireworks on July 4th lifted the K and K^+ concentrations substantially. The mass of crustal material has to include oxygen associated with minerals and can be estimated empirically (e.g., $1.89 \times Al + 2.14 \times Si + 1.4 \times Ca + 1.43 \times Fe + 1.2$) [*Chow et al.*, 1996]. Figure 4.7.1 shows the seasonal variation of the crustal mass. Each 24-hr crustal mass concentration generally remains below the monthly means except during a few special events when the crustal concentration exceeds 20 – 50 times of the monthly means. These events mostly appear in summer and spring. It will be shown in Section 4.4 and Section 5.3 that these high episodes are regional in nature and likely result from distant sources.

The correlation coefficients of these elements with each other and with EC are calculated in Table 3.7.1. Al, Si, and Ca are significantly correlated to each other but only weakly correlated to Fe. Fe is correlated to Cu, Zn, Mn, and Pb that are relatively less

common in crustal material. Therefore, Fe may originate from other sources such as iron/copper smelters or steel furnaces. Se, Zn, Br, and Pb are another group of elements that are likely linked to combustion sources. For example, Se is known to be a tracer for coal combustion [*Rabano et al*., 1989; *Malm and Gebhart*, 1997] while Br is a good tracer for mobile sources or wood smoke [*Malm and Gebhart*, 1997]. Most of the combustion-related elements reach higher concentration in winter than in summer and have almost no correlation with the crustal elements. These tracer elements are very important in aerosol source apportionment techniques and will be discussed further in Chapter 5.

Na^+ and Cl^- can be tracers for marine aerosols. Na^+ is often a good tracer for sea salt. Cl^- may not be as reliable since the volatilization of Cl^- from sea salt aerosols by acid displacement or photochemistry limits the utility of particulate Cl^- as a sea salt indicator. At FME, Cl^- concentration is usually below the detection limit. Na^+ is not correlated to any species in Table 3.7.1. Since FME is near the U.S. east coast, the contribution of marine sources relies on easterly transport while westerly transport usually carries more continental emissions. The seasonal variation of Na^+ is shown in Figure 3.7.2, but no specific pattern is found. Overall, the mass fraction of Na^+ and Cl^- in $PM_{2.5}$ are 0.31% and 0.27%, respectively. Sea salt probably contributes to < 1% of the $PM_{2.5}$ mass due to the relatively low chance of easterly transport (Section 5.3). At FME, the sea salt and crustal material contribution is generally less than 5% in the $PM_{2.5}$ mass.

Table 3.7.1. Correlation coefficients (r) of species in $PM_{2.5}$ at FME. Numbers in bold indicate higher correlations ($r > 0.60$ or $r^2 > 0.36$).

(r)	EC	S	Se	Br	Zn	Pb	Mn	Ni	K+	K	Cu	Fe	Al	Si	Ca	Na+
EC	1.00															
S	0.41	1.00														
Se	0.51	0.46	1.00													
Br	**0.68**	0.33	**0.67**	1.00												
Zn	0.59	0.16	**0.64**	**0.79**	1.00											
Pb	0.56	0.26	0.58	**0.73**	**0.73**	1.00										
Mn	0.52	0.25	**0.60**	0.58	**0.74**	**0.69**	1.00									
Ni	0.54	0.22	0.50	0.53	0.52	0.47	0.48	1.00								
K+	0.19	0.26	0.18	0.21	0.23	0.41	0.27	0.09	1.00							
K	0.16	0.27	0.16	0.19	0.20	0.40	0.26	0.07	**0.99**	1.00						
Cu	0.32	0.11	0.22	0.28	0.34	0.44	0.38	0.36	0.27	0.26	1.00					
Fe	0.46	0.31	0.48	0.47	**0.60**	**0.61**	**0.71**	0.50	0.31	0.33	**0.72**	1.00				
Al	0.06	0.43	0.10	0.04	0.01	0.17	0.30	0.09	0.45	0.53	0.11	0.47	1.00			
Si	0.07	0.38	0.09	0.02	0.04	0.11	0.27	0.11	0.28	0.35	0.05	0.46	**0.89**	1.00		
Ca	0.23	0.30	0.15	0.16	0.20	0.22	0.38	0.17	0.20	0.25	0.10	0.48	**0.65**	**0.66**	1.00	
Na+	0.05	0.08	0.11	0.24	0.20	0.21	0.28	0.24	0.21	0.22	0.07	0.27	0.29	0.27	0.19	1.00

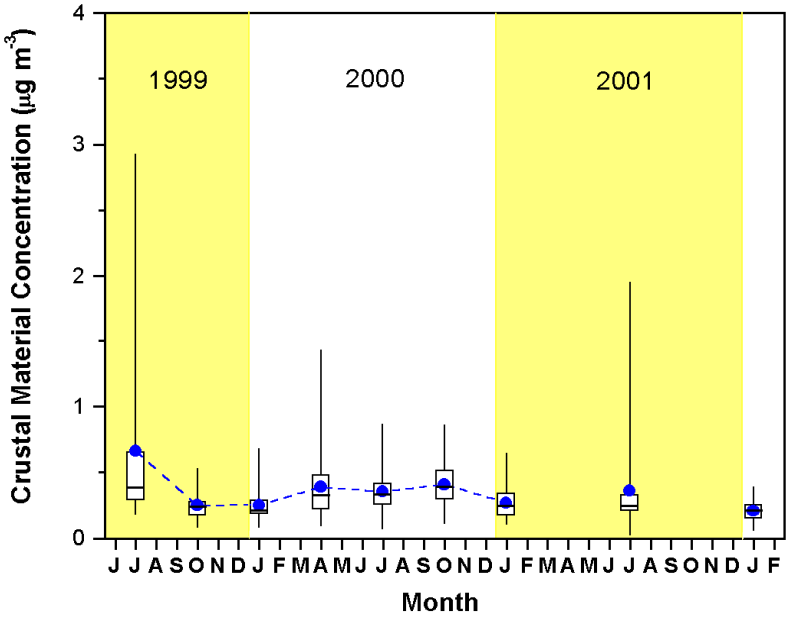

Figure 3.7.1 Seasonal variation of 24-hr crustal material concentration at FME. Monthly means are indicated by circles while median values by short dashes. Boxes indicate the quartiles and vertical bars indicate the maximum and minimum.

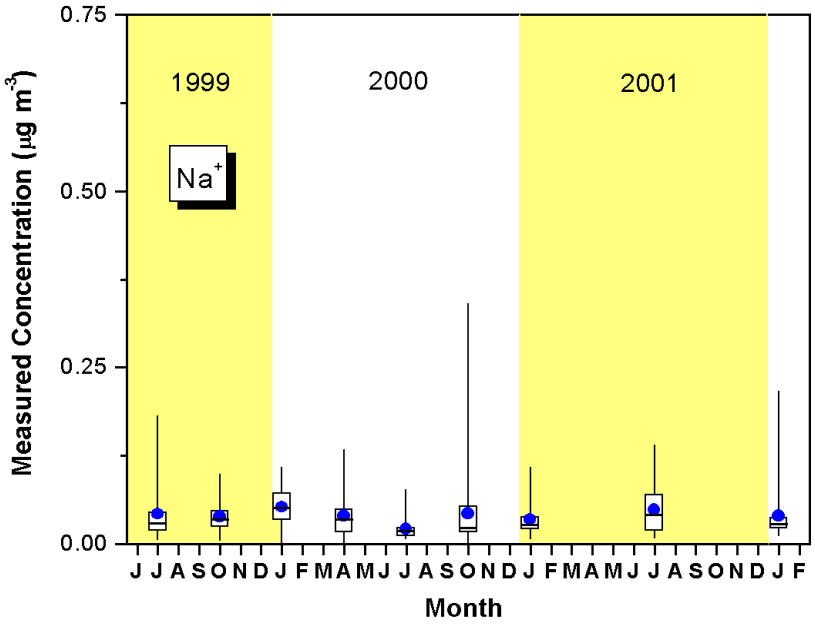

Figure 3.7.2 Seasonal variation of 24-hr Na^+ concentration at FME. Monthly means are indicated by circles while median values by short dashes. Boxes indicate the quartiles and vertical bars indicate the maximum and minimum.

Chapter 4 Discussion

This chapter discusses various analyses of data acquired in this study. It starts with an audit experiment (Section 4.0) in which the accuracy and reliability of our $PM_{2.5}$ measurement are examined. Section 4.1 studies the inorganic fraction of fine aerosol using a thermodynamic model, ISORROPIA. ISORROPIA calculates not only the gas/particle partitioning of T-NO_3^- and T-NH_4^+ but also the aerosol water content at ambient conditions. The correlation between visibility and aerosol mass with/without water is investigated in Section 4.5. Section 4.3 compares EC and CO measurement from various studies, attempting to capture characteristics of mobile emissions and test the current EC emission inventory. Finally, the spatial variation of major $PM_{2.5}$ components is studied in Section 4.4 by comparing data from FME to concurrent measurements at other locations.

4.0 SFS and SGS Audit Experiment

The quality of measurements depends on careful field operation and laboratory analysis. The SFSs and SGSs for this study had been deployed in some other studies and proven to be stable. During our sampling period, the instruments were routinely checked every time filters were replaced. The flow systems were calibrated once a year and little

change was reported (a ~ ± 5% random variation). Filter media used were polymethylpentane ringed, 2.0 μm pore size PTFE Teflon membrane filters (#R2PJ047, Gelman, Ann Arbor, Michigan) and pre-fired quartz fiber filters (#2500 QAT-UP, Pallflex Products Corp., Putnam, Connecticut). Filter diameter was 47 mm, and controlled flow rate was 20 L m^{-1} through each filter (Figure 2.3).

More than 40 species were analyzed at DRI using various techniques. The analytical method and minimum detection limit (MDL) for each species (in μg per filter) is shown in Table 4.0.1. Note that here the MDL indicates the concentration at which instrument response equals three times the standard deviation of the response to a known concentration of zero. Even though the MDLs for ions such as NO_3^-, SO_4^{2-}, NH_4^+, Na^+, and K^+ and carbon are higher than trace elements from XRF, the signal/noise ratio of these ions and carbon are usually better than most of the elements due to their higher ambient concentrations (see Appendix 1). In practice, besides the MDL, one needs to consider the Lower Quantifiable Limit (LQL) in the measurement. LQL can be estimated from the chemical loading on field blank filters. LQL is usually the dominant source of the analytical uncertainty reported [*Chow et al*., 1996].

At FME, since filters were not collected right after each 24-hr sampling period and remained on site for as long as 2.5 days, passive deposition onto the filters and evaporation from the filters could introduce biases to the measurements. To evaluate this uncertainty, an audit experiment was carried out between 8/7/2001 – 8/11/2001. From 8/6/2001 – 8/10/2001 was a haze episode in which the daily high temperature generally exceeded 35 °C. The relatively humidity remained low until 8/11/2001 when precipitation accumulated to end the episode. This is considered the most favorable

condition for such an audit experiment since both the $PM_{2.5}$ concentration and potential sampling artifacts are higher. On 8/7 and 8/9, in each of the SFS and SGS samplers, two filter packs with one identical configuration (e.g. Teflon filter for SFS-1) were installed into the two channels and exposed simultaneously for 24 hrs. One of them (P1) was picked up and put into refrigerated storage immediately after the sampling was completed, and the second pack (P2) was left in the sampling plenum for 72 hours before picked up. Filter pack handling and analysis were identical from then on. On 8/8 and 8/10, filter packs with the other configuration were used (e.g. quartz filter for SFS-1). Therefore, two trials were accomplished for each type of filter pack used during the normal field study. This design is summarized in Figure 4.0.1.

The results of this experiment are summarized in Table 4.0.2. The analytical uncertainty associated with each measurement is presented as well. For trace elements, P2 is generally less than P1, and this suggests losses of material after 72-hour standby. In the first pair, the difference is not significant in comparison with the analytical uncertainty. In the second pair, a significant change is observed for Si, Al, and S, and the mass change exceeds 50% of the Al ambient concentration. There could be many possibilities for the losses. Based on the limited number of observations, crustal material data needs to be interpreted cautiously.

The measurement of soluble ions seems to be reliable except Cl^- and NO_3^-. The Cl^- concentration is low at FME and often below the MDL. NO_3^- is also low in summer (Section 3.4). The mass change of NO_3^- on the front quartz filter and backup cellulous filter is not consistent in the two pairs of experiments. There could be mass exchange in

either direction between the front and backup filters when the pump is turned off. The uncertainty accounts for < 20% of NO_3^- (sum of the front and backup filters).

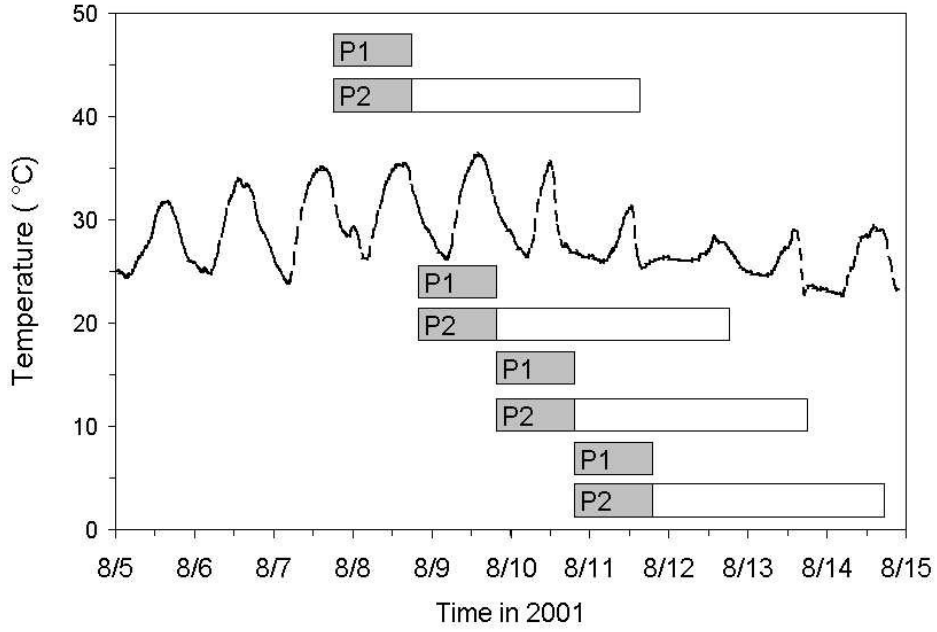

Figure 4.0.1 Design for a SFS and SGS audit experiment at FME. The gray and white bars indicate sampling and standby period, respectively. The first and third pair use one configuration and the second and fourth pair use the other configuration. The dashed line indicates the trend of ambient temperature.

The mass change of carbonaceous material on quartz filters is most interesting. The backup filters (BQ and TBQ) clearly gain OC while the front quartz filter (FQ) loses OC.

This is especially significant in the first pair of the experiment. It is mentioned in Section 2.2 that OC on backup filter likely results from two possibilities: VOC adsorption and semi-volatile OC evaporation. The result of this experiment supports evaporation of semi-volatile OC as a likely cause. Note that the ambient temperature was generally higher during the first pair's sampling and standby period (Figure 4.0.1), and this could explain the more volatilization. Evaporation certainly can occur during sampling as well as during standby. The volatilization of OC is substantial at FME and cannot be ignored in determining OC concentration. Similar mass exchange happens in EC, but it is not consistent. Though volatilization of EC is unlikely, some OC may be mistaken as EC in the TOR analysis due to an ambiguous EC-OC separation, which remains to be a serious problem in carbon measurement [e.g., *Neusüß et al*., 2001].

In SGSs, larger changes appear in denuded samples. For those filters sampling without denuders, the mass loss or gain during the 72-hr standby is negligible for both T-NO_3^- and T-NH_4^+. For those filters sampling with denuders, the mass change is significant. For example, in the second pair sampling in SGS-1 on 8/10/2001 – 8/11/2001, P2 is higher than P1 by ~ 2.4 μg m^{-3}, ~ 250% of the T-NO_3^- ambient concentration. This cannot be possible if only volatilization and analytical uncertainty are considered. Note that P1 and P2 use different denuders in this experiment, and the effectiveness of these denuders could vary. A careful examination of these denuders' efficiency needs to be done perhaps before each sampling. The loss of T-NH_4^+ during standby seems to be smaller, close to the analytical uncertainty. Since the HNO_3 concentration is determined from the difference between the T-NO_3^- amount on denuded and undenuded samples, this finding suggests that some of the HNO_3 data could be questionable.

Table 4.0.1 Summary of analytical methods for $PM_{2.5}$ at FME. The MDL stands for Minimum Detection Limit.

Species	Analytical Method	MDL (μg per filter)	Species	Analytical Method	MDL (μg per filter)
Mass	Gravimetric	12	Se	XRF	0.0049
Cl^-	IC	0.12	Br	XRF	0.0024
NO_3^-	IC	0.12	Rb	XRF	0.0024
SO_4^{2-}	IC	0.12	Sr	XRF	0.0049
NH_4^+	AC	0.12	Y	XRF	0.0049
Na^+	AA	0.072	Zr	XRF	0.0073
K^+	AA	0.072	Mo	XRF	0.011
Al	XRF	0.037	Pd	XRF	0.024
Si	XRF	0.021	Ag	XRF	0.026
P	XRF	0.011	Cd	XRF	0.026
S	XRF	0.0084	In	XRF	0.034
Cl	XRF	0.024	Sn	XRF	0.044
K	XRF	0.011	Sb	XRF	0.053
Ca	XRF	0.011	Ba	XRF	0.19
Ti	XRF	0.0073	La	XRF	0.21
V	XRF	0.0049	Au	XRF	0.020
Cr	XRF	0.0049	Hg	XRF	0.013
Mn	XRF	0.0043	Tl	XRF	0.016
Fe	XRF	0.0024	Pb	XRF	0.011
Co	XRF	0.0024	Ur	XRF	0.019
Ni	XRF	0.0024	OC	TOR	0.49
Cu	XRF	0.0024	EC	TOR	0.49
Zn	XRF	0.0049			
Ga	XRF	0.0073			
As	XRF	0.0049			

Table 4.0.2 (next page) Concentration and uncertainty of SFS and SGS measurements during an audit experiment from 8/7/2001 to 8/11/2001. The AU stands for analytical uncertainty. Values in bold indicate that P2 differs from P1 by greater than the analytical uncertainty.

8/7							8/9					
SFS1	Teflon	unit	(μg m^{-3})		P2-P1		Teflon	unit	(μg m^{-3})		P2-P1	
	P1	P1-AC	P2	P2-AC	(ΔP)	ΔP/P1	P1	P1-AC	P2	P2-AC	(ΔP)	ΔP/P1
Mass	42.5955	2.1643	41.4886	2.1099	-1.1069	-3%	40.9674	2.0821	41.2115	2.0941	0.2441	1%
Na	0.1566	0.5850	0.1831	0.5861	0.0265	17%	0.3181	0.2277	0.0000	0.4963	**-0.3181**	-100%
Mg	0.0370	0.0620	0.0281	0.0605	-0.0089	-24%	0.0115	0.0533	0.0000	0.0528	-0.0115	-100%
Al	0.0313	0.0100	0.0628	0.0103	**0.0315**	101%	0.0506	0.0095	0.0232	0.0090	**-0.0274**	-54%
Si	0.0795	0.0079	0.0813	0.0079	0.0018	2%	0.1011	0.0082	0.0671	0.0072	**-0.0340**	-34%
P	0.0000	0.0460	0.0000	0.0436	0.0000	-	0.0000	0.0356	0.0000	0.0296	0.0000	-
S	7.6804	0.3844	7.2619	0.3635	**-0.4185**	-5%	5.9028	0.2956	4.8569	0.2433	**-1.0459**	-18%
Cl	0.0000	0.1466	0.0000	0.1404	0.0000	-	0.0000	0.1148	0.0000	0.1009	0.0000	-
K	0.0413	0.0029	0.0398	0.0029	-0.0015	-4%	0.0417	0.0029	0.0370	0.0027	**-0.0047**	-11%
Ca	0.0490	0.0039	0.0442	0.0038	**-0.0048**	-10%	0.0326	0.0033	0.0275	0.0032	**-0.0051**	-16%
Ti	0.0054	0.0294	0.0049	0.0286	-0.0005	-9%	0.0074	0.0262	0.0050	0.0270	-0.0024	-32%
V	0.0013	0.0124	0.0011	0.0121	-0.0002	-15%	0.0046	0.0112	0.0055	0.0115	0.0009	20%
Cr	0.0008	0.0022	0.0004	0.0022	-0.0004	-50%	0.0007	0.0021	0.0000	0.0021	-0.0007	-100%
Mn	0.0028	0.0008	0.0027	0.0008	-0.0001	-4%	0.0016	0.0008	0.0012	0.0008	-0.0004	-25%
Fe	0.0687	0.0053	0.0746	0.0055	**0.0059**	9%	0.0692	0.0053	0.0618	0.0050	**-0.0074**	-11%
Co	0.0002	0.0013	0.0001	0.0014	-0.0001	-50%	0.0005	0.0013	0.0002	0.0012	-0.0003	-60%
Ni	0.0005	0.0005	0.0007	0.0005	0.0002	40%	0.0023	0.0005	0.0020	0.0005	-0.0003	-13%
Cu	0.0017	0.0005	0.0011	0.0005	**-0.0006**	-35%	0.0018	0.0005	0.0013	0.0005	-0.0005	-28%
Zn	0.0100	0.0014	0.0106	0.0014	0.0006	6%	0.0105	0.0014	0.0090	0.0014	**-0.0015**	-14%
Ga	0.0007	0.0014	0.0000	0.0014	-0.0007	-100%	0.0003	0.0014	0.0000	0.0014	-0.0003	-100%
As	0.0003	0.0017	0.0006	0.0017	0.0003	100%	0.0006	0.0014	0.0012	0.0009	0.0006	100%
Se	0.0041	0.0005	0.0039	0.0005	-0.0002	-5%	0.0034	0.0005	0.0028	0.0004	-0.0006	-18%
Br	0.0048	0.0005	0.0044	0.0005	-0.0004	-8%	0.0057	0.0008	0.0044	0.0008	**-0.0013**	-23%
Rb	0.0000	0.0008	0.0004	0.0008	0.0004	-	0.0001	0.0007	0.0001	0.0007	0.0000	0%
Sr	0.0008	0.0007	0.0005	0.0010	-0.0003	-38%	0.0006	0.0009	0.0000	0.0009	-0.0006	-100%
Y	0.0000	0.0012	0.0002	0.0012	0.0002	-	0.0000	0.0011	0.0000	0.0011	0.0000	-
Zr	0.0011	0.0010	0.0008	0.0014	-0.0003	-27%	0.0006	0.0013	0.0000	0.0013	-0.0006	-100%
Mo	0.0000	0.0024	0.0000	0.0025	0.0000	-	0.0002	0.0023	0.0004	0.0023	0.0002	100%
Pd	0.0000	0.0045	0.0019	0.0045	0.0019	-	0.0000	0.0041	0.0024	0.0041	0.0024	-
Ag	0.0017	0.0054	0.0000	0.0054	-0.0017	-100%	0.0014	0.0051	0.0000	0.0052	-0.0014	-100%
Cd	0.0004	0.0055	0.0011	0.0058	0.0007	175%	0.0009	0.0052	0.0000	0.0054	-0.0009	-100%
In	0.0000	0.0066	0.0000	0.0069	0.0000	-	0.0013	0.0063	0.0000	0.0064	-0.0013	-100%
Sn	0.0000	0.0093	0.0003	0.0097	0.0003	-	0.0010	0.0089	0.0004	0.0093	-0.0006	-60%
Sb	0.0071	0.0112	0.0076	0.0118	0.0005	7%	0.0000	0.0104	0.0000	0.0106	0.0000	-
Ba	0.0000	0.0548	0.0000	0.0563	0.0000	-	0.0051	0.0518	0.0000	0.0524	-0.0051	-100%
La	0.0000	0.0724	0.0000	0.0741	0.0000	-	0.0129	0.0678	0.0000	0.0699	-0.0129	-100%
Au	0.0003	0.0019	0.0000	0.0020	-0.0003	-100%	0.0006	0.0018	0.0001	0.0018	-0.0005	-83%
Hg	0.0003	0.0012	0.0008	0.0013	0.0005	167%	0.0000	0.0011	0.0008	0.0012	0.0008	-
Tl	0.0000	0.0012	0.0005	0.0012	0.0005	-	0.0000	0.0011	0.0000	0.0011	0.0000	-
Pb	0.0060	0.0016	0.0049	0.0016	-0.0011	-18%	0.0025	0.0015	0.0018	0.0015	-0.0007	-28%
U	0.0000	0.0020	0.0006	0.0021	0.0006	-	0.0002	0.0019	0.0003	0.0019	0.0001	50%

8/8							8/10					
SFS1	Quartz	Unit	(μg m^{-3})		P2-P1		Quartz	unit	(μg m^{-3})		P2-P1	
	P1	P1-AC	P2	P2-AC	(ΔP)	ΔP/P1	P1	P1-AC	P2	P2-AC	(ΔP)	ΔP/P1
Cl^-	0.0227	0.0243	0.0614	0.0244	**0.0387**	170%	0.0000	0.0289	0.0381	0.0290	**0.0381**	-
NO_3^-	0.0557	0.0060	0.0000	0.0009	**-0.0557**	-100%	0.0000	0.0008	0.0709	0.0079	**0.0709**	-
SO_4^{2-}	12.5394	0.6407	12.8908	0.6586	0.3514	3%	5.8078	0.3011	6.0250	0.3120	0.2172	4%
NO_3^- B	0.7227	0.0472	0.8447	0.0539	**0.1220**	17%	1.5279	0.0924	1.3289	0.0808	**-0.1990**	-13%
NH_4^+	6.9132	0.3638	6.6858	0.3519	-0.2274	-3%	2.0766	0.1119	2.1179	0.1140	0.0413	2%
Na^+	0.0297	0.0112	0.0306	0.0112	0.0009	3%	0.0276	0.0105	0.0303	0.0105	0.0027	10%
K^+	0.0424	0.0080	0.0388	0.0075	-0.0036	-8%	0.0213	0.0048	0.0246	0.0052	0.0033	15%
OC	4.9701	0.4822	4.1854	0.4309	**-0.7847**	-16%	2.4207	0.3133	2.1314	0.2975	-0.2893	-12%
EC	1.6907	0.1548	1.3571	0.1275	**-0.3336**	-20%	0.9589	0.0945	0.9491	0.0935	-0.0098	-1%
TC	6.6489	0.5996	5.5343	0.5231	**-1.1146**	-17%	3.3683	0.3766	3.0694	0.3564	-0.2989	-9%

8/7							8/9					
SFS2	T-Q	Unit	(μg m^{-3})		P2-P1							
	P1	P1-AC	P2	P2-AC	(ΔP)	ΔP/P1	P1	P1-AC	P2	P2-AC	(ΔP)	ΔP/P1
OC (TBQ)	2.3363	0.3111	2.6923	0.3464	**0.3560**	15%	2.6030	0.3376	2.6349	0.3422	0.0318	1%
EC (TBQ)	0.0748	0.0451	0.1282	0.0636	0.0534	71%	0.1803	0.0879	0.2688	0.1238	0.0884	49%
TC (TBQ)	2.4147	0.3564	2.8241	0.4037	**0.4094**	17%	2.7834	0.3999	2.9037	0.4150	0.1202	4%

8/8							8/10					
SFS2	Q-Q	Unit	(μg m^{-3})		P2-P1							
	P1	P1-AC	P2	P2-AC	(ΔP)	ΔP/P1	P1	P1-AC	P2	P2-AC	(ΔP)	ΔP/P1
OC (FQ)	5.5164	0.5695	3.0758	0.3460	**-2.4406**	-44%	3.1277	0.3468	2.1345	0.2607	**-0.9932**	-32%
EC (FQ)	1.9166	0.2128	1.4572	0.1629	**-0.4594**	-24%	0.8985	0.1050	1.1377	0.1289	**0.2392**	27%
TC (FQ)	7.4330	0.7498	4.5330	0.4797	**-2.9000**	-39%	4.0296	0.4305	3.2722	0.3647	**-0.7574**	-19%
OC (BQ)	1.9022	0.2672	2.9430	0.3756	**1.0408**	55%	1.1469	0.1930	1.3130	0.2081	0.1661	14%
EC (BQ)	0.08255	0.0491	0.1795	0.0858	**0.0969**	117%	0.0851	0.0468	0.0516	0.0364	-0.0335	-39%
TC (TBQ)	1.98477	0.3097	3.1225	0.4420	**1.1377**	57%	1.2320	0.2245	1.3645	0.2383	0.1325	11%

8/7							8/9					
SGS1	Without denuder		Unit	($\mu g\ m^{-3}$)	P2-P1			unit	($\mu g\ m^{-3}$)		P2-P1	
	P1	P1-AC	P2	P2-AC	(ΔP)	ΔP/P1	P1	P1-AC	P2	P2-AC	(ΔP)	ΔP/P1
$T\text{-}NO_3^-$	6.8118	0.3428	6.6937	0.3373	-0.1182	-2%	4.8922	0.2529	4.8231	0.2497	-0.0691	-1%

8/8							8/10					
SGS1	With denuder		Unit	($\mu g\ m^{-3}$)	P2-P1			unit	($\mu g\ m^{-3}$)		P2-P1	
	P1	P1-AC	P2	P2-AC	(ΔP)	ΔP/P1	P1	P1-AC	P2	P2-AC	(ΔP)	ΔP/P1
$T\text{-}NO_3^-$	1.4178	0.0916	1.2387	0.0834	**-0.1791**	-13%	0.9862	0.0720	3.3657	0.1817	**2.3795**	241%

8/7							8/9					
SGS2	Without denuder		Unit	($\mu g\ m^{-3}$)	P2-P1			unit	($\mu g\ m^{-3}$)		P2-P1	
	P1	P1-AC	P2	P2-AC	(ΔP)	ΔP/P1	P1	P1-AC	P2	P2-AC	(ΔP)	ΔP/P1
$T\text{-}NH_4^+$	7.1750	0.4314	6.8622	0.4135	-0.3128	-4%	5.5905	0.3409	4.9923	0.3068	**-0.5981**	-11%

8/8							8/10					
SGS2	With denuder		Unit	($\mu g\ m^{-3}$)	P2-P1			unit	($\mu g\ m^{-3}$)		P2-P1	
	P1	P1-AC	P2	P2-AC	(ΔP)	ΔP/P1	P1	P1-AC	P2	P2-AC	(ΔP)	ΔP/P1
$T\text{-}NH_4^+$	6.5970	0.3984	6.2541	0.3788	-0.3429	-5%	2.5018	0.1648	2.2901	0.1528	**-0.2117**	-8%

4.1 $PM_{2.5}$ Mass Closure and Chemical Composition

Before discussing the seasonal variation in $PM_{2.5}$ chemical composition, it is important to determine the extent of aerosol mass closure for the species detected. This can be done by comparing aerosol reconstructed mass and gravimetric mass. As shown in Chapter 3 and Appendix 1, major mass contributing species includes SO_4^{2-}, NO_3^-, NH_4^+, EC, OC and crustal material, and therefore the aerosol reconstructed mass is to be determined by the sum of these species. However, SO_4^{2-}, NO_3^-, NH_4^+, EC and OC are sampled and analyzed on quartz filter but the aerosol gravimetric mass is determined on Teflon filter. Teflon and quartz filters have different properties, and this may produce differences between gravimetric and reconstructed mass.

First, OC on Teflon filter needs to be estimated. It is known that the adsorption of volatile organic compounds (VOCs) on quartz filters and evaporation of semi-volatile organic aerosol causes biases in the particulate OC measurement. In Section 3.6, we have seen significant OC detected on backup quartz filters (both behind quartz and Teflon). On average, OC (BQ) and OC (TBQ) reaches 23 ± 12% and 49 ± 19% of OC (FQ), respectively. This suggests that quartz and Teflon filters behave differently relative to adsorbing VOC or evaporating semi-volatile OC. This artifact cannot be ignored in estimating OC on Teflon filters. OC captured by a sequential quartz-quartz filter includes particulate OC (POC, low vapor pressure OC), semi-volatile OC (SVOC), and quartz-philic VOC (QVOC) (Turpin et al., 1994; Warner et al., 2001); thus

$$OC\ (FQ + BQ) = POC\ (FQ) + SVOC\ (FQ) + SVOC\ (BQ) + QVOC\ (FQ) + QVOC\ (BQ)$$

It is assumed that POC only appear on front filter. Since Teflon generally absorbs much less VOC than quartz [*Mader and Pankow*, 2001], a sequential Teflon-quartz filter likely obtains the same POC but less QVOC, thus

$$OC\ (FT + TBQ) = POC\ (FT) + SVOC\ (FT) + SVOC\ (TBQ) + QVOC\ (TBQ)$$

Figure 4.1.1 summarizes the plausible distribution of OC on the two types of sequential filters. In case 1, QVOC >> SVOC, OC on Teflon filter, OC (FT), can be estimated by subtracting OC (TBQ) from OC (FQ), assuming QVOC (FQ) ~ QVOC (TBQ). In case 2, SVOC >> QVOC, Teflon-quartz and quartz-quartz filters would contain more equal OC, and thereby OC (FT) is better estimated by subtracting OC (TBQ) from OC (FQ) + OC (BQ). The difference between OC (FT) determined in case 1 and case 2 is exactly OC (BQ). The actual OC (FT) could be between the two extremes. There is no inarguable choice of OC. However, since in the audit experiment we did observe some OC mass moving from front filter to backup filter (Section 4.0), OC (FT) defined in the second case (the upper limit) is used hereafter as the OC on Teflon filter with the understanding that a ~ 20% uncertainty may apply. To account for mass of elements such as H, O, and N in organics, *White and Roberts* [1977] proposed an average organic molecule weight per carbon weight of 1.4, and this value is widely used in the literature. Therefore, the mass of organic matter (OM) in this study is calculated by $1.4 \times$ OC (FT).

Nitrate is also volatile, and the nitrate evaporating from the single-layer Teflon filter (for mass measurement) is not re-collected by a backup filter. Therefore, the loss of nitrate could cause a deficit in the $PM_{2.5}$ gravimetric mass. Volatile nitrate detected on backup filter (behind quartz; see Section 2.2) reaches the maximum in summer when nitrate is low at 1- 2% of the $PM_{2.5}$ mass. When particulate nitrate becomes a significant

fraction of $PM_{2.5}$ in winter, the volatile nitrate on the backup filter drops to nearly zero. The deviation between reconstructed mass and gravimetric mass due to loss of nitrate is expected to be minor.

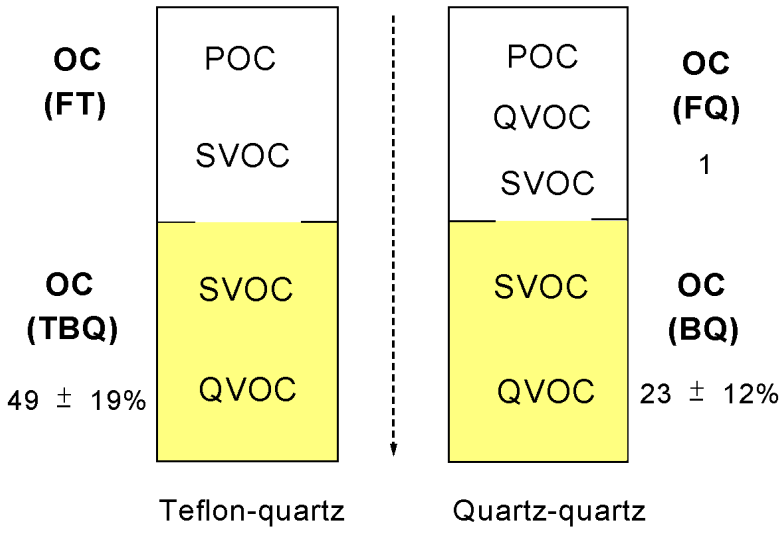

Figure 4.1.1 Illustration of the idealized distribution of OC sampled by sequential Teflon-quartz filter and quartz-quartz filter. The arrow indicates the direction of sampling flow. All abbreviations are defined in the text. In this study, OC (BQ) and OC (TBQ) are 23 ± 12% and 49 ± 19% of OC (FQ), respectively.

The mass of crustal material is estimated using Al, Si, Ca and Fe mass, as described in Section 3.7. Reconstructed mass is then determined by summing SO_4^{2-}, NO_3^-, NH_4^+, EC, OM and crustal material, and it is compared to the gravimetric mass in Figure 4.1.2. The good agreement (r^2 ~ 0.94, slope ~ 0.91, RMS difference ~ 13%) indicates a relatively complete $PM_{2.5}$ mass closure. The deviation is generally within ± 15% on low $PM_{2.5}$ days; this probably reflects analytical errors and the uncertainties in determining OC and

nitrate. A more significant negative bias that appears on high $PM_{2.5}$ days, however, could imply unidentified species. *Malm et al.* [1994] and *Rees et al.* [2002] presented similar results and suggested that water could be part of the unidentified mass. The Teflon filters were weighed at 30 - 40% relative humidity; water associated with sulfate at 30 – 40% relative humidity is expected to be minimum when thermodynamic equilibrium is reached.

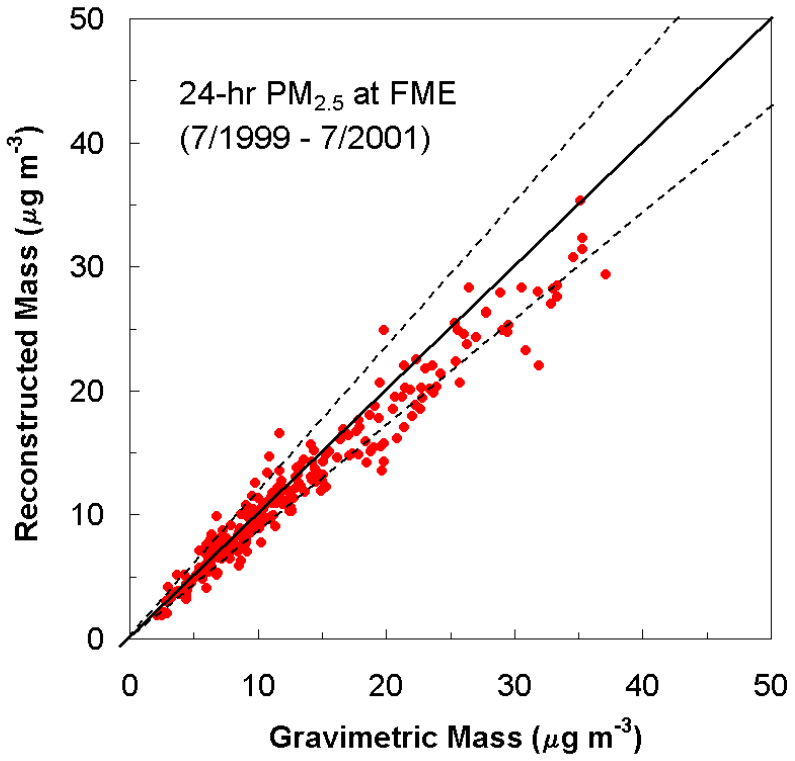

Figure 4.1.2 Comparison of 24-hr $PM_{2.5}$ gravimetric and reconstructed mass at FME. The solid and dashed lines indicate 1:1 and ± 15% lines, respectively. The RMS difference between the two is ~ 13%.

However, water taken up by sulfate at higher relative humidity may not be removed completely when the sample is dried (hysteresis effect). An estimate of the aerosol water content based on thermodynamic equilibrium is to be discussed further in Section 4.5. *Turpin and Lim* [2001] suggests that the OM/OC ratio in an urban environment can be higher than 1.4, and this provides another explanation for the 'missing' mass. Despite uncertainties, sulfate, nitrate, ammonium, and carbonaceous material combined explain a majority of the $PM_{2.5}$ gravimetric mass.

Time series of the 24-hr $PM_{2.5}$ chemical composition across the 9 sampling months is presented in Figure 4.1.3(a)-(c) by showing the fraction of each species with respect to the $PM_{2.5}$ gravimetric mass. Time series of the $PM_{2.5}$ gravimetric mass is also included in the figures for comparison. Clearly, strong day-to-day variations are embedded in the seasonal variations described in Chapter 3. Elevated $PM_{2.5}$ level is generally episodic, and each episode generally lasts for 2 – 4 days. On days of low $PM_{2.5}$ concentration ($PM_{2.5}$ < 5 $\mu g\ m^{-3}$), the reconstructed mass is close to or slightly higher than the gravimetric mass. This is best illustrated by the low episodes in January 2001 and July 2001 (arrow group C and D, Figure 4.1.3(b) and (c), respectively). The small difference most likely results from analytical uncertainties. In April 2000, the $PM_{2.5}$ concentration is very low most of the time; a relatively large uncertainty in the $PM_{2.5}$ mass closure is observed.

In low $PM_{2.5}$ episodes, the mass fraction of inorganic salts ($SO_4^{2-} + NO_3^- + NH_4^+$) is generally lower while carbonaceous material plays a bigger role. In high $PM_{2.5}$ episodes, however, inorganic salts dominate the $PM_{2.5}$ mass. The reconstructed mass is often lower than the gravimetric mass during these high episodes; episodes in July 1999 and October 1999 (arrow group A and B, Figure 4.1.3(a) and (b), respectively) are good examples. On

high $PM_{2.5}$ days, biases due to analytical uncertainty are expected to be minor relative to the aerosol mass, and water associated with the hydroscopic inorganic salts can partly explain the unidentified mass in the $PM_{2.5}$.

The most visible seasonal variation in the $PM_{2.5}$ chemical composition is the 'nitrate substitution'. Ammonium sulfate is most responsible for high $PM_{2.5}$ episodes in summer (mass fraction of $NH_4^+ + SO_4^{2-} > 50\%$ in summer). The mass fraction of nitrate is very low in summer but becomes significant in fall, spring, and winter. In the second half of January 2000, for example, the total mass fraction of sulfate plus nitrate remained nearly constant (~ 55%), but the mass fraction of sulfate varies. This means that nitrate took over when sulfate is low. A late episode in this month is actually driven by nitrate (Figure 4.1.3(a)). As described in Section 3.0, low temperature persisted in the second half of January 2000, and this could favor the formation of particulate nitrate. More available ammonium due to low sulfate can increase the chance of forming ammonium nitrate as well. A similar phenomenon is also observed in January 2001. Compared to sulfate and nitrate, the mass of carbonaceous material is more constant throughout a year, and therefore carbonaceous material can account for > 50% of the $PM_{2.5}$ mass on low $PM_{2.5}$ days. The mass fraction of carbonaceous material (EC + OM) is generally higher in fall and spring; this may be due to relatively low concentrations of both sulfate and nitrate.

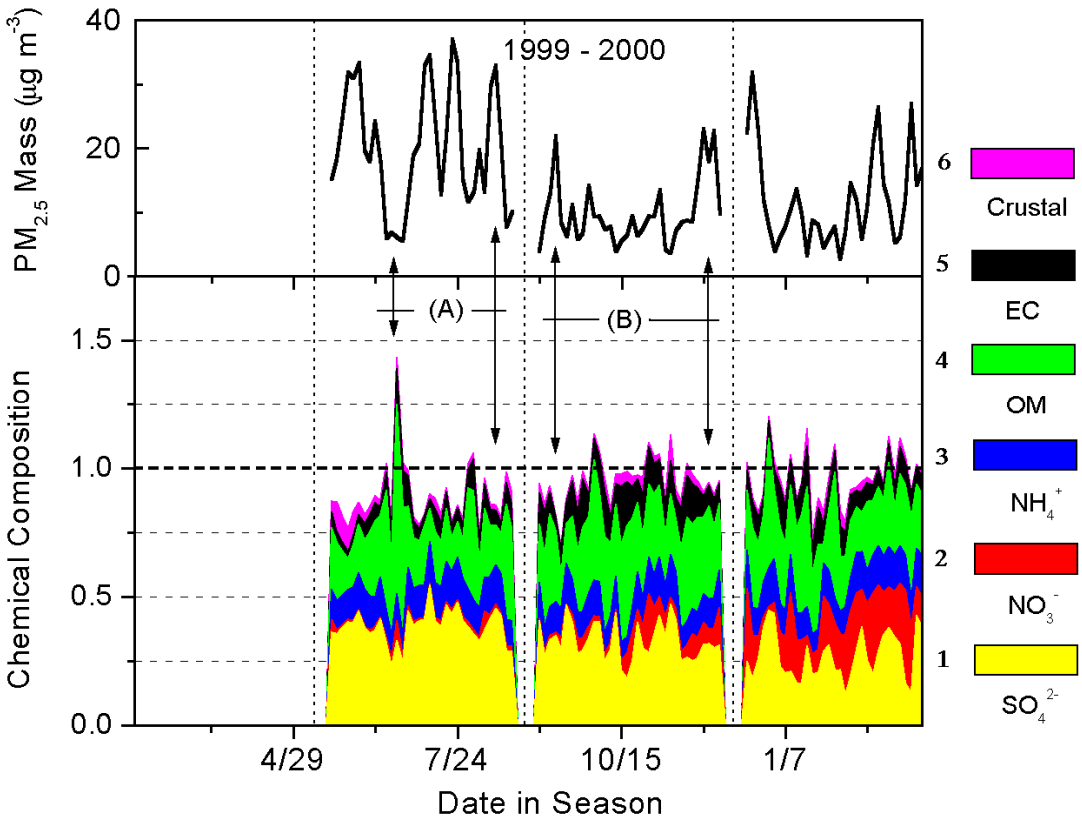

Figure 4.1.3(a) Time series of 24-hr $PM_{2.5}$ gravimetric mass concentration (upper panel) and chemical composition (lower panel) at FME during 1999 – 2000. Color layers, from bottom up, indicate SO_4^{2-}, NO_3^-, NH_4^+, OM, EC, and crustal material, respectively.

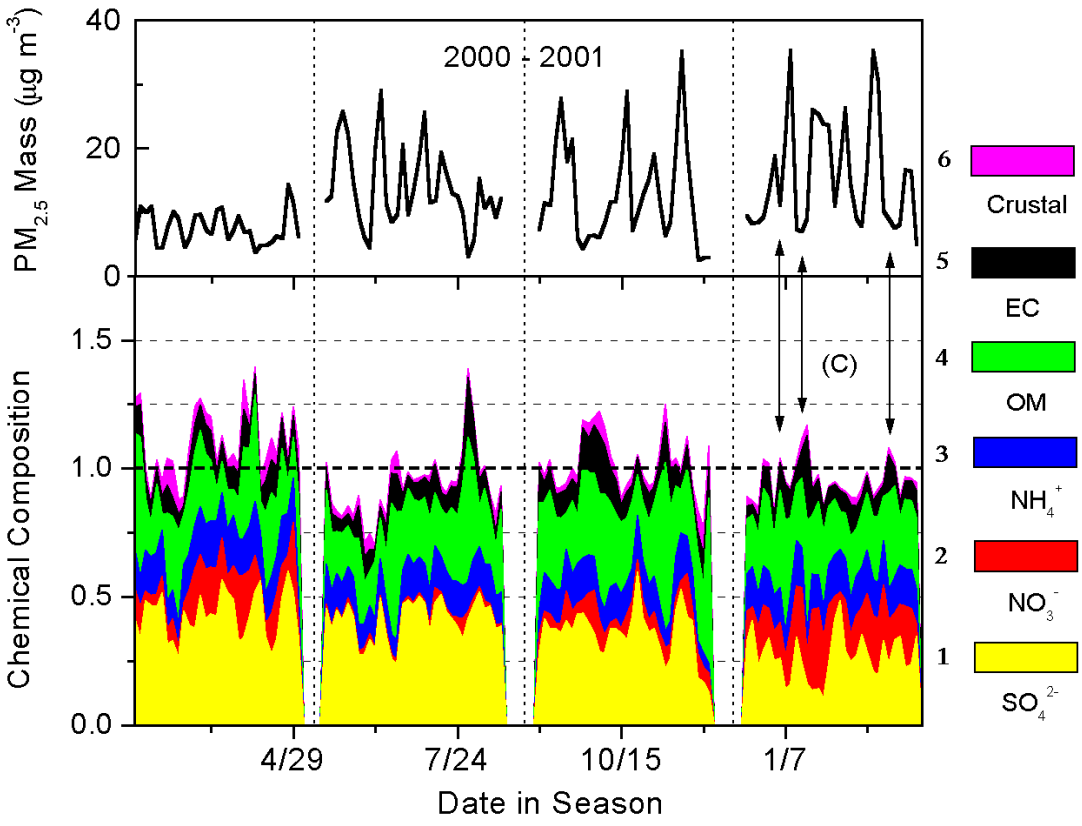

Figure 4.1.3(b) Time series of 24-hr $PM_{2.5}$ gravimetric mass concentration (upper panel) and chemical composition (lower panel) at FME during 2000 – 2001. Color layers, from bottom up, indicate SO_4^{2-}, NO_3^-, NH_4^+, OM, EC, and crustal material, respectively.

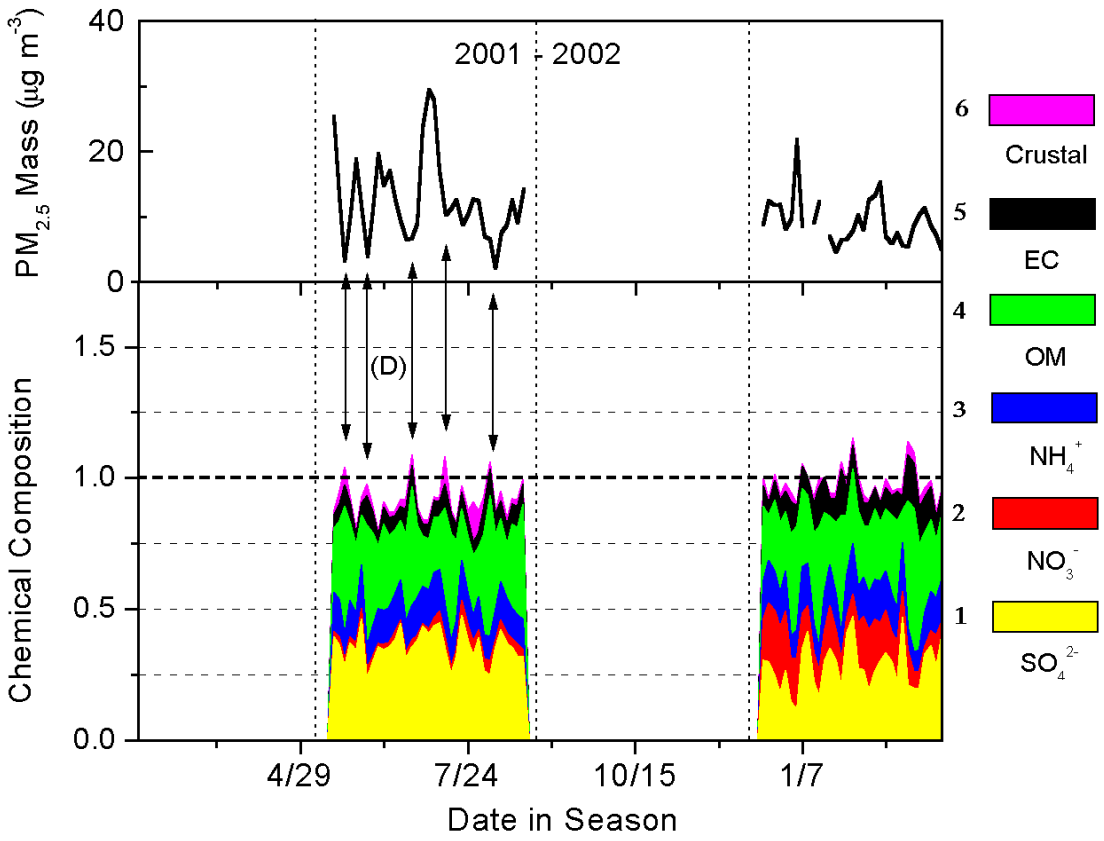

Figure 4.1.3(c) Time series of 24-hr $PM_{2.5}$ gravimetric mass concentration (upper panel) and chemical composition (lower panel) at FME during 2001 – 2002. Color layers, from bottom up, indicate SO_4^{2-}, NO_3^-, NH_4^+, OM, EC, and crustal material, respectively.

4.2 Inorganic Aerosol: Ammonium-Sulfate-Nitrate System

Conventionally, the aerosol inorganic fraction includes the entire aerosol mass except carbonaceous material. Major inorganic species in aerosol are water, salts, minerals, fly ashes, and trace metals, and they usually account for more than half of the fine aerosol mass in urban or rural atmospheres. Inorganic salt is of particular concern in precipitation chemistry since it can dissolve in cloud or rain droplets, changing the acidity of precipitation. Soluble ions measured at FME include SO_4^{2-}, NO_3^-, NH_4^+, Na^+, K^+, and Cl^-, which are commonly detected in precipitation [e.g., *NADP*, 2000]. Figure 4.2.1 shows the molar concentrations of these ions and the gaseous counterparts NH_3 and HNO_3 in our

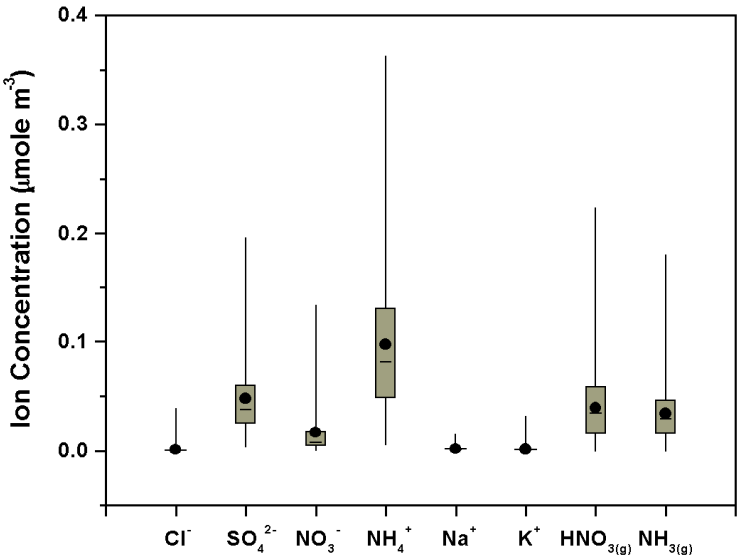

Figure 4.2.1 Molar concentrations of ions measured at FME. Statistics are based on 24-hr data acquired in the first 8 intensive months. Mean values are indicated by solid circles and medians by short dashes. Boxes indicate the quartiles and vertical bars indicate the maximum and minimum.

first eight sampling months. For most of the time Na^+, K^+, and Cl^- concentrations are so low that they have little impact on the mass and charge balance in the inorganic system. Therefore, the $PM_{2.5}$ inorganic fraction can be simplified as an NH_4^+-SO_4^{2-}-NO_3^- system.

Quite a few compounds could exist in the NH_4^+-SO_4^{2-}-NO_3^- system, such as NH_4NO_3, $(NH_4)_2SO_4$, NH_4HSO_4, $(NH_4)_3H(SO_4)_2$, and $(NH_4)_3NO_3SO_4$. These compounds can either be in the form of solid crystal or become liquid solution by absorbing water vapor in the atmosphere, depending on ambient temperature and relative humidity. As shown in Figure 4.2.2, the molar ratio of the basic ion (NH_4^+) over acidic ion ($SO_4^{2-} \times 2 + NO_3^-$) is generally between 0.5 and 1 (mean ratio ~ 0.65), and this suggests unneutralized H^+ that would leads to slightly acidic fine aerosols at FME.

This system can be expanded to include $HNO_{3(g)}$, $NH_{3(g)}$ and $H_2O_{(g\ \&\ aq)}$. $H_2SO_{4(g)}$ has a very low saturation vapor pressure over a H_2SO_4-H_2O solution at all ambient conditions and therefore always condenses into the aqueous phase. If the system has reached a thermodynamic equilibrium, the gas/liquid/solid partitioning of T-NO_3 ($NO_3^- + HNO_3$) and T-NH_4^+ ($NH_4^+ + NH_3$) can, in principle, be determined by equilibrium constants that are usually just functions of ambient temperature. It could be more complicated when some aerosol properties are considered: 1) aerosols are not homogeneous internal mixtures, 2) equilibrium constants (e.g., Henry's Law constant) depend on aerosol size, especially for submicrometer particles that have a higher surface tension, and 3) the equilibrium changes once a salt particle is internally mixed with carbonaceous material (e.g. OC can be hydroscopic or hydrophobic). In this study, an innovative aerosol thermodynamic model, ISORROPIA, is used to study the chemical equilibrium in the aerosol inorganic system. ISORROPIA [*Nenes et al.*, 1998; 1999] is a bulk aerosol model

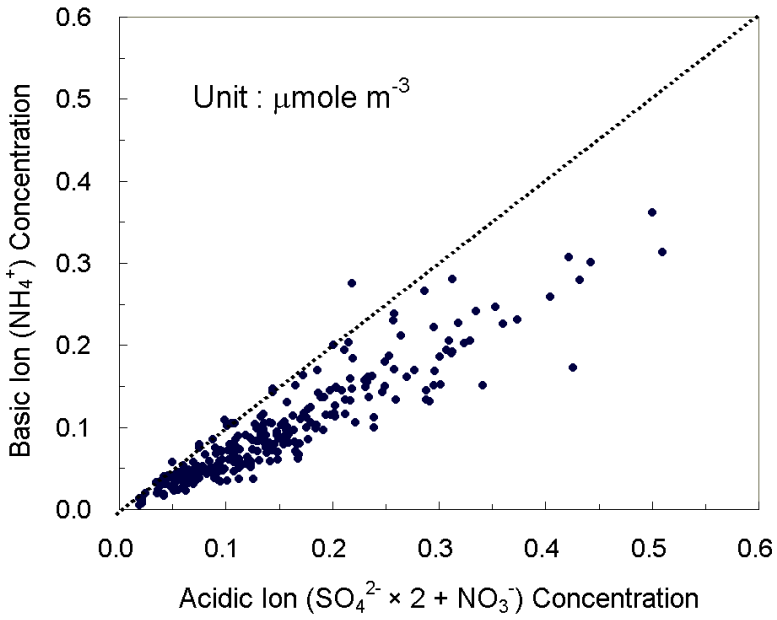

Figure 4.2.2 Comparison of basic and acidic ion molar concentrations at FME. Data used are 24-hr averages in the first 8 intensive months. The dashed line indicates the 1:1 line. Regression slope is ~ 0.65.

designed for a simplified Na^+-NH_4^+-Cl^--SO_4^{2-}-NO_3^--H_2O system. Aerosol is assumed to be internally mixed, meaning that all particles of the same size have the same chemical composition. The possible species for each phase are:

Gas phase:	NH_3, HNO_3, HCl, H_2O
Liquid phase:	NH_4^+, Na^+, H^+, Cl^-, NO_3^-, SO_4^{2-}, HSO_4^-, OH^-, H_2O, $HNO_{3(aq)}$, $HCl_{(aq)}$, $NH_{3(aq)}$, H_2SO_4.
Solid phase:	NH_4SO_4, NH_4HSO_4, $(NH_4)_3H(SO_4)_2$, NH_4NO_3, NH_4Cl, NaCl, $NaNO_3$, $NaHSO_4$, Na_2SO_4.

ISORROPIA considers equilibrium constants of all possible reactions and the mutual deliquescence relative humidity (MDRH) of a salt mixture [*Tang and Munkelwitz*, 1993] to calculate the amount of water taken up by an aerosol. ISORROPIA can handle two types of inputs:

1. The total concentration (i.e., gas and aerosol together) of sodium, ammonia, nitric acid, and sulfuric acid together with the ambient relative humidity and temperature. The model calculates the gas/aerosol partitioning of the species. This type of problem is termed 'forward problem'.
2. The concentration of sodium, ammonium, nitrate, and sulfate in the aerosol phase, together with ambient relative humidity and temperature. The model calculates the concentration of their gas-phase partners. This type of problem is termed 'reverse problem'.

Since gaseous HNO_3 and NH_3 were measured at FME, it is more convenient for us to run the 'forward' approach. The Cl^- and Na^+ concentrations are low, and Cl^- contains significant analytical uncertainties; thereby they are excluded in the calculation. In other

words, we set the Cl^- and Na^+ concentrations zero in the ISORROPIA input. The chemical reactions and equilibrium constants used are summarized:

Equilibrium relation	Constant expression	Equilibrium constant[a] K(298.15)	a	b	Unit
$HSO_4^-(aq) = H^+(aq) + SO_4^{2-}(aq)$	$\frac{[H^+][SO_4^{2-}]\gamma_{H^+}\gamma_{SO_4^{2-}}}{[HSO_4^-]\gamma_{HSO_4^-}}$	1.015×10^{-2}	8.85	25.14	mol/kg
$NH_3(g) = NH_3(aq)$	$\frac{[NH_3(aq)]\gamma_{NH_3}}{P_{NH_3}}$	57.639	13.79	−5.39	mol/kg atm
$NH_3(aq) + H_2O(aq) = NH_4^+(aq) + OH^-(aq)$	$\frac{[NH_4^+][OH^-]\gamma_{NH^+}\gamma_{OH^-}}{[NH_3(aq)]\gamma_{NH_3}a_w}$	1.805×10^{-5}	−1.50	26.92	mol/kg
$HNO_3(g) = H^+(aq) + NO_3^-(aq)$	$\frac{[H^+][NO_3^-]\gamma_{H^+}\gamma_{NO_3^-}}{P_{HNO_3}}$	2.511×10^{6}	29.17	16.83	mol^2/kg^2 atm
$H_2O(aq) = H^+(aq) + OH^-(aq)$	$\frac{[H^+][OH^-]\gamma_{H^+}\gamma_{OH^-}}{a_w}$	1.010×10^{-14}	−22.52	26.92	mol^2/kg^2
$(NH_4)_2SO_4(s) = 2NH_4^+(aq) + SO_4^{2-}(aq)$	$[NH_4^+]^2[SO_4^{2-}]\gamma^2_{NH_4^+}\gamma_{SO_4^{2-}}$	1.817	−2.65	38.57	mol^3/kg^3
$NH_4NO_3(s) = NH_3(g) + HNO_3(g)$	$P_{NH_3}P_{HNO_3}$	5.746×10^{-17}	−74.38	6.12	atm^2
$NH_4HSO_4(s) = NH_4^+(aq) + HSO_4^-(aq)$	$[NH_4^+][HSO_4^-]\gamma_{NH_4^+}\gamma_{HSO_4^-}$	1.383×10^{4}	−2.87	15.83	mol^2/kg^2
$(NH_4)_3H(SO_4)_2(s) = 3NH_4^+(aq) + HSO_4^-(aq) + SO_4^-(aq)$	$[NH_4^+]^3[HSO_4^-][SO_4^{2-}]\gamma^3_{NH_4^+}\gamma_{HSO_4^-}\gamma_{SO_4^-}$	29.72	−5.19	54.40	mol^5/kg^5

[a]Constants a and b are in

$$K = K(T_o)\left[a\left(\frac{T_o}{T} - 1\right) + b\left(1 + \ln\left(\frac{T_o}{T}\right) - \frac{T_o}{T}\right)\right],$$

where $T_o = 298$ K.

(This table is revised from *Kim et al.* [1993], and γ indicates the activity coefficient for each ionic species in the aqueous phase.)

When RH is lower than the deliquescence point of every solid species considered, all the aqueous phase reactions can be ignored and the aerosol phase would only consists of solids. Therefore, relative humidity is an essential parameter determining the mass partitioning between aerosol and gaseous phases. In practice, how to select relative

humidity and temperature representative for a particular day is another difficulty in running ISORROPIA using the 24-hr average $PM_{2.5}$ data. Equilibrium constants K_{eq} depend on ambient temperature, and they are calculated in the model. Generally, K_{eq} varies nearly linearly with temperature in the course of a day so that the daily mean temperature can be a good choice for the model input. The phase equilibrium, however, depends highly nonlinearly (like a step-function) on relative humidity (RH), and the transition occurs at a deliquescence relative humidity (DRH). DRH is the relative humidity at which a solid particle starts taking up water vapor to form aqueous solution. The aerosol water content can be estimated differently by choosing different relative humidity for a particular day [*Malm*, 1994]. In this study, without knowledge of the diurnal variation of aerosol chemical composition, we decided to use the daily mean RH as the ISORROPIA model input, and this could cause a slight underestimation of the aqueous-phase aerosol.

Figure 4.2.3 shows the gaseous HNO_3 and NH_3 as well as aerosol NO_3^- and NH_4^+ measured at FME during four seasonally-representative months in 2000 - 2001. The analytical uncertainty in each single measurement is also presented in the figure. The sum of HNO_3 and NO_3^- ($T\text{-}NO_3^-$) and the sum of NH_3 and NH_4^+ ($T\text{-}NH_4^+$) along with SO_4^{2-}, temperature and RH are used as the ISORROPIA inputs to calculate the gas/aerosol partitioning of $T\text{-}NO_3^-$ and $T\text{-}NH_4^+$ and the amount of water associated the inorganic system. The solid lines in Figure 4.2.3 indicate the calculated aerosol and gas concentrations. The concentration predicted by ISORROPIA generally falls within the uncertainty of the measurement. This close agreement suggests that the aerosol inorganic system is generally at thermodynamic equilibrium. A larger difference occurs in spring

and fall, and this could be explained by a more unstable meteorology that deviates the system from equilibrium. For example, gas-phase NH_3 and HNO_3 are thermodynamically favored at a rapidly decreasing RH following precipitation, but due to the hysteresis effect NH_4NO_3 could remain in the aqueous phase. At FME, aerosol phase (particulate) ammonium always dominates the total ammonium because the air is rich in sulfate and ammonia tends to neutralize the sulfate first. Gaseous ammonia does appear on low sulfate days in summer, spring, and fall but rarely in winter when ammonia seems to be

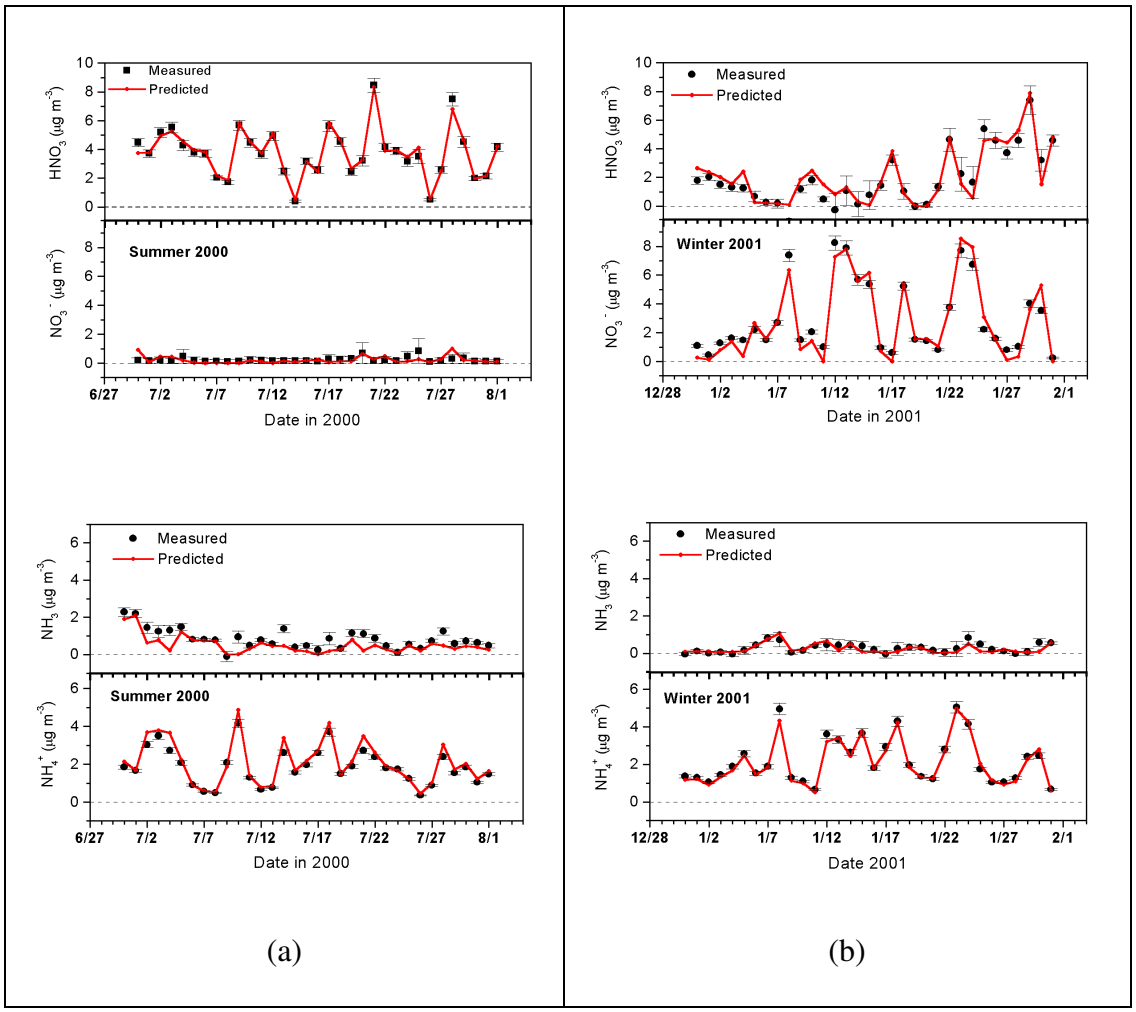

Figure 4.2.3 Measured and predicted (by ISORROPIA) concentration of gaseous HNO_3 and NH_3 as well as aerosol NO_3^- and NH_4^+ in (a) summer 2000 (b) winter 2001 (c) fall 2000 (d) spring 2000.

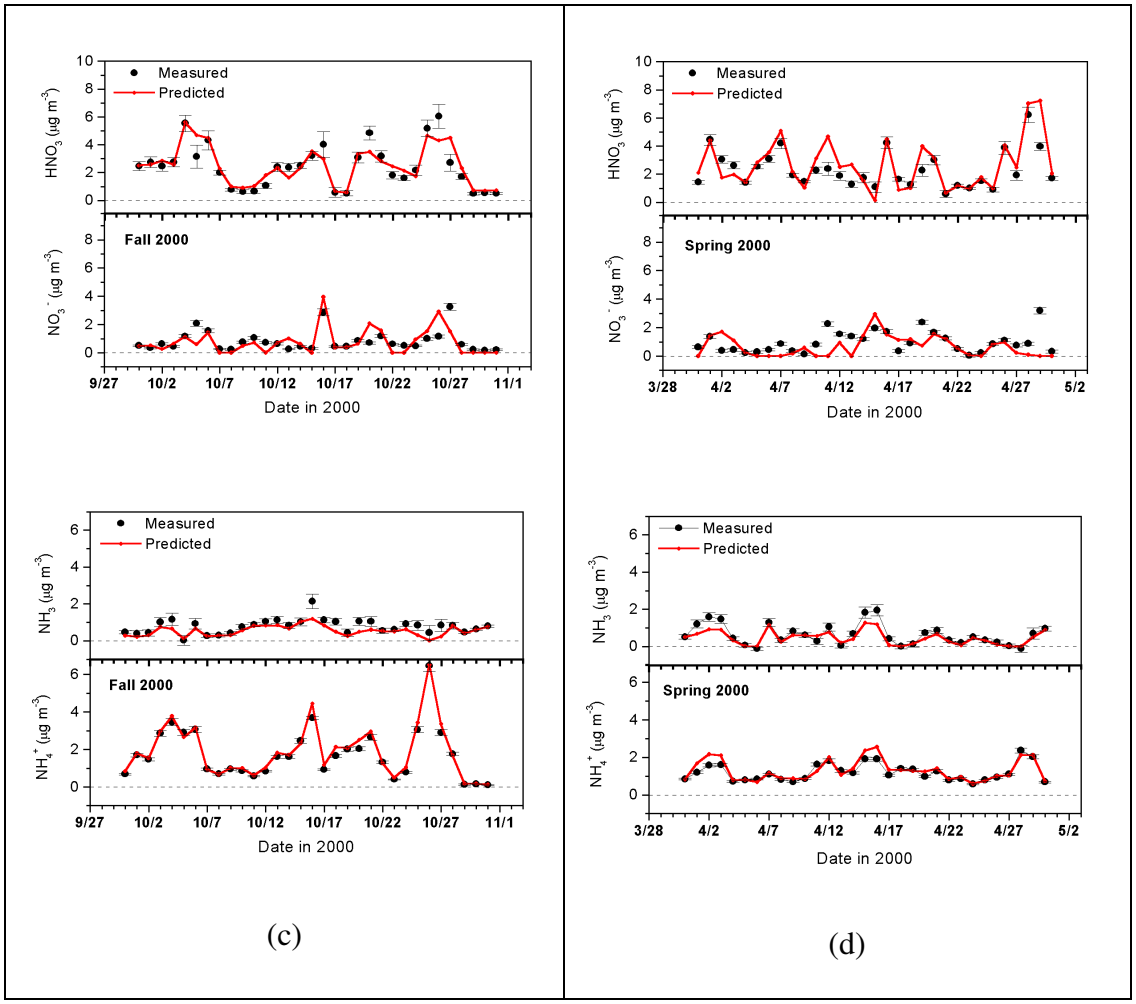

Figure 4.2.3 Measured and predicted (by ISORROPIA) concentration of gaseous HNO_3 and NH_3 as well as aerosol NO_3^- and NH_4^+ in (a) summer 2000 (b) winter 2001 (c) fall 2000 (d) spring 2000.

depleted by nitric acid to form particulate ammonium nitrate. Nitric acid overwhelmingly dominates the total nitrate in summer and coexists with ammonia. In winter, however, particulate nitrate increases and can account for more than half of the total nitrate.

Gas/particle partitioning of total nitrate is an important factor in determining the $PM_{2.5}$ mass. Figure 4.2.4 shows the particulate fraction (percentage) of total nitrate as a function

of T-NO_3^-/SO_4^{2-} ratio, T-NH_4^+/SO_4^{2-} ratio, ambient temperature, and RH based on the ISORROPIA calculations. Figure 4.2.4(a) and (b) uses parameters commonly seen during high sulfate episodes in summer, which feature high temperature and sulfate concentration. The solid diamonds in the figures indicate the high $PM_{2.5}$ days in summer 2000 with the SO_4^{2-} concentration between 6.5 and 9.5 μg m^{-3}. Aerosol NO_3^- does not form until the T-NH_4^+/SO_4^{2-} molar ratio is greater than 2. A comparison of Figure 4.2.4(a) (RH = 0.75) and (b) (RH = 0.9) indicates that the fraction of aerosol NO_3^- in T-NO_3^- increases with relatively humidity. Aerosol NO_3^- does not form at all if RH is < 0.6. Once aerosol nitrate is allowed to form, the NO_3^-/T-NO_3^- ratio depends more on T-NH_4^+ than on T-NO_3^-. At FME, sulfate dominates in summer $PM_{2.5}$ episodes. Ammonia is barely enough to neutralize the sulfate, and this explains the extremely low ammonium nitrate concentration during these episodes.

At a given T-NH_4^+ and T-NO_3^-, the fraction of aerosol NO_3^- in T-NO_3^- at equilibrium increases significantly from summer to winter due to the lower temperature (Figure 4.2.4 (c) and (d)). In winter 2001, the typical SO_4^{2-} concentration on high $PM_{2.5}$ days is lower at 3.5 - 6.5 μg m^{-3}. The T-NO_3^-/SO_4^{2-} and T-NH_4^+/SO_4^{2-} ratios on these days, as indicated by solid diamonds in Figure 4.2.4 (c) and (d), are generally higher than those in summer 2000, and this allows the formation of secondary NH_4NO_3 regardless of relative humidity.

This study contributes information for improving control strategies for $PM_{2.5}$ pollutions in the B-W corridor. Reducing T-NO_3^- in summer (e.g., via controlling NO_x emission) has little direct impact on particulate mass but may substantially reduce HNO_3. (Note that

indirect mechanisms involving gaseous reactions are not considered here.) Reducing T-NO_3^- in winter will increase the NO_3^-/T-NO_3^- ratio unless T-NO_3^- is already very low,

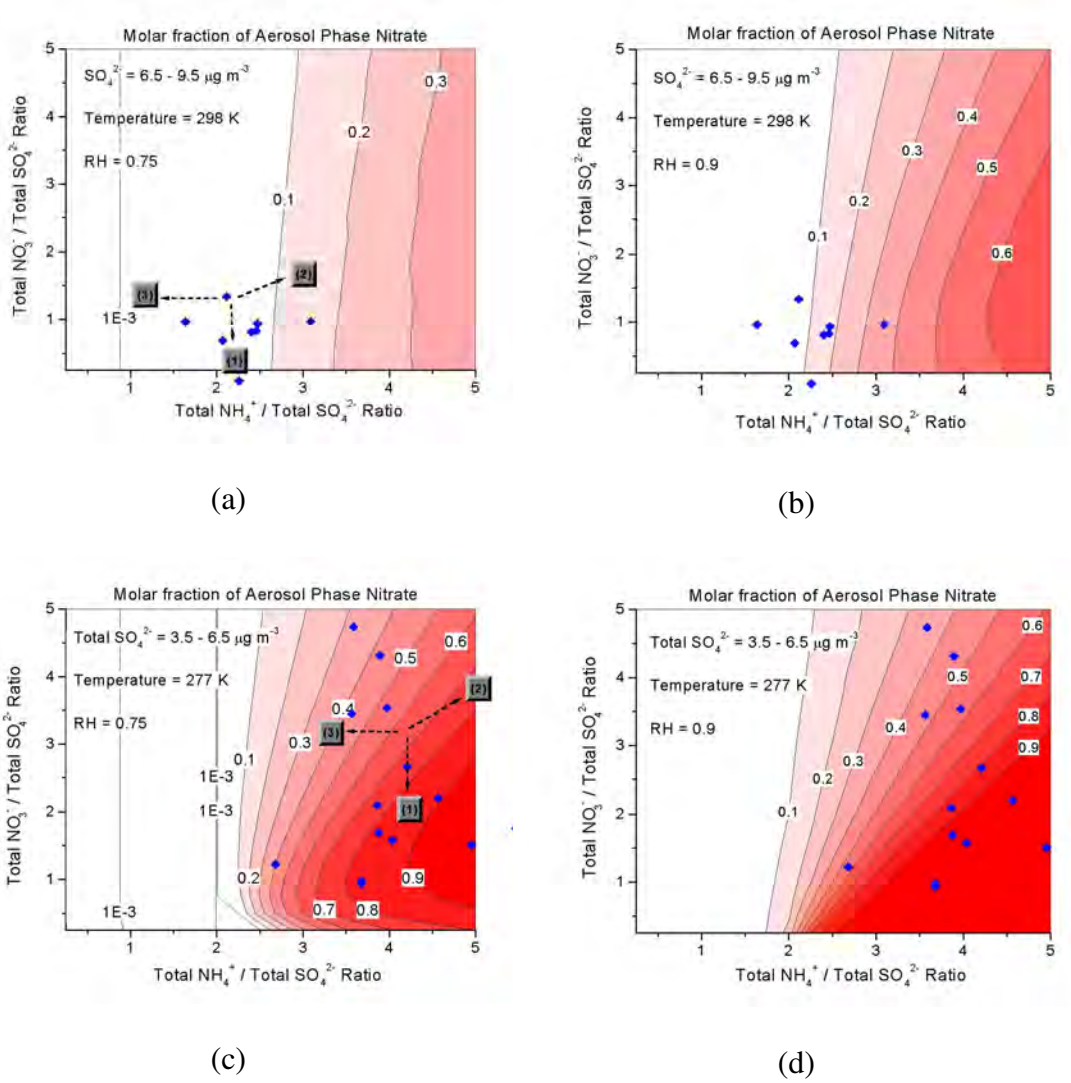

Figure 4.2.4 Molar fraction of aerosol NO_3^- in T-NO_3^- as a function of T-NO_3^-/SO_4^{2-} and T-NH_4^+/SO_4^{2-} ratios at relatively (a) high temperature, high sulfate, and low RH (b) high temperature, high sulfate, and high RH (c) low temperature, low sulfate, and low RH (d) low temperature, low sulfate, and high RH condition. Solid diamonds in (a) and (b) indicate the high $PM_{2.5}$ days in summer 2000, and solid diamonds in (c) and (d) indicate the high $PM_{2.5}$ days in winter 2001. Arrows indicate the shift of equilibrium due to (1) reducing T-NO_3^- (2) reducing SO_4^{2-} (3) reducing T-NH_4^+ concentration.

and therefore it is not effective in lowering the fine PM level, either. Reducing SO_4^{2-} (e.g. via controlling SO_2 emission) will increase the T-NO_3^-/SO_4^{2-} and T-NH_4^+/SO_4^{2-} ratio simultaneously; for PM control this is more effective in summer than in winter since in winter reducing SO_4^{2-} can increase the NO_3^-/T-NO_3^- ratio through producing more particulate NO_3^- (i.e. nitrate substitution). Under any circumstance, fine PM control will benefit from reducing ammonia emission because it can substantially reduce the particulate ammonium nitrate and ammonium sulfate in the atmosphere.

4.3 Elemental Carbon and Carbon Monoxide

Elemental carbon (EC) absorbs strongly in the visible, near UV, and near IR regions due to its graphitic microcrystalline structure [*Rosen et al.,* 1978], and therefore it is usually referred to as 'black carbon' (BC). Among aerosol species, EC contributes substantially to the absorption of radiation in the troposphere. Recent studies point out the impacts of EC on the Earth's radiation budgets, cloud properties [*Kaufman et al.,* 1997; *Ackerman et al.*, 2000; *Jacobson*, 2001] and photochemistry [*Dickerson et al.,* 1997]. An accurate emission inventory is crucial in estimating such influences of EC. *Penner* [1993] took the first step estimating the global EC emission by two different approaches. One approach is based on emission factors of various combustion processes (e.g. motor vehicle, biofuel burning, forest fire, etc) and amounts of combustion activities (e.g. fuel consumption). Similar studies were carried out by *Liousse et al.* [1996] and *Cooke et al.* [1999] with better input data. The other approach utilizes ambient EC/SO_2 ratios

observed in urban and suburban areas along with a well-established emission inventory of SO_2 to estimate EC emission. One has to assume that SO_2 and EC generally originate from the same sources proximate to the receptor sites if the second approach is used.

At FME, correlations between EC and SO_2 are weak (r^2 ~ 0.1 – 0.2), but correlation between EC and CO are much better (r^2 ~ 0.5 – 0.9) (Table 4.3.1). Most of the SO_2 emission in the highly industrialized regions results from coal/oil burning utility plants, which have substantially reduced their particulate emissions since more stringent regulations were applied. It is shown in Section 3.1 that CO at FME is highly influenced by traffic emissions, and this implies that mobile sources, which usually generate little SO_2, contribute to EC. In such a source-dominated environment, ambient concentration

Table 4.3.1 Monthly means and standard deviations of 24-hr average CO and EC measured at FME during nine season-representative months. Linear regressions of EC with CO and OC/EC ratios are included.

Sampling period	Mean CO ±1σ ($\mu g\ m^{-3}$)	Mean EC ±1σ ($\mu g\ m^{-3}$)	Linear regression fit[a]	Correlations (r^2)	OC/EC[c]
Jul. 99 (summer)	281 ± 55	1.2 ± 0.4	[EC] = 0.0067[CO] - 0.70	0.70	3.51
Oct. 99 (fall)	439 ±147	1.1 ± 0.5	[EC] = 0.0027[CO] - 0.07	0.76	2.44
Jan. 00 (winter)	468 ± 208	1.1 ± 0.7	[EC] = 0.0029[CO] - 0.35	0.84	2.68
Apr. 00 (spring)	312 ± 73	0.7 ± 0.3	[EC] = 0.0027[CO] - 0.16	0.52	3.30
Jul. 00 (summer)	301 ± 59	1.1 ± 0.4	[EC] = 0.0041[CO] - 0.14	0.48	2.98
Oct. 00 (fall)[b]	410 ± 155	1.2 ± 0.7	[EC] = 0.0033[CO] - 0.12	0.58	2.56
Jan. 01 (winter)[b]	576 ± 272	1.4 ± 0.9	[EC] = 0.0029[CO] - 0.28	0.77	2.47
Jul. 01 (summer)	234 ± 50	0.8 ± 0.3	[EC] = 0.0056[CO] - 0.51	0.68	3.84
Jan. 02 (winter)					

[a] CO concentrations are converted to $\mu g\ m^{-3}$ based on daily mean temperature before regression.
[b] Construction work going on during the intensives may have caused enhanced mobile emission.
[c] OC is determined only using front quartz filters.

of pollutant released is driven mostly by dispersion. CO, rather than SO_2, can be a good tracer for the EC emission in this region, and perhaps in the whole North America. Since both EC and CO have background levels, the slope of EC versus CO rather than EC/CO ratio represents the production rate of EC relative to CO. Table 4.3.1 shows that the EC/CO slope ranges from 2.7×10^{-3} to 6.7×10^{-3} and has an annual average ~ 3.5×10^{-3} g(EC)/g(CO) at FME. This ratio is compared to those observed at other locations, including the city of Boston, Shenandoah National Park, northern Indian Ocean, and Mace Head, Ireland. These studies will be discussed and the results are summarized in Table 4.3.2.

Hourly CO (by Thermo Environment Instrument Model 48, see Section 2.7) and BC (by Magee Aethalometer) were measured concurrently at an urban site in southern Boston from 1/1995 to 3/1997. The BC sampler was calibrated using a DRI SFS (similar to the SFS-2 at FME) to obtain EC defined by the IMPROVE protocol [*Oh*, 2000]. The correlation (r^2) between the 24-hour EC and CO ranges from 0.5 to 0.7 and is generally stronger in fall and winter. The EC/CO slope at the Boston site is similar to that at FME (Table 4.3.2). Both of them indicate a higher EC/CO slope in summer. The emission of EC versus CO in the metropolitan Northeast likely ranges from 1 : 150 to 1 : 300.

CO at Shenandoah National Park was measured with a trace-level CO detector (Thermo Environment Instrument Model 48C) [*Hallock-Waters et al.*, 1999] while EC was measured as part of the IMPROVE network [*Malm et al.*, 1994]. The Shenandoah site is very rural and generally removed from any significant local source [*Poulida et al.*, 1991]. According to the data acquired between 12/1994 to 12/1997, a good correlation (r^2 ~ 0.6) between EC and CO occurs in summer with an EC/CO slope ~ 3.4×10^{-3}, slightly lower

that at FME and Boston. In summer, EC and CO at Shenandoah is probably dominated by long-range transport from upwind source regions (e.g., the US Midwest), and the lower EC/CO slope could reflect the shorter atmospheric lifetime of EC (days to weeks) relative to CO (1 – 3 months). The correlation of EC with CO is weak in other seasons, especially in winter, suggesting strong influences from other sources. One of the major suspects is residential wood burning. According to the National Emission Trend 1996 [*USEPA*, 2000], the fraction of CO emission from residential wood burning is relatively high in Virginia (13%) and West Virginia (10%). Burning wood for heat is more popular in rural areas during wintertime, and it could produce a much lower EC/CO ratio. This explains the weaker correlation and slope of EC versus CO at the Shenandoah site in winter. The wood-burning source is to be discussed further in Section 5.4.

Table 4.3.2 Linear regressions and correlations of EC versus CO measured at Boston, Shenandoah, Ireland, and Indian Ocean. Unit is μg m^{-3} for both EC and CO. (See text for references.)

Sampling locations	Linear regression fit of EC and CO	Correlations (r^2)
Boston, MA (summer, 95 – 96)	[EC] = 0.0048[CO] - 1.03	0.58
Boston, MA (fall, 95 – 96)	[EC] = 0.0035[CO] - 0.34	0.69
Boston, MA (winter, 95 – 97)	[EC] = 0.0029[CO] - 0.08	0.67
Boston, MA (spring, 95 – 96)	[EC] = 0.0023[CO] - 0.00	0.52
Shenandoah, VA (summer, 95 – 97)	[EC] = 0.0034[CO] - 0.28	0.60
Shenandoah, VA (fall, 95 – 97)	[EC] = 0.0035[CO] - 0.29	0.30
Shenandoah, VA (winter, 94 – 97)	[EC] = 0.0013[CO] - 0.05	0.17
Shenandoah, VA (spring, 95 – 97)	[EC] = 0.0024[CO] - 0.19	0.23
Northern Indian Ocean (spring, 99)	[EC] = 0.0125[CO] - 1.23	0.74
Mace Head, Ireland (spring, 92)	[EC] = 0.0033[CO] - 0.48	0.70

The comparison of EC/CO slopes is extended to Europe and south Asia. The BC at Mace Head, Ireland was also measured by a Magee Aethalometer [*Jennings et al.*, 1996], but it was not compared to the DRI instruments. *Jennings et al.* [1996] used an absorption efficiency of 19 m^2 g $(EC)^{-1}$ to calculate EC from BC. A strong correlation between EC and CO is observed during a severe pollution episode in which air plumes originate from the Ireland and United Kingdom. The EC/CO slope is found to be 3.3×10^{-3}. Considering uncertainties in the absorption efficiency (possibly 7 – 19 m^2 $g(EC)^{-1}$), the EC/CO slope could range from 3.3×10^{-3} to ~ 7×10^{-3}, close to that reported in the U.S. Northeast. The EC and CO over Indian Ocean were measured during the Indian Ocean Experiment (INDOEX) [*Neususess et al.*, 2001; *Stehr et al.*, 2001]. The sampling substrate and analytical method for EC is different from the DRI-TOR technique but should be in reasonable agreement. Again EC is well correlated to CO. However, the EC/CO slope is high at 12.5×10^{-3}, suggesting a very different emission characteristic in this part of the developing world. A more detailed survey of CO and EC emission from south Asia can be found in *Dickerson et al.* [2001].

To investigate if the emission from mobile sources, including diesel and gasoline engines, is the dominant contributor to EC and CO at FME, we compare the ambient EC/CO and EC/OC ratios with the EC/CO and EC/OC ratios derived from tunnel/dynamometer studies. Table 4.3.3 summarizes the typical results in these studies. Even though EC and OC were all measured using filter-based methods, sampling artifacts mentioned earlier prevent very reliable inter-comparisons. However, these results generally suggest that 1) when traveling the same mileage, diesel vehicles produce tens to hundreds times more EC but much less CO than gasoline vehicles; thus EC/CO ratio in

diesel exhaust is much higher, 2) EC/CO ratio from diesel vehicle is generally higher than the ambient values, while that from gasoline vehicle is lower, and 3) diesel emission (both EC and CO) tends to increase in summer while gasoline vehicles emit stronger in winter. Moreover, older vehicles tend to emit more gaseous and particulate pollutants. For example, gasoline vehicles manufactured in 1971 - 1980 can produce 100 times more particulate matter than vehicles manufactured in 1991 - 1996 [*Cadle et al.*, 1999].

Table 4.3.3 Mobile CO, EC, and OC emission measured in recent tunnel and dynamometer studies. HD means heavy-duty diesel vehicles.

Sampling location (type)	Fraction of HD	CO emission ($g\ km^{-1}$)	EC emission ($mg\ km^{-1}$)	EC/CO (10^{-3})	OC/EC
San Francisco, CA (tunnel, 8/21/1996)[a]	0.002	-	-	0.4	-
San Francisco, CA (tunnel, 8/28/1996)[a]	0.048	-	-	3.1	-
San Francisco, CA (tunnel, 7/22/1997)[b]	0.037	-	-	3.1	0.33
San Francisco, CA (tunnel, 8/1/1997)[b]	0.003	-	-	0.4	1.45
Pennsylvania (tunnel, 5/22/1999, #15)[c]	0.096	2.11	24.2	11.4	-
Pennsylvania (tunnel, 5/20/1999, #10)[c]	0.277	0.79	70.8	90.0	0.29
Pennsylvania (tunnel, 5/19/1999, #4)[c]	0.830	0.33	146.0	440.0	0.52
Denver, CO (dynamometer, 7-8/1996, gasoline)[d]	0	2.14	0.40	0.2	2.86
Denver, CO (dynamometer, 1-2/1997, gasoline)[d]	0	10.57	4.18	0.4	3.57
Denver, CO (dynamometer, 7-8/1996, diesel)[d]	1	2.61	136.0	52.0	1.43
Denver, CO (dynamometer, 1-2/1997, diesel)[d]	1	1.12	99.2	88.6	0.52

[a] Data selected runs from *Miguel et al.* [1998].
[b] Data selected runs from *Kirchstetter et al.* [1999].
[c] Data selected runs from *Gertler et al.* [2001].
[d] Data for vehicles of model year 1991 – 1996 and operated in hot stabilized phase [*Cadle et al.* 1999].

There are several highways proximate to FME (Section 2.1), carrying both heavy-duty diesel and light-duty gasoline vehicles. The EC/CO ratio based on 24-hr sampling likely represents an average emission profile. The majority of traffic should consist of newer

model vehicles that comply with the stricter regulations, but emissions from a small fraction of older vehicles can be very significant. According to the 1996 Maryland Periodic Emissions Draft [*MDE*, 1999], diesel vehicles account for 4 – 7% of the total vehicle mile traveled (VMT) in Maryland. Assuming that 7% of the VMT is attributed to diesel and the emission factors obtained in *Cadle et al.* [1999] are typical, we estimate that in summer, diesel is responsible for ~ 96% of EC and ~ 8% of CO released from the mobile source. In winter, these fractions decrease to ~ 64% of EC and ~ 1% of CO. The EC/CO ratio, therefore, should be 4.55×10^{-3} in summer and 1.09×10^{-3} in winter. The predicted EC/CO ratios are generally lower than the ambient values reported at urban sites (Table 4.3.1 and Table 4.3.2) but of the same order of magnitude. The higher EC/CO ratio observed in summer can then be explained by the stronger EC emission of diesel vehicles and the weaker CO emission of gasoline vehicles. Note that ambient EC/CO ratio could be influenced by many other factors such as high emitting vehicles, road types/conditions, transport/mixing, and other sources (e.g., wood burning, forest fires, etc.). Mobile sources probably dominate the EC and CO emission in the B-W corridor, but more quantitative examinations rely on accurate emission inventory and receptor data analysis (Chapter 5).

The OC sampling has more artifacts than EC (see Section 2.2). A single OC measurement could contain an uncertainty up to 50%. The typical OC/EC ratio is 0.3 - 1.5 in the diesel exhaust and 1 - 4 in the gasoline exhaust [*Cadle et al.*, 1997, 1999; *Gillies and Gertler*, 2000; *Gillies et al.*, 2001; *Gertler et al.*, 2001]. The monthly OC/EC ratio at FME is ~ 2 – 4 and generally higher in summer (Table 4.3.1). This ratio suggests a mobile source favoring gasoline engines. A fraction of OC may result from the

formation of secondary organic aerosol in summer and wood burning (with OC/EC ratio ~ 10) in winter. These non-mobile sources usually contribute more OC than EC. At FME, the correlation between OC and EC is weaker in summer (r^2 ~ 0.3) than in winter (r^2 ~ 0.8).

The seasonal variation of EC/CO ratio observed in the mobile source and ambient air implies that temperature may influence the EC and CO emission. A scatter plot of all 24-hr EC and CO data at FME is presented in Figure 4.3.1 with ambient temperature indicated in the z-axis. Data points of the highest and lowest temperatures well depart

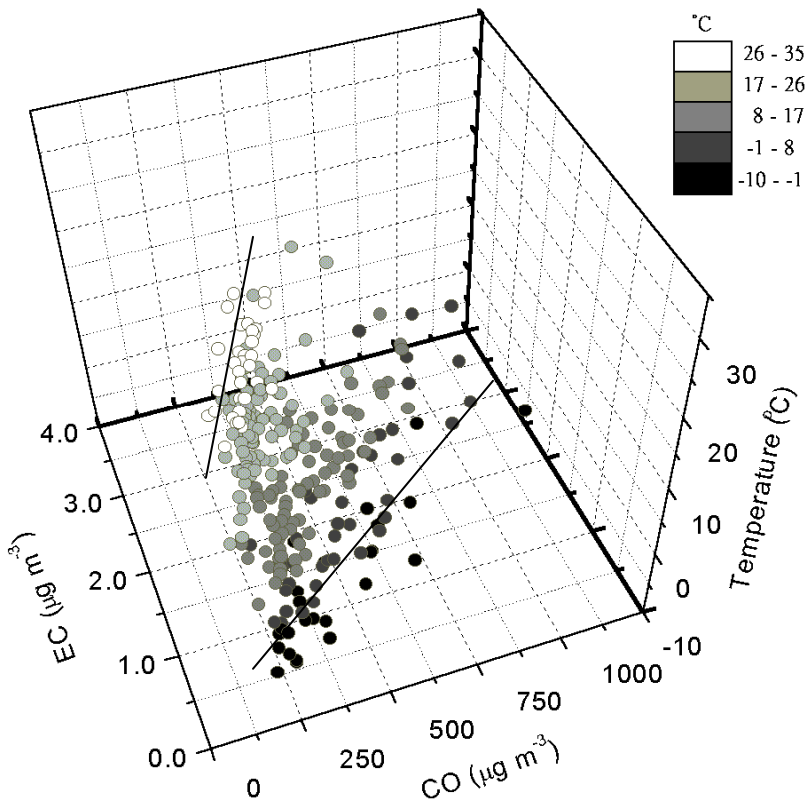

Figure 4.3.1 Scatter plot of 24-hr average EC vs. 24-hr average CO over the first eight intensive sampling months at FME. The z-axis and color code indicate daily mean temperature. The EC/CO slope generally increases with temperature (indicated by the two solid lines).

from each other. The slope of EC versus CO increases significantly when the ambient temperature exceeds 17 °C (290 K). EC emission likely increases with temperature. *Ladommatos et al.* [1998] demonstrated that in a dynamometer study, increasing the temperature of air entering diesel engines generally increases the particulate emission. *Human et al.* [1990] shows that a 20% decrease in air density due to the effect of high altitude can lead to a 2 – 4 folds increase in the particulate emission of heavy-duty diesel engines. This would be a highly nonlinear effect if it results from changes in the air-fuel ratio [*Nuti,* 1998]. The difference of ambient temperature between summer and winter in the B-W corridor can produce a 10 - 15% change in the intake air density, and this may contribute to the higher EC/CO slope observed in summer. However, a fraction of EC and CO is generated by gasoline vehicles, and the role of temperature in those processes warrants further investigation.

Despite that multiple sources are involved and source strengths may vary, the good correlation of EC with CO at FME and Boston can, at least, offer a test for the EC emission inventory of North America. The average and standard deviation of EC versus CO slopes is 0.0035 ± 0.0013 and 0.0034 ± 0.001 at FME and Boston, respectively. Annual CO emission in North America, including U.S. and Canada, is about 90 Tg (CO) [*USEPA,* 1997]. Therefore, EC emission in North America is estimated at $90 \times (0.0035 \pm 0.0013) = 0.32 \pm 0.12$ Tg (EC) yr^{-1}. This value is smaller than a previous estimate, 0.55 Tg (BC) yr^{-1} [*Cooke et. al.,* 1999] for yr. 1984, but the emission controls have become stricter since then. Regarding the EC and CO sources outside urban areas, multi-location monitoring including rural sites like Shenandoah is essential to have a better estimate of

EC emission based on EC/CO ratios. This study suggests that the temperature effect on source strength needs to be considered in such an effort.

4.4 Spatial Variations

To understand the causes of visibility reduction in the U.S. rural areas, the Interagency Monitoring of PROtected Visual Environments (IMPROVE) network has been operating ~ 150 air monitoring sites in the National Parks and Wilderness Areas across the United States since 1988. In each IMPROVE site 24-hr chemically speciated $PM_{2.5}$ is sampled twice a week year around (Wednesday and Saturday) using filter-based methods [*Malm et al.*, 1994; *IMPROVE*, 2000]. The sampling and analytical procedures at FME for the MARCH-Atlantic study (Chapter 2) generally follow the IMPROVE protocol so that data acquired can be reliably intercompared. Figure 4.4.1 shows the locations of the IMPROVE sites in the Mid-Atlantic region. Three sites geographically close to FME are Washington, Shenandoah, and Brigantine. The Washington site (WASH, 38.88°N, 77.05°W; elevation 10 m MSL), located in downtown Washington DC, is one of a few urban sites in the IMPROVE network. WASH is < 20 km south of FME, and therefore the difference between the WASH and FME data can represent the variation of aerosol concentration within the B-W corridor. The Shenandoah site (SHEN, 38.52°N, 78.44°W; elevation 1097 m MSL) is rural, located at Big Meadows, Shenandoah National Park, generally upwind of FME. This site is at the eastern side of the Appalachian Mountains and less influenced by sources below the planetary boundary layer [*Poulida et al.*, 1991]. The Brigantine site (BRIG, 39.47°N, 74.45°W; elevation 5 m MSL) is also rural, located

in the Brigantine National Wildlife Reserve, generally downwind of FME and just several kilometers from the U.S. eastern seashore. Both SHEN and BRIG are ~ 200 km from FME and WASH. The difference between SHEN/BRIG and WASH/FME observations can generally represent the contribution of the urban B-W corridor.

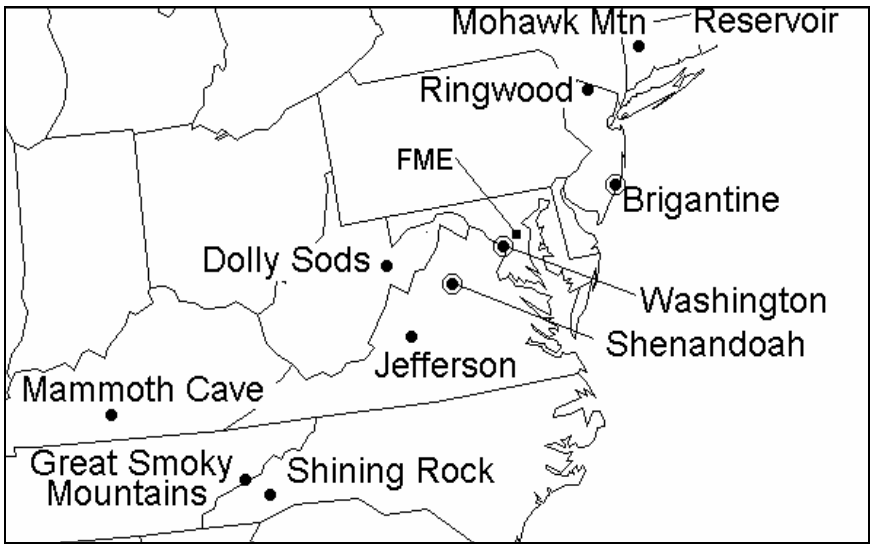

Figure 4.4.1 Locations of FME and IMPROVE sampling sites. The three sites circled are chosen for comparisons with FME in this study.

The sulfate concentrations measured at the three IMPROVE sites between 7/1999 – 2/2001 (available IMPROVE data to date) are compared to the concurrent measurement at FME (Figure 4.1.2). Close agreements between all sampling sites suggest a relatively well mixing of sulfate across a region ~ 400 km in diameter. In other words, the contribution of the urban corridor to aerosol sulfate could be quite limited. Sulfate is more regional than local in character. The correlation between FME and IMPROVE measurements is better in summer likely due to a few high sulfate days, but the r^2 is still good at ~ 0.7 in winter. Summertime haze is usually regional. This finding implies the crucial role of sulfate in the haze formation. Nitrate, however, seems to have a much

narrower distribution. The nitrate concentration at FME and WASH is close but substantially higher than that at SHEN and BRIG (Figure 4.4.3). The lowest nitrate level appears at upwind SHEN, suggesting that nitrate observed at FME could mostly originate inside the B-W corridor (or the greater Philadelphia-Washington corridor). The source of nitrate is most likely to be traffic emission (Section 3.4). A moderate correlation between nitrate at FME and BRIG corroborates the downwind transport.

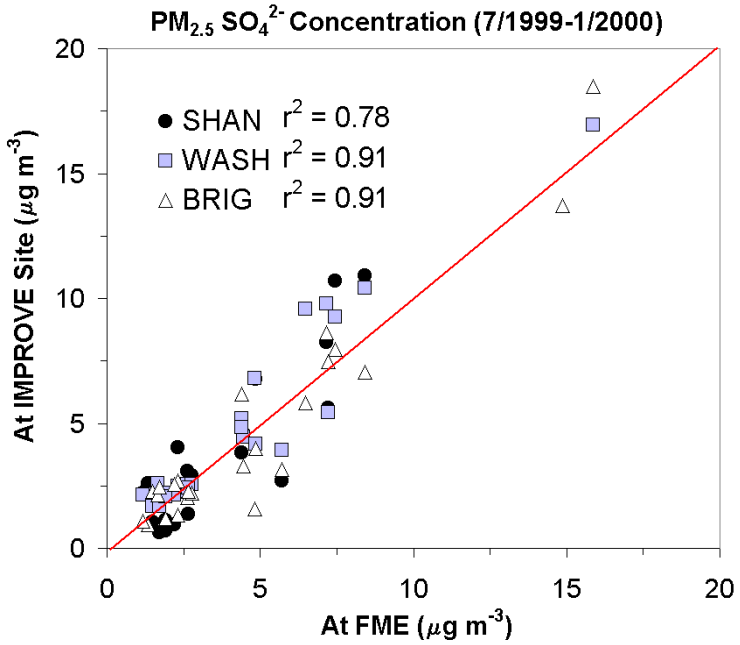

Figure 4.4.2 Scatter plot of 24-hr sulfate concentration at FME versus concurrent measurements at three IMPROVE sites in the Mid-Atlantic region. The solid line indicates 1 : 1 correspondence.

The EC distribution is somewhat like nitrate (Figure 4.4.4). The EC concentration at FME and WASH is close to but generally higher than that at SHEN and BRIG. As mentioned in Section 3.6, EC is likely dominated by traffic emission as well so that EC and nitrate could share a common or co-located source. The aerosol OC (only that from front quartz filter since the IMPROVE network does not use backup filter.) distribution

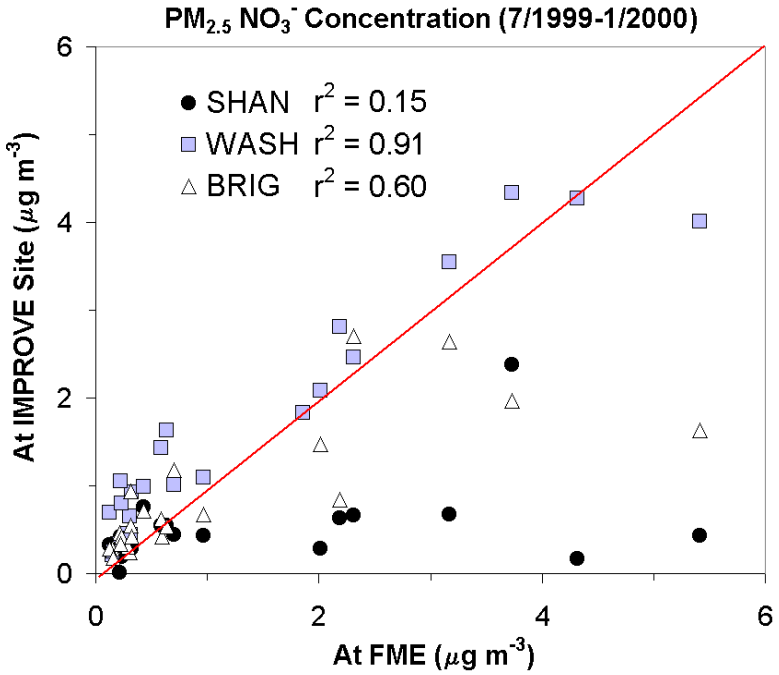

Figure 4.4.3 Scatter plot of 24-hr nitrate concentration at FME versus concurrent measurements at three IMPROVE sites in the Mid-Atlantic region. The solid line indicates 1 : 1 correspondence.

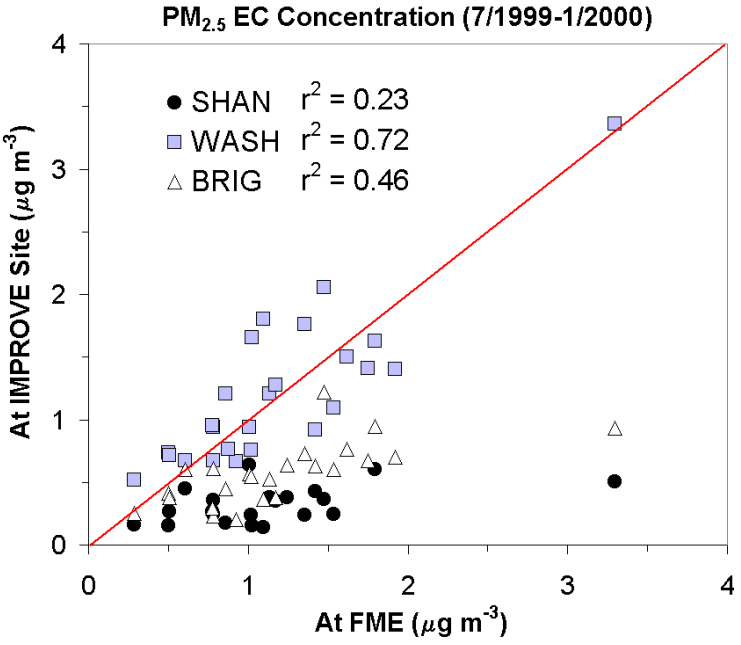

Figure 4.4.4 Scatter plot of 24-hr EC concentration at FME versus concurrent measurements at three IMPROVE sites in the Mid-Atlantic region. The solid line indicates 1 : 1 correspondence.

is similar to EC (Figure 4.4.5). However, a moderate correlation of OC at FME with those at SHEN and BRIG implies some regional OC, though emissions from the urban corridor could still dominate. The regional OC could result from upwind anthropogenic or biogenic sources (e.g., wood burning, plant wax, secondary OC, etc).

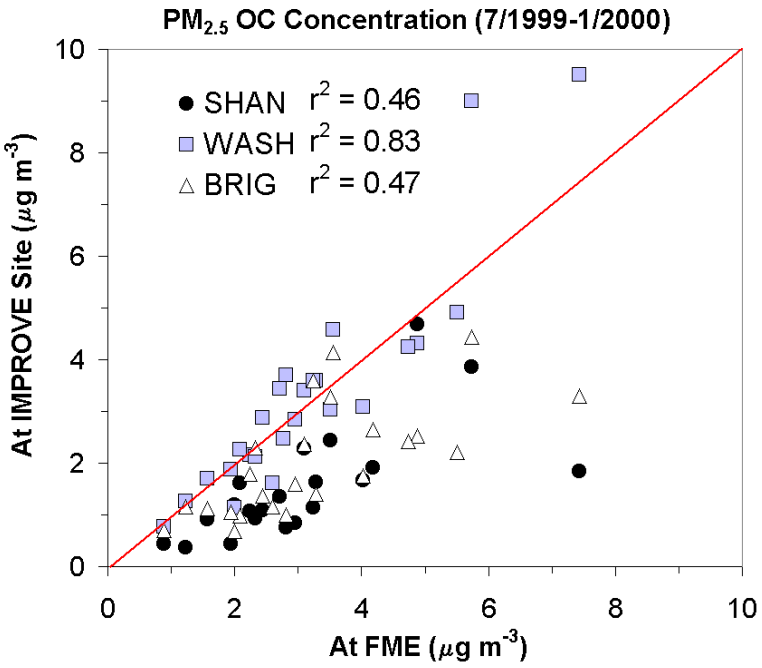

Figure 4.4.5 Scatter plot of 24-hr OC concentration at FME versus concurrent measurements at three IMPROVE sites in the Mid-Atlantic region. The solid line indicates 1 : 1 correspondence.

The crustal material concentration is determined using the empirical formula described in Section 3.7. As shown in Figure 4.4.6, the crustal material concentration remains < 1 μg m^{-3} except on one day (7/3/1999) when it is much higher than the average at every site. The crustal material level is likely driven by special and rare events. Even if the special day (7/3/1999) is excluded, the crustal material concentrations at the four sites are still close and correlated to each other. In other words, crustal material is more regional in

nature. The anthropogenic activities in the corridor can generate substantial dust, but it is primarily in the coarse-particle mode. The fine-mode crustal material in the Mid-Atlantic region, however, seems to originate from more distant sources. For example, air parcel back trajectories on 7/3/1999 link the high-concentration crustal material to the long-range transport of Saharan dust (Section 5.3).

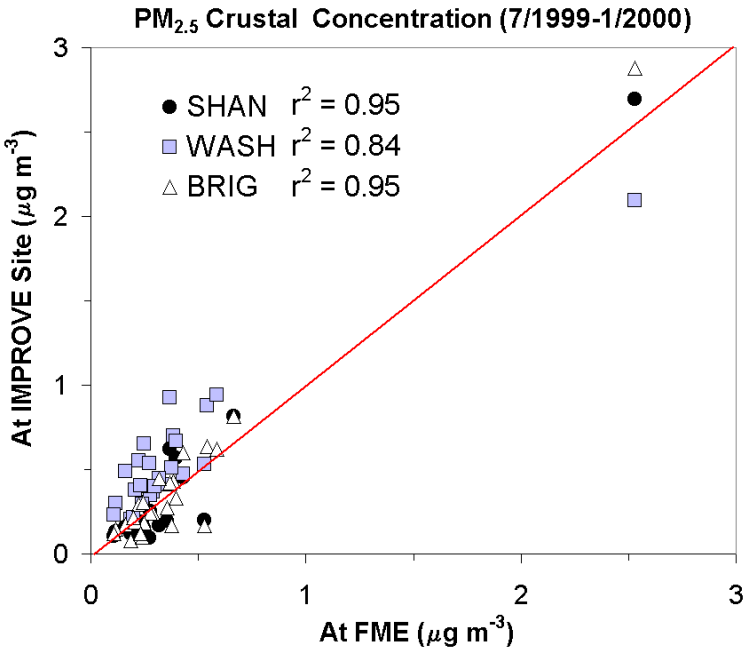

Figure 4.4.6 Scatter plot of 24-hr crustal material concentration at FME versus concurrent measurements at three IMPROVE sites in the Mid-Atlantic region. The solid line indicates 1 : 1 correspondence.

For major species in $PM_{2.5}$, observations at FME and WASH generally agree with each other. This suggests a relatively well mixing of pollutants at least within the B-W corridor, and therefore our 24-hr measurements at FME can be considered representative for the whole urban corridor.

4.5 Visibility and Fine Particulate Matter

4.5.1 Introduction of Light Extinction and Visibility

Visibility is an important part of air resource. The definition of visibility, however, is difficult. Historically, visibility has been defined as 'the greatest distance at which an observer can just see a black object viewed against the horizon sky'. Human eyes detect relative differences in brightness rather than the overall brightness level. Therefore, as mentioned in Section 2.4, visibility is actually a measure of our eyes' ability to distinguish an object from the surrounding background. This ability may differ for each individual and between day and night. An object is usually referred to as at maximum visual range when the difference between the brightness of the background and the brightness of the object is reduced to such a degree that an observer can just barely see the object. To be more objective and quantitative, this means the brightness of the object has been reduced to 2% of the original value at the observer's distance.

Light emitted or reflected by an object in the atmosphere is attenuated by air molecules, particulate matter, and precipitation droplets, etc. through scattering and absorption (Figure 4.5.1). Using the Beer-Lambert law, we get

$$\frac{I}{I_0} = e^{-b_{ext}X}$$

$$b_{ext} = b_{p,scat} + b_{p,abs} + b_{g,scat} + b_{g,abs}$$

Here I/I_0 is the ratio of intensities of the original and attenuated radiation, while X is distance between the object and observer. The first equation defines extinction coefficient

b_{ext} while the second equation indicates that the extinction coefficient includes scattering and absorption by particles and gases. The distance X at which $I/I_0 = 0.02$ is defined as visibility or visual range; thus

$$Visibility \sim \frac{3.912}{b_{ext}} \text{ (}Koschmeider\text{ equation).}$$

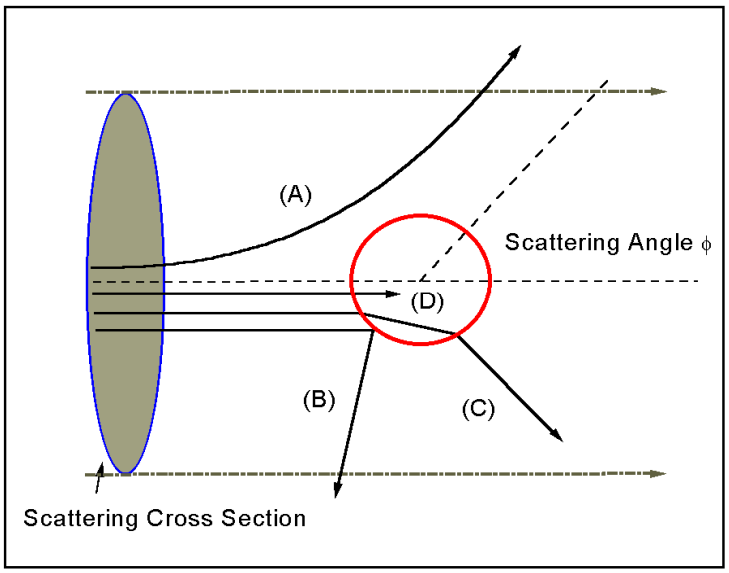

Figure 4.5.1 Interactions between incident radiation and an atmospheric scatter. (A), (B), and (C) indicate scattering while (D) indicates absorption. The area between two undeflected lights indicate the total scattering cross section.

The scattering by molecules $b_{g,scat}$ (Rayleigh scattering) is approximately 13 Mm^{-1} at 520 nm at sea level, and that limits the visibility in the cleanest atmosphere to ~ 300 km. The visibility in the continental U.S. is usually much lower than 300 km [*Malm et al.*, 1994], and this means that $b_{g,scat}$ is a minor term in b_{ext}. Scattering by particles of sizes comparable to the wavelength of visible light (0.4 μm – 0.7 μm: accumulation-mode

particles) is most responsible for the light extinction in the atmosphere though absorption by EC and dust also contributes. NO_2 is the light-absorbing gas present in significant quantity in the troposphere. In spite of the strong blue-absorbing of NO_2, the brown haze characteristic of a smoggy atmosphere is largely a result of aerosol scattering rather than NO_2 absorption [*Charlson and Ahlquist*, 1969].

Light scattering by aerosols depends not only on aerosol size spectrum but also on aerosol chemical composition. While the atmospheric scattering (b_{scat}) is a measure of total scatting cross section per unit volume of media, the aerosol mass scattering efficiency (E_{scat}) represents the total scattering cross section of a unit mass of particulate matter. Figure 4.5.2 shows the mass scattering efficiencies of spherical particles of water,

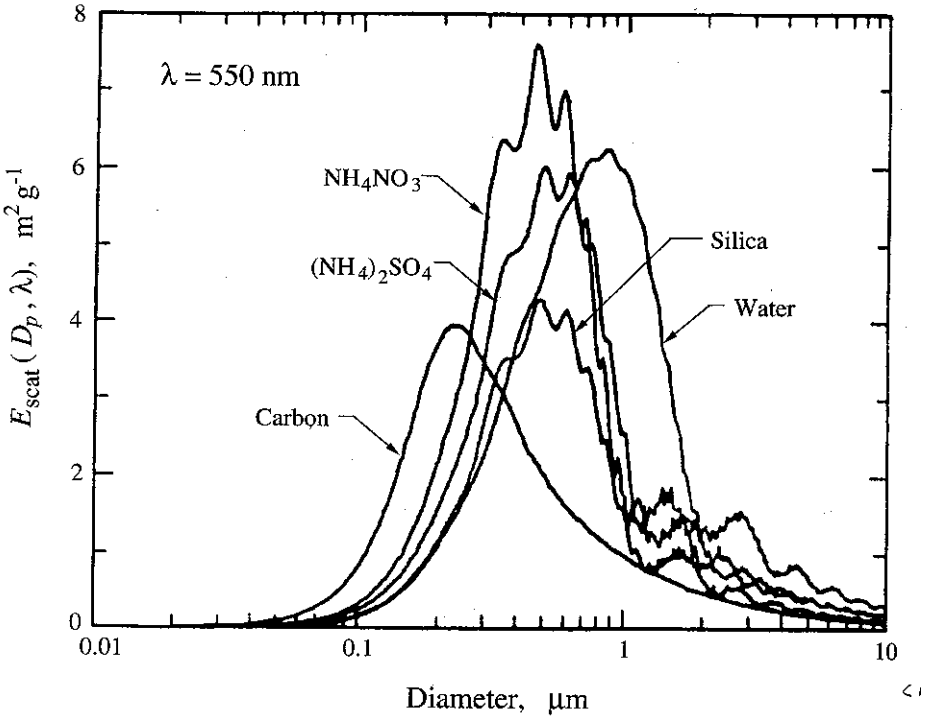

Figure 4.5.2 Mass scattering efficiencies of homogeneous sphere of $(NH_4)SO_4$, NH_4NO_3, carbon, H_2O, and silica at λ = 550 nm. (Adapted from *Seinfeld and Pandis* [1998], pp. 1131-1133.

ammonium nitrate and sulfate, silica (SiO_2), and carbon as a function of particle diameter at 550 nm wavelength. Particles between 0.1 and 1.0 μm diameter scatter light most efficiently. H_2O, NH_4NO_3, $(NH_4)_2SO_4$, and carbon exhibit the maximum scattering efficiency at 0.85 μm, 0.5 μm, 0.5 μm, and 0.2 μm diameter, respectively. This reflects the different optical properties of each species.

4.5.2 Observations

In late January 2002, a special study was carried out to measure the atmospheric scattering (by a Nephelometer; see Section 2.6) and absorption (by a PSAP; see Section 2.5) simultaneously at FME. Figure 4.5.3 shows the results. The fraction of backscattering (scattering angle > 90º) is distinguished from the total scattering. No precipitation was detected until late 1/30/2002. A background-level scattering of ~ 12 Mm^{-1} is observed. Using the *Koschmeider* equation, this scattering corresponds to a visual range ~ 300 km and is likely caused by air molecules. The backscattered fraction is relatively minor, especially when the total scattering is strong. The degree of backscattering depends on the size of a scatter relative to the wavelength (D_p/λ ratio) [*Nemesure et al.*, 1995]; weaker backscattering suggests larger D_p/λ ratio. Therefore, aerosols rather than molecules should be responsible for the periods of stronger scattering in this study. The absorption coefficient (b_{ap}) is generally close to or less than 20% of the total scattering coefficient (b_{scat}) through the entire period (i.e. the single scattering albedo is ~ 0.8 – 0.9). A previous study at urban Denver, CO [*Groblicki et al.*, 1981] suggests that absorption by EC accounts for ~ 30% of the atmospheric extinction. The

mass fraction of EC is lower at FME than at Denver, and this could explain the lower degree aerosol absorption. b_{ap} and b_{scat} are only moderately correlated (r^2 ~ 0.5). It is believed that in general 'forward scattering' dominates the atmospheric extinction, though no extremely high $PM_{2.5}$ episode occurred during this special study.

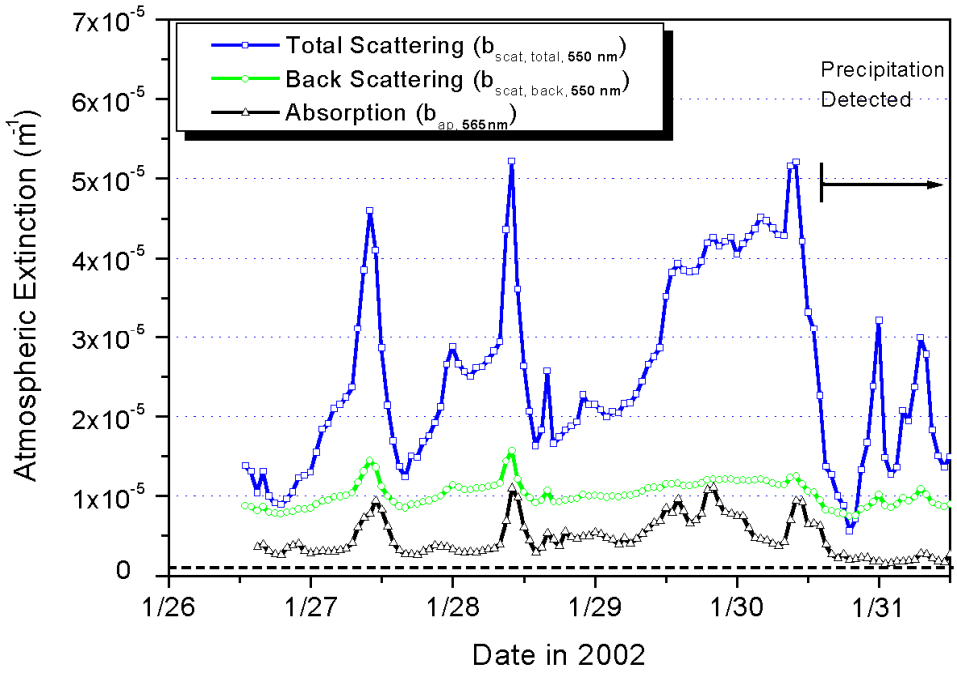

Figure 4.5.3 Time series of hourly total scattering, backscattering, and absorption coefficients at FME. The thick dashed line indicates the detection limits of the Nephelometer and PASP deployed.

One of the goals of the MARCH-Atlantic study is to investigate how fine particles impact the visibility. Unfortunately, *in-situ* measurements of visibility or atmospheric extinction are not available at FME. The most nearby visibility measurement is made at Baltimore-Washington International (BWI) airport through an Automated Surface Observing System (ASOS). ASOS does not directly measure the extinction coefficient,

which is usually determined by using an Optic Transmissometer. Instead, ASOS deploys a forward scatter meter (Belfort model 6220) in which light from a pulsed Xenon flash lamp in the blue portion of the visible spectrum is transmitted twice a second in a cone-shaped beam over a range of angles. A nominal 45° horizontal incident angle is set between the projector and a detector. The detector only receives a portion of the beam that is scattered forward by the intervening medium in the sampling volume. Atmospheric extinction coefficient (b_{ext}) is calculated based on the amount of light detected by the sensor [*Chu*, 1994]. The detection limit for each single b_{ext} measurement is ~ 0.05 km^{-1}. One-minute average b_{ext} is calculated and converted to visual range by using specified algorithms [*Chu*, 1994].

For this study, one-minute extinction data for most of our intensive sampling months were acquired. Extra precautions have to be exercised when one compares the extinction coefficient with the $PM_{2.5}$ data. First, the BWI airport is about 15 km north of FME, though the spatial variation of major $PM_{2.5}$ components is probably not significant over a 15 km distance (Section 4.4). Second, the ASOS extinction is only based on forward scattering so that it likely underestimates the atmospheric extinction due to backscattering and absorption. Third, changes in the visibility not only depend on fine aerosol mass and chemical composition but also on relative humidity. Since RH is usually not a constant in a 24-hr period, it could cause problems in relating the 24-hr $PM_{2.5}$ data to the 24-hr atmospheric extinction. Finally, heavy precipitation reduces visibility more substantially than aerosols and is usually responsible for the lowest-visibility days. Therefore, this study can be considered at best semi-quantitative.

The correlation between dry $PM_{2.5}$ gravimetric mass and 24-hr average b_{ext} is weak (Figure 4.5.4: $r^2 \sim 0.2$). Many low visibility days occur when the $PM_{2.5}$ concentration is low. The correlation r^2 between 24-hr RH and b_{ext} is also ~ 0.3. Even if there is no precipitation, liquid water absorbed by aerosols can scatter light, causing visibility reduction as well. Since neither the liquid water content nor hydroscopic scattering factor was determined experimentally in this study, aerosol water is estimated by ISORROPIA based on thermodynamic equilibrium. As described in Section 4.2, ISORROPIA only

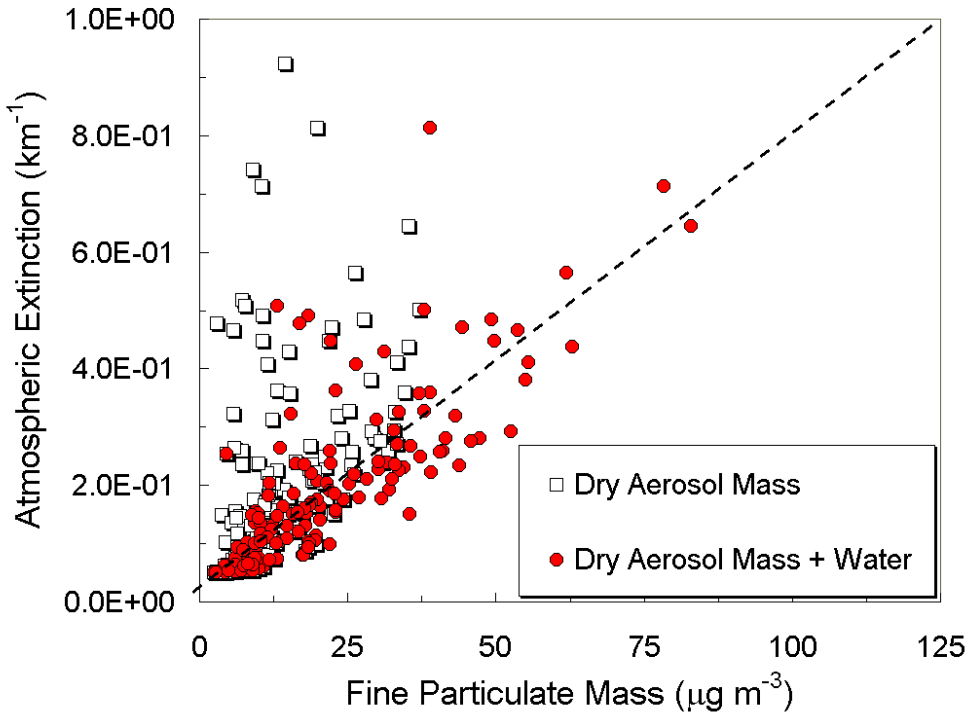

Figure 4.5.4 Scatter plot of extinction coefficient at BWI versus $PM_{2.5}$ mass concentration at FME between 7/1999 and 1/2001. Aerosol water content is calculated by ISORROPIA. The dashed line indicates the linear regression (including water) excluding outlier points.

considers inorganic salts. However, this may not be a serious artifact because carbonaceous material is generally much less hydrophilic than sulfate or nitrate. A comparison of the 'corrected' aerosol mass (dry mass + water) versus extinction coefficient is also shown in Figure 4.5.4. The correlation r^2 improves to ~ 0.55 though several outlier points still appear. All outliers indicate stronger extinction with lower aerosol mass concentration. Some of the outliers correspond to heavily rainy days on which the extinction is mostly caused by raindrops, and others may be due to the spatial inhomogeneity in the $PM_{2.5}$ concentration or atmospheric extinction.

The slope of extinction coefficient versus 'corrected' aerosol mass suggests an aerosol mass extinction efficiency ~ 7 – 8 $m^2\ g^{-1}$. *Hegg et al.* [1997] suggest a scattering efficiency of 4.0 ± 1.1 $m^2\ g^{-1}$ for carbon species (including EC and OM) and 2.7 ± 1.3 $m^2\ g^{-1}$ for ammoniated sulfate on the Mid-Atlantic coast of the United States. According to Figure 4.5.2, these two values correspond to carbonaceous particles of ~ 0.2 μm diameter and sulfate particles of ~ 0.8 μm diameter, respectively. Absorption is suggested to contribute as much as 25% to the total dry extinction in *Hegg et al.* [1997]. Overall, the extinction efficiency suggested by *Hegg et al.* [1997] is significantly lower than 7 $m^2\ g^{-1}$. However, if only very dry days (mean RH < 55%) are considered, the aerosol extinction efficiency at FME drops to 2.1 ± 0.3 $m^2\ g^{-1}$ (21 days; $r^2 = 0.72$). Aerosol water associated with inorganic salts can have a much higher scattering efficiency at ~ 6 $m^2\ g^{-1}$ (Figure 4.5.2), and this partly explains the higher aerosol extinction efficiency on more humid days. The ASOS visibility monitor uses a wavelength shorter than 550 nm, and this could also contribute to the positive bias in b_{ext}. More quantitative chemical apportionment of atmospheric extinction or scattering can be achieved using multiple linear regression

methods if co-located measurements of aerosol chemistry and optical property are available.

Another way to study the relation between visibility and fine particle concentration is to compare their time series. Two months, July 1999 and January 2001 are chosen to represent summer and winter conditions. Figure 4.5.5(a)-(b) shows the averaged diurnal variation of b_{ext} and RH in the two months. Lower RH appears in early afternoon due to a higher temperature. b_{ext} generally follows the pattern of RH in both summer and winter. In other words, despite that the $PM_{2.5}$ concentration could vary from day to day, low visibility occurs more frequently at nighttime than at daytime. July 1999 was warmer and drier than January 2001, and b_{ext} observed in July 1999 was generally stronger in terms of monthly median values. In January 2001, there are, however, some rain/snow days that lift average extinction coefficients. The 24-hr average aerosol mass, extinction coefficient, and relative humidity are compared in Figure 4.5.6(a)-(b). The aerosol water content is calculated using methods mentioned earlier. Four haze episodes appear in July 1999: 7/4-7/6, 7/18-7/19, 7/22-7/24, and 7/30-7/31. The most serious episode is 7/22-7/24 when RH is between 75% and 85%; water contributes to about half of the extinction in this episode. The extinction coefficient closely agrees with the aerosol mass on dry days. On humid days, however, disagreements can be significant even if water is taken into account. In January 2001, mean RH > 90% occurs on a few days, causing precipitation, and the liquid water content in the air cannot be accurately estimated by thermodynamics. Measurements at finer time resolution are needed to study the different hydroscopicities of sulfate, nitrate, and carbon species and the potential hysteresis effect.

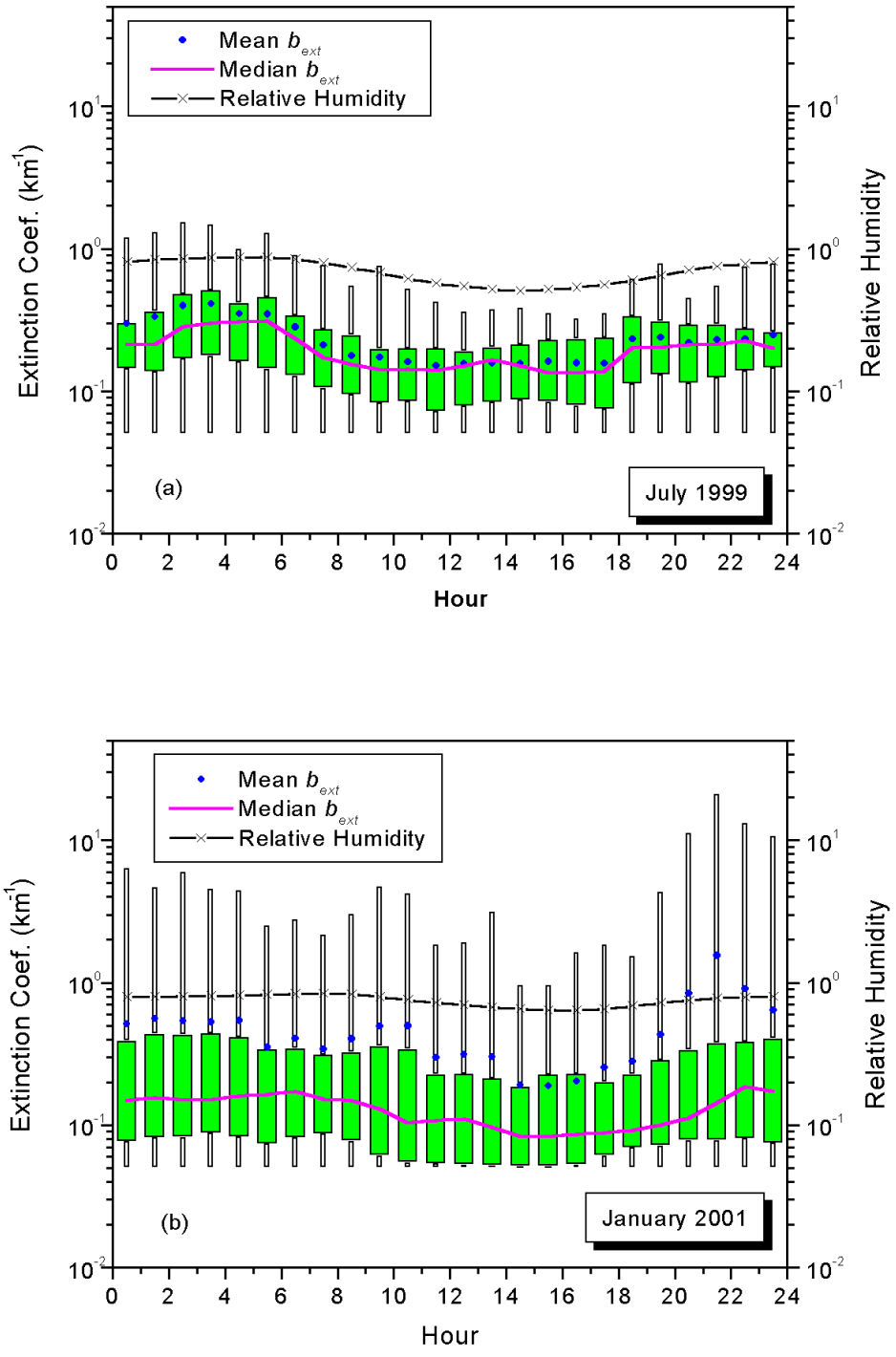

Figure 4.5.5 Diurnal variations of extinction coefficient and relative humidity at BWI in (a) July 1999 (b) January 2001. Monthly means of extinction coefficient are indicated by solid circles and median values by short dashes. Boxes indicate the quartiles and vertical bars indicate the maximum and minimum.

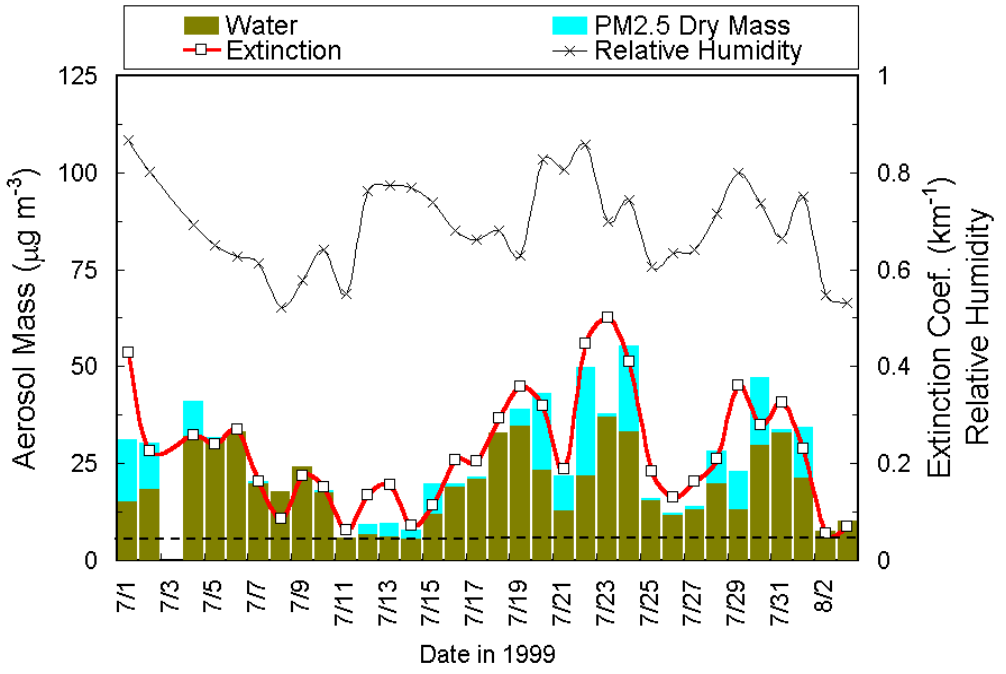

(a)

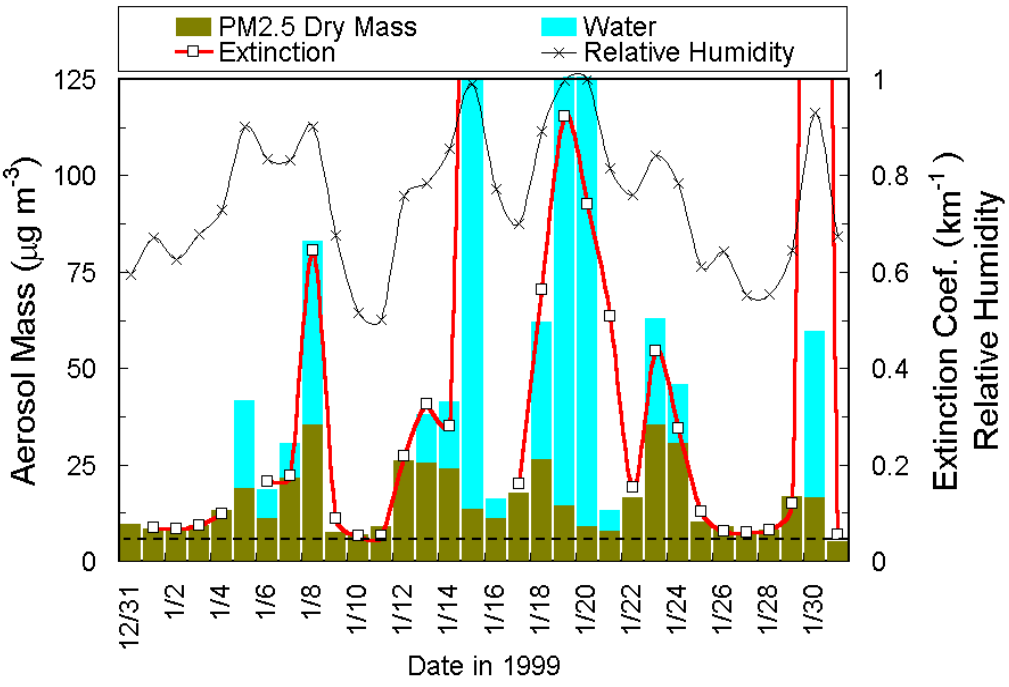

(b)

Figure 4.5.6 Comparison of 24-hr aerosol mass (at FME), extinction coefficient (at BWI) and relative humidity in (a) July 1999 (b) January 2001. Aerosol water content is calculated by ISORROPIA. The dashed lines indicate the detection limit of the ASOS visibility monitor.

Chapter 5 Receptor Data Analysis

5.1 Introduction of Factor Analysis

One of the major challenges in studying fine particulate pollution is to apportion ambient aerosol mass and components to various sources. There are generally two approaches, forward and inverse. A forward approach starts with investigating sources. The first step is to build a reliable database of emissions, including information about locations, types, and strengths of potential sources, in a region that can influence aerosol concentration at a chosen receptor site. A chemical transport model (CTM) that incorporates chemistry and meteorology is then utilized to study the dispersion and evolution of pollutants to predict pollutant concentrations. The model calculation is compared to measurements at the receptor site to evaluate its performance. This approach, though potentially more accurate, required detailed knowledge of sources and atmospheric processes. An inverse approach is based on ambient measurements. What observed at a receptor site is a mix of contributions from all sources. Variations in the concentrations of pollutants usually reflect changes in source contributions. Suitable algorithms can be developed to retrieve source compositions and contributions from ambient observations [e.g. *Gordon*, 1988]. The MARCH-Atlantic study had been sampling chemically speciated $PM_{2.5}$ at FME since 1999 and completed more than 300

days of measurements. The next step is to study the source of fine PM from these data using an inverse approach, multiple variances receptor modeling.

Widely used receptor models include chemical mass balance (CMB) and factor analysis. The CMB techniques [e.g., *Kowalczyk et al.*, 1982; *Chow et al.,* 1992; *Suarez and Ondov*, 2001] assume a known number of sources and source compositions in a receptor region and utilize a least-square approach to retrieve the respective source contribution from ambient measurements. This approach does not need a large number of measurements, but its performance depends highly on accurate information of sources. Factor analysis does not utilize source information. Using the data alone, the factor analysis method attempts to estimate the number of factors in the data and calculate composition and contribution of each factor to the pollutant loading. This kind of approach does rely on a large number of measurements, and usually the more data it uses, the better results it can achieve. Well-known examples include Principal Component Analysis (PCA) [*Koutrakis and Spengler*, 1987; *Ehrman et al.*, 1992], Positive Matrix Factorization (PMF) [*Chueinta et al*., 2000; *Song et al*., 2001], and UNMIX [*Henry et al.*, 1999; *Henry*, 2000]. UNMIX is used here to study the $PM_{2.5}$ data (also see *Chen et al*. [2002]).

All receptor models assume linear combinations. The linear equation that links emissions to ambient concentrations can be written as

$$c_{ik} = \sum_{j=1}^{s} a_{ij} S_{jk} + e_{ik}$$

where c_{ik} is the concentration of the ith species in the kth sample, a_{ij} is the concentration of species i from source j, S_{jk} is the contribution of source j in the kth sample, and s is the number of sources. e_{ik} represent the uncertainty of the ith species in the kth sample. Given

a data matrix of *n* samples by *m* species, UNMIX first calculates the data variance coverage and signal/noise ratio as various numbers of factors are applied [*Henry et al.*, 1999]. This procedure suggests the most probable number of factors *s* in the data matrix. The model then performs a singular value decomposition of the data matrix to reduce the dimensionality of the data to the number of factor *s*. UNMIX further reduces the dimensionality of the data by projecting the data to a plane perpendicular to the principle axis of the *s*-dimensional space. The boundaries or edges of the projected data represent samples that can characterize the factors.

To illustrate the last point, samples (or measurements) of a simplified case that contains only 2 species is shown in Figure 5.1.1. If only one source contributes to the two species, the data points should scatter along the dashed line that characterizes the composition of the source. Actually, the data points generally scatter in an area spanned by two dashed lines, and this implies contributions from two independent sources. The 'edge' points that define the boundaries of the area indicate the source compositions. The same logic can apply to a multi-variant data space. Once source compositions are determined, source contributions can be estimated straightforward.

One of the natural constraints imposed to the UNMIX calculation is the non-negativity condition since both source compositions and contributions must be zero or positive. However, the effects of analytical errors require that UNMIX allow small negative values [*Henry*, 1997, 2000]. Even with the constraint, the factor analysis model may produce a large number of mathematically 'correct' but different answers, many of which are physically implausible [*Henry*, 1987]. One has to rely on the knowledge of nature of sources to eliminate these 'fake' factors. Moreover, UNMIX assumes nearly constant

source compositions and a linear combination of all source contributions. This may not be true since atmospheric lifetimes of various species from a single particulate source may be different due to complex atmospheric processes (e.g., deposition and gas-to-particle transformation). Source signatures gradually decay during atmospheric transport. Therefore, extra caution has to be exercised in linking model-resolved factors to real source emissions. For example, *Poirot et al.* [2001] suggested that a coal-burning source could produce plumes of distinct compositions in summer and winter and split into two factors in the factor analysis

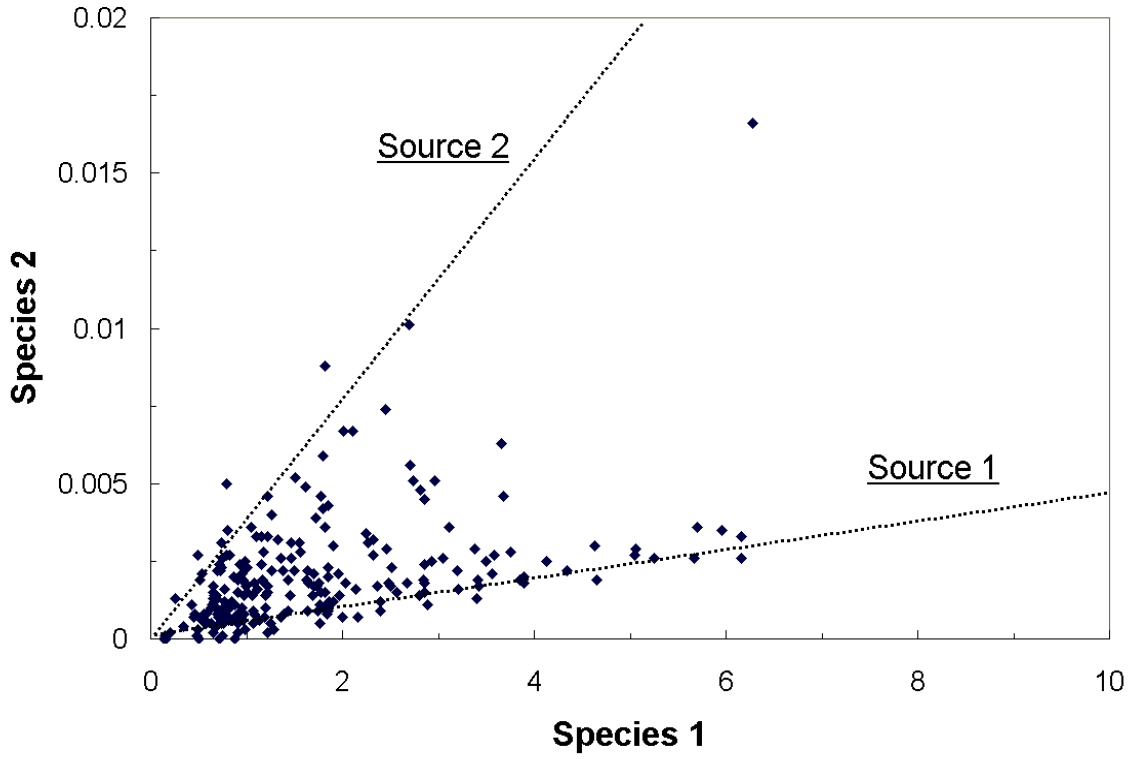

Figure 5.1.1 Scatter plot of concentrations of two species. (These are real data acquired at FME between 7/1999 and 7/2001. Species 1 is 24-hr SO_4^{2-} and Species 2 is 24-hr Se. The unit is μg m^{-3}.)

5.2 $PM_{2.5}$ Factor Analysis with UNMIX

FME is considered suburban. Unlike remote sites, local (< 100 km) and regional (100 - 1000 km) sources probably explain most of the $PM_{2.5}$ mass at FME. This relatively short source-receptor distance is favorable for factor analysis because of the shorter transport time between sources and the receptor. Table 5.2.1 summarizes the measurements of 24-hr $PM_{2.5}$ and trace gases in the first eight intensive months. The major mass contributing species include SO_4^{2-}, NO_3^-, NH_4^+, OC, and EC. Concentrations of other species are much lower and contain larger analytical uncertainties. Trace elements with concentration usually below the analytical uncertainty (AU) are not qualified to be the UNMIX inputs. Only Na^+, K^+, K, Al, Si, S, Ca, Fe, Cu, Zn, Se, and Br have more than half of their values greater than twice the analytical uncertainty (Table 5.2.1). As suggested in Table 3.7.1, Al, Si, and Ca are one group primarily of crustal origin while Se, Br, Zn, and Pb are another group likely linked to combustion sources (Section 3.7). Almost no correlations are found between the two groups. Fe was assumed to be crustal material but its correlations with Cu, Pb, and Zn imply other sources. K and K^+ are also correlated to Br and Pb better than Si or Ca if 3 outlier points (July 4^{th}) are removed. To simplify the factor analysis, we decide to exclude Si, Al, Ca, and Na^+ from the model inputs since 1) crustal and marine sources are minor (Section 3.7) and probably contain little sulfate, nitrate and EC which result mostly from combustion, and 2) crustal sources are diverse and their contributions are likely dominated by special and rare events (Section 4.4).

Using nine input variables, including gravimetric mass, SO_4^+, NO_3^-, NH_4^+, OC (FT), EC, Se, Br, and Cu, a unique 6-factor model is resolved by UNMIX and their

compositions and contributions are calculated. The model explains at least 91% of the variance of each of the fitting species. To test the model stability, an arbitrary one month of data are removed from the UNMIX input, and this causes little difference in the output results. Table 5.2.2 shows the annual mean contribution of each factor (F1 - F6) to mass and each species, from which one also obtains the factor composition. (Notice that Table 5.2.2 shows the factor contributions averaged over the four sampling months in 2000, while Table 5.2.1 lists the overall mean concentrations of each species in the eight sampling months. Therefore, two sets of numbers are slightly different.) The monthly median as well as the 25^{th} and 75^{th} percentile contributions of each factor, relative to the 2000 annual mean, is shown in Figure 5.2.1. UNMIX also estimates uncertainties in factor composition using boot-strapping methods [*Henry*, 2000]; in Table 5.2.2, values shown in bold are greater than twice the calculated uncertainty, and thus the upper limit of uncertainty in these values is 50%. The difference between reconstructed mass (SO_4^{2-} + NO_3^- + NH_4^+ + EC + OM) and gravimetric mass in each factor is within ± 15%. A 5-factor model using the same inputs is available but can explain only ~ 80% of the data variance. Adding K, Fe or Zn to build a 6 or 7-factor model were unsuccessful, generating no solutions. K, Fe and Zn could partly originate from one or more sources that are unexpected in the model (e.g. crustal sources). We estimate the contributions of F1 - F6 to species not included in the model by multiple linear regression, and the results are also shown in Table 5.2.2. The model explains the observations of Zn, Fe, and Pb (r^2 > 0.6) better than Al, Ca, and Si (r^2 < 0.2). Relatively large residues left from regressing Al, Ca, and Si suggest significant contributions from other sources. The model explains the CO variation (r^2 = 0.76) better than SO_2 (r^2 ~ 0.6 with negative loadings). The residue

CO from regression is 154.2 μg m^{-3} (~ 130 ppbv), typical for background CO level over Eastern North America [*Poulida et al*., 1991].

Figure 5.2.2 shows the profile of each factor. Certain species noted in each factor act as tracers, providing information about sources. Factor F1 and F2 together apportion ~ 80% of the sulfate. F2 differs from F1 by a higher Se/SO_4^{2-} ratio. Se is widely used as a tracer for coal burning and smelter operations [*Rabano et al.*, 1989; *Malm and Gebhart*, 1997; *Suarez and Ondov*, 2001] that usually generate SO_2 and sulfate as well. SO_2 should dominate in a freshly emitted plume, but it is gradually converted to sulfate as the plume ages. The Se/SO_4^{2-} ratio is expected to be higher in fresh plumes than aged plumes [*Dodd et al*., 1991]. Table 5.1.2 shows that SO_2 is associated more closely with F2 than with any other factor. Therefore, F1 and F2 suggest a thoroughly oxidized sulfate source and a partially oxidized sulfate source, respectively. The partially oxidized sulfate source should be geographically closer to FME to prevent a thorough oxidation before its plumes arrive at FME; this will be shown later in the ensemble back trajectory analysis. F1 should be relatively far away, and it contributes stronger in summer possibly due to a more efficient long-range transport besides a higher SO_2-to-SO_4^{2-} conversion rate. F1 contains most unidentified mass. A large fraction of secondary sulfate is formed in the aqueous phase [*Pandis et al.*, 1992], and water associated with the sulfate may explain part of the 'missing' mass. The OC and EC apportioned to F1 probably have a proximate source region and share similar seasonal variations.

Factor F3 is the dominant source of secondary ammonium nitrate (NH_4NO_3), and its contribution reaches a distinct maximum in winter. The suspected origin of NO_y, HNO_3, and NO_3^- is mobile emission. The EC/OC ratio in F3 is ~ 0.55. Recent dynamometer and

tunnel studies suggest EC/OC ratios of 0.75 - 3 for heavy-duty (diesel) vehicle emissions and lower values (~ 0.25 - 1) for light-duty (gasoline) vehicles [*Gillies and Gertler*, 2000; *Gillies et al.*, 2001; *Gertler et al., 2001*]. Since both types of vehicular traffic are closely located, our data based on 24-hour sampling may not distinguish one from the other and probably capture an average emission profile. Disregarding that EC/OC-separation can vary when different analytical methods are adopted [e.g., *Chow et al.*, 2001], a 0.55 EC/OC ratio supports the association of F3 with a mobile source favoring gasoline vehicles. F4 features the same EC/OC ratio as F3 but shows a seasonal variation somewhat complementary to F3. Carbonaceous material is the single dominate species in F4. It is suggested that F4 represents the 'summer profile' of the mobile source, and it is separated from F3 (winter profile) because it contains no nitrate (note that HNO_3 is not discussed in the source profile). The linear combination of F3 and F4 may better reproduce the real emission profile of mobile source. Another evidence is that the two factors both apportion significant CO emission. A recent (1999) tunnel study carried out in the Mid-Atlantic region [*Gertler et al.*, 2001] suggests an EC/CO ratio of 1.8×10^{-3} for light-duty vehicles and an unquantified high value ($> 10^{-2}$) for diesels. The EC/CO ratio in F3 is close at 2.6×10^{-3}. In F4, a larger value of 5.9×10^{-3} may result from greater contributions from diesel emissions in summer. In Section 4.3, we have suggested that ambient temperature may influence particulate emission of diesel engines through changing intake air density and air-fuel ratio [e.g., *Chen et al.,* 2001]. The F4 contribution reaches a maximum in fall rather than summer. Factor contributions depend on both source strength and transport efficiency. Though the source strength of F4 should peak in summer (if it is the summer profile), stronger summertime dispersion keeps its

contribution low. The role of meteorology in the source-to-receptor transport will be discussed later.

Br and K are two important tracers in F5. Traditionally, Br and Pb are mostly attributed to mobile sources [*Kowalczyk et al.*, 1982; *Chow et al.*, 1992] since they were standard additives to gasoline fuel in the United States. *Cadle et al.* [1999], however, suggest that vehicles manufactured after 1990 have substantially reduced the Br and Pb emissions. Tunnel studies [*Gillies et al.,* 2001; *Gertler et al.,* 2001] suggest that diesel vehicles dominate Br emission with a Br/EC ratio ~ 10^{-4}. The Br/EC ratio in F5 is higher than that by 2 - 3 orders of magnitude. *Malm and Gebhart* [1997] note a strong correlation of Br with atmospheric absorption at rural sites of low transportation and suggest that the Br is related to residential wood burning. *Turn et al.* [1997] report an EC/OC ratio ranging from 0.1 to 0.3 and a mean Br/EC (also Pb/EC) ratio ~ 10^{-3} for various types of wood burning. These values are close to what we find in F5. The F5 peak in winter and contribution to K and K^+ further supports its association with vegetative burning. Incinerator operation is another likely source of Br and K [*Olmez et al*., 1988; *Dzubay et al*., 1988], but it usually produces little CO. F5 contains significant CO and sulfate. A positive correlation between sulfate and Br is observed here and in *Malm and Gebhart* [1997]. Sources of sulfate and wood smoke may have some overlap spatially.

F6 is relatively minor, contributing to ~ 2% of the $PM_{2.5}$ mass. This factor suggests another sulfate source rich in Cu and Fe. Given that the U.S. Northeast is a highly industrialized region, F6 could be caused by industrial emissions, such as steel furnaces. Compared to F2, F6 contribution is higher in fall and summer when long-range transport is generally more efficient.

Table 5.2.1 Statistics of measurements at FME over the first eight sampling months between 7/1999 and 7/2000. AU, FQ, BQ, and TBQ are defined in the text.

Species	Mean ± 1σ ($\mu g\ m^{-3}$)	# of samples	# of samples > 2 × AU
Mass	13.03 ± 7.74	266	266
SO_4^{2-}	4.59 ± 3.28	266	266
NO_3^-	1.04 ± 1.51	266	257
NH_4^+	1.75 ± 1.16	266	266
EC	1.06 ± 0.57	266	266
OC (FQ)	3.11 ± 1.41	266	265
OC (BQ)	0.72 ± 0.45	263	179
OC (TBQ)	1.43 ± 0.75	264	238
Cl	0.013 ± 0.072	266	16
Cl^-	0.035 ± 0.1	266	36
Na	0.072 ± 0.11	266	69
Na^+	0.04 ± 0.035	266	214
K	0.069 ± 0.13	266	266
K^+	0.056 ± 0.11	266	265
Mg	0.016 ± 0.018	266	28
Al	0.032 ± 0.037	266	219
Si	0.084 ± 0.098	266	227
P	0.0022 ± 0.0031	266	18
S	1.69 ± 1.22	266	266
Ca	0.026 ± 0.017	266	257
Ti	0.003 ± 0.0036	266	0
V	0.021 ± 0.024	266	0
Fe	0.064 ± 0.055	266	266
Mn	0.0017 ± 0.0016	266	63
Ni	0.0012 ± 0.0013	266	78
Cu	0.002 ± 0.0023	266	144
Zn	0.014 ± 0.013	266	265
As	0.0006 ± 0.0006	266	1
Se	0.002 ± 0.0017	266	148
Sr	0.0007 ± 0.0014	266	20
Br	0.0045 ± 0.0031	266	251
Ba	0.0083 ± 0.012	266	0
La	0.0085 ± 0.012	266	0
Pb	0.0047 ± 0.0034	266	118
$HNO_{3(g)}$	2.78 ± 1.94	231	209
$NH_{3(g)}$	0.58 ± 0.49	264	189
NO_y (ppb)	14.3 ± 6.3	194	-
CO (ppb)	314 ± 146	256	-
SO_2 (ppb)	3.8 ± 2.8	216	-

Table 5.2.2 Compositions of six factors contributing to $PM_{2.5}$ at FME. Values (in unit μg m^{-3}) shown are 2000 annual mean contributions of each factor. Values greater than twice the uncertainty calculated by UNMIX are noted in bold. Numbers in brackets indicate percentage of species relative to mass. The r^2 indicates correlation between measured and calculated concentrations.

	F1	F2	F3	F4	F5	F6	Residue	r^2
Mass	**5.28**	0.93	**2.03**	**1.77**	**1.58**	0.19	-	0.98
NO_3^-	0.01 (0)	0.02 (2)	**0.99** (49)	0.02 (1)	0.05 (3)	-0.01 (-5)	-	0.99
SO_4^{2-}	**2.64** (50)	**0.70** (75)	0.10 (5)	0.16 (9)	0.47 (30)	0.11 (58)	-	0.99
NH_4^+	**0.83** (16)	**0.25** (26)	**0.33** (16)	0.08 (3)	0.13 (8)	0.00 (0)	-	0.99
EC	**0.19** (4)	**0.08** (9)	**0.17** (8)	**0.40** (23)	**0.09** (6)	0.05 (26)	-	0.94
OC (FT)	**0.57**	-0.04	**0.31**	**0.75**	**0.55**	0.04	-	0.91
$Cu \times 10^3$	0.07	0.14	0.2	0	-0.03	**1.92**	-	0.99
$Se \times 10^3$	0.3	**1.69**	0.21	0.07	-0.24	0.02	-	0.99
$Br \times 10^3$	**0.61**	**0.6**	**0.48**	**0.32**	**2.68**	0.06	-	0.99
OM	0.80 (15)	-0.06 (-6)	0.43 (21)	1.05 (59)	0.77 (49)	0.06 (32)	-	-
$Pb \times 10^3$	0.39	0.93	0.48	0.45	1.45	0.76	0.47	0.61
$Zn \times 10^3$	0.49	4.22	2.88	1.14	4.72	1.35	0.51	0.70
$Fe \times 10^3$	8.44	16.18	5.47	3.56	3.74	29.59	1.46	0.64
$K \times 10^3$	7.86	4.28	9	10.44	18.25	5.47	1.09	0.45
$K^+ \times 10^3$	6.65	3.78	11.07	8.98	13.45	4.51	-3.08	0.53
$Ni \times 10^3$	0.14	0.39	0.28	0.24	0.07	0.23	-0.11	0.40
$Mn \times 10^3$	0.17	0.67	0.4	0.15	0	0.3	0.1	0.50
$Al \times 10^3$	12.89	-0.58	-0.4	-1.77	-0.18	3.52	15.5	0.19
$Si \times 10^3$	28.56	1.76	-3.81	2.57	1.69	4.63	42.66	0.14
$Ca \times 10^3$	3.66	0.84	-0.32	2.6	1.89	0.94	15.83	0.10
$Na^+ \times 10^3$	1.97	-2.27	2.26	-4.33	10.43	0.41	33.27	0.09
CO	2.6	18.2	66.6	68.1	49.8	15.2	154.2	0.76
SO_2	-0.78	5.69	1.62	0.25	-2.19	-0.3	6.24	0.63

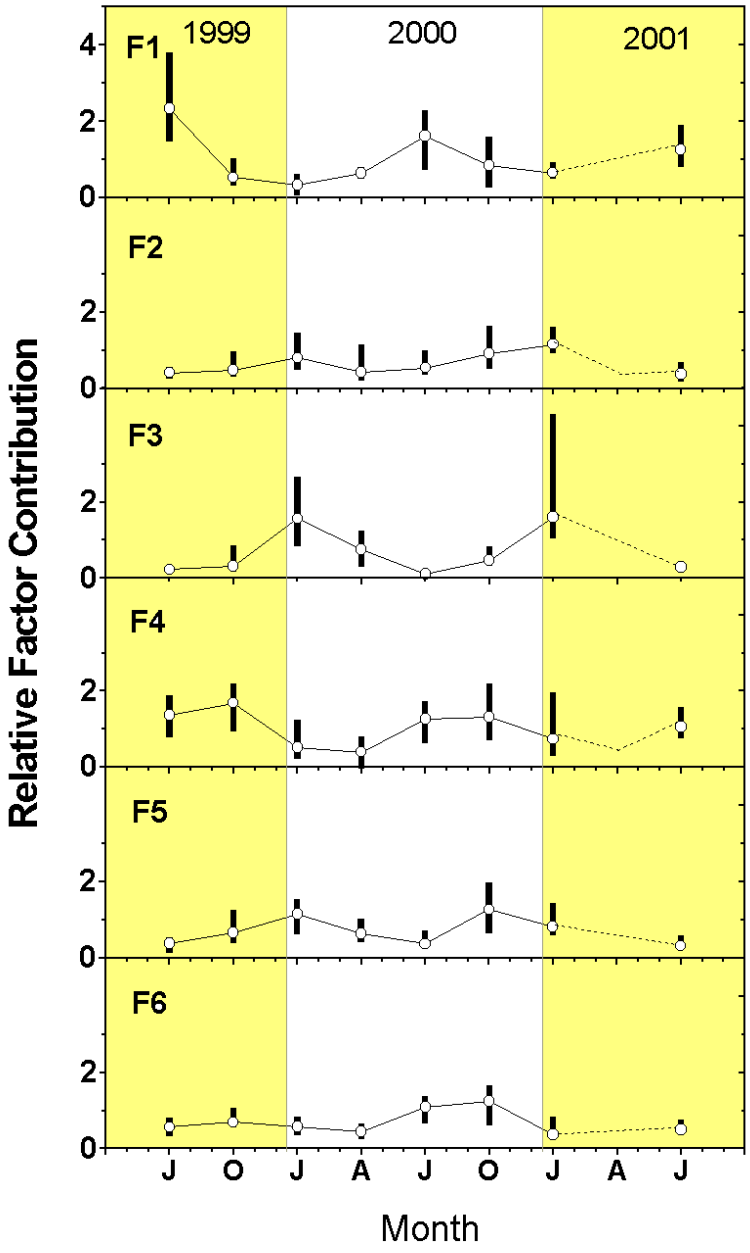

Figure 5.2.1 Seasonal variation of contributions of six factors derived from UNMIX. Monthly medians are indicated by circles and quartiles by vertical bars. The dashed lines are added to reproduce the possible seasonal variation.

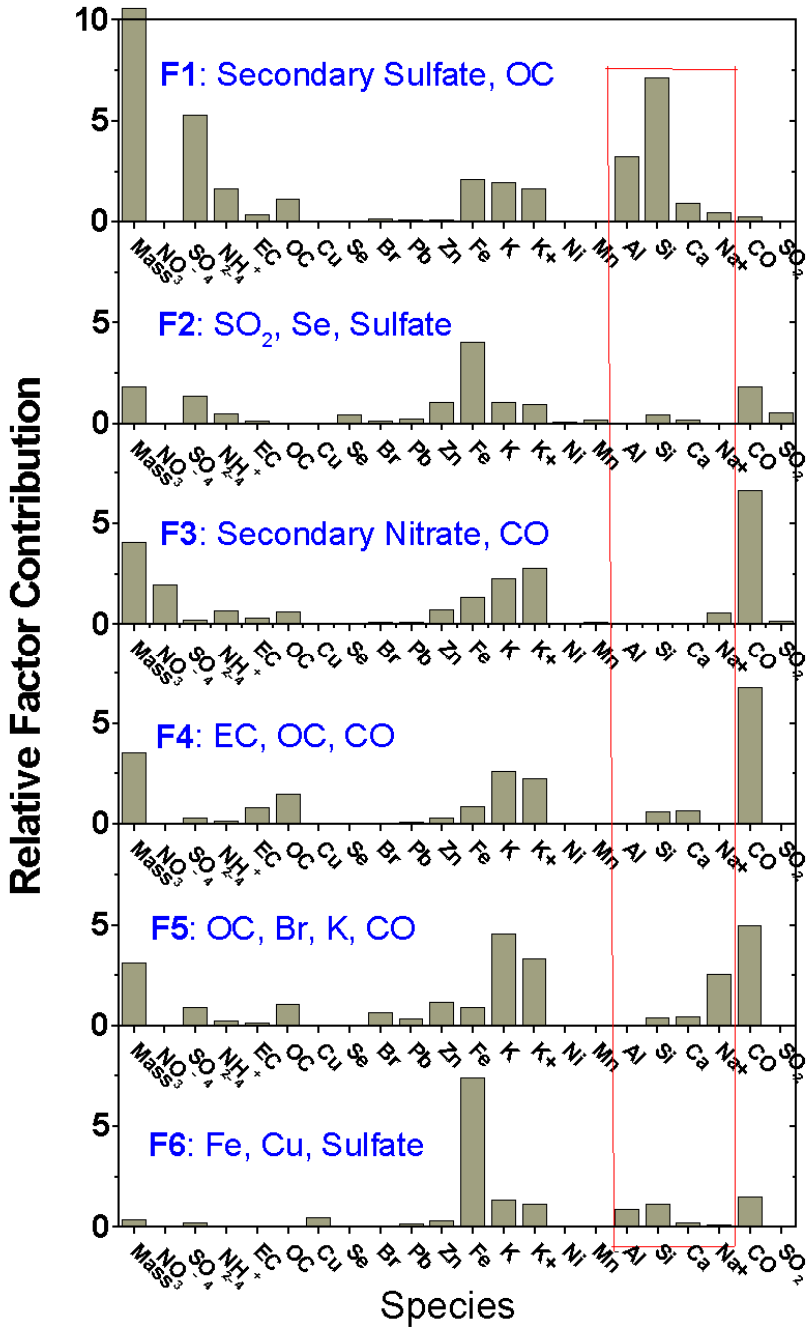

Figure 5.2.2 Profiles of six factors resolved by UNMIX using FME measurements. Values are the 2000 annual mean contributions. The unit for mass, NO_3^-, SO_4^{2-}, NH_4^+, EC, and OC is 0.5 μg m^{-3}, for CO and SO_2 is 10 μg m^{-3}, and for the rest is 0.004 μg m^{-3}. Elements circled are not well explained (regressed) by the model.

Justifying the choice of the number of factors is difficult in factor analysis. Using too few factors may combine sources of different nature together while using too many factors make a real factor dissociate into two or more nonphysical sources. *Kowalczyk et al.* [1982] employ a CMB model of seven sources, including soil, limestone, motor vehicle, coal, oil, refuse, and marine sources to explain 'primary' total suspended particle (TSP) mass in Washington, DC. Each of the last three sources contributes to only ~ 1% of the TSP. Soil is quite dominant but appears mostly in coarse particles. For fine particles, it is essentially a six-source approach if one excludes soil, limestone, and marine sources but adds secondary sulfate and nitrate. *Song et al.* [2001] analyzed the IMPROVE data for Washington D. C. using PMF and also derive six non-crustal and non-sea-salt factors. Though these factors may not be identical to the UNMIX solution in this study, six factors seem to be sufficient for including major $PM_{2.5}$ contributors (except sea salt and crustal) in the B-W corridor. The factors resolved here have such distinct characteristics that six factors are thought to be necessary, too.

5.3 Air Parcel Back Trajectory

Besides types and strengths of sources, another important factor that determines the ambient concentrations of pollutants is meteorology. Meteorology controls transport, dispersion, and deposition of pollutants in the atmosphere. Analyzing meteorological patterns associated with pollution episodes can provide insights into source locations. For example, the wind rose analysis, which measures wind direction at a receptor site and correlates it with high pollutant concentrations, is used to identify the directions from

which pollutants arrive at the receptor site [*Rheingrover and Gordon*, 1988; *Chow et al.*, 1996; *Chueinta et al.*, 2000]. However, on the meteorological microscale surface wind may not be representative of transport and sometimes even misleading since natural terrain, vegetation and man-made structures can influence surface flow significantly and make it different from winds aloft (i.e. wind shear). Mean streamlines of synoptic and meso- scale circulation, important for long-range transport, are usually better described by air parcel trajectories.

A trajectory is the time integration of the position of an air parcel as it is transported passively by wind. In principle, it can be calculated starting from the parcel's initial position $\boldsymbol{P}(t)$ using a 4-dimensional wind velocity field $\boldsymbol{V}(\boldsymbol{r}, t)$:

$$\boldsymbol{P}(t+dt) = \boldsymbol{P}(t) + \boldsymbol{V}(\boldsymbol{P}(t), t)dt \; .$$

It is plausible to describe the entire path that an air parcel travels precisely if continuous 4-dimensional wind fields in the atmosphere are available through measurement or meteorological model. In reality, wind data are discrete in time, and therefore the equation needs to be modified to

$$\boldsymbol{P}(t+\Delta t) = \boldsymbol{P}(t) + \frac{1}{2}[\boldsymbol{V}(\boldsymbol{P}(t), t) + \boldsymbol{V}(\boldsymbol{P}(t+\Delta t), t+\Delta t)]\Delta t$$

for model calculations. The precision of trajectory calculation strongly replies on the accuracy and temporal resolution of the wind data used. Trajectories can be calculated either forward or backward in time, depending on whether a positive or negative Δt is chosen. A back trajectory traces an air parcel backward in time from a receptor site, and therefore it can be utilized to study the possible source region of pollutants observed at the receptor site. Back trajectory analysis is one of the foci of the MARCH-Atlantic project.

The Hybrid Single-Particle Lagrangian Integrated Trajectories (HY-SPLIT) model [*Draxler*, 1988; 1991] was used in this study to calculate air parcel back trajectories. Detailed description of the model can be found in http://www.arl.noaa.gov/ready/hysplit4.html. Comparing HY-SPLIT calculated back trajectory with the path of actual tracer plumes suggests a potential error of 20 – 30% of total travel distance [*Draxler*, 1991].

Figure 5.3.1 is an example of the HY-SPLIT output using FNL wind data (see http://www.arl.noaa.gov/ready-bin/fnl.pl for a detailed description of the FNL data archive). Two 3-dimentional 14-day back trajectories initiating from FME at 00 EST (05 UTC), 7/3/1999 are calculated with starting height 500 m and 1500 m, respectively. From 7/2/1999 to 7/5/1999 was a special event in which a high concentration of crustal material (Si, Al, Ca, and Fe) was observed at FME (Figure 4.1.3(a) and Figure 4.4.6). The back trajectories indicate a southerly transport within the U.S. and an easterly transport from the Atlantic Ocean outside the North America. This pattern is rarely seen since westerly and northwesterly transport strongly dominates at FME (e.g. Figure 5.3.2). The back trajectories may extend to North Africa. Though not conclusive, the elevated crustal level could originate from the burst of Saharan dust storm in summer (also see *Prospero* [1999]).

Since the emphasis is on local and regional particulate matter, another observational (actual) wind field data, Eta Data Assimilation System (EDAS, model range: 20 °N – 55 °N, 60 °W – 130 °W, 0 – ~ 6 km; see http://www.arl.noaa.gov/ss/transport/edas.html), covering only North America with higher resolution is used as the HY-SPLIT model

input. The EDAS data are archived every three hours, but a trajectory can be calculated at every hour using interpolation.

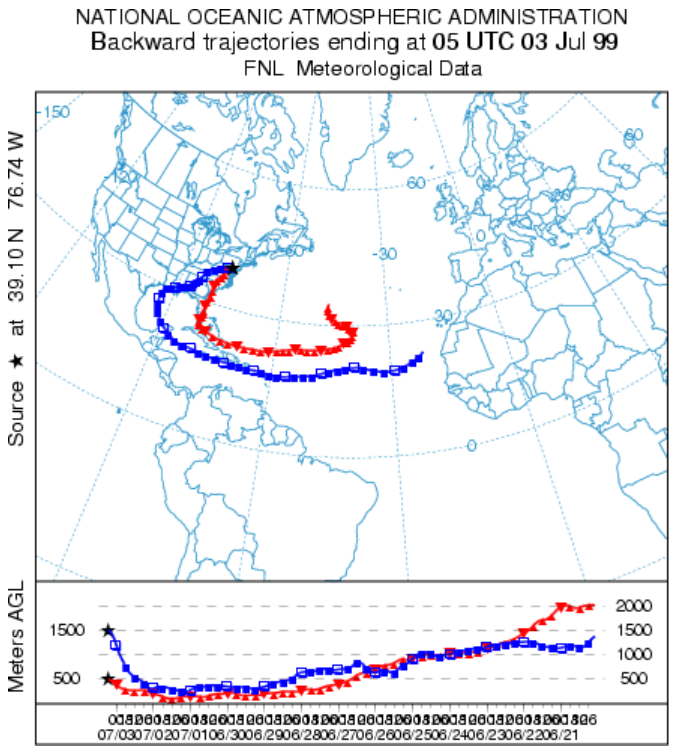

Figure 5.3.1 14-day back trajectories initiating from FME at 00 EST, 7/3/1999.

Meteorological conditions such as wind direction can change significantly within 24 hours. To match with the 24-hr $PM_{2.5}$ data acquired in this study, the back trajectory representative for each day needs to be determined. An ensemble back trajectory method is developed. In this approach, the eastern U.S. (30 °N – 55 °N, 65 °W – 105 °W) is gridded into 1° × 1° areas (~ 40 km × 40 km). The vertical dimension from the surface to 4 km is divided into eight 500-m layers, for a total of 8000 cells in this analysis. Considering that transport over a regional scale (~ 1000 km) generally takes 2 - 3 d and

lifetime of fine particles against wet deposition is ~ 1 week, we decided to use 72-hr back trajectories for this study. Trajectories were calculated every 2 hours to capture diurnal-scale meteorology. To remove surface roughness effects but consider dispersion and mixing across PBL, the initial height of back trajectories is compromised at 500 m (~ 950 mbar) above FME. The history of incoming air on a particular day (i.e., the daily average back trajectory) is determined by counting endpoints of the 12 back trajectories in that day to calculate 'probability field'. A probability field is a matrix of ratios of air parcel residence time in each cell over ensemble time:

$$\text{Ensemble time} = 72\frac{\text{hour}}{\text{Trajectory}} \times 12\frac{\text{Trajectory}}{\text{day}} \times N \text{ Sampling days.}$$

Using this concept we can calculate daily ($N = 1$), monthly ($N = 30$), or annual probability fields for the receptor. This 'averaging' approach reduces random errors created in each trajectory calculation.

Two kinds of probability fields, 'background' (BG) and 'high-day' (HD), are especially useful. The BG probability field is an overall average, containing trajectories of the entire sampling period. To construct a HD probability field, only days of a relatively strong signal are selected. Here, the signal can be ambient concentration, source contribution, etc. The difference between HD and BG probability field (only positive values used), referred to as 'incremental' probability field, contains information about the source location.

Since the size of each cell in the EBT analysis is different and depends on its latitude, it is not the probability but the probability density (probability divided by the cell's size) that better represents the history of air parcels. To compensate for that, the probability reported hereafter has been divided by the cosine of its latitude. (This causes limited

differences in the mid-latitude region, and hereafter we use the term probability with the understanding that it is relative probability density.)

Figure 5.3.2 shows the BG probability field, based on 3192 back trajectories on 266 $PM_{2.5}$ sampling days. Note that the 266 days includes 3 summers (1999, 2000, and 2001), two winters (2000, 2001), two falls (1999, 2000), and one spring (2000). The original 3-dimensional matrix is squeezed into two 2-dimensional charts in order to present its horizontal and vertical components separately. The highest probability of 5 – 6% is at FME where all back trajectories initiate, and higher values extend to its northwest. Throughout the sampling period, northwesterly transport is so dominant that emissions from upwind west Pennsylvania, Ohio, and Michigan may have the greatest impact on our sampling site. In the vertical dimension, the trajectory ensemble generally spends equal time between 0 and 1.5 km (AGL). Usually an air parcel entrains more pollutants if it stays longer near the surface in source regions. However, a high probability of ensemble back trajectory at the lowest level (0 – 499 m) around the receptor, especially in summer, could indicate low-level convection that dilutes pollutants released locally. Trajectories in different seasons are segregated, and background probability field for each season is shown in Figure 5.3.3(a)-(d); the seasonal variation during the period of our study is limited. Major features include 1) northwesterly transport dominates in every season, 2) return flow (northeasterly transport) is more probable in summer and spring, and 3) trajectory residence time over the B-W corridor is significantly shorter in winter. The last point implies that wind is stronger in winter, and it could contribute to lower gaseous pollutant concentrations (fast removal).

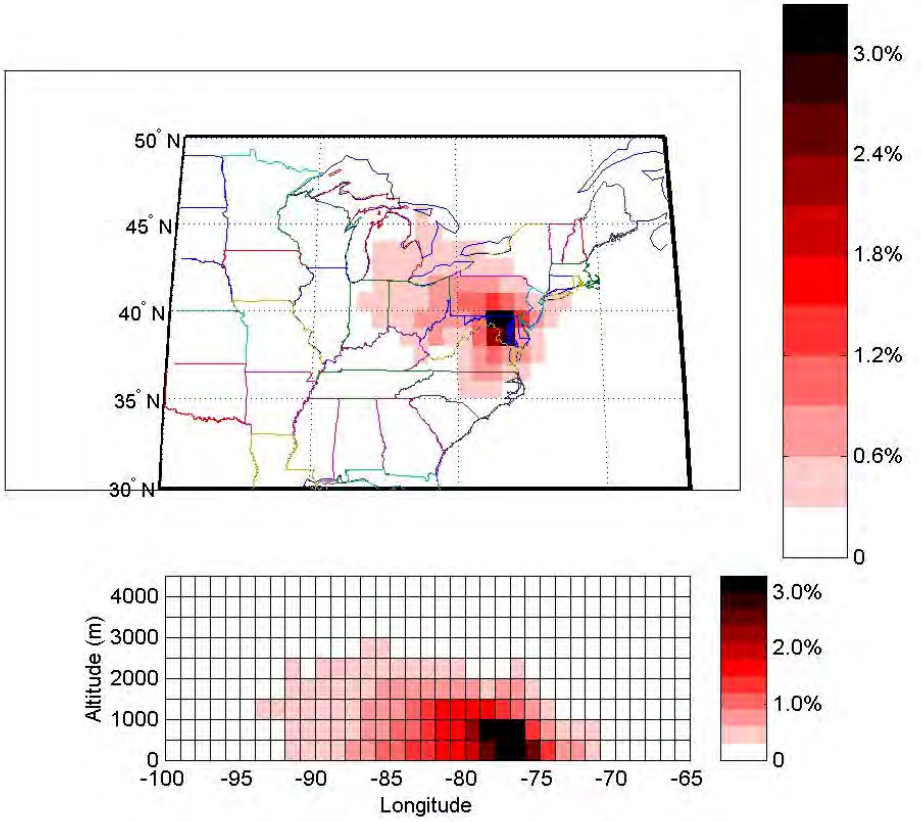

Figure 5.3.2 The background probability field for FME calculated using back trajectories of 266 sampling days between 7/1999 and 7/2001.

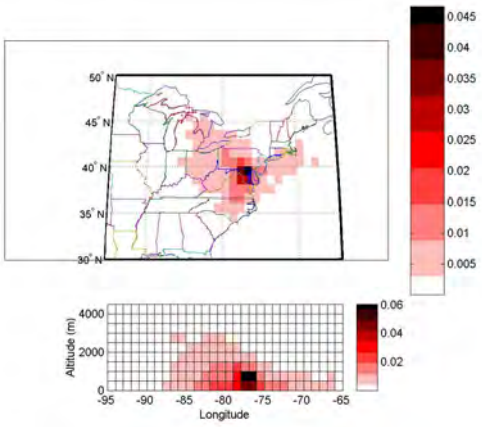

(a) Summer (104 days)

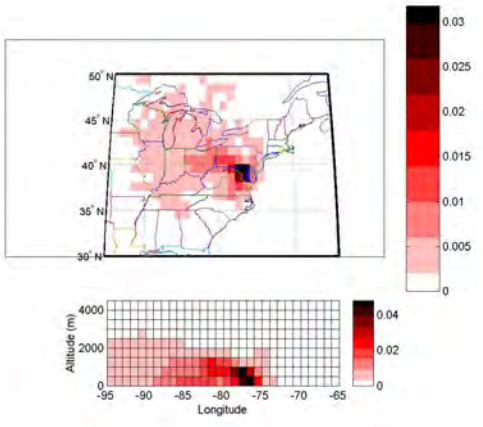

(c) Winter (65 days)

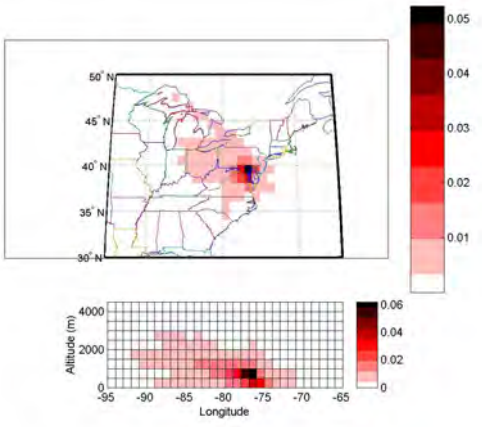

(b) Fall (66 days)

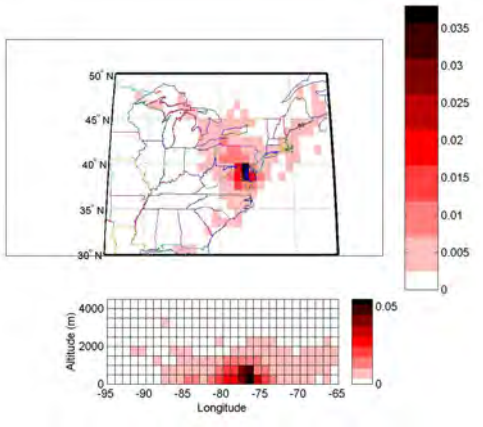

(d) Spring (31 days)

Figure 5.3.3(a)-(d) Seasonal average back trajectory probability field for FME.

5.4 Ensemble Back Trajectory Analysis

The fundamentals of the ensemble back trajectory (EBT) method have been described in Section 5.3. The next step is to apply the method to study transport associated with each fine particulate species to resolve likely source regions. Since the EBT approach depends on the difference between 'high-day' (HD) and background (BG) probability fields, extra caution need to be exercised in selecting days containing relatively strong signal. When using ambient concentration as a signal, trace elements Al, Br, Ca, Cu, Fe, K^+, K, Na^+, Pb, S, Se, Si, and Zn are more suitable for this study because of the higher confidence level in their measurements. K is strongly correlated to K^+ (Table 3.7.1), and thereby only K^+ is chosen to run the EBT analysis; SO_4^{2-} can be represented by S. Since the gas/particle partitioning in the HNO_3/NO_3^- and NH_3/NH_4^+ systems depends on ambient temperature and relative humidity (Section 4.2), T-NO_3^- and T-NH_4^+ could be more conserved and appropriate for running the analyses. Finally, carbonaceous material (EC and OC) is also included despite the potential analytical uncertainties.

To ensure a significant source signal, in this case 'high' days are defined as the first 10% high concentration days for each species considered. A HD probability field, therefore, includes all trajectories in the first 26 high concentration days. The calculated HD and incremental probability field for each species is presented in Appendix 3. There are many different patterns found, and this indicates that origins of fine particles are complicated. The HD probability field for S suggests a dominant westerly transport from the U.S. Midwest, but its incremental probability field implies a minor southerly transport

as well (Figure A.3.1). A relatively low incremental probability over the B-W corridor suggests that S emission from local sources is not significant.

Na^+ is thought to originate from marine sources. The incremental probability field for Na^+ does support this assumption (Figure A.3.2). The source region of Na^+ seems to be broad along the U.S. east coast and extends into the Atlantic Ocean. Northeasterly and southwesterly trajectories likely contribute equally on high Na^+ days. Results from the EBT analysis for S and Na^+ agree with the concepts established earlier so well that we feel confident applying this technique to other species.

Crustal elements Si and Al are well correlated with each other, and their probability fields share a similar pattern (Figure A.3.3 and Figure A.3.4). The source region of Al and Si could be extremely broad. There seem to be three major pathways of transport: 1) southerly transport along the east coast, 2) southwesterly transport through Mississippi, Tennessee, and Kentucky, and 3) northwesterly transport from north Ohio. The high incremental probability region that characterizes the first two pathways extends farther south; the actual source region could be outside the modeled domain. Section 5.3 has introduced the possibility of long-rang transport of Saharan dust. At least, Al and Si are not generated locally, and this explains the regional nature of crustal material described in Section 4.4. Another important component in crustal material is Ca; Ca^{2+} is also important for soil fertility. At FME, Ca is only moderately correlated to Al and Si (Table 3.7.1). Figure A.3.5 indicates that Ca concentration is dominated by a northwesterly transport, similar to the third pathway of Al and Si. Ca originates primarily from limestone erosion. Whether earth in the Great Lakes area is rich in limestone needs further studies. The source region of Fe could be closer and narrower (Figure A.3.6). The

incremental probability field suggests a short northeasterly transport. Cu shows a similar pattern (Figure A.3.10). Fe at FME is not likely to be all crustal. This finding supports the results from factor analysis in Section 5.2.

The incremental probability fields of Pb, Br, Se, K^+, and Zn have a common local maximum. Moreover, the high concentration days of Pb and Se are clearly coupled with atmospheric subsidence over FME (see vertical dimension in Figure A.3.8 and Figure A.3.12). Strong local contributions are implied. Note that these elements are linked to various types of combustions (mobile emission, vegetative burning, coal combustion, and oil burning, etc) and certainly could be urban and released nearby.

T-NO_3^- seems to be local as well, but its source region could be larger than Se, Pb or Zn (Figure A.3.15). This is reasonable if mobile emission in the corridor is a major source of NO_3^- and HNO_3.

The incremental probability field of T-NH_4^+ shows two separate maxima, one local and one around the Ohio River Valley (Figure A.3.16). NH_4^+ appears in the atmosphere mostly in the form of $(NH_4)_2SO_4$, NH_4HSO_4, and NH_4NO_3. Therefore, the two maximum could actually correspond to NH_4NO_3 and $(NH_4)_2SO_4$, respectively. EC is mostly local (Figure A.3.14). Compared to T-NO_3^-, however, the incremental probability field of EC also indicates weak long-range transport. OC shows a complicated probability field (Figure A.3.13). There are certainly local contributions, but long-range transport of OC is possible from two distant regions: the south Midwest (including West Virginia) and the North Carolina/Virginia states.

Major mass contributing species such as sulfate, nitrate, and carbonaceous material usually have multiple sources. Using ambient concentration as signal to construct HD

probability field has a risk of weakening signatures of a particular source and therefore could be misleading in resolving source locations. Source contribution, if available, can serve as a better criterion for selecting 'high' days. The sources of $PM_{2.5}$ at FME has been studied in Section 5.2 using the UNMIX factor analysis. UNMIX calculates both factor composition and contribution. The ensemble back trajectory method can be utilized to study the transport associated each of these factors and attempt to determine the spatial distribution of their likely sources.

The chance of contributing distinguishably is different for each factor. The criterion for selecting 'high' days is a compromise; including too many days will weaken the signal of a factor while including too few days may produce unrepresentative results. The similarity between HD and BG probability fields can be estimated from ||HD - BG||, sum of the absolute values of the incremental matrix elements. (Notice that the sum of incremental matrix elements always vanishes.) Starting with a HD of any daily probability field, ||HD - BG|| is usually ~ 2 (without the correction for latitude); it is gradually reduced to zero as the HD includes more and more days until finally HD becomes BG. We calculate a series of HD probability fields for F1 - F6, starting from the day of the strongest factor contribution, then adding the second, and so on. Figure 5.4.1 shows the ||HD - BG|| of F1 – F6 as a function of number of 'high' days included, in comparison with that obtained by adding days selected randomly. The curves representing factors are higher than the 'random' curve, and this indicates that daily ensemble back trajectories do contain certain degrees of source signal. The F1 curve shows the weakest slope, suggesting that the back trajectory leading to a strong contribution of F1 is most favored. In this study, we adopt the HD probability field in

which ||HD - BG|| equals 0.75 since 1) ||HD - BG|| between 0.5 and 1 is where the factor curves differ from the random curve most, 2) ||HD - BG|| / ||BG|| ratio of 0.75 means a HD 75% different from BG, which provides an adequate contrast between the HD and BG field, and 3) making ||HD - BG|| constant for all 6 factors facilitate analyzing the extent of source region from the incremental probability field. Therefore, the number of days (and the fraction out of 266 days) used to construct HD for F1 – F6 is 56 (21%), 37 (14%), 34 (13%), 29 (11%), 42 (16%), and 38 (14%), respectively. Due to inherent uncertainties, the calculated incremental probability field may not indicate the exact

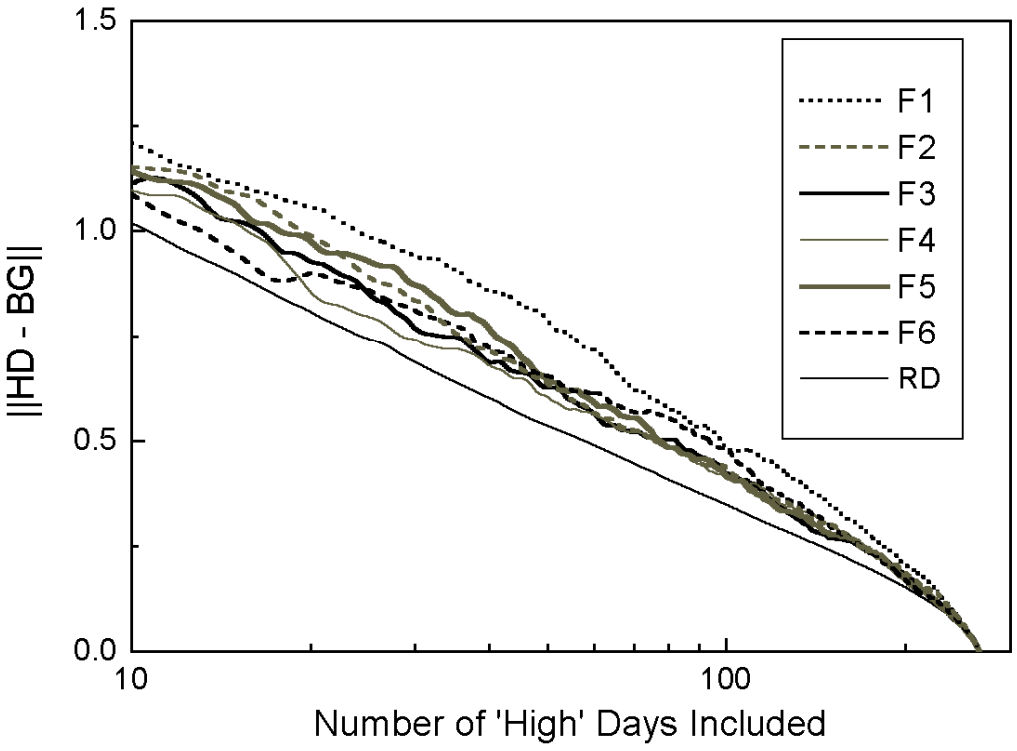

Figure 5.4.1 Deviation of HD from BG probability field as a function of number of 'high' days included. F1 – F6 are 6 $PM_{2.5}$ mass-contributing factors resolved by UNMIX. RD indicates the 'random' curve (see text).

contribution of each cell within the modeled domain. It is, however, useful for comparing direction of transport and extent of source region of the 6 factors.

The incremental probability fields of F1 – F6 are shown in Figure 5.4.2(a)-(f), respectively. In Figure 5.4.2(a), high probabilities appear in a broad area west of FME but excluding FME. Longer residence times of air parcels over FME coupled with lower factor contribution, confirming that F1 is non-local. Regions of higher probability include the Ohio River Valley and Pittsburgh area; trajectories stay near the surface when passing through these suspected source regions. F1 represents regional sulfate that likely originates from the Midwest and moves into the Mid-Atlantic region along the northern border of Maryland. Significant OC and EC in F1 explain most of the non-local carbonaceous aerosols that could originate from the Midwest.

In contrast, the incremental probability field of F2, another sulfate contributor, indicates a strong local maximum (Fig. 5.4.2(b)). F2 generally contributes more strongly under stagnant or stable conditions in which winds are weak and trajectories move slowly in the PBL. This supports the concept that F2 represents a nearby sulfate source. The incremental probability is higher at north of FME; this fine feature links F2 to the cities of Baltimore and Philadelphia, both of which have quite a few coal-burning power plants. The F2 contribution is weaker in summer when turbulence in the PBL is strong. An incremental probability field using only summer trajectories suggests that stronger F2 contribution in summer (still more from north of FME) is usually related to atmospheric subsidence associated with synoptic scale high-pressure systems.

F5 represents a proximate source as well (Figure 5.4.2(e)). Compared to F2, the incremental probability of F5 is less concentrated around FME, and therefore F5 may

have a broader source region. Higher probability remains at low levels, extending from Washington D.C. to rural areas in central and western Virginia, where residential wood stoves and fireplaces are often utilized in winter. According to the National Emission Trend 1996 (USEPA, 2000), the fraction of CO emission from residential wood burning is higher in Virginia (13%) and West Virginia (10%) than in Maryland (3%), Pennsylvania (4%), Delaware (2%) and New Jersey (1%). F5 contributes stronger in winter probably due to the stronger emissions and more stable PBL.

The origin of F6 seems to come from northeast of FME (Figure 5.4.2(f)). Between New York and Philadelphia is a heavily industrialized corridor close to FME. Factories such as blast furnaces and iron smelters can release trace metals (Cu and Fe) appearing in F6. According to the USEPA 1996 National Emission Trend [*USEPA*, 2000], active blast furnaces and steel mills in this region include Atlantic States Cast Iron Pipe, New Jersey Steel Corporation (New Jersey), U.S. Steel Corporation, Lukens Steel Corporation (Philadelphia), and Bethlehem Steel Corporation (Baltimore). A dispersion model with finer spatial resolution is required to investigate contributions of these point sources.

In Figure 5.4.1, the incremental probability fields of F3 and F4 contain the lowest degree of source signature (e.g. their curves are closest to the 'random' curve). These two factors' contributions depend least on the air parcel back trajectory, implying that the mobile emissions are too close to FME to be resolved by the ensemble back trajectory analysis. (Note that major highways within a few miles from FME include I-95, MD-295, US-1 (west), MD-175 (northeast), and MD-32 (south)). F3, similar to F2, has a local maximum probability at the ground level but shows little preferred direction of transport (Figure 5.4.2(c)). The F4 probability field shows no specific region of dominance (Figure

5.4.2(d)). F3 and F4 are thought to represent the same mobile source, but they dominate in different seasons. F3 is stronger in winter when high contribution of a local source is generally caused by stable near-surface conditions. F4 contributes more in fall and summer when air parcels spend less time within the PBL, and atmospheric subsidence under the influence of high-pressure systems is often responsible for strong local contributions. The ensemble back trajectory analysis shown in Fig. 8(c)-(d) clearly corroborates these concepts.

In summary, the 6 factors resolved by the UNMIX factor analysis includes local and regional sources. The aged sulfate source (F1) is clearly regional in nature. Most of the contributions from wood burning (F5) and factory emission (F6) are considered outside the B-W corridor as well. Based on the calculated factor composition and day-to-day contribution, we can calculate the seasonal variation of contribution from each factor and determine the relative importance of local and regional sources. Figure 5.4.3 shows the $PM_{2.5}$ mass contributions, by season, from the 6 factors (F1 – F6). The summertime fine PM is dominated by the regional sulfate source (F1), and the fraction of local contribution, mobile sources (F3 & F4) plus local sulfate (F2), increase from < 30% in summer to > 60% in winter. Though high $PM_{2.5}$ episodes were observed in both summer and winter, they could have completely different causes. Subsequently, this implies that different approaches to control fine PM and haze pollution may be applicable in summer and winter.

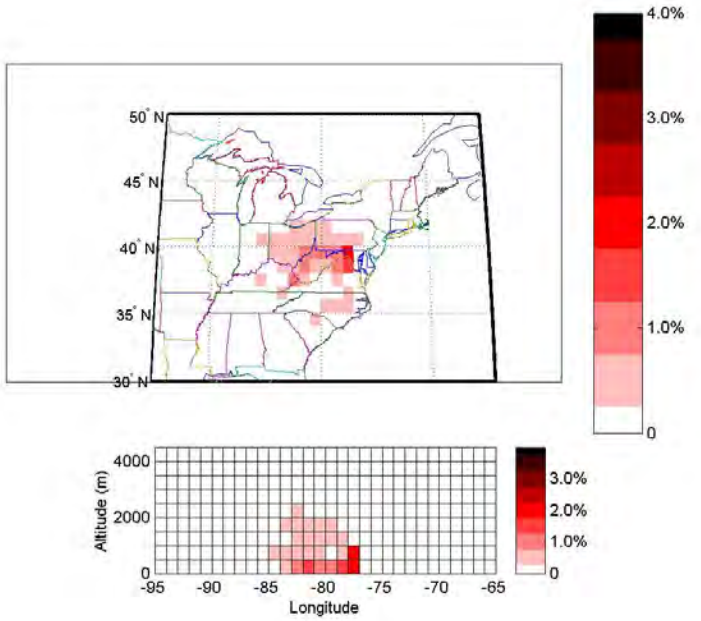

(a) F1 (regional sulfate)

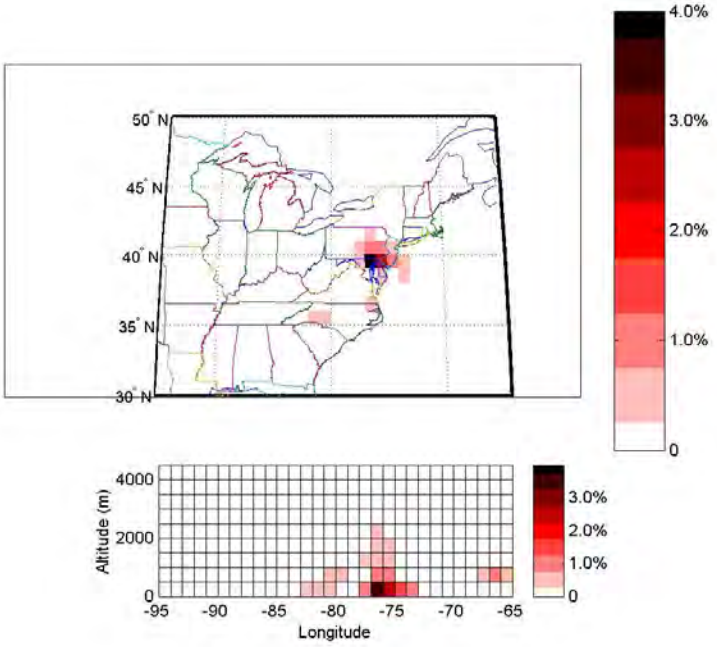

(b) F2 (Se, sulfate)

Figure5.4.2 The incremental probability fields (HD - BG) calculated for factor (a) F1 (b) F2 derived by UNMIX.

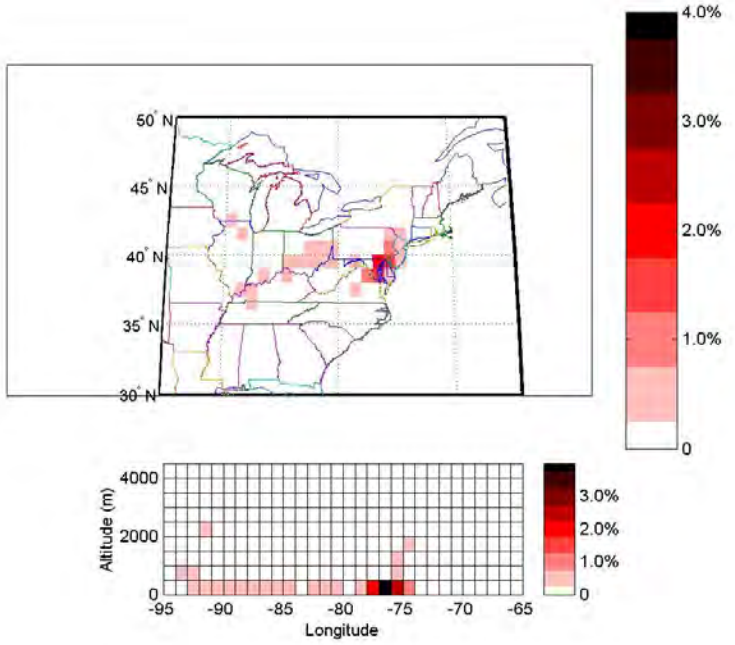

(c) F3 (secondary nitrate, mobile)

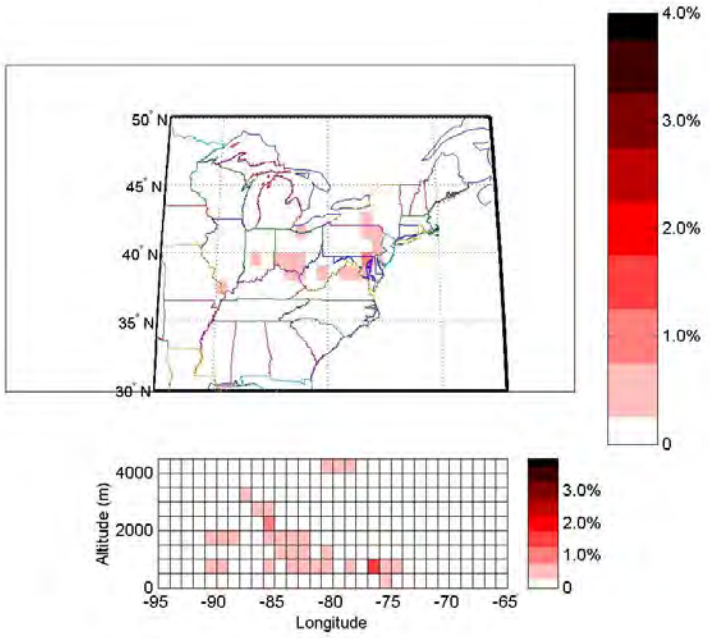

(d) F4 (mobile)

Figure5.4.2 The incremental probability fields (HD - BG) calculated for factor (c) F3 (d) F4 derived by UNMIX.

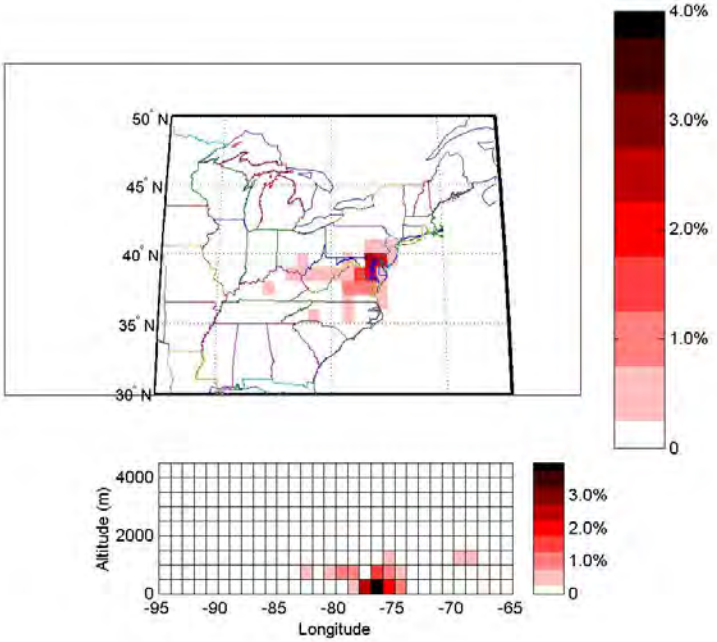

(e) F5 (Br, K, wood smoke)

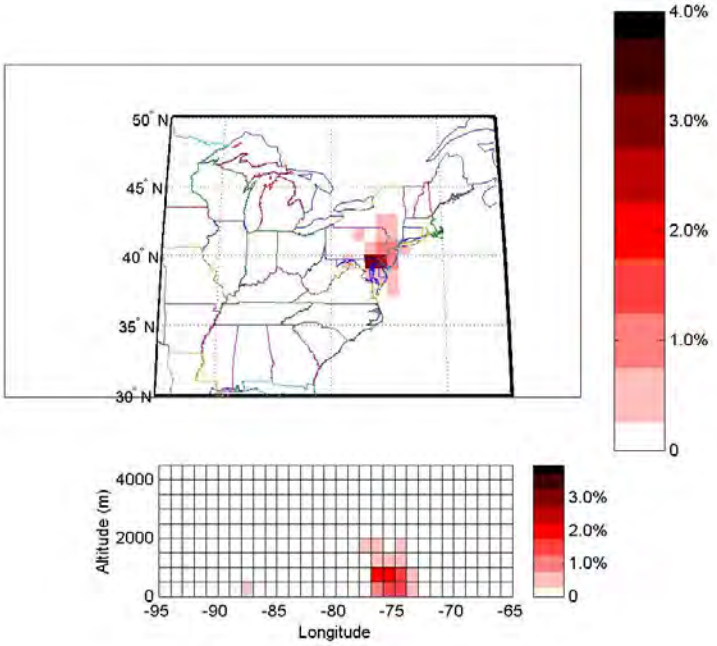

(f) F6 (Cu, Fe, and sulfate)

Figure5.4.2 The incremental probability fields (HD - BG) calculated for factor (e) F5 (f) F6 derived by UNMIX.

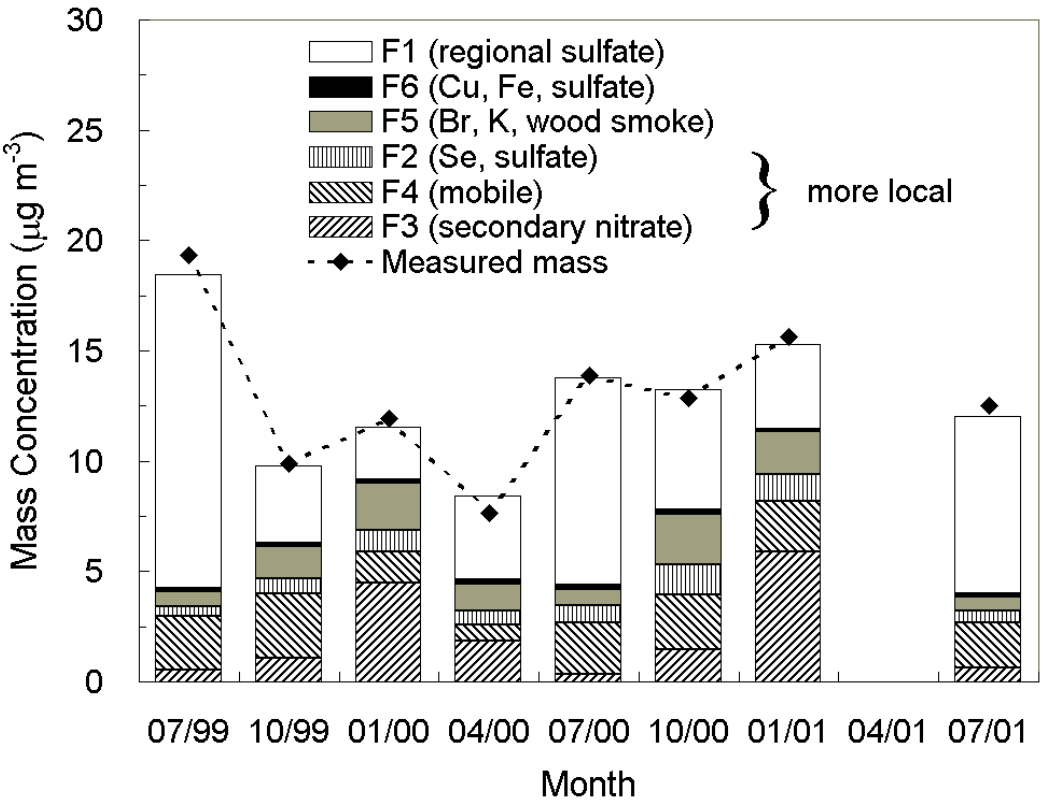

Figure 5.4.3 Monthly mean contribution of six UNMIX-resolved factors to the $PM_{2.5}$ mass at FME.

Chapter 6 Conclusions

6.1 Summary

Twenty-four-hr chemically speciated $PM_{2.5}$ and continuous CO, SO_2, and NO_y measurements have been carried out at FME, a suburban site in the Baltimore-Washington corridor, as the primary field experiment for the Maryland Aerosol Research and Characterization (MARCH-Atlantic) study. A few previous studies have attempted to characterize the ambient fine aerosols in this region. However, the seasonal variation of $PM_{2.5}$ mass concentration and chemical composition in a typical urban environment has not been investigated thoroughly by far. The foci of the MARCH-Atlantic study include 1) studying the seasonal variation in the concentration and composition of urban $PM_{2.5}$, 2) determining the performance of the mass-based FRM in comparison with other aerosol sampling techniques as a compliance tool, and 3) identifying the most likely $PM_{2.5}$ sources to the region studied.

The $PM_{2.5}$ mass was measured independently using three techniques, DRI SFS, FRM, and TEOM. SFS and FRM measured 24-hr average concentration while TEOM performed sub-hourly measurements. The results from SFS and FRM closely agree with each other ($r^2 > 0.98$). FRM is slightly higher than SFS, and this is likely due to the different $PM_{2.5}$ size-cut inlets installed. The 24-hr TEOM data also agree with SFS except

in winter when a significant deficit is observed. This could result from the loss of volatile species as the sample air is preheated to 50 ºC. The annual mean $PM_{2.5}$ mass concentration is ~ 13 μg m^{-3}. Throughout the whole sampling period, only two months have monthly mean $PM_{2.5}$ concentration exceeding 15 μg m^{-3}, the annual NAAQS.

The sulfate concentration is generally higher in summer but its precursor gas, SO_2, peaks in winter. Faster SO_2-to-SO_4^{2-} conversion rates in summer partly explain the observed trend. Aerosol nitrate is very low in summer since most of the nitrate remains gaseous nitric acid at high ambient temperature. Nitric acid coexists with gaseous ammonia in summer, but in winter it depletes ammonia to form ammonium nitrate that becomes a significant fraction of $PM_{2.5}$ in winter. Sulfate, nitrate, and ammonium dominate the inorganic fraction of fine aerosol. The gas/particle partitioning in this inorganic system can be well explained using a thermodynamic model, ISORROPIA, which considers the equilibrium of major inorganic species in the aerosol bulk and in the gaseous phase, disregarding aerosol size effects such as surface energy, heterogeneous chemistry, etc. At FME, ammonium is generally not sufficient to neutralize both sulfate and nitrate, and this suggests $PM_{2.5}$ being a slightly acidic mixture at this location. Compared to the inorganics, carbonaceous aerosol does not show a clear seasonal cycle (except a minimum in spring 2000).

The $PM_{2.5}$ mass closure is examined by comparing the $PM_{2.5}$ gravimetric mass to reconstructed mass that is calculated by summing mass of major $PM_{2.5}$ components, including sulfate, nitrate, ammonium, OM, EC, and crustal material. The sampling artifacts for OC need to be considered; these include 1) adsorption of VOC on quartz filters and 2) evaporation of semi-volatile OC. To compensate for the uncertainty,

specially designed sequential filters are used and analyzed to estimate OC on Teflon filter, which is then multiplied by 1.4 to obtain OM. Crustal material is calculated empirically using 4 trace elements (Al, Si, Ca, and Fe). The reconstructed mass is highly correlated with the gravimetric mass (r^2 ~ 0.94) and generally agrees with the gravimetric mass within ±15%. A minor deficit on high $PM_{2.5}$ days likely results from unaccounted species such as water.

On average, more than 50% of the $PM_{2.5}$ mass is inorganic. Ammoniated sulfate dominates in summer, especially in high $PM_{2.5}$ episodes. In winter, sulfate and nitrate contribute nearly equally. Since the seasonal and day-to-day variations in OC and EC concentration are less significant than sulfate and nitrate, carbonaceous material can account for more than 50% of the $PM_{2.5}$ mass on low $PM_{2.5}$ days but just ~ 30% in high $PM_{2.5}$ episodes.

The spatial variation of major $PM_{2.5}$ components is investigated by comparing our data with concurrent measurements at three IMPROVE sites in the Mid-Atlantic region. Sulfate and crustal material are found to be more regional (~ 1000 km range) in character. Sulfate is believed to be influenced by the long-range transport from the U.S. Midwest. The diurnal variation of SO_2 shows a mid-day high, suggesting that SO_2 could originate from more distant sources as well.

The concentration of crustal material is driven by special and rare events. Air parcel back trajectory links an extreme crustal episode to the long-range transport of Saharan dust. Nitrate and EC concentrations are much higher in the B-W corridor than in the upwind and downwind rural areas, suggesting that nitrate and EC are more influenced by

local emissions. The spatial variation of OC is more complicated. OC could originate from both local and regional sources.

NO_y and CO are good tracers for nitrate and EC, respectively. The diurnal variation of NO_y and CO shows two peaks corresponding to the morning and evening rush hours and a mid-day low likely due to PBL dilution. Traffic emission in the corridor is believed to be a major contributor to nitrate and EC. EC is well correlated with CO in every month, but the EC/CO slope is higher in summer than in winter. In a source-dominated environment (i.e. ambient level driven by dispersion), this suggests either a stronger EC emission in summer or a stronger CO emission in winter. This EC/CO slope leads to an estimation of the EC emission inventory at 0.32 ± 0.12 Tg (EC) yr^{-1} for North America.

The source locations of various species in $PM_{2.5}$ are then studied using an ensemble back trajectory analysis that calculates the difference between probability fields of air parcel back trajectories on 'background' and 'high' days. As expected, the major source region of S and Na^+ are the Midwest and eastern seashore, respectively. Elements that have a broad non-local source region include Al, Si, Ca, and OC, and elements that seem to originate more from local sources include Pb, Zn, Se, EC, K^+, and T-NO_3^-.

To characterize the potential sources of $PM_{2.5}$, the $PM_{2.5}$ and trace gases data were studied using a factor analysis model, UNMIX. UNMIX estimates the number of factors in the dataset and determine both factor composition and contribution. A model of six factors that contribute to the $PM_{2.5}$ mass is constructed using mass, SO_4^{2-}, NO_3^-, NH_4^+, EC, OC, Br, Se, and Cu as the model inputs. Two factors appear to represent contribution of an aged sulfate source and a fresh SO_2/sulfate source. The model also suggests contributions from wood burning and Cu/Fe processing plants. Mobile emission is

represented by two factors distinguished by their nitrate content, and this implies that a source with its composition varying temporally may dissociate into two or more factors in the factor analysis.

The source location for the six factors identified is also studied using the ensemble back trajectory analysis. The aged sulfate source is more regional in character, resulting from emissions in the Midwest, while the fresh SO_2/sulfate mixture likely originates from more proximate urban areas north of FME. The wintertime wood burning occurs more in rural areas of Virginia and West Virginia, and the mobile-related factors are dominated by traffic emissions on the nearby highways. Figure 6.1.1 illustrates the distribution of these source regions. The summertime fine PM is dominated by the regional sulfate

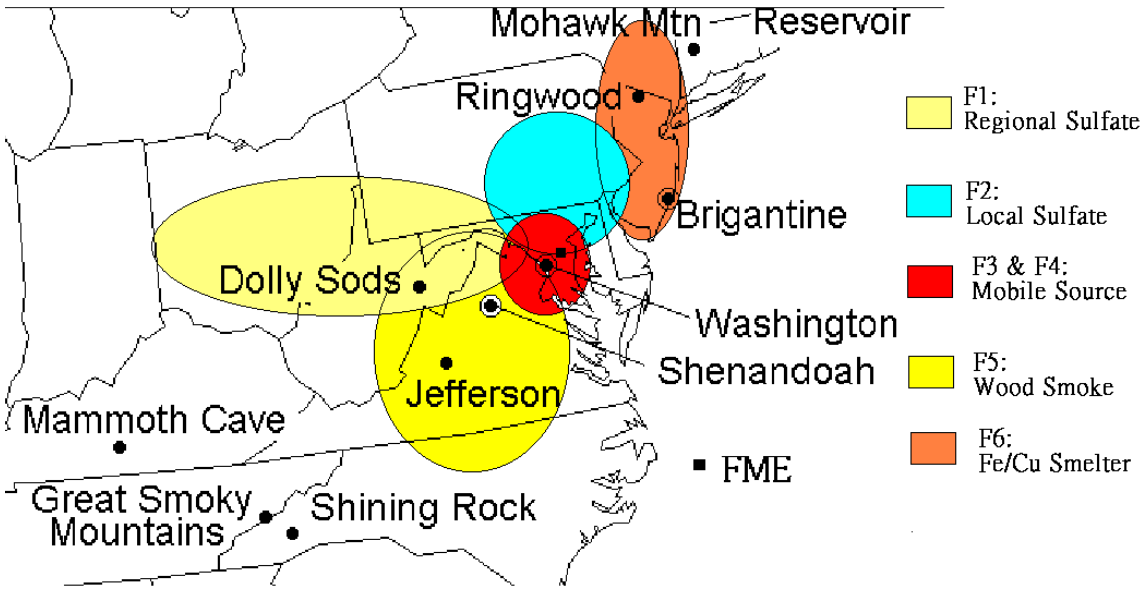

Figure 6.1.1 Schematic plot of probable source regions of the six factors resolved by UNMIX factor analysis in this study.

source, and the fraction of local contribution, mobile sources plus local sulfate, increases from < 30% in summer to > 60% in winter. Though high $PM_{2.5}$ episodes were observed in both summer and winter, the relative importance of local and regional sources could be very different. This finding has implications on the fine PM and haze regulation.

6.2 Recommendations

Due to the increasing concern of aerosol health and environmental effects, the United States Environment Protection Agency (USEPA) has proposed a new National Ambient Air Quality Standard for $PM_{2.5}$, a Federal Reference Method for sampling $PM_{2.5}$ mass concentration, and initiated 7 supersites located in 7 major U.S. cities (Baltimore, Fresno, Houston, Los Angeles, New York, Pittsburgh, and St. Louis) to investigate the characteristics, origins, and effects of urban aerosols. The observation and analysis presented in this dissertation is ahead of major conclusions of the EPA supersite studies in time. Therefore, these results are valuable for EPA as intercomparisons to those from supersites, which will be available in the next few years. The study also provides crucial information for the State of Maryland to consider the $PM_{2.5}$ control strategies.

Haze is one of the most visible forms of air pollution. Visibility reduction is caused primarily by scattering and absorption of visible light by aerosols. The atmospheric extinction coefficient measured at the Baltimore Washington International Airport was compared to the $PM_{2.5}$ data at FME. Extinction is found to depend on not only $PM_{2.5}$ concentration but also relative humidity. Sulfate and nitrate are highly hydroscopic. Water associated with sulfate and nitrate, as estimated by the ISORROPIA

thermodynamic model, is significant on humid days. Aerosol water may have a relatively high scattering efficiency and further reduce the visibility. In a severe haze episode, water is suggested to account for > 50% of the atmospheric extinction. When inorganic aerosol is reduced, visibility improvement may benefit from not only a lower dry PM mass but also less water. More accurate measurements of aerosol water content at ambient condition are required to confirm this concept.

Reducing inorganic aerosol concentration can be achieved by controlling SO_2 and NO_x emissions. For a most simplified scheme in which only aerosol thermodynamic equilibriums are considered (without gas-phase and heterogeneous reactions such as O_3 chemistry), controlling this region's NO_x emission in summer only reduces the HNO_3 concentration and has limited impact on the $PM_{2.5}$ level. Controlling NO_x emission could be more effective in winter though it may still remove more HNO_3 than NO_3^-. Controlling SO_2 emission should be very effective in summer since it lowers the sulfate production that is crucial in summer haze episodes. In winter, nitrate could substitute in an ammonia rich environment when sulfate is low. Note that the $PM_{2.5}$ reduction efficiency through controlling NO_x and SO_2 emission can be different in other regions such as Pittsburgh (higher SO_4^{2-} concentration in any season) or the Maryland Eastern Shore (stronger NH_4^+ and NH_3 sources). In any case, controlling ammonia emission, if possible, will reduce $PM_{2.5}$ most effectively since it prevents the formation of both ammoniated nitrate and sulfate.

Organic matter may be the most important species regarding the $PM_{2.5}$ health effect, but it remains the least known component in $PM_{2.5}$. Mobile emissions certainly contribute to OC. However, the OC/EC ratio is relatively high at FME, implying significant secondary

OC converted from gaseous precursors. Secondary OC can account for 70% of OC in this study if primary OC is estimated using EC as a tracer. Spatial correlations and ensemble back trajectory analysis both suggest that OC is more regional than EC. Chemically speciated OC measurement such as mass spectrometry will be crucial for source apportionment of OC in the future.

Haze is regional in space and episodic in time. The formation of haze depends highly on meteorological conditions such as wind speed, wind direction, PBL depth, temperature, and relative humidity. To further understand this problem, the chemistry and optical properties of fine aerosols need to be measured at multiple locations and higher time resolution (e.g., hourly measurement). Once an hourly resolution is available, the factor analysis and ensemble back trajectory method used in this study need to be refined to handle the data. So far, one of the major difficulties in factor analysis is how to handle secondary species that are formed in the atmosphere. For back trajectory analysis, the coarse grid size and trajectory begin heights selected to remove surface roughness effects limit its application in resolving contributions from more local sources. Improving the receptor modeling tool by using high resolution mesoscale model (MM5) and comparing it with emission inventory data and aerosol chemistry/transport models will be essential for studying PM and haze pollution in the future.

Appendix 1 Monthly Statistics of $PM_{2.5}$

Table A.1.1 Monthly statistics of $PM_{2.5}$ mass, chemical composition, and analytical uncertainty (AU) at FME in July 1999.

Species	Mean*	Std. Dev.*	10%*	25%*	50%*	75%*	90%*	AU (RMS)	# of data	# > 2×AU
Mass	19.8803	9.6056	7.0006	12.6753	19.0104	29.5786	33.2588	5%	33	33
SO_4^{2-}	8.0631	4.7498	2.0161	4.8347	7.1568	12.1868	14.8212	6%	33	33
NO_3^-	0.3080	0.1760	0.1598	0.2153	0.2626	0.3175	0.5022	20%	33	33
NH_4^+	2.6877	1.5216	0.6665	1.6689	2.4647	3.6478	4.9551	7%	33	33
OC	4.1836	1.2495	2.7677	3.3857	3.8541	4.8824	5.6900	9%	33	33
EC	1.1775	0.4356	0.7493	0.8404	1.1575	1.4522	1.8601	9%	33	33
OC (BQ)	1.2665	0.4155	0.7841	0.9776	1.2714	1.6249	1.7716	22%	31	29
OC (TBQ)	2.5202	0.7396	1.5773	1.9047	2.5919	3.1940	3.4607	10%	31	31
Cl^-	0.0135	0.0410	0.0000	0.0000	0.0049	0.0051	0.0181	100%	33	1
Na^+	0.0420	0.0385	0.0125	0.0175	0.0284	0.0448	0.0856	8%	33	33
K^+	0.0639	0.1580	0.0160	0.0206	0.0297	0.0394	0.0650	7%	33	33
Na	0.0250	0.0267	0.0000	0.0042	0.0149	0.0436	0.0693	100%	33	9
Mg	0.0132	0.0121	0.0012	0.0058	0.0118	0.0178	0.0236	100%	33	4
Al	0.0721	0.0819	0.0204	0.0298	0.0443	0.0661	0.1608	11%	33	33
Si	0.1703	0.2025	0.0532	0.0709	0.0888	0.1601	0.4073	7%	33	33
Ph	0.0024	0.0033	0.0000	0.0000	0.0000	0.0047	0.0076	100%	33	0
S	3.1213	1.7728	0.8097	1.8489	2.8905	4.6332	5.6905	5%	33	33
Cl	0.0000	0.0000	0.0000	0.0000	0.0000	0.0000	0.0000	100%	33	0
K	0.0906	0.2214	0.0210	0.0312	0.0427	0.0547	0.0843	7%	33	33
Ca	0.0401	0.0226	0.0200	0.0258	0.0312	0.0478	0.0635	11%	33	33
Ti	0.0026	0.0048	0.0000	0.0000	0.0000	0.0028	0.0103	100%	33	0
Va	0.0009	0.0017	0.0000	0.0000	0.0000	0.0011	0.0033	100%	33	0
Cr	0.0002	0.0003	0.0000	0.0000	0.0000	0.0003	0.0008	100%	33	0
Mn	0.0018	0.0013	0.0006	0.0009	0.0014	0.0024	0.0038	76%	33	9
Fe	0.0740	0.0629	0.0290	0.0390	0.0465	0.0804	0.1464	6%	33	33
Co	0.0001	0.0001	0.0000	0.0000	0.0000	0.0001	0.0002	100%	33	0
Ni	0.0014	0.0011	0.0003	0.0006	0.0012	0.0017	0.0031	53%	33	14
Cu	0.0015	0.0010	0.0007	0.0010	0.0013	0.0018	0.0024	49%	33	15
Zn	0.0090	0.0046	0.0044	0.0059	0.0077	0.0118	0.0150	10%	33	33
Ga	0.0001	0.0003	0.0000	0.0000	0.0000	0.0002	0.0005	100%	33	0
As	0.0002	0.0003	0.0000	0.0000	0.0000	0.0002	0.0007	100%	33	0
Se	0.0018	0.0011	0.0007	0.0009	0.0016	0.0026	0.0035	37%	33	21
Br	0.0035	0.0015	0.0018	0.0023	0.0033	0.0044	0.0054	18%	33	32
Rb	0.0001	0.0001	0.0000	0.0000	0.0001	0.0002	0.0003	100%	33	0
Sr	0.0011	0.0028	0.0000	0.0001	0.0003	0.0006	0.0011	77%	33	3
Yt	0.0003	0.0002	0.0001	0.0001	0.0003	0.0004	0.0006	100%	33	0
Zr	0.0002	0.0003	0.0000	0.0000	0.0001	0.0003	0.0006	100%	33	0
Mo	0.0004	0.0003	0.0000	0.0002	0.0004	0.0005	0.0008	100%	33	0
Pd	0.0003	0.0005	0.0000	0.0000	0.0000	0.0006	0.0011	100%	33	0
Ag	0.0007	0.0011	0.0000	0.0000	0.0000	0.0011	0.0022	100%	33	0
Cd	0.0020	0.0021	0.0000	0.0000	0.0016	0.0030	0.0048	100%	33	0
In	0.0008	0.0011	0.0000	0.0000	0.0000	0.0013	0.0028	100%	33	0
Sn	0.0026	0.0021	0.0000	0.0011	0.0025	0.0039	0.0053	100%	33	0
Sb	0.0016	0.0022	0.0000	0.0000	0.0002	0.0031	0.0056	100%	33	0
Ba	0.0216	0.0127	0.0095	0.0126	0.0188	0.0242	0.0393	100%	33	0
La	0.0103	0.0117	0.0000	0.0000	0.0070	0.0146	0.0241	100%	33	0
Au	0.0001	0.0001	0.0000	0.0000	0.0000	0.0000	0.0002	100%	33	0
Hg	0.0002	0.0003	0.0000	0.0000	0.0000	0.0002	0.0006	100%	33	0
Tl	0.0000	0.0001	0.0000	0.0000	0.0000	0.0000	0.0001	100%	33	0
Pb	0.0041	0.0024	0.0016	0.0026	0.0034	0.0053	0.0060	49%	33	13
Ur	0.0002	0.0002	0.0000	0.0000	0.0001	0.0003	0.0004	100%	33	0
HNO_3	4.3745	2.5056	1.9697	2.7655	3.6525	5.8113	7.0918	10%	33	33
NH_3	0.7115	0.3694	0.2136	0.4172	0.6908	0.8965	1.2256	33%	33	25
$T\text{-}NO_3^-$	5.1426	2.5592	2.5622	3.5386	4.9151	6.4302	7.5741	8%	33	33
$T\text{-}NH_4^+$	3.3620	1.4885	1.5994	2.3188	3.0364	4.4026	5.4812	6%	33	33

* Concentration in unit $\mu g\ m^{-3}$.

Table A.1.2 Monthly statistics of $PM_{2.5}$ mass, chemical composition, and analytical uncertainty (AU) at FME in October 1999.

Species	Mean*	Std. Dev.*	10%*	25%*	50%*	75%*	90%*	AU (RMS)	# of data	# > 2×AU
Mass	9.8894	5.1877	4.7221	6.5519	8.6633	10.8082	17.2349	6%	34	34
SO_4^{2-}	3.1791	1.7455	1.5876	1.9874	2.5066	3.9896	5.7439	7%	34	34
NO_3^-	0.6037	0.5687	0.1162	0.2265	0.3401	0.9769	1.3513	14%	34	30
NH_4^+	1.1516	0.6375	0.5180	0.6983	0.9457	1.4655	2.0771	6%	34	34
OC	2.7174	1.2884	1.2936	1.8650	2.4520	3.2340	4.9459	11%	34	34
EC	1.1121	0.4521	0.5030	0.7796	1.1621	1.3507	1.5169	8%	34	34
OC (BQ)	0.4049	0.3146	0.0391	0.1373	0.3418	0.6303	0.8537	53%	34	14
OC (TBQ)	0.9830	0.4138	0.5209	0.6342	0.9318	1.2545	1.4554	12%	34	34
Cl^-	0.0069	0.0131	0.0000	0.0000	0.0000	0.0102	0.0276	100%	34	0
Na^+	0.0385	0.0211	0.0182	0.0234	0.0345	0.0471	0.0640	27%	34	27
K^+	0.0404	0.0237	0.0172	0.0215	0.0359	0.0482	0.0818	9%	34	34
Na	0.0268	0.0206	0.0028	0.0123	0.0224	0.0342	0.0533	100%	34	6
Mg	0.0067	0.0059	0.0000	0.0004	0.0064	0.0093	0.0131	100%	34	1
Al	0.0165	0.0090	0.0045	0.0097	0.0159	0.0222	0.0290	37%	34	22
Si	0.0512	0.0231	0.0252	0.0421	0.0489	0.0552	0.0870	10%	34	34
Ph	0.0023	0.0027	0.0000	0.0000	0.0008	0.0039	0.0064	100%	34	3
S	1.1850	0.6339	0.5673	0.7455	0.9931	1.4351	1.8886	5%	34	34
Cl	0.0001	0.0007	0.0000	0.0000	0.0000	0.0000	0.0000	100%	34	0
K	0.0553	0.0323	0.0236	0.0303	0.0465	0.0680	0.1115	9%	34	34
Ca	0.0207	0.0101	0.0101	0.0132	0.0195	0.0255	0.0318	21%	34	31
Ti	0.0025	0.0019	0.0000	0.0015	0.0025	0.0035	0.0041	100%	34	0
Va	0.0018	0.0028	0.0000	0.0001	0.0010	0.0021	0.0038	100%	34	0
Cr	0.0002	0.0003	0.0000	0.0000	0.0000	0.0003	0.0006	100%	34	0
Mn	0.0015	0.0014	0.0002	0.0005	0.0013	0.0017	0.0034	100%	34	4
Fe	0.0554	0.0370	0.0187	0.0307	0.0465	0.0704	0.0852	6%	34	34
Co	0.0003	0.0003	0.0000	0.0000	0.0002	0.0004	0.0005	100%	34	0
Ni	0.0009	0.0013	0.0000	0.0002	0.0006	0.0010	0.0018	100%	34	4
Cu	0.0020	0.0015	0.0008	0.0013	0.0016	0.0023	0.0034	43%	34	15
Zn	0.0139	0.0065	0.0062	0.0082	0.0130	0.0188	0.0233	8%	34	34
Ga	0.0001	0.0002	0.0000	0.0000	0.0000	0.0003	0.0005	100%	34	0
As	0.0006	0.0007	0.0000	0.0001	0.0005	0.0008	0.0013	100%	34	1
Se	0.0015	0.0012	0.0004	0.0006	0.0011	0.0018	0.0031	63%	34	12
Br	0.0042	0.0026	0.0016	0.0028	0.0034	0.0053	0.0081	18%	34	31
Rb	0.0001	0.0002	0.0000	0.0000	0.0000	0.0001	0.0002	100%	34	0
Sr	0.0004	0.0008	0.0000	0.0000	0.0002	0.0003	0.0011	100%	34	2
Yt	0.0001	0.0002	0.0000	0.0000	0.0001	0.0002	0.0004	100%	34	0
Zr	0.0001	0.0002	0.0000	0.0000	0.0000	0.0002	0.0003	100%	34	0
Mo	0.0003	0.0004	0.0000	0.0000	0.0002	0.0005	0.0009	100%	34	0
Pd	0.0008	0.0015	0.0000	0.0000	0.0000	0.0008	0.0030	100%	34	0
Ag	0.0003	0.0006	0.0000	0.0000	0.0000	0.0005	0.0008	100%	34	0
Cd	0.0002	0.0007	0.0000	0.0000	0.0000	0.0000	0.0007	100%	34	0
In	0.0004	0.0009	0.0000	0.0000	0.0000	0.0000	0.0020	100%	34	0
Sn	0.0016	0.0023	0.0000	0.0000	0.0004	0.0029	0.0046	100%	34	0
Sb	0.0023	0.0029	0.0000	0.0000	0.0009	0.0042	0.0065	100%	34	0
Ba	0.0017	0.0042	0.0000	0.0000	0.0000	0.0000	0.0068	100%	34	0
La	0.0076	0.0095	0.0000	0.0000	0.0020	0.0141	0.0232	100%	34	0
Au	0.0004	0.0005	0.0000	0.0000	0.0001	0.0007	0.0013	100%	34	0
Hg	0.0001	0.0002	0.0000	0.0000	0.0000	0.0003	0.0005	100%	34	0
Tl	0.0003	0.0003	0.0000	0.0000	0.0004	0.0005	0.0007	100%	34	0
Pb	0.0055	0.0034	0.0024	0.0031	0.0045	0.0070	0.0108	43%	34	17
Ur	0.0002	0.0003	0.0000	0.0000	0.0002	0.0004	0.0006	100%	34	0
HNO_3	1.2856	1.3318	0.1496	0.4392	0.8983	1.6871	2.5774	19%	32	24
NH_3	0.6012	0.7751	0.0049	0.1970	0.3917	0.6914	1.5716	27%	32	24
$T\text{-}NO_3^-$	1.8991	1.5504	0.6286	0.9246	1.4582	2.2352	3.0811	11%	32	31
$T\text{-}NH_4^+$	1.9590	1.3099	0.8914	1.1479	1.5767	2.0574	3.5948	7%	34	34

* Concentration in unit $\mu g\ m^{-3}$.

Table A.1.3 Monthly statistics of $PM_{2.5}$ mass, chemical composition, and analytical uncertainty (AU) at FME in January 2001.

Species	Mean*	Std. Dev.*	10%*	25%*	50%*	75%*	90%*	AU (RMS)	# of data	# > 2×AU
Mass	12.1242	7.4126	4.5733	6.2394	10.5048	14.6357	22.7406	6%	33	33
SO_4^{2-}	3.0241	1.8696	1.2944	1.6662	2.1949	4.3993	5.7923	5%	33	33
NO_3^-	2.2670	2.0375	0.3939	0.8566	1.6074	2.6413	6.1500	22%	33	31
NH_4^+	1.5378	0.9949	0.6357	0.7331	1.3158	2.0426	3.0235	5%	33	33
OC	2.7197	1.6981	0.8704	1.5701	2.5820	3.2410	4.5982	11%	33	31
EC	1.0131	0.6772	0.3487	0.6557	0.8729	1.1422	1.8168	12%	33	32
OC (BQ)	0.3377	0.2659	0.0179	0.1301	0.3064	0.4897	0.7301	75%	33	7
OC (TBQ)	0.8701	0.4487	0.4606	0.5566	0.7442	1.1014	1.4225	12%	32	32
Cl^-	0.0451	0.0855	0.0000	0.0096	0.0097	0.0311	0.1150	56%	33	5
Na^+	0.0517	0.0297	0.0101	0.0321	0.0506	0.0725	0.0913	10%	33	30
K^+	0.0675	0.0673	0.0201	0.0318	0.0508	0.0681	0.1241	8%	33	33
Na	0.0412	0.0274	0.0000	0.0221	0.0409	0.0596	0.0745	79%	33	14
Mg	0.0133	0.0083	0.0026	0.0075	0.0138	0.0179	0.0228	100%	33	6
Al	0.0241	0.0100	0.0126	0.0171	0.0234	0.0320	0.0353	26%	33	29
Si	0.0471	0.0156	0.0299	0.0418	0.0454	0.0533	0.0630	11%	33	33
Ph	0.0024	0.0028	0.0000	0.0000	0.0018	0.0041	0.0062	100%	33	2
S	1.1095	0.6903	0.4809	0.6473	0.7963	1.6299	2.2344	5%	33	33
Cl	0.0257	0.0780	0.0000	0.0000	0.0000	0.0000	0.0483	88%	33	4
K	0.0832	0.0833	0.0270	0.0423	0.0640	0.0817	0.1559	8%	33	33
Ca	0.0198	0.0097	0.0097	0.0138	0.0169	0.0260	0.0303	23%	33	31
Ti	0.0030	0.0050	0.0000	0.0007	0.0015	0.0027	0.0056	100%	33	0
Va	0.0027	0.0029	0.0000	0.0006	0.0017	0.0031	0.0076	100%	33	0
Cr	0.0006	0.0004	0.0000	0.0002	0.0006	0.0009	0.0011	100%	33	0
Mn	0.0021	0.0021	0.0005	0.0010	0.0015	0.0022	0.0039	70%	33	6
Fe	0.0538	0.0557	0.0191	0.0260	0.0335	0.0505	0.1083	7%	33	33
Co	0.0004	0.0003	0.0001	0.0002	0.0003	0.0005	0.0006	100%	33	0
Ni	0.0014	0.0013	0.0005	0.0007	0.0009	0.0015	0.0036	66%	33	7
Cu	0.0020	0.0016	0.0006	0.0012	0.0017	0.0022	0.0039	43%	33	17
Zn	0.0187	0.0145	0.0075	0.0095	0.0141	0.0215	0.0349	7%	33	33
Ga	0.0003	0.0003	0.0000	0.0000	0.0002	0.0005	0.0007	100%	33	0
As	0.0008	0.0008	0.0001	0.0002	0.0006	0.0010	0.0018	100%	33	0
Se	0.0021	0.0018	0.0005	0.0010	0.0015	0.0027	0.0035	42%	33	14
Br	0.0059	0.0040	0.0023	0.0032	0.0048	0.0061	0.0126	14%	33	30
Rb	0.0002	0.0003	0.0000	0.0000	0.0001	0.0003	0.0006	100%	33	0
Sr	0.0007	0.0007	0.0001	0.0002	0.0004	0.0008	0.0015	100%	33	3
Yt	0.0002	0.0002	0.0000	0.0000	0.0002	0.0004	0.0004	100%	33	0
Zr	0.0002	0.0005	0.0000	0.0000	0.0001	0.0003	0.0004	100%	33	1
Mo	0.0001	0.0002	0.0000	0.0000	0.0000	0.0000	0.0003	100%	33	0
Pd	0.0001	0.0004	0.0000	0.0000	0.0000	0.0000	0.0004	100%	33	0
Ag	0.0004	0.0011	0.0000	0.0000	0.0000	0.0000	0.0015	100%	33	0
Cd	0.0013	0.0015	0.0000	0.0000	0.0008	0.0023	0.0035	100%	33	0
In	0.0018	0.0019	0.0000	0.0000	0.0015	0.0035	0.0045	100%	33	0
Sn	0.0040	0.0037	0.0000	0.0006	0.0034	0.0065	0.0092	100%	33	0
Sb	0.0032	0.0034	0.0000	0.0000	0.0029	0.0054	0.0067	100%	33	0
Ba	0.0038	0.0074	0.0000	0.0000	0.0000	0.0031	0.0183	100%	33	0
La	0.0055	0.0089	0.0000	0.0000	0.0000	0.0091	0.0210	100%	33	0
Au	0.0004	0.0004	0.0000	0.0000	0.0003	0.0006	0.0010	100%	33	0
Hg	0.0002	0.0003	0.0000	0.0000	0.0001	0.0004	0.0008	100%	33	0
Tl	0.0001	0.0001	0.0000	0.0000	0.0000	0.0001	0.0003	100%	33	0
Pb	0.0064	0.0047	0.0026	0.0035	0.0052	0.0064	0.0117	36%	33	21
Ur	0.0003	0.0003	0.0000	0.0000	0.0002	0.0005	0.0007	100%	33	0
HNO_3	0.4036	0.8740	-0.5123	-0.0526	0.1894	0.5158	1.7219	100%	33	0
NH_3	0.1882	0.2389	-0.0093	0.0638	0.1245	0.3207	0.5065	82%	33	12
$T\text{-}NO_3^-$	1.3192	1.1347	0.2972	0.5417	0.8146	1.7554	3.0752	69%	33	0
$T\text{-}NH_4^+$	1.8194	1.0652	0.7419	1.0161	1.8199	2.3869	3.4391	7%	33	33

* Concentration in unit $\mu g\ m^{-3}$.

Table A.1.4 Monthly statistics of $PM_{2.5}$ mass, chemical composition, and analytical uncertainty (AU) at FME in April 2000.

Species	Mean*	Std. Dev.*	10%*	25%*	50%*	75%*	90%*	AU (RMS)	# of data	# > 2×AU
Mass	7.6638	2.6579	4.5225	5.6405	7.1597	9.8755	10.8890	7%	31	31
SO_4^{2-}	3.2786	1.5604	2.0051	2.2782	2.8697	3.5978	5.0907	6%	31	31
NO_3^-	0.9836	0.7521	0.2324	0.3763	0.8543	1.3753	1.9611	12%	31	29
NH_4^+	1.1892	0.4622	0.7108	0.8289	1.0937	1.4808	1.9003	6%	31	31
OC	2.2644	1.0637	0.9710	1.5016	2.2171	2.7031	3.4524	17%	31	31
EC	0.6889	0.2731	0.2981	0.5680	0.6873	0.8538	0.9743	19%	31	31
OC (BQ)	0.6052	0.3106	0.2507	0.3903	0.6104	0.7689	0.9793	36%	31	22
OC (TBQ)	1.5277	0.7430	0.5681	0.8772	1.5417	1.8504	2.6777	18%	31	31
Cl^-	0.0287	0.0564	0.0000	0.0000	0.0000	0.0216	0.1175	120%	31	4
Na^+	0.0396	0.0303	0.0081	0.0149	0.0341	0.0497	0.0748	30%	31	22
K^+	0.0315	0.0159	0.0140	0.0188	0.0305	0.0392	0.0479	11%	31	31
Na	0.0356	0.0265	0.0085	0.0168	0.0304	0.0524	0.0652	94%	31	11
Mg	0.0156	0.0132	0.0052	0.0084	0.0111	0.0180	0.0308	100%	31	1
Al	0.0322	0.0240	0.0139	0.0181	0.0232	0.0405	0.0593	22%	31	28
Si	0.0881	0.0757	0.0322	0.0443	0.0713	0.0991	0.1418	51%	31	12
Ph	0.0027	0.0033	0.0000	0.0000	0.0007	0.0055	0.0077	100%	31	5
S	1.0720	0.4707	0.6985	0.7509	0.9107	1.2078	1.7032	5%	31	31
Cl	0.0008	0.0033	0.0000	0.0000	0.0000	0.0000	0.0000	100%	31	0
K	0.0469	0.0227	0.0203	0.0327	0.0406	0.0564	0.0695	10%	31	31
Ca	0.0255	0.0167	0.0112	0.0136	0.0219	0.0287	0.0443	16%	31	31
Ti	0.0020	0.0040	0.0000	0.0000	0.0000	0.0017	0.0056	100%	31	0
Va	0.0005	0.0010	0.0000	0.0000	0.0000	0.0004	0.0021	100%	31	0
Cr	0.0000	0.0001	0.0000	0.0000	0.0000	0.0000	0.0000	100%	31	0
Mn	0.0012	0.0013	0.0000	0.0001	0.0008	0.0018	0.0035	100%	31	4
Fe	0.0715	0.0837	0.0174	0.0293	0.0483	0.0744	0.1250	8%	31	31
Co	0.0001	0.0001	0.0000	0.0000	0.0000	0.0000	0.0001	100%	31	0
Ni	0.0007	0.0008	0.0000	0.0001	0.0005	0.0010	0.0019	100%	31	5
Cu	0.0021	0.0054	0.0004	0.0007	0.0011	0.0016	0.0019	50%	31	6
Zn	0.0132	0.0109	0.0042	0.0065	0.0090	0.0136	0.0295	9%	31	31
Ga	0.0000	0.0001	0.0000	0.0000	0.0000	0.0000	0.0000	100%	31	0
As	0.0009	0.0006	0.0002	0.0004	0.0007	0.0014	0.0015	100%	31	0
Se	0.0013	0.0012	0.0002	0.0006	0.0009	0.0020	0.0027	72%	31	10
Br	0.0036	0.0018	0.0018	0.0023	0.0031	0.0049	0.0060	23%	31	28
Rb	0.0003	0.0002	0.0001	0.0002	0.0003	0.0005	0.0006	100%	31	0
Sr	0.0002	0.0002	0.0000	0.0000	0.0002	0.0003	0.0004	100%	31	0
Yt	0.0000	0.0001	0.0000	0.0000	0.0000	0.0000	0.0000	100%	31	0
Zr	0.0004	0.0003	0.0000	0.0001	0.0003	0.0007	0.0008	100%	31	0
Mo	0.0002	0.0003	0.0000	0.0000	0.0000	0.0001	0.0005	100%	31	0
Pd	0.0009	0.0011	0.0000	0.0000	0.0003	0.0018	0.0023	100%	31	0
Ag	0.0030	0.0023	0.0000	0.0013	0.0030	0.0045	0.0051	100%	31	0
Cd	0.0002	0.0005	0.0000	0.0000	0.0000	0.0000	0.0008	100%	31	0
In	0.0009	0.0015	0.0000	0.0000	0.0000	0.0013	0.0028	100%	31	0
Sn	0.0040	0.0038	0.0000	0.0011	0.0025	0.0055	0.0102	100%	31	0
Sb	0.0011	0.0022	0.0000	0.0000	0.0000	0.0011	0.0034	100%	31	0
Ba	0.0182	0.0133	0.0018	0.0073	0.0161	0.0287	0.0380	100%	31	0
La	0.0187	0.0147	0.0000	0.0109	0.0178	0.0239	0.0374	100%	31	0
Au	0.0001	0.0002	0.0000	0.0000	0.0000	0.0000	0.0001	100%	31	0
Hg	0.0001	0.0002	0.0000	0.0000	0.0000	0.0001	0.0005	100%	31	0
Tl	0.0002	0.0003	0.0000	0.0000	0.0001	0.0004	0.0005	100%	31	0
Pb	0.0036	0.0026	0.0006	0.0020	0.0033	0.0043	0.0055	76%	31	7
Ur	0.0001	0.0002	0.0000	0.0000	0.0000	0.0002	0.0004	100%	31	0
HNO_3	2.3317	1.2943	1.0825	1.4248	1.9231	3.0336	4.2036	11%	31	31
NH_3	0.6277	0.5660	0.0252	0.2152	0.5060	0.9159	1.4753	25%	31	23
T-NO_3^-	4.1276	2.0369	1.9323	2.4205	3.7977	5.4394	6.7469	6%	31	31
T-NH_4^+	1.9247	0.9782	1.0479	1.1861	1.6295	2.4817	3.2461	7%	31	31

* Concentration in unit $\mu g\ m^{-3}$.

Table A.1.5 Monthly statistics of $PM_{2.5}$ mass, chemical composition, and analytical uncertainty (AU) at FME in July 2000.

Species	Mean*	Std. Dev.*	10%*	25%*	50%*	75%*	90%*	AU (RMS)	# of data	# > 2×AU
Mass	13.8887	6.3733	6.5248	9.7300	12.2996	18.7449	22.6002	5%	33	33
SO_4^{2-}	5.8736	3.3231	2.1957	3.4435	5.3461	7.8948	10.3675	6%	33	33
NO_3^-	0.2289	0.1658	0.1169	0.1442	0.1658	0.2303	0.4352	11%	33	33
NH_4^+	1.8483	0.9404	0.6809	1.2351	1.7934	2.3964	2.9709	6%	33	33
OC	3.1661	0.8943	2.0189	2.6697	3.1288	3.6578	4.2937	9%	33	33
EC	1.0638	0.3517	0.6128	0.8143	1.1045	1.2783	1.4610	11%	33	33
OC (BQ)	1.0203	0.3671	0.5984	0.7230	1.0193	1.2775	1.4976	27%	33	31
OC (TBQ)	1.8445	0.7100	1.0220	1.2285	1.6083	2.3683	2.8225	10%	33	33
Cl^-	0.0225	0.0200	0.0000	0.0147	0.0178	0.0283	0.0496	100%	33	4
Na^+	0.0210	0.0153	0.0081	0.0103	0.0180	0.0233	0.0332	43%	33	16
K^+	0.0720	0.2080	0.0180	0.0211	0.0292	0.0389	0.0722	7%	33	33
Na	0.0231	0.0222	0.0000	0.0028	0.0197	0.0354	0.0522	100%	33	4
Mg	0.0127	0.0258	0.0000	0.0000	0.0017	0.0156	0.0365	100%	33	4
Al	0.0321	0.0235	0.0120	0.0201	0.0280	0.0361	0.0463	25%	33	28
Si	0.0877	0.0620	0.0287	0.0513	0.0783	0.0886	0.1531	33%	33	23
Ph	0.0030	0.0037	0.0000	0.0000	0.0015	0.0062	0.0087	100%	33	3
S	2.1894	1.2162	0.7393	1.5003	1.9019	2.8601	3.8314	5%	33	33
Cl	0.0000	0.0000	0.0000	0.0000	0.0000	0.0000	0.0000	100%	33	0
K	0.0879	0.2596	0.0212	0.0265	0.0360	0.0460	0.0755	7%	33	33
Ca	0.0213	0.0095	0.0103	0.0138	0.0197	0.0277	0.0353	22%	33	30
Ti	0.0027	0.0023	0.0000	0.0000	0.0029	0.0042	0.0058	100%	33	0
Va	0.0019	0.0016	0.0000	0.0000	0.0020	0.0032	0.0037	100%	33	0
Cr	0.0003	0.0003	0.0000	0.0000	0.0002	0.0004	0.0007	100%	33	0
Mn	0.0019	0.0010	0.0009	0.0014	0.0020	0.0021	0.0030	78%	33	5
Fe	0.0534	0.0249	0.0226	0.0371	0.0484	0.0672	0.0812	6%	33	33
Co	0.0002	0.0002	0.0000	0.0000	0.0002	0.0003	0.0004	100%	33	0
Ni	0.0009	0.0007	0.0001	0.0004	0.0006	0.0013	0.0017	100%	33	5
Cu	0.0024	0.0012	0.0010	0.0015	0.0023	0.0030	0.0034	38%	33	23
Zn	0.0121	0.0060	0.0054	0.0082	0.0119	0.0140	0.0168	10%	33	33
Ga	0.0005	0.0004	0.0000	0.0001	0.0004	0.0009	0.0010	100%	33	0
As	0.0005	0.0004	0.0000	0.0002	0.0004	0.0007	0.0011	100%	33	0
Se	0.0019	0.0013	0.0006	0.0009	0.0018	0.0023	0.0040	47%	33	17
Br	0.0033	0.0011	0.0020	0.0027	0.0032	0.0040	0.0047	24%	33	32
Rb	0.0002	0.0002	0.0000	0.0001	0.0002	0.0003	0.0005	100%	33	0
Sr	0.0008	0.0020	0.0000	0.0001	0.0003	0.0005	0.0016	100%	33	4
Yt	0.0001	0.0001	0.0000	0.0000	0.0000	0.0002	0.0003	100%	33	0
Zr	0.0006	0.0003	0.0003	0.0004	0.0005	0.0007	0.0008	100%	33	0
Mo	0.0009	0.0005	0.0004	0.0005	0.0009	0.0012	0.0016	100%	33	0
Pd	0.0003	0.0007	0.0000	0.0000	0.0000	0.0000	0.0013	100%	33	0
Ag	0.0009	0.0014	0.0000	0.0000	0.0002	0.0012	0.0030	100%	33	0
Cd	0.0018	0.0021	0.0000	0.0000	0.0014	0.0027	0.0045	100%	33	0
In	0.0006	0.0011	0.0000	0.0000	0.0000	0.0005	0.0023	100%	33	0
Sn	0.0039	0.0030	0.0001	0.0016	0.0037	0.0058	0.0084	100%	33	0
Sb	0.0020	0.0029	0.0000	0.0000	0.0008	0.0030	0.0049	100%	33	0
Ba	0.0092	0.0144	0.0000	0.0000	0.0011	0.0169	0.0254	100%	33	0
La	0.0091	0.0151	0.0000	0.0000	0.0000	0.0110	0.0311	100%	33	0
Au	0.0005	0.0004	0.0000	0.0002	0.0005	0.0009	0.0011	100%	33	0
Hg	0.0000	0.0001	0.0000	0.0000	0.0000	0.0000	0.0000	100%	33	0
Tl	0.0002	0.0003	0.0000	0.0000	0.0000	0.0004	0.0007	100%	33	0
Pb	0.0046	0.0025	0.0016	0.0034	0.0041	0.0061	0.0073	55%	33	13
Ur	0.0001	0.0003	0.0000	0.0000	0.0000	0.0000	0.0006	100%	33	0
HNO_3	3.7626	1.7184	2.0035	2.5699	3.7095	4.5232	5.6111	8%	33	33
NH_3	0.8365	0.5334	0.3136	0.4786	0.7677	1.1570	1.4281	21%	33	30
$T\text{-}NO_3^-$	4.7732	1.8815	2.4316	3.7589	4.6301	5.8935	6.6417	6%	33	33
$T\text{-}NH_4^+$	2.7701	1.2528	1.5051	1.6812	2.2418	3.5746	4.7290	5%	33	33

* Concentration in unit $\mu g\ m^{-3}$.

Table A.1.6 Monthly statistics of $PM_{2.5}$ mass, chemical composition, and analytical uncertainty (AU) at FME in October 2000.

Species	Mean*	Std. Dev.*	10%*	25%*	50%*	75%*	90%*	AU (RMS)	# of data	# > 2×AU
Mass	12.8656	8.0998	4.4572	6.3900	11.5239	18.5466	21.3977	6%	32	32
SO_4^{2-}	4.9267	3.7189	1.4126	2.2678	4.3668	7.1689	8.5794	6%	32	32
NO_3^-	0.8159	0.7263	0.2369	0.4147	0.5997	1.0087	1.5159	11%	32	32
NH_4^+	1.7755	1.3483	0.4164	0.8278	1.6185	2.7040	3.0711	5%	32	32
OC	3.1061	1.2832	1.6329	1.9758	2.8690	4.2881	4.7122	14%	32	32
EC	1.2154	0.6555	0.4444	0.7395	1.1510	1.6314	1.8258	19%	32	32
OC (BQ)	0.6859	0.4156	0.2097	0.3257	0.6578	0.9385	1.2478	31%	32	21
OC (TBQ)	1.1847	0.3520	0.6925	0.8961	1.1868	1.4227	1.6230	15%	32	32
Cl^-	0.0160	0.0410	0.0000	0.0000	0.0037	0.0133	0.0211	100%	32	2
Na^+	0.0428	0.0601	0.0066	0.0150	0.0228	0.0542	0.0819	10%	32	28
K^+	0.0498	0.0283	0.0204	0.0279	0.0416	0.0614	0.0940	12%	32	32
Na	0.0620	0.0596	0.0155	0.0333	0.0537	0.0725	0.0880	57%	32	16
Mg	0.0228	0.0231	0.0034	0.0092	0.0197	0.0269	0.0483	94%	32	5
Al	0.0248	0.0123	0.0124	0.0153	0.0226	0.0328	0.0438	27%	32	29
Si	0.0875	0.0534	0.0436	0.0527	0.0822	0.1078	0.1213	30%	32	24
Ph	0.0018	0.0030	0.0000	0.0000	0.0000	0.0027	0.0068	100%	32	3
S	1.8368	1.3137	0.4560	0.8841	1.6947	2.7023	3.3385	5%	32	32
Cl	0.0060	0.0145	0.0000	0.0000	0.0000	0.0007	0.0145	100%	32	3
K	0.0614	0.0330	0.0277	0.0365	0.0531	0.0738	0.1074	8%	32	32
Ca	0.0391	0.0243	0.0171	0.0259	0.0337	0.0431	0.0690	12%	32	32
Ti	0.0037	0.0033	0.0000	0.0004	0.0038	0.0055	0.0083	100%	32	0
Va	0.0027	0.0023	0.0000	0.0004	0.0028	0.0043	0.0062	100%	32	0
Cr	0.0000	0.0001	0.0000	0.0000	0.0000	0.0000	0.0002	100%	32	0
Mn	0.0020	0.0016	0.0002	0.0007	0.0016	0.0028	0.0044	81%	32	8
Fe	0.0836	0.0559	0.0278	0.0402	0.0780	0.1032	0.1183	7%	32	32
Co	0.0002	0.0003	0.0000	0.0000	0.0000	0.0003	0.0005	100%	32	0
Ni	0.0014	0.0017	0.0000	0.0004	0.0010	0.0020	0.0028	71%	32	10
Cu	0.0027	0.0014	0.0010	0.0014	0.0028	0.0038	0.0044	35%	32	20
Zn	0.0196	0.0169	0.0055	0.0094	0.0145	0.0231	0.0382	8%	32	32
Ga	0.0001	0.0002	0.0000	0.0000	0.0000	0.0001	0.0003	100%	32	0
As	0.0006	0.0005	0.0000	0.0002	0.0005	0.0009	0.0014	100%	32	0
Se	0.0027	0.0033	0.0002	0.0010	0.0018	0.0030	0.0051	36%	32	15
Br	0.0062	0.0039	0.0019	0.0031	0.0055	0.0084	0.0106	15%	32	29
Rb	0.0002	0.0002	0.0000	0.0000	0.0002	0.0003	0.0004	100%	32	0
Sr	0.0006	0.0003	0.0002	0.0004	0.0006	0.0008	0.0009	100%	32	0
Yt	0.0001	0.0002	0.0000	0.0000	0.0000	0.0002	0.0003	100%	32	0
Zr	0.0002	0.0002	0.0000	0.0000	0.0000	0.0003	0.0006	100%	32	0
Mo	0.0007	0.0006	0.0000	0.0002	0.0006	0.0011	0.0016	100%	32	0
Pd	0.0006	0.0012	0.0000	0.0000	0.0000	0.0005	0.0019	100%	32	0
Ag	0.0011	0.0016	0.0000	0.0000	0.0002	0.0016	0.0033	100%	32	0
Cd	0.0014	0.0016	0.0000	0.0000	0.0009	0.0023	0.0039	100%	32	0
In	0.0013	0.0020	0.0000	0.0000	0.0004	0.0017	0.0032	100%	32	0
Sn	0.0029	0.0024	0.0000	0.0006	0.0030	0.0047	0.0060	100%	32	0
Sb	0.0020	0.0026	0.0000	0.0000	0.0010	0.0031	0.0056	100%	32	0
Ba	0.0059	0.0076	0.0000	0.0000	0.0040	0.0087	0.0147	100%	32	0
La	0.0067	0.0101	0.0000	0.0000	0.0000	0.0107	0.0253	100%	32	0
Au	0.0001	0.0002	0.0000	0.0000	0.0000	0.0000	0.0002	100%	32	0
Hg	0.0003	0.0003	0.0000	0.0000	0.0003	0.0005	0.0008	100%	32	0
Tl	0.0002	0.0003	0.0000	0.0000	0.0001	0.0004	0.0007	100%	32	0
Pb	0.0056	0.0036	0.0013	0.0027	0.0049	0.0076	0.0099	49%	32	15
Ur	0.0000	0.0001	0.0000	0.0000	0.0000	0.0000	0.0001	100%	32	0
HNO_3	2.4378	1.5625	0.5385	0.9832	2.4267	3.1629	4.7961	15%	32	31
NH_3	0.7770	0.3917	0.3953	0.4504	0.8331	1.0315	1.1204	24%	32	30
$T\text{-}NO_3^-$	4.5089	2.9181	1.0787	2.4169	4.0668	5.6034	8.5818	7%	32	32
$T\text{-}NH_4^+$	2.7962	1.4741	1.1284	1.7006	2.5418	3.6374	4.9960	6%	32	32

* Concentration in unit $\mu g\ m^{-3}$.

Table A.1.7 Monthly statistics of $PM_{2.5}$ mass, chemical composition, and analytical uncertainty (AU) at FME in January 2001.

Species	Mean*	Std. Dev.*	10%*	25%*	50%*	75%*	90%*	AU (RMS)	# of data	# > 2×AU
Mass	15.3029	8.5547	7.5847	8.8448	12.0528	19.5323	26.3000	6%	32	32
SO_4^{2-}	3.7389	1.7566	1.9557	2.5114	3.3556	4.5610	5.8519	5%	32	32
NO_3^-	2.9275	2.4889	0.8025	1.0726	1.6063	4.3318	7.3207	7%	32	32
NH_4^+	2.1988	1.2323	1.0497	1.2762	1.8425	2.8303	4.1025	6%	32	32
OC	3.4388	1.8768	1.7722	1.8328	3.0240	4.1057	6.6267	9%	32	32
EC	1.3942	0.8968	0.4873	0.5399	1.2588	1.9691	2.6327	9%	32	32
OC (BQ)	0.5141	0.2377	0.2582	0.3159	0.4258	0.6673	0.8413	40%	32	18
OC (TBQ)	1.0423	0.3025	0.7508	0.8028	0.9595	1.2270	1.3530	10%	32	32
Cl^-	0.1213	0.2459	0.0239	0.0274	0.0371	0.0938	0.2382	24%	32	11
Na^+	0.0344	0.0237	0.0142	0.0192	0.0270	0.0381	0.0666	11%	32	32
K^+	0.0649	0.0517	0.0271	0.0304	0.0413	0.0856	0.1175	9%	32	32
Na	0.1289	0.1354	0.0000	0.0000	0.1225	0.1851	0.3368	100%	32	2
Mg	0.0297	0.0218	0.0034	0.0143	0.0291	0.0453	0.0513	100%	32	6
Al	0.0240	0.0096	0.0135	0.0152	0.0245	0.0295	0.0353	41%	32	22
Si	0.0483	0.0201	0.0268	0.0342	0.0450	0.0643	0.0718	17%	32	31
Ph	0.0023	0.0036	0.0000	0.0000	0.0001	0.0040	0.0076	100%	32	2
S	1.2827	0.5882	0.7162	0.8996	1.1603	1.5707	1.9903	5%	32	32
Cl	0.0711	0.1829	0.0000	0.0000	0.0000	0.0573	0.2001	29%	32	9
K	0.0644	0.0467	0.0277	0.0333	0.0461	0.0791	0.1206	6%	32	32
Ca	0.0182	0.0097	0.0092	0.0110	0.0142	0.0223	0.0342	16%	32	32
Ti	0.0029	0.0023	0.0004	0.0017	0.0022	0.0034	0.0051	100%	32	0
Va	0.0033	0.0031	0.0009	0.0011	0.0022	0.0044	0.0079	100%	32	0
Cr	0.0003	0.0002	0.0000	0.0002	0.0003	0.0005	0.0006	100%	32	0
Mn	0.0026	0.0024	0.0009	0.0011	0.0016	0.0032	0.0057	28%	32	20
Fe	0.0661	0.0636	0.0226	0.0310	0.0393	0.0621	0.1427	8%	32	32
Co	0.0001	0.0002	0.0000	0.0000	0.0000	0.0001	0.0004	100%	32	0
Ni	0.0017	0.0018	0.0003	0.0005	0.0009	0.0020	0.0038	28%	32	16
Cu	0.0021	0.0017	0.0007	0.0010	0.0014	0.0024	0.0045	25%	32	23
Zn	0.0194	0.0197	0.0076	0.0081	0.0118	0.0172	0.0476	6%	32	32
Ga	0.0000	0.0001	0.0000	0.0000	0.0000	0.0000	0.0000	100%	32	0
As	0.0008	0.0006	0.0001	0.0004	0.0007	0.0013	0.0015	100%	32	0
Se	0.0029	0.0015	0.0017	0.0019	0.0024	0.0032	0.0046	17%	32	32
Br	0.0064	0.0045	0.0029	0.0037	0.0052	0.0069	0.0127	8%	32	32
Rb	0.0001	0.0002	0.0000	0.0000	0.0000	0.0001	0.0003	100%	32	0
Sr	0.0009	0.0010	0.0002	0.0004	0.0007	0.0010	0.0015	89%	32	4
Yt	0.0000	0.0001	0.0000	0.0000	0.0000	0.0000	0.0001	100%	32	0
Zr	0.0000	0.0001	0.0000	0.0000	0.0000	0.0000	0.0001	100%	32	0
Mo	0.0002	0.0003	0.0000	0.0000	0.0000	0.0003	0.0006	100%	32	0
Pd	0.0005	0.0008	0.0000	0.0000	0.0002	0.0008	0.0010	100%	32	0
Ag	0.0017	0.0018	0.0000	0.0000	0.0016	0.0032	0.0034	100%	32	0
Cd	0.0012	0.0012	0.0000	0.0000	0.0008	0.0021	0.0030	100%	32	0
In	0.0005	0.0010	0.0000	0.0000	0.0000	0.0005	0.0019	100%	32	0
Sn	0.0018	0.0024	0.0000	0.0000	0.0006	0.0032	0.0046	100%	32	0
Sb	0.0017	0.0028	0.0000	0.0000	0.0000	0.0028	0.0046	100%	32	0
Ba	0.0033	0.0075	0.0000	0.0000	0.0000	0.0000	0.0114	100%	32	0
La	0.0043	0.0088	0.0000	0.0000	0.0000	0.0019	0.0151	100%	32	0
Au	0.0000	0.0001	0.0000	0.0000	0.0000	0.0000	0.0000	100%	32	0
Hg	0.0000	0.0001	0.0000	0.0000	0.0000	0.0000	0.0001	100%	32	0
Tl	0.0000	0.0000	0.0000	0.0000	0.0000	0.0000	0.0000	100%	32	0
Pb	0.0050	0.0044	0.0016	0.0024	0.0034	0.0054	0.0118	34%	32	16
Ur	0.0001	0.0001	0.0000	0.0000	0.0000	0.0000	0.0003	100%	32	0
HNO_3	1.9404	1.9327	0.0982	0.6237	1.3842	3.2014	4.5915	28%	32	19
NH_3	0.2796	0.2494	-0.0079	0.0757	0.2266	0.4406	0.5803	64%	32	9
$T\text{-}NO_3^-$	5.2896	3.1208	2.0144	2.7905	4.3035	7.5502	9.9044	8%	32	32
$T\text{-}NH_4^+$	2.6453	1.5166	1.2387	1.3669	2.1840	3.3292	5.0338	5%	32	32

* Concentration in unit $\mu g\ m^{-3}$.

Table A.1.8 Monthly statistics of $PM_{2.5}$ mass, chemical composition, and analytical uncertainty (AU) at FME in July 2001.

Species	Mean*	Std. Dev.*	10%*	25%*	50%*	75%*	90%*	AU (RMS)	# of data	# > 2×AU
Mass	12.5135	6.5645	6.4876	8.7409	11.2137	14.4860	22.0848	6%	35	35
SO_4^{2-}	4.6267	2.8581	1.7026	3.0426	4.0680	5.2141	8.9913	5%	35	35
NO_3^-	0.3586	0.1817	0.1438	0.2519	0.3370	0.4635	0.5579	8%	35	35
NH_4^+	1.6632	1.0700	0.6186	1.0934	1.4165	1.9065	3.0832	6%	35	35
OC	3.0723	1.0165	2.0042	2.2729	3.0149	3.8281	4.2313	12%	35	35
EC	0.7911	0.3388	0.5102	0.5868	0.7155	0.9379	1.1464	11%	35	35
OC (BQ)	0.8518	0.3061	0.4702	0.6775	0.7943	1.0039	1.2460	26%	35	34
OC (TBQ)	1.4906	0.3143	1.0620	1.3337	1.4608	1.7152	1.8614	13%	35	35
Cl^-	0.0338	0.0349	0.0000	0.0000	0.0434	0.0582	0.0796	86%	35	9
Na^+	0.0483	0.0351	0.0131	0.0179	0.0410	0.0703	0.0941	24%	35	23
K^+	0.0584	0.1378	0.0148	0.0214	0.0272	0.0379	0.0647	18%	35	34
Na	0.2222	0.2039	0.0000	0.0563	0.2020	0.3166	0.4977	100%	35	6
Mg	0.0148	0.0146	0.0000	0.0000	0.0135	0.0241	0.0340	100%	35	1
Al	0.0297	0.0320	0.0068	0.0148	0.0224	0.0360	0.0502	33%	35	25
Si	0.0866	0.1166	0.0317	0.0398	0.0486	0.0694	0.1675	9%	35	34
Ph	0.0009	0.0014	0.0000	0.0000	0.0000	0.0019	0.0033	100%	35	0
S	1.6963	1.0228	0.6567	1.1130	1.4675	1.9941	3.2442	5%	35	35
Cl	0.0000	0.0000	0.0000	0.0000	0.0000	0.0000	0.0000	100%	35	0
K	0.0628	0.1386	0.0195	0.0241	0.0296	0.0432	0.0708	7%	35	35
Ca	0.0243	0.0141	0.0136	0.0167	0.0222	0.0267	0.0361	14%	35	34
Ti	0.0047	0.0039	0.0008	0.0025	0.0039	0.0063	0.0094	100%	35	0
Va	0.0027	0.0020	0.0006	0.0014	0.0023	0.0040	0.0055	100%	35	0
Cr	0.0003	0.0004	0.0000	0.0001	0.0002	0.0004	0.0008	100%	35	0
Mn	0.0011	0.0007	0.0003	0.0007	0.0009	0.0016	0.0023	79%	35	7
Fe	0.0577	0.0349	0.0290	0.0368	0.0475	0.0705	0.0952	9%	35	35
Co	0.0005	0.0005	0.0002	0.0002	0.0004	0.0007	0.0009	100%	35	1
Ni	0.0013	0.0012	0.0001	0.0003	0.0008	0.0022	0.0027	44%	35	15
Cu	0.0015	0.0010	0.0007	0.0010	0.0012	0.0018	0.0024	34%	35	22
Zn	0.0089	0.0087	0.0032	0.0044	0.0061	0.0096	0.0183	16%	35	34
Ga	0.0001	0.0002	0.0000	0.0000	0.0000	0.0000	0.0004	100%	35	0
As	0.0006	0.0004	0.0000	0.0001	0.0005	0.0010	0.0011	100%	35	0
Se	0.0016	0.0012	0.0003	0.0008	0.0013	0.0019	0.0032	28%	35	25
Br	0.0027	0.0012	0.0013	0.0021	0.0025	0.0036	0.0043	18%	35	34
Rb	0.0001	0.0002	0.0000	0.0000	0.0001	0.0002	0.0004	100%	35	0
Sr	0.0008	0.0015	0.0000	0.0002	0.0004	0.0007	0.0013	100%	35	4
Yt	0.0001	0.0001	0.0000	0.0000	0.0000	0.0001	0.0002	100%	35	0
Zr	0.0003	0.0003	0.0000	0.0001	0.0003	0.0006	0.0007	100%	35	0
Mo	0.0001	0.0002	0.0000	0.0000	0.0000	0.0002	0.0005	100%	35	0
Pd	0.0008	0.0010	0.0000	0.0000	0.0004	0.0013	0.0022	100%	35	0
Ag	0.0008	0.0009	0.0000	0.0000	0.0003	0.0017	0.0023	100%	35	0
Cd	0.0001	0.0003	0.0000	0.0000	0.0000	0.0000	0.0004	100%	35	0
In	0.0002	0.0007	0.0000	0.0000	0.0000	0.0000	0.0002	100%	35	0
Sn	0.0015	0.0016	0.0000	0.0000	0.0013	0.0026	0.0039	100%	35	0
Sb	0.0018	0.0025	0.0000	0.0000	0.0002	0.0031	0.0055	100%	35	0
Ba	0.0015	0.0040	0.0000	0.0000	0.0000	0.0000	0.0065	100%	35	0
La	0.0049	0.0115	0.0000	0.0000	0.0000	0.0040	0.0155	100%	35	0
Au	0.0002	0.0003	0.0000	0.0000	0.0000	0.0002	0.0005	100%	35	0
Hg	0.0001	0.0002	0.0000	0.0000	0.0000	0.0003	0.0004	100%	35	0
Tl	0.0001	0.0002	0.0000	0.0000	0.0000	0.0001	0.0004	100%	35	0
Pb	0.0028	0.0016	0.0010	0.0018	0.0025	0.0035	0.0049	63%	35	14
Ur	0.0003	0.0004	0.0000	0.0000	0.0002	0.0006	0.0008	100%	35	0
HNO_3	3.1762	1.1773	1.5399	2.4712	3.1791	3.8050	4.5017	6%	35	35
NH_3	0.6140	0.2358	0.4083	0.4869	0.5848	0.7015	0.8054	24%	35	33
$T\text{-}NO_3^-$	3.8767	1.3139	1.9692	3.4566	3.9987	4.6448	5.5079	5%	35	35
$T\text{-}NH_4^+$	2.2004	1.0181	1.1566	1.5578	1.7916	2.6895	3.5581	6%	35	35

* Concentration in unit $\mu g\ m^{-3}$.

Table A.1.9 Monthly statistics of $PM_{2.5}$ mass, chemical composition, and analytical uncertainty (AU) at FME in January 2002.

Species	Mean*	Std. Dev.*	10%*	25%*	50%*	75%*	90%*	AU (RMS)	# of data	# > 2×AU
Mass	9.3245	3.5656	5.6191	6.9884	8.5707	11.5694	12.6064	6%	31	31
SO_4^{2-}	2.4345	0.7833	1.4586	1.9901	2.3810	2.8128	3.6225	7%	33	33
NO_3^-	1.3544	0.9849	0.5028	0.6507	1.1384	1.7307	2.8495	6%	33	33
NH_4^+	1.2396	0.4843	0.7055	0.9038	1.1189	1.4637	1.9540	6%	33	33
OC	2.4397	1.1529	1.2964	1.5791	2.3730	2.9901	3.7743	12%	33	33
EC	0.9094	0.3963	0.4397	0.6185	0.8808	1.1251	1.5102	11%	33	33
OC (BQ)	0.3872	0.1844	0.1852	0.2486	0.3583	0.5474	0.6413	58%	33	10
OC (TBQ)	0.8453	0.3051	0.4827	0.5865	0.8298	1.0598	1.2320	32%	33	30
Cl^-	0.0126	0.0387	0.0000	0.0000	0.0018	0.0039	0.0343	100%	33	1
Na^+	0.0395	0.0373	0.0157	0.0211	0.0281	0.0373	0.0727	9%	33	33
K^+	0.0528	0.0249	0.0273	0.0340	0.0498	0.0666	0.0788	7%	33	33
Na	0.0131	0.0156	0.0000	0.0000	0.0072	0.0195	0.0364	100%	31	4
Mg	0.0096	0.0070	0.0000	0.0039	0.0077	0.0157	0.0184	100%	31	2
Al	0.0134	0.0074	0.0027	0.0076	0.0166	0.0182	0.0215	45%	31	19
Si	0.0394	0.0173	0.0176	0.0271	0.0406	0.0477	0.0577	14%	31	31
Ph	0.0036	0.0037	0.0000	0.0005	0.0030	0.0046	0.0084	100%	31	5
S	0.9875	0.3088	0.5864	0.8168	0.9548	1.1162	1.3778	5%	31	31
Cl	0.0093	0.0464	0.0000	0.0000	0.0000	0.0000	0.0020	100%	31	1
K	0.0613	0.0287	0.0340	0.0423	0.0556	0.0787	0.0893	9%	31	31
Ca	0.0191	0.0091	0.0080	0.0120	0.0195	0.0263	0.0317	25%	31	27
Ti	0.0021	0.0019	0.0000	0.0008	0.0019	0.0029	0.0039	100%	31	0
Va	0.0013	0.0014	0.0000	0.0000	0.0008	0.0022	0.0032	100%	31	0
Cr	0.0003	0.0003	0.0000	0.0000	0.0000	0.0005	0.0008	100%	31	0
Mn	0.0012	0.0007	0.0003	0.0010	0.0013	0.0018	0.0022	100%	31	1
Fe	0.0488	0.0252	0.0212	0.0269	0.0461	0.0617	0.0832	6%	31	31
Co	0.0001	0.0002	0.0000	0.0000	0.0000	0.0002	0.0004	100%	31	0
Ni	0.0009	0.0006	0.0004	0.0005	0.0007	0.0011	0.0015	99%	31	4
Cu	0.0021	0.0012	0.0010	0.0013	0.0017	0.0025	0.0037	40%	31	16
Zn	0.0137	0.0060	0.0079	0.0095	0.0125	0.0162	0.0216	24%	31	30
Ga	0.0002	0.0002	0.0000	0.0000	0.0000	0.0003	0.0006	100%	31	0
As	0.0008	0.0006	0.0001	0.0005	0.0007	0.0011	0.0015	100%	31	0
Se	0.0024	0.0012	0.0011	0.0015	0.0020	0.0027	0.0039	37%	31	18
Br	0.0051	0.0029	0.0025	0.0031	0.0043	0.0061	0.0073	17%	31	31
Rb	0.0002	0.0002	0.0000	0.0000	0.0001	0.0002	0.0004	100%	31	0
Sr	0.0005	0.0006	0.0001	0.0002	0.0004	0.0005	0.0007	100%	31	1
Yt	0.0002	0.0002	0.0000	0.0000	0.0002	0.0003	0.0004	100%	31	0
Zr	0.0004	0.0003	0.0001	0.0002	0.0004	0.0006	0.0009	100%	31	0
Mo	0.0002	0.0003	0.0000	0.0000	0.0000	0.0005	0.0006	100%	31	0
Pd	0.0022	0.0016	0.0000	0.0011	0.0020	0.0032	0.0049	100%	31	0
Ag	0.0017	0.0020	0.0000	0.0000	0.0010	0.0029	0.0036	100%	31	0
Cd	0.0008	0.0015	0.0000	0.0000	0.0000	0.0004	0.0031	100%	31	0
In	0.0011	0.0018	0.0000	0.0000	0.0000	0.0017	0.0032	100%	31	0
Sn	0.0032	0.0032	0.0000	0.0000	0.0022	0.0057	0.0075	100%	31	0
Sb	0.0040	0.0032	0.0000	0.0012	0.0033	0.0068	0.0085	100%	31	0
Ba	0.0049	0.0083	0.0000	0.0000	0.0000	0.0062	0.0128	100%	31	0
La	0.0139	0.0122	0.0000	0.0010	0.0121	0.0218	0.0282	100%	31	0
Au	0.0001	0.0002	0.0000	0.0000	0.0000	0.0000	0.0003	100%	31	0
Hg	0.0002	0.0003	0.0000	0.0000	0.0001	0.0004	0.0007	100%	31	0
Tl	0.0002	0.0002	0.0000	0.0000	0.0000	0.0003	0.0005	100%	31	0
Pb	0.0041	0.0021	0.0017	0.0025	0.0039	0.0056	0.0070	67%	31	10
Ur	0.0003	0.0003	0.0000	0.0000	0.0001	0.0005	0.0008	100%	31	0
HNO_3	1.1343	0.4868	0.4891	0.7679	1.2265	1.4133	1.7055	18%	33	27
NH_3	0.8497	1.2446	0.1550	0.2223	0.4163	0.9179	1.4797	19%	33	21
T-NO_3^-	3.0842	1.2836	1.8862	2.1869	2.6516	3.9035	5.2043	5%	33	31
T-NH_4^+	2.3066	1.3700	1.3776	1.6111	2.0425	2.4686	2.9553	6%	33	31

* Concentration in unit $\mu g\ m^{-3}$.

Appendix 2 Monthly Statistics of CO, NO_y, and SO_2

Table A.2.1 Monthly statistics of CO concentration at FME. Calculation is based on available 24-hr averages.

Month	Mean*	Std. Dev.*	10%*	25%*	50%*	75%*	90%*	# of data
Jun-99	230.8	41.4	187.3	200.0	222.6	258.2	289.0	24
Jul-99	245.7	47.8	187.8	215.5	233.7	285.2	307.0	30
Aug-99	253.6	45.3	193.5	223.2	250.1	292.1	304.4	28
Sep-99	270.7	73.3	167.0	221.4	266.3	314.0	364.0	29
Oct-99	369.1	112.1	225.3	278.9	355.5	452.6	495.6	31
Nov-99	390.6	176.3	180.8	251.1	364.6	497.9	620.3	26
Dec-99	466.7	214.3	230.9	298.1	454.2	553.2	809.4	31
Jan-00	367.5	170.4	204.5	243.9	314.0	476.3	583.2	31
Feb-00	403.4	156.0	252.6	316.6	360.6	453.9	652.9	27
Mar-00	294.8	85.0	203.5	236.4	282.1	346.4	380.3	20
Apr-00	259.6	62.2	199.3	214.2	245.9	279.4	322.6	28
May-00	263.7	50.0	204.1	222.2	266.5	302.0	331.7	30
Jun-00	258.7	60.3	187.1	206.2	264.8	312.0	335.3	23
Jul-00	260.2	49.3	196.8	234.1	258.6	285.9	322.3	30
Aug-00	256.5	53.2	204.4	210.0	241.2	280.7	341.9	20
Sep-00	215.1	58.8	149.1	173.3	197.7	259.5	297.3	20
Oct-00	347.2	134.7	163.8	233.4	345.7	421.0	502.8	30
Nov-00	323.3	144.4	180.8	213.4	303.0	379.7	532.6	30
Dec-00	356.4	160.5	202.9	231.1	311.1	425.4	597.3	29
Jan-01	470.6	216.4	215.8	289.5	422.0	619.0	801.4	31
Feb-01	337.7	106.3	224.5	266.7	318.9	402.5	470.8	28
Mar-01	264.2	67.1	190.2	214.1	256.6	313.5	348.9	31
Apr-01	266.2	59.1	203.9	225.4	247.4	299.0	346.9	30
May-01	226.7	52.7	161.9	193.0	205.1	264.3	301.0	23
Jun-01	248.6	59.7	183.0	206.2	249.7	293.5	317.0	26
Jul-01	200.9	44.5	145.7	176.6	198.6	218.5	264.9	31
Aug-01	238.9	43.9	188.3	206.6	231.6	269.0	302.4	28
Sep-01	222.9	51.4	160.4	176.8	220.6	255.4	283.1	30
Oct-01	264.4	94.5	154.8	183.1	248.7	326.6	407.8	31
Nov-01	357.5	143.5	163.0	248.0	344.6	470.5	531.9	30
Dec-01	347.9	125.8	206.6	235.8	349.4	422.2	528.5	26
Jan-02	356.0	102.5	247.6	280.9	326.3	403.9	514.4	28
Feb-02	298.7	110.5	203.1	229.7	267.5	348.8	435.7	24

* Concentration in unit ppbv.

Table A.2.2 Monthly statistics of NO_y concentration at FME. Calculation is based on available 24-hr averages.

Month	Mean*	Std. Dev.*	10%*	25%*	50%*	75%*	90%*	# of data
Jun-99	11.4	3.6	7.7	8.3	11.2	14.7	16.2	16
Jul-99	13.5	5.0	8.3	9.6	12.0	17.1	20.7	22
Aug-99	11.8	4.2	6.4	8.8	11.0	15.1	18.0	31
Sep-99	11.0	7.0	3.9	6.4	9.3	13.7	20.9	30
Oct-99	15.3	6.6	9.1	11.2	13.5	17.1	22.6	7
Nov-99	15.9	7.1	6.8	10.1	17.1	21.0	25.4	22
Dec-99	18.8	6.3	9.8	14.4	19.6	22.8	26.9	31
Jan-00	16.2	7.5	9.1	10.6	16.1	18.4	21.8	31
Feb-00	19.9	9.6	11.8	14.3	17.0	22.5	34.7	29
Mar-00	16.1	5.1	10.8	11.5	15.3	20.0	22.5	27
Apr-00	11.5	6.3	3.9	7.2	11.1	16.1	20.2	26
May-00	10.5	5.0	5.6	6.7	7.9	14.1	18.1	19
Jun-00	10.5	3.4	6.0	8.4	10.2	13.1	14.9	30
Jul-00	11.1	3.7	6.8	8.0	10.6	13.4	15.8	31
Aug-00	10.6	3.6	6.9	7.8	9.7	12.6	16.5	31
Sep-00	10.0	3.7	5.1	6.7	10.2	12.8	15.0	30
Oct-00	14.4	4.6	8.8	11.6	14.4	17.1	19.8	31
Nov-00	14.7	6.1	8.0	10.8	13.4	17.9	21.0	30
Dec-00	17.5	4.8	11.9	14.7	17.5	21.2	23.0	31
Jan-01	19.2	6.2	10.5	14.5	20.0	22.2	27.6	31
Feb-01	16.2	5.0	9.4	11.4	16.5	19.8	22.2	28
Mar-01	12.9	4.6	7.8	9.1	13.0	15.9	17.8	31
Apr-01	12.1	3.2	8.3	10.1	11.6	14.4	16.5	30
May-01	9.9	3.9	6.0	6.8	8.6	11.9	15.3	26
Jun-01	9.6	3.7	4.2	7.1	9.9	11.8	13.5	30
Jul-01	8.8	3.3	5.3	6.1	9.2	11.2	12.0	31
Aug-01	8.9	3.6	4.9	6.6	8.3	11.4	14.1	31
Sep-01	11.6	5.5	6.1	8.0	10.1	14.7	19.6	30
Oct-01	18.5	13.9	4.8	8.2	17.0	22.1	31.9	31
Nov-01	32.5	21.2	8.7	17.6	25.6	48.4	62.0	30
Dec-01	28.8	20.4	8.8	13.8	23.9	36.0	56.2	31
Jan-02								
Feb-02								

* Concentration in unit ppbv.

Table A.2.3 Monthly statistics of SO_2 concentration at FME. Calculation is based on available 24-hr averages.

Month	Mean*	Std. Dev.*	10%*	25%*	50%*	75%*	90%*	# of data
Jun-99								
Jul-99								
Aug-99								
Sep-99								
Oct-99	2.8	2.3	0.9	1.5	2.5	3.5	4.2	23
Nov-99	3.4	2.7	1.1	1.4	2.6	5.0	5.9	26
Dec-99	5.4	4.5	1.8	2.5	4.0	6.5	10.5	31
Jan-00	4.2	2.4	1.6	2.6	4.1	5.3	8.5	31
Feb-00	4.4	1.8	2.3	3.1	4.1	5.9	6.7	27
Mar-00	3.2	2.0	1.0	1.3	3.0	4.9	6.1	22
Apr-00	2.8	1.8	0.9	1.4	2.6	3.3	5.8	29
May-00	3.9	2.3	1.7	2.4	3.4	4.5	7.6	29
Jun-00	3.3	2.2	1.1	1.9	2.5	4.3	6.2	26
Jul-00	3.5	2.9	1.3	1.8	2.4	3.8	6.7	30
Aug-00	3.5	2.1	1.4	2.1	2.9	4.5	7.0	31
Sep-00	3.0	1.8	1.0	1.7	2.8	3.7	5.6	27
Oct-00	4.4	3.6	1.3	2.4	3.0	5.7	9.6	30
Nov-00	3.2	1.6	1.0	1.9	3.2	4.3	5.2	30
Dec-00	5.3	2.3	2.4	3.3	5.2	6.5	7.9	30
Jan-01	6.0	2.6	3.3	4.0	5.5	7.2	9.0	31
Feb-01	4.0	1.3	2.4	3.3	4.0	4.9	5.6	28
Mar-01	3.6	1.6	1.9	2.4	3.6	4.2	5.6	29
Apr-01	3.4	1.2	1.8	2.9	3.5	4.0	5.3	23
May-01	2.1	1.5	0.4	1.1	1.8	3.1	3.8	31
Jun-01	3.4	2.8	0.4	1.9	3.0	4.3	5.8	29
Jul-01	3.2	2.8	0.6	1.3	2.2	4.3	6.4	31
Aug-01	3.1	2.9	0.2	1.0	2.5	4.6	5.9	28
Sep-01	2.5	2.4	0.8	1.2	1.7	2.8	4.9	30
Oct-01	2.5	1.5	1.1	1.7	2.3	2.7	4.9	31
Nov-01	3.8	2.5	1.1	2.1	3.4	5.2	6.5	30
Dec-01	4.8	3.3	2.4	2.8	4.2	5.3	7.0	26
Jan-02	4.9	1.5	3.4	3.9	4.3	5.9	6.9	31
Feb-02	3.9	1.8	1.5	3.0	3.6	4.9	6.4	24

* Concentration in unit ppbv.

Appendix 3 Probability Fields for $PM_{2.5}$ Species

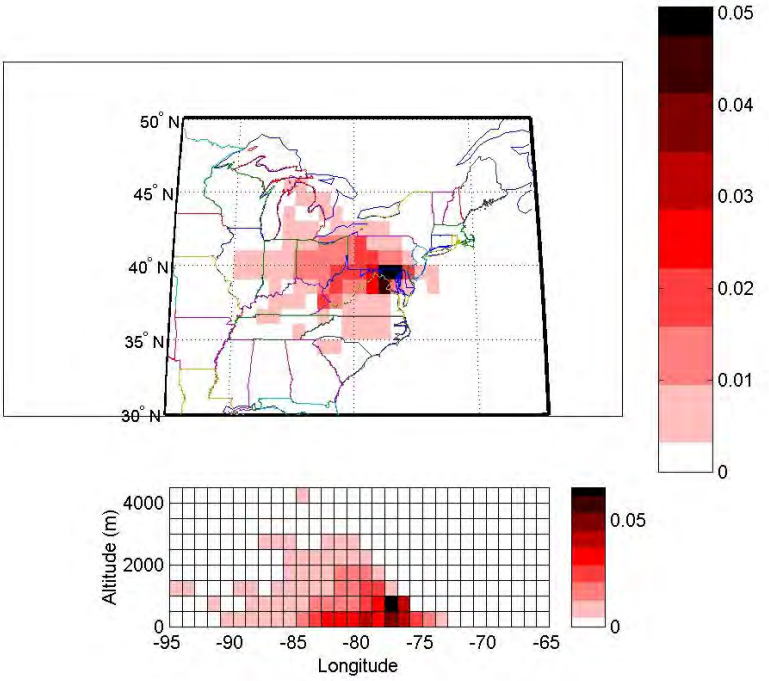

A.3.1(a) High-day (10%) probability field for S.

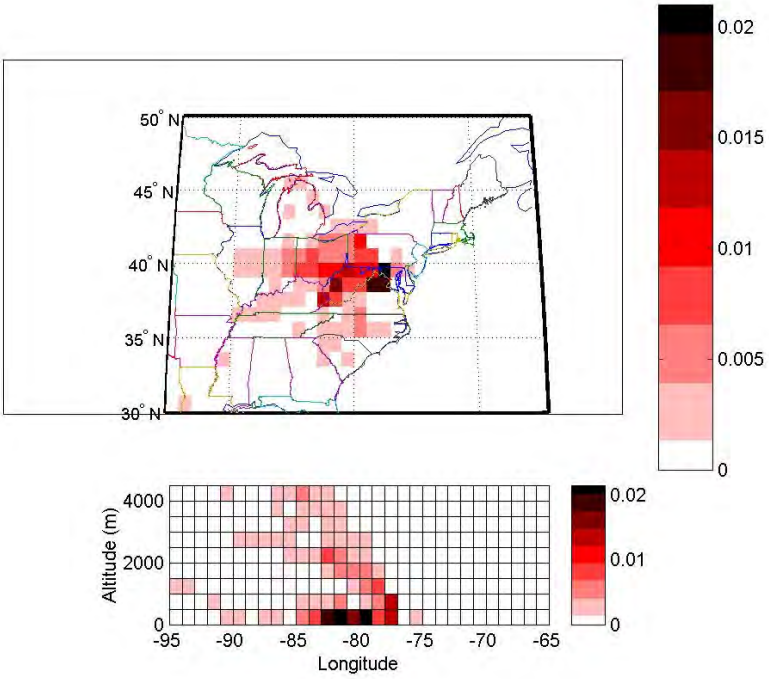

A.3.1(b) Incremental probability field for S.

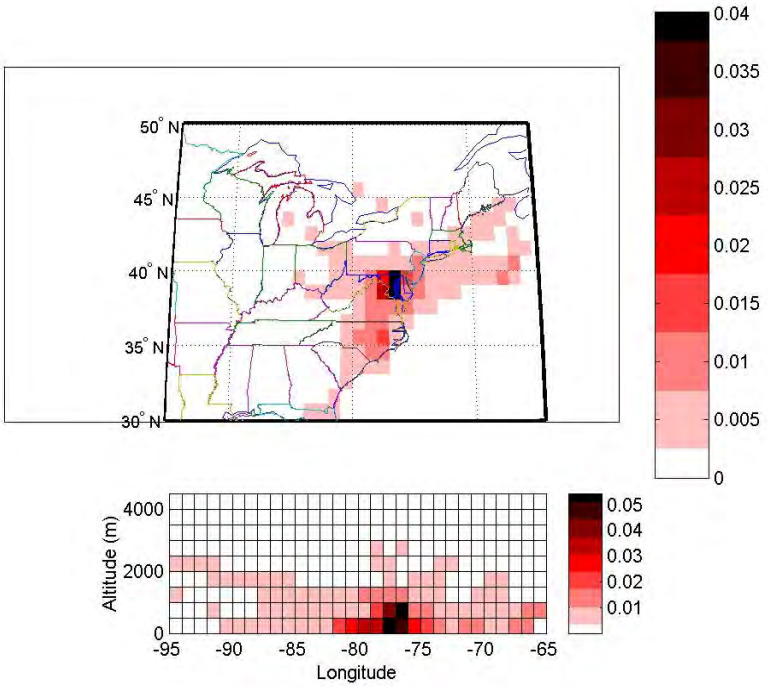

A.3.2(a) High-day (10%) probability field for Na^+.

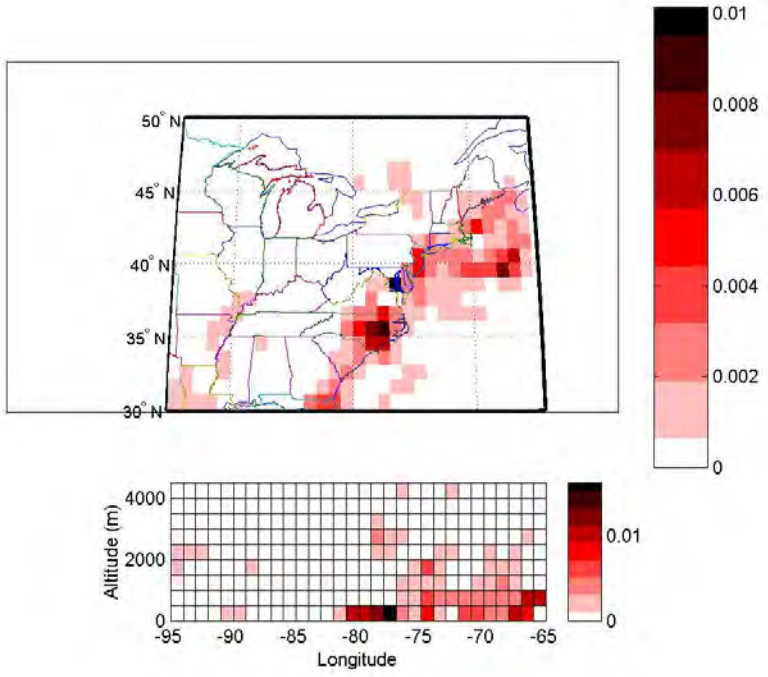

A.3.2(b) Incremental probability field for Na^+.

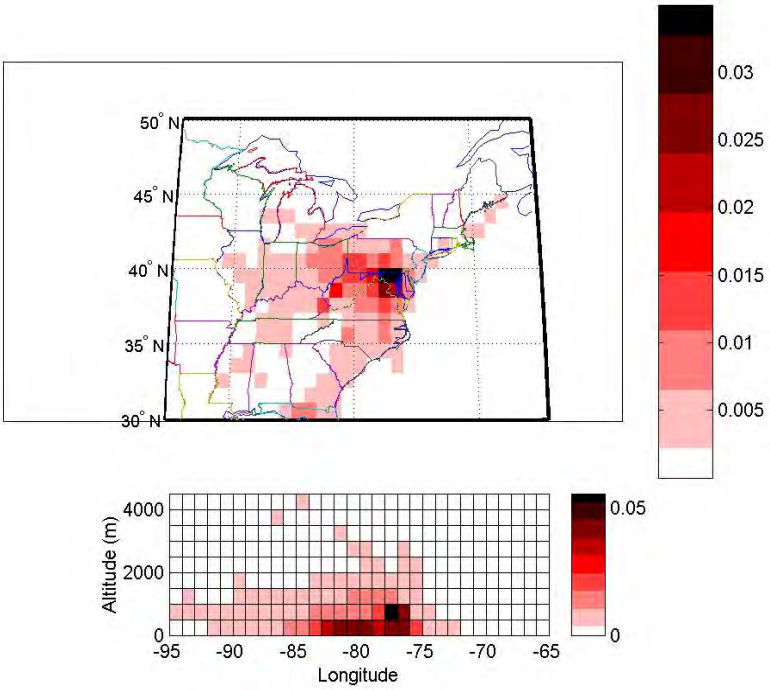

A.3.3(a) High-day (10%) probability field for Si.

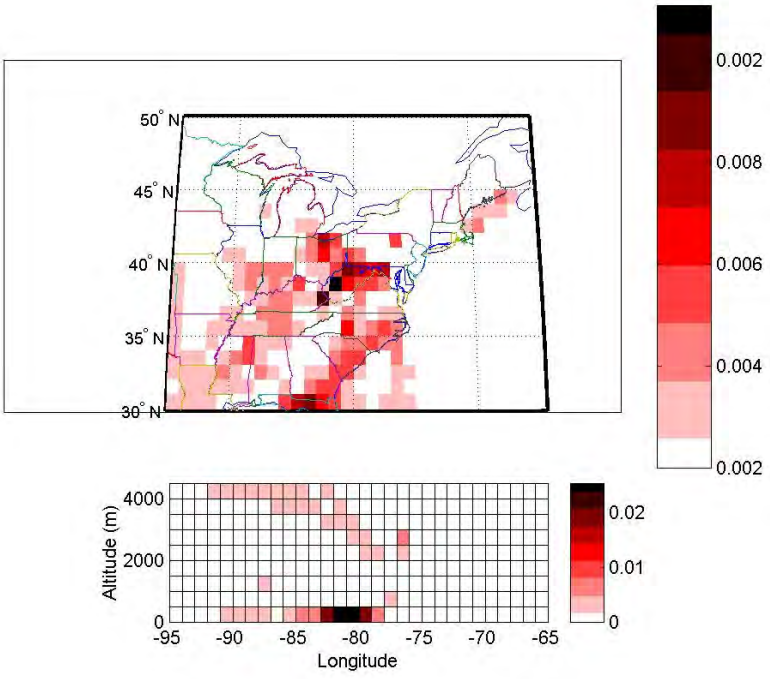

A.3.3(b) Incremental probability field for Si.

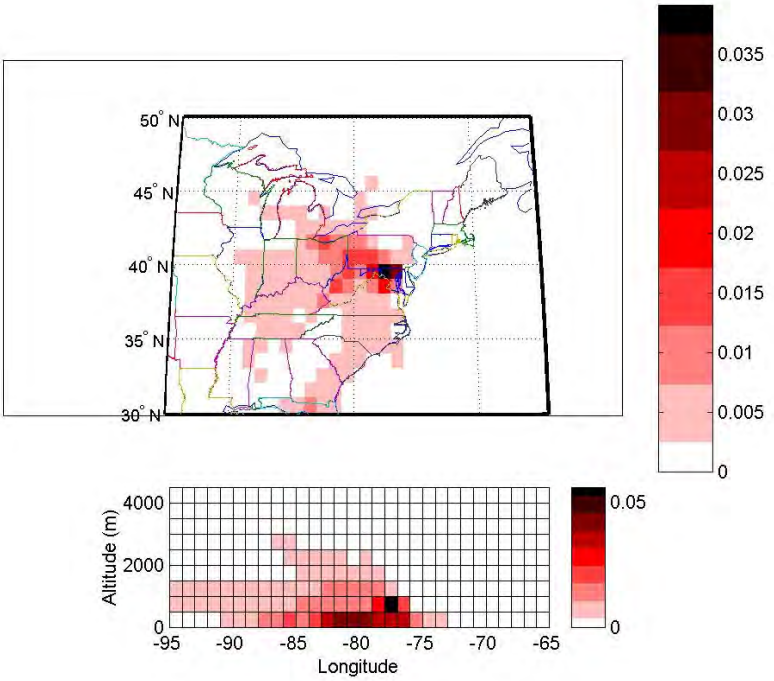

A.3.4(a) High-day (10%) probability field for Al.

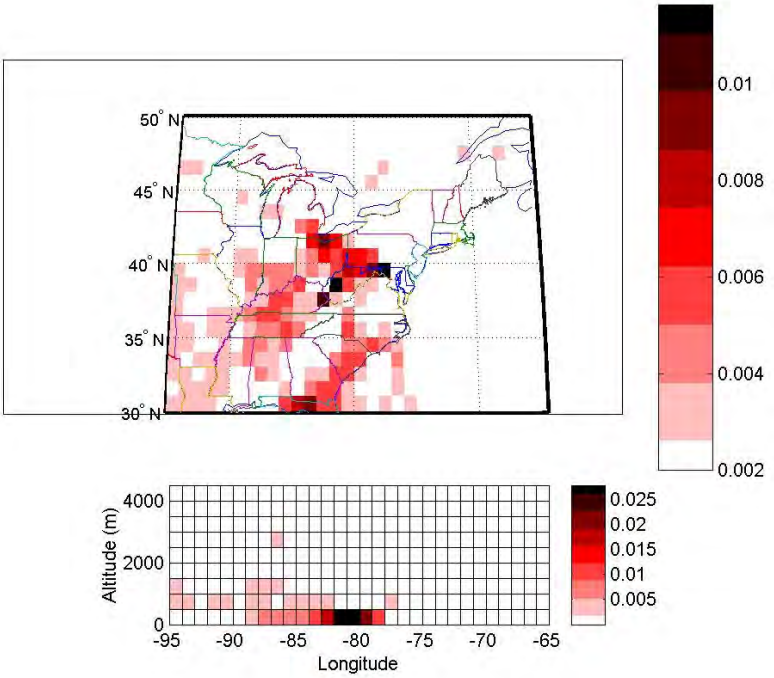

A.3.4(b) Incremental probability field for Al.

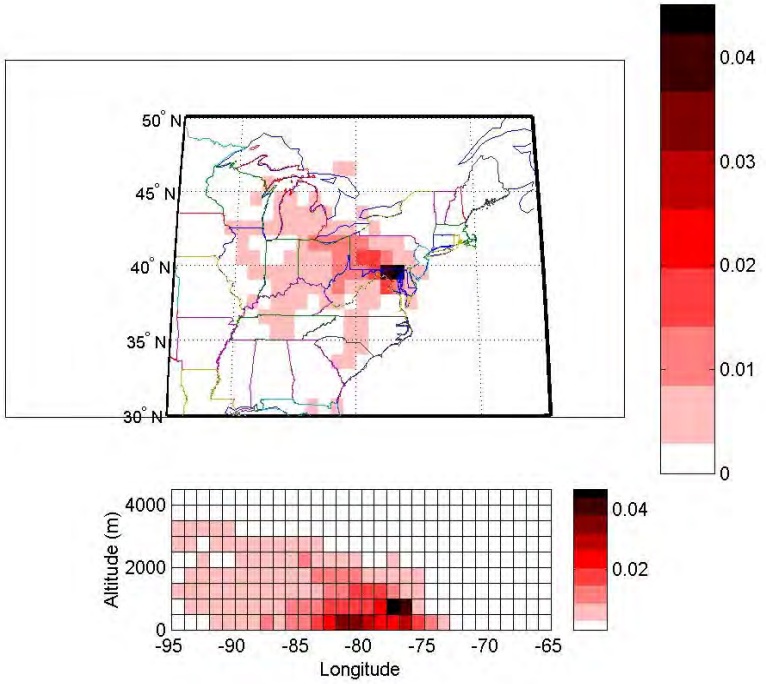

A.3.5(a) High-day (10%) probability field for Ca.

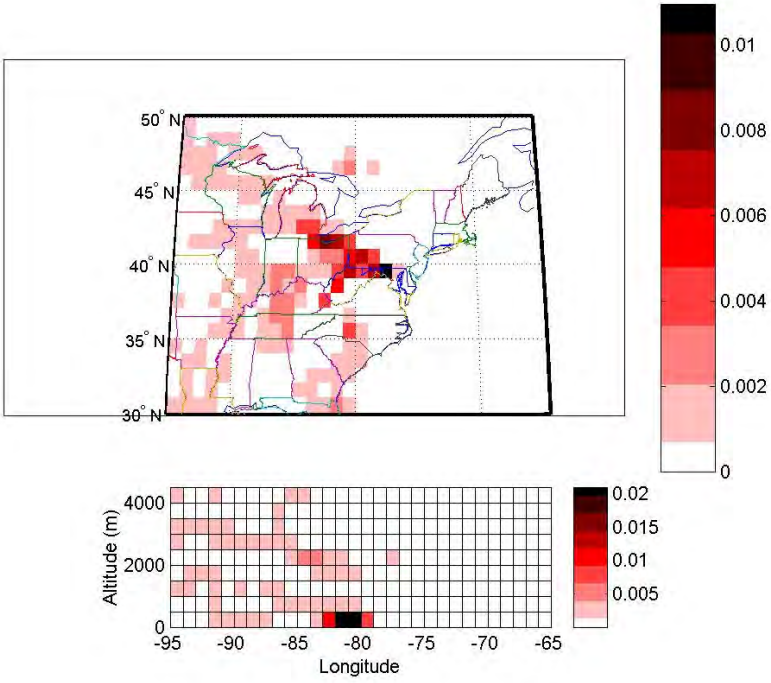

A.3.5(b) Incremental probability field for Ca.

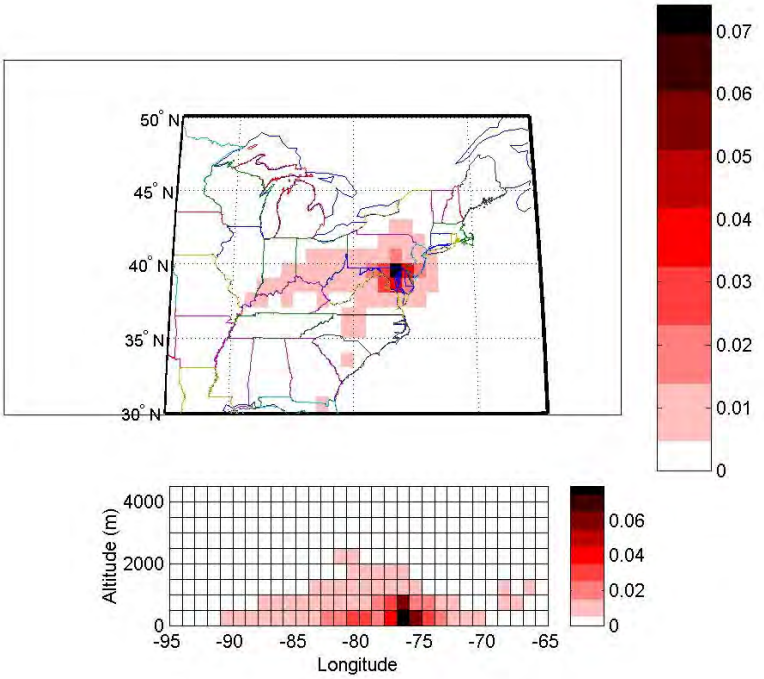

A.3.6(a) High-day (10%) probability field for Fe.

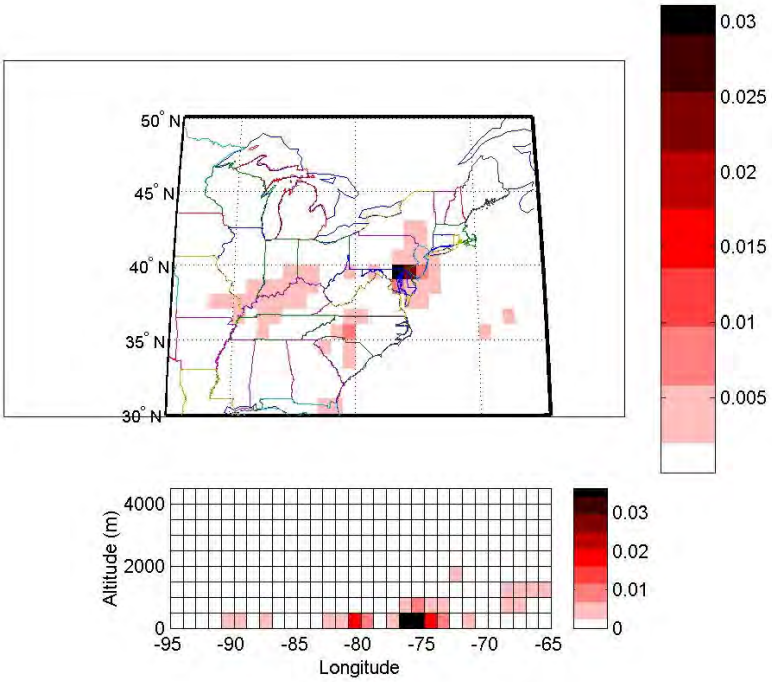

A.3.6(b) Incremental probability field for Fe.

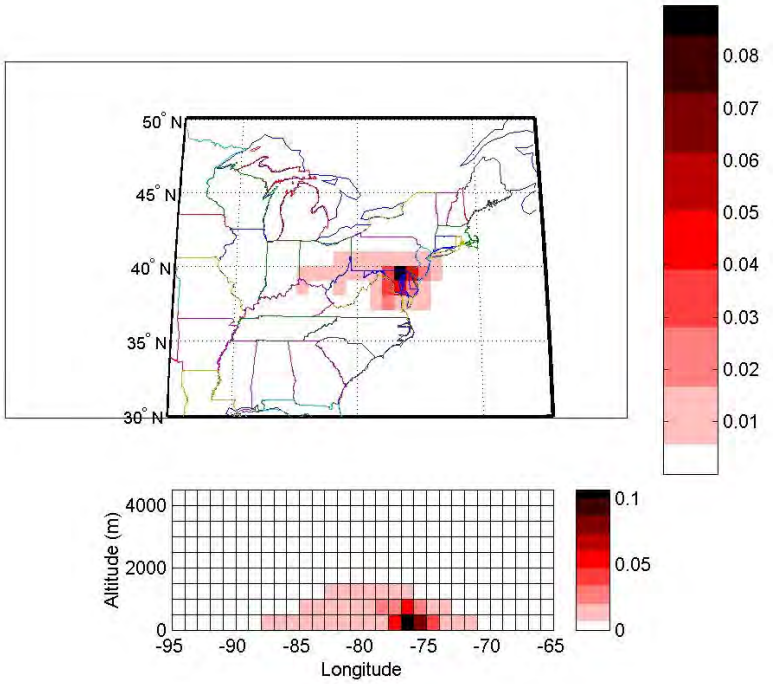

A.3.7(a) High-day (10%) probability field for Zn.

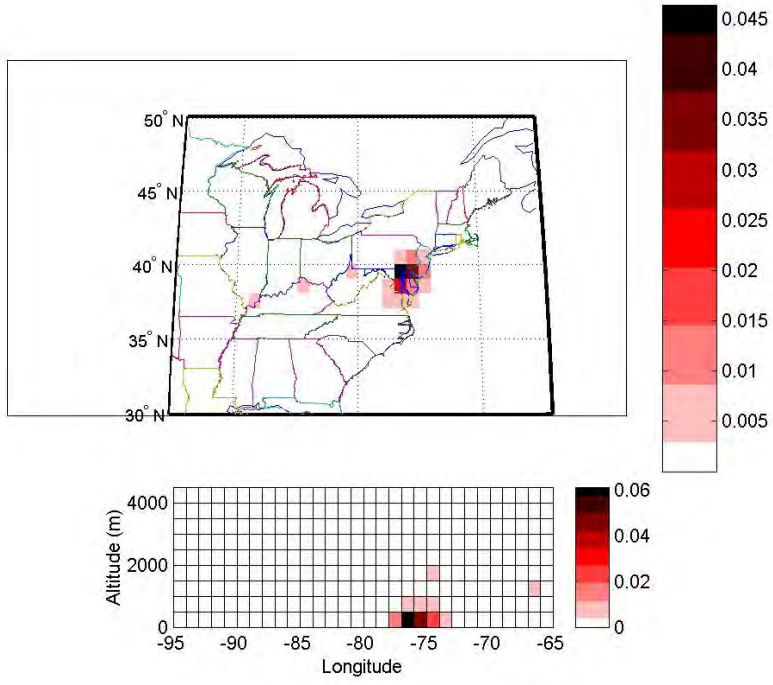

A.3.7(b) Incremental probability field for Zn.

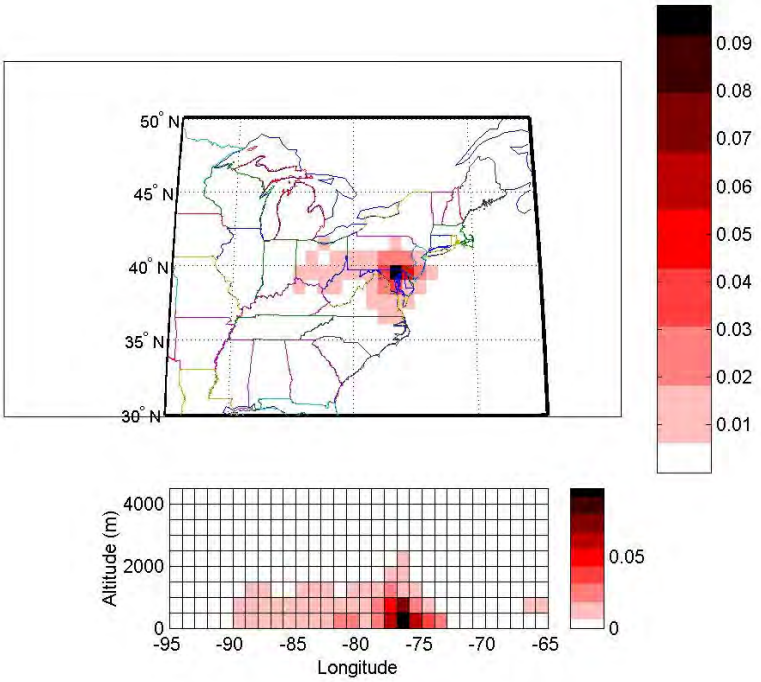

A.3.8(a) High-day (10%) probability field for Se.

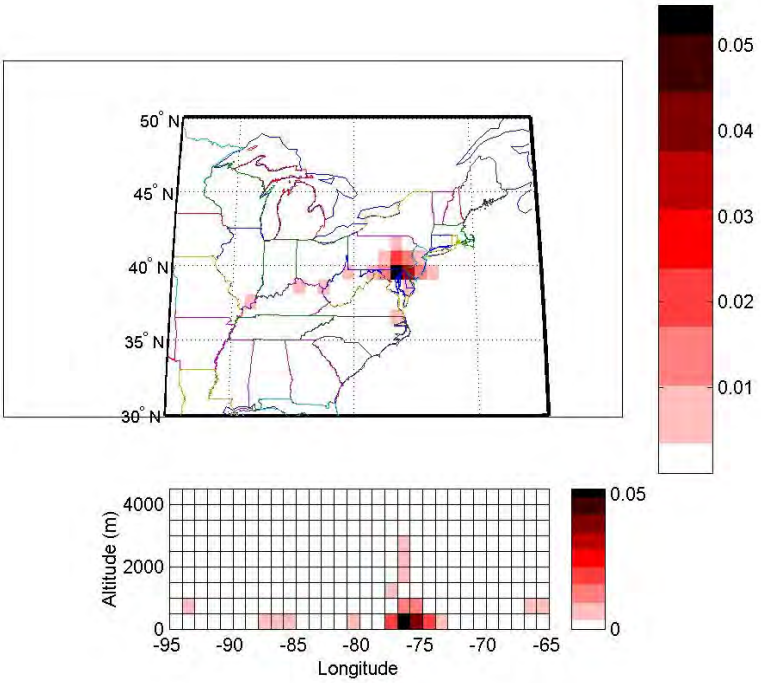

A.3.8(b) Incremental probability field for Se.

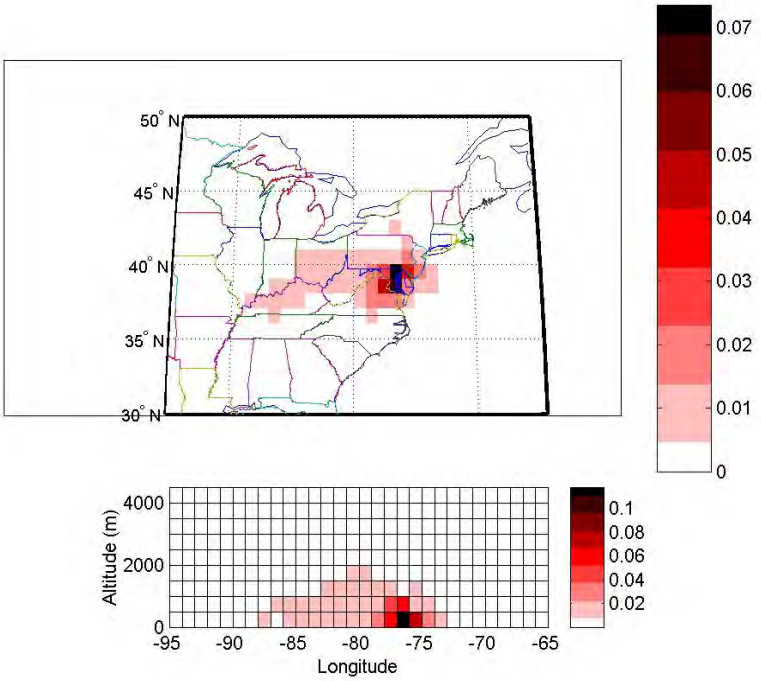

A.3.9(a) High-day (10%) probability field for K^+.

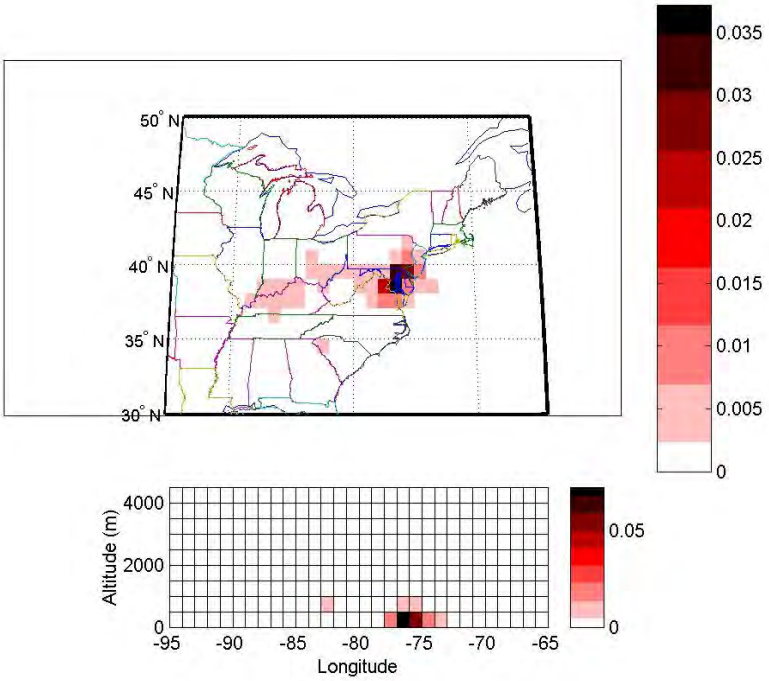

A.3.9(b) Incremental probability field for K^+.

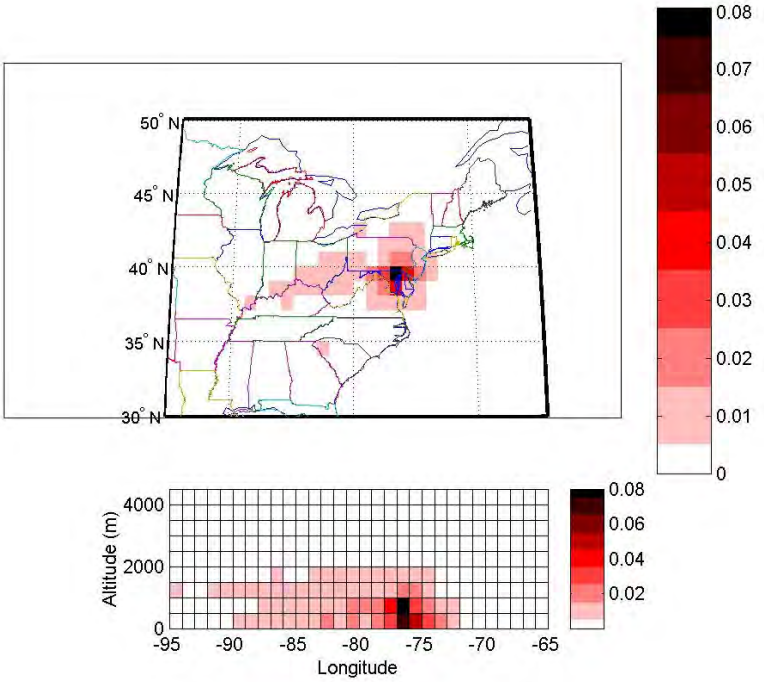

A.3.10(a) High-day (10%) probability field for Cu.

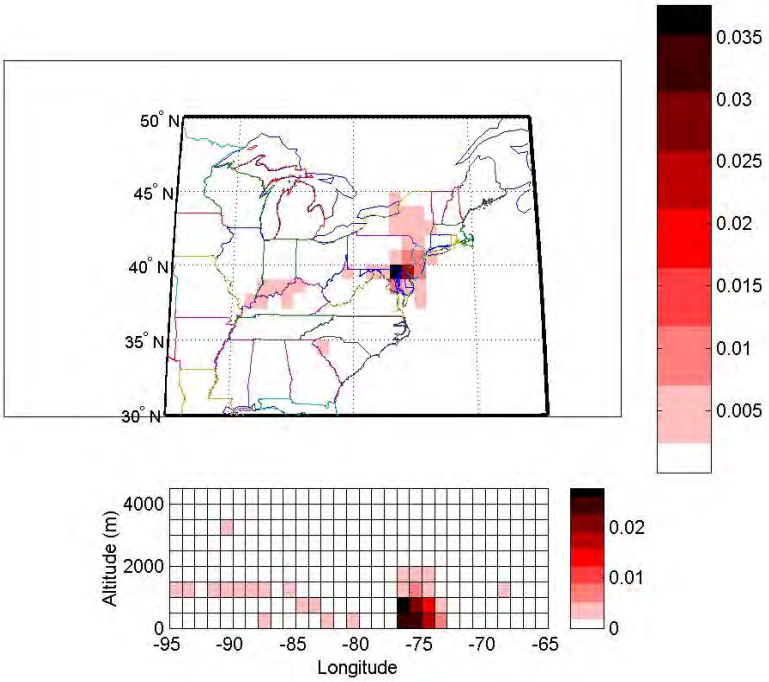

A.3.10(b) Incremental probability field for Cu.

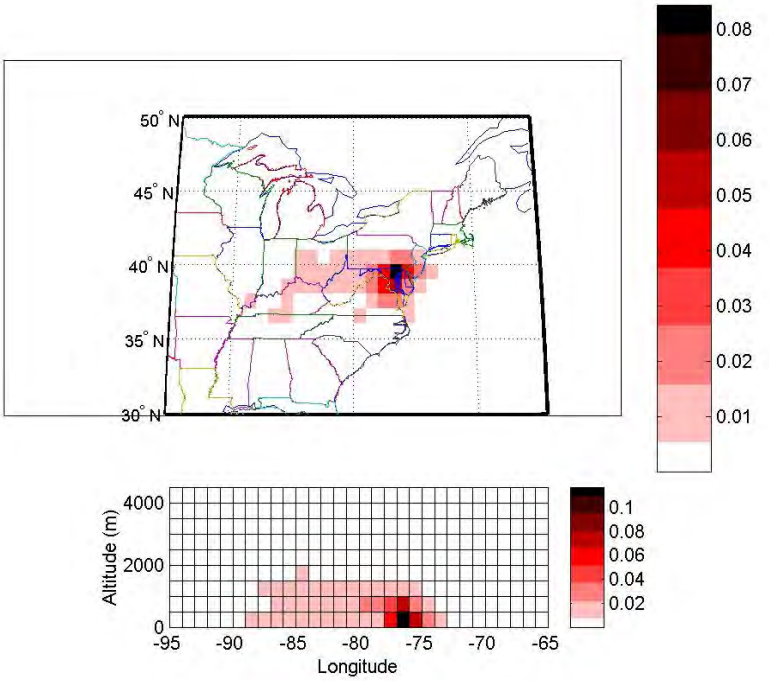

A.3.11(a) High-day (10%) probability field for Br.

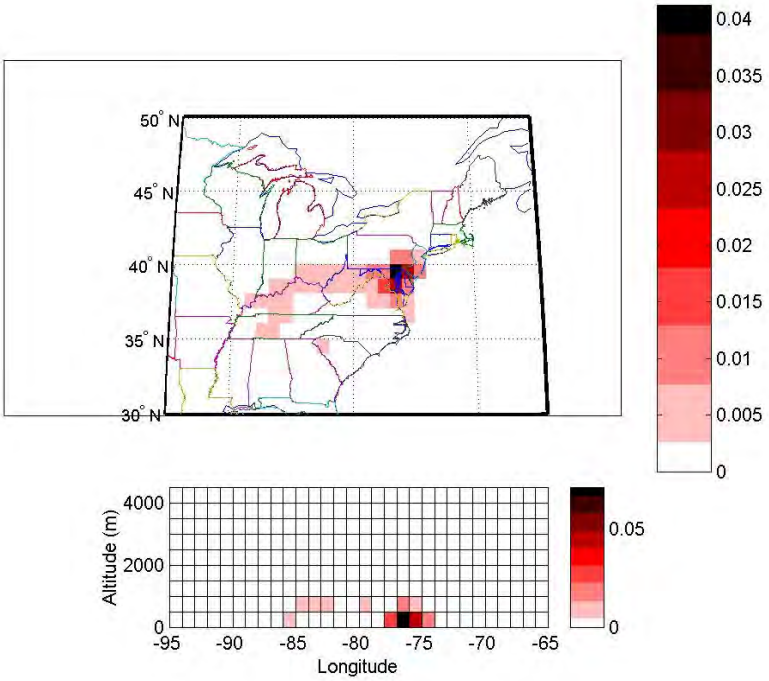

A.3.11(b) Incremental probability field for Br.

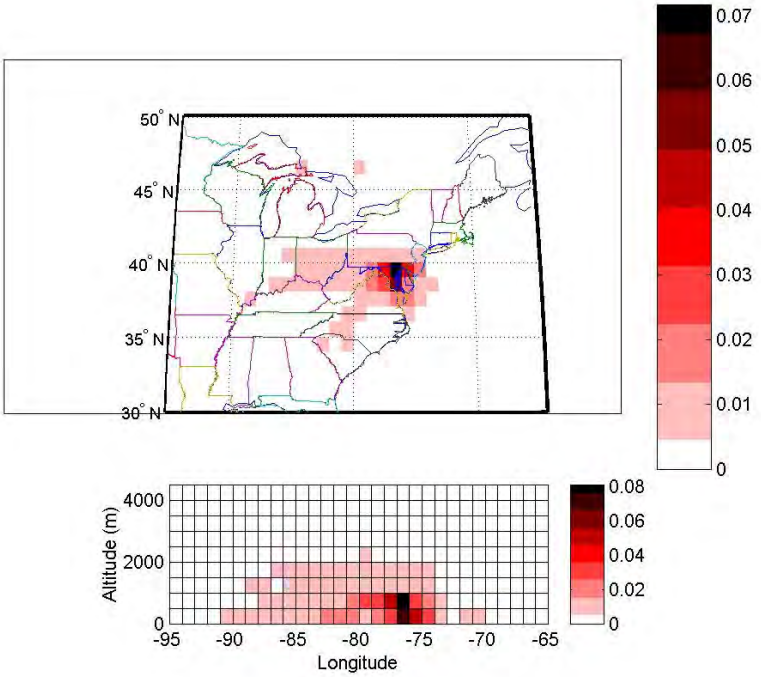

A.3.12(a) High-day (10%) probability field for Pb.

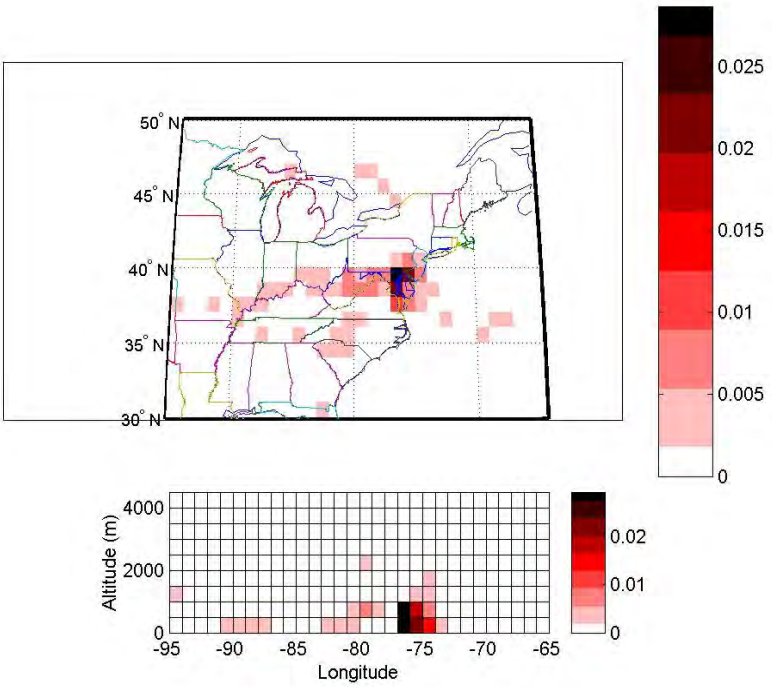

A.3.12(b) Incremental probability field for Pb.

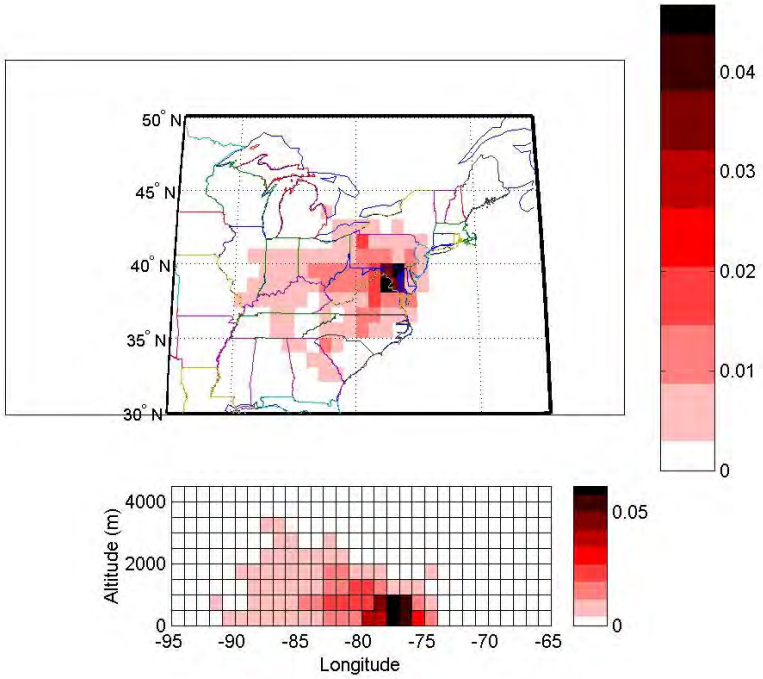

A.3.13(a) High-day (10%) probability field for OC (FQ).

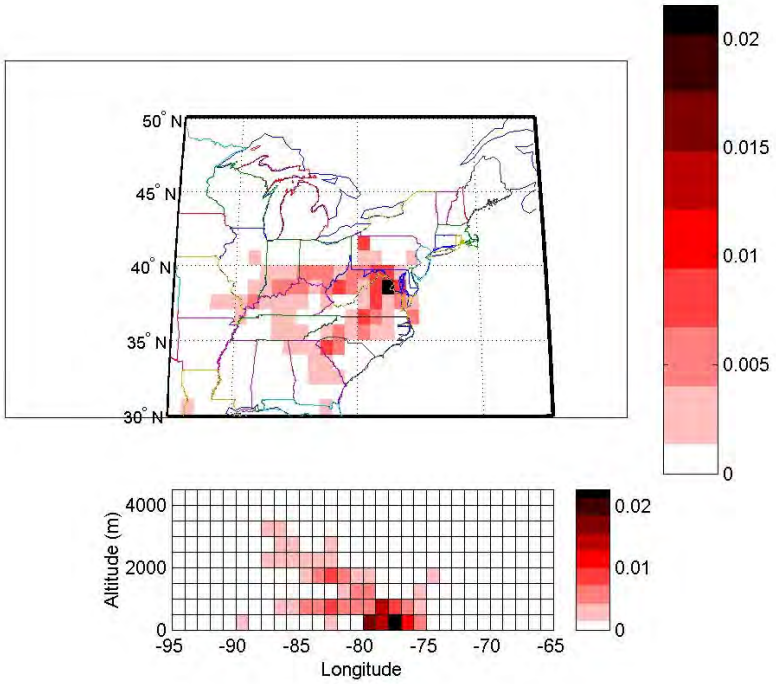

A.3.13(b) Incremental probability field for OC (FQ).

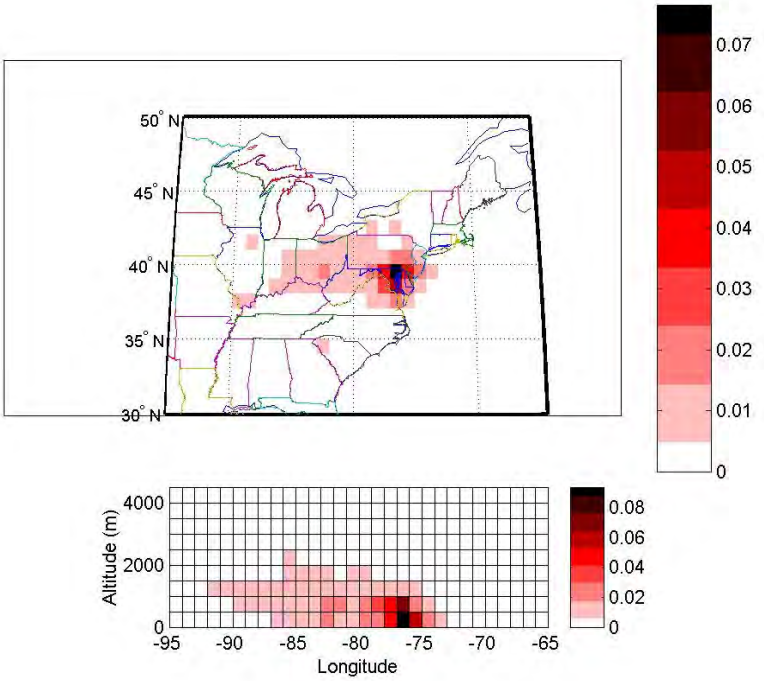

A.3.14(a) High-day (10%) probability field for EC.

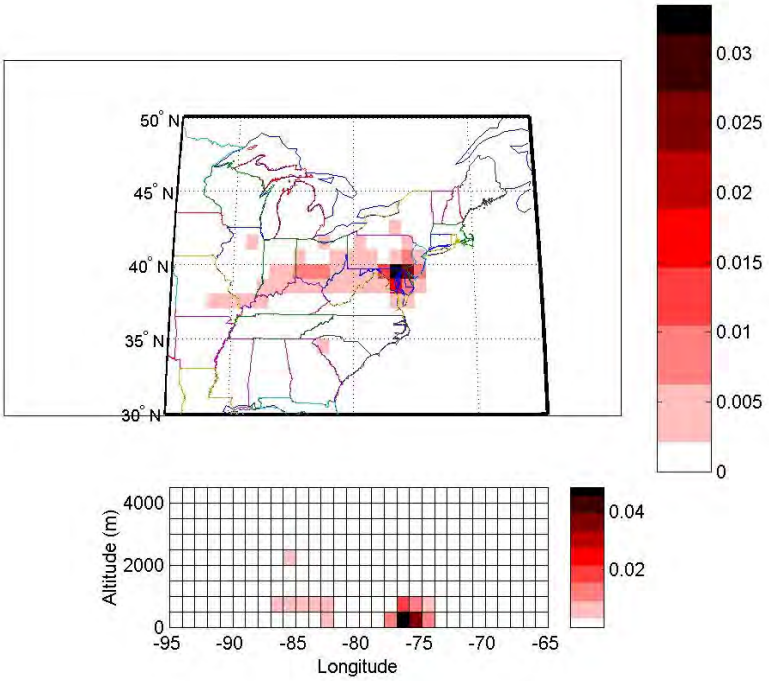

A.3.14(b) Incremental probability field for EC.

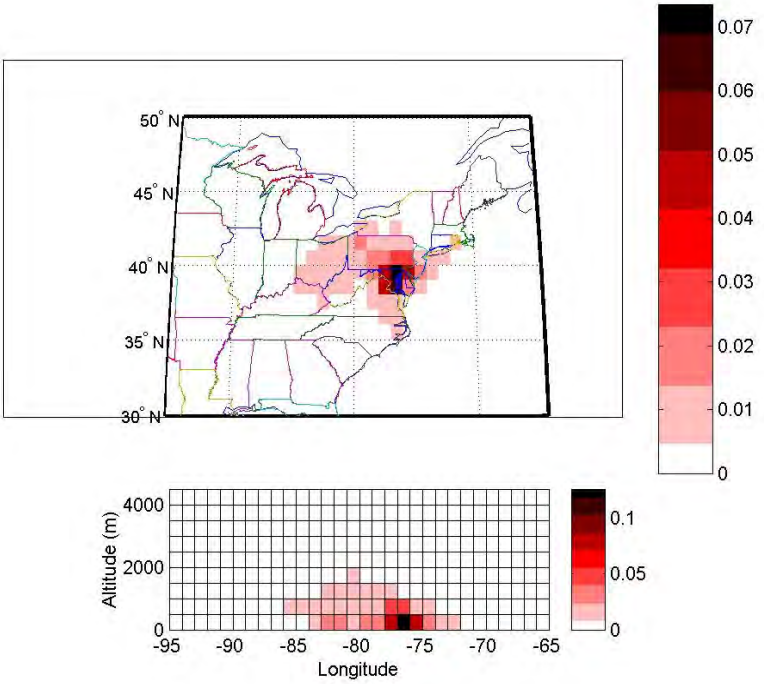

A.3.15(a) High-day (10%) probability field for T-NO_3^-.

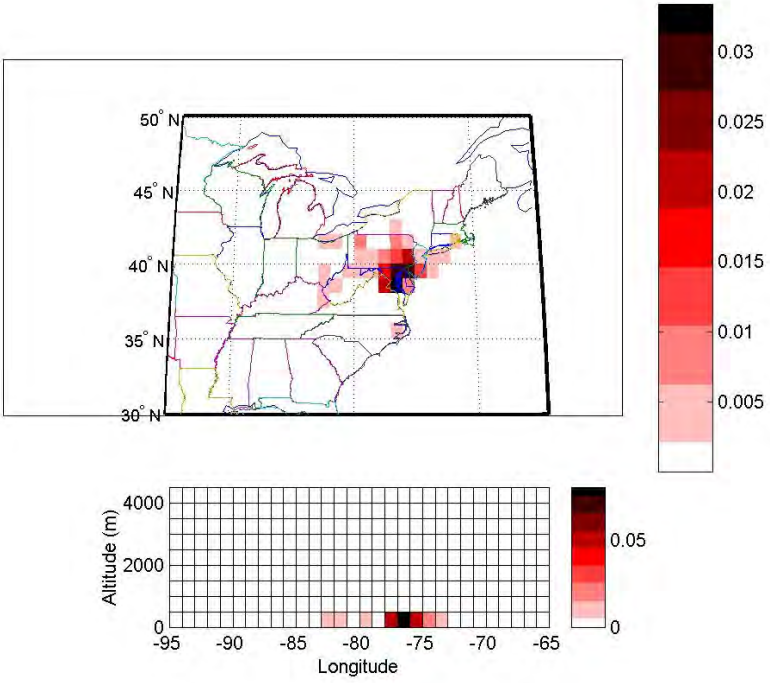

A.3.15(b) Incremental probability field for T-NO_3^-.

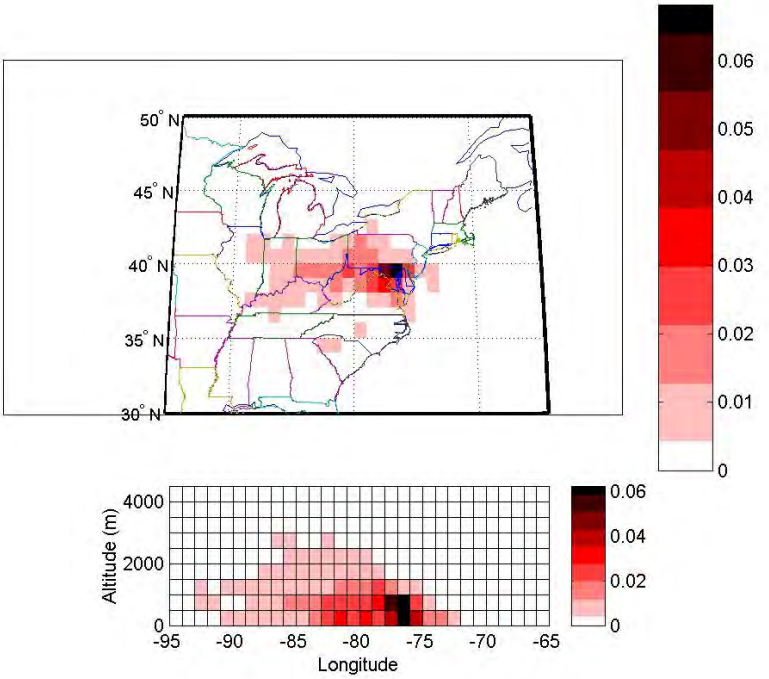

A.3.16(a) High-day (10%) probability field for T-NH_4^+.

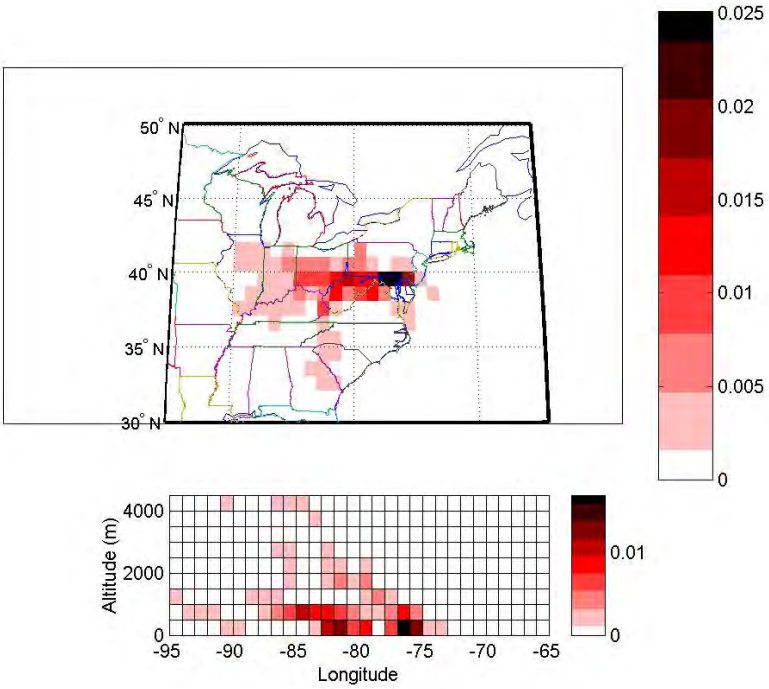

A.3.16(b) Incremental probability field for T-NH_4^+.

References

Ackerman, A. S., O. B. Toon, D. E. Stevens, A. J. Heymsfield, V. Ramanathan, and R. J. Welton, Reduction of tropical cloudiness by soot, *Science*, May 12, 1042-1047, 2000.

Anderson, T. L., D. S. Covert, S. F, Marshall, M. L. Laucks, R. J. Charlson, A. P. Waggoner, J. A. Ogren, R. Caldow, R. L. Holm, F. R. Quant, G. J. Sem, A. Wiedenshhler, A. A. Ahlquist, and T. S. Bates, Performance characteristics of a high-sensitivity, three-wavelength, total scatter/backscatter Nephelometer, *J. Atm. Ocean. Technol.*, 13, 967-986, 1996.

Anderson, T. L., and J. A. Ogren, Determining aerosol radiative properties using the TSI 3563 Integrating Nephelometer, *Aerosol Sci. Technol.*, 29, 57-69, 1998.

Artaxo, P., F. Gerab, M. A. Yamasoe, and J. V. Martins, Fine mode aerosol composition at three long-term atmospheric monitoring sites in the Amazon Basin, *J. Geophys. Res.*, 99, 22857-22868, 1994.

Artaxo, P., H. Storms, F. Bruyndeels, R. Van Grieken, and W. Maenhaut, Composition and sources of aerosols from the Amazon Basin, *J. Geophys. Res.*, 93, 1605-1615, 1988.

Bohren, C. F., and Hiffman, D. R., *Absorption and Scattering of Light by Small Particles*, Wiley, New York, 1983.

Bond, T. C., T. L. Anderson, and D. Campbell, Calibration and intercomparison of filter-based measurements of visible light absorption by aerosols, *Aerosol Sci. Technol.*, 30, 582-600, 1999.

Burkhard, E. G., V. A. Dutkiewicz, and L. Husain, A study of SO_2, SO_4^{2-}, and trace elements in clear air and clouds above the Midwestern United States, *Atmos. Environ.*, 28, 1521-1533, 1994.

Cadle et al., Composition of light-duty motor vehicle exhaust particulate matter in the Denver, Colorado area, *Environ. Sci. Technol.*, 33, 2328-2339, 1999.

Charlson, R. J., and N. C. Ahlquist, Brown haze: NO_2 or aerosol?, *Atmos. Environ.*, 3, 653-656, 1969.

Chen, L.-W. A., B. G. Doddridge, R. R. Dickerson, P. K. Muller, J. C. Chow, W. A. Butler, Seasonal variations in elemental carbon aerosol, carbon monoxide, and sulfur dioxide: Implications for sources, *Geophys. Res. Lett.*, 28(9), 1711-1714, 2001.

Chen, L.-W. A., B. G. Doddridge, R. R. Dickerson, J. C. Chow, and R. C. Henry, Origins of fine aerosol mass in the Baltimore-Washington corridor: Implications from observations, factor analysis, and air parcel back trajectories, *Atmos. Environ*., in press, 2002.

Chow, J. C., J. G. Waston, D. H. Lowenthal, P. A. Solomon, K. L. Magliano, S. D. Ziman, and L. W. Richards, PM_{10} source apportionment in California's San Joaquin Valley, *Atmos. Environ*., 26A, 3335-3354, 1992.

Chow, J. C., J. G. Waston, L. C. Pritchett, W. R. Pierson, C. A. Frazier, and R. G. Purcell, The DRI thermal/optical reflectance carbon analysis system: description, evaluation and applications in U. S. air quality studies, *Atmos. Environ.,* 27, 1185-1201, 1993.

Chow, J. C., J. G. Watson, E. M. Fujita, Z. Lu, and D. R. Lawson, Temporal and spatial variations of $PM_{2.5}$ and PM_{10} aerosol in the southern California air quality study, *Atmos. Environ.*, 28, 2061-2080, 1994.

Chow, J. C., J. G. Watson, L. Zhiqiang, D. H. Lowenthal, C.A. Frazier, P. A. Solomon, R. H. Thuillier, and K. Magliano, Descriptive analysis of $PM_{2.5}$ and PM_{10} at regionally representative locations during SJVAQS/AUSPEX, *Atmos. Environ.*, 30, 2079-2112, 1996.

Chow, J. C., J. G. Watson, D. Crow, D. H. Lowenthal, T. Merrifield, Comparison of IMPROVE and NIOSH Carbon Measurements, *Aerosol Sci. Technol*., 34(1), 1-12, 2001.

Chu, R., Algorithms for the Automated Surface Observing System (ASOS). ISL Office Note 94-4, NWS/OSD, pp. 106 pp, 1994.

Chueinta W., P. K. Hopke, and P. Paatero, Investigation of sources of atmospheric aerosol at urban and suburban residential areas in Thailand by positive matrix factorization, *Atmos. Environ*., 34(20), 3319-3329, 2000.

Cofer, W. R., III, J. S. Levine, D. I. Sebacher, E. L. Winstead, P. J. Riggin, J. A. Brass, and V. G. Ambrosia, Particulate emissions from a mid-latitude prescribed chaparral fire, *J. Geophys. Res*., 93, 5207-5212, 1988.

Cooke, W. F., C. Liousse, and H. Cachier, Construction of a $1° \times 1°$ fossil fuel emission data set for carbonaceous aerosol and implementation and radiative impact in the ECHAM4 model, *J. Geophys. Res.,* 104(D18), 22137-22162, 1999.

De Haan, D. O., T. Brauers, K. Oum, J. Stuz, T. Nordmeyer, and B. J. Finlayson-Pitts, Heterogeneous chemistry in the troposphere: Experimental approaches and applications to the chemistry of sea salt particles, *Int. Rev. Phys. Chem.*, 18(3), 1999.

Dickerson, R. R., A. C. Delany, and A. F. Wartburg, Further modification of a commercial NO_x detector for high sensitivity, *Rev. Sci. Instrum.*, 55, 1995-1998, 1984.

Dickerson, R. R., and A. C. Delany, Modification of a commercial gas filter correlation CO detector for increased sensitivity*, J. Atmos. Oceanic Technol.*, 5(3), 424-431, 1988.

Dickerson, R. R., S. Kondragunta, G. Stenchikov, K. L. Civerolo, B. G. Doddridge, and N. Holben, The impact of aerosols on solar ultraviolet radiation and photochemical smog, *Science*, 278, 827-830, 1997.

Dickerson, R. R., M. O. Andreae, T. Campos, O. L. Mayol-Bracero, C. Neususess, and D. G. Streets, Emissions of Black Carbon and Carbon Monoxide from South Asia, submitted to *J. Geophys. Res.*, 2001.

Dockery, D.W., Pope, C.A., Xu, X.P., Spengler, J.D., Ware, J.H., Fay, M.E., Ferris, B.G., Speizer, F.G., 1993. An association between air-pollution and mortality in 6 United States cities. New England Journal of Medicine 329, 1753-1759.

Dodd J. A., J. M. Ondov, G. Tuncel, and T. G. Dzubay, Multimodal size spectra of submicrometer particles bearing various elements in rural air, *Environ. Sci. Technol.*, 25(5), 890-903, 1991.

Doddridge, B. G., R. R. Dickerson, R. G. Wardell, K. L. Civerolo, and L. J. Nunnermacker, Trace gas concentrations and meteorology in rural Virginia 2: Reactive nitrogen compounds, *J. Geophys. Res., 97*, 20631-20646, 1992.

Doddridge, B. G., R. R. Dickerson, T. G. Spain, S. J. Oltmans, and P. C. Novelli, Carbon monoxide measurements at Mace Head, Ireland, *in Ozone in the Troposphere and Stratosphere*, edited by Hudson, R. D*., NASA Conf. Publ. 3266*, 134-137, 1994.

Doddridge, B. G., R. M. Morales, K. P. Rhoads, J. T. Merrill, P. C. Novelli, R. R. Dickerson, V. S. Connors, and H. G. Reichle, Jr., Ground-based and airborne observations of carbon monoxide during NASA/MAPS missions SRL-1 and SRL-2, *J. Geophys. Res.,* 103, 19305-19316, 1998.

Draxler, R. R., Hybrid single-particle Lagrangian integrated trajectories (HY-SPLIT): Model description, *NOAA Tech. Memo.*, ERL ARL-166, pp. 23, 1988.

Draxler, R. R., The accuracy of trajectories during ANATEX calculated using dynamic model analysis versus rawinsonde observations, *J. Appl. Meteorol.*, 30, 1466-1467, 1991.

Durbin, T. D., R. D. Wilson, J. M. Norbeck, J. W. Miller, T. Huai, and S. H. Rhee, Estimates of the emission rates of ammonia from light-duty vehicles using standard chassis dynamometer test cycles**,** *Atmos. Environ.,* 36(9), 1475-1482, 2002.

Dzubay T. G., R. K. Stevens, G. E. Gordon, I. Olmez, A. E. Sheffield, and W. J. Courtney, A composite receptor method applied to Philadelphia aerosol, *Environ. Sci. Technol.*, 22, 46-52, 1988.

Ehrman, S. H., S. E. Pratsinis, and J. R. Young, Receptor modeling of the fine aerosol at a residential Los Angeles site, *Atmos. Environ*., 26B, 473-481, 1992.

Fehsenfeld, F. C., R. R. Dickerson, G. Hubler, W. T. Luke, L. J. Nunnermacker, E. J. Williams, J. M. Roberts, J. G. Calvert, C. M. Curran, and A. C. Delany, A ground-based intercomparison of NO, NO_x, and NO_y measurement techniques, *J. Geophys. Res*., 92, 14710-14722, 1987.

Ferman, M. A., G. T. Wolff, and N. A. Kelly, The nature and sources of haze in the Shenandoah Valley/Blue Ridge Mountains area, *J. Air Poll. Control Assoc.*, 31(10), 1074-1082, 1981.

Fitzgerald, J. W., Marian aerosols-A review, *Atmos. Environ.*, 25A, 533-545, 1991.

Gertler A.W. et al., *Sampling of ambient diesel particulate matter in the Tuscarora Mountain Tunnel, Pennsylvania*, Final report prepared for Health Effects Institute, Cambridge, MA, by Desert Research Institute, Reno, NV, 2001

Gillies, J. A., and A. W. Gertler, Comparison and evaluation of chemically speciated mobile source $PM_{2.5}$ particulate matter profiles, *J. Air & Waste Manage. Assoc*., 50, 1459-1480, 2000.

Gillies, J. A., A. W. Gertler, J. C. Sagebiel, and W. A. Dippel, On-road $PM_{2.5}$ and PM_{10} emissions in the Sepulveda Tunnel, Los Angeles, California, *Environ. Sci. and Technol*., 35, 1054-1063, 2001.

Gillani, N. V., S. E. Schwartz, W. R. Leaitch, J. W. Strapp, and G. A. Isaac, Field observations in continental stratiform clouds: Partitioning of cloud particles between droplets and unactivated interstitial aerosols, *J. Geophys. Res.*, 100, 18687-18706, 1995.

Glen, W. G., M. P. Zelenka, and R. C. Graham, Relating meteorological variables and trends in motor vehicle emissions to monthly urban carbon monoxide concentrations, *Atmos. Environ.*, 30(24), 4225-4232, 1996.

Goldstein, A. H., S. C. Wofsy, and C. M. Spivakovsky, Seasonal variations of non-methan hydrocarbons in rural New England: Constraints on OH concentrations in northern mid-latitudes, *J. Geophys. Res*., 100, 21023-21033, 1995.

Gordon G. E., Receptor models, *Environ. Sci. Technol*., 22, 1132-1142, 1988.

Groblicki, P. J., G. T. Wolff, and R. J. Countess, Visibility-reducing species in the Denver 'brown cloud'- I. Relationships between extinction and chemical composition, *Atmos. Environ.*, 15, 2473-2484, 1981.

Grosjean, D., and J. H. Seinfeld, Parameterization of the formation potential of secondary organic aerosols, *Atmos. Environ*., 23, 1733-1747, 1989.

Hallock-Waters, K. A., B. G. Doddridge, R. R. Dickerson, S. Spitzer, and J. D. Ray, Carbon monoxide in the U.S. mid-Atlantic troposphere: Evidence for a decreasing trend, *Geophys. Res. Lett*., 26 , 2861-2864, 1999.

Hallock-Waters, K. A., Trace gas observations over rural Virginia: Photochemistry and transport, *Ph. D. dissertation*, Department of Chemistry, Graduate School of the University of Maryland at College Park, 2000.

Hegg, D. A., J. Livingston, P. V. Hobbs, T. Novakov, and P. Russell, Chemical apportionment of aerosol column optical depth off the mid-Atlantic coast of the United States, *J. Geophys. Res*., 102(D21), 25293-25303, 1997.

Heller-Zeisler S. F., and J. M. Ondov, Collection and characterization of a bulk $PM_{2.5}$ air particulate matter material for use inreference materials, *Biolog. Trace Elem. Res*., 71-2, 195-202, 1999.

Henry, R. C., Current factor analysis receptor models are ill-posed, *Atmos. Environ*., 21, 1815-1820, 1987.

Henry, R. C., History and fundamentals of multivariate air quality receptor models, *Chemometrics & Intelligent Laboratory Systems*, 37, 37-42, 1997.

Henry, R. C., E. S. Park, and C. H. Spiegelman, Comapring a new algorithm with the classical methods for estimating the number of factors, *Chemometrics & Intelligent Laboratory Systems*, 48, 91-97, 1999.

Henry, R. C., 2000, *UNMIX theory and applications*, In: Willis, R. D., Final Report of Workshop on UNMIX and PMF as Applied to $PM_{2.5}$, United States Environment Protection Agency, EPA/600/A-00/48.

Hering, S. V. et al., Comparison of sampling methods for carbonaceous aerosols in ambient air, *Aerosol Sci. Technol*., 12, 200-213, 1990.

Hobbs, P. V., Introduction to Atmospheric Chemistry, Cambridge University Press, New York, pp. 103, 2000.

Holloway, T., H. Levy II, and P. Kasibhatla, Global distribution of carbon monoxide, *J. Geophys. Res*., 105(D10), 12123-12147, 2000.

Human, D. M., T. L. Ullman, and T. M. Baines, Simulation of high altitude effects on heavy-duty diesel emissions, *Society of Automotive Engineers (SAE)*, Paper 900883, 1990.

Interagency Monitoring of Protected Visual Environments (IMPROVE), *Spatial and Seasonal Patterns and Temporal Variability of Haze and its Constituents in the Unites States: Report III*, ISSN: 0737-5352-47, 2000.

Intergovernmental Panel on Climate Change (IPCC), *Climate Change 2001: The Scientific Basis*, Cambridge Univ. Press, New York, 2001.
Jacob, D. J., *Introduction to Atmospheric Chemistry*, Princeton University Press, New Jersey, pp. 148, 1999.

Jacobson, M. Z., Strong radiative heating due to the mixing state of black carbon in the atmosphere, *Nature*, 409, 695-697, 2001.

Jacobson, M. C., H.-C. Hansson, K. J. Noone, and R. J. Charlson, Organic atmospheric aerosols: Review and state of the science, *Rev. Geophys*., 38(2), 267-294, 2000.

Jennings, S. G., T. G. Spain, B. G. Doddridge, H. Maring, B. P. Kelley, and A. D. A. Hansen, Concurrent measurements of black carbon aerosol and carbon monoxide at Mace Head, *J. Geophys. Res*., 101, 19447-19454, 1996.

Jones, A., D. L. Roberts, and A. Slingo, A climate model study of indirect radiative forcing by anthropogenic sulphate aerosols, *Nature*, 370, 450-453, 1994.

Kaiser, J., Evidence mounts that tiny particles can kill, *Science*, 289, 22-23, 2000.

Kaufman, Y. J., and R. S. Fraser, The effect of smoke particles on clouds and climate forcing, *Science*, 277, 1636-1639, 1997.

Kiehl, J. T., Clouds and their effects on the climate system, *Physics Today*, 47, 36-42, 1994.

Kiehl., J. T., and H. Rodhe, Modeling geographical and seasonal forcing due to aerosols, in *Aerosol Forcing and Climate*, edited by R. J. Charlson and J. Heintzenberg, Wiley, New York, pp. 281-296, 1995.

Kim, Y. P., J. H., Seinfeld, P. Saxena, Atmospheric gas-aerosol Equilibrium I. Themodynamic model, *Aerosol Sci. Technol.*, 19, 157-181, 1993.

Kley, D., and M. McFarland, Chemiluminescence detector for NO and NO_2, *Atmos. Tech*., 12, 63-69, 1980.

Koutrakis, P., and J. D. Spengler, Source apportionment of ambient particles in Steubenville, OH using specific rotation factor analysis, *Atmos. Environ*., 21, 1511-1519, 1987.

Kowalczyk, G. S., G. E. Gordon, and S. W. Rheingrover, Identification of atmospheric particulate sources in Washington, D. C. using chemical element balances, *Environ. Sci. and Technol*., 16, 79-90, 1982.

Ladommatos N., S. Abdelhalim, H. Zhao, Control of oxides of nitrogen from diesel engines using diluents while minimizing the impact on particulate pollutants, *Appl. Thermal Eng.,* 18(11), 963-980, 1998.

Larsen, R. K., III, Atmospheric exchange of PAHs, PCBs, and ammonia with the Chesapeake Bay, *Ph. D. dissertation*, Chesapeake Biological Laboratory, University of Maryland Center for Environmental Science, 2002.

Liousse, C., H. Cachier, and S. G. Jennings, Optical and thermo measurements of black carbon aerosol content in different environments: Variation of specifoc attenuation cross-section σ, *Atmos. Environ*., 27A, 1203-1211, 1993.

Liousse, C., J. E. Penner, C. Chuang, J. J. Walton, H. Eddleman, and H. Cachier, A global three-dimensional model study of carbonaceous aerosols, *J. Geophys. Res*., 101(D14), 19411-19432, 1996.

Luke, W. T., Evaluation of a commercial pulsed fluorescence detector for the measurement of low-level SO_2 concentrations during the Gas-Phase Sulfur Intercomparison Experiment*, J. Geophys. Res.,* 102(D13), 16255-16265, 1997.

Lusis, M. A., K. G. Anlauf, L. A. Barrie, and H. A. Wiebe, Plume chemistry studies at a Northern Alberta Power Plant, *Atmos. Environ*., 12, 2429-2437, 1978.

Malm, W. C., Characteristics and origins of haze in the continental United States, *Earth-Sci. Rev.*, 33, 1-36, 1992.

Malm, W. C., Sisler, J. F., Huffman, D.Eldred, R. A., and Cahill, R. A., Spatial and seasonal trends in particle concentration and optical extinction in the United States, *J. Geophys. Res.,* 99(D1), 1347-1370, 1994.

Malm, W. C., and K. A. Gebhart, Source apportionment of sulfur and light extinction using receptor modeling techniques, *J. Air & Waste Manage. Assoc*., 47, 250-268, 1997.

Maryland Department of the Environment, Daily VMT mix by roadway type, *The 1996 Periodic Emission Inventroy for Precusors of Ozone in Maryland*, Section 4, pp. 114, prepared by Air Quality Planning Program, 1999.

Mason, C. B., and B. Moore, *Principles of Geochemistry*, 4th ed., Wiley, New York, 1982.

Meng, Z., D. Dabdub, and J. H. Seinfeld, Chemical coupling between atmospheric ozone and particulate matter, *Science*, 277, 116-119, 1997.

Molina, M. J., Heterogeneous chemistry on polar stratospheric clouds, *Atmos. Environ.*, 25A, 2535-2537, 1991.

Nadarajan, A., Development of a model of secondary organic aerosol formation, *M. S. degree thesis*, Department of Chemical Engineering, Graduate School of the University of Maryland at College Park, 2002.

National Atmospheric Deposition Program, *2000 Annual Summary*, National Atmospheric Deposition Program, A cooperative research support program of the State Agriculture Experiment Stations (NRSP-3). (http://nadp.sws.uiuc.edu/lib/)

Nemesure, S., R. Wagener, and S. E. Schwartz, Direct shortwave forcing of climate by the anthropogenic sulfate aerosol: sensitivity to particle size, composition, and relative humidity, *J. Geophys. Res.*, 100, 26105-26116, 1995.

Neusüß, C., T. Gnauk, A. Plewka, H. Herrmann, and P.K. Quinn, Carbonaceous aerosol over the Indian Ocean: OC/EC fractions and selected specifications from size-segregated onboard samples, *J. Geophys. Res*., in press*,* 2002.

Nuti, M. P., *Emissions from two-stroke engines*, Society of Automotive Engineers Inc., pp. 283, Warrendale, Penn., 1998.

Oh, J. A., Characterization and Source Apportionment of Air Pollution in Boston, Massachusetts, *Ph. D. thesis*, Harvard School of Public Health, 2000.

Okabe, H., P. L. Splitsone, and J. J. Ball, Ambient and source SO_2 detector based on a fluorescence method, *J. Air Pollut. Control Assoc*., 23, 514-516, 1973.

Olmez I., A. E. Sheffield, G. E. Gordon, J. E. Houck, L. C. Pritchett, J. A. Cooper, T. G. Dzubay, and R. L. Bennett, Compositions of particles from selected sources in Philadelphia for receptor modeling applications, *J. Air Poll. Cont. Asso*., 38, 1392-1402, 1988.

Ondov, J. M., F. Divita, and A. Suarez, Size-spectra and growth of particles bearing As, Se, Sb, and Zn in Washington, DC area aerosol by instrumental neutron-activation analysis, *J. Radioan. Nucl. Ch. Ar.*, 192(2), 215-228, 1995.

Ondov, J. M., and A. S. Wexler, Where do particulate toxins reside? An improved paradigm for the structure and dynamics of the urban Mid-Atlantic aerosol, *Environ. Sci. Technol*., 32, 2547-2555, 1998.

Pandis, S. N., J. H. Seinfeld, and C. Pilinis, Heterogeneous sulfate production in an urban fog, *Atmos. Environ*., 26A, 2509-2522, 1992.

Penner, J. E., and H. Eddleman, Toward the development of a globe inventory for black carbon emissions, *Atmos. Environ.,* 27A(8), 1277-1295, 1993.

Petzold, A., C. Kopp, and R. Niessner, The depedence of the specific attenuation cross-section on black carbon mass fraction and particle size, *Atmos. Environ*., 31, 661-672, 1997.

Poirot, R. L., P. R. Wishinski, P. K. Hopke, and A. V. Polissar, Comparative application of multiple receptor methods to identify aerosol sources in northern Vermont, *Environ. Sci. and Technol*., 35, 4622-4636, 2001.

Prospero, J. M., Long-term measurements of the transport of African mineral dust to the southeastern United States: Implications for regional air quality, *J. Geophys. Res.*, 104(D13), 15,917-15,927, 1999.

Poulida, O., R. R. Dickerson, B. G. Doddridge, J. Z. Holland, R. G. Wardell, and J. G. Watkins, Trace gas concentrations and meteorology in rural Virginia: 1. Ozone and carbon monoxide, *J. Geophys. Res*., 96(D12), 22461-22475, 1991.

Portmann, R. W., S. Solomon, R. R. Garcia, L. W. Thomason, L. R. Poole, and M. P. McCormick, Role of aerosol variations in anthropogenic ozone depletion in the polar regions, *J. Geophys. Res.*, 101, 22991-23006, 1996.

Quinn T. L., and J. M. Ondov, Influence of temporal changes in relative humidity on dry deposition velocities and fluxes of aerosol particles: Bearing trace elements, *Atmos. Environ.,* 32(20), 3467-3479, 1998.

Rabano, E. S., N. T. Castillo, K. J. Torre, and P. A. Solomon, Speciation of arsenic in ambient aerosols collected in Los Angeles*, J. Air & Waste Manage. Assoc*., 39, 76-80, 1989.

Raes, F., R. V. Dingenen, E. Vignati, J. Wilson, J.-P. Putaud, J. H. Seinfeld, P. Adams, Formation and cycling of aerosols in the global troposphere, *Atmos. Environ*., 34, 4215-4240, 2000.

Rees, S. L., S. Takahama, A. L. Robinson, A. Khlystov, and S. N. Pandis, Seasonal composition of $PM_{2.5}$ and performance of the Federal Reference Method in Pittsburgh. In: *$PM_{2.5}$ and Electric Power Generation: Recent Findings and Implications*, Summaries of a Conference Sponsored by National Energy Technology Laboratory, Pittsburgh, Pennsylvania, April 9-10, pp 69-70, 2002.

Rheingrover, S. W., and G. E. Gordon, Wind-trajectory method for determining compositions of particles from major air-pollution sources, *Aerosol. Sci. Technol*., 8(1), 29-61, 1988.

Rupprecht & Patashnick, *TEOM Series 1400a Operating Manual*, Rupprecht & Patashnick Co., Inc., pp. 1-10, 1996.

Russell, P. B., P. V. Hobbs, and L. L. Stowe, Aerosol properties and radiative effects in the United States East Coast haze plume: An overview of the Tropospheric Aerosol Radiative Forcing Observational Experiment (TRAFOX), *J. Geophys. Res.,* 104(D2), 2213-2222, 1999.

Ryan, W. F., B. G. Doddridge, R. R. Dickerson, R. M. Morales, K. A. Hallock-Waters, P. T. Roberts, D. L. Blumenthal, J. A. Anderson, and K. L. Civerolo, Pollutant transport during a regional O_3 episode in the mid-Atlantic States, *J. Air & Waste Manage. Assoc.*, 48, 786-797, 1998.

Samet J. M., S. L. Zeger, K. Berhane, Particulate air pollution and daily mortality: Replication and validation of selected studies, in *The Phase I Report of the Particle Epidemiology Evaluation Project*, Cambridge, MA, Health Effects Institute, 1995.

Schlesinger, W. H., and A. E. Hartley, A global budget of atmospheric NH_3, *Biogeochemistry*, 15, 191-211, 1992.

Seinfeld, J. H., and S. N., Pandis, *Atmospheric Chemistry and Physics*, John Wiley & Sons, New York, 1998.

Sillman, S., The relation between ozone, NO_x, and hydrocarbons in urban and polluted environments, *Atmos. Environ*., 33, 1821-1845, 1999.

Slinn, W. G. N., L. Hasse, B. B. Hicks, A. W. Hogan, D. Lai, P. S. Liss, K. O. Munnich, G. A. Sehmel, O. Vittori, Some aspects of the transfer of atmospheric trace constituents past the air-sea interface, *Atmos. Environ.*, 12, 2055-2087, 1978.

Song, X.-H., A. V. Polissar, and P. K. Hopke, Sources of fine particle composition in the northeastern US, *Atmos. Environ*., 35, 5277-5286, 2001.

Spivakovsky, C. M., R. Yevich, J. A. Logan, S. C. Wofsy, and M. B. McElroy, Tropospheric OH in a three-dimensional chemical tracer model: An assessment based on observations of CH_3CCl_3, *J. Geophys. Res*., 95, 18441-18471, 1990.

Stehr, J. W., R. R. Dickerson, K. A. Hallock-Waters, B. G. Doddridge, and D. Kirk, Observation of NO_y, CO, and SO_2 and the origin of reactive nitrogen in the eastern United States, *J. Geophys. Res*., 105(D3), 3553-3563, 2000.

Stehr, J. W., W. P. Ball, R. R. Dickerson, B. G. Doddridge, C. A. Piety, and J. E. Johnson, Latitudinal Gradients in O3 and CO During INDOEX1999, *J. Geophys. Res*., in press, 2002.

Stull, R. B., *An Introduction to Boundary Layer Meteorology*, Kluwer Academic Publishers, Dordrecht/Norwell, MA, Fig. 1.7, 1988.

Suarez A. E., and J. M. Ondov, Ambient aerosol concentrations of elements resolved by size and by source: Contributions of some cytokine-active metals from coal- and oil-fired power plants, *Energy & Fuels*, 16(3), 562-568, 2001.

Thermo Environment Instrument Inc., *Instruction Manual for Model 43S High Sensitivity Pulsed Fluorescence SO_2 Analyzer*, Thermo Environ. Instrum. Inc., Franklin, MA, 1992.

Tolocka, M. P., P. A. Solomon, W. Mitchell, G. A. Norris, D. B. Gemmill, R. W. Wiener, R. W. Vanderpool, J. B. Homolya, and J. Rice, East vs. West in the US: Chemical characteristics of $PM_{2.5}$ during the winter of 1999, *Aerosol Sci. Technol*., 34(11), 88-96, 2001.

Turn, S. Q., B. M. Jenkins, J. C. Chow, L. C. Pritchett, D. Campbell, T. Cahill, and S. A. Whalen, Elemental characterization of particulate matter emitted from biomass burning: Wind tunnel derived source profiles for herbaceous and wood fuels, *J. Geophys. Res*., 102(D3), 3683-3699, 1997.

Turpin, B. J., J. J. Huntzicker, and S. V. Hering, Investigation of organic aerosol sampling articles in the Los Angeles basin, *Atmos. Environ*., 28, 3061-3071, 1994.

Turpin, B. J., and J. J. Huntzicker, Secondary formation of organic aerosol in the Los Angeles Basin: A descriptive analysis of organic and elemental carbon concentrations, *Atmos. Environ*., 25A, 207-215, 1995.

Turpin, B. J., H.-J. Lim, Species contributions to $PM_{2.5}$ mass concentrations: Revising common assumptions for estimating organic mass, *Aerosol Sci. Technol.*, 35, 602-610, 2001.

United States Environment Protection Agency, *National Air Pollutants Emission Trends Report, 1990-1994*, EPA/454/R-95/011, 1995.

United States Environment Protection Agency, *National Air Pollution Emission Trends, 1990-1996*, EPA/454/R-97/011, 1997.

United States Environment Protection Agency, Monitoring $PM_{2.5}$ in ambient air using designated reference or class I equivalent methods, *EPA Quality Assurance Guidance Document 2.12*, 1998.

United States Environment Protection Agency, Concentrations, sources, and emissions of atmospheric particles, *Air Quality Criteria for Particulate Matter*, EPA/600/P-99/002a, 1999.

United States Environmental Protection Agency, *National Air Pollutant Emission Trends: 1990-1998*, EPA-454/R-00-002, 2000. (See http://www.epa.gov/ttn/rto/areas/net.htm)

United States Environmental Protection Agency, EPA communication to recipients of Third Draft EPA PM Criteria Document (EPA/600P-99/002aC and EPA/600P-99/002bC), 2002.

Vossler, T. L., C. W. Lewis, R. K. Stevens, T. G. Dzubay, G. E. Gordon, S. G. Tuncel, and G. M. Russwurm, *Atmos. Environ*., 23(7), 1535-1547, 1989.

Warner K. S., D. J. Eatough, and L. Stockburger, Determination of fine particulate semi-volatile organic material at three eastern U.S. sampling sites, *J. Air and Waste Manage. Assoc.*, 51, 1302-1308, 2001.

Watson J. G., P. J. Lioy, and P. K. Mueller, The measurement process: precision, accuracy, and validity, In: Cohen, B. and Hering, S.V. (Eds.), *Air Sampling Instruments for Evaluation of Atmospheric Contaminants* (8^{th} Edn.), American Conference of Governmental Industrial Hygienists, Cincinnati, Ohio, 1995.

Whitby, K. T., and B. Cantrell, Fine particles, in *International Conference on Environment Sensing and Assessment*, Institute of Electrical and Electronic Engineers, Las Vegas, NV, 1976.

White, W. H., and P. T., Roberts, On the nature and origins of visibility-reducing aerosols in the Los Angeles air basin, *Atmos. Environ.*, 11, 803-812, 1977.

Zhang, X. Q., and P. H. McMurray, Theoretical analysis if evaporative losses from impactor and filter deposites, *Atmos. Environ*., 21, 1779-1789, 1987.

Zhang, X., and McMurray, P. H., Evaporative losses of fine particulate nitrates during sampling, *Atmos., Environ.*, 26, 3305-3312, 1992.